Schriften des Forschungszentrum Jülich
Reihe Energietechnik / Energy Technology Volume 21, Part I

Forschungszentrum Jülich GmbH
Institut für Werkstoffe und Verfahren der Energietechnik

Jacqueline Lecomte-Beckers, Marc Carton,
Florian Schubert and Philip J. Ennis (Editors)

Materials for Advanced Power Engineering 2002

Proceedings of the 7th Liège Conference
Part I

EUROPEAN COMMISSION
UNIVERSITE DE LIEGE

Schriften des Forschungszentrum Jülich
Reihe Energietechnik / Energy Technology Volume 21, Part I

ISSN 1433-5522 ISBN 3-89336-312-2

Die Deutsche Bibliothek- CIP-Einheitsaufnahme

Materials for advances power engineering 2002 : proceedings of the 7th Liège Conference / ed.: Jacqueline Lecomte-Beckers ... - Jülich : Forschungszentrum, Zentralbibliothek

(Schriften des Forschungszentrums Jülich : Reihe Energietechnik ; Vol. 21)
ISBN 3-89336-312-2
Pt. 1 . - (2002)

Publisher and Distributor:	Forschungszentrum Jülich GmbH Central Library 52425 Jülich Phone +49 (0) 24 61 61 53 68 · Telefax +49 (0) 24 61 61 61 03 e-mail: zb-publikation@fz-juelich.de Internet: http://www.fz-juelich.de/zb
Cover Design:	Grafische Betriebe, Forschungszentrum Jülich GmbH
Printer:	Grafische Betriebe, Forschungszentrum Jülich GmbH
Copyright:	Forschungszentrum Jülich 2002

Printed on environmentally friendly paper.

The editors cannot accept any responsibility or liability for the accuracy of any statements or information given in the papers.

Schriften des Forschungszentrum Jülich
Reihe Energietechnik / Energy Technology, Volume21, Part 1

ISSN 1433-5522
ISBN 3-89336-312-2

Neither this book nor any part of it may be reproduced or transmitted in any form or by any means, electronic or mechanical, including photocopying, microfilming, and recording, or by any information storage and retrieval system, without permission in writing from the publisher.

FOREWORD

The European Co-operation in the field of Scientific and Technical Research (COST) is now a well established organisation for the co-ordination of national research and development programmes on a European level. This series of Liège Conferences was initiated in order to disseminate the results of the materials related COST Actions, beginning with COST 50 which was mainly concerned with materials for gas turbines and then moving to COST 501 in which materials for power generation plant were investigated. The results of the current COST Action 522 'Ultra Efficient, Low Emission Power Plants' are presented at this, the Seventh Liège Conference. The work is focused on materials for the components that have a decisive influence on the enhancement of power plant performance and efficiency.

Reliable energy supply at reasonable cost is one of the most important factors in the development of the modern industrialised society, but we are becoming increasingly concerned about the environmental impact of energy production and of the need to conserve valuable energy resources for future generations. Therefore, the emphasis is on a sustainable energy supply and the development of advanced energy conversion and power generation technologies taking into account the need for fuel conservation and environmental protection is essential. Although new and emerging energy technologies are of great interest, fossil fuel will continue to make a significant contribution well into the 21st century. Because a by-product of the conversion of fossil fuels is CO_2, the key factor is the thermal efficiency of plant; the higher the efficiency, the lower will be the levels of CO_2 produced for a given energy output. Power plant can be made more efficient by increasing the temperatures and pressures of the process, resulting in the general requirement for improved materials and components that can operate reliably for long times at higher temperatures and pressures.

The materials research and development activities required for the critical components of power generation plant have been based on the principle of work-sharing, bringing together materials scientists, design engineers, alloy producers and component manufacturers, reflecting the need to match materials properties and component behaviour. In order to put the European efforts into a world context, there are several invited review papers covering power plant materials development in the USA, Japan and South Africa. In addition there are over 130 contributions (presented as posters at the Conference) from 26 countries.

The Conference Proceedings reflect the Conference Technical Programme. They are divided in three volumes and the contents are as follows:

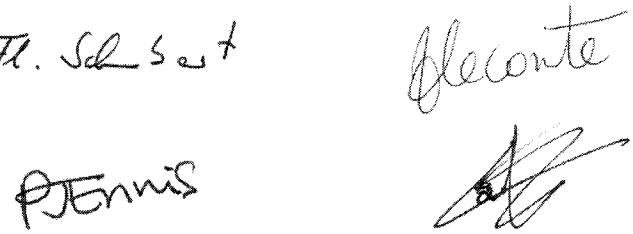
Part I: ADVANCED GAS TURBINE MATERIALS I
Invited Papers
1.1. Single Crystal
1.2. Ni Base Superalloys
1.3. Coatings

Part II : ADVANCED GAS TURBINE MATERIALS II
1.4. Intermetallics
1.5. Miscellaneous Topics
FUEL ISSUES AND NOVEL COMPONENTS
Invited Papers
2.1. Hot Gas Corrosion
2.2. Miscellaneous Topics
ADVANCED STEAM POWER PLANT I
Invited Papers
3.1. Microstructure

Part III: ADVANCED STEAM POWER PLANT II
3.2. Alloy Development
3.3. Mechanical Properties
3.4. Steam Oxidation and Coatings
3.5. Welding
3.6. Applications
OUTLOOK
Invited Papers

As in previous Liège Conferences, many people have made significant contributions to the success of this Conference. The Technical and Editorial Board would like to thank all the members of the COST 522 Management Committee both for their supervision and co-ordination of the considerable research effort in their own countries and across national boundaries, and for their help in the reviewing of the contributed papers.

September 2002



International Advisory Board

Aguero, A.	INTA	Spain
Allen, D.	Alstom Power	UK
Artinger, I.	TU Budapest	Hungary
Auerkari, P.	VTT	Finland
Berger, C.	TU Darmstadt	Germany
Bosansky, J.	Welding Research Inst	Slovenia
Bregani, F.	CESI	Italy
Cerjak, H.	TU Graz	Austria
Czyrska-Filemonowicz, A.	AGH Krakow	Poland
Delannay, F.	UC Louvain	Belgium
Déroulède, A.	DGXII	CEC
Engelen, B.	Min Economic Affairs	Belgium
Ennis, P.J.	FZ Jülich	Germany
Geipel, D.	MBF	Germany
Germain, A.	Université de Liège	Belgium
Hald, J.	TU Denmark	Denmark
Harada, H.	NIMS	Japan
Härkegård, G.	NUST	Norway
Henderson, P.J.	Vattenfall	Sweden
Khan, T.	ONERA	France
Kern, T.U.	Siemens PG	Germany
Koslowski, R.	TU Krakow	Poland
Legros, W.	Université de Liège	Belgium
Lecomte-Beckers, J.	Université de Liège	Belgium
Lupinc, V.	CNR-IENI	Italy
Masuyama, F.	Mitsubishi HI	Japan
Mayer, K.H.	Alstom Energie	Germany
McLean, M.	Imperial College	UK
Oakey, J.	Cranfield University	UK
Perez-Trujillo, F.	UC Madrid	Spain
Pomeroy, M.	University of Limerick	Ireland
Rademakers, P.	TNO	The Netherlands
Sánchez-Pasqual, A.	INTA	Spain
Schubert, F. (Chairman)	FZ Jülich	Germany
Seitz, E.	DGXII	CEC
Singheiser, L.	FZ Jülich	Germany
Sklenicka, V.	Academy of Sciences	Czech Republic
Spiradek-Hahn, A.	ÖFZ Seibersdorf	Austria
Staubli, M.	Alstom Power	Switzerland
Teixeira, V.M.	University of Minho	Portugal
ten Hoeven, H.J.	NRL	The Netherlands
Tiainen, T.	TU Tampere	Finland
Toulios , M.	NTU Athens	Greece
van Duysen, J.C.	EDF	France
Viswanathan, R.	EPRI	USA
Wright, I.	ORNL	USA
Zrnik, J.	TU Kosice	Slovakia

Technical and Editorial Board

J. Lecomte-Beckers (chief editor)	Université de Liège	Belgium
D. Allen	Alstom Power	UK
M. Carton	Université de Liège	Belgium
H. Cerjak	TU Graz	Austria
A. Déroulède	DGXII	CEC
P. J Ennis	FZ Jülich	Germany
H. Nguyen-Dang	Université de Liège	Belgium
J. Oakey	Cranfield University	UK
R. B. Scarlin	Alstom Power	Switzerland
F. Schubert	FZ Jülich	Germany
E. Seitz	DGXII	CEC
M. Staubli	Alstom Power	Switzerland
M. Toulios	NTU Athens	Greece

Organisation of Sessions

Advanced Gas Turbine Materials :	D. Allen
Fuel Issues and Novel Components :	J. Oakey
Advanced Steam Power Plant :	M. Staubli

Local Organisation Committee

F. Schubert (chairman)	Jülich
J. Lecomte-Beckers (vice-chairman)	Liège
P. J. Ennis, R. Herzog	Jülich
M. Carton, Y. Greday	Liège
B. Krahl-Urban (co-ordinator)	Jülich

Conference Secretaries

E. Wittig, Y. Abdel-Fatah, S. Stassar	Jülich
R. Pirson	Liège

The 7th Liège Conference has been organized by the Forschungszentrum Jülich and the Université de Liège.

TABLE OF CONTENTS

PART I

Foreword iii

Table of Contents vii

SECTION 1 – ADVANCED GAS TURBINE MATERIALS

Invited Papers

THE MECHANICAL BEHAVIOUR OF A CLASS OF RHENIUM BASED SX SUPERALLOYS FOR INDUSTRIAL GAS TURBINE APPLICATIONS I.5
Toulios M., Allen D.H.

CONSTITUTIVE MATERIAL FORMULATIONS AND ADVANCED LIFE ASSESSMENT METHODS FOR SINGLE CRYSTAL GAS TURBINE BLADES I.23
Busso E.P., Toulios M., Cailletaud G.

GAMMA TiAl INTERMETALLICS FOR TURBOMACHINERY APPLICATIONS I.43
Nazmy M., Lupinc V.

ADVANCES IN COATING SYSTEMS FOR UTILITY GAS TURBINES I.57
Nicholls J.R., Wing R.

ENVIRONMENTAL DEGRADATION OF GAS TURBINE COATINGS: TOWARDS STANDARDISED TESTING AND DATABASES I.73
Simms N.J., Bale D.W., Baxter D., Oakey J.E.

WROUGHT Ni-BASE ALLOYS FOR ADVANCED GAS TURBINE DISC AND USC STEAM TURBINE ROTOR APPLICATIONS I.89
Rösler J., Böttger B., Wolske M., Penkalla H.J., Berger C.

NEW MATERIALS AND COOLING SYSTEMS FOR HIGH TEMPERATURE, HIGHLY LOADED COMPONENTS IN ADVANCED COMBINED CYCLE POWER PLANTS I.107
Bohn D.E.

OVERVIEW OF US-DOE PROGRAM IN HIGH EFFICIENCY ENGINES AND TURBINES I.121
Layne A.W.

1.1. Single Crystal

THE CREEP BEHAVIOUR OF AS-CAST SX CM186LC AT INDUSTRIAL GAS TURBINE OPERATING CONDITIONS I.139
Wilcock I.M., Lukas P., Maldini M., Klabbers J., Dubiel B., Henderson M.B.

THE LOW CYCLE FATIGUE BEHAVIOUR OF AS CAST SINGLE CRYSTAL CM186LC I.149
Bale D.W., Henderson M., Dubiel B., Czyrska-Filemonowicz A., Guardamagna C., Bontempi P., Mulvihill P., Lukas P., Obrtlik K., Kolkman H.

CREEP BEHAVIOUR OF THE THIRD GENERATION Ni-BASE SINGLE CRYSTAL SUPERALLOY TMS-75 AND ITS γ/γ' TIE-LINE ALLOYS I.159
Murakumo T., Kobayashi T., Nakazawa S., Harada H.

CREEP BEHAVIOUR AND γ' EVOLUTION OF A NEW NICKEL BASE SUPERALLOY FOR SINGLE CRYSTAL BLADE APPLICATIONS I.167
Maldini M., Lupinc V., Li H., Angella G.

CREEP OF [001]-ORIENTED Ni-20 MASS %Cr SINGLE CRYSTALS I.177
Terada Y., Nakamoto Y., Matsuo T.

CHARACTERIZATION OF THE PROPAGATION BEHAVIOR OF SHORT FATIGUE CRACKS IN NICKEL-BASED SINGLE CRYSTAL SUPERALLOY SC16 I.187
Zhang X.P., Wang C.H., Chen W.Y., Ye L., Mai Y.-W.

EFFECT OF γ' VOLUME FRACTION ON THIRD-GENERATION SINGLE-CRYSTAL SUPERALLOYS I.197
Zhou H., Harada H., Ro Y., Koizumi Y., Kobayashi T., Nakazawa S.

ON THE EFFECT OF RHENIUM ON THE EXTENT OF PRIMARY CREEP IN ADVANCED Ni-BASED SUPERALLOYS I.207
Rae C.M.F., Kakehi K., Reed R.C.

INVESTIGATION OF POROSITY IN SINGLE-CRYSTAL NICKEL-BASE SUPERALLOYS I.217
Epishin A., Link T., Brückner U., Portella P.D.

INVESTIGATION AND COMPARISON OF THE MICROSTRUCTURE OF THE NICKEL-BASE SUPERALLOYS CMSX-4 AND SX CM186LC I.227
Danciu D., Klabbers J., Penkalla H.J.

DISLOCATION MICROSTRUCTURE OF CMSX-4 AFTER TENSILE TESTING WITH DIFFERENT STRAIN RATES AT 700 AND 1000°C I.235
Danciu D., Penkalla H.J., Schubert F.

MORPHOLOGICAL CHANGE IN γ' PHASE IN DIFFERENT PORTIONS OF FIRST STAGE HIGH PRESSURE TURBINE BLADE OF PWA1480 I.245
Miura N., Harada N., Kondo Y., Matsuo T.

METALLURGICAL ANALYSIS OF IN SERVICE *CMSX-2* SINGLE CRYSTAL GAS TURBINE BUCKETS I.255
Yoshioka Y., Saito D., Ito S., Fukuyama Y.

CARBIDE PRECIPITATION IN SINGLE CRYSTAL Ni-BASE SUPERALLOYS I.263
Tin S., Pollock T.M.

MODELLING OF HIGH TEMPERATURE TMF TESTS OF SINGLE CRYSTALS BY A PURE CREEP LAW I.273
White P.S., Kong C.N.

A MULTISCALE CONSTITUTIVE APPROACH TO MODEL THE MECHANICAL BEHAVIOUR OF INHOMOGENEOUS SINGLE CRYSTAL SUPERALLOYS: APPLICATION TO AS-CAST SX CM186LC I.283
Regino G.M., Busso E.P., O'Dowd N.P., Allen D.

DEFORMATION MODELLING OF THE SINGLE CRYSTAL SUPERALLOY CM186LC I.293
Daniel R., Tinga T., Henderson M.B., Ward T.J.

TMS-82+: A HIGH STRENGTH Ni-BASE SINGLE CRYSTAL SUPERALLOY I.303
Hino T., Yoshioka Y., Koizumi Y., Kobayashi T., Harada H.

1.2. Ni Base Superalloys

MICROSTRUCTURE OF A 5-COMPONENT Ni-BASE MODEL ALLOY: EXPERIMENTS AND SIMULATION I.315
Warnken N., Böttger B., Ma D., Vitusevych V., Hecht U., Fries S.G., Dupin N.

ALLOY DESIGN FOR ULTRA HIGH TEMPERATURE STEAM TURBINE APPLICATIONS : SIMULATION OF MICROSTRUCTURE DURING FORGING I.325
Kopp R., Wolske M.

MICROSTRUCTURE AND STRUCTURAL STABILITY OF CANDIDATE MATERIALS FOR TURBINE DISC APPLICATIONS BEYOND 700°C I.335
Penkalla H.J., Wosik J., Schubert F.

MATERIAL DEGRADATION AND DAMAGE ASSESSMENT FOR GAS TURBINE COMBUSTION COMPONENTS I.345
Saito D., Yoshioka Y., Fujiyama K.

EFFECT OF SOLUTION HEAT TREATMENT ON THE HOT CORROSION RESISTANCE OF A SECOND GENERATION DS SUPERALLOY I.355
Tamaki H., Okayama A., Onay B., Yoshinari A.

CREEP PROPERTIES DEGRADATION IN A LONG-TIME THERMALLY EXPOSED NICKEL BASE SUPERALLOY I.365
Zrnik J., Strunz P., Vrchovinsky V., Hornak P., Wiedenmann A.

EFFECT OF TENSILE HOLDS ON THE DEFORMATION BEHAVIOUR OF A NICKEL BASE SUPERALLOY SUBJECTED TO LOW CYCLE FATIGUE I.375
Zrnik J., Semenak J., Wangyao P., Vrchovinsky V., Hornak P.

IN-SITU OBSERVATIONS OF THE DEFORMATION AND DAMAGE BEHAVIOUR AROUND LASER-DRILLED COOLING HOLES IN INCONEL ALLOY 617 USING THE SCANNING ELECTRON MICROSCOPE I.385
Klabbers J., Wessel E., Schubert F.

DESIGN OF Ni-BASE DS SUPERALLOYS FOR INDUSTRIAL GAS TURBINES I.395
Sato M., Koizumi Y., Kobayashi T., Karada H., Ono H.

THE INVESTIGATIONS OF DEFORMABILITY AND STRUCTURE OF A-286 ALLOY AT HIGH TEMPERATURE DEFORMATION I.401
Ducki K.J., Hetmanczyk M., Kuc D.

MODELLING THE CREEP BEHAVIOUR OF A WROUGHT NICKEL BASE SUPERALLOY IN A WIDE RANGE OF STRESS/TEMPERATURE CONDITIONS I.409
Maldini M., Lupinc V.

CREEP BEHAVIOUR OF A POWDER METALLURGY UDIMET 720 NICKEL-BASED SUPERALLOY I.419
Dubiez S., Couturier R., Guétaz L., Burlet H.

1.3. Coatings

MCrAlY COATING BY AN ELECTROCHEMICAL ROUTE I.429
Bacos M.-P., Girard B., Josso P., Rio C.

EVALUATION OF THERMOMECHANICAL FATIGUE RESISTANCE OF COATED SUPERALLOYS BY A LASER THERMAL SHOCK SYSTEM I.439
Meriggi M., Rinaldi C.

THERMOPHYSICAL AND MICROSTRUCTURAL CHARACTERISATION OF MODIFIED THICK YTTRIA STABILISED ZIRCONIA THERMAL BARRIER COATINGS I.449
Bianchi P., Cernuschi F., Lorenzoni L., Ahmaniemi S., Vippola M., Vuoristo P., Mäntylä T.

ADVANCED NITRIDE COATINGS FOR OXIDATION PROTECTION OF TITANIUM ALLOYS I.465
Leyens C., Hovsepian P.Eh., Münz W.-D., Peters M., Lewis D.B., Luo Q.

HIGH TEMPERATURE NANOLAMINATE CERAMIC COATINGS PREPARED BY PVD TECHNIQUES I.475
Teixeira V., Monteiro A., Portinha A., Vaßen R., Stöver D.

CYCLIC LIFETIME OF PYSZ AND CESZ EB-PVD TBC SYSTEMS ON VARIOUS Ni-SUPERALLOY SUBSTRATES I.483
Schulz U., Fritscher K., Kaysser W.A.

CHARACTERISATION OF SIX OVERLAY COATINGS I.493
Giannozzi M., Giorni E., Merluzzi M., Pratesi F., Zonfrillo G.

SINGLE CRYSTAL COATING OF SX TURBINE BLADES BY A LASER CLADDING TECHNIQUE I.503
Bezençon C., Wagnière J.-D., Höbel M., Schnell A., Konter M., Kurz W.

COMPARISON OF THERMAL CYCLING LIFE OF YSZ AND $LA_2ZR_2O_7$-BASED THERMAL BARRIER COATINGS I.511
Vaßen R., Barbezat G., Stöver D.

DEPOSITION OF ALUMINIUM + YTTRIUM ON THE INTERNAL SURFACES OF COMPLEX COOLED INDUSTRIAL TURBINE BLADES I.523
Innocenti M., Giorni E., Wing R., Norreys A., Archer N.J.,Yeatman J., Bianchi P., Baxter D., Wahl G., Metz Ch.

CHARACTERIZATION OF THE BOND-COAT MATERIALS FOR THE SUPER HIGH EFFICIENCY GAS TURBINES I.535
Suzuki A., Wu F., Murakami H., Imai H.

ELASTIC BEHAVIOUR OF PLASMA SPRAYED THERMAL BARRIER COATINGS I.543
Steinbrech R.W., Frahm J., Herzog R., Schubert F.

DEFORMATION BEHAVIOUR OF A LOW PRESSURE PLASMA SPRAYED NiCoCrAlY BOND COAT UNDER SHEAR LOADING AT TEMPERATURES ABOVE 750°C I.551
Majerus P., Steinbrech R.W., Herzog R., Schubert F.

VISCO-PLASTIC PROPERTIES OF SEPARATED THERMAL BARRIER COATINGS UNDER COMPRESSION LOADING I.561
Heckmann S., Herzog R., Steinbrech R.W., Schubert F., Singheiser L.

STRUCTURE IN THE SURFACE LAYER OF COATED Ni-BASED SUPERALLOYS DURING ANNEALING IN OXYDATION ENVIRONMENT I.569
Svejcar J., Jirikovsky K., Krejcí J.

MEASUREMENT OF THE DUCTILE BRITTLE TRANSITION TEMPERATURE AND THERMAL MECHANICAL FATIGUE RESISTANCE OF COATINGS USED IN GAS TURBINE ENGINES I.577
Saunders S.R.J., Banks J.P.

AUTHOR INDEX I

KEYWORD INDEX VII

PART II

SECTION 1 – ADVANCED GAS TURBINE MATERIALS

1.4. Intermetallics

MICROSTRUCTURE AND TENSILE CREEP BEHAVIOR OF MULTIPHASE NiAl EUTECTIC ALLOYS MODIFIED WITH Zr OR Hf II.595
Guo J.T., Qi Y.H., Cui C.Y., Li G.S.

CREEP STRENGTH AND MICROSTRUCTURE OF Ti-46Al-2W-0.5Si BASE ALLOYS II.605
Dlouh_ A., Arrell D., Karlsson B., Lapin J., Lupinc V., Nazmy M., Nikbin K., Staubli M.

HIGH TEMPERATURE DEFORMATION OF THE Fe28Al3Cr IRON ALUMINIDE MODIFIED WITH ADDITIVES II.615
Hakl J., Vlasák T., Kratochvil P.

MICROSTRUCTURE AND CREEP OF γ-TIAL BASED INTERMETALLIC ALLOY II.623
Lapin J., Pelachová T.

HIGH CYCLE FATIGUE BEHAVIOUR OF INTERMETALLIC γ-TiAl BASED ALLOYS II.633
Koolloos M.F.J., Arrell D.J., Henderson M.B., Gallet S.

Ti_2AlNb-BASED TITANIUM INTERMETALLIC ALLOYS FOR HIGH TEMPERATURE APPLICATIONS II.643
Hagiwara M., Emura S., Tang F.

MANUFACTURING AND TESTING OF A NOVEL ADVANCED NiAl-BASE ALLOY FOR GAS TURBINE APPLICATIONS II.653
Palm M., Sauthoff G.

HIGH-RATE SPUTTER DEPOSITION OF NiAl ON SAPPHIRE FIBERS II.663
Reichert K., Martinez C., Cremer R., Neuschütz D.

INTERFACIAL THERMAL STABILITY IN BN-COATED CONTINOUS Al_2O_3 FIBER REINFORCED NiAl COMPOSITES II.673
Wen K.Y., Reichert K., Hu W., Frommert M., Gottstein G.

MECHANICAL PROPERTIES AND OXIDATION BEHAVIOUR OF A CAST TiAl INTERMETALLIC II.683
Lupinc V., Marchionni M., Nazmy M., Onofrio G., Staubli M., Tomasi A., Zhou L.Z.

COATING OF Ni-ALUMINIDES ON TiAl INTERMETALLICS THROUGH UP-HILL DIFFUSION II.693
Izumi T., Nishimoto T., Narita T.

INFLUENCE OF MICROSTRUCTURAL EVOLUTION ON HARDNESS OF A γ TiAl INTERMETALLIC CONTAINING W AND Si II.703
Munoz-Morris M.A., Gil I., Morris D.G.

STRENGTHENING MECHANISMS IN DUCTILE FeAl INTERMETALLIC PROCESSED BY MECHANICAL ALLOYING II.711
Morris D.G., Garcia Oca C., Munoz-Morris M.A.

1.5. Miscellaneous topics

EXTRAPOLATION OF LIMITED CREEP DATA BY PARALLEL FITTING WITH DATA FOR SIMILAR MATERIALS II.723
White P.S.

DEVELOPMENT OF A VIRTUAL TURBINE SYSTEM FOR NEW MATERIALS DESIGN II.733
Saeki H., Fukuyama Y., Yokokawa T., Odaka T., Yoshida T., Harada H.

DRILLING OF COOLING HOLES AND SHAPING OF BLOW-OUT FACILITIES IN TURBINE BLADES BY LASER RADIATION II.743
Willach J., Horn A., Kreutz E.W.

REPAIR AND (RE)CONDITIONING OF COMPRESSOR AND TURBINE BLADES BY CO_2 AND Nd: YAG LASER RADIATION II.751
Kelbassa I., Gasser A., Backes G., Keutgen S., Kreutz E.W., Pirch N.

HIGH TEMPERATURE REACTOR (HTR) MATERIALS II.759
Buckthorpe D., Couturier R., Van der Schaaf B., Riou B., Rantala H., Moormann R., Buenaventura A., Friedrich B.-C.

PROPERTIES OF OXIDE/OXIDE CMCs FOR HIGH TEMPERATURE APPLICATIONS IN GAS TURBINES II.769
Innocenti M., Del Puglia P., Pappas Y.Z., Dassios C.G., Steen M., Kostopoulos V., Vlachos D.

SECTION 2 - FUEL ISSUES ANS NOVEL COMPONENTS

Invited Papers

IN-SITU FIRESIDE CORROSION TESTING OF ADVANCED BOILER MATERIALS WITH DIVERSE FUELS II.785
Henderson P.J., Karlsson A., Davis C., Rademakers P., Cizner J., Formanek B., Goransson K., Oakey J.

DEGRADATION OF BOILER AND HEAT EXCHANGER MATERIALS: DATA GENERATION, DATABASES AND PREDICTIVE MODELLING II.801
Saunders S.R.J., Simms N.J., Osgerby S., Oakey J.E.

COMPLEX FIRESIDE CORROSION MECHANISM IN BOILERS USING STAGED COMBUSTION SYSTEMS II.815
Bakker W., Kung S., Blough J., Seitz W.

FABRICATION OF A GAS TURBINE COMBUSTION HARDWARE IN ODS FERRITIC MATERIALS II.833
McColvin G., Munasinghe D., O'Driscoll J., Jacobs M.

DESIGN, CONSTRUCTION AND TESTING OF A CERAMIC HIGH TEMPERATURE HEAT EXCHANGER FOR AN EXTERNALLY FIRED CYCLE PLANT II.845
Mao C., Scarpellini R., Valarani M.

ELECTRICAL SWING ADSORPTION FOR CO_2 SEPARATION AND CAPTURE II.853
Judkins R.R.

2.1. Hot Gas Corrosion

HIGH TEMPERATURE CORROSION IN GAS TURBINES: FUEL MODEL AND EXPERIMENTAL RESULTS II.871
Bordenet B., Boßmann H.P.

REDUCTION OF FIRESIDE CORROSION OF SUPERHEATER MATERIALS IN A BIOMASS-FIRED CIRCULATING FLUIDISED BED BOILER II.883
Henderson P.J., Högberg J., Mattsson M.

EFFECT OF FUEL TYPE ON THE FIRESIDE CORROSION OF BOILER MATERIALS FOR ADVANCED CLEAN COAL TECHNOLOGIES II.893
Pinder L.W., Davis C.J.

FATE OF TRACE CONTAMINANTS FROM BIOMASS FUELS IN GASIFICATION SYSTEMS II.903
Kilgallon P., Simms N.J., Oakey J.E.

MATERIALS FOR GASIFIER HEAT EXCHANGERS II.913
Kilgallon P., Simms N.J., Norton J.F., Oakey J.E.

PERFORMANCE OF GAS TURBINE MATERIALS IN "DIRTY FUEL" ENVIRONMENTS II.923
Simms N.J., Encinas-Oropesa A., Kilgallon P., Oakey J.E.

LOW CYCLE FATIGUE IN AGGRESSIVE ENVIRONMENTS –A NEW TESTING METHOD USING CONTROLLED ATMOSPHERES II.933
Andersson H.C.M., Lindblom J.

CHLORINE CORROSION OF THERMALLY SPRAYED COATINGS AT ELEVATED TEMPERATURES II.945
Uusitalo M.A., Vuoristo P.M.J., Mäntylä T.A.

HIGH TEMPERATURE CORROSION IN STRAW FIRED POWER PLANTS: INFLUENCE OF STEAM/METAL TEMPERATURE ON CORROSION RATES FOR TP347H II.957
Montgomery M., Biede O., Hede Larsen O.

2.2. Miscellaneous Topics

EROSION CORROSION OF STEEL TUBES IN THE LOOP SEAL OF A BIOFUEL FIRED CFB PLANT II.969
Nafari A., Nylund A.

PERFORMANCE OF EROSION CORROSION RESISTANT COATINGS IN DIFFERENT COMBUSTION ENVIRONMENTS II.979
Hjörnhede A., Nylund A.

HAFNON – A POTENTIAL CERAMIC MATERIAL FOR LIQUID SLAG REMOVAL IN PRESSURIZED PULVERIZED COAL COMBUSTION ? II.989
Müller M., Hilpert K., Singheiser L.

HEAT RESISTANT SILICON NITRIDE CERAMICS WITH RARE-EARTH SILICON OXYNITRIDE II.997
Nishimura T., Guo S., Hirosaki N., Yamamoto Y., Mitomo M.

SECTION 3 – ADVANCED STEAM POWER PLANT

Invited Papers

BENEFIT OF ADVANCED STEAM POWER PLANTS II.1009
Blum R., Hald J.

DESIGN AND MATERIALS FOR TURBOSETS IN ADVANCED STEAM POWER PLANTS II.1017
Wieghardt K., Kern T.-U.

BOILER DESIGN AND MATERIALS ASPECTS FOR ADVANCED STEAM POWER PLANTS II.1019
Chen Q., Scheffknecht G.

ALLOY DESIGN AND MICROSTRUCTURAL CONTROL FOR IMPROVED 9-12% Cr POWER PLANT STEELS II.1035
Vanstone R.W.

THE EUROPEAN EFFORT IN DEVELOPMENT OF NEW HIGH TEMPERATURE ROTOR MATERIALS UP TO 650°C – COST 522 II.1049
Kern T.-U., Staubli M., Mayer K.H., Escher K., Zeiler G.

DEVELOPMENT OF CREEP RESISTANT CAST STEELS WITHIN THE EUROPEAN COLLABORATION IN ADVANCED STEAM TURBINE MATERIALS FOR ULTRA EFFICIENT, LOW EMISSION STEAM POWER PLANT / COST 501-522 II.1065
Staubli M., Mayer K.-H., Gieselbrecht W., Stief J., DiGianfrancesco A., Kern T.-U.

WELDABILITY AND WELD PROPERTIES FOR ADVANCED POWER PLANT MATERIALS II.1081
Cerjak H., Letofsky E., Jochum C., Nies H.

NEW BOILER MATERIALS FOR ADVANCED STEAM CONDITIONS II.1091
Scarlin B., Stamatelopoulos G.N.

MATERIALS FOR ULTRA-SUPERCRITICAL COAL-FIRED POWER PLANT BOILERS II.1109
Viswanathan R., Purgert R., Rao U.

THE STEAM OXIDATION RESISTANCE OF 9-12% CHROMIUM STEELS II.1131
Ennis P.J., Quadakkers W.J.

COATINGS FOR STEAM POWER PLANTS UNDER ADVANCED CONDITIONS II.1143
Agüero A., Muelas R., Scarlin B., Knoedler R.

3.1. Microstructure

MARTENSITIC/FERRITIC SUPER HEAT-RESISTANT 650°C STEELS –MICROSTRUCTURE II.1161
Agamennone R., Blum W.

PRECIPITATION OF Z-PHASE AND DEGRADATION BEHAVIOUR OF MOD.9Cr-1Mo STEEL II.1171
Kimura K., Suzuki K., Toda Y., Kushima H., Abe F.

DISTRIBUTION OF MX CARBONITRIDES AND ITS EFFECT ON CREEP DEFORMATION IN 9Cr-0.5Mo-1.8W-VNb STEEL II.1181
Sawada K., Kubo K., Hara T., Abe F.

THE EFFECT OF MICROSTRUCTURAL STABILITY ON LONG-TERM CREEP BEHAVIOUR OF 9-12%Cr STEELS II.1189
Sklenicka V., Kucharova K., Kloc L., Svoboda M., Staubli M.

SYSTEM FREE ENERGY APPROACH TO THE PRECIPITATION OF THE LAVES PHASE IN Fe-Cr-W-C QUATERNARY STEELS II.1201
Murata Y., Koyama T., Morinaga M., Hashizume R., Miyazaki T., Doi M.

MICROSTRUCTURAL PHYSICALLY BASED CREEP MODELLING ON 9-12 % Cr STEELS II.1211
Weinert P.

Z PHASE CHARACTERISTICS IN MARTENSITIC 12CrMoVNb STEELS II.1223
Vodarek V., Strang A.

MICROSTRUCTURAL ISSUES IN THE DESIGN OF AUSTENITIC AND NICKEL BASED MATERIALS FOR SUPERHEATER SYSTEMS IN 700°C STEAM PLANT II.1233
Starr F., Shibli A.

PRECIPITATION OF INTERMETALLIC PHASES DURING MARTENSITE AGING IN STEELS CONTAINING 10% Cr II.1241
Pigrova G.D.

A NEW MODELLING APPROACH TO MICROSTRUCTURAL EVOLUTION IN FERRITIC STEELS II.1247
Yin Y.F., Faulkner R.G.

AUTHOR INDEX I

KEYWORD INDEX VII

DEVELOPMENT OF CREEP RESISTANT CAST STEELS WITHIN THE EUROPEAN COLLABORATION IN ADVANCED STEAM TURBINE MATERIALS FOR ULTRA EFFICIENT, LOW EMISSION STEAM POWER PLANT / COST 501-522 II.1065
Staubli M., Mayer K.-H., Gieselbrecht W., Stief J., DiGianfrancesco A., Kern T.-U.

WELDABILITY AND WELD PROPERTIES FOR ADVANCED POWER PLANT MATERIALS II.1081
Cerjak H., Letofsky E., Jochum C., Nies H.

NEW BOILER MATERIALS FOR ADVANCED STEAM CONDITIONS II.1091
Scarlin B., Stamatelopoulos G.N.

MATERIALS FOR ULTRA-SUPERCRITICAL COAL-FIRED POWER PLANT BOILERS II.1109
Viswanathan R., Purgert R., Rao U.

THE STEAM OXIDATION RESISTANCE OF 9-12% CHROMIUM STEELS II.1131
Ennis P.J., Quadakkers W.J.

COATINGS FOR STEAM POWER PLANTS UNDER ADVANCED CONDITIONS II.1143
Agüero A., Muelas R., Scarlin B., Knoedler R.

3.1. Microstructure

MARTENSITIC/FERRITIC SUPER HEAT-RESISTANT 650°C STEELS –MICROSTRUCTURE II.1161
Agamennone R., Blum W.

PRECIPITATION OF Z-PHASE AND DEGRADATION BEHAVIOUR OF MOD.9Cr-1Mo STEEL II.1171
Kimura K., Suzuki K., Toda Y., Kushima H., Abe F.

DISTRIBUTION OF MX CARBONITRIDES AND ITS EFFECT ON CREEP DEFORMATION IN 9Cr-0.5Mo-1.8W-VNb STEEL II.1181
Sawada K., Kubo K., Hara T., Abe F.

THE EFFECT OF MICROSTRUCTURAL STABILITY ON LONG-TERM CREEP BEHAVIOUR OF 9-12%Cr STEELS II.1189
Sklenicka V., Kucharova K., Kloc L., Svoboda M., Staubli M.

SYSTEM FREE ENERGY APPROACH TO THE PRECIPITATION OF THE LAVES PHASE IN Fe-Cr-W-C QUATERNARY STEELS II.1201
Murata Y., Koyama T., Morinaga M., Hashizume R., Miyazaki T., Doi M.

MICROSTRUCTURAL PHYSICALLY BASED CREEP MODELLING ON 9-12 % Cr STEELS II.1211
Weinert P.

Z PHASE CHARACTERISTICS IN MARTENSITIC 12CrMoVNb STEELS II.1223
Vodarek V., Strang A.

MICROSTRUCTURAL ISSUES IN THE DESIGN OF AUSTENITIC AND NICKEL BASED MATERIALS FOR SUPERHEATER SYSTEMS IN 700°C STEAM PLANT II.1233
Starr F., Shibli A.

PRECIPITATION OF INTERMETALLIC PHASES DURING MARTENSITE AGING IN STEELS CONTAINING 10% Cr II.1241
Pigrova G.D.

A NEW MODELLING APPROACH TO MICROSTRUCTURAL EVOLUTION IN FERRITIC STEELS II.1247
Yin Y.F., Faulkner R.G.

AUTHOR INDEX I

KEYWORD INDEX VII

PART III

SECTION 3 – ADVANCED STEAM POWER PLANT

3.2. Alloy development

EVALUATION OF A NEW 11 % Cr STEEL FOR STEAM CHESTS III.1261
Bates P., Vanstone R.W., Osgerby S., Mulvihill P.

DEVELOPMENT OF HIGH WCoB-CONTAINING 12Cr ROTOR STEELS FOR USE AT 650C IN USC POWER PLANTS III.1269
Arai M., Doi H., Fukui Y., Azuma T., Fujita T.

MARTENSITIC/FERRITIC SUPER HEAT-RESISTANT 650°C STEELS III.1279
Agamennone R., Berger C., Blum W., Ehlers J., Ennis P.J., Granacher J., Inden G., Knezevic V., Quadakkers J.W., Sauthoff G., Scholz A., Singheiser L., Vilk J., Wang Y.

MARTENSITIC/FERRITIC SUPER HEAT-RESISTANT 650°C STEELS – DESIGN OF MODEL ALLOYS III.1289
Knezevic V., Sauthoff G.

MARTENSITIC/FERRITIC SUPER HEAT-RESISTANT 650°C STEELS – THERMODYNAMICS AND KINETICS OF PRECIPITATION REACTIONS III.1299
Vilk J., Schneider A., Inden G.

IMPROVEMENT OF CREEP RUPTURE STRENGTH OF HIGH STRENGTH 12Cr FERRITIC HEAT-RESISTANT STEEL III.1311
Uehara T., Toji A., Komatsubara S., Fujita T.

DEVELOPMENT OF A NEW 18Cr-9Ni AUSTENITIC STAINLESS STEEL BOILER TUBE III.1321
Ishitsuka T., Mimura H.

ALLOY DESIGN FOR ULTRA-HIGH TEMPERATURE STEAM TURBINE APPLICATIONS: PHASE FIELD SIMULATION OF THE REMELTING PROCESS III.1333
Böttger B., Steinbach I., Fries S.G., Chen Q., Sundman B.

WORKABILITY AND DEVELOPMENT OF T/P23 (2.25 % Cr-1.6W-Nb-V STEEL) FOR FOSSIL BOILER AND COMBINED CYCLE APPLICATIONS III.1343
Gabrel J., Lefebvre Bo., Vaillant J.-C., Vandenberghe B.

NEW WROUGHT Ni-BASED SUPERALLOYS WITH LOW THERMAL EXPANSION FOR 700C STEAM TURBINES III.1351
Yamamoto R., Kadoya Y., Kawai H., Magoshi R., Noda T., Hamano S., Ueta S., Isobe S.

DEVELOPMENT OF A NEW 12% Cr-STEEL FOR TUBES AND PIPES IN POWER PLANTS WITH STEAM TEMPERATURES UP TO 650°C III.1361
Bendick W., Gabrel J., Vaillant J.-C., Vandenberghe B.

HIGH PERFORMANCE LOW ALLOY STEEL CASTING FOR STEAM TURBINE III.1371
Ishii R., Tsuda Y., Yamada M., Ikeda K., Kaneko J.

DEVELOPMENT OF HIGH STRENGTH 9Cr STEEL BY COMBINATION OF FINE MX-TYPE NITRIDES AND NO CARBIDE III.1379
Taneike M., Sawada K., Abe F.

DEVELOPMENT STEPS OF NEW STEELS FOR ADVANCED STEAM POWER PLANTS III.1385
Mayer K.H., Blum R., Hillenbrand P., Kern T.-U., Staubli M.

GUIDING PRINCIPLES FOR DEVELOPMENT OF ADVANCED FERRITIC STEELS FOR 650°C USC BOILERS III.1397
Abe F., Okada H., Wanikawa S., Tabuchi M., Itagaki T., Kimura K., Yamaguchi K., Igarashi M.

3.3. Mechanical Properties

LONG TERM CREEP AND CREEP FATIGUE PROPERTIES OF THE MARTENSITIC STEELS OF TYPE (G)X12CrMoWVNbN10-1-1 III.1409
Schwienheer M., Haase H., Scholz A., Berger C.

TWO SPECIMEN COMPLEX THERMAL-MECHANICAL FATIGUE TESTS ON THE AUSTENITIC STAINLESS STEEL AISI 316 L III.1419
Rau K., Beck T., Löhe D.

CREEP PROPERTIES OF AUSTENITIC STAINLESS 353 MA AT 1100°C AND 1200°C III.1431
Wu R., Seitisleam F., Sandström R.

PROPERTIES AND EXPERIENCES WITH A NEW AUSTENITIC STAINLESS STEEL (TEMPALOY AA-1) FOR BOILER TUBE APPLICATION III.1445
Minami Y., Tohyama A., Hayakawa H.

IMPROVEMENTS IN THE SHORT TERM CREEP STRENGTH OF AISI 304L BY MEANS OF GRAIN BOUNDARY DESIGN AND CONTROL III.1453
Spigarelli S., Cabibbo M., Evangelista E., Palumbo G.

MICROSTRUCTURAL FEATURES INFLUENCING THE CREEP PROPERTIES OF 9-12 % Cr-STEELS FOCUSING ON LAVES-PHASE PRECIPITATION III.1459
Stocker Ch., Spiradek K., Zeiler G.

CREEP PROPERTIES OF PRECIPITATION STRENGTHENED CARBON FREE MARTENSITIC ALLOYS III.1469
Muneki S., Okubo H., Okada H., Yamada K., Igarashi M., Abe F.

MICROSTRUCTURE AND PROPERTIES OF MODIFIED 3% Cr STEELS III.1477
Foldyna V., Jakobová A., Vodárek V., Kroupa A., Kubon Z.

AN ASSESSMENT OF CREEP RUPTURE DATA ON STEEL E911 III.1487
Allen D.J., Servetto C.

EFFECT OF Cr CONTENT ON THE CREEP STRENGTH AND MICROSTRUCTURAL CHANGE IN HIGH Cr HEAT RESISTANT STEEL III.1497
Miki K., Azuma T., Ishiguro T., Hashizume R., Murata Y., Morinaga M.

THE EFFECT OF THE ELEMENT CARBON ON THE TOUGHNESS AND THE CREEP RUPTURE STRENGTH IN 12Cr HEAT RESISTANT STEELS III.1505
Ryu S.H., Kim M.S., Lee Y.S., Kang S.T., Kim J.T., Yu J.

STRAIN RANGE PARTITIONING ANALYSIS FOR CREEP-FATIGUE LIFE OF FERRITIC HEAT-RESISTING MATERIALS III.1515
Kimura M., Kobayashi K., Yamaguchi K.

HIGH TEMPERATURE CREEP BEHAVIOUR AND MICROSTRUCTURAL CHANGES OF TAF 650 STEEL III.1521
Svoboda M., Bursik J., Podstranska I., Kroupa A., Sklenicka V., Mayer K.-H.

STRESS CHANGE EXPERIMENTS IN LOW STRESS CREEP REGIME OF P-91 TYPE STEEL III.1531
Kloc L., Sklenicka V.

INVESTIGATIONS AND ANALYSIS ON THE STATIONARY CREEP BEHAVIOUR OF 9-12 % CHROMIUM FERRITIC MARTENSITIC STEELS III.1539
Dimmler G., Weinert P., Cerjak H.

ALLOY DESIGN FOR ULTRA HIGH TEMPERATURE STEAM TURBINE APPLICATIONS: CREEP BEHAVIOUR AND MODELLING OF CREEP III.1551
Thoma A., Scholz A., Berger C.

EFFECT OF ALLOYING ELEMENTS ON CREEP PROPERTIES OF Pd ADDED 9Cr FERRITIC STEELS III.1561
Okada H., Muneki S., Yamada K., Okubo H., Igarashi M., Abe F.

IMPROVEMENT OF CREEP STRENGTH OF PRECIPITATION STRENGTHENED 15Cr HEAT RESISTANT FERRITIC STEELS III.1571
Toda Y., Tohyama H., Kushima H., Kimura K., Abe F.

LONG-TERM CREEP STRENGTH PREDICTION OF HIGH Cr FERRITIC CREEP RESISTANT STEELS III.1581
Kushima H., Kimura K., Abe F.

EVALUATION OF CREEP PROPERTIES AND MICROSTRUCTURES ON THERMO-MECHANICAL AND MAGNETIC TREATED 9Cr FERRITIC STEELS III.1591
Okubo H., Muneki S., Okada H., Yamada K., Igarashi M., Abe F.

3.4. Steam Oxidation and Coatings

OXIDATION OF ADVANCED FERRITIC/MARTENSITIC STEELS AND OF COATINGS IN FLOWING STEAM AT 650°C III.1601
Knödler R., Scarlin B.

STEAM OXIDATION OF 9-12Cr MARTENSITIC STEELS: CHARACTERISATION AND MODELLING THE SPALLING OF OXIDE SCALE III.1613
Osgerby S., Mc Cartney L.N.

MECHANICAL AND OXIDATION TESTING OF ADVANCED MATERIALS FOR STEAM POWER PLANTS III.1621
Bontempi P., Guardamagna C., Ricci N., Torri L.

IMPROVEMENT OF STEAM OXIDATION RESISTANCE FOR FERRITIC HEAT RESISTANT STEELS III.1629
Kutsumi H., Itagaki T., Abe F.

STEAM OXIDATION OF HIGH CHROMIUM FERRITIC STEELS CONTAINING PALLADIUM III.1639
Itagaki T., Kutsumi H., Igarashi M., Abe F.

3.5. Welding

DESCRIPTION OF THE MATERIAL BEHAVIOUR IN GIRTH WELDS DURING WELD FABRICATION AND FOR HIGH TEMPERATURE SERVICE III.1651
Mohrmann R.

AN ASSESSMENT OF CREEP RUPTURE DATA ON E911 STEEL WELDMENTS III.1661
Servetto C., Allen D.J.

CHARACTERIZATION OF MATCHING FILLER METALS FOR NEW FERRITIC-BAINITIC STEELS LIKE T/P23 AND T/P24 III.1671
Heuser H., Jochum C.

EVALUATION OF THE WELDED JOINTS IN P92 AND P122 PIPE STEELS III.1681
Ryu S.H., Lee K.W., Chi B.H., Lee Y.S., Kong B.O., Park S.H., Nam S.W., Lim B.S., Kim B.J.

CREEP STRENGTH AND MICROSTRUCTURES FOR HAZ OF WELDMENTS OF HIGH Cr FERRITIC STEELS III.1691
Matsui M., Tabuchi M., Watanabe T., Kubo K., Abe F.

RESEARCH AND DEVELOPMENT OF NEW MARTENSITIC STEELS III.1701
Artinger A., Rozsavolgyi Z.

3.6. Applications

THE FIRST SUPERCRITICAL POWER UNIT IN POLAND. WELDABILITY EVALUATION OF NEW MARTENSITIC CHROMIUM STEELS WITH TUNGSTEN ADDITIONS AND PROPERTIES OF WELDED JOINTS III.1711
Brózda J., Zeman M., Pasternak J.

APPLICATION OF A NEW ROTOR STEEL FORGING FOR MEDIUM RATING SINGLE CYLINDER STEAM TURBINES III.1721
Yamada M., Tsuda Y., Kaneko J.

THE FIRST INDUSTRIAL CAST OF CrMoCoB ADVANCED STEEL FOR CAST TURBINE COMPONENTS III.1731
Contessi E., Del Vecchio D., Ghidini A., Valenti S., Carosi A., Di Gianfranceso A., Ielpo F.M.

OUTLOOK

Invited Papers

MATERIALS DEVELOPMENT FOR ADVANCED VISION 21 POWER PLANTS III.1745
Ruth L.A.

TRENDS IN POWER ENGINEERING IN JAPAN AND REQUIREMENTS FOR IMPROVED MATERIALS AND COMPONENTS III.1767
Masuyama F.

POWER GENERATION IN SOUTHERN AFRICA III.1783
De Beer J.A., Olsha Z.

ENERGY RESEARCH IN THE SIXTH FRAMEWORK PROGRAMME III.1801
Busquin P.

ADDENDUM

DEGRADATION OF EB-PVI) THERMAL BARRIER COATINGS DURING THERMAL CYCLING III.1809
Sun X.F., Li M.H., Zhang Z.Y., Guan H.R

AUTHOR INDEX I

KEYWORD INDEX VII

Part I

SECTION 1

ADVANCED GAS TURBINE MATERIALS

SECTION 1

ADVANCED GAS TURBINE MATERIALS

Invited Papers

THE MECHANICAL BEHAVIOUR OF A CLASS OF RHENIUM BASED SX SUPERALLOYS FOR INDUSTRIAL GAS TURBINE APPLICATIONS

M. Toulios[1] and D.H. Allen[2]

[1]School of Naval Architecture and Marine Engineering,
National Technical University of Athens, Athens 157 73, Greece

[2]ALSTOM Power Technology Centre
Cambridge Road, Whetstone, Leicester LE8 6LH, UK

Abstract

The superior high temperature properties of Re containing single crystal (SX) superalloys are regarded necessary in industrial gas turbine (IGT) applications in order to increase cycle efficiency and to achieve significant reductions in the NO_x emissions. However, IGT manufacturers seek to use SX superalloys that will also keep production and engine maintenance costs low, even though this may imply a compromise in their high temperature advantage. CMSX-4 and CM186LC are two Re containing nickel base superalloys that have been developed for different gas turbine applications, the former to give maximum properties for use in first stage components, the latter to improve the castability and yield of complex DS columnar aerofoils. One of their key differences is that CM186LC does not require an expensive solution treatment and is designed to have an increased grain boundary tolerance. More recently, CM186LC has become commercially available in SX castings in order to increase its high temperature capability. This paper presents a comparison of the creep and LCF properties of the two SX superalloys across the temperature regime and loading conditions that are relevant to IGT applications. In addition, certain microstructural details are given to highlight the differences between the two SX alloys. Wherever possible comparisons are made to the directionally solidified (DS) form of CM186LC.

Keywords: Creep, Low Cycle Fatigue, Single crystal, CMSX-4, CM186LC, Industrial gas turbine

Introduction

The use of a single crystal (SX) superalloy in an industrial gas turbine (IGT) blade/vane application is dependent on both its high temperature properties and its castability. The chemical composition which, in conjunction with the heat treatment, determines the mechanical and physical properties of the superalloy, is also crucial in being able to cast complex shaped components at an acceptable yield. The key improvement of SX superalloys, over previous polycrystalline and directionally solidified (DS) columnar casting alloys, is the introduction of simpler chemical compositions that do not contain grain boundary strengthening elements. The suppression of these alloying elements made possible the full solutioning of the γ' phase and enabled the design of single crystal superalloys (referred to as first generation) with superior high temperature capability. The addition of Rhenium in SX superalloys produced a further significant improvement in their creep resistance. Superalloys with around 3 wt % Re are now referred to (although not exclusively) as second generation.

IGT manufacturers have demanding targets for efficient and clean power generation. For example, in combined cycle plant thermal efficiencies of greater than 60% are targeted, with proportionate decreases in emissions. These improvements require higher turbine inlet and

invariably necessary. Moreover, the greater the temperature advantage of a particular SX alloy, the less cooling air is required. Second generations alloys, such as the commercially available alloy CMSX-4 [1], offer very good mechanical properties that can, together with thermal barrier coatings and advances in cooling technology, enable IGT manufactures to approach the above targets. However, at the same time production and engine maintenance costs are high as a result of the cost of the raw material, the efficient but expensive multi-step heat treatments, and the high rejection rates of components due to casting defects. This is particularly true for the larger single crystal (stage 1 and 2) blades used in the heavy-duty gas turbines of a combined cycle plant.

The need may therefore arise to use single crystal superalloys in the IGT engine that may offer a somewhat lower temperature advantage but, at the same time, can provide a significant reduction in costs. In this context, the alloy CM186LC has recently become commercially available in single crystal form [2] with significant cost savings since it can be used as cast, or partially solution-treated reducing overall cost. It also has an increased tolerance to grain boundary defects, as discussed further below. The objective of this paper is therefore to examine the relative strength of the single crystal alloys CMSX-4 and SX CM186LC across test conditions that are relevant to IGT applications. Reference is also made to certain mechanical properties of the columnar DS CM186LC, in view of its previous use in service, e.g. see [3], and since the DS and SX variants have identical compositions and heat treatments. The approach followed is to consider the mechanical properties that are used at the initial simplified design stage of a component. Moreover, only the creep and low cycle fatigue (LCF) behaviour are examined since they represent the two most critical loading conditions in a blade/vane. The ultimate selection of either alloy for a particular engine application will require a more extensive study, including a detailed simulation of the component that takes into account the in-service loadings, in conjunction with a careful analysis of the operational details of the engine.

Composition, Castability and Microstructure

The two alloys considered here contain 3% wt Rhenium and a high volume fraction (~70%) of the coherent γ' precipitate phase. CMSX-4 has been primarily developed to achieve maximum mechanical properties, as required in modern turbine blade applications. CM186LC was however originally designed to improve the castability and yield of complex DS columnar aerofoil segments that are typically used for vane applications. The chemical composition of the two alloys, see Table 1, reflects these objectives. Accordingly, CMSX-4 contains only traces of the grain boundary strengthening elements carbon, boron, hafnium and zirconium in order to increase the incipient melting temperature and hence to allow complete (>99%) solutioning of the γ' and most of the γ/γ' eutectic. In contrast, DS CM186LC contains optimum levels of these elements in order to achieve satisfactory mechanical properties in the transverse direction to the columnar grains.

More recently, it has been established that grain boundary strengthening elements, such as C, B, Hf, also significantly improve the mechanical properties of Ni-based SX superalloys that are subjected to loadings transverse to existing grain boundary defects. In general, grain specifications for SX castings only allow low angle boundaries (LABs) with misorientation less than 10-12°, particularly for aerofoil sections. However SX CM186LC intentionally cast as bi-crystals, with a predefined degree of misorientation, were found to retain the creep and

LCF properties of defect free single crystals well in the high angle boundary (HAB) regime [2]; that is, with grain boundary misorientations in excess of 10° and up to 35° and 25° respectively. The available data for SX CM186LC only address a few temperatures and loading conditions. This may be partly due to the complexity of producing the required castings. However similar results have been also reported in a more extensive experimental study for the first generation SX superalloy PWA1483 [4]. In this case SX PWA1483 modified with optimum levels of Hf and B exhibited significant tolerance to HABs in comparison to the original alloy that contained no such additions.

	C	Cr	Co	Mo	W	Al	Ti	Ta	Re	B	Zr	Hf	Nb	Fe	Ni
CM186 LC	0.069	6.0	9.3	0.5	8.4	5.7	0.7	3.4	2.9	0.015	0.006	1.4	-	0.065	Bal.
CMSX-4	0.002	6.4	9.6	0.61	6.4	5.7	1.01	6.5	2.9	<0.002	<0.001	0.1	<0.05	0.03	Bal.

Table 1: Chemical composition of typical CMSX-4 and CM186LC bar stock (wt pct)

One of the key features of SX CM186LC is that it can be used in service in the as cast or partially solutioned condition, hence avoiding difficulties that may arise, particularly for larger and thicker castings, due to the smaller "heat treatment window" resulting from the addition of the grain boundary strengthening elements. In contrast, CMSX-4 requires a multistage solution heat treatment (see [5]) in order to obtain the optimum γ/γ' structure and hence to achieve the enhanced mechanical performance.

The microstructure of the as cast SX CM186LC consists of a eutectic γ/γ' structure (in the interdendritic regions) surrounded by the primary γ with a finely precipitated γ' phase (in the dendrites). For the materials reported here, the morphology of the dendritic structure was found to somewhat differ in bars of different diameter. Both Howmet Castings (Exeter, UK) and PCC Airfoils Inc (USA) supplied castings for the manufacture of test specimens. In thicker bars, of 19mm diameter and 205mm length, a much coarser dendritic structure was observed with the secondary dendrite arms reaching a mean length of around 1mm at the bar end that solidified first. This decreased to around 600μm at the other end of the bar. The dendritic structure was found however to be much more uniform along the span of 16mm diameter bars (of 160mm and 205mm lengths) and the dendritic structure was also much finer. At mid-span of a 16mm diameter bar, the mean secondary dendrite arm length was between 300-400μm with a primary dendrite trunk spacing of 350-450μm.

The heat treatment (solutioning >99% plus ageing, see [5]) of CMSX-4 resulted in a reasonably homogeneous γ/γ' structure with cuboidal γ' particles. Details of the bars cast may be found in [6]. In pre-delivery inspection, one test bar per mould cast was sectioned longitudinally and transversely at the end that solidified first. This showed that the interdendritic porosity was <0.5% to 1.3% and the maximum pore sizes were between 60 to 120μm.

The quantitative characterisation of the γ/γ' structure in both CMSX-4 and SX CM186LC has been carried out using TEM thin foils, e.g. see [7][8] for the latter. The SEM micrographs, shown here in Fig. 1, are useful in highlighting the differences between the two alloys and, to a certain extent, are typical of a fully solutioned versus an as cast SX microstructure. It is evident that the dendritic γ/γ' in SX CM186LC, see Fig. 1(b), is less regular and less cuboidal

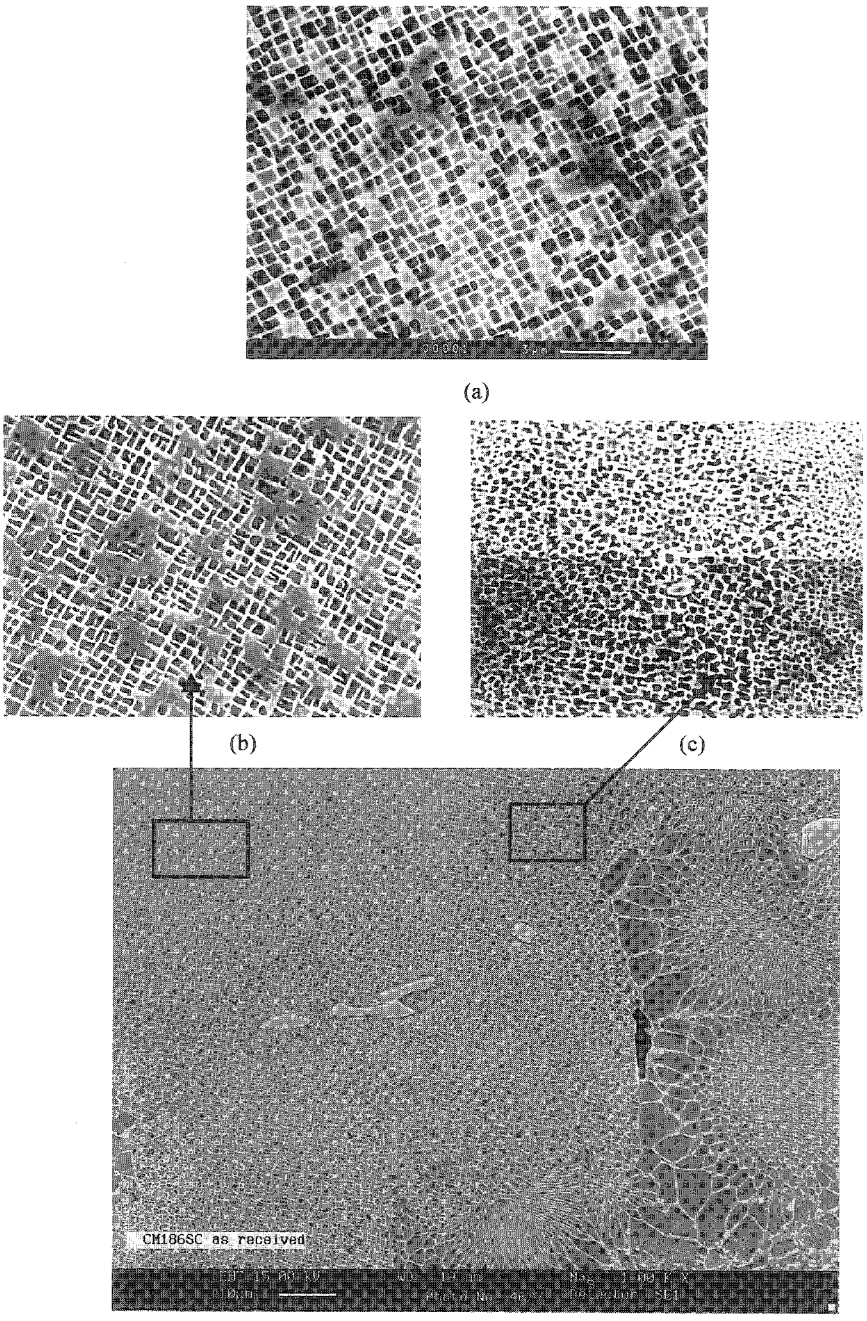


Fig. 1 SEM micrographs of the γ/γ' microstructure: (a) CMSX-4; (b), (c) and (d) [9] SX CM186LC.

than the homogeneous γ/γ′ structure in CMSX-4, Fig. 1(a), with typical precipitate sizes of 0.4 and 0.47μm respectively. The eutectic γ/γ′ in SX CM186LC is however highly irregular with some γ′ particles reaching a maximum width in excess of 10μm, see Fig. 1(d). A further heterogeneity in the superalloy microstructure is shown in Fig. 1(c). This shows that there is a transition region from the coarse eutectic to the 'regular' dendritic structure where the γ′ precipitates are of widely varying shape and size.

Also present in the as cast microstructure of SX CM186LC are carbides of the MC type that are rich in Ta and Hf with small amounts of Ti, W, and Ni. These particles were primarily found at the interdendritic regions, although some were also observed within the dendrites, see Fig. 1(d). SEM of the surface of as cast bars has shown that these particles tend to form a network, see Fig. 2, however their distribution in cross sections normal to the longitudinal axis of the specimen appeared to be random. In the absence of solutioning, there is much less microporosity in SX CM186LC and it is mostly found adjacent to the eutectic islands, Fig. 1(d). These pores are the result of volume shrinkage during the liquid to solid transformation [11].

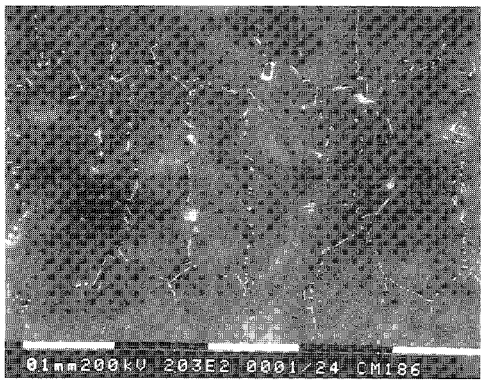


Fig. 2 Network of carbides on the surface of a virgin SX CM186LC bar; SEM micrograph from [10]

Creep Behaviour

The creep strength is a key factor in the selection of an alloy for IGT blades since these operate at high temperatures for long periods of time. Typical aerofoil temperatures are in the range of 700 to 950°C and steady state operation usually exceeds 30 000 hours. In order to compare the creep behaviour of the two superalloys, the creep properties along the <001> and <011> orientations are considered here. This is because of their role in the alloy selection process and in preliminary design calculations. The <001> orientation offers the optimum combination of mechanical properties and is therefore aligned with the main aerofoil axis (within the angle tolerances mentioned above) that is subjected to high centrifugal and thermal loadings. In cross-sections of the aerofoil, the tangential (to the surface) stress components can be parallel to any orientations along the <001> - <011> side of the crystallographic triangle. Accordingly the <011> orientation is also of practical significance in the initial design assessment.

Creep behaviour in the <001> orientation

The creep behaviour in the <001> orientation is presented here in terms of the time to rupture and the time to reach 1% creep strain. The CMSX-4 and SX CM186LC rupture data in Fig. 3(a) have been fitted with the parametric equation used in [6],

$$\log t_r = -C + (1/T).(a + b.f(\sigma) + c.f(\sigma)^2 + d.f(\sigma)^3 + e.f(\sigma)^4) \quad (1)$$

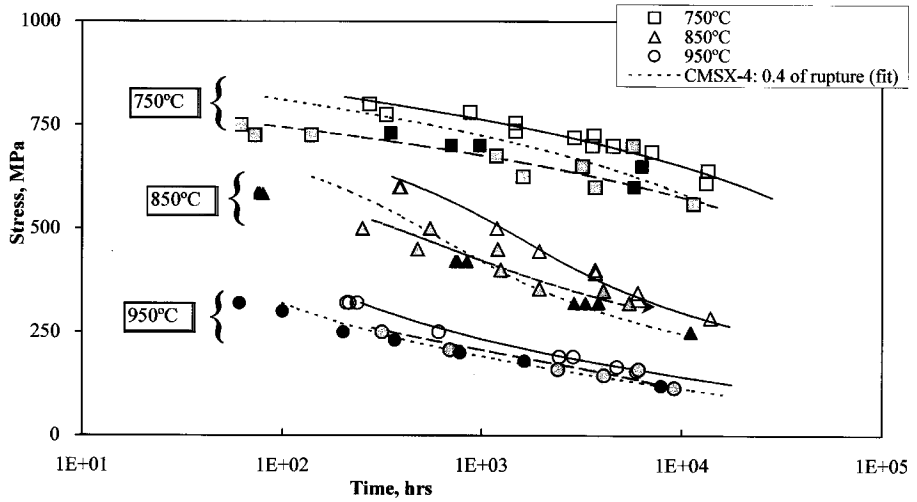
where $f(\sigma) = \sigma^{0.5}$, σ is the initial applied stress, T is the absolute temperature, and C, a, b, c, d, and e, are fitted coefficients. It is evident that transferring the constant C and the temperature T to the left hand side of the above equation gives the well-known Larson Miller Parameter. The values of the constant C and the other polynomial coefficients were determined by multiple regression. In [6] this procedure resulted in C=14.1 for CMSX-4 and a best-fit value of C=17.5 has been obtained for SX CM186LC. The 1% creep strain data in Fig. 3(b) have also been fitted using a similar parametric equation. Based on the data and fits shown in these two figures, the following comments can be made:

(a) The SX CM186LC data show considerably more scatter, particularly at 750°C and 850°C. This is not attributed to the testing being carried out by more than one laboratories and is considered to be a feature of the material. In this context, it should be noted that the scatter found in the 850°C data are from tests carried out by the same laboratory that also conducted the CMSX-4 testing (at similar loads).

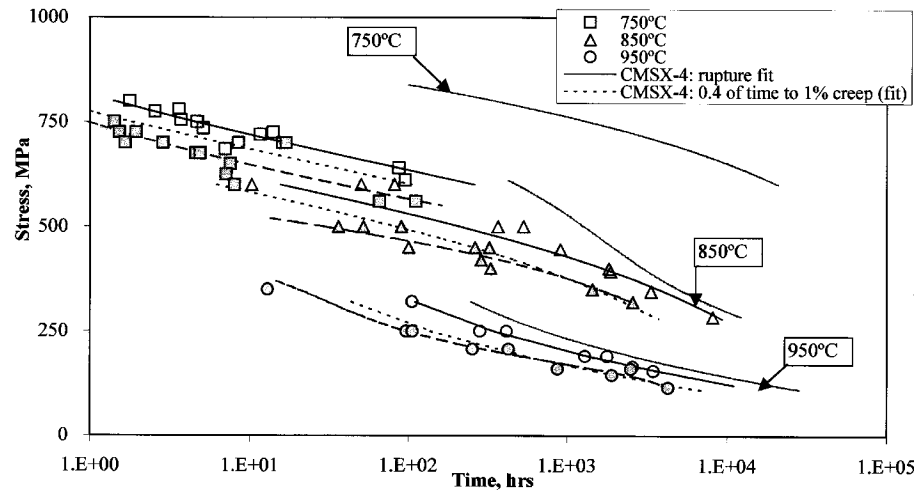
(b) As expected, SX CM186LC is significantly weaker than CMSX-4 particularly at the lower temperatures (i.e. 750°C and 850°C) and high stress regime. A 0.4 factor has been used to scale the CMSX-4 fits in order to facilitate the comparison to the SX CM186LC data. It is evident that at 950°C this factor correctly represents the relative strength of the two alloys, both in terms of rupture and the time to reach 1% creep strain. The 850°C data of Fig. 3(a) suggest that as the applied stress is reduced the rupture times of the two alloys converge. However this may be fortuitous in view of the scatter and the lack of longer-term tests. In addition, the 1% creep strain data at 850°C, see Fig. 3(b), do not show the same trend since they appear to fall on approximately parallel lines at the lower stress regime.

(c) Fig. 3(a) also includes rupture data from the DS (columnar grain) form of CM186LC. These show that there is virtually no difference in the rupture strength of the two alloys, especially if one takes into account the observed scatter. In general, a DS creep specimen (with a gauge length diameter of between 5 to 7mm) consists of a relatively small number of <001> columnar grains that are uniformly loaded in the axial direction. However, incompatibility of the transverse strains, due to misalignment in the secondary orientation of the columnar grains, might be expected to be an additional source of damage initiation in an axially loaded DS specimen in comparison to a SX specimen. The available rupture data suggest that either this effect is minor or the grain boundary strengthening elements in CM186LC minimise its impact.

(d) An important difference in the creep deformation across the temperature range 750°C to 950°C is highlighted in Fig. 3(b). At the lower temperatures (approximately ≤ 800°C) the deformation exhibits significant primary creep that results in the time to reach 1% creep strain being a small fraction of the time to rupture. This is also observed at 850°C but only



(a)



(b)

Fig. 3 Comparison of CMSX-4 and CM186LC creep data in the <001> orientation: (a) stress vs. time to rupture; (b) stress vs. time to reach 1% creep strain. White filled symbols denote CMSX-4 data, grey filled symbols SX CM186LC and black filled symbols DS CM186LC (rupture) data. The solid and long dash lines are fits to the CMSX-4 and SX CM186LC data respectively, as per eq. (1).

in the high stress regime. Tertiary creep dominates the deformation at the high temperatures (approximately ≥ 900°C) and therefore the time to reach 1% creep strain is within one order of magnitude of the rupture time. Although this is shown here using CMSX-4 data, the same is true for SX CM186LC, for example refer to the creep curves given in [8].

It is important to point out here that the above remarks are based on medium term tests, that is tests that ruptured, with a few exceptions, below 15 000 hours. They are therefore less representative of the low stress regime towards which the stresses in the aerofoil should relax and redistribute if the design life can be reached. For example, a few long-term <001> SX CM186LC tests, currently in progress at 950°C [8], suggest that there is a well-defined secondary creep regime (although until tertiary data become available it is not possible to estimate, since taking these tests to rupture is unlikely, the extent of this steady state period in terms of the rupture time).

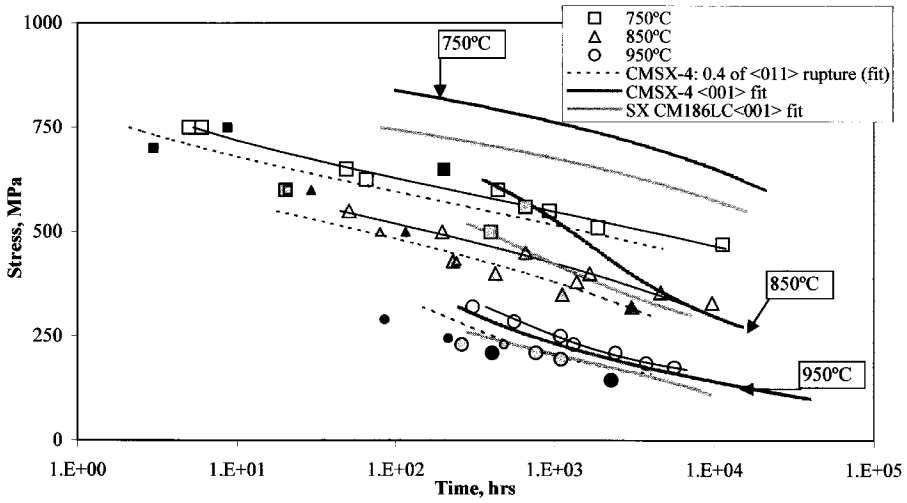


Fig. 4 Comparison of CMSX-4 (white symbols) and CM186LC (grey filled symbols) creep rupture data in the <011> orientation. Smaller symbols are used in the case of the CM186LC data to denote constant stress tests. The black filled symbols are from transversely loaded DS CM186LC specimens (constant stress tests from [12]). The solid lines are fits to the CMSX-4 <011> data, as per eq. (1).

Creep behaviour in the <011> orientation

The <011> behaviour of the two SX superalloys is presented in Fig. 4 in terms of the time to rupture. The CMSX-4 data have again been fitted with the parametric equation (1). Several medium-term SX CM186LC tests are still in progress and therefore no fitting has been carried out at this stage. Accordingly, the remarks below concern primarily its short-term behaviour.

(a) In terms of the <011> time to rupture, SX CM186LC is again significantly weaker than CMSX-4. A 0.4 factor has been used to scale down the CMSX-4 fitted curves at each temperature, as in the case of the <001> data. This is once more a reasonable representation of the relative strength of the two alloys at 950°C, less so however at 850°C and 750°C where SX CM186LC is even weaker.

(b) Fig. 4 also shows the rupture times from a smaller number of creep tests using specimens machined transversely to the columnar grains of DS CM186LC. The key point here is that the rupture strength of these specimens is similar to that of the <011> orientation in

SX CM186LC, particularly at the temperatures of 750°C and 850°C. At 950°C there is approximately a 40% drop in life as the applied stress is decreased. The DS CM186LC specimens consist of an undefined (relatively small) number of transversely loaded grain boundaries with random misorientation. These results therefore suggest that the optimised additions of C, B, Hf and Zr (which are present in both the DS and SX forms of the alloy) effectively strengthen the grain boundaries. However, the secondary orientation of the columnar grains will also have an effect on the rupture life, which cannot be quantified in view of their uncontrolled nature. The RT (pre-test) Young's moduli of the transverse DS CM186LC specimens may be used to detect a preferential alignment of the grains in the specimen. For example, in the 750°C, 650MPa test, which failed closer to the <001> rupture line, the Young's modulus was found to be 160GPa, while the average <001> and <011> moduli of SX CM186LC are 135GPa and 235GPa respectively. In the other constant load tests, for which RT Young's moduli are available, values of between 190 and 210 GPa were obtained.

(c) The anisotropy of the time to rupture is significantly reduced at the temperature of 950°C and in the low stress regime at 850°C. At 750°C the<011> orientation is significantly weaker and, although the rupture data appear to be converging, it is not possible to predict the long-term response. It should be noted that the highest degree of anisotropy occurs during the primary creep stage. When the latter is only a short transient, either by applying a lower stress and/or a higher temperature, the anisotropy in the creep deformation and rupture is also generally reduced. These observations are clearly more evident in the case of CMSX-4 where medium term <011> data are available, however the short term SX CM186LC data point to similar conclusions.

Microstructural characteristics

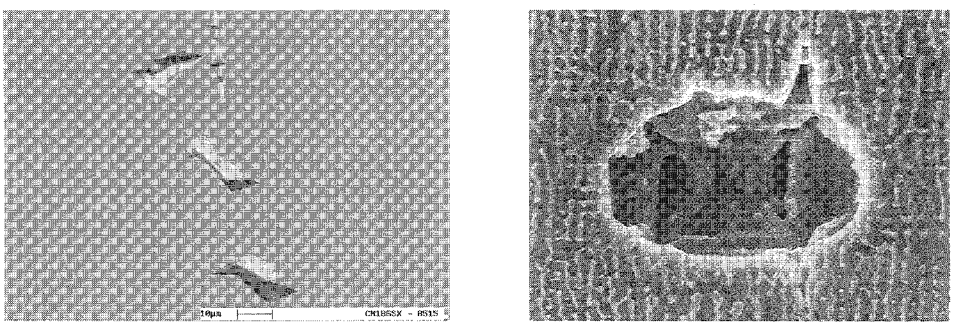
A detailed account here is beyond the scope of this paper. The emphasis is therefore to briefly discuss the role of the eutectic islands and the widespread carbides, these being the two main differences of the virgin SX CM186LC microstructure to that of the fully solutioned CMSX-4.

It has been shown for a number of alloys that at the lower temperatures, 750 to 800°C, the large primary creep strains obtained in <001> tests occur as a result of cutting of the γ' precipitates by partial dislocations on the {111} planes and a Burgers vector a<112> linked by stacking faults. In the case of CMSX-4 this has been extensively observed at 750°C and 750MPa [13][14], although there is currently no information concerning the dislocation mechanisms at lower stresses approaching IGT conditions. For SX CM186LC, ongoing examination of a failed 750°C, 675MPa test [15] has also found frequent shearing of γ' precipitates and the formation of stacking faults and, as expected, the morphology of the γ/γ' microstructure remains unchanged. No work has been carried out so far at this temperature to characterise further the observed dislocation structures. The work in [15] has confirmed however that at low stress levels, 361MPa and 279MPa, after approximately 10 000-12 500 hours and a total strain of around 0.25%, no rafting of the γ' precipitates occurs and there are no visible changes to the morphology of the eutectic islands.

At the higher temperature of 950°C rafting readily occurs and, in the case of <001> specimens, the γ' precipitates coalesce to form rafts perpendicular to the tensile axis. TEM studies on CMSX-4 [13] specimens loaded in creep at 950°C and 185MPa, has found no

evidence of stacking faults in the γ′ particles characteristic of the <112>{111} shear observed at 750°C. Instead both the TEM observations and the implications of the observed shape changes in the specimen cross-section, point to the operation of a <110>{111} slip system[13][16]. Dislocations were observed in the γ channels and, in particular, networks of dislocations had formed along the γ/γ′ interfaces. TEM work on SX CM186LC has also found dense networks of dislocations along the γ/γ′ interfaces at both relatively high stresses (207MPa) and at low stresses (115MPa and 70MPa) close to IGT conditions. However, in the as cast structure of SX CM186LC, dislocations were frequently observed within the γ′ particles in the eutectic colonies which, in view of their large size, may independently activate dislocations [8]. A further observation, found only in the low stress tests, concerns distinct changes in the γ/γ' morphology in the eutectic regions [8]. It is therefore postulated that these deformation mechanisms of the interdendritic microstructure contribute to the lower creep strength of SX CM186LC relative to CMSX-4.

Further differences are found in the mechanisms primarily responsible for the initiation of microcracks that lead to failure under creep conditions. In CMSX-4 microcracks are found to nucleate from micropores (Fig. 5(b)), believed to pre-exist after casting and solutioning [19], which grow and coalesce during the later stages of creep. Although cracking from micropores was also observed in SX CM186LC, microcracks were primarily seen to initiate from fractured carbides and along the carbide/matrix interfaces, for example see Fig. 5(a).



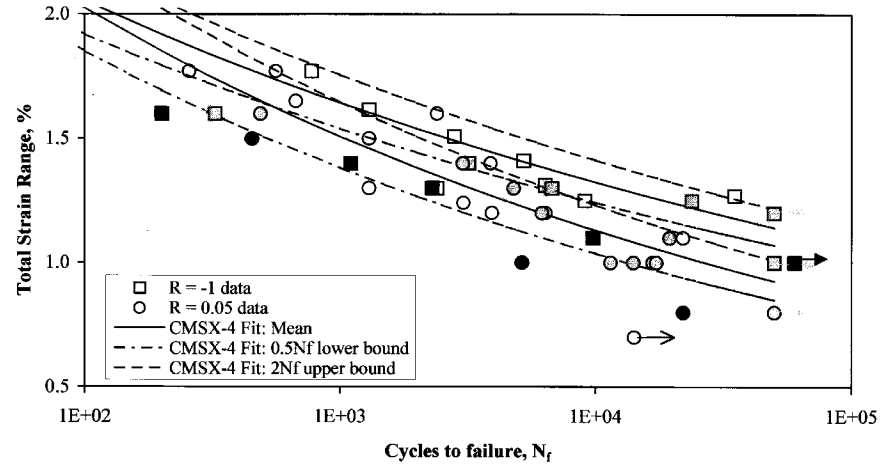
(a) (b)

Fig. 5 Nucleation of microcracks in: (a) SX CM186LC from carbides (800°C, stress direction vertical) [17]; (b) CMSX-4 from a micropore (950°C, stress direction horizontal) [18].

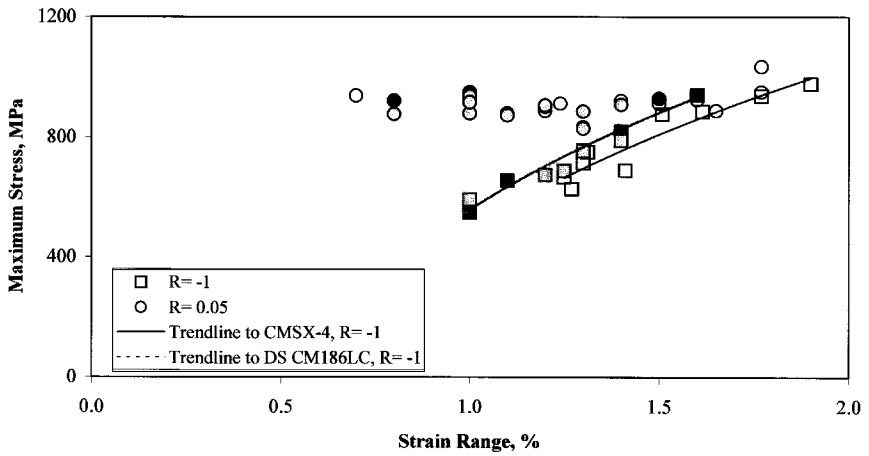
Low Cycle Fatigue Behaviour

The complex geometry of a cooled blade contains several features that give a high stress concentration and hence are susceptible to fatigue damage during each start-up/shut-down cycle. In the aerofoil such features include the fillet regions joining the aerofoil to the platform or the shroud, cooling passages with ribs, and infringement cooling holes. The stress state in the peak regions can be biaxial or uniaxial, e.g. along the surface of an infringement hole[20]. Since single crystal blading is cast without controlling the secondary crystal axes, the tangential stress components can be aligned with any orientation in the crystallographic triangle. As in the previous section, the <001> and <011> orientation are used here to

compare the behaviour of the two alloys. The <001> orientation has the highest LCF strength in view of the low Young's modulus. The <111> high modulus orientation has the lowest LCF strength, however the <011> orientation is selected in view of its relevance when considering the transverse behaviour of the DS form of the CM186LC alloy.



(a)



(b)

Fig. 6 Comparison of CMSX-4 and CM186LC <001> LCF data at 700°C and 6%/min: (a) total strain range vs. cycles to failure; (b) maximum stress at half-life vs. total strain range. White filled symbols denote CMSX-4 data, grey and black filled symbols respectively denote SX and DS CM186LC data.

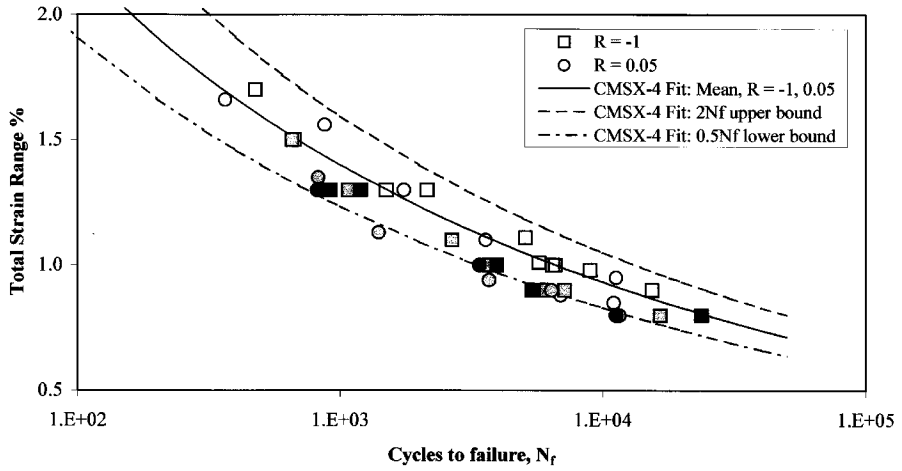
LCF behaviour in the <001> orientation

The LCF behaviour is presented at three typical aerofoil temperatures, 700, 850 and 950°C. The failure data at 700°C (from [6][21]), shown in Fig. 6(a), clearly show that in both alloys there is a strong dependence on the applied R-ratio, particularly in the low to medium strain ranges. This has been reported previously, e.g. [6], and is due to the presence of tensile mean stresses in tests with R =0.05 (& R=0.5, not shown in Fig.6), which are introduced by the strain cycle asymmetry. The mean stresses remain unchanged during load cycling, leading to high maximum stresses, see Fig. 6(b) where the half-life values are shown. Of interest here is the comparison of the two alloys which, despite the data scatter, clearly show that CMSX-4 and single crystal CM186LC have similar LCF strength. However the DS form of CM186LC is evidently weaker. It should be noted here that the scatter in the failure data could not be correlated to the differences in the morphology of the dendritic structure observed in the 16mm and 19mm diameter cast bars.

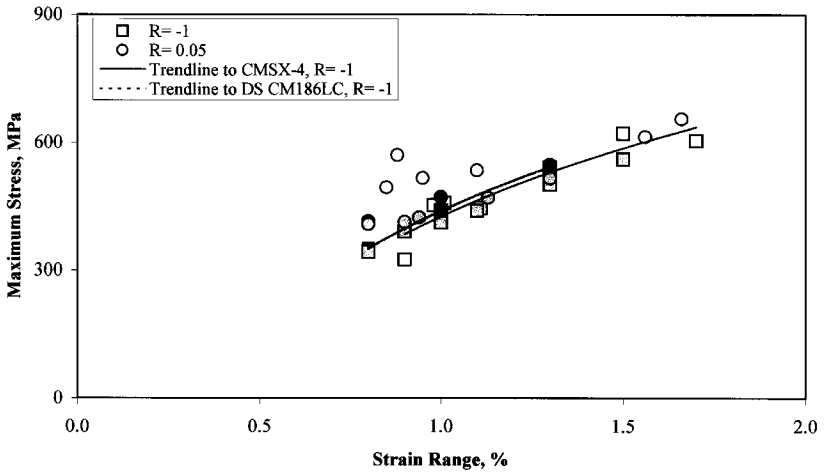
The cycles to failure data at 950°C, Fig. 7(a), indicate that the effect of the strain cycle asymmetry is negligible at this temperature. This can be justified by the half-life maximum stress data, Fig. 7(b), which show small to negligible dependence on the applied R-ratio. The latter can be attributed to creep deformation that fairly quickly relaxes the positive mean stresses induced by the strain asymmetry. At this temperature, the LCF strength of single crystal CM186LC is somewhat lower then that of CMSX-4, see Fig. 7(a) where the SX CM186LC data are consistently below the CMSX-4 mean fit curve and close to the $0.5N_f$ lower bound. Moreover, at this temperature the DS and SX forms of CM186LC have similar fatigue endurance. The LCF failure data at 850°C, not shown here due to shortage of space, indicate that the relative strength of the two single crystal alloys is intermediate to those found at 700 and 950°C. That is, several SX CM186LC data points lie close to the CMSX-4 mean fit curve but no data fall above this curve.

Further investigation is necessary in order to understand the reasons for the varying relative strength of the alloys across the temperature range 700 to 950°C. However, as the maximum stress data in Figs. 6(b) and 7(b) suggest, there appear to be small differences in the stress histories of the two SX and the DS alloys when tested at similar conditions. In general, somewhat higher differences were expected since, as in the case of creep, there is evidence of dislocation activity within the γ' particles in the eutectic colonies[21] (at least at 950°C). This is additional to the dislocation networks observed within the γ channels.

Examination of fractured CMXS-4 and SX CM186LC <001> specimens found that in some cases at 700°C and 850°C, a single (sub-surface or close to the surface) site was responsible for the initiation of the main crack that ultimately induced failure. In CMSX-4 the initiation site is associated with microporosity, as in Fig. 8(a), while in SX CM186LC cracks initiate at carbides, Fig. 8(b). At the higher temperatures, particularly at 950°C, the main crack is usually found to initiate at the surface, for example from surface emergent carbides [21] in SX 186LC test pieces, see Fig. 2 here, or from micropores in CMSX-4 specimens [22], assisted by the oxidising environment (i.e. the air). There is also a marked increase on the number of secondary cracks originating on the surface [9][21]. The fractographic examination of CMSX-4 specimens has been more extensive and there is a suggestion that larger pores result in the most significant loss of life [23]. However, there were cases of rosettes growing from the surface of test pieces with no clear porosity at their centres and some specimens failed prematurely with no evidence of micropores initiating cracks.



(a)

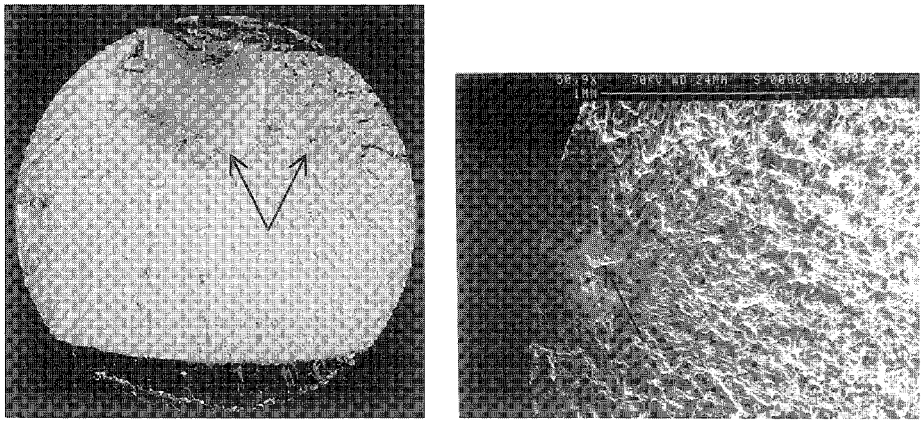


(b)

Fig. 7 Comparison of CMSX-4 and CM186LC <001> LCF data at 950°C and 6%/min: (a) total strain range vs. cycles to failure; (b) maximum stress at half-life vs. total strain range. White filled symbols denote CMSX-4 data, grey and black filled symbols respectively denote SX and DS CM186LC data.

LCF behaviour in the <011> orientation

There are less data available in this orientation and therefore a detailed comparison of CM186LC and CMSX-4 is only possible at the temperature of 850°C. Accordingly, as shown in Fig. 9(a), the two single crystal alloys have comparable strength up to medium strain ranges. At the lower strain ranges, less than 0.7%, there appears to be a distinct advantage of



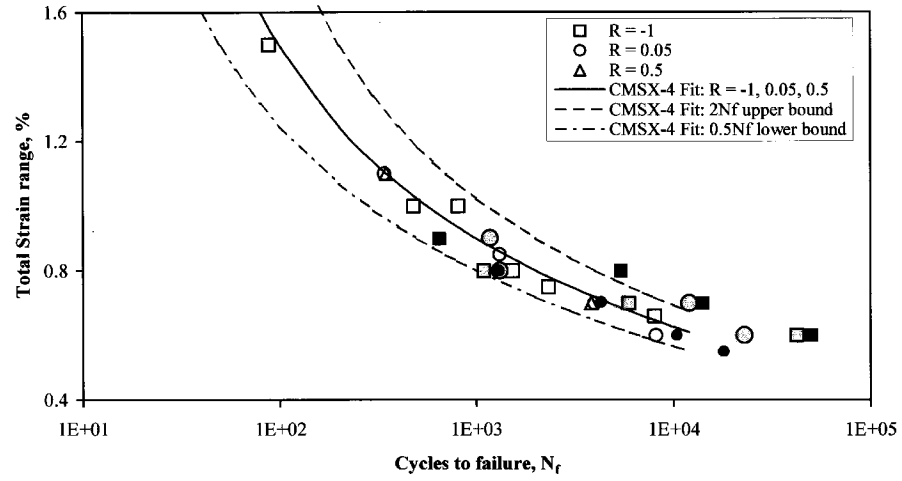
(a) (b)

Fig. 8. (a) CMSX-4: LM photograph of two 'rosettes' (regions of stable crack growth, radius ≈ 2.5mm for the large one) marked by the two arrows, with cracks initiating at micropores [23]; in <001> specimen tested at 850°C and 6%/min. (b) SX CM186LC: SEM micrograph showing close to the surface initiation of a crack from a carbide, marked by the arrow, and a smaller 'rosette' (radius ≈ 130μm) [15]; in <001> specimen tested at 700°C and 6%/min.

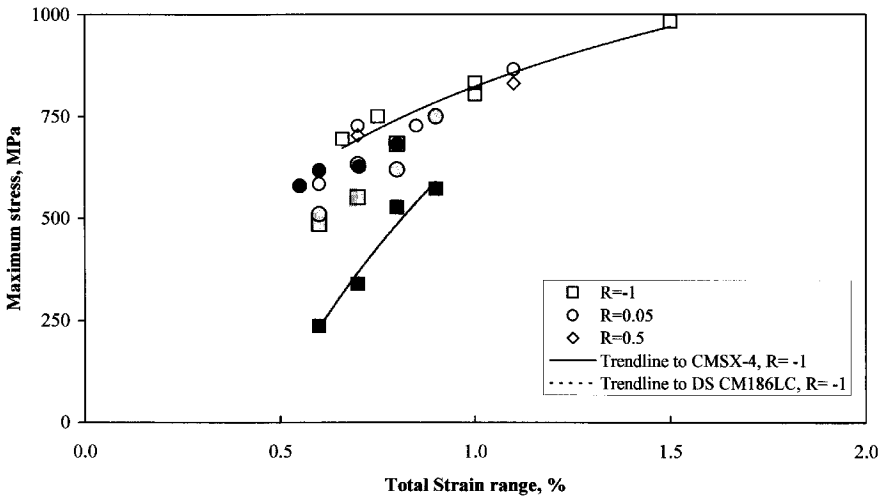
SX CM186LC that CMSX-4, despite the lack of adequate low strain range data, seems unlikely to follow. The comparison of the <011> SX and DS variants of CM186LC is meaningful when for the latter the LCF specimens are machined transversely to the columnar grains. The available cycles to failure data, also included in Fig. 9(a), indicate that at least for R= –1 the LCF endurance of SX and DS CM186LC is similar. The transverse DS data show in addition a dependence on the applied R-ratio that is not evident in the <011> data of the two single crystal alloys. In general, at 850°C (as at 950°C) creep is again expected to reduce the high positive stresses induced by the strain asymmetry and this is supported by the half-life maximum stress <011> data presented in Fig. 9(b). On the contrary for DS CM186LC, the maximum stress data at R=0.05 are significantly higher then the corresponding values at R= –1, which results in the shorter lifetime in the case of R=0.05, as shown in Fig. 9(a). The reasons for this difference are under investigation.

Conclusions

The creep and LCF properties of the single crystal superalloys CMSX-4 and SX CM186LC, and the DS variant of the latter, have been reviewed in order to examine their relative strength under testing conditions of relevance to IGT applications. Both alloys contain 2.9 wt % Rhenium which benefits their high temperature creep resistance. CMSX-4 is known to have very good high temperature properties but component manufacturing costs can be high as a result of the required solution heat treatment and reduced yields due to casting defects. On the contrary, CM186LC (SX & DS) contain optimum additions of grain boundary strengthening elements, increasing yield, and can also be used as cast, hence offering the possibility of significant savings in the cost of a blade/vane component.



(a)



(b)

Fig. 9 Comparison of CMSX-4 and CM186LC [21] LCF <011> data at 850°C and 6%/min: (a) total strain range vs. cycles to failure; (b) maximum stress at half-life vs. total strain range. White and grey filled symbols denote respectively CMSX-4 and SX CM186LC data. The black filled symbols are from transversely loaded DS CM186LC specimens.

The analysis of the creep data presented here indicates that in the temperature range 750°C to 950°C SX CM186LC is significantly weaker then CMSX-4. Both the time to 1% creep strain and the rupture time data show that the <001> creep strength of SX CM186LC is, at best,

approximately 40% that of CMSX-4 at the temperature of 950°C. A similar figure is found to express the relative creep strength of the two alloys in the <011> orientation. Of significant interest is the result that the columnar DS and <001> CM186LC data are virtually the same. Moreover, the <011> and transverse DS rupture times suggest a similar strength at 750-850°C for the two CM186LC variants, however this remark is tentative due to lack of adequate data. Although these conclusions are based on data that are, with a few exceptions, somewhat short of actual IGT operating conditions, they address a stress-temperature regime not previously used to compare this class of SX alloys.

The LCF data presented here lead to different conclusions concerning the relative strength of the two SX alloys. Accordingly at 700°C and 850°C, the LCF endurance of CMSX-4 and SX CM186LC was found to be similar, although at 950°C the latter is to some extent weaker. Somewhat unexpected is the observation that at 950°C the columnar DS and <001> SX variants of CM186LC have equal LCF strength, while at 700°C the columnar DS form is weaker. The comparison of the <011> data suggests that at the low strain ranges there appears to be a distinct advantage of SX CM186LC, although this conclusion is tentative due to lack of CMSX-4 data.

Finally, although the selection of the alloys considered for an engine application will require a much more extensive study then the analysis of the data presented here, it is possible to comment on this issue. Accordingly, in cases where there is a favourable turbine engine service experience using DS columnar blades, a switch to the SX variant of CM186LC seems unlikely. This is because of the relatively similar creep and LCF behaviour of the two variants and the fact that their composition and heat treatments are identical. Equally significant, concerning turbine blading applications, is the result that SX CM186LC lags well behind CMSX-4 in terms of its creep resistance. However, the LCF strength of CM186LC, the SX variant in particular but also in the DS form, is very good and therefore it remains an attractive option for complex shaped vane applications.

Acknowledgements

The authors would like to acknowledge the contributions of all the participants in the Single Crystal Subgroup of COST 501, Round III and in the Blades/Vanes Work Package of the Gas Turbine Group of COST 522 that respectively provided the framework for the mechanical and microstructural characterisation of the CMSX-4 and SX CM186LC superalloys. Without their true spirit of co-operation and their enthusiasm, it is certain that fewer objectives would have been realised. Finally, ALSTOM Power gratefully acknowledges UK DTI for funding of this work.

References

[1] Harris, K., Erickson, G.L., Sikkenga, S.L., Brentnall, W.D., Aurrecoechea, J.M. and Kubarych, K.G., Development of the Rhenium Containing Superalloys CMSX-4 and CM186LC for Single Crystal Blade and Directionally Solidified Vane Applications in Advanced Turbine Engines, *The Metallurgical Society of AIME, 7th International Symposium on Superalloys,* Seven Springs, Pennsylvania (1992), 297-306.

[2] Harris, K. and Wahl, J.B., New Superalloy Concepts for Single Crystal Turbine Vanes and Blades, in *Parsons 2000, Advanced Materials for 21st Century Turbines and Power Plant, Proceedings of the 4th International Charles Parsons Turbine Conference,* A. Strang et al (eds.) (2000), 832-846.

[3] McColvin, G., Sutton, J., Whitehurst, M.F., Fleck, D.G., VanVranken, T.A., Harris, K., Erickson, G.L. and Wahl, J.B., Application of the Second Generation DS Superalloy CM186LC to First Stage Turbine Blading in EGT Industrial Gas Turbines, *Proceedings of the 4th International Charles Parsons Turbine Conference*, Newcastle upon Tyne (1997), 339-357.

[4] Shah, D.M. and Cetel, A., Evaluation of PWA1483 for Large Single Crystal IGT Blade Applications, in *Superalloys 2000*, T.M. Pollock et al (eds.), TMS (2000), 295-304.

[5] Harris, K., Erickson, G.L., Schwer, R.E., Frasier, D.J. and Whetstone, J.R., Process and Alloy Optimisation for CMSX-4 Superalloy Single Crystal Airfoils, in *High Temperature Materials for Power Engineering 1990*, E. Bachelet et al (eds.), Part II (1990), 1281-1300.

[6] Bullough, C.K., Toulios, M., Oehl, M., and Lukáš, P., The Characterisation of the Single Crystal Superalloy CMSX-4 for Industrial Gas Turbine Blading Applications, in *Materials for Advanced Power Engineering 1998*, J. Lecomte-Beckers et al (eds.), Part II (1998), 861-878.

[7] Czyrska-Filemonowicz, A., Dubiel, B. and Danciu, D., Microstructural Investigation of the CM186LC Single Crystal Superalloy by Means of LM and TEM, *COST 522, WP1.1 "Blades/Vanes" Annual Report* (1999).

[8] Wilcock, I.M., Lukáš, P., Maldini, M., Klabbers, J., Dubiel, D. and Henderson, M.B., The Creep Behaviour of As-Cast SX CM186LC at Industrial Gas Turbine Operating Conditions, To appear in the Proceedings of the 7th Liège Conference, *Materials for Advanced Power Engineering*, Sept. 2002.

[9] Bontempi, P., Guardamagna, C. and Ricci, N., Creep and Fatigue Characterisation and Microstructural Observations of SX CM186LC, *COST 522, WP1.1 "Blades/Vanes" Annual Report* (2001).

[10] Lukáš, P. and Kunz, L., Structure and Microstructure of Superalloy Single Crystal CM186LC, *COST 522, WP1.1 "Blades/Vanes" Annual Report* (1999).

[11] Lecomte-Beckers, J., Study of Solidification Features of Nickel-Base Superalloys in Relation with Composition, *Metall. Trans.*, 19A, (1988), 2333-2340.

[12] Wilcock, I.M., *QinetiQ* (2002) Private Communication.

[13] Matan, N., Cox, D.C., Carter, P., Rist, M.A., Rae, C.M.F. and Reed, R.C., Creep of CMSX-4 Superalloy Single Crystals: Effects of Misorientation and Temperature, *Acta Materialia*, 47 (1999), 1549-1563.

[14] Rae, C.M.F., Matan, N. and Reed, R.C., The Role of Stacking Fault Shear in the Primary Creep of [001]-Oriented Single Crystal Superalloys at 750°C and 750MPa, *Materials Science and Engineering*, A300 (2001), 125-134.

[15] Czyrska-Filemonowicz, A. and Dubiel, B., Microstructural Investigation of the CM186LC Single Crystal Superalloy by Means of LM, SEM and TEM, *COST 522, WP1.1 "Blades/Vanes" Annual Report* (2001).

[16] Matan, N., Cox, D.C., Rae, C.M.F. and Reed, R.C., On the Kinetics of Rafting in CMSX-4 Superalloy Single Crystals, *Acta Materialia*, 47 (1999), 2031-2045.

[17] Maldini, M., Angella, G., Lupinc, V. and Signorelli, E., High Temperature Mechanical Properties of Nickel-base Superalloys for Gas Turbines Blades, *COST 522, WP1.1 "Blades/Vanes" Annual Report* (2001).

[18] Henderson, P., Lindblom, J. and Komenda, J., Creep of the Single Crystal Ni-Base Superalloy CMSX-4, *COST 501 - Round III, WP14.2 Progress Report*, No. IM-3380 (1996).

[19] Komenda, J. and Henderson, P.J., Growth of Pores During the Creep of a Single Crystal Nickel-Base Superalloy. *Scripta Materialia*, 37 (1997), 1821-1826.

[20] Toulios, M., Lifing of High Temperature Components, in *MATERIALS WEEK 2000 - Proceedings*, editor and organiser: Werkstoffwoche-Partnerschaft, Frankfurt, 25-28 September 2000,URL: www.materialsweek.org/proceedings.

[21] Bale, D.W., Henderson, M., Dubiel, B., Czyrska-Filemonowicz, A., Guardamagna, C, Bontempi, P., Mulvihill, P., Lukáš, P., Obrtlik, K. and Kolkman, H., The Low Cycle Fatigue Behaviour of As Cast Single Crystal CM186LC, To appear in the Proceedings of the 7th Liège Conference, *Materials for Advanced Power Engineering*, Sept. 2002.

[22] Ott, M. and Mughrabi, H., Dependence of the high temperature LCF behaviour of the monocrystalline nickel base superalloys CMSX-4 and CMSX-6 on the γ/γ' morphology, *Materials Science and Engineering*, A272 (1999), 24-30.

[23] Bullough, C.K., McColvin, G., White, P.S. and Whitehurst, M.F., Mechanical Properties of CMSX-4 Single Crystal Alloy, *COST 501 – Round III, WP14.2 Final Report* (1998).

CONSTITUTIVE MATERIAL FORMULATIONS AND ADVANCED LIFE ASSESSMENT METHODS FOR SINGLE CRYSTAL GAS TURBINE BLADES

E.P. Busso[1], M. Toulios[2] and G. Cailletaud[3]

[1]Department of Mechanical Engineering
Imperial College, London SW7 2BX, UK

[2]School of Naval Architecture and Marine Engineering,
National Technical University of Athens, Athens 157 73, Greece

[3]Ecole Nationale Supérieure des Mines de Paris
Centre des Matériaux, B.P.87, 91003 Evry Cedex, France

Abstract

Constitutive models for single crystal superalloys have been developed for the past fifteen years in response to the increasingly wider use of these materials to manufacture industrial and aerospace gas turbine blading. A number of model formulations are now available that aim to predict correctly the deformation behaviour at loading conditions similar to those experienced in service. Some of the most relevant work in this field is reviewed in this paper. In engineering practice, the complexity of the material models used depends on the required level of accuracy and the ability to effectively perform computationally intensive FE analyses, due to the complex geometry of a cooled blade. However, it is argued that a constitutive formulation should take into account various features of the microstructure to predict correctly the effect of heterogeneities in the material that can be critical to the life of a component. Certain key aspects in the design assessment of cooled blades are also discussed, in particular the implications of the choice of constitutive models in the blade design procedure.

Keywords: constitutive models, multi-scale modelling, single crystal superalloys, cooled blade design

Introduction

Land-based and aerospace gas turbines often rely on more than one row of single crystal blades to expand and speed-up the hot gases from the combustor while they turn the rotor. Nickel based superalloys have become widely favoured as the material of choice for turbine blades since they offer good high temperature properties. The introduction of a new superalloy in an existing or future blade design is a complex and time-consuming process. The comprehensive characterisation of the mechanical behaviour of the alloy contributes significantly to the duration and cost of this process. Often the development cycle time is shortened by using high safety factors, which lead to a more frequent replacement programme to address the uncertainty and/or limitations in the life estimation methods. However, this conservative, experience-based, approach of the past is gradually being substituted with a much shorter and accurate computer-based modelling approach [1][2]. With each new generation of blade materials, advanced materials models are required to predict accurately their high temperature deformation behaviour, including the effects of changes in phase constitution as a function of chemical composition, temperature and time. The need for advanced constitutive models is highlighted by the fact that a major contributing factor to the acceleration of creep rates and to fatigue failures in superalloy components is the localization of the inelastic deformation caused by the heterogeneity of the material microstructure. Most

complex behaviour to assure the accuracy of hot section component design and life assessments.

This paper initially reviews recent developments in the formulation of constitutive models to describe the stress-strain behaviour of single crystal (SC) superalloys. The review is divided in three parts. The first one addresses several formulations developed during the past 10-15 years which, although physically based, do not explicitly take into account the heterogeneities that arise in SC superalloys. In the second part, more recent constitutive approaches, which incorporate the evolution of the microstructure at different length scales to deal with the effects of a heterogeneous microstructure, are briefly described. Finally, the paper describes certain key aspects in the design assessment of cooled blades and discusses the implication of the choice of constitutive models in blade design.

Microstructural Considerations and Constitutive Frameworks

In Ni-base superalloys, material heterogeneities exist at both the microscopic and mesoscopic levels. At the microscale, they can occur due to the changing morphology of the ~ 0.5-1 μm γ' precipitates during service, i.e. the so-called rafting process, and to the breakdown of uniform patterns of plastic deformation into localised deformation modes (i.e. shear bands) from which cracks can initiate, e.g. see [3]. At the mesoscale, heterogeneities may exist in the material in the form of either casting and processing defects (e.g., ~10-30 μm diameter casting micropores , inclusions), or as 20-200 μm eutectic regions, which generally precipitate during the final stages of solidification (e.g. see [4]), occupy interdendritic regions and are composed of a high volume fraction (>90%) of γ' precipitates of irregular shape. During service, local conditions around these homogeneities such as stress-state, anisotropy, temperature and interaction with a free-surface can give rise to microcracks initiating, e.g. from the circumference of embedded casting defects, following an incubation or growth period. Coalescence of these microcracks often leads to failure at the macroscopic level [5][6].

Constitutive models developed to predict the high temperature behaviour of single crystal superalloys follow either a Hill-type or a crystallographic approach. As a common feature, they treat the material as a continuum in order to describe properly visco-plastic effects in the temperature range of interest. Hill-type approaches (e.g. [7][8][9]) are based on a generalisation of the Mises yield criterion proposed by Hill [10] to account for the non-smooth flow potential surface required to describe the anisotropic flow stress behaviour of single crystal materials. In visco-plastic constitutive formulations based on crystallographic slip, the macroscopic stress state is resolved onto each slip system following Schmid's law. Depending on the relative orientation of the slip system with respect to the macroscopic principal stress directions and to the magnitude of the resolved shear stress, the slip system may be activated and slip produced. Internal state variables are generally introduced in both formulations to represent the evolution of the microstructural state during the deformation process.

Although recent developments in these two approaches have now reached an advanced stage, the major improvements have been made by crystallographic models due to their ability to incorporate complex micro-mechanisms of slip within the flow and evolutionary equations of the single crystal models. These include the effects of dislocation interactions [11][12], strain gradient phenomena [13][14][15], precipitate morphologies [13][16] and their spatial

arrangements [17], and general anisotropic visco-plastic behaviour (e.g. [7][11][12][18][19] [20][21][22][23]).

General form of the flow and evolutionary equations

A rate-type formulation for the time rate of change of the stress tensor, **T**, under small strains and rotations and isothermal conditions gives,

$$\dot{\mathbf{T}} = \mathbf{L}\left[\dot{\mathbf{E}} - \dot{\mathbf{E}}^{i}\right] \tag{1}$$

where $\dot{\mathbf{E}}$ and $\dot{\mathbf{E}}^{i}$ are the total and inelastic strain tensors, respectively, and **L** is the fourth order elastic anisotropic moduli.

In an anisotropic constitutive framework, the macroscopic deformation evolves from a flow rule that is derived from a flow potential function, Ω. The evolution of the inelastic anisotropy of the material, represented by $\dot{\mathbf{E}}^{i}$ in Eq. 1, is obtained from

$$\dot{\mathbf{E}}^{i} = \frac{\partial \Omega}{\partial \mathbf{T}} \tag{2}$$

The particular form of the flow potential function varies between the constitutive approaches, as it will be discussed next.

Crystallographic approach

In a crystallographic formulation, the time rate of change of the inelastic strain tensor is derived from the kinematics of dislocation motion. It can be shown that,

$$\dot{\mathbf{E}}^{i} = \sum^{m_\alpha} \dot{\gamma}^{\alpha} \mathbf{P}^{\alpha}, \quad \text{with} \quad \mathbf{P}^{\alpha} = \frac{1}{2}\left(\mathbf{n}^{\alpha} \otimes \mathbf{m}^{\alpha} + \mathbf{m}^{\alpha} \otimes \mathbf{n}^{\alpha}\right) \tag{3}$$

Here, $\mathbf{m}^{\alpha}$ and $\mathbf{n}^{\alpha}$ are unit vectors defining the slip direction and the slip plane normal for the slip system α, respectively, $\dot{\gamma}^{\alpha}$, represents the rate of slip in the slip system α, the summation extends over the m_α active slip systems and the symbol $\otimes$ denotes the outer product of the vectors (i.e. the components of the orientation tensor $\mathbf{P}^{\alpha}$ are, $P_{ij}^{\alpha} = 0.5\left(n_i^{\alpha} m_j^{\alpha} + n_j^{\alpha} m_i^{\alpha}\right)$). For the case of superalloy single crystals, inelastic deformation is generally assumed to take place by crystallographic slip along two families of slip systems, namely twelve octahedral {111}<110> and eight cubic {100}<100> systems. (Note that, even though the latter system has not been experimentally identified from TEM investigations, its inclusion is necessary to predict consistently the effect of crystallographic orientation on the macroscopic response of the superalloy, e.g. see [11][12][20][23]).

The slip rate in Eq. 3 can, in its most general form, be functionally expressed as,

$$\dot{\gamma}^{\alpha} = \dot{\hat{\gamma}}^{\alpha}\left\{\tau^{\alpha}, \theta, S_1^{\alpha}, S_2^{\alpha}, \ldots\ldots, S_{n_S}^{\alpha}\right\} \tag{4}$$

where θ is the absolute temperature, τ^{α} is the resolved shear stress in the slip system defined by,

$$\tau^{\alpha} = \mathbf{P}^{\alpha} : \mathbf{T} \tag{5}$$

and S_i^{α}, for $i=1, \ n_S$, represents a set of internal state variables for the slip system α. The latter accounts for the current microstructural state of the dislocation or obstacle network on

each slip system α. Their evolutionary behaviour should be linked to the dominant hardening and recovery processes in the single crystal (e.g. [21]). For crystallographic formulations which do not incorporate deformation gradient - dependent effects, the time rate of change of each internal slip system variable, $\dot{S}_i^\alpha$, can, in its most general form, be expressed as,

$$\begin{aligned}
\dot{S}_1^\alpha &= \dot{\hat{S}}_1^\alpha \left\{\dot{\gamma}^\alpha, \theta, S_1^\alpha, S_2^\alpha, ..., S_{n_S}^\alpha\right\} \\
\dot{S}_2^\alpha &= \dot{\hat{S}}_{2i}^\alpha \left\{\dot{\gamma}^\alpha, \theta, S_1^\alpha, S_2^\alpha, ..., S_{n_S}^\alpha\right\} \\
&\vdots \\
\dot{S}_{n_S}^\alpha &= \dot{\hat{S}}_{n_S}^\alpha \left\{\dot{\gamma}^\alpha, \theta, S_1^\alpha, S_2^\alpha, ..., S_{n_S}^\alpha\right\}
\end{aligned} \tag{6}$$

The set of non-linear differential equations 1, and 3 to 6 constitute the complete crystallographic formulation, which must be solved numerically. This is typically done using implicit Newton-type algorithms (e.g. see [15]).

Hill-Type approach

In a Hill-type anisotropic framework, the macroscopic deformation evolves from a flow rule that is derived from a Hill-type flow potential function, ψ [10]. The time rate of change of the stress tensor, **T**, is given by an analogous relation to that of Eq. 1. The evolution of the inelastic anisotropy of the material, $\dot{\mathbf{E}}^i$ in Eq. 1, is obtained, in component form, from

$$\dot{\varepsilon}_{ij}^i = \frac{\partial \Omega}{\partial T_{ij}} = \dot{\tilde{\varepsilon}}^i \frac{\partial \psi}{\partial T_{ij}'} \tag{7}$$

where T_{ij}' represents the deviatoric component of the stress tensor, **T**, and $\dot{\tilde{\varepsilon}}^i$ the magnitude of the equivalent inelastic strain rate. In their most general form, ψ and $\dot{\tilde{\varepsilon}}^i$ can be functionally expressed in terms of **T**, the temperature θ, and the current microstructural state represented by a set of one macroscopic tensorial, $\overline{\mathbf{B}}$, and n_S macroscopic scalar internal state variables, $\{\overline{S}_1, \overline{S}_2, \ldots, \overline{S}_{n_S}\}$, respectively. (Note that the bar over the symbols indicates the macroscopic nature of the internal state variables). Then,

$$\psi = \hat{\psi}\left\{\mathbf{T}, \theta, \overline{\mathbf{B}}, \overline{S}_1, \overline{S}_2, \ldots, \overline{S}_{n_S}\right\} \tag{8}$$

$$\dot{\tilde{\varepsilon}}^i = \dot{\hat{\tilde{\varepsilon}}}^i\left\{\mathbf{T}, \theta, \overline{\mathbf{B}}, \overline{S}_1, \overline{S}_2, \ldots, \overline{S}_{n_S}\right\} \tag{9}$$

It should be noted that the internal state variables in Eqs. 8 and 9 can be considered to be the macroscopic equivalent of those introduced at the slip system level in a crystallographic framework, viz. Eq. 4. The formulation is completed with the evolutionary equations for each macroscopic internal state variable. In their most general form, one can write,

$$
\begin{aligned}
\dot{\overline{\mathbf{B}}} &= \dot{\hat{\overline{\mathbf{B}}}}\left\{\dot{\overline{\varepsilon}}^{i}, \theta, \overline{\mathbf{B}}, \overline{S}_1, \overline{S}_2, \ldots\ldots, \overline{S}_{n_S}\right\} \\
\dot{\overline{S}}_1 &= \dot{\hat{\overline{S}}}_1\left\{\dot{\overline{\varepsilon}}^{i}, \theta, \overline{\mathbf{B}}, \overline{S}_1, \overline{S}_2, \ldots\ldots, \overline{S}_{n_S}\right\} \\
\dot{\overline{S}}_2 &= \dot{\hat{\overline{S}}}_2\left\{\dot{\overline{\varepsilon}}^{i}, \theta, \overline{\mathbf{B}}, \overline{S}_1, \overline{S}_2, \ldots\ldots, \overline{S}_{n_S}\right\} \\
&\vdots \\
\dot{\overline{S}}_{n_S} &= \dot{\hat{\overline{S}}}_{n_S}\left\{\dot{\overline{\varepsilon}}^{i}, \theta, \overline{\mathbf{B}}, \overline{S}_1, \overline{S}_2, \ldots\ldots, \overline{S}_{n_S}\right\}
\end{aligned}
\tag{10}
$$

As in the crystallographic approach, the set of non-linear differential equations given by Eqs. 1 and 7 to 10 must be integrated numerically using an appropriate integration scheme (e.g. see [24]).

In the next section, some examples of crystallographic and macroscopic constitutive formulations developed for single crystal superalloys are given.

Constitutive Models for Superalloy Single Crystals

Crystallographic Models

The amount of modelling work done on superalloys has been extensive in the last 15 years or so. In this section, only an outline of some of the most relevant work in this area will be given.

Most superalloy models based on an internal slip system variable framework, such as those of [11][12][14][20][21], describe the microstructure evolution through two internal state variables per slip system: (i) a macroscopically average slip resistance S^{α} (sometimes confusingly referred to as an "isotropic hardening variable", due to its non-directional nature), and (ii) a back or internal stress B^{α}, which represents the current polarisation of the dislocation/obstacle network associated with the macroscopically observed kinematic hardening. Thus, Eq. 4 becomes

$$\dot{\gamma}^{\alpha} = \dot{\hat{\gamma}}^{\alpha}\left\{\tau^{\alpha}, \theta, S^{\alpha}, B^{\alpha}\right\} \tag{11}$$

An alternative and more physically intuitive way of interpreting the inherent differences between flow rules is found by inverting Eq. 11 to obtain the dependence of the flow stress on temperature, strain rate and microstructural state [25]. Thus, one can obtain a general expression of the form,

$$\tau^{\alpha} = \hat{F}_V\left\{\dot{\gamma}^{\alpha}, \theta, S^{\alpha}, B^{\alpha}\right\} + c_S\, S^{\alpha} + c_B\, B + c_0 \tag{12}$$

Here, c_0 is a threshold value, c_S and c_B are scaling coefficients of order unity, and $\hat{F}_V$ is a generic function.

Until relatively recently, almost all crystallographic formulations relied on power law functions of the resolved shear stress for Eq. 11, with and without a threshold stress. A general power law form widely used (e.g. [20]),

$$\dot{\gamma}^{\alpha} = \dot{\gamma}_0 \; e^{\left\{-\frac{G_0}{k\theta}\right\}} \left\langle \frac{\left|\tau^{\alpha} - B^{\varepsilon}\right| - c_0}{S^{\alpha}} \right\rangle^{n} sign\left(\tau^{\alpha} - B^{\alpha}\right) \tag{13}$$

where temperature effects are introduced through the Arrhenius term, and the activation free energy, G_0, the constants $\dot{\gamma}_0, c_0$ and n, and the initial value of S^{α} (note that the initial value of $B^{\alpha}|_{t=0} = 0$) constitute the minimum number of material constants per slip system in the simplest and most commonly used form of Eq. 11. It can be shown that the inversion of Eq. 13 gives

$$\tau^{\alpha} = S^{\alpha} \left\{ \frac{\dot{\gamma}^{\alpha}}{\dot{\gamma}_0} e^{\left\{\frac{G_0}{k\theta}\right\}} \right\}^{1/n} + S^{\alpha} + B^{\alpha} + c_0 \tag{14}$$

Even though Eq. 14 is generally considered to be "a classical one", it also highlights the two main problems with this type of flow rule. Firstly, the viscous term, i.e. first term in Eq. 14, is also affected by the current state through the value of S^{α}. Such coupling poses problems when calibrating the rate dependent response of the constitutive model. Furthermore, some rate-dependent activated mechanisms, such as lattice friction, are known to be independent of the current microstructural state, thus in such cases $F_V = \hat{F}_V\left\{\dot{\gamma}^{\alpha}, \theta\right\}$ only. Secondly, the presence of an athermal and rate independent threshold value, viz. c_0 in Eq. 14, which is independent of the current microstructural state, is inconsistent with most strengthening mechanisms.

In the work of Meric et al. [11][12], a different power law relation is used for the slip rate dependence on the resolved shear stress in each slip system, in that the slip resistance is written in the numerator, in contrast to Eq. 12. Then

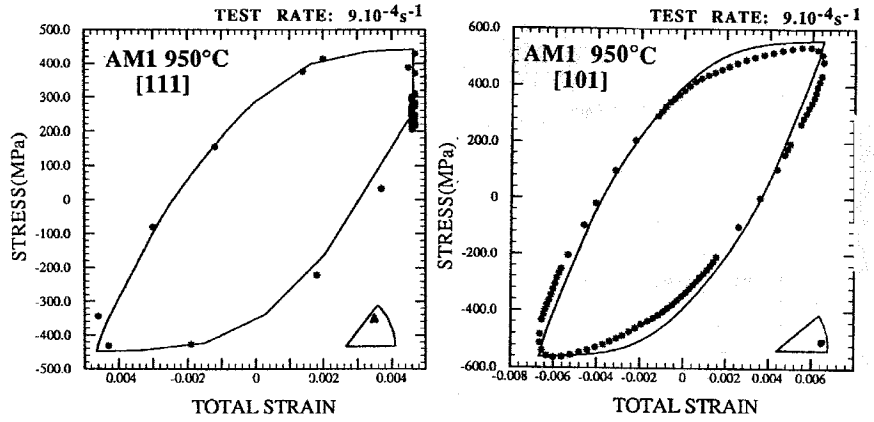
$$\dot{\gamma}^{\alpha} = \dot{\gamma}_0 \; e^{\left\{-\frac{G_0}{k\theta}\right\}} \left\langle \frac{\left|\tau^{\alpha} - B^{\varepsilon}\right| - S^{\alpha}}{\hat{\tau}_0} \right\rangle^{n} sign\left(\tau^{\alpha} - B^{\alpha}\right). \tag{15}$$

By inverting Eq. 15 and expressing it in the form of Eq. 12, one finds

$$\tau^{\alpha} = \hat{\tau}_0 \left\{ \frac{\dot{\gamma}^{\alpha}}{\dot{\gamma}_0} e^{\left\{\frac{G_0}{k\theta}\right\}} \right\}^{1/n} + S^{\alpha} + B^{\alpha} \tag{16}$$

Equation 16 provides a more physically meaningful interpretation of the strengthening mechanisms contributing to the overall flow stress of the single crystal than Eq. 14: the first term describes uniquely the viscous effects, and the second and third terms the contributions from the current microstructural state. Equation 15, in conjunction with the corresponding evolutionary equations, was used by Meric et al. [11][12] to describe the SC behaviour of the nickel base superalloy AM1. The work focused on predictions of uniaxial monotonic and cyclic isothermal tests at 950 °C. Figures 1(a) and (b), taken from [26], show a comparison between experimental and predicted cyclic responses for the superalloy single crystal AM1 at 950°C. It can be seen that correct predictions are obtained for [111] and [101] cycles (a) with and (b) without peak tension strain holds. The Meric et al.'s [11][12] constitutive single

crystal formulation was also numerically implemented into a finite element code (e.g. see [27]) so that the experimentally measured deformation of the cross sectional profiles of tubular specimens subjected to torsion could subsequently be compared with numerical FE predictions. For highly symmetric orientations, viz. <001> and <111>, good agreement was found between experiment and predictions.



(a) *(b)*

Fig. 1. *Comparison between experimental (symbols) and predicted (lines) cyclic responses for the superalloy AM1 at 950°C: (a) with and (b) without peak tension strain holds along [111] and [101] orientations, respectively [26].*

More recently, Golan et al. [28] explored the possibility of using a modified version of the Norton creep power law with an internal stress or back stress internal variable to predict the uniaxial creep behaviour of CMSX-2 at 982°C, along crystallographic orientations close to the [001] axis. It was found that an empirical relation exists between the parameter multiplying the power law term and the exponent n. The existence of such a relation indicates that the activation energy for the creep process is continuously changing as deformation of the single crystal progresses, reaching a peak when a rafted microstructure is obtained. However, the empirical and one-dimensional nature of this type of model limits its usefulness.

One important limitation of the widely used power law relations, such as those in Eqs. 13 and 15, is that at a given temperature and at a constant internal state, the exponent n imposes a constant strain rate sensitivity in the material behaviour, irrespective of the stress level. Thus, it is a limitation when describing the behaviour of materials that exhibit non-linear strain rate sensitivities over stress ranges typical of service. Nevertheless, power law based flow rules have been shown to be suitable under well-defined stress ranges. The effect of this constraint can to some extent be reduced by introducing, at the expense of additional material parameters, a static recovery term in the evolutionary behaviour of the back stress (e.g. see [11][12][20]). For instance, in the work of Jordan & Walker [20], uniaxial tests on PWA 1480 at 889°C along the symmetric orientations <001> and <111> were reasonably correlated using a flow rule of the form given in Eq. 13. Torsion tests, designed to induce a biaxial stress state,

provided reasonable correlation only if both octahedral and cubic slip systems were assumed active.

One way of introducing non-linear strain rate sensitivity into the crystallographic formulation without allowing the power law exponent to be a variable or without rather artificially introducing a static recovery term, is by using either hyperbolic (e.g. [29]) or exponential functions of the resolved shear stress in the flow rule. The former is a purely phenomenological way of introducing this effect, whereas the latter is more useful as it allows for the dependency of the activation free energy on stress to be readily incorporated [21][25].

More recently, the crystallographic framework initially proposed by Busso [25] (see also [14][15][21][23]) for NiAl single crystals was further developed to describe the behaviour of superalloy single crystals. Here, the flow rule relies on a stress-dependent activation energy expressed in terms of a macroscopically average slip resistance S^{α}, and a back or internal stress B^{α}. The flow rule is expressed in terms of an exponential function as,

$$\dot{\gamma}^{\alpha} = \dot{\gamma}_0 \exp\left[-\frac{F_0}{k\theta}\left\langle 1-\left\langle \frac{\left|\tau^{\alpha}-B^{\alpha}\right|-S^{\alpha}\,\mu/\mu_0}{\hat{\tau}_0\,\mu/\mu_0}\right\rangle^{p}\right\rangle^{q}\right]\mathrm{sgn}\left(\tau^{\alpha}-B^{\alpha}\right) \tag{17}$$

where μ, μ_0 are the shear moduli at θ and 0 °K, respectively, and F_0, $\hat{\tau}_0$, p, q and $\dot{\gamma}_0$ are material parameters. Likewise, an inversion of Eq. 17 allows the flow stress to be expressed as a function of its contributing terms. Here,

$$\tau^{\alpha} = \hat{\tau}_0 \frac{\mu}{\mu_0}\left\{1-\left(\frac{\theta}{\theta_0}\right)^{1/q}\right\}^{1/p} + S^{\alpha}\frac{\mu}{\mu_0} + B^{\alpha} \tag{18}$$

where

$$\theta_0 = \frac{\mathrm{F_0}}{\mathrm{k}}\frac{1}{\mathrm{Ln}\left(\dot{\gamma}_0/\dot{\gamma}^{\alpha}\right)} \tag{19}$$

It can be seen that Eqs. 18-19 provide a similar physically intuitive strengthening framework as Eq. 16 since the first term describes uniquely the strain rate and temperature effects, and the second and third terms the contributions from the current dislocation resistance and internal stresses. One shortcoming of Eq. 17 is that the slip rate for $\tau^{\alpha} = 0$ is not zero but equal to a very small residual value (typically $< 10^{-15}$ 1/s.). Nevertheless, for most practical purposes, this residual value has no effect on the overall predicted deformation of superalloy components and it can, in fact, easily be forced to be zero when integrating Eq. 17 numerically.

In contrast to power law relations, the exponential form of Eq. 17 enables the non-linear stress rate sensitivity exhibited by superalloy single crystals to be described correctly. This point is illustrated in Fig. 2, which shows the strain rate versus the steady state flow stress curves obtained for a <111> oriented CMSX4 specimen at 950°C and the corresponding data [23]. In general, the strain rate sensitivity (which for a given state, it is controlled to a great extent by the power law coefficient n) predicted by power law relations of the type given in Eqs. 13 and 15 would underestimate the deformation at both very high and very low stress levels. This

problem can be overcome by using an exponential flow rule of the type shown in Fig. 2. These results also highlight the critical nature of the model parameter calibration, in particular the stress range at which this is done. It is also worth noting that the stress levels seen in turbine blades can be very low, thus the material model calibration must rely on test data obtained under such representative stress conditions.

The evolutionary behaviour of the slip system variables is typically defined within a hardening-dynamic recovery format. The form and type of equations vary within formulations and it would be outside the scope of this work to present the details. As a typical illustration, those given by [14][15][21][25] will be shown. Here, the evolutionary behaviour of the overall slip resistance is defined as,

$$\dot{S}^{\alpha} = \sum_{\beta=1}^{m_{\alpha}} \delta_S^{\alpha\beta} \left[h_S - d_D (S^{\beta} - S_0^{\beta}) \right] | \dot{\gamma}^{\alpha} | \tag{20}$$

where, S_0^{β} is the initial value of S^{β}, d_D is a dynamic recovery parameter, and m_{α} the total number of slip systems. In Eq. 20, $\delta_S^{\alpha\beta}$ is the latent hardening or interaction function [20],

$$\delta_S^{\alpha\beta} = \omega_1 + (1 - \omega_2)\delta_{\alpha\beta} \tag{21}$$

where $\delta_{\alpha\beta}$ is the Kroneker delta so that $\omega_1 = \omega_2 = 0$ corresponds to self-hardening, and $\omega_1 = \omega_2 = 1$ to Taylor hardening.

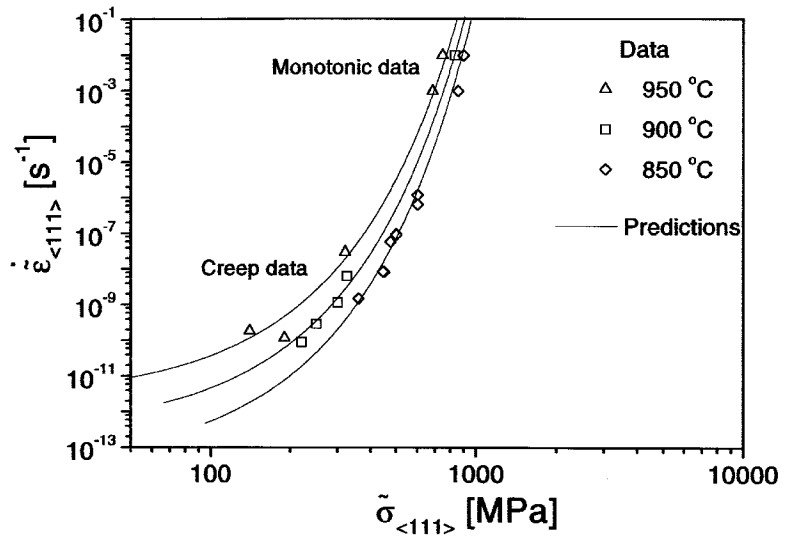


Fig. 2. Evolution of strain rate vs. steady state stress for a <111> oriented CMSX4 specimen at 950°C: non-linear strain rate sensitivity predicted by the exponential slip rate relation Eq. 17 [23].

The back stress evolves according to the well-known Armstrong-Frederic hardening-dynamic recovery framework,

$$\dot{B}^{\alpha} = h_B \dot{\gamma}^{\alpha} - r_D B^{\alpha} \left| \dot{\gamma}^{\alpha} \right| - r_S \left| B^{\alpha} \right|^{r} \tag{22}$$

where h_B is the hardening coefficient, $r_D = \hat{r}_D \{S^{\alpha}\}$ a dynamic recovery function expressed in terms of the current overall deformation resistance, S^{α} [21][25], and r_S and r, static recovery parameters. The model was calibrated to predict the visco-plastic behaviour of single crystal superalloy CMSX-4 using a database of monotonic, cyclic and creep data. No static recovery was considered for simplicity. It was then validated by comparing the predicted response with experimental data obtained from complex thermal-mechanical histories and multi-axial stress states. Figure 3 shows typical predictions of monotonic and cyclic responses obtained experimentally from CMSX4 at 950 and 850°C, respectively [30].

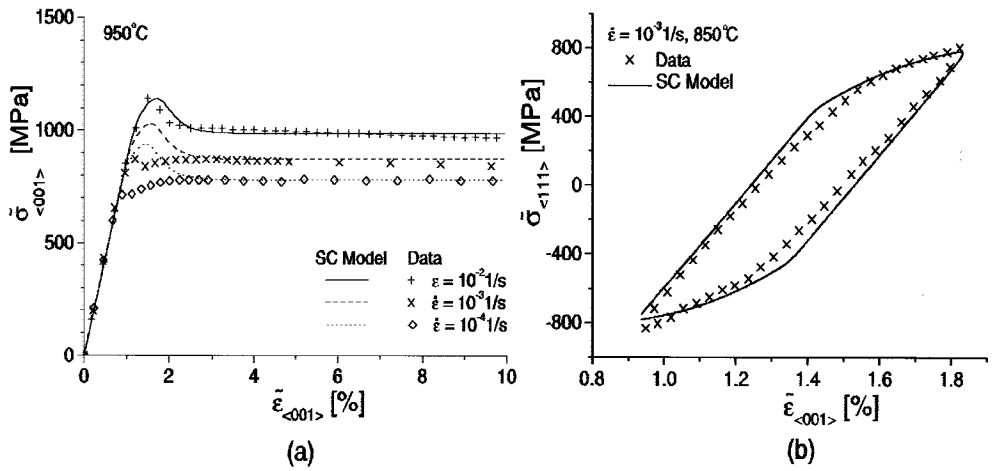


Fig. 3. Comparison between measured and predicted (a) <001> monotonic response at different strain rates and 950°C, and (b) <111> steady state cyclic response at 850°C [30]

Continuum damage mechanics (CDM) concepts have also been used to incorporate the effects of microstructure evolution on the tertiary creep behaviour of superalloys (e.g. through a strain softening mechanism linked to the accumulation of dislocations [18][22][29][31]). CDM – based crystallographic models contain one or more scalar damage variables at the level of the slip system, in addition to or instead of the directional and non-directional hardening variables given in Eq. 11. These models are generally calibrated from uniaxial creep data obtained at different temperatures and stresses, hence their predictive capabilities

are limited to creep deformation and monotonic stress-strain responses at low strain rates close to the minimum ones obtained in creep testing [29]. The prediction of transient monotonic and cyclic stress-strain conditions requires an accurate description of the Bauschinger effect, which can be only clearly identified from cyclic data. A further limitation is the difficulty in formulating a three-dimensional version of CDM models and the mesh sensitivity of FE results in regions where deformation may localise.

A phenomenological approach that has received some attention is based on the use of appropriate mathematical representations of the <001> and <111> creep curves. These models are therefore primarily calibrated from uniaxial creep data and their parameters are related, in a relatively simple manner, to various features of the creep curve. Multiaxial formulations are obtained via Eq. 3 using distinct <001> and <111> parameters. In [32], the creep curves are fitted with a Graham-Walles type equation. This uses a summation of stress and time power law terms, although in [32] an additional term is used and the temperature dependence is now introduced via an exponential form. One of the main differences between the Graham-Walles equation and the CDM approach of [29], is that the latter combines primary and tertiary creep in product form, which implies that primary and tertiary creep mechanisms act in parallel. The creep model proposed in [33] also incorporates a back stress state variable which evolves according to a hardening-static recovery law (with no dynamic recovery and $r=1$ for the static recovery term in Eq. 22). The creep rate expression also includes a tertiary creep softening term that is also combined in product form. The use of these models to predict the transient monotonic and cyclic stress-strain response can also lead to inaccuracies. However, it appears that there is the potential to use this approach for creep-dominated behaviour, see [33].

Although it is well known that directional coarsening of γ' precipitates strongly affects the creep and fatigue behaviour of the material, e.g. [34] [36], there has been only limited amount of work addressing this issue within a crystallographic framework. This is due mostly to the fact that raftening is associated with a loss of cubic symmetry. To accommodate such changes within a slip system based framework requires that groups of slip system within the same family (e.g. octahedral) be calibrated differently. As it will be discussed below, the incorporation of raftening effects may be done more easily using a macroscopic single crystal framework.

Hill-Type Models

Several macroscopic phenomenological formulations have been developed for single crystal superalloys (e.g. [7][8][37][38]). Most of them are modifications of isotropic macroscopic formulations, with a different criterion to account for the cubic symmetry of the material.

The approach of Nouailhas and Freed [8] relies on fourth order tensors to define both the elastic and inelastic anisotropy of a superalloy single crystal. Despite the simplicity of the constitutive equations and the reduced number of state variables, which offers some advantages for finite element structural calculations over crystallographic based models, such type of models have been found to have limited predictive capabilities for some particular cases such as under torsional loading. As they rely on a Hill type criterion, only one free parameter can be specified for the shear behaviour relative to the tensile behaviour. Thus, it was found in [39] that, for the case of a tubular specimen subjected to pure torsion, a uniform stress-strain distribution is predicted along the circumference of the specimen. This is

inconsistent with both Schmid's law and the experimental evidence reported in [40]. In follow-up work, Nouailhas et al. [38] proposed a new improved version of the model presented in [8], whereby the potential function used to describe the initial material anisotropy was now expressed in terms of nine stress invariants. This new model showed improved predictive capabilities and overcame the limitations exhibited by the previous model as cyclic data and slip traces obtained from CMSX-2 torsional tests at room temperature and at 950°C were reasonably well predicted by the model.

Schubert et al [9] relied on an orthotropic Hill-type potential, with the anisotropic coefficients linked to the evolving morphology of the γ' precipitates, to incorporate the effects of precipitate raftening within the macroscopic behaviour of the superalloy CMSX4. The model was calibrated from <001> and <111> creep data and microstructural observations in order to define the stress-temperature regime where raftening occurs. In the absence of raftening, the orthotropic potential used reduces to the cubic form of Hill's potential. The model was found to correctly predict the orientation dependence of the minimum creep rate at 950°C, where raftening readily takes place, and it has successfully simulated the <100> and <111> creep deformation behaviour.

Busso & McClintock [7] studied the anisotropic creep behaviour of the superalloy single crystal CMSX4 using a Hill-type anisotropic creep (or flow) potential for a cubic crystal and the associated flow rule. The anisotropic parameter in the Hill flow potential was calibrated from uniaxial creep data along <110> and <100> crystallographic orientations at different temperatures and stress levels. No hardening or softening behaviour was incorporated in the model. Even though the model was not calibrated against complex multiaxial data, a good representation of the anisotropy of the steady state creep behaviour of the superalloy was obtained.

Advanced Constitutive Models for Superalloy Single Crystals

The main driving force behind the current and future research on superalloy characterisation and modelling is the development of constitutive formulations that can incorporate features of the micro-mechanisms of deformation and damage. This includes the effects of microstructural evolution during service occurring simultaneously at different scales in the microstructure and coupling with kinetics processes such as oxidation. Such approaches are referred to as multi-scale and multi-physics, respectively.

For the case of superalloys, most of the current models are unable to predict the effect of local variations in the precipitate volume fraction on the local material behaviour. Recently, precipitate volume fraction effects were quantified for a range of temperature and strain rate conditions using a strain-gradient crystallographic framework and periodic unit cell-based FE analyses [14][15]. These results have been incorporated into a state variable crystallographic formulation to account for experimentally observed precipitate volume fraction and size effects in a single crystal nickel-base superalloy [23].

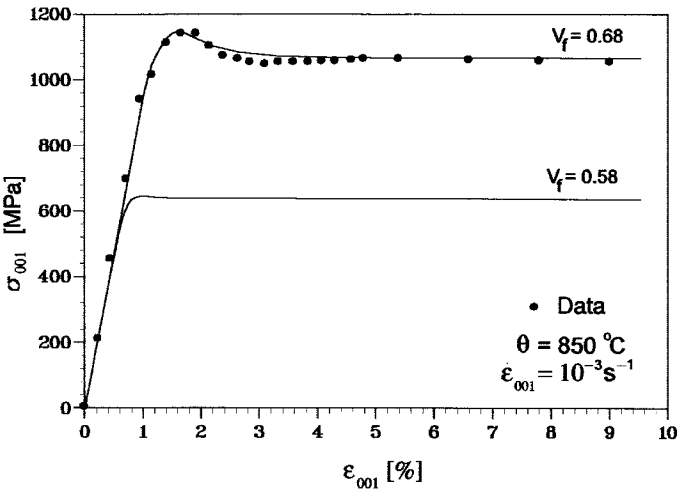


Fig. 4. *Effect of precipitate volume fraction on the <001> monotonic response of CMSX4 at 850°C and 10^{-3} 1/s. Symbols represent experimental data for the 68% vol. fraction case [23].*

The resulting crystallographic formulation incorporates an explicit link between the γ' precipitate population at the microscale, and the behaviour of the homogeneous equivalent material at the macroscale. This link is introduced through the dynamic recovery function d_D and the initial microstructural state, S_0^β, in Eq. 20. Thus they depend on the characteristics of the current precipitate population as follows,

$$d_D = \hat{d}_D\{\theta, l/l_0, V_f\} \tag{23}$$

$$S_0^\alpha = \hat{S}_0^\alpha\{\theta, l/l_0, V_f\} \tag{24}$$

where l/l_0 is the precipitate size, l, normalised by a reference mean value, l_0, and V_f the precipitate volume fraction. Equations 23 and 24 were calibrated from FE analyses of periodic unit cells at the microscale containing the individual precipitates [14][15]. Typical predictions of the monotonic uniaxial behaviour of CMSX4 at 850°C and 10^{-3} 1/s are shown in Fig. 4 for two different γ' volume fractions, namely 58 and 68 %, together with experimental data for the latter case. These results show that a 10 % reduction in volume fraction results in a 40 % decrease in the superalloy steady state flow stress at this temperature and strain rate.

Work to be presented in this conference [41] will describe recent progress made in developing a multi-scale crystallographic framework to characterize the effect of different γ-γ' eutectic regions on the mechanical behaviour of nickel-base superalloys. As the volume fraction of eutectic regions in the superalloy can be controlled by heat treatment, this type of work can have important implications in the selection of adequate homogenisation heat treatments so as to optimise the mechanical properties of the single crystal superalloy.

On the Design Assessment of Industrial Gas Turbine Single Crystal Blading

Thermo-mechanical response of cooled blades

The service cycle of an industrial gas turbine (IGT) consists of rapid transient periods, during start-up and shutdown, and long intervals of steady-state operation. The duration of the transients varies according to the power output of the engine. A small IGT (e.g. 6-12MW) can reach operating speeds of 12,000 rpm within 20 to 80 seconds. A large IGT (e.g. 200MW) will typically take between two to three minutes to reach a speed of 3,000 rpm. There are also varying requirements concerning the steady state operation of an engine. Accordingly, a large GT plant that contributes to base load operation can be subjected to a daily shift. A smaller GT that provides power to a small industrial unit may operate at steady state on a weekly basis.

Cooled high-pressure turbine blades are subjected to complex thermo-mechanical loading. The mechanical loads consist of centrifugal and gas forces, with the latter being the result of pressure differences across the aerofoil surface and between the internal cooling air and the external hot gases. The thermal stresses are induced by non-uniform temperatures in the aerofoil due to temperature differences between the cooling air and hot gases. This difference varies during the transients and peaks during start-up.

In view of the complexity of the loading and, in particular, the geometry of a cooled blade, the stress distribution in the aerofoil can only be estimated through detailed inelastic FE analysis. It is important to highlight two key aspects of blade design. The centrifugal loads introduce high radial stresses that are tensile in nature, while the thermal loading induces biaxial compressive stresses on the hot external surface of the aerofoil. It is also instructive to distinguish further between the response of small and large blades when addressing the key issues related to blade design procedures [42]. For instance, in a large blade with a typical 3 mm wall thickness, the thermal stresses are sufficiently high so that the biaxial stress state on the surface of the blade is compressive. In contrast, in a small blade with a 1mm wall thickness, the thermal stresses are lower and the radial stresses are predominantly tensile while the tangential stresses are compressive. It should be noted that these remarks do not account for stress redistributions during steady state operation.

The aerofoil section of a cooled blade has a number of geometric features that can lead to a significant increase in the local stresses. Such features include the fillet regions joining the aerofoil to the platform or the shroud, cooling passages with ribs, and infringement cooling holes. Due to computational constraints, when constructing a three dimensional FE model of the blade to determine its (overall) inelastic stress-strain response, such features are either left out or not modelled with the required detail to capture the peak (localised) stresses. In such cases, elastic FE analyses of candidate blade components have shown that the stress state in the aerofoil is well below yield and that during each load cycle the aerofoil is only experiencing elastic-creep deformation. This is shown in Fig. 5 in terms of an upper bound curve of the resolved shear stresses in typical IGT blades with metal temperatures between 550 to 950°C. The curve has been constructed by plotting the maximum octahedral and cubic shear stresses in the aerofoil at each temperature. The upper bound values are compared to the critical resolved shear stresses (CRSS) for CMSX-4 which have been obtained from <001> and <111> tensile data at 0.6%/min (dashed/dotted lines) and 6%/min (dashed lines) [43].

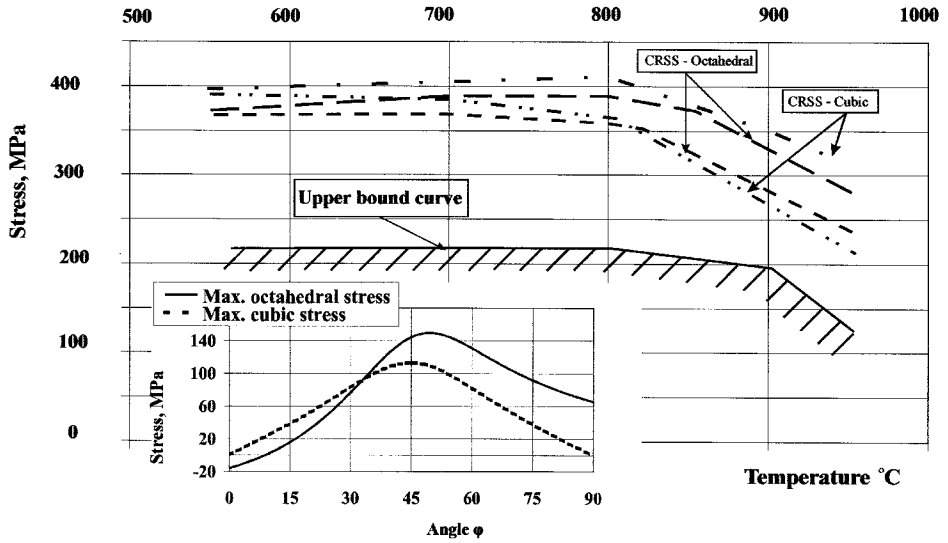


Fig.5: Upper bound curve of the elastically calculated resolved stresses in typical IGT aerofoils compared to the CRSS values of CMSX-4. The inset, based on the simplified method of [42], shows the graphs of the octahedral and cubic stresses that give the maximum values at a cross-section in the aerofoil root of a large blade. The angle φ measures the in-plane rotation from the secondary [100] crystal axis.

The peak stresses present in the stress concentration regions mentioned above can lead to creep-fatigue problems, particularly in applications that are expected to experience a large number of start/stop cycles. For example, the elastic stress concentration factor at an infringement cooling hole can be greater than two, depending on the combination of the far field radial and tangential stresses. Also the peak stress, tangential to the hole surface, can be tensile or compressive. That is, in a large blade the far field compressive stresses lead to a compressive stress while, in a small blade, it is mostly tensile but changes to compressive in the upper half of the aerofoil. Such detailed estimates are currently possible using submodeling FE techniques which, in practice, are only used in elastic analyses. Otherwise it is necessary to specify not only the magnitude and distribution of the transmission loads from the adjoining structure to the submodel, but also their evolution during cycling. In the inelastic regime, it is also more difficult to identify a representative submodel that has a negligible effect on the overall solution, particularly during steady state operation where creep deformation can lead to widespread redistribution of the stresses.

Current and future applications of inelastic analysis methods

The above discussion points to a three-level application of inelastic analysis methods in the life assessment of turbine blades. The first level, believed to be current practice in blade design, involves the computation of the stresses and strains in the aerofoil section of the blade during steady state (i.e. constant load) operation. Since the geometrical features that lead to high stress concentration factors cannot be efficiently included in such analyses, an FE model of the aerofoil is experiencing pure creep deformation, as shown in Fig. 5. Thus, it is the creep behaviour of SC superalloys that should be reliably predicted. This conclusion has prompted

the development of some of the creep calibrated models mentioned above, e.g. [9][33], and also the acquisition of medium to long-term deformation data that are closer to IGT operating conditions, e.g. [43]. It should also be mentioned here that peak stresses in the aerofoil will generally redistribute and relax fairly quickly. Thus the average stresses in the blade should be such that rupture will occur in excess of 10^5 hours. Accordingly, the emphasis here at this first design level is to obtain long-term engineering predictions neglecting various microstructural features that can also be critical to the life of the component.

The second level of application concerns the inelastic analysis of a blade that includes sufficient refinement, either in the geometric or the FE idealisation, to capture the local (peak) stresses in some of the stress concentration features mentioned above. In this case, the behaviour is no longer elastic-creep since additional visco-plastic deformation occurs in the initial loading (i.e. the first start-up) and possibly also during the ensuing loading cycles (in addition to that incurred during each dwell period, i.e. in steady state operation). It is possible here to provide an indication of the allowable strain levels during load cycling, assuming a minimum design life of 3000 cycles. On the basis of CMSX-4 data from continuous LCF tests [43], this implies that the total strain range at typical stress concentration regions should be less than 1.2% to 1.4%. For these strain values, as Fig. 6 shows, the amount of visco-plastic strain incurred during cycling is small. Note that using failure data from LCF tests that include hold periods will reduce the allowable strain ranges even further. The emphasis therefore firstly shifts to predicting accurately the visco-plastic deformation incurred during the initial monotonic loading as in Fig. 3(a). Secondly, during load cycling, the constitutive models should be capable of correctly representing the mean stress relaxation at low strain values. Computational constraints still limit this application in engineering design practice. However, recent advances in numerical techniques and parallel processing are expected to lead to wider usage, e.g. [44].

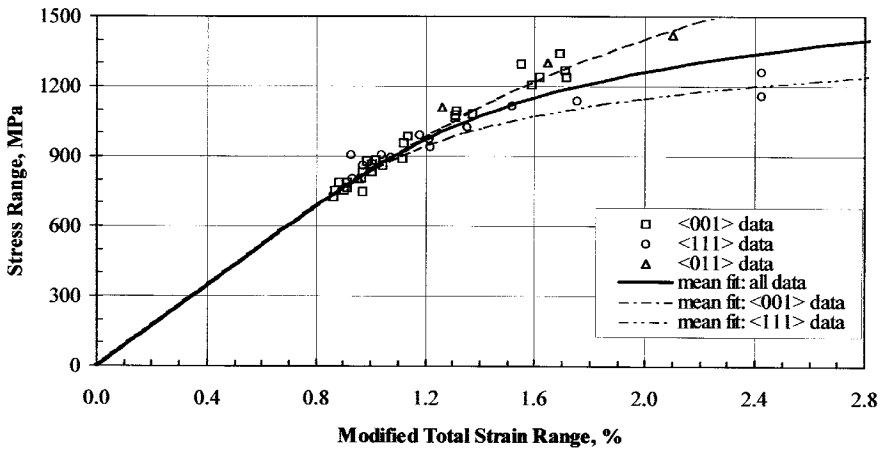


Fig. 6. Cyclic stress-strain curve constructed from CMSX-4 half-life LCF data at 950°C and 6%/min [43]. The modified strain range, used to eliminate the effect of anisotropy (up to around 1.4%), equals the applied strain range multiplied by the ratio of the Young's modulus of the specimen over the Young's modulus in the <001> orientation.

The third level of application involves the use of advanced single crystal models, such as those outlined above, which are capable of properly accounting for the effects of the initial and the evolving microstructure on the deformation and damage behaviour. Clearly, the hot metal temperatures of gas turbine blading, coupled with the complexity of the resulting stress state, can lead to drastically different changes in the microstructure. For example, the compressive stress state in a large blade will induce different coarsening of the γ' precipitates than that found in typical creep tests in tension. A different precipitate morphology will result in significantly different deformation rates, e.g. [45]. Further differences appear to arise at the mesoscale, e.g. specimens loaded in compression show little or no evidence of micro-cracking, originating at either micropores, carbides or in eutectics, as observed under a tensile load [45]. Advanced single crystal models, e.g. of the type outlined above, are now beginning to be used in the analysis of actual blade components operating under steady-state conditions [46].

Concluding Remarks

This paper has reviewed a number of constitutive material formulations for single crystal superalloys that have been developed during the past fifteen years or so. Both crystallographic and macroscopic (Hill-type) approaches have been considered, although the former was discussed in greater detail in view of its wider acceptance. Emphasis was given to constitutive formulations which rely on internal state variables to describe the microstructural evolution during service. The need for advanced constitutive models was highlighted in view of the (intrinsic) microstructural and deformation-induced heterogeneities which are present in the material and which can have a significant effect on component lifetimes. A three level application of the constitutive models in the design of cooled blades has been put forward, based on certain aspects of their thermo-mechanical response and the ability to carry out computationally intensive FE analyses.

References

[1] Seth, B.B., Superalloys – The Utility Gas Turbine Perspective, in *Superalloys* 2000, T.M.Pollock et al. (eds), The Minerals, Metals & Materials Society (TMS), USA (publ.), 2000, 3-16.

[2] Toulios, M. and McKenzie, D.O., Efficient Use of Materials in Gas Turbines Through Advanced Inelastic Analysis. *GEC ALSTOM Technical Review*, 17 (1995), 25-40.

[3] Mukherji, D., Gabrisch, H., Chen, W., Fecht, H.J. and Wahi, R.P., Mechanical Behaviour and Microstructural Evolution in the Single Crystal Superalloy SC16., *Acta Mater.*, 45, (1997), 3143-3154.

[4] Lecomte-Beckers, J., Study of Solidification Features of Nickel-Base Superalloys in Relation with Composition, *Metall. Trans.*, 19A, (1988), 2333-2340.

[5] Ai, S.H., Lupinc, V. and Maldini, M., Creep Fracture Mechanisms in Single Crystal Superalloys. *Scripta Mater.*, 26, (1992) 579-584.

[6] Komenda, J. and Henderson, P.J., Growth of Pores During the Creep of a Single Crystal Nickel-Base Superalloy. *Scripta Mater.*, 37, (1997) 1821-1826.

[7] Busso, E. P. and McClintock, F.A., Stress-strain Histories in Coatings on Single Crystal Specimens of a Turbine Blade Alloy, *Int. Journal Solids and Structures*, V. 24, (1988), 1113-1130.

[8] Nouailhas, D. and Freed, A.D.; A Viscoplastic Theory for Anisotropic Materials. *J. Eng. Mat. Tech.*, 114, (1992) 97-104.

[9] Schubert, F., Fleury G and Steinhaus, T., Modelling of the Mechanical Behaviour of the SC Alloy CMSX4 during Thermomechanical Loading. *Modelling Simul. Sci. Eng.*, V. 8 (2000), 947-957.

[10] Hill, R., *The Mathematical Theory of Plasticity*, Oxford: Clarendon Press (publ.), 1950.

[11] Meric, L., Poubanne, P. and Cailletaud, G., Single Crystal Modelling for Structural Calculations: Part 1 – Model Presentation. *J. Eng. Mat. Tech.* 113, (1991a) 162-170.

[12] Meric, L. and Cailletaud, G. Single Crystal Modelling for Structural Calculations: Part 2 - Finite Element Implementation. *J. Eng. Mat. Tech.* 113, (1991b) 171-182.

[13] Busso, E.P., Meissonnier, F., O'Dowd, N.P. and Nouailhas, D., Length Scale Effects on the Geometric Softening of Precipitated Single Crystals, *J. Physique IV*, V. 8, (1998), 55-61.

[14] Busso, E.P., Meissonnier, F. and O'Dowd, N. P., Gradient-Dependent Visco-Plastic Deformation of Two-Phase Single Crystals. *J. Mech. Phys. Solids*, V. 48, Issue 11 (2000), 2333-2361.

[15] Meissonnier, F., Busso, E.P., and O'Dowd, N.P., Finite Element Implementation of a Generalised Non-Local Rate-Dependent Crystallographic Formulation for Finite Strains. *Int. J. Plasticity,* V. 17, Issue 4, (2001), 601-640.

[16] Busso, E.P. and Cheong, K. S., Length Scale Effects on the Macroscopic Behaviour of Single and Polycrystalline FCC Materials. *J. Physique IV*, V. 11 (2001), 161-170.

[17] Fedelich, B., A Microstructure Based Constitutive Model for the Mechanical Behaviour at High Temperatures of Ni-Base Single Crystal Superalloys, *Comp. Mat. Sci.*, 16, (1999), 248-258.

[18] Dyson, B.F. and McLean, M., Creep Deformation of Engineering Alloys: Developments from Physical Modelling, *ISIJ International*, V. 30, (1990), 802-811.

[19] Anand, L. and Kothari, M., A Computational Procedure for Rate-Independent Crystal Plasticity. *J. Mech. Phys. Solids.*, 44, (1996) 525-558.

[20] Jordan, EH and Walker, K.P., A Viscoplastic Model for Single Crystals, *ASME J. Eng. Mat. Technol.*, V. 114, (1992), 19-26.

[21] Busso, E.P. and McClintock, F.A., A Dislocation Mechanics-Based Crystallographic Model of a B2-Type Intermetallic Alloy, *Int. J. Plasticity*, V. 12, (1996), 1-28.

[22] MacLachlan, D.W. and Knowles, D.M. Creep behaviour modellinbg of the single crystal superalloy CMSX4, *Met. Trans.* 31 A, (2000), 1401-1411.

[23] Busso, E.P., A Crystallographic Formulation for Superalloy Single Crystals with Explicit Microstructural Length Scales. Part I: Model Formulation. Submitted for publication (2002).

[24] Besson, J., Leriche, R., Foerch, R. and Cailletaud, G., Object Oriented Programming Applied to the Finite Element Method: Part II: Application to Material Behaviours, *Revue Europeene des Elements Finis*, V. 7, (1998), 567-588.

[25] Busso, E.P., PhD Thesis, Department of Mechanical Engineering, Massachusetts Institute of Technology, Cambridge, USA, (1990).

[26] Hanriot, F., Cailletaud, G. and Remy, L., Mechanical Behaviour of a Ni-Base Superalloy Single Crystal, in *High Temp. Constitutive Modelling-Theory and Application*, ASME, Book H00667, A.D. Freed and K.P. Walker (eds.), (1991), 139-150.

[27] Foerch, R., Azzouz, F., Quilici, S., and Cailletaud, G., New Tools for a Simplified Access to UMAT, ABAQUS User Conference, Chester, UK, HKS Inc., Rhode Island, USA (publ.), 1999.

[28] Golan, O., Arbel, A., Eliezer, D. and Moreno, D., The Applicability of Norton's Creep Power Law and its Modified Version to a Single-Crystal Superalloy Type CMSX-2. *Mat. Sci. Eng.*, A216, (1996), 125-130.

[29] Pan, L-M, Shollock, B.A, and McClean, M., Modelling of High Temperature Mechanical Behaviour of A Single Crystal Superalloy. *Proc. R. Soc. London A*, V. 453, (1997), 1689-1715.

[30] Busso, E.P., N.P. O'Dowd and Dennis, R., A Rate Dependent Formulation for Void Growth in Single Crystal Materials, in *Proc. Fifth IUTAM Symposium on Creep in Structures*, April 2000, Japan, S. Murakami and N. Ohno (eds), Kluwer Academic Publishers, (2001), 41-50.

[31] Othman, AM, BF Dyson, DR Hayhurst and J Lin, Continuum Damage Mechanics Modelling of Notched Bars UnderTertiary Creep with Physically-based Constitutive Equations, *Acta Met.*, V. 42, (1994), 597.

[32] Homewood, T., Ward, T.J., Henderson, M.B., Harrison, G.F., The DERA Slip System Creep Law for the Modelling of Face Centred Cubic Single Crystal Material Behaviour, in the *Proc. Conf. On Modelling of Microstructural Evolution in Creep Resistant Materials*, Imperial College, London (1998).

[33] White, P.S. and Kong, C.N., Modelling of High Temperature TMF of Single Crystals by a Pure Creep Law. To appear in the Proceedings of the 7th Liège Conference, *Materials for Advanced Power Engineering*, Sept. 2002.

[34] Muller, L., Glatzel, U., Feller-Kneipmeier, M. Modelling Thermal Misfit Stresses in Nickel-Base Superalloys Containing High Volume Fraction of γ' Phase. *Acta Mater.*, V. 40, (1992), 1321-1327.

[35] Biermann, H., Spangel, S. and Mughrabi, H., Local Lattice Parameter Changes in Monocrystalline Turbine Blades Subjected to Service-like Conditions. *Z. Metallkd*, V. 87, (1996) 403-410.

[36] Pollock, T.M., Argon, A.S., Directional Coarsening in Nickel-Base Single Crystals with High Volume Fractions of Coherent Precipitates. *Acta Mater.*, V. 42, (1994), 1859-1874.

[37] Choi, S.H. and Krempl, E., Viscoplasticity Theory Based on Overstress Applied to the Modeling of Cubic Single Crystals, *European J. Mechanics A/Solids*, V. 8, (1989), 219.

[38] Nouailhas, D., Culié, J.-P., Cailletaud, G., and Méric, L., FE Analysis of the Stress-Strain Behaviour of Single Crystal Tubes, *European. J. Mech. A/Solids*, V. 14 (1995), 137-154.

[39] Nouailhas, D. and Cailletaud, G., Comparaison de Divers Critères Anisotropes pour Monocristaux Cubiques à Face Centrée (CFC), *Note aux Comptes Rendus de l'Académie des Sciences de Paris*, t. 315, série II, (1992), 1573-1579.

[40] Nouailhas, D., Pacou, D. Cailletaud, G., Hanriot, F., and Rémy, L., Experimental Study of the Anisotropic Behaviour of the CMSX-2 Single Crystal Superalloy under Tension-Torsion Loadings, in *Advances in Multiaxial Fatigue*, D.L. McDowell and R. Ellis (eds). ASTM STP1191, (1993) 244-258.

[41] Regino, G.M., Busso, E.P., O'Dowd, N.P., and Allen, D.H., A Multiscale Constitutive Approach to Model The Mechanical Behaviour of Inhomogeneous Single Crystal Superalloys: Application to As-Cast SX CM186LC. To appear in the Proceedings of the 7th Liège Conference, *Materials for Advanced Power Engineering*, Sept. 2002.

[42] Toulios, M., Lifing of High Temperature Components, in *MATERIALS WEEK 2000 - Proceedings*, editor and organiser: Werkstoffwoche-Partnerschaft, Frankfurt, 25-28 September 2000,URL: www.materialsweek.org/proceedings.

[43] Bullough, C.K., Toulios, M., Oehl, M., and Lukáš, P., The Characterisation of the Single Crystal Superalloy CMSX-4 for Industrial Gas Turbine Blading Applications, in *Materials for Advanced Power Engineering 1998*, J. Lecomte-Beckers et al (eds.), Part II (1998), 861-878.

[44] Cailletaud, G., Chaboche, J-L., Forest, S., and Remy, L., On the Design of Single Crystal Turbine Blades. Dimensionnement des Aubes de Turbines Monocristallines. *Journées d'Automne de la SFM* (2001). Also, submitted for publication to *La Revue de Métallurgie*, (2002).

[45] Lukáš, P., Čadek, J., Šustek, V., and Kunz, L., Creep of CMSX-4 Single Crystals of Different Orientations in Tension and Compression. *Materials Science and Engineering*, A208 (1996), 149-157.

[46] Busso, E.P., O'Dowd, N.P, and Dennis, R., A Crystallographic Formulation for Superalloy Single Crystals with Explicit Microstructural Length Scales. Part II: Model Validation and Finite Element Implementation. Submitted for publication (2002).

GAMMA TiAl INTERMETALLICS FOR TURBOMACHINERY APPLICATIONS

M. Nazmy* and V. Lupinc°

*ALSTOM Ltd., Baden, CH
°CNR-IENI, Milano, Italy

Abstract

Gamma titanium aluminide intermetallics possess a unique combination of physical and mechanical properties. The low density, high stiffness and good creep strength, at intermediate temperature range, are beneficial for a variety of components in turbomachinery. The application of gamma TiAl base intermetallics as a lightweight blade in last stage blading will result in much lower centrifugal stresses, in turn, will allow the use of larger blades which lead to improved efficiency and power output. The use of gamma TiAl in turbochargers to replace the nickel-base superalloy turbines, leads to an improved performance i.e. shorter reaction time during engine transients and reduced particulate emissions during load changes. In the framework of COST522, Work Package 1.2, an extensive effort has been carried out to evaluate the different aspects of physical and mechanical properties of the cast TiAl alloy ABB-IMN23. Additionally, efforts are being carried out to manufacture and test components from wrought extruded TiAl intermetallic. In this paper, an overview is given on the different types of evaluated properties of the cast alloys.

Keywords: gamma-TiAl, intermetallics, creep, fatigue, tensile strength.

Introduction

Gamma-TiAl base alloys exhibit several attractive properties for structural applications in turbomachinery industries. These unique properties include high elastic modulus, low density, competitive creep properties to Ni-base superalloys, and good oxidation and fire resistance [1-2]. The development of cast γ-TiAl alloys has progressed significantly within the last decade [3]. The intensive efforts have led to a better understanding of the fundamental correlation between alloy composition, microstructure, processing behaviour and mechanical properties [4-6]. The payoff for γ-TiAl in turbomachinery can be summarised in three areas [7, 8]. The first is that γ-TiAl has a specific Young's modulus, E/ρ where E is Young's modulus and ρ is the density, nearly 50 % greater than the structural materials commonly used in gas turbines. It is well known that Young's modulus is of value whenever clearances are concerned. In addition, higher specific Young's modulus shifts acoustically excited vibrations towards higher frequencies, which is usually beneficial for turbine blades. Additionally, the low density of γ-TiAl alloys makes them particularly attractive for components in which the stresses arise primarily from inertia, such as low pressure turbine blades, compressor blades, turbocharger rotors and valves for internal combustion engines [8-10]. The second payoff area is the improved creep strength of advanced γ-TiAl based alloys in the temperature range of 600-750°C, where for certain applications Ni-base alloys, with twice the density of γ-TiAl alloys, could be substituted. The third payoff area is the high fire resistance of γ-TiAl base alloys that enables the substitution of heavy and expensive fire-resistant designed Ti-based alloy components [11].

The need for gas turbine with higher efficiency was the motivation for the collaborative efforts for COST522 Work Package 1.2. A means to achieve improved efficiency is to

increase the exit area of the low pressure turbine by using longer turbine blades. The application of longer turbine blades is closely related to two issues. First, large blades are heavy and therefore increase the turbine disc loading. The second issue is as the blade length increases, the natural frequency of the blade decreases thereby reducing the tolerance of the blade to vibrations. Actually, the γ-TiAl base alloys belong perhaps to the only class of materials that offer unique solutions for these two issues. A disadvantage of γ-TiAl-based alloys is their low ductility and toughness, which lead to a material with limited inherent damage tolerance. Therefore, it is essential to develop appropriate design and lifing procedures to ensure the structural integrity of components made from γ-TiAl alloys.

The general objective of the activities in the subtask on γ-TiAl of COST522 Work Package 1.2 was to evaluate the different aspects of mechanical properties, oxidation resistance and coating development by the different partners of the cast γ-TiAl ABB-IMN2 and the fine grain size version ABB-IMN23 under engine relevant conditions. The emphasis was made to compare this behaviour with that of the Ni-base superalloy IN738LC.

The aim of the present paper is to present and report on the achieved results of the activities carried out within the framework of this COST522 subtask.

Materials and Microstructures

The nominal compositions of the γ-TiAl ABB-IMN2 and ABB-IMN23 alloys, in atomic percent are Ti-47Al-2W-0.5Si and Ti-47Al-2W-0.5Si-0.5B [12]. Several batches, in round bars 16 mm in diameter, plates 25 mm thick, and last stage gas turbine blades ca 600 mm long, of both alloys, had been cast and acquired from Howmet Corp., Whitehall MI USA.

The HIP and heat treatment schedules aimed to produce a nearly lamellar microstructure for balanced mechanical properties. The HIP was done at 1260°C for 4 h at 172 MPa. The heat treatment consisted of 1 h at 1350°C followed by 6 h at 1000°C. The typical microstructural features of this alloy are mainly colonies of lamellar γ/α_2. In addition, Ti and W rich β phase particles as well as Ti_5Si_3 silicides can be observed; in particular secondary silicides appear within all the three main phases: γ, α_2 and β [13, 14]. Figure 1 shows the typical microstructures of alloy ABB-IMN23. Detailed description of the microstructures of different batches of the two alloys as well as of the gas turbine blades are given in the publications of the COST522 Work Package 1.2 γ-TiAl Subtask partners [14].

Duplex ABB-IMN2 alloy (HIP + 20 h at 1300°C followed by 6 h at 900°C) properties are sometimes also shown for comparison.

Physical Properties

The density of γ-TiAl alloys investigated within COST522 activity is 4.12 g/cm^3 which is about half of that of IN738LC, i.e. 8.10 g/cm^3. The dynamic modulus of elasticity of γ-TiAl ABB-IMN2 has been determined in the framework of COST501 III, and compared with that of IN738LC [13]. Figure 2 shows this comparison as well as the modulus of elasticity of ABB-IMN23 as determined from tensile testing. It can be seen that the γ-TiAl alloys have excellent modulus retention at elevated temperatures which can be exploited for the design of light-weight structural parts with high stiffness. The thermal parameters, i.e. conductivity, specific heat and thermal diffusivity of the γ-TiAl alloy ABB-IMN2 have been measured within COST501 Action by Chalmers University. One should not expect to find differences, in the thermal properties, between ABB-IMN2 and its fine grain size version ABB-IMN23.

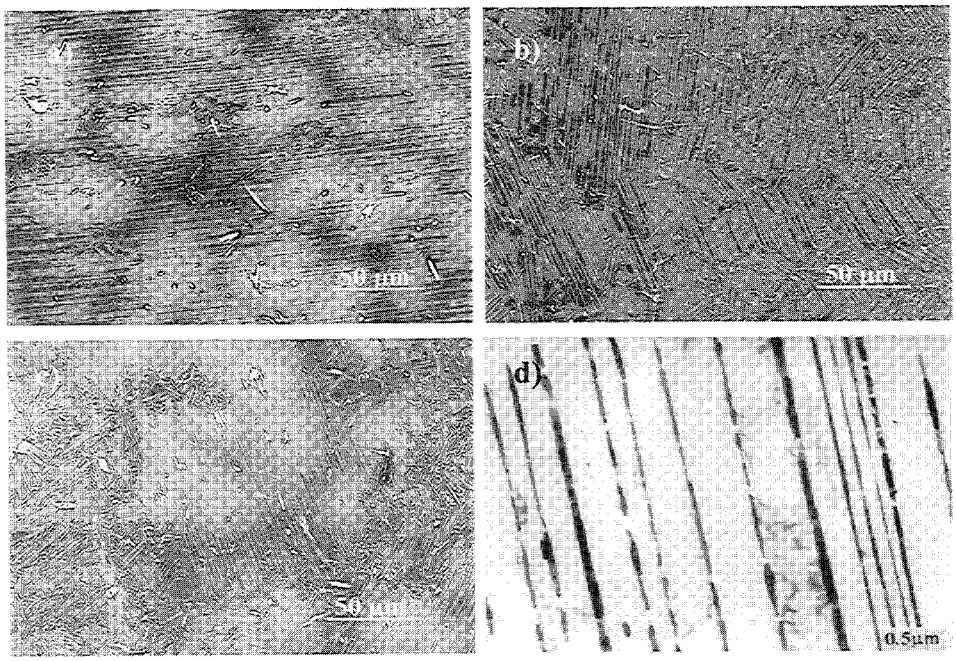


Figure 1: Microstrusture of ABB-IMN23 cast plate after HIPing and heat treatment. BSE SEM images of : a) cellular-grain area, b) casting edge area, c) plate core area and d) TEM image showing details of lamellar microstructure.

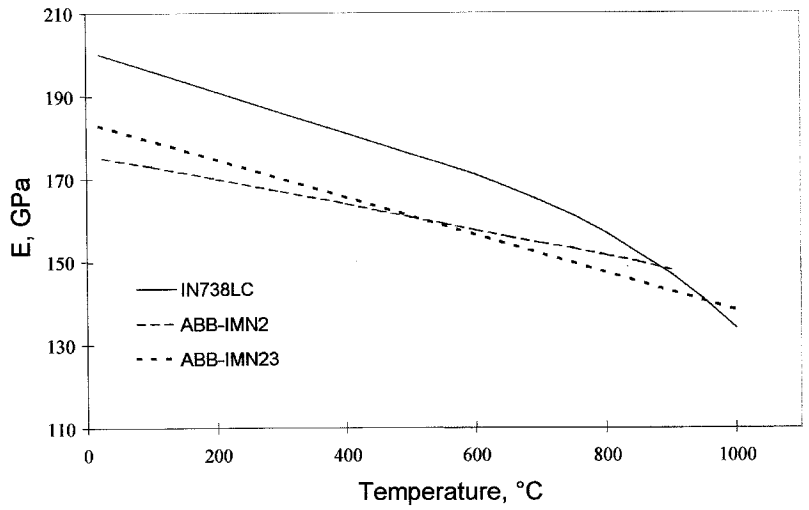


Figure 2: The moduli of elasticity of ABB-IMN2 and ABB-IMN23 both show better high temperature retention than modulus of elasticity of IN 738 LC alloy.

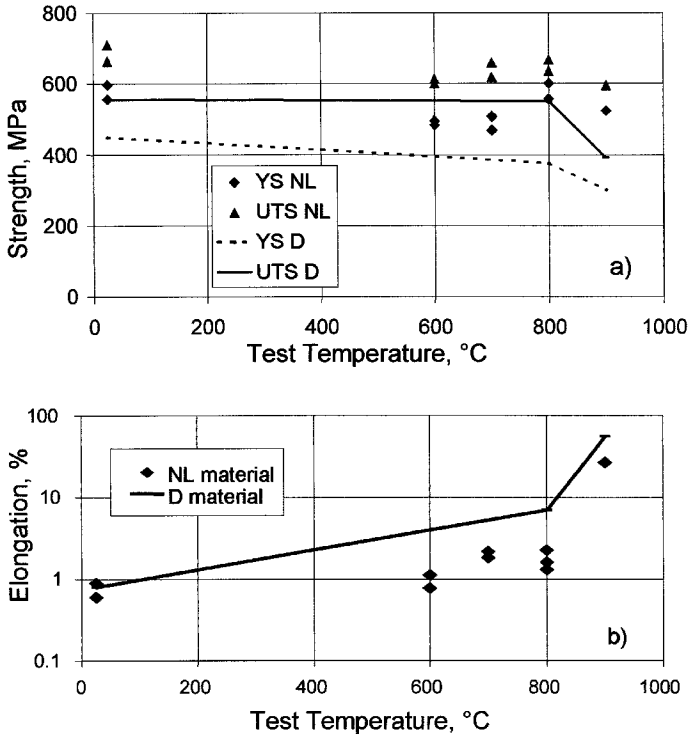


Figure 3a and b: Tensile properties at $7x10^{-4}s^{-1}$ strain rate as functions of temperature show (a) slightly better strength and lower elongation of ABB-IMN2 nearly lamellar (points) compared to duplex (lines) material with a ductile to brittle transition between 800 and 900°C.

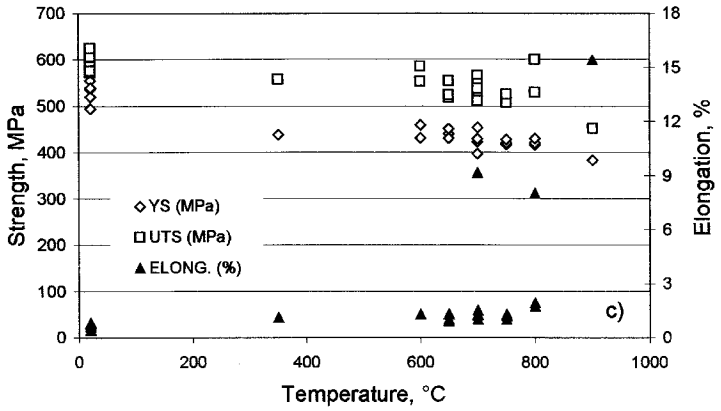


Figure 3c: Tensile properties at $7x10^{-4}s^{-1}$ strain rate as functions of temperature show excellent strength behaviour of the small grain version ABB-IMN23 alloy that is equivalent to the ABB-IMN2 alloy behaviour.

Tensile Properties

The tensile properties of both cast alloys as a function of temperature, are given in Figures 3. Figures 3a and b compare tensile strength and elongation, respectively, of the nearly lamellar (NL) and duplex (D) ABB-IMN2, showing comparable properties, although slightly higher strength and slightly lower elongation of the nearly lamellar material compared to duplex material. Figure 3c shows tensile behaviour of the ABB-IMN23. The yield and ultimate tensile strengths of the two intermetallic alloys are comparable, and they are comparable also with those of IN738LC, on a density corrected basis , as shown for ABB-IMN2 in [13]. Elongation to fracture exhibits rather low values, as compared with those of IN738LC, up to 700°C and then shows a brittle to ductile transition behaviour between 800 and 900°C. The results of tensile tests on specimens from different batches and components can be correlated to the different microstructures, i.e. colony size [9, 11].

Creep Properties

The creep strength is of essential importance for components subjected to constant loading at high temperatures, e.g. turbine blades and turbocharger rotors. Therefore a large number of creep tests were carried out, by the different participants of the γ-TiAl Work Package 1.2 group, at different stresses and temperatures. Additionally, the scatter in the creep behaviour in both γ-TiAl alloys was investigated in details and correlated to the microstructural variations in the components [14].

Figure 4a shows the density normalised stress rupture of both intermetallic alloys and of IN738LC in the form of Larson-Miller plot. The nearly lamellar ABB-IMN2 exhibited better creep strength than that of its fine grain size version ABB-IMN23. Nevertheless, both γ-TiAl alloys, including the duplex version of ABB-IMN2 material, showed comparable density normalised stress rupture to that of IN738LC. Figure 4b shows the density normalised time to 1 % creep strain resistance of specimens of both intermetallic alloys and of IN738LC machined from bars and plates, and of specimens machined out of a thick ABB-IMN2 component. As in the stress rupture Larson-Miller graph, also the 1% creep strain resistance graph shows some lower creep strength of ABB-IMN23 compared to ABB-IMN2 and some creep strength loss of the specimens from blade compared to bars and plates. Nevertheless, both γ-TiAl alloys, including the specimens excised from the component, showed comparable density normalised creep strength to that of IN738LC.

In Figure 5 minimum creep rate data of ABB-IMN23 (nearly lamellar) and ABB-IMN2 (duplex) are plotted as a function of true stress. The two alloys, after different heat treatments that produce different microstructures, have comparable creep strengths. Detailed account on the creep behaviour of the two γ-TiAl alloys including notch effects, is given in this proceedings [14].

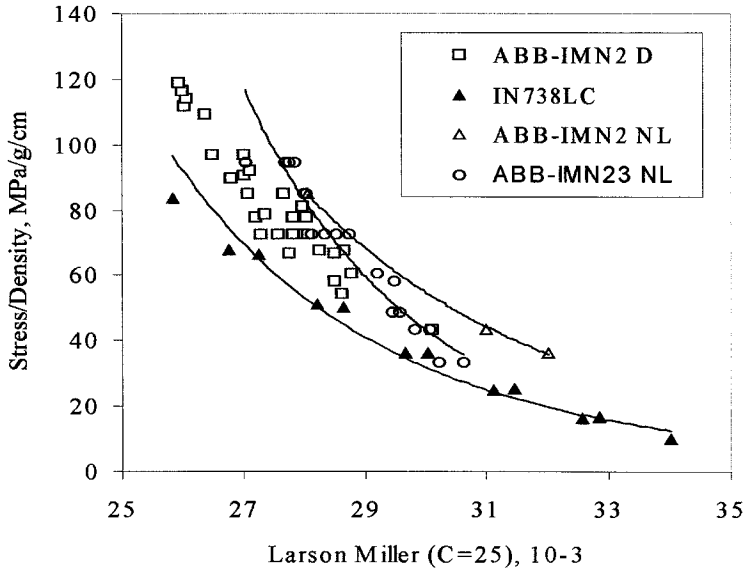


Figure 4a: Density normalised stress rupture Larson-Miller plot of ABB-IMN2 (duplex (D) and nearly lamellar (NL)) and ABB-IMN23 (NL), compared to IN738LC superalloy.

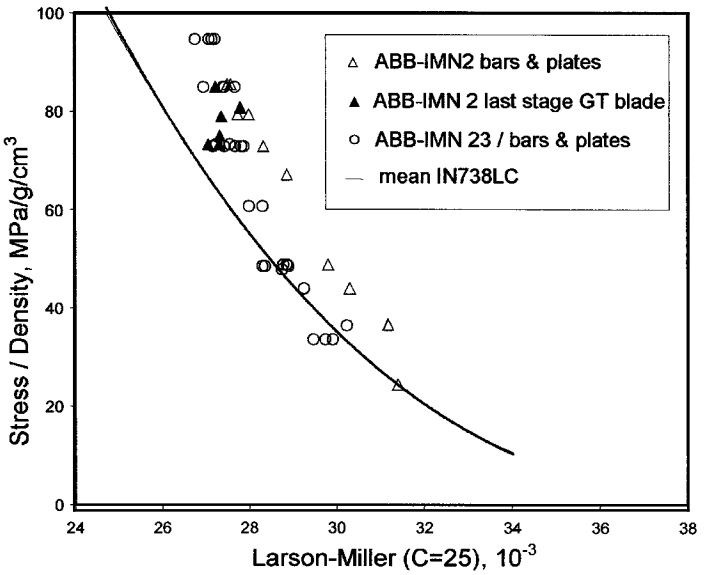


Figure 4b: Density normalised 1 % creep Larson-Miller plot of ABB-IMN2 and ABB-IMN23, compared to IN738LC superalloy.

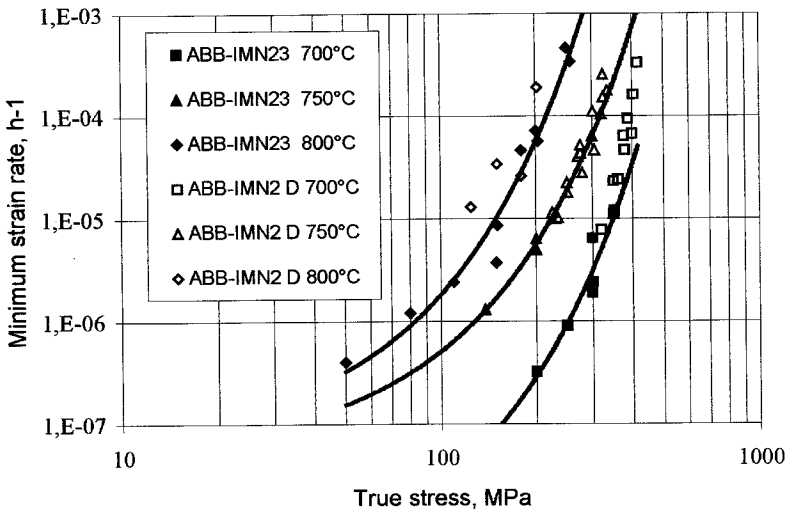


Figure 5: Comparison of minimum creep rate vs. true tensile stress of ABB-IMN23 (nearly lamellar) and ABB-IMN2(duplex).

Low Cycle Fatigue Behaviour

A sizable number of low cycle fatigue (LCF) tests were carried out, under completely reversed total strain controlled conditions, on specimens from both alloys as well as on specimens excised from components.

In general, the cyclic stress response of γ-TiAl ABB-IMN23, under LCF conditions, exhibited cyclic hardening behaviour during the entire life time, with decreasing rate towards the end of the test. Figure 6 shows the LCF results from the project of IENI (ex TeMPE), at 600°C and 700°C of the ABB-IMN2 alloy compared with the mean value curves for IN738LC superalloy. LCF results of the ABB-IMN23 alloy are also shown. The LCF properties of the two γ-TiAl base alloys are comparable and, in spite of the low ductility, they are equivalent to those of IN738LC superalloy. Additionally, no influence of 300 s tensile hold time was observed on LCF lives of the ABB-IMN2 alloy. Therefore, one can conclude that, in the investigated temperature range, fatigue mechanisms in the intermetallic material were predominant over creep mechanisms.

The LCF results of specimens, excised from the thick cross-section of the large GT blades, showed somewhat lower endurances. ABB-IMN23 specimens from blade at 700°C are somewhat better than ABB-IMN2 specimens from blade but their number is limited. This may indicate that the fine grain size version ABB-IMN23 can have an advantage in cast components with thick cross-sections.

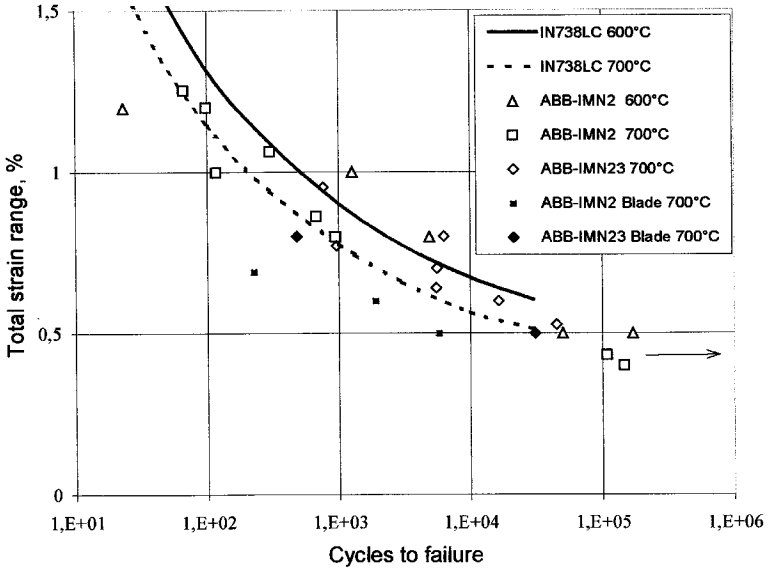


Figure 6: Comparison of LCF life of ABB-IMN2 , ABB-IMN23 and IN738LC.

High Cycle Fatigue Behaviour and Foreign Object Damage Effects

The high cycle fatigue behaviour of γ-TiAl ABB-IMN2 and ABB-IMN23 has been extensively studied by ALSTOM CH, UK and S, and NLR NL. The results of Figure 7 indicate typical HCF properties of this material. In general, the HCF behaviour of γ-TiAl alloys is characterised by: a) low slope of S-N curves, b) endurance limits being a high fraction of the ultimate tensile strength and c) strong dependence on the stress ratio R, indicating maximum stress control rather than stress range control behaviour. The S-N curves are much flatter than the curves for most metallic materials, a fact which can be directly attributed to the narrow interval between the threshold stress intensity factor and fracture toughness [15]. Therefore, the inherent brittleness of γ-TiAl alloys requires the use of the so called initiation, rather than propagation based design. However, although the material exhibits little damage tolerance, the endurance limits are high compared to most other metallic alloys. The endurance limit at R = 0 can be 70 % of the ultimate tensile strength. The tolerance of ABB-IMN2 to surface defects has been studied at 700°C [16]. One could successfully correlate the HCF endurances to the size of surface defects using the threshold stress intensity factor in the form of Kitagawa diagram [16]. The effect of foreign object damage (FOD) on HCF behaviour of γ-TiAl alloys has been studied in details by ALSTOM, CH and NLR, NL [17, 18]. It was experimentally found that the fatigue threshold and not tensile properties, determines the post-impact fatigue strength [17].

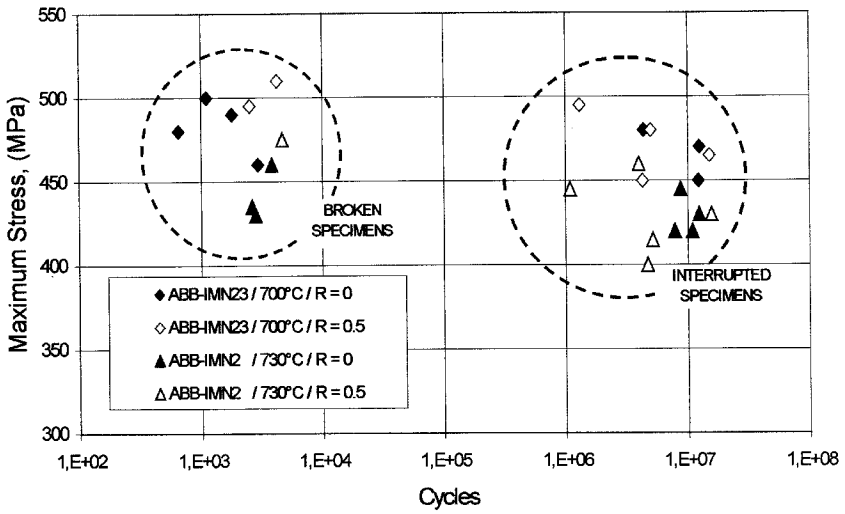


Figure 7: HCF results of the ABB-IMN2 and ABB-IMNB32 alloys, rationalised on σ_{max} rather than on $\Delta\sigma$ basis, showing a high stress sensitivity.

Fatigue Crack Growth

The fatigue crack growth (FCG) behaviour of the ABB-IMN2 and ABB-IMN23 alloys has been investigated [19]. In general, it can be observed that both γ-TiAl base alloys exhibited similar FCG behaviour in the investigated temperature range when heat treated to produce the nearly lamellar microstructure. A non significant temperature effect and a marked stress ratio effect on the FCG rates in ABB-IMN23 appear in Figure 8. The small temperature effect was observed also in the ABB-IMN2 alloy of nearly lamellar microstructure. The marked stress ratio effect on the FCG rates is consistent with a crack closure phenomenon that disappears when the minimum load in the cycle approaches the opening load. The frequency effect on the FCG rate in ABB-IMN23 at 700°C is shown in Figure 9, where it is apparent that the FCG threshold increases when the frequency decreases from 10 to 0.01 Hz.

Oxidation Resistance and Coating Development

The oxidation and corrosion behaviour of γ-TiAl alloys is an important aspect for their applications in turbomachinery. Recent studies have been carried out on the oxidation and corrosion behaviour of ABB-IMN2 in the temperature range of 600-800°C [13]. The thermogravimetric results of ABB-IMN2 showed good oxidation resistance up to 700°C.

Hence, coating development activities for γ-TiAl base alloys were started within COST522 for applications in the temperature range 700-800°C. Several approaches for coating development were followed including typical MCrAlY, ion implantation, surface treatment with phosphoric acid and pack cementation. The most promising technique was the pack cementation. Figure 10 shows the long-term cyclic oxidation of coated and uncoated ABB-IMN2 in air at 800°C [20].

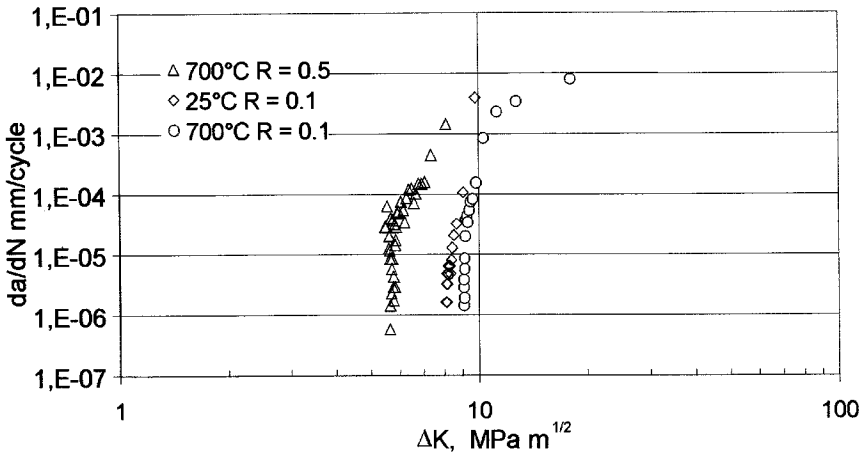


Figure 8: Effect of temperature and R ratio on fatigue crack propagation of ABB-IMN23 at 10 Hz.

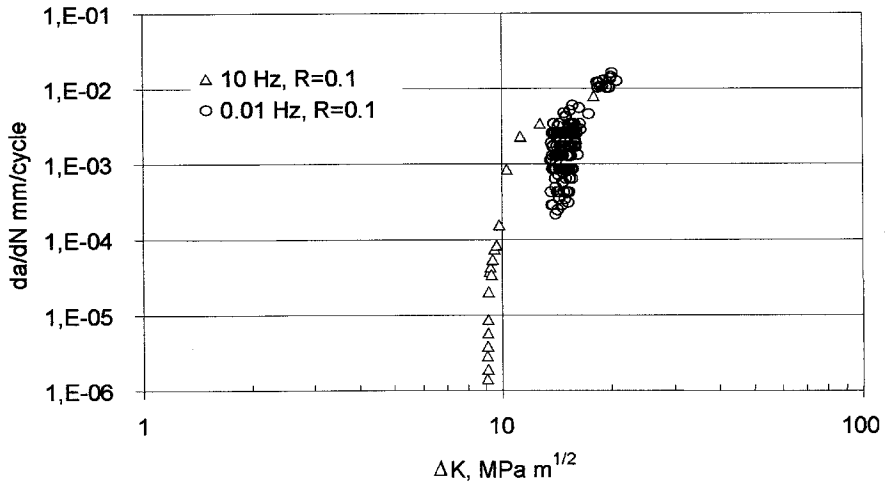


Figure 9: Effect of test frequency on fatigue crack propagation rate of ABB-IMN23 at 700°C.

The corrosion resistance of ABB-IMN2 at 700°C was shown to be better than that of IN738LC superalloy [13].

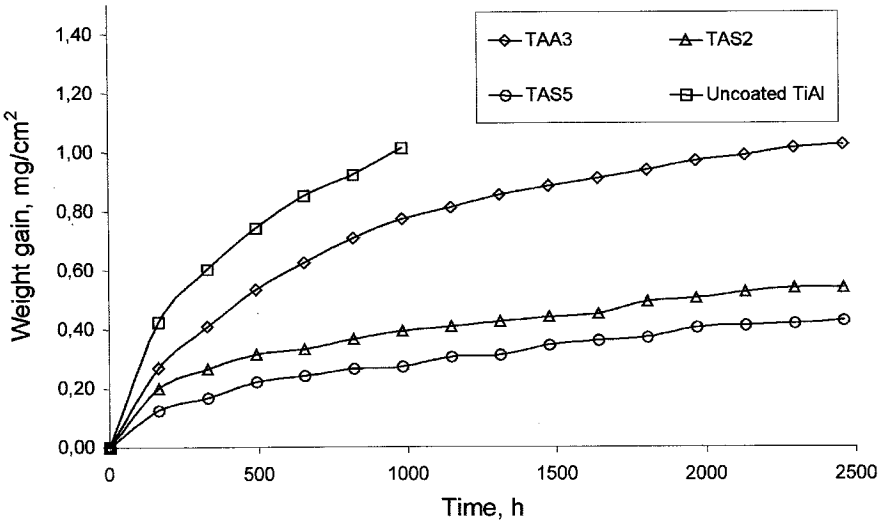


Figure 10: Long-term cyclic oxidation testing (cycle of 164 h) of coated and uncoated ABB-IMN2 in air at 800°C. Aluminised coating TAA3 showed the least protection compared to Si and Al containing TAS2 and TAS5 coatings [20].

Manufacturing of Components and Engine Testing

Four last stage gas turbine blades were cast from both alloys. Figure 11 shows two of them.

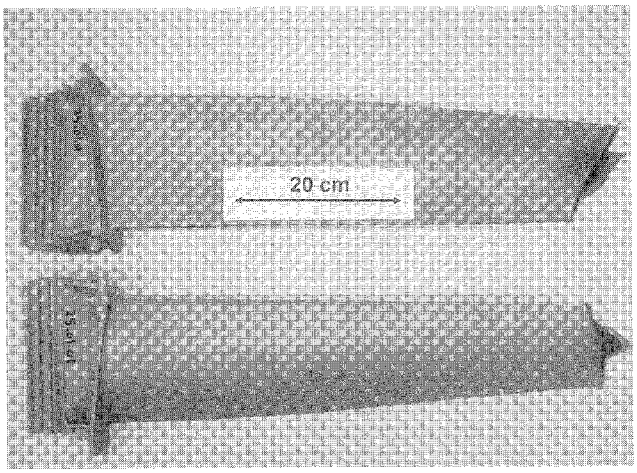


Figure 11: Example of last stage gas turbine blades that were cast in ABB-IMN2 and ABB-IMN23. Specimens for mechanical testing and metallographic examination were then machined out of such components.

Several specimens were excised from these components for carrying out different types of tests. As expected, the different parts of the components exhibited gradients in microstructure, i.e. grain size and colony size. These microstructures were responsible for the observed scatter in the mechanical properties data as discussed in details in reference [14].

Hence, one has to take the effect of section size into consideration in designing with cast γ-TiAl. Nevertheless, no dramatic deteriorations were observed in the mechanical properties in the different locations in the components. It is obvious that the size of such gas turbine blades is considered a challenge for the casting technology of γ-TiAl.

First results at Lufthansa Technik on weld repair of components from ABB-IMN2, using TiAl wire and TIG welding were encouraging.

It is noteworthy to present the results of a successful engine testing using ABB-IMN2 in turbocharger application [9, 10]. Figure 12 shows the γ-TiAl ABB-IMN2 turbine of one of the two ABB RR151 turbochargers after 1800 h operation on the fast ferry M/S Koegelwick. These turbocharger turbines were not coated. The M/S Koegelwick was equipped with two ABB RR151 turbochargers to boost one of the two Deutz T BD620V16 diesel engines with ca 2 MW. It is interesting to state that the two RR151 turbochargers have accumulated, at the present time, more than 6200 hours of operation.

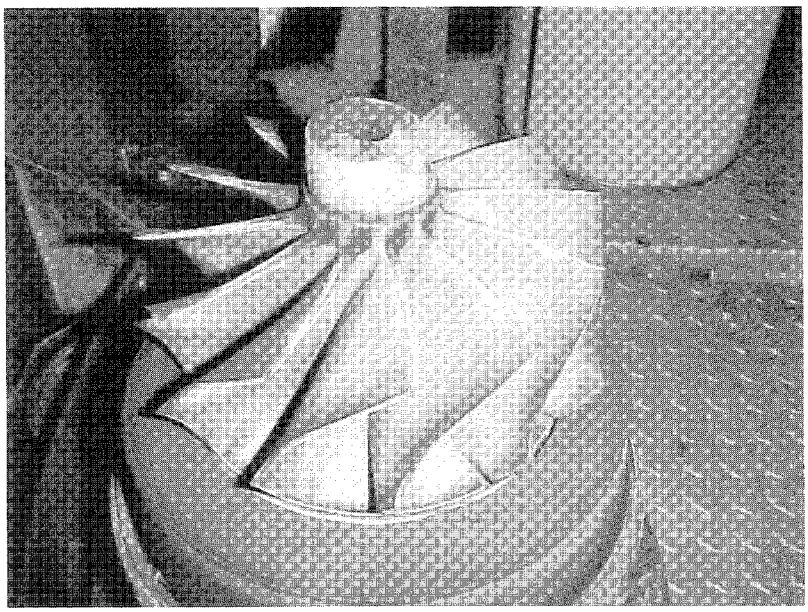


Figure 12: Turbocharger turbine after the field test of 1800 hours of operation.

Efforts have also been carried out recently, at Plansee AG, to manufacture, evaluate and test small blades of a wrought γ-TiAl alloy. The first results of the evaluation of mechanical properties of the material are encouraging.

Conclusions

A detailed evaluation of the cast γ-TiAl ABB-IMN2 and its fine grain size version ABB-IMN23 alloys have been carried out and the conclusions of this activity are:

1) The γ-TiAl materials exhibited improved density corrected tensile and creep strengths when compared with the IN738LC Ni-base superalloy. However, the tensile ductility of the γ-TiAl materials was lower than that of IN738LC.
2) Both γ-TiAl alloys, including the specimens excised from the component, showed comparable density normalised creep strength to that of IN738LC.
3) The LCF properties of the γ-TiAl alloys, at 600 and 700°C, were comparable with those of IN738LC. The specimens excised from the component, showed somewhat lower endurances ,especially for ABB-IMN2 and at high strain-ranges, as compared with those from cast bars.
4) The HCF behaviour differed from that of IN738LC with a) less steep S-N curves and b) higher ratio of the endurance limit / ultimate tensile strength.
5) The fatigue crack propagation behaviour indicated lower fracture toughness compared to IN738LC and an environmental effect balanced by a stress relaxation effect at high temperature.
6) The oxidation and corrosion resistance of the γ-TiAl material showed improvement over those of IN738LC. Nevertheless, a protective coating seems to be necessary for the γ-TiAl at temperatures > 700°C.
7) Casting and HIP has proved to be a viable processing route for manufacturing large turbomachinery components.
8) An engine testing of two RR151 turbochargers equipped with γ-TiAl ABB-IMN2 turbines, accumulated successfully more than 6000 hours of operation.

Acknowledgements

The authors wish to acknowledge the successful collaborations of all partners in the following projects within the γ-TiAl subtask in COST 522 Work Package 1.2: - ALSTOM (CH, S, UK) – CNR-IENI (ex TEMPE) (I) – Chalmers Univ. (S) - Cranfield Univ. (UK) – ITC-IRST (I) – IMMM (SK) – Imperial College (UK) – IPM (CZ) – IRC (UK) – Lufthansa (D) - NLR (NL) – Northumbria Univ. (UK) - Plansee (A) – QinetiQ (ex DERA) (UK). The valuable discussions and technical support of M. Staubli and A. Künzler are highly appreciated. The financial support for M. Nazmy by the Gas Turbine Development division at ALSTOM Ltd. CH is also appreciated.

References

1) Y-W. Kim, Journal of Metals, 46 (7), 30 (1994).

2) H. A. Lipsitt, M. J. Blackburn, and D. M. Dimiduk, in proceedings of 3rd Symp. on "Structural Intermetallics", Eds. K. J. Hemker et al., p. 73, TMS publication (2001).

3) Y-W. Kim and D. M. Dimiduk, in proceedings of 2nd Symp. On "Structural Intermetallics", Eds. M. V. Nathal et al., p. 531, TMS publication (1997).

4) P. I. Gouma et al. in Mat. Res. Soc. Symp. proceedings vol. 552, KK 2.11.1, (1999).

5) M-C. Kim et al. in Mat. Res. Soc. Symp. proceedings vol. 522, KK 3.1.1 (1999).

6) F. Appel et al. in proceedings of 3rd Symp. on "Structural Intermetallics", Eds. K. J. Hemker et al., p. 63, TMS publication (2001).

7) C. Austin et al., in proceedings of 2nd Symp. on "Structural Intermetallics", Eds. M. V. Nathal et al., p. 413, TMS publication (1997).

8) W. Smarsly et al., in proceedings of 3rd Symp. on "Structural Intermetallics", Eds. K. J. Hemker et al., p. 25, TMS publication (2001).

9) M. Nazmy et al., in "Processing and Design Issues in High Temperature Materials", N. S. Stoloff and R. H. Jones Eds., p. 159, TMS publication (1997).

10) B. Phillipsen, in Diesel and Gas Turbine World, p. 52, March (2001).

11) M. Oehring et al., in proceedings of 3rd Symp. on "Structural Intermetallics", Eds. K. J. Hemker et al., p. 157, TMS publication (2001).

12) M. Nazmy and M. Staubli, U.S. Pat # 5, 207, 982 and European Pat. # 45505 BI.

13) M. Nazmy and V. Lupinc, in proceedings of "Materials for Advanced Power Engineering 1998", J. Lecomte-Beckers et al. Eds., p. 933, publication Forschungszentrum Juelich (1998).

14) A. Dlouhy et al. in this proceedings.

15) R. I. Prihar, in proceedings of 3rd Symp. on "Structural Intermetallics", Eds. K. J. Hemker et al., p. 819, TMS publication (2001).

16) M. Nazmy et al., Scripta Materialia 45, p. 787 (2001).

17) S. L. Draper et al., in proceedings of 3rd Symp. on "Structural Intermetallics", Eds. K. J. Hemker, p. 295, TMS publication (2001).

18) M. Kolloos et al., in this proceedings

19) V. Lupinc et al., in proceedings of Symposium on "Structural Intermetallics", Eds. K. J. Hemker, p. 709, TMS publication (2001).

20) P. K. Datta et al., in this proceedings.

ADVANCES IN COATING SYSTEMS FOR UTILITY GAS TURBINES

J. R. Nicholls and R. Wing*
Cranfield University, Cranfield, Bedford MK43 0AL
* Chromalloy United Kingdom Ltd, Somercotes, Derbyshire DE55 4RH

Abstract

This paper aims to review current research into coating systems applicable to utility gas turbines. Both environmental resistant coatings and thermal barrier technologies will be discussed, in light of targeted aims:

1) to increase turbine operating temperatures by 100°C,
2) to increase the turbines ability to operate on a wide range of fuels
3) to increase the time between inspection/overhaul to greater than 10 000 h.

The paper reviews research undertaken as part of COST 522 relative to other strategies worldwide, published in the open literature. The environmental resistant coatings review focuses on performance issues associated with multi-fuel capable turbines and the performance of commercial, developmental and novel coating concepts are evaluated. Coating strategies aimed at increasing turbine operating temperatures focus on thick, air plasma sprayed thermal barrier coatings (up to 1.5mm) for use in combustors and thin, EB-PVD thermal barrier coatings (100-300μm) for use on both rotating and static turbine components.

Keywords: COST 522, gas turbine, coating, thermal barrier, APS, EBPVD, arc PVD, corrosion resistant, platinum aluminising, MCrAlY overlay, cyclic oxidation

Background

Gas Turbines form an integral part of modern advanced power plant engineering. They are featured in the most efficient design, where they are used as a means of converting raw fuel into electrical energy, plus the exhaust residual heat from the turbine can also be used to raise steam [1]. Their versatility allows them to burn many fuel types, including natural gas, synthetic gas produced from coal or other feedstock such as biomass, or liquid fuels. Thus modern, advanced design, power plants can be quite complex involving combined cycles, intercoolers, re-heat reformers and recuperation to improve the overall efficiency of the plant. Efficiencies up to 55-60% have been projected for combined cycle plant [1,2], requiring heavy duty gas turbine inlet temperatures of 1450°C [2].

With the strategic view (COST 522) that alternative fuels/cycles will play a major part in future world power generations, the challenge to the gas turbine sector (COST 522- gas turbine work group) is to increase turbine efficiency (a 10% increase is targetted), whilst reducing emissions (10 ppm natural gas derived NO_x at 1300°C) in engines with a multi-fuel capability.

These targets have major influence on the choice of materials for hot gas path components. Higher firing temperatures and reduced cooling, implies that turbine blades and vanes must be fabricated from single crystal materials with the highest temperature capability, in combination with advanced coatings.

From a coatings perspective, the turbine engine requirements can be translated into the following generic targets:

- +100°C increase in operating temperature
- + 10 000 h on project service life
- a factor of two increase in inspection interval
- wide fuel capability – natural gas, liquid fuels, and 'dirty' fuels.

Furthermore, a greater understanding of the "material system" is required, as increased temperatures lead to a greater interaction between the coating system and both the substrate and combustion environment.

Protective Systems for Future Industrial Gas Turbines (COST 522 – Work Package 2)

The purpose of this work package is to improve current knowledge of existing coatings and evaluate novel coating systems and technologies to enhance gas turbine component life of the hot gas path components. The research builds on earlier coating work undertaken in COST 501 Round III [3-6] which investigated improvements to both platinum aluminide and MCrAlY coating systems [3,4] and thermal barrier coating technologies [5,6]. For the platinum aluminides, improvements focused on their cyclic oxidation performance and hot corrosion resistance [3]. CN91, a single phase, CVD platinum aluminide produced by Chromalloy United Kingdom Ltd, is representative of this next generation platinum aluminide and has been adopted as the reference bondcoat system for comparing EB-PVD thermal barrier coatings within this COST 522 work package. Overlay coating developments within COST 501 Round III [3,4] focused on developing high strength MCrAlYs to overcome rumpling/cracking problems and also aimed at improving thermal stability, thus reducing inter-diffusion problems. These developments demonstrated that NiAlTaCr intermetallics showed promise. Thus, Amdry 997, a vacuum plasma sprayed NiCrAlTaY overlay, has been adopted as the reference bond coat system for air plasma sprayed thermal barrier coatings in COST 522.

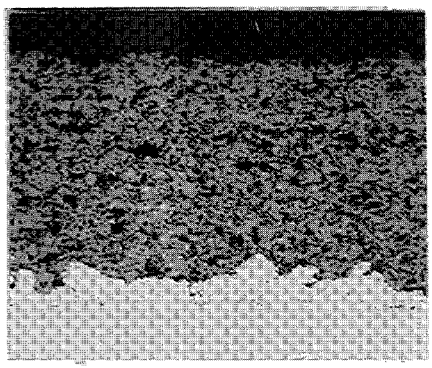
Thus, these reference coatings are:

- IN738LC, with a VPS MCrAlY (Amdry 997) bond coat and an APS (204NS powder) ZrO_2-8% Y_2O_3 thermal barrier coating (Figure 1a).

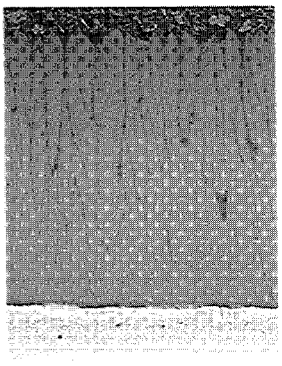
- CMSX4, with a monophased platinum aluminide (CN91) and an EB-PVD ZrO_2-8% Y_2O_3 thermal barrier coating (Figure 1b).

The 'new coatings/processes' initiative focused on the following:

1) Thick thermal barrier coatings for combustors and ducting
2) Thin thermal barrier coatings for turbine blades and vanes
3) Novel environmental corrosion resistant coatings.



a) Plasma sprayed thermal barrier coating



b) EB-PVD thermal barrier coatings

Figure 1 Coating microstructures of reference coatings used within COST522, work package 2 (coating details provided in the text)

Improvements to Thick Thermal Barrier Coatings

The major participants in this research activity are Ansaldo Energia and Tampere University and details of their thick TBC development work is presented in a companion paper at this meeting [7]. The aim is to develop an air sprayed TBC system ≥ 1.5 mm thick, but containing porosity levels in excess of 20%, together with an improved bond coat technology based on modified MCrAlY alloys, at lower manufacturing cost. The major application is as a thermal protection coating for combustor tiles.

Ansaldo Richerche has considerable research experience in this area, having developed a spraying process that produces air sprayed TBCs with vertically segmented cracks [8] and controlled density. The control of porosity is instigated by simultaneous spraying of zirconia + plastic mixed powders and this has enabled porosity levels up to 25% to be achieved [8] in sprayed TBCs of 1.5 mm thickness. A thick, porous, segmented TBC microstructure is shown in Figure 2. For this 1.5 mm thick coating a temperature drop of 320°C was achieved, giving a thermal conductivity of 0.77 W/mK (a state-of-the-art plasma sprayed TBC of 0.5 mm thick has a thermal conductivity of 0.8 W/mK [9]).

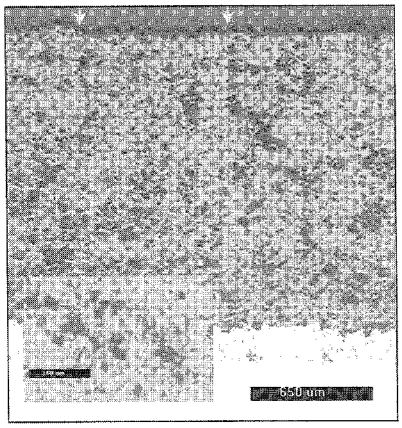


Figure 2 Micrograph of a thick, porous, segmented thermal barrier coating [7]:
inset enlargement of the cracked, porous ceramic microstructure;
arrows indicate segmentation cracks.

The bondcoat technology used was Sicoat 2453 (Ni10Co23Cr12Al3Re0.6Y), originally developed by Siemens Gas Turbines. Bondcoats were deposited using both vacuum plasma spraying (VPS) and high velocity oxy-fuel spraying (HVOF). These coatings were spray deposited onto IN738 substrates.

After deposition and heat treatment, this coating has a three-phase microstructure consisting of NiAl and CrRe intermetallic phases in a NiCoCr matrix. When oxidation occurs during deposition, lamella-shaped alumina particles are formed at splat boundaries. This was most noticeable in APS bond coats but was not evident in VPS or HVOF deposited coatings [8]. Thus the low-cost, air plasma spray technology results in a bond coat with 10% alumina content and 31% β-NiAl phase. The VPS, state of the art deposition technique, has no detectable oxide content and 79% β-NiAl phase content. To achieve similar quality to the VPS coating, but at reduced cost. Tampere University in collaboration with Ansaldo Richerche has researched the HVOF spray deposition of Sicoat 2453 as part of COST 522 as reported in detail in references 7 and 8. Preliminary results are most encouraging; alumina inclusions are barely detectable and the average β-NiAl content is 74%.

To evaluate the performance of HVOF deposited bond coats, relative to the state-of-the-art VPS process, Sicoat 2453 was sprayed onto IN738 test pieces, then over-coated with a standard thickness (0.5 mm) air plasma sprayed PSYZ ceramic coating. Samples were oxidised (discontinuous oxidation with occasional sample removal, mass change measurements and sample replacement) at 950 and 1000°C for a planned exposure of 10 000 h. The tests are still on-going and have achieved 5 000 h as reported in this paper.

Metallurgical examination of the VPS and HVOF coatings at various periods within the testing revealed that the HVOF coating had lowered the oxidation rate (measured as thickness of oxide film) as shown in Figure 3. Retention of the beta phase (Figure 4) is similar for both bond coat

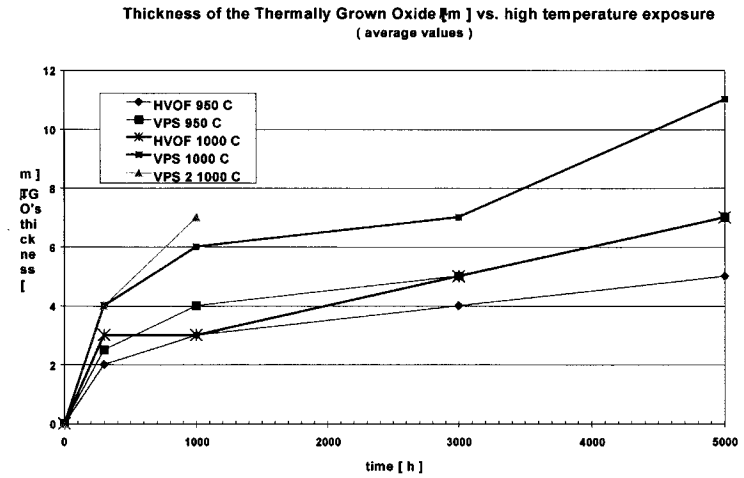


Figure 3 Variation in oxide thickness formed on SiCoat 2453 as a function of the spraying process and temperature

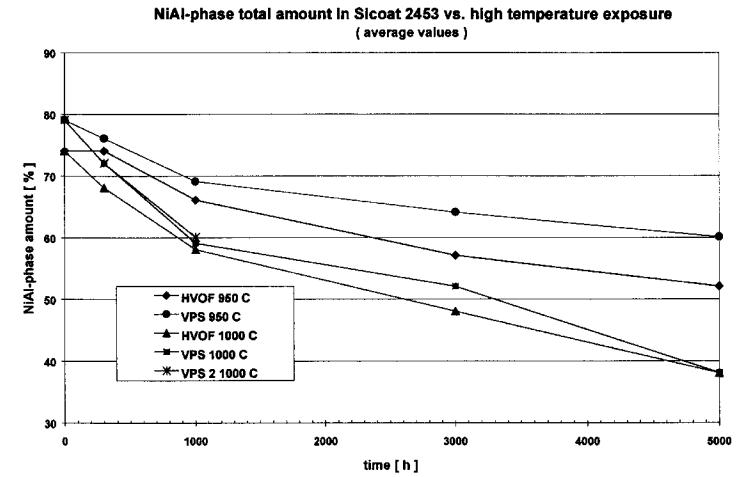


Figure 4 Variation in β-NiAl phase content for Sicoat 2453 as a function of spraying processes and temperature.

production routes, although the retained β phase fraction is marginally lower for the HVOF coating. It was noted that pores formed at the Sicoat 2453/base material interface following exposure with an almost continuous network being formed after 3000 h at 1000°C as shown in Figure 5; this was seen on both HVOF and VPS coatings and is being further investigated.

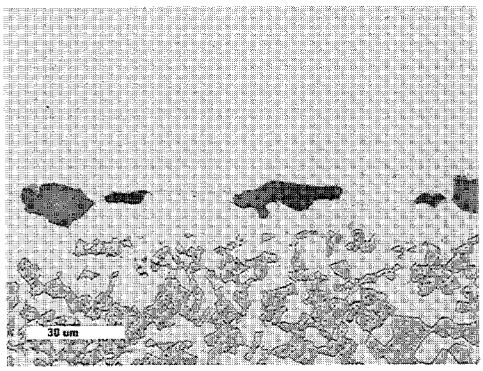


Figure 5 Pore network formed at the bond coat/substrate interface
for Sicoat 2453 coated IN738 after 3000 h at 1000°C

Thermal cycling testing has also been undertaken on the best thick (1.5 mm) APS ceramic topcoat and a Sicoat 2435 APS, VPS or HVOF bond coat. This combustion thermal cycling test is designed to produce a thermal gradient across the ceramic topcoat [7]. The test is set-up to achieve 1300°C at outer ceramic surface in 90 seconds (825-850°C in the base material) and the pass condition is set at 1000 cycles without failure of ceramic. Good thermal cycle resistance was seen for all thermal barrier coating systems tested but none achieved the 1000 cycle life criterion; average lifetimes for the various bond coats being; APS 770 cycles, VPS 689 cycles, HVOF 660 cycles. Testing is continuing.

Surface Modification of Thick Thermal Barrier Coatings

Alternative ceramic compositions and surface modifications are also under investigation within COST 522. At Tampere University, in addition to the reference 8 wt% yttria/zirconia ceramic, other compositions including zirconia-25 wt% ceria-2.5 wt% yttria and zirconia-22 wt% magnesia, all of which are deposited by air plasma spraying, are being investigated [10]. At the Forschungszentrum, Julich, lanthanum zirconate air plasma sprayed ceramics are under investigation [11]. Surface modification technologies, including laser glazing and a phosphate sealing, are under investigation at Tampere University [7].

The microstructural changes observed following laser and aluminium phosphate sealing are shown in Figures 6a-c.

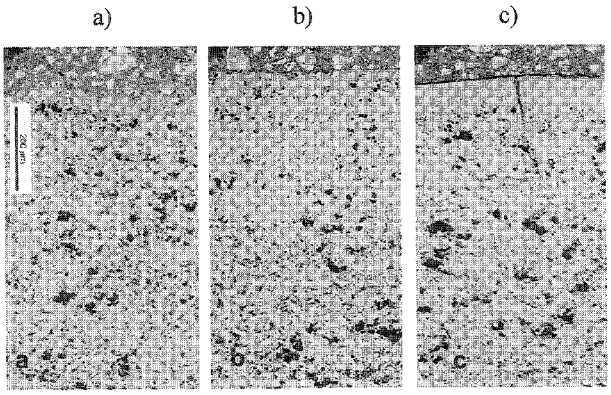


Figure 6 Micrographs of a) a standard APS PYSZ ceramic topcoat,
b) a coating sealed with aluminium phosphate and
c) a coating that has been laser glazed.

Analysis of the test results from this work is still largely on-going although some interesting results have been seen on the thermal properties of 8 wt% yttria/zirconia. Laser glazing appears to have negligible effect on thermal conductivity, whilst aluminium phosphate sealing appears to double this value, as shown in Figures 7 and 8.

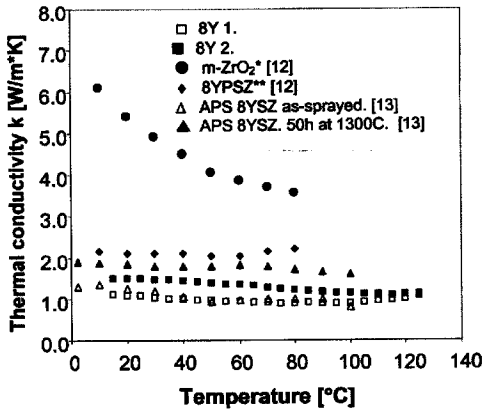


Figure 7 Thermal conductivity of air plasma sprayed ZrO_2-8 wt% Y_2O_3 TBCs, compared to hot pressed and sintered material (*uniaxial pressed and sintered ZrO_2, density 99% **uniaxial pressed and sintered ZrO_2 –8 wt% Y_2O_3,

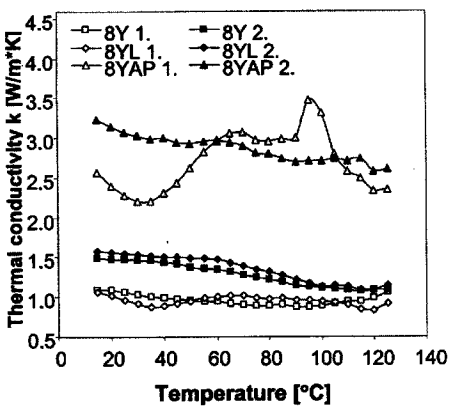


Figure 8 Influence of surface treatments on the thermal conductivity of air plasma sprayed ZrO_2-8 wt% Y_2O_3 (Y1, Y2 as sprayed: YL1, YL2, laser glazed; YAP1, YAP2 aluminium phosphate sealant

Improved Processing of EB PVD Thermal Barrier Coatings

The objective of this part of the programme was to investigate improved bond coat technologies for an EB-PVD thermal barrier coating system for application to turbine blades and nozzle guide vanes.

Chromalloy United Kingdom Ltd is the major participant in this investigation and selected outward diffusion platinum aluminising as the improved bondcoat technology for application in conjunction with an EB-PVD 8 wt% yttria/zirconia ceramic top coat. CMSX-4 test pieces were coated with 2 thicknesses of platinum and each platinum thickness was aluminised using vapour phase and CVD processes. These 4 groups of test pieces are to be compared with a thermal barrier system which had the "older" RT22LT platinum aluminising as the bond coat.

Using an EB-PVD ZrO_2-8wt%Y_2O_3 ceramic top coat onto an inward grown platinum aluminide bondcoat (RT22LT type) on a CMSX4 substrate as a reference coating, then the relative cyclic oxidation performance of various coating/substrate system can be evaluated, albeit tested in different cyclic oxidation rigs. This approach has been adopted for data presented in Figures 9, 10 and 11, where the influence of various diffusion, overlay coatings and surface treatments are evaluated on cyclic oxidation life at 1135°C. The term 'life capability ratio' is the relative performance in cyclic oxidation behaviour of these various systems compared to the RT22LT type reference coating system on a CMSX4 substrate.

Prior testing of an EB-PVD thermal barrier coating with a CN91 platinum aluminide bond coat, one of the 4 variants to be tested in this programme, demonstrated an increase in cyclic life to spallation of the 8 wt% yttria/zirconia ceramic layer as shown in Figure 9 [14]. These new EB-PVD thermal barrier coating/platinum aluminide bondcoats developed within COST 522 will be evaluated using a similar 1135°C, 1 h test cycle and are also expected to outperform the RT22LT reference system. However, problems have been experienced during the thermal cycle testing of the EB-PVD thermal barrier coated test pieces at Chromalloy United Kingdom Ltd and no reliable results have been produced to date; the testing is to be repeated.

The same EB-PVD thermal barrier coating has also been evaluated in a joint Cranfield/Rolls Royce/ Chromalloy United Kingdom Ltd programme with a range of alternative bondcoat technologies [15], and on various substrate materials. Tests were conducted at 1135°C, using a 1 h cycle. These results are reproduced in Figures 10 and 11, using RT22LT as the reference coating system.

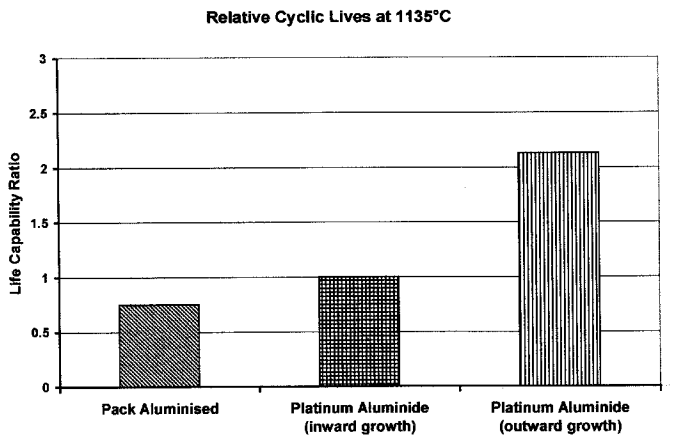


Figure 9 Thermal cycling performance of various diffusion bondcoats over-coated with an EB-PVD PYSZ ceramic topcoat, tested at 1135°C using a 1 h hot test cycle [14].

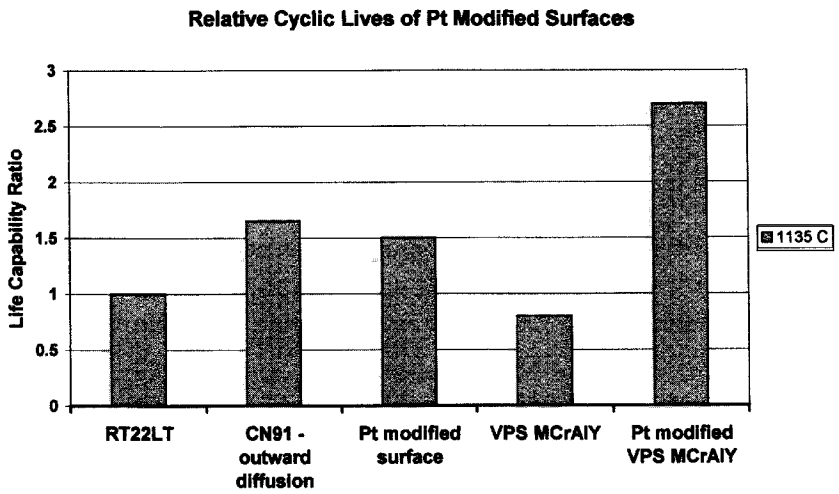


Figure 10 Influence of various bondcoat technologies on EB-PVD thermal barrier coatings life, following cyclic oxidation testing (1135°C; 1 h) (substrate CMSX4, reference bondcoat system RT22LT).

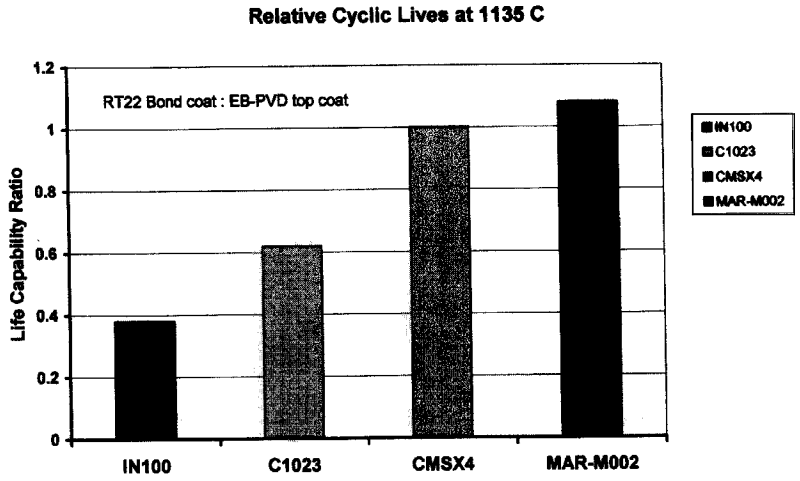


Figure 11 Influence of substrate alloy on EB-PVD thermal barrier coating life for an RT22LT platinum aluminide bond coat, following cyclic oxidation (1135°C; 1 h)

Results shown in Figures 9 and 10 are in general agreement with each other and also with independent, recently published data from the USA [16,17], which show that an outwardly grown, CVD platinum aluminide has a life increase of 1.7 to 2.1 when compared with inwardly formed, RT22LT type of platinum aluminide diffusion coating. Both platinum aluminide types out-perform a standard high activity aluminide.

A further point worth noting is the role of the substrate (Figure 11). For the inwardly grown, RT22LT type of coating, substrate effects are significant, due to the greater incorporation of substrate elements into the coating system. Alloys such as IN100 and C1023 contain relatively laarge amounts of titanium compared with CMSX4, leading to a possible contamination of the thermally grown oxide with associated reduction in cyclic life. On the other hand, MarM002, which contains hafnium, shows a marginal increase in cyclic life.

The benefit of platinum within bond coat systems (when tested in cyclic oxidation) is clearly shown in Figures 9 to 11 with the platinum modified VPS MCrAlY bond coat out-performing the standard MCrAlY and the platinum modified aluminides out-performing conventional aluminides. Recent published work within the USA by Meier and Pettit's research group [16,17] concur with these observations. Following cyclic oxidation tests (1 h duration) at 1100°C they have shown that platinum surface modification of various NiCoCrAlY coatings increases the cyclic life by a factor of between 10-12. This is attributed to the role platinum plays in producing a smoother surface, effectively burying grit-line manufacturing defects. The deposited platinum layer, once heat treated, extracts aluminium from the bondcoat forming a platinum aluminide intermetallic overlay on top of the MCrAlY. For the study reported in Figure 10 the benefits of the platinum overlay, once diffused, is x 3.4 at 1135°C.

Novel Environmental, Corrosion Resistant Coating

The Silesian Technical University is the major participant in this part of the COST 522 coatings development programme. They have produced a number of arc PVD coatings on both CMSX-4 and Rene 80, these being;

NiCoCrAlY , NiCoCrAlY + Al-Si, Al-Si, Pt +Al-Si

An interesting feature of this process method is that intermetallic "diffusion type" coatings can be produced contain less of the detrimental elements from the substrate that adversely effect oxidation and hot corrosion resistance compared to conventional CVD routes [18]. The microstructure of the Pt + Al-Si coating is shown in Figure 12; platinum was deposited by electroplating and the total coating, after arc PVD, was diffused at 1050C for 4 h. The chemical composition of the coating, through the platinum enriched outer zone (Table 1), approximates *to* NiPtAl (with equi-atomic ratios of Ni, Pt and Al). This intermetallic phase is iso-structural with NiPt but with aluminium substituted on each sub-lattice, as identified in recent phase diagram studies by Gleeson et al [19].

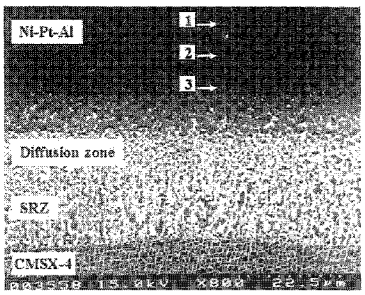


Figure 12 Platinum aluminide coating produced by Arc PVD and thermal diffusion [20]

measurement	Al		Si		Cr		Co		Ni		Pt	
point	at. %	wt. %	at. %	wt. %	at. %	wt. %	at. %	wt. %	at. %	wt. %	at. %	wt. %
1	36.47	11.34	-	-	1.59	0.95	2.67	1.81	30.15	20.40	29.12	65.49
2	36.56	13.05	-	-	2.32	1.60	4.18	3.26	35.97	27.95	20.97	54.14
3	28.12	12.60	6.28	2.93	3.11	2.68	7.24	7.08	46.04	44.91	9.19	29.79

Table 1 Results of elemental analyses of Pt-AlSi Coatings on CSX-4 alloy (see Figure 12 for the reference points).

The arc PVD coatings have been thermal cycle oxidation tested at 1100°C and the results obtained on CMSX-4 are shown in Figure 13. Each cycle was 24 h, with approximate 1 h to cool to room temperature and reheat to 1100°C.

The order of oxidation resistance revealed the Pt + Al-Si coating to be the best. By way of comparison, Figure 14 presents cyclic oxidation data, obtained at 1100°C, 1 h cycle, for modified CVD coatings on IN738 that were produced at Cranfield. This shows that low activity platinum aluminide and yttrium modified aluminides show promise, lasting in excess of 1000 h hours at 1100°C [21]. The yttrium modified aluminide was observed to out-perform the low activity, outward diffusion platinum aluminide (currently the best performing commercial platinum aluminide coating). A comparison of Figures 13 and 14 (note that each cycle represents 23 h at temperature in Figure 13 and 1 h at temperature in Figure 14), suggests that the Pt+AlSi coatings perform similarly to a low activity, outward diffusion platinum aluminide, out to the 300 h data measured at Silesian Technical University. In the Cranfield tests, the low activity, outward diffusion platinum aluminide lasted over 1000 h at 1100°C; further testing will establish whether these new Arc PVD coatings perform as well. The test is still on-going, being only halfway through the planned test programme. The poor performance of the MCrAlY coatings (R150+HT; RT150+R151+HT) is unexpected and is under investigation; their lives were only 2-3 times that observed for un-coated CMSX4.

Silesian Technical University has also developed new MCrAlY spray powder compositions containing intermetallic and ceramic phases for deposition using APS or HVOF for use in erosive or corrosive conditions. Coatings containing FeAl, Cr_xC_y, TiC and Al_2O_3 have been produced and the microstructure and properties are being investigated [20] and are reported elsewhere in this meeting.

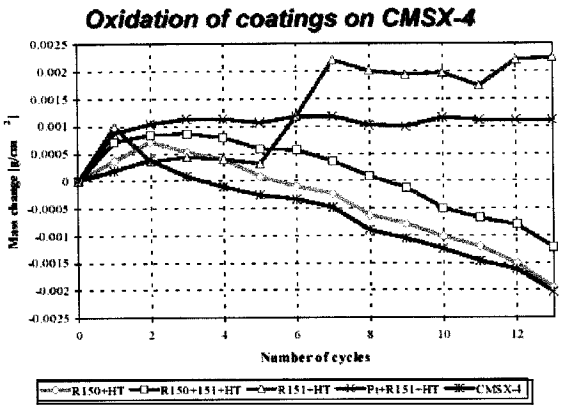


Figure 13 Mass change curves for thermal cycle tests at 1100°C of new PtNiAlSi intermetallic arc PVD coatings. The duration of each cycle is 24h.

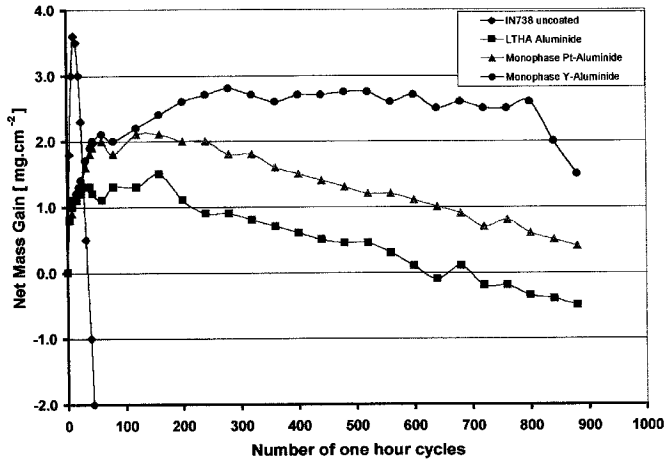


Figure 14 Cyclic oxidation performance, 1 hour cycles at 1100°C, of modified aluminide coatings on IN738 [21]

Conclusions

This paper has reviewed the progress to date of the "new coatings/processes" programme within the work package 2 of COST 522. Three strategies have been addressed.

1) *Improved thick, sprayed TBC systems for combustor and liner applications*
Here, thick *PSYZ* TBC systems have been produced up to 1.5mm thick. The TBCs contain up to 25% porosity, are segmented and microcracked and can provide a temperature drop of 320°C. The bondcoat technology is based on the latest generation Re-modified MCrAlY. HVOF spraying of this bondcoat provides cyclic oxidation performance similar to the vacuum plasma sprayed state-of-the-art, but at reduced cost.

2) *EB-PVD thermal barrier coatings on platinum modified bondcoats offering extended life components for turbine blade and vane applications*
In this work package, research has focussed on the low activity, outward diffusion vapour phase platinum aluminide (CN91 type). Cyclic oxidation data at 1135°C has shown that this bondcoat system out-performs the older, inward diffusion (RT22LT type) when deposited onto CMSX4 and both platinum aluminide variants offer increased spallation lives compared to a conventional high activity aluminide. Published data in the literature, from research in Europe and the USA, further show that platinum surface treatments of the base alloy [22,23] and an MCrAlY bondcoat [15-17] can offer significant advantage, providing a smoother, stronger, more defect free surface, thus improving TBC cyclic life.

3) *Novel corrosion resistant coatings*

Finally, the Arc PVD manufacturing route has been investigated to produce new, more pure (less influence of outward substrate element diffusion) platinum modified aluminide environmental coatings. Initial trials show that these platinum-aluminium-silicon modified surface out-perform the unmodified MCrAlY overlay coatings under cyclic oxidation conditions at 1100°C. This work is continuing to evaluate the coatings performance under hot corrosion conditions within the remaining period of this COST 522 programme.

References

1. J. E. Oakey, D. H. Allen and M. Staubli "Power Generation in the 21st Century – The New European COST Action" , Euromat '99.
2. T. Schulenberg, "New Developments in Land Based Gas Turbine Technology" in "Materials for Advanced Power Engineering, 1998" (Eds. J. Lecomte-Becker, F. Schubert and P. J. Ennis) part II, p849-859, Forschungszentrum Julich Germany (1998).
3. D. F. Bettridge, R Wing and S. R. J. Saunders, "The Exploration of Protective Coatings and Deposition Processes for Nickel Based Alloys and Gamma Titanium Aluminides" in "Materials Engineering, 1998 (Eds. J. Lecomte-Becker, F. Schubert and P. J. Ennis) part II, p61-976 Forschungszentrum Julich Germany (1998).
4. L. Peichl and D. F. Bettridge "Overlay and Diffusion Coatings for Aerogas Turbines" in "Materials for Power Engineering" (ed. D. Coutsouradis et al). Part I, p717-740, Kluwer Academic Publishers, Netherlands (1994).
5. Z. Babiak, Fr. W. Bach, L. Bertamini, F. Hinydryckx, P. J. Krugers, Ch. Mertens, B. Michel, S. Sturlese and W. Unterberg, "Innovative Plasma Sprayed 7% YSZ-Thermal Barrier Coatings for Gas Turbines" in "Materials Engineering, 1998 (Eds. J. Lecomte-Becker, F. Schubert and P. J. Ennis) part III, p1611-1618 Forschungszentrum Julich Germany (1998).
6. R. Vassen, F. Tietz, G. Kerkhoff and D. Stover, "New Materials for Advanced Thermal Barrier Coatings", in "Materials Engineering", 1998 (Eds. J. Lecomte-Becker, F. Schubert and P. J. Ennis) part III, p1627-1636 Forschungszentrum Julich Germany (1998).
7. P. Bianchi, F. Cernuschi, L. Lorenzoni, S. Ahmaniemi, M. Vippola, P. Vuoristo and T. Mantyla "Thermophysical an Microstructural Characterisation of Modified Thick Yttria Stabilised Zirconia Thermal Barrier Coatings" in "Materials for Advanced Power Engineering", (2002), Liege, Belgium..
8. G. C. Gualco, E. Cordano, F. Fignino, C. Gambarao, S. Ahmaniemi, S. Tuurna, T., Mantyla and P. Vuoristo, "An Improved Deposition Process for Very Thick Porous Thermal Barrier Coatings", Int. Thermal Spray Conference 2002, Essen Germany, 4-6 March (2002).
9. J. R. Nicholls "Design of Oxidation Resistant Coatings" JoM 52 (1) 28-35 (2002).
10. M. Vippola, P. Vuoristo and T. Mäntylä, COST 522 Report, June (2001).
11. R. Vassen, A. Pesl and D. Stover "Comparison of Thermal Cycling Life of YSZ and La_2ZrO_7-based Thermal Barrier Coatings" in "Materials for Advanced Power Engineering (2002), Liege, Belgium, Oct 2002.
12. Raghaven et al cited in reference 10.
13. R. Dullan et al cited in reference 10.
14. R. G. Wing, Private Communication (2002).
15. R. Jones and D. S. Rickerby, Private Communication (2002)
16. N.M. Yanar, G. M. Kim, F. S. Pettit and G. H. Meier, "Advanced Coatings for High Temperatures" Turbine Forum, Nice, April 2002
17. A. G. Evans, D. R. Mumm, J. W. Hutchinson, G. H. Meier and F. S. Pettit, Progress in Materials Science 46, 505, (2001).

18. J. G. Smeggil and N.S. Bornstein, "Study of Interdiffusion Effects on Oxidation/Corrosion Resistant Coatings for Advanced Single Crystal Superalloys" in Conf on "High Temperature Protective Coatings", Atlanta, AIME, 61-74 (1983).
19. B. Gleeson, D. Sordelet and W. Wang, "Portion of 1100°C Ni-Al-Pt Phase Diagram", Office of Naval Research, Contract No. N00014-00-1-0484 (2000).
20. L. Swadzba, S. R. J. Saunders, M. Hetmanczyk, B. Mendala, "Formation and Degradation of Overaluminisive of MCrAlY Coatings Deposited by Arc PVD Process on Ni-base Superalloys" in "Materials for Advanced Power Engineering" (2002), Liege, Belgium Oct. 2002.
21. G. Amperiawan PhD Thesis, Cranfield University (2002).
22. D. S. Rickerby and R. G. Wing, "Thermal Barrier Coating for a Superalloy Article and a Method of Application Thereof", US Patent 5,942,337, August 24, (1999).
23. D. S. Rickerby, S. R. Bell and R. G. Wing, "Article Including Thermal Barrier Coated Superalloy Substrates", US Patent 5,981091, November 9 (1999).

ENVIRONMENTAL DEGRADATION OF GAS TURBINE COATINGS: TOWARDS STANDARDISED TESTING AND DATABASES

N J Simms*, D W Bale#, D Baxter+ and J E Oakey*

*Power Generation Technology Centre, Cranfield University,
Cranfield, Bedfordshire, MK43 0AL, UK
ALSTOM Power Technology Centre, Cambridge Road, Whetstone, Leicestershire, UK
+Institute for Energy, JRC Petten, 1755 ZG Petten, The Netherlands

Abstract

The development of a database of quantitative information on the environmental degradation of industrial gas turbine coatings has been a major activity within the European COST522 programme. The database is intended to facilitate the comparison of coating performances in different degradation regimes, as well as providing basic data on coating properties. Components targeted in this activity have been gas turbine blades and vanes manufactured from CMSX-4 and IN738LC, with current standard and new coatings.

The database has been produced using data generated within parallel performance testing activities in the COST522 programme. This test work has covered degradation due to isothermal oxidation, cyclic oxidation, laboratory hot corrosion and burner rig testing, as well as synergistic degradation from erosion-oxidation and thermal fatigue. In addition, tests have been carried out to determine the mechanical and thermal properties of the coatings, for example: ductile-brittle transition temperatures and thermal conductivity. The preferred method of obtaining data that describes the damage caused by corrosion and oxidation has been dimensional metrology before and after sample exposure, to obtain a distribution of damage measurements. To ensure the quality of the data being generated, a round robin exercise has been carried out between all the organisations carrying out these types of measurements.

For the data to be incorporated into the database, it has been necessary to develop and apply standardised methods of data collation and presentation of the results for each of the test types, especially since the testing activities have been carried out by 16 different companies and research institutes within Europe. The database contains information that precisely specifies the coating and substrate combination, as well as accurately describing each test environment and the raw data produced from each test.

Keywords: gas turbine coatings; corrosion; mechanical properties; physical properties; database

Introduction

Gas turbines are at the heart of many current power stations [1-3], usually as part of combined cycle systems fired on natural gas. It is anticipated that gas turbines will be used even more widely in the future, with increasing numbers of natural gas fired combined cycle systems being installed [1-3] and as new solid fuel (coal, biomass, waste) combined cycle power generation systems move from development through demonstration to commercialisation [1,4]. However, the distribution in the usage of gas turbines and the uptake of these various potential power systems will continue to vary significantly between countries due to the availability of fuels, economic factors, national policies and regulatory frameworks (both for the power markets and environmental restrictions).

Industrial gas turbines (IGTs) have been developed to use increasingly higher firing temperatures and pressures to increase their efficiency of power generation [1-3], with current models firing at temperatures up to ~1400°C at pressures of ~ 30 bar. To cope with these progressive increases in firing conditions, the materials used for blades and vanes in the hot

gas paths of IGTs have needed considerable development and a series of new alloys have been produced since the 1960s with increased creep and thermal fatigue resistance [2,5]. Until the 1970s, increased high temperature oxidation and corrosion resistance of these new materials was targeted as a compromise to alloys with improved high temperature mechanical properties. However, since then alloy development has concentrated on optimising the mechanical properties of the alloys, in order to permit usage of the highest possible metal temperature consistent with economically viable component life times. Thus, coatings that protect the base alloys from the surrounding environment have become critical parts of IGT hot gas path components. To enable combustion gas temperatures to continue to rise, increasingly sophisticated air-cooling has been required to allow the operating temperatures of the blades and vanes to remain at viable levels. However, the use of air bleeds from the compressor to provide air-cooling to hot gas path components has an efficiency penalty for the gas turbine operation. This has provided the driving force for the development and application of thermal barrier coatings (TBC's) to such components to reduce the cooling air requirements and/or component metal temperatures.

Thus, coatings have been developed to provide:

- a hot corrosion/oxidation resistant barrier layer to protect the base alloys from the potential of damage from the surrounding environments
- a low conductivity thermal barrier to reduce cooling air requirements and/or base alloy operating temperatures

Many classes of coatings have been developed to meet these needs. These are reviewed elsewhere [e.g. 5,6] and their continuing development is summarised in another review paper in this conference [7].

The performance of coatings in advanced gas turbines in power generation systems is critical to the viability of these systems. Thus, it is increasingly important that the correct coatings are selected for particular applications. In order to achieve this, the properties and performance of the candidate coatings must be thoroughly investigated and the data generated on coating performances from different sources needs to be both consistent and compatible. A large amount of data on the performance of candidate gas turbine coatings already exists; unfortunately much of this data is neither consistent nor compatible.

The COST522 activities described in this paper have been targeted at:

- comparing different test methods for the generation and measurement of oxidation/corrosion damage, and the determination of mechanical and physical properties
- standardising the assessment methods for coating performance
- producing a database of coating performance under well characterised test conditions

The database that is the major product of these activities allows the systematic comparison of the various test methods using data arising from tests on common (reference) coatings. It also provides a comprehensive set of test results for current and candidate coatings that allows coating performances to be compared. This database provides a valuable resource for information on coating performance and assisting in coating selections.

Relevance of Coating Properties

There are many specific properties of coatings that need to be characterised to fully evaluate their potential usage as integral parts of IGT hot gas path components. As coatings can have different primary uses (e.g. thermal barrier or corrosion resistance), not all coating performance properties need to be evaluated for every type of coating. The relevance of the different coating properties is outlined below.

Oxidation and Hot Corrosion Performance

Many coatings are applied to enable a protective oxide layer to be formed and maintained on their surfaces to protect the underlying alloy [5,6,8]. Such coatings may degrade by reaction with the surrounding environment or by interdiffusion with the underlying alloy. Coating compositions are usually targeted so that they form slow growing aluminium or chromium oxides; to resist oxidation/type I and type II hot corrosion respectively. The coating degradation by oxidation, hot corrosion and interdiffusion have been well documented and reviews are available elsewhere [5,6,8]. These coatings need to have lives of at least one year (and preferably three years) in their target operating environment(s), so low oxidation/ corrosion rates are required. Oxidation and hot corrosion are particularly sensitive to trace contaminants in the fuel and air supplies to the gas turbine combustor, component operating temperatures, local component gas temperature/pressure and the temperature cycling of the gas turbine.

Mechanical Properties

In general coatings do not need to have particularly good mechanical properties, but need to have sufficient strength and adhesion to remain firmly attached to the component surfaces and not impair the performance of the underlying alloy (e.g. by acting as fatigue crack initiation sites) [6]. Strong adhesion also prevents the coating from impinging the flow of hot gas around the turbine components. The stresses that arise in the coatings can be caused by thermal expansion mismatch between the coating and the substrate alloy, thermal gradients within the components, operation of the gas turbine (e.g. centrifugal forces from blade rotation), thermal cycling of the gas turbine, impacting particles. Thus, important mechanical properties for coatings include creep, fatigue, Young's modulus, thermal expansivity, ductile-brittle transition temperatures and erosion resistance.

Thermal barrier coatings (TBCs) are parts of multi-layered coating systems. Therefore, both the absolute and relative mechanical properties of each individual coating layer and the substrate are important (e.g. as they may give rise to thermal expansion mismatches). As the ceramic TBCs are inherently brittle, the microstructure and adhesion of these coatings are particularly important when considering their behaviour during heating, cooling, cyclic stressing and particle impaction.

Thermal Properties

The thermal properties of TBCs are inherently important [6,7]. Current TBC technology can achieve temperature reductions of approximately 150°C across typical coating thicknesses. This capability is reliant on the low thermal conductivity of the TBC, with typical values in the range ~0.8 – 2 W/m/K. Therefore, all factors that contribute to this thermal conductivity must be well characterised, e.g. thermal diffusivity, specific heat, density and microstructure, and their dependence on coating application routes and compositions, as well as component heat treatments.

Coating Property Characterisation

Within the COST522 programme the properties of coatings are being investigated by 16 companies, research institutes and universities in 10 European countries as part of the 'Protective Systems' work package of the Gas Turbine Group. The various work programmes in the different organisations have started since 1998 and are scheduled to be completed in 2003. Many of these test programmes are reported in much more detail elsewhere in these conference proceedings.

Reference Coatings

A common set of reference coatings (Table 1) were agreed by the participating organisations to enable comparison between the different test methods and results from different organisations, as well as allowing the assessment of the relative performance of a wider range of materials included in each test.

Table 1 Reference Materials for COST522 Protective Systems Coating Characterisation

Base Alloy	Coating	Comments / Nominal Compositions (wt%)
IN738LC	-	IN738LC = Ni – 16 Cr –8.5 Co–3.4 Al – 3.4 Ti – 2.6 W – 1.7 Mo – 1.7 Ta – 0.9 Nb – 0.11 C
IN738LC	LCO22#	LCO22 = Co – 32 Ni – 21 Cr - 8 Al – 0.5 Y
IN738LC	Air plasma sprayed (APS) TBC* on LCO22# bond coat	
CMSX-4	-	CMSX-4 = Ni –6.5 Cr –10 Co – 5.6 Al – 4.9 Ti – 6 W – 0.6 Mo – 6 Ta – 1 C – 2.9 Re – 0.1 Hf
CMSX-4	CN91	Modified aluminised (Pt-Al) coating
CMSX-4	Electron beam physical vapour deposited (EB PVD) TBC* on CN91 bond coat	

* 8%Y_2O_3 partially stabilised zirconia (PSYZ); # or equivalent

Corrosion and Oxidation Testing

Within this COST activity, nine partners are carrying out corrosion and oxidation test work. This work encompasses isothermal oxidation, thermal cycling, laboratory hot corrosion testing and burner rig hot corrosion/deposition testing (as summarised in Table 2).

Test Methods

Tests are being conducted using a range of test equipment at the different organisations. For entry into the database, it has been necessary to characterise the operation of each test system, so that the various different exposure conditions of samples are known within each test rig, for example

- gas composition at exposure temperature, heating / cooling environments;
- gas temperature, metal temperature, heating / cooling rates;
- deposit compositions, deposition fluxes

Table 2 Corrosion and Oxidation Testing

Organisation	Isothermal Oxidation	Thermal Cycling	Laboratory Hot Corrosion	Burner Rig Corrosion & Deposition
ALSTOM POWER	Y		Y	Y
Ansaldo	Y	Y		Y
Cranfield University				Y
Innogy				Y
Julich		Y		Y
Petten				Y
PowerGen	Y			
Silesian Technical University		Y		
Tampere University			Y	

The test methods have included:

- *Isothermal oxidation* - carried out in laboratory furnaces in either air, air-SO_2 or combustion gas environments at temperatures of up to 1100°C for periods of up to 10,000 hours (with gas mixtures being either non-equilibrated or catalyst equilibrated).
- *Thermal cycling tests* - carried out in either air or combustion gas environments at temperatures of up to 1250°C. A range of cycle durations, heating and cooling rates, etc, are being used in the various test rigs, using electrical or gas heating.
- *Laboratory hot corrosion tests* - carried out in controlled atmosphere furnaces using air-SO_2 gas mixtures (either non-equilibrated or catalyst equilibrated), and deposit compositions/fluxes of varying degrees of realism [9-11]

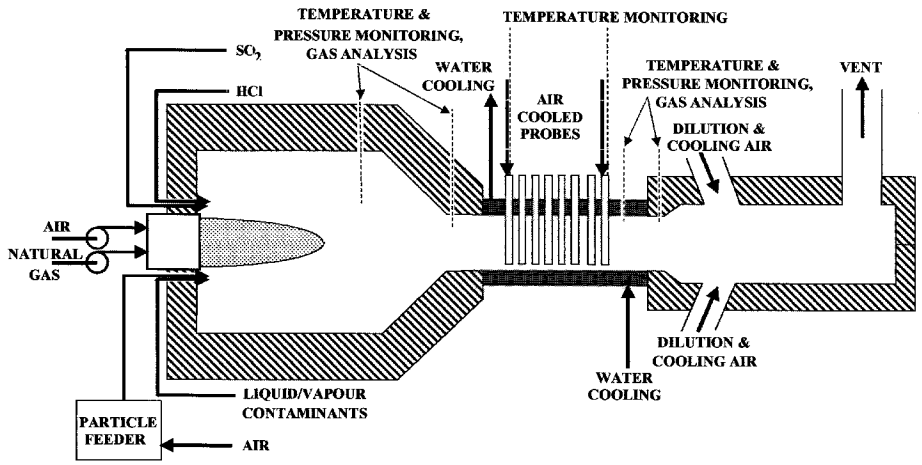


Figure 1 Cranfield University's Burner Rig Test Facility [9]

- *Burner rig tests* - carried out by six partners using rigs with different unique operating characteristics; the rigs range from those that operate with realistic combustion gas stream temperatures and flows, with samples cooled to typical operating temperatures (e.g. Figure 1 [9]) to those rigs that operate isothermally with very low combusted gas flows.

For all the burner rigs, characterising the operating conditions and resulting sample exposure environments is particularly important if the results are to be compared and contrasted usefully via the coatings performance database.

Performance Evaluation

In order to compare data from the various different oxidation and corrosion tests within a database structure, it has been necessary to agree a methodology for collecting such data in a standardised way. The route adopted is based on dimensional metrology of samples before and after exposure to determine the performance of the materials at a number (at least 24) of points in each different anticipated zone of behaviour around each sample (so differently shaped samples in the various different tests had varying numbers of measurements taken, but at least 24 in each distinct environment). Before exposure samples have to be measured using accurate contact metrology. After exposure, it is necessary to make cross-sections through each sample and carry out measurements on these sections (Figure 2). Metal losses can be determined by comparison of the measurements made before and after the sample exposure. Then it is possible to carry out statistical interpretation of the oxidation/corrosion degradation data, as illustrated in Figure 3, which shows the degree of metal damage (defined as the loss of metal during exposure, i.e. from Figure 2 the change in value of the sum of $A+B+C$) in terms of percentage probability of this level of damage not being exceeded.

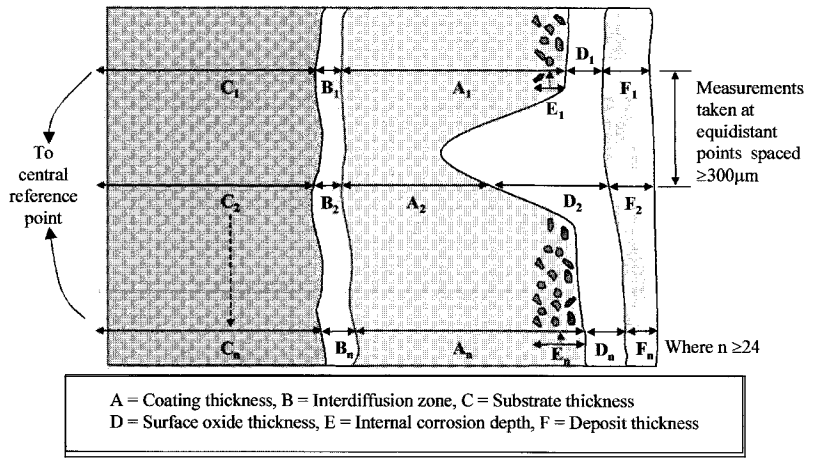


Figure 2 Schematic diagram of features to be measured on a cross-section through an exposed oxidation/corrosion sample [10]

This approach to evaluating the performance of materials in corrosion tests and plant exposures was developed in the UK as part of development programmes for advanced coal-fired power generation systems in the late 1980s [eg 12] and has since been used in a series of EU and ECSC funded programmes [e.g. 10]. This approach to the assessment of sample performance forms one of the bases for the EU funded TESTCORR programme that investigated the development of standardised test methods for high temperature corrosion testing [13].

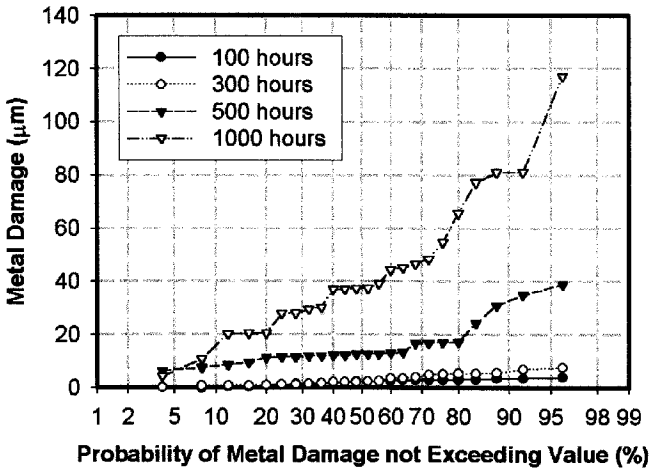


Figure 3 Example of a probability plot from a laboratory hot corrosion test [10] (IN738LC exposed at 700°C in air-260 vpm SO_X-300 vpm HCl, with flux of 1.5 µg/cm^2/hour of 80/20 $(Na/K)_2SO_4$)

Mechanical Property Characterisation

Within this COST activity, mechanical property characterisation is being carried out by seven partners (Table 3). These activities are investigating the erosion, thermo-mechanical fatigue (TMF), high and low cycle fatigue (HCF & LCF), ductile-brittle transition temperatures (DBTT), thermal expansivity and Young's modulus of selected coatings.

Table 3 Mechanical Property Characterisation

Organisation	Erosion	Thermo-Mechanical Fatigue (TMF)	High & low cycle fatigue (HCF & LCF)	Ductile-brittle transition Temperature (DBTT)	Thermal expansion	Young's modulus
ALSTOM POWER			Y			
Cranfield University	Y					
Jülich					Y	Y
Lufthansa	Y					
NPL		Y		Y		Y
Nuovo Pignone						Y
PowerGen		Y				

Test Methods and Performance Evaluation

Each of the mechanical properties is being characterised using well established test methods:

- Erosion testing is being carried out by Cranfield University in a test rig capable of achieving particle velocities of up to 300 m/s in heated air of temperatures up to 900°C [14]. The damage level is determined by mass loss measurements.
- Thermo-mechanical fatigue (TMF) is being carried out using two different test methods:
  - Temperature and load cycling (out of phase) using standard tensile test samples in a servo-hydraulic mechanical test machine. The numbers of cycles to coating cracking were determined.
  - Induction heating of coated test samples and determination of the numbers of cycles to the commencement of TBC spallation (Figure 4).
- High and low cycle fatigue (HCF and LCF) testing is being carried out at temperatures up to 950°C using Amsler vibrophore and servo-hydraulic mechanical test machines respectively.
- Ductile-brittle transition temperature (DBTT) is being determined at NPL using the small punch test method (Figure 5); DBTT can be determined in the temperature range 400 – 1000°C with coating strains of up to 10% [15].
- Thermal expansivity in the temperature range ~20 - 1400°C is being determined using a dilatometer
- Young's modulus is being determined using two distinct test methods:
  - impact resonance at NPL
  - 4-point bend tests at Nuovo Pignone

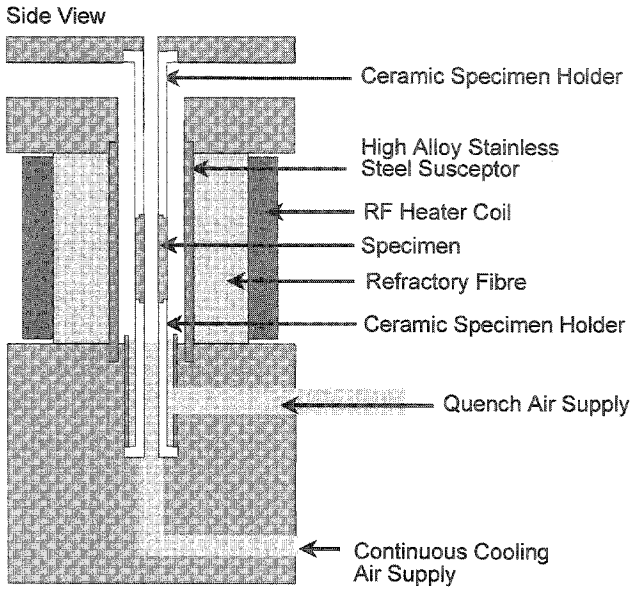


Figure 4 Simultaneous thermo-mechanical fatigue and oxidation being carried out by PowerGen

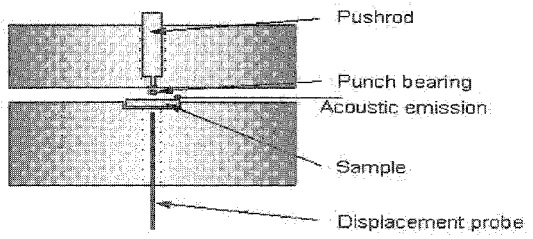


Figure 5 NPL's small punch test method for the determination of coating DBTT [15]

Thermophysical Property Determination

Three partners are investigating the thermophysical properties of selected current and candidate gas turbine coatings (Table 4). These properties include thermal diffusivity (see Figure 6 for equipment details), specific heat capacity and density (and/or porosity) [16].

Test Methods and Performance Evaluation

Each property determination has used a distinctive test method, the details of which are beyond the scope of this paper, but are given elsewhere [16] - the methods and temperature ranges over which the properties are being determined are listed below. An example of the data obtained by combining the results of these tests is given in Figure 7.

Table 4 Thermophysical Property Test Matrix

Property	Test method	Temperature range	Organisation
Thermal diffusivity	Laser flash (Figure 6)	~20 – 1300°C	CESI, Jülich
Specific heat capacity	Differential scanning calorimeter (DSC)	~100 – 1250°C	CESI
Coating density / porosity	Mercury porosimetry; image analysis	-	Ansaldo, CESI, Jülich

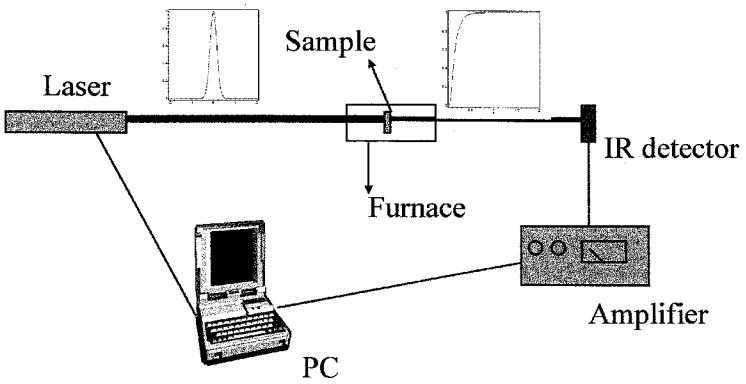


Figure 6 Diagram of Laser Flash Technique for determining thermal diffusivity [16]

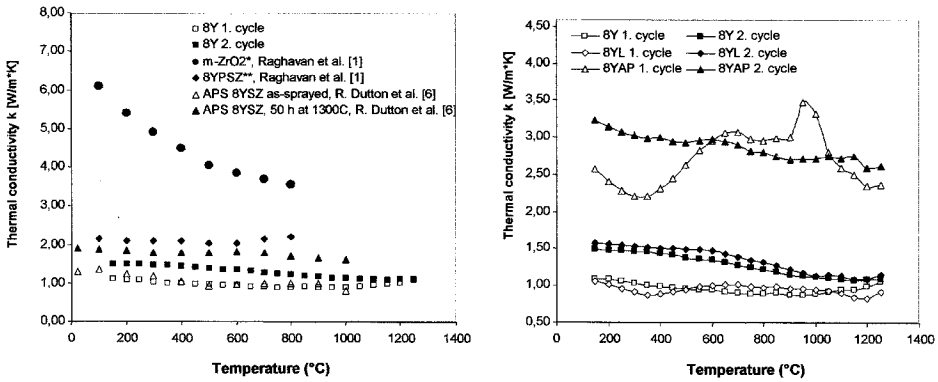


Figure 7 Examples of results of thermal conductivity determinations [16] (thermal conductivity = thermal diffusivity x specific heat x density)

Database of Coating Performance

The database structure was designed to incorporate two basic types of information. Firstly the database was to include the results of all testing conducted within the COST522 Protective Systems testing programme: details of all these tests and performance measurements have been described previously within this paper. Secondly, the database was to accommodate information resulting from microstructural characterisation of as-received and tested coating systems. This was to incorporate example images of the microstructure at critical regions of the coating system.

As with many other materials database systems there are three broad categories of materials data to be considered:

- *Material Information* - incorporating all data that relates to the specification of the material system, encompassing both the substrate material and the applied coating. This includes composition, heat treatment and other material processing parameters.
- *Test Environment* - including all information regarding the environment and conditions that the test specimen was exposed to. For example this could include test temperature, applied stress or strain, and compositions of gases or corrosive deposits applied.
- *Test Results* - the raw test results that arise from each test, presented both in a tabular and graphical manner. Standard graphical formats have been generated for each property type.

Each of these categories was considered when developing the data model for the database.

Data Model

A data model that reflects the inherent structure of the electronic database was developed. Entity relation diagrams were used to describe the relationship between the different data types. An example is given in Figure 8, which describes the data model for the coatings database system. Each rectangle represents a group of properties, which is linked to another group of properties in a "one to many" relationship. Examples of database fields within each

group are given in the circles. The three rectangular category boxes have been used to identify which property groups belong to which data category.

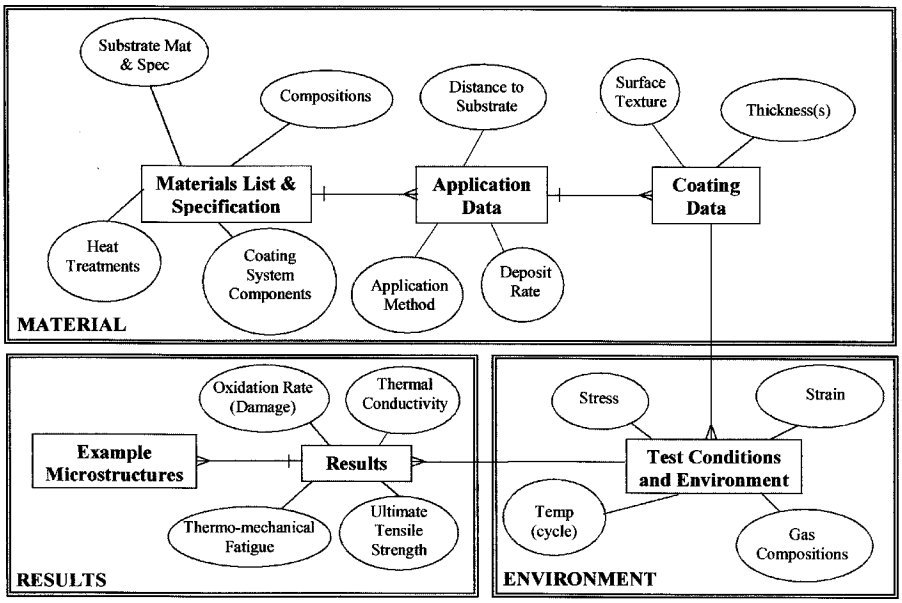


Figure 8 Entity Relationship Diagram for the Coatings Database

Database Implementation and Population

With the data model in place, the database was built by using a series of Microsoft Excel spreadsheets, which were linked together using a web page. Standard data collation spreadsheets were produced for each property type and issued to each partner. This allowed data generated at multiple test sites to be collated together in a standard format that was suitable for addition to the database.

Materials List

Central to the entire database structure is a list of materials that precisely defines each substrate material and coating, it also provides each one with a unique reference number (material number). This practise allows material properties to be explicitly linked to specific material systems, as described by Piearcey [17], and is a prerequisite for any future exploitation of the material systems in gas turbine applications.

An extract from the materials list is given in Table 5. This highlights how materials and coatings are defined in terms of material specification, product form, thermo-mechanical condition, and basic chemistry. It also shows how this definition is linked to a material identification number and common name. All populated property tables are linked back to the materials list via the materials identification number. Substrate materials and coatings are listed individually, and one or more of each are combined to create a materials system (e.g.

Table 5 Extract from the Coatings Database Materials List

Material Number	Common Name	Form of Material	Powder ID	Material System Components	Manufacturing/ Apllication Method	Thermo-mechanical Condition	Part types	Chemical Type
55	CMSX-4	Casting	-	-	Investment SXL	Full HT	Blades, Vanes Segments	Ni:9.7Co6.5Cr6.5Ta6.4W5.6 Al3Re1Ti0.6Mo0.1Hf
65	Inconel 738	Casting	-	-	Investment CC	Soln HT & Aged	Blades, Vanes Segments	Ni-16Cr8.5Co3.5Al3.5 Ti2.6W1.7Ta1.7Mo
152	Sicoat 2453	Coating			Plasma sprayed			Ni-10Co28Cr12Al3Re0.6Y
168	RT22LT	Coating			Electroplate & aluminised			Pt-Al
201	CMSX-4 RT22LT	Mat System	-	MATS 55,168	-	Full HT	Blades, Vanes Segments	Ni-19.5Cr2.2Ti1.4Al0.1C / Pt-Al
202	CMSX-4 Sicoat 2453	Mat System	-	MATS 55, 152	-	Full HT	Blades, Vanes Segments	Ni-19.5Cr2.2Ti1.4Al0.1C / Ni-10Co28Cr12Al3Re0.6Y
203	Inconel 738 RT22LT	Mat System	-	MATS 65, 168	-	Full HT	Blades, Vanes Segments	Ni-16Cr8.5Co3.5Al3.5 Ti2.6W1.7Ta1.7Mo / Pt-Al
204	Inconel 738 Sicoat 2453	Mat System	-	MATS 65, 152	-	Full HT	Blades, Vanes Segments	Ni-16Cr8.5Co3.5Al3.5 Ti2.6W1.7Ta1.7Mo / Ni-10Co28Cr12Al3Re0.6Y

Table 6 Example Data Collation Table for Hot Corrosion Tests

Material Number	Test ID	SO_2 in Gas	HCl in Gas	O_2 in Gas	N_2 in Gas	Deposit Na_2SO_4	Deposit K_2SO_4	Re-deposit Time	Test Temp	Exposure Time	Mean Damage	Median Damage	Max Damage	Image file
-		vppm	vppm	%Vol	-	Wt%	Wt%	hours	°C	hours	µm	µm	µm	(path)
203	1_Cr	2686	293	20	Bal.	8.31	91.69	20	650	100	2.18	2.3	5.3	1Cr_100a.gif
203	1_Cr	2686	293	20	Bal.	8.31	91.69	20	650	200	3.58	3	8.5	1Cr_200a.gif
203	1_Cr	2686	293	20	Bal.	8.31	91.69	20	650	500	4.85	5.8	8.8	1Cr_500a.gif
203	1_Cr	2686	293	20	Bal.	8.31	91.69	20	650	1000	5.86	6.25	14.3	1Cr_1000a.gif
203	1_Cr	2686	293	20	Bal.	8.31	91.69	20	650	2000	16.96	14.8	48.7	1Cr_2000a.gif

material number 201). Additional property tables that are not shown here are used to define the specified composition and mechanical properties of substrate alloys and the properties of the original coating powders.

As explained previously the database has been designed to accommodate many different property data types. Examples of how the database can be used to store property data of various kinds follow.

Hot Corrosion Data

An extract from a data collation table for a series of hot corrosion tests conducted on IN738LC specimens coated with RT22LT (material number 203) is provided in Table 6. The database also provides the results in graphical form. Standard graphical presentation formats have been generated for each of the main properties and an example for the data in Table 6 is given in Figure 9. It shows the variation of corrosion damage with time for material 203 at 650°C, and the affect of different deposit compositions. Interpretation of this type of graph needs to be carried out carefully in conjunction with an appreciation of the errors involved in determining the corrosion damage: this information is provided by damage probability type plots (of the form illustrated in Figure 3). Table 6 also highlights the provision for storage of electronic image files. The final column in the table provides an electronic link to a microstructural image that is representative of the material system exposed to the conditions described in that data row. An example is given in Figure 10 for test 1_Cr after 2000 hours, with test conditions described in Table 6.

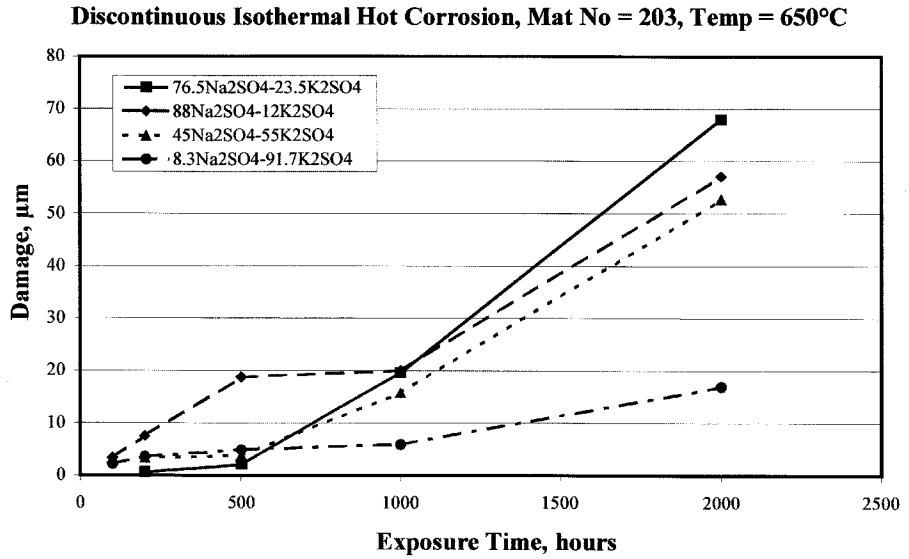


Figure 9 One of the Standard Graphical Formats for Hot Corrosion Data

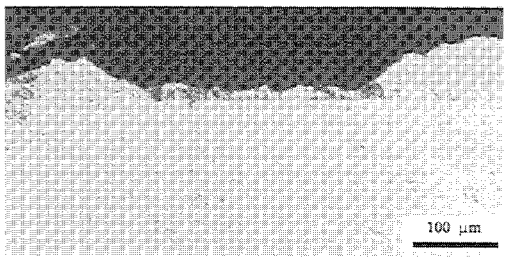


Figure 10 Microstructure of Material Number 203 exposed in Hot Corrosion Test 1_Cr for 2000 hours

Ductile Brittle Transition Temperature Data

NPL has conducted small punch testing to obtain the Ductile Brittle Transition Temperatures (DBTT) for a number of material systems, using the methods described above under mechanical property characterisation. A standard data collation spreadsheet was again used to record the results. An extract from this spreadsheet is given in Table 7, and these results are presented graphically using the standard format for DBTT data in Figure 11. It can be seen that the results for material 201 were inconclusive as all tests conducted in between room temperature and 930°C cracked. However, the results for material 202 indicate the DBTT to be somewhere between 650 and 675°C.

Table 7 Example Data Collation table for DBTT results

Material Number	Test ID	Test Temp	Cracked	AE Peak Energy	Strain	Image file
-	-	°C	Yes/No		%	(path)
201	1_NPL	20	Yes	65600	1.48	1_NPL_20a.gif
201	2_NPL	801	Yes	59400	4.31	2_NPL801a.gif
201	3_NPL	801	Yes	8051	4.08	3_NPL801a.gif
201	4_NPL	820	Yes	3308	0.21	4_NPL820a.gif
201	5_NPL	840	Yes	4244	2.64	5_NPL840a.gif
201	6_NPL	930	Yes	1297	3.39	6_NPL930a.gif
202	7_NPL	20	Yes	65000	1.25	7_NPL20a.gif
202	8_NPL	500	Yes	65100	3.9	8_NPL500a.gif
202	9_NPL	600	Yes	65300	5.98	9_NPL600a.gif
202	10_NPL	650	No	42900	10	10_NPL650a.gif
202	11_NPL	675	Yes	4941	7.7	11_NPL675a.gif
202	12_NPL	700	No	767	10	12_NPL700a.gif
202	13_NPL	750	No	1603	10	13_NPL750a.gif

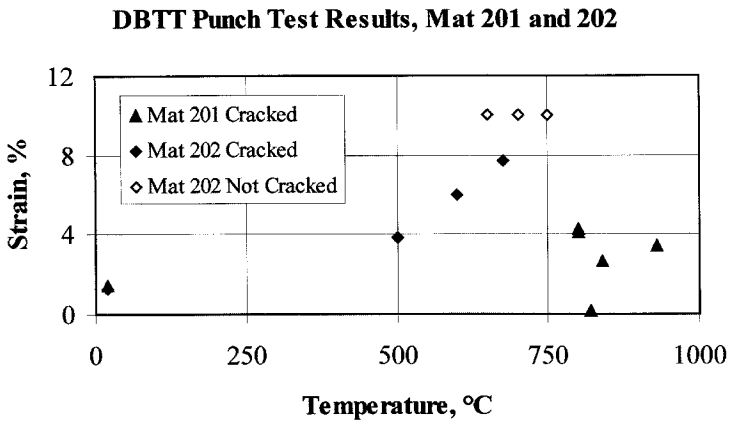


Figure 11 Example of DBTT results obtained from NPL's small punch test method

Summary

The development of a database of quantitative information on the environmental degradation of industrial gas turbine coatings is being carried out within the Protective Systems Work Package of the European COST522 programme. Materials systems targeted in this activity are current standard and new coatings applied to CMSX-4 and IN738LC substrates.

Test work on these coatings is covering degradation due to isothermal oxidation, cyclic oxidation, laboratory hot corrosion and burner rig testing, as well as synergistic degradation from erosion-oxidation and thermal fatigue. In addition, tests are being carried out to determine the mechanical and thermal properties of the coatings, for example: ductile-brittle transition temperatures and thermal conductivity.

The data being produced by these extensive testing activities are being compiled into a database. This database is being populated with large quantities of data that are being produced by the partners in this COST522 programme. These data can be displayed in the form of tables or graphically, as required.

The database is intended to facilitate the selection of coatings for industrial gas turbines by allowing the comparison of coating performances in different degradation regimes, as well as mechanical and thermal properties, produced using standardised test and reporting methodologies.

Acknowledgements

The work described in this paper has been made possible by the collaboration of all the partners within the COST522 Protective Systems Work Package. Funding for these participants has been supplied by individual companies and by some national government funded programmes. The authors wish to acknowledge funding from ALSTOM POWER and

the UK Department of Trade and Industry Cleaner Coal Programme. For one author, DB, work was carried out within the European Commission's Research and Development Programme.

References

[1] D.H. Allen, J.E. Oakey and B. Scarlin, *'The New COST Action 522 – Power Generation in the 21st Century:- Ultra Efficient, Low Emission Plant'*, Materials for Advanced Power Engineering 1998, Eds J Lecomte-Beckers et al (1998) pp1825-1838.

[2] S.T. Scheirer and R. Viswanathan, *'Evolution of Hot Section Technology'*, ASM Materials Solution Conf. 2000.

[3] T. Schulenberg, *'New development in Land-based Gas Turbine Technology'*, Materials for Advanced Power Engineering 1998, Eds J Lecomte-Beckers et al (1998) pp849-859.

[4] Proc. Corrosion in Advanced Power Plants, Special Issue of Materials at High Temperatures 14 (1997).

[5] C.T. Sims., N. S. Stoloff and W.C. Hagel, "Superalloys II", Wiley (1987).

[6] J.R. Nicholls, Designing Oxidation Resistant Coatings, JoM (2000).

[7] J.R. Nicholls and R. Wing, 'Advances in Coating Systems for Utility Gas Turbines', Materials for Advanced Power Engineering (2002).

[8] "Hot Corrosion Standards, Test Procedures and Performance", High Temperature Technology 7 (4) (1989).

[9] N.J. Simms, J.R. Nicholls and J.E. Oakey, 'Materials for Solid Fuel Fired Gas Turbines: Burner Rig and Laboratory Studies', Materials Science Forum Vols 369-372 (2001) pp 833-840.

[10] N.J Simms, P.J. Smith, A. Encinas-Oropesa, S Ryder, J.R. Nicholls and J.E. Oakey, Development of Type II Hot Corrosion in Solid Fuel Fired Gas Turbines', *in* Lifetime Modelling of of High Temperature Corrosion Processes, eds M Schütze et al, EFC No. 34 (2001) pp 246-260.

[11] B Waschbüsch and H-P Bossmann, Influence of the Salt Composition on the Hot Corrosion Behaviour of Gas Turbine Materials, *in* Lifetime Modelling of of High Temperature Corrosion Processes, eds M Schütze et al, EFC No. 34 (2001) pp 261-273.

[12] N. J. Simms and J. E. Oakey, 'Measurement of Erosion/Corrosion Damage to Gas Turbine Components', ASME Turbo Expo '96, Paper No. 96-GT-396, ASME, Atlanta (1996).

[13] 'Draft Code of Practice for Discontinuous Corrosion Testing in High Temperature Gaseous Atmospheres', European Commission Project SMT4-CT95-2001 'TESTCORR', ERA Technology, UK (2000).

[14] R.G. Wellman, 'Modelling the erosion of electron beam physical vapour deposited thermal barrier coatings', Ph.D. Thesis, Cranfield University (2001) p96.

[15] S.R.J Saunders, J.P. Banks and M. Wright, Measurement of Ductile Brittle Transition Temperature of Coatings Using the Small Punch Test, NPL Report MATC (A) 60 (2002).

[16] F Cernuschi and S Ahmaniemi, COST522 Protective Systems, Progress Reports (2002)

[17] B J Piearcey, "Materials Design Databases - Towards an Expert System", Materials Engineering in Turbines and Compressors - 3rd International Charles Parsons Turbine Conference, Newcastle (1995).

WROUGHT NI-BASE ALLOYS FOR ADVANCED GAS TURBINE DISC AND USC STEAM TURBINE ROTOR APPLICATIONS

J. Rösler[1], B. Böttger[2], M. Wolske[3], H.J. Penkalla[4] and C. Berger[5]
[1]Technical University Braunschweig, 38106 Braunschweig, Germany
[2]ACCESS e.V., 52072 Aachen, Germany
[3]RWTH Aachen, 52056 Aachen, Germany
[4]Forschungszentrum Jülich, 52425 Jülich, Germany
[5]TU Darmstadt, 64229 Darmstadt, Germany

Abstract

Future requirements for gas turbine disc and ultrasupercritical (USC) steam turbine rotor applications necessitate advanced wrought Ni-base alloys, exhibiting excellent fabricability in addition to sufficient long term microstructural and mechanical stability. In this article, potential candidates are discussed. It is concluded that material solutions are available for operation conditions around 600°C but not for temperatures of 700°C and above, as required for the construction of future USC steam turbines. Alloy development strategies are suggested in order to close this gap.

Keywords: Superalloys, alloy development, casting, forging, phase transformation, creep, creep crack growth.

Introduction

Wrought Ni-base alloys are of increasing interest for rotor applications in stationary gas turbines for two reasons: (i) turbine inlet temperatures and compressor pressure ratios are steadily elevated for efficiency reasons. Consequently, heat input from the hot gas side into the rotor is increasing in parallel with the cooling air temperature. Both effects drive rotor temperatures up unless intercooling is used, which is costly and diminishes efficiency; (ii) high mass flow engines offer usually lower investment costs per unit of installed power. Thus, the trend to larger machines continues, leading to larger blades and increased centrifugal loading of the rotor [1].

Similar trends can be noted in the steam turbine industry. The objective of the European THERMIE project is to construct ultrasupercritical (USC) steam turbines with steam inlet temperatures of 700°C and above, leading to efficiency levels of about 55% (today: < 48%) [2, 3]. As steam turbine components are uncooled, replacement of ferritic steels by Ni-base alloys will be mandatory in the hottest engine sections. This statement holds true for piping, casing and rotor applications. Nevertheless, the discussion in this article will concentrate on the latter component as it is probably the most challenging.

On first sight one would tend to believe that numerous Ni-base alloys which are used in the aeroindustry are available for the above applications [4]. However, closer inspection reveals several requirements surpassing aeroengine needs: (i) due to component size and weight (sometimes more than 10 tons), alloy fabricability is of paramount importance. Highly alloyed materials with good strength characteristics at service temperature may be unsuitable as their flow strength at forging temperature may be too high and / or their tendency for defect

formation upon remelting of large ingots may be unacceptable. Powder metallurgy, which avoids the latter issue, seems also impractical for the component size of interest here; (ii) service durations of about 200000 hours at 700°C in case of future USC steam turbine applications necessitate exceptional microstructural stability and long term strength. In addition, the loading scenario is quite different with emphasis on creep and creep crack growth rather than on fatigue (crack growth), as stationary turbines are operating under full load for most of the time. Crack growth is of interest, because rotor design in stationary turbines requires damage tolerance. Thus, component integrity must be demonstrated for defect sizes up to the detection limit of the ultrasonic inspection method.

Some of the wrought Ni-base alloys under consideration for advanced gas- and steam turbine disc applications are listed in table 1. They can be categorized in three groups according to their main hardening mechanism, namely solid solution and carbide strengthened (group 1), γ' strengthened (group 2) and γ' / γ'' strengthened (group 3). Amongst those materials, only Inconel 706 is currently used as disc material in stationary gas turbines, while Inconel 718 seems in the state of introduction [35]. A unique feature of these " group 3" materials is the high lattice parameter misfit between γ'' and γ-phase. It ensures excellent ambient temperature yield strength at moderate precipitate content, i.e. moderate amount of alloying elements. This can be best appreciated on the example of Inconel 706, exhibiting a yield strength above 1000 MPa despite a relatively lean composition. Consequently, fabricability is excellent compared to γ'-hardened materials of similar strength. Furthermore, the sluggish precipitation kinetics of the γ''-phase ensures good weldability as residual stresses upon cooling remain low. However, the disadvantage of this material class is the limited stability of the γ''-phase, which is also a consequence of the large lattice misfit. Consequently, Inconel 706 or 718 for rotor applications are excellent choices provided temperatures are moderate (say below 500°C). Under the prospective loading conditions of future USC steam turbines, the situation might be quite different. Thus, it is worthwhile considering other classes of wrought Ni-base alloys as well.

It is the objective of this article to review the potential of wrought Ni-base alloys for rotor and disc applications under extreme temperature conditions as outlined above. To keep this task feasible, the discussion concentrates in section 2 on typical representatives of each material group, namely Inconel 617, Waspaloy and Inconel 706. Consideration is given to important fabricability aspects (remelting and forging), microstructural stability and mechanical performance (creep and creep crack growth) during long term service. Based on this discussion, general conclusions regarding advantages and disadvantages of the different alloys and alloying concepts are drawn and suggestions for advanced alloy designs are given in chapter 3. The presented results have been obtained in a collaborative research effort of the 5 research establishments listed above, funded by the Deutsche Forschungsgemeinschaft.

Group	Alloy	Composition						
1	Inconel 617	Ni	Cr	Co	Mo	Nb	Al	Ti
		Bal.	22.0	12.9	9.0	-	1.1	0.5
		Fe	Mn	Si	C	B	Zr	W
		0.5	0.03	0.14	0.06	0.001	-	-
	Haynes 230	Ni	Cr	Co	Mo	Nb	Al	Ti
		Bal.	22.0	-	2.0	-	0.3	-
		Fe	Mn	Si	C	B	La	W
		-	0.5	0.4	0.10	0.000	0.02	14.0
2	Waspaloy	Ni	Cr	Co	Mo	Nb	Al	Ti
		Bal.	19.4	14.0	4.5	0.01	1.2	3.1
		Fe	Mn	Si	C	B	Zr	W
		0.5	0.05	0.04	0.033	0.005	0.06	-
	Nimonic 263	Ni	Cr	Co	Mo	Nb	Al	Ti
		Bal.	20.0	20.0	5.9	-	0.5	2.1
		Fe	Mn	Si	C	B	Zr	W
		-	0.4	0.3	0.06	0.001	0.02	-
	Udimet 500	Ni	Cr	Co	Mo	Nb	Al	Ti
		Bal.	18.0	18.5	4.0	-	2.9	2.9
		Fe	Mn	Si	C	B	Zr	W
		-	-	-	0.08	0.006	0.05	-
3	Inconel 706	Ni	Cr	Co	Mo	Nb	Al	Ti
		Bal.	16.0	-	-	3.0	0.2	1.6
		Fe	Mn	Si	C	B	Zr	W
		37.0	-	0.08	0.01	0.003	-	-
	Inconel 718	Ni	Cr	Co	Mo	Nb	Al	Ti
		Bal.	19.0	0.0	3.0	5.1	0.5	0.9
		Fe	Mn	Si	C	B	Zr	W
		18.5	0.2	0.2	0.04	0.000	0.00	0.0
	Inconel 625	Ni	Cr	Co	Mo	Nb	Al	Ti
		Bal.	21.5	0.0	9.0	3.6	0.2	0.2
		Fe	Mn	Si	C	B	Zr	W
		2.5	0.2	0.2	0.05	0.000	0.00	0.0

Table 1: Chemical composition (in wt.-%) of selected wrought Ni-base alloys. They are grouped in three classes according to their main hardening mechanism (group 1: solid solution and carbide strengthened; group 2: γ'-strengthened; group 3: γ'/γ''-strengthened). Note that most particle strengthened alloys (groups 2 and 3) contain also considerable amounts of solid solution strengtheners (Mo, W) [7]. The composition of Inconel 706, Inconel 617 and Waspaloy corresponds to the material tested by the authors.

2. Analysis of commercial Ni-base alloys

2.1 Remelting

After vacuum induction melting, ingots are refined by electroslag or vacuum-arc remelting. Main objectives are to remove trace elements as well as to eliminate macro-segregation, defects and porosity. As ingot size increases, it becomes increasingly difficult to keep the solidification parameters in an acceptable range. For example, sufficient power input is needed to avoid white spots, which in turn diminishes the temperature gradient G at the solidification front and, thus, increases the risk of freckle formation. Freckling is a kind of macrosegration caused by an unstable density distribution in the liquid due to microsegregation. When microsegregation during solidification is such that light elements are concentrated in the interdendritic liquid, convective flow of interdendritic liquid is triggered even in the case of a planar solidification front, leading to segregation of macroscopic dimensions (fig. 1) [5, 6].

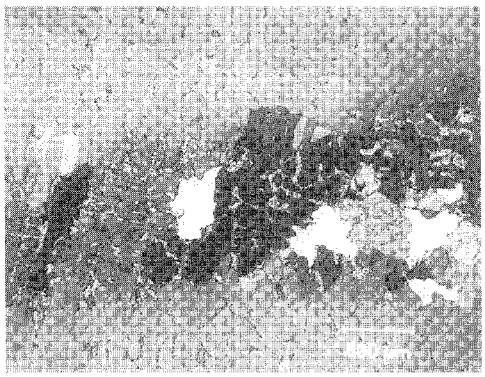


Fig. 1: Freckle formation in a Ni-base superalloy.

In this paper a freckle criterion is used which does not describe the effects of the solidification process parameters as done by other authors [8-11], but focuses on the specific tendency of the alloys for freckle formation. This tendency can be assessed from the composition distribution along the mushy zone which has to be calculated by an appropriate microsegregation model. In this work a unit cell phasefield model has been used. The liquid compositions from the simulation are transformed to the local liquid density ρ using the empirical approach of Sung et al [12]:

$$\rho^{-1} = \sum_k \frac{c_{liq}^k}{\rho_{\mathrm{Re}f}^k + \Lambda^k\left(T - T_{\mathrm{Re}f}^k\right)}. \tag{1}$$

According to this approximation, ρ can be calculated from the densities of the pure element melts ρ^k_{Ref} and the thermal expansion coefficients Λ^k given at a reference temperature T^k_{Ref} by molar volume averaging with the molar compositions c^k_{liq}.

Now a buoyancy force $f_B(h)$ is calculated for all positions h in the mushy zone. This is done by integration of the liquid density differences in the melt between this point and the top of the mushy zone, weighting with the liquid fraction $f_L(z)$:

$$f_B(h) = \int_{z=0}^{h} f_L(z)(\rho(z) - \rho(0))dz . \tag{2}$$

To obtain a freckle criterion which is independent of the temperature gradient, integration is done over the temperature T instead of the height h:

$$f_B^*(T) = \int_{T=T^{Liq}}^{T(h)} f_L(T)(\rho(T) - \rho(T^{Liq}))dT . \tag{3}$$

The formation of a freckle will be initiated at the point where the value of f^*_B is at a maximum, defining the freckle parameter f_{FR}:

$$f_{FR} = \max(f_B^*(T)). \tag{4}$$

If no liquid density inversion occurs at all, the value of f^*_B is arbitrarily taken at the temperature where the fraction liquid is 0.5.

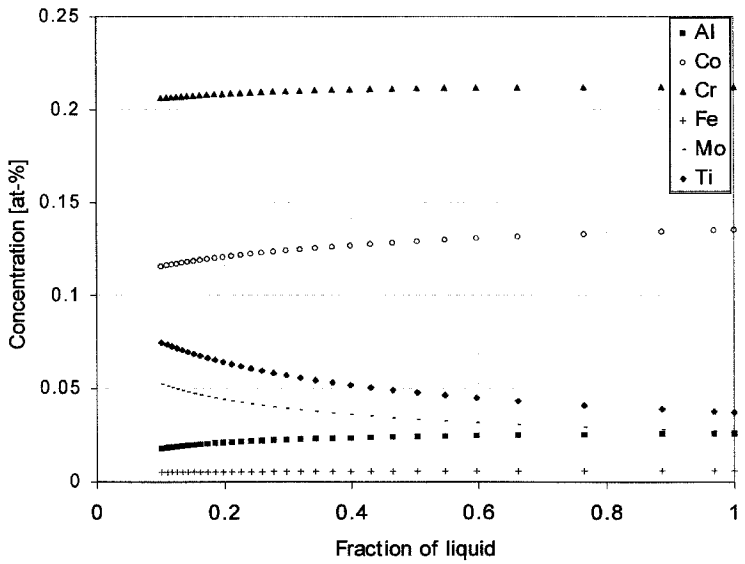


Fig. 2: Calculated element partitioning during solidification of Waspaloy.

Fig. 2 illustrates element partitioning for Waspaloy during solidification. It is clearly seen that titanium is the main cause for freckle formation as it has a low density and is segregating interdendritically. Beneficial are the heavy elements Mo and – not shown here – Nb. This qualitative finding is reflected in the calculated freckle-numbers (fig. 3). Inconel 617 and Inconel 706 are predicted to be freckle-safe (density inversion does not happen under the solidification conditions assumed here) because of high Mo and Nb contents, respectively. In contrast, Waspaloy is predicted to be at risk. This is in good agreement with experimental findings, showing that it is virtually impossible to remelt freckle-free Waspaloy ingots with diameters > 1 m. This conclusion can be extended to all "group 2" alloys shown in table 1.

Although Nb helps to prevent freckle-formation in "group 3" alloys according to the above consideration, its strong susceptibility to interdendritic segregation can impede mechanical performance [13, 14]. This seems to be a considerable challenge in case of Inconel 718, whereas remelting of large Inconel 706 ingots to acceptable quality is standard practice in industry [15]. Furthermore, it is should be noted that freckles are found experimentally in large Inconel 706 ingots under unfavorable solidification conditions [35]. Thus, the shown freckle-numbers give trends but no guarantee for safety against freckle-formation under all solidification conditions.

In summary we note a serious shortcoming of current γ'-forming alloys with high Ti-content as far as freckle formation upon remelting of large ingots is concerned. Solid solution strengthened Ni-base alloys and Nb-containing alloys exhibit better performance, provided the Nb-content does not significantly exceed the level used in Inconel 706.

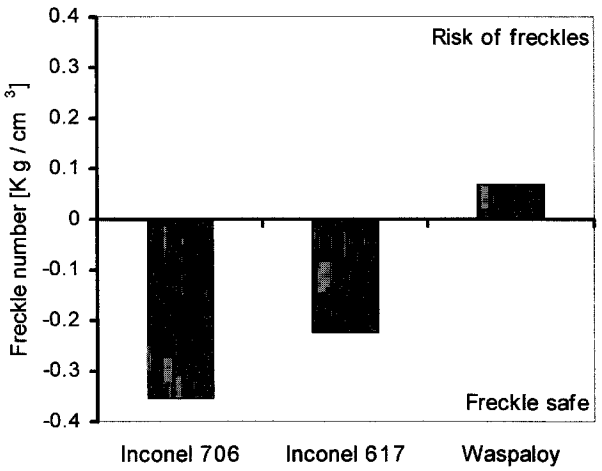


Fig. 3: Calculated freckle-numbers for Waspaloy, Inconel 706 and Inconel 617. Positive numbers indicate a risk of freckle-formation.

2.2 Forging

Forging of the remelted ingot to the final shape of the turbine disc is accomplished in several steps. Upset and hammer forging operations are performed to break up the large as-cast grain structure, while final shape is usually obtained in a closed die or, as investigated here, using several hammer forging operations. As the capacity of the largest forge presses is limited, alloy selection for stationary gas and steam turbine rotor applications must consider the flow strength at forging temperature (typically between 950°C and 1050°C). As illustrated in fig. 4, there is a considerable difference between the three alloys investigated here. Interestingly, Inconel 617 exhibits the highest load level even though Waspaloy is the stronger material at service temperature. The reason is that the strengthening phases of Waspaloy and Inconel 706 are dissolved at forging temperature, leaving solid solution strengthening as the remaining hardening mechanism. Consequently, there is a direct correlation between the molybdenum content of the investigated alloys, being highest in Inconel 617 and lowest in Inconel 706, and the flow strength.

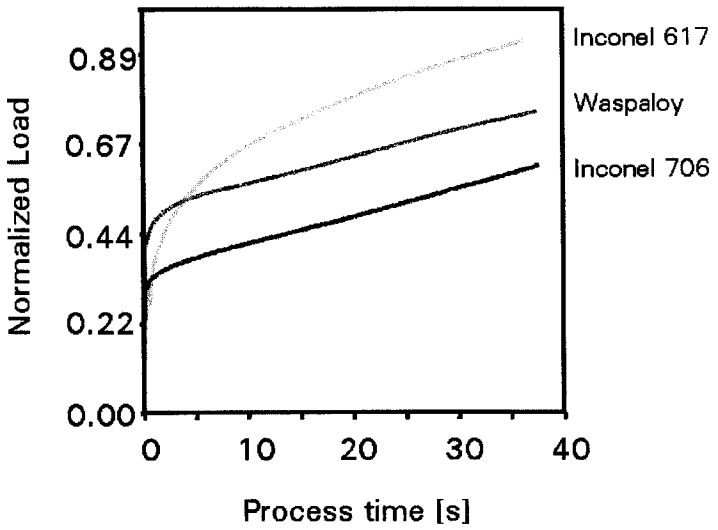


Fig. 4: FEM calculation of the normalized load for Waspaloy, Inconel 706 and Inconel 617 during upsetting (height reduction $\varepsilon_h = \Delta h / h_0 = 0.75$) using an initial grain size of 220µm.

To assess alloy performance during complex forging operations, a FEM coupled microstructure model was used, monitoring grain size and flow stress evolution as a function of temperature and deformation rate [16]. Microstructure models for simulating recrystallization and grain growth on the basis of empiric-phenomenological equations have been developed for each alloy [17, 18]. These models are in excellent agreement with experimental findings [18]. To compare forgeability of the above mentioned alloys, a sequence of upsetting and hammer forging operations were simulated via FEM coupled

microstructure simulation, assuming an initial grain size of 220 µm for all alloys. The process route describes the first forging steps of large components for USC steam turbine applications. As discussed before, fig. 4 illustrates the required loads for the first production step after remelting, i. e. upsetting of a large ingot with a height reduction of $\varepsilon_h = \Delta h / h_0 = 0.75$. Following the process route, fig. 5 shows calculated flow stresses after hammer forging of the compressed ingot in several steps to a ratio of extension by hammer forging of $\lambda_R = l_1 / l_0 = 1.345$. Calculated stresses in Inconel 617 exceed those in Inconel 706 by a factor 2. Also evaluated were the grain size evolution and the tendency to crack formation. Again, Inconel 617 showed unfavorable results as deformability is rather low and grain size distribution tends to be less homogeneous.

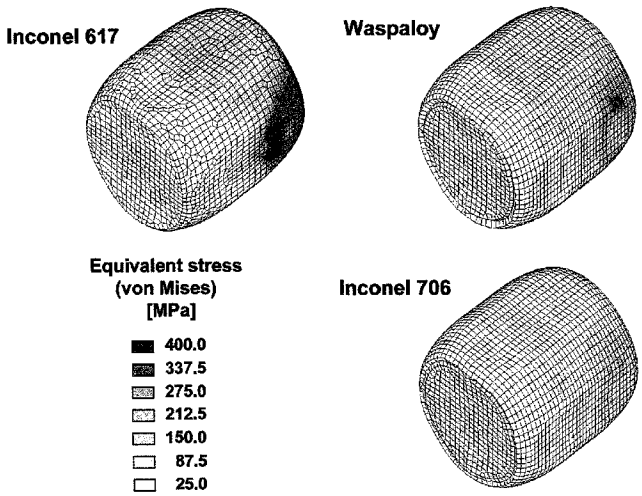


Fig. 5: Von Mises stress for Inconel 617, Inconel 706 and Waspaloy after hammer forging (initial grain size: 220µm). Three strokes of hammer forging, 90° turning of the forging dies followed by three additional strokes were needed to forge the square cross section.

In summary, group 1 alloys such as Inconel 617 turn out to be the least suitable as they rely primarily on solid solution strengthening. Inconel 706 shows the best forgeability because precipitates are completely dissolved at forging temperature and molybdenum is not present as solid solution strengthener. Establishing a suitable forging route for large Inconel 617 rotor components seems to be a formidable challenge.

2.3 Creep crack growth

Sufficient resistance against creep crack growth is an important design criterion for gas and steam turbine rotor applications, as mentioned above. While Waspaloy and Inconel 617 exhibit acceptable performance at 700°C (see fig. 6) after heat treatment according to table 2,

the situation is remarkably different in case of Inconel 706. Creep crack growth is extremely fast with propagation rates of several millimeters per hour at stress intensity factors as low as 20 $MPam^{-1/2}$ after heat treatment according to fig. 7a. This is due to environmental embrittlement of the grain boundaries [19], often referred to as SAGBO (SAGBO: stress accelerated grain boundary oxidation) [20-22] or dynamic embrittlement [23-25]. The problem is well known in industry and treatment "Bst" (see fig. 7b) is normally used as the remedy. The basic idea is to stabilize grain boundaries against embrittlement by decoration with η-phase upon exposure at 850°C. As the η-phase is consuming some of the available titanium content, less γ'/γ'' is formed during consecutive heat treatment at lower temperatures, so that the yield strength is somewhat reduced. This drawback is the reason why treatment "A" is typically used at lower temperatures (say below 500°C) while procedure "Bst" is recommended under creep conditions. Unfortunately, treatment "Bst" fails to significantly improve creep crack growth resistance when a relatively slow cooling rate of 4K/min is selected to represent large components [19, 26, 27].

The above result can be understood as follows [19, 27, 28]: as demonstrated by hardness measurements, the supersaturated solid solution at 980°C is quenched in at cooling rates of 40K/min and above, while γ'/γ''-precipitation occurs upon slow cooling. Consequently, the driving force for subsequent η-formation is greatly diminished in the latter case and grain boundary decoration does not occur to the required extent. Based on this interpretation, a revised heat treatment cycle was proposed [26, 28], whereby cooling from solutioning temperature is interrupted at the η-precipitation temperature (treatment "B", fig. 7c), as suggested earlier for other reasons by Shibata et al. [29]. The effect of this simple measure is remarkable. It diminishes the creep crack growth rate by several orders of magnitude and the data become comparable with those obtained for Waspaloy and Inconel 617 (see fig. 6).

The above results demonstrate the need for a grain boundary phase to prevent fast crack growth along grain boundaries under static high temperature loading. While η is the relevant phase in Inconel 706, similar effects can be attributed to carbides and γ'-particles along grain boundaries in case of Inconel 617 and Waspaloy, respectively.

In summary, it is noted that sufficient creep crack growth resistance can be obtained for all three materials investigated here. However, care must be taken to ensure appropriate microstructure evolution during heat treatment.

Material	Heat Treatment Step 1	Heat Treatment Step 2
Inconel 617	2 h / 1180 °C; 4 K / min to 700 °C / then AC to RT	2 h / 800 °C; AC
Waspaloy	4 h / 1080 °C; 4 K / min to 700 °C / then AC to RT	4 h / 850 °C then AC to RT 16 h / 760 °C

Table 2: Heat treatment conditions of Inconel 617 and Waspaloy (AC: air cooling, FC: furnace cooling, RT: room temperature).

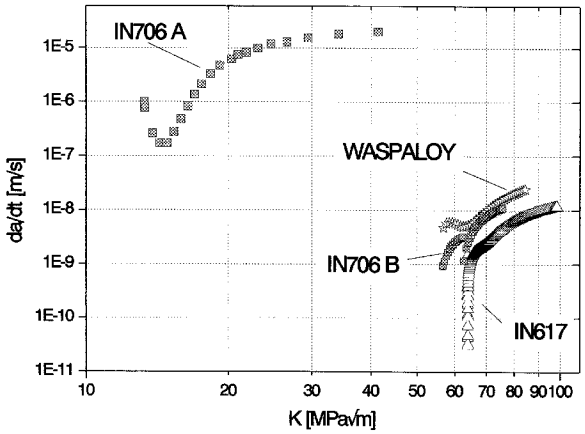


Fig. 6: Creep crack growth data of the investigated alloys at 700°C. Tests were performed using 1" compact tension (CT) specimen with 2.5 mm deep side grooves according to ASTM E 1457-92 [30].

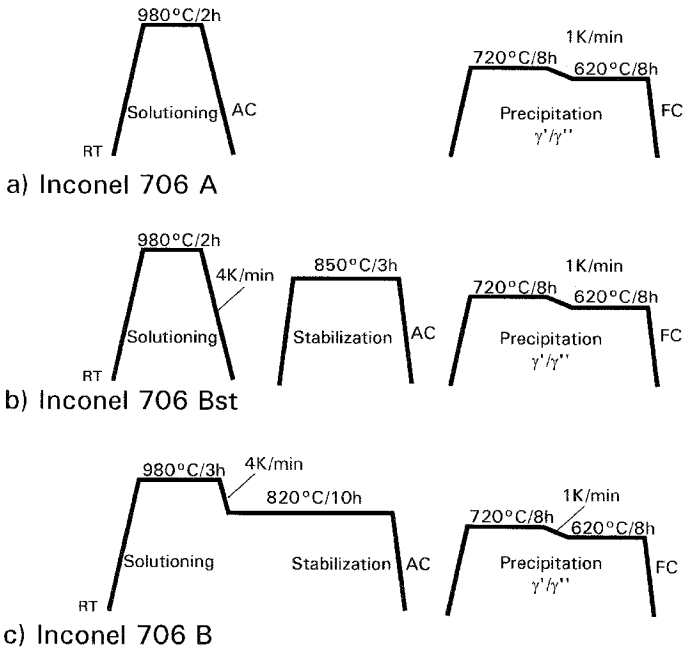


Fig. 7: Heat treatment cycles for Inconel 706 (RT: room temperature, AC: air cooling, FC: furnace cooling). The cycles shown in (a, b) are according to current industrial practice [31], while the procedure shown in c) has been suggested in [26, 28] for improved creep crack growth resistance.

2.4 Phase stability

As mentioned above, mechanical properties must not deteriorate during the component life time, thus requiring sufficient microstructural stability. This is a particular challenge for future USC steam turbine applications with 700°C/200000 h as intended operation conditions. Stationary gas turbine requirements are less severe as rim temperatures are not normally above 600°C so that phase stability is not expected to pose a particular problem for any of the three alloys investigated here. Consequently, the focus in this paragraph is on the more severe steam turbine application.

Relevant microstructural changes are summarized in figs. 8-10, whereby 750°C/5000 h is roughly equivalent to 700°C/100000 h. As a consequence of the aging cycle (850°C/2 h plus 760°C/16 h), Waspaloy exhibits a bimodal γ' size distribution with mean diameters d_{av} of 184nm and 11,3nm for the coarse and fine particle fraction, respectively (fig. 8a). After 750°C/5000 h, the fine particles are completely dissolved, leading to a monomodal distribution with d_{av} = 273nm (fig. 8b). The effects are much more severe in Inconel 706. The γ'/γ''-precipitates coarsen quickly during thermal exposure, irrespective of the initial heat treatment. Partial transformation of γ'/γ'' into intragranular η-plates occurs even after 750°C/1000 h (fig. 9b). It continues towards longer exposures and is completed after 5000 h, demonstrating that γ' and γ'' are truly metastable phases at this temperature (fig. 9c). The major microstructural change observed in Inconel 617 is the formation of film-like carbides along grain boundaries (fig. 10b). Clearly, grain size will play a role in this process and it stands to reason that film-like precipitation would not happen to the same extent at smaller grain dimensions. However, noting the tendency of the material to develop a heterogeneous grain size distribution during forging (see chapter 2.2), it seems difficult to avoid entirely large grain dimensions in a large turbine disc or rotor.

In summary, group 2 alloys such as Waspaloy, containing relatively stable γ'-precipitates, show the best microstructural stability and are well suited for applications at 700°C in that respect. The other two alloys show severe limitations, whereby phase changes are most dramatic in Inconel 706. This excludes application of Inconel 706 and other γ''-strengthened alloys in the hottest sections of future USC steam turbines, but not necessarily in advanced gas turbines.

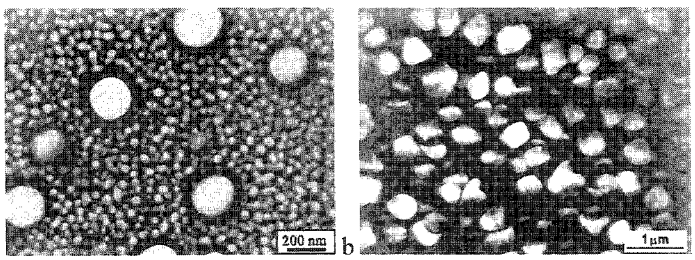


Fig. 8a,b: γ'-structure of Waspaloy after precipitation heat treatment (a) and exposure at 750°C/5000 h (b).

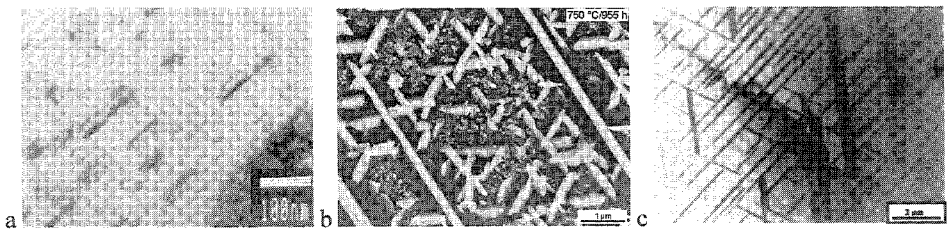


Fig. 9a-c: Microstructure of Inconel 706 after precipitation heat treatment (a), and thermal exposure (b: 750°C/1000 h; c: 750°C/5000 h). Clearly visible is the transformation of the γ′- and γ′′-phases to η-platelets.

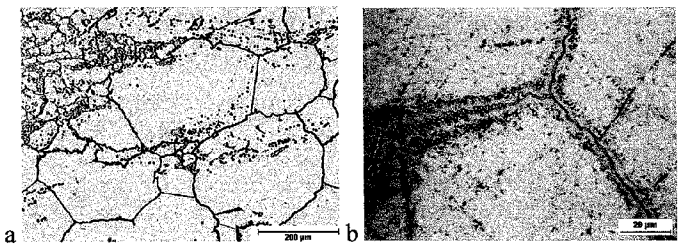


Fig. 10: Microstructure of Inconel 617 after precipitation heat treatment (a) and exposure at 650°C/15000 h (b). Note formation of film-like carbides at grain boundaries.

2.5 Creep

Creep tests were performed in a temperature range from 600°C to 800°C and durations up to approximately 15000 h. Additional tests were conducted after preaging at 750°C/5000 h, resembling a "mid-of-life" condition after 100000 h at 700°C. Even though operation conditions of future USC steam turbines are not fully defined at present, a rupture strength of 100 MPa at 700°C/100000 h is a realistic requirement. In this context, it is illustrative to inspect extrapolated values for $R_{u,10^5}$ in fig. 11. Despite the relatively high extrapolation values, a clear trend is visible. Waspaloy and Inconel 617 exceed the goal considerably. The influence of preaging on $R_{u,10^5}$ is minimal, reflecting the excellent thermal stability of the microstructure. In contrast, the strength of Inconel 706 drops dramatically with temperature, so that the target at 700°C is not met. This result is a direct consequence of the fast transformation kinetics from fine γ′/γ′′-precipitates into the η-phase (see chapter 2.4). As phase transformation is not completed after creep deformation at 650°C, pre-exposure at 750°C/5000 h leads to a drastic strength reduction compared to the as heat treated material. Conversely, prior aging barely influences the creep strength at 700°C (fig. 11), as phase transformation is already fast at that temperature.

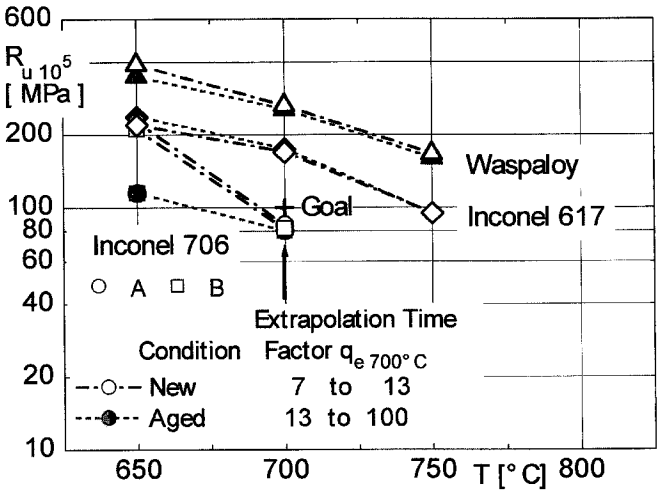


Fig. 11: Extrapolated creep rupture strength $R_{u,10^5}$ for Waspaloy, Inconel 617 and Inconel 706. Shown are data of two material conditions: as heat treated and pre-aged at 750°C/5,000h. The given extrapolation values q_e are defined as ratio between the extrapolated time (here: 100,000h) and the actual duration of the creep tests.

In summary, Inconel 706 turns out to be unsuitable for USC steam turbine applications, while Inconel 617 and Waspaloy meet the target. However, it should also be noted that the strength of Inconel 706 is quite high at temperatures typical for gas turbine applications. Noting an extrapolation factor q_e of approximately 10 at 650°C, a 100000 h creep rupture strength of about 230 MPa is expected [32].

3. Alloy development concepts

The results obtained in chapter 2 are summarized in table 3. One alloy, namely Inconel 706, exhibits excellent fabricability and is well suited for large forging products in this respect. However, application temperatures are limited to about 600°C as microstructural transformation and loss in strength is severe when this limit is exceeded considerably. Furthermore, creep crack growth can be a serious problem and the heat treatment practice used today seems unsuitable to solve that issue. It is, therefore, mandatory to modify the heat treatment along the lines discussed here and elsewhere [26, 28] to fully exploit the temperature potential of Inconel 706.

Waspaloy, representing γ′-strengthened alloys, shows a quite different behavior. Its mechanical performance is excellent. However, freckling is a serious problem and ingot diameters are limited to about 1m for that reason [34]. It means that none of the materials investigated here are satisfactory for USC steam turbine applications, while solutions for stationary gas turbines are available.

Alloy	Solification Behavior	Forgeability	Long Term Stability	Phase Stability	Creep Crack Growth
Inconel 706	+	+	-	-	0 / -*)
Inconel 617	0	-	0	0	0
Waspaloy	-	0	+	+	+

*) Depending on the heat treatment

Table 3: Ranking of the investigated alloys with respect to their fabricability, mechanical performance and microstructural stability (+:good; 0:acceptable; -:unacceptable).

Starting from the above finding, alloy development concepts for USC steam turbine applications were evaluated, following two lines:

- Development of a γ′-strengthened alloy based on Waspaloy with substantially reduced risk of freckle formation.
- Modification of Inconel 706 for improved microstructural stability and creep rupture strength.

Following the results and interpretation given in chapter 2.1, addition of Mo is one possibility for reducing the risk of freckle formation in Waspaloy. However, this measure would very likely increase the flow strength at forging temperature due to the higher concentration of solid solution strengthening elements (see comparison of Inconel 617 with Waspaloy in chapter 2.2). Another option, favored here, is to replace Ti partially by Nb[1]. As Waspaloy exceeds the creep strength target by far, some reduction of the γ′-content seems acceptable, so that the required Nb-content is relatively moderate. Consequently, the alloy composition DT 750 shown in table 4 was selected for further analysis. The calculated freckle number changes from +0.069 K·g/cm³ for Waspaloy to –0.150 K·g/cm³ for the modified composition, so that reduced tendency to freckle formation is expected. The calculated molar γ′-content at 700°C, using THERMOCALC, is 18.3% instead of 23.9%, which seems acceptable in view of the excellent creep strength of the base material.

[1] Note that similar effects can be obtained by addition of Ta. Nb was selected here as it is less costly than Ta.

Alloy	Composition						
DT 750	Ni	Cr	Co	Mo	**Nb**	Al	**Ti**
	Bal.	19.35	14.0	4.52	**1.4**	1.22	**1.5**
	Fe	Mn	Si	C	B	Zr	W
	0.57	0.05	0.04	0.033	0.005	0.06	-
DT 706	Ni	**Cr**	Co	Mo	Nb	**Al**	**Ti**
	Bal.	**18**	-	-	3	**0.55**	**1.9**
	Fe	Mn	Si	C	**B**	**Mg**	W
	22	-	0.08	0.01	**0.012**	**0.06**	-

Table 4: Compositions of the modified alloys in wt.-%. Concentration changes are highlighted.

The main cause for the severe strength loss of Inconel 706 at 700°C is the complete transformation of the strengthening phases (i.e. γ'/γ'') to η, demonstrating that γ' and γ'' are metastable at that temperature. Consequently, one must ensure sufficient stability of the strengthening phase(s) by compositional modification to meet USC steam turbine requirements. As γ'' exhibits a large misfit to the matrix, its coarsening kinetics is fast in any case, so that it appears logical to stabilize the γ'-phase. This can be achieved by slight increase of the Al-content which, at the same time, destabilizes the γ''-phase. There is, however, a further aspect to be considered. As γ'-stability and solvus temperature increase with the Al-content, it becomes more difficult to find a heat treatment window where η-precipitation at grain boundaries occurs prior to γ'-precipitation. Consequently, creep crack growth resistance may become unacceptable unless the solvus temperature of the η-phase is raised at the same time (see chapter 2.3). According to THERMOCALC simulations, two options may be explored, namely to increase the Ti-content and / or to reduce the amount of iron. Both measures were employed, leading to alloy DT 706 as illustrated in table 4. As phase stability increases with decreasing iron content, it was also possible to raise the chromium concentration from 16% to 18% for improved oxidation / corrosion resistance.

Both alloys are presently being produced in 75 kg quantities and further analysis is under way to evaluate their performance under USC steam turbine conditions.

4. Summary

Inconel 617, Inconel 706 and Waspaloy were discussed as candidate materials for gas turbine disc and USC steam turbine rotor applications. Provided operation temperatures do not exceed 600°C, Inconel 706 appears to be a viable choice as it combines excellent fabricability with acceptable microstructural stability and long term mechanical strength. It is, however, mandatory to select a heat treatment procedure along the lines outlined here to ensure sufficient creep crack growth resistance. In contrast, none of the alloys investigated here appear to be satisfactory for USC steam turbine applications with steam inlet temperatures of

700°C and above. Based on that finding, directions for further alloy development were outlined and two novel compositions suggested.

Acknowledgement

The authors would like to thank the Deutsche Forschungsgemeinschaft for financial support of this research project.

5. References

[1] G.Härkegård, J.Y.Guédon: Disc Materials for Advanced Gas Turbines, Materials for Advanced Power Engineering, 1998, 913-931.

[2] R.W. Vanstone: Advanced ("700°C") Pulverized Fuel Power Plant, Proceedings of the 5th International Charles Parsons Turbine Conference, 2000, 91-97.

[3] A. Feldmüller, T.U. Kern: Design and Materials for Modern Steam Power Plants - An Actual Concept, Proceedings of the 5th International Charles Parsons Turbine Conference, 2000, 143-156.

[4] M.J. Goulette: The Future Costs Less – High Temperature Materials from an Aeroengine Perspective, Superalloys, 1996, 3-6.

[5] A.F. Giamei, B.H. Kear: On the Nature of Freckles in Nickel Base Superalloys, Metall. Trans., 1A, 1970, 2185-2192.

[6] S.M. Copley, A.F. Giamei, S.M. Johnson, M. F. Hornbecker: The Origin of Freckles in Unidirectionally Solidified Castings, Metall. Trans., 1A, 1970, 2193-2192.

[7] C.T. Sims, N.S. Stoloff, W.C. Hagel: Superalloys II, Vieweg 1987, 587-589.

[8] P. Auburtin, S. L. Cockcroft, A. Mitchell: Liquid Density Inversions during the Solidification of Superalloys and their Relationship to Freckle Formation in Castings, Superalloys 1996, 443-450.

[9] R. Schadt, I. Wagner, J. Preuhs, P.R. Sahm: New Aspects of Freckle Formation during Single Crystal Solidification of CMSX-4, Superalloys 2000, 211-218.

[10] C. Beckermann, J.P. Gu, W.J. Boettinger: Development of a Freckle Predictor via Rayleigh Number Method for Single-Crystal Nickel-Base Superalloys, Metall. Mater. Trans. A, 31, 2000, 2545-2557.

[11] P. Auburtin, T. Wang, S.L. Cockcroft, A. Mitchell: Freckle Formation and Freckle Criterion in Superalloy Castings, Metall. Mater. Trans. B, 31, 2000, 801-811.

[12] P.K. Sung, D.R. Poirier, E. McBridge: Estimating Densities of Liquid Transition-Metals and Ni-Base Superalloys, Mat. Sci. Eng. A, 231, 1997, 189-197.

[13] T. Shibata, T. Takahashi, J. Taira, T. Kure: Superalloy 706 Large Forgings by ESR, Superalloys 718, 625, 706 and Various Derivatives 2001, 161-172.

[14] T. Takahashi, T. Shibata, J. Taira, T. Kure: Compositional Modification of Alloy 706, Superalloys 718, 625, 706 and Various Derivatives 2001, 269-278.

[15] A.D. Helms, C.B. Adasczik, L.A. Jackman: Extending the Size Limits of Cast / Wrought Superalloy Ingots, Superalloys 1996, 427-433.

[16] K. Karhausen: Integrierte Prozeß- und Gefügesimulation bei der Warmumformung, Umformtechnische Schriften, 52, 1994.

[17] C.M. Sellars: The physical metallurgy of hot working, Hot Working and Forming Processes, 1979, 3-15.

[18] R. Kopp, M. Wolske: Microstructure simulation of Ni based alloys, Proc. 'IV[a] Conferência Internacional de Forjamento', 2000, 42-53.

[19] J. Rösler, S. Müller, D. Del Genovese, M. Götting: Design of Inconel 706 for Improved Creep Crack Growth Resistance, Superalloys 718, 625, 706 and Various Derivatives, 2001, 523-534.

[20] W. Carpenter, B.S.-J. Kang, K.M. Chang: SAGBO Mechanism on High Temperature Cracking Behavior of Ni-base Superalloys, Superalloys 718, 625, 706 and Various Derivatives, 1997, 679-688.

[21] C.J. McMahon, Jr. L.F. Coffin: Mechanisms of Damage and Fracture in High-Temperature, Low-Cycle Fatigue of a Cast Nickel-Based Superalloy, Met. Trans. A, 1970, 3443-3450.

[22] M.M. Morra, S. Nicol, L. Toma, I.S. Hwang, M.M. Steeves, R.G. Ballinger: Stress Accelerated Grain Boundary Oxidation of Incoloy Alloy 908 in High Temperature Oxygenous Atmospheres, Adv. Cryog. Eng., 40, 1994, 1291-1298.

[23] D. Bika, C.J. McMahon Jr: A Model for Dynamic Embrittlement, Acta metall. mater., 43, 1995, 1909-1916.

[24] D. Bika, J. A. Pfaendtner, M. Menyhard, C.J. McMahon Jr: Sulfur-Induced Dynamic Embrittlement in a Low-Alloy Steel, Acta metall. mater., 43, 1995, 1895-1908.

[25] J.A. Pfaendtner, C.J. McMahon Jr: Dynamic Embrittlement in Alloy 18, Superalloys 718, 625, 706 and Various Derivatives, 2001, 701-707.

[26] J. Rösler, S. Müller, D. Del Genovese, M. Götting: Concepts for the Design of INCONEL 706 against Creep Crack Growth, HTM, 56, 2001, 359-362.

[27] S. Müller, J. Rösler: On the Creep Crack Growth Behavior of INCONEL 706, Steels and Materials for Power Plants (EUROMAT 99), 7, 2000, 352-357.

[28] S. Müller, J. Rösler: Microstructural Design of IN706-type Disc Materials for Improved Creep Crack Growth Resistance, Life Assessment of Hot Section Gas Turbine Components, 1999, 49-58.

[29] T. Shibata, T. Takahashi, Y. Shudo, M. Kushuhashi: Effect of Cooling Rate from Solution Treatment on Precipitation Behaviour and Mechanical Properties of Alloy 706, Superalloys 718, 625, 706 and Various Derivatives, 1997, 379-388.

[30] ASTM E 1457-92: Standard Test Method for Measurement of Creep Crack Growth Rates in Metals, American Society for Testing and Materials, 1992, 945-957.

[31] Inconel alloy 706, Huntington Alloys, 1974.

[32] C. Berger, J. Granacher, A. Thoma: Creep Rupture Behaviour of Nickel Base Alloys for 700°C-Steam Turbines, Superalloys 718, 625, 706 and Derivatives, 2001, 489-499.

[33] T. Shibata, Y. Shudo, T. Takahashi, Y. Yoshino, T. Ishiguro: Effect of Stabilizing Treatment on Precipitation Behavior of Alloy 706, Superalloys 1996, 627-636.

[34] K.-H. Schönfeld, Saarschmiede GmbH, Völklingen, Germany, private communication, 2000.

[35] P.W. Schilke, R.C. Schwant: Alloy 706 Use, Process Optimization, and Future Directions for GE Gas Turbine Rotor Materials, Superalloys 781, 625, 706 and Various Derivatives, 2001, 25-34.

NEW MATERIALS AND COOLING SYSTEMS FOR HIGH TEMPERATURE, HIGHLY LOADED COMPONENTS IN ADVANCED COMBINED CYCLE POWER PLANTS

Dieter E. Bohn

Institute of Steam and Gas Turbines
Aachen University
Templergraben 55
52056 Aachen, Germany
Phone: +49-241-8025450, Fax: +49-241-8022307

Abstract

Preservation of natural resources and economic points of views are the most important challenges for the future supply of electrical energy. Therefore, increasing the efficiency of combined cycle power plants towards 65% is an essential contribution.

The collaborative research center (SFB) 561 at Aachen University will create the technical and scientific know-how required to set up such power plants with elevated temperatures and a total efficiency of 65 % by the year 2025. The high maximum temperatures of these power plant cycles can only be realized by innovative material solutions, cooling concepts with porous materials for effusion / transpiration cooling and thermal barrier coatings. Design concepts of thermally and mechanically highly loaded components have to be specified by joint research of experts of fluid dynamics, experts of structure mechanics, material scientists and production engineers.

Keywords: combined cycle power plants, material science, cooling technology

Introduction

In the field of energy supply the market pressure has been the driving force for the improvement of thermal power plants in order to generate electrical energy at a minimum of costs. Therefore it is the aim to increase the efficiency of the process of energy conversion. Not only these economic but also ecological reasons like the worldwide discussion about the CO_2-reduction show the need of further development of modern power plants, especially the fuel provided, challenging parameters, component efficiency, new concepts for power plants and the use of combined heat and power.

At the present time the technical researches are focussed on gas- or oil-fired combined steam and gas turbine power plants, because with these thermal power plants an electrical efficiency up to 58 % can be achieved. The development of the efficiency of thermal power plants shows that for a significant improvement of the energy efficiency the utilizable temperature gradient between gas turbine inlet and steam turbine outlet has to be increased [1].

Especially for the gas turbine process, an increase of the turbine inlet temperature offers a great potential for enhancing the efficiency. The increasing hot gas temperature necessitates more and more complex cooling configurations for the blading in gas turbines. Due to the

decreasing gas temperature during the expansion in the turbine, the thermal load of the stages varies (see fig. 1). The complexity of the cooling concept decreases from the highly thermal loaded first guide vane to the last guide vane. In the first guide vane, extensive film cooling is used to enhance the cooling efficiency and to eliminate the need for an external air cooling system. The cooling system of the first rotating blade rows utilizes e.g. straight-through cooling paths for the leading and trailing edges of the blade and a serpentine cooling system for the center section. Cooling air is supplied through the rotor disk and discharges at the tip, the trailing edge, and through a large number of film cooling discharge holes, especially at the leading edge.

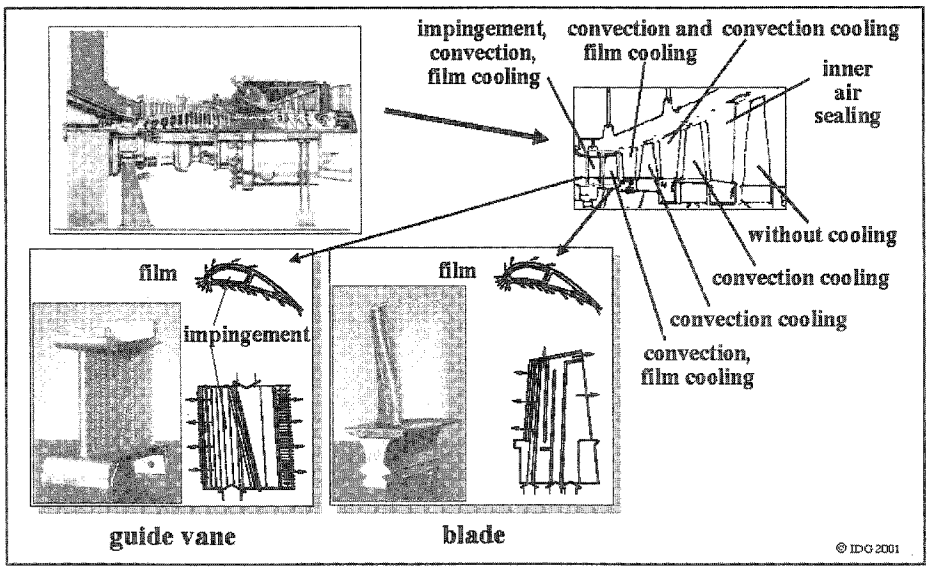


Fig. 1: Cooling in modern gas turbines

An advanced cooling method is the use of superheated steam instead of compressor air for internal blade cooling [2]. Figure 2 gives a comparison of the internal vane temperatures of a steam cooled blade in the cutting plane at 50 % blade height for two cases of a parametric study. The solid body temperature field shows a nearly homogeneous distribution inside the cooling passage arrangement. For the two cases no. 1 and no. 6 which differ in the steam pressure and steam mass flow temperatures are about 150 K lower for case no. 1. The difference is higher than the difference of the external temperature distributions. This is not astonishing as a more intensive convection cooling leads to higher temperature gradients in the solid body outside the cooling passage arrangement. In the trailing edge region, the temperature increase is leading to very high temperature gradients. Thus, this has to be taken into account in the subsequent thermal stress analysis. In contrast to the use of compressor air as cooling fluid, the use of superheated steam requires due to the very high cooling potentials only about half the mass flow which is needed for air cooling. [2]

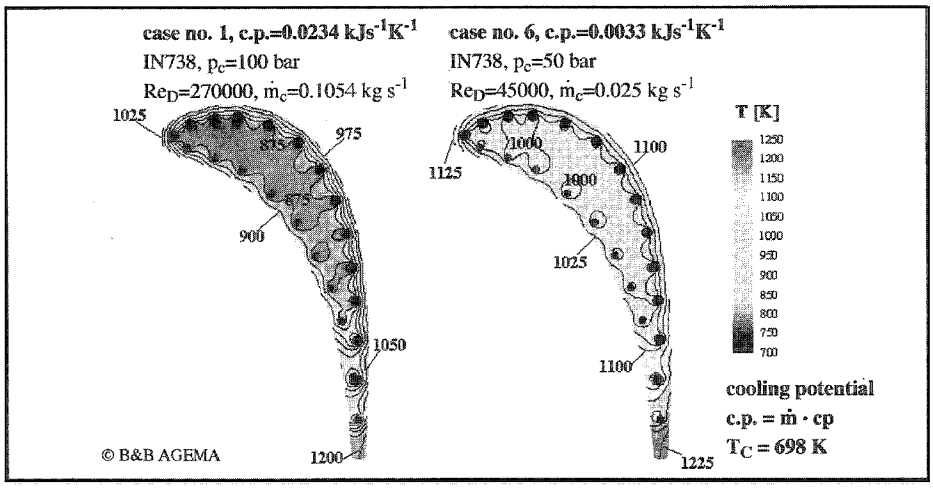


Fig. 2: Parametric study on steam cooled gas turbine blades

But even with these methods a maximal efficiency of only 61 % can be achieved. In order to satisfy the demand of research in the technical bases of fluid mechanics, material science and product engineering for thermally high loaded components of next generation combined cycle power plants the collaborative research center (SFB) 561 was founded at Aachen University.

There are several objectives of research in turbo machinery to realize an increasing efficiency of modern power plants. First of all the aerodynamics of both compressor and turbine have to be improved, although this will have relatively small effect on the total efficiency. Another aspect that requires further investigation and an increase of understanding is the combustion process. The new developments will lead to higher turbine inlet temperatures. The increased thermal load of the gas turbine parts requires special attention on the internal and external cooling systems. An increase of temperature also requires the development of new materials [3].

These new techniques and materials have to be tested both numerically and experimentally. Therefore a validation and improvement of numerical tools is important. And lastly, the new parts have to be tested on scaled down machines.

In addition, the SFB 561 also comprises the development and analysis of new materials and production technologies. Here the aerodynamic, structural and material aspects are integrated in the research of several experts so that the newly developed components can withstand the challenges of the next generation power plant.

The application of drilled fine-porous structures or perforated grid sheets as well as that of porous metallic foams or sintered materials in power plant components is a novelty in

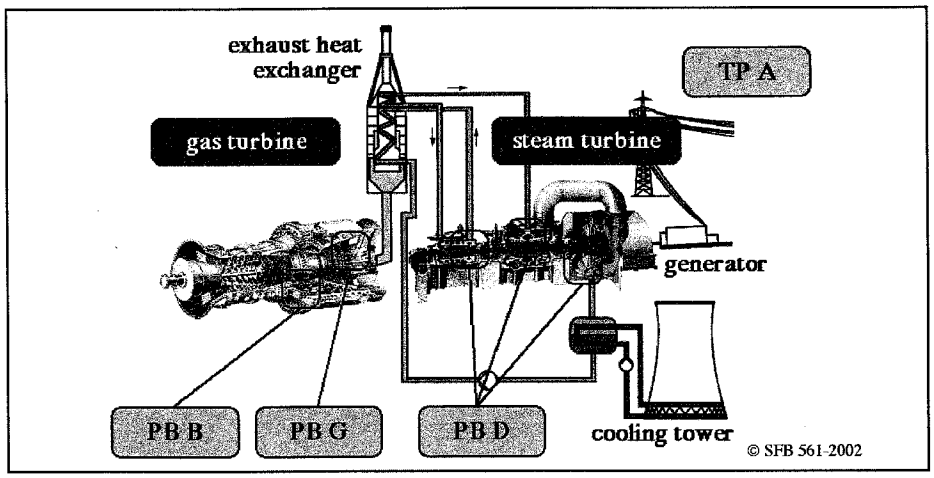


Fig. 3: Principal scheme of a combined cycle power plant

engineering. This applies to the manufacturing, the ascertainment of the characteristics, and structural mechanics as well as the interaction between operational and cooling fluid. The constructional and fluid dynamical development of effusion cooling and the development and testing of new alloys is done in different task forces (fig. 3).

The basis for the realization of newly designed components for a modified combined cycle technique has to be set up by interdisciplinary research work of fluid dynamics experts, structural mechanical engineers, material scientists and production engineers. The main stress is on the following components: the combustion chamber of the gas turbine, the gas turbine blades, the high temperature steam turbine and the low pressure steam turbine. Task

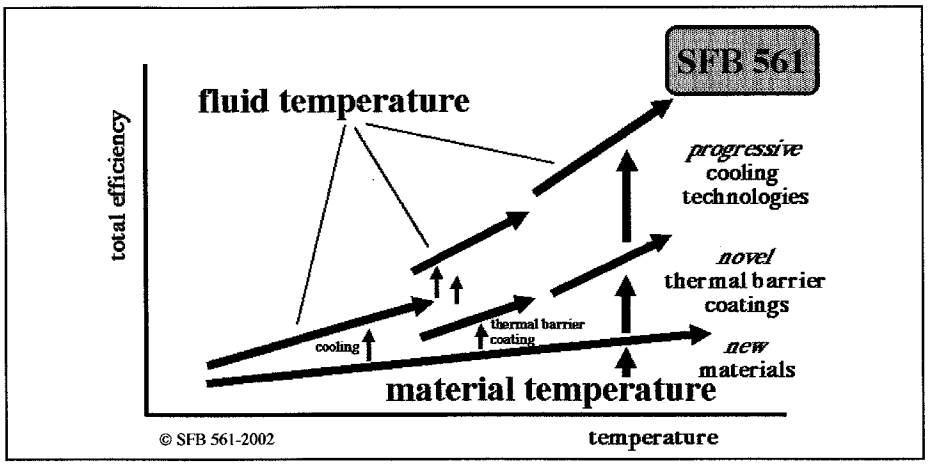


Fig. 4: Increase of total efficiency

force A focusses on the overall analysis of the process, task force B on the combustion chamber, task force G on the gas turbine blades and task force D on the steam turbine components.

The main goal of SFB 561 is the improvement of the total efficiency of a combined cycle power plant by improving materials, thermal barrier coating and cooling technologies. The optimum combination of the different factors enables a significant increase of the turbine inlet temperature.

Figure 4 shows the relationship between turbine inlet temperature and efficiency of the combined cycle process and the contribution of the different technological concepts.

Development of novel highly efficient cooling systems and materials

In modern gas turbines the turbine inlet temperature is considerably higher than the permissible material temperatures. In order to decrease the thermal stress on the component parts and the blades to an acceptable level, intensive cooling is necessary. Furthermore thermal barrier coatings are used, which lead to a further decrease of the temperature in the metal. The most effective cooling method, which is already applied in working plants, is film cooling. With this method the cooling air is transported from the inside of the part, through holes, on to the surface, where it protects the parts against a too intensive contact with the hot operating gas. It also achieves additional cooling in the holes by means of convection [4,5]

The logical next step in this cooling principle is the development of effusion cooling, which is achieved by applying porous metals or fine-drilled hole-fields. The result is the cooling air is not only locally effective, but, because of its escaping over the whole surface, a protective film is formed around the part that needs to be protected. The best example for this in nature is the skin, which transfers a fluid through pores to the surface of the body in order to regulate the body temperature. The film is formed here because the fluid seeps out on a very low speed.

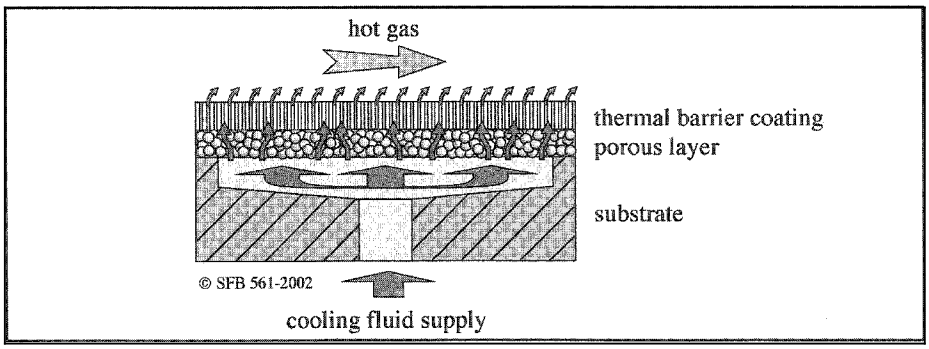


Fig. 5: Principle setup of transpiration cooling

So in the development of technically applicable effusion cooling we have to bear in mind that a cooling film only develops when the density of the pores or holes is so high that the cooling fluid escapes at a low speed on the surface and therefore disturbs the main flow as little as possible [6,7]. Figure 5 shows the basic structure of the outer wall of a part cooled by effusion cooling. Additionally a thermal barrier coating is used because this makes a decrease of the cooling fluid and by that an increase of the total efficiency possible.

Compared to cooling concepts in use today, this enables an increase of the turbine inlet temperature while the amount of cooling fluid stays constant or a decrease of the amount of cooling fluid while the temperature stays constant. Both ensure a significant improvement of the total efficiency and increase of power density.

The development of effusion cooling requires developing material, production and construction techniques further and a detailed aerodynamic and thermal analysis of the parts concerned [8]. For the construction of porous metallic materials which can handle the thermal stress in gas turbines the SFB 561 develops new casting techniques which ensure the mechanical load capacity of the materials. The realization of effusion cooling by means of perforated grid sheets is part of a numerical analysis being done at the moment at the Institute of Steam and Gas Turbines. The grid sheets are made at the Institute for Laser Technology with pulsed Nd:YAG lasers, where the parameters laser energy, duration of pulse and pulse frequency are optimized for the machining of multi-layer sheets.

The result of the optimization of the perforated sheets has to be a geometry of the position and form of the holes which enables a reliable and sufficient cooling of the gas turbine components with an as small as possible amount of cooling fluid. For a flat plate it is already proven that a homogeneous cooling film develops on the top side of the component when cylindrical, inclined holes are shaped both in the area where the cooling fluid escapes and inside the cooling hole (fig. 6). By hole shaping a considerable reduction of the secondary flow is achieved, so the hot gas cannot reach the surface of the component between the separate rays of the cooling fluid [9].

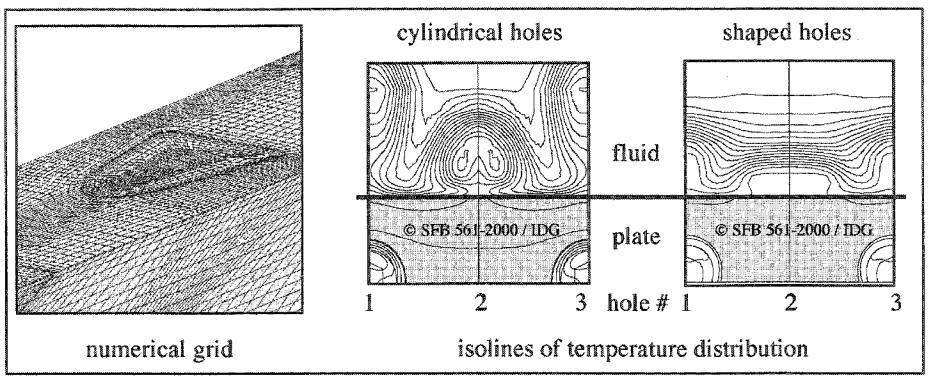


Fig. 6: Homogeneous cooling film by application of hole shaping

The mechanical strength of the drilled alloy is being calculated at the Institute of Materials and Processes of Energy Engineering with the help of numerical calculations of cracking and creep tests [10]. By homogenizing the material parameters the material properties for an equivalent material are calculated at ACCESS e.V. These will make the numerical calculation of complex effusion cooled parts possible at a later stage, without the necessity of projecting every pore or hole individually in the model.

For the development of new material systems and cooling technologies it is necessary to consider the real application and general conditions. The combustion chamber components of the gas turbine have to be cooled more effectively and at the same time be equipped with thermal barrier coating in order to keep the temperatures of 1800 °C in the centre of the combustion chamber and the high proportion of radiation in the heat transfer to the combustion chamber walls under control within the margins of the maximum thermal stress. Therefore structures of porous multi-layer materials are under development. In doing this the cooling technique is switched from the cooling by discrete cooling channels to effusion cooling. Fig. 7 shows schematically the cooling of the wall of the combustion chamber on the basis of a drilled multi-layer system.

The combustion chamber with its special combustion gas, combustion air and cooling air transport system has to be able to withstand turbine inlet temperatures (ISO) of 1350 °C. When thermal barrier coatings of 2-3 mm are made available, it is necessary to develop for the combustion chamber and hot gas guidance components materials with a thermal stability up to 1250 °C and to provide these with porous structures. The goal is a effusion cooled layer material and a heat barrier on the side of the combustion chamber and a good resistance to oxidation. In this field the production and application of metallic foams is investigated. For this purpose is a new casting method under development in the Institute for

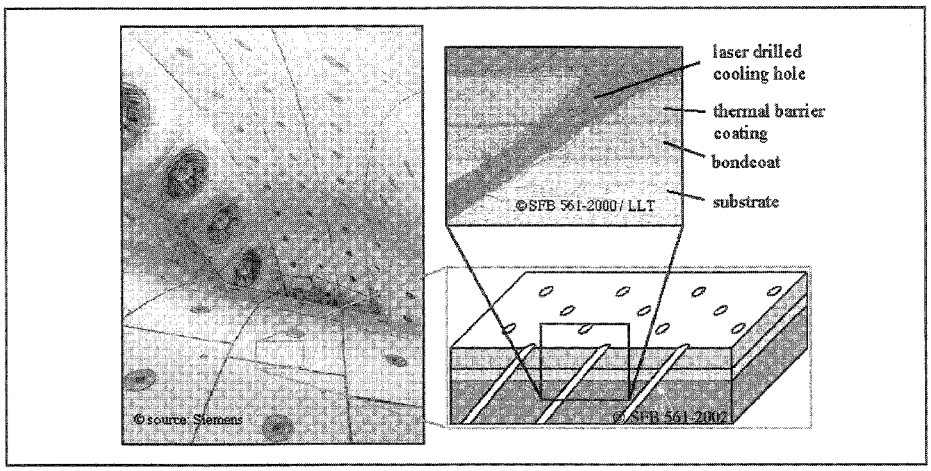


Fig. 7: Multi-layer systems with laser drilled, shaped cooling holes

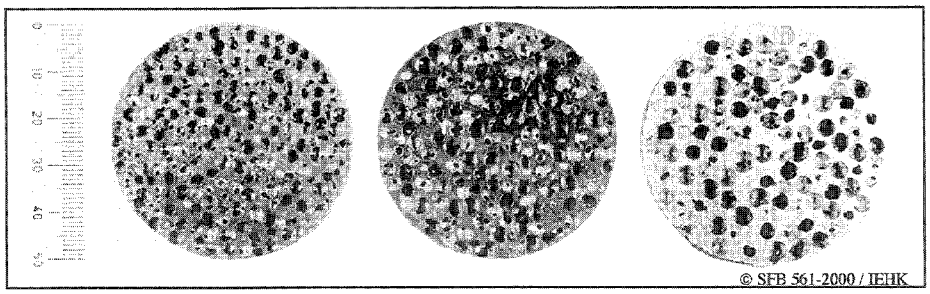


Fig. 8: Cast structure with open porosity on basis of cast iron

Ferrous Metallurgy in which the open porous structure is made with the help of placeholders. The result of this is shown in fig. 8.

For gas turbine blades in the first turbine stages constructive measurements and new materials, which enable effusion cooling, are being developed. An increase of the hot gas temperatures when using single-crystal superalloys of the third generation as the load-bearing blade material requires an improvement of the layer systems with regard to hot gas corrosion, high temperature oxidation and thermal barriers as well as the optimizing of the cooling techniques.

In the long run the employment of fibre reinforced NiAl-alloys seems to be most likely to guarantee success [11]. This is from the point of view of casting a special challenge since the moulds which have been used so far for the casting of NiAl-alloys cannot be used. The process is being developed at the Foundry Institute. For the formulation of the technology

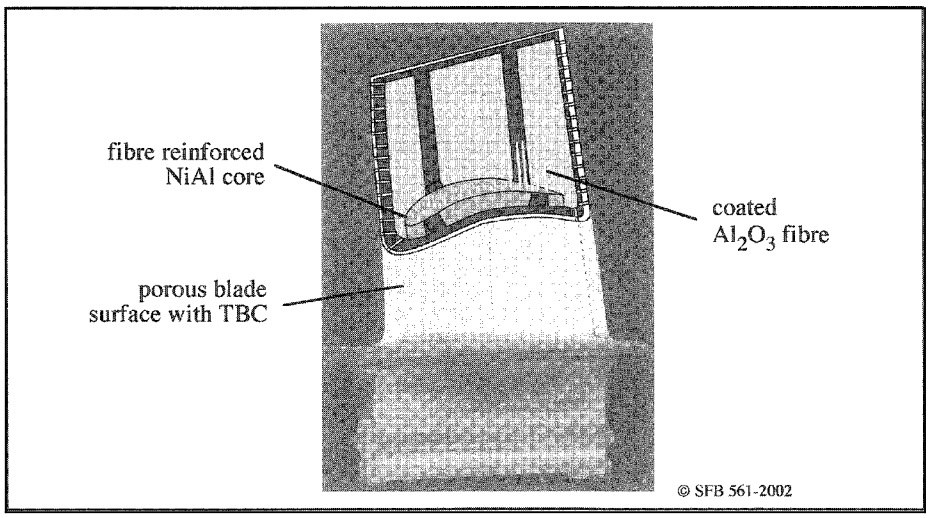


Fig. 9: New concept for gas turbine baldings

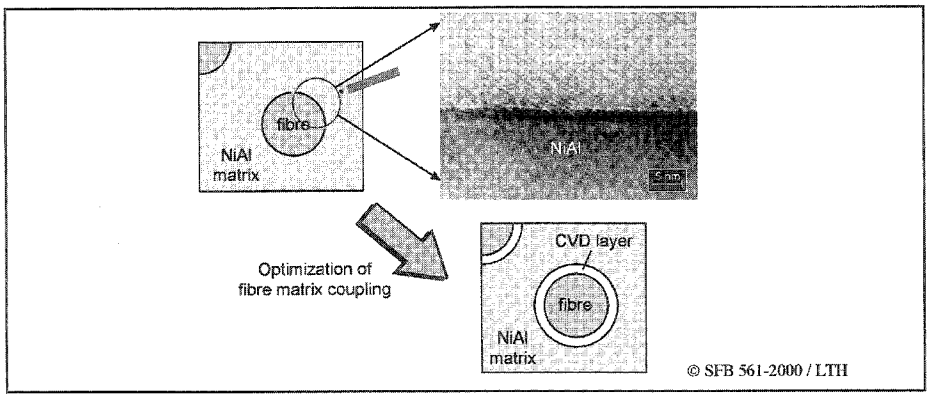


Fig. 10: Fibre matrix coupling for fibre reinforced NiAl

for the production of this new alloy research is done at the Department of Theoretical Process Metallurgy in the coating of long fibres (Al_2O_3) by CVD for optimizing of the fibre-matrix coupling.

Subsequently so-called preforms are manufactured from the NiAl-sheets and the fibres at the Institute of Metallurgy. Then these preforms are incorporated into the NiAl-matrix. This material system will eventually have a higher thermal capacity than is the case with current systems.

Round this core of the fibre-reinforced alloy a "mantle" of porous and thereby gas permeable NiAl is cast, which is in turn coated with a ceramic thermal barrier coating. A pre-requisite for the barrier coating is it has to be expansion tolerant and sinter only slowly. Fig. 9 shows the design of the conceptional blade, fig. 10 the fibre-matrix coupling.

Realizing high initial steam temperatures of 700 °C and more and the raising of the initial steam pressure which is connected with this requires a new design of the high temperature steam turbines, especially of the rotors. Without cooling precautions for the rotor and the casing components it would be necessary to use Ni-alloys which are not sufficiently developed yet for the use to which it would be put, i.e. components weighing 10 tons and the long-term use in steam turbines.

Using ferritic high-temperature materials 9-12 % Cr-steels at temperatures of 700 °C and more means a suitable cooling has to be realized. Ferritic steels are preferred because of their positive start-up characteristics. The 9-12 % Cr-steels under development in the moment have at 620 °C the required long-term creep resistance ($R_{p0.2;100000h}$ >100 MPa), but show, dependant on the Cr percentage, a too rapid steam oxidation by temperatures of about 650 °C [12]. The cooling of the rotor and casing surfaces will be taken over by a process in which initial steam flows through perforated grid sheets in the components. Fig. 11 shows the cooling on the basis of perforated grid sheets.

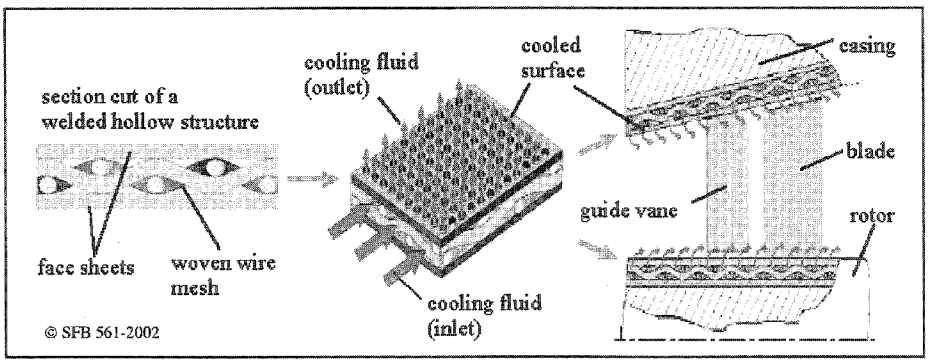


Fig. 11: Cooling of high temperature steam turbine with perforated grid sheets [13]

Techniques for the water drain at the last stages on the cold end of the process, the low pressure steam turbine, are being developed at the Institute of Metallurgy. The aim is to remove the water film on the blades and casing walls with a method different from the drain slits which are used now. The new method consists of open porosity powder metallurgical in-situ composites which drains the water from the surfaces. The manufacturing of this open porosity powder metallurgical in-situ composite is the main concern in this part of the SFB. Therefore stress corrosion cracking and erosion/wet steam corrosion are analyzed. Fig. 12 shows the water drain of a steam turbine stage with open porosity schematically. Furthermore the sample of a layer material is shown here.

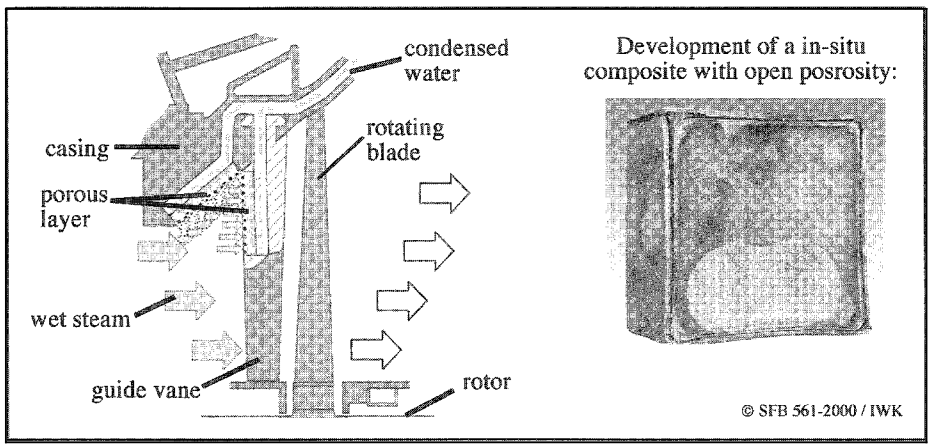


Fig. 12: Water removal in low pressure steam turbine with open porosity metallurgical in-situ composite

Future Combined Cycle Power Plants with High Plant Efficiency

For the validation of the attainable increase of efficiency in future combined cycle power plants by means of newly developed material, cooling and drain techniques a state-of-the-art power plant is taken as the basis of the calculations. Therefore the process of the power plant "Tapada do Outeiro" is modelled in detail [14]. Characteristic of this modern power plant are the single-shaft construction of gas and steam turbine, the non-fired heat recovery steam generator and the 3-pressure-evaporation with reheat. The total efficiency level of the combined cycle with the discussed gas turbine is 55.4 %.

Because of the in-depth modelling the different cooling air flows on the different pressure levels are depicted very accurately. The same is valid for the heat recovery steam generator by the parallel arrangement of the heating surfaces of the high pressure and second middle pressure superheaters, the high pressure economizer and the first middle pressure superheater and the middle pressure evaporator and the low pressure superheater in the waste gas mass flow of the gas turbine.

The combined process of "Tapada do Outeiro" is modelled and calculated exactly on the basis of complex models for the characteristics of the components and assumptions based on real power plant data [15]. The model for the cooling air in gas turbines used in the actual calculations is based upon both the data from a real turbine under working load and the results of a 2D-calculation of temperature and flow. The 2D-calculations furthermore form the basis for the calculation of the reduced cooling air needs of effusion cooling. The results show that the application of effusion cooling reduces the cooling air needs in the gas turbine by approximately 67 %. Parallel calculations for the cooling air model of thermal highly stressed steam turbines were performed, which took the different fluid and material characteristics and the smaller surface that needs to be cooled (compared to that of the gas turbine) into account. For the low pressure part of the steam turbine a model for the wetness losses was implemented [16]. The results of the calculation showed that by draining the condensate and the centrifuged water completely the wetness losses can be decreased by up to 21 %.

As reference process for the estimate of the efficiency increase by the application of effusion cooling on the basis of open porous materials the gas turbine is modified to reflect the original turbine inlet temperature of 1207 °C. The changed parameters lead to a changed net total efficiency for the reference process of 56.14 %.

When the film cooling is changed to effusion cooling, the total efficiency increases by 4.8 % This is the result of the decrease in total efficiency losses by cooling air because of higher efficiency of the effusion cooling. At the same time the initial steam parameter increase with identical temperature difference in the heat recovery steam generator because of the higher gas turbine outlet temperature, so the steam turbine process is improved as well. Because of the decreased cooling air needs of 9.9 % compared to that of the compressor inlet mass flow when using film cooling the gas turbine inlet temperature can be raised to 1328 °C.

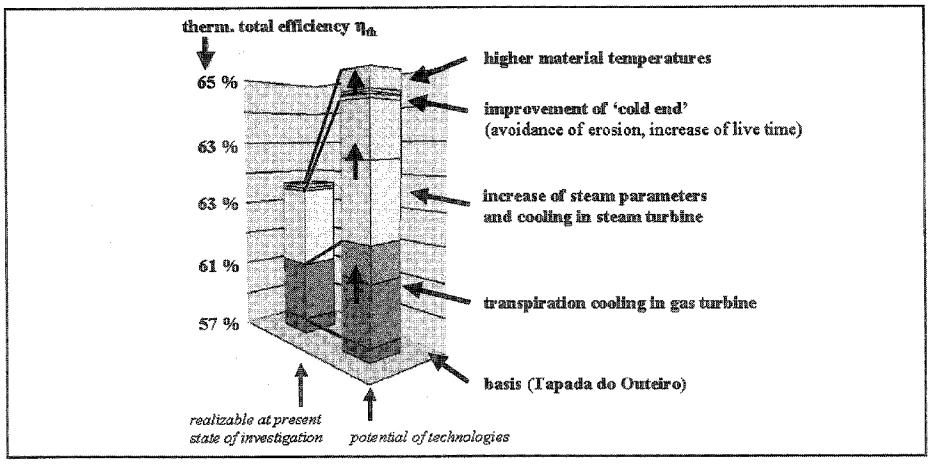


Fig. 13: Increase of total efficiency

After a first three years period of scientific research of the collaborative research center (SFB) 561 the new knowledge base was used to improve the detailed model of the combined cycle power plant. This first period proved that the principle methods that were focussed by the involved institutes are qualified for application in gas and steam turbines to increase the plant efficiency by use of porous materials. At this point of the scientific work a net thermal efficiency of 61.7 % could be reached for the described combined cycle (see fig. 13).

On the basis of this detailed model of the combined cycle power plant the thermodynamic parameters for the goal of a net total efficiency of 65 % were determined by application of a conjugate-gradient-method. For a relative cooling fluid mass flow of 9.9 % with a temperature of 420 °C the gas turbine inlet temperature was predicted as 1473 °C. The gas turbine inlet pressure was determined as 1.698 MPa. The high pressure steam turbine inlet temperature of 620 °C will lead to a need of cooling steam of 0.17 %. In the middle pressure steam turbine 0.12 % cooling steam will be necessary for a inlet temperature of 691 °C to ensure acceptable material temperatures. The pressure at the high pressure steam turbine inlet was calculated to be 29.8 MPa.

Summary and Conclusions

With the founding of the collaborative research center 561 "Thermally Highly Loaded, Porous and Cooled Multi-Layer Systems for Combined Cycle Power Plants" at Aachen University a basis was formed to satisfy the research demand in fluid mechanics, material science and product engineering for thermally high loaded components. The state of the research tasks shows, that a thermal efficiency of up to 65 % is realizable for the next generation of combined cycle power plants. Therefore, originating from the developed basis within the scope of the collaborative research center, work will be focussed on the production of first specimens of the new materials in the next step. After testing those

specimens, experimental components for gas turbines and steam turbines will be developed using the new cooling technologies. The final work will be to transfer the new knowledge to manufacturers with the result of novel products in turbo machinery.

Acknowledgement

The authors gratefully acknowledge the financial support of the Deutsche Forschungsgemeinschaft (DFG) within the Collaborative Research Center (SFB) 561 "Thermally Highly Loaded, Porous and Cooled Multi-Layer Systems for Combined Cycle Power Plants". The responsibility for the content of this publication lies upon the authors.

References

[1] Kail, C., Rukes, B.: Fortschrittliche Gas- und Dampfturbinenprozesse zur Wirkungsgrad- und Leistungssteigerung bei GUD-Kraftwerken. VDI Berichte Nr.1182, 1995, S. 71 - 87

[2] Krüger, U., Kusterer, K., Lang, G., Rösch, H., Bohn, D., Martens, E.: Analysis of the Influence of Cooling Steam Conditions on teh Cooling Efficiency of a Steam-Cooled Vane using the Conjugate Calculation Technique, ASME 2001-GT-0166, Munich, 2001

[3] Keppel, W., Bohn, D.: Gasturbinen und Kombikraftwerke - Anforderungen an Werkstoffe und Werkstoffentwicklung heute und morgen. "Werkstoffe für die Energietechnik", Proceedings Werkstoff-Wochen 96, Stuttgart, ed. H.W. Grünling, DGM Informationsgesellschaft Verlag, 1997

[4] Berhe, M. K., Patankar, S. V.: A Numerical Study of Discrete-Hole Film Cooling. ASME, 96-WA/HAT-8, ASME International Mechanical Engineering Congress & Exhibition Atlanta, Ga, USA, November 17-22, 1996

[5] Kercher, D. M.: A Film-Cooling CFD-Bibliography: 1971-1996. Int. Journ. of Rot. Mach., Vol. 4, No. 1, 1998, pp.61-72

[6] Martiny, M., Schulz, A., Wittig, S.: Mathematical Model Describing the Coupled Heat Transfer in Effusion Cooled Combustor Walls. ASME, 97-GT-329, International Gas Turbine & Aeroengine Congress & Exhibition Orlando, Fl., USA, June 2 - June 5, 1997

[7] Kirkpatrick, K., Chai, J., Munukutla, S.: Computational Study of Flow in a Porous Pipe with Wall Suction/Injection. AIAA 99-1013, 37TH AIAA Aerospace Science Meeting and Exhibit, Reno, NV, 1999

[8] Roos, F. W.: Combined Effects of Surface Porosity and Pressure Gradient on Turbulent Boundary Layers. AIAA 99-1014, 37TH AIAA Aerospace Science Meeting and Exhibit, Reno, NV, 1999

[9] Bohn, D., Moritz, N.: Influence of Hole Shaping of Staggered Multi-Hole Configurations on Cooling Film Development, AIAA 2000-2579, Denver, 2000

[10] Fleury, G., Schubert, F., Nickel, H.: Modelling of the thermo-mechanical behaviour of the single crystal superalloy CMSX-4. Computational Materials Science, 342, 1996

[11] Noeber, R. D., Waltson, W. S.: Perspects for the Development of Structural NiAl Alloys. Proceedings "Structural Intermetallics 1997", Seven Springs, USA, Sept. 1997

[12] Schubert, F., Thiele, M., Williams, C., Quadakkers, W. J.: Wasserdampf- und Rauchgaskorrosion der neuen Kraftwerksstähle im Temperaturbereich oberhalb 550°C. "Werkstoffe für die Energietechnik", Proceedings Werkstoff-Wochen 96, Stuttgart, ed. H.W. Grünling, DGM Informationsgesellschaft Verlag, 1997

[13] 1. Workshop zum Sonderforschungsbereich 561 "Thermisch hochbelastete, offenporige und gekühlte Mehrschichtsysteme für Kombi-Kraftwerke. Einzelbeiträge der am SFB 561 beteiligten Institute, RWTH Aachen, 15.Mai 2000

[14] Siemens AG Power Generation Group: Tapada do Outeiro brings V94.3A Combined-Cycle Efficiency to Portugal. Nachdruck aus Modern Power Ssytems, May 1996, Wilmington Publishing Ltd. Dartford, Großbritannien

[15] Bohn, D., Lepers, J., Sürken, N.: Einsatz von Prozeßberechnungsprogrammen zur Optimierung fortschrittlicher Dampfkraftprozesse. CIT, 72. Jahrgang, 7/2000, S. 683-687

[16] Bohn, D., Kerpicci, H.: Lagrangian / Eulerian Calculation Approach in the Computation of Homogeneous Condensation in a Nozzle Guide Vane of a LP-Steam Engine. 8th Intenational Symposium on the Transport Phenomena and Dynamics of Rotating Machinery (ISROMAC-8), Honolulu, USA, 2000

OVERVIEW OF US-DOE PROGRAM IN HIGH EFFICIENCY ENGINES AND TURBINES

Abbie W. Layne
National Energy Technology Laboratory
U.S. Department of Energy
3610 Collins Ferry Road
Morgantown, WV 26507-0880

Abstract

The overall goal of the USDOE Program in High Efficiency Engines and Turbines (HEET) is to develop technologies for ultra-clean, reliable, and high-performance power systems. One of the objectives of the program is to reduce the life-cycle cost of advanced turbine power plants by at least 15 percent compared to current systems, and improve the reliability, availability and maintainability (RAM) of the existing and future turbine power-plant infrastructure. The Program supports the development and demonstration of ultra-clean, high-performance turbine power systems for near-term power markets and long-term integration into solid-fueled power plants. Consequently, advanced materials, combustion systems, computational tools, and sensors/controls/instrumentation to solve crosscutting technical barriers related to condition assessment are key elements of the Program which aims to collaborate with regulatory agencies and develop sound technical information to produce appropriate and beneficial regulatory decisions related to gas turbine power plants.

Keywords:

1. Introduction

During the last decade, gas turbine (GT) based advanced combined cycle power plants have gained favor for electric generation sector owing to the low installation cost, short construction time, and high efficiency. High efficiency engines and turbines will provide clean, efficient power systems to meet the predicted increase in electricity demand over the next 20 years. These advanced systems will also alleviate transmission congestion by encouraging distributed generation and facilitate co-generation. In addition, the HEET Program will ensure that goals and objectives of DOE's Clean Coal Power Initiative can be met. The Program will provide the power block modules needed in the Vision 21 and Distributed Generation programs, including hybrid turbine-fuel cell modules. And the Program will help develop technologies to sequester carbon dioxide, a greenhouse gas.

Taken together these advantages provide the developer the means to take relatively quick decisions regarding new capacity additions and navigate the permitting process with confidence. Low NO_x combustion advances have led to new GT power plants which have significant environmental advantages compared to other technologies. Gas turbine based power plants are likely to further increase their share of the total power generation capacity as new "Clean Coal" concepts such as APFBC and IGCC expand the use of gas turbines to low grade liquid and solid fuels through gasification. Similarly the new trend towards the use of distributed energy resources is expected to further expand the share of GT based power plants.

Advances in gas turbine technology have raised gas turbine firing temperatures to over 1260 °C (2300°F) and pressure ratios to about 30:1, resulting in increased turbine power system efficiencies

to greater than 60 percent (LHV) on natural gas fuels [1] and potentially up to 52%(HHV) on coal fuels. However, the increases have also caused some reductions: availability has been reduced by as much as 10 percent, nozzle life and first-stage blade life have been reduced to less than 25,000 hours, and combustor liner life has been reduced to 4,000 hours. A performance-based condition monitoring approach to improving power plant performance will enable turbine operation at major utility and process plants to be safer, more environmentally friendly, more flexible, more reliable, and more profitable than is possible today.

Condition monitoring research in the HEET Program managed by the National Energy Technology Laboratory (NETL) is aimed at doubling current power plant efficiencies with no reduction in operating and maintenance costs, flexibility of 400 starts per year for gas fueled systems and load change on a daily basis for coal systems, RAM improvement, and operation of coal syngas. Options for reducing operation and maintenance costs include (1) limiting degradation, (2) operating at optimal design conditions while the system is at off-design conditions, (3) improving component life, and (4) increasing the time between major overhauls. RAM improvement studies will include performance-based maintenance and total condition, overhaul, and low-NO_X combustion monitoring. Natural gas will be used as the baseline for fuel flexibility work, with the ultimate goal for high reliability operation on coal-derived fuels. Fuel treatment, fuel tracing and special designs for heavy fuels, and on-line turbine washing will be investigated.

2. Program Objectives

Specific HEET Program objectives are listed below.

- ***Ultra-High Efficiency.*** HEET systems will have ultra-high efficiencies: 60 percent for coal-based systems (higher heating value [HHV]), and 75 percent for natural-gas-based systems. Turbines developed under the HEET Program will be successfully integrated with fuel cells into hybrid systems for use in distributed generation and Vision 21 power modules.
- ***Environmental Superiority.*** Advanced turbine plants developed under the HEET Program will ultimately have near zero emissions – no carbon, and negligible NO_x, SO_x, and trace contaminants.
- ***Reduced Life-Cycle Cost.*** The life-cycle cost of electricity produced from advanced turbine power plants developed in the HEET Program will be reduced by at least 15 percent compared to current systems.
- ***Fuel Flexibility.*** Advanced high-efficiency engines and turbines developed under the HEET Program will demonstrate fuel and operational flexibility, operating on coal syngas or hydrogen, and have adequate load-following capability.
- ***Improved Electricity Reliability.*** Technology developed under the HEET Program will improve the electricity reliability of the existing and future power-plant infrastructure. These technologies will ensure that coal-fired turbine power plants will have high reliability, availability, and maintainability.
- ***Reduced Water Consumption.*** Technologies developed under the HEET Program will significantly reduce the amount of water needed in power-plant operation.

Leapfrog advances and breakthrough technologies, rather than evolutionary advances, are needed to develop turbine systems that demonstrate ultra-high efficiency, reduced life-cycle cost, environmental superiority, fuel flexibility, improved electricity reliability, and reduced water consumption. HEET Program objectives directly support the clean coal technology recommendations identified in the *National Energy Policy* report (National Energy Policy Development Group, 2001) and specific objectives noted in the *Vision 21 Technology Roadmap* (National Energy Technology Laboratory, 2001). Achieving the objectives of HEET will be required to attain the goals of the Administration's Clean Coal Power Initiative.

3. Program Strategy

The HEET Program strategy is to focus on environmental, performance, life-cycle cost, and reliability issues related to turbine power plants. To find solutions to these issues, technology development is needed in five areas: Materials, combustion and emission reduction, aero-thermal, instrumentation / condition monitoring, and design tools. The strategy is based on significant input from the private sector and other public organizations. This approach offers the best chance of success in achieving the Nation's energy policy goals while yielding environmental benefits and reduced electricity costs for the consumer. The relationship between technical issues, program strategy and program structure is shown in Figure 1 below.

Technology roadmaps have been developed with industry and academia in these five development areas. These roadmaps chart technology development pathways that will produce advanced components for Vision 21 power modules. Technologies will be developed and integrated into industrial turbine and hybrid power systems. Component validation and integration will be coordinated with the Clean Coal Power Initiative to promote demonstration of HEET power systems by the private sector.

The five development areas are described below.

3.1 Materials

A roadmap for materials R&D was developed with input from gas turbine developers and researchers. Current land-based gas turbines have incorporated advancements in cooling technology, aerodynamic design, and mechanical innovation. Traditionally, the primary driver for applications other than military aircraft has been to increase fuel efficiency, with emission reduction rapidly rising to prominence in recent years. Both goals require a combination of higher temperature capability in the hot-gas path components and lower requirements for cooling air. A strategic plan to meet these goals, as well as system life assessment, has been developed with stakeholder input. A materials roadmap has been established, and potential benefits have been outlined.

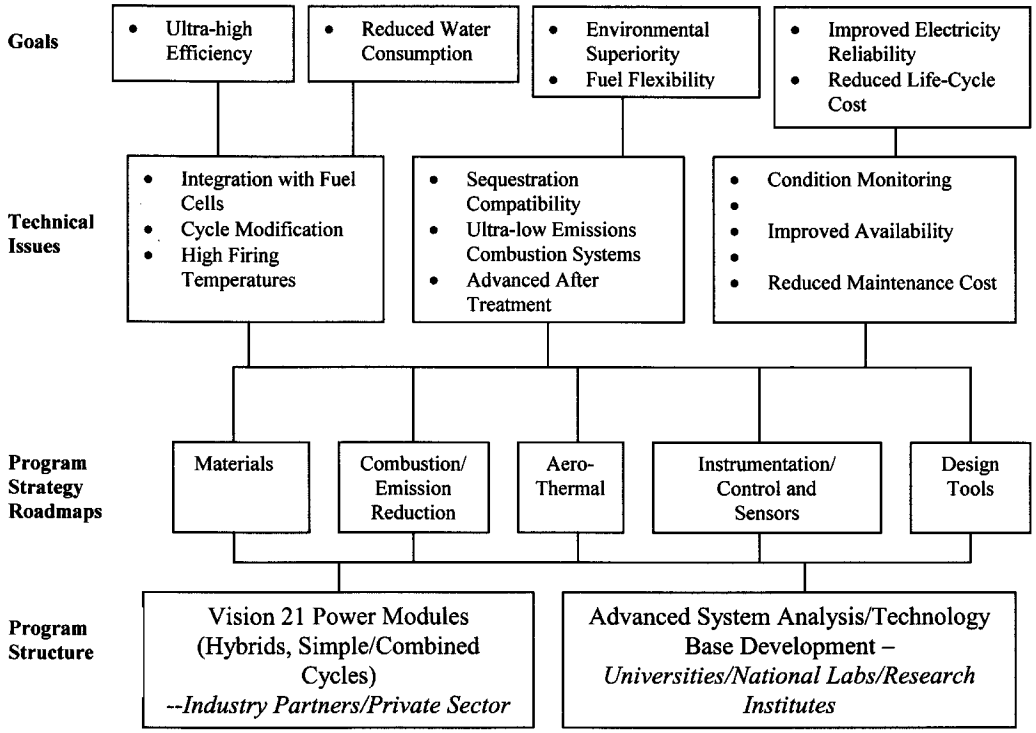


Figure 1. HEET Technology Required to Achieve Vision 21 Goals

Materials technology is keeping pace with advancements for key components exposed to the hot gas path combustor, transition pieces, and turbine vanes, blades, and disks. Progress is specifically being made in single crystal blades and vanes, wider use of thermal barrier coatings, coatings improvements for oxidation and corrosion protection, and nickel-based alloys for discs. Innovations being studied for future land-based turbines include limited use of structural ceramics, increased use of advanced welding and joining methods, and condition assessment. Materials R&D in the HEET Program addresses unmet needs and challenges for future land-based systems that will be affected by cycle configuration, firing temperature, fuel type, and duty cycle. Advanced materials developed under the program should enable cycle innovations and turbine design changes that promise 60 percent efficiency for coal-based systems (HHV), and 75 percent for natural-gas-based systems. Establishing a mechanistic base for models is a research priority.

Non-intrusive methods that can monitor the physical state of a turbine component during service are needed for the gas turbine operator. Kinetics of evolutionary processes that lead to failure of hot gas components will be facilitated by smart materials, a term used to include materials or probes that can provide information on the material or coating while in service. The information can then be used with suitable process control to assess remaining life, as well as to regulate the operating conditions.

Materials issues are relevant to the near-term need to demonstrate/confirm the efficacy of conventional gas turbines in a coal-derived synthesis gas system. Different hot gas environments are obtained and there is a dearth of long-term performance data for these environments. Industry is interested in deep cleaning technologies that are less expensive and more efficient than current technologies. The goal is to achieve the performance of Rectisol at a cost equal to or less than conventional amine based systems. Although improved cold gas cleaning technologies would be acceptable, there is a strong desire for technologies that operate in the 150-380°C range, i.e. temperatures commensurate with downstream applications such as gas turbines and synthesis gas conversion technologies.

Priorities in the program include the selection and verification testing of turbine hot path component materials and protective coatings. Differences in syngas composition relative to natural gas and syngas variability due to different gasifier type must also be researched with respect to the interaction of trace contaminants with advanced turbine blade materials and coatings. Syngas contains traces of heavy metals not found in natural gas. Petcoke-derived gas may contain nickel and vanadium. The interactions of these trace constituents with the materials and coatings currently being used needs to be investigated. In addition, the presence of particulates may cause erosion or deposition, and gaseous species (e.g. SO_x, alkali compounds, HCl) may cause deposition and/or enhance corrosion. Synergistic effects between these various degradation processes are also likely under gas turbine operating conditions. These various potential degradation modes may be life limiting for gas turbine hot gas components (e.g. combustion chamber, vanes and blades), rather than creep and fatigue processes. Thus, hot corrosion and erosion-corrosion models to predict the lives of candidate gas turbine hot gas path materials in realistic environments for a gas turbine operating on coal-derived gases are necessary to assess potential lives of such components, and establish changes to these environments which would significantly extend these lives.

3.2 Combustion and Emission Reduction

Power generation from fuels generated by coal or biomass gasification could provide a clean energy source for U.S. energy needs. New concepts, such as environmentally superior power plants, will use radically different turbine engine configurations to produce a sequesterable CO_2 stream, thereby virtually eliminating greenhouse gas emissions.

Proposed hybrid turbine-fuel cell systems may achieve unprecedented fuel efficiencies, saving both fuel and reducing CO_2 , but these technologies use significantly different operating cycles compared to conventional power plants. In each of these applications, a key technical challenge is designing and controlling the turbine combustion process without compromising reliability or environmental performance.

The focus of combustion and emission reduction research in the HEET Program covers four major topics:

1.) Improving the simulation of combustion so that the behavior of proposed systems can be evaluated at greatly reduced cost;

2.) Addressing the problem of combustion stability so that low-emission engines can operate with greater fuel flexibility and reliability;

3.) Developing sensors and control systems that can improve the reliability of hot-section components in very high efficiency systems or hybrid systems;

4.) Investigating novel strategies for combustion that can provide low-emissions on a wide variety of fuels without the cost and environmental tradeoffs of ammonia-based after-treatment.

3.3 Aero-Thermal

To achieve the efficiency goals of the HEET program, advanced turbines will need to operate at higher temperatures and pressures under more severe conditions. Currently, manufacturers utilize air and steam to cool the hot components in turbine power plants. Other components of the turbine power plant, such as air-cooled condensers, are still inefficient and could be improved with advanced heat transfer applications to reduce water consumption. Several barrier issues exist in the area of heat transfer and aerodynamics/mechanics.

The focus of aero-thermal research in the HEET Program covers five major topics:

1.) Advanced cooling fabrication (surface enhancements);

2.) Robust gas turbine blade components and increased durability;

3.) Transpiration hot-gas path cooling;

4.) Heat transfer for highly loaded aero-thermal designs (wake and shock effects); and

5.) Compressor cooling at higher pressure ratios, generator cooling and insulation, and advanced cooling for balance of plant (BOP) equipment.

3.4 Instrumentation/Condition Monitoring

Advances in gas turbine technology have raised gas turbine firing temperatures to 2600°F (1427°C) and pressure ratios to about 30:1, resulting in increased turbine power system efficiencies to greater than 60 percent (LHV) on natural gas fuels, and potentially up to 52 percent (HHV) on coal fuels. However, the increases have also caused some reductions: Availability has been reduced by as much as 10 percent; nozzle life and first-stage blade life have been reduced to less than 25,000 hours; and, combustor liner life has been reduced to 4,000 hours. Leapfrog technology advances are needed to develop advanced technology that is both able to withstand the higher temperatures and pressures and is reliable.

For the past three years, NETL has been developing dynamic models as part of collaboration with the National Fuel Cell Research Center located at the University of California at Irvine. Dynamic models and control systems need to be developed to design and operate engine/fuel cell hybrid systems. Following a detailed design phase, NETL is constructing an experimental hybrid simulator.

This facility will be used (1) for experimental validation of dynamic models, and (2) to provide a test bed for the control systems needed for hybrid systems.

A performance-based condition monitoring approach to improving power plant performance will enable turbine operation at major utility and process plants to be safer, more environmentally friendly, more flexible, more reliable, and more profitable than is possible today. Condition monitoring research in the HEET Program is aimed at doubling current power plant efficiencies with no reduction in operating and maintenance costs, flexibility of 400 starts per year for gas fueled systems and load change on a daily basis for coal systems, RAM improvement, and operation of coal syngas. Options for reducing operation and maintenance costs include (1) limiting degradation, (2) operating at optimal design conditions while the system is at off-design conditions, (3) improving component life, and (4) increasing the time between major overhauls. RAM improvement studies will include performance-based maintenance and total condition, overhaul, and low-NO_x combustion monitoring. Natural gas will be used as the baseline for fuel flexibility work, with the ultimate goal of high reliability operation on coal fuels. Fuel treatment, fuel tracing and special designs for heavy fuels, and on-line turbine washing will be investigated.

3.5 Design Tools

Benchmark quality data on low-emission turbine combustion flames is a critical need. The HEET Program will address this need using data obtained in national lab and university projects. Design tools, using advanced numeric simulations, can assess new engine performance while greatly reducing the time needed for development and testing. With continued advances, large-scale computing facilities, as well as distributed computing resources, it may become possible to predict full-engine behavior. This will allow virtual tests of the complex interactions expected to occur in hybrid energy plants. If successful, this could save the cost of building less than optimal prototype plants, because many of the component interactions could be explored before building a physical system.

Because engine manufacturers do not directly profit from software and computing techniques, development of these techniques is often under-funded in the private sector. Emerging high-tech companies that produce software are seldom able to address the huge cost and technical hurdles needed to develop full-engine simulation. For example, the needed experimental data that must accompany simulation development is not readily available to software companies. To address these barriers, the HEET Program will develop advanced computing methods at national laboratories, universities, and small businesses. The work will be coordinated with related activities supported by NASA and DoD for flight-engine applications, but will cover the significantly different problems of stationary power. For example, none of the propulsion applications will include hybrid turbine-fuel cells, or adaptations for variable coal or biomass gas.

Perhaps the greatest technical challenge of developing new energy plants is the combustion system. The cost of developing new low-emission turbine combustors usually exceeds tens of millions of dollars, even when using natural gas as the fuel. Adapting a low-emission combustor to a fuel with a different composition, such as coal fuels, may require a similar investment of time and money. The high development cost is one factor that prevents routine engine deployment where low emissions are sought on opportunity fuels such as biomass or hydrogen-rich coal syngas. Likewise, candidate

combustor strategies for advanced hybrid power plants can ordinarily be expected to be a high-risk, long-term, capital-intensive venture that industry cannot be expected to undertake on its own. Industry sees no near-term payback from developing new combustors for biomass or syngas. This is slowing efforts to develop innovative, zero-emission power systems, even though the public benefits will be huge.

A reliable, low-cost method to evaluate combustor performance on different fuels could address this dilemma. Progress in numeric simulation of combustion has advanced to the point where basic design features are now routinely assessed using computer simulations. These simulations often provide useful qualitative information about the effect of proposed design changes. However, quantitative accurate prediction of pollutant emissions, and the effects of specific fuel chemistries, are beyond the state of the art in current numeric models. Technical progress on this issue will provide a low-cost method to evaluate the behavior of new fuels in proposed combustor designs. Technical progress in combustion simulation is linked to available data for model development.

A central problem is providing an accurate, computationally tractable representation of key processes in the flame. Data are not available for the type of premixed flames that are used in low-emission turbine combustors. Because turbine combustors operate at high pressures with short residence times and high turbulence levels, creating representative test conditions requires specialized facilities. The required pressures and flow rates are typically found only in commercial turbine development laboratories. These commercial facilities are often occupied with hardware testing for near-term product development. Experimental data to support models for pre-commercial concepts, such as hydrogen-fueled turbines, is even more difficult to obtain. The research payback is too long and speculative to justify investigation by commercial laboratories.

4. Program Structure

The HEET Program portfolio consists of four elements: Advanced System Analysis, Simple/Combined Cycle Development, Hybrid Cycle Development, and Technology Base Development. These four elements are described below. The five technology development areas discussed in the previous section are interwoven into the work areas within these program elements.

The Program will be implemented through competitive solicitations and consortia involving industry, national laboratories, and universities. During fiscal year (FY) 2000, several competitive selections were made to evaluate technology needs and benefits of advanced turbine systems. These studies will provide information for program planning, and will define the direction and focus of the R&D portfolio. A follow-on solicitation is planned for FY 2002 to begin implementation of the technology base development element.

Prior to the establishment of the HEET Program, several relevant projects were initiated with teams of industry, academia, and research institutions under FY 2000 broad-based solicitations. These teams are developing gas turbine-fuel cell hybrids and computational tools to (1) improve low-emission combustion design, and (2) test engine concepts such as the Clean Energy Systems (CES) gas generator and the Ramgen engine. Targeted and broad-based solicitations were issued in FY 2001 to continue activities in the five technology development areas, many of which are crosscutting

R&D activities. Current projects that will continue as essential activities under the HEET Program are discussed in Section 5.

4.1 Advanced System Analysis

This element contains one program work area, ***Concept Development***. In this element, systems analysis will be performed to evaluate new, promising concepts such as hydraulic compression or advanced cycles. Information derived from this element will be transferred into the other program elements for further development or assessments.

4.2 Simple/Combined Cycle Development

This element contains five work areas: Syngas Combustion, Durable Materials, Condition Monitoring, Design Tools and Aero-Thermal Technology.

The ***Syngas Combustion*** element will provide the technology to produce clean electricity from coal fuels in advanced clean-coal power systems. Technologies such as catalytic combustion, trapped vortex, or other advanced after-treatment configurations will be developed and validated to reduce emissions from coal-fired turbine plants to near zero levels.

Durable Materials will be developed (1) to withstand ultra-high temperature, corrosive coal-fueled environments; and (2) to reduce the cooling loads on hot turbine parts. This will enable increased firing temperatures and pressures to achieve Vision 21 performance goals.

Condition Monitoring in the HEET Program is aimed at (1) doubling current power plant efficiencies with no increase in operating and maintenance costs, (2) flexibility of 400 starts peryear for gas fueled systems and load change on a daily basis for coal systems, (3) RAM improvement, and (4) operation on coal syngas. Options for reducing operation and maintenance costs include (1) limiting degradation, (2) operating at optimal design conditions while the system is at off-design conditions, (3) improving component life, and (4) increasing the time between major overhauls. RAM improvement studies will include performance-based maintenance and total conditioning, overhauling, and low-NO_x combustion monitoring. Technologies developed in this area include high temperature sensors, prognostics, diagnostics, controls systems, and instrumentation hardware.

Aero-Thermal Technology will address advanced cooling, aerodynamic designs, and durability under high loaded conditions. Activities will include new design configurations and testing to ensure that advanced materials and combustion systems are capable of high performance levels. Increased performance of air cooled condensers to reduce water consumption will be achieved.

Design Tools using advanced numeric simulations can assess new engine performance while greatly reducing the time needed for development and testing. With continued advances, large-scale computing facilities as well as distributed computing resources may make it possible to predict full-engine behavior. This will allow virtual tests of the complex interactions expected to occur in hybrid energy plants. If successful, this could save the cost of building less-than-optimal prototype plants, because many of the component interactions could be explored before building a physical system.

4.3 Hybrid Cycle Development

The specific program objective is to achieve the required cost reductions for hybrid systems by combining HEET turbines with Fuel Cell product line resources. Current gas turbines cannot meet the pressure ratios, mass flows, and other critical operating and performance parameters of high-temperature fuel cells. Currently available small-scale fuel cells and turbines will be used to evaluate and resolve some of these integration issues. The DOE Fuel Cells Program is focusing on the Solid State Energy Conversion Alliance (SECA) with the goal of producing a core solid-state fuel cell module that can be produced at a cost of no more than $400/kW. The aim of the Hybrid Cycle Development element is to produce turbine technology for SECA turbine-fuel cell hybrids, and the ultimate goal is testing a near-commercial-scale multi MW Vision 21 coal-fired hybrid power system.

The ***Hybrid Teams*** work area will consist of one consortium of industry members. The ultimate goal will be to conduct near-commercial-scale demonstrations of Vision 21 hybrid power systems. The industry team will consist of power system developers, sub-system developers, system packagers, and customers. One near-term team will focus on producing a virtual simulation that can visualize and model system performance and manage distributed generation through information technology. Technologies deployed will use heat engines as a major component of the hybrid power system. These heat engines will undoubtedly include new mini gas turbines and other advanced heat engines. The goal for the team will be Vision 21 performance targets.

4.4 Technology Base Development

To support the development and operation of HEET power systems, R&D will be conducted by teams of U.S. government organizations, universities, and DOE national laboratories. These teams will be structured to leverage government and private-sector resources and guided by industrial review boards. Roadmaps for the technology base research and development elements have been prepared with industry, university, and academia. Key R&D technology needs are combustion and low emissions technologies, materials, advanced computing, and condition monitoring. The R&D will support the related private sector activities for development of HEET technology.

5. Current Projects Under the HEET Program

The activities listed below describe currently funded projects that relate to the goals of the HEET program.

5.1 Hybrid Cycles

The intent of the hybrids work in the HEET Program is to resolve integration issues, using very small turbines as an expedient method for investigating interface issues. The focus is to develop a suitable larger-size (mini) turbine for use in a SECA turbine-fuel cell hybrid that costs $400/kW or less.

Fuel Cell Energy is working with various gas turbine manufactures to develop a hybrid power system that will combine a fuel cell and a gas turbine to generate electricity at ultra-high efficiencies. Integration issues are being resolved by coupling a micro-turbine with a molten carbonate fuel cell. This information will be used to develop an engineering conceptual design of a 40 MW Vision 21 hybrid power module. This project was awarded under the first Vision 21 solicitation in March 2000.

Siemens Westinghouse Power Corp. is producing a modular natural gas turbine with extended fuel-use capabilities and the ability to work within a turbine-fuel cell hybrid system.

Honeywell International is working on the first stages of development for a new type of planar solid-oxide fuel-cell hybrid system. In the mature version of the technology, the fuel cell will be linked with a micro-turbine to use the energy remaining in the high-temperature exhaust gases exiting the fuel cell.

5.2 Simple/Combined Cycle Development

5.2.1 Advanced Concept Studies

Six projects were selected in April 2000 to begin examining innovations that could enhance the efficiency and environmental performance of gas turbines systems greater than 30 MW in output. About half the U.S. demand for gas turbine systems through 2020 is expected to be for industrial turbines suitable for both central and distributed power applications. The goal is to develop low-cost, zero-emission natural gas/coal fired power plants with efficiencies close to double that of today's fleet; while reducing operations, maintenance, and capital costs by at least 15 percent compared to comparable size units operating today. These turbine systems are planned for use as power modules in Vision 21 energy plants. This will be achieved by integrating the turbines into a simple or combined cycle configuration.

Pratt & Whitney will work to develop an intercooled gas turbine with high efficiency without a bottoming cycle and at low capital cost. The study will configure a dry, low emissions combustor, improve cooling and turbine technology, and extend current turbine materials technology.

Rolls-Royce Corporation will develop a highly efficient and economically viable power system based on the latest aero-derivative gas turbine and low emissions combustion technologies. The system will incorporate steam injection, recuperation, and intercooling technologies. The study will feature an outline of a plant that could lead to commercialization of the technology.

Siemens Westinghouse Power Corp. will work to develop a modular gas turbine with new enabling technologies in a single, low-cost system design that holds worldwide applications. The turbine will be fuel flexible, operating on natural gas and syngas derived from coal or biomass.

GE Power Systems will conduct feasibility studies of three broad categories of gas turbines: aero-derivative, heavy duty, and potential hybrids. GE will recommend an engine configuration based on these studies.

Two projects announced in March and June 2000 are developing alternative engine concepts. ***Ramgen Power Systems Inc.*** is developing a novel concept that uses ramjets to spin a wheel and generate power. The technology is exciting because it has the potential to significantly lower power-generation initial and maintenance costs, perhaps by as much as 50 percent. The Ramgen engine concept accepts waste fuels and very lean fuels such as the unutilized fuel from a fuel cell. The goal of the project is to develop a pre-prototype ramjet-like engine that can be a component in Vision 21 energy plants. Use of the engine on opportunity fuels, especially on coal-bed methane, is of interest. Ramgen will test a 10- to 15-MW engine, synchronize the engine to the power grid, and initiate analysis and design work for a second engine.

Clean Energy Systems is designing and testing a 10-MW high-temperature gas generator that would be used in a zero-emissions power plant. The gas generator, which burns a clean fuel (methane or practically any gaseous fuel or synthetic fuel), is based on rocket engine technology. The project was selected in the first group under the Vision 21 Program solicitation. NETL believes that the CES approach is a highly innovative approach that has substantial promise for increasing the efficiency and reducing the cost of power generation using coal.

5.2.2 Innovations for Environmentally Superior Power Plants

General Electric Co. was selected in December 2000 to improve the environmental performance and efficiencies of tomorrow's high-efficiency turbines. In one project, GE will develop a prototype combustor that will reduce smog-causing Nox emissions by 50 percent or more compared to current lean, premixed gas turbine combustors.

In a second project, GE will develop a "smart power turbine" sensor and control system. GE will work to develop a suite of novel sensors that will measure combustor flame temperature and hot-gas-component life directly. These sensors and controls would be applicable to both new and existing turbines.

5.2.3 Durable Materials

High-strength materials will be one of the critical requirements for Vision 21 high-tech power plants. Two projects were selected in June 2001 in the third round of the Vision 21 competition. These projects will help improve the strength and durability of tomorrow's metals.

Texas A&M University will develop a model that describes how single-crystal turbine blades respond to high temperatures and how defects form and move through turbine blades.

The University of Pittsburgh will work to improve the durability of turbine blade coatings, a critical issue in industrial engines because of the greater variety of fuels utilized, many of which contain sulfur, alkali metals, vanadium, or a mixture.

5.2.4 Electricity Reliability

DOE is supporting an effort with private industry to extend the life and improve the operation of advanced turbine power plants. Two of four projects selected in August 2001 will focus on protecting turbine components from erosion; the other two will study ways to improve turbine stability and performance.

Siemens Westinghouse Power Corp. will work to improve the life cycle of advanced gas turbines by developing, building, and installing an on-line system to monitor thermal barrier coatings (TBCs). TBCs protect the engine and components against high temperatures.

Solar Turbines Inc. will team with CFD Research Corp., Siemens Westinghouse Power Corp., and Los Alamos National Laboratory to produce a laser-stabilization system. The purpose is to reduce combustion vibrations that can lead to turbine instability.

EPRI, along with South West Research Institute, will develop a technology that assesses and manages the life of protective coatings used on natural gas turbine blades and vanes to protect them against high temperatures.

In another project, ***EPRI*** will team with Impact Technologies LLC, Boyle Engineering International, and Carolina Power & Light/Progress Energy to develop a computer program that assesses the total health of natural gas turbines and improves their RAM.

5.2.5 Technology Base Projects

DOE national laboratories are involved in turbine-related R&D. These projects are technology-base development activities. Several projects support R&D on higher performance materials for demanding turbine environments. NETL on-site work is in several technology development areas.

Oak Ridge National Laboratory (ORNL) is working on welding and weld repair of single crystal gas-turbine alloys. ORNL will determine the welding behavior of single crystal nickel-based superalloys and develop methodologies to fuse parts without stray grain formation. Currently, large parts that have a single crystal microstructure yield high performance, but require exotic and expensive casting procedures.

Argonne National Laboratory is working on two projects that involve structural ceramics. The goal in one project is to develop non-destructive evaluation (NDE) technology for environmental barrier coating and residual life estimation. Argonne will explore the use of NDE techniques to examine accumulated damage in turbine blade environmental barrier coatings. In a second project, Argonne is working on a new approach for evaluating the mechanical reliability of ceramic gas turbine components. Argonne will develop mechanical testing procedures that use miniaturized specimens from ceramic turbine components.

Sandia National Laboratories and ***NETL*** are collaborating to investigate the structure of high-pressure pre-mixed flames. The research community developing advanced turbine combustion simulations has repeatedly stated the need for this data. Successful simulation of turbine combustion that accounts for fuel variability could allow turbine developers to market engines that operate on a wide range of fuels.

NETL continues R&D on coal syngas combustion and ultra-low emissions. Activity includes the design of a reheater for the CES rocket concept, testing of a trapped vortex combustor under high pressure/temperature conditions, development of a novel flame sensor, and an international

collaborative program called "Energy Fuels Simulation Validation." This is a collaborative partnership with the European Union, NASA, and DOE to develop the most accurate design tools for fossil fuel energy gases and hydrogen.

Clemson University administers the Advanced Gas Turbine Systems Research (AGTSR) consortium. The national network of universities under the AGTSR is mobilizing the scientific talent needed to understand the fundamental mechanisms impeding turbine performance gains and to identify pathways to overcome them. The AGTSR is a university/industry consortium that has grown into a vibrant virtual laboratory with national scope and worldwide recognition. Several projects in HEET Program technology development areas are highlighted below.

Georgia Tech (combustion and emissions control) is developing active control approaches to prevent combustion instabilities that have caused excessive noise, vibration damage, and removal of turbines from commercial service for repair. Georgia Tech has demonstrated active control, which has produced a factor of four times reduction in combustor pressure oscillations. Georgia Tech has also been granted two patents and another is in the process, and is working to transfer the technology to four turbine companies.

University of California, Irvine (combustion and emissions control) is using several fuels to acquire data for design rules to avoid auto-ignition in lean, premixed, fuel-flexible turbine combustion systems. A knowledge of fuel auto-ignition characteristics as a function of operating parameters is needed for the design of low NO_x combustors. Fuel-air residence times in the premixers of turbine combustors must be sufficiently long for the thorough mixing needed to inhibit Nox formation, but not so long that premature auto-ignition or damaging flashback into the premixer chambers occurs.

Mississippi State and the ***Air Force Institute of Technology*** (aero-thermal) are working to improve aero/cooling design of turbines. The team is providing turbine manufacturers with a database of measured surface roughness and resulting parameters significant to aerodynamic and cooling performance, determined from over 100 parts that had experienced service in turbines. Past analyses of vanes and blades that had operated in turbines have shown that methods established by turbine manufacturers to represent airfoil surface roughness for aerodynamic and heat transfer analyses are not universally appropriate.

University of Connecticut and University of California, Santa Barbara (materials) are developing advanced TBC coatings to protect turbine materials from high temperatures and to provide longer lifetimes [2,3]. Achievement of the project goal of 300°F higher temperature capability for TBC coatings could increase turbine efficiency, thereby producing a national fuel cost savings of $2.2 billion over 10 years with corresponding substantial reductions in CO_2 emissions. Several U.S. gas turbine manufacturers, a coating supplier, and an instrument maker are actively involved in a University of Connecticut project to develop a low cost and portable prototype of a non-destructive inspection (NDI) instrument to be utilized by turbine manufacturers, overhaul facilities, and coating suppliers. NDI methods are needed to alleviate manufacturing quality issues and operational lifetime inconsistencies that have impeded the full implementation of the power and efficiency benefits of TBCs for industrial and utility turbines.

IPITEK, a small business, is investigating phosphor materials to develop temperature and pressure dependent non-contact probe integrated into turbine thermal barrier coatings, while Advanced Fuel Research is developing dual wavelength infra-red sensor system for in-use turbine blade coating diagnostics. The efforts are being supported by other projects in the Advanced Research Program developing optical techniques for surface temperature measurement based on the fluorescent emission of rare earth ion-doped phosphors [4].

6. Concluding Remarks

The United States will need to rely on fossil fuels for electricity and transportation fuels well into the 21st century. It makes sense to rely on a diverse mix of fossil energy resources rather than on a limited subset of resources. Benefits of the HEET Program match those of the Vision 21 Program:

1.) ***Removes Environmental Barriers to Fossil Fuel Use*** – smog- and acid-rain-forming pollutants, particulate and hazardous air pollutants, solid waste, and CO_2

2.) ***Keeps Energy Costs Affordable*** – wide range of low-cost fossil fuel options available.

3.) ***Continues U.S. Leadership Role in Clean Energy Technologies*** – promotes export of U.S. fossil energy and environmental technologies, equipment, and services.

4.) ***Provides the Most Certain Route to Achieving US Energy, Environmental, and Economic Objectives*** – technology innovation is the best way to address the challenges to our electric power and fuel supply infrastructure.

The HEET Program will result in significant public benefits. Lower energy consumption leads to fuel cost savings, which will mean electricity cost savings for the U.S. consumer. Improved efficiencies will also yield reduced emissions and a cleaner environment for the U.S. consumer. HEET systems offer conservation of natural resources (water and land), especially critical in water-sensitive areas like the southwest U.S. HEET systems will promote system reliability and electric grid stability. Because HEET systems will be fuel flexible, they will expand the options for high-efficiency conversion of domestic fossil energy resources into electric power. They will provide early entry high efficiency technologies for distributed generation at substations and other critical locations in the grid system. Enabling technologies developed under the HEET

Program will benefit and support other missions of the U.S. government, such as enhancing defense capabilities and serving the needs of future military operations. The U.S. power generation industry currently exports more than $3 billion in power generation systems annually, and about one third of this is turbine systems. According to the 2000 Frost and Sullivan report on North American Gas and Steam Turbine Markets, $8 billion in turbine power plant sales occurred in 1999 in the United States. When turbine-fuel cell hybrid systems penetrate the U.S. market, these systems will produce less than 1-ppm Nox emissions and virtually no Sox emissions. They are at least 70-percentefficient, have a concentrated Co2 stream, and no particulates even when utilized as electric generation modules in the coal-fired power plants of Vision 21 energy facilities.

References:

1. Islas, J., *The Gas Turbine: A New Technology Paradigm in Electricity Generation*, in Technological Forecasting and Social Change 60 (1999) 129-148
2. Tolpygo, V.K., Clarke, D.R., and Murphy, K.S., Surface and Coatings Tech. 2001 (146-147) 124-131.
3. Sohn, Y.K., Vaidyanathan, K., Ronski, M., Jordan, E.H., and Gell, M., Surface and Coatings Tech. 2001 (146-147) 102-109.
4. Noel, B.,Turley, W., Lewis, W., Tobin, K., and Beshears, D., in *Temperature, Its Measurement and Control in Science and Industry,* Vol. 6. American Institute of Physics, 1992, pp 1249-54.

SECTION 1

ADVANCED GAS TURBINE MATERIALS

1.1. Single Crystal

THE CREEP BEHAVIOUR OF AS-CAST SX CM186LC AT INDUSTRIAL GAS TURBINE OPERATING CONDITIONS

I. M. Wilcock[1], P. Lukáš[2], M. Maldini[3], J. Klabbers[4], B. Dubiel[5] and M.B. Henderson[6]

[1]QinetiQ, Farnborough, Hampshire, GU14 0LX, UK
[2]Academy of Sciences, Brno, Czech Republic
[3]CNR-Tempe, Milan, Italy
[4]Institute for Materials and Processes in Energy Systems, Jülich, Germany
[5]University of Mining and Metallurgy (AGH), Kraków, Poland
[6]ALSTOM Power Technology Centre, Leicester, UK

Abstract

Increases in the operating temperature of industrial gas turbines are driving the requirement for high temperature, single crystal nickel alloys for turbine blade applications. A candidate for this application is the aerospace alloy CM186LC, and this is being investigated as part of a COST 522 programme WP1.1. The creep behaviour of the SX CM186LC has been studied to assess its suitability for use in the industrial gas turbine environment. A fully quantitative microscopic characterisation of cast SX CM186LC has been made which provides details of the complex microstructure of this alloy without any heat treatment. Creep tests have been conducted at a variety of stresses and temperatures relevant to operating conditions in a typical industrial gas turbine and the results are compared to other single crystal nickel alloys. Similarly, the effect of crystal orientation on the creep behaviour of CM186LC single crystals has also been assessed. Microscopic analysis of the failed creep specimens has aided understanding of initiation and failure mechanisms operating within the alloy.

Keywords: Creep, Single Crystal, CM186LC, Industrial Gas Turbine

Introduction

Continual demand for improvements in gas turbine engine power, efficiency and durability over the years has been closely related to improvements in turbine blade materials and cooling systems. Single crystal nickel based superalloys have been proven to possess superior creep properties over conventionally cast and directionally solidified materials, and hence are widely used in the aero industry; they have only fairly recently been introduced into industrial gas turbines (IGT). Single crystal (SX) CM186LC is seen as a potential low cost alternative to blade alloys such as CMSX-4. The aim of the COST522 WP1.1 is to characterise the mechanical properties of SX CM186LC at conditions relevant to IGT applications.

The main differences in the chemical compositions of CM186LC and CMSX-4 (Table 1) are the addition of carbide-forming and grain boundary strengthening elements, such as carbon, hafnium and boron. The driving forces behind the development of SX CM186LC are the potential cost and performance benefits arising from having defect tolerant SX components without the need for an expensive solution heat treatment stage; the disadvantage being an extremely complex multi-phase microstructure.

	Ni	Co	Cr	Mo	Al	Ti	Ta	W	Re	Nb	B	Hf	Zr	Fe	C
CMSX-4	60	9.7	6.5	0.6	5.6	1.04	6.5	6.4	2.9	<0.05	0.002	0.11	0.001	0.038	0.0025
CM186LC	60	9.3	6.1	0.51	5.7	0.73	3.4	8.4	2.9	-	0.016	1.4	0.004	0.027	0.062

Table 1. Chemical composition of the second generation nickel alloys CMSX-4 and CM186LC (wt. %).

IGT engines often operate under constant load, steady state conditions for long periods of time; the expected life of a cooled turbine blade is between $3x10^4$ and 10^5 hours [1]. The gas turbine inlet temperature in modern industrial turbines often exceeds 1300°C, leading to a blade metal temperature of between 750 to 950°C and this range was chosen for the laboratory tests to be conducted within the current study. Turbine blades are primarily cast with the <001> orientation along the blade axis due to both ease of casting and this orientation providing the optimum combination of mechanical properties. As well as the principle stresses acting along the <001> axis of the blade, there are tangential stresses that act along orientations close to the <001> - <011> side of the crystallographic triangle. Therefore, the majority of the testing has been on <001> specimens, but a number of <011> tests were also conducted, together with <111> for the purpose of the CM186LC deformation models. The creep data are required for preliminary design and also to support development of life prediction techniques based on inelastic finite element stress analysis.

Experimental Procedure

Material was supplied in the form of solid cast bars of 16, 14 or 12 mm diameter and a detailed structural investigation was conducted using light microscopy (LM), scanning electron microscopy (SEM) and transmission electron microscopy (TEM). Standard metallographic preparation procedures were employed for observations by LM and SEM. Foils for TEM were prepared by mechanical polishing and twin jet thinning in a solution of 95% acetic and 5% perchloric acid at a temperature of 12°C and voltage of 95V.

Creep tests have been conducted at 50°C intervals between 750 and 950°C at a range of stresses considered relevant to those seen by an IGT blade. A number of higher stress tests were also conducted to obtain a full stress/rupture curve for modelling the creep behaviour. Tests were conducted under either constant load or constant stress, and extensometry was used with digital data recording software for continual time and strain measurements. Strain-time data from individual tests were analysed to determine times to various levels of strain and presented using the Larson Miller Parameter. Representation of creep data in terms of the Larson Miller Parameter allows extrapolation of short times and high temperature data to longer times at lower temperatures representing service conditions [2], assuming similar deformation mechanisms are operating over the range of the test conditions.

Both fractured and specimens from interrupted tests have been sectioned to allow detailed SEM and TEM investigation. For the fractured specimens, examination using SEM allowed crack initiation sites to be identified and investigated.

Results and Discussion

Microscopy of Virgin Material

The microstructure of SX CM186LC is very different to the regular "cuboidal" γ' structure seen in the traditional fully solution treated SX superalloys such as CMSX-4. SX CM186LC basically consists of two components: dendritic regions and eutectic colonies. Figure 1 shows a LM image of a typical section taken perpendicular from a <001> bar with secondary and tertiary dendrites growing in the [100] and [010] directions. From pictures such as Figure 1, secondary dendrite arm lengths were determined and found to be between 0.2 and 1.0 mm. The volume fraction of the eutectic colonies is between 20-25 %.

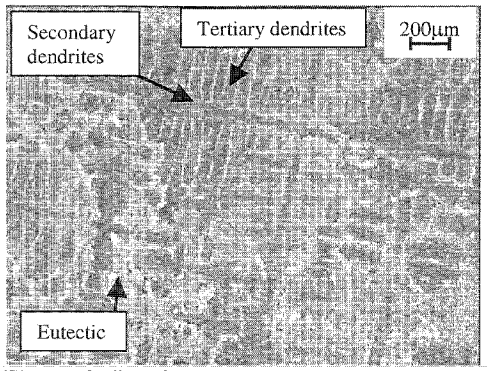


Figure 1. Dendrite structure in a <001> CM186LC bar showing dendrite arms in the [100] and [010] directions.

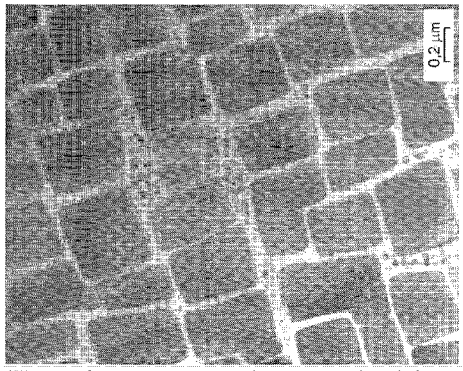


Figure 2. TEM image showing cuboidal γ' particles separated by γ channels with secondary spherical γ' precipitates within a dendritic region in CM186LC.

The dendritic regions consist of a more or less regular distribution of cuboidal γ' particles with a typical size of 0.4 µm. The estimated total volume fraction of the γ' particles is 70 to 80 %, and within the dendritic region it is ~70%. In some of the γ channels spherical γ' particles were found; their diameter lies between 20 and 50 nm (Figure 2). Figure 3 shows that within the eutectic colonies the morphology of the γ/γ' structure is irregular, characteristic of eutectic solidification; the major constituent being γ' with a feature size of 10 µm.

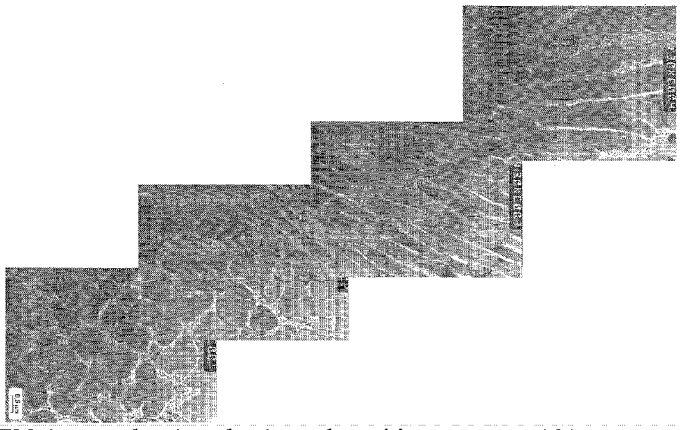


Figure 3. TEM image showing the irregular γ/γ' structure within a eutectic region in CM186LC.

Primary carbides rich in Ta and Hf were found in the eutectic colonies. The carbides are irregular in shape and often in the form of curved platelets (Figure 4) with the largest dimension exceeding 30 µm. The material also contains pores, which were found predominantly in and near to the eutectic colonies. This suggests that the eutectic may represent areas of weakness in the material.

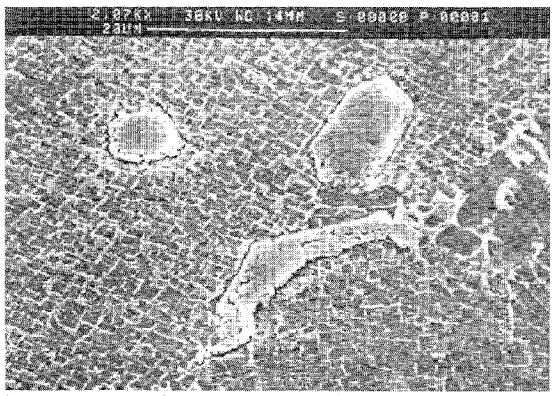


Figure 4. SEM image of primary MC carbides within interdendritic region.

Creep Testing

SX CM186LC generally exhibits a dominant tertiary stage during high temperature creep deformation, whereas the primary and secondary stages often appear less important and sometimes negligible, both in magnitude and in duration (Figure 5). However, lower temperature tests (750 and 800°C) do show significant sigmoidal primary deformation as often found in creep tests on single crystal superalloys at high stresses/low temperatures (Figure 5), where the threshold stress for particle cutting is exceeded. Figure 6 shows a strain softening response and a linear dependence of the strain rate on the strain is manifested during tertiary creep up to large strains, corresponding to 80-90% of the creep life of the specimens.

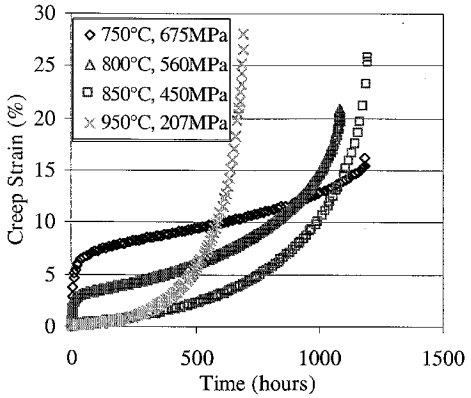


Figure 5. Creep strain versus time plot showing the reduction in the primary creep strain as temperature increases.

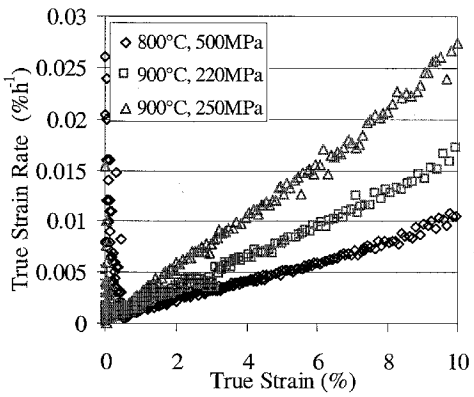


Figure 6. Plot of strain rate versus strain showing linear strain softening up to large values of strain.

Figure 7 shows the creep curves from four low stress tests conducted at 950°C, which demonstrate stabilised secondary creep regimes. The two lower stress tests are on-going at the time of publication, whilst the two higher stress tests have ruptured. Analysis of the <001> rupture data showed that a Larson Miller parametric form with the constant C=20 gave a good

representation of the data, Figure 8. Unbroken tests are indicated with an arrow and these have been excluded from the data used to input the linear regression fitting equation. Figure 8 shows a good fit to the parameter across the whole range of temperatures. It must also be noted that in general (particularly for the shorter tests) whether the test was conducted under constant stress or constant load did not greatly effect the test life. Hence, it was decided not to distinguish between the two test types when fitting the trend line to the data.

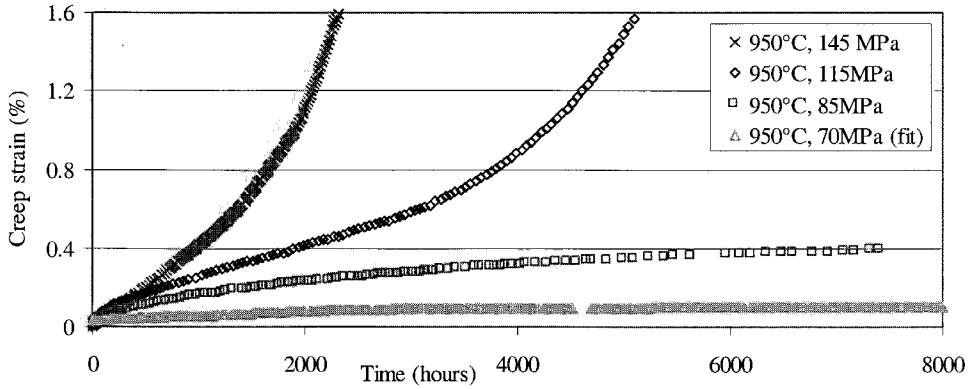


Figure 7. Creep strain versus time plot showing the differences in short and long term creep curves at 950°C.

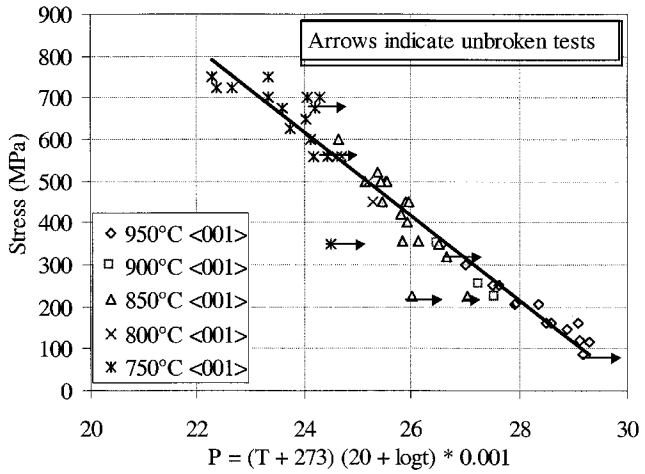


Figure 8. Rupture results in the <001> direction with Larson Miller Parameter (C=20).

The effect of orientation is shown in Figure 9 (data from the <111> and <011> tests are shown plus the trend line taken from Figure 8) and the ranking can be seen to be dependent on both stress and temperature. As with Figure 7, the trend lines are fitted using linear regression excluding the unbroken tests which are labelled with arrows. At high stresses the <111> specimens displayed the longest lives followed by <001> and then <011>. However, the data from all three orientations appear to converge at stresses more relevant to IGT components.

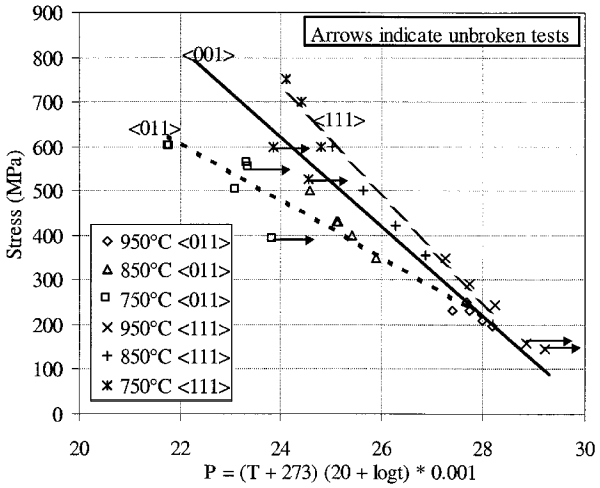


Figure 9. Comparison of the rupture results for <001>, <011> and <111> CM186LC.

Of more relevance to the IGT designer is the time taken to reach 0.1% creep strain rather than time to rupture. Figure 10 shows these data, once again in terms of Larson Miller, for <001>, <111> and <011> orientated CM186LC. This plot shows there is little difference between the time taken to reach 0.1% strain for <001> and <011>, and as with rupture, <111> displays the superior creep properties.

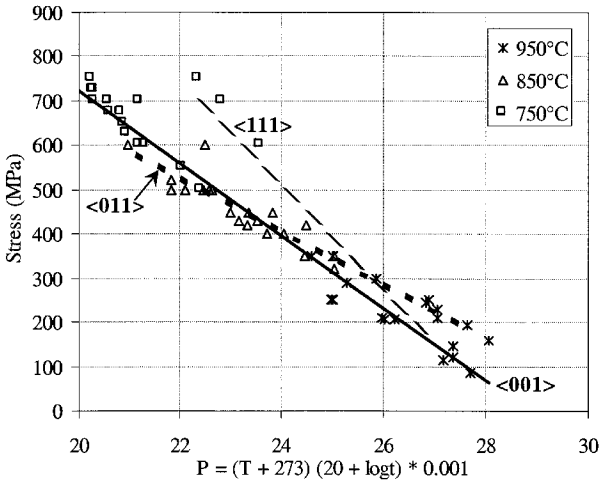


Figure 10. Comparison of time to 0.1% strain for <001>, <011> and <111> CM186LC.

Comparing the rupture data from the current work with results for CMSX-4 [1] and SRR99 [3], CM186LC is seen to have inferior creep strength at high stress/low temperature conditions (Figure 11). SRR99 is a 1st generation SX alloy that contains no rhenium, which may be expected to demonstrate inferior creep properties to both CM186LC and CMSX-4.

These data underline the importance of the solution treatment stage for single crystal superalloys in producing a homogeneous and uniform distribution of strengthening precipitates and elements that are rejected to the eutectic colonies during solidification. Also, the benefits of Re additions in providing longer term creep strength are illustrated. CM186LC is seen to have inferior creep strength compared to CMSX-4 at all test conditions, but it is superior to SRR99 at the low stress/high temperature regime and demonstrates the attractiveness of CM186LC to IGT designers over first generation SX superalloys, such as SRR99.

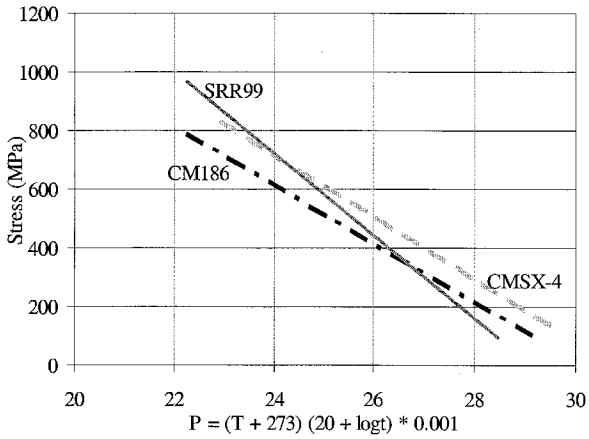


Figure 11. Comparison of the rupture results in the <001> orientation for CM186LC, CMSX-4, and SRR99.

Post Creep Microscopy and Fractography

A limited amount of fractography has been conducted. Creep cracks were seen to initiate at fractured carbides, carbide/matrix interfaces and casting pores, with propagation along (001) planes (Figure 12), perpendicular to the applied stress. The fracture surface morphology did not change substantially with test temperature.

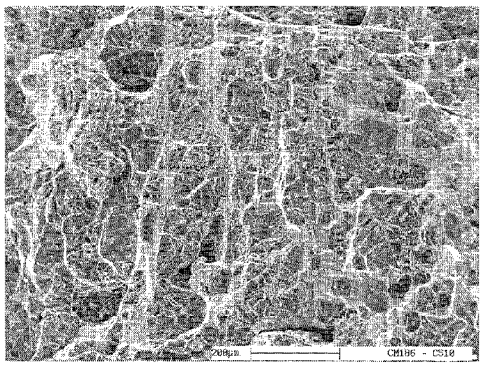


Figure 12. SEM image of fracture surface of C510 (800°C, 560MPa).

Rafting of the γ/γ' structure was found in all the specimens tested at 900 and 950°C, but not in the lower temperature tests. High temperature medium to long term creep (shown in Figure 7) is of prime relevance to IGT conditions and hence requires detailed analysis. SEM and TEM examination of a specimen tested at low stress at 950°C revealed rafting in both the dendritic regions and the eutectic colonies (Figure 13). However, the specimen tested at 950°C at a higher stress had rafting in the dendrites only; the γ/γ' structure in the eutectic colonies remained unchanged. Rafting, or coagulation, of the eutectic γ' in the lower stress test has occurred due to the increased exposure time (~900 hours c.f. ~9000 hours). It should be noted that there are significant differences in primary γ/γ' volume fractions between samples. At all stresses, the dislocations were piled-up mainly at the γ/γ' interfaces, with evidence of dislocations within the large γ' (Figure 14a) in the eutectic colonies.

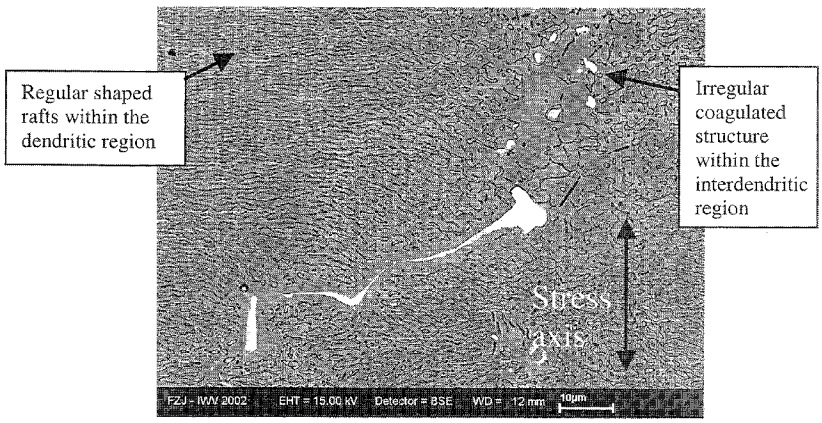


Figure 13. SEM image of irregular and large γ' rafts after creep deformation at 950°C, 115MPa (specimen cut longitudinally to the cast axis of the bar).

Further analysis of the specimens tested at 950°C and low stresses has revealed the presence of TCP phases. The composition measured by EDX corresponds well with data taken from the literature. The chromium contents of TCP- phases in rhenium containing alloys, for σ-phase as well as P- phase, is reported to be lower and similar to the chromium- content in the γ- matrix [4, 5]. This was also found for CM186LC. The needle-shaped phases (Figure 15) were seen to be strongly enriched with rhenium and tungsten, however, as the composition of σ- phase and P- phase are reported to be identical, it was impossible to state which type of TCP was present in this CM186LC sample. The number of needle shaped precipitates present was approximately the same for all investigated specimens (only high temperature-low stress samples), and this number was very low and it is unlikely that the deformation behaviour is influenced by these needle precipitates under the test conditions examined.

Mechanisms of creep deformation in CM186LC

TEM examination of virgin specimens found the γ/γ' in the dendritic regions to be largely free of dislocations. As SX CM186LC is a negative misfit alloy, the effective stress at the outset of testing will be higher in the horizontal γ channels compared with the vertical γ channels. Thus, generation of dislocations starts in the horizontal channels and is assisted by percolation of

dislocations from eutectic colonies through to the dendrite cores, followed by piling-up at the γ/γ' interfaces to reduce misfit strains. Little evidence of dislocation cutting of the γ' particles was found, and it is proposed that deformation was confined predominantly to the γ channels. Dislocation creep is the dominant mechanism with dislocations moving by a combination of glide in the matrix, aided by climb and cross-slip processes along the γ/γ' interfaces to by-pass the particles and assist recovery processes, such as the reaction and annihilation of dislocations with opposite sign to decrease dislocation density. Particle cutting is largely dependent on the stress and temperature conditions. Diffusion becomes more important at higher temperatures and lower stresses where more rafting was observed.



Figure 14a. Dislocation structure in interdendritic region of specimen tested at 950°C, 207MPa; dislocations observed within the large γ' particles.

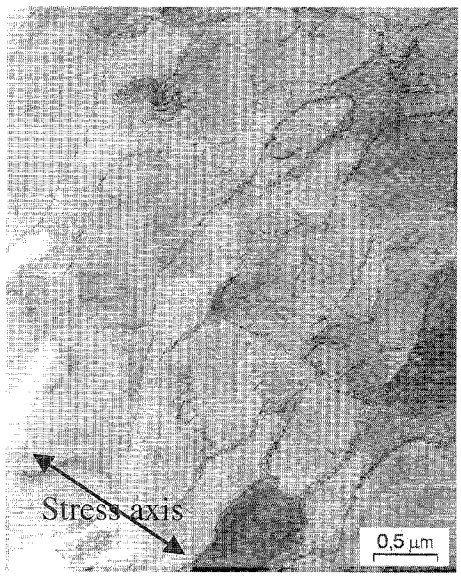


Figure 14b. Dislocation structure in dendritic region of specimen tested at 950°C, 207MPa; fewer dislocations observed within the γ' particles.

The size of the γ' particles in the eutectic colonies are sufficiently large for independent activation of dislocation sources within the γ'. Thus, deformation of the large γ' particles occurs independently of the deformation in the adjacent γ matrix and so contributes to the overall deformation of the specimen.

At higher temperatures (above 900°C), rafting of the γ' particles to form "infinite", thin plates (thickness ~0.5 µm) occurs by means of stress and strain driven diffusion process. This, generally, "closes" many of the vertical γ channels and encourages cutting of the γ' rafts. However, the post creep dislocation structure observed by TEM was found to be similar at both lower and higher temperatures with dislocations being present mainly at the γ/γ' interfaces (Figure 14). The eutectic colonies were found to play a similar role to that seen at lower temperatures.

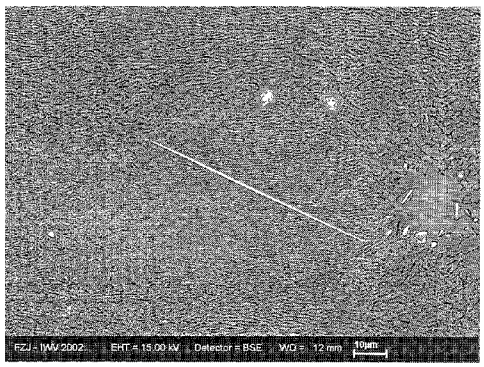


Figure 15. SEM image of needle shaped TCP shaped precipitate (TCP-phase).

Conclusions

- As-cast SX CM186LC consists of dendritic cuboidal γ/γ' regions and 20-25% eutectic.
- At high stress/low temperatures <111> specimens displayed higher creep strength than <001>, and <001> displayed a higher creep strength than <011> at the same conditions.
- The creep strength for the three principle orientations appeared to converge at lower stresses.
- Specimen failures were predominantly seen to initiate from the eutectic colonies, carbides and microporosity.
- For a range of stress and temperature loading conditions, dislocation structure is mainly confined to the matrix channels with little evident cutting of the γ' particles. Dislocation activity was found within the eutectic γ' phase.

Acknowledgements

ALSTOM Power and QinetiQ gratefully acknowledge UK DTI for funding of this work. PL wishes to thank MSMT for grant support under contract OC522.80.

References

[1] C.K. Bullough, M. Toulios, M. Oehl, and P. Lukáš, Materials for Advanced Power Engineering 1998, J. Lecomte-Beckers et al, Editors, Part II, 861-878, Forschungszentrum Julich (1998)
[2] R.F. Larson and J. Miller, Trans ASME, Vol. 74, pp 765 (1952)
[3] Homewood, T., Ward, T.J., Henderson, M.B. and Harrison, G.F., Proc. Conf. on Modelling of Microstructural Evolution in Creep Resistant Materials, McLean et al., Eds., Imperial College London, (1998)
[4] Dariola R.; Lahrmann D. F.; Fields R. D., Superalloys 1988, ed. S. Reichmann, D. N. Duhl, G. Maurer, S. Antolovich, and C. Lund, (Warrendale, PA: The Metallurgical Society 1988), pp. 255 – 264
[5] Simonetti M.; Caron P., Materials Science and Engineering A, 254, 1998, pp.1 –12

THE LOW CYCLE FATIGUE BEHAVIOUR OF AS CAST SINGLE CRYSTAL CM186LC

D.W. Bale *, M Henderson *, B Dubiel ^, A Czyrska-Filemonowicz ^, C Guardamagna #, P Bontempi #, P.Mulvihill @ P. Lukas +, K.Obrtlik +, H. Kolkman –

* ALSTOM POWER Technology Centre, Leicestershire, UK
^ University of Mining and Metallurgy (AGH), Krakow, POLAND
# CESI SpA, Milan, ITALY
@ Powergen, Power Technology Centre, Nottingham, UK
+ Academy of Sciences of the Czech Republic, Brno, CZECH REPUBLIC
- National Aerospace Laboratory NLR, The Netherlands

Abstract

CM186 LC DS is well established as a first stage Industrial Gas Turbine (IGT) blade material and has been adopted by leading IGT manufacturers due to significant grain boundary tolerance and cost benefits. To increase the temperature capability, single crystal (SX) casting practices have been applied. The composition and heat treatment are identical to those of the DS variant meaning that the cost savings remain. The following paper characterises the Low Cycle Fatigue (LCF) properties of CM186LC SX, and considers the effects of orientation, temperature, strain rate and mean stress on the cyclic stress-strain and strain-life characteristics. The impact of LCF and creep loading interactions has also been studied by applying tensile and compressive dwell periods during the fatigue cycle. Fractographic and microstructural analysis of as-received and fatigued specimens has been conducted.

Keywords: Low Cycle Fatigue, Single Crystal, CM186LC, Industrial Gas Turbine

1. Introduction

To achieve improved efficiency and lower emissions targets, Industrial Gas Turbine (IGT) engine manufacturers are being challenged to increase the temperature capability of the materials used for a range of hot section IGT components. Engine testing and service experience of single crystal (SX) first stage turbine blades and vanes have demonstrated enhanced temperature capability, service life and reliability over conventional polycrystalline parts [1, 3]. However, strict limitations placed on the allowable low angle and high angle boundaries (LAB's and HABS's) within SX components often result in relatively low yields and, therefore, increased costs that are compounded by the expensive solution treatments that the alloys require.

CM186LC is a directionally solidified (DS) columnar grain superalloy [3] that has been adopted by a number of manufacturers for first stage vane and blade applications. The alloy has good castability, resulting in high yields and does not require a solution treatment. However, DS castings suffer from the presence of grain boundaries in highly stressed, none aerofoil locations such as the inner and outer shroud sections of multiple aerofoil segments [1]. Application of SX casting methods to produce CM186LC SX parts has been successful with an increased tolerance to HAB'S of up to 30° [2]. The cost savings delivered by DS CM186 LC remain in the SX form, resulting in much reduced costs compared with conventional SX alloys. The nominal alloy chemistry is provided in Table 1.

The alloy undergoes a two stage ageing treatment that consists of 4 hours at 1080°C ± 10 °C in vacuum, followed by 20 hours at 870 °C ± 5 °C. Rapid gas fan quenching in the presence of high purity Argon is utilised after each stage.

Ni	Cr	Co	Mo	W	Ta	Re	Al	Ti	Hf	C	B	Zr
Bal.	6	9	0.5	8	3	3	5.7	0.7	1.4	0.07	0.015	0.005

Table 1. Nominal Composition (wt %) of CM186 LC superalloy

The aim of COST 522 Work Package 1.1 has been to develop advanced life prediction methods for CM186LC SX turbine blades. A key property for gas turbine engineers is the material response to cyclic loading at high temperatures and this paper focuses on recent work to characterise the Low Cycle Fatigue (LCF) properties of CM186LC SX.

2. Low Cycle Fatigue Properties

The mechanical properties of single crystals are anisotropic with significantly different Young's Modulus values found for test bars cast in the three primary crystallographic orientations; namely <001>, <011> and <111>. The Young's modulus of <001> oriented crystals is significantly lower than for the other orientations; this provides improved thermal fatigue resistance for <001> aligned specimens and components, as well as lower plastic strain ranges and therefore greater LCF strength for the same applied strain range.

Testing has focussed on the properties of the <001> orientation, however a number of tests have also been conducted on <011> and <111> aligned specimens. Tests were performed at 550, 700, 850 and 950°C and the effect of strain rate was investigated by conducting selected tests at 0.6, 6 and 60 %/minute. Mean stress effects were studied by conducting tests at Rε ratios of 0.5, 0.05 and –1 (Rε = ε_{min} / ε_{max}). Finally, the interaction of LCF and creep was investigated by subjecting a number of specimens to compressive and tensile dwell periods during each successive cycle.

3.1 Cyclic Stress Strain Response

It can be seen from the <001> cyclic stress-strain data presented in Figure 1 that the plastic strain ranges are small with little variation between the elastic and plastic regions of the curves. There is a strong temperature dependence of the cyclic stress-strain response in the 700 to 950°C temperature range, however, the influence of temperature is much weaker below 700°C and little difference between the 550 and 700°C results is found. A limited effect of strain rate for tests conducted at 850°C at the higher strain rates of 60 and 6%/minute was observed and a single curve was fitted to the two data sets. However, a small reduction in stabilised cyclic strength was observed for specimens tested at a strain rate of 0.6%/minute. This is probably caused by stress relaxation due to creep at the lower ramp rate.

The effect of orientation on the cyclic response has also been investigated. To exclude the orientation dependence of Young's Modulus the total stress amplitude vs. plastic strain range data at half-life have been plotted, as shown in Figure 2. In most cases the <001> stress ranges are somewhat lower than those for the <011> and <111> orientations. The <111> data show a potential to fall outside the scatter band at plastic strain ranges >0.04%, however, further testing

would be required to confirm this trend. All present data can be contained within a +/-2 standard deviation scatter band. The apparent weak orientation dependence suggests that the data may be merged by normalising the elastic contribution of the cyclic stress strain response to that observed in the <001> direction. This method has been applied successfully and reported previously for CMSX-4 [4].

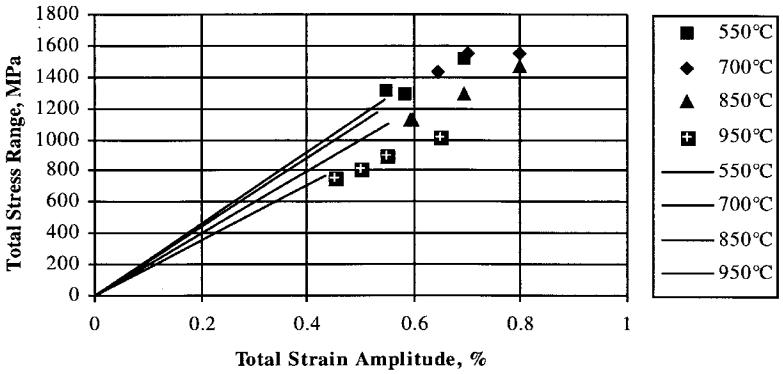


Figure 1. The effect of temperature on <001> aligned cyclic stress strain curves for Rε = -1 tests conducted at a strain rate of 6%/minute.

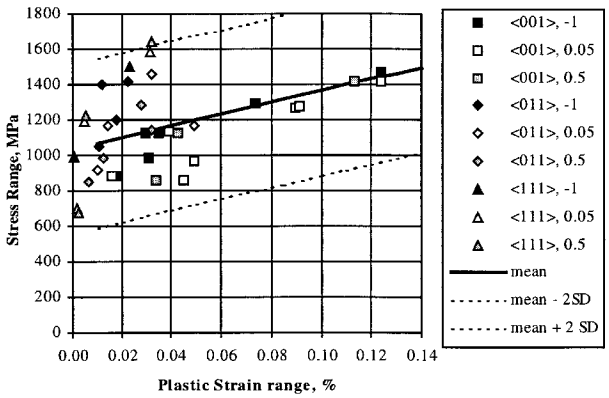


Figure 2: Total stress range versus plastic strain range for 850°C and 6%/minute tests.

Normalisation of the data can be achieved by modifying the total strain range, as follows:

$$\Delta\tilde{\varepsilon}_{<hkl>} = \left[E_{<hkl>}/E_{<001>}\right]\Delta\varepsilon_{<hkl>} \qquad (1)$$

Where $E_{<hkl>}$ is the Young's Modulus in the specimen and $E_{<001>}$ the Young's modulus in the precise <001> orientation, both measured at the appropriate test temperature.

The total strain range for each of the 850°C tests conducted at a strain rate of 6%/minute has been modified according to equation 1. The modified data versus stress range are plotted in Figure 3, all Rε ratios have been included and it can be seen that the data for all three orientations fall close to the mean line.

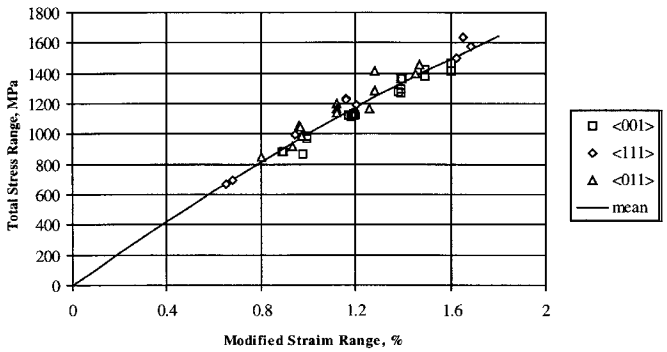


Figure 3: Modified strain range versus total stress range for 850°C and 6%/minute tests

3.2 Strain-Life Behaviour

In all cases, the <001> aligned data shows the greatest number of cycles to failure for a given strain range, followed by <011> and then <111>. Following the procedure identified previously [4], the total strain range data has been modified to account for the different Young's Moduli. This allows the data for all orientations to fit to a single curve. Figure 4 shows the modified strain range versus number of cycles to failure at 850°C and 6%/minute; whilst some degree of scatter remains, all the data points fall within a 2.5 factor scatter band on life. This implies that the modified strain-life data is independent of orientation, as was found for CMSX-4 [4].

Mean stress effects on the strain-life response of <001> aligned specimens was studied by applying Rε-ratios of 0.5 and 0.05 and comparing the results with Rε = -1 data. As shown in Figure 5, at 700°C (and below) substantial differences between the strain-life response for the three Rε ratios were observed, particularly at lower Δε. At higher Δε the maximum stress in the positive Rε ratio tests reduces to levels similar to those observed in the Rε = -1 tests, thus little difference in life is observed. At smaller strain ranges a high maximum and therefore mean stress is maintained throughout the test and this results in a shorter lifetime for a given strain range for the Rε = 0.05, and shorter still for the Rε = 0.5 tests. At higher temperatures (above 850°C) the mean stress influence diminishes. The maximum stress is reduced for the positive Rε ratio tests to similar levels to those of the Rε = -1 tests even at the lower strain ranges as a consequence of creep relaxation of peak and mean stress levels.

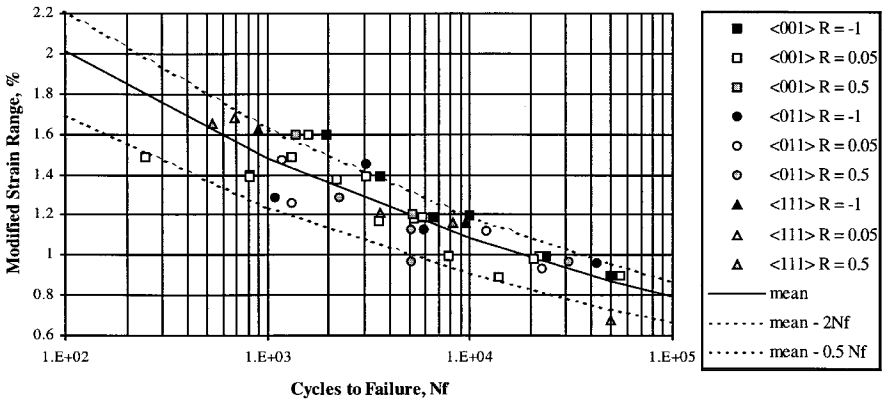


Figure 4. Modified strain range versus cycles to failure for 850°C, 6%/minute tests.

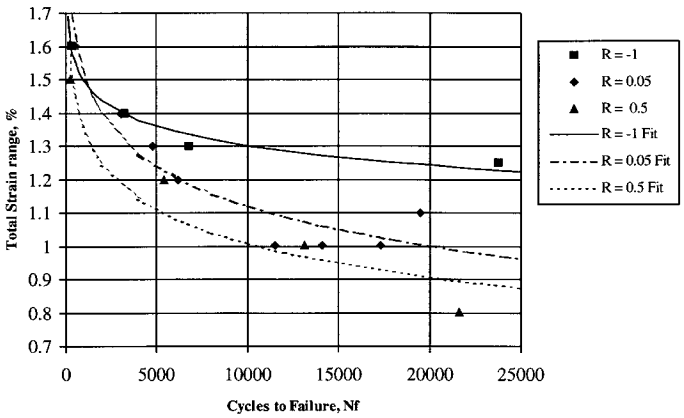


Figure 5. Effect of Rε ratio on the cycles to failure for <001>, 700°C and 6%/minute tests.

3.3 Interaction of Creep and Low Cycle Fatigue Behaviour

A series of tests have been conducted at 850 and 950°C, Rε = 0.05, using 2 minute peak tensile and compressive dwell periods (i.e., Creep-Plastic (CP) and Plastic-Creep (PC) cycles). Test data has been compared with the corresponding zero dwell period tests, as shown in Figure 6 for tests conducted at 950°C. Similar behaviour was observed at both temperatures. Both compressive and tensile dwell periods caused a substantial life reduction, with compressive dwell periods causing the most significant damage. Tensile dwell periods appear to be least damaging at the intermediate strain ranges.

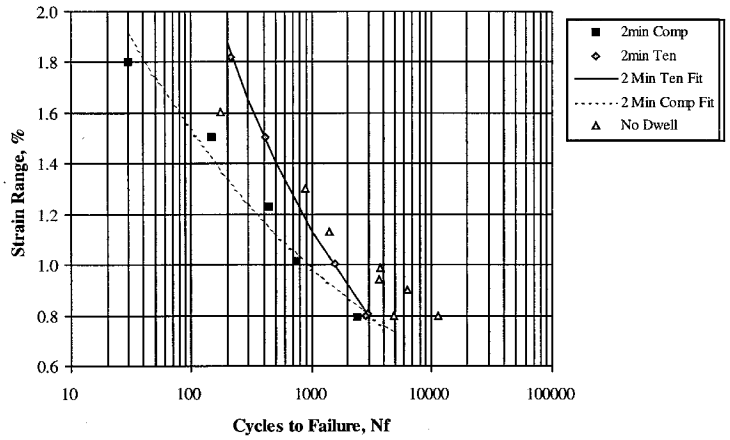


Figure 6. Effect of dwell on the fatigue life of <001>, 950 °C, R =0.05 and 6%/minute tests.

4. The Microstructure of CM186LC SX

Microstructural characterisation of the as-received (un-solutioned, aged) and fatigue exposed CM186LC SX test bars and specimens has been conducted using optical macroscopic and microscopic examination, SEM and TEM/STEM and energy dispersive X-ray spectrometry to identify constituent phases.

4.1 As-received Material Characterisation

Figure 7 shows a typical example of the fairly coarse, dendritic microstructure found for a cylindrical casting of CM186LC SX. The secondary dendrite arm length was found to range from 0.2 to 1 mm. The material is comprised of distinct regions of dendrite cores, that consist of regular and irregular (near-ogdoadical) cuboidal γ/γ' structure, and interdendritic γ/γ' eutectic colonies.

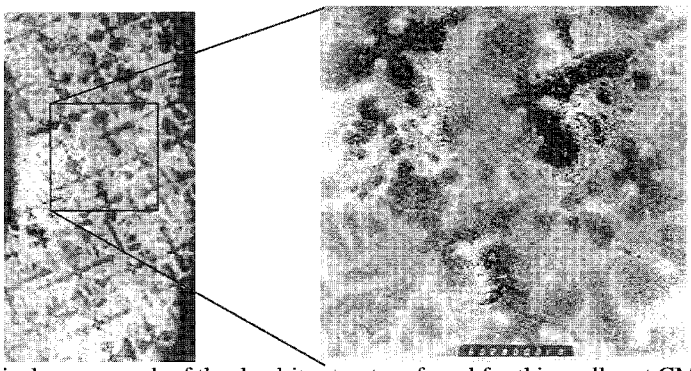


Figure 7. Optical macrograph of the dendrite structure found for thin wall cast CM186LC SX.

Figure 8 shows an example of regular γ/γ' dendritic regions lying adjacent to coarser γ/γ' eutectic colonies. Interdendritic microporosity was evident, as were blocky, Ta and Hf-rich primary MC carbides. Several examples of irregular and Chinese-script morphology carbides were also observed, as were smaller Hf-rich phases. Examination of specimen surfaces using SEM found a regular distribution of surface emergent eutectic and carbide particles.

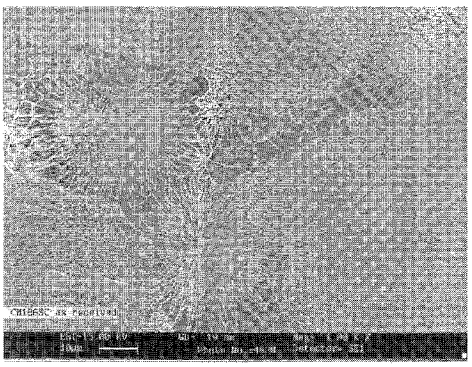


Figure 8. SEM micrograph showing regular γ/γ' dendritic regions adjacent to coarser eutectic colonies.

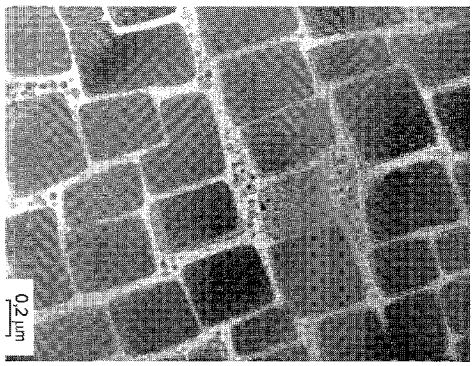


Figure 9. TEM micrograph of the regular γ/γ' cuboids found in dendritic cores of CM186LC SX. Cooling γ' are also evident.

The volume fraction of eutectic was found to be between 20-25%, whilst the volume fraction of γ' within the dendrite regions (see Figure 9) was estimated to be ~70%, with a typical particle size of 0.4 μm, though this was found to vary slightly along the dendrite arms. Several examples of spherical, cooling γ', 20 – 50 nm in diameter were observed within the γ channels.

4.2 Fractured Specimen Characterisation

Examination of <001> LCF specimens tested at 700°C without dwell found the fractures generally lay perpendicular to the loading axis, with often a single sub-surface initiation site. Figure 10 shows a typical example, which is associated with a sub-surface carbide particle and microporosity. Similar observations were made for specimens tested at 850°C. Examples of fatigue striations were evident at both temperatures. For <001> oriented specimens tested at 950°C, fractures were again largely perpendicular to the specimen axis, however, initiation was associated with surface cracking. The density of surface cracks was found to increase markedly compared with lower temperatures and the number present increased with a reduction in applied strain range. Initiation was due to a combined effect of oxidation of surface emergent carbides and coarse interconnecting slip on non-parallel planes.

For <111> specimens tested at 700°C (6%/min, $R\varepsilon = -1$, $\Delta\varepsilon = 0.5$ and 0.7%) the fracture surfaces tended to be inclined to the specimen axis with multiple surface crack initiation resulting in more irregular fracture surfaces. Nucleation of secondary cracking intermixed with regions of fatigue and brittle type failure modes was evident.

Examination of LCF plus dwell samples tested at 850°C (6%/min, Rε = 0.05, 2 min compressive or tensile hold time) found numerous small cracks on the specimen surfaces (Figure 11) with initiation sites evenly distributed around the gauge circumference (Figure 12) that link up during propagation. Despite heavy oxidation, fatigue striations were evident within the propagation zones. Fewer surface initiation sites were evident for the 2 min compressive dwell test examined. Longitudinal sectioning, as shown in Figure 13, found heavily oxidised cracks which contained an inner Al oxide layer with outer Cr and Co oxides. No evidence for γ' rafting was found for tests conducted at 850°C.

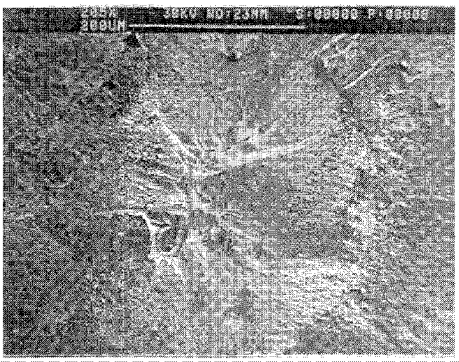


Figure 10.F SEM micrograph of sub-surface crack intiation site in <001> CM186LC SX tested at 700°C (6%/min, Rε= -1, Δε= 1.25%) without dwell.

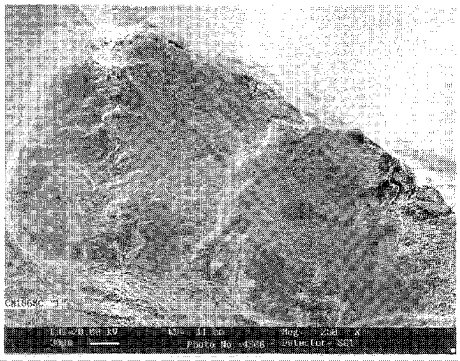


Figure 11. SEM micrograph of surface crack initiation site in <001> CM186LC SX tested at 850°C (6%/min, Rε = 0.05, 2 min tensile dwell, Δε= 1%).

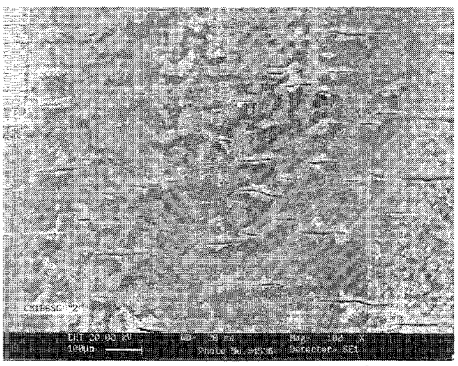


Figure 12. SEM micrograph of surface crack initiation sites on <001> CM186LC SX tested at 850°C (6%/min, Rε = 0.05, 2 min compressive dwell, Δε= 1%).

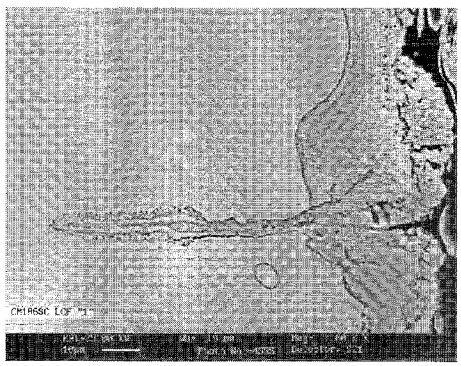


Figure 13. SEM micrograph of secondary surface crack initiation in <001> CM186LC SX tested at 850°C (6%/min, Rε = 0.05, 2 min tensile dwell, Δε= 1%).

Tests conducted at 950°C (6%/min, Rε = 0.05, 2 min tensile or compressive dwell) showed a much increased surface crack initiation density, with numerous secondary cracks distributed around the gauge surface. Specimen failure, however, was largely driven by propagation of one dominant crack, as shown in Figure 14. Rafting of the cuboidal γ/γ' within the dendrite core regions was observed (see Figure 15) for the 2 min tensile dwell test, however, no evidence was found for the formation of rods/rafts during the 2 min compressive dwell test. This may be attributed to the higher stress levels endured during the hold period for the tensile dwell tests.

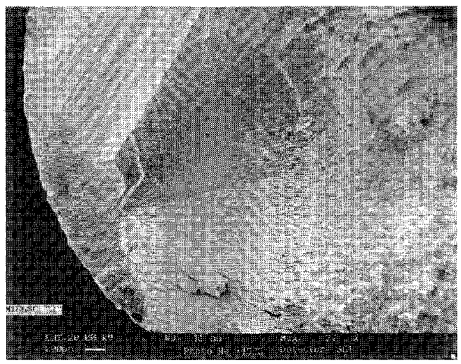


Figure 14. SEM micrograph of crack initiation site in <001> CM186LC SX tested at 950°C (6%/min, Rε = 0.05, 2 min tensile dwell, Δε= 1%).

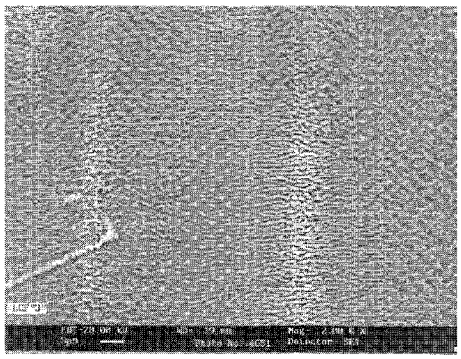


Figure 15. SEM micrograph of γ/γ' rafting in dendrite cores in <001> CM186LC SX tested at 950°C (6%/min, Rε = 0.05, 2 min tensile dwell, Δε= 1%).

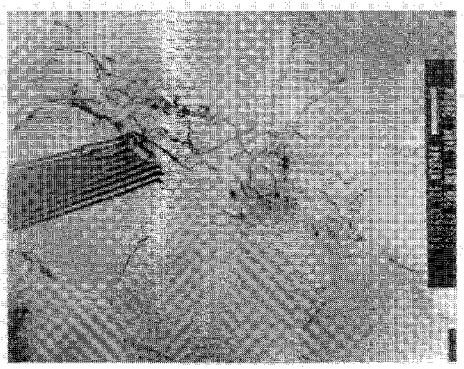


Figure 16. TEM micrograph of <001> aligned CM186LC SX tested at 700°C (6%/min, Rε=-1, Δε=1.25%)

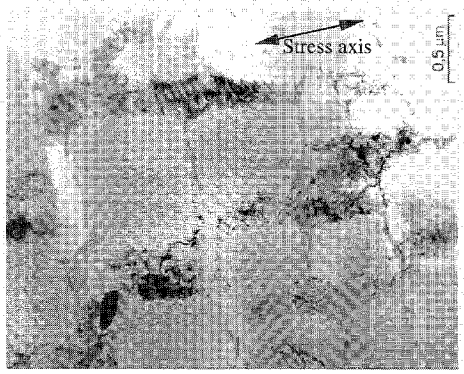


Figure 17. TEM micrograph of <001> aligned CM186LC SX tested at 950°C (6%/min, Rε=-1, Δε=1.5%)

TEM examination of <001> specimens tested at 700°C (6%/min, Rε= -1, Δε= 1.25%) revealed a high density of dislocations within the γ channels (see Figure 16) and occasional dislocation

pile-ups. Numerous examples of superlattice stacking faults (SISF/SESF) were observed within the γ' particles. TEM examination of a specimen tested at 850°C (6%/min, Rε= 0.05, Δε= 1%) found an increase in dislocation density within the γ channels. For <111> oriented specimens tested at 700°C (6%/min, Rε= -1, Δε= 0.7% and 0.5%) a low density of single dislocations was observed in the γ channels with frequent bands of stacking fault crossing the γ/γ' structure. Reducing the applied strain range resulted in an increased dislocation density within the γ phase.

Examination of <001> specimens tested at 950°C (Figure 17) found the dislocation network within the dendritic regions to be confined to the γ channels. Little evidence of γ' particle cutting or formation of persistent slip bands was found. For triangular loading cycles no preference for either horizontal or vertical channels was observed, however, under tensile or compressive dwell loadings there appeared to be a tendency for higher dislocation densities within the horizontal channels. Examination of the interdendritic eutectic colonies found dislocations to be present within the large γ' particles, indicating a plastic deformation response for these regions.

5. Summary

The high temperature LCF properties of CM186LC SX have been investigated at various strain rates and Rε ratios, as well as under tensile and compressive dwell loading cycles. The influence of orientation on cyclic stress-strain and strain-life behaviour was normalised using an established method that accounts for the variation in elastic modulus for each of the primary orientations. Fractographic examination of failed test samples found low temperature failures to be dominated by sub-surface primary carbides and associated porosity, whilst higher temperature failures were largely due to a combination of oxidation and coarse multiple slip at surface emergent eutectic and carbide particles.

6. Acknowledgements

CESI acknowledge support of "ricerca di sistema" D.L MICA 26/01/2000 and 17/04/2001. ALSTOM and Powergen acknowledge support of UK DTI. Many thanks to Dr C. K. Bullough and colleagues at ALSTOM POWER Technology Centre.

7. References

[1] K.Harris, J.B.Wahl, "New Superalloy Concepts for Single Crystal Turbine Blade and Vanes", Proc. 5th Int. Charles Parsons Conf., Cambridge, July 2000, pp. 822-846.
2] Phil.S.Burkholder et al, "CM186 LC Alloy Single Crystal Turbine Vanes" International Gas Turbine and Aeroengine Congress and Exhibition, Indianapolis, June 1999.
3] G. McColvin et al, "Application of the Second Generation DS Superalloy CM186LC to First Stage Turbine Blading in EGT Industrial Turbines", Proceedings of the 4th International Charles Parsons Conference, November 1997, pp. 339-357.
[4] C.K. Bullough, M. Toulious, M. Oehl and P. Lukas, "The Characterisation of the Single Crystal Superalloy CMSX-4 for Industrial Gas Turbine Blading Applications", Proc. 6th Liege Conf., Liege, 1998, pp. 861-878.

CREEP BEHAVIOUR OF THE THIRD GENERATION Ni-BASE SINGLE CRYSTAL SUPERALLOY TMS-75 AND ITS γ/γ' TIE-LINE ALLOYS

Takao Murakumo, Toshiharu Kobayashi, Shizuo Nakazawa and Hiroshi Harada

High Temperature Materials 21 Project,
National Institute for Materials Science (NIMS),
1-2-1 Sengen, Tsukuba Science City, Ibaraki 305-0047, Japan

Abstract

Creep tests at 900°C/392MPa and 1100°C/137MPa were performed on a third generation Ni-base single crystal superalloy TMS-75 and its γ/γ' tie-line alloys. These alloys are designed to have different fractions (0, 20, 40, 60, 80, 100%) of the γ' phase, while the composition of each phase is kept the same. The rupture life is longest at the vicinity of 60% γ', which is similar to that of polycrystalline Inconel713C in an earlier work by one of the authors (H. Harada). However, the dependence of the creep rupture life on the amount of γ' is more evident in single crystals than in a polycrystals. It was found, by SEM observation of the ruptured specimens, that the raft structure in the 80% γ' alloy formed parallel to the stress axis, in contrast to the usual perpendicular rafts observed in the 40~60% γ' alloys. This parallel raft structure can be explained by the change in the relative role between the matrix and the dispersed phase.

Keywords: Ni-base superalloys, microstructure, creep, rafting, fraction of precipitates

1. Introduction

Ni-base superalloys show good creep strength when its γ' fraction is 60~70%. It was previously shown in an earlier study on polycrystalline Inconel713C by one of the authors [1, 2] that the creep rupture life was the longest in the vicinity of 65% γ' under any creep condition. This tendency is also expected to be applicable to single crystal superalloys. Actually, many studies in the vicinity of 60~70% γ' have been carried out in the last two decades to find the optimum chemical composition for the development of better single crystal superalloys. However, when the composition of each phase is changing, it is difficult to evaluate the effect of the γ' fraction because the behaviour of γ and γ' will also change. Therefore, investigating tie-line alloys is important, but there are no readily available tie-line single crystal superalloys.

Figure 1 shows a pseudo-binary phase diagram for a (Ni,X)-(Al,Y) system. Now, assuming that a Ni-base superalloy has a composition indicated by A in Fig. 1 and consists of a γ/γ' two phase structure in equilibrium at a given temperature, then the compositions of the γ and γ' phase in this alloy should be indicated by B and C. In other words, all alloys on the tie-line BC can be made by mixing two alloys that have the composition B and C. This logic can be applied to multi-component systems. When the compositions of γ and γ' are given as X_i and X_i' respectively, the composition (C_i) of a Ni-base superalloy for a given γ' fraction (f) is obtained by Eq. (1), which is the equation of a tie-line combining the compositions of γ and γ' in a state of equilibrium.

$$C_i = (1 - f) X_i + f X_i' \qquad (i : \text{Ni, Al, Co, Cr, Mo, etc...}) \qquad (1)$$

In this study, the creep behaviour and microstructure evolution during creep in Ni-base single crystal superalloys which have different γ' fractions are investigated.

2. Materials and experimental procedure

The equilibrium compositions of the γ and γ' phases in the third generation single crystal superalloy

TMS-75 [3] are calculated by the alloy design program (ADP) which was developed by our group [4, 5], as shown in Table 1. The γ and γ' single phase alloys were cast as master alloys at first. These alloys were mixed to make six single crystal superalloys which had been designed to contain 0, 20, 40, 60, 80, and 100 at% γ' phase at 900°C. For reason of clarity, each alloy is henceforth referred to in terms of the originally designed γ' volume fraction values, e.g. 20% γ', etc. The single crystals were produced in a directional solidification furnace at NIMS in the form of bars with a diameter of 10 mm. The longitudinal direction is near [001] in the 0~80% γ' alloys; however, it is near [111] in the 100% γ' alloys, according to the preferred growth direction of the primary crystal. Solution and two step aging heat treatment was carried out on each alloy under an optimum condition for standard TMS-75 as follows:

1300°C/1h + 1320°C/5h → GFC(Gas Fan Cool) → 1120°C/5h → GFC → 870°C/20h → GFC

Constant load tensile creep tests were performed at 900°C/392MPa and 1100°C/137MPa. After the heat treatment and creep rupture, SEM observation was carried out.

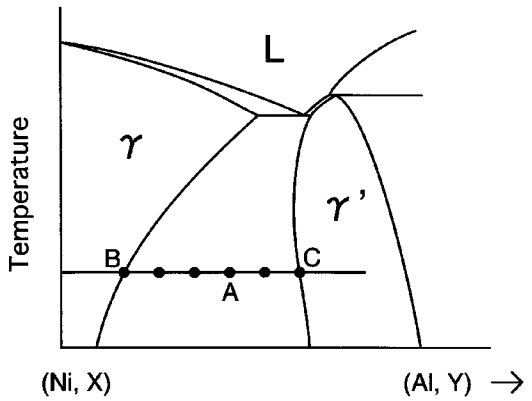


Fig.1 Schematic drawing of pseudo-binary phase diagram for a (Ni,X)-(Al,Y) system

Table 1 Chemical composition (wt%) of γ and γ' phases in TMS-75 calculated by ADP

	Ni	Co	Cr	Mo	W	Al	Ta	Hf	Re
TMS-75	59.90	12.00	3.00	2.00	6.00	6.00	6.00	0.10	5.00
γ	52.05	17.85	5.87	3.41	6.23	2.40	1.82	0.03	10.35
γ'	65.69	7.72	0.89	0.95	5.83	8.64	9.06	0.15	1.07

3. Results

3.1 Initial microstructure

Figure 2 shows initial microstructure of each alloy after heat treatment. The 0% γ' fraction alloy consists mostly of a single γ phase; however, a very small amount of γ' was observed particularly in the interdendritic areas. In the 20% γ' alloy, fine spherical γ' precipitates were observed (2(b)). The spherical shape of γ' should be derived from the relatively larger interfacial energy as compared with the elastic strain energy in the case of smaller precipitates. The size of these randomly distributed precipitates is about 30~50nm. This microstructure suggests that the 20% γ' alloy consisted of only a γ phase during the first aging heat treatment at 1120°C. In the case of the 0 and 20% γ' fraction, the actual volume fraction of γ' in the interdendritic regions was somewhat larger than that in the dendrites due to the segregation, during solidification, of refractory elements

that have small diffusion coefficients. Figure 2(c) shows the initial microstructure of the 40% γ' alloy. Cuboidal γ' precipitates with sides of 200~500nm were aligned along <100> during the aging treatment because of the elastic interaction between precipitates. Many fine spherical γ' particles that precipitated at the second step aging treatment, at 870°C for 20h, were also observed among the cuboidal γ' precipitates. In the 60% γ' alloy, as shown in Fig. 2(d), the microstructure was the same as that of coherent γ/γ' two phase structure in TMS-75, and other modern Ni-base superalloys. There were no significant differences in the dendritic and interdendritic regions in the 40 and 60% γ' alloys. The γ' volume fraction of the initial microstructures was in accordance with the calculated value for the 0~60% γ' alloys.

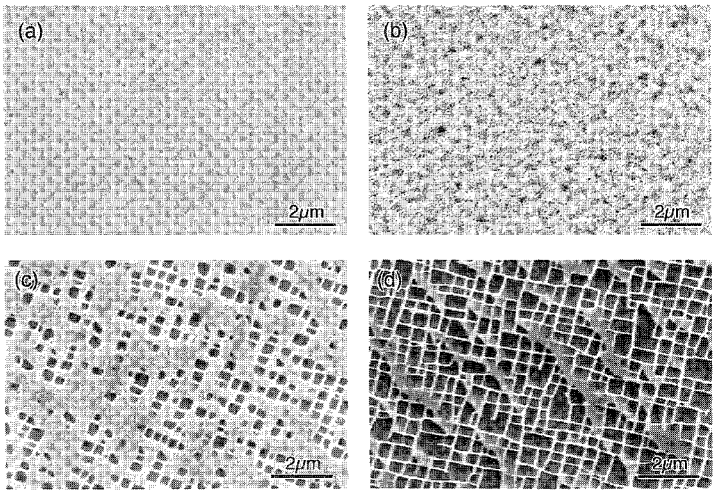


Fig.2 Initial microstructure in each alloy: (a) 0%, (b) 20%, (c) 40% and (d) 60% γ' volume fraction.

Figure 3 represents the initial microstructure in a superalloy designed to contain an 80% γ' phase. Three kinds of microstructures were observed in different contrasts (as indicated by b~d in Fig. 3(a)). The microstructure in region b consists of cuboidal γ' and narrow γ channels, as in the 60% γ' alloy. In region c, the γ/γ' structure is coarser, so γ' appears like the matrix. The wavy γ/γ' interfaces suggest that the interfaces are in a semi-coherent state. In the interdendritic region, a single phase of γ' was observed as a dark contrast (Fig. 3(d)). It is known that the single γ' phase region extend to the left side under a eutectic temperature in an equilibrium phase diagram of Ni-base superalloys, as shown in Fig. 1. Therefore, in this alloy, it is probable that the eutectic γ/γ' was formed in the interdendritic region during solidification and transformed to the single γ' phase during cooling and heat treatments. This single phase of γ' is called eutectic γ'. The existence of a large amount of eutectic γ' indicates that this alloy cannot be solution-treated completely under the conditions applied in this study.

The initial microstructure in the 100% γ' alloy is shown in Figure 4. The dendrites consisted of a γ' phase only. There was no γ phase, however, two other types of precipitates were observed. The interdendritic regions were densely populated with round precipitates in the γ' matrix. Mostly, plate-like precipitates were observed in the dendrites. Generally, precipitates, called topologically close-packed (TCP) phases, are formed in long annealed Ni-base superalloys, particularly in the cases of Re-added alloys. The phases σ, P, μ, and R are reported as TCP phases with different

crystallographic structures [6, 7]. In this study, round-shaped and plate-like precipitates are expected to be TCP phases, but this is difficult to identify clearly by EDX because the four types of TCP phases have similar compositions. Analysis of the crystallographic structure by X-ray or TEM is needed for the identification of TCP phases.

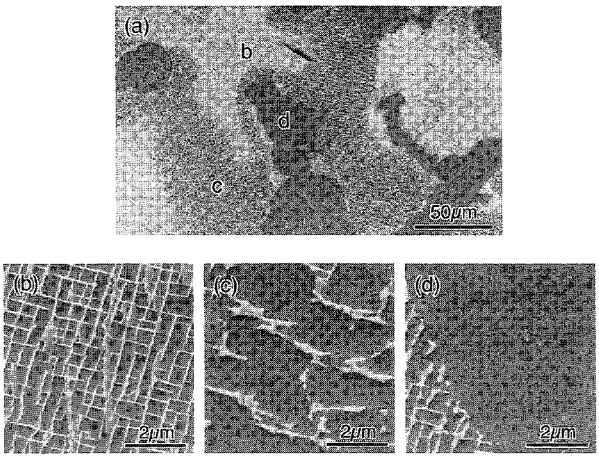


Fig.3 Initial microstructure in the 80% γ' alloy: (a) Three kinds of microstructures were observed as indicated by b~d. (b) fine cuboidal γ' and narrow γ channels, (c) coarsened γ/γ' structure with semi- coherent interface, (d) a single phase of γ' in the interdendritic region.

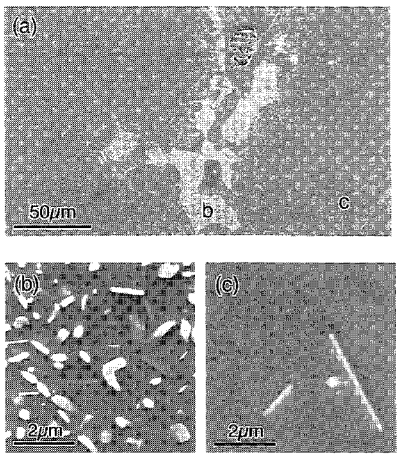


Fig.4 Microstructure in the 100% γ' alloy after heat treatment: (a) Most of the alloy consists of a γ' matrix, but small amount of precipitates were observed in interdendritic region. (b) round-shaped TCP phases in the interdendritic region, (c) plate-like TCP phases in a dendrite

3.2 Creep behaviour

Figure 5 shows the resultant variation of creep rupture life against the designed amount of γ' at 900°C/392MPa and 1100°C/137MPa, accompanied with the results in an earlier study on Inconel713C [1, 2] for comparison. In both conditions, the single γ phase (0% γ') alloys were ruptured instantly when the load was applied. The alloy containing 20% γ' also ruptured quickly at 1100°C. As expected, the longest rupture life was obtained at the 60% γ' fraction under each condition. These results are similar to those of an earlier study, however, this dependence is more evident in single crystals than in polycrystals.

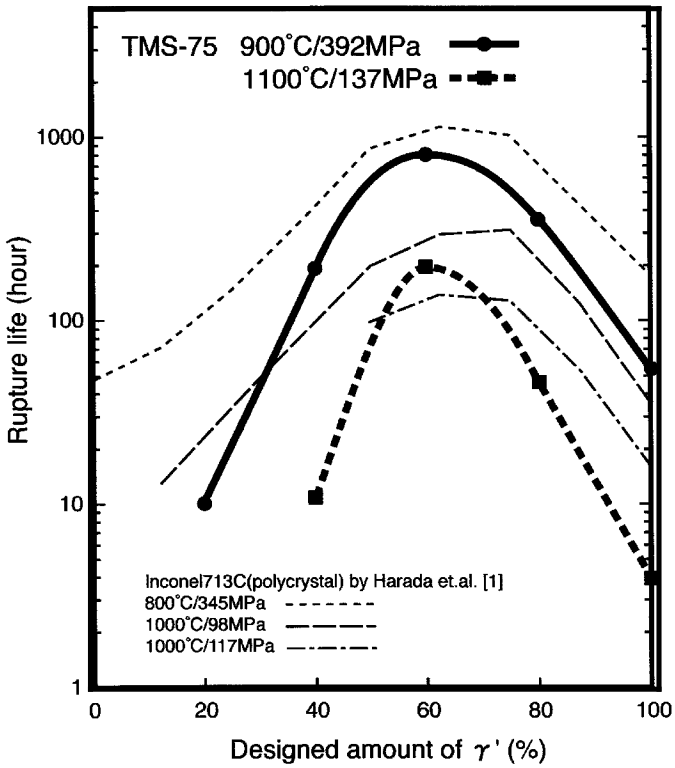


Fig. 5 Relationship between the designed amount of γ' and the creep rupture life obtained from creep testing

3.3 Microstructure in ruptured specimens

Figure 6 shows the microstructure in the creep ruptured specimens. The shape of the γ' precipitates in the 20% γ' alloy remained spherical after a 10hour creep at 900°C/392MPa but seemed to have somewhat coarsen (Fig. 6(a)). Broad and narrow rafts perpendicular to the stress axis were observed in the 40% γ' alloy crept at 900°C (Fig. 6(b)). This result means that not only cuboidal but also fine γ' precipitates can be linked to each other. As shown in Fig. 6(c), only broad wavy rafts were observed after creep at 1100°C. The fine γ' precipitates should have re-dissolved into the γ matrix under this condition. In the 60% γ' alloys (Fig. 6(d), (e)), the microstructure is completely the same to that reported in detail before [8]. In the 80% γ' alloys, the direction of the rafts is quite different from that in the 40~60% γ' alloys. At 900°C/392MPa, fine flat rafts formed

in the dendrites parallel to the stress axis, as shown in Fig. 6(f). Interdendritic regions consisted of only the γ' phase, which is the same as the initial microstructure. At 1100°C/137MPa, parallel rafts were also observed in the dendrites. However, the microstructure was coarser and the interfaces of the rafts were wavy in the ruptured specimen (Fig. 6(g)). Rafts parallel to the stress axis have been reported before in compressed Ni-base single crystal superalloys having a negative lattice misfit [9~11] and in the tensile creep of Ni-base alloys with a positive lattice misfit [12, 13]. In this study, creep tests were performed under tension, and the lattice misfit of TMS-75 was -0.15% at 900°C and -0.18 at 1100°C, as previously reported [8]. This is the first time that a raft structure parallel to the stress has been observed under such conditions. The formation mechanism of these parallel rafts is discussed in detail in a separate paper [14]. A brief explanation is as follows. When an alloy has a negative lattice misfit and consists of a γ matrix and γ' precipitates, perpendicular rafts should be formed, as is well known. On the other hand, if the morphology of γ and γ' in this alloy is reversed, parallel rafts can be formed because the lattice misfit will switch to positive from negative due to the change in the relative role between the matrix and the dispersed phase. The initial microstructure of the 80% γ' alloy is not so simple, but it contains the area consisting of γ phases surrounded by γ' phase as shown in Fig. 3(c). Finally, in the 100% γ' alloys the raft structure was not formed because of the absence of γ phase. At 900°C (Fig. 6(h)), some of the plate-like phases were cut to pieces, but the shapes of the rounded phases in the interdendritic region were not changed as they had in the initial microstructure. At 1100°C, the shearing of TCP phases was observed frequently, as shown in Fig. 6(i). In both conditions, the cracks were observed at interdendritic regions near the rupture surface.

4. Discussion

An instant rupture of the single γ phase alloy means that the yield stress of this alloy at each temperature was the same or smaller than the creep stress under each condition, namely, the viscous resistance for dislocation motion in the γ phase was very low in spite of the large quantities of solution hardening elements that were added. The single γ' phase alloy did not rupture instantly, but its creep rupture life was short. While the weak phases were combined, the longest life was obtained at the 60% γ' fraction under both conditions. In the light of these facts, it can be said that Ni-base superalloys are strengthened by interface rather than dispersed precipitates.

In tie-line alloys, the chemical compositions in each phase are kept fairly the same, but the fractions of the γ and γ' phases are different. If the same number of cuboidal γ' precipitates were dispersed and the volume fraction of γ' was changed, the Ni-base alloy would be expected to be stronger, with an increase in the γ' fraction, because the γ channels would become narrower. However, the creep test of the tie-line alloys revealed that the creep rupture life decreases with an increasing amount of γ' when the fraction is over 80%. From the observation of the initial microstructure, it was found that heat treatment cannot solution fully the alloys containing over 80% γ'. In such a case, the single γ' phase region appears in the interdendritic regions. Increasing the γ' fraction to over 80% decreases the gross area of the γ/γ' interface. Consequently, the creep strength also decreases.

The coherency between the matrix and the precipitates has a great influence on the mechanical properties. Generally, the creep strength of Ni-base superalloys decreases when the γ/γ' interfaces in the initial microstructure are semi-coherent. The coarsened two phase region observed in the 80% γ' alloy is considered to be in a semi-coherent state because the interfaces are rounded and wavy. This can be attributed to an increase in the creep rate because the semi-coherent interfaces act as dislocation sources.

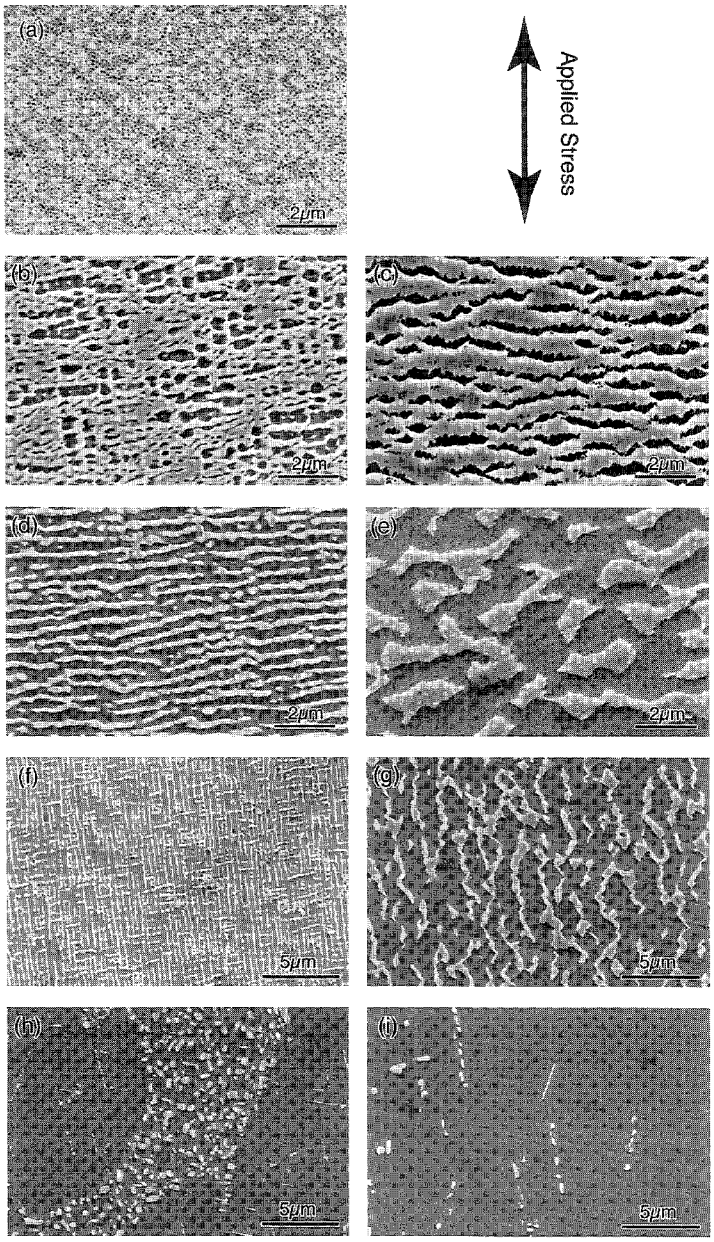


Fig.6 Microstructure after creep rupture: the 20% alloy crept at 900°C/392MPa; the 40% γ' alloy crept at (b)900°C and (c) 1100°C/137MPa; the 60% γ' alloy crept at (d) 900°C and (e) 1100°C; inside of the dendrite in the 80% γ' alloy crept at (f) 900°C and (g) 1100°C; (h) interdendritic region in the 100% γ' alloy crept at 900°C; (i) Plate-like TCP phases sheared at 1100°C.

5. Conclusions

Creep tests at 900°C/392MPa and 1100°C/137MPa were performed on a third generation Ni-base single crystal superalloy TMS-75 and its γ/γ' tie-line alloys, and the microstructure in these alloys was observed by SEM. The summary is as follows:

- The γ' volume fraction of the initial microstructure was in accordance with the original design values. The 0~60% γ' alloys have an almost homogeneous microstructure; however, there were differences in the dendrite and interdendritic regions in the 80~100% γ' alloys.
- Creep rupture life is the longest for the 60% γ' fraction, which is similar to that of polycrystals, but this tendency is more evident in single crystals.
- In a ruptured specimen, a raft structure perpendicular to the stress axis was observed in the 40~60% γ' alloys. On the other hand, parallel rafts were observed in the 80% γ' alloy. The change of raft direction with increasing the γ' fraction was observed for the first time in this study.
- This parallel raft structure can be explained by the change in the relative role between the matrix and the dispersed phase.

References

[1] H.Harada, M. Yamazaki, Y. Koizumi, N. Sakuma, N. Furuya and H. Kamiya, Proc. of a Conf. on High Tempeature Alloys for Gas Turbines, Liège, Belgium (1982) 721.
[2] Y. Ro, Y. Koizumi and H. Harada, Mater. Sci. Eng. A223 (1997) 59.
[3] T. Kobayashi, Y. koizumi, S. Nakazawa, T. Yamagata and H. Harada, Proc. of the 4th Int. Charles Parsons Turbine Conf. on Advances in Turbine Materials, Design and Manufacturing (1996) 766.
[4] H. Harada, T. Yamagata, S. Nakazawa, K. Ohno and M. Yamazaki, Proc. of the Conf. on High Temperature Materials for Power Engineering, 1990, Liège, Belgium (1990) 1319.
[5] H. Harada, T. Yamagata, T. Yokokawa, K. Ohno and M. Yamazaki, Proc. the 5th Int. Conf. on Creep and Fracture of Engineering Materials and Structures, Swansea, UK (1993) 255.
[6] R. Darolia, D. F. Lahrman and R. D. Field, Superalloys 1988, 255.
[7] C. M. F. Rae, M. S. A. Karunaratne, C. J. Small, R. W. Broomfield, C. N. Jones and R. C. Reed, Superalloys 2000, 767.
[8] T.Murakumo, T. Kobayashi, S. Nakazawa, Y. Koizumi and H. Harada, submitted to Mat. Sci. Eng. A.
[9] M. Véron, Y. Bréchet and F. Louchet, Superalloys 1996, 181.
[10] J. K. Tien and S. M. Copley, Metall. Trans. 2 (1971) 215.
[11] J. K. Tien and R. P. Gamble. Metall. Trans. 3 (1972) 2157.
[12] T. M. Pollock and A. S. Argon, Acta metall. mater. 42 (1994) 1859.
[13] T. Miyazaki, K. Nakamura and H. Mori, J. Mater. Sci. 14 (1979) 1827.
[14] T. Murakumo, T. Kobayashi, S. Nakazawa and H. Harada, submitted to Acta mater.

CREEP BEHAVIOUR AND γ' EVOLUTION OF A NEW NICKEL BASE SUPERALLOY FOR SINGLE CRYSTAL BLADE APPLICATIONS

M. Maldini ,V. Lupinc, H. Li and G. Angella

CNR – IENI
Via Cozzi 53, 20125 Milano, Italy

Abstract

The creep curves of nickel base superalloys are often characterised by a dominant tertiary creep stage that has been attributed to the accumulation of internal damage not directly related to fracture mechanisms, but rather to a change in the density/mobility of the moving dislocations. A close examination of the experimental creep accelerating stage shows different regimes of strain accumulation depending on the value of the applied stress/temperature. These experimental behaviours can be rationalised in terms of evolution, during creep, of the reinforcing γ' phase morphology.

Keywords: creep, nickel base superalloy, single crystal, microstructure, raft.

1 Introduction

After the initial heat treatment, the microstructure of well established single crystal nickel base superalloys consists in ordered quasi-cubic shape γ' precipitates coherently embedded in the solid solution γ matrix. The γ' particles are arranged along the <001> orientations and are separated by narrow γ channels. During creep tests at temperatures lower than 800°C, the initial cuboidal microstructure is stable even in creep tests lasting thousands of hours. At temperatures higher than 1050°C, the rafted microstructure develops during the first creep, i.e. within the first 1-3% of creep life, and the real structure of the material at such a high temperature can be better simulated by the rafted instead of the cuboidal structure. Around 900°C, the rafted microstructure continues to develop through a considerable portion of creep life and the major portion of lamellar microstructure builds up during tertiary creep.

One of the most significant factors in determining the creep strength of the high volume reinforcing phase nickel base superalloys is the resistance that matrix dislocations encounter in shearing the γ' phase. This is the reason why the initial γ' precipitate morphology, which is obtained after heat treatment, and its evolution during component life can strongly influence the high temperature mechanical behaviour of nickel base superalloys.

The objective of this paper is to show the preliminary results of a research on the effect of γ' morphology evolution on creep strain rate in single crystal nickel base superalloy SMP14.

2 Material and experimental procedure

The material studied in this work is SMP14, a rhenium-containing alloy developed by CSIR, Pretoria, RSA for single crystal turbine blade and vanes applications. The nominal chemical composition of SMP14 superalloy is shown in Table 1. Fully heat treated 12 mm diameter bars were supplied by Ross & Catherall Ltd, Sheffield (U.K). The heat treatment consisted in

Table 1 – Nominal composition of SMP14 alloy

Cr	Co	Mo	W	Re	Ta	Al	Nb	Ni
4.8	8.1	1.0	7.6	3.9	7.2	5.4	1.4	Bal.

complete solutioning of the alloy by a six-stage heat treatment up to 1308°C followed by 16h/1080°C + 16h/870°C. The mean size of the γ' cuboids was 0.45 μm and the hardening phase occupied approximately 2/3 of the alloy volume [1]. Deviations of <001> crystallographic direction from the rod axis were within 6°. Micrographs of original cuboidal and rafted microstructures were obtained through SEM from sections taken along planes parallel to the stress axis, after polishing mechanically and etching the section surfaces with 3 HCL + 1 HNO_3 + 4 glycerine. The creep specimens had a cylindrical geometry of 5.6 mm diameter and 28 mm gauge length. Creep strain was continuously monitored using capacitive transducers connected to extensometers that were clamped to the shoulders of the specimen. Three thermocouples were placed in the gauge length to control and monitor temperature gradients during creep. The creep tests were run at constant load.

3 Experimental results

The creep tests analysed in this work were performed in the stress/temperature range 135-425MPa/900-1050°C producing rupture times between 300 and 3000 h. The results of the experimental creep tests are reported in Table 2 and the plots of strain against the time are shown in Fig. 1.

Table 2 - Experimental creep results on SMP14 alloy

Temp. (°C)	Stress (MPa)	Time in h to strain 0.5%	1%	2%	Time to rupt. (h)	Elong. (%)	Zu (%)
900	425	31.5	208	254	450.1	25.7	27
	400	154	242	331	605.2	19.3	31.3
	400				51.5*	0.15*	
	375	266	342	455	806.8	29.2	32.6
	325	613	787	965	1692.5	27.7	35.2
	300				630*	0.32*	
	300	1028	1220	1460	2433.9	22.9	33.7
950	320	124	151	183	302.9	25.5	32.3
	275	266	320	394	665.1	27.1	34.6
	220	572	837	1100	1798.2	25.8	32.3
	215	778	1074	1363	2178.2	24.7	32.3
1000	230	120	145	176.5	276.6	22	29.4
	200	121.5	227	364	622.9	21.6	28.7
	175	307	630	820	1188.7	17.4	30.9
	150	2057	2317	2512	3073	16.3	31.4
	125				3000*	-0.1*	
1050	165	241	292	335	391.7	21.7	28.5
	150	217	488	660	722.9	16.3	30.9
	135	1030	1317	1554	1570.6	13.7	30.5

* interrupted test

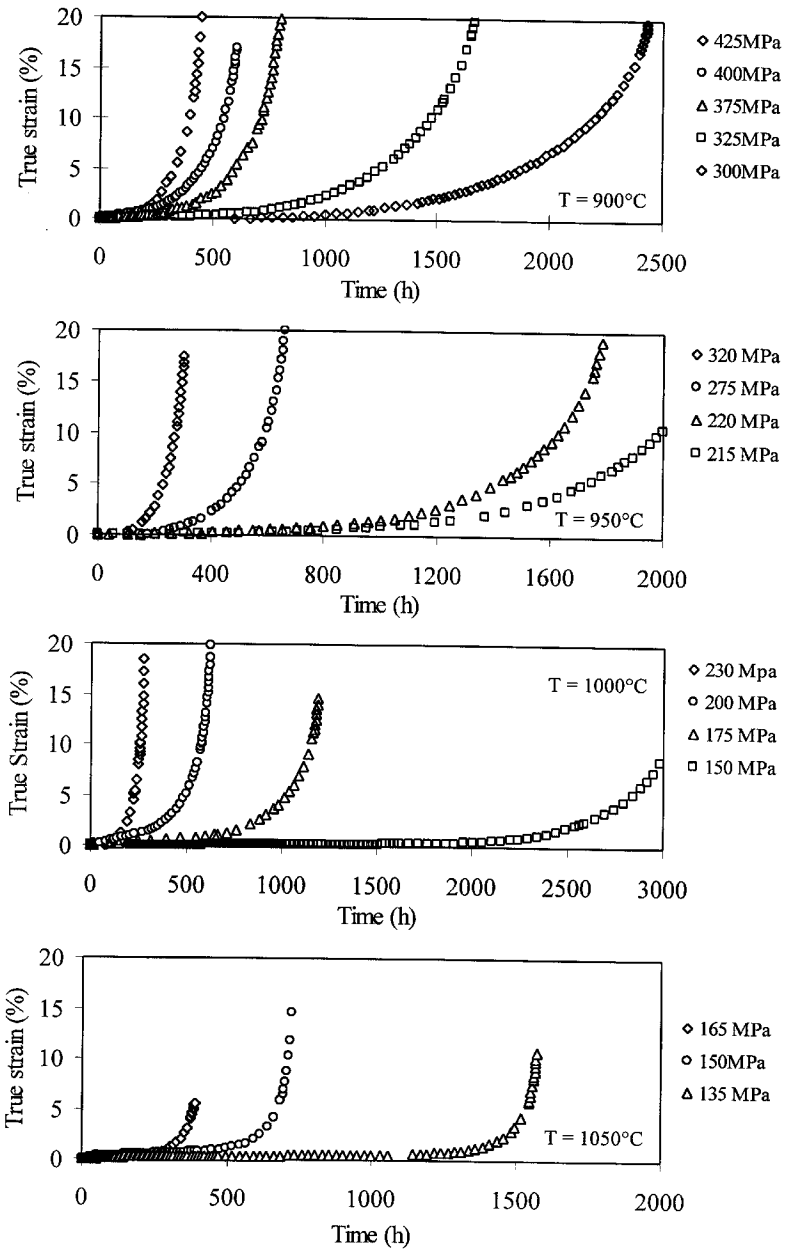


Fig. 1 - Experimental creep curves at different temperatures and stresses.

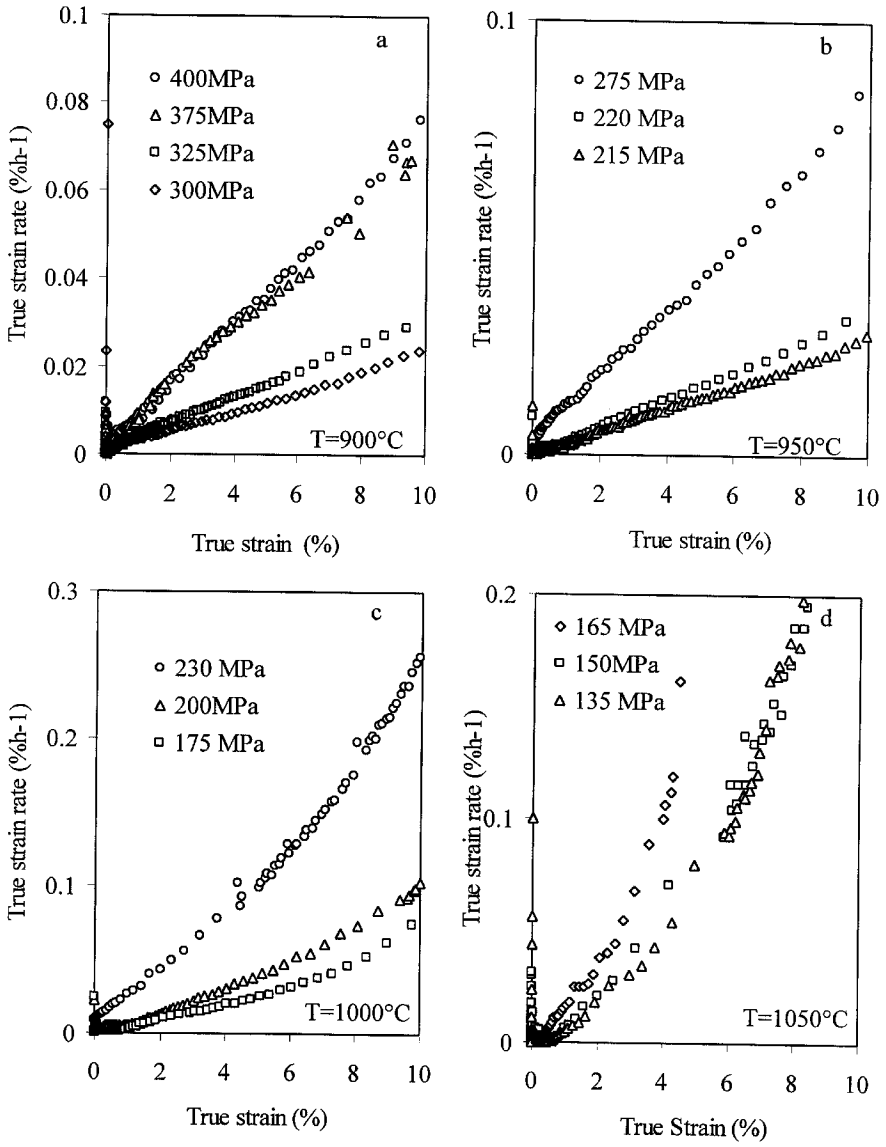


Fig. 2 – Strain rate vs. strain at a) 900°C, b) 950°C, c) 1000°C and d) 1050°C. Linear strain softening appears up to large value of strain.

For the explored test conditions, the creep curves exhibit near no or a short small primary stage with a strain always smaller than 0.1%, while the major part of each single creep curve consists of tertiary creep. These results are consistent with those obtained on other single crystal nickel base superalloys [2-5] for equivalent stresses/temperatures. The shape of the creep curves depends on the test conditions: the curvature of the creep curves seems continuously increasing with the decreasing /increasing of the applied load/temperature.

When $\dot{\varepsilon}$ vs. ε is plotted, see Fig. 2, a linear dependence between the tertiary strain rate and the accumulated strain for a large portion of the creep curve can be observed: up to about 10% of strain for the tests performed at 900-950°C and to a smaller strain interval for the tests run at 1000-1050°C. It is worth noting that the linear relationship can describe the material behaviour up to about 90% of the creep life in all the test conditions even if the time to rupture spans in a large time interval.

Although the results suggest that the strain acceleration in the tertiary creep is mainly due to a damage related only to the accumulated strain and independent on the evolution of the reinforcing phase γ', actually, an effect of the particle instability on the strain rate can not be excluded in early tertiary creep, when the γ' microstructure quickly changes and the deformation is not substantial.

In order to better analyse the initial phase of tertiary creep, compressed in the plots of Fig. 2, the same experimental creep curves are proposed as plots log $\dot{\varepsilon}$ vs. time. It is noteworthy that plots $\dot{\varepsilon}$ vs. ε and log $\dot{\varepsilon}$ vs. time are qualitatively equivalent, since experimental points showing a straight line in the former plot must also show a linear relationship in the latter one. Nevertheless the plots of Fig. 3 expand the initial portion of the experimental creep curves, where effects of γ' evolution can be expected at high temperature. In fact, after the initial primary creep stage, where the strain rate decreases to a minimum, the plots log $\dot{\varepsilon}$ vs. time clearly reveal new unusual features, hidden in the $\dot{\varepsilon}$ vs. ε plots. The experimental results show where effects of γ' evolution can be expected at high temperature. In fact, after the initial primary creep stage, where the strain rate decreases to a minimum, the plots log $\dot{\varepsilon}$ vs. time clearly reveal new unusual features, hidden in the $\dot{\varepsilon}$ vs. ε plots. The experimental results show a dependence of creep curve shape on applied temperature and stress as outlined in the following points:

- At 900°C and at high stress, the tertiary creep can be approximated by a single straight line. In the last portion of creep curve, fracture mechanisms produce a further increment of creep strain rate leading to final fracture. At lower stresses two different rates of damage accumulation during the dominant tertiary creep are clearly exhibited before fracture mechanisms start influencing the creep curves. The first tertiary creep stage A starts after the minimum creep rate and it influences the creep curves up to about 1% of strain. A decrement of the creep slope in Fig. 3 demarcates the beginning of a second phase of the tertiary creep B where most of the creep strain was accumulated. Both stages can be described by a straight line, but with different slope.
- At 950°C and at the highest applied stress, the shape of the creep curve is qualitatively similar to the curve at 900°C at low stress. Decreasing the applied stress, a further regime of strain accumulation is found: the initial tertiary creep stage A is followed by a new

stage C, characterised by a slope decreasing with applied stress. Then a further stage, similar to the B stage at 900°C, is detected.

- At 1000°C the behaviour detected at 950°C is enhanced: the slope of stage C continues to decrease with stress, becoming negative for the lowest stresses, which produced a deceleration of the creep strain.
- At 1050°C a clear deceleration after the initial stage appears. The combination of hardening and softening processes during stage C and B respectively produce a second and longer minimum creep rate.

After fracture, necking is observed to be more localised at lower applied stress/higher temperature. This beehaviour is generally observed in single crystal superalloys at high temperatures and, in extreme cases, it tends to localise fracture on a single shear plane.

4 Discussion

To describe the evolution of tertiary creep strain rate in nickel base superalloy for test temperatures lower than those studied in this work [3,5-6] the following equation has been often utilised:

$$\dot{\varepsilon} = \dot{\varepsilon}^{\circ}(1 + C\varepsilon) \qquad (1)$$

with $\dot{\varepsilon}$ the instantaneous strain rate, $\dot{\varepsilon}^{\circ}$ the strain at the beginning of the tertiary creep, ε the tertiary creep strain and C a parameter controlling the curvature of the creep curve. According to Eq. 1 tertiary creep is not associated to fracture mechanisms, but it is due to an increase of mobile dislocation density with strain or to an increase of recovery rate [7,8], whereas the reinforcing-particle coarsening plays a secondary role in this softening mechanism. At the high temperatures here analysed, neglecting the microstructure instability is an oversimplification, since the raft development can strongly influence the dislocation mobility, particularly at the low stresses, when the dislocations cannot easily cut the long rafted γ'.

The experimental creep results of SMP 14 alloy are hereafter rationalised supposing a single strain softening damage, described by Eq. 1, and supposing that the development of raft structure mainly influences dislocation velocity rather than mobile dislocation density.

At all the test temperatures, during stage A of tertiary creep the raft structure was developing [9], producing an acceleration of creep strain due to following reasons:

- The thickness of the horizontal γ channels, perpendicular to the applied stress, shows a remarkable increase [9], see Fig. 4, producing a reduction of the Orowan resistance the dislocations must exceed to move in the γ channels.
- The development of rafting produces an increment of the alloy volume that can be easily deformed. In fact, the external applied stress and the coherency (misfit) stresses combine giving rise to local stresses in the γ channel oriented perpendicular and parallel to the load axis [10]. For negative misfit alloys ($a\gamma' < a\gamma$), as in the alloy here investigated, the external applied tensile stress along [001] is compensated, in some measure, by a component of the compressive misfit stress in the γ channel parallel to [001]. As a result, the misfit stresses can interdict the dislocation activity in the vertical channels. Then, at the beginning of

creep, see Fig. 4, when the microstructure is still cuboidal γ', only about 10% of the alloy volume (1/3 of the γ phase) contributes to the creep strain, while all the γ volume contributes to the creep strain when the rafts are completely developed, see Fig. 4.

An opposite effect on the strain acceleration of the latter mechanisms can occur, when rafts are developed, since mobile dislocations within the γ phase can not circumvent anymore the γ' phase by glide/climb mechanisms, which should promote a deceleration of the strain. In fact the accumulation of plastic strain in γ phase only provides a local redistribution of stress in the alloy: stress is decreased in γ phase and amplified in γ' phase, as it is expected during creep in a composite material with 'soft' (γ) and 'hard' (γ') components deforming in parallel. Hence the creep behaviour is determined by the effective stress in γ phase where all the mobile dislocations are confined, producing stage C in the plots of Fig. 3. The redistribution of the stress continues and the stress in γ' phase increases with strain until the cutting threshold stress is achieved, which should occur at stage B in Fig. 3 plots. Mughrabi et al [11], studying the single crystal superalloy SRR 99 at 900°C and 305 MPa, have found that a γ' lattice distortion was built up during the first portion of the tertiary creep and it remained then constant until the rupture, showing there was no further redistribution of the stress occurring between the two phases during the second portion of tertiary creep. This observation is consistent with our interpretation of the creep behaviour.

The effects on the creep curve of the above sketched processes are expected to be more evident at low applied stresses, while they should disappear at higher stresses, since the elevated stress allows the dislocations to move easily in the vertical γ channel and/or cut the reinforcing γ' phase. Since the higher is the value of the applied stress, the smaller must be the redistribution of the stress between the two phases before the cutting threshold stress is achieved, the tests at low stresses/high temperatures show a more evident C stage, producing even a reduction of the strain rate in the tests at 1000-1050°C and applied stress ≤ 200 MPa.

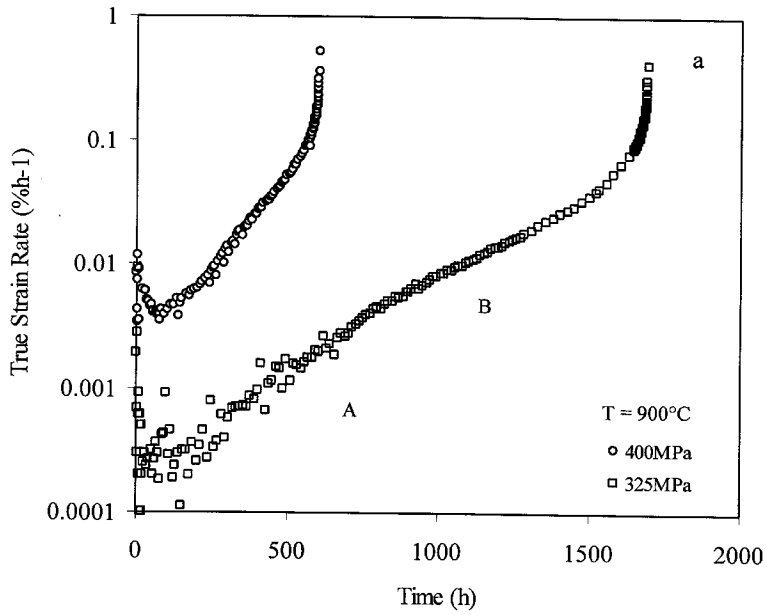
5 Conclusions

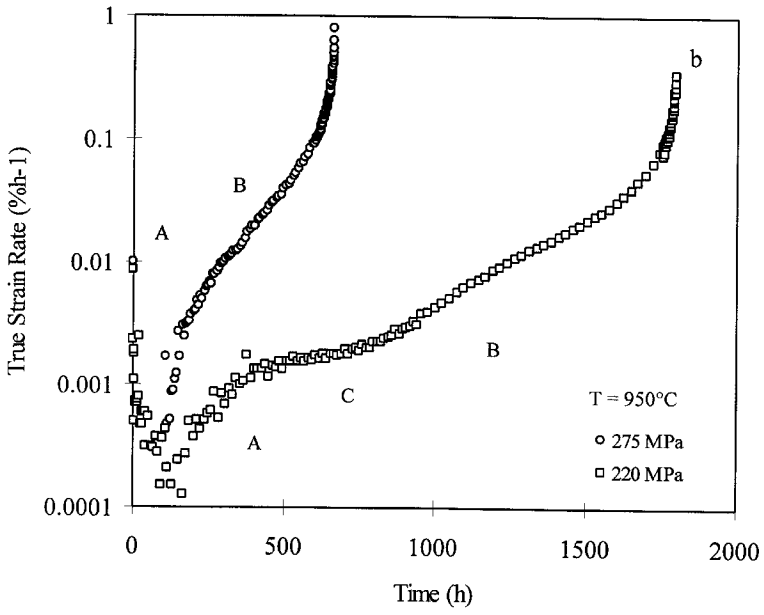
The analysis of the experimental creep curves of the SMP 14 alloy in the 135-425 MPa/900-1050°C has shown:

- In the explored stress/temperature range, a rafted microstructure is developed during creep.
- The tertiary creep dominates the creep curves.

During tertiary creep, different stages can be distinguished:

- A strongly accelerated stage, that occurs during the raft evolution.
- A stage that can produce a reduction of the strain rate for the highest temperatures/lowest stresses explored. This stage has been attributed to a redistribution of the local stresses between the γ and γ' phases and it disappears in the highest stresses tests.
- A further stage where the strain accelerates again, with the strain rate following a linear strain softening relationship in the 900-1000°C interval.
- The fastest and shortest final accelerated stage, leading to fracture.


1
0.1
0.01
0.001
0.0001
True Strain Rate (%h-1)
0
500
1000
1500
2000
Time (h)
a
A
B
T = 900°C
400MPa
325MPa


1
0.1
0.01
0.001
0.0001
True Strain Rate (%h-1)
0
500
1000
1500
2000
Time (h)
b
A
B
C
T = 950°C
275 MPa
220 MPa

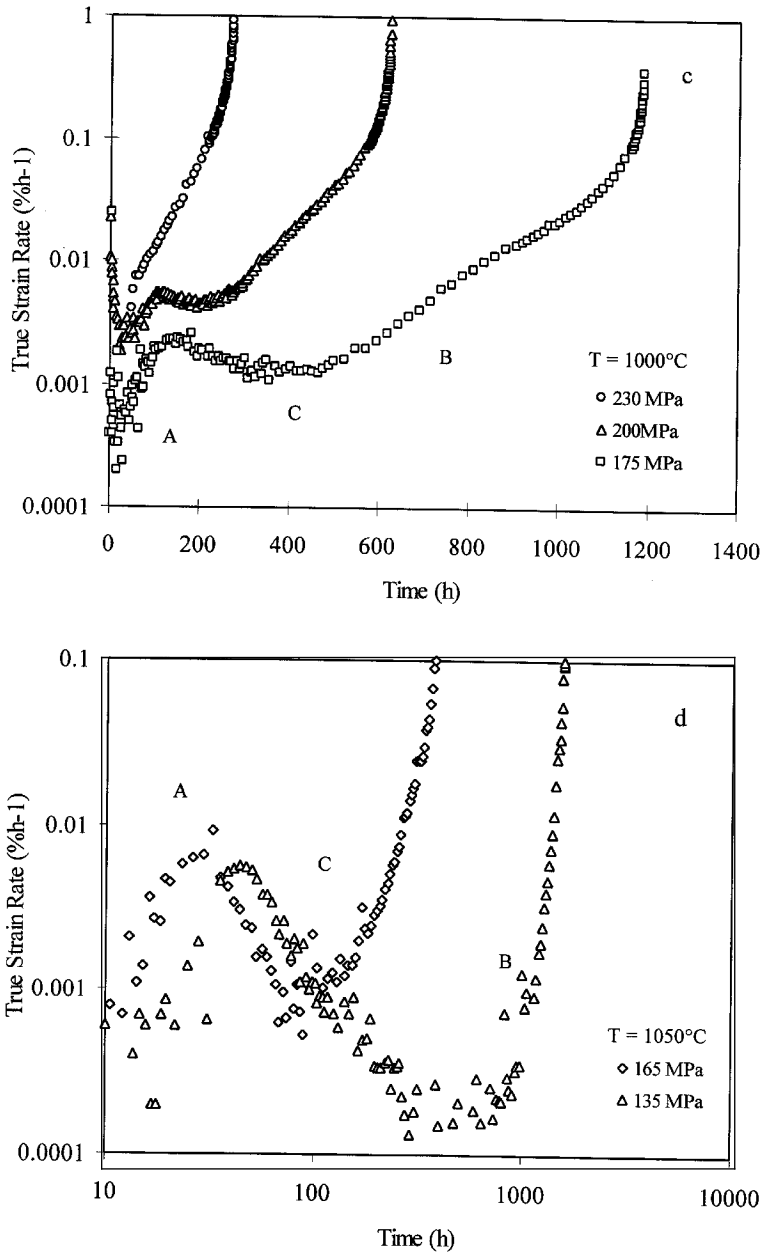


Fig. 3 - Plots of log $\dot{\varepsilon}$ vs. time in tests a) 900°C, b) 950°C and c) 1000°C and log $\dot{\varepsilon}$ vs. log time in d) tests at 1050°C. Different stages of damage accumulation during tertiary creep.

Acknowledgements: The authors are grateful to Ross & Catherall Ltd, Sheffield (U. K.) for supplying the SMP 14 alloy.

References

[1] J.M. Benson et al . "SMP 14 advanced high strength single crystal superalloy" report of CSIR, Pretoria, RSA.
[2] P.J. Henderson and J. Lindblom, "High temperature creep in a <001> single crystal nickel-base superalloy", Scripta Materialia, **37** (1997) p. 491.
[3] M. Maldini, V. Lupinc: "A constitutive equation for creep strain analysis and prediction of a single crystal superalloy". Materials at High Temperatures, **14** (1997) p. 47.
[4] M. Maldini, V. Lupinc: "Cyclic creep behaviour of nickel base superalloys". Proc. Inter. Conf. ICSMA 10, August 1994 Sendai. In "Strength of Materials", Eds. H.Oikawa et al., publ. The Japan Institute of Metals, Sendai, (1994) p. 697.
[5] M. Maldini, V. Lupinc: "A representation of tertiary creep behaviour in a single crystal nickel-based superalloy", Script. Met., **22** (1988) p. 1737.
[6] L.M. Pan, B.A. Shollock, M. McLean " Modelling of high-temperature mechanical behaviour of a single crystal superalloy", Proc. R. Soc., London, **453** (1997) p. 1689.
[7] J.J. Gilman, Micromechanics of Flow in Solids. New York: McGrow-Hill, 1969.
[8] B.F. Dyson " Creep and fracture of metals: mechanisms and mechanics" Revue Phys.Appl., **23** (1988), p. 605.
[9] M. Maldini et al.: "Tertiary creep behaviour of a new single crystal superalloy at 900°C". Scripta Materialia, **43** (2000) p. 637
[10] T. M. Pollock, A. S. Argon: "Creep resistance of CMSX-3 nickel base superalloy single crystals" Acta Metall.et Mater., **40** (1992) p. 1.
[11] H. Mughrabi et al.: "High–Temperature X-Ray Measurements of the Lattice Mismatch of Creep-Deformed Monocrystals of the Nickel-Base Superalloy SRR 99",Proc. Superalloys 1992 ed. by Antolovich et al., TMS, Warrendale (1992) p. 599.

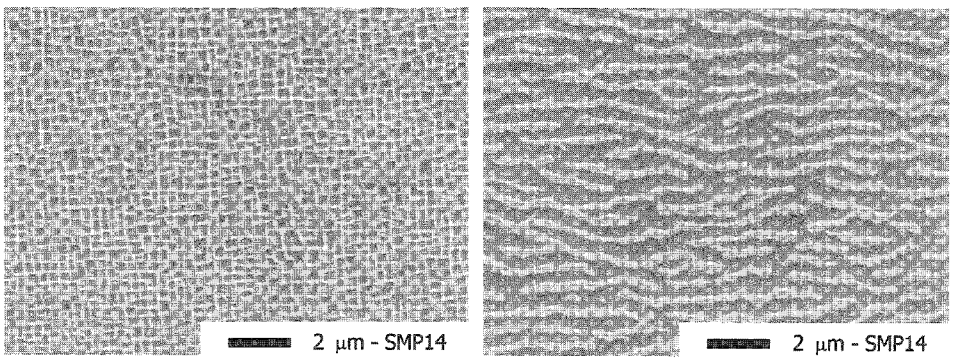


Fig. 4 - SEM microstructure observed in the material after heat treatment and on longitudinal section of the interrupted creep test after 392 h, at 1050°C and 150 MPa.

CREEP OF [001]-ORIENTED Ni-20MASS%Cr SINGLE CRYSTALS

Yoshihiro Terada, Yoshiro Nakamoto and Takashi Matsuo

Department of Metallurgy and Ceramics Science, Tokyo Institute of Technology, Meguro-ku, Tokyo 152-8552, Japan

Abstract

Creep of a [001]-oriented Ni-20mass%Cr single crystal with a single γ phase is investigated at 1173 K at stresses between 14.7 and 68.6 MPa. The shape of the creep curves and the ruptured microstructure at higher stresses are different from those at lower stresses. The decrease in the creep rate during the transient stage is negligible and the accelerating creep is prematurely initiated above 32 MPa, whereas the transient stage is pronounced and the onset of accelerating creep is retarded below 32 MPa. The formation of dynamically recrystallized grains is restricted in the vicinity of the ruptured portion above 32 MPa, while dynamic recrystallization occurs homogeneously in the whole gage portion below 32 MPa. It is demonstrated that instantaneous plastic strain is introduced above 32 MPa at 1173 K, at the application of stress. The creep rate of the early stage of transient creep is controlled by the shear stress, irrespective of crystal orientation. However, the creep rate during the transient creep and the ratio of transient creep duration to rupture life are strongly dependent on crystal orientation. The transient creep is most pronounced for the [001] single crystal typically at the lower stresses, which results in the marked evolution of the dislocation substructure.

Keywords: Creep, Single crystal, Nickel based alloy, [001] orientation, Microstructure

1. Introduction

A major part of the high temperature creep deformation process in nickel based superalloys takes place in the γ matrix [1,2]. We have previously reported the creep curves for the γ single phase Ni-20mass%Cr single crystal, which is the model alloy of the γ matrix of nickel based superalloys. The creep rate - time curves for the [001] oriented Ni-20mass%Cr single crystal at 1173 K - 29.4, 49.0 and 68.6 MPa obtained in our previous study are shown in Fig. 1 [3]. The shape of the creep curves for the [001] oriented single crystal is different, depending on the applied stress. At 49.0 and 68.6 MPa, the decrease in creep rate during transient stage is negligible, followed by the abrupt creep acceleration. On the contrary, the creep rate decreases over two orders of magnitude during transient stage and the onset of accelerating creep is retarded at 29.4 MPa.

The purpose of this study is twofold. Firstly, to determine the critical value of stress at 1173 K dividing the high and low stress regime, and secondly, to obtain the creep curves at the lower stresses, below 29.4 MPa. The creep tests at 39.2 and 34.3 MPa are conducted for the former purpose, and at 24.5, 19.6 and 14.7 MPa for the latter one. The measurement of the instantaneous strain introduced at the stress application in the creep tests is available to identify the critical stress dividing the higher and the lower stresses. It has been reported for the ferritic steel [4] and the TiAl-based alloy [5] that the accelerating creep is prematurely initiated at stresses above the yield stress, in which the plastic strain, in addition to the elastic strain, is introduced at the stress application. In this study, the instantaneous strain at the stress application is also investigated for the Ni-20mass%Cr single crystal with the [001] orientation.

2. Experimental

A Ni-20mass%Cr alloy, designated as Ni-20Cr in this paper, was prepared for this study. The chemical composition of the alloy is shown in Table 1. The alloy was melted in a high frequency induction furnace in a vacuum and cast into a 4 kg ingot in an argon atmosphere. The ingot was hot-forged into rods with a diameter of 13 mm. The single crystals with the [001] orientation were successfully grown by a modified Bridgman furnace in a flow of purified argon and then homogenized at 1523 K for 36 ks. The crystal orientation corresponding to the stress axis was determined by the Laue back-reflection X-ray technique. Only the crystals within three degrees of the [001] orientation were employed for creep tests. Full size creep specimens with the gage portion of 30 mm in length and 6 mm in diameter were machined from the crystals.

Table 1. Chemical composition of single crystals used in the present study (mass%).

Elements	C	Si	Mn	Cr	Ni
Ni-20Cr	0.001	0.49	0.30	19.3	Bal.

Tensile creep tests were carried out at 1173 K under the constant stresses of 14.7, 19.6, 24.5, 34.3 and 39.2 MPa using the single-lever type creep machines. During the creep tests, stress was kept constant by adjusting the auxiliary weights in an accuracy within one per cent against the initial stress. Creep strain was automatically recorded using linear variable-differential transducers via extensometer fitting onto annular ridges machined at both ends of the specimen gage portion. Microstructures subjected to creep deformation were observed by the optical microscope.

3. Results

3.1. Instantaneous strain

The instantaneous strain introduced at the stress application in the creep tests is plotted against the applied stress in Fig. 2. The data obtained in the measurement of elastic modulus are shown by open symbols, while the data measured at the stress application in each creep test are shown by the solid symbols. The instantaneous strain increases linearly with increasing stress. The elastic modulus for the crystal is estimated to be 86 GPa at 1173 K. The instantaneous strain above 32 MPa is larger than that predicted by the elastic deformation. It is deduced that plastic strain is introduced at stresses above 32 MPa, that is, the yield stress may be 32 MPa at 1173 K.

3.2. Creep curves

Creep rate - time curves are shown in Fig. 3, where the creep rate is a true strain rate [6]. The curves at 68.6, 49.0 and 29.4 MPa obtained in the previous study [3] are reproduced in the figure by thin lines. At 39.2 and 34.3 MPa, the decrease in creep rate during transient stage is negligible, followed by the abrupt creep acceleration. The shape of the creep curves is similar to those at 68.6 and 49.0 MPa. The critical value of stress dividing the higher and the lower stresses is placed between 34.3 and 29.4 MPa, which is in good agreement with the yield stress evaluated from the measurement of instantaneous strain. In the lower stresses, below 29.4 MPa, the marked decrease in creep rate is observed during transient stage. The creep rate decreases two orders of magnitude at 24.5 and 19.6 MPa, while the decrease in creep rate is still one order of magnitude at 14.7 MPa. Note that these three tests are currently in progress and that the creep deformation is still in the transient stage.

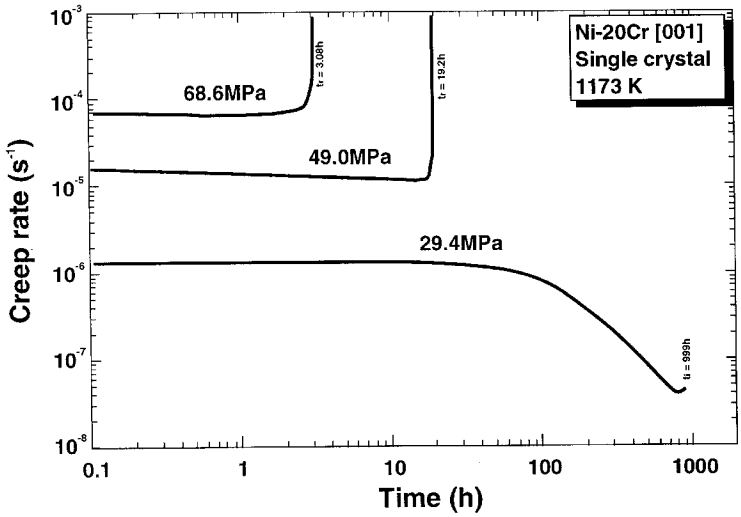


Fig. 1. Creep rate - time curves for [001] oriented Ni-20Cr single crystal at 1173 K / 29.4, 49.0 and 68.6 MPa [3].

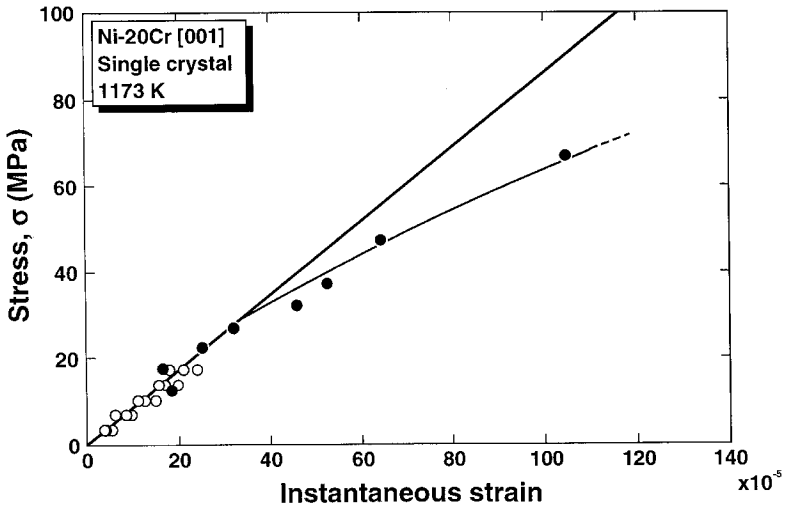


Fig. 2. Plot of instantaneous strain vs stress for [001] oriented Ni-20Cr single crystal at 1173 K.

Creep rate - strain curves are shown in Fig. 4. At 39.2 and 34.3 MPa, the accelerating creep is initiated at the strain of 1.0, as in the tests at 68.6 and 49.0 MPa, and the rupture strains are around 1.3. On the contrary, the strain hardening continues up to a strain greater than 1.0 at the lower stresses below 29.4 MPa. The threshold strain at which the creep rate begins to decrease rapidly is 0.5 at 29.4 MPa, and it monotonically decreases with a decreasing stress.

The creep rates at the strain of 0.01 and the minimum creep rates are plotted against stress in Fig. 5. The creep rates at the strain of 0.01 fall on a straight line in the whole stress region. The slope of this line is 5. The minimum creep rates above 34.3 MPa also fall on a straight line with a slope of 5. However, the minimum creep rate at 29.4 MPa is two orders of magnitude smaller than that at 34.3 MPa, and the discontinuity occurs between 34.3 and 29.4 MPa. The stress exponent of the minimum creep rates, n, cannot yet be determined in the lower stress region.

3.3. Microstructures

Optical micrographs of the specimen ruptured at 1173 K and 39.2 MPa are shown in Fig. 6, where 39.2 MPa is larger than the critical stress. Note that the measured rupture strain is 1.29. The specimen is slightly necked near the ruptured portion (Fig. 6a). Well-developed subgrains are observed in the vicinity of the ruptured portion (Fig. 6b), while subboundaries and dynamically recrystallized grain boundaries are not observed elsewhere in the specimen (Fig. 6c).

At 34.3 MPa, which is just above the critical stress, the specimen is necked near the ruptured portion (Fig. 7a), as in the case at 39.2 MPa. The dynamically recrystallized grains with a diameter of 30 μm are observed only in the vicinity of the ruptured portion (Fig. 7b), whereas no grain boundaries and no subboundaries are observed elsewhere in the specimen (Fig. 7c).

The specimen crept at 29.4 MPa, which is lower than the critical stress, is shown in Fig. 8. Note that the creep test was interrupted at the strain of 1.5 which is the start of accelerating stage. The specimen homogeneously deforms and no necked portions are observed even at the strain of 1.5. Dynamically recrystallized grains with a diameter of approximately 1 mm are generated in the whole gage portion (Fig. 8a). A magnified view of the interrupted specimen (Fig. 8b) shows that twins are extensively observed, and that cracks generate at dynamically recrystallized grain boundaries.

4. Discussion

In the previous section, it was demonstrated for the [001] oriented Ni-20mass%Cr single crystal that the creep behavior at the stresses higher than 32 MPa is different from that at the lower stresses. At the higher stresses, the decrease in the creep rate during the transient stage is negligible and the dynamic recrystallization occurs heterogeneously. On the contrary, at the lower stresses, the creep rate decreases to a large extent during the transient stage and dynamic recrystallization occurs homogeneously in the whole gage portion. In this section, the creep of the [001] single crystal is compared with those of the [011] and the [-111] single crystals.

For the creep of Ni-20mass%Cr single crystal, the following two experimental results have been presented at lower stresses [7,8]. Firstly, easy glide predominantly occurs and dislocation substructure scarcely evolves in the early stage of transient creep, in which the decrease in the creep rate is negligible (the early stage of transient creep is named hereafter "stage I"). Secondly, multiple slip occurs and the dislocation substructure evolves in the latter stage of transient creep, in which the creep rate decreases continuously (named "stage II"). To characterize the creep of the [001] single crystal in comparison with those of the [011] and the [-111] single crystals, we pay attention to the creep rate at stage I, the decrease in the creep rate during the transient stage and the transient creep / accelerating creep ratio.

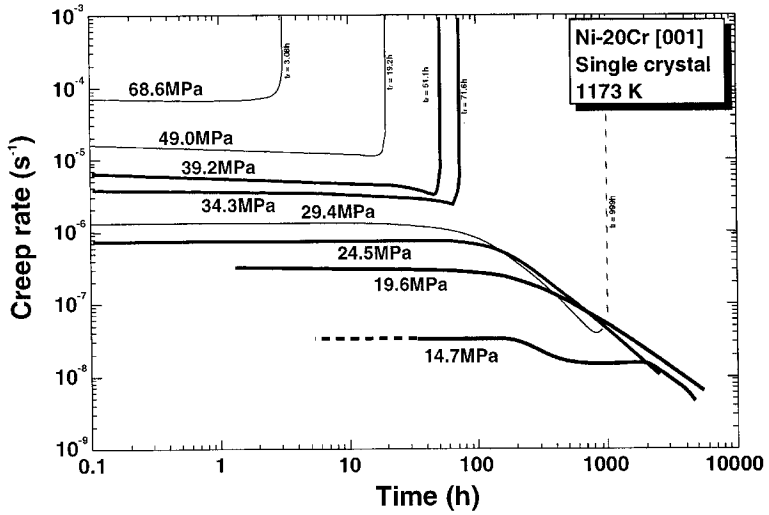


Fig. 3. Creep rate - time curves for [001] oriented Ni-20Cr single crystal at 1173 K.

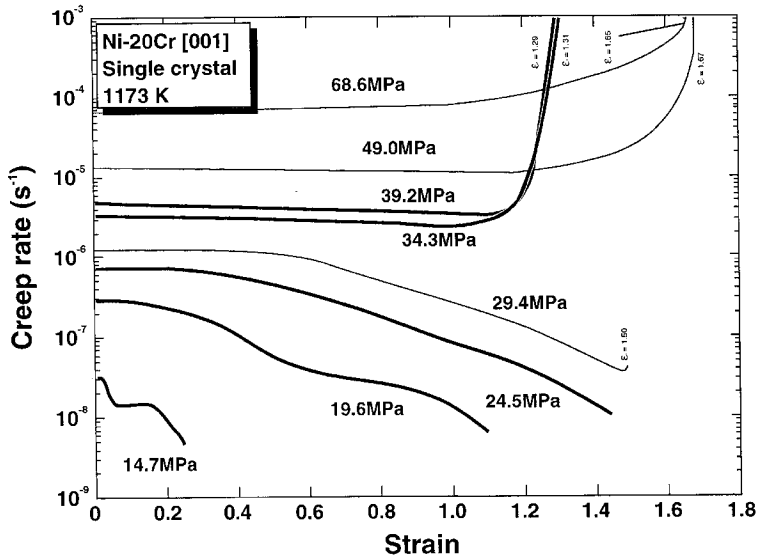


Fig. 4. Creep rate - strain curves for [001] oriented Ni-20Cr single crystal at 1173 K.

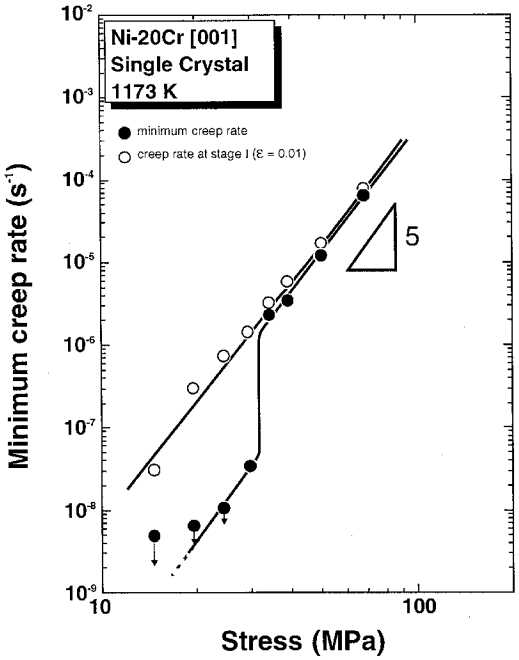


Fig. 5. Plot of minimum creep rate vs applied stress for [001] oriented Ni-20Cr single crystal at 1173 K. The creep rates at the strain of 0.01 are also included.

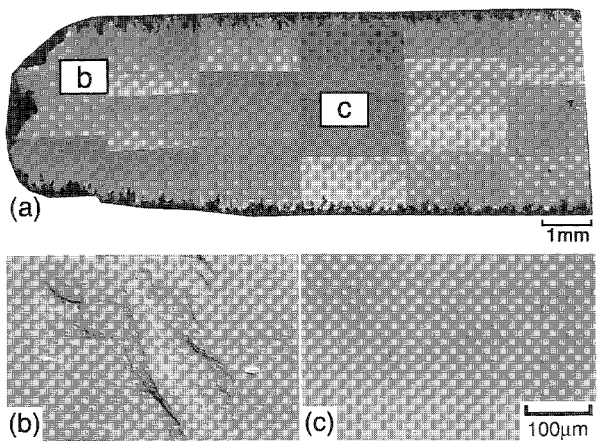


Fig. 6. Optical micrographs of [001] oriented Ni-20Cr single crystal creep-ruptured at 1173 K and 39.2 MPa.

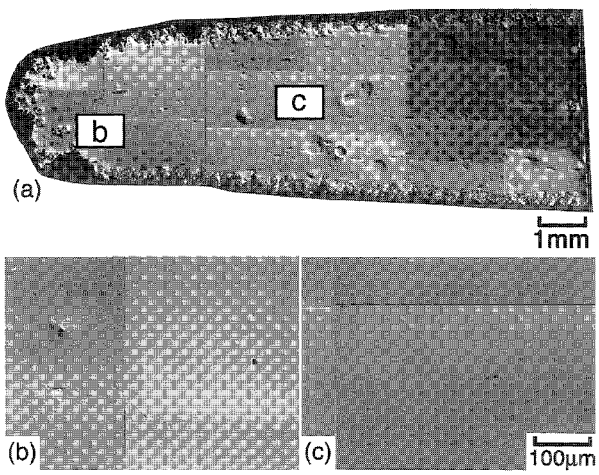


Fig. 7. Optical micrographs of [001] oriented Ni-20Cr single crystal creep-ruptured at 1173 K and 34.3 MPa.

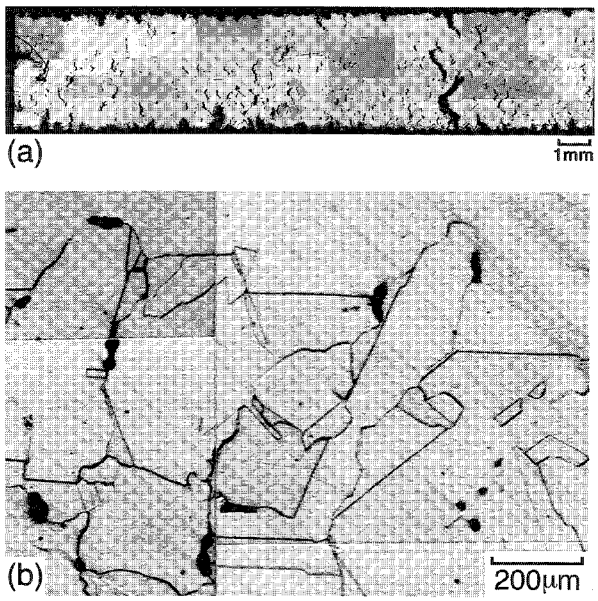


Fig. 8. Optical micrographs of [001] oriented Ni-20Cr single crystal creep-interrupted at the strain of 1.5 at 1173 K and 29.4 MPa.

4.1. Shear stress versus shear stain rate

The creep rates in stage I are plotted against the shear stress for the [001] oriented Ni-20Cr single crystal in Fig. 9. Note that the creep rate is indicated by the shear strain rate on the slip planes and that is plotted against the maximum resolved shear stress. The data for the [011] and the [-111] single crystals, obtained in the previous study [3], are also shown in the figure. The shear strain rates data for the [001] single crystal lie on a straight line with the slope of 5. The plots for the [011] and the [-111] orientations fall well on the line. In conclusion, the creep rate in stage I for the single crystal is a function of the shear stress on the slip planes.

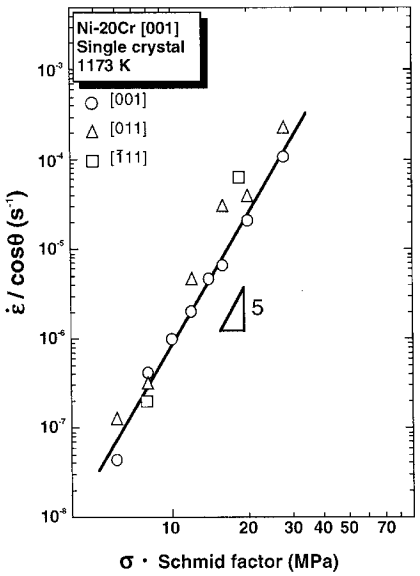


Fig. 9. Plot of shear strain rate vs shear stress for [001], [011] and [-111] oriented Ni-20Cr single crystal at 1173 K.

4.2. Creep rate ratio during the transient stage

The decrease in the creep rate during the transient stage, as characterized by the ratio $\dot{\varepsilon}_{min}$ / $\dot{\varepsilon}_{stageI}$, is summarized as a function of stress for the [001], [011] and [-111] single crystals in Fig. 10, where $\dot{\varepsilon}_{min}$ is the minimum creep rate and $\dot{\varepsilon}_{stageI}$ is the creep rate at stage I. Note that the value of $\dot{\varepsilon}_{min}$ / $\dot{\varepsilon}_{stage\ I}$ is representative of the evolution of the dislocation substructure during the transient creep stage. For the [001] single crystal, the value of $\dot{\varepsilon}_{min}$ / $\dot{\varepsilon}_{stageI}$ is larger than 0.6 above 32 MPa, while the ratio decreases drastically below 32 MPa. The value of $\dot{\varepsilon}_{min}$ / $\dot{\varepsilon}_{stageI}$ is $3x10^{-3}$ below 32 MPa for the [001] single crystal. This ratio is also decreasing as the stress is reduced for the [-111] single crystal, while its magnitude is much larger than that for the [001] single crystal. The value of $\dot{\varepsilon}_{min}$ / $\dot{\varepsilon}_{stageI}$ is 0.3 at 29.4 MPa for the [-111] single crystal, which is one order of magnitude larger than that for the [001]. The variation of the $\dot{\varepsilon}_{min}$ / $\dot{\varepsilon}_{stageI}$ ratio for the [011] single crystal is rather complicated, however, its value ranges between 0.1 and 0.3 in every stress. It is elucidated that the evolution of dislocation substructure is most pronounced in the lower stresses for the [001] single crystal.

4.3. Transient creep / accelerating creep ratio

The ratio of transient creep duration to rupture life, t_{min} / t_r, is summarized for the [001], [011] and [-111] single crystals in Fig. 11, where t_{min} is the elapsed time at the minimum creep rate and t_r is the rupture life. Note that the left side of plots means the ratio of transient creep to rupture life and the right side means the ratio of accelerating creep. For the [001] single

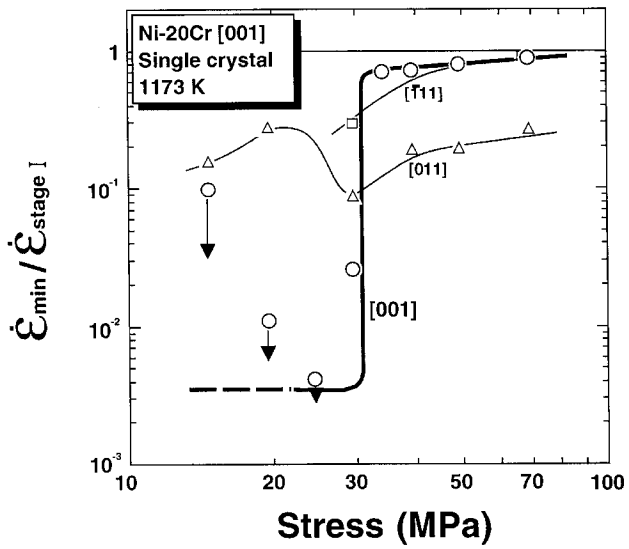


Fig. 10. Plot of $\dot{\varepsilon}_{min}$ / $\dot{\varepsilon}_{stage\ I}$ vs applied stress for [001], [011] and [-111] oriented Ni-20Cr single crystal at 1173 K, where $\dot{\varepsilon}_{min}$ is the minimum creep rate and $\dot{\varepsilon}_{stage\ I}$ is the creep rate of plateau region at the beginning of the creep tests.

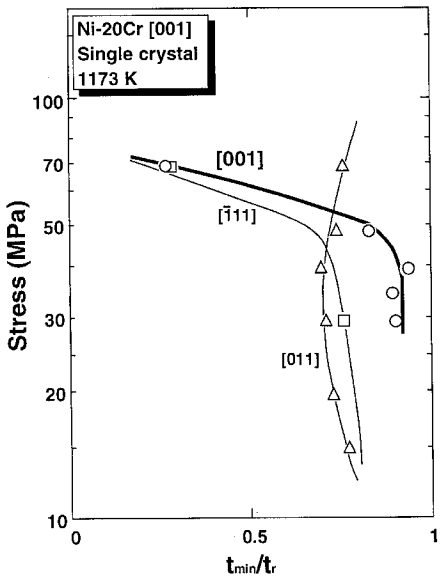


Fig. 11. Plot of t_{min} / t_r vs applied stress for [001], [011] and [-111] oriented Ni-20Cr single crystal at 1173 K, where t_{min} is the time at the minimum creep rate and t_r is the rupture life.

crystal, the value of t_{min} / t_r is 0.27 at 68.6 MPa, indicating that the creep deformation is dominated by the accelerating stage. The value of t_{min} / t_r abruptly increases with decreasing stress, and it reaches 0.9 at the lower stresses. The transition from accelerating to transient stage dominance with decreasing the stress is observed also for the [-111] single crystal. However, the value of t_{min} / t_r in the lower stresses is 0.76 for the [-111] single crystal, which is smaller than that for the [001] single crystal. For the [011] single crystal, the value of t_{min} / t_r is around 0.7 in every stress, indicating that transient rather than accelerating creep dominate the creep deformation. It is found that the transient creep is most pronounced in the lower stresses for the [001] single crystal. In conclusion, the transient stage predominantly occupies creep for the [001] single crystal, typically at lower stresses, which results in the marked evolution of dislocation substructures.

5. Conclusions

The creep tests were conducted for the [001] oriented Ni-20mass%Cr single crystal at 1173 K under a constant stress between 14.7 and 68.6 MPa. The results are summarized as follows:
1. Plastic strain, in addition to the elastic strain, is introduced at the stress application in creep tests with stresses above 32 MPa.
2. The decrease in the creep rate during the transient stage is negligible above 32 MPa, while a marked decrease in the creep rate is observed during the transient stage below 32 MPa.
3. The deformation of the creep specimens and the evolution of the substructure occur heterogeneously above 32 MPa, while they occur homogeneously at the start of the accelerating creep stage for the tests with an applied stress below 32 MPa.
4. The creep rate in the early stage of transient creep is decided by the shear stress on the slip planes, irrespective of crystal orientation. The evolution of substructure and the extent of transient creep are functions of crystal orientation. These are most pronounced for the [001] orientation, typically at the lower stresses.

References

[1] V.Sass and M.Feller-Kniepmeier, Orientation dependence of dislocation structures and deformation mechanisms in creep deformed CMSX-4 single crystal, Mater. Sci. Eng., **A245** (1998), 19-28.
[2] N.Matan, D.C.Cox, C.M.F.Rae and R.C.Reed, On the kinetics of rafting in CMSX-4 superalloy single crystals, Acta Mater., **47** (1999), 2031-2045.
[3] Y.Terada, D.Kawaguchi and T.Matsuo, Creep deformation of Ni-20mass%Cr single crystals with [001], [011] and [-111] orientations, Proc. of the 9th Intern. Conf. on Creep & Fracture of Engineering Materials & Structures, Ed. by J.D.Parker, The Institute of Materials, London, (2001), p.427-435.
[4] T.Matsuo, D.Serino and Y.Terada, Change in feature of transient creep with decreasing stress, Proc. of the 7th Intern. Conf. on Creep and Fatigue at Elevated Temperatures, Ed. by Y.Asada, The Japan Society of Mechanical Engineers, Tokyo, (2001), p.551-555.
[5] S.Hirata, Creep deformation of Ti-48at%Al PST crystals with fully lamella structures, Thesis, Tokyo Institute of Technology, Tokyo, (2001).
[6] R.W.Hertzberg, Deformation and Fracture Mechanisms of Engineering Materials, 4th edn., Wiley, New York, (1996).
[7] T.Matsuo, S.Takahashi, Y.Ishiwari and Y.Terada, Creep in single crystals of γ single phase Ni-20Cr alloy and evolution of dynamic recrystallization, Key Eng. Mater., **171-174** (2000), 553-560.
[8] T.Matsuo, T.Kashiwa, M.Nijyo and Y.Terada, Effects of tantalum and rhenium on creep in single crystals of nickel-20%chromium, Aerospace Materials, Eds. by B.Cantor et al., Institute of Physics, London, (2001), p.285-293.

CHARACTERIZATION OF THE PROPAGATION BEHAVIOR OF SHORT FATIGUE CRACKS IN NICKEL-BASED SINGLE CRYSTAL SUPERALLOY SC16

X. P. Zhang[1], C. H. Wang[2], W. Y. Chen[3], L. Ye[1] and Y.-W. Mai[1]

[1] School of Aerospace, Mechanical and Mechatronic Engineering, the University of Sydney, NSW 2006, Australia
[2] Aeronautical and Maritime Research Laboratory, DSTO, Melbourne 3001, Australia
[3] Institute for Metal Physics, Technology University Berlin, 10623 Berlin, Germany

Abstract

As a comparative study to poly- crystal materials, the present work focused on investigating the growth behaviour of microstructurally short fatigue cracks in a nickel-based single crystal superalloy SC16 by *in-situ* SEM fatigue testing at room temperature. From the present results, it was concluded that for single- crystal superalloy SC16, there does exist the so-called anomaly of short fatigue crack growth, similar to poly-crystal alloys. In addition, it was found that a short fatigue crack in single crystal SC16 propagated predominantly along microstructural slip bands which were nearly perpendicular to the globe mode **I** loading direction or the [001] crystallographic orientation of SC16. Moreover, it was also observed that fatigue crack growth in single crystal alloy exhibited a less deflected crack path and fairly flat fracture surfaces, as compared to poly-crystals. This implies that there is almost no fracture surface roughness induced crack closure, while the dominant crack closure mechanism is plasticity induced.

Keywords: Microstructurally short crack, growth behaviour, single crystal SC16, slip bands, *in-situ* SEM fatigue

1. Introduction

Failure of engineering structures and components due to fatigue is most common in a range of industries. Fatigue is often the primary cause of aircraft accidents, power plant and automobile failures, bridge fractures, railway-line breakages, and so forth. To manufacture more reliable high-performance structures and products, and to improve reliability and safety and to reduce maintenance costs, without compromising structural integrity and hence safety, it is essential to develop means of assessing the growth behaviour of small cracks in both traditional and advanced materials, especially under cyclic stresses [1-3]. Although it is widely recognised that fatigue-induced damage is often related to crack size, it remains a significant challenge for scientists and engineers to analytically predict fatigue crack growth right from an initiation/small crack to final failure. However, the growth behaviour of short (or small) fatigue cracks has been widely recognised to significantly differ from that of long fatigue cracks, i.e. the anomalously high crack growth rates that are found in short crack regime. The importance of the short crack issue has therefore been of great concern to researchers and engineers for the past two decades. The short fatigue crack problem remains a critical factor in fatigue design, lifetime prediction and elongation ever since. In particular,

ignoring short fatigue cracks can result in serious overestimates of the damage-tolerant life of engineering structures [3,4].

Recently, the fatigue and fracture behavior of single crystal structural components, especially the lifetime prediction and failure assessment, have been giving many attentions since single crystal structural alloys have excellent reliability and superior resistance to high temperature deformation and are being used in some important engineering applications [5~8]. In addition, there is also an acute demand to understand the growth characteristics of small cracks in single crystal alloys, since lifetime prediction and failure assessment based on *'retirement for cause'* (**RFC**) rule of aircraft safety assessment for some critical components or structures made of single crystals or directionally solidified alloys, such as aero-engines and turbines, depend upon their fatigue performance in single crystal structures. The **RFC** program utilises techniques of damage tolerant design, taking account of crack initiation life and allowing for a certain crack growth within the critical scale. Although the behaviour of small cracks is now well documented for traditional polycrystalline metallic materials, far less information is available for the small fatigue crack growth behaviour in single crystal structural alloys. Our present understanding for small fatigue crack behaviour in single crystal and directionally solidified alloys is fairly poor [9-11]. Existing results are mainly for high purity single crystal metals (*not alloys*), such as copper single crystal [12] and nickel single crystal [13] where the cracks grew rapidly in the very small crack regime, for example less than 10 ~20μm. There is not much research work on small crystallographic fatigue crack growth behaviour in single crystal alloys, especially the interaction between a small crack and the crystallographic orientations or sub-structures, as well as the crack closure problem. Moreover, a major difficulty with small cracks has always been the difficulty of experimentally determining small-crack data, particularly for design purposes [14]. On the other hand, as the grain-boundary blocking effect has been recognised as a major factor contributing to the anomaly of small fatigue crack growth in polycrystalline metallic materials [15-17], studying the small fatigue crack growth behaviour in a single crystal material would have the advantage of eliminating this complication factor, and allowing us to examine in detail the interaction between a small crack and crystallographic orientations. Research on this aspect will also deepen and enrich our understanding of small crack growth in traditional polycrystalline metallic materials.

2. Experimental material and method

2.1 Test material and specimen preparation

The material used in the present research is a high chromium nickel-based single crystal superalloy SC16 developed by ONERA in France (French National Aerospace Research Establishment) last decade for manufacturing high-performance gas-turbine blades and vanes components [18]. Its chemical compositions and mechanical properties at room temperature are shown in Tables 1 and 2. The heat treatment for this material in the as-supplied condition (unimodal distribution of γ'-phase precipitates) is as follows: (1) Solution treatment: 1250 °C/3 hrs/air cooling (AC), and followed by (2) Ageing treatment: 1100 °C/1 hrs/cooling at a rate of 15 °C per hour to 850 °C, 850 °C/24 hrs/AC. Single crystal superalloy SC16 derives its high temperature strength from the ordered (Ll_2) precipitate of γ'-phase dispersed in a nickel solid solution matrix of γ phase (f.c.c). The typical microstructure of SC16 after heat

treatment is shown in Fig.1, where cuboidal γ'-phase precipitates are coherently embedded in the γ phase matrix. The average size of γ' particles is 450 nanometres and the volume fraction of γ' particles is about 40%. The specimen geometry used for *in-situ* SEM fatigue testing is 40 × 10 ×0.8 (length × width × thickness, mm). Both faces of each specimen were well polished, and the face to be observed in SEM was polished to the level of 0.5 micron diamond suspension solution. After polishing, specimens were etched slightly by Florge's reagent. Very short cracks with a crack length ranging from a few microns to tens of microns were machined at one edge of the specimens.

Table 1 Nominal composition of the nickel-based single crystal superalloy SC16 (wt%)

Cr	Ti	Ta	Al	Mo	Ni
15.4	3.5	3.5	3.5	2.8	Balance

Table 2 The mechanical properties of superalloy SC16 at room temperature (22 °C) [a)]

$\sigma_{0.2}$, MPa	σ_{uts}, MPa	E, GPa	δ_5 [b)] (%)
810.8	992.4	123.0	>16

[a] Longitudinal direction of tensile specimens is in [001] orientation of the single crystal alloy, and the strain rate in the tensile test was 1.0E-03 1/s.

[b] δ_5 (%) is percentage elongation.

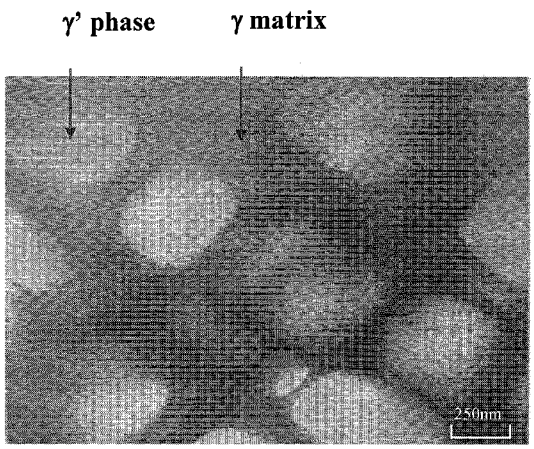
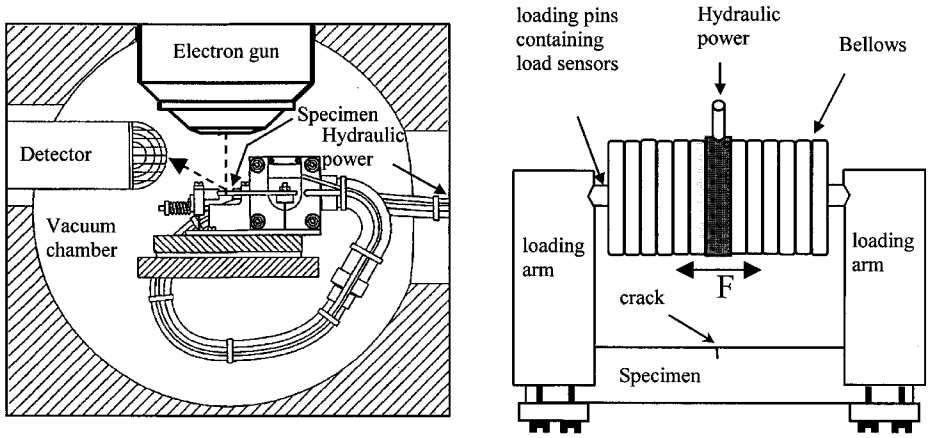


Fig.1 Microstructure of single crystal superalloy SC16 (as heat treated condition)

2.2 In-situ SEM fatigue test procedure

The *in-situ* observation on fatigue crack growth behaviour was conducted, at room temperature, using a Phillip 505 scanning electron microscope where a cyclic loading stage was mounted in the vacuum specimen chamber, as illustrated in Fig.2. The cyclic loading

stage was driven by the hydraulic power system where the mean load and single overload can be varied by an adjustable piston and a plunger operated through an eccentric gear. The eccentric gear was controlled by a frequency-modulated motor which can provide loading frequency up to 15 Hz. In the present work, *in-situ* SEM fatigue testing was carried out at a frequency of 5 Hz in sinusoidal waveform pulsating tension loading mode with a stress ratio of R=0. The fatigue load consists of a cyclic tensile stress with the constant amplitude of 29 MPa and a cyclic bending stress with the maximum stress amplitude of 525 MPa at the specimen edge (bending movement M=7.0 N.m). Crack growth processes were recorded by a series of digital photographs, and could also be monitored by TV and recoded by videotape. The testing system was stopped intermittently to perform measurements by taking SEM digital images, from which crack length and the crack tip opening displacement were measured. Experimental conditions in SEM were optimised to get the best resolution of images, where a secondary electron beam was used. The specimen was tilted by a maximum 15° angle away from the detector of the SEM because the limited chamber room can not allow the specimen to be rotated fully, this may improve the contrast by filtering out the backscattered electrons and the higher energy secondary electrons [19].



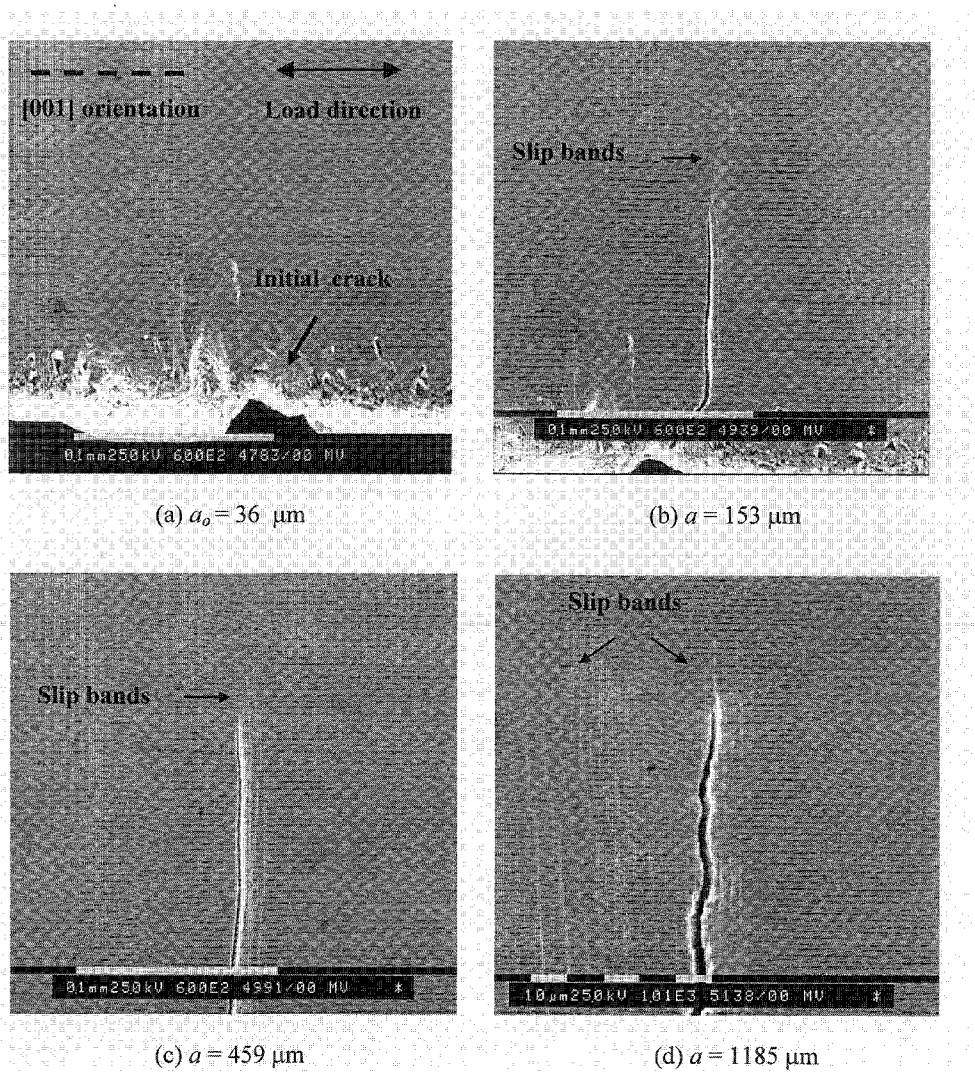
(a) Configuration of *in-situ* SEM fatigue system (b) Schematic of the cyclic loading stage

Fig.2 Illustration of *in-situ* SEM fatigue testing system

3. Results and discussions

Observations of the propagation process of a short fatigue crack emanating from an initial micro-notch (the depth is 36 microns) were recorded by a series of digital SEM images as shown in Fig.3. Since the mode I pulsating tension loading direction is nearly coincident with the [001] crystallographic orientation of single crystal SC16 (the angle between them is less than 5 degree) and the crack propagation direction is nearly perpendicular to the mode I loading direction, therefore the crack propagated nearly perpendicular to the [001] orientation.

In these photos, the shear slip bands are clearly shown paralleled to the crack propagation direction, and occur alternately on both sides of the crack body. Since the shear slip bands are perpendicular to the mode I loading direction, the crack propagation path is virtually co-planar, with little deflection. This actually also implies that there is almost no crack closure induced by fracture surface roughness. In addition, it was noticed that the short fatigue crack started growing as a corner crack with its surface length equal to the depth, and then it changed into a through-thickness crack when its length reached the thickness of the specimen. The results of fatigue crack growth rate versus the fatigue crack length are shown in Fig.4.



(a) $a_o = 36$ μm (b) $a = 153$ μm

(c) $a = 459$ μm (d) $a = 1185$ μm

Fig.3 In-situ SEM observations of short fatigue crack growth in single crystal SC16

To assess the applicability of the stress intensity factor in correlating the crack growth rates, the experimental results are plotted against the stress intensity factor range, ΔK, as shown in Fig.5. For a corner crack with length a, the stress intensity factor is given by the following equation,

$$K = (\sigma_m + \sigma_b)\sqrt{\pi a}F(a/t) \ , \quad a/t < 1, \ t/W << 1 \tag{1}$$

where σ_m and σ_b are the membrane stress and maximum bending stress respectively; t and W are the thickness and width of the specimen respectively; F is the geometry factor that can be estimated referring to the stress intensity factor handbook [20]. After the crack becomes a through-thickness edge crack, the stress intensity factor is estimated by

$$K = [\sigma_m F_m(a/W) + \sigma_b F_b(a/W)]\sqrt{\pi a} \ , \quad a/t \geq 1 \tag{2}$$

where the geometry factors F_m and F_b can also be obtained from the handbook [20].

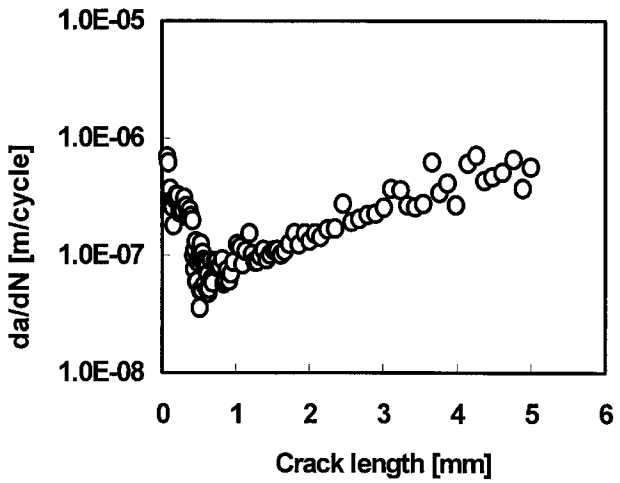


Fig.4 Crack growth rates (da/dN) versus crack length

In Figs. 4 and 5, an obvious deceleration in the crack growth rate, till a crack length of ~0.5 *mm* and a stress intensity factor range of ~24 MPa$\sqrt{m}$ (i.e. $\Delta K = 24$ MPa$\sqrt{m}$ for R=0), can be seen clearly. Then the crack growth rates increase again. This means that the growth of short fatigue cracks in the single crystal superalloy SC16 also shows an anomalously high rate

in the short crack regime. This also implies that the anomaly of short fatigue crack growth is a common feature for metallic materials, it does not matter whether they are polycrystalline or single crystal. Moreover, it was noticed that in F.C.C. single crystals the expected crystallographic planes of the slip bands are the [111] planes, the short fatigue cracks follow the [111] planes at least at the onset of the propagation, for example, cracking close to the specimen surface was actually along the [111] slip bands for Ni_3Al single crystal alloy [10]. Although it is shown that the short fatigue crack in single crystal SC16 propagates along slip bands which are perpendicular to the [001] orientation, it is yet unclear where the preferable crystallographic planes are so as slip bands and short cracks can follow. Also it is unknown whether a short fatigue crack grows differently from a long crack, since no long fatigue crack growth data are currently available for this single crystal alloy. Further investigation is needed to address the above issues.

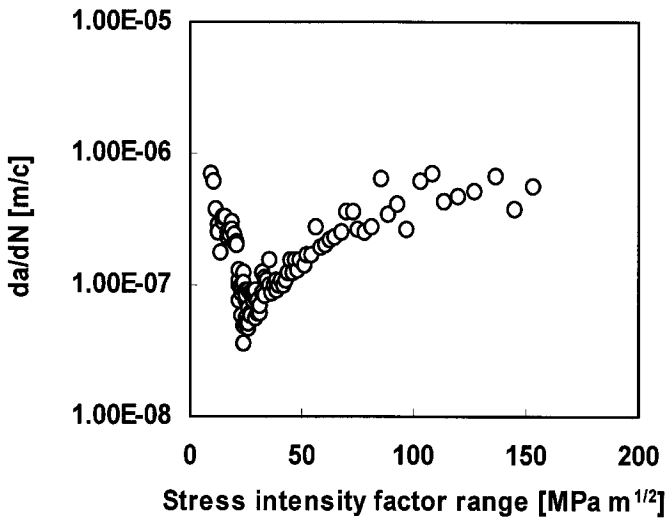
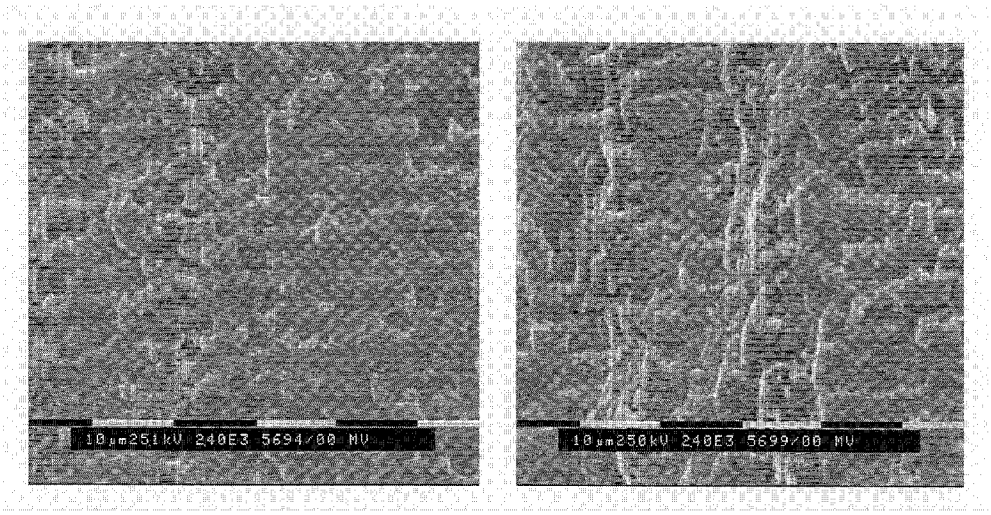


Fig.5 Crack growth rates versus the stress intensity factor range, ΔK

In addition, as seen in Fig.3, the short fatigue crack propagated along shear slip bands which were perpendicular to loading direction, and exhibited fairly flat fracture surfaces and less deflected propagation path. The morphologies of fatigued fracture surfaces both in the short crack regime (a is less than 0.25 mm) and in the long crack stage (a =2.1 mm) consisted of small flat facets, as shown in Fig.6. These facets are actually a clear indication of shear decohesion as the main fatigue crack propagation mechanism under the present test conditions.



(a) In short crack regime (a = 0.25 mm) (b) In long crack stage (a =2.1mm)

Fig.6 Morphologies of fatigued fracture surfaces for short and long cracks

4. Conclusions

1) For the single crystal superalloy SC16, there does exist the so-called anomaly of short fatigue crack growth, similar to poly-crystal alloys. The crack length and the stress intensity factor range corresponding to the lowest crack growth rate are 0.5 mm and 24 MPa·m$^{1/2}$ respectively by the present *in-situ* SEM fatigue experiment.
2) Fatigue crack growth in SC16 exhibited a less deflected crack path and fairly flat fracture surfaces, as compared to poly-crystals. This implies that there is almost no fracture surface roughness induced crack closure, while the dominant crack closure mechanism is plasticity induced.
3) A short fatigue crack in SC16 propagated predominantly along slip bands which were nearly perpendicular to the globe mode **I** loading direction or the [001] crystallographic orientation.
4) Analysis of the morphologies of fatigued fracture surfaces showed that shear decohesion is the main fatigue crack propagation mechanism in this single crystal alloy for the test conditions studied.

Acknowledgements

Authors XPZ, YWM and CHW wish to thank the Australian Research Council (ARC) for financial support through the Large Research Grant (A10009166), and the support from DSTO (Australia) through the Centre of Expertise in Damage Mechanics established in the University of Sydney.

References

[1] Newman Jr., J.C., Phillips, E.P. and Swain, M.H., Fatigue-life prediction methodology using small-crack theory, International Journal of Fatigue, Vol.21, 1999, 109-119.

[2] Tiffany, C.F., Aging of US Air Force Aircraft, National Academy Press, Washington, 1997.
[3] Ritchie, R.O., Small crack growth and the fatigue of traditional and advanced materials, Plenary Lecture, Fatigue'99, Beijing, China, 1999, 3-14.
[4] Ritchie, R.O., Gilbert, C.J. and McNaney, J.M., Mechanics and mechanisms of fatigue damage and crack growth in advanced materials, International Journal of Solids and Structures, Vol.37, 2000, 311-329.
[5] Mukherji, D. Gabrisch, H, Chen, W., Fecht, H.J. and Wahi, R.P., Mechanical behaviour and microstructural evolution in the single crystal superalloy SC16, Acta Materialia, Vol.45, 1997, 3143-3154.
[6] Mercer, C., Soboyejo, A.B.O. and Soboyejo, W.O., Micromechanism of fatigue crack growth in a single crystal Inconel 718 nickel-based superalloy, Acta Materialia, Vol.47, 1999, 2727-2740.
[7] Koizumi, Y., Nakano, T. and Umakoshi, Y., Plastic deformation and fracture behaviour of Ti_3Al single crystals deformed at high temperatures under cyclic loading, Acta Materialia, Vol.47, 1999, 2019-2029.
[8] Okazaki, M. and Yamazaki Y., Creep-fatigue small crack propagation in a single crystal Ni-based superalloy, CMSX-2-Microstructural influences and environmental effects, International Journal of Fatigue, Vol.21, 1999, S79-S86.
[9] Suresh, S., Fatigue of Materials, Cambridge University Press, 2nd Ed., Cambridge, 1998.
[10] Zhang, G.P. and Wang, Z.G., Short fatigue crack growth under mixed mode loading in Ni_3Al alloy single crystals, Materials Science and Engineering, A229, 1997, 129-136.
[11] Okazaki, M., Yamada, H. and Nohmi, S., Temperature dependence of the intrinsic small fatigue crack growth behaviour in Ni-base superalloys based on measurement of crack closure, Metallurgical and Materials Transactions A, ASME, Vol.27A, 1996, 1021-1031.
[12] Ma B.T. and Laird C., Overview of fatigue behavior in copper single crystals-V, Acta Metallurgica, Vol.37, 1989, 369-379.
[13] Blochwitz C., Heinrich D. and Frenzel R., Microcrack propagation in fatigued f.c.c. monocrystals-I: Crack-depth distribution and propagation rate, Materials Science & Engineering, A118, 1989, 71-81.
[14] Ritchie, R.O. and Peters, J.O., Small fatigue cracks: mechanics, mechanisms and engineering applications, Materials Transactions, Vol.42, 2001, 58-67.
[15] Miller, K.J., Metal fatigue-past, current and future, Proceedings of the Institution of Mechanical Engineers, Vol.205, 1991, 1-14.
[16] Hong, Y., Qiao, Y., Liu, N. and Zheng, X., Effect of grain size on collective damage of short cracks and fatigue life estimation for a stainless steel, Fatigue and Fracture of Engineering Materials and Structures, Vol.21, 1998, 1317-25.
[17] Sehitoglu, H., Gall, K. and Garcia, A.M., Recent advances in fatigue crack growth modelling, International Journal of Fracture, Vol.80, 1996, 165-192.
[18] Khan, T. and Caron, P., Development of a new single crystal superalloy for industrial gas turbine blades, in High Temperature Materials for Power Engineering *1990*, Proceedings of a conference held in Liege, Belgium, 24-27 Sept. 1990, Eds: Bachelet, E., Brunetaud, R. and Coutsouradis, D. et al. Vol.2, 1261-1270.
[19] Zhang, X.P., Wang, C.H., Ye, L. and Mai, Y.W., *In-situ* investigation of small fatigue crack growth in poly-crystal and single-crystal alloys, Fatigue and Fracture of Engineering Materials and Structures, Vol.25, 2002, 141-150.
[20] Murakami, Y., Stress Intensity Factors Handbook, Vol.1, Pergamon, London, 1997, 9-12.

EFFECT OF γ' VOLUME FRACTION ON THIRD-GENERATION SINGLE-CRYSTAL SUPERALLOYS

H. Zhou, H. Harada, Y. Ro, Y. Koizumi, T. Kobayashi and S. Nakazawa
High Temperature Materials 21 Project, National Institute for Materials Science (NIMS),
1-2-1 Sengen, Tsukuba-shi, Ibaraki 305-0047, Japan

Abstract

Creep and thermo-mechanical fatigue (TMF) behaviors of two third-generation single-crystal superalloys, TMS-75 and TMS-113, were investigated. The two alloys have similar chemical composition (TMS-113 is simply TMS-75 + 0.6 wt.% Al) with a γ' volume fraction of 60% (TMS-75) and 70% (TMS-113). Compared with TMS-113, the TMS-75 superalloy showed superior TMF behavior between 400 °C and 900 °C under out-of-phase conditions. TMS-75, showed, however, inferior creep behavior at 900 °C. Microstructural study of the surface fracture morphologies, dislocations and stacking faults by electron microscopy was done to reveal the deformation mechanisms for the two superalloys. The microstructures developed during TMF differed for the two superalloys, probably due to the difference in γ' volume fraction. Compressive stress relaxation behaviors also differed, which played a key role in the different yield stresses and rupture lives. Our results suggest that making a compromise between creep and TMF behaviors by changing the volume fraction of γ' phase is important for designing new superalloys.

Keywords: Thermo-mechanical fatigue, creep, Ni-based superalloy, single crystal.

1 Introduction

Many components in gas turbine engines and aircraft engines are subject to a complex combination of temperature and stress cycling during operation. The stresses arise from temperature gradients in the airfoils during start-up and shut-down operations or from gradients within the cooled airfoils. Such cyclic loading is termed *thermo-mechanical fatigue,* or *TMF* [1, 2]. High-temperature materials are also subject to creep during operation [3-6]. Therefore, the design of high-temperature materials must consider both TMF and creep behavior.

Because singe-crystal superalloys offer improved creep and fatigue resistance compared to conventionally cast superalloys, such as equiaxed and directionally solidified (DS) columnar grain components, single crystal superalloys have been developed since the early 1990's. For example, TMS-75 was developed at the National Institute of Materials Science (NIMS), Japan, as a third-generation single crystal superalloy [7]. The γ' volume fraction plays an important role in the performance of single crystal superalloys [7]. Although the influence of γ' volume fraction on the creep behavior of TMS-75 superalloy has been studied [8], TMF behavior plays a more important role when considering practical applications of such superalloys. Despite such importance, no studies have been done on the effect of γ' volume fraction on both the creep and TMF behaviors of single-crystal superalloys. In this study, to help in the design of new single-crystal superalloys, we clarified the effect of γ' volume fraction on third-generation single-crystal superalloys by comparing the creep and TMF behaviors of two superalloys, TMS-75 and TMS-113.

example, TMS-75 was developed at the National Institute of Materials Science (NIMS), Japan, as a third-generation single crystal superalloy [7]. The γ' volume fraction plays an important role in the performance of single crystal superalloys [7]. Although the influence of γ' volume fraction on the creep behavior of TMS-75 superalloy has been studied [8], TMF behavior plays a more important role when considering practical applications of such superalloys. Despite such importance, no studies have been done on the effect of γ' volume fraction on both the creep and TMF behaviors of single-crystal superalloys. In this study, to help in the design of new single-crystal superalloys, we clarified the effect of γ' volume fraction on third-generation single-crystal superalloys by comparing the creep and TMF behaviors of two superalloys, TMS-75 and TMS-113.

2 Experimental procedure

Deformation mechanisms of creep and TMF were determined and compared for two third-generation superalloys with similar composition but different γ' volume fractions. Table 1 lists the compositions of the two superalloys, TMS-75 and TMS-113, where TMS-113 is simply TMS-75 + 0.6 wt.% Al.

Table 1. Chemical composition of TMS-75 and TMS-113 superalloys (in wt.%).

	Co	Cr	Mo	W	Al	Ta	Hf	Re	Ni
TMS-75	12.00	3.00	2.00	6.00	6.00	6.00	0.1	5.0	balance
TMS-113	11.93	2.98	1.99	5.96	6.56	5.96	0.1	4.97	balance

To obtain different γ' volume fractions, the superalloys were cast at NIMS and heat-treated as follows. TMS-75 superalloy was solution-treated in argon at 1320°C for 8h, air quenched, aged in argon at 1150 °C for 4h, and finally aged at 870 °C for 20 h. TMS-113 superalloy was solution-treated in argon at 1320°C for 5h, air quenched, aged in argon at 1150 °C for 4h, and finally aged at 870 °C for 20 h.

The microstructure of the heat-treated TMS-75 and TMS-113 bars consisted of about 60 vol.% and 70 vol.% of principally cuboidal γ' precipitates, respectively. The edge length of the γ' precipitates was approximately 0.4 μm for TMS-75 and 0.45 μm for TMS-113, as shown in Fig. 1. Specimens with [001] orientation were machined parallel to the longitudinal direction of the bars. Parallel sections of the Ø4 × 20 mm and Ø6 × 20 mm specimens were made for the creep and TMF tests, respectively. Deviations of <001> crystalline direction from the sample axis were within 10°.

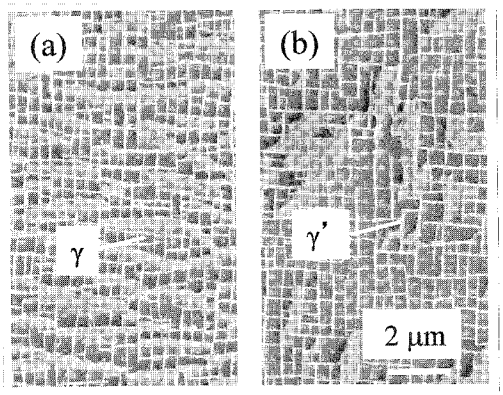


Figure 1. Photographs showing the coherency of γ/γ' structure of (a) TMS-75 and (b) TMS-113.

Creep tests were done at a constant temperature (900 °C) and constant load (40 Kg/mm^2) on a creep machine. The creep strain (ε) was measured as a function of time under load using an axial extensometer. TMF tests were done on a servo-hydraulic, closed-loop machine under strain control. Radio frequency induction heater with a closed- loop control was used. Again, the total strain ($\Delta\varepsilon_t$) was measured using an axial extensometer. Out-of-phase TMF behavior was recorded for simplified thermal cycles between minimum (400 °C) and maximum temperature (900 °C). A dwell time was introduced at the maximum strain in compression for parts of the TMF tests. The stress response and hysteresis loop were recorded at intervals. Figure 2 shows a schematic plot of an out-of-phase TMF cycling, in which, $\Delta\varepsilon_t$ is total strain,

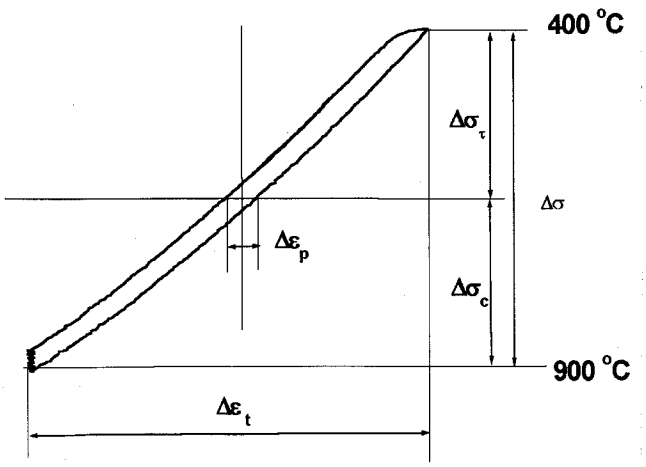


Figure 2. Schematic of out-of-phase TMF cycling.

$\Delta\varepsilon_p$ is total plastic strain, $\Delta\varepsilon_e$ is total elastic strain, $\Delta\sigma$ is full stress, $\Delta\sigma_t$ is maximum stress in tension and $\Delta\sigma_c$ is maximum stress in compression. The total cycle period is ranged from 6 min. to 16 min., depending on the dwell time at the maximum strain in compression.

Deformed specimens after the creep and TMF tests were sectioned parallel to the (100) plane for metallography and scanning electron microscopy (SEM) characterization. The SEM was a Philips XL30 operating at 15 kV. TEM specimens were prepared only from sections of TMF specimens, perpendicular to the longitudinal axis or parallel to the (100) plane by mechanical grinding and subsequent electro-chemical polishing. These slices were examined by using a Phillips CM200 TEM operating at 200 kV. For the convenience of TEM observations, some specimens were also sectioned along the {111} planes of these superalloys.

3 Experimental results and discussion

Figure 3 shows the creep curves of TMS-75 and TMS-113 superalloys obtained at 900 °C and 40 Kg/mm^2. Compared with TMS-75, TMS-113 exhibited higher creep strength. The corresponding rafted structures after rupture are shown to the right of the figure.

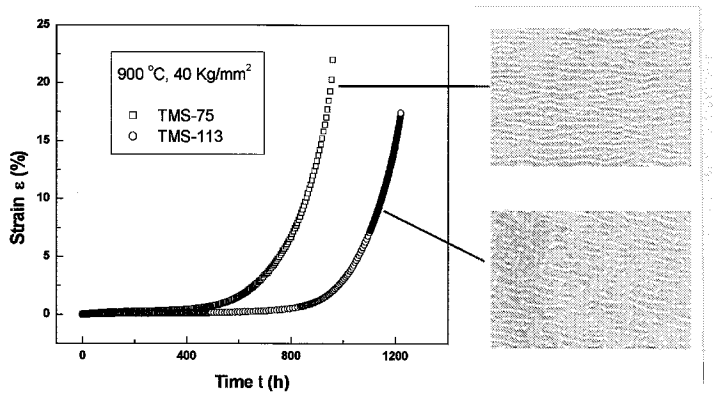


Figure 3. Creep curves for TMS-75 and TMS-113 superalloys at 900 °C and under a load of 40 Kg/mm^2.

Table 2 summarizes the TMF results. The plastic strain range $\Delta\varepsilon_p$ was defined as the difference between the maximum and minimum plastic strain amplitudes at half-life. The plastic strain was calculated as $\varepsilon_p = \varepsilon_t - \sigma/E(T)$, where σ is the axial stress and E(T) is the elastic modulus.

Table 2. Thermo-mechanical fatigue (TMF) data for TMS-75 and TMS-113 single-crystal superalloys, where t_H is dwell time at the maximum stress in the compression phase, N is cycle number, N_f is number of cycles to failure, σ_t is maximum stress in tension, σ_c is maximum stress in compression and $\Delta\sigma$ is full stress.

Type	T (°C)	Cyclic period	Sample	$\Delta\varepsilon_t$ (%)	t_H (min.)	N_f	N=N_f/2, $\Delta\varepsilon$ (%) and σ(Kg/mm^2)				
							$\Delta\varepsilon_p$	$\Delta\varepsilon_e$	$\Delta\sigma$	σ_t	σ_c
TMF (out of phase)	400 ↔ 900	6 min/ cycle	TMS -75	1.28	-	985	0.00	1.28	134.9	89.6	-45.2
				1.28	10	158	0.13	1.15	132.6	86.0	-46.6
			TMS -113	1.28	-	500	0.03	1.25	138.0	83.1	-54.9
				1.30	10	74	0.10	1.20	132.0	75.3	-56.7

Figure 4 shows the total strain range $\Delta\varepsilon_t$ versus number of cycles to failure N_f for the two superalloys. For both alloys, the introduction of dwell time led to a drastic reduction in lifetimes of TMF by one order of magnitude. Although TMS-113 had higher creep strength, for the conditions studied here, it had lower TMF strength with about half the life of TMS-75.

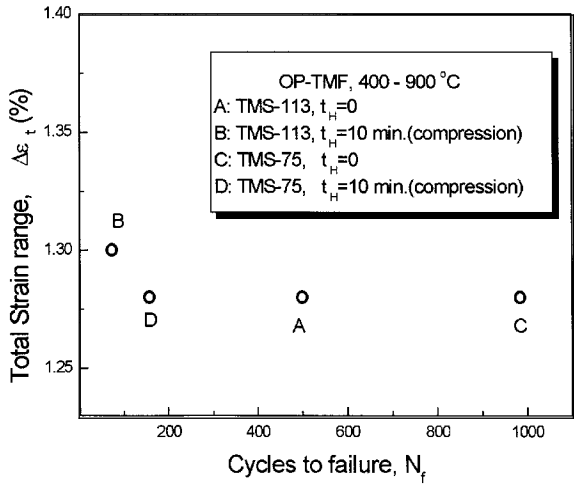


Figure 4. Total strain range $\Delta\varepsilon_t$ versus number of cycles to failure N_f at two different dwell times t_H for TMS-75 and TMS-113.

The curves of the variation in the maximum stresses under tension (σ_t) and compression (σ_c) during TMF cycling are shown in Fig. 5. For the out-of-phase TMF tests, the low temperature coincided with the maximum tensile strain, and hence, the tensile stress amplitude was high. Overall, the variations in the stress-versus-cycle during TMF are similar for the two superalloys. When t_H =0, the curves (denoted by ◑) show slightly cyclic hardening in tension and cyclic softening in compression. In contrast, when t_H =10 min, the curves (denoted by ▲) show no cyclic hardening in tension and only an initial slight softening in compression during the first cycles. This latter case (i.e., t_H =10 min.) for TMS-113 differs slightly from that for TMS-75, where there was an apparent softening during the first cycles [9]. For the two alloys concerned, the initial hardening for TMF cycles without a dwell time is associated with an increase in dislocation density. However, the little difference in softening between the two superalloys is supposedly due to the difference in γ' volume fraction, i.e., TMS-113 superalloy has higher compressive deformation resistance than does TMS-75 superalloy. The variation in full stress Δσ remained relatively constant during TMF cycles without a dwell time, whereas Δσ decreased slightly for TMF cycles with a dwell time. For the case of TMS-75 superalloy, higher strain amplitude leads to higher Δσ [9]. The final decrease in stress level just before failure was caused by macro-cracks in the material.

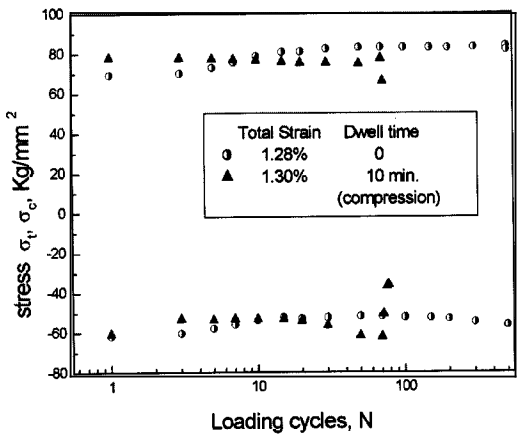


Figure 5. Cyclic softening /hardening curves for TMS-113 superalloy during TMF cycling.

Figure 6 shows the evolution of the strain-stress hysteresis loop for TMS-113. The variations in the loops of TMS-75 are similar to those shown in Fig.6. The sharp increase in stress at the compression phase is due to the stress relaxation during the dwell period. The variations in the range of stress relaxation reflect the mobility of defects during the TMF cycling. The yielding in the tension phase is caused by a transition from plastic strain to

elastic strain. Figure 7 shows the curves of the stress relaxation versus relaxation time of the two superalloys, taken at half-life. Compared with TMS-75, TMS-113 had higher stress relaxation resistance. Overall, compared with TMS-75, TMS-113 superalloy exhibited higher compressive stress relaxation resistance and lower tensile maximum stress.

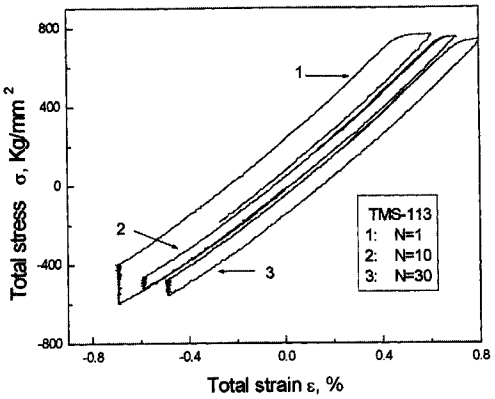


Figure 6. Evolution of the strain-stress hysteresis loop of TMS-113 superalloy during TMF cycling.

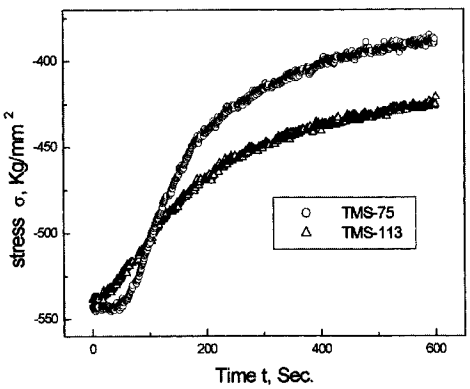


Figure 7. Stress relaxation of TMS-75 and TMS-113 superalloys at half-life during the dwell period.

Figure 8 shows the difference in the microstructure of ruptured samples after TMF tests of TMS-75 and TMS-113 superalloys. Deformation by slip is the characteristic for both superalloys. Higher slip bands density was found in the TMS-75 superalloy. The fatigue deformation of TMS-113 was more localized, and thus TMS-113 had a shorter life, compared

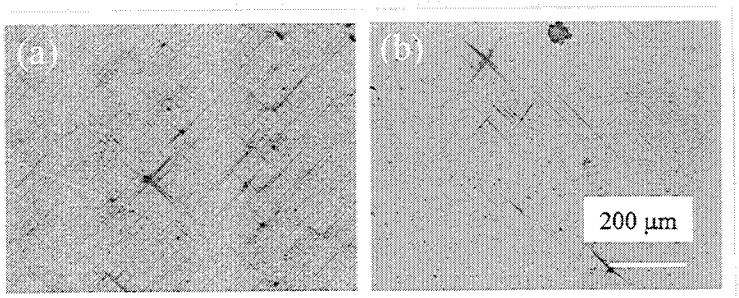


Figure 8. Metallographs of (a) TMS-75 and (b) TMS-113 superalloys, taken from the failed samples after TMF cycling.

with that for TMS-75. Recent TEM studies indicate that the crept specimens of TMS-75 showed rafted structure, and the dislocation structure was rather homogeneous [8]. In contrast, inhomogeneity in defect structure was observed in the fatigued specimens. At the early stage of creep, matrix dislocations glided along the {111} planes, which is similar to what occurred in the fatigued specimens, as shown in Fig. 9(a). The γ/γ' structure gradually lost its coherency, i.e., rafting occurred after the primary creep stage. Most dislocations were of the a/2<1$\underline{1}$0> type. In addition to the dislocations similarly observed in the crept specimens, stacking faults were often observed in the fatigued specimens. Fig. 9(b) shows a slip band consisting of many faulted areas. Slip bands were the result of linkage and development of faulted areas. Fig. 9(c) shows the SFs taken from a {111}foil. Detailed inspection of the SFs indicates that one type of dislocation reaction described by equation 1 occurred frequently. A perfect matrix dislocation dissociated into two partials with respective Burgers vectors of

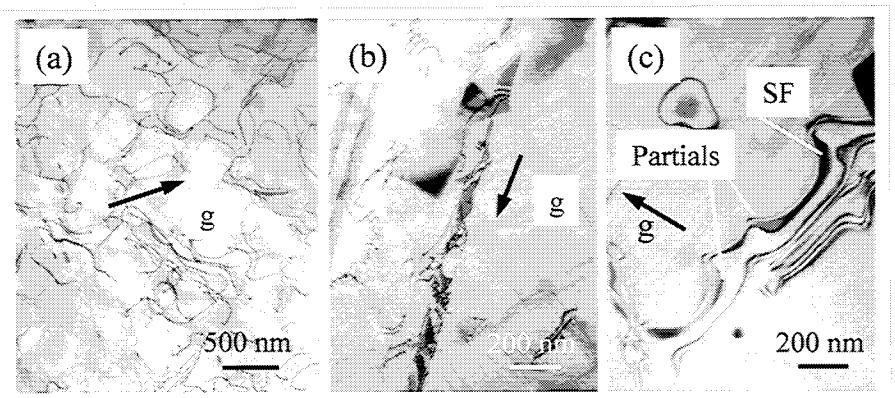


*Figure 9. TEM photographs taken from fatigued specimens of TMS-75 at $\Delta\varepsilon_t$ = 1.28% and t_H=10 min. with reflections of (a) **g**= 1$\underline{1}$1, (b) **g**= 111, (c) **g**=1$\underline{1}$1.*

a/3[$\underline{2}$11] and a/6[1$\underline{2}$1]. A superlattice intrinsic stacking fault (SISF) was generated by the former partial cutting into one γ' particle and the other partial remaining on the γ/γ' interface. This deformation mechanism plays an important role in the TMF process, because the path of crack propagation was sometimes along slip bands and thus facilitated the crack propagation.

$$a/2\,[\underline{1}10] \rightarrow a/3[\underline{2}11] + (SISF) + a/6\,[1\underline{2}1] \qquad (1)$$

Stacking faults were in different configurations as shown in Fig.9. The dislocation reaction described by Eq. (1) is unfavorable in terms of energy, because the dislocation line energy increased by 33%. The prerequisite that this dislocation reaction occurs is the generation of local stresses [10]. As shown in Fig. 8, deformation in TMF was characterized by local shearing, indicating the existence of localized stresses, and thus the dislocation reaction would not have difficulty occurring. This characterization of the stacking faults discussed here is consistent with reports in the literature [6, 10].

The γ' volume fraction is a key parameter in creep behavior [7, 8]. The shorter creep lifetime of TMS-75 superalloy is attributed to the easier glide of dislocations in the matrix and easier shearing of the γ' precipitates. The γ' volume fraction is also supposedly a key parameter in TMF behavior. Assuming that the temperature dependence of flow stress of TMS-75 and TMS-113 is similar to that of Ni-Cr-Al alloys [11], TMS-113 with a higher volume fraction of γ' precipitates would have a higher stress relaxation resistance at 900 °C and lower maximum stress at 400 °C. As expected, TMS-113 superalloy had a 70 vol.% of γ' precipitates that led to a higher stress relaxation resistance and lower maximum stress, compared with that for TMS-75 consisting of 60 vol.% of γ' precipitates. However, compared with TMS-75, TMS-113 did not have superior TMF resistance, despite TMS-113 having superior creep strength.

4 Conclusions

The effect of γ' volume fraction on the performance of third-generation single-crystal superalloys was clarified by comparing the creep and TMF behaviors for two such superalloys, TMS-75 and TMS-113, that had nearly the same chemical composition but contained 60 % and 70 % γ' volume fractions, respectively. Comparison between the two superalloys revealed the following. TMS-75 showed a superior TMF resistance when tested under out-of-phase conditions between 400 °C and 900 °C, whereas TMS-113 showed superior creep behavior at 900 °C. TMS-113 had a higher stress relaxation resistance and a lower tensile stress amplitude during TMF cycling. The lower resistance of TMS-113 to crack

propagation in TMF tests was associated with the more local slip deformation. The shorter creep lifetime of TMS-75 was attributed to the easier glide of dislocations in the matrix and easier shearing of the γ' precipitates. The most likely mode of creation of stacking faults under the conditions studied here is as follows. First, a matrix dislocation disassociates into two partials. Then, the leading partial a/3<112> cuts into one γ' particle, thus creating a SISF stacking fault, while the other partial remains on the γ/γ' interface. This work suggests that achieving a balance between creep and TMF behaviors by changing the volume fraction of γ' phase is important for designing new superalloys.

5 Acknowledgements

We thank Mr. Y. Kadoya and Mr. I. Okada for doing some of the thermo-mechanical fatigue experiments at the Takasago Research & Development Center, Mitsubishi Heavy Industries, LTD, Japan.

6 References

[1] S. Kraft, R. Zauter and H. Mughrabi, Fatigue Fract. Eng. Mater. Struct., 16 (1993), 237.

[2] S. Müeller, J. Röster, C. Sommer and W. Hartnagel, in proceedings of Superalloys 2000, ed. T.M. Pollock et al, p.347, TMS, Warrendale, PA (2000).

[3] T.M. Pollock and A.S. Argon, Acta Metall. Mater., 40 (1992), 1.

[4] C.M.F. Rae, N. Matan and R.C. Reed, Mater. Sci. Eng., A300 (2001), 125.

[5] G. Eggeler and A. Dlouhy, Acta Mater., 45 (1997), 4251.

[6] M. Feller-Kniepmeier, and T. Kutink, Acta Metall Mater., 42(1994), 3167.

[7] H. Harada and H. Murakami, Springer Series in Materials Science, Vol. 34, Ed. T. Saito, Springer-Verlag Berlin Heidelberg ,1999, p. 39.

[8] T. Murkumo et al, to be published in the same proceedings book.

[9] H.Zhou, H. Harada, Y. Ro, Y. Koizumi, T. Kobayashi and I. Okada, in proceedings of David L. Davidson symposium on Fatigue, ed. K.S. Chan et al, p.203, TMS, Warrendale, PA (2002).

[10] P. Caron, T. Khan and P. Veyssiere, Phil.Mag., A 57 (1988), 859.

[11] P. Beardmore, R.G. Davies and T.L. Johnston, TMS-AIME, 245 (1969), 1537.

ON THE EFFECT OF RHENIUM ON THE EXTENT OF PRIMARY CREEP IN ADVANCED NI-BASED SUPERALLOYS

C.M.F. Rae*, K. Kakehi**, and R.C. Reed*

*University of Cambridge / Rolls-Royce University Technology Centre
Department of Materials Science and Metallurgy
Pembroke Street, CAMBRIDGE CB2 3QZ, UK

**Department of Mechanical Engineering, Tokyo Metropolitan University,
Minami Osawa 1-1, Hachioji TOKYO, 192-0397 Japan

Abstract

The addition of rhenium to Ni-based single crystal superalloys has improved the high temperature creep resistance of these alloys considerably, however it is not clear whether this is the case at lower temperatures (~750°C) where significant amounts of primary creep can occur. These temperatures are characteristic of the load-bearing internal webs of cooled turbine blades. Primary creep at lower temperatures has been demonstrated to occur by the movement of ribbons of dislocations separated by superlattice stacking faults cutting through the γ' precipitates.

We report some preliminary results of a systematic study of the stress dependence of primary creep in three alloys: TMS82+, CMSX-4 and TMS 75, containing 2.4, 3.0 and 5.0 wt % Re respectively. Creep tests were performed at a range of stresses on specimens cut from a single bar; orientations between 8-12° from [001] were chosen to promote a reasonable amount of primary creep and provide consistency in orientation across the series of alloys. It has been found that the amount of primary creep increases as the amounts of rhenium and cobalt in the alloys increase, and for each alloy a stress threshold for the occurrence of a distinct regime of primary creep is identified. TEM observations of the dislocation mechanism of deformation show a higher occurrence of stacking fault shear with increasing primary creep. Considerable differences in the extent of dislocation penetration into the γ phase and in the configuration of the mobile dislocation ribbons point to a combination of factors governing mobility and hardening being responsible for high primary creep.

Keywords: Nickel-based Superalloys, Creep, Stacking fault energy, Rhenium

Introduction

The addition of rhenium to nickel based single crystal alloys has produced an incremental improvement in the creep resistance of these alloys [1] and, as testament to the effectiveness of the addition, alloys have been classified as first, second and third generation alloys principally (but not exclusively) by the rhenium content. Rhenium is most effective in reducing creep rates at intermediate temperatures 850°C-1000°C where the principal deformation mechanism is the climb of dislocations trapped at the γ/γ' interface around these precipitates, [2]. Rhenium has the lowest diffusion rates in the γ phase of any of the alloy additions [3]. At lower temperatures the dislocations are able to cut through the precipitates as stacking fault ribbons [4] and at higher temperatures the development of the γ' morphology to produce the rafted structure provides additional resistance to dislocation motion, [5]. As the performance of alloys at the crucial intermediate temperature range has improved with the addition of rhenium, it has become apparent anecdotally [6] that there is a significant increase in the primary creep observed at lower temperatures. In cooled blades the internal webs,

which bear the majority of the load, can operate at temperatures as low as 700°C, [7]. However no systematic study of the effect of rhenium on the creep performance at low (750°C-850°C) temperatures and in particular on the extent of primary creep has been undertaken.

Creep behaviour in the temperature range of 700°C-850°C is distinct from creep at other temperatures both in the shape of the creep curve and in the mechanism. Following a short incubation period [8] during which dislocations multiply and spread through the gamma matrix, there is a rapid burst of high strain-rate primary creep which can be in excess of 10%. This occurs by the cutting of the γ' precipitates by planar faults consisting of four dislocations lying on the close packed planes and of overall Burgers vector a<112> [9]. These are separated by superlattice stacking faults and anti-phase boundaries. This Burgers vector is a lattice vector of the $L1_2$ lattice and is thus able, in principle, to pass through both phases without leaving dislocation loops around the precipitates. It is formed from the combination of at least four matrix dislocations two each of two different Burgers vectors at 60° from each other. The progress through the γ/γ' lattice is also complex; involving a complete change in the dislocation configuration each time it passes from matrix to precipitate [10]. The lattice rotations demonstrate that the strain of primary creep comes largely from the movement of these ribbons; and thus the extent of primary creep depends on the density of mobile ribbons and the rate at which these can move without encountering obstacles.

Thus we have chosen three alloys containing different levels of Re to explore the differences in the extent of primary creep. All alloys show excellent creep resistance, TMS82+ noteably despite the low rhenium content [11]. These alloys also show varying levels of cobalt, titanium and tantalum and γ' volume fraction, factors which may also play an important role. It was anticipated that the differences in the microstructures might reveal the mechanisms most important in determining the extent of primary creep.

Experimental

The alloys TMS75, TMS82+ and CMSX-4 were supplied with the full proprietary heat treatments; the compositions are given in Table 1. Single bars of the alloys TMS75 and TMS82+ were cut into three test-pieces for creep testing at 750°C and the three stresses 750MPa, 650MPa and 550MPa. By cutting the test-pieces from the same bar the effects of orientation are eliminated for each alloy, and the effect of stress alone on the primary creep can be gauged. The results for the alloy CMSX-4 were obtained by cutting the test-pieces from a single crystal slab as described elsewhere [12]. The orientations were determined by back-reflection Laue patterns and are indicated in Figure 1. They were chosen to give a substantial amount of primary creep and such that the orientations were similar for the alloys to allow the best comparison between the behaviour of the different alloys. In addition creep test were performed on each of the alloys at 750°C and 750MPa and interrupted at approximately 1.4% strain to allow for the examination of the deformed microstructure. Unfortunately there was not enough material to allow the interrupted tests to be of the same orientation as the other tests. These orientations are also indicated in Figure 1, and are all somewhat closer to the [001] orientation than the varying stress tests indicating that a smaller amount of primary creep would be anticipated.

Wt %	Co	Cr	Mo	W	Re	Al	Ti	Ta	Hf	GP vf
TMS75	12.0	3.0	2.0	6.0	5.0	6.0	0.0	6.0	0.1	70.6
TMS82+	7.8	4.9	1.9	8.7	2.4	5.3	0.5	6.0	0.1	69.7
CMSX-4	9.0	6.5	0.6	6.0	3.0	5.6	1.0	6.5	0.1	72.8

Table 1. Alloy compositions wt % together with the calculated γ' volume fraction at 750°C

Specimens for TEM examination were cut from the interrupted creep tests so that the specimen normal is parallel to the tensile axis and also with the specimen normal parallel to the primary slip plane normal. This was done by identifying the {111} plane with the highest resolved shear stress using the back reflection Laue X-ray technique and rotating the specimen to this orientation before cutting. Specimens were prepared from discs by twin jet electro-polishing using a solution of 15% Perchloric acid in methanol at 25V and 5°C.

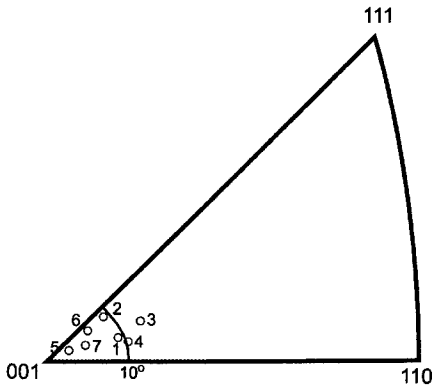


Figure 1. Orientations of the creep tests:

1. TMS75; 750, 650, 550MPa
2. TMS82+; 750, 650, 550MPa
3. CMSX-4; 750, 650, 550MPa
4. TMS75 Interrupted
5. TMS82+ Interrupted
6. CMSX-4 Interrupted

Results:

Creep testing

The stress strain graphs of the creep tests performed at 750°C for each of the alloys at 750MPa, 650MPa and 550MPa are presented in Figures 2(a) and 2(b). The three alloys all displayed characteristic three stage creep curves with an initial incubation period, followed by rapid primary creep decreasing to give stable secondary creep before rapid tertiary failure. At lower stresses the test were interrupted after stable secondary creep was established. The extent of the incubation period was similar for the three alloys but increased substantially as the stress dropped; at 750MPa this was 2h, at 650MPa 15h and at 550h 200h, essentially increasing 10 times with each 100MPa drop in stress. The extent of primary varies greatly with the alloy composition: TMS75 shows extremely high primary creep, CMXS-4 shows considerably less, and the alloy TMS82+ the lowest of all, (although at the lowest stress 550MPa the order changes slightly with the alloy CMSX-4 showing the lowest primary creep). Indeed, TMS75 showed 25% primary creep at the highest stress of 750MPa, and although some hardening occurred with a decrease in creep rate, secondary creep was not fully established before the specimen entered tertiary creep.

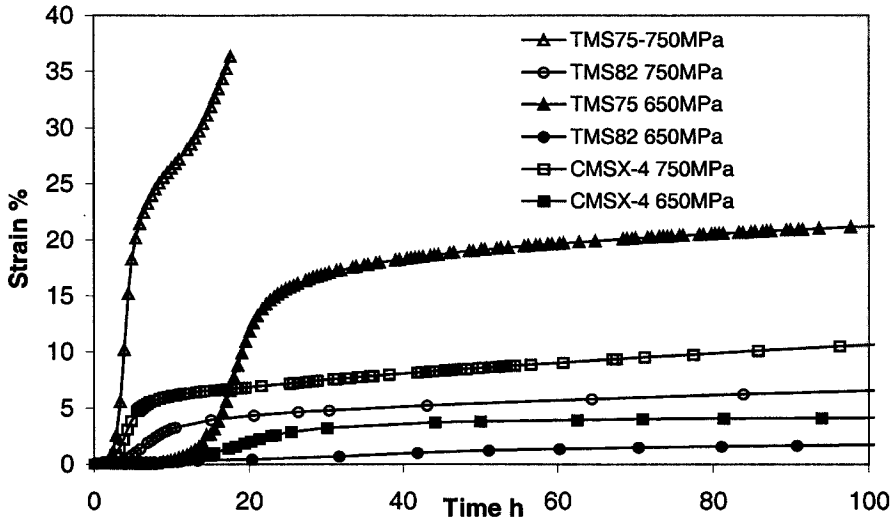


Figure 2(a). Strain-time graphs for creep tests at 750°C; 750MPa and 650MPa

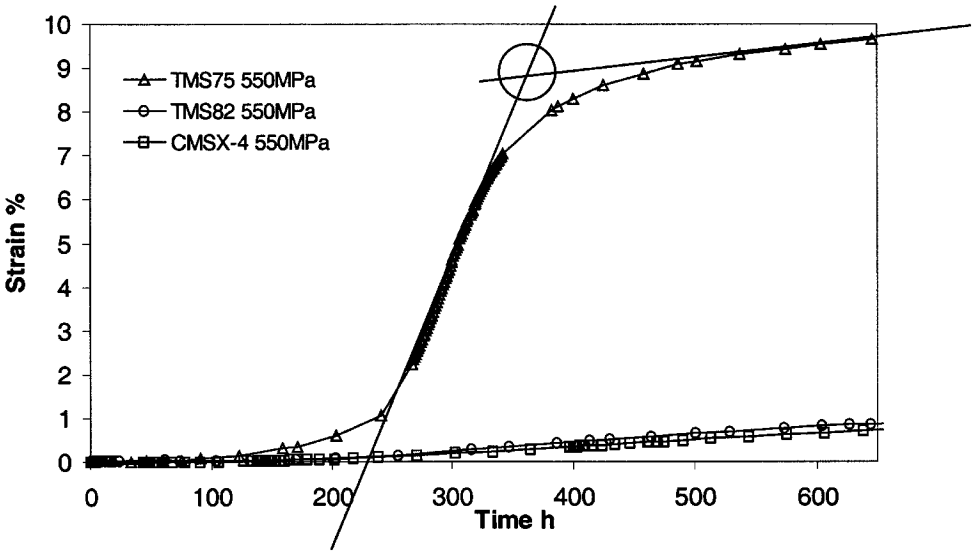


Figure 2(b). Strain-time graphs for creep tests at 750°C; 550MPa. The method used for measuring the primary creep strain is indicated.

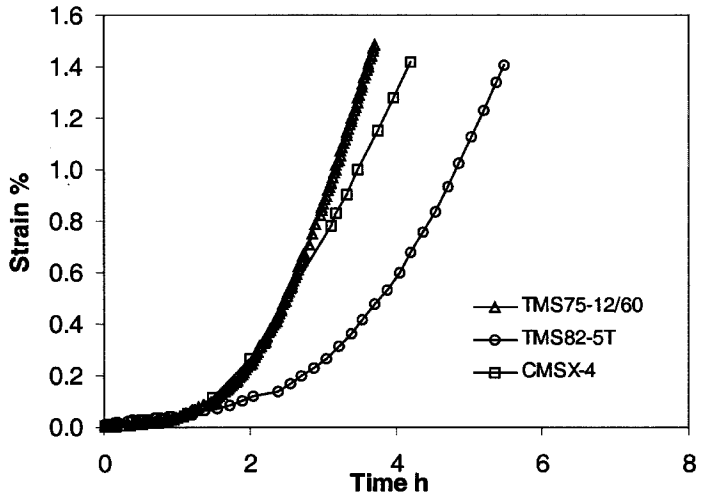


Figure 3. Stress strain graph for the creep tests interrupted at 1.4% strain, 750°C, 750MPa

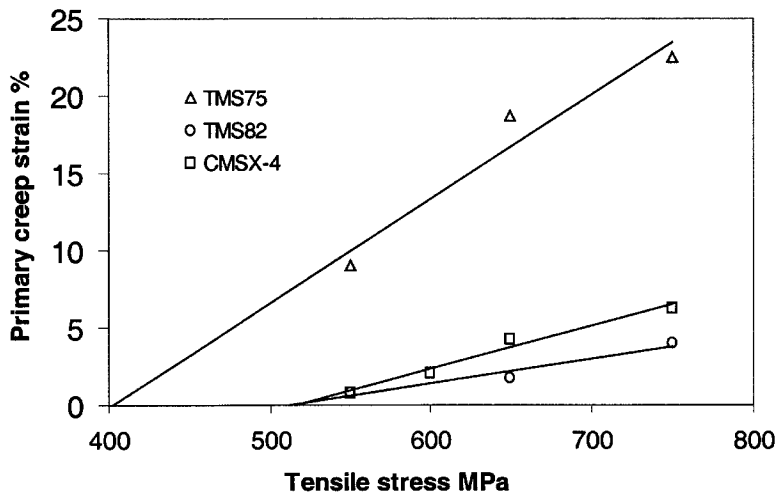


Figure 4. Extent of primary creep plotted as a function of the stress, tests at 750°C.

Orientation is known to have a strong effect on the extent of primary creep [2, 4, 12, 13] at low temperatures. However the test on alloy TMS82+ is oriented to produce slightly more primary creep than that of TMS75 because the tensile axis lies closer to the [001]-[111] boundary and the maximum in the resolved shear stress for the <112>{111} slip system. The extent of the primary creep strain drops as the stress decreases. The extent of primary creep has been measured in these alloys by extrapolating the asymptotes for primary and secondary creep and measuring the primary creep strain at the point where they meet, as shown in Figure 2(b). This method differs from that used previously [12] where the secondary creep curve was extrapolated back to the stress axis, and gives a more accurate reflection of the amount of strain resulting from the initial transient particularly where very different incubation periods are observed. These values are plotted against the stress, Figure 4.

At the lowest stress of 550MPa the primary creep of the alloys TMS82+ and CMSX-4 has almost disappeared but TMS75 retains 9% primary creep. When the extent of primary creep strain is plotted as a function of the applied stress the strain decreases sharply and extrapolating linearly to zero strain provides an estimate of the stress threshold for the onset of primary creep. This value is approximately the same for TMS82+ and CMSX-4 at 512MPa and 516MPa but very much smaller for TMS75 at 402MPa. These correspond to resolved shear stresses of 254MPa, 256MPa and 200MPa for TMS82+, TMS75 and CMSX-4 respectively.

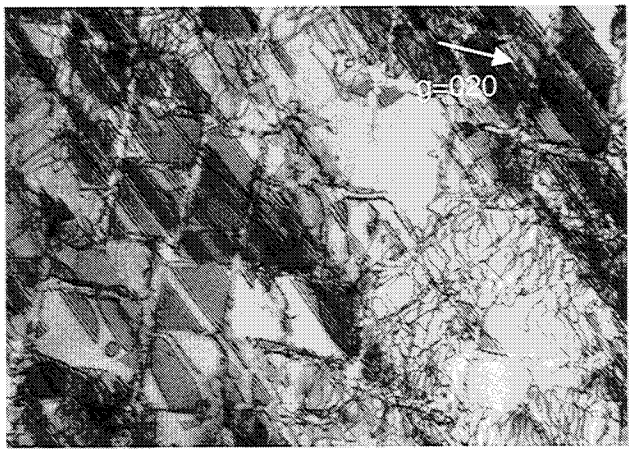
Microstructure

Figure 5 shows sections cut perpendicular to the tensile axis for each of the three alloys interrupted at 1.4% strain. Although there were variations in the microstructures throughout the specimens examined, the figures are representative of the microstructures. In the alloys TMS75 and TMS82+ many more of the gamma channels were filled with dislocations than in CMSX-4. CMSX-4 also has the lowest density of stacking fault ribbons and TMS75 has approximately 50% more dislocations ribbons per unit area in the section plane than TMS82+. The indications are that the densities of stacking fault ribbons are not sufficiently different to account alone for differences in primary creep strain, and hence the differences in the primary creep are due, in large part, to the mobility of the dislocations ribbons.

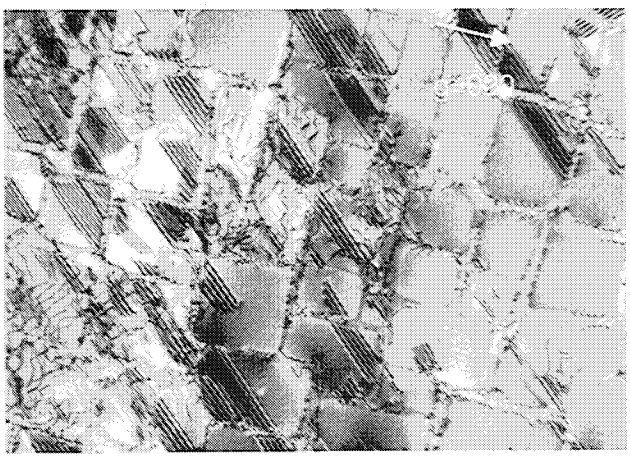
Figure 6 shows the dislocation ribbons sectioned on the {111} primary slip plane for the alloys TMS75 and TMS82+. The stacking faults are very extended in the alloy TMS75 and the faults are frequently continuous across the gamma channels as indicated by the arrows. In TMS82+ the stacking fault ribbons are much more contained and, in general, the stacking faults do not extend across the γ, although some instances of this happening where the γ channel is very narrow were noted. Thus the ribbons tend to be less spread but the dislocations in the ribbon are more convoluted as they follow the γ/γ' interface. The ribbons in CMSX-4 are very similar to TMS82+ (see ref [2] for example).

Alloy	TMS75	TMS82+	CMSX-4
Re + Co (at%)	14.2	9.0	10.2
Ta + Ti (at%)	2.05	2.71	3.45
γ' vol fraction % (750°C)	70.6	69.7	72.8

Table 2. Compositional indicators for high primary creep.

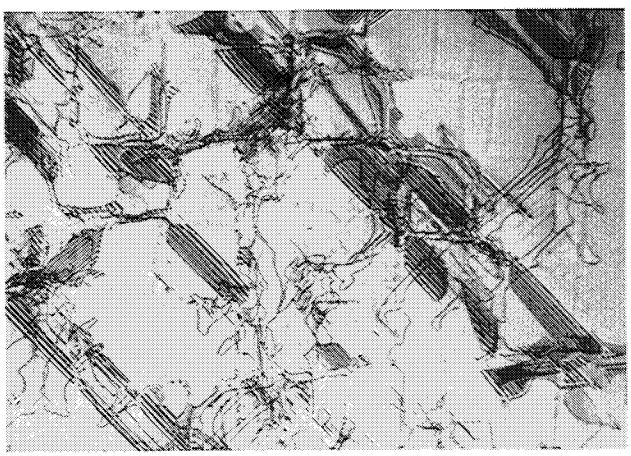


5(a) TMS75



1μm

5(b) TMS82+



5(c) CMSX-4

Figure 5. Microstructures of alloys crept at 750°C 750MPa to 1.4% strain, {001} sections.

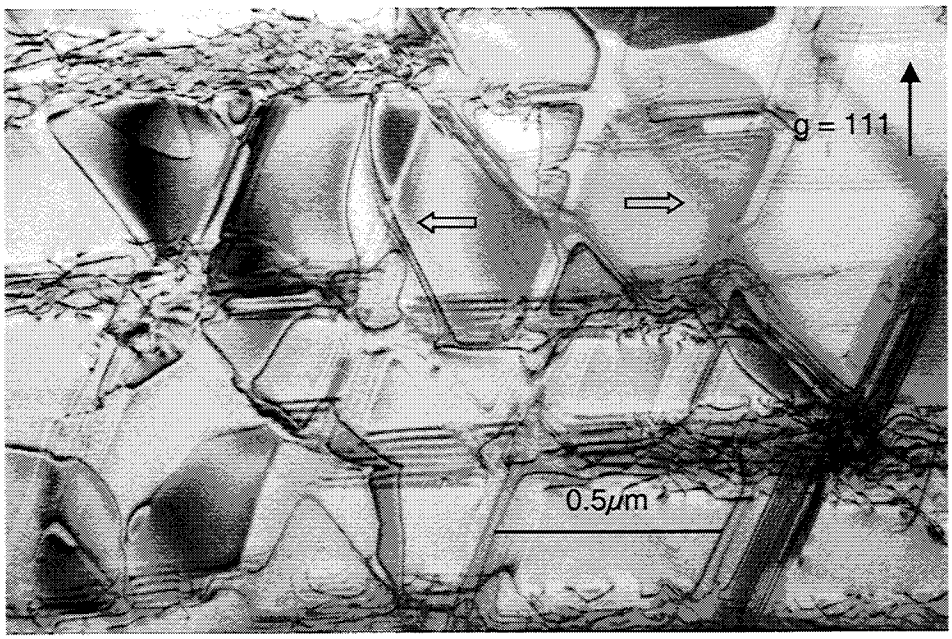


Figure 6(a) TMS75 deformed 750MPa 750°C to 1.4% sectioned on the primary slip plane.

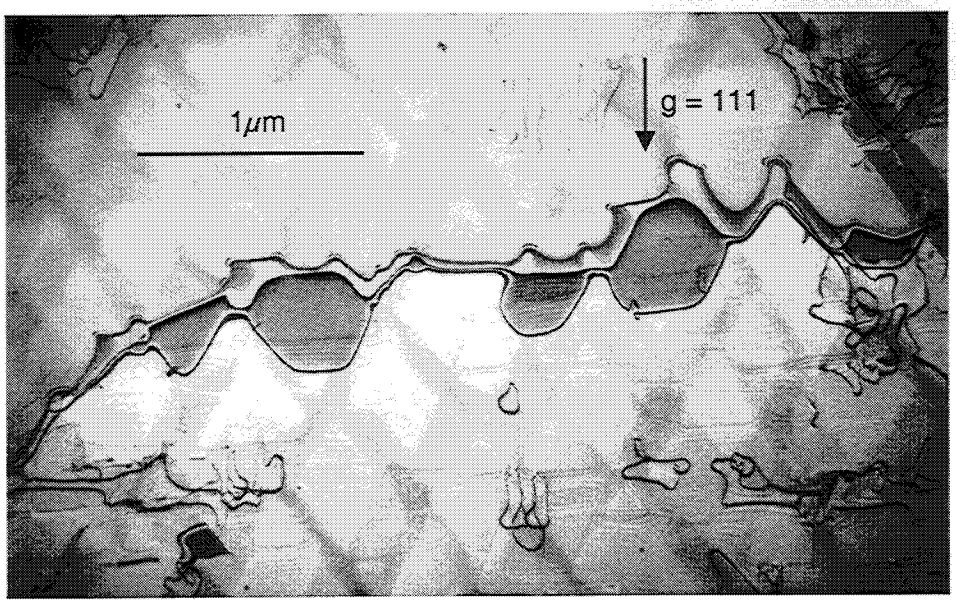


Figure 6(b) TMS82+ deformed 750MPa 750°C to 1.4% sectioned on the primary slip plane.

Discussion

We can divide the factors affecting the extent of primary creep into two categories: those *directly* affecting the mobility of the dislocation ribbons, and those affecting the rate of propagation of octahedral slip in the γ channels to populate the γ/γ' interfaces and thus *indirectly* impeding the movement of the ribbons.

Direct effects: Detailed observations of the ribbons in CMSX-4 show that generally the dislocations pass through the γ' phase as superlattice stacking faults; intrinsic followed by extrinsic for a tensile stress applied close to the [001] axis. In the γ phase the fault constricts and the dislocation appears to be a closely associated pair of different a/2<110> dislocations which are separated by an anti-phase boundary fault. Thus for every γ' precipitate through which the dislocation ribbon passes it must change structure twice, on entry and exit. Kear [9] points out that this process will involve diffusive shuffles and the time taken for these to occur is likely to contribute to the drag on the ribbon reducing mobility. If, however, the dislocation ribbon can pass through the γ channels between the γ' precipitates without a change in structure it should be able to move more quickly.

The ribbons in the interrupted test of TMS75 are wider than those and more often cross the γ without constriction, Figure 6, whereas in TMS82+ the dislocations very rarely cross the γ. The role of cobalt in reducing the stacking fault energy of the γ phase and promoting primary creep is well established, [[14] and it is likely to be enhanced by rhenium which is also a hexagonal metal. High atomic fractions of these elements might therefore be expected to facilitate the passage of the ribbon through the γ without the constriction of the stacking fault. The atomic fractions of Re + Co for the three alloys follow the trends in primary creep for the three alloys TMS75, TMS82+ and CMSX-4: Table 2. The combination of high rhenium and cobalt reducing γ stacking fault energy could thus be a major factor in promoting the high primary creep in TMS75.

The elements tantalum and titanium partition to the γ' and are both γ' strengtheners. It is also likely that these two elements might segregate to the SSF since they both form ordered inter-metallics with nickel but with hexagonal (Ti) and complex (Ta) structures. This would give rise to a Suzuki locking effect of these elements on <112>{111} slip. One effect of increasing the tantalum: aluminium ratio content is to substantially increase the stress rupture life at 750°C, [15]. We note that TMS 75 has the lowest Ti + Ta at% content of the three alloys discussed here: Table 2. This too, could contribute to the rapid primary creep rate.

Indirect effects: The a/2<110> dislocations gliding through the γ have to overcome the narrow channels, back-stress from the γ/γ' misfit and the solid solution hardening produced by alloying additions such as rhenium, tungsten and molybdenum. Negotiating the obstacle course that is the inside of a superalloy is greatly assisted by the ability to climb around the precipitates and particularly to cross slip onto the alternative {111} plane. This will be inhibited by a decrease in the stacking fault energy in the γ phase allowing the dissociation of the dislocations into two Shockley partials. Hence both rhenium and cobalt can have a role in decreasing the amount of dislocation movement in the γ phase, and increasing the time during which primary creep can effectively occur.

The two alloys TMS75 and TMS82+ both have more dislocations in the gamma channels than CMSX-4. One factor may be the 10% increase in the γ content of the former alloys (see Table 2). This would lead to greater difficulty in propagating dislocations in the gamma and the reduced dislocation density in CMSX-4 may account for the higher primary creep levels in CMSX-4 as compared with TMS82+ despite the lower stacking fault density and the very similar dislocation ribbon configurations.

It is clear that there is not one single factor determining the extent of primary creep: rather that it is the balance between a number of alloy characteristics that is responsible for the wide range of behaviours found. Further work is in progress on a wider range of alloys to confirm and refine the observations reported here.

Conclusions.

1. The amount of primary creep increases strongly with stress for all alloys
2. The incubation period for the start of primary creep is roughly the same for all of the alloys examined here but increases exponentially with decreasing stress.
3. The amount of primary creep increases with the rhenium and cobalt content of the alloys; the alloy TMS 75 shows extremely high levels of primary creep.
4. The dislocations ribbons are wider in the alloy TMS75 with an increased tendency to cross the γ channels whilst retaining the extended configuration characteristic of the dislocation in the γ'; we suggest this increases the mobility of the defect.
5. The dislocation density in the γ phase is lowest in the alloy CMSX-4 which has the highest γ' volume fraction: this may explain why this alloy shows a higher primary creep than the alloy TMS82+ despite the similar dislocation ribbon densities and configurations.

Acknowledgements

The authors are grateful to Rolls-Royce plc and DSTL for their support of this work, to Prof. H. Harada of NIMS, Japan, for the provision of materials and H. Tamaki of Hitachi Ltd for performing some of the creep tests.

1. A.F. Gaimei and D.L. Anton, Metallurgical Transactions A, Vol. 6A (1985), 1997-2005.
2. N. Matan, D.C. Cox, P. Carter, M.A. Rist, C.M.F. Rae, R.C. Reed, Acta Mater., 47, (1999), 1549-1563.
3. M.S.A. Karunarate, P Carter and R.C. Reed, Materials Science and Engineering, A281 (2000) 229-233.
4. C.M.F. Rae, N. Matan and R.C. Reed, Materials Science and Engineering, A300, (2001) 125-134.
5. R.C. Reed, N. Matan, D.C. Cox, M.A. Rist and C.M.F. Rae, Acta Mater. Vol 47, (1999), 3367-3381
6. R.W. Broomfield, Rolls-Royce plc, Derby, Priv. Com.
7. G.F. Harrison, 'The Role of Material Modelling Techniques in Stress Analysis and Life Assessment of Modern Aero-engine Components', Proc. Instn. Mech. Engrs. Vol. 208, (1993) 19-31.
8. T.M. Pollock and A.S. Argon, Acta Metall. Mater., 40, (1992), 1-30.
9. B.H. Kear and J.M. Oblak, Journal de Physique, 35, C7, (1974), 35-45.
10. B.H. Kear, A.F. Gaimei, G.R. Leverant and J.M. Oblak, Scripta Metal. Vol. 3, (1969), 455-460.
11. T. Hino, T. Kobayashi, Y. Koizumi, H. Harada and T.Yamagata, Superalloys 2000, Eds. T.M. Pollock, R.D. Kissinger et. al., TMS (The Metals and Materials Society) 2000, 729-735.
12. Rae Smeeton Rist and Reed Mat Sci and Engineering, in press. 2002.
13. R.A. MacKay and R.D. Meier, Met. Trans., 13A, (1982), 1747-1754.
14. H. Murakami, T. Yamagata, H. Harada and M. Yamazaki, Mat. Sci. and Eng., A223, (1997), 54-58.
15. P. Spilling and M. Goulette 'The Effect of Major Element Chemistry on the Heat Treatment and Creep Strength of a series of Single Crystal Alloys' Rolls-Royce report, 1982.

INVESTIGATION OF POROSITY IN SINGLE-CRYSTAL NICKEL-BASE SUPERALLOYS

A. Epishin[1], T. Link[2], U. Brückner[1] and P. D. Portella[1]

[1]Federal Institute for Materials Research and Testing, 12205 Berlin, Germany
[2]Technical University Berlin, 10623 Berlin, Germany

Abstract

Different types of microporosity were investigated in SC superalloys of 1st, 2nd and 3rd generation. It was shown that development of superalloys by increasing the total level of strongly segregating refractory elements, results in high microporosity forming during homogenization. A pronounced growth of microporosity, correlating with steady creep, was found after creep tests at high temperatures (1050-1100°C). It is proposed that mechanism for growth of this microporosity is dislocation climb transverse to the stress axis along the interfaces of the rafted γ/γ′-microstructure. Climb parallel to the stress axis is retarded by γ′-rafts. Such anisotropic climb creates a powerful flux of vacancies agglomerating into pores by fast diffusion through the interfacial dislocation networks.

Keywords: superalloys, microporosity, creep

Introduction

Pores in single-crystal (SC) nickel-base superalloys are very undesirable defects because they cause concentration of stresses which initiate rupture. Inspite of their small size and low volume fraction, pores significantly influence the mechanical behaviour of SC superalloys, especially fatigue. One can distinguish the following types of microporosity in SC superalloys: microporosity forming during solidification (S), microporosity growing during homogenization (H) and microporosity developing during creep deformation (D). The increase in the total level of refractory elements in new nickel-base superalloys improves their creep resistance but at a cost of a pronounced increase of H-microporosity. Moreover, rising operation temperatures for turbine blades results in growth of D-microporosity, the volume fraction of which, is comparable with the initial level of microporosity (S+H) in the undeformed material. Therefore, investigation of the microporosity generation and its consequences in practice, is an important task. The phenomenon of S- and H-pores in superalloys has been investigated in detail in [1-3], but little is known about D-pores [4]. This work investigates different types of micoporosity in SC superalloys. It was found that an increase in D-microporosity correlates with accumulated steady creep strain. It was concluded that the increase in D-microporosity and steady creep are caused by the same mechanism, namely climb of dislocations transverse to the stress axis along the interfaces of the rafted γ/γ′-microstructure. Climb parallel to the stress axis is retarded by γ′-rafts. Such anisotropic climb creates a powerful flux of vacancies agglomerating into pores by fast diffusion through the interfacial dislocation networks.

Experimental

The materials investigated were the SC nickel-base superalloys SC16, SRR99, CMSX-4 and CMSX-10. SC16 and SRR99 are SC superalloys of the 1st generation without rhenium, CMSX-4 and CMSX-10 superalloys of the 2nd and 3rd generation, respectively containing

about 1 and 2 at% rhenium. The composition of the superalloys is shown in Table 1. The [001] single-crystals of these superalloys were solidified by Doncasters Precision Casting, Bochum, Germany using the grain selector technique. The primary dendrite arm spacing was 250-300 μm for all superalloys. After solidification the superalloys were fully heat treated (homogenization and a two-stage anneal). Specimens of SC16 and SRR99 were investigated in the undeformed condition only while specimens of CMSX-4 and CMSX-10 were creep tested at temperatures 1050 and 1100°C.

Table 1
Composition of the superalloys investigated in at%

Alloy	Al	Ti	Cr	Co	Ni	Mo	Ta	W	Re
SC16	7.3	4.1	16.8	-	rest	1.7	1.1	-	-
SRR99	12.2	2.7	9.7	5.0	rest	-	0.9	3.1	-
CMSX-4	12.7	1.3	7.5	10.0	rest	0.4	2.2	2.1	1.0
CMSX-10	13.0	0.3	2.8	3.5	rest	0.3	2.9	1.9	2.1

Microporosity in the undeformed material was investigated in the scanning electron microscope (SEM) with backscattered electrons which produce a sharp image of the pores. SEM images with a resolution of 512×512 pixels were taken from areas 460×460 μm^2 (magnification ×200) to distinguish pores with a minimum size of 2 μm. The area fraction of microporosity and the pore size were obtained by processing 30-100 images depending on the scatter of the results. The pore size was characterized by the circular diameter, i.e. the diameter of a circle with the same area as the pore analyzed. An increase in D-microporosity was measured by a change in the material density during creep deformation. Unlike SEM analysis this method has a higher accuracy and it is not so time consuming. For density measurement, cylinders were machined from the creep specimens, approximate diameter 5 mm, length 40 mm, mass 10 g. When ruptured specimens were investigated, the cylinders were cut far from the rupture surface to exclude the influence of cracking and large local straining on the results. The weight of each specimen was measured in air and water using a Satorius balance with an accuracy of 0.1 mg. To avoid gas bubbles adhering to the specimen surface during measurements in water, the specimen corners were rounded and the surface was polished. The weight difference in air and water enables calculation of the volume of the cylinder and thus its density. The reproducibility of the measured densities was shown to be better than $\Delta\rho/\rho \leq 3 \cdot 10^{-4}$.

Results

Microporosity in undeformed superalloys. The results of SEM investigation of microporosity in fully heat treated, undeformed SC superalloys of different generations, are presented in Table 2. It shows that the increase in the total level of refractory elements (Mo+Ta+W+Re), which requires a homogenisation treatment of longer duration t and at a higher maximum temperature T_{max}, results in a pronounced increase in microporosity. In CMSX-10, containing about 2 at% rhenium, it is especially high (≈0.57%).

Microporosity measured in undeformed superalloys is the sum of S- and H-microporosity. Fig. 1 shows these types of pores in CMSX-10. S-pores form during solidification of the interdendritic regions (IRs) during the final stages of the dendritic growth, when melt flow is not sufficient to compensate for the volume shrinkage due to the liquid/solid transformation.

Therefore, S-pores are concentrated in the IRs, have ragged shape and very different sizes. A detailed model of formation of S-microporosity was proposed in [1]. H-pores are also concentrated in the IRs, but they are smaller on average and have a spherical shape similar to gas bubbles in a liquid. Indeed simple calculations show that oxygen and nitrogen dissolved in a melt can cause a small gas pressure of a few MPa inside H-pores at the homogenization temperature.

Table 2

Microporosity in fully heat treated SC superalloys of different generations

Superalloy	Generation	Mo+Ta+W+Re, at%	T_{max}, °C	*t*, h	Microporosity area.%
SC16	1	2.8	1255	3	0.09
SRR99	1	4.0	1303	5	0.16
CMSX-4	2	5.6	1303	9	0.23
CMSX-10	3	7.2	1366	20	0.57

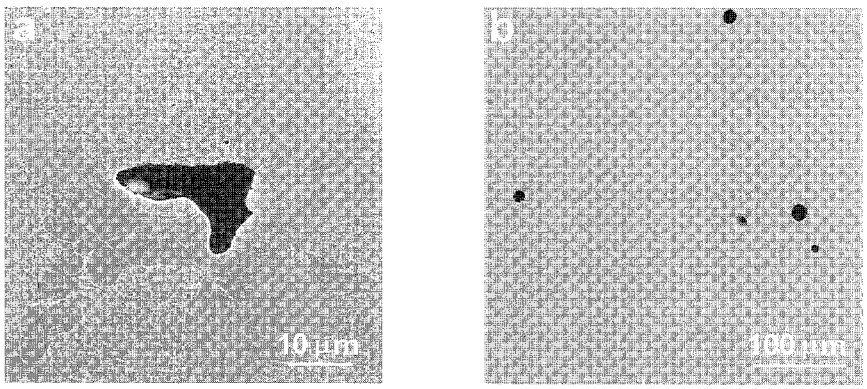


Fig 1. Pores in undeformed CMSX-10.
a. - S-pores after solidification, b. - H-pores after homogenization.

To check which type of pores (S or H) is responsible for the high level of microporosity in CMSX-10, the microporosity was measured in as-cast and heat treated conditions. The measurement showed that in as-cast CMSX-10 the area fraction of S-pores is ≈0.1% (a level of fully heat treated SC16) while after heat treatment the area fraction of S+H-pores is 0.57%. It is seen from the histogram of the distribution of the pore size in fully heat treated CMSX-10 (Fig. 2) that this increase is mostly caused by the development of smaller H-pores. H-pores with sizes ranging from 5 up to 15 μm produce a large peak in the histogram, while S-pores with sizes ranging from 15 μm up to ≈ 50 μm produce a long tail on the right side of the peak. This clearly shows that microporosity in the new superalloys mostly develops during homogenization. A homogenization treatment of longer duration and at a higher maximum temperature increases the pore size. For example, the average size of (S+H)-pores measured in CMSX-4 homogenized for 9 h at T_{max}=1303°C is about 8 μm, in CMSX-10 after 20 h homogenization at T_{max}=1366°C it is about 11.5 μm.

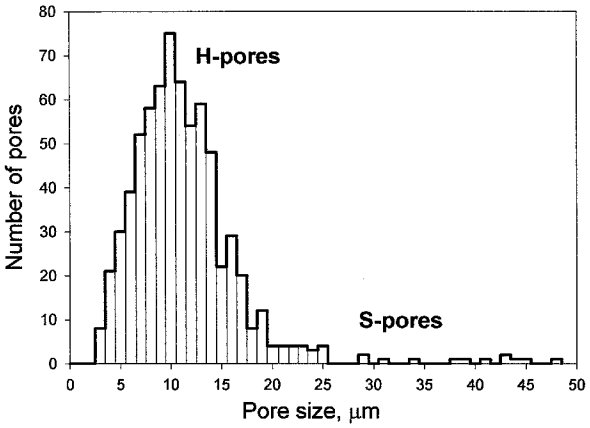


Fig. 2 Distribution of the pore size in fully heat treated CMSX-10.

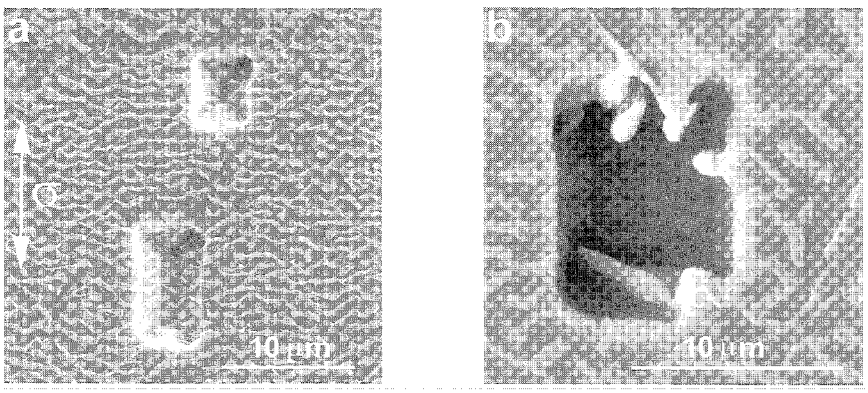


Fig. 3 Deformation induced microporosity after creep at 1100°C and 120 MPa.
a.-Dodecahedronal pores with {011} faces in CMSX-4 (292 h),
b.- Cuboidal pore with {001} faces in CMSX-10 (654 h).

Microporosity in superalloys after creep. Under high temperature creep conditions in superalloys, a new type of microporosity develops - D-microporosity. Fig. 3 shows D-pores in CMSX-4 and CMSX-10 after creep at 1100°C. D-pores are smaller than S- and H-pores, in the specimens tested at temperatures 1050-1100°C for up to 700 h their size does not exceed 10 μm. The shape is crystallographically typical of vacancy agglomeration. It changes with the alloy. D-pores in CMSX-4 have {011} faces (Fig. 3a), while in CMSX-10 they have {001} faces (Fig. 3b). Their spatial distribution is also different. In CMSX-4 they are mostly concentrated in the IRs along the subgrain boundaries (Fig. 4a), in CMSX-10 they are distributed more uniformly within the dendritic cell (Fig. 4b). The crystallographic shape of D-pores can be understood from the minimization of the energy of the total pore surface (the Gibbs-Curie principle)[1]. If the specific surface energy γ^{hkl} is not orientation dependent, the minimization simply leads to spheres. This is the case for the H-pores, forming at very high

[1] Detailed theoretical analysis of the pore shape in the solid state is presented in [5].

temperatures, where the anisotropy of γ^{hkl} nearly vanishes. D-pores form at lower temperatures, where γ^{hkl} is anisotropic. The formation of D-pores can be considered as a negative crystal growth, where vacancy condensation generates faces {hkl} with low γ^{hkl}. The connection between the anisotropy of γ^{hkl} and alloy composition is complex and needs further investigation.

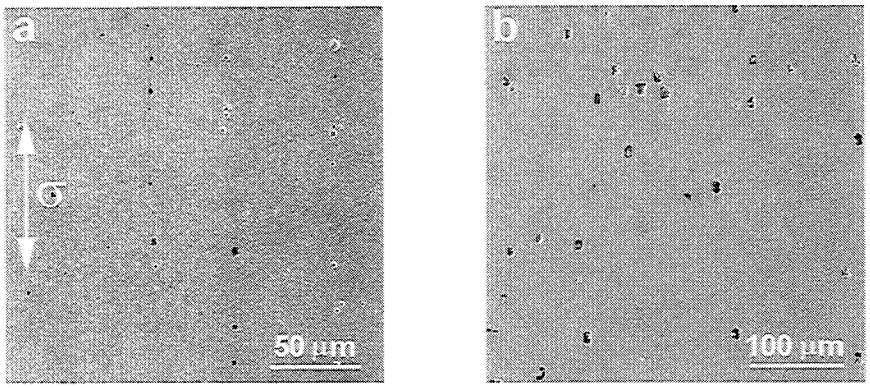


Fig. 4 Spatial distribution of D-microporosity (longitudinal section).
a.- On the subgrain boundaries in CMSX-4 (1100°C, 117 MPa, 393 h),
b. – Randomly distributed in CMSX-10 (1100°C, 120 MPa, 645 h)

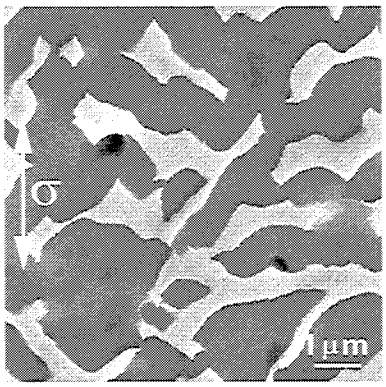


Fig. 5 Nucleation of D-pores in the γ/γ'-interface (CMSX-10, 1100°C, 120 MPa, 645 h).
The γ'-phase is dark.

In the first approximation the difference found in the spatial distribution of D-pores in CMSX-4 and CMSX-10 can be referred to the homogeneity of their macrostructure: the more homogenised the macrostructure - the more uniform the pore distribution (CMSX-10 was much better homogenised compared with CMSX-4). Figure 5 shows an indication of the formation of D-pores. In CMSX-10 very small pores (< 0.5 µm) were found at the γ/γ'-interfaces on the γ'-side. They could have nucleated at the corners of the interface zigzags or at intersections of the γ/γ'-interfaces with low angle boundaries (LABs) between the mosaic blocks.

Additional proof that D-pores are formed by vacancy agglomeration is precipitation of particles on the surface of D-pores (see Fig. 3b). Investigation of these precipitates in the transmission electron microscope (TEM) by energy dispersion X-ray spectroscopy (EDXS) and convergent beam electron diffraction (CBED) was performed. EDXS analysis of the precipitates showed, that they consist mostly of rhenium (about 30 at%), tungsten (about 12 at%), nickel (about 38 at%) the remainder being aluminum, titanium, chromium, cobalt, molybdenum and tantalum. The lattice type was analyzed by CBED. Fig. 6 shows the precipitate (Fig. 6a) and its CBED-pattern (Fig. 6b). The Laue spot pattern in the centre and in the surrounding ring (zero order Laue zone ZOLZ and first order Laue zone FOLZ) gives a lattice constant a=b= 8,85Å and an angle of 90°. The ring diameter of the FOLZ gives the c-parameter c= 4.64Å. Thus this phase is tetragonal. Darolia *et al* [6] reports similar results from a sigma phase in alloy 800 with lattice parameters a=b= 9.3Å, c= 4.86Å. It is clear that formation of these precipitates results from the diffusion mechanism of pore growth. During pore growth vacancies drain to the pore, while atoms diffuse away. Slow diffusion of rhenium and tungsten leads to their supersaturation around the pore and precipitation of the phases with a high concentration of rhenium and tungsten.

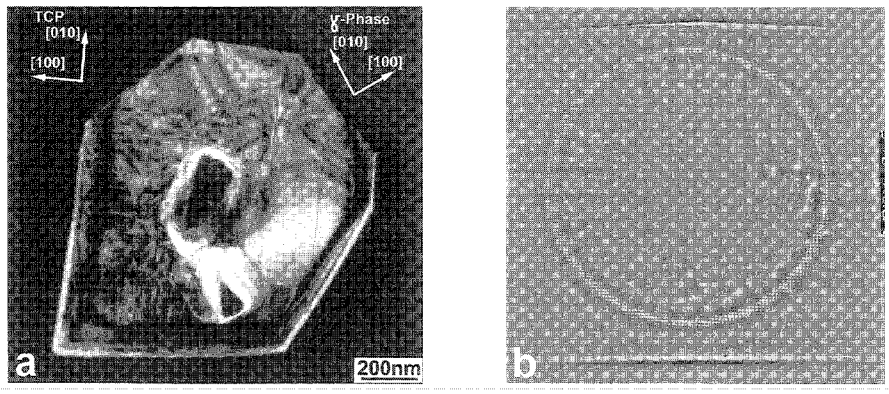


Fig. 6. Precipitate in CMSX-10 after 654h creep at 1100°C, 120MPa.
a.- TEM-image, corrected dark field,
b. - CBED pattern of the precipitate. Image processed by Fourier filtering.

Correlation of D-microporosity with steady creep. At high temperatures and low stress levels (e.g. 1100°C, 120 MPa) the creep curves of [001] single-crystals show a pronounced steady creep with nearly constant creep rate (see Fig. 7). In [4] it was found that microporosity (measured far from the rupture surface) increases nearly as a linear function of time. Because of similar kinetics of the steady creep and microporosity growth, the correlation between these processes was investigated. The steady creep strain was determined as multiplication of the minimum creep rate $(d\varepsilon/dt)_{min}$ by the testing time after the end of primary creep $t-t_p$ (see Fig. 7), i.e. $\varepsilon_{st}=(d\varepsilon/dt)_{min}\cdot(t-t_p)$. It was assumed that steady creep starts at the end of primary creep (at $t=t_p$) and continues until rupture in areas far from the rupture surface, where microporosity was measured. The growth of microporosity was characterized by the relative decrease of the material density $\Delta\rho/\rho$ which is equal to volume fraction v_D of accumulated D-microporosity. The absolute change of density was measured as $\Delta\rho(t-t_p)=\rho(t)-\rho(t_p)$. Fig. 8 shows $v_D = -\Delta\rho/\rho$ versus ε_{st} measured in specimens of CMSX-4 and CMSX-10 tested at 1100°C, for different stress levels and testing times.

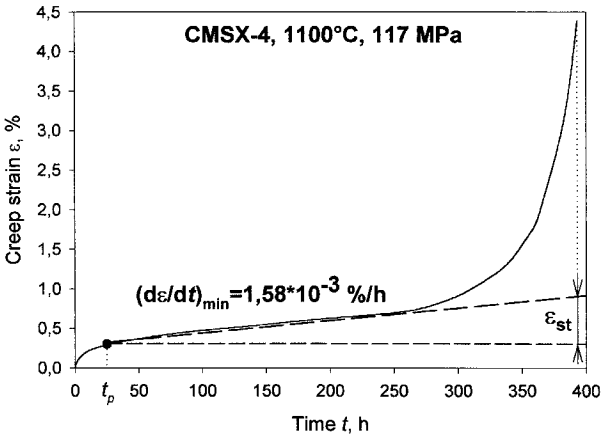


Fig. 7 Typical creep curve of CMSX-4 with pronounced steady creep at high temperature and low stress level. Determination of the steady creep strain ε_{st}.

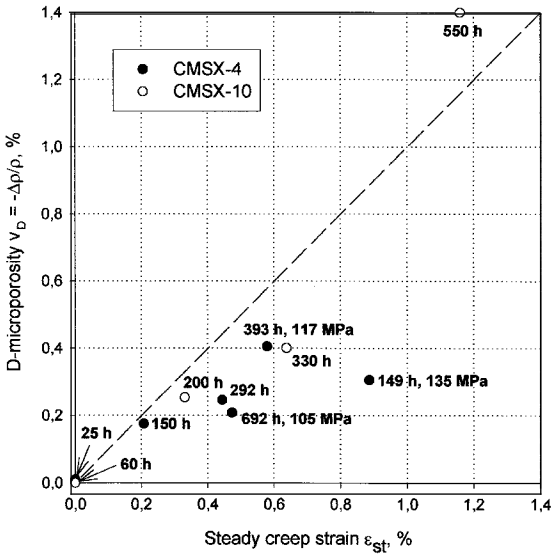


Fig. 8 Correlation of accumulated steady creep strain with volume fraction of D-microporosity at 1100°C. The black dots - CMSX-4, the white dots - CMSX-10. The dots without a stress level correspond to 120 MPa.

One can see a clear increase in D-microporosity with an increase of the steady creep strain. It is important to mention that v_D nearly reaches ε_{st} (dashed line in Fig. 8: $v_D = \varepsilon_{st}$). Points measured at lower stress levels 105-120 MPa are closer to this line than a point measured at a higher stress level 135 MPa. One can conclude from the correlation found between v_D and ε_{st} that growth of D-microporosity and steady creep probably result from the same mechanism. This will be discussed in detail below.

Discussion

Microporosity in undeformed superalloys. Superalloys of the new generation have a high concentration of refractory elements (Mo+Ta+W+Re). A strong dendritic segregation and slow diffusion of these elements make a long-term, high temperature homogenization necessary. During this homogenization the microporosity grows significantly. For example, in as-cast CMSX-10 the S-microporosity is about 0.1% while, after homogenization, the microporosity increases up to 0.57%. There are several factors relevant for the development of H-pores, such as chemical inhomogeneity after solidification, volume fraction of γ/γ'-eutectics, temperature and duration of homogenization. These factors are interdependent: stronger segregation causes more γ/γ'-eutectics and removal of these inhomogeneities needs a longer high temperature heat treatment. Because the mechanism of pore formation is complex, different hypotheses exist for this mechanism [2, 3]. S+H-microporosity can be strongly reduced by high temperature isostatic pressing however this does not solve the problem, because under high temperature creep a new type of microporosity develops, D-pores, which can have an even higher volume fraction than S+H-pores.

Mechanism of D-microporosity growth. To understand, how pores form during creep in superalloys, it is necessary to discuss the mechanism of high temperature creep in general and then the special effects in superalloys. According to the classical concept of high temperature creep of metals, the creep controlling process is the climb of dislocations having a Burgers vector with an edge component $\vec{b}_{edge}$ [7]. Climb is controlled by two forces, the elastic force F_{el}/L, caused by the applied stress σ:

$$F_{el}/L = \sigma\left(\vec{b}_{edge} \cdot \vec{k}\right) \tag{1}$$

(F_{el}/L has the direction $\vec{b} \times \vec{u}$, $\vec{u}$ is the line vector of the dislocation, $\vec{k}$ the stress direction). and the osmotic force F_{os}/L, caused by the difference between the vacancy concentration at the dislocation core c and in the standard-state c^0:

$$F_{os}/L = -\frac{kTb_{edge}}{V_a} \ln\frac{c}{c^0} \tag{2}$$

(kT is the thermal energy per atom, V_a the atomic volume).

From (1) it follows that dislocations with a half plane perpendicular to the applied stress ($\vec{b} \parallel \vec{k}$) experience the maximum elastic force. This means, that under load, the half planes of these dislocations grow perpendicular to the stress direction, thus increasing the specimen length. This process of climb is from here on referred to as a transversal (T) climb. For dislocations with a half plane parallel to the stress direction ($\vec{b} \perp \vec{k}$) the elastic force is zero[2]. For the osmotic force (2) the direction of $\vec{b}_{edge}$ is irrelevant. Osmotic climbing is possible for both types of dislocations. The sign of F_{os}/L is opposite to that of F_{el}/L, i.e. F_{os}/L makes the half planes shrink. Shrinking of half planes of dislocations with ($\vec{b} \perp \vec{k}$) under osmotic force reduces the specimen diameter. We will call this process longitudinal (L) climb. During deformation, the T-climbing dislocations, driven by F_{el}/L, build up the half planes by removal of atoms from neighbour lattice sites. Thus they create vacancies, i.e. increase c. This

[2] Because only the edge component is relevant, only edge dislocations are discussed.

increase of c above c^0 activates F_{os}/L and consequently L-climb. Vacancies diffuse from T-climbing dislocations to L-climbing dislocations where they condense on the half planes and make them shrink. Hypothetically, all vacancies created by T-climb can reach the L-climbing dislocations and be destroyed by them. In this case the specimen does not change the volume V during deformation, i.e.

$$\Delta v = \varepsilon_L + 2\varepsilon_T = 0$$

Where $\Delta v = \Delta V/V$, ε_L is the longitudinal strain of the specimen due to T-climb and ε_T is the transversal strain due to L-climb.

In reality, many vacancies created by the T-climb do not reach the L-climbing dislocations and condense on other defects in the crystal structure, e.g. grain boundaries. Agglomeration of condensed vacancies into micropores increases the specimen volume by the pore volume fraction v_D, i..e.

$$\Delta v = \varepsilon_L + 2\varepsilon_T = v_D \neq 0$$

In superalloys, creeping at high temperatures, the direction of dislocation climb is determined by the morphology of the γ/γ'-microstructure. Under tensile loading the γ'-cubes coalesce into extended γ'-rafts orientated perpendicular to the load axis. Because penetration of the γ'-rafts is difficult, the dislocation climb is restricted to the γ/γ'-interfaces and the matrix channels, i.e. to the transversal direction. This strong imbalance between T- and L-climb generates a powerful source of vacancies which condense at the interfacial dislocations and agglomerate into pores. At low stress levels the L-climb is strongly retarded, $\varepsilon_T \approx 0$ and $\varepsilon_L \approx v_D$. The experimental check of these consideration is the comparison of the creep strain with volume fraction of the microporosity v_D. In CMSX-4 and CMSX-10 crept at 1100°C and stresses ≤120 MPa it was found, that the increase in the steady creep strain ε_{st} is nearly the same as the growth of microporosity v_D, i.e. $dv_D/d\varepsilon_{st}$ is close to 1. Thus the above considerations about climb-controlled deformation are valid for steady creep. Raising the stress up to 135 MPa decreases the slope $dv_D/d\varepsilon_{st}$. This also fits with the model presented, because higher stresses should activate some L-climb, reducing the vacancy flux towards pores.

Pore nucleation. Vacancies created by T-climb diffuse through the γ/γ'-interfaces and LABs to pre-existing S- and H-pores, or to nucleating D-pores, increasing the total level of microporosity. In SC superalloys, D-pores can nucleate: in the LABs between subgrains and mosaic blocks, on precipitates of the topologically closed packed phases, at interfacial dislocations or dislocations within the γ- and γ'-phases. The nucleation process depends on the test parameters. For example, no new pores with sizes greater than those resolvable in a light microscope were found during creep at temperatures ≤950°C [4], while the present investigation showed that creep at 1100°C results in generation of D-pores with sizes of few microns. This effect can be explained by a difference in the vacancy concentration: the probability of agglomeration of vacancies to form pores increases with an increase in vacancy concentration. An increase in temperature from 950 to 1100°C results in a rapid increase in the concentration of thermally generated vacancies (e.g. for nickel by 5-6 times). Moreover at higher temperatures and low stresses rafting has a stronger effect on climb anisotropy, increasing the flux of D-vacancies generated according to our model.

Further investigation of the mechanism of high temperature creep of superalloys is needed for a detailed understanding the phenomenon of D-microporosity.

Conclusions

1. Investigation of microporosity in undeformed superalloys of different generations; SC16, SRR99, CMSX-4 and CMSX-10, showed that the volume fraction of pores significantly increases with raising the total level of refractory elements (Mo+Ta+W+Re). This increase is caused by pore growth during high temperature, long-term homogenization which is necessary to reduce segregation of refractory elements and, hence, to suppress precipitation of topologically closed packed phases.
2. Creep deformation at 1050-1100°C results in pronounced growth of D-microporosity exceeding the initial level of microporosity in undeformed material. It was found that at low stress levels, the volume fraction of D-microporosity correlates with the steady creep strain. Deformation induced pores have clear crystallographic shape typical of vacancy agglomerations. The crystallography of D-pores and their distribution within the dendritic cell was found to be quite different in CMSX-4 and CMSX-10.
3. Consideration of dislocation movement in the rafted γ/γ'-microstructure shows that the reason for the D-microporosity is strong anisotropy of the dislocation climb. In this plate-like microstructure, dislocations climb mostly perpendicular to the stress direction creating vacancies which agglomerate into pores by fast diffusion through the interfacial dislocation network.
4. D-microporosity is expected to reduce the fatigue strength of superalloys. Therefore the danger of fatigue rupture in turbine blades due to accumulation of D-microporosity needs to be investigated.

Acknowledgements

The authors are grateful to the Deutsche Forschungsgemeinschaft (DFG Project No. 100212119) for financial support for this work. The authors also would like to thank Mr. J. Schwerdt for performing the creep experiments.

References

1. J. Lecomte-Beckers, Study of microporosity formation in nickel-base superalloys, *Metall. Trans. A*, Vol. 19A, No. 9 (1988), pp. 2341-2348
2. D. L. Anton and A.F. Giamei, Porosity distribution and growth during homogenization in single crystals of a nickel-base superalloy, *Mater. Sci. and Eng.*, Vol. 76 (1985) , pp. 173-180
3. V. N. Toloraja, A. G. Zuev and I. L. Svetlov, Influence of regimes of directional solidification and heat treatment on porosity in single-crystal nickel-base superalloys, Izv. AN. USSR, Metalls,, No. 5 (1991) pp. 70-76 (in russian)
4. J. Komenda and P. J. Henderson, Growth of pores during the creep of a single crystal nickel-base superalloy, *Scripta Mater.*, Vol. 37 (1997), pp. 1821-1826
5. R. S. Nelson, D. J. Mazey and R. S. Barnes, The thermal equilibrium shape and size of holes in solids, *Phil. Mag*, Vol. 11 (1965), pp. 91-111
6. R. Darolia, D.F. Lahrman, R.F. Field, Formation of topologically closed packed phases in nickel base single crystal superalloys, Superalloys 1988, edited by D.N. Duhl, G. Maurer, S. Antolovich, C. Lund, S. Reichman, TMS 1988, pp. 255-264
7. J. Weertman and J. R. Weertman, Mechanical Properties, strongly temperature dependent, In: Physical Metallurgy, ed. by R. W. Cahn and P. Haasen, North-Holland Physics Publishing, 1983

INVESTIGATION AND COMPARISON OF THE MICROSTRUCTURE OF THE NICKEL-BASE SUPERALLOYS CMSX-4 AND SX CM186LC

Danciu D.[1,2], Klabbers J.[1], Penkalla H.J.[1],

[1] Forschungszentrum Juelich GmbH (FZJ), Institute for Materials and Process in Energy Systems IWV-2: Microstructure and Properties of Materials, 52425 Juelich, Germany

[2] University of Mining and Metallurgy Krakow (AGH), Poland

Abstract

Microstructure investigations of CMSX-4 and SX CM186 LC have been performed by the mean of light and scanning electron microscopy in order to evaluate the potential of SX CM186LC for CMSX-4 replacement. Such a replacement would involve lower production cost of turbine gas components. Using EDX-SEM, detailed chemical analyses of the identified phases was performed before and after the heat treatment proposed by producer in order to estimate the effect of the heat treatment on materials microstructure. While the heat treatment of CMSX-4 generated a very homogeneous microstructure, the proposed heat treatment for SX CM186LC was less effective without reducing γ/γ' eutectic areas and causing additionally a transition from primary Ta-rich MC carbides to Hf-rich carbides in eutectic regions. The addition of carbide-forming elements (especially the high amount of Hf) to the chemical composition of SX CM186LC prohibited its full homogenisation. Except for dendrites and eutectic regions which are always present in SC nickel-base superalloys, thermally unstable carbides were precipitated. Trials aimed at finding a higher temperature heat treatment which could lead to elimination of eutectics and microstructural inhomogeneity have not been successful. Microstructural homogeneity is often a strict requirement for many of the theoretical assumptions used for example, in life prediction models.

Keywords: nickel-base superalloys, CMSX-4,CM186LC, microstructure, carbides, heat treatment

Introduction

The introduction of single crystal casting technology, formerly developed for aero engines, in industrial gas turbine vanes and blades requires the optimisation of the chemical composition to achieve a material which possesses carefully balanced long term mechanical properties [1]. An important step in the development of single crystal nickel-base superalloys was the elimination of grain boundary strengthening elements such as C, B, Zr and Hf. This preventive measure increased considerably the temperature of the incipient melting and allowed the almost complete elimination of γ/γ' eutectic areas by using a super-solvus high temperature solution heat treatment [2]. The next step towards evolution of these materials was the introduction of Re to the chemical composition of nickel base single crystals which offered an additional strengthening of the γ matrix and substantially slowed downthe γ'coarsening kinetics [3]. All these measures involved enormously increased costs for large IGT-components.

A new trend imposed by the economic constraint for lower manufacturing costs is the re-introduction of grain boundary strengthening elements such as C, B, Hf and Zr which were used in the second generation of single crystal nickel-base alloys. The addition of carbon allows a cleaner melting procedure because it helps to reduce the oxides, thus improving the castability. The intentional addition of C could also inhibit grain defect formation in certain high refractory alloys [4]. In order to minimize the possible deleterious effects of low angle

boundaries (LABs) which are inevitably present in the 'single crystal' components, low amounts of C, B and Hf are also added in order to strengthen the LABs. This may also result in a higher tolerance for secondary grains. These additions improve the manufacturing yields of the components, because LAB with misorientations up to 15° are accepted, instead of the value of 6° generally fixed for rejection of the castings when the grain boundary strengthening elements are omitted [5,6].

Experimental procedure

The investigated materials are :

- CMSX-4 – a typical Re-containing single crystal superalloy evaluated for first stage vanes and blades in the COST activities 501
- SX CM186LC- a single crystal Re-containing superalloy primarily developed for DS columnar grain turbine airfoils with an addition of grain boundary strengthening elements : C, Hf, B and Zr (*Table 1*).

The specimens were both hollow and solid bars with <001> orientation provided by Doncasters Precision Castings- Bochum. The applied heat treatment is presented in *Table 2.*

Material	Chemical composition wt (%)														
	Ni	Co	Cr	Mo	Al	Ti	Ta	W	Re	Nb	B	Hf	Zr	Fe	C
CMSX-4	60	9,7	6,5	0,6	5,6	1,04	6,5	6,4	2,9	<0,05	0,002	0,11	0,001	0,038	0,0025
SX CM186LC	60	9,3	6,1	0,51	5,7	0,73	3,4	8,4	2,9	---	0,016	1,4	0,004	0,027	0,062

Table 1: Chemical composition of CMSX-4 and SX CM186LC* (wt-%)*
*trade names of Cannon Muskegon

Material	Heat treatment
CMSX-4	a) 2h/ 1280°C (vacuum) + 2h/ 1290°C (vacuum) + 2h/ 1305°C (vacuum) followed by rapid gas fan quenching in high purity argon to RT b) 6h/ 1140°C (Ar-atmosphere) followed by cooling in argon, and 20h/ 871°C (Ar-atmosphere) followed by cooling in argon
SX CM186LC	a) 4h/ 1080°C; (vacuum), followed by rapid gas fan quenching in high purity argon to RT b) 20h/ 870°C; (vacuum or high purity argon) followed by rapid gas quenching in high purity argon

Table 2. Heat treatment of SX CM186LC and CMSX-4 alloys

Microstructural investigations were performed by means of light microscopy (LM), scanning electron microscopy (SEM and EDX-SEM) on specimens cut parallel and perpendicular to the bars axis before and after the proposed heat treatment. Specimens for light microscopy and scanning electron microscopy were prepared in the same manner. Mounted specimens were ground to 1200 grit surface finish using SiC abrasive paper. After their polishing with 6, 3 and 1 μm diamond paste, the specimens were chemically etched in a solution of 8 g Cr-(VI)-oxide + 85 ml H_2PO_4 (85%) + H_2SO_4 (95-97%).

Results and discussion

Microstructure characterisation

As-cast CMSX-4

The microstructure of CMSX-4 solid bar after solidification is presented in *Fig 1 a), b), c)* and *d)*. A well developed dendrite structure consisting of primary, secondary and tertiary dendrite arms growing in the three orthogonal directions <001> is shown in *Fig.1 a)* and *b)*. In the dendrite cores the structure consists of very fine cubic-shaped γ' particles with an edge length of 400-500 nm, as shown in *Fig.1 c)*. Between the dendrite arms, large γ/γ' eutectic areas of low melting temperature *(Fig.1 d)* were found.

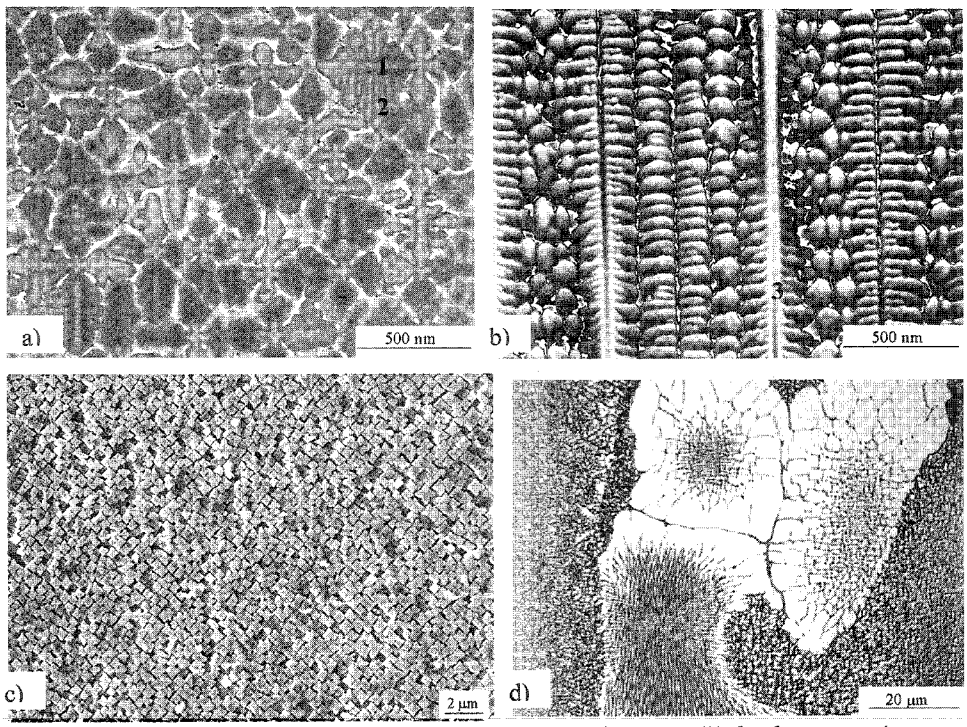


Fig.1. CMSX-4 as-cast microstructure a) secondary (1) and tertiary (2) dendrite arms (cross section, LM), b) primary dendrite arms (3) (longitudinal section, LM), c) fine cubic-shaped γ'-particles in a dendrite core (cross section, SEM), d) γ/γ'- eutectic areas (cross section, SEM)

Chemical analyses performed by the means of EDX-SEM revealed a very strong segregation of chemical elements as shown in *Fig. 2*, the most significant difference being the segregation of Re and W to the dendrite cores and Ta to the eutectic areas.

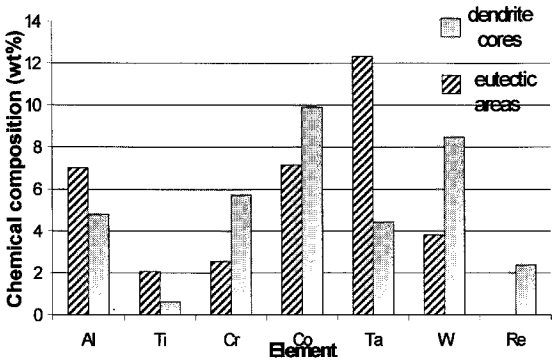


Figure 2. CMSX-4 chemical composition of γ/γ' eutectics and dendrite cores in the as-cast structure

Heat –treated CMSX-4

After the applied heat treatment (Table 2), the microstructure of CMSX-4 became more homogeneous, almost all γ/γ' eutectic areas were eliminated *Figure 3.* In the dendrite cores no significant changes occurred. The shape of γ' particle in the dendritic cores was more regular and well aligned (Figure 3 a)) than in ex-eutectic areas (Figure 3 b)).

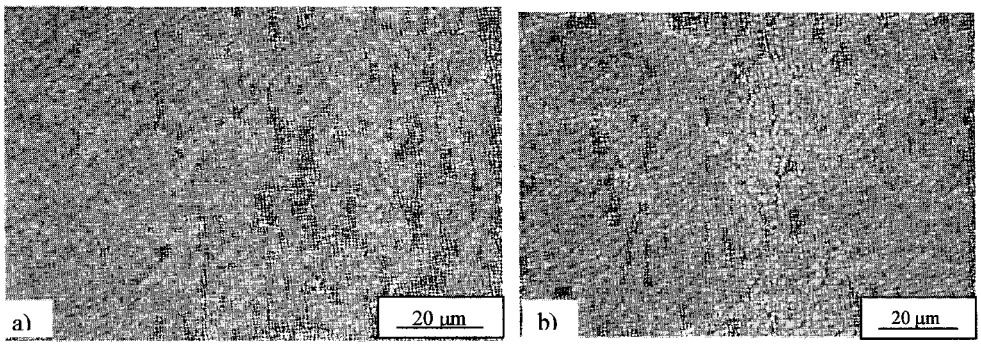


Figure 3. CMSX-4 after heat treatment (SEM): a) dendritic area b) ex-eutectic area

EDX-SEM analyses revealed no significant differences in the chemical composition of dendrite cores and areas that earlier were eutectic regions, just a minimal difference in the amount of Re with a higher content in the dendrite cores (*Figure 4*). This could lead to a slight decrease of solid solution hardening in the matrix volume of ex-eutectic regions.

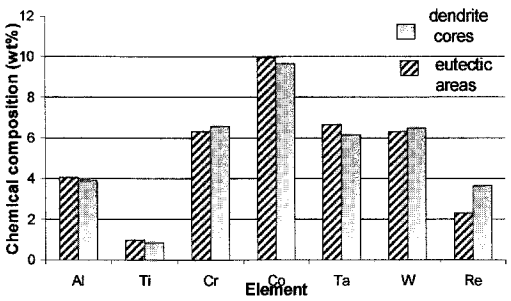


Figure 4. CMSX-4 chemical composition of eutectic and dendrite cores in as heat-treated microstructure

As-cast SX CM186LC

The microstructure of SX CM186LC as-cast (*Fig.5*) is similar to the microstructure of CMSX-4 (primary, secondary, tertiary dendrite arms and eutectics) with the main difference that the addition of C, Hf, B caused a change in the element segregation between eutectic and dendritic areas and favoured the formation of Ta - rich carbides (TaC). Dendritic areas of very fine γ' particles and large, irregular γ/γ' eutectic areas of very high Hf content were observed. Ta-rich MC carbides in intermediate regions were very large and very irregular, script-like shaped.

The difference between the chemical composition of dendrite cores and eutectic areas is presented in *Fig.6* indicating about the strong partition of Hf to eutectics and Re to the dendrite cores. In the intermediate areas Ta-rich MC carbides were formed (*Table 3*). The large difference in the distribution of Re and W between the dendrite cores and eutectic regions (without Re content) gave rise to a variety of γ' morphology and alignment.

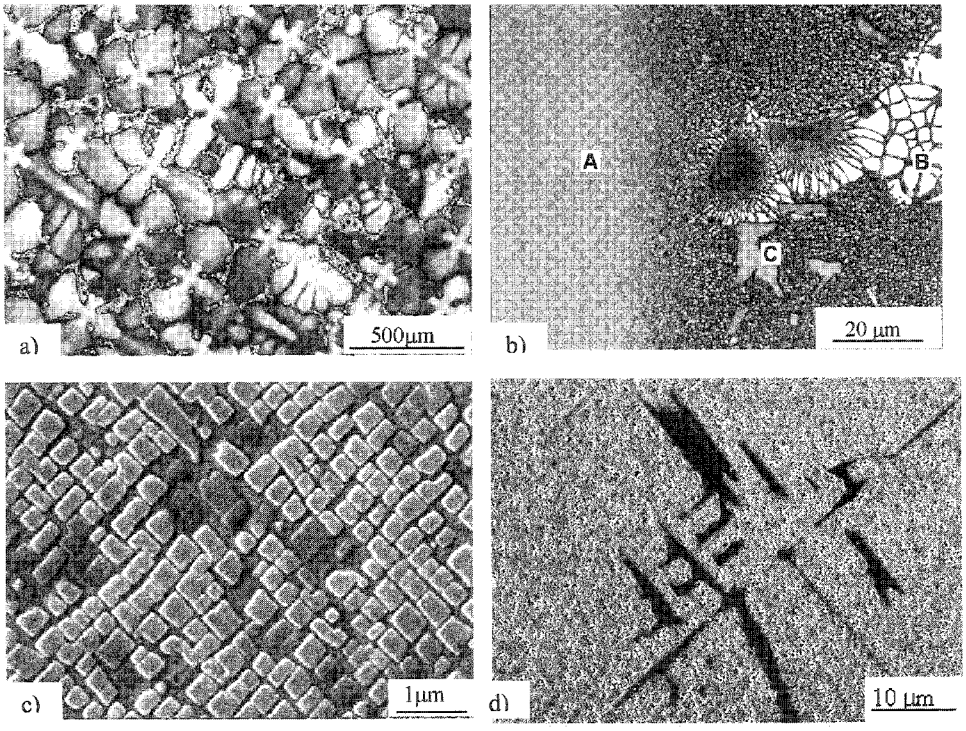


Fig.5. SX CM186LC as-cast microstructure a) Secondary and tertiary dendrite arms (cross section, LM) b) Primary dendrite arm (A), γ/γ' eutectic (B) and primary carbide (C) (longitudinal section, LM) c) Fine γ' particles cubic-shaped in dendritic areas (cross section, SEM) d) Primary Ta-rich carbide in intermediate region (cross section, SEM)

Although the addition of C favourably changed the segregation behaviour of Ta, its partition to eutectics and dendrite cores being more equalised than in the case of CMSX-4 after casting, it did not affect the segregation behaviour of other constituent elements, for example Re which does not segregate to the eutectics (Figure 6).

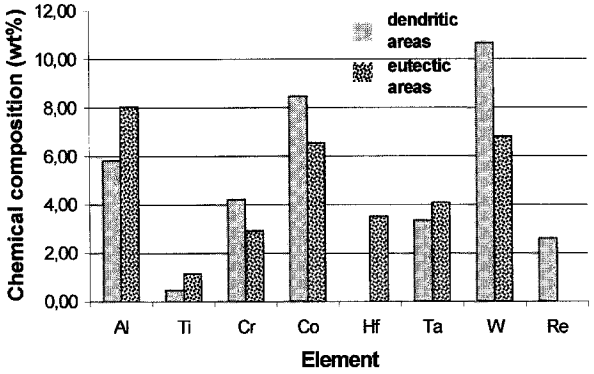


Figure 6
Chemical composition of SX CM186LC in dendrite cores and eutectic areas after solidification

Element	C	Al	Ti	Cr	Co	Ni	Ta	W	Hf
wt (%)	7.54	-	5.8	0.62	-	2.2	53	8.95	21.89

Table 3 SX CM186LC: chemical composition of a primary Ta-rich MC carbides in intermediate regions

Heat –treated SX CM186LC

The applied first heat treatment step (4h/1080°C) did not change significantly the microstructural features of SX CM186LC, there seemed to be no effect regarding the homogenisation. An additional generation of Hf-rich carbides in the eutectic areas was observed (*Figure 7*). Gradually, a reduction of Ta-rich carbides from intermediate regions occurred accompanied by a diffusion of C to the eutectics and its combination with Hf, leading to the Hf-rich carbides formation in γ/γ' eutectics. In the dendrite cores and eutectic areas the segregation of the other chemical elements remained similar to the as-cast structure before the applied high temperature heat treatment (Figure 8). The chemical composition of a typical Hf-rich carbide is presented in Table 4. HfC carbides are small compared with TaC carbides of various shapes and grouped mainly in eutectics. The transition from Ta-rich carbides to Hf carbides can be explained by a higher affinity of Hf to form monocarbides at high temperatures.

Element	C	Al	Ti	Cr	Co	Ni	Ta	W	Hf
wt (%)	7.19	-	1.4	0.41	0.96	4.16	16.86	7.05	62.06

Table 4 Chemical composition of a typical Hf-rich carbide in γ/γ' eutectics in SX CM186LC after first heat treatment step

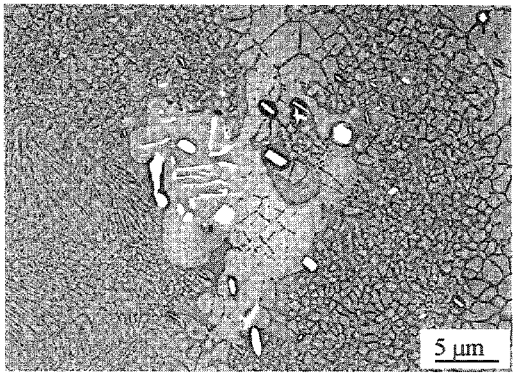


Figure 7. Hf-rich carbides grouped in eutectic areas in SX CM186LC after high temperature heat treatment step-a

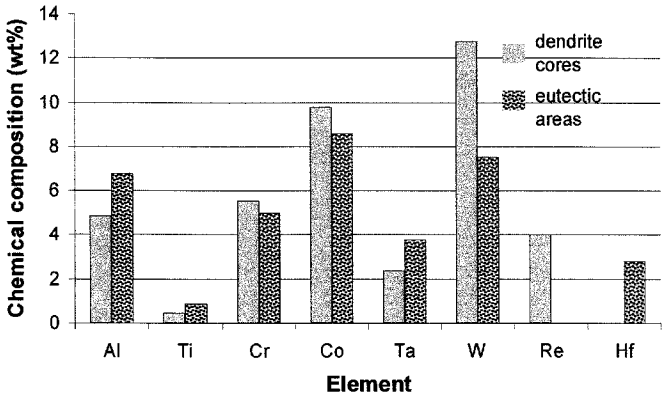


Figure 8. Chemical composition of SX CM186LC in dendrite cores and eutectic areas after the heat treatment step-a

In order to have additional information about the possible microstructural changes at higher temperatures, heat treatments in the temperature range from 1280°C to 1300°C followed by a rapid cooling in Ar atmosphere were applied. In the specimens heat treated at 1290°C pores

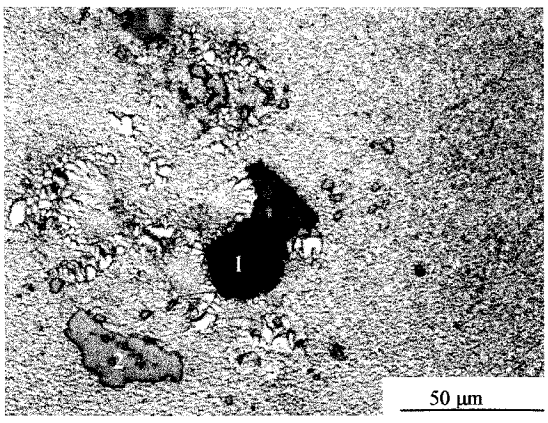


Figure 9. SX CM186LC after 1290 °C/4h. pore on eutectic region (1) and carbide (2)

could be observed in the places where eutectics were initially located. Such a structure is presented in *Fig.9*. It can be assumed that pores occurred as a result of incipient melting of γ/γ' eutectics.

Conclusions :

- CMSX-4 as-cast microstructure is characterized by dendrite arms growing in <001> orthogonal directions containing a higher amount of Re and W and lower amount of Ta than γ/γ' eutectic regions;

- the application of a heat treatment using theparameters presented in *Table 2*, led to a very homogeneous microstructure in the case of CMSX-4;

- SX CM186LC as-cast microstructure consists of orthogonal dendrite arms containing a large amount of Re and W, eutectics (where almost all the Hf is concentrated) and Ta-rich mono carbides in areas between dendrite cores and eutectics;

- as a result of application of the high temperature heat treatment step proposed in *Table 2* for SX CM186LC, the homogenization of the microstructure could not be achieved;

- a higher heat treatment temperature which could lead to a homogenization of SX CM186LC microstructure usually required in many theoretical assumptions is detrimental, leading to an instability of carbides and incipient melting of the γ/γ' eutectic areas.

Literature

[1] N.Matan, D.C.Cox, P.Carter, M.A.Rist, C.M.F. Rae, R.C.Reed 'Creep of CMSX-4 superalloy single crystals: effects of misorientation and temperature', Acta mater., Vol 47, No 5, 1999, pp.1549-1563

[2] T.E.Strangman, G.S.Hoppin, C.M Phipps, K.Harris, R.E.Schwer 'Superalloys 1980', J.K.Tien (ed), American Society for Metals, Metals Park, OH, USA, 1980, p.215

[3] P.Caron, T.Khan 'Third generation superalloy for single crystal blades', Proc. 6th Liege Conference on Materials for advanced power engineering, Belgium, J.Lecomte-Beckers, F. Schubert, P.J. Ennis (eds), ISBN389336 228-2, Forschungszentrum Julich, 1998, pp.897-912

[4] S.Tin, T.M. Pollock, W.T.King 'Carbon addtions and grain defect formation in high refractory nickel-base single crystal superalloys', Superalloys 2000, T.M.Pollock, R.D.Kissinger, R.R.Bowman, K.A.Green, M.McLean, S.Olson, J.J.Schirra (eds), TMS (The Minerals, Metals & Materials Society), 2000, pp.201-210

[5] J.R.Davis 'Directionally solidified and Single-Crystal Superalloys', Heat resistant materials, II Series, ASM International, 1997, pp.255-271

[6] K.Harris, J.B.Wahl 'New superalloy concepts for single crystal turbine blade and vanes', Proc. 5th Int. Charles Parsons Conf., Cambridge, July 2000, pp.832-846

DISLOCATION MICROSTRUCTURE OF CMSX-4 AFTER TENSILE TESTING WITH DIFFERENT STRAIN RATES AT 700 AND 1000°C

D Danciu [1,2], H J Penkalla [1], F Schubert [1]

[1] Research Centre Juelich (FZJ), Institute for Materials and Processes in Energy Systems IWV-2, 52425 Juelich, Germany

[2] University of Mining and Metallurgy (AGH), Krakow, Poland

Abstract

An overview of dislocation structure evolution has been performed using of TEM techniques on <001> orientated CMSX-4 specimens after tensile testing at 700 and 1000°C with strain rates in the range from 10^{-3} s^{-1} to 10^{-8} s^{-1}. TEM specimens were prepared from sections cut parallel to (001) planes perpendicular to the stress axis, along the specimen axis parallel to (011) planes and parallel to (111) gliding planes. The aim of the applied conventional TEM methods was to provide with more details about the influence of temperature and deformation rate on the deformation behaviour of CMSX-4, a nickel-base single crystal alloy. A correlation of the γ' phase deformation mechanisms and associated mechanical responses for different tensile testing conditions has been made. Using a simple TEM method, dislocation dipole identification and characterisation of stacking faults characteristics have been carried out for specimens deformed at 700°C with different strain rates.

Keywords: single crystal, CMSX-4, tensile, microstructure, transmission electron microscopy

Introduction

In the last few decades, the energy industry has stimulated the development of high temperature superalloys. Industrial gas turbines will play an important role in the future either as single –cycle facilities or as integrated parts of a combined cycle plant [1]. In the most advanced gas turbines, single crystal superalloys are currently used for production of critical parts, such as turbine blades and vanes [2-4].

The development of single crystal cast technology was associated with aero engines and industrial gas turbine blades and vanes, and included the development of new chemical compositions to balance and optimise the mechanical properties of the material. Nickel-base superalloys have long recognised as important engineering materials because of their excellent resistance to high temperature deformation [5,6]. Different deformation characteristics are possible depending on the working temperature and applied stresses [7,8].

Nickel-based single crystal alloys benefit from a low content of solidus depressing elements, such as boron, carbon and zirconium generally used as grain boundary strengthening elements in conventionally cast materials. In case of single crystal superalloys the elimination of γ/γ' eutectics and solutioning of all the secondary γ' precipitates using appropriate high temperature heat treatments is facilitated. This results in a homogeneous microstructure consisting of fine cube-shaped γ' particles (≈ 70% volume fraction) surrounded by γ matrix channels [3, 9].

Since <001> crystal orientation offers the best combination of the required mechanical properties (creep resistance, thermal induced low cycle fatigue) which is also the direction of

natural growth, the investigations of technically used single crystals are mainly focused on <001> oriented specimens.

It is known that in Ni-base superalloys at lower temperatures (600°-750°C) the deformation involves cutting of γ' particles which is mainly responsible for the high level of strength [10,11]. The shearing of γ' precipitates by partial matrix dislocations leads to various types of planar defects in the γ' phase, e.g. superlattice intrinsic and extrinsic stacking fault (SISF or SESF), antiphase boundary (APB) and complex stacking fault (CF). Shearing of the γ' particles has been the subject of many experimental and theoretical studies in the past. Two shearing processes, one involving the formation of APB and the other leading to superlattice stacking fault within the γ' phase have been identified in nickel-base alloys containing high volume fractions of γ'. While the shearing mechanism by pairs of a/2<110> type matrix dislocations coupled by APB is relatively better understood, disagreement exists in the literature regarding the details of the shearing process leading to stacking fault formation [12].

The following TEM investigation presents an overview of dislocation structure evolution and microstructure stability of CMSX-4 single crystal superalloy after tensile tests at two different temperatures and with different strain rates. For specimens deformed at 700°C and different strain rates, simple TEM method for dislocation dipoles identification as well as for identification of the stacking fault nature has been performed.

Experimental procedure

The CMSX-4 single crystal solid bars (chemical composition presented in *Table 1*) were provided by Doncasters Precision Castings Bochum, Germany. The solid bars were heat-treated accordingly to the procedure presented in *Table 2*. The specimen orientations did not exceed 10° from the <001> orientation. For tensile testing investigations, specimens were machined from solid bars to a shape presented schematically in *Fig.1*.

Table 1. Chemical composition of CMSX-4 alloys (Ni-bal.)*

Material	Cr	Mo	Ti	Ta	W	Co	Al	Re	Hf	B	Zr	C
CMSX-4	6.45	0.6	1.03	6.5	6.4	9.6	5.62	2.9	0.1	0.002	0.001	0.0022

* trade name of Cannon Muskegon

The tensile specimens were deformed in an Instron test facility at different strain rates and at two temperatures, 700 and 1000°C. When on the resulting stress – strain curve a 'plateau' corresponding to the steady state seemed to have been reached, the test machine was switched from strain control to load control mode and the specimens were cooled down to room temperature. This procedure was carried out to preserve the microstructure. At 700 °C and high strain rates (10^{-3} s^{-1} to 10^{-5} s^{-1}), the constant load during the cooling down was limited to 0.5 kN in order to avoid specimen fracture. It is likely that such a cooling did not allow the dislocation structure to be preserved, as mentioned in [13].

Table 2. Heat treatment of CMSX-4 alloy

Material	Heat treatment
CMSX-4	a) 2h/ 1280°C (vacuum) + 2h/ 1290°C (vacuum) + 2h/ 1305°C (vacuum) followed by rapid gas fan quenching in high purity argon to RT b) 6h/ 1140°C (Ar-atmosphere) followed by cooling in argon and 20h/ 871°C (Ar-atmosphere) followed by cooling in argon

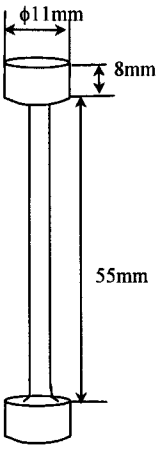


Fig. 1. CMSX-4 tensile test specimen <001> oriented

Specimens deformed at 1000°C were cooled down after tensile testing under constant stress, which represented the last value of the applied stress during deformation. At this temperature even for the applied high strain rates it was possible without the risk of a specimen fracture during cooling.

TEM specimens were prepared from sections cut parallel to (001) planes perpendicular to the stress axis (and perpendicular to the axis of the tensile specimens), along the specimen axis parallel to (011) planes and parallel to (111) slip planes. Such a complex investigation should provide precise information concerning the dislocation structure in the deformed specimens. The electrolytic polishing conditions for the thin foil preparation were : temperature – 18°C, voltage 20 V, solution : 66 ml perchloric acid, 680 ml ethanol, 340 ml butyl glycol. The applied TEM methods are briefly described in the following paragraph.

Dislocation dipoles identification

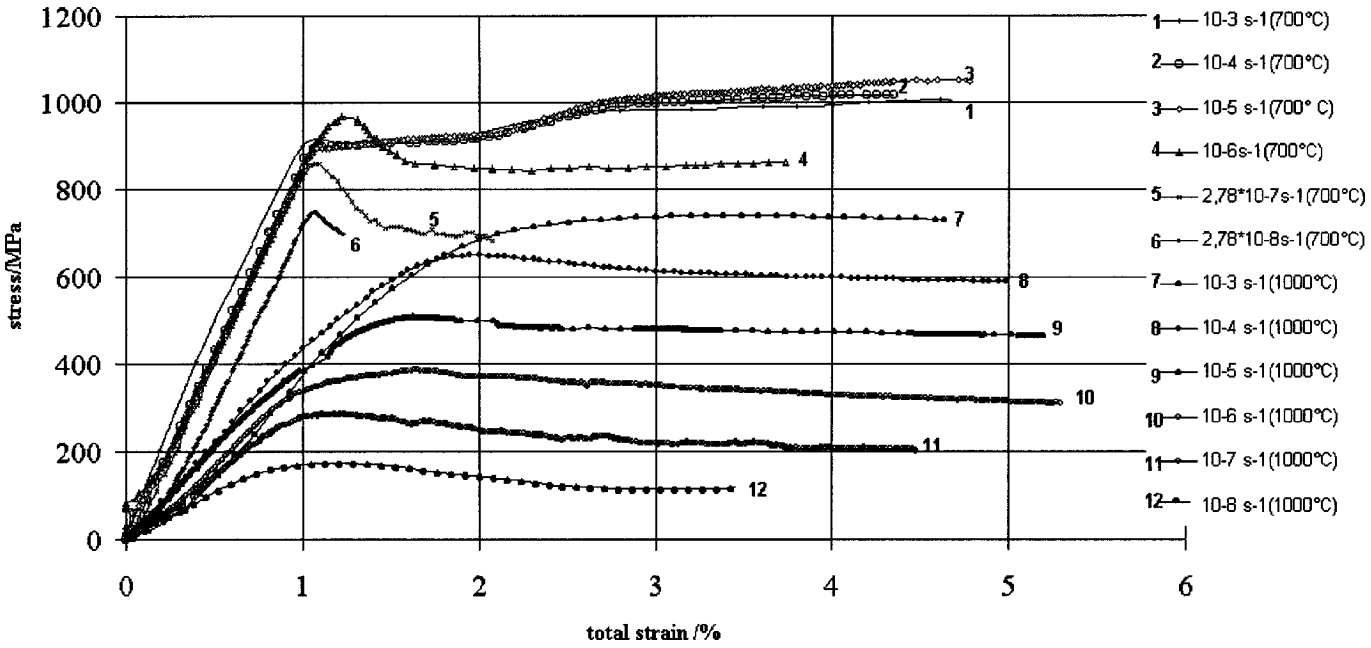
It was performed accordingly to a method described in [14]. Two parallel dislocations having opposite Burgers vectors **b** constitute a dislocation dipole. Another description is that **b** is the same for both dislocations but their line vectors are opposite. If such a dipole is imaged ($\mathbf{g}*\mathbf{b}\neq 0$) the contrast of the two dislocations is displaced in opposite directions: the distance between the two contrast lines is either smaller or larger than the true projected distance between the dislocations. If **g** is changed into **–g** the two cases are interchanged.

Stacking faults determination

For the determination of the intrinsic/extrinsic nature of the stacking faults the following procedure can be applied:

- a BF and a DF image are obtained in order to verify if the defect has fault characteristics BF image symmetric, DF asymmetric)
- a diffraction pattern in BF mode is done
- **g** is drawn on the negative from the transmitted spot to the diffraction spot used to form the image
- **g** is transferred to the positive print making allowance for the lens rotation and the 180° rotation setting the origin of **g** to the fault centre
- use the following rule to determine the sense of the fault:

Fig.2. Technical strain-stress dependence of CMXS-4 specimens deformed with different strain rates at 700°C and 1000°C



If the origin of **g** vector is placed at the centre of the fault in a DF image, **g** points away from the light outer fringe if the fault is extrinsic and towards it if it is intrinsic for all {200}, {222} and {440} (type A) reflections regardless of the sense of inclination of the fault. If the operative reflection is of the type B {400}, {111}, {220} the reverse is true [15].

Results and discussion

A) Mechanical behaviour during tensile test

The stress –strain dependence of the tensile tested specimens at 700°C and 1000° C and applied strain rates from 10^{-3} s^{-1} to 10^{-8} s^{-1} are presented in Fig. 2.

On the base of stress-strain behaviour, strengthening coefficient **m** was calculated accordingly to the expressions 1) and 2). The dependence of **m** on the total strain for two different strain rates (10^{-3} s^{-1} to 10^{-6} s^{-1}) is illustrated in *Fig.3* and *Fig.4*.

$$m = \frac{1}{\sigma}\frac{\partial\sigma}{\partial\varepsilon_p} \qquad (1)$$

$$\varepsilon_p = \varepsilon - \sigma E \quad (E = \text{Youngs modulus}) \qquad (2)$$

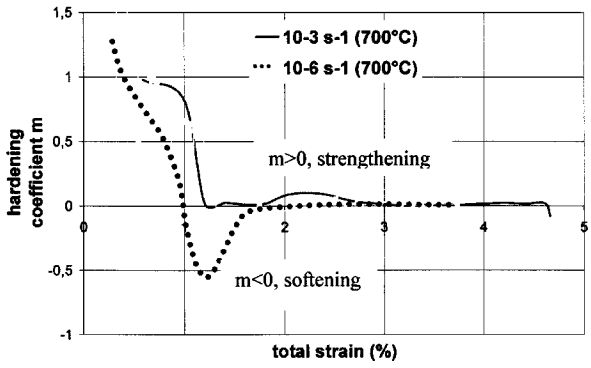


*Fig.3. Dependence of strengthening coefficient **m** on the total strain at 700°C for high strain rate (10^{-3} s^{-1}) and low strain rate (10^{-6} s^{-1})*
E=84615 MPa

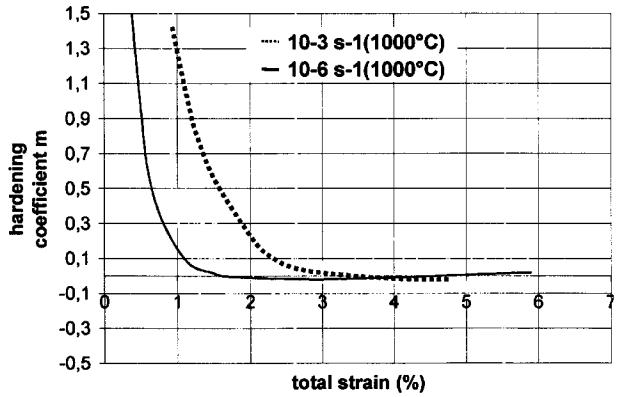


*Fig.4. Dependence of strengthening coefficient **m** at 1000°C on the total strain for high strain rates (10^{-3} s^{-1}) and low strain rate (10^{-6} s^{-1})*
E=48780 MPa

It should be noted that at 700°C, the strain-stress characteristics can be divided into two regimes (*Fig.3*):

- high strain rates ($10^{-3}s^{-1}$ - 10^{-5} s^{-1}) where the influence of the strain rate on the stress–strain behaviour is insignificant. A further strengthening during deformation correlated with a positive value of **m** coefficient occurs in the range 2-3% total strain. The independence of the stress-strain behaviour on the strain rate indicates a time-independent plastic deformation ;
- low strain rates ($10^{-6}s^{-1}$ - 10^{-8} s^{-1}) where the stress level is more sensitive to the applied strain rate. The softening during deformation is correlated with a negative value of **m** and occurs after 1 % total strain. This indicates a time-dependent deformation (creep).

At **1000°C** stress-strain curves suggest about a very high sensitivity of the stress level on the applied strain rate (*Fig.2*) but a dominant mechanism of strengthening or softening could not be noticed for any of the applied strain rates (*Fig.4*), the behaviour seems to become purely viscose.

Microstructure evolution during tensile test

Dislocation microstructure at 700°C and high strain rates

The microstructure of CMSX-4 after heat treatment consists of fine (about 400 nm) cubic-shaped γ' particles surrounded by narrow matrix channels (*Fig.5*). It is already known that in the first stadium of deformation the dislocations fill up the matrix channels. In conditions of high stresses and low temperature, the deformation proceeds by gliding on {111}<110> slip systems (octahedral slip) and by cutting the γ' particles.

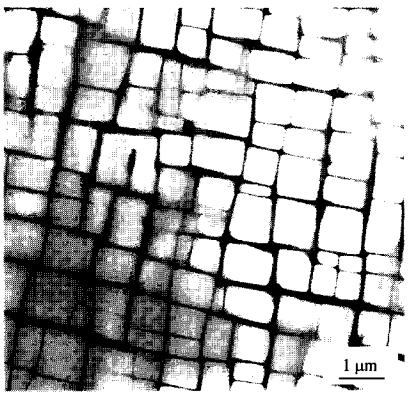


Fig.5. Microstructure of a nickel base superalloy (CMSX-4) after heat treatment consisting of aligned cubic-shaped γ' particles(~70 %) separates by γ channels

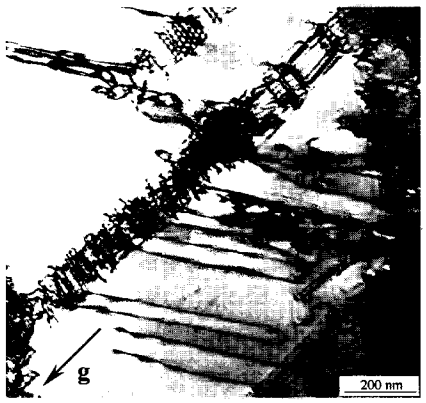


Fig.6. Long dislocation dipoles in γ' particles in a specimen deformed with $\dot{\varepsilon}= 10^{-3}\ s^{-1}$.The TEM foil was parallel to $\{111\}$ planes, $\mathbf{g}=(111)$

The main deformation mechanism of γ' particles is cutting by dislocation dipoles (*Fig.6.*) of partial dislocations. Dislocation dipoles are generated by two partial screw dislocations separated by an antiphase boundary (APB). In the ordered phase A_3B, APB faults are similar to stacking faults and are generated by the sliding of one atom layer by a vector $\mathbf{b}_A = 1/2[101]$

referred to its neighbour atom layer generating nearest-neighbour bonds (two atoms B become neighbours). More details are given in literature [8]. APBs can lie on each plane, the most important are {111} and {100}. It had been suggested [8,12] that it is the cross slip of dislocation dipoles on {100} cube planes the reason for the very high strength level reached in nickel-base superalloys.

Dislocation microstructure at 700°C and low strain rates

With decreasing strain rate, a change in the gliding system of dislocations from {111}<110> slip system to {111}<112> occurs. This is equivalent with the dissociation of matrix dislocations at the γ/γ' interfaces into two partials, one dislocation passing through γ' particle creating a stacking fault and the other remaining at the interface. The passing dislocation is responsible for the shifting of one atom layer by a vector $\mathbf{b}_s$ = 1/3[211] relative to its neighbour atom layer. With increasing strain rate, this mechanism of γ' particle cutting becomes dominant (*Fig.7*) and for strain rates of 10^{-7} s^{-1} and 10^{-8} s^{-1} cutting of γ'particles by dislocation dipoles is completely absent.

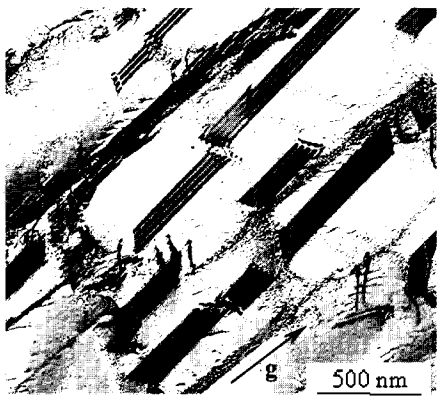


*Fig.7. Stacking fault in γ' particles particles in CMSX-4 specimen deformed at 700°C with $\dot{\varepsilon}$= 10^{-7} s^{-1} parallel to {111} planes, **g**=(200)*

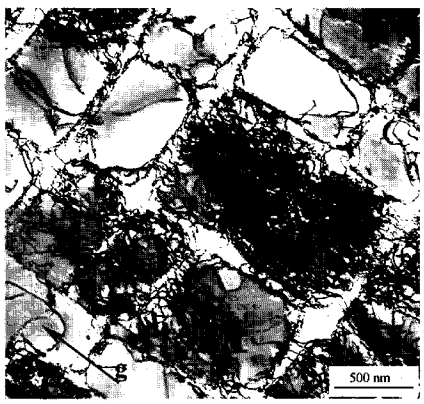


*Fig.8. Dislocation networks at γ/γ' interfaces (matrix/precipitates) in a specimen deformed with intermediate strain rates at 1000°C in a foil cut parallel to (001), $\dot{\varepsilon}$= 10^{-5} s^{-1}, **g**=(020)*

Dislocation microstructure at 1000°C

At this temperature the interaction between γ' particles and dislocations is dependent on the applied strain rate. With higher strain rates in the range > 10^{-4} s^{-1} a strong random cutting of γ' particles by dislocations of various types was found. At intermediate strain rates, the dislocations tend to generate a dislocation network along the γ/γ' interfaces perpendicular to the applied stress. An example with $\dot{\varepsilon} = 10^{-5} s^{-1}$ observed parallel to the (001) plane is shown in Fig. 8. With further decreasing the strain rate a tendency for narrowing of the channels in the planes parallel to the applied stress was observed. Dislocations passing through the γ' particles could be only occasional found while the rafting process of γ' particles in directions perpendicular to the applied stress is favoured (Fig. 9). Simultaneously, TCP phases containing a very large amount of Re and W are precipitated in the dendrites (Fig. 10).

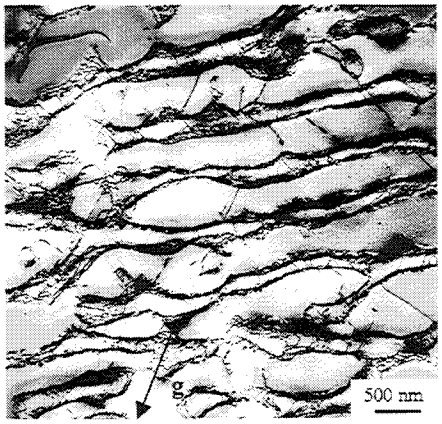


Fig 9. γ' particles rafting and networks at γ/γ' interfaces (matrix/precipitates) in a specimen deformed with low strain rate of $\dot{\varepsilon}= 10^{-7} s^{-1}$ at 1000°C on a plane cut parallel to (011), $\mathbf{g} = (11\bar{1})$

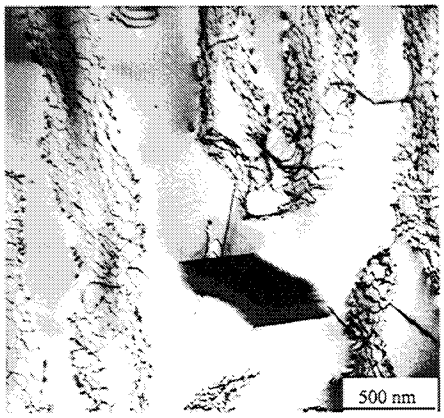


Fig 10. TCP phase and γ' particles rafting in specimens deformed with low strain rates at 1000°C on a plane cut parallel to (011), $\dot{\varepsilon}= 10^{-7} s^{-1}$

Dislocation dipoles identification

The identification of dislocation dipoles has been performed accordingly to the method presented in experimental procedure. Two two-beam pictures for $\pm \mathbf{g} = \pm (\bar{1}11)$ were taken and the distances between the two constituent dislocations were compared (*Fig.11*). The changing distance between the two dislocations 2 and 2' when tilting from $\mathbf{g} = (\bar{1}11)$ to $\mathbf{g}=(1\bar{1}1)$ suggests they are constituents of a dislocation dipole.

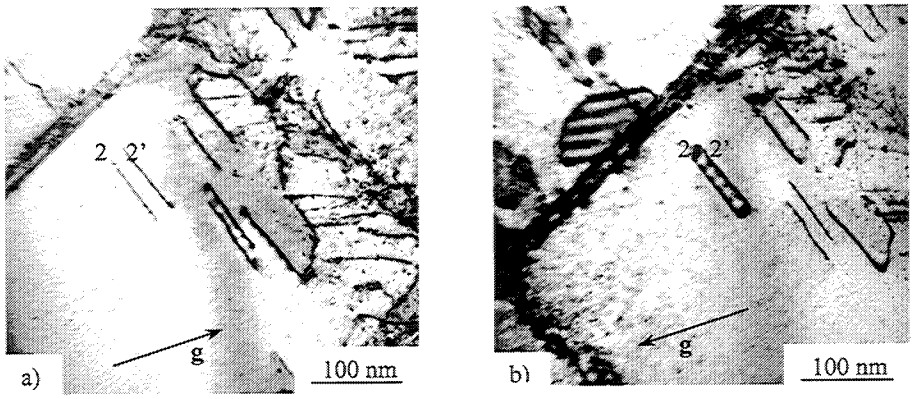


Fig.11. Diffraction contrast of dislocation dipole taken with $\pm \mathbf{g} = \pm (\bar{1}\bar{1}1)$ (Bright field). The distance between the dipole dislocation 2 and 2' is wide in a) and narrow in b) (specimen deformed with $\dot{\varepsilon}= 10^{-4} s^{-1}$, cut parallel to (001) plane).

Identification of stacking faults

The approach described in the experimental procedure was applied. It should be mentioned that almost all the stacking faults were parallel to each other (*Fig.7, Fig.12*) and in the same

TEM conditions they behaved identically leading to the conclusion that they are of the same type. *Fig.12* shows that the **g** points towards the light outer fringe for an operative reflection of the type A {200}. Accordingly to the described procedure the stacking faults are all intrinsic. This is in agreement with the results presented in ref. [16], where the investigations were performed by the mean of high resolution imaging.

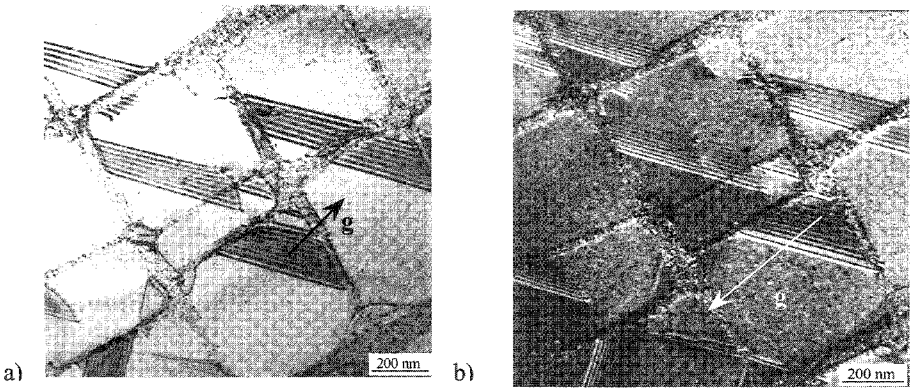


Fig.12. Stacking faults in CMSX-4 after deformation at 700°C with $\dot{\varepsilon}= 10^{-7}\ s^{-1}$ parallel to {001} planes
*a) bright field (image symmetric), **g**= $(\bar{2}00)$ b) dark field (image asymmetric), **g**= (200)*

Conclusions

- At 700°C, two regimes could be distinguished, depending on the applied strain rate: the high strain rates regime in which the change of strain rate does not influence significantly the strain-stress behaviour (time-independent plastic deformation); and the regime of low strain rates, in which a decrease in the strain rate leads to a significant decrease in the stress level (creep deformation).

- The first regime (700°C) is characterised by a strengthening of the material after 2% total strain probably caused the rotation of the crystallographic orientation of the specimen. This could cause a change in the gliding system from (111) $[\bar{1}01]$ primary slip system to $(\bar{1}\bar{1}\bar{1})$ [110]. Detailed TEM investigations (unpublished) revealed the presence of dislocation dipoles of at least two possible Burgers vectors: $\mathbf{b_1}=1/2\langle 101\rangle$ and $\mathbf{b_2}=1/2\langle 110\rangle$. The cutting of γ' particles by dislocation dipoles could be correlated with this regime of high level stress and 'low' temperature.

- The second regime (700°C) is characterised by a softening of the material after 1% total strain. The cutting mechanism of γ' particles is related with dissociation of dislocation into partials and generation of stacking faults in the particles. Deformation mechanism changed progressively from $\{111\}\langle 110\rangle$ to $\{111\}\langle 112\rangle$. All the stacking faults identified by a simple TEM diffraction method were of the intrinsic type.

- At 1000 °C and high strain rates, cutting of γ' particles by dislocations occurs and the tendency for γ' particles to coagulate and form rafts decreases with increasing strain rate. Because of the time dependency of the rafting for a given strain limit, the rafts were more pronounced at lower strain rates.

Literature

[1] R. Theenhaus, F. Schubert - 'The impact of materials research for energy technologies providing for the twenty-first century', Proc. 6th Liege Conference on Materials for advanced power engineering, Belgium, J.Lecomte-Beckers, F. Schubert, P.J. Ennis (eds), ISBN389336 228-2, Forschungszentrum Juelich, 1998, pp.1769-1788

[2] N.Matan, D.C.Cox, P.Carter, M.A.Rist, C.M.F. Rae, R.C.Reed -'Creep of CMSX-4 superalloy single crystals: effects of misorientation and temperature', Acta mater., Vol 47, No 5, 1999, pp. 1549-1563

[3] P.Caron, T.Khan -'Third generation superalloys for single crystal blades', Proc. 6th Liege Conference on Materials for advanced power engineering, Belgium, J.Lecomte-Beckers, F. Schubert, P.J. Ennis (eds), ISBN389336 228-2, Forschungszentrum Juelich, 1998, pp. 897-912

[4] J.Svoboda, P.Lukas -'Creep deformation modelling of superalloy single crystals', Acta Mater., Vol 48, No 10, 2000, pp. 2519-2528

[5] K.P.L. Fullagar, R.W.Bromfield, M.Hulands, K.Harris, G.L.Erickson, S.L.Sikkenga -'Aero engine test experience with CMSX-4 alloy single crystal turbine blades', Transactions of the ASME, Vol 118, 1996, pp. 380-388

[6] T.M. Pollock, A.S. Argon - 'Creep resistance of CMSX-3 nickel base superalloy single crystals', Acta Mater., Vol 40, No 1, 1992 pp. 1-30

[7] T.M.Pollock, R.D.Field, W.H.Murphy - 'Creep deformation and the evolution of precipitate morphology in nickel-based single crystals', International Conference on ,Modelling on Microstructural Evolution in Creep Resistant Materials' 29-30.09.1998, London U.K Institute of Metals, book 723, A. Strang , McLean (eds), University Press, Cambridge 1999, pp. 193-212

[8] D.P Pope, S.S. Ezz - 'Mechanical properties of Ni_3Al and nickel-base alloys with high volume fraction of γ'', International Metal Reviews, Vol 29, No 3, 1984, pp. 136-167

[9] W.Schneider, J.Hammer, H.Mughrabi -'Creep deformation and rupture behaviour of the monocrystalline superalloy CMSX-4', Superalloys 1992, S.D Antolovich, R.W. Stusrud (eds), TMS (The Minerals, Metals & Materials Society), 1992, pp. 589-598

[10] S.Neves, H.J.Penkalla, F.Schubert -'Microstructure study of the N18PM nickel-base superalloy after tensile deformation and crack growth experiments and of the CMSX-4 single-crystal' *to be published*

[11] D.Mukherji, F.Jiao, W.Chen, R.P.Wahi -'Stacking fault formation in γ' phase during monotonic deformation of IN738LC at elevated temperatures', Acta metal. mater. Vol 39, No 7, 1991, pp. 1515-1524

[12] G.Scheunemann-Frerker, H.Gabrisch, M.Feller-Kniepmeier -'Dislocation microstructure in a single crystal nickel based superalloy after tensile testing at 823 K in the [001] direction', Philosophical magazine A, Vol 65, No 6, 1992, pp. 1353-1368

[13] V.Sass, M.Feller-Kniepmeier -'Orientation dependence of dislocation structures and deformation mechanisms in creep deformed CMSX-4 single crystals', Mat. Science and Engineering A, 245, 1998, pp. 19-28

[14] M.Ruhle, M.Wilkens 'Transmission electron microscopy', Physical Metallurgy, Vol II, R.W.Cahn, P.Haansen (eds), 1996, pp. 1059-1061

[15] J.A.Edington -'Practical electron microscopy in material science', Monograph II 'Electron diffraction in the electron microscope'(pp.1-10), (28-29), Monograph III 'Interpretation of transmission electron micrographs'(pp. 10-75)

[16] B.Decamps, J.M.Penisson -'High resolution imaging of shearing configurations of γ' precipitates in Ni-based superalloys', Scripta Met. et Mater., Vol 30, No 11, 1994, pp. 1425-1430

MORPHOLOGICAL CHANGE IN γ' PHASE IN DIFFERENT PORTIONS OF FIRST STAGE HIGH PRESSURE TURBINE BLADE OF PWA1480

Nobuhiro Miura*, Naoki Harada*, Yoshihiro Kondo* and Takashi Matsuo**

*National Defense Academy, 1-10-20 Hashirimizu Yokosuka, Kanagawa 239-8686, Japan
**Tokyo Institute of Technology, 2-12-1 Oookayama Meguro-ku, Tokyo 152-8552, Japan

Abstract

The morphology of the γ' phase of a single crystal nickel-based superalloy, PWA1480, serviced as the first stage high pressure turbine blade of an aircraft engine was examined. The aim of this examination was to estimate the difference in the morphology of γ' phase among the thirty portions of the serviced turbine blade, and to estimate the distribution of the temperature and the stress in the blade. The thirty portions of the serviced turbine blade are as follows. Firstly, the blade was cut into three parts parallel to (001) plane. They are named as the tip, middle and root parts. Secondly, each part was cut into two sides of the pressure and suction one. Finally, these six parts were cut into five portions from the leading to the trailing edge. The most marked morphological changes of the cuboidal γ' arose at the portion of the pressure side of the middle part. At the leading edge, rafted γ' plates perpendicular to the [001] direction were observed. On the contrary, at the trailing edge, rafted γ' plates perpendicular to the [010] direction were found. Consequently, the portions under the highest temperature and stress were determined to be the leading and trailing edges of the pressure side of the middle part. However, the stress direction was estimated to be different between the leading and trailing edges. At the leading edge, the tensile stress is acting along the [001] direction. Contrary to this, at the trailing edge, the uni-axial tensile stress perpendicular to the blade surface or biaxial compressive stress parallel to the blade surface is expected.

Keywords : PWA1480, Turbine blade, Microstructure, γ' Phase, Rafted structure

1 Introduction

As the material for the first stage high pressure turbine blades in aircraft engines, single crystal nickel-based superalloys have been employed because of their excellent in creep rupture strength, rupture ductility, and thermal fatigue [1]-[3]. Through the appearance of the serviced blades, the distributions of the temperature and the stress of the turbine blade in service has been estimated as follows; the tip part is under the high temperature and low stress conditions, while the root part is under the low temperature and high stress conditions [4]. By subjecting specimens to creep deformation under a high temperature, the cuboidal γ' ($Ni_3(Al, Ti)$) in single crystal nickel-based superalloys with the orientation of [001] turns to a rafted one normal to the stress axis [5]-[11]. In our previous work, creep tests of [001] orientated single crystal nickel-based superalloy, CMSX-4, were conducted in a wide stress range, from 100 to 400MPa, at 1273 and 1323K, and the cuboidal γ' turned into rafts that are normal to the stress axis [12]-[15]. It has been also elucidated that the shape of rafted γ' plates differs by changing the stress, temperature and creep testing time [10], [16]. In the case of simple aging at the high temperature, the cuboidal γ' in CMSX-4 was coarsened to the [100] and [010], without rafting. Moreover, difference were found in the rafting of the γ' among [001], [011] and [111] single crystals of CMSX-2, crept at

1273K was investigated and it was elucidated that the rafted γ' formed as the plate perpendicular to the [001] [17]. The experimental evidence on the morphological change of the cuboidal γ' as a function of the temperature and the stress applied on {100} are available to estimate the conditions applied to the turbine blade. Based on the above conception, the detailed microstructural observation must be conducted on the serviced turbine blade.
In this study, the morphology of the γ' phase in the single crystal nickel-based superalloy, PWA1480, serviced as the first stage high pressure turbine blade of the jet engine was investigated to estimate the distribution of the temperatures and the stresses, and the stress direction in the blade.

2 Experimental Procedure

The single crystal nickel-based superalloy PWA1480, with a chemical composition (in weight per cent) 10.0Cr, 5.0Cr, 4.0W, 5.0Al, 12.0Ta, 1.5Ti, balance Ni, was cast in the form of an air-cooled turbine blade. The crystal growth direction of [001] was attained in the turbine blade by directional precision casting. After employing the defined solution treatment and the aging, the aluminide coating was deposited on the surface of the airfoil. This blade was in-service for about 1000 hours as the first stage high pressure turbine blade of the F-100 jet engine on JASDF F-15 fighter aircraft. The exact crystal orientation of the longitudinal direction of the turbine blade was determined by the X-ray Laue back-reflection technique. Microstructural examinations by a field emission scanning electron microscope (FE-SEM) were carried out on the thirty portions of the blade cut by a electron discharge machine (EDM), as follows. Firstly, the blade was cut into sections perpendicular to the longitudinal direction, at 5, 25 and 45mm from the tip. These parts were designated as the tip, middle and root parts, respectively. Secondly, each part was cut into two sections corresponding to the pressure and suction sides. Finally, these six specimens were cut into five portions from the leading edge to the trailing one at an interval of 8mm, that is, parallel to (100), as shown in Fig.1. Specimens for the SEM observation were prepared metallographically and electroetched with a supersaturated oxialic aqueous solution. The hardness

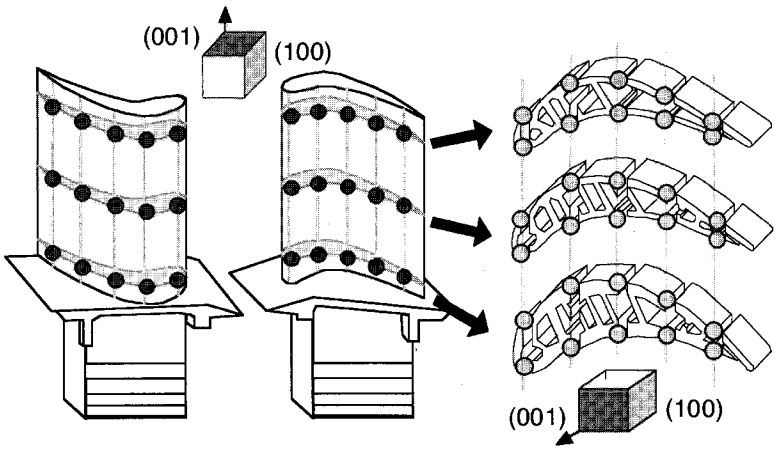


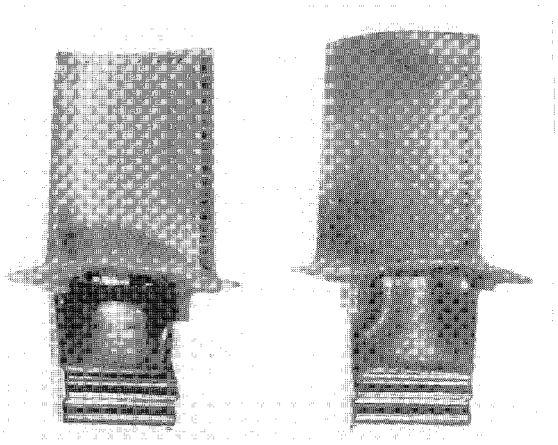
Fig.1. Schematic illustration of the thirty portions cut from the blade

test by a micro-Vickers hardness testing machine were done for the specimen sectioned parallel to (001).

3 Results and discussion

3.1 Appearance of turbine blade

The appearance of the turbine blade is shown in Fig.2. The size of the blade is about 77mm length, about 44mm width and about 22mm thick. The size of the airfoil is about 45mm length, about 32mm width and about 7mm thick. Cooling holes are positioned in a row at the pressure side and at the trailing edge in the airfoil.



Pressure side Suction side

Fig.2. Appearance of the turbine blade

3.2 Crystal direction of turbine blade

The exact crystal orientation of the longitudinal direction of the turbine blade is inclined about 3° from the [001] to [011] in the stereographic triangle. The orientation between the [100] direction and the line joining the leading edge to the trailing edge is 15° as shown in Fig.3.

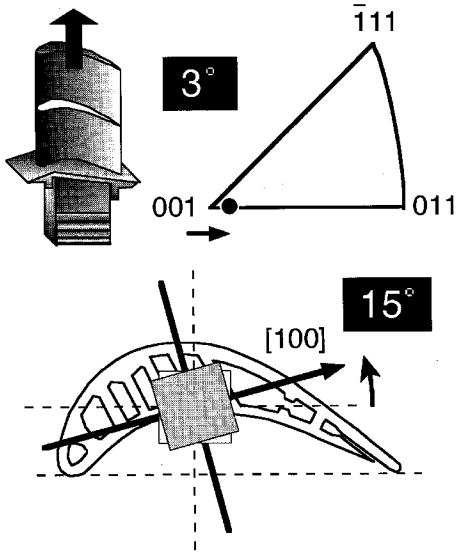


Fig.3. Crystal orientation of the turbine blade

3.3 Morphology of γ' phase in different parts

3.3.1 Tip part

The scanning electron micrographs at the vicinity of the surface of the five portions in the suction side of the tip part are shown in Fig.4. The cuboidal γ' remains and there is no change in microstructures among the five positions (Fig.4-(a)-(e)).

The scanning electron micrographs at the vicinity of the surface of the five portions in the pressure side of the tip part are shown in Fig.5. At the leading edge, the cuboidal γ' still remains (Fig.5-(a)). At the portions with the distance of 8 and 16 mm from the leading edge, most of the cuboidal γ' still remain, whereas some of the cuboidal γ' contact each other in the specific direction at the vicinity of interface (Fig.5-(b) and (c)). However, at the portion with the distance of 24mm from the leading edge and at the trailing edge, rafted γ' plates appears in the direction parallel to the

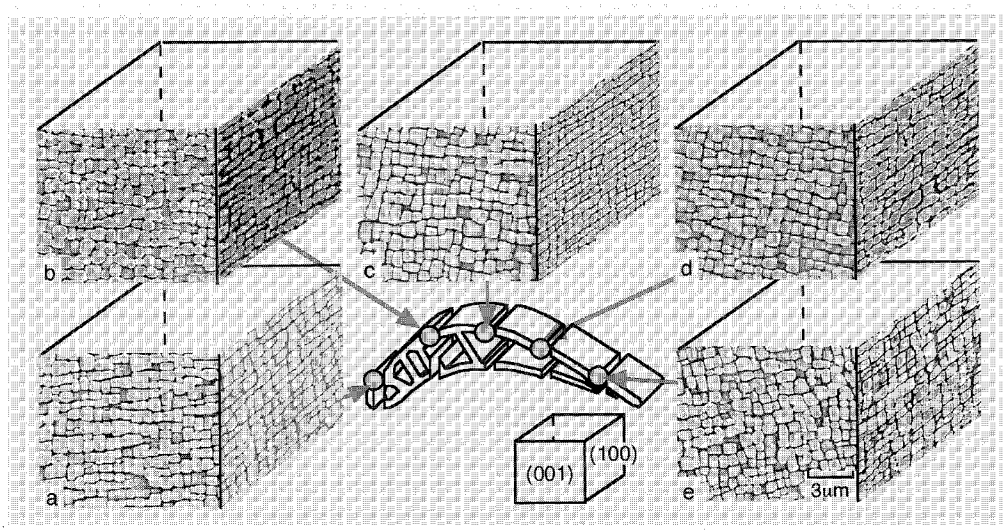


Fig.4. Scanning electron micrographs at the vicinity of the surface of the five portions in the suction side of the tip part : the leading edge (a), portion with the distance of the 8mm (b), 16mm (c), 24mm (d) from the leading edge and, the trailing edge (e)

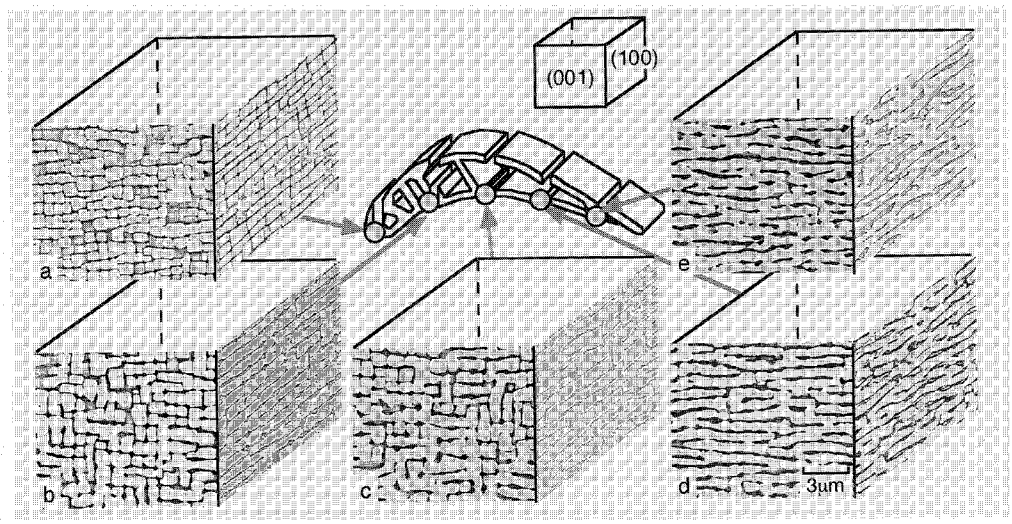


Fig.5. Scanning electron micrographs at the vicinity of the surface of the five portions in the pressure side of the tip part : the leading edge (a), portion with the distance of the 8mm (b), 16mm (c), 24mm (d) from the leading edge and, the trailing edge (e)

longitudinal direction of the blade, that is, perpendicular to the [010] direction (Fig.5-(d) and (e)).

3.3.2 Middle part

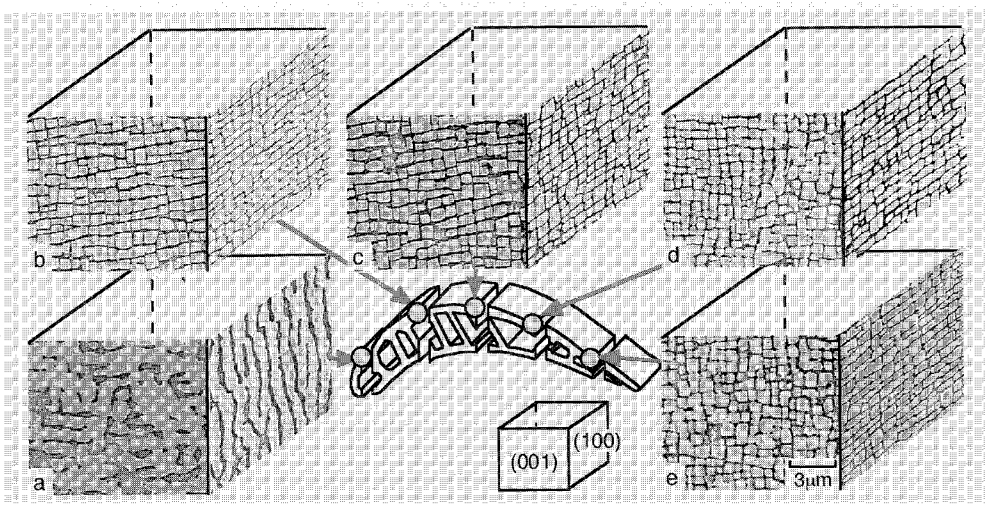


Fig.6. Scanning electron micrographs at the vicinity of the surface of the five portions in the suction side of the middle part : the leading edge (a), portion with the distance of the 8mm (b), 16mm (c), 24mm (d) from the leading edge and, the trailing edge (e)

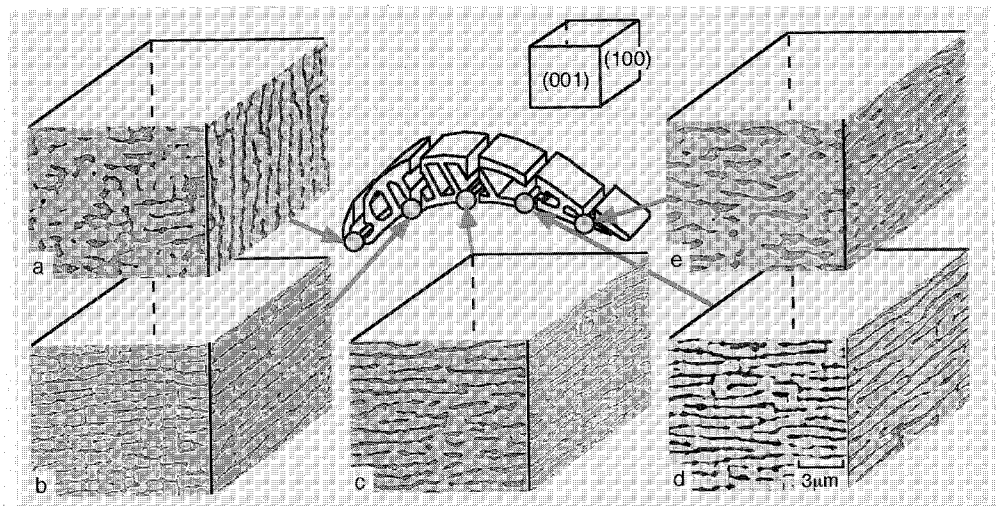


Fig.7. Scanning electron micrographs at the vicinity of the surface of the five portions in the pressure side of the middle part : the leading edge (a), portion with the distance of the 8mm (b), 16mm (c), 24mm (d) from the leading edge and, the trailing edge (e)

The scanning electron micrographs at the vicinity of the surface of the five portions in the suction side of the middle part are shown in Fig.6. At the leading edge of (100), the cuboidal γ' is connected with perpendicular to the [001] direction of the blade, and the well aligned rafted γ' plates are observed. While in (001), the cuboidal γ' connect with each other in random directions

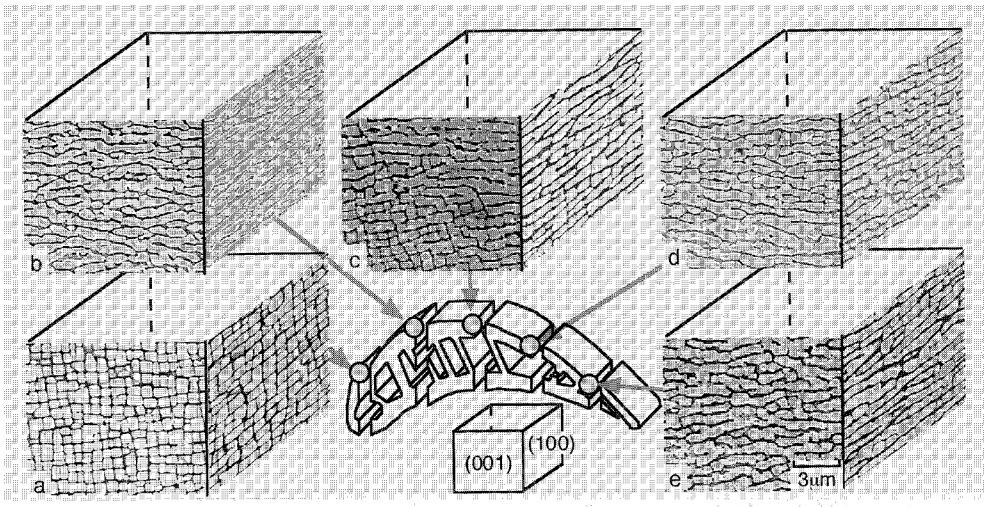


Fig.8. Scanning electron micrographs at the vicinity of the surface of the five portions in the suction side of the root part : the leading edge (a), portion with the distance of the 8mm (b), 16mm (c), 24mm (d) from the leading edge and, the trailing edge (e)

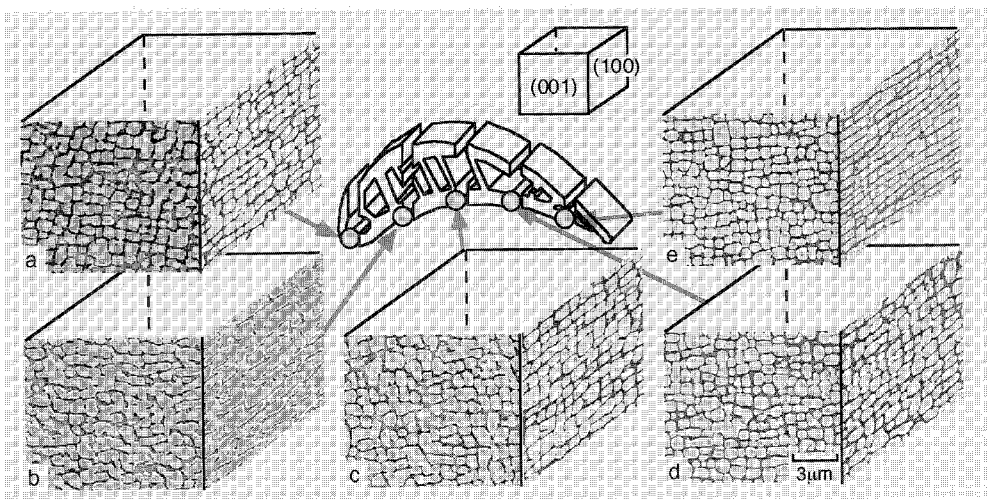


Fig.9. Scanning electron micrographs at the vicinity of the surface of the five portions in the pressure side of the root part : the leading edge (a), portion with the distance of the 8mm (b), 16mm (c), 24mm (d) from the leading edge and, the trailing edge (e)

(Fig.6-(a)). At the other positions, the cuboidal γ' is still maintained (Fig.6-(b)-(e)).
The scanning electron micrographs at the vicinity of the surface of the five portions in the pressure side of the middle part are shown in Fig.7. At the leading edge, rafted γ', with plates that are perpendicular to the [001] direction, is observed in (100) (Fig.7-(a)). On the contrary, at the

portions with the distance of 16 and 24mm from the leading edge, rafted γ' plates perpendicular to the [010] direction are observed (Fig.7-(c) and (d)). At the trailing edge, rafted γ' starts to collapse (Fig.7-(e)). The direction of rafted γ' plates at the trailing edge is different from that of the leading edge.

3.3.3 Root part

The scanning electron micrographs at the vicinity of the surface of the five portions in the suction side of the root part are shown in Fig.8. At the leading edge, the cuboidal γ' still remains (Fig.8-(a)). At the portion with the distance of the 8 mm from the leading edge, rafted γ' plates perpendicular to the [010] direction are observed (Fig.8-(b)). At the portions with the distance of the 16 and 24 mm from the leading edge, rafted γ' plates are observed at the vicinity of interface between the coating layer and the matrix, whereas the cuboidal γ' remains in the inside (Fig.8-(c) and (d)). At the trailing edge, some of the cuboidal γ' contact with each other toward the [100] and [001] directions are observed in (001) and (100) respectively (Fig.8-(e)). In this way, at the suction side of the root part, the morphology of γ' is different from those at the suction side of the tip and middle parts and the rafted γ' is observed. The interface of the γ / γ' phases is also wavy compared with those of the pressure side of the tip and root parts.

The scanning electron micrographs at the vicinity of the surface of the five portions in the pressure side of the root part are shown in Fig.9. At the portions with the distance of 8 mm from the leading edge, some of the cuboidal γ' contact with each other toward the [001] and [100] directions (Fig.9-(b)). In other portions, the cuboidal γ' becomes rounded (Fig.9-(a), (c)-(e)).

From the above results, the differences in rafting manner of the cuboidal γ' will be related to the differences in the distribution of the temperature and the stress, and the stress directions.

3.4 Relation between the hardness and morphology of γ' phase

As mentioned above, marked morphological changes of the cuboidal γ' to a rafted structure in each part of the blade are observed. Then, the hardness is measured on the middle part of the blade where the marked γ'morphological changes are detected, and the effect of the γ' morphology on the hardness is investigated.

The Vickers hardness of (001) plane in the middle part is shown in Fig.10. From the leading

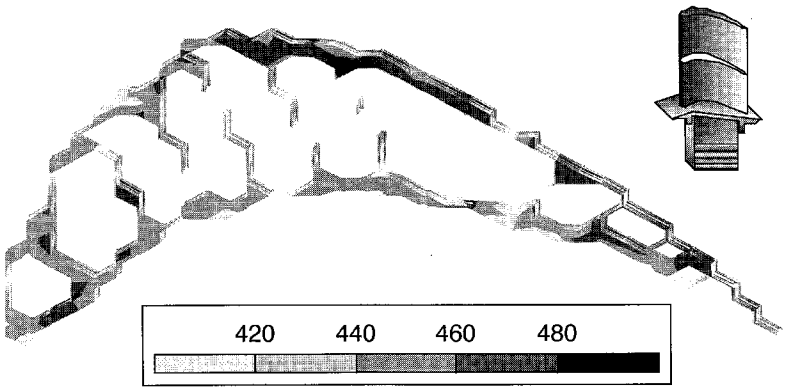


Fig.10. The result of Vickers hardness at (001) plane of the middle part

edge to the trailing one in the suction side, the hardness is high with over Hv=460. On the other hand, the hardness of the pressure side is less than that of the suction side, and the smallest hardness of Hv=440 or less is detected.
Therefore, it is obvious that the decrease in the hardness arises from the progression in the coarsening of rafted γ'.

3.5 Distribution of temperature and stress of blade in service

The distribution of the temperatures and the stresses in the blade in service based on the microstructural observations and the results of the hardness test is estimated. Fig.11 shows the schematic illustrate of the distribution of the temperature and the stress, and the stress direction of the turbine blade in service. The distribution of the temperature is shown in shades from light to dark and the distribution of the stress and the stress direction are shown in the direction and the length of the arrow. Firstly, the distribution of the temperatures and the stress magnitudes will be discussed.
At the leading edge of the suction side of the middle part where the cuboidal γ' turns to the well aligned rafted γ' plates, the surface is exposed to the highest temperature and stress conditions. At the suction side of the root part where the rafted γ' plates are observed, the temperature and the stress are comparatively high. The other portions of the suction side where the cuboidal γ' still remains, the surface is not exposed to the high temperature and stress conditions.
At the pressure side, it is suggested that the temperature and stress conditions are higher than those of the suction side because the morphological change of the cuboidal γ' is more extensive. Especially, at the leading and trailing edges of the middle part where the rafted γ' plates and the

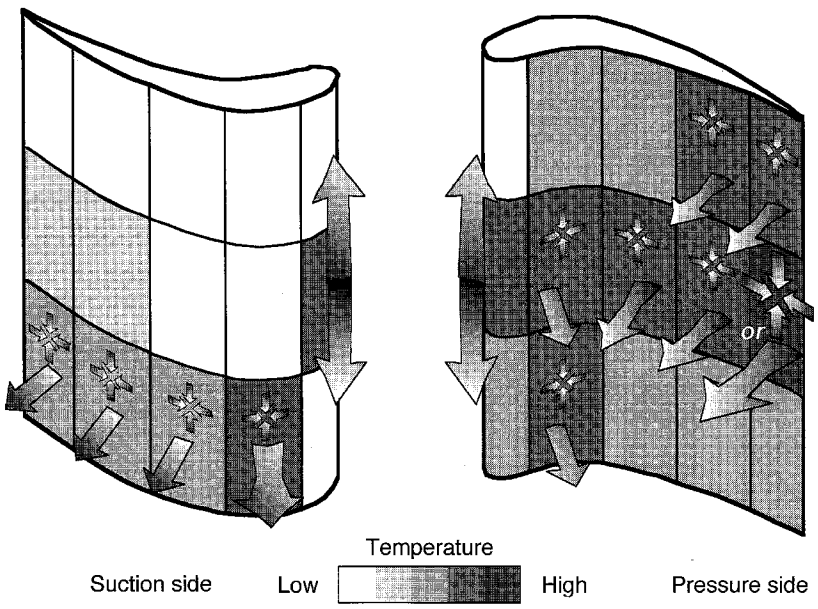


Fig.11. Schematic illustrations of the distribution of the temperature and the stress of the turbine blade in service

coarsened rafted ones are observed, the surfaces are exposed to the highest temperature and stress conditions. The temperature and the stress are comparatively high at the trailing edge of the pressure side of the tip part where the rafted γ' is observed. At the root part, where the cuboidal γ' turns to a rounded shape, the temperature is comparatively high but the stress is not expected.

It is well understood that the cuboidal γ' turns to a rafted one perpendicular to the stress axis by subjecting [001] oriented specimens to tensile creep [13], [15], and that the cuboidal γ' turns its shape to the rod-shaped structure parallel to the stress axis by subjecting the same specimens to a compressive stress [18]. Based on the above understanding and this experimental result, the stress direction of the turbine blade in service is evaluated. At the leading edge of the pressure and suction sides of the middle part where the cuboidal γ' turns to a rafted one with plates that are perpendicular to the [001] direction, a tensile stress is acting along the longitudinal direction. This tensile stress is considered to result from the centrifugal stress. However, at the trailing edge of the pressure side of the tip and middle parts, and the suction side of the root part where the cuboidal γ' turns to a rafted one perpendicular to the [010] direction, the microstructural evidence indicates that the uni-axial tensile stress perpendicular to the blade surface is expected. The appearance of the uni-axial tensile stress means the operating a biaxial compressive stresses parallel to the blade surface. The biaxial compressive stresses are supposed to result from difference between the coefficient of thermal expansion of the coating layer (Al_2O_3) and the metal matrix (γ).

4. Conclusions

To elucidate the distribution of the temperature and the stress, and the stress direction in a turbine blade in service is investigated using the single crystal nickel-base superalloy, PWA1480, serviced as the first stage high pressure turbine blade.

The following conclusions are obtained.

1) Marked morphological changes of the cuboidal γ' are observed in the leading and trailing edges of the pressure side of the middle part. Especially, at the trailing edge, rafted γ' starts to collapse
2) The rafted γ', with plates that are perpendicular to the [010] direction, is observed at the trailing edge of the pressure side of the tip and middle parts, and the suction side of the root part. On the contrary, at the leading edge of the middle part, rafted γ' plates perpendicular to the [001] direction is found.
3) The decrease in the hardness arises from the progression in the coarsening of the rafted γ'.
4) The turbine blade in service, at the leading and trailing edges of the pressure side of the middle part and the leading edge of the suction side of the middle part are exposed to the highest temperature and stress conditions.
5) From these results, at the leading edge of the pressure and suction sides of the middle part, a tensile stress is acting along the longitudinal direction. Contrary to this, at the trailing edge of the pressure side of the tip and middle parts, and the suction side of the root part, the evidence that the uni-axial tensile stress perpendicular to the surface or a biaxial compressive stresses parallel to the surface are expected is detected.

5. References

[1] H. Hiroshi, Superalloys and Heat-resistant Alloys for Jet Engine Application, 123rd Committee on Heat Resisting Metals and Alloys Rep., 38(1997), p.248
[2] A. Nitta, Energy Problem and High-Temperature Materials Technology in the 21st Century, 123rd Committee on Heat Resisting Metals and Alloys Rep., 38(1997), p.157
[3] Y. Yoshioka, Advances of Gas Turbine Hot-Section Materials in Electric Utility Applications, 123rd Committee on Heat Resisting Metals and Alloys Rep., 38(1997), p.257
[4] R. J. E. Glenny, J. E. Northwood and A. B. Smith : Int. Met. Rev. 20(1975), p.1
[5] J. K. Tine and R. P. Ganble, Effects of Stress Coarsening on Coherent Particle Strengthening, Metall. Trans, 3A(1972), p.2157
[6] R. A. MacKay and L. J. Ebert, Factors which Influence Directional Coarsening of Gamma Prime Creep in Nickel-base Superalloy Single Crystals, Proc. of the 5th Int'l Conf. Superalloys1984, (1984), p.135
[7] Y. Kondo, Creep Deformation of Single Crystal Ni-based Superalloy, CAMP ISIJ, 11(1998)3, p.473
[8] T. M. Pollock and A. S. Argon, Creep resistance of CMSX-3 Nickel Base Superalloy Single Crystals, Acta Metall. Mater., 40(1992)1, p.1
[9] V. Sass, V. Glatzel and M. F. Kniepmeier, Anisotropic Creep properties of the Nickel-Base Superalloy CMSX-4, Acta Metall. Mater., 44(1996)5, p.1967
[10] R. A. MacKay and L. J. Ebert, The Development of γ / γ' Lamellar Structures in a Nickel-base Superalloy during Elevated Temperature Mechanical Testing, Crystal Metall. Trans, Metall Trans, 16A(1985), p.1969
[11] M. V. Nathal and L. J. Ebert, Elevated Temperature Creep-Rupture Behavior of the Single Crystal Nickel-base Superalloy NASAIR 100, 16A(1985), p.427
[12] K. Ishibashi, Y. Kondo, J. Namekata, N. Ohi and H. Hattori, Long Time Creep Rupture Properties of Single Crystal Nickel-based Superalloy, CMSX-4, 123rd Committee on Heat Resisting Metals and Alloys Rep., 37(1996), p.1
[13] Y. Kondo and T. Matsuo, Creep of Single Crystal Superalloys, 123rd Committee on Heat Resisting Metals and Alloys Rep., 38(1997)3, p.269
[14] Research group on strengthening of heat resisting steel and alloy of ISIJ : Final Report of Research Group on Strengthening of Heat Resisting Steel and Alloy, (2000), p.121
[15] N. Miura, Y. Kondo and T. Matuso, Stress Dependence of Strain Attained to Rafting of γ' phase in Single Crystal Nickel-based Superalloy, CMSX-4, Proc. of the 9th Int'l Conf. on Creep and Fracture of Engineering Materials and Structures, (2001), p.437
[16] Y. Kondo, N. Kitazaki, J. Namekata, N. Ohi and H. Hattori, Effect of Aging and Stress Aging on Creep Resistance of Single Crystal Nickel-base Superalloy CMSX-4, Tetsu-to-Hagane, 80(1994), p.568
[17] K. Ishibashi, Y. Kondo, J. Namekata, N. Ohi and H. Hattori, Effect of Tensile Orientation on Rafting Structure of Gamma Prime Precipitates in Single Crystal Ni-base Superalloy CMSX-2, 123rd Committee on Heat Resisting Metals and Alloys Rep., 34(1993), p.2
[18] J. K. Tien and S. M. Copley, The Effect of Uniaxial Stress on the Periodic Morphology of Coherent Gamma Prime Precipitates in Nickel-Base Superalloy Crystals, Metall. Trans, 2(1971), p.215

METALLURGICAL ANALYSIS OF IN SERVICE *CMSX*-2 SINGLE CRYSTAL GAS TURBINE BUCKETS

Yomei Yoshioka, Daizo Saito, Shoko Ito, Yoshitaka Fukuyama

Power & Industrial Systems Research & Development Center
Power Systems & Services Company Toshiba Corporation
2-4, Suehiro-cho, Tsurumi-ku, Yokohama, 230-0045, JAPAN

Abstract

The microstructural characterization of a single crystal *CMSX*-2 bucket, in service for 500 hours with a 15 MW heavy-duty gas turbine, was conducted in order to understand the type, distribution and direction of the stresses. Before the destructive evaluation of the bucket, tension and compression creep tests using [001] specimens were conducted and γ' rafting perpendicular to the tensile stress and parallel to the compressive stress were observed. Thermo-elastic FE analyses of the bucket were also carried out in order to determine the stress and temperature distributions in the airfoil. Based on those tests and analyses, a microstructural evaluation of the bucket, which was sectioned longitudinally ([001] direction) and transversely, was conducted. The raft structure of the γ' phases was observed around the area of 50 – 100 μm below the airfoil external surface. Investigations of the rafting morphology were conducted in order to ascertain the stress state during operation. The results were compared with those of the FE stress-temperature analyses. The main factor to cause the observed rafting morphology was found to be the dominant compressive thermal stresses that were induced by the temperature gradients across the walls of the cooled bucket and, less so, the contribution of the tensile centrifugal stresses.

Keywords: Single crystal, Rafting, γ' phase, Bucket, *CMSX*-2

1 Introduction

In recent years, the inlet gas temperature of heavy-duty gas turbines is increasing at a remarkable rate, which requires advances in high temperature materials as well as cooling technologies. The use of advanced cooling technologies leads to geometrically more complex turbine buckets that are also subjected to complex tri-axial stresses during service. These stresses are due to superposition of a centrifugal loading that is applied along the [001] axis, thermal loads, internal pressure, and vibration loading.

Single crystal superalloys contains a high volume fraction of the γ' phases and currently are usually designed to have negative γ/γ' lattice misfit [1]. When it is annealed under a tensile stress applied along the [001] axis, the cubic γ' particles are reported to form flat raft-like structure perpendicular to the [001] axis [2], and this phenomenon is confirmed in specimen from laboratory creep tests and also from serviced aero engine buckets [3].

This paper described the microstructure characterization of a single crystal *CMSX*-2 bucket in service with a 15 MW heavy-duty gas turbine. The objective is to investigate the extent and morphology of the γ' rafting in a heavy-duty gas turbine bucket, in conjunction with laboratory tested *CMSX*-2 materials and finite element (FE) stress-temperature analyses.

2 Procedure

2.1 Materials and testing

The single crystal alloy *CMSX*-2 was casted to the plates of 150mm X 100mm X 15mm and heat-treated at the condition of 1315°C X 2h/GFC+1080°C X 4h/GFC+871°C X 20h. Specimens were then cut parallel to the [001] direction of the plate and used for the tension and compression creep tests. The chemical composition of the material is shown in Table I. Creep tests were carried out with tensile and compressive stresses of 245MPa at 950°C and a tensile stress of 410MPa at 850°C. Samples were cut, from the gauge length of each specimen, with cross-sections parallel and normal to the stress axis in order to conduct a SEM study.

Table I Chemical composition of the *CMSX*-2 alloy studied here (mass %)

	Ni	Cr	Co	W	Mo	Ta	Ti	Al
CMSX-2	Balance	8.0	5.0	8.0	0.6	6.0	1.0	5.5

2.2 FE analysis

The nonlinear finite element analysis program ABAQUS was used for the stress and temperature analyses of a 15MW gas turbine stage 1 air cooled bucket. Heat transfer analysis was conducted at first, followed by a thermo-elastic stress analysis with centrifugal loading. The anisotropy of Young's modulus was considered here.

2.3 Turbine buckets

The gas turbine buckets of CMSX-2 used in this study were in service for around 500 hours in a 15 MW heavy-duty gas turbine TGT. The inlet gas temperature of a stage 1 bucket, which uses a return-flow air cooling type, was 1340°C. The operating mode is a daily start up and shut down.

The bucket was cut parallel and perpendicular to the longitudinal directions of the airfoil and then metallurgical evaluations were conducted. Cutting sections and microstructure observation points are shown in Figure 1.

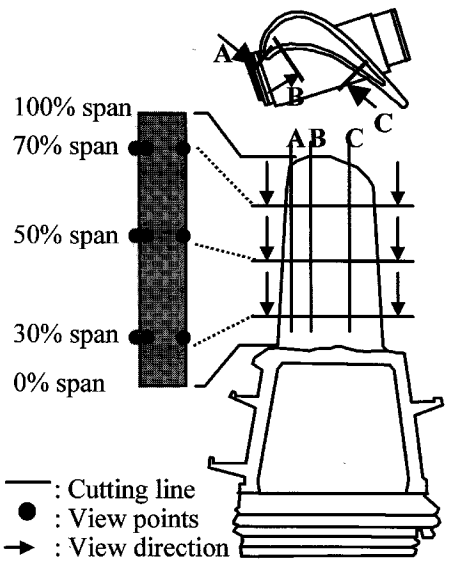


Figure 1 Sampling locations in the stage 1 bucket of a 15 MW gas turbine, in service for 500 hours

3 Results and discussions

3.1 Microstructural analyses of specimens under tension and compression creep

The single crystal alloy CMSX 2 contains a high volume fraction of γ' phases with a negative γ/γ' lattice misfit [4], [5]. When it is annealed under a tensile stress applied along the [001] axis, the γ' cubes are reported to form flat raft-like structures perpendicular to the [001] axis [4], [5], [6]. To confirm these phenomena, both tensile and compressive creep tests were conducted. The results are shown

in Figure 2. The test specimen were cut along the [001] axis which is the direction of the applied stress. A rafted structure was observed at every test conditions. Tensile creep induced γ' rafting perpendicular to the stress-axis at both 850 and 950°C, but compressive creep

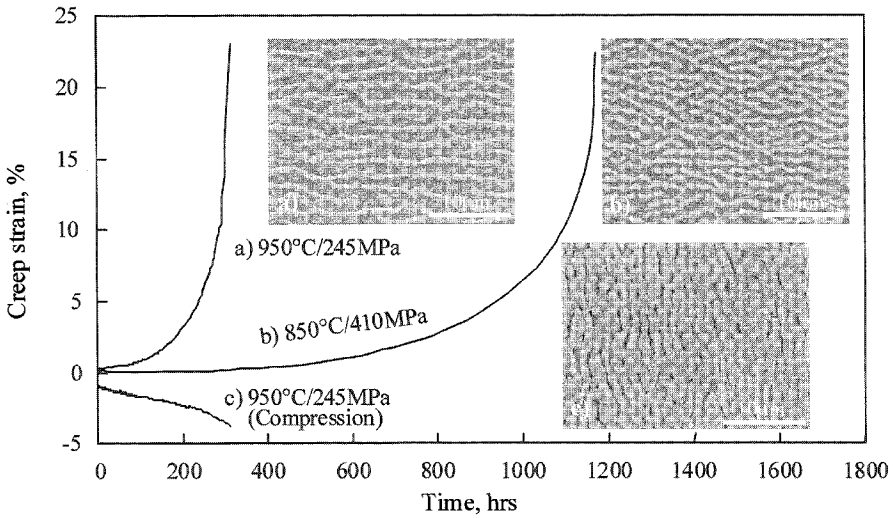


Figure 2 Creep test results under the tensile and compressive stresses of 245 MPa at 950°C and under the tensile stress of 410 MPa at 850°C with SEM microphotographs of the samples cut along the direction of the stress-axis.,

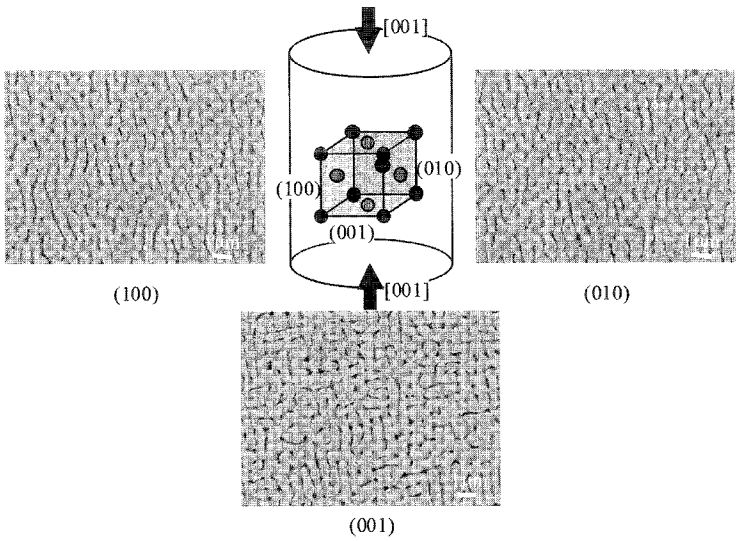


Figure 3 Creep test results under the compressive stress of 245 MPa at 950°C with SEM microphotographs of the samples cut along the (100), (010) and (001) planes.

induced γ' rafting parallel to the stress-axis. Figure 3 shows the γ/γ' structures on sections cut along the three different planes (001), (100), and (010). Rafting of the γ' is well developed in a direction parallel to the stress-axis of [001] on (100) and (010) planes, but on the (001) plane symmetrically interpenetrating sets of platelets γ/γ' can be seen.

3.2 FE analysis of the stage 1 bucket

Figure 4 shows the surface temperature analysis results at 0%, 30%, 50%, 70%, and 100% airfoil spans in the bucket. Figure 5 shows the surface stress analysis results at 30%, 50%, and 70% airfoil spans, with and without considering the centrifugal force. In these figures the horizontal axis defines positions along the airfoil surface using normalized length scales and with the leading edge as the origin. Accordingly, a negative region is the pressure side of the airfoil and a positive region is the corresponding suction side.

The vertical axis in Figure 4 defines temperature deviation from the normal. The highest temperature in each span was found to be at the leading edge, with big temperature drops calculated on either side. Plateau zones exist along the downstream sides from these locations (Figure 4).

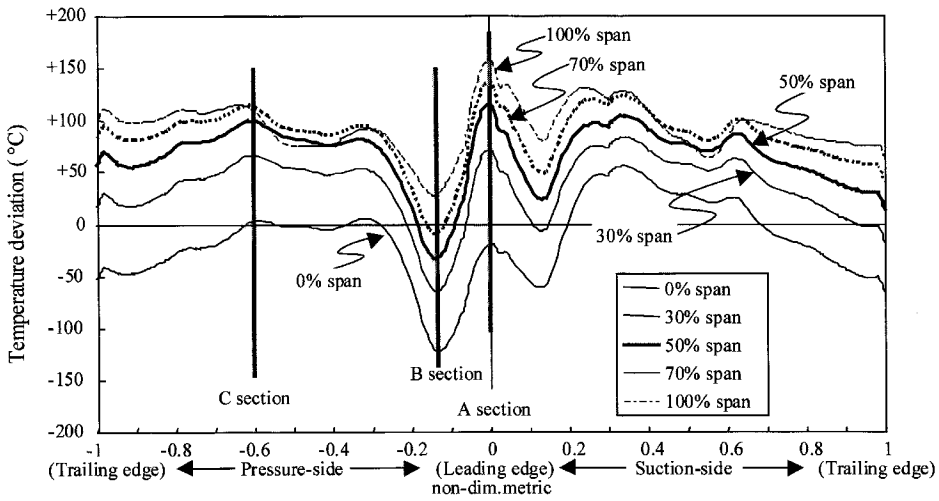
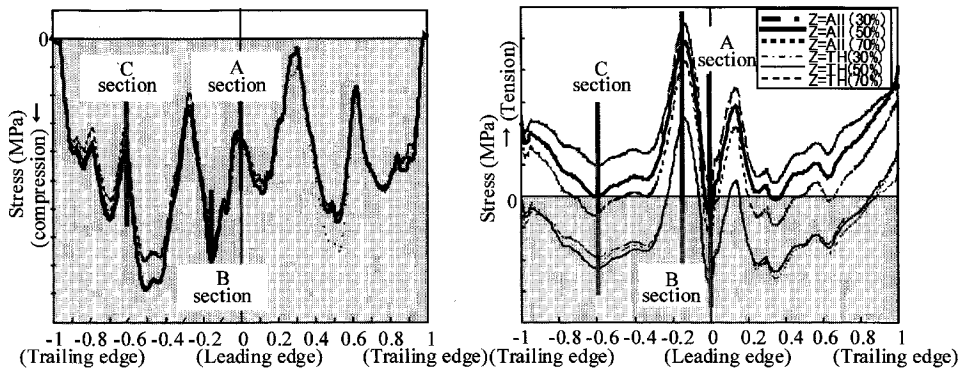


Figure 4 FE analysis results of the surface temperature distributions at 0, 30, 50, 70, and 100% spans of the airfoil

The dominant stream-wise stress along the whole of the airfoil surface was compressive due to the thermal loading. The span-wise thermal stress distribution shows an inverse relationship with reference to the temperature distribution on the airfoil surface. At the portions where the temperature drops were observed, that is, on either side of the leading edge, a tensile thermal stress is calculated while in the other parts the thermal stress is compressive. The span-wise stresses consist not only of the thermal stress but also a centrifugal stress, which shifts the surface stress distributions to the tension side (Figure 5(b)).

In this work, microstructural observations were performed at three locations along each of the airfoil cross-section at 30%, 50%, and 70% airfoil spans. Section A was selected because a compressive stress was dominant, section B because a span-wise tensile stress was dominant, and section C because the stress changed from compression to tension, at cross sections towards the root of the airfoil, when the centrifugal load was included.



(a) stream-wise (tangential) surface stress (b) span-wise (radial) surface stress

Figure 5 FE analysis results of the surface stress distributions at 30%, 50%, and 70% spans of the airfoil (All : thermal and centrifugal stresses) and without the centrifugal force(TH : thermal stresses only).

3.3 Destructive evaluation of the turbine buckets

The microstructure at the leading edge (section A) of the 50% airfoil span is shown in Figure 6. A low magnification SEM image is shown in 6-a. A gray layer, of 50 to 150 μm from the surface just below the scale and precipitation free zone, was observed. The image of this layer is shown in 6-b. Formation of γ' rafting parallel to the centrifugal stress (span-wise γ' rafting) was observed. The microstructure in the (001) cross section is shown in 6-e. Formation of γ' rafting slightly inclined to the airfoil circumference was observed, which is evidence that span-wise and stream-wise compressive surface stresses, normal to each other, were present.

The microstructure of section B, at which a span-wise tensile stress was analytically predicted, is shown in Figure 7. The microstructure at the 70% span of the airfoil surface was observed to have span-wise rafting, which means that a compressive stress was dominant. Stream-wise γ' rafting formation was observed at the 50% span of the airfoil surface which means that the centrifugal stress was dominant. No microstructural changes were observed at the 30% span, which is believed to be the result of the predicted extremely low temperature.

The microstructure of section C is shown in Figure 8. Span-wise rafting was observed along the whole surface area, which means this surface area was subjected to a compressive stress and that the thermal loading was dominant. In this section stream-wise γ' rafting was expected at the 30% airfoil span, but the thermal stress contribution is thought not to be so low as predicted from the FE analysis.

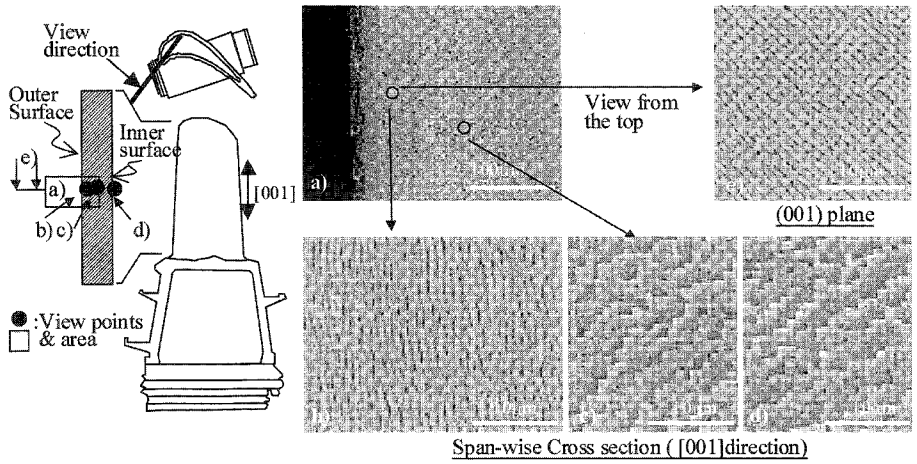


Figure 6 SEM micrographs at the 50% span of the airfoil leading edge portion (Section A), in the stage 1 bucket.

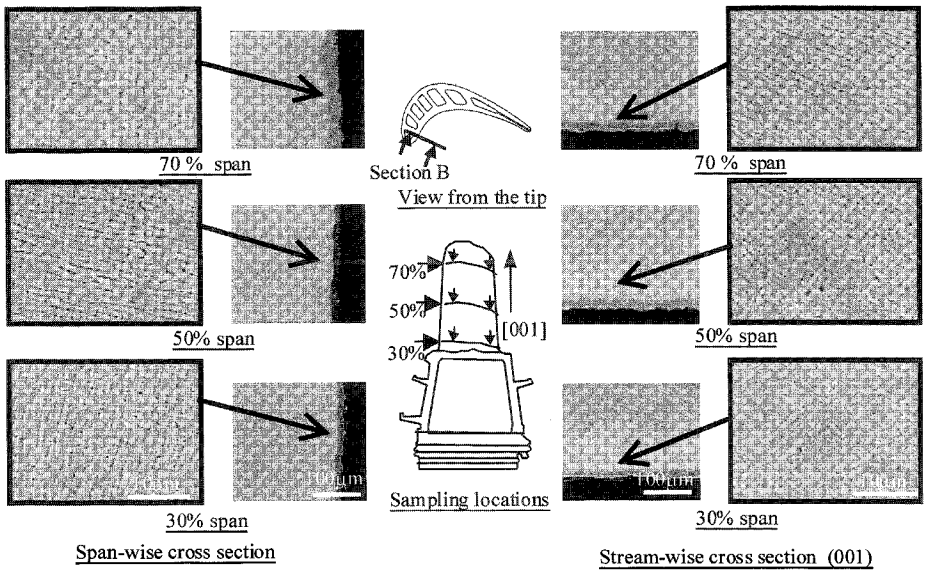


Figure 7 SEM micrographs at the 30, 50, 70% span of the airfoil, surface section B, in the stage 1 bucket.

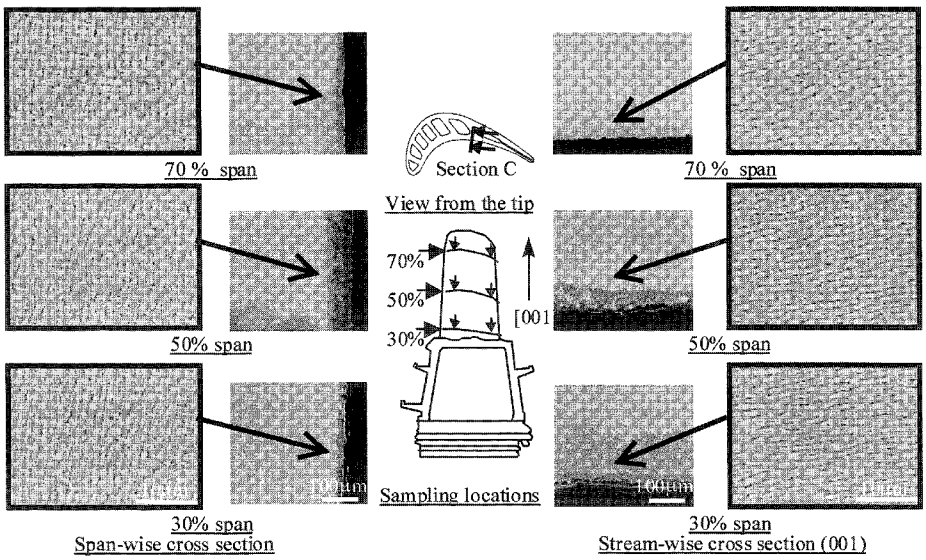


Figure 8 SEM micrographs at the 30, 50, 70% span of the airfoil, surface section C, in the stage 1 bucket.

4. Conclusions

A metallurgical investigation was conducted in order to identify the stress state of a bucket in service with a 15MW gas turbine TGT. This work was carried out in conjunction with a fundamental study of crept specimens and FE stress/temperature analyses. The conclusions obtained here are as follows.

1) It was confirmed from the creep tests that rafting occurs normal to the stress-axis under the tensile stress and parallel to the stress-axis under the compressive stress.

2) Rafting of the γ' was observed just below the outer surface of the airfoil. The direction of the γ' rafting was dependent on the relative contribution of the thermal and centrifugal stresses. The microstructure at the surface portion near the leading edge in the 50% span, where the surface temperature was predicted to be rather low, showed stream-wise γ' rafting perpendicular to the centrifugal stress axis. Span-wise rafting was observed in the remaining surface area of the airfoil, which means that the compressive thermal stress due to the temperature gradients was dominant.

3) The results from the microstructure observation and the FE analysis showed generally good agreement. However, the actual thermal stress on the airfoil surface was thought to be somewhat higher than that predicted from the FE analysis, which shifted the actual state of stresses somewhat back towards the compression side.

5 References

[1] Harada H, Ohno K, Yamagata T, Yokokawa T, Yamazaki M, Phase Calculation and its use in alloy design program for Nickel-base superalloys, Superalloys 1988, (1988), p.733
[2] Tien JK and Gamble RP, Metall. Trans., 3(1972), p.2157
[3] H. Biermann, B.Grossmann, T. Schneider, H.Feng, G. Mughrabi, Investigation of the γ/γ' morphology and internal stresses in a monocrystalline turbine blade after service:determination of the local thermal and mechanical loads, Superalloys 1996, (1996) p.201
[4] Gabb TP, Draper SC, Hull DR, MacKay RA, Nathal MV, Mater. Sci. Engng. A, 118, (1989) , p.59
[5] Fredhholm A. and Strudel JL, On the creep resistance of some Nickel base single crystals, Superalloys 1984, (1984), p211
[6] N. Kitazaki, Y.kondo, J.Namekata, N. Ohi, H. Hattori, Effect of tensile orientation on rafting structure gamma prime precipitation in nickel-base superalloy *CMSX*-2, 123rd committee on heat resistance metals and alloys Rep., Vol.34, No.2 (1993), p.165

CARBIDE PRECIPITATION IN SINGLE CRYSTAL NI-BASE SUPERALLOYS

S. Tin and T.M. Pollock

University of Michigan
Department of Materials Science and Engineering
Ann Arbor, MI 48019, USA

Abstract

Carbide precipitation during solidification of Ni-base superalloy René N5 has been investigated in a series of single crystals cast under varying thermal gradients. The investigation was focused on establishing a relationship between solidification parameters and resultant carbide morphology. Microstructures of single crystals unidirectionally solidified using liquid metal cooling were compared to single crystals solidified in a conventional Bridgman furnace. Differences in thermal gradients experienced during solidification were found to influence the development of both dendrite and carbide morphology. Detailed analyses of carbides, segregation characteristics and phase transformation temperatures are presented. The mechanisms of MC carbide formation in Ni-base superalloys are discussed.

Keywords: Carbides, liquid metal cooling, Ni-base single crystals and solidification

Introduction

Technologies for land based gas turbines designed for power generation applications have typically been derived from advances established in the aircraft engine sector. With regard to materials technologies, development of new processes and alloys in the past 40 years has been driven by the increasingly stringent requirements of high-performance aircraft turbines. Compared to aircraft engines, the operating conditions for industrial gas turbines have been less demanding and have previously provided a greater degree of flexibility for materials selection. Currently, aircraft engines require the exclusive use of highly alloyed single crystal turbine blades, while most large power generation turbines operate with less creep resistant polycrystalline and directionally solidified blades. However, recent requirements for highly efficient (~60% efficiency) power generation turbines capable of producing in excess of 400MW has necessitated a need to improve creep resistance and implement large single crystal turbine blades into these applications[1].

Manufacture of large single crystal blades for power generation turbines has proved to be quite challenging. During unidirectional solidification of these heavily alloyed Ni-base superalloys in Bridgman furnaces, micro-segregation of the solute occurs within the dendritic mushy zone. Since solidification occurs in a direction anti-parallel to gravity and the density

of the segregated solute is less than the density of the bulk liquid, the solute can accumulate within the mushy zone and form flowing plumes denoting the onset of thermosolutal convection[2, 3]. These convective instabilities result in the formation of freckle chains and misoriented grains which significantly degrade the mechanical properties of the component and cause the breakdown of single crystal solidification[4, 5].

Advances in process modeling and furnace design have enabled sufficiently high thermal gradients to be maintained during the solidification of small (~15cm length and >1kg mass) aircraft engine turbine blades. The application of high thermal gradients during solidification results in the formation of a fine dendritic microstructure and tends to suppress the onset of thermosolutal convection[6]. Turbine blades required for land-based gas turbines, however, can measure up to 1m in length and weigh in excess of 25kg. Due to the sheer size of these components, heat transfer during unidirectional solidification becomes limited across large cross-sectional areas and low internal thermal gradients can develop. These low gradient conditions are particularly favorable for thermosolutal convection and cause these components to be highly susceptible to the formation of freckles and misoriented grains.

Recently, the authors have shown that minor additions of carbon to high refractory content Ni-base superalloys are extremely effective in preventing freckle formation during low gradient solidification[7, 8]. Following from these investigations, new single crystal Ni-base superalloy compositions containing carbon are currently being developed and marketed exclusively for applications in large power generation turbines. To truly optimize and carefully balance the composition of the alloy to be amenable to low gradient solidification, a mechanistic understanding of the carbon/carbide interactions with the mushy zone is required. Both changes in refractory element segregation and carbide precipitation have been associated with the beneficial influence of carbon on the solidification characteristics of Ni-base single crystals[7, 8]. In this study, the relationship between solidification parameters and carbide morphologies was investigated in the commercial single crystal Ni-base superalloy René N5.

Experimental

Experimental trials were conducted to investigate the mechanisms of carbide precipitation and the subsequent development of characteristic carbide morphologies. The influence of cooling rates, particularly thermal gradients, during solidification was studied with respect to the development of carbide morphologies. A series of casting trials using René N5 were conducted in a pilot-scale Bridgman furnace with a 150mm diameter chill. The nominal composition of René N5 is listed in Table I. Single crystal bars were solidified in an investment cluster mold containing four 19mm diameter bars approximately 150mm in length. The molds were withdrawn from the hot zone of the furnace at a rate of 200mm/h. For the high gradient trial, the solid-liquid interface was quenched into the liquid metal (Sn at 250°C) cooling (LMC) media after solidifying approximately 100mm along the length of the bar.

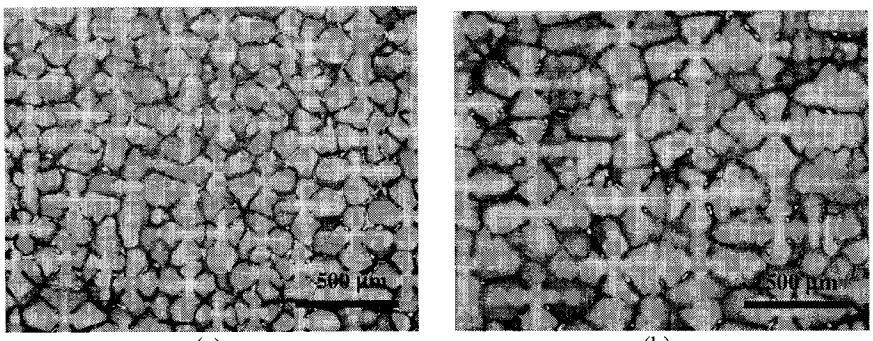
Microstructures of the as-solidified crystals were carefully analyzed and carbides were extracted from the samples for further characterization. Quantitative segregation mapping was used to characterize the partitioning behavior of the constituent elements during

solidification. Finally, samples from the single crystals were also prepared for differential thermal analysis (DTA). Additional details of the experimental procedures can be found in the previous investigations by Tin and Pollock[7, 8].

Results

Carbon additions to single crystal Ni-base superalloys were previously shown to be beneficial with respect to preventing the breakdown of single crystal solidification due to thermosolutal convection. In addition to changes in the characteristic segregation behavior of the constituent elements, the physical presence of carbides within the mushy zone was shown to be important in preventing the formation of freckles and misoriented grains. The addition of carbon to these high-refractory content Ni-base superalloys results in the formation of three distinct carbide morphologies: blocky, script and nodular. The potential interaction of each carbide morphology with the mechanisms that result in freckle formation were investigated in René N5.

Systematic changes in the cooling rate during unidirectional solidification of René N5 influenced the development of the dendritic microstructure in these single crystals. Figure 1 shows the dendritic microstructures of René N5 solidified with thermal gradients ranging from high to low. Representative primary dendrite arm spacings and pertinent solidification parameters for the single crystal bars are shown in Table II. Consistent with previous solidification studies, primary dendrite arm spacings decreased with the increasing thermal gradients. No freckles were observed to form in any of the single crystal castings. In addition to changes in dendrite morphology and the magnitude of the spacing between primary dendrite arms, carbide morphologies were also affected. Although the overall carbide volume fractions remained constant, metallographic observations indicated that the fraction of blocky carbides increased with increasing gradients. Carbides extracted from sample UM1-1, which was solidified under a high thermal gradient using the molten tin bath, contained some nodular carbides, but the majority of carbides were identified to exhibit a blocky morphology, Figure 2. Processed using the conventional Bridgman furnace under low gradients, the large majority of the carbides extracted from sample UM6-3 exhibited script-like features, Figure 3.



(a) (b)

Figure 1: Dendritic microstructure of René N5 solidified at R=200mm/hr using a) liquid metal cooling (UM1-1) and b) conventional DS (UM6-3).

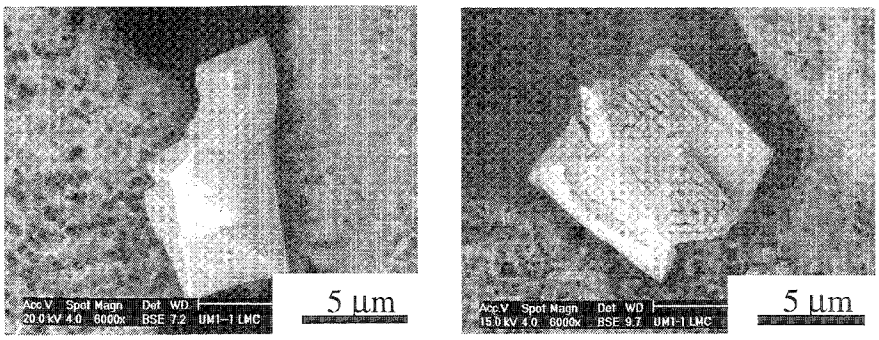


Figure 2: SEM micrographs showing the small blocky carbides extracted from sample UM1-1 solidified under a high thermal gradient using liquid metal cooling.

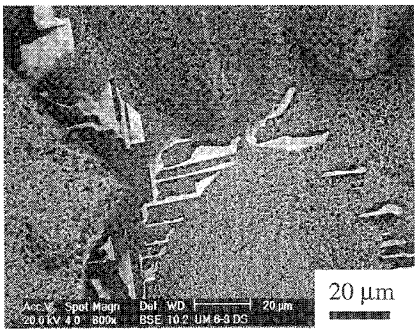


Figure 3: SEM micrograph showing the script carbides present in sample UM6-3 solidified under a low thermal gradient using the conventional Bridgman process.

These observations are also consistent with the results from the DTA analyses performed on these specimens. Although the solidus and liquidus temperatures measured in these samples remain constant in all instances (T_S=1351°C and T_L=1388°C), Figure 4 uncovers the presence of an extra peak just below the liquidus temperature corresponding to the dissolution temperature of the blocky carbides in sample UM1-1. With a much smaller volume fraction of the blocky carbides, this peak is absent in UM6-3. Solutioning of the nodular carbides in UM1-1 and the script carbides in UM6-3 was measured to occur at the same temperature, 1363°C.

Table I: *Composition of René N5 (wt.%) and Assessed Distribution Coefficients*

	Al	*Ta*	*W*	*Mo*	*Re*	*Co*	*Cr*	*C*	*Ni*
René N5	6.2	6.5	5.0	1.5	3.0	7.5	7.0	0.05	Bal.
$k = C_S/C_L$	0.90	0.80	1.25	1.20	1.38	1.07	1.11	-	-

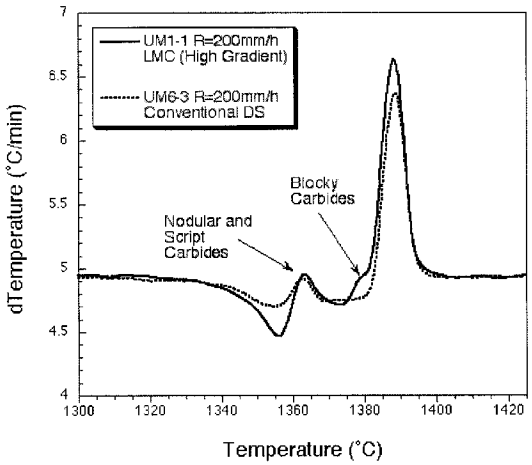
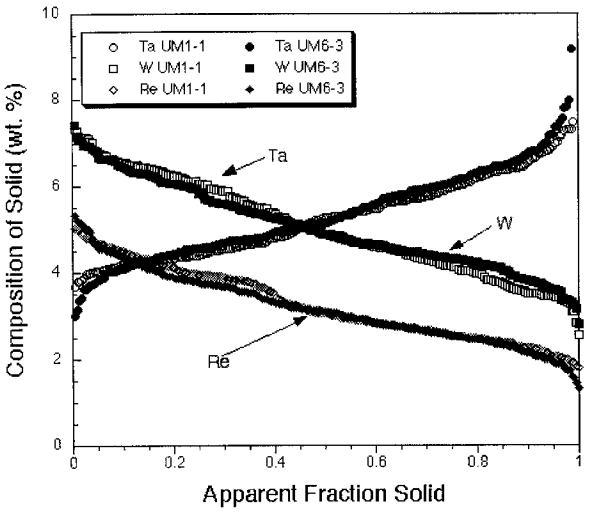


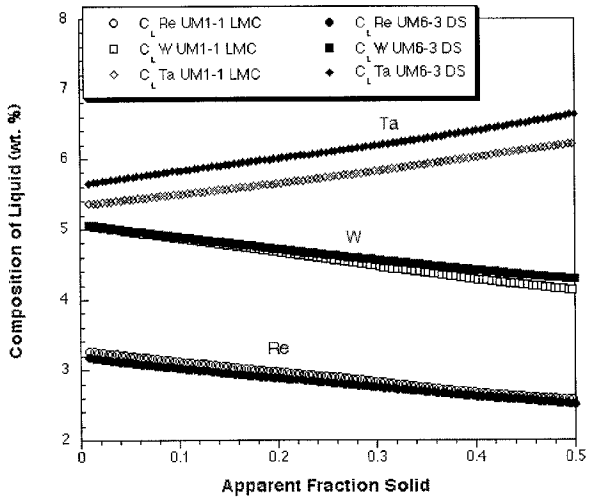
Figure 4: DTA results from the René N5 alloys solidified under different thermal gradients.

Results from the segregation analysis also indicate that large fractions of blocky carbides are only formed when the thermal gradients during solidification are sufficiently large. A comparison of the ranked distributions for tantalum, tungsten and rhenium in samples UM1-1 and UM6-3 can be seen in Figure 5. For a specified composition, the segregation characteristics for the constituent elements did not vary significantly with changes in solidification parameter and are all within the expected range of error. Assessed distribution coefficients for René N5 are listed in Table I. Upon closer examination of the ranked distributions, the segregation of tantalum appeared to be slightly affected by the changes in thermal gradient. Calculation of the liquid solute composition using the data from the segregation analysis reveals that there was consistently ~0.3 wt.% less tantalum present in UM1-1. Precipitation of blocky Ta-rich MC carbides close to the liquidus temperature in the sample solidified under high gradients would partially consume some of the tantalum in the solute during the initial stages of solidification.

Using X-ray diffraction, bulk lattice parameter measurements from the extracted carbides reveal the majority of the blocky carbides from UM1-1 to be non-stoichiometric, Table II. A noticeable shift in the diffraction pattern is evident from the X-ray diffraction patterns corresponding to the carbides extracted from UM1-1 and UM6-3, Figure 6. With a larger fraction of script and nodular carbides present in the bars solidified under low gradient conditions, differences in the lattice parameters were measured due to the presence of minor amounts of Ni, Co, Cr and Mo in the carbides. Despite the low gradient solidification conditions, no freckle defects developed during these casting trials.



(a)



(b)

Figure 5: Segregation analyses from UM1-1 and UM6-3. (a) Ranked distributions of Ta, W and Re reveal no significant differences in segregation behavior due to changes in solidification parameters. (b) Calculation of the liquid composition suggests that slightly less tantalum was present in the solute during solidification in UM1-1.

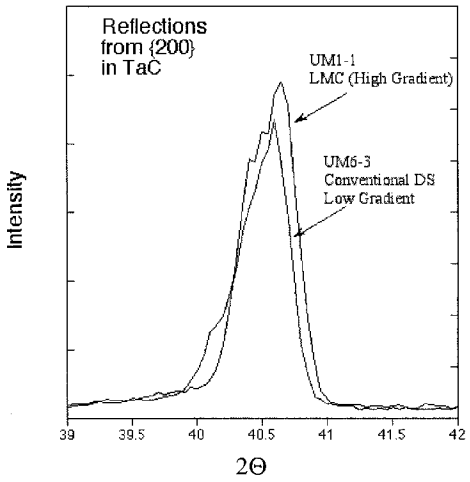
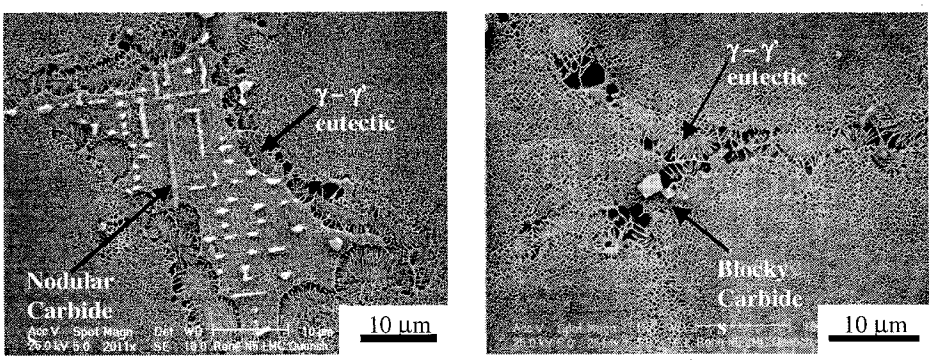


Figure 6: Comparison of the X-ray powder diffraction patterns taken from the carbides extracted from the René N5 alloys.

Experiments in which the solid/liquid mushy zone was quenched into the molten tin bath during unidirectional solidification led to the development of interesting microstructures, Figure 7. Corresponding primary dendrite arm spacing (PDAS) measurements taken from these quenched regions were in the range of ~60μm. Solidification under these extremely high gradients led to the absence of carbides with the script morphology. Lamellar nodular carbides were dispersed within patches of the γ - γ' matrix contained within the interdendritic regions and surrounded by eutectic pools of γ - γ', Figure 7a. The blocky carbides were observed to reside directly adjacent to the eutectic pools of γ - γ', Figure 7b.



(a) (b)

Figure 7: SEM micrographs taken from the René N5 sample solidified at R=300mm/min in the liquid metal media. The high thermal gradients resulted in the formation of $\gamma - \gamma'$ eutectic pools adjacent to the blocky carbides.

Table II: *Solidification Processing Conditions and Lattice Parameters of René N5 Alloys*

	Alloy	*Casting Media*	*Withdrawal Rate*	*PDAS*	*Majority Carbide Morphology*	*Lattice Parameter (Å)*
UM1-1	René N5	LMC	200cm/h	317μm	Blocky	4.443
UM6-3	René N5	Conventional DS (Low Gradient)	200cm/h	443μm	Script + Nodular	4.451

Discussion

Development of new alloys amenable to low gradient processing requires knowledge of the carbon/carbide interactions with the various mechanisms that ultimately result in thermosolutal convection and freckle formation. The present investigation has concentrated on identifying the morphological dependence of the carbides with changes in solidification parameters. Development of carbide morphologies in single crystal specimens of René N5 was shown to be highly sensitive to thermal gradients during solidification. Large thermal gradients during solidification are required to induce the formation of blocky carbides, Figure 2, while the intricate script carbides develop only under lower gradient conditions associated with conventional Bridgman furnaces. These findings are consistent with those of previous studies that have reported a morphological dependence of carbides on solidification rates[9-12].

Changes in the solidification processing parameters also led to changes in the dendritic microstructure. At a constant withdrawal rate of 200mm/h, the resulting magnitude of the primary dendrite arm spacings in UM1-1 was measured to be smaller than UM6-3, Figure 1 and Table I. Changes in the thermal gradient during solidification resulted in physical changes in the mushy zone. The height of the mushy zone (h) can be described as a function of the freezing range of the alloy ($\Delta T = T_L - T_S$) and the thermal gradient (G), $h=\Delta T/G$. Hence, the height of the mushy zone was reduced in UM1-1 and the compositional gradient associated with the segregated solute was also altered. As evidenced by the difference in measured lattice parameters, Figure 6, the growth of the blocky carbides within the mushy zone of UM1-1 resulted in a slight difference in carbide composition when compared to carbides extracted from UM6-3. Despite these differences, only minor changes in the degree of segregation could be measured in the as-solidified samples.

The characteristic segregation behavior of tungsten and rhenium additions in UM1-1 and UM6-3 were not influenced by the changes in thermal gradient, Figure 5. Between the two samples, only a slight change in the distribution of tantalum was apparent. This is due to the primary dendrites in UM1-1 solidifying in a solute field that has been slightly depleted of tantalum due to the precipitation of blocky Ta-rich MC carbides. Since the carbides contain primarily tantalum, the segregation behavior of the other constituent elements are not affected.

The experimental results in this paper appear to be consistent with previous studies on the ternary Ni-Ta-C system[13]. Composite structures consisting of γ + TaC were investigated as potential successors to Ni-base superalloys for turbine blade applications. In the Ni-rich region of the ternary system, it has been proposed that formation of γ + TaC

occurs along a trough that connects the Ni-C eutectic and the Ni-Ni_3Ta eutectic[13]. With only 0.05 wt.% C and 6.5 wt.% Ta in René N5, the γ + TaC eutectic would typically be suppressed until dendritic segregation enabled a sufficient amount of tantalum and carbon to accumulate in the solute. The strong orientation relationships exhibited between the carbides and γ along with the invariant carbide dissolution temperatures measured over a wide range of compositions indicate that the formation of script and nodular carbides are most likely due to this eutectic reaction[7, 8].

Based on the proposed ternary projection, the atomic ratio of carbon to tantalum in the solute would have to exceed unity in order to enable the precipitation of blocky carbides from the liquid. Thus, solidification at high gradients would have to induce a higher concentration of carbon in the solute to form the blocky carbides. By physically reducing the height of the mushy zone, the composition gradient in the liquid associated with the segregated solute is confined to a smaller volume. Hence, blocky carbides are rarely seen in samples solidified under low gradients since precipitation would be limited to occurring only when the solute becomes supersaturated with carbon.

Understanding the mechanisms associated with carbide precipitation in single crystal Ni-base superalloys has become increasingly important as carbon additions are being viewed as viable methods of preventing the breakdown of single crystal solidification. Formation of the script and nodular carbides within the interdendritic regions of the microstructure can be attributed to the TaC – γ eutectic reaction. Carbon supersaturation within the solute contained in the mushy zone potentially enables the formation of blocky carbides ahead of the solidifying interfaces. In summary, utilization of minor alloying additions to enhance the solidification characteristics of Ni-base superalloys without significantly compromising the physical and mechanical properties of the alloy has become a promising alternative for the continued development of commercial alloys.

Conclusions

1) Carbides in single crystal Ni-base superalloy, René N5, exhibit a strong morphological dependence with cooling rates during solidification.
2) High thermal gradients promote the formation of blocky carbides, while thermal gradient associated with conventional casting processes lead to the formation of intricate script carbides.
3) Script and nodular carbides develop as part on a TaC – γ eutectic reaction.
4) Blocky carbides form in the liquid and deplete the solute of tantalum.

References

1. B.B. Seth, *Superalloys - The Utility Gas Turbine Perspective*, in *Superalloys 2000*, 2000, Warrendale, PA, TMS, p. 3-16
2. A.F. Giamei and B.H. Kear, *On the Nature of Freckles in Nickel-Base Superalloys,* Metall. Trans., 1970, **1**, p. 2185-2192.
3. S.M. Copley, A.F. Giamei, S.M. Johnson, and M.F. Hornbecker, *The Origin of Freckles in Unidirectionally Solidified Castings,* Metall. Trans., 1970, **1**, p. 2193-2204.
4. T.M. Pollock and W.H. Murphy, *The Breakdown of Single-Crystal Solidification in High Refractory Nickel-Base Alloys,* Metall. Mater. Trans., 1996, **27A**, p. 1081-1094.

5. T.M. Pollock, W.H. Murphy, E.H. Goldman, D.L. Uram, and J.S. Tu, *Grain Defect Formation During Directional Solidification of Nickel Base Single Crystals*, in *Superalloys*, 1992, Warrendale, PA, TMS, p. 125-134
6. J.S. Tu and R.K. Foran, *The Application of Defect Maps in the Process Modeling of Single-Crystal Investment Casting,* JOM, 1992, **44**(6), p. 26-28.
7. S. Tin, T.M. Pollock, and W.T. King, *Carbon Additions and Grain Defect Formation in High Refractory Nickel-Base Single Crystal Superalloys*, in *Superalloys*, 2000, Warrendale, PA, TMS, p. 201-210
8. S. Tin, T.M. Pollock, and W. Murphy, *Stabilization of Thermosolutal Convective Instabilities in Single Crystal Ni-Base Superalloys: Carbon and Freckles,* Metall. Mater. Trans., 2001, **32A**, p. 1743-1753.
9. J. Chen, J.H. Lee, C.Y. Jo, S.J. Choe, and Y.T. Lee, *MC Carbide Formation in Directionally Solidified MAR-M247 LC Superalloy,* Mater. Sci. Eng., 1998, **A247**, p. 113-125.
10. A.K. Bhambri, T.Z. Kattamis, and J.E. Morral, *Cast Microstructure of Inconel 713C and its Dependence on Solidification Variables,* Met. Trans., 1975, **6B**, p. 523-537.
11. R. Fernandez, J.C. Lecomte, and T.Z. Kattamis, *Effect of Solidification Parameters on the Growth Geometry of MC Carbide in IN-100 Dendritic Monocrystals,* Metall.Trans., 1978, **9A**, p. 1381-1386.
12. W.R. Sun, J.H. Lee, S.M. Seo, S.J. Choe, and Z.Q. Hu, *The Eutectic Characteristics of MC-type Carbide Precipitation in a DS Nickel-Base Superalloy,* Mater. Sci. Eng. A, 1999, **A271**, p. 143-149.
13. M.R. Jackson, *Composites of Gamma + TaC in the Ni-Ta-C Ternary System,* Metall. Trans., 1977, **8A**, p. 905-913.

MODELLING OF HIGH TEMPERATURE TMF TESTS OF SINGLE CRYSTALS BY A PURE CREEP LAW

P S White
ALSTOM POWER, Cambridge Rd, Whetstone, Leicester, LE8 6LH, England
C N Kong
Department of Mechanical Engineering, University of Bristol, Bristol, BS8 1TR, UK.

Abstract

A uniaxial primary-secondary-tertiary creep law, the basis of multiaxial laws for isotropic and cubic materials, is outlined with emphasis upon the inclusion of data from high-temperature tensile tests. Experimental data for high temperature LCF and TMF tests in the single crystal alloys CMSX4, CM186 are also described and comparisons are made with predictions from the creep law. Qualitative and partially quantitative agreement is found and it is concluded that such a creep law is capable of representing these forms of cyclic behaviour.

Keywords: Creep, Modelling, Single crystal, LCF, TMF

Introduction

From ambient to moderately elevated temperatures the Ni-based superalloys usually show little time-dependence at experimentally practicable (sub-dynamic) time-scales. The chief exceptions are in behaviour of the 'strain-burst' or 'serrated yield' types, which may appear beyond certain *thresholds* of time-scale (and temperature). Such phenomena apart, a classical elastic-plastic material model is then adequate. But at higher temperatures all the usual material tests show clear time-dependence and fig 1 shows an example of tensile test results (mostly including a sudden change of strain-rate) for IN939 at 850°C.

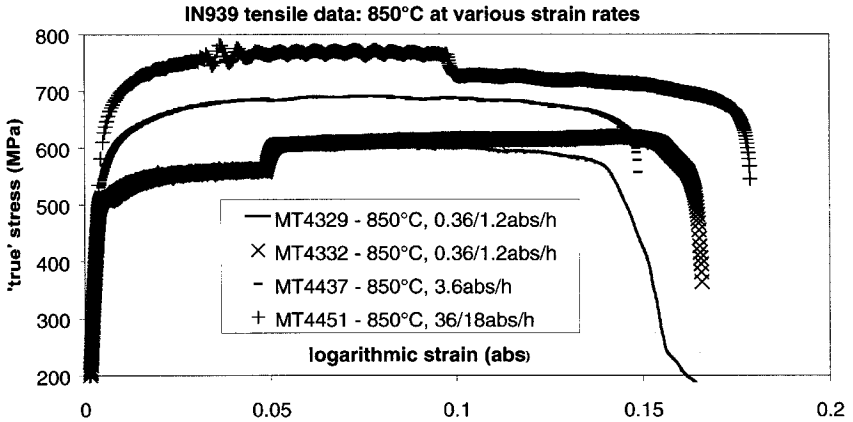


Fig 1

Moreover, when the applied strain-rates and 'true' flow stresses of fig 1 are plotted on fig 2 with secondary rate data from creep tests for the same batch, a consistent trend appears (and similarly for failure times etc), suggesting essential similarity of the underlying mechanisms. Therefore it is surmisable that *all* high-temperature inelastic behaviour might be modelled as

creep. Such observations and postulates are far from novel, even for Ni-based superalloys alone [1], but the consequences have generally been followed only for monotonic behaviour. The present work shows, for particular single crystal materials in the <001> direction, that a suitable creep law may also have good predictive power for high temperature isothermal cyclic (LCF) tests and even TMF tests provided that no 'low-temperature plasticity' occurs. Note however that only stress/deformation behaviour is considered here and that corresponding life-prediction - especially for TMF conditions - remains under study.

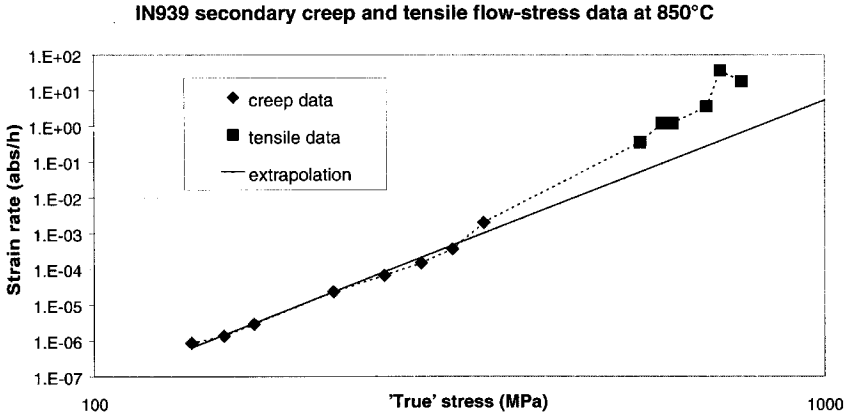


Fig 2

Assumed form of creep law and fitting of creep data

For *uniaxial* stress σ, the corresponding creep strain ε^c is assumed to be governed by two state variables β (back-stress, giving primary effects) and $\mathbf{s}$ (tertiary softening) according to

$$d\varepsilon^c/dt = (1-\theta)^{-1} |\sigma|^{-(1+\theta)} \{\varepsilon^*(|\sigma|) / t^*(|\sigma|)\} \Omega(\mathbf{s}) |\sigma - \beta|^{\theta} (\sigma - \beta) \quad (1)$$

$$d\beta/dt = \{|\sigma| / \varepsilon^*(|\sigma|)\} d\varepsilon^c/dt - \{\mathbf{G}(|\beta|) / |\beta|)\} \beta \quad (2)$$

$$d\mathbf{s}/dt = \{t_3(|\sigma|)\}^{-1} \quad (3)$$

In these relations θ [$0 < \theta < 1$] is a parameter while ε^*, $\mathbf{t}^*$, Ω [$\Omega = 1$ if $\mathbf{s} < 1$] and $\mathbf{G}$ are functions of the indicated arguments. All these quantities may also depend upon temperature $\mathbf{T}$. Here $\mathbf{t}_3$ is identified with the time to the start of tertiary creep in a test at given stress while θ and the functions ε^*, $\mathbf{t}^*$, Ω, $\mathbf{G}$ are determined less directly through the implied relations (see below) with correlations of various features of experimental data. *Specific* forms of the above functions are *not* pre-assumed, apart from certain constraints as $|\sigma|$ approaches zero. Equation (2) expresses changes of back-stress as a combination of 'strain-hardening' and 'thermal recovery' so that, except for the included tertiary effect, the equations may be regarded as extending Lagneborg's primary-secondary description [2]. However the *manner* of joint dependence upon σ and β implied by (1,2) is specifically chosen to give a physically reasonable form of time-dependent response (otherwise akin to that of kinematic plasticity) in cyclic conditions. Multiaxial versions have been derived for isotropic materials in a natural tensorial generalisation and for cubic single crystals via a Schmid model with distinct <001> and <111> parameters. However, for present considerations a uniaxial description suffices.

For purposes of fitting, experimental tensile creep curves are assumed to be approximated by classical 'three-stage' forms, with each curve represented principally in terms of various 'curve descriptors' as defined geometrically on fig 3. Further details of the evaluations and correlations with σ and $\mathbf{T}$ - with statistical allowances for experimental errors, batch-to-batch variability, etc - are given in [3,4]. In particular, so as to maximise the synergy of information, data for different but essentially similar material types are fitted together, with all parameters treated as common *except* for certain pre-multipliers. The latter have statistically based average and bounding forms for each type. Specific types of function *are* used for the correlation of curve descriptors and, though others are possible, the 'double Norton' forms have been employed here. These are fully described in [3,4] but should be noted as containing independent parameters for limiting behaviour at high and low stresses respectively.

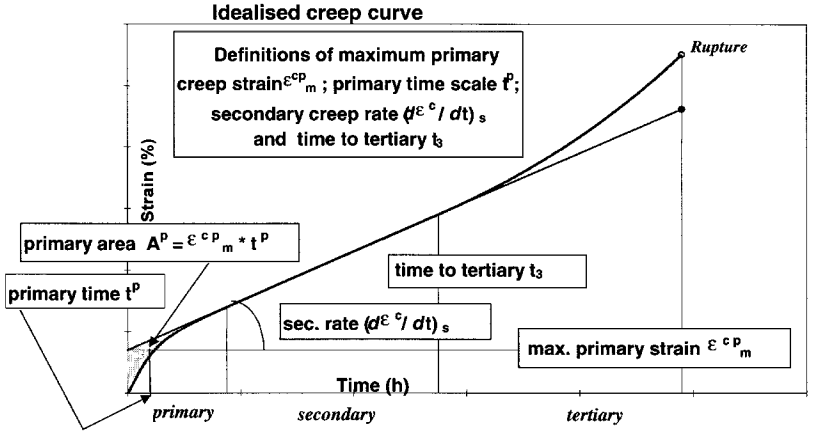


Fig 3

Identification of material functions for FE implementation and inclusion of tensile data

With the assumption that the secondary stage is represented by a 'steady' value $\beta_s(\sigma)$ of β, the above equations imply for the steady state and for the evaluation of primary behaviour that

$$(d\varepsilon^c(\sigma)/dt)_s = (1-\theta)^{-1}\{\varepsilon^*(\sigma) / t^*(\sigma)\}\ \{\delta(\sigma)\}^{1+\theta} \quad \text{where } \delta(\sigma) = 1 - \beta_s(\sigma)/\sigma \tag{4}$$

$$\mathbf{G}(\beta_s(\sigma)) = \{\sigma / \varepsilon^*(\sigma)\}\ d\varepsilon^c_s(\sigma)/dt \tag{5}$$

$$\varepsilon^{cp}_m = \varepsilon^*\sigma^{-1} \int_0^{\beta_s} \mathbf{U}(\beta)[\mathbf{U}(\beta)+\mathbf{V}(\beta)]^{-1} d\beta \tag{6}$$

$$\varepsilon^{cp}_m t^p = \varepsilon^* t^* (1-\theta)\ \sigma^{-2} \int_0^{\beta_s} \{\int_\beta^{\beta_s} \mathbf{U}(\beta')[\mathbf{U}(\beta')+\mathbf{V}(\beta')]^{-1} d\beta'\}\ [\mathbf{U}(\beta)+\mathbf{V}(\beta)]^{-1} d\beta \tag{7}$$

where $\mathbf{U}(\beta) = (1-\beta/\sigma)^{1+\theta} - \delta^{1+\theta}$, $\mathbf{V}(\beta) = \delta^{1+\theta}\ [1 - \mathbf{G}(\beta)/\mathbf{G}(\beta_s)]$ (8)

with the measurable quantities $(d\varepsilon^c(\sigma)/dt)_s$, ε^{cp}_m and t^p defined on fig 3. No closed form solution exists for the unknowns ε^*, t^*, and $\mathbf{G}$ but, given that $(d\varepsilon^c(\sigma)/dt)_s$ is *small* compared with the initial rate $(d\varepsilon^c(\sigma)/dt)_0$, a perturbation expansion may be used in terms of δ since

$$\delta = \{\ (d\varepsilon^c(\sigma)/dt)_s / (d\varepsilon^c(\sigma)/dt)_0\ \}^{1/(1+\theta)} \qquad << 1 \tag{9}$$

In a crude *lowest* approximation two material functions and the *early* creep curve are given by

$$\varepsilon^*(\sigma) = \varepsilon^{cp}{}_m(\sigma),\ \mathbf{t}^*(\sigma) = \mathbf{t}^p(\sigma),\ \varepsilon^c/\varepsilon^{cp}{}_m = \{1-(1+[\theta/(1-\theta)]\,[\mathbf{t}/\mathbf{t}^p])^{-1/\theta}\} \qquad (10)$$

so that θ may be evaluated from tests, with a value of about 1/3 often being adequate. In practice primary data are usually too inconsistent to justify closer estimates but θ only significantly influences the predicted primary curve-shape. With such an estimate the material functions ε^*, $\mathbf{t}^*$ and **G** may then be evaluated more accurately from (4-9) in terms of suitable correlations of test data for $\varepsilon^{cp}{}_m$, $\mathbf{t}^p$ and $(d\varepsilon^c/dt)_s$. However the calculation is not explicit and is performed by an iterative scheme contained in appropriate material subroutines for FE programs. Material data then need *only* to be supplied directly in terms of the correlations for test data while average or bounding parameters may be automatically applied in FE work.

Fig 2 for an isotropic superalloy, with a gradually changing Norton index, indicates the danger in direct extrapolation of creep data to the higher stresses commonly seen in high temperature tensile or fatigue tests (error of up to two magnitudes). For single crystal superalloys the picture is comparable [3] and it is desirable to include tensile information in fitting if behaviour at fatigue stress-levels is to be simulated. If all information is treated in terms of estimated *true* stresses (at the mid-secondary stage for creep tests) then tensile flow stress data may reasonably be taken as equivalent to secondary creep data. Likewise, the time to the start of significant fall of true stress and the fracture time may be reasonably identified with the times to tertiary creep and to rupture. But there is *no* simple equivalent of the primary curve descriptors of fig 3 since the *early* stress in tensile tests is not constant in any approximate sense and, when simple extrapolation from creep data appears inadequate, a special procedure is needed. In this process 'effective' values of $\varepsilon^{cp}{}_m$ and $\mathbf{t}^p$ for each tensile test are computed for 'notional' creep tests at tensile flow stresses. The 'high stress' parameters of existing correlations for $\varepsilon^{cp}{}_m$ and $\mathbf{t}^p$ are varied in simulations until an adequate representation of the tensile curve is obtained. The 'effective' values are then taken from the adjusted correlation of each tensile test and added to the data-base of curve descriptors, which is finally used in an overall refitting. This rather complex process allows account to be taken of scatter, variability etc among tensile tests. Note however that the cyclic simulations to be described below do *not* employ this refinement though it will be used in future reported work.

Difficulties arise with single crystals for which *initial* tensile loading, as in fig 4a, often displays a characteristic 'hump' in the stress-strain curve before a steady flow stress, though the phenomenon usually disappears in *subsequent* cycles of fatigue tests, as shown in fig 4b.

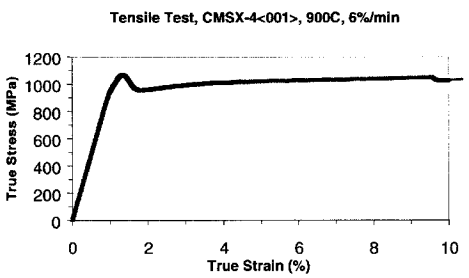


Fig 4a

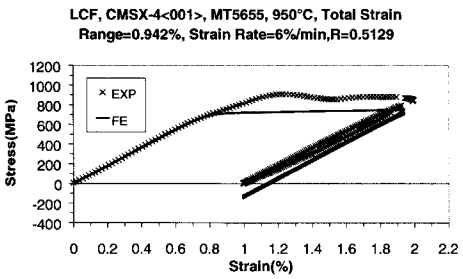


Fig 4b

Whatever the explanation, this amounts to *temporary* hardening similar to the temporary (but substantial) reduction of creep rate often seen part way through the primary stage of a creep test. Such effects being short-term, they may be legitimately ignored in constitutive models for long-term *engineering* predictions and are *not* covered by the above model. However, the 'humps' complicate data fitting and the 'high-stress' parameters of the present work are preliminary values, which will be revised after further consideration.

Predictive calculations and outline of the corresponding experimental situation

As outlined above, parameter sets have been established for several single crystal Ni-based superalloys, including CMSX4 and CM186. These sets were included in a Schmid-based UMAT subroutine for the ABAQUS FE program. Yet in order to justify subsequent engineering predictions, such a model and subroutine must be tested against data *independent* of those used in fitting. But all available creep and high temperature tensile data (apart from <011> tests) had already been used so that checking was through cyclic tests at constant (LCF) and variable (TMF) temperatures. The potential additional freedoms of cyclic behaviour, common in gas turbines, were considered to give adequately stringent checks.

LCF data of CMSX4 studied in this paper were generated within the concluded co-operative programmes CARAD (UK, supported by DTI) and COST501 (European Commission). Creep data from the latter activity were included in the study of [3]. Most LCF tests were conducted at ALSTOM Power Technology Centre in Whetstone, UK during COST 501. In this paper, attention is restricted to <001> oriented single crystal material. LCF data for CMSX4 involved uncoated solid test pieces at various strain rates, temperatures, mechanical strain (R) ratios and total strain ranges. Applied strain rates were 0.6%/min, 6%/min and 60%/min. Test temperatures were 850°C and 950°C, R-ratios used were -1, 0.5 and 0.05 while strain ranges were between 0.9% and 2.3%. There was a database of 28 tests in which the combination of 850°C and 6%/min was well represented at all three R-ratios.

Within CARAD, coated and uncoated hollow TMF test pieces were supplied by ALSTOM Power and TMF tests were performed at QinetiQ (then DERA) at Farnborough, UK. The material, single crystal CM186, is very similar to CMSX4 but weaker in many aspects, especially creep strength, and also has an (as-cast) heterogeneous structure. Hollow test pieces were used and experimental details may be found in [5]. Both out-of-phase (OP) and in-phase (IP) tests were performed with R-ratios -1 and 0.05 and total mechanical strain ranges between 0.6% and 1.0%. In OP tests, the maximum strain was applied at minimum temperature and the strain decreased as the temperature increased, reaching a minimum at maximum temperature. In IP tests conversely, minimum strain was applied at minimum temperature then both strain and temperature varied linearly until reaching maximum values. The temperature varied in linear heating and cooling cycles between 350°C and 950°C at 6°C/s so that the strain rate altered with the mechanical strain range. Thus, strain rates applied in an OP or IP test with 0.6% and 0.8% mechanical strain ranges were 0.36%/min and 0.48%/min respectively. The oxidation-resistant coating significantly reduced TMF lives, especially in OP tests. This was due to premature cracking of the coating at low temperatures, which induced cracks on the substrate during early parts of the tests. However, the coating, being very thin (about 80μm), was assumed to have little effect on the deformational behaviour of the specimens. Hence the stress-strain loops from both coated and uncoated test pieces were treated or compared with the FE simulation results in the same manner.

Outline of Calculations Performed

FE simulations were performed of high temperature uniaxial LCF tests of CMSX4 and TMF tests of CM186. Since the creep/tensile test data for all available <001> materials (from the CARAD/COST501 programmes and other sources) were fitted together as indicated above, the same set of creep coefficients was used for both simulated materials, *except* for different pre-multipliers. It is also important to note that the same set of elastic constants, actually derived for CMSX4, was used in the FE calculations for both materials. This was due to the current unavailability of a complete set of elastic constants for CM186. Nevertheless, the use of the CMSX4 constants for CM186 seemed adequate in providing good elastic predictions even in TMF conditions with strongly varying temperatures. FE simulations were carried out using the ABAQUS FE program and a user material subroutine (UMAT) implemented for single crystal material in *implicit* form (with exact Newton-Raphson iteration to allow good convergence during varying loads) based upon the creep law outlined above.

A 3-D single element model was used, which provided pure material response, ie without any structural influences. The element type used was C3D20, a solid 3-D 20 noded brick element, with 27 integration points. Each side of the element was of unit length. The boundary conditions in simulating LCF and TMF tests were identical, where all the nodes on one face of the element were fixed in the uniaxial (Z) direction. Additional constraints were applied to two other nodes on the same side, where one of the nodes was constrained in the y-direction and the other one in the x and y-directions, as shown in fig 5. This was necessary to hold the model in space and prevent any rotation during the FE analysis. To simulate a cyclic test, a fixed displacement (positive for tension and negative for compression) was applied to all the nodes on the loading face of the single element model, as shown in fig 5. Each reversal of loading and unloading was simulated in one step, where two steps contributed to one cycle of loading. To simulate LCF tests, the temperatures of all the nodes were fixed to the test temperature throughout the analysis. For TMF tests, the loading conditions for strain were the same as the LCF tests, but the temperature was varied throughout the test. The temperature of all the nodes within each step was set according to the type of TMF cycle, as indicated above The strain rate was taken into account by setting the appropriate total time for each step. During the analysis, the stress and strain history data was collected from the first integration point. The analysis was performed using average creep coefficients, for about 1000 cycles.

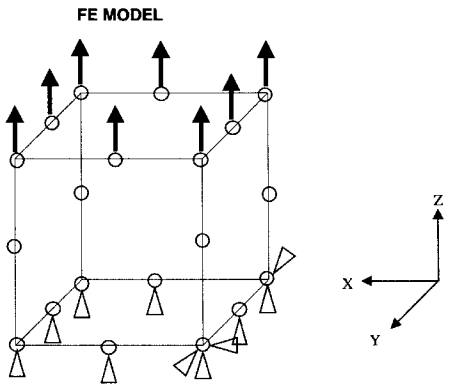


Fig 5

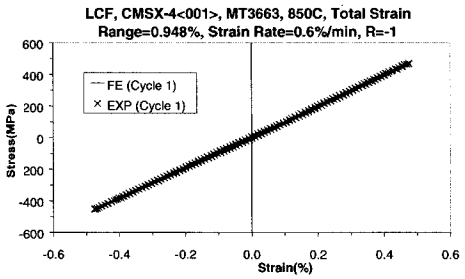


Fig 6

Comparison of calculations and tests

For CMSX4 LCF tests, experimental results showed that for R=-1 there was little or no variation in the mean stress which was seen to be zero or close to zero throughout, while the stress-strain loops showed almost completely elastic deformation, see fig 6 above. The results, especially for tests with low strain ranges, not unexpectedly showed good agreement on the variation of stresses, as in fig 7. For non-symmetrical strain ranges, ie R=0.5 and R=0.05 tests, significant mean stresses were seen, as shown in figs 8 and 9. These were tensile, decreasing rapidly during early cycles before approaching stabilisation. The model was generally able to predict qualitatively the mean stress effects observed, but in many cases failed to predict the correct stress magnitudes, as shown in fig 8.This appears to be related to the result shown in fig 4b where the calculation under-predicted the maximum stress during initial loading and consequently the subsequent cyclic mean stress. In other cases the prediction was better, as in fig 9. However, the early stresses were again under-predicted.

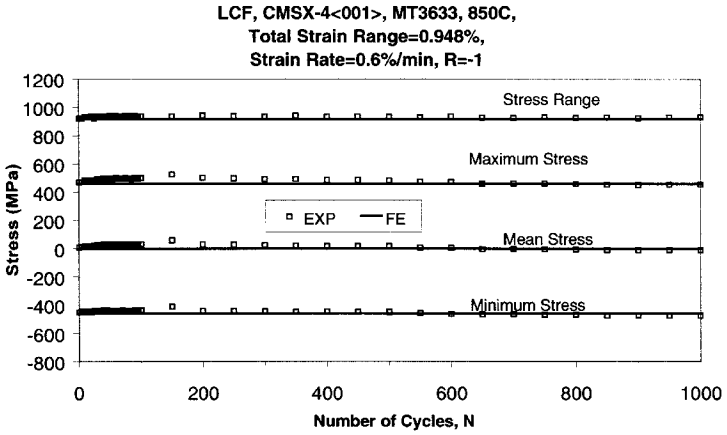


Fig7

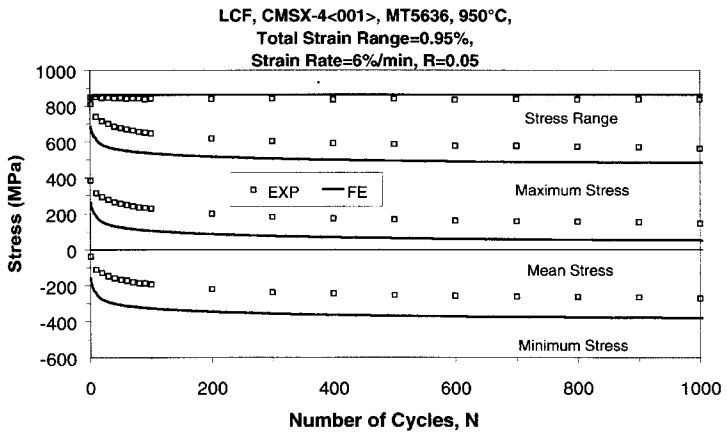


Fig 8

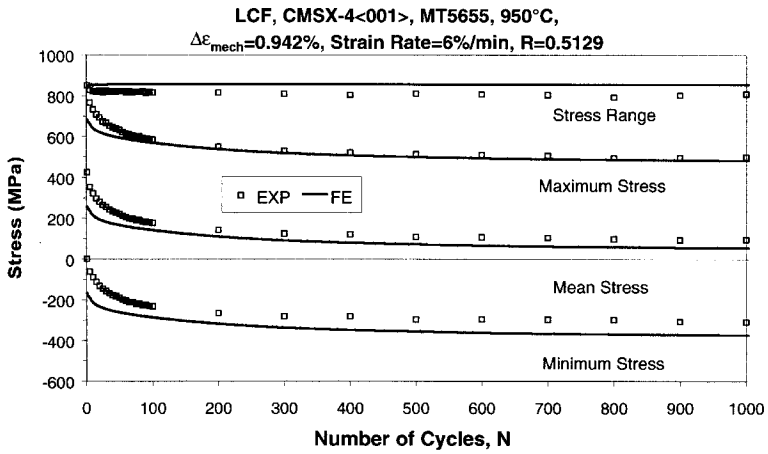


Fig 9

For CM186 TMF tests, OP and IP tests produced different shapes of stress-strain loop. The model was able to predict such shapes, as shown in figs 10a and 10b respectively, though the dominant behaviour here is evidently the change of elastic modulus with temperature. Measured inelastic strain ranges were too small for reliable resolution and the most significant check of inelastic predictions concerned mean stresses. Changes of mean stress were observed in all cases, with greater effects in R=0.05 tests, with the mean stress shift being consistently *away* from the *high*-temperature ends of the loops, as in figs 11 and 12. This is to be expected in terms of creep since, for a steady-state cycle, the general stress levels at the *lower* temperatures must be numerically *greater* than those of opposite sign at the *higher* temperatures in order that the 'hot' and 'cold' halves of the cycle should produce equal and opposite strain contributions. In this respect the mean stresses of IP tests behaved like those of LCF tests with R>-1 (figs 8 and 9) where the loading pattern creates early *tensile* mean stresses which subsequently reduce. For OP tests conversely, compressive mean stress was observed and shifting upwards, as would be expected in LCF tests with R<-1. LCF mean stresses would be expected to approach zero (otherwise equal and opposite strains would *not* be produced within the tensile and compressive halves of the steady cycle). But such is not the case for TMF owing to the temperature asymmetry, and in fig 11 the mean stress actually changes sign in order to achieve the necessary balance. The model predicted the trends of shifting of the mean stress and, in at least some cases, was able to provide reasonable numerical prediction, as shown in fig 11. Stress range was almost constant in all LCF and TMF tests, and tended to be somewhat over-predicted in the calculations. In the TMF tests, as illustrated by figs 11 and 12, the high temperature stresses tended to be rather better predicted in both IP and OP cases. This might be associated with the greater influence of data-extrapolation at low temperatures, since almost no single crystal creep information was available below 750°C. All the stress-levels were well below low temperature yield stresses (~1000MPa for the materials involved) so that *no* time-independent plasticity effects are suspected. However the present model ought not to be applied if such effects should arise. It is finally noted that in nearly all comparisons, as in most of those illustrated, the major discrepancies were associated with the first cycle and the agreement tended to improve in later cycles or at least not to worsen.

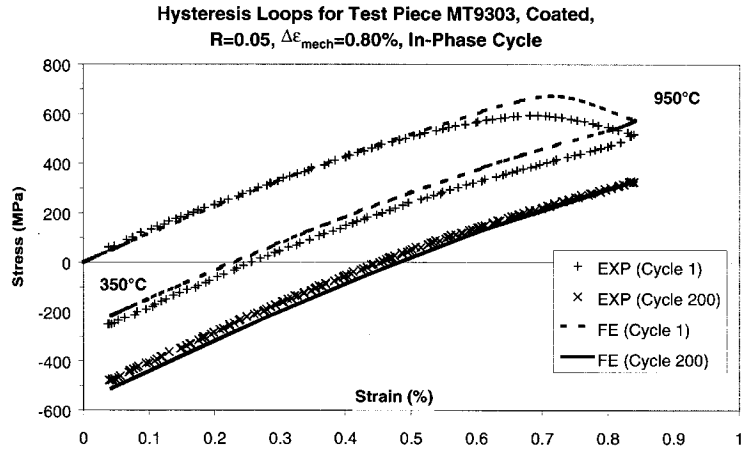


Fig 10a

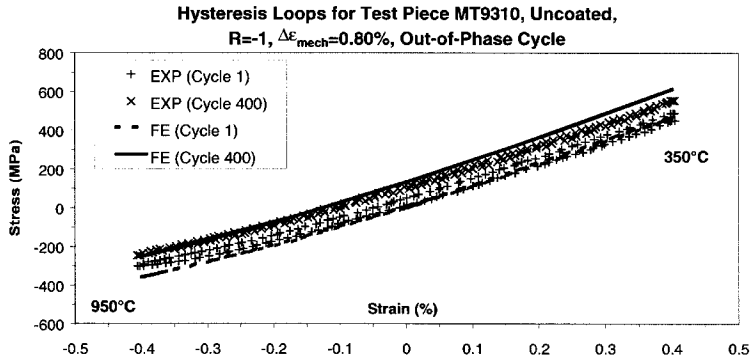


Fig 10b

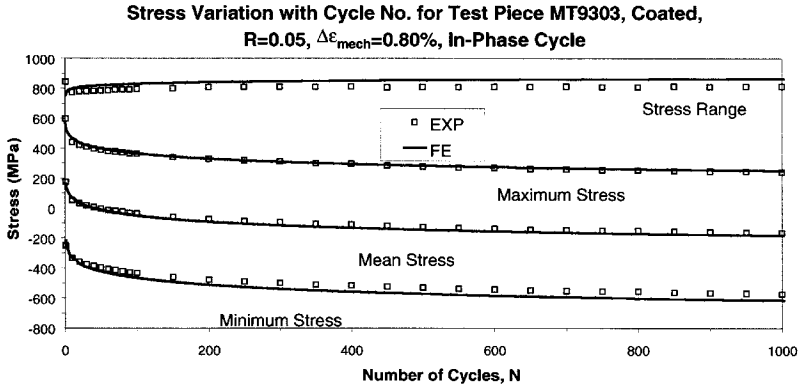


Fig 11

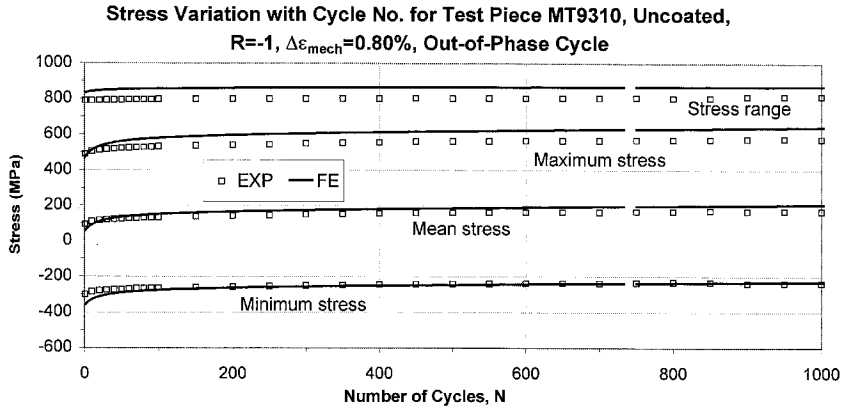


Fig 12

Conclusions

The comparisons described show that a suitable creep law, fitted only to high temperature creep data and strain-controlled tensile data, is able to simulate qualitatively, and to at least some degree quantitatively, the long-term high temperature cyclic mechanical response of <001> single crystal materials in LCF and TMF tests. However the characteristic 'humps' of initial loading in tensile and LCF tests are not modelled. The association of quantitative discrepancies with the *initial* cycle of loading may therefore be largely a question of the *primary* creep parameters employed *not* including tensile test information. It remains to see whether a fuller treatment of such data (as indicated) would bring significant improvements.

Acknowledgement

The authors thank ALSTOM Power for the permission to publish this article.

References

[1] Reppich B, Listl W and Meyer T *'Particle-Strengthening Mechanisms in ODS Superalloys'*, in ' Proc. Liège Conf. High Temperature Alloys for Gas Turbines and Other Applications (ed Betz W and others)', p1023, Reidel, Dordrecht, 1986.
[2] Lagneborg R 'A Modified Creep-Recovery Model and its Evaluation', Met. Sci. J, 1972, **6**, 127,
[3] White P S '*An Investigation of the Anisotropy of the Secondary Creep Rate in CMSX4*', in 'Proc. 6th Liège Conference (ed Lecomte-Beckers J, Schubert F and Ennis P J)', vII p1059, Univ. de Liège & Eur. Commission, Forschungszentrum Julich, 1998.
[4] White P S '*Statistically Based Fitting of Creep Data for FE Analysis, Covering Material Variability'*, in 'Proc. 5th Parsons Conference (ed Strang A, Banks W M, Conroy R D, McColvin G M, Neal J C and Simpson S)' p1022, IOM Communications Ltd, London, 2000.
[5] Kong C N, Bullough C K and Smith D J 'Thermomechanical Response of Single Crystal Nickel-base Superalloy CM186', *Thermomechanical Fatigue Behaviour of* Materials, *ASTM STP 1428, Vol 4*, ASTM, 2002 (to be published).

A MULTISCALE CONSTITUTIVE APPROACH TO MODEL THE MECHANICAL BEHAVIOUR OF INHOMOGENEOUS SINGLE CRYSTAL SUPERALLOYS: APPLICATION TO AS-CAST SX CM186LC

Gabriel M. Regino, Esteban P. Busso, Noel P. O'Dowd, and Derek Allen†

Department of Mechanical Engineering, Imperial College,
London SW7 2BX, UK
†ALSTOM Power Technology Centre,Whetstone, UK

Abstract

The as-cast microstructure of nickel-base single crystals generally consists of two regions: a dendritic one with a regularly arranged cuboidal $\gamma - \gamma$' microstructure, and the interdendritic region containing a high γ' volume fraction eutectic microstructure. In this work, we examine the effect of the eutectic microstructure on the mechanical behaviour of a typical Ni-base single crystal superalloy. Representative volume elements (RVEs) are used to obtain the homogenised behaviour of the heterogeneous superalloy microstructure. The behaviour of each region within the RVE is described by a large strain, rate-dependent crystallographic constitutive formulation. The overall uniaxial stress-strain response of a typical Ni-base single crystal alloy (viz. CM186LC) along different crystallographic orientations and at different strain rates and temperatures is obtained numerically from finite element computations of RVEs and compared with experimental data.

Keywords: Single Crystal Superalloys, Homogenisation, Non-Linear Finite Element Analyses, Crystallographic Models, CM186.

Introduction

The microstructure of nickel-base superalloys is greatly affected by chemical composition, cooling rates during casting and any subsequent heat treatments. In the as-cast condition, the microstructure typically consists of coherent γ' precipitates (typically $Ni_3(Al,Ti)$). At the mesoscale, the microstructure is composed of 50–200 μm γ/γ' eutectic regions, generally occupying the interdendritic regions. These eutectic regions, which precipitate during the final stages of solidification [1][2], contain a high volume fraction ($> 90\%$) of γ' precipitates of irregular shape. Figure 1(a) shows the different regions of a typical as-cast microstructure, namely that of the commercial superalloy CM186LC. Figure 1(b) displays a higher magnification view of the microstructure where the irregular shapes of the γ/γ' eutectic and the high γ' volume fraction are evident (the white phases correspond to γ'). Note also the presence of 'chinese script'-shaped carbides within the dendritic region (labelled B in Figure 1(b)), which are also a feature of this alloy.

The existence of eutectic regions was first reported in the first generation of cast nickel-base superalloys, such as SM200, IN100, INCO713 [3][4]. The effect of these eutectic regions was examined by Viatour *et al.* [2] while studying the influence of casting conditions on internal defects and creep properties of rotor blades cast in the Mar-M-002

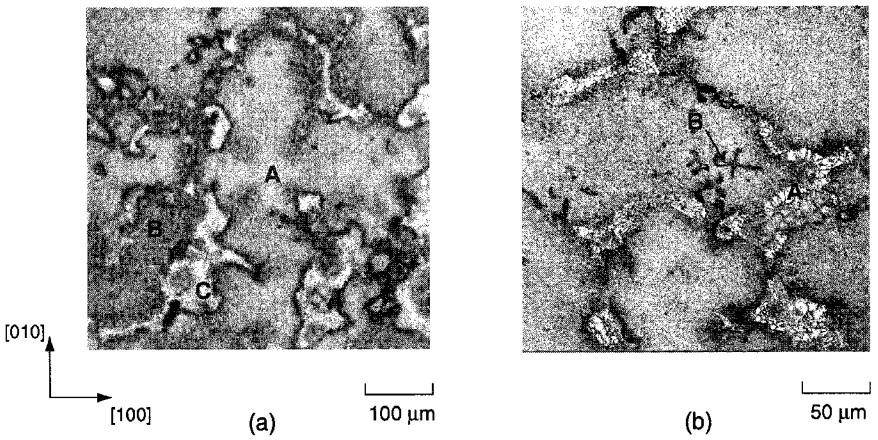


Figure 1: Typical SX CM186LC as-cast microstructure (a) overall microstructure, **A** dendritic region, **B** interdendritic region containing eutectic pools, **C** (b) γ/γ' eutectic microstructure **A** and 'chinese script' carbides, **B**

alloy. It was shown that the morphology of the γ' precipitates in the eutectic regions could affect the high temperature deformation and fracture behaviour of the material —cracks were often found to nucleate in eutectic pools with coarse γ', which are depleted of Cr, shortening the secondary (steady state) stage in a creep test. However, due to the existence of the coarse γ', it was found that the crack propagation rate was reduced. On the other hand, crack nucleation is more difficult in castings with finer γ' in the eutectic region, because of the presence of Cr, but propagation is easier.

Other attempts have been made to characterize the effect of γ/γ' eutectic regions on the mechanical behaviour of nickel-base superalloys. Walston *et al.* [5] examined the role of eutectic regions in the deformation of PWA1480 single crystals. Different heat treatments were employed to vary the volume fraction of eutectic in the alloy and room temperature tests were subsequently carried out. It was concluded that the presence of γ/γ' eutectic regions did not change the room temperature yield strength, but decreased both the ultimate tensile strength (UTS) and strain to failure. However, in their work the volume fraction of eutectic regions was reported to be small (near 6%) compared to other alloys, such as CM186LC, and the deformation mechanisms at room temperature are different from those relevant to service conditions at intermediate and high temperatures [6].

Further research has been carried out by Gayda *et al.* [7] and Caruel *et al.* [8] on PWA1480 single crystals and directionally solidified CM186LC, respectively, but no attempt was made in their work to include the effect of eutectic regions within a constitutive formulation. Furthermore, most of the current models are unable to predict the effect of local variations in the precipitate volume fraction on the local material behaviour. Recently, precipitate volume fraction effects were quantified for a range of temperature and strain rate conditions using a strain-gradient crystallographic framework and unit cell-based FE analyses [9][10]. These results have been incorporated into a state variable crystallographic formulation to account for experimentally observed precipitate volume

fraction and size effects in a single crystal nickel-base superalloy [11]. The present work is concerned with the development of a multiscale constitutive framework to quantify the role played by the size, volume fraction and spatial arrangement of both precipitates and γ/γ' eutectic in the mechanical behaviour of nickel-base superalloys.

Material Description

The alloy is assumed to be comprised of two regions, as mentioned previously, one that includes dendritic and interdendritic regions with an assumed regularly arranged cuboidal $\gamma - \gamma$' microstructure, and the second region formed by the eutectic microstructure. It has been found that, for the CM186LC alloy, the eutectic regions typically constitute 22% of the total volume.

The behaviour of the regularly arranged γ' regions within the CM186LC alloy (e.g. **A** and **B** in Fig. 1(a)) is assumed to be identical to that of a eutectic-free superalloy single crystal with the same γ' volume fraction. Due to the high precipitate volume fraction of the eutectic regions (e.g. **C** in Fig. 1(a)), these can be considered to have the same elasto-visco-plastic behaviour as that of the intermetallic compound Ni_3Al.

The stress-strain behaviour of both regions of the alloy is described by the multi-scale rate-dependent crystallographic formulation proposed by Busso [11]. The flow rule is expressed in terms of two internal variables per slip system (α): a macroscopically average slip resistance, S^α, and an internal or back stress, B^α. Thus,

$$\dot{\gamma}^\alpha = \dot{\gamma}_o \exp\left[-\frac{F_o}{k\theta}\left\langle 1 - \left\langle \frac{|\tau^\alpha - B^\alpha| - S^\alpha \mu/\mu_o}{\hat{\tau}_o \mu/\mu_o} \right\rangle^p \right\rangle^q\right] sgn(\tau^\alpha) \tag{1}$$

where k is the Boltzmann constant, τ^α the resolved shear stress on a slip system α, θ the absolute temperature, μ, μ_o the shear moduli at θ and 0 K, respectively, and F_o, $\hat{\tau}_o$, p, q and $\dot{\gamma}_o$ are material parameters. The evolutionary behaviour of the slip resistance and the back stress for an arbitrary slip system can be functionally expressed as,

$$\begin{aligned} \dot{S}^\alpha &= \hat{\dot{S}}^\alpha \{\dot{\gamma}^\alpha, S^\alpha, B^\alpha, v_f, l/l_m, \theta\} \\ \dot{B}^\alpha &= \hat{\dot{B}}^\alpha \{\dot{\gamma}^\alpha, S^\alpha, B^\alpha, \theta\}\,. \end{aligned} \tag{2}$$

Equation 2 contains an explicit link between the characteristics of the γ' precipitate population at the microscale and the homogeneous equivalent material at the macroscale, through the precipitate volume fraction, v_f, and the precipitate size l, here normalized by a mean reference value, l_m. Note that, for the eutectic regions, the evolution of the slip resistance and back stress in each slip system are assumed to be independent of v_f or l/l_m since they are, by definition, composed of pure Ni_3Al.

The elastic constants for the $\gamma - \gamma$' region were taken to be the same as those for the commercial superalloy CMSX4 [11], as its microstructure is similar to that of the dendritic regions in the superalloy of interest in this work, CM186LC. For the eutectic regions, the elastic constants were expressed as a function of an equivalent Al concentration, following the work of Prikhodko and co-workers [12], where the equivalent Al % was calculated depending on whether the other elements in the γ' composition in eutectic pools replace Ni or Al sites in the Ni_3Al lattice.

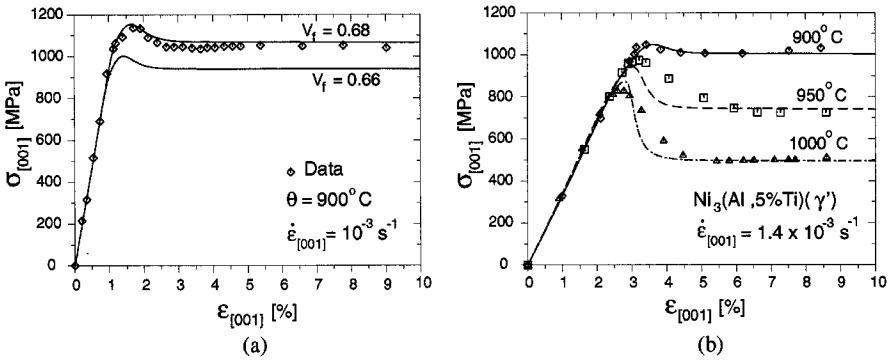


Figure 2: Comparison between model predictions (lines) and monotonic [001] tensile test data (symbols) for (a) CMSX4 and (b) Ni_3(Al, 5%Ti) single crystals [13]. Also shown in (a) is the predicted response of the regularly arranged γ' region within the heterogeneous SX CM186LC, for which $v_f = 0.66$.

Typical predictions of the monotonic uniaxial behaviour of CMSX4 and Ni_3(Al, 5% Ti)[13] at different temperatures and strain rates are shown in Figs. 2 (a) and (b), respectively, together with experimental data. Here, the ability of the model to predict the behaviour of a completely homogenised nickel-base superalloy and an intermetallic compound can be seen.

Note that the average γ' volume fraction in CMSX4 is 68%, while that in the regularly arranged $\gamma - \gamma$' regions in CM186LC was estimated as 66%. In this work, the effect of the difference in γ' volume fraction on the mechanical behaviour of the dendritic regions is taken into account through the calibration of Eqs. 2 using the results of [10].

Finite Element Framework

The crystallographic formulation was implemented numerically into the finite element method using a large strain algorithm with an implicit time integration procedure [10]. The material parameters in Eq. 1 and the functional relations in Eqs. 2 were calibrated based on data for the commercial superalloy CMSX4 [11] and Ni_3(Al, Ti) single crystals [13].

Finite element (FE) calculations of periodic unit cells of the RVEs were performed under 2D generalized plane strain conditions in conjunction with multiphase elements, whereby the constitutive behaviour of each material point within the finite elements is defined based on the material region/phase to which it belongs [14]. The advantage of this type of method over the conventional way of using the same constitutive law for all the integration points within each FE, is that it offers an economical way of modelling heterogeneous materials with complex microstructures [15]. When using multiphase elements, one can use any arbitrarily generated FE mesh, such as a regular one. A digitised image of a typical microstructure, where each of the regions of interest has been identified with the help of a quantitative image analyser, can then be easily superimposed onto the FE mesh. Figure 3(a) shows a typical digital image of the SX CM186LC microstructure,

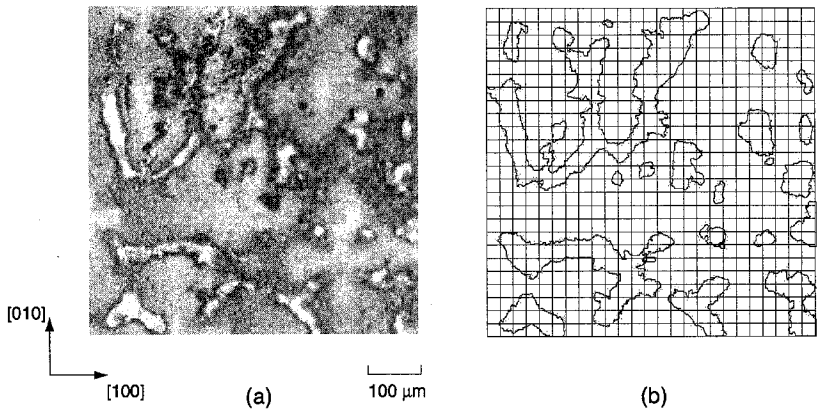


Figure 3: Discretisation of a typical RVE used in FE computations: (a) actual CM186LC microstructure, and (b) the corresponding eutectic region discretisation and FE mesh

with the distribution of eutectic regions on a (001) plane. In Fig. 3(b), the corresponding regular FE mesh and the irregular boundaries of the eutectic regions are shown.

Results and Discussions

Finite element analyses of periodic unit cells of RVEs similar to the one shown in Fig. 3 have been carried out. The RVE unit cell size for each analysis was varied from ~ 250 to ~ 1800 μm on a randomly located area of 2.8×2.8 mm^2 in the SX CM186LC microstructure [14]. These studies have shown that the overall material behaviour depends strongly on the volume fraction of the eutectic regions, and more weakly on their morphology, and that the smallest RVE size which correctly represents the overall uniaxial material response is $\sim 650 \times 650$ μm^2.

Having identified an appropriate size for the RVE, FE simulations of monotonic tensile tests along the [001], [010], and [100] crystallographic orientations for different strain rates at 900°C were carried out. Figures 4 (a) and (b) show the RVE contour plots of uniaxially equivalent accumulated inelastic strain, $\bar{\varepsilon}^p$, after a 10% deformation at a strain rate of 10^{-3} 1/s along the [010] and [100] orientations, respectively. It can be seen that the level of inelastic deformation within the eutectic regions is somewhat lower than that in the dendritic regions and that localisation of inelastic strain occurs in the vicinity of the eutectic regions.

The overall stress-strain response of the SX CM186LC when loaded along the [001] orientation is shown in Fig. 5, together with the experimental data [16]. It can be seen that the model accurately predicts the steady state response of the material. However, in the elastic regime, there is some disagreement between the experimental results and the RVE model. There are also some differences in the softening behaviour of the material at strains between 1.0 and 3.0%.

The single crystal data used to calibrate the behaviour of the eutectic regions was taken from [13] for an aluminium rich Ni_3Al with 5% Ti alloy. It is known that the elastic

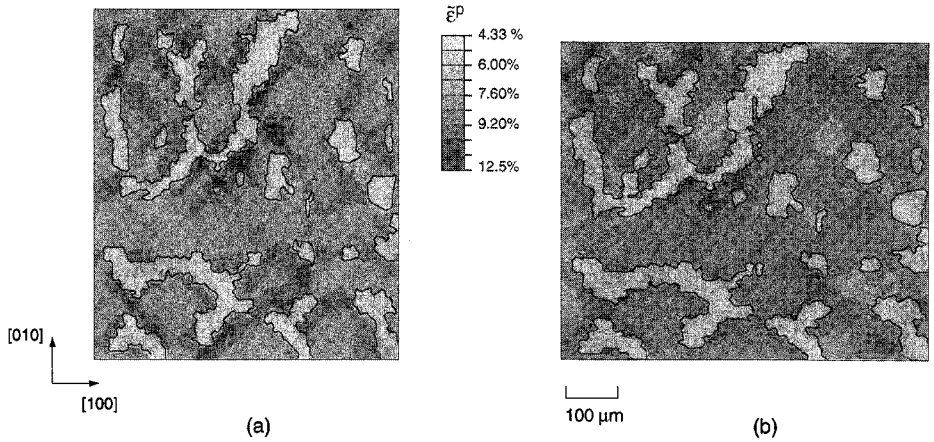


Figure 4: Contour of accumulated inelastic strain of a typical RVE, after a 10% macroscopic uniaxial strain loaded in (a) [010] orientation and (b) [100] orientation

moduli of the intermetallic compound Ni_3Al increases with a reduction in Al content [12]. In SX CM186LC, the measured composition of γ' particles was 64.4 Ni, 14.7 Al, 6.7 Co, 3.1 Cr, 3.0 W, 2.6 Ta, 1.0 Ti, and 0.5 Re (at.%) [17]. Bearing in mind that Ti, Ta, and W take up Al positions in the lattice, and Cr those of Al and Ni [18][19], one can calculate a resulting equivalent Al concentration of $\sim$ 23 at.%. Figure 6 shows the overall monotonic tensile behaviour using the elastic moduli obtained from [12] based on this eutectic composition —note that the inlelastic response is still based on that for Ni_3(Al, 5% Ti) as the effect of Al concentration on the inelastic response is not known. It is seen that the use of this improved estimate of the elastic moduli results in a better overall

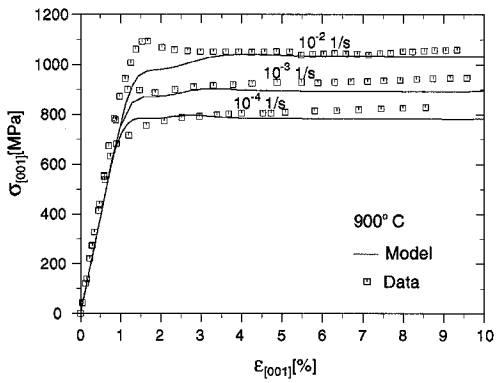


Figure 5: Comparison between [001] experimental data and the predicted monotonic response along the [001] orientation of the RVE at different strain rates with eutectic composition as in [13].

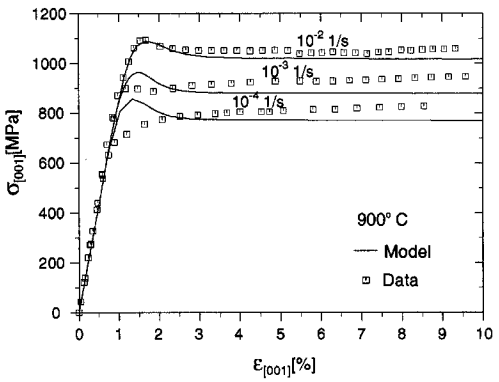


Figure 6: Comparison between [001] experimental data and the predicted monotonic response along the [001] orientation of the RVE at different strain rates with 23% Al_{eq} at.%.

agreement with the experimental data of the transient uniaxial stress-strain response.

Concluding Remarks

In this work, it has been shown that the use of a homogenisation technique based on representative volume elements of the microstructure provides a valuable tool to determine the stress-strain behaviour of heterogeneous single crystals superalloys. In particular, the proposed approach should enable material designers to predict the effect of different morphological characteristics of the microstructure, such as the volume fraction and shape of γ' precipitates and eutectic regions, on the mechanical behaviour of the superalloy.

The results of the FE RVE calculations also revealed that the eutectic regions' elastic moduli, linked to the equivalent Al concentration, play a role on the transient part of the uniaxial response of the heterogeneous superalloy. Ongoing work deals with the effect of the 3D nature of the eutectic regions on the macroscopic response of the superalloy and on the formulation and calibration of an equivalent single crystal formulation for the macroscopically homogenised superalloy, based on the types of parametric periodic unit cell FE results presented here.

References

[1] J. Lecomte-Beckers, Study of Solidification Features of Nickel-Base Superalloys in Relation with Composition, Metall. Trans., 19A, 1988, pp. 2333–2340.

[2] P. Viatour, D. Coutsouradis, and L. Habraken, Casting Conditions, Microstructure and Creep Properties of MAR-M-002 Blades, in High Temperature Alloys for Gas Turbines, D. Coutsouradis, P. Felix, H. Fischmeister, L. Habraken, Y. Lindblom, and M. O. Speidel ed., Applied Science Publ., London, 1978, pp. 875–891.

[3] C. G. Bieber and T. E. Kihlgren, A New Cast Alloy for Use at 1900°F, Met. Prog., 79, April, 1961, pp. 97–99.

[4] R. A. Gregg and B. J. Piearcey, Solute Distribution and Eutectic Formation in As-Cast Nickel-Base Superalloys, Trans. AIME, 230, 1964, pp. 599–600.

[5] W. S. Walston, I. M. Berstein, and A. W. Thompson, The role of the γ/γ' Eutectic and Porosity on the Tensile Behaviour of a Single-Crystal Nickel-Base Superalloy, Metall. Trans., 22A, 1991, pp. 1443–1451.

[6] W.W. Milligan and S.D. Antolovich, Yielding and Deformation Behavior of the Single Crystal Superalloy PWA 1480, Metall. Trans., 18A, 1987, pp. 85–95.

[7] J. Gayda, R.L. Dreshfield, and T.P. Gabb, The Effect of Porosity and $\gamma-\gamma$' Eutectic Content on the Fatigue Behavior of Hydrogen Charged PWA 1480, Scripta Metal. Mater., 25, 1991, pp. 2589–2594

[8] F. Caruel, S. Bourguignon, B. Lallement, S. Fargeas, A. DeBussac, K. Harris, G.L. Erikson, and J.B. Wahl, SNECMA Experience with Cost-Effective DS Airfoil Technology Applied Using CM 186 LC Alloy, J. Eng. Gas Turbines and Power, 120, 1998, pp. 97–104.

[9] E.P. Busso, F. Meissonnier, and N.P. O'Dowd, Gradient-Dependent Visco-Plastic Deformation of Two-Phase Single Crystals, Journal of the Mechanics and Physics of Solids, V. 48, Issue 11, 2000, pp. 2333–2361.

[10] F. Meissonnier, E.P. Busso, and N.P. O'Dowd, Finite Element Implementation of a Non-Local Visco-Plastic Crystallographic Formulation, Int. J. Plast., 17, 2001, pp. 601–640.

[11] E.P. Busso, A Crystallographic Formulation for Single Crystals with Explicit Microstructural Length Scales. Part I: Model Formulation, Submitted for Publication.

[12] S.V. Prikhodko, J.D. Carnes, D.G. Isaak, and A. J. Ardell, Temperature and Composition Dependence of the Elastic Constants of Ni_3Al, Metall. Trans., 30A, 1999, pp. 2403–2408.

[13] S. Ochiai, S. Miura, Y. Mishima, and T. Suzuki, High Temperature Yielding of Ni_3(Al, Ti) Single Crystals, J. Jpn. Inst. Metals, 51, 1987, pp. 604–615.

[14] G.M. Regino, A Multiscale Constitutive Approach to Model the Mechanical Behaviour of Inhomogeneous Single Crystals, MPhil Thesis, Imperial College, London, 2002.

[15] Th. Steinkopff, Multiphase Element Method, in Third Workshop on Computational Modellingof the Mechanical Behaviour of Materials, Stuttgart, Germany, 1993.

[16] ALSTOM Power, Mechanical Testing, COST522 Progress Report, May 2001.

[17] A. Czyrska-Filemonowicz, B, Dubiel, D. Danciu, M. Biel, and M. Lucki, Microstructural Investigation of the CM186 SC Superalloy by Means of LM, SEM, and TEM, COST522 Annual Report, 2000.

[18] R.W. Guard and J.H. Westbrook, Alloying Behaviour of Ni_3Al (γ' Phase), Trans. AIME, 215, 1959, pp. 807–814.

[19] Y. Mishima, S. Ochiai, N. Hamao, M. Yodogawa, and T. Suzuki, Solid Solution Hardening of Ni_3Al with Ternary Additions, Trans. Jpn. Inst. Metals, 27, 1987, pp. 648–655.

DEFORMATION MODELLING OF THE SINGLE CRYSTAL SUPERALLOY CM186 LC

R. Daniel*, T.Tinga[Ψ], M.B. Henderson[+], T.J. Ward*

*QinetiQ, UK; [Ψ]NLR, Netherlands; [+]ALSTOM Power, UK,

Abstract

Single crystal nickel-based superalloys are being used increasingly to manufacture the turbine blades for both aero and land-based gas turbine engines. These alloys provide significant increases in component endurance and reliability, as well as engine performance due to the increased turbine entry temperature levels that can be achieved. To ensure full utilisation and determination of safe component lifetimes, accurate modelling of the non-linear deformation suffered during typical duty cycles is needed. In recent years a number of anisotropic creep data analysis and modelling methods have been developed, largely based on the determination of constitutive parameters for the <001> and <111> crystallographic directions. These models have been incorporated within a Schmid's Law slip-system analysis to determine local shear creep strain accumulation and resolved shear stresses. Any appropriate creep formulation can be included within this framework. The present paper describes the development of two models: i) the QinetiQ Creep Law and ii) the creep law used by the National Aerospace Laboratory (NLR) in The Netherlands, that have been incorporated into user material subroutines for the ABAQUS and MSC Marc finite element programmes, respectively. The models allow full three-dimensional analysis with elastic, inelastic and thermal deformations and can be used to simulate the high temperature creep and thermomechanical fatigue behaviour of specimens and turbine blades under service loading conditions. Predictions have been generated for the anisotropic creep behaviour of a number of specimen tests and blade designs for the as-cast (non-solutioned) single crystal nickel based superalloy CM186LC.

Keywords: Creep, Anisotropy, CM186LC, Single Crystal, Finite Element Analysis

Introduction

The demands placed on gas turbine engine hot section components are extreme. Typical metal temperatures range from 850 to >1000°C, with component creep lives expected to run between 10,000–100,000hrs, depending on the duty cycle imposed. The need to meet these demands, in terms of creep and fatigue life has led to the development of a range of single crystal (SX) nickel based superalloys specifically designed for first and second stage, turbine blade applications. First generation alloys, such as SRR99, have been superseded by second-generation, higher creep strength materials containing additions of Rhenium, such as CMSX-4. These alloys were developed specifically for aero-engines, where the turbine blades experience for short durations, higher peak temperatures and stresses than are generally found in land based power generation systems. SX castings are susceptible to low and high angle grain boundary defects that can result in low yields and high manufacturing costs. For certain land based turbine duty cycles, it should be possible to use lower cost components, and therefore, a defect tolerant CMSX-4 derivative alloy, called CM186LC has been developed [1-3]. This alloy is intended for use in the as-cast form to minimise solution heat treatment costs and contains grain boundary strengthening additions to overcome defect susceptibility and improve casting yields. Removal of the solution treatment schedule enables a significant cost saving, but results in a complex microstructure containing residual levels of eutectic. The following paper forms part of a large body of research conducted under the COST 522 European collaborative programme, focused on determining the properties of CM186LC SX.

During service exposure turbine components such as blades and nozzle guide vanes undergo creep and thermo-mechanical fatigue. Utilisation of these components requires that the

response of the materials to deformation mechanisms, as a function of engine conditions, be understood. For instance, the creep life has been shown to be highly dependent on operating temperatures; a 10° to 15° increase in temperature can reduce the creep rupture life by 50% [4]. The single crystal nature of the components used mean that the complex anisotropic response must be included in any model of the elastic or inelastic behaviour. Even though most engine components are cast in the nominally <001> direction, variations in blade orientation occur during casting and the non-uniform shape of components, particularly around cooling holes and platform shoulders, results in a multi-axial stress state and an anisotropic response. For components where the crystal orientation deviates significantly from the <001> direction the need for an anisotropic analysis is even more apparent. This has led to the development by QinetiQ of the UK and NLR of The Netherlands of full 3-D, anisotropic creep deformation materials models which can be used within commercial Finite Element analysis software.
(Note the models do not take into account for the inhomogeneity of the material.)

The QinetiQ creep model

Under static loading at elevated temperatures, most engineering materials exhibit a three-stage creep deformation response. It should be possible to describe the creep strain accumulation with an expression involving the stress (σ), temperature (T) and time-on-load (t) as follows:

$$\varepsilon_c = f(\sigma, t, T) \qquad (1)$$

The QinetiQ creep law, based on that first developed by Graham and Walles [5], represents the total creep strain (ε_c) by the sum of a number of independent terms expressed by a power law summation, hence:

$$\varepsilon_c = \sum_j \sum_i \sigma^{\beta_j} t^{\kappa_i} e^{\left(\Lambda_{T\beta_j\kappa_i} T + \Lambda_{S\beta_j\kappa_i}\right)} \qquad (2)$$

where κ_i = 1/3, 1, 3, 9; and β_j is chosen such that the ratio $-\frac{\kappa_i}{\beta_j}$ = ½, ¼, 1/8, 1/16...etc. $\Lambda_{T\beta_j\kappa_i}$ and $\Lambda_{S\beta_j\kappa_i}$ are constants.

The original Graham-Walles equations omitted the rupture term $\kappa_4 = 9$, and had a temperature function of the form $(T'_{\beta_j} - T)^{-20\kappa_i}$ where T'_{β_j} are constants. Analysis of a significant creep database has identified a limitation in the form of the temperature term in the original Graham-Walles approach that restricted the predictive accuracy. An exponential function was found to be more accurate over a wide temperature range. A fuller description of the model and the parameter determination methods can be found elsewhere [6].

The NLR creep model

As mentioned previously, under static loading at elevated temperatures, most materials exhibit a three-stage creep deformation response. Moreover, the creep rate is a function of temperature and stress level. These two requirements are met by the creep law presented by Pan, Shollock and McLean [7], which has been applied here.

The shear strain rate at the k-th slip system $\dot{\gamma}^k$ is defined as

$$\dot{\gamma}^k = \dot{\gamma}_i^k \left(1+\omega^k\right)\left(1-S^k\right) \tag{3}$$

where ω^k is a dimensionless damage parameter, whose initial value is zero and which evolves with time according to the following relationship:

$$\dot{\omega}^k = \beta^k \dot{\gamma}^k \tag{4}$$

and S^k is a dimensionless internal stress parameter, whose initial value is also 0 and which evolves with time according to the following:

$$\dot{S}^k = H^k \dot{\gamma}_i^k \left(1-\frac{S^k}{S_{ss}^k}\right) \tag{5}$$

The internal stress parameter S controls the primary part of the creep behaviour, whereas the damage parameter ω controls the tertiary part.

The four parameters $\dot{\gamma}_i^{\,k}$, β^k, H^k and $S_{ss}^{\,k}$ all have the same functional dependence on resolved shear stress and temperature.

$$\dot{\gamma}_i^k = a_1^k \exp\left(b_1^k \tau^k - \frac{Q_1^k}{RT}\right) \tag{6}$$

$$\beta^k = a_2^k \exp\left(b_2^k \tau^k - \frac{Q_2^k}{RT}\right) \tag{7}$$

$$H^k = a_3^k \exp\left(b_3^k \tau^k - \frac{Q_3^k}{RT}\right) \tag{8}$$

$$S_{ss}^k = a_4^k \exp\left(b_4^k \tau^k - \frac{Q_4^k}{RT}\right) \tag{9}$$

The parameters a_1 to a_4, b_1 to b_4 and Q_1 to Q_4 must be determined for both the octahedral and cuboidal slip systems from experiments.

Single crystal anisotropy

The QinetiQ and NLR Slip System Models assume that all non-linear deformation within a single crystal superalloy occurs on 12 octahedral and 6 cuboidal slip systems (Figure 1). When subjected to a uniaxial load, the degree of slip activity is dependent on the resolved shear stress for that system, determined by the Schmid factor [8] using the following equation:

$$d\tau^{(\alpha)} = \underline{\mu}^{(\alpha)^T} d\underline{\sigma} \tag{10}$$

where τ is the shear stress, $\underline{\sigma}$ the global stress, and $\underline{\mu}$ are the Schmid factors.

The shear stress τ can be applied within the creep law at the temperature of interest to determine the amount of shear creep deformation γ on the slip system for a given increment of time. The increment of creep strain on a slip system is resolved back into a global strain vector also using the Schmid factors. The contribution from each slip system is resolved and summed to give the total creep strain on the global axes of the model as follows:

$$d\underline{\varepsilon}_C = \sum_{\alpha} \underline{\mu}^{(\alpha)} d\gamma_c^{(\alpha)} \tag{11}$$

where $d\gamma_c$ is the incremental shear strain on the α slip system and $d\underline{\varepsilon}_c$ is the incremental global creep strain. The general summation covers all 18 slip systems with the contribution from each to the overall global creep strain being determined by the magnitude of the appropriate Schmid factor. By means of substitution the parameters for equation (2) or (6) to (9) are calculated for the octahedral and cube slip systems by using the single shear stress and strain values from equations (10) and (11).

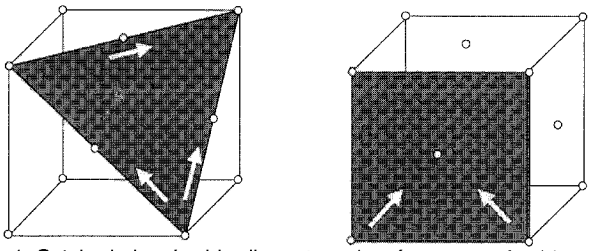


Figure 1. Octahedral and cubic slip systems in a face centred cubic unit cell.

Uniaxial loading along the <001> direction activates 8 identically stressed octahedral systems, the remaining slip systems being subject to zero stress. This allows the associated stress-strain values to be related to single crystal <001> creep test data, and the Λ_S constant in equation (2), or a_i, b_i and Q_i (i =1..4) in equations (6) to (9) for the octahedral slip systems to be determined. Loading along the <111> direction activates 6 identical octahedral systems and 3 identical cubic systems. Having calculated the octahedral contribution, the Λ_S or a_i, b_i and Q_i for the cubic slip system can be determined.

The octahedral and cuboidal parameters are used to predict the creep deformation on each of the 18 slip systems. Shear strains are transformed onto the global axes to contribute to the incremental creep strain vector, using equation (11).

For an arbitrary orientation the Schmid factors determine the stress component on the individual slip systems from which the creep strain component on each slip system - and hence the creep strain on the global axis - can be calculated.

A computer program has been developed at both QinetiQ and NLR to determine the creep model parameters for the constitutive equations described above. In addition, the constitutive models have been incorporated within user materials subroutines (UMAT's) for ABAQUS and MSC.MARC, for QinetiQ and NLR respectively [9]. Full 3-D isotropic or anisotropic creep strain analysis for a range of stress, temperature and time on load conditions is possible for any pre-defined crystallographic orientation and specimen or aerofoil design.

Results

Analysis of CM186LC creep data

The QinetiQ and NLR creep models have been used to analyse data generated under uniaxial creep at the temperatures 750, 850 and 950°C for stresses ranging between 115-750MPa for the crystallographic directions <001> and <111>. These analyses provide the macroscopic creep parameters for the <001> and <111> orientations from which the slip system parameters were calculated. Using the models, the macroscopic creep parameters for the <001> direction

can be used to predict the <001> creep behaviour of CM186LC for any stress and temperature. Similarly the macroscopic creep parameters for <111> can be used to predict the <111> creep behaviour for any stress and temperature. A set of predictions have been made for the <001> and <111> directions at 850°C independently by QinetiQ and NLR, these have been compared with corresponding uniaxial creep test data, generated within the COST 522 Work package 1.1 programme. The predicted and actual uniaxial creep test curves for <001> and <111> at 850°C and for various stresses are shown in Figures 2 to 5. The data are presented as linear-log plots of creep strain (%) versus time (Hrs), the "M" before the stress in the legend denotes the curves predicted by the model.

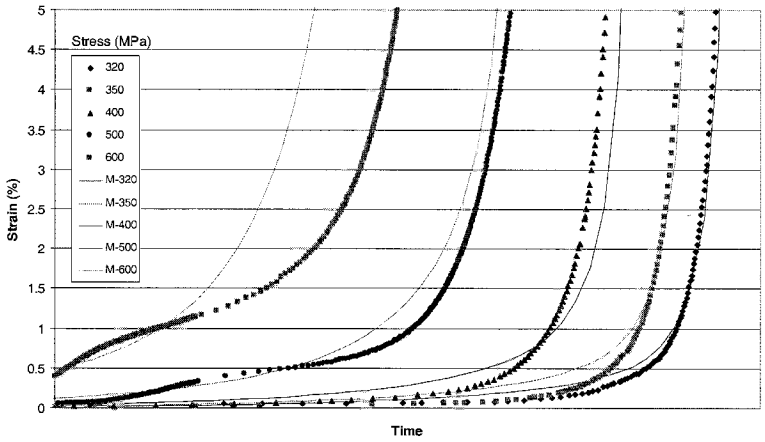


Figure 2. A comparison of uniaxial creep test results and their corresponding curves produced by the QinetiQ creep law model for <001>, 850°C and various stresses.

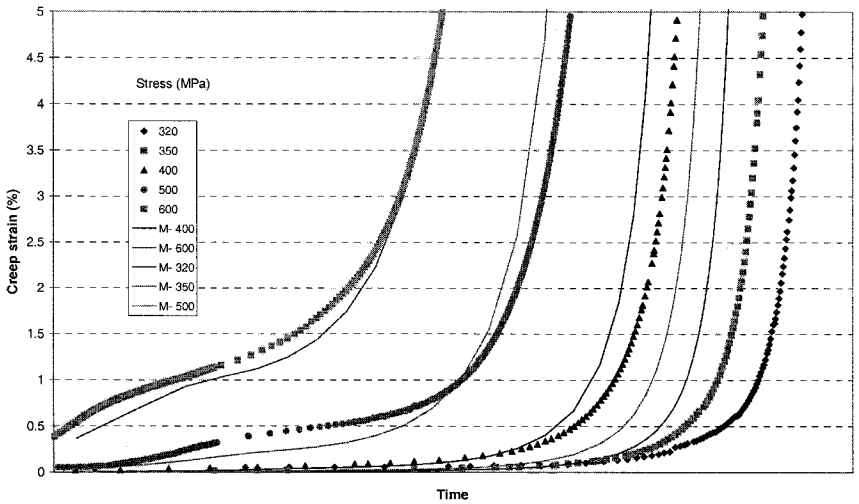


Figure 3. A comparison of uniaxial creep test results and their corresponding curves produced by the NLR creep model for <001>, 850°C and various stresses.

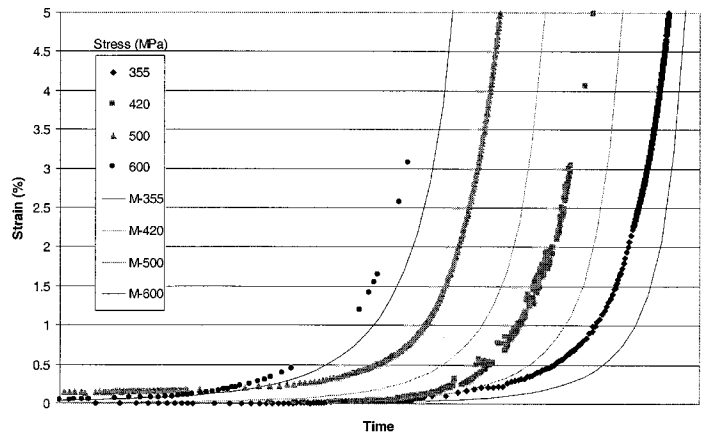


Figure 4. A comparison of uniaxial creep test results and their corresponding curves produced by the QinetiQ creep law model for <111>, 850°C and various stresses.

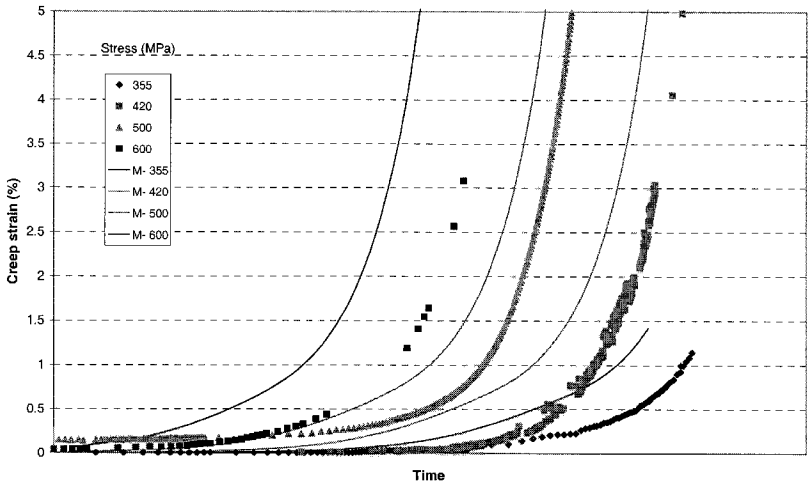


Figure 5. A comparison of uniaxial creep test results and their corresponding curves produced by the NLR creep model for <111>, 850°C and various stresses.

It can be seen from the comparisons that there is a general agreement between the actual data and the re-plotted, predicted data. The <001> analysis has a closer match than the <111> analysis except for the high stress case (600 MPa) for the QinetiQ model, where the prediction begins to breakdown, and conversely in the low stress case (320 MPa) for the NLR model. A comparison between the two models for the <111> direction shows that there is greater agreement. Further optimisation of the fitting to the data is anticipated to reduce the discrepancies found thus far.

FEA of creep behaviour

Modelling of diametral strain

When a cylindrical CM186LC SX test bar is loaded in a non-symmetrical direction, the cross section becomes elliptical due to the anisotropic deformation. The NLR creep model was used to calculate this diametral strain distribution, the results of which can be seen in the left-hand side of Figure 6. The Polar plot shown on the right hand side is taken from measurements made from different directions during the course of the creep tests. It can be seen from Figure 6 that the maximum strain is observed in the <001> direction, whereas the minimum is in a <011> direction. This is predicted correctly by the model. Moreover, the absolute value of diametral strain is predicted quite well. Only some details in the shape of the strain distribution are not predicted very well.

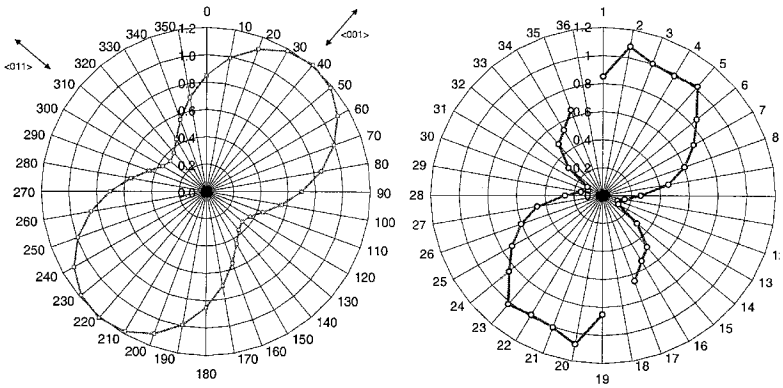


Figure 6. Calculated (left) and measured (right) diametral strain distribution in a cylindrical creep test bar after 875 hrs creep at 850°C and 355 MPa.

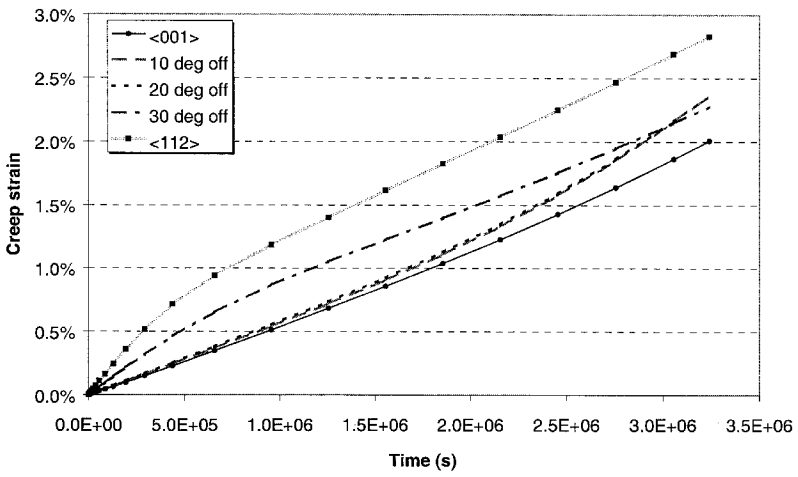


Figure 7 Effect of crystal misorientation on creep behaviour (NLR model).

Effect of crystal misorientation

For gas turbine applications single crystals are oriented with the superior <001> orientation in the most highly loaded direction (radial direction for turbine rotor blades). However, the alignment of crystal axis and component axis is not always perfect. Figure 7 shows the effect of misorientation of the crystal on creep behaviour. The <001> direction has been shifted towards the <112> direction in steps of 10 degrees along the <001>-<111> boundary line in the stereographic triangle. It appears that the creep rate increases rapidly with increasing misorientation angle, although the increase in creep rate is small between 10 and 20 degrees off the <001> axis.

Creep strain distribution in gas turbine components

The creep strain distribution in a high pressure turbine blade has been calculated, using the NLR model, for a simplified mission (start-up / steady-state at max power / shut-down). The resulting predicted Von Mises equivalent creep strain after 100 hrs at max power for an SR99 SX blade and a IN100 polycrystalline blade, for reference, are shown in Figure 8.

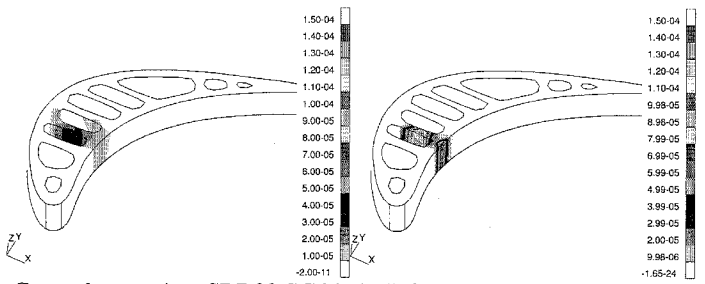
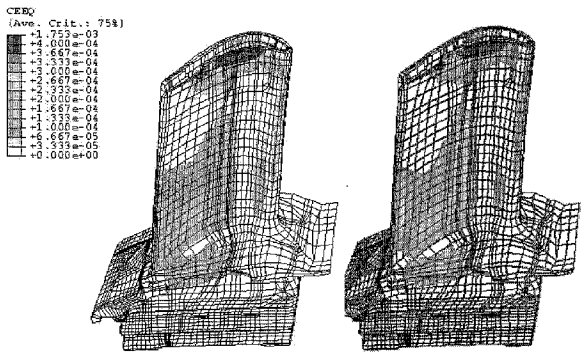


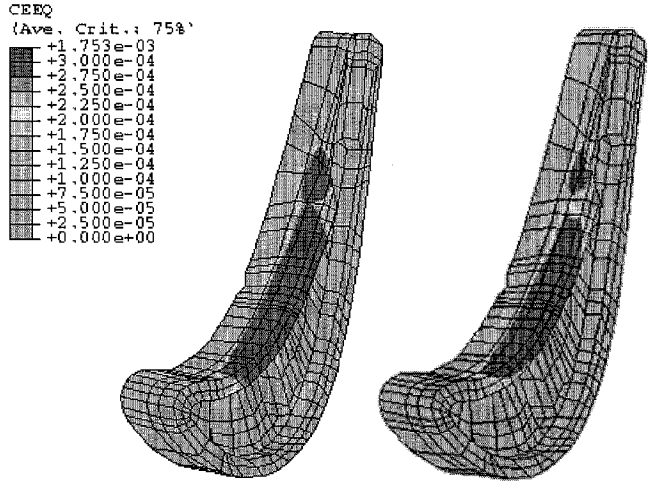
Figure 8. Creep damage in a SRR99 SC blade (left) and a polycrystalline IN100 blade.

Figure 9 is a picture of the model blade mesh with the creep damage plotted for the isotropic and anisotropic analyses, calculated for a typical industrial gas turbine duty cycle using the QinetiQ creep model. At first sight the results appear fairly similar, though there are important differences (NOTE the blade root is modelled elastically).



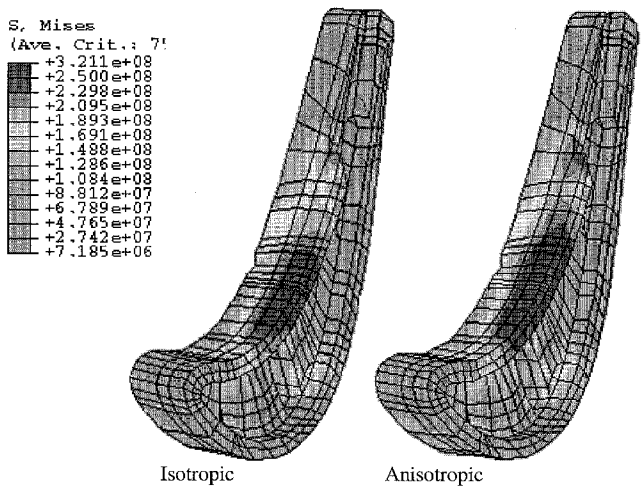
Isotropic Anisotropic

Figure 9. Contour plots of Von Mises Stress - Anisotropic Analysis.



Isotropic Anisotropic

Figure 10. Detail Contour plots of creep damage at tip of aerofoil.



Isotropic Anisotropic

Figure 11. Detail contour plots of Von Mises stress at tip of aerofoil

Figures 10 and 11 show the detail at the tip of the aerofoil, where it can be seen that the isotropic analysis predicts a greater degree of creep damage (Fig. 10). As creep strain has the effect of relaxing the stress locally, this explains why the isotropic model predicts a lower Von Mises stress (Fig. 11) distribution.

Discussion:

- Application of the QinetiQ and NLR creep models to modelling the anisotropic creep behaviour of CM186LC SX using a slip system approach has found similar results. The largest difference between the models is the creep law formulation used by each organisation. However, both formulations are capable of describing the three-stage creep behaviour and therefore predict the CM186LC SX creep deformation quite well.

- Implementation of the anisotropic creep models in finite element codes (ABAQUS and MSC.Marc) offers the potential to conduct a large variety of calculations and simulations that demonstrate the effects of orientation and multiaxial stress states on the deformation response and damage accumulation in complex component geometries. A selection of the simulations available has been presented. Significant differences are found between the predictions due to isotropic and anisotropic formulations specifically located around features such as cooling holes and sharp radii. The results underline the necessity for anisotropic analysis, rather than isotropic that is sometimes carried out in engineering design practice for reasons of simplicity, as they show that there are implications for the creep and fatigue life calculations in high pressure turbine blades.

Acknowledgements
QinetiQ and ALSTOM Power gratefully acknowledge the support of UK DTI for this work. In addition the authors would to thank CESI, FZ – Jülich, IPM –Brno for the creep data results.

References:

1. K.Harris, J.B.Wahl, "New Superalloy Concepts for Single Crystal Turbine Blade and Vanes", Proc. 5th Int. Charles Parsons Conf., Cambridge, July 2000, pp. 822-846.
2. P.S.Burkholder, M.C. Thomas, R. Helmink, D.J. Frasier, K. Harris and J,B, Wahl, "CM186 LC Alloy Single Crystal Turbine Vanes" International Gas Turbine and Aeroengine Congress and Exhibition, Indianapolis, June 1999.
3. G. McColvin, J, Sutton, M. Whitehurst, D.G. Fleck, T.A. van Vranken, K. Harris, G.L. Erickson and J,B, Wahl, "Application of the Second Generation DS Superalloy CM186LC to First Stage Turbine Blading in EGT Industrial Turbines", Proceedings of the 4th International Charles Parsons Conference, November 1997, pp. 339-357.
4. G.F. Harrison, "The Influence of New Materials on Future Engine Design, Component Lifing and Reliability", Proc. Eurpean Forum, The Royal Aeronautical Society (1993), pp.3.1-3.16.
5. A. Graham and K.J. Walles, Iron and Steel Institute, 179, 1955.
6. T. Homewood, T.J. Ward, M.B. Henderson and G.F. Harrison, "The DERA Slip System Creep Law for the Modelling of Face Centred Cubic Single Crystal Material Behaviour." Proc. Conf on Modelling of Microstructural Evolution in Creep Resistant Materials, Imperial College, London, September 1998.
7. L-M Pan, B. Shollock, M. McLean, "Modelling of High-Temperature Mechanical Behaviour of a Single Crystal Superalloy", Proc. R. Soc. Lond. A, 453 (1997), 1689-1715.
8. E. Schmid and W. Boas, Plasticity of Materials, F.A. Hughes & Co, 1950.
9. T.J. Ward and M.B. Henderson, "Writing and Applying a User Material Subroutine (UMAT) for the Analysis of Single Crystal Turbine Blades", Proc. of the ABAQUS Users Group Conf., September 1998.

TMS-82+ : A HIGH STRENGTH NI-BASE SINGLE CRYSTAL SUPERALLOY

Takehisa Hino*, Yomei Yoshioka*,
Yutaka Koizumi**, Toshiharu Kobayashi**, Hiroshi Harada**
*Power & Industrial Systems R&D center, Toshiba Corporation
2-4, Suehiro-Cho, Tsurumi-ku, Yokohama, 230-0045, Japan
**National Institute for Materials Science
1-2-1, Sengen, Tsukuba Science City, Ibaraki, 305-0047,Japan

Abstract

A new single crystal (SC) superalloy with a moderate Re addition (2.4wt%),TMS-82+, has been developed. TMS-82+ shows a higher creep rupture strength than the second and even the third generation single crystal superalloys. The composition of the alloy were designed to have a large negative lattice misfit with a computer aided alloy design program which was developed in National Institute for Materials Science (NIMS-ADP) . TMS-82+ had a stress rupture temperature advantage over 30℃ in comparison with the second generation SC superalloys on 137MPa under 10^5 hours duration. The large negative lattice misfit enhances the formation of continuous γ' platelets, which is called raft structure, and leads to fine interfacial dislocation networks during creep tests, which are considered to prohibit the movement of dislocations and increase creep strength. The other properties such as high temperature tensile strength, low cycle fatigue and oxidation resistance are equivalent to those of second generation SC superalloys.

Keywords : Gas turbine, Single crystal superalloys, Raft structure, Creep strength

1.Introduction

The thermal efficiency of the gas turbine can be improved by increasing the turbine inlet gas temperature. To increase the turbine inlet gas temperature, the materials for turbine blades and nozzles are required to have higher temperature capability. Ni-base single crystal (SC) superalloys have higher creep strength in comparison with conventional and directionally solidified superalloys. So advanced gas turbine plant is adopting Ni-base single crystal superalloys for use in blades and nozzles[1].

Creep rupture strength of SC superalloys are reported to be improved by adding Re. Accordingly, the second generation SC superalloys which contain 3% Re[2][3][4], and the third generation SC superalloys which contain 5 to 6 % Re [4][5][6] have been developed. On the other hand, it is also reported that excess additions of Re to the Ni-base superalloys tend to increase the sensitivity of Re-rich TCP phase precipitation[7][8], which is known to reduce the creep rupture strength. It is reported that *CMSX*-10, which is a third generation SC superalloy, precipitates TCP phases during high temperature aging and the creep rupture strength becomes equivalent to that of the second generation SC superalloy *CMSX*-4 after 20000 hours exposure at 982°C[5].

So, the key objective was to develop a new SC superalloy which has excellent phase stability and creep strength with a moderate amount of Re addition.

3. Material Properties of TMS-82+

Microstructure and Heat-Treatment

Figure 2 shows the microstructures of TMS-82+ in the as-cast condition and as heat treated for 2 hour between 1280°C and 1360°C. Most of the γ' precipitates are dissolved into the γ phase at 1280°C but at temperatures higher than 1340°C, incipient melting is observed. TMS-82+, therefore, has a wide solution heat treatment window over 60°C, which means very good heat-treatment temperature capability. Figure 3 shows the micrograph after the following heat treatment. Average edge dimension of cuboidal gamma prime phase is about 0.4-0.5 μm with regular alignment.

Solution heat-treatment :1280-1300°C/1-2 hours→1300-1320°C/5hours→R.T.(A.C.or G.F.C.)
Aging heat-treatment : 1100°C/4hours→R.T. (A.C. or G.F.C.)
+ 780°C/20hours→R.T. (A.C. or G.F.C.)

Microstructural Stability

Figure 4 shows TTT diagram of *CMSX*-10 cited from reference[5] and the aging test results of TMS-82+. Third generation SC superalloys, which have a high Re content, exhibit greater propensity for TCP phase formation with exposure at about 1090-1150°C[5]. The Re content of TMS-82+ was designed to be less than 2.5wt% in order to reduce propensity for TCP formation. So the reduction of creep strength due to the formation of TCP phase under high temperature and low stress conditions is expected to be less.

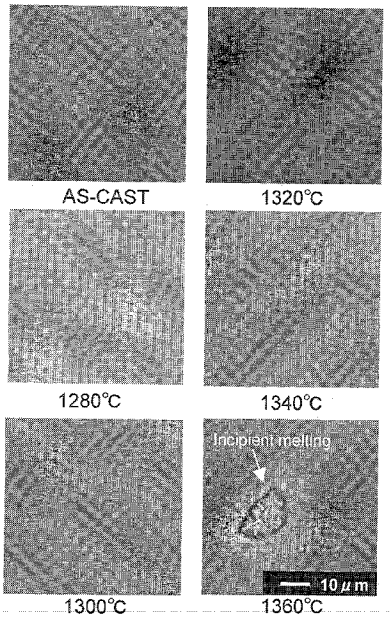


Figure2: The result of solution heat-treatment trials at different temperature for 2 hours.

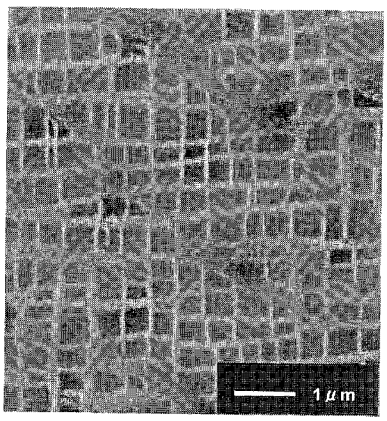


Figure3: Micrograph at the as heat treated condition.

2.Alloy Design

Alloy design was conducted using NIMS-ADP. This program can estimate material properties (creep rupture life, heat-treatment window, phase stability, concentrations of solid solution elements in γ and γ' phases, volume fraction of γ' phase, lattice misfit between γ and γ' phases etc.) by equations derived empirically from mechanical properties of SC superalloys [9]. A schematic flow diagram of this program is shown in Figure 1.

The developed alloy was designed to have superior creep rupture strength by an effective use of negative lattice misfit ($a\gamma > a\gamma'$). The target of creep rupture life at 1100°C/137MPa was designed to be longer than 200h (e.g., 100h for *CMSX*-4). The Re content was restricted to be less than 2.5%, which is designed to prevent precipitation of TCP phases and reduce the raw materials cost. The alloy density was set to below 8.9g/cm^3 and the solution heat treatment window was designed to be larger than 50°C. Other properties, such as long-term phase stability, corrosion/oxidation resistance and castabilty were also considered. The phase stability was estimated by the Solution Index (SI) value[9]. The latter is defined as, $SI = \Sigma (Ci/CLi)$, where Ci is the atomic fraction of i-th element in the γ' phase and CLi is the solubility limit of i-th element in γ' phase of the Ni-Al-i-th element ternary system. If the SI value exceeds 1.25, precipitation of TCP phases is expected. After some calculations with NIMS-ADP and experimental screening tests, we obtained TMS-82+. The alloy composition of TMS-82+ is shown in Table I with other second and third generation SC superalloys.

Table I Typical chemical composition of tested and referenced superalloys.

mass%

Alloy	Co	Cr	Mo	W	Al	Ti	Ta	Hf	Re	Ni	SI value
TMS-82+	7.8	4.9	1.9	8.7	5.3	0.5	6.0	0.1	2.4	Bal.	1.20
TMS-75	12.0	3.0	2.0	6.0	6.0	-	6.0	0.1	5.0	Bal.	1.10
*René*N5	7.5	7.0	1.5	5.0	6.2	-	6.5	0.15	3.0	Bal.	-
CMSX-4	9.0	6.5	0.6	6.0	5.6	1.0	6.5	0.1	3.0	Bal.	-
*René*80	9.5	14.0	4.0	4.0	3.0	5.0	-	-	-	Bal.	-

**René*80 is a equiaxial alloy and C0.07%,Zr0.04%,B0.016%are contained

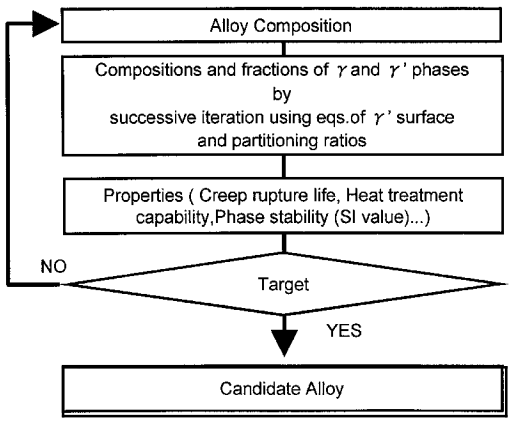


Figure1: Schematic flow diagram of NIMS Alloy Design Program.

Creep Property

Figure 5 shows the creep rupture curves of TMS-82+, with those of *CMSX*-4[3], TMS-75[6], *René*N5[4], *René*N6[4][10] and *MC-NG* (MC544) [11][12]. *MC-NG* (MC544) is a fourth generation SC superalloy[12] which contains the element Ru.

The creep rupture strength of TMS-82+ is superior to those of the second generation SC superalloys, such as *CMSX*-4 and *René*N5, in all the stress and temperature range. In particular, the temperature capability of TMS-82+ is 30°C higher than the second generation SC superalloys at 137MPa. Moreover, in the higher temperature and lower stress range, TMS-82+ is stronger than the third generation SC superalloys such as TMS-75 and *René*N6, and fourth generation SC superalloy *MC-NG* (MC544).

Figure 6 shows the creep strain rate of TMS-82+ plotted against creep time under 1100°C/137MPa, together with the third generation SC superalloy TMS-75 [13]. The creep strain rate of TMS-82+ is lower than that of TMS-75 at all test times and TMS-82+ also has a long secondary creep region. Figure 7 shows the raft structures and dislocation networks formed in TMS-75 and TMS-82+ at the initial stage of secondary creep. The morphology of the raft structure normal to the stress direction is more continuous in TMS-82+ and the dislocation network spacing is finer than in TMS-75 .

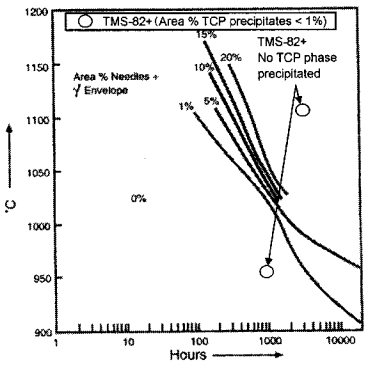


Figure 4: TTT diagram of *CMSX*-10[5] and TMS-82+ .

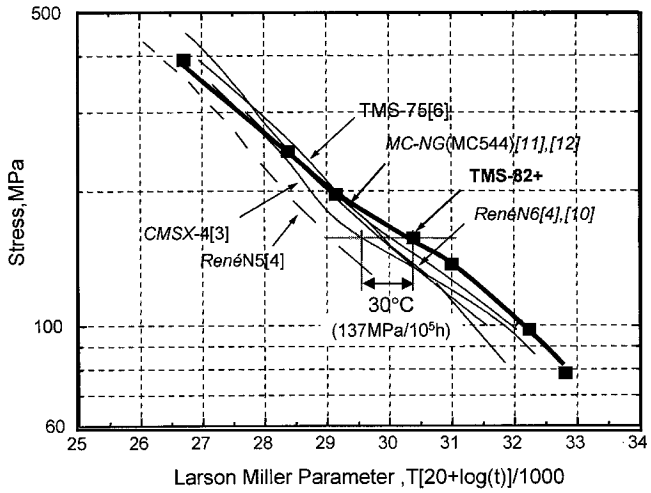


Figure 5: Creep rupture strengths of TMS-82+, *René*N5, *CMSX*-4, *René*N6,TMS-75 and *MC-NG* (MC544).

The raft structure improves the creep resistance effectively by providing effective barriers to dislocation climb around γ' platelets[14] and a more continuous raft structure can disturb the dislocation movement effectively. Once a well formed good raft structure is established, dislocation climb becomes very difficult. In this condition dislocation cutting into γ' platelet is supposed to be the predominant creep mechanism. Finer dislocation network can act as a very effective barrier to this. This seems to be the reason that TMS-82+ has good creep strength.

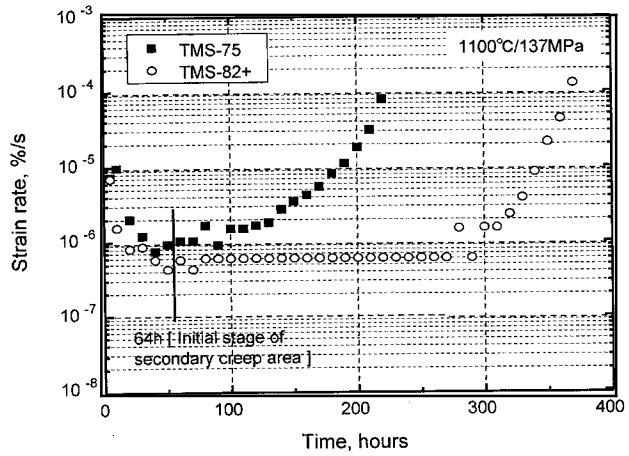


Figure 6 : Creep strain rate of TMS-82+ and TMS-75 plotted against time at 1100°C/137MPa.

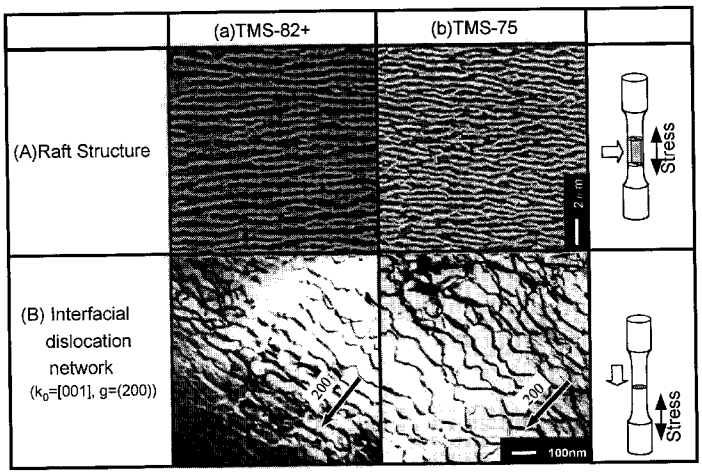


Figure 7 : Raft structure (A) and dislocation network on γ/γ'interface(B) in TMS-82+ (a)and TMS-75(b); creep test interrupted at 64 hours under 1100°C/137MPa.

It is considered that a larger negative lattice misfit promotes the formation of a more continuous raft structure and a finer dislocation network [15]. Table. II shows the lattice misfit of TMS-82+, TMS-75 and *CMSX*-4 measured at 1100°C by X-ray diffraction techniques [16][17]. The lattice misfit of TMS-82+ is more negative than that of both TMS-75 and CMSX-4. This is considered to be the reason that TMS-82+ has a more continuous raft structure and finer interfacial dislocation network, as Figure 7 shows in comparison to TMS-75, leading to the enhanced creep properties mentioned above.

Table II : Lattice misfit of TMS-82+,TMS-75 and *CMSX*-4.

	TMS-82+	TMS-75	*CMSX*-4
Lattice Misfit (1100°C)	-0.24	-0.17	-0.13

Tensile Properties

Figure 8 compares the tensile strength of TMS-82+ and *CMSX*-4[18]. The yield strength and the ultimate tensile strength of TMS-82+ are similar to those of *CMSX*-4. Accordingly the tensile properties of TMS-82+ seem to be equivalent to those of a second generation SC superalloy.

Low Cycle Fatigue Properties

Figure 9 shows the low cycle fatigue properties of TMS-82+ and *CMSX*-4[19]. The solid line shows low cycle fatigue lives under compression hold (C-H) wave condition at 1000°C. A broken line shows low cycle fatigue lives at 900°C under no hold triangular wave condition (N-H). Low cycle fatigue lives of TMS-82+, with and without compression holding, is almost the same as that of *CMSX*-4. This shows that the low cycle fatigue behavior of TMS-82+ is equivalent to that of a second generation SC superalloys.

Oxidation Resistance

Figure 10 shows the weight gain of TMS-82+, *Rene*80 and *CMSX*-4 through an isothermal oxidation test at 950°C for 1000 hours and relevant cross section micrographs of TMS-82+ and *Rene*80. The weight gain of TMS-82+ is much smaller than that of *Rene*80 and equivalent to that of *CMSX*-4. The oxidized area of TMS-82+ is also much thinner than that of *Rene*80. These results shows that TMS-82+ has a good oxidation resistance.

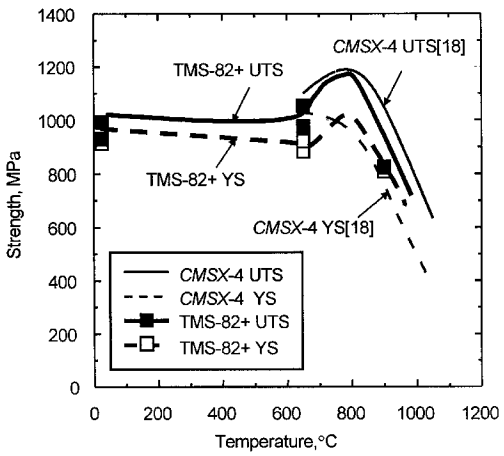


Figure 8 : Tensile strengths of TMS-82+ and *CMSX*-4.

Production Experience

The castability of TMS-82+ was evaluated by producing gas turbine blade for a 15MW engine. Figure 11 shows the test casting after heat treatment and machining. There are no visible defects such as freckles, slivers and so on even at this first trial casting.

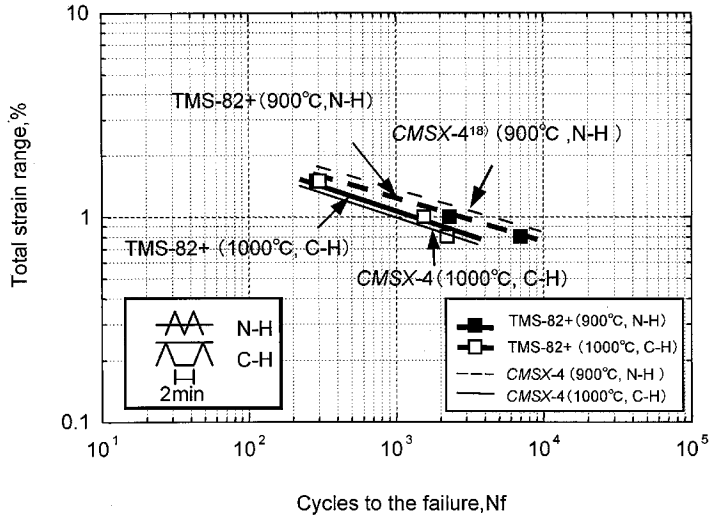


Figure9: Low cycle fatigue failure of TMS-82+ and *CMSX*-4.

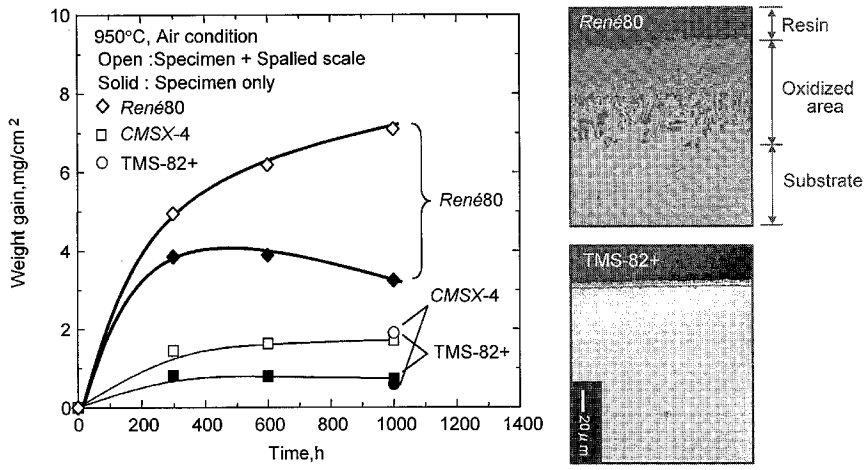


Figure 10: Weight gains of TMS-82+, *René*80 and *CMSX*-4 and cross section micrographs of TMS-82+ and *René*80 during oxidation test at 950°C for 1000 hours.

Rainbow Rotor Test

For a final evaluation of this alloy, 15MW gas turbine blades were made and placed in service in an actual turbine test. The turbine inlet gas temperature was about 1300°C. Turbine blades after one year service are shown in Figure 12. There is no evidence of damage due to oxidation, erosion, fatigue cracking and creep deformation.

4.Conclusions

In this study, we described a newly developed SC superalloy that has excellent creep properties in comparison with present second generation SC superalloys. The following results were obtained.

1. We developed a new SC superalloy,TMS-82+ aided by the NIMS-ADP. The creep strength of the developed alloy is higher than those of second generation SC superalloys, and even higher than third generation SC superalloys at high temperature and low stress conditions.

2. Microstructual observations have shown that in TMS-82+, the morphology of the raft structure normal to the stress direction is more continuous and that the dislocation network spacing is finer than in the third generation SC superalloy TMS-75. These are considered to be the reasons for the creep properties of TMS-82+ being superior to those of other SC superalloys, especially at high temperature and low stress conditions.

3. TMS-82+ has good high temperature tensile strength, low cycle fatigue strength and oxidation resistance, equivalent to those of *CMSX*-4, with excellent phase stability.

4. Following a rainbow rotor test, there were no damage due to oxidation, erosion, fatigue cracking and creep deformation.

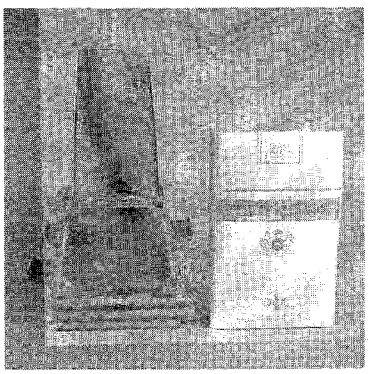


Figure 11 : Trial casting of TMS-82+

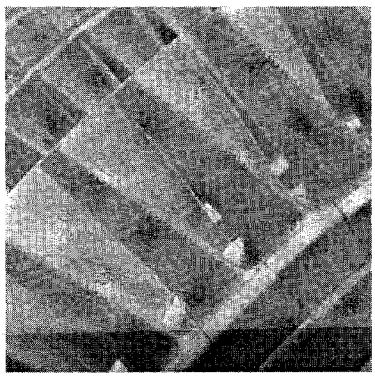


Figure12 : TMS-82+ blades after one year service in a 1300°C class 15MW gas turbine

5.Acknowledgements

This work has been carried out within the research activity of High Temperature Materials 21 Project. We would like to express sincere thanks to Mr.T.Yokokawa, Dr.H.Murakami (Now at Tokyo Univ., Japan), Dr.M.Maldini (Now at CNR-TEMPE, Italy), Dr.Y.Yamabe-Mitarai, Mr. S.Nakazawa, Dr.M.Osawa and Mr.M.Sato (Now at Kawasaki Heavy Industries co. ltd., Japan), of National Institute for Materials Science for their advice. We would like to express sincere thanks to Dr.P.E.Waudby of Ross & Catherall ltd. for making the master ingot and analyzing the compositions of developed alloys.

6.References

[1] Y.Iida and S.Shibuya,"1500°C-class combined cycle system", Toshiba Review, Vol.56 No.6, 2001,pp.8-12

[2] A.D.Cetel and D.N.Duhl,"Second-generation nickel-base single crystal superalloy ", Proceeding of the 6th Symposium on Superalloys, 1998, pp. 235-244.

[3] G.L.Erickson and K.Harris, "DS and SX superalloys for industrial gas turbines", Proceedingof 5th Liège conference, Part I, 1994, pp.1055- 1074.

[4] W.S.Walston, K.S O'hara, E.W.Ross, T.M.Pollock and W.H.Murphy,"*René*N6 : Third generation single crystal superalloys", Proceeding of the 8th Symposium on Superalloys, 1996, pp.27-34.

[5] G.L.Erickson, "The development and application of *CMSX*-10", Proceeding of the 8th Symposium on Superalloys, 1996, pp. 35-44.

[6] Y.Koizumi, T.Kobayashi, T.Yokokawa, T.Kimura, M.Osawa and H.Harada, "Third generation single crystal superalloys with excellent processability and phase stability", Proc.of 6th Liège conference , Part II, 1998, pp.1089-1098.

[7] R.Darolia, D.F.Lahrman, R.D.Field, "Formation of topologically closed packed phases in nickel base single crystal superalloys" Proceeding of the 6th Symposium on Superalloys, 1988, pp.255-264.

[8] T.Hino, Y.Yoshioka, K.Nagata, H.Kashiwaya, T.Kobayashi, Y.Koizumi, H.Harada and T.Yamagata, "Design of high Re containing single crystal superalloys for industrial gas turbines", Proceeding.of 6th Liège conference, Part.II, 1998, pp.1129- 1137.

[9] H.Harada, K.Ohno, T.Yamagata, T.Yokokawa and M.Yamazaki., "Phase calculation and its use in alloy design program for nickel-base superalloys", Proceeding of the 6th Symposium on Superalloys,1988, pp.733-742.

[10] K.S.O'hara, W.S.Walston, E.W.Ross, R.Darolia, U.S.Patent 5,482,789 "Nickel Base Superalloy and Article".

[11] P.Caron, "High γ' solvus new generation nickel-based superalloys for single crystal turbine blade applications", Proceeding of the 9th Symposium on Superalloys, 2000, pp.737-746.

[12] D.Argence, C.Vernault, Y.Desvallées and D.Fournier, "MC-NG: A 4th generation single-crystal superalloy for future aeronautical turbine blades and vanes", Proceeding of the 9th Symposium on Superalloys, 2000, pp.829-837.

[13] T.Hino, Y.Yoshioka, Y.Koizumi and H.Harada, "Development of high strength Ni-base single crystal superalloys TMS-82+ for gas turbine blade and vane", Proceeding of the 123rd committee on heat resisting metals and alloys, Vol.42, No.3, 2001, pp.307-314.

[14] R.A.MacKay and L.J.Ebert, "Factors which influence directional coarsening of γ' during creep in nickel-base superalloy single crystals", Proceeding of the 5th Symposium on Superalloys, 1984, pp.135-144.

[15] H.Harada et.al., "Phase calculation and its use in alloy design program for nickel-base superalloys", Proceeding of the 6th Symposium on Superalloys, 1988, pp.733-742.

[16] Private communication from T.Yokokawa and M.Osawa, National Institute for Materials Science, 2000.

[17] Private communication from T.Yokokawa, National Institute for Materials Science, 2002.

[18] C.K. Bullough et.al.,"The characterisation of the single crystal superalloys *CMSX*-4 for industrial gas turbine blading applications" Proceeding of 6th Liège conference, Part II, 1998, pp.861-878.

[19]Subcommittee on Superalloys and coatings, "Collaborative research on thermo-mechanical and isothermal low-cycle fatigue strength of Ni.base superalloys and the protective coating at elevated temperatures in Japan", 2001, p4.4

SECTION 1

ADVANCED GAS TURBINE MATERIALS

1.2. Ni Base Superalloys

MICROSTRUCTUR OF A 5–COMPONENT Ni–BASE MODEL ALLOY: EXPERIMENTS AND SIMULATIONS

N. Warnken, B. Böttger, D. Ma, V. Vitusevych, U. Hecht, S. G. Fries, N. Dupin*

ACCESS e.V., Intzestr. 5, D–52072 Aachen

*Calcul Thermodynamique, 3, rue de l'avenir, F–63670 Orcet

Abstract

A model alloy containing the five elements Ni, Cr, Al, Ta and W was designed and produced in order to investigate solidification microstructure and microsegregation for a simple, yet representative alloy composition, both by experimental and numerical methods. Experimental investigations were carried out by (a) *unidirectional solidification* in a Bridgman type furnace to provide benchmark data for simulations, (b) *isothermal heat treatments* at several temperatures ranging from 1584–1643 K followed by quenching to provide equilibrium partition ratios and (c) *DTA analysis* to determine liquidus and solidus temperatures.
Numerical modeling was done by using the ACCESS Multiphase Multicomponent Phase Field software (MICRESS) using the thermodynamic alloy database provided by LTH, RWTH–Aachen. With this we simulated microstructure evolution for solidification and subsequent homogenisation. The simulation results show reasonable agreement with the experimental data regarding the formation of the primary and secondary phases.

Keywords: Phase–field, Superalloys, Thermodynamic coupling, Microstructure simulation, Solidification, Ni–Al–Cr–Ta–W

Introduction

The ever increasing demand for high performance alloys for high temperature applications has led to the development of todays Ni–base superalloys. These alloys are nowadays routinely used as turbine blades in gas turbine engines [1,2]. Their development, e.g. alloying, casting, heat treatments, homogenisation, was done based on experimental observation and metallurgical intuition. Indication of trends, correlation between measurable quantities, determination of detrimental effects, etc. deduced by numerical simulations, even if qualitative, are very welcome as these informations can bring economy in time and expenses as well as improve efficiency when compared to the usual trial and error methods. Not many steps in these alloys design and production can, nowadays, be quantitatively simulated. Nevertheless, the state of the art of solidification simulations achieved a stage where it is already possible to revise these empirical methods bringing more understanding, which implies in the improvement of the whole process.

The work done by our group within the frame of the Collaborative Research Center SFB 370 "Integrated Modeling of Materials" and partially reported in this paper, aims at understanding, controlling and optimising the microstructure evolution during solidification for the second generation of Ni–base superalloys, e.g. CMSX–4. In order to diminish the number of variables to be controlled during the process, the high alloyed (usually more than 10 components) second generation material, is substituted by a model alloy, complex enough to reproduce the main features of the commercial alloy, but with less components: Ni–13at%Al–10at%Cr–2.7at%Ta–3at%W.

Much attention is given to a close control of all the tools used in the project, therefore a realistic thermodynamic database is prepared by one of the project partners, the LTH at the RWTH–Aachen, by means of the Calphad method [3,4] which quite successfully describes phase equilibria for multicomponent systems with the accuracy desired for technological applications. Details about the thermodynamic database constructed specifically for the model alloy is not given in this paper, however some equilibrium experimental data is presented here that can be used to validate the thermodynamic database. To simulate realistic microstructure evolution in multicomponent alloys, coupling of the phase–field code to a thermodynamic database is mandatory. Figure 1 schematically shows the coupling as it is implemented in the ACCESS phase–field code "MICRESS" used throughout this work. Details are given in the contribution "Alloy design for ultra high temperature steam turbine applications: Phase–field simulation of the remelting process" at this conference.

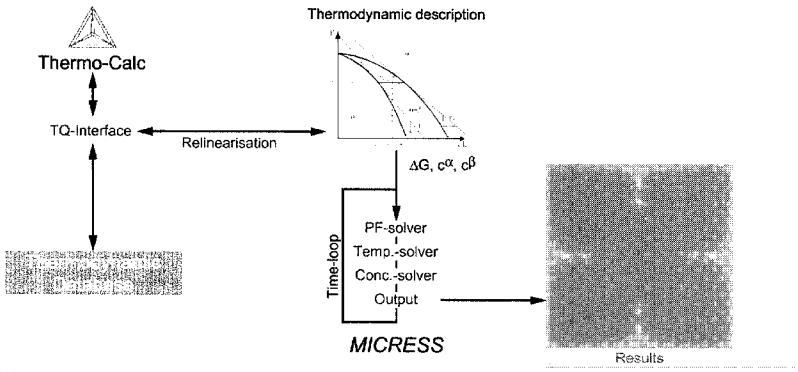


Figure 1: The MICRESS approach for coupling the phase–field solver with thermodynamic calculations [5] for microstructure simulations.

Experimental work

Experimental work is performed on the model alloy Ni–13at%Al–10at%Cr–2.7at%Ta–3at%W with the aid of different methods: First, the effective chemical composition of the alloy is measured by wet chemical analysis, secondly, DTA–analysis is employed to measure liquidus and solidus temperatures. Several samples are subjected to isothermal heat treatment at different temperatures from within the solidification interval followed by quenching, as to allow for measurement of the equilibrium partition coefficient. This information is needed for adjustment of the thermodynamic database of the quinary system Ni–Al–Cr–Ta–W.

Finally, samples of the alloy are subjected to unidirectional solidification, as to give morphological and element distribution patterns that can be compared to those, obtained by numerical simulation of the solidification microstructure. Today, the experimental work is far from being completed, therefore we report in the following on the present state.

The model alloy: Chemical composition and DTA

In order to control the composition of the alloy, samples were extracted from different parts of the logs and submitted to wet chemical analysis. The results indicate a small deviation of the compositions as compared to the data provided by the manufacturers of the model alloy,

but still inside the range of variation previously defined. Table 1 shows both results.

Table 1: Model alloy composition determined by manufacturers (grey) and by chemical analysis (white).

Element	Al	Cr	Ta	W	Ni
at%	13.06	10.49	2.67	2.92	Bal.
wt%	5.80	8.98	7.94	8.84	Bal.
at%	13.08	11.22	2.74	2.98	Bal.
wt%	5.80	9.50	8.15	9.00	Bal.

For determination of the liquidus and solidus temperature of the alloy DTA runs were performed using the Perkin Elmer Pyris DTA 7. Cylindrical samples ∅2×6 [mm] in the as cast state were processed in alumina crucibles under high–purity (5N) argon gas at atmospheric pressure. Three samples from different parts of the log were heated up to 1450°C at 5 K/min and subsequently cooled with 5 K/min, rates that are small enough to provide data close to thermodynamic equilibrium but at the same time high enough to avoid long operating periods at elevated temperatures with risk of contamination.

Figure 2 shows the thermal effects measured by DTA, compared to the evolution of phase fractions with temperature as calculated for the model alloy using ThermoCalc and the first version of the thermodynamic database provided by LTH, RWTH–Aachen. The comparison indicates that the calculated liquidus temperature differs from the experimental one in less than 20K which is rather good as first approximation, as the databases is constructed only by extrapolation from ternary subsystems. The experimental and calculated solidus temperatures are in a slightly better agreement when referring to the heating curve of the DTA–measurement. More detailed DTA measurements will follow for samples in the homogenised state for different heating and cooling rates as to allow for extrapolation to a rate of 0 K/min, meaning equilibrium. Moreover, the thermodynamic database will be adjusted to these experimental data by LTH, RWTH–Aachen.

Microstructure of isothermally heat treated samples

Figure 3 shows a solidification–microstructure diagram of the model alloy. To create this diagram, a number of samples were cooled down from the liquid to different temperatures within the solid/liquid interval. Each sample was held at the respective temperature for three hours. After this time the samples were quenched to freeze the remaining liquid. Their structure was investigated under the optical microscope.

The coarse white phase in the micrographs is the solid formed at the temperature of isothermal holding, which is embedded in the fine–structured frozen liquid. Formation of γ' from the liquid is only found for samples held at lower temperatures, with no visible amount of frozen liquid. This encourages one to think, that the formation of interdendritic γ' from the liquid occurs at the very end of the solidification path, as a non–equilibrium phase, and is dissolved by diffusion if temperature and time are high and long enough. With the aid of WDX the partitioning of alloying elements between solid and liquid can be measured from these samples [6]. This work is on going and the results will be used for thermodynamic database adjustment.

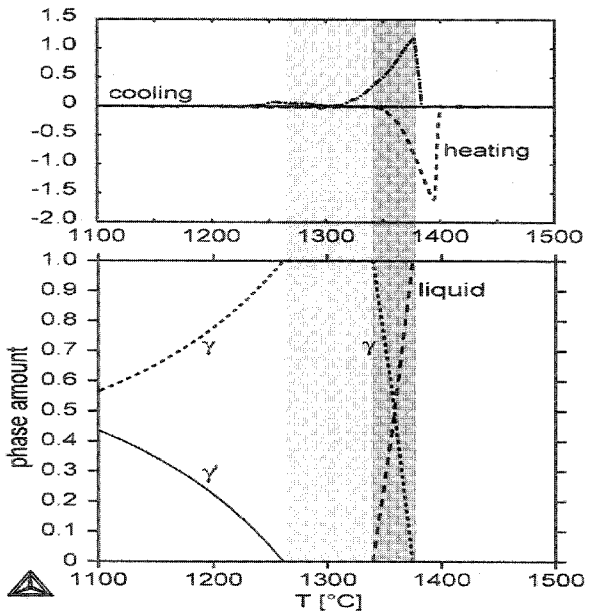


Figure 2:
DTA experimental curves obtained on heating/cooling rate of 5K/min compared to the equilibrium phase evolution with temperature calculated using the thermodynamic database, showing a reasonable agreement of the experimental and calculated liquidus, solidus temperatures.

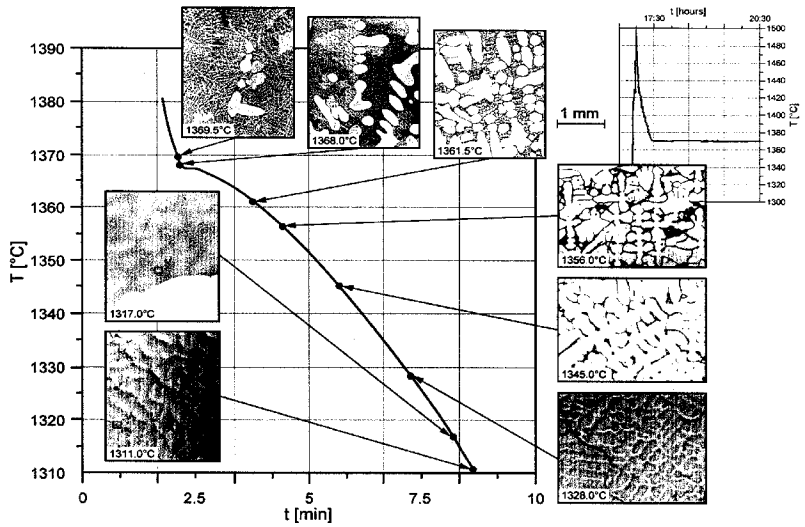
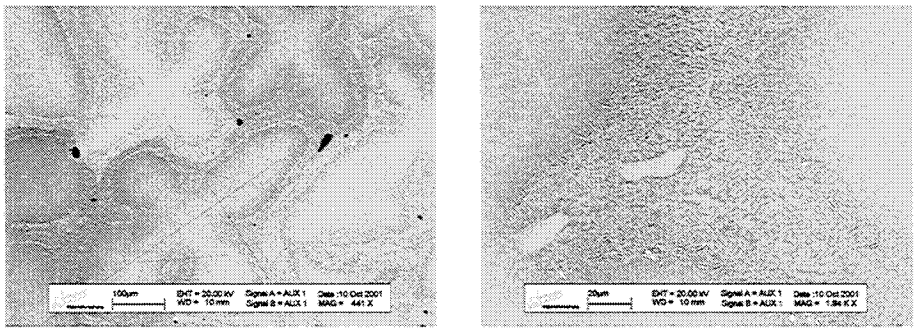


Figure 3: Solidification–microstructure diagram of the model alloy, showing the micro structural features obtained when cooling the respective samples from the liquid state to different temperatures indicated by the dots on the overall cooling curve of the alloy. The thermal history of a typical sample is shown in the small diagram upside right. After isothermal holding the samples are quenched.

Microstructure of unidirectionally solidified samples

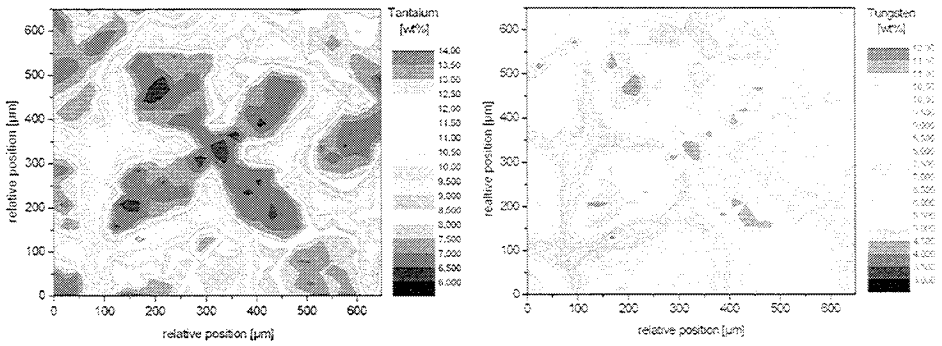
Figure 4.a and 4.b show micrographs obtained in cross sections of a unidirectional solidified sample of the model alloy (G=4K/mm, v=3mm/min). After solidification the sample was isothermally heat treated at 1300°C for three days. Both frames are back scattered electron images taken in SEM. The dendritic structure of the primary phase can clearly be seen. Figure 4.b shows the interdendritic region at higher resolution with almost oval secondary phases; EDX measurements have identified these oval phases as γ' and the primary phase as γ. At the boundary between the γ dendrites and the interdendritic region, small white precipitates with needle like shapes can be observed. These phases were formed during the heat treatment, being absent in the unidirectionally solidified state.



4.a 4.b

Figure 4: SEM /BSE images of the model alloy Ni–13at%Al–10at%Cr–2.7at%Ta–3at%W after directional solidification and heat treatment at 1300°C for 3days.

Metallographic sections of a unidirectionally solidified sample were submitted to microprobe analysis (WDX) as to map element distributions within the area of a primary dendrite and it's interdendritic surrounding. The results for the distribution of the strongly segregating elements Ta and W are given in figure 5.a and 5.b respectively.



5.a 5.b

Figure 5: WDX–mapping of the elements Ta and W performed with a beam defocus of 5µm at a step size of 6 µm in x–direction and 13 µm in y–direction. The direct segregation of Ta and the inverse segregation of W can be observed straight forward.

Microstructure Simulation

Model

Simulation is done using MICRESS, the multiphase multicomponent phase field model [7,8]. Phase–field models are known to be quite successful for description of moving phase boundaries during microstructure formation. For multicomponent systems like the model alloy investigated in this paper the demands for the simulation tool are not only to handle multiphase and multicomponent differential equations, but also thermodynamics have to be described properly. This is done by using thermodynamic databases. For this reason online thermodynamic calculations have been incorporated into MICRESS, using the software package Thermo–Calc and the Fortran TQ interface. The way how this coupling is done, is described in detail in [9].

Directional dendritic solidification is simulated using a unit cell model for the isothermal dendritic cross section, which is chosen under the assumption of a fourfold symmetry of the dendrite and the surrounding dendritic array. The size of the unit cell corresponds to the primary dendrite spacing. The unit cell model also is described in [5]. A constant cooling rate is applied for solidification which corresponds to a constant velocity in the Bridgman furnace. Nucleation of secondary phases is done, when a certain undercooling, calculated from Thermo–Calc via TQ, is reached.

Results

The following section shows calculated microstructures of the five–component model alloy, obtained from simulations done with the coupled phase–field model. The overall composition of the alloy is listed in Table 1. The images shown in figure 6 present distribution maps for tantalum (Ta) and tungsten (W) within isothermal sections through the mushy zone. The time labels correspond to the local solidification time. The upper row shows the Ta distribution while the lower row shows the W distribution, respectively. The first two images of each row show the growth of the primary phase into the liquid, the last images exhibit the final microstructure after solidification. Due to the large difference in solubility of the two elements Ta and W, the secondary γ' phase can easily be identified as light spots in the Ta, and dark spots in the W maps. The morphology of the primary γ phase has a large influence on the size and distribution of the secondary γ' phase.

Figure 7 shows the distribution maps for tungsten as calculated (the right hand side) and as measured by WDX (left hand side). Both images refer to the same grey level coded fraction of tungsten range, from 0.015 to 0.035 at%. The primary γ–phase can clearly be distinguished as the tungsten–rich light region with fourfold symmetry, surrounded by the darker, tungsten–poor interdendritic region. The negative segregation is well reproduced by the calculation. The secondary γ' contains less then 0.01 at% W and can therefore be identified as dark spots in the images.

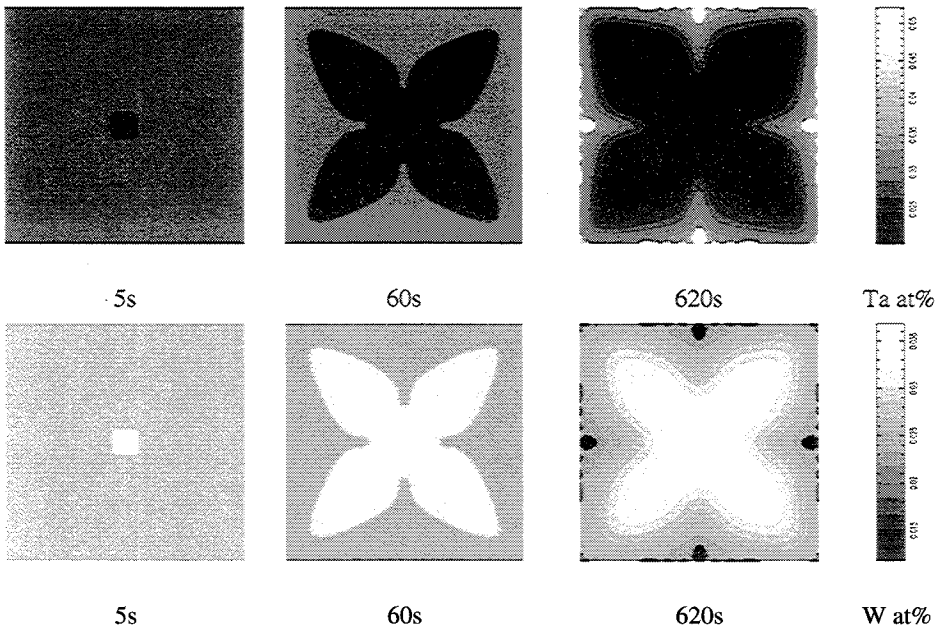


Figure 6: Calculated distribution maps for tantalum and tungsten within isothermal cuts through the mushy zone for directional solidification; cooling rate: 0.25K/s.

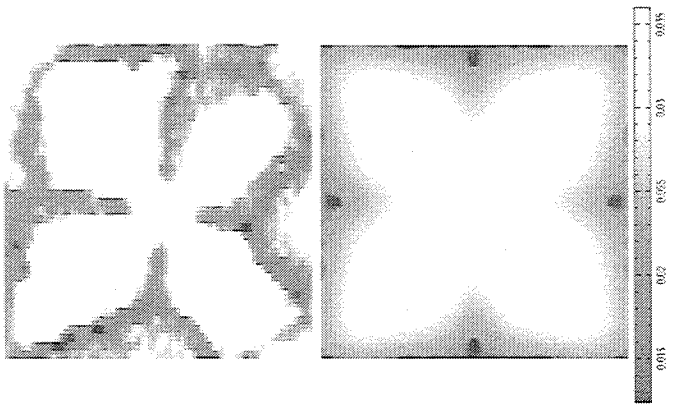
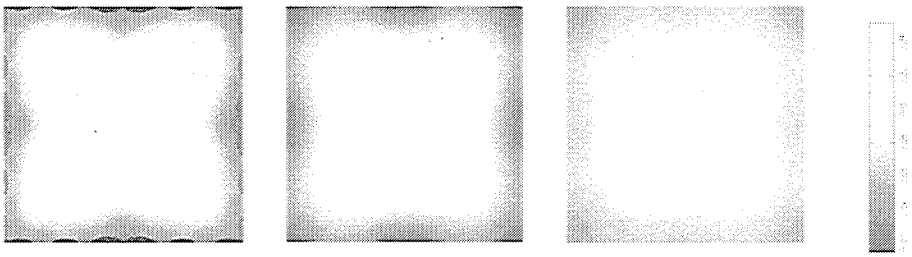


Figure 7: Measured and calculated distribution maps, scaled to the same range of grey levels for tungsten, from 0.015 at% to 0.035 at%.

The results of a solidification simulation have been used as a starting point to simulate a homogenisation treatment. Figure 9 shows the calculated W distribution map at different times. After seven hours the γ' precipitations have already dissapeared. At the end of the homogenisation, the segregation of W has significantly decreased, but is still not completely vanished. The element fraction profiles along the <001> direction are plotted in figure 9 for all alloying elements. All plots start from the center of the primary phase (dendrite). The

curves show the profiles at the same timesteps as the images in figure 8. At the end of the initial curves (t=0h), around 200 µm relative position, the influence of the secondary γ' phase can clearly be seen as steep change in slope of the curves. In this simulation the elements Al and Cr achieve a flat profile after seven hours of heat treatment, while for W the segregation remains until the end.



0h 7h 18h X(W)

Figure 8: Calculated distribution maps for W during solidification. With evolving time the precipitates disappear first. At the end of the heat treatment the W segregation is not completely vanished.

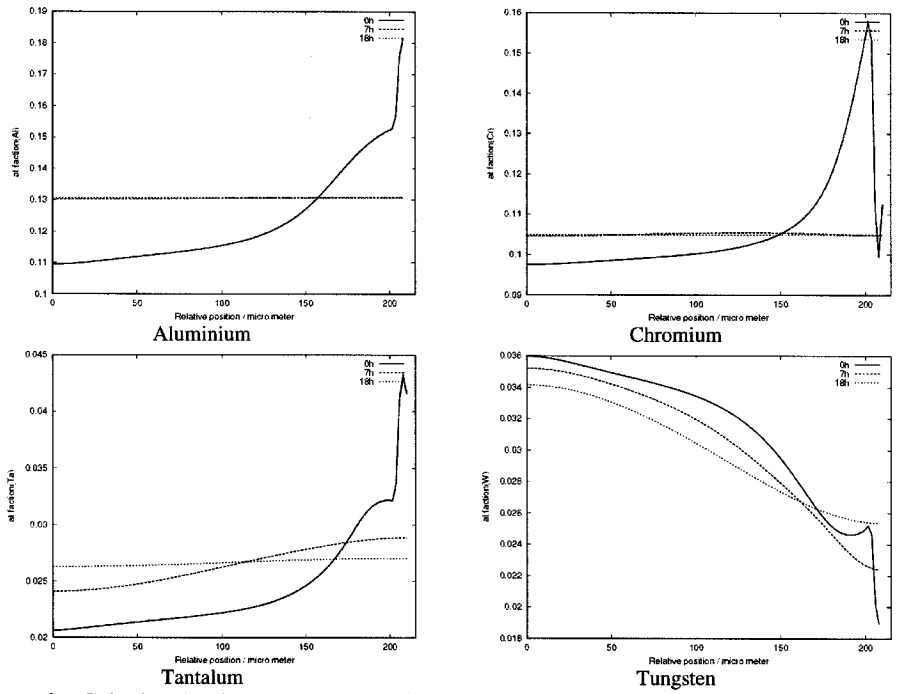


Figure 9: Calculated Element concentration profiles along the <001> direction during homogenisation. Starting from the solidification the curves show the evolution of the profiles during the heat treatment.

Discussion

Although the results shown here look very promising, a few odds need to be discussed, regarding the comparison between real 3D structures and simulated 2D–structures. The measured element distribution patterns shown so far, relate to an arbitrary transversal cut, in an arbitrarily selected dendrite of a dendrite array consisting of many more dendrites. To make sure, that the measurements are representative for the dendritic segregation pattern, more mappings need to be done. A statistical analysis of several maps will provide us with better benchmark data for the simulation. One could also attempt to simulate microstructure evolution in 3D. This will be addressed in future simulations, using a 3D unit cell approach, but calculation times, especially with the phase field code being coupled to the thermodynamic database will be high.

A second aspect, more straight forward to handle, but not definitely independent from the above discussed problem, regards the fact that simulated dendrites of the γ phase develop a more compact morphology then real ones do. Recent theories [10,11] have shown, that interfacial anisotropy has a significant influence on the dendrite morphological features. Interfacial anisotropy is one of the parameters that can be accounted for in phase–field simulations, and future simulations will focus on matching real and simulated morphologies more closely.

Despite of these limitations, the qualitative agreement between experimental and simulated results is quite good. This means, that the main factors determining microstructure evolution are already integrated into our model. Future work will concentrate on a quantitative comparison between experiments and simulations.

Conclusion

A five component model alloy representative for single crystal application, Ni–13at%Al–10at%Cr–2.7at%Ta–3at%W was produced and first experiments were performed regarding the measurement of data relevant to thermodynamic equilibrium like liquidus and solidus temperatures, partition coefficients etc. Moreover unidirectional solidification has been applied to generate dendritic off–equilibrium microstructures, needed for comparison with numerical simulation obtained by a phase–field model coupled to the thermodynamic database of the Ni–Al–Cr–Ta–W system.

At this time the experimental work is still in progress and will give more detailed data in future, as to assure the fine–tuning of the thermodynamic database on one hand, and the quantitative comparison of solidified structures obtained by experiment and simulation respectively.

The phase–field model MICRESS coupled to the thermodynamic database was applied to simulate the formation and evolution of microstructures. Realistic microstructures which reproduce the influence of the primary phase morphology on the formation and distribution of the secondary phase were simulated. The results show that the segregation of species is in good qualitative agreement with experimental results. Future work will focus on evaluating the quantitative agreement between simulation and experiment. Moreover we have shown, that the model can be applied not only for solidification but also for the homogenisation treatment.

The results obtained so far look very promising for future work, as with some fine tuning a comprehensive model to describe microstructure evolution in directional solidified superalloys for solidification and homogenisation will be available. [12]

Acknowledgement
The authors gratefully acknowledge the financial support of the Deutsche Forschungsgemeinschaft (DFG) within the Collaborative Research Center 370 "Integrated Modeling of Materials".

References

[1] M.Durand–Charre, "The Microstructure of Superalloys", ISBN 90–5699–097–7, 1997
[2] M.S.A. Karunaratne, D.C. Cos, P. Carter, R.C. Reed, "Modelling of the microsegregation in CMSX–4 superalloy and its homogenisation during heat treatment", Proc. of Superalloy 2000, ed. TM. Pollock, R.D. Kissinger, R.P. Bowman, 2000
[3] N. Saunders and A. P. Miodownik, CALPHAD (CALculation of PHase Diagrams) A Comprehensive Guide, Pergamon Materials Series: vol. 1, ed. R. W. Cahn (Elsevier, Oxford, 1998)
[4] U. R. Kattner, "Thermodynamic Modeling of Multicomponent Phase Equilibria", JOM 49 (12), 1997, 14–19
[5] G. Eriksson, H. Sippola and B. Sundman, CALPHAD, 18 (1994) 345–345, http://www.thermocalc.se/download/pdf/tq99.pdf
[6] P.K.Sung, D.R.Poirier, "Liquid–Solid Partition Ratios in Nickel–Base Alloys", Met. and Mat. Trans. A, 30A, August 1999, p.2174–2181
[7] I. Steinbach et al., "A Phase Field Concept for Multiphase Systems", Physica D, 94 (1996) 135–147.
[8] J. Tiaden et al., "The multiphase–field model with an integrated concept for modelling solute diffusion", Physica D, 115 (1997) 73–86.
[9] B.Böttger, I.Steinbach, S.G.Fries, Q.Chen, B.Sundman, „Alloy Design for Ultra–Hightemperature steam turbine applications", This conference, 2002
[10] J.S.Langer, "Lectures in the Theory of Pattern Formation", in Chance andMatter, Proceedings of the Les Houches Summer School, Session XLVI (Elsevier, New York, 1987)
[11] H.Mueller–Krumbhaar, W. Kurz, "Solidification" in Materials Science and Technology, Vol. 5/Phase Transformations in Materials, Ed P.Haasen, VCH–Verlag, Weinheim 1991
[12] The figures shown in this presentation can be viewed in color at: http://www.access.rwth–aachen.de/~nilsw/luettich/figures.html

Alloy Design for Ultra High Temperature Steam Turbine Applications: Simulation of Microstructure during Forging

R. Kopp[1], M. Wolske[1]
[1] Institute of Metal Forming, RWTH Aachen, 52056 Aachen, Germany

Abstract

The improvement of future generations of steam turbines mainly includes an increase in efficiency to levels of about 55%, leading to steam inlet temperatures of 700°C and higher. The achievement of this goal needs not only new design principles but also advanced wrought alloys in the hottest turbine sections. This article will focus on the manufacturability by forging of large Ni-base rotor applications for ultrasupercritical (USC) steam turbines. Potential candidates for further alloy development will be proposed by this mean.

Keywords: Superalloys, Forging, FEM, Microstructure simulation, Workability

Introduction

Current developments in stationary gas turbines in power plants commonly use ferritic steels in the large turbine components. The demand for higher efficiency in power plants with respect to energy and environmental aspects could be reached by exceeding steam inlet temperatures of 700°C or higher with a corresponding increasing compressor pressure of app. 350 bar. These circumstances requires new material solutions for the turbine rotors.
For higher efficiency levels of about 55%, modern ultrasupercritical (USC) steam turbines with service temperatures of 700°C and higher are in planning [1, 2]. One possibility to reach this goal is the implementation of cooled areas of piping, casing and rotor applications in the hottest engine sections, which is cost consuming. Fundamentals for the adaptation to the materials and design principles of turbine components in combined cycle power plants are developed for instance in the Collaborative Research Center 561 at the RWTH Aachen [3]. Another possibility is to replace ferritic steels by Ni-base alloys in the areas of high temperature loading, because of their high temperature strength, long-time stability and corrosion resistance at high temperatures [2, 4].
In this article, the workability of three groups of wrought Ni-base alloys, classified by their main hardening mechanisms (group 1: solid solution and carbide strenghtened, group 2: γ'-strenghtened and group 3: γ'- and γ''-strenghtened) is discussed.
Three types of Ni-base alloys have been investigated to ascertain the best suitable material group for advanced gas- and steam turbine applications at elevated service temperatures. The analysed materials in this case are Inconel* 617 (group 1), Waspaloy (group 2) and Inconel* 706 (group 3). For comparing the workability, the forming behaviour of the materials was analysed in two ways: (i) microstructure models for each alloy have been developed and used in FEM coupled forging simulations to investigate the flow stress development in process and (ii) experimental investigations of the formability of the alloys have been performed.

* Inconel is a tradename of the INCO group of companies. In the following of the paper this naming is used.

1. Experimental Procedure

1.1 Analysed Materials

In the present study, three commercial Ni-base alloys were selected for understanding fundamental mechanisms and principles in case of above mentioned topics: Inconel 706 as a representative for γ'- and γ''-strengthened alloys, Inconel 617 as a solid solution hardener and Waspaloy, hardened by γ'-particles. The chemical compositions are given in table 1.

Alloy	Ni	Fe	Cr	Co	Mo	Nb	Al	Ti	C	Zr
INCONEL 617	53.70	0.50	22.00	12.90	9.05	-	1.11	0.55	0.060	-
INCONEL 706	41.96	36.97	16.02	0.05	-	3.02	0.20	1.55	0.010	-
WASPALOY	57.10	0.57	19.35	14.00	4.52	0.01	1.22	3.13	0.033	0.06

Table 1: Chemical compositions of investigated Ni based alloys in wt-%

1.2 Flow stress testing

For FEM simulations of forming processes, the knowledge of the flow stress is necessary to improve the accuracy of the numerical calculation. Flow stress testing at IBF (Institut of Metal Forming of RWTH Aachen) was performed on the computer controlled, 1200 kN servohydraulic testing system of Servotest Ltd., with which uniaxial hot compression tests up to temperatures of 1280°C at strain rates of up to 100/s can be obtained.
Throughout the examination of the experimental data, the specimen, tools and surrounding atmosphere were kept at a constant forming temperature by a furnace, installed in the testing system [5, 6]. Before compression, all specimen were annealed for 15 min in the machine furnace to attain the accurate forming temperature.
Cylindrical compression samples, 16 mm diameter by 24 mm height, were machined. To eliminate friction as far as possible, Rastegaev specimen were used [5]. The recessed end faces of the specimen were filled with glass lubricant. Constant strain rate is arranged by setting the crosshead velocity of the testing machine via displacement control. Hot compression tests were carried out in a temperature range from 900°C to 1100 °C for Inconel 706 and Waspaloy and from 950 °C to 1150 °C for Inconel 617. For all materials the strain rates were set to 0.001/s, 0.01/s, 0.1/s, 1/s and 10/s. The compressed samples were rapidly quenched in water spray just after deformation with assistance of a quenching unit, which is directly connected to the upsetting machine [6, 7].

1.3 Metallography

Metallographical investigations are needed to fit the microstructure model's equations with use of the initial microstructural state and dynamically recrystallized (DRX) grain sizes after deformation. The observed specimen of Inconel 617 and Waspaloy were etched in a V_2A mordant at 60°C for 2 to 5 minutes resp. 20 minutes. The specimen of Inconel 706 were etched electrolytically with a reagent of 10% oxalic acid at 10 V for 25 seconds.
The determined initial average grain size is 223 µm (ASTM 1.4) for Inconel 617, 43.5 µm (ASTM 6.1) for Inconel 706 and 69.2 µm (ASTM 4.8) for Waspaloy.

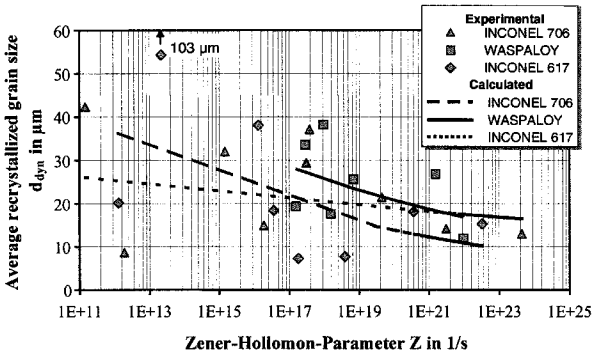


Fig. 1: Experimental and calculated values of average dynamic recristallized grain sizes for the investigated materials

The microstructural state of compressed samples was observed over the whole range of forming conditions as well. The specimen were prepared with the same etching as for the observation of the initial state. Under forming conditions leading to partial recrystallization, characteristic 'necklace' structures were observed.
The combined influence of strain rate and temperature was taken into consideration by use of the Zener-Hollomon-parameter Z,

$$Z = \dot{\varepsilon} \cdot \exp\left(\frac{Q_{def}}{R \cdot T}\right) \qquad (1)$$

where R is the universal gas constant, T the temperature in K and $\dot{\varepsilon}$ the strain rate in 1/s.
In consideration of these forming conditions, the average grain size decreases with increasing forming conditions, caused by dynamic recrystallization, as shown in fig. 1.

1.4 Formability tests

The term formability $\varphi_{eff,fr}$ (or fracture strain) is used to describe the maximum deformation of a material without the appearance of fractures or cracks during a forming process in accordance with the term effective strain φ_{eff} or the local fracture strain $\varepsilon_{eff,fr}$, according to the effective local strain ε_{eff}.
The global formability is exhausted when the stresses occurring in the material lead to cracks. In metallurgical terms, discontinuities occur within the plastic zone, the material structure can thus no longer withstand the internal stresses and breaks open.
Technically speaking, there are local stresses which are responsible for cracking. These are not distributed homogeneously over the entire material. Therefore it is practical to define a parameter that describes the local material failure: the local formability $\varepsilon_{eff,fr}$. This parameter describes the maximum local effective strain at which the material is still not damaged. If the material fails locally during forming, the global formability has of course been reached, too. Thus, both parameters are reached at the same time, whereby $\varphi_{eff,fr}$ is calculated from the externally applied true strain φ_{eff}, and $\varepsilon_{eff,fr}$ from the local effective strain ε_{eff} and thus assumes a knowledge of the point of material failure.
The global formability $\varphi_{eff,fr}$ can be determined in basic tests (compression, tensile, torsion tests) by calculating the true strain φ_{eff} which leads to a fracture of the test piece. However, if a number of materials are tested in one basic test, they can be compared with each other in

terms of their global formability. The local strain ε_{ij} must be known to calculate the local formability $\varepsilon_{eff,fr}$. An analysis by using the Finite Element Method (FEM) is used for many forming processes to determine the deformation tensor in this case.
In this paper, a strategy for comparing the global formability of different materials is shown, by upsetting a manufactured cylindrical sample with a collar. The collar of the sample is loaded by highest tangential tensile stresses, which normally leads to early material failure during compression. This sample 'Flange' has been deformed up to crack initiation by using acoustic emission analysis for registering the beginning of cracking.
Compression tests up to crack initiation with the sample type 'Flange' have been performed with all investigated alloys at temperatures of 800°C and 950°C. The samples were placed within a furnace, which is installed in the testing system, and annealed for 15 min before compression to attain the accurate forming temperature. Afterwards, the samples were compressed up to crack initiation. For detection of the crack initiation, acoustic emission has been monitored during the tests with the help of acoustic emission analyse system from the company Physical Acoustics Corp. [8, 9]. The ascertained moment of crack initiation was set in correspondence to the specific height reduction up to crack initiation of the prevailing compression test, after correction of elasticity of workpiece and tool during deformation and heading of the sample after cooling:

$$\varepsilon_{h,c} = \left| \frac{h_1 - h_0}{h_0} \right| \qquad (2)$$

2. Set-up of microstructure models and validation

Isothermal flow stress curves have been calculated by an iterative method for providing material models on the basis of empirical equations. From the measured data, the activation energy for hot deformation Q_{def} was calculated in a first step at the prevailing maximum of each flow curve. In the next step the dependence of the maximum flow stress on forming temperature and strain rate was formulated by use of Z. Activation energies for hot deformation were found to be 411.8 kJ/mole for Inconel 617, 372.3 kJ/mole for Inconel 706 and 511.2 kJ/mole for Waspaloy. These determined activation energies were in good agreement with data from literature. Thus, Karhausen 389 kJ/mole and Jonas 400±50 kJ/mole, both for Inconel 718, Shivpuri et al. 536 kJ/mole and McQueen et al. 410 kJ/mole, both for Waspaloy [10, 11, 12, 13].
As shown in fig. 1, the dynamic recrystallized grain size d_{dyn} decreases with increasing forming conditions, represented by the Zener-Hollomon-parameter Z. The dynamically recrystallized grain size does not depend on the initial grain size but could be described in dependence from the hot working conditions, as reported by various authors [14, 15, 16]. Using previously measured values of d_{dyn}, two different regimes were found for Inconel 706 and Waspaloy: one for temperatures nominally below the γ' solvus (subsolvus) and one for temperatures above γ' solvus (supersolvus):

Inconel 706: subsolvus: $d_{dyn} = 0.0393 \cdot Z^{-0.016}$ (3a)

supersolvus: $d_{dyn} = 0.0188 \cdot Z^{-0.062}$ (3b)

Waspaloy: subsolvus $d_{dyn} = 0.0171 \cdot Z^{-0.046}$ (4a)

supersolvus: $d_{dyn} = 0.2265 \cdot Z^{-0.114}$ (4b)

This circumstance could probably be attributed to the presence of γ' particles during hot forming in subsolvus regime, which could lead to influences on further dynamic recrystallization by grain-particle interactions [17]. For Inconel 617, the correlation to different forming temperatures has not been found. Therefore, following equation summarize the dependency of the average recrystallized grain size d_{dyn} from the hot working conditions:

Inconel 617: $$d_{dyn} = 0.0182 \cdot Z^{-0.111} \qquad (5)$$

The dynamically recrystallized fraction X_{dyn}, which corresponds to the dynamically recystallized grain size d_{dyn} could be expressed by an Avrami type equation [14]. Because the coefficients of the equations have an effect on each other during a simulation, a combined interdependence optimisation was carried out to determine the whole set of coefficients. This was realised automatically with a program developed at the IBF.

After completion of recrystallization further grain growth is modelled [19]. In case of all alloys, a relationship between final grain size d_{GG}, initial grain size d_0, annealing time t, activation energy for grain growth Q_{GG} and temperature T was developed, basically described by Sellars [18]:

$$d_{GG}^{h_4} = d_0^{h_4} + h_5 \cdot t \cdot \exp\left(\frac{-Q_{GG}}{R \cdot T}\right) \qquad (6)$$

Laboratory annealing experiments at 4 temperatures (1000°C, 1040°C, 1080°C and 1120°C), 5 annealing times (10min, 20min, 30min, 60min and 120min) and further metallographic observations lead to a set of coefficients for equation (6) for each alloy as presented in table 2. A complete description of the microstructure models could be found in [19].

Alloy	h_4	h_5 in µm/s	Q_{GG} in J/mole
Inconel 706	4.5	3.5×10^{21}	395,000
Waspaloy	4.5	9.0×10^{19}	310,000
Inconel 617	4.5	3.0×10^{17}	375,000

Table 2: Coefficients to fit grain growth function, calculated from annealing experiments

In order to use a complete set of phenomenological equations to simulate a multistage forming operation, a comprehensive model called STRUCSIM is available at IBF [10]. The fundamental idea of STRUCSIM is to identify different microstructural fractions within the material, showing different grain size evolution and work hardening states due to different deformation histories. The program STRUCSIM calculates the volume fractions of recrystallised material and the actual grain size. A new flow curve is computed by use of the calculated material structure. The coupling of STRUCSIM to the implicit FEM code LARSTRAN/SHAPE was developed at IBF and described in detail in [10]. STRUCSIM receives current local forming conditions (strain, strain rate and temperature) from LARSTRAN/SHAPE and simulates microstructural changes based on the forming data. Flow stress depending on the microstructure is calculated by STRUCSIM and given back to the FEM.

The validation of the developed microstructure models was performed with the help of laboratory tests. Here, nonsteady-state and inhomogenous compression tests with cylindrical samples at constant tool velocity of 1 mm/s have been performed. The test conditions are given in table 3.

The experimental tests with 1st step compression, annealing and 2nd step compression were simulated by a coupled FEM-STRUCSIM simulation. The material data as density, thermal

conductivity and specific heat capacity were taken for each material from product informations of Inco Alloys Int. Inc. The values for boundary conditions have been set in case of heat transfer from workpiece to the tool to $\alpha = 0.0011$ W / (mm² K) and in case of the radiation coefficient to $\varepsilon = 0.86$. Coulomb's friction coefficients were set by comparing the bulged FEM shape with the contour of the experimental samples.

Test condition	Step 1	Step 2	Step 3
Forming temperature	1050 °C	-	1050 °C
Tool speed	1 mm/s	-	1 mm/s
Total deformation degree	0.4	-	0.8
Annealing temperature	-	1160 °C	-
Annealing time	-	77 min	-

Table 3: Test conditions for laboratory validation of microstructure models

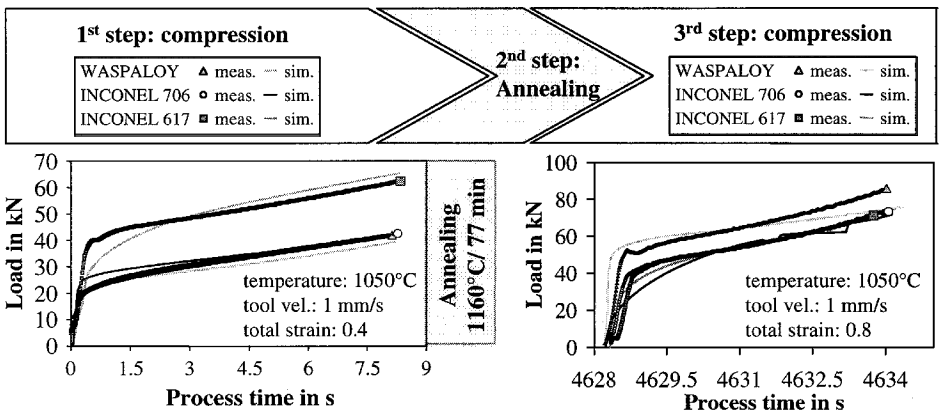


Fig. 2: Comparison of measured (meas.) and FEM simulated (sim.) loads for Waspaloy, Inconel 706 and Inconel 617 during 3-stage laboratory compression tests for validation of microstructure models. The first compression step (left) is shown as well as the last compression step after annealing (right)

The experimental and numerical microstructures were compared as well as the measured and simulated loads, as shown in fig. 2. As one can see, the prediction of the microstructure models as shown in the comparison between measured and simulated loads is reasonably well.

3. Microstructure modeling of forging

Forging of remelted ingots to the final shape of a turbine rotor is accomplished in several steps. At first, an upsetting operation is performed to break up the large as-cast grain structure. The final shape is usually obtained in succession of several hammer forging and upsetting operations. Because the capacity of the largest forge presses in the world is limited to 14,000 tons, the identification of the alloy, which meets best the demands of manufacturing

large steam turbine rotor applications, must consider the flow strength at forging temperature. For Ni-base alloys, the starting temperature for forging lays typically narrow between 950°C and 1050°C, while re-heating temperatures are at higher levels.

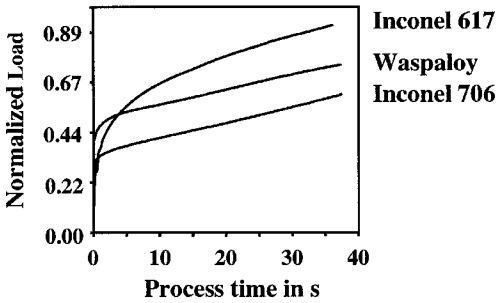


Fig. 3: Calculated normalized loads for the first forging step of rotor forgings. Microstructure models for Waspaloy, Inconel 706 and Inconel 617 were used (initial grain size: 220 µm).

For comparison of the workability of the three investigated Ni-base alloys, a sequence of upsetting and hammer forging operations was simulated via FEM coupled microstructure simulation. The process data as e.g. initial ingot and tool geometries, starting temperatures and tool velocities were provided by Saarschmiede GmbH Freiformschmiede, Germany. With the help of equation (6) the grain sizes of Inconel 706 and Waspaloy were brought to a value of 220µm. Therefore, uniform starting grain sizes for each alloy were put into the thermo-mechanical microstructure FEM forging simulation to equalize the influence of grain size on the resulting flow stress. In this context, the same FEM mesh was used for all initial simulation models to equalize numerical influences on the calculated results.
Fig. 3 demonstrates the result of needed loads for the first production step after remelting, the upsetting of a large ingot with a height reduction of $\varepsilon_h=\Delta h/h_0=0.75$.
Interestingly, Inconel 617 exhibits the highest load level even though Waspaloy is the stronger material at service temperature. The reason is that the strengthening phases of Waspaloy and Inconel 706 are dissolved at forging temperature, leaving solid solution strengthening as the remaining hardening mechanism. Consequently, for the selected alloys a direct correlation between the molybdenum content and the Al/Ti-ratio, being highest in Inconel 617 and lowest in Inconel 706, and the level of flow stress could be found.
Following the process route, fig. 4 shows calculated flow stresses after hammer forging of the compressed ingot in several steps to a ratio of extension by hammer forging of $\lambda_R=l_1/l_0=1.345$. Calculated stresses in Inconel 617 exceed those in Inconel 706 by a factor 2. Also evaluated were the grain size distribution in the forging billets. Again, Inconel 617 showed unfavorable results as grain size distribution tends to be more inhomogeneous, showing high gradients within the forged billet.
Summarizing this part, different criteria have to assess forgeability resp. workability of materials: One aspect is the flow stress level in consideration of the microstructure. By these means, beneath low forging forces, the refinement and homogeneity of grain sizes are also important. In this context, Inconel 617 turns out to be the least suited while Inconel 706 shows best forgeability. Establishing a suitable forging route for large Inconel 617 rotor components seems to be a immense challenge.

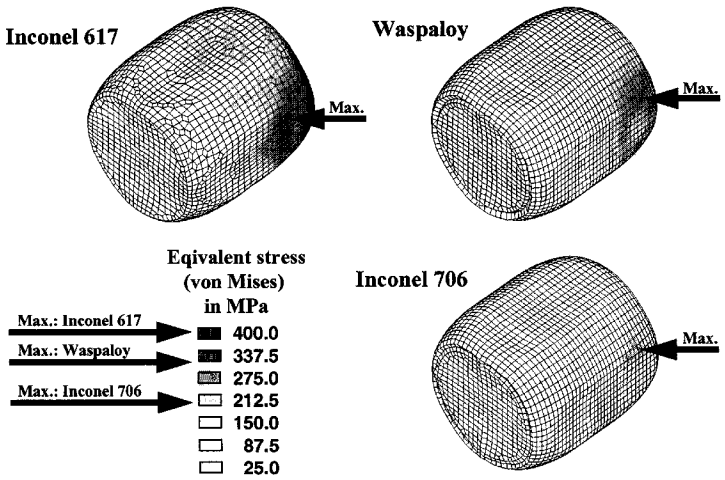


Fig. 4: Hammer forging from round to square cross section for Inconel 617, Waspaloy and Inconel 706, showing von Mises stress distribution at the last stroke. To forge the square cross section, three strokes of hammer forging, then 90° turning of the dies and following three strokes of hammer forging were needed.

4. Formability of analysed materials

After analysing the flow stress behaviour of each alloy during manufacturing of large turbine components, the formability of each alloy is analysed with the help of laboratory tests.
As previously described in chapter 1.4, compression tests with sample geometry 'Flange' have been performed at temperatures of 950°C and 800°C and a constant strain rate of 0.05/s. The tested temperature of 800°C should be seen as the lowest border for forging. However, this temperature could be reached during forging in the contact area of the forging billet to the cool forging die. Here, a local drop under the lowest suitable forging temperature could cause cracking at the surface of the forged billet.
To quantify the level of formability, the specific height reduction up to crack initiation is used. The results of the tests are summarized in fig. 5. At 950°C, Inconel 706 showed no appearance of cracks at the given forming conditions, as could be seen in the picture of the compressed sample in fig. 5.
This corresponds to its good dynamic recrystallization behaviour, which could also be noticed in the lowest determined value of activation energy for hot forming of all alloys: $372.3\,\mathrm{kJ/mole}|_{\mathrm{Inconel\,706}} < 411.8\,\mathrm{kJ/mole}|_{\mathrm{Inconel\,617}} < 511.2\,\mathrm{kJ/mole}|_{\mathrm{Waspaloy}}$. Therefore, the other alloys show cracking at average values of $\bar{\varepsilon}_{h.c}$ at 0.66 for Inconel 617 and at 0.69 for Waspaloy, with a slightly better ductility at this temperature. The formability at test temperature of 800°C shows a significant loss of ductility for all alloys. In this case, Inconel 706 has got best formability due to highest average value of specific height reduction up to crack initiation ($\bar{\varepsilon}_{h.c}$ = 0.71) of all investigated Ni-base alloys. The effect of decrease in ductility with decreasing temperature is dramatical for Inconel 617 and Waspaloy, as could be observed in fig. 5. The reason of loss in formability below 950°C is not only because of solid solution, but also, in case of Waspaloy, because of γ'-precipitations, which further inhibits

dynamic recrystallization [13]. For both alloys a forging should be done under any circumstances within the given narrow temperature band.

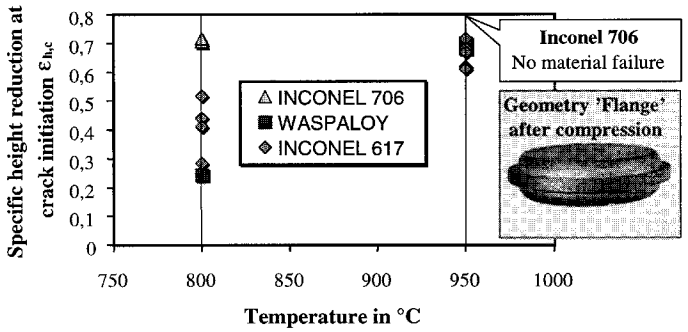


Fig. 5: Temperature dependency of formability for the investigated Ni-base alloys. For example, the final shape of sample of Inconel 706 is shown, after compression at 950°C.

5. Summary

The forging of large components for gas turbine discs and USC steam turbine rotor applications mainly depends on the flow stress level of the forged material, due to component size (up to 2000mm diameter) and weight (up to 100 tons) and limited forge press capacity (worldwide: 14,000 tons) [1]. Therefore, new alloy developments for USC steam turbine applications with steam inlet temperatures of 700°C and above have to meet these demands in manufacturing.
In this context, the workability of the wrought Ni-base alloys Inconel 706, Waspaloy and Inconel 617 were analysed in two ways: (i) microstructure models for each alloy have been developed and used in FEM coupled forging simulations to investigate the flow stress behaviour in process and (ii) experimental investigations of the formability of the alloys have been performed. Inconel 706 was found to be a good choice due to its combination of low forging forces, its grain refinement behaviour and the good formability. On the other side, Inconel 617 seems to be no good solution, mainly caused by its solid solution strengthening behaviour which leads to highest flow stress level during forging.

Acknowledgement

The authors would like to acknowledge the financial support given by the Deutsche Forschungsgemeinschaft (DFG), Germany, within the joint research project DT5. The authors would like to thank Mr. K.-H. Schönfeld from Saarschmiede GmbH Freiformschmiede and Dr. Kern from Siemens Power Generation for fruitful discussions.

6. References

[1] Potthast, E.; Schönfeld, K.-H., Stein, G.: 'Schmiedestücke für den Energiemaschinenbau', in *Werkstoffe für die Energietechnik* (Ed.: Grünling, H.), Werkstoffwoche '96, DGM Informationsgesellschaft (1997), p. 71-79.

[2] Vanstone, R.W.: 'Advanced ("700°C") PF power plant', 3rd EPRI Conf. on Adv. in Mat. Techn. for Fossil Power Plants, Swansea, UK (2001).

[3] Dilthey, U.; Ghandehari, A.; Kopp, R.; Hohmeier, P.; Beiss, P.; Figueredo, E.I.; El-Magd, E.; Kranz, A.: 'Development of Porous Steel Structures for Steam Turbines', Advanced Engineering Materials 3 (2001), No. 3, p. 111-119.

[4] Kern, T.-U.; Wieghardt, K.: 'The application of high-temperature 10Cr materials insteam power plants', VGB Power Tech 5 (2001), p. 125-131.

[5] Herbertz, R.; Wiegels, H.: 'Der Zylinderstauchversuch – ein geeignetes Verfahren zur Fließkurvenermittlung?', Stahl und Eisen 101 (1981), No. 11, p. 47-52.

[6] Kopp, R.; Bernrath, G.: 'Fließkurvenaufnahme bei hohen Umformgeschwindigkeiten', Stahl und Eisen 118 (1998), No. 4, p. 71 – 76.

[7] Kopp, R.; Luce, R.; Leisten, B.; Wolske, M.; Tschirnich, M.; Rehrmann, T.; Volles, R.: 'Flow stress measuring by use of cylindrical compression test and special application to metal forming processes', steel research 72 (2001) No. 10, p. 394-401.

[8] Kopp, R.; Bernrath, G.: ' The determination of formability for cold and hot forming conditions', steel research 70 (1999) No. 4+5, p. 147-153.

[9] Kopp, R.; Wolske, M.; Parteder, E.: 'Investigations on the formability of a tungsten alloy by use of acoustic emission analysis', Proc. 15th Int. Plansee Seminar, (Eds.: Kneringer, G.; Rödhammer, P.; Wildner, H.), Plansee Holding AG, Reutte / Tyrol, Vol. 3 (2001), p. 49-59.

[10] Karhausen, K.: 'Integrierte Prozeß- und Gefügesimulation bei der Warmumformung', Dr.-Ing. Thesis, Institute of Metal Forming, (1994).

[11] Guimaraes, A.A.; Jonas, J.J.; 'Recrystallization and aging effects associated with the high temperature deformation of Waspaloy and Inconel 718', Met. Trans. 12A (1981), p. 1655-1666.

[12] Shen, G.; Semiatin, S.L.; Shivpuri, R.: 'Modeling Microstructural Development during Forging of Waspaloy', Met. and Mat. Trans. 26A (1995), p. 1795 – 1803.

[13] McQueen, H.J; Gurewitz, G.; Fulop, S.: 'Influence of dynamic restoration mechanisms on the hot workability of Waspaloy and concentrated FCC alloys', High Temp. Technol. 2 (1983), p. 131-138.

[14] Luton, M.J.; Sellars, C.M.: 'Dynamic recrystallization in nickel and nickel-iron alloys during high temperature deformation', Acta Metal. 17 (1969), p.1033 – 1043.

[15] Roberts, W.; Bohden, H.; Ahlblom, B.: 'Dynamic recrystallization kinetics', Metal Science 13 (1979), p. 195-205.

[16] McQueen, H.J.; Bourell, D.L.: 'Summary Review of Comparative Hot Workability of Metals in Different Crystal Structures', in *Inter-Relationship of Metallurgical Structure and Formability,* (Eds.: Sachdev, A.K.; Embury, J.D.), TMS-AIME, Warrendale, USA, (1986), p. 341 – 368.

[17] Humphreys, F.J., Hatherly, M.: 'Recrystallization and related annealing phenomena', Pergamon Press, Oxford (1995), p. 381.

[18] Sellars, C.M.: 'The physical metallurgy of hot working', in *Hot Working and Forming Processes*, (Eds.: Sellars, C.M.; Davies, G.J.), TMS, London, UK, (1979), p. 3-15.

[19] Kopp, R.; Wolske, M.: 'Microstructure simulation of Ni based alloys', *Proc. 'IV*[a] *Conferência Internacional de Forjamento'*, Porto Alegre, Brazil, (2000), p. 42-53.

MICROSTRUCTURE AND STRUCTURAL STABILITY OF CANDIDATE MATERIALS FOR TURBINE DISC APPLICATIONS BEYOND 700 °C

H.J. Penkalla, J. Wosik , F. Schubert
Research Centre Jülich, Institute for Materials and Processes in Energy Systems
D-52425 Jülich, Germany

Abstract

Three Ni-base wrought alloys with different hardening mechanisms (Inconel 706, Waspaloy and Inconel 617) are candidates for steam turbine disc applications with temperatures up to 700 °C and were examined in respect to their microstructure and microstructural stability. The materials were investigated after different heat treatments and after short and long term ageing by metallography, scanning and transmission electron microscopy. The Nb containing alloy Inconel 706 shows a complex microstructure containing γ', γ'' and η phases which are stable under long term service up to about 620 °C. At higher temperatures a strong particle coarsening and phase transformation was observed. Waspaloy is hardened by γ' particles with a bimodal size distribution. After ageing at 700 °C and higher a coarsening was observed by loss of the bimodal size distribution. Inconel 617 is a solid solution hardened material additionally hardened by homogeneously distributed fine $M_{23}C_6$ carbides. After long term ageing at temperatures of 650 °C to 750 °C the carbides tended to form carbide films along the grain boundaries and at 700 °C and higher γ' precipitated to homogeneously distributed particles with low coarsening under long term service.

Keywords: Microstructure of Inconel 706, Inconel 617 and Waspaloy, influence of ageing

1. Introduction

An increase in the efficiency of steam power plants can be achieved by increasing the steam temperature. In future, power plant for electricity generation will, for thermal efficiency and ecological reasons, operate with steam temperatures as high as 700°C. The currently used martensitic/feritic steels are limited to application temperatures of about 600 °C [1]. Ni-base wrought superalloys with good formability, high yield strength, sufficient creep strength, creep crack growth resistance, as well as good steam oxidation resitance and high structural stability during long term service are candidate materials for large components and application temperatures of 700 °C.

In the German DFG research project "Production and life-time models for the application of Ni-base alloys in steam turbines at temperatures above 700 °C" different aspects of the use of Ni-base superalloys should be modelled. In order to collect a data base for the modelling, in a first screening step three candidates, Inconel 706, Inconel 617 and Waspaloy, have been investigated in respect to their casting, forgeability, heat treatment, structure, microstructural stability and mechanical properties such as creep strength and creep crack growth behaviour in the temperature range 650 to 750 °C.

An important criterion for the selection of these material selections was the difference in the hardening mechanisms of these alloys. Inconel 617 is representative for solid solution hardened Ni-base alloys, Waspaloy is hardened by coherent γ'particles and by solid solution and the alloy Inconel 706 is hardened due to a complex microstructure consisting of MC carbides, γ', γ'' and η phase. In the following contribution the aspects of the alloy microstructure and the structural stability will be reported.

2. Experiments

2.1 Materials and heat treatment

Inconel 706 is a Nb containing Ni-Fe-base superalloy derived from Inconel 718 with higher Fe and Ti content to improve the forgeability and to reduce the tendency for segregation [2-4]. The microstructure consists of fine γ' and γ'' precipitates, homogeneously distributed in the γ matrix, and, depending on the heat treatment, η-phases along the grain boundaries as a cellular structure. Additionally M(C,N) carbonitrides can be found. Inconel 617 is a solid solution hardened material and shows after heat treatment a distribution of small $M_{23}C_6$ precipitates with the matrix and along the grain boundaries. Waspaloy is hardened by γ' precipitates in a bimodal size distribution of primary and secondary particles and a small amount of $M_{23}C_6$ particles, which tend to precipitate at the grain boundaries in a globular shape.

The chemical compositions of the investigated alloys are shown in Table 1. From Inconel 706 two variants A and B were investigated to determine the influence of the heat treatment.

Element	Inconel 706	Inconel 617	Waspaloy
Ni	42	54	57.1
Fe	37.1	0.5	0.57
Cr	16	22	19.35
Ti	1.54	0.55	3.13
Al	0.26	1.11	1.22
Nb	2.96	0	0.01
C	0.01	0.55	0.033
B	0.0034	0.001	0.005
Co		12.9	14
Mo		9.05	4.52
Si	0.05	0.14	0.04

Table 1: Nominal chemical composition of Inconel 706, Inconel 617 and Waspaloy

Inconel 706 A has been solution treated at 980 °C for 2 h with subsequent cooling to room temperature at a cooling rate of 25 K/min (Figure 1). The two-stage precipitation heat treatment was performed at 720 °C for 8 h and at 620 °C for 8 h. This heat treatment results in a homogeneous distribution of small γ' and γ'' precipitates; the η phase is absent.

In order to precipitate the η phase, a different heat treatment was applied (Inconel 706B). This heat treatment according to the results of Shibata [4] includes a stabilising step at 820 °C for 8 h following solution annealing. In contrast to Shibata's heat treatment, however, stabilising directly follows solution annealing by cooling down from 980 °C to 820 °C at a cooling rate of 4 K/min. This procedure should avoid initial γ' and γ'' precipitation during the cooling down before η phase precipitates.

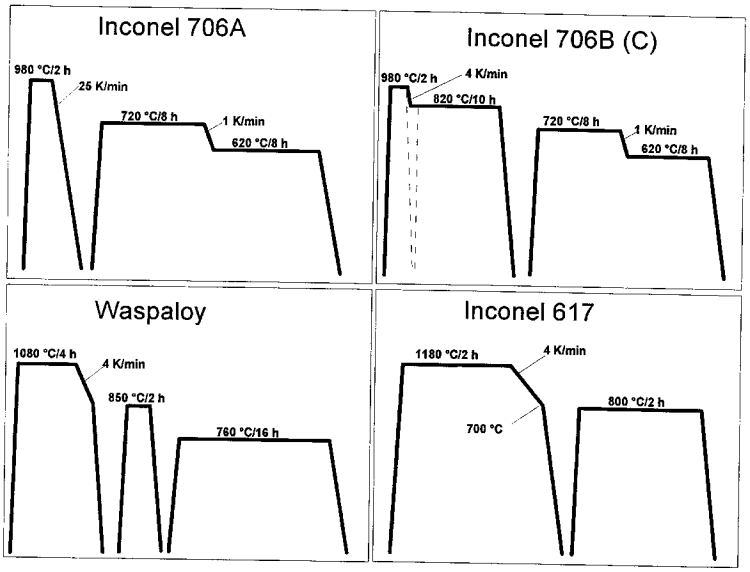


Figure 1: Heat treatments of the investigated alloys. The dashed lines indicate the heat treatment proposed for Inconel 706 by Shibata [5].

The heat treatment of Inconel 617 consists of two steps, an initial solution annealing at 1180 °C for 2 h and a precipitation heat treatment at 800 °C for 2 h. After solution annealing, the specimen was cooled down to room temperature. In the range to 700 °C the cooling rate was limited to 4 K/min to avoid a supersaturation of C in the matrix. This procedure led to a homogeneous distribution of $M_{23}C_6$ during the stabilising annealing. The temperature of 800 °C was chosen to avoid additional γ' precipitation, which may occur at heat exposure in the temperature range of 650 °C to 750 °C.

Waspaloy was solution annealed at 1080 °C for 4 h, followed by precipitation heat treatment at 850 °C for 2 h and at 760 °C for 16 h. Between the three annealing steps the specimens

were cooled down to room temperature, after the solution annealing up to 700 °C with a definite cooling rate of 4 K/min.

Table 2 shows the grain size and hardness HV10 of the investigated materials. The γ' and γ'' hardened Inconel 706 A shows the highest hardness. The η phase in the variants Inconel 706 B led to a loss of hardness of about 10% compared with the variant Inconel 706A.

Material	mean grain size (μm)	hardness HV10
Inconel 706 A	39	426
Inconel 706 B	69	378
Inconel 617	223	169
Waspaloy	44	328

Table 2: Grain size and hardness of the investigated alloys

2.2 Methods of investigations

The microstructural investigations were carried out using scanning and transmission electron microscopy (SEM, TEM). Thin foil specimens for TEM examinations were prepared by mechanically thinning to about 80 μm thickness, followed by double jet polishing (Tenupol) to 5 μm residual thickness in the etching dimple. The last step of thinning was done by small-angle ion beam milling (Gatan PIPS) with angles of -3, and +4° and an energy of 5keV. The conditions of the electrolytic polishing process were: temperature –25°C, voltage 22V, solution: 60 ml perchloric acid, 620 ml ethanol, 310 ml butylglycol. For TEM replicas, the specimens were thinned to about 40 μm thickness and covered on both side with a thin carbon film. Then the matrix was dissolved in a solution of 10% bromium in ethanol. TEM investigations were carried out using a JEOL 200 CX and Philips (FEI) CM200 combined with a Gatan Image Filter (GIF); the SEM investigations were carried out using LEO1530/Gemini scanning electron microscope.

Specimens for SEM investigation were prepared to a polished surface and etched with 10% phosphoric acid at a voltage 3V. The measurement of particle sizes and the evaluation of size distributions was carried out by the image analysis system KS400 from Kontron. The images were taken from the electron micrographs in digital format or, if the contrast was too low, redrawn from a printed copy and scanned from the image analysis system.

3. Results and discussion

3.1 Inconel 706

3.1.1 Microstructure after heat treatment.

The variant Inconel 706 A exhibited after heat treatment two types of precipitation, the coherent γ' phase of Ni_3(Ti, Al) and the metastable semi-coherent γ'' phase of Ni_3(Nb, Ti). In Figures 2 and 3, TEM images of Inconel 706 A alloy are shown. The spherical precipitates observed inside the grains were identified as γ' phase and the disc shaped precipitates as γ'' phase. The γ' and γ'' particles were homogeneously distributed inside grains with volume fractions of lower than 3% for γ' and about 4% for γ''. The mean length of γ'' particles was

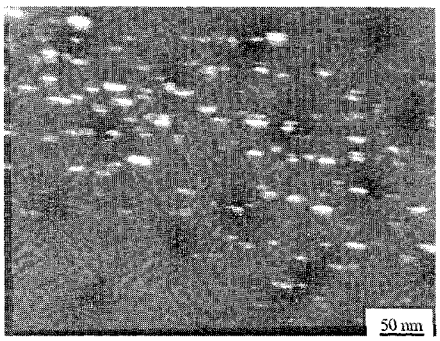


Figure 2: Homogeneously distributed γ' and γ'' particles in Inconel 706 A (TEM dark field)

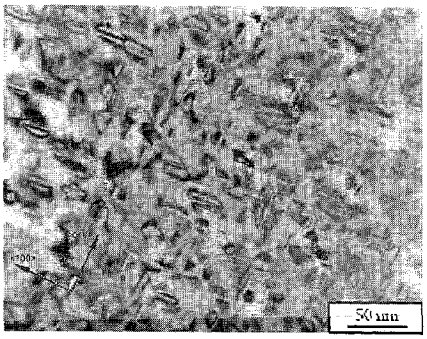


Figure 3: Coherence contrast of γ'' particles demonstrates the orientation to the <100> and <010> directions in the matrix

about 20 nm and the diameter of the spherical γ' particles 10 to 15 nm. Figure 3 shows the orientation of γ'' particles related to the matrix where the coherent planes of γ'' are parallel to the <100> or <010> planes of the matrix.

A typical microstructure of the variant Inconel 706 B is presented by Figure 3. The γ' and γ'' particles were homogeneously distributed comparable to the variant Inconel 706 A. The η phase precipitated at the grain boundaries in a cellular manner (Figure 4) or as a grain boundary film, dependent on the grain boundary orientation.

The platelets grew parallel to the (111) planes of the matrix and had one partly coherent interface with the {111} plane The orientation relationship between γ and η phase is given by the relationship $<011>_\gamma \| <2110>_\eta$, $\{111\}_\gamma \| \{0001\}_\eta$ and was established using electron diffraction technique.

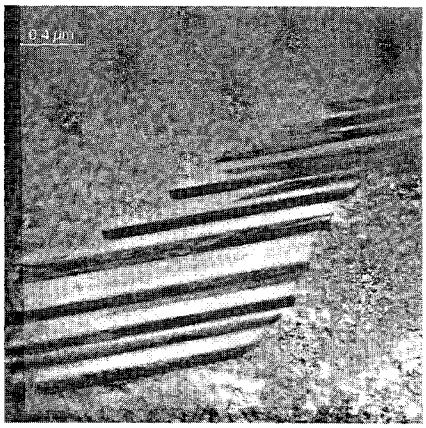


Figure 4: Cellular precipitated h phase along the grain boundary in Inconel 706B

3.1.2 Microstructure after ageing.

To observe the structural changes in Inconel 706 at elevated temperatures, some ageing experiments were carried out at temperatures of 600, 650, 700 and 750 °C with exposure times up to 30 000 h. At temperatures up to 620 °C and exposure times up to 10 00 h, no significant changes of the γ' and γ'' particle size were observed in the variant Inconel 706 A, but the Laves phase of the Fe_2Nb type appeared at 600 °C after less than 3000 h. It was found as clusters of small platelets near to MC carbides. Figure 4 demonstrates this fact by a TEM

replica image, where the larger spherical particles are MC carbides and the small plates or needles are the Laves phase.

At temperatures of 650 °C and higher the γ'' particles grew significantly. The changes in particle size and morphology in Inconel 706 A after ageing at 650°C and 30 000 h is presented in Figure 5. The main aspect of this image is the directional coarsening process of γ''. The γ'' platelets grew in defined <001> direction of the matrix (γ). This behaviour can be explained by a minimisation of coherency strain during the particle growth [5].

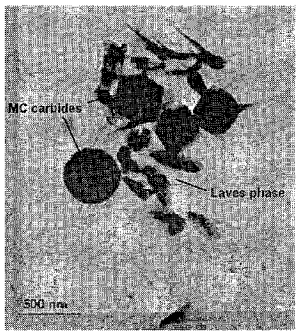


Figure 5: Laves plates in Inconel 706 A after 10000 h at 650°C (replica)

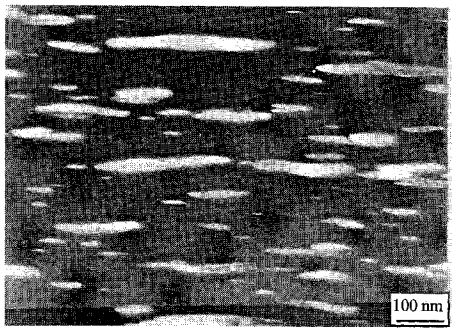


Figure 6: Microstructure of Inconel 706 A after ageing at 650°C and 30 000 h (TEM dark field)

Table 3 and Figures 7 and 8 present the γ'' particle size distribution and aspect ratio for the variant Inconel 706 A after long term exposure at 650 °C.

	Time (h)	3000h	10000h	30000h
as received	Temperature (°C)	650	650	650
18.1 ± 9.8	γ'' particle length	44.1 ± 29.8	93.6 ± 74	155.6 ± 142
0.42 ± 0.14	particle aspect ratio	~0.4	~0.3	0.24± 0.12

Table 3: The changes in γ'' size (length) and aspect ratio during long term ageing at 650 °C

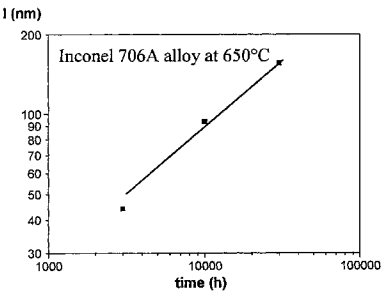


Figure 7: The growth of γ'' precipitates in Inconel 706 A alloy aged at 650°C.

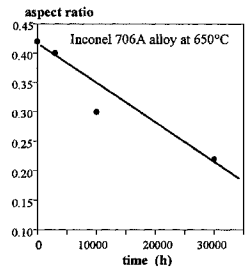


Figure 8: The γ'' particles aspect ratio (morphology) vs. ageing time

The results confirm the preferred growing directions for γ'' phase during coarsening. The regression analysis shown in Figure 6 results to the equation $l = 0.547 \cdot t^{1/2}$ where l represents the particle length. This result is different to the growth of γ'-particles in a number of Ni-base alloys which follow the $d \propto t^{1/3}$ rule of the LSW theory [6,7] and is in agreement with the observation of a mainly planar growth of the γ'' particles.

At temperatures above 650 °C and after exposure times of about 3000 h the η phase appeared additionally on grain boundaries and twins. The volume fraction was very small and could not be measured. At 700 °C and more than 4000 h, the η phase appeared homogeneously distributed in the grain interior and at the grain boundaries. As a result of η precipitation the hardness of the aged material decreased. Figure 9 demonstrates the loss of hardness in dependence on ageing temperature and time. The coarsening of γ' and γ'' at 600 °C to 650 °C caused only a small loss of hardness.

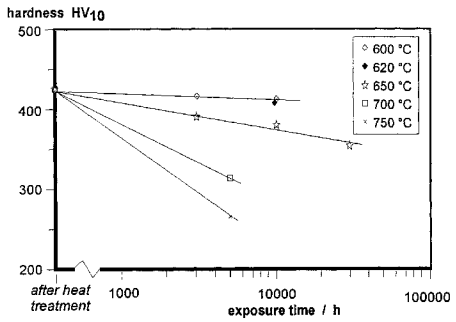


Figure 9: Hardness of Inconel 706A in dependence on ageing time and temperature

Two examples of the microstructural features of Inconel 706 B alloy after ageing at 750 °C for different ageing times are given in Figure 10.

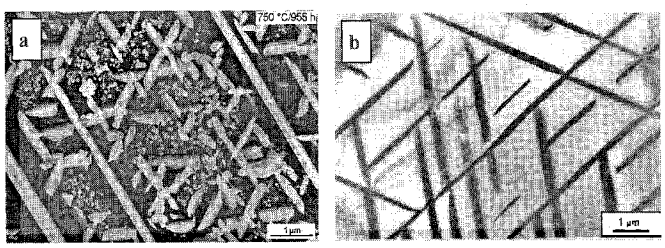


Figure 10: Microstructure of Inconel 706 after ageing at 750 °C for 1000 h (a) and 5000 h (b)

The amount of η phase after ageing at 750 °C was much higher than that after ageing at 700 °C. At 750 °C after 1000 h, the transformation to the η phase was not completed and the parts of small spherical γ' and prismatic γ'' particles between the large η platelets is visible (Figure 10a). In the case of extending the exposure time up to 5000 h, both of the strengthening phases γ' and γ'' disappeared and the η phase dominated (Figure 10b).

3.2 Waspaloy

3.2.1 Structure after heat treatment.

The microstructure of Waspaloy after heat treatment consisted of bimodal distribution of coherent γ' particles $Ni_3(Ti,Al)$ with a volume fraction of about 0.25 and $M_{23}C_6$ precipitates along the grain boundaries with a volume fraction below 0.002. Figure 11 shows TEM dark field images of γ' precipitates in Waspaloy from specimens taken either from a surface near zone (a) or from the centre (b) of a billet of 200 mm in diameter. The large γ' precipitates, the primary γ' differ obviously from the fine secondary γ'. The primary γ'

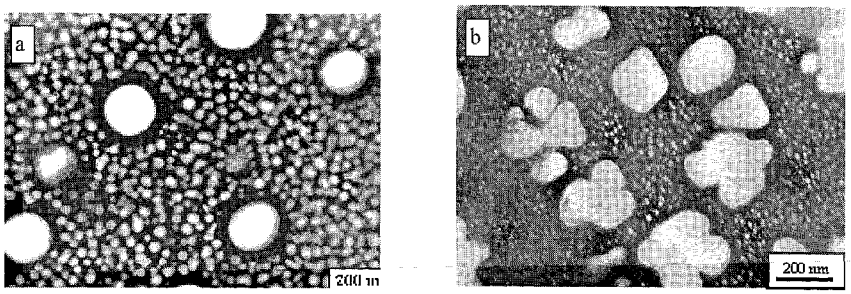


Figure 11: Microstructure of Waspaloy after heat treatment a) closed to surface and b) in the centre of a billet (TEM dark-field image).

precipitates tended to form spheres in the specimen from the edge and more complex shapes in the billet centre. The secondary γ' particles at the centre of the specimen were smaller compared to those in the near surface specimen. It seems that the complex form of primary γ' particles is a result of attraction of γ' particles during the cooling down of the heat treatment.

3.2.2 Microstructure after ageing

In order to observe the ageing behaviour of Waspaloy, a set of creep specimens tested at 650, 700 and 750 °C were investigated. After 6700 h at 650 °C no significant change in γ' particle amount and shape has been observed. After exposure at 700 °C a reduction of secondary γ' and a coarsening of primary γ' particles was detected. The volume fraction of secondary γ' decreased from 4.8 % as received to about 0.1 % after 2500 h and the volume fraction of primary γ' increased. After 5000 h at 750°C the small secondary γ' particles disappeared completely and the dimensions and volume fraction of large primary γ' particles increased from 13.8% in as-received condition to about 22-24% (Figure 12). That means that after heat treatment, the system is not in equilibrium state, not all of possible γ' has been precipitated.

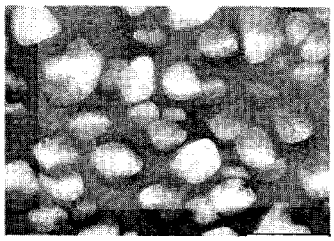


Figure 12: γ' particle coarsening in Waspaloy after ageing at 750 °C/5000 h

3.3 Inconel 617

3.31 Microstructure after heat treatment.

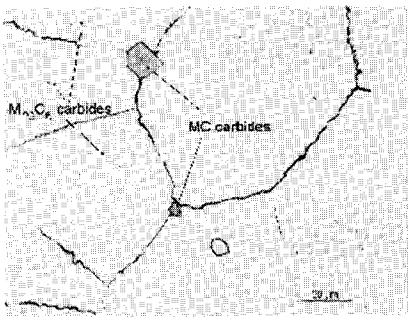


Figure 13: Micrograph of Inconel 617 showing M(C,N) carbo-nitrides and small M23C6 carbides

Inconel 617 is a solid solution hardened Ni-base alloy which is additionally strengthened by M(C,N) carbonitrides and by homogeneously distributed $M_{23}C_6$ carbides with a size of about 60 - 100 nm (Figure 13). The distribution of carbides is dependent on the cooling rate after solution annealing and tend slightly to form clusters at lower cooling rates leading to differences in the hardness values within the grains. The influence of carbides mentioned above on the properties of Inconel 617 depends on their morphology. After heat treatment $M_{23}C_6$ carbides are usually globular and strengthen the matrix and the grain boundaries. The volume fraction of $M_{23}C_6$ carbides was estimated to be 0.006 – 0.007 [7]. The volume fraction of the homogeneously distributed carbonitrides of the Ti(C,N) type was about 0.004 %. Because of the high Mo content the formation of M_6C carbides (Mo_6C type) is possible and has been detected (volume fraction about 0.001) in TEM analysis.

3.3.2 Microstructure after ageing.

During ageing at temperatures of 650 – 750 °C the $M_{23}C_6$ carbides tended to grow along the grain boundaries and to form carbide films (Figure 14). Additionally fine lamellar structures of $M_{23}C_6$ needles clustered to islands in the matrix near the grain boundaries have been found.

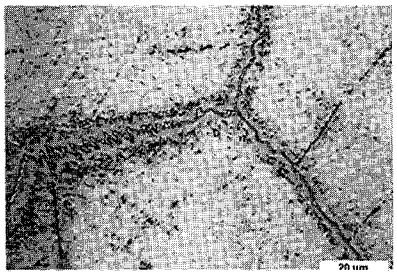


Figure 14: M23C6 carbide film along the grain boundaries in Inconel 617 after ageing at 650 °C/15000 h

An unexpected effect of the ageing of Inconel 617 at 700 to 750 °C was the precipitation and growth of very homogeneously distributed γ' particles. The precipitation of γ' particles of a mean size of about 20 nm was still observed after 83 h at 700 °C. After ageing at 750 °C and 5000 h γ' particles with a size of about 80 – 90 nm at a volume proportion of about 4 % were detected .

4. Conclusions

Three Ni-base wrought alloys, Inconel 706, Waspaloy and Inconel 617, representative for alloys with different hardening mechanisms were investigated with respect to their microstructure and microstructural stability at temperatures from 650 °C to 750 °C. Inconel 706 is hardened by γ', γ'' and η phases The presence of η phase along the grain boundaries can be controlled by the heat treatment. The microstructure is not stable at temperatures above 650 °C and the microstructural changes are characterised by particle coarsening after medium service life and long term phase transformation into the platelets forming η phase.

The alloy Waspaloy exhibits a bimodal size distribution of primary and secondary γ' particles strongly dependent on the cooling rate after solution annealing during the heat treatment. During service life at temperatures above 700 °C, γ' particles coarsen to a homogeneous microstructure containing with γ' particles of about 250 nm diameter.

Inconel 617 is a solution hardened Ni-base alloy exhibiting small $M_{23}C_6$ carbides after heat treatment. During service life above 700 °C the carbides tend to form carbide films at the grain boundaries and small needle like precipitates inside the grains. Because of the Al and Ti content of this alloy γ' will be precipitated in a homogeneous distribution and a volume fraction of maximum 0.04.

5. References

[1] F. Tarcet, H.K.D.H. Bhadeshia and D.J.C. Mac Kay, "Design of new creep-resistant nickel-base superalloys for power plant applications", Key Engineering Materials 171-174 (2000), 529-536.

[2] K.A. Heck, "The Time-Temperature-Transformation Behaviour of Alloy 706", Paper presented on the Conference Superalloys 718, 625, 706 and Various Derivatives, 1994, 393-404.

[3] G.W. Kuhlman, "Microstructure-Mechanical Properties Relationships in Inconel 706 Superalloy" Proc. Conf. Superalloys 718, 625, 706 and Various Derivatives, 1994, 441-450.

[4] T.Shibata, et al. "Effect of Stabilizing Treatment on Precipitation Behaviour of Alloy 706", Proc. Conf. Superalloys 1996, pp. 153-636.

[5] J. Rys and K. Wiencek, Koagulacja faz w stopach, Wydawnictwo Slask, Poland, 1979)

[6] I.M. Lifshitz, V.V. Slyozow "The Kinetics of Precipitation From Supersaturated Solid Solution", Journal Phys. Chem. Solids, 19 (1/2) (1961), 35-50

[7] C. Wagner, "Theorie der Alterung von Niederschlägen durch Umlösen (Ostwald-Reifung)", Zeitschrift für Elektrochemie, 65 (7/8) (1961), 581- 591

[8] F. Schubert, H. J. Penkalla, A. Weisbrodt - „PHASCALC*: An improved computer programme for the calculation of phase kinetics, microstructural parameters and microstructural instabilities in Nickel base Superalloys", Paper on the European Conference on Advanced Materials and Processes, Aachen, Germany, 1989,

Acknowledgement

This work is part of the DFG - research programme "Herstellungs- und Lebensdauermodelle für den Einsatz von Nickel-basis Werkstoffen in Dampfturbinen oberhalb 700°C". The financial support of the Deutsche Forschungsgemeinschaft is gratefully acknowledged.

Material Degradation and Damage Assessment for Gas Turbine Combustion Components

Daizo Saito, Yomei Yoshioka, Kazunari Fujiyama
Power & Industrial Systems Research & Development Center

Power Systems & Services Company Toshiba Corporation
2-4, Suehiro-cho, Tsurumi-Ku, Yokohama, 230-0045, JAPAN

Abstract

Extensive microstructural changes were observed in the after end of a combustion liner made of *Hastelloy* X. In addition to the material degradation, a large creep deflection was observed in the picture frame of the transition piece. This paper describes the influence of long time aging on microstructure and mechanical properties of *Hastelloy* X, an alloy often used for combustion components. By using specimens aged at temperatures of 750-900°C up to 10000 hours, carbides and the intermetallic compound μ phase were found to precipitate at grain boundaries and inside grains. The density of intragranular precipitates was found to be correlate well with hardness, tensile strength and proof stress. Concerning the effect of precipitates on the creep properties, grain boundary precipitates contribute to the strengthening of the creep resistance while intragranular precipitates and μ phases weaken the creep resistance.

Keywords: Gas turbine, Combustion liner, Transition piece, Material degradation, *Hastelloy* X

Introduction

The damage modes and service life of hot gas path components of gas turbines differ from component to component depending upon the operating modes, fuel, material and operating environment of a power station etc., which leads to the definition of different life criteria for each component. It is, therefore, important to develop the assessment technology for specific life-dominated factors which are based on the correct understanding of the actual in-service phenomena experienced by the component.

The Ni-base, solid-solution strengthened, alloy *Hastelloy* X is used for gas turbine combustion liner and transition piece. It has good oxidation resistance, formability and high temperature strength. In recent years, the turbine inlet gas temperature is becoming higher for the purpose of improving thermal efficiency and output. Therefore, the material degradation of combustors has been observed to be extensive, and creep deflection has also appeared in transition pieces [1]. This paper clarifies the microstructural changes and creep damage which have been observed in combustors operated in-service. It also describes Toshiba's microstructural assessment methodology developed for long time aged materials.

Degradation and damage of in-service combustion components

In-service combustion liners, made of *Hastelloy* X, are observed to have several kinds of damage, such as fatigue cracking of the welded portions, wearing of fitting portions and spallation of the thermal barrier coating. Material degradation is also observed. The microstructure of a combustion liner in-service for about 24000 hours is shown in Fig. 1 and is compared with that of a new combustion liner. Although microstructural changes were not

observed in the main body, many precipitates were found in the after end portion of the liner.

In-service transition pieces, made of *Hastelloy* X, are also observed to have damage, such as creep deflection, thermal fatigue cracking of welded portions and of the picture frame, wear of fitting portions, and spalling of the thermal barrier coating, with heavy material degradation. Those damages and degradation are refurbished, repaired, reformed at the combustion inspection time when the damage exceeds the repair criteria of the component. Fig. 2 shows changes of creep deflection in axial and radial directions of picture frames against service hours. One example of radial deflection in the picture frame of a transition piece is shown in Fig. 3. This deflection is measured at every inspection and any acceleration of the deflection rate is detected. The microstructure of the transition piece after 12000 hours in-service are also shown in Fig. 4. Many precipitates were observed at grain boundaries and in the grains and these coarsened during service. There seems to be some correlation between this microstructural change and the deflection in this material and therefore the investigation of the microstructure of these hot gas path components is thought to be very important.

Experimental procedures

Test Material

The chemical composition of the *Hastelloy* X alloy studied here is shown in Table 1. After a solution heat treatment of 1150°C/50min., aging was conducted to a 20mm thick rolled material (AMS55365). Long-term aging heat treatments, up to 10000 hours, at 750°C, 800°C, 850°C and 900°C were applied to the 20 mm thick rolled material and then microstructural observations and mechanical tests were conducted.

Test Methods

Microstructural observations were conducted by an optical microscope. The etching reagent contained HNO_3, HCl and glycerin in the ratio of 1:3:3 respectively. The microstructure was quantified using an image analyzer. Here, intergranular and intragranular precipitates were separately recorded and measurements were taken of the grain boundary coverage ratio and the density and volume fraction of intragranular precipitates.

The precipitates were extracted, and characterized by X-ray diffraction analyzer. The electrolyte contained HCl, tartaric acid and CH_3OH in the ratio of 10:1:89 respectively. The conditions of extraction were 4 hours at a current density of $0.06A/cm^2$.

Mechanical tests were also conducted. Hardness and tensile test were performed at room temperature. Creep tests were also conducted at three different temperatures and two different stresses. The test specimens used for tensile and creep tests have a diameter of 6mm and a gauge length of 30mm.

Test results

Microstructural Observations

The observation results of the material aged at 750-900°C up to 10000 hours using an optical microscope are shown in Fig 5. Table 2 shows X-ray diffraction test results of the residue extracted from various aged materials. Fig. 6 shows changes in the element composition of the extracted residues. M_6C type carbide was slightly observed in the as-solution-treated material, but $M_{12}C$ and $M_{23}C_6$ type carbides were observed in the materials aged at 750-850°C. M_6C type carbide was also observed in the materials aged at 900°C. The

precipitation of a μ phase (Fe_7Mo_6), which is an intermetallic compound, was also observed. The ratio of the μ phase to carbide became larger with aging time up to 6000 hours. In connection with this, an increase of Mo content in precipitates was observed. Moreover, the ratio of μ phase in precipitates was observed to increase with aging temperature.

A quantitative description of the precipitates, obtained using an image analyzer, is shown in Fig.7. Intragranular precipitates mostly precipitated up to 1000 hours and then increased more gradually or saturated. Grain boundary coverage ratio also increased as aging time increased.

Mechanical testing

The results of tensile strength, 0.2% proof stress, elongation, reduction of area and hardness are shown in Fig. 8. Increases in the tensile strength, proof stress and hardness are observed up to 1000 hours for every aging temperatures, and then these decreased further or saturated. On the other hand, the elongation and reduction of area significantly decreased after the agings of 1000 hours and the reductions became larger at the lower aging temperature.

The results of creep testing conducted under the stresses of 78.5MPa, 49.0MPa and 29.4MPa at 850°C are shown in Fig. 9. Rupture life decreased and minimum creep rate increased up to 6000 hours for every aging temperatures, but a recovery of rupture life was observed in specimens aged for 10000 hours.

The effect of test temperature on the creep properties has been investigated at three temperatures, 830°C, 850°C and 900°C, for the stress of 49.0MPa, and at 800°C, 850°C and 870°C, for the stress of 78.5MPa. The results are shown in Fig. 10. A good correlation between test temperature and rupture life or minimum creep rate was observed.

Discussion

Limited precipitation is observed in the as-solution-heat-treated condition of *Hastelloy* X. However, many precipitates of carbides and intermetallic compounds were found in the aged sample at the temperatures of 750 - 900°C, and also, in-service combustion liner and transition pieces. Here, we will discuss the effect of long time aging on hardness, tensile properties and creep properties based on the results of microstructural evaluation and mechanical tests of aged specimens.

Effect of microstructure on hardness and tensile properties

This material is solid solution strengthened and normally no precipitation is observed. But the intermetallic compound μ phase and the carbides $M_{12}C$ or M_6C precipitate during aging leading to strengthening of the material. This particle strengthening mechanism is considered to be a shear model, with dislocations cutting through the precipitates, or a by-pass model, with dislocations bowing around them. The former one has a correlation with the diameter of precipitates and the latter one has an inverse relationship with the interparticle distance, which also has an inverse relationship with the density of precipitates, as described below.

$$\lambda \propto N^{-\frac{1}{2}}$$

where

λ: interparticle distance, N: density of intragranular precipitate

Fig. 11 shows the relationship of hardness, tensile strength and 0.2% proof strength at room temperature with the density of intragranular precipitates. It is clear that a good correlation is obtained across the available data. Consequently, it can be argued that Orowan's by-pass

model is the dominant strengthening mechanism. The following equations are obtained.

$$HV = HV_0 + \frac{C_{HV}}{\lambda} = HV_0 + C_{HV} N^{\frac{1}{2}} \quad (1), \quad TS = TS_0 + \frac{C_{TS}}{\lambda} = TS_0 + C_{TS} N^{\frac{1}{2}} \quad (2)$$

$$PS = PS_0 + \frac{C_{PS}}{\lambda} = PS_0 + C_{PS} N^{\frac{1}{2}} \quad (3)$$

where

HV: Vickers hardness, *TS*: tensile strength, *PS*:0.2 % proof strength
N: density of intragranular precipitate, HV_0, C_{HV}, TS_0, C_{TS}, PS_0, C_{PS}: material constants

Effect of microstructure on minimum creep rate

The effect of precipitation on the creep resistance is thought to be grain boundary strengthening (2) due to intergranular precipitation, strengthening due to intragranular precipitation, and precipitation weakening by the decrease of solid solution strengthening elements in the matrix due to the precipitation of the carbides etc..

The creep test results show a decrease for aging up to 6000 hours, but a recovery of the strength is observed after 10000 hours aging. The amount of intergranular precipitates increased with aging time, but that of intragranular ones saturated at 1000 hours aging. The transformation of precipitates from carbides to μ phase continued even after 1000 hours aging, but this saturated after 6000 hours.

The following creep strength degradation mechanism, related to the observed microstructural changes, is proposed. The intragranular precipitates do not contribute to an increase in the creep strength. This precipitation reduces the concentration of solid solution strengthening elements, mainly Mo, in the matrix and hence decreases the creep resistance. Moreover, although intergranular precipitates increase the creep strength since they restrain the deformation near the grain boundaries, their positive effect is small compared to the negative effect of the intragranular precipitates. The intergranular precipitation strengthening effect, therefore, is thought to have appeared after 6000 hours aging when the precipitation and the transformation of precipitates was completed and the concentration of the solid solution strengthening elements in the matrix had stabilized at a lower level. The effects of inter- and intra- granular precipitates on the creep resistance are shown in Fig.12, where $\dot{\varepsilon}_m$ is the minimum creep rate, $\dot{\varepsilon}_{mo}$ is the minimum creep rate without intergranular precipitates. It has been assumed that the effect of intergranular precipitates acts independently of intragranular precipitation.

A study of the intergranular precipitates strengthening mechanisms in creep has been conducted for the Ni-20Cr-20W alloy (3). The reduction ratio of the creep rate was found to be proportional to the ratio of grain boundary without intergranular precipitation of bcc-W phase, (1-ρ), where ρ is grain boundary coverage ratio with a bcc-W phase. According to these results, intergranular precipitate strengthening mechanism was verified. This strengthening mechanism was also confirmed in *Nimonic* 263, which is a γ' precipitation strengthened alloy (4), and IN 617 which is carbide precipitation strengthened (5).

$$\dot{\varepsilon}_m / \dot{\varepsilon}_{mo} = 1 - \rho \quad (0 \le \rho < 1) \quad (4)$$

This formula was introduced empirically under the condition that intragranular precipitates do not appear during creep testing, but actually both precipitates appear during service. For the

material studied here, therefore, we should consider that both inter- and intra- granular precipitation occurred. However, as a first approximation, based on the model described previously, the cause for the decrease in the resistance to creep deformation in the matrix is supposed to be due to the reduction of solid-solution strengthened elements. The change in the minimum creep rate from the as-solution-treated condition was calculated in terms of the change in the volume fraction of intragranular precipitates. The result is shown in Fig.13. The minimum creep rate varies linearly with the volume fraction, with a slope of 2 in a logarithm-logarithm diagram, for every aging temperature.

$$(\dot{\varepsilon}_m - \dot{\varepsilon}_o)/(1-\rho) = \dot{\varepsilon}_1/(1-\rho) = A(V - V_o)^2 \tag{5}$$

where, $\dot{\varepsilon}_1$: $\dot{\varepsilon}_m - \dot{\varepsilon}_o$

Here, $\dot{\varepsilon}_o$ and V_o are minimum creep rates and volume fraction of intragranular precipitates before aging, and $\dot{\varepsilon}_m - \dot{\varepsilon}_o$ and $V - V_o$ are the changes in the minimum creep rate and in the volume fraction of intragranular precipitates due to aging. The coefficient A in equation (5) is estimated, at each aging temperature, from the intercepts of the straight line fits in Fig.13. The values obtained can then be plotted as a function of aging temperature, for each of the applied stress, as shown in Fig.14, leading to the exponential type expression.

$$A = A' \exp(-Q_a / kT_a) \tag{6}$$

where, A', Q_a : material constant, T_a : aging temperature

Consequently, equation (5) can be expressed in terms of the following equation.

$$\dot{\varepsilon}_m - \dot{\varepsilon}_o = A'(1-\rho)(V - V_o)^2 \exp(-Q_a / kT_a) \tag{7}$$

Q_a is obtained to be 5.18×10^{-19}J here. The amount of μ phase within the precipitates is thought to have introduced an aging temperature dependence. The change of the element composition in the precipitates is shown in Fig. 6. The concentration of Mo has significantly changed. The activation energy of diffusion of Mo in Ni is reported to be 4.78×10^{-19}J [6], which is similar to this result. It is, therefore, thought that the value of Q_a obtained here is the activation energy of diffusion of Mo in this alloy.

Effect of temperature and stress on minimum creep rate

Generally the minimum creep rate can be expressed as a function of temperature and stress [7], as described below.

$$\dot{\varepsilon}_m = B\sigma^n \exp(-Q_c / kT) \tag{8}$$

Where, B is a parameter of microstructure, temperature and environment, n is material constant Q_c is the activation energy of creep. Under a fixed temperature, equation (8) becomes.

$$\dot{\varepsilon}_m = B' \sigma^n \tag{9}$$

If $\dot{\varepsilon}_o$ and $\dot{\varepsilon}_1$ are described using equation (9) and each n is set to n_0 and n_1, the following

equations, result.

$$\dot{\varepsilon}_o = B_o \sigma^{n_o}, \quad \dot{\varepsilon}_1 = B_1 \sigma^{n_1} \tag{10}$$

where, B_0 and B_1 are material constants. $A' = A_1 \sigma^{n_1}$ is derived from equation (7) and (10). $\dot{\varepsilon}_o$ and A' are plotted against stress as shown in Fig.15. Good correlation is obtained and both lines have a slope of 5.03. Equation (7), therefore, can be expressed as shown below.

$$\dot{\varepsilon}_m = (B_o + B_1)\sigma^n = [B_o + A_1(1-\rho)(V - V_o)^2 \exp(-Q_a / kT_a)]\sigma^n \tag{11}$$

A temperature dependency was also introduced using equation (8). Arrhenius plot of $\dot{\varepsilon}_m / \sigma^n$ is shown in Fig. 16. Consequently, minimum creep can be finally expressed by the following equation.

$$\dot{\varepsilon}_m = [B_0^* + A_1^*(1-\rho)(V - V_o)^2 \exp(-Q_a / kT_a)]\sigma^n \exp(-Q_c / kT) \tag{12}$$

where, A_1^*, B_0^*: material constant

The activation energy of the creep here is 8.19×10^{-19}J which is quite high in comparison with the self-diffusion energy of nickel, which is 4.68×10^{-19}J. This is considered to be the reason that the addition of solid-solution strengthened elements and the effect of inter- and intra-granular precipitates retard the recovery rate of dislocations during creep.

Correlation between creep rupture life and minimum creep rate

It is well known that a relationship between creep rupture life and minimum creep rate is expressed as equation (13), which is called Monkman-Grant equation [8].

$$\dot{\varepsilon}_m \cdot t_R^m = \dot{\varepsilon}_R^* \tag{13}$$

where, t_R : creep rupture time, $\dot{\varepsilon}_R^*$, m : material constant

Based on this equation, all the data are plotted in Fig.17. It is clear that a Monkman-Grant relationship can be applied to the degraded material of *Hastelloy* X. Here, the value of constant $\dot{\varepsilon}_R^*$ was 0.352 and m was 1.15.

Conclusions

(1) Microstructural changes was observed in the after end of in-service combustion liner, and the creep deflection was also recorded in the picture frame of in-service transition piece.
(2) Carbides and the intermetallic compound μ phase precipitate at the grain boundaries and inside the grains of the specimens aged at temperatures of 750-900°C for up to 10000 hours.
(3) The hardness, tensile strength and proof strength can be expressed as linear functions of the density of intragranular precipitates.

(4) The minimum creep rate was shown to be a function of the volume fraction of intragranular precipitate, grain boundary coverage ratio, applied stress, and test temperature.
(5) The Monkman-Grant relationship is applicable tothe degraded *Hastelloy* X.

References

[1] Yomei Yoshioka, The Japan Society of Mechanical Engineers, No.920-6, 1992, p41
[2] H.M.Tawancy, Long-term Aging Characteristics of *Hastelloy* X, J.Mater.Sci., 18, 1983, p2976-2986
[3] Masao Takeyama, Kaoru Kawasaki , Takashi Matsuo, Ryohei Tanaka, Effect of grain boundary precipitate on the high temperature creep property of Ni-20Cr-Nb-W alloy, Iron and Steel, 72, 1986, p1605 -1612
[4] Abdel Monem ElBatahgy and Takashi Matsuo, Hiroshi Kikuchi, Grain boundary strengthned by γ' of Nimonic 80A, Japan Society for the Promotion of Science Report, 30, 1989, p41-49
[5] Ryuuichi Ishii, Abdel Monem ElBatahgy, Yoshihiro Terada, Takashi Matsuo, Hirishi Kikuchi, Grain boundary precipitate strengthening by the carbide in high temperature creep of *Inconel* 617, material and process, 2, 1989, p1857
[6] Metal data book, The Japan Institute of Metals, 1984, p27-28
[7] J.Harper and J.E.Dorn, Viscous Creep of Aluminum near its Melting Temperature, Acta.Met., 5, 1957, p654-665
[8] F.C.Monkman and N.J.Grant, An Empirical Relationship between Rupture Life and Minimum Creep Rate in Creep Rupture Tests, Am.Soc.Test.Mater.Proc., 56, 1956, p593-620

Table 1 Chemical composition of *Hastelloy* X studied

mass%

C	Cr	Mo	Fe	Co	W	Mn	Si	S	P	Ni
0.06	22.3	8.9	17.4	1.0	0.6	0.7	0.4	<0.1	0.01	Bal.

Table 2 X-ray diffraction test results of extracted residue of *Hastelloy* X aged at 750-900°C for 1000-10000 hours

	As heat treated	1000 hours	3000 hours	6000 hours	10000 hours
750°C	M_6C +++	$M_{12}C$+++ μ + ($M_{23}C_6$)	$M_{12}C$+++ μ +	–	–
800°C		$M_{12}C$+++ μ + ($M_{23}C_6$)	$M_{12}C$+++ μ ++ ($M_{23}C_6$)	$M_{12}C$+++ μ +++ $M_{23}C_6$	$M_{12}C$+++ μ +++ $M_{23}C_6$
850°C		$M_{12}C$++ μ +++ ($M_{23}C_6$)	$M_{12}C$+ μ +++ ($M_{23}C_6$)	–	$M_{12}C$+ μ +++ $M_{23}C_6$
900°C		M_6C+++ μ +++	M_6C+++ μ +++	M_6C+++ μ +++	M_6C+++ μ +++

++++ : Very strong intensity +++ : Strong intensity
++ : Middle intensity + : Weak intensity
(+) : Very weak intensity

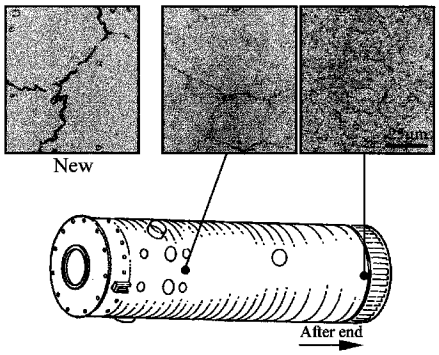


Fig.1 Optical micrographs of a new and an in-service combustion liner

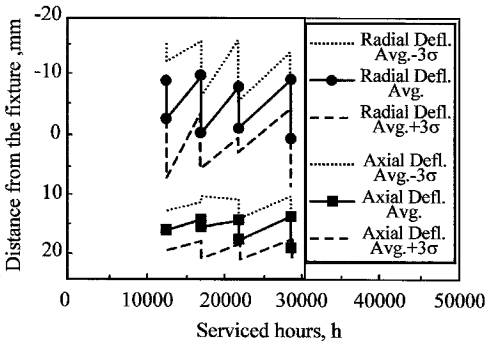


Fig.2 Results of measurement of the deflection of the transition pieces

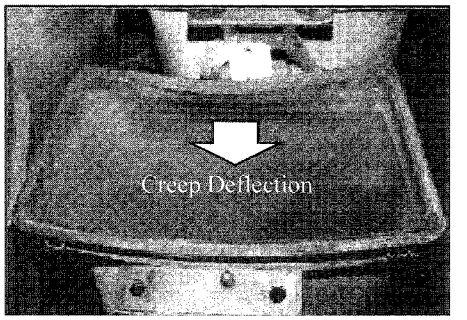


Fig.3 Photograph of typical creep deflection of the in-service transition piece

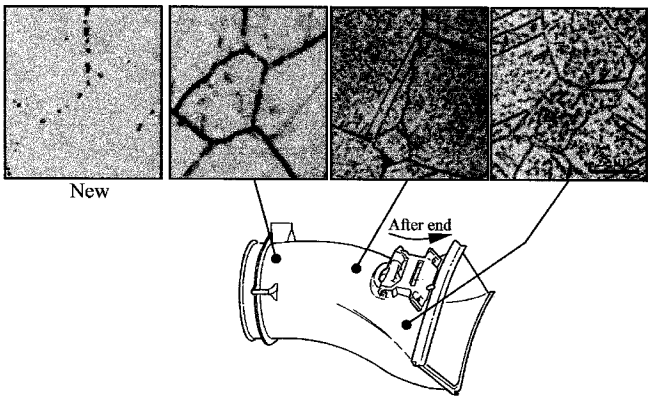


Fig.4 Optical micrographs of a new and an in-service transition piece

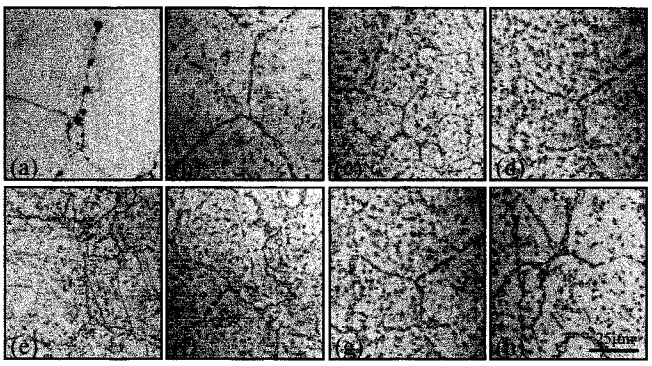


Fig.5 Optical micrographs of *Hastelloy* X (a)as-solution-treated and aged at 850°C for (b)1000h, (c)3000h, (d)10000h, and aged for 10000h at (e)750°C, (f)800°C, (g)850°C, (h) 900°C

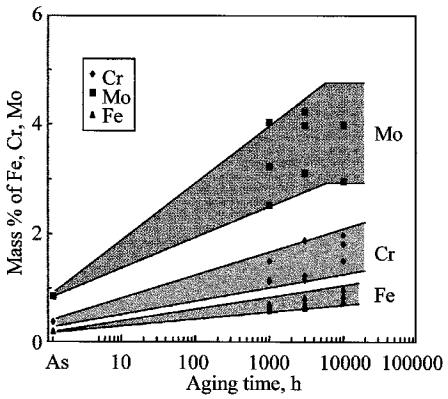


Fig.6 Chemical compositions of extracted residue of *Hastelloy* X aged at 750-900°C for 1000-10000h

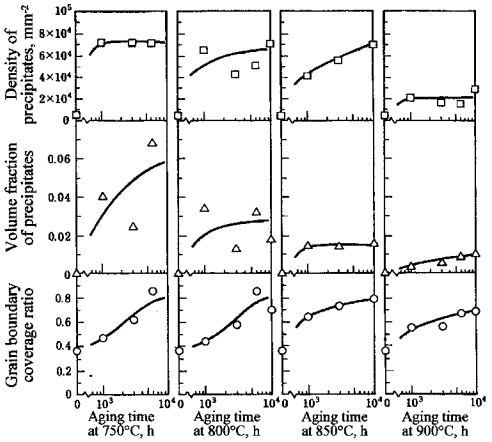


Fig.7 Image analysis results of *Hastelloy* X aged at 750-900°C up to 10000h

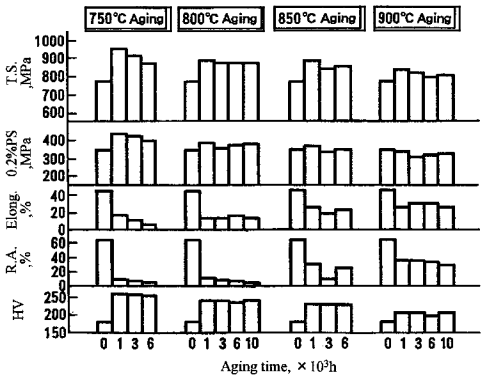


Fig.8 Mechanical properties at room temperature of *Hastelloy* X aged at 750-900°C for 1000-10000h

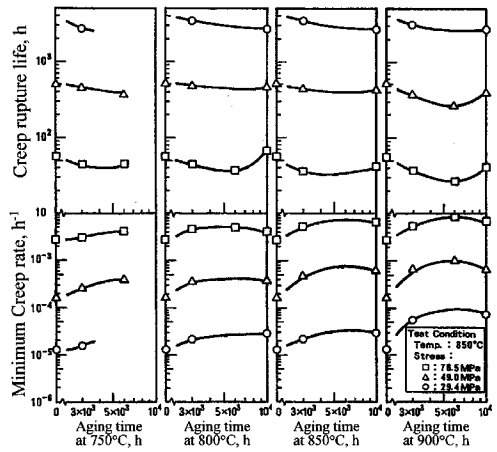


Fig.9 Creep properties tested at 850°C under the stress of 78.5, 49.0, 29.4MPa in *Hastelloy* X aged at 750-900°C for 1000-10000h

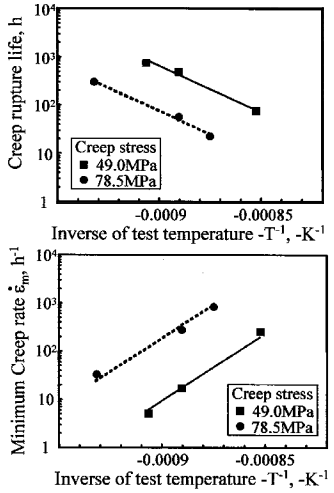


Fig.10 Creep properties tested at 830-900°C under the stress of 49.0, 78.5MPa

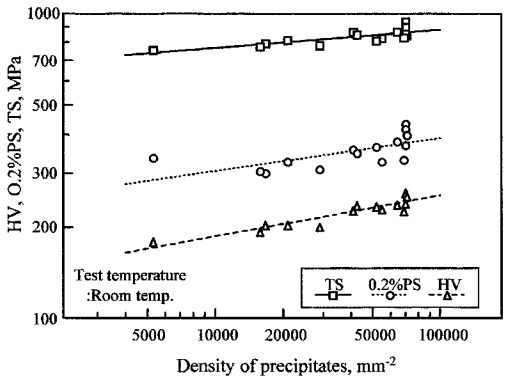


Fig.11 Relationship of hardness, the tensile strength and the 0.2% proof stress with density of precipitates

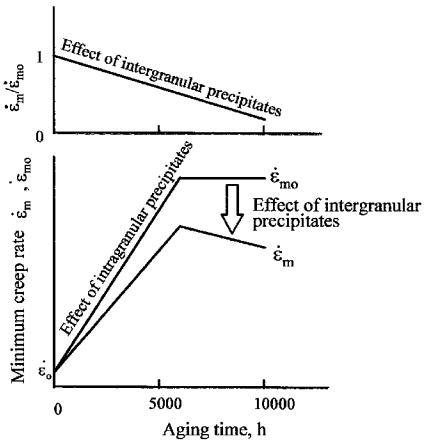


Fig.12 Effect of intragranular and transgranular precipitates on the creep resistance

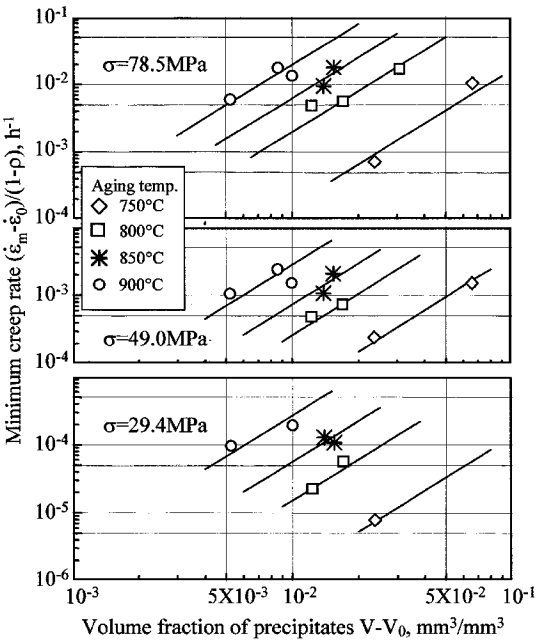


Fig.13 Relationship between the minimum creep rate at 850°C under the stresses of 78.5, 49.0 and 29.4MPa and the precipitates of *Hastelloy* X aged at 750-900°C for 1000-10000h

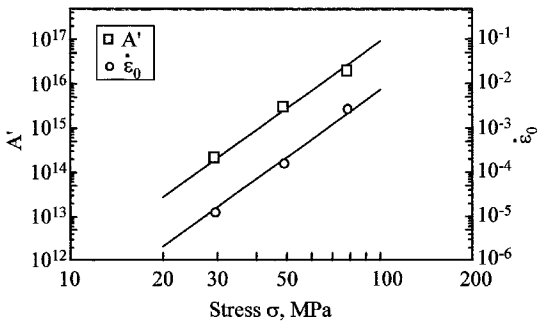


Fig.15 Relationship between the minimum creep rate at 850°C and the stresses in *Hastelloy* X aged at 750-900°C for 1000-10000h

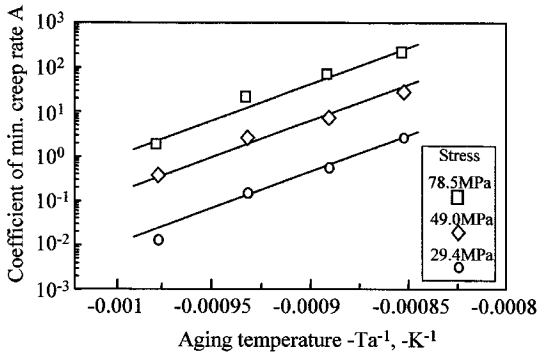


Fig.14 Arrhenius plot of creep rate coefficient A at 850°C under the stresses of 78.5, 49.0 and 29.4MPa of the *Hastelloy* X aged at 750-900°C for 1000-10000h

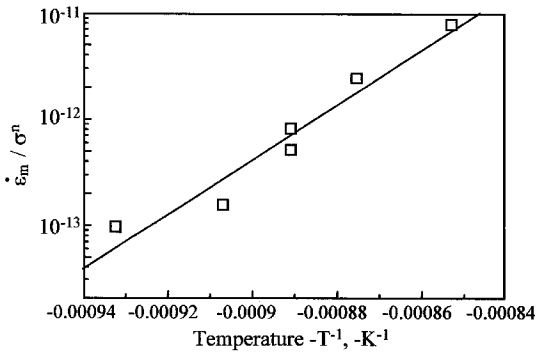


Fig.16 Relationship between the minimum creep rate and the test temperature in *Hastelloy* X aged at 750-900°C for 1000-10000 h

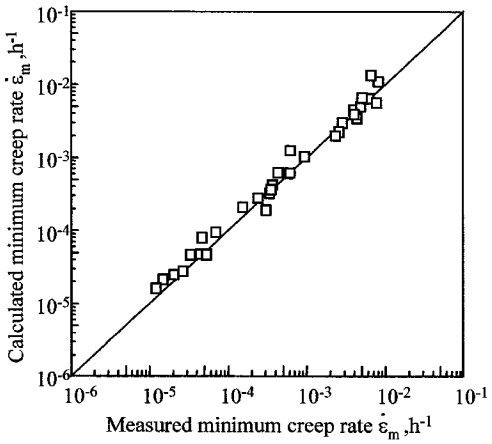


Fig.17 Relationship between the creep rupture life and the minimum creep rate

EFFECT OF SOLUTION HEAT TREATMENT ON THE HOT CORROSION RESISTANCE OF A SECOND GENERATION DS SUPERALLOY

H. Tamaki, A. Okayama, B. Önay and A. Yoshinari

Hitachi Research Lab., Hitachi, Ltd., MD#840 7-1-1 Ohmika, Hitachi, Ibaraki, 319-1292, Japan (hidekit@hrl.hitachi.co.jp)

Abstract

The effect of solution heat treatment on the high temperature corrosion resistance of the 2nd generation DS (Directionally solidified) superalloy CM186LC was studied. Solution heat treatments were conducted between 1150 and 1274°C for times ranging from an hour to 40 hours. Following these treatments, the high temperature corrosion resistance of the alloy specimens was evaluated in a burner rig at 900°C. The corrosion resistance of the alloy was found to improve with increasing solution heat treatment temperature and time. Microstructural characterization of the alloy specimens showed that interdendritic areas which contained complex carbides of refractory elements were selectively attacked. However, protective aluminum-rich layers were able to develop over the dendrite core regions which were increased as a result of solution heat treatment of the alloy. Other positive effects of solution heat treatment were decreased segregation in the cast superalloy and decreased amount of carbides which acted as initiation sites for hot corrosion. Solution heat treatment also affected the mechanical properties of the alloy. Creep rupture life in the longitudinal direction increased while its life in the transverse direction decreased after the solution heat treatment. It was concluded that, when determining the solution heat treatment conditions for DS superalloys, it is necessary to consider both the positive and negative effects of such a treatment on the alloy's high temperature properties.

Keywords: Superalloy, Directional solidification, Solution heat treatment, Hot corrosion, CM186LC

1 Introduction

Although single crystal (SC) buckets and vanes have already been introduced in some industrial gas turbines (IGTs) [1][2], DS buckets and vanes are still the mainstream technology for IGT, especially in the case of large heavy-duty machines. The reason for this is the relatively higher cost of SC castings for large heavy-duty machines as a result of some grain defects in SC castings. Second generation DS superalloys which contain rhenium also have limited in-service operation in large IGTs while they have been widely used in aero-engines and small IGTs [3]. Thus, it is necessary to investigate properties such as hot corrosion resistance, long-term phase stability and castability of 2nd generation DS superalloys in conditions applicable to IGT. It is well known that the solution heat treatment of 2nd generation DS superalloys affects some of their properties. Several studies have shown that increasing the maximum temperature and period of the solution heat treatment has a positive effect on the longitudinal mechanical properties but causes a deterioration to the corresponding transverse properties [4][5]. However, very few studies have been carried out on the effect of solution heat treatment on their hot corrosion resistance. In this study, the relationship between solution heat treatment conditions and hot corrosion resistance of a 2nd generation DS superalloy was investigated as part of a study for evaluating the adaptability of 2nd generation DS superalloys to IGT.

2 Experimental procedure

A commercial 2nd generation DS superalloy, CM186LC which was developed by Cannon-Muskegon Corp. MI, USA [3] was used in this study. The nominal composition of the alloy is shown in Table 1. DS slabs (100 x 15 x 250 mm) were cast from master ingots of the alloy by a mold withdrawal method. Heat treatment conditions used for samples, in this study, are listed in Table 2. It should be noted that the solvus temperature of the alloy is about 1220°C [6]. Thus, under conditions 1 and 2, samples were heat-treated below the solvus temperature.

Table 1: Nominal composition of CM186LC (mass%) [3]

C	Cr	Co	Mo	W	Ta	Re	Al	Ti	B	Zr	Hf	Ni
0.07	6	9	0.5	8	3	3	5.7	0.7	0.015	0.005	1.4	Bal.

CM186LC is a registered trademark of the Cannon-Muskegon Corp.

Table 2: Heat treatment conditions used in this study

No.	Solution heat treatment	Aging
0	(as-cast)	1080°C/4h/GFC +871°C/20h/GFC
1	1150°C/4h/GFC	
2	1200°C/4h/GFC	
3	1225°C/4h/GFC	
4	1250°C/4h/GFC	
5	1274°C/1h/GFC	
6	1274°C/4h/GFC	
7	1274°C/8h/GFC	
8	1274°C/20h/GFC	
9	1274°C/40h/GFC	

GFC: Gas Fan Cooling

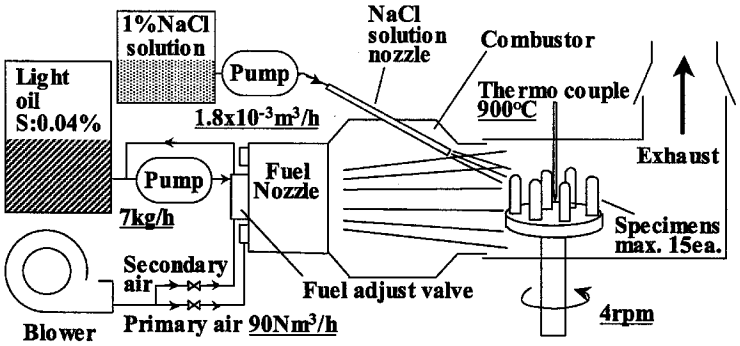


Figure 1: A schematic view of the burner rig

The hot corrosion resistance of the alloy was evaluated in a burner rig. Test specimens were machined from heat-treated DS slabs to have the same grain growth direction as that of the DS slabs. Figure 1 shows a schematic view of the burner rig used in this study. The fuel used was light oil which contained 0.04mass% sulfur. A solution of 1mass% NaCl solution was sprayed into the combustion gases at the rate of $1.8 \times 10^{-3} m^3/h$. The test temperature was controlled to be 900°C at the center of the specimen holder. A single test cycle was 7h and the weight change of the specimens was measured after either one or two cycles. Before each measurement, the specimens were washed by hot water to remove combustion products other than the scale. After the test, cross sections of the specimens were investigated by optical microscopy and scanning electron microscopy (SEM). Corrosion products were analyzed by WDX or EDX attached to the SEM chamber.

3 Results

3.1 Effect of solution heat treatment on the microstructure

Figure 2 shows the microstructure of specimens heat-treated under the conditions 0, 5, 6, 7, 8 and 9. In this figure, region (A) corresponds to a dendrite core and is the region where γ' phase completely dissolved into the γ phase during the solution heat treatment. In this region, fine γ' particles, which improve the mechanical properties along the longitudinal direction of the alloy, re-precipitated during the following aging process. It is observed in this work that this region (A) enlarged with increasing solution heat treatment time. If a "solution index (SI)" is defined as the volume percentage of the region (A) in the test specimens, the relationship between SI value and the solution heat treatment time at 1274°C can be described as in Figure 3. The SI value is therefore indicative of the extent of the solutioned microstructure and the amount of the remaining eutectic islands. It may also be related to both the DS longitudinal and transverse creep-rupture lives, as shown in Figure 4. It is clear from Figure 4 that increasing the extent of solution heat treatment improves the creep-rupture life of the DS superalloy in the longitudinal direction but not in the transverse direction. This effect must therefore be taken into account when defining the solution heat treatment conditions of DS superalloys.

In DS castings, depending on the solution heat treatment conditions, element segregation is reduced as a result of diffusion. Figure 5 shows EPMA mappings for tantalum and tungsten after heat treatment conditions of 0 and 9. In the only aged specimen (condition 0), significant segregation of tungsten to the dendrite core and tantalum to the interdendritic area was observed. Such tungsten and tantalum segregations almost disappeared after the solution heat treatment of 1274°C/40h. Aluminum, titanium and hafnium behaved similar to tantalum while chromium and rhenium behaved the same as tungsten. However, some segregation of rhenium to the dendrite core and an enrichment of tantalum, titanium and hafnium at the carbides were still observed for the heat-treated specimen under condition 9.

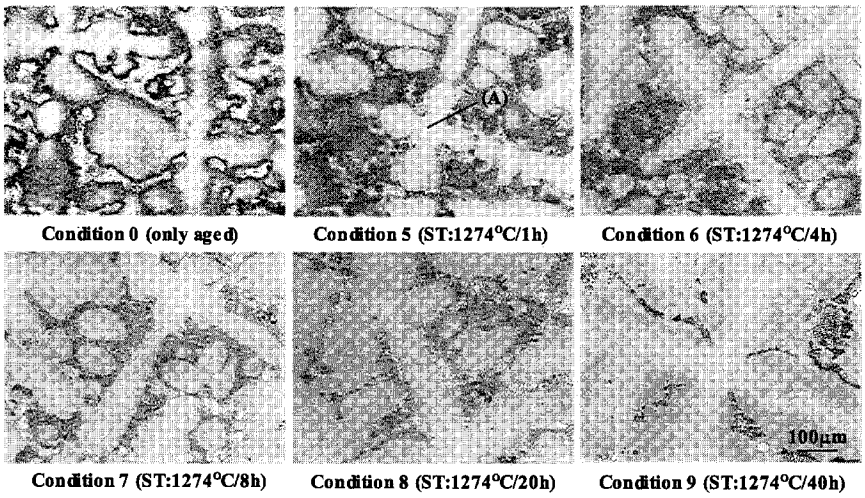


Figure 2: Effect of solution heat treatment on the microstructure of DS CM186LC

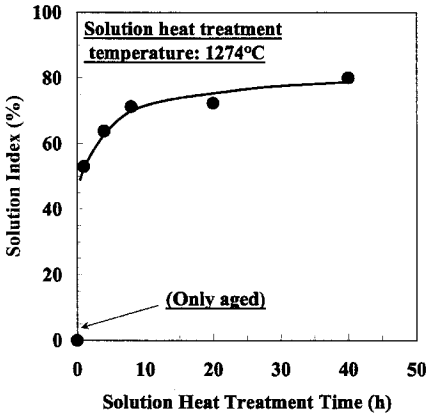


Figure 3: Relationship between solution heat treatment time and the solution index

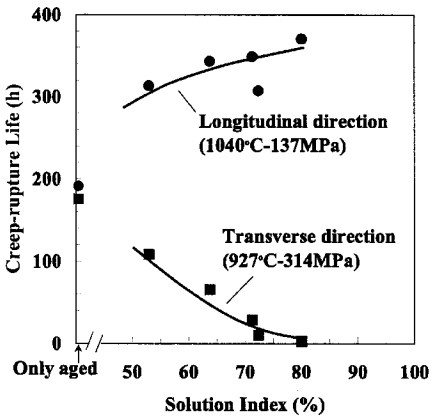
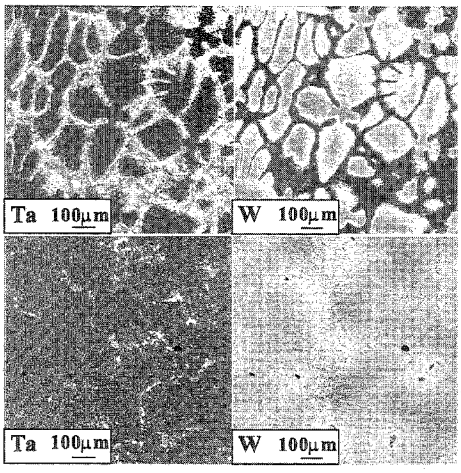


Figure 4: Effect of solution heat treatment on the creep-rupture life of DS longitudinal and transverse direction



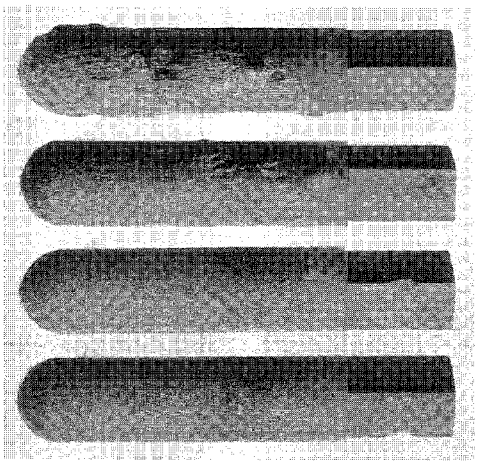
(a) Condition 0
Only aged

(b) Condition 9
ST:1274°C/40h

Figure 5: EPMA mappings for tantalum and tungsten of only aged (a) and solution-heat-treated (b) specimens

3.2 Effect of solution heat treatment on the hot corrosion resistance

The surface condition of representative specimens after the burner rig test is shown in Figure 6. Weight changes of specimens as a function of cumulative test time are plotted in Figure 7 for each heat treatment condition. The effect of solution heat treatment on the hot corrosion resistance of the alloy can be observed clearly in Figure 8 where the weight changes after 35h are plotted as a function of the SI value. The plot indicates that the weight change due to hot corrosion decreased with increasing SI values. This result suggests that a longer solution heat treatment time improves the hot corrosion resistance of this DS superalloy.



(a) Condition 0
Only aged

(b) Condition 5
ST: 1274°C/1h

(c) Condition 8
ST: 1274°C/20h

(d) Condition 9
ST: 1274°C/40h

Figure 6: The Surface condition of the representative specimens after the burner rig test (900°C/35h)

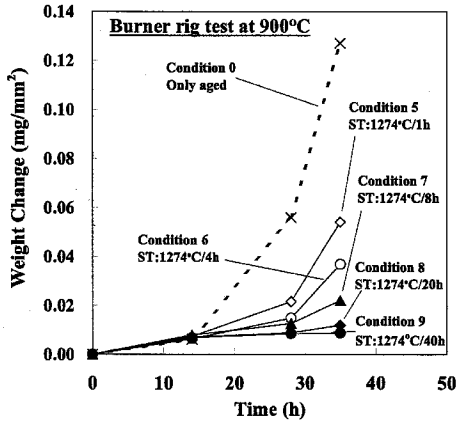


Figure 7: Weight change of specimens due to hot corrosion as a function of cumulative test time

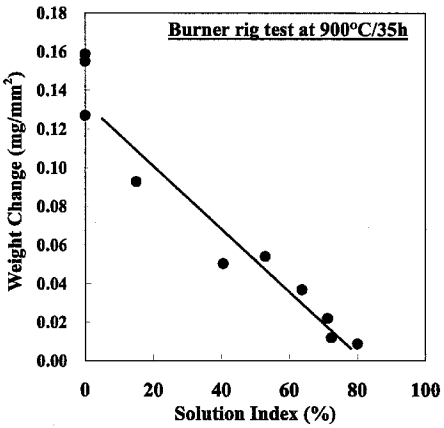
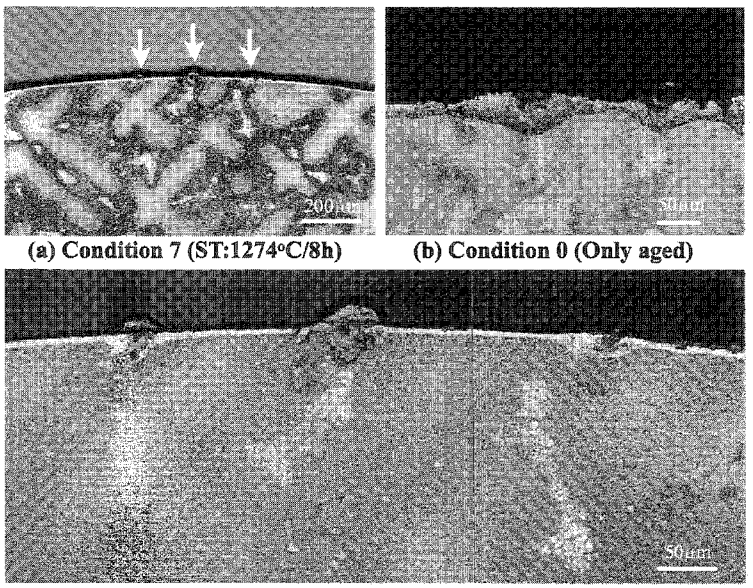


Figure 8: Effect of solution heat treatment on the hot corrosion resistance of DS CM186LC



(a) Condition 7 (ST:1274°C/8h)

(b) Condition 0 (Only aged)

(c) Higher magnification of a photograph-a (Condition 7)

Figure 9: Cross-sectional view after the burner rig test (900°C/35h) for specimens heat-treated with condition 0 and 7

4 Discussion on the effect of solution heat treatment on the hot corrosion resistance of DS CM186LC

Numata et al. [7] observed different corrosion rates for the dendrite core region and the interdendritic area in an as-cast DS superalloy. They suggested that element concentration inhomogeneity in the DS casting caused the observed difference in corrosion rates. In the present study, a similar selective corrosion behavior was observed for the alloy investigated. Corrosion was more pronounced in the interdendritic area of the test specimens. In the case of the specimens which did not show severe corrosion, isolated corrosion sites which are thought to be the initiation points for corrosion were observed mainly in the interdendritic area (Figure 9-a, c). In the specimens which had significant corrosion, the attack was in the form of deep penetrations in the interdendritic area rather than the dendrite core (Figure 9-b).

In order to understand the mechanism of this selective corrosion behavior, SEM-WDX and EDX analyses were performed on the cross sections of some of the representative burner rig test specimens. Figure 10 shows the secondary electron image and the corresponding characteristic X-ray images (dot-maps) of an interdendritic area in the specimen heat-treated under condition 9. The blocky precipitate visible at the center of the selectively corroded area was rich in tantalum, hafnium and oxygen, according to dot-maps of these elements obtained for this precipitate. The result of the semi-quantitative EDX analysis conducted on the same precipitate is shown in Table 3, results of a similar analysis conducted on carbides found in the same specimen (condition 9) and some other samples are also shown in Table 3. In these test samples, carbides were present in the interdendritic areas adjacent to the γ-γ' eutectic constituent (Figure 2). These results suggested that the precipitates which were found at the center of the selectively corroded region were mixed oxides of refractory elements, like tantalum and hafnium, which had formed upon oxidation of their corresponding carbides. The simple thermodynamic calculations [8] shown below show that TaC and HfC phases would have been oxidized to Ta_2O_5 and HfO_2 , respectively in the test environment.

1200K(927°C)

$$2TaC+9/2O_2 \rightarrow Ta_2O_5+2CO_2 \qquad \Delta G^\circ = -2032kJ/mol$$
$$HfC+2O_2 \rightarrow HfO_2+CO_2 \qquad \Delta G^\circ = -1080kJ/mol$$

These non-protective oxides (former carbides) are thought to obstruct formation of a protective oxide (Al_2O_3) scale at the surface and help sulfur to access to the metal underneath. In Figure 10, sulfur was detected under these non-protective oxide inclusions in the interdendritic area. However, for the same specimen, surface regions corresponding to the dendrite core were covered with a uniform scale rich in aluminum and oxygen. Detectable amount of sulfur was not present under this oxide layer after 35h at 900°C (Figure 11). These results suggest the following hot-corrosion degradation mechanisms for these specimens:

(1) In both the as-cast and solution-heat-treated samples, refractory element (tantalum, hafnium) carbides, present mainly in the interdendritic areas, oxidized preferentially and disrupted formation of a protective surface oxide layer. This allowed ingress of sulfur into the alloy matrix. Upon increased sulfur concentration, the Ni-Ni_3S_2 eutectic phase, which was in a liquid state at the test temperature, formed beneath these preferential sites and accelerated corrosion of the test specimens.

(2) An aluminum-rich protective oxide scale was able to form over the dendrite core regions.

After long exposure times, increased diffusion of sulfur into the dendrite core from the neighboring interdendritic areas also caused the formation of the Ni-Ni_3S_2 liquid phase in the dendrite core region. As a result of this, the oxide scale over these regions also lost its protectiveness.

(3) The well-accepted explanation of hot-corrosion in superalloys, due to the oxide scale solution into the molten salt, can also be invoked here. It is known that refractory oxides enhance this type of electrochemical corrosion mechanism by changing the local acid-base condition in the salt. It is possible that oxides, formed from carbides of refractory elements in this alloy, promoted the acidic dissolution of the scale thus increasing the corrosion of the test specimens.

Regardless of the actual corrosion mechanism, a positive contribution of solution heat treatment on the extent of corrosion of the alloy was made clear in this study. The first proposal that carbides acted as initiation sites for hot corrosion is supported by the observation that the volume fraction of carbides was lower for the specimens of higher solution index (Figure 12). Piearcey and Smashey [9] showed that MC-type carbides (where M= titanium, niobium) in Mar-M200 slowly decomposed, enriching the surrounding matrix with titanium and causing nucleation of γ'. In CM186LC, although tantalum is considered to behave similar to titanium in Mar-M200, the decomposition of carbides was also observed after solution heat treatment (Figure 13). Besides decreasing the overall segregation in the material, solution heat treatment promoted the decomposition of carbides thus improving its corrosion resistance during subsequent oxidation. As shown in Figure12, solution heat treatment possibly affected the alloy corrosion behavior by modifying the chemistry of carbides.

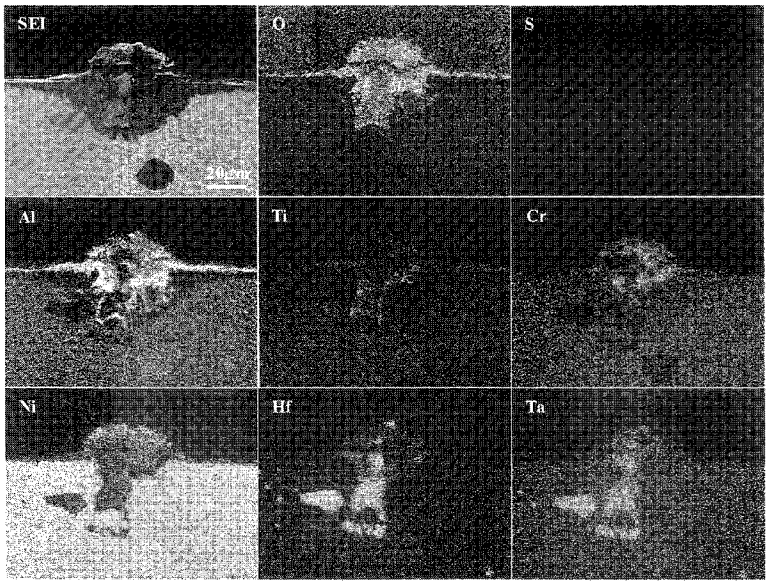


Figure 10: Secondary electron image and the corresponding characteristic X-ray images of an interdendritic area in the specimen heat-treated under condition 9 (after the test of 900°C/35h)

Table 3: Semi-quantitative EDX analysis of the blocky oxide found after the burner rig test (condition 9) and of carbides found in some typical specimens (sum of following elements is 100%, at%)

Precipitate	Al	Ti	Cr	Co	Ni	Ta	W	Re	Hf	Mo	Hf/(Ti+Hf+Ta)
Oxide in condition 9	0	4.4	6.9	4.2	8.2	28.8	0.8	0	46.6	0	0.58
Carbide in condition 9	0	5.8	0.6	1.8	9.6	35.0	0.7	0	46.5	0	0.53
Carbide in condition 5	0	10.2	1.6	1.8	16.2	37.0	0	0	33.4	0	0.41
Carbide in condition 0	0	21.6	1.1	1.2	7.9	43.4	5.8	0	18.7	0.3	0.22

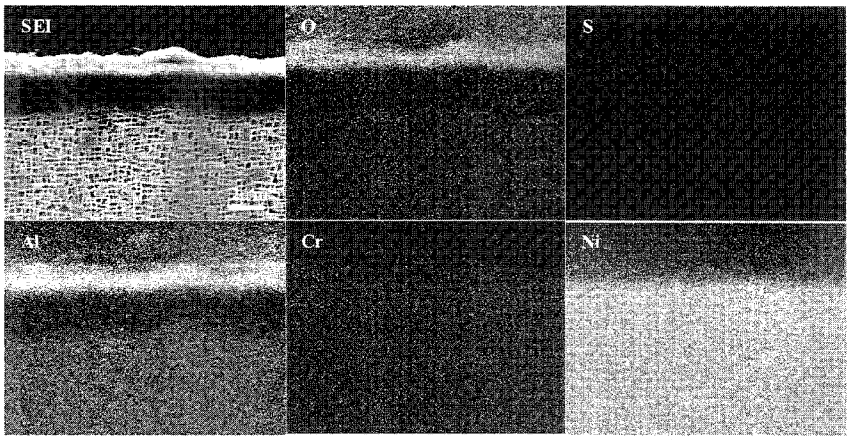


Figure 11: Secondary electron image and the corresponding characteristic X-ray images of a dendrite core region in the specimen heat-treated under condition 9 (after the test of 900°C/35h)

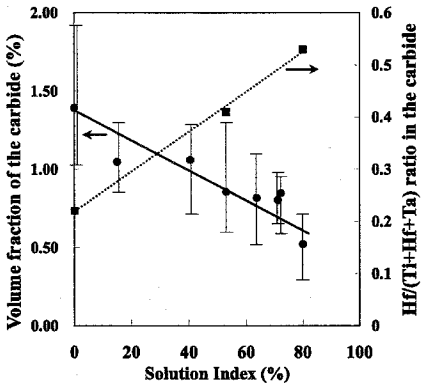


Figure 12: Effect of solution heat treatment on volume fraction of the carbide and ratio of MC former elements in the carbide

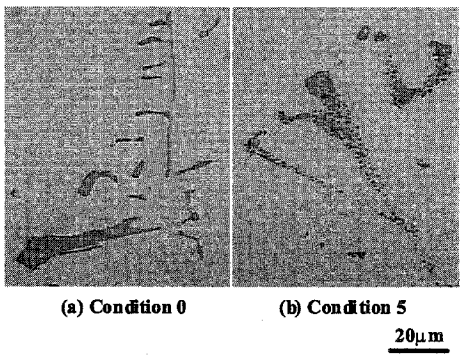


Figure 13: Carbide morphology of only aged (a) and solution-heat-treated (b) specimens

5 Conclusions

In this study, the effect of solution heat treatment on the high temperature corrosion resistance of the 2nd generation DS superalloy CM186LC was investigated. Microstructural characterization of the alloy specimens after the burner rig tests showed that interdendritic areas, which contained complex carbides of refractory elements, were selectively attacked. However, protective aluminum-rich layers were able to develop over the dendrite core regions which were increased as a result of solution heat treatment of the alloy. Other positive effects of solution heat treatment were decreased segregation in the cast superalloy and decreased amount of carbides which acted as initiation sites for hot corrosion. Although the creep rupture life in the longitudinal direction of this DS alloy was increased by solution heat treatment, its life in the transverse direction was decreased. Therefore, when determining the solution heat treatment conditions for DS superalloys, it is necessary to consider its positive and negative effects on the high temperature properties of the alloy. Many studies have investigated the hot corrosion resistance of Ni-based superalloys. However, very few of them attempted to characterize the initiation of the hot corrosion attack. It is believed that this investigation has provided, for 2nd generation DS superalloys, useful information on their properties. Such information is important for both the adoption of these alloys to IGTs and the development of new superalloys.

References

[1] H.-J. Kiesow and D. Mukherjee, "The GT24/GT26 Family Gas Turbine: Design for Manufacturing", Advances in Turbine Materials, Design and Manufacturing, ed. A. Strang et al., (London, UK: The Institute of Materials, 1997), 159-172.

[2] T. Barker, "Siemens' New Generation", Turbomachinery International, 1995, Jan/Feb: 20-22.

[3] G. M. McColvin et al., "Application of the Second Generation DS Superalloy CM186LC® to First Stage Turbine Blading in EGT Industrial Gas Turbines", Advances in Turbine Materials, Design and Manufacturing, ed. A. Strang et al., (London, UK: The Institute of Materials, 1997), 339-357.

[4] A. D. Cetel and D. N. Duhl, "Second Generation Columnar Grain Nickel-Based Superalloy", Superalloys 1992, ed. S.D. Antolovich et al., (Warrendale, PA: TMS, 1992), 287-296.

[5] H. Tamaki, A. Yoshinari, A. Okayama and S. Nakamura, "Development of A Low Angle Grain Boundary Resistant Single Crystal Superalloy YH61", Superalloys 2000, ed. T.M. Pollock et al., (Warrendale, PA: TMS, 2000), 757-766.

[6] F. Caruel et al., "SNECMA Experience with Cost Effective DS Airfoil Technology Applied Using CM186LC® Alloy", ASME Paper 96-GT-493, (New York, NY: ASME, 1996).

[7] H. Numata, I. Tomizuka, H. Harada, Y. Koizumi, S. Nakazawa, K. Hirano and M. Yamazaki, "Effects of Manufacturing Processes on Ni-base Superalloy", Corrosion Engineering, 38 (1989), 293-301.

[8] F. Sauert, E. Schultze-Rhonhof and W. S. Sheng, Thermochemical Data of Pure Substances, (Weinheim, Germany: VCH, 1993).

[9] B. J. Piearcey and R. W. Smashey, "The Carbide Phases in Mar-M200" Transactions of The Metallurgical Society of AIME, 239 (1967), 451-457.

CREEP PROPERTIES DEGRADATION IN A LONG-TIME THERMALLY EXPOSED NICKEL BASE SUPERALLOY

J. Zrník[1], P. Strunz[2], V. Vrchovinský[1], P. Horňák[1], A. Wiedenmann[3]

[1]Department of Materials Science, Technical University of Košice, Park Komenského 11, Košice, Slovak Republic
[2]Nuclear Physics Institute, CSAV, 25068 Řež near Prague, Czech Republic
[3]Hahn-Meitner Institut, Berlin, Germany

Abstract

Numerous studies have been conducted on the structure-properties relationship of nickel base superalloys in last two decades with aim to understand them in order to improve their performance. Their main advantages include good resistance to creep and high structural stability under the conditions of static and dynamic loading in an oxidation-corrosive environment. A study on the structural stability of the wrought nickel base superalloy EI698 VD exposed for a long time under thermal conditions was performed in this work. In order to evaluate the prolonged thermal effect on structural changes, the alloy was exposed to over 25000 hours at two different temperatures, 430°C and 650°C, prior the creep. The creep deformation behavior of alloy exposed to different period was then evaluated. The results of the creep tests have shown that the deformation ability of alloy changed and the creep life of exposed specimens shortened regardless the time and the temperature of pre-exposure. The change was more expressive as the time of exposure was more prolonged. The structure characteristics changes including the γ' size, morphology and grain boundary carbide precipitation were investigated using TEM and SEM analyzing techniques. While those microstructral structure analyses showed no evidence of morphological and/or dimensional γ' changes, the Small Angle Neutron Scattering (SANS) diffraction technique was able to reveal significant changes in the morphology of γ' phase already present after the shortest thermal exposure of the alloy. The SANS experiment contributed to clarification on resulting size distributions, distance distributions, mean sizes and mean distances among the γ' and provided evident that both the size and the inter-precipitate distance increased in the bulk of the alloy with increasing thermal exposure, even at relatively low exposure temperature of 430°C.

Keywords: Superalloy, thermal exposition, structure, creep, neutron diffraction, SANS

1. Introduction

Nickel base superalloys are structural materials with chemical composition and microstructure, which predisposes them to high temperature applications. The structure of nickel base superalloys results from their thermal processing. The stability of the microstructure and the properties of nickel base superalloys at high temperatures, under the conditions of either creep or fatigue loading, was the subject of a number of studies conducted in the past. These found that some superalloys maintain their adequately high strength and good ductility even after long time thermal exposure [1-5].

The exposure of the alloys at elevated temperatures in combination with stress or without it, can result in microstructural changes and, subsequently, alter their properties and stability. In general, the higher is the temperature of exposure the higher is the probability of structural changes taking place in the alloy. A decrease in the temperature to which the alloy is exposed can change the type of its microstructural degradation. The stability of the microstructure and the ability to resist the potentially destructive effects of overheating, or long time heating,

is important and essential properties for the superalloys which are considered for use in land base gas turbines.
The excellent mechanical properties of nickel base superalloys result from their two-phase structure, where the coherent γ' precipitates are embedded in a matrix formed by a γ phase. One of the most important characteristics of these materials (determining their use for high-temperature applications) is their creep resistance. Therefore, investigations considering their creep properties is one of the basic themes of research. In the polycrystalline superalloy EI698VD [6], large differences in its creep characteristics (time to fracture, deformation ability) were observed when the samples were previously exposed to isothermal loading, at relatively low temperatures, for a long time. However, these differences in the creep behavior were not practically reflected in the microstructural changes observed by classical methods of microstructural investigation (TEM, SEM, light metallography) [6]; rather more significant microstructural changes than those observed were expected to support the deterioration in creep. They were possibly not revealed either due to the "local-information" character of the used methods or due to their low sensitivity to the evolved microstructural changes.

The small-angle neutron scattering method (SANS) has been proved to contribute substantially to the investigation of the microstructure of Ni-base superalloys. Important is its contribution in the field of determination of the γ' phase bulk-averaged morphology [7-10]. Generally, the SANS technique concerns the characterization of inhomogeneities in solids, as well as in the soft matter, in the range 20Å-5μm. Because of the low absorption of cold neutrons by the majority of elements, it provides bulk-averaged information on the morphology of particles. In fact, the term small-angle scattering means the coherent elastic scattering of radiation (e.g. neutrons) to small values of scattering vector magnitudes Q [$Q = |\mathrm{Q}| = 4\pi\sin\theta/\lambda$], $\mathrm{Q} = \mathrm{k}-\mathrm{k}_0$; k_0, k being the wavevectors of the incident and scattered neutrons, respectively, $|\mathrm{k}|=|\mathrm{k}_0|=2\pi/\lambda$; 2θ is the full scattering angle, λ is the incident neutron wavelength] when compared e.g. with the commonly used Bragg diffraction which studies a crystal lattice. The small-angle neutron scattering is caused by fluctuations of the scattering length density $\rho(\mathrm{r})$ due to connected with compositional and/or structural inhomogeneities, which give rise to the scattering contrast $\Delta\rho(\mathrm{r})$ [$\mathrm{r} = (x, y, z)$ being the coordinate in the real space]. A comprehensive introduction to the application of this technique in material science can be found in [11].

The aim of the study was to evaluate the influence of long time thermal exposure, up to 25 000 hours, on microstructural changes and their subsequent effect on the high temperature creep deformation and rupture of the nickel base superalloy EI 698 VD. The creep resistance of the thermally exposed material was evaluated with respect to its microstructural changes and deformation behavior. The SANS experiment was carried out in order to contribute to the understanding of the above-mentioned discrepancy, between creep experiments, and electron microscopy observations.

2. Experimental material

Experiments were carried out on commercial nickel base superalloy EI 698 VD, used in crankshaft manufacture for aircraft gas turbines. This is a complex alloy that is highly alloyed. Special alloying elements are present which aim to provide an advantageous combination of

properties, as required for exploitation at higher temperatures. The chemical composition of the alloy (in weight %) is presented in Table 1.

Table 1. Chemical composition of EI 698 VD superalloy in wt. %.

C	Cr	Al	Ti	Mo	Fe	Nb	Mn	Ni
0.08	13 -16	1.3– 1.7	2.3-2.7	2.8-3.2	max. 2.0	1.8-2.2	max.0.4	balance

The nickel base superalloy EI 698 VD is a solution and precipitation strengthened two phase alloy. The γ phase matrix is a solid solution of Ni. The principal strengthening phase is the γ' $Ni_3(Al)$ alloyed and modified with other substitution elements. The volume fraction of the γ' strengthening phase was determined to be ~ 40%. In order to obtain the required mechanical properties of alloy, under normal and elevated temperatures, the alloy was subjected to the following three stage heat treatment:
- solution annealing at 1100°C / 8 h, air cooling
- precipitation aging at 1000°C / 4 h, air cooling
- precipitation aging at 775°C / 16 h, air cooling.

The micrographs representing the alloy microstructure and the γ' distribution and morphology prior to the alloy heat treatment are illustrated in Fig.1 and Fig.2.

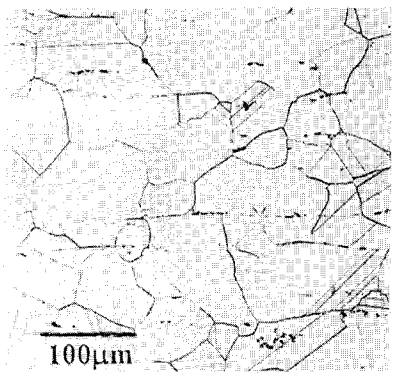


Fig. 1. Micrograph of the alloy equiaxed structure.

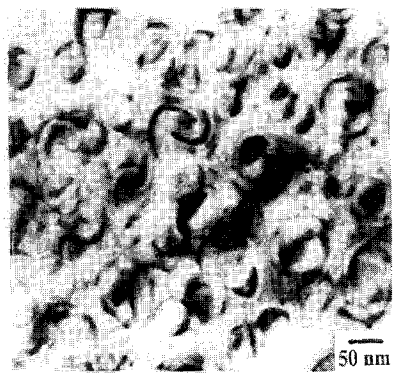


Fig. 2. Micrograph of γ' morphology.

3. Experimental procedure

The prism shaped specimens, which were used to machine the creep specimens after the thermal exposure, were exposed for 2000, 5000, 8000, 10000, and 25000 hours at two different temperatures, 430°C and 650°C. The exposure was carried out in electric furnace. The exposure temperatures were chosen on the basis of gas turbine manufacturer requirements and they resulted from temperature measurement records on the cross section of a crankshaft at the time of turbine loading regime.

The study of the microstructural characteristics of the virgin, i.e. after heat treatment, superalloy and after thermal exposure was conducted by means of light metallography. Substructure characteristics of the virgin alloy and specimens subjected to different conditions of thermal exposure were analyzed by transmission electron microscopy (TEM) of thin foils as well.

The creep tests were carried out using exposed specimens. The specimens were machined according to the required standards with a gauge length of l_o = 30 mm. A maximum loading force of 19.62 kN was applied which corresponded to 706 MPa. The testing temperature of 650°C was measured by two thermocouples of NiCr-Ni. The testing temperature was maintained within the accuracy of ± 2°C. The absolute elongation of each specimens was measured by an extensometer. The creep deformation ε versus time were frequently logged. fracture was plotted. The creep resistance of the differently exposed alloy was evaluated through the elongation at fracture ε and the time to fracture t_f.

The qualitative and statistical quantitative fractography analyses of the fracture surfaces were conducted by scanning electron microscopy. The aim of these analyses was to identify the main failure mechanism and to evaluate the contribution the other individual fracture mechanisms participating in the failure process in dependence of the exposure time and temperature. The results are reported in [6].

Samples of approximately 1.5 mm thickness were cut from the head of the creep specimen, to perform SANS diffraction measurements. The measurements were performed at room temperature at the V4 SANS facility [12, 13] in the Berlin Neutron Scattering Center (BENSC) at the HMI Berlin, employing a standard sample exchanger. The data were collected by a 2D position sensitive detector with a sample-to-detector distance equal to 16 m and λ = 12.0 Å. This geometry was selected in order to enable the observation of the large γ' precipitates and distances between them. Due to the low flux of the neutron source at such a wavelength, it was possible to measure without the beam-stop, which usually protects the 2D position-sensitive detector (PSD) against overloading by non-scattered neutrons in the primary beam. The bottom limit of the measured Q-range is therefore restricted only by the resolution of the facility (ΔQ □ 0.0013 $Å^{-1}$) for such geometry. The collected data thus covered the scattering vector magnitude range that is suitable for determining particle sizes between approximately 150 Å and 2000 Å. The measured isotropic scattering curves were corrected for the background and set to the absolute scale [14].

4. Results

4.1 Microstructure

The microstructure of the virgin alloy exhibited equiaxed grain characteristics with a relatively uniform grain size defined by the average diameter d_{mean} ~0.06 mm. The initial microstructure is shown in Fig. 1. The figure shows that in addition to the presence of annealing twins, two types of carbides were observed with different morphology and size, which precipitated in the interior of grainsand/or along grain boundaries. The first type, coarser, blocky-like carbide particles of eutectic type MC, were distributed mainly throughout the volume of grains but also on their boundaries. The heterogeneity of their distribution in the matrix is affected by the forming process. This type of carbides as failure initiation sites

can exert a local influence (mainly due to carbide agglomeration) on creep properties of the alloy. According to expectations, the the creep strength should be affected more by the finer carbides of $M_{23}C_6$ that precipitated along grain boundaries. They stabilize the grains and, as a result of that, increase the creep resistance of the alloy. A representative substructure of the virgin alloy is shown in Fig. 2. The γ' precipitate morphology, which strengthens the matrix, is spherical. The coherent interfacial bond between precipitates and the matrix is maintained.

The results of the microstructural analysis of the thermally exposed specimens confirmed that the exposure of 2000 hours at 430°C and 650°C was sufficient to promote additional precipitation of the carbide phase locally along sections of grain boundaries, as it is illustrated in Fig.3. No other microstructural changes, such as change in the size of γ' particles, a change of their interfacial coherency with the matrix, or changes in their volume fraction, were observed. The exposure to over 10000 hours produced no additional microstructural changes. Likewise no additional precipitation of morphologically different or topologically close packed phases were observed, which long time thermal exposure can induce in of nickel base superalloys [6]. Only further carbide precipitation at grain boundaries and also carbide precipitation along twin boundaries was observed after the exposure of 25000 hours at both temperatures, Fig. 4.

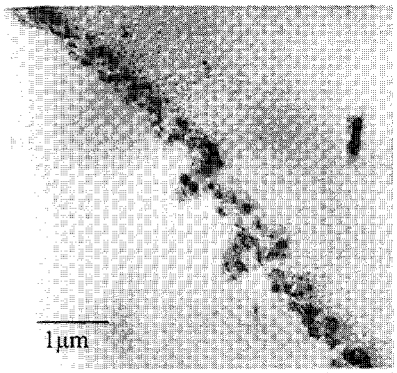


Fig. 3. TEM micrograph of carbid precipitates on a grain boundary afte 2000 h of thermal exposure.

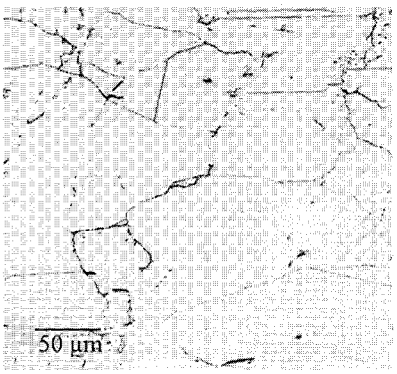


Fig. 4. Microstructure resulting after 25000 h of thermal exposure.

4.2. Creep tests.

The creep deformation of specimens that were previously exposed at 430°C are shown in Fig. 5 and those that were exposed at 650°C are in Fig. 6. Fig. 5 shows that the thermal exposure reduced the rupture life of all the specimens when compared with the creep life of specimens that were only heat treated. In general, it is possible to state that the longer was the exposure time the more detrimental was its effect on the recorded lifetime. This phenomenon could be observed already in the early stages of secondary creep where different steady state creep rates were detected for the individual specimens. The only exception was in the behavior of the pre-exposed specimens at 430°C for 10000 and 25000 hours where the rate of steady state creep rate followed a similar course up to the time of about 8000 minutes to that observed in

the specimen with a 430°C and 8000 hours exposure. The creep rate in tertiary creep stage has also surprisingly similar course for the specimens 8000, 10000 and 25000 hours of exposure.

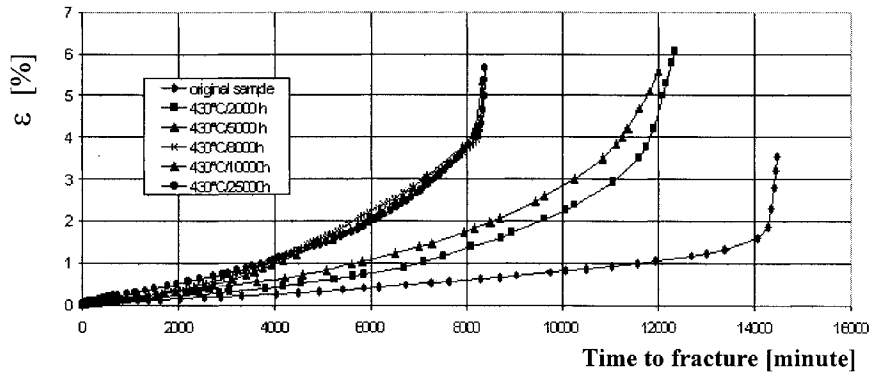


Fig. 5. Creep curves for specimens previously exposed at 430°C. Testing temperature T_{test} = 650°C, applied stress R = 706 MPa.

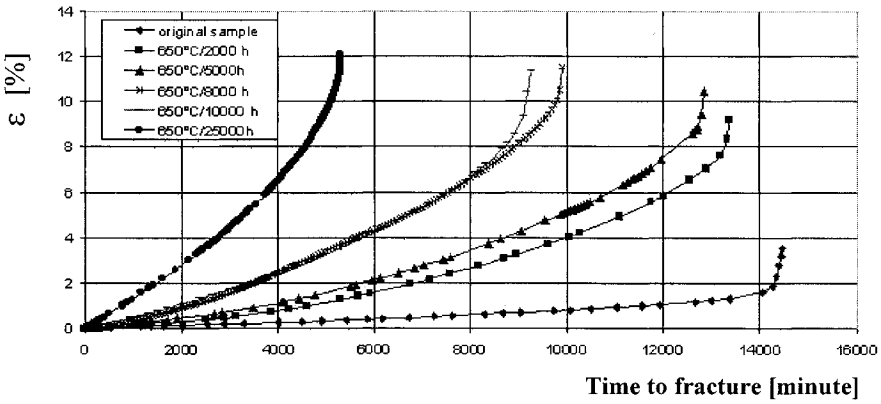


Fig. 6. Creep curves for specimens previously exposed at 650°C. Testing temperature T_{test} = 650°C, applied stress R = 706 MPa.

The elongation values of differently exposed specimens show some scatter. The comparison of the measured elongation data reveals that the lowest value of deformation ε was reached for the heat treated specimens and that all the exposed specimens exhibited higher deformation ductility to fracture. From Fig. 5 and Fig. 6 can be seen as well that for most of the exposed specimens modified for the least-square fit of the isotropic data as well. The model used the

values of deformation are surprisingly equal. Only small differences were recorded for the specimen pre-exposed for 2000 hours.

In the case of the previous thermal exposure at 650°C, it can be concluded (on the basis of the obtained creep results which are presented in Fig. 6) that the prolonged exposure at high temperature had a adverse effect on the lifetime of specimens and, as a rule, the longer was the exposure time the shorter was the time to fracture. However, the comparison of specimen elongation ε with different exposure periods shows the greater increase of deformation for the longer exposure times.

The presented results in Fig. 5 and Fig. 6 indicates that the lifetime of some of the pre-exposed specimens were, within the usual scatter, very similar. The plotted results confirm unambiguously the influence of prolonged annealing period on the increase of the deformation ability of the alloy. On the other side this also leads to increased strain rates. Such behavior the strong by evidence suggests that some changes of the microstructure evolve which unfavorably affect the subsequent creep behavior of the pre-exposed alloy. The increase of deformation in the specimens pre-exposed at 650°C was by about 50% higher than in those pre-exposed at the lower exposure temperature.

4.3. SANS results.

The conducted SANS measurements resulted in the isotropic scattering curves. The resulting differential cross-sections $d\Sigma/d\Omega$ are displayed in Fig. 7 and Fig. 8 in logarithmic scale for different time of the thermal exposure. Each curve exhibits an interparticle-interference maximum that indicates to a certain extent ordered precipitate microstructure.

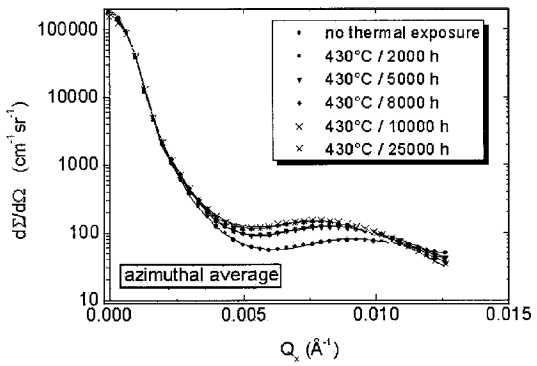


Fig. 7. Measured (points) and fitted (solid lines) SANS data from thermally exposed nickel base superalloy at temprature of 430°C.

The curves were evaluated by a special procedure [15] suited to anisotropic data evaluation but recently modified for the least-square fit of isotropic data as well. The model used his Transformed Model Fitting evaluation method [16], was a size distribution of cuboids forming a 3D binary map in real-space. Both size and distance distributions were locally randomly smeared in order to obtain a realistic approximation of the precipitation morphology. A long-size distribution was included as well. The results of the fit for the presented isotropic SANS data were not signifificantly sensitive to the shape of the modeled precipitates. Therefore, the shape parameter was fixed to simulate a rather spherical form which can be deducted also from the micrograph in Fig. 2. The scattering from large-scale inhomogeneities had to be included as well in order to approximate the background on which the intensity from the investigated γ' precipitates was superimposed.

5. Discussion

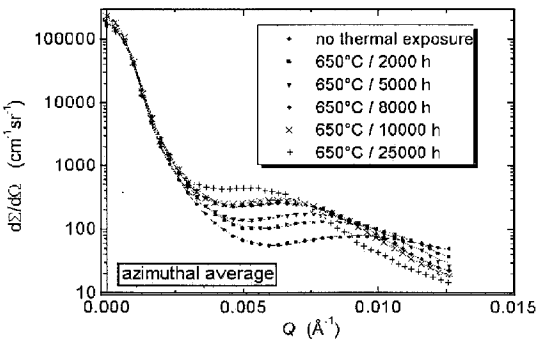


Fig. 8. Measured (points) and fitted (solid lines) SANS data from thermally exposed nickel base phase superalloy at temperature of 650°C.

The results from the creep testing of previously thermally exposed specimens of this nickel base superalloy provided basic proof of an adverse effect manifested by a reduction in the time to fracture and higher values of deformation to fracture. The microstructural analysis of the exposed specimens suggested that additional precipitation of carbide phases observed mainly at grain buondaries, might be the decisive cause of the reduction in the time to fracture. When summarizing and evaluating the creep deformation behaviour, it is apparent that the increase in strain rate and in the total deformation to fracture ε is progressively increasing with the time of exposure. This can be related not only to the process of carbide precipitation but also to possible changes in γ' precipitates during long time thermal exposure. The TEM microscopy of thin foils did not provide the clear evidence of substructure changes as to the morphological characteristics of the γ' strengthening phase, which might be an evidence of the observed improved matrix deformation ability. This ought to be due to the local character of TEM method.

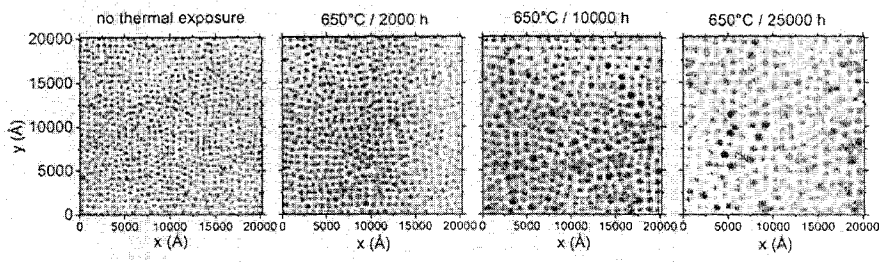


Fig. 9. Some of the real-space model distributions resulting from the SANS data evaluation.

The SANS experiments revealed significant changes to the γ' morphology and distribution which became more pronounced as the time of exposure increased. Some of the model distributions corresponding to the measured data (optimised by a least square fit) for differently exposed samples are displayed in Fig. 9. The global change of the microstructure is evident. These changes can be considered as evidence of the creep properties degradation with respect to the applied period of alloy thermal exposure.

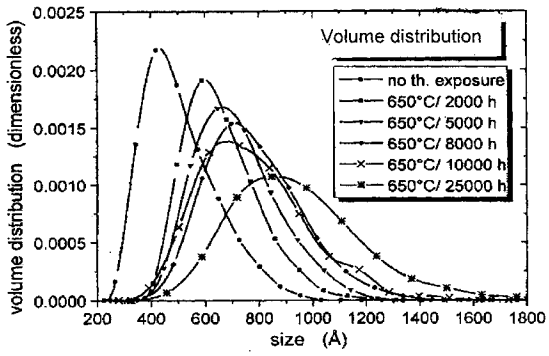


Fig. 10. Distributions of gamma prime precipitate size resulting from the SANS evaluation.

The resulting precipitate parameters, which were extracted from the SANS curves, are displayed in Figs. 10 and 11. The maximum of the volume distribution (Fig. 10) shifts towards larger particle sizes with the increasing thermal exposition. A similar shift can be observed also for the center-to-center distance between γ' precipitates (see Fig. 11).

The determined parameters are evidence that both the precipitate size and their distance increase in the bulk of the material with the increasing thermal exposure. The determined mean distance of precipitate (volume weighted) ranges from 570 Å (no thermal exposition) to 1070 Å (25000 hours of exposition at 650°C); the mean size increases from 510 Å (no thermal exposition) to 940 Å (25000 hours of exposition). However, the distributions are rather broad and it can explain why this increase is not observed when using experimental techniques providing local information only. The revealed evolution of the microstructure can affect strongly the creep properties and is most probably the reason of the large differences of the time to fracture and of the deformation ability due to the previous thermal exposure at relatively low temperature.

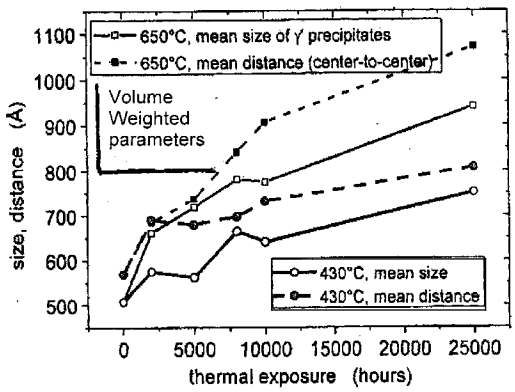


Fig. 11. Volume-wighted mean size and distance of precipitates

Conclusions

On the basis of the obtained results the following conclusions can be drawn:
- the creep behaviour of the nickel base superalloy, is influenced by previous long term thermal exposure.
- a longer thermal exposure leads to higher creep rates, increased elongation (alloy softening), and a reduction in the failure time.

- the microstructural analyses of thermally exposed samples did not provide sufficient evidence to support and explain the creep deformation behavior.
- the SANS analysis was helpful to detect and quantify the γ' morphology and distribution changes resulting in the alloy structure due to thermal exposure and hence contributed significantly to the understanding of the degradation mechanism.

Finally, it should be noted that despite the negative effect of long time thermal exposure on the lifetime of the alloy and on the deformation behavior, the lifetime reached still complies with the requirements set by the specification for use of the respective nickel base superalloy under the prescribed conditions of loading.

Acknowledgement

One of the authors (J. Zrník) is grateful for support provided by the European Commission under the Access to Research Infrastructures action under the Human Potential Programme, which enabled him to perform the experiment at BENSC.

References

[1] J. F. Barker, E. W. Ross, and J. F. Radawich: J. of Metals, 1, 1970, 31.
[2] J. W. Brooks, P. J. Bridges: Supealloys 1988, Publication of TMS, 1988, 31.
[3] J. F. Radavich: Supealloy 718 - Metallurgy and Applications, Publication of TMS, 1989, 257.
[4] J. F. Radavich, A. Fort: Superalloys 718, 625, 706 and Various Derivatives, and Publication of TMS, 1994, 635.
[5] N. S. Stoloff: in Sims, T.M. & Hagel, C.W. (eds), The Superalloys, Interscience, and New York, 1972.
[6] J. Zrnik, V. Vrchovinsky and M. Bercak: *Proc. of the Eight International Conferences on the Mechanical Behaviour of Materials ICM8*, Victoria, B.C. Canada, F. Ellyin and J.W. Provan (Eds.) May 1999, Vol II.4, p.676-681.
[7] P. Strunz, A. Wiedenmann, J. Zrnik and P. Lukas: *J. Appl. Cryst.* 30, (1997), p.597-601.
[8] P. Strunz, D. Mukherji, R. Gilles, A. Wiedenmann, J. Rosler and H. Fuess: *J. Appl. Cryst.* 34, (2001), accepted.
[9] P. Strunz, R. Gilles, D. Mukherji, A. Wiedenmann, R. Wahi and J. Zrnik: *Materials Structure* 6, No. 2 (1999), p.1-5, *Proc. of 18th European Crystallographic Meeting*, August 15-20, 1998, Prague, Czech Rep..
[10] R. Gilles, D. Mukherji, P. Strunz, S. Lieske, A. Wiedenman and R.P. Wahi: *Scripta Materialia* 39, (1998), p.715-721.
[11] G. Kostorz: *In: Neutron Scattering (Treatise on materials science and technology)*, ed. G. Kostorz, Academic Press, New York (1979), p.227-289.
[12] U. Keiderling and A. Wiedenmann: *Physica* B 213-214, (1995), p.895-897.
[13] BERLIN NEUTRON SCATTERING CENTER: *V4 Small Angle Neutron Scattering Instrument*, (2001), http://www.hmi.de/bensc/instrumentation/instrumente/v4/v4.html.
[14] P. Strunz, J. Šaroun, U. Keiderling, A. Wiedenmann and R. Przeinoslo: *J. Appl. Cryst.* 33, (2000b), p.829-833.
[15] P. Strunz, A. Wiedenmann, R. Gilles, D. Mukherji, J. Zrnik and G. Schumacher: *J. Appl. Cryst.* 33, (2000), p.834-838.
[16] P. Strunz: *Materials Structure* 4, (1997), p.136-143.

EFFECT OF TENSILE HOLDS ON THE DEFORMATION BEHAVIOUR OF A NICKEL BASE SUPERALLOY SUBJECTED TO LOW CYCLE FATIGUE

J. Zrnik, J. Semenak, P. Wangyao, V. Vrchovinsky, P. Hornak

Department of Materials Science, Technical University of Kosice, Park Komenskeho 11, Kosice, Slovak Republic

Abstract

The deformation behaviour of the wrought nickel base superalloy EI698 VD has been investigated in conditions of low cycle fatigue. The tensile hold periods, imposing a constant stress into the fatigue loading, have been introduced at the maximum stress value. The individual hold periods were in the range of 1 minute to 10 hours. The fatigue tests were of tension-tension type defined by a stress ratio R = 0.027 and were conducted at temperature of 650°C. The tests were performed until fracture. The time to failure, the time to failure corresponding to total load at peak amplitude and the number of cycles to failure have been criteria to evaluate the deformation behaviour of the alloy subjected to complex cyclic creep loading. In order to predict lifetime of alloy, regarding the respective types cyclic test , the Kitagawa's modified the linear cumulative damage criterion has been considered. The two regression functions for applied hold period interval were proposed time to calculate the time to failure. The formulae can be used to predict the life of nickel base superalloy considering the specific conditions of low cycle fatigue with tensile hold period introduced at stress amplitude peaks. The failure analysis of fracture surfaces contributed to evaluation of the role of repeatedly reduced stress in damage process.

Keywords: fatigue, creep, hold time, life prediction, damage evaluation.

1. Introduction

The superalloys have been developed for specific applications and have, specialized properties and applications. One of the main applications for nickel base superalloys is gas turbine components for land based power generation and aircraft propulsion system. The various parts within this type of power generation system have specific and unique requirements. Various components of industrial gas turbines and aircraft engine experience periods of both fluctuating and steady stress, due to complex situation of mechanical and thermal stress originating from centrifugal force, high frequency vibrations and temperature transients during engine service [1]. These components to operate under complex stress conditions, involving creep, fatigue and thermal fatigue.

In the past considerable effort has been brought into characterising the deformation process of nickel base superalloys that were stressed under the conditions of time-dependent load at elevated temperatures [2-6]. Permanently increased attention has been paid to the study of creep and fatigue interaction in either isothermal or anisothermal fatigue condition .In such cases both creep and fatigue can contribute to degradation of the material. The creep-fatigue interaction can be judged as two specific cases in dependence on the way of stressing. The first case involves two subsequent simultaneous interactions with the creep and fatigue stress components separated in the process of loading which results in separate processes of damage. The second case involves subsequent simultaneous interactions with the presence of both components of damage in each single deformation or stress cycle. Simultaneous interactions are frequently applied at the fatigue cycle controlled through constant

deformation while the holds are introduced into the fatigue cycle either at the tensile or compressive stress or both simultaneously. The hold constitutes the creep stress component in the fatigue cycle. Deformation characteristics under the creep-fatigue stress than can differ considerably from those of the static creep.

The study presents results of analysis gathered at deformation process of wrought nickel base superalloy EI 698 VD subjected to low cycle fatigue where creep stress component have been introduced imposing hold time into fatigue stress amplitude. The evaluation of deformation process and life prediction of the alloy was done in relation to the hold periods introduced into low fatigue stress cycle at tensile amplitude peaks. The service life prediction in relation to the respective type of applied stress is presented using modified Kitagawa's criterion being suitable for static and cyclic creep. The fracture mechanisms analysis was employed to investigate the onset of fatigue mechanisms in participating at crack nucleation process.

2. Experimental

The creep resitant wrought nickel base superalloy EI 698 VD was selected for this experimental study. This alloy is suitable for the manufacturing of discs and shafts of aircraft engines and can be exposed at operating temperatures up to 760°C. Chemical composition of the alloy in mass % is given in Table 1. The alloy was given a three step heat treatment to produce a uniform equiaxed grain structure where alloyed nickel fcc matrix is strengthened by coherent gamma prime precipitates with an average size of about 60 nm and a the volume fraction of ~ 40%, Fig. 1. Carbides of MC and $M_{23}C_6$ types, that do not contribute substantially to the matrix strengthening but stabilize and strengthen grain boundaries, were present in the alloy.

Table 1. Chemical composition of nickel base superalloy EI698 VD in mass %.

C	Cr	Al	Ti	Mo	Fe	Nb	Mn	Ni
max.0.08	13-16	1.3-17	2.3-27	2.3-3.8	max 0.2	1.8-2.2	max 0.4	balance

The load controlled cyclic tests were conducted at the temperature of 650°C using a microprocessor controlled hydraulic dynamic system INSTRON 8511. The cyclic creep tests were of trapezoidal wave pattern shown schematically in Fig. 2. The nine different hold times

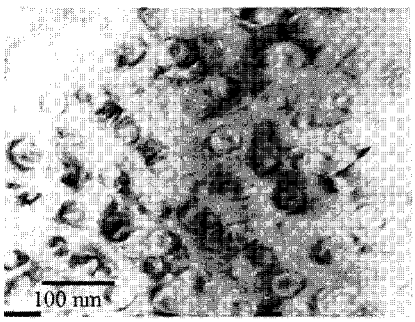


Fig. 1. TEM micrograph of the alloy structure.

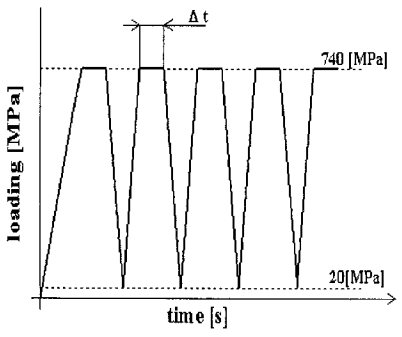


Fig. 2. Illustration of the loading pattern.

of Δt = 0 (pure fatigue), 1, 3, 7.5, 15, 30 minute and Δt = 1, 3, 5 and 10 hours were introduced at the maximum tensile stress of σ = 740 MPa. The net effect of these hold times is to impose a creep stress component into the fatigue load cycling. The cycling frequency range was between 5.5×10^{-3} and 2.7×10^{-5} Hz and the stress ratio was R = 0.027. The load ramp rate in one cycle, either during the on-load or the off-load period, was 7.4 kN/min. No hold time was introduced at the minimum, i.e. at the stress of 20 MPa. The specimen longitudinal deformation, the failure lifetime or the total time of the cyclic test, the number of cycles to fracture, and the total time at maximum load were recorded and compared with appropriate static creep data. Creep tests, under stress equal to the maximum stress amplitude of σ = 740 Mpa, were also carried out in this work.

The fracture surfaces were examined using scanning electron microscopy (SEM) with the aim to evaluate the contribution of the introduced fatigue stress component to the crack initiation process.

3. Results and discussion

3.1 Mechanical testing

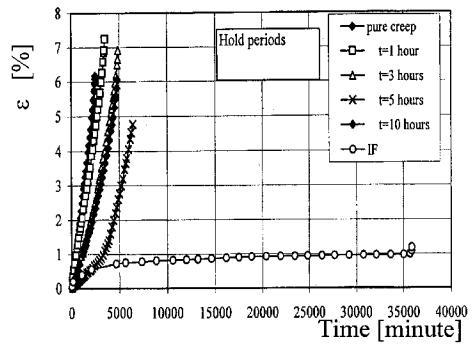


Fig.3. Strain–time to failure dependencies.

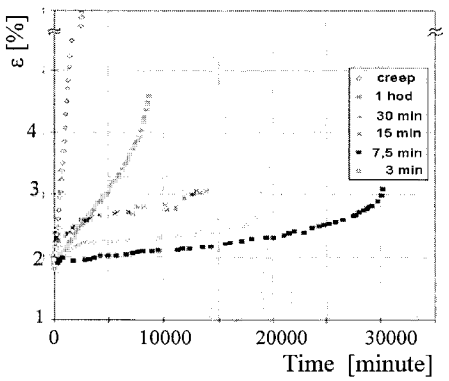


Fig. 4. Strain-time to failure dependencies.

The strain – time data, measured when strain was at the maximum load, corresponding to initial stress of 740 MPa, for isothermal cyclic creep tests for longer hold periods are presented in Fig. 3. The longer hold periods varied between 1 hour to 10 hours. The strain - time when shorter hold periods in range of 1 minute to 30 minute were applied is presented in Fig. 4. Comparing the results of the cyclic tests with that of pure creep data the introduction of any hold period in cycling resulted in fracture life increase and decrease in creep strain rate $\dot{\varepsilon}$. There is only slight scattering of $\dot{\varepsilon}$ values observed for 10, 5, 3, 1, 0.5 hours of the hold periods respectively. However, the introduction of the shorter hold periods caused the creep strain to drop down to more than half compared with that of the creep.

The results on the total time to failure (TTF), the total time corresponding at the maximum (creep) load (MLT), the numbers of cycles to failure (NCF), and the fracture strain obtained in the cyclic creep experiments with the shorter hold periods, are summarised in Table 2.

Evaluating the number of cycles N_f to failure vs. hold time Δt, which are recorded in Table 2 indicates sharp transient in the lifetime response corresponding to hold periods in the range of 7.5 minute to 15 minutes. These stated numbers do not include the N_f value obtained from the low cycle fatigue test conducted without hold periods but with the same stress amplitude values.

Table 2. Experimental data obtained from LCF and creep tests

Parameter	Hold period [minute]							
	fatigue	creep	1	3	7.5	15	30	60
TTF [min]	44 268	2 500	54 972	18 942	30 300	13 896	5 662	3 406
MLT [min]	-	2 500	10 741	8 003	19 591	10 911	4 981	3 188
NCF [min]	22 120	-	10 778	2 668	2 612	728	166	53
ε_f	3.2	6.3	3.3	3.5	3.6	3.1	3.9	6.9

In order to evaluate the creep fatigue resistance of this superalloy the time criteria, such as time to failure and/or time to failure corresponding only to total sum of holds at the maximum applied load (MLT) can be used for this purpose. The evaluation of lifetime behaviour according to the time to failure corresponding to the sum of hold periods at maximum load is presented in Fig. 5. The corresponding hold period of $\Delta t = 7.5$ minute at maximum load

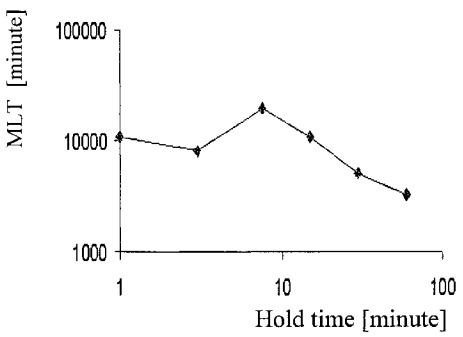


Fig. 5. Plot of time to failure in terms of to sum of hold time at maximum load.

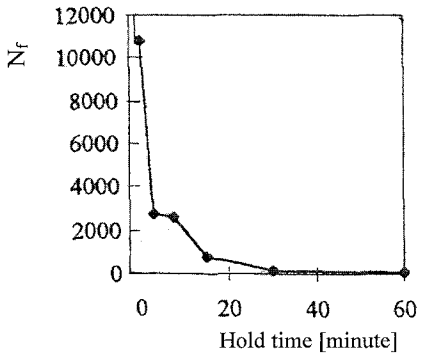


Fig. 6. The dependence of hold time and the number of cycles to failure.

seems to have specific influence on the lifetime behaviour of alloy. Probably, in the cyclic creep with the hold period shorter than $\Delta t = 7.5$ minute, in damage process more fatigue would contribute at crack nucleation and its propagation. If hold time is over this critical hold period in the the life prediction dominating role in damage process would be taken over by creep. Comparing these results with those determined using the total time to fracture, a clear contradiction appears, (see Table 2). The longest life corresponds to the test with the hold period of $\Delta t = 1$ minute. In case that total number of cycles to fracture was the criterion to evaluate the lifetime of the alloy the plot representing the dependence is documented in Figure 6. Regardless the fact that there is observed continuous decrease in number of cycles to failure with increasing hold period Δt the the relationship can not be interpreted simply as

the effect of prior creep damage on the fatigue mechanisms and/or as the influence of creep on cycles reduction. The main reason not to follow such interpretation is the fact that creep damage, which is time-controlled process, simply dominates in cyclic deformation process with longer hold periods introduced, i.e. when time needed for creep deformation advancement in one cycle would be sufficient.

Another interesting experimental result of was observed in case of the hold times of $\Delta t = 3$ and 7.5 minutes. The recorded number of cycles to failure showed very small difference. To verify these findings these tests were repeated, however no differences were obtained, hence discounting the possiblity of scatter. Considering this fact, the explanation on such lifetime behaviour could be based on the balanced contribution from creep and fatigue damage in these two specific hold periods.

To predict creep fatigue life of the alloy under considered laboratory test condition the linear damage summation rule [7] would be hardly appropriate to employ it in case when creep damage may arise due to the cyclic loading condition. To separate the creep caused by the applied stress and the creep damage caused by the strain accumulation the equation of Kitagawa et al. [8] which is a modification of the linear rule of damage accumulation is more practical to be used. The Kitagawa's equation where $\boldsymbol{a}$ parameter is assumed as the frequency dependent can be written than in the following form:

$$\left(\frac{N}{N_f}\right)+\left(\frac{t}{t_{rcyc}}\right)+\boldsymbol{a}\left(\frac{\varepsilon}{\varepsilon_{stat}}\right)=1 \qquad (1)$$

N is total number of cycles to failure, N_f is number of fatigue cycles to failure corresponding to pure fatigue, t is the total time to failure at cyclic creep, ε_{stat} is creep ductility, and $\boldsymbol{a}$ is Kitagawa's parameter, expressing the process frequency dependence.

This equation considers explicitly the creep life modification under the cyclic creep condition. However, it fails in evaluation of fatigue degradation by creep, i.e. by the time-dependent process. The parameter $\boldsymbol{a}$ can be expressed as $\boldsymbol{a} = 1 - 1/\boldsymbol{k}$. Parameter $\boldsymbol{k}$ determines the difference in a material life exposed in condition of cyclic creep and can be stated as $\boldsymbol{k} = t_{rcyc}/t_{stat.}$, where t_{rcyc} is the life corresponding to the conditions of cyclic creep when only creep process is considered, and t_{stat} is life corresponding to the course of static creep. When substituting these parameters the equation can be adjusted to the following form:

$$\left(\frac{N}{N_f}\right)+\left(\frac{t}{kt_{stat}}\right)+\left(1-\frac{1}{k}\right)\left(\frac{\varepsilon}{\varepsilon_{stat}}\right)=1 \qquad (2)$$

The equation in such form expresses the simplest modification of the linear damage summation rule that enables to evaluate the creep fatigue interaction when lifetime increase is involved. The only limitation of using it for life evaluation was an assumption that creep damage resulting from hold period and from on-load and off-load period in one cycle was proposed to be equal. To summarise the creep damage resulting from fluctuating load, creep damage resulting from constant load and from fatigue damage the modified equation can be written as:

$$\left(\frac{N}{N_f}\right)+\left(\frac{N}{kN_c}\right)+\left(\frac{t_h}{kt_f}\right)=1 \tag{3}$$

where N_f is cycles to failure under fatigue, and N_c is number of cycles representing pure creep when fluctuating load is applied, t_h is the sum of holds at maximum load, t_f is time to failure at applied static creep, k is the parameter to characterise the different deformation behaviour of material under cyclic and static creep.

If we consider the cyclic creep as deformation process where fatigue and creep (cyclic) participate there together with respect to time-controlled degradation, then the resulting degradation should arise due do superposition of both these contributions. Of course, we cannot generalise this assumption to whole frequency reductions interval of the applied stress because, exclusively at low frequencies of load reduction, dominantly only simple static creep would control the deformation process. That is why any important changes between the parameters t_{cyc} and t_{stat} can not be expected there. However, a continuous transition must exist between them due to the change in stress reduction frequency. Kitagawa resolved the problem of the ***a*** parameter frequency dependence by introducing a third member into the Eqn. (1). The limitation must be introduced in order to validate this equation over the entire frequency interval. A contribution resulting from cyclic deformation to total deformation would be only a negligible. It would be therefore more advantageous, to satisfy above limitation, to use only the first two terms of Eqn. (2) and to assume the frequency dependence of the ***k*** parameter. However, in order to simplify the calculation procedure the creep process was separated in to the periods of hold time and periods of ramping time, and the number of cycles was formally used as the parameter of damage although time-controlled process was involved. After these adjustments and using the experimental data for creep life corresponding to total sum of holds at amplitude peaks and data from pure fatigue test to calculate the number of cycles to fracture corresponding to fluctuating load the following equation was received for applied loading cycle:

$$\left(\frac{N}{60000}\right)+\left(\frac{N}{k.13000}\right)+\left(\frac{t_h}{k.2500}\right)=1 \tag{4}$$

where t_h is hold time at the maximum load. The realised laboratory test did not provide the satisfactory data for precise determination of the time during which the creep at static load does not contribute to damage accumulation. However, according to the deformation dependence in Figure 6 it can be assumed that hold periods of Δt =1 and 3 minute are only involved to comply with this assumption. In order to guarantee the stated prediction, the calculation was based on an extreme hold limit Δt = 1 minute, when the effective period of static creep will be the longest. After subtracting this value from applied hold period the effective holds related to maximum load were calculated and they are presented in Table 3.

Table 3. Fracture effective hold periods at the maximum load.

Δt [minute]	1	3	7.5	15	30	60
MLT_{ef}	0	5 335	16 979	10 183	4 815	3 153

Substituting this effective hold time to Eqn. (4) and employing additional experimentally obtained data the ***k*** parameter and ***a*** parameter as a function of hold time at the maximum load was determined. The results of this calculation are presented in Table 4.

Table 4. Parameters ***k*** and ***a*** as a function of hold period.

Δt [minute]	1	3	7.5	15	30	60
k	1.03	2.62	7.5	4.2	1.95	1.25
a	0.03	0.62	0.87	0.76	0.48	0.2

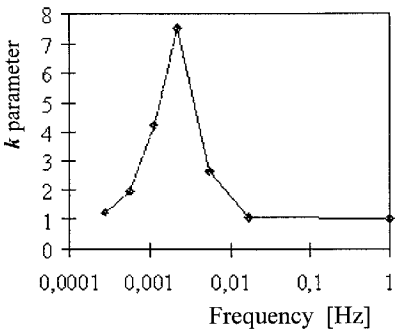


Fig. 7. Frequency dependence of ***k*** parameter.

It was already stated that ***k*** and ***a*** parameters are frequency dependent. The frequency dependence of ***k*** parameter can be related to frequency dependent process corresponding to, for example, the ability of storing and recovery of anelastic creep deformation. It is possible to assume that, in process of cyclic creep it should be a defined frequency at which the maximum dissipation of deformation energy resulting from the storing and recovery of anelastic creep deformation will be reached because the frequency effect was introduced into the loading process as a result of different hold periods. Another possible example supporting of the ***k*** parameter frequency dependence is equilibrium frequency dependence of hardening and softening process due to stress relaxing within the load off-times. The frequency dependence of the ***k*** parameter, which was introduced into process by creep load reduction or by introduction of hold time onto low cycle fatigue, is presented in Figure 7.

To model the life prediction behaviour of alloy the modified Eqn. (4) of the linear rule of damage accumulation was used. For the applied load – temperature condition to calculate the time to failure (MTF) as a function of the applied hold time t_h at the maximum load with respect to ***a*** and ***k*** parameters the following explicit formula was determined:

$$\mathrm{MTF} = \frac{60937.5k(t_h)}{24.375(t_h - 1) + 4.6875}\, t_h \qquad (5)$$

For other parameters, which may be suitable for life prediction, the following relations were calculated:

$$\mathrm{NCF} = \mathrm{MLT}/t_h \quad \text{and} \quad \mathrm{TTF} = \mathrm{MLT} + 4\,\mathrm{NCF} \qquad (6)$$

To calculate the ***k*** parameter values it is not easy to find the regression function, which would describe its value with good reliability for whole interval of the applied hold periods. That is why for interval of used short hold times $t_h < 7.5$ minutes and for interval of longer hold

times, interval t_h > 7.5 minutes the different regression function has been used. The discontinuity at the boundary of the interval corresponding to hold time of Δt = 7.5 minutes on plotted curve presenting the alloy model life prediction was the result. For the shorter hold time the regression functions $\boldsymbol{k}$ = 1.0105 t_h – *0.1567* and for longer hold time the another one $\boldsymbol{k}$ = 44.53 $t_h^{-0.8862}$ were calculated.

If these regression functions expressing the $\boldsymbol{k}$ parameter dependence on hold time would be substituted into the Eqn. (5) the following formulae for life prediction, to differentiate the effect of shorter and longer hold time on superalloy behaviour subjected to cyclic creep would be resulting:

$$\mathrm{MTF} = \frac{60937.5\left(1.0105\ t_h - 0.1567\right)}{24.357\left(t_h - 1\right) + 4.6875 + \left(1.0105 t_h - 0.1567\right)} t_h \quad \text{for holds } t_h < 7.5 \text{ minutes} \qquad (6)$$

$$\mathrm{MTF} = \frac{60937.5\left(44.53 t_h^{\ -0.8862}\right)}{24.375\left(t_h - 1\right) = 4.6875 + \left(44.53 t_h^{\ -0.8862}\right)} t_h \quad \text{for holds } t_h > 7.5 \text{ minutes} \qquad (7)$$

The graphic presentations of the model life parameters prediction MTF and NCF for defined testing condition of cyclic creep using the Eqn. (6) and Eqn.(7) are shown in Figure 8 and in Figure 9.

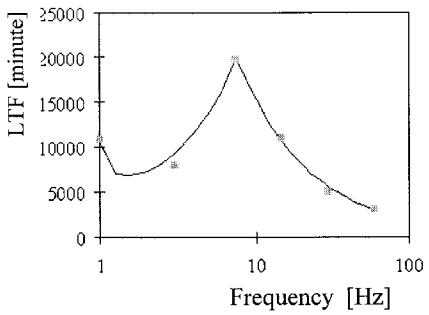


Fig. 8. The plot of alloy model life prediction in condition of cyclic creep.

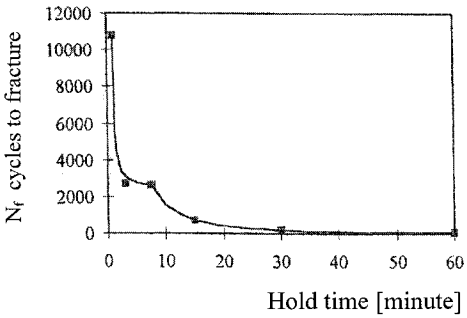


Fig. 9. Model prediction dependence of N_f as the function of hold time.

3.2. Fracture analysis.

The SEM fracture analysis was used to investigate the crack initiation site and its morphology in relation with cycling frequency, i.e. with holds periods. Structure investigation along the plane normal to the crack propagation revealed that the crack initiation was located dominantly at the intersections of grain boundaries with the specimen surface regardless the hold time. Secondary cracks, which were few on cross section, prevailingly nucleated along grain boundaries perpendicular to the applied stress and had either wedge or flat appearance. All fractures formed either at creep or under cyclic creep with long hold periods had characteristic intergranular crack initiation and propagation mode as it shown in Fig. 10.

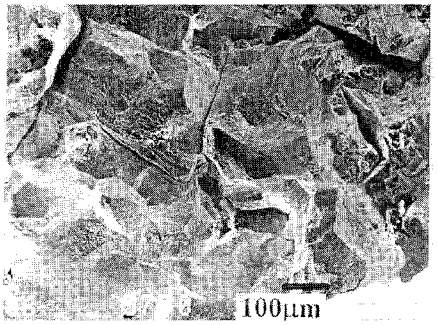


Fig. 10. Micrograph of intergranular fracture.

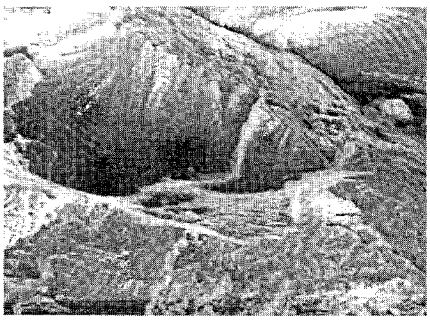


Fig. 11. Crack intiation by fatigue.

On the basis of fracture mechanism investigation at damage process, regardless the hold periods, the cleavage was dominant mechanisms of intergranular failure. This fact proves the decisive contribution to deformation process from the creep process. However, this conclusion is apparent and cannot be accepted as only a proof of assetion that fatigue was absent in damage. It was found and verified that when only fatigue was involved, without any holds, the intragranular cleavage dominated for defined stress amplitude. In case of cyclic creep testing, when hold periods have been introduced at stress amplitude peaks, it was evident that participation of fatigue mechanism in damage process appeared first time when hold time of 30 minute was applied. The facet with characteristic fatigue striations appeared on fracture surface. The shorter hold was introduced in fatigue cycle more fatigue facets were manifested and in these cases the intragranular crack initiation of fatigue origin were present, Fig. 11. Later in advanced stage of fracture the crack proceeded by intergranular mechanism. The effect of fatigue was more pronounce as hold time became shorter.

Very often was observed, after critical crack opening, the further propagation of crack was of mixed fracture mode, intergranular and intragranular cleavage. As hold period was cut down more intragranular facets with fatigue striations appeared on fracture surfaces. To relate results on mechanical testing with failure analysis results the conclusion can be made that if fatigue dominates in deformation process a substructure of narrow dislocation shear bands was observed and dislocation slip was more localised what reflected in higher strengthening.

Conclusions

The mechanisms of deformation and damage at high temperature in wrought nickel base superalloy subjected to low cycle fatigue where creep stress component have been imposed were investigated. The obtained results serve to demonstrate that introduction of creep deformation into fatigue process or vice versa resulted in modification of the deformation behaviour of superalloy in dependence of the introduced parameters representing individual loading regime. The following conclusions can be drawn from the present study:

1) The creep-fatigue interaction represented by tensile hold period introduced into low cycle fatigue regime showed detrimental effect in fatigue life no matter what periods of holds have been used.

2) Introduction of tensile hold period has been shown to result in decrease in the number of cycles to failure as hold period prolonged. The increase in the strain rate resulted from creep participation in deformation process. The more pronounced strain rate increase can be related to more active creep participation in deformation process.
3) The presence of fatigue stress participation became dominant in deformation process when hold period was below 0.25 h.
4) The creep-fatigue interaction reflected in change of failure mode. Whereas in the creep process the intergranular fracture mechanisms dominated in crack nucleation and propagation at introducing fatigue into failure process the intragranular crack nucleation with characteristic striation mode appeared.
5) For the laboratory test condition of low cycle fatigue where creep process was involved the modified linear damage summation rule was used to the model life prediction in dependence on hold periods, representing the creep stress in fatigue cycle, introduced.

Acknowledgement
The authors gratefully acknowledge the support of the present research by the Grant No. 1/6008/99 of the Scientific Grant agency of Slovak republic.

References

[1] G. Härkegard, J. Y. Guedon: Proc. of the 6th Liege Conf. on materials for Advanced Power Engineering, Liege, Belgium, 1998, 913.
[2] T. G. Gabb, G. Welsch: Acta Met., 37, (1998), 2507.
[3] P. D. Portela, A. Bertram, E. Fahlbusch, H. Frenz, J. Kinder: In: Fatigue'96, Lütjering, G., Nowack, H. (Eds). Beijing, 1996, 795.
[4] J. Zrnik, J.A. Wang, Y. Yu, L. Peijing, P. Hornak: Mater.Sci. Eng. A, (1987), 884.
[5] Bosimer, D.A. and Sheitogolu, H. Trans. ASME, 112, (1989), 68.
[6] J. Y. Wang, W. Chen, D. Mukherji, T. Kutner, R.P. Wahi: Z. Metallkd. 86, (1995), 365.
[7] S. Taira: Creep in structures, Nicholas, H. J. (Eds). Academic Press, N.Y. 1962, 99
[8] M. Kitagawa, K. Tamura, A. Ohtomo, 1983 J. of SMSJ, 32, (1983), 662.

IN-SITU OBSERVATIONS OF THE DEFORMATION AND DAMAGE BEHAVIOUR AROUND LASER-DRILLED COOLING HOLES IN INCONEL ALLOY 617 USING THE SCANNING ELECTRON MICROSCOPE

J Klabbers, E Wessel, F Schubert

Research Centre Juelich (FZJ)
Institute for Materials and Process in Energy Systems IWV-2
D-52425 Juelich, Germany

Abstract

Subject of the present work is an investigation of short crack behaviour (length approx. <100 μm) around laser-drilled cooling holes in a nickel-base-alloy. The investigation of short cracks by light microscopy is impossible due to the very small diameter of laser-drilled cooling holes (approx. 200 μm), therefore uniaxial tensile tests with flat tensile specimens were carried out in a scanning electron microscope. A tensile test rig and a heating device specially designed for the SEM were used. The tests were conducted with the nickel-base INCONEL alloy 617. For the description of the deformation and damage behaviour, especially at high temperatures, the experiments were carried out under uniaxial tensile load at 650°C. The formation of a technical crack length (approx. 1 mm) in metallic materials will be mainly determined by the crack growth of short cracks. Therefore it seemed to be important to look at the evolution of accumulated fatigue damage in this region, for developing fracture mechanics concepts.

Keywords: INCONEL 617; deformation/damage behaviour; cooling holes; short cracks

Introduction

The conservation of fossil fuel resources, the growth of the world demand for energy and the satisfaction of the increasingly stringent environmental criteria are the driving forces for the continuing development of fossil fired, heavy duty industrial gas turbines for electrical power generation. The introduction of single crystal technology for vanes and blades and the use of thermal barrier coatings for highly exposed components may help to realise a very high inlet temperature in the gas turbines, which is one of the most important indicator for high efficiency. Efficiency values higher than 38 % for IGT, however, will not be realised without an optimisation of the cooling technology. Today a combination of convection and film cooling is used, but in the future, effusion or even transpiration cooling will be required. The porous structures needed for film and effusions cooling are obtained by laser-drilling of the required configuration of holes in cooled Ni-base alloys [1, 2]. The drilled holes may be locations for crack initiation. In the open literature there is only limited information regarding the behaviour of arrays of laser-drilled holes in vanes and blades under operational loading conditions. The deformation behaviour under tensile loading was therefore observed in-situ using the scanning electron microscope SEM. The yield strength of a single crystal alloy like CMSX-4 at up to 750°C was too high for the available equipment in the SEM, which does not allow test temperatures above 650°C; therefore the weaker alloy INCONEL 617 was used for the first experimental work. In the case of a material with high potential for deformation at higher temperatures, like Alloy 617, the treatment of technical cracks with C*-concept seemed to be adequate for higher temperatures. Former experiences [3 - 5] demonstrate that up to 650°C the application of a K_I-concept may be tolerable. A laser-drilled cooling hole

may be treated as a kind of inhomogeneity in the continuum structure. Using an SEM equipped with a stress loading facility, in-situ investigations of the behaviour of very small laser-drilled cooling holes in small flat tensile specimens can be observed only in vacuum. Conventional uniaxial tests of specimens without cooling holes have been carried out on INCONEL 617 to check the tensile test device and the controlling system of the SEM.

The influence of single cooling channels, of cooling channel arrays and their mutual interaction under loading conditions is totally uncertain. For this reasons investigations on initiation and propagation behaviour of short cracks emanating from specimens with cooling holes were performed with the polycrystalline material INCONEL alloy 617 by in-situ SEM observations.

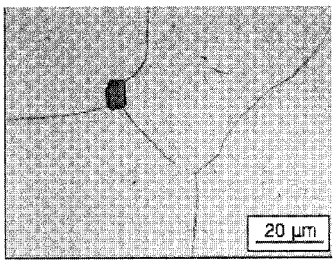
Material

INCONEL alloy 617 is a solid-solution hardened Ni-Cr-Co-alloy, originally developed as a hot-workable sheet material for aero-turbine combustion chambers and has been evaluated for tubes and heavy forgings for the high temperature gas reactor (HTGR). The mechanical short term strength properties, such as yield strength, depend on $M_{23}C_6$ precipitates which form during first stage of operation. Normally this alloy is, however, used in solid soluted version. This alloy is a typical example for a forgeable material without any important content of γ`precipitates. This example stands for an alloy with good deformability. The nominal chemical composition (Table 1) and the used heat treatment are given in Figure1. The material was delivered as polycrystalline plates and fully heat treated.

Table1: Nominal chemical composition (wt.-%)

Material	Ni	Co	Cr	Mo	Al	Ti	Fe	C
INCONEL* 617	Bal.	12	23	9.0	1.0	0.5	<2	0.05

*trade name of Special Metals



polycrystalline solid solution hardened equiaxed
heat treatment: 1120°C / 2h / air
grain size: ASTM: 3-4

Figure 2: Heat treatment and microstructure after heat treatment of INCONEL 617

All specimens were manufactured by electric discharge machining (EDM).Cooling channels were simulated by specimens with a different number of laser-drilled holes (1 – 5 holes), see details in Figure3. Holes were drilled by an µs-SLAB-Laser, notches with a ns-Starline-Laser.

The diameter of a hole is approx. 0.2 mm, the distance between the holes parallel to the load axis is 0.6 mm and perpendicular to the load axis 1.2mm.
Generally three types of tensile specimens were tested:

- Type I with one laser-drilled hole
- Type II with three laser-drilled holes in one row
- Type III with five laser-drilled holes in different rows,

see Figure 3. For the measurement of crack growth and fatigue crack growth it was tried to use notched specimens, maximum notch width 0.025 mm, see detail in Figure 4.

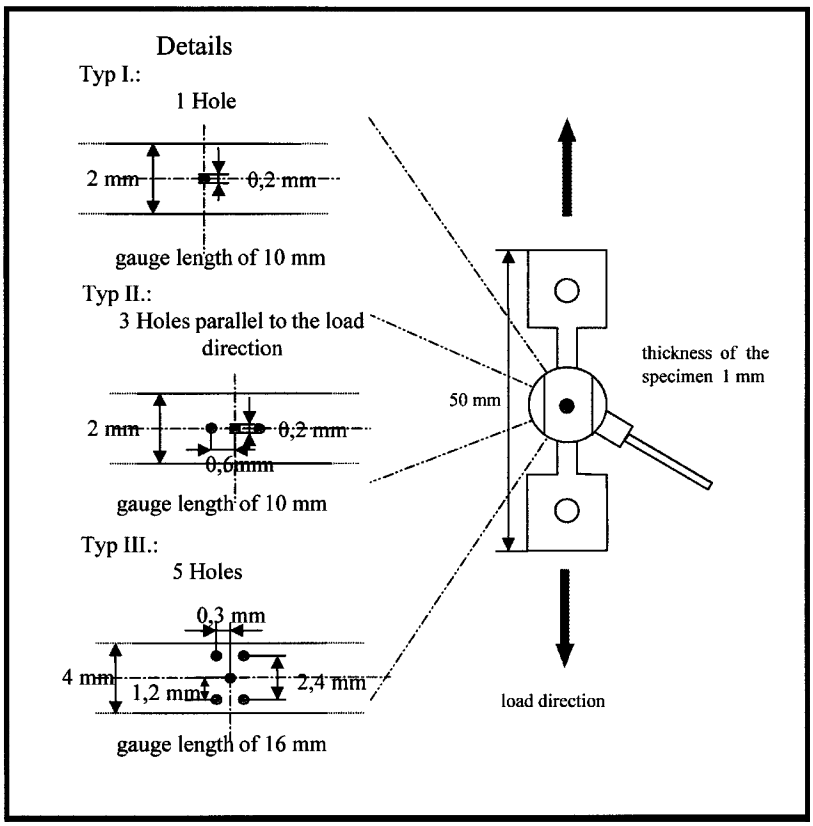


Figure 3: Diagram of tensile specimen with a different number of holes

In a 3-D finite element model of a thin wall cylinder, created by the ABAQUS-program, the stress-response around laser-drilled cooling channels carried out at uniaxial tensile load has been calculated. High stress concentrations were detected by the FEM-analysis in the ground of the holes, perpendicular to the stress axis and between the holes of different rows.

In those regions crack formation, initiation and propagation may be initiated. In-situ SEM can greatly enhance the chance of description the deformation and damage behaviour and identifying very small cracks at its very early stage.

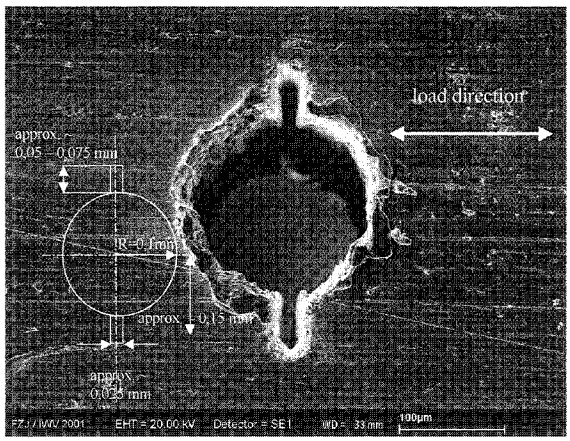


Figure 4: Notched specimen

SEM Device

The experiments were carried out in a scanning electron microscope (LEO 440, Oberkochen, Germany) with a mechanical tensile device (Kammrath & Weiss, Dortmund, Germany) which allowed loads up to 5000 N (Figure 5). To carry out the tensile experiments at high temperatures a small graphite furnace has been used which allowed temperatures up to 800°C. For controlling the temperature a NiCr-Ni thermocouple was mounted directly under the tensile sample (Figure 5). To avoid high temperatures at the ends of the sample and at the sample holders copper wires with a diameter of 5 mm were used as heat conductors, which were connected with one end to the sample holders and with the other end to a water flashed heat exchanger. The load, elongation and the temperature were controlled by an electric controlling system. To acquire the data the controlling system was connected to a personal computer.

The sample was heated up with a heating rate of around 10 C/h. At temperatures higher than 650°C it was impossible to acquire SEM pictures, because of disturbing the secondary electron detector by emission of light and thermal electrons from the furnace and the sample. Back scattered imaging was also impossible because of disturbing the semiconductor detector by infra red light. So all in-situ experiment were carried out at temperatures around 650°C.

Results and discussion

The tests have been conducted with the nickel-base INCONEL 617. For the description of deformation and damage behaviour at high temperatures, the experiments were carried out at first under uniform tensile load at 650°C.

A typical stress-strain diagram measured by in-situ SEM tensile testing for INCONEL 617 is shown in Figure 6.

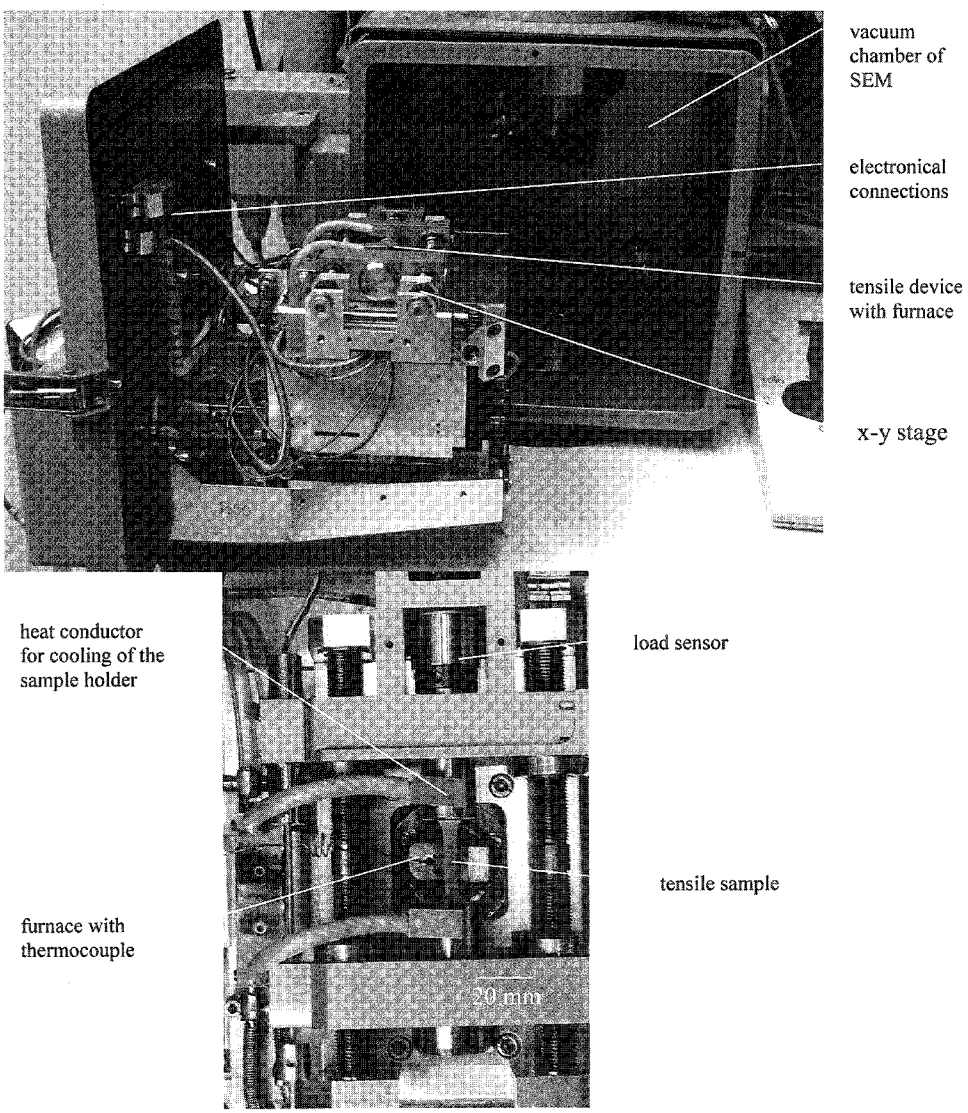


Figure 5: Scanning electron microscope with tensile and heat device (Detailview: Tensile device with sample and furnace)

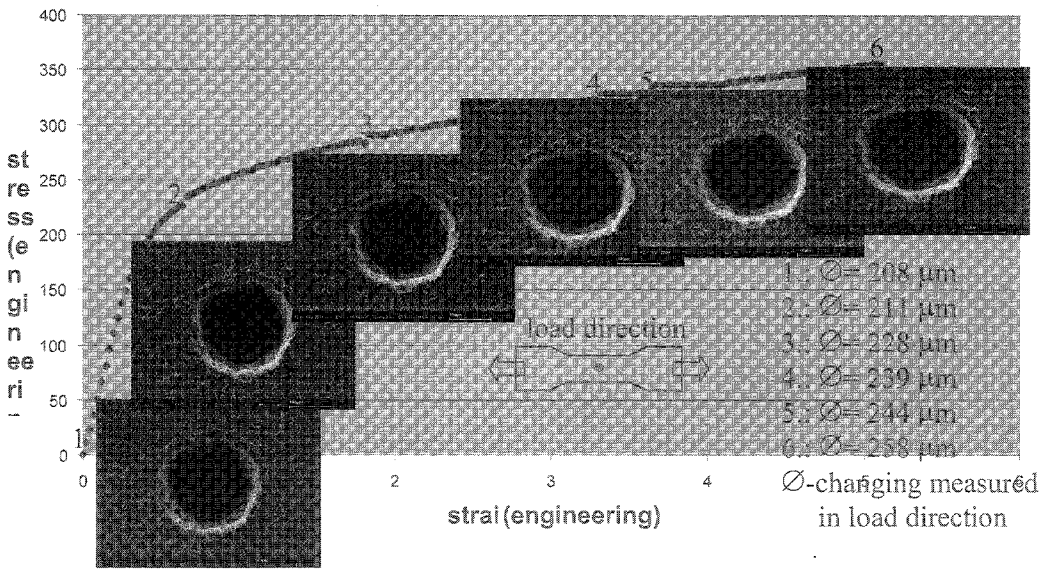
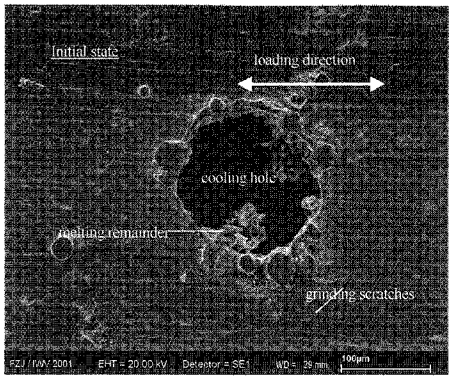
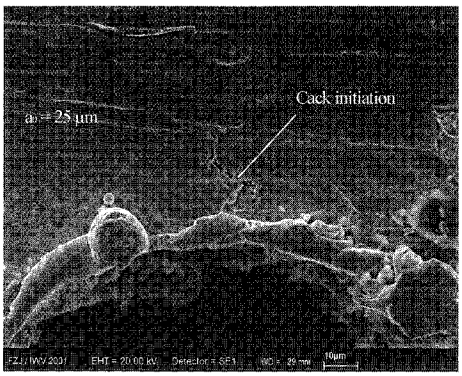


Figure 6: Stress-strain diagram (engineering) from a specimen with one hole for INCONEL 617

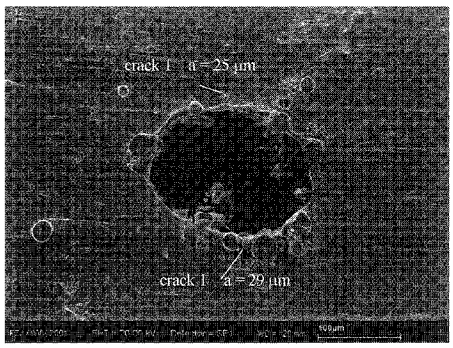
Figure 7 shows the deformation behaviour of specimen Typ I. and the propagation process of a short crack at uniform tensile load at 650°C. The micro-macroscopic crack growth path is basically perpendicular to the mode I loading direction which is the horizontal direction in the SEM-photos. At the top and at the bottom side of the hole crack formation starts, in addition at both sides of the cracks, deformation lines on the specimen surface can be detected.



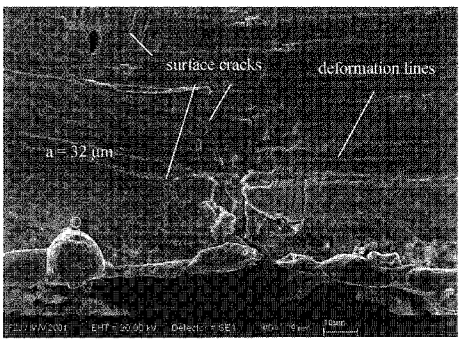
a.) Initial state



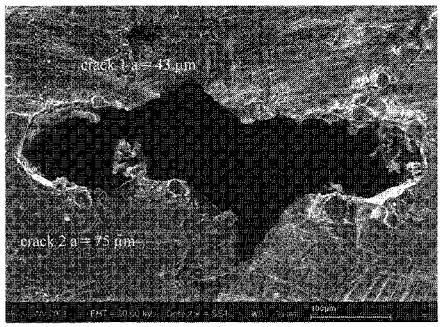
b.) In-hole ground cracking perpendicular to the load direction (top side of the hole)



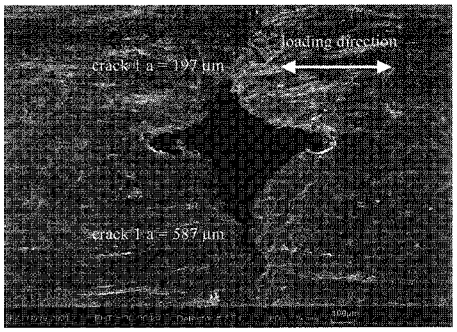
c.) Crack formation perpendicular to the load direction at the top and at the bottom side of the hole



d.) Crack at the top side of the hole



e.) Crack opening and blunting after high deformation



f.) Specimen failure

Figure 7: A typical process of short crack formation for INCONEL 617 at 650°C and uniform tensile load

Comparing the SEM micrograph photo, shown in Figure 8, with checking the recorded stress strain curve, it was observed that with increasing of the force, initial multiple microcracks occurred continuously at the top and at the bottom side of a cooling hole. A dominant crack is formed as a result of the competition among different multiple microcracks, while most microcracks slowed down or fully arrested being non-propagating cracks. In **figure9** different stress-strain curves for the tensile specimens without cooling hole and with one, three and five holes are shown. The load is concerned to the load bearing cross section of the specimen.

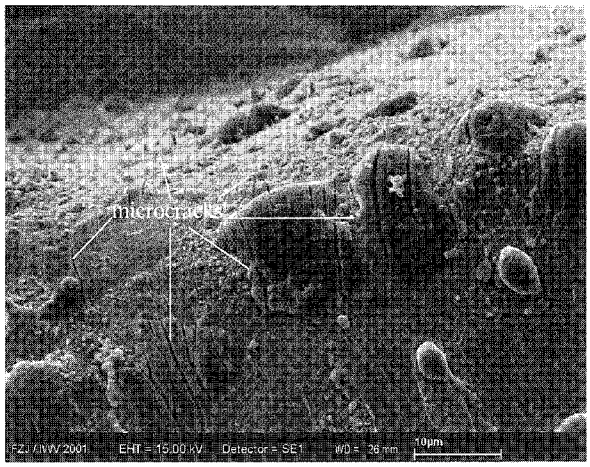


Figure 8: Formation of microcracks at the bottom side of a cooling hole

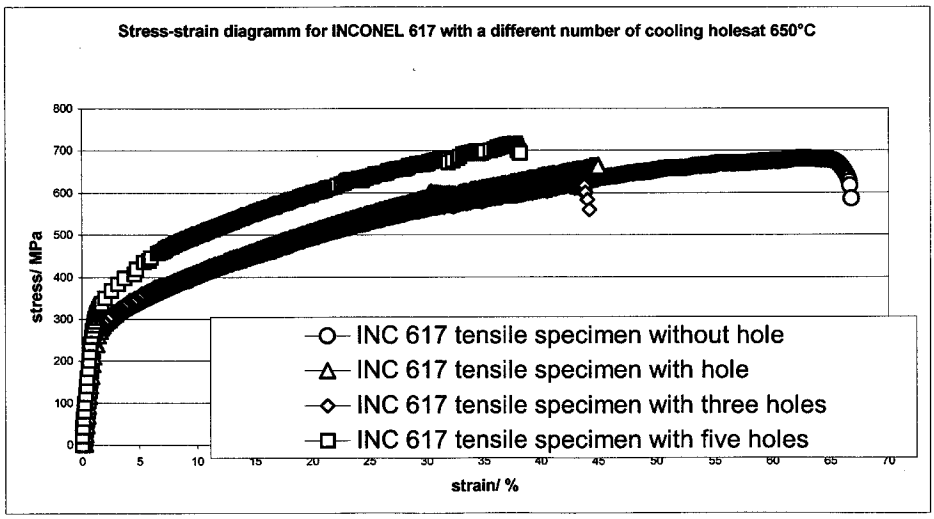


Figure 9: Stress-strain diagrams for INCONEL 617 with a different number of holes

A comparison of an un- and a notched specimen is given in (Figure7 and Figure10). For INCONEL 617 an influence of a notched specimen could not detected. This is an typical example for the enormous plasticity of INCONEL 617 at higher temperatures and its high resistance to a notch in the hole.

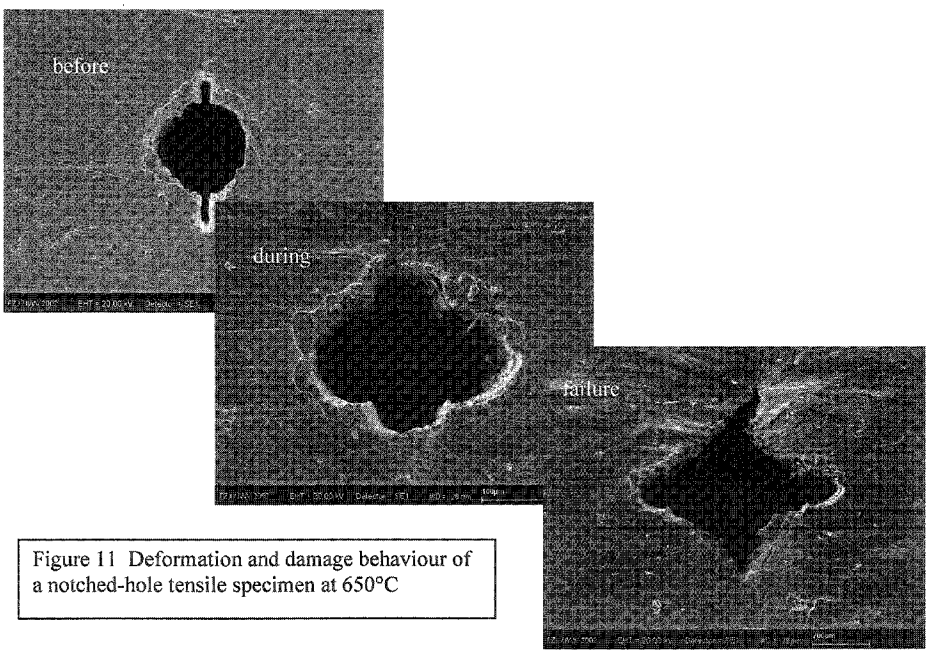


Figure 11 Deformation and damage behaviour of a notched-hole tensile specimen at 650°C

Conclusions

Based on the present investigation of the deformation, damage and short crack growth behaviour in the polycrystal superalloy INCONEL 617, it can be concluded that:

- Crack initiation starts in the ground of cooling holes perpendicular to the loading direction where the stress-concentration becomes the highest value
- in INCONEL 617 short cracks propagated along deformation lines, which were nearly perpendicular to the mode I loading direction
- the early stage propagation of a dominant short crack is a process of the competition among different multiple micro-cracks, most of them become non-propagating cracks while one of them becomes a dominant and critical crack

References

[1] Bohn, D.: New materials and cooling systems for high temperature, highly loaded components in advanced combined cycle power plants; these Proceedings, 2002

[2] Schubert F., Rieck T., Ennis P. J.: The Growth of Small Cracks in the Single Crystal Superalloy CMSX-4 at 750 and 1000°C, Proceedings of the 9th International Symposium on Superalloys, Seven Springs, The Minerals, Metals & Materials Society, 2000, pp. 341 – 346

[3] Rieck T.: Wachstum kleiner Risse bei hohen Temperaturen und Zug-Schwellbeanspruchungen in den einkristallinen Superlegierungen CMSX-4 und SC16, Dissertation RWTH-Aachen, Berichte des Forschungszentrums Jülich,ISSN 0944-2952, Jül-3706, 1999

[4] Antolovich B. F., Saxena A., Antolovich S.D.: Fatigue crack propagation in single crystal CMSX-2 at elevated temperature, Superalloys 1992 (Ed. By Antolovich S.D. et al.), The Minerals, Metals & Materials Society, 1992, pp. 727 – 736

5] Sengupta A., Putatunda S., Balogh M., Fatigue crack growth behavior of a new single crystal nickel-based superalloy (CMSX-4) at 650°C, journal of Materials Engineering and Performance, 3, 1994, pp. 540 – 550

DESIGN OF Ni-BASE DS SUPERALLOYS FOR INDUSTRIAL GAS TURBINES

M. Sato, Y. Koizumi, T. Kobayashi, H. Harada and H. Ono*

National Institute for Material Science,
1-2-1 Sengen, Tsukuba, Ibaraki, 305-0047, Japan
*Kawasaki Heavy Industries, Ltd.,
2-4-1 Hamamatsu-cho, Minato-ku, Tokyo, 105-6116, Japan

Abstract

For industrial gas turbines with a power output below 10MW, operation using corrosive fuel such as diesel oil and heavy oil is often needed, and hot corrosion resistance is an important property in addition to the creep strength for blade materials. In this work, the effects of alloying elements and microstructures on hot corrosion resistance and creep strength were evaluated with experimental DS alloys and some commercial alloys. Burner rig hot corrosion tests were performed, and the regression analysis of test results showed that Cr clearly improved the hot corrosion resistance in a wide temperature range, while Re was effective only at over 900°C of metal temperature. This suggests that Re is effective in reducing oxidation rather than sulfidation. Creep tests were conducted at 900°C-392MPa, and the regression analysis of the results showed that the effective factors for creep strength were γ' fraction, Ta content, etc.. From microstructural observations, the grain boundary structure was also considered to be an important factor affecting the creep strength. With using the regression equations and experimental results, it has become possible to design DS superalloys having excellent hot corrosion resistance and creep strength.

Keywords: DS superalloy, hot corrosion resistance, creep strength, regression analysis, microstructure

1. Introduction

For small class industrial gas turbines as on-site use below 10MW range, the operation with multi fuel including corrosive oil such as diesel oil and heavy oil is often needed, and hot corrosion resistance is an important property in addition to the creep strength for blade materials. From a viewpoint of chemical compositions of superalloys, high temperature strength were improved mostly by decreasing Cr content and increasing Al content with adding W, Ta and Re. This type of alloys tend to have good oxidation resistance but poor hot corrosion resistance. While considering the crystal structures, creep strengths of DS alloys are lower than those of SC alloys, but the tolerance of DS alloys is better than SC in case of some grain defects such as misorientation and recrystallisation occurring. This character of DS alloys contributes to higher yields of casting and heat-treatment process, higher applicability to complicated shape, and higher cost-performance.

In this work, the effects of alloying elements and microstructures on hot corrosion resistance and creep strength were evaluated with experimental DS alloys, whose compositions were systematically designed, to develop a new DS alloy having good properties in both environmental and mechanical performance.

2. Experimental procedure

2.1 Alloy design

Experimental DS alloys were designed using NIMS-Alloy Design Program [1]. Chemical

Table 1 Chemical compositions (wt%) of experimental DS superalloys.

	Ni	Co	Cr	Mo	W	Al	Ti	Nb	Ta	Hf	Re	C	B	Zr
20 alloys	Bal.	9 ~ 12	3 ~ 14	0 ~ 4	3 ~ 6	3 ~ 6	0 ~ 6	0 ~ 2	0 ~ 6	0.1 ~ 1.1	0 ~ 5	0.07 ~ 0.16	0.01 ~ 0.03	0 ~ 0.06

compositions of them are shown in Table 1. Most of alloys were set to have more than 10wt% Cr content, and other elements were systematically changed within the range of practical Ni-base superalloys. The third generation DS superalloy TMD-103 [2], which we developed as high strength DS alloy containing 3wt% Cr and 5wt% Re, was also examined.

2.2 Casting and heat treatment

DS bars of 12mm diameter and 140mm length were cast with solidification rate at 200mm/h. The partial solution temperature was examined to find the optimum condition to dissolve the γ' phases without the incipient melting at grain boundaries, which affects the creep strength.

2.3 Burner rig test

Hot corrosion resistances were examined by burner rig test at gas temperature 1050°C for 500h with kerosene fuel containing some sulfuric oil and artificial seawater, which simulate the combustion gas atmosphere of heavy oil fuel. The test conditions are shown in Table 2. Test pieces, 10mm diameter and 100mm length, were held at bottom side and exposed to burner flame with revolving. The surface temperature of a test piece was not uniform because of the created thermal gradient along the longitudinal direction. After the test, two cross sections of each test piece were evaluated by measuring the maximum penetration depth at about 910°C and 810°C part (70mm and 55mm from the bottom end respectively) of metal temperature, and corroded zone were analyzed.

2.4 Creep test

Test pieces were machined to 4mm diameter and 22mm gauge-length size from DS bars, which were almost in the <100> orientation as longitudinal direction. Creep tests were conducted at 900°C-392MPa condition. Creep curves of each sample were measured, and microstructures in the creep-ruptured samples were observed.

Table 2 Burner rig hot corrosion test conditions.

Atmosphere				Test piece		Time
Gas temp., °C	SO_x, vol.ppm	Cl, mass ppm	Na, mass ppm	Size, mm	Surface temp., °C	Exposure time, hours
1050	100 ~ 500	5 ~ 40	5 ~ 30	10 diameter 100 length	910 (at 70mm) 860 (at 55mm)	500 (100 x 5)

3. Results and discussion

3.1 Hot corrosion resistance

In the burner rig test, IN792Hf and Rene80H were also tested as references as well as experimental alloys. The corrosion depth (maximum penetration depth) of alloys were relatively evaluated. The data of maximum penetration depth and metal temperature were

considered by regression analysis. Corrosion depth was estimated by this equation;

$$y = C + \Sigma a_i x_i \quad (1)$$

where y is the penetration depth and C is a constant and a_i is the regression coefficient and x_i is the atomic fraction of element i.

Figure 1 shows the regression coefficient and the t-value of corrosion depth by regression analysis. If the regression coefficient is negative, the element decreases the corrosion depth. This means the negative parameters are effective for hot corrosion resistance. At 910°C, Cr and Re are effective with sufficient reliability, while at 860°C, Cr is effective but Re is not. This data suggests that Re is effective at over 900°C range of metal temperature. Cross sectional X-ray maps of corrosion layer are shown in Figure 2. Sulfide layer was formed inner than oxide layer, and some parts of sulfide were supposed to be melted, which suggests that the penetration was accelerated by sulfidation. Figure 3 shows the correlation between experimental and calculated data of burner rig test. The estimation by new equation shows a very good correlation, especially at 910°C position. This equation is also applicable to commercial alloys.

3.2 Creep strength

The creep rupture life of experimental alloys at as-cast condition was examined by regression analysis. Creep strength was estimated by this equation;

$$y = C + \Sigma a_i x_i \quad (2)$$

where y is the creep strength and C is a constant and a_i is the regression coefficient and x_i is the parameters including γ' composition of element i, γ' volume fraction and lattice misfit. These parameters were calculated by NIMS-ADP.

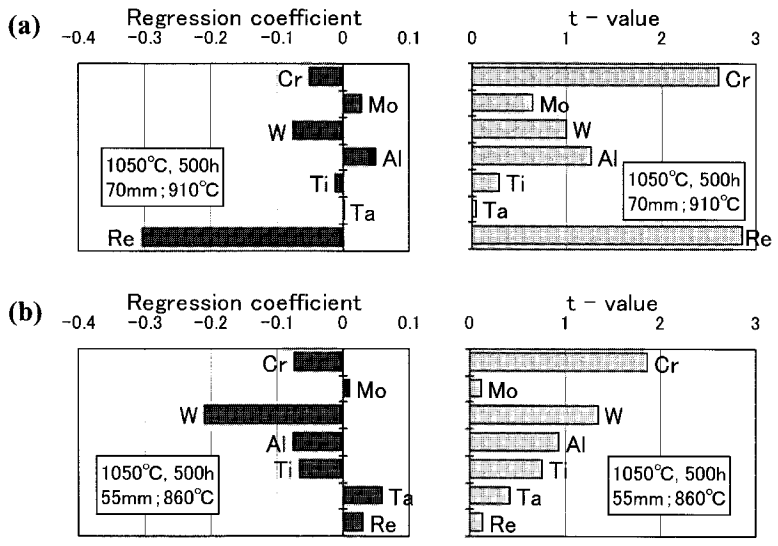


Figure 1 Regression coefficient and t-value from penetration depth of experimental alloys by burner rig test. (a) 70mm position, (b) 55mm position.

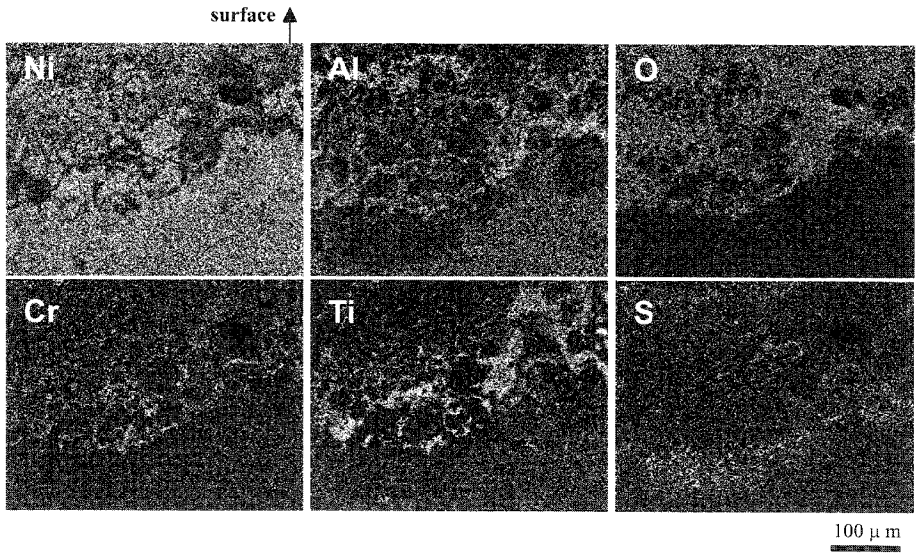


Figure 2 Cross sectional X-ray maps of an experimental sample after burner rig test.

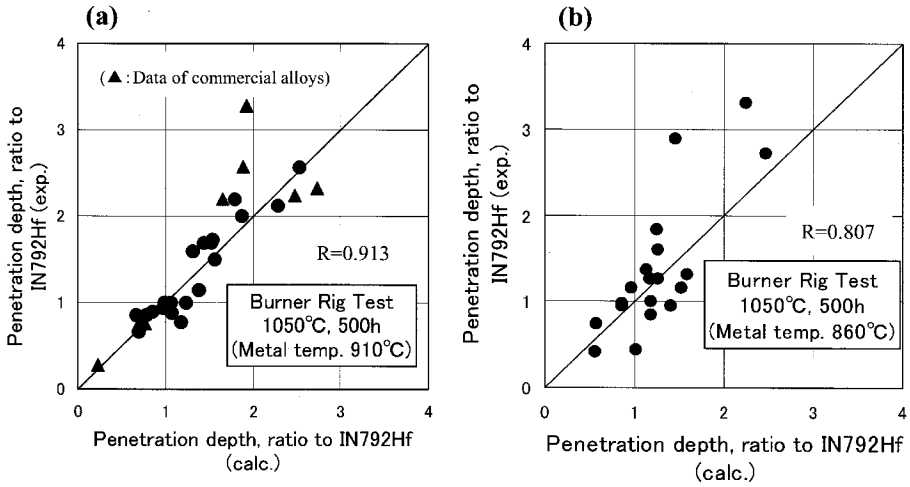


Figure 3 Correlation between experimental and calculated data of burner rig test. (a) 70mm position, (b) 55mm position.

Figure 4 shows the regression coefficient and the t-value of creep strength by regression analysis. If the regression coefficient is positive, the parameter increases the creep strength. This means the positive parameters are effective for creep strength. The result shows that the effective factors are γ' fraction and Ta content. In addition, the lattice misfit term has a large negative coefficient, which suggests the negative lattice misfit is good for the creep strength, too. These effects of parameters are almost same as the case of SC alloys.

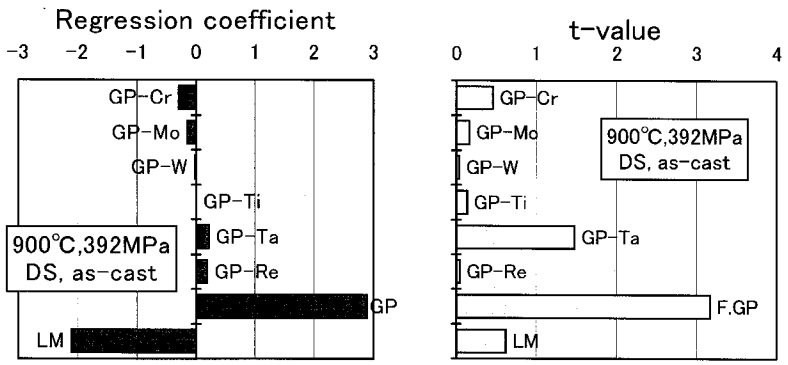


Figure 4 Regression coefficient and t-value from creep-rupture life of experimental alloys by creep test.

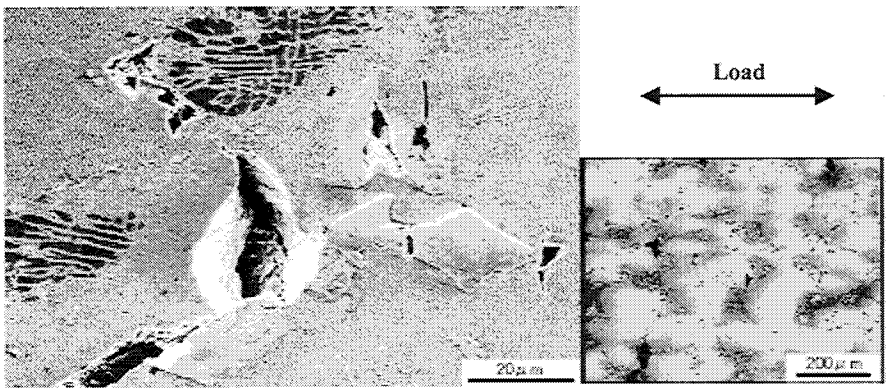


Figure 5 Microstructures in a longitudinal section of a heat-treated sample after creep test.

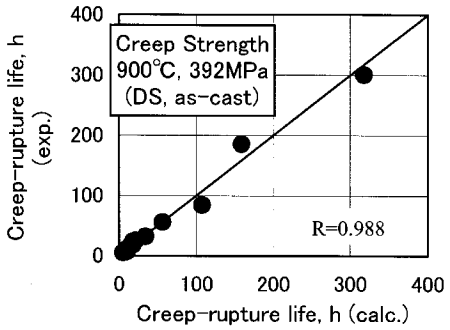


Figure 6 Correlation between experimental and calculated data of creep test.

Figure 5 shows the microstructures of creep-ruptured samples. The rafted structure was made and the initial crack occurred at grain boundaries, where were the final solidified regions including many γ/γ' eutectic phases and carbides. Increasing the amount of γ' phase may increase the strength of inner grain, but the amount of undisolved eutectic phases at grain boundaries after the partial solution treatment are also increased, then the strength of grain boundaries are relatively decreased. At the partial solution treated condition of DS alloy, the optimum ratio of γ' phase is found to be 55-60%. Figure 6 shows the correlation between experimental and calculated data of creep test. The estimation by new equation shows a good correlation for DS as-cast condition.

4. Conclusions

A design of Ni-base DS superalloys for small class IGT blade was conducted. The effects of alloying elements and microstructures on hot corrosion resistance and creep strength were evaluated with experimental DS alloys, whose compositions were systematically designed. For the hot corrosion resistance, amount of Cr clearly affects, and Re is effective at over 900°C range of metal temperature. For the creep strength, γ' volume fraction is effective at DS as-cast condition, and 55-60% of γ' volume fraction is optimum for the partial solution heat treatment of DS alloys. From these parameters, new equations estimating hot corrosion resistance and creep strength of DS superalloys were established. And now oxidation resistance was added into consideration to prepare for rising up of gas temperature. Next series of DS alloys were designed with new equations of hot corrosion, creep strength and oxidation, and evaluating tests are being conducted.

Acknowledgements
This work is a part of the KHI-NIMS collaborative research in the High Temperature Materials 21 Project. The authors wish to thank Dr.N.Akikawa of KHI Akashi Works and Dr.A.Tamura of KHI Yachiyo Works for their cooperation in experiments.

References

[1] H.Harada, M.Yamazaki, Y.Koizumi, N.Sakuma, N.Furuya, "Alloy Design for Nickel-base Superalloys", Proc. of High Temperature Alloys for Gas Turbines 1982, 721-735.
[2] T.Kobayashi, M.Sato, Y.Koizumi, H.Harada, T.Yamagata, A.Tamura, J.Fujioka, "Development of a Third Generation DS Superalloy", Proc. of Superalloys 2000, 323-328.

THE INVESTIGATIONS OF DEFORMABILITY AND STRUCTURE OF A-286 ALLOY AT HIGH TEMPERATURE DEFORMATION

K. J. Ducki, M. Hetmańczyk, D. Kuc

Silesian University of Technology, Materials Science Department,
Krasińskiego 8, 40-019 Katowice, Poland

Abstract

The influence of initial austenite grain size and parameters of plastic deformation on the deformability and structure of high-temperature austenitic alloy type A-286 have been presented. The hot deformation characteristics of alloy were investigated by hot torsion tests using torsion plastometer. The tests were executed at constant strain rates of 0.1 and 1.0 s^{-1}, and testing temperature in the range of 900 to 1150°C and were conducted until total fracture of the samples. The structural inspections were performed on microsections taken from plastometric samples after so called "freezing", i.e. rapid cooling of samples in water from deformation temperature. Plastic properties of the alloy were characterized by worked out flow curves and the temperature relationships of flow stresses and the strain limits. The flow stress of the torsion tests showed a single peak in the flow stress–strain curves, and indicated that a recovery and dynamic recrystallization took place during the hot deformation. The relationship between the peak stresses (σ_{pmax}) and the Zener-Hollomon parameter (Z) were described by $\sigma_{pmax} = A \cdot Z^n$ power function. Activation energy for hot working (Q) was assessed for the alloy after two variants of previous heating, i.e. 1100°C/2h and 1150°C/2h. In the samples deformed at temperatures bellow 950°C partially recrystallized structures of „necklace" type austenite were observed. At higher deformation temperatures (above 1000°C) completly recrystallized structures with austenite grain size depending on plastic deformation parameters were revealed in the samples.

Keywords: A-286 alloy, hot deformation, Zener-Hollomon parameter, structure

1. Introduction

The behaviour of metals and alloys during hot working has a complex nature and it varies along with changing such process parameters as [1]: deformation, strain rate and temperature. A high-temperature plastic deformation is related with dynamic processes of recovery and recrystallization, which have influence on the structure and properties of alloys. These processes have particular significance for determination of the mechanisms of hot plastic deformation and the relationships between strain parameters and the structure and properties of material.

The creep-resisting austenitic Fe-Ni alloys, precipitation hardened by intermetallic phases are featuring with high values of flow stress in high temperatures and are more difficult to hot working than the low-alloy and stainless steels [2]. At optimization of the processes of hot working of austenitic alloys, the following factors should be taken into account [3]: grain size, course of dynamic recrystallization and strain parameters. A particular role in processes of hot plastic working is played by the size of grain, as the refinement of grain is increasing the speed of recovery and dynamic recrystallization but reducing the size of recrystallized grain. This is particularly important in high-temperature Fe-Ni alloys, where grain size of austenite influence on their creep characteristics [4].

In this work are performed examinations of the influence of grain size and parameters of hot plastic deformation on the deformability and structure of high-temperature austenitic Fe-Ni alloy, precipitation hardened by γ' -type intermetallic phase.

2. Material and procedure

The tests were executed on specimen of rolled bars 16 mm diameter of the austenitic A-286 type alloy, having the chemical composition as specified in table 1.

Table 1. Chemical composition of tested austenitic alloy

Content of elements; [%]weight													
C	Si	Mn	P	S	Cr	Ni	Mo	V	W	Ti	Al	Co	B
0.05	0.61	1.32	0.03	0.01	13.7	24.3	1.30	0.42	0.15	1.90	0.22	0.10	0.01

To model the heating conditions of alloy before mechanical working, examinations were conducted on the samples pre-heated in high temperatures. The specimens of rolled bars used as samples for examinations were subjected to soaking at 1100°C / 2h and 1150°C / 2h with subsequent cooling in water. This type of heat treatment corresponds with heating parameters of tested alloys prior to hot working [2].

Examinations of alloy formability were performed by a hot torsion method at Setaram torsion plastometer. The plastometric tests were conducted every 50°C in the range of temperatures 900 ÷1150°C, maintaining a constant soaking time 10 min. at given temperature. The full cylindrical samples (6.0 dia. x 50 mm) were twisted with rotational speed 50 and 500 rpm, which corresponds to strain rate 0.1 and 1.0 s^{-1}. The samples after deformation were water cooled by direct introduction of liquid to the heating chamber of furnace. From the recorded data was determined the true strain (ε) as a function of rpm of sample during torsion [5,6]:

$$\varepsilon = \frac{2}{\sqrt{3}} \times \operatorname{arcsinh}\left(\frac{\pi \bar{R} N}{L}\right) \tag{1}$$

where: $\bar{R}$ – equivalent radius corresponding to 2/3 outer radius of R sample,
L – measured length of sample, N – rpm of sample.

The flow stress (σ_p) was defined by relation (2) considering the torque (M), sample radius (R), parameters (m, p) and axial force (F) [5,6]:

$$\sigma_p = \left[\left(\frac{\sqrt{3} \cdot M}{2\pi R^3}\right)^2 \times (3 + p + m)^2 + \left(\frac{F}{\pi R^2}\right)\right]^{0,5} \tag{2}$$

where: p – parameter defining the stress sensitivity to strain volume,
m – parameter defining the stress sensitivity to strain rate.

Relationships between the flow stress and deformation of alloy and the conditions of deformation are described by a Zener-Hollomon (Z) parameter [5,6]:

$$Z = \dot{\varepsilon} \cdot \exp\left(\frac{Q}{RT}\right) = A \cdot \left[\sinh\left(\alpha \sigma_{p\,max}\right)\right]^n \tag{3}$$

where: $\dot{\varepsilon}$ – strain rate, Q – activation energy for hot working,
R – molar gas constant, T – temperature,
σ_{pmax} – peak stress,
A, α, n – constants depending on grade of material.

Activation energy for hot working (Q) was defined according to procedure given in the work by Schindler and Boruta [6]. The algorithm of solution comprised transformation of equation (3) to the form:

$$\dot{\varepsilon} = A \cdot \exp\left(\frac{-Q}{RT}\right)\left[\sinh\left(\alpha\sigma_{p\,max}\right)\right]^n \qquad (4)$$

Further proceedings comprised a solution of equation (4) by graphical method with application of regression analysis.

The structure of alloy after hot torsion was analysed on microsections perpendicular and parallel to plastometric sample axis. Examinations of alloy substructure were conducted with use of thin foils technique at transmission electron microscope.

3. Experimental results and discussion

After preliminary soaking at 1100°C / 2h the microstructure of the examined alloy is characterized by austenite grains of mean size $\bar{A} = 1813\mu m^2$ and occurrence of insignificant minor of undissolved precipitations (Fig. 1a). Increase of preliminary soaking temperature of alloy to 1150°C / 2h is causing a distinct growth of austenite grains ($\bar{A}=3242\mu m^2$) and dissolution of a certain proportion of existing precipitations (Fig.1b). In the phase composition of extracted precipitations was revealed appearance of titanium compounds, i.e. the carbide (TiC), nitride (TiN), carbosulfide ($Ti_4C_2S_2$) and Laves phase (Fe_2Ti).

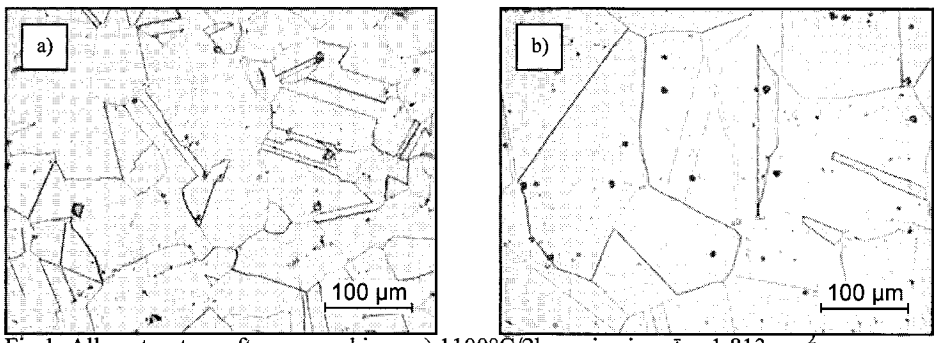


Fig.1. Alloy structure after pre-soaking: a) 1100°C/2h: grain size $\bar{A} = 1.813\ \mu m^2$, b) 1150°C/2h: grain size $\bar{A} = 3.242\ \mu m^2$. Magn. 150×.

Results of plastometric examinations in form of calculated torsion curves of alloy, after pre-soaking in two variants are presented in fig. 2÷5. The deformation curves obtained for pre-soaking variant 1100°C/2h and a torsion rate $0.1s^{-1}$ are showing the form being characteristic for material where are taking place the processes of recovery and dynamic recrystallization (fig. 2). At some flow curves were observed effects of cyclic dynamic recrystallization. High values of strain were obtained for alloy in a wide range of torsion temperatures, i.e. 950 ÷ 1100°C. An increase of torsion rate to $1.0s^{-1}$ is raising considerably the values of flow stress and decreases distinctly the formability of alloy at all tested temperatures (fig. 3). This phenomena could be explained by higher rate of alloy hardening and too slow removal of hardening due to recovery and dynamic recrystallization.

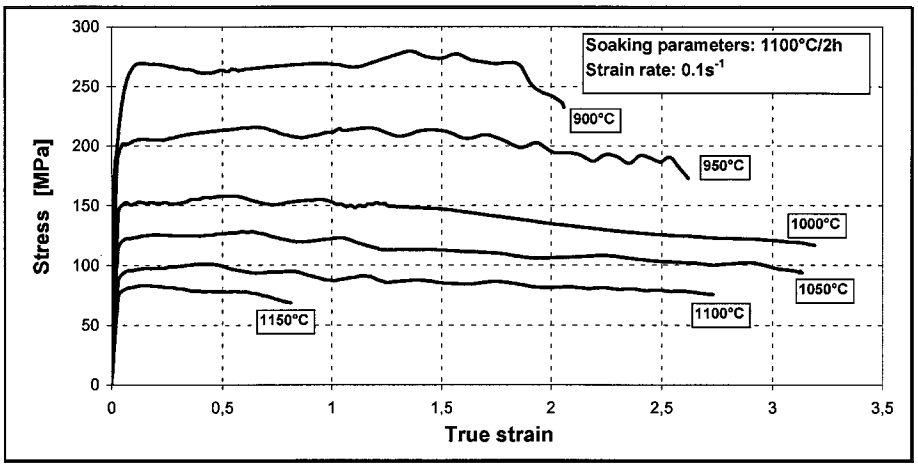


Fig. 2. Influence of deformation temperature on the form of flow curves after pre-soaking at 1100°C/2h. Strain rate: $0.1s^{-1}$.

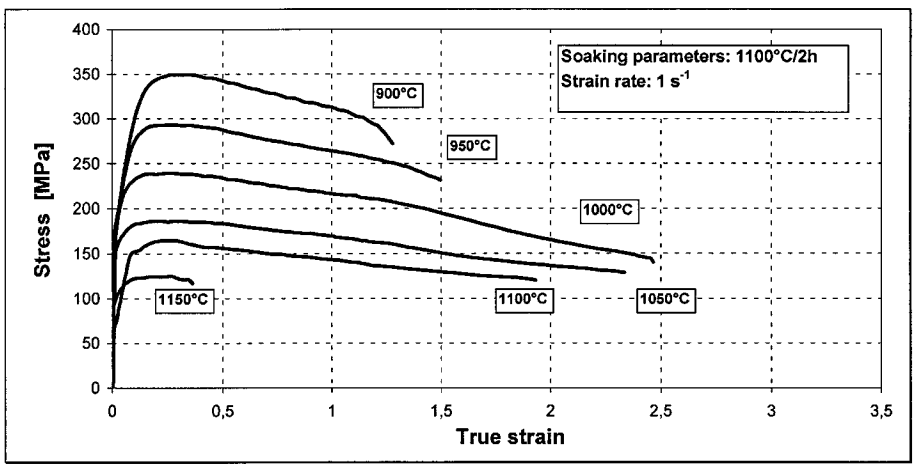


Fig. 3. Influence of deformation temperature on the form of flow curves after pre-soaking at 1100°C/2h. Strain rate: $1.0s^{-1}$.

The raising of pre-soaking temperature to 1150°C/2h is results in a reduction of the formability of alloy for both torsion speeds, at the low and the high deformation temperatures do well (fig. 4, 5). In this case there were obtained comparable high values of strain for the alloy in a narrow range of torsion temperatures, i.e. 1000 ÷ 1050°C. Such behaviour of alloy could be explained by a greater growth of austenite grains at this soaking temperature before the deformation, and respectively lower rates of recovery and dynamic recrystallization during deformation.

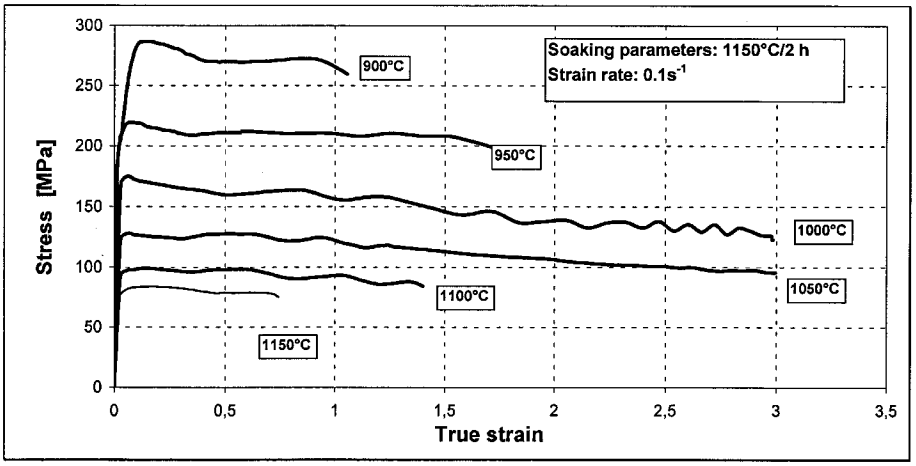


Fig. 4. Influence of deformation temperature on form of alloy flow curves after pre-soaking at 1150°C/2h. Strain rate: $0.1s^{-1}$.

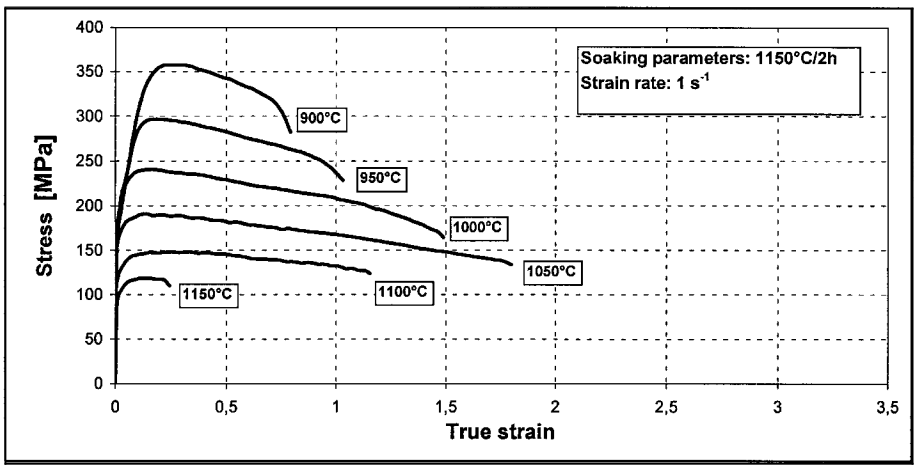


Fig. 5. Influence of deformation temperature on form of alloy flow curves after pre-soaking at 1150°C/2h. Strain rate: $1.0s^{-1}$.

Relationships between the peak stress ($\sigma_{p\,max}$) and Zener-Hollomon parameter (Z) are presented in fig. 6. For both variants of pre-soaking was obtained a power relation with of correlation coefficient $R^2=0.92 \div 0.93$ of peak stress in function of Z parameter. The defined relationships had the form of power function:

- for alloy after pre-soaking at 1100°C/2h: $\sigma_{p\,max} = 0.52 \times Z^{0.13}$ (5)
- for alloy after pre-soaking at 1150°C/2h: $\sigma_{p\,max} = 0.37 \times Z^{0.12}$ (6)

The higher values of Z parameter for the alloy after pre-soaking at 1150°C/2h are resulting from higher values of activation energy for hot working. For the alloy after pre-soaking

1100°C/2h, the estimated activation energy is Q = 483 kJ/mole. In case of deformation of alloy after pre-soaking at 1150°C/2h the activation energy was higher and its value determined to Q= 563 kJ/mole.

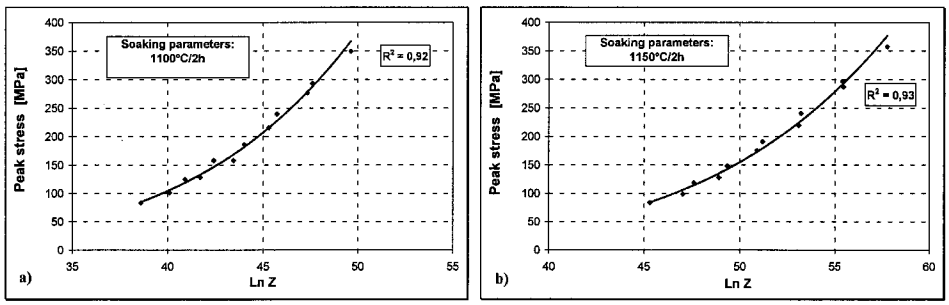


Fig. 6. Relation between maximum flow stress of alloy and Zener-Hollomon parameter: a) pre-soaking: 1100°C/2h, b) pre-soaking: 1150°C/2h.

Results of microstructure examinations of the alloy strained to failure for two variants of pre-soaking, for selected temperatures and both torsion speeds are presented in fig. 7, 8.

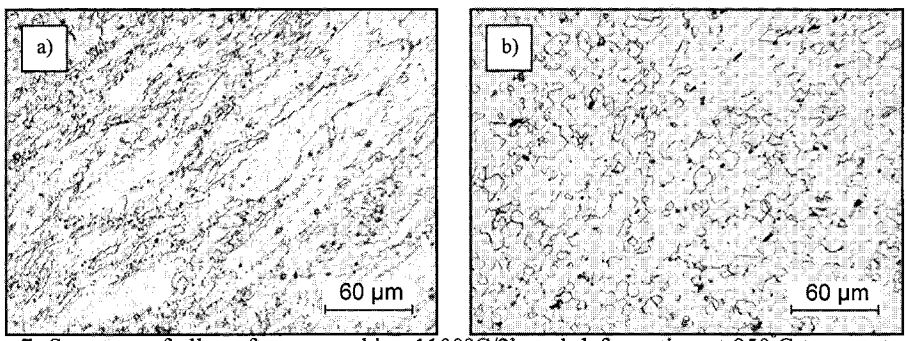


Fig. 7. Structure of alloy after pre-soaking 1100°C/2h and deformation at 950 C temperature with the rate: a) $0.1s^{-1}$, b) $1.0s^{-1}$. Magn. 250×.

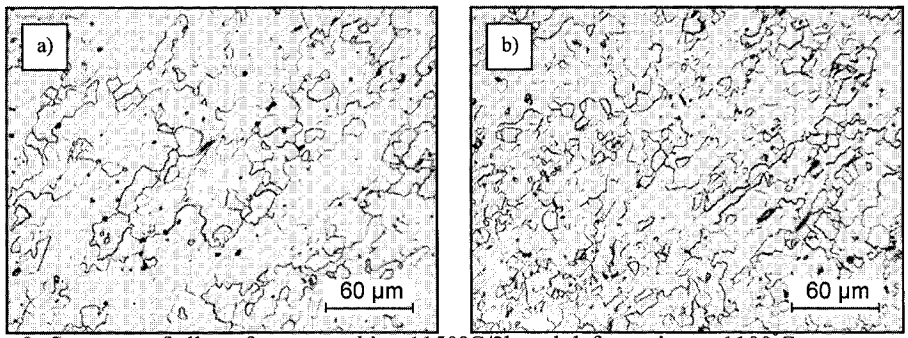


Fig. 8. Structure of alloy after pre-soaking 1150°C/2h and deformation at 1100 C temperature with the rate: a) $0.1s^{-1}$, b) $1.0s^{-1}$. Magn. 250×.

The microscope observations showed that in case of samples strained at the rate of $0.1s^{-1}$ and deformation temperatures up to 950°C, the dominating process of structure rebuilding is the dynamic recovery (fig. 7a). Increase of strain rate to $1.0s^{-1}$ initiates intensification of the recovery processes and dynamic recrystallization, and the first recrystallized subgrains started to appear in the structure in 950°C temperature (fig. 7b). At higher temperatures of deformation in the structure of alloy was observed a dominating participation of recrystallized grains for both strain rates, what is the proof of developing dynamic recrystallization (fig. 8).

The structural examinations at transmission electron microscope showed that the substructure of tested alloy deformed at 1000°C temperature for both variants of pre-soaking is composed mainly of recrystallized austenite subgrains (fig. 9, 10). In alloy structure after pre-soaking 1100°C/2h and strain rate $0.1s^{-1}$ discovered dominating share of fine subgrains and micro-twins of recrystallized austenite (fig. 9a). During twisting with a higher rate ($1.0s^{-1}$) in the alloy structure are observed a dynamic polygonized austenite subgrains and dynamic recrystallized fine austenite subgrains (fig. 9b).

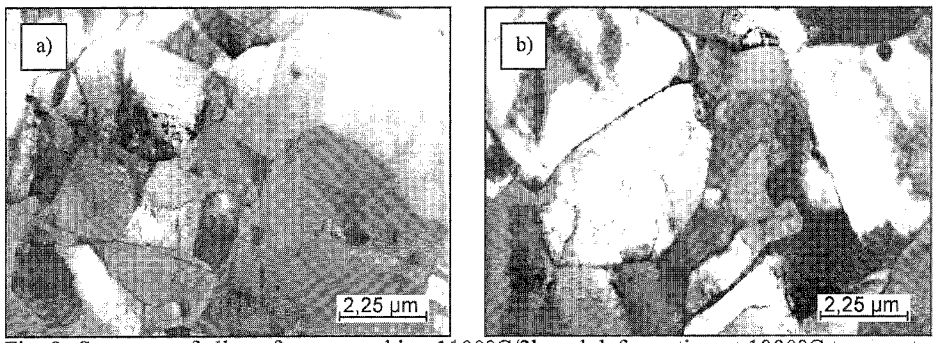


Fig. 9. Structure of alloy after pre-soaking 1100°C/2h and deformation at 1000°C temperature with the rate: a) $0.1s^{-1}$, b) $1.0s^{-1}$. Magn. 6.700×.

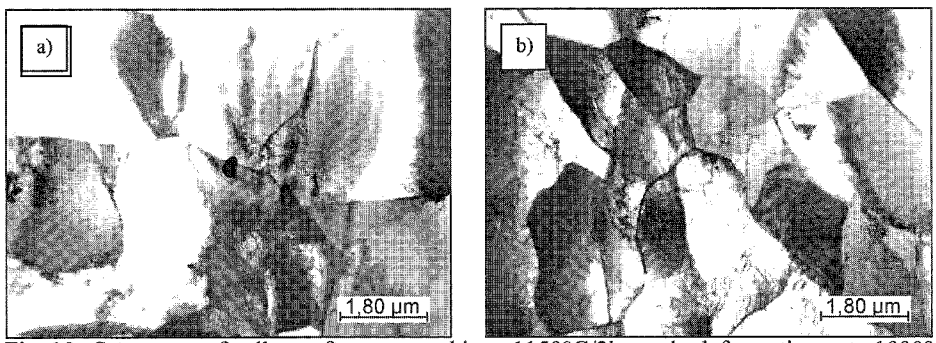


Fig. 10. Structure of alloy after pre-soaking 1150°C/2h and deformation at 1000°C temperature with the rate: a) $0.1s^{-1}$, b) $1.0s^{-1}$. Magn. 8.300×.

After pre-soaking 1150°C/2h and deformation at 1000°C temperature with the rate $0.1s^{-1}$ in the structure of alloy are predominating the subgrains of dynamic recrystallized austenite with subgrains after dynamic recovery (fig. 10a). An increase of torsion speed to $1.0s^{-1}$ is causing refinement of austenite structure composed of dynamic polygonized and dynamic recrystallized subgrains (fig. 10b).

4. Conclusions

1. The tested alloy type A-286 characterizing by high values of flow stress in high temperatures and could cause some difficulties during hot working. The character of stress-strain curves and characteristics of deformability of alloy during hot working depend considerably on the temperature of pre-soaking and deformation speed.
2. The optimum values of the flow stress and strain limit were obtained for the alloy after pre-soaking at 1100°C/2h and strain rate $0.1s^{-1}$. Application of higher pre-soaking temperatures and greater strain rates is not recommended because of the grow of austenite grain, difficulties in processes of dynamic recrystallization and recovery, and reduction of alloy deformability.
3. A pre-soaked (1100°C/2h) alloy is recommended to be hot worked in the range of temperatures 1050÷950°C. At temperatures of forming below 950°C one can account for high resistance to deformation and increased tendency of alloy to cracking. Application of too high temperatures of deformation, i.e. over 1100°C is disadvantageous because of the grow of austenite grain and reduction of useful properties of alloy.
4. The tested alloy is showing a high activation energy for hot working, while its value depends on pre-soaking conditions. For an alloy pre-soaked at 1100°C/2h the estimated activation energy in the range of applied deformation temperatures (900÷1150°C) amounted to Q = 483 kJ/mole. In case of deformation of alloy after soaking at 1150°C/2h the activation energy was higher and amounted to Q =563 kJ/mole.
5. In samples of alloy strained to failure in temperatures below 950°C were revealed the structures of partially recrystallized austenite of "necklace" type. At higher deformation temperatures in alloy structure are predominating recrystallized subgrains and micro-twins of austenite of diversified size.

5. Acknowledgements

This work was sponsored by the Committee of Scientific Research of Poland under the Contract No. 7 T08A 038 18.

6. References

[1] L.X. Zhou, T.N. Baker : Effects of strain rate and temperature on deformation behaviour of IN718 during high temperature deformation, Materials Science and Engineering, A 177, 1994, pp.1÷9.

[2] M. Kohno, T. Yamada, A. Susuki, S. Ohta : Heavy disk of heat resistant alloy for gas turbine, Internationale Schmiedetagung 1981, Dusseldorf, 1981, pp. 4.1.1÷4.1.22.

[3] K.J. Ducki, M. Hetmańczyk, D. Kuc, K. Rodak: Inspections of deformability and structure of Fe-Ni austenitic alloy precipitation hardened by intermetallic phases, Proc. of the Int. Conf.: FORMING'2001, Stara Lesna (Slovakia), 2001, pp.35÷43.

[4] S.M. Zhu, F.G. Wang, S.J. Zhu : Grain size dependence of creep crack growth in Ni-Cr austenitic steels, Mater. Trans. JIM, vol.34, No.5, 1993, pp.450÷454.

[5] I. Schindler, E. Hadasik : Description of deformation behaviour as a base of metal forming processes design, Int. Conf. Pap.: Challanges to Civil and Mechanical Engineering in 2000 and beyond. CCME'97, Wrocław, vol.II, pp.397÷406.

[6] I. Schindler, J. Boruta: Utilization Potentialities of the Torsion Plastometer, Department of Metal Forming, Silesian University of Technology, Katowice, 1998.

MODELLING THE CREEP BEHAVIOUR OF A WROUGHT NICKEL BASE SUPERALLOY IN A WIDE RANGE OF STRESS/TEMPERATURE CONDITIONS

M. Maldini and V. Lupinc

CNR – IENI
Via Cozzi 53, 20125 Milano, Italy

Abstract

The creep curves of Nimonic 263 alloy are dominated by primary or tertiary stage respectively in the high stress/low temperature and in the low stress/high temperature field. The evolution of mobile dislocation density, rather than changes in dislocation velocity, seems to control the shape of the creep curves. A steady state creep is reached only at high temperature when fracture occurs after large creep strain.

Keywords: creep, nickel superalloys, high temperature, modelling

1. Introduction

The aim of the present paper is to model the creep behaviour of the γ' reinforced nickel base superalloy Nimonic 263, a polycrystalline material used for combustion chambers of aeroengines. As different regions of such components can experience very different stress/temperature conditions, the establishment of constitutive equations capable of describing material creep behaviour in a wide stress/temperature field is of primary interest.
The creep curves of γ' reinforced nickel base superalloys do not usually exhibit the three stages of creep that typically occur in pure metals and many simple alloys, in which most of the creep curve is due to a steady state characterised by constant creep rate. In opposition, in γ' reinforced nickel base superalloys, particularly at high temperatures/low stresses, the creep curve is often dominated by an extensive accelerating creep rate that is not necessarily associated with the development of cavitation and cracking. The primary creep is generally small and short, but its contribution to the overall strain increases strongly at high stress/low temperature. In this work we have analysed and modelled the creep curves until fracture mechanisms become operative and modify the creep strain rate.

2. Material and experimental procedure

The nominal chemical composition of the alloy studied in this work, Nimonic 263, is given in Table 1. The γ' solvus temperature is around 920°C. The heat treatment sequence was 2 h/1150°C + water quenching + 8 h/800°C + air-cooling, resulting in 0.1 mm average grain size, a volume fraction of the reinforcing phase γ' of 20% and an average γ' spheroid particle size ~ 20 nm. Constant load creep tests were run on cylindrical specimens in the stress/temperature field 750-36MPa/600-950°C producing rupture times in the 10 - 1250 h range. The creep specimens had 5.6 mm gauge diameter and 28 mm gauge length. Creep strain was continuously monitored using capacitive transducers connected to extensometers clamped to the specimen ledges which delimit the gauge length. Three thermocouples were

Table 1 - Nominal chemical composition (wt. %) of Nimonic 263

Ni	Co	Cr	Mo	Ti	Fe	Mn	Al	Si	C
Bal.	20	20	5.8	2.1	0.7	0.6	0.45	0.4	0.06

Table 2 – Nimonic 263 bar creep test parameters

Temp. (°C)	Nominal Stress (MPa)	True Stress after Initial Inelastic Strain (MPa)	Time to Rupture (h)	Total Strain to Rupture, ε_r (%)	Initial Inelastic Strain, ε_{pr} (%)	Creep Strain to Rupture, ε_r-ε_{pr} (%)
600	750	878	11.4	22.8	17.06	5.7
	700	761	56.4	11.6	8.75	2.8
	680	730	122.6	10.7	7.40	3.3
	650	681	281	10.7	4.75	5.9
	610	628	1012.9	5.9	2.93	3.0
700	600	606	8.1	5.6	1.02	4.6
	545	547	27.1	3.8	0.35	3.4
	480	480	74.0	2.4	≈0.04	2.4
	440	440	230.6	3.1	≈0.02	3.1
	380	380	594.3	2.6	0	2.6
	380	380	437.7	2.2	0	2.2
800	330	330	10.4	9.3	0	9.3
	280	280	24.1	5.8	0	5.8
	225	225	94.0	4.5	0	4.5
	180	180	270.8	3.6	0	3.6
	135	135	902.3	3.4	0	3.4
900	120	120	13.5	26.4	0	26.4
	100	100	31.4	29	0	29
	80	80	119.6	19	0	19
	70	70	254.7	19	0	19
	55	55	1254.1	13	0	13
950	80	80	3.5	100	0	100
	70	70	11.0	84	0	84
	55	55	26.5	85	0	85
	50	50	77.5	60	0	60
	45	45	165.7	43	0	43
	36	36	492.9	40	0	40
	30.5	30.5	1236.5	23	0	23

placed along the gauge length allowing to manually control the longitudinal temperature gradients and the furnace power was automatically controlled by the central thermocouple.

3. Analysis of the constant load creep tests

The performed creep tests are summarised in Table 2. The shape of the creep curves reported in Figs. 1-2 shows a strong dependence on the applied stress/temperature and is outlined in the following points.

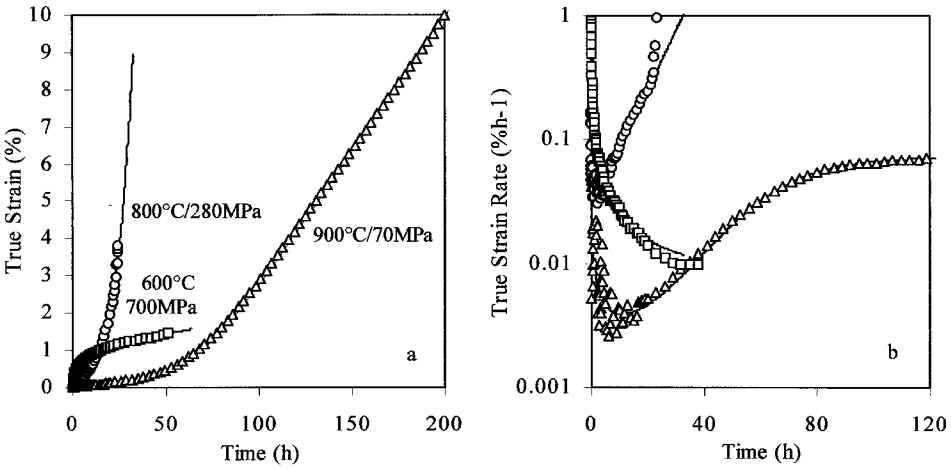


Fig. 1 Creep curve shape comparison of a selection of creep curves at different temperatures. At the highest applied stress the creep curve is characterised by a large primary creep. At lower applied stresses the creep curves are dominated by the tertiary creep. The creep curves are interpolated through Eqs. 7. The creep curves of Fig. 1a are reported in Fig. 1b as Log(strain rate) vs. time.

- At 600°C during the initial loading, an instantaneous plastic strain that increases with the applied stress, occurs. The creep curve is characterised by a long and large primary creep stage. The creep strain due to the primary stage, ε_p, is always larger than the elastic strain obtained during the initial loading, i.e. $\varepsilon_p > \sigma/E$. Only for the lowest stress (610 MPa) the size of the primary stage is comparable to the initial elastic strain. The long primary creep is interrupted by the fracture, before a secondary and tertiary stage appear.
- At 700 and 800°C, during the initial loading no instantaneous plastic deformation occurs with the exception of the tests at the highest applied stresses at 700°C (Table 2). The primary creep strain generally results smaller than σ/E and is less significant if compared to the tests at 600°C. Decreasing the applied stress, the primary creep loses importance and concurrently the importance of the tertiary creep stage increases becoming dominant in all the tests performed at 800°C and at low stress at 700°C. The tertiary creep can be interpolated with a straight line in a plot strain rate vs. strain and, consequently, in a plot log(strain rate) vs. time. The observed rupture creep strains are respectively comparable and lower to the values obtained in the tests at 600°C and 900-950°C.
- In the 900-950°C temperature range the primary creep is negligible. During tertiary creep, different regimes of accumulation of strain can be detected. In particular, at the lowest applied stresses, the tertiary creep is characterised by an initial rapid accelerating stage followed by a long steady state (Figs. 1). A further accelerating stage leads then to fracture (Fig. 2) through necking and loss of section.

4. Creep strain constitutive model

The creep strain rate is proportional to the density of the mobile dislocations, ρ, and their average velocity, v, according to the Orowan equation:

$$\dot{\varepsilon} = b\rho v \qquad (1)$$

where b is the Burgers vector.
Before the fracture mechanisms, like cavitation and necking, become operative, the creep curve shape depends on the evolution of the parameters ρ and v.

Evolution of the mobile dislocations during a creep test
According to Gilman [1] the kinetics of the development of mobile dislocation density can be described by the following differential equation:

$$\dot{\rho} = \delta v\rho - h\rho^2 \qquad (2)$$

where δ and h are parameters and v represents the average velocity of the mobile dislocations.
In Eq. 2, the density of the mobile dislocations evolves from an initial value ρ°, at the beginning of the test, to an equilibrium value $\rho_{SS} = \delta v/h$ when $\dot{\rho} = 0$.
Eq. 2 can describe two different transient regimes depending on the initial value of the dislocation density, ρ°: i) $\rho^\circ > \delta v/h$ and ii) $\rho^\circ < \delta v/h$.
The first case applies to the test results at 600°C, i.e. at low temperatures/high stresses, when a large instantaneous plastic strain is accumulated, and a large quantity of dislocations are injected in the material, during the initial loading. In this transient regime the rate at which the dislocations are immobilised is higher than the rate at which the dislocations are multiplied and the mobile dislocation density and the strain rate, decrease toward a steady state, i.e. $\dot{\rho} < 0$ and $\rho^\circ > \rho_{SS}$. Li has used Eq. 2 to describe the primary creep of stainless steels [2].
In the tests at high temperatures/low stresses, the initial density of dislocations ρ° is low and the second regime, i.e. $\rho^\circ < \delta v/h$, fits the experimental data. The mobile dislocation density and, in turn, the strain rate increase approaching a steady state, i.e. $\dot{\rho} > 0$ and $\rho^\circ < \rho_{SS}$. In both cases, the number of mobile dislocations tends to reach a constant value producing a steady state creep, $\dot{\varepsilon}_{SS}$, in creep tests at 900-950°C, since fracture does not intervene early. In both situations, in the long time limit, and if fracture mechanisms do not modify the strain rate, the density of mobile dislocations reaches a steady state and the specimen deforms at a constant rate. Supposing that the average dislocation velocity is constant, Eq. 2 can be integrated using Eq.1, to give the following expression for the strain rate $\dot{\varepsilon}$ as a function of time:

$$\dot{\varepsilon} = \dot{\varepsilon}_{ss}\left(1 - \frac{\rho^\circ - \rho_{ss}}{\rho^\circ}\exp(-\delta v t)\right)^{-1} \qquad (3)$$

Evolution of the dislocation velocity during a creep test
The dislocation velocity is driven by an effective stress, i.e. the applied stress reduced by an internal stress σ_{back} and the average dislocation velocity can be represented by the following expression:

$$v = v^\circ \sinh(\beta\sigma_{eff}) \qquad (4)$$

with v° and β constants and $\sigma_{eff} = \sigma - \sigma_{back}$. The internal stress evolution strongly depends on plastic strain accumulated during the initial loading.

Tests at high stress/low temperature
In tests at high stress/low temperature, when creep curve is dominated by primary creep, the internal stress builds up mainly before the beginning of the creep test, during the instantaneous plastic strain accumulated at the initial loading. Using Li's model [2], we assume constant dislocation velocity during the whole creep test. In this case the strain rate reduction is proportional to dislocation density reduction.

Tests at low stresses/high temperatures
In the tests at low stresses/high temperatures, when the creep curves are dominated by the tertiary creep stage, no inelastic strain is accumulated during the initial loading. As creep starts, the internal stress builds up causing a reduction of mobile dislocation velocity and producing strain deceleration during the small primary creep. In these tests the small size of the primary creep ($\varepsilon_p < \sigma/E$) suggests that the internal stress is due to a redistribution of stresses between different creep resistance regions of the material [3], such as, for instance, between grains with different Schmidt factor of the dominant gliding planes. At the end of the primary creep the redistribution of the stress can be considered completed and both the internal stress and the dislocation velocity almost constant, particularly when during tertiary creep no long-range stresses are built up due to, for instance, subgrain development.

The evolution of the internal stress can be described using the following equation due to Dyson [3]:

$$\dot{\sigma}_{back} = H\dot{\varepsilon}(1 - \frac{\sigma_{back}}{\sigma^*_{back}}) \qquad (5)$$

where H is a hardening coefficient, and σ^*_{back} the saturated value of the internal stress.
It is evident, from Eq. 1, that the mean dislocation velocity plays a primary role to determine the strain rate and then the time to rupture in a creep test. However it seems to have smaller influence than the dislocation density on affecting the shape of the creep curve. In fact, it explains the existence of the small primary creep in tests characterised by a dominant tertiary creep caused by a continuous dislocation density increase.

5. General constitutive equations

Accumulation of creep strain through evolution of ρ and v can be described combining the Eqs. (1-3 and 5) in the following set of equations:

$$\begin{cases} \dot{\varepsilon} = b\rho v = A\rho \sinh(\beta\sigma_{eff}) \\ \dot{\sigma}_{back} = H\dot{\varepsilon}(1 - \frac{\sigma_{back}}{\sigma^*_{back}}) \\ \dot{\rho} = \delta v\rho - h\rho^2 \end{cases} \qquad (6)$$

density of dislocations and their velocity can not be easily quantified. From an engineering point of view, it is better to describe the creep curves as proposed by Kachanov, i.e. in terms of parameters having value = 0 at the beginning of the test and approaching a constant value at the end of the test.

According to this approach, two parameters can be defined as follows:

$$w = 1 - \frac{\rho^\circ}{\rho} \qquad \text{and} \qquad S = \frac{\sigma_{back}}{\sigma},$$

and the Eqs. 6 result in:

$$\begin{cases} \dot{\varepsilon} = A \dfrac{\rho^\circ}{(1-w)} \sinh(\beta\sigma(1-S)) \\ \dot{S} = \dfrac{H}{\sigma}\dot{\varepsilon}(1 - \dfrac{S}{S^*}) - \dfrac{S}{\sigma}\dot{\sigma} \\ \dot{w} = \delta v (w^* - w) \end{cases} \tag{7}$$

with parameters A, H, δv, ρ°, S* and w* depending on stress and temperature. Parameter ρ° represents the dislocation density at the beginning of the creep test, while $S^* = \sigma_{back}/\sigma^*_{back}$ and $w^* = \rho^\circ/\rho_{SS}$ represent the saturated (asymptotic) values of the parameters S and w, respectively. Dyson and McLean [4] have developed a set of equations similar to our Eqs. 6, but without the recovery term $h\rho^2$.

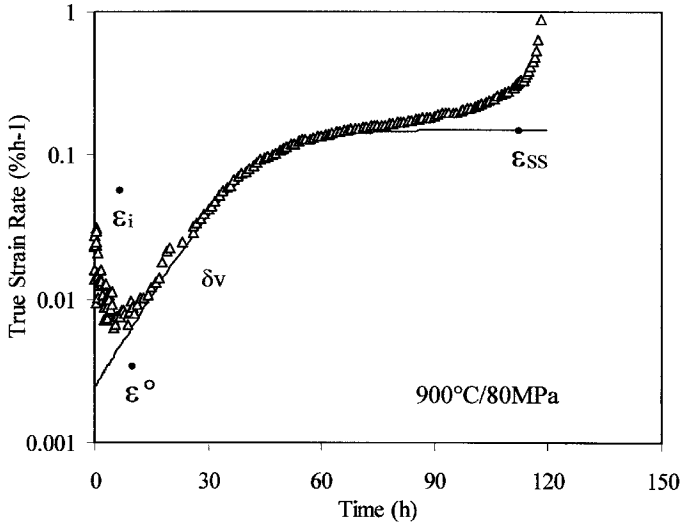


Fig. 2 Interpolation of a tertiary curve through Eq. 3. Graphic interpretation of the parameters $\dot{\varepsilon}_i$, $\dot{\varepsilon}^\circ$, $\dot{\varepsilon}_{ss}$. Parameter δv controls the acceleration during the first tertiary creep. The strain deceleration during primary creep is controlled by parameter H which is not graphically interpolated here.

Equations 7 represent the *general* constitutive equation set capable of describing the different creep behaviours that occur in Nimonic 263 alloy in the explored stress/temperature field. Under particular creep test conditions Eqs. 7 can be simplified. For instance, the second equation of the set can be neglected to interpolate creep curves characterised by large primary creep and absence of the tertiary stage, as in the tests performed at 600°C. Furthermore the value of the parameter w* is reduced to unity, w* = 1, to describe the creep curves obtained at 700 and 800°C where tertiary strain rate increases linearly with strain.

6. Application of the constitutive equations to analyse Nimonic 263 creep curves.

In an engineering context, it is important that the model parameters of the constitutive equations can be related in a simple manner to macroscopically measurable quantities. In Fig. 2 a creep curve composed of all the various stages found in our tests is reported in a plot $\log \dot{\varepsilon}$ vs. time. Four parameters can be easily measured from the creep curves, that allow reconstructing the shape of the curve with significant precision. They are listed below:

$\dot{\varepsilon}_i = A\rho^{\circ}\sinh(\beta\sigma)$	initial strain rate
$\dot{\varepsilon}^{\circ} = A\rho^{\circ}\sinh(\beta\sigma(1-S^*))$	initial strain rate extrapolated from tertiary creep
δv	parameter controlling the acceleration during tertiary creep
$\dot{\varepsilon}_{SS}$	steady state strain rate appearing when tertiary creep saturates

Parameter $\dot{\varepsilon}^{\circ}$ represents the creep strain rate due to dislocation density ρ° and dislocation velocity $v = v^{\circ}\sinh(\beta(\sigma-\sigma^*_{back}))$. It represents the initial strain rate of creep curves in the case of tests starting with an instantaneous plastic strain during loading (as shown in Fig. 3) or it represents the extrapolated creep strain rate at the beginning of the tests from the tertiary creep data, as shown in Fig. 2. Parameter $\dot{\varepsilon}_i$ represents the initial strain rate in the tests at high temperature/low stress. Parameter δv can easily be obtained interpolating the plot of Fig. 2 through Eq. 3. Another parameter is needed to determine the kinetics of creep deceleration during primary creep in high temperature/low stress tests. Since the creep curves display very little primary creep at these test conditions, it is inevitable that all the relevant parameters related to the primary are subject to large uncertainties. This is the reason why a constant value of the parameter H of Eqs. 4-6 is used, independent of the test conditions.

Figures 3-5 show a comparison between a selection of experimental ε vs. time and $\log\dot{\varepsilon}$ vs. time creep curves and the interpolation through the proposed equations. The good match between the experimental data and the fit obtained through Eqs. 7 show that the same set of equations can be used to describe the different shapes of the creep curves.

In order to predict the creep behaviour under other temperature/stress combinations, within the range value examined, it is necessary to have a description of the stress and temperature dependence of the model parameters, which is the subject of a work in progress. It seems to be a quite demanding task particularly in the 900-950°C temperature range, where the γ' phase dissolves (solvus temperature ~ 920°C), causing a strong decrease of the material creep resistance.

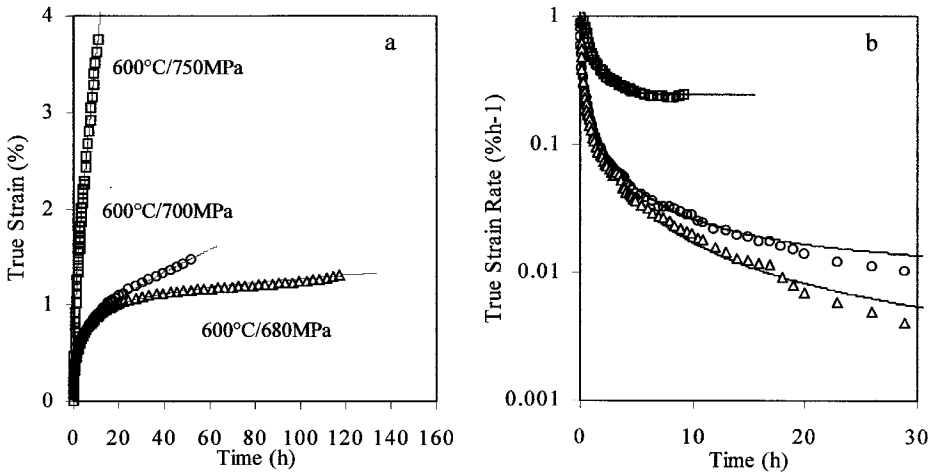


Fig. 3 a) Strain vs. time and b) log(strain rate) vs. time plots of a selection of creep tests at 600°C. The curves are fitted through Eqs. 7.

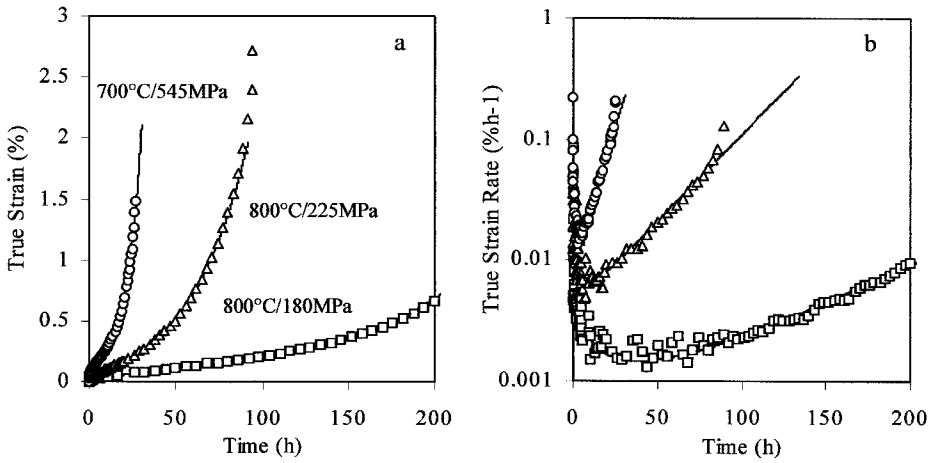


Fig. 4 a) Strain vs. time and b) log(strain rate) vs. time plots of a selection of creep tests at 700-800°C. The curves are fitted through Eqs. 7.

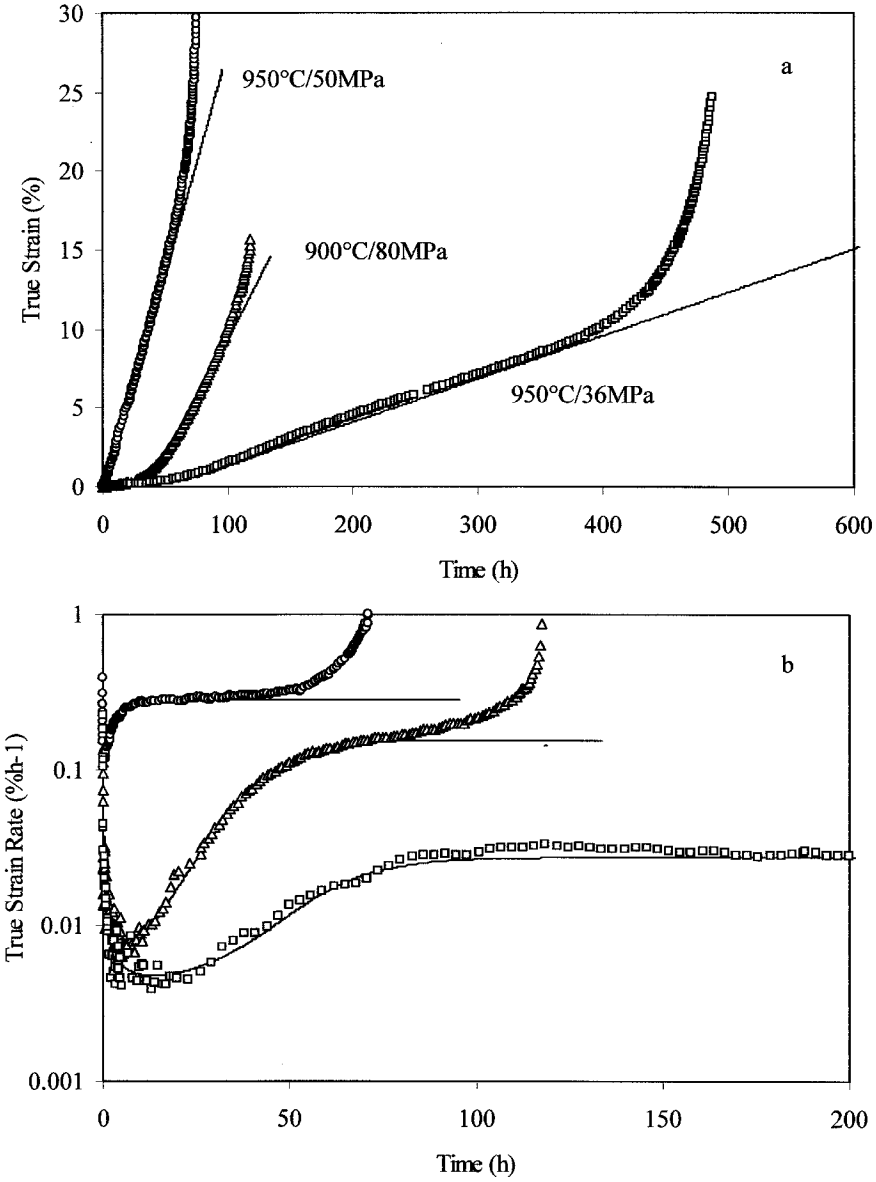


Fig. 5 Strain vs. time and log(strain rate) vs. time plots of a selection of creep tests at 900-950°C. The curves are fitted through Eqs. 7.

7. Conclusions

The examined creep curves of Nimonic 263 alloyare dominated by primary creep stage in the tests run at applied stress > 600 MPa, since large instantaneous plastic strain is accumulated during the initial loading. At stresses <600 MPa, generally below the yield stress, the creep curves consist mainly of tertiary creep.

In the tests run in the 700-950°C temperature range, the minimum creep rate, appearing after the primary creep, must not be confused with steady state. The steady state stage appears only in tests run at 900-950°C after large deformation in tertiary creep.

In the tests at 700-800°C, early fracture mechanisms interrupt the creep curve before the steady state is reached. At these temperatures the tertiary creep exhibits a linear relationship between strain rate and strain.

The proposed constitutive equation based on the evolution of mobile dislocation density and their velocity, has been shown to be capable of describing the creep curves in the wide explored stress/temperature field.

Acknowledgements

This work has been performed within the Brite Eu-Ram III CPLIFE project BRPR-4034 (1997-2001) partly supported by EC Brussels. The project partners are: Rolls Royce UK (co-ordinator), Alstom Power S, CNR-IENI I, JRC Petten NL, Fiat Avio I, MTU D, QinetiQ UK, Rolls Royce D, Sener E and Turbomeca F.

References

[1] J.J. Gilman, " Micromechanics of Flow in Solids", McGraw-Hill, New York (1969) p.194.
[2] J.C.M. Li, "A dislocation mechanism of transient creep", Acta Metall., **11** (1963) p.1269.
[3] B.F. Dyson, "Mechanical testing of high-temperature materials: data scatter", Modelling in High Temperature Structural Materials, London, Chapman&Hall, (1996), p.161
[4] B.F. Dyson and M. McLean, "Microstructural Stability of Creep Resistant Alloys for High Temperature Plant Applications", ed. by Strang et al., Institute of Materials, London (1998).

CREEP BEHAVIOUR OF A POWDER METALLURGY UDIMET 720 NICKEL-BASED SUPERALLOY

Sophie Dubiez, Raphaël Couturier, Laure Guétaz, Hélène Burlet

CEA-Grenoble, DTEN-SMP, 38054 Grenoble cedex 9, France

Abstract

Powder metallurgy Udimet 720 is a high strength nickel-based superalloy considered for high temperature turbine disks for nuclear gas cooled reactors. For these applications a material with high creep strength is required. The 650°C and 750°C creep behaviour of a powder metallurgy Udimet 720 was investigated. In order to have similar creep duration at both temperatures, the applied stresses have been in the range of 700-800 MPa at 650°C and of 140-280 MPa at 750°C.

Both fine-grained and coarse-grained microstructures have been obtained by applying respectively a subsolvus or a supersolvus solution treatments, followed by aging treatments. In both microstructures, the distribution of the strengthening γ' precipitates has been characterized by transmission electron microscopy (TEM).

At 650°C, the creep curves of the fine-grained microstructure show a transition directly from primary to tertiary creep with no obvious steady state. On the contrary, the creep curves of the coarse-grained microstructure show the classical three stages.

For both microstructures, the dislocation structures in crept alloy have been analyzed by TEM. Large stacking faults inside γ' precipitates are observed in the fine-grained microstructure whereas the dislocations observed in the coarse-grained microstructure form loops around the γ' precipitates. These observations suggest that the smaller spacing of the γ' precipitates analyzed in the fine-grained microstructure promotes shearing of the precipitates, whereas the larger spacing of the γ' precipitates analyzed in the coarse-grained microstructure promotes an overcoming of the precipitates by an Orowan mechanism. These different deformation mechanisms can explain the different creep behaviours between the two microstructures.

At 750°C, the grain boundary sliding seems to become the predominant deformation mechanism.

Some specimens have also been analysed by scanning electron microscopy (SEM) after creep rupture for damage analysis (fractographic examinations). At 650°C, micro-cracks are observed near the fracture surface, mostly along the grain boundaries and along powder prior particles boundaries. At 750°C damage is by contrast distributed in the bulk of the specimen.

Keywords: Ni-based superalloy, powder metallurgy, Udimet 720, creep, turbine disk.

Introduction

Nickel-based superalloys processed by the powder metallurgy are considered for high temperature gas turbine of nuclear Gas Cooled Reactors (GCR). The components of the primary circuit operate at temperatures up to 850°C in order to reach high efficiencies. The gas turbine is expected to work with uncooled disks and blades during around 60 000 h without significant maintenance. These disks have a diameter reaching 1.5 meters. In accordance with GCR creep specifications, the potential use of Hot Isostatically Pressed (HIPed) superalloys is considered.

According to CEA's selection studies of the most relevant materials and processes for disks, HIPed Udimet[1] 720 is considered as a potential superalloy [1]. Udimet 720 is a high strength

[1] Udimet is a registered trademark of Special Metals Corporation (AFNOR designation is NC17KTDAW).

nickel-based superalloy that was first developed for aeronautical applications. The γ', which is an ordered intermetallic precipitate ($L1_2$) in the γ matrix, constitutes a large volume fraction (about 50 %) of the alloy microstructure. Among the elements in solid solution, the high chromium content (16 % weight) provides a good oxidation resistance. This high strength superalloy is rather difficult to cast and isothermal forging is today limited to small diameter disks. Powder metallurgy processing makes it possible to produce segregation-free parts, with a geometry close to the final shape of the component. The purpose of this paper is to show how HIPed Udimet 720 microstructural parameters (γ-grain size, γ' precipitation size and distribution and prior particle boundaries) influence deformation and damage mechanisms, in order to predict creep lifetime from creep models based on physical parameters.

Experimental methods

Composition and processing of the Udimet 720 LI (U720) superalloy

Starting material is Udimet 720 LI processed by Hot Isostatic Pression (HIP). The composition is given in table 1. The acronym LI standing for Low Interstitial is related to Udimet 720 alloy with low carbon and boron contents. This particular composition prevents the degradation of the mechanical properties of the alloys by limiting the coarse and continuous agglomeration of carbides and borides during aging at high temperature. Powder particles are obtained by atomisation under argon atmosphere. The particles diameters range from 10 µm to 90 µm with an average diameter of about 30 µm. Powder billets used in this study have been HIPed by Tecphy under standard conditions.

Ni	Cr	Co	Ti	Mo	Al	W	Fe	Zr	C	Cu	B	Si	S	Mn	P
Balance	16.2	15.3	5.18	3.06	2.47	1.33	0.06	0.039	0.023	0.02	0.018	0.007	0.003	0.002	0.001

Table 1. Chemical composition (weight %) of the Udimet 720 LI.

Heat treatments

The two heat treatments employed are the usual ones applied to cast and wrought Udimet 720. They are so-called « High Strength » (HS), improved for tensile strength and low cycle fatigue resistance, and « Creep Resistant » (CR), improved for creep strength. HS treatment consists of a 4h solutioning treatment at 1110°C, followed by two precipitation heat treatments for 24h at 650°C and 16h at 760°C. The CR heat treatment consists of a 4h solutioning at 1170°C, then a second 4h solutioning at 1080°C followed by two precipitation heat treatments for 24h at 845°C and 16h at 760°C.

Creep tests

Creep tests have been performed at 650°C and 750°C under air on cylindrical specimens (ϕ 4 mm) after either HS or CR heat treatment. Stress range applied to the specimens was selected to reach fracture between 300 to 5000 h. This corresponds to creep stresses ranging from 650 MPa to 850 MPa at 650°C and from 140 MPa to 280 MPa at 750°C.

Transmission Electron Microscopy (TEM) examinations

For TEM observations, thin foils were mechanically and then electrochemically thinned in a monobutyl ethylene glycol ether solution with 10% perchloric acid, under 18 V tension. To

analyse the dislocation structure in the strained specimens, thin foils were machined out from specimens crept up to 1% strain under 750 MPa at 650°C.

Scanning Electron Microscopy (SEM) observations
Specimens were observed with SEM after creep testing for damage analysis. Longitudinal cross-sections of the gauge length were observed after polishing to 1 µm using standard metallographical techniques, and slight etching of the surface in a 100 ml ethanol, 100 ml HCl, and 5g $CuCl_2$ reagent.

Experimental results

Microstructure
HS and CR heat treatments resulted in two microstructures with different γ-grain size and γ' precipitate distribution and sizes.

The two heat treatments mainly differ by their solutioning temperature. For the U720 HS, subsolvus solutioning does not allow dissolution of primary γ' precipitates. γ-grain growth is therefore restrained. The γ-grain size of U720 HS ranges from 1 to 10 µm.
Supersolvus solutioning of the U720 CR dissolves most of the primary γ' precipitates and γ-grain size ranges from 10 to 30 µm, close to the average powder particle diameter.

Figure 1 shows the distribution of the γ' phase in the two heat treatments. For U720HS, there are three different types of γ' precipitate (figure 1-a) : Primary γ' precipitates formed during HIP treatment, with a 500 nm diameter and secondary and tertiary γ' precipitates which have nucleated during cooling after solutioning treatment and coarsened during ageing (with respective average diameters of 50 nm and 10 nm). For U720CR, there are also two types of γ' precipitate formed during cooling (figure 1-b). The so-called secondary γ' precipitates have a diameter of 500 nm and the tertiary ones a diameter ranging from 30 to 60 nm.

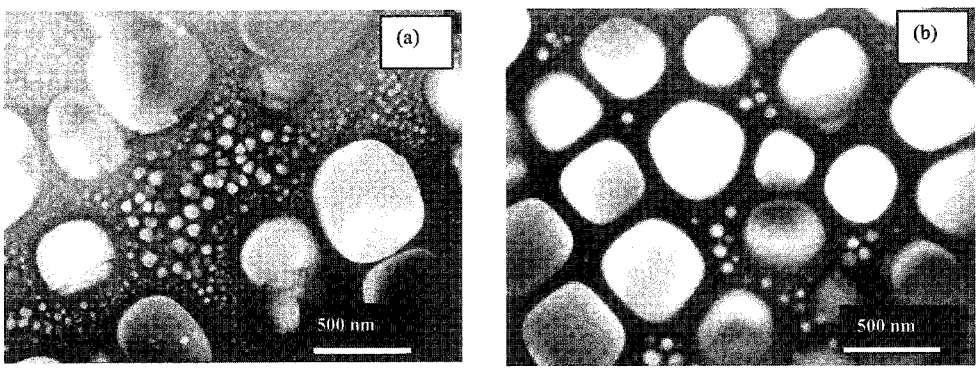


Figure 1. *γ' precipitate distribution in (a) Udimet 720 HS, and in (b) Udimet 720 CR (TEM dark-field micrographs using γ' diffraction spots).*

Creep behaviour

Creep tests performed at 650°C on the U720 HS and CR show different behaviours between the two microstructures (Figure 2). The U720 HS has a specific behaviour without any steady-state creep and an apparent tertiary stage arising early in the creep life. By contrast the U720 CR shows the classical three stages. At 750°C, the difference between the two creep modes is less pronounced. Under the same stresses at 650°C, U720 HS rupture time is greater than U720 CR. After testing at 750°C, U720 CR exhibits the highest creep resistance.

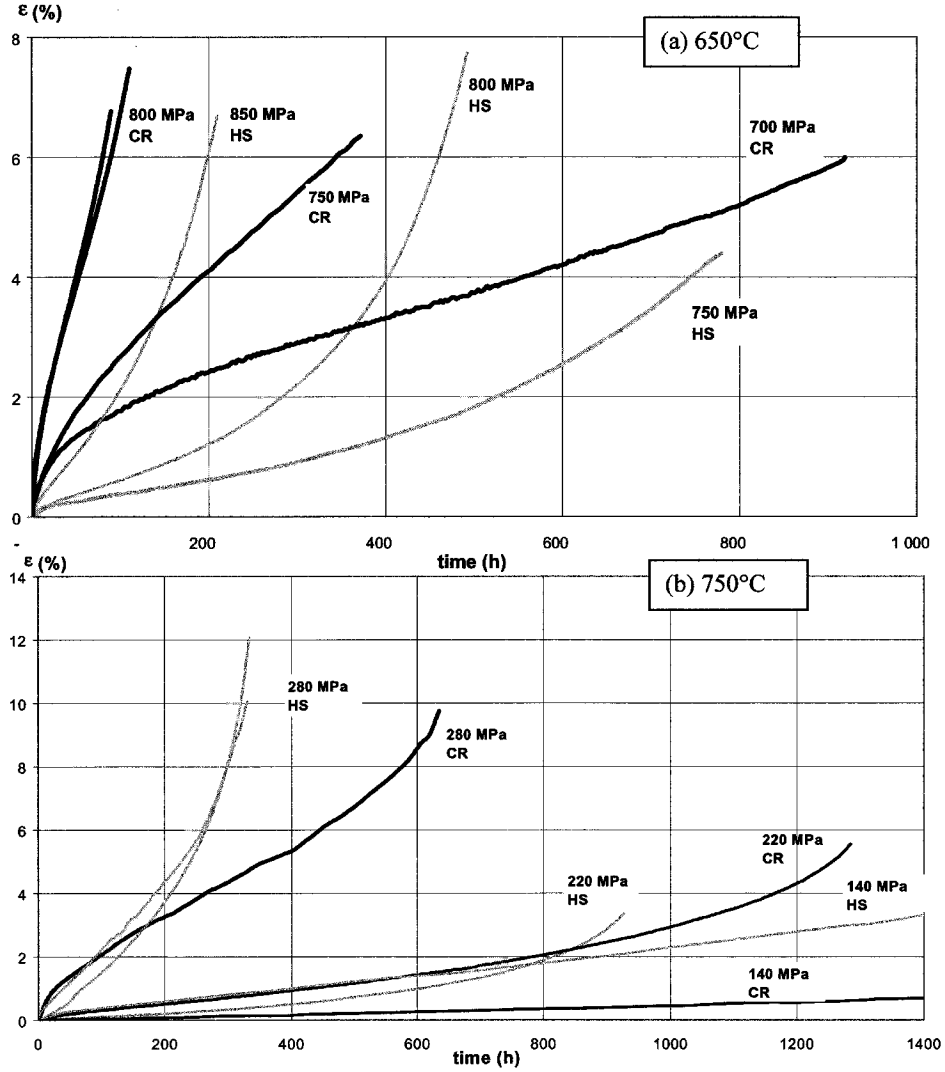


Figure 2. *Creep curves of the Udimet 720 HS and CR (a) at 650°C under 850 MPa, 800 MPa, and 750 MPa stresses and (b) at 750°C under 280 MPa, 220 MPa and 140 MPa stresses.*

The power law creep exponent n ($\dot{\varepsilon} = A\sigma^n$) determined from these tests was calculated by using the minimum creep rate for the U720 HS and by using the steady-state creep rate for the U720 CR. At 650°C, n values are higher than 20 for both U720 HS and CR. These values are usual for superalloys strengthened by a large volume fraction of γ' precipitates. By contrast, at 750°C, n values are much lower : $n \approx 4$ for U720 CR and n close to 1 for the U720 HS.

Dislocation structure after creep at 650°C

The examinations of crept specimen of U720 HS show large stacking faults inside the γ' precipitates (Figure 3a). These faults are clearly observed inside the primary and secondary γ' precipitates.

For the U720 CR dislocations form loops around the γ' precipitates (Figure 3b). These observations suggest that the deformation mechanism differs between the two microstructures ; for the U720 HS, γ' precipitates are sheared, whereas in the U720 CR γ' precipitates are bypassed by an Orowan mechanism.

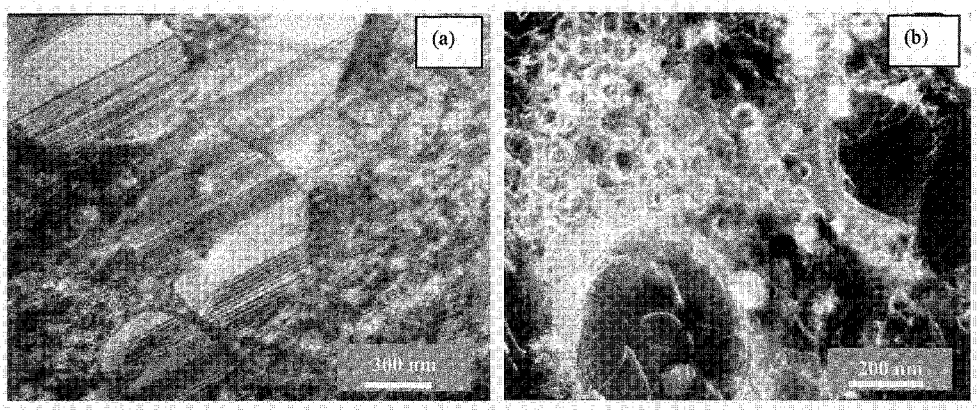


Figure 3. *Dislocation structure in (a) the Udimet 720 HS (TEM bright-field) and (b)Udimet 720 CR (TEM weak-beam) in interrupted specimens crept after 1% strain under 750 MPa.*

Creep damage for the Udimet 720 HS and CR at 650°C and 750°C

After creep, broken specimens and longitudinal cross sections were examined by scanning electron microscopy (SEM) for damage analysis. Micro-cracks are observed mostly along the grain boundaries and along the powder particle boundaries for both creep temperatures (Figure 4). At 650°C, damage is only observed close to the fracture surface, whereas at 750°C, damage is distributed in the bulk of the specimen along the entire gauge length.

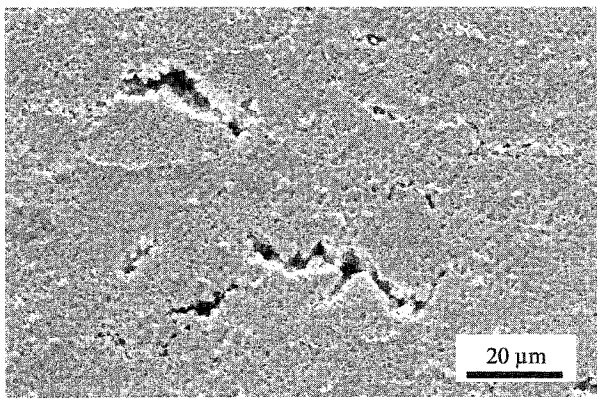


Figure 4. *Micro-cracks in the bulk of a specimen after creep testing at 750°C under 220 MPa (SEM observation on a longitudinal cross section)*

Discussion

The different dislocation structures observed at the beginning of the creep test clearly show that the deformation mechanisms are different in the two heat treatments. For U720HS, the dislocations shear the γ' precipitates whereas for U720CR dislocations bypass the precipitates by an Orowan mechanism.

These two mechanisms, already observed in other recent powder metallurgy nickel-based superalloys [2,3] seems to depend on the γ' distribution. As the Orowan stress required to have a dislocation overcoming mechanism depends on the width of γ corridors between γ' precipitates, this parameter has to be a key parameter. The large corridors observed in U720CR promotes an Orowan mechanism whereas in U720HS the presence of tertiary γ' decreases the corridor width and promotes a shearing mechanism.

The fact that steady-state creep stage is not observed in the U720 HS may be attributed either to an early damage of the specimen, or to a degradation of the microstructure related to ageing during high temperature deformation. In order to discriminate these two effects, a creep test has been conducted at 750°C under 280 MPa and stopped at 3.5 % strain. Then, the microstructure was restored by applying the full HS heat treatment cycle to the specimen (under vacuum), and the creep test was started again under the same conditions (Figure 5). The behaviour of this rejuvenated specimen is then compared to the behaviour of a as-heat treated specimen. Figure 5 shows that the rejuvenated specimen has a creep behaviour similar to that of the virgin material. This special test suggests that the specimen did not contain any cracks or voids after 3.5% strain. This indicates that apparent tertiary creep stage is due to the thermal ageing of the alloy. This ageing is often related to coarsening of the fine γ' precipitates. Nevertheless at 650°C, it was shown that aging up to 5000 h has no measurable effect on γ' precipitate size, according to TEM observations. In this case, the lack of steady-state creep stage could be due to the shearing of the γ' precipitates leading to an apparent softening of the U20 HS. On the contrary, the overcoming mode may lead to an apparent work hardening for U720 CR tested in the same conditions.

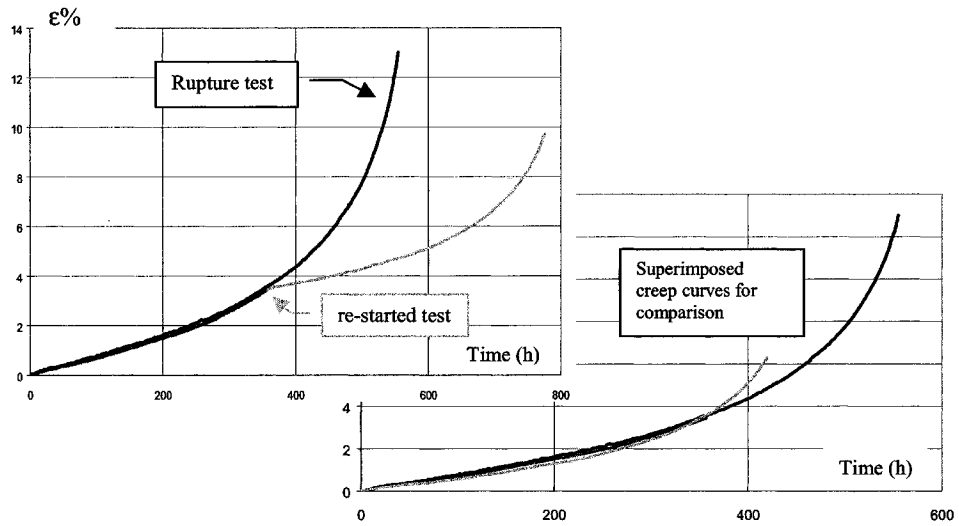


Figure 5. *Comparison of the creep test performed at 750°C under 280 MPa and the same test stopped after 3.5 % and re-started after rejuvenation (HS microstructure)*

For creep tests at 750°C, under 140 to 280 MPa, n values in the U720 CR is much lower than at 650°C under 750 to 850 MPa. This strongly suggests a change of dominant creep-controlling mechanism. At 750°C, n value is close to 1 for U720HS and this would correspond to a grain boundary sliding mechanism. This could explain the longer creep life of the U720 CR with slightly larger γ-grain size. Precise effect of the grain boundary sliding still needs to be clarified in order to optimise the HIPed U720 microstructure for long term creep endurance.

Conclusions

The study of two microstructures of HIPed U720 has shown how the γ-grain size and the γ' distribution have an influence on deformation mechanisms and creep strength. In the 720 CR, the large spacing of the γ' precipitates promotes an overcoming of the γ' by Orowan mechanism. In contrast the smaller spacing of the γ' in the U720 HS promotes shearing of the precipitates. This may explain the creep curves without any apparent steady-state creep regime. Moreover, the apparent tertiary stage arising at the beginning of the test may not be due to an early damage of the material (cracks, voids) but rather to the deformation mechanism.

During creep tests at 750°C, grain boundary sliding seems to become a controlling deformation mechanism and may explain the longer creep life observed for U720 CR with coarse grain microstructure.

The potential use of specific creep models developed by Dyson and MacLean [4] for superalloys including physical damage parameters (intergranular damage, aging of the

microstructure) will be evaluated in the near future to precisely describe the creep behaviour of HIPed Udimet 720.

REFERENCES

[1] Couturier R, Escaravage C, High temperature alloys for the HTGR gas turbine : required properties and development needs, IAEA Technical committee meeting on 'Gas Turbine Conversion Systems for modular HTGRs", Palo Alto California, 2000.

[2] Bhowal P.R, Wright E.F., Raymond E.L., Effects of cooling rate and γ' morphology on creep and stress-rupture properties of a powder metallurgy superalloy, Metallurgical transaction A, vol. 21A, 1990, p.1709-1717.

[3] Locq D., Marty M., Caron P., Optimisation of the mechanical properties of a new PM superalloy for disk applications, Superalloys 2000, Edition TMS, 2000, p. 395-403.

[4] McLean M., Dyson B.F., Modeling the effects of damage and microstructural evolution on the creep behaviour of engineering alloys, Journal of Engineering Materials and Technology, vol 122, 2000, p. 273-278.

SECTION 1

ADVANCED GAS TURBINE MATERIALS

1.3. Coatings

MCRALY COATING BY AN ELECTROCHEMICAL ROUTE

Marie-Pierre Bacos[Θ,*], Benoît Girard[♣], Pierre Josso[Θ], Catherine Rio[Θ]

[Θ] Office National d'Etudes et de Recherches Aérospatiales, Département Matériaux Métalliques et Procédés, Unité Recherches Transversales. France
[♣] Chromalloy France

Abstract

MCrAlY coatings are increasingly being used in gas turbine applications where high corrosion resistance is needed. In this paper a relatively new coating process, based on an electrochemical route, is presented. Results show that simple MCrAlY coatings or two-layers protective coatings, composed of one phase β nickel aluminide and a two-phase β-γ coatings, can be obtained. The microstructure of these coatings are as good as conventional plasma spray or electroplated ones and the non directionality of this process has been assessed .

Key words : autocatalytic electroless MCrAlY coating, turbine blade, engine, microstructure.

Introduction

Improvement in efficiencies of gas turbine can be achieved by increasing the gas inlet turbine temperature. This leads to increased blade and vane temperatures and therefore to enhanced oxidation and corrosion attack of these components coatings. Such coatings are usually of MCrAlY type where M is equal to nickel, cobalt or nickel-cobalt alloy.
Different routes to produce MCrAlY coatings exist including plasma spray or electrolysis way.
Plasma spray is convenient and permits a large range of MCrAlY composition [1-4] to be obtained, but the directionality of the process leads to a non uniformity of the thickness distribution, resulting in local corrosion and oxidation attack. Therefore this route is defective in it usefulness for coating blades with a pocket on the tip.
More recently an electroplating way has been developed [5-14] using typically, sulfamate or sulphate baths that contaminate MCrAlY coatings with impurities such as sulphur that may have a detrimental effect on the adherence of the protective oxide scale [15].
The aim of this study was to develop a new electrochemical process and to characterise the microstructure of such MCrAlY coatings. An outline of the experimental procedure will first be given followed by a summary of the experimental results.

Experimental procedure

An experimental approach which can achieve the goals of this research program is outlined in this section.
The deposit experiments were performed using a classical three-electrode cell, a reference electrode, a working electrode and a counter electrode, as shown on figure 1.
A bath using nickel-II-tri(ethylenediamine) hydroxide, with the ethylenediamine as the complexing agent, was prepared at a pH greater than 11, as described in [16]. This bath

has been developed in order to perform electroless autocatalytic nickel deposition process. Electroless nickel deposition is a chemical reduction process which depends upon the catalytic reduction process of nickel ions in an aqueous solution (containing a chemical reducing agent) and the subsequent deposition of nickel metal without the use of electrical energy. In the electroless nickel deposit process, the driving force for the reduction of nickel metal ions and their deposition is supplied by a chemical agent in solution (the reducer). The electrons needed to reduce the metal ions are provided through a catalytically surface (in this case nickel deposit which can both initiate and sustain the catalytic deposition) by the reducing agent during its oxidation reaction. Deposition of a metal from solutions containing reducing agents on a catalytically active surfaces is the strictest definition of electroless deposition but as sometime uncontrolled deposition out the reaction is also called "electroless" deposition, the first one is often called "electroless autocatalytic deposition".
In a part of the bath described in [16], other agents are added in order to obtain a new bath with the following composition :

Nickel	Ni	0,17M
Ethylenediamine	$NH_2(CH_2)_2NH_2$	1M
Sodium hydroxide	NaOH	1M
Arsenic pentoxide	As_2O_5	$6.4\ 10^{-3}$ M

In a double walled and thermostated stainless steel cell, connected to a potentiometer device composed of a high impedance voltmeter, a regulation device and a stabilised power supply, the bath was stirred with a mechanical stirring device (figure 1).

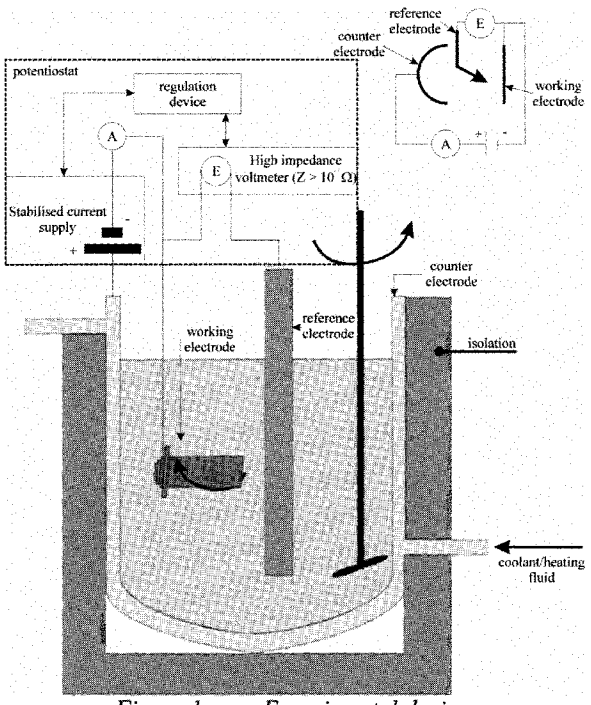


Figure 1 : Experimental device.

CoCrAlYTa with the mass composition as following : Co : 39.3%, Cr : 35.7%, Al : 16.1%, Y: 1.1%; Ta : 7.8% and an average grain size of 4 micrometers, were defloculated with the use of Coatex P 90 (iron stabilised methacrylate of methyl). Defloculated particles were added to the bath as 50 g/litre of bath, and were kept in this suspension by this stirring. This bath was then heated up to 85°C by circulating oil through the double wall of the cell.

Samples of nickel-base superalloys were sandblasted to roughen the surface and improve adhesion of the coating. These samples were linked to the working electrode in the bath.

Hydrazine, the reducing agent, as 0,3 mole/litre, was added (10 ml/hour) while applying to the working electrode an overpotential equal to -150 mV against the reference electrode. Fixing the potential of the working electrode leads to a new stationary reactions equilibrium at the working electrode interface and to higher nickel deposition rate. Indeed without overpotential the nickel deposition rate is quite low. This rate is related to the hydrazine concentration that must be kept low in order to keep the bath stabilised.
After 16 hours of nickel and particles co-deposition experiments, samples coatings on the order of 75 micrometers thick were produced.
Then the samples were either annealed under vacuum for 2 hours at 1080°C or aluminised using high Al activity pack cementation (inward process). In the last case they were packed in a Al-Cr alloy (65wt.% and 35wt.% respectively) alumina powder mixture. The pack cementation process was chloride salt activated and heated at 700°C during 7 hours 30 minutes under hydrogen atmosphere. After cooling under argon atmosphere (and cleaning by ethylic alcohol and ultrasound) the samples were heat treated depending on the superalloy type. For instance nickel- base single cristalline superalloy are heat treated 6 hours at 1080°C while nickel- base polycristalline superalloy are heat treated 5 hours at 1085°C both under hydrogen atmosphere.
The alloy used as substrate in this study is a new nickel-base single cristalline superalloy with the following composition (table 1) [17].

Table 1. MC-NG composition

	Ni	Cr	W	Mo	Re	Ru	Al	Ti	Ta	Si	Hf	C	S
Wt.%	base	4	5	1	4	4	6	0,5	5	0,1	0,1	-	-

Experimental results
In the following paragraph, experimental results are summarised. The bulk chemical analysis results will be shown first followed by information from electron microscope examinations.

Chemical analysis of the matrix
Bulk chemical analysis of minor elements (as sulphur) was conducted by GDMS (Glow Discharge Mass Spectrometry) both for the electrochemical nickel matrix realised as described above and for an electroplated cobalt matrix realised according the electroplating process [7, 9-14]. Among the numerous examples given in ref. 7 and ref. 9 to 14, the used electroplated deposit has been realised with a cobalt sulphate bath

(400g/l) containing sodium chloride (15 g/l) and boric acid (20g/l), at a low pH (4,5), low temperature (45°C) and a low current density (0.3 A/dm²).
This analysis reveals that the electrochemical process leads to a low sulphur content (less than 1 ppm wt.).
Table 2 : Sulphur analysis of electroless autocatalytic MCrAlY coating

Ppm mass.	S
Electroless autocatalytic coating	0.92 ppm wt
Electroplated MCrAlYTa coating [7, 9-14]	42 ppm wt.

Electron microscope examinations.
The following paragraph summarises the results of the electron microscope examinations of metallography prepared cross-sections of coatings : the as-deposited coating, the coating annealed under vacuum (1080°C, 4 h at a pressure less than 10^{-4} Pa) and the aluminised coating.

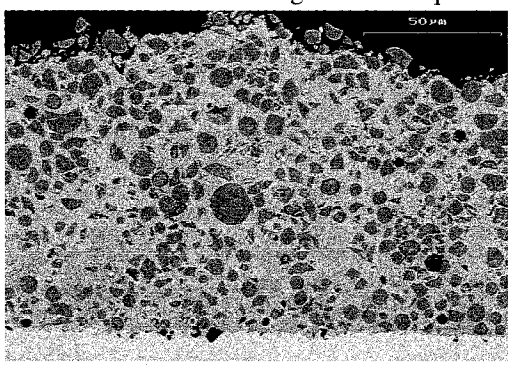


Figure 2: Micrograph showing the morphology of an as deposited composite Ni + CoCrAlYTa. x 625. SEM-BSE.

As-deposited coating
Figure 2 illustrates the morphology of an as-deposited coating as well as the structure of the outer coating layer. The distribution of the particles, whatever their size, was quite uniform in the coating 120 micrometers thick.
As demonstrated in figure 3, the adherence between the particles and the matrix was very good, there was not porosity visible at this interface. The included particles ratio of the annealed coating was measured by image analysis using the APHELION software. Calculations have been performed on 256 grey levels 512 * 512 pixel scanning electron micrographs. It leads to an average included particles ratio up to 50 vol% . The porosity level is quite low (below 5 vol.%).

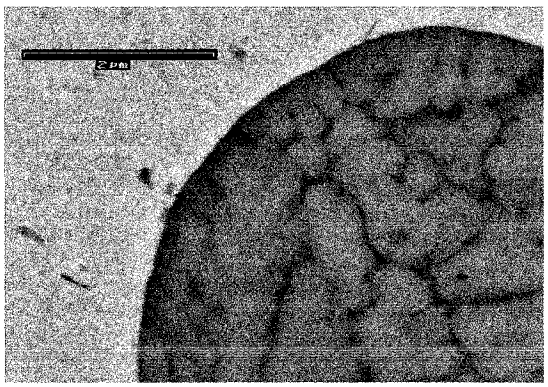


Figure 3 : Micrograph showing the adherence between a particle and the matrix of pure nickel. x 20000. SEM-BSE.

Coating annealed in an argon atmosphere
Figure 4 and 5 illustrate the morphology of an annealed coating deposited on a blade as well as the structure and the composition of the outer coating layer.

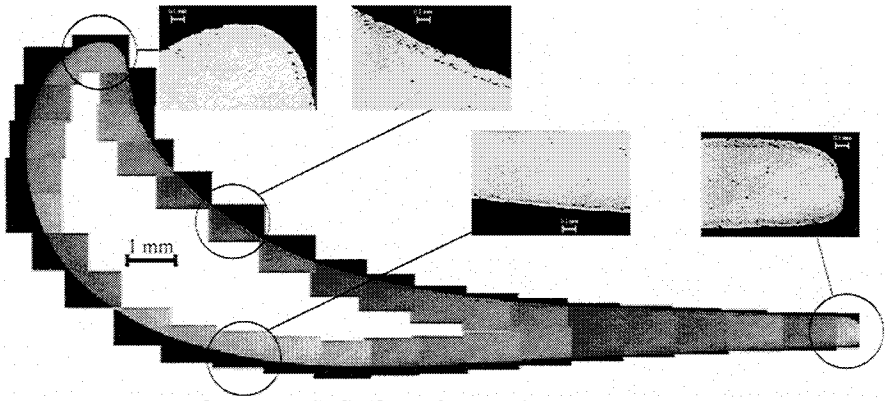


Figure 4 : Autocatalytic Ni + CoCrAlYTa deposited an a AM3 blade after annealing under argon. x 10. Optical microscopy.

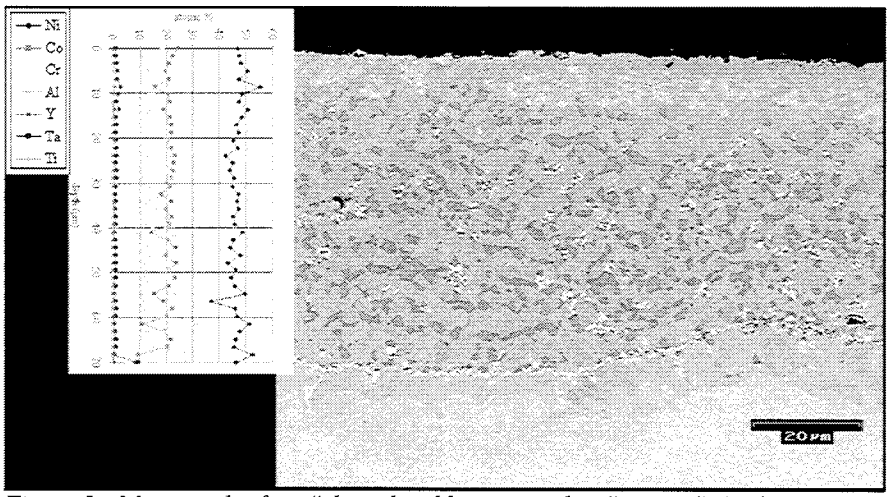
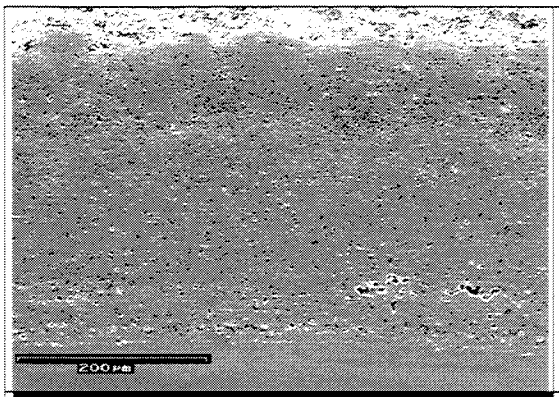
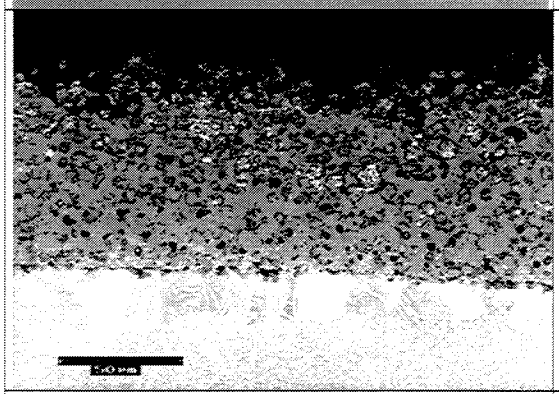


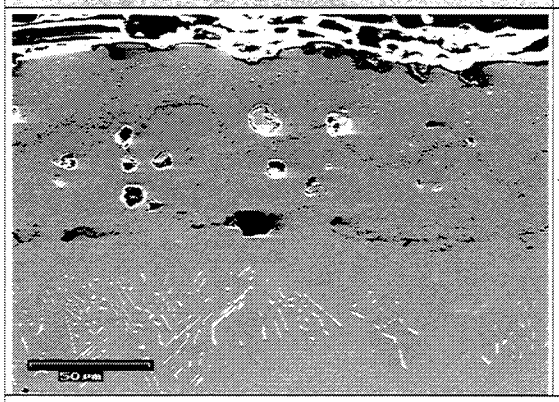
Figure 5 : Micrograph of an "electroless-like autocatalytic" Ni + CoCrAlYTa coating deposited on a AM3 blade after annealing under argon. Picture x 1000; EDS analysis by 2 µm steps. SEM-BSE.



a : "electroless-like autocatalytic" deposit. x 200.



b : commercial electrolytic deposit. x 500



c : commercial low pressure plasma spray (LPPS). x 500.

Figure 6: Micrographs of three MCrAlYTa deposit. SEM-BSE.

Uniformity of the coating all around the blade was good. The microstructure of the coating was composed of β and γ phases (dark and grey phases on figure 5 respectively) and tantalum particles (white particle on figure 5).
Figure 6 shows comparison between this autocatalytic chemical coating (6a) and two commercial coatings, an electroplated one and a plasma sprayed one (6b and 6c respectively). The porosity level of the annealed coatings is comprised between 5 and 15 vol.% according to the metallic powder particles included (30 to 50 vol.% respectively).

Aluminised coating
After the aluminization treatment, the microstructure of the electrochemical coating showed a two layers microstructure (figure 7). The upper aluminium enriched layer, about 80 micrometers thick, is composed of a constant aluminium and nickel concentrations, in the 40/60 atomic ratio (analysis of figure 8), enriched with cobalt, chromium, yttrium and tantalum. It was also revealed that the inside region of aluminised layer did not contain any chromium precipitate but had a constant aluminium concentration up to the inner two-phases β/γ layers. Inside the typically β/γ MCrAlY inner layer, the nickel concentration increased, until it reached its matrix nominal concentration, as the aluminium concentration decreased. Between this two-layers coatings and the substrate there was a thin continuous diffusion zone ensuring good adhesion.

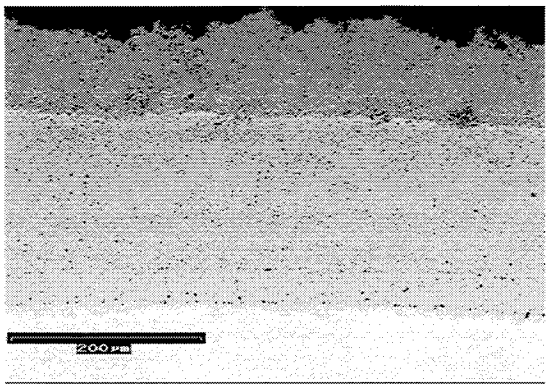


Figure 7 : Cross section of a chemical MCrAlY after an inward aluminisation. SEM-BSE.

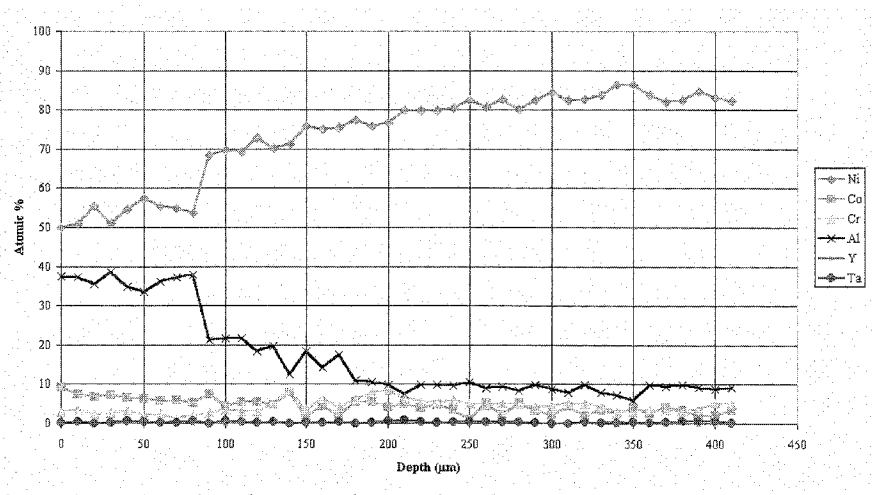


Figure 8 : EDS analysis by steps of 2 µm of an electroless-like autocatalytic deposit of MCrAlYTa after an inward aluminisation.

Complex shapes

In order to check the non directionality of the process, complex shapes as a grooved specimen have been coated by the electrochemical route (figure 9). As forecast shadowed zones are covered by a chemical composite deposit. This microscopic examination show that the experimental deposit process used is nearest an electroless process than an electroplating one. Indeed one of the major drawback of electroplated deposit lies in the fact that thickness of the deposited metal is not uniform over the entire surface of the substrate but is dependant of its geometry and shape. With our experiment process, all parts of the surface have been catalytically activated ad are wetted by the solution.

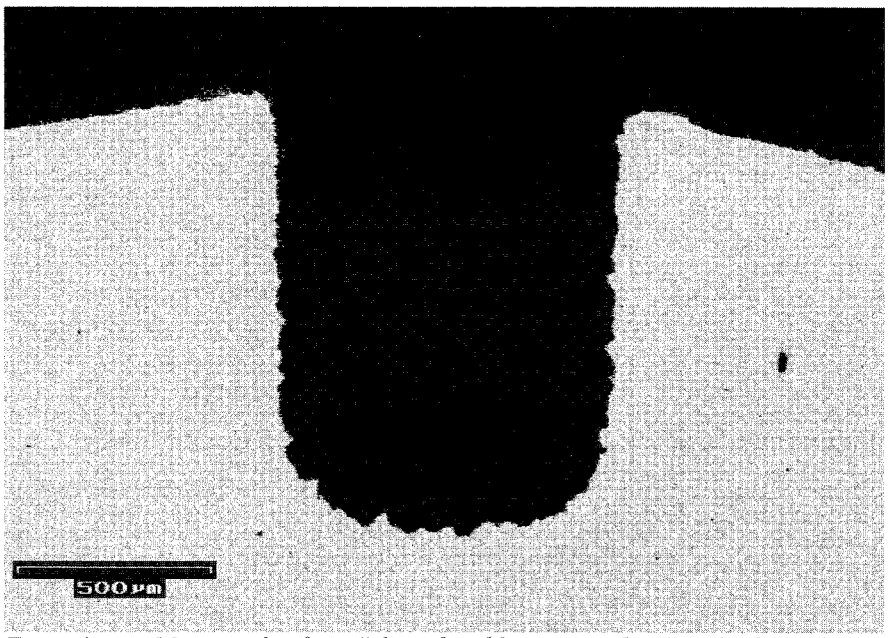


Figure 9: Micrograph of an "electroless-like autocatalytic" MCrAlYTa deposit showing a good penetration in a grooved sample. x 50. SEM-BSE.

Conclusion

1. According to the experimental results, the formation of a high quality MCrAlY coating is feasible by the electrochemical process. Deposits containing up to 50 vol%. of pre-alloyed powder, which after treatment, would produce alloys typically used as protective blades'coating can be produced.
2. With the proposed process, a simple MCrAlY coating or a two-layers protective coating, composed of one phase β nickel aluminide and a two-phase β-γ coating, can be obtained. The porosity level of the annealed coatings is comprised between 5 and 15 vol.% according to the metallic powder particles included (30 to 50 vol.% respectively).
3. The experimental results showed the good uniformity and the good microstructure properties of these coatings -compared to the conventional plasma spray or

electroplated ones- and the non directionality of the process. Oxidation and corrosion tests are in progress.

References

[1] Wood J.H, Goldman E.H, *Protective coatings,* In Superalloys II--High Temperature Materials for Aerospace and Industrial Power, edited by Sims C.T., Stoloff S. and Hagel W.C., 1987, p. 359-384.

[2] Godard G.W., *Protective Coatings -purpose, role and design,* Materials Science and Technology, vol 2, March 1986, p 194-200

[3] Nichols J.R., Hancock P., *Advanced high temperature coatings for gas turbines,* Industrial corrosion, vol 5, July 1987, p 8-17

[4] Patnaik P.C., *Coatings for high temperature corrosion in aero and industrial gas turbine,* in Proceedings of Surface Modification technologies II, edited by Sudarshan T.S. and Bhat D.G. The Minerals, Metals & Materials Society, 1989, p 37-61

[5] Kedward et al., *Processes for the electrodeposition of composite coatings,* United States Patent 4,305,792 December 15, 1981.

[6] Honey et al., *Overlay coating,* United States Patent 4,810,334 March 7, 1989.

[7] Foster J, *Production of coatings,* United States Patent 5,037,513 August 6, 1991.

[8] Wride et al, *Gas turbine blades,* United States Patent 5,076,897 December 31, 1991.

[9] Foster J, *Electrodeposited composite coatings,* United States Patent 5,558,758 September 24, 1996.

[10] Foster J et al.; *Jig for coating rotor blades,* United States Patent 5,702,574 December 30, 1997.

[11] Foster J, *Protective coating,* United States Patent 5,824,205 October 20, 1998.

[12] Foster J, *Protective coating* ,United States Patent 5,833,829 November 10, 1998.

[13] Foster J, Cameron B.P, Carew J.A, *The production of multi-component alloy coatings by particle codeposition,* Trans. Inst. Met. Finish., vol 63 n°3-4, 1985 , p 115-119.

[14] Averill A.F, Nuvoloni U, Orin J, Foster J, *Prediction of thickness distribution of electrodeposited coatings using a low-cost boundary element method,* Plating & surface Finishing, May 1997, p 127.

[15] Rivoaland L., *Etude de la ségrégation du soufre à la surface de NiAl à haute température,* PhD thesis, Université Paris 6, 26 septembre 2001.

[16] Josso P. et al.; *Hydrazine bath for chemically depositing nickel and/or cobalt, and a method of preparing such a bath,* United States Patent 4,844,739, July 4, 1989.

[17] Caron P., *High γ' solvus new generation nickel-based superalloys for single crystal turbine blade applications,* Proceedings of the 9th International Symposium on Superalloys SUPERALLOYS 2000, Champion (USA) September 17-21, 2000, p 737-746.

EVALUATION OF THERMOMECHANICAL FATIGUE RESISTANCE OF COATED SUPERALLOYS BY A LASER THERMAL SHOCK SYSTEM

Monica Meriggi, Claudia Rinaldi

CESI – B.U. GEN Via Reggio Emilia, 39 - 20090 Segrate (Milano) – Italy
tel +390221258439- fax +390221258474, e-mail rinaldi@cesi.it

Abstract

As the thermomechanical characterization of coated superalloys is very expensive, because the tests are long and complex, an alternative technique was developed, based on the use of a Nd:YAG laser thermal shock system, developed in CESI to locally and automatically apply the thermal cycles chosen by the operator onto the coating surface. During tests the thermal cycling is continued until the first surface cracks appear.
FEM methods were used to calculate the stress-strain field around the heated zone and the $\Delta\varepsilon$ obtained in several different cycling conditions. From the simulation results, a typical test matrix was established, able to evaluate a $\Delta\varepsilon$ range from 1.5 to 0.4, so that the number of cycles to fracture between one hundred and one thousand can be expected. Results are plotted on a fatigue resistance plot ($\Delta\varepsilon$ vs Number of cycles to surface cracking).
The proposed test method was applied on AMDRY995 coatings sprayed on IN738 superalloy, both with LPPS and with HVOF technique, the last one being almost three times cheaper. Thermal shock test results show that HVOF coatings have a resistance to thermomechanical fatigue comparable to LPPS sprayed coatings.

Keywords: thermomechanical fatigue, laser thermal shock, AMDRY 995 coatings, LPPS and HVOF coatings

Introduction

Thermomechanical fatigue is one of the most important damage mechanisms of the MCrAlY coatings used on hot parts of gas turbines and on combustion chambers to increase gas temperature and reduce hot corrosion. These coatings are under continuous development to optimise resistance and reduce gas turbine maintenance costs; the qualification of innovative coatings requires long, complex thermomechanical fatigue (TMF) tests on coated samples.
To reduce such characterization costs an alternative technique is here proposed. An innovative laser thermal shock system was developed in CESI (ex CISE/ENEL research), able to verify the resistance of samples, or local critical regions of components, during speeded up laboratory tests.
In the present paper both numerical simulation and experimental test results are presented for a two layered specimen under thermal shock conditions, obtained by means of local heating induced by the laser beam impingement at the centre of the coated surface.
Numerical analyses were carried out by means of finite elements code ABAQUS [1].
The simulated experimental conditions are cycles which heat up the specimen surface to the required temperature, by means of a laser power flow, and then cooling it to room temperature, by natural air convection on the top surface and by a nitrogen jet on the bottom surface. The thermal analysis results are in good agreement with experimental temperature values (measured by the pyrometer and by two thermocouples on the sample surface). The temperature fields due to the cycles were used as input of the thermomechanical analysis of the two layered specimen, to determine the stress-strain fields inside the specimen thickness, during the two simulated cycles. Only two cycles were simulated because it was

experimentally verified that stationary thermal conditions are reached by the specimen after this small number of cycles.
The test methodology was applied to compare the resistance to abrupt thermal cycles of AMDRY 995 coatings sprayed by LPPS (low pressure plasma sprayed) and HVOF (high velocity oxygen fuel) techniques on a Ni based superalloy.

Experimental details

Materials and size of the sample
The sample is a rectangular sheet of IN738 (4 mm thick and 25 x 40 mm wide) coated on one side by AMDRY 995 (thickness about 300 μm) by LPPS or by HVOF technique. After the coating process the samples were fully heat treated (solution and ageing of IN738 alloy).

Laser Thermal Shock system
The laser thermal shock system present in CESI was home made (see Fig. 1) and designed to obtain a fast thermal cycling of metallic materials and coatings.

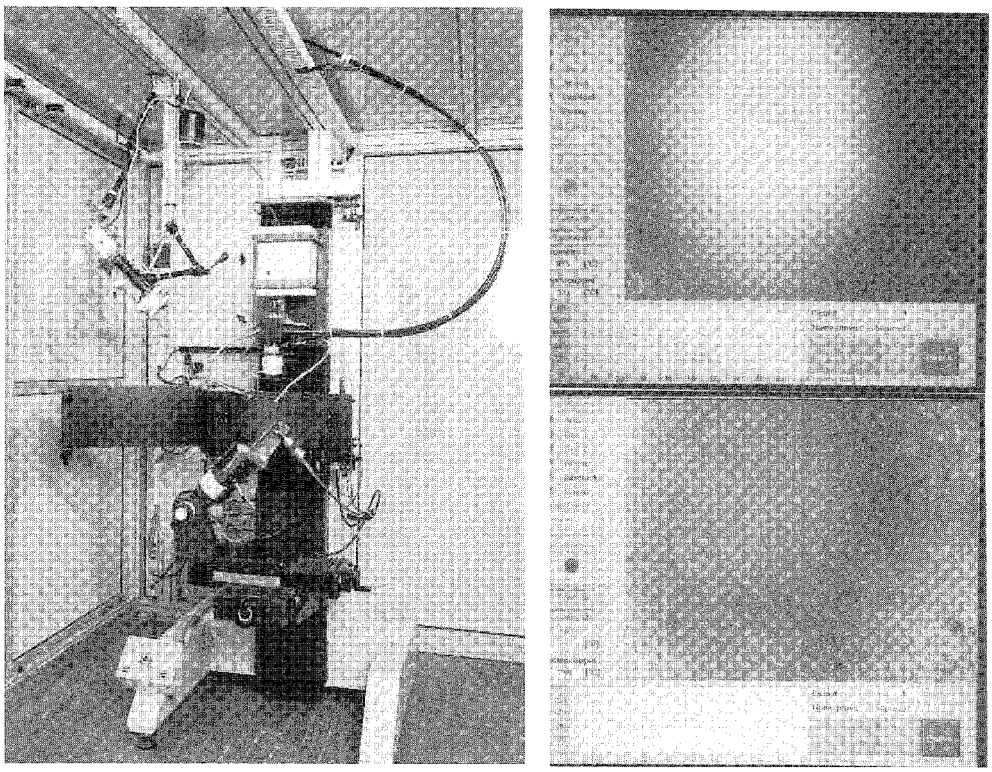


Figure 1 Laser thermal shock system (left): the laser beam arrives through an optical fiber to the optical head sending it onto the sample surface (here a gas turbine blade).

A Nd:YAG laser (1kW maximum power) heats up the surface of a sample or a component, locally. A pyrometer measures the surface temperature in the region heated by the laser spot; its signal is used as a feed back control of the laser power, through a dedicated software, to obtain the thermal cycle chosen by the operator. For safety reasons the system control console is outside the laser cabin.
The operator can choose the characteristics of the thermal cycle (size of the hot spot, minimum and maximum temperatures, duration of the hot and cold phases of the cycle, number of cycles,...). The surface image is on line monitored by a videocamera, so that the operator can follow surface changes (e.g. crack appearance) on the screen of the control panel. On this both, the plot of the thermal cycles on line recorded and the image of the sample surface are shown. Left pictures in Fig. 1 are two examples relative to the hot (top) and the cold (bottom) phase of the cycle.
For each test the control system records a group of files containing the cyclic conditions chosen by the operator, the thermal cycles monitored by the pyrometers (both Temperature and laser power versus time) and the images of the surface (after groups of cycles chosen by the operator).
The distance between the laser head and the sample was chosen to heat up a small region at the center of it; the shape of the laser power distribution was measured by the Prometec laserscope UFF100 and is selfsimilar at the different nominal power values used (see Fig. 2); a decreasing value of laser power is automatically delivered during the hot part of the cycle, to obtain the required constant temperature (with a trend similar to that shown in Fig.3).
The cooling to room temperature happened by natural air convection on the top surface and was accelerated by a nitrogen jet on the bottom surface.
The thermal cycling was continued until the appearance of surface cracks; this damage mechanism was chosen as it is similar to the cracks which start at the specimen surface and cause the end of the life in standard TMF tests.

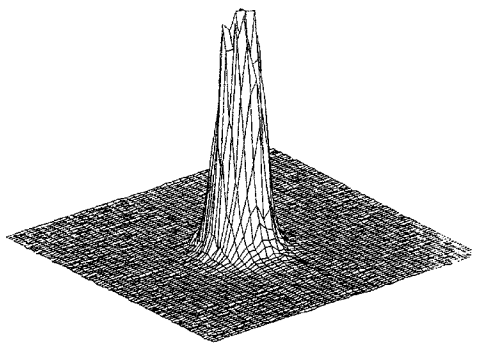


Figure 2 Laser power spatial distribution (the whole area is 20x20mm)

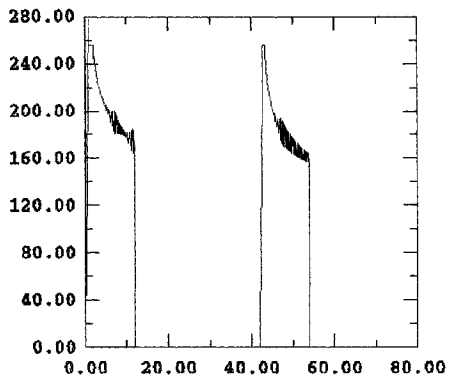


Figure 3 – Input leading power (W) versus time (s) calculated by the new software

Numerical simulation of layered specimens under "thermal shock" conditions

Thermal analyses

Some thermal analyses were performed to evaluate the temperature distribution due to the laser power flow. Calculations were repeated with different power input, varying both shape and peak value of the laser power flow to obtain different thermal cycles on the specimen.

The same specimen used for experimental tests was discretized by means of a finite elements model constituted by composite shell linear quadrilateral elements (Fig. 4). For the calculations, the specimen was constituted of IN738 4 mm thick and 25x40mm wide, with a 310 μm AMDRY995 layer on one side. Onto the coated specimen surface a "load" (the laser power flow) was applied constituted by the matrix of values measured by means of the Laserscope UFF 100 (PROMETEC): the laser power is distributed on a 20x20 mm area with the concentration at the centre as shown in Fig. 2; the intensity spatial distribution of the laser beam remains selfsimilar while the nominal total laser power changes due to the feed-back control.

Material data were found in [2], [3], [4], [5]; the analyses were performed taking into account the elastoplastic behaviour of materials (creep was excluded due to the short cycle duration).

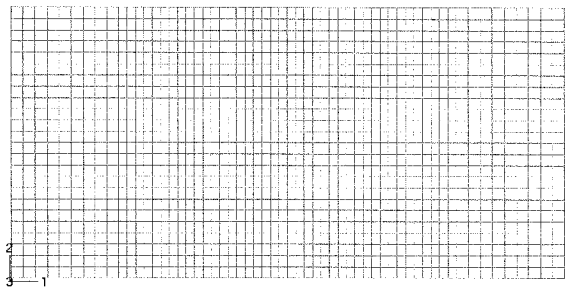


Figure 4 – Finite element model (25x40mm).

The laboratory test was executed with the maximum temperature value chosen by the operator as "input" for the thermal shock system, recording the driving power (as an "output") modulated by the system during the hot part of the cycle. On the opposite the numerical simulation is usually carried out considering the laser power flow as "input" and finding the temperature distribution during the cycles as "output" of the calculation.

In order to make these procedures similar a software was developed, able to modify the leading power input data during the numerical analysis execution, so that the temperature on the surface of the specimen can be controlled, as it happens in the laser thermal shock system. In this way from the numerical point of view the calculations were carried out following the same methodology of the laser system which "retrofits" the entering power starting from the temperature values recorded by the pyrometer during thermal shock test, in order to maintain the temperature set up for the wished time. Such software is constituted from some user's subroutine for code ABAQUS, executed during the numerical simulations of the thermal shock test.

In fig. 3 an example is shown of the power values versus time calculated during the two simulated cycles for one of the examined cases.
Using the new software some numerical tests were performed in the same conditions of experimental tests; a good agreement was found between the temperature values resulting from the simulations and the measurements with the pyrometers of the system (Figs. 5-6).
Beyond this also a comparison with temperatures measured from two thermocouples was done, in order to estimate the effectiveness of the described software procedure. During one test the temperature was recorded not only by means of the laser thermal shock system pyrometers, but also by two thermocouples, placed near the region hit from the laser spot on the upper surface of the specimen, both at a distance from the laser spot centre of 2,7 mm. (see Fig. 7).
A good agreement with the measures supplied from the thermocouples was obtained: the recorded maximum experimental value was 830°C ± 8°C and a numerical temperature of approximately 740°C was obtained as an average of the calculated temperatures at the two nearest nodes, shown in Fig. 8 (this because numerical data at exactly 2.7 mm from the center of the spot were not available).

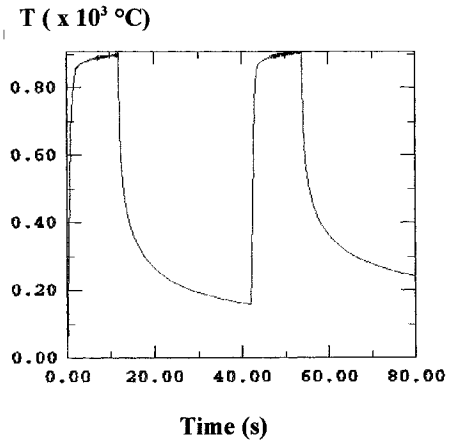


Figure 5 – Calculated temperature (average evaluated on the same area used by the laser system pyrometer) vs. time (s).

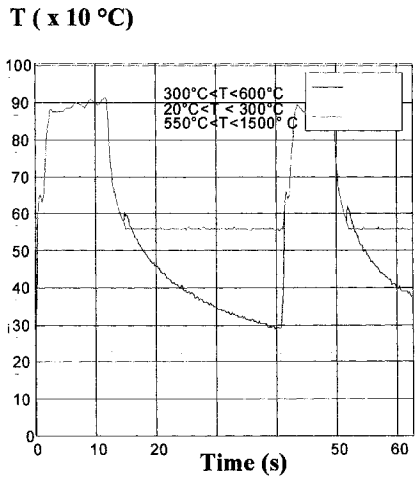


Figure 6 – Temperature (°C) vs. time (s) measured by the pyrometers; the straight line is relative to the pyrometer measuring the bottom surface of the sample (working for 20°C <T < 300°C). The other curve is the temperature at the hot surface measured by two pyrometers working respectively between 600° and 300° and between 550°C and 1500°C

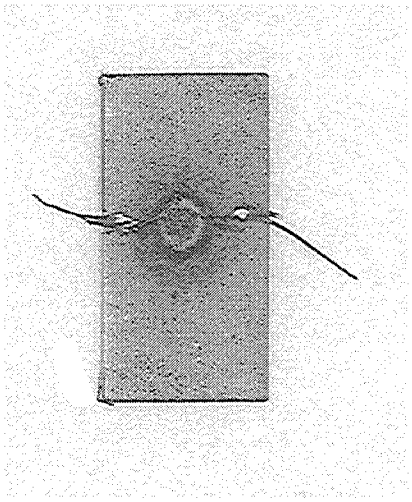


Figure 7 – Specimen with the two thermocouples both placed at 2,7mm from the laser spot centre.

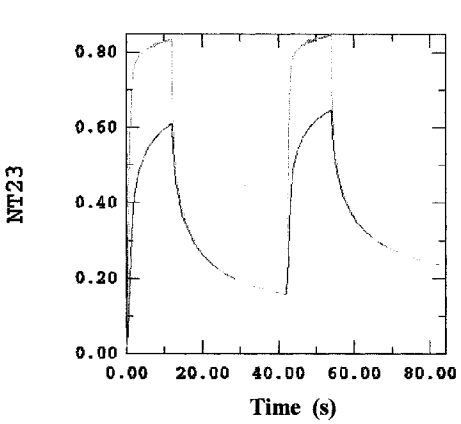


Figure 8 – Numerical temperatures calculated at the two nodes nearest to the thermocouples placed at 2,7mm from the laser spot centre: the higher curve is relative to the position at 3 mm from the spot center; the lower to the position at about 2 mm from the spot center

Thermomechanical evaluations for the two layer specimen

Themomechanical analyses were performed as follows for different cycles, with different ΔT:

- the first step is a thermal analysis to evaluate the temperature distribution over the specimen due to different laser power input;
- starting from the temperature distribution given by the thermal analysis, a mechanical calculation was performed to evaluate the stress-strain fields all over the specimen;
- the strain values were analysed and the critical $\Delta\varepsilon$ was considered for each cycle, considering maximum and minimum strain values over a cycle;

In figures 9-11 we can observe one example of the calculated leading power input for a cycle between 900°C and 200°C, the corresponding "numerical pyrometer" temperature and the ε-T plot during the cycle. (the "numerical pyrometer" temperature is here defined as the temperature evaluated as an averaged value over the area (a 5 mm circle), on the top surface of the specimen corresponding to the area measured by the pyrometer of the laser thermal shock system; the temperature gradient inside the hot spot is approximately 250°C).

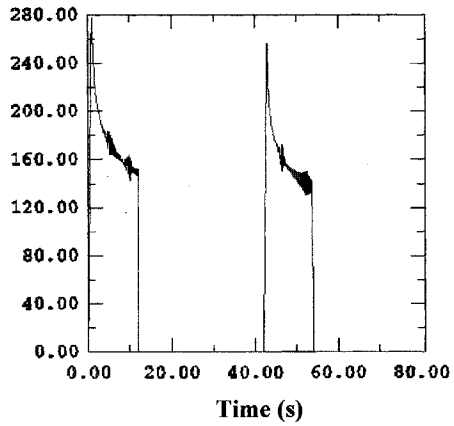


Figure 9 – Experimental input power (W) versus time (sec).

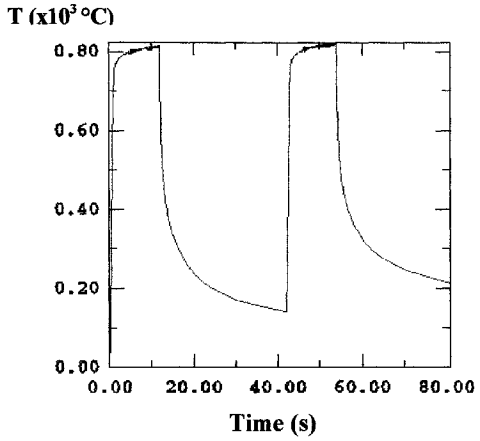


Figure 10 – Temperature (C°) versus time (sec).

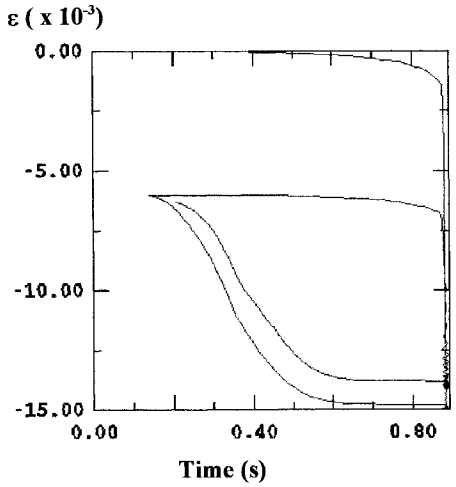


Figure 11 - Calculated Δε vs temperature T (x10^{-3} C°).

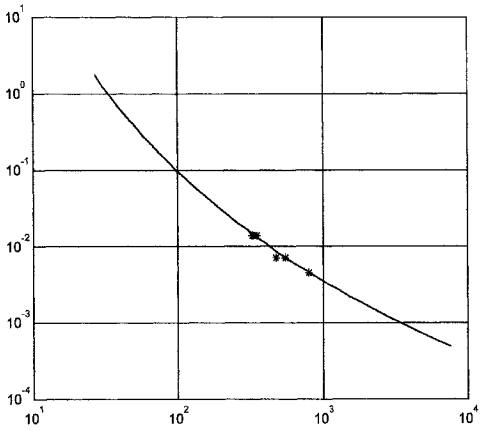


Figure 12 - Δε versus N_f(10-10000) data and Manson Coffin "interpolated" curve.

Experimental results and Thermomechanical curve

In order to supply the results of the activity performed with the laser thermal shock system, in a way comparable to traditional thermomechanical fatigue, it is necessary to produce a specific curve Δε-Nf , typical of the specimen type and size used here in the laser thermal shock tests.
Therefore some numerical and experimental tests were carried out in different thermal cycling conditions, so that the calculation supplied the values of Δε corresponding to each thermal cycle and the experimental tests supplied the value of Nf related to each Δε. Thermal cycles with the maximum temperature variable between 800°C-950°C and the minimum temperature between 200°C-650°C were considered, to obtain Δε values distributed over an as wide range as possible with this experimental configuration.

The results of simulations and of the experimental tests are shown in Table 1.
In the right column of this table a good reproducibility of test results can be observed in tests repeated in the same conditions (see tests between 900 and 200°C) for both type of coatings. Moreover the N_f values measured on both coatings increase with the decrease of the applied Δε. Finally the results relative to the two different coatings are similar in all the three thermal cyclic conditions used.

Table 1 Test matrix summarising simulation and experimental results

Temperature interval (ΔT)	Numerically evaluated maximum Δε	Numerical $R = \varepsilon_{min} / \varepsilon_{max}$ values over each cycle	Experimentally evaluated N_f	
			LPPS	HVOF
800°C-200°C	1.12e-02	2.1739		
850°C-200°C	1.28e-02	2.0833		
900°C- 200°C	1.41e-02	2.0408	330-350	325-325
950°C- 200°C	1.52e-02	2.0408		
900°C–600°C	7.2e-03	1.3333	550	480
850°C–650°C	4.5e-03	1.25	800	800

These sets of data allowed to examine the possibility to draw a thermomechanical fatigue curve. It is interesting to point out that such points have a "distribution" similar to the typical curve thermomechanical fatigue. It is possible to find out a Manson-Coffin type curve

$$\Delta\varepsilon_{pl} = C_1 N^{\nu_1} + C_2 N^{\nu_2}$$

"describing" the obtained data, shown in Fig. 12; for this curve the characteristic parameters have been obtained applying the least-squares method relatively to the calculated points. Such curve represents a best fit of the data and could constitute a thermomechanical fatigue curve for two-layers specimens under different thermal cycles.
Furthermore for all the examined cycles, with different temperature intervals, using the relative ε-T plots, the R strain ratio parameter was evaluated, as follows:

$$R = \frac{\varepsilon_{min}}{\varepsilon_{max}}$$

Such values are shown in the last column of Table 1. The six examined cases are characterised from 2 values of R and, based on that two values, the results can be subdivided in two groups: one group at R=2.17-2.04 and the other one at R=1.33-1.25. It was also observed that the values obtained for the parameter R are always positive because they have been obtained by the ratio of two negatives numbers, and it means that the surface of the specimen is always subjected to compression stresses.
Based on the two groups tests carried out, related to the different values of the parameter R, even if the number of experimental data appears to be insufficient in order to draw definitive conclusions, it can be noticed from Fig. 13 that it is possible to characterise two different curves of TMF type. Therefore it can be concluded that the next step of the activity is to perform further experimental tests to confirm such these results.

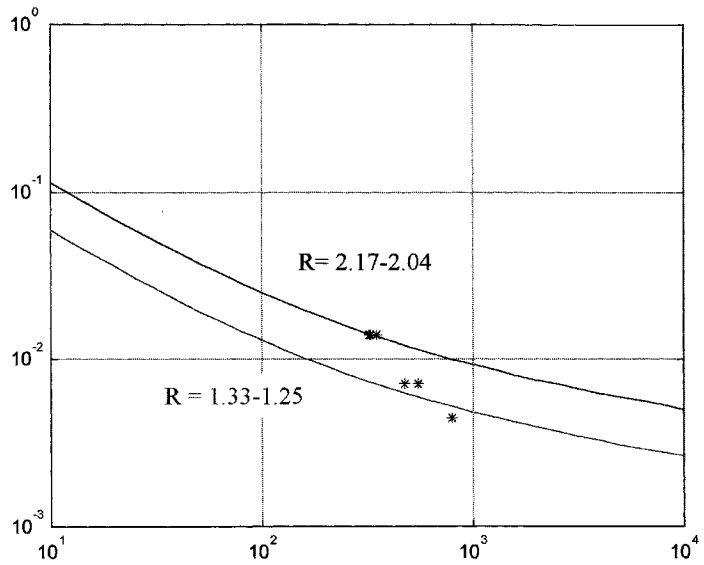


Figure 13 - Δε versus N_f : Thermal shock test results and Manson Coffin curves

Since in the examined cases the strain values are always negative, that is compression during the whole cycle, it can be necessary to perform thermal shock tests and numerical simulations, with a different cooling method, for example with gas jets impinging onto the sample surface, to produce tensile stresses and obtain cycles more similar to those experienced by real gas turbine blades (simulated in classical TMF with tests with R= -1 and LOP type cycle [6]).
Finally it can be noticed in figure 13, that the tests carried out with the laser thermal shock methodology, in the experimental configuration adopted here, are characterized from strain values placed in a small range in comparison to the range of classic TMF tests. This is due to the fact that stress and strain fields are only due to thermal effect in thermal shock tests,

while, in the traditional TMF, mechanical loads and strain can be imposed on the specimen independently from the thermal cycle and a larger range of strain can be explored.
Nevertheless the test methodology here proposed with the laser thermal shock system seems to have a certain validity, since it supplies quantitative information with very fast tests (some hours each) on the coating capability to resist to the thermal cycles applied to the external surface, as happens when the coating is exposed to jets of cooling air or warm gas.

Conclusive remarks

A thermomechanical fatigue testing methodology was developed, based on the use of a Nd:YAG laser thermal shock system, able to automatically apply the thermal cycles chosen by the operator onto the coating surface. During tests the thermal cycling is continued until the first surface cracks appear.
FEM analyses were performed to determine the stress-strain field in the sample. Such analyses allowed to point out some critical aspects of simulation; the fundamental point was the development of the dedicated software able to simulate the modulated power delivery typical of the experimental laser system to keep the sample surface at constant temperature during the hot part of the thermal cycle. This software allowed to obtain a good agreement between experimental and measured temperatures.
The thermomechanical calculations were performed starting from the thermal calculation results on 6 different thermal cycles. Results let to define a "test matrix " where $\Delta\varepsilon$ values vary in the range from 1.5 to 0.4 and the number of cycles to fracture from 100 to 800.
Experimental tests have been performed to compare the behaviour of two AMDRY 995 coatings sprayed onto IN738 substrate with two different thermal spray techniques. The thermal shock test results show that HVOF coatings have a resistance to thermomechanical fatigue comparable to LPPS sprayed coatings in the $\Delta\varepsilon$ range analysed.

Acknowledgements

This activity was performed in the frame of "Ricerca di Sistema", D.L. MICA 26-01-2000.

References

1. Hibbit, Karlsson & Sorensen Inc., ABAQUS Manual, Version 6.2, 2001.
2. Martinella R., Rinaldi C., Materiali ceramici e rivestimenti, CISE 4932, 1989.
3. Giovanardi S., Martinella R., Menetti L., Determinazione della conducibiltà termica di tubi saldati, CISE-SMR-93-10, 1993.
4. Cook L. S., Wolfenden A., Brindley W. J., Temperature dependence of dynamic Young's modulus and internal friction in LPP NiCrAlY, Journal of Material Science, vol. 29, pp. 5104-5108, 1994.
5. ASM Metals Handbook Ninth Edition, vol.3 Properties and selection: Stailess Stees, Tool Materials and Special-Purpose Metals, p.242, 1980
6. Taylor N., Rinaldi C., Bontempi P. and Casaroli F., Thermomechanical Fatigue of Gas turbine Blading Materials, in Proc. Int. Symposium on Materials Ageing and Component Life Extension, Milan 1995, EMAS pub., eds. V. Bicego et al, vol I, 327-336.

THERMOPHYSICAL AND MICROSTRUCTURAL CHARACTERIZATION OF MODIFIED THICK YTTRIA STABILISED ZIRCONIA THERMAL BARRIER COATINGS

P. Bianchi, F. Cernuschi, L. Lorenzoni
CESI
Via Reggio Emilia, 39
20090 Segrate , Italy

S. Ahmaniemi, M. Vippola, P. Vuoristo, T. Mäntylä
Tampere University of Technology/Institute of Materials Science
P. O. Box 589
33101 Tampere, Finland

Abstract

Increasing the turbine hot gas inlet temperature is a potential way to improve the efficiency of the land base gas turbines. Since the nickel and cobalt based superalloy materials can not face temperatures higher than 950°C, thermal barrier coatings (TBC) with better insulation properties are needed. A possible way to achieve this is the use of thicker TBCs (> 500μm) are needed to improve the thermal insulation. However, the increased thickness of TBCs may lead to a reduced coating lifetime. In order to overcome this drawback, two modifications of the thick $8Y_2O_3$-ZrO_2 TBC's structure were studied. Within these two modifications the TBC coating surface layer was sealed by using phosphate impregnation or laser glazing. These procedures are expected to improve coating hot corrosion and thermal cycling resistance, due to the denser coating surface or with the controlled vertical crack network.

In this study thermal diffusivity and specific heat analysis together with microstructural characterization were carried out considering the sintering effect and possible phase transformations at elevated temperatures, up to 1250°C. Qualitative explanation of experimental results was taken account by modelling the effect of porosity on the thermal properties of TBC. Broad variations in microstructural and thermophysical properties were observed within modified coatings.

Keywords: TBC, sealing, thermal diffusivity, thermal conductivity, specific heat, zirconia

1. Introduction

Thermal barrier coatings (TBC) are widely used in gas turbine hot section components such as combustors, transition ducts, shrouds and blade and vane segments. The most common TBC material is $8Y_2O_3$-ZrO_2 because of its high temperature stability, low thermal diffusivity and high coefficient of thermal expansion (CTE) as ceramic material. Combustion section components of the gas turbine are typically coated by atmospheric plasma spray (APS) process, while the electron beam physical vapor deposition (EB-PVD) is the state-of-the-art coating process in manufacturing strain tolerant TBCs for turbine components. The vertically oriented columnar structure of the EB-PVD TBCs offers better strain tolerance for the component under thermal cycling, if compared to the lamellar microstructure of the APS coatings. In addition, the surface finish of the EB-PVD coatings is aerodynamically advantageous in rotating turbine aerofoils. However, there are also certain drawbacks in EB-PVD TBC coatings, such as their thermal diffusivity is higher than that of the APS coatings [1-4], their manufacturing costs are higher than that of APS coatings [5] and the coating

process is not so flexible when coating for instance large components or the components with complex shape or inside diameter surfaces [6]. For these reasons, the EB-PVD coatings are mainly used in rotating turbine aerofoils in aeroturbines.

A major TBC failure mechanism that causes coating spallation in gas turbine components is typically bond coat oxidation. When the thickness of the thermally grown oxide (TGO) exceeds the certain limit, it induces the critical stress for the coating failure [7-8]. The risk of this failure mechanism is even increased by sintering of the zirconia top coating. In addition, TBCs are exposed to thermal and mechanical loads as well as to hot corrosion.

There have been several attempts to enhance the properties of the APS TBCs by various sealing and modification processes. The primary interest has been on thick TBCs for gas turbine and diesel engine combustion chamber components. The modification of the open porosity in TBC coating can be made by liquid metal impregnation [9], laser-glazing [10-14], hybrid spray process [15], solar furnace heat treatment [16], hot isostatic pressing (HIP) [17,18], sol-gel processing [19-21], phosphate impregnation [22,23] or by thin CVD overlay - coatings [24]. Organic sealants are mainly used for corrosion protection at lower temperatures [25]. When modifying the TBC structures one should remember that the coating primary functions, such as thermal insulation and strain tolerance, should not be deteriorated.

Low thermal conductivity (~0,5-1,5 W/mK) of the plasma sprayed yttria stabilized zirconia coating is consequence of the crystalline properties of the t-ZrO_2 and c-ZrO_2 phases in addition to its characteristic porous microstructure. The ionic charge imbalance ($Zr^{4+} \Rightarrow Y^{3+}$) generates oxygen vacancies in to the crystal lattice when replacing ZrO_2 with Y_2O_3. Crystal lattice point defects, such as oxygen vacancies are very effective phonon scatters and thus lower the thermal conductivity of the $8Y_2O_3$-ZrO_2 coatings [26,27]. In some recent studies the thermal conductivity of partially stabilized zirconia has tried to further decrease by structural modifications. S. Raghavan et al. [28] doped the zirconia crystal lattice using pentavalent oxides (Nb^{5+} and Ta^{5+}) in order to introduce substitutive point defects in addition to, or instead of, oxygen vacancies. S. Raghavan et al. [29] have also studied the effect of grain boundaries, as structural defects, on thermal conductivity using nanocrystalline (grain sizes 30-400nm) yttria stabilized zirconia. Anyway, the thermal conductivity change in both previous studies was quite limited. P. K. Schelling et al. [26] suggested that the grain size should be reduced down to 10 nm to get significant effect on thermal conductivity. J. R. Nicholls et al. [30] presented promising results of reducing thermal conductivity of the $7Y_2O_3$-ZrO_2 EB-PVD coatings by doping (colouring) and by layering the coating microstructure. By using 4 mole% of dopants, such as ytterbia, neodymia, gadolinia the thermal conductivity values were reduced by 35-45 %. In layering, the coating density was varied in 0,2-2,0 µm thick layers by pulsing the D.C. bias of the substrate during the coating deposition. Thermal conductivity reduction by layering was as effective as in doping.

In this study the thermophysical properties of modified $8Y_2O_3$-ZrO_2 were studied. The goal was to find methods to produce a dense top layer on a TTBC without losing the beneficial thermal properties of the coating. We present here the results of the thermophysical properties of the coatings, linked with the coating characterization data and compare our results with the other studies. We also used the model, which predicts the thermal diffusivity of the coating as a function of the coating porosity.

2. Experimental

Sample preparation

$8Y_2O_3$-ZrO_2 coatings were air plasma sprayed with plasma spray equipment (Plasma-Technik A3000S, Sulzer Metco AG, Wohlen, Switzerland) using the spray parameters recommended by the powder manufacturer. HOSP (hollow oven spherical powder) powder, Metco 204 NS (Sulzer Metco AG, Wohlen, Switzerland) was used as a feedstock material. Coatings were sprayed on the cleaned and slightly grit blasted AISI4142 steel substrates (∅ = 25 mm, h = 5) from which they were easily detached during after-spraying cooling using pressurized air. The substrate temperature during the spraying was kept below 200°C. Targeted coating thickness was 1000 µm. For porosity and characterization studies some coatings were heat treated at 1250°C for 5 hours in order to simulate the thermal exposure (time, temperature) of three successive thermal diffusivity measurements.

Laser glazing

8Y coatings were laser-glazed using a 4 kW continuous wave fiber coupled HAAS HL4006D lamp-pumped Nd-YAG laser (HAAS-laser GmbH, Schramberg, Germany). In the glazing experiments the laser was equipped with an integrated water-cooled copper mirror with an effective focal length of 100 mm. The optimised continuous laser power in glazing processing was 4.0 kW and coating surface speed was 3500 mm/min. The width of the laser beam was 10 mm at the focused area, which was at the distance of 80 mm from the mirror. The specific energy density of the laser beam with the above mentioned parameters is 6.9 J/mm^2. Three parallel 10 mm wide tracks, with 2 mm overlapping, were used to glaze the whole specimen. Before the final preparation of the studied coatings, laser glazing parameters were optimised by comparing coating microstructures with different specific laser energy densities using continuous and pulsed laser beams. In the optimisation stage of the laser glazing the predetermined melting depth of the coating surface was reached, without causing coating spallation. Also formation of vertical cracks, which pass through thickness of the coating, was avoided. The abbreviation for the laser-glazed coating is 8YL.

Aluminium phosphate impregnation

8Y coating was sealed with an $Al(OH)_3$-(85%)H_3PO_4 solution diluted with 20 wt% of deionized water. The ratio of $Al(OH)_3$:(85%)H_3PO_4 was 1:4.2 by weight which corresponds to the molar ratio P/Al of about 3. The solution was slightly heated and mixed with a magnetic stirrer until it became clear. The sealant was spread onto the coating surface just before the heat treatment. Heat treatment was performed at 300°C for 4 hours in air. The abbreviation for the phosphate sealed coating is 8Y AP.

Characterization

Polished microsections and fracture planes were prepared for microscopy studies. The coating microstructure was determined by optical microscopy (Leitz, Wetzlar, Germany), scanning electron microscopy (SEM, Model XL-30, Philips, Eindhoven, Netherlands) and transmission electron microscopy (TEM, Model JEM 2010, Jeol, Tokyo, Japan). In TEM studies selected area electron diffraction (SAED) was used to study the crystal structures. Coating phase structure was characterized by X-ray diffractometry (XRD, Rigaku Model IIID Max, Tokyo, Japan) using CuK_α radiation (scan step 0.02°, step time 1.2 s.). XRD analysis for the phosphate sealed coatings were made after grinding a 50 µm layer from the surface, because reaction products on the coating surface normally differ considerably from those below the

surface. Quantitative phase analysis and texture determination was performed with MAUD software (Material Analysis Using Diffraction, version 1.81, Luca Lutterotti, University of Trento, Italy). The porosity evaluation was performed both before and after laser flash thermal diffusivity measurements by using the Q500 Quantimet Image Analysis System (IA, Leitz, Wetzlar, Germany). Porosity was estimated by its different gray level if compared with bulk material. The uncertainty sources of this type of evaluation are mainly the sample preparation (the polishing procedure can produce some porosity artifacts) and the arbitrary choice of the gray level threshold. In order to minimize the effects of sample preparation, TBCs were impregnated with resin under vacuum both before and after cutting. Prior the optical analysis, the sample section was coated by a thin gold layer to improve the light contrast between porosity and bulk material. This procedure makes easier and less arbitrary fixing the gray level threshold for a skilled operator. Porosities were measured also with mercury infiltration porosimetry (MIP, models Pascal 140 and Porosimeter 2000, CE-instruments, Milan, Italy) at pressure range 0,1 kPa – 200 MPa.

Thermal property determination

Samples for thermal property study were either 10mm (thermal diffusivity) or 6mm (specific heat) diameter disk shaped free standing TBCs. Thermal diffusivity $\alpha(T)$ measurements were carried out with laser flash apparatus Theta (Theta Industries Inc., Port Washington, NY, USA) under vacuum and at the temperature range T_R-1250°C. Prior to evaluating the thermal diffusivity, in order to make the sample surfaces opaque, thin layers of colloidal graphite were painted on both the front and the rear faces. In the laser flash method a short laser pulse heats the front surface of the sample and by measuring the time corresponding to the half rise of the temperature increase at the rear surface the thermal diffusivity $\alpha(T)$ can be determined. At high temperature the time-temperature curves were analysed by the ratio method to account for radiation losses. At each temperature, the final value resulted from the average of five repeated measurements carried out for statistical purposes. Furthermore each measurement cycle was repeated 3 times in order to find out irreversible structural changes in coatings. Specific heat $C_P(T)$ measurements were performed with differential scanning calorimeter DSC 404 C (Netzsch-Gerätebau GmbH, Selb, Germany), at the same temperature range, but in air with a scanning rate of 15°C/min. Specific heat measurements were repeated twice. Alumina crucibles were used in all measurements and sapphire samples as DSC standards. Thermal conductivities $k(T)$ were calculated using the equation $k(T) = \alpha(T)*C_P(T)*\rho$, where ρ is the density of the coating.

3. Results and discussion

Coating characterization

In laser-glazed coating the melted region was highly densified, but some vertical cracks were detected, especially at the melted zone. The depth of the melted zone was 80-120 μm. Melting had occurred at quite uniform layer. 8YL coatings had transparent and glassy-like surface after the glazing treatment. The colour of the yttria stabilized zirconia coatings changed from light grey to transparent yellow due to the laser glazing process. SEM studies showed that the melted zone consisted of two variant layers. The uppermost layer was formed of pentagon and hexagon shaped plates and the underneath layer of columnar/dendritic grains; see the marked layers in Fig 1a. From the fracture surface of the coating, some voids could be detected at the lower region of the melted zone, marked with an arrow in Fig. 1 b. Large voids are probably developed from coating porosity during the melting process.

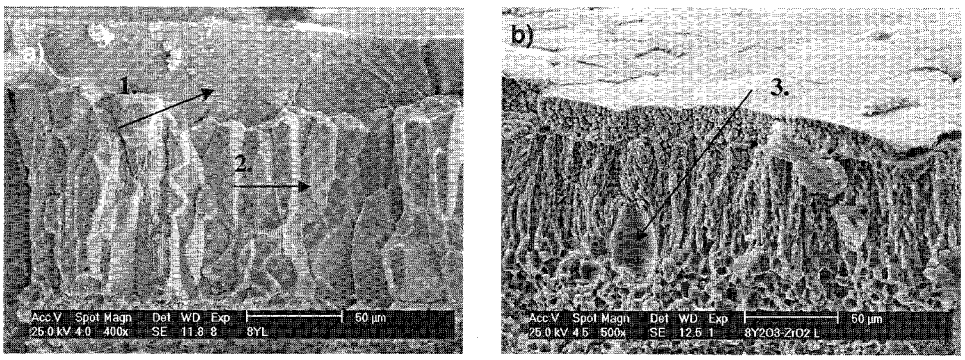


Figure 1. Fracture surfaces of the 8YL coating. a) the melted zone composed of dense plate like top layer and vertically oriented columnar grains and b) closed pores were detected at the melted zone.

In the laser-glazed 8Y coating the phase structure of the coating surface was purely nontransformable tetragonal zirconia, t'-ZrO_2 as it was in the case of the as-sprayed coating. The formation of the nontransformable t'-ZrO_2 indicates rapid solidification of crystals in both plasma spraying and laser glazing. The relative intensity of the individual diffraction peaks was changed strongly due to the glazing process. This is due to the columnar grain orientation, induced by laser glazing process. The full pattern x-ray analysis showed the preferred crystal orientation in direction (002). Optical microscopy studies showed that the phosphate based sealant penetrated approximately 300-400 µm into the coating. Our earlier studies, ref. [22-23], showed also the presence of the aluminium rich bonding phase in coating structure. Any reaction products caused by phosphate sealing treatment could not be found by XRD form the 8Y AP coatings. This is either due to the low concentration of the bonding phases or their amorphous microstructure. After the heat treatment at 1250°C for 5 hours, the XRD studies showed 40 vol-% of m-ZrO_2 in 8Y AP coatings. Monoclinic zirconia was not detected from reference 8Y or laser-glazed 8YL coatings after the heat treatment. Phosphate sealant, penetrated into the interlamellar crack, is presented in TEM micrograph in Fig. 2.

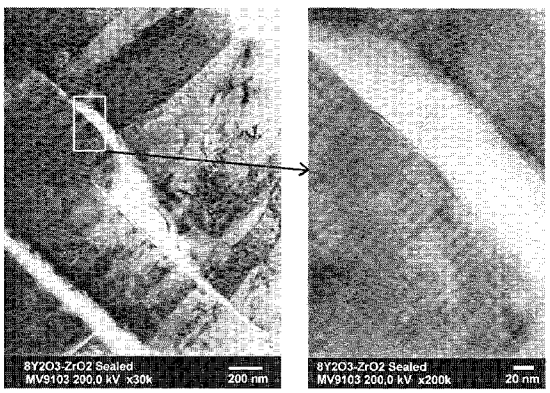


Figure 2. TEM micrograph of the 8Y AP coating.

SAED ring patterns verified the amorphous structure of the sealant. Our previous studies [31,32] of the aluminium phosphate sealed plasma sprayed Al_2O_3 and Cr_2O_3 coatings showed also the amorphous nature of the sealant.

The original total porosity of the as-sprayed coatings, measured by image analysis, was at the range of 14-25 % and the values after the three α(T) measurement cycles were reduced at the level of 14-20%, see Table 1. The open porosity values, measured by mercury infiltration porosimetry (MIP), were much lower and at the range of 5,3-9,3 %, see Table 1. The total porosity, determined by image analysis, is always higher that the real total porosity due to the specimen preparation caused defects on the coating cross sections. So for that reason we could expect that the absolute total porosity is between the values of measured total and closed porosity.

Table 1. Porosities measured by image analysis and mercury infiltration.

	Image analysis			Mercury infiltration		
Specimen	As-sprayed [%]	Heat treated* [%]	Change [%]	As-sprayed [%]	Heat treated** [%]	Microporosity change*** [%]
8Y	24,9 ± 3,2	19,7 ± 1,5	21	9,3 ± 1,0	10,0 ± 1,0	- 40
8YL	20,2 ± 1,9	16,3 ± 2,3	19	-	-	-
8Y AP	14 ± 2,2	14,7 ± 2	-5	5,3 ± 1,0	9,0 ± 1,0	118

* after the three α(T) measurement cycles ** after heat treatment at 1250°C for 5hours *** when counted only the pores with radius < 0,1 μm.

The mercury infiltration porosimetry data could be utilized well when explaining the sintering behaviour of the reference coating 8Y. MIP studies showed slightly increased open porosity in the heat treated 8Y coating, but significant reduction of microporosity at the pore size range of < 0,1 μm. Respectively, image analysis showed porosity reduction of 21 % in heat treated 8Y coating. With image analysis, the detected porosity was mainly macroporosity within the pore size range of > 1 μm. However, the sintering of the structure could be seen in image analysis results indirectly as lower porosity. The reason for that was the specimen preparation caused defects on the cross section of the heat treated coating which were reduced due to sintering of the splat boundary microcracks. SEM studies showed also the evidences of the splat boundary sintering, see Fig. 3. The Fig. 3a shows the typical lamellar structure of the plasma sprayed coating. In Fig. 3b it can be seen the closed splat boundary cracks with remaining strings of closed pores. These areas are marked with the arrows in Fig. 3b.The data obtained from the sealed coatings was more difficult to interpret, because the results could not be focused only to the sealed top layer, but the whole coating. The porosity values of the aluminium phosphate sealed coating increased when measuring with both two methods. The reason for that was probably the volume change, that is linked to the phase change of t'-ZrO_2 ⇒ m-ZrO_2. This could explain also the significant increase of microporosity in form of new microcracks.

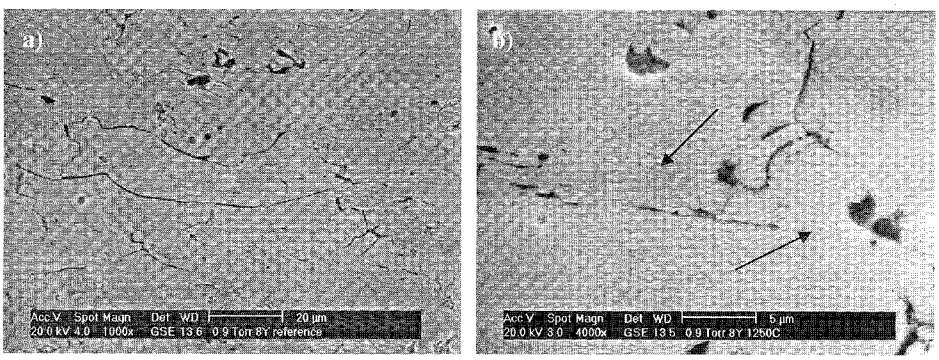


Figure 3. SEM micrograph of the polished 8Y coatings a) in as-sprayed state and b) after the heat treatment at 1250°C for 5hours.

Thermal properties

Thermal diffusivity $\alpha(T)$ and specific heat $C_P(T)$ of the studied coatings were determined as a function of temperature from 100°C up to 1250°C, which is the maximum service temperature for the state-of-the-art thermal barrier coatings. Both measured values $\alpha(T)$ and $C_P(T)$ as well as calculated $k(T)$ values of the unsealed 8Y coatings were compared with the data from the literature [29,33-36]. Specific heat $C_P(T)$, thermal diffusivity $\alpha(T)$ and thermal conductivity $k(T)$ data are presented in Figs. 4, 5 and 6.

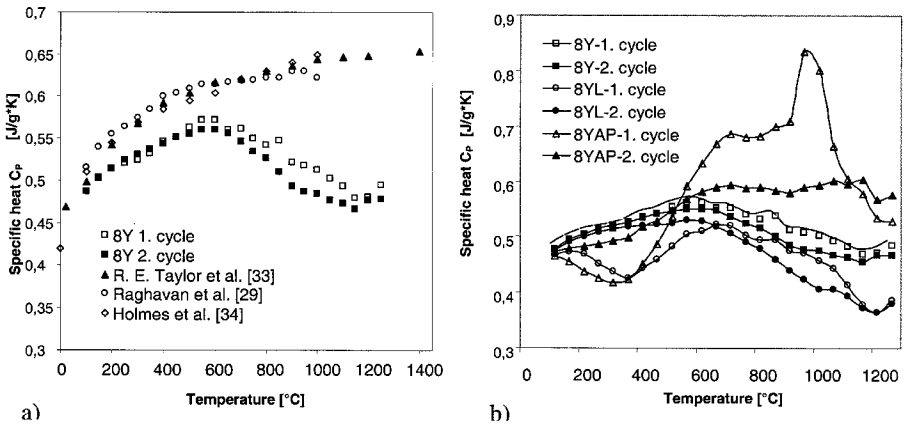


Figure 4. Specific heat $C_P(T)$ data for the $8Y_2O_3$-ZrO_2 coatings. a) comparative graph of the 8Y coatings with the values found in literature and b) first and second cycle data for all studied coatings.

Comparative graph, Fig 4a, shows the difference of our results and the $C_P(T)$ values reported earlier. The difference is below 10% at temperature range 100-600°C, but increases at higher temperatures at 600-1250°C. The measurements with calibration specimen did not show any divergence, but we believe that the deviation was mainly caused by the use of alumina

crucibles. The new set of experiments is in progress with platinum crucibles in order to clarify this difference. Specific heat curves in Fig. 4b indicated the structural changes that took place in coatings during the first heating cycle. In all coatings there was a C_P difference between the first and the second cycle at temperature range around 800-1000°C. This could be explained by the possible exothermal reaction of absorption of oxygen within the unstoichiometric YPSZ lattice. The colour changes of the coatings in the heat treatment support this argument. For better understanding this phenomenon we will perform some comparative analysis in air and in argon atmosphere. In laser-glazed and phosphate sealed coatings there was a minimum in first cycle at about 300°C. The disappearing of the minimum refers to endothermal reaction which was possibly caused by the residual stress relieve or their redistribution in sealed coatings. We will get more information to support this argument when the ongoing measurements for the pulverized specimens are performed. However, our earlier study [22] showed the compressive stress states that arise normally in phosphate sealed $8Y_2O_3$-ZrO_2 coatings. The strong exothermal peak in 8Y AP at 950-1000°C could be explained by the phase change of t-ZrO_2 ⇒ m-ZrO_2.

The comparable α(T) data is presented in Fig. 5a. Our results agree quite well with the literature data. The effect of splat boundary sintering, caused by the heat treatment, can be seen clearly as an increase of α(T) values. There has been lots of research activity on this topic lately [4,33,36]. Sintering starts to appear at temperature around 1000°C, see the ascending curves of the as-sprayed coatings. The differences of the as-sprayed coatings are probably related to the slightly different porosities in their as-sprayed state, but also can be affected by the temperature scanning rate used in measurement. This means that with lower scanning rates there is more time for sintering. From Fig. 5b it can be observed that the thermal diffusivity difference between second and third cycle is very narrow. We can say that almost all the sintering has taken place already in the first cycle. D. Zhu et al. [4] demonstrated by isothermal k measurements at 990, 1100 and 1320°C that the major increase in k occur during the first 5-10 hours, depending on the temperature.

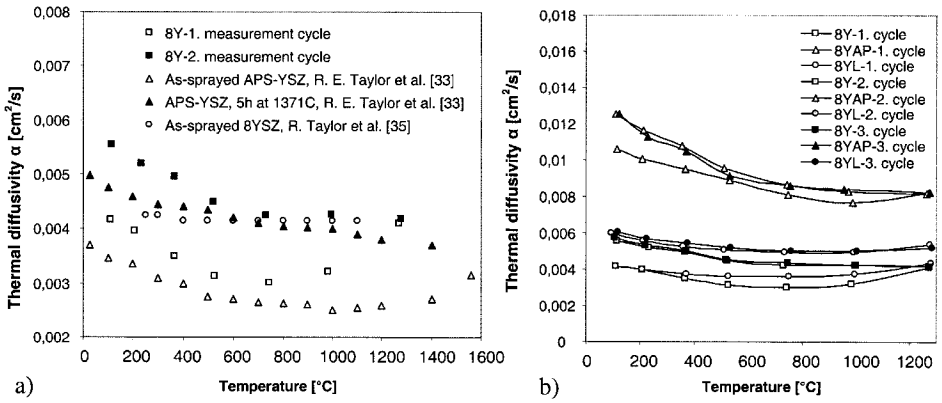
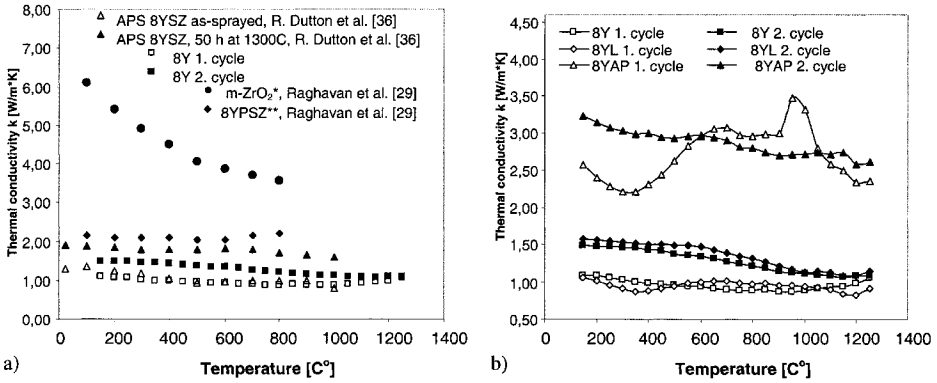


Figure 5. Thermal diffusivity data α(T) for the $8Y_2O_3$-ZrO_2 coatings. a) comparative data from the literature and b) three cycle data for the studied coatings.

The results for laser-glazed coating were almost similar than for as-sprayed coating. The relatively thin glazed zone (80-120 μm) had just slight increasing effect on $\alpha(T)$ values at high temperatures and only after the first measurement cycle. On the contrary, aluminium phosphate sealing treatment had clear increasing effect on thermal diffusivity. The $\alpha(T)$ values of the phosphate sealed coating were rather high if compared to as-sprayed coating and the values were almost doubled at the whole measured temperature range. The sealant penetration in to the interlamellar cracks, as could be detected in TEM studies, is only one reason for higher $\alpha(T)$ values. The sealant had evidently filled part of the vertical microcracks in addition to splat boundary porosity. If the $\alpha(T)$ of the sealant is higher than zirconia, which is quite probable, the sealant acts like thermal diffusion bridge through the coating structure. This could be a reason for why the thermal conductivity $k(T)$ values of the phosphate sealed coatings were even higher than that of bulk yttria stabilized zirconia. The $k(T)$ data is presented in Fig. 6.



* uniaxial pressed and sintered, density 98%, 0 wt% of Y_2O_3 ** uniaxial pressed and sintered, density 96%, 8 wt% of Y_2O_3

Figure 6. Calculated thermal conductivity k(T) values for the $8Y_2O_3$-ZrO_2 coatings. a) comparative graph of the 8Y coatings with the values found from literature and b) first and second cycle data for all studied coatings.

If compared the $k(T)$ values of the as-sprayed $8Y_2O_3$-ZrO_2 coatings with the values obtained from the ref. [36], the data is almost identical. In the case of the heat treated coatings, Dutton et al. [36] used higher heat treatment temperature and longer treatment time, what explains the higher $k(T)$ values. Thermal conductivity values of 7,0 W/mK and 2,2 W/mK were presented for the bulk specimens of m-ZrO_2 and $8Y_2O_3$-ZrO_2, respectively [29]. Thermal conductivity of the monoclinic zirconia showed strong decreasing tendency as a function of temperature, while it was almost constant up to 800°C in the case of $8Y_2O_3$-ZrO_2. In heat treated phosphate sealed coating also the 40 -vol% fraction of m-ZrO_2 could explain the high $k(T)$ values especially at low temperature region.

The modelling of the thermal properties vs. coating porosity

In order to compare the results of porosimetry carried out by IA and by MIP with the thermal conductivity k data referring to the first and the third measurement cycles, some modelling of the thermal conductivity in porous materials should be introduced. Several models describing

the effect of spherical and ellipsoidal-shaped porosity on *k(T)* have been presented in the literature [37-40]. Generally these models consider a binary mixture of bulk material and pores with a fixed shape and orientation in respect to the heat flux. In order to model a coating constituted by a matrix and by two different kinds of porosity (closed porosity with a given shape and orientation, and open randomly oriented porosity, respectively) a three-phase model was proposed by applying in an iterative way a two-phase modelling [41]. In particular if p_0 is the total amount of porosity and p_1 and p_2 are the percentages of open and closed porosity respectively, the thermal conductivity of the three-phase mixture is:

$$k = \frac{k_0}{2}\left\{\Phi\left[\frac{p_2}{(1-p_1)}\right]\Psi(p_1)+\Psi\left[\frac{p_1}{(1-p_2)}\right]\Phi(p_2)\right\} \tag{1}$$

where k_0 is the matrix thermal conductivity, and $\Psi(p)$ and $\Phi(p)$ are the functions describing the effect (in the two-phase model) of open and closed porosity on matrix thermal conductivity.

Since three different kinds of porosity (randomly oriented open porosity, ellipsoidal shaped oriented closed porosity and microcracks perpendicularly oriented to the heat flux) could be distinguished in the coatings studied here, a further iterative process should be applied. In particular, if $\Theta(p)$ is the function describing the contribution of the microcracks to the thermal conductivity, the symmetrical expression giving the final k of the four phase system is:

$$k = \frac{k_0}{6}\left\{\begin{array}{l}\Phi\left[\frac{p_2}{(1-(p_1+p_3))}\right]\Psi\left(\frac{p_1}{(1-p_3)}\right)\Theta(p_3)+\Psi\left[\frac{p_1}{(1-(p_2+p_3))}\right]\Phi\left(\frac{p_2}{1-p_3}\right)\Theta(p_3)+\\ \Phi\left[\frac{p_2}{(1-(p_1+p_3))}\right]\Theta\left(\frac{p_3}{1-p_1}\right)\Psi(p_1)+\Psi\left[\frac{p_1}{(1-(p_2+p_3))}\right]\Theta\left(\frac{p_3}{1-p_2}\right)\Phi(p_2)+\\ \Theta\left(\frac{p_3}{(1-(p_1+p_2))}\right)\Phi\left[\frac{p_2}{1-p_1}\right]\Psi(p_1)+\Theta\left(\frac{p_3}{(1-(p_1+p_2))}\right)\Psi\left[\frac{p_1}{(1-p_2)}\right]\Phi(p_2)\end{array}\right. \tag{2}$$

Ψ, Φ and Θ functions describe the influence of porosity (supposed ellipsoidal) following the equation [2]:

$$\Psi(p),\Phi(p),\Theta(p) = (1-p)^X \text{ and } X = \frac{1-\cos^2\vartheta}{1-F}+\frac{\cos^2\vartheta}{2F} \tag{3}$$

where ϑ is the angle between the heat flux and the axis of revolution, and F is the shape factor of the ellipsoid. The main advantage in modelling porosity as revolution ellipsoids is that by varying the ratio between the two ellipsoid axes it is possible to obtain either lamellas or cylinders or any intermediate case such as spheres.

In the specific case of open randomly oriented porosity, the correct value for X is 1,66 (F=0.5 and $\cos^2\vartheta$=1/3), while for closed lightly lamellar porosity oriented perpendicular to the flux X could be fixed equal to 2 (F=0,25 and $\cos^2\vartheta$=1). In order to correctly represent microcracks as porosity, lamellae can be very flat; this means that the ratio between the major b and minor a ellipsoid axes can be quite high. Fig. 7 gives an idea of the influence of the shape and the orientation of porosity on the normalized thermal conductivity k/k_0.

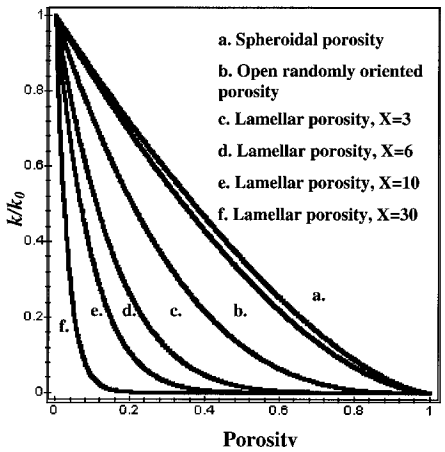


Fig. 7. Normalized thermal conductivity (k/k_0) vs. volumetric fraction of porosity. Curves refer to porosity with different shape. In particular the effects of spheres, of open randomly oriented porosity, and of lamellar porosity (X=3, 6, 10 and 30). In the case of lamellae the minor axis always is parallel to the heat flux direction. In fact due to the spraying process porosity is generally flattened along the thickness direction.

In order to semi-quantitatively explain the experimental results, in the specific case of 8Y sample we could assume that closed porosity fraction is the difference between the total porosity measured by IA and the total open porosity estimated by MIP. Microcracks porosity is assumed to correspond to open porosity in the range < 0,1 μm while the rest of open porosity (the range 0,1-10 μm in MIP analysis) was fixed as the open randomly distributed porosity. For microcracks, considering 8.5 as a reasonably average value for the ratio *b/a*, X resulted as equal to 6.

Thus, considering the bulk thermal conductivity of 8YPSZ and the relative percentages of open randomly oriented, lamellar and microcracks porosity in the sample 8Y both before and after the thermal cycling, two curves have been obtained by using Eq.(2) and (3) as shown in Fig. 8. Note that at about 0,25 (total porosity before heat treatment) and 0,20 (total porosity after heat treatment) the values on the two curves resulted 1,15 W/mK and 1,71W/mK respectively. Since a very satisfactory agreement between the modelling is shown - as a matter of fact the experimental values for thermal conductivity are 1,15 W/mK and 1,55 W/mK respectively - it is possible to conclude that the thermal conductivity increase after the thermal cycling can be really explained with the porosity transformation and reduction.

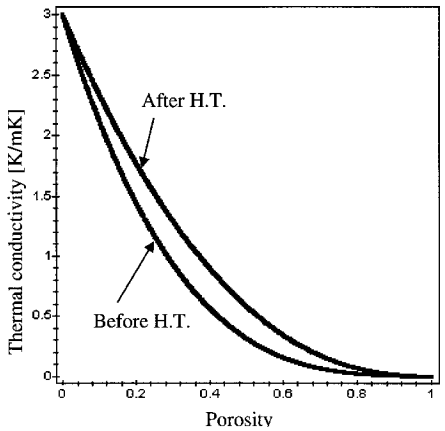


Fig. 8. Thermal conductivity vs. total porosity volumetric fraction. Curves were obtained by using Eq.(2) and Eq.(3) with k_0=3W/mK [42]. Curve before the heat treatment refer to a porometric distribution of 59% lamellar porosity (X=2), 4% of open randomly oriented porosity (X=1.66) and 37% of microcrack porosity (X=6) respectively. The corresponding values after the treatment were 59%, 27% and 14%.

4. Conclusion and summary

In this paper we introduced and characterised two modified TTBC structures, namely laser-glazed and aluminium phosphate sealed $8Y_2O_3$-ZrO_2 coatings. Thermal properties ($C_P(T)$, $\alpha(T)$, $k(T)$) of the coatings were determined in cycles and the relation of thermal properties and microstructures was discussed. Finally we introduced a model in which thermal conductivity was considered as a function of porosity and combination of different porosity geometries. The main results of this study were:

- Sintering of the splat boundaries in heat treatment (measurement cycle) was obvious. This microstructural change was clarified with OM, SEM and MIP studies in addition to thermal diffusivity $\alpha(T)$ measurements.
- Laser-glazing had negligible effect on coating thermal conductivity values. On the contrary, aluminium phosphate sealing doubled the thermal conductivity values of the $8Y_2O_3$-ZrO_2 coating.
- The modelled thermal conductivities were in good agreement with measured values. Also the effect of sintering could be considered in the model.

5. Acknowledgements

Results in this paper have been collected from the work carried out in COST522 Work Package 2 "Protective Systems" at TUT/IMS and CESI during the years 2001 and 2002. The authors are grateful to their national financial supporters.

6. References

1. K. An, K.S. Ravichandran, R.E. Dutton, S. Semiatin, Microstructure, Texture and Thermal Conductivity of Single-Layer and Multilayer Thermal Barrier Coatings of Y_2O_3-Stabilized ZrO_2 and Al_2O_3 Made by Physical Vapor Deposition, Journal of American Ceramic Society, 82 [2], 1999, p. 399-406.
2. K.S. Ravichandran, K. An, Thermal Conductivity of Plasma-Sprayed Monolithic and Multilayer Coatings of Alumina and Yttria-Stabilized Zirconia, Journal of American Ceramic Society, 82 [3], 1999, p. 673-682.
3. D. Zhu, R. A. Miller, B. A. Nagaraj, R. W. Bruce, Thermal conductivity of EB-PVD thermal barrier coatings evaluated by a steady-state laser heat flux technique, Surface and Coatings Technology, 138, 2001, p. 1-8.
4. D. Zhu, R. A. Miller, Thermal Conductivity and Elastic Modulus Evolution of Thermal Barrier Coatings under High Heat Flux Conditions, Journal of Thermal Spray Technology, 9(2), 2000, p. 175-180.
5. W. P. Parks, E. E. Hoffman, W. Y. Lee, I. G. Wright, Thermal Barrier Coatings Issues in Advanced Land-Based Gas Turbines, Journal of Thermal Spray Technology, 6(2), 1997, p. 187-192.
6. W. Beele, G. Marijnissen, A. Van Lieshout: The Evolution of Thermal Barrier Coatings – Status and Upcoming Solutions for Today's Key Issues. Surface and Coatings Technology, 120-121, 1999, p. 61-67.
7. J. P. Singh, B. G. Nair, D. P. Renusch, M. P. Sutaria, M. H. Grimsditch, Damage Evolution and Stress Analysis in Zirconia Thermal Barrier Coatings during Cyclic and Isothermal Oxidation, Journal of American Ceramic Society, 84 [10], 2001, p. 2385–2393.
8. A. G. Evans, D. R. Mumm, J. W. Hutchinson, G. H. Meier, F. S. Pettit, Mechanisms Controlling the durability of thermal barrier coatings, Progress in Materials Science, 46, 2001, p. 505-553.
9. A. Ohmori, Z. Zhou, K. Inoue, K. Murakami, T. Sasaki, Sealing and Strengthening of Plasma-Sprayed ZrO_2 Coating by Liguid Mn Alloy Penetration Treatment, Thermal Spraying: Current Status and Future Trends, Akira Ohmori (Ed.), High Temperature Society of Japan, Osaka University, Osaka 567, Japan, 1995, p. 549-554.
10. I. Zaplatynsky, Performance of Laser-Glazed Zirconia Thermal Barrier Coatings in Cyclic Oxidation and Corrosion Burner Rig Test, Thin Solid Films, 95, 1982, p. 275-284.
11. R. Sivakumar, B. L. Mordike, Laser Melting of Plasma Sprayed Ceramic Coatings, Surface Engineering, 4(2), 1988, p. 127-140.
12. K. M. Jasim, D. R. F. West, W. M. Steen, R. D. Rawlings, Laser Surface Sealing of Plasma Sprayed Yttria Stabilized Zirconia Ceramics, in conference proceedings of the Laser Materials Processing 1988, Springer-Verlag, Heidelberger Pl. 3, D-1000 Berlin, 1989, p. 17-31.
13. H.L. Tsai, P.C. Tsai, Microstructures and Properties of Laser-glazed Plasma-sprayed ZrO_2-$YO_{1.5}$/Ni-22Cr-10Al-1Y Thermal Barrier Coatings, Journal of Materials Engineering and Performance, 4(6), 1995, p. 689-696.
14. K. A. Khor, S. Tana, Pulsed Laser Processing of Plasma Sprayed Thermal Barrier Coatings, Journal of Materials Processing Technology, 66, 1997, p. 4-8.
15. Z. Zhou, N. Eguchi, H. Shirasawa, A. Ohmori, Microstructure and Characterization of Zirconia-Yttria Coatings Formed in Laser and Hybrid Spray Process, Journal of Thermal Spray Technology, 8(3), 1999, p. 405-413.

16. A. Ferriere, L. Lestrade, A. Rouanet, A. Denoirjean, A. Grimaud, P. Fauchais, Solar Furnace Surface Treatment of Plasma-Sprayed Thermal Barrier Coatings, Journal of Thermal Spray Technology, 3(4), 1994, p. 362-370.
17. H. Kuribayashi, K. Suganuma, Y. Miyamoto, M. Koizumi, Effect of HIP Treatment on Plasma-Sprayed Ceramic Coating onto Stainless Steel, American Ceramic Society Bulletin, 65(9), 1986, p. 1306-1310.
18. K. A. Khor, N. L. Loh, Hot Isostatic Pressing of Plasma Sprayed Thermal Barrier Coating Systems, Materials and Manufacturing Processes, 10(6), 1995, p. 1241-1256.
19. K. Moriya, Wenxhen Zhao, A. Ohmori, Improvement of Plasma-Sprayed Ceramic Coatings Treated by Sol-Gel Process, Thermal Spraying: Current Status and Future Trends, A. Ohmori (Ed.), High Temperature Society of Japan, Osaka University, Osaka 567, Japan, 1995, p. 1017-1021.
20. G. John, T. Troczynski, Surface Modification of Thermal Sprayed Coatings, Thermal Spray: Practical Solutions for Engineering Problems, ASM International, C.C. Berndt (Ed.), Materials Park, OH-USA, 1996, p. 483 – 488.
21. T. Troczynski, Q. Yang, G. John, Post-Deposition Treatment of Zirconia Thermal Barrier Coatings Using Sol-Gel Alumina, Journal of Thermal Spray Technology, 8(2), 1999, p. 229-234.
22. S. Ahmaniemi, P. Vuoristo, T. Mäntylä "Effect of Aluminum Phosphate Sealing Treatment on Properties of Thick Thermal Barrier Coating", Thermal Spray: Surface Engineering via Applied Research, C. C. Berndt (Ed.), ASM International, Materials Park, OH-USA, 2000, p. 1087-1092.
23. S. Ahmaniemi, P. Vuoristo, T. Mäntylä: "Comparative Study of Different Sealing Methods for Thick Thermal Barrier Coatings", Thermal Spray: New Surfaces for a New Millenium, C. C. Berndt, K. A. Khor, E. F. Lugscheider (Eds.), ASM International, Materials Park, OH-USA, 2001, p. 157-165.
24. V. A. C. Haanappel, J. B. A. Scharenborg, H. D. Corbach, T. Fransen, P. J. Gellings, Can Thermal Barrier Coatings be Sealed by Metal-Organic Chemical Vapour Deposition of Silica and Alumina, High Temperature Materials and Processes, 14(2), 1995, p. 57-66.
25. J. Knuuttila, P. Sorsa, T. Mäntylä, Sealing of Thermal Spray Coatings by Impregnation, Journal of Thermal Spray Technology, 8(2), 1999, p. 249-257
26. P. K. Schelling and S. R. Phillpot, Mechanism of Thermal Transport in Zirconia and Yttria-Stabilized Zirconia by Molecular-Dynamics Simulation, Journal of American Ceramic Society, 84(12), 2001, p. 2997–3007.
27. P. G. Klemens, Phonon scattering by oxygen vacancies in ceramics, Physica B, 263–264, 1999, p. 102–104.
28. S. Raghavan, H. Wang, W. D. Porter, R. B. Dinwiddie and M. J. Mayo, Thermal Properties of Zirconia Co-doped with Trivalent and Pentavalent Oxides, Acta Materiali, 49, 2001, p. 169–179.
29. S. Raghavan, H. Wang, R. B. Dinwiddie, W. D. Porter, and M. J. Mayo, The Effect of Grain Size, Porosity and Yttria Content on the Thermal Conductivity of Nanocrystalline Zirconia, Scripta Materialia, 39(8), 1998, p. 1119-1125.
30. J. R. Nicholls, K. J. Lawson, A. Johnstone, D. S. Rickerby, Methods to reduce the thermal conductivity of EB-PVD TBS's, Surface and Coatings Technology, in print, 2001.
31. M. Vippola, S. Ahmaniemi, J. Keränen, P. Vuoristo, T. Lepistö, T. Mäntylä, and E. Olsson, Aluminum Phosphate Sealed Alumina Coating: Characterization of Microstructure, Materials Science & Engineering, 323(1-2), 2002, p. 1 – 8.

32. M. Vippola, S. Ahmaniemi, P. Vuoristo, T. Lepistö, T. Mäntylä, and E. Olsson, Microstructural Study of Aluminum Phosphate Sealed Plasma-Sprayed Chromium Oxide Coating, Journal of Thermal Spray Technology, In Print, 2001.
33. R.E. Taylor, X. Wang, X, Xu, Thermophysical Properties of Thermal Barrier Coatings, Surface and Coatings Technology 120–121, 1999, p. 89–95
34. R.R. Holmes, T.N. McKechnie, Vacuum application of thermal barrier plasma coatings, in: R.J. Richmond, S.T. Wu Eds., NASA Marshall Space Flight Center, Advanced Earth-To-Orbit Propulsion Technology, 1, 1988, p. 692-702.
35. R. Taylor, J. R. Brandon, P. Morrel, Microstructure, Composition and Property Relationship of Plasma Sprayed Thermal Barrier Coatings, Surface and Coatings technology 50, 1992, p. 141.
36. R. Dutton, R. Wheeler, K. R. Ravichandran, K. An, Effect of Heat Treatment on the Thermal Conductivity of Plasma-Sprayed Thermal Barrier Coatings, Journal of Thermal Spray Technology, 9(2), 2000, p. 204-209.
37. J. C. Maxwell "A treatise on Electricity and Magnetism" Clarendon Press, Oxford, UK, 1904.
38. B. Shultz, "Thermal conductivity of porous and highly porous materials", High Temp.-High Press., 13, 1981, p. 649-660.
39. D.S. McLachlan, "An equation for conductivity of binary mixtures with anisotropic grain structures", Journal of Phyics. C: Solid State Physics, 20, 1987, p. 865-877.
40. A. Bjorneklett, L. Haukeland, J. Wigren and H. Kristiansen, "Effective medium theory and the thermal conductivity of plasma-sprayed ceramic coatings", Journal of Materials Science, 29, 1994, p. 4043-4050.
41. P. Scardi, M. Leoni, F. Cernuschi, A. Figari, "Microstructure and heat transfer phenomena in ceramic Thermal Barrier Coatings", Journal of American Ceramic Society, 84(4), 2001, p. 827-35.
42. D.H. Hasselmann, L.F. Johnson, L.D. Bentsen, R. Syed, H.L. Lee, M.V. Swain, American Ceramic Society Bulletin, 66(5), 1987, p.799-806.

ADVANCED NITRIDE COATINGS FOR OXIDATION PROTECTION OF TITANIUM ALLOYS

C. Leyens[1], M. Peters[1], P. Eh. Hovsepian[2], D.B. Lewis[2], Q. Luo[2], W.-D. Münz[2]

[1]DLR-German Aerospace Center, Institute of Materials Research, Cologne, Germany
[2]Sheffield Hallam University, Materials Research Institute, Howard Street, Sheffield, UK

Abstract

CrN/NbN, TiAlCrYN and TiAlYN/CrN coatings were deposited onto aerospace titanium alloy TIMETAL 834 using combined cathodic arc/unbalanced magnetron sputtering. Specimens were Nb- and Cr-ion etched before coating deposition, respectively. Isothermal and cyclic oxidation tests were performed in air at 750°C for 1000h. While CrN/NbN coatings as well as metal ion etching alone did not improve oxidation resistance of the substrate alloy, monolithically grown TiAlCrYN and superlattice TiAlYN/CrN coatings demonstrated enhanced oxidation resistance. Careful post-oxidation microstructural investigations using SEM, EDS, Raman spectroscopy, and TEM revealed that the TiAlCrYN and TiAlYN/CrN formed a thin protective alumina scale which was interrupted by titania agglomerations originating from substrate oxidation that dominated oxidation behaviour after extended exposure times. Despite the presence of coating defects leading to substrate attack, these novel coatings are considered as promising candidates for oxidation protection of titanium alloys.

KEYWORDS: oxidation resistant nitride coating, titanium alloys, combined cathodic arc/unbalanced magnetron sputtering, superlattice coating

Introduction

Due to their low density and their well-balanced mechanical properties, near-α and α+β titanium alloys are widely used for aircraft engine parts, for example, as compressor components such as disks, vanes and blades. The maximum useful service temperature of titanium alloys for these applications is limited to about 500°C [1], mainly due to the insufficient environmental resistance of the structural material.

Surface treatments, first and foremost various types of coatings, aiming at improved environmental resistance of titanium alloys have been investigated for more than three decades [2]. One major problem of coating development for titanium alloys has been that, although reasonable short-term oxidation resistance was achieved in many cases, most of these coatings tended to be inherently brittle or formed brittle phases with the substrate material, thus degrading its mechanical properties, especially fatigue behavior. Since the embrittlement problem has never been acceptably solved, none of the coatings proposed for improved oxidation resistance has been brought into service. Recently, promising avenues for coating development have been demonstrated with sputter-deposited Ti-Al-based coatings [3]. In addition to enhanced oxidation resistance, these coating systems demonstrated reasonable mechanical properties such as creep [4] and fatigue behaviour [5]. Cr additions to Ti-Al-base coating demonstrated significantly improved environmental resistance [6]. Furthermore, silver additions to γ-TiAl-base coatings have shown excellent oxidation resistance [7].

In the present paper, a new approach is described to improve the environmental resistance of titanium alloys by nitride overlay coatings produced by combined cathodic arc/unbalanced

magnetron sputtering. The coating systems selected were reported to have reasonable oxidation resistance in cutting applications [8-11]. Furthermore, due to the high hardness of the coatings, protection against wear and erosion can be expected, both of which can be critical issues in certain fields of application. This paper reports results of an oxidation study under isothermal and cyclic conditions and post-oxidation microstructure investigation of the coatings systems after exposure.

Experimental

Monolithically and superlattice coatings grown by combined cathodic arc/unbalanced magnetron technique

This sections gives only a brief description of the deposition procedure; details are provided in [12]. An industrially sized HTC 100-4 ABS (ABS: Arc Bond Sputtering) [13] coating unit was used to deposit monolithic TiAlCrYN and the superlattice TiAlYN/CrN and CrN/NbN coatings. The system comprises four vertically arranged rectangular cathodes (target size 600x 200 mm), which can be operated either in steered arc or in unbalanced magnetron mode (figure 1). The cathodes surround a turntable providing threefold planetary rotation of the parts to be coated. Prior to coating deposition, the substrate surfaces were subjected to an intense metal ion bombardment, either using Cr^+ or Nb^+ ions. TiAlCrYN coatings were deposited by the use of two TiAl targets and one TiAlY target, all powered at 8 kW, and one Cr target at 0.5 kW. Using 8 kW power on all four targets leads to clear superlattice coating architecture, (TiAlN/CrN), with a bi-layer thickness defined by the frequency of the primary rotation and the power dissipated on the targets. Similarly, CrN/NbN superlattice coatings were produced using a pair of Cr (99.8% pure) and pair of Nb (99.8% pure) targets, reactively sputtered in an (Ar + N_2) atmosphere. The microstructure of the TiAlCrAlYN and the TiAlYN/CrN coatings is single phase NaCl, whilst the TiAlYN/CrN coating exhibits a superlattice structure consisting of alternating layers of Y-free TiAlN, Y-rich TiAlYN, and CrN [14]. The TiAlYN/CrN coating, however, was found to be single phase as it was not possible to resolve the individual reflections of the TiAlN, Y-rich TiAlYN, and CrN phases.

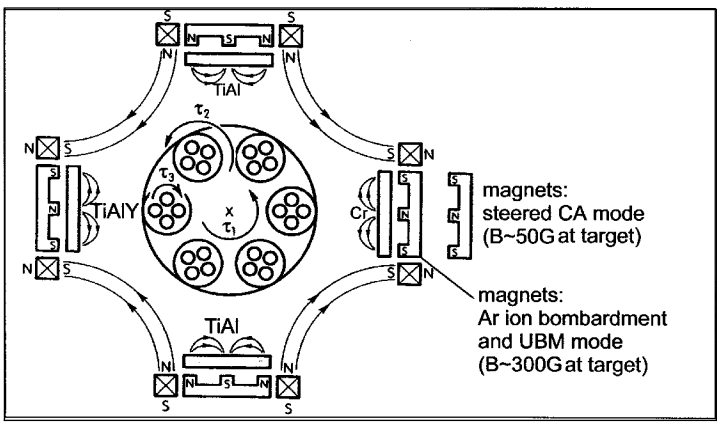


Figure 1: Schematic cross section of the Hauzer HTC 100-4 coating unit.

Oxidation tests and characterisation

The coatings were deposited on coupon specimens (dia. 15mm x 1mm) of aerospace titanium alloy TIMETAL 834 (nominal composition: Ti-5.8Al-4.0Sn-3.5Zr-0.7Nb-0.5Mo-0.35Si, in wt.%). Quasi-isothermal oxidation tests were performed in box furnaces at 750°C in air. The specimens were placed in alumina crucibles covered with alumina lids to collect any spalled oxide during cooling of the specimens. Specimens were weighed and visually inspected before exposure and once every week up to a total exposure time of 1000h. Cyclic oxidation tests were carried out in automated rigs in air at 750°C for up to 1000 cycles. One cycle consisted of 1h at temperature and 10min cooling down to 70°C. The specimens were suspended from Pt hooks. For the first 100 cycles specimens were weighed every 20 cycles and then after 50 additional cycles.

After the tests, the samples were examined by SEM (Philips XL40 SEM-EDS , 20 kV, ultra-thin window), both on the oxidised surface and on a fractured and/or polished cross-section surface. XRD measurements using Bregg-Brentano (Θ/2Θ) geometry as well as glancing angle X-ray diffraction (GA-XRD) were performed at 0.5, 2 and 10° incidence. Moreover, Raman spectroscopy was used to identify phase composition of the oxide layers formed. Then analytical TEM examination was applied to cross-sectioned samples, with a Philips CM20 STEM instrument (200 kV, with ultra-thin window EDS system). EDS analysis of interesting areas employed a focused electron beam of 50 nm in diameter.

Results and Discussion

Oxidation behavior

Mass change vs. time data indicated considerable mass gain of the reference TIMETAL 834 specimens during the first 350 h as a result of rapid oxide scale growth, and mass loss during continued exposure (Figure 2). The mass loss of the specimen is clearly attributed to oxide spallation during cooling down from 750°C to room temperature. The Cr-etched specimen behaved similarly to the reference sample, however, oxide scale adherence might have been

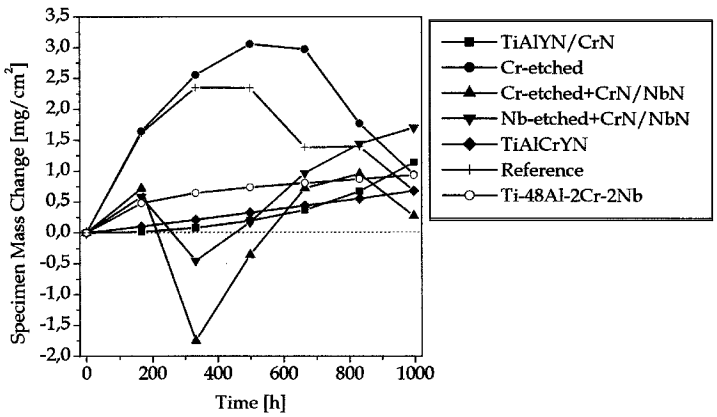


Figure 2: Specimen mass change vs. time for coated and bare TIMETAL 834 isothermally exposed to air at 750°C. γ-TiAl alloy Ti-48Al-2Cr-2Nb was included for comparison.

improved slightly. The CrN/NbN superlattic coatings, both with Cr- and Nb-etching, demonstrated moderate mass gain during the first week of exposure but significant mass loss was measured after the second week. Visual inspection of the specimens revealed that mass loss was, at least partly, attributed to loss of the coating rather than oxide scale alone. As mass change data suggest, adhesion of the CrN/NbN coating was somewhat better on the Nb-etched specimen than on the Cr-etched counterpart. However, once part of the coating was lost, the bare substrate material started to oxidize heavily with oxidation kinetics similar to that of the reference material in the initial state of oxidation. Similarly, mass loss due to oxide scale spallation was observed for the CrN/NbN coated specimens after extended exposure times. On the contrary, the TiAlYN/CrN (Ti (11 at %), Al (12 at %), Y (1 at %), Cr (26 at %), N (50 At %)) superlattice coating and the monolithically grown TiAlCrYN (Ti (22 at %), Al (25.5 at%), Cr (1.5 at %), Y (1 at %), N (50 at %)) coating exhibited relatively good oxidation resistance. The TiAlCrYN coating followed linear oxidation kinetics but with a fairly slow growth rate, whereas oxidation kinetics gradually accelerated with continued exposure for the TiAlYN/CrN superlattice coating. Although oxidation kinetics of both coatings did not follow a parabolic rate law indicative of protective oxide scale formation, oxidation behavior was significantly better compared with that of commercial γ-TiAl alloy Ti-48Al-2Cr-2Nb over a long period of time. However, after 1000 h exposure, the mass gain of the TiAlCrYN coating was only slightly lower than that of the reference material Ti-48Al-2Cr-2Nb, while for the TiAlYN/CrN superlattice coating mass gain was slightly higher. The reason for the increase in mass gain of the coatings will be addressed later.

Mass change vs. number of cycles data indicated the identical ranking of specimens as obtained from isothermal testing (figure 3). The bare TIMETAL 834 reference material as well as the Cr- and also the Nb-etched variants exhibited rapid mass gain during the initial several hundred cycles before oxide scale spallation occurred. The onset of scale spallation was somewhat earlier for the Nb-etched variant than for the reference material and was, similar to the isothermal tests, somewhat retarded for the Cr-etched variant. The CrN/NbN layers spalled partly off the specimens during the initial cycles, leading to rapid oxide scale growth after exposure of bare substrate material. Visual inspection as well as mass change data indicated that the CrN/NbN layers on the Cr-etched substrate had somewhat better adherence than the Nb-etched counterparts resulting in moderate mass gain due to oxidation; however, the oxide scale spalled off the coating after roughly 300 cycles, then reformed, but spalled again after 600 cycles, finally resulting in substantial mass loss of the specimen after 1000 cycles. The TiAlYN/CrN superlattice coating and the monolithic TiAlCrYN coating both showed low mass gain in the first few hundred cycles but, similar to isothermal testing, accelerated mass gain was observed for the superlattice coating after roughly 500 cycles resulting in significantly higher mass gain after 1000 cycles compared to Ti-48Al-2Cr-2Nb. After 1000 cycles, the TiAlCrYN coating exhibited identical mass gain as Ti-48Al-2Cr-2Nb, again indicating a tendency towards accelerated oxidation. So, in conclusion, the results indicate that the TiAlYN/CrN and the TiAlCrYN provided good protection for near-α alloy TIMETAL 834 under isothermal and cyclic testing conditions, however, accelerated oxidation occurred after a few hundred hours of exposure, resulting in oxidation resistance as good as or poorer than that of reference Ti-48Al-2Cr-2Nb alloy.

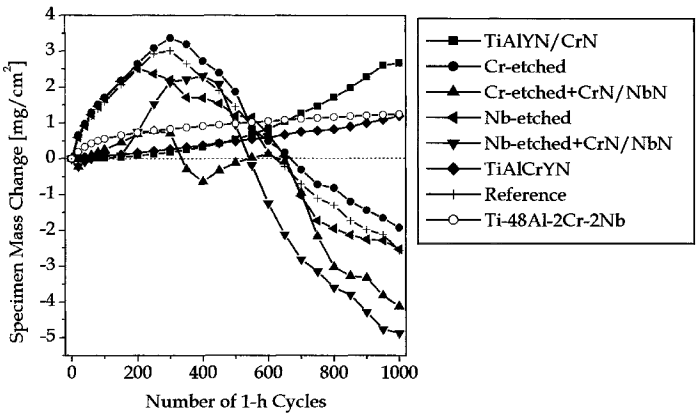


Figure 3: Specimen mass change vs. number of 1-h cycles for coated and bare TIMETAL 834 cyclically exposed to air at 750°C. γ-TiAl alloy Ti-48Al-2Cr-2Nb was included for comparison. TiAlCrYN and TiAlYN/CrN coatings demonstrated good oxidation resistance.

The beneficial effect of Cr additions to the oxidation resistance of γ-TiAl alloys in certain parts of the Ti-Al-Cr system was discovered by Perkins and Meier [15], developed for coatings on titanium aluminides [16, 17] and extensively studied by Brady et al. [18, 19]. Ti-Al-Cr alloys with Cr contents from 6-35 at.% and Al contents from 47-55 at.% form thin alumina scales in the temperature range between 760 and 1000°C [16] and thus exhibit excellent oxidation resistance. The $Ti(Cr,Al)_2$ Laves phase is considered to play a key role with regards to the Cr effect by formation of protective alumina as a result of low oxygen permeability [18]. Furthermore, the Cr negates the adverse effects on oxidation of the nitrogen present in air [19]. In the present study, apart from the coating defects, at 750°C in air the nitride coatings formed protective alumina at the outermost scale followed by three zones with varying alumina/titania content as will be outlined below, although for the TiAlYN/CrN coating the Cr level was fairly high (26 at.%) while the Al level was low (12 at%) whilst for the TiAlCrYN coating Al was higher (25.5 at%) and Cr was only 1.5 at.%. In earlier work, the formation of a mixed alumina and titania scale after short oxidation times (1h) at relatively high temperatures (900°C) was reported [20]. Y segregates to the grain boundaries of the nitride layers and is thought to act as a barrier against inward diffusion of oxygen and outward diffusion of substrate elements [20]. It is not clear yet whether Y has also an effect on the critical Cr level needed to form protective alumina scales.

Microstructural characterisation of the TiAlYN/CrN superlattice coatings

The oxidised surface of the TiAlYN/CrN superlattice coating after 1000h exposure at 750°C was smooth, however, showed pronounced dispersion of oxide agglomerations (figure 4); the morphology of the oxide agglomerations was indicative of titania, while the smooth part of the oxide scale was alumina, as confirmed by XRD and Raman spectrocopy. SEM cross-section investigations revealed that the thickness of the smooth surface oxide layer was only ~0.6-0.8 μm compared to the entire thickness 4μm of the coating structure (figure 5). The titania agglomerations were associated with subsurface oxidation of the titanium alloy,

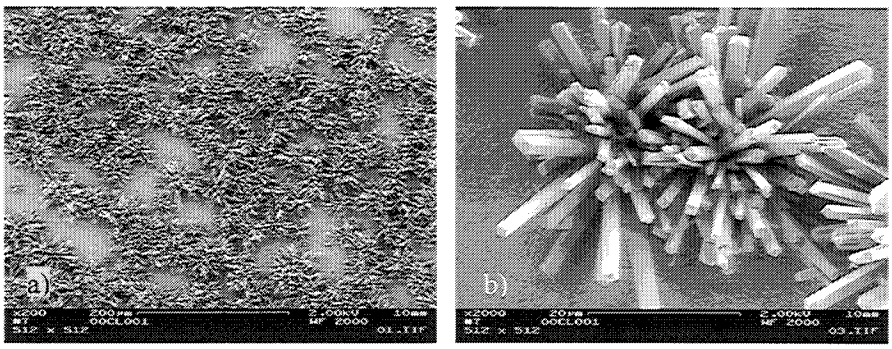


Figure 4: SEM top view of the TiAlN/CrN coating after 1000h cyclic oxidation exposure at 750°C. The smooth surface oxide layer is interrupted by oxide agglomerations (a) the morphology of which is indicative of titania formation (b).

through defects in the nitride coating. The arrangement of the titania agglomerations suggested that single cylindrical-shaped channels were formed during exposure; thus, oxygen had direct access to the titanium alloy, resulting in local oxide formation underneath the nitride layer, spreading along the interface. The resultant volume expansion from the oxidation process led to upward bending of the coating and interfacial cracks. Considering the continuously increasing oxidation rate as obtained from both isothermal and cyclic oxidation tests (figures 2 and 3) it was concluded that the amount of "active" defects in the nitride coating increased with increasing exposure time, thus promoting formation of a significant amount of rapidly growing titania.

TEM analysis of the TiAlYN/CrN after high temperature exposure indicated a layered substructure consisting of an ~0.8μm oxide layer with varying phase composition across the thickness, a 95nm transition layer between the oxide and the nitride layer, 3.8μm retained nitride layer with an unchanged columnar morphology (35-90nm in column width) and B1 NaCl structure, and a 275nm transition layer between the titanium alloy and the nitride

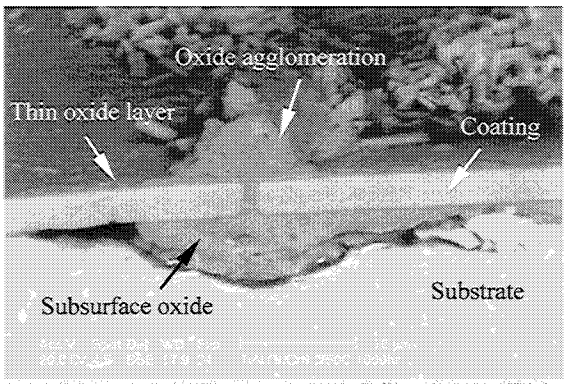


Figure 5: SEM tilted angle view of the surface region of TIMETAL 834 coated with TiAlYN/CrN after exposure to air at 750°C for 1000h.

coating. Underneath the transition zone, the titanium alloy was recrystallised with fine grains in a 460nm layer; neither oxygen nor nitrogen or chromium were found in this layer, indicating both excellent protection of the nitride layer against diffusion of nitrogen and oxygen from the gas atmosphere during exposure as well as very little interdiffusion between the nitride coating and the substrate alloy. Where the titanium alloy was oxidized underneath defects in the nitride coating, EDS analysis revealed Ti 84.2%, Al 2.0%, Cr 0.1%, remainder oxygen, suggesting that rutile was the predominant oxide which is in good agreement with earlier results on oxidation of TIMETAL 834 [21].

Microstructural characterisation of the monolithically grown TiAlCrYN coatings

The oxidised surface of the TiAlCrYN coatings was generally smooth as observed by secondary electron imaging (figure 6a), whilst oxide agglomerations were dispersed over the surface (figure 6b). As observed from cross-section by back-scattered electron imaging, the oxidised top layer and the retained nitride coating was approximately 1.1 μm thick each (compared to ~0.6-0.8μm for the TiAlYN/CrN superlattice coating. However, the amount of the oxide agglomerations was less than that on the TiAlYN/CrN coating (see figures 4 and 6). The morphology of the oxide agglomeration was somewhat different from that on the superlattice coating (see Figures 4b and 6b) with regard to column diameter and length as well as number of the agglomerations. Corresponding to the surface oxide rods, subsurface oxidation of the Ti alloy substrate developed ~9 μm in depth and spreading along the interface, similar to what was observed for the superlattice coating.

Similar to the TiAlYN/CrN coatings, TEM analysis of the oxidised TiAlCrYN coatings revealed a layered substructure, starting with an outer oxide layer of 1.1μm thickness, a transition layer of 40-70 nm, the retained TiAlCrYN coating of 1.4μm, and a transition layer of 320nm (figure 7). Again, close to the coating/substrate interface, the titanium alloy was refined within a depth of ~1μm. The oxide layer itself consisted of three single layers. As typical for TiAlN coatings [22] and in agreement with the GA-XRD results, the outermost part of the oxide scale contained predominantly alumina followed by three zones with varying alumina/titania content where titania was the major oxide.

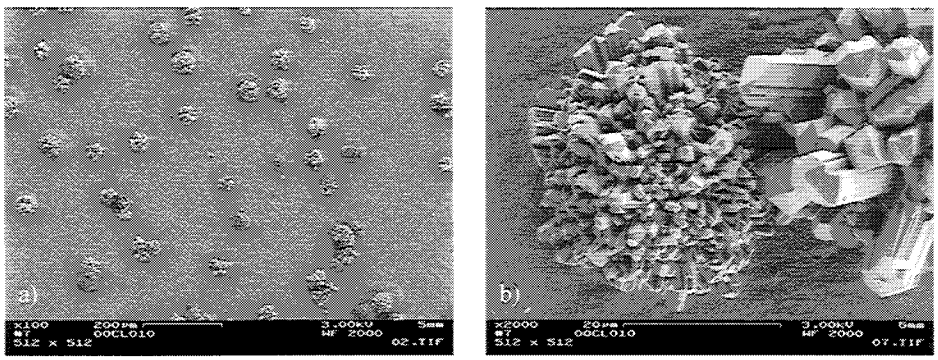


Figure 6: SEM top view of the TiAlCrYN coating after 1000h cyclic oxidation exposure at 750°C. The smooth surface oxide layer is locally interrupted by oxide agglomerations (a) the morphology of which is indicative of titania formation (b).

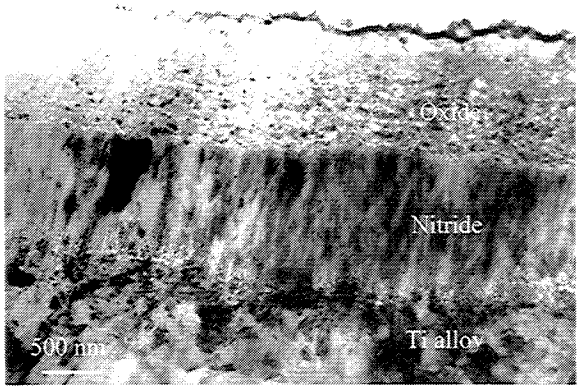


Figure 8: TEM overview image of TiAlCrYN coating isothermally oxidised for 1000 h at 750°C in air.

The retained TiAlCrYN was 1.4μm in entire thickness with a uniform distribution of Al, Ti, and Cr (no oxygen detectable), still exhibiting columnar morphology (70-140nm in column width) and dense grain boundaries. The B1 NaCl cubic structure (a_0=0.432nm) was determined by electron diffraction. At the transition from oxide to nitride, a Cr peak was detected. Only little interdiffusion between the nitride coating and the titanium alloy was measured (320nm) resulting in increasingly high titanium concentration from the nitride coating to the substrate, balanced by lower Al concentrations. EDS analysis of the fine grained recrystallized outer zone of the titanium alloy recorded no oxygen diffusion in the coating or the substrate.

Conclusions

Among the coatings systems and surface modifications tested in this study, monolithically grown TiAlCrYN coatings and TiAlYN/CrN superlattice coatings demonstrated best oxidation protection of aerospace titanium alloy TIMETAL 834 under isothermal and cyclic oxidation conditions at 750°C up to 1000h. The TiAlCrYN coating even outperformed γ-TiAl alloy Ti-48Al-2Cr-2Nb, at least for a few hundred hours test duration. TiAlCrYN and TiAlYN/CrN coatings formed thin protective outer alumina scales (followed by zones with varying alumina/titania content) of 1.1μm and 0.6-0.8μm thickness, respectively. During extended exposure defects in the nitride coatings led to substrate oxidation and formation of rapidly growing titania which then dominated oxidation behavior. Although the alumina scale was thinner on the uniformly oxidised surface, the amount of titania agglomerations on the surface was significantly higher on the TiAlYN/CrN superlattice coatings compared to the TiAlYN. Nevertheless, both coating systems are promising candidates for environmental protection of titanium alloys, since interdiffusion between the coatings and the substrate alloy was very limited, and neither oxygen nor any other element from the nitride coating was recorded in the titanium alloy subsurface zone. The coating structure itself appeared very stable after long-term exposure, with basically no changes in chemistry and crystallographic

structure. The next steps in this ongoing research effort are focussed on minimisation of the coating defects in order to limit local substrate alloy attack.

References

1. R.R. Boyer, *Titanium for Aerospace: Rationale and Applications.* Advanced Performance Materials, 1995. **2**: p. 349-368.
2. C. Leyens, *Oxidationsverhalten und Oxidationsschutz von Titanlegierungen für den Hochtemperatureinsatz in Flugtriebwerken.* Ph.D. thesis, RWTH Aachen. 1997, Aachen: Verlag Shaker. 113.
3. C. Leyens, M. Peters and W.A. Kaysser, *Intermetallic Ti-Al Coatings for Protection of Titanium Alloys - Oxidation and Mechanical Behavior.* Surface and Coatings Technology, 1997. **94-95**: p. 34-40.
4. C. Leyens, M. Peters and W.A. Kaysser, *Influence of Intermetallic Ti-Al Coatings on the Creep Properties of TIMETAL 1100.* Scripta Materialia, 1996. **35**(12): p. 1423-1428.
5. C. Leyens, K.-H. Trautmann, M. Peters and W.A. Kaysser, *Influence of Intermetallic Ti-Al Coatings on the Fatigue Properties of TIMETAL 1100.* Scripta Materialia, 1997. **36**(11): p. 1309-1314.
6. C. Leyens, M. Schmidt, M. Peters and W.A. Kaysser, *Sputtered Intermetallic Ti-Al-X Coatings: Phase Formation and Oxidation Behavior.* Materials Science and Engineering, 1997. **A239-240**: p. 680-687.
7. L. Niewolak, V. Shemet, A. Gil, L. Singheiser and W.J. Quadakkers, *Alumina-forming coatings for titanium and titanium aluminides.* Advanced Engineering Materials, 2001. **3**(7): p. 496-500.
8. I. Wadsworth, I.J. Smith, L.A. Donohue and W.D. Münz, *Thermal Stability and oxidation resistance of TiAlN/CrN multilayer coatings.* Surface and Coatings Technology, 1997. **94-95**: p. 315-321.
9. P.E. Hovsepian, D.B. Lewis, Q. Luo, W.-D. Münz and M. Meyer. *High temperature performance of CrN/NbN superlattice coatings deposited on Ti alloy substrates.* in *Euromat 99.* 1999.
10. L.A. Donohue, I.J. Smith, W.D. Münz, I. Petrov and G. J.E., *Microstructure and oxidation-resistance of Ti-1-x-y-zAlxCryYzN layers grown by combined steered-arc/unbalanced-magetron-sputter deposition.* Surface and Coatings Technology, 1997. **94-96**: p. 226-231.
11. W.-D. Münz, *Oxidation resistance of hard wear resistant $Ti_{0,5}Al_{0,5}N$ coatings grown by magnetron sputter deposition.* Werkstoffe und Korrosion, 1990. **41**: p. 753-754.
12. C. Leyens, M. Peters, P.E. Hovsepian, D.B. Lewis, Q. Luo and W.-D. Münz, *Novel Coating Systems Produced by the Combined Cathodic Arc/Unbalanced Magnetron Sputtering for Environmetla Protection of Titanium Alloys and Titanium Aluminides.* Surface and Coatings Technology, 2002, in press.
13. W.D. Münz, D. Schulze and F.J.M. Hauzer, Surface and Coatings Technology, 1992. **50**: p. 169.
14. D.B. Lewis, L.A. Donohue, M. Lembke, W.-D. Munz, R. KuzelJr., V. Valvoda and C.J. Blomfield, *The influence of the yttrium content on the structure and properties of Ti1-x-y-zAlxCryYzN PVD hard coatings.* Surface and Coatings Technology, 1999. **114**(2-3): p. 187-199.

15. R.A. Perkins and G.H. Meier; in *Proc. of the Industry-University Advanced Materials Conference II.* 1989. Golden, CO.
16. R.L. McCarron, J.C. Schaeffer, G.H. Meier, D. Berztiss, R.A. Perkins and J. Cullinan, *Protective Coatings for Titanium Aluminide Intermetallics*, in *Titanium '92 - Science and Technology*, F.H. Froes and I. Caplan, Editors. 1992, TMS: Warrendale, PA. p. 1971-1978.
17. J.C. Schaeffer, R.L. McCarron, G.H. Meier, R.A. Perkins and J.R. Cullinan, *Ti-Cr-Al protective coatings for alloys*, 1998: U.S. Patent No. 5,783,315.
18. M.P. Brady, J.L. Smialek, J. Smith and D.L. Humphrey, *The Role of Cr in Promoting Protective Alumina Scale Formation by γ-Based Ti-Al-Cr Alloys Part I: Compatibility with Alumina and Oxidation Behavior in Oxygen.* Acta Materialia, 1997. **45**(6): p. 2371-2382.
19. M.P. Brady, J.L. Smialek, D.L. Humphrey and J. Smith, *The Role of Cr in Promoting Protective Alumina Scale Formation by γ-Based Ti-Cr-Al Alloys Part II: Oxidation Behavior in Air.* Acta Materialia, 1997. **45**(6): p. 2357-2369.
20. M.I. Lembke, D.B. Lewis, W.-D. Münz and J.M. Titchmarsh, *Significance of Y and Cr in TiAlN hard coatings for high speed cutting.* Surface Engineering, 2001. **17**(2): p. 153-158.
21. C. Leyens, M. Peters and W.A. Kaysser, *Influence of Microstructure on Oxidation Behaviour of Near-Alpha Titanium Alloys.* Materials Science and Technology, 1996. **A12**: p. 213-218.
22. D. McIntyre, J.E. Greene, G. G. Håkansson, J.-E. Sundgren and W.-D. Münz, J. Appl. Phys., 1990. **67**: p. 1542.

475

HIGH TEMPERATURE NANOLAMINATE CERAMIC COATINGS PREPARED BY PVD TECHNIQUES

V. Teixeira , A. Monteiro, A. Portinha, R. Vaßen*, D. Stöver*

University of Minho, Physics Department, GRF-Functional Coatings Group

Campus de Azurém, PT-4800-058 Guimarães-PORTUGAL

* Forschungszentrum Jülich, IWV1- Institute for Materials and Processes in Energy Systems,

D-52425 Jülich- GERMANY

keywords: stabilised zirconia, nanocomposite ceramic coatings, nanolayer, PVD, sputtering, thermal stability

Abstract:

Zirconia coatings are very interesting materials because of their outstanding mechanical, thermal, optical and electrical properties. Recently there was a special attention on research of nanostructured thin coatings, since the nanosized grains presented in these systems strongly influence the chemical and physical properties of the material. Magnetron sputtering is a powerfull method for synthesis of nanostructured ceramic thin coatings. In this contribution we studied the structural properties of ZrO_2/Al_2O_3 nanolayered coatings. These films were deposited by DC reactive magnetron sputtering. X-ray diffraction measurements were used to characterize the film structure. The surface microtopography was analyzed by atomic force microscopy (AFM). EDX was used to get thin film composition. SEM was used to measure the film thickness and to observe microstructure of the film cross-section. The ZrO_2/Al_2O_3 films are composed by nanolayers with 3/3.5, 6/7 and 12/14 nanometers each, and the total thickness is 2.2 microns. The nanolayered films present a ZrO_2 polycrystalline phase (monoclinic and tetragonal phases depending on the ratio of thicknesses of the nanolaminated structure) and an Al_2O_3 amorphous phase. The ZrO_2 high temperature tetragonal phase content increases as the nanolayers in the structure get thinner. The Al_2O_3 nanolayers are used to stabilize the ZrO_2 tetragonal phase at room temperature. After annealing in air at 1000°C the Al_2O_3 is presented on amorphous state and the quasi-amorphous tetragonal ZrO_2 nanosized grains crystallizes to tetragonal phase without any monoclinic transformation.

1-INTRODUCTION

As the grain size decreases to the nanometer range, there is a significant increase in the volume fraction of grain boundaries or interfaces. This characteristic strongly influences the chemical and physical properties of the material. For example, nanostructured ceramics are sometimes tougher and stronger than the coarser grained ceramics. Nanophase metals exhibit significant increases in yield strength and elastic modulus. It has also been shown that other properties (electrical, optical, magnetic, etc) are influenced by the fine grained structure of these materials. Magnetron sputtering is a powerfull method for synthesis of nanostructured ceramic thin coatings [1].

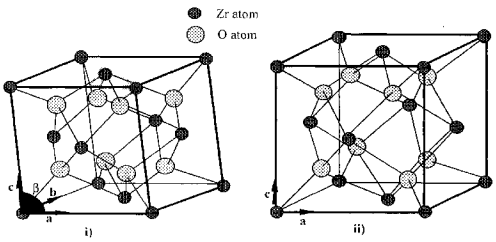


*Fig. 1- Unit cell structure for ZrO_2 **i)** monoclinic (baddeleyite) **ii)** tetragonal phase*

Zirconia coatings are very interesting materials because of their outstanding mechanical, thermal, optical and electrical properties. Zirconia has a high melting point, high resistance to oxidation, low thermal conductivity, high hardness, and high coefficient of thermal expansion [2]. These ceramic coatings are widely use in many technological applications such as heat resistant layers and TBC's [3], optical coatings [4], buffer layers for growing superconductors [5], for memory cells [6], oxygen sensors and ion conductors [7,8], etc.

Bulk ZrO_2 crystallizes in different polymorphs under different conditions of temperature and pressure. Three main equilibrium solid phases have been reported: monoclinic phase, tetragonal phase, and cubic fluorite phase (see fig. 1), [9-11]. Monoclinic phase is stable at room temperature. The cubic and tetragonal phases of zirconium oxide can be stabilized at room temperature by doping with cations such as Y^{3+}, Ca^{2+}, etc [2,9,12-13].

In technological applications which involve coatings of pure zirconia, microcracking results upon cooling from 1150 °C to room temperature due to the phase transformation tetragonal to monoclinic. This is a consequence of the 3% volume change which accompanies this phase transition. As referred the transformation of t-ZrO_2 to m-ZrO_2 can be suppressed by alloying with Y_2O_3, CeO_2 , CaO, etc [9-12]. Besides this method to retain the high temperature tetragonal phase two others can be employed : i) mixture of ZrO_2 with an oxide such as Al_2O_3 [9,14] and ii) by decreasing the particle size of the crystalline domains, i.e., using small zirconia crystals with radii lower than 6 nm (the surface energy of the tetragonal phase is lower than the one of the monoclinic phase which results in stable tetragonal crystal at room temperature) [15,16]. The ZrO_2/Al_2O_3 bulk composite is a classic model of the transformation-toughening ceramic system. The Al_2O_3 is not soluble with ZrO_2 and alters the stability through constraint. Alumina has a Young's modulus higher than zirconia and it is suggested that it forms a rigid matrix around the zirconia crystals which causes a local compressive stress and hinders the mechanism of the martensic phase tranformation [14].

Zirconia thin films have been produced using different methods such sol-gel processing [17], chemical vapor deposition [18], plasma spraying [2,19], and sputtering [20-23]. In the present study DC magnetron sputtering was used. A possible application of these multilayer coatings is as thermal barrier coatings in gas turbine components.

2. EXPERIMENTAL DETAILS

ZrO_2, $ZrO_2Y_2O_3$-Al_2O_3 and ZrO_2/Al_2O_3 coatings (as single layer, nanocomposite and nanolaminate structure) were prepared by DC reactive magnetron sputtering in an Ar and O_2 gas mixture and were deposited on glass, Inconel 617 and Hastelloy X (Ni-alloy substrates). All coatings were deposited at constant temperature, bias voltage, sputtering power, and target-substrate distance.

Table 1- Deposition conditions for the ZrO_2, $ZrO_2Y_2O_3$ and $ZrO_2Y_2O_3$-Al_2O_3 nanocomposite coatings

Coating type / Parameter	ZrO_2	$(ZrO_2)_{1-x}(Y_2O_3)_x$	$(ZrO_2)_{1-x}(Al_2O_3)_x$
Target-substrate dist. (mm)	60	60	60
Current (A)	1.00	0.75	1.00
Voltage (V)	400	380	380
Base pressure (mbar)	$1.2*10^{-5}$	$1.2*10^{-5}$	$1.2*10^{-5}$
Substrate temperature (°C)	150	150	150
P O_2 (mbar)	$1.3*10^{-3}$	$5*10^{-4}$	$6*10^{-4}$
Total Pressure Ar+O_2(mbar)	$8*10^{-3}$	$6.8*10^{-3}$	$1.2*10^{-2}$
% wt stabiliz. dopant in the coating	0	4 or 11	25

The alloy substrates were polished, and ultrasonically cleaned before the deposition process. Glass substrates were also ultrasonically cleaned. Before deposition the vacuum chamber was evacuated to $2*10^{-6}$ mbar. Both targets and substrates were pre-cleaned at same time in argon atmosphere for

20 minutes. During deposition, the substrates change position, rotating between two metal targets (Zr and Al) with a purity of 99.5%, stopping in front of targets during the estimated deposition time for each ceramic nanolayer. The Y additions were made by putting some Y pieces in the main area of erosion of the metallic Zr target. (see table 1 and 2 with the main sputter deposition conditions for the zirconia nanocomposite coatings).

Table 2- Sputtering deposition conditions for the nanolaminated ZrO_2-Al_2O_3 coatings

Base pressure	$2x10^{-6}$ mbar
Sputtering power	1000 W
Bias voltage	-50 V
Target-substrate distance	60 mm
Deposition temperature	300 °C
Oxygen pressure (ZrO_2)	$5.8x10^{-4}$ mbar
Argon pressure (ZrO_2)	$4.6x10^{-3}$ mbar
Oxygen pressure (Al_2O_3)	$7.8x10^{-4}$ mbar
Argon pressure (Al_2O_3)	$4.2x10^{-3}$ mbar
Total work pressure	$6x10^{-3}$ mbar

3- RESULTS AND DISCUSSION

3.1- COATING MICROSTRUCTURE

Composite coatings (mixed oxides such as Y_2O_3 or/and Al_2O_3 with the ZrO_2) and nanolaminate coatings of ZrO_2-Al_2O_3 with nanosized layer thicknesses were prepared. In table 3 and 4 the structures and thicknesses of the coatings investigated are presented. All deposited films were transparent. The coating microstructure was studied by SEM. The usual columnar and dense structure found in sputtered coatings prepared at low temperature is clearly identified in the SEM analysis (see fig. 2). The AFM analysis presented in fig. 3 shows the surface roughness for the sample nanolaminated ZrO_2-Al_2O_3 with a thickness relation of 6nm/7nm. The composite coatings $ZrO_2Y_2O_3$ also show a columnar structure. However, the fracture edge of the composite coatings with alumina ($ZrO_2Y_2O_3$-Al_2O_3) analysed by SEM revealed a glassy, amorphous and dense structure.

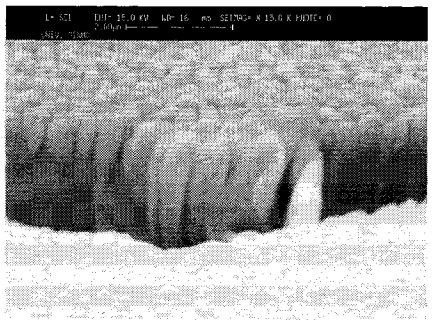


Fig. 2- SEM micrograph showing the columnar structure for the nanostructured zirconia-alumina multilayered coating (structure 6nm/7nm, sample Z6A7)

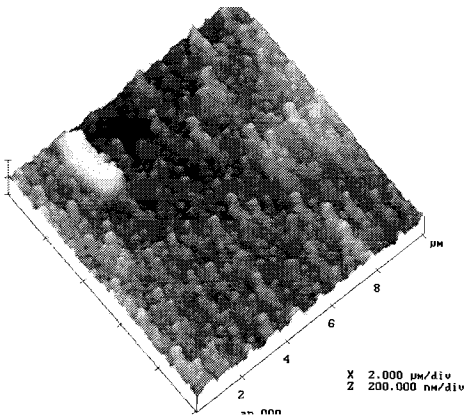


Fig. 3- AFM image for the nanolaminated structure zirconia-alumina (sample Z6A7).Axis scale for X and Y (in µm) and Z (in nm) are presented at bottom in the left.

3.2-STRUCTURAL ANALYSIS BY X-RAY DIFFRACTION

The coatings were analysed by XRD to study the phase composition and crystallite sizes. For the pure ZrO_2 coatings without dopants the main phase presented is monoclinic with traces of tetragonal (see fig. 4 and 5b). Unstabilized Zirconia exists in the monoclinic phase with traces of tetragonal on all substrates. Annealing in air at 1000 °C does not modify the phases present. The coatings are textured with the [111] direction normal to the substrate surface. A peak at approximately 30° is attributed to diffraction from (111) planes of the tetragonal phase of ZrO_2 and the peaks at ~28°C and ~31°C correspond to the monoclinic phase.

Table 3- Sample structure for the nanocomposite zirconia based sputtered coatings

Sample structure	ZrO_2	$ZrO_2Y_2O_3$	$ZrO_2Y_2O_3$	$ZrO_2Y_2O_3Al_2O_3$
Sample code	Z1A0	Z1A0Y5	Z1A0Y11	Z1A25Y5
%wt Y_2O_3	0	5.2	11	11
%wt Al_2O_3	0	0	0	25
Number of layers	1	1	1	1
Layer thickness (nm)	950	2000	6750	800

Table 4- Structure of individual layers and coating thickness for the nanolaminates

Sample structure	ZrO_2	Al_2O_3	ZrO_2/Al_2O_3	ZrO_2/Al_2O_3	ZrO_2/Al_2O_3
Sample code	Z1	A1	Z3A3	Z6A7	Z12A14
Number of layers	1	1	375/375	188/188	94/94
Layer thickness (nm)	520	772	3/3.5	6/7	12/14
Total thickness (nm)	520	772	2440	2440	2440
Deposition time (s)	3600	3600	14/24	28/48	56/96

A non-transformable tetragonal phase of ZrO2 can be produced by adding 5% to 12% wt. of Y2O3 to ZrO2. The coatings, which are, as-deposited, in the tetragonal phase, show also a preferred orientation with the (111) crystallographic plane parallel to the surface. The $ZrO_2Y_2O_3$ coatings are stable even at high temperature, presenting the tetragonal phase with predominant peak t(111). The average crystallite dimension is about 30 nm (see table 5), without any significant changes after annealing in air at 1000°C for 48 h [9].

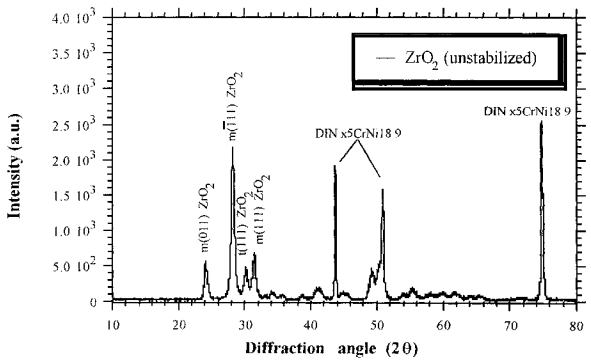
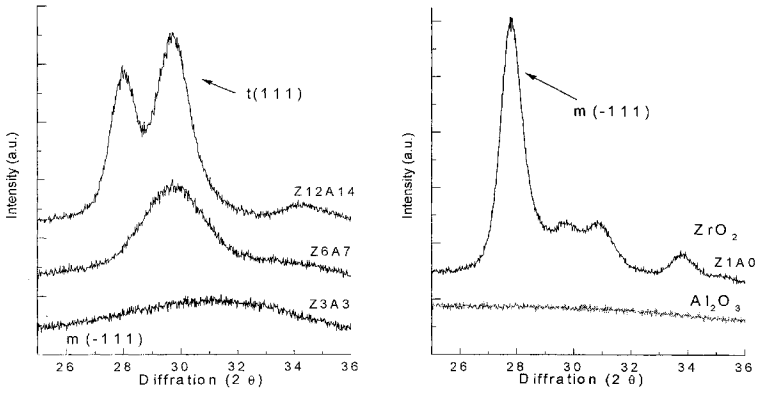


Fig. 4- XRD spectrum for a non-stabilised zirconia coating presenting the monoclinic phase (m) on a steel substrate.



a) *b)*

Fig. 5- XRD patterns of a) ZrO_2-Al_2O_3 nanostructured coatings prepared with different nanolayers thickness b) the individual layers , monoclinic ZrO_2 layer (sample Z1A0) and amorphous Al_2O_3

$ZrO_2Y_2O_3$-Al_2O_3 nanocomposites coatings were X-ray amorphous after deposition with evidence of zirconia tetragonal phase and amorphous alumina. After annealing in air at 1000 °C the tetragonal phase of ZrO_2 crystallizes in the tetragonal phase with the alumina particles showing an amorphous structure. The crystallite size were much lower than in the $ZrO_2Y_2O_3$ coatings and was found to be about 15 nm. The nanostructured coatings with the lowest layer thickness of ZrO_2 and Al_2O_3 (3nm/3.5nm) has a quasi-amorphous X-ray structure with evidence of tetragonal phase. For higher nanolayer thickness the tetragonal phase is found clearly with the (111) crystallographic plane parallel to the interface (see fig. 5a). We found that most tetragonal crystallites grow with their (111) planes parallel to the interface as was the case for the nanocomposite coatings of $ZrO_2Y_2O_3$. The t(111) planes are the most densely packed in tetragonal zirconia, and as such are thermodynamically favored to grow parallel to the substrate surface [9,13,16]. The estimation of the nanocrystallite size of the zirconia-alumina multilayer films by the XRD peak broadening indicates that they have an average crystallite dimension approximately equal to the nanolayer thickness, as can be seen in table 5.

Table 5- Grain sizes of the zirconia composite coatings and the nanolaminates

Sample	Structure	Type of coating	Phase	Thickness (nm)	Grain size (nm)
Z1A0	950nm/0nm	Single layer	m(11-1)*	950	52
Z1A0Y11	6750nm/0nm	Nanocomposite	t(111)	6750	34
Z1A0Y5	2000nm/0nm	Nanocomposite	t(111)	2000	29
Z1A25Y5	800nm/0nm	Nanocomposite	amorphous	800	15
Z12A14	12nm/14nm	Nanolaminate	t(111)**	2440	12.8
Z6A7	6nm/7nm	Nanolaminate	t(111)	2440	7.3
Z3A3	3nm/3.5nm	Nanolaminate	amorphous	2440	4.9

**the main phase is monoclinic m(11-1) with traces of tetragonal t(111)*
*** the main phase is t(111) with some m(11-1)*

The excellent mechanical properties of partially stabilized zirconia, such as the good toughness is associated with the martensitic t => m transformation which increases the toughness by two distinct mechanisms. Firstly, if a restricted number of particles undergo the transformation during cooling from the fabrication temperature, a fine distribution of microcracks is produced, which increase the

toughness. The stress field at a crack tip can induce a metastable t-particle to transform in monoclinic. This the basis of the second toughening mechanism, transformation toughening, where the propagation of a crack is hindered by both the transformed particles in the crack wake [24]. Transformation toughening, unlike microcrack toughening, does not have a detrimental effect on strength.

This transformation toughening technique was applied recently to thin coatings [9,14,16,25-26] and is discussed in the frame of this work. We applied the model presented in ref. [16] to predict the layer thickness at which tetragonal phase is produced in any zirconia-based nanolaminate, independent of the materials of the restart layer provided its interface with the growing zirconia crystallites is incoherent. The stable tetragonal zirconia phase is produced when the thickness of each zirconia layer is less than the radius at which a unconstrained, unstressed hemispherical tetragonal zirconia crystallite spontaneously transforms to monoclinic at the growth temperature [16,27]. Aita *et al.* [16] derived, using thermodynamics analysis, the expression for the critical radius, R_c, at which a tetragonal-to-monoclinic zirconia growth transformation occurs:

$$R_c=3.79\,[1 - (T/1448\ K)]^{-1}\quad nm \qquad [1]$$

Where T is the temperature of deposition. For the growth temperature used in our experiments, eq. (1) gives R_c=6.3 nm. We have deposited multilayers of zirconia and alumina in which the layer spacing were scaled to ensure nanosized zirconia crystallites, thus depositing nanolaminates with amorphous or tetragonal structure at room temperature without the use of dopants. At the growth temperature used in our experiments this gives a critical radius of about 6 nm.

The nanolaminates fabricated with ZrO_2 nanolayer thickness of 3 nm, 7 nm and 12 nm are in good agreement with the model described in ref. [16]. In fact, for the samples where the layer thickness of ZrO_2 in the laminate structure is 12 nm they present some monoclinic grains in the tetragonal matrix (see fig. 4). With layer thicknesses lower than this a quasi-amorphous or tetragonal phase is retained at room temperature. Other studies [26], shows that the layer thickness of Al_2O_3 can also influence the critical thickness of the ZrO_2 layer at which the monoclinic phase starts to appear. In the present study we use the same thickness for both Al_2O_3 and ZrO_2 layers, but with a constant Al_2O_3 layer thickness (8 nm) it was found that ZrO_2 layers with thickness up to 20 nm have retained the tetragonal phase and did not show any transformation into monoclinic when annealed in air at 1000 °C [26].

4-CONCLUSIONS

With a sputtering technique it was possible to produce dense, adherent and stabilized zirconia thin coatings employing three different methods:

i) by substitution of some Zr atoms by Y (composite coatings of $ZrO_2Y_2O_3$);

ii) by mixing Al_2O_3 with $ZrO_2Y_2O_3$ (composite coatings of $ZrO_2Y_2O_3$-Al_2O_3);

ii) by decreasing the ZrO_2 crystal dimensions through the growing of nanosized laminates where the ZrO_2 nanolayers are constrained between Al_2O_3 layers (nanolaminates of ZrO_2-Al_2O_3).

With the aim to stabilize the tetragonal phase of zirconia we grew composite sputtered coatings of zirconia, yttria and alumina. For the deposition of stabilized zirconia it is possible to control at an atomic level the addition of these elements to the zirconia matrix, and thus providing an improved uniformization of the crystalline phases presented in the coating. The $ZrO_2Y_2O_3$-Al_2O_3 coating, which is amorphous in the as-deposited state, crystallizes in the high temperature tetragonal phase when annealed in air at 1000 °C.

With the objective of developing transformation-toughening high temperature ceramic coatings, we also deposited multilayers of ZrO_2-Al_2O_3 in which the layer spacing were scaled to ensure nanosize zirconia crystallites, thus depositing nanolaminates with amorphous or tetragonal structure at room temperature without the use of dopants. The nanocrystallite size of the ZrO_2-Al_2O_3 multilayers was close to the nanolayer thickness.

ACKNOWLEDGMENTS

This work is supported by German-Portuguese Co-operative Programme ICCTI-DAAD and European Commission-DG-XII under contracts: ICCTI-DAAD/ 423/2000, "Composite Coatings for high temperature applications" and COST 522, WP2/SP2-1999/01: "Residual stresses and failure in multilayered and functionally graded coatings for advanced energy systems". A. Monteiro and A. Portinha are gratefully for the Research Grants supported by F.C.T.- Portuguese Foundation for Science and Technology .

REFERENCES

[1] S. Vepek, P. Nesládek, A. Niederhofer,F. Glatz, *Nanostructured Materials, Vol. 10-5, (1998),679-689*
[2] A. Duparré, E. Welsch, H.G. Walther, N. Kaiser, H. Müller, E. Hacker, H. Lauth, J.Meyer, P. Weissbrodt, *Thin Solid Films*, 187 (1990) 275-288.
[3] V. Teixeira, M. Andritschky, W. Fischer, H. P. Buchkremer, D. Stöver, *Surf. Coat. Tech.*, 120-121 (1999) 103-111
[4] T. Sikola, J. Spousta, L. Dittrichova, I. Benes, *Nucl. Instr. Methods Phys. B.*, 1(4) (1999), 673
[5] Y. Komatsu, T. Sato, S. Ito, K. Akadi, *Thin Solid Films*, 341 (1999), 132
[6] M.S.R. Rao, C.P D'souza, P.R. Apte, R. Pinto, L.C. Gupta, *J. Appl. Phys*, 79 (1996), 940
[7] G. Z. Cao, H. W. Brinkman, J. Meijerink, K. J. De Vries, A. J. Burggraaf, *J. Am. Ceram. Soc.* 76 (1993), 2201
[8] A. Bastianini, G. A. Battiston, R. Gerbasi, M. Porchia, S. Daolio, *J. Phys. IV 5* , (1995), 525
[9] V. Teixeira, M. Andritschky, *High Temperature-High-Pressures*, 25, (1993), 213
[10] J. S. Kih, H. A. Marzouk, P. J. Reucroft, *Thin Solid Films*, 254 (1995) 33-38
[11] R. Guinebretiere, B. Soulestin, A. Douger, *Thin Solid Films,* 319 (1998) 197-201
[12] H. G. Scott, *J. Mat. Sci.*, 10, (1975), 15227
[13]] P. Gao, L. J. Meng, M.P dos Santos, V. Teixeira, M. Andritschky, *Applied Surface Science*, 6748 (2000) 1-7
[14] S. B. Qadri, C. M. Gilmore, C. Quinn, E. F. Skelton, C. R. Gosset, *J. Vac. Sci. Technol.* A7(3), (1989), 1220-1224
[15] B. E. Yoldas, *J. Mat. Sci.*, 21, (1986), 1080
[16] C. R. Aita, M. D. Wiggins, R. Whig, C. M. Scanian, M. G-Josifovska, *J. Appl. Phys.*, 79(2), (1996), 1176-1178
[17] R. Brenier, A. Gagnaire, *Thin Solid Films*, 392 (2001) 142-148
[18] J. Holgado, J. Espinós, F. Yubero, A. Justo, M. Ocaña, J. Benítez, A. G-Elipe, *Thin Solid Films*, 389 (2001) 34-42
[19] L. Bianchi, A.C. Leger, H. Vardelle, A. Vardelle, P. Fauchais, *Thin Solid Films*, 305 (1997) 35-47
[20] J. S. Kim, H. A. Marzouk, P. J. Reucroft, *Thin Solid Films*, 254 (1995) 33-38
[21] P. Gao, L. J. Meng, M. P. dos Santos, V. Teixeira, M. Andritschky, *Thin Solid Films*, 377-378 (2000) 557-561
[22] P. Gao, L. J. Meng, M. P. dos Santos, V. Teixeira, M. Andritschky, *Vacuum*, 56 (2000), 143
[23] M. Andritschky, V. Teixeira, L. Rebouta, H. P. Buchkremer, D. Stöver, *Surf. Coat. Tech.,* 76/77, (1995), 101
[24] F. F. Lange, *J. Mat. Sci.*, 17, (1982), 225
[25] M. Andritschky, I. Cunha, P. Alpuim, *Surface and Coatings Technology*, 94/95, (1997), 144
[26] P. Gao, L. J. Meng, M. P. dos Santos, V. Teixeira, M. Andritschky, *Vacuum*, 64,(2002), 267-273
[27] R. C. Garvie, M. V. Swain, *J. Mater. Sci.,* 20, (1985), 1193

CYCLIC LIFETIME OF PYSZ AND CESZ EB-PVD TBC SYSTEMS ON VARIOUS NI-SUPERALLOY SUBSTRATES

U. Schulz, K. Fritscher, W.A.Kaysser

DLR-German Aerospace Center, Institute of Materials Research, 51170 Cologne, Germany

Abstract

EB-PVD TBCs applied on several polycrystalline, directionally solidified, and single crystalline substrate alloys were thermally cycled with T_{max}=1100°C. Two different TBC chemistries were deposited onto EB-PVD NiCoCrAlY bond coats: P-YSZ and CeSZ. The microstructure and composition of the CeSZ can be correlated with processing conditions during EB-PVD. Spallation of the TBCs does not only correlate with TGO thickness, but also depends on the substrate alloy. The longest lifetimes have been achieved with P-YSZ TBCs on Hf containing alloys while they suffer from early spallation on the SX alloy. Application of CeSZ TBCs on the same SX-alloy, however, increases the time to failure, although fluctuations of chemistry across the thickness have been found.

Keywords: thermal barrier coating, EB-PVD, Ceria-stabilized zirconia, thermally grown oxide

1. Introduction

Thermal barrier coatings (TBCs) on advanced turbine blades considerably increase the engine efficiency and blade performance. State-of-the-art TBCs consist of a metallic bond coat (BC) and a ceramic top coat of partially yttria stabilized zirconia (P-YSZ), deposited by electron beam physical vapor deposition (EB-PVD) or plasma spraying (PS). The EB-PVD process provides a columnar microstructure of the ceramic coating exhibiting superior strain and thermal shock tolerance. P-YSZ as a standard material for current TBC applications has low thermal conductivity, a relatively high coefficient of thermal expansion and is chemically inert in combustion atmospheres. However, its application temperature reaches a limit at around 1200°C. Consequently, the search for alternative ceramic top coats is of uppermost interest. Ceria-stabilized zirconia (CeSZ) was considered to be a potential candidate material, providing a good corrosion resistance and superior phase stability at high temperature [1, 2]. Furthermore, the thermal conductivity is found to be lower than for P-YSZ, and benefits for lifetime and thermocyclic resistance are reported for EB-PVD CeSZ TBCs [3, 4] and PS TBCs as well [5]. As the vapor pressures of zirconia and ceria differ extensively, the evaporation from one source containing both zirconia and ceria turns out to be critical. Two source evaporation was identified to offer a possibility to overcome the problem, but the sublimation of ceria in vacuum imparts new challenges for process control, especially if constant evaporation and condensation rates are mandatory [6].

The thermally grown oxide (TGO) plays an important role for TBCs performance; failure in EB-PVD TBCs is almost always initiated at or near the TGO, mostly along the TGO/BC interface. Some investigations have already shown the high sensitivity and decisive role of the interplay between the constituents of a TBC system consisting of substrate, BC, TGO, and ceramic top coat [7, 8, 9]. To give an example, a dramatic decrease of TBC spalling life is re-

ported as soon as conventionally cast polycrystalline substrate material is exchanged for directionally solidified (DS) or single crystalline (SX) alloys [9, 10, 11].
The aim of this study is to determine the effect of the variation of Ni-base substrate materials belonging to the conventionally cast, DS, or SX alloy group with identical EB-PVD NiCoCrAlY BCs and the variation of the ceramic top coat chemistry like P-YSZ or CeSZ on cyclic lifetime.

2. Experimental

100 to 120µm thick NiCoCrAlY (Ni-22Co-20Cr-12Al-0.1 to 0.2Y, in wt%) bond coats were deposited onto cylindrical Ni-base superalloy substrates by EB-PVD. The composition of the substrates alloys used in this study is given in table 1. The cylinders had a diameter of 6mm. After BC densification by peening and vacuum annealing at 1080°C for 4h, 200 to 250µm thick P-YSZ ceramic top coats containing 7wt%Y_2O_3 were deposited by EB-PVD in rotation mode at 12 rpm. During deposition of the P-YSZ, the average substrate temperature was adjusted between 980°C and 1040°C. A controlled amount of oxygen was bled into the deposition chamber in order to get stoichiometric zirconia coatings.

Table 1: Chemical composition of substrate materials (wt%, Nickel is balanced)

alloy	condition	Co	Cr	Al	Mo	W	Ta	Ti	Hf	Re	C	B	other
IN 100 DS	DS [1]	14	9	5	2.3			5			0.18	0.015	0.05 Zr, 1V
Rene 142	DS	12	6.8	6.1	1.5	5	6.4		1.5	2.8	0.12	0.015	0.02 Zr
MAR M002	DS	10	9	5.5		10	2.5	1.5	1.5		0.15	0.015	0.05 Zr
CMSX-4	2nd gen. SX	9	6.5	5.6	0.6	6	6.5	1	0.1	3			

DS... directionally solidified
SX... single crystal
[1] IN 100 is originally a conventionally cast polycrystal but has been manufactured as DS

CeSZ TBCs were processed analogously by EB-PVD in the same equipment, but by use of the jumping beam technique and two evaporation sources [6]. One of the two source ingots was manufactured out of 3wt% Y_2O_3 stabilized zirconia, the other one of pure CeO_2. The evaporation sources were arranged side by side in the evaporation chamber but in perpendicular orientation to the axis for sample transfer and rotation. The deposition temperature was adjusted close to 1000°C. The coating thickness was 220µm by maintaining similar deposition rates as also used before. The composition of the TBC analyzed by energy dispersive X-Ray Fluorescence on the sample surface was $27.65CeO_2$-$2.0Y_2O_3$-$0.85HfO_2$-$69.5ZrO_2$ (wt%) which has come close to the intended target composition of $25CeO_2$-$2.5Y_2O_3$-$72.5ZrO_2$.
Samples were thermal-cyclically tested with T_{max}=1100°C using one hour cycles (50 min heating, 10 min forced air cooling to room temperature, for details see [12]). Failure of the TBCs was defined as TBC spallation of an area with one dimension greater than 5mm. Representative samples were cross sectioned after deposition and after failure. They were prepared by conventional metallographic preparation techniques for examination by SEM and EDX.

3. Results

The microstructure of as-processed EB-PVD P-YSZ TBCs is sufficiently well documented in literature [13, 14] and is therefore omitted here. The corresponding microstructure of an EB-PVD CeSZ TBCs is shown in Fig. 1. It shows a cross sectional view through a CeSZ TBC. The EDX linescan exhibits a scatter in the CeO_2 content in two different respects. Firstly, there are minor periodical fluctuations in the order of ±2% bringing about a stratified structure of layers having an average thickness or periodicity of approximately 1.25 µm. Secondly, there are gradual changes caused by unsteady evaporation conditions mainly of the CeO_2 source that range over the entire coating thickness, leading to a variation of the ceria content between 15 and 50 wt%. The cracks that propagate through the TBC are discussed later.

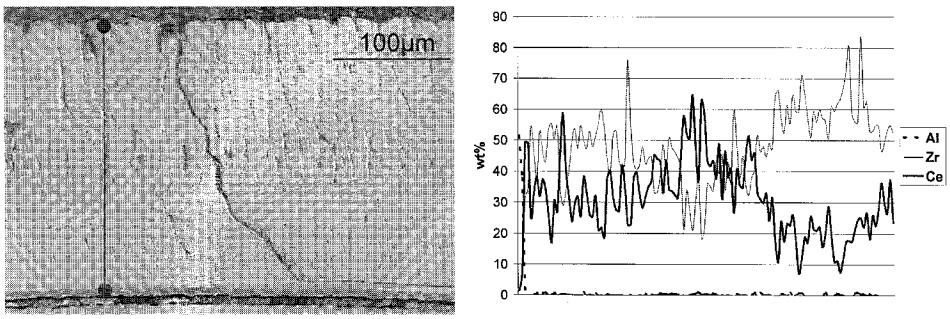


Fig. 1: Cross section (left) and EDX line scan (right) of an EB-PVD CeSZ TBC on NiCoCrAlY / CMSX-4 after testing

The lifetime of the various TBC systems are shown in Fig. 2 in a Weibull plot. Whereas the two DS alloys (Rene 142 and MAR M002) showed no visible damage of their TBCs after extended 2000h cyclic testing (according to ln(cycles to failure) > 7.6 on the abscissa of a Weibull plot) and thus were suspended from further testing (details are given in [15]), the two other alloys with their respective TBCs showed following average lifetimes: 836 cycles for IN100/P-YSZ, 311 cycles for CMSX-4/P-YSZ, and 926 cycles for CMSX-4/CeSZ. Comparing the two different top coats on the CMSX-4 substrate, a threefold longer lifetime is observed for the CeSZ coat on identical substrate/ bond coat-systems, although composition and microstructure of the CeSZ TBC version was far from optimized (see Fig. 1). Samples of P-YSZ on IN 100 showed a lifetime close to CeSZ on CMSX-4 which is for the P-YSZ versions between the two extremes of DS and SX.

In Fig. 3 representative cross sections of the TGO region are shown after testing. EDX line scans and point measurements revealed the following features. In all cases, the TGO consists mainly of alumina with inclusions of other oxides. At the interface between metal oxide and P-YSZ a mixed zone (MZ) has formed consisting of bright zirconia particles embedded in an alumina matrix (dark). The MZ is porous and contains in most cases traces of chromium (oxide). The interface between TGO and ceramic top coat is relatively planar with only minor microscopic roughness due to the intermixing. For both P-YSZ and CeSZ on CMSX-4, an yttria rich outer layer was found just at the outer portion of the mixed zone close to the interface between MZ and ceramic top coat. This was more pronounced for the CeSZ version than for P-YSZ, leading to a mixed zone of mainly alumina-yttria with only minor zirconia content.

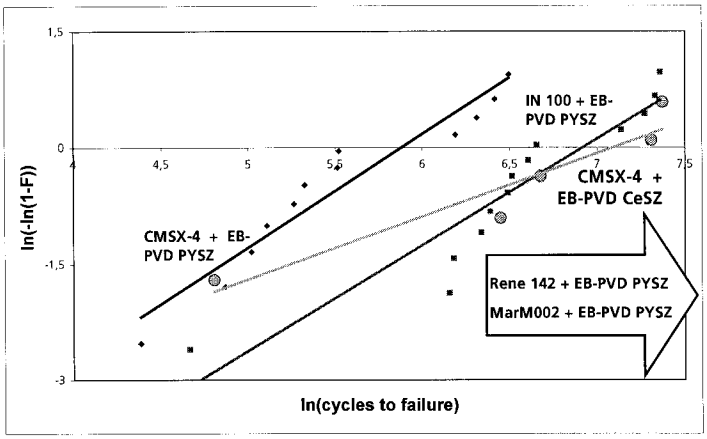


Fig. 2: Cycles to failure of P-YSZ and CeSZ TBCs on cyclic furnace testing at 1100°C. All versions had an EB-PVD NiCoCrAlY bond coat

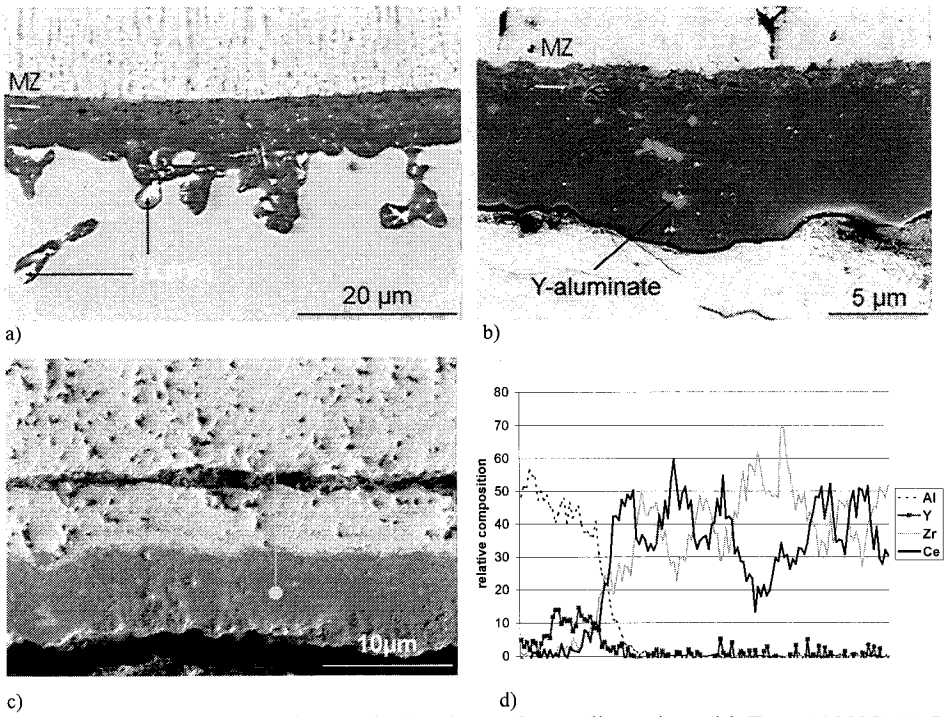


Fig. 3: TGO formation on NiCoCrAlY bondcoat after cyclic testing with T_{max}=1100°C. (a) P-YSZ on MAR M002 after 1122 cycles, (b) P-YSZ on IN 100 after 1527 cycles, (c) CeSZ on CMSX-4 after 1493 cycles showing debonding within the CeSZ 5µm apart from the TGO/CeSZ interface, (d) line scan of (c) showing Y enrichment in the MZ and periodical fluctuations in Ce content.

All TGOs contain rounded particles rich in Yttrium, Aluminum, and Oxygen. There was no systematic but a more random distribution found for the arrangement of these Y-aluminates within the TGO. The interface between TGO and CeSZ ceramic top coat, however, appears to be slightly rougher and hence less planar whereas the remainder of the TGO seems to be equivalent to the TGO/P-YSZ version on CMSX-4 (see Fig. 1 and 3). For the two substrates with lives > 2000 cycles (MAR M002 and Rene 142), a very rough BC/TGO interface was observed, characterized by large oxide pegs protruded into the BC and occasional oxide regions in the BC matrix apparently disconnected from the TGO, the latter ones tentatively labeled as internal oxides. In the center of the protrusions and of the internal oxides, hafnium oxide particles embedded in alumina were identified. These features have occurred more pronounced for MAR M002 than for Rene 142 as detailed in [15].
The location of separation for the failed P-YSZ TBCs was at the BC/TGO interface, regardless of the substrate alloy. This was also the location of further crack formation in all systems during metallographic preparation indicating this interface to be the weakest link in the entire system. As typical for MCrAlY overlay coatings, below the TGO a β-NiAl phase depleted layer was observed with a thickness depending on the testing time.
However, the location of separation for the failed CeSZ TBCs was within the ceramic, approximately 5 to 7μm above the TGO/TBC interface regardless of short or long lifetime of the individual samples. Only occasionally the crack was deflected into a nearly perpendicular direction (Fig. 1). The major location of the crack within the TBC above the TGO/TBC interface corresponds to a local minimum in ceria concentration. This minimum was caused on the third to forth revolution of the samples by the movement pattern above the two ceramic sources on deposition as can be followed on the respective EDS line scan (Fig. 3d). This is apparently the weakest part in this particular CeSZ TBC. The thickness of the respective TGOs, however, is in the same scatter band as found for various P-YSZ coated substrates (see Fig. 4).
The measured thickness of the TGOs is plotted versus the number of cycles in Fig. 4. Note that the graph shows data obtained from multiple samples and not from the kinetics of only one sample. For all samples, TGO thickness follows nearly the same growth kinetics. For thickness measurements on MAR M002 and Rene 142 only the portion of the relatively flat TGO consisting mainly of α-Al_2O_3 was considered. The oxide pegs and internal oxides stretching down to a thickness of 15μm or more were neglected as they were judged inconsistent with the pertinent growth kinetics. The thickness of the mixed zone stays nearly constant between 1.1 and 1.8μm on all substrate materials and for both TBC compositions during the entire duration of the thermal-cyclic experiments. Data were given in detail in [15].

4. Discussion

The small periodical fluctuations of the ceria content in Fig. 3 (d) can be simply correlated with the rotational frequency of the samples. Since during each rotation the samples pass through two compositionally different vapor clouds that penetrate each other but possess at each position a different vapor density, the ratio of the two condensing species will vary on the samples accordingly. The fluctuations compare well to earlier findings on alumina-zirconia coatings that were processed in a analogous two source jumping beam manner [16]. The larger gradual changes of ceria through the entire thickness of the CeSZ TBC clearly show the problems which may arise on co-evaporation of a sublimating material like CeO_2. Further optimization of the processing routes is under way to establish constant evaporation rates and constant mass ratios of the evaporated materials.

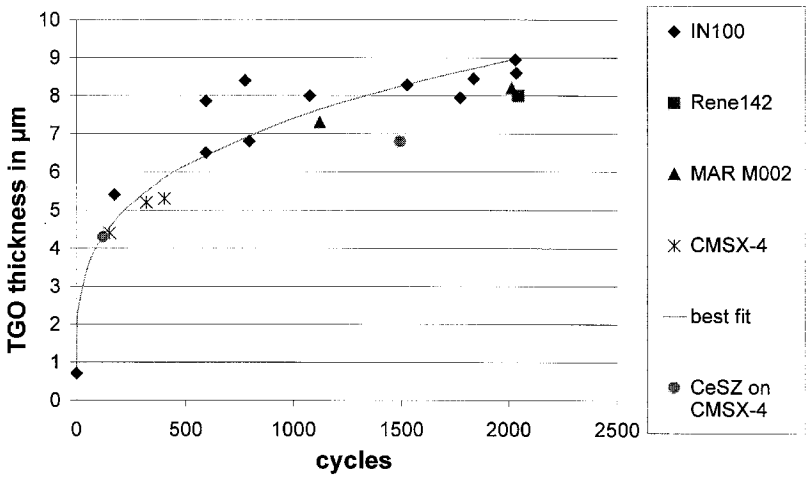


Fig. 4: TGO thickness at failure on EB-PVD NiCoCrAlY bond coats with P-YSZ and CeSZ TBCs

The cyclic lifetime of identical PYSZ TBCs not only depends on the bond coat but also and even more significantly on the substrate alloy. Similar to some other studies [8, 9, 10], the longest lifetimes were found for DS alloys while PYSZ on SX alloys suffered from early TBC spallation. For the latter item, several hypotheses were taken into account for shortening the lifetime:

- Less carbon in the SX alloys that otherwise ties up "detrimental" elements like Ta, W, Mo, Ti) in DS or polycrystalline alloys diffusing from the substrate through the bondcoat to the TGO [10]. In addition, no boron is commonly alloyed in single crystals that may probably account for life extensions.
- Absence of grain boundaries should advantageously avoid faster diffusion along grain boundaries, but obviously this does not work [11].
- The coefficient of thermal expansion is commonly lower for SX alloys than for the other substrates, which causes less stresses in TGO and TBC due to a lower extension mismatch, but this is again not effective. The anisotropy in SX alloys specially of the Young's modulus also varies the stress state. However, at what amount and in which direction is unclear.
- The total amount of refractory elements is highest in SX alloys.

The growth rate of the TGO on the NiCoCrAlY bond coats is very similar regardless of the substrate alloys and TBC composition (Fig. 4), suggesting that the predominant growth mechanism is the same. The TGO growth does not strictly follow a parabolic law but calms down with time, probably due to grain growth and decreasing portions of grain boundary diffusion. Obviously, for the present NiCoCrAlY/P-YSZ system, the spallation life of the TBC can not be correlated to TGO thickness in a simple manner. Moreover, only slight differences were found in the mixed zone of the TGO on the different substrates with some yttrium enrichment below it on the SX alloy. Since this area is normally not the location of failure, the interface between TGO and bond coat is of great interest instead. No enrichment of refractory elements like Ta, W, and Mo were found in that region.

In the present study and also in most other studies, the longest lifetimes were achieved with substrate alloys that contain large amounts of hafnium. Surprisingly, the TGO on samples with the longest lifetimes showed a very rough BC/TGO interfaces (Fig. 3). This is in contradiction to models that have been developed suggesting that imperfections in that area might be initiation sites for large scale buckling and subsequent spallation of the TBC [17]. In the present case, large hafnia containing oxide pegs have developed on the Hf containing alloys Rene 142 and MarM002. These pegs may act as crack stoppers since an interfacial crack has to change its propagation direction very often if it would follow intimately the BC/TGO interface that possesses the lowest interface toughness. The TGO is tightly bonded to the metal by these pegs, with a potential but well known positive effect of the rare earth element hafnium, that for instance may have tied-up sulfur or may have lowered the activity of detrimental refractory elements. Normally, traces of Hf, Y, or Zr are most helpful for alumina scale adherence especially on Al diffusion BCs [18], and the alarmingly high level of 1.5 wt% hafnium in both Rene 142 and MAR M002 could lead to an over-doping of the bondcoat. But in spite of it the irregular TGO interface with pegs sticking down to 15µm, and even worsened by isolated internal oxide regions , behaved best in the cyclic tests. Careful analysis of the metal underneath the TGO will be necessary to get a better understanding of the large differences in cyclic lifetime, initiated most probably by diffusion of substrate elements to the bond coat and to the TGO [11].

The existence of the mixed zone in the as-coated condition suggests that its formation is governed by outward diffusion of aluminum through a very thin oxide scale that forms during vacuum heat treatment and pre-heating prior to P-YSZ deposition with concurrent precipitation of zirconia particles [19]. This was confirmed by constant values of the MZ found in SEM for all substrates after the initial oxidation times. Once a certain thickness of a continuous α-alumina layer has formed, aluminum outward diffusion into the mixed zone is no longer possible. During subsequent thermal exposure, the growth mechanism of the TGO is dominated by inward diffusion of oxygen. The growth front is then always at the interface between alumina and bond coat. This observation is different from the mechanism of continuously increased aluminum outward diffusion proposed in [20, 21]. Differences might be caused by different bond coats as well as different deposition techniques as detailed above. Since the diffusivity of aluminum in an α-Al_2O_3 scale is in general much smaller than that of oxygen, the growth of an α-alumina scale on alumina-forming alloys is dominated by inward diffusion of oxygen moving mainly along grain boundaries of the columnar oxide grains.

The location of the life-limiting main separation crack within the CeSZ close to the TGO/CeSZ interface can be assumed to be a consequence of a critical low content of stabilizing oxides of CeO_2 and Y_2O_3 to make the t` structure less stable. On the other hand, it is a classic location for the failure of APS TBCs showing "white failure". Obviously, enhanced internal stresses in that area have accumulated that result in this chemically and mechanically related failure mode. Interestingly, for both ceramic top coats on CMSX-4 an Y enrichment in the mixed zone was found. The yttria deficient ceria stabilized zirconia version clearly indicates the bond coat as the primary source for Yttrium. More investigations are needed to detail the mechanism that accounts for the Y-rich mixed zone on CMSX-4 substrates.

The gain in lifetime of the CeSZ version on CMSX-4 is at the current stage of evaluation not easy to explain. So far we know the oxide growth rates are too similar compared to P-YSZ to account unequivocally for the variations in lifetime. There is only a slight indication that the growth rate data are at the lower range of the scatter band. The only noticeable difference between CeSZ and P-YSZ TBCs observed so far is the higher content of Y in the mixed zone for the CeSZ version. Although there is no proof for interactions between the different ce-

ramic top coat compositions and the TGO that may account for life extensions, a similar promising behavior was found in burner rig for CeSZ. There, a different failure mechanism (quasi-continuous step-wise weight loss and a degradation in thin layers in stead of spallation of the whole P-YSZ TBC) was identified [3]. One major reason for a step-wise loss was, of course, the extensive fluctuation of composition across the thickness of the TBC that was attacked by a high speed gas stream. Both aspects are at some variance to this investigation since the favorable two source evaporation has lowered the fluctuations in CeO_2 content significantly and the gas stream in furnace cyclic testing is only moderate.
The large scatter of the lifetimes of the CeSZ TBC system needs some comment. Without having much proof by analytical evidence it seems to be somehow related to the individual composition of the CeSZ TBC on the various samples. They were all prepared and coated in the same batch so they should be identical. But if the coating process of the CeSZ TBC in the rotation mode is analyzed in more detail, in the very beginning of ceramic deposition a part of the samples will cross the CeO_2 rich vapor cloud first whereas the other samples will pass the ZrO_2 rich cloud. So chemically different compositions and TGO/CeSZ interfaces on the samples will result. They are assumed to affect the lifetime. The critical layer near the interface will be $< 1.25\mu m$ which is the size of one layer per rotation.

Conclusions

EB-PVD NiCoCrAlY/zirconia based TBCs on several polycrystalline, directionally solidified, and single crystalline substrate alloys were thermally cycled with T_{max}=1100°C. The following conclusions can be drawn.
(1) Hafnium containing alloys (MAR M002 and Rene142) improve adhesion of the TGO on the bondcoat, leading to the longest lifetimes. A rough interface between TGO and bondcoat with hafnia pegs was characteristic for these alloys.
(2) SX alloys suffer from early P-YSZ TBC spallation, although no difference in TGO growth rate or segregation of refractory elements was observed. Yttrium enriches in the outer portion of the mixed zone.
(3) TBC spallation cannot be simply correlated to the TGO thickness while the substrate alloy plays a crucial role for TBC spallation life.
(4) Ceria stabilized zirconia TBCs brought about significant longer lifetimes on the CMSX-4 substrate compared to P-YSZ, reaching similar cycles to failure as PYSZ on a conventional superalloy (IN100 substrate in spite of serious compositional fluctuations in the CeSZ). They show an atypical white failure within the TBC just 5 to 7μm above the TBC/TGO interface.

Acknowledgements

The authors gratefully acknowledge careful manufacture of the coatings by J. Brien, C. Kröder, H. Mangers, and H. Schurmann as well as helpful comments on the manuscript by M. Peters at DLR. J. Münzer and U. Kaden performed some of the TGO thickness measurements in SEM. The manufacture of the ceria and 3Y-PSZ ingots by Prof. Teja Reetz, HTM Reetz GmbH Berlin, is kindly appreciated.

References:

[1] B.A. Nagaraj, A.F. Maricocchi, D.J. Wortmann, J.S. Patton, and R.L. Clarke, "Hot corrosion resistance of thermal barrier coatings", ASME paper 92-GT-44, (1992),

[2] P. Vincenzini, G. Appiano, F. Brossa, and S. Meriani, "Stability of thermal barrier coatings.

Proc. 3th Int. Symp. "Ceramic Materials and Components for Engines"", ed. V.J. Tennery, (1989), 201-210.

[3] U. Schulz, K. Fritscher, and M. Peters, "Thermocyclic Behavior of Variously Stabilized EB-PVD Thermal Barrier Coatings," *J. Engineering for Gas Turbines and Power,* 119(1997), 917-921.

[4] U. Schulz, K. Fritscher, M. Peters, C. Leyens, and W.A. Kaysser, "Thermocyclic Behavior of Differently Stabilized and Structured EB-PVD Thermal Barrier Coatings," *Materialwissenschaft und Werkstofftechnik,* 28(1997), 370-376.

[5] P.A. Langjahr, R. Oberacker, and M.J. Hoffmann, "Langzeitverhalten und Einsatzgrenzen von plasmagespritzten CeO2- und Y2O3- stabilisierten ZrO2-Wärmedämmschichten," *Materialwissenschaft und Werkstofftechnik,* 32(8)(2001), 665-668.

[6] U. Schulz, K. Fritscher, and C. Leyens, "Two-source jumping beam evaporation for advanced EB-PVD TBC systems," *Surface and Coatings Technology,* 133-134(2000), 40-48.

[7] O. Unal, T.E. Mitchell, and A.H. Heuer, "Microstructures of Y2O3-stabilized ZrO2 electron beam-physical vapor deposition coatings on Ni-base Superalloys," *J. Am. Ceram. Soc.,* 77(4)(1994), 984-992.

[8] J.G. Goedjen and G.P. Wagner, "Evaluation of commercial coatings on MARM-002, IN-939 and CM-247 substrates," *ASME,* 96-GT-458(1996),

[9] J. Kimmel, Z. Mutasim, and W. Brentnall, "Effects of alloy composition on the perfomance of yttria stabilized zirconia-thermal barrier coatings," *ASME IGTI congress and exhibition 1999,* 99-GT-350(1999), 1-9.

[10] P. Morrell and D.S. Rickerby, "Advantages/disadvantages of various TBC systems as perceived by the engine manufacturer", AGARD report 823 "Thermal barrier coatings", Aalborg, Denmark: (1998), 20-1 to 20-9.

[11] U. Kaden, C. Leyens, M. Peters, and W.A. Kaysser, "Thermal Stability of an EB-PVD Thermal Barrier Coating System on a Single Crystal Nickel-Base Superalloy", in: *Elevated Temperature Coatings: Science and Technology III,* ed. J.M. Hampikian and N.B. Dahotre TMS, 1999), 27-38.

[12] K. Fritscher, U. Schulz, and M. Schmücker, "EB-PVD TBC Lifetime Response to Various Bond Coat Pretreatments", in: *Cyclic Oxidation of High Temperature Materials,* ed. M. Schütze and W.J. Quadakkers (London, UK: The Institute of Materials, 1999), 383-391.

[13] U. Schulz and M. Schmücker, "Microstructure of ZrO_2 Thermal Barrier Coatings Applied by EB-PVD," *Materials Science and Engineering,* A276(2000), 1-8.

[14] S.G. Terry, J.R. Litty, and C.G. Levi, "Evolution of porosity and texture in thermal barrier coatings grown by EB-PVD", Elevated temperature coatings: science and technology III, ed. J.M. Hampikian and N.B. Dahotre, The Minerals, Metals & Materials Society, (1999), 13-25.

[15] U. Schulz, M. Menzebach, C. Leyens, and Y.Q. Yang, "Influence of substrate material on oxidation behavior and cyclic lifetime of EB-PVD TBC systems," *Surface and Coatings Technology,* 146-147(2001), 117-123.

[16] T. Krell, U. Schulz, M. Peters, and W.A. Kaysser, "Graded EB-PVD alumina-zirconia thermal

barrier coatings- an experimental approach", FGM 98, ed. W.A.Kaysser, Trans Tech Publications LTD, (1999), 396-401.

[17] D.R. Mumm, A.G. Evans, and I.T. Spitsberg, "Characterization of a cyclic displacement instability for a thermally grown oxide in a thermal barrier system," *Acta Materialia,* 49(12)(2001), 2329-2340.

[18] B.A. Pint, J.A. Haynes, K.L. More, I.G. Wright, and C. Leyens, "Compositional effects on aluminide oxidation performance: objectives for improved bond coats", Superalloys 2000, Seven Springs: TMS, Warrendale, PA, (2000),

[19] C. Leyens, U. Schulz, W. Braue, and Y.Q. Yang, "Formation of the Alumina-Zirconia Bonding Zone in EB-PVD Thermal Barrier Coatings", in High Temperature Corrosion Materials Chemistry III, eds. E.J.Opila et al., The Electrochemical Society, Pennington, NJ, (2001), 28

[20] M.J. Stiger, N.M. Yanar, F.S. Pettit, and G.H. Meier, "Mechanisms for the failure of electron beam physical vapor deposited TBCs induced by high temperature oxidation", Elevated Temperature Coatings: Science and Technology III, ed. J.M. Hampikian and N.B. Dahotre, TMS, (1999), 51-65.

[21] M.J. Stiger, N.M. Yanar, M.G. Topping, F.S. Pettit, and G.H. Meier, "Thermal barrier coatings for the 21st Century," *Zeitschrift für Metallkunde,* 90(12)(1999), 1069-1078.

CHARACTERISATION OF SIX OVERLAY COATINGS

M.Giannozzi°, E.Giorni°, M.Merluzzi*, F.Pratesi*, G.Zonfrillo*

° GEPS Nuovo Pignone – Firenze
* DMTI – Facoltà di Ingegneria, Università di Firenze

Abstract

Six different overlay coatings, deposited on the same substrate, GTD111, a nickel superalloy, have been investigated. In order to determine the relative performance of each coating at high temperatures, two sets of specimens were submitted to programmed exposure: a set of samples has been exposed to temperatures of 850 and 980°C for fixed times and another set submitted to cyclic oxidation tests at 1000, 1050 and 1100°C. All the samples were then examined with several metallographic techniques. In particular, thickness, micro-hardness, and depletion were systematically measured and reported. An analysis of the different methods used for characterisation was also carried out, with the conclusion that the most reliable technique for these coatings is the determination of depletion. A new way of performing this kind of measurement has been introduced (on the basis of image analysis during SEM observation) leading to an improved standard procedure for characterisation. Measures of coating thickness, on the other hand, were found to be affected by excessive standard deviations in the experimental data. The experimental results are reported, summarised in tables and diagrams, and discussed, in particular with the aim of deducing the comparative behaviour of the individual coatings examined.

Keywords: coatings, cyclic oxidation, ageing, depletion

Introduction

In the surface protection of turbine blades, special care must be devoted to the coating, which often represents the critical part of the blade systems. In actual practice, both diffusion and overlay coatings are used, and the choice depends on the particular component or application. The general metallurgical background for protection is known, but many laboratories are still attempting to improve the properties of the standard coatings commonly used.

Several modifications have been suggested, firstly the addition of given chemical elements in the composition of the coating [1]. Notwithstanding the large number of proposals, the effect of given chemical additions to the standard coatings is still uncertain, especially from the quantitative point of view. One reason is that many aspects are involved. If a modification of the coating is to be beneficial, it has to improve several properties at the same time, such as the growth rate of the oxide, its adherence, its resistance to spallation and similar phenomena occurring at the interfaces involved, with the aim of keeping good quality after exposure to high temperatures and thermal stresses [2-5].

Experimental results

Sample Preparation

The investigation was based on the selection of six different overlay coatings. As substrate, the same GTD111 alloy has been used for all the specimens. It is a nickel based superalloy, developed by General Electric, with composition ranges of its elements indicated in table 1.

Table 1. Composition of the GTD 111 superalloy (wt%).

Cr	*Co*	*Al*	*Ti*	*W*	*Mo*	*Ta*	*C*	*Zr*	*B*	*Fe*	*Si*
13.7-14.3	9. - 10.	2.8-3.2	4.7-5.1	3.5-4.1	1.4-1.7	2.5-3.1	0.08-0.12	0.005-0.04	0.005-0.02	0.35 max	0.3 max
Mn	*Cu*	*P*	*S*	*Nb*	*V*	*Hf*	*Pt*	*Rh*	*O*	*N*	*Mg*
0.1 max	0.1 max	0.015 max	0.005 max	0.15 max	0.1 max	0.15 max	0.3 max	0.15 max	< 25 ppm	< 50 ppm	< 50 ppm

This alloy has been commonly employed in turbine blades, for years. It has often been employed in components produced by GEPS Nuovo Pignone. The six coatings deposited and investigated are reported in table 2.

Table 2. Coatings investigated.

Abbreviation	Composition	Deposition technique
NCP	NiCoCrAlY+Pt	Low-Pressure Plasma Spray + Pt electroplated and diffused on the surface
NCT	NiCoCrAlY+Ta	Electroplated
NCHS	NiCoCrAlY+Hf+Si	Electroplated
NC	NiCoCrAlY	Electroplated
NCHV	NiCoCrAlY	High Velocity Oxygen Fuel
NHV	NiCrAlY	High Velocity Oxygen Fuel

All of the six coatings investigated show satisfactory adhesion to the substrate, and the amount of impurities at the interface is acceptable. The microstructure of all these coatings is formed (Fig. 1) of the β-NiAl phase dispersed in the γ matrix consisting of the solid solution of Co, Cr, Al and minor alloying elements in Ni. NC and NCHV have the same ranges of composition.

High-Temperature Static Exposure

In order to obtain an evaluation of the relative resistance at high temperatures, the six coatings were exposed to high temperatures according to two different programs. Temperatures were chosen so that they were sufficiently near to working conditions, and the resulting times were adequate to show the evolution of the properties of the coating. A first set of samples was exposed for fixed times to two different high temperatures (850 and 980°C). Two different furnaces were used, each for the given temperature, and the time intervals were also set differently. This is due to the fact that coating damage roughly depends on time (at constant temperature) according to a power law, and exponentially on temperature (for constant times).

Interruptions have thus been introduced at 2000 and 5000 hours for the lower temperature of 850°C and at 1000, 2000 and 3000 hours in the case of 980°C. Further interruptions at longer times have been programmed, but these results are not yet available. During each interruption, a thin slice was cut from every sample and prepared for metallographic observation.

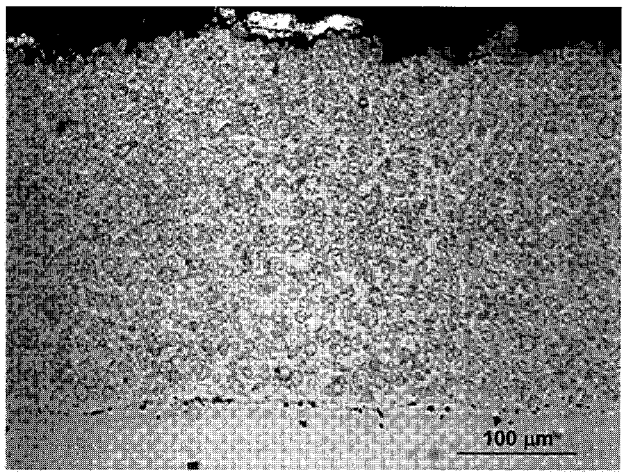


Fig. 1. NCHS as coated; optical microscope (x200).

High-Temperature Cyclic Oxidation

The static tests described in the previous paragraph are useful for characterisation. However, it is necessary to add information on cyclic behaviour. As a matter of fact, working conditions involve start-ups and interruptions with great temperature variations and corresponding expansions and contractions of substrate, coating and surface oxide that induce severe mechanical stresses in these elements. In particular, variation in volume differs in the various surface and subsurface layers and one of the possible consequences is spallation of the oxide layer, due especially to its brittleness. Continuing with the exposure to normal working conditions and the inherent start-up-interruption cycles, the whole surface layer may become less adherent, also due to the manifestation of rumpling phenomena. Accordingly, another set of samples has been submitted to cyclic oxidation tests, as is current practice for a reliable characterisation of these coatings.

Three temperatures (1000, 1050 and 1100°C) have been selected for this experimentation. The furnace used is similar to those employed for creep testing, with suitable modifications. In particular, it has the top section closed and the bottom one opened for inserting the sample holder; the latter is mounted on a piston programmed for times of exposure to high temperature and outside of the furnace. As soon as the piston is lowered, compressed air is blown onto the sample to increase its cooling rate. The cycle includes one hour of high-temperature exposure alternating with five minutes holding outside of the furnace. After each cooling step, the samples are weighed three times and the mean value is recorded. One section of each sample was prepared for metallographic observation, in order to investigate the effects of thermal cycling on the microstructure.

Examination Procedure

After the programmed exposure to high temperature, as mentioned above, the specimens to be characterised consisted of slices of the original samples. These sections were examined with several metallographic techniques. In particular the following properties were measured: thickness, micro-hardness, depletion. Moreover, all specimens were observed under optical and SEM microscopes: details of their microstructure were recorded and in a few cases semi-quantitative microanalysis was carried out for confirmation.

Thickness was determined under the microscope, at 500x, as the average of six measurements made in equidistant positions all around the surface. For measuring depletion, the same six positions were observed at the same magnification. In particular in these zones, in which the β-NiAl phase is still present, the thickness of the band is measured as the thinnest layer observed at 500x. The final value (namely, the mean value of the six measures) is considered a sensitive and reliable parameter for indicating the residual life of the coating. Vickers microhardness was determined with a Leitz RZD-DO apparatus with 100 g load.

The microstructure was first observed at various magnifications and two images of each sample were taken at 200x and 500x and kept as a record for comparison. As a second step in the analysis, samples were submitted to electrolytic attack in a 2% solution of chromic acid. Greater contrast was thus obtained between the phases and the matrix. Two photos at the same magnification were taken and kept for comparative observation. Microanalysis, at a semiquantitative level, accompanied in some cases morphological observation in the SEM, in order to clarify the chemical background of observed changes in the microstructure. A particular use of backscattered electrons will be described below.

Critical Analysis of the Characterisation

An a-posteriori analysis of the different methods used for characterisation has also been carried out. Measurements of coating thickness were found to be affected by great standard deviations of the experimental results. More significant appear to be measurements of micro-hardness, although they yield insufficiently precise results too. The conclusion is that the determination of depletion must be considered as the most reliable technique for determining modifications due to ageing in these coatings.

A New Method for Determining Depletion

As known, one parameter of damage in the coatings sector is represented by NiAl depletion [6, 7]. This mechanism is due to the alumina scale formation that is necessary for protection against oxidation. During start-up, shut down and service the alumina scale, once having reached critical thickness, tends to spall. Therefore this layer must be replaced by new aluminium coming from the coating. This phenomenon produces a progressive β-phase depletion and the effectiveness of the coating protection is exhausted when the β-phase is no longer present. For this reason systematic measurement of β-phase has been performed on the specimens in question. The simplest method is to measure the β-phase band of aged samples in relation to the total thickness.

A more accurate method has been introduced taking into account also the volume fraction of the β-phase, leading to an improved standard procedure for characterisation. It systematically uses image analysis during SEM observation. It is based on the introduction of a new parameter

$$\%\beta_{NEW} = \underbrace{\frac{L_\beta}{L_{tot}} \cdot 100}_{\text{Depletion factor}} \cdot \underbrace{\frac{S_\beta}{S_{tot-b}}}_{\text{Image analysis constant}}$$

where $\%\beta_{NEW}$ is the modified depletion factor, L_β the layer thickness of the NiAl phase, L_{tot} the total thickness of the coating, S_β the surface area of the NiAl phase, $S_{tot\text{-}b}$ the total surface area of the band. Accordingly, the modified depletion factor accounts for the actual fraction of Al in the coating, no longer depending on the individual measurement of band thickness. This new parameter gives results that in some cases follow the same trend of the commonly used parameter, but in other cases the oxidation resistance ranking of the various coatings changes.

Study of Depletion

The experimental curves of Fig. 2 – and especially those corresponding to higher temperatures – show that the three coatings produced by electroplating have greater resistance. As a matter of fact, the band thickness of the NiAl phase decreases more slowly and thus retains a larger quantity of Al available for protection – at the same working conditions. Moreover, it can be observed that the addition of Ta in NCT (except at 850°C) and of Hf and Si in NCHS induces a remarkable slowing down in Al diffusion as compared to the same coatings without additions (NC). The behaviour of NCP is intermediate, whereas the two coatings obtained by HVOF deposition are those showing the lowest resistance to static oxidation.

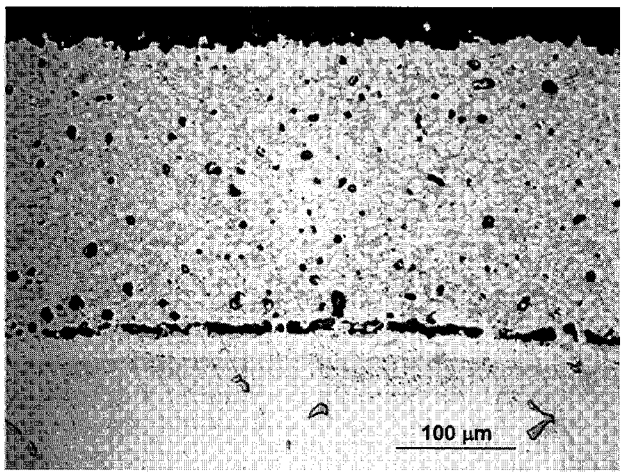


Fig. 3: NC, 1000 hours 980°C, optical microscope (x200).

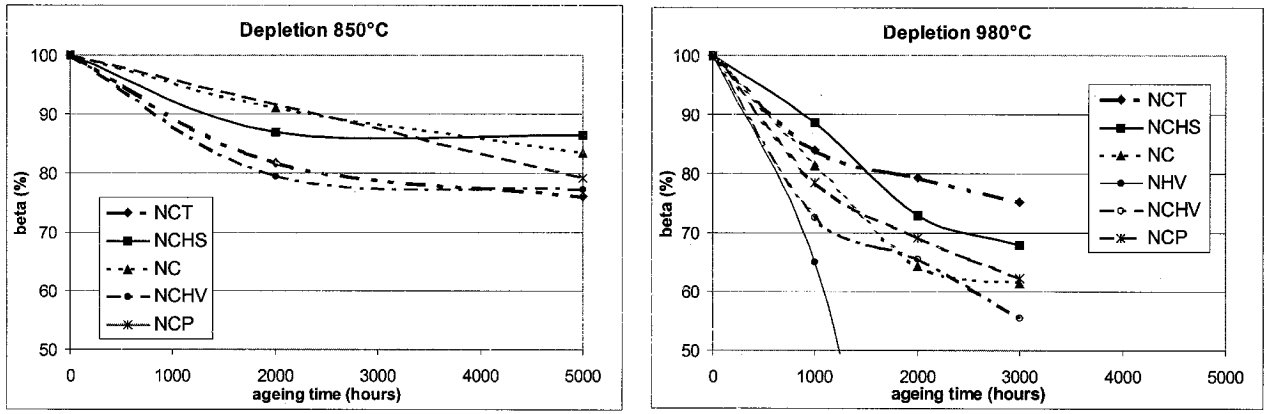


Fig. 2. Depletion behaviour of coating subjected to static ageing.

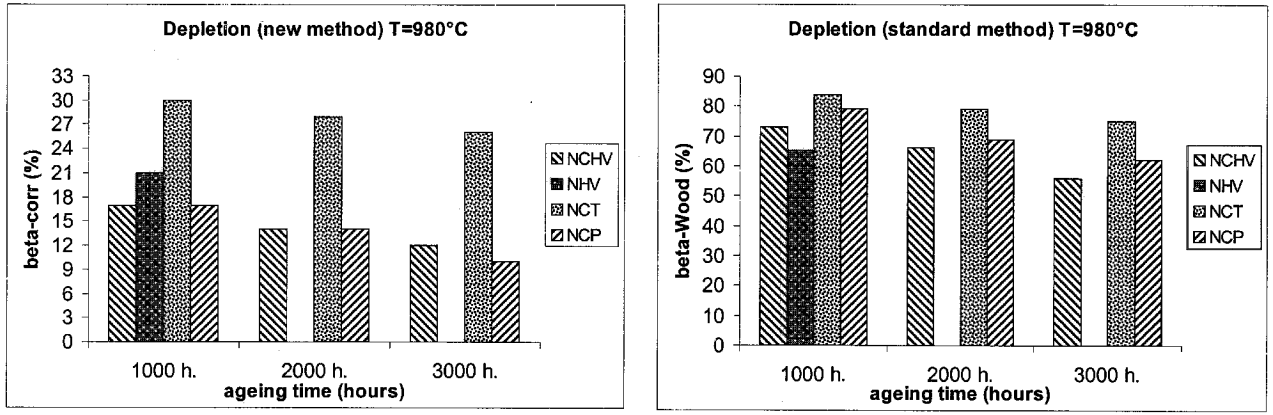


Fig. 4. Comparison between standard and new method for depletion procedure.

A first analysis thus indicates that electroplated coatings provide the best protection for the underlying superalloy. However, at room temperature some brittleness has been detected at the interfaces between NiAl particles and the coating matrix, owing to a preferential accumulation of oxides and impurities in these regions. This may lead to a detachment of the β phase and the manifestation of porosity to an unacceptable degree (Fig. 3).

It is possible that these negative phenomena can be strongly reduced through a stricter control of the deposition and particularly a reduction of the impurities that are usually present in any electrolytic solution.

As an example of the application of the new method, the different mutual locations of the curves for four coatings in the 980°C test are shown in Fig. 4. Note that with the new method proposed here NHV contains an amount of Al greater than NCHV and NCP up to 1000 hours.

On the other hand, the two latter coatings contain about the same quantity of Al, whereas in the traditional determination NCHV showed a greater depletion than NCP for all exposure times. Moreover, NCT is confirmed as the most resistant coating, as already found with the standard method, but the improvement in performance as compared to the other coatings is now greater.

Resistance To Thermal Shock

The results are reported in Fig. 5. All coatings initially follow a similar behaviour, although the individual kinetics may differ in detail. At first an abrupt increase in weight is found, due to the growth of the oxide. In this first stage, spallation cannot occur because the oxide layer is so thin that it will not develop during the thermal shock a notable amount of microcracks, especially rather long ones. However, oxide thickness increases with increasing cycle numbers and microcracks correlated with the stress conditions at the coating-oxide interface can now initiate the spallation process, in correspondence with the first drop in the curve.

Later on, most curves show a inversion of concavity with a cycle interval in which the weight of each specimen remains constant. This is probably due to the increase in the composition ratio between mixed oxides (NiM_2O_4) and stable oxide (Al_2O_3). Since Ni oxides are brittle and grow with low adherence to the support, the whole amount of oxides formed during a cycle is immediately lost due to spallation in the subsequent thermal shock.

The intermediate stage outlined above is followed by the final irreversible failure of the coatings due not only to oxide spallation but also to rumpling phenomena with loss of coating parts. Stresses at the coating-oxide boundary lead to an increasingly corrugated interface that implies greater stress concentrations at the lowest radii of curvature. In such zones a fracture of coating fragments thus becomes inevitable. This damaging process can be followed by visual inspection and quantitatively determined by weight loss as shown in Fig. 5. In particular the test at highest temperature (1100°C) shows above 230 cycles, a remarkable decrease in weight for all coatings.

The same curves can be examined for varying temperatures. The effect of temperature is – as expected – pronounced. As often occurs in high-temperature exposures, small variations in temperature are equivalent to great changes in time. This general behaviour is qualitatively confirmed. Further data will be collected with the aim of finding quantitative relations, which

may be used, in particular, to determine damage, life assessment and residual life prediction. The visual inspections and the diagrams reported show that the most resistant coatings, as regards thermal shocks, are NCT and NCP. In particular, the latter also shows very little rumpling in the test at 1100°C. It may be deduced that rumpling in NCP is remarkably reduced by the Pt interlayer, placed between overlay and oxide, able to smooth thermally induced tensions with its ductile behaviour. Optical observations of the specimen confirm this hypothesis.

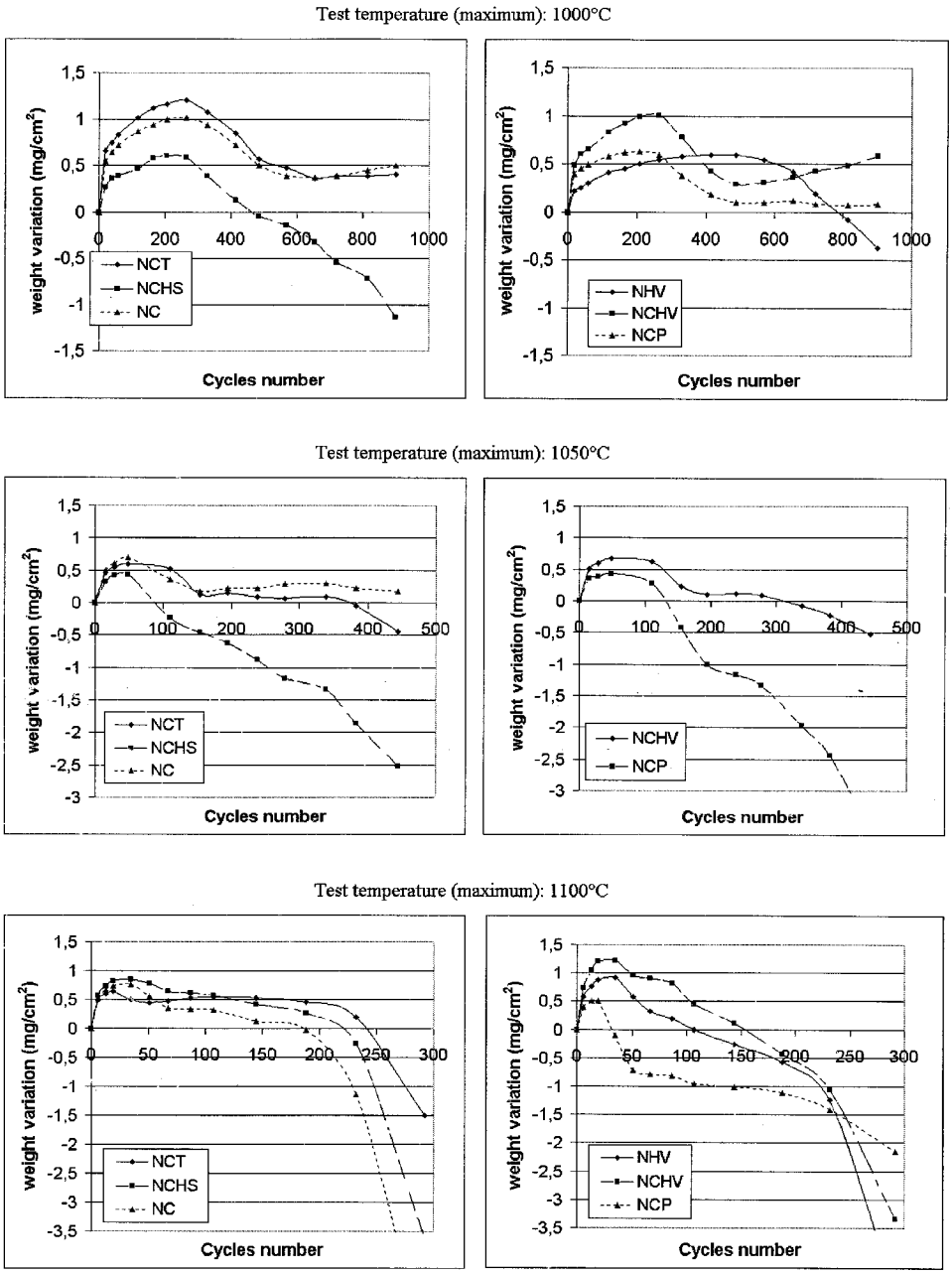
Among HVOF deposited coatings, NCHV shows a greater resistance than NHV. NCHS shows an unsatisfactory resistance in comparison with the two electroplated coatings, both in the 1000°C and in the 1050°C tests. Apparently, the positive effect of Hf and Si of inducing a slower diffusion of Al is counterbalanced by the silicon diffusion into the oxide layer, making it more brittle.

Concluding remarks

A comparison among the different performances of the various coatings has been performed on the basis of traditional and innovative techniques. In particular, a new method has been suggested and used for determining depletion.

The conclusion has been that NCT and NCP show the best behaviour at high temperatures. Of the two, NCT would of course be preferable, because it also shows the best resistance to static high-temperature ageing among all the coatings investigated. In particular, the gap in performance between this coating and the others is further increased by the new method of depletion analysis suggested in this work. In addition to this property, NCT shows a good resistance to spallation. On the other hand, another significant advantage derives from its manufacturing costs, by far lower than the LPPS process required for producing NCP.

However, a drawback for selecting NCT (as well as the two other electroplated coatings investigated) is represented by its lower adhesion at room-temperature, indicated by metallographic means. More work is required to increase this specific property to make this interesting process more reliable.



a) b)

Fig. 5. Thermal shock behaviour (a: electroplated coatings; b: sprayed coatings).

References

[1] B.A. Pint, I.G. Wright, W.Y. Lee, Y. Zhang, K. Prussner, K.B. Alexander, *Substrate and bond coat compositions: factors affecting alumina scale adhesion*, Materials Science and Engineering vol.245, 1998.
[2] A. Boudot, F. Crabos, D. Fournier, *Thermo-mechanical fatigue of coating for HP turbines*, ASME 1998, 98-GT-324.
[3] K.S. Chan, N.S. Cheruvu, G.R. Leverant, *Cyclic oxidation behaviour of aluminide, Pt aluminide and MCrAlY coatings on GTD111*, ASME 1998.
[4] K.S. Chan, N.S. Cheruvu, G.R. Leverant, *Coating life predictions for combustion turbine blade*, ASME 1998, 98 -GT-478.
[5] R.C. Pennefather, D.H. Boone, *Mechanical degradation of coating systems in high temperature cyclic oxidation*, Int. J. Pres. Ves. & Piping vol.66, 1996.
[6] J.H. Wood, *Methodology for remaining beta phase measurements on exposed GT33 coating*, MPE-663, 1998.
[7] J.H. Wood, *Methodology for GT33 coating life/remaining life prediction using beta phase depletion measurements*, MPE-678, 1999.

SINGLE CRYSTAL COATING OF SX TURBINE BLADES BY A LASER CLADDING TECHNIQUE

C. Bezençon[1], J.-D. Wagnière[1], M. Höbel[2], A. Schnell[2], M. Konter[2], W. Kurz[1]

[1] Department of Materials, Centre de Traitement des Matériaux par Laser (CTML), Ecole Polytechnique fédérale EPFL, 1015-Lausanne, Switzerland;

[2] ALSTOM Power Technology, 5401-Baden, Switzerland

Abstract

Present day HP/HT blades for aircraft and stationary gas turbines mostly consist of single crystal (SX) Ni-base superalloys, protected by a MCrAlY coating (with M for Ni or Co). The oxidation and corrosion resistance of the blades is improved by the high Cr and Al content of the coating, but the thermal fatigue resistance of the blade is reduced by the polycrystalline nature of the layer. Differences in the elastic moduli of the single crystal substrate and the random crystal orientation of the coating lead, during thermal cycling, to incompatibility stresses. One way to improve the component life is to produce SX coatings, with the same crystal orientation as the substrate. A single-crystal coating can only be produced when epitaxial and directional solidification is ensured. In this paper, it is shown that such a coating can be produced by a laser cladding technique, when the cladding alloy is adapted to the process and when the processing parameters are precisely controlled. Defects which must be avoided and the results of SX coatings of MCrAlY alloys deposited onto single crystal CMSX-4 superalloy will be presented.

Keywords : single crystal coating, laser cladding, solidification microstructure.

1. Introduction

Present day high pressure/high temperature turbine blades are usually made of single-crystal (SX) Ni-base superalloys, coated with a Ni or Co base layer rich in Cr and Al (MCrAlY alloy). SX blades have been developed to improve the mechanical behaviour at elevated temperatures (creep and thermal fatigue). The coating protects the blade surface against oxidation and corrosive atmospheres [1]. Deposition techniques such as the plasma spray process produce polycrystalline layers. Due to this polycrystalline nature, the mechanical compatibility of the layer with the single-crystal substrate is limited. Indeed, the thermo-mechanical strength of those components is reduced by incompatibility stresses induced by the high anisotropy of the elastic modulus of the Ni-base alloys [2].

It has been recently shown that a single crystal deposition of protective layers can be achieved by a laser cladding technique [3, 4]. In this process, the coating material in powder form is molten by a high intensity laser beam then solidifies on the treated surface. Single crystal solidification is obtained through epitaxial and columnar growth [5]. The application of such a deposit should lead to an increase in the life of the gas turbine blades.

In this paper, following a brief description of the laser cladding process, the two major defects of a single crystal laser deposition are described: (i) loss of the crystal orientation of the substrate and (ii) formation of hot tears. It is shown that both phenomena occur during the solidification of the liquid pool obtained by laser heating. The solidification of the clad is analysed, by means of recent solidification models [5, 6], in order to determine the conditions required for (i) single-crystalline and (ii) crack-free solidification. The main process and alloy parameters controlling successful deposition are discussed.

2. Experimental procedure

During laser cladding, metallic powder is injected into a melt pool produced by laser heating. By scanning the laser beam over the substrate a coating can be deposited layer by layer [7], with only slight re-melting of the substrate. The process is shown schematically in fig. 1. The main processing parameters are: laser power, P, scanning velocity, V_b, laser beam diameter, D_b, substrate temperature, T_0, mass (powder) feeding rate, $\dot{m}$, and the displacement between two successive laser tracks, Δy.

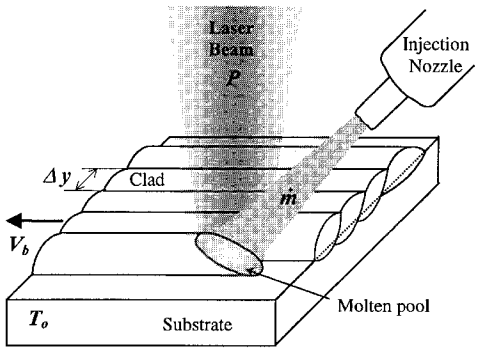


Figure 1 : *Schematic of the laser cladding process.*

Laser cladding of MCrAlY alloys was performed on fully heat-treated CMSX-4, a commercial single crystal Ni-base superalloy [8]. A Rofin-Sinar 1.7 kW cw CO_2 laser was used for all experiments. The beam intensity profile was a near top hat mode (TEM_{00} + TEM_{01}) with circular polarisation. The feeding powder, produced by atomisation in a protective atmosphere, was injected through a lateral nozzle. Laser treatment was carried out under a lamina flow of argon for oxidation protection of the molten pool. The melt pool temperature was measured with a pyrometer.

The microstructures of the solidified materials were observed by conventional metallographic techniques. Transverse and longitudinal sections of samples were polished with diamond paste and chemically etched with a MoO_3 solution (Al-rich etching).

3. Solidification of the melt pool

The solidification microstructure of the deposit is directly influenced by the solidification conditions prevailing at the transformation front, namely the temperature gradient, G, and the solidification velocity, V. During laser cladding, the high energy density of the beam leads to high temperature gradients (G ~10^5-10^6 K/m) and laser beam velocities are generally in the range of 1 to 50 mm/s. Under these conditions, the solidification morphology for nickel-base alloys is mainly dendritic.

The columnar dendritic solidification mode is characterised by a well defined tip radius and tip undercooling (T_l-T*), which is a function of the solidification velocity V [9]. Due to solute redistribution at the solid/liquid interface, a mushy zone where solid and liquid coexist forms.

In this zone, the development of secondary and tertiary dendritic arms is accompanied by a decrease of the temperature. The permeability of the mushy zone decreases with increasing solid fraction, f_s. At the roots of the dendrites, secondary arms of neighbouring dendrites coalesce and join to form a coherent solid. The corresponding temperature is the coherency temperature, T_{coh}. The end of solidification (i.e. $f_s = 1$) is reached at T_{end} (fig. 2).

In cubic crystals, dendrites generally grow following one of the six <100> crystallographic directions. The <100> orientation which is closest to the heat flux is selected. Therefore, a change in the growth direction may be observed in the melt pool (i.e. secondary arms which are orthogonal to the trunk may become primary trunks).

Moreover, the solute redistribution at the tip leads to a zone of constitutionally undercooled liquid ahead of the columnar front. In this zone, the local temperature, as imposed by the heat flux through the solid dendrites, is below the local equilibrium temperature of the liquid : this being the driving force for a potential columnar to equiaxed transition [9] (fig. 2).

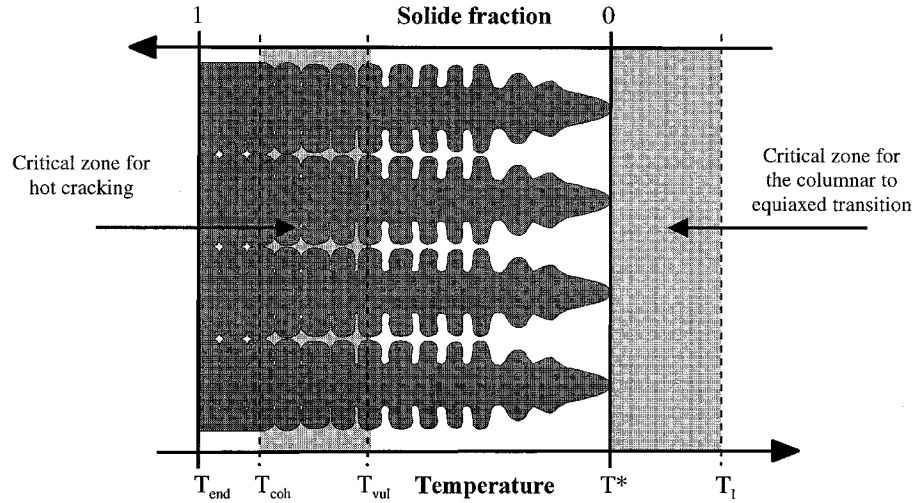


Figure 2 : *Schematic representation of a columnar dendritic solidification front showing the liquidus temperature of the alloy, T_L, the tip temperature, T^*, the vulnerable temperature, T_{vul}, where liquid feeding becomes difficult, and the coherency temperature, T_{coh}. Deep in the mushy zone, when f_s approaches 1, the poor permeability of the mush and the presence of a continuous interdendritic liquid film may lead to hot tearing.*

4. Single crystal solidification

Solidification usually occurs in two steps [9] : (i) nucleation and (ii) growth. A single crystal deposit will only be obtained if the substrate is itself a single crystal and if this crystallographic structure and orientation is propagated into the deposit. In other words, a SX deposit will be produced if the nucleation of new grains is avoided during the solidification process. Two kinds of nucleation have been observed : (i) nucleation on an non-remelted substrate, known as loss of epitaxy and (ii) nucleation in the undercooled liquid ahead of the tips, called columnar to equiaxed transition (CET).

3.1 Loss of epitaxy

When the substrate is slightly remelted and the primary solidification phase of the clad material is similar in crystal structure to that of the substrate, epitaxial growth will occur. At the fusion line the solid substrate is in contact with the liquid and, locally, the thermal gradient is positive (i.e. the liquid temperature is higher than that of the substrate). This leads to an epitaxial and columnar growth.

However, if the substrate surface is not remelted during the process, the liquid clad alloy will solidify on the oxide layer at the substrate surface, leading to nucleation and growth of grains of different orientations to the single crystalline substrate. This case is mainly observed when the solidus temperature of the clad is much lower than the solidus temperature of the substrate. A discontinuity in the solidus temperature at the interface may lead to a non-remelted zone between the traces of the clad. Figure 3 shows a transversal section of a MCrAlY layer deposited onto single crystalline CMSX-4 with four successive traces spaced by a lateral step Δy = 500 µm. The solidus temperature of the clad alloy is approximately 100°K lower than that of CMSX-4. The dashed lines shows the position of each successive trace, where the laser beam moved perpendicularly to the page. Non-remelted zones and misoriented grains are clearly visible between traces.

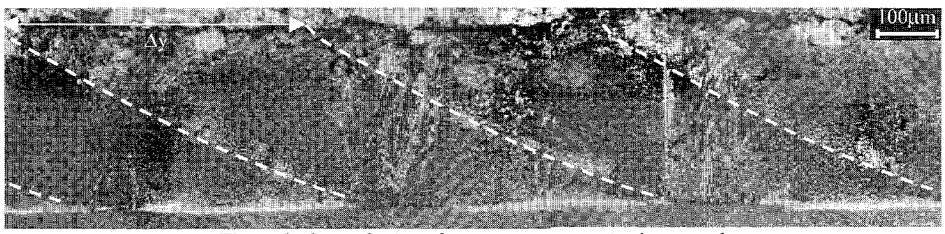


Figure 3 : *Loss of epitaxy between two successive laser tracks.*

By adjusting the lateral shift, Δy, and the mass feeding rate, $\dot{m}$, a regular remelted layer of the entire substrate can be produced and the epitaxial growth of the deposit can be assured. However, a second condition for a single crystal solidification of the clad is imposed : the growth of epitaxial dendrites must be columnar during the whole of the solidification process.

3.2 Columnar to equiaxed transition (CET)

When the solidification conditions are not appropriate, the growth of columnar dendrites can be interrupted by the formation of equiaxed grains in the undercooled liquid ahead of the solidification front (fig. 2). Indeed, the growth of nuclei in the undercooled zone leads to the formation of randomly oriented grains in the deposit (fig. 4-a). These nuclei are due either to heterogeneous nucleation (if the local undercooling is larger than the nucleation undercooling of the alloy) or from dendritic fragments (by remelting of secondary arms) [10]. The growth and size of these equiaxed grains are a function of the extent of the undercooled zone, characterised by the alloy composition and the local solidification conditions G and V. The volume fraction of equiaxed grains can be derived from Avrami's equation, if the nucleation site density of the alloy, N_0, is known (an effective nucleation site density considering the sum of heterogeneous nuclei and dendritic fragments should be taken into account) [11].

It has recently been shown by Gäumann et al. [5] that the columnar to equiaxed transition can be described, for laser solidification conditions (i.e. high G, high V), by the following relation:

$$\frac{G^n}{V} > K \qquad \text{(eq. 1)}$$

where K and n are alloy parameters which are functions of the nuclei density and the dendritic growth kinetics of the alloy.

This criterion defines the solidification conditions necessary to avoid the CET : a sufficiently high temperature gradient and/or low solidification velocity. These local solidification conditions can be related to the laser processing parameters (e.g. laser power, P, scanning velocity, V_b) by heat flux simulation of the process. Processing maps, showing the window for successful SX processing have been drawn [5].

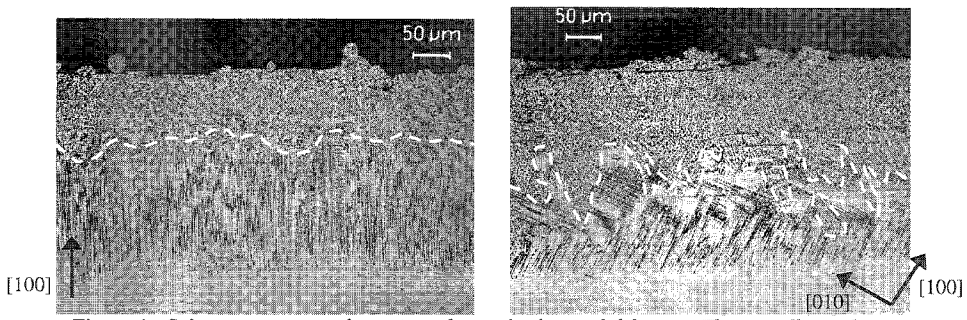


Figure 4 : *Columnar to equiaxed transition during dendritic solidification. The crystallographic direction normal to the substrate surface is (a) <100> and (b) close to <110>. Same processing conditions in both case. (MCrAlY alloy on CMSX-4)*

However, figure 4 shows that the CET is also dependent on the crystallographic orientation of the substrate. For instance, when the surface-normal of the sample is parallel to a <110> direction (fig. 4-b), the CET is favoured. Indeed, the epitaxial/columnar zone is reduced and the main part of the deposit shows equiaxed microstructure, with a random crystallographic orientation[1]. The influence of the crystallographic orientation of the substrate can be taken into account by introducing the angle ψ [12], that is the angle between the heat flux direction and the dendritic growth direction <100>. The criterion for columnar growth becomes [13] :

$$\frac{G^n}{V}(\cos\psi)^{n+1} > K \qquad \text{(eq. 2)}$$

From this criterion, it is shown that the process window for a columnar growth is reduced when the dendritic growth direction is not collinear with the heat flux ($\psi \neq 0$).

---

[1] It can be seen from this figure that the epitaxial dendrites still grow following one of the six <100> directions. A growth direction transition (between [100] and [010]) is observed. This transition, imposed by the heat flux, does not affect the crystallographic structure, as in cubic systems (such as fcc Ni), both directions are identical.

When the columnar to equiaxed transition is avoided and epitaxial growth is ensured, a single crystal clad is obtained. Such a deposit is shown in figure 5. A transition of the dendritic growth direction is observed in the center of the deposit : dendrites grow from the back of the melt pool, in a <001> direction. No grain boundaries are present between the <100> and the <001> zones, as both directions are identical in cubic systems. However, a polycristalline layer is still observed at the top of the deposit. This layer is mainly due to the presence of partially un-melted particles from the injected powder. Those particles will promote the formation of equiaxed grains. The equiaxed layer can be removed by a final machining operation or by laser remelting treatment without powder injection.

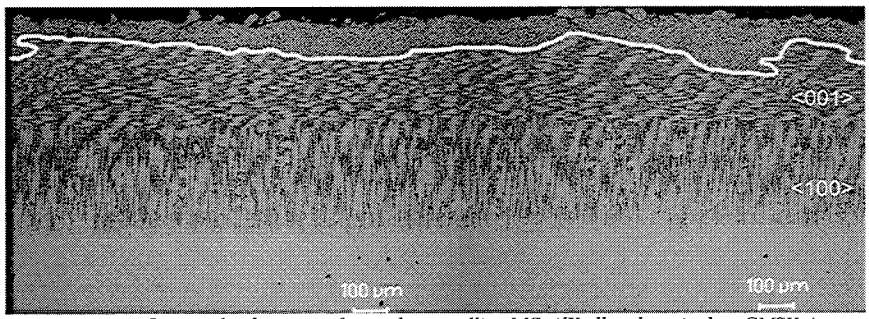


Figure 5 : *Longitudinal section of a single crystalline MCrAlY alloy deposited on CMSX-4. The scanning direction of the laser is from right to left of the photograph.*

4. Formation of cracks.

In the last section, it was shown that, due to the high temperature gradient of the laser process, columnar dendritic growth can be obtained during solidification (cf. eq. 2). A high temperature gradient also results in high thermal stresses in the clad. In some cases, these stresses lead to cracking of the deposit and the substrate (fig. 6). In a successful process cracking during laser deposition must be avoided. One way to decrease the risk of cracking is to preheat the part during the deposition with an induction coil [14], so that the temperature gradient and the thermal stresses are reduced. However, preheating of the substrate considerably reduces the thermal gradient in the melt pool too. As a consequence, it may become impossible to avoid the CET.



Figure 6 : *Transverse section of a cracked deposit. MCrAlY alloy on CMSX-4.*

It has been observed that the cracking mechanism follows two steps: (i) initiation of cracks by hot tearing, during solidification and (ii) propagation of the crack into the substrate and into the solid deposit, during cooling. Figure 7 clearly shows the presence of interdendritic cracks with the characteristic form of a hot tear [15].

The hot cracking phenomenon occurs at the root of the mushy zone, above the coherency temperature (fig. 2), when an external stress is applied [6, 15]. In this zone, (i) the presence of a continuous interdendritic liquid film ($T > T_{coh}$) leads to zero shear strength of the mushy zone and (ii) the permeability is too small for sufficient liquid feeding to compensate for the deformation. If the liquid pressure decreases below a critical pressure for cavitation, a void or a crack can form. A criterion for the initiation of such a crack has recently been developed by Rappaz et al. [6]. They show that the hot cracking susceptibility (HCS) of an alloy is highly dependant on the evolution of the solid fraction with temperature, $f_s(T)$ and on the coherency temperature, T_{coh} :

$$HCS \approx \int_{Tcoh}^{Tl} \frac{E(T)\cdot fs(T)^2}{(1-fs(T))^3} dT \quad ; \quad E(T) = \int_{Tcoh}^{T} fs(T)dT \qquad \text{(eq. 3)}$$



Figure 7 : *Hot cracking in a MCrAlY alloy deposited on CMSX-4.*

The problem of cracking during the laser process can be avoided by a careful selection of the clad alloy composition, rather than by substrate preheating. Thermal analysis of alloys has been undertaken to determine the evolution of the solid fraction with temperature. Based on these experimental results and on equation 3, a classification of the HCS of each alloy can be made. Well designed MCrAlY alloys with low hot cracking susceptibility can lead to single crystal, crack-free laser cladding (fig. 5).

5. Conclusions

A laser process allowing the deposition of single crystal MCrAlY layers on single crystal Ni-base superalloys has been developed. For a successful SX processing, three defects have to be avoided:

- loss of epitaxy with the substrate
- growth of equiaxed grains in the liquid ahead of the columnar zone
- hot tearing of the deposit.

It is shown that both the process parameters and the alloy composition must be well controlled for a successful deposition :

- The energy density must be sufficiently high to ensure a slight and regular remelting of the substrate surface (a required condition for epitaxial growth).
- The temperature gradient must be sufficiently high and the solidification velocity low to avoid the columnar to equiaxed transition. The process window is decreased when the heat flow direction is not parallel to <100>.
- An optimal coating alloy has low hot cracking susceptibility (HCS) with low risk of columnar to equiaxed transition (CET). The hot cracking susceptibility decrease with a small solidification interval and a large volume fraction of eutectic. The risk of CET is reduced when both the nucleation site density, N_0, and the dendritic growth kinetic parameters are low.

Acknowledgments – The authors would like to acknowledge Jean-Marie Drezet and Sélim Mokadem for their helpful discussions as well as Brian Neal for his help with metallography. This work has been undertaken with financial support of the CTI from the Swiss federal office for professional education and technology.

References

[1] C. T. Sims, N.S. Stoloff, W.C. Hagel : *Superalloys II : High-Temperature materials for aerospace and industrial power*, John Wilew ans Sons, New-York, 1987

[2] D. Siebörger, H. Knake, U. Glatzel : *Temperature dependence of the elastic moduli of the nickel-base superalloy CMSX-4 and its isolated phases*, Mater. Sci. Eng., **A298** (2001) 26

[3] C. Bezençon, M. Konter, J.-D. Wagnière, W. Kurz : *Microstructure development in laser cladding of single crystal nickel based alloys,* In the Proc. of Laser in Manufacturing, eds. German Scientific Laser Society – WLT, June 18-22, 2001, Munich, Germany, p. 580-589

[4] European Patent: EP1001055A1

[5] M. Gäumann, C. Bezençon, P. Canalis, W. Kurz : *Single-crystal laser deposition of superalloys: processing-microstructure maps*, In Acta mater., **49** (2001) 1051

[6] M. Rappaz, J.-M. Drezet, M. Gremaud : *A new hot-tearing criterion*, Met. Trans. **30A** (1999) 449

[7] A. Frenk, M. Vandyoussefi, J.-D. Wagnière, A. Zryd, W. Kurz : *Analysis of the Laser-Cladding Process for Stellite on Steel*, In Metall. Mater. Trans. B, **28B** (1997) 501

[8] K. Harris, G.L. Erickson, S.L. Sikkenga, W.D. Brentnall, J.M. Aurrecoechea, K.G. Kubarych : *Development of the rhenium containing superalloys CMSX-4* ;in 7th Inter. symposium on superalloys, eds. S.D. Antolovich et al, Metals Park, Seven springs, OH:TMS, 1992, p. 297

[9] W. Kurz, D.J. Fisher : *Fundamentals of Solidification*, 4th ed, Trans Tech Publication, Switzerland, 1998

[10] S.C. Flood, J.D. Hunt : *Columnar to equiaxed transition*; 9th edn, in Metals Handbook, Vol. 15. ASM International, Materials Park, OH, (1998) 130

[11] J.D. Hunt, *Steady state columnar and equiaxed growth of dendrites,* In Mater. Sci. Eng., **65** (1984) 75

[12] M. Rappaz, S.A. David, J.M. Vitek, L.A. Boatner : *Analysis of Solidification Microstructures in Fe-Ni-Cr Single-Crystal Welds*, In Met. Mat. Trans. A, **21A** (1990) 1767

[13] C. Bezençon, S. Mokadem, J.-D. Wagnière, W. Kurz : *Microstructure development during laser remelting of cylindrical single-crystal Ni-base superalloys*, to be published

[14] S.A. David, J.M. Vitek, S.S. Babu, L.A. Boatner : *Welding of nickel base superalloy single crystals*; Sci. Technol. Weld. Joining, **2** (1997) 79

[15] J. Campbell : *Castings*, Butterworth-Heinemann, Oxford, UK, 1991

COMPARISON OF THERMAL CYCLING LIFE OF YSZ AND $LA_2ZR_2O_7$-BASED THERMAL BARRIER COATINGS

R. Vaßen, G. Barbezat*, D.Stöver

IWV1, Forschungszentrum Jülich GmbH, D-52134 Jülich, Germany
*Sulzer Metco, Wohlen, Switzerland

Abstract

Three different kinds of ceramic top coats have been investigated: standard YSZ coatings, single layer $La_2Zr_2O_7$ coatings and double layer YSZ/$La_2Zr_2O_7$ coatings. The thermal cycling coatings were deposited on disk-shaped CM186 substrates with a NiCoCrAlY bondcoat supplied by industry. Additionally, the YSZ coatings were manufactured by industry and by IWV1. In former investigations the double layer systems show a superior thermal cycling behavior compared to the other systems. Also in the present investigation the performance of the double layer system was by orders of magnitude better than the one of the single layer system made of the new material alone. At moderate surface temperatures the behavior of the double layer and the YSZ systems were quite similar. However, at high temperatures, in our test rigs above 1340 °C, the double layer systems performed much better.

Keywords: plasma-spraying, thermal cycling, double layer, new thermal barrier coatings, temperature capability

Introduction

In thermally highly loaded parts of gas turbines as the combustion chamber or transition ducts often plasma-sprayed thermal barrier coating (TBC) systems consisting of a vacuum plasma-sprayed MCrAlY (M=Ni,Co) bondcoat and a porous atmospheric plasma-sprayed yttria partially stabilized zirconia (YSZ) topcoat are used [1, 2]. For long-term operation these systems perform well up to surface temperatures of about 1200 °C. However, the need for a further improvement of the efficiency of the gas turbines is accompanied by increasing surface temperatures. At these higher application temperatures YSZ coatings are becoming increasingly unstable. The porosity of the coating is reduced due to sintering effects. This leads to a reduction of the strain tolerance in combination with an increase of the Young's modulus [3]. Higher stresses will originate in the coating, which lead to a reduced life under thermal cyclic loading. The second detrimental mechanism is a phase change of the t'-phase, which does not undergo a direct phase transition to the monoclinic phase and which is typically the major phase in the as-sprayed YSZ coating. At elevated temperatures the t'-phase transforms into the equilibrium tetragonal and cubic phase. During cooling the tetragonal phase will further transform into the monoclinic phase, which is accompanied by a volume change and the resulting damage of the coating [4].These disadvantages of the YSZ based TBCs in combination with the need for further improvement of the efficiency of gas turbines promoted world wide activities in the area of new TBC materials [5, 6, 7, 8, 9, 10].

Materials that show promising properties for an application as TBC are those with pyrochlore structure. One material of this class is $La_2Zr_2O_7$. It has been shown that this material has several excellent physical properties, i.e. thermal conductivity below the values of YSZ and high thermal stability [7]. On the other hand the thermal expansion coefficient is lower ($9 \cdot 10^{-6}$/K) than the value of YSZ ($10\text{-}11 \cdot 10^{-6}$/K) giving higher thermal stresses in the TBC system as the substrate and the bondcoat have high thermal expansion coefficients (about $15 \cdot 10^{-6}$/K). In addition, no toughening effects are expected in this new material compared to

the behaviour of YSZ. This fact gives lower toughness values of the $La_2Zr_2O_7$ coatings. As a result, the thermal cycling properties are expected to be relatively poor compared to YSZ coatings. It is expected that this problem will occur for most of the new TBC materials, as these materials crystallize in thermally stable structures which probably do not have the ability to show transformation toughening effects. A way to overcome this shortcoming was found in the use of layered or graded topcoats. The failure of TBC systems often occur within the TBC close to the interface bondcoat/topcoat (white failure, [11]). At this location YSZ is used as a TBC material with a relatively high thermal expansion coefficient and high toughness. The YSZ layer is then coated by the new TBC material (e.g. $La_2Zr_2O_7$) which is able to withstand the higher temperatures at the outer surface of the thermal barrier coating[12]. In the present paper the performance of new TBC systems is compared with YSZ coatings supplied by industry and by IWV1.

Experimental

The investigated thermal barrier coating systems have been partially supplied by Sulzer Metco, Wohlen. Sulzer Metco produced an about 150 µm thick VPS bondcoat using an Amdry 997 NiCoCrAlY powder with about 4 wt.% Ta. Also one type of standard YSZ coatings were supplied by Sulzer Metco. For some specimens no heat treatment for diffusion bonding was made. Fortunately the missing heat treatment led only in one sample to a failure at the bondcoat/substrate interface. Even in this case this crack did not significantly influence the life time of the sample as spallation of the top coat, which led to the termination of the cycling, took place at a different location within the TBC. The heat treated samples were annealed at 1080 °C for 4 hours in vacuum.

The coatings made of $La_2Zr_2O_7$ were produced in the IWV1, Forschungszentrum Jülich GmbH, using a Triplex I gun in a Sulzer Metco atmospheric plasma spraying unit. The powders were also prepared in the institute using solid state method with oxides as starting materials. Spray - able powders were obtained by a subsequent spray drying process. Details are presented elsewhere [13]. In the case of the double layer systems additionally the YSZ powder Metco 204 NS, Sulzer Metco GmbH, Hattersheim, Germany, has been used. The spraying parameters were kept constant for both powders, giving slightly higher densities within the $La_2Zr_2O_7$ coatings [14]. Porosity was in the range between 11 and 14 vol.%. The thickness of the coatings showed a certain variation, 250 to 310 µm for the YSZ, 270 µm for the single layer and about 220 – 300 µm for the double layer systems. In addition, also standard YSZ coatings prepared by IWV1 were tested.

As substrate the nickel base, directionally solidified superalloy CM186 DS supplied by Alstom, UK was used. Disk shaped thermal cycling samples with 30 mm diameter and 3 mm height were machined, which had at the outer edge a radius of curvature of 1.5 mm. These geometries were designed to minimize the effect of stresses originating at the free edge of the specimens. Thermal cycling was performed in a gas burner test facility operating with natural gas and oxygen (s. Fig. 1). The back of the substrates were cooled by compressed air. The surface temperature was measured with a pyrometer operating at a wavelength between 8 and 13 µm and a spot size of 12 mm. For YSZ and $La_2Zr_2O_7$ the emissivity E for this wavelength interval was determined to be close to 1, by measuring the reflectance R and the transmittance T of coatings and calculating the emissivity E using the relation 1 = E - R - T. Additionally,

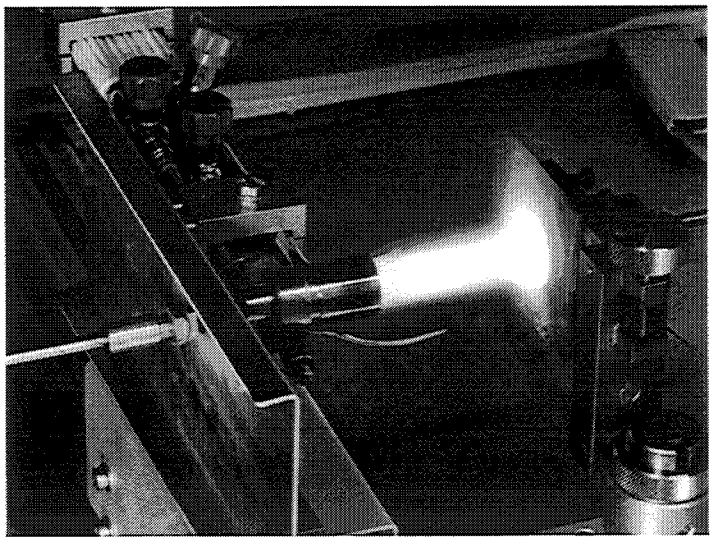


Fig. 1 Photograph of the major components of one of the thermal cycling test facilities at IWV1, Forschungszentrum Jülich.

the substrate temperature was measured using a thermocouple. This thermocouple was located in the centre of the substrate. From the two measured temperatures the temperature at the bondcoat/TBC interface was calculated by assuming a thermal conductivity of 1 W/m/K for the TBC.

The surface temperature was varied between about 1240 and 1378°C, the substrate temperature was adjusted between 976 and 1073°C. Using the thermal conductivities of the coatings and the substrate one can estimate that the bondcoat temperature is about 40-60 K higher than the substrate temperature. In the test facility a gas burner with a broad flame was used giving a rather homogeneous temperature distribution in the central part of the specimens. At the outer edges of the samples the temperature is typically slightly lower. After heating for about 20 s the maximum temperature is reached. After 5 minutes the burner is automatically removed for 2 minutes from the surface and the surface is cooled at a rate of more than 100 K/s using compressed air.

Thermal cycling experiments were automatically stopped when the temperature data from the pyrometer deviates more than a certain value (typically 40 K) from the desired surface temperature. This process is not sensitive to small spallations or spallations at the outer rim because the pyrometer measures the temperature at the centre of the coating. Therefore, in addition, specimens are inspected regularly to detect a visible spallation of the coating, which will then lead to a termination of the cycling. As the specimens are not inspected after each cycle, it might occur that even after spallation a certain number of cycles will be performed. Metallographical sections have been prepared from all samples to investigate the microstructure.

Results and discussion

In Fig. 2 the microstructures of the as-sprayed coatings are shown. The coatings supplied by industry consist of the system which was also used for cycling experiments, i.e. a CM186DS substrate, a NiCoCrAlY bondcoat and an atmospheric plasma-sprayed YSZ TBC. For the investigation of the microstructure of the as-sprayed coatings prepared by IWV1 steel substrates have been used. Obviously, the microstructure of the YSZ coatings supplied by Metco (Fig. 2a) reveals certain microstructural differences compared to the coatings prepared at IWV1 (Fig. 2b) – d)). In Fig. 2b) a YSZ coating, in Fig. 2c) a single layer $La_2Zr_2O_7$ coating, and in Fig. 2d) a double layer system with a YSZ layer at the interface substrate / TBC is shown. The industrial coating shows an increased porosity level and relatively broad microcracks compared to all coatings prepared at IWV1.

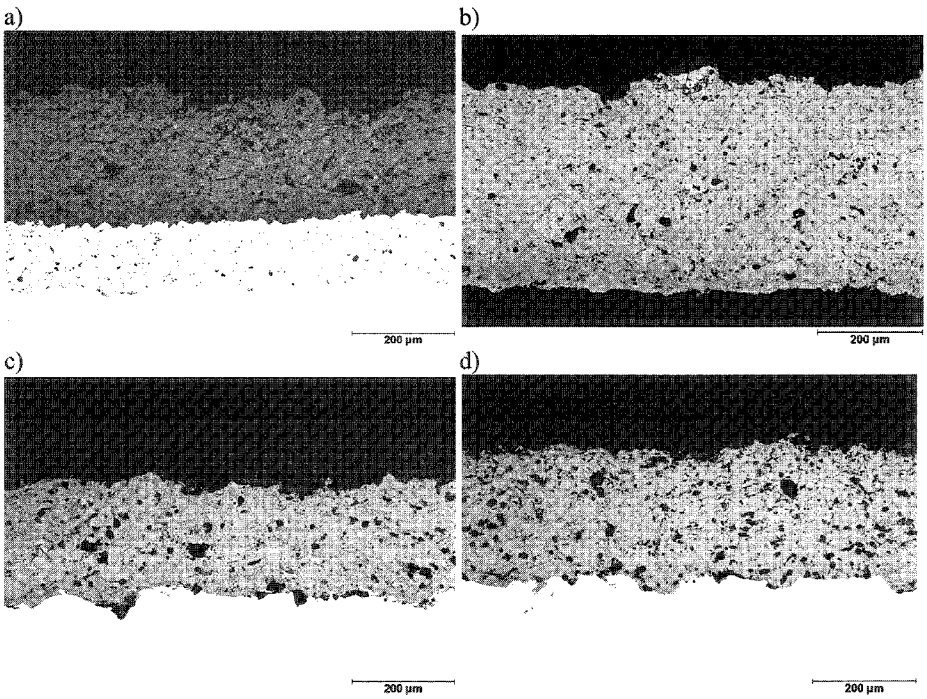


Fig. 2 Optical micrographs of as-sprayed coatings made of YSZ prepared by Metco (a) and IWV1 (b) and a single layer of $La_2Zr_2O_7$ (c) and a double layer of YSZ/$La_2Zr_2O_7$ (d) both prepared by IWV1.

YSZ and double layer $La_2Zr_2O_7$ coatings were tested in the gas burner test facility at two different surface temperature regimes. The so-called "low" surface temperature was about 1250°C, the "high" surface temperature about 1350°C. Only the single layer system was tested twice at the low surface temperature. The bondcoat temperatures were between 1020 and 1094°C with the exception of one sample, which was tested at a higher bondcoat temperature of 1119 °C.

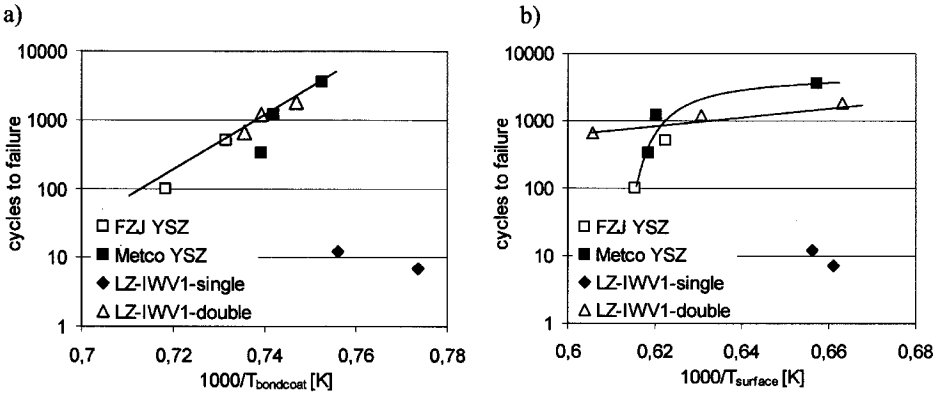


Fig. 3 Number of cycles to failure for the different systems as a function of inverse bondcoat (a) and surface temperature (b).

In Fig. 3a) the cycle number to failure is plotted for the different systems as a function of inverse bondcoat temperature. Obviously, the life-time of the single layer system is much lower than the cyclic life of a YSZ system and of the double layer system. This was found earlier and has been explained by the low fracture toughness of the $La_2Zr_2O_7$ and the relatively high mismatch in thermal expansion coefficient between substrate and coating [12]. Additional stress levels in the coatings induced by substrate curvatures are sufficient to induce subcritical crack growth and hence early failure of these coatings. These can be proved by microstructural findings. In Fig. 4 b the microstructure of a cycled single layer system after failure is shown. A long crack within the coating in the region of the bevel - edge of the thermal cycle specimen was found. The argumentation also corresponds with the observation that only a thin thermally grown oxide (TGO) is found after the cycling tests as the time at temperature was too short (Tab. 1, s. discussion below).

The life-time of both YSZ systems are strongly decreasing with increasing bondcoat temperature. This has also been observed in numerous studies and can be explained by the strong temperature dependence of the growth rate of the thermally grown oxide (TGO). This scale formation at the interface between TBC and bondcoat is assumed to be one of the dominant mechanisms which lead to spallation of the coatings. For the data points of the YSZ samples tested at relatively low surface temperatures and for all data points of the double layer systems a linear dependence of the logarithm of the cycle number on the inverse bondcoat temperature was found. This behavior can be explained by a life time modeling in which stresses due to TGO formation are considered [11, 15]. In this model it is expected that the crack will grow within the TBC close to the interface bondcoat / TBC. These kind of cracks can be found in the micrographs shown in Fig. 4 a) and more clearly in Fig. 4 c). It should be mentioned that for the double layer system for all tested surface temperatures the failure can be attributed to the TGO growth and hence the limited performance of the bondcoat and the YSZ interlayer. Even for the highest surface temperatures (1378 °C) life time is not limited by the ceramic top coat. More indication of the superior temperature capability of the new system will be given below.

For the so far discussed moderate surface temperatures failure was mainly located at the edges of the samples (s. Fig. 5), which can be explained by the substrate curvature and the additional stresses due to this curvature. In earlier investigations with a different substrate (IN738) and bondcoat, we found that the spalled areas were often located at the centre of the sample, which we then attributed to a slight radial temperature gradient in the coating, i.e. a reduced temperature at the outer rim due to the fixing of the sample.

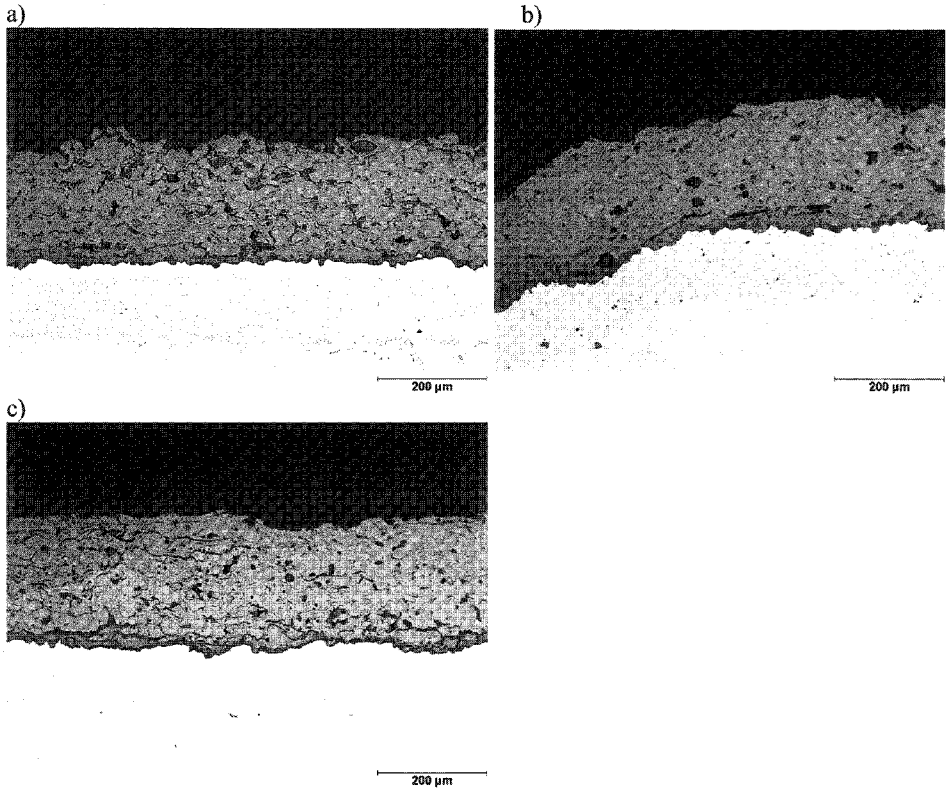


Fig. 4 Optical micrographs of a cycled YSZ coating (a), prepared by Metco, 3633 cycles, $T_{surf/BC}$ 1249°C/1056°C), a cycled single layer $La_2Zr_2O_7$ system (b), prepared at IWV1, 31 cycles, $T_{surf/BC}$ 1240°C/976°C), a cycled double layer YSZ/$La_2Zr_2O_7$ system (c), prepared at IWV1, 1800 cycles, $T_{surf/BC}$ 1235°C/1066°C).

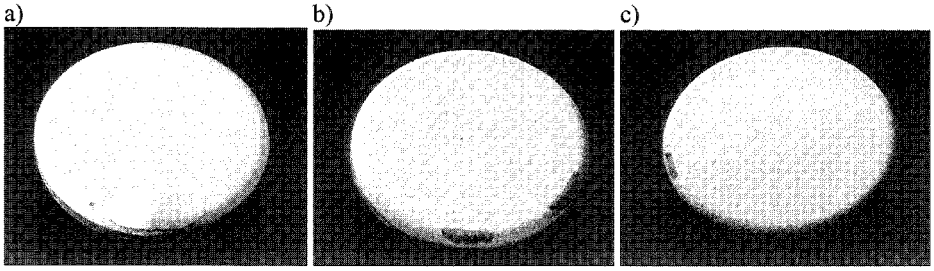


Fig. 5 Photographs of cycled specimens (a, b, c correspond to Fig. 4)

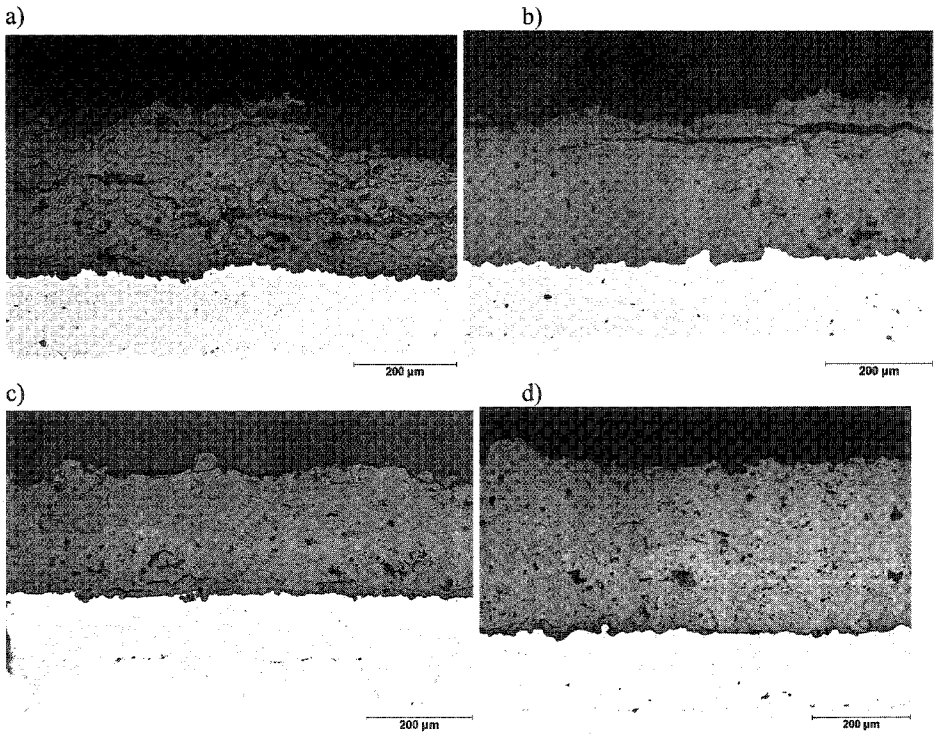


Fig. 6 Optical micrographs of a cycled YSZ coating (a), prepared by Metco, 331 cycles, $T_{surf/BC}$ 1344°C/1080°C), a cycled YSZ coating (b), prepared at IWV1, 100 cycles, $T_{surf/BC}$ 1352°C/1119°C), two cycled double layer YSZ/$La_2Zr_2O_7$ system (c), prepared at IWV1, $T_{surf/BC}$ left 1218 cycles, 1313°C/1080°C, right 652 cycles, 1378/1087°C).

In Table 1 the thickness of the TGO and the thickness of the depleted zone are given. The depleted zone is the region in which the β phase (corresponding to NiAl phase) diminishes due to the formation of alumina. Typically a TGO thickness of 4 - 5 µm is observed in most systems after failure. In agreement with the above given argumentation the thickness of the

TGO in the single layer $La_2Zr_2O_7$ system is extremely thin. Due to the low toughness of this material additional stresses which arise from the growth of the TGO are not necessary to promote spallation. As the failure in the double layer systems can be attributed to the formation of TGO in all cases and not to a limited stability of the $La_2Zr_2O_7$ the TGO and depleted zone thickness is similar to the ones of the YSZ specimens.

The samples with a double layer system showed a large improvement of life time compared to the single layer system (several orders of magnitude). Up to about 1340 °C the double layer systems show a similar performance as the YSZ systems. However, for higher surface temperatures the life time of the conventional YSZ systems is limited by the spallation within the ceramic close to the surface, i.e. the limited temperature capability of the YSZ. This is clearly shown in Fig. 6, in which micrographs of the coatings cycled at high surface temperatures are shown. The large cracks close to the surface in both YSZ coatings a) and b) are obvious. The two presented double layer systems c) and d) remain nearly unchanged. The surface temperature of the system shown in d) was the highest of all tests (1378 °C).
This result corresponds with the photographs of the samples after cycling shown in Fig. 7. Clearly damaged areas can be detected on the surface of the YSZ systems while the double layer systems are still intact in the inner region.

As the life time of the YSZ systems is for high surface temperatures limited by these it makes sense to plot the number of cycles to failure as a function of surface temperature (s. Fig. 3 b). A dramatic decrease is observed above about 1340°C while the life time of the double layer systems remains unaffected and is only limited by the TGO growth (s. Fig. 3 a) and discussion above). This is in agreement with earlier investigations in which we found an improvement of cyclic life in our new systems compared to YSZ systems at high surface temperatures [16].

Table 1: Thickness in µm of the TGO d and the depleted zone z for the investigated systems after cycling at different surface temperatures T_{surf} given in [°C] and different cycles to failure N. * indicates strong , + slight spallation at the ceramic surface

system	low surface temperature N / T_{surf} / d /z	high surface temperature N / T_{surf} / d /z
YSZ-Metco	3633 / 1249 / 5.0 / 31	1198 / 1339 / 4.6 / 27^{+} 331 / 1344 / 3.2 / 13*
YSZ-FZJ	-	504 / 1334 / 4.0 / 17 100 / 1352 / 4.0 / 14*
single layer $La_2Zr_2O_7$	7 / 1240 / < 1 / 6 12 / 1251 / < 1 / 8	-
double layer $La_2Zr_2O_7$ / YSZ	1800 / 1235 / 4.2 / 39	1218 / 1313 / 4.1 / 25 652 / 1378 / 4.4 / 22

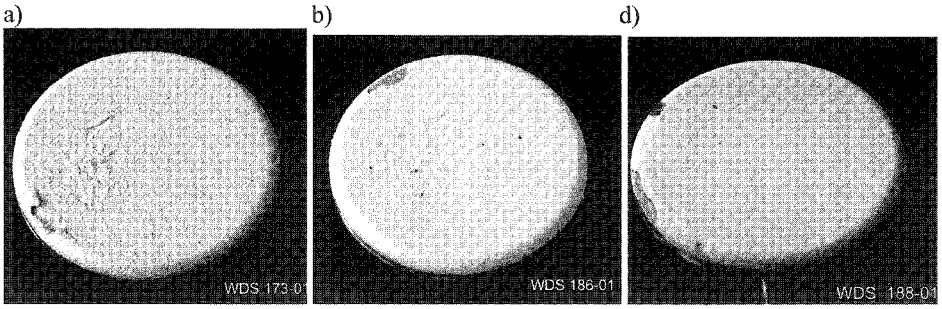


Fig. 7 Photographs of cycled specimens (a, b, d correspond to Fig. 6)

Summary and outlook

$La_2Zr_2O_7$ based thermal barrier coating materials have been compared with industrially produced and our own YSZ based systems in a thermal cycling test facility. The single layer $La_2Zr_2O_7$ systems showed a low thermal cycling life. The double layer systems, in which YSZ is applied on the bondcoat and the new ceramic on top, improved the performance of the system by several orders of magnitude. The thermal cycling life is comparable to that of industrial YSZ based systems for moderate surface temperatures below 1340°C for our tests conditions. For higher surface temperatures failure within the ceramic close to the surface was found for the YSZ systems. This led to a dramatic decrease of life time of the YSZ systems while the life time of the double layer systems was still limited by the bondcoat oxidation and hence longer then the YSZ systems. The investigation confirms the superior performance of the double layer concept especially for applications at high temperatures.

Acknowledgement

The authors would like to thank Mr. K.H. Rauwald and Mr. R. Laufs (both IWV1, FZ Jülich) for the manufacture of the plasma-sprayed coatings and the thermal cycling of the specimens. The authors also gratefully acknowledge the work of Mrs S. Schwartz-Lückge and Mr. M. Kappertz (both IWV1, FZ Jülich) who performed the characterization of the specimens.

Literature

1 W.A Nelson,. R.M. Orenstein, "TBC Experience in Land-Based Gas Turbines" *Journal of Thermal Spray Technology* **6** [2] 176-180 (1997).

2 D. Stöver, C. Funke, "Directions of Developments of Thermal Barrier Coatings in Energy Applications" *Materials Processing Technology* **92-93** 195-202 (1999).

3 C. Funke, B. Siebert, R. Vaßen, D. Stöver, "Properties of ZrO_2 – 7 wt. % Y_2O_3 Thermal Barrier Coatings in Relation to Plasma Spraying Conditions" pp. 277-284 in the Proceedings of the United Thermal Spray Conference (15.-19. September 1997, Indianapolis, Indiana), C.C. Berndt (ed.), ASM International, Materials Park, OH, (1998).

Literature

4 R. A. Miller J.L. Smialek, R.G. Garlick, "Phase Stability in Plasma-Sprayed Partially Stabilized Zirconia-Yttria" pp. 241-251 in Science and Technology of Zirconia, Advances in Ceramics, Vol. 3, A.H. Heuer and L.W. Hobbs (eds.), The American Ceramic Society, Columbus, OH, USA, (1981)

5 R.L. Jones, R.F. Reidy, D. Mess, "Scandia, Yttria Stabilized Zirconia for Thermal Barrier Coatings" *Surface Coating and Technolgy* 82 70-76 (1996).

6 R. Vaßen, F. Tietz, G. Kerkhoff, R. Wilkenhöner, D. Stöver, "New Materials for Advanced Thermal Barrier Coatings" pp.1627-35 in Proceedings of the 6th Liège Conference, Part III, Materials for Advanced Power Engineering. Edited by J. Lecomte-Beckers, F. Schubert, P.J. Ennis, Forschungszentrum Jülich GmbH, Jülich, Germany, 1998.

7 Subramanian, R., Sabol, S.M., Goedjen, J., and Arana, M. (1999), "Advanced Thermal Barrier Coating Systems for the ATS Engine" 1999 ATS Review Meeting, Nov. 8-10, 1999.

8 R. Vassen, X. Cao, F. Tietz; Basu, D. Stöver, "Zirconates as New Materials for Thermal Barrier Coatings" *J. Am. Ceram. Soc.* 83 [8] 2023-28 (1999).

9 R. Vaßen, D. Stöver, "Conventional and new materials for thermal barrier coatings" in Functional Gradient Materials and Surface Layers Prepared by Fine Particle Technlogy, NATO Science Series II: Mathematics , Physics and Chemistry - Vol. 16, Kluwer Acadmic Publishers, Dordrecht, The Netherlands (2001) 199-216.

10 Schäfer, G. W.; Gadow, R., "Lanthane Aluminate Thermal Barrier Coating" *Ceram. Eng. Sci. Proc.* (1999), 20 (4), 291-297

11 R. Vaßen, G. Kerkhoff, D. Stöver, "Development of a Micromechanical Life Prediction Model for Plasma Sprayed Thermal Barrier Coatings" *Materials Science and Engineering A*, 303, 1-2 (2001) 100-109.

12 R. Vaßen, M. Dietrich, H. Lehmann, X. Cao, G. Pracht, F. Tietz, D. Pitzer, D. Stöver, "Development of Oxide Ceramics for an Application as TBC" *Materialwissenschaft und Werkstofftechnik* 8 (2001) 673-677.

13 X. Cao, R. Vassen, S. Schwartz, W. Jungen and D. Stöver, "Spray-Drying of Ceramics for Plasma-Spray Coating" *J. Eur. Ceram. Soc.*, 20 (2000) 2433-2439.

14 R. Vaßen, G. Pracht, D. Stöver, "New Thermal Barrier Coating Systems with a Graded Ceramic Coating" in Proc. of the International Thermal Spray Conference 2002, Verlag für Schweißen und verwandte Verfahren DVS-Verlag GmbH, Düsseldorf, 2001, pp. 202-207.

15 F. Träger, M. Ahrens, R. Vaßen, D. Stöver, "A Life Time Model for Plasma-Sprayed Thermal Barrier Coatings", *submitted to Materials Science and Engineering A.*

16 Robert Vaßen, Xueqiang Cao, Detlev Stöver, "Improvement of New Thermal Barrier Coating Systems using a Layered or Graded Structure", *Ceramic Engineering & Science Proceedings*, 22, 4 (2001) 435- 442. 16 W.A Nelson,. R.M. Orenstein, "TBC Experience in Land-Based Gas Turbines" *Journal of Thermal Spray Technology* **6** [2] 176-180 (1997).

16 D. Stöver, C. Funke, "Directions of Developments of Thermal Barrier Coatings in Energy Applications" *Materials Processing Technology* **92-93** 195-202 (1999).

16 C. Funke, B. Siebert, R. Vaßen, D. Stöver, "Properties of ZrO_2 – 7 wt. % Y_2O_3 Thermal Barrier Coatings in Relation to Plasma Spraying Conditions" pp. 277-284 in the

Literature

Proceedings of the United Thermal Spray Conference (15.-19. September 1997, Indianapolis, Indiana), C.C. Berndt (ed.), ASM International, Materials Park, OH, (1998).

16 R. A. Miller J.L. Smialek, R.G. Garlick, "Phase Stability in Plasma-Sprayed Partially Stabilized Zirconia-Yttria" pp. 241-251 in Science and Technology of Zirconia, Advances in Ceramics, Vol. 3, A.H. Heuer and L.W. Hobbs (eds.), The American Ceramic Society, Columbus, OH, USA, (1981)

16 R.L. Jones, R.F. Reidy, D. Mess, "Scandia, Yttria Stabilized Zirconia for Thermal Barrier Coatings" *Surface Coating and Technolgy* 82 70-76 (1996).

16 R. Vaßen, F. Tietz, G. Kerkhoff, R. Wilkenhöner, D. Stöver, "New Materials for Advanced Thermal Barrier Coatings" pp.1627-35 in Proceedings of the 6th Liège Conference, Part III, Materials for Advanced Power Engineering. Edited by J. Lecomte-Beckers, F. Schubert, P.J. Ennis, Forschungszentrum Jülich GmbH, Jülich, Germany, 1998.

16 Subramanian, R., Sabol, S.M., Goedjen, J., and Arana, M. (1999), "Advanced Thermal Barrier Coating Systems for the ATS Engine" 1999 ATS Review Meeting, Nov. 8-10, 1999.

16 R. Vassen, X. Cao, F. Tietz; Basu, D. Stöver, "Zirconates as New Materials for Thermal Barrier Coatings" *J. Am. Ceram. Soc.* 83 [8] 2023-28 (1999).

16 R. Vaßen, D. Stöver, "Conventional and new materials for thermal barrier coatings" in Functional Gradient Materials and Surface Layers Prepared by Fine Particle Technlogy, NATO Science Series II: Mathematics , Physics and Chemistry - Vol. 16, Kluwer Acadmic Publishers, Dordrecht, The Netherlands (2001) 199-216.

16 Schäfer, G. W.; Gadow, R., "Lanthane Aluminate Thermal Barrier Coating" *Ceram. Eng. Sci. Proc.* (1999), 20 (4), 291-297

16 R. Vaßen, G. Kerkhoff, D. Stöver, "Development of a Micromechanical Life Prediction Model for Plasma Sprayed Thermal Barrier Coatings" *Materials Science and Engineering A*, 303, 1-2 (2001) 100-109.

16 R. Vaßen, M. Dietrich, H. Lehmann, X. Cao, G. Pracht, F. Tietz, D. Pitzer, D. Stöver, "Development of Oxide Ceramics for an Application as TBC" *Materialwissenschaft und Werkstofftechnik* 8 (2001) 673-677.

16 X. Cao, R. Vassen, S. Schwartz, W. Jungen and D. Stöver, "Spray-Drying of Ceramics for Plasma-Spray Coating" *J. Eur. Ceram. Soc.*, 20 (2000) 2433-2439.

16 R. Vaßen, G. Pracht, D. Stöver, "New Thermal Barrier Coating Systems with a Graded Ceramic Coating" in Proc. of the International Thermal Spray Conference 2002, Verlag für Schweißen und verwandte Verfahren DVS-Verlag GmbH, Düsseldorf, 2001, pp. 202-207.

16 F. Träger, M. Ahrens, R. Vaßen, D. Stöver, "A Life Time Model for Plasma-Sprayed Thermal Barrier Coatings", *submitted to Materials Science and Engineering A.*

16 Robert Vaßen, Xueqiang Cao, Detlev Stöver, "Improvement of New Thermal Barrier Coating Systems using a Layered or Graded Structure", *Ceramic Engineering & Science Proceedings*, 22, 4 (2001) 435- 442.

DEPOSITION OF ALUMINIUM + YTTRIUM ON THE INTERNAL SURFACES OF COMPLEX COOLED INDUSTRIAL TURBINE BLADES

M. Innocenti°, E. Giorni°, R. Wing•, A. Norreys•, N. J. Archer□, J. Yeatman□, P. Bianchi■, D. Baxter◊, G. Wahl■, Ch. Metz■

° GE Oil & Gas – Nuovo Pignone S.p.A,. Via F. Matteucci n° 2 – 50127 Florence Italy
• Chromalloy United Kingdom Limited, Brandle Way Clover Nook Ind. Estate Somercotes, Derbyshire DE55 4Rh - England.
□ Archer Technicoat Ltd - Progress Road High Wycombe Bucks HP12 4JD – England
■CESI S.p.A. - Via Rubattino n° 54 – 20134 Milan Italy
◊ JRC-Joint Research Centre - Westerduinweg, 1755 ZG Petten The Netherlands
■ Technische Universität Braunschweig IOPW - Bienroder Weg 53 38108 Braunschweig

Abstract

In mechanical drive, electric power generation or co-generation applications, the efficiency of the equipment is increased by raising the gas inlet temperature; pursuant to this the metal must be cooled by letting cold air pass through internal holes or through specially designed cavities. The high temperature of the metal causes oxidation on the internal cooling cavities, making it necessary to slow down the oxidation process by applying a protective coating such as the aluminide coating. The higher inlet temperature results in not only improved performance but also reduced emissions of polluting compounds through better control of the combustion process. To increase the resistance to oxidation and hot corrosion we experimented with adding other elements such as Y to the Al. Processes such a slurry cementation, gas phase of the out-of pack type and CVD, developed by the aeronautic industry for aluminide coating of cavities, fail to achieve a comparable or acceptable quality standard when applied to larger components, either with straight-through ducts or cooling coils.The aim of this project was to investigate CVD deposition techniques with high throwing power that will deposit aluminide coatings in a consistent and uniform manner all over the complex internal surfaces of large turbine blades.
Modelling was first approached by coating with aluminide some ≈ 1 mm internal diameter tubes, in Inconel 600 and blade material, up to 360 mm long, in a laboratory equipment. The results of the modelling were used to design the demonstrator, a pilot plant for direct aluminide coating of the critical parts of gas turbines. The samples coated in the laboratory were submitted to coating characterisation obtained through thermal cycling, flowing oxidant test, corrosion tests and other tests. The results were compared with those from samples coated only with aluminium by traditional techniques. The improvement in the coating characteristics after the addition of Y was also investigated. Structural examinations, after the different tests, were carried out according to traditional micrographic techniques such as optical and electron microscopy and also according to advanced techniques. Regarding the design of the demonstrator, owing to the high temperatures required for the aluminide coating process, it was necessary to use a special alloy, Haynes 230, for the inner retort. In designing the crucible for AlCl generation inside the retort we considered the Y and aluminium co-deposition. This was done by interposing a special disc inside the crucible. With the aid of the demonstrator it was possible to coat blades with both simple and complex geometry of the cooling paths (traditional and aero derivative cooling systems). The possibility of coating large blades as well with aluminide was verified by treating tubes in Inconel 600 and GTD 111DS, up to 360 mm long, coated in the demonstrator. The optimum process parameters established are:

Aluminide coating temperature:	1000-1100 °C
Pressure:	100 Torr (13KPa)
Carrier gas:	Hydrogen

Tests conducted on parts coated in the demonstrator and simulating the operating conditions have given satisfactory results.

Keywords: Al; Al+Y; CVD; Coating, Blade.

1. Introduction

This research project concerns a study carried out to provide the basis for the industrialisation of an aluminide coating process for the cooling cavities in critical components (rotor blades and nozzles) of gas turbines for industrial use operating at high temperature.
In mechanical drive, electric power generation and cogeneration applications, one of the chief aims in gas turbine engineering is to raise the turbine inlet temperature so as to improve efficiency. The blading and nozzle materials, especially those used for the first stage, are subjected to particularly severe operating cycles which seriously affect durability. At present gas turbines are limited in their operating temperature due to oxidation and corrosion of the turbine blades. An improved corrosion and oxidation resistance is of great importance, since engine manufacturers demand longer component life at higher turbine inlet temperatures in order to achieve higher cycle efficiency and lower pollution gas emission and maintenance costs.
Major damage factors including oxidation, hot corrosion, and thermomechanical fatigue also affect the cooling ducts of the above-mentioned components. Internal cooling has been introduced to limit the temperature level on these components since the size of the components prohibits, at present and in the near future, use of the materials and technologies developed for the aeronautic industry. At the temperatures in question, over 850°C, the internal flow of cooling air gives rise to processes of oxidation of the superalloy material, which drastically reduce the life of blades and nozzles. This results in increased operating risks for the machine as well as higher maintenance costs due to the need for frequent replacement of critical components.
Processes such as slurry cementation gas phase of the out-of-pack type and CVD, developed by the aeronautic industry for aluminide coating of cavities, fail to achieve a comparable or acceptable quality standard when applied to larger components, either with straight-through ducts or cooling coils.
The aim of this project was to investigate CVD deposition techniques with high throwing power that would deposit aluminide coatings in a consistent and uniform manner throughout the complex internal surfaces of large turbine blades. To this aim, two methods were planned:

1. The first method involved modifying existing aluminide coating processes to adapt them to the shape of industrial turbine blades and nozzles. Basically, modification would concern the architecture of the coating equipment and the process parameters, such as: gas activity, gas pressure, deposition rate, temperature, gas flow rate and carrier gas.
2. The second method consisted of adding other elements to aluminium to improve resistance to oxidation, corrosion and thermal cycles, applying the process developed in aluminide deposition.

2. Experimentation

The development of this project was divided into several stages. The first of these concerned a study of the reaction kinetics in order to derive a mathematical model of the deposition of Al and the codeposition of Al+Y.
The model developed was subsequently confirmed through deposition tests on discs in IN600 and GTD111 utilising a suitably modified micro-balance.
Using this instrumentation and with subsequent microstructural examination carried out on discs coated only with Al or Al+Y it was possible to determine the optimal parameters for

deposition, such as temperature, pressure, time and carrier gas. The parameters derived in this way were utilised to conduct experiments with a laboratory scale demonstrator.
Coatings were applied to small tubes in IN600 and GTD111 with internal diameter of ≈ 1 mm and length of 120 or 360 mm which simulated the internal cooling cavities in the turbine blades.
The tubes aluminised in this way were suitably sectioned to conduct further tests, in controlled environments characteristic of the operating conditions of the machine, and to determine the microstructural characteristics and composition of the coating.
Considering the satisfactory results obtained, the last stage of the project consisted of designing a demonstrator for the aluminising of entire blades with both simple and complex internal cooling system.

2.1. Kinetic investigation of Al deposition

The evaporation behaviour of $AlCl_3$ and YCl_3 was modelled with the computer code 'Fluent'. The physical properties (Lennard-Jones-parameters [1], molecular weights) of the species and the boundary conditions (temperature, gas velocity, pressure) were supplied to the program. By this modelling the evaporation data were transformed into vapor pressure data. The modelling work was not only carried out for the evaporation but also the deposition processes. The modelling results were in good accordance with the experimental values. (Ch. Metz to be published). The modelling was based on the subdivision into elementary cells representing a small part of the total length of the tube to be coated. For each cell the following parameters were calculated: composition of the gas flow, pressure, activity of aluminium, deposition rate, etc. Kinetic investigations were performed with the modified microbalance equipment. This consists of an evaporator for volatilising the $AlCl_3$ and a hot wall CVD-reactor in which aluminium is evaporated through reaction (1) and IN600/GTD111 samples are coated through reaction (2).

$$Al + AlCl_3 \Leftrightarrow AlCl + AlCl_2 \qquad (1)$$

$$AlCl + AlCl_2 + Ni(\text{sup}eralloy) \rightarrow NiAl(coating) + AlCl_3 \qquad (2)$$

The samples to be weighed were connected to microbalances outside the vacuum system by means of magnetic suspension. As carrier gases, either hydrogen or argon was supplied by thermal mass flow controllers. The pressure was measured with a capacitor pressure sensor and kept within the range between 1000 and 10000 Pa with a PID-Controller and a butterfly valve.
First the evaporation kinetics of $AlCl_3$ was measured as function of the temperature, total pressure and gas flow.
Then the deposition kinetics were measured by the weight variation of the $AlCl_3$ crucible and the deposition rate in IN600 and GTD111 sample discs.
The evaporation temperature was between 90°C and 130°C at a total pressure of 5000 or 10000 Pa.

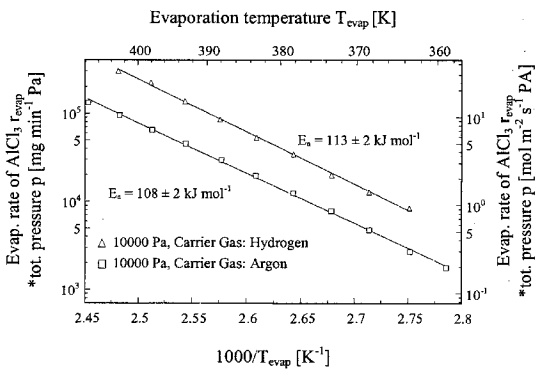


Figure 1: Arrhenius-plot for the evaporation of $AlCl_3$

The evaporation rate is given by the Arrhenius law with an activation energy of E_a = 113 ±2 kJ mol^{-1}. This value is in good accordance with the activation energy measured with argon as carrier gas (E_a = 108 ±2 kJ mol^{-1}), see figure 1.

2.2. Preliminary samples: Short aluminium and aluminium plus Y coated discs of Inconel 600 and GTD 111

Flat samples of IN600 were aluminised during the kinetic investigations in the microbalance equipment. The operating conditions were: pressure 5000 Pa, temperature between 950°C and 1050°C, carrier gas argon or hydrogen with a total flow of 3.75 l h^{-1}. The analysis performed after heat treatment showed the formation of high quality coatings with chemical composition and thickness according to specifications (Al 18-25%: thickness 50-100 µm)

To validate the coating quality, other GTD111 samples were aluminised at a total pressure of 5000 Pa and with deposition temperatures of 1000°C and 1050°C. Also in this case the chemical composition and the thickness of the layers met the specifications.

For the codeposition of aluminium and yttrium a GTD111 sample was connected with the microbalance and placed in the middle heating zone of the furnace. The YCl_3 was placed in a carbon crucible and located in the lower heating zone [2]. At the same time, for the codeposition process $AlCl_3$ was evaporated in the temperature range between 80°C and 130°C. Furthermore an aluminium-containing crucible was placed in the middle heating zone of the furnace. The deposition temperature was 1000°C. As carrier gas, hydrogen with a flow of 3.75 l h^{-1} (STP) was used. The total pressure was kept constant at 5000 Pa. The experiments showed a parabolic mass gain of the substrate due to the dominating aluminium deposition.

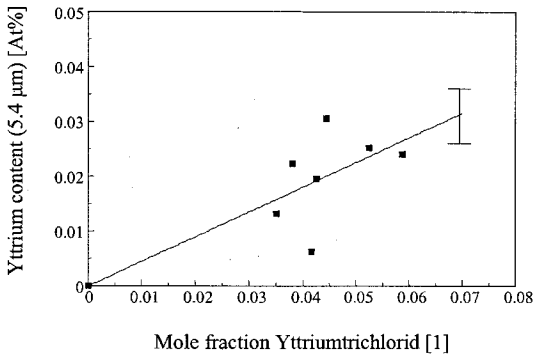


Fig. 2: Yttrium content of the codeposition layer

The depth profile of the element concentrations, analysed by SIMS measurement with a detection area of 50 µm in diameter, showed a decreasing yttrium content beginning from the surface. The mean yttrium content of the aluminide layer in relation to different mole fractions of YCl_3 in the gas phase is shown in figure 2. The results revealed an increasing yttrium content in the layer with increasing YCl_3 gas-phase concentration.

2.3. Design and modelling of a CVD laboratory equipment

For the coating of the internal passages of IN600 or GTD111 tubes (length = up to 360 mm, internal diameter d = 1 to 3 mm) a new CVD laboratory apparatus having the features describe below was designed and manufactured, see figure 3:

- Deposition temperature up to 1100°C
- Evaporation temperature of the AlCl3 up to 150 °C
- Codeposition process of YCl3 in the temperature range between 800°C and 1000°C

- Deposition pressure between 1000 Pa and 10000 Pa
- The sealing line close to the maximum deposition temperature
- The sealing connection suitable for different tube diameters and easy to open after the deposition process
- For the deposition process hydrogen or argon as carrier gas with a gas flow between 0.5 and 50 l h^{-1} (STP) controlled with thermal mass flow controller.

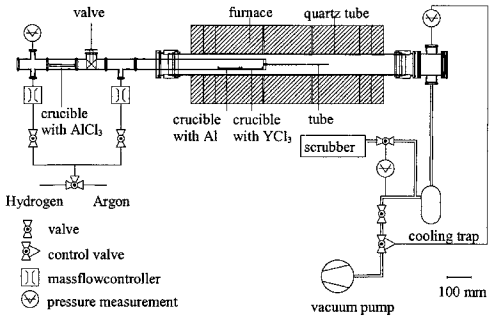


Fig. 3: Schematic flow chart of the CVD equipment for the coating of tubes

Long and complex Al coated tubes in blade material

To investigate the quality and the profiles of the deposited aluminium layers in relation to the deposition parameters, tubes of IN600 and GTD111 were coated with the laboratory CVD equipment.

The samples showed that, with increasing temperature and deposition time, the amount of deposited aluminium increased. The same behaviour was observed if hydrogen instead of argon was used. With increasing operating pressure the amount of deposited aluminium decreased. In addition, with longer deposition time there was less difference between the layer thickness at the inlet and the outlet of the tubes.

Long, complex Al and Y coated tubes in blade material

To improve the oxidation resistance of the aluminium layers the Al+Y codeposition was investigated. Several tubes made of GTD111 with length of 120 mm were coated with different $AlCl_3/YCl_3$ evaporation ratios in order to obtain aluminide layers with different yttrium contents. The sample composition, especially the aluminium and the yttrium content, was measured to estimate the optimal deposition conditions for the coating requirements.

2.4. Performance testing of coatings produced in the laboratory setup.

All of the coatings were subjected to characterisation through laboratory tests simulating the main operating conditions of an industrial gas turbine, after which they underwent microstructural examination.

The performance tests consisted of:

- Oxidation with flowing oxidant;
- Thermal cycling at 900° C and 1000 °C up to 1500 cycles;
- Burner rig hot–corrosion test .

The structural and compositional examinations were carried out utilising different analytic techniques including: optical microscope analyses, scanning electron microscopy and X-ray microanalysis with energy dispersing spectrometry. To determine the Y content in codeposition of Al and evaluate coating morphology, analysis by means of the GDOES technique, EMPA, SIMS and SEM+EDS were performed.

2.5. Test results

Microstructural analysis of coatings

The coating application parameters defined after some experimentation were successful in producing coatings on the inside surfaces of tubes that were relatively uniform in thickness (~30 μm) and uniform in chemical composition (18 to 30 wt% Al). Samples with coatings containing both Al and Y were analysed by SEM, EPMA and GDOES. Cross-sections were taken of the samples. The total coating and inter-diffusion thickness was almost constant at approximately 30 μm. The analyses performed by EPMA revealed that the concentration of Y was always below detection limits (<0.5%). Yttrium instead was detected by a qualitative method using GDOES.

For metallographic and chemical analysis the tubes were cut at different distances from the original CVD gas inlet. The IN600 tubes, after heat treatment, usually contained voids at the interface and a two-layer coating structure with an Al percentage between 25 and 30% in the outer layer and between 10 and 15% in the inner layer. This undesirable structure does not appear on the GTD111 material. In the GTD111 alloy tubes produced with argon carrier gas, the coating microstructure is typical of that of a low activity deposition process [3, 4] and no voids are present in the interface. The use of hydrogen as carrier gas increases both the thickness and the Al concentration in the coating.

The correlation between tube length, thickness and Al concentration for GTD111 tubes is reported in Figs. 4 and 5, confirming the ability of the deposition system to achieve the predetermined coating specification [5, 6, 7, 8].

The influence of the roughness of the internal tubes on the coating morphology and thickness has also been studied on specifically produced tubes. The results show no evident correlation.

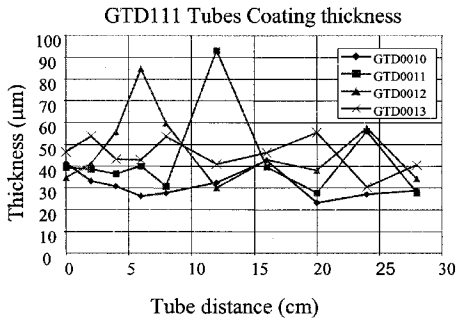


Fig. 4: Correlation between tube length and thickness

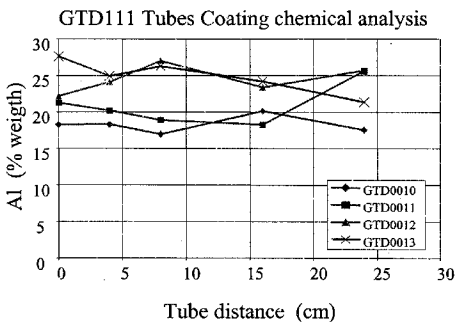


Fig. 5: Correlation between tube length and Al percentage

Thermal cycling oxidation tests

The results of thermal cycling tests, burner rig tests and oxidation with flowing oxidant conducted on samples coated with the new process were compared with the results obtained on similar samples coated by standard pack cementation. In Figs 6 and 7 below the "new" (DEPAC) coatings are denoted by the letter I, while the standard pack cementation aluminised coatings are denoted by the letter C. Cycling tests between room temperature and 900°C and 1000°C were run for a total of 1500 cycles on cylindrical samples 5 mm diameter and 30 mm long.

Cycling to 900°C generally resulted in a progressive increase in weight due to the growth of protective surface oxide scales on the aluminide coatings. An exception to this general behaviour was shown by the sample, I1, which lost some of the thermally grown oxide due to spallation at sample edges.

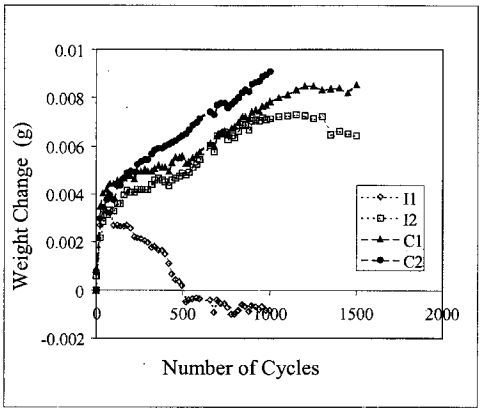


Fig. 6: Weight change data for coated samples under thermal cycling conditions in air: upper temperature of cycle 900°C

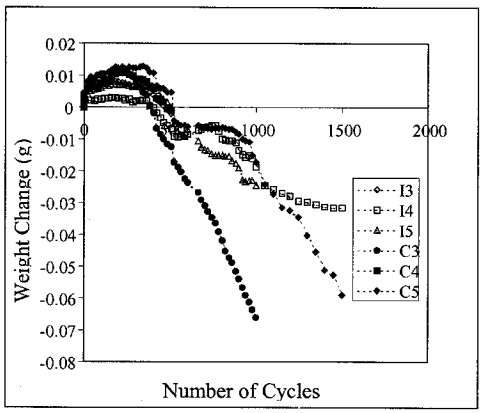


Fig. 7: Weight change data for coated samples under thermal cycling conditions in air: upper temperature of cycle 1000°C

For the 1000°C test weight gains were observed for all samples up to approximately 250 cycles. Thereafter, spallation of the alumina-rich surface scale occurred resulting in weight loss for both C and I coatings. Spallation of the surface oxide layer occurs after a thickness is reached when stresses caused by the thermal cycling can lo longer be accommodated. The inability of the oxide to deform at low temperatures results in mechanical failure and spallation. The main conclusion from the 900°C and 1000°C tests was that the new and conventional coatings behaved in a similar manner, indicating that the new process was capable of meeting the level of thermal cycling performance of an accepted aluminised coating.

Subsequently two batches of Al+Y coated samples (before and after an ageing heat treatment) were tested for either 500 or 1000 cycles (1000°C). In Figure 8 the weight change data for un-heat treated Al+Y coated samples are compared with data for the new Al coated samples. The data for the Al+Y samples show a low rate of oxidation and no spalling of the surface oxides within 500 cycles, whereas for the Al-only coated samples, spallation started after approximately 300 cycles.

Weight change data for the two batches of Al+Y coated samples are compared in Fig. 9. The weight changes occurring with the heat treated (second) batch of Al+Y samples were less than in the first batch (Fig. 9). The trend of increasing weight and absence of spalling over the first 500 cycles was similar. The test was extended for the second batch to 1000 cycles, with breakaway oxidation starting after 800 cycles (spallation causing a loss of weight) for one sample. While the number of samples tested was small and some variability in performance of the Al+Y coatings was observed, the improvement over simple Al coated material was at least a factor of two (when measured in terms of time or number of cycles to the initiation of spallation).

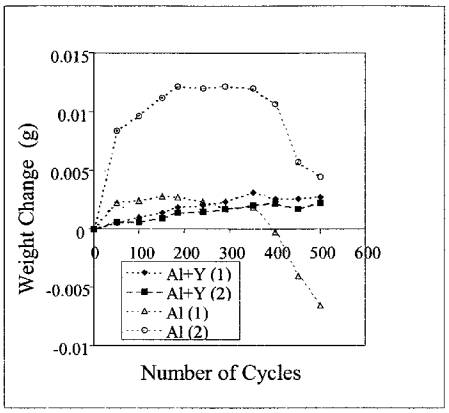


Fig. 8: Weight change data for Al+Y and Al coated samples under thermal cycling conditions in air: upper temperature in cycle 1000°C

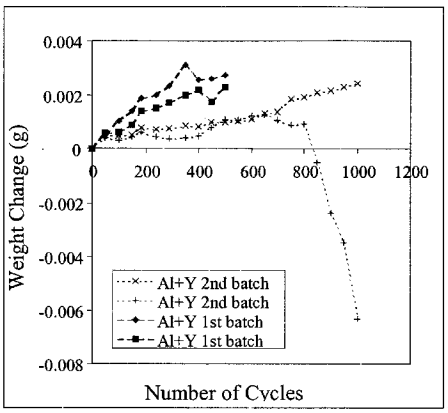


Fig. 9: Weight change data for two batches of Al+Y coated samples under thermal cycling conditions in air: upper temperature in cycle 1000°C

Burner rig hot-corrosion test

The corrosion testing on disc samples of Al+Y and Al-coated, both standard and new/DEPAC, and was carried out using a laboratory low-velocity burner rig. The test conditions were based on the guidelines for hot-salt corrosion testing of superalloys [9]. While internal cooling passages should not be exposed to the type of combustion gas used in this test, the conditions are aggressive enough to expose weaknesses in coating in a relatively short time.

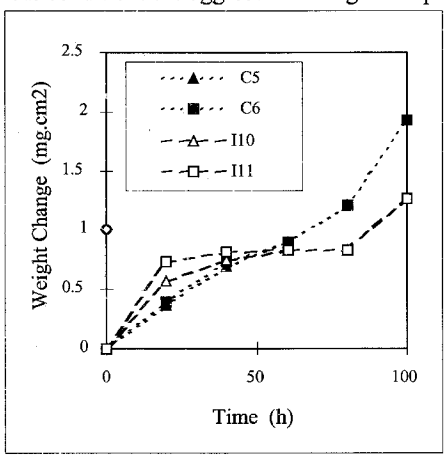


Fig. 10: Weight change data for coated samples exposed to burner rig combustion gas at 900°C under thermal cycling conditions

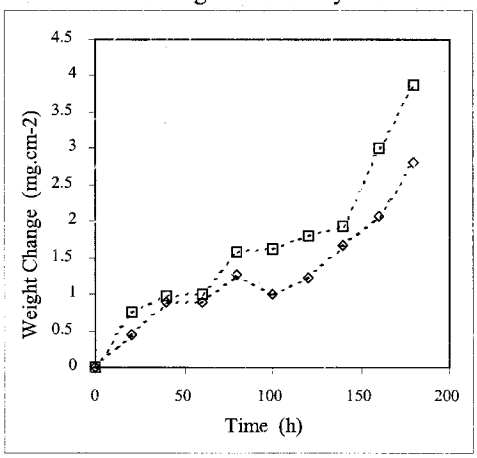


Fig. 11: Weight change data for Al+Y coated samples exposed to burner rig combustion gas at 900°C under thermal cycling conditions

The weight changes in the Al-coated samples are shown in Fig.10. The time to breakaway of the coatings (accelerated rate of weight change) containing only Al, both standard and new/DEPAC type, was about 60 hours. Some sample were exposed for up to 500 hours. For the Al+Y coating, breakaway corrosion occurred after about 120 hours (Fig.11). Microstructural examination was carried out after test time of 180 hours.
All Al coated samples originating from new and conventional processes were fully microstructurally examined after exposure times of 100, 200 and 500 hours.
In C specimens the corrosion initially produces, inside the coating, a low aluminium phase which forms a network; then through this network the corrosion spreads to the interface where base material corrosion may then occur, Fig. 12. In I specimens the corrosion affects all the coating, and the base material corrosion begins after the destruction of the complete coating, Fig. 13. For both types of coating the base material corrosion begins after 200 hours.

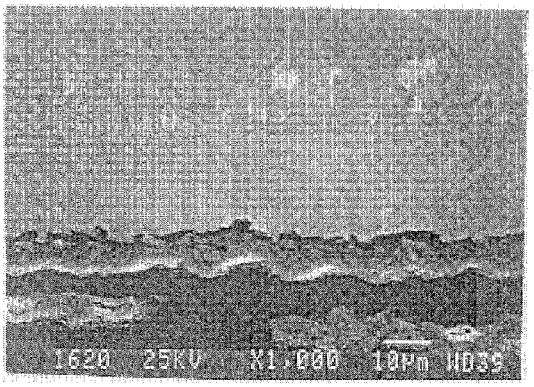


Fig. 12: Conventional coatings corrosion test.

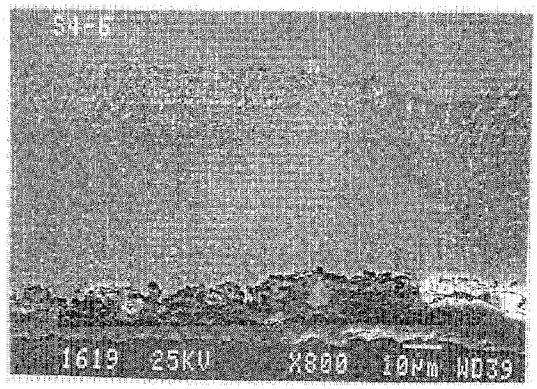


Fig. 13: New coatings corrosion test.

In the specimens coated with Al+Y, the coating remained intact after 180 hours of exposure with the formation of a low Al phase, the globularisation of the interface zone and the presence of σ phase in the base material.

Oxidation with flowing oxidant (Al and Al+Y coated tubes)
Specimens made of GTD 111 DS, which had been drilled and vacuum aluminised, were used for the oxidation with flowing oxidant tests.
The parameters testing was conducted at temperatures of 1000°C, 1020°C, 1050°C, 1020°C+1120°C for a total of about 170 hours . The temperature and the time had been established pursuant to considerations on the damage occurring during the tests conducted on specimens coated with Al only.
The temperature of the specimen was checked with a contact thermocouple and the air blown through the holes at 2 l/min was heated before being applied to the specimens.
In a further test: two tubes were aluminised with Al+Y and subsequently subjected to an oxidation test with flowing oxidant at 1050°C for 100 hours, and another two tubes were subjected to an oxidation test at 1000°C and 1050°C for 200 hours.

Microstructural analysis of Al coated tubes

The Al coated specimens were sectioned prior to oxidation tests with gas flow to measure coating thickness (inlet avg = 45 μm, outlet avg. = 28 μm), values within the specified range. After testing the specimens were sectioned especially for SEM and opticalexamination to observe the damage to the coating.

The results can be summarised as follows.

It was observed that the two-phase oxide scale formation (dark area=Al and white area=Al, Ti, Cr) is not continuous but includes only some superficial zones of the coating.

Significant structural degradation of the coating occurs at the test temperature of 1050°C, at which the coating is formed of two phases: dark with Al 18% (β phase) and white (perhaps γ' phase) with Al 8%.

An increase in the dimensions of the basaltic interface zone was observed with the presence of white phases (Cr, Mo, W) and substantial formation of the brittle needle phase (σ).

Complete structural degradation of the coating with an initial penetration of oxide in the base material is evident at 1120°C.

However the above-mentioned temperatures, used to accelerate the degradation process, are never reached on gas turbine blades in service.

See Fig. 14 and 15 showing the holes and microstructures before and after the oxidation process.

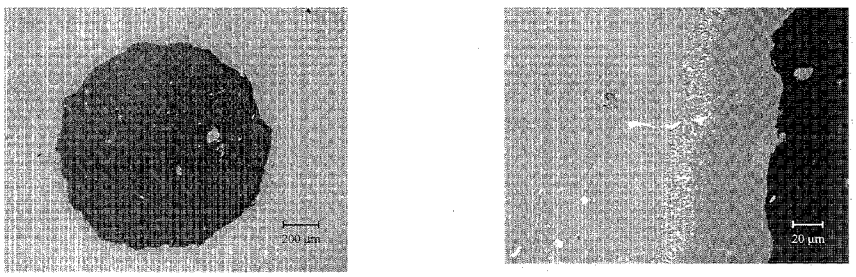


Fig. 14: Aluminising of holes GTD111 DS (sample 5\1) before oxidation

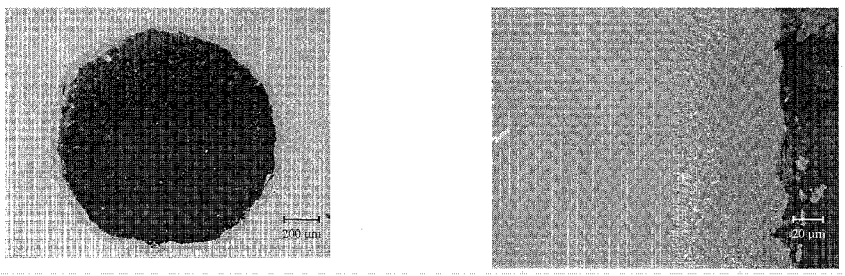


Fig. 15: Aluminising of holes GTD111 DS (sample 5\1) after oxidation (1000°C for 1 week)

Microstructural analysis of Al+Y coated tubes after oxidation

The microstructural observations conducted on a thin Al+Y coating after oxidation test (1050°C for 100 hours) showed similar degradation of the coatings.

On an area of the internal tube surface the formation of a thick, adhering oxide scale, whose degree of penetration sometimes reaches the base material was observed.

The oxide scale is comprised of three phases: external white phase rich in Yttrium, intermediate grey phase rich in aluminium, titanium and yttrium and internal dark phase near the base material rich in aluminium.
The Al+Y coating is decomposed and occupied by the γ'-phase.
Some part of the β-phase (NiAl) was observed in the middle section of the tube GTDR0016.
In those parts the percentage content of Al is equal to ≅ 13.8% and that of Y ≅ 0.48%.
Microstructural examinations performed on the other Al+Y coated tubes (with thicker coatings) after oxidation test (1000°C sample GTDR 0018 and 1050°C sample GTDR 0017 for 200 hours) showed better behaviour of the coatings

3. Comments on the results of the sample coated with CVD laboratory demonstrator

The new CVD coating process is useful and efficient for aluminising the internal surface of turbine blade cooling cavities.
Microstructural characterisation performed on long tubes and samples, after the tests carried out to evaluate the behaviour of the coating and to simulate the service condition of the blade, has been essential to evaluate the achievement of satisfactory coating in terms of thickness and Al percentage.

A. The coating application parameters defined after some experimentation produced coatings on the inner surfaces of tubes that were relatively uniform in thickness (~30 μm) and uniform in chemical composition (18 to 30 wt% Al). The Y content was below detection limits for EPMA (its presence was confirmed by SIMS).
B. For Al-coated samples, the CVD DEPAC laboratory scale coatings exhibited oxidation resistance under thermal cycling conditions at least as good as the conventional standard current generation Al coatings.
C. The presence of Y in addition to Al resulted in a marked increase in oxidation resistance as compared to Al coatings alone under thermal cycling conditions. Based on weight change data, the time to the initiation of breakaway oxidation is increased by a factor of 2 when Y is present. The consequence of this improvement should be longer coating life between service/repair and reduced tendency for thermally grown oxide to spall and block cooling passages.

These satisfactory results have been utilised for the design and construction of the demonstrator for aluminising the critical parts of the gas turbines.

4. Design & construction of the CVD Demonstrator reactor

In the design, the following points were taken into account: the need to attain a suitable degree of vacuum, to operate at high temperature and in the presence of hydrogen, and to add yttrium to the aluminium .
To resolve these problems, it was decided to use a retort of size no more than 600 mm diameter and made of the special alloy Haynes 230, possessing high mechanical strength at high temperatures.
Special care was taken in constructing the inner crucible of graphite, so as to be able to insert an additional part for the co-deposition of Al+Y.
The entire system is controlled by a dedicated computer allowing monitoring at any moment of the deposition parameters and, when necessary, intervening appropriately and, in case of emergency, shutting down the system before problems arise.

With this system, after the preliminary trials for optimising the deposition parameters, it was possible to perform aluminising of gas turbine blades having cooling holes of simple geometry, as well as those of complex geometry typical of aeronautical derivation.
Micrographic examinations as well as oxidation and thermal cycling tests have confirmed the satisfactory properties of the coatings produced, in line with the preliminary results obtained on samples coated with aluminium conducted in the laboratory CVD equipment.

5. Conclusion

With the new CVD process operating using $AlCl_3$ and H_2, Al coatings can be applied on the internal cooling systems of gas turbine blades of recent design. The coatings obtained with the new CVD process present good performance, in terms of homogeneous coatings along the entire length of cooling channels.
Furthermore, the co-deposition of Al plus Yttrium improves the resistance of Al to hot corrosion/oxidation.

6. Reference list

[1] R.C. Reid, J. M. Prausnitz, B. E. Poling, The properties of gases & liquids, McGraw-Hill Book Co., New York, 4th edition, 1987
[2] Ch. Metz, G. Wahl, P. Bianchi, M. Innocenti, D. Baxter, N. Archer, R. Wing, Yttrium containing aluminide layers, Journ de Physique IV Vol. 11 (2001), Pr3-869
[3] C.T. Sims, W.C. Hagel, The superalloys, Wiley Interscience Publication, 1972.
[4] E. Lang, Coatings for High Temperature Applications, Applied Science Publishers, 1983
[5] C.Labatut, C.Metz, R.Stolle, G.Wahl, P.Bianchi, L.Pelacchi, Deposition of Aluminium on the Internal Surfacer of Tubes, 9°International Conference on Modern Materials & Technologies, Florence, 14-19 June 1998.
[6] P.Bianchi, C.Labatut, L.Pelacchi, R.Stolle, N.Archer, R.Wing, Ricoprimenti protettivi di tipo alluminiuri nelle superfici interne di palette turbogas a canali di raffreddamento con geometria complessa, Study Day "Ricoprimenti protettivi metallici e ceramici per applicazioni industriali", Rovereto (TN), 23 April 1998.
[7] C. Labatut, C. Metz, G. Wahl, P. Bianchi, M. Innocenti and J.-P. Hirvonen, AlNi coatings on the internal surfaces of tubes, Journal de Physique IV, Vol. 9 (1999), Pr8-987.
[8] C. Labatut, C. Metz, R. Stolle, G. Wahl, P. Bianchi, L. Pelacchi, Deposition of Aluminum on the internal surfaces of tubes, in: Surface Engineering (1999), Ed. P. Vincenzini, p. 675 -682.
[9] S.R.J.Saunders and J.R.Nicholls, "The need for a standard procedure in hot-salt corrosion testing", High Temperature Technology, 7 (4) (1989) 232-240.

7. Acknowledgements

This work has been sponsored by the European Commission within the DEPAC Brite Euram III project (New Technique for the Deposition of Protective Aluminide Coatings on the Internal Surfaces of Complex Cooled Industrial Turbine Blades (DEPAC)

CHARACTERIZATION OF THE BOND-COAT MATERIALS FOR THE SUPER HIGH EFFICIENCY GAS TURBINES

A.Suzuki[1], F.Wu[2], H.Murakami[3] and H.Imai[1]
1) Shibaura Institute of Technology
3-9-14 Shibaura, Minato-ku, Tokyo, Japan
2) High Temperature Materials 21 Project
National Institute for Materials Science (NIMS)
1-2-1 Sengen, Tsukuba Science City, Ibaraki, Japan
3) Dept. of Mater. Eng. School of Eng., the University of Tokyo
7-3-1, Hongo, Bunkyo-ku, Tokyo, Japan

Abstract

Novel bond coat materials with higher heat resistant properties are developed in order to achieve high efficiency in gas turbine systems. In this study, we propose an Ir-Ta underlying metallic bond coat material. The material proposed is coated by an electron beam physical vapor deposition (EB-PVD) method on a Ni-base single crystal superalloy, TMS-75, followed by a conventional low activity Al pack cementation process. The oxidation and corrosion properties of the Ir-Ta coated and Al pack cemented specimens were compared with those of uncoated and Al pack cemented alloys. The cyclic oxidation and hot corrosion tests revealed that Ir-Ta coated specimens show better oxidation and hot corrosion resistance than uncoated specimens. SEM-EDX analysis revealed that a reduction of Al concentration of the substrate in the vicinity of substrate/coating interface is much lower in coated material, suggesting that the Ir-Ta coating works as a diffusion barrier of Al. It is also found that the Ir-Ta coated specimen after the oxidation test has a lower amount of detrimental phases such as topologically close packed (TCP) phases than the others, suggesting that the Ir-Ta coated material developed here is advantageous in terms of phase stability of the base alloy.

Keywords: EB-PVD, Ir-Ta coating, low activity Al pack cementation process, Diffusion Barrier, Ni-base single-crystal superalloy

1. Introduction

High temperature capability and oxidation resistance are required for heat-resistant structural materials. To achieve these properties, thermal barrier coatings [1] (TBCs) and oxidation-resistant coatings are being developed. However, at higher temperatures over 1273K, interdiffusion of elements, such as Al, between the coated materials and substrate often assists the formation of detrimental phases, resulting in the deterioration of creep properties of the substrate. To avoid this problem, Narita [2] et al. has recently proposed the Re-modified aluminide coatings as a diffusion barrier, in which Re and Cr from the substrate form a σ phase. Unfortunately, the σ phase formation takes place only when the Cr amount of substrate is sufficiently high.

Above this as backgrounds, we propose a new metallic under-coat material for Ni-base superalloys working as a diffusion barrier, ie. an Ir-Ta binary alloy. Ta has a problem of the oxidation resistance, but the diffusibility into the Ni-base alloys is low [3]. Ir is thus added to improve oxidation resistance as well as to works as a diffusion barrier.

The purpose of this study is to evaluate the high temperature characteristics of the

newly proposed material. Cyclic oxidation tests and hot corrosion tests were carried out to evaluate the high temperature performance of the specimens. The change in microstructure and chemical concentration of solute elements of the specimens during the tests were also investigated.

2. Experimental Details

2.1 Coating Procedure

All substrates used in the present investigation were prepared from a Ni-base single crystal superalloy, TMS-75 (Ni: 63.1, Co: 12.6, Cr: 3.5, Mo: 1.29, W: 2.02, Al: 13.7, Ta: 2.05, Hf: 0.04, Re: 1.66 in at%)[4,5]. The substrates of dimensions 17mm x 17 mm x 2mm were cut and were then polished with emery paper up to 600#, buffed with 0.25μm diamond, and were cleaned with acetone by ultrasonic bath before coating. The EB-PVD method was used for coating. Arc melted pure Ta and Ir-20at%Ta were selected as the source material. The typical coating condition was as follows: the vacuum chamber pressure : $1.2\sim3.5\times10^{-3}$Pa, the acceleration voltage of electron beam : 10kV, current: 450mA, and the deposition rate : approximately 10μm per hour.

2.2 Al pack cementation

As polished and uncoated TMS-75 substrates, Ta-coated, and Ir-Ta-coated specimens were Al-pack cemented by setting the specimen embedded in the mixture of Al, Fe, Al_2O_3 and NH_4Cl powder. The pack cementation was carried out at 1373K for 5hours under Ar atmosphere. Hereinafter, these Al-pack cemented specimens are denoted as 'TMS-75+Al', 'Ta+Al' and 'Ir-Ta+Al', respectively.

2.3 Cyclic oxidation tests

In order to evaluate the oxidation resistance of these specimens, cyclic oxidation tests were carried out. For the test, we used uncoated TMS-75 (hereafter 'TMS-75'), Ta and Ir-Ta-coated specimens ('Ta' and 'Ir-Ta', respectively), and the three Al-pack cemented specimens described above (TMS-75+Al, Ta+Al, Ir-Ta+Al,). The test temperature was 1373K in air, the holding time was 20 hours per cycle followed by air-cooling to room temperature. The tests were carried out for 10 cycles. The oxidation resistance of the specimens was evaluated by measuring the weight of the sample after each cycle.

2.4 Hot corrosion tests

In order to evaluate the hot-corrosion resistance of the specimens, cyclic hot-corrosion tests in dipped molten salt were carried out [6]. Test specimens used were the same as in the cyclic oxidation tests. Na_2SO_4 was used as the molten salt; test temperature was 1173K; the holding time was 20 hours per cycle followed by air-cooling, and the tests were carried out in air for 10 cycles. The hot-corrosion resistance was evaluated by measuring the weight of the sample after each cycle.

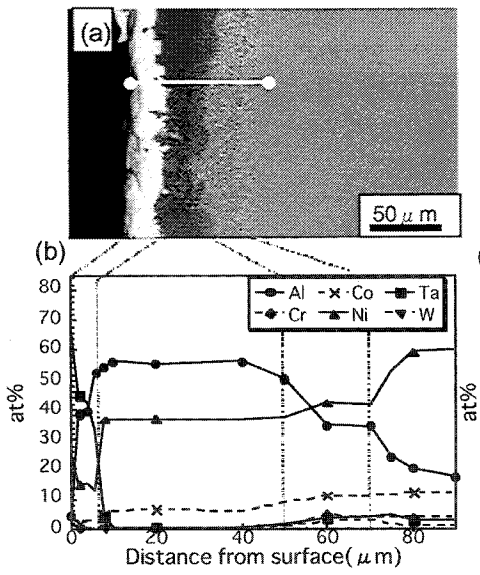


Fig.1 (a) The cross-sectional microstructure and (b) corresponding chemical composition profile of the 'Ta+Al' specimen.

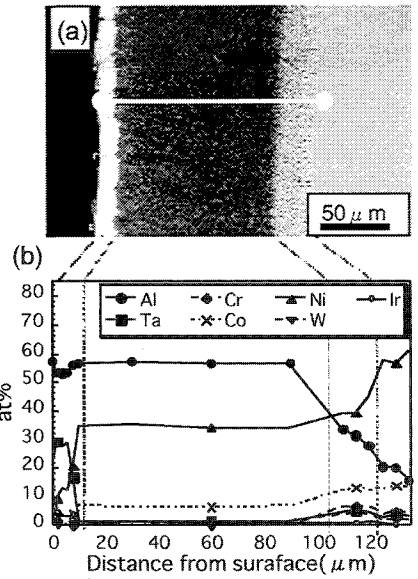


Fig.2 (a) The cross-sectional microstructure and (b) corresponding chemical composition profile of the 'Ir-Ta+Al' specimen [7] .

3. Results

3.1 Microstructure and chemical composition of the Ta-coated specimens

The thickness of Ta in the 'Ta' specimen was about 10μm. EDX analysis revealed that the chemical composition of the Ta layer was almost homogeneous. Figure 1 shows the cross-sectional microstructure and corresponding composition profiles of solute elements in the 'Ta+Al' sample. Between the coated Ta layer and the substrate, a Ni and Al-enriched layer (Ni-Al layer) with a thickness of about 40μm is formed. Consequently, the 'Ta+Al' specimen has 3 layers over the substrate: a Ta-rich layer, Ni- and Al-enriched layer originated from the Ta-coated layer, a Ni-Al layer, and a γ' layer, stacking in this order from the surface.

3.2 Microstructure and chemical composition of the Ir-Ta-coated specimens

Figure 2 shows the cross-sectional microstructure and corresponding composition profiles of solute elements in the 'Ir-Ta+Al' sample. The thickness of the Ir-Ta layer in the 'Ir-Ta' specimen was about 6μm. EDX analysis revealed that the chemical composition of the Ir-Ta layer was Ir-70at%Ta. Between the coated Ir-Ta layer and the matrix, a Ni-Al layer with a thickness of about 100μm is observed. Consequently, similar to the 'Ta+Al' sample, the 'Ir-Ta+Al' sample has 3 layers over the substrate: an Ir-Ta-, Ni- and Al-enriched layer originated from the Ir-Ta coated layer, a Ni-Al layer, and a γ' layer, stacking in this order from the surface.

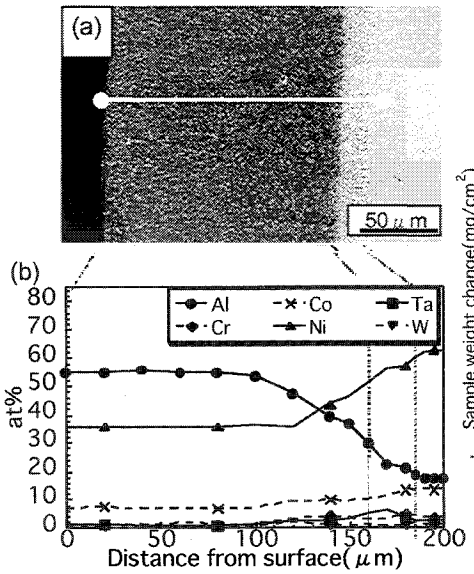


Fig.3 (a) The cross-sectional microstructure and (b) corresponding chemical composition profile of the 'TMS75+Al' specimen [7] .

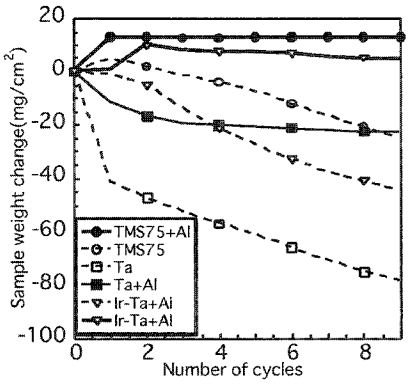


Fig.4 The weight change of specimens as a function of oxidation cycle. The specimen were kept at1373K for 20hours for each cycle.

3.3 Microstructure and chemical composition of the 'TMS-75 +Al'

Figure 3 shows the cross-sectional microstructure and corresponding chemical composition profiles of solute elements in the 'TMS-75+Al' sample. A Ni-Al layer with a thickness of about 160μm is observed. Consequently, the TMS-75 +Al has 2 layers: the Ni-Al layer and the γ' layer, stacking in this order from the surface.

3.4 Cyclic oxidation tests

In order to evaluate the oxidation resistance of the 6 specimens described in 2.2 and 2.3, cyclic oxidation tests were carried out. Figure 4 shows the changes in sample weight as a function of oxidation cycle. From the results, we found that the 'TMS-75+Al' and the 'Ir-Ta+Al' show better oxidation resistance than the other samples. It should be noted that further cyclic oxidation tests up to 30 cycles did not cause the significant mass changes especially in the case of the 'Ir-Ta+Al'coatings [8]. It is also found that the Ta-coated specimens have poor oxidation resistance with or without Al-pack cementation.

3.4.1 Change in microstructure and chemical composition of the 'TMS-75+Al' after cyclic oxidation tests

Figure 5 shows the cross-sectional microstructure and corresponding chemical composition of the 'TMS-75+Al' after 10 cycles of oxidation tests. The Al_2O_3 and the Ni-Al layers are observed in this order from the surface.

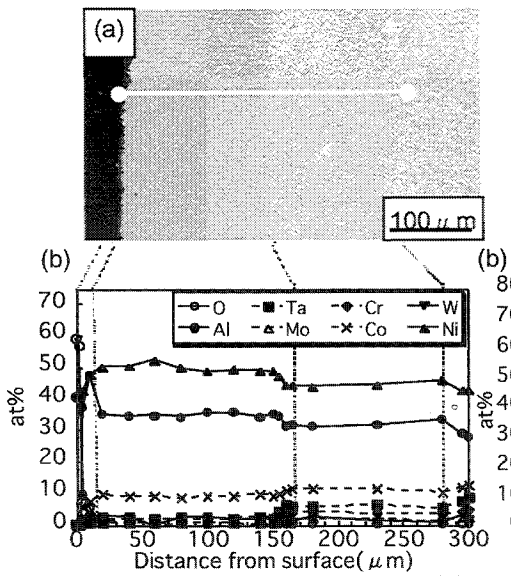


Fig.5 The changing in (a) microstructure and (b) chemical composition profile of the 'TMS-75+Al' specimen after cyclic oxidation tests.

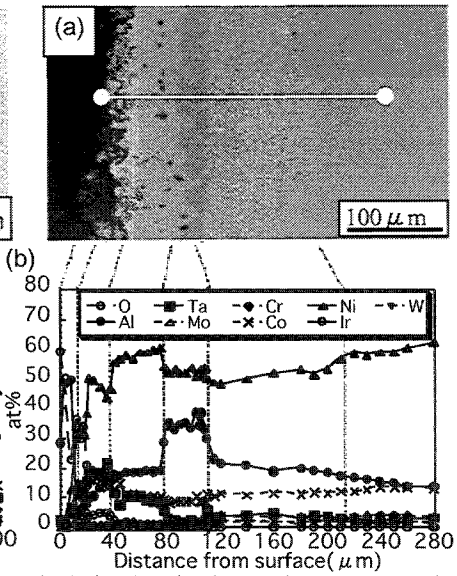


Fig.6 The changing in (a) microstructure and (b) chemical composition profile of the 'Ir-Ta+Al' specimen after cyclic oxidation tests.

At the same time, the precipitation of the detrimental phases, such as topographically close packed phases (TCP), were spreading over 300 μm from the surface.

3.4.2 Change in microstructure and chemical composition of the 'Ir-Ta+Al' after cyclic oxidation tests

Figure 6 shows the cross-sectional microstructure and corresponding chemical composition of the 'Ir-Ta+Al' after 10 cycles of oxidation tests. The Al_2O_3 layer, the Ir-, Ta-, Ni- and Al-enriched layer originated from the Ir-Ta-coated layer, the Ni_3Al layer, the Ni-Al layer, and the γ' layer are observed in this order from the surface. The volume fraction of the detrimental phases, considered as an enriched layer of W and Re and regarded as the σ phase, is smaller than that of the TMS-75 +Al. The detrimental phases are spreading less than 200 μm from the surface.

3.5 Hot-corrosion tests

Cyclic hot corrosion tests in dipped molten salts were also carried out to compare the corrosion resistance of the samples.

Figure 7 shows the sample weight change as a function of hot-corrosion cycles. The surface morphology of each sample after 10 cycles of hot-corrosion tests is displayed in Figure 8. As clearly indicated in these figures, the 'TMS-75+Al and the 'Ir-Ta+Al' show better hot corrosion-resistance than others.

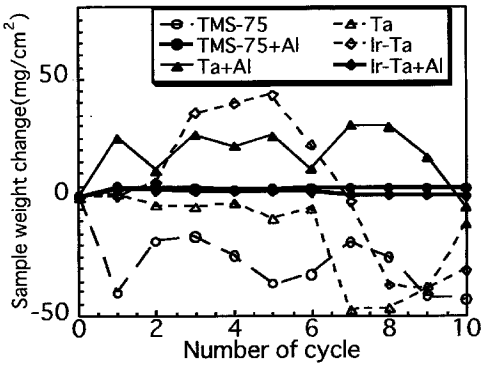


Fig.7 The weight change of specimens as a function of hot-corrosion cycle. The specimen were kept 1173K for 20hours for each cycle.

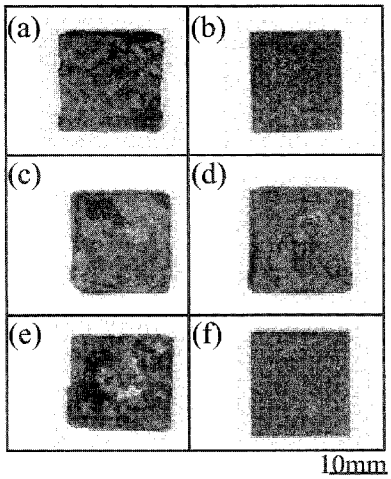


Fig.8 The surface morphograpy of each sample after 10 cycles of hot-corrosion tests with molten salts.
(a) TMS-75, (b) TMS-75+Al,
(c) Ta coating, (d)Ta+Al,
(e) Ir-Ta coating, (f) Ir-Ta+Al

4. Discussion

4.1 Difference in chemical composition between the coated layer and the source material

As described in 3.2, the chemical composition of the Ir-Ta-coated layer, analyzed by EDX, was Ir-70at%Ta, which is far different from the composition of the source material, Ir-20at%Ta, suggesting that 'preferential deposition' occurred during the EB-PVD process This 'preferential deposition' is caused by the the difference in the vapor pressure Ir and Ta [9].Under our experimental conditions, the evaporation pressure of Ta is much lower than that of Ir, and which resulted in the higher deposition yield of Ta.

It is planned to perform experiments to investigate this effect of Ir-Ta composition on the high temperature properties of the Ir-Ta coated alloy by precisely controlling the Ir/Ta ratio by taking into account the difference in vapor pressure of Ir and Ta.

4.2 Comparison of microstructural evolution by cyclic oxidation tests

Although the 'TMS-75+Al' and the 'Ir-Ta+Al' both showed good oxidation resistance with small difference in weight change during cyclic oxidation change, the microstructure and the distribution of solute elements drastically differ between the two materials.

Figure 9 shows the Al and Ni concentration profiles of the 'TMS-75+Al' and the 'Ir-Ta+Al'. In the case of 'TMS-75+Al', concentration changes of both Ni and Al are small and

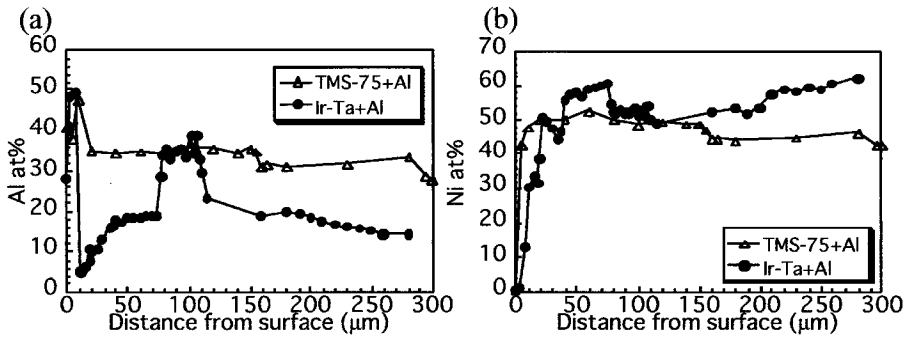


Fig.9 Concentration profiles of (a) Al and (b) Ni after cyclic oxidation tests, in the case of 'TMS-75+Al' and 'Ir-Ta+Al'.

the Al-enriched layer completely disappeared, suggesting that the inward / outward diffusion of Al is rapid. On the other hand, the 'Ir-Ta+Al' specimen has several layers, and still has the Al-enriched layer, suggesting that the Ir-Ta layer worked as a diffusion barrier for Al. In addition, there is the most distinctive difference between the two specimens: the precipitation morphology of the detrimental phases. In the case of 'Ir-Ta+Al' coating, the detrimental phases are not observed over, 300μm from the surface, whereas the 'TMS-75+Al' still shows detrimental phases. The detrimental phase precipitation occurs by the lack of Ni in the matrix, segregation of refractory elements such as Mo and Re and the excessive amount of Al, all caused by the diffusion of solute elements. Therefore if the diffusion barrier layer exists, the precipitation of detrimental phases is suppressed. The result of precipitation kinetics also supports that the Ir-Ta layer works as a diffusion barrier. Though pure Ta has a high melting point, it has poor oxidation resistance and therefore, the Ta layer is not stable under oxidation atmosphere. This study confirmed that the addition of Ir to Ta improves the oxidation resistance. Although Ir and Ta are relatively expensive elements, they are much cheaper than Pt, which has already commercially been used for turbine blade coatings. It is thus expected that the Ir-Ta alloys are promising material for the next-generation turbine technologies.

5. Conclusions

We proposed an Ir-base underlying metallic bond coat material. The coating is carried out by EB-PVD on a Ni-base single crystal super alloy, TMS-75, followed by Al-pack cementation. Cyclic oxidation tests and hot corrosion tests with dipped molten salt (Na_2SO_4) were conducted for the characterization of the coatings at high temperatures. The following results were obtained:

1. The Ir-Ta-coated superalloy with Al-pack cementation showed good oxidation and corrosion resistance. In addition, with the coating, the precipitation of the third phase was suppressed. Ir-Ta is thus a promising new metallic under-coat material.
2. The Ir-Ta layer works as a diffusion barrier.

3. The Ta coating shows poor oxidation and corrosion resistance with or without Al pack cementation.

Further improvement of process control will be carried out to control the composition of coated layer, so that we could find out the best combination of oxidation and hot corrosion resistance and the diffusion barrier effect of the coated Ir-Ta layer.

6. Acknowledgements

A part of this work was carried out under the auspices of Industrial Technology Research Grant Program, JAPAN New Energy and Industrial Technology Development Organization (NEDO). The authors wish to thank Toshiba Co. Ltd for assisting in Al pack cementation, and are also grateful to Dr. P. Kuppusami, Dr. M. Osawa, Mr. T. Yokokawa, Mr. Y. Koizumi, Mr. T. Kobayashi and Mr. M. Sato for assistance and helpful discussion during experiments.

7. References

[1] M. J. Stinger, N. M. Yanar, M. G. Topping, F. S. Pettit and G. H. Meier: Z. Metalkd , 90 (1999) 12, 1069-1078
[2] T. Narita, M. Shoji, Y. Hisamatsu, D. Yoshida, M. Fukumoto, S. Hayashi: High-temperature corrosion and protection 2000, 351-357
[3] C. E. Campbell, W. J. Boettinger, U. R. Kattner: Acta Materialia, 50 (2002), 775-792
[4] Y. Koizumi, T. Kobayashi, T. Yokokawa, T. Kimura, M. Osawa and H. Harada: Materials for Advanced Power Engineering proceedings, 1998,P.2-1089
[5] Y. Yamabe, Y. Koizumi, H. Murakami, Y. Ro, T. Maruko, and H. Harada : Scripta Materialia,Vol.35 (1996) , P.211
[6] D. He, H. Guan, X. Sun and X. Jiang: Thin Solid Films, 376 (2000) 144-151
[7] F. Wu, H. Murakami and A. Suzuki, submitting to Surface & Coatings Technology
[8] A. Suzuki, F. Wu, H. Murakami, H. Imai, submitting.
[9] S. Dasushman: 'scientific foundation of vacuum technique' second edition, 1962,696-700

ELASTIC BEHAVIOUR OF PLASMA SPRAYED THERMAL BARRIER COATINGS

Steinbrech, R.W., Frahm, J., Herzog, R., Schubert, F.

Institute for Materials and Processes in Energy Systems
Forschungszentrum Jülich GmbH, D-52435 Jülich

Abstract

The elastic behaviour of air plasma sprayed (APS) thermal barrier coatings (TBCs) of 8 wt.% yttria stabilised zirconia was studied using various mechanical tests with global and local resolution. Results are presented, which reveal the complex relationship between lamellar APS-microstructure and stiffness and illustrate scaling aspects. Also the influence of residual stresses is addressed. The obtained stiffness values for as-sprayed TBCs show a systematic variation between 10 and 100 GPa. Typically results from bending tests of free-standing TBCs are at the low end, whereas results from depth sensitive indentation tests with TBCs bonded to a substrate are found at the high end. When heat treated above 950°C the TBCs exhibit a rapid increase in stiffness which can be attributed to defect healing within the spraying lamellae. Discussion of the results focuses on the implications of a non-uniform stiffness modulus for the mechanical characterisation of thermal barrier systems.

Keywords: elastic behaviour, thermal barrier coating (TBC), plasma sprayed TBC, yttria stabilised zirconia

1. Introduction

Ceramic top layers of yttria stabilised zirconia are increasingly exploited as thermal barrier coatings for high temperature components of advanced gas turbines [1,2]. Thereby advantage is taken from the low inherent thermal conductivity of zirconia containing ceramics, which in the case of APS - TBCs, is further diminished by microstructral defects introduced during the spraying process. Some of the frequently observed defects are related with incomplete melting of powder agglomerates, pores, quenching cracks due to rapid solidification of the spraying splats and lack of splat contact.

The influence of these defects on the macroscopic coating properties has to be known in order gain insight in the mechanical performance of the TBCs. In this respect the elastic behaviour of the TBC is of particular interest.

Elasticity studies, predominantly carried out with thick free-standing APS-TBCs in the past, show a decrease of stiffness with increasing porosity. A summarising plot of the results and relevant references are compiled in [3]. In the relevant porosity regime of 10 - 15 % the measured values are about one order of magnitude lower than the elastic modulus of dense YSZ. There is typically large scatter in the results indicating considerable material heterogeneities.

However, also systematic differences in apparent TBC stiffness have been reported [4-15]. They are related with variations in processing [4], anisotropy of lamellar microstructure [5,6], residual stress [7], sign of applied load [8,9] and heat exposure [10-14]. Even the experimental testing method has influence on the obtained results [12,15].

It is the aim of the present work to elucidate some of the systematic variations in apparent stiffness and to correlate the results with microstructural features. The paper concludes with some implications of the non-uniform stiffness behaviour of APS-TBCs for the mechanical characterisation of thermal barrier systems.

2. Experiments

2.1 Material

Zirconia stabilised with 8 wt.% yttria was air plasma sprayed in various thickness (0.3-2.5 mm) on different substrates. All spraying activities were carried out at the Institue for Materials and Processes in Energy Systems (IWV 1), FZ-Juelich. To simulate the geometrical conditions of gas turbine components the thin TBCs were sprayed on NiCoCrAlY coated Ni-superalloy substrates. The thick TBCs had a mild steel substrate. For measuring the elastic properties of free-standing TBCs all thick and also some of the thin TBCs were separated from the respective substrates using a HCl acid. Some of the free-standing TBCs were fractured to examine the microstructure of the APS-TBC.

The SEM micrograph of such a through-thickness fracture surface (Fig. 1) reveals the typical lamellar appearance of APS coatings. The individual spraying splats with columnar, submicron-diameter grains are clearly visible. In addition to less frequent pores many crack-shaped defects exist between and within the individual spraying splats, termed subsequently as inter- and intra-splat cracks, respectively.

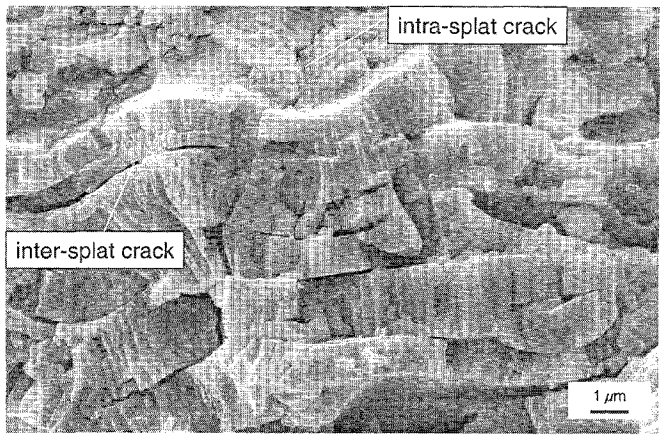


Fig. 1: Lamellar microstructure of APS-TBC. Through thickness fracture surface reveals the columnar, sub-micron grain morphology within the spraying splats. Also the numerous crack-shaped defects between and within the splats are visible (inter- and intra-splat cracks).

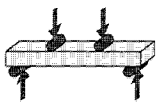
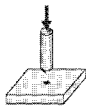
2.2 Testing methods

The apparent stiffness of APS-TBCs was measured using global (integrating) and local methods with respect to the typical splat dimensions of the microstructure. Global results were obtained from bending and compression tests with the thick free-standing coatings, whereas depth sensitive micro-indentation tests with high lateral resolution provided localised results for both, separated and bonded 300 μm thick TBCs (Table 1).

The bend bars (2.5 x 4 x 30 mm^3) were machined from thick (2.5 mm) separated TBCs. The tubular specimens ($\varnothing \approx 14$ mm, length $L \approx 12$ mm, wall thickness $\approx 500\ \mu$m) for the compression tests had been initially plasma sprayed on a cylindrical rod of mild steel.

For indentation measurements perpendicular to the spraying direction the specimens were embedded in a resin following standard metallographic procedures.

Table 1: Matrix of global and local testing methods applied for APS-TBCs of various thickness.

Test			APS-TBC condition		
approach	method		sep.	bond.	thickness [mm]
global	4-point bending (2.5x4x50 mm³)		x		2.5
	Compression (ϕ = 14 mm, L = 12 mm)		x		0.5
localised	depth sensitive indentation (1N load)		x		0.3
				x	0.3

Most of the tests were carried out with as sprayed TBC material. In addition separated TBCs (300 μm thick) were given heat treatments at 950, 1050, 1100 and 1200°C up to 100 h prior to RT testing with depth sensing micro-indentation.

3. Results and Discussion

3.1 Separated TBCs

Besides the small intra-splat cracks (Fig. 1) often also larger vertical cracks develop in APS-TBCs, which relieve the tensile stresses from the rapid cooling of a larger TBC volume. Fig. 2 shows an example of such a vertical "macro-crack" on the tentative tensile surface of a free-standing TBC bend bar.

Considering the tensile stress situation in the global approach of a bending test it is very likely that the crack opening displacement (COD) of such larger cracks determines the specimen compliance [8]. As a consequence, the measured apparent "global" stiffness of the TBC primarily reflects orientation, amount and size of such vertical cracks. Average stiffness values of about 10 GPa (Fig. 3) were obtained from the bending tests with variation between 5 and 15 GPa. Note that also non-linearity in deformation behaviour occurs as soon as the vertical cracks start growing under the applied bending stress [9].

Contrary to the situation in the presence of tensile stresses the intra-splat and the larger vertical cracks experience closure forces when loaded under compression. The more sites along the crack surfaces develop physical contact the stiffer the TBC appears [8]. Again a

non-linear elastic response is observed in a global measurement, i.e. the slope of the stress-strain curve increases with increasing compressive stress [9]. By applying compressive stresses in the order of 50 MPa apparent stiffness values of about 43 GPa were measured (Fig. 3).

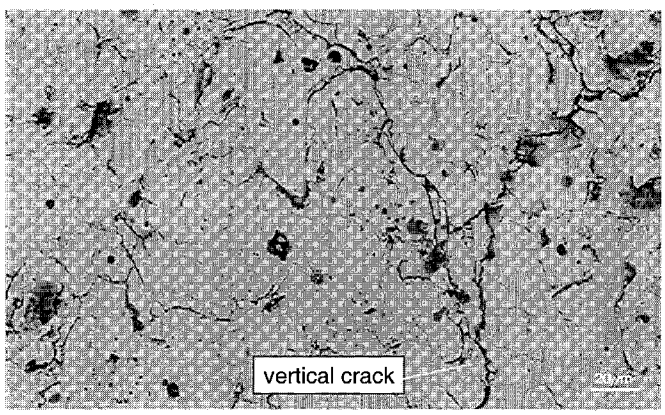


Fig. 2: Polished surface of free-standing thick APS-TBC with larger vertical cracks. Under tensile stress in a (global) bending test the specimen compliance is significantly increased by the crack opening displacement of such "macro-cracks".

In the case of the highly localised micro-indentation measurements the larger vertical cracks are of less importance. Predominantly the smaller inter- and intra-splat cracks are the defects, which influence the deformation and fracture behaviour in the vicinity of the impression. These defects also govern to a large extent the elastic recovery of the TBC during unloading, which is taken as a measure of stiffness in depth sensitive indentation [16]. Since local heterogeneities exist in the TBC, typically a large scatter of data is obtained. The summarising results of the indentation tests, which are plotted in Fig. 3, represent the characteristic values derived from a statistical Weibull analyses of at least 30 indentation measurements.
A stiffness of 45 GPa results from indentations with 1 N maximum load parallel to the spraying direction. As has been reported elsewhere [11] the apparent stiffness increases with decreasing indentation load. Obviously, the more the impression size approaches the dimensions of a single spraying splat, the more the bulk properties of dense zirconia dominate the stiffness. In fact, nano-indentation results with apparent stiffness values of about 135 GPa have been published previously [12]. But it should be also noted that in addition to the higher lateral resolution of indentation measurements, the testing method also generates compressive stresses which contribute to a higher modulus by crack closure.
The mechanical microprobe of an indentation test also allows elastic measurements in the cross-section of the thin 300 μm TBCs, i.e. perpendicular to the spraying direction. Thus anisotropy effects of the lamellar microstructure are recognised. The stiffness is about 65 % higher in the perpendicular direction compared to measurements parallel to the spraying direction (Fig. 3). The elastic anisotropy correlates qualitatively with the geometrical differences between inter- und intra-splat cracks. Obviously the large gaps between the splats make the TBC more compliant than the narrow intra-splat cracks (Fig. 1).

3.2 Bonded TBC

In the multi-layered thermal barrier components the TBC is bonded to the substrate via an oxidation resistant metallic interlayer (bond coat). The ceramic TBC has a lower thermal expansion than bond coat and substrate and thus experiences compressive residual stresses upon cooling from spraying or operation temperature. Considering the crack closure effect of a compressive stress for the defect permeated TBC microstructure a higher apparent stiffness can be expected in the case of bonded TBCs. Compared to free-standing TBCs the results from indentation tests (Fig. 3) show an increase by more than a factor of two in the bonded state, i.e. 98 GPa compared to 45 GPa [11]. By superimposing an external tensile stress to the bonded TBC, e.g. in a bending test, the compressive mismatch stress is reduced and accordingly the apparent indentation stiffness decreases [17].

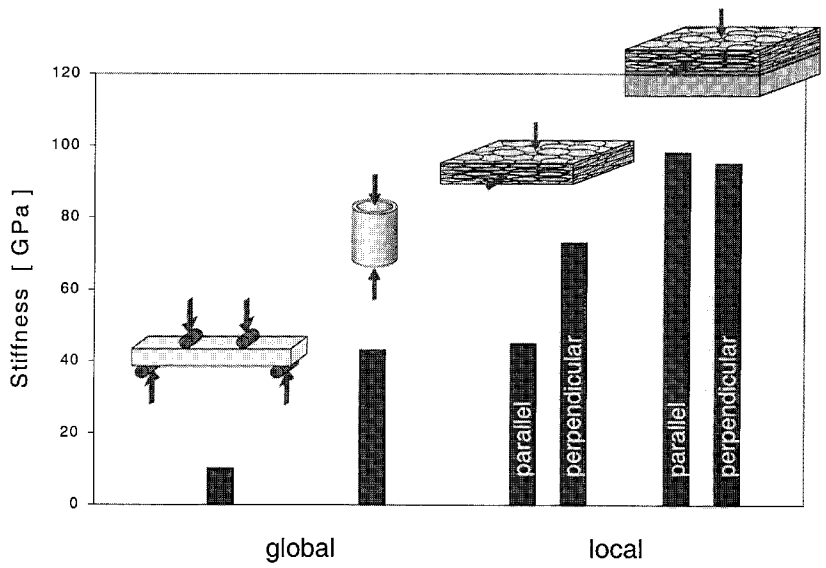


Fig. 3: Summarising plot of APS-TBC stiffness results from global and local testing methods.

3.3 Heat treatment

The above stiffness results of free-standing and bonded TBCs in as-sprayed condition emphasise the importance of crack-shaped defects, i.e. large vertical cracks, inter- and intra-splat cracks for the elastic behaviour. In service the coated gas turbine components face severe heat exposure and develop temperature gradients in the regime between 1200°C (free surface) and 950°C (interface to bond coat). Simulation of the heat exposure by isothermal annealing at temperatures between 950°C and 1200°C with dwell times up to 100 h yield TBC stiffening. Fig. 4 shows results from indentation tests with separated TBCs, measured at room temperature after annealing. The stiffness increases with annealing temperature and time, e.g. a 50 % increase is obtained after 100 h annealing at 1200°C. Similar results and even larger stiffing effects (factor 2) are reported in literature for the same annealing conditions [14].

However, stiffening might be less pronounced in the case of bonded TBCs due to straining effects related with the larger thermal expansion of substrate and bond coat [13].

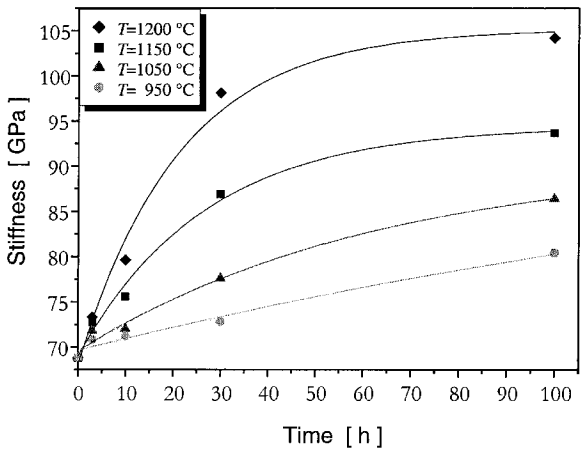


Fig. 4 Stiffness increase of APS-TBC after annealing at temperatures between 950°C and 1200°C.

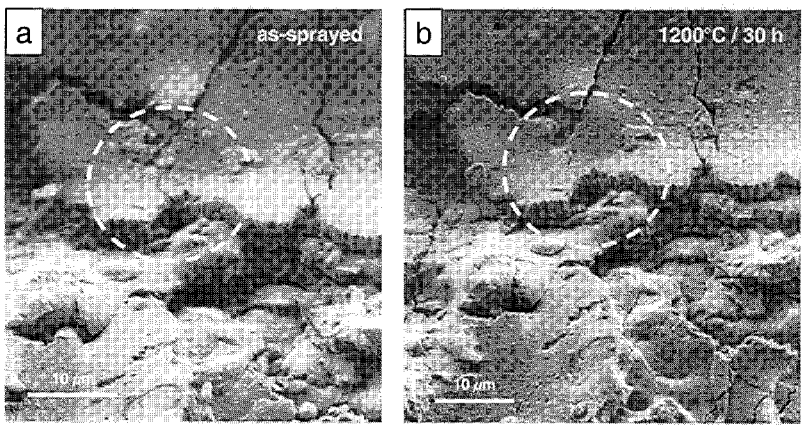


Fig. 5: Microstructural changes in TBC due to annealing. a) as sprayed condition and b) after heat treatment at 1200°C for 30 h. The encircled healing of an intra-splat crack documents the general impression of preferred densification within rather than between the spraying splats.

Microstructurally, the stiffening of the TBC can be again attributed to changes in the morphology and population of the defects with crack shape. With increasing temperature the intra-splat cracks tend to heal. Also sintering effects between the spraying splats, i.e.

stiffening by increase of the contact area, may occur. Fig. 5 shows a heat treatment experiment with inspection of exactly the same microstructural location prior and after annealing. Similar to the densification mechanism recognised in Fig.5, in general closure and healing of intra-splat cracks is observed up to 1200°C. This finding is in agreement with similar interpretations of in situ small angle neutron scattering (SANS) studies of TBCs [18]. However, since evidence of preferred sintering and elimination of inter-splat cracks is also given in literature [8], future work should address the stiffening aspect by heat treatment in more detail. In particular, TBCs with a systematic variation of the ratio between inter- and intra-splat cracks should be examined.

4. Conclusions

The mechanical tests with free-standing and bonded APS-TBC of 8 wt.% YSZ revealed systematic variations of stiffness, when global measurements (bending-, compression-test) are compared to those with high lateral resolution (indentation tests). Also the anisotropy of the lamellar microstructure and the existence of residual TBC stresses have significant influence on the elastic behaviour. Moreover the TBC stiffness increases after heat exposure.
The results of the present work strongly indicate that a matrix of stiffness values rather than a single unique elasticity modulus has to be considered when estimating the thermoelastic and fracture behaviour of TBCs in service. With respect to a global elasticity treatment, in particular, the differences between tension and compression are of interest. Complimentary, the stiffness data from measurements with high lateral resolution seem necessary, when modelling of TBC failure mechanisms is intended.
Finally it should be emphasised again that TBC stiffness generally increases with thermal exposure, but may be also significantly influenced by the residual stress state of the TBC. A quantitative description of the elastic behaviour of TBCs thus becomes even more complex.

5. Acknowledgements

The authors are grateful to Dr. R. Vaßen and K.H. Rauwald, who provided the plasma sprayed thermal barrier composites and to J. Mönch for his experimental support.

References

[1] J.Wigren, L. Pejryd, "Thermal Barrier Coatings – Why, How, Where and Where to", Proceedings of the 15th International Spray Conference, 1998, Nice, France, pp. 1531 – 1542, ASM International, Materials Park, OH, 1998
[2] N. P. Padture, M. Gell, E.H. Jordan „Thermal Barrier Coatings for Gas Turbine Engeine Applications", Science, Vol 296 (2002) 280-284
[3] G. Blandin, "Thermomechanical Behaviour of Plasma-Sprayed Multilayer Composites for Thermal Barriers" (in German), Doctoral Thesis, University of Aachen (2001)
[4] A. Kucuk, C.C. Berndt, U. Senturk, R.S. Lima, C.R.C. Lima, "Influence of Plasma Spray Paramters on Mechanical Properties of Yttria Stabilized Zirconia Coatings: Four Point Bend Test", Mat. Science and Engineering A284 (2000) 29-40
[5] S.-H. Leigh, C.-K. Lin, C.C. Berndt, "Elastic Response of Thermal Spray Deposits under Indentation Tests", J. Am. Ceram. Soc. 80 [8] 2093-99 (1997)

[6] A. Wanner, E. Lutz, "Elastic Anisotropy of Plasma Sprayed, Free-Standing Ceramics", J. Am. Ceram. Soc. 81 [10] 2706-708 (1998)
[7] T.W. Clyne, S.C. Gill, "Residual Stresses in Thermal Spray Coatings and Their Effect on Interfacial Adhesion: A Review of Recent Work", Journal of Thermal Spray Technology, 5 (4) (1996) 401-418
[8] J.A. Thomson, T.W. Clyne, "The Effect of Heat Treatment on the Stiffness of Zirconia Top Coats in Plasma-Sprayed TBCs", Acta Mater. 49 (2001) 1565-1575
[9] S.R. Choi, D. Zhu, R.A. Miller, "Deformation and Strength Behaviour of Plasma Sprayed ZrO_2 – 8Wt% Y_2O_3 Thermal Barrier Coatings in Biaxial Flexure and Trans-Thickness Tension", Ceramics Engineering and Science Proceedings, Vol. 21, 2000, p. 653-661
[10] A.J. Allen, G.G. Long, Y. Wallace, Y. Llavsky, C.C. Berndt, H. Hermann, "Microstructural changes in YSZ Deposits During Annealing", in Unified Thermal Spray Converence (1999), ed. E. Lugscheider and P.A. Kammer, DVS,1999, p. 228-233
[11] D. Basu, C. Funke and R.W. Steinbrech, "Effect of Heat Treatment on Elastic Properties of Separated Thermal Barrier Coatings", J. Mat. Res., 14 [12] (1999) 4643-50
[12] J.A. Thompson, T.W. Clyne, "Stiffness of Plasma Sprayed Zirconia Top Coats in TBCs", in United Thermal Spray Conference", ed. E. Lugscheider and P.A. Kammer, DVS,1999, p. 835-840
[13] J.A. Thompson, W. Yi, T. Klocker and T.W. Clyne, "Sintering of the Top Coat in Thermal Spray TBC Systems Under Service Conditions", in Superalloys 2000, T.M. Pollock et al. (eds.), Seven Springs, USA, TMS (2000) p. 685-692
[14] G. Thurn, G.A. Schneider, H.-A. Bahr, F. Aldinger, "Toughness Anisotropy and Damage Behavior of Plasma Sprayed ZrO_2 Thermal Barrier Coatings", Surface and Coatings Technology 123 (2000) 147-158
[15] R.W. Steinbrech, "Thermomechanical Behavior of Plasma Sprayed Thermal Barrier Coatings", Proceedings of the 26th International Conference on Advanced Ceramics and Composites, Cocoa Beach, 2002, in print
[16] W.C. Oliver and G.M. Pharr, "An Improved Technique for Determining Hardness and Elastic Modulus Using Load and Displacement Sensing Indentation Experiments", J. Mater. Res.,7 (1992) 1564-1583
[17] D. Basu, A.K. Mukhopadhyay, L. Singheiser, R.W. Steinbrech and R.Vasen, "Influence of Residual Stress on Elastic Behaviour of Thermal Barrier Coatings", to be published
[18] J. Ilavsky, G.G. Long, A.J. Allen, C.C. Berndt, "Evolution of the Void Structure in Plasma Sprayed YSZ Deposits during Heating", Mat. Science and Engineering A 272 (1999) 215-221

DEFORMATION BEHAVIOUR OF A LOW PRESSURE PLASMA SPRAYED NiCoCrAlY BOND COAT UNDER SHEAR LOADING AT TEMPERATURES ABOVE 750°C

P Majerus, R W Steinbrech, R Herzog, F Schubert

Research Centre Juelich (FZJ)
Institute for Materials and Processes in Energy Systems (IWV-2)
52425 Juelich, Germany

Abstract

A new testing method has been developed to analyse the visco-plastic properties and the deformation behaviour of thin bond coat layers in thermal barrier systems for advanced gas turbines. The test allows a symmetrical, in-plane shear-deformation to be applied to specimens with thermal barrier coatings. At temperatures above the ductile-brittle transition temperature, the MCrAlY bond coat exhibits a much higher ductility than the CMSX-4 substrate and the ceramic top coat. Thus it is possible to concentrate nearly the all the shear deformation in the bond coat. Relaxation experiments as well as tests with constant load have been performed on samples with bond coat thicknesses of 70 µm and 130 µm. The maximum observed in-plane displacement between substrate and ceramic coat was 500 µm. It could be demonstrated that the creep behaviour of the bond coat was independent of the loading condition. Thus power law equations for shear creep deformation in the temperature regime 750-1050°C could be derived. The Norton creep factor n between 3.3 and 4.4 was obtained, which increased with decreasing temperature.

Keywords: shear test, MCrAlY, bond coat, relaxation, creep

1. Introduction

An effective measure to increase the efficiency of land-based gas turbines is to increase the operation temperature, but the more arduous service conditions demand the development of new materials. Major improvements have been achieved in recent years with the introduction of single crystal superalloys for the blades of the first row [1]. Further enhancement has been realised with the introduction of thermal barrier coatings (TBCs). To draw maximum advantage from such coatings it has to be guaranteed that no major delamination of TBC occurs during service. Although the mechanisms that drive failure of the complex thermal barrier composites are not well understood, it is generally agreed that the adherence of TBC strongly depends on bond coat creep behaviour [2]. Stress relaxation of the bond coat at high temperature is expected to result in significant increase of out-of-plane residual stresses after cooling down to room temperature. Brindley [3] could demonstrate that the residual stresses calculated for different bond coats are directly correlated with the measured thermal cycle lives. On the other hand, bond coat deformation at high temperature reduces the growth stresses of the oxide layer (TGO). In any case experimental data of the deformation behaviour are essential for modelling the stress situation and the damage process.

In the present study, the creep properties of the bond coat were investigated at elevated temperatures using a specially developed symmetrical shear testing method. Creep shear tests have been described by various authors [4, 5], but an application to TBC coatings has not yet been reported in the open literature. In contrast to classical material testing, the shear test

allows the bond coat to be deformed in the thickness dimensions relevant for gas turbine applications. In addition several effects, such as interface roughness and inter-diffusion processes, which might affect the deformation behaviour, are also considered. At temperatures above 750°C, in the regime of higher bond coat ductility, exclusively the bond coat deforms. Up to now the new test was applied to obtain information about the creep behaviour of the bond coat.

The paper describes details of the test method and experimental results obtained from relaxation and constant load creep experiments in the temperature range between 750°C and 1050°C. From both types of experiment, a unifying set of parameters is deducted, describing the shear deformation with a temperature-dependent power law equation.

2. Experimental

2.1 Specimens and material

The single crystal Ni-based superalloy CMSX-4 was used as substrate material. 5 mm wide rectangular bars of CMSX-4 were coated on the two side faces with a low pressure plasma sprayed (LPPS) bond coat of average thickness of 70 µm and 130 µm for two different specimen variants respectively. The chemical composition of the bond coat is given in Table 1. An air plasma sprayed thermal barrier layer (ZrO_2/8wt%Y_2O_3) of 2 mm thickness was coated onto the bond coat. All plasma spraying was carried out at the Research Centre Juelich (IWV-1). After coating, thin specimen slices were machined from the bar. Figure 1 shows the specimens in the as-received state, the match-head indicates the scale, the dimensions of the specimens varying between 5 and 10 mm in length and 1.8 to 2.3 mm in height. More details about manufacturing and heat treatment of the specimens are given elsewhere [6].

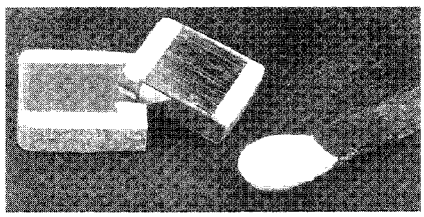


Figure 1: Symmetric shear creep test specimens compared to the size of a match-head

Ni	Co	Cr	Al	Y
48.3	21.1	17.1	12.6	0.61

Table 1: Chemical composition of the bond coat in wt. % (powder analysis from the producer).

The microstructure of the bond coat before testing was mainly composed of the cubic body centred β-phase (B2-structure) and the cubic face centred γ-phase. The volume fractions were about 65% β-phase and 28% γ-phase. The volume fraction was determined from optical micrographs using the analySIS software programme. By this method a remaining 7% volume cannot be assigned to one of the phases. Both phases are homogeneous, texture-free and distributed over the coating thickness. Because the morphology of the relatively fine phases was not comparable to any geometrical shape, reasonable quantification of their size could not be obtained. Average distances between phase boundaries, as estimated by counting the number of intersections with a defined line, were around 7-8 µm.

2.2 Symmetric shear creep testing method

The experimental approach is based on the simple concept of a symmetric shear test, illustrated in Figure 2. The device, made of alumina, is divided in an upper and lower part,

connected by guidance rods allowing only vertical movements. The lower part is designed with a plane top surface 5.3 mm wide with a 3-mm deep rectangular slot in the centre. This allowed positioning and centring of the specimen with respect to pushing piston and load support. In order fix the specimen to its position after adjustment, the upper and lower part were pressed together. The upper part guided the pressure punch. The punch was of a rectangular shape (5 x 10mm) at the contact side with the specimen and widened to a large cylindrical shape of 30 mm diameter at the top. The load was applied by an electromechanical testing machine. A displacement sensor (LVDT-system) monitored the shear deformation as indicated in Figure 2 (left side). The temperature inside the electric resistance furnace was controlled with a single Pt-Pt/Rh thermocouple positioned close to the specimen. Preliminary temperature calibration tests using a supplementary thermocouple fixed to the sample showed a homogeneous temperature in the relevant testing volume after approx. 45 minutes of isothermal soaking. All the tests were conducted in ambient atmosphere.

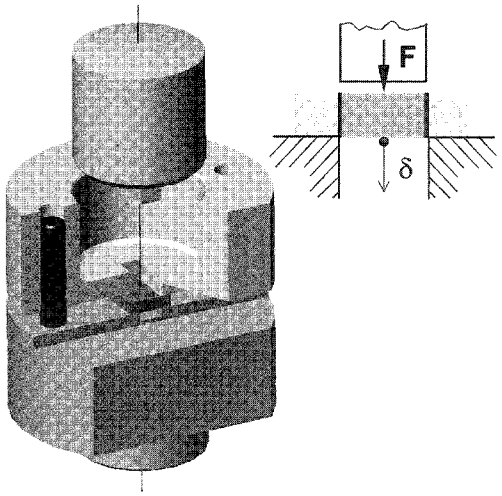


Figure 2: Device (left side) and concept (right side) for double shear creep testing. The displacement δ is measured at the lower surface of the specimen.

2.3 Testing procedure

The closed loop system of the testing machine allowed load controlled and displacement controlled operations during the shear tests. Loads up to 1000 N and displacements between –1000 µm and +1000 µm could be achieved. The experimental load/displacement data were converted into the deformation specific values shear stress and shear rate. The equation (1) for the calculation of the shear stress considers the reduction in shear area due to a continuous displacement of the substrate relative to the TBC. More details about the specific interpretation of the measured data and the corrections of the displacement measurements will be discussed later in this paper.

$$\tau = \frac{F}{2 \cdot h_{sp.} \cdot l_{sp.}} \cdot \left(\frac{h_{sp.}}{h_{sp.} - \delta} \right) \qquad \gamma = \frac{\delta}{d_{BC}} \qquad (1)$$

τ = shear stress [MPa]; F = load [N]; $h_{sp.}$ = high of the specimen [mm]; $l_{sp.}$ = length of the specimen [mm]; δ = displacement [mm]; γ = shear strain; d_{BC} = thickness of the bond coat

3. Results

3.1 Deformation behaviour

Figure 3 shows the shape of a deformed bond coat after a large total deformation, $\delta \approx 500$ µm ($\gamma > 700\%$) at 950°C. At such high temperatures, the MCrAlY material was able to sustain large deformations without losing contact to the substrate and the TBC. On the other hand, the sharp edges of the substrate material and the TBC demonstrate that neither noticeably deformed. Both interfaces remained parallel over the whole deformation process, indicating that the test was producing the expected shear deformation with almost no bending effects. This favourable shear behaviour is probably due to the very low and ideal ratio between coating thickness and specimen high ($d_{BC}/h_{Sp.} < 1/12$).

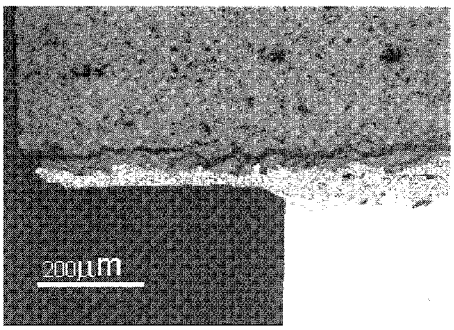


Figure 3: Optical micrograph of a deformed bond coat tested at 950°C with a total displacement of approx. 500µm.

The delamination crack in the TBC (Figure 3) probably developed after the creep test during cooling to room temperature. Since the shrinkage of the metal substrate was higher than that of the ceramic punch thermal mismatch stresses normal to the interface occurred. Superimposed shear stress concentrations on the specimen surface as described by Zhu et al. [7], certainly increased the trend for TBC delamination. The probability for the occurrence of such cracks and even complete delamination of the TBC increased with increasing shear displacement.

3.2 Relaxation experiments

Displacement controlled stress relaxation tests were conducted at temperatures between 750 and 1050°C. After initial deformation at constant displacement rate up to a certain load level, the movement was stopped and the displacement was kept constant. The load decrease was monitored as a function of time for up to 5000 s after the strain signal was kept constant. The loading sequence was then continued with an increased displacement rate to a significantly higher load. Subsequent relaxation followed. The loading sequence for two strain controlled relaxation experiments with a single specimen is schematically illustrated in Figure 4. Up to four sequences were performed, applying displacement rates $\dot{\delta}$ between 0.1 and 100 µm/min during straining.

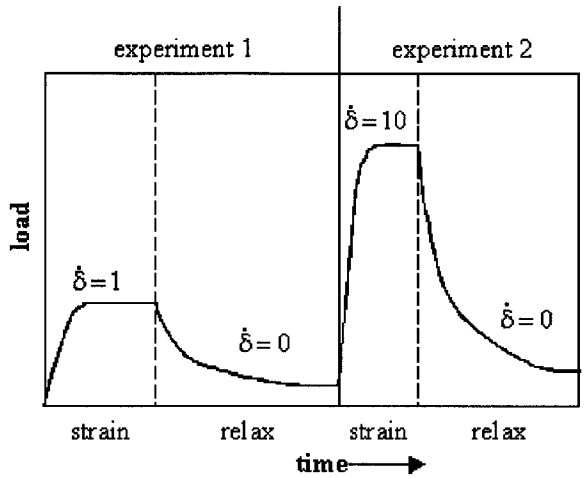


Figure 4: Schematic diagram of loading and relaxation sequences used to determine relaxation behaviour. Up to four sequences, have been performed, applying displacement velocities $\dot{\delta}$ between 0.1 and 100 µm/min during straining to reach each time an increased stress level.

The relaxation results are conveniently plotted as log stress rate versus log stress curves, which allows comparison of the relaxation data obtained from different stress levels. Figure 5 compares four successive relaxation experiments conducted at 1050°C. Although there is a relatively large scatter of data for low stresses it is possible to fit the data by a power law relationship. Regardless of the starting stress and the accumulated deformation, the same creep relaxation mechanism seems to be activated. This effect has also been observed by Brindley [3] in multiple creep and relaxation tests with bulk MCrAlY specimens under tension.

Shear relaxation experiments with specimens of different high or length showed comparable results. This indicates an excellent reproducibility of the test.

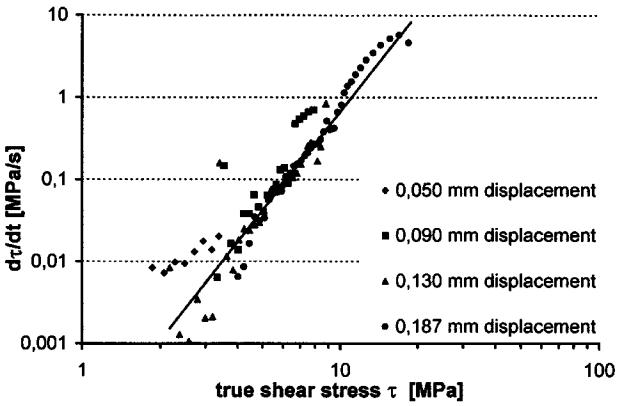


Figure 5: Stress rate versus stress data points determined from the relaxation curves of a single sample at 1050°C. Relaxing was initiated from different starting stresses and accumulated deformation.

3.3 Constant load experiments

The constant load experiments were conducted in the same temperature regime as the relaxation tests, but exclusively with specimens of 130 µm bond coat thickness. The load was increased with a rate of 50N/s until a pre-defined load was reached. This load was then kept constant and the displacement was monitored as a function of time. Tests were mainly conducted until secondary creep or minimum creep rate was reached. In contrast to the relaxation experiments, each creep test was conducted with a new specimen. In Figure 6 data of 4 different applied shear stresses at 950°C are displayed in a typical shear rate versus shear

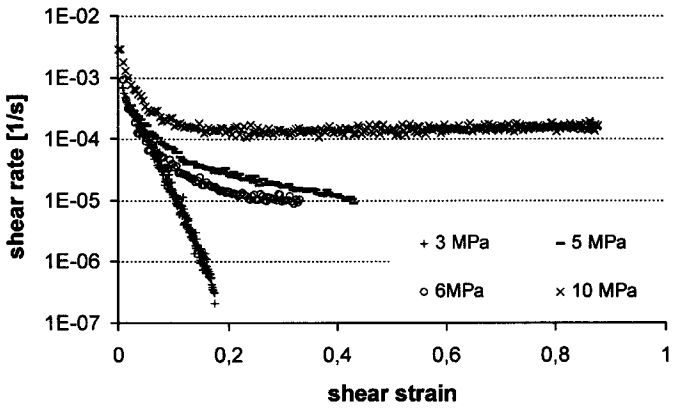


Figure 6:
Shear rate versus shear strain for 4 different shear stresses at 950°C.

strain plot. The shear strain is normalised to the displacement value measured after the load was applied. The minimum creep rates obtained by these experiments are used in Figure 8 to describe secondary creep.

5. Discussion

The described symmetric shear creep test proved to be successful but limitations with respect to load range need to be addressed first. At high shear stresses above 30 MPa, the probability of failure of the TBC increases. Especially the constant load experiments are sensitive to an instantaneous fracture of the ceramic coating, probably because the load is applied more spontaneously. The lower limit for shear creep testing range is given by a small drift of the displacement signal (<1 μm/h). Thus measured shear rates below 2×10^{-6} 1/s cannot be considered as reliable results.

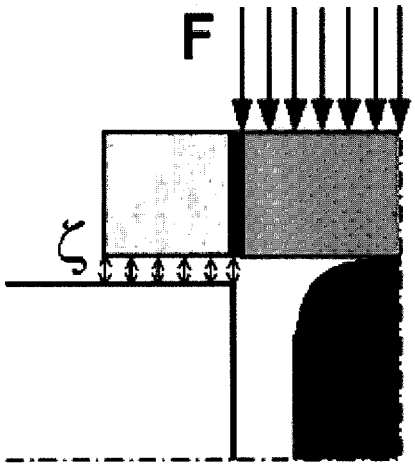


Figure 7:Load dependent gap between specimen and lower part of the test device, influencing the displacement signal

Within the regime of valid relaxation experiments a higher relaxation rate was observed with specimens of thicker bond coat. This indicates that either the bond coat thickness has an influence on the creep behaviour and creep mechanisms or a systematic error occurs during testing. As the morphology of γ-phase and β-phase did not change and differences in the chemical composition could not be detected, the first explanation seems rather unlikely. On the other hand tests with stiff dummy specimens of different size, always resulted in a displacement signal while increasing the load. Detailed analyses revealed that the

displacement resulted partially from the elastic deformation of the loading piston (~0.5 µm at 1000 N), and from small gaps at surface to surface contacts. Figure 7 shows as an example a possible gap between specimen and testing device.

The measurements revealed a reproducible effect at loads between 1000 N and 200 N which could be described mathematically using a linear approach ($d\zeta/dF = 5 \times 10^{-6}$ mm/N, where ζ is the displacement correction factor). Below 200 N the contact effect is not reproducible and changes with different specimen sizes and different temperatures.

The relaxation data were corrected, neglecting relaxation loads below 200 N by applying the equations:

$$\dot{\gamma}_{tot} = \dot{\gamma}_{inel.} + \dot{\gamma}_{el.} = \dot{\gamma}_{inel.} + \frac{1}{G} \cdot \left(\frac{d\tau}{dt} \right) = \frac{1}{d_{BC}} \cdot \frac{d\zeta}{dF} \cdot \frac{dF}{dt} \tag{2}$$

(3)

where G = shear modulus [MPa] (measured by the use of the resonance method : $G_{1050°C}$ = 21.6 GPa, $G_{950°C}$ = 32.2 GPa, $G_{850°C}$ = 40.2 GPa, $G_{750°C}$ = 45.8 GPa; τ = shear stress; d_{BC} = bond coat thickness [mm]; ζ = displacement correction factor [mm]; F = force [N]; $h_{sp.}$ = high of the specimen [mm]; $l_{sp.}$ = length of the specimen [mm]; δ = measured displacement [mm]

The equation (3) allows calculation of a shear rate for each load measured during the relaxation. The data couples (inelastic shear rate versus load and shear stress, respectively) obtained from equation (3) can be plotted as shown in Figure 8 and interpreted as a description of secondary creep of the bond coat under shear loading. Confirmation is given by the fact that the data points based on relaxation experiments (and performed with samples of different bond coat thickness) coincided with the results of minimum shear rate versus shear stress, measured within the steady load experiments. Power law approximations of creep under shear load could be given for the four temperatures. The stress exponent was 3.3 at 1050°C and increased with decreasing temperature to a value of 4.4 at 750°C.

4. Conclusion

A symmetric shear technique for testing bond coat creep deformation in a thermal barrier composite has been introduced. Above 750°C large deformations of the bond coat material between CMSX-4 and YSZ-TBC are possible. Performing two types of experiments, relaxation and creep, a set of parameters describing secondary creep could be given. Additionally the reliability, but also the limits of this testing method were elaborated.

5. Acknowledgements

The authors are grateful to Dr. R. Vaßen and K.-H. Rauwald for plasma spraying the coatings and J. Mönch for his support in the carrying out the shear tests.

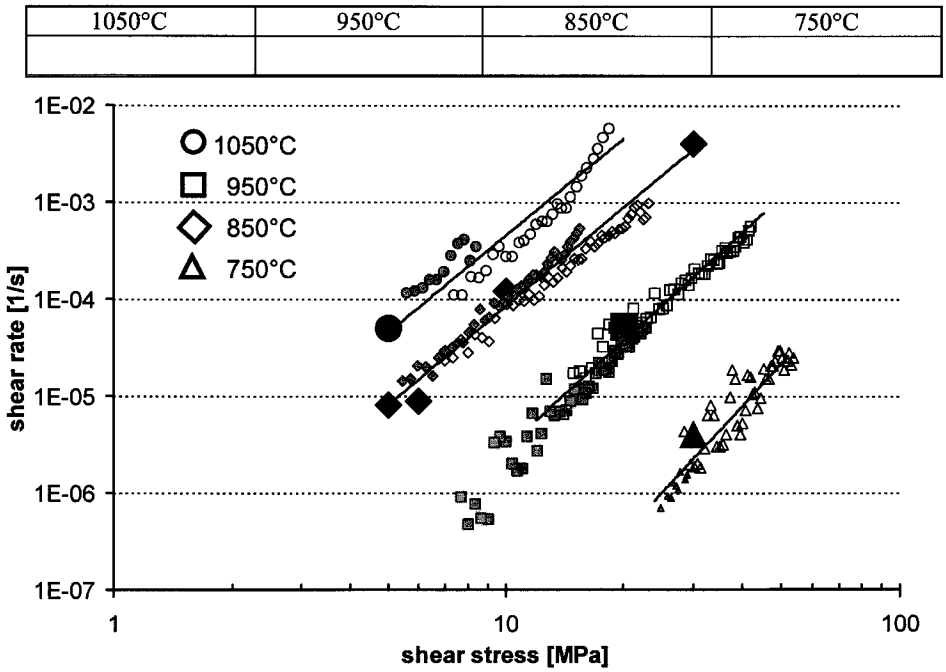


Figure 8: Minimum shear rate versus shear stress. The large filled symbols represent minimum creep rates of constant load experiments, symbols with grey background (d_{BC} = 130μm) and open symbols (d_{BC} = 70 μm) represent calculated shear rates from the relaxation experiments. In the table above, the mathematical relationships for the line fits in the analysed temperature range are listed.

6. References

[1] T. Rieck, F. Schubert, Growth of Small Fatigue Cracks in the Single Crystal Superalloys SC16 and CMSX-4, Proceedings of the 6th Liège Conference, volume 5, part2, 1998

[2] J.A. Haynes, Potential Influences of Bond Coat Impurities and Void Growth on Premature Failure of EB-PVD TBC's, Scripta Materialica 44, 2001

[3] W.J. Brindley, Properies of Plasma Sprayed Bond Coats, NASA Conference Publication 3312, 1995

[4] D. Y. Seo, C. H. Wu, T. R. Bieler, Shear creep deformation in poly-synthetically twinned (PST) Ti-47Al-2Nb-2Cr with <110> and <112> orientations, Materials Science and Engineering, A239-240, 1997

[5] C. Mayr, G. Eggeler, G.A. Webster, G. Peter, Double shear creep testing of superalloy single crystals at temperatures above 1000°C, Materials Science and Engineering A199, 1995

[6] P. Majerus, J. Mönch, R.W. Steinbrech, R. Herzog, F. Schubert, Stress Relaxation Behaviour of the Low-Pressure-Plasma-Sprayed-NiCoCrAlY Bond Coat PWA 1386-2 at Temperatures above 750°C, Proceedings of the MATERIALS WEEK, Munich 1.-4. October, 2001

[7] D. Zhu, L.J. Ghosn, R.A. Miller, Effect of Layer-Graded Bond Coats on Edge Stress Concentration and Oxidation Behavior of Thermal Barrier Coatings, 193rd Meeting of The Electrochemical Society, San Diego, 1998

VISCO-PLASTIC PROPERTIES OF SEPARATED THERMAL BARRIER COATINGS UNDER COMPRESSION LOADING

S. Heckmann, R. Herzog, R. W. Steinbrech, F. Schubert, L. Singheiser

Institute for Materials and Processes in Energy Systems 2, Research Centre Jülich, Germany

Abstract

Thermally induced stresses in the vicinity of the metal/ceramic interface affect substantially the integrity of thermal barrier coatings (TBCs) for advanced gas turbines. The stress level in the TBC near the interface is controlled by the thermoelastic mismatch of metallic bond coat and ceramic top coat and is also influenced by time dependent deformation and stress relaxation at high temperature. In order to characterize the deformation properties of plasma-sprayed TBCs, thin, separated coatings of zirconia stabilized with 7-8 wt% yttria and approximately 11-12% porosity have been prepared and were subjected to isothermal constant compression load tests at various temperatures (RT, 850, 950, 1050 and 1150°C). Additionally, the elastic modulus has been measured using unloading steps.

A continuously decreasing deformation rate was observed during test duration up to a maximum compression creep strain of 2.5% at 1150°C. A time dependent deformation response after load application has also been observed at RT. The deformation rates and the extent of primary creep at 1150°C are similar to those of partially stabilized zirconia (3 mol% yttria, grain size: 0,3-0,8 μm), but significantly different from 8YSZ (grain size: 2-7 μm). The deformation properties are discussed in comparison with the deformation properties of dense YSZ. The elastic moduli increased after constant compression loading for temperatures $\geq$ 950°C. The maximum increase from approximately 20 GPa up to 120 GPa was found at 1150°C after a time dependent compressive deformation of 2.5%.

Keywords: thermal barrier coating, visco-plastic properties, time dependent deformation, elastic modulus

Introduction

Coating systems that provide corrosion protection and thermal insulation are widely used to improve gas turbine efficiency and durability of high temperature components. Currently used protective coating systems consist of a ceramic thermal barrier coating (TBC) of zirconia partially stabilized with yttria and a metallic corrosion protective layer (bond coat, BC) between the structural material and the TBC. Under service conditions, the metal/ceramic interface (BC/TBC) is frequently the critical and life-limiting region of the composite. Due to different thermal expansion and the formation of a thermally grown oxide (TGO) at the BC/TBC interface, the interface regions are subjected to high stresses. However, the stress level is affected not only by thermoelastic properties but also by time dependent deformation and stress relaxation during prolonged exposure to high temperatures. Thus the time dependent deformation properties of both coatings are of particular interest. The present investigations focus on the deformation properties of plasma-sprayed thermal barrier coatings [1,2,3,4] under compression loading. Additionally, the deformation tests provided data for the elastic properties, which have been obtained as the strain response of the material during unloading steps.

Experimental

For the preparation of the TBC specimens, cylindrical rods of conventional low carbon steel (St35) with an outer diameter of 14 mm were coated with zirconia (partially stabilized with about 7-8 wt% yttria) by air plasma spraying (APS). The surface of the 650 μm thick coating

was ground and each cylinder was cut into segments of 12 mm length. The faces of the segments were ground at right-angles to the circumferential surface. Afterwards the steel core was dissolved completely by etching. After preparation, the separated thermal barrier coatings had a hollow cylindrical shape with an inner diameter of 14 mm, a height of 12 mm and a wall thickness of approximately 500 μm. The porosity of the ceramic coating was approximately 11-12% determined by mercury porosimetry. Fig. 1 shows an example of an as-prepared separated TBC.

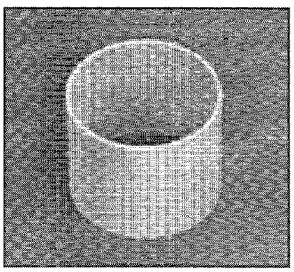


Fig. 1: Separated TBC; d = 14 mm, h = 12 mm, t_{TBC} = 500 μm.

The deformation experiments were carried out using an universal testing machine (Instron 1361, 5 kN load cell). The specimen compression was monitored using two opposing resistance foil strain gauges from Hottinger Baldwin Messtechnik, located near the top and bottom contact plane of specimen and push rod. The load was A 3-zone resistance furnace from Heraeus equipped with Pt/PtRh-thermocouples allowed temperature control within ± 3°C over the gauge length.

The tests have been carried out isothermally at RT, 850, 950, 1050 and 1150°C under constant compression load. The initially applied stress values were 40, 80 and 120 MPa. The load had been applied with approximately 0.5 MPa/s. The strain change during loading was substracted afterwards from the total strain. The presented compression strain vs. time or deformation rate vs. time curves comprise the strain data from the point when the load has reached its constant value. The maximum test duration was 100 h.

Results

Fig. 2 shows typical compression strain vs. time curves for an initial stress of 80 MPa at various temperatures. The deformation rate vs. time and vs. strain curves are shown in Figs. 3 and

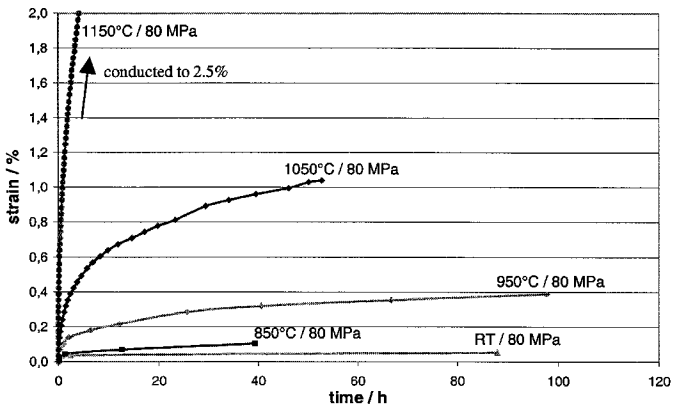


Fig. 2: Compression strain vs. time; influence of temperature for 80 MPa initially applied stress.

4. The deformation rate in all cases continuously decreased, namely until a deformation of 2.5% at 1150°C, 1% at 1050°C and 0.4% at 950°C has been reached during the test duration of 100 h. Even at room temperature, the deformation response after load application was time dependent. Fig. 5 represents the influence of stress on the deformation rate at 1050°C. The deformation rate increased only slightly with increasing stress in the range 40-120 MPa, when rate values are compared at equal times.

Fig. 6 shows the typical microstructure of cross-sections after preparation before testing and after constant loading at 1050°C (80 MPa, 1% deformation, 100 h). The microcrack density appeared to be lower after deformation, but a quantitative analysis has not yet been carried out.

The elastic modulus was measured at RT, 600, 850, 950, 1050 and 1150°C by monitoring the instantaneous strain change during rapid unloading to a stress value of approximately 1 MPa.

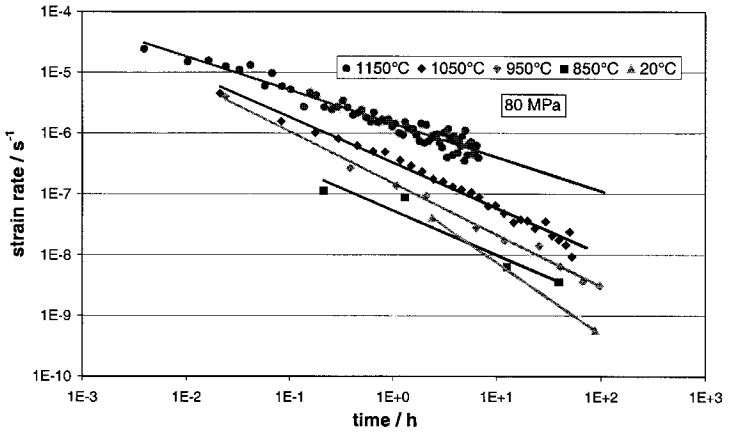


Fig. 3: Deformation rate vs. time; influence of temperature for 80 MPa initially applied stress.

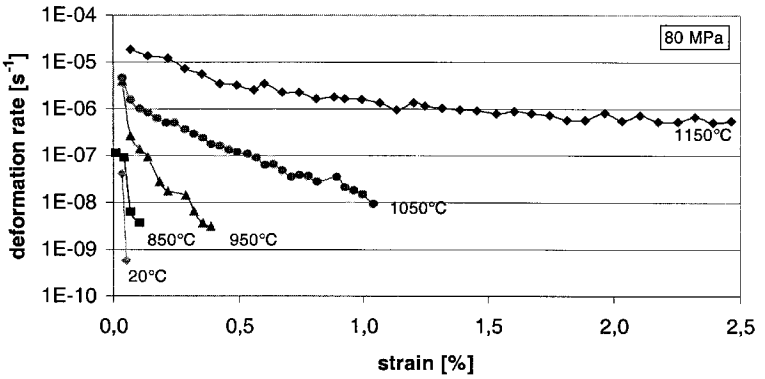


Fig. 4: Deformation rate vs. time; influence of temperature for 80 MPa initially applied stress.

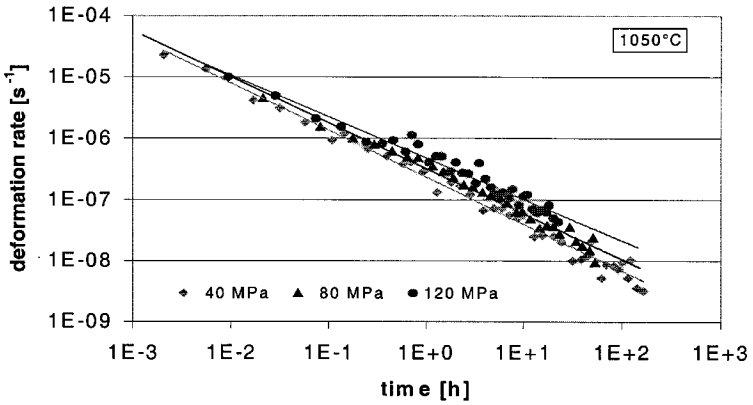


Fig. 5: Compression strain rate vs. time, influence of stress at a temperature of 950°C

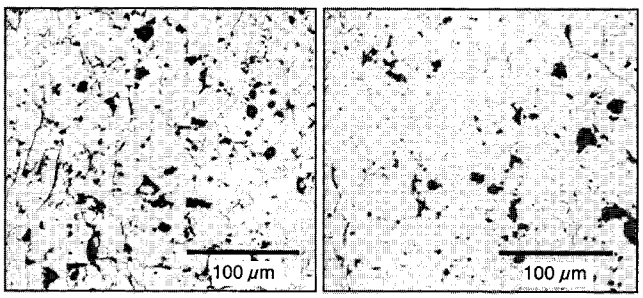


Fig. 6: Micrographs of cross-section of separated TBC; left: as prepared; right: after constant compression loading at 1050°C, 80 MPa for 100 h, deformation: 1%

The elastic modulus has been measured for as-prepared specimens without long-term compression loading and after time dependent deformation at constant load. Furthermore, repeated loading and unloading has been conducted (up to three times) with the as-prepared specimens in order to obtain information about a cyclic effect. The values for the elastic modulus are illustrated in Fig. 7 for various test temperatures. The resulting values vary between about 20 GPa at RT and 120 GPa at 1150°C after constant load deformation. The instantaneous strain drops were 0.1-0.3%.

At RT the elastic modulus determined from the first and the repeated loading and unloading steps as well as from the unloading after constant load deformation do not vary significantly. At 600°C the first and three repeated loading and unloading steps also resulted in similar values. At temperatures ≥ 1050°C, the repeated loading and unloading resulted in increasingly higher values than the first unloading with as-prepared specimens (one square and three diamond symbols at 1050°C and 1150°C, respectively). However, the elastic moduli after constant compression loading at temperatures ≥ 950°C (triangle symbols) were significantly higher than those after repeated unloading.

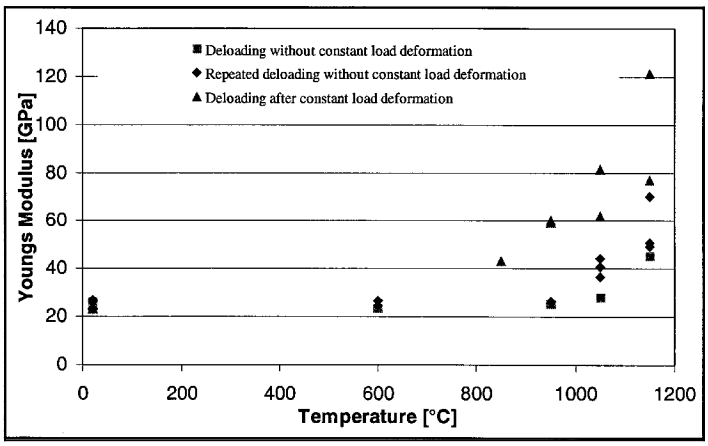


Fig. 7: Elastic modulus of separated TBCs at various temperatures deduced from the instantaneous strain change after a deloading step

Discussion

In order to compile the differences and similarities between the present plasma-sprayed TBC material and fully dense sintered YSZ with regard to their creep properties, some literature data (Lakki [5], Caspers [6], Nauer and Carry [7]) has been taken into account for comparison. These data, which had been determined on pure, dense 3 mol% and 8 mol% yttria doped zirconia, are summarised in Table 1. The dense, sintered zirconia materials did not contain glassy phases. The grain size, which had been shown to be one of the major deformation rate controlling parameters, varied between 0.3 and 6.8 μm. Note that an yttria content of 8 wt% is equal to about 5 mol%.

Characteristic microstructural parameters that may influence the deformation behaviour of the plasma-sprayed TBC material, are the total amount of porosity, the mean dimensions of spraying splats and the size of columnar grains within one splat. The present material is characterized by a splat thickness of approximately 10 μm and a lateral diameter of approximately 100 μm. The mean diameter of columnar grains within one splat is of the order of 0.5 μm. No evidence for glassy phase was found in the TBC material.

Regarding the creep data, a minimum deformation rate of $5 \cdot 10^{-7}$ s^{-1} was determined for the APS-TBC material at 1150°C at a stress of 80 MPa. This is a factor 25-500 higher than the steady state values of dense 8YSZ at the same temperature and approximately the same stress [5] (see Table 1). The minimum deformation rate of pure, partially stabilized, 3 mol% zirconia with 0.3 μm grain size at 1150°C and 75 MPa has been determined as $7 \cdot 10^{-6}$ s^{-1} [6]. In contrast to 8YSZ, this value is one order of magnitude higher than that of the TBC material. Furthermore, for 3 mol% material, minimum creep rates in the range of $1\text{-}8 \cdot 10^{-6}$ s^{-1} were determined at 1200°C and 75 MPa and a mean grain size in the range 0.4-0.8 μm [7]. Taking into account the temperature difference of 50°C between these and the present data of the TBC coating, the differences between the deformation rate values became relatively small.

	stress	min. deformation rate	respective deformation	stage	extension of prim. transient
APS-TBC, 1150°C	80 MPa	$5 \cdot 10^{-7}$ s^{-1}	3 %	primary transient	> 3 %
APS-TBC, 950°C	80 MPa	$7 \cdot 10^{-9}$ s^{-1}	0,4 %	primary transient	> 0,4 %
3YSZ, 1150°C grain size: 0,3 μm [6]	75 MPa	$7 \cdot 10^{-6}$ s^{-1}	-	steady state	1-4%
3YSZ, 1200°C grain size: 0,4 μm [7]	75 MPa	$7{,}4 \cdot 10^{-6}$ s^{-1}	-	steady state	-
3YSZ, 1200°C grain size: 0,8 μm [7]	75 MPa	$1{,}1 \cdot 10^{-6}$ s^{-1}	-	steady state	-
8YSZ, 1150°C grain size: 2,4 μm [5]	75 MPa	$2 \cdot 10^{-8}$ s^{-1}	-	steady state	< 0,2 %
8YSZ, 1150°C grain size: 6,8 μm [5]	75 MPa	$1 \cdot 10^{-9}$ s^{-1} (extrap.)	-	steady state	-

Table 1: Comparison of creep data for separated TBC and pure, dense 3PSZ and 8YSZ

In summary, it can be concluded that the minimum deformation rates of the TBC material are significantly higher (factor 25-500) than that of 8YSZ (8 mol% yttria, grain size: 2.4-6.8 μm) and comparable or lower (up to a factor of 16) than that of partially stabilized zirconia (3 mol% yttria, grain size: 0.3-0.8 μm).

A second criterion for a comparison of creep behaviour is the extent of the primary (transient) creep stage, i.e. the deformation which corresponds to the minimum of the deformation rate (transient strain). The values for the transient strain differ significantly for the present TBC material (> 3%) and 8YSZ (< 0,2%), whereas they are similar for the TBC coating and the partially stabilized material (1-4%).

Thurn et al [1] assumed that locally enhanced stresses at contact areas between splats could generate high local creep rates and could therefore be related to a certain extent to the high creep rates obtained from plasma-sprayed thermal barrier coatings. He explained the extended primary creep in the temperature range 900-1100°C partly by a homogenisation of initially highly enhanced local stresses. Zhu and Miller [2] argued that stress enhanced diffusion, fast diffusion paths along grain and splat boundaries, volume compaction and mechanical sliding may all contribute significantly to the macroscopic deformation. Furthermore it is conceivable that crack growth parallel to the load axis, which is known for some ceramic materials, affects the macroscopic deformation [8]. However, a systematic identification and understanding of the mechanisms that are rate controlling above 1000°C and which generate relatively high macroscopic deformation rates also at RT are not yet available.

In the case of 3 mol% yttria doped zirconia with a mean grain size in the range 0.3-0.8 μm, the authors reported superplastic deformation as rate controlling in the temperature range 1150-1200°C [6,7], as widely known. The deformation rates and transient strains in this temperature range are similar to those of the partially stabilized fine grained material and the plasma-sprayed TBC coatings. Even the mean diameter of the columnar grains within one splat (roughly 0.5 μm) lies within the grain size range of the compared 3 mol% material.

Therefore, superplastic contributions to the deformation of plasma-sprayed thermal barrier coatings above 1000°C cannot be excluded.

The elastic data that have been determined from the compressive deformation tests comprise the modulus of the as-prepared state of the investigated thermal barrier coatings, the change after constant compression loading at various temperatures for normally 100 h test duration and the effect of repeated loading and unloading.

The obtained RT values (20-30 GPa) are lower than values that had been determined on the same coating material using micro-indentation technique (70 GPa) [9]. Singh [10] reported values of 35 GPa for plasma-sprayed thermal barrier coatings measured by Knoop indentation. Data for the elastic modulus obtained from compression testing on plasma-sprayed 8YSZ were reported to be below 50 GPa [11].

The present data show a temperature effect in the range > 600°C (see Fig. 7) and confirm results of other workings. In the temperature regime up to 500°C, Beghini [12] stated no significant change in elastic behaviour using four-point bending tests. Szücs [13] investigated the elastic properties between room temperature and 1000°C by a dynamic three-point bending technique. Up to 600°C the modulus was roughly constant, but started to rise from 600 to 1000°C by a factor of 1.5.

The present investigations show that at 950°C the elastic modulus was a factor of two higher after constant compression loading for 100 h (80 MPa, 0.4% time-dependent deformation) than before creep testing. Annealing without stress loading, which had been investigated using micro-indentation technique on the same material, resulted in an increase of the elastic modulus of 18% after 100 h at 950°C [9]. At 1150°C the elastic modulus increased by more than a factor of four after constant compression loading for 100 h (80 MPa, 2.5% time-dependent deformation). In contrast, annealing for 100 h at 1150°C resulted in an increase of the elastic modulus of 50% [9]. This comparison shows that compressive deformation of plasma-sprayed TBCs results in a significantly larger increase of stiffness than annealing without stress loading. Even the process of (repeated) loading and unloading at 1150°C, which lasted less than 0.5 h, resulted in a larger increase of the elastic modulus (by a factor of three after three repeats of loading and unloading with respect to the RT value) than annealing for 100 h at this temperature.

Conclusions

The constant compression load tests on separated thin plasma-sprayed thermal barrier coatings at RT, 850, 950 1050, and 1150°C revealed high deformation values without failure of the coatings. The deformation rates in all cases continuously decreased during test duration. The minimum deformation rate values were significantly higher than those of dense, polycrystalline 8YSZ, but similar or lower than those of dense, fine-grained 3 mol% partially stabilized zirconia. Comparison of these data and consideration of the respective rate controlling deformation mechanisms led to the conclusion that superplastic contributions amongst others, which are currently discussed, cannot be excluded for deformation at temperatures above 1000°C. However, a systematic understanding of the time-dependent deformation of plasma-sprayed thermal barrier coatings is not yet available. Particularly, the time-dependent deformation at RT has not been understood.

The investigation of the elastic properties using unloading steps revealed that constant compression loading resulted in a fairly large increase of the elastic modulus for temperatures

≥ 950°C. The effect of compressive deformation for 100 h on the elastic modulus was significantly higher than that of annealing for 100 h. Even repeated loading and unloading at 1050 and 1150°C for short exposure times resulted in a larger effect than annealing for 100 h.

Acknowledgments

The authors are grateful to Dr. R. Vaßen and K.-H. Rauwald (IWV 1) for manufacturing the coatings and B. Werner (IWV 2) for conducting some of the deformation tests.

References

[1] G. Thurn, G.A. Schneider, F. Aldinger: *High-temperature deformation of plasma-sprayed ZrO_2 thermal barrier coatings*, Materials Science and Engineering, A233, 1997, 176-182

[2] D. Zhu, R.A. Miller: *Determination of Creep Behavior of Thermal Barrier Coatings Under Laser Imposed Temperature and Stress Gradients*, NASA Technical Memorandum 113169 (ARL-TR-1565), Nov., 1997

[3] J.T. DeMasi, K.D. Sheffler, M. Oritz: *Thermal barrier coating live Prediction Develoopement* (Phase I, Final Report), NASA Contractor Report 182230, Dec., 1989

[4] E.F. Rejda, D.F. Socie, T. Itoh: *Deformation behavior of plasma-sprayed thick thermal barrier coatings*, Surface and Coatings Technology, 113, 1999, 218-226

[5] A. Lakki, R. Herzog, M. Weller, H. Schubert, C. Reetz, O. Görke, M. Kilo, G. Borchardt: *Mechanical loss, creep, diffusion and ionic conductivity of ZrO_2-8 mol% Y_2O_3 polycrystals*, J. Europ. Ceram. Soc., 20 (2000), 285-296

[6] B. Caspers: *Hochtemperaturverformung von Zirkonoxidkeramiken*, Dissertation Universität Stuttgart, 1992

[7] M. Nauer, C. Carry: *Creep Parameters of Yttria doped Zirconia materials and superplastic deformation mechanisms*, Scripta met. 24 (1990), 1459-1463

[8] R.W. Trice, D.W. Prine, K.T. Faber: *Deformation Mechanisms in Compression-Loaded, Stand-Alone Plasma-Sprayed Alumina Coatings*, J. Am. Ceram. Soc., 83, 2000, 3057-3064

[9] R.W. Steinbrech: this conference

[10] J.P. Singh, M. Sutaria, M. Ferber: *Use of indentation technique to measure elastic modulus of plasma-sprayed zirconia thermal barrier coating*, Ceramic engineering & science proceedings, 18, 1997, 191-200

[11] K.F. Wesling, D.F. Socie, B. Beardsley: *Fatigue of Thick Thermal Barrier Coatings*, J. Am. Ceram. Soc., 77, 1994, 1863-1868

[12] M. Beghini, L. Bertini, F. Frendo, E. Giorni: *Determination of thermal sprayed coatings elastic modulus using four point bending test*, Surface Treatment III: Computer Methods & Experimental Measurements, 1997, 61-70

[13] F. Szücs: *Thermomechanische Analyse und Modellierung plasmagespritzter und EB-PVD aufgedampfter Wärmedämmschicht-Systeme für Gasturbinen*, Fortschr.-Ber. VDI Reihe 5, 518, 1998

STRUCTURE IN THE SURFACE LAYER OF COATED Ni-BASED SUPERALLOYS DURING ANNEALING IN OXIDATION ENVIRONMENT.

Jiří Švejcar, Karel Jiřikovský, Jan Krejčí

Dept. of Structure and Phase Analysis, PIME, FME, TU of Brno, Technická 2, 616 69 Brno
Czech Republic

Abstract

Different techniques were used to follow the structure changes caused by annealing of SC 16 and CMSX-4 single crystals with and without different plasma-sprayed coatings. Namely light microscopy, image analysis, SEM, and EDS microanalysis (some attempts were made to employ TEM), were used. Oxidation was also characterized by weight measurement. The results are complex. Briefly, it was shown that two diffusion processes govern structure development. First, the elements present in the substrate diffuse outward and interact with the elements of the coating. Second, oxygen penetrates the specimen and modifies the diffusion processes - diffusion of elements with high affinity toward oxygen is more rapid. Resulting structure in the surface layer then consists of different oxides (usually "sheet-like") and original superalloy structure in different stages of decay (coarsening of Ni_3Al particles, vanishing of LRO, recrystallization of original single crystal structure).

Keywords: superalloys, annealing, structure, diffusion, oxidation

Introduction

Two main problems must be coped with in the coated Ni-based superalloys namely: corrosion (mainly oxidation) resistance and structure stability at high temperatures. When superalloy single crystals are used, structure stability is more complicated as, apart from loss of LRO, we may encounter also loss of "single-crystallinity". Favorable mechanical properties of superalloys for extreme temperatures applications are the result of the strengthening effect of intermetallic long-range ordered $Ni_3(Al+Ti)$ γ'-phase. Usually the surface of superalloys is protected by various layers produced by plasma spraying or some other technique (e.g., aluminization), see e.g., [1,2]. Interaction between superalloy and coating at high temperatures with assistance of oxygen is very complex. Disappearance of existing (strengthening) phases and nucleation, and growth of (detrimental) new phases is accompanied by massive redistribution of elements in substrate and coating (see e.g. [3]). The extent of material affected is increasing with time and temperature. Our aim is to describe structure changes during the annealing in oxidation environment and eventually contribute to the identification of the causes.

Materials and Experiments

Two single crystal Ni-based superalloys were used as substrates.

(wt.%)	Ni	Cr	Al	Ti	Ta	Co	Mo	W	Re	Hf
SC 16	B	16.0	3.5	3.5	3.5		3.0			
CMSX-4	B	6.5	5.6	1.0	6.5	9.0	0.6	6.0	3.0	0.1

These superalloys were plasma coated by Ni, and by TBC coatings OT3 (93% Al_2O_3+3% Y_2O_3), PSZ (92% ZrO_2 + 8%Y_2O_3) and $ZrSiO_4$. Some specimens were provided with

NiCrAlY layer under the TBC coating. Different specimens were annealed for different time at temperatures from 850 °C to 1200 °C. Pure Ni coating was used because of its good adhesion and also to test the case when the coating consist of γ forming element only.

The structures were evaluated by usual metallographic techniques, image analysis, SEM + microanalysis and X-ray diffraction. Image analysis procedure developed for measurement of the thickness of different structural layers was described elsewhere [4].

The process of oxidation was also followed by weight measurement.

Results and Discussion

Generally processes taking place in the material during annealing could be described as follows: Structural changes are controlled by diffusion of γ'-phase forming elements from substrate into the coating (or toward the free surface), some elements present in coating into the substrate and diffusion of oxygen into the both materials. The diffusion of oxygen (especially at higher temperature) gradually becomes the main factor because all elements present with high affinity to oxygen follow its diffusion paths. Deficiency of these elements in the specimen interior then causes further diffusion in remaining material and dramatic structural changes.

The prevailing structure on cross section consists of original coating, in the case of uncoated specimen it is substituted by scale, below the coating there is a complex layer of oxides and diffusion interlayer. Under the original superalloy surface there is a region where strengthening particles of γ' $Ni_3(Al+Ti)$ phase have dissolved and recrystallisation of original single crystal structure has taken place, Fig.1.

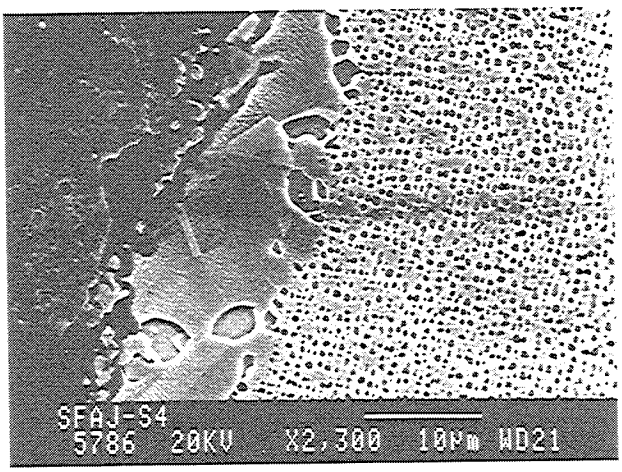


Fig.1 Coating (far left), diffusion interlayer (left), layer of original structure decomposition and substrate γ + γ' structure (right). Dark horizontal line is the trace of EDS microanalysis (contamination). (SE)

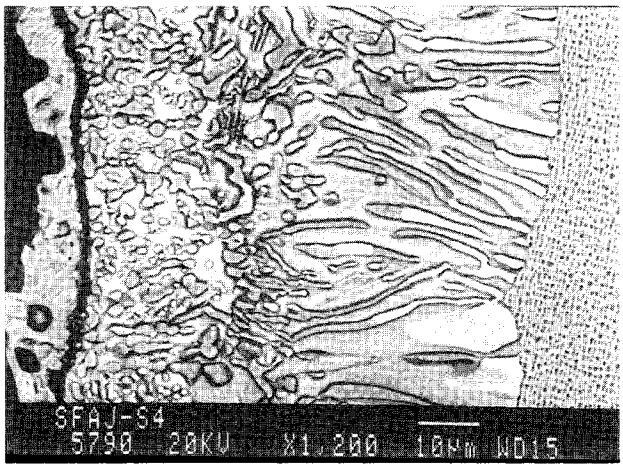


Fig. 2 Lamellae formed by "squeezing" of Cr (and other BCC elements) from γ solid solution after the structure is depleted of Al (and other γ' formers). (BSE)

Both micrographs were obtained on the cross sections of SC 16 single crystal superalloy coated with Ni and annealed for 500 hrs at 950 °C.

Backscattered electron contrast of particles in Figure 2 is caused by differences in composition. Table 1 contains the average composition of bright and dark parts of lamellar particles.

Table 1

Element [wt.%]	Dark region	Bright region
Al	0.40	0.75
Ti	0.91	1.08
Cr	86.08	50.92
Ni	6.83	35.78
Mo	5.54	11.43
Ta	0.25	0.54

Removal of elements with high affinity to oxygen (Al, Ti, eventually Ta) from superalloy causes the deterioration of long-range order, LRO, (i.e. of γ'-phase) and phase transformations of matrix with high nickel content according to modified Ni-Cr phase diagram. Nevertheless most microstructural objects in the region of intensive diffusion are apparently non-equilibrium (e.g. lamellar particles in Fig.2).

The results of image analysis of these two main structure elements are summarized in Figures 4 and 5. Figure 3 shows an example how the thickness of different regions was measured. The colored individual regions of structure showed in Fig. 3 were obtained by thresholding and

minor manual corrections. Than the mask consisting of parallel lines one pixel apart was overlayed and lengths of these lines coincident with particular region counted and averaged.

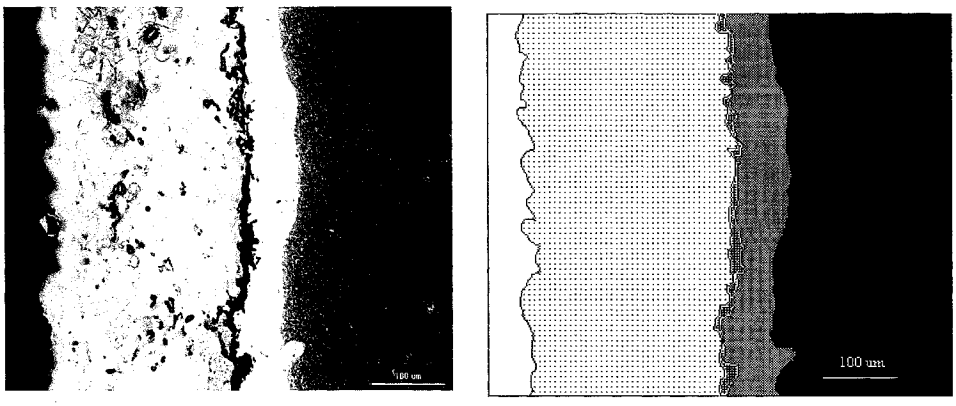


Fig. 3 Original micrograph and the result of image processing preceding the final thickness measurement. Ni coating on SC16 superalloy. Annealing 1050 °C/200hrs. From left: Coating surface, Coating (light grey), Inter-diffusion layer, thin (very dark grey), Modified structure, originally γ+γ' (dark grey), Unaffected superalloy (black).

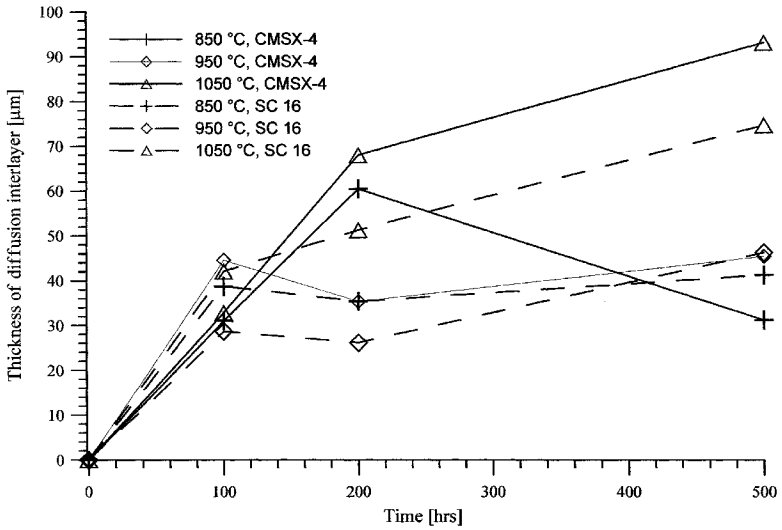


Fig. 4 Thickness of diffusion interlayer between the Ni coating and superalloys substrate as depends on annealing time, temperature and substrate.

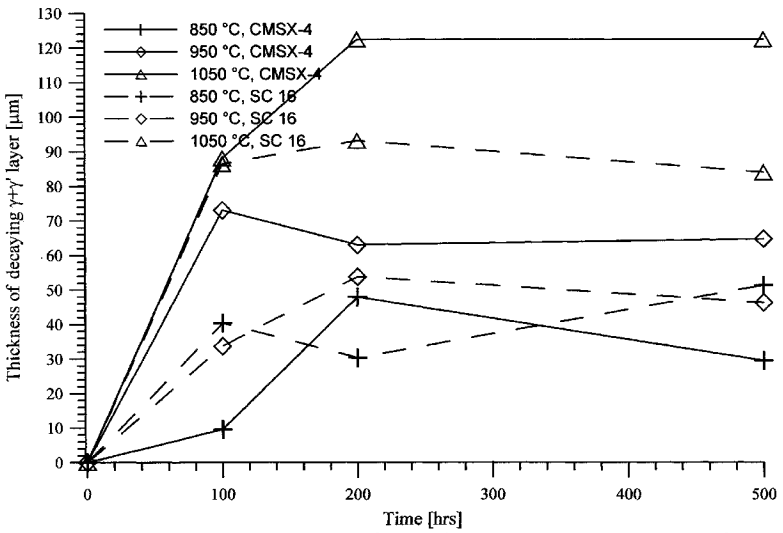


Fig. 5 Thickness of layer at substrate surface where, as a consequence of complicated diffusion, $\gamma + \gamma'$ structure of substrate gradually decomposes. Dependence on annealing time, temperature and substrate.

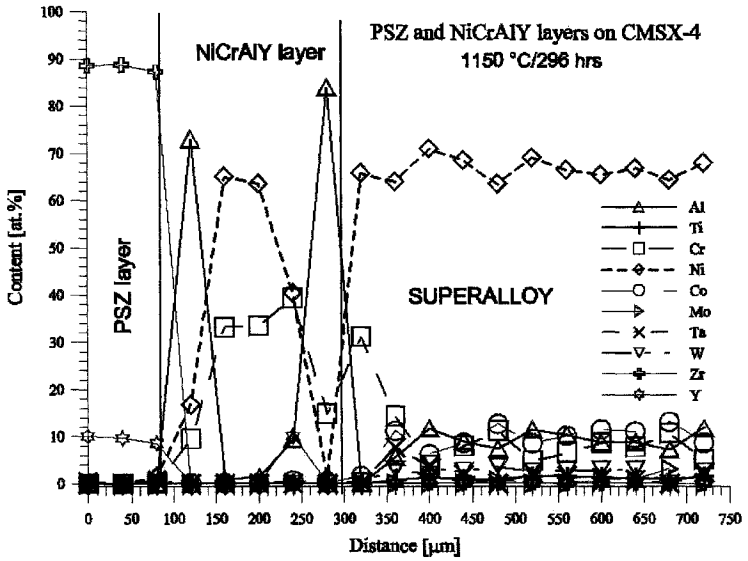


Fig. 6 EDS line microanalysis across the surface region of CMSX-4 single crystal coated by NiCrAlY covered by partially stabilized zirconia (PSZ) TBC coating. Annealed for 300 hrs at 1150 °C.

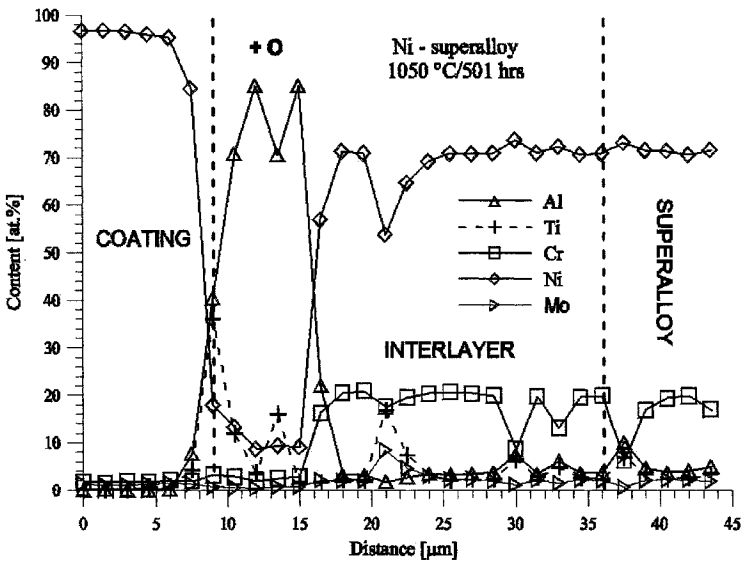


Fig. 7 Ni coating on SC16 superalloys single crystal. Note left part of the interlayer with high Al and O content (accompanied by Ti), while Cr, third in the affinity to oxygen, is lagging behind.

There is no space to discuss in detail complicated diffusion patterns encountered in these materials. After LRO vanishes, the diffusion of elements present is affected by the presence of fast-diffusion paths and differences of elements concentrations in various specimen regions leads to the formation of cavities and cracks that further accelerate diffusion in some directions. An illustration of complicated composition pattern is in Figure 6 (TBC coating) and 7 (pure Ni coating).

Figures 4 and 5 characterize the processes occurring in the materials. It is clear that fast diffusion is taking place at the beginning of the annealing, slow down and products of diffusion (remnants of destroyed and new phases, oxides, cavities) gradually block further diffusion. This would be desirable structural state but for spalling. We can assume that during service these diffusion processes are repeated due to the spalling off of corrosion products.

Weight measurements showed that minimal weight change exhibits $ZrSiO_2$ coating on CMSX-4 alloy and PSZ coatings (regardless of substrate) are better (lesser change in weight) than OT3 coating. Weight measurements are difficult in our case to interpret exactly as many factors influence the result - the quality and compactness of the coating, its adhesion to the substrate, exact composition, size and shape of plasma sprayed particles etc. [e.g. 5]

The results also show that diffusion processes in the surface region of the superalloy are slower in material with higher Cr and Mo and lower Al and Co content (SC16). Thus the combination coating - substrate must be selected with respect to the diffusion processes. Our results also showed that the process of coating deposition is important - best quality is obtained when professional (patented) procedures are used.

Acknowledgment
Authors gratefully appreciate financial support of GA CR through grant No. 106/97/S008 - Surface Engineering, and of the Faculty of Mechanical Engineering TU Brno, grant No. FP 390017 (1999).

References
[1] ASM International Handbook, Volume 5-Surface Engineering, 1994, pp 497-605
[2] Bradley E.F.: Superalloys - a technical guide, ASM International, 1988, pp 187-195
[3] Basuki E., Crosky A., Gleeson B.: Interdiffusion behaviour in aluminide-coated René 80H at 1150 °C. Materials Science & Engineering A **A224** (1997), pp 27-32
[4] Krejčová J. et al.: Application of image analysis in the study of NiCr-Al diffusion couples produced by plasma spraying. Prakt. Metallographie **XXXIV** (1998), pp 71-79
[5] Liu Zhenyu, Gao Wei, Dahm Karl, Wang Fuhui: The effect of coating grain size on the selective oxidation behaviour of Ni-Cr-Al alloy. Scripta Materialia **37** (1997), pp 1551-1558

MEASUREMENT OF THE DUCTILE BRITTLE TRANSITION TEMPERATURE AND THERMAL MECHANICAL FATIGUE RESISTANCE OF COATINGS USED IN GAS TURBINE ENGINES

S R J Saunders and J P Banks

Materials Centre, National Physical Laboratory, Teddington, Middlesex, TW11 0LW, UK

Abstract

Test procedures for measurement of the ductile brittle transition temperature (DBTT) and thermal mechanical fatigue (TMF) resistance are described. For the case of DBTT determination, a procedure using a small punch test has been developed. Coated samples are strained in tension by pressing a small diameter SiC ball into the top surface of the sample where the coating is on the underside. Finite element analysis was used to determine the tensile strain imposed. Cracking events were determined by use of acoustic emission (AE) in which monitoring the energy of the AE gave good correlation with cracking events. Overlay MCrAlY and diffusion Pt aluminide coatings have been examined using this method and fracture strain determined as a function of temperature up to 900 °C.

TMF resistance was assessed using a rig designed at NPL in which the sample was directly heated by passage of a large electrical current, and the strain was imposed using a hydraulic actuator. The temperature strain cycles were controlled using Labview® software. Two cycles have been simulated for industrial and aero use of gas turbines. MCrAlY and Pt diffusion coating systems have been investigated and tested to failure. Metallographic examination of the failed samples yielded information on the fracture process.

Key words: Coatings, Fracture, Thermal mechanical fatigue, Test development

1 Introduction

Coatings designed for use in the hot section of a gas turbine are required to withstand high temperatures and mechanical stressing. A coating is used for either corrosion or thermal resistance, and will be effective only if it remains intact. Thus the mechanical properties of the coating can have a marked effect on the performance of the system, and data are required to provide designers with assurance that the coating system will be fit for purpose. Additionally, during service ageing effects occur due to oxidation and interdiffusion that alter the coating properties from the as-produced values. It is important, therefore, to be able to measure the properties of the coating in the aged state and this may involve testing small samples taken from a blade that is to be refurbished.

The strain that a coating can tolerate before fracture changes as a function of temperature. Brittle behaviour is frequently observed at low temperatures, and, as the temperature is increased, the material becomes increasingly ductile. In some materials this transition is relatively well defined so that a ductile/brittle transition temperature (DBTT) can be defined. In practice, the information should allow the designer to define conditions under which a coating will crack when subjected to the anticipated service stresses. A pragmatic criterion used by some turbine manufacturers is that the coating should be able to withstand 1% strain [1]. In this case, therefore, the DBTT corresponds to the temperature below which a strain of 1% would result in cracking the coating. The small punch test has been used to measure the fracture behaviour of bulk and coated samples [2,3,4], and is ideally suited to extraction of samples from service-exposed components. Indeed, the test was first developed to allow

examination of small volumes of irradiated materials, and samples as small as 3 mm diameter have been used [2].

The DBTT also becomes important when considering thermal mechanical fatigue (TMF) resistance. In service a blade develops a hot spot in the centre. The material at this point is constrained from expanding by the cooler material surrounding it, and thus is compressively stressed. At high temperatures creep can relieve the stress in the coating, as its creep resistance is generally lower than that of the substrate. On cooling, depending on the extent of the creep relaxation and differences in thermal expansion coefficients, the coating may be placed in tension, and will crack if the fracture strain, ε_f, is exceeded (Figure 1).

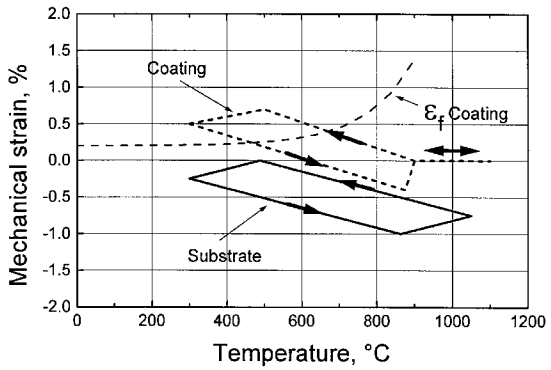


Figure 1 *Schematic TMF cycle (total mechanical strain versus temperature) of an aluminized component showing the effect of creep relaxation during heating and subsequent tensile cracking on cooling*

TMF resistance is usually assessed in complex rigs involving closed loop servo controlled hydraulic testing machines with induction heating [5]. Problems with many test procedures are temperature measurement and the ability to control cycle shape. Often thermocouples are welded directly to the sample and there is a concern that this could initiate cracking: some workers have used spot focussed radiation pyrometers to overcome this difficulty. The large size of normal TMF samples is one of the major constraints in imposing realistic cycles.

The approach adopted at NPL was to use relatively small samples so that realistic heating and cooling rates could be achieved. In an earlier design of a novel rig for TMF resistance measurement [6] the samples were only 10 x 2 x 2 mm, however such small samples would be inappropriate for coatings as the edge effect would dominate behaviour. A new rig was designed in which sample size was increased, but which nevertheless would allow heating and cooling rates to be imposed that permitted a good simulation of service conditions.

2 Materials

Coatings were deposited on IN738, CMSX4 and Rene 80 substrates. Table I lists the coatings systems examined and the tests carried out. All coating systems received the appropriate heat treatment before testing.

Table I: Coating systems studied

Substrate	*Coating*	*Supplier*	*DBTT*	*TMF*
IN738	SE20 (NiCrAlYTaSi)	Praxair		✓
IN738	2453	Siemens	✓	
IN738	2231	Siemens	✓	
CMSX4	Pt Al (3 types)	Chromalloy	✓	
CMSX4	TM312S (LCO22 – CoNiCrAlY)	Praxair		✓
CMSX4	2453	Siemens	✓	
CMSX4	SE20	Praxair		✓
Rene 80	PVD MCrAlY (3 types)	Silesian Technical Univ.	✓	

3 Experimental

3.1 DBTT Tests

3.1.1 Test Equipment

The test jig is illustrated schematically in Figure 2. The samples were fitted within a recess and a 2.4 mm diameter Si_3N_4 ball, mounted into the loading train of a bench-top Instron electro-mechanical test machine, was pressed into the centre of the sample that was located above a 3.4 mm hole.

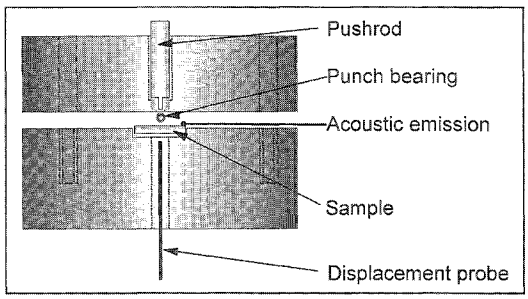


Figure2 Schematic diagram of the small punch test jig

The coated sample was placed in the rig such that the coating was strained in tension. The sample was held in place using clamping screws and the whole jig placed within a split furnace. A linear variable displacement transducer (LVDT) that had a spring loaded alumina rod extension to allow contact with the hot sample was placed at the centre of the lower surface of the sample to measure the vertical displacement.

With this arrangement tests at up to 1000 °C could be carried out. The sample was placed in the jig with both a Fecralloy® waveguide, to detect acoustic emission (AE) signals, and a thermocouple attached. It was then heated in air to the test temperature at 10 °C min^{-1}. The sample was also subjected to a small load (30 N) during heating which compensated for system expansion during the heating cycle. Samples were then strained in about three minutes up to a maximum vertical displacement of 250 μm. The sample was cooled in the furnace. The tensile strain values were validated using finite element analysis. After

completion of the test the samples were examined by optical or scanning electron microscopy.

Cracking of the coating was detected by monitoring AE using a waveguide that was welded to the sample. Tests were carried out with uncoated samples to determine the "background" AE signals. The Physical Acoustics Corporation supplied the AE equipment; a MISTRAS system was used which allowed a range of different AE signals to be stored. Specifically, HITS, COUNTS, ENERGY and AMPLITUDE of the signals were stored as a function of time and displacement.

3.1.2 Finite Element Analysis

In the small punch test the vertical displacement was monitored by the LVDT. In order to determine the tensile strain imposed on the sample, it was necessary to convert the vertical displacement measured at the centre of the sample into tensile strain parallel to the coating. This was carried out numerically using a finite element analysis. ANSYS was used for the calculation and the input values, (Young's modulus, Poisson's ratio and yield strength) required were obtained from the literature. Calculations were carried out for the pure elastic and elastic plastic cases for room temperature and 750 °C. It should be noted that above the DBTT creep relaxation effects would change the shape of the calibration curve and this has not been considered in the FE analysis. This numerical analysis was then used to obtain a calibration curve for the relationship between the vertical displacement at the centre of the sample and the in-plane tensile strain in the coating and this is shown in Figure 3. For a given vertical displacement above 50 μm the greater strain in the elastic/plastic compared with the elastic case is believed to be due to membrane stretching. This calibration was used for all subsequent work described below.

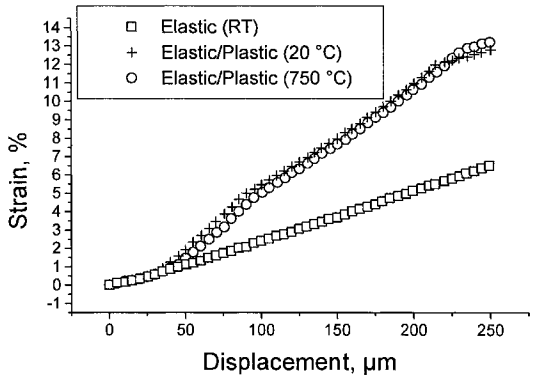


Figure 3 *Calibration curve of coating in-plane tensile as a function of the vertical displacement strain in the small punch test*

3.2 TMF Tests

The test sample has an overall length of 66 mm and was 4.37 mm diameter in the gauge length; two wings define the 6 mm gauge length (Figure 4), and these were used in conjunction with a video extensometer (Messphysik Gmbh model ME-64), having a sub-micron resolution, to measure strain. The sample was heated by passing a large direct current

of up to 800 A; at 400 A the heating rate was 140 °C s^{-1}, which is comparable with that achieved during normal gas turbine operation. Cooling rates of 25 °C s^{-1} were possible under ambient conditions. The load was applied using a hydraulic system with a maximum load of 20 kN. Figure 5 is a photograph of the test rig.

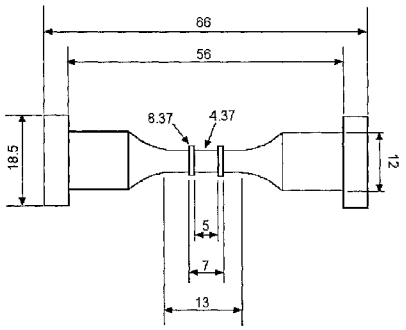


Figure 4 *Schematic diagram of the TMF test sample – all dimensions in mm.*

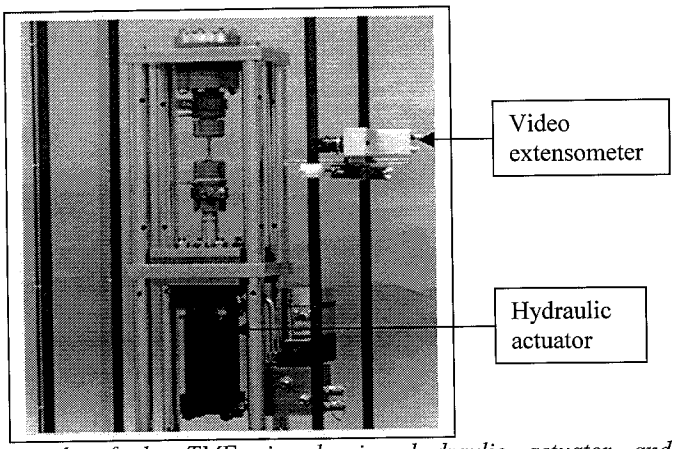


Figure 5 *Photograph of the TMF rig showing hydraulic actuator and video extensometer*

The temperature of the sample was controlled by a thermocouple welded on to one of the wings. The specimen and associated loading train were housed in a polymer box to allow the system to be purged with argon to reduce oxidation during the tests. The strain temperature cycles were controlled using bespoke software based on LABVIEW®. The procedure involved first assessing the thermal strain imposed during the test by heating the sample under zero loading and monitoring the strain. This information was then the baseline against which the mechanical stain was imposed.

A pure out-of-phase cycle, which simulates an industrial gas turbine, was used in which the heating and cooling rates were 8.5 °C s^{-1} with a 10-minute hold at 850 °C (Figure 6). A pure out-of-phase cycle was also used to simulate aero engine operation, and in the case the

heating rate was 25 °C s^{-1} to 1100 °C with a 10 second hold period followed by cooling at about 12 °C s^{-1}

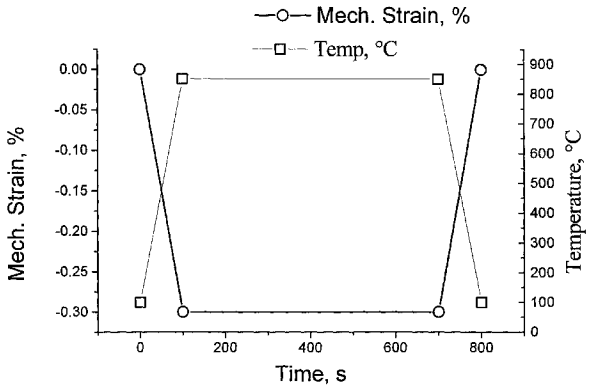


Figure 6 An industrial TMF out-of-phase cycle

It was originally hoped that fracture of the coating could be detected using AE using a Fecralloy® waveguide spot-welded to the grip end of the sample. Unfortunately the hydraulic system proved to be too "noisy", and as will be seen later the type of failure observed would not be expected to generate significant acoustic signals. Furthermore, it was also believed that failure could be defined by a fall in the maximum (tensile) load at the coldest part of the cycle, but again this proved not be a reliable indication of coating cracking. Thus cracking was detected by removing the sample from the rig at intervals during the test and then inspection of the sample using a scanning electron microscope at intervals during the test. Crack initiation was confirmed metallographically by inspecting the sample in a scanning electron or light microscope.

4 Results and Discussion

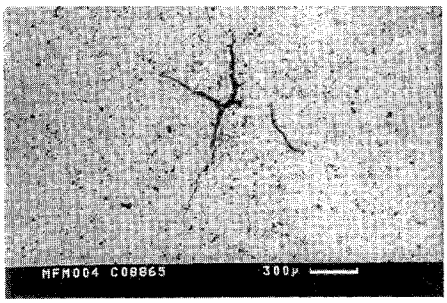
4.1 DBTT

4.1.1 Crack detection – Optimising Acoustic Emission

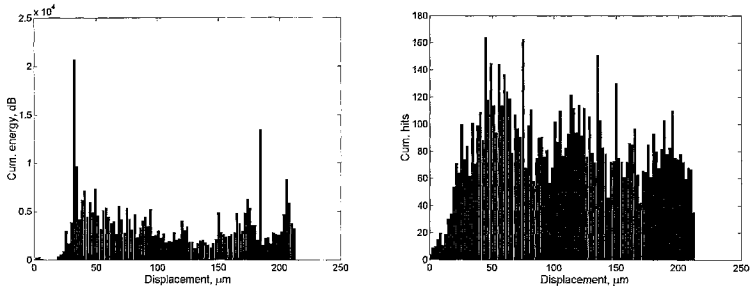
During the initial experiments it was observed that while all AE signals showed a transition in behaviour during the straining cycle, it was often difficult to determine a precise time for the change in behaviour. Examination of the sample after deformation to various extents gave a good indication of the onset of cracking. Figure 7 shows a micrograph of a cracked sample and the associated AE signal (hits and energy).

It was concluded from these initial experiments that the onset of the cracking could not be clearly discerned from the increase in the number a hits, but that the first high energy signals was a good indication of coating cracking. Additional tests were performed in which the same coating was strained to different extents (2.5 and 5%) and it was observed that a high AE energy signal occurred at very similar strain values (1.5 and 1.7%), giving confidence

that AE energy signals were an effective indicator of cracking (Figure 8). Furthermore the AE energy values corresponding to the first cracks have similar values at about 1.6 x 10^4 dB. In all other experiments the first high energy AE was used to determine the onset of coating cracking.

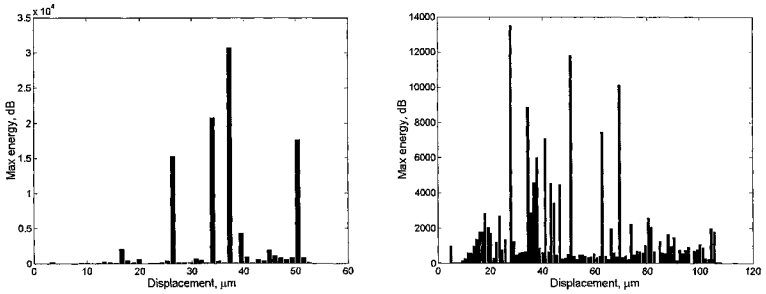


(a)



(b) (c)

Figure 7 *(a) Scanning electron micrograph a Pt aluminide coating on CMSX4 after straining to in plane to 10%, at 800 °C and the associated AE ENERGY (b) and HITS (c) as a function of vertical displacement*



(a) (b)

Figure 8 *AE signals obtained from a Pt aluminised coating deposited on CMSX4 after testing at 750 °C strained to (a) 2.5% and (b) 5%*

4.1.2 DBTT Curve determination

The DBTT was determined by carrying out a series of experiments with the same coating over the temperature range of interest. Single samples were strained generally to 10% and examined after the test to determine whether the coating had cracked. For some samples tested at the highest temperatures ductile tearing was observed, and an example of this behaviour is shown in Figure 9. These samples did not generate high energy AE signals and are considered to be ductile. Accordingly, the fracture strain versus temperature graph shown in Figure 10a for a MCrAlY coating was constructed by determining the onset of coating cracking to coincide with the first AE energy signal greater than 20 x 10^3 dB. Figure 10b shows a similar plot for a typical Pt aluminide coating, and as expected the MCrAlY coating exhibited much more ductile behaviour. This approach was used for all subsequent interpretation of the data.

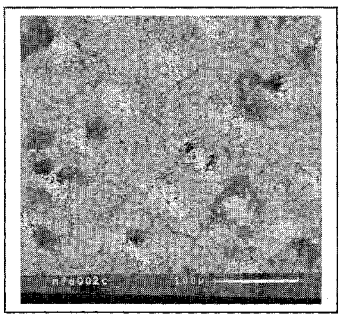
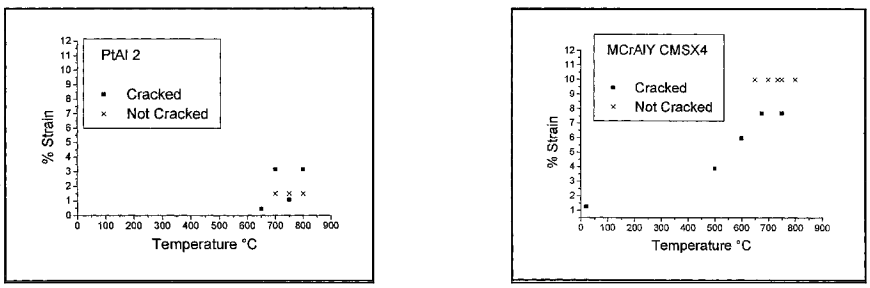
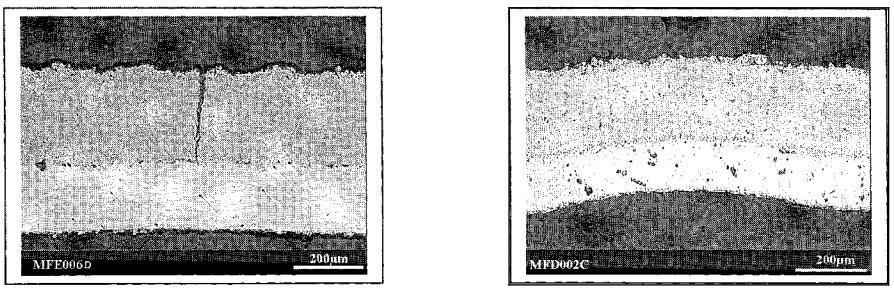


Figure 9 *Scanning electron micrograph of MCrAlY (2453) strained to 10% at 800 °C showing ductile tearing.*



(a) (b)

Figure 10 *DBTT curves for (a) Pt aluminide and (b) for Sicoat 2453 applied to CMSX4*



(a) (b)

Figure 11 *Optical micrographs of cross-sections through MCrAlY (Sicoat 2453) deposited on (a) CMSX4 and deformed at room temperature, and (b) IN738 and deformed at 650 °C*

Metallographic cross-sections were prepared through the deformed samples firstly, as added confirmation that the coatings were fractured or not as indicated by the AE energy signals, secondly, to determine whether the crack in the coating propagated into the substrate. Figure 11 shows two such micrographs and for these cases, there were no examples of crack propagation into the substrate. It can also be clearly seen that significant plastic deformation occurred for the sample deformed at high temperature whereas very little bending of the substrate was observed in the sample tested at room temperature

4.1.3 Data Generation

A criteria sometimes used to define DBTT is the temperature at which the strain to first crack is a certain level, in Table II below temperatures are listed at which the fracture strain is 1, 3 and 10%.

Table II: Temperature Required for Fracture of Various Coating Systems

Substrate	***Coating***	***Temp for fracture at 1% strain, °C***	***Temp for fracture at 3% strain, °C***	***Temp for fracture at 10% strain, °C***
Rene 80	MCrAlY 1		800	900
Rene 80	MCrAlY 2		700	
Rene 80	MCrAlY 3		800	900
IN738	MCrAlY 2453		~500	770
IN738	MCrAlY 2231		>600	750
CMSX4	MCrAlY 2453		<500	700
CMSX4	RT22	20	930	
CMSX4	PtAl 1	750	~825	
CMSX4	PtAl 2		700	

The dataset is incomplete due to the limited numbers of samples that were available for this work. It is clear however that MCrAlY coatings are more ductile than the Pt-aluminised systems. Comparisons within the different types of MCrAlY show that the experimental PVD coatings were in general more brittle than the 2453 or 2231, with possibly the former exhibiting slightly more ductile behaviour. Of the three Pt-aluminised coatings examined,

PtAl 2 would appear to be the most ductile, although additional work is required to confirm this. The same coating deposited on different alloys was investigated in just one case; 2453 deposited on IN738 and CMSX4. These data suggest that the coating on CMSX4 exhibited the more ductile behaviour, which may be related to differences in heat treatment for the two coating systems. It should be emphasised that in this work the coatings were tested in the as-received condition, and it might be anticipated that after ageing, behaviour could be modified by interdiffusion effects.

4.1.4 Summary and conclusions

During this work the small punch test has been developed for determination of DBTT determination of coatings. The work has demonstrated that the test can yield useful data.

There have been a number of difficulties in specimen preparation that have caused erroneous data to be produced, and while the sample has a simple shape, it has been found that even small departures from the specified sample geometry, can cause serious errors. Thus great care is needed over specimen preparation.

It is evident that the data are somewhat scattered. This could be the result of slight differences in specimen geometry between the different samples, as discussed above, but it should also be remembered that fracture is very dependent up on the presence of defects. Thus, some of these discrepancies could arise from local defects in some coatings. The repeatability of the test needs to be validated further by using a large number of samples to define the DBTT curve and also by taking greater care at the specimen preparation stage to ensure uniform geometry.

4.2 TMF

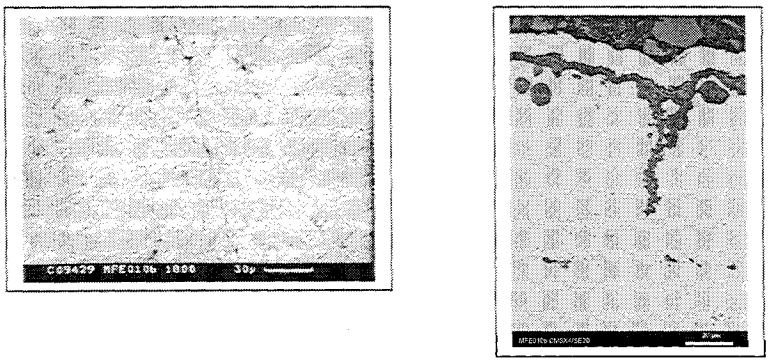
4.2.1 TMF data

The most successful tests were with coatings applied to CMSX4, and here two industrial and one aero cycle test were performed with SE20 and TM312 coatings. The number of cycles to failure of the different coating systems tested is listed in Table III.

Table III: Coating Behaviour in TMF Out-of-Phase Tests

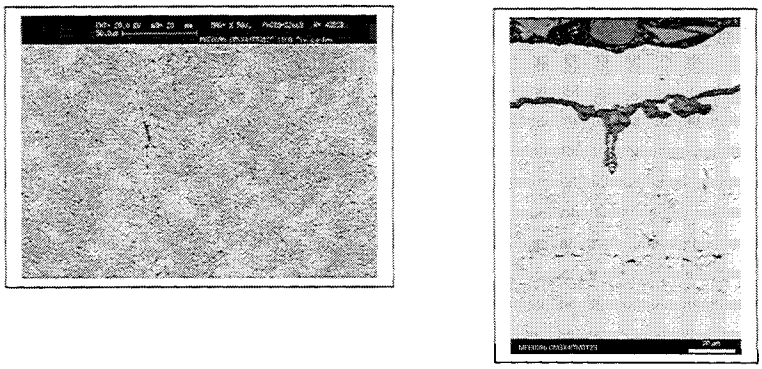
Coating system Substrate/coating	*TMF test cycle, temp °C*	*Latest cycle when cracking not observed*	*First cycle when cracking was observed*
CMSX4/SE20	*Industrial, 850*	*1371*	*1803*
CMSX4/TM312	*Industrial, 850*	*800*	*1100*
CMSX4/SE20	*Aero, 1100*	*423*	*500*

Figures 12-14 show micrographs of surface cracking and cross-section through the exposed samples. The cross-sections show that there was significant oxidation during the tests despite the presence of an inert atmosphere. In no case did the crack penetrate into the substrate.



(a) (b)

Figure 12 CMSX4 coated with SE20 after 1800 cycles in the industrial out-of-phase TMF cycle at 850 °C (a) Scanning electron micrograph of the surface, and (b) an optical micrograph of a cross-section through a cracked region



(a) (b)

Figure 13 (a) Scanning electron micrograph of the surface CMSX4 coated with TM312 after 1100 cycles in the industrial out-of-phase TMF cycle at 850 °C, and (b) an optical micrograph of a cross-section through a cracked region of the same sample

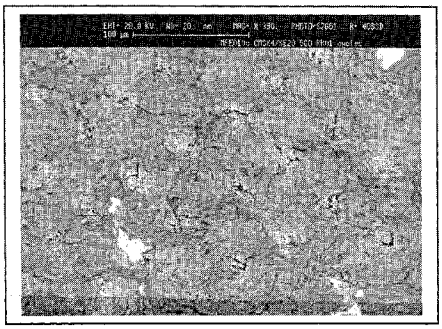


Figure 14 *Scanning electron micrograph of the surface CMSX4 coated with SE20 after 500 cycles in the aero out-of-phase TMF cycle at 1100 °C.*

This dataset is somewhat limited so that it is difficult to make comparisons, but it would seem clear that SE20 has superior TMF resistance to TM312, while the aero TMF cycle caused significantly more damage than the industrial cycle used in this work. Additional comparison with data in the literature was not possible as most of the published TMF data on coated components is concerned with a determination of the effect of coating on the life of the component rather than assessment of the TMF resistance of the coating itself.

It is perhaps understandable that such data are not available in view of the difficulties encountered in this work in detecting the onset of cracking. As stated previously use of acoustic emission (AE) and drop in maximum load were investigated as a means of crack detection, but these attempts were unsuccessful. In the case of AE, the hydraulic system generated significant noise and, furthermore, the nature of the crack formed suggested slow crack growth rather than a single event, so that it would be difficult to detect an AE response about the background noise.

It is clear therefore that further work is required to develop an crack detection systems if the TMF resistance of the coating *per se* is to be determined using this method.

4.2.2 Summary and Conclusions

A TMF test facility has been developed and preliminary results have indicated that TMF failures were induced in MCrAlY type coatings. At this stage it has not been possible, however to develop a means of on-line crack detection, so that data on the number of cycles to initiate coating cracking could only be obtained by use of interrupted tests.

For the coatings investigated differences in behaviour were observed when tested under similar conditions, but care should be exercised in interpreting these results due to the very limited data set. It was also clear that, as expected, the aero TMF cycle led to coating failure in fewer cycles than the industrial TMF cycle.

5 Acknowledgements

The research at NPL was part of the "Degradation of Materials in Aggressive Environments Programme", a programme of underpinning research financed by the UK Department of Trade and Industry. The authors are also grateful for the support of Alstom Power and Rolls Royce, who supplied substrate alloys and advice on TMF cycles; Chromalloy UK, Siemens, Praxair, Silesian Technical University who provided coatings; and PowerGen for the samples extracted from a blade.

6 References

[]] Werner Stamm, Siemens, private communication

[2] J Kameda and X Mao, *J Mats Sci*, **27** (1992) 983-989

[3] J Kameda and R Ranjan, *Materials Science and Engineering*, **A183** (1994) 121-130

[4] J R Foulds, P J Woytowitz, T K Parnell and C W Jewett, *J Testing and Evaluation,* **23** (1995) 3-10

[5] K Tate, R Ohtani, M Kaku, T Takenaka and H Masuo, in Proc Materials for Advanced Power Engineering 1998, Eds J Lecomte-Beckers, F Schubert and P J Ennis, Forschungszentrum Jülich GmbH, 1998, p1569-1578

[6] B Roebuck and M G Gee, *Materials Science and Engineering*, **A209** (1996) 358-365

AUTHOR INDEX

A

Abe F., II.1171, II.1181, III.1379, III.1397, III.1469, III.1561, III.1571, III.1581, III.1591, III.1629, III.1639, III.1691
Agamennone R., II.1161, III.1279
Agüero A., II.1143
Ahmaniemi S., I.449
Allen D., I.5, I.283, III.1487, III.1661
Andersson H.C.M., II.933
Angella G., I.167
Arai M., III.1269
Archer N.J., I.523
Arrell D., II.605, II.633
Artinger I., III.1701
Azuma T., III.1269, III.1497

B

Backes G., II.751
Bacos M.-P., I.429
Bakker W., II.815
Bale D.W., I.73, I.149
Banks J.P., I.577
Barbezat G., I.511
Baxter D., I.73, I.523
Beck T., III.1419
Bendick W., III.1361
Berger C., I.89, III.1279, III.1409, III.1551
Bezençon C., I.503
Bianchi P., I.449, I.523
Biede O., II.957
Blough J., II.815
Blum R., II.1009, III.1385
Blum W., II.1161, III.1279
Boβmann H.P., II.871
Bohn D.E., I.107
Bontempi P., I.149, III.1621
Bordenet B., II.871
Böttger B., I.89, I.315, III.1333
Brozda J., III.1711
Brückner U., I.217
Buckthorpe D., II.759
Buenaventura A., II.759
Burlet H., I.419
Bursik J., III.1521
Busquin P., III.1806
Busso E.P., I.23, I.283

C

Cabibbo M., III.1453
Cailletaud G., I.23
Carosi A., III.1731
Cerjak H., II.1081, III.1539
Cernuschi F., I.449
Chen Q., II.1019, III.1333
Chen W.Y., I.187
Chi B.H., III.1681
Cizner J., II.785
Contessi E., III.1731
Couturier R., I.419, II.759
Cremer R., II.663
Cui C.Y., II.595
Czyrska-Filemonowicz A., I.149

D

Danciu D., I.227, I.235
Daniel R., I.293
Dassios C.G., II.769
Davis C., II.785, II.893
De Beer A.J., III.1783
Del Puglia P., II.769
Del Vecchio D., III.1731
Di Gianfrancesco A., II.1065, III.1731
Dimmler G., III.1539
Dlouhý A., II.605
Doi H., III.1269
Doi M., II.1201
Dubiel B., I.139, I.149
Dubiez S., I.419
Ducki K.J., I.401
Dupin N., I.315

E

Ehlers J., III.1279
Emura S., II.643
Encinas-Oropesa A., II.923
Ennis P.J., II.1131, III.1279
Epishin A., I.217
Escher K., II.1049
Evangelista E., III.1453

F

Faulkner R.G., II.1247
Foldyna V., III.1477
Formanek B., II.785
Frahm J., I.543
Friedrich B.-C., II.759
Fries S.G., I.315, III.1333
Fritscher K., I.483
Frommert M., II.673
Fujita T., III.1269, III.1311
Fujiyama K., I.345
Fukui Y., III.1269
Fukuyama Y., I.255, II.733

G

Gabrel J., III.1343, III.1361
Gallet S., II.633
Garcia Oca C., II.711
Gasser A., II.751
Ghidini A., III.1731
Giannozzi M., I.493
Gil I., II.703
Giorni E., I.493, I.523
Girard B., I.429
Giselbrecht W., II.1065
Goransson K., II.785
Gottstein G., II.673
Granacher J., III.1279
Guardamagna C., I.149, III.1621
Guétaz L., I.419
Guo J.T., II.595
Guo S., II.997

H

Haase H., III.1409
Hagiwara M., II.643
Hakl J., II.615
Hald J., II.1009
Hamano S., III.1351
Hara T., II.1181
Harada H., I.159, II.197, I.303, II.733
Harada N., I.245
Hashizume R., II.1201, III.1497
Hayakawa H., III.1445
Hecht U., I.315
Heckmann S., I.561
Hede Larsen O., II.957
Henderson M., I.139, I.149, I.293, II.633
Henderson P.J., II.785, II.883
Herzog R., I.543, I.551, I.561
Hetmanczyk M., I.401
Heuser H., III.1671
Hillenbrand P., III.1385
Hilpert K., II.989
Hino T., I.303
Hirosaki N., II.997
Hjörnhede A., II.979
Höbel M., I.503
Högberg J., II.883
Horn A., II.743
Hornak P., I.365, I.375
Hovsepian P. Eh., I.465
Hu W., II.673

I

Ielpo F.M., III.1731
Igarashi M., III.1397, III.1469, III.1561, III.1591, III.1639
Ikeda K., III.1371
Imai H., I.535
Inden G., III.1279, III.1299
Innocenti M., I.523, II.769
Ishiguro T., III.1497
Ishii R., III.1371
Ishitsuka T., III.1321
Isobe S., III.1351

Itagaki T., III.1397, III.1629, III.1639
Ito S., I.255
Izumi T., II.693

J

Jacobs M., II.833
Jakobová A., III.1477
Jirikovsky K., I.569
Jochum C., II.1081, III.1671
Josso P., I.429
Judkins R.R., II.853

K

Kadoya Y., III.1351
Kakehi K., I.207
Kaneko J., III.1371, III.1721
Kang S.T., III.1505
Karada H., I.395
Karlsson A., II.785
Karlsson B., II.605
Kawai H., III.1351
Kaysser W.A., I.483
Kelbassa I., II.751
Kern T.-U., II.1017, II.1049, II.1065, III.1385
Keutgen S., II.751
Kilgallon P., II.903, II.913, II.923
Kim B.J., III.1505, III.1681
Kim J.T., III.1505
Kimura K., II.1171, III.1397, III.1571, III.1581
Kimura M., III.1515
Klabbers J., I.139, I.227, I.385
Kloc L., II.1189, III.1531
Knezevic V., III.1279, III.1289
Knödler R., II.1143, III.1601
Kobayashi K., III.1515
Kobayashi T., I.159, I.197, I.303, I.395
Koizumi Y., II.197, I.303, I.395
Kolkman H., I.149
Komatsubara S., III.1311
Kondo Y., I.245
Kong B.O., III.1681
Kong C.N., I.273
Konter M., I.503
Koolloos M.F.J., II.633
Kopp R., I.325
Kostopoulos V., II.769
Koyama T., II.1201
Kratochvil P., II.615
Krejcí J., I.569
Kreutz E.W., II.743, II.751
Kroupa A., III.1477, III.1521
Kubo K., II.1181, III.1691
Kubon Z., III.1477
Kuc D., I.401
Kucharova K., II.1189
Kung S., II.815
Kurz W., I.503
Kushima H., II.1171, III.1571, III.1581
Kutsumi H., III.1629, III.1639

L

Lapin J., II.605, II.623
Layne A.W., I.121
Lee K.W., III.1681
Lee S.Y., III.1505, III.1681
Lefebvre Bo., III.1343
Letofsky E., II.1081
Lewis D.B., I.465
Leyens C., I.465
Li G.S., II.595
Li H., I.167
Lim B.S., III.1681
Lindblom J., II.933
Link T., I.217
Löhe D., III.1419
Lorenzoni L., I.449
Lukas P., I.139, I.149
Luo Q., I.465
Lupinc V., I.43, I.167, I.409, II.605, II.683

M

Ma D., I.315
Magoshi R., III.1351
Mai Y.-W., I.187
Majerus P., I.551
Maldini M., I.139, I.167, I.409

Mäntylä T.A., I.449, II.945
Mao C., II.845
Marchionni M., II.683
Martinez C., II.663
Masuyama F., III.1767
Matsui M., III.1691
Matsuo T., I.177, I.245
Mattsson M., II.883
Mayer K.H., II.1049, II.1065, III.1385, III.1521
Mc Cartney L.N., III.1613
McColvin G., II.833
Meriggi M., I.439
Merluzzi M., I.493
Metz Ch., I.523
Miki K., III.1497
Mimura H., III.1321
Minami Y., III.1445
Mitomo M., II.997
Miura N., I.245
Miyazaki T., II.1201
Mohrmann R., III.1651
Monteiro A., I.475
Montgomery M., II.957
Moormann R., II.759
Morinaga M., II.1201, III.1497
Morris D.G., II.703, II.711
Muelas R., II.1143
Müller M., II.989
Mulvihill P., I.149, III.1261
Munasinghe D., II.833
Muneki S., III.1469, III.1561, III.1591
Munoz-Morris M.A., II.703, II.711
Münz W.-D., I.465
Murakami H., I.535
Murakumo T., I.159
Murata Y., II.1201, III.1497

N

Nafari A., II.969
Nakamoto Y., I.177
Nakazawa S., I.159, I.197
Nam S.W., III.1681
Narita T., II.693
Nazmy M., I.43, II.605, II.683
Neuschütz D., II.663
Nicholls J.R., I.57
Nies H., II.1081
Nikbin K., II.605
Nishimoto T., II.693
Nishimura T., II.997
Noda T., III.1351
Norreys A., I.523
Norton J.F., II.913
Nylund A., II.969, II.979

O

O'Dowd N.P., I.283
O'Driscoll J., II.833
Oakey J.E., I.73, II.785, II.801, II.903, II.913, II.923
Obrtlik K., I.149
Odaka T., II.733
Okada H., III.1397, III.1469, III.1561, III.1591
Okayama A., I.355
Okubo H., III.1469, III.1561, III.1591
Olsha Z., III.1783
Onay B., I.355
Ono H., I.395
Onofrio G., II.683
Osgerby S., II.801, III.1261, III.1613

P

Palm M., II.653
Palumbo G., III.1453
Pappas Y.Z., II.769
Park S.H., III.1681
Pasternak J., III.1711
Pelachová T., II.623
Penkalla H.J., I.89, I.227, I.235, I.335
Peters M., I.465
Pigrova G.D., II.1241
Pinder L.W., II.893
Pirch N., II.751
Podstranska I., III.1521
Pollock T.M., I.263

Portella P.D., I.217
Portinha A., I.475
Pratesi F., I.493
Purgert R., II.1109

Q

Qi Y.H., II.595
Quadakkers J.W., II.1131, III.1279

R

Rademakers P., II.785
Rae C.M.F., I.207
Rantala H., II.759
Rao U., II.1109
Rau K., III.1419
Reed R.C., I.207
Regino G.M., I.283
Reichert K., II.663, II.673
Ricci N., III.1621
Rinaldi C., I.439
Rio C., I.429
Riou B., II.759
Ro Y., II.197
Rösler J., I.89
Rozsavölgyi Z., III.1701
Ruth L.A., III.1745
Ryu S.H., III.1505, III.1681

S

Saeki H., II.733
Saito D., I.255, I.345
Sandström R., III.1431
Sato M., I.395
Saunders S.R.J., I.577, II.801
Sauthoff G., II.653, III.1279, III.1289,
Sawada K., II.1181, III.1379
Scarlin B., II.1091, II.1143, III.1601
Scarpellini R., II.845
Scheffknecht G., II.1019
Schneider A., III.1299
Schnell A., I.503
Scholz A., III.1279, III.1409, III.1551
Schubert F., I.235, I.335, I.385, I.543, I.551, I.561
Schulz U., I.483
Schwienheer M., III.1409
Seitisleam F., III.1431
Seitz W., II.815
Semenak J., I.375
Servetto C., III.1487, III.1661
Shibli A., II.1233
Simms N.J., I.73, II.801, II.903, II.913, II.923
Singheiser L., I.561, II.989, III.1279
Sklenicka V., II.1189, III.1521, III.1531
Spigarelli S., III.1453
Spiradek K., III.1459
Stamatelopoulos G.-N., II.1091
Starr F., II.1233
Staubli M., II.605, II.683, II.1049, II.1065, II.1189, III.1385
Steen M., II.769
Steinbach I., III.1333
Steinbrech R.W., I.543, I.551, I.561
Stief J., II.1065
Stocker Ch., III.1459
Stöver D., I.475, I.511
Strang A., II.1223
Strunz P., I.365
Sundman B., III.1333
Suzuki A., I.535
Suzuki K., II.1171
Svejcar J., I.569
Svoboda M., II.1189, III.1521

T

Tabuchi M., III.1397, III.1691
Tamaki H., I.355
Taneike M., III.1379
Tang F., II.643
Teixeira V., I.475
Terada Y., I.177
Thoma A., III.1551
Tin S., I.263
Tinga T., I.293
Toda Y., II.1171, III.1571

Tohyama A., III.1445
Tohyama H., III.1571
Toji A., III.1311
Tomasi A., II.683
Torri L., III.1621
Toulios M., I.5, I.23
Tsuda Y., III.1371, III.1721

U

Uehara T., III.1311
Ueta S., III.1351
Uusitalo M.A., II.945

V

Vaillant J.-C., III.1343, III.1361
Valarani M., II.845
Valenti S., III.1731
Van der Schaaf B., II.759
Vandenberghe B., III.1343, III.1361
Vanstone R.W., II.1035, III.1261
Vaßen R., I.475, I.511
Vilk J., III.1279, III.1299
Vippola M., I.449
Viswanathan R., II.1109
Vitusevych V., I.315
Vlachos D., II.769
Vlasák T., II.615
Vodarek V., II.1223, III.1477
Vrchovinsky V., I.365, I.375
Vuoristo P., I.449
Vuoristo P.M.J., II.945

W

Wagnière J.-D., I.503
Wahl G., I.523
Wang C.H., I.187
Wang Y., III.1279
Wangyao P., I.375
Wanikawa S., III.1397
Ward T.J., I.293
Warnken N., I.315
Watanabe T., III.1691
Weinert P., II.1211, III.1539
Wen K.Y., II.673
Wessel E., I.385
White P.S., I.273, II.723
Wiedenmann A., I.365
Wieghardt K., II.1017
Wilcock I.M., I.139
Willach J., II.743
Wing R., I.57, I.523
Wolske M., I.89, I.325
Wosik J., I.335
Wu F., I.535
Wu R., III.1431

Y

Yamada K., III.1469, III.1561, III.1591
Yamada M., III.1371, III.1721
Yamaguchi K., III.1397, III.1515
Yamamoto R., III.1351
Yamamoto Y., II.997
Ye L., I.187
Yeatman J., I.523
Yin Y.F., II.1247
Yokokawa T., II.733
Yoshida T., II.733
Yoshinari A., I.355
Yoshioka Y., I.255, I.303, I.345
Yu J., III.1505

Z

Zeiler G., II.1049, III.1459
Zeman M., III.1711
Zhang X.P., I.187
Zhou H., II.197
Zhou L.Z., II.683
Zonfrillo G., I.493
Zrnik J., I.365, I.375

KEYWORD INDEX

γ' phase: I.245, I.255
[001] orientation: I.177
0.2 % proof stress: III.1581
10 % Cr steel: II.1049, III.1385
11% Cr steels: II.1131
12 % Cr steel: II.1161, III.1269, III.1279, III.1289, III.1299, III.1361
2.25 % Cr1.7 % NiMoVNbW steel: III.1721
700°C power plant: II.1009
8 wt.% YSZ: I.543
9 % Cr steel: II.1171, II.1181, III.1691
9-12 % Cr steel: II.1035, II.1189, II.1211, III.1505, III.1539, III.1409, III.1459, III.1681, III.1731
A-286 alloy: I.401
Advanced 700C class steam turbine: III.1351
Advanced power plant: II.1019
Ageing: I.335, I.493
Agressive environnements: II.933
AISI 316L: III.1419
Al: I.523
Al + Y: I.523
Alloy 122: III.1261
Alloy design program: II.733
Alloy development: I.89, III.1333, III.1351, III.1361, III.1745
AMDRY 995 coatings: I.439
Anisotropy: I.293
Annealing: I.569, II.711
APS: I.57
Austenitic: II.1233
Austenitic stainless 353 MA: III.1431
Austenitic stainless steel: III.1445
Austenitic steels: II.1091
Autocatalytic electroless deposit: I.429
Back-stress concept: III.1539
Bayonet tubes: II.845
Biomass: II.903, II.957, II.969
Blade: I.523
Boiler: II.1091, II.1109
Boiler design principles: II.1019
Boiler tube: III.1321, III.1445
Bond coat: I.551
Bucket: I.255
Burner rig tests: II.923
Carbides: I.227, I.263, II.1171, II.1247, III.1477
Carbon free: III.1469
Carbon-free martensitic alloys: III.1629
Casing: III.1371
Cast component: I.89, II.605, III.1385, III.1731
Cast steel: II.1065
Cavitation: III.1431
Ceramic: II.845, II.989, III.1745
Ceramic matrix composites: II.769
Ceria-stabilized zirconia: I.483
CFB-boiler: II.969
Chaboche: III.1651
Chlorination: II.815
Chlorine: II.893, II.945
Chromium steels: II.893, III.1521
Clean coal: II.1009
CM186: I.285
CM186LC: I.5, I.139, I.149, I.227, I.293, I.355
CM247: II.871
CMSX-2: I.255
CMSX-4: I.5, I.227, I.235, II.871
Coal: II.785, II.903, II.1109
Coal-fired boilers: II.815
Coating: I.57, I.465, I.493, I.523, I.577, II.945, II.979, II.1143
Cobalt: III.1311
Cold bending: III.1343
Combined cathodic arc/unbalanced magnetron sputtering: I.465
Combined cycle power plant: I.107, III.1721
Combustion liner: I.345
Combustion power plant: II.979
Composite: II.673, II.853
Composition: II.643
Composition changes of precipitates: II.1223
Computer simulation: II.1247
Constitutive models: I.23
Cooled blade design: I.23
Cooling holes: I.385, II.743
Cooling technology: I.107

Corrosion: I.73, I.107, II.785, II.801, II.883, II.945, II.989
Corrosion resistance: I.57, III.1279
Cost 522: I.57, II.1035, II.1049, III.1487
Cr content: III.1497
Cr_2N: III.1571
Creep: I.5, I.43, I.89, I.139, I.159, I.167, I.177, I.197, I.207, I.217, I.273, I.293, I.365, I.375, I.409, I.419, I.551, II.595, II.605, II.623, II.723, II.997, II.1161, II.1189, II.1211, III.1361, III.1379, III.1397, III.1431, III.1453, III.1459, III.1469, III.1487, III.1497, III.1521, III.1531, III.1561, III.1621, III.1661
Creep behaviour: II.615, II.1181, III.1539, III.1551
Creep crack growth: I.89
Creep equations: III.1409, III.1551
Creep fatigue: III.1409
Creep fracture: II.623
Creep life: II.1189, III.1521
Creep strength: I.303, I.395, II.1065, II.1081, II.1091, II.1189, III.1269, III.1289, III.1311, III.1321, III.1371, III.1409, III.1445, III.1505, III.1521, III.1571, III.1691, III.1711, III.1767
Creep-fatigue: III.1397, III.1515
CrVN: III.1321
Crystallographic models: I.283
CVD: I.523
Cyclic oxidation: I.57, I.493
Damage: I.375, II.1211, III.1409
Database: I.73, II.801
Deformation/damage behaviour: I.385
Degradation: I.345, III.1477
Depletion: I.493
Deposits: II.913, II.957
Design: I.121, II.1017, II.1049
Diffusion: I.569
Diffusion Barrier: I.535
Directional solidification: I.355
Dislocations: II.711
Double layer: I.511
Downtime corrosion (DTC): II.913
DS superalloy: I.395
Ductility: III.1571
Ductility normalized strain-range partitioning method: III.1515
Duplex microstructure: II.605
E911: III.1487
EB-PVD: I.57, I.483, I.535
EFCC plants: II.845
Efficiency: II.1109, II.1143
EF-TEM: II.1181
Elastic behaviour: I.543
Elastic modulus: I.561
Electric power plants: III.1745
Electrochemical particle isolation: III.1459
Energy: III.1806
Engine: I.429
Erosion corrosion: II.969
ESR method: III.1269
European commission: III.1806
Experience: II.1065
Extrapolation: II.723
Extrapolation of creep rupture time: III.1539
Fatigue: I.43, I.375
FATT: III.1505
FEM: I.293, I.325, III.1731
FePd: III.1561
Ferrite matrix: III.1571
Ferritic steel: II.1091, II.1143, II.1201, II.1247, III.1311, III.1379, III.1397, III.1487, III.1515, III.1561, III.1581, III.1591, III.1601, III.1621, III.1629, III.1639, III.1661
Fiber coating: II.663
Filler metals: III.1671
Fireside corrosion: II.893
Forging: I.89, I.325
Fraction of precipitates: I.159
Fractography: II.633
Fracture: I.577, III.1431
Gamma TiAl: I.43, II.605, II.633
Gas: II.759
Gas separation process: II.853
Gas turbine: I.57, I.303, I.345, II.923
Gas turbine coatings: I.73
Gas turbine design program: II.733
Gasification: II.903
Gasifier: II.913
Grain boundary: II.1247, III.1453
Graphite: II.759
Growth behaviour: I.187
Hafnon: II.989
Hastelloy X: I.345
HAZ: III.1661, III.1691
Heat exchanger: II.801, II.845, II.913
Heat flux: II.957

Heat input: III.1701
Heat resistance: II.997
Heat resistant steel: III.1269, III.1321, III.1445, III.1767
Heat treatment: I.227
High cycle fatigue: II.633
High steam parameters: II.1019
High temperature: I.409, II.1049, II.1143, III.1431
Hold time: I.375
Homogeneous deformation: III.1469
Homogenisation: I.283
Hot corrosion: I.355, I.395, II.871, II.923, III.1445
Hot deformation: I.401
HP-LP single cylinder steam turbine rotor: III.1721
HTGR: III.1783
HTR: II.759
IGCC: III.1767
Impact: III.1505, III.1701
IN 738: I.871
Inconel 617: I.335, I.385
Inconel 706: III.1551
Industrial gas turbine: I.5, I.139, I.149
In-situ SEM fatigue: I.187
Interfaces: II.673
Intermetallic: I.43, II.595, II.633, II.653, II.1241
Intermetallic compound: II.673, II.703, II.711, III.1469, III.1571
Intermetallic matrix composite: II.663
Iron aluminides Fe_3Al: II.615
Irradiation: II.759
Ir-Ta coating: I.535
Johnson-Mehl-Avrami: III.1651
Kinetics: III.1299
$L1_0$ type ordered intermetallic phase: III.1561
Laboratory tests: II.923
Laser cladding: I.503, II.751, II.979
Laser drilling: II.743
Laser thermal shock: I.439
Laves: II.1171, II.1201, III.1289, III.1459, III.1497
LCF: I.5, I.149, I.273, II.933, III.1621, III.1681
Life prediction: I.375, III.1409
Liquid metal cooling: I.263
Long-term: III.1279, III.1497, III.1571, III.1581
Loop seal: II.969
Low activity Al pack cementation process: I.535
Low alloy steel: II.893, III.1343, III.1371
Low NOx combustors: II.815
Low thermal expansion: III.1351
LPPS and HVOF coatings: I.439
$M_{23}C_6$: III.1571
Magnetic field: III.1591
Magnetron sputtering: II.663
Manufacturing: III.1731
Maraging steel: II.1241
Martensitic steel: II.1223, III.1379, III.1397, III.1613, III.1701
Material development: II.1019, II.1009
Material science: I.107
Materials: I.121, II.759, II.1109, II.1049, II.1017, III.1745
MCrAlY: I.57, I.429, I.551, II.871
Mechanical properties: I.73, II.615, II.643, II.683, II.703, II.711, II.833, II.1081, III.1261, III.1385, III.1671, III.1681, III.1731
Medium rating thermal power plant: III.1721
Microporosity: I.217
Microstructural stability: II.1189, III.1279
Microstructurally short crack: I.187
Microstructure: I.159, I.167, I.177, I.227, I.235, I.245, I.335, I.365, I.395, I.401, I.429, I.503, I.569, II.595, II.623, II.633, II.643, II.703, II.1035, II.1171, II.1211, III.1261, III.1505, III.1521, III.1561, III.1681, III.1731
Microstructure evolution: II.1201, II.1223
Microstructure simulation: I.315, I.325
Modelling: I.273, II.801, I.409, II.1211, III.1613
Modified Garofalo equation: III.1551
Multi-scale modelling: I.23
MX carbonitrides: II.1181, III.1289
Nanocomposite ceramic coatings: I.475
Nanolayer: I.475
Nearly lamellar microstructure: II.605
Neutron diffraction: I.365
NiAl base alloy: II.595, II.653
Ni-Al coating: II.663, II.693
Ni-Al-Cr-Ta-W: I.315
Ni-base SC superalloy: I.263, I.535, II.733

Ni-base superalloy: I.159, I.167, I.177, I.197, I.207, I.227, I.409, I.419, II.1233, III.1351
Nitride: II.1171
No-destructive evaluation: II.769
Non-isothermal model: III.1651
Non-linear finite element analyses : I.283
Notch behaviour: III.1409
ODS Alloys: II.833
Orientation relationship: II.1223
Oxidation: I.569, II.683, II.693, II.997, II.1091, II.1143, III.1397, III.1621
Oxidation resistant nitride coating: I.465
Oxide/oxide: II.769
Oxide scales: III.1601
P 23: III.1671
P 24: III.1671
P92 steel: II.1131
Palladium: III.1639
Particulate composites: II.643
PD 6605: III.1487
Phase formation: II.1241
Phase transformation: I.89, III.1651
Phase-field: I.315, III.1333
Physical properties: I.73
Pipe: III.1361
Plasma sprayed TBC: I.543
Plasma-spraying: I.511
Platinum aluminising: I.57
Post-weld heat treatment: III.1701
Powder metallurgy: I.419
Power generation: III.1711, III.1783
Power plant: II.743, III.1767
Precipitation: II.1161, II.1171, II.1247, III.1299, III.1691
Precipitation strengthening: III.1351, III.1379, III.1477, III.1571
Prediction: III.1581
Pressurized pulverized coal combustion: II.989
Prior austenite grain boundary: II.1171
Processing: II.615
Protective oxide layer: III.1629, III.1639
PVD: I.57, I.475
PWA1480: I.245
PWHT: III.1671
Rafted structure: I.245
Rafting: I.159, I.167, I.255, I.303
Recovery: II.1171, III.1497
Regression analysis: I.395
Reheater: II.893
Relaxation: I.551
Research: III.1806
Rhenium: I.207
Rupture: II.595
SANS: I.365
Scale fracture: III.1613
Sealing: I.449
Shaping: II.743
Shear test: I.551
Short cracks: I.385
Silicon carbide: II.845
Silicon nitride: II.997
Simulation: III.1333
Single crystal: I.5, I.23, I.139, I.149, I.167, I.177, I.187, I.197, I.235, I.255, I.273, I.283, I.293, I.303
Single crystal coating: I.503
Slag: II.989
Slip bands: I.187
SO_2: II.933
Solid fuels: II.801, II.923
Solid solution: III.1459, III.1477
Solidification: I.315
Solution heat treatment: I.355
Spallation: III.1601, III.1613
Specific heat: I.449
Sputtering: I.475
Stabilised zirconia: I.475
Stacking fault energy: I.207
Stainless steel: III.1321
Stationary creep rate: III.1539
Steam chest: III.1261
Steam oxidation: II.1131, III 1445, III.1601, III.1613, III.1629, III.1639
Steam plant: II.1143, III.1681
Steam turbine: III.1371
Steam/metal temperature: II.957
Steel: II.759, III.1531
Straw: II.785
Stress exponent: III.1531
Stress range partitioning method: III.1581
Stress rupture: II.1233
Subgrain: II.1161
Sulfidation: II.815
Superalloy: I.89, I.217, I.315, I.325, I.355, I.365, I.569, II.723, II.751, III.1333

Supercritical boiler: II.1019
Superheated steam: III.1621
Superheater: II.785, II.883, II.893, II.945, II.969
System free energy: II.1201
T and P 23: III.1343
TBC: I.57, I.449, I.483, I.511, I.561
TEM: I.235, II.673
Temperature capability: I.511
Tensile: I.235
Tensile strength: I.43
Test: I.577, II.759, II.933
Thermal barrier: I.543
Thermal conductivity: I.449
Thermal cycling: I.511
Thermal diffusivity: I.449
Thermal efficiency: III.1767
Thermal exposition: I.365
Thermal mechanical fatigue: I.577
Thermal spray: II.979
Thermal stability: I.475
Thermally grown oxide: I.483
Thermocalc: III.1477
Thermodynamic modelling: I.315, II.871, II.903, III.1299, III.1333, III.1477
Thermo-mechanical fatigue: I.197, I.273, I.439, III.1419
Thermomechanical heat treatment: III.1591
Thermo-mechanical properties: II.769
Ti-Al-Ni phase diagram: II.693
TiAl: II.623, II.683
Time dependant deformation: I.561
Titanium alloy: I.465, II.643, II.751
Titanium aluminides: II.623, II.693
TP347H: II.957
Trace contaminants: II.903
Transition piece: I.345
Tube: III.1361
Tube alloys: II.1233
Tungsten: III.1311
Turbine blade: I.245, I.429
Turbine components: I.419, II.751, II.769, III.1269
Turbines: II.743
Type 347: II.933
Type IV cracking: III.1661
Udimet 720: I.419
Under deposit corrosion: II.815
USC: II.1009, II.1109, II.1233, III.1311, III.1397, III.1469, III.1515, III.1591, III.1629, III.1639, III.1767
Valve: III.1371
Virtual gas turbine system: II.733
Visco-plastic: I.561, III.1651
Viscous creep: III.1531
Vision 21: III.1745
Waspaloy: I.335, III.1551
Waste: II.785, II.933
Weldability: II.1065, II.1081, III.1711
Welded joint: III.1397, III.1661, III.1691, III.1711
Welding: II.1091, III.1343, III.1671, III.1681, III.1701
Wood: II.785, II.883
Workability: I.325
$Yb_4Si_2O_7N_2$: II.997
Z phase: II.1171, II.1223
Zener-Hollomon parameter: I.401
Zirconia: I.449

Schriften des Forschungszentrums Jülich
Reihe Energietechnik/Energy Technology

1. **Fusion Theory**
   Proceedings of the Seventh European Fusion Theory Conference
   edited by A. Rogister (1998); x, 306 pages
   ISBN 3-89336-219-3

2. **Radioactive Waste Products 1997**
   Proceedings of the 3rd International Seminar on Radioactive Waste Products
   held in Würzburg (Germany) from 23 to 26 June 1997
   edited by R. Odoj, J. Baier, P. Brennecke et al. (1998), xxiv, 506 pages
   ISBN 3-89336-225-8

3. **Energieforschung 1998**
   Vorlesungsmanuskripte des 4. Ferienkurs „Energieforschung"
   vom 20. bis 26. September 1998 im Congrescentrum Rolduc und
   im Forschungszentrum Jülich
   herausgegeben von J.-Fr. Hake, W. Kuckshinrichs, K. Kugeler u. a. (1998),
   500 Seiten
   ISBN 3-89336-226-6

4. **Materials for Advances Power Engineering 1998**
   Abstracts of the 6th Liège Conference
   edited by J. Lecomte-Beckers, F. Schubert, P. J. Ennis (1998), 184 pages
   ISBN 3-89336-227-4

5. **Materials for Advances Power Engineering 1998**
   Proceedings of the 6th Liège Conference
   edited by J. Lecomte-Beckers, F. Schubert, P. J. Ennis (1998),
   Part I xxiv, 646, X pages; Part II xxiv, 567, X pages; Part III xxiv, 623, X pages
   ISBN 3-89336-228-2

6. **Schule und Energie**
   1. Seminar Energiesparen, Solarenergie, Windenergie. Jülich, 03. und
   04.06.1998
   herausgegeben von P. Mann, W. Welz, D. Brandt, B. Holz (1998), 112 Seiten
   ISBN 3-89336-231-2

7. **Energieforschung**
   Vorlesungsmanuskripte des 3. Ferienkurses „Energieforschung"
   vom 22. bis 30. September 1997 im Forschungszentrum Jülich
   herausgegeben von J.-Fr. Hake, W. Kuckshinrichs, K. Kugeler u. a. (1997),
   505 Seiten
   ISBN 3-89336-211-8

Schriften des Forschungszentrums Jülich
Reihe Energietechnik/Energy Technology

8. **Liberalisierung des Energiemarktes**
   Vortragsmanuskripte des 5. Ferienkurs „Energieforschung“
   vom 27. September bis 1. Oktober 1999 im Congrescentrum Rolduc und
   im Forschungszentrum Jülich
   herausgegeben von J.-Fr. Hake, A. Kraft, K. Kugeler u. a. (1999), 350 Seiten
   ISBN 3-89336-248-7

9. **Models and Criteria for Prediction of Deflagration-to-Detonation Transition (DDT) in Hydrogen-Air-Steam-Systems under Severe Accident Conditions**
   edited by R. Klein, W. Rehm (2000), 178 pages
   ISBN 3-89336-258-4

10. **High Temperature Materials Chemistry**
    Abstracts of the 10th International IUPAC Conference, April 10 - 14 2000, Jülich
    edited by K. Hilpert, F. W. Froben, L. Singheiser (2000), 292 pages
    ISBN 3-89336-259-2

11. **Investigation of the Effectiveness of Innovative Passive Safety Systems for Boiling Water Reactors**
    edited by E. F. Hicken, K. Verfondern (2000), x, 287 pages
    ISBN 3-89336-263-0

12. **Zukunft unserer Energieversorgung**
    Vortragsmanuskripte des 6. Ferienkurs „Energieforschung“
    vom 18. September bis 22. September 2000 im Congrescentrum Rolduc und
    im Forschungszentrum Jülich
    herausgegeben von J.-Fr. Hake, S. Vögele, K. Kugeler u. a. (2000),
    IV, 298 Seiten
    ISBN 3-89336-268-1

13. **Implementing Agreement 026**
    For a programme of research, development and demonstration on advances fuel cells
    Fuel Cell Systems for Transportation
    Annex X. Final Report 1997 - 1999
    edited by B. Höhlein; compiled by P. Biedermann (2000), 206 pages
    ISBN 3-89336-275-4

14. **Vorgespannte Guß-Druckbehälter (VGD) als berstsichere Druckbehälter für innovative Anwendungen in der Kerntechnik**
Prestressed Cast Iron Pressure Vessels as Burst-Proof Pressure Vessels for Innovative Nuclear Applications
von W. Fröhling, D. Bounin, W. Steinwarz u. a. (2000) XIII, 223 Seiten
ISBN 3-89336-276-2

15. **High Temperature Materials Chemistry**
Proceedings of the 10th International IUPAC Conference
held from 10 to 14 April 2000 at the Forschungszentrum Jülich, Germany
Part I and II
edited by K. Hilpert, F. W. Froben, L. Singheiser (2000), xvi, 778, VII pages
ISBN 3-89336-259-2

16. **Technische Auslegungskriterien und Kostendeterminanten von SOFC- und PEMFC-Systemen in ausgewählten Wohn- und Hotelobjekten**
von S. König (2001), XII, 194 Seiten
ISBN 3-89336-284-3

17. **Systemvergleich: Einsatz von Brennstoffzellen in Straßenfahrzeugen**
von P. Biedermann, K. U. Birnbaum, Th. Grube u. a. (2001), 185 Seiten
ISBN 3-89336-285-1

18. **Energie und Mobilität**
Vorlesungsmanuskripte des 7. Ferienkurs „Energieforschung“
vom 24. September bis 28. September 2001 im Congrescentrum Rolduc und im Forschungszentrum Jülich
herausgegeben von J.-Fr. Hake, J. Linßen, W. Pfaffenberger u. a. (2001),
205 Seiten
ISBN 3-89336-291-6

19. **Brennstoffzellensysteme für mobile Anwendungen**
von P. Biedermann, K. U. Birnbaum, Th. Grube u. a. (2002)
PDF-Datei auf CD
ISBN 3-89336-310-6

20. **Materials for Advances Power Engineering 2002**
Abstracts of the 7th Liège Conference
edited by J. Lecomte-Beckers, M. Carton, F. Schubert, P. J. Ennis (2002),
c. 200 pages
ISBN 3-89336-311-4

Schriften des Forschungszentrums Jülich
Reihe Energietechnik/Energy Technology

21. **Materials for Advances Power Engineering 2002**
Proceedings of the 7th Liège Conference
edited by J. Lecomte-Beckers, M. Carton, F. Schubert, P. J. Ennis (2002),
Part I c. 600 pages; Part II c. 600 pages; Part III c. 600 pages
ISBN 3-89336-312-2

Schriften des Forschungszentrum Jülich
Reihe Energietechnik / Energy Technology Volume 21, Part II

Forschungszentrum Jülich GmbH
Institut für Werkstoffe und Verfahren der Energietechnik

Jacqueline Lecomte-Beckers, Marc Carton,
Florian Schubert and Philip J. Ennis (Editors)

Materials for Advanced Power Engineering 2002

Proceedings of the 7th Liège Conference
Part II

EUROPEAN COMMISSION
UNIVERSITE DE LIEGE

Schriften des Forschungszentrum Jülich
Reihe Energietechnik / Energy Technology Volume 21, Part II

ISSN 1433-5522 ISBN 3-89336-312-2

Die Deutsche Bibliothek- CIP-Einheitsaufnahme

Materials for advances power engineering 2002 : proceedings of the 7th Liège Conference / ed.: Jacqueline Lecomte-Beckers ... - Jülich : Forschungszentrum, Zentralbibliothek

(Schriften des Forschungszentrums Jülich : Reihe Energietechnik ; Vol. 21)
ISBN 3-89336-312-2

Pt. 2 . - (2002)

Publisher and Distributor:	Forschungszentrum Jülich GmbH Central Library 52425 Jülich Phone +49 (0) 24 61 61 53 68 · Telefax +49 (0) 24 61 61 61 03 e-mail: zb-publikation@fz-juelich.de Internet: http://www.fz-juelich.de/zb
Cover Design:	Grafische Betriebe, Forschungszentrum Jülich GmbH
Printer:	Grafische Betriebe, Forschungszentrum Jülich GmbH
Copyright:	Forschungszentrum Jülich 2002

Printed on environmentally friendly paper.

The editors cannot accept any responsibility or liability for the accuracy of any statements or information given in the papers.

Schriften des Forschungszentrum Jülich
Reihe Energietechnik / Energy Technology, Volume21, Part 2

ISSN 1433-5522
ISBN 3-89336-312-2

Neither this book nor any part of it may be reproduced or transmitted in any form or by any means, electronic or mechanical, including photocopying, microfilming, and recording, or by any information storage and retrieval system, without permission in writing from the publisher.

FOREWORD

The European Co-operation in the field of Scientific and Technical Research (COST) is now a well established organisation for the co-ordination of national research and development programmes on a European level. This series of Liège Conferences was initiated in order to disseminate the results of the materials related COST Actions, beginning with COST 50 which was mainly concerned with materials for gas turbines and then moving to COST 501 in which materials for power generation plant were investigated. The results of the current COST Action 522 'Ultra Efficient, Low Emission Power Plants' are presented at this, the Seventh Liège Conference. The work is focused on materials for the components that have a decisive influence on the enhancement of power plant performance and efficiency.

Reliable energy supply at reasonable cost is one of the most important factors in the development of the modern industrialised society, but we are becoming increasingly concerned about the environmental impact of energy production and of the need to conserve valuable energy resources for future generations. Therefore, the emphasis is on a sustainable energy supply and the development of advanced energy conversion and power generation technologies taking into account the need for fuel conservation and environmental protection is essential. Although new and emerging energy technologies are of great interest, fossil fuel will continue to make a significant contribution well into the 21st century. Because a by-product of the conversion of fossil fuels is CO_2, the key factor is the thermal efficiency of plant; the higher the efficiency, the lower will be the levels of CO_2 produced for a given energy output. Power plant can be made more efficient by increasing the temperatures and pressures of the process, resulting in the general requirement for improved materials and components that can operate reliably for long times at higher temperatures and pressures.

The materials research and development activities required for the critical components of power generation plant have been based on the principle of work-sharing, bringing together materials scientists, design engineers, alloy producers and component manufacturers, reflecting the need to match materials properties and component behaviour. In order to put the European efforts into a world context, there are several invited review papers covering power plant materials development in the USA, Japan and South Africa. In addition there are over 130 contributions (presented as posters at the Conference) from 26 countries.

The Conference Proceedings reflect the Conference Technical Programme. They are divided in three volumes and the contents are as follows:

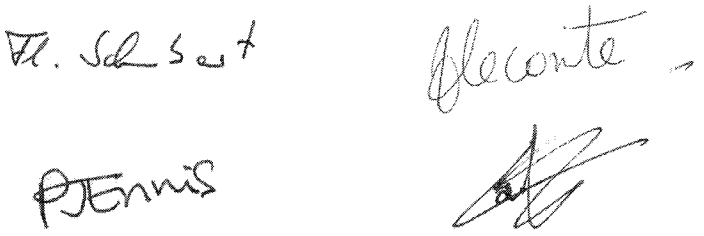
Part I : ADVANCED GAS TURBINE MATERIALS I
Invited Papers
1.1. Single Crystal
1.2. Ni Base Superalloys
1.3. Coatings

Part II : ADVANCED GAS TURBINE MATERIALS II
1.4. Intermetallics
1.5. Miscellaneous Topics
FUEL ISSUES AND NOVEL COMPONENTS
Invited Papers
2.1. Hot Gas Corrosion
2.2. Miscellaneous Topics
ADVANCED STEAM POWER PLANT I
Invited Papers
3.1. Microstructure

Part III: ADVANCED STEAM POWER PLANT II
3.2. Alloy Development
3.3. Mechanical Properties
3.4. Steam Oxidation and Coatings
3.5. Welding
3.6. Applications
OUTLOOK
Invited Papers

As in previous Liège Conferences, many people have made significant contributions to the success of this Conference. The Technical and Editorial Board would like to thank all the members of the COST 522 Management Committee both for their supervision and co-ordination of the considerable research effort in their own countries and across national boundaries, and for their help in the reviewing of the contributed papers.

September 2002



International Advisory Board

Aguero, A.	INTA	Spain
Allen, D.	Alstom Power	UK
Artinger, I.	TU Budapest	Hungary
Auerkari, P.	VTT	Finland
Berger, C.	TU Darmstadt	Germany
Bosansky, J.	Welding Research Inst	Slovenia
Bregani, F.	CESI	Italy
Cerjak, H.	TU Graz	Austria
Czyrska-Filemonowicz, A.	AGH Krakow	Poland
Delannay, F.	UC Louvain	Belgium
Déroulède, A.	DGXII	CEC
Engelen, B.	Min Economic Affairs	Belgium
Ennis, P.J.	FZ Jülich	Germany
Geipel, D.	MBF	Germany
Germain, A.	Université de Liège	Belgium
Hald, J.	TU Denmark	Denmark
Harada, H.	NIMS	Japan
Härkegård, G.	NUST	Norway
Henderson, P.J.	Vattenfall	Sweden
Khan, T.	ONERA	France
Kern, T.U.	Siemens PG	Germany
Koslowski, R.	TU Krakow	Poland
Legros, W.	Université de Liège	Belgium
Lecomte-Beckers, J.	Université de Liège	Belgium
Lupinc, V.	CNR-IENI	Italy
Masuyama, F.	Mitsubishi HI	Japan
Mayer, K.H.	Alstom Energie	Germany
McLean, M.	Imperial College	UK
Oakey, J.	Cranfield University	UK
Perez-Trujillo, F.	UC Madrid	Spain
Pomeroy, M.	University of Limerick	Ireland
Rademakers, P.	TNO	The Netherlands
Sánchez-Pasqual, A.	INTA	Spain
Schubert, F. (Chairman)	FZ Jülich	Germany
Seitz, E.	DGXII	CEC
Singheiser, L.	FZ Jülich	Germany
Sklenicka, V.	Academy of Sciences	Czech Republic
Spiradek-Hahn, A.	ÖFZ Seibersdorf	Austria
Staubli, M.	Alstom Power	Switzerland
Teixeira, V.M.	University of Minho	Portugal
ten Hoeven, H.J.	NRL	The Netherlands
Tiainen, T.	TU Tampere	Finland
Toulios , M.	NTU Athens	Greece
van Duysen, J.C.	EDF	France
Viswanathan, R.	EPRI	USA
Wright, I.	ORNL	USA
Zrnik, J.	TU Kosice	Slovakia

Technical and Editorial Board

J. Lecomte-Beckers (chief editor)	Université de Liège	Belgium
D. Allen	Alstom Power	UK
M. Carton	Université de Liège	Belgium
H. Cerjak	TU Graz	Austria
A. Déroulède	DGXII	CEC
P. J Ennis	FZ Jülich	Germany
H. Nguyen-Dang	Université de Liège	Belgium
J. Oakey	Cranfield University	UK
R. B. Scarlin	Alstom Power	Switzerland
F. Schubert	FZ Jülich	Germany
E. Seitz	DGXII	CEC
M. Staubli	Alstom Power	Switzerland
M. Toulios	NTU Athens	Greece

Organisation of Sessions

Advanced Gas Turbine Materials :	D. Allen
Fuel Issues and Novel Components :	J. Oakey
Advanced Steam Power Plant :	M. Staubli

Local Organisation Committee

F. Schubert (chairman)	Jülich
J. Lecomte-Beckers (vice-chairman)	Liège
P. J. Ennis, R. Herzog	Jülich
M. Carton, Y. Greday	Liège
B. Krahl-Urban (co-ordinator)	Jülich

Conference Secretaries

E. Wittig, Y. Abdel-Fatah, S. Stassar	Jülich
R. Pirson	Liège

The 7th Liège Conference has been organized by the Forschungszentrum Jülich and the Université de Liège.

TABLE OF CONTENTS

PART I

Foreword iii

Table of Contents vii

SECTION 1 – ADVANCED GAS TURBINE MATERIALS

Invited Papers

THE MECHANICAL BEHAVIOUR OF A CLASS OF RHENIUM BASED SX SUPERALLOYS FOR INDUSTRIAL GAS TURBINE APPLICATIONS I.5
Toulios M., Allen D.H.

CONSTITUTIVE MATERIAL FORMULATIONS AND ADVANCED LIFE ASSESSMENT METHODS FOR SINGLE CRYSTAL GAS TURBINE BLADES I.23
Busso E.P., Toulios M., Cailletaud G.

GAMMA TiAl INTERMETALLICS FOR TURBOMACHINERY APPLICATIONS I.43
Nazmy M., Lupinc V.

ADVANCES IN COATING SYSTEMS FOR UTILITY GAS TURBINES I.57
Nicholls J.R., Wing R.

ENVIRONMENTAL DEGRADATION OF GAS TURBINE COATINGS: TOWARDS STANDARDISED TESTING AND DATABASES I.73
Simms N.J., Bale D.W., Baxter D., Oakey J.E.

WROUGHT Ni-BASE ALLOYS FOR ADVANCED GAS TURBINE DISC AND USC STEAM TURBINE ROTOR APPLICATIONS I.89
Rösler J., Böttger B., Wolske M., Penkalla H.J., Berger C.

NEW MATERIALS AND COOLING SYSTEMS FOR HIGH TEMPERATURE, HIGHLY LOADED COMPONENTS IN ADVANCED COMBINED CYCLE POWER PLANTS I.107
Bohn D.E.

OVERVIEW OF US-DOE PROGRAM IN HIGH EFFICIENCY ENGINES AND TURBINES I.121
Layne A.W.

1.1. Single Crystal

THE CREEP BEHAVIOUR OF AS-CAST SX CM186LC AT INDUSTRIAL GAS TURBINE OPERATING CONDITIONS I.139
Wilcock I.M., Lukas P., Maldini M., Klabbers J., Dubiel B., Henderson M.B.

THE LOW CYCLE FATIGUE BEHAVIOUR OF AS CAST SINGLE CRYSTAL CM186LC I.149
Bale D.W., Henderson M., Dubiel B., Czyrska-Filemonowicz A., Guardamagna C., Bontempi P., Mulvihill P., Lukas P., Obrtlik K., Kolkman H.

CREEP BEHAVIOUR OF THE THIRD GENERATION Ni-BASE SINGLE CRYSTAL SUPERALLOY TMS-75 AND ITS γ/γ' TIE-LINE ALLOYS I.159
Murakumo T., Kobayashi T., Nakazawa S., Harada H.

CREEP BEHAVIOUR AND γ' EVOLUTION OF A NEW NICKEL BASE SUPERALLOY FOR SINGLE CRYSTAL BLADE APPLICATIONS I.167
Maldini M., Lupinc V., Li H., Angella G.

CREEP OF [001]-ORIENTED Ni-20 MASS %Cr SINGLE CRYSTALS I.177
Terada Y., Nakamoto Y., Matsuo T.

CHARACTERIZATION OF THE PROPAGATION BEHAVIOR OF SHORT FATIGUE CRACKS IN NICKEL-BASED SINGLE CRYSTAL SUPERALLOY SC16 I.187
Zhang X.P., Wang C.H., Chen W.Y., Ye L., Mai Y.-W.

EFFECT OF γ' VOLUME FRACTION ON THIRD-GENERATION SINGLE-CRYSTAL SUPERALLOYS I.197
Zhou H., Harada H., Ro Y., Koizumi Y., Kobayashi T., Nakazawa S.

ON THE EFFECT OF RHENIUM ON THE EXTENT OF PRIMARY CREEP IN ADVANCED Ni-BASED SUPERALLOYS I.207
Rae C.M.F., Kakehi K., Reed R.C.

INVESTIGATION OF POROSITY IN SINGLE-CRYSTAL NICKEL-BASE SUPERALLOYS I.217
Epishin A., Link T., Brückner U., Portella P.D.

INVESTIGATION AND COMPARISON OF THE MICROSTRUCTURE OF THE NICKEL-BASE SUPERALLOYS CMSX-4 AND SX CM186LC I.227
Danciu D., Klabbers J., Penkalla H.J.

DISLOCATION MICROSTRUCTURE OF CMSX-4 AFTER TENSILE TESTING WITH DIFFERENT STRAIN RATES AT 700 AND 1000°C I.235
Danciu D., Penkalla H.J., Schubert F.

MORPHOLOGICAL CHANGE IN γ' PHASE IN DIFFERENT PORTIONS OF FIRST STAGE HIGH PRESSURE TURBINE BLADE OF PWA1480 I.245
Miura N., Harada N., Kondo Y., Matsuo T.

METALLURGICAL ANALYSIS OF IN SERVICE *CMSX-2* SINGLE CRYSTAL GAS TURBINE BUCKETS I.255
Yoshioka Y., Saito D., Ito S., Fukuyama Y.

CARBIDE PRECIPITATION IN SINGLE CRYSTAL Ni-BASE SUPERALLOYS I.263
Tin S., Pollock T.M.

MODELLING OF HIGH TEMPERATURE TMF TESTS OF SINGLE CRYSTALS BY A PURE CREEP LAW I.273
White P.S., Kong C.N.

A MULTISCALE CONSTITUTIVE APPROACH TO MODEL THE MECHANICAL BEHAVIOUR OF INHOMOGENEOUS SINGLE CRYSTAL SUPERALLOYS: APPLICATION TO AS-CAST SX CM186LC I.283
Regino G.M., Busso E.P., O'Dowd N.P., Allen D.

DEFORMATION MODELLING OF THE SINGLE CRYSTAL SUPERALLOY CM186LC I.293
Daniel R., Tinga T., Henderson M.B., Ward T.J.

TMS-82+: A HIGH STRENGTH Ni-BASE SINGLE CRYSTAL SUPERALLOY I.303
Hino T., Yoshioka Y., Koizumi Y., Kobayashi T., Harada H.

1.2. Ni Base Superalloys

MICROSTRUCTURE OF A 5-COMPONENT Ni-BASE MODEL ALLOY: EXPERIMENTS AND SIMULATION I.315
Warnken N., Böttger B., Ma D., Vitusevych V., Hecht U., Fries S.G., Dupin N.

ALLOY DESIGN FOR ULTRA HIGH TEMPERATURE STEAM TURBINE APPLICATIONS : SIMULATION OF MICROSTRUCTURE DURING FORGING I.325
Kopp R., Wolske M.

MICROSTRUCTURE AND STRUCTURAL STABILITY OF CANDIDATE MATERIALS FOR TURBINE DISC APPLICATIONS BEYOND 700°C I.335
Penkalla H.J., Wosik J., Schubert F.

MATERIAL DEGRADATION AND DAMAGE ASSESSMENT FOR GAS TURBINE COMBUSTION COMPONENTS I.345
Saito D., Yoshioka Y., Fujiyama K.

EFFECT OF SOLUTION HEAT TREATMENT ON THE HOT CORROSION RESISTANCE OF A SECOND GENERATION DS SUPERALLOY I.355
Tamaki H., Okayama A., Onay B., Yoshinari A.

CREEP PROPERTIES DEGRADATION IN A LONG-TIME THERMALLY EXPOSED NICKEL BASE SUPERALLOY I.365
Zrnik J., Strunz P., Vrchovinsky V., Hornak P., Wiedenmann A.

EFFECT OF TENSILE HOLDS ON THE DEFORMATION BEHAVIOUR OF A NICKEL BASE SUPERALLOY SUBJECTED TO LOW CYCLE FATIGUE I.375
Zrnik J., Semenak J., Wangyao P., Vrchovinsky V., Hornak P.

IN-SITU OBSERVATIONS OF THE DEFORMATION AND DAMAGE BEHAVIOUR AROUND LASER-DRILLED COOLING HOLES IN INCONEL ALLOY 617 USING THE SCANNING ELECTRON MICROSCOPE I.385
Klabbers J., Wessel E., Schubert F.

DESIGN OF Ni-BASE DS SUPERALLOYS FOR INDUSTRIAL GAS TURBINES I.395
Sato M., Koizumi Y., Kobayashi T., Karada H., Ono H.

THE INVESTIGATIONS OF DEFORMABILITY AND STRUCTURE OF A-286 ALLOY AT HIGH TEMPERATURE DEFORMATION I.401
Ducki K.J., Hetmanczyk M., Kuc D.

MODELLING THE CREEP BEHAVIOUR OF A WROUGHT NICKEL BASE SUPERALLOY IN A WIDE RANGE OF STRESS/TEMPERATURE CONDITIONS I.409
Maldini M., Lupinc V.

CREEP BEHAVIOUR OF A POWDER METALLURGY UDIMET 720 NICKEL-BASED SUPERALLOY I.419
Dubiez S., Couturier R., Guétaz L., Burlet H.

1.3. Coatings

MCrAlY COATING BY AN ELECTROCHEMICAL ROUTE I.429
Bacos M.-P., Girard B., Josso P., Rio C.

EVALUATION OF THERMOMECHANICAL FATIGUE RESISTANCE OF COATED SUPERALLOYS BY A LASER THERMAL SHOCK SYSTEM I.439
Meriggi M., Rinaldi C.

THERMOPHYSICAL AND MICROSTRUCTURAL CHARACTERISATION OF MODIFIED THICK YTTRIA STABILISED ZIRCONIA THERMAL BARRIER COATINGS I.449
Bianchi P., Cernuschi F., Lorenzoni L., Ahmaniemi S., Vippola M., Vuoristo P., Mäntylä T.

ADVANCED NITRIDE COATINGS FOR OXIDATION PROTECTION OF TITANIUM ALLOYS I.465
Leyens C., Hovsepian P.Eh., Münz W.-D., Peters M., Lewis D.B., Luo Q.

HIGH TEMPERATURE NANOLAMINATE CERAMIC COATINGS PREPARED BY PVD TECHNIQUES I.475
Teixeira V., Monteiro A., Portinha A., Vaßen R., Stöver D.

CYCLIC LIFETIME OF PYSZ AND CESZ EB-PVD TBC SYSTEMS ON VARIOUS Ni-SUPERALLOY SUBSTRATES I.483
Schulz U., Fritscher K., Kaysser W.A.

CHARACTERISATION OF SIX OVERLAY COATINGS I.493
Giannozzi M., Giorni E., Merluzzi M., Pratesi F., Zonfrillo G.

SINGLE CRYSTAL COATING OF SX TURBINE BLADES BY A LASER CLADDING TECHNIQUE I.503
Bezençon C., Wagnière J.-D., Höbel M., Schnell A., Konter M., Kurz W.

COMPARISON OF THERMAL CYCLING LIFE OF YSZ AND $LA_2ZR_2O_7$-BASED THERMAL BARRIER COATINGS I.511
Vaßen R., Barbezat G., Stöver D.

DEPOSITION OF ALUMINIUM + YTTRIUM ON THE INTERNAL SURFACES OF COMPLEX COOLED INDUSTRIAL TURBINE BLADES I.523
Innocenti M., Giorni E., Wing R., Norreys A., Archer N.J.,Yeatman J., Bianchi P., Baxter D., Wahl G., Metz Ch.

CHARACTERIZATION OF THE BOND-COAT MATERIALS FOR THE SUPER HIGH EFFICIENCY GAS TURBINES I.535
Suzuki A., Wu F., Murakami H., Imai H.

ELASTIC BEHAVIOUR OF PLASMA SPRAYED THERMAL BARRIER COATINGS I.543
Steinbrech R.W., Frahm J., Herzog R., Schubert F.

DEFORMATION BEHAVIOUR OF A LOW PRESSURE PLASMA SPRAYED NiCoCrAlY BOND COAT UNDER SHEAR LOADING AT TEMPERATURES ABOVE 750°C I.551
Majerus P., Steinbrech R.W., Herzog R., Schubert F.

VISCO-PLASTIC PROPERTIES OF SEPARATED THERMAL BARRIER COATINGS UNDER COMPRESSION LOADING I.561
Heckmann S., Herzog R., Steinbrech R.W., Schubert F., Singheiser L.

STRUCTURE IN THE SURFACE LAYER OF COATED Ni-BASED SUPERALLOYS DURING ANNEALING IN OXYDATION ENVIRONMENT I.569
Svejcar J., Jirikovsky K., Krejcí J.

MEASUREMENT OF THE DUCTILE BRITTLE TRANSITION TEMPERATURE AND THERMAL MECHANICAL FATIGUE RESISTANCE OF COATINGS USED IN GAS TURBINE ENGINES I.577
Saunders S.R.J., Banks J.P.

AUTHOR INDEX I

KEYWORD INDEX VII

PART II

SECTION 1 – ADVANCED GAS TURBINE MATERIALS

1.4. Intermetallics

MICROSTRUCTURE AND TENSILE CREEP BEHAVIOR OF MULTIPHASE NiAl EUTECTIC ALLOYS MODIFIED WITH Zr OR Hf II.595
Guo J.T., Qi Y.H., Cui C.Y., Li G.S.

CREEP STRENGTH AND MICROSTRUCTURE OF Ti-46Al-2W-0.5Si BASE ALLOYS II.605
Dlouhy A., Arrell D., Karlsson B., Lapin J., Lupinc V., Nazmy M., Nikbin K., Staubli M.

HIGH TEMPERATURE DEFORMATION OF THE Fe28Al3Cr IRON ALUMINIDE MODIFIED WITH ADDITIVES II.615
Hakl J., Vlasák T., Kratochvil P.

MICROSTRUCTURE AND CREEP OF γ-TIAL BASED INTERMETALLIC ALLOY II.623
Lapin J., Pelachová T.

HIGH CYCLE FATIGUE BEHAVIOUR OF INTERMETALLIC γ-TiAl BASED ALLOYS II.633
Koolloos M.F.J., Arrell D.J., Henderson M.B., Gallet S.

Ti_2AlNb-BASED TITANIUM INTERMETALLIC ALLOYS FOR HIGH TEMPERATURE APPLICATIONS II.643
Hagiwara M., Emura S., Tang F.

MANUFACTURING AND TESTING OF A NOVEL ADVANCED NiAl-BASE ALLOY FOR GAS TURBINE APPLICATIONS II.653
Palm M., Sauthoff G.

HIGH-RATE SPUTTER DEPOSITION OF NiAl ON SAPPHIRE FIBERS II.663
Reichert K., Martinez C., Cremer R., Neuschütz D.

INTERFACIAL THERMAL STABILITY IN BN-COATED CONTINOUS Al_2O_3 FIBER REINFORCED NiAl COMPOSITES II.673
Wen K.Y., Reichert K., Hu W., Frommert M., Gottstein G.

MECHANICAL PROPERTIES AND OXIDATION BEHAVIOUR OF A CAST TiAl INTERMETALLIC II.683
Lupinc V., Marchionni M., Nazmy M., Onofrio G., Staubli M., Tomasi A., Zhou L.Z.

COATING OF Ni-ALUMINIDES ON TiAl INTERMETALLICS THROUGH UP-HILL DIFFUSION II.693
Izumi T., Nishimoto T., Narita T.

INFLUENCE OF MICROSTRUCTURAL EVOLUTION ON HARDNESS OF A γ TiAl INTERMETALLIC CONTAINING W AND Si II.703
Munoz-Morris M.A., Gil I., Morris D.G.

STRENGTHENING MECHANISMS IN DUCTILE FeAl INTERMETALLIC PROCESSED BY MECHANICAL ALLOYING II.711
Morris D.G., Garcia Oca C., Munoz-Morris M.A.

1.5. Miscellaneous topics

EXTRAPOLATION OF LIMITED CREEP DATA BY PARALLEL FITTING WITH DATA FOR SIMILAR MATERIALS II.723
White P.S.

DEVELOPMENT OF A VIRTUAL TURBINE SYSTEM FOR NEW MATERIALS DESIGN II.733
Saeki H., Fukuyama Y., Yokokawa T., Odaka T., Yoshida T., Harada H.

DRILLING OF COOLING HOLES AND SHAPING OF BLOW-OUT FACILITIES IN TURBINE BLADES BY LASER RADIATION II.743
Willach J., Horn A., Kreutz E.W.

REPAIR AND (RE)CONDITIONING OF COMPRESSOR AND TURBINE BLADES BY CO_2 AND Nd: YAG LASER RADIATION II.751
Kelbassa I., Gasser A., Backes G., Keutgen S., Kreutz E.W., Pirch N.

HIGH TEMPERATURE REACTOR (HTR) MATERIALS II.759
Buckthorpe D., Couturier R., Van der Schaaf B., Riou B., Rantala H., Moormann R., Buenaventura A., Friedrich B.-C.

PROPERTIES OF OXIDE/OXIDE CMCs FOR HIGH TEMPERATURE APPLICATIONS IN GAS TURBINES II.769
Innocenti M., Del Puglia P., Pappas Y.Z., Dassios C.G., Steen M., Kostopoulos V., Vlachos D.

SECTION 2 - FUEL ISSUES ANS NOVEL COMPONENTS

Invited Papers

IN-SITU FIRESIDE CORROSION TESTING OF ADVANCED BOILER MATERIALS WITH DIVERSE FUELS II.785
Henderson P.J., Karlsson A., Davis C., Rademakers P., Cizner J., Formanek B., Goransson K., Oakey J.

DEGRADATION OF BOILER AND HEAT EXCHANGER MATERIALS: DATA GENERATION, DATABASES AND PREDICTIVE MODELLING II.801
Saunders S.R.J., Simms N.J., Osgerby S., Oakey J.E.

COMPLEX FIRESIDE CORROSION MECHANISM IN BOILERS USING STAGED COMBUSTION SYSTEMS II.815
Bakker W., Kung S., Blough J., Seitz W.

FABRICATION OF A GAS TURBINE COMBUSTION HARDWARE IN ODS FERRITIC MATERIALS II.833
McColvin G., Munasinghe D., O'Driscoll J., Jacobs M.

DESIGN, CONSTRUCTION AND TESTING OF A CERAMIC HIGH TEMPERATURE HEAT EXCHANGER FOR AN EXTERNALLY FIRED CYCLE PLANT II.845
Mao C., Scarpellini R., Valarani M.

ELECTRICAL SWING ADSORPTION FOR CO_2 SEPARATION AND CAPTURE II.853
Judkins R.R.

2.1. Hot Gas Corrosion

HIGH TEMPERATURE CORROSION IN GAS TURBINES: FUEL MODEL AND EXPERIMENTAL RESULTS II.871
Bordenet B., Boßmann H.P.

REDUCTION OF FIRESIDE CORROSION OF SUPERHEATER MATERIALS IN A BIOMASS-FIRED CIRCULATING FLUIDISED BED BOILER II.883
Henderson P.J., Högberg J., Mattsson M.

EFFECT OF FUEL TYPE ON THE FIRESIDE CORROSION OF BOILER MATERIALS FOR ADVANCED CLEAN COAL TECHNOLOGIES II.893
Pinder L.W., Davis C.J.

FATE OF TRACE CONTAMINANTS FROM BIOMASS FUELS IN GASIFICATION SYSTEMS II.903
Kilgallon P., Simms N.J., Oakey J.E.

MATERIALS FOR GASIFIER HEAT EXCHANGERS II.913
Kilgallon P., Simms N.J., Norton J.F., Oakey J.E.

PERFORMANCE OF GAS TURBINE MATERIALS IN "DIRTY FUEL" ENVIRONMENTS II.923
Simms N.J., Encinas-Oropesa A., Kilgallon P., Oakey J.E.

LOW CYCLE FATIGUE IN AGGRESSIVE ENVIRONMENTS –A NEW TESTING METHOD USING CONTROLLED ATMOSPHERES II.933
Andersson H.C.M., Lindblom J.

CHLORINE CORROSION OF THERMALLY SPRAYED COATINGS AT ELEVATED TEMPERATURES II.945
Uusitalo M.A., Vuoristo P.M.J., Mäntylä T.A.

HIGH TEMPERATURE CORROSION IN STRAW FIRED POWER PLANTS: INFLUENCE OF STEAM/METAL TEMPERATURE ON CORROSION RATES FOR TP347H II.957
Montgomery M., Biede O., Hede Larsen O.

2.2. Miscellaneous Topics

EROSION CORROSION OF STEEL TUBES IN THE LOOP SEAL OF A BIOFUEL FIRED CFB PLANT II.969
Nafari A., Nylund A.

PERFORMANCE OF EROSION CORROSION RESISTANT COATINGS IN DIFFERENT COMBUSTION ENVIRONMENTS II.979
Hjörnhede A., Nylund A.

HAFNON – A POTENTIAL CERAMIC MATERIAL FOR LIQUID SLAG REMOVAL IN PRESSURIZED PULVERIZED COAL COMBUSTION ? II.989
Müller M., Hilpert K., Singheiser L.

HEAT RESISTANT SILICON NITRIDE CERAMICS WITH RARE-EARTH SILICON OXYNITRIDE II.997
Nishimura T., Guo S., Hirosaki N., Yamamoto Y., Mitomo M.

SECTION 3 – ADVANCED STEAM POWER PLANT

Invited Papers

BENEFIT OF ADVANCED STEAM POWER PLANTS II.1009
Blum R., Hald J.

DESIGN AND MATERIALS FOR TURBOSETS IN ADVANCED STEAM POWER PLANTS II.1017
Wieghardt K., Kern T.-U.

BOILER DESIGN AND MATERIALS ASPECTS FOR ADVANCED STEAM POWER PLANTS II.1019
Chen Q., Scheffknecht G.

ALLOY DESIGN AND MICROSTRUCTURAL CONTROL FOR IMPROVED 9-12% Cr POWER PLANT STEELS II.1035
Vanstone R.W.

THE EUROPEAN EFFORT IN DEVELOPMENT OF NEW HIGH TEMPERATURE ROTOR MATERIALS UP TO 650°C – COST 522 II.1049
Kern T.-U., Staubli M., Mayer K.H., Escher K., Zeiler G.

DEVELOPMENT OF CREEP RESISTANT CAST STEELS WITHIN THE EUROPEAN COLLABORATION IN ADVANCED STEAM TURBINE MATERIALS FOR ULTRA EFFICIENT, LOW EMISSION STEAM POWER PLANT / COST 501-522 II.1065
Staubli M., Mayer K.-H., Gieselbrecht W., Stief J., DiGianfrancesco A., Kern T.-U.

WELDABILITY AND WELD PROPERTIES FOR ADVANCED POWER PLANT MATERIALS II.1081
Cerjak H., Letofsky E., Jochum C., Nies H.

NEW BOILER MATERIALS FOR ADVANCED STEAM CONDITIONS II.1091
Scarlin B., Stamatelopoulos G.N.

MATERIALS FOR ULTRA-SUPERCRITICAL COAL-FIRED POWER PLANT BOILERS II.1109
Viswanathan R., Purgert R., Rao U.

THE STEAM OXIDATION RESISTANCE OF 9-12% CHROMIUM STEELS II.1131
Ennis P.J., Quadakkers W.J.

COATINGS FOR STEAM POWER PLANTS UNDER ADVANCED CONDITIONS II.1143
Agüero A., Muelas R., Scarlin B., Knoedler R.

3.1. Microstructure

MARTENSITIC/FERRITIC SUPER HEAT-RESISTANT 650°C STEELS –MICROSTRUCTURE II.1161
Agamennone R., Blum W.

PRECIPITATION OF Z-PHASE AND DEGRADATION BEHAVIOUR OF MOD.9Cr-1Mo STEEL II.1171
Kimura K., Suzuki K., Toda Y., Kushima H., Abe F.

DISTRIBUTION OF MX CARBONITRIDES AND ITS EFFECT ON CREEP DEFORMATION IN 9Cr-0.5Mo-1.8W-VNb STEEL II.1181
Sawada K., Kubo K., Hara T., Abe F.

THE EFFECT OF MICROSTRUCTURAL STABILITY ON LONG-TERM CREEP BEHAVIOUR OF 9-12%Cr STEELS II.1189
Sklenicka V., Kucharova K., Kloc L., Svoboda M., Staubli M.

SYSTEM FREE ENERGY APPROACH TO THE PRECIPITATION OF THE LAVES PHASE IN Fe-Cr-W-C QUATERNARY STEELS II.1201
Murata Y., Koyama T., Morinaga M., Hashizume R., Miyazaki T., Doi M.

MICROSTRUCTURAL PHYSICALLY BASED CREEP MODELLING ON 9-12 % Cr STEELS II.1211
Weinert P.

Z PHASE CHARACTERISTICS IN MARTENSITIC 12CrMoVNb STEELS II.1223
Vodarek V., Strang A.

MICROSTRUCTURAL ISSUES IN THE DESIGN OF AUSTENITIC AND NICKEL BASED MATERIALS FOR SUPERHEATER SYSTEMS IN 700°C STEAM PLANT II.1233
Starr F., Shibli A.

PRECIPITATION OF INTERMETALLIC PHASES DURING MARTENSITE AGING IN STEELS CONTAINING 10% Cr II.1241
Pigrova G.D.

A NEW MODELLING APPROACH TO MICROSTRUCTURAL EVOLUTION IN FERRITIC STEELS II.1247
Yin Y.F., Faulkner R.G.

AUTHOR INDEX I

KEYWORD INDEX VII

PART III

SECTION 3 – ADVANCED STEAM POWER PLANT

3.2. Alloy development

EVALUATION OF A NEW 11 % Cr STEEL FOR STEAM CHESTS III.1261
Bates P., Vanstone R.W., Osgerby S., Mulvihill P.

DEVELOPMENT OF HIGH WCoB-CONTAINING 12Cr ROTOR STEELS FOR USE AT 650C IN USC POWER PLANTS III.1269
Arai M., Doi H., Fukui Y., Azuma T., Fujita T.

MARTENSITIC/FERRITIC SUPER HEAT-RESISTANT 650°C STEELS III.1279
Agamennone R., Berger C., Blum W., Ehlers J., Ennis P.J., Granacher J., Inden G., Knezevic V., Quadakkers J.W., Sauthoff G., Scholz A., Singheiser L., Vilk J., Wang Y.

MARTENSITIC/FERRITIC SUPER HEAT-RESISTANT 650°C STEELS – DESIGN OF MODEL ALLOYS III.1289
Knezevic V., Sauthoff G.

MARTENSITIC/FERRITIC SUPER HEAT-RESISTANT 650°C STEELS – THERMODYNAMICS AND KINETICS OF PRECIPITATION REACTIONS III.1299
Vilk J., Schneider A., Inden G.

IMPROVEMENT OF CREEP RUPTURE STRENGTH OF HIGH STRENGTH 12Cr FERRITIC HEAT-RESISTANT STEEL III.1311
Uehara T., Toji A., Komatsubara S., Fujita T.

DEVELOPMENT OF A NEW 18Cr-9Ni AUSTENITIC STAINLESS STEEL BOILER TUBE III.1321
Ishitsuka T., Mimura H.

ALLOY DESIGN FOR ULTRA-HIGH TEMPERATURE STEAM TURBINE APPLICATIONS: PHASE FIELD SIMULATION OF THE REMELTING PROCESS III.1333
Böttger B., Steinbach I., Fries S.G., Chen Q., Sundman B.

WORKABILITY AND DEVELOPMENT OF T/P23 (2.25 % Cr-1.6W-Nb-V STEEL) FOR FOSSIL BOILER AND COMBINED CYCLE APPLICATIONS III.1343
Gabrel J., Lefebvre Bo., Vaillant J.-C., Vandenberghe B.

NEW WROUGHT Ni-BASED SUPERALLOYS WITH LOW THERMAL EXPANSION FOR 700C STEAM TURBINES III.1351
Yamamoto R., Kadoya Y., Kawai H., Magoshi R., Noda T., Hamano S., Ueta S., Isobe S.

DEVELOPMENT OF A NEW 12% Cr-STEEL FOR TUBES AND PIPES IN POWER PLANTS WITH STEAM TEMPERATURES UP TO 650°C III.1361
Bendick W., Gabrel J., Vaillant J.-C., Vandenberghe B.

HIGH PERFORMANCE LOW ALLOY STEEL CASTING FOR STEAM TURBINE III.1371
Ishii R., Tsuda Y., Yamada M., Ikeda K., Kaneko J.

DEVELOPMENT OF HIGH STRENGTH 9Cr STEEL BY COMBINATION OF FINE MX-TYPE NITRIDES AND NO CARBIDE III.1379
Taneike M., Sawada K., Abe F.

DEVELOPMENT STEPS OF NEW STEELS FOR ADVANCED STEAM POWER PLANTS III.1385
Mayer K.H., Blum R., Hillenbrand P., Kern T.-U., Staubli M.

GUIDING PRINCIPLES FOR DEVELOPMENT OF ADVANCED FERRITIC STEELS FOR 650°C USC BOILERS III.1397
Abe F., Okada H., Wanikawa S., Tabuchi M., Itagaki T., Kimura K.,
Yamaguchi K., Igarashi M.

3.3. Mechanical Properties

LONG TERM CREEP AND CREEP FATIGUE PROPERTIES OF THE MARTENSITIC STEELS OF TYPE (G)X12CrMoWVNbN10-1-1 III.1409
Schwienheer M., Haase H., Scholz A., Berger C.

TWO SPECIMEN COMPLEX THERMAL-MECHANICAL FATIGUE TESTS ON THE AUSTENITIC STAINLESS STEEL AISI 316 L III.1419
Rau K., Beck T., Löhe D.

CREEP PROPERTIES OF AUSTENITIC STAINLESS 353 MA AT 1100°C AND 1200°C III.1431
Wu R., Seitisleam F., Sandström R.

PROPERTIES AND EXPERIENCES WITH A NEW AUSTENITIC STAINLESS STEEL (TEMPALOY AA-1) FOR BOILER TUBE APPLICATION III.1445
Minami Y., Tohyama A., Hayakawa H.

IMPROVEMENTS IN THE SHORT TERM CREEP STRENGTH OF AISI 304L BY MEANS OF GRAIN BOUNDARY DESIGN AND CONTROL III.1453
Spigarelli S., Cabibbo M., Evangelista E., Palumbo G.

MICROSTRUCTURAL FEATURES INFLUENCING THE CREEP PROPERTIES OF 9-12 % Cr-STEELS FOCUSING ON LAVES-PHASE PRECIPITATION III.1459
Stocker Ch., Spiradek K., Zeiler G.

CREEP PROPERTIES OF PRECIPITATION STRENGTHENED CARBON FREE MARTENSITIC ALLOYS III.1469
Muneki S., Okubo H., Okada H., Yamada K., Igarashi M., Abe F.

MICROSTRUCTURE AND PROPERTIES OF MODIFIED 3% Cr STEELS III.1477
Foldyna V., Jakobová A., Vodárek V., Kroupa A., Kubon Z.

AN ASSESSMENT OF CREEP RUPTURE DATA ON STEEL E911 III.1487
Allen D.J., Servetto C.

EFFECT OF Cr CONTENT ON THE CREEP STRENGTH AND MICROSTRUCTURAL CHANGE IN HIGH Cr HEAT RESISTANT STEEL III.1497
Miki K., Azuma T., Ishiguro T., Hashizume R., Murata Y., Morinaga M.

THE EFFECT OF THE ELEMENT CARBON ON THE TOUGHNESS AND THE CREEP RUPTURE STRENGTH IN 12Cr HEAT RESISTANT STEELS III.1505
Ryu S.H., Kim M.S., Lee Y.S., Kang S.T., Kim J.T., Yu J.

STRAIN RANGE PARTITIONING ANALYSIS FOR CREEP-FATIGUE LIFE OF FERRITIC HEAT-RESISTING MATERIALS III.1515
Kimura M., Kobayashi K., Yamaguchi K.

HIGH TEMPERATURE CREEP BEHAVIOUR AND MICROSTRUCTURAL CHANGES OF TAF 650 STEEL III.1521
Svoboda M., Bursik J., Podstranska I., Kroupa A., Sklenicka V., Mayer K.-H.

STRESS CHANGE EXPERIMENTS IN LOW STRESS CREEP REGIME OF P-91 TYPE STEEL III.1531
Kloc L., Sklenicka V.

INVESTIGATIONS AND ANALYSIS ON THE STATIONARY CREEP BEHAVIOUR OF 9-12 % CHROMIUM FERRITIC MARTENSITIC STEELS III.1539
Dimmler G., Weinert P., Cerjak H.

ALLOY DESIGN FOR ULTRA HIGH TEMPERATURE STEAM TURBINE APPLICATIONS: CREEP BEHAVIOUR AND MODELLING OF CREEP III.1551
Thoma A., Scholz A., Berger C.

EFFECT OF ALLOYING ELEMENTS ON CREEP PROPERTIES OF Pd ADDED 9Cr FERRITIC STEELS III.1561
Okada H., Muneki S., Yamada K., Okubo H., Igarashi M., Abe F.

IMPROVEMENT OF CREEP STRENGTH OF PRECIPITATION STRENGTHENED 15Cr HEAT RESISTANT FERRITIC STEELS III.1571
Toda Y., Tohyama H., Kushima H., Kimura K., Abe F.

LONG-TERM CREEP STRENGTH PREDICTION OF HIGH Cr FERRITIC CREEP RESISTANT STEELS III.1581
Kushima H., Kimura K., Abe F.

EVALUATION OF CREEP PROPERTIES AND MICROSTRUCTURES ON THERMO-MECHANICAL AND MAGNETIC TREATED 9Cr FERRITIC STEELS III.1591
Okubo H., Muneki S., Okada H., Yamada K., Igarashi M., Abe F.

3.4. Steam Oxidation and Coatings

OXIDATION OF ADVANCED FERRITIC/MARTENSITIC STEELS AND OF COATINGS IN FLOWING STEAM AT 650°C III.1601
Knödler R., Scarlin B.

STEAM OXIDATION OF 9-12Cr MARTENSITIC STEELS: CHARACTERISATION AND MODELLING THE SPALLING OF OXIDE SCALE III.1613
Osgerby S., Mc Cartney L.N.

MECHANICAL AND OXIDATION TESTING OF ADVANCED MATERIALS FOR STEAM POWER PLANTS III.1621
Bontempi P., Guardamagna C., Ricci N., Torri L.

IMPROVEMENT OF STEAM OXIDATION RESISTANCE FOR FERRITIC HEAT RESISTANT STEELS III.1629
Kutsumi H., Itagaki T., Abe F.

STEAM OXIDATION OF HIGH CHROMIUM FERRITIC STEELS CONTAINING PALLADIUM III.1639
Itagaki T., Kutsumi H., Igarashi M., Abe F.

3.5. Welding

DESCRIPTION OF THE MATERIAL BEHAVIOUR IN GIRTH WELDS DURING WELD FABRICATION AND FOR HIGH TEMPERATURE SERVICE III.1651
Mohrmann R.

AN ASSESSMENT OF CREEP RUPTURE DATA ON E911 STEEL WELDMENTS III.1661
Servetto C., Allen D.J.

CHARACTERIZATION OF MATCHING FILLER METALS FOR NEW FERRITIC-BAINITIC STEELS LIKE T/P23 AND T/P24 III.1671
Heuser H., Jochum C.

EVALUATION OF THE WELDED JOINTS IN P92 AND P122 PIPE STEELS III.1681
Ryu S.H., Lee K.W., Chi B.H., Lee Y.S., Kong B.O., Park S.H., Nam S.W., Lim B.S., Kim B.J.

CREEP STRENGTH AND MICROSTRUCTURES FOR HAZ OF WELDMENTS OF HIGH Cr FERRITIC STEELS III.1691
Matsui M., Tabuchi M., Watanabe T., Kubo K., Abe F.

RESEARCH AND DEVELOPMENT OF NEW MARTENSITIC STEELS III.1701
Artinger A., Rozsavolgyi Z.

3.6. Applications

THE FIRST SUPERCRITICAL POWER UNIT IN POLAND. WELDABILITY EVALUATION OF NEW MARTENSITIC CHROMIUM STEELS WITH TUNGSTEN ADDITIONS AND PROPERTIES OF WELDED JOINTS III.1711
Brózda J., Zeman M., Pasternak J.

APPLICATION OF A NEW ROTOR STEEL FORGING FOR MEDIUM RATING SINGLE CYLINDER STEAM TURBINES III.1721
Yamada M., Tsuda Y., Kaneko J.

THE FIRST INDUSTRIAL CAST OF CrMoCoB ADVANCED STEEL FOR CAST TURBINE COMPONENTS III.1731
Contessi E., Del Vecchio D., Ghidini A., Valenti S., Carosi A., Di Gianfranceso A., Ielpo F.M.

OUTLOOK

Invited Papers

MATERIALS DEVELOPMENT FOR ADVANCED VISION 21 POWER PLANTS III.1745
Ruth L.A.

TRENDS IN POWER ENGINEERING IN JAPAN AND REQUIREMENTS FOR IMPROVED MATERIALS AND COMPONENTS III.1767
Masuyama F.

POWER GENERATION IN SOUTHERN AFRICA III.1783
De Beer J.A., Olsha Z.

ENERGY RESEARCH IN THE SIXTH FRAMEWORK PROGRAMME III.1801
Busquin P.

ADDENDUM

DEGRADATION OF EB-PVI) THERMAL BARRIER COATINGS DURING THERMAL CYCLING III.1809
Sun X.F., Li M.H., Zhang Z.Y., Guan H.R

AUTHOR INDEX I

KEYWORD INDEX VII

Part II

SECTION 1

ADVANCED GAS TURBINE MATERIALS

SECTION 1

ADVANCED GAS TURBINE MATERIALS

1.4. Intermetallics

MICROSTRUCTURE AND TENSILE CREEP BEHAVIOR OF MULTIPHASE NIAL EUTECTIC ALLOYS MODIFIED WITH ZR OR HF

J.T.Guo* Y.H.Qi** C.Y.Cui* G.S.Li*
* Institute of Metal Research, Chinese Academy of Sciences, Shenyang 110016, PR China
** Department of Material and Chemical Engineering, Liaoning Institute of Technology, Jinzhou 121001,PR China

Abstract

The microstructures and tensile creep behaviors of HIPed NiAl-33.5Cr-0.5Zr and DS NiAl-28Cr-5.8Mo-0.2Hf alloys have been investigated. The microstructure of HIPed NiAl-Cr(Zr) alloy consists of NiAl matrix, Cr phase and non-continuous white Zr-rich phase, which distributed on the NiAl/Cr phase boundary. As to the DS NiAl-Cr(Mo,Hf) alloy, it is composed of a combination of dendritic and eutectic microstructures. The dendritic arms are of NiAl phase, the interdendritic region is the NiAl and Cr(Mo) phase eutectic region, and there also existed a Hf-rich phase in the NiAl and Cr(Mo) interface. The creep results indicated that the creep curves of both alloys have similar shapes, which are composed of primary creep stage, steady-state creep stage, longer accelerated creep stage, and about 25-45% creep strain. The apparent stress exponents are in the range of 4.8-7.5 and the apparent activation energies of 520-584 kJ/mol were also analyzed. The creep deformations were controlled by the sub-grain boundary formation for the HIP NiAl-Cr(Zr) and dislocation climb for the DS NiAl-Cr(Mo,Hf). The creep rupture data of both alloys obey the Monkman-Grant relationship.

Keywords: Intermetallic, NiAl-based alloy, Microstructure, Creep, Rupture.

1. Introduction

The intermetallic compound NiAl possesses a number of promising properties, such as its low density, high melting point and excellent oxidation resistance at high temperature, that make it an attractive replacement material for superalloys[1]. But the poor fracture toughness at ambient temperature and low creep strength at elevated temperature have inhibited its application. The creep strength has been successfully improved by precipitation strengthening[2] or particulate composite reinforcement[3] and the ductility at room temperature has also been increased by some form of slip homogenization process in the NiAl [110] single crystal doped with Fe, Mo, Ga[4]. It was also necessary to simultaneously improve the fracture toughness and creep resistance of NiAl alloy to compete with currently used superalloys. Cahn[5] has postulated that multiphase intermetallics may be more promising as compared to monolithic alloys in combining high temperature creep strength and room temperature fracture toughness.

It is now well established that transition element addition to NiAl can improve the creep-resistance by solid-solution effects and precipitate hardening through the formation of Ni_2AlX (β') Heusler phase precipitates, where X=Ti, Hf, and Zr[6-8]. But these alloys containing Heusler phase are more brittle than binary NiAl at low temperature. Ductile phase toughening is an attractive approach to enhance the fracture resistance of brittle intermetallics, such as γ-Fe, γ'-Ni_3Al, α-Cr, α-Mo etc. Up to now, only the NiAl-Cr and NiAl-Cr(Mo) alloys toughened by refractory phases possess a better balance between high temperature creep

strength and low temperature toughness[9,10]. However, the creep strengths of these pseudo-binary eutectic alloys are still lower than the superalloys[11]. To further improve the properties from the perspective of processing of multiphase intermetallic alloy, two alloys were selected. One was cast NiAl-33.5Cr-0.5Zr alloy (Unless otherwise stated, all alloys are in atomic percent), followed by hot isostatically pressing. The other was directionally solidified NiAl-28Cr-5.8Mo-0.2Hf alloy. Creep of the NiAl-based alloys has been studied by many investigators[7,8,12], but most of which were tested by compression. Little information was concerned with the tensile creep behavior. This paper aimed at understanding the tensile creep behavior of the HIPed NiAl-33.5Cr-0.5Zr and DS NiAl-28Cr-5.8Mo-0.2Hf multiphase intermetallic alloys.

2. Experimental procedures

The NiAl-33.5Cr-0.5Zr alloy used in this study was prepared by induction melting in vacuum, and processed by hot isostatically pressing (HIP) at 1573K /100MPa for 2h. The NiAl-28Cr-5.8Mo-0.2Hf alloy was directionally solidified in an Al_2O_3–SiO_2 mold by the standard Bridgman technique. The growth rate was about 5 mm/min and the thermal gradient through the solid-liquid interface ranged from 70~80℃/cm. The creep specimens were electro-discharge machined from the alloy ingots with gauge dimensions of 2.5 mm×2 mm×16 mm, with the length direction parallel to the growth direction of the DS alloy. Prior to testing, all samples were ground through 600-grit SiC paper. The creep tests were performed on a DC-25 experimental machine and the creep deformations were recorded by dial indicators. Specimens for microstructural observation were electropolished in a solution containing 25% perchloric acid and 75% glacial acetic acid. Scanning electron microscope (SEM) analysis was performed in a JSM6301F microscope. The transmission electron microscope (TEM) samples were prepared using conventional procedures, including cutting discs with a thickness of 0.3 mm, mechanically polishing them to a 35 μm thickness, dimpling to 20 μm and finally ion milling. TEM observations were performed with a Philips TEM 420 analytical electron microscope operating at 120 kV.

3. Results and discussion

3.1 Microstructure

The microstructure of the HIPed alloy consists typically of eutectic colonies of β-NiAl and α-Cr phase with a non-continuous Zr-rich phase, as shown in Fig.1(a). The composition of the Zr-rich phase is Zr 83.77, Ni 5.40, Cr 10.65 (at,%), and almost no Al is detected by EDS analysis. A typical microstructure of the as-grown NiAl/Cr(Mo, Hf) alloy is shown in Fig.1(b),(c). It is a β+Cr(Mo) two-phase alloy with a dendritic and a eutectic microstructure. Since the directionally solidified ingot was processed at near-equilibrium condition, the dendritic microstructure represents an off-eutectic alloy. The dendrite cores are composed of the NiAl matrix (dark phase), whereas the interdendritic regions are Cr(Mo) single phase. As to the eutectic region, it is formed by the NiAl matrix (dark phase) and Cr(Mo) phase (white phase). It is noted that there existed whiter phase at the NiAl and Cr(Mo) interface. The composition of this whiter phase by EDXS is as follows: Hf 82.19, Ni 6.07, Cr 8.62, Mo 2.26, Al 0.86, which indicated that this white phase is the Hf-rich precipitate with high levels of the elements Cr and Ni.

According to the NiAl-Cr(Mo) phase diagram[9] and NiAl-Ni_2AlHf pseudobinary phase diagram[13], the maximum solubility of Hf in NiAl is less than 5% at the eutectic (NiAl-Ni_2AlHf) temperature of approximately 1350℃. Therefore Hf can be fully dissolved in the NiAl matrix at the NiAl and Cr(Mo) eutectic temperature. The solidificated process of DS NiAl-28Cr-5.8Mo-0.2Hf alloy could be deduced as follows: the Cr(Mo) and NiAl eutectic reaction occurs at about 1445℃ firstly,

$$L \rightarrow NiAl + Cr(Mo) \qquad (1)$$

The NiAl phase becomes enriched in Hf and the Hf-rich phase precipitates with decreasing temperature from the NiAl phase.

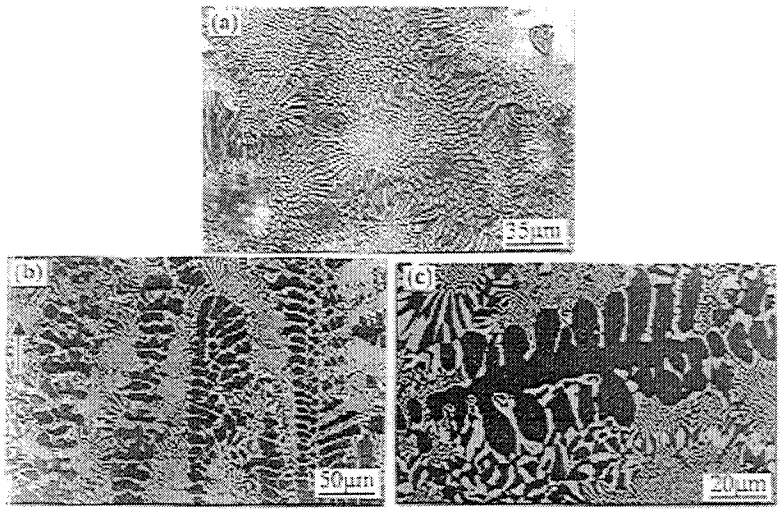


Fig.1 The microstructures of the alloys (a) Secondary electron image of the HIPed NiAl-Cr(Zr) alloy, (b) and (c) The microstructure of the longitudinal section and the transverse section for the DS NiAl-28Cr-5.8Mo-0.2Hf alloy, respectively

The TEM image of the NiAl and Cr(Mo) in the DS NiAl-28Cr-5.8Mo-0.2Hf alloy is shown in Fig.2(a). The selected area diffraction pattern of NiAl and Cr(Mo), as shown in Fig.2(b), establishes a cube-on–cube orientation relationship between the NiAl and Cr(Mo) phases, i.e. $[111]_{NiAl}//[111]_{Cr(Mo)}$, $(10\bar{1})_{NiAl}//(10\bar{1})_{Cr(Mo)}$, which is consistent with our previous report[14]. Diffraction patterns obtained parallel to the growth direction of the crystal also indicate a <111> growth direction for both phases. In addition to the Cr(Mo) phase, fine Cr(Mo) precipitates with an average size of 30nm were also observed in the NiAl matrix.

3.2 The creep behavior

Tensile creep curves of HIPed NiAl-Cr(Zr) alloy are shown in Fig.3(a), and those of DS NiAl-Cr(Mo,Hf) alloy are shown in Fig.3(b). It can be seen that the creep curves are composed of primary creep stage, steady-state (second) creep stage and longer accelerated creep stage. For the DS alloy, the primary creep strains tend to increase with increase in applied stress and test temperature. The steady state creep rate increases with increasing in applied stress at a fixed temperature and in test temperature at a fixed applied stress. It is

found that the elongation to fracture of all samples under the present experimental conditions are about 25-45%, which is similar to that of the DS Ni_3Al-based alloy[15], and far more than that of DZ17G superalloy[16], It is suggested that at least two factors could be responsible for the relatively large elongation to failure: creep cavitation and cross slip to non-basal planes[17]. The activity of additional slip-systems in addition to the basal ones can explain the large elongations to fracture[18].

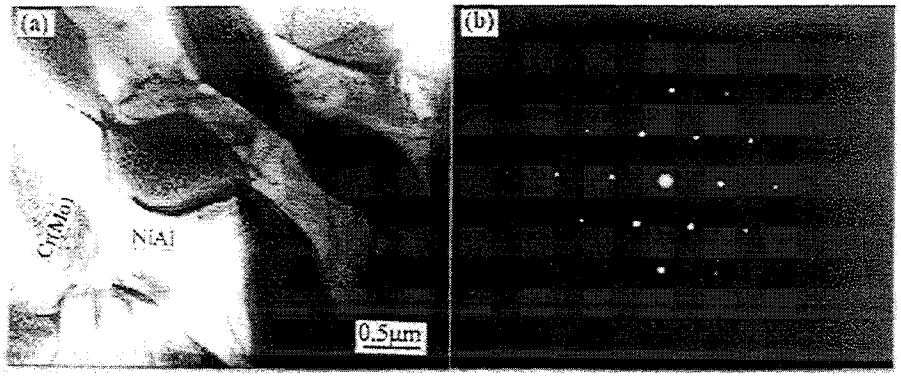


Fig.2 (a) TEM image of NiAl and Cr(Mo) phase in the DS NiAl-28Cr-5.8Mo-0.2Hf alloy, (b) The selected area diffraction pattern of NiAl and Cr(Mo) phases

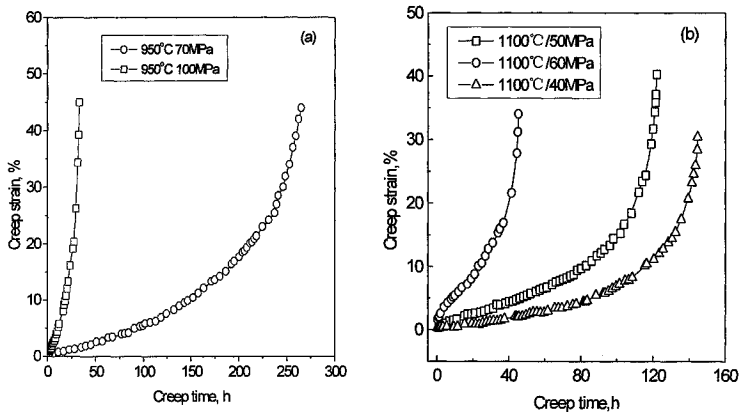


Fig.3 Tensile creep curves of the alloys (a) For the HIPed NiAl-Cr(Zr) alloy, (b) For the DS NiAl-28Cr-5.8Mo-0.2Hf alloy

The creep behavior of B2 aluminides follows that for metals and alloys and can be analyzed accordingly. The steady state (or minimum) creep rate, $\dot{\varepsilon}$, can be described by a power-law equation:

$$\dot{\varepsilon} = A\sigma^n \exp(-Q_c/RT) \qquad (2)$$

where A is constant for a given material, R the gas constant, σ the applied stress, n the apparent stress exponent, Q_c the apparent activation energy for creep.

For pure metals and simple alloys, the value of the apparent stress exponent (n) is between 4 and 6, while the apparent activation energy for creep (Q) is close to that of self-diffusion activation energy. The dependences of applied stress on steady state creep rate at constant temperature between 900~1000℃ are shown in Fig.4. The stress exponents are approximate 6.1~6.9 for the HIPed NiAl-Cr(Zr) alloy, and 4.8 for the DS alloy. These values are somewhat larger than that characteristic of dislocation creep in metallic systems, demonstrating the effects of solid solution strengthening by partially substituting Zr or Hf for Ni or Al elements and precipitation strengthening by forming the Zr-rich or Hf-rich phases.

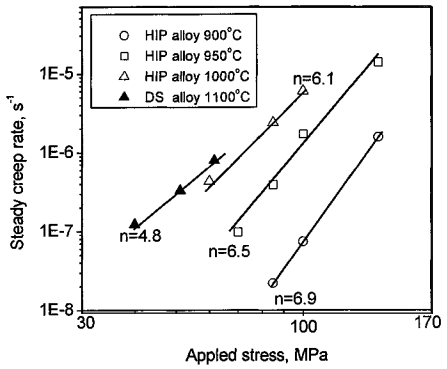


Fig.4 Dependence of the steady state creep rate on the applied stress of the alloys

The temperature dependence of the steady state creep rate at constant applied stress is shown in Fig.5. The apparent creep activation energy determined for the HIPed alloy is approximately 520~584kJ/mol for stresses 50~150MPa. These values are much higher than that for self-diffution of pure Ni in austenite (265-285kJ/mol) and in the NiAl (220-300 kJ/mol)[19]. In general, the higher Q value is typical for dislocation creep in engineering alloys. TEM observation (Fig.6) indicates that subgrain boundaries were formed in the crept HIPed NiAl-Cr(Zr) alloy, which imply that dynamic recovery and dynamic recrystallization occurred. The TEM observations of the crept DS NiAl-Cr(Mo,Hf) alloy specimen revealed a strong attractive interaction between the dislocations and the precipitates (See Fig.7). The apparent stress exponent and the interaction between the dislocations and the precipitates suggested that there exists a threshold stress, where the threshold stress is defined as a lower limiting stress below which no measurable strain rate can be achieved. Such a threshold stress is usually observed for alloys with finely distributed precipitate particles. Accordingly, the present threshold stress in the DS NiAl-Cr(Mo,Hf) alloy is attributed to the small Cr(Mo) particles in the NiAl grains.

The creep characteristics for the present alloys are compared to those of several NiAl-based alloy in references [7,11,20,21]. It is found that the stress exponent of the DS NiAl-Cr(Mo,Hf) alloy is less than that of the DS NiAl/Cr(Mo) alloy and that of the HIPed NiAl-Cr(Zr) alloy is the same as that of the DS NiAl/Cr(Mo) alloy. Such differences can be attributed to the addition of Zr or Hf and their different processing routes. The stress exponent n is believed to provide an insight into creep mechanisms. The values of 1,3,5,7,or 8 are considered to represent the processes of grain boundary diffusion controlled creep (Coble creep), viscous

glide of mobile dislocations (class I), high temperature climb controlled creep due to lattice self-diffusion (class II), low temperature climb controlled creep due to core diffusion or a constant structure model controlled by lattice self diffusion, respectively. The n values for the creep reported by a number of authors range between 3 and 10.2[1]. The origin of this wide scatter is not clear but the n values are dependent on temperature, stress and processing history. The stress exponent of the DS NiAl-Cr(Mo,Hf) alloy leads to the conclusion that the creep behavior of this alloy is class II type.

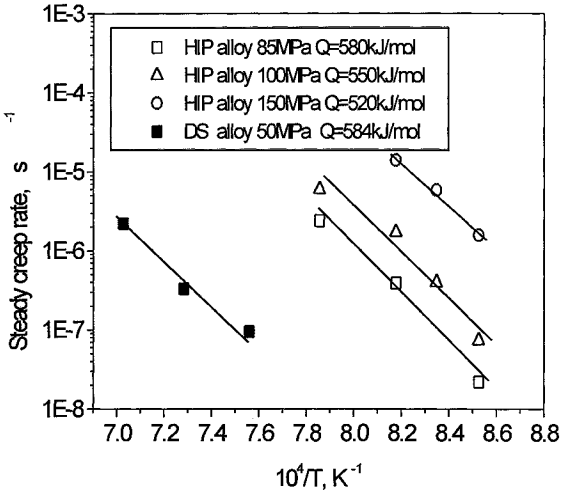


Fig.5 Dependence of the steady state creep rate on the temperature of the alloys

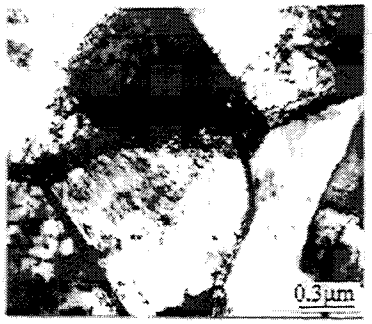


Fig.6 TEM image showing the formation of sub-grain boundary in the HIPed NiAl- Cr(Zr) sample crept at 1173K under 150MPa

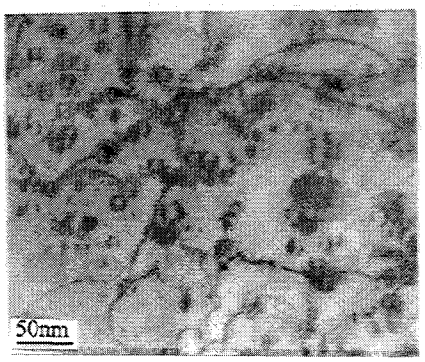


Fig.7 Dislocations interaction with Cr(Mo) precipitates in the DS NiAl -28Cr -5.8Mo -0.2Hf alloy crept to 10% at 1100 ℃ under a tensile stress of 50MPa

For some pure metals and alloys with stable structures during the creep deformation, it was thought that the time to onset of tertiary creep (t_t) was linearly related to the time to fracture (t_f), and the ratio of t_f/t_t is about 1.5 [22]. The ratio of t_f/t_t is between 1.48 and 1.71 for the HIPed alloy, and that is 1.75 for the DS alloy. SEM observations (as shown in Fig.8) on the

post creep samples also confirm this. This microstructural stability can give the material higher resistance for creep deformation than precipitation strengthening [23]. SEM observations of the side surface showed that the creep cracks can initiate at the phase boundary of NiAl and Cr or Cr(Mo) phase, which is almost the same as the fracture behavior of DS NiAl/Cr(Mo,Hf) alloy[24]. The tensile fractographs of multiphase Ni-25Al-15Cr investigated by Chen and Guo [25] are also characterized by complete debonding along the interface. So the bonding of the phase boundary in multiphase alloy is very weak and much work needs to be done to improve bonding of the interface.

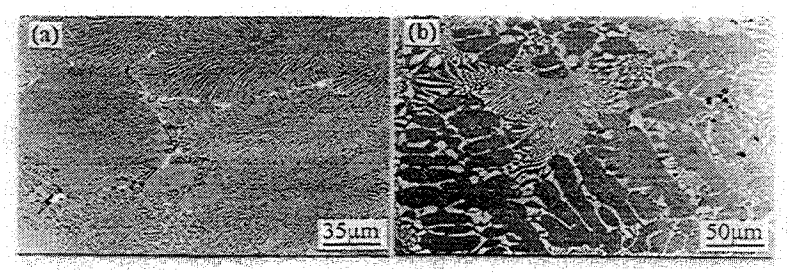


Fig.8 The stable microstructure of the crept alloy, which the creep cracks were formed at the phase boundaries of NiAl and Cr or Cr(Mo) phases. (a) The HIPed NiAl-Cr(Zr) sample crept at 1173K under 150MPa, (b) The DS NiAl-28Cr-5.8Mo-0.2Hf alloy crept at 1100℃ under 50Mpa

The SEM observations (Fig.9(a)) of the creep fracture surfaces of the HIPed alloy indicated that the fracture surfaces were oxided severely, and there are two characteristic: (1) ductile regions consisting of dimple at the eutectic cell region, (2) the chisel prism region at the cell boundary. The ductile region is created by the growth and coalescence of voids formed in eutectic cells, and the chisel prism is created by decohesion along the cell boundary. In general, the proportion of ductile region increased when the test temperature increased and the applied stress decreased. The SEM observations of the creep-rupture surfaces of DS NiAl-Cr(Mo,Hf) alloy at 50MPa and 1100℃ show that the creep fracture mode is ductile transgranular with apparent dimples, as shown in Fig.9(b).

Under all test conditions, creep-rupture data of the present alloys follow the Monkman-Grant relationship[26], as shown in Fig.10, and can be described as:

$$t_f(\dot{\varepsilon}_s)^M = C_{MG} \qquad (3)$$

where M=0.8868 and $C_{MG}=6.38\times10^{-5}$ for the HIPed alloy. M=0.778 and $C_{MG}=8.33\times10^{-4}$ for the DS alloy. The result of fitting equation (3) to the data for both alloys is M=0.8869 and $C_{MG}=1.77\times10^{-4}$.

Moreover, the stress and temperature dependence of creep life can be written as [22]:

$$t_f = B\sigma^m \exp(Q_f / RT) \qquad (4)$$

where t_f is creep life, B is a material constant, σ is the applied stress, R is the gas constant, m is the stress exponent, Q_f is the creep rupture activation energy, T is the absolute temperature. As shown in Fig.11, the creep rupture activation energy is 338, 392, and 523kJ/mol for stresses of 85, 100, and 150MPa for the HIPed NiAl-Cr(Zr) alloy, and 469kJ/mol for the DS

NiAl-Cr(Mo,Hf) alloy. This dependence of t_f on the creep behavior suggests that the rate of development of cracks is determined by the deformation process.

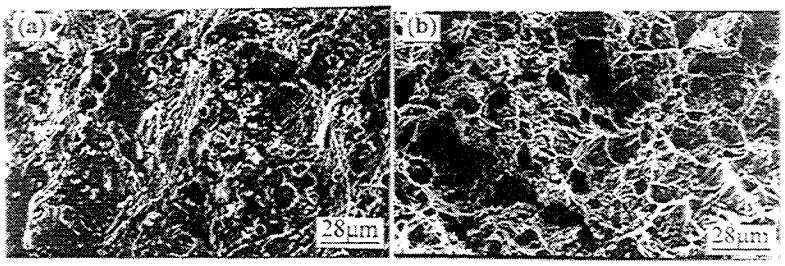


Fig.9 The creep fractograph of the alloys (a) The HIPed NiAl-Cr(Zr) sample crept at 1273K under 100Mpa, (b) SEM photograph showing the transgranular failure with dimple for theDS NiAl-28Cr-5.8Mo-0.2Hf alloy crept at 1100 ℃ under 50 MPa

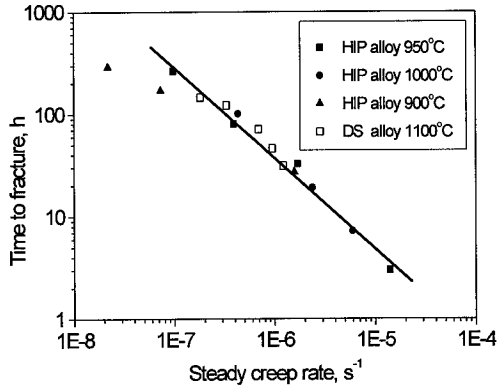


Fig.10 Dependence of the time to fracture on the steady state creep rate of the alloys

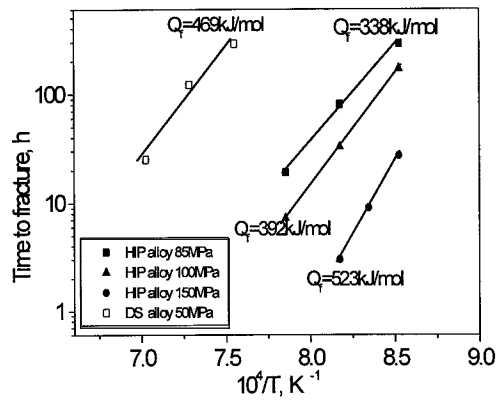


Fig.11 Dependence of the time to fracture on the temperature of the alloys

4. Conclusions

(1). The microstructure of HIPed NiAl-33.5Cr-0.5Zr alloy consists of β-NiAl and α-Cr eutectic cells surrounded by a non-continuous Zr-rich phase. Small addition of Hf to the NiAl/Cr(Mo) system resulted in a dendritic and eutectic two phase (NiAl+Cr(Mo)) alloy. The Hf-rich phase existed at the NiAl/Cr(Mo) phase boundary.
(2). All of the creep curves is these experiments exhibited similar shapes of primary creep stage, steady-state creep stage and longer accelerated creep stage, and the creep strains are about 25~45%. The microstructures of crept samples are stable.
(3). The creep mechanism is dynamic recovery and dynamic recrystallization for the HIPed NiAl-Cr(Zr) alloy., and the climb of dislocation for the DS NiAl-Cr(Mo,Hf) alloy. The creep fracture behavior obeys the Monkman-Grant relationship.

5. Acknowledgements

This work was supported by the National Natural Science Foundation of China (No. 59895152) and National Advanced Materials Committee of China (No. 863-715-005-0030), to whom we are very grateful.

6. References

[1] R.D. Noebe, R.R. Bowman and N.V. Nathal, Physical and mechanical properties of the B2 compound NiAl, Int.Mater.Rev., **38**, 1993, 193.
[2] R. Darolia, NiAl alloy for high-temprature structural applications, JOM, **43**, 1991, 44.
[3] J.T. Guo and Z.P. Xing, Investigation of NiAl-TiB_2 in situ composites, J.Mater.Res., **12**, 1997, 1083.
[4] R. Darolia, D. Lahrman and R. Field, The Effect of Iron, Gallium and Molybdenum on the room temperature tensile ductility of NiAl, Scripta.Mater., **26**, 1992, 1007.
[5] R.W. Cahn, Multiphase intermetallics, Phil.Trans. R. Soc. Lond. A, **351**, 1995, 497.
[6] P. R. Strutt, R. S. Polvani and J. C. Ingram, Creep behavior of the Heusler type structure alloy Ni_2AlTi, Metall. Mater. Trans. A, **7A**, 1976, 23.
[7] J. D. Whittenberger and R. D. Noebe, Elevated temperature compressive properties of Zr-modified NiAl, Metall. Mater.Trans. A, **27A**, 1996, 2628.
[8] J. D. Whittenberger, I. E. Locci, R. Darolia, and R. R. Bowman, 1300K creep behavior of [001] oriented Ni-49Al-1Hf (at.%) single crystal, Mater. Sci. Eng. A, **A268**, 1999, 165.
[9] H. E. Cline and J. L. Walter, The Effect of alloy additions on the rod-plate transition in the eutectic NiAl-Cr, Metall. Trans., **1**, 1970, 2907.
[10] H. E. Cline, J. L. Walter, E. Lifshin and R. R. Russell, Structures, faults, and the rod-plate transition in eutectics, Metall. Trans., **2**, 1971, 189.
[11] D. R. Johnson, X. F. Chen, B. F. Oliver, R. D. Noebe and J. D. Whittenberger, Processing and mechanical properties of in situ composites from the NiAl-Cr and the NiAl-(Cr,Mo) eutectic systems, Intermetallics, **3**, 1995, 99.
[12] E. Arzt and P. Grahle, High temperature creep behavior of oxide dispersion strengthened NiAl intermetallics, Acta Mater., **46**, 1998, 2717.
[13] M. Takeyama and C.T. Liu, Microstructures and mechanical properties of NiAl-Ni_2AlHf alloys, J.Mater.Res., **5**, 1990, 1189.
[14] C.Y. Cui, Y.X. Chen, J.T. Guo, Y.H. Qi and H.Q. Ye, Brittle-to-ductille transition in

multiphase NiAl alloy, Mater.Sci. Eng., **A325**, 2002, 187.

[15] J. Lapin, Creep behavior of directionally solidified Ni_3Al-Based alloy, In 'Proceedings of the 6th Liège conference Part III, Materials for Advanced Power Engineering 1998', ed. J. Lecomte-Beckers, F. Schubert and P. J. Ennis, Liège, Univerte de Liege, European Commission, 1998, pp1337.

[16] J.T. Guo, C.Yuan, H.C. Yang, V. Lupinc and M. Maldini, Creep-rupture behavior of a directionally solidified Nickel-based superalloy, Metall. Mater. Trans. A, **32A**, 2001, 1103.

[17] M. Regev, E. Aghion, A. Rosen and M. Bamberger, Creep studies of coarse-grained AZ91D Magnesium castings, Mater. Sci. Eng., **A252**, 1998, 6.

[18] M Regev, A. Rosen and M. Bamberger, Qualitative model for creep of AZ91D Magnesium alloy, Metall. Mater.Trans., **32A**, 2001, 1335.

[19] R. D. Noebe, C. L. Cullers and R. R. Bowman, The Effect of strain rate and temperature on the tensile properties of NiAl, J. Mater. Res., **7**, 1992, 605.

[20] D.R. Johnson, X.F. Chen, B.F. Oliver, R.D. Noebe and J.D. Whittenberger, Directional solidification and mechanical properties of NiAl-NiAlTa alloys, Intermetallics, **3,** 1995, 141.

[21] C.T. Liu, J. Yang, Z. Suo, A.G. Evans, R. Hecht and R. Mehrabian, Matrix cracking in intermetallic composites caused by thermal expansion mismatch, Acta mater., **39**, 1991, 1883.

[22] J.T. Guo, D. Ranucci, E. Picco and P. M. Strocchi, An investigation on the creep and fracture behavior of cast Nickel-base superallloy IN738LC, Metall.Mater. Trans. A, **14A,** 1983, 2329.

[23] Y. Yamabe-Mitarai, S. Nakazawa and H. Harada, Creep behavior of Ir-Nb and Ir-Zr alloys, Scripta mater., **43**, 2000, 1059.

[24] J.T. Guo, C.Y. Cui, Y.X. Chen, D.X. Li and H.Q. Ye, Microstructure, interface and mechanical property of the DS NiAl/Cr(Mo,Hf) composite, Intermetallics, **9,** 2001, 287.

[25] R.S. Chen, J.T. Guo, W.L. Zhou and J.Y. Zhou, Brittle-to-ductile transition of a multiphase intermetallic alloy, Intermetallics, **8**, 2000, 663.

[26] F.C. Monkman and N.J. Grant, An empirical relationship between rupture life and minimum creep rate in creep-rupure tests, Proc. ASTM, **56**, 1956, 593.

CREEP STRENGTH AND MICROSTRUCTURE OF Ti-46Al-2W-0.5Si BASE ALLOYS

A. Dlouhý[1)], D. Arrell[2)], B. Karlsson[3)], J. Lapin[4)], V. Lupinc[5)], M. Nazmy[6)], K. Nikbin[7)] and M. Staubli[6)]

[1)]Institute of Physics of Materials, AS CR Brno, Czech Republic, [2)]Alstom Power Sweden AB, Finspång, Sweden, [3)]Chalmers University of Technology, Göteborg, Sweden, [4)]Institute of Materials and Machine Mechanics, SAS Bratislava, Slovak Republic, [5)]CNR IENI, Milano, Italy, [6)]Alstom Ltd., Baden, Switzerland, [7)]Imperial College, London, United Kingdom

Abstract

The present study summarizes data on the tensile creep strength of ABB-2 and ABB-23 alloys (base chemical composition Ti-46Al-2W-0.5Si (at-%)) collected at 700 and 750°C within the framework of the COST 522 – GT – WP 1.2 γ-TiAl action. Participating laboratories tested different cast parts including test pieces cut directly from gas turbine blades. Both, uniaxial and notched bar tests were performed. It is shown that the alloy microstructure in the as-received condition (after casting, HIPping and heat treatment) varies with the position in the cast part. While regions below the casting surface exhibit columnar grains and a nearly lamellar microstructure, the central part is often composed of globular grains and a duplex microstructure in which the fully lamellar grains coexist with the equiaxed-γ grains free of lamellae. These microstructural variations represent the important contribution to the scatter of the creep strength data. In agreement with earlier studies, it has been found that the creep strength of the duplex material is inferior to the creep strength of the fully lamellar parts. This effect should be considered in the case of thick wall cast sections where redistribution of stresses during service may occur due to the microstructurally based variations of the creep strength. Boron additions are shown to accelerate creep in the range of low applied stresses.

Keywords: Creep, gamma-TiAl, nearly lamellar microstructure, duplex microstructure, cast components.

Introduction

In recent years, there has been a considerable effort directed towards a development of creep resistant γ-TiAl based alloys that would meet strong mechanical and oxidation requirements set for specific applications in gas turbines (GTs). As a result, the alloy ABB-2 with the chemical composition Ti-46Al-2W-0.5Si (at-%) was patented [1]. Further research was performed to optimise the heat treatment, microstructure and related properties of the ABB-2 alloy [2]. The component processing is a next step towards the final application of the ABB-2 alloy. Precision casting represents one of the most cost effective routes used for the production of GT components. However, this processing route yields microstructures that are later difficult, if possible at all, to break and homogenize during subsequent heat treatments. Therefore, certain degree of microstructural inhomogeneity has to be accepted as the consequence of the selected processing path. The relation between the casting process and the final properties of ABB-2 casts has recently been investigated in the COST522 GT-WP1.2 γ-TiAl work package. A considerable effort has been spent to understand how the non-homogeneous microstructure of the ABB-2 casts forms and how this microstructure influences final mechanical properties. The present study summarizes creep data obtained in the participating laboratories and relates these data to the characteristic microstructures observed in the ABB-2 cast parts after their processing and heat treatment.

Experimental details

Investigated alloy – microstructure after casting and heat treatment

The ABB-2 alloy cast by Howmet Research Corp. and supplied by ALSTOM Power Baden has been investigated in the present study. Two different batches, which are further referred to as ABB-2 and ABB-23, were subjected to microstructure analysis and creep. The chemical composition of the two batches is given in Table 1 where the boron content represents the main difference between the two materials. While the batch ABB-2 was free of boron, the batch ABB-23 was alloyed with 0.7 at% of boron. Two different shapes were cast and investigated using the ABB-2 material, namely 15 and 25 mm thick plates and two GT blades. Similarly, 16 mm diameter rod and 25 mm thick slab were cast and subjected to the analysis in the case of ABB-23 material. After casting, all the investigated parts received the same heat treatment which consisted of HIP (1260°C/172 MPa/4 hours), annealing at 1350°C for 1 hour and final aging at 1000°C for 6 hours after which the parts were furnace cooled to room temperature. The macrostructure in some of the investigated cast parts, formed during processing and heat treatment, is shown in Figure 1.

Table 1 Chemical composition of the investigated alloys

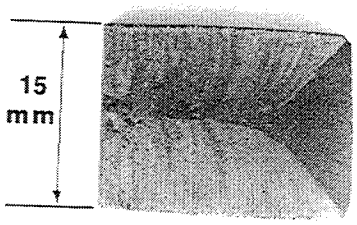
element	Ti	Al	W	Si	Fe	Cu	C	O	N	H	B
	ABB-2										
wt %	bal	30.5	9.1	0.33	0.02	0.001	0.005	0.066	0.032	0.001	-
at %	bal	46.1	2.0	0.48	0.02	0.001	0.017	0.168	0.093	0.040	-
	ABB-23										
wt %	bal	30.2	9.0	0.38	0.04	0.001	0.045	0.087	0.017	0.001	0.182
at %	bal	45.3	2.0	0.55	0.03	0.001	0.152	0.220	0.049	0.040	0.682

Creep testing

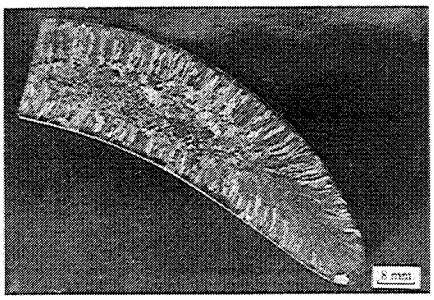
Seven laboratories contributed to the investigation of creep in ABB-2 and ABB-23 alloys: (i) Institute of Physics of Materials in Brno, Czech Republic, (ii) Alstom Power Sweden in Finspång, Sweden, (iii) Chalmers University of Technology in Göteborg, Sweden, (iv) Institute of Materials and Machine Mechanics in Bratislava, Slovak Republic, (v) CNR IENI in Milano, Italy, (vi) Alstom Power in Baden, Switzerland and (vii) Imperial College of Science Technology and Medicine in London, United Kingdom. These laboratories are further referred to respectively as (i) IPM, (ii) AP Sweden, (iii) ChUT, (iv) IMMM, (v) IENI, (vi) AP Baden and (vii) ICSTM to facilitate the identification of individual data points in creep strength plots.

Creep experiments were performed in tension according to high standards followed in the individual laboratories. In all the laboratories, strain-time readings were continuously recorded by data acquisition systems. Tests were performed at 700 and 750°C either under the constant load or under the constant stress in air or in purified argon. These variations in the testing method were assessed based on round robin exercises and it was concluded that (i) the difference associated with the load application (constant load versus constant stress) does not influence the ABB-2 and ABB-23 minimum creep rate (MCR) data since these minima are observed after about 1 to 2% of creep strain where the load difference is negligible and (ii) there is no influence of the environment (air versus argon) on the creep strain accumulation

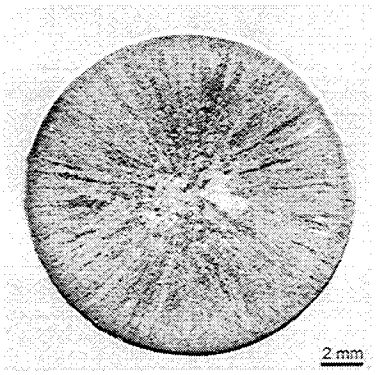
kinetics up to testing times of the order of 2000 hours [3]. Much more influence on the creep strength stem from the varying microstructure throughout the cast parts [4] (Figure 1). These microstructurally based variations are reported on later in the result section. An effort was also made to economize the expensive testing material and time and thus some of the MCR data were acquired in the incremental load creep tests described earlier [5]. The MCR data obtained in this type of tests were shown to agree well with the similar data measured in the conventional creep tests [6].



(a)



(b)



(c)

Figure 1: The macrostructure after casting and heat treatment observed in the cross-sections of: (a) the ABB-2 plate, (b) the ABB-2 GT blade and (c) the ABB-23 rod.

A program focused on the notched bar creep testing has been running at the ICSTM in London. Three notch geometries, including sharp, medium (shown in Figure 2) and blunt notches, were investigated, for details see [7]. Double-notched tensile bars were tested in dead weight lever arm machines at 750°C. The axial and, in some cases diametral, displacements were recorded using an LVDT. Notched bar strain was computed in percent by dividing the creep displacement by the gauge length of the specimen which was 38 mm.



Figure 2: Two medium size notches machined on the tensile bar for creep testing.

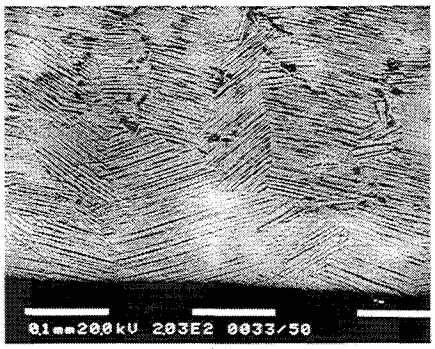
Metallographic methods

The microstructure of the as-cast and heat treated ABB-2 and ABB-23 batches was investigated using light microscopy - LM, scanning electron microscopy – SEM and transmission electron microscopy – TEM (equipped with the Ultra-Thin window EDAX Phoenix analyzer). The fraction of interdendritic regions and its variation with the position in the as-cast and heat treated parts was quantitatively assessed using a PC-based DIPS image analysis system. A special care was taken during the preparation of TEM foils to avoid any damage due to thinning operations. Slices cut out of the creep specimen gauge length were ground on emery papers to the thickness of 0.3 mm. From this point on only chemical methods were applied. The double jet TENUPOL equipment was used for final perforation of the foil. The electrolyte $HClO_4$ (5%) and methanol (95%) was kept at -50°C.

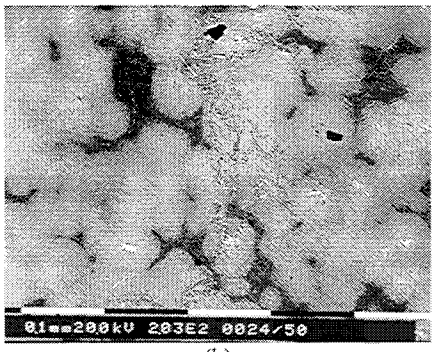
Results and discussion

As-cast and heat treated state

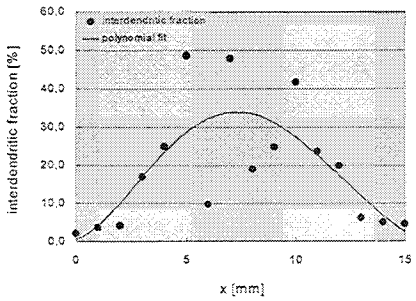
The macrostructure of the cast parts shown in Figure 1 always consists of columnar grains situated below the cast surface that continue into the cast interiors. These columnar grains usually exhibit a nearly lamellar microstructure as it is documented in the back scattered electron SEM image (BSE) in Figure 3a. On the other hand, the central regions of the casts are composed of a duplex microstructure in which nearly lamellar grains are mixed with



(a)



(b)



(c)

Figure 3: SEM micrographs (a) and (b) were obtained in BSE mode. (a) the lamellar grains close to the cast surface, (b) the dendritic lamellar and interdendritic γ regions inside the cast, 6 mm from the cast surface. (c) the fraction of interdendritic regions in the Ti-46Al-2W-0.5Si (at-%) cast increases with distance from the cast surface, the x-coordinates 0 and 15 mm correspond respectively to the top and bottom surface of the cross-section in Figure 1a.

equiaxed γ-grains. This irregular microstructure builds up during the cast solidification because the interdendritic regions are enriched with aluminium and this promotes the formation of pure γ-phase on the expense of the lamellar γ-α_2 microstructure [8]. The Al-rich interdendritic regions in the central part of the ABB-2 cast plate (Figure 1a) give rise to a good contrast in the BSE image shown in Figure 3b since they appear darker than the surrounding Ti-rich dendritic areas. In order to quantify the volume fraction of the interdendritic regions, sixteen BSE images were taken from the metallographic cross-section shown in Figure 1a. The individual images (600 x 400 μm^2) sampled the cross-section area from the top edge to the bottom edge of the cast plate with the sampling step of 1 mm. The complete set of sixteen BSE images was subjected to the quantitative image analysis the result of which is presented in Figure 3c. The plot in Figure 3c clearly shows that the fraction of interdendritic regions increases towards the central part of the ABB-2 cast plate.

The TEM analysis confirmed that the grains inside the columnar regions are nearly lamellar with the mean interface spacing of (450 ± 35) nm, Figure 4. The TEM study also confirmed that the microstructure in the central part of the cast is more irregular. In this region the lamellar grains often coexist with the γ-grains that do not exhibit any lamellae, Figure 5.

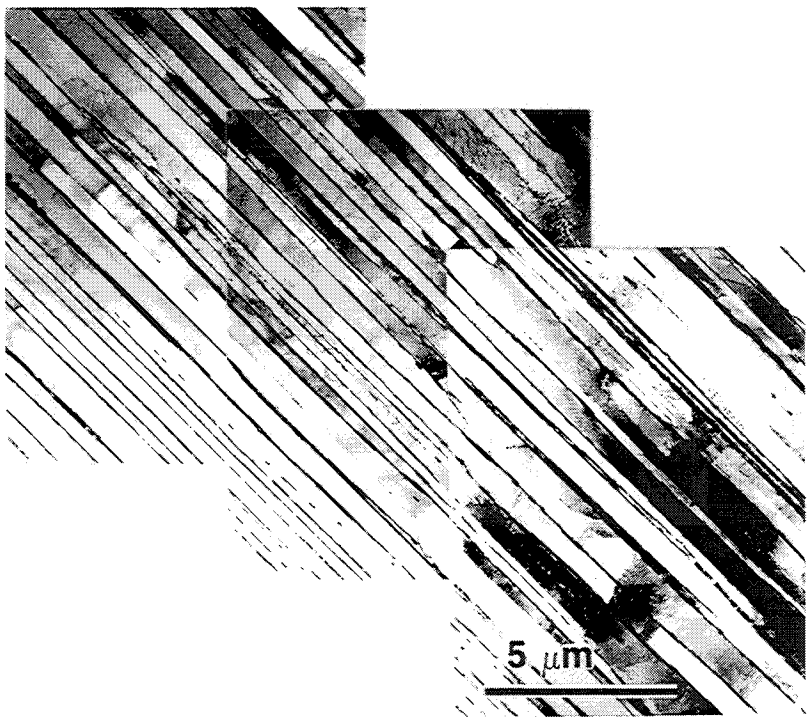


Figure 4: The TEM micrograph shows the lamellar structure of the Ti-46Al-2W-0.5Si (at-%) alloy inside the grain situated in the columnar region of the ABB-2 cast plate. The mean lamellar spacing (interface to interface) was estimated as 450 ± 35 nm.

The chemical composition of the alloy has been studied in the STEM mode. The composition of the matrix γ-phase corresponds, within the accuracy of the measurement, to the nominal composition stated by the alloy producer. In addition to the matrix γ-phase and α_2 lamellae in

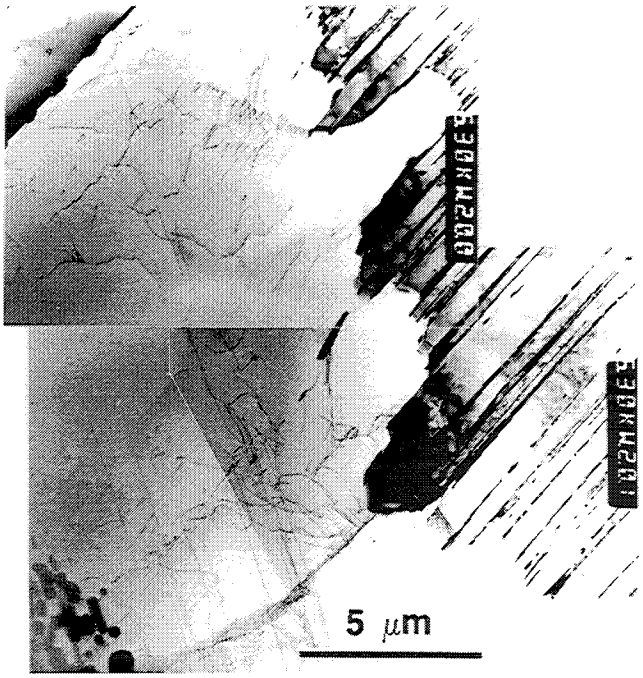
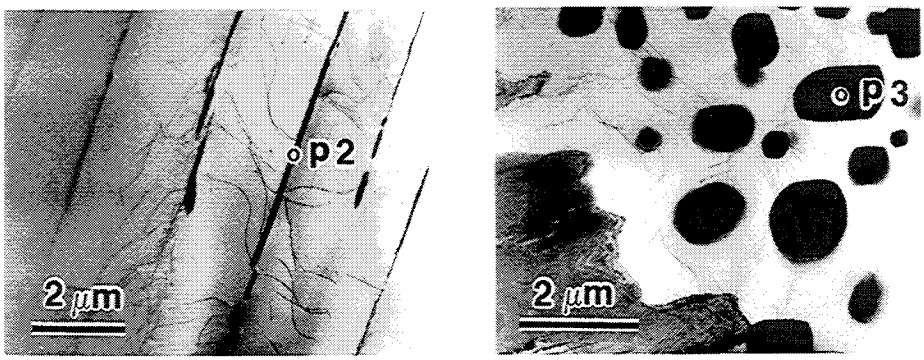


Figure 5: The TEM micrograph showing the boundary between a lamellar grain and a γ-grain in the central part of the Ti-46Al-2W-0.5Si (at-%) cast plate where duplex microstructure is observed.



(a) (b)

Figure 6: TEM micrographs showing the distribution of W-rich B2 (a) and Si-rich Ti_5Si_3 (b) phases in the as-cast microstructure of the Ti-46Al-2W-0.5Si (at-%) alloy. B2 particles like the particle P2 are always associated with lamellar boundaries, while Ti_5Si_3 particles like the particle P3 can be found inside γ- or B2-grains where they form larger conglomerates.

the nearly lamellar grains, two other secondary phases were found. The first type of precipitates is documented in Figure 6a. These W-rich particles decorate the interfaces between γ and α_2 lamellae and there are some indications in the literature that the particles belong to the ordered B2 phase, e.g. [9]. The other precipitates (shown in Figure 6b) are Si-rich and contain only limited amount of tungsten. These particles have chemical composition of Ti_5Si_3 and their structure and orientation relationship with respect to the matrix are also known [10,11]. These globular Ti_5Si_3 particles precipitate inside the γ- or B2-grains and are frequently found in larger groups as it is documented in the lower left corner of Figure 5.

Creep

Uniaxial tension

In view of the microstructural variations in the investigated casts, the creep performance of the individual microstructural types was assessed [4]. Typical creep curves obtained at 750°C for specimens with either nearly lamellar or duplex microstructure are presented in Figure 7. At the same external conditions, the specimen cut from the nearly lamellar region of the ABB-2 cast exhibits the lowest creep rate (the highest creep strength) while two specimens cut out of the duplex regions creep clearly faster. These microstructurally based variations of the creep strength were systematic [4] and gave rise to a scatter band delimited by the two dashed lines in Figure 8a. The lower dashed line represents the MCR measured for the nearly lamellar samples while the upper dashed line fits similar data obtained for the duplex specimens [4]. The plot in Figure 8a also summarizes all the MCR data obtained within our work package testing program. We note that all the data points collected at 750°C in different participating laboratories for ABB-2 batch casts are located inside the scatter band. Thus we can conclude that the varying microstructure of the ABB-2 casts (nearly lamellar below the surface versus duplex microstructure in the central part) provides a relevant contribution to the scatter of creep strength data. However, the scatter is not too dramatic and is usually lower than one order of magnitude in terms of MCR. It should be highlighted that the creep strength differences observed for the nearly lamellar and duplex type of specimens in the present study are in agreement with some earlier results obtained for similar materials [12]. These creep strength variations are also in line with the generally accepted view that the duplex microstructure possesses lower creep strength as compared to the fully lamellar one [13].

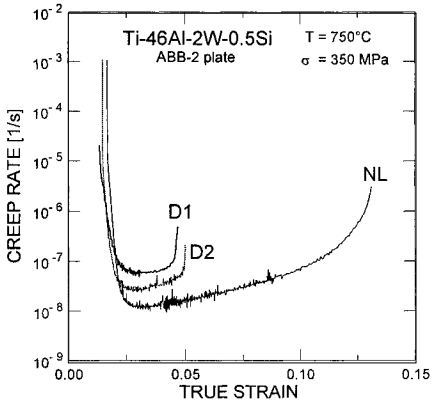


Figure 7: Creep curves measured at 750°C and 350 MPa for specimens which were cut out of different positions in the ABB-2 cast plate. The nearly lamellar specimen (NL) exhibits the lowest creep rate, the two duplex specimens D1 and D2 creep clearly faster; for further details see [4].

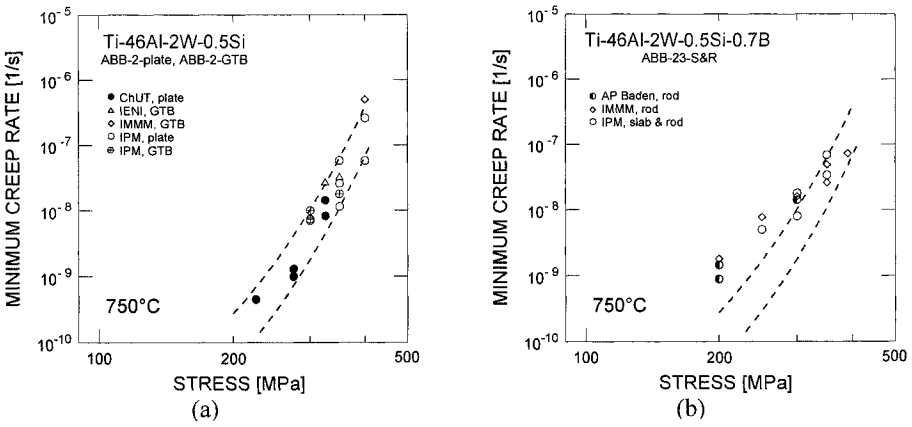


Figure 8: Dependencies of minimum creep rate on the applied stress obtained at 750°C for (a) the boron-free ABB-2 alloy and (b) the boron-alloyed ABB-23 material. The two dashed lines delimit the scatter of data expected on the basis of microstructural variations in ABB-2 casts [4]. Individual data points from partner laboratories as well as the cast type can be identified.

The dependence of MCR on the applied stress obtained for the boron alloyed batch ABB-23 at 750°C is shown in Figure 8b. The two dashed lines in Figure 8b represent again the scatter band found for the boron free ABB-2 batch and plotted first in Figure 8a. There are two important features related to the ABB-23 data. The comparison with the ABB-2 scatter band clearly shows that the MCR of the boron alloyed material is comparable to the MCR of the ABB-2 in the range of high applied stresses. However, for stresses below 300 MPa, the ABB-23 batch exhibits distinctly higher MCRs than the boron free material. The microstructures of the ABB-2 and ABB-23 in their as-received state are very similar. Nevertheless, the lamellar colony or γ-phase grain size is approximately five times smaller for the ABB-23 casts (~100

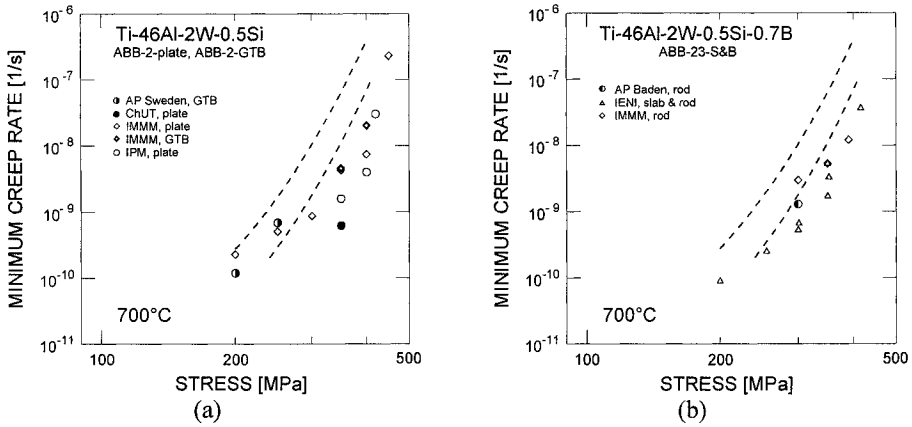


Figure 9: Dependencies of minimum creep rate on the applied stress obtained at 700°C for (a) the boron-free ABB-2 alloy and (b) the boron-alloyed ABB-23 material. The two dashed lines delimit the scatter of 750°C data expected on the basis of microstructural variations in ABB-2 casts [4]. Individual data points from partner laboratories as well as the cast type can be identified.

μm) as compared to the ABB-2 alloy (~500 μm). A reduced stability of the ABB-23 grain structure thus could contribute to the observed decrement of creep strength at low applied stresses. The higher creep rates observed for the ABB-23 alloy may also be due to a lower long-term stability of B2 and Ti_5Si_3 precipitates associated with boron alloying effects. A further work is needed to provide conclusive evidence. Similar data on applied stress dependence of MCR measured at 700°C are presented in Figure 9.

Notched bars

The effect of a multiaxial loading on the creep life of ABB-2 and ABB-23 casts has been investigated at 750°C. Test were performed on sharp, medium and blunt notched bars an example of which is shown in Figure 2. The comparison of creep rupture times obtained for flat and notched tensile bars cut out of the ABB-2 alloy is shown in Figure 10. At the same net-section stress (applied load divided by the smallest specimen cross-section), the notched bars take a considerably longer time before the final failure. This notch strengthening, with respect to net-section stress, which can be as much as a factor of 2 at the low applied stresses is observed to different extent in other materials [14]. The local stress due to the notch effectively redistributes the damage development region and failure occurs with strains of about 1.5% (measured across the notch region, as compared to the uniaxial failure strains of about 10%). The damage development modelling is ongoing to account for the observed effect on a microstructural basis.

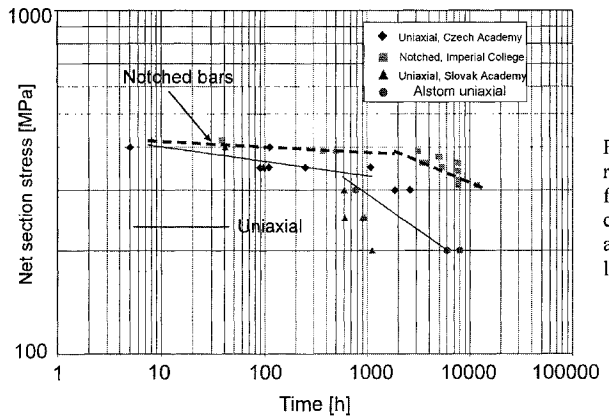


Figure 10: Comparison of creep rupture times versus net-section stress for the ABB-2 notch bar tests and the corresponding uniaxial tests performed at 750°C in different participating laboratories.

Summary and conclusions

The microstructure and creep properties of the boron-free and boron-enriched cast Ti-46Al-2W-0.5Si-(0.7B) (at-%) alloys were investigated in the present study. The experimental results support following conclusions.

1) All the investigated cast parts contain two distinct microstructural types (i) the columnar grains below the cast surface which exhibit nearly lamellar structure (mean interface spacing of 450 ± 35 nm) and (ii) the duplex microstructure in the central region of the casts.

2) The lamellar colony size and the grain size of the boron-enriched ABB-23 alloy (~100 μm) is approximately five times smaller as compared to the boron-free ABB-2 material.
3) After casting and heat treatment, elongated W-rich B2 precipitates decorate the γ/α_2 boundaries. The Si-rich globular Ti_5Si_3 precipitates were also found inside the γ-grains.
4) An anisotropy of creep in the cast ABB-2 alloy has been investigated at 750°C. The specimens taken out of the nearly lamellar cast region exhibited higher creep strength than the specimens cut out of the region with duplex microstructure.
5) The variations of microstructure throughout the ABB-2 and ABB-23 casts cause a scatter of the minimum creep rate that is less than one order of magnitude in terms of creep rate.
6) The relevant notch strengthening effect (with respect to net-section stress) has been observed for the ABB-2 alloy tested at 750°C. This can be as much as a factor 2 at low stress levels and exposure times exceeding 1000 h.

Acknowledgement

The authors individually acknowledge the financial support received for their COST 522 subtasks from various institutions on the national as well as European level.

References

[1] M. Nazmy and M. Staubli: U.S. Pat. no. 5,207,982 and European Pat. no. 4555005 B1.
[2] M. Nazmy and V. Lupinc: Gamma TiAl Intermetallic for Gas Turbine Applications, in: *Materials for Advanced Power Engineering 1998, Part II, Proceedings of the Sixth Liège Conference*, J. Lecomte-Beckers et al. (Eds.). Forschungszentrum Jülich, Jülich, 1998, pp. 933-944.
[3] A. Dlouhý: Microstructure and Creep Strength of near-γ TiAl Alloys for Gas Turbine Applications, *IPM second progress report*, COST 522 – Gas Turbines – WP 1.2 γ-TiAl, Brno, June 2001.
[4] A. Dlouhý, K. Kuchařová, M. Svoboda, R. Válek and J. Březina: Microstructure and Anisotropy of Creep in Ti-46Al-2W-0.5Si Castings, in: *Materials Structure and Micromechanics of Fracture, Proceedings of the 3rd International Conference MSMF-3*, P. Šandera (Ed.), Vutinum, Brno 2001, pp. 240-247.
[5] V. Lupinc, W. M. Yin and M. Maldini: Microstructure and Creep Resistance at 650-750°C of the Ti-47Al-2W-0.5Si Cast Alloy, in: *Materials for Advanced Power Engineering 1998, Part III, Proceedings of the Sixth Liège Conference*, J. Lecomte-Beckers et al. (Eds.). Forschungszentrum Jülich, Jülich 1998, pp. 1239-1248.
[6] A. Dlouhý: Microstructure and Creep Strength of near-γ TiAl Alloys for Gas Turbine Applications, *IPM third progress report*, COST 522 – Gas Turbines – WP 1.2 γ-TiAl, Brno, March 2002.
[7] M. Ahmad and K. Nikbin: Multiaxial Failure in gamma Titanium Aluminide, *ICSTM third progress report*, COST 522 – Gas Turbines – WP 1.2 γ-TiAl, London, March 2002.
[8] S. Naka: Considerations on Solidification Paths and Development of new Castable gamma Titanium Aluminides, in: *Materials for Advanced Power Engineering 1998, Part II, Proceedings of the Sixth Liège Conference*, J. Lecomte-Beckers et al. (Eds.). Forschungszentrum Jülich, Jülich 1998, pp. 945-960.
[9] I. Gil, M. A. Munoz-Morris and D. G. Morris: The Effect of Heat Treatments on the Microstructural Stability of the Intermetallic Ti-46.5Al-2W-0.5Si, *Intermetallics* 9 (2001) 373-385.
[10] R. Yu, L. L. He, J. T. Guo, H. Q. Ye and V. Lupinc: Orientation Relationship and Interfacial Structure between ζ-Ti_5Si_3 Precipitates and γ-TiAl Intermetallics, *Acta Mater.* **48** (2000) 3701-3710.
[11] R. Yu, L. L. He, Z. X. Jin, J. T. Guo, H. Q. Ye and V. Lupinc: On the Orientation Relationship between Ti_5Si_3 Precipitates and B2 Phase in a Ti-47Al-2W-0.5Si Alloy, *Scripta Mater.* 44 (2001) 911-916.
[12] D. Lundström, M. Knutson-Wedel and B. Karlsson: Microstructures, Development of Defects and Creep Behaviour in a γ-TiAl Alloy for Gas Turbine Applications, in: *Materials for Advanced Power Engineering 1998, Part III, Proceedings of the Sixth Liège Conference*, J. Lecomte-Beckers et al. (Eds.). Forschungszentrum Jülich, Jülich 1998, pp. 1229-1238.
[13] F. Appel and R. Wagner: *Mat. Sci. Eng.* R22 (1998) 187.
[14] O. Kwon, K. Nikbin and G.Webster: Failure mechanism in Carbon Manganese steel at 360°C under multi-axial stress states, in: *CREEP 7*, Conf. Tsukuba 2001.

HIGH TEMPERATURE DEFORMATION OF THE Fe28Al3Cr IRON ALUMINIDE MODIFIED WITH ADDITIVES

Jan Hakl, Tomáš Vlasák

SVUM a.s., Research Centre, Prague, Czech Republic

Petr Kratochvíl

Department of Metal Physics, Charles University, Prague, Czech Republic

Abstract

The high temperature creep and tensile properties of high corrosion resistant iron aluminide Fe28Al3Cr (at.%) with cerium as an additive in the range between 500 and 900°C and the related deformation substructure were investigated. The data on creep rupture time and on the creep strength are mathematically evaluated and compared with those of other high temperature corrosion resistant materials.

Keywords: iron aluminides Fe_3Al, processing, mechanical properties, creep behaviour

Introduction

Iron aluminides are well known for their excellent resistance to oxidation and sulfidation. The main drawbacks are their bad workability at room temperature [1-3]. The influence of environmental effects was identified as the main reason for small plasticity of iron aluminides at room temperature. Only in recent years [2,3], the improvement of the plasticity was achieved using both the off-stoichiometric compositions (e.g., 28 at.%Al) and the ternary additives (especially chromium, molybdenum and manganese) in combination with grain refinement agents such as TiB_2 and Ce and TMT (thermal and mechanical treatment). In contrast to the advantages (low material costs, low density, corrosion resistance) low ductility, brittle fracture and processing problems hampered the commercial use. Nevertheless, there already exist the first examples of application of Fe_3Al-type alloys. Most of them are connected with the use of iron aluminides at high temperatures. Therefore, the creep testing of this material is very important.

The knowledge on the creep of Fe_3Al - type alloys could be summarized as follows: Most of the creep studies were made in the B2 phase field. Creep rupture properties of binary Fe_3Al were reported to be poor, which was attributed to the easy tendency of grain boundaries to crack under tensile stresses [4-6]. Addition of the alloying elements [7-10] like Nb, Mo, Zr and W was shown to improve the rupture life and to reduce the minimum creep rate. In addition, it was shown in a complex alloy [10], that it is possible to improve the creep strength using changes of the heat treatment condition. The improvement was also achieved through the presence of a second phase.

Recent most important creep measurement on Fe_3Al-based alloys are due to McKamey and coworkers [10], who studied the behaviour of a very complex alloy Fe-28Al-5Cr (at.%) with 0.5 Nb, 0.8 Mo, 0.025 Zr, 0.05 C and 0.005 B (Oak Ridge National Laboratory - ORNL - designation FA 180). They had shown that the creep rupture strength is strongly dependent on the microstructure. The creep rupture resistence of this alloy could be improved by solution annealing at 1150°C followed either by air cooling or by oil quenching. The

strengthening was due to a dispersion of fine Nb- and Zr- based MC precipitates in the matrix and along the grain boundaries. During their creep tests (200 - 250 MPa) performed at 600 and 650°C the minimum creep rate (MCR) was between 10^{-8} to 10^{-10} s^{-1}.
Also Chen and coworkers [11] investigated the possibility to improve the high temperature properties of Fe_3Al based aluminides by allying Mo, Nb, Cr and some minor additives. Neither the alloying nor the microstructure enhanced the creep resistivity to values obtained by McKamey [10].
It is the purpose of the present investigations to perform first creep tests with an iron aluminide alloy of the type Fe28Al3Cr (at.%) modified mainly by Ce, Mn and C.

Experimental procedure

The alloy was melted in a vacuum furnace and cast under argon atmosphere in the Research Institute of Metals, Ltd. Panenské Břežany. The rolling of the original sheet (thickness 40 mm) to the final one (13mm) was performed at 1100°C. Finally the sheet was quenched in oil. No further heat treatment was applied before creep testing. The composition of the studied alloy is (at.%): 28.44 Al, 2.64 Cr, 0.4 Mn, 0.16 C, 0.02 Ce. The alloy was denoted as FA 282 [12, 13]. The creep samples were prepared with a gauge length of 25mm and a diameter of 5mm. The creep testing was performed in air at constant load conditions, the temperature range was 500 - 900°C. The range of loads was 5 - 100 MPa for 600 to 900°C and 100 to 200 MPa for 500°C. The accuracy of the temperature adjustment was ±3°C for testing temperatures up to 600°C, ±4°C for the range 600 - 800°C and ±6°C for 800 - 1000°C. The deformation was measured with the accuracy of 10μm.

Results

Creep rupture strength
One of the most important characteristics of the creep process is the creep rupture strength, i.e. dependence of time to rupture on temperature and stress, see Fig.1. For a mathematical evaluation of this quantity we used the procedure in accordance with [14] given by the relationship

$$\log t_r = A_1 + A_2 \cdot \log\left|\frac{1}{T} - \frac{1}{A_5}\right| + A_3 \cdot \log[\sinh(A_6 \cdot \sigma \cdot T)] + A_4 \cdot \log\left|\frac{1}{T} - \frac{1}{A_5}\right| \cdot \log[\sinh(A_6 \cdot \sigma \cdot T)], \quad (1)$$

where t_r is time to rupture (h), T is temperature (K), σ is stress (MPa), A_1-A_6 are material constants.
Material parameters from Eq. (1) were evaluated from experiments and their numerical values are given in Tab.I. Calculated values of creep rupture strength and stresses for 1% strain are given in Tab.II. The effect of the exposure time is also obvious.

Tab.I. - Material constants from relationships (1), (3).

(1)		(3)	
A_1	21.893726	B_1	79.698138
A_2	5.295915	B_2	25.717630
A_3	4.561839	B_3	10.198438
A_4	14.507374	B_4	29.064450
A_5	13.122461E+2	B_5	37.224609E+2
A_6	5.832893E-05	B_6	1.443611E-05

Constants are valid for T [K], σ[MPa], t[h].

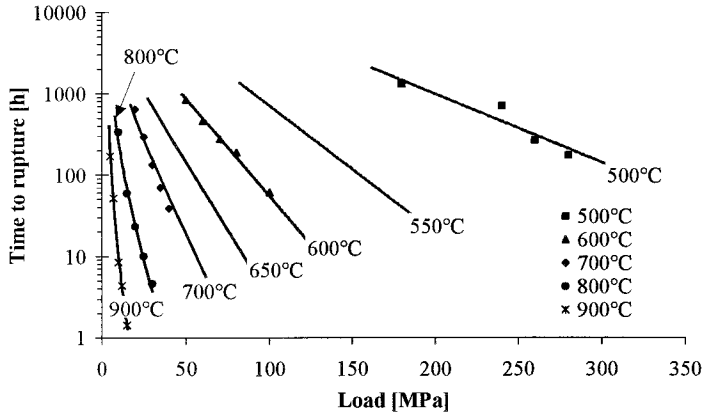


Fig.1 - Creep rupture strength evaluated for some temperature levels

Tab.II Creep properties of investigated aluminide

Temperature (°C)	Creep rupture strength (MPa)			Stress for 1% strain (MPa)	
	10 h	100 h	1000 h	10 h	100 h
500	436	318	199	325,9	182,4
550	219	154	90	161,4	68,7
600	131	89	47	74,6	28,4
650	85	55	26	35,8	14,4
700	56	34	15	19,5	8,5
750	37	21	9	11,9	5,6
800	25	13	6	8,0	4,0
850	16	9	4	5,7	3,0
900	10	6	3	4,3	2,4

Strain behaviour

Data from series of creep curves were evaluated by the following model [15]

$$\varepsilon_c = \varepsilon_0 \cdot \left[\left[\frac{\varepsilon_m}{\varepsilon_0} \right]^{[g(\pi(t))]} - 1 \right], \tag{2}$$

$$g(\pi(t)) = \pi^N \cdot \left[\frac{1+\exp(-2\cdot\pi^K)}{1+\exp(-2)} \right]^M, \tag{2a}$$

$$\pi = \frac{t}{t_r}, \tag{2b}$$

$$\varepsilon_0 = \frac{\sigma}{E(T)} \cdot 10^2, \tag{2c}$$

$$E(T) = E_1 + E_2 \cdot \exp\left(\frac{E_3}{T}\right), \tag{2d}$$

where ε_c is total creep strain (%), t is time (h), ε_o is elastic deformation (%), K,M,N, ε_m, $E_{1\text{-}3}$ are material constants.

Time to specific creep strain in dependence on temperature and stress was evaluated by the regresion model [15]

$$\log t_1 = B_1 + B_2 \cdot \log\left|\frac{1}{T} - \frac{1}{B_5}\right| + B_3 \cdot \log[\sinh(B_6 \cdot \sigma \cdot T)] + B_4 \cdot \log\left|\frac{1}{T} - \frac{1}{B_5}\right| \cdot \log[\sinh(B_6 \cdot \sigma \cdot T)], \qquad (3)$$

where t_1 is time for reaching 1% total strain (h) and/or minimum creep rate (s^{-1}), respectively, B_1-B_6 are material constants.
The plots corresponding to Eq. (3) are displayed in Figs. 2 and 3.

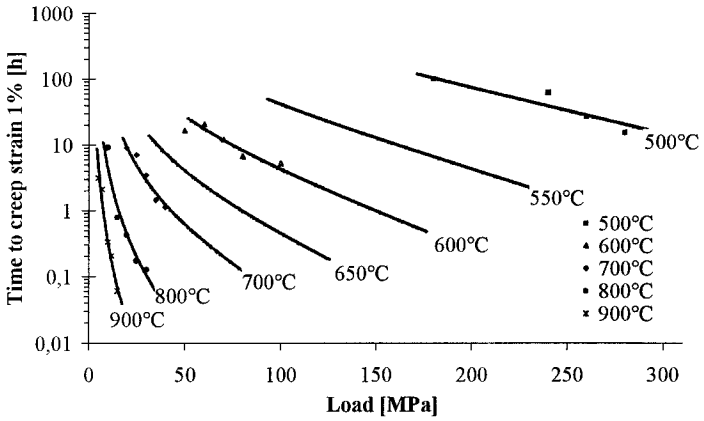


Fig. 2 - Dependence of creep stress for 1% strain on temperature and time

The detailed investigation of the creep process is necessary to improve the creep resistance of the material. The activation energy of creep Q and the stress exponents n were determined using the relation

$$d\varepsilon_o/dt = A\sigma^n.\exp(-Q/kT), \qquad (4)$$

where $d\varepsilon_o/dt$ is the minimum creep rate (MCR) or steady state creep rate (s^{-1}), σ the stress (MPa), Q the activation energy for creep (kJ/mol).

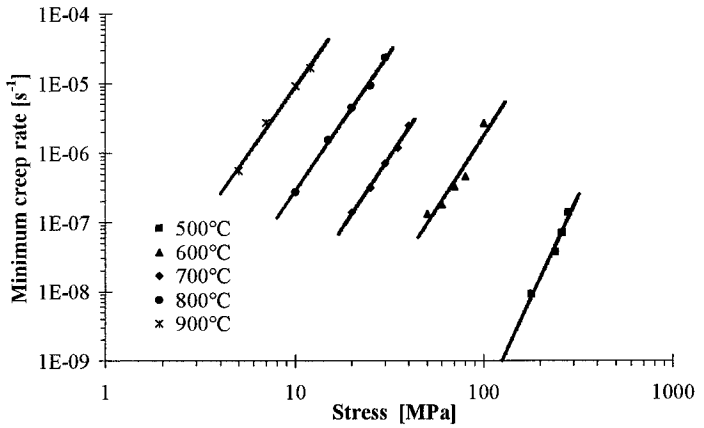


Fig. 3 - Minimum creep strain rate as a function of temperature and stress

The dependence of MCR on the load for different temperatures are given in Fig.3. The stress exponents determined for different temperatures are represented in Table III. The activation energy Q was determined from the $\ln\dot{\varepsilon}$ vs 1/kT dependence plotted at constant stress - see Eq.(4). The values obtained for Q are 500 and 320 kJ/mol for loads 10 and 20 to 30 MPa respectively. The type of the experimental results (creep under constant load) enables to use the evaluation for constant stress experiments. The reason is following: MCR was reached at deformations of approximately 3%. For this value the load is very near to the stress, which differs only by a factor of 1.03. So the values of n and Q can be compared with experiments using constant stress.

Table III.

	Temperature [°C	n
DO_3	500	5.92
B2	600	4.23
	700	4.10
	800	3.96
	900	3.86

The value of the time to rupture for 600°C cannot be directly compared with those of McKamey et al. [10], while the time to rupture for constant load experiments is approximately the half of that obtained during the creep experiments with constant stress. The studied material may be therefore taken as a material with properties comparable to that with Nb, Mo, Zr, C and B additives (amounts are mentioned above) [10].

The microstructure after creep was observed and compared to the unstrained microstructure. The microstructure of the unstrained specimen (obtained by rolling at 1100°C followed by quenching in oil) is characterised by grains, which are elongated along the direction of rolling. The start of the dynamic or metadynamic recrystallization process was identified during creep at temperatures near to 800°C. Finally, the recrystallization process with fully polygonal recrystallized grains takes place during creep at 900°C.

All specimens were determined to be composed of a mixture of a B2 structure matrix (which occurs at temperatures above approximately 550°C) with fine $D0_3$ structure domains (which occur bellow 550°C). Network dislocations appear after creep at 700 and 900°C (Fig.4) forming subgrain walls as a result of dynamic softening processes during creep. The microstructure developed in the gage section of samples creep tested at 600°C to rupture is shown in Fig. 5 . In this case the creep induced dislocation structure consists of a nearly uniform distribution of dislocation segments, subgrain boundaries and sparse substructure components of two fold superdislocations. These configurations are partly held on small particles, which were identified as σ-phase FeCr. Ce containing precipitates were also identified in the material [13].

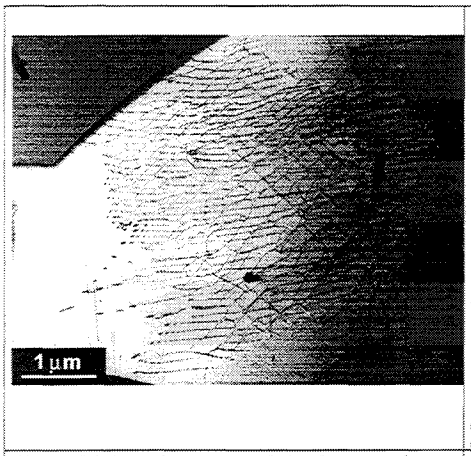


Fig. 4 Dislocation network in the sample crept at 700°C



Fig.5 Dislocation configuration in the sample crept at 600°C held partly at precipitate particles

Discussion - the conditions for the use as a structural material

Temperature dependencies of basic mechanical properties [15] and creep rupture strength at 1000 h are shown for the investigated aluminide in Fig.6. It is obvious that strength characteristics (yield limit and tensile strength) do not change to a great extent up to a temperature of about 580°C and only above this temperature they gradually decline. Therefore, in the region of lower temperatures (approximately up to 450-500°C), it is possible to use room temperature strength characteristics for design purposes (of course, diminished by an adequate safety factor). In this case, yield limit is about 300-380 MPa and tensile strength about 530-720 MPa. Elongation gradually growths from a level of 8% at room temperature up to about 28% at 700°C.

The dependence of the creep rupture strength on temperature, which is plotted in Fig. 6 for a time of 1000 h, determines the area, where it is necessary to include creep damage in life-time calculations. The limit of elongation measured during the creep tests at temperatures 700 - 900°C was in the range 95-150%.

The following Fig.7 shows the temperature dependence of the minimum yield limit of austenitic steels 800 H (32Ni20CrTiAl), AC 66(32Ni28CrNbCe) and Ni-base alloy 45 TM (NiCr28FeSiCe) [17] in comparison with the investigated aluminide (hatched area). The alloys mentioned were chosen as examples of materials which are typical for applications in sulphur or oxidizing environments at higher temperatures. It is obvious that this aluminide has significantly better properties up to 600°C.

However, it is necessary to notice that at temperatures higher than 500°C, where creep processes determine life-time, the creep rupture strength of the investigated aluminide will be worse than those of austenitic steels and/or Ni-base alloys.

Concerning the creep process itself the values of n and Q (of a given material) depend on the stress (load) and on temperature, which influence the creep process. The higher n and (independently) Q are, the better is the creep resistance. MCR in the material having a good creep resistance is generally smaller compared to the material with the worse resistance. The possibilities to enhance the creep resistance (e.g. the stress to rupture and time for rupture) are the use of solid solution hardening and/or precipitation strengthening. Comparing our

data with those of McKamey et al. [10], who investigated the creep behaviour at 600°C, the values of Q and n observed in the present paper are lower. It is believed that the difference is due to combined effects of solid solution and precipitation strengthening after high temperature annealing at 1150°C followed by cooling to room temperature. The material used in this paper contains little Ce, C and Mn (in the basic composition Fe-28at.%Al-3at.%Cr). The material was hot rolled at 1100°C and hold at that temperature one hour prior to rolling. This might be taken as comparable to solution treatment at 1150°C. We were not able to reach the creep resistivity described by n = 10 - 12 which corresponds to annealing at 1150°C and to a completely different composition of the additives. Nevertheless the method may be used in future to prepare better creep resistant materials.

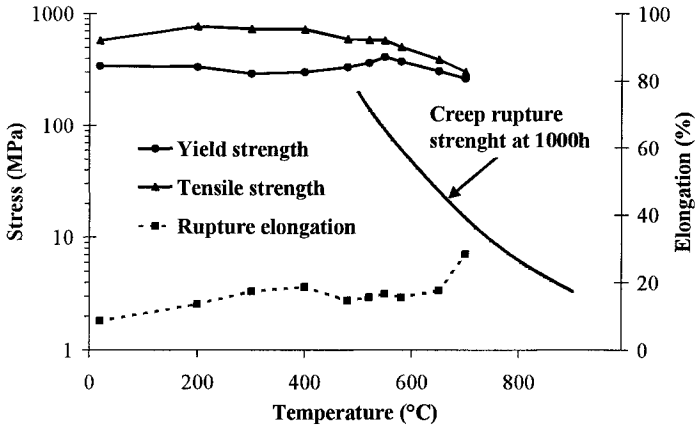


Fig. 6 - Definition of design area

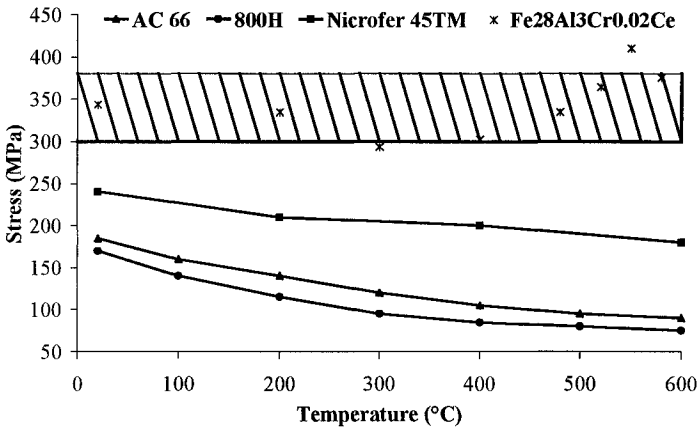


Fig.7 - Temperature dependence of Fe28Al3Cr0,02Ce yield limit in comparison with AC66, 800H a Nicrofer 45TM

Conclusions

- The iron aluminide Fe-28at.%Al-3at.%Cr with Ce, C and Mn as small amount additives was presented as a material with promissing creep properties.
- A modified thermomechanical processing is expected to improve the creep properties of the investigated material.
- The use of other combination of additives can enhance the solid solution and precipitation strengthening .

Acknowledgement

The authors thank the Grant Agency of the Charles University in Prague, Czech Republic, who covered the expenses of the Research Project No. 162 / 2000.

References

[1] Vedula, K.: in *Intermetallic Compounds*, eds. J. H. Westbrook & R. L. Fleischer, John Wiley & Sons, New York, 1995, vol. 2, p. 199.
[2] Deevi, S. C. - Sikka, V. K.: Intermetallics 4, 1996, p. 357.
[3] McKamey, C.G. et al.: J. Mater. Res. 6, 1991, p.1779.
[4] Lawley, A. - Coll, J.A. - Cahn, R.W.: Trans. AIME 218, 1960, p.166.
[5] Sastry, D. A. - Sundar, R. S.: in *Inter. Symp. on Ni and Fe Aluminides Processing, Properties and Applications,* eds. Deevi S.C., Sikka V.K., Masiasz P.J., Cahn R.W., ASM, 1996, p. 123.
[6] McKamey, C. G. - Masiasz, P. J. - Jones, J.W.: J. Mater. Res. 7, 1992, p.2089.
[7] Morris, D. G. - Nazmy, M. - Noseda, C. : Scr. Metall. Mater. 31, 1994, p.173.
[8] Yangshan, S. - Zhongua, Z. - Feng, X. - Xingquan, Y.: Mater.Sci.Eng. A258, 1998, p.167.
[9] Morris, D.G. - Nazmy, M. - Noseda, C.: Scr. Metall. Mater. 31, 1994, p.173.
[10] McKamey, C.G. - Masiasz, P.J.: Intermetallics 6, 1998, p.303.
[11] Chen, G. - Huang, Y. - Yang, W. - Sun, Z.: in *Processing, Properties, and Applications of Iron Aluminides,* eds.Stollof N.S., Sikka V. K., Chapman and Hall, 1996, p. 131.
[12] Hotař, A. - Kratochvíl, P.: Metallic Materials, 2002, in press.
[13] Karlík, M. - Cieslar M.: Mat. Sci. Eng. A324, 2002, p.5.
[14] Pech, R. - Koucký, J. - Bína, V.: Strojírenství 29, 1979, p.389 (in Czech).
[15] Bína, V. - Hakl, J.: Mat. Sci. Eng. A234-236, 1997, p. 583.
[16] Karlík, M. - Kratochvíl, P. - Janeček, M. - Siegel, J. - Vodičková, V.: Mat.Sci.Eng, A289, 2000, p 182.
[17] High-Performance Materials. KRUPP VDM, Werdohl, publ. No. N52492-11.

MICROSTRUCTURE AND CREEP OF γ-TiAl BASED INTERMETALLIC ALLOY

J. Lapin, T. Pelachová

Institute of Materials and Machine Mechanics, Slovak Academy of Sciences,
Racianska 75, 831 02 Bratislava, Slovak Republic

Abstract

The microstructure of γ-TiAl alloy with chemical composition Ti-46Al-2W-0.5Si (at.%) was investigated before and after creep testing using optical microscopy, scanning and transmission electron microscopy. The constant load creep tests were performed in air at applied stresses ranging from 150 to 400 MPa and temperatures from 700 to 800°C. The creep specimens were cut from central part of cast plate and turbine blade after HIP-ing and heat treatments. Before creep testing the microstructure of specimens consisted of well-aligned lamellar α_2/γ colonies, misaligned lamellar regions and γ-rich regions. In addition, B2-phase and fine Ti_5Si_3 precipitates were identified in the microstructure. Long-term creep exposure resulted in some structural changes including the precipitation of fine B2 particles within the lamellae and local transformation of the α_2/γ lamellae to the α_2/B2–γ structure. The minimum creep rate was found to depend on the applied stress and temperature. The power law stress exponent was determined to vary between 7.9 to 8.9.

Keywords: titanium aluminides, TiAl, microstructure, creep, creep fracture

1. Introduction

In recent years ordered TiAl based intermetallic alloys have been extensively studied as potential high-temperature materials in gas turbine industry. The low density, high stiffness, good oxidation resistance and interesting mechanical properties have made TiAl based alloys attractive candidate for use in low-pressure stage of gas turbine engines or for turbocharger of diesel engines [1-6]. Of the numerous microstructures that can be developed in TiAl based alloys, the fully lamellar or nearly lamellar microstructure consisting of TiAl (γ-phase) and small volume fraction of Ti_3Al (α_2-phase) exhibits better creep resistance than duplex material [7]. A lamellar structure with fine interlamellar spacing decreases the mobility of dislocations in soft oriented grains and increases the difficulty for shear in hard oriented grains. Interlocked lamellae along grain boundaries provide greater resistance to intergranular cracking [8]. However, large cast components such as turbine blades may exhibit various microstructures ranging from fully or nearly lamellar in columnar grain regions to duplex ones in the equiaxed grain region. Such microstructural changes will result in a variation of creep properties of investment cast polycrystalline blades. Therefore, evaluation of creep properties of specimens prepared from defined regions of the investment cast and heat-treated large turbine blades is of great interest.

Several alloy compositions have been developed to meet specific property requirements of γ-TiAl based alloys: e.g. Ti-47Al-2Nb-2Cr (at.%) for maximum room temperature ductility and Ti-47Al-2W-0.5Si (at.%) for maximum creep resistance [5]. In creep resistance alloys, tungsten is known to act most effectively as solid solution strengthener and stabiliser of β phase. It has been shown that TiAl alloy modified by 2 at.% of

W contains numerous fine β precipitates on lamellae interfaces and within some equiaxed γ grains that improve the creep resistance [9]. However, tungsten can segregate in dendrite cores producing a detrimental effect on creep resistance. The addition of silicon to γ–TiAl alloy improves high temperature oxidation resistance. The coherent Ti_5Si_3 particles formed through eutectoid transformation along lamellar interfaces and grain boundaries enhance creep resistance and inhibit dynamic recrystallisation [10].

The aim of this paper is to characterise the microstructure and to study creep behaviour of creep specimens prepared from defined regions of investment cast and heat treated γ-TiAl plate and turbine blade before and after creep testing. In addition, creep fracture data of the creep specimens prepared from the turbine blade are reported and fracture mechanisms are discussed. This work was performed in the frame of European program COST 522 - Work Package 1.2 γ-TiAl.

2. Experimental procedure

Creep experiments were conducted on ABB2 alloy with the chemical compositions given in Table 1. The material was provided by Alstom Power in the form of cast plate with a width of 75 mm, thickness of 15 mm and length of 121 mm and a part of investment cast turbine blade. Table 2 summarises the treatments of the material before creep testing according to supplier data. Creep specimens were positioned to the central part of the cast components. The creep specimens with a gauge length of 20 mm and gauge diameter of 4 mm were water jet cut from the material and lath-machined. After turning, the specimen surface was polished to a roughness better than 0.3 μm. Constant load creep tests were performed at temperatures of 700, 750 and 800°C under initial tensile stresses ranging from 150 to 400 MPa. The test temperature was monitored with two thermocouples touching the specimen gauge section and held constant within ± 1°C for each individual test. Specimen displacement was measured using high-temperature extensometer attached to the ridges of the creep specimen. The extensometer was equipped with a linear variable displacement transformer (LVDT) SATEC. The acquisition of time-elongation data was accomplished by a computer and data processing was performed by a computer program Jandel Scientific.

Optical microscopy (OM), scanning electron microscopy (SEM), and transmission electron microscopy (TEM) were conducted on samples before and after creep testing. After grinding and mechanical polishing the specimens were etched in a solution of 100 ml H_2O, 6 ml HNO_3 and 3 ml HF. TEM samples were thinned mechanically to a thickness of 4 μm and then by ion milling.

Table 1. Chemical composition of studied ABB2 alloys (at.%)

Material	Ti	Al	W	Si	C	Fe	Cu	O	N	H
Plate	Balance	46.1	2.0	0.48	0.017	0.017	<0.001	0.168	0.093	0.04
Blade	Balance	46.2	2.0	0.48	0.017	0.015	0.001	0.086	0.043	0.08

Table 2. Treatments of ABB2 alloys

Material	Treatments
Plate	Hot isostatic pressing at 1260°C and 172 MPa for 4 h Heat treatments: annealing at 1350°C for 1 h and gas fun cooling followed by annealing at 1000°C for 6 h and furnace cooling
Turbine blade	Hot isostatic pressing at 1270°C and 172 MPa for 4 h Heat treatments: annealing at 1350°C for 1 h and gas fun cooling followed by annealing at 1000°C for 6 h and furnace cooling

3. Results

3.1. Microstructure of as-received material

The macrostructure of the cast plate and turbine blade with chemical compositions given in Table 1 consisted of columnar grains (C) growing from the surface towards the central part of the castings. The central part contained equiaxed grain structure (E). Fig. 1 shows typical macrostructure on a transverse section of the turbine blade composed of columnar and equiaxed grain regions. It should be noted that similar macrostructure was observed in the cast plate. The creep specimens were positioned to the central minor axis of the cast components. Such procedure resulted in equiaxed or mixed columnar and equiaxed grain structure in the gauge region of the creep specimens. In the case of the turbine blade, the longitudinal axis of creep specimens was parallel to the longitudinal axis of the turbine blade.

Fig. 2 shows typical microstructure in the gauge region of creep specimens machined from the turbine blade. The creep specimens machined from the plate showed similar type of microstructure. Three basic regions can be distinguished in each creep specimen: lamellar

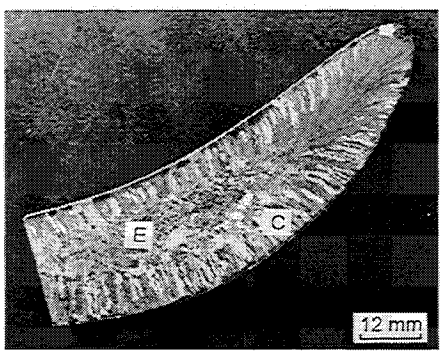


Fig. 1. Optical micrograph showing typical macrostructure composed of columnar and equiaxed grains on a transverse section of the investment cast turbine blade.

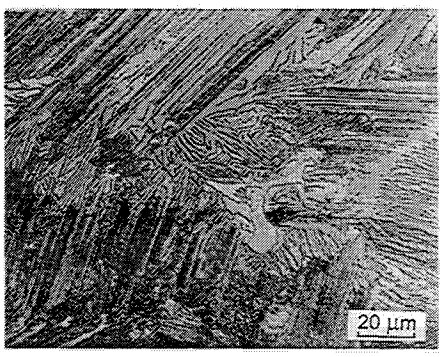


Fig. 2. Optical micrograph showing microstructure in the gauge region of creep specimens machined from the turbine blade before creep testing.

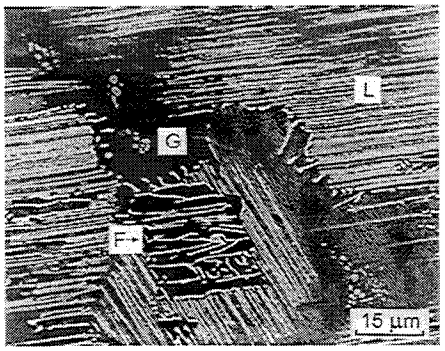


Fig. 3. SEM micrograph showing microstructure in the gauge region of creep specimens machined from the plate before creep testing.

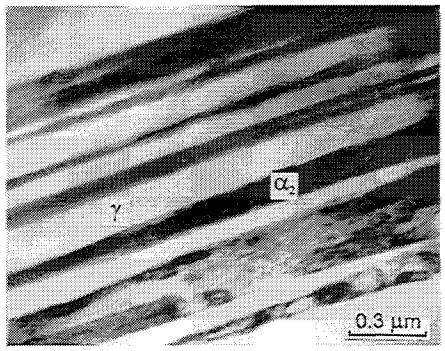


Fig. 4. TEM micrographs showing regular lamellae of creep specimen machined from the turbine blade before creep testing.

region containing perfectly aligned lamellae (L), feathery structure with misaligned lamellae (F) and γ-rich region containing small volume fraction of spherical precipitates (G), as shown in Fig. 3. The feathery structure was formed preferentially at the grain boundaries. Table 3 summarises the results of quantitative metallography analysis of the microstructure in the gauge region of creep specimens prepared from the plate and turbine blade. As seen from this table, both types of creep specimens contained similar volume fraction of lamellar region but differed in volume fraction of feathery and γ-rich regions.

TEM observations and selected diffraction patterns revealed that the lamellar region consists of ordered TiAl (γ) and Ti_3Al (α_2) intermetallic phases, as shown in Fig. 4. Well-known crystallographic orientation relationships:

$$(0001)_\alpha \,||\, (111)_\gamma \text{ and } \langle 1120\rangle_\alpha \,||\, \langle 110\rangle_\gamma$$

were confirmed between the coexisting phases. Table 4 summarises the results of quantitative metallography analysis of the lamellar regions performed on deeply etched specimens using SEM and computerised image analyser. However, some regular lamellar regions contained coarse bright colour particles enriched in tungsten (48-52Ti (at.%), 36-42Al (at.%), 7-12W (at.%)), as seen in Fig. 5. TEM analysis revealed that these particles belong to B2-phase. Three types of B2–phase were observed in the present alloy: coarse B2-particles formed within the lamellar regions, fine B2-precipitates within the γ-rich regions and fine

Table 3. Volume fraction of lamellar, feathery and γ-rich regions

Material	Lamellar (L) (vol. %)	Feathery (F) (vol. %)	γ-rich region (G) (vol. %)
Plate	68	12	20
Blade	66	26	8

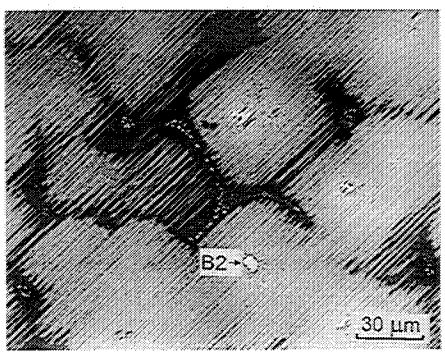


Fig. 5. Backscattered SEM micrograph showing B2 particles formed within lamellar region of the turbine blade before creep testing.

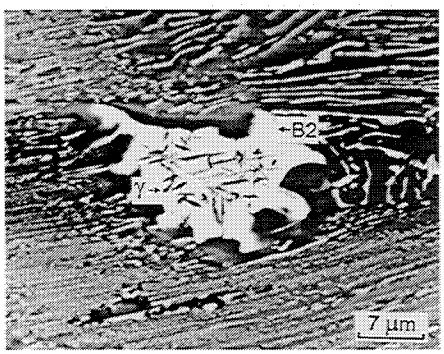


Fig. 6. Backscattered SEM micrograph showing B2 particle with needle like γ-precipitates before creep testing.

B2-precipitates formed along α_2/γ-interfaces. The average volume fraction of coarse B2-particles in the gauge region of creep specimens was measured to be about 3 vol.%. It should be noted that some coarse B2-particles contained fine γ-needles, as illustrated in Fig. 6. Fig. 7 shows the morphology of fine B2–precipitates within the γ-rich region. Small volume fraction of needle like B2-precipitates was also observed within feathery structure region. In addition, TEM analysis revealed that the creep specimens contain fine Ti_5Si_3 precipitates. Orientation relationships between Ti_5Si_3 precipitates and γ- and β-phases in Ti-47Al-2W-0.5Si alloy were recently determined by Yu et al. [10, 11].

3.2. Creep properties

All of the creep curves obtained in this study have the same basic shape, as shown in Fig. 8. The creep curves exhibit short primary creep stage that is directly followed by tertiary creep. Fig. 9 shows the variation of instantaneous creep rate with the strain. During the primary creep stage the creep rate decreases with increasing strain. After reaching a minimum at a strain of about 1%, the creep rate increases with increasing strain. No steady-state creep stage was observed over the studied temperature range from 700 to 800°C and applied stresses from 150 to 400 MPa. During tertiary creep stage the specimens underwent plastic deformation that represents 8 to 16% of total elongation before fracture. The minimum creep

Table 4. Volume fraction of α_2 lamellae, interlamellar spacing and width of α_2 and γ lamellae

Material	Volume fraction (%)	α_2–α_2 spacing (nm)	Width of α_2–lamellae (nm)	Width of γ–lamellae (nm)
Plate	33	640	230	440
Blade	28	660	180	410

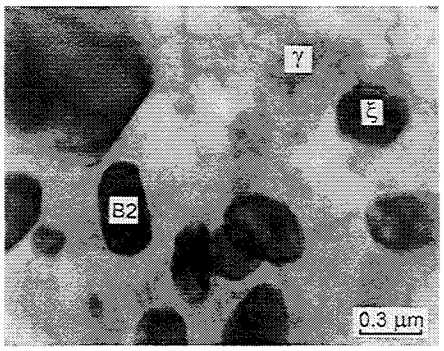


Fig. 7. TEM micrograph showing fine B2 and ξ-Ti_5Si_3 precipitates in the turbine blade before creep testing.

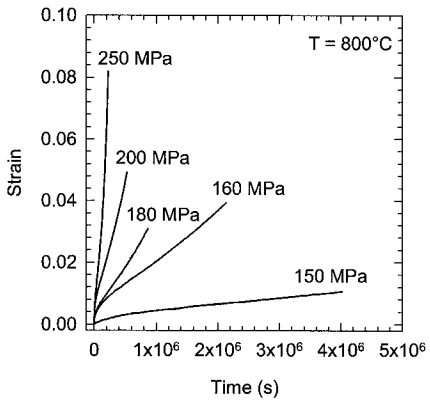


Fig. 8. Examples of creep deformation curves at 800°C. The applied stresses are indicated in the figure.

rates $\dot{\varepsilon}_{min}$ and applied stresses σ were fitted to the power law

$$\dot{\varepsilon}_{min} = A\sigma^{n}, \tag{1}$$

where A is a constant and n is the stress exponent. It should be noted that a scatter of minimum creep rates and time to 1% creep deformation were measured for creep specimens tested under the same creep conditions. Therefore, selection of creep data was performed to fit

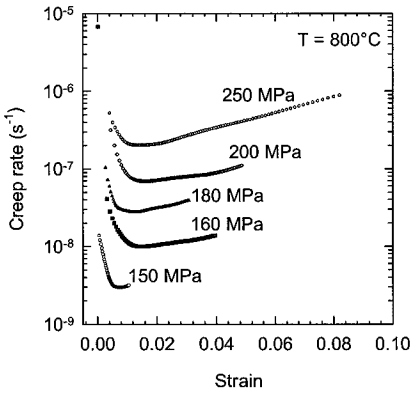


Fig. 9. Dependence of the creep rate with the strain at 800°C. The applied stresses are indicated in the figure.

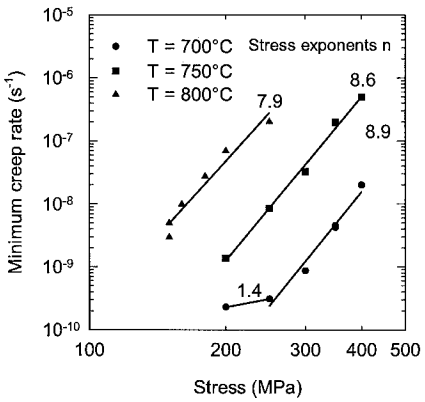


Fig. 10. Dependence of minimum creep rate on the applied stress. Creep temperatures are indicated in the figure.

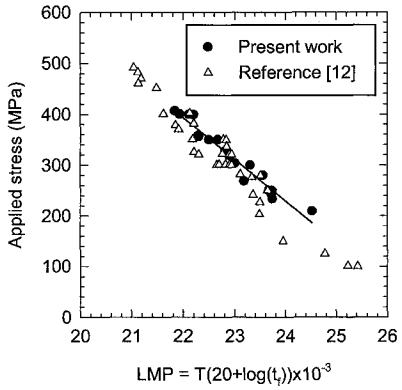


Fig. 11. Stress rupture Larson-Miller graph of creep specimens prepared from the turbine blade.

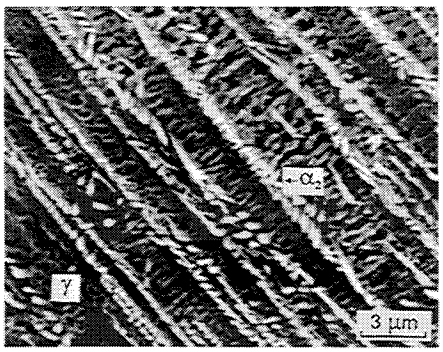


Fig. 12. TEM micrograph showing regular lamellar region after creep testing at 700°C for 7277 h.

the measured minimum creep rates as a function of stress. Fig. 10 shows the variation of the selected minimum creep rate with applied stress for the temperatures varying between 700 to 800°C. From the selected creep data, the stress exponent was determined to vary from 7.9 to 8.9. It should be noted that minimum creep rate measured at 700°C and 200 MPa deviates significantly from fitted power law. Fitting this point resulted in a stress exponent of 1.4 which indicates different creep regime.

Fig. 11 shows the dependence of the applied initial stress on Larson-Miller parameter measured from the creep specimens prepared from the turbine blade. Comparison of the

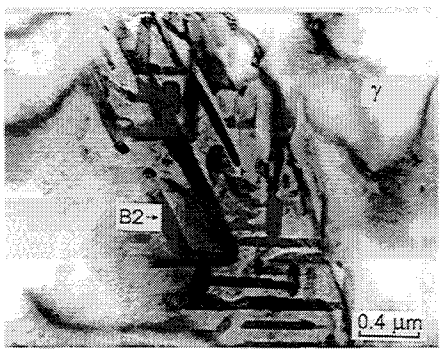


Fig. 13. TEM micrograph showing needle-like B2 precipitates formed in the feathery structure region during creep testing at 700°C for 7277 h.

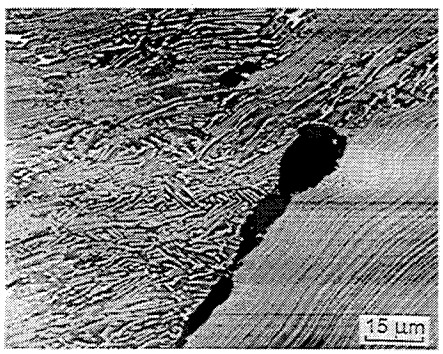


Fig. 14. Backscattered SEM micrograph showing the cavities formed during creep testing at 800°C/250 MPa for 200 h.

present data to those of Nazmy and Lupinc [12] for Ni-47Al-2W-0.5Si (at.%) alloy shows that the present creep specimens show comparable creep fracture properties at higher applied stresses and improved properties at lower applied stresses and higher temperatures.

3.3. Microstructure of material after creep

During creep testing some microstructural changes were observed in the gauge region and unloaded parts of creep specimens. Fig. 12 shows discontinuous lamellae formed in some regular lamellar regions. Long-term creep testing resulted in thinning of the α_2–lamellae. The most important structural changes observed in the crept specimens were the transformation of some α_2–lamellae and formation of γ/B2-regions in the feathery structure regions. Fig. 13 shows fine needle B2 precipitates formed by a transformation of α_2-lamella. In addition, spheroidisation of regular α_2-lamellae was observed in some regions. The precipitation of B2 particles was also observed to take place at γ/α_2 interface in the lamellar regions. Similar microstructural changes were also observed in unloaded parts (button heads) of the creep specimens.

The creep specimens showed necking before fracture. Microstructural analysis revealed that nucleation of cavities occurred preferentially at the boundaries between the lamellar and feathery regions, within the feathery structure and around the spherical Ti_5Si_3 and B2 precipitates. The number of cavities and small cracks was significantly higher in a macroscopically necked region. Fig. 14. shows a crack formed at the boundary between feathery and regular lamellar regions that propagates along lamellar α_2/γ interface. The final fracture of the material was caused by coalescence of voids and small cracks.

4. Discussion

During investment casting of the turbine blade the solidification starts by the nucleation of fine grains at the ceramic walls and continues by the growth of columnar grains. The primary solidification phase in Ti-46Al-2W-0.5Si alloy is the α-phase. As was observed in directionally solidified specimens, during columnar grain growth tungsten segregates into the melt and forms elongated β-particles in the interdendritic region [13]. Hence, growth of columnar grains region in large investment cast components is also connected with such tungsten segregation resulting in a small enrichment of the central equiaxed region by tungsten and aluminium. Recent work of Yin et al. [5] showed that the addition of tungsten and lower aluminium content favour the formation of B2 phase in γ-TiAl alloys containing 45.3 to 47.2 Al (at.%) and 1.5 to 2.1 W (at.%). However, the effect of tungsten on formation of B2 phase is more important than aluminium. Lower content of tungsten (1.5 at.%) results in very small amount and size of B2 phase in the interdendritic region. Higher content of tungsten increases volume fraction of B2 phase which precipitates both inside the lamellar colonies and along the grain boundaries. On the contrary, Recina et al. [14] attributed large variation of the microstructure to small variation in aluminium content in Ti-48Al-2W-0.5Si (at.%) alloy. Hence, variations in chemical composition of an investment cast components result in formation of a complex microstructure in the equiaxed region where locally β or α phase can be the primary solidification phase. The applied hot isostatic pressing and two successive heat treatments including homogenisation annealing at high temperature and $\alpha_2+\gamma$

decomposition at intermediate temperature (Table 2) are not sufficiently effective to eliminate such variations in chemical composition caused by the segregation. Heat treatments experiments of Gil et al. [15] showed that high temperature homogenisation annealing and rapid cooling result in a regular α_2/γ–lamellar microstructure. However, during annealing at lower temperatures such microstructure transforms rapidly into a structure composed of γ-matrix and equiaxed B2 particles, occasionally of remnant α_2 phase. In spite of some structural changes observed in the crept specimens from the unloaded and gauge regions, long-term creep testing did not confirm such large structural changes which might have a significant detrimental effect on the creep resistance of the cast components.

The central part of equiaxed region of the turbine blade characterised by a large variation of the microstructure represents the less creep resistance part of the turbine blade. The minimum creep rates measured on the creep specimens prepared from this regions are generally higher than those obtained from other parts of the casting. As mentioned before, these variations in creep behaviour are connected with specific structural characteristics of the equiaxed region. In spite of the volume fraction of the different regions (lamellar, feathery and γ-rich) the creep behaviour strongly depends on the size and distribution of these regions in the creep specimens.

5. Conclusions

1. Before creep testing the microstructure of creep specimens consisted of lamellar, feathery and γ–rich regions. Within the lamellar colonies the lamellae of $\alpha_2(Ti_3Al)$ and $\gamma(TiAl)$ phases were identified. Misaligned α_2- and γ-lamellae formed a feathery structure. In addition, the lamellar and feathery regions contained coarse B2 particles and Ti_5Si_3 precipitates. Fine B2 precipitates were found at the α_2/γ interfaces.
2. During creep tests some structural changes were observed in the creep specimens. The specimens which were subjected to long creep testing showed spheroidisation of some α_2–lamellae and transformation of some α_2-lamellae to needle-like B2 precipitates in local regions. The transformation of α_2-lamellae to B2 precipitates resulted in final microstructure consisting of γ-matrix with B2 precipitates and spherical α_2-particles.
3. The creep curves showed primary creep stage that was directly followed by a tertiary creep. The minimum creep rate was found to be function of the applied stress and temperature. For the selected creep data, the power law stress exponent was determined to vary between 7.9 to 8.9.
4. During tertiary creep stage formation of cavities was observed around the precipitates in the γ-rich region, within the feathery structure and at boundaries between regular lamellar and feathery regions and grain boundaries. The creep specimens failed by coalescence of cavities and small cracks formed along α_2/γ-interfaces.

Acknowledgments
The authors would like to thank to Dr. M. Nazmy of Alstom Power, Baden for providing the material within COST522 - Work Package 1.2 European research programme. The authors gratefully acknowledge the financial support of the Slovak Academy of Sciences under the

contract COST 51-98-9209-00/1999 and the Slovak Grant Agency for Science under the contract VEGA 2/1044/21.

References

[1] D.M. Dimiduk: Gamma titanium aluminide alloys - an assessment within the competition of aerospace structural materials. Mater. Sci. Eng. A, A263, 1999, pp. 281-288.

[2] M. Nazmy, M. Staubli, G. Onofrio and V. Lupinc: Surface defect tolerance of a cast TiAl alloy in fatigue. Scripta Mater., 45, 2001, pp. 787-792.

[3] E. Evangelista, W.J. Zhang, L. Francesconi, M. Nazmy: Toughening mechanism in the lamellar and duplex TiAl-base alloys at ambient temperature. Scripta Metall. Mater., 33, 1995, pp. 467-472.

[4] W.J. Zhang, E. Evangelista and L. Francesconi: Microstructural variation of a cast Ti48Al2W0.5Si alloy during quenching and tempering. Mater. Sci. Eng. A, A220, 1996, pp. 15-25.

[5] W.M. Yin, V. Lupinc and L. Battezzati: Microstructure study of a γ-TiAl based alloy containing W and Si. Mater. Sci. Eng. A., A239-240, 1997, pp. 713-721.

[6] D. Lundström, M. Knutson-Wedel and B. Karlsson: Microstructures, development of defects and creep behaviour in a γ-TiAl based alloy for gas turbine applications. In: Materials for advance Power Engineering 1998 (Eds. J. Lecomte-Beckers, F. Schubert and P.J. Ennis), Forschungszentrum Jülich GmbH, Vol. 5, Part III, 1998, pp. 1129-1238.

[7] V. Lupinc, W.M. Yin and M. Maldini: Microstructure and creep resistance at 650-750°C of the Ti-47Al-2W-0.5Si cast alloy. In: Materials for advance Power Engineering 1998 (Eds. J. Lecomte-Beckers, F. Schubert and P.J. Ennis), Forschungszentrum Jülich GmbH, Vol. 5, Part III, 1998, pp. 1239-1248.

[8] W.R. Chen, J. Triantafillou, J. Beddoes and L. Zhao: Effect of fully lamellar structure on creep of a near γ-TiAl intermetallic. Intermetallics, 7, 1999, pp. 171-178.

[9] L. Zhao, J. Beddoes, D. Morphy and W. Wallace: Microstructure and mechanical properties of a PM TiAl-W alloy processed by hot isostatic pressing. Mater. Sci. Eng. A, A192/193, 1995, pp. 957-964.

[10] R. Yu, L.L. He, Z.X. Jin, J.T. Guo, H.Q. Ye and V. Lupinc: On the orientation relationship between Ti_5Si_3 precipitates and B2 phase in a Ti-47Al-2W-0.5Si alloy. Scripta Mater., 44, 2001, pp. 911-916.

[11] R. Yu, L.L. He, J.T. Guo, H.Q. Ye and V. Lupinc: Orientation relationship and interfacial structure between ξ-Ti_5Si_3 precipitates and γ-TiAl intermetallics. Acta Mater., 48, 2000, pp. 3701-3710.

[12] M. Nazmy and V. Lupinc: Gamma TiAl intermetallic for gas turbine applications. In: Materials for advance Power Engineering 1998 (Eds. J. Lecomte-Beckers, F. Schubert and P.J. Ennis), Forschungszentrum Jülich GmbH, Vol. 5, Part II, 1998, pp. 933-944.

[13] J. Lapin, Ľ. Ondrúš and M. Nazmy: Directional solidification of intermetallic Ti-46Al-2W-0.5Si alloy in alumina moulds. In preparation.

[14] V. Recina, J. Ahlström and B. Karlsson: Sample preparation and microstructural characterisation of the gamma titanium aluminide Ti-48Al-2W-0.5Si. Materials Characterisation, 38, 1997, pp. 287-300.

[15] I. Gil, M.A. Muñoz-Morris, D.G. Morris: The effect of heat treatments on the microstructural stability of the intermetallic Ti-46.5Al-2W-0.5Si. Intermetallics, 9, 2001, pp. 373-385.

HIGH CYCLE FATIGUE BEHAVIOUR OF INTERMETALLIC γ-TiAl BASED ALLOYS

M.F.J. Koolloos[a], D.J. Arrell [b], M.B. Henderson[c] and S. Gallet[c]

[a] National Aerospace Laboratory NLR, P.O.Box 153, 8300 AD Emmeloord, The Netherlands
[b] ALSTOM Power Sweden AB, SE-612 82 Finspång, Sweden
[c] ALSTOM Power Technology Centre, Cambridge Road, Whetstone, Leicester LE8 6LH, UK

Abstract

The high cycle fatigue behaviour of two versions of a high strength TiAl-based alloy (ABB-2 and ABB-23) have been investigated. The plain and notched (K_t = 3) axial high cycle fatigue behaviour of ABB-2 has been studied at 20 and 700°C under two different R ratios, and that of ABB-23 has been studied at 20°C (R=0.1 and 0.5) and 550°C (R=0.1). The fatigue tests showed flat S-N plots with high fatigue strength to UTS ratios (≈1). The notched fatigue strength depended on the colony size relative to the specimen size and was often higher than the unnotched fatigue strength. The fatigue strength of both ABB alloys compare well with trendline data presented for Ti-4722XD however the degree of scatter in the endurance data is often excessive. The increased fatigue strength for ABB-2 and ABB-23 is commensurate with the increased tensile properties of the ABB alloys. After the fatigue tests metallographic investigation of fracture surface cross-sections was carried out to determine the fracture modes and fractography was done to reveal the initiation sites and crack growth directions. It is concluded that although both the ABB alloys show very high fatigue strength relative to their tensile strength, their behaviour strongly depends on the microstructure.

Keywords: Intermetallic, gamma TiAl, High Cycle Fatigue, Fractography, Microstructure

1. Introduction

Gamma based intermetallic TiAl alloys show great promise as candidate materials for gas turbine rotating parts exposed to intermediate temperatures, owing to their relatively low density compared with nickel-based alloys. In the temperature range from 20 to 750°C, titanium aluminides exhibit attractive density-corrected mechanical properties and a high oxidation resistance. However, the low ductility (<2% at room temperature) and fracture toughness of γ-TiAl are commonly recognised as its main drawbacks [1-4]. Much research has been done over the last decades to increase the ductility and improve the mechanical properties. This research has led to the development of titanium aluminides from simple Ti-48Al to several more complex alloys of Ti-(47-49)Al-(1-3)X_1-(1-10)X_2-(0-1)X_3 (in at.%) where X_1 = V, Cr, Mn; X_2 = Nb, Mo, Ta, Hf, W; and X_3 = Si, B, Fe, C, N [2,5-7]. Several investigations have shown that the microstructure greatly affects the mechanical properties [8]. Small changes in composition, casting and heat treatment procedures may cause changes in the microstructure and hence changes of material properties. It is therefore of utmost importance to perform detailed studies when a new alloy is being developed.

The γ-TiAl alloy ABB-2 with nominal composition Ti-46Al-2W-0.5Si (at.%) was developed in the framework of the European COST501 project (1994 to 1998) and several batches of material were characterised [9]. The present study has been conducted within COST522 (1999-2003), where specimens extracted from low pressure turbine (LPT) blades manufactured from the ABB-2 alloy have been characterised and compared with the properties for the new, fine grained ABB-23 alloy.

This article presents the results of an investigation on the high cycle fatigue (HCF) behaviour of ABB-2 and ABB-23. Axial HCF testing of ABB-2 has been conducted in air at 20 and 700°C at R=0.1 and 0.5, and ABB-23 has been tested at 20 and 550°C at R = 0.1 and 0.5. Both smooth and notched (K_t=3) specimens have been used. Post-test fractographic and metallographic examination of longitudinal cross-sections was conducted for a number of specimens to determine the fracture modes and reveal the initiation sites and crack growth directions.

2. Materials and experimental procedures

2.1 Materials

The materials used for the present study were ABB-2 and ABB-23, provided by ALSTOM Power (Switzerland). The materials were cast, HIPped (1260°C, 4h, 172 MPa) and heat-treated (1350°C for 1h followed by gas fan cool, then held at 1000°C for 6h and furnace cooled) resulting in a nearly lamellar structure. The ABB-2 alloy with nominal composition Ti-46Al-2W-0.5Si (at.%) was supplied in the form of a cast plate and sections removed from a LPT blade for an industrial gas turbine engine. It showed a generally inhomogeneous microstructure with large areas having a nearly lamellar microstructure, and a colony size of 0.5-2 mm. The ABB-23 alloy is an improved version of ABB-2, containing boron to homogenise and refine the microstructure. Its nominal composition is Ti-45Al-2W-0.55Si-0.6B (at.%) and it was supplied as round cast bars in two diameters.

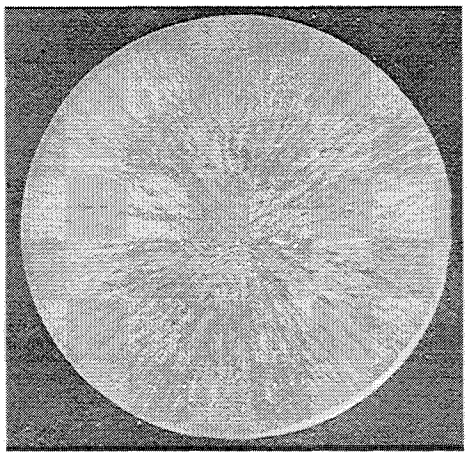


Figure 1. *Optical macrograph of ABB-23 Ø16 mm cast bar structure.*

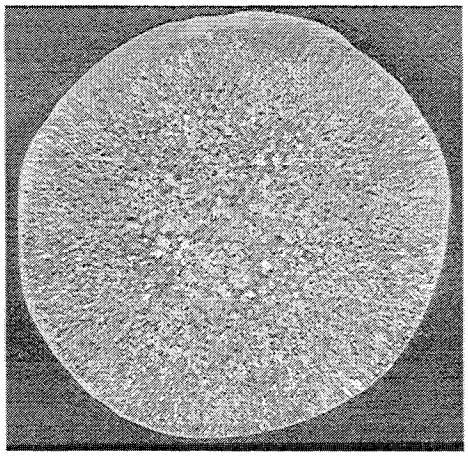


Figure 2. *Optical macrograph of ABB-23 Ø25 mm cast bar structure.*

The microstructure of ABB-23 was duplex with a small amount of equiaxed γ-TiAl grains. The colony size in the Ø16 mm bars (see Figure 1) varied from 20-50 μm at the centre of the bars to 200 μm near the edge of the bar. The colony size in the Ø25 mm bars (see Figure 2) was 200-300 μm over the entire cross-section. However, due to the casting process the shape of the colonies changed from equiaxed in the centre to columnar near the edge of the bar. Table 1 shows the actual compositions of the investigated materials.

Table 1. *Designation and composition (wt.%) of materials studied.*

Material	Batch	Ti	Al	W	Si	B	Fe	O	N
ABB-2	Plate	Bal.	30.5	9.1	0.33	-	0.023	0.066	0.032
ABB-2	FTR	Bal.	30.6	9.0	0.33	-	0.020	0.034	0.013
ABB-2	Blade	Bal.	30.6	9.0	0.33	-	0.020	0.034	0.013
ABB-23	1, Ø16mm	Bal.	29.6	9.3	0.38	0.163	0.022	0.053	0.013
ABB-23	1, Ø 25 mm	Bal.	29.6	9.3	0.38	0.163	0.022	0.053	0.013
ABB-23	2, Ø 16 mm	Bal.	29.9	9.1	0.41	0.193	0.044	0.071	0.011

FTR = Fir Tree Root

2.2 Testing Procedure

The plain specimen HCF behaviour of ABB-2 has been studied in air at 20 and 700°C at R = 0.1 and 0.5, and plain ABB-23 specimens (from two batches and two test bar diameters) have been tested at 20 and 550°C at R = 0.1 and 0.5. The notched (K_t = 3) behaviour for both alloys has been studied at 20°C and R = 0.1 only. Each sample was cycled until either failure or run-out, which was defined as 10^6 or 10^7 cycles depending on the test frequency used. For tests achieving run-out, the load was raised stepwise at each successive run-out until specimen failure occurred.

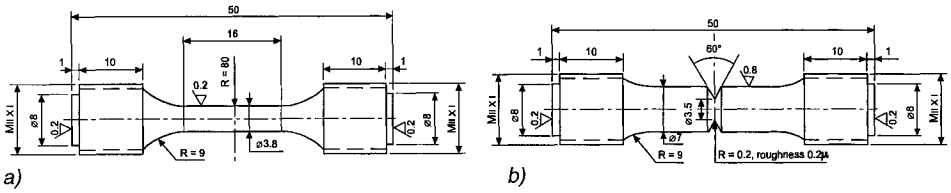


Figure 3. *Test specimens used for the NLR HCF tests. a) smooth, K_t=1; b) notched, K_t=3.*

Tests were carried out using 100 kN Amsler HFP machines, running at frequencies ranging from 90 to 160 Hz, depending on the loading conditions and specimen geometry (K_t =1 or 3) or using a 100kN Instron/Losenhausen servo-hydraulic test machine at 30 Hz (runout of 10^6 cycles). Figure 3 shows typical examples of the HCF specimens used in the study, which were machined from either the cast LPT blade (ABB-2), cast and HIPped slabs (ABB-2) or cast rods (ABB-23, Batches 1 and 2 as described above) as necessary.

To enable a baseline estimate of the HCF life to be made, room temperature tensile tests were also carried out using 250 kN and 100 kN Schenk Trebel test machines at a displacement rate of 1mm/min and 6%/min, respectively. Simple tensile specimens were used having a diameter of 7 mm (ABB-2 specimens) and 3.8 mm (ABB-23 specimens).

3. Results and Discussion

3.1 Tensile tests

The tensile test results showed large scatter within each batch and there was also batch-to-batch variation. Table 2 gives the average yield strength and ultimate tensile strength for some of the batches of ABB-2 and ABB-23.

Table 2. *Average room temperature tensile properties for batches of ABB-2 and ABB-23.*

Material	Batch	$R_{0.2}$ (MPa)	R_m (MPa)
ABB-2	Plate	473	546
ABB-2	FTR	491	507
ABB-2	Blade	523	619
ABB-23	1, Ø16mm	530	606

FTR = Fir Tree Root

3.2 HCF life

Figures 4 and 5 show the HCF results for ABB-2 (FTR + blade) and ABB-23 (all batches) respectively, both for R=0.1. The main body of data presented in Figure 4 are derived from the fir tree root (FTR) specimens. The tests with the ABB-2 blade specimens (K_t=1 only) are pointed out.

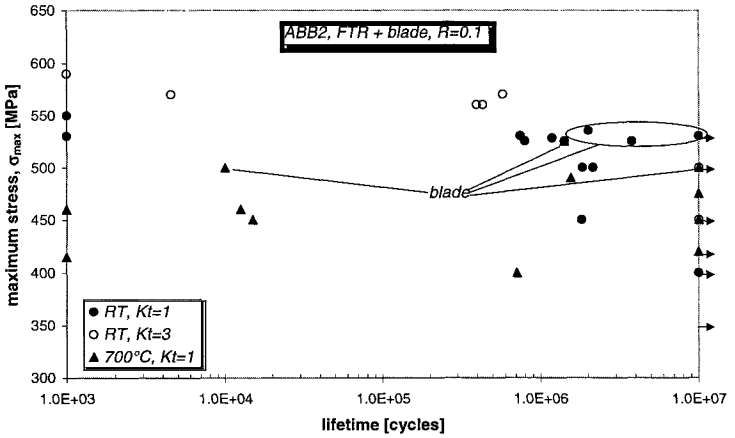


Figure 4. *Fatigue life for ABB-2 with R=0.1, K_t=1 or 3, at 20 and 700°C. Run-out at 10^7 cycles*

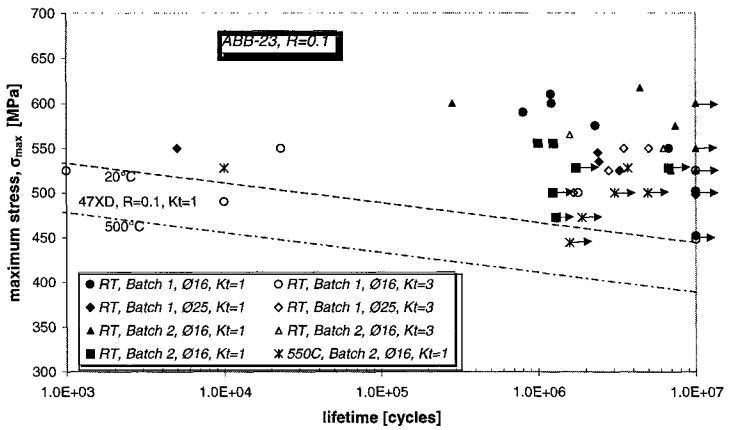


Figure 5. *Fatigue life of ABB-23 for R=0.1, K_t=1 at 20 and 550°C and K_t = 3 at 20°C. Run-out at 10^7 cycles. Trend lines for Ti-47-2-2XD at 20 and 500°C are added for comparison.*

The unnotched ABB-2 specimens show very flat fatigue curves with a high fatigue strength to R_m ratio (~1). The 700°C fatigue strength is lower than that at 20°C, although the tensile strength is fairly temperature independent at temperatures up to 700°C [8]. Apparently the fatigue strength decrease with temperature is not due to a decrease in R_m, but to a change in fatigue cracking mechanism (see Section 3.3). The fatigue strength of the notched ABB-2 specimens is higher than that of the unnotched specimens. This remarkable result can be explained by consideration of the coarse colony size in these castings (see Section 3.3). Furthermore, it is seen that the fatigue strength of the ABB-2 blade specimens is slightly higher than that of the ABB-2 FTR specimens, both at 20°C and at 700°C. This is probably caused by the difference in microstructure, which is known to have a large effect on the mechanical properties [8].

The ABB-23 alloy also shows very flat fatigue endurance curves (Figure 5) with a high fatigue strength to R_m ratio (~1). The fatigue strength for the unnotched ABB-23 specimens is higher than that of ABB-2, which corresponds with the higher tensile strength. Generally, the specimens from the Ø16 mm bars, batches 1 and 2, show similar fatigue behaviour, both for unnotched and for notched specimens. Unlike that found for ABB-2, the ABB-23 notched fatigue strength is lower than that for the unnotched specimens. The Ø25 mm bar specimens, Batch 1, show somewhat lower unnotched fatigue strengths compared with the Ø16 mm bar specimens and a notched fatigue strength similar to that of the unnotched specimens. This can be attributed to the larger colony size in the ABB-23 Ø25 mm bars. Increasing the test temperature to 550°C causes a reduction in fatigue strength in ABB-23 of similar magnitude as in Ti-47-2-2XD for which the trend lines are presented.

Figure 6 shows the plain specimen fatigue results for ABB-2 (plate) and ABB-23 (batch 1) at 20°C and R = 0.5. For both alloys the HCF curves are very flat, giving a transition from HCF to short life LCF behaviour over a cyclic stress range of around 10 MPa. This behaviour is presumably due to the rather low ductility of both alloys (under 1%). The high R-ratio fatigue strength of ABB-2 is greater than that for ABB-23.

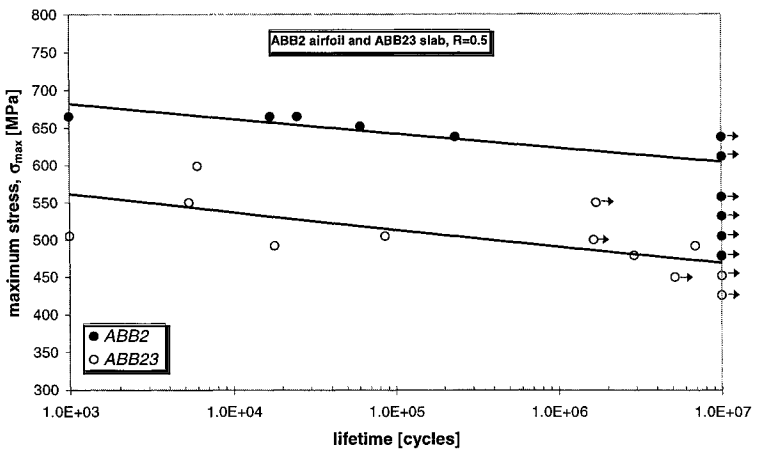


Figure 6. *Fatigue life of ABB2 and ABB23 at 20°C and R = 0.5. Run-out at 10^7 cycles.*

In order to compare the different fatigue tests, all results are plotted on a Haigh diagram (Figures 7 and 8) along with the Goodman lines for the ultimate tensile strength ($\sigma_m+\sigma_a=R_m$) and the 'first guess' life estimate using Hempels equation, as follows:

$$\sigma_D = \sigma_W \left[1 - \sigma_m \cdot \frac{1-Z}{R_m} \right] \tag{1}$$

where σ_m is the mean stress under HCF, R_m is the ultimate tensile strength, σ_w is the fatigue limit when σ_m =0, often taken to be $0.45R_m$, σ_d is the fatigue limit when $\sigma_m \neq 0$ and Z is the area reduction after fracture in a tensile test. For ABB2 two Goodman lines and two Hempel lines are drawn. This is because the R=0.1 data are based on specimens from the FTR and the R=0.5 data are based on specimens from the blade. Since the tensile properties differed for these two parts of the blade, the Goodman and Hempel lines differ also.

Haigh diagrams are usually considered to be a convenient method for extrapolating the fatigue behaviour from one R ratio to another, thereby limiting the amount of mechanical testing needed to construct a fatigue limit surface. However, the data in figures 7 and 8 show that there can be some discrepancies and inconsistencies. Figure 7 shows that the ABB-2 R=0.1 data fall below the FTR Goodman line, but the R=0.5 data agree well with the blade Goodman line. Figure 8 shows that the ABB-23 R=0.1 and R=0.5 data fall below the Goodman line, especially the R=0.5 data. This latter result is rather unexpected, as a finer grain structure is generally considered to improve grain structure, whereas the effect of grain refinement shown here is the opposite (compare to R=0.5 data of ABB-2, figure 7). Thus, not only are there discrepancies of fits to the Goodman lines, but comparison of the two materials shows that for ABB-2 the R=0.5 fatigue strength is relatively higher than the R=0.1 fatigue strength, while for ABB-23 the opposite is true.

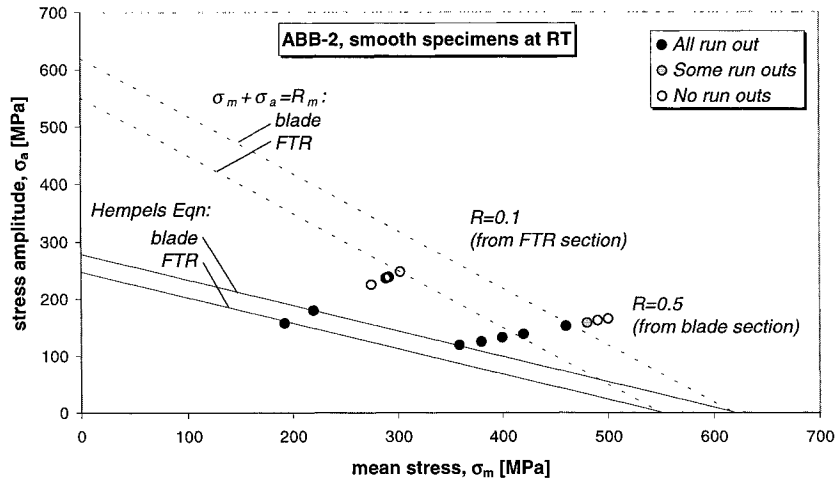


Figure 7. *Haigh diagram for ABB-2 with Goodman lines and Hempels equation lines.*

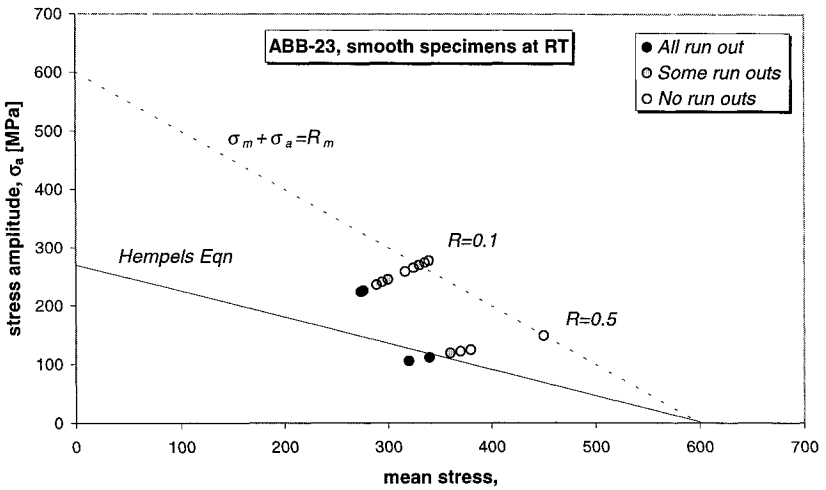


Figure 8. *Haigh diagram for ABB-23 (batch 1) with Goodman line and Hempels equation line.*

3.3 Fracture surfaces

Longitudinal sections

To reveal the fracture path, post-test, cross-sectional samples were prepared from a number of specimens and investigated using Optical Microscopy (OM) and Scanning Electron Microscopy (SEM). Figure 9 shows a cross-section through the fracture surface of an ABB-2 FTR specimen, tested at 20°C and R = 0.1. It can be seen that fracture occurred by transgranular failure of the lamellar colonies: interlamellar failure when the lamellae were oriented favourably, *i.e.* within an envelope of ±45° with the ideal plane of fracture (perpendicular to loading direction), and translamellar when the lamellae were oriented outside this envelope. At 700°C, not shown here, fracture occurred in a mixed intergranular / transgranular mode.

A large lamellar colony with favourably oriented lamellae and situated at or near the free surface was found to be detrimental to the fatigue strength. This is because the colony size is larger than the expected critical crack size resulting in instant failure after initiation [10]. The large colonies have also a size effect in the notched specimens: the notched area of the K_t=3 specimens is small, and so is the probability of the presence of a large colony with favourably oriented lamellae. Hence cracks are forced to initiate translamellarly, and the fatigue strength will be higher than in the unnotched specimens.

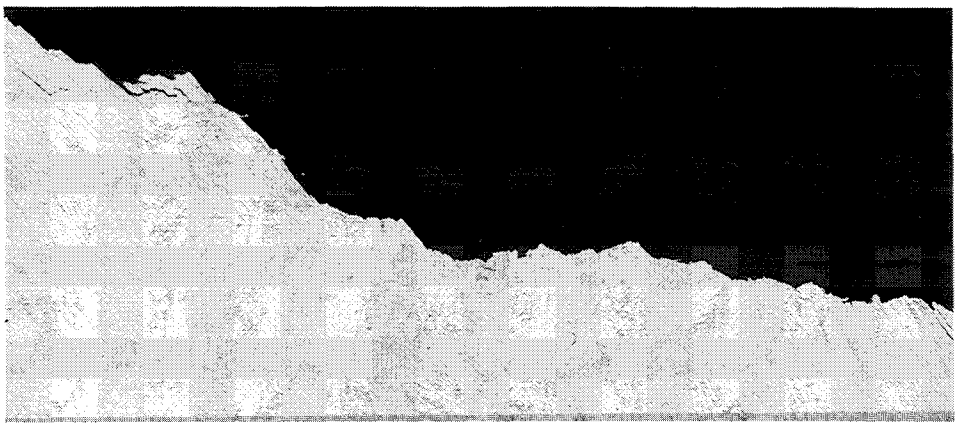


Figure 9. *Cross-section (OM) of fracture surface of unnotched ABB-2 specimen, tested at 20°C and R= 0.1.*

The ABB-23 colony size was too small to reveal the crack path by optical microscopy and hence SEM was used to analyse the cross-section. Figure 10 shows a cross-section through the fracture surface of an ABB-23 batch 1 Ø16 mm specimen, tested at 20°C and R = 0.1. Again, there is a strong tendency for transgranular fracture of lamellar colonies and γ-grains. This is notably observed by inspection of secondary cracks. Also, there is a tendency for interlamellar fracture when the lamellae are oriented favourably. However, this is less so than for ABB-2.

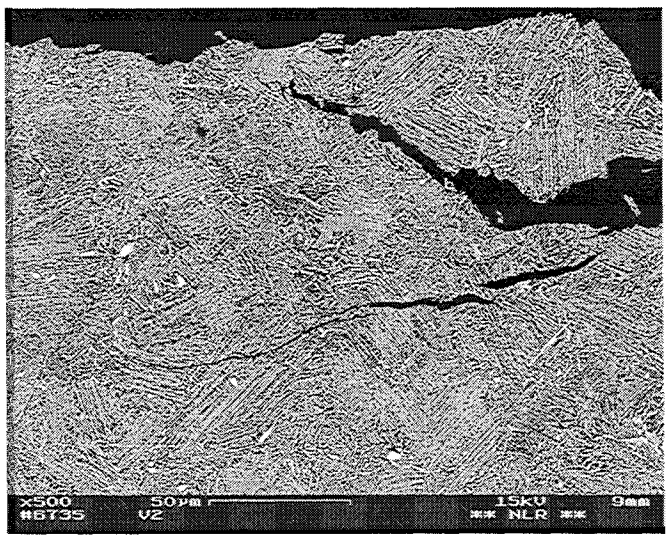


Figure 10. *Cross-section (SEM, Back Scattered Electron) of fracture surface of unnotched ABB-23 specimen, tested at 20°C and R = 0.1.*

Fractography

The ABB-2 (FTR) and ABB-23 (batch 1, Ø16 mm) fracture surfaces were investigated by stereo microscopy, for first impression and global fatigue crack features, and by SEM for more detailed investigation. Table 3 summarises the results.

Table 3. *Summary of fractographic examinations.*

	Stereo Microscopy	**SEM**
ABB-2	• very rough fracture surface • large faceted grains visible (interlamellar fracture) • no observable indications for crack initiation and cgd*	• practically no indication for crack initiation and cgd* • interlamellar fractured grains observed, but no river patterns indicating cgd*
ABB-23	• crack initiation region traceable • indications for global cgd* (see figure 11)	• global cgd* still visible • crack initiation site retraceable • local average cgd*, deduced from river patterns on transgranular fractured γ-grains (see Figure 12), agrees with global cgd*

* *cgd = crack growth direction*

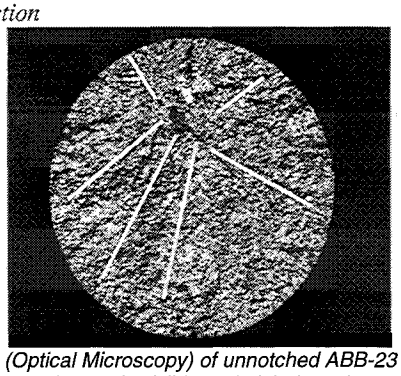
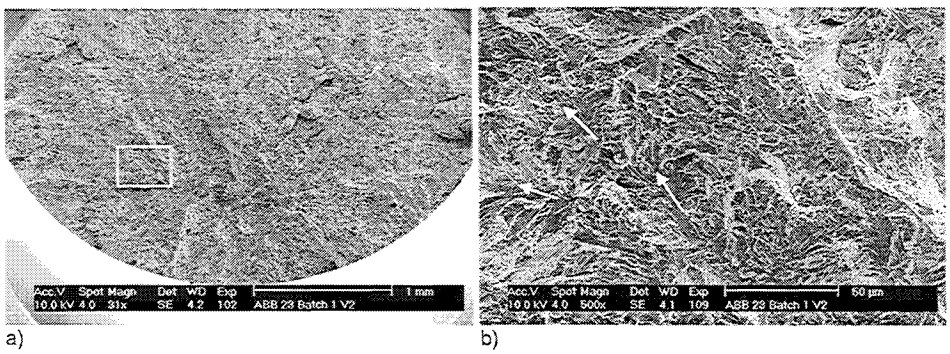


Figure 11. *Fracture surface (Optical Microscopy) of unnotched ABB-23 specimen tested at 20°C. Crack initiation region is clearly visible and global crack growth direction is indicated.*



a) b)

Figure 12. *Fracture surface (SEM) of unnotched ABB-23 specimen, tested at 20°C. a) overview of crack initiation area; b) detail of area above and left of the initiation site. Crack growth directions are indicated on river patterns on transgranular fractured γ-grains.*

4. Conclusions

- ABB-2 and ABB-23 show both at 20°C and at 700°C flat fatigue curves with a high fatigue strength to UTS ratio.
- For R=0.1 the unnotched fatigue strength of ABB23 is higher than that of ABB-2. For R=0.5 the unnotched fatigue strength of ABB23 is lower than that of ABB-2.
- For R=0.1 the notched fatigue strength of ABB-23 is lower than that of ABB-2. The reason for this is a size effect (notch area vs. lamellar colony size).
- Fracture was predominantly transgranular in both alloys, with interlamellar fracture for colonies with favourably oriented lamellae.
- Fatigue crack features on transgranular fractured grains were visible for ABB23 (γ-grains) but not for ABB2.

Acknowledgements

The authors thank Alstom Power Switzerland for providing the test material and performing some of the tensile tests.

References

[1] Y.W. Kim and D.M. Dimiduk, "Progress in the Understanding of Gamma Titanium Aluminides," *JOM*, Vol. 43, 1991, pp. 40-47.

[2] Y.W. Kim, "Ordered Intermetallic Alloys, Part III: Gamma Titanium Aluminides," *JOM*, Vol. 46, 1994, pp. 30-39.

[3] I.J. Perrin, "Designing with Low Ductility Intermetallic Alloys," *Gas Turbines – Materials Make the Difference*, Workshop at DERA Farnborough, Hampshire, UK, 21/22 January 1999.

[4] D.M. Dimiduk, "Gamma Titanium Aluminide Alloys – an Assessment within the Competition of Aerospace Structural Materials," *Mater. Sci. Eng.*, Vol. A263, 1999, pp. 281-288.

[5] T.T. Cheng, M.R. Willis and I.P. Jones, "Effect of Major Alloying Additions on the Microstructure and Mechanical Properties of γ-TiAl," *Intermetallics*, Vol. 7, 1999, pp.89-99.

[6] F.S. Sun, C.X. Cao, S.E. Kim, Y.T. Lee and M.G. Yan, "Alloying Mechanism of Beta Stabilisers in a TiAl Alloy," *Metall. Mater. Trans. A*, Vol. 32A, 2001, pp. 1573-1589.

[7] H. Clemens, A. Lorich, N. Eberhardt, W. Glatz, W. Knabl, and H. Kestler, "Technology, Properties and Applications of Intermetallic γ-TiAl Based Alloys," *Z. Metallkd.* Vol. 90, 1999, pp. 569-580.

[8] V. Recina and B. Karlsson, "Tensile Properties and Microstructure of Ti-48Al-2W-0.5Si γ-Titanium Aluminide at temperatures between room temperature and 800°C," *Mater. Sci. Technol.*, Vol. 15, 1999, pp. 57-66.

[9] M. Nazmy and V. Lupinc, "Gamma TiAl Intermetallic for Gas Turbine Applications," *Proc. 6th Liège Conference, Part II*, J. Lecomte-Beckers, F. Schubert and P.J. Ennis (Ed.), 1998, pp. 933-944.

[10] V. Recina and B. Karlsson, "High Temperature Low Cycle Fatigue Properties of Ti-48Al-2W-0.5Si gamma Titanium Aluminide," *Mater. Sci. Eng.*, Vol. A262, 1999, pp. 70-81.

Ti_2AlNb-BASED TITANIUM INTERMETALLIC ALLOYS FOR HIGH TEMPERATURE APPLICATIONS

M. Hagiwara, S. Emura and F. Tang
National Institute for Materials Science
1-2-1 Sengen, Tsukuba 305-0047, Japan
e-mail: HAGIWARA.Masuo@nims.go.jp

Abstract

The effects of microstructural and compositional modifications on the mechanical properties of an orthorhombic Ti2AlNb-based intermetallic alloy were investigated. In addition, Ti-22Al-27Nb alloy-based particulate composites reinforced with 6.5%TiB were produced and evaluated.
A Ti-22Al-27Nb alloy with a prior B2 grain size ranging from 10 μm to 200 μm was successfully obtained by using spherical α2 particles as obstacles against grain growth. An alloy with a B2 grain size of 50 μm and a lamellar microstructure within the grains exhibited higher tensile strength (1371 MPa) and elongation (7 %) at room temperature. The substitution of 2%W for 7%Nb in a Ti-22Al-27 Nb was quite effective in increasing tensile strength at temperatures above 923 K. This substitution was also effective in reducing the steady state creep rate and primary creep strain. The mechanical properties of the composites, including the yield stress, tensile strength, Young's modulus, resistance to creep, and high cycle fatigue strength were greatly superior to those of the matrix alloy.

Keywords: orthorhombic titanium alloy, microstructure, composition, particulate composites, mechanical properties

1. Introduction

A new class of titanium intermetallic alloy based on the Ti_2AlNb phase has been receiving a lot of attention as a candidate material for high temperature applications [1-4]. These alloys are often called orthorhombic alloys because of the ordered orthorhombic structure of the Ti_2AlNb phase.

A wide range of microstructures and, hence, a variety of properties can be developed in orthorhombic alloys through control of their chemistry and processing. Of various orthorhombic alloys so far studied, Rowe has shown that a Ti-22Al-27Nb alloy, which consists mainly of the O phase and B2 phase, has the best balance of tensile, creep, and fracture properties [1]. The primary disadvantage of a Ti-22Al-27Nb alloy is, however, that the room temperature tensile elongation is very low, ranging from 0 % to 7 % depending on the microstructures. Another disadvantage of this alloy is that it exhibits a relatively large primary creep strain, as compared to that of nickel-based super-alloys. Furthermore, its yield stress drops sharply at temperatures higher than 923K.

This paper summarizes our recent research efforts to overcome these drawbacks and develop novel orthorhombic alloys for temperatures above 923 K. The research objectives were threefold. The first one dealt with the microstructural modification, which was aimed at improving the room temperature ductility and tensile strength of a Ti-22Al-27Nb alloy. To achieve this goal, the possibility of refining prior B2 grains was examined. The second one dealt with the compositional modification, which was aimed at improving the tensile strength and creep strength at temperatures above 923 K by substituting β phase-stabilizing elements such as W, Mo, or V for a portion of Nb in a Ti-22Al-27Nb alloy. The third one dealt with the powder metallurgy (P/M) synthesis of orthorhombic alloy-based composites with 6.5%TiB particulate, which was aimed to further improve the physical and mechanical properties of

orthorhombic alloys over those for the above microstructurally and/or compositionally modified alloys.

2. Experimental procedure

Since an orthorhombic alloy contains a large amount of Nb, the gas atomization powder metallurgy processing route was employed to ensure the homogeneity of the alloy. Melting stocks with and without boron (B), which were previously prepared by plasma arc melting, were melted by a high frequency induction coil, and a high speed argon gas jet was simultaneously bombarded on the melt and finally the melt was atomized to very fine spherical powder. In the case of the B-containing melting stocks, B reacted with Ti during solidification, forming an in-situ TiB compound in each powder. In the present case, the fraction of TiB in each powder was calculated to be 6.5 mass percent. Although we intended to make Ti-22Al-27Nb alloy-based composites, the actual composition of the composites was Ti-23.5Al-25.5Nb. The powder particles with the diameters ranging between 45 μm and 150 μm were contained in an evacuated can, and the powder was then compacted by hot isostatic pressing (HIP) at 1373 K with 200 MPa pressure. The HIP'ed materials were hot-rolled in the B2 phase region or in the (B2+α_2) phase region into bars. After hot-rolling, various heat treatments were performed to modify the microstructure.

The alloys, which were used for the study of compositional modification, were prepared using a non-consumable electric arc furnace. The alloy ingots, which weighed 200g each, were first forged at 1423 K in the B2 phase region. These forged ingots were annealed at 1423 K for 3.6ks, and then slowly cooled to produce a lamellar microstructure.

High temperature tensile tests were performed in a vacuum with specimens of 3.5 mm diameter by a 16 mm gauge length. The high temperature Young's modulus was determined by the ultrasonic pulse echo method. Creep tests were performed in air with specimens of 4.0 mm diameter by a 25 mm gauge length using a constant load creep frame. High cycle fatigue tests were performed in air using specimens with a 3.0 mm diameter by 14 mm gauge length, an R ratio of 0.1 in the load-control mode, and a frequency of around 80 Hz.

3. Results and discussion

3.1. Microstructural modification

3.1.1 Thermo-mechanical treatments for microstructural modification

The microstructural modification, which corresponded to the B2 grain size control, was achieved using the following three thermo-mechanical treatments, in which the spherical α_2 particles were successfully used as obstacles against grain growth.

(a) Hot rolling in the (α_2+B2) phase region and annealing in the (α_2+B2) phase region

The pseudo binary phase diagram of Ti-22at.%Al-Nb [4] is shown in Fig.1. It was found that the hot rolling of a Ti-22Al-27Nb alloy in a (α_2+B2) phase region (1273 K to 1343 K) could be easily done. The elongated α_2 phases formed after hot-rolling tended to become spherical during subsequent annealing in the (α_2+B2) phase region, even though the alloy was not subjected to heavy deformation during hot rolling.

Fig.2 shows the distribution of the spherical α_2 phases after hot-rolling at 1273 K and subsequent annealing at 1323 K and 1273 K (Fig.2a and Fig.2b, respectively). It was seen that when the hot-rolled alloy was annealed at the lower temperature of 1273 K, the size of these

α_2 particles was much smaller, and their distribution was much more dense (Fig.2b). These uniformly dispersed α_2 phases acted as obstacles against grain growth, and, therefore, fine B2 grains ranging from 10 μm to 50 μm in diameter were obtained. As shown in Fig.2c, the lamellar microstructure could be formed within these small B2 grains by slow cooling from the annealing temperature.

Fig.3 shows that there is a linear relationship between the average size of the B2 grain and the Larson-Miller parameter for a Ti-22Al-27Nb alloy that was hot-rolled at 1273 K and annealed in the (α_2+B2) phase region with various combinations of temperature and time.

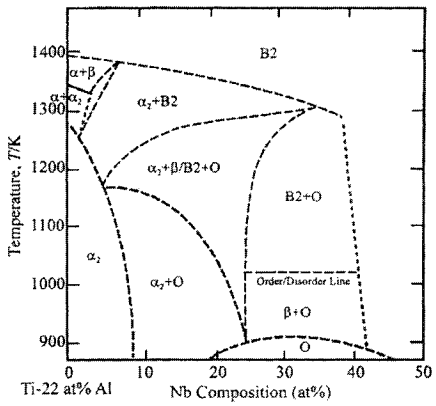


Fig.1 The pseudo binary phase diagram of Ti-22at.%Al-Nb [4]

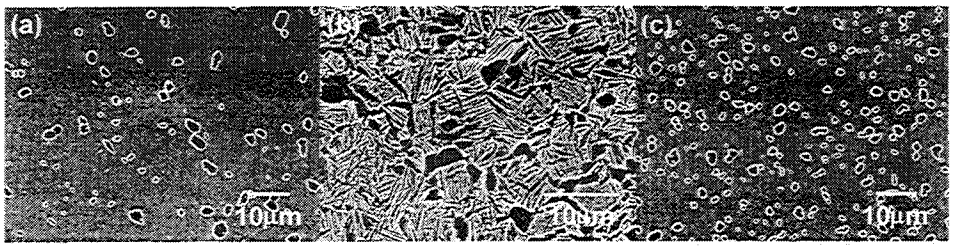


Fig.2 Distribution of the spherical α_2 phases. The material was hot-rolled at 1273 K and then annealed at (a):1323 K for 72 ks followed by water-quenching, (b): same as (a) but followed by slowly cooling, and (c): 1273 K for 72 ks followed by water-quenching.

(b) Hot rolling in the (α_2+B2) phase region and annealing in the B2 phase region

The resolution rate of these spherical α_2 phases was found to be quite slow when the spherical α_2 particles-containing material was heated in the B2 phase region. Relatively fine B2 grains could therefore be obtained due to the pinning effect of these α_2 particles on the B2 grain growth. As shown in Fig.3, there is a linear relationship between the average size of the B2 grain ranging from 50 μm to 80 μm in diameter, and the Larson-Miller parameter for a Ti-22Al-27Nb alloy that was hot-rolled at 1273 K and subsequently annealed in the B2 phase region with various combinations of temperature and time.

(c) Hot rolling in the B2 phase region and annealing in the B2 phase region

During slow cooling after hot rolling in the B2 single region (e.g., 1423 K), a small

amount of spherical α_2 particles were found to form. These particles were therefore used to control the B2 grains to a size above 80 μm in diameter by annealing the hot-rolled material in the B2 phase region, as shown in Fig.3.

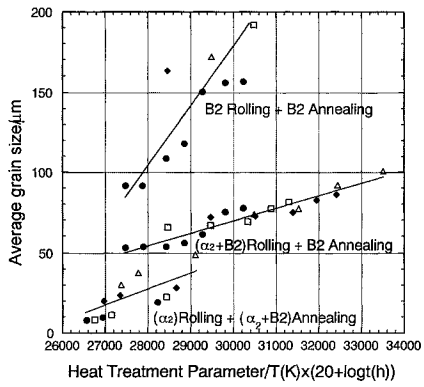


Fig.3 The relationship between the average B2 grain size and the Larson-Miller parameter.

3.1.2 Tensile properties for a Ti-22Al-27Nb alloy with reduced B2 grains

Fig.4 shows the tensile properties for a Ti-22Al-27Nb alloy with B2 grain sizes of 50 μm and 200 μm. The materials were cooled at a cooling rate of 0.5 K/s from the annealing temperature. This faster cooling rate resulted in a fine lamellar microstructure within the grains. It was clearly demonstrated that by reducing the grain size from 200 μm to 50 μm, the room temperature proof stress and tensile strength increased from 1021 MPa and 1174 MPa to 1115 MPa and 1371 MPa, respectively, and the room temperature elongation increased from 4 % to 7 %.

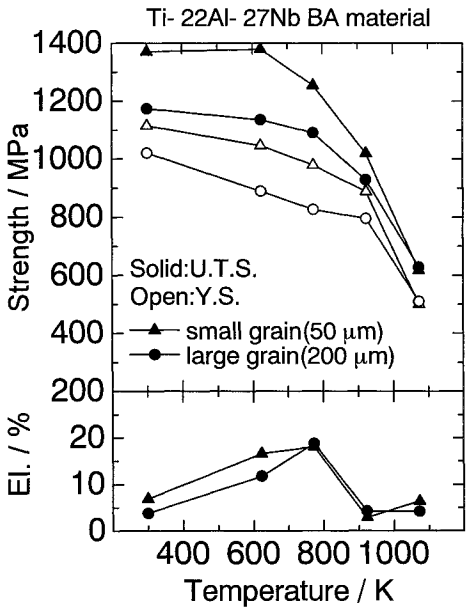


Fig.4 Tensile properties of a Ti-22Al-27Nb alloy with two different grain sizes.

3.2. Compositional modification

3.2.1 Guideline for alloy modification

The guideline governing the alloy modification is based on the fact that the total sum of the β phase stability from each β-stabilizing element in the modified alloy should correspond to a baseline Ti-22Al-27Nb alloy. This guideline suggests that the phase diagram for the modified alloy needs to be equal or very similar to that of a baseline alloy, and, therefore, the same phase constitutions may be obtained with the same heat treatment for both modified and baseline alloys.

Table 1 shows the critical concentration of various beta stabilizers in titanium necessary to retain a 100 % β phase (bcc structure) at room temperature [5], indicating that the β phase stabilizing ability becomes strong in the order of Nb, V, W, and Mo. For example, Mo is Nb (22.5) / Mo (5.3) = 4.25 times stronger than that of Nb. Therefore, it is reasonable to consider that one atomic percent addition of Mo corresponds to the replacement of the 4.25 atomic percent of Nb. Similarly, one atomic percent addition of W corresponds to the replacement of the Nb (22.5) / W(6.7) = 3.36 atomic percent of Nb. According to this guideline, various modified alloys were produced.

Table1 Critical concentration, βc, of various beta stabilizers necessary to retain a 100 % beta phase at room temperature [5].

β-stabilizer	Mn	Fe	Cr	Co	W	Ni	Mo	V	Nb	Ta
βc (at.%)	5.6	3.0	5.8	5.8	6.7	7.5	5.3	14.2	22.5	17.8

3.2.2 Composition, density, and phase constitutions of each modified alloy

The lamellar morphology for the modified alloys and a baseline Ti-22Al-27Nb alloy was highly dependent on the cooling rate. A slower cooling rate of 0.03 K/s resulted in coarsely aligned laths within the grains (See Fig.2b).

The composition, density, and phase constitution of each modified alloy are shown in Table 2. The density of these modified alloys was in the range of 4.9 to 5.4 g/cm^3, which is almost equal to or somewhat lower than that of the baseline alloy. When solution-treated at 1323 K, a single B2 phase was obtained in all of the alloys. Although we expected that the same phase constitutions would be obtained for both the modified alloys and the baseline alloy, the alloys having a higher Nb content, such as the Ti-22Al-24Nb-2V and baseline alloys, had a higher B2 transus temperature. In a Ti-22Al-11Nb-4Mo alloy, which has the lowest Nb content, O phases existed only at temperatures below 1053 K. When aged at 1123 K after the B2 solution treatment, the volume proportions of the residual B2 phase in the modified alloys were almost comparable to that in the baseline alloy.

3.2.3 Creep properties

Fig.5 shows the creep curves of the modified alloys and a baseline Ti-22Al-27Nb alloy. A creep test was conducted at 923 K at an applied stress of 310 MPa. It was demonstrated that the Ti-22Al-20Nb-2W alloy exhibited a marked decrease in primary creep strain as well as in steady state creep rate as compared to those of other modified alloys and the baseline alloy.

Table 2 Composition, density and phase constitution of each modified alloy

Alloy (at.%)	Density (Mg/m^3)	1,323K/3.6ks/WQ	1,323K/3.6ks/WQ + 1,223K/61.2ks/WQ	1,323K/3.6ks/WQ + 1,123K/360ks/WQ	1,323K/3.6ks/WQ + 1,003K/165.6ks/WQ
Ti-22Al-19Nb-2Mo	5.1	B2	B2+α_2	B2+O	B2+O
Ti-22Al-11Nb-4Mo	4.9	B2	B2+α_2	B2+α_2	B2+O+α_2
Ti-22Al-20Nb-2W	5.3	B2	B2+α_2	B2+O	B2+O
Ti-22Al-14Nb-4W	5.4	B2	B2+α_2	B2+α_2+O	B2+α_2+O
Ti-22Al-24Nb-2V	5.3	B2	B2+O	B2+O	B2+O
Ti-22Al-21Nb-4V	5.2	B2	B2+α_2	B2+O	B2+O
Ti-22Al-12Nb-2Mo-2W	5.1	B2	B2+α_2	B2+α_2	B2+O+α_2
Ti-22Al-27Nb	5.4	B2	B2+O	B2+O	B2+O

3.2.4 High temperature tensile properties

The 0.2 % yield stress of the W-modified Ti-22Al-20Nb-2W alloy was compared with that of the baseline Ti-22Al-27Nb alloy, and is represented in Fig.6. Since the yield strength of these two alloys changed depending on the alloy's lamellar morphology, the yield strength data were depicted as a scatter-band. In this scatter-band, a coarser lamellar morphology resulting from the slower cooling rate corresponded to the lower boundary, whereas a finer lamellar morphology resulting from the faster cooling rate exhibited the highest yield strength.

It is obvious that the critical temperature above which the yield stress began to decrease rapidly is 100 K higher in a Ti-22Al-20Nb-2W alloy than in the baseline alloy.

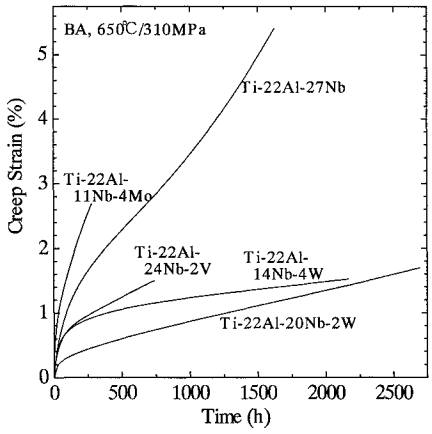


Fig.5 Creep property of modified alloys with lamellar microstructure.

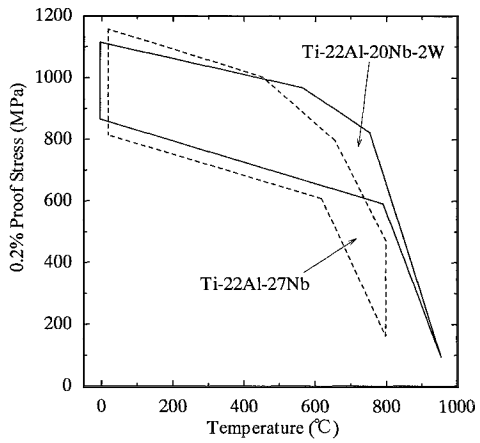


Fig.6 0.2 % yield stress of W-modified Ti-22Al-20Nb-2W alloy.

3.3. P/M synthesis of orthorhombic alloy-based composites reinforced with TiB particulates

The HIP'ed and hot-rolled Ti-22Al-27Nb alloy and Ti-22Al-27Nb/6.5%TiB composites were slowly cooled from the annealing temperature of 1323 K at the cooling rate of 0.03 K/s.

3.3.1 Microstructure of the composites

Fig.7 shows the microstructure of the composites. It can be seen that the TiB particulates in the composites are extremely fine, with a diameter less than 1 μm and a length ranging from 1 μm to 10 μm, and are uniformly distributed throughout the matrix (Fig.7a). The microstructure of the matrix in the composites consists of a fine colony-like O (dark phase) +B2 (light phase) microstructure (Fig.7b). The prior B2 grain size could not be determined, but was presumed to be very small because of the narrow spacing of the TiB particulates.

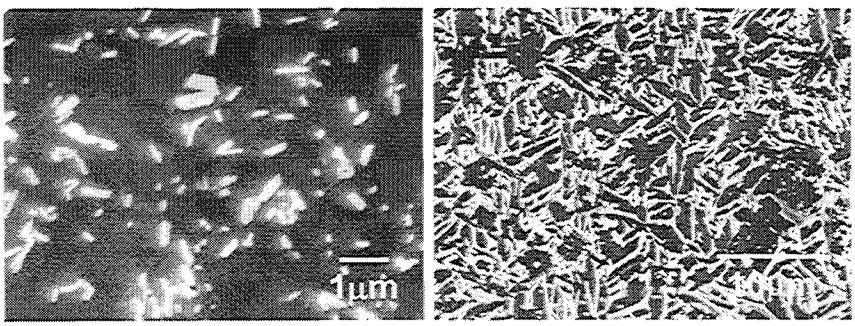


Fig.7 Microstructure of the composites in the polished (left) and etched conditions (right).

3.3.2 Mechanical properties of the composites

Fig.8 shows the results of the high temperature tensile tests for the baseline Ti-22Al-27Nb alloy and the composites. It is seen that the composites exhibited higher yield and tensile strength in the entire temperature range up to 1074 K. The elongation of the composites increased gradually with increasing temperature. A 10 % elongation was obtained at 1074 K. Both specimens tested at room temperature and 1073 K exhibited a ductile fracture mode, as shown in Fig.9.

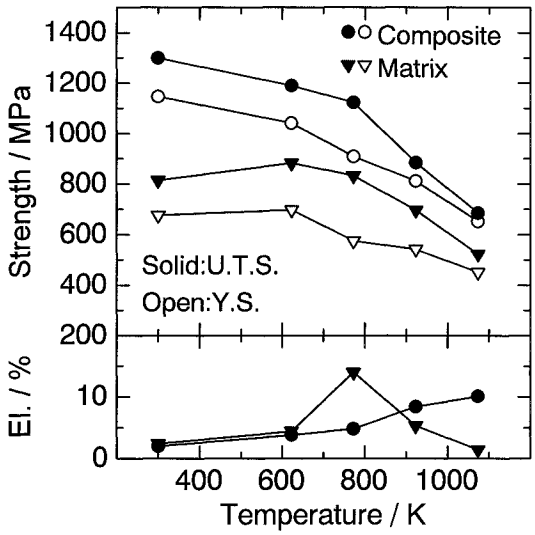


Fig.8 High temperature tensile properties of the Ti-22Al-27Nb alloy and the Ti-22Al-27Nb /6.5%TiB composites.

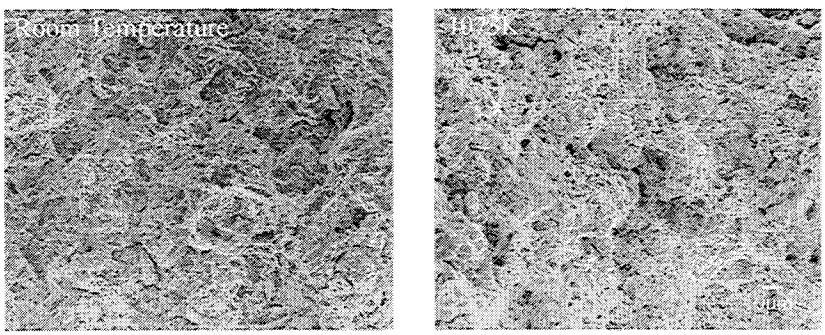


Fig.9 Tensile fracture surfaces of the composites.

Fig. 10 shows the creep curves for the baseline Ti-22Al-27Nb alloy and the composites, tested at 923 K and at an applied stress of 310 MPa. The composites showed a lower primary creep strain, a lower steady state creep rate and a longer creep life than the baseline alloy.

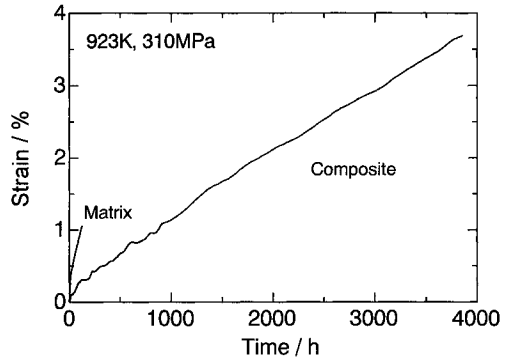


Fig.10 Creep curves for the Ti-22Al-27Nb alloy and the Ti-22Al-27Nb /6.5%TiB composites.

Fig.11 shows the high temperature Young's modulus for the baseline Ti-22Al-27Nb alloy and the composites. The Young's modulus for the baseline alloy at room temperature was 119 GPa, which is somewhat higher than those of conventional titanium alloys such as Ti-6Al-4V, but considerably lower than that of γ-TiAl. The Young's modulus for the baseline alloy increased to 127 GPa by the dispersion of 6.5%TiB. The composites exhibited higher Young's modulus in the entire range of temperatures up to 973K.

Fig.12 shows the room temperature high cycle fatigue life for the baseline Ti-22Al-27Nb alloy and the composites. The composites exhibited higher high cycle fatigue strength in the entire cycle range than those for the baseline alloy. For example, the fatigue strength at 10^7 cycles increased from 430 MPa to 600 MPa with 6.5%TiB. Such a large increase in fatigue strength seems to be due to the increase in Young's modulus, the microstructural refinement of the matrix, and the Orowan strengthening. Further study is needed, however, to clarify the actual contribution of each factor to the increase in fatigue strength.

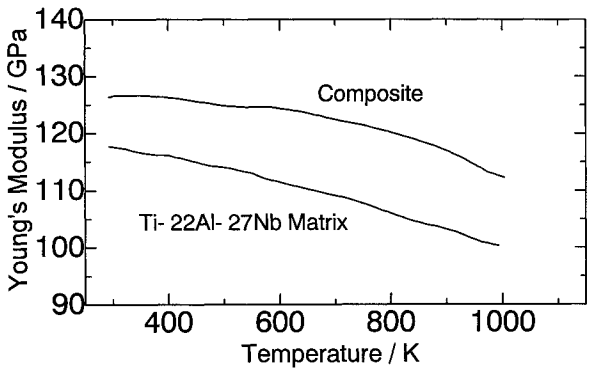


Fig.11 High temperature Young's modulus for the Ti-22Al-27Nb alloy and the Ti-22Al-27Nb /6.5%TiB composites.

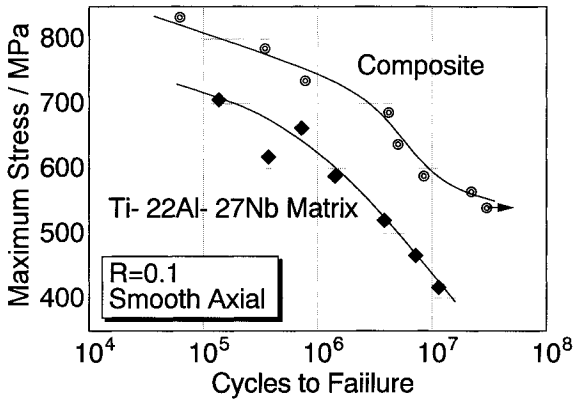


Fig.12 Room temperature high cycle fatigue life for the Ti-22Al-27Nb alloy and the Ti-22Al-27Nb /6.5%TiB composites.

4. Conclusion

A Ti-22Al-27Nb alloy with a prior B2 grain size ranging from 10 μm to 200 μm was successfully obtained by using spherical α_2 particles as obstacles against grain growth. An alloy with a B2 grain size of 50 μm and a lamellar microstructure with thin laths exhibited higher tensile strength (1371 MPa) and elongation (7 %) at room temperature.

The substitution of 2 %W for 7 %Nb in a Ti-22Al-27Nb was quite effective in increasing tensile strength at temperatures above 923 K. This substitution was also effective in reducing the steady state creep rate and primary creep strain.

The Ti-22Al-27Nb alloy-based composites reinforced with 6.5%TiB were successfully produced using a gas atomization P/M method. The size of the TiB particulates was extremely small, with a diameter less than 1 μm and a length ranging from 1 μm to 10 μm. Most of the mechanical properties, such as the high temperature tensile strength, creep, high temperature Young's modulus and high cycle fatigue strength were superior to those of the baseline alloy.

5. References

1. R.G. Rowe, Microstructure/Property Relationship in Titanium Aluminides and Alloys Y.-W. Kim and R.R.Boyer, eds., TMS, Warrendale, PA, (1991), pp.387-398.
2. J. Kumpfert and C. Leyens, Structural Intermetallics, B.D. Miracle, R. Wagner and M. Yamaguchi, eds., TMS, Warrendale, PA, (1997), pp.895-904.
3. A.K. Gogia et al, Intermetallics, 6(1998), pp.741-748.
4. C.J. Boehlert, B.S. Majumdar, V. Seetharaman and D.B. Miracle, Met. Trans., 30A(1999), pp.2305-2329.
5. S. Ankem and S.R. Seagl, Beta Titanium Alloys in the 1980's, R.R. Boyer and H.W. Rosenberg, eds., TMS-AIME, Warrendale, PA, (1983), pp.107-126.

MANUFACTURING AND TESTING OF A NOVEL ADVANCED NiAl-BASE ALLOY FOR GAS TURBINE APPLICATIONS

M. Palm & G. Sauthoff

Max-Planck-Institut für Eisenforschung GmbH, D-40074 Düsseldorf, Germany

Abstract

A novel NiAl-base alloy has been developed for gas turbine applications. The alloy with nominal composition 45 Ni, 45 Al, 2.5 Ta and 7.5 Cr (in at.%, IP75 for short) has a NiAl matrix with precipitates of Laves phase and α-Cr. By different methods of processing, e.g. powder metallurgical processing, investment casting or hot forging, the distribution of these precipitates can be controlled, thus varying the mechanical properties of IP75 within a wide range. Compared to conventional Ni-based superalloys the alloy has lower density, higher thermal conductivity, higher melting point and excellent oxidation and corrosion resistance at least up to 1300°C. The coefficients of thermal expansion, the heat capacity and Young's modulus are comparable or slightly superior to those of the superalloys, and in contrast to Ni-base alloys IP75 exhibits excellent microstructural stability without marked coarsening or dissolution of second phases at temperatures up to 1400°C. The alloy has a higher strength and creep resistance above 1100°C than that of the superalloys, which is correlated with a poor ductility at room temperature.
Methods have been established to produce the alloy by investment casting and powder metallurgy on an industrial scale. Various components have been produced and the material has been tested up to 1300°C including thermo-shock behaviour, long-time static and cyclic oxidation resistance, hot gas corrosion and creep properties. Possible applications are discussed.

Keywords: NiAl base alloys, intermetallics

Introduction

In view of gas turbine applications at or above 1200°C a novel intermetallic NiAl-base alloy with strengthening Laves phase has been developed. Compared to conventional Ni-base superalloys, this new alloy allows a higher application temperature and has advantageous properties such as lower density, higher thermal conductivity and a better oxidation resistance, which make this alloy promising for structural applications in more efficient low-pollution energy-converting systems. As part of a materials development in progress, the processing of this alloy has been studied on an industrial scale, the mechanical and oxidation behaviour has been evaluated and components have been tested.
Based on a detailed exploratory investigation of alloys in the systems NiAl-Ta, NiAl-Ta-Nb, NiAl-(Ta,Nb)-(Cr,Mo) and NiAl-Ta-Nb-C with strengthening Laves phase [1,2], two-phase NiAl-Ta-Cr alloys were identified as promising candidate alloys [3,4]. The subsequent development lead to an alloy of composition of 45 Ni, 45 Al, 2.5 Ta and 7.5 Cr (in at.%) - IP75 for short [5-8]. The basic physical and mechanical properties including flow stress, brittle-to-ductile transition temperature, creep, fatigue, corrosion and thermal shock resistance were screened [9] as well as effects of processing on properties, which allows adjusting of properties to specific applications [10].

The investment-cast alloy variant (IC75) as well as the powder-metallurgically processed variant (PM75) are considered for gas turbine applications. The current efforts aim at

transferring IP75 into industrial application by establishing a comprehensive data base including mechanical and corrosion data under service conditions. For this, components have been produced on an industrial scale [11].

Basic properties

IP75 shows superior properties compared to Ni-base superalloys. Superalloys melt between about 1200 and 1360°C (data for superalloys were obtained from [12]) while eutectic regions in IP75, which may be present in the IC75 variant of the alloy, melt at 1470°C and the melting point of the NiAl matrix is about 1638°C. The density of IP75 is 6.3 g/cm^3, which is significantly lower than that of the superalloys (7.8 – 9.0 g/cm^3). The thermal conductivity at 1000°C of IP75 (57 W/mK) is about one and a half time to three times higher than those of the superalloys (21 – 40 W/mK) and the thermal expansion coefficient of IP75 at 1000°C (14.7 x 10^{-6} K) is up to a quarter lower than those of the superalloys (15.0 – 19.5 x 10^{-6} K). The specific heat capacity of IP75 at 1000°C is 670 J/kgK which is within the range of that of the superalloys (525 – 790 J/kgK) while the dynamic Young´s modulus of elasticity (157 Gpa) is at the high end of the range of the superalloys (80 – 155 GPa) at 1000°C. Thus replacement of Ni-base superalloys by IP75 could increase the efficiency of a gas turbine by allowing higher service temperatures with less cooling and reduced weight of moving parts.
The microstructure of IP75 consists of 85 to 90 vol.% NiAl (B2-structure) with a composition slightly on the Ni-rich side with several at.% chromium and a small amount of tantalum. Precipitated within the NiAl matrix, there are up to 10 vol.% of a Cr-rich hexagonal (C14) Laves phase and up to 5 vol.% of α-Cr solid-solution (A2) [13]. The distribution of the precipitates and thus the mechanical properties can be varied within a wide range by the processing of the alloy [10].

For the two alloy variants under consideration for gas turbine applications the microstructures are shown in Figure 1. For the investment cast alloy IC75 (Figure 1a) the primary NiAl grains of about 100 to 150 µm size are surrounded by a network of Laves phase and α-Cr with additional fine precipitates of both phases within the NiAl grains. The PM75 material that was produced from a pre-alloyed powder by hot isostatic pressing (HIP) at 1250°C/150 MPa/4 h exhibits a much finer microstructure. Small precipitates of Laves phase and α-Cr (< 5 µm) are randomly distributed within a NiAl matrix with a grain size of about 10 µm (Figure 1b).
The stability of the microstructure at high temperatures has been checked by annealing samples of IC75 and PM75 between 1200 and 1400°C for several hundred hours. Except for coarsening of the fine microstructural details in PM75, the microstructure, phase content and compositions of the phases did not change [13]. Impurities such as carbon, oxygen and iron typical for production-scale processing, i.e. up to several hundred weight ppm, do not sensitively affect the properties of IP75 with the possible exception of silicon. Silicon, which is released from the binder of the crucible during melting, was found to promote segregation during casting which is believed to result in embrittlement of IC75 [14].
IP75 exhibits an excellent oxidation behaviour due to the formation of adherent Al_2O_3 scales (see below). The oxidation resistance under cyclic temperature conditions is further enhanced by alloying with a small amount of hafnium (0.1 wt.% Hf) without affecting other properties.

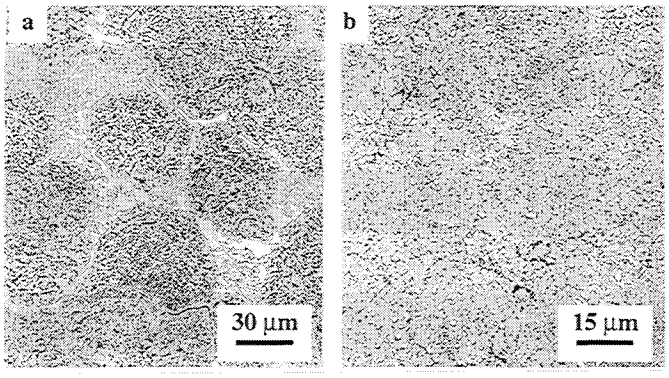


Figure 1: Light optical micrographs of IC75 (a) and PM75 (b); grey phase: NiAl; light precipitates: Laves phase and α-Cr (the black voids result from the etching process with dissolution of the fine precipitates of Laves phase and α-Cr and thus indicate the presence of these fine precipitates).

The brittle-to-ductile transition temperature (BDTT) of IP75 varies considerably for the differently processed variants of the alloy [10]. The BDTT of PM75 is about 650°C (at a deformation rate of 10^{-4} 1/s) while a BDTT of about 900°C is found for the coarse grained IC75.

Manufacturing

Though all variants of IP75 are brittle at ambient temperatures, machining of the alloy is possible. Besides manufacturing components by electro-discharge machining (EDM) a number of specimens were produced successfully by grinding and careful turning on a lathe. On a laboratory scale, the production of material of IP75 by investment casting, hot extrusion of the investment cast alloy, direct solidification, powder metallurgical preparation with HIP and subsequent isothermal forging has been demonstrated [10].

The manufacturing of the alloy on an industrial scale has been investigated. In view of the brittleness of IC75 at low and ambient temperatures, components are best manufactured by near net-shape techniques such as investment casting or metal injection molding (MIM).

Investment casting

Because standard molds are very close to their application limits at the conditions for the casting of IC75 [13] an optimised casting procedure has been developed for NiAl-Ta-Cr-alloys [15]. A ceramic mold with SiO_2-free front layer and low SiO_2 backup layers has been applied for the casting of IC75 which can be manufactured in the standard shell mold process using a steam autoclave for dewaxing and a furnace to sinter the mold. Numeric simulations were performed for optimising the casting parameters such as mold temperature, casting temperature, cooling rate and geometry of the feeder and ingate system. Based on these results a casting process has been established which gives maximum mold filling and minimizes thermal stresses in the cast components [16,17]. In addition, grain-refining front layers have been tested and successfully employed for the reduction of the grain size [18,19]. Figure 2 shows a crack-free combustion liner panel for an industrial gas turbine of IC75 which was cast using optimised casting parameters in a low SiO_2-poor mold.

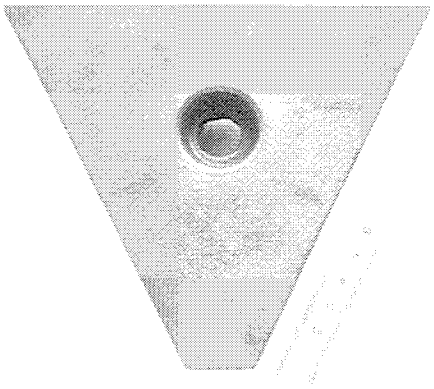


Figure 2: Combustor liner panel of IP75 produced by investment casting with optimised ceramic mold system (casting parameters T_{cast}= 1700°C, T_{mold} = 1300°C; cooling rate = 2.5 K/min between 1100°C and 600°C) [11].

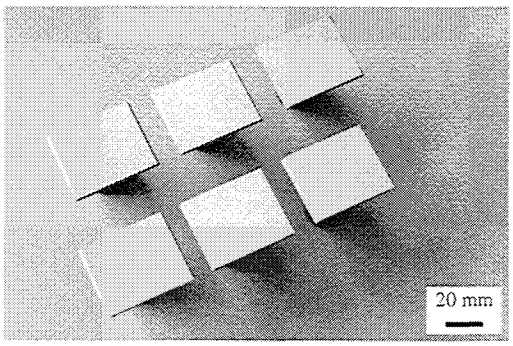


Figure 3: PM75 panels prepared by electro discharge machining [13].

Panels with dimensions 100 mm x 160 mm x 16 mm have been produced by an industrial-scale casting process at DONCASTERS Precision Castings – Bochum GmbH [14]. By using a furnace and casting equipment otherwise employed for directional solidification of superalloys, clusters of 4 panels each were cast from melts with max. 40 kg weight. A mold temperature between 1200 and 1300°C and a cooling rate of 2.5 K/min were chosen according to the above results. Extensive testing of the production scale material revealed that properties such as yield stress, creep resistance and oxidation resistance are not very sensitive to production-scale processing [14]. However, a decreased toughness of the panels compared with laboratory-scale material was found which is attributed to the presence of segregations because of contamination by silicon during the melting process.

Powder-metallurgical processing

For smaller parts with complex shape powder-metallurgical processing is an alternative to investment casting. Batches of IP75 powder each weighing about 150 kg have been produced by gas atomisation of the elements at about 1750°C using argon at H.C. Starck, Laufenburg. At DONCASTERS Precision Castings - Bochum GmbH cylindrical bolts of 80 mm diameter and 115 mm height each weighing about 3.5 kg were produced from the powders by HIP at 1250°C/150 Mpa/4 h [20]. The bolts showed no porosity and mechanical testing and evaluation of the oxidation behaviour did not reveal any differences between this production-scale material and laboratory-scale material that had been tested before [10,20]. Figure 3 shows a number of panels which were cut from the PM75 bolts by electro discharge machining. These panels have been used in burner tests in order to evaluate the potential of IP75 for application in industrial gas turbines.

For mass production of small parts up to a weight of several grams the MIM process is suitable. At GKN Sinter Metals Service GmbH heat-exchange tubes of 5 mm diameter and 300 mm length with a wall thickness of 1 mm have been produced by MIM. Figure 4 shows several components which have been produced by powder-metallurgical techniques.

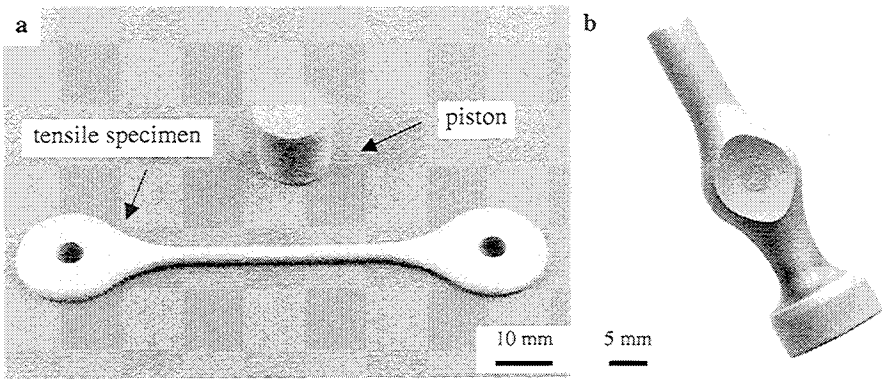


Figure 4: Components produced by powder metallurgical techniques. The piston in Figure 4a (above) has been produced by sintering of the pre-alloyed powder while the specimen for tension testing in Fig. 4a (below) was produced by MIM (GKN Sinter Metals Service GmbH, Radevormwald). Figure 4b shows a pin for a Diesel engine pre-chamber produced by MIM [1,3].

Mechanical behaviour

Thermal fatigue

As IP75 has a considerably high BDTT, the behaviour under thermal fatigue conditions was evaluated. The IP75 material apparently has a very good thermo-shock resistance. No visible damage was detected in specimens after 400 cycles with heating in hot Diesel exhaust gas to temperatures above 1100°C, holding for 1 min. and quenching in cool air [9]. Samples of PM75 and IC75 showed no cracks after cyclical heating at 1200 and 1250°C in air except for one sample of IC75 which exhibited a crack that originated from a notch at the surface of the sample [13,21].

Fracture toughness K_{IC}

The fracture toughness (K_{IC}) of PM75 and IC75 was evaluated between room temperature and 850°C by 4-point bending tests on notched samples at a deformation rate of 2×10^{-7} s^{-1}. The results presented in Figure 5 reveal that the fine grained PM75 has a higher fracture toughness at all temperatures within the investigated temperature range. The increase in fracture toughness between room temperature and 200°C for PM 75 and between 600 and 700°C for IC75 is attributed to the brittle-to-ductile transition by thermal activation.

0.2% yield strength

The compressive 0.2% yield stress as a function of temperature for several variants of IP75 is shown in Figure 6. As to the powder-metallurgically processed alloys, the MIM variant (PM75-GKN) shows a very high yield strength up to 600°C presumably because of its very fine-grained microstructure. Compared to the laboratory-scale material (PM75-MPI), the production-scale PM75-DPC material shows a slightly lower yield strength at all temperatures except for 1200°C which has been attributed to a higher level of impurities in the production-scale material [20]. As to the two investment cast variants, the production- scale IC75-DPC material has a somewhat lower yield strength below 900°C compared with the laboratory-

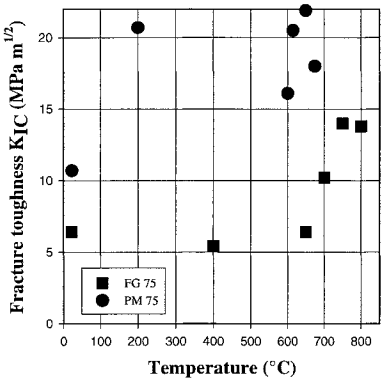


Figure 5: Fracture toughness K_{IC} as a function of temperature for PM75 and IC75 (4-point bending of notched samples, deformation rate: 2 x 10^{-7} s^{-1}).

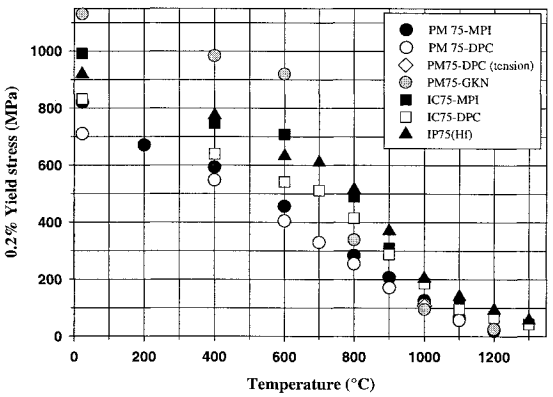


Figure 6: 0.2% yield strength as a function of temperature for several variants of IP75 (see text for details, deformation rate: $10^{-4}s^{-1}$).

scale IC75-MPI material [14]. At all temperatures above 600°C the variant with 0.1 wt.% Hf (IP75(Hf)) shows the highest 0.2% yield strength. While all these results have been determined in compression, some tests were carried out for PM75-DPC in tension at 1000°C. No significant difference between testing in compression and tension is found.

In Figure 7 the compressive 0.2% yield strength of IC75 and IP75(Hf) is compared with that of several Ni-base and Co-base superalloys. Above 1100°C the variants of IP75 show the highest 0.2% yield strength of the tested materials and at 1300°C a 0.2% yield strength of IP75 is still about 50 MPa.

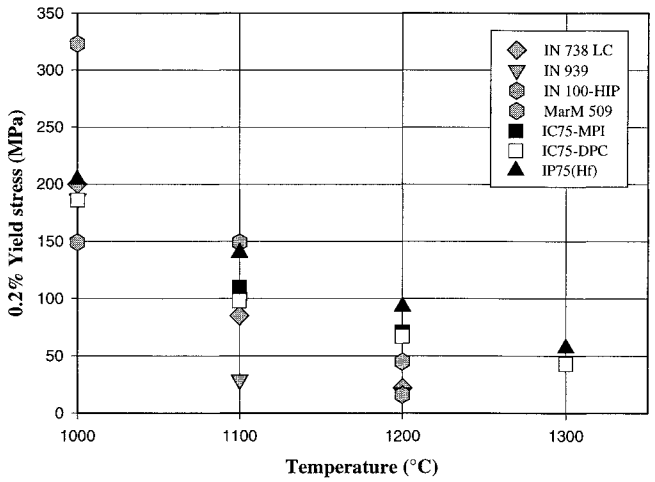


Figure 7: Compressive 0.2% yield strength as a function of temperature for three variants of IP75 and various Ni- and Co-base alloys (deformation rate: $10^{-4}s^{-1}$).

Fatigue

Though the fatigue behaviour of IP75 has not been studied in detail some tests have been performed at room temperature in compression. At a constant stress amplitude up to 800 MPa and 1 Hz frequency a fatigue life of more than 10^5 cycles was observed [9].

Creep

The creep resistance and secondary creep rates of IP75 have been determined in the temperature range 800 to 1300°C for differently processed alloys [10,21]. Up to 1000°C the creep properties of the Ni-base superalloys are superior to those of IP75, but above 1100°C, when the strength of the superalloys becomes negligible, IP75 still shows sufficient creep resistance. Figure 8 illustrates the creep properties of IP75. At 1250°C secondary creep rates have been determined by step-wise increase of the load as well as at constant load. The fine-grained PM75 exhibits creep rates which are about two orders higher than those of IC75. Coarsening of the microstructure by a prior heat treatment or during long time testing at 1250°C at a constant load causes some reduction in the secondary creep rate of PM75. As the microstructure of IC75 is less uniform compared to that of PM75 two series of tests have been performed with as-cast material. The results of both tests are in good agreement, i.e. the effects of the microstructure inhomogeneities of IC75 are negligible. A prior heat treatment has no effect on the creep rate of IC75 and the results of testing with step-wise loading and at constant load are in agreement within the scatter of the experimental data. The addition of impurities (IC75d) leads to a decreased creep rate only at stresses below 5 MPa. Only the production-scale material IC75-DPC shows a creep rate which is different to the other tested variants of IC75. Due to the larger grain size of the material the secondary creep rates are about one order lower compared to those of the other investment-cast variants.
In view of gas turbine applications, the long-term creep behaviour is of particular interest. In Figure 9 the stress dependence of time to rupture (in tension) of IP75 is shown for 900 and 1000°C in comparison to the Ni-base superalloy IN 738 DS. The investment cast alloy IC75 (grain size of NiAl: 75 μm) has a higher creep strength than the powder-metallurgically produced PM75 (grain size of NiAl: 10 μm), but has a somewhat lower creep strength than the directionally solidified Ni-base superalloy IN 738 DS at these temperatures.

Oxidation behaviour

Detailed studies of the oxidation behaviour in air of IP75 have been performed [13,21]. High-temperature X-ray diffraction studies and combined Auger electron spectroscopy (AES), scanning Auger microscopy (SAM) and X-ray photoelectron spectroscopy investigations of samples oxidised at 1000 to 1200°C between 4 and 48 h showed the formation Al_2O_3 scales right from the start of the oxidation. Thermogravimetric oxidation tests of IP75 between 600 and 1300°C in air showed that these adherent Al_2O_3 scales give rise to parabolic growth of the oxide layer. Investigation of cross sections of various oxidised samples confirmed the formation of adherent Al_2O_3 scales and also showed that no preferential oxidation of the Laves phase takes place. The parabolic rate constants for IP75 compare favourably with those for ternary NiAl-Cr alloys [22]. Long-term oxidation tests at 1200°C for 17904 h showed that the formation of protective Al_2O_3 scales results in an effective oxidation resistance which enables long-time service of PM75 and IC75 without any protective coatings at temperatures beyond those of the superalloys.

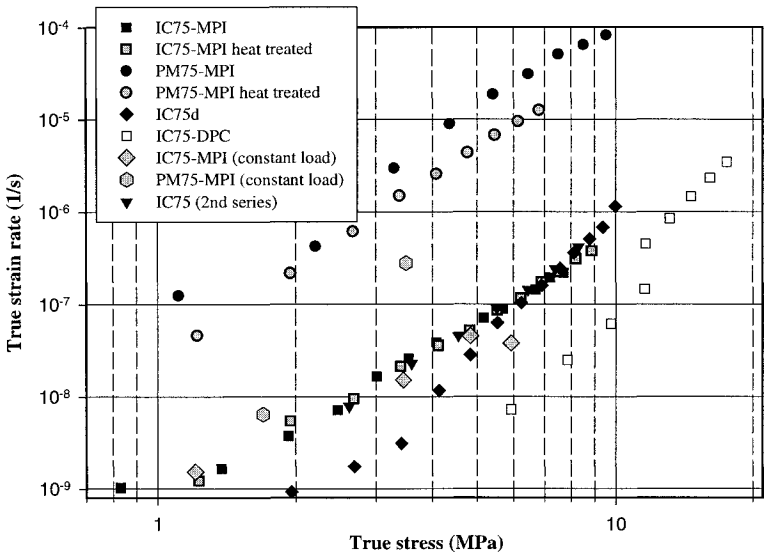


Figure 8: Stress dependence of secondary creep rate of IP75 in compression with step-wise load increases and at constant load at 1250°C (MPI: laboratory scale, DPC: production scale, heat treated: annealed at 1250°C for 300 h before testing, IC75d: additional Fe and O).

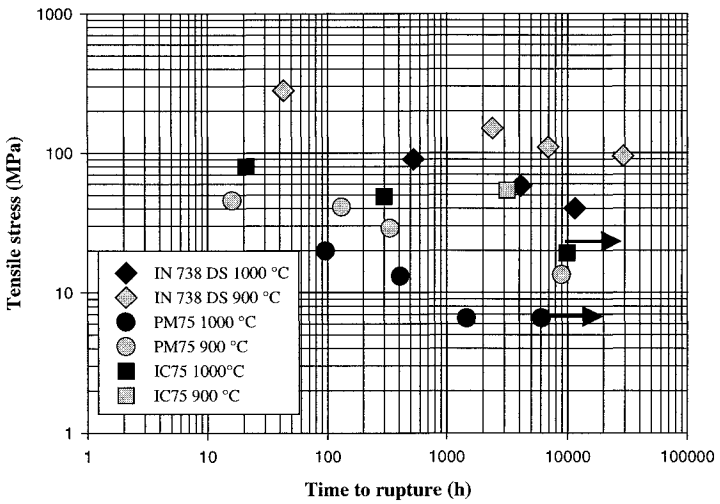


Figure 9: Stress dependence of time to rupture for IP75 and IN 738 DS at 900 and 1000°C (in tension, arrows indicate tests terminated before rupture).

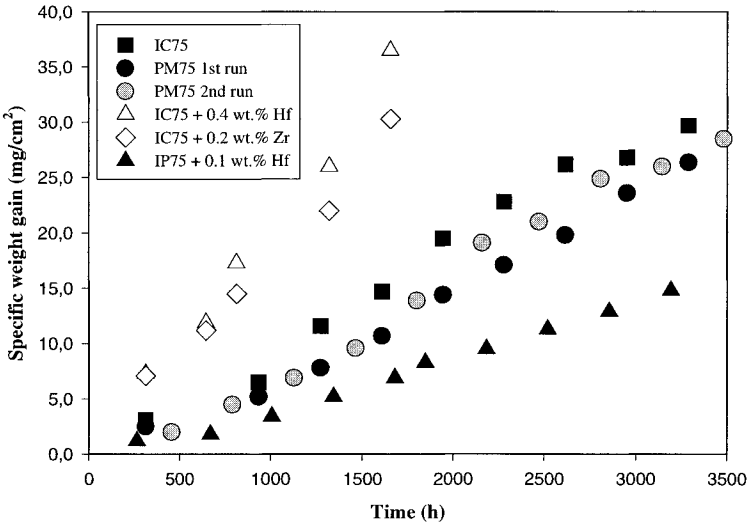


Figure 10: Specific weight gain as a function of time for IP75 and IP75 with various alloying additions during cyclic oxidation at 1200°C in air.

In cyclic thermogravimetric oxidation tests at 1000 and 1200°C no spalling of the scales was observed and the resulting parabolic rate constants are about those for static oxidation [13]. Long-term cyclic oxidation tests revealed that some spalling of the scales may occur under more severe cooling conditions. This does not affect the excellent oxidation resistance of IC75, whereas samples of PM75 showed considerable oxidation attack after cyclic oxidation at 1200°C for 11540 h and 12672 h [21]. The alloying of IP75 with about 0.1 wt.% hafnium improves the adherence of the scales during cyclic oxidation effectively (Figure 10).

Conclusions

The ongoing materials development has resulted in the novel intermetallic NiAl-Ta-Cr alloy IP75 with attractive physical, mechanical and corrosive properties for gas turbine applications at 1200°C. The material can be produced by ingot metallurgy including investment casting as well as by powder metallurgy including metal injection molding (MIM). A database for estimating the potential of IP75 for specific applications is available. The present results demonstrate the feasibility of IP75 material for application as combustor liner panels in stationary gas turbines. Further work is necessary for adjusting the properties of IP75 by proper processing to other more demanding applications.

Acknowledgment

The financial support by the Bundesministerium für Bildung und Forschung (BMBF) is gratefully acknowledged.

Literature

[1] Zeumer, B.: Zur Entwicklung von Laves-Phasen-verstärkten NiAl-Basis-Legierungen für Anwendungen bei hohen Temperaturen; Thesis, VDI Verlag, Düsseldorf, (1994) 1-140.

[2] Zeumer, B., Sauthoff, G.: Intermetallic NiAl-Ta alloys with strengthening Laves phase for high-temperature applications. I. Basic properties; *Intermetallics*, **5** (1997) 563-577.

[3] Sauthoff, G., Kleinekathöfer, W.: Höchstwarmfeste NiAl-Basis-Legierungen für Strukturbauteile im Verbrennungsmotor; In: *Effizienzsteigerung durch innovative Werkstofftechnik*, VDI-Verlag, Düsseldorf, (1995) 647-654.

[4] Zeumer, B., Sauthoff, G.: Deformation behaviour of intermetallic NiAl-Ta alloys with strengthening Laves phase for high-temperature applications. II. Effects of alloying with Nb and other elements; *Intermetallics*, **5** (1997) 641-649.

[5] Sauthoff, G., Zeumer, B.: German patent P4417936.7-24; (1995).

[6] Sauthoff, G., Zeumer, B.: International patent PCT/EP95/01921; (1997).

[7] Sauthoff, G., Zeumer, B.: Russian Federation Pat.-Nr. 2148671; (2000).

[8] Sauthoff, G., Zeumer, B.: Europ. Patent EP 0760869 B1; (2001).

[9] Zeumer, B., Sauthoff, G.: Deformation behaviour of Intermetallic NiAl-Ta alloys with strengthening Laves phase for high-temperature applications - III. Effects of alloying with Cr; *Intermetallics*, **6** (1998) 451-460.

[10] Zeumer, B., Sanders, W., Sauthoff, G.: Deformation behaviour of intermetallic NiAl-Ta alloys with strengthening Laves phase for high-temperature applications - IV. Effects of processing; *Intermetallics*, **7** (1999) 889-899.

[11] Hermann, W., Paul, U., Palm, M., Sauthoff, G., Rablbauer, R., Frommeyer, G., Rothe, H., Scheppe, F., Sahm, P.R., Preuhs, J.: Intermetallische NiAl-Komponenten für Systeme zur umweltfreundlichen Energiewandlung; In: A. Kranzmann, U. Gramberg (Eds.), *Werkstoffwoche '98*, Wiley-VCH, Weinheim, (1999) 43-48.

[12] Anonymous: High Temperature High Strength Nickel Base Alloys; INCO Data Sheet, 1-52.

[13] Palm, M., Sauthoff, G.: Characterization and processing of an advanced intermetallic NiAl-base alloy for high-temperature applications; In: K.J. Hemker, D.M. Dimiduk, H. Clemens, R. Darolia, H. Inui, J.M. Larsen, V.K. Sikka (Eds.), *Structural Intermetallics 2001 - ISSI3*, TMS, Warrendale, (2001) 149-156.

[14] Palm, M., Preuhs, J., Sauthoff, G.: Production-scale processing of a new intermetallic NiAl-Ta-Cr alloy for high-temperature application - Part I: Production of master alloy remelt ingots and investment casting of combustor liner model panels; *J. Mater. Process. Technol.*, accepted for publication.

[15] Scheppe, F.: Feingusstechnik für NiAl-Basis-Legierungen; Thesis, Shaker Verlag, Aachen, (2001) 1-108.

[16] Scheppe, F., Rothe, H., Sahm, P.R.: Progress in adapting the investment casting of NiAl; In: E.P. George, M.J. Mills, Y. Yamaguchi (Eds.), *High-Temperature Ordered Intermetallic Alloys VIII*, MRS, Warrendale, (1999) KK5.21.21-KK25.21.25.

[17] Scheppe, F., Sahm, P.R., Hermann, W., Paul, U., Preuhs, J.: Comparison of the numerical simulation and the cast process of nickel aluminides; In: P.R. Sahm, P.N. Hansen, J.G. Coinley (Eds.), *Modeling of Casting, Welding and Advanced Solidification Processes IX*, Shaker Verlag, Aachen, (2000) 207-214.

[18] Scheppe, F., Rothe, H., Sahm, P.R., Hermann, W., Paul, U.: Einfluß verschiedener Kornfeinungsmechanismen auf das Werkstoffverhalten von NiAl-Legierungen; In: *Erstarrung metallischer Schmelzen in Forschung und Gießereipraxis*, DGM, (1999) 175-180.

[19] Scheppe, F., Sahm, P.R., Hermann, W., Paul, U., Preuhs, J.: Nickel aluminides: A step toward industrial application; In: *5th International Conference on Structural & Functional Intermetallics*, TMS Warrendale, (2001) accepted for publication.

[20] Palm, M., Preuhs, J., Sauthoff, G.: Production scale processing of a new intermetallic NiAl-Ta-Cr alloy for high-temperature application - Part II: Powder metallurgical production of bolts by hot isostatic pressing; J. Mater. Process. Technol., submitted.

[21] Palm, M., Sauthoff, G.: Long-term creep and oxidation behavior of a Laves phase-strengthened NiAl-Ta-Cr alloy for gas turbine applications; In: J.H. Schneibel, K.J. Hemker, R.D. Noebe, S. Hanada, G. Sauthoff (Eds.), *High-Temperature Ordered Intermetallic Alloys IX*, MRS, Warrendale, (2001) N6.8.1-N6.8.6.

[22] Brumm, M.W., Grabke, H.J.: The oxidation behaviour of NiAl - I. Phase transformations in the alumina scale during oxidation of NiAl and NiAl-Cr alloys; *Corrosion Science*, **33** (1992) 1677-1690.

HIGH-RATE SPUTTER DEPOSITION OF NiAl ON SAPPHIRE FIBERS

K. Reichert, C. Martínez, R. Cremer, D. Neuschütz

Lehrstuhl für Theoretische Hüttenkunde, RWTH Aachen, D-52056 Aachen, Germany

Abstract

Once the fiber-matrix bonding has been optimized to meet the different requirements during fabrication and operation of the later composite component, sapphire fiber reinforced NiAl will be a potential candidate to substitute conventional superalloys as structural material for gas turbine blades. To improve the composite fabrication process, a direct deposition of the intermetallic matrix material onto hBN coated sapphire fibers prior to the consolidation of the fiber-matrix composite is proposed. It is believed that this will simplify the fabrication process and prevent pore formation during the diffusion bonding. In addition, the fiber volume fraction can be quite easily adjusted by varying the NiAl coating thickness. For this, a high-rate deposition of NiAl is in any case necessary. It has been achieved by a pulsed DC magnetron sputtering of combined Al-Ni targets with the fibers rotating between the two facing cathodes. The obtained nickel aluminide coatings were analyzed as to structure and composition by means of X-ray (GIXRD) as well as electron diffraction (RHEED) and X-ray photoelectron spectroscopy (XPS), respectively. The morphology of the NiAl coatings was examined by SEM.

Keywords: Intermetallic matrix composite; NiAl; Fiber coating; Magnetron sputtering

Introduction

The use of single-crystal nickel-base superalloys as structural material for the turbine blades of the first stages in modern gas turbines appears limited, so that in the long run innovative materials that are able to withstand an even higher thermal and mechanical load have to be investigated. Especially the intermetallic phase NiAl is an attractive candidate due to its combination of high melting point, low density, and excellent oxidation resistance [1]. Despite several advantages over today's superalloys, NiAl is so far unsuitable for structural applications because of a lacking strength at elevated temperatures and an insufficient ductility at room temperature. The highest potential to compensate these deficits is evaluated for a reinforcement of the intermetallic matrix by continuous ceramic fibers, primarily single-crystal sapphire fibers [2,3]. The performance of intermetallic matrix composites is determined by the character of the bonding between fiber and matrix. In fact, the interfacial requirements in IMCs are more complicated than those in typical metal or ceramic matrix composites [4].

For that reason a new concept of a tailored fiber-matrix interface for sapphire fiber reinforced NiAl matrix composites, which consists of an initial hexagonal boron nitride (hBN) fiber coating and selected interface reactions, has been recently [5,6] developed to satisfy the varying demands, i.e. a weak fiber-matrix bonding during the fabrication of the composites and a strong fiber-matrix bonding during the later operation of the composite component, respectively. Aim of this work was to establish an appropriate process to deposit the matrix material with a sufficient thickness onto the hBN coated fibers prior to their consolidation, thus simplifying the processing route for the IMC fabrication (Fig. 1) because of the improved ability to control the fiber volume fraction as well as the uniformity of fiber spacing. The consolidation of such single fiber composites is an already often applied fabrication technique [7].

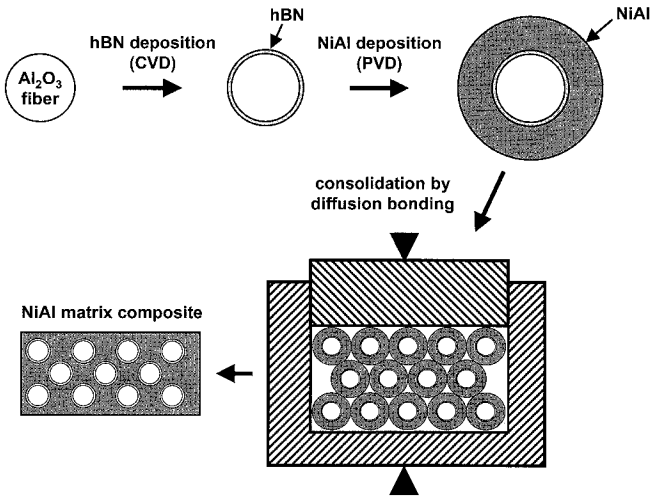


Fig. 1. Processing route for the fabrication of sapphire fiber reinforced NiAl matrix composites, consisting of CVD-hBN and PVD-NiAl fiber coatings prior to the consolidation by means of diffusion bonding.

Mainly depending on the according application of the nickel aluminide coating, there are several deposition techniques to choose from. Classic diffusion coatings are deposited by chemical vapor deposition (CVD) [8], which is however limited by the outward diffusion of nickel atoms to the substrate surface. Another possibility to deposit nickel aluminides is by various thermal spray approaches [9-11], whose application for the deposition of NiAl fiber coatings suffers from the tendency for spallation due to thermal stresses generated during processing. Furthermore, the open literature provides some investigations on the deposition of nickel aluminide coatings by means of physical vapor deposition (PVD), for instance by magnetron sputtering. But especially for the sputter deposition of NiAl quite different approaches exist as to target selection, i.e. sputtering of a compound target [12,13] or a combined Ni-Al target [14], alternate sputtering [15] or co-sputtering [16] of two different targets, and the type of plasma generation (RF or DC mode). As far as specified in the literature, the rate of deposition for the mentioned sputter processes appears insufficient for a high-rate deposition of NiAl fiber coatings. Therefore, a modified high-rate sputter process is presented in this paper. To verify its applicability for the composite fabrication as displayed in Fig. 1, the structure, composition, and morphology of the deposited coatings were investigated.

Experimental

Deposition of NiAl by Means of Magnetron Sputtering

The nickel aluminide coatings were deposited onto single-crystal 125 µm diameter Al_2O_3 fibers (Saphikon Inc.) as well as planar alumina or graphite substrates, for a simplified film characterization, in a Leybold L 560 HV magnetron sputtering system equipped with CemeCon CK288 cathodes. NiAl was sputter deposited in either single cathode DC or dual cathode pulsed DC mode. In dual cathode mode the substrate holder with the fibers rotates between the two opposite cathodes resulting in a homogeneous deposition. The deposition parameters for both processes are given in Table 1.

Table 1. Parameters for single and dual cathode deposition of NiAl.

	Single cathode deposition	Dual cathode deposition
Plasma generation	DC	bipolar pulsed DC (40 kHz)
Cathodes	1×CK288	2×CK288
Target	aluminum (99.5%) with 10 nickel strips (40×12 mm^2) and 4 nickel strips (40×13 mm^2)	
Distance target – substrate	40 mm	45 mm
Sputter power	1×2000 W	2×2000 W
Argon partial pressure	0.6 Pa	0.8-1.0 Pa
Residual gas pressure	4×10^{-4} Pa	

On each cathode a 99.5% pure aluminum target was positioned with 2.0 mm thick strips of nickel foil (99.0% pure) mounted on it. This combined nickel-aluminum target was designed to provide a sufficient electrical, but a relatively poor thermal contact between the nickel foil strips and the aluminum target. As displayed in Fig. 2, the nickel foil strips begin to glow during the sputtering of this combined Ni-Al target, whereas the aluminum target itself is water-cooled. It is therefore insured that the temperature of the sputtered nickel exceeds its Curie temperature and that the magnetic field of the cathodes is not distorted during the deposition process.

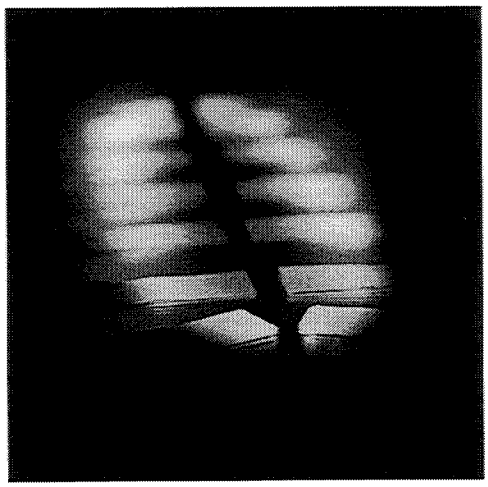


Fig. 2. Combined Ni-Al target during sputtering at 2000 W DC in pure argon atmosphere.

Film Characterization by GIXRD, RHEED, XPS, and SEM

The crystallographic structure of the nickel aluminide coatings was analyzed by means of grazing incidence X-ray diffraction (GIXRD) in a Siemens D 500 diffractometer at an angle of incidence of 3° to the surface. Diffractograms were taken in the 2θ range of 20-90° using 900 W Cu Kα radiation (λ = 0.154186 nm).

Further structural analyses were performed in an UHV analytical chamber by means of reflection high-energy electron diffraction (RHEED). The RHEED system consists of an electron gun (energy range 5-35 keV) with a beam diameter of about 100 µm, which is equipped with deflection coils that allow the scanning of the beam across the sample. The diffracted beams reach a phosphorescent screen where the patterns are displayed and at the same time recorded by a computer controlled CCD camera. The diffraction system was calibrated using an in-situ deposited polycrystalline copper film. The patterns of the NiAl coatings were recorded at 35 keV beam energy (λ = 0.006446 nm).

The composition of the films as well as the chemical binding states of the components were analyzed by X-ray photoelectron spectroscopy (XPS) in the above mentioned UHV analytical chamber, which is equipped with a double-pass cylindrical mirror analyzer (CMA) suitable for XPS and a non-monochromatic X-ray source with Al and Mg anodes. The system was calibrated with respect to the Ni $3p_{3/2}$ (66 eV) and Cu $2p_{3/2}$ (958.6 eV) lines as well as the Fermi level of Ni. Survey spectra were taken in the range of 0-1100 eV with an energy resolution of 3 eV. The spectra of the Ni 2p peaks as well as of the Al 2p and Ni 3p peaks were taken with a resolution of 0.5 eV. The spectra were acquired using Al Kα radiation (1486.6 eV) at a power of 300 W (15.0 keV, 20.0 mA).

The morphology of the NiAl coatings was examined in a Zeiss DSM 982 Gemini field emission scanning electron microscope (SEM). The operating voltage was 10 kV and the lateral resolution was less than 4 nm.

Results and Discussion

The X-ray diffraction patterns in Fig. 3 indicate that the magnetron sputtering of the above described combined Ni-Al target in pure argon atmosphere results in the deposition of single-phase coatings in the primitive cubic B2 structure of the nickel aluminide NiAl. The main difference between the two patterns for single and dual cathode deposition, respectively, lies in the intensity distribution. The peak intensities of the coating deposited by a single cathode roughly correspond to the ones listed in the ICDD powder diffraction file, thus implying the absence of a texture in the coating. On the other hand the intensity of the (100) peak incomparably rises for the dual cathode deposition. This suggests a slight [100] texture. Another difference for this type of deposition is the reduced FWHM of the X-ray reflexes, indicating an increase in grain size as compared to the single cathode deposition.

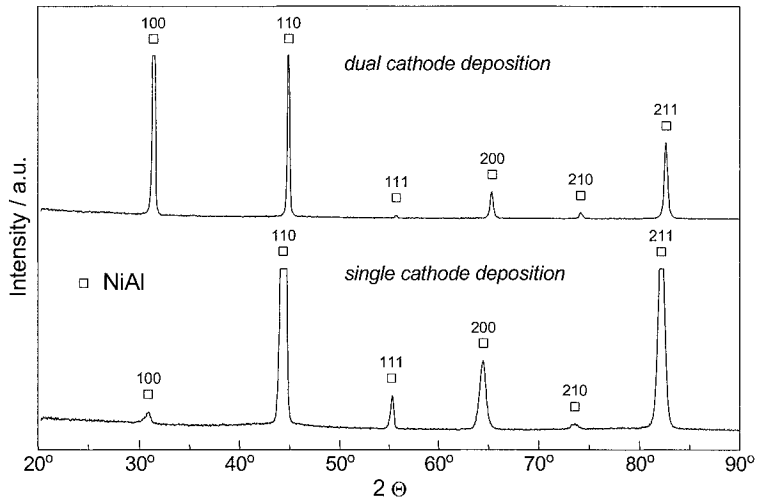


Fig. 3. GIXRD patterns of single-cathode and dual-cathode deposited NiAl coatings.

For a precise determination of the lattice parameter a of a deposited NiAl coating, the calculated lattice parameters for each reflex were plotted versus

$$\frac{1}{2}\cdot\left(\frac{\cos^2\theta}{\sin\theta}+\frac{\cos^2\theta}{\theta}\right)$$

and extrapolated to $a_0 = 2.8732$ Å (Fig. 4). Disregarding residual stresses in the PVD coating, the composition of the deposited nickel aluminide would thus be approximately $Ni_{0.56}Al_{0.44}$ according to the relation between the lattice parameter and the stoichiometry of the nickel aluminide as determined by Taylor and Doyle [17]:

$$a_0 = 2.99839\ \text{Å} - 0.222\cdot x_{Ni} \qquad 0.5 \le x_{Ni} \le 0.6$$

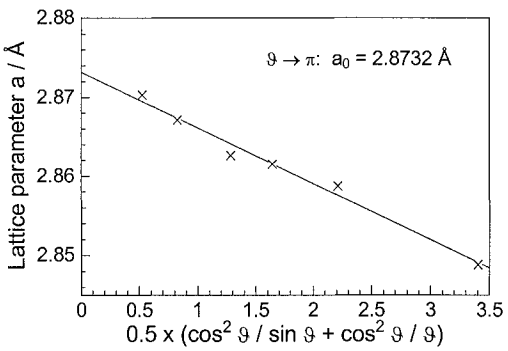


Fig. 4. Precise lattice parameter determination from the GIXRD pattern of a dual-cathode deposited coating.

For further characterization of the film composition and the binding states of its components a sample coating deposited in dual cathode mode was analyzed by means of XPS. Fig. 5 shows the corresponding survey spectra taken with a energy resolution of 3 eV in the binding energy range of 0-1100 eV before and after a 30 min surface treatment by RF etching in pure argon atmosphere. Apart from the photoelectron lines of nickel and aluminum the O 1s and C 1s peaks can be observed. The latter is attributed to a minor contamination of the coating surface by hydrocarbons, whereas the significant decrease of the oxygen signal due to the RF etching indicates a surface oxidation during the transfer from the magnetron sputtering system into the UHV analytical chamber. Furthermore, a substantial change of the Ni/Al ratio between the two spectra in Fig. 5 can be noted.

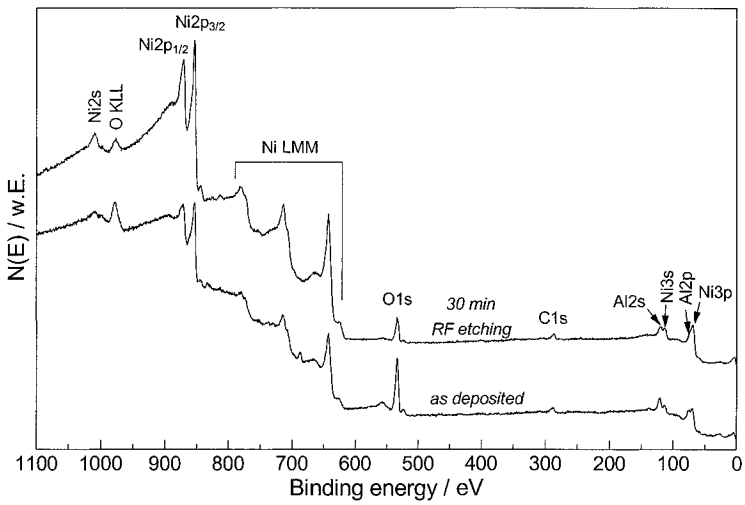


Fig. 5. Photoelectron spectra of a deposited NiAl coating and after 30 min RF etching.

A closer examination of the Al 2p and Ni 3p photoelectron lines (Fig. 6b) reveals an alteration of the aluminum binding state, i.e. from a predominantly oxidic state before the etching to a rather metallic binding state in case of the etched sample. The binding state of nickel on the contrary remains metallic, which is also recognizable in the spectra of the Ni 2p level recorded with an energy resolution of 0.5 eV (Fig. 6a). The position of the Ni $2p_{3/2}$ peak is 853.2 eV and corresponds well with the measured value for NiAl of 853.0 eV as specified by Silvain et al. [18].

The XPS analyses indicate a slight oxidation of the NiAl coatings due to exposing to air during the transportation of the sample. On this occasion a thin alumina layer had formed which was effectively removed by RF etching. Based on these results a formation of either NiO or $NiAl_2O_4$ can be excluded, because nickel remains in the metallic or actually intermetallic binding state both before and after the etching. A quantification of the XPS spectrum of the etched surface whose composition should presumably be close to the bulk composition of the sputtered coating resulted in a somewhat Ni-rich composition, thus consistent with the previously performed energy dispersive X-ray analysis (EDX).

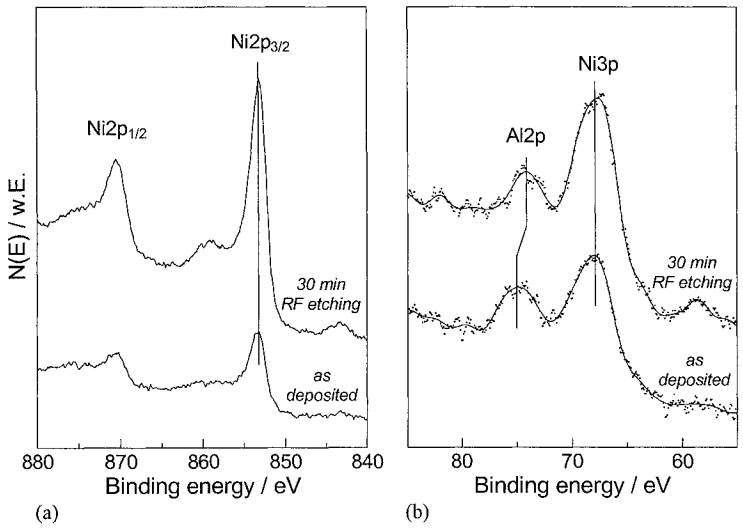


Fig. 6. Photoelectron spectra of the Ni 2p (a) as well as Al 2p and Ni 3p peaks (b).

Furthermore, a NiAl coating deposited on graphite was examined as to crystallographic structure and texture by RHEED. The corresponding pattern of the sample surface before etching is shown in Fig. 7. Sharp diffraction rings of the primitive cubic B2 structure exhibiting a distinct [100] texture are clearly detected. This kind of texture for coatings deposited in dual cathode mode were already implied by the GIXRD results. The fact that no further crystalline phase besides NiAl was identified by RHEED indicates that the alumina film, which has formed on the aluminide coating, consists of only a few amorphous monolayers.

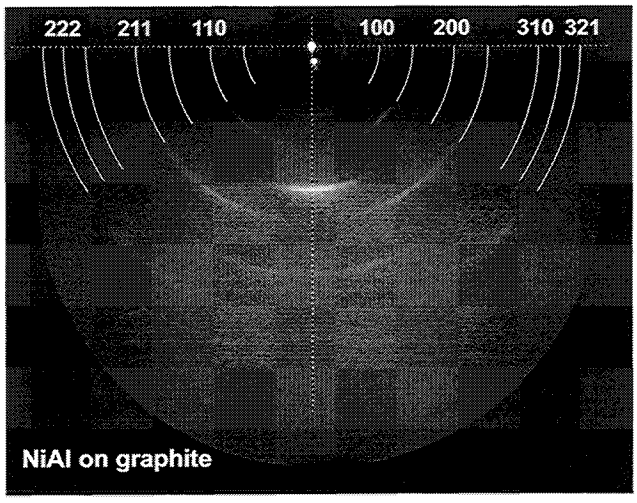


Fig. 7. RHEED pattern of a NiAl coating as deposited on graphite.

Fig. 8 shows the morphology of a 40 μm thick NiAl coating as deposited in dual cathode mode on a single-crystal sapphire fiber, i.e. up to 3 μm wide columnar crystallites. The rate of the bipolar pulsed DC deposition using two opposing cathodes is 0.35 μm min^{-1}, which is an acceptable rate for the deposition of 25 to 80 μm thick NiAl fiber coatings resulting in a fiber volume fraction of 20 to 50%. SEM observations of the single cathode deposited coatings showed a different, rather fine-grained morphology, which had been already indicated by the GIXRD results. It is believed that an apparent difference in substrate temperature between the two deposition processes is the main reason for the variation of the morphology.

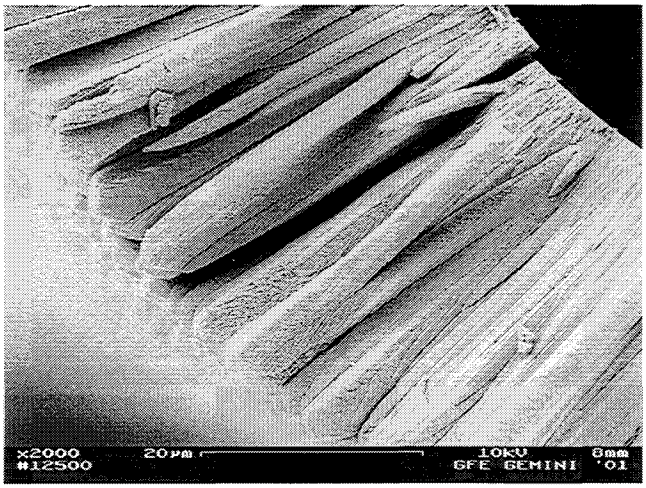


Fig. 8. SEM image of a NiAl coating deposited on a single-crystal sapphire fiber.

Conclusions

An appropriate magnetron sputtering process for the deposition of NiAl onto sapphire fibers with a sufficiently high deposition rate has been developed. This was accomplished by bipolar pulsed DC magnetron sputtering of two facing cathodes, each equipped with a combined Al-Ni target. Comprehensive investigations on the structure, composition, and morphology of the coatings revealed that a slightly Ni-rich, yet single-phase aluminide in the primitive cubic B2 structure of NiAl was deposited by this dual cathode deposition. The intermetallic binding states of the nickel and aluminum atoms were confirmed by XPS measurements. In addition, RHEED analyses indicated a distinct [100] texture. The columnar shape of the crystallites as well as the exact deposition rate (0.35 μm min^{-1}) was determined by SEM observations.

Acknowledgments

The authors gratefully acknowledge the financial support granted by the Deutsche Forschungsgemeinschaft (DFG) within the Collaborative Research Center SFB 561 "Thermally highly loaded, porous, and cooled multi-layer systems for combined cycle power plants".

References

[1] R. Darolia, NiAl alloys for high-temperature structural applications, *J. Met.* 43 (1991) 44.

[2] R.D. Noebe, R.R. Bowman, J.I. Eldridge, Initial evaluation of continuous fiber reinforced NiAl composites, in: D.L. Anton, R. McMeeking, D. Miracle, P. Martin (Eds.), *Intermetallic Matrix Composites*, Mater. Res. Soc. Symp. Proc., Vol. 194, Materials Research Society, Pittsburgh, 1990, p. 323.

[3] R.R. Bowman, Influence of interfacial characteristics on the mechanical properties of continuous fiber reinforced NiAl composites, in: D.B. Miracle, D.L. Anton, J.A. Graves (Eds.), *Intermetallic Matrix Composites II*, Mater. Res. Soc. Symp. Proc., Vol. 273, Materials Research Society, Pittsburgh, 1992, p. 145.

[4] J.-M. Yang, S.M. Jeng, Interface and mechanical behavior of $MoSi_2$-based composites, *J. Mater. Res.* 6 (1991) 505.

[5] K. Reichert, K. Wen, R. Cremer, W. Hu, D. Neuschütz, G. Gottstein, Influence of BN fiber coatings on the interfacial structure of sapphire fiber reinforced NiAl composites, *Appl. Surf. Sci.* 179 (2001) 150.

[6] K. Reichert, R. Cremer, D. Neuschütz, K. Wen, W. Hu, G. Gottstein, Tailoring the fiber-matrix interface of sapphire fiber reinforced NiAl composites through BN fiber coatings, in: *EUROMAT 2001 Conf. Proc.*, Associazione Italiana di Metallurgia, 2001, ISBN 88-85298-39-7.

[7] S.L. Semiatin, R.L. Goetz, W.R. Kerr, Consolidation of continuous fiber, intermetallic-matrix composites, in: D.B. Miracle, D.L. Anton, J.A. Graves (Eds.), *Intermetallic Matrix Composites II*, Mater. Res. Soc. Symp. Proc., Vol. 273, Materials Research Society, Pittsburgh, 1992, p. 351.

[8] A. Reich, L. Singheiser, G. Wahl, CVD-deposition of aluminium on nickel-based alloys from $AlCl_3/H_2$-gas-mixtures, in: J. Bloem, G. Verspui, L.R. Wolff (Eds.), *Proc. 4th Eur. Conf. on Chemical Vapour Deposition*, Philips Centre Manuf. Technol., Eindhoven, 1983, p. 122.

[9] L. Pawlowski, D. Lombard, F. Tourenne, F. Kassabji, P. Fauchais, Thermal diffusivity of plasma sprayed NiAl, NiCr, NiCrAl, and NiCoCrAlY coatings, *High Temp. – High Pressures* 16 (1984) 611.

[10] S.E. Hsu, I.C. Hsu, Study on VPS-cladding of NiAl intermetallics on the TiAl-based intermetallics, *Corr. Sci.* 41 (1999) 1431.

[11] J.A. Hearley, J.A. Little, A.J. Sturgeon, The effect of spray parameters on the properties of high velocity oxy-fuel NiAl intermetallic coatings, *Surf. Coat. Technol.* 123 (2000) 210.

[12] D. Zhong, J.J. Moore, J. Disam, S. Thiel, I. Dahan, Deposition of NiAl thin films from NiAl compound target fabricated via combustion synthesis, *Surf. Coat. Technol.* 120-121 (1999) 22.

[13] S.L. Yang, F.H. Wang, W.T. Wu, Y. Niu, Effect of a NiAl coating on the oxidation resistance of a NiAl-TiC composite, *Oxid. Met.* 56 (2001) 33.

[14] Y. Ding, Y. Zhang, D.O. Northwood, A.T. Alpas, PVD NiAl intermetallic coatings: microstructure and mechanical properties, *Surf. Coat. Technol.* 94-95 (1997) 483.

[15] J.-K. Ho, K.-L. Lin, Preparation of Al-Ni alloy films by alternate sputter deposition, *J. Vac. Sci. Technol. A* 13 (1995) 2170.

[16] P. de Almeida, R. Schäublin, A. Almazouzi, M. Victoria, F. Lévy, Microstructure and growth modes of stoichiometric NiAl and Ni_3Al thin films deposited by r.f.-magnetron sputtering, *Thin Solid Films* 368 (2000) 26.
[17] A. Taylor, N.J. Doyle, Further studies on the nickel-aluminium system, *J. Appl. Cryst.* 5 (1972) 201.
[18] J.F. Silvain, J.C. Bihr, M. Alnot, J. Lambert, J.J. Ehrhardt, XPS studies of the $NiAl/Al_2O_3$ interfacial chemical compatibility, in: P. Vincenzini (Ed.), *Advanced Structural Fiber Composites*, Techna, Srl, Faenza, 1995, p. 163.

INTERFACIAL THERMAL STABILITY IN BN-COATED CONTINUOUS Al_2O_3 FIBER REINFORCED NiAl COMPOSITES

K. Y. Wen, K. Reichert*, W. Hu, M. Frommert and G. Gottstein

Institut für Metallkunde und Metallphysik der RWTH
52056 Aachen Germany
* Lehrstuhl für Werkstoffchemie der RWTH
52056 Aachen Germany

Abstract

The microstructural changes at the interfaces in a NiAl composite reinforced with BN-coated continuous single crystal Al_2O_3 fibers were studied by analytical electron microscopy and high-resolution electron microscopy after annealing at 1000°C for 100h and 500h. Both NiAl/BN and BN/ Al_2O_3 interfaces exhibited excellent stability during annealing, as did the AlN layer formed at NiAl/BN interface during processing. In the case of contamination which was introduced through the use of a glue during diffusion bonding of the composite, significant changes of the microstructure at both NiAl/BN and BN/Al_2O_3 interfaces were observed. A continuous reaction layer formed at the BN/Al_2O_3 during annealing. The reaction product was identified by electron diffraction as $Al_{18}B_4O_{33}$. We propose to attribute this to the reaction: $9Al_2O_3 + 2B_2O_3 \rightarrow Al_{18}B_4O_{33}$. Many nanoparticles were observed in the BN matrix near the BN(AlN)/NiAl interface in the as-fabricated composite. Neither the AlN layer nor these nanoparticles grew during annealing. HREM images of the precipitates revealed a structure distinctly different from that of the BN matrix. B, C, N and Al were detected in these precipitates by EELS analysis.

Keywords: Composites, Interfaces, TEM, Intermetallic compounds.

1. Introduction

The low high-temperature strength and poor ambient-temperature toughness are the main drawbacks for the practical application of NiAl as a high-temperature structural material, in spite of its other attractive properties such as high melting temperature, low density, high thermal conductivity and excellent oxidation resistance. Several ways have been explored recently to improve the high temperature mechanical properties of NiAl. Addition of Ti has been shown to significantly improve the creep strength of single crystal NiAl. The creep rates for the single crystal NiAl alloy containing 2.5~3 at. pct Ti were observed to be as much as three to four orders of magnitude lower than those for unalloyed NiAl [1]. Considerable improvement of high-temperature strength was also achieved for discontinuously reinforced NiAl composites. NiAl composites containing 20 vol.% of 5μm or larger TiB_2 and/or Al_2O_3 particles or Al_2O_3 whiskers are 50% stronger than the monolithic NiAl at 1273K [2]. The drag of solute atmospheres was suggested to control the creep of NiAl(Ti) solid-solution single crystals. For discontinuously reinforced NiAl composites, the rate controlling mechanism of high-temperature deformation was postulated to be the thermally activated motion of vacancies producing jogged screw dislocations.

An alternative approach for improving both strength and damage tolerance is to introduce continuous fibers into the NiAl matrix. Among various continuous metal and ceramic fibers, Al_2O_3 fibers have received much attention because of their high modulus, low density and

especially high strength at elevated temperatures. The mechanical properties of NiAl-matrix composites reinforced by 125-μm diameter single crystal Al_2O_3 (Sapphire) fibers, however, fall well below expectation primarily because of fiber strength degradation [3]. For single crystal Al_2O_3 fibers sputter-coated with various metal, alloy and intermetallic matrices and exposed to temperature profiles simulating fabrication cycles for the different composite systems, a severe fiber strength degradation was observed. For NiAl coated fibers, the strength decreased by 53% [4]. The mechanisms for fiber strength degradation is as yet unknown. Applying a coating on the surface of fibers is therefore indispensable to avoid fiber strength degradation during fabrication and service of the composites. The coating can also serve to improve the bond between fiber and matrix.

In recent work [5], a BN coating was applied to the surfaces of single crystal Al_2O_3 (Sapphire) fibers in a Al_2O_3/NiAl composite. It was shown that there is excellent chemical compatibility between Al_2O_3 and BN, and a thin AlN layer formed at the NiAl/BN interface during hot-pressing of the composite. High-temperature long-term stability of the interface is crucial for a composite expected to be used in a high temperature environment, because interfaces in composites are well known to have significant influence on the mechanical properties of a composite. In the present study, the microstructural changes of the interfaces in a NiAl composite reinforced with BN-coated continuous single crystal Al_2O_3 fibers were studied by analytical electron microscopy (TEM) and high-resolution electron microscopy (HREM) after annealing at 1000°C for 100h and 500h.

2. Experimental Procedures

The composite samples used in this study were fabricated by diffusion bonding. A detailed description of the fabrication process can be found in Ref. [5]. Annealing was conducted in a vacuum of $5x10^{-5}$ mbar ($5x10^{-3}$ Pa). For fabrication of the composite samples by annealing at 1000°C for 100h, a small amount of liquid glue was used to fix the Al_2O_3 fibers on the surface of a NiAl plate. The glue was observed to quickly wet the surfaces of the BN-coated Al_2O_3 fibers. Contamination at the fiber/matrix interface may arise from wetting by the glue. To prevent possible contamination, the BN-coated Al_2O_3 fibers were first glued to two small pieces of Mo for the fabrication of the composite samples by annealing at 1000°C for 500h. The fibers were checked by light microscopy to ensure that the segments of the fibers, which were put between two NiAl plates, were not wetted by the glue. Conventional mechanical grinding, dimple and ion milling were employed to prepare the samples for TEM using a JEOL 2000FX equipped with an energy dispersive x-ray spectrometer (EDS) and an electron energy loss spectrometer (EELS), and HREM using a JEOL 2000EX.

3. Results

3.1. Al_2O_3/BN interface

3.1.1. *Al_2O_3/BN interface in the composite annealed at 1000°C for 100h*

A continuous interlayer between Al_2O_3 and BN was observed in the composite annealed at 1000°C for 100h as shown in Fig. 1. The thickness of the interlayer was not uniform, with the thickest part being about 200nm thick and having an average thickness of about 125nm. Electron diffraction studies were performed to determine the crystal structure and lattice parameter(s) of the interlayer. In the electron diffraction pattern in Fig. 2(a), which was taken

from one of the grains in the interlayer in Fig. 1, the two coordinate axes **A** and **B** are orthogonal. Systematic tilting experiments around both A and B were performed, and a series of electron diffraction patterns were obtained. Tilting around the **B** axis revealed a systematic absence along **B** axis, only those (0k0), k=2n reflections appeared. No systematic absence was observed along **A** axis when tilting around **A** axis. For the whole pattern of Fig. 2(a), the allowable reflection condition is k+l=2n for all h. From this an A-centred unit cell can be concluded. By combining other diffraction patterns, the crystal structure of the reaction product was determined to be A-centred orthorhombic with lattice parameters: a = 0.768 nm, b = 1.497nm and c = 0.568nm. Both structure and lattice parameters were found to be in good agreement with those of an aluminum borate ($Al_{18}B_4O_{33}$), which has an orthorhombic A-centred lattice with parameters a=0.76874nm, b=1.50127nm and c=0.56643nm, space group Amam (JCPDS 32-0003). The interfacial reaction product is therefore determined to be $Al_{18}B_4O_{33}$. Fig. 2(a) and Fig. 2(b) are indexed as the [001] and $[10\bar{1}]$ zone axis patterns of $Al_{18}B_4O_{33}$, respectively.

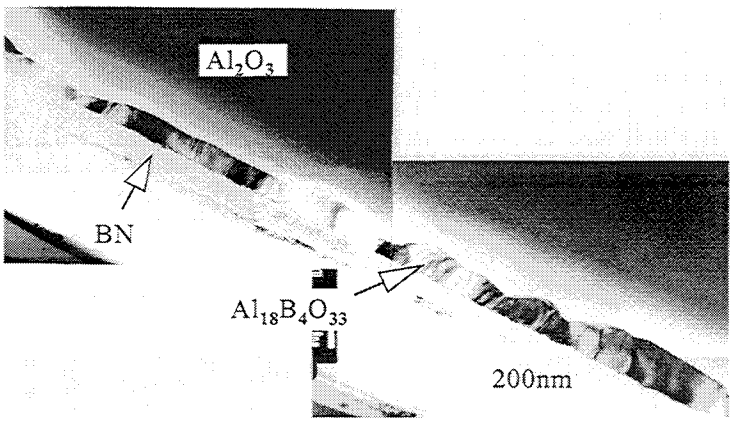


Fig. 1. Reaction layer formed at the Al_2O_3/BN interface during annealing at 1000°C for 100h.

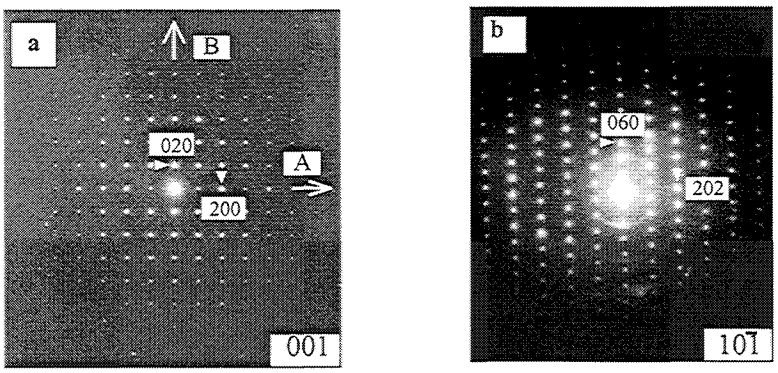


Fig.2. (a) [001] and (b) [101] zone axis patterns of $Al_{18}B_4O_{33}$.

EDS analysis, which is incapable of detecting light elements, showed that aluminum is the only element detected in the interlayer. In the EELS analysis, which is sensitive for detecting light elements, Al, O and B were detected. This confirmed the above reported determination of the interfacial reaction product by electron diffraction.

3.1.2. *Al_2O_3/BN interface in the composite annealed at 1000°C for 500h*

The microstructure of the Al_2O_3/BN interface in the composite annealed at 1000°C for 500h is shown in Fig. 3. No interlayer was observed between Al_2O_3 fiber and BN layer, the interface appeared very stable.

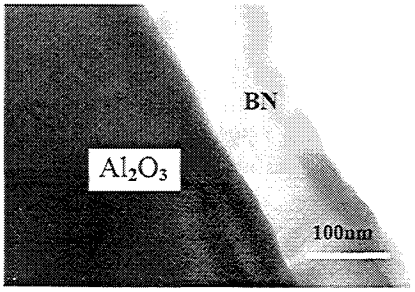


Fig. 3. Diffraction contrast image of Al_2O_3/BN interface in the composite annealed at 1000° for 500h.

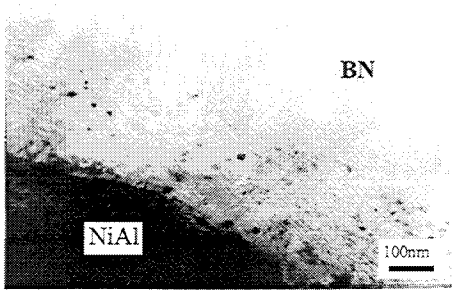


Fig. 4. TEM image of NiAl/BN interface in the composite annealed at 1000°C for 100h.

3.2. NiAl/BN interface

3.2.1. *NiAl/BN interface in the composite annealed at 1000°C for 100h*

Fig. 4 shows a bright field micrograph of the NiAl/BN interface in a composite annealed at 1000 for 100h. Apart from a thin AlN layer which was formed at the NiAl/BN interface during processing of the composite, many small particles, with the largest about 30nm in size, were observed in the BN matrix near the NiAl(AlN)/BN interface, forming a continuous precipitation layer. On the other hand, the thickness of the AlN layer seemed to remain unchanged when compared to that observed in the as-fabricated composite. HREM micrographs taken from these particles are shown in Fig. 5. The bright dots in Fig. 5(a) exhibit a hexagonal symmetry, therefore, it can be deduced that the precipitate belongs to a cubic, a hexagonal or a rhombohedral crystal system and Fig. 5(a) is a [111] or a [0001] projection.

Twin-like growth defects can be observed in Fig.5(a) as indicated by arrows. It is known that for hexagonal close packed crystals, twinning normally occurs on the basal (0001) plane and rhombohedral planes ($\{10\bar{1}2\}$), and that for face centred cubic crystals (f.c.c.) and body centred cubic (b.c.c.) crystals, twinning normally occurs on {111} or {112} planes, respectively. The twins in Fig. 5(a) are then suggested to be {112} twins. The structure of the small precipitated particles belongs tentatively to a cubic crystal system with a lattice parameter a=1.07 nm. Fig 5(a) is a [111] projection of the cubic phase. The measurement of interplanar spacings showed that Fig 5(b) is the [112] projection of a cubic phase. From EDS analysis on these small particles, both Al and Ni were detected, but the counts of both the Al

and Ni peaks were much smaller than those of the Al and Ni peaks from the NiAl matrix. The EELS analysis (Fig. 6) shows that the particles contain B, C, N and Al.

3.2.2. *NiAl/BN interface in the composite annealed at 1000°C for 500h.*

The microstructure of the NiAl/BN interface in the composite annealed at 1000°C for 500h is shown in Fig. 7. Only the AlN layer was observed at the NiAl/BN interface and the thickness of the layer did not change. Small particles were occasionally observed in the BN matrix near the NiAl(AlN)/BN interface, but these particles were distributed locally, not like those observed in Fig. 3 which formed a continuous layer.

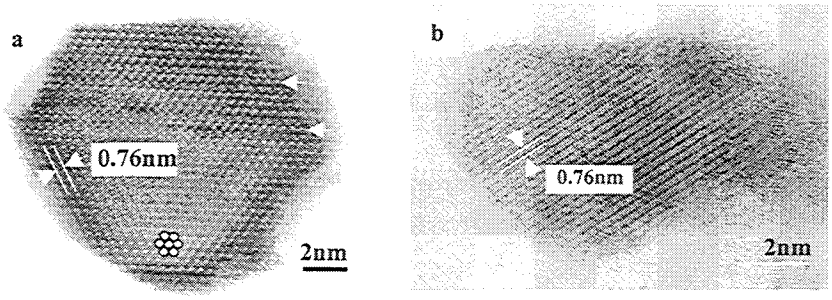


Fig. 5. HREM images of the nanoparticles in Fig.4, (a) [111] projection, (b) [112] projection.

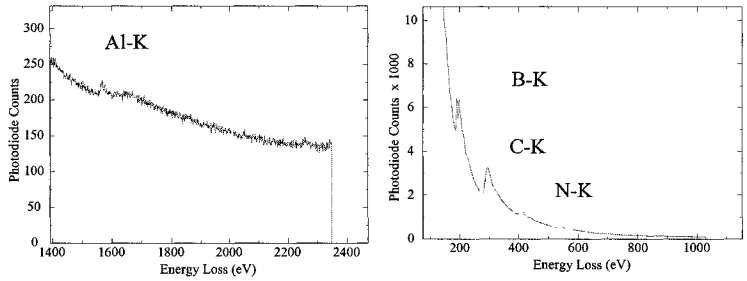


Fig. 6. EELS spectrum taken from the nanoparticles in Fig.4.

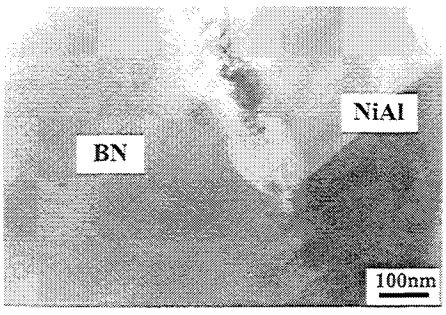


Fig. 7. TEM image of the NiAl/BN interface in the composite annealed at 1000°C for 500h.

4. Discussion

4.1 Formation of a cubic phase

A cubic phase was observed in the composite annealed at 1000°C for 100h in the form of nanoparticles distributed in the BN matrix near the NiAl(AlN)/BN interface. Similar small precipitate particles occurred occasionally in the composite annealed at 1000°C for 500h. The only difference in the preparation procedure of the two composite samples was the use of a glue to fix the fibers on the surface of the NiAl plates during the preparation of the composite which was subsequently annealed at 1000° for 100h. The glue wetted the surface of the fibers and is therefore assumed to have caused the abundant precipitation of the nanoparticles.

In order to determine whether the nanoparticles in Fig. 3 precipitated during the processing of the composite or during the annealing of the composite, TEM observations were conducted on the as-fabricated composite, and a similar interfacial microstructure to that in Fig. 3 was observed. Therefore it is concluded that the precipitation of the nanoparticles in Fig.3 had already taken place during processing of the composite. There was no obvious change of size of the nanoparticles during annealing.

Like other organic substances, the glue used was likely to contain mainly carbon, hydrogen and oxygen. Under the conditions of composite fabrication, the glue decomposed and most but not all of such elements evaporated during processing. It is highly probable that part of the C, and maybe some O diffused into to BN layer during the fabrication of the composite. This assumption is supported by the observation of a graphite-decorated Al_2O_3/NiAl interface in a Al_2O_3/NiAl composite fabricated by the powder cloth method which involved the use of organic substances as binders [6]. The appearance of the graphite phase at the Al_2O_3/NiAl interface is an indication that not all C from the binder volatilized during fabrication process of the composite.

Because the continuous nanoparticles precipitation layer appeared only when a glue was used during processing of the composite, the diffusion of C into the BN layer apparently played an important role in the precipitation of these particles. A ternary B-C-N compound was reported recently which had a structure similar to that of h-BN [7]. The structure of the nanoparticles as revealed by HREM indicated that these nanoparticles are unlikely to be such a B-C-N compound. The formation of the nanoparticles might require the diffusion of both C and Al into the BN matrix. Quantitative composition analysis would be needed to clarify the mechanisms of the formation of the nanoparticles. In addition, no known binary or ternary compound from B, C, N and Al seem to give rise to the observed HREM images in Fig. 5.

The C and O contents in a CVD-coated BN coating vary greatly depending on the type of precursor(s) and the process parameters to obtain a BN coating. Up to 10% of O and 15% of C was reported in a CVD-coated BN [8]. When a BN coating has such a high C content, the precipitation of the cubic nanoparticles may take place even if no contamination is introduced.

The BN coating used in the present study contained ~1 at% of O and ~1 at% of. C [9]. The fact that small particles were only occasionally observed indicated that without an additional source of carbon, the C concentration in the BN coating used in present study was not high enough for the formation of abundant nanoparticles. The occasionally observed particles may

be the result of local contamination on the surface of the NiAl plates or on the surface of the fibers.

4.2 Formation of the $Al_{18}B_4O_{33}$ phase

It was clearly shown that a thin $Al_{18}B_4O_{33}$ layer formed at the interface between BN and Al_2O_3 in the composite annealed at 1000°C for 100h, but in the composite annealed at 1000°C for 500h, no interlayer was observed. Apparently, the formation of the $Al_{18}B_4O_{33}$ layer at the BN/ Al_2O_3 interface was related to the appearance of the nanoparticles in the BN matrix near the NiAl(AlN)/BN interface. In the as-fabricated composite, in which the precipitation of the nanoparticles in the BN matrix was observed, no reaction product was found at the BN/ Al_2O_3 interface. The formation of the $Al_{18}B_4O_{33}$ phase at the BN/ Al_2O_3 interface occurred definitely during annealing of the composite.

The formation of a $Al_{18}B_4O_{33}$ phase was also observed at the interface between Pt and α-Al_2O_3 diffusion bonded at 1200°C [10]. This was attributed to trace impurities of B in Pt diffusing into the oxide to replace the Al in the oxide. The overall reaction for the formation of $Al_{18}B_4O_{33}$ phase was proposed to be [10]:

$$11\ Al_2O_3\ (s) + 4\ B[Pt] \rightarrow Al_{18}B_4O_{33}\ (s) + 4Al[Pt] \quad (1)$$

Reaction (1) did not proceed at or below 1100°C [11]. The $Al_{18}B_4O_{33}$ phase observed in the present study formed during annealing at 1000°C. The formation mechanism of the $Al_{18}B_4O_{33}$ phase observed in the present study is therefore different from the substitution mechanism of Al by B in the oxide. It is proposed that the $Al_{18}B_4O_{33}$ phase at the BN/ Al_2O_3 interface formed via the following reaction [12]:

$$9\ Al_2O_3 + 2\ B_2O_3 \rightarrow Al_{18}B_4O_{33} \quad (2)$$

Because at 1000°C B_2O_3 is only stable in both the liquid and gas states, reaction (2) should be rewritten as follows

$$9\ Al_2O_3 + 4\ [B]_{BN} + 6\ [O]_{BN} \rightarrow Al_{18}B_4O_{33} \quad (3)$$

According to this reaction equation, the amount of oxygen which diffused from the BN layer to the BN/ Al_2O_3 interface to form a 125nm thick $Al_{18}B_4O_{33}$ layer can be calculated using the following data: fiber diameter: 125μm, thickness of the BN coating: 3μm, theoretical density of $Al_{18}B_4O_{33}$: 2.93g/cm^3 [10], theoretical density of BN: 2.27g/cm^3 [9]. Considering a segment of a fiber of unit length (1cm) along its longitudinal direction, the calculated oxygen content in BN coating was 0.37 at.%.

As to the oxygen content in the as-coated BN (~1 at.%, as mentioned above), the layer of the $Al_{18}B_4O_{33}$ phase in Fig. 1 ought to have been thicker. Furthermore, the same oxygen content was expected in the as-coated BN layer in the composite annealed at 1000°C for 500h, but no interfacial $Al_{18}B_4O_{33}$ phase was observed. Evidently the oxygen in as-coated BN did not participate in reaction (3).

The nitrogen to boron ratio (N/B) is generally not equal to 1 and can be smaller [8] or greater [9] than 1, depending on the type of boron precursor(s) and deposition temperature. A deficiency of nitrogen (boron) with respected to boron (nitrogen) was suggested to be partly compensated for by oxygen and carbon [8]; the oxygen and carbon in as-coated BN has then

become part of the hexagonal BN structure and do not remain as free atoms. This may be the reason for the absence of an interfacial phase at the BN/Al_2O_3 interface in the composite annealed at 1000°C for 500h.

The oxygen atoms have to come from somewhere other than the as-deposited BN layer. As suggested above, some oxygen atoms probably diffused into the BN layer during the decomposition of the glue. When considering the vacuum conditions (5×10^{-3} Pa) during annealing, it might be also possible that some oxygen atoms in the vacuum chamber diffused along the BN/Al_2O_3 and/or NiAl/BN interface into the composite to a certain depth. The positions of the TEM foils investigated were not determined.

It seems that the boron atoms in reaction (3) were not provided by a decomposition of the hexagonal BN because in both samples a growth of the AlN layer was not observed. However the formation of the AlN layer at the NiAl/BN interface during composite fabrication did result in the liberation of some boron atoms. These boron atoms which were suggested to diffuse into the grain boundaries of NiAl might actually have diffused into the BN layer. When free oxygen atoms are available and the temperature condition favorable, both B and O atoms may diffuse from the BN layer to the BN/Al_2O_3 interface, and the formation of $Al_{18}B_4O_{33}$ may take place via reaction (3).

The melting point of $Al_{18}B_4O_{33}$ was reported to be 1440± 20°C [12]. Okada et al. reported the decomposition of bulk $Al_{18}B_4O_{33}$ at 1400°C [13]. In contrast, in the Al_2O_3-B_2O_3 phase diagram given by Gielisse and Foster, $Al_{18}B_4O_{33}$ was stable up to 1950°C [14]. The observation that the $Al_{18}B_4O_{33}$ phase did not form during processing of the composite but formed during annealing in the present study indicated that $Al_{18}B_4O_{33}$ was not stable at 1400°C in vacuum.

5. Conclusions

Because of the chemical inertness of BN, both NiAl/BN and BN/ Al_2O_3 interfaces in a NiAl matrix composite reinforced with BN-coated single crystal Al_2O_3 fibers exhibited excellent stability after annealing at 1000°C for up to 500h. The AlN layer formed during the processing of the composite did not grow during annealing.

In the presence of contamination by carbon and oxygen which resulted from the use of a glue to fix the fibers, significant changes in the microstructure of both BN/Al_2O_3 and NiAl/BN interfaces were observed. A continuous $Al_{18}B_4O_{33}$ interlayer formed at the interface between BN and Al_2O_3 during annealing. Apart from a thin AlN layer at the NiAl/BN interface, many nanoparticles with possibly a cubic structure (a=1.07nm) were observed in the BN matrix near the NiAl(AlN)/ BN interface in the as-fabricated composite.

Acknowledgements

The authors would like to acknowledge the financial support from the Deutsche Forchungsgemeinschaft through the collaborative research center SFB 561: "Thermally highly loaded porous and cooled Multi-Layer Systems for Combined Cycle Power Plants".

References

1. P. H. Kitabjian, A. Garg, R. D. Noebe and W. D. Nix, High-temperature deformation behavior of NiAl(Ti) solid solutionsingle crystals, Metall. Trans. A, 30A, 1999, 587-600.
2. K. Xu and R. J. Arsenault, High temperature deformation of NiAl matrix composite, Acta mater., 47, 1999, 3023-3040.
3. R. R. Bowman, A. K. Misra and S. M. Arnold, Processing and mechanical properties of Al_2O_3 fiber-reinforced NiAl composites, Metall. Mater. Trans. A, 26A, 1995, 615-628.
4. S. L. Draper and I. E. Locci, Al_2O_3 fiber strength degradation in metal and intermetallic matrix composites, J. Mater. Res., 9, 1994, 1397-1411.
5. K. Y. Wen, W. Hu, K. Reichert and G. Gottstein, Interfacial microstructure and reaction of BN-coated single crystal Al_2O_3 fiber reinforced NiAl matrix composites, J. Mater. Sci., to be published in 2002.
6. L. Wang, K. Xu, R. R. Bowman and R. J. Arsenault, Interface in continuous filament-reinforced Al_2O_3/NiAl composites, Metall. Mater. Trans. A, 26A, 1995, 897-903.
7. J. L. He, Y. J. Tian, D. L. Yu, T. S. Wang, F. R. Xiao, A. D. Li, D. C. Li, Y. G. Peng and L. Li, Chemical synthesis of crystalline hexagonal B-C-N compound, J. Mater. Sci. Lett., 19, 2000, 2061-2063.
8. E. Pippel, J. Woltersdorf, D. Dietrich, S. Stöckel, K. Weise and G. Marx, CVD-coated boron nitride on continuous silicon carbide fibers: structure and nanocomposition, J. Euro. Ceram. Soc., 20, 2000, 1837-1844.
9. A. Jörg, Ph. D thesis, RWTH Aachen, 1996.
10. M. J. Murtagh, J. Hulvat, R. Dieckmann and S. L. Sass, Impurity controlled phase formation at platinum-sapphire interfaces, Acta. Mater., 49, 2001, 3493-3504.
11. Y. C. Lu, S. Agnew, R. Dieckmann and S. L. Sass, Further characterization of the aluminum peroxide oxide, AlO_2, formed by interfacial reaction between Pt and α-Al_2O_3. Acta. Metall. Mater., 43, 1995, 1885-1893.
12. H. Scholze, Über aluminiumborate, Z. Anorg. Allgem. Chem., 284, 1956, 272-276.
13. K. Okada, H. Mutoh, N. Otsuka and T. Yano, Formation of Al_2O_3 whisker by thermal decomposition of 9 $Al_2O_3.2B_2O_3$ whiskers. J. Mater. Sci. Lett., 10, 1991, 588-590.
14. P. J. Gielisse and W. R. Foster, The system Al_2O_3-B_2O_3. Nature, 195, 1962, 69

MECHANICAL PROPERTIES AND OXIDATION BEHAVIOUR OF A CAST TiAl INTERMETALLIC

V. Lupinc(°), M. Marchionni(°), M. Nazmy(*), G. Onofrio(°), M. Staubli(*), A. Tomasi(+) and L.Z. Zhou(°,++)

(°) CNR-IENI, Milano, Italy
(*) ALSTOM POWER Ltd, Baden, Switzerland
(+) ITC-IRST, Trento, Italy
(++) Institute of Metal Research, Chinese Academy of Sciences, Shenyang, China

Abstract

In the present investigation, the effect of microstructure on the tensile strength, creep, low cycle fatigue and fatigue crack propagation properties has been studied in the new cast and HIP'ed Ti-47Al-2W-0.5Si-0.5B ABB-23 alloy and, as a comparison, in the Ti-47Al-2W-0.5Si ABB-2 alloy. The latter has been studied in the duplex (D) and in the near lamellar (NL) microstructural conditions, while the ABB-23 has been heat treated to achieve the NL microstructure. For these alloys tensile strength at the temperature up to 900°C and creep behaviour, in the temperature range of 600-850°C, have been determined and correlated to the corresponding microstructures and chemical composition. In addition, low cycle fatigue and fatigue crack propagation behaviour has been studied at different temperatures. The overall mechanical behaviour has shown that the boron containing alloy with a near lamellar microstructure has the best combination of properties for high temperature applications. Oxidation resistance in the 600-800°C temperature range has also been examined.

Keywords: cast TiAl intermetallic , mechanical properties, oxidation behaviour

Introduction

Gamma titanium aluminide alloys based on the ordered TiAl phase are of great interest for high temperature applications due to their low density, high stiffness, and attractive mechanical properties at elevated temperature [1,2]. Research and development of γ-TiAl alloys have progressed significantly within the last decade [3]. This research effort has resulted in better understanding of the correlation among the alloy composition, heat treatment and microstructure, processing and mechanical properties [4]. The cast alloys have shown a significant improvement of their performance and an encouraging possibility to be used for industrial applications [5].

In applications with high load, adequate knowledge of the critical mechanical properties, e.g. creep strength, low cycle fatigue (LCF), and toughness, of these materials, is essential [6]. It has been shown that, for γ-TiAl base alloys, the microstructure can have a significant effect on these properties [3]. For example, a duplex structure can improve the tensile ductility, while fracture toughness and creep strength are improved by a lamellar microstructure [3]. Hence, it is essential to define the most crucial properties required for a specific application in order to achieve the optimum microstructure by applying the right composition, processing, and heat treatment. Recently, the refinement of the microstructure by microalloying with boron resulted in a significant homogeneity of the lamellar colonies dimension and, as a consequence, in more reproducible mechanical properties.

The goal of the present work is to study effect of addition of 0.5 at.% boron on the tensile strength, creep resistance, LCF, and fatigue crack propagation behaviour of the new cast ABB-23 alloy. The alloy has been heat treated to produce the near lamellar microstructure.

Material and experimental procedure

The ABB-2 alloy nominal composition is: Ti-47Al-2W-0.5Si at.% [7]. Its properties are considered as a reference and were measured in cast bars HIP'ed at 1260°C/172 MPa/4 h and heat treated at 1300°C/20 h/GFC (gas fan cooling) + 900°C/4 h/FC (furnace cooling) to obtain duplex structure (D) and at 1350°C/1 h/GFC + 1000°C/6 h/FC for near lamellar (NL) structure [9]. The new alloy, called ABB-23, has the nominal composition Ti-47Al-0.5Si-0.5B at.%. It was obtained in cast bars and plates, HIP'ed and heat treated to obtain near lamellar microstructure.

Tensile testing has been performed at the strain rate of $7x10^{-4}$ s^{-1} from room temperature to 900°C. Tensile creep tests at constant load and temperature have been done in the 700-800°C temperature range with the longest creep test duration of about 9000 h.

Low cycle fatigue tests have been carried out in longitudinal strain controlled conditions with a triangular wave form (R = -1) on cylindrical specimens with 7 mm minimum diameter and 12 mm gauge length. The strain rate applied was 10^{-3} s^{-1}. The samples were heated by induction coil at 700 °C. The temperature was controlled within ± 3 °C. During the experiments, the stress response and the hysteresis loop were recorded at intervals.

Fatigue crack propagation tests have been carried out on single edge notch tension (SENT) specimens with a rectangular cross section of 12 x 4.5 mm^2 and a 1 mm deep starter notch. The fatigue crack propagation rate (FCPR) tests have been run in load control with triangular wave shape (R = 0.1) at frequency ranging from 0.01 to 10 Hz and temperature from 25 to 700°C. The specimens were fatigue pre-cracked at room temperature with a frequency of 10 Hz and induction heated with temperature controlled within ±3°C. The crack length was measured by the direct current potential drop technique, and the crack propagation rate was correlated to the stress intensity factor range $\Delta K = K_{max} - K_{min}$ that is calculated as follows [8]:

$$\Delta K = (1-R)\sigma\sqrt{\pi a}\left[1.12 - 0.23\left(a/W\right) + 10.6\left(a/W\right)^2 - 21.7\left(a/W\right)^3 + 30.4\left(a/W\right)^4\right] \qquad (1)$$

High temperature oxidation resistance of the ABB-2 and ABB-23 samples was investigated by thermogravimetric methods with isothermal treatment between 600-800°C performed in dry air. The degradation process due to oxidation and the thermal stability of the developed oxide were followed up to 1000 h. The oxide scale morphology was studied by SEM and the microstructure evolution after the heat treatment was studied by X-ray diffraction (XRD).

Experimental results and discussion

Microstructure

The microstructure of ABB-23 cast plate is shown in Fig. 1. Fig. 1a shows a cellular grain zone which represents the major part of the examined 25 mm thick plate, where some of the creep

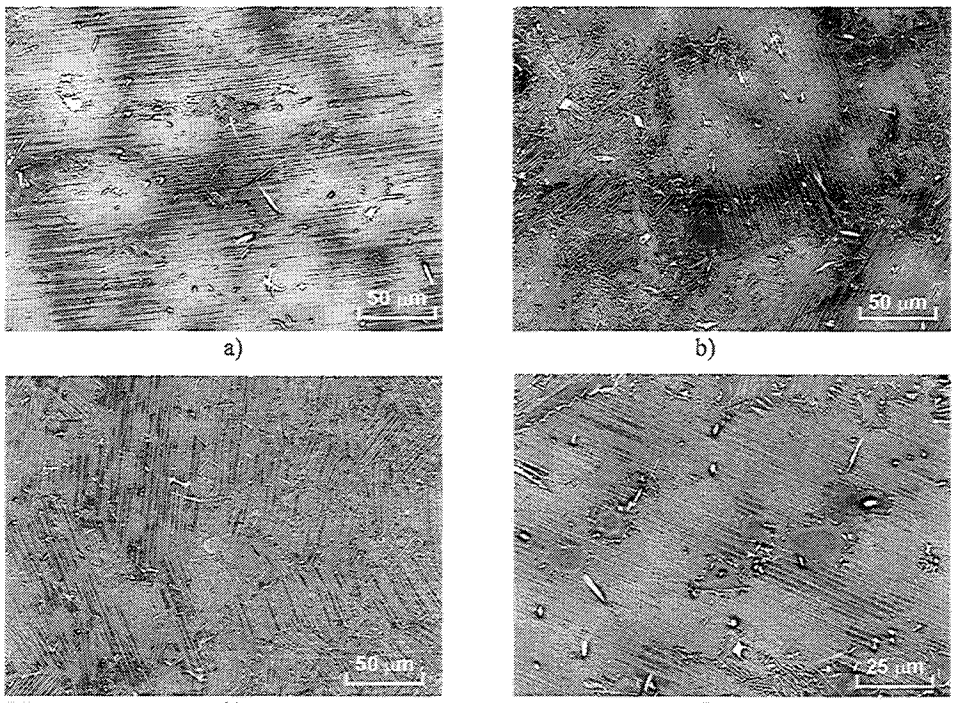


Fig. 1 – BSE SEM images of ABB-23 cast plate: a) as-received, cellular-grain area; b) as-received, centre of plate; c) as-received, casting edge; and d) cellular-grain area after 1000 h ageing at 800°C.

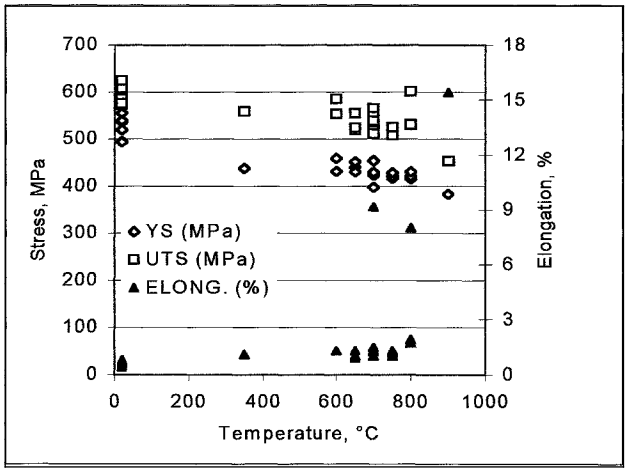


Fig. 2 - Tensile properties of the ABB-23 alloy.

specimens were machined from. Fig. 1b shows a small central zone of the plate where globular grains and some coarsened lamellae typically appear. Fig. 1c shows the microstructure at edge of casting where small grains and some ribbon-like borides can be observed. The microstructure of this alloy is near lamellar γ/α_2, as expected from the 1350°C/1 h/GFC + 1000°C/6 h FC heattreatment. Microstructure features similar to those observed in the plate were observed also in cast bars of ABB-23.

In general, ABB-23 microstructure is made of finer grains and is more homogeneous than ABB-2 microstructure. A comparison of microstructure of ABB-23 specimens of this work with microstructure of ABB-2 specimens of previous work [9,10] is not straightforward, if microstructure relevant to mechanical testing specimens is to be considered. Test-pieces of ABB-23 were machined from cast bars and from cast plates, while test-pieces of ABB-2 were all machined from cast bars. Since the specimens obtained from bars contain the central globular grain zone in the gauge length and the specimens obtained from plate have the gauge length machined out of the cellular region of the casting, part of scatter of the creep properties of ABB-23 measured in this work could be due to the microstructure differences of the specimens from bars and plates.

The ABB-23 microstructure seems to be quite stable up to 1000 h ageing at 800°C. After this ageing treatment, the ABB-23 microstructure shows only small changes, i.e. new small equiaxed γ islands appear in the lamellar colonies. This can be seen from comparison of the cellular grain zone microstructure after ageing shown in Fig. 1d, and the initial microstructure shown in Fig. 1a, although the different magnification of the two photographs makes the comparison more difficult.

Tensile properties

The tensile behaviour of the ABB-23 alloy in the temperature range 25 – 900°C is presented in Fig. 2, where it is possible to observe a good tensile strength retention of this alloy up to 800°C. At the same temperature the ductile to brittle transition is evident in the figure. Comparing the tensile properties of ABB-23 with those of ABB-2 alloy, reported in previous work [9], it can be said that the tensile properties of the ABB-23 alloy lay between the duplex and the near lamellar versions of the ABB-2 alloy.

Creep properties

The Larson-Miller graph in Fig. 3 shows stress rupture data of ABB-23 alloy in the 700-800°C temperature range, and compares them to stress rupture data of both microstructures of ABB-2 alloy in the 650-850°C temperature range and to density corrected stress rupture data of IN738LC alloy. It can be seen, that the stress rupture data of ABB-23 lay between the two different microstructure versions, the duplex and the near lamellar microstructure, of alloy ABB-2. Furthermore, it can be seen that ABB-23 stress rupture data are higher than density corrected data of cast superalloy IN738LC, often used for rotating high temperature components.

Time to 0.5% creep strain is often even more important than stress rupture data for design purposes. These data of ABB-23 lay again between the two different microstructure versions of alloy ABB-2 in the Larson-Miller plot of Fig. 4 where three typical commercial cast alloys data (i.e. the GE 48-2-2 alloy and the two XD Howmet alloys), taken from [11], are also shown for comparison.

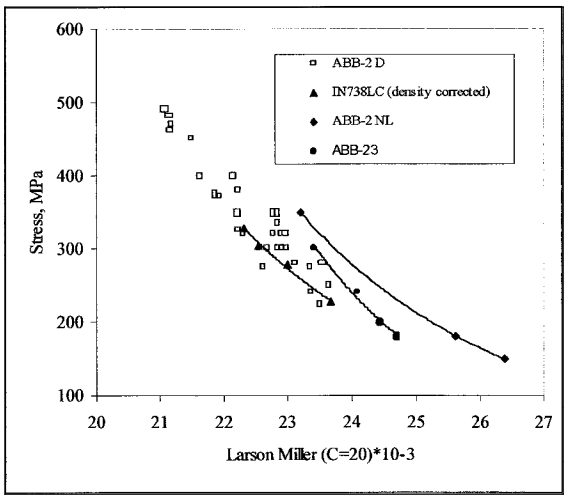


Fig. 3 – Stress rupture plot of ABB-23, ABB-2 duplex and near lamellar and density corrected IN738LC alloy.

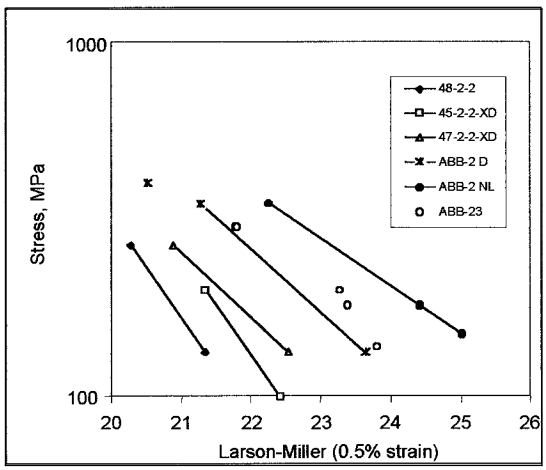


Fig. 4 - Comparison of ABB alloys with commercial alloys in 0.5% creep strain Larson-Miller plot.

Low cycle fatigue

The low cycle fatigue data on ABB-23 alloy have been collected and compared with ABB-2 duplex and near lamellar material.

Figure 5 shows the fatigue results plotted as total strain range versus the number of cycles to failure. The fatigue life of ABB-23 NL alloy is comparable with the duplex ABB-2 alloy even

material are expected to produce a reduction of fatigue life. The NL materials LCF data at low strain are also comparable, at least on the basis of the single test done on NL ABB-2 alloy.
The results have also been analysed by the following Basquin (2) and Coffin – Manson (3) relationships:

$$\Delta\varepsilon_e = AN^{-\alpha} \qquad (2)$$

$$\Delta\varepsilon_p = BN^{-\beta} \qquad (3)$$

where $\Delta\varepsilon_e$ and $\Delta\varepsilon_p$ are the elastic and plastic strain components, N the number of cycles to failure (all evaluated at half-life), A, B, α and β constants of the material. The values of the constants for the ABB-23 alloy are reported in table I, in which r^2 is the confidence parameter. The value of r^2 is good for the Coffin-Manson relationship, while is worse for Basquin equation as the fatigue data of the elastic strain component are more scattered.
In Fig. 6 the elastic and plastic strain components versus the number of cycles to failure N are reported for the two alloys. As it can be observed, the lines describe the behaviour of the experimental data with good accuracy and low scatter-band, confirming the correct description of the materials behaviour with the same parameters of the Eq.s 2 and 3. The position of the transition point (less than 200 cycles) confirms the low ductility of the alloys.

Table I - Values of the fatigue parameters for Eq.s 2 and 3.

A	α	r^2	B	β	r^2
0.0086	0.0626	0.64	0.0258	0.312	0.92

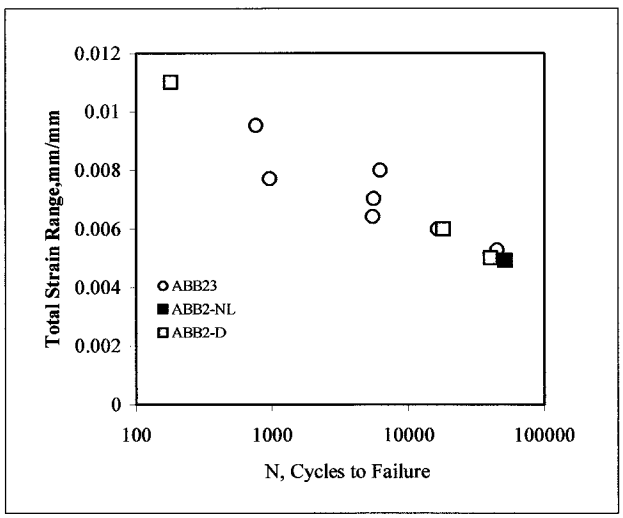


Fig.5 – Comparison of LCF life of ABB-23 and ABB-2 alloys.

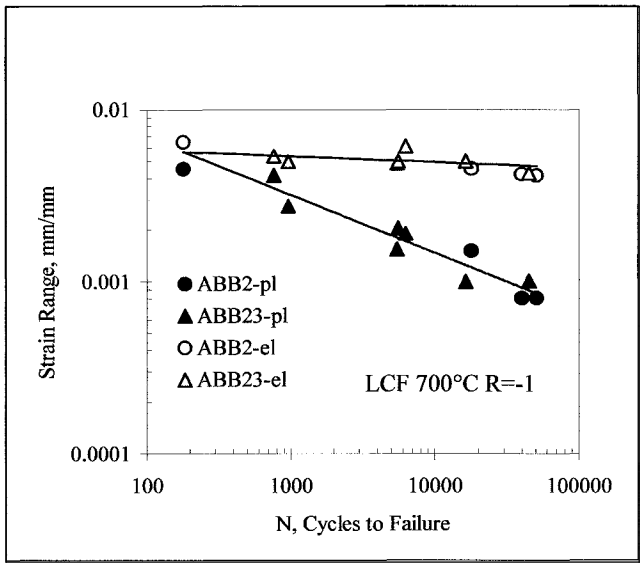


Fig. 6 – Elastic and plastic strain components of ABB-23 and ABB-2 alloys.

Fatigue crack propagation results.

Fig. 7 shows the fatigue crack propagation behaviour of the examined alloys at the temperature of 700°C and at the loading frequency of 10 Hz. The alloys with near lamellar microstructure ABB-2 and ABB-23 show higher fracture toughness (K_{IC}) as well as higher threshold values when compared with the duplex microstructure ABB-2 alloy. This observation confirms the general trend found in literature comparing high temperature behaviour of duplex and nearly lamellar microstructure γ-TiAl alloys [9]. Examining this figure, a similar fatigue crack propagation behaviour of ABB-23 and ABB-2 with the NL microstructure alloy is apparent.

The effect of temperature on FCPR of ABB-23 alloy, in the 25 – 700°C temperature range, is shown in Fig. 8. As already observed for the near lamellar ABB-2 alloy in the 500 – 750°C range [6], very limited effect of temperature on fatigue crack propagation behavior is observable in ABB-23 in the examined range. The only exception is a slight increase in the threshold at 700°C with respect to the 25°C test, that should be attributed to a crack closure mechanism that is more effective at higher temperature. In the same figure the curve obtained at 700°C and at the R ratio value of 0.5 is also reported. The threshold value decreases from 8-9 to 5-6 MPa$\sqrt{m}$ when the R-ratio is increased from 0.1 to 0.5. It is generally accepted that closure effect tends to disappear increasing R ratio when the minimum load in the cycle approaches the opening load, this behaviour could be related to the less effective closure mechanism at this relatively high R ratio. On the other hand the threshold increases when the frequency decreases from 10 to 0.01 Hz, as it can be observed in Fig. 9 for ABB-23 alloy. This behaviour could be ascribed to an oxidation closure mechanism operative at the lower frequency.

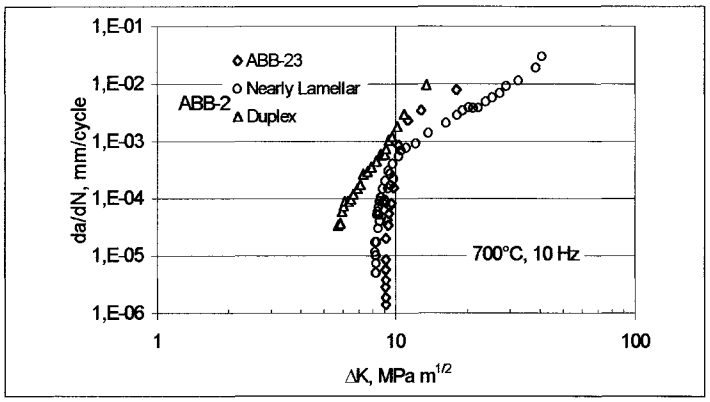


Fig. 7 - Fatigue crack propagation behaviour of ABB-2, with duplex and nearly lamellar microstrucure, and ABB-23.

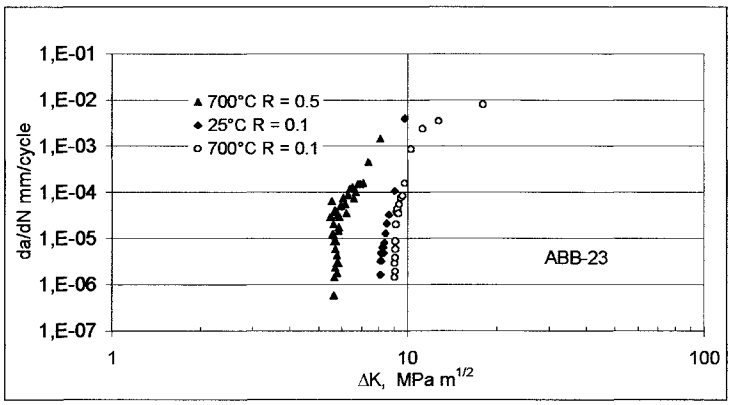


Fig. 8 – Effect of temperature and R ratio on fatigue crack propagation of ABB-23 at 10 Hz.

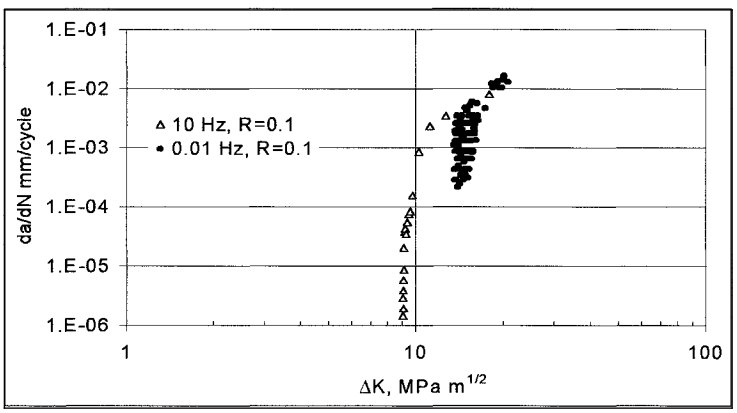


Fig. 9 - Effect of test frequency on fatigue crack propagation rate of ABB-23.

Oxidation

Fig. 10 shows the weight change versus time curves for isothermal heat treatments at 600, 700 and 800°C for ABB-2 and ABB-23 samples. At 600 and 700°C the oxidation degradation process is very poor and, after 100 h only, the SEM and XRD analyses show the presence of a well adherent and protective alumina oxide scale on the surface of the materials. At 800°C the

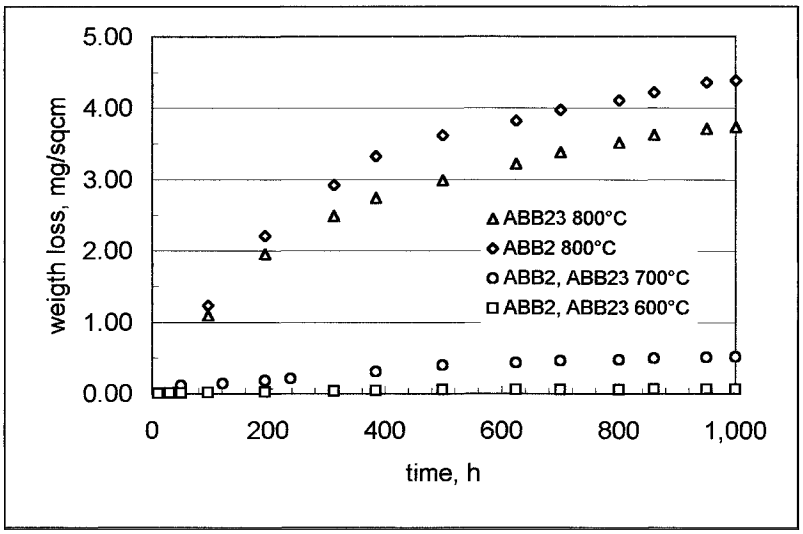


Fig.10 - Oxidation behaviour of the studied alloys.

kinetics data show a parabolic behaviour due to the formation of an oxide scale and the presence of alumina and titania is clearly detected by XRD and SEM. In this range of temperature the oxidation data of the ABB-23 samples exposed at 600 and 700°C are identical with the data of ABB-2 alloy. On the contrary the samples heat treated at 800°C show a similar trend, the same chemical composition of the oxide scale, but a reduced oxidation rate with respect to the ABB-2 alloy. The main reason for the observed difference in the oxidation kinetics can possibly be ascribed to the presence of boron in the ABB-23 alloy. Even if present in small amount, boron is known to effect oxidation kinetics through precipitation at grain boundaries reducing the ion diffusion.

Conclusions

The cast γ-TiAl materials examined in the present study have shown very interesting mechanical properties at high temperature.

The tensile properties of the boron containing ABB-23 alloy in the 25 to 800°C range lay in general between the tensile properties of the two versions of the ABB-2 alloy.

In general the creep properties of the new ABB-23 alloy are comparable or better than the duplex microstructure ABB-2 alloy but they are lower compared to the NL ABB-2 material. All these alloys show higher stress rupture values than that of density corrected IN738LC stress rupture values.

The low cycle fatigue behaviour of ABB-23 and ABB-2 alloys is similar in the explored experimental range.

The fatigue crack propagation behaviour of ABB-23 alloy is similar to that of the ABB-2 NL alloy, both having near lamellar microstructure.

The oxidation behaviour of ABB-2 and ABB-23 alloys have been studied in the 600-800°C temperature range. All weight gain curves follow the parabolic rate indicating the growth of a compact oxide scale on the surface of the alloys. Microstructural investigations show that boron in ABB-23 alloy tends to influence and reduce the oxidation kinetics only at 800°C.

References

1. Y.W. Kim and D.M. Dimiduk, Journal of Metals, Vol. 43 (8), 1991, p.40.
2. C. Austin and T.J. Kelly, Proc. of 1st Symp. on "Structural Intermetallics", eds. R. Darolia et al., TMS publ., 1993, p. 1433.
3. Y.W. Kim, Journal of Metal, Vol. 46 (7), 1994, p. 30.
4. Y.W. Kim and D.M. Dimiduk, Proc. of 2nd Symp. on "Structural Intermetallics", eds. M.V. Nathal et al., TMS publ., 1997, p. 531.
5. D.E. Larsen, Materials Science & Engineering, A213m, 1996, p.128.
6. V. Lupinc et al., Proc. of "Structural Intermetallics 1997", eds. M.V. Nathal et al., TMS Publ., 1997,p. 515.
7. M. Nazmy and M. Staubli, US Patent 5,207,982 & EP. 45505 B1
8. W.F. Brown and J.E. Srowley, ASTM-STP, 410, 1966, p.1.
9. V. Lupinc et al., Proc. of "Gamma Titanium Aluminides 1999" TMS Conf. San Diego, eds. Y.W. Kim et al., TMS Publ., 1999, p. 349.
10. M. Nazmy and V. Lupinc, Proc. of the 6th Liege Conference "Materials for Advanced Power Engineering 1998", eds. J. Leconte-Beckers et al., 1998, p. 933.
11. W. Voice, Proc. of the 5th International Charles Parsons Turbine Conference, Cambridge UK, eds. A. Strang et al., IOM Publ., 2000, p. 865.

COATING OF Ni-ALUMINIDES ON TiAl INTERMETALLICS THROUGH UP-HILL DIFFUSION

Takeshi Izumi*, Takumi Nishimoto*, and Toshio Narita

Research Group of Interface Control Engineering,
Graduate School of Engineering, Hokkaido University
Kita-13 Nishi-8 Kita-Ku Sapporo 060-8628 Japan

* Graduate student, Hokkaido University

Abstracts

A TiAl intermetallic was electrolytic-plated with 10μm Ni, followed by high Al activity pack cementation at 1273K for 5h to form a coated layer with an inner $TiAl_2$ / $TiAl_3$ / Al_2TiNi layer and an outer Ni_2Al_3 layer. The coated layer grew due to inward, up-hill, diffusion of Al.

The Ni-aluminized TiAl was oxidized in air for up to 1,000h under a thermal cycling condition between room temperature and 1173K. Mass gain per unit surface area was 8 g/m^2 after 1,000h and there was little exfoliation of the Al_2O_3 scale. After oxidation for up to1,000h it was found that the coated layer maintains a duplex layer structure of an inner $TiAl_2$/Al_2TiNi layer and an outer Al-rich β-NiAl layer; the inner layer contains more Al than the outer layer. Both the Ni_2Al_3 and the Al rich β-NiAl contain less than 0.5at% Ti, in accordance with the experimentally determined phase diagram.

Key words: Titanium aluminides, Nickel-aluminides coating, Oxidation, Ti-Al-Ni phase diagram

1 Introduction

There are many reports dealing with addition of alloying elements [1,2], surface processing [3～7], ion implantation [8], sulfidation processing [9～11], and Cr-Al diffusion treatment [12] to improve the oxidation resistance of the γ-TiAl intermetallics, However, further investigation are needed to improve the oxidation resistance of TiAl intermetallics subjected to long-term exposure at temperatures higher than 1123K.

It has been widely accepted that nickel-aluminides such as β-NiAl have very good oxidation resistance in long-term exposure at high temperatures. Therefore, a coating of Ni aluminides would be a candidate for coating of TiAl intermetallics. Several papers [13,14] investigated Ni-Al coatings on TiAl alloys, showing anti-oxidation properties of such coatings against high temperature oxidation. However, there are still uncertainties in the coating process and oxidation behavior of the Ni aluminized TiAl.

In the present investigation so-called up-hill diffusion was achieved to form a Ni aluminized coating with a duplex layer structure of an inner layer containing more Al than the outer layer. To prepare the coating, a two-step process was adopted by electroplating of nickel followed by high Al activity pack cementation.

2. Experimental

2.1 Alloy preparation

The Ti-50at%Al alloy was prepared using Ar-arc melting with pure 99.99% Al and 99.5% sponge Ti. The alloy ingot was heat-treated in vacuum at 1373K for 9h and then cut into 1mm thick plates with surface areas of about 2 cm^2. The alloy surface was finished using waterproof SiC abrasive paper up to #400.

2.2 Coating of Ni aluminized layers on TiAl

Nickel was electroplated in a Watt-type solution containing $NiSO_4$, $NiCl_2$, and H_3BO_3 at 328K for 2h with a current density of 5mA/cm^2, forming a Ni film of about 10μm. High Al activity pack cementation was used to aluminize the Ni-plated TiAl in vacuum at 1273K for 5h in a powder mixture containing 15mass% Al; 10mass% NH_4Cl, and 75mass% Al_2O_3.

2.3 Oxidation test

Batch type oxidation experiments were carried out under a thermal cycle between 1173K and room temperature in flowing air for up to 1,000h. The specimens were suspended with a platinum wire in an alumina crucible to collect oxide scales exfoliated during cooling. The mass gain was measured from the difference in specimen weight before and after oxidation. The mass of the exfoliated oxide was also measured. The amount of oxidation was obtained from the mass gain divided by the original alloy surface area.

Cross-sectional microstructures of the oxidized TiAl were observed using a scanning electron microscope equipped with an energy dispersion X-ray analyzer (SEM-EDX) and quantitative analysis for each element was carried out by an electron-probe micro analyzer (EPMA).

2.4 Solubility of Ti in Ni_2Al_3 and NiAl

According to a Ti-Al-Ni ternary system in Villars et al. [15] the maximum solubility of Ti is 7mass% in Ni_2Al_3 and 16mass% in NiAl at 1273K. Recently, Ding et al. [16] reported that the Ti contents in both the Ni_2Al_3 and the NiAl are much smaller than those reported by Villars et al. [15].

To understand the disagreement between the two phase diagrams and also to know the phase relationships in the Al-rich corner of the Ti-Al-Ni system, several ternary alloys were arc-melted and then heat-treated in vacuum at 1373K for 24h. The alloys were finally heat-treated in air at 1273K for 24h followed by rapid cooling in water. The quantitative analysis for each element in the cross-section of the alloys were made with EPMA to determine the concentration of each constituent.

3. Results

Fig.1 shows the microstructure and concentration profiles of Ti, Al, and Ni across the as-coated TiAl, (below the compositions are given in at%, except where otherwise specified). The coated layer consists of a duplex layer structure, an outer layer (1) and an inner layer (2) to (6). The (1) layer is Ni_2Al_3 with a little Ti. Layer (2) is Al_2TiNi with a composition of Ti-55%Al-24%Ni. Layer (3) is $TiAl_3$ and (4) is $TiAl_3$ containing 7%Ni with a $L1_2$ structure. Layer (5) is $TiAl_3$ again, but this time non-continuous. A Layer (6) adjacent to the substrate is $TiAl_2$. The Ni content in both the $TiAl_3$ and the $TiAl_2$ is negligible. That was a maximum concentration of Al close to 73%Al in the inner layer, higher than the 60%Al in the outer layer.

Fig.2 shows changes in total mass gain with time for the Ni aluminized TiAl alloy with thermal cycling in air at 1173K. The thermal cycling of one sample was stopped at 36h and the other was continued up to 1,000h. The exfoliated oxide scale was carefully collected in an alumina crucible. However, the amount of exfoliated oxide was negligible at every measurement and therefore it is not shown in Fig.2. As demonstrated in Fig.2, oxidation proceeded slowly to become approximately $8g/m^2$ after 1,000h.

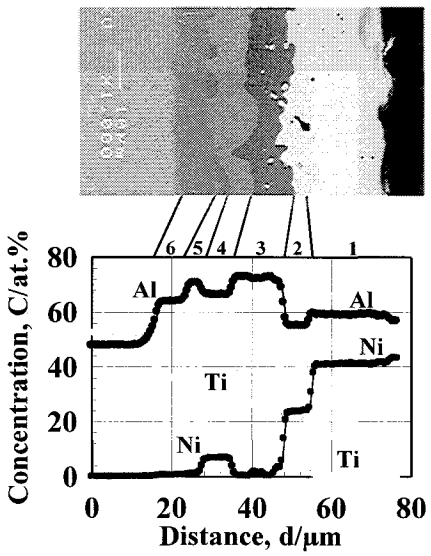


Fig. 1 Cross-sectional microstructures of the coating layer and concentration profiles of Ti, Al and Ni for Ni-Al coated TiAl alloy.

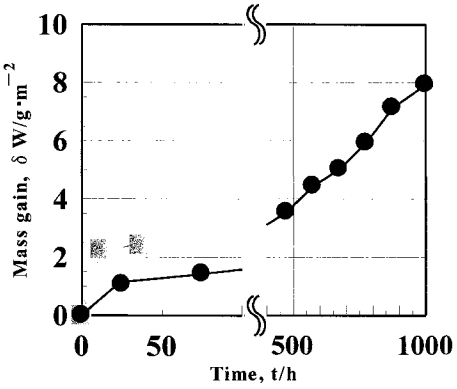


Fig.2 Changes in oxidation mass gain with time for Ni-Al coated TiAl alloy under the thermal cycles in air at 1173K. (■=36h oxidation, ●=1,000h oxidation)

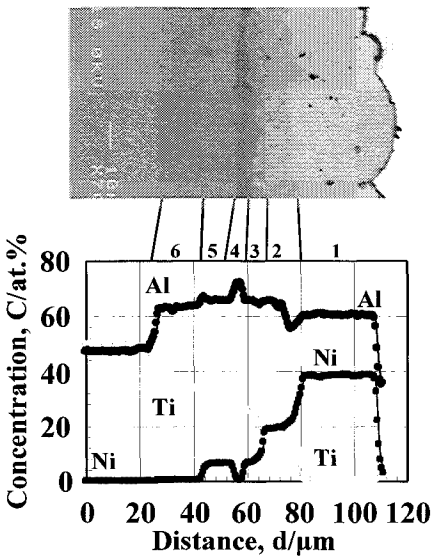


Fig. 3 Cross-sectional microstructures of the coating layer and concentration profiles of Ti, Al and Ni for Ni-Al coated TiAl alloys oxidized at 1173K in air for up to 129.6ks.

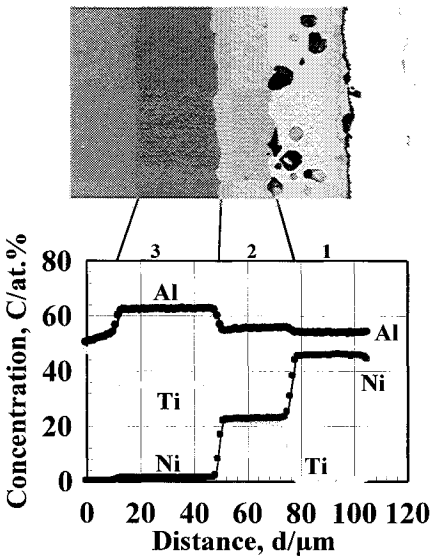


Fig. 4 Cross-sectional microstructures of the coating layer and concentration profiles of Ti, Al and Ni for Ni-Al coated TiAl alloys oxidized at 1173K in air for up to 3600ks.

Figs.3 and 4 show cross-sectional microstructures and concentration profiles of Ti, Al, and Ni for the alloys oxidized for 36h and 1,000h, respectively. There are α-Al_2O_3 surface scales of several μm thickness after both 36h and 1,000h oxidation, and there was no cracks or exfoliation in the surface scale. Observations of the cross-sections showed that the coated layer after oxidation for 36h is sound without flaws such as cracks and voids, after oxidation for 1,000h there are defects like voids in the outer layer of β-NiAl. There appears to be soft matter embedded in the defects, although details of this soft matter have not been established.

As shown in Fig.3, the coated layer structure after oxidation for 36h is essentially the same as that of the as-coated specimen, except that the $TiAl_3$ layer was thinner after 36h. After oxidation for up to 1,000h, as shown in Fig.4, the coated layer consisted of three layers. An outer layer (1) of Al-rich β-NiAl containing less than 0.5%Ti, altered from Ni_2Al_3. Layer (2) is Al_2TiNi with a composition of Ti-55%Al-23%Ni. Layer (3) is the $TiAl_2$ containing less than 1%Ni.

Table 1 summarizes the concentrations of each phase in different Ti-Al-Ni alloys equilibrated at 1273K for 24h, followed by water quenching. Fig.5 shows cross-sections and Ti, Al and Ni concentration profiles measured along the X-X lines in the photograph of alloys No.1, No.5, and No.12 in Fig.5a-c, as examples of two or three phase co-existence. It was found that concentration profiles in each phase were almost flat in Fig.5, showing that the phases are in equilibrium at 1273K.

Fig.6 shows tied-lines among each phase in the Ti-Al-Ni phase diagram, and compositions of both the Ni_2Al_3 and NiAl phases are plotted in the magnified diagram inserted to the left in Fig.6. The shaded area in Fig.6 shows the composition range of each phase in the Ti-Al-Ni phase diagram after Villars et al. [15]. In the magnified diagram the results reported recently by Ding et al. [16] are shown by a dotted line. From these results it was concluded that the solubility of Ti in both the Ni_2Al_3 and the Al-rich β-NiAl range from 0.3 to 0.5 at%, close to those given by Ding et al. [16]. With increasing Al content in the Ni aluminides, the solubility of Ti tended to increase rapidly, especially for the Ni-rich β-NiAl.

As demonstrated in Fig.6, the Ni_2Al_3 was tie-lined with the Al_2TiNi with a composition of 19.1%Ti-57.1%Al-23.8%Ni, and further the Al_2TiNi was tie-lined with the $L1_2$-Ti(Al, Ni)$_3$ with a composition of 26%Ti-65.8%Al-8.2%Ni. The Al-rich β-NiAl was also tie-lined with both the Al_2TiNi and the Ni_2Al_3. Meanwhile, the Ni-rich β-NiAl was tie-lined with two phases, one of them has a composition of 32.7%Ti-44.8%Al-24.7%Ni and the other is 50.2%Ti-32.3%Al-17.5% Ni. These two phases do not appear in the phase diagram in Villars et al. [15], while the τ_1 phase in the diagram after Ding et al. [16] may correspond to these two phases, because the τ_1 phase has a wide composition range. Further investigation should is required to establish more details.

Table 1 Composition data(at.%) of the alloys

Alloy No	nominal composition	matrix	precipitate
1	0.5Ti-59.8Al-39.7Ni	0.3Ti-59Al-40.7Ni	19.1Ti-57.1Al-23.8Ni and 26Ti-65.8Al-8.2Ni
2	2.7Ti-58.4Al-38.9Ni	0.1Ti-56.9Al-43Ni	20.8Ti-55.2Al-24Ni
3	5.4Ti-56.8Al-37.8Ni	0.1Ti-56.5Al-43.4Ni	19.1Ti-57Al-23.9Ni
4	1.7Ti-59Al-39.3Ni	0.1Ti-56Al-43.9Ni	20.8Ti-54.6Al-24.6Ni
5	0.6Ti-53.7Al-45.7Ni	0.2Ti-53.7Al-46.1Ni	21.3Ti-54.5Al-24.2Ni
6	1.7Ti-53.1Al-45.2Ni	0.3Ti-53.3Al-46.4Ni	20.5Ti-55.3Al-24.2Ni
7	2.8Ti-52.5Al-44.7Ni	0.8Ti-51.7Al-47.5Ni	21.9Ti-53.8Al-24.3Ni
8	5.3Ti-51.2Al-43.5Ni	1.3Ti-50.7Al-48Ni	22.6Ti-52.6Al-24.8Ni
9	1.7Ti-49.3Al-49Ni	1.2Ti-50.1Al-48.7Ni	—
10	0.6Ti-49.7Al-49.7Ni	0.7Ti-49.4Al-49.9Ni	—
11	2.8Ti-48.6Al-48.7Ni	3.3Ti-48.4Al-48.3Ni	29.2Ti-44.8Al-26Ni
12	5.4Ti-47.3Al-47.3Ni	3.9Ti-47.8Al-48.3Ni	32.7Ti-42.6Al-24.7Ni and 50.2Ti-32.3Al-17.5Ni

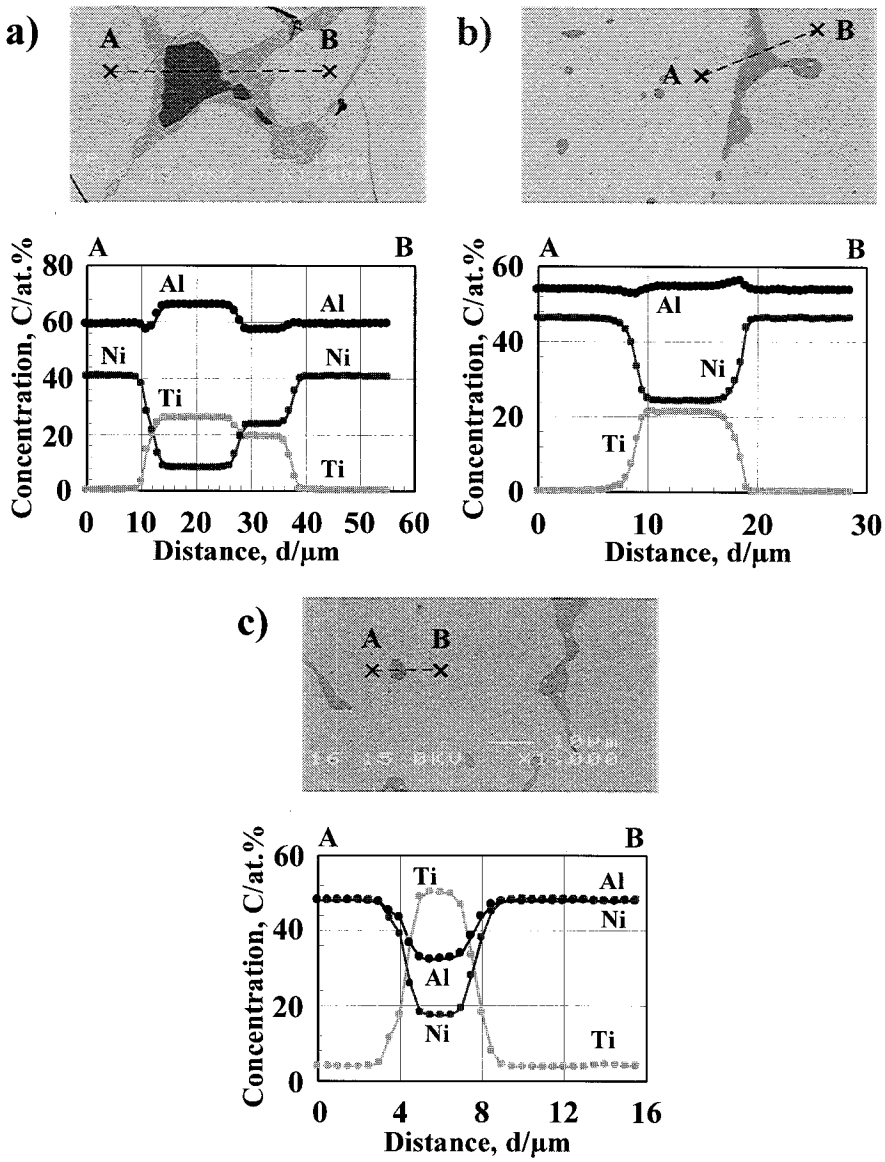


Fig. 5 Microstructures and concentration profiles of Ti, Al, and Ni for Ni-Al-Ti alloys anealed at 1173K.
a) Alloy No.1; b) Alloy No.5; c) Alloy No.12

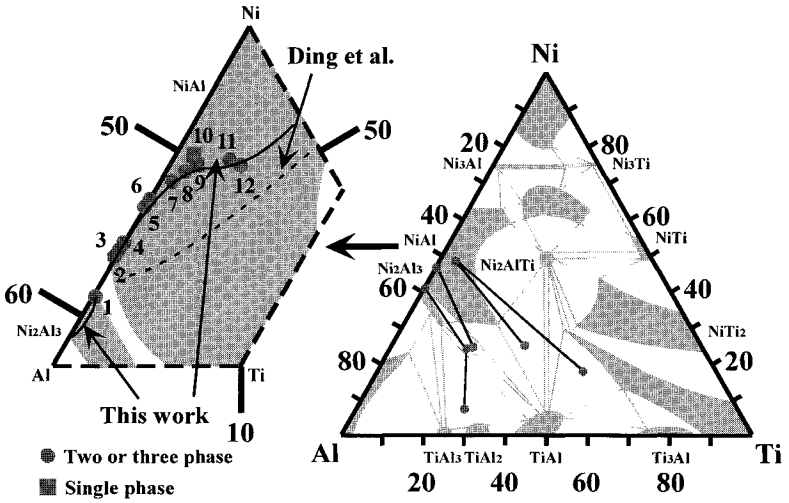


Fig.6 Ti-Al-Ni system phase diagam (isothermal section at 1273K) The 1-12 numbers in the enlarged portion refer to the alloy numbers in Table 1.

4. Discussion

The formation mechanism of the coated layer structure shown in Fig.1 may be explained as follows. At the initial stage of aluminizing the plated Ni reacted with both Al vapor and TiAl substrate, forming the Ni_2Al_3 on the surface side and the Ti-Al-Ni intermetallic compound on the alloy side. With further aluminizing the Ti-Al-Ni intermetallic compound changed to Al_2TiNi and the TiAl changed to $TiAl_2$ and further $TiAl_3$. This layer structure could be formed as Al is the fastest diffusing species among these aluminides. Accordingly, Al diffuses into the inner ($TiAl_3$, $TiAl_2$, and Al_2TiNi) layer through the outer Ni_2Al_3 due to so-called "up-hill diffusion", although it appears that Al activity decreased gradually through the coated layer. The solid line in Fig.7 would give the composition path for the as-coated TiAl.

Diffusion proceeded among the phases during oxidation, resulting in inward Al and Ni diffusion as well as outward Ti diffusion. The broken line in Fig.7 would give the composition path after oxidation for 36h. Both composition paths coincide, because they have essentially the same layer structure, except that the $TiAl_3$ layer with the 36h oxidation is thinner.

After oxidation for 1,000h the coating has a three-layer structure, $TiAl_2$, Al_2TiNi, and an Al-rich β-TiAl, and the dotted line in Fig.7 gives the composition path. It was found that each composition path the inner layer shows higher Al than the outer layer, even after 1,000h oxidation.

It must be emphasized that the Ti content in both the Ni_2Al_3 and the Al-rich β-NiAl are very low, between 0.3 and 0.5at%. This agrees well with the results obtained in the present experiments and also with data in Ding et al. [16]. The low solubility of Ti into the Ni-aluminides contributed significantly to form the protective Al_2O_3 scale.

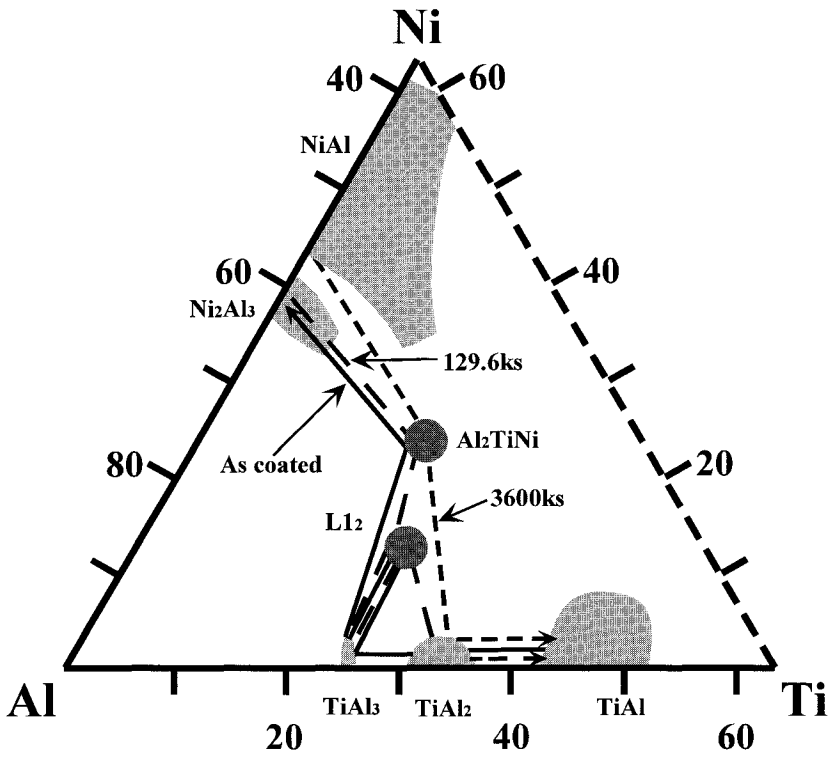


Fig.7 Composition paths on the Ti-Al-Ni system phase diagam (isothermal section at 1173K)

5. Conclusion

A novel coating was developed on a TiAl intermetallic with Ni plating followed by high Al activity diffusion, and the Ni aluminized TiAl was oxidized at 1173K in air for up to 1,000h under a thermal cycling condition. The results may be summarized as follows.

1. About 10μm Ni film was electroplated on TiAl and the Ni-plated TiAl was exposed to high Al activity diffusion at 1273K in vacuum for 5h in a $Al+NH_4Cl+Al_2O_3$ powder mixture. The developed layer consisted of an outer Ni_2Al_3 and an inner Al_2TiNi, $TiAl_3$, $Ti(Al, Ni)_3$ with a $L1_2$ structure and $TiAl_2$ in this sequence.

2. The duplex coated layer with an inner layer containing more Al than the outer layer could be formed due to up-hill diffusion of Al. The whole coated layer was sound with no cracks and the outer Ni_2Al_3 layer contained less than 0.5at% Ti.

3. The coated TiAl oxidized slowly due to formation of a protective α-Al_2O_3 scale with little exfoliation, resulting in an oxidation amount of 8 g/m^2 after oxidation for 1,000h at 1173K under thermal cycling.

4. After oxidation for 1,000h the outer layer changed from Ni_2Al_3 to Al-rich β-NiAl, and both $TiAl_2$ and Al_2TiAl existed in the inner layer, maintaining the Al content higher than in the outer layer.

5. The composition paths were drawn on the Ti-Al-Ni phase diagram for the as-coated alloy and for alloys after oxidation for 36h and 1,000h. The Ti contents in the Al-rich β-NiAl are between 0.3 and 0.5at%, and this coincided with the experimentally determined results that the solubility limits of Ti are between 0.3 and 0.5at%.

6. The novel coating method reported here involved what may be termed as an "up-hill diffusion process".

References

[1] Shida.Y, Anada.H: The effect of various ternary additives on the oxidation behavior of TiAl in high-temperature air, Oxid Met, 45(1996), 197.

[2] McKee.D.W, Huang.S.C: The oxidation behavior of gamma-titanium aluminide alloys under thermal cycling conditions, Corros Sci, 33(1992), 1899.

[3] Suzuki.T, Goto.M, Yoshihara.M, Tanaka.R: Improvement in oxidation resistance of the Ti-31~39mass%Al alloys by heat treatment under a low partial pressure oxygen atmosphere, Mater Trans, JIM, 32(1991), 1017.

[4] Yoshihara.M, Imamura.N, Kobayashi.I, Miura.K, Mishima.Y, Suzuki.T, Tanaka.R: Oxidation resistance and effects of the heat treatment under low partial pressure oxygen atmosphere in intermetallic compound TiAl containing Nb, J Japan Inst Metals, 57(1993), 574.

[5] Kawakami.T, Mabuchi.H, Tsuda.H, Matsui.T, Morii.K: Oxidation resistant coating of $L1_2$-$(Al, Cr)_3Ti$ on the TiAl alloys by pack cementation, Mater Trans, JIM, 40(1999), 381.

[6] Lei.M.K, Zhu.X.P, Han.S.Q, Wang.D.Y, Wang.F.G, Wang.F: Effect of borate coating on oxidation resistance of γ-TiAl intermetallic compound, Materials Chemistry and Physics, 65(2000), 249.

[7] Zhou.C, Xu.H, Gong.S, Yang.Y, Kim.K.Y: A study on aluminide and Cr-modified aluminide coatings on TiAl alloys by pack cementation method, Surface and Coating Technology, 132(2000), 117.

[8] Li.X.Y, Taniguchi.S, Zhu.Y.-C, Fujita.K, Iwamoto.N, Matsunaga.Y, Nakagawa.K: Oxidation behavior of TiAl protected by Al and Nb combined ion implantation at high temperature, Nuclear Instruments and Methods in Physics Research B,187(2002), 207.

[9] Yoshioka.T, Narita.T: Anti-oxidation property and reaction diffusion process of pre-sulfidized TiAl alloy, Zairyo-to-Kankyo, 45(1996), 712.

[10] Narita.T, Izumi.T, Yatagai.M, Yoshioka.T: Sulfidation processing and Cr addition to improve oxidation resistance of TiAl intermetallics in air at 1173K, Intermetallics, 8(2000), 371.

[11] Izumi.T, Yoshioka.T, Hayashi.S, Narita.T: Oxidation behavior of sulfidation processed TiAl-2at%X (X=V, Fe, Co, Cu, Nb, Mo, Ag, and W) alloys at 1173Kin air, Intermetallics, 9(2001), 547.

[12] Nishimoto.T, Izumi.T, Narita.T: Formation of oxidation resistance coating on TiAl alloy by Cr, Al pack cementation method, Report of the 123rd

Committee on the High TemperatureMetals and Alloys. Jpn SocFor Promotion of Science, 42(2001), 327.
[13] Kasahara.K, Takei.A, Yamashita.T: High- temperature oxidation of Ni-Al composite coating formed by a combination of wet and dry processes, Hyomen-Gijutsu, 45(1994), 428.
[14] Katsman.A, Ginzburg.A, Werber.T, Cohen.I, Levin.L: Nickel-aluminide coating of TiAl by a tow-stage process, Surface and Coating Technology, 127(2000), 220.
[15] Villars.P, Prince.A, Okamoto.H: Handbook of ternary alloy phase diagrams. ASM international, (1995), 4195.
[16] Ding.J.J, Rogl.P, Schmidt.H: Phase relation in the Al-rich corner of the Ti-Ni-Al system, Journal of Alloys and Compounds, 317-318(2001), 379.

INFLUENCE OF MICROSTRUCTURAL EVOLUTION ON HARDNESS OF A γTiAl INTERMETALLIC CONTAINING W AND Si

M.A. Muñoz-Morris, I. Gil and D. G. Morris

Department of Physical Metallurgy, CENIM, CSIC, Avenida Gregorio del Amo 8, 28040 Madrid, SPAIN

Abstract

The initial microstructure of a cast and heat treated commercial γ-based TiAl alloy component has been examined within an on-going COST 522 project. The fine lamellar microstructure produced after fairly rapid cooling from high temperatures consists mostly of $\alpha_2+\gamma$ lamellae but transforms surprisingly rapidly (over times of the order of 50-100h) at temperatures between 900-1000ºC into a globular structure composed of a γ matrix and fairly equiaxed particles of B2 phase, occasionally of remnant α_2 phase or of Ti_5Si_3 silicide. It has been confirmed that the driving force leading to microstructural change is the phase change to complete thermodynamic equilibrium (in order to accommodate the chemical species present), from a mixture of mostly $\alpha_2+\gamma$ lamellae, into a mixture of α_2+B2+γ phases, and possibly eventually a B2+γ mixture. One important consequence resulting from the destabilisation of the initial lamellar structure is the decrease in mechanical strength as measured by the evolution of hardness during annealing. During the early stages of globularization of the lamellar structure the material loses a quarter of its initial hardness after 50-100h exposure at 900-1000°C but hardness remains rather constant thereafter. In addition to producing a significant fall in hardness, the break-up of the initial α_2 lamellae into discrete particles will probably be associated with a significant loss of creep resistance and fracture toughness.

Key words: microstructure, intermetallic compound, mechanical properties.

Introduction

Titanium aluminides containing elements that stabilise the B2 phase have been extensively studied in the past years because such additions can also improve the oxidation properties necessary for high temperature applications [1-3]. Microstructural stability studies [4] of one of these alloys have shown that high temperature anneals can substantially modify the distribution of the three phases ($\alpha_2+\gamma$+B2) present without altering the strength of the material. A more recent study of microstructural evolution during annealing of another alloy with composition Ti-46.5Al-2W-0.5Si [5] confirmed that the alloy was rather unstable. In particular the lamellar structure, containing $\alpha_2+\gamma$ lamellae, was shown to destabilise rapidly into a globular structure composed of a γ matrix and fairly equiaxed globules of B2 phase, occasionally of remnant α_2 phase or of Ti_5Si_3 particles. It was also shown that the material strength fell rapidly as the initial lamellar microstructure transformed to the globular one and that the extent of the fall was dependent on the initial volume fraction of B2 phase. The aim of the present study was to analyse the kinetics of softening of as a function of annealing time between 900-1000ºC .

Experimental Procedure

The alloy had a composition Ti-46.5Al-2W-0.5Si (at%), supplied by ALSTOM POWER, CH. The as-received material had been HIP processed at 1260°C and 172 MPa followed by heat treatment at 1350°C/ 1h and furnace cooled to 1000°C and maintained for 6h to stabilise the microstructure. The material here was given a heat treatment at 1390°C for 1h where [4] the microstructure consisted of a mixture of lamellar zones and globular/equiaxed zones with γ, α_2 and B2 phases present. This material was given additional annealing treatments at temperatures between 900-1000ºC for times between 24 and 800 hours to study softening in the different zones (lamellar and globular). For this, the hardness evolution of the samples was measured as a function of exposure time by Vickers microhardness using loads of 300 and 500g. Compression tests were carried out for information on dislocation interactions within the

different types of microstructures. In all cases microstructural studies were carried out by electron microscopy, both SEM and TEM. Samples were prepared by electropolishing [5].

Results

Examples of the initial microstructure, after the heat treatment at 1390°C/ 1h followed by air cool, are shown in Figure 1. In the SEM image we see the mixture of lamellar and equiaxed/globular zones and within these the bright particles which have been identified as the B2 phase [5]. TEM images confirm the continuous nature of the lamellae within the lamellar zones as well as the small particles within the globular ones. The lamellar microstructure destabilizes rather quickly during the lower temperature anneals, in particular at 1000°C where the softening process is also faster. Figures 2 and 3 show examples of the different microstructural zones after annealing for different times. Already after 48h at 1000°C, the α_2 lamellae have decomposed into α_2 and B2 phases [4] while the B2 particles initially present within the equiaxed/ globular zones have coarsened substantially. After 762 h at that temperature the phase transformation of the lamellar zones is practically completed and from then on there is no distinction between the lamellar and globular zones except for the different stage of coarsening of the B2 particles at the expense of the dissolution of the α_2 phase. In Figure 3 we observe similar phase transformation and coarsening after annealing at 900°C but at this lower temperature it was necessary to anneal for 1500h to complete the phase transformation of the lamellar zones. Figure 4 shows examples of the microstructures observed by TEM after annealing 96h at 1000°C and also after deforming annealed samples in compression to 1% strain. We note the presence of two phases (α_2 and B2) in the lamellae[5] and also the accumulation of dislocations at the lamellar interfaces and between the globules.

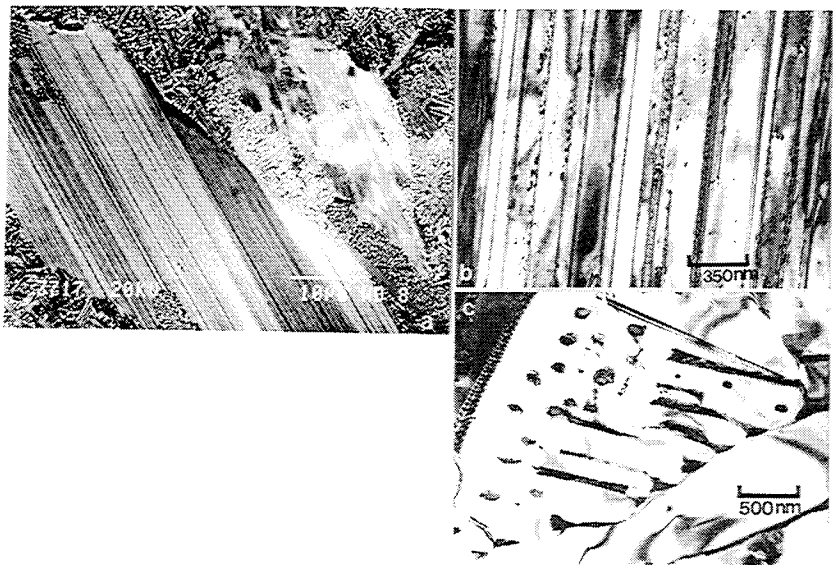


Figure 1. General microstructure observed in the material heat treated at 1390°C/1h and air cool.(a)SEM image using backscattered electrons. b) and c) Detailed TEM images of the lamellar and globular zones.

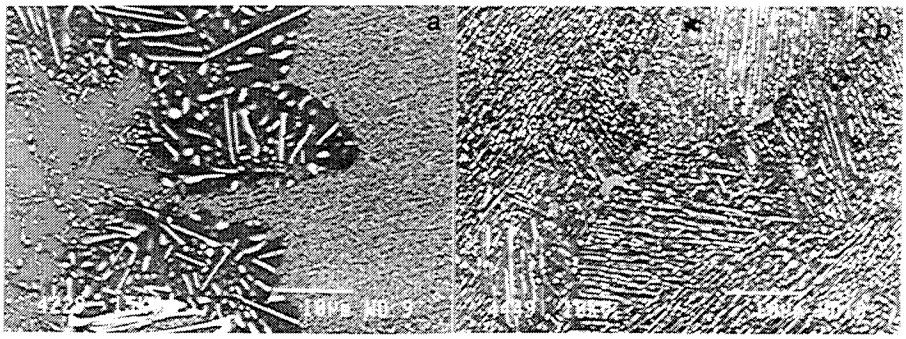


Figure 2. Examples of microstructures observed by atomic number contrast in the SEM after annealing at 1000°C the samples treated at 1390°C/1h. (a) 1000°C/ 48h and (b) 1000°C/ 288 h.

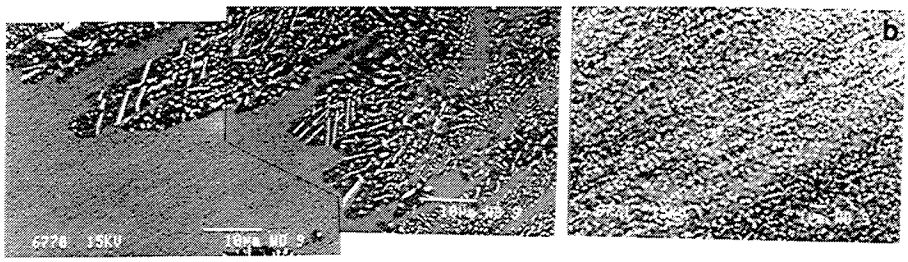


Figure 3. Examples of microstructures observed by atomic number contrast in the SEM after annealing at 900°C the samples treated at 1390°C/1h. (a) 900°C/ 288h and (b) 900°C/ 792 h.

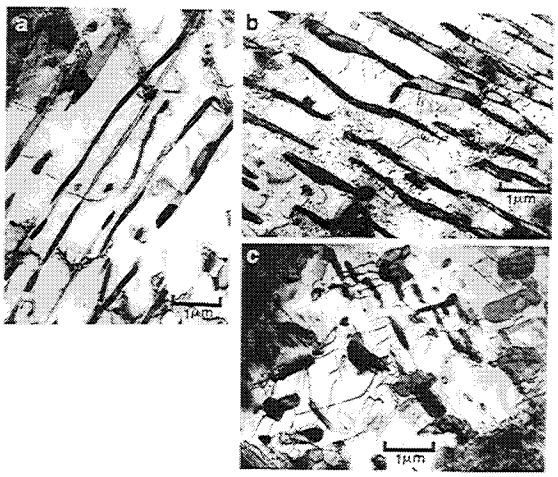


Figure 4. Examples of TEM microstructures from annealed and deformed samples: (a) Lamellar structure after annealing at 1000°C/ 96h (b) Same structure as in (a) after deforming to 1% strain. (c) Globular structure after annealing at 1000°C/ 96 h and deforming to 1% strain.

The hardness fall and coarsening processes in the different lamellar and globular zones are shown in Figure 5. The softening process is much faster in the lamellar zones where the total hardness decrease is also larger. We have analysed the kinetics of softening by considering a time dependent equation of the type $\Delta H_v{}^m = k_0 + Kt$. We have plotted the values of hardness decrease versus annealing time to obtain the value of the exponent **m** providing the best fit.

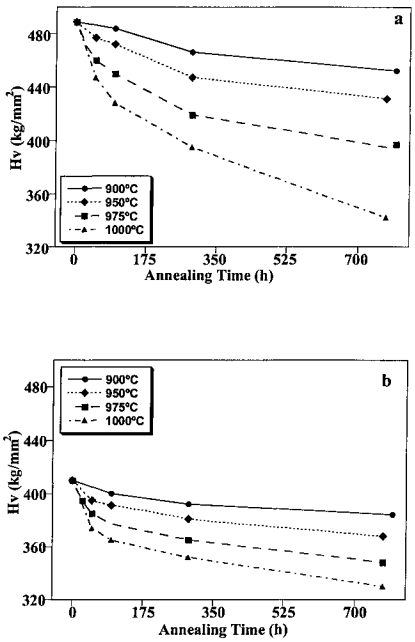


Figure 5. Hardness variation measured from the different microstructures as a function of annealing time. (a) Zones with lamellar microstructure; b) Globular zones.

Figures 6a and 6b illustrate that the best fit corresponds to the value **m=2** for the lamellar zones and **m=3** for the globular ones. The constants from the lines of figure 4 provide the dependence on temperature of the softening process as $\mathbf{K = K_0 \exp(-Q/RT)}$ (Q is the activation energy, R the gas constant and T the temperature). In figure 7 we show the logarithmic plots of K versus 1/T and from the slopes of the lines we have obtained the corresponding activation energies $Q_l = 349 \pm 10$ kJ/mol and $Q_g = 415 \pm 20$ kJ/mol for the lamellar and globular zones.

Discussion

The results obtained from the hardness testing as a function of annealing time at different temperatures confirm that the softening process is related to the microstructural changes occurring in the material. Below we attempt to relate the hardness changes to these microstructural changes and thereby to the controlling diffusional processes.

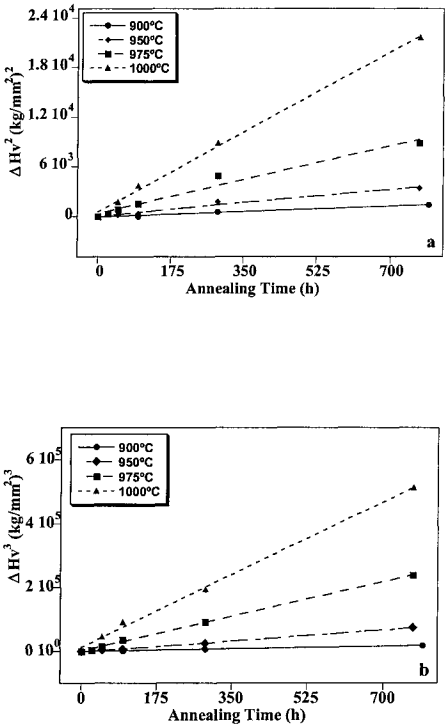


Figure 6. Hardness decrease versus annealing time plotted as a) ΔH_v^2 for the lamellar microstructure and b) ΔH_v^3 for the globular microstructure.

For lamellar regions the important change is from initial lamellar α_2 into connected elongated particles of α_2, γ and B2 phase[5]. Small amounts of silicide are also produced. Initially strong α_2/γ interfaces are replaced by weaker γ/γ ones where the transformation from α_2 phase to elongated γ zones (see figure 4) occurred. This change involves chemical composition changes of all the elements present (the γ phase is rich in aluminium, and the B2 phase rich in W, compared to parent α_2 lamellae) we expect diffusion of the slower diffusing species to control the rate of chemical interchange. This will be diffusion of Al in TiAl and Ti_3Al, rather than Ti diffusion, which is faster [6] although the role of W diffusion in modifying kinetics is not clear.

Since the lamellae of α_2 phase or of elongated α_2 and B2 phases are strong barriers to dislocation motion we can expect their strengthening contribution to be described by a Hall-Petch type relationship [7], and the hardness decrease will be expressed as $\Delta Hv \propto 1/\sqrt{\lambda}$, where λ is the interlamellar spacing. The average interlamellar spacing will increase as the phase change (from α_2 phase to a mixture of α_2+ γ + B2 phases) takes place and the new elongated γ phase regions will appear effectively as a much softer region than the original lamellar zones. We can consider that the nucleation process (of γ or B2 phase) is easy/rapid along the α_2 lamellae or α_2/γ interface and the growth of these effective holes of γ phase in the lamellae will be controlled by the chemical diffusivity of the slow Al species. It is the sum of these various processes that leads to the observed parabolic time dependence of softening , and

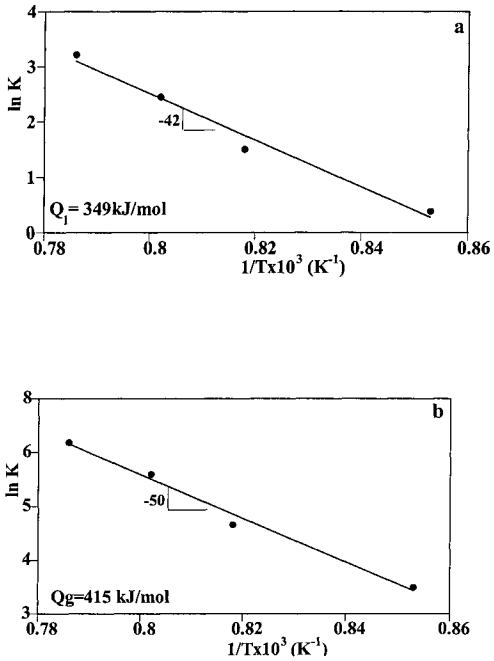


Figure 7. Logarithmic plots of the constants K, obtained from the lines of Fig. 2, versus 1/T. a) Lamellar microstructure zones, b) Globular microstructure zones

the activation energy deduced in Figure 7a, 349± 30 kJ/mol, agrees well with the phase change being controlled by Al diffusion in either TiAl or Ti_3Al [6]. Note also that, as for the globular regions below, we are using Hall-Petch or Orowan strengthening models which relate essentially to yield stress to describe hardness variations. While hardness is more properly correlated with flow stress after a certain amount of work hardening, it is nevertheless common to observe a proportionality between hardness and yield stress variations.

For the globular regions, where the chemical composition is already close to equilibrium at 900-1000°C since they were previously stabilised at this temperature prior to the 1390°C and 900-1000°C treatments [5], the changes occurring can be associated with structural coarsening, rather than composition or phase change. In this case (coarsening/dissolution of globules of α_2 phase by an Ostwald ripening process) the globule size, ϕ, can be expected to increase with a size cubed dependence on time, and the separation L between the globules in the dislocation glide planes, will also increase with a $L^3 \propto t$ dependence in view of the linear dependence of L on ϕ ($L = \phi/\sqrt{f}$, where f is the volume fraction of the globule phase). The hardening contribution of these globule particles can be described by an Orowan dislocation strengthening process, namely $\Delta Hv \propto 1/L$ since dislocations are able to bow through the γ matrix channels between the α_2 or B2 globule particles. As such, the hardness drop in the globular regions will be expected to follow a cube root dependence of annealing time as confirmed in Figure 6b. The activation energy of softening (415± 25 kJ/mol, see Fig. 7b)

should again correspond to that for diffusion of the slowest species (probably Al, or again perhaps W, in TiAl).

Based on these analyses, the time dependencies of the hardness changes in the respective lamellar and globular regions are expected to be different, as observed. For the lamellar region the instability and softening is driven by the change of phase of the material constituting some of the lamellae, namely the α_2 phase regions, and the time dependence is shown to be consistent with a parabolic softening-ageing time dependence. For the globular regions, instability and softening is driven solely by the interface energy of the α_2 /B2 globule-γ matrix interfaces, and a softening cubed ageing time dependence is observed. In both cases we expect a similar diffusion process to control instabilities, namely Al diffusion in TiAl or Ti_3Al. The two activation energies deduced, 349± 30 kJ/mol for the lamellar region and 415± 25 kJ/mol for the globular region are reasonably close to literature values for Al diffusion in TiAl and Ti_3Al (358-394 kJ/mol, ref [6]) and the difference between these experimental values is ascribed to experimental error in their determination.

As a final point, we may note that the two different strengthening mechanisms invoked, namely strong barrier interfaces to dislocation motion and Hall-Petch strengthening for lamellar regions and dislocation bowing between discrete obstacles as Orowan strengthening for the globular regions, are consistent with the observed accumulation of dislocations at lamellar interfaces and bowing between globules in the two regions, Fig. 4.

Conclusions

Microstructural instabilities occurring during high temperature annealing have been examined in a commercial TiAl alloy (ABB) and related to the loss of hardness observed. In the fine lamellar regions, hardness falls according to a parabolic time relation and is dependent on the phase change from the B2 cubic phase to the γ and α phases. In the coarser, globular regions, hardness falls according to a time-cubed dependence and is determined by coarsening processes.

Acknowledgements

We should like to thank especially our colleagues at ALSTOM POWER, CH for the supply of the material. This work was funded by a MCYT-FEDER under project MAT2FD1997-1398

References

[1] Nobuki M., Vanderschueren D., and Nakamura M. (1994), Acta Metall. Mater., 42, 2623.
[2] Baker I., (1995), Mater. Sci. Eng., A192/193, 1.
[3] Li Y.G., Loretto M.H, (1992), .Acta Metall. Mater., 40, 1121.
[4] Morris M. A., Li Y.G and Leboeuf M., (1994), Scripta Metall. Mater., 31, 449.
[5] Gil I., Muñoz-Morris, M. A., Morris D., (2001) Intermetallics, 9, 373.
[6] Mishin Y. and Herzig Ch., (2000) Acta Materialia, 48, 589.
[7] Chan K. S., (1995) in Gamma Titanium Aluminides, ed. Y.W-Kim, R. Wagner and M. Yamaguchi, Pennsylvania ,USA, 835.

STRENGTHENING MECHANISMS IN DUCTILE FeAl INTERMETALLIC PROCESSED BY MECHANICAL ALLOYING

D.G. Morris, C. Garcia Oca and M.A. Muñoz-Morris

Department of Physical Metallurgy, CENIM, CSIC, Avenida Gregorio del Amo 8, 28040 Madrid, SPAIN

Abstract

An iron aluminide alloy of base composition Fe-40Al has been prepared by mechanical alloying and processed using a variety of powder consolidation methods within an on-going European project. Variations of processing conditions and subsequent heat treatments lead to a range of grain sizes and oxide dispersoid sizes. Material strengths have been determined and related to the microstructure. It is the fine dispersoid particles that are mostly responsible for determining the grain size by pinning grain boundaries, and contribute most to material strength. Grain size strengthening is a rather small component of the material strength, with the matrix strength being rather high. Other contributions to strength, for example due to textural changes, are also discussed. In addition to good strength, such materials can show good tensile ductility with ductility being insensitive to the testing environment and to the state of the component surface before testing. Such behaviour may be correlated with the difficulty of crack nucleation in these fine-grained materials and the subsequent slow crack propagation.

Keywords: Intermetallic compounds; Mechanical properties; Dislocations; Annealing

Introduction

Iron aluminides of composition around Fe-40Al (atomic percentage) remain of interest as structural materials because of their reasonable strength combined with good ductility and excellent oxidation and corrosion resistance in some industrial environments [1-5]. Considerable effort has been devoted to improving mechanical properties by developing a mechanically-alloyed version of this intermetallic to make use of strengthening by fine grain size and by the introduction of oxide particles [6-8]. These materials also have small amounts of elements (e.g. B, C, Zr) to strengthen grain boundaries and improve ductility [6-8].

Recent work has developed such materials from the stage of laboratory curiosities to engineering materials by attempting industrial-scale processing, so it is important to understand the microstructural aspects that lead to good strength and ductility. Earlier studies have analysed strengthening [9-12] and ductility [13]: grain size strengthening was interpreted from literature data to have a strong Hall-Petch effect [2,6,14-16], a similar strengthening contribution due to fine oxide particles and an equal contribution from the matrix. Texture played some role in modifying matrix strength [10,11], and vacancies or other solute also playing some role [10,11,17].

The present study re-examines strengthening in mechanically alloyed FeAl with more materials and microstructural variants available. A re-analysis of strengthening is also justified since recent studies have shown that fine grain sized materials may not suffer vacancy hardening since the many interfaces are sinks for easy elimination of vacancies [17,18]. Such vacancy hardening contributes significantly to the hardness unless the vacancies are carefully annealed out [19]. The analysis of strengthening mechanisms can also be compared with recent studies of oxide dispersion strengthened iron, where the relative roles of matrix, dispersion, and grain size strengthening have been established, and notably very strong grain size strengthening is deduced [20].

Experimental Details

Materials were supplied by CEREM, CEA (Centre de Recherche en Materiaux, Atomic Research Centre) of Grenoble, France, as part of a European Research Network (CEASI), or by PLANSEE AG of Germany, as part of a European Research Project (FIAC). Samples have been designated as CH and F samples for the initial ones, and D samples for the later ones. Materials were prepared by milling pre-alloyed powders of composition Fe-40Al-0.05Zr-50ppmB with 1 vol.% of Y_2O_3, and consolidated to bar or plate by extrusion, forging or rolling at 1100°C. Preparation conditions ensured excellent powder particle adhesion with full density, and no inter-powder particle decohesion during mechanical testing. Materials were prepared in large dimensions: for example, as bars/plates of diameter/thickness of the order of 30mm and a metre in length, such that the final natural cooling stage after processing was very slow. Some materials were given thermal or thermo-mechanical treatments, and others aged at low temperatures to ensure removal of excess vacancies. D materials were not heat treated after processing, because natural cooling after fabrication was slow and because excess vacancies are now known to be easily lost from fine grained materials [18]. Table 1 lists the various materials and treatments.

Tension and compression samples were tested along the axial direction of the extruded bars and along the compression direction of forged/rolled plates. These tests were carried out in air at a strain rate of about 3-5 x 10^{-4}/s. Vickers hardness testing was also carried out.

Microstructures were determined by Scanning Electron Microscopy (SEM) using a JEOL 840 microscope using back-scattered electrons to determine grain size and coarse yttria particle sizes and distributions, and by Transmission Electron Microscopy (TEM) using a JEOL 2010FX microscope at 200kV on electropolished foils to determine fine yttria particle size and distribution as well as to examine dislocations. Grain and particle sizes and average sizes were determined from SEM and TEM micrographs using standard quantitative methods.

Results

Initial Microstructures

Samples were studied by SEM and by TEM to determine grain size and shape and the distribution and sizes of Y_2O_3 particles. It was confirmed by EDS that the majority of particles were Y_2O_3 with only a small amount of Al_2O_3. Fig. 1 shows typical grain sizes, and also that some Y_2O_3 remains as coarse particles. The extruded materials contained elongated grains of about 2:1 aspect ratio, while the forged/rolled materials had flattened disk grains of aspect ratio about 1:2. Average grain size was determined as the mean of the maximum and minimum values. The volume fraction of coarse Y_2O_3 phase visible by SEM was about 0.33%, and hence the amount of unresolvable Y_2O_3 phase, present as particles smaller than 100-200nm, is about 0.66% (the total volume fraction of Y_2O_3 phase was 1%). This determination of coarse Y_2O_3 particles was made on electro-polished samples at low accelerating voltage in the SEM to avoid detecting subsurface Y_2O_3 particles.

Grain and particle sizes and distributions were determined by TEM, Figs. 2 and 3. Fig. 2 shows material after tensile deformation which therefore has many dislocations. The Y_2O_3 particles are uniformly distributed with sizes from a few nm to 100nm with a grain size of about 1μm. Fig. 3 shows the uniform distribution of 20-30nm Y_2O_3 particles in material D1 where a few larger particles (50-100nm) are also seen. Fig. 4 illustrates typical size distributions of particles and grains. An average particle size of about 20nm is seen in Fig. 4a, and an average grain size of about 2μm in Fig. 4b. These particle sizes are averages from TEM micrographs of the 0.66% fraction of Y_2O_3 phase important for strengthening, taking no account of the small fraction of coarse particles.

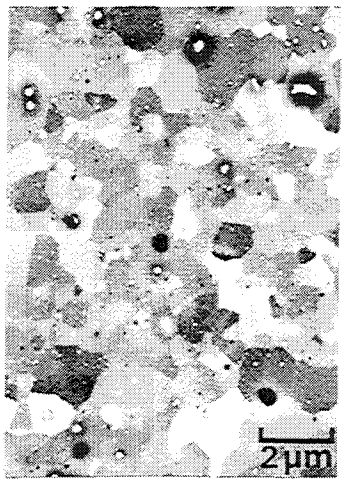


Figure 1: SEM micrograph illustrating grain size and particles in material F1. Transverse section.



Figure 2: TEM micrograph showing grain size and Y_2O_3 particles in material F1. S Sample previously strained 2%.

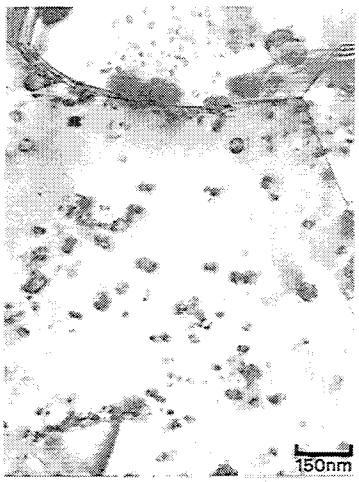


Figure 3: TEM micrograph showing Y_2O_3 particles inside a grain and at the grain boundaries in material D1.

Table 2 shows grain and fine particle sizes. In as-fabricated material, particle sizes were 10-30nm and grain sizes 1-2µm, while heat treatments coarsened particles to 50-150nm and grains to 50-350µm. Changes of particle and grain size have been examined [10], and secondary recrystallization seen on annealing at 1300°C, as particles coarsen and liberate grain boundaries (materials CH3 and F3). Prior deformation allows grain boundaries to break

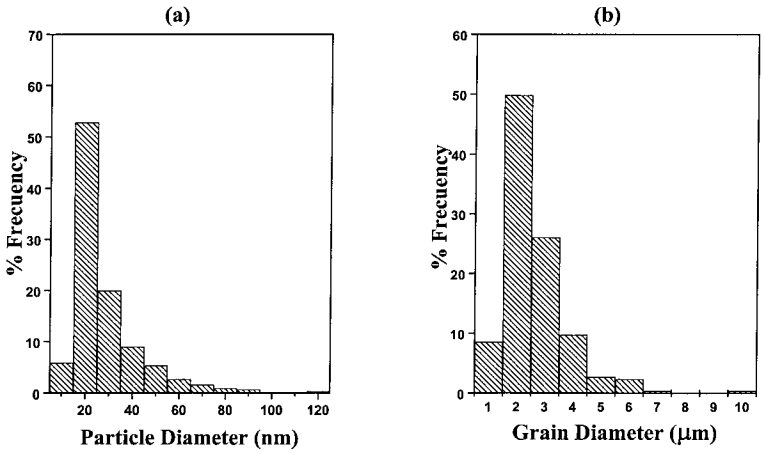


Figure 4: Histograms of particles size in (a) material D1 measured from TEM micrographs, showing average particle size of about 20nm, and (b) of grain size in material D2 measured from SEM micrographs.

away at lower temperatures before particle coarsening (material CH4). Texture changes during annealing [10], and the as-extruded moderate <110> fibre texture changes to a weak <111> texture on annealing, remaining a mostly <110> fibre texture and weak <111> texture component after the strain-anneal treatment.

Mechanical testing results

Compression testing was carried out to a strain of 8-10% and tension testing to failure. Tensile ductility varied from 2% to 10% according to material and surface preparation [13]. Hardness, yield stress and flow stress at 8% plastic strain are given in Table 2.

Studies of dislocation arrangements

At both low and high strains dislocations were homogeneously and uniformly distributed across the grains. Bowed dislocations were seen attempting to pass around Y_2O_3 particles situated close to grain boundaries. Weak beam images showed that the dislocations were two-partial, dissociated superdislocations, and Burgers vector analysis confirmed that the total Burgers vector was of the type <111>.

Discussion

Fig. 5 shows a graph of the grain sizes compared to the oxide particle sizes. The line drawn is that corresponding to the Zener relation considering that the stable grain size is determined by particles pinning grain boundaries. Apart from the three recrystallized materials, all materials have grain sizes that correspond approximately to that given by the Zener relationship. The data is consistent with the grain boundaries produced during/after consolidation being pinned when the grain size approaches the Zener value. While the observed grain sizes correspond approximately to that of the Zener relationship, the agreement is not exact and the range of experimental grain and particle sizes is too small to draw a definitive conclusion. Some of the materials, with rather small grain sizes for their particle sizes, may not yet have attained the stable Zener grain size after primary recrystallization, and other materials, with rather large

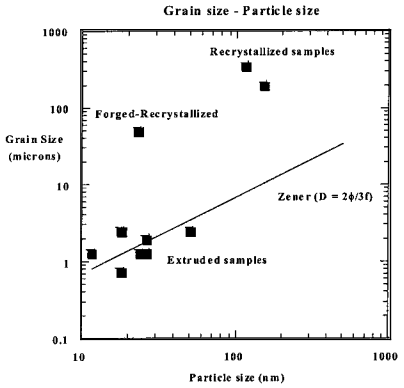


Figure 5: Correlation of grain size with particle size in as-fabricated and annealed materials. The shows grain size based on particle pinning of boundaries (Zener relationship).

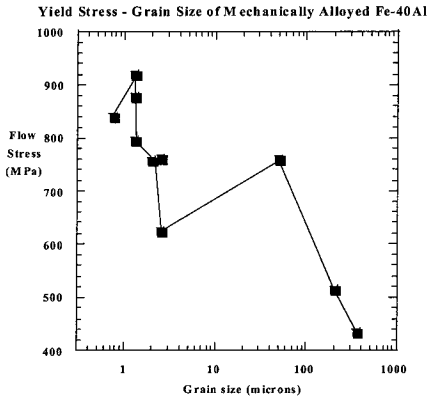


Figure 6: Variation of yield stress (flow stress at 0.2% plastic strain) with grain size.

grain sizes for their particle sizes, may already have some boundaries breaking away from the pinning particles. On higher temperature annealing, or annealing after prior straining, oxide particles coarsen but there is also a break away of grain boundaries from their pinning points and secondary recrystallization occurs, such that the final grain size is far from that of the Zener relationship.

The evolution of particle size with temperature has been compared with the coarsening of similar yttria particles in mechanically-alloyed commercial Fe-Cr base alloy, PM2010 [21]. For Fe-Cr base alloys, rapid coarsening is avoided even above 1300°C. In FeAl, rapid coarsening of particles is observed at 1300°C, previously associated with a reaction between Y_2O_3 and FeAl leading to the formation of complex Y-Al-Fe spinel oxides [9].

The yield stress is shown in Fig. 6 in terms of the grain size. Parameters other than grain size play a significant role in determining the yield stress. The relationship between hardness and flow stress, Table 2, is not the generally expected relationship of hardness being 3 times flow stress, but rather the hardness is typically about 5 times yield stress. An attempt was made to relate the hardness to the flow stress at 8% strain, which corresponds to the strain below the diamond indenter [22], but again no simple proportionality was observed.

The flow stress increase due to uncuttable particles can be estimated using the Orowan-Ashby [23] equation:

$$\sigma_{OR} = \frac{m * 2 * \mu * b}{(1.18) * 4 * \pi * (\lambda - \phi)} * \ln(\frac{\phi}{2b}) \qquad \text{(i)}$$

(m - Taylor factor, 2.5 for the bcc structure, μ - shear modulus, b - Burgers vector, λ - interparticle spacing, and ϕ - particle size). Values of elastic moduli for Fe-Al alloys are known [24] for the highly elastically anisotropic FeAl intermetallic. For this reason energy factors K have been calculated [25] and used instead of μ and values of the order of 65GPa to 85GPa determined for near-edge and near-screw dislocations. The Burgers vector is taken as 5.02×10^{-10}m, from the lattice parameter of FeAl [26] since the total Burgers vector of the

superdislocations is a<111>. The use of the total Burgers vector instead of that of the individual partials is justified since the separation of the partials, 10nm, is smaller than the particle diameters and spacings and hence the superdislocation can be considered to interact with the particles as a single elastic line. The interparticle spacing λ on the slip plane is calculated from the number of particles, N_S, as $\lambda = 1/\sqrt{N_S}$, where $N_S = N_V.\phi$, and the number of particles per volume N_V is determined from the volume fraction of oxide phase as small particles, f_V, and the particle size as $f_V = (4/3)\pi(\phi^3/8).N_V$.

Fig. 7 shows experimental flow stresses after subtracting values of Orowan stress, ($\sigma_{0.2}$-σ_{OR}), as a function of the reciprocal square root of grain size. The Orowan stress has been calculated for K values of 65-85 GPa, corresponding to the stress to move edge and screw dislocations. Fig. 7 shows reasonable fit to the data for K = 85 GPa, i.e. the stress required for both edge and screw dislocations to move. For K = 85 GPa:

$$\sigma_{0.2} = 420\text{MPa} + \frac{115MPa}{\sqrt{D(\mu m)}} + \sigma_{OR} \qquad \text{(ii)}$$

The remaining data scatter in Fig. 7 can be analysed in several ways. It can be argued that texture plays only a small part in affecting strength. All materials had a moderate <110> fibre texture, with the exception of two samples recrystallized to very large grain size ($1/\sqrt{D} \approx 0.05$ - Fig. 7). One sample was much weaker than the corresponding Hall-Petch line, while the other lay exactly on the line, suggesting that texture plays little role in determining strength. No more precise analysis is possible with the limited texture data available here.

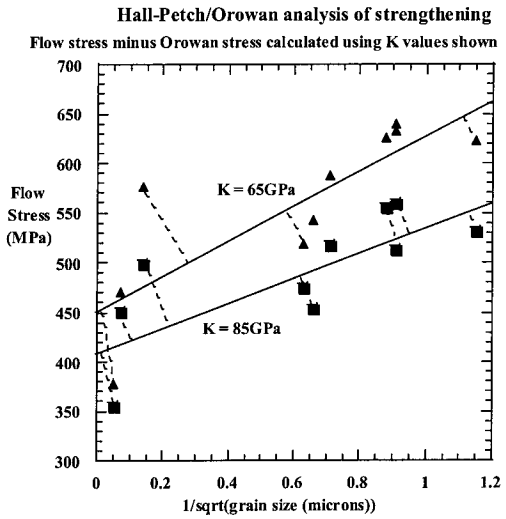


Figure 7: Hall-Petch representation of flow stress after removing Orowan strengthening ($\sigma_{0.2}$-σ_{OR}). Orowan strengthening has been calculated using values of the energy factor K of 65GPa-85GPa. Triangles represent data (i.e. $\sigma_{0.2}$-σ_{OR}) with Orowan strengthening calculated using a K = 65GPa, and the squares equivalent data calculated with K = 85GPa. Data points lying far off the best-fit line are connected to this by dashed lines.

A second way of examining data is to separate compression data and tension data. The data points close to the best-fit line in Fig. 7 are consistently compression data, and the few points significantly below the line are tensile data. A much better fit to the data can be obtained by considering only compression data. Now:

$$\sigma_{0.2} = 460\text{MPa} + \frac{70MPa}{\sqrt{D(\mu m)}} + \sigma_{OR} \qquad \text{(iii)}$$

The processes used to consolidate powders (extrusion, rolling, forging) all involve compression loading and the materials may show a compression-tension asymmetry. The effect is similar to the Bauschinger effect, where re-testing in one sense after first deforming in the opposite sense leads to lower initial flow stress. It is perhaps for this reason that it is not possible to include tension and compression data on the one plot.

From the analysis, the relative contributions of various strengthening mechanisms to strength can be described:

(i) The matrix strength is about 460MPa. This corresponds roughly to literature values [9].

(ii) Grain size strengthening, through the Hall-Petch relationship $\sigma_{0.2} = \sigma_0 + k_{HP}.D^{-0.5}$, contributes only 5-80MPa, because of the low value of k_{HP} ($70\text{MPa}\mu\text{m}^{0.5}$). In an earlier analysis [9] a high value of k_{HP} ($260\text{MPa}\mu\text{m}^{0.5}$) was deduced from literature data, which show very wide scatter. Most of the literature data [2,6,8,9,14] fit a Hall-Petch line with a matrix strength of 400 MPa and a slope of 260 $\text{MPa}\mu\text{m}^{0.5}$, while purer binary alloys [15,16] fit a Hall-Petch line of slope 700 $\text{MPa}\mu\text{m}^{0.5}$ and matrix strength of 200 MPa. A high value of Hall-Petch slope ($500\text{MPa}\mu\text{m}^{0.5}$) was also suggested in a recent analysis of mechanically alloyed iron [20]. The present deduction of a limited strengthening by grain boundaries appears consistent with the uniform distribution of dislocations after straining, suggesting that particles serve as efficient obstacles to dislocations with grain boundaries being much weaker obstacles. There appears, thus, to be a loose association of low Hall-Petch slope and high matrix strength by particle strengthening. A possible explanation of low Hall-Petch slope is shielding of grain boundaries by the particles, such that strengthening by the boundary is weakened. A second possibility may be a texure effect - generally a moderate <110> fibre texture here. The presence of this texture may imply that average boundary misorientations are lower than for randomly oriented grains, and hence dislocations can readily pass through.

(iii) Orowan strengthening contributes about 40-400MPa to strengthening for the present materials.

(iv) There is no evidence of excess vacancy hardening in the materials. As shown elsewhere [18], the many grain boundaries and finely distributed particles ensure that there are many sinks for vacancy annihilation.

(v) There is little evidence of any influence of texture on the strength of materials here, apart from the possible role in modifying the strength of grain boundaries and the Hall-Petch slope, as discussed above in (ii).

Finally, it of interest to compare the matrix strength here (460MPa) with the literature, which suggests a matrix strength of 400MPa [2,6,8,9,15], but binary alloys showing matrix strength near 200MPa [15,16]. B and/or Zr in solution may be responsible for this high strength. B is known to produce strong hardening [4,27-29] and increase Hall-Petch slope [30].

Conclusions

Strengthening mechanisms in mechanically alloyed Fe-40Al have been examined. Milling has not refined all the dispersoids to a very fine level and about 1/3 of the oxide phase present is

retained as coarse particles. Y_2O_3 particles in FeAl show lower high temperatures stability than the same particles in FeCr alloys. Fine particles are major obstacles to grain boundary movement and define the grain size after processing. The hardness-flow stress relation is complex and does not respect the usual proportionality relationship. Particles provide an important part of the strength, much more than grain boundaries. Finely distributed particles are major obstacles and act to shield boundaries. Processing methods (extrusion, forging, rolling) use compressive forces. Tensile testing leads to a lower yield stress than compression testing, a phenomenon which appears similar to the Bauschinger effect.

Acknowledgements

We should like to thank CEREM, CEA, Grenoble and PLANSEE for material supply. The work was funded under a European GROWTH project, FIAC, contract number G5RD-CT-99-00070. We should also like to thank the Spanish Ministry of Science and Technology for complementary support under MAT2000-1885-CE.

Table 1

Materials examined, preparation methods, and additional heat treatments given

Material Code	Fabrication Method	Additional Heat Treatment
CH1	Extrusion	1day 500C, 1week 400°C
CH2	Extrusion	24h 1100°C, 1day 500C, 1week 400°C
CH3	Extrusion	1h 1300°C, 1day 500C, 1week 400°C
CH4	Extrusion	Compressed 10%, 1h 1100°C, 1day 500C, 1week 400°C
F1	Extrusion	As supplied (extruded 1100°C then slow cool)
F2	Extrusion	3h 1100°C, furnace cool to 900°C, air cooled
F3	Extrusion	1h 1300°C, furnace cool to 475°C, 1week 475°C
D1	Extrusion	1h 1000°C then slow cool
D2	Rolling	As supplied (rolled 1100°C then slow cooled)
D3	Forging	As supplied (forged 1100°C then slow cooled)

Table 2

Microstructural parameters and mechanical properties

Material Code Name	Grain size (D) (μm)	Particle size (ϕ) (nm)	Hardness Hv (MPa)	Yield stress ($\sigma_{0.2}$) (MPa)	Flow stress (σ_8) (MPa)
CH1	0.75	18	3950	840	-
CH2	2.5	50	-	625	-
CH3	200	150	3290	515	-
CH4	50	23	3320	760	-
F1	1.3	11.5	3640	920	1425
F2	1.3	26.1	3480	795	1350
F3	356	113	3100	435	1065
D1	1.3	23.7	3380	823	1340
D2	2.0	25.9	3620	758	1360
D3	2.5	17.9	3280	761	1100

References

1: McKamey, C.G., DeVan, J.H., Tortorelli, P.F. and Sikka, V.K., J. Mater. Res., 1991, 6, 1779.
2: Gaydosh, D.J., Draper, S.L., Noebe, R.D. and Nathal, M.V., Mater. Sci. and Eng., 1992, A150, 7.
3: Stoloff, N.S. and Liu, C.T., Intermetallics, 1994, 2, 75.
4: Baker, I. and Munroe, P.R., Int. Mater. Rev., 1997, 42, 181.
5: Morris, D.G. and Morris-Muñoz, M.A., Intermetallics, 1999, 7, 1121.
6: Tassa, O., Testani, C., Bocher, P. and Lefort, A., Proc. Materials Development in Rail, Tire, Wing, Hull Transportation, Genoa, 22-24 September, 1992, Elsevier Applied Science, London, 1992, p2.101.
7: Lefort, A., Webb, G., Wolski, K., Lecoze, J., Thevenot, F., Franzoni, U. and Tassa, O., in A. Niku-Lari (ed.), Proc. MATTEC-92, Grenoble, 14-16 October 1992, IITT-International, Paris, 1992, p. 327.
8: Baccino, R., San Filippo, D., Moret, F., Lefort, A. and Webb, G., Proc PM'94, Powder Metallurgy World Congress, Paris, June 1994, Vol. II, Editions de Physique, Les Ulis, 1994, p. 1239.
9: Morris, D.G. and Gunther, S., Mater. Sci. and Eng., 1996, A208, 7.
10: Morris, D.G., Gunther, S. and Briguet, C., Scripta Mater., 1997, 37, 71.
11: Briguet, C. and Morris, D.G., Acta Mater. 1997, 45, 4939.
12: Briguet, C. and Morris, D.G., Acta Mater. 1998, 46, 5053.
13: Chao, J., Morris, D.G., Muñoz-Morris, M.A. and Gonzalez-Carrasco, J.L., Intermetallics, 2001, 9, 299.
14: Gaydosh, D.J., Draper, S.L. and Nathal, M.V., Metall. Trans. 1989, A20, 1701.
15: Xiao, H. and Baker, I., Scipta Metall. Mater. 1993, 28, 1411.
16: Baker, I., Nagpal, P., Liu, F. and Munroe, P.R., Acta Metall. Mater. 1991, 39, 1637.
17: Garcia Oca, C., Morris, D.G. and Muñoz-Morris, M.A., Scripta Mater. 2001, 44, 561.
18: Montealegre, M.A., Muñoz-Morris, M.A., Gonzalez-Carrasco, J.L. and Morris, D.G., Scripta Mater. 2001, 44, 2673.
19 Nagpal, P. and Baker, I., Metal.. Trans., 1990, 21A, 2281.
20: Badmos, A.Y., Bhadeshia, H.K.D.H. and MacKay, D.J.C., Mater. Sci. and Tech. 1998, 14, 793.
21: Krautwasser, P., Czyrska-Filemonowicz, A., Widera, M. and Carsughi, F., Mat. Sci. and Eng., 1994, A177, 199.
22: Cottrell, A.H., The mechanical properties of matter, Wiley series on the science and technology of materials, New York, 1963.
23: Ashby, M.F., in A. Kelly and R.B. Nicholson (eds.), Strengthening Methods in Crystals, Elsevier, New York, 1971, p. 165.
24: Leamy, H.J., Gibson, E.D. and Kayser, F.X., Acta Metall., 1967, 15, 1827.
25: Hirth, J.P. and Lothe, J., Theory of Dislocations, McGraw Hill, New York, 1968.
26: Okamoto, H. and Beck, P.A., Metall. Trans., 1971, 2, 569.
27: Baker, I., Klein, O., Nelson, C. and George, E.P., Scripta Metall. Mater., 1994, 30, 863.
28: Baker, I., Li, X., Xiao, H., Carleton, R. and George, E.P., Intermetallics, 1998, 6, 177.
29: Calonne, O., Fraczkiewicz, A., and Louchet, F., Scripta Mater., 2000, 43, 69.
30: Li, X. and Baker, I., Scripta Mater., 1996, 34, 1219.

SECTION 1

ADVANCED GAS TURBINE MATERIALS

1.5. Miscellaneous Topics

EXTRAPOLATION OF LIMITED CREEP DATA BY PARALLEL FITTING WITH DATA FOR SIMILAR MATERIALS

P S White
ALSTOM POWER, Cambridge Rd, Whetstone, Leicester, LE8 6LH, England

Abstract

Extrapolation of creep properties is discussed with special reference to the inclusion of transitions between regions of different dependence. A methodology is described in which expressions allowing for two distinct regions are treated in terms of assumed parallel behaviour for all batches within groups of essentially similar materials. This allows low-stress trends seen for relatively weak materials at practical test times to be combined with high stress data available for strong materials at comparable or shorter times. A practically motivated example is given for NIM115 data extrapolated by data for similar materials including the much weaker NIM90.

Keywords: Creep, Extrapolation, Superalloys

Introduction

For a few materials truly long-term creep data are available and little if any extrapolation is needed, even for service-periods of twenty or more years, so that numerous fitting methods are likely to be reasonable. However for many other materials the only available information is for time-scales of a tenth or less of intended component lives. This is necessarily true for *recently* introduced highly creep-resistant materials for extended service. But it is equally so for many 'old' materials of which, for example, the creep properties had not originally seemed important but later become of concern owing to raised operating temperatures. In such cases reliable means of extrapolation in terms of stress σ and temperature T are needed but, despite a long history of research, not much is universally agreed.

Most of the available methods rely *only* upon the evaluation, at the relatively low stress-temperature combinations of interest, of expressions giving - for a particular material - a reasonable fit to available short-term data. However it is argued here that such methods are inherently incapable of accounting reliably for any *transitions* of behaviour that arise beyond (or are poorly represented within) the data-range. Such transitions, which often occur, can only be dealt with through *guidance* of the extrapolation by inclusion of *further* knowledge. In particular it is suggested that a principle of *parallel* fitting and extrapolation may often be adopted systematically within certain groups of 'essentially similar' materials. That is, for which the same functional dependence upon stress and temperature occurs but which differ in pre-multiplying coefficients expressing differences of strength in terms of characteristic time-scales. Thus 'weak' members may be tested over *moderate* time-scales at relatively *low* stress-temperature levels and their behaviour may be used for a *guided* 'parallel extrapolation', down to these levels, of shorter-term information for 'strong' members. This method is outlined in general terms and is then applied to the secondary creep rates required for relaxation predictions in NIM115, a material proposed for a certain long-term application but for which only short-term data are currently available to the Company.

Traditional approaches

The Larson-Miller method [1] of 1952 remains widely used for rupture time t_r, has often been extended to secondary (minimum) creep rate $(d\varepsilon^c/dt)_s$ etc, and appears still to be regarded as

wholly satisfactory by some [2]. On the other hand, criticisms of its real ability to extrapolate have been made from the early days, as by Betteridge [3]. He found unconservative predictions with respect to rupture times of materials NIM80A and NIM90, with similar conclusions for the Orr, Sherby and Dorn parameter, but better predictions for that of Manson and Haferd. In particular the standard assumption 'C=20' of the Larson-Miller method gave poor results and Betteridge recommended case-by-case re-estimation of any such coefficient. Since the original proposal of [1], a variety of more complex 'time-temperature parameters' have been suggested, usually in the form

$$\mathbf{P}(\sigma) = \alpha(\mathbf{T})\,[(log(\mathbf{t}_r) - \beta(\mathbf{T})] \qquad \text{ie} \qquad log(\mathbf{t}_r) = \beta(\mathbf{T}) + \mathbf{P}(\sigma) / \alpha(\mathbf{T}) \qquad (1)$$

(with similar forms for $(d\varepsilon^c/dt)_s$ etc) and a voluminous literature has developed, of which [4, ch6] gives a useful summary. Dissatisfaction with these parameters, or various alternative ideas - an early example being that of Graham and Walles [5], have prompted generalisations:

$$log(\mathbf{t}_r) = \phi(\sigma,\mathbf{T}) \qquad , \qquad log((d\varepsilon^c/dt)_s) = \psi(\sigma,\mathbf{T}) \qquad (2)$$

in which the functions ϕ and ψ *cannot* be reduced to the form of (1) and are more capable of representing significantly different trends in different parts of the σ-**T** plane. The same aim remains, of directly extrapolating short-term data for a given material to longer times, but - as demonstrated in [3] for the method of [5] - more complex functions by themselves do not necessarily improve extrapolation.

The supposition of *all* such methods is that a correlation function found to hold for a given material in a *part* of the σ-**T** plane - in particular corresponding to conveniently *short* creep tests - may be expected *also* to hold (adequately well) when applied elsewhere - usually to *long*-time service conditions. This might well be so in *particular* circumstances but there are reasons to assert that it will not hold in general.

Thus, it is implicit in the idea of 'deformation/damage maps' (see [6]) that *different* micro-mechanisms are expected to dominate in *different* parts of the σ-**T** plane. In particular, as emphasised in [7], long time-scales are likely to activate metallurgical instabilities not seen for shorter times (at relevant temperatures). Even *without* specific mechanistic explanations, transitions either gradual or sharp in the form of dependence are often *empirically* evident, as exemplified by the data [8] plotted in fig 1a using a logarithmic representation of stress. The essential difficulty is that little or no evidence of a significant transition might be contained within the range of *available* data - in which case how may a fitting method be expected to see round an invisible or indistinctly viewed corner?

It is true that *different* forms of transition, or none at all, might be exhibited in *other* representations (linear etc) of stress. Other things being equal, it is legitimate to extrapolate in a representation for which any apparent changes of trend are relatively *simple* - but *only* if the predicted limiting behaviour for small or large stress is physically reasonable. For example, fig 1b replots the data of fig 1a but using a linear stress scale. The data points *might* then be regarded as simply forming straight lines - but such a fitting predicts unacceptable non-zero rates at zero stress.

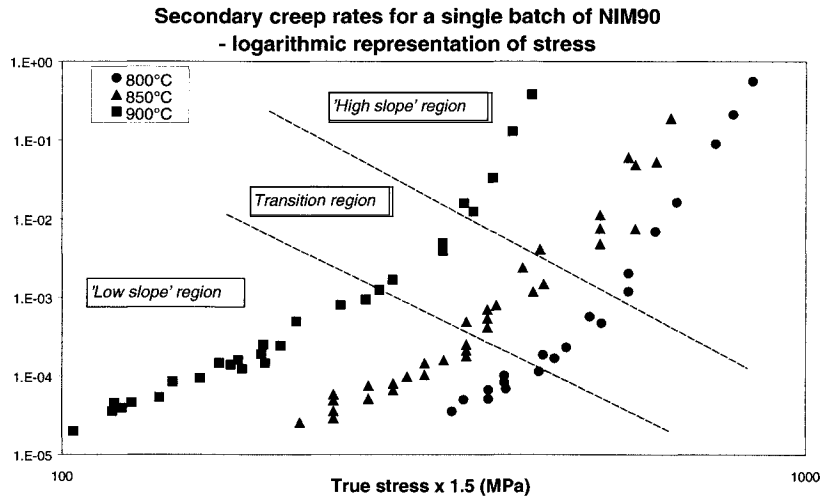


Fig 1a

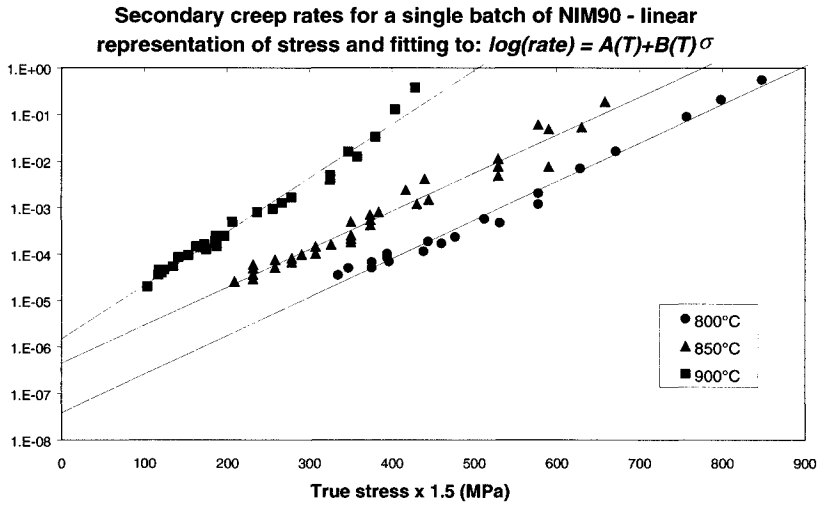


Fig 1b

Now it is mathematically correct that a function, at least if assumed sufficiently smooth, is defined over its *entire* domain (if of sufficiently simple topology) by its behaviour over an arbitrarily small *open* subset - the principle of analytical continuation. But the available data for creep are invariably discrete and are always subject to random uncertainties (however small). Therefore not only are there infinitely many *possible* extrapolations (corresponding in effect to *potential* transitions) but any one of them is liable to contain *arbitrarily large* errors at sufficient distance from the data. In other words, a good fit over the *data range* implies in

itself very *little* for the quality of extrapolation. Indeed, it hardly matters whether the chosen fitting function contains a minimal number of free coefficients or many more than required to satisfy the data themselves with small error. In the former case there is little scope even to *express* a poorly defined transition; in the latter case the *additional* freedoms, *able* to express a transitional trend but insignificant *on* the data range, may easily attain *spurious* values from random aspects of the data.

It is concluded that the *sole* use of information in a *limited* range is dangerous for *any* mathematical technique for extrapolation. On the contrary, in view of transitions of behaviour and scatter it seems evident that three conditions are required for reasonably reliable extrapolations. First, the expressions *must* contain sufficient free coefficients to allow (at least) two regimes of behaviour to be *independently* described. Second, since at least some of the coefficients are then indeterminate over a single regime, there *must* be some source of *supplementary* information for a second regime. Finally, uncertainties require inclusion within a reasonable *statistical* framework.

Parallel dependence and fitting

Parallel dependence and fitting are intended to supply such supplementary information. The idea comes from the common observation that, when data for secondary creep rate, rupture time, etc are plotted against stress σ at a given temperature **T** on a logarithmic scale, curves for *different* batches of a *given* material type are very often sensibly *parallel* to within the apparent scatter. Such behaviour is indicated on fig 2a ([9] and various other sources) though the scatter is very appreciable.

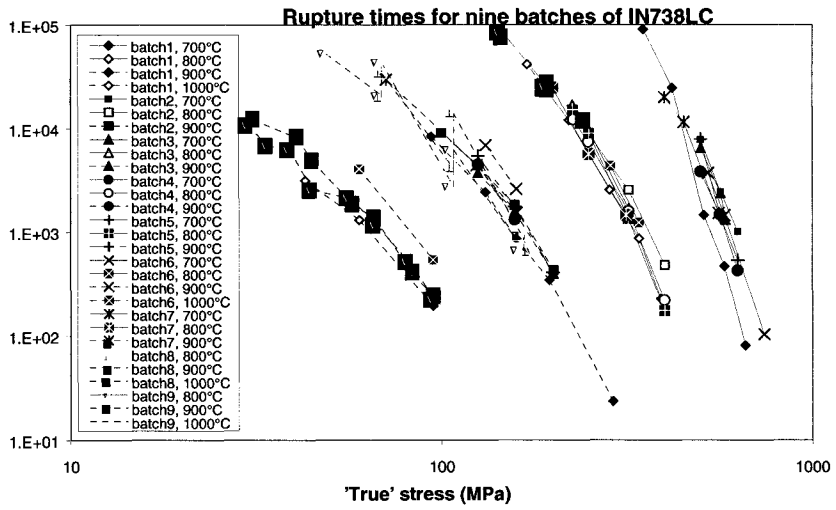


Fig 2a

That is, observed values of such a quantity **Q** (or its reciprocal if more convenient) behave as

$$ln(\mathbf{Q}) = ln(\mathbf{A}_p) + ln(\mathbf{f}(\sigma,\mathbf{T})) + \mathbf{D} \qquad (3)$$

where **D** is a simply distributed *random* variable (with zero mean) to account for scatter. The 'kernel function' **f** - containing enough free coefficients for two regimes - is *identical* for all batches **p** which differ *only* in their pre-multipliers $\mathbf{A}_p$. These pre-multipliers then usually represent characteristic *time* (or frequency) *scales* for each batch and these scales express *strength-factors*. In most cases **D** appears fairly *homoscedastic* and it has usually been found (Anderson-Darling test) that a *normal* distribution is adequate for each **Q** so that the 'maximum likelihood principle' justifies fitting through the 'least squares' method (or variants to account for any constraints among the various **Q**). An advantage is that the pre-multipliers may be eliminated analytically from the minimisation conditions to leave a nonlinear calculation in a *moderate* number of unknowns. It cannot be overemphasised that the appropriate fitting method and all conclusions depend *strongly* upon the statistical model. The notion of such 'batch coefficients', and corresponding 'dummy variables', is long-established (see [10]) within general statistical methodology for the regression of samples involving so-called 'blocked data' (pre-identified sub-populations). In the context of time-temperature parameters for rupture time (also sometimes for secondary rate etc), it has been widely adopted for over thirty years within American practice [11], often under the name of 'lot-centered' (or 'heat-centered') analysis, and has been used to extrapolate for batches with limited data. [This work sometimes extends the idea to formulae with a *second* batch-dependent coefficient, but caution seems required since if no *very simple* regularity occurred - especially if the derived trend-curves *crossed* for different batches - then the adopted material classification might be nugatory.]

Here - as indeed has been suggested [12] in the more limited formulation of (1) - an *extended* hypothesis is made; that the same 'parallelism' *also* generally applies among batches of *different* materials which are 'essentially similar' in a suitable sense. Specifically:

> (a) Among which the basic crystalline *matrix* (γ-nickel in the case of many superalloys) is the same. [NB: varying proportions of highly *compatible* elements, such as Ni and Cr, may usually be regarded as not changing the matrix.];
> (b) Among which any particles of *high* volume fraction are much the same in *all* aspects (size, shape, volume fraction and geometrical distribution within the matrix);
> (c) Among which any instabilities of structure are effectively identical.

Thus, *low* volume fractions of interstitial strengtheners or particles with *low* volume fraction are assumed *only* to influence creep properties through pre-multipliers. However, otherwise closely comparable CC and SX γ'-strengthened superalloys are regarded as essentially *different* - owing to the respectively *random* and *cubic* distributions of γ' particles. Conversely, various SX alloys of different detailed compositions (at least first and second generations) are essentially similar - see [13] for evidence of parallel behaviour. But much care may be needed in deciding whether instabilities, such as 'rafting' in γ'-strengthened materials, have the *same* quantitative influence for entire groups of materials. An example of parallelism (within the expected scatter) is shown for single batches of three related superalloys in fig 2b (data from [9,14]) where, however, it is possible to suspect a change of the relative strengths at the highest temperature of 1000°C where γ' instability is known to occur even for moderate times.

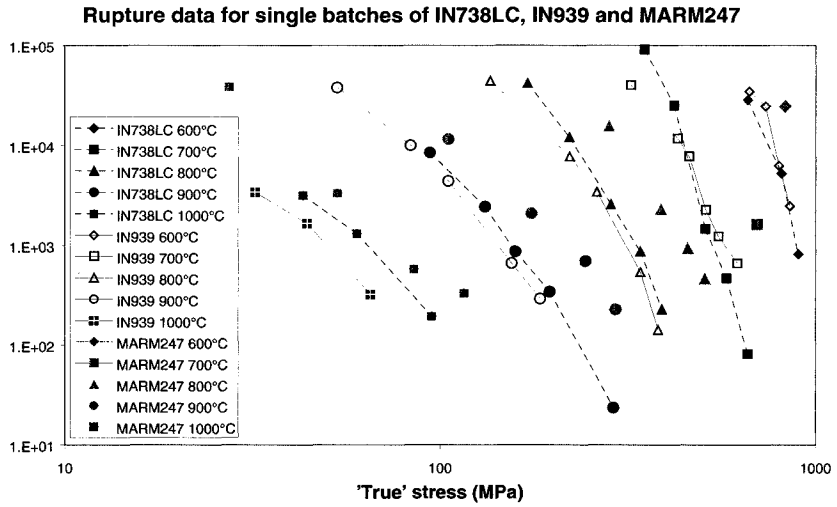


Fig 2b

A physical argument for parallelism may be based upon the idea that the time-scales of high-temperature creep are essentially controlled by processes of 'climb' (transverse diffusion) of dislocations *around* the various obstacles but 'glide' *between* such obstacles is relatively instantaneous. It is then plausible that the mean diffusion times - at a certain stress-temperature combination, for a given matrix and for a given pattern of any particles with high volume fraction - would be simply proportional to certain functions of the sizes and spacings of *widely spaced* obstacles but independent of their chemistry.

The advantage of this extended hypothesis is that data for 'strong' and 'weak' types of a given group may be processed *together* to produce *common* trends with respect to stress and temperature. The data for 'weak' types, obtainable at *lower* stress-temperature combinations for the *same* testing time, may well be available across the transition to a regime in which few or no results are available for a 'strong' material. That is, 'weak' types give a *guided* extrapolation for 'strong' types. The necessary mathematical and statistical procedures for parallel fitting are outlined in [13,15], the former reference explicitly dealing with secondary creep rates in SX superalloys. There are, of course, significant assumptions involved - especially involving uncertainties from potential instabilities such as rafting, which can only be *finally* checked by *systematic* comparisons with long-term data. However this is regarded as a safer approach than *blind* extrapolation wherein some purely mathematical correlation at high stress-temperature conditions is assumed to apply equally well when evaluated in other conditions. In particular, it allows play for metallurgical understanding from which it might well be clear that two materials would behave in parallel even though a *quantitative* theoretical statement for either material might be too daring.

A practical engineering problem

Gas turbine combustors provide numerous high temperature problems and a recent question arose concerning modification of a heat-shield for which it was desired to alter the fixing

arrangements so as to give better control of relative movements in service. One suggested answer involved bolts which would be exposed to gas temperatures in excess of 800°C. In order to limit undesirable bolt relaxation, a highly creep-resistant wrought material was needed. It appeared that the alloy NIM115, readily available though not of significant previous use by the Company, would be a suitable candidate on various grounds. A creep law suitable for relaxation assessments was therefore requested. In practice long-term relaxation is predominantly influenced by secondary creep in most cases (primary creep is soon exhausted while creep strains are too small for tertiary effects), so that only this aspect of creep properties was required - but it transpired that scarcely any secondary test data were available.

In fact it was thought necessary to predict relaxation rates down to between about 15 and 150 MPa per year. With typical elastic moduli these correspond to creep rates of 10^{-8} to 10^{-7} abs/h but data were only available above 10^{-5} abs/h. However, the material was considered to be essentially similar to other γ'-strengthened alloys - NIM90, IN738, IN939 and MARM247 - which had already been fitted together. Therefore a parallel extrapolation was proposed to allow the meagre and short-time information for NIM115 to be extended down to suitable stress-levels. The data ranges for all materials concerned are shown on fig 3 where it is clear that the relatively weak material NIM90 is generally represented at lower stress levels than the others. However, in view of likely instabilities, data above 1000°C were *not* fitted.

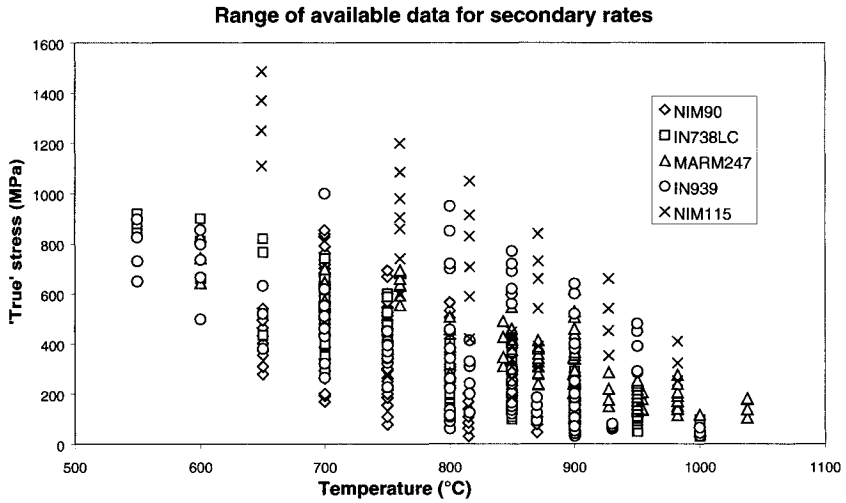


Fig 3

Extrapolation of the available data

There were only two immediately available data sources for NIM115: [16] with creep tests at 850°C *only*, [17] with flow-stress information at *other* temperatures from tensile tests of a different batch. With the assumptions that the two batches concerned were both fairly typical and that the scatter band is similar to those of the related materials, this information was enough for design estimates. [Note that flow-stress data are treated within the present approach as equivalent to secondary creep data and it is then important, especially whenever

loading strains are significant, for creep data to be in terms of the estimated true stress at the mid-secondary stage.] On this basis over 850 data points for some 90 batches were available for the comparison materials and had been fitted using the 'double Norton' kernel function:

$$\mathbf{f} = (\mathbf{f}_1^{\,1/\xi} + \mathbf{f}_2^{\,1/\xi})^{\xi} \tag{4}$$

$$ln(\mathbf{f}_i) = \mathbf{L}_i - \mathbf{C}_i/\mathbf{T} + \{\mathbf{m}_i - \mathbf{n}_i\mathbf{T}_0\,(\mathbf{T}_0/\mathbf{T} - 1)\}\, ln(\sigma/\sigma_0) \quad (i = 1, 2;\ \mathbf{L}_1 = 0) \tag{5}$$

Here $\mathbf{T}_0$ and σ_0 are arbitrary scaling numbers (usually taken as typical values for the data set) while $\mathbf{f} \sim \mathbf{f}_1$ or $\mathbf{f}_2$ at small or large stress, rapidly if the 'blending coefficient' ξ is small. Distinct sets of coefficients then govern low- and high-stress behaviour, thus permitting transition between two regimes This form readily allows physically reasonable constraints to be imposed among the limiting low- or high-stress behaviours of different quantities $\mathbf{Q}$. The results of fitting for $\mathbf{Q} = (d\varepsilon^c/dt)_s$ are shown on figs 4a,b at various temperatures.

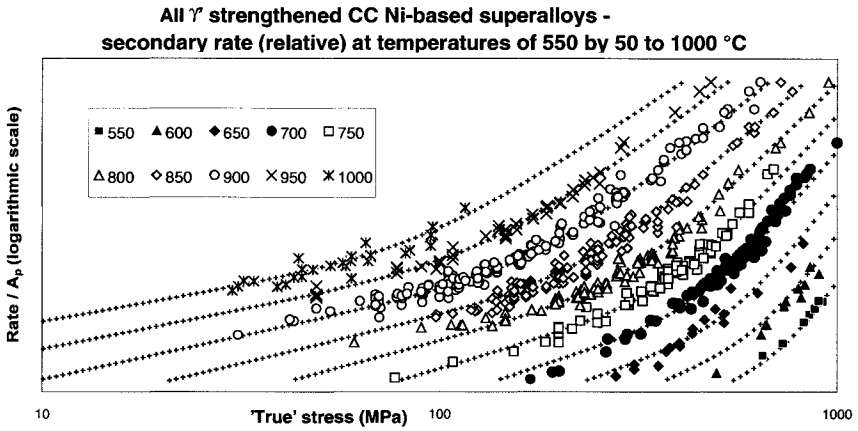


Fig 4a

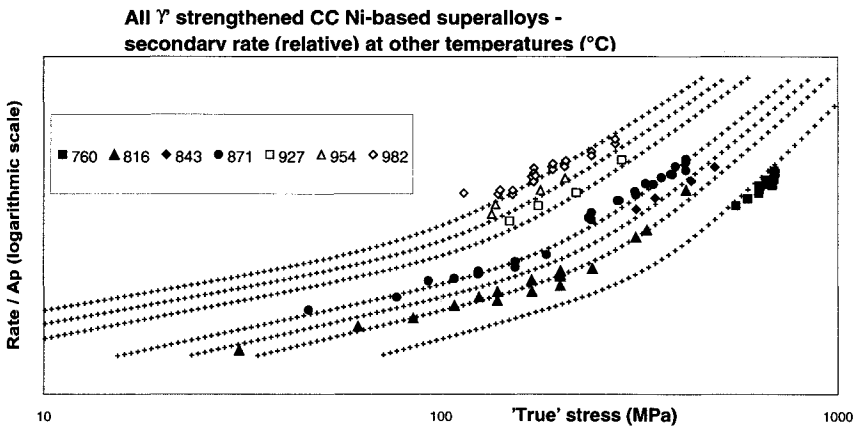


Fig 4b

These are in terms of plots against 'true' stress of the quantity $\mathbf{Q/A_p}$ where the calculated value of $\mathbf{A_p}$ for the appropriate batch is used for each data point. Since by (3)

$$ln(\mathbf{Q/A_p}) = ln(\mathbf{f}(\sigma,\mathbf{T})) + \mathbf{D} \qquad (6)$$

the vertical spacing on the logarithmic scale, between each plotted point and the corresponding curve of **f** against σ, is precisely the discrepancy **D**. The visible scatter therefore indicates the overall success of simultaneous fitting to (3) for several materials.

Results and comments

'Spreadsheet' software is used for fitting and automatically provides, using the 'common' coefficients obtained for (5) and without further optimisation, pre-multipliers $\mathbf{A_p}$ for any batches *subsequently* added to the data file. The information for NIM115 was so added and the two batches proved to have very similar $\mathbf{A_p}$ values. The data are shown on fig 5, with the predicted extrapolations at the same temperatures (and over roughly within the stress levels covered by the data range of fig 3) using as pre-multiplier $\mathbf{A_{mean}}$ the geometrical mean of the two $\mathbf{A_p}$. The corresponding secondary creep law was then used in 'average property' predictions of relaxation, hence allowing decisions to be made about the proposed bolting arrangement. Check calculations were also made using 'minimum properties' estimated with $\mathbf{A_{mean}}$ adjusted according to the known scatter band for IN738.

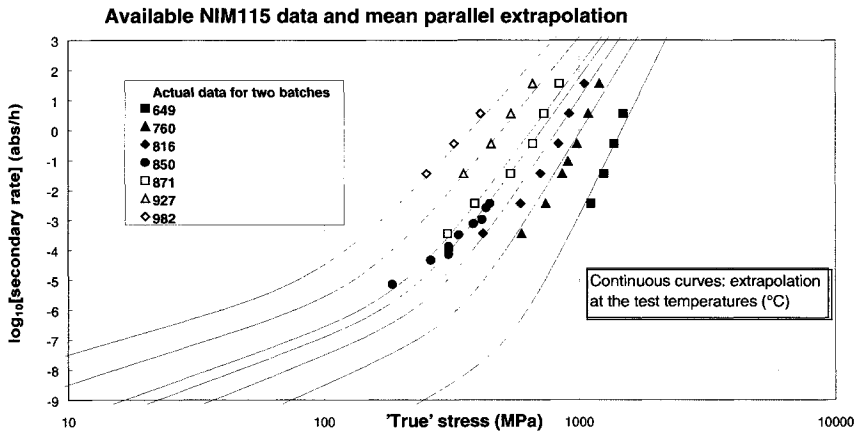


Fig 5

It is noteworthy that the stress-temperature combinations and corresponding creep rates of most significance (10^{-8} to 10^{-7} abs/h) not only lay entirely in the *extrapolation* range but also lay *beyond* a transition barely evident in the available NIM115 data. *Much* of the relevant information was therefore provided by the comparison materials - especially the weak NIM90. Hence the engineering conclusions relied heavily upon trends visible *only* for materials other than that of interest.

In fact the suggested re-design was not adopted (but for reasons unconnected with relaxation) so that no long-term tests are planned to verify the extrapolations produced. However, the author would be delighted to compare notes with anyone in possession of longer-term creep data or relaxation data for NIM115.

Acknowledgement

The author thanks ALSTOM Power for the permission to publish this article.

References

[1] Larson F R and Miller J, Trans. Amer. Soc. Mech. Eng. , 1952, **74**, p765.
[2] Daleo J A and Wilson J R, '*GTD111 Alloy Study*', ASME paper GT-520, 1996.
[3] Betteridge W, Inst. Metals J., 1957, **86**, p232.
[4] Penny R K and Marriot D L, 'Design for Creep (second edition)', Chapman and Hall, London, 1995.
[5] Graham A and Walles K F A, J Iron Steel Inst., **169**,105,1955.
[6] Frost H J and Ashby M F, 'Deformation-Mechanism Maps', Pergamon, Oxford, 1982.
[7] Greenfield P 'A Review of the Properties of 9-12%Cr Steels for Use as HP/IP Rotors in Advanced Steam Turbines', Commission of the European Communities, EUR11887, 1988.
[8] Harrison G F and Evans W J, '*A Creep deformation Map for Nimonic 90*', I. Mech. E Conference paper C211, London, 1980.
[9] Preussler T, Dr.-Ing. Diss. Technische Hochschule Darmstadt D17, 1991
[10] Draper N R and Smith H, 'Applied Regression Analysis', Wiley, New York, 1966.
[11] Manson S S and Ensign C R , 'A Specialised Model for Analysis of Creep-Rupture Data by the Minimum Commitment - Station Function Approach', NASA TM X 52999, 1971.
[12] Park J and Manson S S '*A New Approach for the Characterisation of Creep Rupture Properties for a Newly Fabricated Material*', in 'Sixth Int. Conf. on Creep and Fatigue p71', I Mech E, London, 1996.
[13] White P S '*An Investigation of the Anisotropy of the Secondary Creep Rate in CMSX4*', in 'Proc. 6th Liège Conference (ed Lecomte-Beckers J, Schubert F and Ennis P J)', vII p1059, Univ. de Liège & Eur. Commission, Forschungszentrum Julich, 1998.
[14] Kloos K H, Granacher J and Pfenning A '*Rechnerische Beschreibung des Kriechverhaltens ausgewählter hochwarmfester Legierungen, Teil I*', Mat.-wiss. und Werkstofftech. **25**, 125-132, 1994.
[15] White P S '*Statistically Based Fitting of Creep Data for FE Analysis, Covering Material Variability*', in 'Proc. 5th Parsons Conference (ed Strang A, Banks W M, Conroy R D, McColvin G M, Neal J C and Simpson S)' p1022, IOM Communications Ltd, London, 2000.
[16] Davies P W and Dennison J P '*The Use of Heat-Treatment to Recover the Creep Properties of Nimonic 115 after High-Temperature Creep*', Metal Science, **9**, 1975, p319.
[17] Jensen R J and Tien J K '*Temperature and Strain rate Dependence of Stress-Strain Behavior in a Nickel-Base Superalloy*', Met. Trans., **16A**, 1985, p1049.

DEVELOPMENT OF A VIRTUAL TURBINE SYSTEM FOR NEW MATERIALS DESIGN

*Hiroshi Saeki, *Yoshitaka Fukuyama, **Tadaharu Yokokawa,
**Toshiko Odaka, +Toyoaki Yoshida, and **Hiroshi Harada

*Toshiba Corporation
2-4 Suehiro, Tsurumi, Yokohama 230-0045, Japan
**National Institute for Materials Science (NIMS)
1-2-1 Sengen, Tsukuba Science City 305-0047, Japan
+National Aerospace Laboratory (NAL)
7-44-1 Jindaiji-higashi, Chofu, Tokyo 182-8522, Japan

Abstract

In " High Temperature Materials 21 project ", we construct a virtual gas turbine system (VT) as a combination of an alloy design program (ADP) and a gas turbine design program. By using the VT, we estimate the plant performance (thermal efficiency and CO_2 emission rate) as well as the life of components (such as the creep rupture life of blades) for any new superalloys with arbitrary alloy compositions.

The VT performs simplified aerodynamic, cooling, and structural analysis calculations based on prefixed design parameters, which were tuned up for a medium-size 1300 °C class land-base gas turbine. We estimate the relationship between the turbine inlet gas temperature (TIT) and the thermal efficiency. It is clear that the combined-cycle thermal efficiency can reach 55% (higher heating value : HHV) if the TIT is increased to 1700°C using our SC superalloy TMS-82+ (2.4% Re), which has a temperature capability 25 °C higher than CMSX-4. Further improvement of the thermal efficiency is expected with a more sophisticated cooling system which will be applied to the real 1700 °C turbine system.

Keywords

Virtual gas turbine system, Ni-base SC superalloy, Alloy design program, Gas turbine design program

1. Introduction

The increase of the thermal efficiency of a combined-cycle power plant is achieved by an increase of gas turbine (GT) pressure and temperature. However, in using GT blades made of conventional materials, the increase of coolant consumption with the increase of GT working temperature reduces the efficiency of the plant. Therefore, the development of advanced high-temperature materials, such as new generation Ni-based single crystal (SC) superalloys or possible alternative materials are expected to realize a higher temperature GT with less coolant consumption. Unfortunately, however, the opportunity has been limited for materials scientists and GT designers to evaluate newly developed materials in actual GTs. To improve the situation, a simplified gas turbine design simulation program, called as a virtual gas

turbine system (VT), has been developed as a combination of a materials design program and a gas turbine design program. In this paper, the principal features of the present VT and its application for materials design are described.

2. Outline of a virtual gas turbine system

Figure 1 shows the schematic diagram of the VT. The present VT is unified with the materials design program and the GT design program with the cooling characteristics program (CCP). The GT design program is used for the estimation of the aerodynamic characteristics of a turbine. The materials design program is used to estimate the mechanical properties of the blade / vane in a gas turbine operating condition for arbitrary compositions of SC superalloys. In the present VT, the materials design program is available for Ni-base superalloys. We have developed an alloy design program (ADP) for γ' precipitation-hardened Ni-base superalloys [1, 2]. Several alloys with superior properties have been developed using this ADP. the CCP is used for the estimation of the cooling effectiveness versus the coolant flow rate. When the gas turbine conditions (power level and inlet gas temperature) and arbitrary compositions of SC superalloys for gas turbine materials (or selected materials from a database) are defined, the combined-cycle heat balance, the high-temperature strengths of the turbine blade / vane, and the cooling characteristics under the given conditions are evaluated. The principal features of each program are described below.

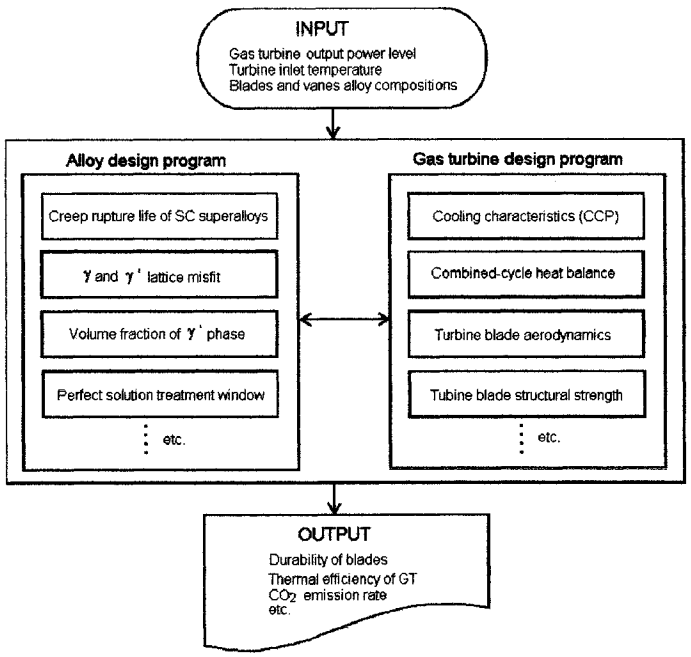


Fig. 1 Schematic diagram of the virtual gas turbine (VT).

2.1 Gas turbine design program

Figure 2 shows the thermal cycle schematics of the combined cycle plant. The ambient air is compressed through the compressor (from ① to ⑤) and introduced into the combustor (from ⑤ to ⑦). High-temperature and high-pressure gas flows, which are generated in the combustor, are then introduced to the turbine. The hot gas is expanded to the atmospheric pressure to generate power (from ⑦ to ⑩). The hot exhaust gas energy is utilized by the heat recovery boiler to generate new power in dashed block.

Usually, the evaluation of turbine system performance, such as heat balance, structural parameters, and total efficiency, requires an enormous number of calculations and a considerable amount of time. In this gas turbine design program, simplified equations based on the prefixed design conditions, which were tuned up for medium-size 1300 °C class land-base GT, are used for aerodynamic, cooling, and structural calculations. The aerodynamic design is based on the stage-to-stage velocity triangle calculation taking the cooling effects into account. The structural design is based on information regarding size, working conditions, and metal temperatures. The points of assessment are as follows: the metal surface temperature for the oxidation or corrosion life evaluation, the vane bending stress, and the blade centrifugal stress and bulk temperature for the creep rupture life evaluation. The GT coolant flow is determined to clear all these design limitations that come from the blade life consideration. However, this process requires a considerable amount of computational time, since the rate of coolant flow must be given for all the nozzles and blades in all the stages, and the changes in the coolant flow rates influence the basic thermal cycle calculations. To solve this highly complicated system, the VT has the outer convergence loop to balance all the dependent variables by the iterative procedure.

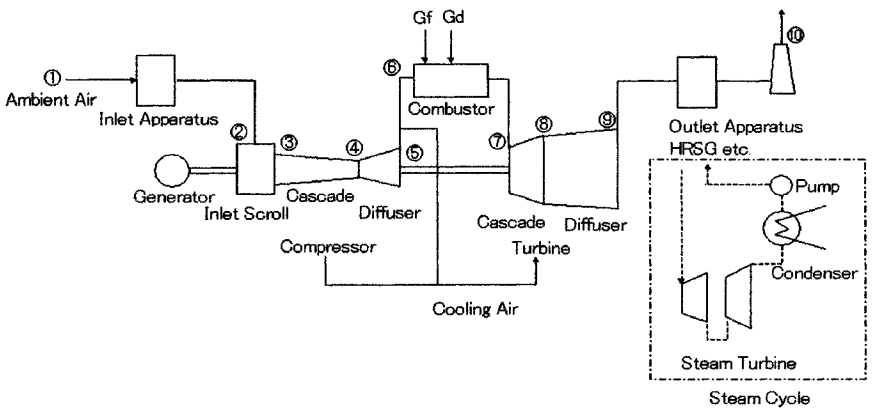


Fig. 2 The thermal cycle schematics of the combined-cycle plant

The CCP is developed by using the database and the advanced computational fluid dynamics technology available at the National Aerospace Laboratory (NAL) [3, 4]. This program is integrated to the VT for the evaluation of the wall temperatures of a turbine vane and blade through the cooling characteristics of internal cooling, film cooling, and external heat transfer. For example, the average and minimum cooling effectiveness for the first stage vane and blade is expressed as,

<Vane>
average: $\eta_{ave} = 0.714\ \{1\text{-}\exp(-0.468(Gc/Gg))\}$
minimum: $\eta_{min} = 0.660\ \{1\text{-}\exp(-0.468(Gc/Gg))\}$
<Blade>
average: $\eta_{ave} = 0.608\ \{1\text{-}\exp(-0.427(Gc/Gg))\}$
minimum: $\eta_{min} = 0.507\ \{1\text{-}\exp(-0.427(Gc/Gg))\}$

where Gg is the principal gas flow rate and Gc is the cooling air flow rate. Figure 3 shows an excellent agreement of the cooling effectiveness between experimental data and prediction formulas.

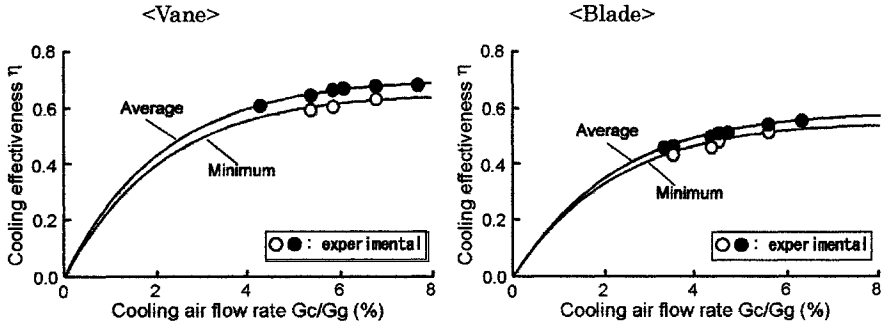


Fig. 3 Agreement of the cooling effectiveness between experimental data and prediction formulas.

2.2 Alloy design program

The ADP is developed at the National Institute for Materials Science (NIMS) and has been integrated into the VT, and used for the evaluation of the creep strength in a gas turbine operating condition for arbitrary compositions of SC superalloys. Many researchers were tried to predict of the creep rupture life, e.g. G. Durber [5] have been developed the prediction equation for the Larson-Miller parameter. His prediction equation shows good agreement between actual and calculated Larson-Miller parameters, but it does not take into account the structural parameters such as γ/γ' lattice misfit, volume fraction of γ' phase. These structural parameters strongly affect the creep rupture life, especially on SC superalloys. we developed the prediction equation of creep rupture life at arbitrary temperature and stress by using alloy composition, γ/γ' lattice misfit and volume fraction of γ' phase. The equation is shown below, where t_r is the creep rupture life in hours, σ is the applied stress in MPa, T is the temperature

in Kelvin, A, B, C, and D are the regression coefficients obtained from 197 creep rupture data of 36 different SC alloys, X_i is the composition of the i-th alloying element in at%, δ is the γ/γ' lattice misfit, and V_f is the volume fraction of γ' phase. Figure 4 shows excellent agreement between the calculated and measured creep rupture lives with the Larson-Miller parameter ($=T\{20+\log(t_r)\}$). Table 1 shows structural parameters and properties that can be predicted by the ADP.

$$log_{10}(t_r) = A+(B+CT/\sigma)\ log_{10}\sigma+D/T \qquad (1)$$

$$A = a_0 + \Sigma a_i X_i + a_j\delta + a_k V_f, \quad B = b_0 + \Sigma b_i X_i + b_j\delta + b_k V_f,$$
$$C = c_0 + \Sigma c_i X_i + c_j\delta + c_k V_f, \quad D = d_0 + \Sigma d_i X_i + d_j\delta + d_k V_f,$$

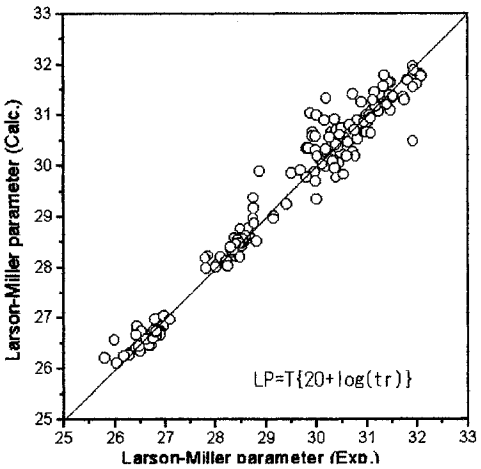


Fig. 4
Agreement between calculated and experimental creep rupture lives with the Larson-Miller parameter ($=T\{20+\log(t_r)\}$).

Table 1 Structural parameters and high-temperature properties predicted in the alloy design program.

Structural parameters	Properties
Fraction and composition of γ / γ' phases	Creep rupture life of SC alloys at arbitrary temperature and stress
Lattice parameter	Ultimate tensile strength at 900 °C
Alloy density	Yield strength at 900 °C
Liquidus temperature	Hot corrosion resistance
Solidus temperature	Elongation at RT
Perfect solution treatment window	

3. Applications

The present VT was constructed on a Microsoft® Excel worksheet to provide an easy-to-use environment, as shown in Fig. 5. The main inputs and outputs are listed below,

Inputs: Gas turbine output power level (e.g., 200 MW)
Turbine inlet temperature (e.g., 1700 °C)
Alloy composition (e.g., TMS-82+, or a new SC alloy composition)
Outputs: Thermal efficiency
CO_2 emission rate
Durability of blade, etc.

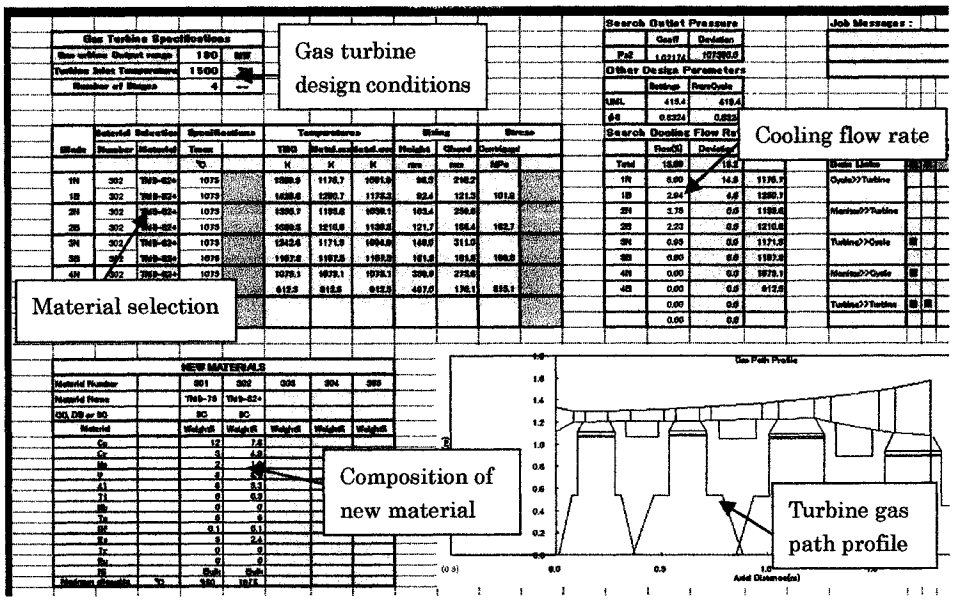


Fig. 5 A part of Input/Output worksheet of VT system.

For example, the centrifugal stress created in the blade operated in a 1300 °C - 15MW class turbine is calculated and compared with the SC superalloy creep strength (Fig. 6). In this figure, the dashed line shows the centrifugal stress, and the solid line shows the estimated creep strength of 10^5 h. If these lines crossed each other as shown in the left-hand side, the material strength would not be enough for the given turbine condition. On the other hand, if optimal material or newly designed material with ADP were used in a blade, the relationship

between centrifugal stress and material strength would change, as shown in the right-hand side of the figure; the alloy strength is well agree the required strength.

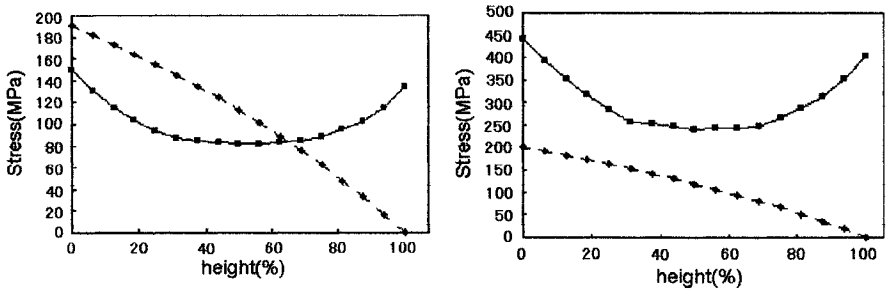


Fig. 6 Relationship between blade centrifugal stress and the alloy creep strength.
(dashed line: average centrifugal stress, solid line: estimated 10^5 h creep rupture strength).

Figure 7 shows the relationship between the turbine inlet temperature (TIT) and the combined-cycle thermal efficiency estimated by the VT. Table 3 shows the turbine design conditions and the turbine material used in this estimation. It is shown that the combined-cycle thermal efficiency can reach 55% (HHV) if TIT is increased up to 1700 °C using our SC superalloy TMS-82+ (2.4% Re) [6], which has a temperature capability 25 °C higher than CMSX-4. The efficiency is expected to be further improved by the application of a more sophisticated cooling system that has not yet been realized.

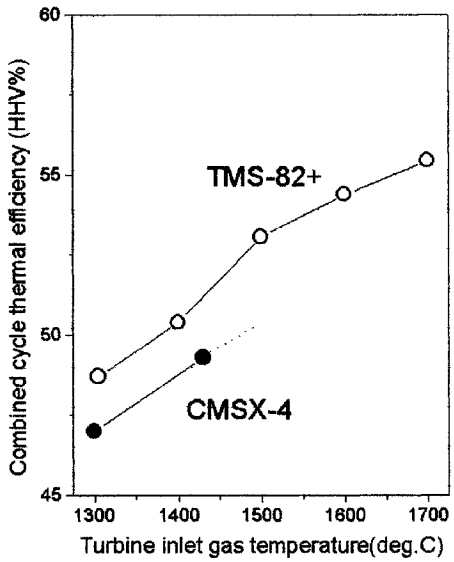


Fig. 7
Relationship between the turbine inlet gas temperature (TIT) and the combined-cycle thermal efficiency estimated by the VT.

Table 3 Design conditions used for the estimation of the combined cycle thermal efficiency shown in Fig. 7.

Item	Condition
Fuel	LNG
Blade and Vane	4 stages
Materials	TMS-82+ (blade, vane) with TBC (YSZ)
Principal flow rate	560.6 kg/s
Outlet gas temperature	624.4 °C

4. Conclusions

A virtual gas turbine system (VT) has been developed by a combination of an alloy design program for Ni-base superalloys, a gas turbine design program with a cooling characteristics program. By using the VT, we can estimate the plant performance (e.g., thermal efficiency, CO_2 emission rate) as well as the life of the components (e.g., creep rupture life of blade) for any new superalloys with arbitrary alloy compositions. The VT performs simplified aerodynamic, cooling, and structural strength calculations based on the prefixed design parameters which were tuned up for a medium-size 1300 °C class land-base gas turbine and combined-cycle plant. We estimated the relationship between the turbine inlet gas temperature (TIT) and the thermal efficiency, and clarified that the combined-cycle thermal efficiency can reach 55 % (higher heating value) if TIT is increased up to 1700 °C using our SC superalloy TMS-82+ (2.4 % Re), which has a temperature capability 25 °C higher than CMSX-4. The efficiency is expected to be further improved by the application of a more sophisticated cooling system.

The development of the VT is being continued, e. g., so-called alternative materials including ceramics, Ir-base refractory superalloys [7], etc. are ready to be evaluated as un-cooled vanes in the VT. A demonstration version will be released on our World Wide Web soon [8].

Acknowledgment

This work was performed as a part of the research activities of "High Temperature Materials 21 project", being conducted at NIMS under collaborations with Japanese and overseas private companies and research organisations.

References

[1] H. Harada, K. Ohno, T. Yamagata, T. Yokokawa, and M. Yamazaki, Superalloys 1988, Proc. of the 6th International Symposium on Superalloys (Warrendale, PA: The Metallurgical Society, 1988), 733.

[2] H. Harada, T. Yokokawa, K. Ohno, T. Yamagata, and M. Yamazaki, Proc. of the Conference on High Temperature Materials for Power Engineering 1990, Liege, Belgium, 24-27 September 1990, 1319.

[3] M. Matsushita and T. Yoshida, Proc. of the 15th Gas Turbine Fall Lecture Meeting, Gas Turbine Society of Japan, November 2001, 83.

[4] T. Yoshida, H. Harada, Y. Fukuyama, A. Ogawa, O. Nozaki, T. Nishizawa, M. Matsushita, and F. Zhou, Proc. of the High Temperature Materials 2001, Materials Science and Engineering A, Elsevier Science, to be published.

[5] G. Durber, Superalloys 1996, Proc. of the 8th International Symposium on Superalloys (Seven Springs, PA: The Metallurgical Society, 1996), 111.

[6] T. Hino, T. Kobayashi, Y. Koizumi, H. Harada, and T. Yamagata, Superalloys 2000, Proc. of the 9th International Symposium on Superalloys (Seven Springs, PA: The Metallurgical Society, 2000), 729.

[7] ex., Y. Yamabe-Mitrai, Y. Ro, T. Maruko, H. Harada, Structural Intermetallics 1997, (Minerals, Metals & Materials Society, 1997)

[8] our WWW address; http://sakimori.nims.go.jp

DRILLING OF COOLING HOLES AND SHAPING OF BLOW-OUT FACILITIES IN TURBINE BLADES BY LASER RADIATION

J. Willach, A. Horn, E.W. Kreutz

Lehrstuhl für Lasertechnik, RWTH Aachen, Steinbachstraße 15, 52074 Aachen, Germany

Abstract

Drilling of cooling holes (diameter 200µm) by melt expulsion with microsecond pulsed laser radiation in a multilayer system (Ni-superalloy CMSX-4, VPS-MCrAlY, EB-PVD-zirconia) of turbine blades is reported. The quality of drilled holes, e.g. conicality determined by optical (OM) and electron (SEM) microscopy, heat affected zone (HAZ) and recast analyzed by SEM after metallographical preparation and chemical composition of the resolidified zone measured by EDX are presented for different processing gases (oxygen, argon and nitrogen).

To avoid hot spots on the cooled blade surface shaping of aerodynamic blow-out facilities in the TBC (zirconia) is done by laser radiation of different pulse length and wavelength. Two different strategies to structure the zirconia are investigated: mask-projection and scanning. The average removal depth and average surface roughness determined by white light interference microscopy (WIM) are presented in dependence on average laser power and overlap of the laser pulses. The formation of cracks while shaping is analyzed by SEM.

Keywords: cooling holes, laser drilling, shaping, turbines, power plants

Introduction

Since the first development of turbines for power plants in the early 19th century their efficiency has been improved dramatically in increasing the gas combustion temperature by the development of superalloys [1]. Continous optimization of the superalloys e.g. by directional and single crystal soldification has introduced the alloys to critical parts of turbines like combustion chamber plates and turbine blades. These high-technology materials can sustain working temperatures above 1000°C and very high temperature stress [1].

In order to extend the lifetime of thermally highly loaded turbine parts protective coatings have been developed. Using a MCrAlY coating as an antioxidant barrier and a TBC (zirconia) this multilayer coating opens a new generation of gas turbines working at temperatures above 1200°C with a net efficiency of about 38% [2, 3]. In the seventies and eighties of the last century an active material protection by thin film cooling was introduced. Air is blown through small holes drilled in the blades in order to cover the surface with a protective cooling film. In the last years multicoated turbine blades and combustion chamber plates were drilled with about 300 holes per blade having a diameter of 800-1000µm arranged on an area of 400cm² (hole density 0.75 per cm²) in order to withstand high working temperatures resulting in high efficiency [4].

Today, the aim is to further increase the efficiency up to 65% for combined cycle power plants consisting of gas and steam turbines. By increasing the hole density to 100 per cm² and reducing the hole diameter to 200µm effusion cooling can be obtained with reduced mass flux of coolant [5]. By shaping blow-out facilities (e.g. hoppers) into the TBC the cooling efficiency can be improved by an aerodynamic spread of the cooling gas.

Experimental Setup

Drilling

Cooling holes are drilled in turbine blades and combustion chamber plates with pulsed laser radiation from a flash lamp pumped Nd:YAG slab laser at λ=1064nm with pulse durations in the range of 100 to 500µs. For the drilling the pulse repetition frequency is fixed to 20Hz. Intensities up to 280MW/cm² are reached using a lens with a focal length of f=100mm. Therefore, the slab laser enabels the drilling and cutting of metal sheets with a thickness up to 5mm. Because of the diffraction limited beam quality ($M^2 \approx 1.01$) hole diameters and cutting kerf widths of about 60µm and nearly parallel kerf walls are reached. A conical nozzle with an exit diameter of 1mm is positioned 0.5mm above the top surface in order to remove the molten material by a supersonic gas flow collinear to the laser beam.

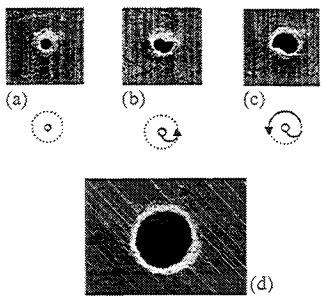


Fig. 1: Principle of trepanning

Holes (diameter 200µm) are drilled in 2.5mm thick Ni-superalloy CMSX-4 by trepanning. Starting with percussion drilling a transit hole is brought into the material by a fixed laser beam (Fig. 1, a). The hole diameter (60µm) corresponds nearly to the beam diameter (40µm). During trepanning the fixed laser beam is moved along the circumference of the hole to be drilled by workpiece movement (cutting, b-d) done by a 5 axis positioning stage with a positioning accuracy of 1µm. Using microsecond laser pulses the drilling process is mainly achieved by melt expulsion. Main difference between material removal during percussion drilling and trepanning is the direction of melt expulsion: during percussion drilling the melt is ejected through the entrance of the hole and resolidifies on the top surface. During trepanning the melt ejects through the hole exit on the bottom surface reducing the recast on the top surface.

The pulse energy and the pulse duration are measured by a calibrated detector included in the laser system. The utilized processing gases are of technical quality: oygen 3.5, nitrogen 4.6 and argon 4.6. For metallographical investigations cross-sections of holes are prepared by cutting and polishing (some including etching). The hole diameter and the melt thickness in the holes are measured by optical and electron microscopy. The chemical composition of the alloy is analyzed by EDX.

Shaping

Aerodynamic shapes (e.g. a hopper, Fig. 2) are structured by pulsed laser radiation into the TBC (zirconia, thickness 250µm) using two strategies: mask-projection or scanning.

An ArF excimer laser (λ=193nm) is used for the mask-projection. A mask with a square opening (4.6x4.6mm²) is illuminated by the laser radiation (beam size 13x29mm², behind a demagnification optic about 8.7x19.3mm²) and projected (demagnification 11.5x) on the zirconia surface in order to remove a cuboid of material. In order to structure a blow-out ramp the workpiece is moved by a 2 axis positioning stage with a positioning accuracy of 1µm. The pulse duration (full width half maximum) is determined to be 25ns. At a pulse repetition frequency of 10Hz pulse energy densities up to 4J/cm² are used.

For the scanning a Nd:YAG laser (diode pumped, regenerative amplified, λ=1064nm) with a pulse duration of 40ps is used at a pulse repetition frequency of 500Hz. The focal diameter is determined by wedge method to be $2w_0$=14.8µm. In order to remove a cuboid of material the workpiece is moved in a meandering way by a 3 axis positioning stage with a positioning accuracy of 1µm while the laser beam is fixed (perpendicular incidence of laser radiation). The movement of the axis is controlled by a CAD/CAM tool in which the hopper is designed (Fig. 2). The average removal depth and the average surface roughness are evaluated in circular areas with a diameter of 500µm after four scans. After each scan the focus is tracked in order to maintain constant removal.

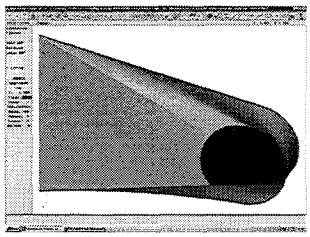


Fig. 2: Shape of a blow-out hopper designed in a CAD/ CAM tool

The geometry of structured shapes, the removal depths and the surface roughness are characterised by white light interference microscopy (WIM).

Results and Discussion

Drilling

Trepanning is done using different processing gases. The mean melt thickness in the holes trepanned with nitrogen is determined by electron microscopy to be 30µm. Chemical composition measurements in the resolidified melt by EDX show a nitration of the superalloy forming a melt with high viscosity which can not be removed properly by the processing gas stream (Fig. 3). Using oxygen the mean melt thickness is measured at 20µm. Bubbles and cracks are found in the resolidified melt. EDX measurements show an enrichment of oxygen compared to measurements in the bulk material (Fig. 4). In comparison to nitration the oxidation forms a melt with a lower surface tension but the melt is not removed completely by the processing gas as well. Argon is found to be the most effective processing gas having the smallest mean melt thickness of 10µm. For all used processing gases no HAZ is detectable by etching the surface of the cross-section and anlyzing the structure of material by electron microscopy [5].

The melt expulsion using argon as processing gas while trepanning is analyzed by reducing the thickness of the superalloy at constant gas pressure. Starting with the thinnest alloy (s_1=550µm) the melt thickness reaches its maximum at the hole entrance because of congestion of the gas stream at the hole entrance and decreases to zero at the hole exit having a mean melt thickness of $\bar{d}_1$=2.4µm. Increasing the alloy thickness shows a rise in the mean melt thickness because of decreasing gas pressure at the exit of the drill channel. The distribution of the melt thickness in the hole shows an oscillatory behaviour (Fig. 5). In order to blow out the melt at the bottom side the gas pressure P has to be >10bar. The polished cross-section of a 2.5mm thick material reveals that at pressures P≤10bar the melt formed during trepanning closes the hole again (Fig. 6).

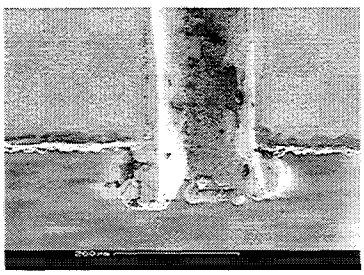


Fig. 3: Cross-section of a hole exit trepanned in CMSX-4 (λ=1064nm, E_P= 0.35J, t_P=0.35ms, processing gas: N_2, P=20bar, SEM)

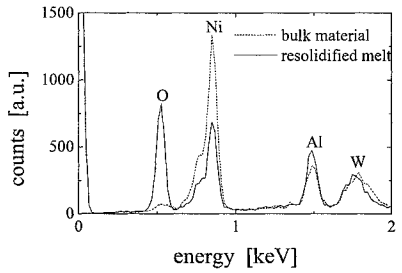


Fig. 4: EDX spectra in bulk material (CMSX-4) and resolidified melt in a trepanned hole (λ=1064nm, E_P=0.35J, t_P=0.35ms, processing gas: O_2, P=15bar)

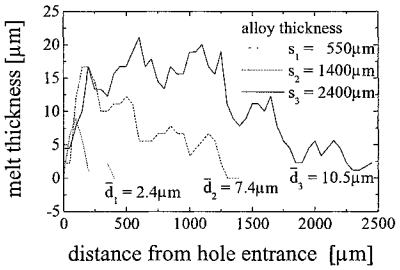


Fig. 5: Distribution of the melt thickness in a trepanned hole in dependence on alloy thickness and distance from hole entrance (CMSX-4, λ=1064nm, E_P=0.35J, t_P=0.35 ms, processing gas: Ar, P=20bar, SEM)

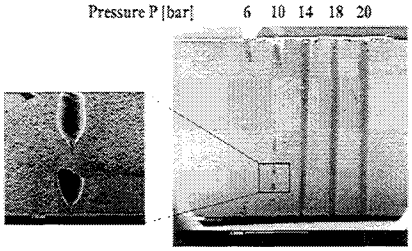


Fig. 6: Cross-section of holes trepanned at different processing gas pressures (CMSX-4, λ=1064nm, E_P=0.35J, t_P=0.35 ms, pro-cessing gas: Ar, P=6, 10, 14, 18, 20bar, SEM)

The conicality of the trepanned holes using argon and P=20bar is determined by measuring the diameters with optical and electron microscopy. Small conicality is achieved by increasing the pulse duration to 0.35ms and the pulse energy to 0.7J (Fig. 7). At v=36mm/min a trepanning time of 1s is realized.

Inclining the surface of the alloy with respect to the laser beam means an increase of the effective length of the hole (Fig. 9) and of the needed time for percussion drilling [6]. For trepanning with argon as processing gas a pressure P>16bar is necessary in order to maintain a sufficient melt expulsion at the hole exit. When drilling the multilayer system the zirconia layer has to be protected against the expelled melt that is mainly deposited during percussion drilling. This can be achieved by covering the zirconia layer with a TiO_2-based lacquer before drilling. After drilling the lacquer and the deposited melt are removed by an alcoholic solvent [5]. Using EB-PVD-zirconia no cracks are formed during drilling and the ceramic layer (TBC) is undercut without fracture (Fig. 8). Because of the small thickness of the two

covering layers compared to the thickness of the CMSX-4 the trepanning parameters for CMSX-4 can be used for the multilayer system as well.

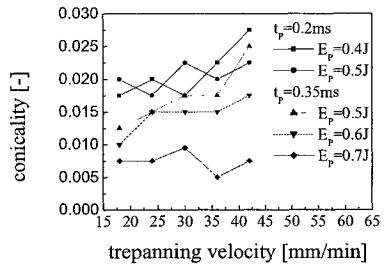


Fig. 7: Conicality of trepanned holes in dependence on pulse energy, pulse duration and trepanning velocity (CMSX-4, λ=1064nm, OM, SEM)

The conicality c of the trepanned holes is defined to

$$c = \frac{d_{top} - d_{bottom}}{2 \cdot l_{eff}}$$

d_{top}	:	hole diameter at the entrance
d_{bottom}	:	hole diameter at the exit
l_{eff}	:	effective length of the hole = thickness of material if the hole is not inclined

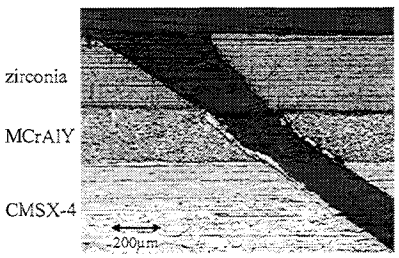


Fig 8: Cross-section of a trepanned hole in the multilayer system at 45° inclination (λ=1064nm, E_P=0.35J, t_P=0.35ms, processing gas: Ar, P=20bar, OM)

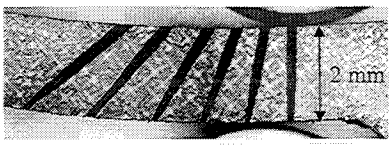
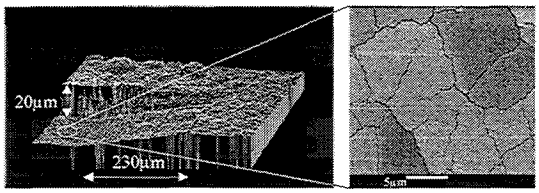


Fig. 9: Cross-section of holes drilled under various inclination angles in CMSX-4 (λ=1064nm, E_P=0.2J, v=36mm/min, processing gas O_2, P=10bar, OM)

Shaping

The absorption of radiation in EB-PVD-zirconia is determined by optical spectroscopy to be >90% at λ=193nm (excimer laser) and 5% at λ=1064nm (Nd:YAG laser) but while structuring the zirconia with the excimer laser radiation energy losses >85% occur on the mask and losses of about 10%/m while transmitting the laser radiation through atmosphere (formation of O_3 at λ=193nm). Therefore, pulse energy densities ≤4J/cm² are measured directly in front of the workpiece. At 4J/cm² the average removal depth is determined by WIM to be about 70nm/pulse. Heat induced surface cracks generated during removal are investigated by SEM (Fig. 10). The average surface roughness (estimated by WIM, scan length 5µm) between the cracks does not exceed 500nm. The cracks can be reduced but not avoided by decreasing the pulse energy density to 0.6J/cm² (average removal depth about 18nm/pulse). In order to structure an inclined (5°) blow-out ramp the workpiece is moved at

8µm/s while structuring (Fig. 10). In addition to the observed cracks the flexibility of realizable shapes is limited by the non-flexible mask geometry.



a) b)

Fig. 10: Surface geometry (a) of a blow-out ramp in zirconia structured by excimer laser radiation (λ=193nm, ε_P=4J/cm², t_P=25ns, v=8µm/s, WIM) showing surface cracks (b) on the bottom of the ramp (SEM)

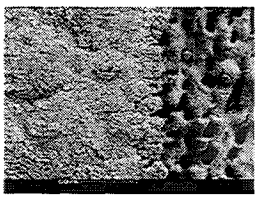


Fig. 11: Surface of zirconia (rigth side) structured by focused Nd:YAG laser radiation (λ=1064nm, P_{av}=20mW, t_P=40ps, o=0.9, SEM)

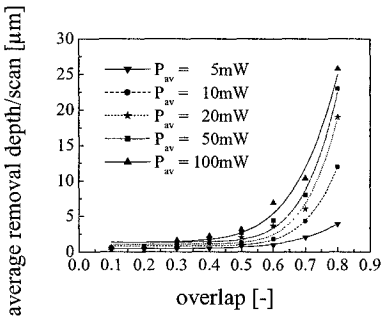


Fig. 13: Average removal depth/scan in relation to average power and overlap (zirconia, λ=1064nm, t_P=40ps, f_P=500Hz, focus diameter 15µm, WIM)

Using focused Nd:YAG laser radiation with a pulse duration of 200µs and 10ns, respectively, surface cracks are also observed [7]. The length and number of cracks can be reduced by decreasing the pulse duration into the picosecond time scale (Fig. 11). While structuring the zirconia with focused Nd:YAG laser radiation with t_P=40ps at λ=1064nm average removal depths of 0.8-6.5µm/scan are reached at 5-100mW (average power) using a pulse overlap $o=1-v/(2w_0 \cdot f_p)$ in the range of 0.4-0.6 (Fig. 13). In this range the average surface roughness (WIM, scan length 300µm) can be kept <2µm (Fig. 14). The roughness increases for an overlap >0.7.

As given by the CAD data the blow-out hopper (meandering movement in 12 planes with P_{av}=20mW at o=0.5) reveals a symmetric geometry taking a processing time of 25s. The maximum depth of the hopper is measured to be about 20µm (WIM) which means a removal depth of about 1.7µm/scan. The average surface roughness throughout the hopper is <3µm (WIM, scan length 300µm). Deposited recast around the structured blow-out hopper is detected by WIM (Fig. 15) with an average width of the recast of about 100µm and an average height of about 4.5µm.

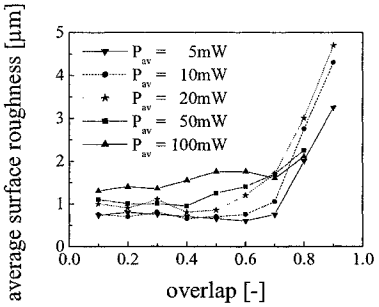


Fig. 14: Average surface roughness in relation to average power and overlap (zirconia, λ=1064nm, t_P=40ps, f_P=500Hz, focus diameter 15µm, WIM, scan length 300µm)

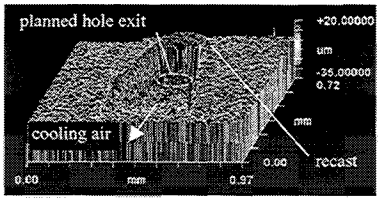


Fig. 15: Surface of structured blow-out hopper (see Fig. 2) in zirconia (λ=1064nm, P_{av}=20mW, t_P=40ps, f_P=500Hz, o=0.5, WIM)

Conclusion

Cooling holes are drilled in 2.5mm thick Ni-base superalloy (CMSX-4) by trepanning with pulsed laser radiation (λ=1064nm) using oxygen, nitrogen and argon as processing gases. Using argon as processing gas the mean melt thickness in the holes is reduced to 10µm. The chemical composition of the melt influences the melt dynamics: when using nitrogen as processing gas the nitration of the melt forms a viscous melt. Oxidation increases the viscosity as well and causes bubbles in the melt. The most effective expulsion of melt is achieved using argon. The mean melt thickness in the trepanned holes shows dependence on the pressure of the processing gas and on the thickness of the alloy, respectively, on the effective length of the hole. The pressure has to be increased when increasing the effective length of the hole in order to maintain the melt expulsion on the exit of the hole during trepanning. The conicality of the holes is reduced to 0.5% by increasing the pulse duration and the pulse energy. Inclined holes need an increase of processing gas pressure and pulse duration in order to maintain melt expulsion.

Drilling in multilayer systems consisting of EB-PVD-zirconia, VPS-MCrAlY and CMSX-4 alloy does not need any changes in parameters that are used for drilling holes in CMSX-4. Trepanning through the multilayer system shows no crack formation in the EB-PVD-zirconia layer demonstrating the advantage of the columnar grown zirconia.

Blow-out facilities are structured in the thermal barrier coating (zirconia) of turbine blades by pulsed laser radiation using mask-projection (excimer) and scanning (Nd:YAG) strategy.

Mask-projection achieves an average removal rate of 70nm/pulse at 4J/cm² and a surface roughness of 500nm. An inclined blow-out ramp (5°) is structured by moving the workpiece relative to the laser beam. Due to the nanosecond pulse duration heat induced surface cracks are generated during the processing at 0.6-4J/cm².

Meandering scanning strategy increases the flexibility of structuring. In order to avoid surface cracks the pulse duration is decreased into the picosecond time scale. Average removal depths of 0.8 to 6.5µm/scan yield an average surface roughness <2µm if the pulse overlap is <0.7. Exceeding an overlap >0.7 the removal depth and the surface roughness increase. A blow-out hopper with aerodynamic properties is structured.

Acknowledgments

The authors gratefully acknowledge the financial support by the Deutsche Forschungsgemeinschaft (DFG) within the Collaborative Research Centre (SFB) 561 "Thermally highly loaded, porous and cooled multilayer system for combined cycle power plants".

References

[1] C. Sims, N. Stoloff and W. Hagel, Superalloys II, John Wiley an Sons, 1987
[2] R. Bürgel, Handbuch Hochtemperatur-Werkstofftechnik, Vieweg Verlag, Braunschweig/ Wiesbaden, 1998
[3] M. Boyce, Gasturbinen Handbuch, Springer Verlag, Berlin, 1999
[4] X. Chen, W. Lotshaw, A. Oritz, P. Staver, C. Erikson and M. McLaughlin, Laser drilling of advanced materials: Effects of peak power, pulse format and wavelength, LIA 80, 1995, pp. 835-840
[5] A. Horn, R. Weichenhain, S. Albrecht and E.W. Kreutz, Microholes in zirconia coated Ni-superalloys for transpiration cooling of turbine blades, Proc. SPIE, High Power Laser Ablation (HPLA) 4065, 2000, pp. 218-226
[6] M. Islam and G. Campbell, Laser machining of ceramics: a review, Materials and Manufacturing Proc. 8 (6), 1993, pp. 611-630

REPAIR AND (RE)CONDITIONING OF COMPRESSOR AND TURBINE BLADES BY CO_2 AND Nd:YAG LASER RADIATION

I. Kelbassa[1], A. Gasser[2], G. Backes[1], S. Keutgen[1], E.W. Kreutz[1], N. Pirch[2]

[1]Lehrstuhl für Lasertechnik, RWTH Aachen, Steinbachstraße 15, 52074 Aachen, Germany

[2]Fraunhofer Institut Lasertechnik, Steinbachstraße 15, 52074 Aachen, Germany

Abstract

Closed-center process chain and an on-line temperature control for turbine component repair were validated. Laser cladding on turbine components by CO_2 and Nd:YAG laser radiation is carried out using powder additive materials of the same sort (e.g. titanium-based alloys: Ti Al6 V4, Ti 6242, Ti 6246 etc. and nickel-based high temperature alloys: In 625, In 718, In 738 etc.). Processing basics and specifications like single-stage processing, powder feeding, gas shielding etc. are described. The dependencies of microstructure, epitaxy, micro-porosity, metallurgical bond defects, mixing, geometry of HAZ, geometrical accuracy and roughness on processing parameters like laser power, scanning speed, powder mass flow and gas shielding flow etc. are discussed on selected clads and materials. Applications like repair of blade tips and seals (e.g. Ti Al6 V4, In 718) and generating of whole blades (e.g. stainless steel) are presented.

Keywords: laser cladding, turbine components, titanium alloys, superalloys

1. Introduction

Increasing the specific efficiency of aero engines (gas turbines) is possible by an increase of the HPT (High Pressure Turbine) temperature and by a reduction of the weight. New developed aero engine components like BLISKs (Blade Integrated Disks) are already in use in several jet engines in order to achieve weight reductions in the LPC (Low Pressure Compressor) and HPC (High Pressure Compressor). BLISKs are compressor disks with integrated blading compared to compressor disks with blades individually attached to the rotor. BLISKs are up to 30 % lighter than conventional disks, involving lower leakage levels and larger tip to hub ratios. Engineering materials for BLISKs are Ti based α, near-α- and α-β-alloys for the LPC (Ti 6Al 4V, Ti 6242, Ti 6246 etc., [1]) and Ni based superalloys for the HPC (In 718, In 625 etc.). SX-components out of Ni based superalloys (CMSX 2, CMSX 4 etc.) are used in the HPT allowing higher turbine temperatures.

The disadvantages of BLISKs become evident when damage occurs. To date worn or damaged BLISK blades necessitate complex and expensive repair work. In the worst case an entire BLISK has to be replaced as a result of the failure of only one blade. The widespread use of BLISKs in aero engines depends strongly on the availability of appropriate repair methods when blade breakage occurs.

In comparison to conventional manufacturing processes laser cladding offers a cost effective alternative for repair and (re)conditioning of gas turbines, steam turbines and aero engine components. Laser cladding fulfills desired process specifications like geometrical accuracy, small heat affected zone (HAZ), metallurgical bond between clads and substrate with small dilution grade, low roughness etc.

Laser cladding with powder additive materials of the same sort allows repair and reconditioning of (BLISK) blades. The results and applications described were achieved with cw-CO_2 wavelength 10.64 μm and cw-Nd:YAG wavelength 1.064 μm laser radiation.

Tip repair and generating of whole blades were carried out. The materials used for tip repair were Ni based superalloys René 80, Waspalloy XX, In 625 and In 718 and for generating whole blades stainless steel 316 L.

2. Processing and Experimental

Cladding is a single-step process: The powder additive material to be clad is directly injected in the interaction zone (fig. 1). In the interaction zone the powder additive material and the substrate surface melt and form the melt pool. The melt solidifies to the clad and the bonding zone with high cooling rates and temperature gradients. [2]

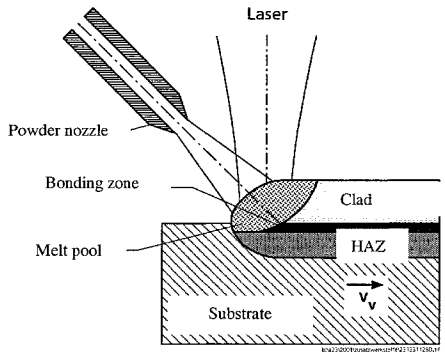


Fig. 1: Scheme of laser cladding [2]

With single or multilayer cladding a typical layer height from 100 µm to several mm can be achieved. If 3D structures are built up by multilayer cladding (typical height: 10 – 100 mm), the process is called laser generating. The macro (geometry, roughness etc.) and micro structural (bonding defects, pores, cracks, microstructure etc.) cladding results depend on the processing parameters:

- Laser power (100 – 2000 W)
- Scanning velocity (100 – 1000 mm/min)
- Powder mass flow (1 – 20 g/min)
- Beam diameter (300 µm – 3 mm)
- Carrier gas flow and pressure (10 – 100 l/min, 1 bar)
- Shielding gas flow and pressure (10 – 100 l/min, 3 – 6 bar)
- Grain size distribution of the powder additive material (20 – 150 µm)

Advantages of laser cladding/generating compared to other processes like TIG (Tungsten Inert Gas), EBW (Electron Beam Welding), MPW (Micro Plasma Welding) and MPTAW (Micro Plasma Transfer Arc Welding) are [2]:

- High accuracy of cladding achieving smallest structures (500 - 800 µm)

- Automatic cladding of layers with a height from 100 µm to more than 100 mm
- No burning notches
- Low heat input
- Small dilution grade
- Small heat affected zone
- Cladding with powder additive material of the same sort

Depending on the cladding application the powder injection (fig. 2) can be realized in different ways:

- Off axis powder nozzle
- Coaxial powder nozzle

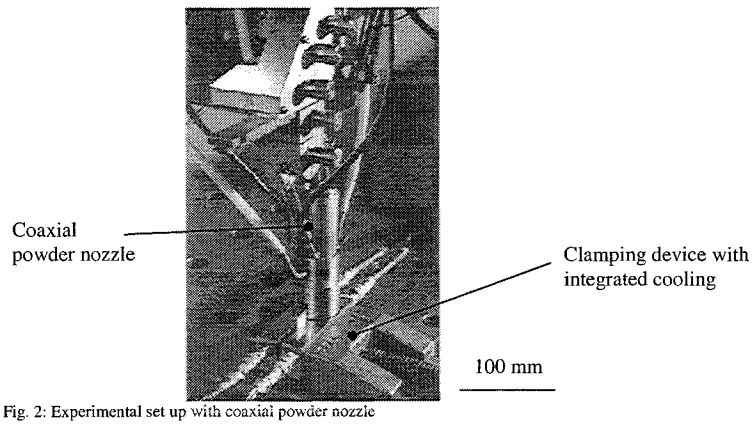


Fig. 2: Experimental set up with coaxial powder nozzle

First steps realizing a closed-center process chain (fig.3) were carried out. Starting point is a damaged BLISK blade. For reconditioning of the blade by laser generating the CAD Data of the component can be used to generate NC trajectories (tracks to be cladded). If the CAD Data is not available, a reference and the milled down damaged blade have to be digitized. The volume difference of the reference and the milled down damaged blade is the volume which has to be reconditioned by laser generating considering a volume offset for finishing. This volume is sliced in different layers (layers to be cladded) and ISO NC trajectories are generated with processing parameters like laser power, scanning velocity, overlapping and filling or building up strategy by a CAD/CAM system and CAD/CAM implemented macros. These ISO NC trajectories are converted into NC control readable machine NC trajectories by a post processing step. The generated NC program is transferred to the NC control and the laser generating process can be initialized. The generated component is finished by milling, grinding and polishing.

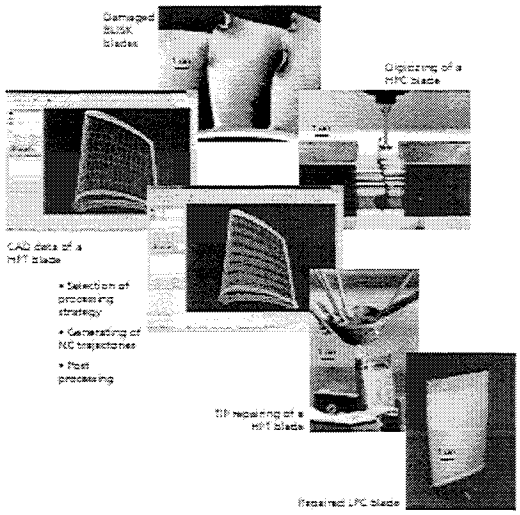


Fig. 3: Flow chart of a closed-center process chain for the repair of a damaged compressor or turbine blades

3. Results and Discussion

The macro and micro structural cladding results depend on the processing parameters (section 2). The dependence of the average cladding height and the cladding result by cladding with cw-CO_2 laser radiation on the line powder mass (cladded mass per distance, cladding rate) and the scanning velocity is shown in figure 6. A low line powder mass leads to an undesired high dilution. A high line powder mass results in bonding defects (lack of fusion) and increased porosity. The adapted and therefore the working point is achieved in between. [2]

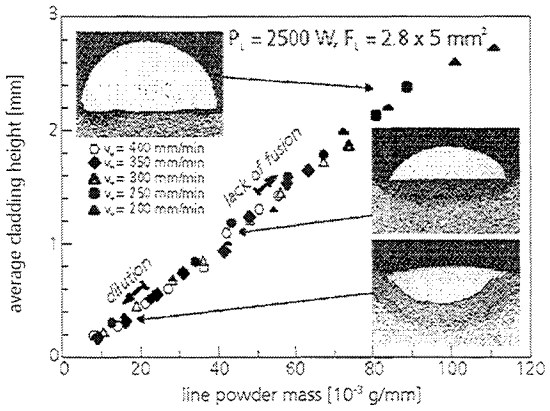


Fig. 6: Dependence of the average cladding height and clad geometry by cladding with cw-CO_2 laser radiation on the line powder mass and the scanning velocity [2]

To determine the best adapted processing parameters for reconditioning of turbine components (HPC blades) out of Ni based superalloy Inconel 718 basic trials on generating webs on Inconel 718 substrates were carried out (fig. 8). Generating was carried out with the processing parameters listed in table 1 in order to avoid bonding defects, pores and oxidations.

	Thin web (50*1.5*20 mm^3)	**Thick web (50*3.5*20 mm^3)**
Laser power (lamp pumped cw-Nd:YAG)	390 – 240 W (adapted bottom to top)	1. track: 990 W (adapted for an improved bonding), elsewhere: 840 W
Scanning velocity	300 mm/min	200 mm/min
Working distance	200 mm	220 mm
Defocusing	0 mm	20 mm
Powder mass flow	$\dot{m}_P = 1.6 - 2\,\%$	$\dot{m}_P = 8\,\%$

Table 1: Processing parameters for generating webs out of In 718

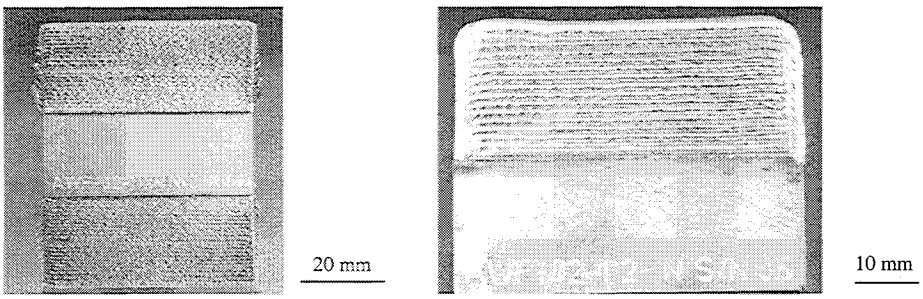


Fig. 8: Thin (left) and thick (right) webs generated by cw-Nd:YAG laser radiation

The surface of the webs is slightly oxidized. The expected geometrical dimensions are met. Cross sections with micro structures of the cladded areas are shown in figure 9. In the bonding zone of the thin webs fine equiaxed grains are observed. The depth of the heat affected zone (HAZ) is about 250 μm. About the half-height of the generated thick web two large grains (length: more than 5 mm) with different dendrite orientations occur. The different dendrite orientations can be verified by dark field illumination. No (micro)pores and (micro)cracks are detected. The average hardness in the cladded area is between 240 (top of the web) and 300 HV 0.3 (near bonding zone). The average hardness of the heat treated base material is 460/470 HV 0.3.

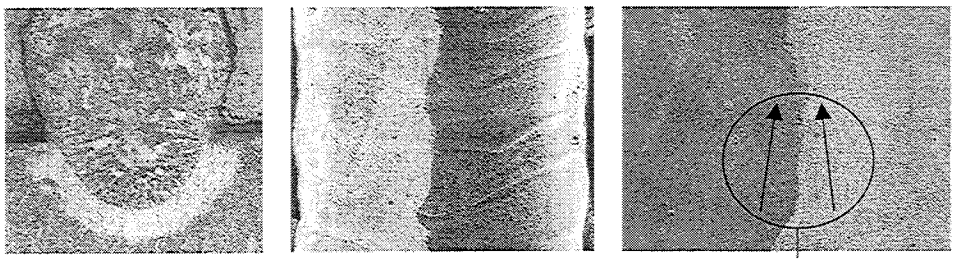


Fig. 9: Cross sections: bonding zone (left, thin web, magnification 50x), middle area (middle, thick web, magnification 25x), middle area (dark field, right, thick web, magnification 50x). The arrows represent the dendrite orientations of the grains.

3D FEM simulations of the temperature field (fig. 7), cooling and solidification rates for web generating were carried out to correlate the results of the basic trials with mathematical modeling. Good correlations between 3D simulations and experimental results are observed. The aim is to develop a mathematical model for generating 3D structures based on laser generating with powder additive materials. [3]

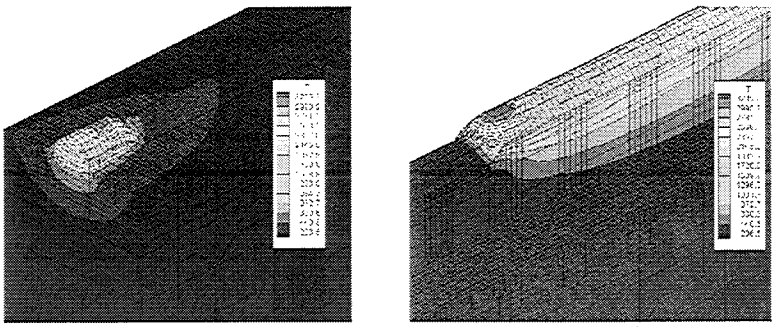


Fig. 7: Temperature field (FEM simulation) within the interaction zone in the turning area first to second layer (left) and after some layers (right) during generating a web [3]

4. Applications

Tip repair and generating of whole blades were carried out (fig. 10, 11 [4]). The powder additive materials used for tip repair on HPT blades were Nickel based superalloy René 80 and on HPC blades Nickel based superalloy Inconel 718. For generating whole blades stainless steel 316 L powder additive material was used. The repaired components are finished by milling, grinding and polishing.

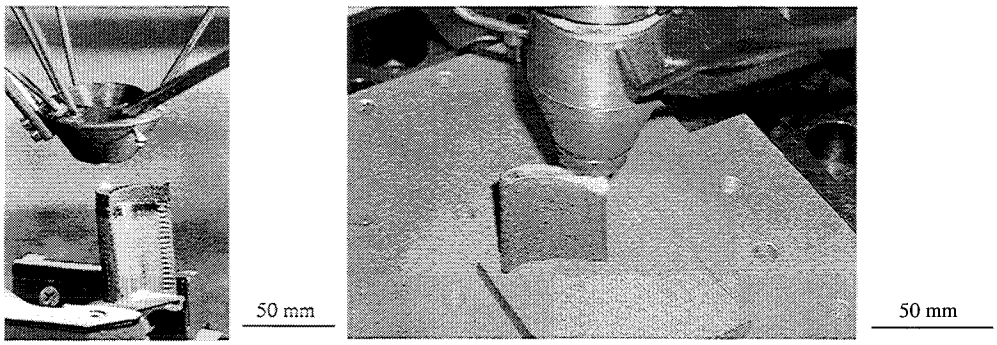


Fig. 10: Tip repair (left) and generating (right) of turbine blades

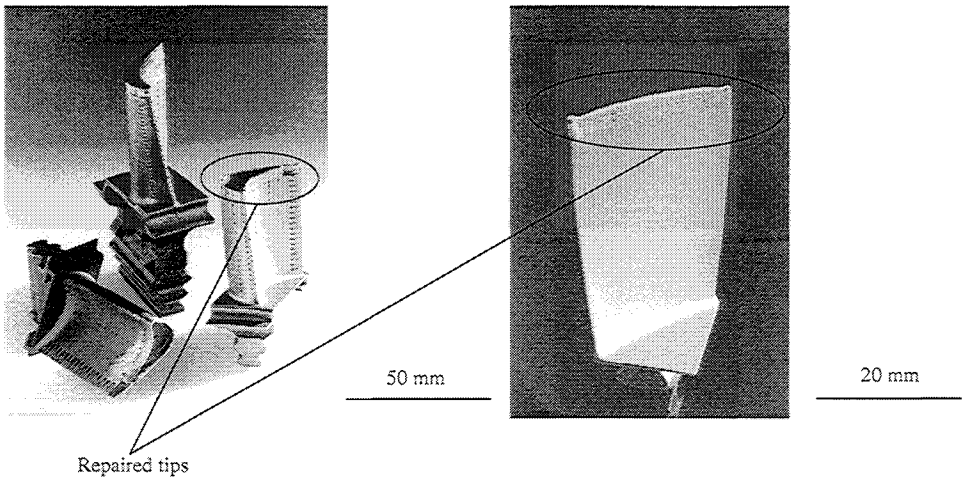


Fig. 11: Tip repaired HPT (left, René 80, [4]) and HPC (right, In 718) blades

Laser cladding and generating also can be used for the repair of other aero engine and gas turbine components such as labyrinth (fig. 12, [4]) and blade seals, z notches etc.

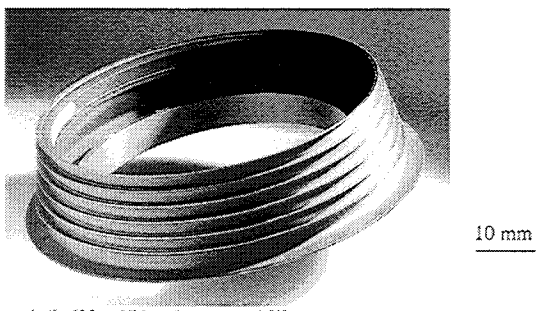


Fig. 12: Repaired labyrinth seals (In 625 on Ni based component) [4]

5. Conclusion and Outlook

Appropriate processing parameters for cladding and generating high temperature Ni based superalloys were determined for repair and reconditioning of HPC blades by FEM simulations and basic trials building up webs (thin: 50*1.5*20 mm^3, thick: 50*3.5*20 mm^3). The corresponding processing parameters minimizing bonding defects, pores and oxidations are in a range of 240 (thin web) to 990 (thick web) Watt for the laser power, 200 to 300 mm/min for the scanning velocity, 200 to 220 mm for the working distance and 1.6 to 8 % for the powder mass flow. No (micro)pores and (micro)cracks are detected. The average hardness in the cladded area is between 240 (top of the web) and 300 HV 0.3 (near bonding zone).

Based on these processing parameters many repair applications have been realized to date like tip repair of HPT and HPC blades or repair and reconditioning of other gas turbine components like blade and labyrinth seals, z notches etc.

In laser cladding and generating research and development are concentrating on new materials and components, used in the gas turbine and aero engine industry, like SX Ni based superalloys (CMSX 2 and 4) and components as well as new designed components like BLISKs out of polycrystalline (PX, In 718) Ni based superalloys. Concerning a reproducible and automatic cladding or generating processing great efforts are taken to realize a closed-center process chain for reverse engineering applications.

In the last years high power diode lasers were pushed onto the market so that it is expected that new (fiber coupled) high power diode lasers with a higher beam quality become more and more utilized for cladding and generating applications.

Acknowledgments

The authors gratefully acknowledge the financial support by the European Union within the GROWTH project "AWFORS: Advanced welding technologies for repair and salvage of high valued engine components on Nickel and Titanium based alloys"

References

[1] M. Peters, C. Leyens, J. Kumpfert, Titan und Titanlegierungen, Werkstoff-Informationsgesellschaft, Oberursel, 1998

[2] A. Gasser, Oberflächenbehandlung metallischer Werkstoffe mit CO_2-Laserstrahlung in der flüssigen Phase, Dissertation RWTH Aachen, Verlag Mainz, 1993

[3] N. Pirch, private communication, 2002

[4] G. Backes, E. W. Kreutz, A. Gasser, E. Hoffmann, K. Wissenbach, R. Poprawe, Laser-Shape Reconditioning of Tools and Machine Parts, Proceedings ICALEO, Orlando, 1998, part 2, section E, pages 48 – 56

HIGH TEMPERATURE REACTOR (HTR) MATERIALS

D. Buckthorpe[1], Couturier[2], B. van der Schaaf[3],,B. Riou[4], H. Rantala[5], R.Moormann[6], A. Buenaventura[7], B-C. Friedrich[8],

Affiliations: NNC Ltd., UK.[1]; Commissariat à l' Energie Atomique (CEA.), France[2], Nuclear Research and Consultancy Group (NRG), Netherlands[3], Framatome ANP, France[4], European Commission, Joint Research Centre (JRC), Institute for Energy, Netherlands[5], Forschungszentrum Juelich GmbH (FZJ.ESS), Germany[6], Empresarios Agrupados Internacional S A (EASA.MD), Spain[7], Framatome ANP (GmbH), Germany[8]

Abstract

Issues concerned with the material selection and behaviour of the main component reactor materials are examined for the Modular High Temperature Reactor. The work considers materials for the reactor vessel, certain high temperature regions including the control rod and turbine and the graphite core. The work is being performed within a European development initiative supported by the European Union Fifth Framework programme. This paper reviews the main elements of the materials work program and presents some initial results. Future actions with regard to experiments and assessment are discussed.

Keywords: HTR, materials, irradiation, tests, steels, graphite, gas

Introduction

European Community Framework Programmes have been launched to consolidate and advance the modular HTR technology in Europe [1]. These involve six coordinated projects that look at important technological issues associated with its development in key technical areas (HTR-F, HTR-M, HTR-N, HTR-E, HTR-L and HTR-C). HTR-C deals with co-ordination of the collective whole, whilst the others cover issues on Fuel, Materials, Nuclear Physics, Equipment, and Licensing. The projects involve partnerships between principal industrial and research organisations from different countries of the European Union, and have the individual aim to develop and consolidate European expertise and experience in each of these areas.

The project on materials (denoted HTR-M & M1) deals with the selection and development of materials for the reactor pressure vessel, high temperature resistant alloys for the internal structures and turbine and graphite for the reactor core. The work started in November 2000 and involves eight partners from five European countries. The main elements of the programme have previously been reviewed and discussed with respect to feasibility and structural integrity requirement [2]. This paper gives a brief outline of the HTR-M programme and presents and discusses some of the initial results and ongoing actions.

Development of HTR Technology

The first commercial gas cooled reactor used for the generation of electricity was commissioned in 1956 at Calder Hall in the UK. This used CO_2 gas as the primary coolant. Over the next decades a total of 26 Magnox Stations and 15 Advanced Gas Cooled Reactors were built most of which are still operating today (the last station starting service in 1989).

Alongside this the helium cooled graphite moderated reactor was developed. The use of helium as a coolant meant that the reactor could operate at higher temperatures and increased efficiency. Such a reactor however called for a new approach to both the core design and the engineering structures. The concept used coated ceramic fuel particles and a dispersed graphite matrix and moderator. In the years 1960 to 1990 HTR prototypes were built and tested in Europe (DRAGON (UK) - 1964 to 1975, AVR (Germany) 1966 to 1988, THTR 300 (Germany) 1983 to 1989). Introduction of a commercial system seemed promising in the early 1980's with the HTR-MODUL plant developed in Germany for industrial process heat applications (based on the passive safety features and a side by side modular arrangement). However the decision to decommission the THTR-300 demonstration plant eventually led to the HTR program being stopped.

Since that time two high temperature test reactors have been built and commissioned outside Europe, the HTTR in Japan in 1998, and HTR-10 in China in 2000. Two international industrial projects are also underway with the aim of commissioning prototype reactors before 2010. The PBMR led by ESKOM (South Africa) with participation of the UK (BNFL), Exelon and South African companies and GT-MHR led by a consortium (MINATOM, General Atomics, Framatome ANP and Fuji Electric). Both of these projects have a strong European involvement. The GT-MHR is being developed for burning Russian military plutonium and the PBMR as the first of a new generation of cost-effective and inherently safe power plants that use the modular approach.

In April 2000 a European HTR Technology Network (HTR-TN) was established to coordinate and encourage work-shared actions within European companies involved in HTR's. This would also serve as a channel for international collaboration [3]. This network involves over 20 organisations from industry, research and development, utilities, universities together with the Joint Research Centre (JRC) of the European Commission who have agreed to work collectively on longer term issues to established a firm basis for continued development of HTR's in Europe.

Objectives and description of the HTR Materials Projects

The development of Advanced HTR concepts requires material data information and an understanding of material behaviour under representative reactor operating

conditions. For components important to the safety and feasibility of designs such as the main steel structures (vessel, internal structures, turbine) and the graphite structures (core), investigation of the different materials to be used and their behaviour in the reactor environment is an important necessary requirement for feasibility and design. The objective of the HTR-M programme therefore was to identify materials of interest for key components, establishing a database of information and support any unresolved technological issues with tests on the most promising options for future application. Two projects are ongoing (HTR-M & HTR-M1 -managed together) that cover three areas: the Reactor vessel, High temperature materials (internal structures and turbine) and Graphite structures (including oxidation). A description of the main activities and project time-scales is shown in Fig. 1. Since no new design work has so far been performed the programme aims to solve technological issues important to the future development of HTR's based on current understandings of the two international project concepts PBMR and GT-MHR.

Reactor Vessel

Design information is needed for the Reactor Pressure Vessel (RPV) under HTR conditions. For the vessel two design options exist:

(1) to keep the vessel temperatures at a similar level to PWR vessels by cooling (this option has been selected for the PBMR) or

(2) to allow the vessel temperatures to reach the core inlet temperature (option selected for the GT-MHR).

It is necessary to investigate and confirm the choice of candidate material options for these two concepts. It is important also to compile their design properties, in relation to both normal and accident conditions. The integrity of the welded joints is seen as a critical feasibility issue and information is needed on the behaviour of welded joints under the influence of the HTR environment. The programme on the vessel material is focused therefore on qualification through a series of tests to look at the integrity of welded joints under irradiated and non-irradiated conditions. An irradiation test of thick section welded joints is being prepared that will start at the end of 2002. It is planned to irradiate specimens in the High Flux Reactor (HFR) at Petten.

In summary the work (performed in HTR-M) on vessel steels covers the following:

- review of existing materials used in gas-cooled reactors and previous high temperature reactors
- setting up of a materials database on design properties (which will lead to identification of data omissions for future R& D testing)
- carrying out of specific tests on welded joints under irradiated and non-irradiated conditions.

High Temperature materials

For the HTR primary circuit components metallic and ceramic materials are possible. Some data exist on such materials but the information and experience for the HTR environment are not well established. The structures to be investigated include the control rods and the turbine. For the former carbon-carbon composites provide an option for which some work has been performed [4]. For the turbine (disc and blades) nickel based alloy steels are possible although the expected working conditions and environment are beyond current industrial experience (with respect to lifetime and in-service inspection).

Work is underway to establish a short list of materials for the control rod and turbine that takes account of the experience from existing high temperature and gas cooled reactors and current manufacturing techniques.

For the turbine, the most critical stage is the first stage discs and blades. The most promising grades are to be investigated initially using short term mechanical tests (tensile, fatigue, short term creep and creep / fatigue tests (in air, vacuum, helium). Within HTR-M1 the test programme includes intermediate term creep effects to confirm the suitability of the chosen alloys for longer-term high temperature exposure. The tests cover specific grades, fabrication routes, and heat treatments. Tests will also be carried out on aged material and damage analysis and lifetime modeling is planned (based on results from notched specimens) to gain a fuller understanding of failure mechanisms.

In summary the work (performed in HTR-M & M1) on high temperature materials covers the following:

- review of existing materials used in gas-cooled reactors and previous high temperature reactors
- setting up of a materials database on design properties (which will lead to identification of data omissions for future R& D testing)
- specific tests on control rod, turbine disc and blade materials (carbon-carbon composites, high alloy steels) at temperature and under short term and intermediate times in air, vacuum and helium.

Graphite

The need for reliable graphite data is a crucial issue for existing and new HTR projects. Graphite plays an important role as a moderator and structural component and has important safety implications because of structural and other property changes that occur when it is irradiated. Its selection also has important consequences for future decommissioning activities. Oxidation resistance of graphites at high temperature requires special attention due to its relevance for safety analyses of air and water ingress accidents, licensing procedure and normal operation.

The HTR-M project provides a limited review of existing graphite information plus some tests on graphite oxidation. The review work focuses on graphite data and selection issues and future needs. Many graphites used in previous core designs are no longer manufactured commercially, and currently available grades limited to a few specific sources of raw materials. Very few of the grades may turn out to be suitable or desirable for a European based modular HTR. The graphite oxidation work involves tests to investigate the effect of oxidation from severe air ingress with core burning. It also looks at protective coatings and innovative C- based materials.

Recognising the shortage of and need for information, the HTR-M1 project concentrates on performing irradiation tests on new graphites for which no data are currently available. The work includes discussions with graphite manufacturers to provide samples and investigate the possibility of producing small quantities of alternative graphites (in the laboratory) which would have a better combination of desirable properties. Also tests to determine variations in physical and mechanical properties up to low/medium irradiation doses (making use of the results from HTR-M as a basis for estimation and extrapolation to higher doses). Although the project falls short of the ultimate selection criteria for the graphite, which will mainly be based on long-term irradiation behaviour, it does provide the groundwork for continuation of the irradiation programme on the most desirable graphite(s). It also makes use of the valuable diminishing experience from experts in design, experiments and testing of graphite within Europe serving to reinstall graphite irradiation and qualification methods within Europe while the available experience and facilities exists.

In summary the work (performed in HTR-M & M1) on graphite covers the following:

- Review of graphite materials data identifying new graphites suitable for HTR and formulating a database of available information.
- Selection of and performing of irradiation testing on new graphites.
- Investigate graphite oxidation and the consequences of severe air ingress with core burning including the development of HTR models and data, protective coatings and innovative C-based materials.

Results from ongoing actions

The work is well into its second year with the emphasis so far on completing and assembling the review and database for the component materials and defining the needs and requirements for the experiments. The following sections provide the results to date from ongoing actions and the basis on which some of the decisions taken so far have been made.

Data Base information

The database is required to cover three main areas:

- The reactor pressure vessel (and other pressure vessels used to contain primary circuit components)
- The high temperature components focusing in particular for the reactor internals on the control rod system and for the turbine on the blades and discs
- The graphite core and its components.

The work is considered to be well advance in certain areas. The overall aims and composition of the database have been defined and Alloys-DB developed at JRC is being considered to house the resulting data. A few selected materials have been chosen for each category and an intermediate spreadsheet is being used to collect and assemble the information from the different partners. The key issues are ease of access, security, quality assurance, central control and the need for web access. The data is being input through a PC version of the software with updating of the web-based information being done in stages.

Reactor Vessel

The vessel review work has concentrated on materials used in new and developing plants to make sure that the most up to date vessel steels are considered. LWR type steel is proposed for the insulated design of the current PBMR and modified 9Cr 1Mo steel for the inlet temperature vessel design of the GT-MHR and both types of steel will be included in the database. The project resources however only permit one type of steel to be tested in the HFR. Since modified 9Cr 1Mo steel has the wider applicability and most uncertainties on data base and fabrication experience (with respect to HTR vessel characteristics), this was chosen as the material for the irradiation test programme.

The irradiation tests will involve the use of the Lyra rig (Fig 2), which allows accurate control of the temperatures and use of a helium atmosphere. The heaters in the rig will be used to correct the temperature levels obtained from gamma heating. Post irradiation tests will include tensile, creep, Charpy and CT toughness tests. The fabrication and characterisation of the welded specimens involves tests on 40 and 150mm thick plate. The former provides a suitable vehicle for trials using different weld bead lengths and different weld parameters before producing the final weld specimens with the thicker plate. The conditions used will simulate the accumulated dose at the end of life. For the tests the lowest temperature condition needs to be considered as higher temperatures are expected to act to anneal out any irradiation damage effects.

Work has started in defining the tests for post-irradiation and reference properties. The database analyses on Mod 9Cr steel weldments together with actions to bound the operating and design conditions will determine the final test selections and boundary condition. The procurement of the material and fabrication of the thick section welded test pieces will be done following characterisation tests. These characterisation tests are underway. Test programme details are expected to be finalised by mid 2002 to allow the test programme to start at the end of 2002.

High Temperature Materials

For the work package on high temperature materials, actions to establish representative design and operating information are in hand. This is needed in order to use the most appropriate conditions for the test. The material review and data base activity on the control rod materials is underway with special attention paid to C/C Composite materials as an alternative to metals. The review and data base work is expected to determine the candidate material for the tests. Actions needed to procure suitable material have started.

For the Turbine (disc and blades) the review and data base work has shown a potential list of alloys which will be considered in detail before selecting the final list of materials for the data base and before confirming the alloy to use for the experiments. Discussions are underway with a turbine materials manufacturer. Testing of turbine materials in helium will require some test facility development. Designs have been initiated and preliminary work is underway in order to have the facilities ready when the materials have become available. Decision on procurement of material is expected to be taken shortly to allow the short-term experiments to start in 2002. Intermediate creep testing of material is planned to start in 2002 under the HTR-M1 project and material selection will be made to maximise the amount of testing time available.

Corrosion problems are known in Helium atmospheres as a result of the decomposition of methane under extremely low oxygen partial pressures. Tests show that such atmospheres are heavily carburising with the carbon forming from water and hydrogen reactions. Such an effect on turbine disc and blade alloys may result in significant reductions in creep strength. Doping the atmosphere with carbon monoxide alleviates the carburising effect. Since carburising can also occur in the tests in helium, the choice of conditions used has to be made very carefully in order to ensure good representative results are obtained. The presence of alloying elements such as cobalt (which is in most of the currently available turbine disc and blade materials) is a further area of investigation. The main issues are the potential for plate out and lift off of particles and their activation and prevention of them flowing through the core.

The current view is to avoid single crystal materials for the blades and test three grades of material under tensile and creep conditions, at temperatures up to 850°C. Manufacturing considerations are a major factor for the disc, producing large ingots without porosity and segregation is a major challenge for the size of disc being considered. The tests on the proposed disc material will be carried out at 700 and 750°C. The ageing will be performed on one grade (that offers the best properties for blades) and post ageing mechanical tests will be performed (tensile and creep tests).

Graphite

The work on the graphite properties has so far looked at the current understanding of knowledge and considered the information available in the IAEA database. Activity has also started on the selection of graphites and for the experimental programme to be performed within HTR-M1 project. Irradiation damage can have a significant effect on the physical and mechanical properties of graphite and the HTR-M1 project will test a small number of graphite types that are to be irradiated within the High Flux Reactor to identify such changes. Progress on this work is underway to set the characteristics of the test programme and shortlist the types of graphites and numbers of tests to be performed. The main graphite suppliers have already indicated their willingness to participate in the test programme.

The work on graphite oxidation involves tests in the THERA and INDEX facilities (Fig. 3). This work is well advanced with some early results in air available. Measurements have been taken on the kinetics of graphite in oxygen for temperatures between 550 and 750°C and partial pressures of between 2 and 20kPa. Measurements in steam have required some improvements to be incorporated in the test rig. Oxidation resistance of three-selected Carbon-Fibre-Composites (CFC's) developed for the Fusion Reactor has so far been measured in air. Further tests in steam are planned for mid 2002 and results from the high flow rate facility expected by the end of 2002. Experiments are also being carried out to determine the thermal conductivity of such CFC materials, and so far reference measurements have been made in non-irradiated material with tests on irradiated samples to be completed in 2002.

Summary and Conclusions

This paper outlines the work program and reviews and discusses important issues concerning material needs for feasibility and results of some of the ongoing actions. Overall the project is progressing to programme with review and data base investigations in hand and planning for experiments started. Graphite oxidation experiments are well underway and results available. The next phase of the work will involve decisions on materials and the setting up of the tests on the vessel material, the disc and blade high temperature alloys, and for the graphite irradiation tests to enable them to start as early as possible in the programme.

Acknowledgements

The projects HTR-M & HTR-M1 mentioned in this paper are being co-sponsored under the Fifth Framework programme of the European Atomic Energy Community ("Euratom"), contracts FIKI-CT-2000-0032 and FIKI-CT-2001-20135. The information provided herein is the sole responsibility of the authors and does not reflect the Community's opinion. The Community is not responsible for any use that might be made of the data appearing in this publication.

References

[1] J Martin-Bermejo, M. Hugon, G. Van Goethem
Research activities on High Temperature Gas-cooled Reactors (HTRs) in the 5th EURATOM RTD, Framework Programme. Smirt 16, Washington, Aug 2001

[2] D. Buckthorpe, R. Couturier, B. van der Schaaf, B. Riou, H. Rantala, R.Moormann, F. Alonso, B-C. Friedrich, Investigation of High Temperature Reactor (HTR) Materials, NEA/OECD, 2nd Information Exchange meeting on High Temperature Engineering, Paris, on 10-12 October 2001

[3] W. Von Lensa, D. Hittner, J. Guidez, F. Sevini, A. Chevalier, M. T. Dominguez, G. Brinkmann, T. Abram, J. Martin- Bermejo. "The Role of International Collaboration within the European High-Temperature Reactor Technology Network (HTR-TN)" Seminar on HTGR Application and Development, Beijing, China, March 19-21, 2001.

[4] Development of carbon/ carbon composite control rod for HTTR (II) - Concept, specification and mechanical test of materials - JEARI research 98-003.

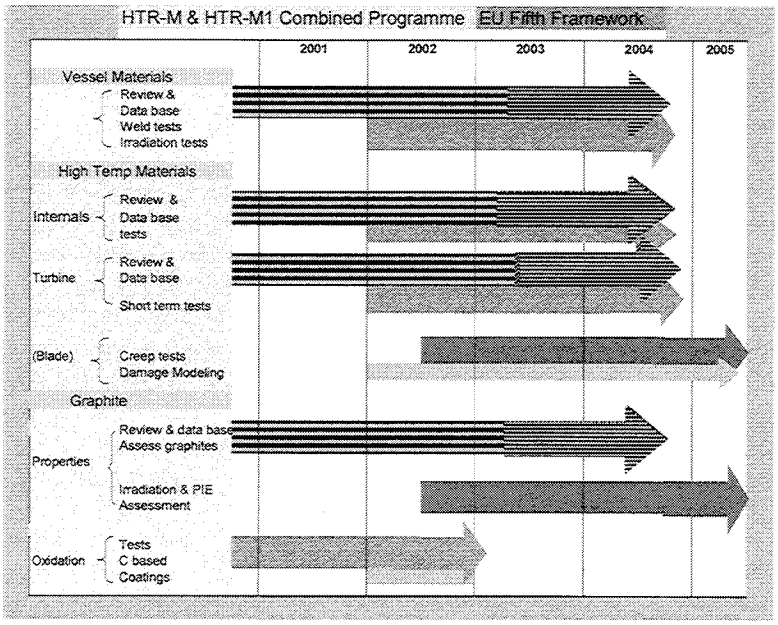


Figure 1 Description of Overall HTR-Materials Programme

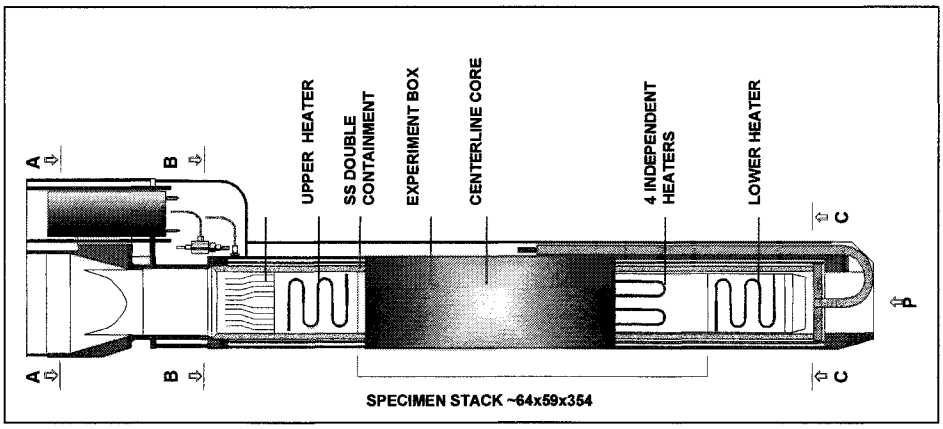


Figure 2 Lyra Test Rig

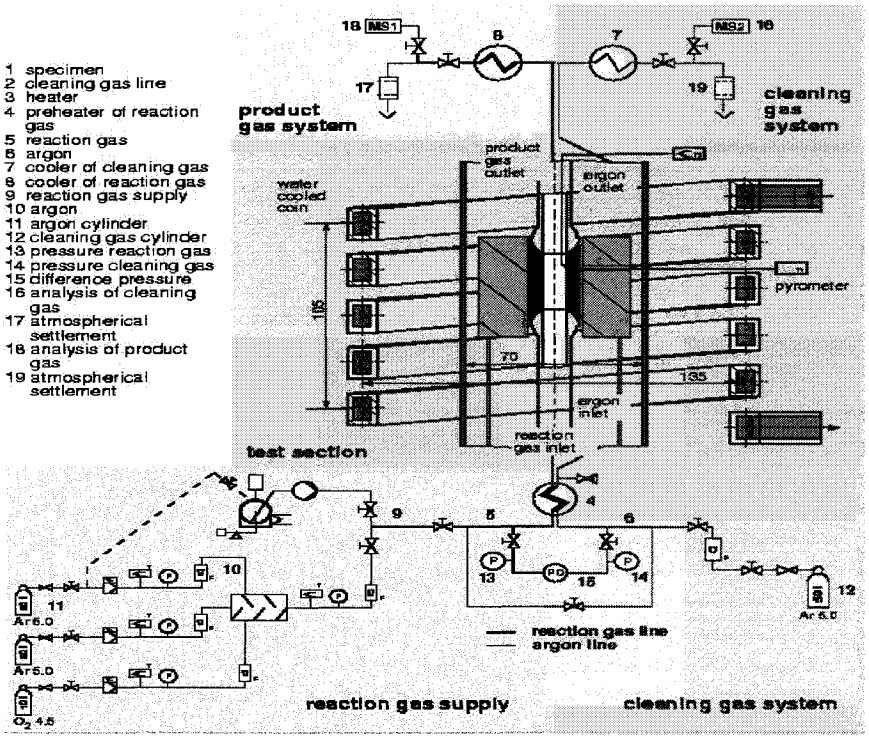


Figure 3 Schematic of the Oxidation Facility INDEX

PROPERTIES OF OXIDE/OXIDE CMCs FOR HIGH TEMPERATURE APPLICATIONS IN GAS TURBINES

M. Innocenti[1], P. Del Puglia[1,2], Y.Z. Pappas[3], C. G. Dassios[3]
M. Steen[3], V. Kostopoulos[4], D. Vlachos[4]

[1] GE Oil & Gas - Nuovo Pignone S.p.A., Via F. Matteucci 2, 50127 Firenze (I),
[2] Università degli Studi di Firenze, Dipartimento di Meccanica e Tecnologie Industriali (DMTI), Via di Santa Marta 3, 50139 Firenze (I),
[3] JRC-Institute for Energy, Westerduinweg 3, 1755 ZG Petten (NL),
[4] University of Patras, Dept. of Mechanical Engineering and Aeronautics & ICE-HT/FORTH, GR 26500 Patras, Greece

Abstract

Ceramic composites with continuous oxide fibres and an oxide matrix have potential for combining high damage tolerance (due to low brittleness compared to monolithic ceramics) with extreme temperature resistance. There are a lot of world-wide activities at laboratory level with Nextel™ type fibres. To prevent brittleness and increase fracture toughness, different material tailoring approaches based on a weak interface between the fibre and the matrix, and porous matrices are under development. Up to now, the limited thermal resistance of commercially available fibres and of the fibre/matrix interface restricts thermal stability. However, an increase of thermal stability up to more than 1200°C for 1000 hours lifetime is necessary for CMCs to represent valid substitutes of alloys, used so far in gas turbine applications. The target is to achieve 1200°C wall temperature by film cooling and convection without using a thermal barrier coating. Some prototypes, e.g. liners for gas turbine and exhaust tubes for aero-engines, have already been produced and successfully tested at moderately high temperature level.
An oxide-based CMC material with Nextel™ 720 fibre and mullite matrix was developed for high temperature application in gas turbines. The composite laminate was characterised in terms of mechanical performance and thermal stability during and after high temperature exposure. Comparisons with a commercially available oxide/oxide material from COI are presented where data are available.
Additionally, in order to explain the mechanical behaviour of the produced oxide/oxide composite, the Nextel™ 720 fibres were investigated in terms of high temperature behaviour in fibre bundle tests. The strong reduction of the Young's Modulus increasing temperature, as well as the unexpected reduction of the Weibull Modulus was monitored. The tested samples were subjected to different non-destructive evaluation (NDE) methods prior, during and after mechanical testing in order to assist interpretation of the obtained results and to identify characteristic damage mechanisms and their evolution during loading.

Keywords: Ceramic matrix composites, oxide/oxide, turbine application, thermo-mechanical properties, non-destructive evaluation.

Introduction

The prominent mechanical properties and the excellent fracture behaviour of Continuous Fibre-reinforced Ceramic-matrix and Carbon/Carbon Composites (CFCCs & C/C) under high thermal and mechanical loads place them today among the ideal candidate materials for structural applications for use at moderate and high temperatures. Their increased fracture resistance and their ability to retain strength in the presence of holes and notches that results from active stress redistribution mechanisms is deployed today to maintain the toughness and durability of structural components that must perform with reliability under severe thermo-mechanical conditions.
So far CFCCs have been used to applications ranging from high performance breaking systems to heat shields for re-entry vehicles. One of the main disadvantages of conventional

CFCC materials is their vulnerability to oxidation at high temperature environment. Although a number of oxidation protection top layer gradient coating systems have been developed and liquid silica infiltration techniques have been used the problem is far from being solved. The use of oxide/oxide composite systems allows the material to withstand high temperature structural applications, with no oxidation protective layers or cooling systems. This is an attractive alternative [1-5].
Recently, one of the most active research and development efforts in the field of oxide/ oxide composites is underway in the gas turbine industry. The main goal is to increase the machine working temperature, reducing the cooling air supply, and thus to increase the plant efficiency (and reduce the fuel consumption) enabling a consistent reduction in pollutant emission.
The present work deals with the characterisation of a mullite matrix based Nextel^{TM} 720 fibre reinforced composite. A complete mechanical characterisation of ceramic matrix composites (CMCs) is rather difficult due to the large variety of mechanical tests needed, e.g. tensile, creep, low cycle fatigue, high cycle fatigue and the material inherent scatter. Therefore, only preliminary studies can be performed, as a limited number of samples are available. In this work some first results on the mechanical behaviour of the oxide based CMC under investigation are presented.

Material description

The material under investigation is a mullite matrix NEXTEL 720 (3000 denier) fibre reinforced composite with a fugitive fibre/matrix carbon interface applied by Sol/Gel technique. The composite laminate was made using a symmetric 0°/90° fibre lay-up orientation, with a total fibre content of 41%. The fabrication process is the polymer infiltration process (PIP) [6].
A similar, commercially available material supplied by Composite Optics Inc, was selected as a reference material for comparison purposes. This composite consists of Nextel 720 (8 harness-satin weave - 8HSW) fibres in a porous aluminosilicate matrix. According to the supplier no additional interface is used between fibre and matrix [7, 8].
These two materials will be referred to as Material Batch 3a and Material Batch 3b respectively.
Since the aim of the present work is to explore the potential of the above-described materials for application in stationary gas turbines, one of the critical issues is to study their mechanical performance after prolonged exposure to the actual operating conditions at different temperatures. For this purpose, an electric resistance furnace equipped with a gas supply system was used as a conditioning chamber simulating combustor gas turbine operating conditions.

Material testing

The material characterisation procedure can be divided into four parts:
Part A: Non-destructive characterisation and quality control tests
Part B: Room temperature tests, containing tension and ILSS tests applied on virgin and long term exposed to operating environment samples.
Part C: High temperature tests, containing tension, creep and low cycle fatigue tests
Part D: Fibre bundle tests at different temperature levels.

A. Preliminary Characterisation and Quality Control Tests, Material Conditioning

Prior to mechanical characterisation at Room Temperature (RT) and High Temperature (HT) conditions, ultrasonic inspection tests were conducted on virgin and tested coupons. This to ensure an uniform density distribution and to identify any possible delamination areas.

The ultrasonic inspection was performed using the "double through-transmission" technique, placing the samples inside a water path and using a 5 MHz ultrasonic transducer. Problems with water absorption due to the material high porosity were tackled by applying a thin varnish coating on the samples. The information obtained from the analysis of the digital images, captured by the use of the C-Scan method, was very useful for the interpretation of the mechanical test results.

As a general statement, both the Batch 3a and the Batch 3b materials seem to feature uniform porosity distribution and to be free from defects and delamination.

B. Tests at Room Temperature

Tensile and interlaminar shear tests were performed on "as produced" specimens and on specimens exposed to the gas turbine simulated operating conditions. Examination of fracture surfaces and characterisation of microstructures were also performed after each test. Room temperature tensile tests were performed on specimens (150 mm x 10 mm or 180 mm x 10 mm), using a Zwick Universal Testing Machine 1474, under displacement control with a crosshead speed of 2 mm/min, according to EN658-1 [9].

Interlaminar shear testing was performed in short beam bending according to the ASTM standard D2344 [10], with specimens of 20 mm length and 10 mm width. The same testing machine was used with a crosshead speed of 0.5 mm/min.

The exposed specimens were subject to a temperature of 1150°C and 1200°C for a period of 1000 and 5000 hours.

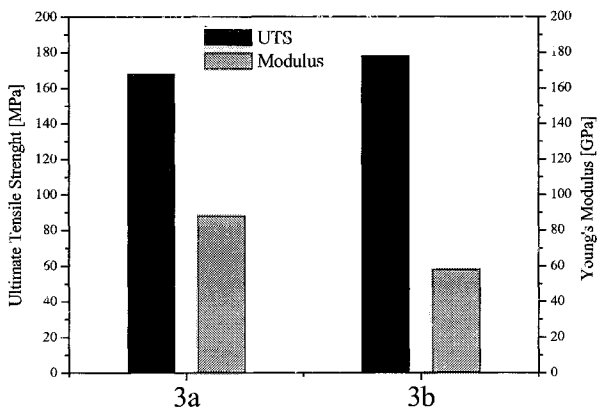


Figure 1 : Ultimate Tensile strength and Young's Modulus (normalised to 35% fibre volume) at room temperature

Figure 1 shows Ultimate Tensile Strength (UTS) and Young's modulus measurements at room temperature for Batches 3a and 3b, calculated for a normalised fibre volume fraction of 35% for comparison purposes. Batch 3a and 3b materials feature almost similar tensile strength values (170 to 180 MPa). However, Batch 3a stiffness is higher than that of Batch 3b.

Fibre properties are degraded by grain growth above 1100°C. Moreover, the matrix structure and the porosity level change, which is expected to alter the crack structure through the material and significantly affects the fracture type. In particular, the relative porosity reduction in material Batch 3b matrix has severely reduced the ability to redistribute stresses and to absorb energy prior to final failure. In the case of material Batch 3a, the fibre debonding and pull-out are hindered by the fibre and matrix sintering across the fugitive gap, created after the burn out of the fugitive coating.
Figure 2a reports the results for UTS before and after the temperature exposure for both material Batches and for different temperatures and duration of exposure. Both materials loose their strength after thermal treatment and the tensile strength drops to around 50 MPa after 1000 hours exposure time. This is due to re-crystallisation processes in the fibres and is consistent with high temperature treatments of fibres only. The slight increase in strength after 5000 hours is probably due to sintering effects in the matrix.
Figure 2b shows the thermal treatment effect on the ILSS. The relative reduction of ILSS values is not as high as in the case of tensile strength, however it is still present. For the material Batch 3a, an ILSS increase after 5000 hours is identified, whereas the material Batch 3b does not show any further variation after the initial reduction of ILSS, after 1000 hours. As for Batch 3b, the higher the exposure temperature the higher the drop off. Moreover, the ILSS values of Batch 3a are higher than the values of Batch 3b.

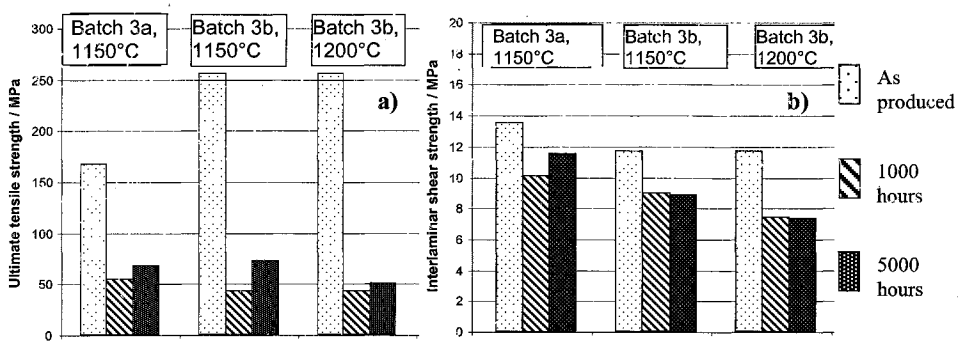


Figure 2: (a) Tensile strength after high temperature exposure and (b) Interlaminar shear strength after high temperature exposure

Acoustic Emission (AE) results and Ultrasonic Measurements
During the tensile tests (done according to EN 658-1), continuous AE monitoring was performed for all the tested samples. The analysis of the monitored AE activity was used to identify the damage mechanisms, the failure modes and their evolution during load increase.
AE analog signals were captured and digitised by a MISTRAS 2001 data acquisition system by Physical Acoustics Corporation (PAC), using two piezoelectric transducers NANO 30, with operating frequency range 120-750 kHz. The transducers were attached to each specimen, while silicon grease was used as coupling agent. Pre-amplification of 40 dB was applied through PAC 1220B pre-amplifiers. Acquisition parameters for the two active channels were: Threshold 40 dB, Peak Definition Time 50 μs, Hit Definition Time 100 μs and Hit Lockout Time 500 μs.

The recorded events were analysed using Pattern Recognition (PR) methodology [11, 12]. In this work, an unsupervised PR procedure (i.e. without any a priori knowledge) was used to identify the major damage accumulation mechanisms in Oxide/Oxide coupons, tested in tension until final failure. Several algorithms were used to achieve an optimum classification based on common mathematical clustering evaluation criteria. The initiation and further activation of the district damage mechanisms are successfully characterised by using the cumulative events of each of the resulting classes. The clustering methodology resulted in three clusters for material Batch 3a and four clusters for material Batch 3b. The results of the clustering process are presented in Figures 3 and 4 (Batch 3a) and 5 and 6 (Batch 3b).
The association of these clusters to the specific failure mechanisms is rather difficult, especially in the case of Oxide/Oxide composites, where only limited experience for their failure modes is available.
However, in this analysis the use of parameters such as cluster activation in time along with systematic microscopic examination of the fracture surfaces leads to a safe interpretation of the clusters. For Batch 3a, three major clusters (no noise cluster) associated with the same damage mechanisms were recognised, as shown in Figures 3 and 4. Further testing on exposed specimens can reveal differences in the activation loads for each mechanisms, thus providing a useful insight for further material development.
In the case of Batch 3b (Figures 5 and 6), cluster 1 corresponds to matrix cracking as it manifests its presence from the beginning of the loading, cluster 2 to fibre failure since it is the dominant cluster in the final stage, cluster 3 to interfacial failure and sliding of the woven structure and cluster 4 to noise, weak AE signals and secondary reflections of the AE signals.

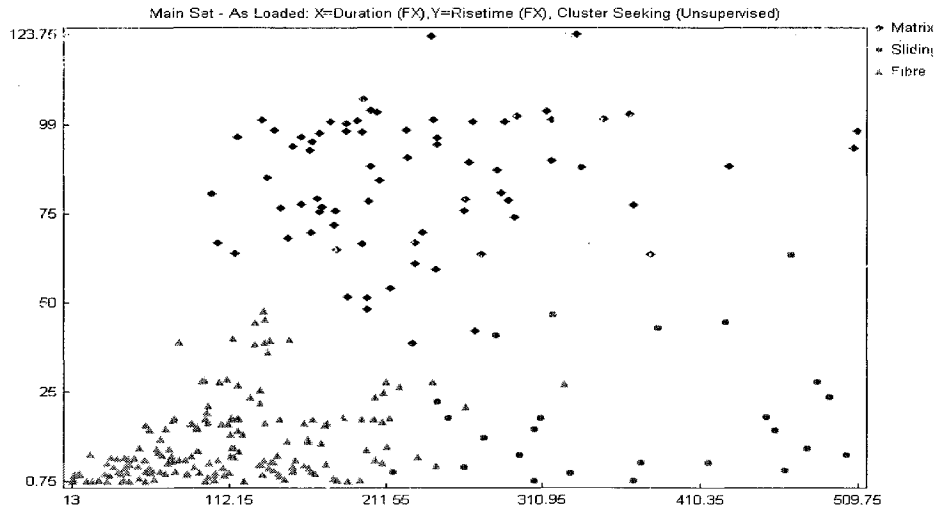


Figure 3 : Clusters identified for material Batch 3a, presented on a Rise Time versus Duration plot

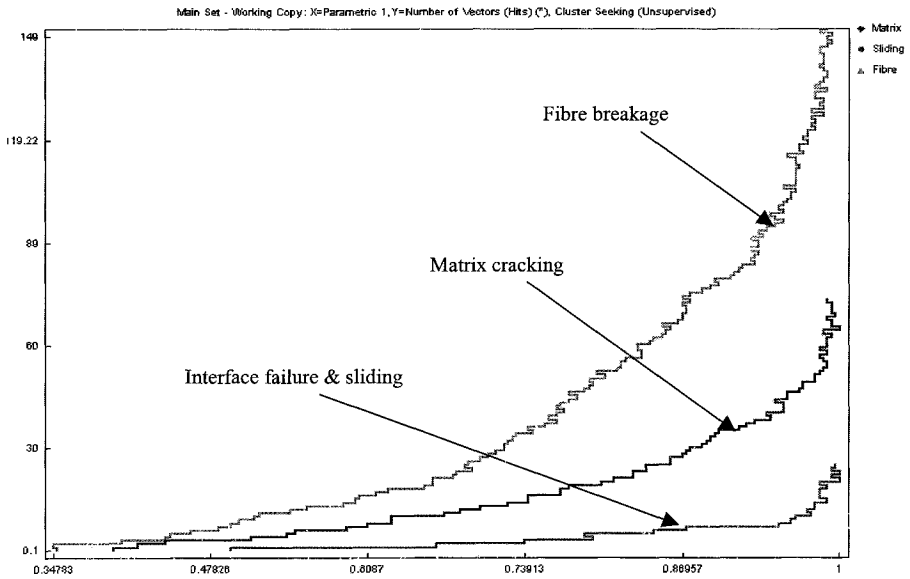


Figure 4 : Clustering results for material Batch 3a, presented in a cumulative energy versus normalised applied load plot

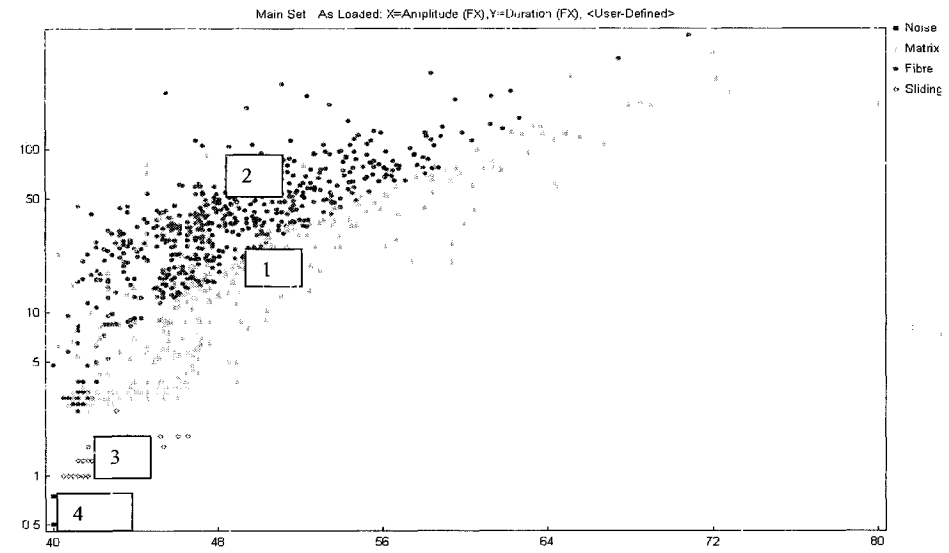


Figure 5 : Clusters identified for material Batch 3b, presented on a Rise Time versus Duration plot

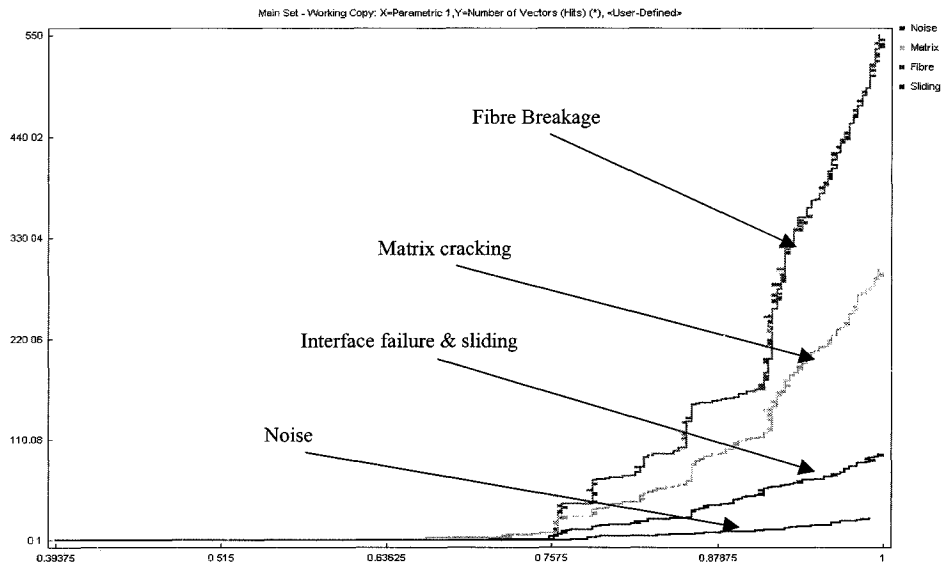


Figure 6 : Clustering results for material Batch 3b, presented in a cumulative energy versus normalised applied load plot

C. High Temperature Tests

High Temperature Uniaxial Tensile Tests

Uniaxial tensile tests at temperatures from 60°C to 1200°C have been performed on coupons from Batches 3a and 3b, using an electromechanical Instron-Schenck machine. The specimens are heated indirectly by induction, via a SiC susceptor centred on the coupon. A Zirconia insulation tube surrounds the susceptor with high open porosity to avoid heat losses. Temperature is measured by means of a pyrometer and B-type thermocouples along the gauge length.

The deformations and therefore the longitudinal strains are obtained by using a low contact force mechanical extensometer, which is mounted sideways on the specimen and placed in a water-cooled Faraday cage to avoid thermal drifts and electromagnetic interference.

Figure 7 shows ultimate tensile strength results for two loading rates as a function of temperature. UTS for material Batch 3a slightly decreases after 800°C and then remains almost constant, while for Batch 3b it increases up to 1000°C, but then decreases at 1200°C.

Creep and Post-Creep Tests

Creep tests were performed at 1050°C. Stress levels were 25 and 50 MPa. Tensile tests at room temperature were performed after them. The first matrix cracking stress and modulus depend on temperature, as was shown in tensile tests. This is confirmed by loading traces up to creep stress at 1050°C. Furthermore, UTS and failure strain are considerably reduced compared to results on unexposed material, whereas modulus is similar to that of virgin material.

Composite-like mechanical behaviour is lost to a great extent.

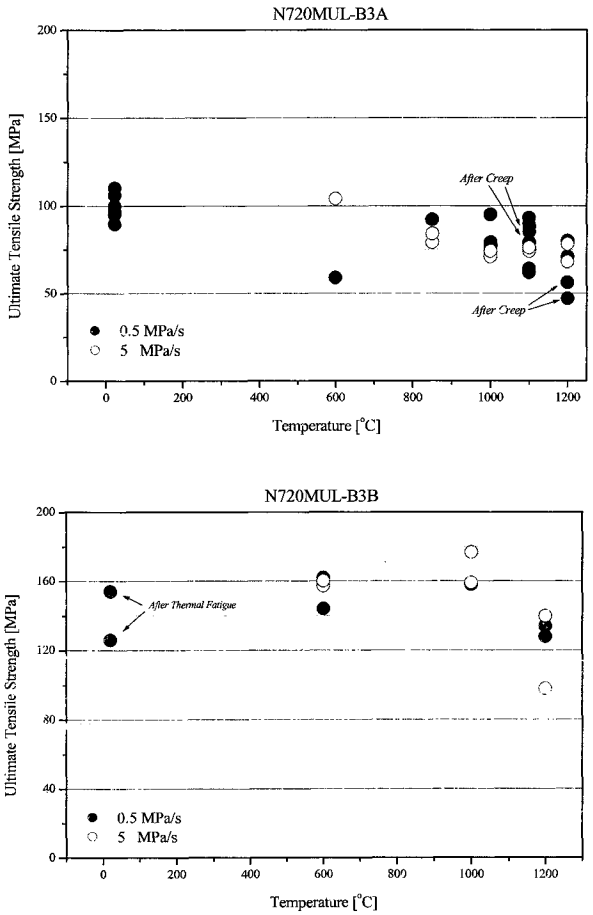


Figure 7 : Ultimate Tensile Strength plots as a function of temperature for material (a) Batch 3a and (b) Batch 3b, for tests performed using loading rates of 0.5 and 5 MPa/s

Thermal Fatigue and Post-Fatigue Tests

A number of Thermal Fatigue tests have been executed between temperatures of 800°C and 1100°C on specimens from Batch 3a, with or without a superimposed mechanical stress. Figures 8a and 8b show typical examples of thermal fatigue experiments with no mechanical loading and in the presence of mechanical loading respectively.

The presence of an external mechanical stress increases the accumulation of the total strain during the thermal fatigue test, especially in the first phase of the fatigue cycles. This leads to higher total strain ranges for each thermal cycle, as shown in Figure 8b.

This indicates that damage is mostly due to creep, accumulated during thermal cycling. This is confirmed by the results shown in Figures 9a and 9b.

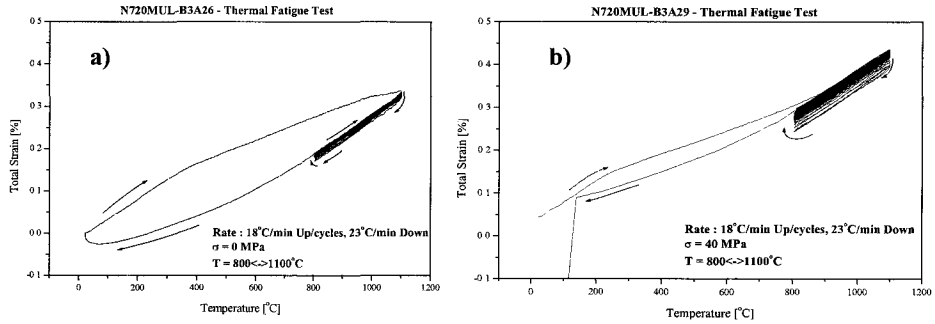


Figure 8: (a) Total strain vs temperature for the case of Batch 3a, under no external mechanical stress, and (b) Total strain vs temperature for the case of Batch 3a, under external mechanical stress of 40 MPa

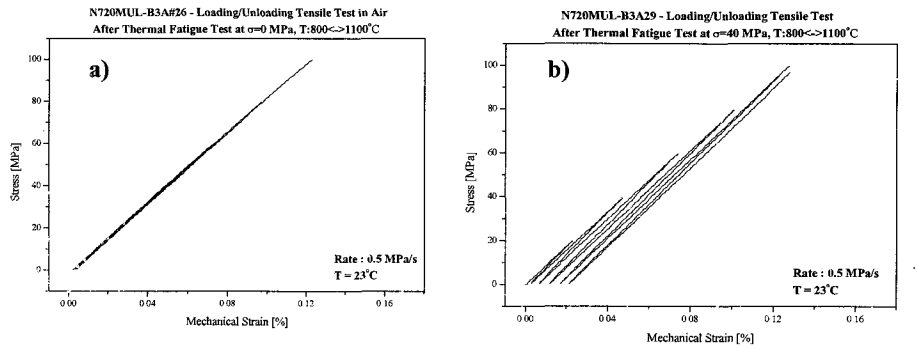


Figure 9: Post-Fatigue Loading/Unloading tensile test for Batch 3a, (a) under no external mechanical stress during thermal fatigue, and (b) under external mechanical stress during thermal fatigue of 40 MPa

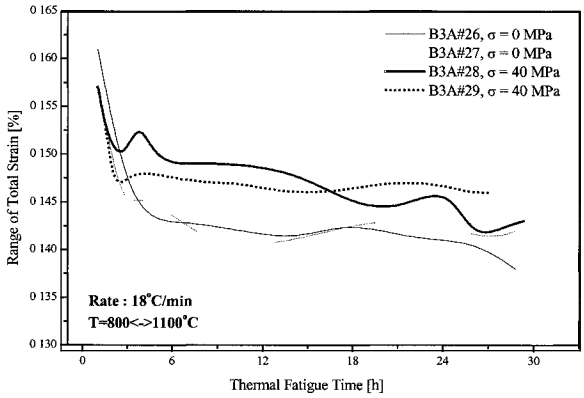


Figure 10 : Range of total strain during thermal fatigue tests as a function of fatigue time, for two cases of external mechanical stress, for Batch 3a specimens

When no external mechanical load is applied during thermal fatigue, the material behaviour is almost linear. While thermal fatigue in the presence of externally applied mechanical loading presents a large amount of irreversible strain, confirming the existence of creep damage. Finally, Figure 10 sums up the thermal fatigue test results.

D. Fibre Bundle Testing

Nextel™ 720 fibre bundle tests, at room and high temperatures, have been carried out to understand the tensile behaviour on the Nextel™ 720/mullite composites [13-17]. In fact, the modulus and strength values recorded in the investigated composites are lower than those reported by 3M, which is the manufacturer [18]. The statistical Nextel™ 720 tensile strength and flexural Young's modulus has been investigated as a function of temperature, gauge length, load rates and effect of sizing.

Tensile tests have been performed on fibre bundles (1500 Denier, 400 filament) extracted from a tow supplied by 3M Corporation. Room temperature specimens of 140, 100, 75 and 50 mm gauge lengths were tested at various extension rates (0.1-0.5 mm/min), both in the as-received and de-sized (heat cleaning at 700°C) conditions. High-temperature cold-end testing was performed in a chamber under inert gas (Argon) at 600, 800, 1000, 1100 and 1200°C; the heated length was kept constant at 20 mm according to ENV 1007-5 [19].

Direct strain measurements could not be performed on the fibres in real testing time and a compliance-derived approach was followed to determine the fibre strain from the recorded extension. The parasitic contribution to strain at room temperature was quantified following the zero-gauge length extrapolation approach. Additional parasitic contributions, due to the different temperature zones along the specimen length during the high-temperature cold-end testing, were also quantified accordingly. By exclusion of these contributions from the total strain the net fibre strain could be determined. The experimental results were analysed using Weibull statistics to deduce the Weibull modulus and characteristic strength of Nextel™ 720 fibres. The equivalent fibre strength at a 25 mm gauge length was calculated using the Weibull gauge length correction to compare it with the reported values.

The room temperature tests agreed with the reported values in Weibull modulus and elastic modulus but the bundle strength appeared to be significantly decreased. No effect on the presence of sizing or the strain rate was noticed on the mechanical properties of the fibres. Non Weibull-smooth failure regions were associated with gauge lengths of 100 and 140 mm. These abrupt stress drops could reflect a higher energy accumulation (an effect on the larger fibre volume) that subsequently leads to a need for a drastic release.

Temperature [°C]	Room	600	800	1000	1100	1200
Weibull modulus m_ε	6.98	1.76	1.66	1.36	2.68	3.68
Young's modulus [GPa]	261.0	125.9	143.5	148.5	53.7	25.2
Strength [MPa]	1149.0	1161.3	1031.8	933.2	753.8	634.9

Table 1 : Summary of fibre bundle test results on Nextel™ 720 - the room temperature values reported by 3M : $m\varepsilon$ =7.1, E = 260 GPa, σ (25 mm) = 2100 MPa

A degradation of the mechanical properties was noted with increasing temperature. Bundle strength remained in the region of the room-temperature value for tests at 600 and 800°C. Above 1000°C, alumina properties decrease as a consequence of creep phenomena.
Table 1 summarises the results obtained up to now. The bundle strength presented is normalised to a 25 mm gauge length for the sake of cross-comparison. For the bundle strength, these values correspond to the mean fibre strength normalised to a reference gauge length of 25 mm.

Conclusions

The properties of oxide based CMCs have been evaluated in the case of two different Oxide/Oxide composites.
Different types of test (destructive, non destructive, cyclic and quasi-static) have been carried out on virgin material and on aged material, both at room temperature and high temperature.
The extensive mechanical testing reveals that the porous matrix concept without a fibre coating as a fibre-matrix interface leads to a slightly higher strength at high temperature (Batch 3b) and to lower stiffness characteristics. However, in both cases the temperature of 1200 °C seems to be the upper bound working temperature for the oxide/oxide composites based on the Nextel™ 720 fibre reinforcement.

References

[1] D. B. Marshall and J. B. Davis, 'Ceramics for future power generation : fiber reinforced oxide composites', Current Opinion in Solid State & Materials Science. Vol 5, 2001, 283-289.
[2] R. S. Hay, E. Boakeye, M. D. Petry, Y. Berta, K. Von Lehmden and K. Welch, 'Grain growth and tensile strength of 3M Nextel 720 after thermal exposure', Ceram Eng Sci Proc, Vol 20, 1999,165-172.
[3] G. Evans, D. B. Marshall, F. Zok and C. Levi, 'Recent advances in oxide-oxide composite technology', Adv Composite Mater Vol 8, 1999,17-23.
[4] R. John, L. Zawada and D. Buchanan, 'Fracture and creep rupture behavior of a notched woven oxide/oxide CMC', presented at the 24th Annual Conference on Composites, Materials and Structures, Coco Beach, FL, January, 2000.
[5] Szweda, et al., 'Exposure of CFCC to high temperature, high pressure combustor environments', presented at the 24th Annual Conference on Composites, Materials and Structures, Coco Beach, FL, January, 2000.
[6] H. Knabe, T. Haug, W. Schafer and T. Waldenmaier, 'Oxide ceramic composites for aerospace applications',(report) Dornier GmbH, and Dornier Luftfahrt GmbH, 2001.
[7] F. W. Zok and C. G. Levi, 'Mechanical properties of porous-matrix composites', Adv Eng Mater, Vol 3, 2001, 15-23.
[8] E. Carelli, H. Fujita, J. Yang and F. W. Zok, 'On the mechanical properties of a porous-matrix ceramic composite following thermal aging', J. Eur Ceram Soc, Vol 20, 2000, 607-618.
[9] EN 658-1:1998 - Advanced technical ceramics - Mechanical properties of ceramic composites at room temperature - Determination of tensile properties.
[10] D2344/D2344M-00e1 Standard Test Method for Short-Beam Strength of Polymer Matrix Composite Materials and Their Laminates

[11] Y. Z. Pappas, Y. P. Markopoulos and V. Kostopoulos, 'Failure mechanisms analysis of 2D carbon/carbon using acoustic emission monitoring', NDI & E International, Vol 31, 1998, 157-163.
[12] G. Sotiriadis, A. Kontsos, T. Loutas, Y. Z. Pappas and V. Kostopoulos, 'On the identification of failure mechanisms of oxide/oxide composites using acoustic emission', accepted for presentation in the 25th European Conference on Acoustic emission testing, Prague, Czech Republic, 2002.
[13] M. L. Antti, E. Lara-Curzio and R. Warren, 'Thermal degradation of an oxide fibre (Nextel 720)/Aluminosilicate composite', 18th ESIS TC6 Meeting, Teddington, Junary 2002.
[14] R. Paar, P. Bonnel and M. Steen, 'Compliance-derived strain determination in fibre (Bundle) tests at high temperatures', Advanced Composites Letters, 7 Vol 3, 1998, 69-73.
[15] H. Schneider, J. Goering, M. Schmeucker and F. Flucht, 'Thermal stability of Nextel 720 Alumino silicate fibers', Ceramic Microstructure: Control at the Atomic Level, Edited by A.P. Tomsia and A. Glaeser, New York 1998, 721-729.
[16] F. Deleglise, M. H. Berger, D. Jeulin and A. R. Bunsell, 'Microstructural stability and room temperature mechanical properties of the Nextel 720 Fibre' Journal of the European Ceramic Society, Vol 21, 2001, 569-580.
[17] G. Dassios et al, 'The Statistical Properties of Alumina Fibres to 1200oC', accepted for publication at Journal of Engineering Materials, 2002.
[18] 3M Nextel Ceramic Fiber Technical Notebook, 3M Ceramic Fiber Products, 2001.
[19] ENV 1007-5:1998 - Advanced technical ceramics - Ceramic composites - Methods of test for reinforcements - Determination of distribution of tensile strength and of tensile strain to failure of filaments within a multifilament tow at ambient temperature.

Acknowledgements

This study has been performed within the frame of R&D programme BRITE/EURAM, 'Ceramic Components for Industrial Gas Turbines - CERCO' of the European Commission. EADS/Dornier GmbH supplied the used materials.

SECTION 2

FUEL ISSUES AND NOVEL COMPONENTS

SECTION 2

FUEL ISSUES AND NOVEL COMPONENTS

Invited Papers

IN-SITU FIRESIDE CORROSION TESTING OF ADVANCED BOILER MATERIALS WITH DIVERSE FUELS

P. J. Henderson[1], A. Karlsson[2], C. Davis[3] , P. Rademakers[4],
J. Cizner[5], B. Formanek[6], K. Göransson[7] and J. Oakey[8]

[1]Vattenfall AB, Sweden, [2]formerly Energi E2, Denmark, now at F. L. Smidth A/S, Denmark,
[3]PowerGen, UK, [4]TNO Industrie, The Netherlands, [5]SVÚM, Czech Republic,
[6]Silesian Technical University, Poland, [7]Sandvik Steel, Sweden, [8]Cranfield University, UK,

Abstract

In the Boilers Work Package of the Plant Integration Group, COST 522, fireside corrosion tests of superheater and waterwall materials have been performed *in-situ* in industrial boilers or combustion test facilities. The results presented in this paper are restricted to superheater materials tested in power station boilers, because of the large amount of data collected. The fuels used included industrial and household waste, straw, wood (logging residues) and coal. The fuels burnt in these boilers depended on local availability and/or established practice and reflect the wide diversity of fuels available or utilised in Europe.

An increase in the steam temperature of a power station increases the electrical efficiency of the turbine. This in turn leads to a reduction in the cost of electricity and in environmental emissions produced per unit of electricity generated. Higher steam temperatures give rise to more aggressive corrosive environments and the choice of superheater material becomes more important. However, the aggressiveness of the fuels also depends on their chemical compositions. Goals for the work package were thus set at different maximum steam temperatures and lifetimes according to the fuel. The targets were:

coal 650°C/100,000 h, wood 580°C/40,000 h, straw 580°C/20,000 h and waste 500°C/40,000 h.

The materials tested included high nickel alloys (intended for coatings or composite tubes), austenitic stainless steels, high chromium martensitic alloys, low chromium and C-Mn steels. An overriding constraint was that the materials must be economically viable and not impose exceptional fabrication requirements. Some materials were tested in a number of combustion environments, allowing useful comparisons to be made.

The corrosion rates measured during straw-firing were similar to those from waste. Wood was much less corrosive than straw, with corrosion rates similar to those from medium to high chlorine coal. It is concluded that the goals can be reached with the use of suitable materials and in the case of straw with changes in boiler design.

Keywords: corrosion, superheaters, waste, straw, wood, coal.

Introduction

Many different fuels are utilised in Europe's power station boilers and the type of fuel burnt often depends on local availability and/or established practice. For example, coal is mined in Great Britain, Germany and Poland and is an important fuel in these countries. Sweden and Finland have indigenous supplies of peat and vast areas of the countryside are forested. The forestry and timber industries are thriving. Not surprisingly, increasing use is being made of peat and wood as fuels in combined heat and power (CHP) stations. In countries with an important agricultural industry, like Denmark, straw used to be burnt in the fields by farmers after the cereal crops had been harvested. Today the straw is sent to be burnt in CHP stations, making a useful energy contribution to the economy, whilst removing the local environmental problem of smoke-filled fields. The only fuel that can be said to be indigenous to the whole of

Europe, is waste. Producing energy from waste by burning under controlled conditions, rather than depositing it in a landfill, has a very positive impact on the environment. A greater use of bio-fuels as a substitute for fossil fuels is also to be encouraged because these fuels are CO_2 neutral. Table 1 shows some typical chemical compositions of bio-fuels and coal.

Table 1. Average properties of selected biofuels, municipal solid waste and one coal analysis (wt%)

	MSW	Straw	Bark	Wood	Peat	Coal
Moisture (%)	20-40	8-16	45-65	10-50	40-60	5-15
Ash (%)	20-30	3-12	2-10	1-10	3-7	20
Sulphur (% in ds)	~ 0.2	0.05-0.07	0.03-0.1	0.03-0.15	0.2-0.4	0.35
Chlorine (% in ds)	~ 0.5	0.01-1.5	0-0.3	0.01-0.04	0-0.1	0.02
Na (% in ash)	N/A*	0.06-2.2	0.1-1.2	0.3-0.8	0.05-0.6	1
K (% in ash)	N/A*	5-32	1-4	3-8	0.03-1.2	1
Ca (% in ash)	N/A*	2-13	16-32	5-40	7-30	2

N/A*information not available
Coal from Ref.1, waste from Ref. 2 and straw, bark, wood and peat from Ref. 3.

At the same time that the fuel range is being widened to include more renewable fuels, the steam temperature is being increased. An increase in the steam temperature of a power station increases the electrical efficiency of the turbine. This in turn leads to a reduction in the cost of electricity and in environmental emissions produced per unit of electricity generated. In the Boilers Work Package of the Plant Integration Group, COST 522, fire-side corrosion tests of superheater and waterwall materials have been performed *in-situ* in industrial boilers or combustion test facilities. Because of the wide range of materials tested and variety of fuels used the results presented in this paper are restricted to superheater materials tested in power station boilers. The fuels used included industrial and household waste, straw, wood and coal. The aggressiveness of the fuels depends on their chemical composition. Straw and waste are the most corrosive of the fuels tested and this affects the maximum steam temperature utilised.

Goals for the work package were thus set at different maximum steam temperatures and lifetimes according to the fuel. The targets were:

coal 650°C/100,000 h, wood 580°C/40,000 h,
straw 580°C/20,000 h, waste 500°C/40,000 h.

The materials tested included high nickel alloys (intended for coatings or composite tubes), austenitic stainless steels (superheaters only), high chromium martensitic alloys and low chromium and C-Mn steels. An overriding constraint was that the materials must be economically viable and not impose exceptional fabrication requirements. Some materials were tested in a number of combustion environments, allowing useful comparisons to be made.

In this paper corrosion data are presented for a wide range of materials tested under waste, straw, wood and coal combustion and where possible, comparisons are made of the same alloy tested under different environments.

Experimental and Results – Project specific

Materials have been exposed as tube components, in cooled probes or as uncooled rings in the flue gases of operating power plants. Typical chemical compositions of the materials used are given in Table 2. The experimental and results are described first project by project in this section.

Table 2. Typical chemical compositions, in weight %, of the steels tested. The balance is Fe.

Steel	Cr	Ni	Mo	Mn	Other
15Mo3	--	--	0.5	0.5	C 0.15, Si 0.25
10CrMo910, T22	2.25	--	1.0	0.5	C 0.15, Si 0.25
Esshete 1250	15	10	1	6	C 0.08, Si 0.6, Nb 1, V 0.22, B 0.006
TP 347 H	18	12	--	1.5	C 0.05, Si 0.5, Nb 0.6,
TP 347H FG	18	12	--	1.5	C 0.05, Si 0.5, Nb 1
Sanicro 28	27	31	3.5	1.5	C 0.015, Si 0.5, Co 0.06, Cu 0.9, N 0.07
Alloy 625, Sanicro 63	21	63	9.0	0.5	Si 0.2, Ti 0.2, Al 0.2, Nb+Ta 3.5.

Waste Incineration in The Netherlands and in The Czech Republic

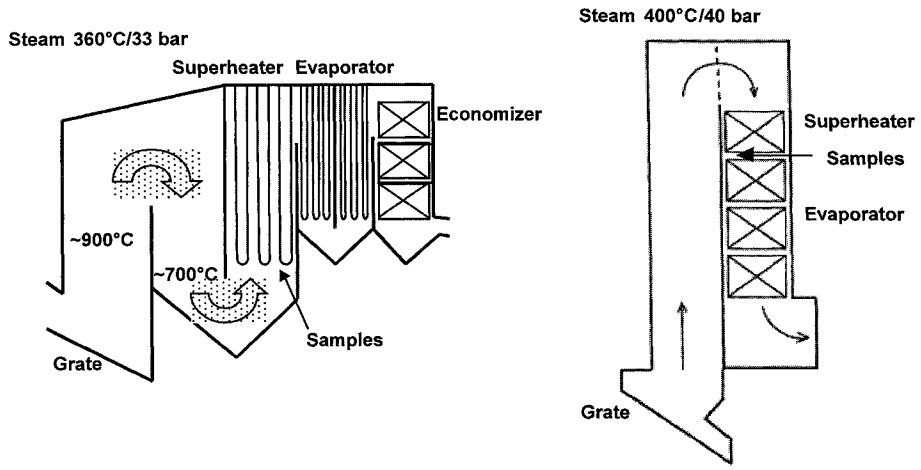


Fig. 1. Waste incinerators AVR 3, Rotterdam (left) and AVIRA 1, Arnhem (right)

Coated tubes were tested in the waste incinerators in AVR 3, Rotterdam and AVIRA 1, Arnhem. These boilers use a mixture of municipal and industrial waste and typical heating values are 9 to 10 MJ/kg. Fig. 1 shows the position of the specimens in the boilers. Coatings were applied by high velocity oxy-fuel (HVOF) spraying. Uncoated material and weld overlay Alloy 625 were tested for comparison. The HVOF coating thicknesses were about 0.5 mm and the weld overlay 1.5 mm. The exposures were performed at the most critical locations in the boilers for times ranging between 4000 and 10,000 hours and results presented are from the

areas with the highest attack (hit by the gas flow). In the AVR 3 boiler the pending superheater bends were made of 15Mo3, dimensions 38x6 mm. The coatings applied were XPT 489 (Cr50Ni) and Diamalloy 1005 (Alloy 625). The gas temperature was 775°C and the metal temperature 440°C at the superheater bends. The steam conditions were 360°C/33 bar.

In the AVIRA boiler, superheater tube parts were mounted horizontally as uncooled tubes, D1 and D2 about 150 cm long, in between the two horizontal superheater bundles, (see Fig. 1). The tube material was 15Mo3, 38 x 4.5 mm, which was coated in two 50 cm sections with XPT 489 (Cr50Ni) and Diamalloy 1005 (Alloy 625). The gas temperature was about 500°C. The steam conditions were 400°C/40 bar. The results are shown in Figs. 2 and 3.

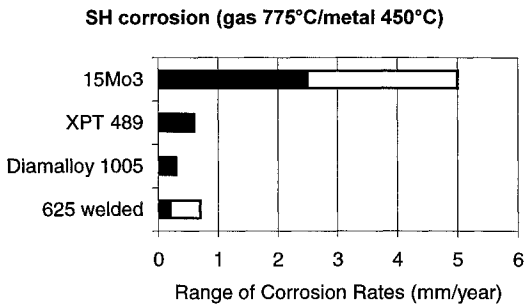


Fig. 2. *Corrosion results from the AVR 3 boiler in Rotterdam. Maximum metal loss rates from each specimen are reported. Where a number of specimens of the same material have been tested the results are given as a spread in metal loss rates.*

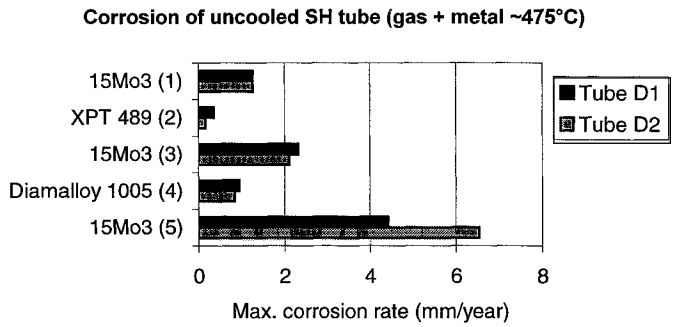


Fig. 3. *Corrosion results from the AVIRA 1 boiler in Arnhem given as maximum metal loss rates. The coatings were applied to tubes of 15Mo3, D1 and D2. Corrosion rates varied with position along the tube. Position (1) was furthest in and (5) was nearest the back wall.*

The HVOF coatings behaved well; the adherence was good, the porosity very low and they

showed no signs of spallation or cracking. The main degradation process for the coatings was metal loss by more or less uniform corrosion. The lifetimes of coatings are obviously limited by thickness. However, it was concluded that an attractive extension of component life is achievable with coatings. The metal losses observed for the '625 type' coatings and weld overlays, and for the 15Mo3 boiler steel fitted very well with previously published extrapolated corrosion data for waste incinerator superheater conditions, [7,8].

Ring specimens, from superheater tube material, were exposed, uncooled, in the waste-fired grate boilers in Prague and Brno. These two boilers are of the same design with steam conditions of 325°C/13.7 bar and produce 36 tonnes of steam per hour. The rings were exposed for 5328 hours in Prague and 4746 hours in Brno. The rings at the three highest temperatures were placed in an empty pass before the heat exchangers. Rings at the lowest temperature were exposed in the convective pass containing heat exchangers. 8 materials were tested; the results of four are reported here. Wall thicknesses were measured before and after testing and the maximum metal wastage rate is given in Table 3 below.

Table 3. Corrosion rate in mm/year at different flue gas temperature ranges in °C. P=Prague, B=Brno

Material	357-397°C	445-520°C	522-555°C	548-562°C	575-620°C	680-715°C	685-705°C
	P	P	B	P	B	P	B
15Mo3	1.37	1.33	2.27				
T22	0.80	0.81	4.89				
SAN 28		0.02	0.25	0.08	1.66	7.15	6.01
Alloy 625		0.01	0.07	0.03	0.27	1.68	0.35

Straw-firing in Denmark

Corrosion tests were performed at the Masnedø straw-fired CHP Plant. This plant has a 8MWth moving-grate boiler and produces steam at 520°C and 80 bar. Some tubes were welded into place into a specially constructed test steam loop which had an outlet temperature of 585°C. Some tubes were exposed during 1998-99 for 3462 hours and others during 1998-2000 giving a total time of 8690 hours over 2 years. Corrosion, given as the sum of metal loss and internal corrosion, was measured at 24 points around the circumference of the tube samples. Internal corrosion varied between 3 and 50% as a percentage of the total. The internal corrosion decreased as a percentage of the total corrosion with an increase in metal loss.

The flue gas temperature during 1998-99 was measured as 900-1050°C, but during 99-2000 it had decreased to around 850-900°C. It can be seen, in Fig 4, that the corrosion rate for TP 347H increased with calculated metal temperature (based on steam temperature), but also depended on the flue gas temperature. The corrosion rates were also higher if the superheater tubes were not shielded from the flue gas. Corrosion data were also obtained for TP 347H FG, Sanicro 28 and Esshete 1250, shown later in this paper.

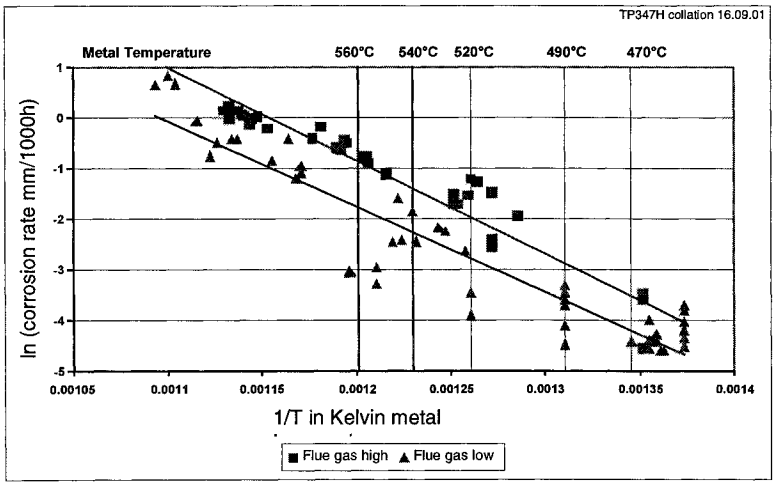


Fig 4. *Ln. corrosion rate in mm per 1000 hours against inverse temperature in Kelvin for TP347H superheater tubes in a straw fired boiler. The corrosion rate depended on the metal temperature, but also the heat flux. (After Refs. 4 and 5)*

Wood-firing in Sweden

A number of steels were tested in internally cooled corrosion probes in the boiler of the Nässjö CHP station. The Nässjö boiler, situated in the southern part of Sweden, is a 30 MW circulating fluidised bed boiler, which produces steam at 80 bar/480°C and generates 9 MW electricity. The fuel is 100% wood (logging residues). Probes were positioned immediately above the first superheater, (or immediately before in terms of the flue gas passage) and were thus heated by the flue gases, which had a temperature of 880°C at full load. The wall thickness of each ring was measured at 8 or 24 points equally spaced around the circumference before and after testing to obtain values of metal loss. Measurements were made on two parallel circumferences separated by 1 cm, giving a total of 16 or 48 measurement points for each ring. Internal corrosion (or selective corrosion such as grain boundary attack) was also measured. The total corrosion is the sum of metal loss and internal corrosion values. Average corrosion rates are presented in Fig. 5.

The three stainless steels tested in probes showed similar corrosion rates and some internal grain boundary corrosion. However, a superheater section of Esshete 1250, which had been in service for 11,500 hours with 480°C steam, showed only negligible grain boundary attack. The total corrosion rate, though, was similar to those of the probe samples at 530°C. The two final stage superheaters, which had previously been made of T22, have been changed to Esshete 1250, resulting in much lower corrosion rates.

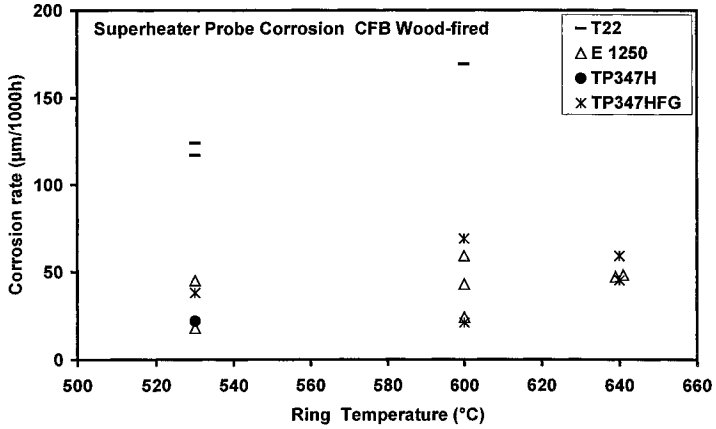


Fig. 5 *Total corrosion per 1000 hours for steels exposed in probes near the superheaters in a wood-fired CFB boiler.*

Coal firing in Great Britain

Much work has been done by the CEGB and its successors in the UK to produce a predictive formula to understand the high temperature fireside corrosion of ferritic steels in coal fired plant. However, with the many variables to be considered, including metal temperature, gas temperature, alloy composition, position within an element and coal composition, no clear understanding has been possible.

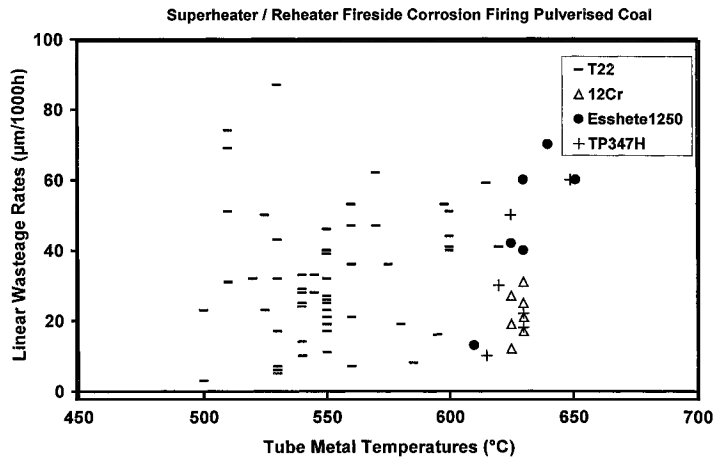


Fig. 6 *Metal loss rates in µm per 1000 hours for superheaters in coal-fired PF boilers. Chlorine content of the coal 0.2-0.4 wt%.*

The difficulty is illustrated by the large scatter in wastage rate data for T22 steel tubing presented in Fig. 6. The data given are derived from actual tubing in a variety of different boilers firing coals with medium to high chlorine contents ranging from 0.2 to 0.4 wt%. The data are limited to those tubes on the leading edge of tube banks or elements, *i.e.* those exposed to the greatest heat flux in the bank or element. Metal losses were determined using a variety of techniques including ultrasonic thickness measurement, calliper measurement and destructive examination of tube samples. Measurements were made at routine outages separated by tens of thousands of operating hours. Some metal temperatures were measured using thermocouples, but, in most cases, have been estimated from metal temperature measurements in the boiler dead spaces, microstructural degradation or from plant modelling exercises.

Data are also presented for 12%Cr 1%Mo steel superheater tubing, again with coal chlorine contents in the range 0.2 – 0.4%, Fig. 6. This material was employed where the operating temperature exceeded that at which T22 steels would be expected to operate due to limitations of creep performance.

Excessive operating temperatures and metal wastage rates lead to unacceptably short operating lives for T22 steels. Original T22 tubing was replaced by austenitic alloys, such as Esshete 1250 and TP347H, possessing greater creep strengths and corrosion resistance. The data presented in Fig. 6, for these alloys, are derived from ultrasonic thickness measurements made on superheater and reheater tubing during boiler overhauls and is again restricted to plants firing coal with chlorine contents between 0.2 and 0.4%.

Superheater probe testing is presently being performed in a 500 MW pulverised fuel coal-fired boiler with metal temperatures ranging from 550 to 700°C to simulate steam temperatures up to 650°C. The materials being tested are TP347 H and HFG, Sanicro 28, Super 304H, Save 25, HR3C, HR11N and IN671. The exposure times range from 2500 to 4000 hours.

Discussion

Scatter in corrosion results

For people accustomed to performing corrosion tests in furnaces in a controlled laboratory environment, the scatter in corrosion rates presented in this paper may seem horrendous. Utility boilers, even if operated continuously, seldom operate under constant conditions. Flue gas temperatures vary daily with load, leading to changes in heat flux and steam temperature, (see Fig. 7). In addition, unplanned outages, often caused by problems with auxiliary equipment, give rise to temperature cycling effects.

Fig 7 shows the spread in steam temperature in the secondary superheater outlet steam over a period of 9330 hours, at the Masnedø straw-fired plant. As can be seen, the spread is considerable, with the temperature lying mostly in the range 420-500° C.

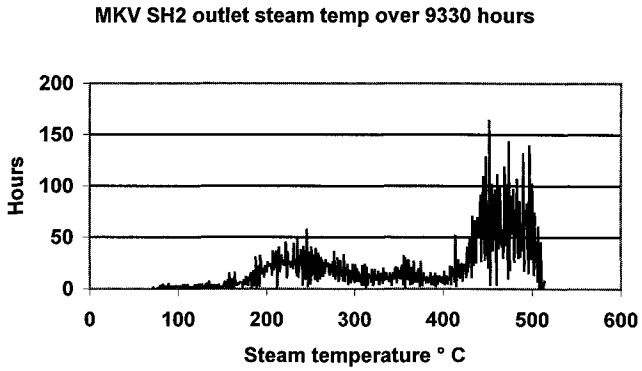


Fig. 7 *Variation of steam outlet temperature for superheater 2 at the Masnedø straw-fired power plant.*

It is evident that the thermal history of the superheater tubes cannot easily be transformed into one alternative temperature which the superheater material could have been subjected to over 9330 hours and still develop the same corrosion. However, the thickness of the steam side layer of magnetite can be used to determine the thermal history of the material, [4,5]. This method of estimating the thermal history of a material has the advantage of being as direct as possible in the sense that it gives a magnetite thickness on the inside of a tube where the flue gas corrosion is measured on the outside of the tube. The magnetite thickness has to be averaged over a number of points but is one of the more accurate methods available.

Comparison of results

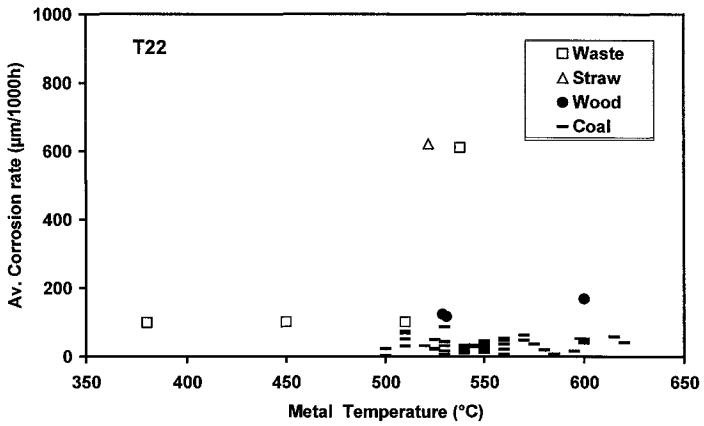


Fig. 8 *Comparison of plant corrosion data for T22 (10CrMo910) with a variety of fuels.*

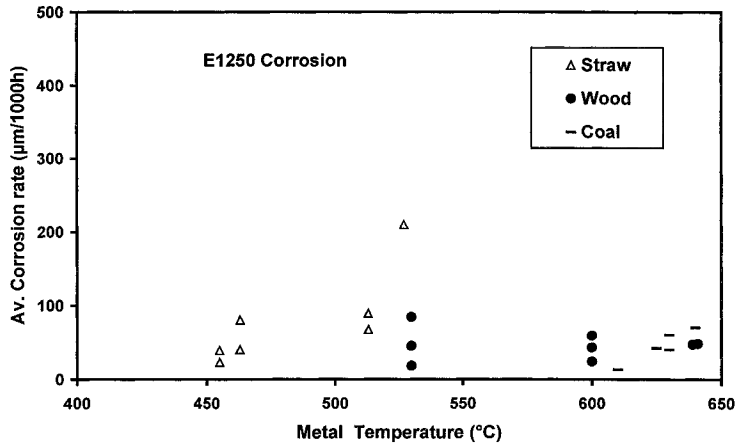


Fig. 9 *Comparison of plant corrosion data for Esshete 1250 with a variety of fuels.*

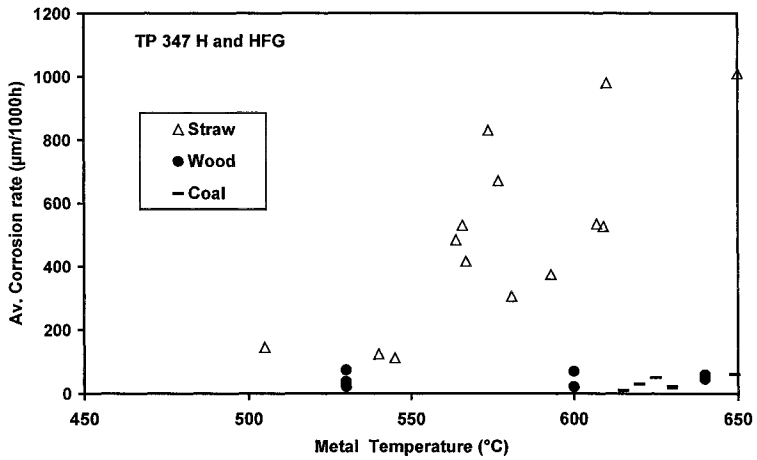


Fig. 10 *Comparison of plant corrosion data for TP 347 H and TP 347H FG with a variety of fuels. There is no difference in the corrosion rates between these two steels under the conditions tested.*

Corrosion rates in different environments are compared in Figs. 8-11. It is apparent, that straw is a very aggressive fuel, and that there is an enormous difference in corrosion rates between straw and wood. (The wood referred to here is in its "as-logged" condition and is not recycled wood). Straw and wood are collectively known as "bio-fuels", but the corrosion rates of steels in straw-fired plant are more similar to those from waste-firing, while the results from wood-firing bear more similarity to those from coal with medium to high chlorine contents.

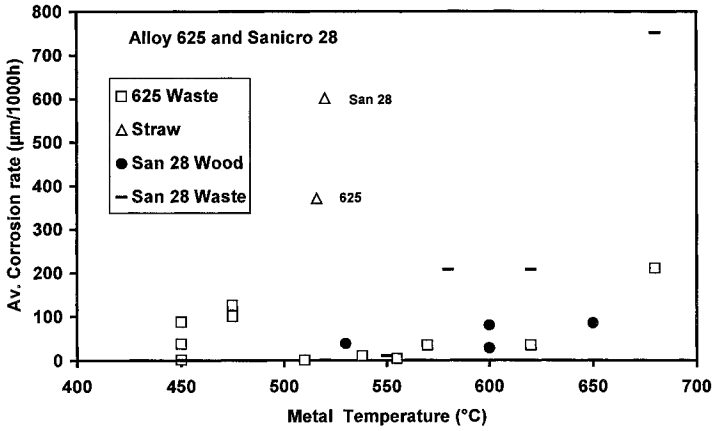


Fig. 11 Comparison of plant corrosion data for Alloy 625 and Sanicro 28.

A comparison of corrosion rates for Alloy 625 (Sanicro 63) and Sanicro 28 is shown in Fig. 11. The corrosion rates for these two alloys were at least 4 times greater for straw than for wood or waste at similar temperatures. In straw it has been found that medium chromium alloys containing 12-18% Cr offer the best resistance because of large amounts of internal corrosion seen in high chromium alloys, [5,6].

Corrosion mechanisms – differences between fuels

Most biomass fuels have a high content of alkali metals and chlorine, and they contain very little sulphur compared to fossil fuels. In Table 1, the average properties from a selection of biofuels are presented together with those for a coal. Most abundant mineral impurities in coal are often associated with alumino-silicate clay minerals together with quartz. These alkali compounds are in general not easily volatilised. In biomass, alkali metals are primarily organically associated, or present as simple salts. The alkali metal of major concern is potassium. The majority of potassium is released into the gas phase during combustion and is mainly present as potassium chloride, KCl, and potassium hydroxide KOH. The alkali metals form compounds having low melting points and can condense either as chlorides or sulphates causing widespread fouling of superheater tubes and other operational problems during combustion.

The most severe corrosion problems are thought to be associated with deposits containing alkali chlorides on the superheater tubes, [9]. The presence of alkali chlorides in deposits may cause accelerated corrosion well below the melting point of KCl. The exact corrosion mechanism is not yet fully understood, but may occur by a process known as "active oxidation", [10], in which alkali chlorides like KCl react with iron oxide (or chromium oxide) to form potassium-iron oxides and release chlorine. The chlorine produced diffuses into the metal-scale interface and reacts with iron to form $FeCl_2$. The $FeCl_2$ evaporates and diffuses outwards where it is oxidised to Fe_2O_3 and chlorine is liberated again. In this scenario Cl is

not consumed, but acts as a catalyst, [10]. It is noteworthy that although Cl is often detected in deposits, it is seldom detected in the metal or oxide, [22,23].

The sulphation of alkali chlorides is important from the corrosion and fouling point of view since a deposit containing only sulphates has a higher first melting point than deposits containing alkali chlorides, [11]. Molten phases increase the corrosion rate, and the presence of a liquid phase on the surface of a metal is usually necessary for high corrosion rates [14,15]. In this sense, alkali sulphates are preferred to alkali chlorides in the deposits.

Results from investigations of corrosion during combustion of chlorine-containing biosludge and bark showed that an increased S/Cl molar ratio suppressed corrosion and the chloride content in the deposits, [3]. This demonstrated the importance of the S/Cl molar ratio in the fuel and supported previous findings of coal or sulphur additions in reducing corrosion in waste fired boilers, [12,13]. Corrosion tests performed during the co-firing of coal and wood and also during combustion of 100% wood in a CFB boiler showed that co-firing led to reduced corrosion rates and deposits with greatly reduced Cl contents, [16, 19]. The sulphur content of the deposits was of course increased during co-firing. Addition of sulphur to 100% wood fuel resulted in the same effect, [16]. This is also backed up by work on straw-fired plant. Severe superheater corrosion was found by combustion of straw alone due to KCl in the deposits, but in co-combustion with coal, the deposits contained no Cl and the corrosion rates were much lower, [17,18].

A glance at Table 1 shows that the S/Cl ratio is higher for coal and wood than for straw and waste and can be used to explain the higher corrosion rates in the latter two fuels. Another factor which influences corrosion is the presence of moisture in the fuel or flue gas. It is known that the presence of water vapour increases the oxidation rate of martensitic and austenitic stainless steels, see for example references 15, 20 and 21.

Are higher steam temperatures possible?

For the lifetime goals mentioned in the Introduction to be fulfilled, and assuming an extra 2mm wall thickness to allow for corrosion, the maximum corrosion rates allowed are given in Table 4.

Table 4. Maximum corrosion rates allowed according to the goals set in the Boilers Work Package.

Fuel	Corrosion rate (µm per 1000h)	Metal Temperature (°C)
Coal	20	680-700
Wood	50	610-630
Straw	100	610-630
Waste	50	550

From the results presented in this paper it is seen that E1250 and TP347 H and HFG are suitable for wood-fired plant and Alloy 625 is suitable for waste-fired. A number of high strength, high Cr and Ni alloys are still under evaluation for use with coal at the stated temperatures. The suitability of alloys for use with straw-firing at metal temperatures of 610-

630°C is more problematic. To reach the goals for straw, special requirements are needed for the design and operation of straw-fired boilers. The heat flux at the superheater material must be kept low (~10% of the heat flux in a coal-fired boiler) and the combustion of straw in the furnace must be divided into gasification followed by combustion. Co-firing with coal will also reduce corrosion, [11-13, 16-19]. As with combustion in any boiler, at any steam temperature, it is important that the combustion is homogeneous in order to reduce corrosion. Incomplete mixing of air and alternating oxidising-reducing conditions accelerate corrosion. Too high a temperature at the superheaters caused by the final combustion of fine or light particle fractions in the superheater area will also exacerbate corrosion.

The corrosion rates are, of course, not the only requirements that have to be fulfilled. The materials must have adequate creep strength and ductility at these higher temperatures. Fortunately, higher chromium and nickel contents usually result in higher strength. Where the requirements are not met, compound tubes can be used.

Conclusions

Fireside corrosion tests of superheater materials and coatings have been performed *in-situ* in industrial boilers as part of the activities of the COST 522 Boiler Work Package, Plant Integration Group. Results for the alloys T22, Esshete 1250, TP 347H, TP 347 HFG, Alloy 625 and Sanicro 28 have been compared in waste-, straw-, wood- and coal-fired boilers at similar metal temperatures.

For a given alloy, temperature and fuel, the corrosion rate depends on the alloy's position in a superheater bank. Tubes on the outside, exposed to the flue gas, will corrode faster than those positioned deeper in a bank. Tubes experiencing a greater heat flux will corrode more rapidly. Poorly controlled combustion will also increase corrosion.

Straw was as corrosive as waste and much more corrosive than wood (logging residues). The difference in corrosiveness increased with increasing temperature above a metal temperature of about 520°C. The corrosion rates of the alloys tested during wood-firing were only a little higher than those from firing coal with a medium to high chlorine content. Straw and wood are often collectively known as "biomass", but the corrosion they cause can vary by a factor of 5 or more.

In straw- and wood-firing no difference could be found in the corrosion rates of the steels TP 347H and TP 347HFG. Esshete 1250 also showed similar fireside corrosion rates to 347 in straw, wood and coal boilers at the temperatures tested. Steels with high chromium contents performed less well in straw environments. HVOF coatings performed well in the waste-fired boilers.

The difference in the corrosiveness of the fuels was explained in terms of their chemical compositions. It is thought that a higher alkali content and a decrease in the S/Cl molar ratio leads to an increase in corrosiveness. A high moisture content in the flue gas is also expected to increase the corrosion rate.

It is expected that the goals set in the Work Package can be achieved with the use of suitable alloys in the case of waste, wood and coal. The goal set for straw firing was ambitious, a steam temperature of 580°C, and in this case a combination of material, combustion technology and boiler design are needed.

References

1. A. Nordin, Chemical elemental characteristics of biomass fuels, *Biomass and Bioenergy*, **6**, pp. 339-347, (1994).
2. D. A. Tillman. Trace Elements in Combustion Systems. Academic Press, USA (1994)
3. K. Salmenoja, Field and laboratory studies on chlorine–induced superheater corrosion in boilers fired with biofuels, Thesis, Report 00-1, Åbo Akademi, Åbo, Finland, 2000
4. M. Montgomery, A. Karlsson and O. H. Larsen. Corrosion Investigations at the Masnedo Combined Heat and Power Plant. Technical University of Denmark, February 2000.
5. M. Montgomery, A. Karlsson and O. H. Larsen: Field test corrosion experiments in Denmark with biomass fuels. Part 1: Straw firing. *Materials and Corrosion* **53**, pp. 121-131 (2002).
6. M. Montgomery and A. Karlsson.. In-situ experiments at the Masnedo Straw-fired power plant. Presented at Eurocorr 1999, Aachen.
7. P. Rademakers, G. Grossmann, A. Karlsson, M. Montgomery, T. Eriksson and L. Nylof, Materials for waste incinerators and biomass plants, Proc. 6th Liège Conference 'Materials for Advanced Power Engineering', 1998, Liège, Belgium, pp. 679-694.
8. P. Rademakers, R.W.A. Wetzel and E. Kokmeijer, Increase of waste incinerator potential by advanced superheaters, Proc. 6th Liège Conference 'Materials for Advanced Power Engineering', 1998, Liège, Belgium, pp751-760.
9. H.P.Nielsen, F.J. Frandsen, K. Dam-Johansen, and L.L.Baxter, The implication of chlorine-associated corrosion on the operation of biomass-fired boilers, *Progress in Energy and Combustion Science*, **26**, pp 283-298, (2000)
10. M. Spiegel "Reactions between gas phase, deposits and metallic materials in chlorine containing atmospheres", *Materials at High Temperatures*, **14**, pp. 221-226, (1997).
11. K. Iisa, , Y. Lu, and K. Salmenoja, Sulfation of potassium chloride at combustion conditions. *Energy & Fuels*, **13**, pp. 1184-1190, (1999).
12. H. J. Grabke, E. Reese and M. Spiegel: The effects of chlorides, HCl and sulphur dioxide in the oxidation of steels below deposits, *Corrosion Science*, **37**, pp. 1023-1043, (1995).
13. H. H. Krause, D. A. Vaughan, P. W. Cover, W. K. Boyd and R. A. Olexsey, Corrosion and deposits from combustion of solid waste. Part VI: *Trans. ASME, Journal of Engineering for Power,* **101**, pp. 592-597, (1979).
14. A. Karlsson, P. Møller, and V. Johansen: Iron and steel corrosion in a system of O_2, SO_2 and alkali chloride. The formation of low melting point salt mixtures. *Corrosion Science*, **30**, pp. 153-158, (1990).
15. P. Kofstad, High Temperature Corrosion, Elsevier Applied Science, New York, 1988
16. P. J. Henderson, P. Ljung, S-B Westberg and B. Hildenwall. Corrosion testing of Superheater Steels for biomass.fired boilers and the effects of co-firing with coal. Proc Conf. *Advanced Materials for 21st Century Turbines and Power Plant*, pp 1094-1104. Eds. A. Strang et al. IOM communications, Book 736, (2000).

17. B. Sander, Emissions, corrosion and alkali chemistry in straw fired combined heat and power plants, *1st World Conference on Biomass for Energy and industry*, Seville, 2000
18. M. Montgomery and O H Larsson. Field Investigation into the effect of co-firing of straw and coal on high temperature corrosion. Presented at *EuroCorr 2000, IoM*, London.
19. P. J. Henderson, P. Ljung, P Kallner and J. Tollin. Fireside corrosion of superheater materials in a wood-fired CFB boiler. Presented at *EuroCorr 2000, IoM*, London.
20. M. Thiele, H. Teichman, W. Schwartz and W. J. Quadakkers. *VGB Kraftverkstechnik*, no 2, p77 (1997).
21. H. Asteman, K. Segerdahl, J-E Svensson, and L-G Johansson. The influence of water vapour on the corrosion of chromia-forming steels. *Mater. Sci Forum.*, **369**, pp277-286, (2001).
22. C. Liu, J. A. Little, P.J. Henderson and P Ljung. Corrosion of TP347H FG stainless steel in a biomass fired boiler. *J. of Mater Sci.*, **36**, pp1015-1026, (2001).
23. P. J. James and L. W. Pinder. Effect of coal chlorine on fireside corrosion of boiler furnace wall and superheater tubing. *Mater. At High Temps.* , **14**, pp187-196, (1997).

Acknowledgements

All the authors are grateful for the financial support which has allowed them to participate in the COST 522 Programme. In particular the support of the Czech Ministry of Education (Project COST 522.30) is gratefully acknowledged. The TNO project on HVOF coatings was coordinated by the *'Projectbureau voor Materiaalonderzoek en Produktietechnieken (PMP)'*, and was financed by participating companies and the Ministry of Economic Affairs in The Netherlands. The work on wood fuel was financed by Vattenfall AB's research programme "Sustainable Energy Solutions".

DEGRADATION OF BOILER AND HEAT EXCHANGER MATERIALS: DATA GENERATION, DATABASES AND PREDICTIVE MODELLING

S R J Saunders*, N J Simms#, S Osgerby* and J E Oakey#

* NPL Materials Centre, National Physical Laboratory, Teddington, Middlesex, TW11 0LW, UK

Power Generation Technology Centre, Cranfield University, Cranfield, Beds., MK43 0AL, UK

Abstract

There is a need to generate and compile quantitative information on the degradation of boiler and heat exchanger materials in the combustion environments being encountered in power plants using new and/or dirtier fuels, as well as with components operating at higher metal temperatures. Within the European COST522 programme this topic is being addressed within the Plant Integration Group. The overall objective of the activity is to produce a database of materials performance and related exposure parameters for candidate materials in plant operating under novel environments and/or at higher metal temperatures. To generate the required data, the materials have been exposed in a range of combustion plant and simulated laboratory environments. The fuels used in the plants have included biomass (e.g. wood and straw), waste (e.g. RDF) and coal. The laboratory tests have been targeted at particular environments to investigate different specific degradation effects in more detail. The database is intended to facilitate the comparison of candidate materials and to enable some of their limitations to be identified, in terms of metal temperature and sensitivity to particular corrosive conditions. The database has been produced by NPL using data generated within the COST522 programme and available from the open literature. The most valuable data for inclusion in such a database are those reported in terms of metal loss (or metal loss distribution) and with a well characterised exposure environment. For the data to be readily incorporated into the database, it has been necessary to develop and apply standardised methods of data collection and presentation (in a spreadsheet). The preferred method of obtaining corrosion damage data has been by dimensional metrology on polished cross-sections, obtaining a distribution of damage measurements. The structured format of the data in the database is being used to produce models of materials performance as a function of environmental exposure parameters (e.g. metal temperature, SO_x, HCl, exposure time). Both neural network and more conventional empirical modelling of these data are being investigated.

Keywords: heat exchangers; solid fuels; corrosion; database; modelling

1 Introduction

Modern power plants have to be operated in an increasingly competitive market place, but also within the context of strict regulatory controls. Thus, plants have to be economically viable and meet increasingly stringent environmental emission regulations [1]. For coal fired power systems, these regulations restrict the emissions of SO_X, NO_X and particulates; other fuels, e.g. waste, have additional restrictions on emissions of trace metal species, etc [2]. The move towards reducing CO_2 emissions, initially in line with the Kyoto agreement, imposes further restrictions on future plant emissions. These factors encourage the use of cheaper fuels (e.g. waste products) and those fuels that are regarded as CO_2 neutral (e.g. biomass), as well as cleaner coals and/or clean coal technologies. Unfortunately, whilst waste products and biomass may apparently have economic and environmental benefits, the contaminants in these fuels have the potential to cause significant degradation of the hot gas path components in power plants. Such components may include heat exchangers, ductwork, filters/gas cleaning devices, gas turbine blades/vanes, etc. This paper is targeted at heat exchangers in such systems.

One approach to overcoming the rapid corrosive degradation of heat exchanger tubing in power systems using dirtier fuels is to reduce the operating temperature of the heat exchanger. This enables longer component lives to be achieved, but with the penalty of reduced plant efficiencies (i.e. producing more CO_2 per unit of electricity). Information on the performance of heat exchangers in coal combustion environments has been gathered over many decades [e.g. 3], during which heat exchanger operating conditions (e.g. steam temperatures) have slowly evolved (e.g. leading to increasingly higher surface temperatures). However, the modern power plant market place requires rapid changes in fuel usage and increased plant efficiencies coupled with decreased environmental emissions.

Within the COST522 programme, the Plant Integration Group has been addressing the issues associated with the performance of heat exchanger tubing at higher operating temperatures and / or with mixed fuels (biomass, waste and/or coal). This work has included exposures of current and candidate heat exchanger materials in plants, pilot plants, and laboratory tests by 17 partners. Detailed reports on the testing and results of many of these studies are contained in papers elsewhere in these conference proceedings.

2 Materials Performance Data Requirements and Generation

Three issues need to be addressed to define the materials performance data requirements [4]:

- The data collection methods must allow all relevant forms of materials damage to be assessed. Destructive methods of monitoring metal damage are required which provide measurements of metal loss, depths of internal corrosion, pit depths, etc. The calculation of metal losses requires dimensional measurements to be made before and after exposure.
- The accuracy of the data must reflect its potential use. More accurate data is needed if trial exposure periods are short when compared to required component life. Different target lives and corrosion allowances for components will lead to a requirement to characterise different levels of acceptable damage within the test period. The overall metrology system must be capable of greater accuracy than the target acceptable damage levels.
- Data must allow the assessment of both average and maximum damage. If sufficient data are produced for statistical analysis, it becomes possible to define and evaluate statistical parameters that describe the damage. The number of data points needed to assess the behaviour of a material in a single environment, e.g. in a laboratory test, has been found to be at least 24 [3]. However, components in plants tend to be exposed to a number of different physical/chemical environments around their surfaces and so require far more data points to be measured so that different zones of behaviour can be assessed independent of each other.

In order to generate the materials performance data required the optimum method uses dimensional metrology before and after exposure. For example, contact metrology before exposure and optical/image analysis measurements on polished sections after exposure. These methods have been developed over the past fifteen years, starting from developments of coal-fired combined cycle power systems carried out within the UK [e.g. 4-6].

3 Database

A metal loss database (MLOSS) has been developed by NPL (using Microsoft ACCESS™) for high temperature corrosion of a range of alloys exposed to a variety of gaseous atmospheres; in some cases solid deposits were also present in the environment. The

database was started in a previous COST programme (COST501 Round III) and was developed using information in the literature and data generated at NPL in laboratory tests. Only metal loss data have been used. For the data generated at NPL mostly 24 metal loss values randomly distributed around the sample were obtained for each test piece, but in the case of the literature information, frequently only a single metal loss value was quoted. In the current state of development there are 770 datasets comprising 43 different alloys, and the gas composition is listed in terms of partial pressures of active species (pO_2, pS_2 etc) atmosphere as well as the detailed composition. Figure 1 is an example of information in the database, and shows the page for alloy HCM2S exposed to a particular atmosphere with the partial pressures of O_2, S_2 and Cl_2. This indicates that 6 datasets are available for tests at 813 K in a simulated "low NO_x" atmosphere. The mean and maximum metal loss is quoted for the series of measurements made, which in this case varied between 24 and 30; the individual metal loss values are viewed by clicking on the "data" button. The database is searchable for alloy type and temperature.

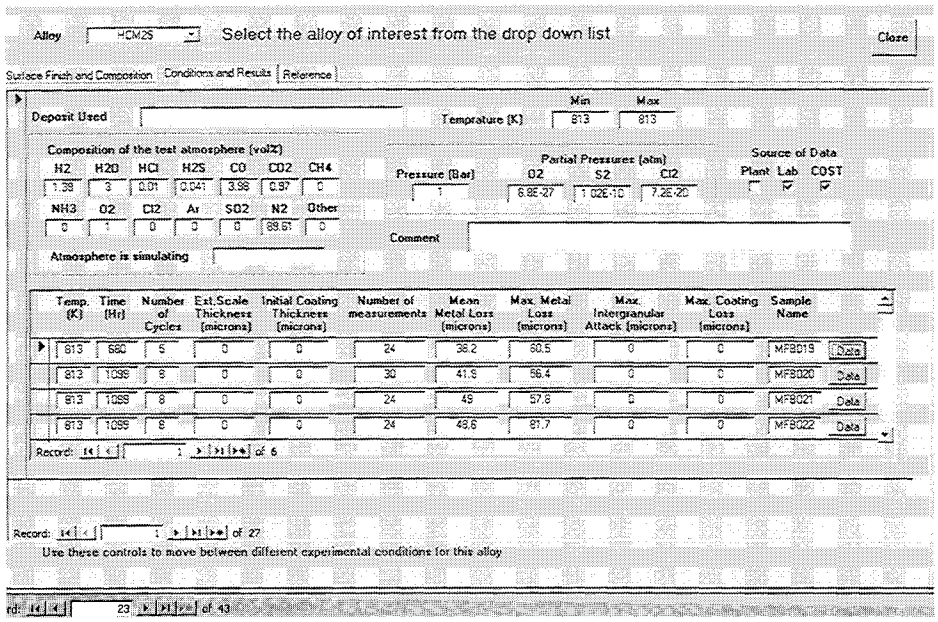


Figure 1 *Page from the NPL MLOSS database showing information available for alloy HCM2S exposed to a specific gas atmosphere*

At the present stage of development the database is not capable of graphical representation of the data. However the metal loss data can be exported to suitable graph plotting software and thus presented in the form of probability plots as shown, for example, in Figure 2.

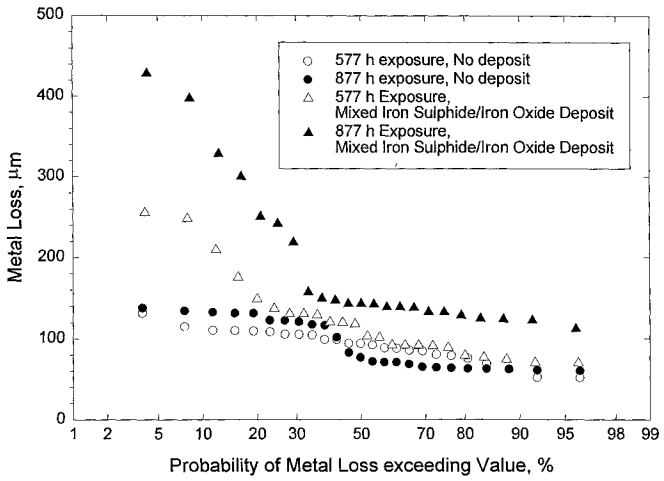


Figure 2 *Probability plot showing the influence of exposure time and surface deposits on metal loss for a 2¼Cr steel (HCM2S) exposed at 500 °C under a gaseous atmosphere simulating low NO_x combustion conditions*

In the current COST522 programme this database is being extended to include additional laboratory experimental data, and, importantly, data from pilot plants and operating power plant. The latter data are obtained from sections of tubing or from probes inserted into the boiler or heat exchanger. As previously indicated, an important consideration in the analysis of power plant data is knowledge of the distribution of metal loss around the tube, since metal loss values could well vary around the circumference of the tube to reflect deposit accumulation and/or gas velocity effects. The thermal history is recorded differently by the various participants in the COST522 programme and care needs to be taken in the further development of the database to ensure proper comparisons are made that take account of the different ways of recording thermal history.

4 Modelling

There are two activities within this COST programme that are aiming to produce models of the corrosive degradation of materials. These two activities both need to use large numbers of materials performance data generated under well characterised conditions, but use distinctly different approaches: (i) empirical modelling and (ii) neural network modelling.

4.1 Empirical Modelling

The first approach has been successfully developed over a number of years for coal gasification systems, and was a particular target for a previous COST activity (COST501 Round III) [7].

4.1.1 Degradation Modes

The performance of materials in various simulated and real coal-gasification gases has been investigated by research groups in the US, Japan and Europe for more than 25 years. The

initial generic studies investigated the performance of materials in a range of highly reducing atmospheres with varying levels of sulphidation at high temperatures. Later studies have tended to concentrate on higher alloyed materials and/or lower exposure temperature. Following plant experience, more recent studies have been targeted at increasingly realistic exposure simulations (Table 1) to match the degradation morphologies observed in practise.

Table 1 Gasifier Gas Compositions

Gas Species	Units	Oxygen Blown Gasifiers			Air Blown Gasifier
		Entrained Slagging		Fluidised Bed	Fluidised Bed
		Dry Feed	Slurry Feed		
CO	%	62 – 64	35 – 45	30 – 40	15 - 20
CO_2	%	2 – 4	10 – 15	10 – 15	5 - 8
H_2	%	27 – 30	27 – 30	24 – 28	10 - 15
H_2O	%	0 – 3	15 – 25	11 – 20	5 - 12
N_2	%	1 – 5	0 – 2	0 – 2	40 - 50
CH_4	%	n/a	n/a	3.5	2 - 4
H_2S *	vppm	2 000 – 12 000	2 000 – 12 000	2 000 – 12 000	300 – 5 000
NH_3	vppm	200 – 500	2 000 – 5 000	200 – 500	500 – 1 500
HCl *	vppm	50- 1 000	50 – 1 000	50 – 1 000	50 - 500

* Dependent on coal S and Cl content

There are several potential degradation processes possible in these environments [8-13], including:

- elevated temperature gas phase induced corrosion: this includes oxidation, sulphidation, carburisation/metal dusting and chlorination;
- corrosion induced by surface deposits: either particles from the gasifier, species condensed onto those particles or species condensed onto the component surfaces;
- dewpoint corrosion: induced by high temperature deposits becoming damp during plant idling, gaseous species (e.g. HCl, H_2S, etc) reacting with condensing water during idling (e.g. forming HCl and polythionic acids) or deposits forming on cooler gas path surfaces;
- downtime corrosion: induced by high temperature deposits becoming damp during plant shut-down, gaseous species (e.g. HCl, H_2S, etc) reacting with condensed water during plant shut-down (e.g. forming HCl and polythionic acids) or hygroscopic deposits being exposed to damp air during plant shut-downs (e.g. during the course of maintenance operations);
- interaction of any of the above degradation modes with mechanical factors, e.g. creep or fatigue, to produce synergistic degradation, e.g. creep-corrosion or corrosion-fatigue;
- spallation of corrosion products: important on the clean side of the filter unit from where spalled scale may enter the gas turbine and cause erosion damage.

In practise, with the complex exposure environments within gasification systems, several materials degradation modes will occur on each component in the hot gas path. In any one gasification system, different combinations of degradation modes will be found on components along the hot gas path due to differences in operating temperature and local plant environment (deposition, local gas composition, i.e. the extent of gas clean-up, gas temperature at that point in the system, component temperature, etc).

As a result of these considerations, the models for materials degradation in gasification conditions considered were developed initially for high temperature isothermal gaseous corrosion and downtime corrosion [4,7,14].

One of the aims of COST501 Round III was to develop the capability of predicting materials performance in gasification systems. For many of the complex synergistic modes, the limited number of laboratory tests possible meant that this was restricted to the particular conditions investigated in those tests. However, for isothermal corrosion in gaseous gasification conditions, a large amount of materials performance data was generated from a number of laboratories in that COST programme, other EU programmes and collected from the literature. Thus, sufficient data was available to model the performance of at least some materials in such conditions.

4.1.2 Isothermal Gaseous Corrosion

A framework isothermal corrosion model for gasifier hot gas path conditions was developed for an EC JOULE programme and applied to Alloy 800H and AISI 310 [13]. The model was based on materials performance data available to the contractors for that project from previous collaborative projects and published literature data; sets of approximately 30 data points obtained from British Coal, JRC Petten, KEMA, ENEL and EPRI covering the temperature ranges 500-900°C (though at some temperatures only single datum points were available). The models were based on an assumption that gaseous corrosion in gasifier product gases followed parabolic kinetics and was either oxidation or sulphidation:

$$\log Kp = A + (B \times R) + \left(\frac{C}{T}\right) \tag{1}$$

where, R is the oxygen excess parameter [9,10],

$$R = 1.5 \log pO_2 - \log pS_2 + \frac{D}{T} + E \tag{2}$$

where A, B, C, D and E are alloy specific constants; T is the metal temperature in Kelvin.

Another model for gaseous gasifier product gas corrosion is reported in the literature. This model has been produced by Shell during development of their oxygen blown 'full' gasification system [15,16] and is targeted only at the gas compositions anticipated for that process. The mathematical form of this model is not fully available, but it is known that for high alloy steels parabolic rates constants are calculated (for exposures in excess of 500 hours) using pS_2, pO_2 and temperature, and that

$$Kp \propto \left(\frac{pS_2}{pO_2^{3/2}}\right)^x \tag{3}$$

For modelling isothermal gaseous corrosion within COST501 Round III, a much larger set of materials performance data was available [7]. Unfortunately, much of these data were available only in the form of mass change data. That meant that more extensive data sets, of up to 100 points for the more commonly researched alloys, were available for producing models of average corrosion damage. More limited data sets, up to ~40 points, were available for producing maximum damage models.

It was found that the best model for the dependence of corrosion rate on gas composition and temperature took a logistic, or sigmoidal, form (e.g. Figure 3 shows the form for AISI 310):

$$CorrosionRate = \frac{a-d}{1+\left(\frac{\log pS_2 - 1.5\log pO_2}{c}\right)^b} + d \qquad (4)$$

where, a, b, c and d are temperature dependent constants of the form,

$$a = a_o \exp(-Q_o/T) \qquad (5)$$

where T is the metal temperature in Kelvin; a_o and Q_a are constants. In theory, the constants a and d should also be dependent on the pO_2 and pS_2 levels, but the corrosion data currently available are not sufficiently detailed to show this effect.

This form of the model compares well with the data generated by Shell for the dependence of corrosion rate on gas composition for their gasification process (e.g. Figure 11 in reference [16]). The Shell data relates to the higher pS_2/lower pO_2 part of the model, where the corrosion rate increases rapidly in the oxidation/sulphidation regime with increasingly sulphidising conditions and then increases more slowly on entering the sulphidising regime. It should be noted that the Air Blown Gasification Cycle process operates under somewhat more oxidising conditions around the change from the oxidation regime to the rapidly increasing oxidation/sulphidation regime. It is interesting to note that recent work on modelling furnace wall fireside corrosion has also produced a sigmoidal dependence on the local environment under increasing reducing conditions [17].

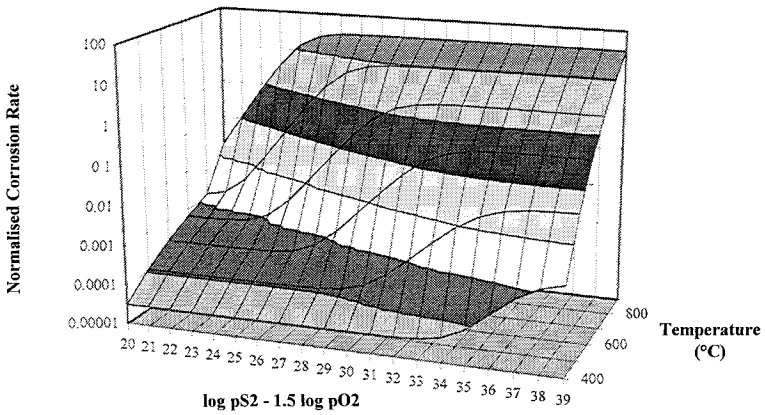


Figure 3 *Corrosion behaviour modelling of AISI 310 in gasification environments [14]*

4.1.3 Model Validation

Validation of the materials performance models requires the prediction of damage in pilot plant hot gas paths from the known exposures conditions to be compared with the actual damage observed to materials exposed under those conditions.

A selection of candidate materials was exposed during the operation of atmospheric and pressurised fluidised bed gasification plants [e.g. [7,13]. The performance of the materials was determined from accurate dimensional metrology before and after exposure. Predictions for typical and maximum high temperature corrosion damage levels were calculated using Eq. 4, with constants evaluated for each material and both evaluations of damage [4].

Figure 4 illustrates the results of the comparison of predicted and measured damage for AISI 310. As expected there is some scatter of data in this comparison. There are several sources of this scatter:

- measurement errors in all stages of materials performance monitoring in both the laboratory and pilot plant exposures;
- mixing different methods of data gathering with different degrees of accuracy and sensitivities to types of corrosion damage (e.g. weight change, optical microscope, contact metrology);
- data analysis and curve fitting in the materials performance modelling;
- plant exposure conditions: gas composition, deposition, gas/metal temperatures, etc.

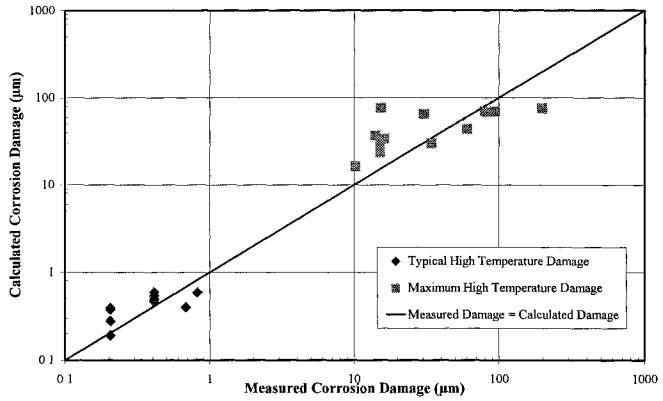


Figure 4 Comparison of Predicted and Measured Gaseous Corrosion Damage for AISI 310 exposed in ABGC Pilot Plants

Of all these factors, by far the most important for model validation is the uncertainties associated with the plant exposure conditions. As the pilot plants were dedicated to process performance evaluation, materials exposure conditions have varied in terms of gas/metal temperatures, gas composition, deposition, etc. For the purposes of these validations, ranges of exposure conditions have been determined and appropriate values of the most important variables taken (e.g. metal temperature and gas H_2S content).

Examination of cross-sections during the course of this data generation allowed the morphology of the damage to be checked to ensure that models were generated and validated for the same types of corrosion behaviour.

4.2 Neural Network Modelling

4.2.1 Basics of neural network models

This is a relatively novel approach to modelling high temperature corrosion data and the authors are aware of only one application in cyclic oxidation of superalloys [18]. However, a similar approach has been successfully used to model a number of aqueous corrosion cases [19-24]. This approach to modelling relies on having a large number of high quality data sets, but the data do not have to be obtained as systematically as for empirical modelling and thus can be used for more incomplete data sets obtained from a number of sources. However, it is still important to use large, good quality datasets obtained under well characterised conditions. The development of the neural network model is an on-going activity, with the model developing as more data is gathered from the COST Plant Integration Group testing activities. However, the basic approach to this modelling is outlined below.

A neural network is essentially a type of information processing technology inspired by studies of the structures in the brain and nervous system. It consists of many simple, highly interconnected processing elements (called neurons) that dynamically interact with each other to "learn" or "respond to" information rather than simply carry out programmed instructions [25]. A single neuron together with the connections from its input and output make up a unit that is referred to as a perceptron.

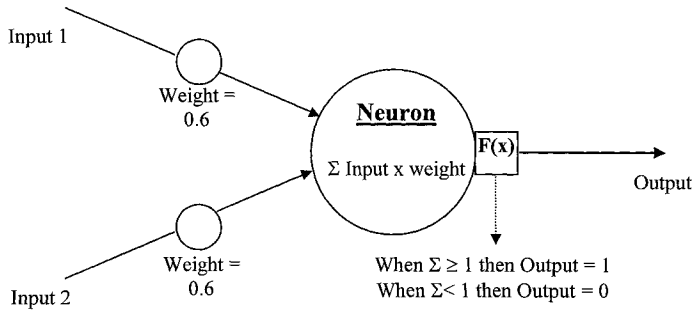


Figure 5 The overall structure and function of a simple perceptron.

As an example consider a simple perceptron, with only two inputs, that has learnt to reproduce Table II below:

Table II. Example input/output pattern.

INPUT 1	INPUT 2	OUTPUT
0	0	0
0	1	0
1	0	0
1	1	1

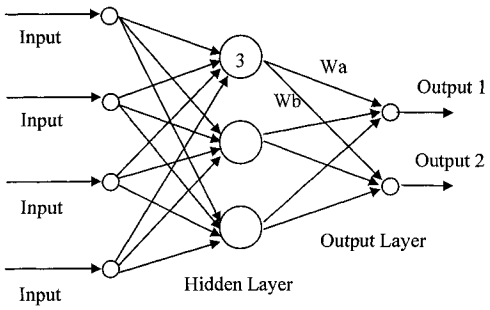
Figure 5 illustrates a perceptron that can reproduce Table II and includes associated weights. Every input to the neuron also has an associated "weight" attached. The neuron simply adds together all the weighted inputs connected to it and calculates the output to be transmitted.

This output is then modified by a function, which in simple cases is a binary transfer function. If the case in which both inputs are zero is presented to the neuron, the total sum will be zero, and therefore the output will be zero. Likewise, if only one input is 1, the total sum calculated by the neuron will be less than 1 (i.e. [1 x 0.6]+[0 x 0.6]<1), and therefore the output will also be zero. Only in the case where both inputs are 1 will the output be 1 (i.e. analogous to a logic "AND" gate).

There are a number of different approaches to neural networks that include the Multi Layer Feed Forward network (MFF), Kohonen network [26, 27] and the Fuzzy Neural network. At present the particular neural network to be used is still undecided, but the MFL model has been found to be successful in modelling stress corrosion cracking behaviour in duplex stainless steels [24] and cyclic oxidation behaviour in Ni-base superalloys [18] so that approach will be tried in the first place. The MFL network methodology is outlined below.

4.2.2 Multi-Layer Feed Forward Network

Single perceptrons can only be used to output simple patterns such as the previous example. For more complex patterns, a multi-layer perceptron (MLP) is required. This is also commonly known as a Multi-Layered Feed-Forward (MLF) neural network. In these networks (Figure 6), neurons are arranged in layers with the input data fed to the network at the input layer. These data then pass through the trained network to the output layer to provide the output, i.e. the prediction.



Wa and Wb are the respective weights on the connections between Neuron 3 and the outputs 1 and 2.

Error on Output 1 = Target value - Output Value = X_1
Error on Output 2 = Target value - Output Value = X_2
Error on Neuron 3 = (X_1 x Wa) + (X_2 x Wb) = X_3
New Wa = Wa + F(X_3)
New Wb = Wb + F(X_3)
And so on...

Figure 6 A multi-layer feed-forward neural network.

Before such networks can be used to generate outputs given a pattern of input variables, they must be trained so that the weights on each connection are correctly assigned. This is

achieved using Back-Propagation, during which sets of training data are presented to the network along with their respective outputs (i.e., the outcomes). This process is known as supervised learning. Quite simply, an error from the network is calculated by subtracting the value of the calculated output, R, from the actual output (or target), T. The errors of the neurons in the previous layer are then calculated. These are worked out simply by multiplying the error in the output layer by the weight on the connection from the previous layer, and summing this for all the relevant connections (see Figure 6). The weights are then recalculated by adding to the original ones a function of the calculated error. This process is iterated until the error from the output is less than a pre-set level. The network is then said to be trained and (following validation and testing) can be used to make predictions given a set of data presented to it at the input layer.

In order to successfully develop predictive algorithms using MLF neural networks, it is necessary to pre-process the database data by: dealing with any missing parameter values; balancing the data such that the neural network can be trained, validated and tested using a full range of environmental conditions; and organising the data such that they can be split (i.e., partitioned) into separate training, validation and test sets.

5 Summary

High temperature corrosion is a complex multivariable process and thus to obtain a set of data that can be used to predict performance is extremely labour intensive. The other major difficulty is to relate corrosion behaviour observed in simulated tests in the laboratory to operation of power plant. In an attempt to develop a predictive capability it is necessary to firstly develop an adequate database, and secondly, a model to accurately predict behaviour. The work described in this paper reports progress made in COST programmes towards achieving this objective.

In the first place a database is being developed that encompasses information from the literature and on-going laboratory tests, and in addition data from operating plant is now being included. An essential requirement for the database is to agree a basis for reporting the data. It has been agreed that one of the best methods is to report metal loss, and at present this can only be reliably obtained using destructive cross-sectioning of the sample. Both pre- and post-test metrology are clearly important in determining the metal loss. Also, in order to obtain statistically useful information for laboratory exposed samples at least 24 measurements around the sample are recommended, and, in the case of plant exposed material, many more measurement are required to allow for the expected variation around the circumference of exposed boiler tubes or heat exchangers. These requirements dictate that the database is capable of storing large amounts of information for just one single exposure condition, and this is even more of a problem when one considers the information needed to adequately describe plant conditions where temperature can be expected to be varying significantly and often randomly throughout the exposure.

A major advantage of working in a collaborative programme such as COST is that large amounts of data can be obtained within a reasonable period.

Life prediction of components depends on modelling and two different approaches have been described. One is based on an empirical approach in which relationships between corrosion

rate and exposure conditions are developed and then used to predict behaviour. The second approach is to use neural networks. Both approaches are unsuitable for extrapolating much beyond the envelope of conditions used to develop the models and can only be expected to provide reliable predictions when interpolating within this envelope. The models are obviously improved with a large data set such as in envisaged in the current project. At present the neural network approach is still under development, but its success has been demonstrated by other workers in a number of aqueous corrosion environments.

6 Acknowledgements

The work at NPL was carried out under the Degradation of Materials in Aggressive Environments and Lifetime Prediction of Materials Programmes, programmes of underpinning research funded by the United Kingdom Department of Trade and Industry (UK DTI). The work at Cranfield University was carried out as part of the UK DTI funded Cleaner Coal Programme.

The authors are grateful to the NPL staff, Mr M U Sheriff and Mr D D Gohil who carried out much of the experimental work, and Dr A Turnbull who provided guidance on neural network systems. The contributions of data from COST522 partners in the Plant Integration Group are gratefully acknowledged.

7 References

[1] J van Liere, *in* 'Corrosion in Advanced Power Plants', Materials at High Temperature **14** (2/3) (1997), pp7-12

[2] 'Incineration of Waste', Directive 2000/76/EC of the European Parliament and of the Council of 4 December 2000

[3] 'Corrosion in Advanced Power Plants', Eds. W Bakker, J F Norton and I Wright, Materials at High Temperature, **14** (2/3) (1997)

[4] N J Simms, J E Oakey and J R Nicholls, in Proc 'High Temperature Corrosion and Materials Chemistry: Per Kofstad Memorial Symposium', Eds M McNallan et al, The Electrochemical Society PV99-38 (2000) pp305-316

[5] N. J. Simms and J. E. Oakey, *in* Microscopy of Oxidation 3, (The Institute of Materials, 1997) pp. 647-658

[6] Draft Code of Practice for 'Discontinuous Corrosion Testing in High Temperature Gaseous Atmospheres', EC Project SMT4-CT95-2001, ERA Technology, UK (2000)

[7] N J Simms, F Bregani, W M M Huijbregts, E Kokmeijer and J E Oakey., *in* Materials for Advanced Power Plant 1998, J Lecomte-Beckers et al Eds, (Forschungszentrum Julich GmbH, Germany 1998) pp. 663-678

[8] J Stringer, in High Temperature Materials Corrosion in Coal Gasification Atmospheres, ed J F Norton, Elsevier (1984).

[9] F Gesmundo, in High Temperature Materials for Power Engineering 1990, eds E Bachelet et al, pp67-90, Kluwer, (1990).

[10] F Gesmundo, Advanced Materials for Power Engineering Components: The Corrosion of Metallic Materials in Coal Gasification Atmospheres - Analysis of Data from COST 501 (Round 1) Gasification Subgroup. EUCO/MCS/08/1991 (1991).

[11] W T Bakker, in Proceedings of Seventh EPRI Annual Conference on Coal Gasification, EPRI, Palo Alto, California, USA (1987).

[12] Proc. First Inernational Workshop on Materials for Coal Gasification Power Plant, Petten, The Netherlands, June, 1993, in Materials for Coal Gasification Power Plant, Special Issue of *Materials at High Temperature*, **11** (1993).
[13] Erosion/Corrosion of Advanced Materials for Coal-Fired Combined Cycle Power Generation, Final and Summary Reports on JOUF-0022 (1994).
[14] N. J. Simms, J. R. Nicholls and J.E. Oakey, in *Materials Science Forum,* **369-372** (2001) 947-954.
[15] R C John, in Proc. Symposium on Life Prediction of Corrodible Structures, Cambridge, UK, 1991, pp33/1-21, National Association of Corrosion Engineers, Houston, USA (1991).
[16] R C John, W C Fort and R A Tait, in Materials for Coal Gasification Power Plant, Special Issue of *Materials at High Temperature*, **11** (1993) 124-132 .
[17] P J James and L W Pinder, Materials at High Temperatures **14** (1997) 187.
[18] K L Cios, L Berke, A Vary and S Sharma, "Soft computing methods in the design of superalloys", NASA Tech Memo 106888, 1996
[19] E M Rosen and D C Silverman, "Corrosion Prediction from Polarisation Scans Using an Artificial Neural Network Integrated with an Expert System", *Corrosion*, NACE, September 1992, pp. 734-745.
[20] J Cai, R A Cottis and S B Lyon, "Phenomenological modelling of atmospheric corrosion using an artificial neural network", *Corrosion Science*, **41** (1999) 2001-2030
[21] M Urquidi-Macdonald and D Macdonald, "Performance Comparison Between a Statistical Model, a Deterministic Model, and an Artificial Neural Network Model for Prediction Damage from Pitting Corrosion", *J. Research of National Institute Standards and Technology*, **99** (1994) 495-504.
[22] H M G Smets and W F L Bogaerts, "SCC Analysis of Austenitic Stainless Steels in Chloride-Bearing Water by Neural Network Techniques", *Corrosion*, NACE, August 1992, pp. 618-623.
[23] M Urquidi-Macdonald and P Egan, "Validation and Extrapolation of Electrochemical Impedance Spectroscopy Data", *Corrosion Reviews*, **15** (1997) 169-194.
[24] S Zhou, D Coleman and A Turnbull, NPL Report MATC(A)21, 2001.
[25] Liebowitz, J., (ed.), *The Handbook of Applied Expert Systems*, CRC, 1998, pp. 13-2.
[26] Tarassenko, L., *A Guide to Neural Computing Applications*, Arnold, UK, 1998.
[27] Kohonen T, "Self-organized formation of topologically correct feature maps", *Biological Cybernetics,* **43** (1982) 59-69

COMPLEX FIRESIDE CORROSION MECHANISM IN BOILERS USING STAGED COMBUSTION SYSTEMS

Wate Bakker, EPRI
Steve Kung, McDermott Technology, Inc
Jeff Blough, Foster Wheeler Development Co
Werner Seitz, Foster Wheeler Development Co

Abstract

Corrosion of water walls in fossil fueled boilers and gasifiers has traditionally been considered the result of gaseous corrodants such as H_2S and HCl, reacting with the heat exchanger tube surfaces. Under reducing conditions these corrodants prevent the formation of a protective oxide scale, leading to increased metal loss. Recent field experience in boilers, using staged combustion systems have shown much greater corrosion rates than predicted by simple gas/solid corrosion processes. The presence of large quantities of unoxidized iron sulfide in deposits in areas where high corrosion rates were found suggests that deposits play a role as well. Subsequent laboratory corrosion studies found that the presence of FeS can indeed lead to very high corrosion rates, but only under oxidizing conditions. Since FeS usually deposits only where reducing conditions are present, the accelerated corrosion observed requires alternating reducing and oxidizing conditions. Such conditions may exist in areas in staged boilers where the overfire air mixes with substoichiometric fluegas from the burner zone. It will further be shown that chlorine corrosion may be caused or at least accelerated by chloride containing deposits in fossil fueled boilers instead of or in addition to corrosion due to HCl in the fluegas. Due to the high sulfur content of fossil fuels, chloride deposits most likely form under reducing conditions only. However once formed they can be highly corrosive under oxidizing conditions. It is therefore likely that the basic chlorine corrosion mechanisms in fossil fueled boilers are the same as those in waste incinerators as in fossil fueled boilers.

Key Words: Low NOx combustors, Coal fired Boilers, Sulfidation, Chlorination, Under Deposit Corrosion

Introduction

Fireside corrosion of carbon or low alloy steel waterwall tubes in fossil, mainly coal-fired boilers has been a minor but persistent problem. Recently the problem has become more severe in the United States due to the introduction of staged combustion systems, designed to lower NOx emissions. In these systems, the fuel is initially combusted at a stoichiometric ratio of 0.7-0.9. Additional air is added through overfire airports above the burner zone, so that the complete combustion is achieved at the furnace exit at the usual stoichiometric ratio of 1.2. Under these conditions corrosion rates in excess of 2 mm/yr are frequently experienced over relatively large areas, especially in supercritical boilers, presumably due to higher wall temperature here. In subcritical boilers corrosion rates up to 2 mm/yr are also occasionally reported, although corrosion rates here are generally less than 1 mm/yr. A survey of waterwall corrosion studies indicates that the observed losses are usually attributed to the presence of corrosive sulfur or chlorine species. Sulfur related corrosion mechanisms include:

1. The presence of molten alkali pyrosulfates, $(Na,K)_2S_2O_7$, with a melting range starting at 407°C [1]. The drawback of this mechanism is that it requires high SO_3 levels and thus a strongly oxidizing environment. The fact that waterwall corrosion increased under more reducing conditions makes this mechanism less likely under present operating conditions.
2. The presence of reducing conditions. Such conditions were previously the result of flame impingement and deposition of carbon rich deposits, due to burner malfunction or boiler designs not suitable for the coal used. However, with the introduction of staged low NOx combustion, reducing conditions are created on purpose to reduce NOx emissions.

According to most researchers [2-4] the corrosion mechanism involved is simple sulfidation of the steel in the presence of reduced sulfur species, mainly H_2S, in the flue gas. Thus, under reducing conditions iron sulfide or mixed iron sulfide/iron oxide scales are formed. These are less adherent and more prone to spalling than iron oxide scales, resulting in high corrosion rates.

This theory holds up quite well in extremely reducing conditions, for instance in gasifiers. Here corrosion rates in H_2S and CO rich environments found in isothermal laboratory studies correspond quite well with those found in actual service [5]. The corrosion of low alloy or carbon steel was found to be a function of the H_2S partial pressure of the syngas. If one extrapolates the corrosion rates to the H_2S levels usually found in boilers, 500-1500 ppm, the predicted corrosion rates are relatively low, generally less than 0.5 mm/yr. This finding has recently been confirmed by laboratory experiments carried out by Kung [4]. Based on his studies he proposed a new corrosion algorithm, describing the corrosion rate as a function of the H_2S content of the flue gas, the Cr content of the steel and the temperature. In some boilers Kung's algorithm has correctly predicted the corrosion rate [4,6], but in many other boilers corrosion rates 2-5 times higher have been experienced. These high corrosion rates are frequently assumed to be caused by higher tube temperatures, but unrealistically high temperatures are needed to arrive at the rates experienced in service. Thus, although there is no doubt that sulfidation is the basic corrosion mechanism, it is clear that the corrosion process is more complex than simple sulfidation by H_2S containing gases.

Corrosion by chlorine or chlorides has also been extensively studies, especially in Great Britain [7-11]. Originally it was thought that chlorine corrosion in coal-fired boilers could be due to both chloride deposits, mainly alkali chlorides as well as gaseous HCl. Based on experimental work carried out by Gibb[12], the majority opinion is now that chloride deposits play at most a minor role and that HCl is the major corrosive agent. The actual corrosion mechanism is still not fully explained, but the work reported in Reference 11 suggests that the corrosion rate is a linear function of the Cl content of the coal and a power function of the local heat flux, provide reducing conditions (CO>3%, O_2< 0.5% approximately) are present.

However, in waste incinerator plants chloride corrosion is strongly associated with chloride deposits and usually occurs under oxidizing conditions as well [13]. Corrosion

is accelerated by high thermal gradients in the deposits and can be reduced by the addition of sulfur compounds; e.g., high sulfur coal, which promotes formation of sulfates instead of chlorides [14]. In this paper we hope to demonstrate that chloride deposits, even in small quantities may well play a significant role in coal-fired boilers as well as in waste incinerators.

Recent Field Experience

The field experience related here concerns boilers with staged low NOx combustion systems only. Figure 1 shows annual corrosion rates of such boilers as a function of coal sulfur content. A few boilers burning high chlorine coals were omitted from the data base. The data reported here relate generally to boilers burning coals with less than 0.2% Cl although the actual Cl content for each plant was frequently unknown.

From Figure 1 it can be deduced that the correlation between corrosion rate and sulfur content is weak to nonexistent. Corrosion rates reported are also generally much higher than predicted from available H_2S corrosion models [4].

To investigate possible corrosion mechanisms and find cost effective coatings and weld overlays to combat corrosion, EPRI carried out long term corrosion studies in one boiler [16]. Standard low alloys steel tubes (T-2, 0.5% Cr,) were exposed alongside various tubes with thermal spray coatings, diffusion coatings and weld overlays. During the first 12,633 hour exposure T-2 steel tubes were exposed in two locations in the boiler. Fluegas measurements near the panels indicated highly reducing conditions with about 7% CO and 500 ppm H_2S in the flue gas at both locations. After exposure the thickness loss of the tubes was measured using an ultrasonic thickness gauge and thickness measurements by microscope. In one location the maximum corrosion rate was 1.5 mm/yr, while in the other location the loss rate was only 0.37 mm/yr, despite the fact

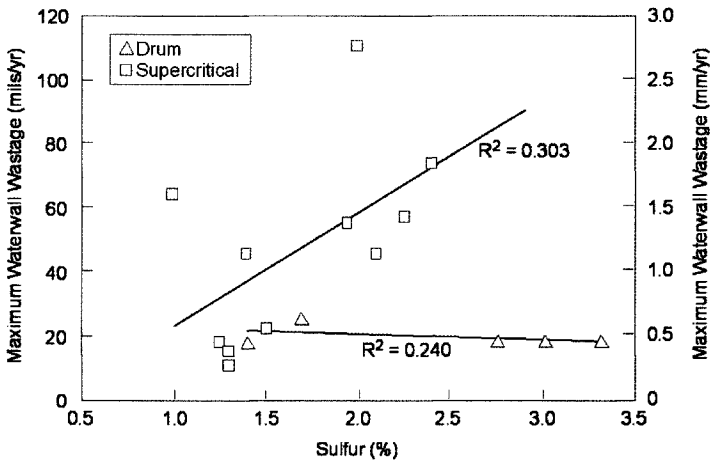


Figure 1 Waterwall Wastage as a Function of Coal Sulfur Content

that the fluegas composition during full load operation was the same in both locations. Further investigations revealed that the deposit in the high corrosion area consisted mainly of FeS (~90%) and fly ash (~10%); while the deposit in the low corrosion area consisted mainly of Fe_3O_4 and flyash. From this it was concluded that FeS deposits probably played a key role in the corrosion process. Based on this information laboratory corrosion tests were initiated to clarify the role of FeS in deposits.

In a later exposure test in the same boiler another panel containing T-2 tubes was exposed for 17,155 hours in an area where FeS rich deposits were common. The FeS content of the deposits varied from 40 to 90%. In contrast to the deposits in the first exposure the deposits also contained significantly more Cl, 500-1800 ppm vs. 90 ppm. In this exposure corrosion rates were about 33% higher on the average, but much more variable, ranging from 0.25 to 3.5 mm/yr over distances less than 1000 mm.

SEM analysis of the tubes indicated simple sulfidation corrosion during the first exposure, while chloride corrosion, as indicated by a $FeCl_2$ layer at the metal/scale interface, was found in addition to sulfidation after the second exposure, at least in some locations (Figure 2). Precise data on the Cl content of the coals used was not available, but the plant consistently used coals from local mines, producing Pittsburgh 8 seam coals, containing 0.1-0.15% Cl. From these observations it was concluded that chlorine deposits may play a role in the corrosion process even at relatively low Cl levels, when using staged combustion systems.

The latter observation was confirmed in a staged cyclone boiler. In a cyclone boiler coal combustion occurs mainly in an external combustor called a cyclone. Under staged conditions the fluegas exiting the cyclones has a stoichiometric ratio less than 1.0 and contains high levels of CO. In the boiler under study a blend of two coals was used, one had about 0.4%Cl, the other almost no Cl but large amounts of available alkali; i.e., alkali not associated with silicate minerals. Six months after firing this coal blend under staged conditions, severe corrosion of low alloy steel tubes (T-11, 1¼ Cr-0.5% Mo) was noted. Corrosion rates were in excess of 2 mm/yr and possibly higher than 3 mm/yr. Exact corrosion rates were not available since the tubes were coated with a 22% Cr thermal spray coating, which almost completely disappeared. Analysis of tube deposits and scales indicated the presence of up to 20% alkali chlorides in the deposits about equally divided between Na and KCl. The structure of the deposit indicated that the chlorides were molten during service (Figure 3). The corrosion scales contained Fe_3O_4, FeS and $FeCl_2$ (at the scale/metal interface) indicating combined sulfidation-oxidation-chlorination (Figure 4).

The service experiences cited above indicate that waterwall corrosion is not a simple case of corrosion by H_2S and HCl in the gas, but that deposits mostly likely play an important role as well. A program to study the effect of deposits on waterwall corrosion was therefore initiated at EPRI.

Corrosion in the Presence of FeS Deposits

Details on this laboratory corrosion study have been reported previously [15,16]. Coupons of low alloy steels, such as T-2 (0.5% Cr) were exposed to flowing synthetic fluegas in a laboratory muffle furnace. After exposure the remaining thickness of the coupons was measured, from which the annual corrosion rate was calculated using linear extrapolation. Initially, two tests were performed: a 600 hour test, with a reducing fluegas composition (7 CO, 12 CO_2, 6 H_2O, 0.13 H_2S, 0.008 HCl, bal. N_2)(vol%) at 450°C and a 400 hour test in which the samples were exposed for 16 hours to the reducing fluegas at 450°C and 8 hours to an oxidizing fluegas (17 CO_2, 6.3 H_2O, 1 O_2, 013 SO_2, 0.008 HCl, bal N_2) (vol %) at 400°C. The latter test simulated a two-shift operation, where the boiler is run at reduced load during the night. Tables 1 and 2 give the test results.

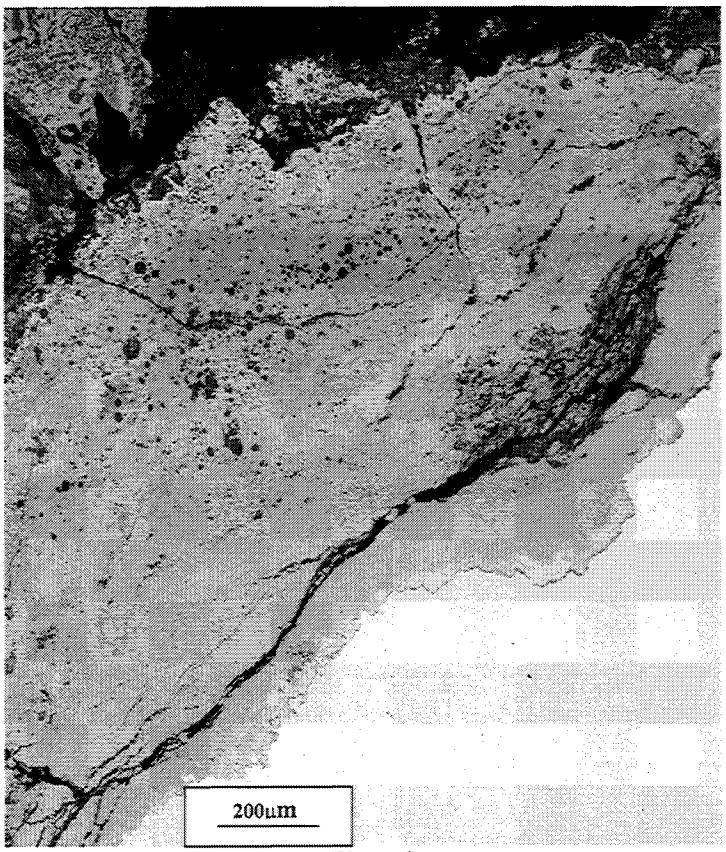


Figure 2
Chloride Corrosion under Deposits Containing 500-1500 ppm Cl and 40-60% FeS

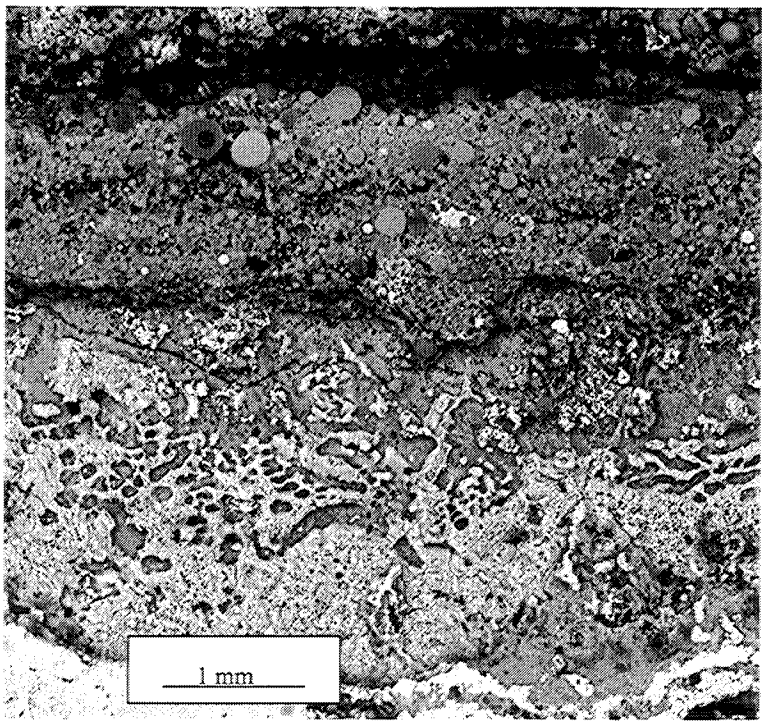
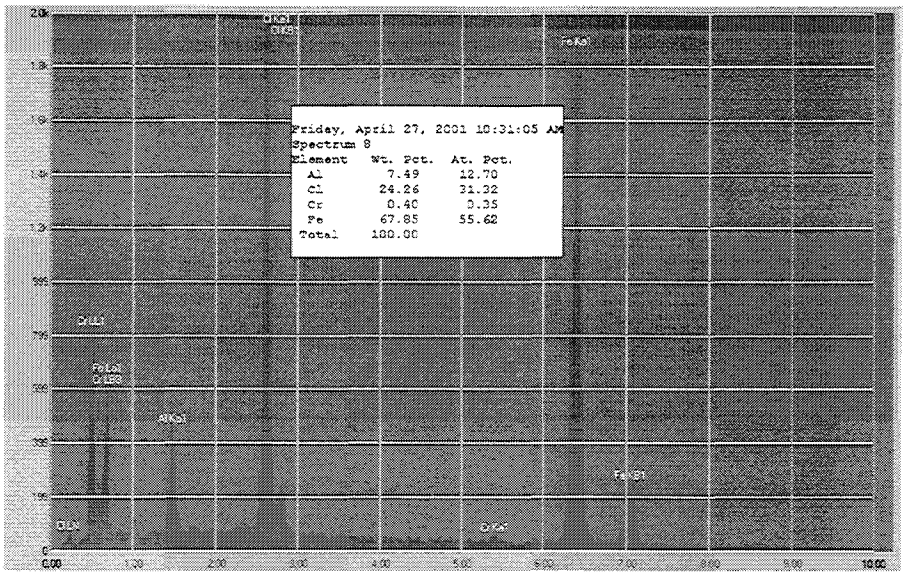


Figure 3
Molten NaC1-KC1 Deposits from Cyclone Boiler, Burning a Coal Blend Containing 0.2%C1



Spectrum #8: Analysis of material observed at the interface between the deposit/scale and tube.

Figure 4
SEM/EDAX Spectrum of Iron Chloride Corrosion Layer
Below Chloride Rich Boiler Deposits

The test run under constantly reducing conditions showed that FeS in the deposit does not increase the corrosion rate. The FeS deposit acted instead as an inert deposit, such as flyash, which usually reduces the corrosion rate somewhat. However, as shown in Table 2, the presence of FeS increases the corrosion rate significantly under alternating reducing/oxidizing conditions.

Table 1
Results of Test 1600 Hours, Reducing Conditions

Sample		Corrosion Rate mm/yr
T-2	No Deposit	0.42-0.57
T-2	30% FeS, 70% Flyash	0.1-0.3
T-2	60% FeS, 40% Flyash	0.1-0.17
T-2	60% FeS, 20% Carbon, 20% Flyash	0.2-0.6
T-2	90% FeS, 10% Flyash	0.1-0.27

Table 2
Results of Test 2, 400 Hours, Alternating Reducing and Oxidizing Conditions

Sample		Corrosion Rate mm/yr
T-2	No Deposit	0.37-0.5
T-2	30% FeS, 70% Flyash	1.0
T-2	60% FeS, 40% Flyash	0.82
T-2	60% FeS, 20% Carbon, 20% Flyash	1.2

The data strongly suggest that the presence of FeS is only detrimental during the oxidizing part of the cycle. It was therefore decided to run tests under oxidizing conditions only, with bare and coated steel samples. A preliminary 100 hour test showed very high corrosion rates (Table 3). Therefore all additional tests were run for 100 hours only, to obtain data under a wide variety of conditions in a short time.

Generally corrosion rates obtained during such short-term tests are higher than those obtained in 1000-2000 hour tests, which are more comparable to field data. Therefore, the results must be multiplied by 0.3-0.5 to obtain corrosion rates, comparable to long term laboratory tests and field data. This is shown in Figure 5 [16], which shows the calculated linear corrosion rate of T-2 steel at 850°F (450°C) as a function of time, with and without an inert flyash deposit. The data from the test without deposits show that the corrosion rate measured at 1000 hours is about 50% of that measured after 100 hours. When a somewhat protective flyash deposit is present, the corrosion rate after 1000 hours is only about 30% of that found after 100 hours. For the above reason, the data of the individual tests are presented in terms of micrometer wastage/100 hours, which were later converted to a probable rate of expected long term corrosion rates, by multiplying the nominal corrosion rate by a correction factor of 0.3-0.5, indicating the average and maximum expected long term corrosion rates.

Table 3
Results of Test 3, 100 Hours Oxidizing Conditions (1%O_2 in Fluegas)

	Corrosion Rate (mm/yr)	
Sample	Nominal	Adjusted
T-2 bare	0.5	0.18-0.25
T-2 10% FeS, 20% Carbon, 70% Flyash	3.5	1.25-1.75
T-2 20% FeS, 20% Carbon, 60% Flyash	3.5	1.25-1.75
T-2 30% FeS, 20% Carbon, 50% Flyash	5.0	1.75-2.5
T-2 60% FeS, 20% Carbon, 20% Flyash	9.0	2.25-4.5

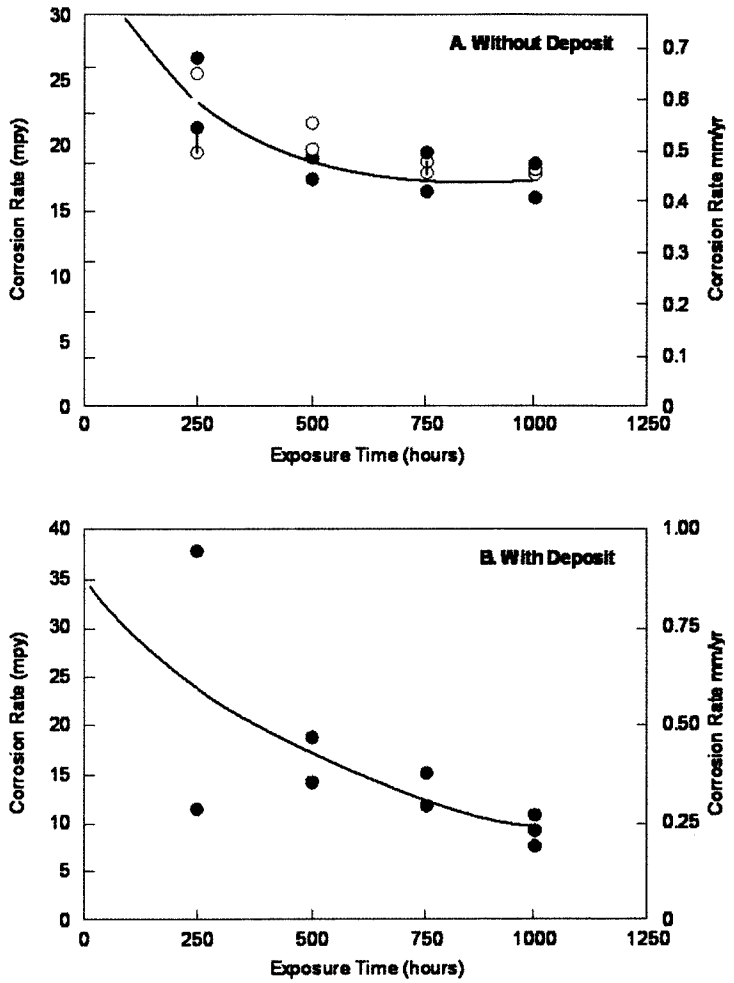


Figure 5
Apparent Linear Corrosion Rate of T-2 Steel with and without Flyash Deposit in a H_2S/CO Rich Environment

During the 100 hour test the deposits were replenished twice at 33 and 66 hours, to make sure that the FeS in the deposit would not be depleted.

In general very high corrosion losses were experienced, which increased with increasing oxygen in the fluegas and strongly decreased with increasing CO content. However, there was no consistent correlation between the FeS content of the deposit and the corrosion loss. Therefore, we decided to average the results from all FeS containing deposits (10-60% FeS) and indicate the variation between different deposits for each data point. Figure 6 shows the data obtained as a function of oxygen or CO content of the fluegas at 450°C (850°F). Figure 7 shows the effect of temperature on corrosion rates for fluegas containing 1% O_2. The results indicate that the highest corrosion rates will occur, when a FeS containing deposit is in contact with an oxidizing flue gas with 1-20% O_2. However, FeS deposits will accelerate corrosion even when mildly reducing conditions (0-3% CO) exist. They only become inert under extremely reducing conditions (7% CO or more). This suggests that the H_2 and CO_2 in the fluegas also act as oxidants.

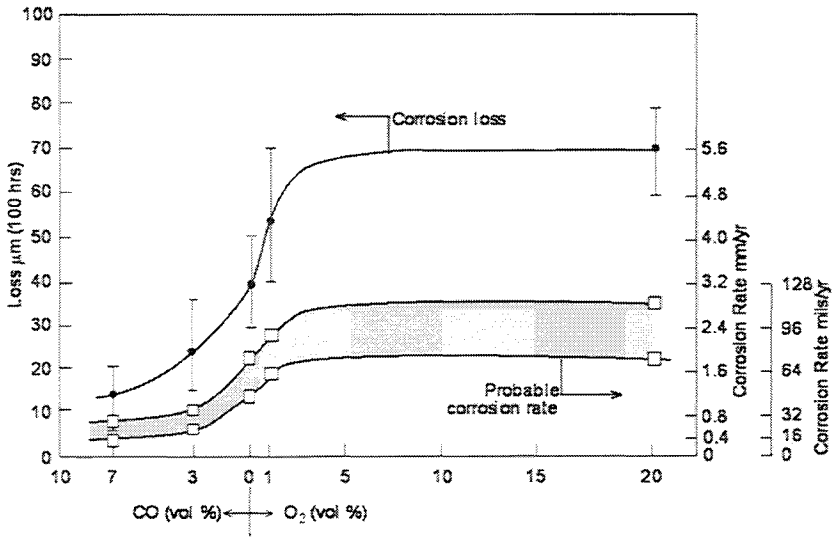


Figure 6
Corrosion Loss of T-2 Steel under FeS Rich Deposits
as a Function of O_2 and CO Content (450°C)

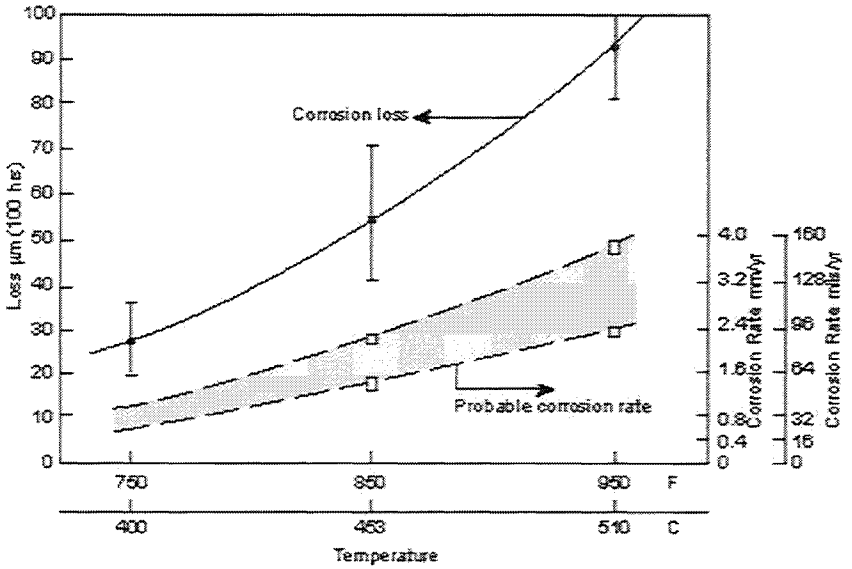


Figure 7
Corrosion Loss of T-2 Steel under FeS Rich Deposits
as a Function of Temperature (1%O_2)

It was also observed that the bare T-2 samples, although exposed to oxidizing conditions, suffered from sulfidation/corrosion with metal losses in the 10-20 µm range, quite similar to those observed in H_2S containing environments. This indicates that corrosive sulfur compounds are indeed generated when the oxidizing fluegas reacts with the FeS deposit.

Decomposition of FeS-Carbon Deposits in the Presence of Oxygen

The corrosion tests provided strong evidence that corrosive, gaseous sulfur species are formed when an oxidizing fluegas is in contact with a FeS-carbon-flyash deposit. However, it was felt useful to carry out a few tests to determine which compounds are formed and their concentration. Therefore a stainless steel reaction chamber, containing a mixture of 60% FeS, 20% carbon black and 20% flyash was installed in a furnace and held at 950°F (500°C), about 100°F (50°C) hotter than the tube temperature. Two tests were carried out. In the first air containing 6% H_2O was flown through the reactor. In the second test a fluegas containing 1% O_2, 17% CO_2, 0.13% SO_2 and 6.3% H_2O was used. The gas composition exiting the reactor was measured at 15-minute intervals. The results of the first test are given in Table 5.

Table 5
Results of Test 1: Oxidant: Humidified Air (6% H_2O),
Composition of Gases at Reactor Exit (Vol. %)

Time (min)	N_2	O_2	CO_2	SO_2	H_2S ppm	COS ppm	S	H_2O
15	85.8	3.4	10.7	3.5	238	147	0.6	1.9
45	81.9	10.2	6.3	4.7	10	197	0.4	3.6
75	82.4	9.8	5.6	3.9	18	34	1.7	3.4
105	82.1	10.9	4.3	2.5	13	18	2.8	5.8
135	82.4	12.2	4.0	2.1	10	13	1.8	2.0
Original Gas Composition (Approx.)	74	20						6

Examination of Table 5 shows that at high oxygen levels, about half the available oxygen and water are consumed and very high levels of SO_2 are generated. More importantly very high levels of elemental sulfur, which is in the gas phase above 830°F (440°C) are generated, up to 2.8%. Production of H_2S and COS on the other hand is limited. Nevertheless the gas composition produced is very corrosive and could, based on experience in gasifiers and the petrochemical industry easily result in corrosion rates exceeding 2 mm/yr. Although SO_2 generally is not considered very corrosive, at the usual level of 0.1-0.3%, it may contribute significantly to wastage at the 2-4% level. The results of the second test at 1%O_2 were similar, but generally produced lower quantities of reduce sulfur species.

In summary it is clearly demonstrated that reactions between oxygen containing fluegas and FeS rich deposits will generate large quantities of corrosive sulfur species in the immediate vicinity of the tube wall. The amount of sulfur, H_2S, and COS generated, can produce corrosion rates in the 1.5-2.5+mm/yr range, based on gasification and petrochemical experience.

Corrosion in the Presence of Chloride Deposits

Laboratory studies are still in progress. Thus results reported here must be considered preliminary. Since it has been well established that thermal gradients enhance chloride corrosion, an existing corrosion test facility was modified to create a significant thermal gradient. This was done by exposing a low alloy steel, air cooled tube in a hot furnace. Thermal gradients in deposits on boiler walls are very high, since the absorbed heat flux is typically in the 250-300 kw/m^2 range, with maximum heat fluxes in the 400 kw/m^2 range in flame impingement areas. These heat fluxes are difficult to achieve in laboratory corrosion experiments, using air cooling, which is relatively inefficient. However, in order to induce melting of chlorides it was found important to obtain a maximum deposit temperature above 650°C, the melting point of a KCl-NaCl mixture.

This was achieved with a deposit thickness of about 3 mm. To hold the tube metal temperature at about 450°C, the following experimental parameters were used:

- Flue gas temperature 1000°C
- Maximum deposit temperature 650°C
- Metal temperature 450-470°C
- Cooling air temperature at exit 320°C

Calculated absorbed heat flux under these conditions ranged from 48-51 kw/m^2, which is 5-6 times lower than in actual boilers. Deposits consisted of char, FeS and flyash with 0, 0.1,0.2, 2.0,10 and 20% KCl + NaCL in equal amounts. The flue gas was oxidizing with 1-10% oxygen. The tube temperature in the first test was about 25°C higher than desired. Further adjustments were made in Test 2 to reduce the temperature to the desired range. In both tests an increase of about 10°C was noted along the length of the tube, which is difficult to reduce further. Figure 8 shows the results of the first 3 tests. The samples without chloride additions had corrosion losses of 22 - 28 μm/100 h, which is close to the losses found in isothermal tests at 450°C. The addition of only 0.2% chloride (~0.1%Cl) already increased the corrosion rate to 44-50 μm/100 h. Higher additions of chloride further increased the corrosion loss, but at a slower rate of about 3 micrometers/% chloride. Chlorides were detected intermittently at chloride levels of 2% and above, indicating that chloride corrosion indeed occurred (Figure 9).

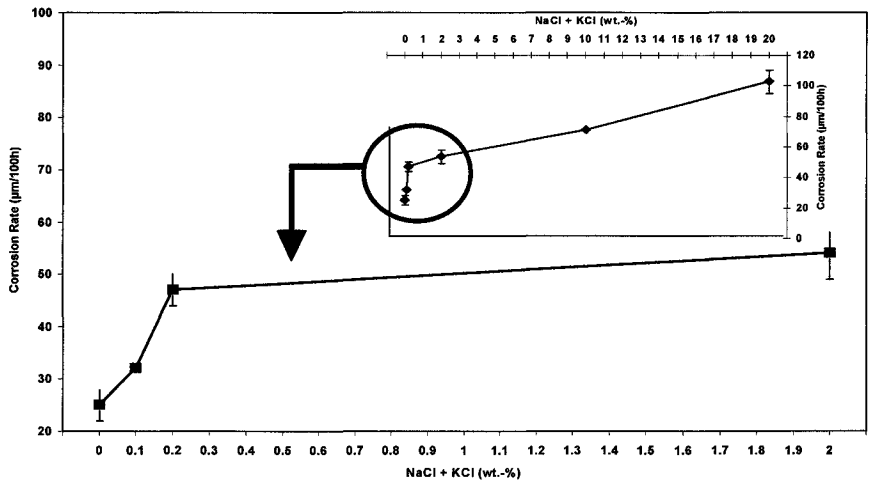


Figure 8
Corrosion Loss of T-2 Steel under FeS/char Deposits Containing 0-10% Cl
(Thermal gradient 450-650°C, 0_2 1-10%)

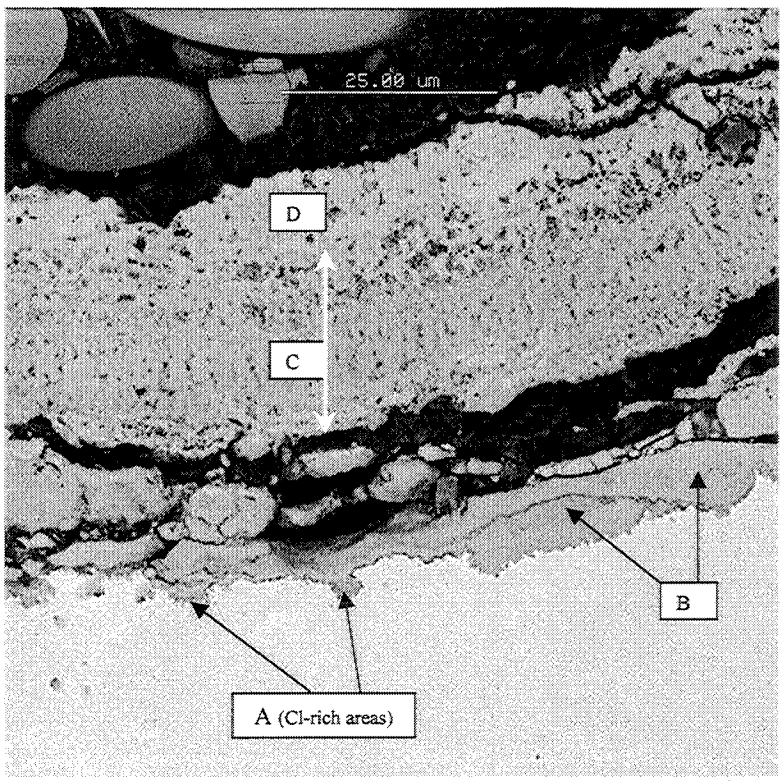


Figure 9
Chloride Corrosion under Deposit Containing 1% Cl in Laboratory Thermal Gradient Corrosion Test under Oxidizing Conditions

Discussion

Field experience in boilers, using staged combustion systems, supported by laboratory corrosion experiments, indicate that waterwall corrosion is more complex than originally thought. The available data indicate that iron sulfides and chlorides in the boiler tube deposits, together with alternating oxidizing and reducing conditions, strongly affect the corrosion rates observed in the field.

The effect of FeS has been the most thoroughly researched and is now rather clear cut. Under reducing conditions incompletely combusted char containing FeS as well as incompletely oxidized, excluded FeS can accumulate on the furnace wall. Deposits with 20-90% FeS are frequently observed in the field. Combustion Fluid Dynamic Modeling shows that areas, where high corrosion rates are observed, agree well with areas, where

partially combusted char or FeS accumulate [17]. Laboratory corrosion tests show that FeS is inert under reducing conditions, as may be expected, as it is the main corrosion product, but decomposes to several corrosive reduced sulfur species as well as SO_2 under oxidizing conditions. The amount of corrosive species produced is very high and often exceeds that formed in gasifiers, fueled by coals with a similar sulfur content. This explains the high corrosion rates observed in service, without the need to assume unrealistically high tube temperatures.

The effect of chlorides in deposits in less well established, at least for fossil fueled boilers. Research is presently in progress to elucidate this area. In waste and biomass incineration the role of chlorides is well established [13] and occurs mainly under oxidizing conditions at waterwalls as well as superheaters. Most laboratory experiments with HCl as the only corrodent indicate that by itself HCl does not increase corrosion either under oxidizing or reducing conditions [18,19] at temperatures and HCl levels of interest for waste incinerators (300-500°C, 200-1500 ppm HCl). This changes when chlorides are present in deposits. Large increases in corrosion rates are observed, generally more so under oxidizing than under reducing conditions [20,21]. Further studies showed that laboratory corrosion rates under thermal gradients are much higher than under isothermal conditions and approach those observed in the field [22]. This strongly indicates that molten phases and/or high chloride vapor pressures play a role in the corrosion process. The actual corrosion process is frequently "active oxidation [23]". Here chlorides or HCl react with oxygen or oxides to form elemental chlorine. The latter will penetrate the oxide scale, and react with Fe to form $FeCl_2$, which may evaporate and decompose in cracks and pores of the scale, thus destroying the oxide scale [24].

This understanding of Cl corrosion is considerable different than that of Cl corrosion in fossil fueled boilers. Here Cl corrosion is thought to occur only under reducing conditions and is reportedly caused primarily by HCl in the fluegas. There appears to be a need to reconcile these two points of view, since it is unlikely that the corrosion mechanism is so radically different in closely related applications. Pending further research, we will make such an attempt here.

As has been previous reported by Miller and Krause [14], additions of sulfur reduce Cl corrosion in waste incinerators, presumably due to the formation (and deposition) of sulfates instead of chlorides, at least under oxidizing conditions.

Thermodynamic calculations by Daniel [25] and more recently by Baxter [26] indicate that gaseous Na and KCl are the thermodynamically stable species at high temperature (>1100°C), provided sufficient alkalies are available. Under oxidizing conditions these convert to sulfates in the presence of SO_2/SO_3 at lower temperatures. However, under reducing conditions, the chlorides may be stable at low temperatures as well, presumably due to the lack of available SO_2/SO_3 as indicated by the presence of chlorides in boiler deposits and predicted by thermodynamic modeling. Thus under reducing conditions the condensation of alkali chlorides appears possible for fuels with a relatively high sulfur content. Experiments are presently under way to quantify this assumption. Corrosion experiments under thermal gradients and oxidizing conditions reported here have already

shown that only small amounts of chloride are needed to increase the corrosion rates under FeS/(Na,K)Cl deposits. Thus the proposed Cl corrosion mechanism for fossil fueled boiler waterwalls is as follows:

1. Under reducing conditions alkali chlorides remain stable and will deposit at waterwall tube surfaces, together with FeS.
2. The already high corrosion rates, due to FeS decomposition under oxidizing conditions are further enhanced by to the formation of $FeCl_2$ under the FeS/Fe_3O_4 scales. Evaporation and decomposition of $FeCl_2$ leads to deposition of Fe_3O_4 and possibly FeS in the already poorly protective scales leading to cracking and spalling.
3. Large thermal gradients will increase the vapor pressure of the alkali chlorides present and cause melting of chloride mixtures. This will further increase the corrosion rate.

This proposed corrosion mechanism is consistent with recent field observations in coal fueled boilers as well as waste incinerators/biomass boilers. Reducing conditions are needed to eliminate the protective effect of the coal sulfur. Chloride deposition is probably a function of the total Cl content in the coal, providing enough available alkali is present to form the thermodynamically stable chlorides. The effect of heat flux on chloride corrosion[11] is due to increases in the vapor pressure of alkali chlorides and/or increases the fluidity of molten salt mixtures in the presence of a thermal gradient.

Conclusions

1. Iron sulfides in boiler tube deposits accelerate fireside corrosion under alternating reducing and oxidizing conditions present in most coal-fired power plants.
2. FeS deposition occurs mainly under reducing conditions, while corrosion rates are highest under oxidizing conditions, due to decomposition of FeS, which produces high amounts of corrosive reduced sulfur species.
3. Small amounts of chlorides (500-1500 ppm) in FeS rich deposits further increase waterwall fireside corrosion rates due to $FeCl_2$ formation below a Fe_3O_4/FeS scale, when burning coals containing as little as 0.1-0.15%Cl.
4. Laboratory tests using FeS-(Na,K)Cl deposits under a 450-650°C thermal gradient, showed a 50-100% increase in corrosion loss at chloride levels as low as 0.2% (Na,K)Cl, without HCl in a fluegas, under oxidizing conditions (1-10%O_2). This indicates that chloride deposits are indeed a major factor in Cl corrosion in coal fired boilers.

References

1. Reed, W.R., "External Corrosion and Deposits – Boilers and Gas Turbines," Elsevier, NY, 1971.
2. Chou, S.F., Daniel P.L., Blascewisz A.J., Dudek A.J., "Hydrogen Sulfide Corrosion in Low NOx Combustion System," p. 327 in High Temperature Corrosion in Energy Systems, M.F. Rothman ed, AIME, 1985.
3. Kung, S.C., Eckhard C.F., "Corrosion of Iron base Alloys in Reducing Combustion Gases," NACE, CORROSION/93, paper 242, New Orleans, LA, March 1993.
4. Kung, S.C., "Prediction of Corrosion Rates for Alloys Exposed to Reducing/Sulfidizing Combustion Gases, Material Performance, Vol. 36, 12, p. 36-40, December 1997.
5. Bakker, W.T., "Effect of Gasifier Environment on Materials Performance," p. 81 in Materials at High Temperatures, Vol. 11, No. 1-4, 1993.
6. Bakker, W.T., et.al., "Long Term Testing of Protective Coatings and Weld Overlays in a Super Critical Boiler, Retrofitted with Low NOx Burners," NACE, CORROSION 2002, paper 02384.
7. Clarke, F., Morris C.W., "Combustion Aspects of Furnace Wall Corrosion," p. 97 in "Corrosion Resistant Materials for Coal Conversion Systems", D.B. Meadowcroft, M.I. Manning ed., Applied Sciences publishers 1983.
8. Lees, D.J., Whitehead M. E., "Micro Analysis of Scales and Deposits formed on Corroding Furnace Tubes in Coal-fired Boilers," Ref. 7, p. 63.
9. Latham, E., Meadowcroft D. B., Pinder L., "The Effects of Coal Chlorine on Furnace Wall Corrosion," p. 207 in Chlorine in Coal, J. Stringer, Banerjee D.D., ed. Elsevier, 1991.
10. James, P.J., Pinder, L., "The Effect of Coal Chlorine on the Fireside Corrosion of Boiler Furnace Walls and SH/RH Tubing," p.117 in Materials at High Temperatures, Vol. 14, No. 2/3, 1997.
11. Davis, C.J, James P.J., L.W. Pinder, Mehta A.K., "Effect of Fuel Composition and Combustion Parameters on Furnace Wall Fireside Corrosion", p. 875 in Materials at High Temperatures 5, Streiff et al ed., Trans tech publ.2001
12. Gibb, W.H., "The Nature of Chlorine in Coal and its Behavior During Combustion," Ref. 7, p. 25.
13. Sorell, G, "The Role of Chlorine in High Temperature Corrosion in Waste to Energy Plants," Ref. 10, p. 137.
14. Miller, P.D., Krause H. H., Proceedings 1972 National Incinerator Conference, p. 300, ASME, NY 1972.
15. Bakker, W.T., Kung S.C., "Waterwall Corrosion in Coal-fired Boiler, a New Culprit FeS," paper 00246, CORROSION 2000 NACE, Houston, TX, USA 2000.
16. Kung, S.C., Bakker W. T., "Furnace Wall Corrosion in Reducing, Sulfidizing Combustion Gas," Ref. 10, p. 109.
17. Bakker, W.T., Waterwall Corrosion in Low NOx Boilers, Root Causes and Remedies, p. 13-17, Proceedings EPRI-DOE-EPA Combined Utility Air Pollution Control Symposium, August 1999, EPRI report TR-113187, V.2, 1999.
18. Smith, G.D., Ganesan, P., Shoemaker, L.E., paper 280 CORROSION 90 NACE, Houston, TX 1990.

19. Kung, S.C., Daniel, P.L., Seeley, R.R., paper 165 CORROSION/96 NACE International, Houston, TX (1996)
20. Slusser, J.W., Dean, S.W., Watkin, W.R., Goff, S.P., paper 217, CORROSION/93 NACE, Houston, TX (1993)
21. Paul, L.D., Daniel, P.L., paper 216, CORROSION/93, NACE, Houston, TX (1993)
22. Kawahara,Y, Masahara, K., Minoru,Y. , p. 625, High Temperature Corrosion and Protection, 2000, Science Reviews, Elsevier A'dam
23. Bremhoff, D., Grabke, H.J., Smidt, H.P., Werkstoffe and Korrosion 40, 135 (1989)
24. Spiegel, M., Reactions between Gas Phase, Deposits and Metallic Materials in Chlorine Containing Atmospheres, p. 151, Ref 10.
25. Daniel, P.L., The Effect of Coal Chloride, or Furnace Wall Corrosion, p.207, in Ref 9.
26. Baxter, L.L., unpublished result.

FABRICATION OF GAS TURBINE COMBUSTION HARDWARE IN ODS FERRITIC MATERIALS

G.McColvin[1], D. Munasinghe[2], J.O'Driscoll[3], M.Jacobs[4].

[1] ALSTOM Power UK Ltd, Lincoln,UK.
[2] Plansee Metals Ltd, Slough, UK.
[3] Special Metals Wiggin Ltd, Hereford, UK
[4] IRC in Materials for High Performance,
University of Birmingham, UK

Abstract

The temperature capability of the ODS ferritic materials in terms of oxidation and creep resistance has proved an enticing but as yet unachieved opportunity in Gas Turbine combustion engineering. One of the most significant barriers to this development is related to the fabrication difficulties experienced with these materials in terms of sheet metal forming and joining. This is particularly challenging for traditional sheet metal fabricated combustion cans and transition ducts, where deep drawing and conventional welding methods play significant roles in the fabrication process.

Within the framework of COST 522, a programme has been established to evaluate alternative metal forming procedures aimed at reducing / eliminating joints from critical regions of the fabrication. Some joints are unavoidable, so investigations are being made using currently available advanced bonding methods to evaluate the thermo-mechanical joint efficiency as an aid to component redesign for ODS materials.

Keywords:

Introduction

Within Europe, one of the main barriers to the development of 4 - 40 MW range power generation gas turbines with >37% efficiency is the temperature and strength limitations of the combustor materials used. The nickel-based sheet materials used currently are increasingly temperature capability limited, operating at peak metal temperatures in excess of 950°C, and are primarily reliant on thermal barrier protection systems and cooling air to limit severe thermal fatigue, creep damage and oxidation cracking. These failure mechanisms restrict the operational lifetimes to less than 24,000 hours and impact severely upon the reliability, availability and costs. Conventional materials are unlikely to allow further benefits, in terms of reduced emissions and increased efficiencies, to be gained. To meet the needs for reduced CO_2 and NOx emissions to mitigate the potential harmful effects due to climate change, more advanced materials such as the ODS alloys are required.

The ODS materials, such as the nickel-based alloys PM1000* and INCONEL ^{R} MA754 and the iron-based alloys PM2000* and INCOLOY ^{R} MA956, represent excellent candidates for a number of gas turbine and power generation applications. In terms of directly fired gas turbine combustion hardware, the iron-based alloys offer the greatest potential due to their high melting point and well renowned oxidation resistance. Implementation of ODS materials will enable a step change in the temperature capability of GT combustion hardware of in excess of 150°C, from the current 950°C metal temperature capability limit to 1100°C. For a directly-fired 5 MW GT engine this represents a 1.25% increase in engine efficiency and a reduction in fuel consumption of 0.75%, providing a CO_2 emissions

reduction and, by reducing the demand for cooling air, enabling improved combustion temperature control for NOx reductions.
These innovative iron-base ODS alloys take advantage of an efficient high temperature hardening mechanism and high levels of alloying (chromium, aluminium and yttrium) to promote the development of stable and adherent oxide scales during exposure to high temperatures. The alloys are manufactured by mechanical alloying to produce an extremely fine-grained powder that incorporates a fine, homogeneous dispersion of spherical yttria (Y_2O_3) particles, 20 – 50 nanometers in diameter. These demonstrate long-term stability at temperatures up to 1200°C, which is in excess of that achievable with conventional superalloys, (Figure 1). Hot compaction of the MA powder is achieved using hot isostatic pressing (HIPping), followed by extrusion and rolling, if necessary, to form sheet products. Application of a thermal processing procedure is crucial to the coarsening of the sub-micron grain size and development of high temperature creep and thermal fatigue strength. The high temperature capability of ODS materials is crucial to the success of this project, however, joining methods and protective coatings need to be developed further and the manufacturing capability validated.

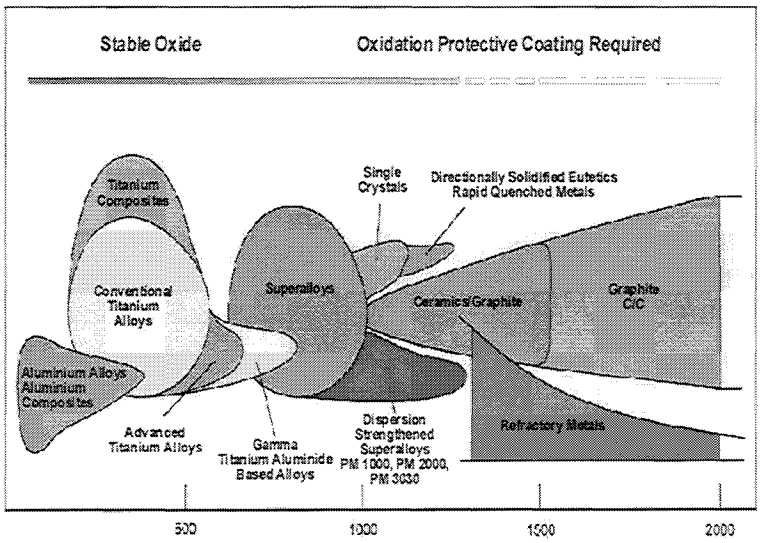


Figure 1. Temperature capability of ODS alloys.

A project was established within the framework of COST 522 work package 3 on Plant Integration to investigate the fabrication of gas turbine combustor hardware using the iron-based oxide dispersion strengthened (ODS) materials. Using the ALSTOM Power UK Ltd. RM Typhoon small industrial gas turbine (figure 2) as the model, the plan was to attempt the manufacture of a canular combustor system (Figure 3).

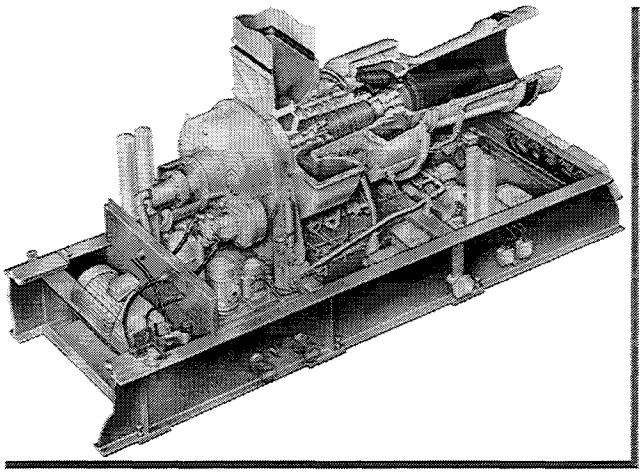
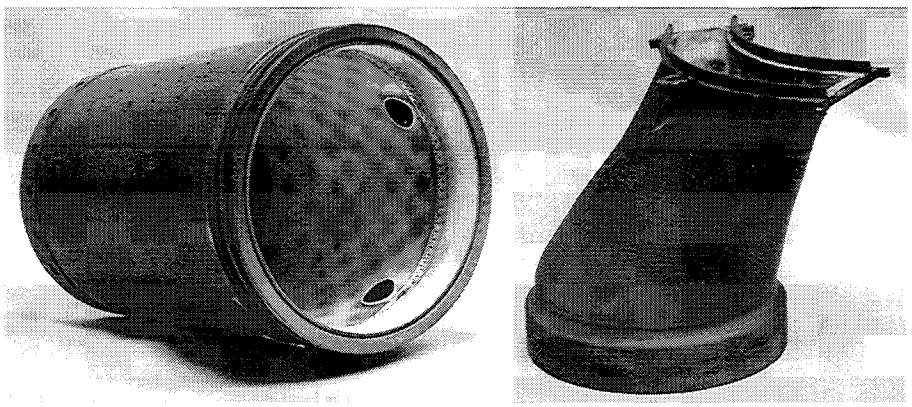


Figure 2. ALSTOM Power UK Ltd. RM Typhoon Industrial Gas Turbine.



(a) (b)

Figure 3. Photograph of RM DLE can (a) and transition duct (b).

Forming

The iron-base ODS alloys have ferritic microstructures which are inherently more difficult to deform at ambient temperatures than an austenitic matrix. Face centred cubic (FCC) crystals have high symmetry and 12 potential slip systems. In the body centred cubic (BCC) lattice of the ferritic materials, slip occurs in the <111> direction. A dislocation reaction has been suggested that appears to lead to the formation of immobile dislocations in the BCC lattice, which has been shown to be one of the mechanisms for producing a crack nucleus for brittle fracture. Two dislocations come together to react and lower their strain energy by providing a pure edge dislocation which lies on the (001) plane. Since the (001) plane is not a close-packed slip plane in the BCC lattice, the dislocation is immobile. Moreover, the

(001) plane is the cleavage plane along which brittle fracture occurs [1]. These ferritic alloys also have a ductile to brittle transition temperature (DBTT), which is a function of chemical composition and grain size. For severe deformations, it is recommended that ODS alloy and its tooling be warmed to at least 150^0C-200^0C i.e. well above the ductile-brittle transition temperature of around 70^0C. Removal of the alumina film on the ODS alloy before forming is recommended, to prevent cracks which originate in the oxide film from propagating through the substrate.

Pressing and Deep Drawing

Simple shapes have been successfully pressed in ODS alloy sheet. In deep drawing the metal is subject to both tensile and compressive forces and a considerable amount of thinning is usually involved. At room temperature the plasticity of the ODS alloys is much less than that of austenitic materials, but is comparable at higher temperatures, above the DBTT. Generally, it is not practical to carry out the process at elevated temperatures. Some gentle heating of the press tools is possible but is limited by the tool material capabilities and practical access issues. Tool materials with higher temperature capability are available but at very high cost. In terms of the RM DLE combustion hardware only the transition duct is produced by sheet metal pressing, involving significant depth of draw. The practical difficulties of pressing ODS sheet material even at slightly elevated temperatures has precluded detailed investigations in this area.

Metal Spinning

Metal Spinning can be used to produce axi-symmetric shapes starting with flat sheet or plate. The process can be carried out at room or elevated temperature and can involve simple bending, folding or flow forming with significant metal thinning. The blank for spinning is usually a flat disc or square, cut from sheet or plate which is clamped by the tailstock of the spinning lathe against a rotating forming tool in the shape of the finished part. One or more, hydraulically driven roller tools progressively form the blank onto the tool shape. The instantaneous deformation zone is very small compared to many other processes, hence the forces are relatively small. The strain rate may be very high e.g. 100 sec^{-1} or more [2]. This is significant for the ODS materials as the process increases the stored energy within the component, which then drives the secondary recrystallisation reaction, producing the coarse grain structure necessary for high temperature creep strength.

Initial spinning trials using a single forming tool were conducted on small-scale demonstration pieces. These initial trials proved successful in producing small, flow formed "pots", (figure 4) and a larger conical form that could be used as the precursor for a spinning full-length combustor can.

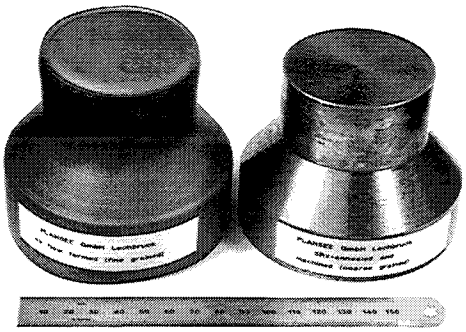
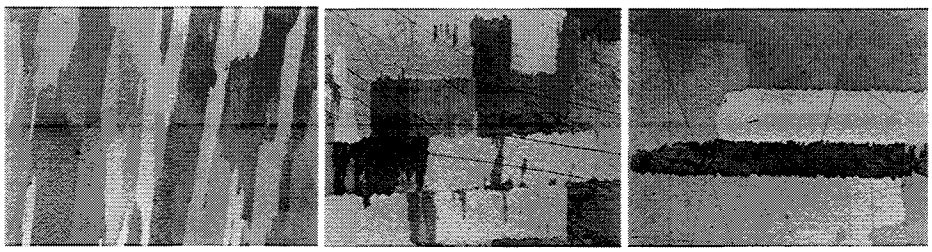


Figure 4. Demonstration spun "pots" on PM2000.

Metal spinning processes frequently impart tangential material flow that will have the effect of elongating the grain structure in the circumferential direction after heat-treatment. Depending on the combination of forming parameters, different grain morphologies can be produced (figure 5) relative to the component axis, from fully axial (a) to fully circumferential (c).



(a) (b) (c)

Figure 5. Variation of grain elongation with material flow from spinning.

Scale-up of the process to a full size combustor can was not successful due to buckling of the rim of the sheet when attempting to fold down onto the barrel section of the forming tool. Two new approaches have been suggested for the manufacture of a land-based gas turbine (LBGT) combustor can. In the first, staged tooling is used to produce a series of cones of diminishing apex angle. The front-end shape (top end) of the can is spun after the second stage. A second approach is to form the front end shape by forging, but leaving sufficient excess metal to flow form the walls of the can.

Hydromechanical forming

Hydromechanical forming enables the production of pressings that are either impossible by conventional means, or that would normally take up to six separate stages. The process provides an ideal method for producing parts with complex shapes or where draw ratios up to the order of 1:2.9 are required. The technique can be used to great advantage when close tolerances and fine surface finishes are required or where there are problems with intermediate annealing. Tooling for the forming process is simple, comprising a punch, draw ring and blank holder ring. The tooling material is the same as for conventional tooling. The process uses a thick walled steel chamber containing the pressure medium. A

draw ring is attached to the top of this chamber and as the punch enters the pressure medium (oil), pressure immediately builds up to a pre-determined setting. Blank holding from above is by means of a third cylinder. As the punch continues into the oil the material is pressed against the punch by the pressure inside the chamber.

Hydroforming.

Hydroforming is a process employing the flexible die technique where only one rigid tool half, either the punch or die is necessary, the other half being a rubber diaphragm which serves as both blank holder and flexible tool member. Under hydrostatic pressure, the rubber diaphragm transfers fluid pressure to the blank, which is forced to assume the shape of the rigid tool. The diaphragm supports the entire area of the blank during the forming process thus giving excellent control of the material, keeping local stress concentrations to a minimum therefore inhibiting thinning and cracking. This in turn enables a thinner blank to be used. Hydroforming has all the advantages of Hydromechanical forming but also allows an increase in draw ratio of up to 50% due to the way the material performs during the forming process. As permanent tooling is not essential tooling is also considerably cheaper.

Joining

Fusion welding

ODS materials can be joined for some applications using conventional fusion processes [3-5], such as gas tungsten arc welding. Fusion welding disrupts the oxide distribution causing agglomeration of the oxide dispersion [4] in the weld zone, with some of the yttria floating to the top of the weld pool. Fusion welding also destroys the interlocked, elongated grain structure replacing it with a much weaker cast structure [3]. These effects result in a loss of the high temperature properties, in particular, a drastic reduction in creep strength [4, 5].

Recent preliminary TIG welding trials by the authors, in which ODS sheet was either welded to itself or to superalloy sheet (Haynes^{R} 230, INCONEL 617, Haynes 214), using matching filler wire (Haynes230W, INCONEL 617 and Sulzer-Metco 8443) indicated problems with post-weld distortion and delayed post-weld cracking. Figure 6 shows a cross-section of a TIG-welded Haynes 230 – PM2000 joint.

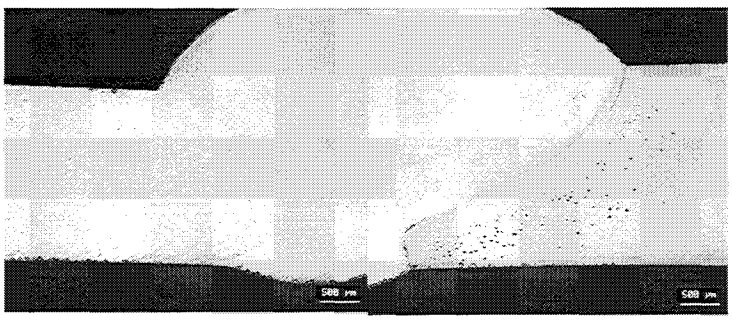


Figure 6. Cross section of a TIG welded HA230 – PM2000 joint.

Other fusion welding processes such as electron beam welding and laser welding, which minimize the extent of the fusion zone, have been used with some success [3-5]. Compared

with TIG welding, porosity and oxide dispersoid agglomeration are significantly reduced [4]. Weld quality may be improved by aligning the energy beam with the grain orientation of the base metal [4]; however, this may be difficult to achieve in practice with real component geometries, such as those being considered in this paper.

Vacuum Brazing

It is reported [6] that successful vacuum brazing of ODS materials may be accomplished in a 'clean' (all metal) vacuum furnace, provided that the vacuum level in the chamber is ~ 5 x 10^{-5} mbar, or higher. Wettability of the molten braze alloy is strongly influenced by the surface condition, particularly the cleanliness of the ODS mating surfaces to be brazed. A basic fact of vacuum brazing is that the filler braze alloy will have a lower melting point than the ODS mating surfaces, and may have poorer mechanical properties. Hence, it is imperative that the composition of the braze alloy is carefully selected. Detailed studies [6, 7] have been carried out with BNi-5 (71Ni, 19Cr, 10Si, 0.03B, 0.06C; Wall Colmonoy Ltd) and Pd-40Ni (60Pd,40Ni; Engelhard) braze alloys. Shear creep testing at 800-900°C showed that the joint strengths of BNi-5 and Pd-40Ni brazed PM2000 ODS test samples were considerably lowered with decreasing stress or strain rate. However, strengths were judged to be suitable for a selected practical application. Transient liquid phase bonding, which employs an interface layer of a sputtered coating of amorphous Fe-B-Si composition, has also been investigated, again with some success [3,8].

Solid State Bonding

A potential technique for the fabrication of high quality joints between ODS alloys is diffusion bonding in a hot isostatic press (HIP). Diffusion bonding is a process that involves the simultaneous application of heat (between 0.5-0.8T_m) and inert gas pressure (of the order of 100-200 MPa) to produce a solid state bond with a minimum of macroscopic deformation. The limited data available in the open literature suggests that the joining of ferritic ODS alloys is feasible since oxide agglomeration can be avoided. However, the fabrication of high quality diffusion bonds in ODS materials requires careful control of surface cleanliness, surface roughness, material recrystallization and process parameters [9]. Also, a non-trivial practical detail is that the bond-line must be isolated from the high-pressure gas during the HIPping operation. This is conventionally achieved by encapsulation, but this may not always be feasible and, therefore, some other form of sealing must be devised. Plasma sprayed encapsulation has been examined [11], but with only limited success. Since joining processes invariably alter the microstructure of the parent material at the interface, a fundamental understanding of the metallurgical changes induced by the HIP diffusion bonding process is essential if the high temperature properties of the material are to be retained.

Uni-axial diffusion bonding with a press should also be considered [4]. If the mating ODS surfaces are diffusion bonded in the unrecrystallized condition, then a subsequent recrystallization treatment can lead to some grain growth across the bond line, which enhances the mechanical properties of the bond. Tooling for the press may be expensive if the components to be bonded are of a complex shape.

Joining of dissimilar materials.

Many potential applications of ODS alloys in power generation and heat exchangers [11] require the ODS alloy to be joined not just to itself but to dissimilar, high temperature alloys. The fabrication of dissimilar metal joints between ODS alloys and nickel-based superalloys and stainless steel introduces additional complications if the required performance characteristics are to be achieved. In general, when joining ferritic materials to austenitic ones, the main problem is the mismatch between the thermal expansion coefficient of the two materials [11]. Ferritic ODS alloys have a thermal expansion coefficient of ~15 x 10^{-6} K^{-1} (between 20°C and 1000°C) whilst those of nickel-based superalloys and stainless steel are 16-18 x 10^{-6} K^{-1} and 19 x 10^{-6} K^{-1}, respectively. Mismatch in the thermal expansion coefficient of the two materials are very likely to give rise to high thermal stresses, which can cause fracture in the joint, either during cooling from the joining temperature or during thermal cycling in service. One possible method to alleviate these thermal stresses is to introduce a tailored interface between the two materials in the form of an appropriate interlayer material or a functionally graded interface. To date, no research appears to have been carried out to study the potential of this approach.

The ability, when demonstrated, to join successfully either ferritic ODS to ferritic ODS or ferritic ODS to high temperature austentic materials may be satisfactory as far as it goes. However, the stability of such joints during exposure to high temperature for long periods, their responses to thermal cycling and, last but not least, their stabilities in corrosive and erosive gas environments must also be examined and proved to be satisfactory.

Mechanical Properties

In order to produce data suitable for design and lifing of combustor hardware, mechanical property data (tensile, creep, low and high cycle fatigue) needs to be generated on commercially produced candidate virgin sheet materials. Ideally this should be repeated over several different batches of material to build in a statistical balance to the data. This data can then be compiled with the existing (supplier and literature) data to provide a reliable database for component design and lifing.

Conventional sheet materials used for combustion hardware (e.g. NIMONIC^{R} 75, Haynes 230) do not show significant influence of the normal fabrication processes on the grain structure and resultant mechanical properties after final heat treatment. In contrast, It is well known that the mechanical properties of the ferritic ODS alloys (MA956 and PM2000) being considered in this project are extremely sensitive to grain size and grain orientation both of which are strongly governed by applied forming methods [12-14].

Hot sheet metal pressing, hot spinning and flow forming processes are the most likely forming methods to be applied to these materials in the course of manufacture of combustion hardware. Hot pressing and hot spinning are most effectively conducted on sheet material in the micro-fine "as-rolled" grain size condition with the coarse grain recrystallization heat treatment process being applied after forming. Hot sheet metal pressing is likely to produce grain structures similar to that of standard flat sheet. In comparison, metal spinning is a considerably more severe forming process. The starting material is usually much heavier section plate or sheet material, which is then subjected to extensive material flow and changes of section in order to achieve the final part shape. In this case the exact forming parameters applied will have a controlling influence on the size,

shape and orientation of the grains within the finished piece after the recystallization heat treatment. The aim within the processing window is to not only achieve the part dimensions required but to also leave a residual "work content", such that a coarse grain sheet type microstructure is formed on recrystallization heat treatment in order to achieve optimum mechanical properties in the part.

A major task within this COST 522 project, therefore, has been to establish a sound design database for ODS ferritic materials. The basis for this has been taken from available literature, primarily ASMH reference Fe-1451 and the suppliers' handbooks, enhanced by an extensive mechanical testing programme on virgin sheet material from several production batches. Using samples taken from both longitudinal and transverse sheet directions of the two candidate ODS ferritic alloys, PM2000 and MA956 a composite database design chart for tensile strength has been compiled, figure 7.

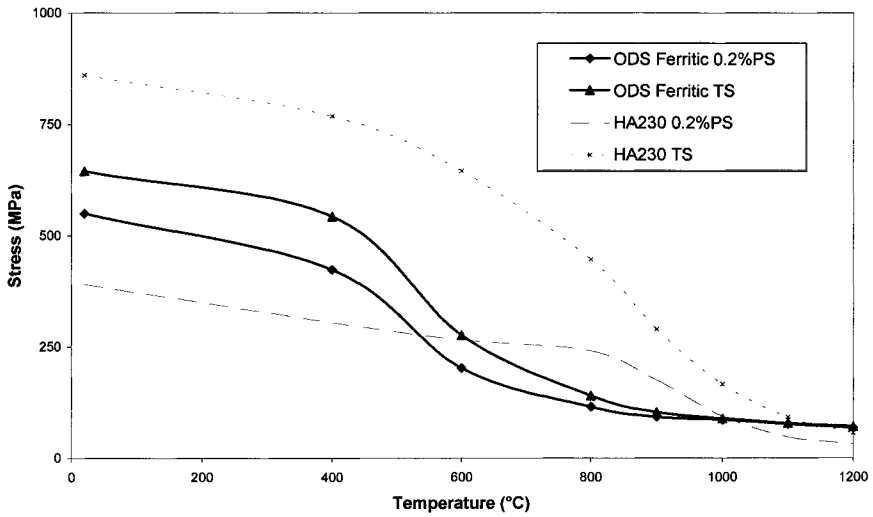


Figure 7. Tensile strength data for ODS ferritic and HA230 sheet material.

In terms of the short-term tensile strength the ODS materials show no significant advantage benefit over the traditional sheet material. The proof strengths of the two materials are generally similar but the tensile strength of the conventional sheet alloy, HA230, is significantly higher until temperatures of 1100°C and above are reached. The tensile ductility (figure 8) also shows an advantage for the conventional material. In view of the nature of the microstructures of the two materials, these results are not unexpected.

It is in the realm of creep properties that the ODS ferritic materials really show their true advantage, this is what they were designed to do. Creep rupture data is presented in classical stress –log time format in figure 9, comparing the ODS sheet materials with both HA230 and INCONEL 617 sheet materials.

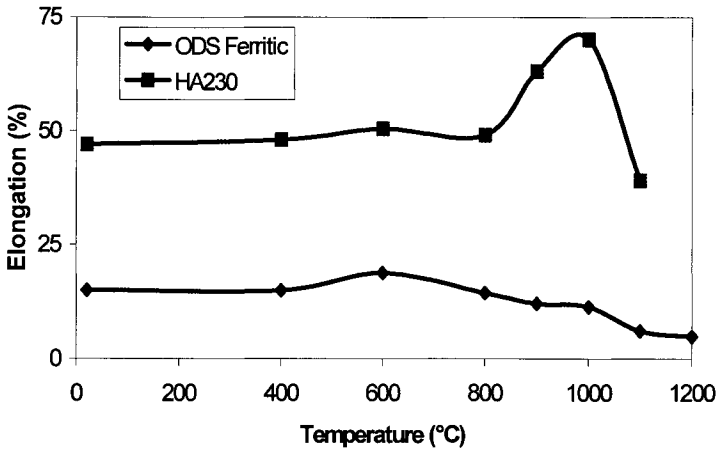


Figure 8. Tensile ductility of ODS Ferritic and HA230 sheet materials.

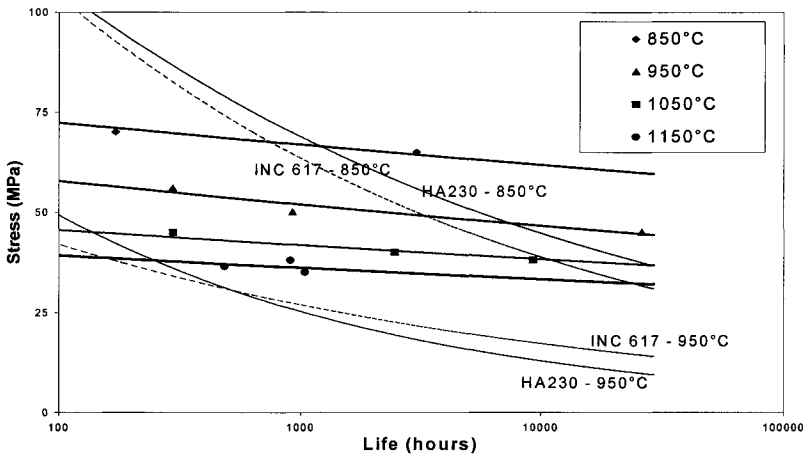


Figure 9. Creep rupture properties of ODS ferritic and conventional nickel-base sheet materials.

From this chart it is easy to see why there is so much interest in using these ODS materials in creep limited situations, the ODS materials showing an advantage of about 200°C for useful lifetimes of 20 000 hours. It is also very clear that at 950°C the conventional solid solution strengthened materials traditionally used for combustion hardware are severely limited in creep strength for long service times, whereas the ODS materials maintain a very flat creep rupture characteristic.

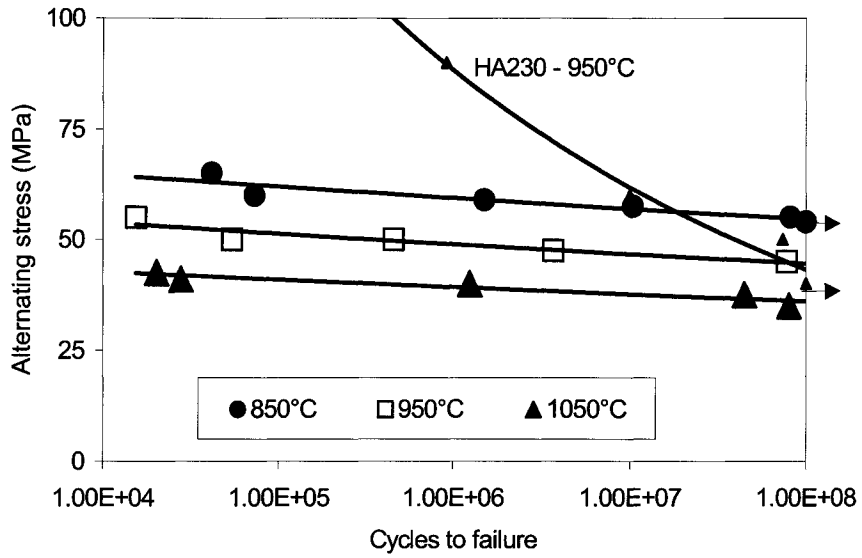


Figure 10. Comparative axial high cycle fatigue properties of ODS ferritic and HA230 sheet materials, at R = 0.05.

Axial high cycle fatigue tests show a similar characteristic of material behaviour, (figure 10). These results do not show any advantage for the ODS sheet materials, but they do show an effective endurance limit type behaviour, albeit starting at a low number of cycles to failure. In terms traditionally used for axial HCF the stress for 10^8 cycles to failure is the same for both materials.

Conclusion

The work presented here is clearly a long way from being completed. Many lessons have been learned regarding forming and joining of these ODS ferritic materials, mostly about things that do not work, but these are just as important conclusions as successful ones. A material database has been established suitable for design and lifing of the engineering components; all we have to do now is to prove reliable practical manufacture of the components.

The future work within the current COST 522 WP3 working group will continue to focus on the forming routes involving the hybrid and composite methods described. Joining continues to be a major issue, but some success in ODS to conventional material joints has been achieved. These joints need to be evaluated to assess their engineering value whilst work continues on the more exotic processes.

Acknowledgements

The authors would like to thank their respective organizations for their support and permission to publish this paper.

References

1. Dieter G.E., *"Mechanical Metallurgy"*, (McGraw Hill), 2nd Edition, 1976

2. Kalpakcioglu S. *"Power Spinning"* from Fundamentals of Deformation Processing. 9th Sagamore Army Materials Research Conference, Raquette Lake, New York, August 28th-31st, 1962 (Syracuse University Press) Chapter 4, 1964, pp. 71-103

3. McKimpson, M.G. and O'Donnell, D., *JOM,* **7**, 1994, p.49-51.

4. Tomkings, A.B. and Cotgrove, R.M., *Joining of Advanced Structural Materials*, ERA Technology report 96 – 0139R, Feb 1996.

5. Wright, I.G., McKamey, C.G., Pint, P.J. and Maziasz, P.J., in Proceedings of the 13th Annual Conference on Fossil Energy Materials, Knoxville, Tennessee, USA, May 11-13, 1999.

6. Holmstrom, S., Siren, M., Auerkari, P. and Heikinheimo, L., *Performance of an ODS material in high temperature service*, Final report VALD292, COST 501 Round 3 WP13 / 13SF2, VVT Manufacturing Technology, Espoo, Finland, 15 January, 1998.

7. Holstrom, S., Siren M., Heikinheimo, L., Auerkari, P., Varmavuo J. and Saarinen, R., pp 769-777 in Materials for Advanced Power Engineering, 1998, LeCompte-Beckers, J., Schubert, F. and Ennis, P.J., Eds, Forschungszentrum Juelich Zentralbibliothek, Germany (1998).

8. Khan, T.I. and Wallach, E.R., *Journal of Materials Science*, **31**, 1996, p.2937-2943.

9. Verpoort, C., Nazmy, M. and Jongenburger, C.P., *Metal Powder Report*, **43**, [2,], 1988, p 107-113.

10. Hammelmann, K.H., Buchkremer, H.P. and Stöver, D., *in Proceedings of the 2nd International Conference on Diffusion Bonding*, Cranfield Institute of Technology, UK, 28-29 March, 1990, p.250-260.

11. Rees, M., Hurst, R.C. and Parker, J.D., *J. Mater. Sci.*, **31**, 1996, p4493

DESIGN, CONSTRUCTION AND TESTING OF A CERAMIC HIGH TEMPERATURE HEAT EXCHANGER FOR AN EXTERNALLY FIRED CYCLE PLANT.

C. Mao*, R. Scarpellini*, M. Valarani°

(*) Ansaldo Ricerche S.r.l., Corso Perrone 25,16152 Genova (Italy)

(°) DIP Università degli Studi di Genova,Via Opera Pia 15, 16145 Genova (Italy)

Abstract

Ansaldo Ricerche (ARI) with the financial support of the Italian Ministry of Research and University (MURST) developed a project for the design, construction and experimental testing of a High Temperature Heat Exchanger (HTHE). Such a project has been included in "Plant Integration & Ancillary Components - Novel Component Working Group" of COST 522 Programme; in particular, it is part of the "Cogeneration and Externally Fired Combined Cycle (Cogen & EFCC)" project. The HTHE, namely the "SCAT" prototype, was thought to act as the "key" component of an Externally Fired Cycle (EFC), enabling the use of a wide variety of ash bearing fuels to provide thermal energy to a gas turbine, without exposing the engine to a potentially corrosive flue gas.
Starting from a reference design of a modular arrangement heat exchanger, two modules, each of them consisting of twenty "in line" or "staggered" bayonet elements, have been built. Taking into account the design temperature of heat exchanger hot fluid is up to 1400°C, reference materials for HTHE tubes were SiC based; metallic elements can replace ceramic ones when the component is operated at lower temperature.
The heat exchanger prototype has been mounted and installed in the existing Heat Exchanger Platform (HEPLA) at ARI's Engineering Laboratories; the plant includes:

- a hot fluid generator, consisting of a thermally insulated combustion chamber and a natural gas burner producing a uniform and stable hot gas;
- a cold fluid generator, consisting of a natural gas axial burner and a thermally insulated cylindrical body for the inlet of the dilution air;
- a pressuring system and a corrosive/erosive species injection device.

The final aim of SCAT was to demonstrate the HTHE feasibility i.e. study integration systems of the heat exchanger, evaluate the heat transfer and investigate thermo-mechanical degradation of sub-components. The test campaign was conducted in different heat exchanger arrangements; bayonet assemblies and joint structures showed good performance; no important size modification and structural damage was detected. Thermodynamic analyses were carried out to assess the thermal behaviour of the heat exchanger.
Keywords: EFCC plants, heat exchanger, bayonet tubes, ceramic materials, silicon carbide.

1. Introduction

Combined cycle plants play an important role in the field of power generation as they provide high efficiency. At the same time, a lot of energy production technologies are under development aiming at using other fuels than natural gas and more especially coal, wood and biomass. Within this scenario, Externally Fired Combined Cycle (EFCC) technology seems to be a promising solution for the coming decades: market studies show that EFCC has a good chance vs. Integrated Gasification Combined Cycle (IGCC) and Pressurised Fluid Bed Cycle (PFBC), particularly when applied to small-to-medium size plants. In the EFCC plants (Fig. 1), fuel is combusted in an atmospheric chamber; hot combustion gases flow to a heat exchanger where air from the compressor is heated up to the combustion turbine inlet

temperature. Exhaust flue gas from the air heat exchanger flows to a steam generator to produce steam and drive a steam turbine [1].
The heat exchanger (HE) turns out to be the "key" component of the EFCC plant, the most novel and the most critical one as it enables the gas turbine to work even when dirty fuels are used. The HE architecture includes two main sections characterised by the increase of the operating temperature: a "low and medium temperature" heat exchanger (LMHE) and a "high temperature" heat exchanger (HTHE). The arrangement of such types of HEs is usually a modular one; the number of modules in series and parallel is linked to operating parameters e.g. the required increase of cold fluid temperature and/or the mass flow rate of fluids. Obviously, owing to technical and economic reasons, advanced ceramic materials are used only in the hottest modules: the border temperature separating the LMHE from the HTHE is the maximum one allowable for metallic materials. Depending on the environmental gas compositions, working pressure and expected component lifetime, such a border temperature, which represents a "technological limit", can vary in the range 850°C - 950 °C.

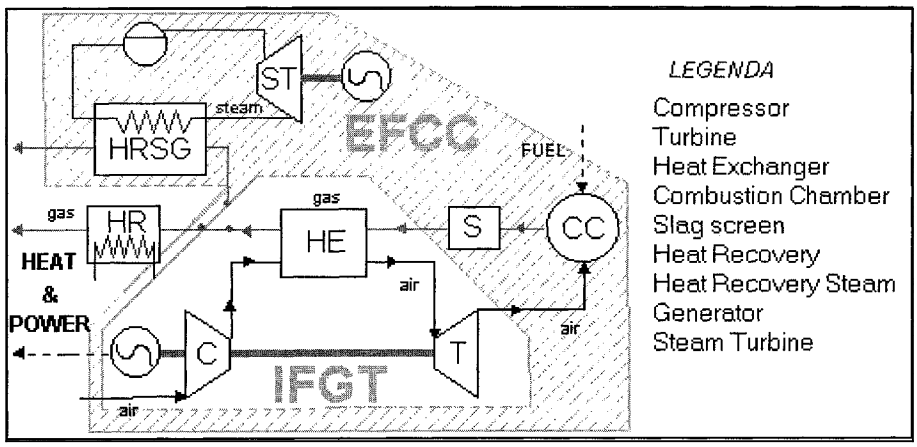


Fig.1 - EFCC configuration.

2. The SCAT prototype

To investigate the thermodynamic behaviour of a large size heat exchanger, a small size prototype is usually manufactured to produce a "reference model": tests conducted therewith are expected to provide significant results duly transferable to the full size component. Following these considerations and taking into account the working conditions for a HTHE to be installed in a coal fuelled EFCC plant e.g. 1400 °C for combustion products and the existing test facility, a "scale down" criterion has been applied to design a HTHE prototype: the present paper refers to the design, construction and testing of a high temperature heat exchanger prototype, named "SCAT".

Its geometrical specifications were worked out; properties of materials for tubes manufacturing as well as constructive considerations about tube-sheets, tube to tube-sheet joining and insulating systems were defined. Furthermore, considering that the component is operated under pressure, structural analyses have been conducted supported by F.E.M. calculation code. The main features of SCAT prototype were:

- modular arrangement i.e. two modules in series working at high temperature;
- shell and tube architecture;
- cross - counter flow configuration;
- bayonet tube assemblies;
- rectangular geometry of the hot side gas channel;
- vertical mounting;
- metallic vessel insulated structure.

The following nominal thermodynamic parameters for the SCAT prototype were fixed:

- Cold gas inlet temperature: 1040 °C
- Hot gas inlet temperature: 1290 °C
- Cold gas pressure: 4.5 bar
- Hot gas pressure: 1.06 bar
- Cold gas mass flow rate for each tube: 0.0272 kg/s
- Hot gas mass flow rate: 0.55 kg/s

A single "bayonet tube assembly" consists of two concentric tubes (Fig.2): the inner tube is open at both ends, the outer tube is sealed on one end; it is assumed that cold air enters the inner tube and flows up the annulus or vice versa and the flue gas flows outside the bayonet assembly. Inner and outer tubes are suspended vertically from higher and lower tube-sheets at one end only, so that no mechanical stress arises under temperature variations.

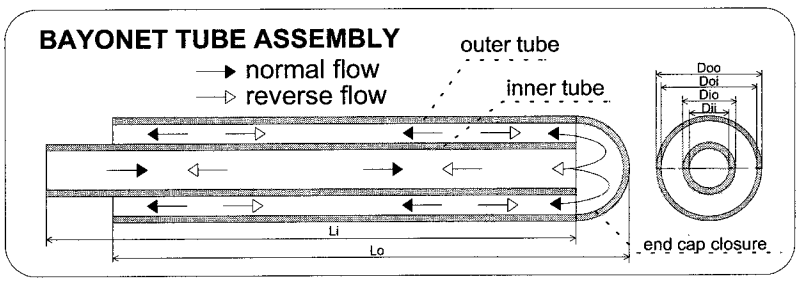


Fig.2 - Bayonet tube assembly.

Bayonet tubes, which can be either metallic or ceramic, depending on the process high temperature and aggressive environment involved, are expected to show advantages such as to ease maintenance and best deal with problems associated with thermal stress, leakage and stress related corrosion [2].

Dimensions of outer and inner tubes of the SCAT prototype are reported in Tables 1 and 2, together with their relevant tube collar size.

Taking into account that only HE modules working at high temperature had to be tested, three sets of tubes withstanding medium to high temperature, were purchased:

- sintered α-SiC outer tubes (single open end);
- sintered nitride bonded silicon carbide inner tubes (double open ends);
- super alloy (INCONEL 600) inner tubes (double open ends).

OUTER TUBE DIMENSION	*Nominal [mm]*	*Tolerance*
OUTER DIAMETER	*50,8*	*±1*
INNER DIAMETER	*40,8*	-
THICKNESS	*5*	*±1*
LENGTH	*850÷1000*	*±2,5*
COLLAR DIMENSION	*Nominal [mm]*	*Tolerance*
OUTER DIAMETER	*65*	*±0,5*
THICKNESS	*10*	*±0,5*
NET WIDTH	*4,6*	*±0,5*

Table 1 - SCAT prototype outer tube geometrical size.

INNER TUBE DIMENSION	*Nominal [mm]*	*Tolerance*
OUTER DIAMETER	*30*	*±1*
INNER DIAMETER	*22*	-
THICKNESS	*4*	*±1*
LENGTH	*Outer tube length + 760*	*±2,5*
COLLAR DIMENSION	*Nominal [mm]*	*Tolerance*
OUTER DIAMETER	*45*	*±0,5*
THICKNESS	*10*	*±0,5*
NET WIDTH	*4,6*	*±0,5*

Table 2 - SCAT prototype inner tube geometrical size.

The SCAT tube-sheets divide each module into three main zones: 1st zone, for the entering of cold gas between the inlet to the module and the inlet to the inner tubes; 2nd zone, for the outlet of cold gas between the two tube-sheets; 3rd zone, for the hot gas flow between the inlet and the outlet (Fig.3). The inner tubes tube-sheet separates the cold gas before and after the heat transfer, supporting the inner tubes weight and the pressure drops due to the bayonet path. The outer tubes tube-sheet separates the cold gas outlet zone from the hot gas zone; therefore it supports the outer tubes weight, the differential pressure between the two gases and the inversion force in the end cap closure.

The tube-sheets, which have been manufactured from standard stainless steel (AISI 304), are air-cooled and insulated by three layers of insulating/refractory materials. They are supported at their edge by the metallic vessel which prevents leakage from inside to outside of the vessel itself. Both ceramic and metallic tubes have been mechanically clamped; such joints which represent the only supporting point, shall be demountable in case of tube replacement/repair. Tubes need to be individually provided with a sealing system, which shall become more and more efficient when the pressure difference between the faces of the tube-sheets increases.

Traditional clamping systems were not considered as difficult to adapt: an *"ad-hoc"* tube to tube-sheet joining system was designed. In order to test this system feasibility, assess the behaviour of different types of gaskets and verify tube tightness, one tube per type was subjected to a high pressure test in a dedicated test rig available at ARI's Engineering Laboratories. It consists of a series of vertically coupled flanges, separated by gaskets, that permit the pressurisation of the internal chamber where the tube is placed through a gate.

The SCAT prototype design was completed by sizing the metallic vessel which is protected by means of an insulating structure; its whole thickness is 300 mm.

All the sections of the prototype were instrumented with diagnostic systems i.e. high temperature thermocouples, flow and pressure measurement devices for assessing the recuperator thermal performance.

A control / regulation system consisting of software and hardware sequences was designed, procured and mounted in order: 1) to start, operate and stop the prototype and the whole test-bed; 2) to manage emergency events.

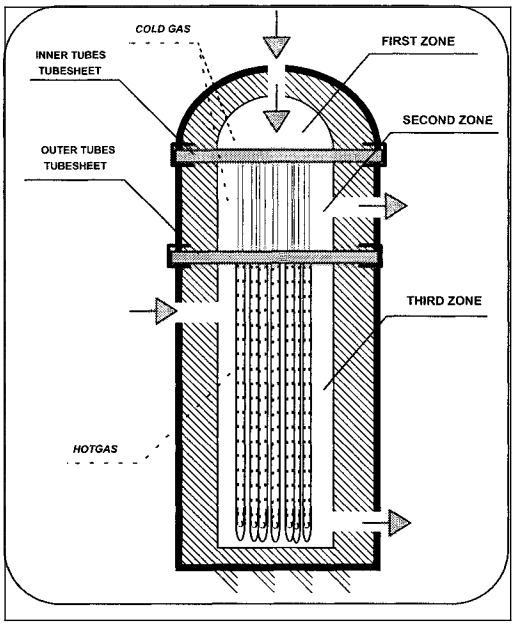


Fig.3 - Tube-sheets schematic in SCAT heat exchanger

3. The experimental campaign

Assembling activities of the SCAT prototype were conducted in five steps in series and completed in the first half of 2000.
Photos of the heat exchanger during mounting phase are in Fig.4.
The SCAT five main sub-components (lower body, lower tube-sheet, central body, upper tube-sheet, header), were installed in the test section i.e. in the existing Heat Exchanger Platform (HEPLA) at ARI's Engineering Laboratories. In particular, the recuperator was connected to:

- the hot fluid generator, through a hot channel that stabilises velocity and temperature fields of flue gas entering the HE; the combustion chamber is a thermally insulated "swirl type" equipped with a natural gas burner;
- the cold fluid generator, which is composed of a natural gas axial burner and a thermally insulated cylindrical section.

Pressuring and seeding systems were set-up; the former consists of a section variable orifice through the hot side channel, the latter of an injection system which distributes silica in the hot gas flow to simulate erosion effect of an actual plant combustion products. Piping for tube-sheets air cooling and pipes for emergency water cooling were included. A combustion products ejection device has been adopted, consisting of a crown of nozzles for the water

injection to decrease the hot gas temperature and a stack to eject the flue gas into the atmosphere.

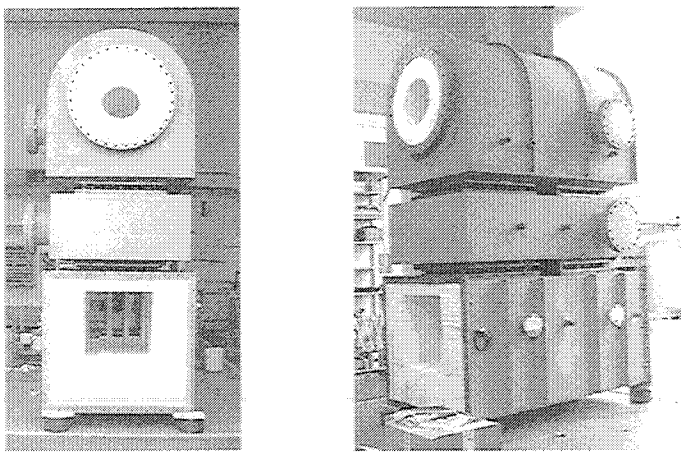


Fig.4 - The SCAT prototype during assembling.

After the installation, a preliminary phase was conducted, to clean the gas piping, check the mechanical and electrical connections, control of tube-sheet cooling and simulate emergency events. In order to limit risks on ceramic tubes, no dangerous velocity of the cold fluid inside tube assemblies was applied, thermal differences between inlet and outlet of the tubes were kept low, the pressure of cold side fixed and continuously monitored. The slow heating up and the drying of the refractory walls was carried out according to the insulating materials supplier's specifications.

Few modifications were done, then the test campaign was started; its aim was to assess the heat exchanger performance, in particular:

- to study the structural resistance of bayonet tubes, tube-sheets and vessel;
- to test the soundness of the tube to tube sheet joining system;
- to evaluate the local and global heat transfer;
- to study the corrosion/erosion effects on the ceramic tubes.

To obtain these objectives, a test matrix consisting of five different sets of increasingly severe testing were worked out. The first and the fourth one were devoted to test the functional behaviour at high temperature and one bar pressure: hot gas and cold air temperature should vary respectively in the range 750 - 1250 °C and 600 - 900 °C. The second and the third sets aimed to monitor leakage from cold side to the hot one and verify the tubes fixing system seal. The purpose of the fifth set was to investigate erosion effects on HTHE tubes. To perform all the tests, three different arrangements of the SCAT prototype were defined; they correspond to three different groups of tests, in particular:

- the arrangement "A" i.e. two modules separated by a wall;
- the arrangement "B" i.e. only one module;
- the arrangement "C" i.e. two modules without any separation wall.

A complete view of SCAT prototype is shown in Fig. 5.

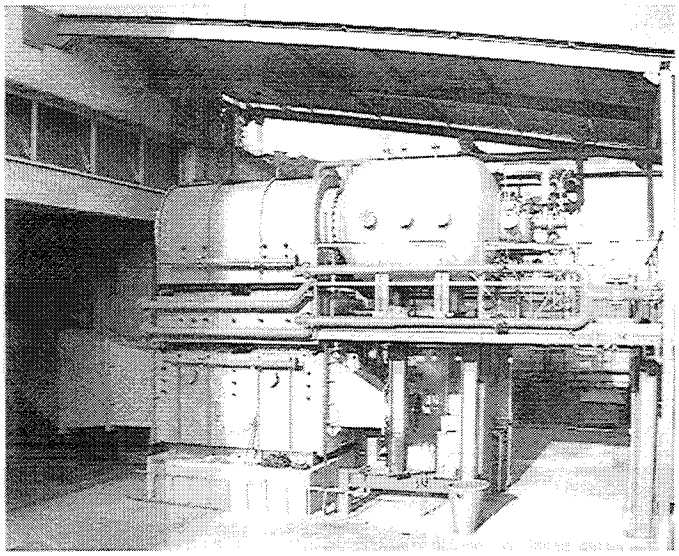


Fig. 5 - The SCAT prototype after installation.

During the drying phase, the HE arrangement was the "A" one, the pressure was 1 bar: when only the 1st burner was ON for 24 hours, temperatures measured in the HE ranged from 90 – 110 °C and when all the burners were ON (100 KW hot side, 60 KW cold side) for 48 hours, temperatures measured in the HE ranged from 185 – 225 °C; in these cases all the checks were positive. When the thermal power of burners was increased, the HE temperature was increased at the rate 25 °C/hr up to 450 °C (hot side), 400 °C (cold side) followed by the holding period: high values of the header temperature close to the separating wall were detected. Monitoring of different thermal parameters was done.
The testing phase was stopped and the cooling down commenced in order to enable the inspection of the HE inner side.
After the positive inspection of the HE structure and the positive check of the operative sequences, the "C" group was started. The first set was devoted to test the HE functional behaviour at high temperature. Nine runs were conducted: HE temperatures ranging from 700 °C to 1300 °C. The second set was devoted to monitor leakage from the cold side to the hot side. Positive controls allowed the leakage test to be repeated when the arrangement of the HE was the "B" one. Nine runs were conducted in the "B" configuration to study the HE functional behaviour at high temperature: HE temperatures ranged from 400 °C to 1015 °C. A new set of tests were performed to assess heat transfer changes when increasing the mass flow rate of cold fluid.
The last set of tests were done specifically to investigate erosion effects on HE tubes, keeping fixed the "B" arrangement.
The total duration testing campaign was about 500 hours.

4. Results

Testing of different types of high temperature gaskets for the integration systems was carried out by increasing the load on the ceramic collar: amongst mica, ceramic felt, ceramic paper, AISI 316, ceramic glass, graphite/AISI 316, only the last gasket appeared suitable for the application as the only one able to withstand the testing pressure.
Sintered α-SiC outer tube showed a perfect impermeability; in constrast, during the test on the sintered nitride bonded SiC inner tube, the collar broke off the joint at the joint level, consequently it seemed worth using this type of tubes only at one bar and replacing them with the Inconel tubes for the testing campaign under pressure.
The maximum temperature obtained on the "hot side" was around 1290-1300 °C i.e. exactly the target one for hot fluid. Bayonet assemblies and critical elements of the HE (tube-sheet and integration systems) showed good performance as expected when operated without differential pressure: no important size modification and/or structural damage has been detected during a visual inspection. Analyses were conducted on a sintered α-SiC outer tube to understand whether chemical and microstructural changes have been occurred modifying the tube mechanical properties as well. Measurements of thermal properties showed no meaningful variations after testing.
From the heat transfer point of view, tube-sheets appeared to be very critical sub-components as, whereas their thermo-structural behaviour was better than expected, from the analysis of the component heat balance, it turned out that the thermal losses on the two tube-sheets were significantly higher than ones calculated in the design phase. These thermal losses and the ones on the external walls of the vessel influenced the thermal efficiency of the heat exchanger which resulted in values lower than anticipated.

5. Conclusions

To reduce tube-sheet heat losses and improve the performance of the component, some interventions are recommended to be adopted:
- to reduce the cooling air mass flow;
- to increase the inlet cooling air temperature;
- to use an insulating material with a lower thermal conductivity.

Furthermore, the experimental results indicated that additional improvements of the technological aspects should be desirable above all to properly scale-up the prototype design e.g. 1) the availability of a joining process at an industrial level or tubes with greater length to facilitate the assembling phase and the heat exchanger operation; 2) ceramic material showing higher structural resistance at high temperature such composite ones.
Another important factor to be carefully considered in future development is the economic one to assure a full size high temperature heat exchanger can be profitably used in combined cycles.

References

[1] P. Mathieu, D. De Soleil, Off-Design Performance of EFCC Plants, Power-Gen, Vol. 2, 1996, pp 21-33
[2] M. Luu, K. W. Grant, Heat Transfer and Pressure-Drop Characteristics of a Ceramic Bayonet-Element Heat Exchanger for Waste Heat Recovery, ASME paper 84 - HT - 98.

ELECTRICAL SWING ADSORPTION FOR CO_2 SEPARATION AND CAPTURE

Roddie R. Judkins

Fossil Energy Program Director
Oak Ridge National Laboratory
Oak Ridge, TN 37831

Abstract

Background information on the deliberations of a government-industry-university team in assessing the state of the science and technology of CO_2 separation and capture is presented. This background information provides, in part, the motivation for pursuit of non-waste generating physical approaches to CO_2 separation and capture. A novel physical adsorbent gas separation process, called "electrical swing adsorption," developed by Oak Ridge National Laboratory is described. The process uses a carbon fiber composite molecular sieve, an activated carbon-bonded-carbon-fiber composite, from which adsorbed gases can be desorbed through electrical stimulation. The electrical swing adsorption technology is being developed under the sponsorship of the U. S. Department of Energy, Office of Fossil Energy, Advanced Research Materials Program. The status of the development of the materials and process is discussed. The electrical swing adsorption approach, which is limited to about 100°C, is extremely versatile in its adsorption capabilities and is especially efficacious for separation and capture of carbon dioxide. The material system and process are in advanced stages of development, but are not yet commercialized. Some remaining issues that should be addressed prior to commercialization are reviewed.

Background

In 1999, the U. S. Department of Energy's (DOE's) Offices of Science and Fossil Energy issued a report entitled *Carbon Sequestration Research and Development* [1], which provided considerable detail on the state of relevant carbon sequestration science and technology, including that related to the separation and capture of CO_2. The conclusions reported were that numerous options, including many commercial processes, were possible for CO_2 separation and capture. However, the study also concluded that none of the possible options had been applied at a sufficiently large scale nor had they been applied to the majority of the myriad of anthropogenic CO_2 sources. Further, it was concluded that a major science-based and applications-oriented R&D program was needed to establish the efficacy of current and novel CO_2 separation processes as important contributors to carbon emissions mitigation.

In this section, the anthropogenic emissions of CO_2 are identified, and an attempt is made to identify those sources most amenable to various separation and capture methods. [Much of the material that follows in this section is adapted from *Carbon Sequestration Research and Development.* The author of this paper also led the U.S. effort that was the basis for the DOE report.]

Most anthropogenic greenhouse gas emissions result from energy production and use, and the principal greenhouse gas emitted is CO_2. Technologies that separate and capture anthropogenic CO_2 have consistently been ranked, in numerous forums, among the most critical of technologies for achieving the overall goal of long-term, safe, and environmentally acceptable sequestration of carbon. The costs of separation and capture are generally estimated to be about three-fourths of the total costs of ocean or geologic sequestration. A study conducted for the International Energy Agency (IEA) Greenhouse Gas R&D

Programme suggests significant penalties on power generation costs resulting from CO_2 separation and capture. In that study, the added costs for avoided CO_2 emissions from advanced power generation plants ranged from $35 to $264 per ton of CO_2. A base-case pulverized-coal plant with flue gas desulfurization was used for comparison; power cost increases ranged from 25 to 215 mills/kWh. Thus, to achieve an acceptable cost element, considerable R&D on emerging and novel CO_2 separation and capture techniques will be required. In addition, it is prudent to conduct a cost-reduction R&D program on currently available technologies, because it cannot be assumed, a priori, that one or even a few technologies will be applicable to all anthropogenic sources of CO_2 emissions.

In the United States, 85 % of our energy is based on fossil fuel. Therefore, CO_2 emissions largely come from the use of fossil fuels. The amount of carbon requiring separation and capture in the United States is assumed to be 1 billion metric tons per year. Large point sources of CO_2 appear to be sources that lend themselves to separation and capture. However, post-combustion removal of CO_2 from the exhaust streams of conventional pulverized coal steam power plants, gas turbines, and natural-gas-fired combined-cycle plants require very large systems because of the volumes of diluent gases, primarily nitrogen, involved. Advanced power generation systems such as coal-or natural-gas-combustion plants employing enriched-air or oxygen to support combustion with CO_2 recycle, integrated coal gasification (especially oxygen-based) combined cycles, hydrogen turbines, and fuel cells are more amenable to CO_2 separation and capture. The equipment used for combustion and processing will range from essentially existing technology (e.g., coal-fired steam plants and gas turbines) to advanced technology (e.g., production of hydrogen).

In addition to power plants, numerous large CO_2-emitting industrial sources are being considered for application of capture and sequestration technologies. In natural gas production, CO_2 is generated as a by-product. Natural gas may contain significant amounts of CO_2 (20% or more by volume), most of which must be removed to produce pipeline-quality gas. Therefore, sequestration of CO_2 from natural gas operations is a logical first step in applying CO_2 capture technology, as witnessed by the Sleipner West project in Norway and the Natuna project in Indonesia. Other significant industrial sources include oil refineries, iron and steel plants, and cement and lime producers. Although these sources contribute only a small fraction of total CO_2 emissions, separation and capture of these emissions is feasible and would contribute significantly to overall goals for the reduction of CO_2 emissions.

Dispersed sources of CO_2 emissions, particularly emissions from the residential-sector and from mobile-spark ignition and diesel engines, seem especially onerous for cost-effective separation and capture and, although collectively large sources, they are not a primary focus of this paper. However, the introduction of fuel cells for vehicular propulsion and power generation may occur within the same time frame as for the deployment of industrial sequestration technologies, and, depending on the extent of their deployment, the hydrogen production needs for fuel cells could have a significant impact on CO_2 separation and capture. For example, buses and fleet operations may move towards on-board H_2 storage which suggests that central H_2 production facilities would exist and would require CO_2 separation and capture. These central H_2 production facilities are considered in this paper. Other advanced power systems, such as hydrogen turbines, that would use H_2 as fuel also have important implications with respect to the need for central H_2 production facilities and for CO_2 separation and capture technology.

Carbon dioxide concentrations will range from ~5% for much existing technology to almost 100% for some advanced technologies. Separation and capture feed streams will, at a minimum, contain small amounts of impurities such as oxygen, sulfur oxides, and nitrogen oxides from combustion of natural gas or advanced processing of fossil fuels to yield hydrogen. At the other extreme, for current and emerging technologies involving combustion of coal, the feed streams will also contain large amounts of nitrogen, oxygen, water vapor, particulates, and volatile and semi-volatile chemical species. The feed stream may be contaminated with chemicals used to remove other constituents (e.g., sulfur or nitrogen oxides). Feed stream pressures will range from essentially ambient for current technologies to tens of atmospheres for some advanced processes. Feed stream temperatures will range from very warm (~50°C) to hot (hundreds of degrees).

Current and Potential Science & Technology Requirements (Needs)

The goal of the separation and capture function requires that carbon be isolated from its many sources in a form that is suitable for transport and sequestration. The technology required to perform this function depends on the nature of the carbon source and the carbon form(s) that are suitable for subsequent steps leading to sequestration. The general end state assumed for the CO_2 is that it has been separated from the feed stream and converted to a form suitable for transport and sequestration. Assumptions on the end-state specification for the separation and capture function are as follows. A variety of carbon sequestration options will be considered, and most are not well developed. The variety of carbon sequestration options suggests that a range of carbon forms may be required from the separation and capture function, including concentrated carbon dioxide or other solid chemical forms for ocean or geologic sequestration. The identity and required characteristics of solid forms of carbon have not yet been specified. Carbon dioxide will be the assumed end-state product until promising solid chemical forms have been identified. The carbon dioxide product will be 99+% pure. The impurities in the product must be at sufficiently low concentrations that transportation and sequestration operations are not compromised. The purity requirements imposed by sequestration operations are not known because sequestration technology is being developed concurrently. This aspect of the end-state specification requires some initial investigation to develop provisional specifications that will be reviewed and modified as the requirements of various sequestration options become clear. This may be the final product of separation and capture or an intermediate product that is converted to another form (e.g., a carbonate) before transport. Separation and capture processes that operate on an effluent stream as well as those that are integrated, (i.e., are part of an optimized advanced processing flow sheet), will be considered. Effluent stream processing will be the initial focus until advanced technologies are better defined.

Based on the source terms (or initial states) and end states of the carbon separation and capture function, and the assumptions summarized above, several generic operations are required to reach the desired end states. The volume and composition of carbon-bearing feed from each source must be determined, and the end-state carbon forms (from the separation and capture function) that are acceptable and promising for each sequestration option must be identified. In turn, specifications for each carbon form for each sequestration option need to be developed, and if carbon forms (other than CO_2) are required, R&D on conversion of CO_2 to the required form for the particular sequestration option will be needed. The identified separation and capture techniques are more or less susceptible to capturing impurities and diluents along with CO_2, and therefore carbon source pretreatments may be necessary. The identified separation and capture techniques are in various stages of development, but R&D ranging from incremental process improvements to dramatic advances will be required.

Although the concepts are straightforward and in some instances demonstrated, none is proven on the scale under consideration here. Of course, R&D is also needed on the disposition of the variety of by-products that these several generic operations will produce. In some scenarios, the separation and capture function will be remote from the sequestration function; therefore, carbon transport to the sequestration site must be included in any R&D program. Systems aspects to address include optimization and integration of the carbon sources, the separation and capture function, the transportation function, and the sequestration function.

In the presumed time frame, the possession of the scientific understanding of CO_2 separation and capture options and the preferred options capable of capturing 95% of the potential carbon releases from large, fixed sources will have been developed to the stage of deployment readiness by 2020 (i.e., five years before the sequestration options have reached a similar state of development). Therefore, it is essential that we begin to escalate R&D on cost-effective and energy-efficient separation and capture methods to help minimize energy and cost penalties should carbon sequestration eventually be required.

Current and Potential Science & Technology Capabilities

The separation and capture options for anthropogenic CO_2 emissions are categorized here in what are believed to be conventional ways. It is not presumed that the categories or methods within categories are exhaustive; certainly, novel techniques that are not widely publicized, or even invented, may not be included, even though some could ultimately become preferred options. For those CO_2 separation and capture methods identified, performance characteristics such as CO_2 product purity and operating conditions differ because of operational or technical considerations. These characteristics of the CO_2 separation and capture technologies are the basis for matching them with the technologies that are the anthropogenic sources of CO_2.

The most likely options presently identifiable for CO_2 separation and capture include physical and chemical absorption, physical and chemical adsorption, membranes, mineralization and biomineralization, cryogenic or low-temperature distillation, and uptake by vegetation.

These options were identified and included as probable options due to process simplicity, environmental impact, and economics. In some instances, the separation and capture methods are also sequestration methods, (e.g., vegetation uptake and some mineralization schemes), and are also included.

Physical and Chemical Absorption

Carbon dioxide can be removed from gas streams through the use of physical or chemical absorption. Physical absorption is typically used when the partial pressure of CO_2 is high (>75 psig). Typical solvents for physical absorption include cold methanol and glycol-based solvents (e.g., the dimethylether of polyethylene glycol). Henry's law governs physical absorption processes, (i.e., they are temperature and pressure dependent with absorption occurring at high pressures and low temperature).

Chemical absorption is preferred for low to moderate CO_2 partial pressures. Since carbon dioxide is an acid gas, chemical absorption of CO_2 from gaseous streams such as flue gases depends on using basic solvents in acid-base neutralization reactions. Most common among the solvents in commercial use are alkanolamines such as monoethanolamine (MEA), diethanolamine (DEA), and methyldiethanolamine (MDEA). Other chemical solvents in

use are ammonia and hot potassium carbonate. Flue gases are typically at atmospheric pressure. Depending on the CO_2 content of the flue gas, the partial pressure of CO_2 can vary from 0.5 to 3.0 psia. At such low partial pressures, alkanolamines are the best chemical solvents to enable good CO_2 recovery levels.

Flue gases typically contain contaminants such as SO_x, NO_x, O_2, hydrocarbons, and particulates. The presence of these impurities can cause reduction in the absorption capacity of the amine as well as create operational difficulties such as corrosion. To avoid such problems, these contaminants are often reduced to acceptable levels through the use of suitable pretreatment techniques. Some commercial processes handle these difficulties through pretreatment and/or the use of chemical inhibitors in the absorption process. However, such processes tend to be more expensive than conventional alkanolamine-based absorption processes. Better options need to be developed to reduce total system costs for CO_2 recovery.

Some of the typical operating problems when using conventional trayed or packed columns for gas-liquid contact are foaming, vapor entrainment of solvent, and the need for replenishment of the solvent in low quantities. However, these limitations have a relatively small effect on the total system costs of the alkanolamine-based absorption process. Membrane contactors that typically use polymeric membranes can offer some advantages over conventional contactors and are being addressed in R&D programs. Potential benefits include the elimination of foaming and vapor entrainment as well as the ability to maintain liquid and gas flow rates independently. However, significant developmental work is needed to improve the chemical compatibility with alkanolamines and high-temperature resistance as well as lower costs of such membrane contactors. Such membrane contactors are expected to be most advantageous where system size and weight need to be minimized, such as on ocean platforms.

Commercially available alkanolamines such as MEA, DEA, and MDEA have different costs, rates of reaction with CO_2, absorptive capacities, and corrosion rates. This presents an opportunity to optimize existing solvents or to develop new solvents to reduce total capital and operating costs.

Some development of chemical and physical solvents and systems will be required to achieve the goals outlined in this paper. Capital and energy costs are currently prohibitive for flue gas treatment. It may be possible to develop novel solvents and contactors to reduce these costs. Investments in R&D on novel solvents, particularly those that are amenable to use in advanced systems, and in system studies to identify the best possible configurations of processes and equipment, particularly as these relate to cost and process simplicity, are prudent courses of action.

Physical and Chemical Adsorption.
Selective separation of CO_2 may be achieved by the physical adsorption of the gas on high-surface-area solids in which the high surface area is achieved by creating very fine surface porosity through surface activation methods using, for example, steam, oxygen, or carbon dioxide. Some naturally occurring materials, such as, zeolites, have high surface areas and have good gas adsorption properties for some gases. Adsorption capacities and kinetics are governed by numerous factors, including adsorbent pore size, pore volume, surface area, and affinity of the adsorbed gas, (the adsorbate), for the adsorbent.

The IEA study [11] evaluated physical adsorption systems based on zeolites operated in pressure swing adsorption (PSA) and thermal, or temperature, swing adsorption (TSA) modes. In PSA operation, gases are adsorbed at high pressures, isolated, and then desorbed by reducing the pressure. In TSA operation, gases are adsorbed at lower temperatures, isolated, and desorbed by heating. These processes are somewhat energy intensive and expensive. The IEA report concludes that PSA and TSA technologies have little attraction for the gas- and coal-fueled power systems included in that study. That conclusion notwithstanding, PSA and TSA are commercially practiced methods of CO_2 separation and capture, particularly in hydrogen production via reforming of natural gas and in removal of CO_2 from subquality natural gas, so these methods have applicability for separation and capture of CO_2 from these relatively large point sources of CO_2. However, H_2 plants that use PSA produce an impure CO_2 stream containing unrecovered hydrogen, methane, carbon monoxide, and nitrogen, and this stream is recycled to the reformer as fuel. The fate of this CO_2 is then the flue gas from the reformer. Currently, absorption is the common practice in those plants that recover CO_2. Physical adsorbents also suffer from low selectivity, low capacity, and operation at low temperatures. Development of adsorbents that can operate at higher temperatures in the presence of steam need to be developed and are already under consideration.

An R&D program is indicated to develop (1) adsorbents with increased adsorptive capacity, improved kinetics, and the capability to produce a pure CO_2 product, and (2) improved methods for effecting the adsorption-desorption process. One such approach, dubbed electrical swing adsorption (ESA), uses a novel carbon-bonded activated-carbon fiber as the adsorption medium. Activation conditions for these adsorbents may be varied to increase or decrease pore size and surface area to improve its effectiveness as a CO_2 adsorbent. This material is also highly electrically conductive, and adsorbed gases can be rapidly, effectively, and efficiently desorbed by passage of a low-voltage electrical current through it. This adsorption-desorption process may be used without variation of system pressure and with only minimal variation in system temperature. Electrical energy required for desorption is very nearly equal to the heat of adsorption of the adsorbed gas; thus, the ESA process is promising as an energy-efficient and economical gas separation and capture method.

Other novel adsorption concepts for CO_2 separation and capture are likely, and R&D on novel concepts should be pursued. Adsorbents capable of adsorption at high temperature and desorption by yet-to-be-determined processes could significantly improve the ability to control CO_2 emissions from fossil-fueled power systems. Examples include cryogenic separation, membrane diffusion, and other advanced concepts.

Cryogenic (Low-Temperature Distillation) Processes.
Cryogenic separation of CO_2 is achieved by lowering the temperature of a gas mixture to condense the CO_2. Increasing the total system pressure may increase the effectiveness of low temperature distillation processes. Generally, removal of other condensable gases, such as water, is a necessary preliminary step. The IEA study suggests that low temperature distillation for separation and capture of CO_2 is cost-effective for those systems that are amenable to that type of processing.

Membranes
Gas separation membranes are of many different types, and although the efficacy of only a few of these types in separating and capturing CO_2 has been demonstrated, their potential is generally viewed as very good. Diffusion mechanisms in membranes are numerous and

differ greatly, depending on the type of membrane being used. Generally, gas separation is accomplished via some interaction between the membrane and the gas being separated. For example, polymeric membranes transport gases by a solution-diffusion mechanism, (i.e., the gas is dissolved in the membrane and transported through the membrane by a solution diffusion process,) whereas porous membranes transport gases by molecular diffusion or molecular sieving. Polymeric membranes, although effective, typically achieve low gas transport flux and are subject to degradation. Palladium membranes are effective in separating H_2 from CO_2, but are subject to degradation in sulfur-containing environments. Porous metallic or ceramic inorganic membranes, are attractive as molecular sieve membranes because of their potential for operation at higher pressures and temperatures and in corrosive environments as compared with the other membrane types. Considerable R&D is required to realize the potential of membranes for separation and capture of CO_2, particularly at higher temperatures and pressures.

Advanced Concepts.
Other advanced processes have been identified and/or advocated as having significant potential for CO_2 separation and capture. For example, in one advanced concept, CO_2-containing gases are first dissolved in water and then CO_2 hydrates are formed in a second step. The process requires gases at about 0°C and 10 to 70 atm, depending on the other gases present and the partial pressure of the CO_2 in the gas stream. This process may be especially amenable to removal of CO_2 from pressurized gas streams with minimal energy losses.

Overall R&D prioritization should be done in conjunction with understanding the potential magnitude of the application in terms of impact on CO_2 emissions versus the complexity of the separation. Each required separation application will have a different magnitude and degree of difficulty. A mix of R&D programs could focus on the applications that, in the short term, would be less complex and thus would be more amenable to today's technologies but would have less of an immediate impact on emissions. In the longer term, the focus must be on the more complex but higher yield opportunities. Short-term successes can provide valuable input to the longer-term programs.

A DOE Workshop on Research and Development Priorities for Carbon Sequestration was held in Washington, DC, in September 1999. Some of the significant conclusions reached at that workshop are presented in the balance of this section. One important conclusion of that workshop was that a methodology that could aid the process of determining the CO_2 sources that could most effectively be adapted to CO_2 separation and capture strategies. The consensus was that, obviously, impact on an overall carbon mitigation strategy would be greater for some sources than for others simply based on the magnitude of emissions. The methodology would also consider the complexity and difficulty associated with integrating the systems with these CO_2 separation and capture techniques. One methodology for displaying the magnitude and the complexity relationships of various sources of CO_2 emissions was proposed by the group in the form of Fig. 1. This is only a qualitative, incomplete example and work would need to be done to make it quantitative and complete. However, such a methodology, albeit qualitative, can and has been used as a basis for selection of CO_2 emitting systems to address and the CO_2 separation and capture technologies to apply to these systems.

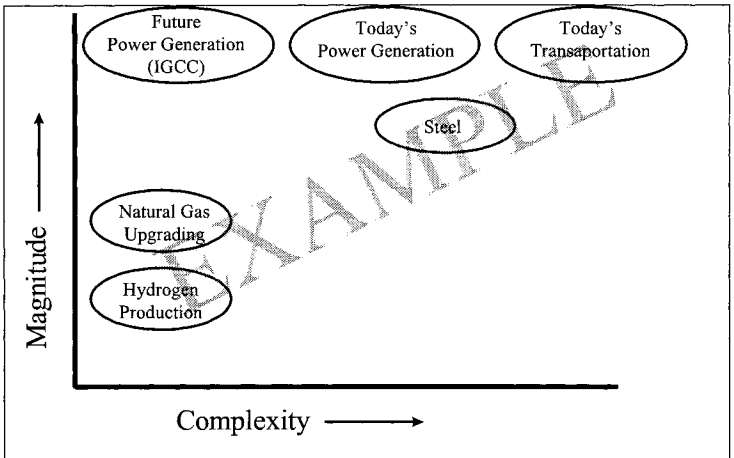


Figure 1. Example of Methodology of Displaying Prioritization Issues.

Currently, a framework for this R&D does not exist. There are too many options with no current prioritization. Whether incentives exist for any actual projects is unclear, especially considering that there are no current legislative mandates in the United States. While some demonstration projects are progressing, predominately outside the United States, there is no overall strategy guiding them. While there are many projections of the mix of CO_2 emission sources in the time frame being proposed (2025), it is clear that many of today's sources will still exist. In addition, there will be new ones that will also need to be addressed. Therefore a program sponsored by DOE is needed to focus future R&D efforts and to provide criteria for evaluation and targets while addressing both business and economic aspects of carbon sequestration.. Completion of the background material discussed in this paper would provide an essential foundation to the program.

Specific Recommendations

- Future efforts must focus on specific problems. Broad, unfocused R&D on general separation technology development will be less effective than focusing on specific CO_2 sources and sequestration requirements.
- Efforts must also focus on longer-term, order-of-magnitude changes in cost if carbon sequestration is ultimately to be viable. However, this should not preclude short-term, incremental improvements that can be demonstrated quickly and provide valuable early feedback to the overall program.
- Real applications that have the potential for a material contribution to CO_2 capture and the interest of an industrial partner should be chosen and supported. DOE needs to provide economic support of a program during all phases (R&D, demonstration, and implementation).
- DOE needs to engage industry, both technology users and equipment suppliers, more than is done today. (N.B. – the general consensus was that the DOE Workshop on Research and Development Priorities for Carbon Sequestration was a good start to such an objective but there were still many potentially critical participants who were not at the workshop.)

Introduction to ORNL Physical Adsorbent Development

Researchers at the Oak Ridge National Laboratory (ORNL) have developed and patented a novel activated-carbon adsorbent called the carbon fiber composite molecular sieve (CFCMS). The monolithic carbon structure is quite macroporous (see Fig. 2), which allows for fairly unrestricted bulk gas flow. The adsorption of gases occurs in micropores created in the fibers by conventional activation techniques. The CFCMS is a carbon-bonded-carbon-fiber structure that is electrically conductive. This electrical conductivity provides for a unique desorption technique called "electrical swing adsorption," ESA, in which an electric current (typically, low voltage) is passed through the material, resulting in desorption of adsorbed gases. The electrically stimulated desorption is a very energy-efficient process; empirical results indicate that the electrical energy required for desorption is approximately equal to the heat of adsorption of the adsorbate, which suggests a significant energy advantage over conventional pressure swing and thermal swing methods.

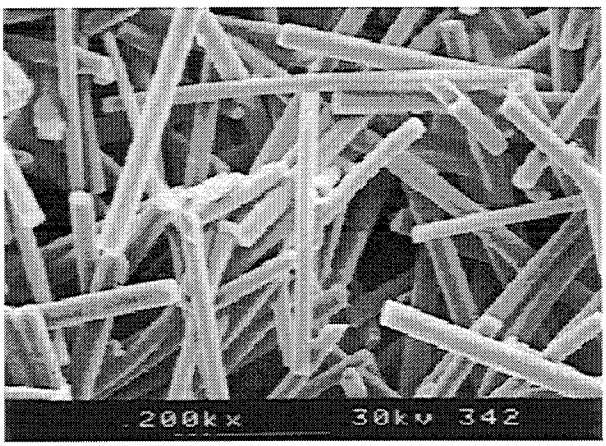


Figure 2. Scanning electron micrograph of CFCMS.

The U. S. DOE Fossil Energy Advanced Research (AR) Materials Program funded development of the ESA system. The AR Materials Program work has been directed toward the material development, fabrication process, activation process, and characterization of the material. The CFCMS has been determined to be a very versatile adsorbent that can be made more-or-less selective for a variety of gases. The continuing AR Materials Program activity addresses the development to determine how the material can be modified or manipulated to alter its selectivity for various gases of interest, and it addresses materials characterization and properties studies. This work is leading to a sound fundamental understanding of the material and its properties, including its electrical properties. This AR Materials Program work has led to variants of CFCMS for specific applications. Variants have been developed that have potential for oxygen separation from air; hydrogen separation and purification; removal of sulfur compounds such as hydrogen sulfide, thiophenes, and mercaptans from gas mixtures such as natural gas; carbon dioxide separation and capture; and methane storage.

Each of these variants has specific development needs to optimize them for these applications, and funding has been obtained or is being obtained for some of them. For example, The DOE Office of Energy Efficiency and Renewable Energy's Office of Transportation Technology is funding work on the use of CFCMS as a natural gas storage medium. The AR Materials Program work continues to address important generic issues that relate to separations and gas storage technology.

The CFCMS is very effective in adsorbing polar molecules, such as H_2S, as well as flat, nonpolar molecules, such as CO_2. The investigation of the CFCMS indicates that it is a highly effective CO_2 adsorbent for the broad range of concentrations and conditions that exist in coal and natural gas systems. For example, experimental results indicate a high degree of effectiveness for separation and capture of CO_2 from: natural gas containing up to 33 vol. % CO_2; coal-derived synthesis gas; exhaust gases of turbines fueled with natural gas or coal-derived synthesis gas; H_2-CO_2 mixtures, and even air containing about 350 ppm CO_2. The AR Materials Program has, appropriately, investigated the CFCMS for these various applications only to the extent that its versatility and potential have been established. That is, the AR Materials Program activity has not addressed details of the separations for specific applications. Specific applications are being addressed on other programs, including coal gasification, coal combustion and carbon sequestration. Because of the considerable interest in separation and capture of CO_2, considerable resources have been applied to the investigation of ESA as a CO_2 separation and capture method.

ESA as a CO_2 Separation and Capture Method

Work is beginning with several energy companies to develop the material and systems needed specifically for CO_2 capture for emissions control with the aim of integrating their technology into carbon sequestration schemes.

- A project application has been submitted for approval to the CO_2 Capture Project, (CCP), which is a consortium of eight oil companies: BP Amoco, Chevron Texaco, Statoil, Norsk Hydro, Suncor Energy, Shell, ENI, and PanCanadian. This project, which teams ORNL, SGL Carbon, and Air Products and Chemicals, Inc., will investigate the applicability of ESA to the capture of CO_2 from gas turbine exhaust streams, which contain about 3% CO_2
- ORNL is engaged in a project jointly funded by the DOE Office of Fossil Energy and Chevron Texaco to remove CO_2 from the exhaust stream of a turbine fueled by synthesis gas. This project has been included in a project called the "Early Entrance Coproduction Plant," involves a team led by Chevron Texaco and has the objective to produce at least one product from at least two of the following three categories; 1) electric power (or heat), 2) fuels, and 3) chemicals. The objective is to have these products produced by technologies capable of using synthesis gas derived from coal, or, coal in combination with some other carbonaceous feedstock. to develop a turbine fueled by coal-derived synthesis gas. This operation results in a turbine exhaust stream with about 9.1% CO_2.
- A project application has been submitted for approval to the CCP precombustion team to remove CO_2 from synthesis gas prior to combustion.
- ZeTek Power Company has licensed CFCMS and ESA patents and was a party to a funds-in cooperative research and development agreement (CRADA) with ORNL, to use these technologies to remove CO_2 from the fuel (H_2) and oxidant (oxygen in air) for their alkaline fuel cells. (A CRADA is an agreement that stipulates the terms of a

cooperative R&D project conducted by a national laboratory and a private concern, usually a U. S. company.)

- The CFCMS/ESA technology is also being investigated for removal of CO_2 from natural gas reformate for other fuel cells.
- Testing of CFCMS/ESA for upgrading subquality natural gas has been conducted on gases simulating the natural gas found in Shell's Fandango field near Laredo, Texas. The specific tests were directed to simulated natural gas with a 2:1 molar ratio of CH_4 to CO_2.

All of these projects have been initiated to address specific CO_2 capture applications. A discussion of the tests to determine the efficacy of CFCMS/ESA for upgrading subquality natural gas will be instructive in demonstrating the usefulness of this technology.

Removal of CO_2 from Subquality Natural Gas

As used here, "subquality" natural gas refers to natural gas containing contaminants and diluents in sufficiently high concentrations that the gas either cannot be used when environmental constraints are considered or is so dilute that it is uneconomical to transport. Early tests have shown that the CFCMS/ESA can separate and isolate CO_2 from natural gas. Figure 3 shows the adsorption characteristics of CFCMS, for CO_2 and CH_4 gas at pressures up to 850 and 550 psi, respectively. The data clearly show the material has a stronger affinity for CO_2 than for CH_4. This difference in adsorption characteristics is the basis for the separation process.

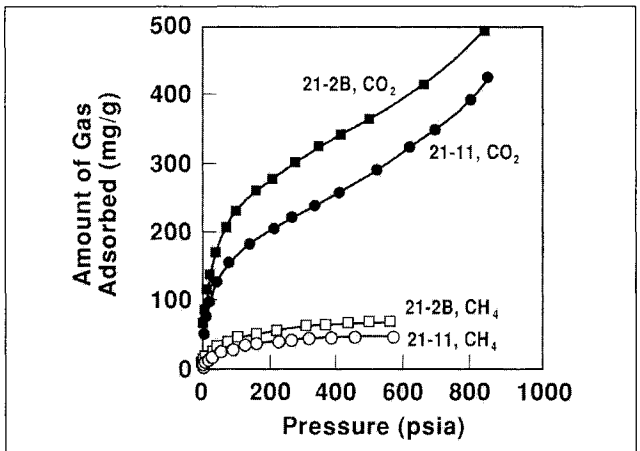


Fig. 3. Adsorption isotherms of CO_2 and CH_4 CFCMS specimens at 25°C.

The ability of the material to separate CO_2 from CO_2/CH_4 mixtures has been confirmed in dynamic separation experiments. Figure 4 shows a breakthrough plot for a 2:1 molar ratio CH_4-CO_2 gas mixture through a CFCMS sample 25 mm diameter by 75 mm long. The sample was purged with He to dry the adsorbent CFCMS, and then the feed gas switched to the 2:1 CH_4/CO_2 mixture. The CH_4 was seen to break through immediately, whereas the CO_2

was retained on the carbon and did not break through for approximately 6 minutes. Thus, during this period a pure CH_4 product stream was produced. The efficiency of this separation would be further enhanced by operating at pressure, as indicated by the data in Fig. 3. Moreover, the adsorbate may be recovered by electrical stimulation of the carbon with very little pressure or temperature change, thus demonstrating that ESA is an energetically efficient separation process for upgrading natural gas.

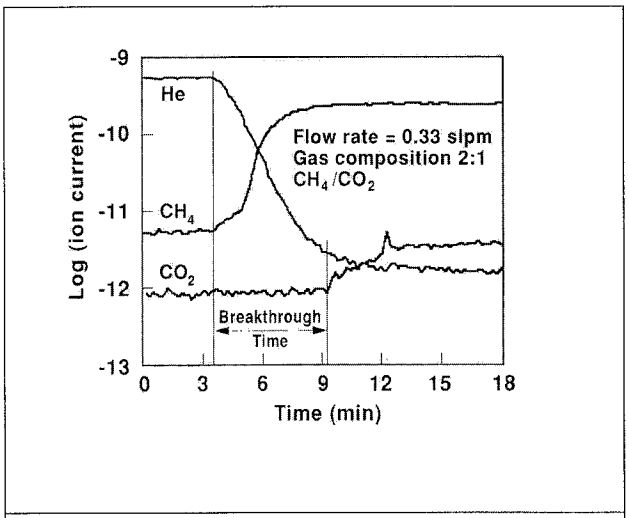


Fig. 4. Typical CO_2/CH_4 breakthrough on a CFCMS pecimen.

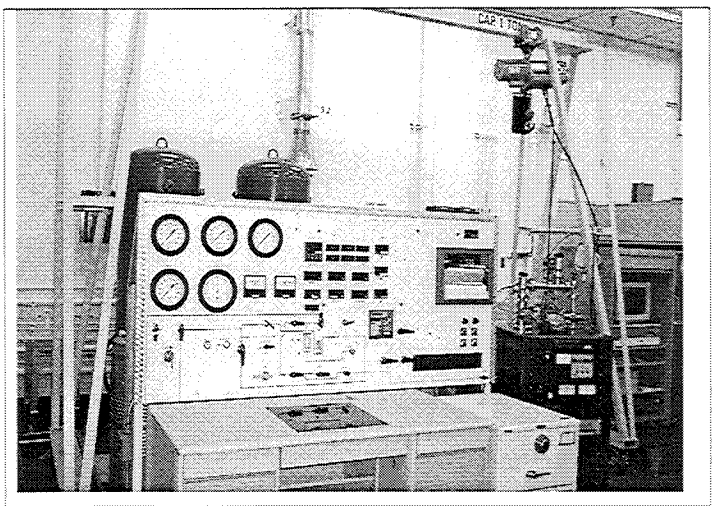


Fig. 5. ORNL's gas flow loop for the evaluation of CFCMS/ESA.

A test facility has been constructed at ORNL to further the development of separations technologies based on CFCMS/ESA. Figure 5 shows the ORNL test system, and Fig. 6 shows one type of separation cell, which consists of a piece of CFCMS 100 mm diameter by 250 mm long. In this cell, the CFCMS has copper contact rings at each end, which are electrically connected through the cell end plates to a direct current power source, allowing the material to be electrically regenerated.

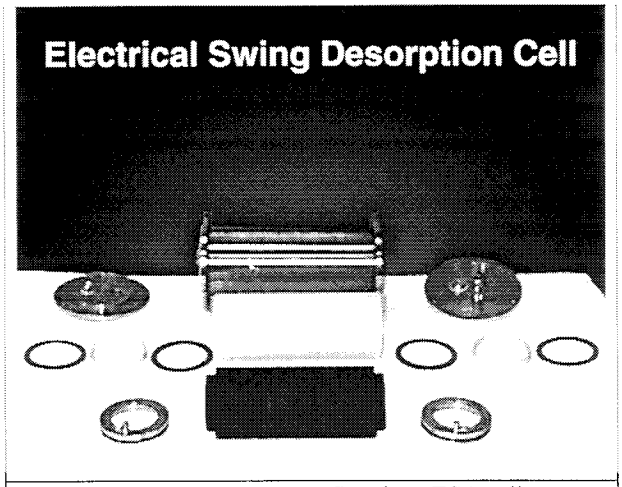


Fig. 6. The ORNL gas flow loop ESA cell.

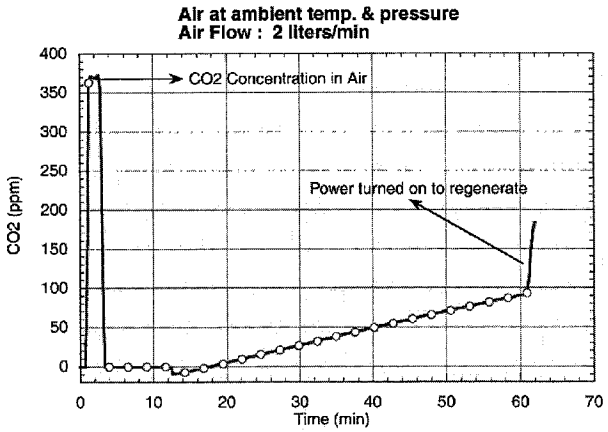


Fig. 7. Demonstration of the effectiveness of CO_2 removal from air (from time = 4 minutes to time = 60 minutes) and desorption of the CO_2 using ESA.

Figure 7 is presented to illustrate the principles of operation of ESA. In this experiment, air, the oxidant for an alkaline fuel cell was passed through an ESA cell to remove CO_2.

The ESA process depicted in Fig. 7 proceeds as follows:

1. Air flows through a cell bypass line and a gas analysis device.
2. The CO_2 concentration in air is confirmed at about 350 ppm, which is consistent with the nominal concentration of CO_2 in air.
3. The air stream is then diverted to flow through the ESA cell, resulting in total removal of CO_2.
4. After about twenty minutes, the CO_2 concentration begins to rise.
5. The concentration of CO_2 reaches a threshold that triggers the desorption cycle, and the CO_2 concentration in the outlet stream increases immediately. (In this experiment, the power supply was turned on when the concentration of the CO_2 in the outlet stream reached about 100 ppm.)

An operating ESA system could be constructed by assembling, for example, three CFCMS elements in an array to permit redirection of gas flow to any one of the three elements. In operation, gases would be fed to one of the elements until it was saturated with the gas being adsorbed, or until a pre-determined concentration was reached. Flow would then be diverted to a second CFCMS element and regeneration of the first element would proceed. On saturation of the second CFCMS element, this process would be repeated with the gas flow directed to the third element. By repeating this cycle, continued and uninterrupted processing of gases could be accomplished.

A project is being negotiated with an industrial partner that will lead to field-testing of an ESA system for removal of CO_2 from natural gas. The activity will begin with an analysis of data already obtained for differential break-through of CO_2 and methane at atmospheric pressure, and will build on information already in hand on the higher-pressure pure gas adsorption behavior. These data will guide the selection of tests to measure the reversible capacity at high pressure and to optimize the material activation process to achieve target objectives. A large part of these studies will be to recover the maximum selective capacity for CO_2 in the presence of other natural gas components. This will require establishing the optimum exposure times, recycle steps, electrical swing desorption parameters, and physical material forms. The results of the studies will be used to size the components of the intermediate-scale reactor of phase 2, and to establish a baseline material for manufacturing scale-up efforts.

The second phase will center on the building and testing of an intermediate-size ESA system, or process development unit (PDU). This unit will be able to handle 15,000 scfd under 635 psi and will be fully equipped for continuous ESA. The system will have enough versatility to handle different forms of the carbon fiber media under different process conditions. The PDU will be skid-mounted for testing at different venues. The process control and instrumentation systems of the PDU will be designed and assembled by ORNL staff.

Additional Research Needs

Development of alternate CFCMS adsorbent media
The CO_2-bearing gas streams to be separated vary widely in concentration, from a few hundred ppm in air to as much as 30 to 40 mol % in shifted synthesis gas, and the nature of

the other diluent gases is infinitely variable. Because of this, the CFCMS media must be tested and tuned (through processing) to best match the targeted separation. Moreover, certain separations are very sensitive to the pressure drop through the ESA bed, creating a need for the development of alternate CFCMS forms that are less dense and that offer a more open structure for gas flow (and hence a lower pressure drop).

Fundamental ESA design issues for CO_2 separation
Several design issues need to be addressed before the ESA bed can be scaled up. These include engineering problems such as sealing the CFCMS media in the beds so that by-pass flow does not occur, determining the optimum method of attaching the electrical power leads, and determining the best insulation material to electrically insulate the CFCMS from the bed. Other issues are related to optimizing the ESA process for the separation of CO_2 and include selection of appropriate bed/vessel geometry, determination of the cycle swing time, or determining the regeneration time and power requirements.

ESA instrumentation and control
An ESA system will require an instrumentation and control system such that the process operates automatically. Therefore, a series of sensors will be required to allow the process to be controlled. These might include CO_2 concentration sensors and detectors, temperature and pressure probes, and gas flow meters. The inputs from these devices need to be monitored and logic circuits need to be applied to determine appropriate points for the beds to switch from adsorption to regeneration. A rugged and robust control system will be required because it is probable that ESA systems will be installed in harsh environments.

Multiple-bed ESA demonstration system
The culmination of this project will be the construction and operation of a small multi-bed ESA system. Such a system could be tested at ORNL for a wide variety of gas mixtures and under numerous operating scenarios. The system will be sled-mounted, thus making it transportable, and could be deployed for field trials at various partner's installations.

Large-Scale Systems
Larger-scale ESA systems will demonstrate the ability to build CFCMS cells that contain, perhaps, on the order of hundreds of pounds of CFCMS each. This scale-up would be, it is believed, a relatively straightforward scaling of the basic fabrication and activation processes.

Integration Into Sequestration Schemes
The ESA systems may need to be integrated into different sequestration schemes, depending on the type and location of the source of the CO_2. These schemes are many and varied, and the sequestration method selected will dictate the options available for integrating ESA into the overall carbon mitigation strategy. It is important to identify and incorporate ESA into field tests to ensure the timely implementation of CO_2 demonstrations.

Conclusions

Based on laboratory data obtained to date, a CO_2 separation and capture system based on CFCMS and ESA appears to be a viable option for integration into a carbon mitigation strategy. The development is moving rapidly into larger-scale units that will be used to confirm the efficacy of the material and system to be effective in the separation and capture of CO_2 emissions from coal and gas systems. ORNL is teaming with industrial partners to

demonstrate the technology for a variety of applications. The successful deployment of the ESA technology could prove quite useful in limiting emissions of CO_2.

Bibliography

1. U.S. Department of Energy. Carbon Sequestration Research and Development, DOE/SC/FE-1, December 1999

2. T. D. Burchell, R. R. Judkins, M. R. Rogers, and A. M. Williams, *CARBON* Vol. 35, No. 9, (1997), pp. 1279-94.

3. T. D. Burchell, "Porous Carbon Fiber-Carbon Binder Composites," Chapter 6 of *Carbon Materials for Advanced Technologies*, T. D. Burchell, Editor, Pergamon, 1999, pp. 169–203.

4. T. D. Burchell, in *Fossil Energy Program Annual Progress Report for April 1997 Through March 1998.* **ORNL-6943**, (1998), pp. 45–50.

5. T.D, Burchell and R.R. Judkins, *Energy Convers. Mgmt.* **37** Nos 6-8 (1996), pp.947-954.

6. T.D, Burchell and R.R. Judkins,. *Energy Convers. Mgmt.* **38** Suppl., (1997), pp.S99-S104.

7. FETC (Federal Energy Technology Center) 1998. *Proceedings of the Government Workshop on Carbon Sequestration,* Morgantown, West Virginia, July 23-24, 1998 (forthcoming).

8. C. E. Fox, 1999. Personal communication from C. E. Fox, Vice President of Operations and Technology, Shell CO_2 Co. Ltd., to H. J. Herzog, Massachusetts Institute of Technology, October 18, 1999.

9. H. J. Herzog, 1998. "The Economics of CO_2 Capture," presented at the Fourth International Conference on Greenhouse Gas Control Technologies, Interlaken Switzerland, August 30-September 2.

10. H. J. Herzog, 1998. *Proceedings of the Stakeholders' Workshop on Carbon Sequestration,* MIT EL 98-002, Massachusetts Institute of Technology Energy Laboratory, June.

11. IEA (International Energy Agency) 1998. *Carbon Dioxide Capture from Power Stations,* available at www.ieagreen.org.uk/sr2p.htm.

12. J. A. Valencia, and R. D. Denton 1985. "Method and Apparatus for Separating Carbon Dioxide and Other Acid Gases from Methane by the Use of Distillation and a Controlled Freezing Zone," U.S. Patent 4,533,372, August 6.

13. D. J. Victory, and J. A. Valencia 1987. "The CFZ Process: Direct Methane Carbon Dioxide Fractionation," presented at the 66th Annual Gas Processors Association Convention, Denver, Colo., March.

14. G. C, Wei and J. M. Robbins,. *Ceramic Bulletin,* **64** No. 5 (1985), pp. 691-699.

SECTION 2

FUEL ISSUES AND NOVEL COMPONENTS

2.1. Hot Gas Corrosion

HIGH TEMPERATURE CORROSION IN GAS TURBINES: FUEL MODEL AND EXPERIMENTAL RESULTS

B. Bordenet, H.P. Boßmann
ALSTOM (Schweiz) AG, Haselstrasse 18, CH-5401 Baden, Switzerland

Abstract

The corrosion in gas turbines is caused by the interaction of the combustion gas and the materials. The risk of sulfate-induced hot corrosion arises if impurities of fuel, air and water can form corrosive compounds and condense on the materials. The compositions and the dewpoints of such deposits depend on the pressure and on the amount of impurities, e. g. Na, K, S. Thermodynamical modelling of the dewpoints was performed to determine the zones in the gas turbine with a risk of hot corrosion. Beside the theoretical approach, corrosion experiments were done with blading materials and protective coatings. The hot corrosion behaviour of three base materials, IN738®, CM247® and CMSX-4®, and SV20, a NiCrAlY-coating material, was studied in a salt-spraying test. For each material, specimens coated with Na_2SO_4 and Na_2SO_4/K_2SO_4 were exposed between 750 and 950°C in air with 300ppm SO_2. The present investigation has established that the addition of K_2SO_4 to Na_2SO_4 causes shorter incubation periods and higher corrosion rates. IN738 has shown a good resistance against hot corrosion. The corrosion resistance of CM247 and CMSX-4 was very poor. In a corrosive environment, both alloys have to be protected by an oxidation- and corrosion-resistant coating. SV20 has exhibited an excellent corrosion resistance with incubation times >1000h at 800°C. The present study has shown that the combination of thermodynamical modelling and corrosion experiments is a suitable approach to assess the risk of hot corrosion in gas turbines.

Keywords: thermodynamical modelling, hot corrosion, NiCrAlY, IN738, CM247, CMSX-4

ChemSage® is a registered trademark of GTT TECHNOLOGIES; IN738® is a registered trademark of Special Metals Corporation; CM247® and CMSX-4® are registered trademarks of Cannon-Muskegon Corporation

---

1. Introduction

Hot corrosion in gas turbines is caused by deposits, which are formed by impurities of the combustion gas. The impurities have their origin in the fuel, in the air and in the water. Water is injected to raise the power output of the gas turbine or to lower the NO_x-values. The compositions and the dewpoints of such deposits depend on the pressure and on the amount of impurities. The present investigation focuses on Na, K and S as main corrosion-relevant species. Thermodynamical calculations were performed with ChemSage®, to determine the dewpoints of the different salts. With a given composition of the combustion gas, the dewpoint and the composition of the deposits can be calculated and the hot corrosion risk can be evaluated at each position in the gas turbine.

To guarantee the production of electricity, stationary turbines have, in addition to the standard fuel, a back-up fuel. Diesel is often used as back-up fuel for gas-fired turbines. The back-up fuel is usually fired for several hours per month. As a general rule, the amount of impurities in diesel is higher than in gas, which leads to an increased risk of corrosion. To reproduce hot corrosion in the laboratory, a salt-spraying test [1-3] was chosen because the amount of salt and the atmosphere during the test is well defined. For the simulation of gas-fired turbines with a diesel back-up fuel, the salt was applied once before exposure to temperature. The results of such corrosion tests can be implemented in lifetime prediction modelling for components in gas turbines.

In order to discuss hot corrosion of superalloys it is convenient to define two stages: the incubation stage and the propagation stage [4]. The incubation stage is characterised by a behaviour close to the behaviour without deposit. During the propagation stage, the initially formed oxide scale is no longer protective and the corrosion rate is increased. The deposit affects the time during which the alumina or chromia scales are protective for the superalloys. Under such conditions, the hot corrosion of nickel-base superalloys was categorised in literature as type I (high temperature) and type II (low temperature) corrosion [5-7]. Type I is characterised by internal sulfidation and a depletion zone below a non-protective oxide scale. Type II shows a pitting morphology with little or no internal attack.

2. Thermodynamical modelling

The computer program ChemSage Version 4.0 [8] was used to calculate the thermodynamic equilibrium of sulfate condensation. This program is derived from SOLGASMIX – PV, which has been successfully applied for calculation of stability of Mg-vanadates in crude oil fired industrial gas turbines [9]. The calculation of the thermodynamic equilibrium is done in this program by minimising the Gibbs free energy of chemical reaction system [8]. The amount and composition of compounds in complex chemical reaction systems can be calculated for a wide temperature and pressure range. The high flow velocity of the combustion gas and its short dwell time near the blading was not taken into account for the following calculations.

For the calculations performed a model composition for the fuel and the air was taken. The composition of the combustion gas was calculated with an excess of air. Twice the amount of necessary O_2, which is needed for a complete combustion, is provided as air. The evaluation of the corrosion risk of special turbine must consider site-specific composition of the surrounding air and the used fuel. As reference, the amount of impurities was set to 350ppm S, and 0.5ppm for Na, K, Ca in the fuel. The dewpoint of Na_2SO_4 was plotted as a function of the pressure for different amounts of impurities in figure 1.

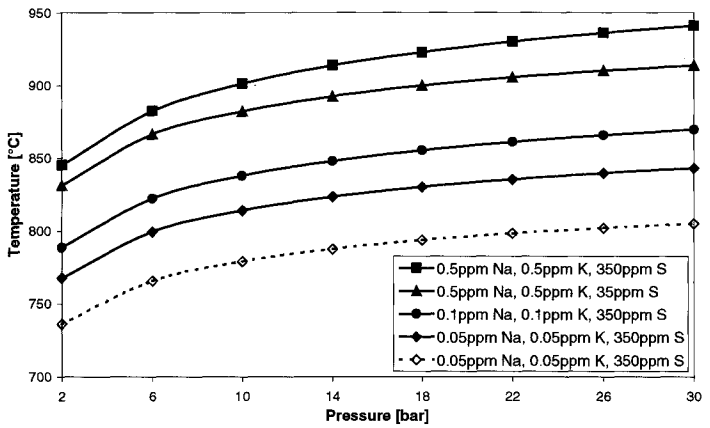


Figure 1 Dewpoints of Na_2SO_4 (filled symbols) and K_2SO_4 (open symbols) in function of the pressure for different impurity level. The impurity levels are given as fuel-equivalent in ppm.

These results indicate that for a given impurity level Na_2SO_4 can be present in the condensed or gaseous form, depending upon the compression ratio of the particular engine [10]. The dewpoint increases with increasing pressure. The decrease in the S-content by a factor of 10, reduces the dewpoint slightly (at 14bar by ~23K). Only the reduction of the alkali-content

causes a significant drop of the dewpoint. A reduction of the alkali-metal content by a factor of 10, decreases the dewpoint of Na_2SO_4 at 14bar by nearly 90K. The dewpoint of K_2SO_4 shows the same dependencies and is 30-40K below the dewpoint of Na_2SO_4 for these conditions. For one impurity level, the dewpoint of K_2SO_4 is given (open symbols) in figure 1. These thermodynamical calculations indicate that condensation of sulfates can only be prevented with a very low impurity level in the fuel and the air.

In a gas turbine, the risk of hot corrosion arises, when the material temperature is below the dewpoint. With known temperature and pressure distribution of the blading, the maximum area with hot corrosion risk can be determined for each blade and vane. This evaluation is conservative because it is based only on thermodynamic calculations. The consideration of aerodynamic or kinetic would shift the dewpoint to lower temperatures and pressures, which corresponds to a reduction of the area with hot corrosion risk.

3. Experimental

Three commercial base material alloys, IN738 (conventionally cast), CM247 (directional solidified) and CMSX-4 (single crystal), and a NiCrAlY-coating SV20 were tested in this study. Their chemical composition was mentioned in table 1. The specimens of CM247 and CMSX-4 were cut perpendicular to <001>. Powder of the coating material SV20 was hot isostatically pressed to bulk material and then cut into specimens. All the specimens were manufactured by spark erosion to the dimensions 10 x 10 x 1mm.

For each material, Na_2SO_4-coated and Na_2SO_4/K_2SO_4-coated specimens were exposed in the short-term test at temperatures between 750 and 950°C up to 250h. In the long-term test at 800°C, the test duration was 1000h. The salt mixture of Na_2SO_4/K_2SO_4 was composed of 80mol% Na_2SO_4 and 20mol% K_2SO_4, which is a composition near the eutectic point with a melting point of 831°C [11]. The reference state was a specimen without any salt deposit exposed to the same conditions.

mass.%	Ni	Co	Cr	Al	Y	Si	Ta	Ti	Nb	Hf	Re	W	Mo
IN738	62.6	8	16	3.4	-	-	1.7	3.3	1	-	-	2.5	1.5
CM247	62.3	9	8	5.6	-	-	3.2	0.7	-	1.4	-	9.5	0.5
CMSX-4	60.4	10	6.6	5.5	-	-	6.5	1	-	0.1	3	6.4	0.6
SV20 (NiCrAlY)	bal.	-	23-27	3-7	0.2-2	1-3	0.2-2						

Table 1 Chemical composition of the investigated materials in mass.%

The specimens were ground up to 800grit and ultrasonically cleaned in ethanol for 5 minutes. The water-soluble salts were sprayed on the specimen, which were heated onto a plate at ~80°C. The water evaporates rapidly and the salt forms a thin salt layer on the specimen. Only one side was coated with a salt-deposit of 1mg/cm² (±0.03mg). The specimens were isothermally exposed to synthetic air and 300ppm SO_2. The flow rate was 60L/h. The specimens were pulled out of the furnace every 2 days and cooled down to room temperature to measure the mass change.

4. Results

4.1 Reference samples without salt (oxidation in air + 300ppm SO_2)

Oxidation treatment was performed in the same atmosphere (air + 300ppm SO_2) without any salt-coating. The four investigated materials can be divided into two groups: IN738 is a chromia-former, CM247, CMSX-4 and SV20 are alumina-formers [11, 12].

4.2 Short time test : 750-950°C up to 250h [11]

Between 750 and 950°C, Na_2SO_4- and Na_2SO_4/K_2SO_4- coated specimens were exposed to air + 300ppm SO_2 for ~250h. The corrosion attack is more severe when K_2SO_4 is present in the salt. The maximum depth of penetration is plotted over temperature in figure 2 and 3. In the investigated temperature range (750-950°C), all salt-coated samples showed type I hot corrosion behaviour, except CMSX-4 at 750°C.

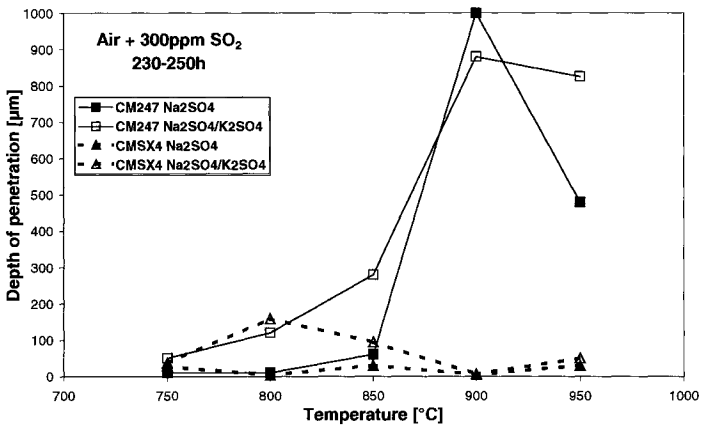


Figure 2 Depth of penetration of CM 247 and CMSX-4 in air + 300ppm SO_2 between 750-950°C (1mg/cm^2 of salt deposit)

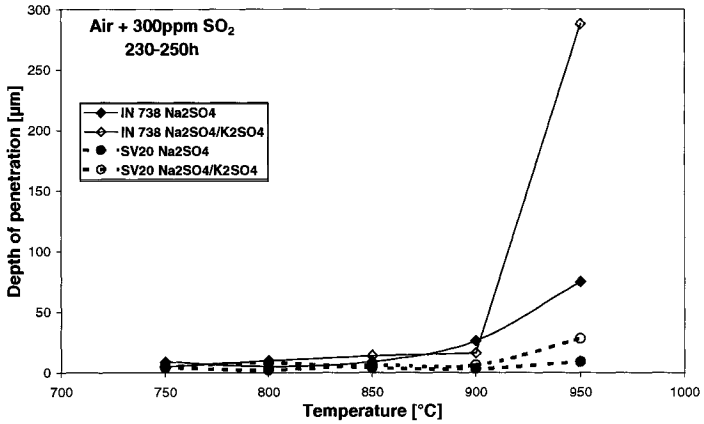


Figure 3 Depth of penetration of IN738 and SV20, NiCrAlY-coating, in air + 300ppm SO_2 between 750-950°C (1mg/cm^2 of salt deposit)

CMSX-4 and CM247

At 750°C, CMSX-4 exhibits type II corrosion. The morphology is illustrated in figure 4. The outer oxide scale is composed of porous Ni- and Co- oxides. Below this outer scale, a layered structure of the corrosion product can be seen (~30µm). The dark layers are composed mainly of oxides of Ni, Cr, Ti and Al. The bright ones contain mainly Ni-W-oxide, which was identified as $NiWO_4$. At the interface between corrosion product and metal, S is enriched in

mixed oxides of Al, Ta and Cr (figure 4, point 5); maybe sulfates/sulfides have been formed. No internal sulfidation or any depletion zone could be detected.

At 850-950°C, CMSX-4 and CM247 show a similar morphology of the corrosion product for type I, although their maximum depth of penetration is different. Up to 850°C, the depth of corrosion is comparable after this short time test. At 900°C and 950°C, CMSX-4 exhibits less penetration. This result is in accordance with the findings of Koizumi et al. [13]. The typical morphology of type I corrosion is represented in figure 5. The outer scale is composed by non-protective Ni-Co-oxides. This leads to the inner zone of mixed oxides. The dark oxides consist mainly of Al-, Cr-, Ta-oxides, the bright ones mainly $NiWO_4$. Deeper, internal sulfidation of chromium takes place.

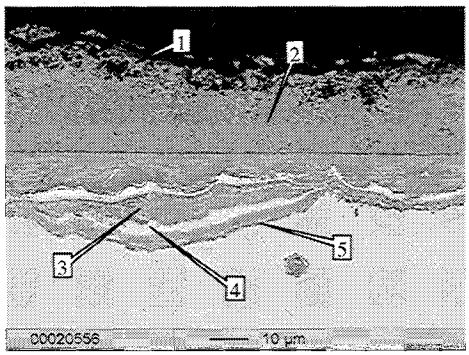


Figure 4 CMSX-4, 750°C/244h, air + 300ppm SO_2, Na_2SO_4-deposit; **1**: Ni-Co-oxides; **2**:NiO; **3**: Ni-Cr-Al-Ti-oxides; **4**: $NiWO_4$; **5**: S-enrichment

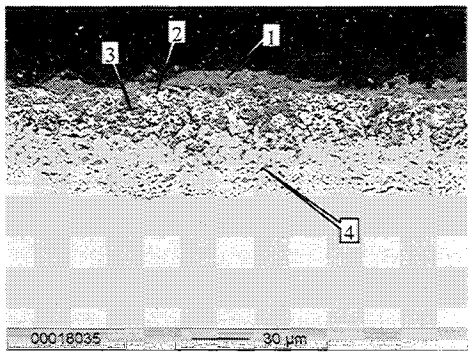


Figure 5 CM 247, 850°C/ 231h, air + 300ppm SO_2, Na_2SO_4-deposit; **1**: Ni-Co-oxides; **2**: $NiWO_4$; **3**: porous oxides of Cr, Al; **4**: Cr-sulfides;

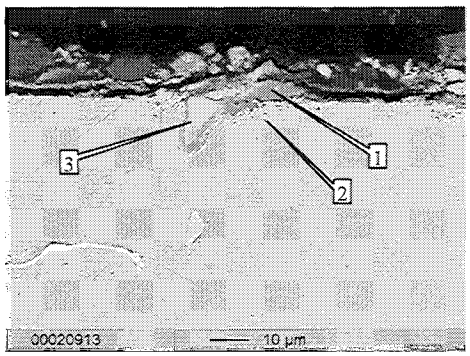


Figure 6 IN738, 750°C/244h, air + 300ppm SO_2, Na_2SO_4 /K_2SO_4-deposit; **1**: Cr-Ti-oxides, **2**: Cr-sulfide, **3**: precipitate of Ti, Nb, W, Ta

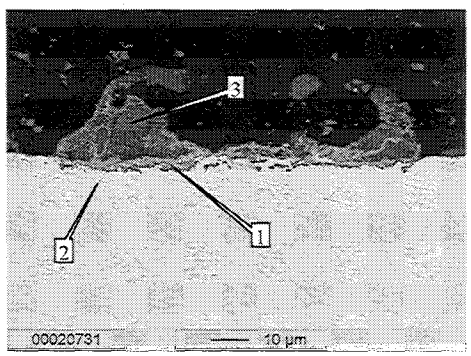


Figure 7 SV20, 800°C/223h, air + 300ppm SO_2, Na_2SO_4-deposit; **1**: Cr-Al-oxides; **2**: Y-sulfides; **3**: Na_2SO_4

IN738

Over the investigated temperature range, IN738 shows a type I corrosion. Between 750°C and 900°C, the depth of penetration is very small and corrosion consists only in internal sulfidation of Cr. Precipitates of Ti, Nb, W and Ta are preferentially oxidised (figure 6). The internal sulfidation seems to start close to these precipitates. At 950°C, the depth of corrosion increases. The corrosion product composition has changed slightly and spalls off easily [11].

SV20

Over the whole investigated temperature range, SV20 shows a type I corrosion. The depth of corrosion is nearly negligible in this short-term test between 750°C and 900°C. Below the salt, the formation of Y-sulfides occurs (figure 7). Yttrium sulfides are thermodynamical more stable than Cr-sulfides [14]. Hence, yttrium can act as a sulfur-getter. Between the Y-sulfides and the salt, a small oxide scale of Cr- and Al-oxide appears. No other corrosion product can be detected.

4.2 Long-term test: 800°C up to 1000h [12]

At 800°C, Na_2SO_4- and Na_2SO_4/K_2SO_4- coated specimens were exposed to air + 300ppm SO_2 for 500h and 1000h. The specific mass gain of CMSX-4, CM247 and IN738 is plotted versus time in figure 8, 9 and 10, respectively. The mass gain and depth of corrosion are increased if K_2SO_4 is present. Although morphology and composition of the corrosion product are the same for both salt deposits, Na_2SO_4/K_2SO_4-salt leads to the highest mass gain and the deepest penetration.

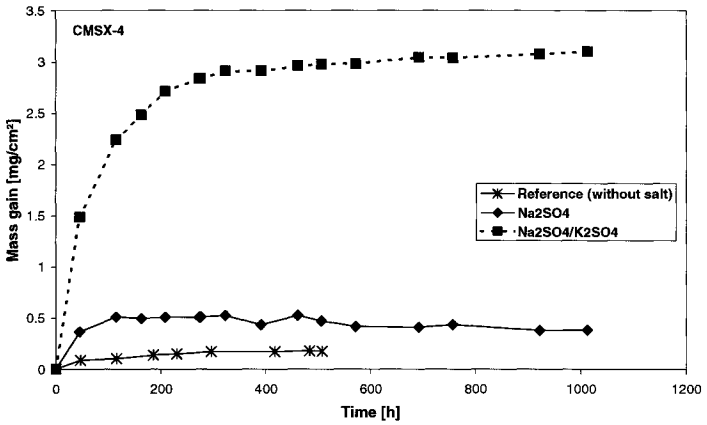


Figure 8 Specific mass gain of CMSX-4 in dry air and 300ppm SO_2 at 800°C

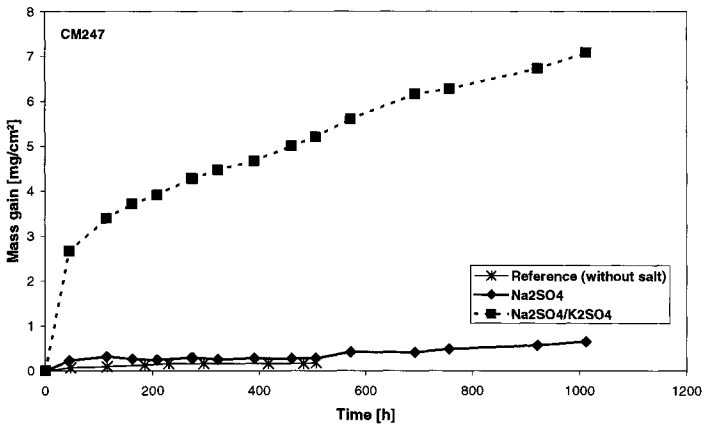


Figure 9 Specific mass gain of CM247 in dry air and 300ppm SO_2 at 800°C

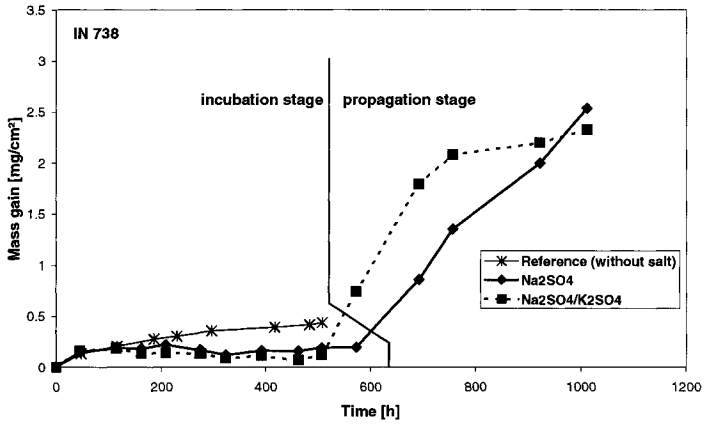


Figure 10 Specific mass gain of IN738 in dry air and 300ppm SO_2 at 800°C

CMSX-4 and CM247

At 800°C, CM247 and CMSX-4 show in principle similar hot corrosion behaviour and morphology, although the mass gain is different. After 500h, the corrosion of CMSX-4 is localised directly below the applied salt (figure 11). It consists mainly of internal sulfidation of Cr and first corrosion pits. After 1000h, the pits are more pronounced (figure 12). The corrosion has a similar morphology as reported for the short-term test above [11]. The growing of the pits can not be detected in the weight gain curve (figure 8). The specific mass gain of the samples with salt is significantly higher as for the reference sample without salt. According to the definition of propagation stage mentioned above, the duration of the incubation stage is shorter than 45h for CMSX-4 as well as for CM247 (table 2).

Salt mixture / Material	1 Na_2SO_4	2 Na_2SO_4/ K_2SO_4
CMSX-4	<45 h	<45 h
CM247	<45 h	<45 h
IN738	600-700 h	500-600h
SV20	>1000 h	>1000 h

Table 2 Duration of the incubation time as function of the applied salt composition

IN738

For both salt-coatings, IN738 shows the typical behaviour for type I corrosion with incubation and propagation stage. Up to 200h, the mass gain of the salt-coated specimens is comparable to the reference sample (figure 10). Until the end of the incubation stage, the salt-coated specimens show a small mass loss, which could be explained by evaporation of sulfates. The incubation period takes 600-700h for the Na_2SO_4-coating and 500-600h for Na_2SO_4/K_2SO_4-coated sample (table 2). Within this period the material has a protective behaviour. During the propagation stage the mass gain is nearly linear. After ~800h, the Na_2SO_4/K_2SO_4-coated sample does not follow linear kinetics. Partial spallation of corrosion products could be a reason for this behaviour.

Both type of salt deposits induce the same morphology of the corrosion attack. During the incubation stage, the corrosion consists only of a small internal sulfidation of chromium

(figure 13). After 1000h (propagation stage), the corrosion starts preferentially on the precipitates, carbides, of heavy elements as W, Ta, Nb. The outer scale consists still of oxides of Cr and Ti (figure 14). Below is a mixture of oxides of Cr, Ti, Ni and heavy metals like W, Ta, Nb. A small scale of alumina separates these mixed oxides from the metal. Under these oxides, a zone of internal sulfidation of Cr and Ni appears.

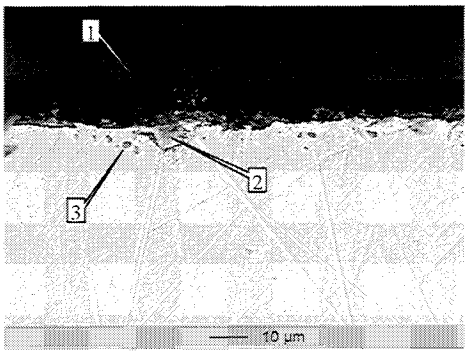


Figure 11 CMSX-4, 800°C/500h, air + 300ppmSO_2, Na_2SO_4-deposit, **1**: Na_2SO_4; **2**: corrosion pit; **3**: Cr-sulfides

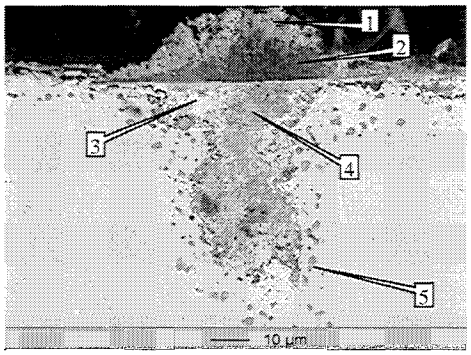


Figure 12 CMSX-4, 800°C/1000h, air + 300ppm SO_2, Na_2SO_4-deposit, **1**: Ni-oxides, **2**: Cr-, Al-oxides, **3**: Ni-W-oxides, **4**: Al-Cr-oxides, **5**: Cr-sulfides

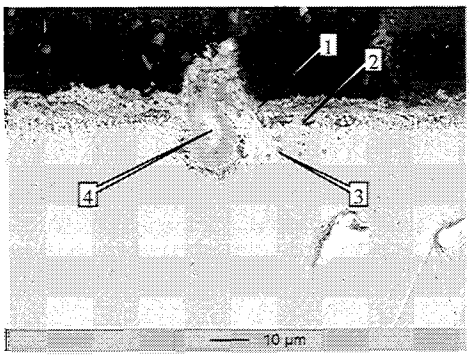


Figure 13 IN738, 800°C/507h, air + 300ppm SO_2, Na_2SO_4-deposit; **1**: Cr- and Ti-oxides; **2**: internal oxidation of Al, **3**: Cr-sulfides, **4**: precipitate of W, Ta, Nb

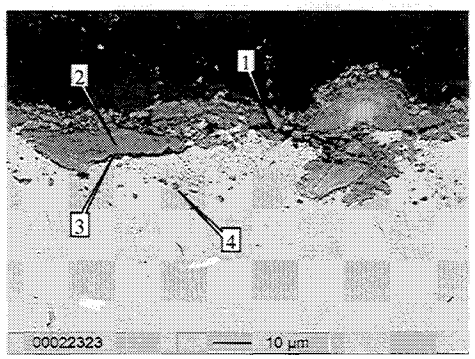


Figure 14 IN738, 800°C/1000h, air + 300ppm SO_2, Na_2SO_4/K_2SO_4-deposit, **1**: Cr- and Ti-oxides; **2**: mixed oxides of Cr, T, Ni, W, Ta, Nb; **3**: alumina; **4**: Cr-, Ni-sulfides

SV20

Up to 1000h, SV20 is still in the incubation stage. As for the short time exposure, the only sign of corrosion attack is the localised formation of Y-sulfides below the salt. The Y-sulfides are growing with exposure time (figure 15). The metal is covered by a more or less protective oxide scale (1-2µm) consisting of Cr- and Al-oxides.

5. Discussion

The reference samples were oxidised as the same atmosphere than the samples with salt deposit. They show no internal corrosion attack, like sulfidation. These results indicate a good resistance against gaseous corrosion and support the assumption that a salt deposition is necessary to induce hot corrosion.

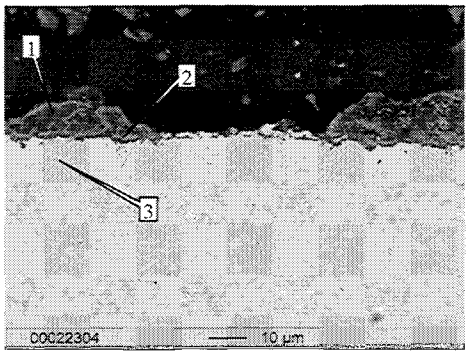


Figure 15 SV20, 800°C/1000h, air + 300ppmSO_2, Na_2SO_4-deposit, **1**: Na_2SO_4; **2**: Al-Cr-oxides; **3**: Y-sulfides

The addition of K_2SO_4 to Na_2SO_4 results in higher corrosion rates (figure 2-3, 8-10) and shorter incubation periods (table 2). A reason for this behaviour could be the lower melting point compared to pure Na_2SO_4. An influence of K_2SO_4 on the corrosion mechanism could not be identified in this study. The composition and morphology of the corrosion product is comparable to that caused by pure Na_2SO_4.

In the investigated temperature range (750-950°C), all salt-coated samples showed type I hot corrosion behaviour, except CMSX-4 at 750°C. The corrosion of CMSX-4 at 750°C was classified type II, but did not show the typical pitting morphology as mentioned by different authors [5-7]. A similar uniform attack was reported for CM247 at 700°C in an embedded ash test by Bayerlein et al. [15]. As a first approach, the corrosion resistance is dependent on the chromium content. The four tested materials can be ranked with decreasing corrosion resistance: SV20 > IN738 > CM247, CMSX-4.

SV20, the NiCrAlY-coating, was developed to achieve a good oxidation and corrosion resistance [16], which is obtained by the high chromium-content and the absence of heavy elements. In the short term test over whole temperature range and in the long-term test at 800°C, the corrosion of SV20 consists of minor internal sulfidation of Y. The fact that no other corrosion product could be detected shows the high resistance against sulfate-induced corrosion. The high chromium and aluminium content are responsible for the formation of a protective oxide scale. Yttrium improves the oxidation behaviour and acts as sulfur-getter by the formation of Y-sulfides [14].

IN738, a base material, shows quite good corrosion resistance due to a high Cr-content (table 1) and the relatively low content of refractory elements like W [17]. At 800°C, the weight gain curve (figure 10) indicates well the transition between incubation and propagation stage. Fryburg et al. [18] have investigated the hot corrosion behaviour of Na_2SO_4-coated IN738 in pure O_2 at 975°C. They propose a corrosion mechanism where the basic fluxing, typical for type I, changes to alloy-induced acidic fluxing. Refractory elements are involved in these reactions and are present in the corrosion product, e.g. Na_2WO_4 or $NiWO_4$. In the present investigation, $NiWO_4$ is detected in the corrosion product. This indicates that the corrosion could proceed by the mechanism proposed by Fryburg et al. [18]. The validation of this assumption needs further investigation.

CMSX-4 and **CM247** are two base materials with a chemical composition optimised for a good mechanical behaviour. Both alloys are alumina-former at higher temperatures. The high tungsten and low chromium content compared to IN738 (table 1) seem to be detrimental for hot corrosion resistance. The deleterious effect of tungsten is reported by different authors [14, 17, 19]. Above 850°C, CMSX-4 is more corrosion resistant than CM247, below it is slightly less resistant. The worse corrosion resistance of CMSX-4 at lower temperatures and the change to type II at 750°C is probably due to the lower chromium content. At 800°C, the corrosion behaviour of both alloys is similar. The incubation period of the samples with salt deposit ends before the first measurement was taken at 45h. As for IN738, $NiWO_4$ was also identified in the corrosion products of CMSX-4 and CM247. The presence of $NiWO_4$ indicates a similar corrosion mechanism as proposed for IN738 [18]. Fryburg et al. suggests such a mechanism for alumina-formers as B-1900 and NASA-TRW VIA [20].

6. Conclusion

The present study has established an approach for corrosion in gas turbines, which includes thermodynamical modelling and laboratory experiments. The thermodynamical modelling determines the dewpoints of the corrosion relevant species in dependence of the composition of the combustion gas and the pressure. With known pressure and temperature distribution in the gas turbine, the areas can be defined, where salt condensation occurs, hence where the corrosion risk is high. To keep these areas as small as possible the amount of corrosive species, e.g. alkali metals, must be limited via a specification for the combustion gas. This means the sum of impurities out of the fuel, the in-take air and injected water must be below the specified limit.

The experimental work exhibits the reaction of the used material on the corrosive deposits. The chosen salt-spraying test is a suitable method for studying hot corrosion behaviour. The base materials, CM247 and CMSX-4, with their excellent mechanical behaviour show a poor corrosion resistance and must be protected by a corrosion-resistant coating. IN738 has the best corrosion resistance of the investigated base materials. The long-term test at 800°C has shown that only one contamination with salt is sufficient to cause hot corrosion. From this results one can conclude that the maximum content of impurities is crucial and not the average. SV20, the NiCrAlY-coating exhibits a very good corrosion resistance. It is a suitable coating to protect the base materials from hot corrosion. For lifetime prediction with respect to corrosion, the propagation stage has to be investigated for longer times over the full temperature range.

References

[1] K.L. Luthra, D.A. Shores, J. Electrochem. Soc., Vol. 127, No. 10 (1980) 2202-2210
[2] K.L. Luthra, J. Electrochem. Soc., Vol. 132, No. 6 (1985) 1293-1298
[3] K.L. Luthra, J.H. Wood, Thin Solid Films, 119 (1984) 271-280
[4] F.S. Pettit, G.H. Meier,in M.Gell et al. (eds.), 'Superalloys 1984', (Warrendale, PA: The Metallurgical Society of AIME), (1984) 651-687
[5] J.R. Nicholls, D.J. Stephenson, Corrosion Science, 33 (8) (1992), 1313-1325
[6] G.H. Meier, Mat. Sci. Eng. A120 (1989) 1-11
[7] J. Stringer, Surf. Coat. Technol. 108-109 (1998) 1-9
[8] G. Eriksson, K. Hack, Met. Trans. B, 21B (1990) 1013
[9] L. Singheiser, H.W. Grünling, 'Hochtemperaturkorrosion in stationären Gasturbinen bei alternierender Betriebsweise' , Report for BMFT (1990)

[10] M.A. Decrescente and N.S. Bornstein, Corrosion, Vol.24, No. 5 (1968), 127-133
[11] B. Waschbüsch, H.P. Bossmann, L. Singheiser, Proceedings of EUROCORR 2000, London, UK, Paper 014-80, published as CD-Rom, Institute of Materials, London (2000)
[12] B. Waschbüsch, H.P. Bossmann, in M.Schütze et al. (eds.) 'Lifetime modelling of high temperature corrosion processes', Publication No. 34 in European Federation of Corrosion Series, Institute of Materials, London (2001), 261-273
[13] Y. Koizumi et al., in J. Lecomte-Beckers et al. (eds.), 'Materials for Advanced Power Engineering 1998', Part II, Forschungszentrum Jülich (1998) 1089-1098
[14] L. Singheiser: 'Untersuchung zur Reduktion der Hochtemperaturkorrosion metallischer Werkstoffe durch legierungstechnische Maßnahmen und Beschichtungen' , Habilitationsschrift, Erlangen 1991
[15] M. Bayerlein, W. Hartnagel, 'Leit- und Laufschaufeln für Gasturbinen (ODS und DS)', COST 501 / II, Projekt 1 D 1, Abschlußbericht für BMFT (1994)
[16] L. Singheiser, Europäische Patentschrift, Veröffentlichungsnr.: 0 318 803 B1 (1993)
[17] F.S. Pettit, G.W: Goward, in E.Lang (ed.) 'Coatings for High Temperature Applications', Elsevier Barking (1983) 1-32
[18] G.C. Fryburg, F.J. Kohl, C.A. Stearns, J. Electrochem. Soc., Vol. 131, No.12 (1984) 2985-2997
[19] P. Steinmetz, J.J. Rameau, Mat. Sci. Eng. A120 (1989) 267-275
[20] G.C. Fryburg, F.J. Kohl, C.A. Stearns, W.L., J. Electrochem. Soc., Vol. 129, No.3 (1982) 571-585

REDUCTION OF FIRESIDE CORROSION OF SUPERHEATER MATERIALS IN A BIOMASS-FIRED CIRCULATING FLUIDISED BED BOILER

P J Henderson[1], J Högberg[2] and M. Mattsson[2]

Vattenfall Utveckling AB,
[1] 162 87 Stockholm, Sweden
[2] 814 26 Älvkarleby, Sweden

Abstract

Corrosion testing of candidate superheater materials has been performed using cooled probes in a 30MWth wood-fired circulating fluidised bed (CFB) boiler. The chromium content of the steels ranged from 2% to 28%. Two probes, temperatures 530°C and 600°C, were exposed at the final superheater in a convective pass and therefore heated by the flue gas. Two probes, temperatures 600°C and 650°C, were placed in the cyclone loop seal and were heated by the sand, which is at the same temperature as the flue gas, and which is then circulated back into the bottom of the furnace. As the heat transfer coefficient between sand and superheater tube wall is greater than that between the flue gas and the tube wall, the temperature of the probes in the loop seal was set at 50-70°C higher than the other probes. This was done to simulate the same steam temperature.

The chemical composition of the flue gas at the superheaters and the environment in the cyclone loop seal were determined by Fourier Transform InfraRed Spectroscopy. Deposits were collected on probes and analysed by energy dispersive x-ray analysis in a scanning electron microscope.

In spite of a higher metal temperature the corrosion rate in the loop seal was at least 50% lower than that in the convective pass, for the same materials. For some materials, the corrosion resistance improved 5-fold if the steel was positioned in the loop seal. The improvement in the corrosion resistance was explained on the basis that the water vapour content in the loop seal is much lower than in the convective pass and that the deposits formed were much thinner. Austenitic steels containing 15-18% Cr performed much better than 2-12% Cr ferritic/martensitic steels and marginally better than high Cr/Ni alloys, when positioned in the convective pass.

Key words: Wood, corrosion, superheaters,

Introduction

In recent years, in many European countries, there has been a move away from burning fossil fuels to biomass, in order to reduce CO_2 emissions. However, burning of 100% biomass causes severe corrosion problems. The chlorine contents of wood, peat and coal are relatively similar, but there is considerably more sodium and potassium and less sulphur in wood fuels and it is thought to be the formation of complex alkali chlorides which principally causes the corrosion problems. Experience from Swedish power stations fired with 100% wood-based biofuels (i.e. not co-firing with fossil fuels) has shown that conventional superheater steels (low chromium ferritic steels) have to be replaced after about 20,000 hours if the steam temperature is 470°C or higher.

This paper reports the results of probe corrosion testing of some commercially available steels which were exposed in probes in a circulating fluidised bed (CFB) utility boiler operating with 100% wood fuel. The probes were heated externally by the flue gases or sand and cooled internally to a constant metal temperature. Corrosion was assessed as the amount of metal loss plus the amount of internal/selective grain boundary attack.

Experimental

A number of steels were tested in corrosion probes in the boiler of the Nässjö Combined Heat and Power (CHP) station, which is owned and operated by Vattenfall AB and situated in the southern part of Sweden. The Nässjö boiler is a 30 MW circulating fluidised bed boiler, which produces steam at 80 bar/480°C and generates 9 MW electricity. The heat is distributed in the town as district heating. The plant was commissioned in the spring of 1990 and at first burnt 70% wood (logging residues) co-fired with 30% coal, in terms of thermal energy produced. Since November 1995 the plant has been run on 100% wood (logging residues) which allows the fly-ash from the power station to be returned to the forests, thus completing the environmental cycle.

Probes were exposed in two positions, as shown in Fig. 1. Probes were positioned immediately above the first superheater, (or immediately before in terms of the flue gas passage) and were thus heated by the flue gases. Probes were also placed in the cyclone loop seal and were heated by the sand, which is at the same temperature as the flue gas. The sand in the loop seal is fluidised by air to aid its circulation back into the bottom of the furnace.

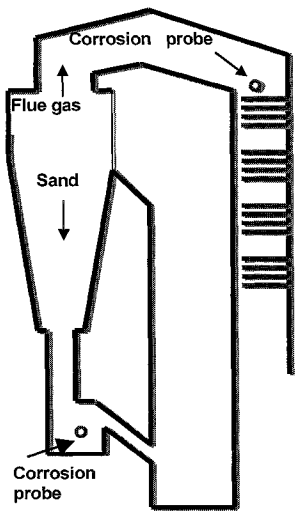


Fig. 1
Schematic diagram of the Nässjö CFB boiler showing one corrosion probe near the top of the boiler at the superheaters and one at the bottom in the cyclone loop seal.

The probes were inserted into the boiler through openings made in existing inspection hatches; different steels were tested in the form of rings attached to the probes. The probes were internally cooled to maintain a constant temperature. The temperature was measured by 6 thermocouples in two dummy rings, one at each end of the test length. The thermocouples

were separated by 120° in the dummy rings and the material temperatures were stored and collected at 2 minute intervals. The flue gas (and sand) temperatures during full load were about 860-880°C in the probe regions. A list of steels tested, with the probe conditions is shown in Table 1 and the chemical compositions of the steels are given in Table 2.

Table 1. List of materials tested, together with the position and probe temperature. Probes N1:3 (Loop seal 650°C) and N2:3 (Superheater 600°C) were exposed for 3360 hours between December 1999 and April 2000. Probes N1:4 (Loop seal 600°C) and N2:4 (Superheater 530°C) were exposed for 2921 hours between November 2000 and March 2001.

Material	**Temp (°C)**	**Position**	**Mat. ring ID no.**	**Material**	**Temp (°C)**	**Position**	**Mat. ring ID no.**
X20	650	Loop Seal	8.6	Sanicro 28	600	Superheater	1.1
X20	600	Loop seal	8.10	Sanicro 28	530	Superheater	1.7
X20	600	Superheater	8.2	TP 347 H FG	600	Superheater	5.2
10 Cr	600	Loop seal	12.8	TP 347 H FG	530	Superheater	5.5
10 Cr	530	Superheater	12.7	TP 347 H FG	650	Loop seal	5.1
10 Cr	600	Superheater	12.2	TP 347 H FG	600	Loop seal	5.6
Esshete 1250	600	Superheater	9.2	HCM12A	650	Loop seal	4.6
Esshete 1250	530	Superheater	9.16	HCM12A	600	Loop seal	4.7
Esshete 1250	650	Loop seal	9.1	HCM12A	600	Superheater	4.3
Esshete 1250	600	Loop seal	9.17	AC 66	600	Superheater	6.2
				AC 66	530	Superheater	6.6

Table 2. Chemical composition, in weight percent, of the steels tested. The balance is Fe.

Steel	**Cr**	**Ni**	**Mo**	**Mn**	**Other**
10CrMo910	2.1	--	0.92	0.43	C 0.12, Si 0.22
X20CrMoV12 1	10.5	0.73	0.89	0.6	C 0.18, Si 0.24, V 0.27
HCM12A	12.0	0.26	0.32	0.65	W 1.9, Si 0.3, Nb 0.06, N 0.06, V 0.02, B 0.003, C 0.08
Esshete 1250	14.9	9.65	0.94	6.25	C 0.084, Si 0.58, Nb 0.86, V 0.22, B 0.004
TP 347H FG	18.5	11.9	--	1.5	Si 0.42, Nb 0.9, C 0.09
AC 66	27.3	31.7	--	0.49	Ce 0.06, Nb 0.8, Si 0.2, C 0.05
Sanicro 28	26.7	30.6	3.32	1.73	C 0.015, Si 0.42, Co 0.06, Cu 0.87, N 0.07

Metallography

The wall thickness of each ring was measured at 8 or 24 points equally spaced around the circumference before and after testing to obtain values of metal loss caused by erosion or corrosion. Measurements were made on two parallel circumferences separated by 1 cm, giving a total of 16 or 48 measurement points for each ring. Internal corrosion (or selective corrosion such as grain boundary attack) was also measured. The total corrosion is the sum of metal loss and internal corrosion values. Specimens were ground and polished using ethanol, because chloride salts are easily dissolved in water. The microstructures of the exposed rings were examined by light optical- and scanning electron microscopy and energy dispersive x-ray analysis.

Gas and deposit analysis

Boiler measurements were made on two occasions, during December 1999 and February 2001. The chemical composition of the flue gas at the superheaters and the environment in the cyclone loop seal was determined by Fourier Transform InfraRed (FTIR) Spectroscopy. Cooled probes were exposed in these environments for 3 hours to collect deposits. The deposits were then analysed by energy dispersive x-ray analysis in a scanning electron microscope.

Results

Metal loss and internal corrosion

The average corrosion values are given in Figs. 2 – 4. The corrosion values are the sum of the metal loss plus internal corrosion and are plotted per 1000 hours (assuming linear corrosion kinetics).

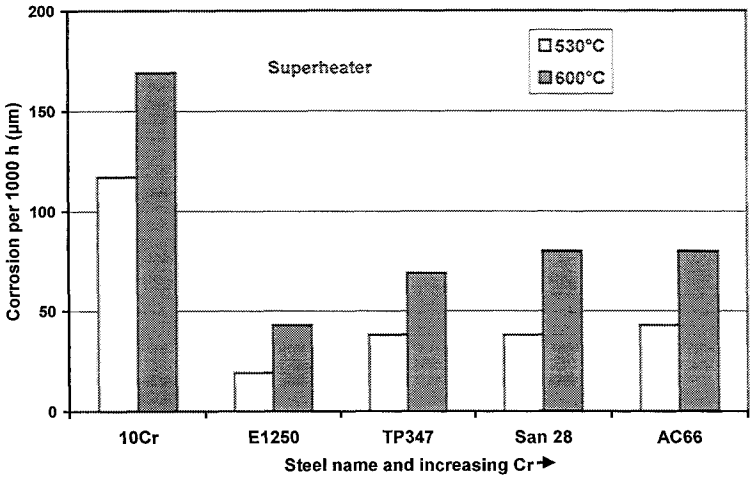


Fig. 2 *Total corrosion per 1000 hours for steels exposed in probes near the superheaters at metal temperatures of 530°C and 600°C. The corrosion rate was higher at 600°C than 530°C.*

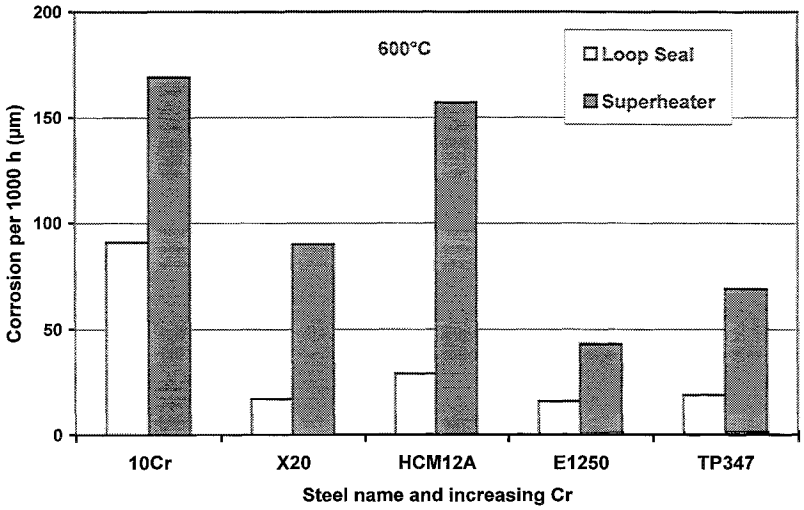


Fig. 3 *Comparison of corrosion rates at 600°C for steels exposed in probes near the superheaters and in the cyclone loop seal. The corrosion rates in the loop seal were considerably lower than at the superheaters.*

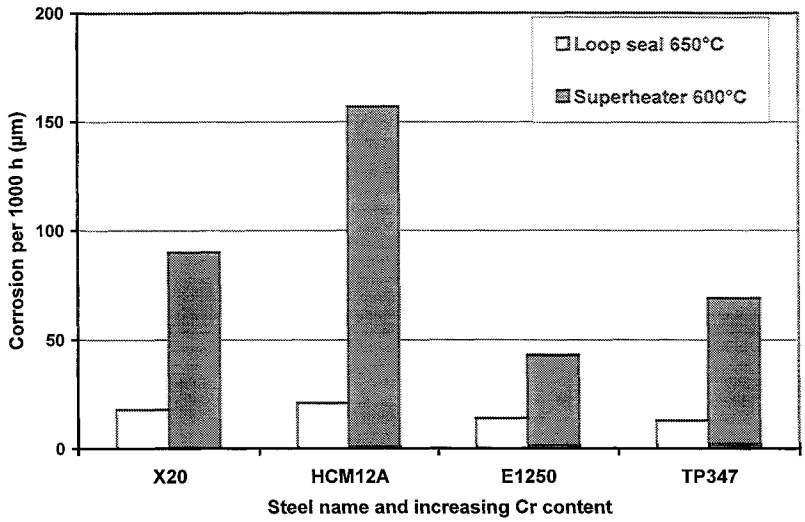


Fig. 4 *Comparison of corrosion/erosion rates for steels exposed in probes near the superheaters at 600°C and in the cyclone loop seal at 650°C, simulating the same steam temperature of about 550°C.*

The amount of internal corrosion in the loop seal probe was small and thus the corrosion results presented for the loop seal represent metal loss. However, in the superheater probes considerable amounts of internal corrosion were seen in Esshete 1250, TP 347HFG and HCM12A. In the 600°C superheater probe (Fig. 3) the corrosion rate per 1000 hours measured for HCM12A was 157 µm; however, internal corrosion accounted for a third of the total corrosion. Fig. 5 shows an optical micrograph of HCM12A. The steels Esshete 1250 and TP 347HFG performed best in the superheater environment and all steels (apart from the 2 % Cr steel 10CrMo910) performed well in the loop seal.

Figure 6 shows typical results of the scanning electron microscopy. The steels that performed relatively well showed an oxide layer enhanced in chromium underneath a top layer of an iron rich oxide. In stainless steels like 347 and Esshete some grains directly under the Cr-rich oxide layer were depleted in chromium, while other adjacent grains appeared not to have been affected in this way. It was difficult to detect sulphur or chlorine in the metal of the steels although these elements were found easily in the deposits on the corrosion probes and to some extent in the oxide. Steels that performed less well (e.g. 10Cr) showed no oxide layer enriched in chromium, only iron oxide. It was not possible to find any differences in the corroded microstructures of the same steels exposed in the loop seal and superheater environments, apart from a larger amount of internal corrosion (as a proportion of the total) in the superheater environment. It appeared that the same type of corrosion mechanisms was operating, only operating faster at the superheater.

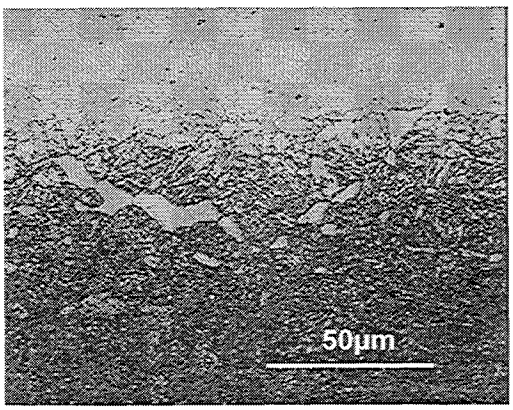


Fig. 5
Optical micrograph of HCM12A, unetched, 600°C, ring 4.3.
The lower part of the micrograph was nearest the outside of the ring and shows considerable internal or selective corrosion. This type of corrosion was not seen in X20.

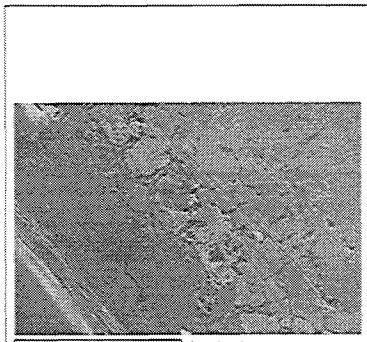


Fig. 6a. Electron micrograph of oxide and internal corrosion in Esshete 1250 (ring 9.17). The marker bar is 60 μm long.

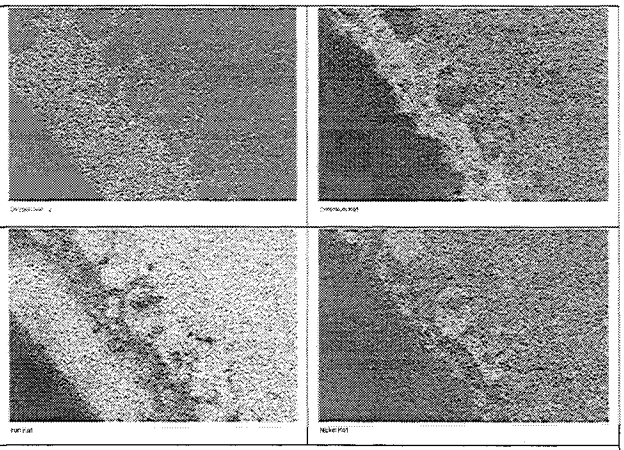


Fig 6b-e. Mapping pictures of oxygen (top, left), chromium (top, right) iron (bottom, left) and nickel (bottom, right). Light areas indicate a high concentration of the element.

Environmental measurements

The deposits formed after three hours exposure in the loop seal were much thinner than those formed on the probes near the superheaters. This made quantitative chemical analysis very difficult, but both S and Cl were detected in the deposits at both locations. Gas sampling in the loop seal was also difficult, because of the sand and fluidisation air. However the gas analyses showed that the levels of SO_2 and H_2O were consistently lower in the loop seal than in the convective pass. O_2 levels were higher in the loop seal because of the fluidisation air, but both CO_2 and O_2 levels were found to vary with boiler load and height in the loop seal. HCl levels were broadly similar in the range of 2-6 ppm at both positions. Levels of H_2O in the flue gas at the final superheater were in the range 22-25% (by volume) as opposed to 3-6 % in the loop seal. SO_2 levels were 13-20 ppm at the superheaters and 3-7 ppm in the sand loop seal. O_2 levels were 3-5 % at the superheaters and 5-15% in the loop seal.

Discussion

For superheater steels in utility boilers fired with coal or a mixture of predominantly coal and biomass it has generally been found that an increase in the chromium content leads to an increase in corrosion resistance [1-3, 11]. The results presented here for 100% wood fuel show that alloys with 15-18% chromium exhibited optimum corrosion resistance in a superheater environment and that there is little to be gained by increasing the chromium and nickel levels to 28-30%. In addition, all the steels tested in the loop seal, apart from 10Cr, performed well.

Considerable amounts of internal corrosion were seen in some alloys, especially E1250, TP 347H FG and HCM12A in the superheater environment at 600°C. Large amounts of internal

corrosion have been seen after corrosion testing in straw-fired boilers, [4,5]. This grain boundary corrosion was thought to be due to preferential attack of chromium carbides by chlorine because the amount of internal corrosion was found to increase with the chromium content of the alloy, [5]. However, microstructural examination of TP 347 H FG, exposed on a probe in the flue gases of a PF wood-fired boiler, showed that the grain boundary corrosion was linked to sulphidation, [6]. Sulphur, but no chlorine, could be detected at the grain boundaries, in spite of a large amount of chlorine in the deposit, [6].

Notably, the corrosion of the steels exposed in the loop seal was much less than the corrosion occurring at the normal superheater position. FTIR spectroscopy showed that the moisture content of the gas in the loop seal was considerably lower than that of the flue gas at the superheaters, (5 vol. % as opposed to 25 vol. %) and oxygen levels were generally higher, although variable. It is known that the presence of water vapour increases the oxidation rate of steels, see for example references 7-9. The oxidation rate at 650°C of P91, a 9% Cr steel that forms mainly iron-rich oxides, depended strongly on the water vapour content, [8]. The oxidation of chromia forming alloys was also found to be affected by the water vapour content of the gas, [9]. It was thought that the critical amount of Cr needed to form a protective oxide scale increased when the moisture content increased, [9]. The oxidation of Type 304L stainless steel (18Cr 10 Ni) at 600°C in dry oxygen resulted in the formation of a Cr-rich oxide, but in the presence of water vapour a non- protective Fe-rich oxide was formed instead, [7]. This was shown to be caused by the evaporation of Cr in the form of $CrO_2(OH)_2$ and the evaporation increased with the gas flow rate and water content, [7].

In the loop seal the sand is fluidised by air to aid the transfer of sand back into the bottom of the furnace. The environment is considerably less aggressive there, from a chemical point of view, although erosion problems would be expected to be greater. However, the results of Figs. 2 - 5 clearly show that the loop seal is an ideal position for a final superheater and sand erosion does not seem to be a problem. In addition, the deposits collected on probes in the loop seal were much thinner than those collected at the superheaters. It is possible that sand erodes the deposits, thereby removing a corrosive source.

Another advantage to be gained, in addition to reduced corrosion, is that the superheater can be considerably smaller in size (about a third of the size of a conventional superheater, [10]) since the heat transfer per unit area of tube surface is more intensive in the loop seal. This leads to savings in material and labour costs. The heat transfer is greater in the loop seal because: -

(i) the temperature drop in the sand, as it gives up its heat to the superheater, is much less than the temperature drop in the flue gas which means that a greater temperature difference between sand and steam is maintained and

(ii) the heat transfer coefficient is greater between sand and the superheater tube wall than between the flue gas and the superheater tube wall.

The result of this, and a possible disadvantage, is that the superheater wall temperature will be higher in the loop seal, for the same steam temperature. For superheaters heated by flue gas (but shielded from radiation from the furnace) the temperature difference between the steam and the tube wall, ΔT, is typically assumed to be 50°C. If a superheater is heated by sand then ΔT can be in the range 70-100°C. This means that a steel with a superior creep strength is needed. However, it is expected that the cost savings by the reduction in size of the

superheater will more than offset any increase due to the use of a more highly alloyed material.

Table 3 shows 100,000 hour creep and tensile strength values for the steels tested in this work. For normal superheater tube dimensions a pressure of 200 bar would require a creep strength of about 85 MPa (including a safety factor of 1.5). The Nässjö power plant produces steam at 80 bar which would require a strength of about 35 MPa. A steam temperature 500°C (c.f. present steam temperature in Nässjö of 480°C) would produce a metal temperature of about 600°C in the loop seal. All materials would be suitable from a strength point of view in Nässjö for use in the loop seal, but 10Cr can be excluded because of its poor corrosion properties. For a steam temperature of 550°C (metal temp 650°C) all steels apart from 10 Cr and X20 could be used.

Table 3 *The stress which causes creep failure in 100,000 hours at metal temperatures of 600°C and 650°C, $\sigma_{B10^5\,h}$ in MPa. The 0.2% proof stress, $\sigma_{0.2}$, is given instead if it is less than $\sigma_{B10^5\,h}$.*

Steel	**Cr (wt %)**	**Ni (wt %)**	**600°C ($\sigma_{B10}5_h$)**	**650°C ($\sigma_{B10}5_h$)**
10CrMo910	2.1	--	34	--
X20CrMoV12 1	10.5	0.73	59	23
HCM12A	12.0	0.26	134*	70*
Esshete 1250	14.9	9.65	$133\sigma_{0.2\%}$	100
TP 347H FG	18.5	11.9	$132\sigma_{0.2\%}$	105
AC 66	27.3	31.7	$90\sigma_{0.2\%}$	$85\sigma_{0.2\%}$
Sanicro 28	26.7	30.6	--**	--**

* extrapolated values
** use as co-extruded/composite tube

The superheaters in Nässjö were previously made of 10CrMo910, but after approximately 19,000 hours of operating on 100% wood fuel the last two superheaters, operating at the highest steam and flue gas temperatures, had to be replaced. Esshete 1250 was chosen as the replacement material.

Conclusions

The corrosion of superheaters heated by flue gas in wood fired boilers can be reduced by selection of the correct material. In the Nässjö CHP plant Esshete 1250 has replaced 10CrMo910 in the last two superheater stages in the convective pass.

The corrosion of superheater tubes in a biomass-fired circulating fluidised bed boiler can also be greatly reduced by positioning the superheater in the cyclone loop seal so that it is heated by sand instead of the flue gas. The superheater can also be more compact as the heat transport per unit area of tube surface is more intensive, which leads to savings in material and labour costs. The reduction in corrosion is thought to be partly due to the reduced amount of water vapour in the loop seal as opposed to the flue gas and a decreased tendency for deposit formation. The metal temperature of a superheater in the cyclone loop seal will be greater than that of a superheater in the convective pass, assuming the same steam temperature. Therefore the strength of the material also has to be taken into consideration.

References

1. E P Latham, T Flatley and C W Morris. "Corrosion Resistant Mateirals for Coal Conversion Systems", pp 137-158. Eds. D B Meadowcroft and M I Manning. Applied Science Publishers, 1983.
2. F Gesmundo. Proc. Conf. "High Temperature Materials for Power Engineering, 1990", p 67. Eds E. Bachelet et al. Kluwer Academic, (1990).
3. P J Henderson, Th Eriksson, J Tollin and T Åbyhammar. Proc Conf "Advanced Heat Resistant Steels for Power Generation." Eds. R Viswanathan and J Nutting. p 507, IOM Communications, London, (1999).
4. N. Henrikssen and O. H. Larsen. *Materials at High Temperatures*, **14**, p 227, (1997).
5. M. Montgomery and A. Karlsson. Presented at Eurocorr 99. Aachen.
6. C Liu, J A Little, P J Henderson and P Ljung. *J. Mater Sci.*, **36**, p 1015, (2001)
7. H Asteman, J-E Svensson, L-G Johansson and M Norell. *Oxid. of Metals*, **52**, p 161, (1999)
8. M Thiele, H Teichman, W Schwarz and W J Quadakkers. *VGB Kraftwerkstechnik*, no. 2, p 77, (1997).
9. P Kofstad. High Temperature Corrosion, p 382. Elsevier Applied Science, London, (1988).
10. A. Berglund. Private Communication, SwedPower AB, (April 2000).
11. P J Henderson, P Ljung, Th. Eriksson, S-B Westberg, B. Hildenwall and T. Åbyhammar. Proc. Conf "Advanced Materials för 21st Century Turbines and Power Plant". Eds A Strang et al. p 1095, IOM Communications, London, (2000).

Acknowledgements

We thank Håkan Kassman (SwedPower AB), Peter Svensson (Vattenfall AB Nässjö) and Annika Stålenheim (Vattenfall Utveckling AB) for their valuable assistance. This work was funded by Vattenfall's research programme "Sustainable Energy Solutions".

EFFECT OF FUEL TYPE ON THE FIRESIDE CORROSION OF BOILER MATERIALS FOR ADVANCED CLEAN COAL TECHNOLOGIES

L.W. Pinder & C.J. Davis

Powergen Power Technology Centre, Ratcliffe - on - Soar, Nottingham, NG11 0EE, United Kingdom

Abstract

In order to meet the demands for future high efficiency coal fired plant in the 21st century, significant increases in the currently employed operating pressures and temperatures will be required. Temperature increases in particular have important implications in terms of materials properties. One important aspect is the fireside corrosion response of the materials. Furnace wall tubes may be expected to operate at metal temperatures approaching 550°C, whilst superheater and reheater materials may be required to operate at metal temperatures in excess of 700°C. This program is examining furnace wall conditions using short term exposures (50 hours) in a $1MW_{TH}$ Combustion Test Facility, and superheater / reheater conditions by conducting long term exposures in a 500MW pulverised coal fired boiler.

Furnace wall fireside corrosion testing is examining the influence of metal temperature, combustion environment, coal chemistry and alloy composition. Five candidate furnace wall alloys, with chromium content varying from 0 to 12%, together with high chromium metallic coatings, are being exposed to both oxidising and reducing environments, whilst burning 3 different UK coals. Results to date show that increasing chromium content offers improved corrosion resistance, and that reducing conditions are more aggressive than oxidising conditions. Dependant upon the coal chemistry, the relationship between metal temperature and corrosion rate is not always simple, with pronounced peaks in wastage rates at intermediate temperatures being observed. Where peaks in wastage rate occur, all alloys and the normally highly protective, high chromium sprayed coatings are seen to suffer unacceptably high wastage rates.

Prolonged exposures are required to accurately reproduce the conditions that are experienced in coal fired superheater / reheater stages, particularly when examining corrosion resistant high alloy materials. 3 corrosion probes, each comprising 19 separate specimens of 8 candidate superheater alloys are undergoing exposure for several thousand hours within a 500MW, pulverised coal fired power station boiler. The alloys range from typical 300 series austenitic stainless steels (18%Cr) to 50% Cr containing IN671. The temperature profile along the corrosion probes permits a range of metal temperatures to be examined for each alloy. The probes are being exposed at 2 separate positions within the boiler to provide information on heat flux effects. A range of open cast and deep mined bituminous United Kingdom coals are burnt in the boiler, reflecting the types of coal routinely delivered to United Kingdom power stations. These exposures are planned to continue until late 2002 / early 2003.

Keywords: chlorine, chromium steel, fireside corrosion, low alloy steels, superheater.

1. Introduction

Whilst a number of new boiler materials are being promulgated by the steel producers as being adequately developed for use under the higher anticipated stresses and metal temperatures in ultra-supercritical plant, little effort has thus far been directed towards their anticipated corrosion performances. Where corrosion tests have been carried out, these have usually only comprised laboratory simulated plant conditions. Tests of this nature have little relevance to the long-term corrosion performance of tubing in boilers under the individual and combined influence of the many operating variables. This project examines the influence of coal composition on the

furnace wall and superheater/reheater fireside corrosion mechanisms during coal-fired combustion under ultra-supercritical conditions.

2. Experimental Program

The alloys selected for testing comprise the most likely candidates to be employed as boiler tubing in the next generation of ultra-supercritical plant [1,2 & 3]. In addition, reference materials are simultaneously being exposed to allow comparisons to be drawn with the corrosion tests of other partners in the Plant Integration Group of COST 522. Sample exposure conditions, particularly metal temperatures, have been chosen as being representative of the conditions likely to be encountered by the candidate alloys during normal and upset conditions in the next generation of ultra-supercritical plant.

2.1 Furnace Wall Fireside Corrosion

2.1.1 Furnace Wall Materials

The compositions of the furnace wall alloys under test are shown in Table 1.

Table 1: Materials Selected for Furnace Wall Fireside Corrosion Tests

Material	Nominal Composition (w/o) (Minimum and Maximum where two values given)								
	C	Si	Mn	Cr	Ni	Nb	N	Mo	Other
15Mo3	0.12 0.22	0.10 0.35	0.40 0.80					0.25 0.35	
HCM2S *	0.04 0.10	0.5	0.10 0.60	1.90 2.60		0.02 0.08	0.03	0.5 3.0	B 0.006, Al 0.03, V 0.20-0.30 W 1.45-1.75
E911	0.09 0.13	0.10 0.30	0.30 0.60	8.50 9.50	0.10 0.35	0.06 0.10	0.05 0.08	0.90 1.10	Al 0.025, V 0.15-0.25, W 0.90-1.10
HCM12	0.14	0.50	0.30 0.70	11.0 13.0		0.20		0.80 1.20	V 0.20-0.30, W 0.80-1.20
50Cr / 50Ni *	0.1	1.7	0.49	49.3	Bal.				Fe 0.22

* Primary Reference Material

15Mo3 is a 0.3% Mo-steel steel which is widely utilised in European power plant. Its furnace wall corrosion performance is expected to be similar to that of the plain carbon steel utilised in the furnace walls of UK sub-critical coal-fired power plant and it is included here as a reference material. HCM2S (2%Cr), E911 (9%Cr) and HCM12 (12%Cr) represent the new family of tungsten-strengthened, chromium containing steels being considered for furnace wall tubing in ultra-supercritical plant. Each contains extensive minor alloying additions to optimise their mechanical properties. However, it is currently not known whether the increased operating temperatures or these alloying additions will have any detrimental effect on the furnace wall corrosion performance of the candidate alloys. The 50%Cr/50%Ni is a High Velocity Oxy-Fuel (HVOF) sprayed coating applied to E911 substrates. It is similar to the corrosion resistant Amdry 350C (50%Cr/50%Ni) successfully applied by plasma sprayed coating to the waterwalls of UK pf-fired boilers suffering severe furnace wall corrosion

during the 1980s. For Runs 5 and 6, the HVOF samples have been coated on one half of their surface with 50%Cr/50%Ni and on the other half with 57%Cr, 38%Ni, 2.5%MoBSi.

2.1.2 Furnace Wall Exposure Conditions

Exposure of the test alloys to simulated furnace wall corrosion environments are being carried out in the $1MW_{TH}$ pulverised coal fired Combustion Test Facility (CTF) at Power Technology. The CTF was purpose designed to recreate real plant conditions and provide a low cost combustion-testing environment. The furnace shape gives aerodynamic patterns typical of power generation boilers, reproducing near-burner flame conditions and giving realistic in-furnace residence times. It is equipped with a comprehensive array of ports on the walls of both the furnace chamber (Figure 1) and convective duct. Overall, the CTF affords near-laboratory control over a range of environmental parameters representative of full-scale plant, many of which have been absent from previous laboratory based studies of furnace wall corrosion.

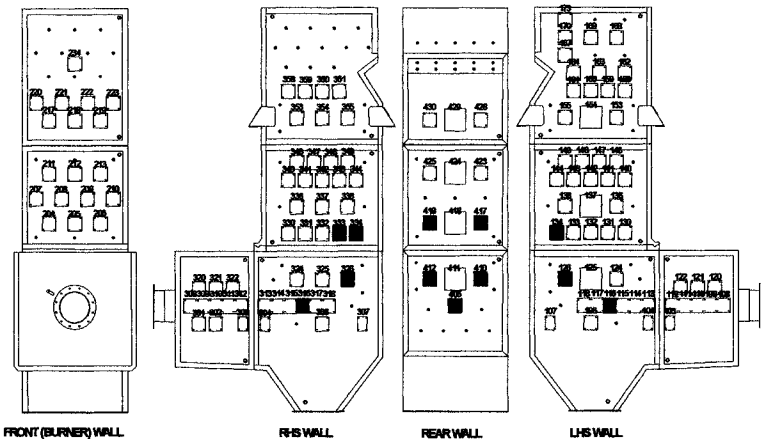


Figure 1: Schematic Diagram Showing Layout of Combustion Test Facility and Location of Sampling Ports (Shaded Ports Indicate Position of Probes)

A total of 6 CTF runs are scheduled, (Table 2), each of nominally 50 hours duration, and each comprising the exposure of 12 specimens of the various alloys to predominantly reducing gaseous environments. The effect of various coal chemistries is being examined by burning three differing United Kingdom coals, chosen primarily on the basis of their chlorine contents.

The specimens are carried into the combustion environment on the front face of air-cooled, precision metrology, furnace wall corrosion probes (Figure 2), designed and proven under a previous programme carried out to examine the influence of coal composition on the furnace wall corrosion rate of plain carbon steel [4 & 5].

2.1.3 Measurement of Metal Loss

The nature of the furnace wall corrosion process results in aggressive linear wastage rates with negligible initiation time, permitting the short term corrosion rates to be measured using

an image analysis technique, developed previously under a Powergen/EPRI collaborative programme [5]. This technique has been proven to measure corrosion losses to an accuracy of better than ±1μm. In addition, the corrosion mechanisms are being characterised by optical and scanning electron microscopy, coupled with EDAX analysis of the corrosion scales and ash layers.

Table 2: Furnace Wall Exposure Program

Coal 1 (High Chlorine (0.39%))				Coal 2 (Very Low Chlorine (<0.1%))				Coal 3 (Medium Chlorine (0.2%))			
Run 1		Run 2		Run 3		Run 4		Run 5		Run 6	
Alloy	T (°C)	Alloy	T (°C)	Alloy	T (°C)	Alloy	T (°C)	Alloy	T (°C)	Alloy	T (°C)
15Mo3	500	15Mo3	550	15Mo3	500	15Mo3	475	15Mo3	450	15Mo3	450
15Mo3	525	15Mo3	575	15Mo3	525	15Mo3	550	15Mo3	475	15Mo3	500
HCM2S	500	HCM12	500	HCM2S	500	HCM12	500	HCM2S	475	HCM12	475
HCM2S	525	HCM12	525	HCM2S	525	HCM12	525	HCM2S	500	HCM12	500
HCM2S	550	HCM12	550	HCM2S	525	HCM12	525	HCM2S	525	HCM12	525
HCM2S	575	HCM12	575	HCM2S	550	HCM12	550	HCM2S	525	HCM12	525
HCM2S	600	HCM12	600	HCM2S	575	HCM12	575	HCM2S	550	HCM12	550
E911	500	50Cr/50Ni	500	E911	500	50Cr/50Ni	500	E911	475	50Cr/50Ni	475
E911	525	50Cr/50Ni	525	E911	525	50Cr/50Ni	525	E911	500	50Cr/50Ni	500
E911	550	50Cr/50Ni	550	E911	525	50Cr/50Ni	525	E911	525	50Cr/50Ni	525
E911	575	50Cr/50Ni	575	E911	550	50Cr/50Ni	550	E911	525	50Cr/50Ni	525
E911	600	50Cr/50Ni	600	E911	575	50Cr/50Ni	575	E911	550	50Cr/50Ni	550

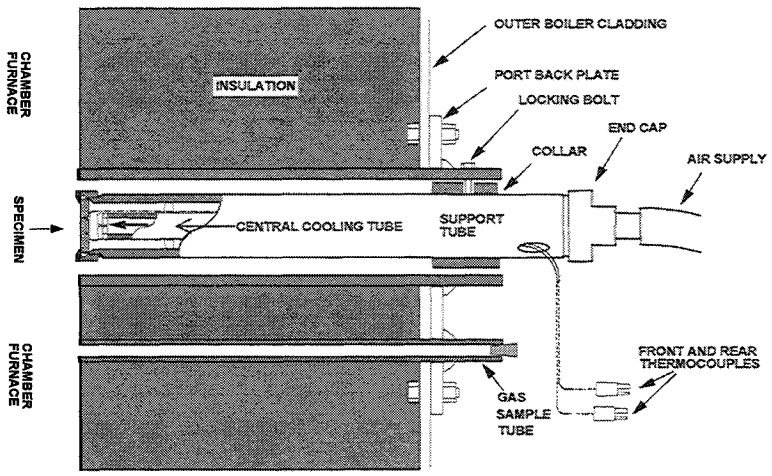


Figure 2: Schematic Diagram Showing Probe and Port Layout in CTF

2.1.4 Evaluation of Alloy Performance

The previous Powergen/EPRI collaboration programme identified that furnace wall fireside corrosion rates of plain carbon steels are dependent upon surface metal temperature, absorbed heat flux, coal chlorine content and the oxidising/reducing potential of the local combustion environment [5]. In total, 109 specimens were exposed during 11 individual CTF runs. Even this large number of samples was insufficient to conduct a full polynomial regression analysis of the individual and interactive contributions of all of the suspected experimental variables. However, a satisfactory algorithm relating corrosion rate to the major variables was derived and this was validated by the successful prediction of a number of historic plant corrosion rates, both in UK and US plant. With material composition as an additional variable in the current programme, it would be even more impractical to attempt a full statistical analysis of the experimental data. Accordingly, the performance of each alloy is being evaluated with reference to the corrosion rate predicted by the aforementioned algorithm. In particular, the new data are being analysed to determine whether the previously determined chlorine dependence holds at the higher anticipated metal temperatures and to identify whether the alloys are more or less corrosion resistant than plain carbon steels.

2.2 Superheater / Reheater Corrosion

2.2.1 Materials

The eight alloys selected for inclusion within the trial are shown in Table 3, and include a COST522 primary reference material (TP347H) and two secondary reference materials. The alloys selected have a range of chromium contents and as such would be expected to posses a range of corrosion resistances. Super 304H is a copper-containing derivative of TP304H, with a higher creep rupture strength. It has the lowest chromium content of all of the superheater/reheater candidate alloys on trial. TP347HFG is a grain-refined variant of TP347H. The finer grain size is claimed to enhance corrosion resistance via increased chromium diffusion rates to the corroding surfaces. Both of these alloys possess similar chromium levels to those of the conventional austenitic alloys commonly employed in Powergen's current 500MW coal fired units. SAVE25 is a 21-24% chromium steel, containing nitrogen, copper and tungsten to increase its creep rupture strength. HR3C is a nitrogen containing derivative of the 25%Cr/20%Ni T310Nb steel currently employed as the outer layer of coextruded furnace wall and superheater tubing in Powergen coal-fired plant. The nitrogen improves the creep rupture strength of T310Nb to such an extent that an inner creep resistant layer is no longer required. Hence, the material has recently been utilised as monobloc tubing in those areas of the final superheater and reheater stages at Ratcliffe power station which are suffering the highest fireside corrosion rates. For the current test programme, this alloy is being exposed at significantly higher metal temperatures than those currently being seen at Ratcliffe-on-Soar. Sanicro28, HR11N and IN671 all contain higher chromium and nickel contents than any alloys used as superheater and reheater tubes in any UK plant to date. As such, they are expected to be highly resistant to fireside corrosion at conventional plant temperatures. The extent to which this corrosion resistance is retained at the higher temperatures predicted for ultra-supercritical plant will be established by the current programme.

Table 3: Alloys Selected for Superheater/Reheater Corrosion Testing

Material	Nominal Composition (%) (Minimum and Maximum where two values given)									
	C	Si	Mn	Cr	Ni	Nb 0.3	N	Mo	Cu	Other
Super304H	0.07 0.13	0.3	1.0	17.0 19.0	7.5 10.5	0.3 0.6	0.05 0.12		2.5 3.5	
TP347H *	0.04 0.10	1.0	2.0	17.0 19.0	9.0 13.0	10 * C				
TP347HFG	0.06 0.10	0.75	2.0	17.0 20.0	9.0 13.0					(Nb+Ta) 8*C
SAVE25	0.05 0.12	1.5	2.0	21.0 24.0	15.0 22.0	0.3 0.6	0.15 0.30		2.0 4.0	W 0.8-2.8
HR3C	0.04 0.10	0.75	2.0	24.0 26.0	17.0 23.0	0.2 0.6	0.15 0.35			B 0.005
Sanicro28 **	0.02	0.6	2.0	27	31			3.5	1.0	
HR11N	0.03	0.6	2.0	27.0 30.0	38.0 42.0			0.5 1.5		
IN671 **	0.05			48	51.5					Ti 0.35

* Primary Reference Material
** Secondary Reference Material

2.2.2 Corrosion Exposures

During a previous fully funded EPRI programme to study the effect of coal chemistry on superheater/reheater fireside corrosion it was established that an extended initiation period of approximately 2,000 hours is required before the corrosion mechanism becomes fully established [6]. Consequently, it is not possible to conduct representative alloy exposures to simulated environments in the CTF. Accordingly, the candidate superheater/reheater alloys are being exposed for a nominal test duration of 10,000 hours on corrosion probes (Figure 3) inserted in the gas passes of a 500MW pf-fired station. Two of the probes are being exposed local to the final reheater stage, whilst the third probe is positioned behind the platen superheater stage. This arrangement permits the investigation of the effects of gas temperature and heat flux, as well as alloy composition, on the fireside corrosion response of the alloys. Each probe holds 19 specimens which are positioned on the probes such that samples from each alloy are exposed over a range of metal and gas temperatures (Table 4).

Superheater/Reheater Probe exposures are planned to continue until around March 2003, by which time it is hoped that they will have accumulated around 10,000 hours of exposure.

2.2.3 Measurement of Metal Loss

As with the furnace wall probe samples, metal losses will be measured using an image analysis technique, this time developed under an EPRI Fully Funded Programme [6]. This technique has been proven to measure corrosion losses to an accuracy of around ±4μm. Again,

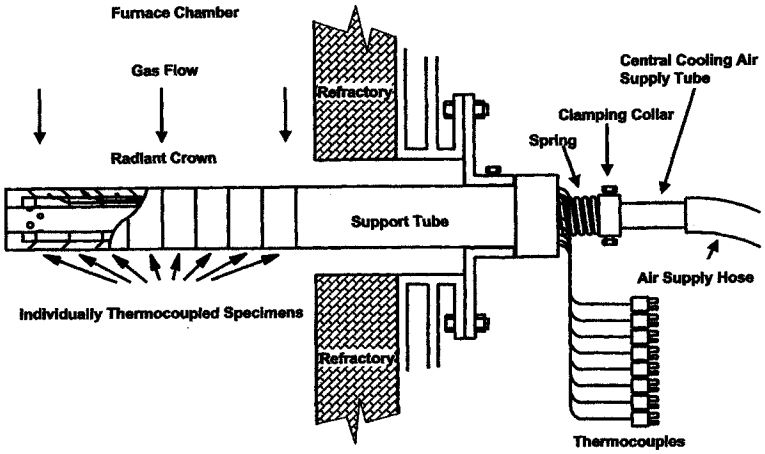


Figure 3: Schematic Diagram Showing Superheater/Reheater Corrosion Probe and Port Layout in U1 Ratcliffe-on-Soar

Table 4: Test Material Location and Temperatures on Superheater/Reheater Probes

Sample	Probe A		Probe B		Probe C	
	Material	Temp. (°C)	Material	Temp. (°C)	Material	Temp. (°C)
1	TP347H	655	Super304H	692	Super304H	550
2	Sanicro28	668	TP347HFG	693	TP347HFG	585
3	Save25	673	HR3C	694	HR3C	610
4	TP347H	678	HR11N	694	HR11N	626
5	Sanicro28	682	IN671	695	IN671	638
6	Save25	688	Super304H	696	Super304H	650
7	TP347H	691	TP347HFG	696	TP347HFG	662
8	Sanicro28	695	HR3C	696	HR3C	672
9	Save25	696	HR11N	696	HR11N	682
10	TP347H	697	IN671	696	IN671	691
11	Sanicro28	698	Super304H	695	Super304H	697
12	Save25	698	TP347HFG	694	TP347HFG	703
13	TP347H	699	HR3C	693	HR3C	706
14	Sanicro28	698	HR11N	692	HR11N	708
15	Save25	698	IN671	692	IN671	710
16	TP347H	697	Super304H	690	TP347HFG	710
17	Sanicro28	697	TP347HFG	688	HR3C	707
18	Save25	696	HR3C	687	HR11N	706
19	TP347H	694	HR11N	685	IN671	701

the corrosion mechanisms will be characterised by optical and scanning electron microscopy, coupled with EDAX analysis of the corrosion scales and ash layers.

2.2.4 Evaluation of Alloy Performance

The high temperature, fireside corrosion performance of conventional ferritic and austenitic superheater and reheater materials has been well characterised by in-plant corrosion probe exposures over the years. Simple comparison of the performance of the new alloys following long term exposure at the higher metal temperatures will be indicative of their anticipated performance under ultra-supercritical conditions.

3. Results to Date

3.1 Furnace Wall Fireside Corrosion

The first four of the scheduled six CTF rig runs have been completed. Figure 4 shows the metal losses measured to date on the 15Mo3 reference material as a function of metal temperature. It can be seen that, at 525°C, one data point for the 0.39% Cl coal falls exactly on the line predicted for a 0.39% Cl coal using the Powergen/EPRI furnace wall corrosion algorithm. However, above 525°C, most of the new metal loss data for 15Mo3 closely follows the predicted line for a 0.04% Cl coal, irrespective of the coal chlorine content.

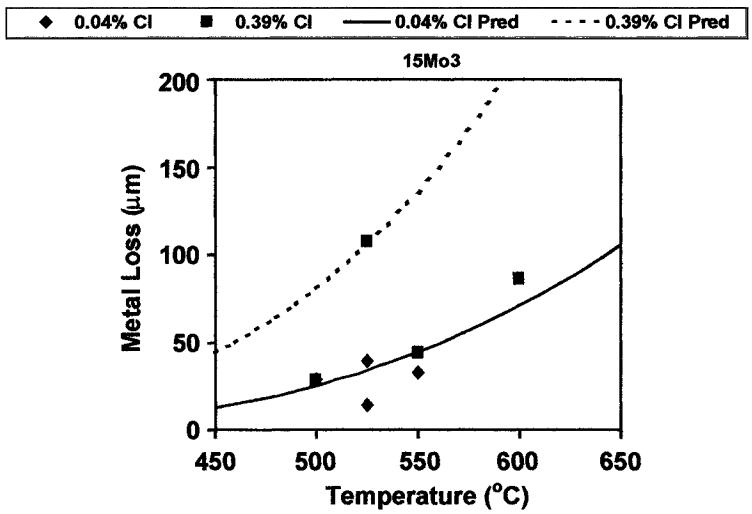
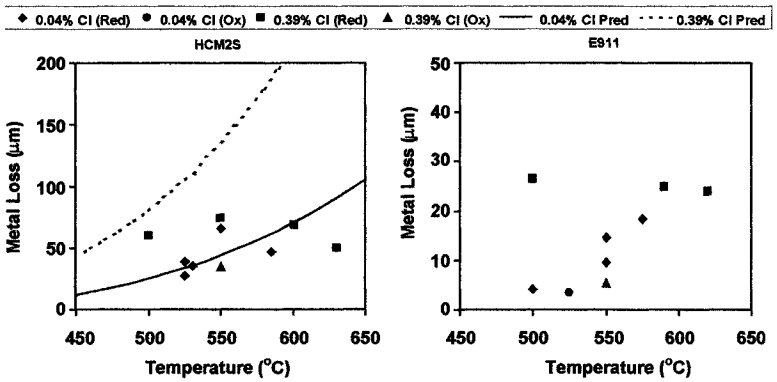
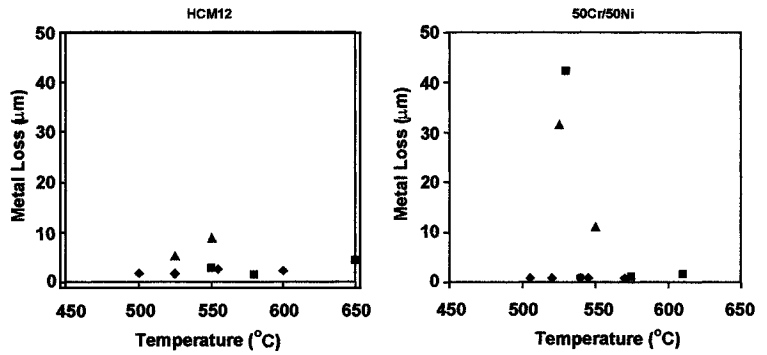


Figure 4: Furnace Wall Metal Loss as a Function of Exposure Temperature for 15Mo3 Compared with Predicted Values

Similar behaviour is mirrored to a greater or lesser extent by the other materials (Figures 5 to 8). Hence, up to around 525°C, and under reducing conditions, corrosion rates appear to be enhanced by increasing coal chlorine content, as would be predicted for classic, furnace wall corrosion behaviour [4]. However, at temperatures above 525-550°C, the data for all of the alloys suggest that metal losses under reducing conditions in the presence of chlorine are similar to those under reducing conditions in the virtual absence of chlorine. Hence, at these temperatures, coal chlorine appears to contribute little, if anything, to the overall corrosion rate. Together, these observations might imply that the chlorine mechanism in furnace wall corrosion is only operative up to around 525°C.



Figures 5 & 6: Furnace Wall Metal Loss as a Function of Exposure Temperature for HCM2S (Compared with Predicted Values) and E911



Figures 7 & 8: Furnace Wall Metal Loss as a Function of Exposure Temperature for HCM12 and 50Cr50Ni (Legend as Figures 5 & 6)

4. Discussion

In classic furnace wall corrosion, a chlorine-rich phase is generally observed interposed between the mixed oxide/sulphide corrosion scale and the metal surface [4]. Whilst this phase has never unambiguously been identified, it is thought to comprise $FeCl_2$ or FeOCl and enhanced chlorine transfer through this chlorine-rich phase under an heat flux is considered to be responsible for the rapid metal loss experienced under reducing conditions when burning high chlorine coals [5]. Theoretical calculations imply that this chlorine-rich phase should become thermodynamically unstable at temperatures much above 450-475°C. Hence, the observation that the chlorine mechanism may not have been operative on the samples exposed at metal temperatures above 525-550°C may confirm this expectation.

Examination of Figures 4 to 8 also show that, whilst the measured corrosion rates for HCM2S are similar to those for 15Mo3, those for the E911 and HCM12 steels fall progressively lower than the predicted corrosion rate with increasing chromium content within the alloy. The

results for the 50%Cr/50%Ni HVOF coating are somewhat surprising in that severe chlorination was seen under both oxidising and reducing conditions at 525°C. The reasons for this anomaly are currently unclear. Again, however, corrosion rates fell dramatically at temperatures above 525°C.

5. Further Work

The final two CTF rig runs (Table 2) will be completed early in 2002. All of the morphological and furnace wall metal loss data will then be interrogated to determine:

- whether the chlorine influence on furnace wall corrosion rates does indeed decline above around 525°C, (sample exposure temperatures have been adjusted to concentrate more data in this area),
- to what extent increasing the chromium content of the steel reduces the corrosion rate, and
- what benefit, if any, might be expected from the use of high chromium and nickel HVOF coatings.

The superheater/reheater corrosion exposures in the 500MW pf-fired plant will continue into early 2003. The samples will again be subjected to detailed morphological analysis to investigate the relative merits of the proposed alloys for use under ultra-supercritical conditions.

6. Acknowledgements

This paper is published with the kind permission of Powergen UK plc. Powergen acknowledge the support of the UK DTI.

7. References

[1] Metcalfe, E. and Scarlin, B., "Advanced High Efficiency Steam Power Plant" in "Materials for Advanced Power Engineering 1998" Edt. Lecomte-Beckers, J. et al. Forschungszentrum Jülich Gmbh (1998) pp 35-52

[2] Fleming, A., Maskell, R.V., Buchanan, L.W. and Wilson, T., "Material Developments for Supercritical Boilers and Pipework" in Materials for High Temperature Power Generation and Process Plant Applications Edt STRANG, A. Institute of Materials Publication Book No. 728. pp 32-77, 2000

[3] Viswanathan, R. and Bakker, W., "Materials for Ultrasupercritical Coal Power Plants - Boiler Materials: Part 1". Journal of Materials Engineering and Performance, Vol. 10, No 1, (2001), pp 81 to 95.

[4] James, P.J. and Pinder, L.W., "Effect of Coal Chlorine on the Fireside Corrosion of Boiler Furnace Wall and Superheater/Reheater Tubing". Materials at High Temperatures 14(3) (1997) 187

[5] Davis, C.J., James, P.J., Pinder, L.W. and Mehta, A.K. "Effects of Fuel Composition and Combustion Parameters on Furnace Wall Fireside Corrosion in Pulverised Coal-Fired Boilers", Materials Science Forum, in Press. (2001)

[6] Davis, C.J., James, P.J. and Pinder, L.W., "Fireside Corrosion in Pulverised Coal-Fired Boilers: Effect of Coal Chlorine and Combustion Parameters" EPRI Report 1001350, May 2001.

FATE OF TRACE CONTAMINANTS FROM BIOMASS FUELS IN GASIFICATION SYSTEMS

P Kilgallon, N J Simms and J E Oakey

Power Generation Technology Centre, Cranfield University, Cranfield, Beds MK Al, UK

Abstract

There is growing interest in the use of biomass and other renewable CO_2 neutral fuels in power generation systems. This interest is being stimulated by the search for electricity generation methods, which minimise environmental emissions and utilise readily renewable fuel sources, but have the attraction of allowing a diversification in power generation fuel sources. Unfortunately, compared to coals, these fuels contain different relative and absolute levels of trace contaminants (sometimes far in excess of coal) so existing plant designs/material specifications based on coal firing may need modification. An extensive list of compositions for potential fuels such as pine wood, wheat straw, a range of grasses, sewage sludge and peat, has been compiled together with coal data for comparison. Most compositions reported in the literature are only partial analyses of the fuels, often targeted at their bulk combustion and/or gasification behaviour with far fewer reports of composition data that include analyses of all minor and trace metal species that are required for assessing the impact of the fuels and processes on material performance. From these data, the fate of typical levels of contaminants has been estimated throughout the hot gas paths of the various candidate power systems, using a software thermochemical modelling package (MTDATA). Plant measurements of both trace elements and minor species in gasification processes have been gathered for comparison with these estimates.

Keywords: Trace contaminants, thermodynamic modelling, biomass, coal, gasification.

Introduction

There is growing interest in the use of biomass and other renewable CO_2 neutral fuels in power generation systems [1]. This interest is being stimulated by the search for electricity generation methods, which minimise environmental emissions and utilise readily renewable fuel sources, but have the attraction of allowing a diversification in power generation fuel sources. One possible approach is for the advanced combined cycle power systems originally developed for coal-firing alone to be introduced with coal/biomass co-firing, to encourage the more rapid introduction of such systems into commercial operation [2,3]. Such systems were originally devised to generate power from coal with much greater efficiencies and far less environmental emissions (SO_x, NO_x and CO_2) than conventional pulverised coal power generation. In the development of these systems for co-firing, it is necessary to ensure that potentially vulnerable component parts are manufactured from appropriate materials and that adequate, reliable and predictable component lifetimes will be achieved with unusual fuels and fuel mixes. For such systems to be competitive with other potential power sources, they must be designed to maximise their efficiency and reliability whilst minimising construction and operating/maintenance costs.

A number of gasification systems have been developed [1,4-8], based on different types of gasification processes, e.g. entrained flow, fixed bed, fluidised bed. Variations on these processes may use either oxygen or air as the oxidant in the gasifier vessel and can be controlled to give varying degrees of conversion of the solid fuel to fuel gas, from complete (>99% conversion) to partial (e.g. 75% conversion). Once generated, the fuel gases need to be cooled and cleaned before being burnt in gas turbines. It is possible to carry out the gas cleaning by water scrubbing the cooled fuel gases, but this leads to lower cycle efficiencies and requires the provision of a scrubbing and waste water treatment facility, which generates liquid waste for

later disposal. Hot dry gas cleaning, using barrier filters to remove particulates and catalysts/sorbents to remove gaseous species (e.g. sulphur, chlorine, ammonia), offer higher cycle efficiencies as well as lower capital and operating/disposal costs and is the target of most second generation gasification systems [9]. There are many significant differences between the various gasification systems [4,7], both in terms of the operation of the actual gasification process and the requirements for different downstream components with distinct ranges of operating conditions. These give rise to economic and efficiency differences between the systems that are beyond the scope of this paper. However, from the perspective of materials performance and optimum materials selection, it is critically important to understand the component operating conditions and the environments produced in each of the systems. Published bulk gas compositions showing the significantly different ranges produced by some of these gasification systems using coal are available (e.g. [4,7]); further differences arise from the minor and trace gas species also generated.

Co-firing biomass fuels introduces further significant differences, particularly in terms of the minor and trace gas species. The use of such co-firing will only prove viable where efficient, reliable, low emission systems can be developed which require a minimum of fuel pre-treatment (if any) and can use existing state-of-the-art components, such as hot gas filters, gas cleansing systems and high efficiency gas turbines. While the selection and life prediction of materials for components in coal-based gasification systems has been the subject of a few extensive studies [e.g. 10], the use of biomass fuels introduces a different balance of contaminants into the fuel gas produced. This can affect components throughout the hot gas paths of the gasifier and gas turbine, as well as altering the trace element emission levels from such systems. For all the components exposed to the fuel gases and combusted fuel gases, the presence of particles may cause erosion, abrasion or deposition, and gaseous species (e.g. H_2S SO_X, HCl, alkali and other trace metal species) may cause deposition and/or enhanced corrosion.

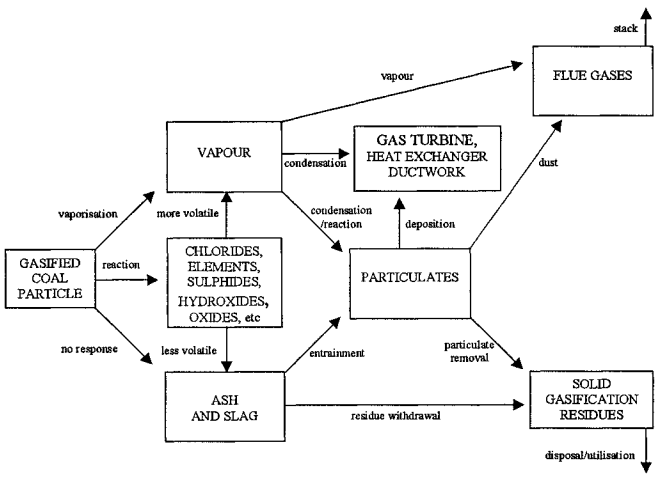


Figure 1. Flow Diagram Summarising the Fate of Minor and Trace Elements in Gasification Systems with Hot Gas Clean-up [2]

There are several possible routes for minor and trace elements to take within a gasification system and through into the gas turbine (Figure 1). These routes vary from no response to the

gasification process (and so exit with the ash/char/slag) through to the formation of vapour species that can pass through the whole hot gas path (and so be emitted from the process). In between these two extremes, there is a range of possible behaviours including (a) reactions to form particles and (b) vapour species that can condense on to particles or different components (depending on their specific operating conditions) throughout the hot gas paths. The fate of the various trace elements is element-specific and in addition can be influenced by both the relative and absolute levels of other elements present in the fuels (e.g. sulphur and chlorine) and in any sorbents, as well as the composition of materials used for hot gas path components.

This paper reports some of the findings of an on-going study into the potential fate of trace elements within gasification systems (and their associated gas turbines) when using coal and biomass fuels. This study has used a commercial thermodynamic package, MTDATA, to carry out theoretical predictions of trace element behaviour and then compared the trends identified by these predictions to plant measurements and known operating experience (both published and confidential). One of the aims of this work is to enable materials studies to be more closely focused onto using realistic deposit compositions when carrying out corrosion testing on materials intended for use within gasifier and gas turbine hot gas paths.

Biomass Fuel Compositions

Extensive composition information has been gathered on potential European biomass fuels [2]; few of these analyses have been carried out for all minor and trace metal species. Average parameter values are given in Table 1 for pine wood, wheat straw, a range of grasses, sewage sludge and peat, with coal for comparison; but it should be noted that there are significant differences in the errors associated with each of these values due to inherent fuel variations, the varying numbers of references used to determine each value and the various analytical methods used. These data were used as the basis for the thermochemical modelling.

Thermochemical Modelling

Gasification Systems

A thermodynamic study was carried out, using MTDATA, to determine which trace elements are more/less likely to enter the hot gas paths of gasification systems, condense onto system components and/or pass through into the gas turbine (for details of the considerations and assumptions needed in such a study see, for example, reference [13]). This study investigated the stability of potential product compounds in gasifier fuel gases and their sensitivity to a number of important process variables:

- two example gasifier processes: an oxygen blown entrained flow process (Prenflo) and an air blown fluidised bed process (ABGC) [2,4,7]
- atmospheric and pressurised operation
- temperature ranges covering gasification and hot gas cleaning processes, as well as component operating temperatures
- a range of S and Cl levels to cover the potential ranges of fuel compositions expected in systems fired on typical European coals with biomass additions of 0 to 100%
- the elements As, B, Ba, Be, Ca, Cd, Co, Cu, Hg, K, Mn, Mo, Na, Pb, Sb, Se, Sn, V, Zn (Cr, Ni and Fe were not investigated as they are major alloying elements in materials used in components throughout the fuel gas paths)

Table 1. Average Compositions of Potential Biomass and Coal Feedstocks

(a)

	Proximate analysis (dry)					
	Wood	Straw	Grass	Sewage	Coal	Peat
Moisture (wt%)	20.7	10.7	14.9	19.5	8.2	27.9
LHV, MJ/kg	18.6	17.3	18.3	10.7	26.2	20.1

(b)

	Ash (%)					
	Wood	Straw	Grass	Sewage	Coal	Peat
Al_2O_3	5.5	1.8	2.8	15.0	18.1	10.4
CaO	34.5	6.0	7.4	17.3	10.3	26.6
Fe_2O_3	3.6	1.0	1.6	10.6	12.3	5.7
K_2O	9.3	22.2	15.3	1.4	2.4	0.8
MgO	4.5	2.9	3.4	3.1	3.8	1.4
MnO	0.8			0.1	0.1	0.3
Na_2O	1.7	3.7	0.7	1.0	3.5	0.6
P_2O_5	5.6	2.6	8.6	10.0	0.4	4.3
SO_3	5.5	3.3	1.4	1.3	6.2	
SiO_2	24.3	49.6	59.5	34.6	40.8	28.2
TiO_2	0.4	0.1	0.2	1.0	0.8	

(c)

	Others (ppm-wt, dry)					
	Wood	Straw	Grass	Sewage	Coal	Peat
Na	139	197			821	288
K	1076	10028			1637	434
Ca	633	3250			2517	2453
Al	100				11300	3467
Fe	50				10160	9463
Mg	100				1160	4750
B	146			83	7	
Li	58			69		
S	500	1175				1290
P	900					110
Cl	280	3250			559	225

(d)

	Ultimate analysis (wt%dry)					
	Wood	Straw	Grass	Sewage	Coal	Peat
S	0.2	0.1	0.2	1.0	1.7	0.4
Cl	0.1	0.8	0.2	0.1	0.2	
Ash	1.7	5.9	5.2	43.4	12.7	4.4

(e)

	Selected Trace Metals (mg/kg, dry)					
	Wood	Straw	Grass	Sewage	Coal	Peat
As	26	32	30	19	32.2	5.75
Ba	1565	90	70	649	677	7.4
Be	1			3	5	
Cd	19	3	2.95	3.7	2.2	0.29
Co	55	20	20	14	23	1.05
Cr	346	58	30	183	123	5.85
Cu	420	85	30	492	217	5.2
Hg	5	5	5	7	3.6	0.35
Mn	4935			569	104	26
Mo	22			14	57	
Ni	268	45	30	87	193	4
Pb	461	45	30	199	234	25
Sb	14	20	20	12	20	
Se	17	30	30	16	21	
V	54	28	38	80	58	0.4
Zn	1074	125	226	1102	433	39

Published literature surveys [e.g. 11-14] were critically evaluated and care taken to avoid the pitfalls identified. For a power plant it is important to note that kinetic effects may arise due to short gas residence times and/or slow reaction rates that could limit movement towards thermodynamic equilibrium. These effects apply especially to the bulk gases and will be less significant in the slower moving boundary layers adjacent to components.

The results of this thermodynamic study are summarised in Tables 2-4. Table 2 indicates which elements are found in gasifier gases as mostly solids or gases throughout the temperature ranges considered (i.e. no phase changes in the major species) and whether process pressure, sulphur or chlorine levels influenced any of the phase transitions found. It should be noted that even elements with condensed phases can have significant vapour pressures. Table 3 lists the major gaseous and condensed phases and the temperature ranges for these transitions. Finally, Table 4 groups the elements in terms of their 'volatility', i.e. in order of the transitions from gaseous to condensed phases. This table does not correspond with the frequently quoted three-group classification of trace elements [14]. This classification was originally developed for combustion systems and some reports directly translate this to gasification systems. As sometimes noted before [e..g. 11,13] and found in this study, the same classification of elements is not applicable to combustion and gasification systems (and indeed there are several significant differences between gasification systems).

Table 2. Summary of Predicted Fate of Trace and Alkali Metal Species in Gasification Gases and Sensitivity to Changes in Conditions

Trace Element	Majority species always in vapour phase		Majority species always in solid phase		Gas → solid transformation sensitivity			
	ABGC	Prenflo	ABGC	Prenflo	Pressure	Cl	S	Process
As	✔	✔	X	X	-	-	-	-
As (+ Ni)	X	X	S	S	✔	✔	✔	(✔)
B	✔	✔	X	X	-	-	-	-
B (+ Ca)	X	-	X	-	X	X	X	✔
Ba	X	X	S	-	✔	✔	✔	✔
Be	X	X	X	X	X	X	X	X
Ca	X	X	S	S	(✔)	(✔)	(✔)	(✔)
Cd	S	S	X	X	✔	✔	✔	X
Co	X	X	S	X	✔	✔	✔	(✔)
Cu	X	X	X	X	(✔)	✔	✔	(✔)
Hg	✔	✔	X	X	-	-	-	-
K	X	X	X	X	✔	✔	✔	(✔)
Mn	X	X	S	X	X	✔	✔	(✔)
Mo	X	X	S	X	(✔)	✔	✔	(✔)
Na	X	X	X	X	✔	✔	✔	(✔)
Pb	S	S	X	X	X	✔	✔	X
Sb	✔	✔	X	X	-	-	-	-
Se	✔	✔	X	X	-	-	-	-
Sn	S	S	X	X	X	✔	✔	X
V	X	✔	✔	X	-	-	-	-
Zn	S	?	X	X	X	✔	✔	X

✔ = Yes; X = No; S = under some pressure, Cl, S conditions; - = not applicable; ( ) = under some conditions.

Table 3. Summary of Behaviour of Trace and Alkali Metal Species in Gasifier Gases in Terms of Major Gaseous and Solid Species as well as Gas→Solid Transformation Temperature Ranges Indicated by Thermodynamic Study. ( ) = Prenflo only

Element	Major Gas Species	Major Solid Species	Gas → Solid Transformation Temperature Range (°C)
As	As, As_2, As_4, AsS	-	-
As (+Ni)	AsS (As)	As_2Ni_5, As_8Ni_{11}	1020-1460
B	BHO_2, $B(OH)_3$	-	-
B (+Ca)	$B(OH)_3$ (BHO_2)	$B_2Ca_3O_6$	Solid→gas 420-840
Ba	$BaCl_2$, BaClHO	$BaCl_2$, BaS $BaCO_3$	900-1040 (or >1200)
Be	BeH_2O_2	BeO	840-960
Ca	-	$CaCl_2$, CaS, $CaCO_3$	-
Cd	Cd, $CdCl_2$	CdS	400-540 (or <400)
Co	$CoCl_2$ (Co)	Co, Co_9S_8	600-1340
Cu	CuCl, Cu_3Cl_3 (Cu, CuH)	Cu, Cu_2S	520-960
Hg	Hg	-	-
K	KCl, K_2Cl_2	KCl	700-900
Mn	$MnCl_2$ (MnCl)	MnO, MnS	440-1260
Mo	$MoClO_2$, $MoCl_2O$, $MoCl_2O_2$ ($MoHO_2$)	MoS_2	700-1200
Na	NaCl, Na_2Cl_2	NaCl	670-900
Pb	Pb, PbCl, $PbCl_2$ PbS	Pb, PbS	560-640 (or <400)
Sb	SbCl (Sb)	-	-
Se	SeH_2 (SeH)	-	-
Sn	SnS, $SnCl_2$	SnO_2, SnS	460-560 (or <400)
V	(VCl_2, VCl_3, $VOCl_3$)	V_2O_3	-
Zn	Zn, $ZnCl_2$	ZnS	460-780

Table 4. Summary of Predicted Volatility of Trace and Alkali Metals in Gasification Gases from Thermodynamic Study

Increasing Volatility	Element
↑	Hg, Sb, Se (As, V, B)
	Cd, Pb, Sn, Zn (As, B)
	Co, Cu, K, Mn, Mo, Na
	As, Ba, Be
	Ca (V, As, B)

( ) = significant differences in behaviour predicted for different gas conditions

Figures 2 and 3 illustrate some of the data generated during the thermochemical modelling and highlight some of the complexities. Figure 2 shows the effect of increasing the pressure on the potassium equilibrium diagram for an ABGC generated fuel gas. The gas to solid transformation temperature of the major species, KCl, is increased from ~700°C to ~900°C when the pressure increases from 1 to 20atm. Figure 3 shows how the data from some of elements can be greatly affected by the inclusion (or omission) of another element, with the example of the effect of nickel on the equilibrium diagram for arsenic; nickel will be found in many materials used in components in gasifier hot gas paths and its influence on the equilibrium models for other trace elements needs to be considered. Without the inclusion of nickel, the arsenic data are comprised of gaseous species but with nickel present solid As_2Ni_5 is predicted to be the major species formed up to 1000°C. Other particularly significant variables are the sulphur and chlorine levels of the fuel gas stream (mostly present as H_2S and HCl). For example, increased levels of H_2S can give, for different elements, higher or lower dewpoints (e.g. Zn or Sn) or different gas phase and/or condensed species (e.g. Pb).

Prediction of Dewpoints For Vapour Phase Deposition In Gas Turbine

The same methods for thermodynamic predictions can be applied to the gas turbine, using the results of the gasifier fuel gas study to identify the elements that can pass through the fuel gas paths (elements from rows 1 to 3 of Table 4 in decreasing order of volatility) into the gas turbine, as well as realistic ranges for the different contaminant levels. Some of these elements (e.g. Hg) will pass through the turbine as well, whereas others (e.g. Pb, Zn, Na, K) may form deposits on hot gas path components. Figure 4 illustrates the results obtained in predicting dewpoint temperatures for K, which are plotted as a function of contaminant levels for different SO_X and HCl levels and gas pressures. Figure 4 shows that the K_2SO_4 dewpoint increases with increasing K or SO_X levels in the gas stream, as well as gas pressure, but decreases with increasing HCl levels in the gas stream.

Gasification Plant Gas and Solid Stream Composition Data

As summarised in Figure 1, there are several different potential routes for trace contaminants to pass through or remain within a solid fuel gasification plant. Sampling of trace metals in gasifier product gas streams has been carried out occasionally [e.g. 11], but more extensive data are available on the analysis of the solid process products [e.g. 14]. Some of these data have been summarised in Figure 5. These data show that, in agreement with the current thermodynamic study, there is a wide range of behaviour of different trace elements in gasification gases, however, many elements show similar removal trends. For example, in every system Co, Cr and Cu show high removal rates with the solid products collected as bottom product/char/ash and primary cyclone (if present), whilst Cd, Hg, Pb, Se and Sn show significantly lower removal rates by this route (in line with the thermodynamic predictions summarised in Table 4).

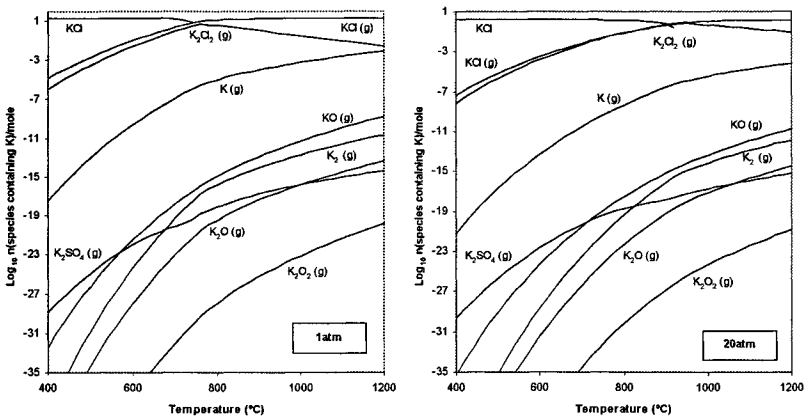


Figure 2. Effect of Pressure on Equilibrium Diagram for Potassium in ABGC Gas.

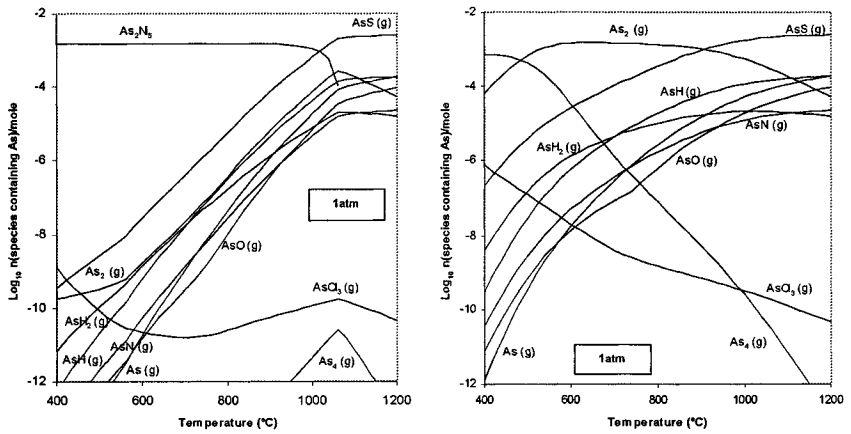


Figure 3. Effect of Nickel on Equilibrium Diagram for Arsenic in ABGC Gas

There are some data for the removal of alkali, trace metals and chlorine species in gasification systems incorporating hot gas filters [11,14-20]. These data are not comprehensive and as each gasification system has used different filtering temperatures, it is difficult to separate process differences from differences arising from the use of different filter temperatures. In addition, many of these data sets show significant errors in the mass balance closures, so their interpretation has to be approached with caution. For example, none of these data sets include a factor for the loss of alkali/trace metals by condensation/deposition on to hot gas path components. This route of losing such species will significantly reduce the levels measured in the gas stream and will be particularly significant in smaller scale plants, where such detailed measurements have usually been carried out (due to the higher ratio of internal plant surface area to gas flow rate). In many cases (e.g. for alkali metals, Zn, etc.), the intended route of removal is by condensation/reaction with the fine particles present in the gas stream followed by particle removal by the hot gas filter, but the coldest component in this hot gas path will be the heat exchanger that cools the gases prior to entry into the hot gas filter.

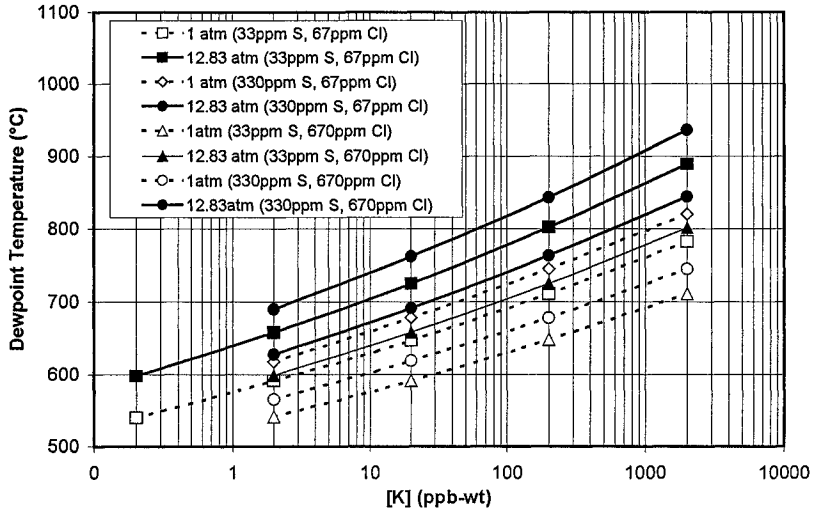


Figure 4. Dependence of K_2SO_4 dewpoint on gas pressure, S, Cl and K levels

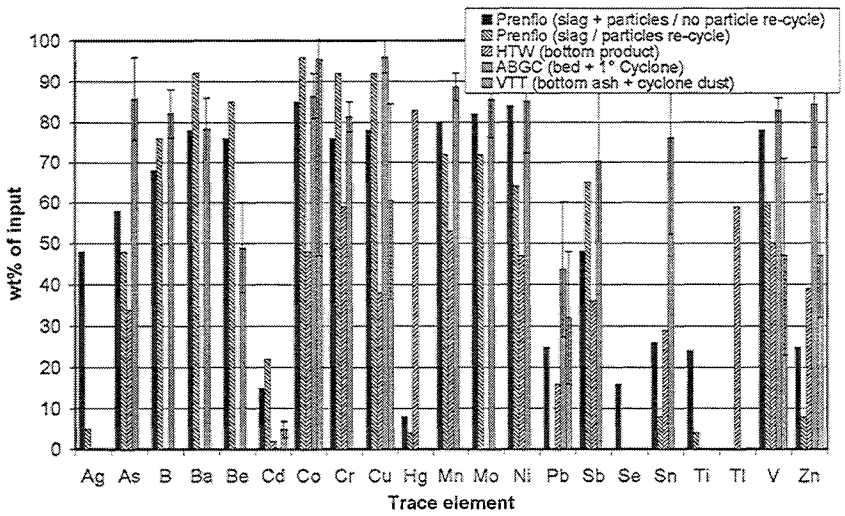


Figure 5. Distribution of Trace Elements Recovered in Bottom Product/Slag and First Cyclones in Five Gasification Systems [data from 11,14-16]

The presence of 'trace' metals in heat exchanger deposits at levels of several wt% has been frequently observed during component examinations and assessments (but only occasionally reported [e.g. 6]). The large internal surfaces of the filter unit itself provide another potential sink for alkali/trace metal removal, especially if it is cooler than the gas stream. In a pressurised air blown fluidised bed gasifier pilot plant [11], deposits of the more volatile 'trace' metals at levels of several wt% were observed on the surfaces of pipes on the 'clean' side of the filter unit (several metres upstream from the location of the trace metal sampling

system). In addition, a reduction in sulphur and chlorine species has been noted across hot gas filter units, presumably as a result of reactions with the filter cake formed on the dirty side of the filter units.

The information available for alkali and trace metal species all show that lowering the filter temperature reduces the amount of vapour phase species present in the remaining fuel gas stream (and enriches the filter fines in these elements) [e.g. 9,11], in agreement with the trends indicated in Table 3. Unfortunately, filter operating temperatures can not simply be lowered to the levels needed to remove most of these vapour species, as the lower limits for filter operation are dictated by other gasification processes parameters: e.g. tar compounds, if formed, need to be kept in the vapour phase to avoid blinding of the filters. The available data are much more comprehensive for alkali species (on which much work has been targeted, despite the importance of other elements, e.g. Pb, which are present at similar, if not higher, levels in gasification fuel gas streams and are also important in determining gas turbine component lives) [11,17-19]. In work carried out at VTT [16], the most significant levels of elements found in the fuel gas were for Cd, Pb and Zn. The levels of several trace metals (e.g. Pb) and alkalis (e.g. Na, K) reported in these studies are higher than those currently acceptable for gas turbines, and in some cases it is likely that the true values of vapour phases species in the gasifier product gases are higher still [11].

Summary

Large amount of data have been gathered on coal/biomass fuel compositions and gas compositions in gasification plant, and an extensive thermodynamic modelling programme has been carried out. Much of this work has been targeted at investigating the fate of trace and alkali metal species that can pass from the fuel(s) through the gasification systems to the gas turbine, determining likely routes for the removal/loss of these elements and their sensitivity to process parameters. The main points arising from this work are summarised as follows:

- fuel composition: on a mass comparison basis, the critical contaminants species (S, Cl, alkalis and trace metals) of many biomasses are similar or lower than coal – notable exceptions are K and Cl in straw; P, Cd, Pb and Zn in wood (as well as Ba, Cr, Cu, Mn); V and Zn in sewage sludge (as well as Cr, Cu, Mn, Hg)
- fuel gas compositions vary significantly between gasification systems at the trace contaminant level (as well as the frequently report bulk gas composition level)
- most trace and alkali metals are more volatile in gasification systems than in combustion systems – the same classification of volatility as for combustion gases is not applicable (different species are volatile)
- S and Cl levels (both absolute and relative), as well as operating pressure and gasification process can influence the volatility of trace and alkali metal species
- potentially damaging levels of Pb, Zn, Cd and Sn (and V in some systems) can all pass through the fuel gas path to the gas turbine, as well as alkali metals (Hg, B, Sb and Se can also pass through the gas turbine)
- the high levels of trace metals present in gasifier product gases can be reduced by use of low filter operating temperatures (e.g. 250-450°C dependent on gasification systems)

Acknowledgements
Funding has been provided by UK Department of Trade and Industry (Cleaner Coal Project 109) and European Coal and Steel Community programme (contract 7220-PR/053).

References

[1] A.V. Bridgwater, 'Biomass gasification for power generation', Fuel, Vol 74 No 5 (1995) pp631-653

[2] 'Gas turbines in advanced co-fired energy systems', ECSC Project 7220-PR/053

[3] N.J. Simms, J.R. Nicholls and J.E. Oakey, 'Materials Performance in Solid Fuel Gasification Systems', Materials Science Forum Vols 369-372 (2001) pp947-954

[4] T. Takematsu and C.W. Maude, 'Coal Gasification for IGCC Power Generation', IEACR/37, IEA Coal Research, London, UK (1991)

[5] J. van Liere, 'Present Status of Advanced Coal-fired Power Plants', Materials at High Temperatures, 14 (2/3), (1997) pp7-12

[6] W.T. Bakker, 'Effect of Gasifier Environment on Materials Performance', Materials at High Temperature, 11 (1-4), (1993), pp81-89

[7] J.E. Oakey and N.J. Simms, 'Materials Requirements for Advanced Coal-fired Power Generation Technologies', Materials for Advanced Power Plant 1998, J Lecomte-Beckers et al Eds, (Forschungszentrum Julich GmbH, Germany, 1998) pp. 651-662

[8] "Co-gasification of Coal/Biomass and Coal/Waste Mixtures", Final Report EC APAS Contract COAL-CT92-0001, University of Suttgart, Germany (1995)

[9] S.C. Mitchell, 'Hot gas clean-up of sulphur, nitrogen, minor and trace elements', IEA Coal Research, UK (1998)

[10] N.J Simms, F. Bregani, W.M.M. Huijbregts, E. Kokmeijer and J.E. Oakey, 'Coal Gasification for Power Generation: Materials Studies', Materials for Advanced Power Plant 1998, J Lecomte-Beckers et al Eds, (Forschungszentrum Julich GmbH, Germany 1998) pp. 663-678

[11] G.P. Reed, 'Control of Trace Elements in Gasification', Ph.D. Thesis, Imperial College, London, 2000

[12] F. Frandsen, K. Dam-Johansen and P. Rasmassen, 'Trace Elements from Combustion and Gasification of Coal – an Equilibrium Approach', Prog. Energy Combustion Sci., Vol. 20, pp115-138, 1994

[13] I.R. Fantom, 'An Assessment of Trace Element Concentrations in the British Coal Topping Cycle', Power Generation Report No. 121, CRE, British Coal, 1991

[14] L.B. Clarke and L.L. Sloss, 'Trace elements – emissions from coal combustion and gasification', IEACR/49, IEA Coal Research, London, 1992

[15] 4th International Conference on Gas Cleaning at High Temperatures, Karlsruhe, Germany, Sept. 1999

[16] M. Nieminen et al., 'Raskasmetallien käyttäytyminen turpeen ja kivihiilen leijukerros-kaasutuksessa'. LIEKKI-Combustion Research Program. Project report (1991). 33 p.

[17] E. Kurkela et al., 'Pressurized fluidized-bed gasification experiments with biomass, peat and coal at VTT in 1991-1994. Part 3. Gasification of Danish wheat straw and coal'. VTT Publication 291, (1996), 41 p. + app. 5 p.

[18] E. Kurkela et al., 'Pressurized fluidized-bed gasification experiments with wood, peat and coal at VTT in 1991-1992. Part 1. Test facilities and gasification experiments with sawdust'. VTT Publication 161, (1993), 55 p. + app. 2 p.

[19] E. Kurkela et al., 'Pressurized fluidized-bed gasification experiments with wood, peat and coal at VTT in 1991-1994. Part 2. Experiences from peat and coal gasification and hot gas filtration'. VTT Publication 249, (1995), 58 p. + app. 10 p.

[20] 'Integrated hot fuel gas cleaning for advanced gasification combined cycle processes'. LIEKKI- Combustion and Gasification Research Programme. LIEKKI- vuosikirjat 1996, projekti: 410.

MATERIALS FOR GASIFIER HEAT EXCHANGERS

P Kilgallon, N J Simms, J F Norton and, J E Oakey

Power Generation Technology Centre, Cranfield University, Cranfield, Beds MK43 0AL, UK

Abstract

Gasification systems were originally developed to be fired on coal, but there is now interest in co-firing coal with waste or biomass or using low-grade coals and heavy fuel oils in order to reduce environmental impact and fuel costs. All gasification technologies require a heat exchanger between the gasifier and the gas cleaning system. However, gasifier hot gas path environments are potentially very aggressive for materials both during plant operation and downtime periods. The potential corrosive effects of deposits formed on coal-fired and co-fired gasifier heat exchangers in ABGC and IGCC systems have been assessed. Data on the formation of deposits on gasifier heat exchangers have been gathered and a literature survey of downtime corrosion testing relating to gasifier heat exchangers carried out. Laboratory studies have been carried out to investigate the potential response of current and candidate gasifier heat exchanger materials (such as Alloy 800 and Sanicro 28) to such deposits. Electrochemical tests in aqueous solutions are being used to give a ranking of the materials in typical environments anticipated for ABGC and IGCC heat exchangers. A modified EPRI downtime corrosion test has been employed which involves exposing candidate materials covered with a simulated deposit to a humid atmosphere. Preliminary results from baseline tests are given. This work is leading towards the identification of combinations of fuels, operating conditions and materials that could produce rapid heat exchanger failures due to interactions with the deposits formed during operation.

Keywords: Gasifier, heat exchanger, downtime corrosion (DTC), deposits

Introduction

A wide variety of gasification systems continue to be developed around the world, including many Integrated Gasification Combined Cycles (IGCCs) and the UK developed Air Blown Gasification Cycle (ABGC) systems. Originally, these systems were developed to be fired on various grades of coal, but there is now interest in using a more diverse range of solid fuels (e.g. co-firing coal with waste or biomass, using low grade coals and heavy fuel oils) in order to reduce environmental impact and fuel costs. All gasification technologies require a heat exchanger (often called either a syngas cooler or fuel gas cooler) between the gasifier and the gas cleaning system. The function of this heat exchanger varies depending on the type of gasifier, gas cleaning requirements (e.g. hot dry cleaning or wet scrubbing) and steam cycle needs. However, gasifier hot gas path environments are potentially very aggressive for materials both during plant operation and off-line periods. This has the effect of imposing a temperature window for the safe operation of these heat exchangers (with current materials restricting their use to modest steam conditions and preventing their use as superheaters with commercially viable lives). Thus, in different gasification systems evaporators are used to produce saturated steam at 10 MPa/320 °C with metal temperatures of 320-400 °C depending on the syngas temperature [1]. However, there is a drive towards raising evaporator steam conditions to 18 MPa/350 °C, with corresponding metal temperatures of 380-450 °C. Under these steam conditions, the use of highly alloyed materials such as Alloy 800 (Fe-32Ni-20Cr) or Sanicro 28 (Fe-31Ni-27Cr-3Mo) will be required to give economically viable heat exchanger lives in gasifier hot gas paths [2]. However, some gasification cycles would be more efficient (and viable) if at least some superheating could be carried out by a heat exchanger in this location in the hot gas path: this would involve steam at temperatures of 500-550 °C with corresponding metal temperatures of 550-600 °C [1]. Both water tube and

smoke tube heat exchanger design are reported in the literature for gasifier heat exchangers: these radically diverse types of designs will have dissimilar characteristics in terms of deposit formation, due to the different gas flows around/through them. Significant differences in the hot gas path environment exist between the various gasification systems and with the use of different fuels, but unfortunately these simply have the effect of changing the balance between different potential degradation modes arising. In this paper deposit formation on gasifier hot gas path components and downtime corrosion testing are reviewed and initial results are given from a new study of dewpoint and downtime corrosion phenomena in gasifier heat exchangers. The overall aim of the work is to assess the potential corrosive effects of deposits formed on coal-fired and co-fired gasifier fuel-gas/syngas heat exchangers in ABGC and IGCC systems. This includes assessing the effects of such deposits on downtime corrosion (including the effects of potential preventative measures) and synergistic interactions. These activities will lead to the identification of combinations of fuels, operating conditions and materials that could produce rapid heat exchanger failures due to interactions with the deposits formed during gasification plant operation.

Degradation Modes

The performance of materials in various simulated and real coal-gasification atmospheres has been investigated by research groups in the US, Japan and Europe for more than 25 years [1-20]. The initial generic studies investigated the performance of materials in a range of highly reducing atmospheres with varying levels of sulphidation at high temperatures. Later studies have tended to concentrate on higher alloyed materials and/or lower exposure temperatures. Following plant experience, more recent studies have been targeted at increasingly realistic exposure simulations to match the degradation morphologies observed in practice [e.g.13].

Several potential degradation processes have been established during the studies carried out in these types of for these environments [1-20], including:

- elevated temperature gas phase induced corrosion: this includes oxidation, sulphidation, carburisation/metal dusting and chlorination;
- corrosion induced by surface deposits either as particles from the gasifier or by species condensing onto those particles or directly onto the component surfaces;
- dewpoint corrosion: induced by high temperature deposits absorbing moisture during part-load plant operation, gaseous species (e.g. HCl, H_2S, etc.) reacting with condensing water during part-load operation (e.g. forming HCl and polythionic acids) or deposits forming on cooler gas path surfaces;
- downtime corrosion: induced by high temperature deposits becoming damp during plant shut-down, gaseous species (e.g. HCl, H_2S, etc.) reacting with condensed water during plant shut-down (e.g. forming HCl and polythionic acids) or hygroscopic deposits being exposed to damp air during plant shut-downs (e.g. during the course of maintenance operations);
- interaction of any of the above degradation modes with mechanical factors, e.g. creep or fatigue, to produce synergistic degradation, e.g. creep-corrosion or corrosion-fatigue;
- spallation of corrosion products: important on the clean side of the filter unit from where spalled scale may enter the gas turbine and cause erosion damage.

In practice, several materials degradation modes will occur on each component in the hot gas path. In any gasification system, different combinations of degradation mode will be found on components along the hot gas path due to variations in operating temperature and local plant

environment (deposition, local gas composition, i.e. the extent of gas clean-up, gas temperature at that point in the system, component temperature, etc.).

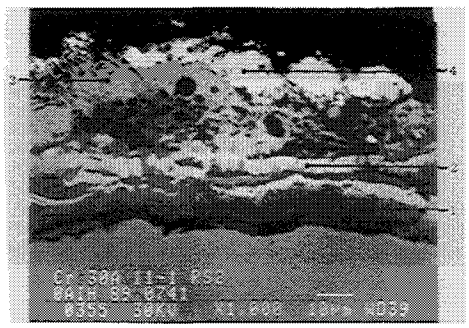
Most studies of gasifier heat exchangers materials have targeted elevated temperature gas phase induced corrosion with increasing levels of realism allowing the successful development of predictive models for sulphidation/oxidation [e.g. 10,19-20]. As a result, heat exchanger metal temperatures have been selected to give viable lives under such conditions. However, pilot plant tests have shown that deposit covered components can suffer rapid failures due to both dewpoint and downtime corrosion. Thus, it is important to avoid (or at least minimise) damage by these degradation modes in gasifier heat exchangers.

Deposit Formation on Gasifier Hot Gas Path Components

Limited data have been reported on the compositions of deposits found on gasifier heat exchangers. For the ABGC system, a DTI Coal Report [10] gave a detailed analysis (Table 1) for a deposit formed on cooled probes upstream of a hot gas filter unit (i.e. in the location of a gasifier heat exchanger in an ABGC system). Later work on this spouted fluidised bed gasification plant showed that the deposits that formed could also contain significant levels of As, Cd and Se. Literature reports of the performance of materials in heat exchangers and probes in other gasification systems also indicate the presence of significant levels of Pb, As, Se, Ge, Pb, Sb [11]. Again, significant levels (up to 80wt%) of these elements were observed (Figure 1), even though these would only have been present in the fuel gas stream at trace levels (<100 ppm).

Table 1. ABGC Deposit Analysis for Cooled Probe Upstream of Filter Unit [10]

	Crystalline phases (by XRD)
Major	SiO_2, CaO, CaS, $CaCO_3$, $CaSO_4$, $CaSO_4.2H_2O$, NH_4Cl
Minor	$(Ca, Na)(Si, Al)_4O_8$, FeS, PbS, ZnS, $PbSO_3$, $ZnSO_4$
	Elements (by EDX)
Major	C, Al, Si, Ca, S, O
Minor	Pb, Zn



Element	**Concentration**			
	Area 1	**Area 2**	**Area 3**	**Area 4**
Se				4.3
Si				1.5
S	10.8	1.6	0.2	12.9
Ti	0.4			
Cr	69.0	4.4	0.9	0.3
Fe	6.1	2.7	7.7	0.7
Ni	2.9	31.4	30.3	
Ge	2.0	2.6	8.3	
As	0.9	8.1	43.2	
Mo	5.0			
Pb	3.0			80.4
Sb		49.7	9.4	

Figure 1. Condensed Trace Element Deposits on Heat Exchanger Tube from an Entrained Slagging Coal Gasifier with a Metal Temperature of ~425 °C [11].

Downtime Corrosion (DTC) Testing

Tests to investigate downtime corrosion of materials in coal gasification environments have utilised different simulations of gasifier heat exchanger deposits (Table 2). These compositions have been produced by EPRI [12] and KEMA [14], from their experience of entrained gasification processes, and British Coal, from their experience of a fluidised bed partial gasifier [10,13]. Other research laboratories have used these types of deposit composition in various downtime corrosion test programmes [e.g.15]

Previous work

Research of downtime corrosion (DTC) testing in gasifier systems has been investigated using similar methods. Samples have usually been exposed to simulated gasifier environments at 550-600 °C for up to 250 hours followed by exposure to a moisture-saturated atmosphere at 25-70 °C for up to 250 hours [12-13,16-18]. The 'EPRI' test [12] has become the basis for most investigations and includes in the above method the coating (and subsequent re-coating) of the specimens with a simulated deposit (Table 2) during the test. Modifications to the test have been made by altering the composition of the simulated deposits (Table 2) to produce more realistic and/or aggressive simulated deposits by adding sulphide [10] or using $FeCl_3$ instead of $FeCl_2$ [15,18] or using char instead of slag (for ABGC systems). The $FeCl_3$ containing deposit was added prior to the high temperature cycle and so could be reduced to $FeCl_2$ but initially the deposit would be higher in chloride than the typical EPRI deposit. NPL [17] modified the test by withdrawing the samples to a cooler region of the furnace so a condensate (pH 1-3) would form on the samples. In the EPRI test dewpoint corrosion was avoided by inert gas flushing of the furnace during heating and cooling.

In terms of materials it is difficult to compare results as there is little overlap between studies and most test parameters vary. Some studies have indicated the effects of certain alloying elements [15-16,18] but work that has used a comprehensive number of materials can give the best indication of the effect of alloy composition. Simms et al [10] found that the ranking of the materials varied slightly between tests, but in general the trend in behaviour followed the ranking given by the pitting resistance equivalence number.

Table 2. Deposit Compositions used in Literature Downtime Corrosion Testing.

Component	Composition (wt%)								
	EPRI [12]		KEMA [1]	NPL [17]		Simms et al [10]			Norton et al [15,18]
	1	2	[13]	1	2	1	2	3	
Slag	100	90	Yes	-	-	-	-	-	80
Char	-	-	-	100	90	100	90	90	-
Carbon	-	-	-	-	-	-	-	-	10
NaCl	-	3.74	37.4	-	3.74	-	3.74	2	5
KCl	-	-	-	-	-	-	-	1	-
PbS	-	-	-	-	-	-	-	4	-
ZnS	-	-	-	-	-	-	-	1	-
$FeCl_2$	-	6.26	62.6	-	6.26	-	6.26	2	-
$FeCl_3$	-	-	-	-	-	-	-	-	5

[1] Ratio of fly ash to eutectic salt mix not specified

Where investigated the least aggressive deposit was that consisting of char or slag alone [12,10]. The chloride/char deposit caused more attack in most studies (although one study

found the addition of chloride to have little effect [13]) but the chloride/sulphide/char deposit could be more aggressive [10]. A synergistic effect has been suggested for the combination of high and low temperature exposure cycles when compared to either cycle alone [10].

There have been few electrochemical studies of gasifier heat exchanger candidate materials in relation to downtime corrosion. One study [16] carried out an electrochemical evaluation to assess the passive behaviour of samples with and without scale. The sample scales were formed in a simulated gasifier environment at 600 °C for 100 hours and were anodically polarised in 0.5 M NaCl solution at room temperature. It was found that the scaled samples did not show passive behaviour whilst the unscaled samples did. Tests were also carried out in 0.1 M $K_2S_4O_6$ to investigate the influence of polythionic acid formation on downtime corrosion. It was concluded that the presence of polythionic acid could cause downtime corrosion in chloride free environments.

In general, electrochemical studies in aqueous chloride environments have studied stainless steels intended for use in chloride containing environments. For testing involving the gasifier heat exchanger materials, the test parameters have not been relevant to downtime testing and generally very simple test environments have been used. Overall, the data for all stainless steels do show trends that can indicate the effects of environmental conditions. The pitting resistance of stainless steels in aqueous environments generally reduces with increasing chloride concentration, decreasing pH and increasing temperature [19,20].

Materials

The nominal composition of the materials used in the work are given in Table 3 together with the corresponding pitting resistance equivalent number (PRENW (including tungsten)) as given by:

$$PRENW = \%Cr + 3.3(\%Mo + 0.5\%W) + 16\%N$$

It has been established that the pitting behaviour of stainless steels can be broadly related to composition using empirical relationships such as PREN. Crevice corrosion is influenced by many factors and therefore PREN is generally not so useful for prediction of this type of behaviour.

Table 3. Compositions of Alloys

Alloy	Nominal Composition (wt %)					PRENW
	Cr	Ni	Fe	Mo	Others	
Alloy 800H	21	32	Bal		0.75Mn	21.0
AISI 316L	16.8	11.2	Bal	2.3	1.5Mn	24.0
AISI 310	25	20	Bal		1.5Mn 1.5Si	25.0
Haynes 160	28	Bal.	3.5	1.0	0.5Mn 30Co 2.7Si 1W	29.7
Haynes 556	21.6	19.9	Bal.	2.8	18Co 2.4W 0.2N	38.0
Sanicro 28	27	31	Bal.	3.5	2Mn	38.6
IN 625	21.5	Bal.	2.5	9.0	0.5 Mn	51.2

Experimental

DTC testing was carried out using a modified EPRI test. Specimens were coated with a deposit consisting of 6.26 % $FeCl_2$, 3.74 % NaCl and 90 % char. The composition (wt %) of

the char was 56.48 %C, 0.7 %H, 0.46 %N, 0.36 %S, 0.65 %Cl and 41.35 %ash. Specimens were exposed to water saturated air at 30 °C for 25 hour cycles initially. After exposure the deposit was removed and the specimens cleaned and examined before repeating the test. Longer cycles were also used to investigate whether the more resistant materials had an initiation period greater than 25 hours. Damage was assessed by visual inspection, weight loss and depth of attack (assessed using microscope technique) [21].

Weighing deposit samples in open glass containers before and after exposure gave the moisture content of the deposit after a continuous 75 hour exposure to the water-saturated environment. The average moisture content was found to be 0.63 g per g of dry deposit which equates to a chloride concentration of ~1 M in the deposit in the DTC test and a pH of ~3 (from 1 M chloride solution made from 6.26:3.74 $FeCl_2$/NaCl ratio but no char).

Electrochemical testing using a triple electrode system in naturally aerated 1 M NaCl at 30 °C has been used to measure the pitting potential, repassivation potential and hysteresis of the candidate materials. The test method is based upon ASTM G61 [22] with modifications for test solution and temperature. Electrochemical tests for pitting corrosion usually measure the pitting potential or the repassivation potential that either indicates the kinetics of nucleation or the kinetics of repassivation. Therefore neither potential relates to an incubation period or the propagation kinetics once initiation has occurred, so the DCT testing is required to gain this information. Nevertheless, these measurements provide a useful method for ranking the susceptibility of a set of materials in a given environment and to establish the aggressive species. Figure 2 shows a schematic representation of an anodic polarisation curve where the sample potential is increased and the resulting current measured. The flat region of fixed low current flow is where the material is passive (no significant corrosion), at the pitting potential (E_{np}) passivity is lost and with potential rise the current increases. If the polarisation is then reversed, the point at which the line crosses the passive region is the repassivation potential (E_{cp}). E_{np}, E_{cp} and the hysteresis in the loop created are a measure of pitting resistance and to some degree crevice resistance.

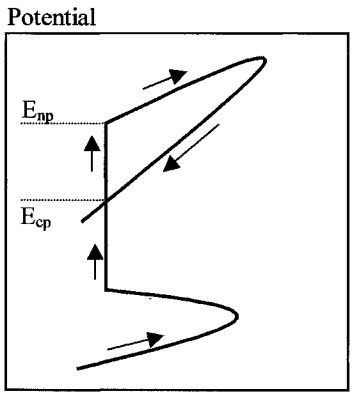


Figure 2. Schematic Representation of Anodic Polarisation Curves Showing Pitting (E_{np}) and Repassivation Potential (E_{cp})

Results and Discussion

Downtime Corrosion Tests

As the type and severity of attack on the materials tested varied significantly (Figure 3), a number of measurements have been used to quantify the degree of attack. In Table 4 the type of attack and depth of attack is shown and the materials are also ranked (Note AISI 310 had many more pits than Haynes 160 and Sanicro 28). Only Alloy 800H and AISI 316 were severely attacked even after the first 25 hours as shown in Figure 3. The other materials showed little or no attack and no effect of increasing the test cycle time from 25 to 75 hours was evident. The degree of attack on AISI 316 and Alloy 800H was so great that weight loss has been used as a measure as shown in Figure 4. Alloy 800H was very severely attacked almost all over the exposed surface. A feature of the attack was that over intense areas of attack the deposit formed a hard crust.

Table 4. DTC Test Results in Terms of Degradation Type and (Depth of Attack (μm))

Alloy	Downtime Corrosion Exposure Time (hours)						PRENW	Rank
	25	50	75	100	145 [1]	175 [2]		
Alloy 800H	CI	CI (235)	CI (>400)	CI (>400)	-	CI (>400)	21.0	5
AISI 316L	C	C (30)	CP (138)	CP (255)	-	CP (278)	24.0	4
Haynes 160	P	P (46)	P (45)	-	P (46)	-	29.7	3
AISI 310	P	P (13)	P (13)	-	P (14)	-	25.0	2
Sanicro 28		P (10)	P (14)	-	P (15)	-	38.6	
Haynes 556				-		-	38.0	1
IN 625				-		-	51.2	

(P = pitting, C = crevice and I = intergranular attack), [1] after 70 hour cycle, [2] after 75 hour cycle.

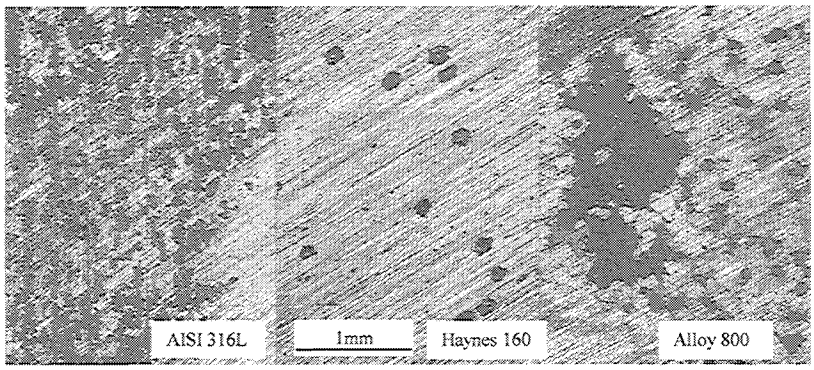


Figure 3. Corrosion Damage on AISI 316L, Haynes 160 and Alloy 800 after 25 Hours Exposure to DTC Test.

The attack on the AISI 316 changed from an under-deposit/crevice type observed for periods of up to 50 hours to predominately pitting after longer exposures. This is apparent in Figure 4 where the weight loss curve after 50 hours becomes flatter, this being associated with the very local increase in size and depth of pits, which does not show up well in weight loss data.

The ranking of the overall resistance of the materials to the DTC test matches the PRENW ranking well (Table 4).

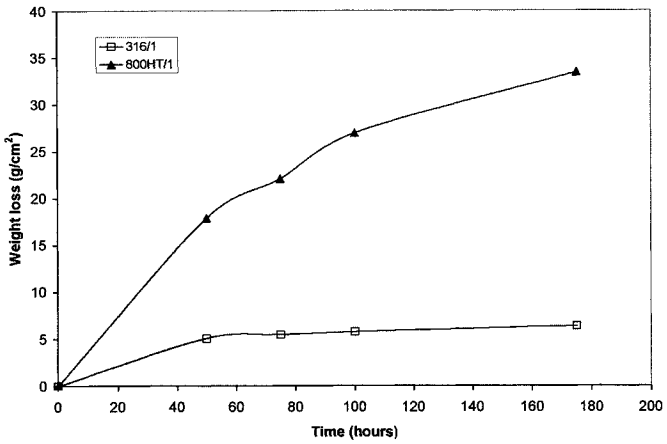


Figure 4. DTC Testing Weight Loss Data for Alloy 800 and AISI 316.

Electrochemistry

Electrochemical tests have been carried out in 1M NaCl at 30 °C to produce baseline data; further work is continuing using more complex solutions. From this data the materials can be ranked in terms of pitting potential, repassivation potential and the hysteresis in the reverse sweep (i.e. difference in E_{np} and E_{cp}), mean values are given in Table 5. The ranking of materials in this environment is generally the same for all three electrochemical measures and also matches the ranking found for the DTC test with the exception that IN 625 could be separated from Haynes 556 as the best performer. Figure 5 shows typical potential versus current density data obtained for IN 625 and Alloy 800. The IN 625 has a high pitting potential and almost no hysteresis in the repassivation loop. In contrast Alloy 800 has a much lower pitting potential and large hysteresis loop.

Table 5. Mean Pitting Potential, Repassivation Potential and Hysteresis in Reverse Polarisation Results for Materials in 1 M NaCl at 30 °C.

Alloy	E_{np} (mV(SCE))	E_{cp}(mV(SCE))	E_{cp}- E_{cp} (mV)	Rank
Alloy 800H	107	-200	307	6
AISI 316L	158	-100	258	5
AISI 310	175	-33	208	4
Haynes 160	146	15	131	3
Sanicro 28	-	-	-	-
Haynes 556	157	67	90	2
IN 625	771	742	29	1

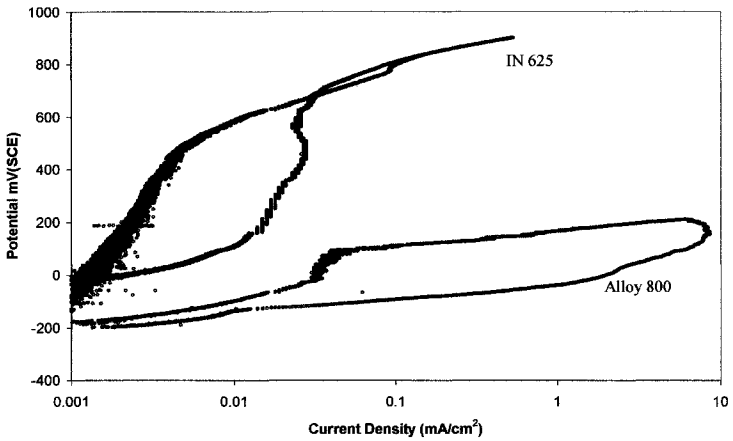


Figure 5. Typical Potential Versus Current Density Plot for IN 625 and Alloy 800 in 1 M NaCl at 30 °C

Conclusions

1. Very little data exists in the literature about the compositions of the various different deposits that can form on gasifier heat exchangers.
2. A 'standard' test exists has been modified to more accurately simulate real deposits observed in service.
3. Alloy ranking given by DTC testing and electrochemical studies have shown a strong correlation with that predicted by PRENW.
4. Alloy 800 and AISI 316 showed very poor corrosion resistance in the DTC test used.
5. IN625 demonstrated the greatest resistance to the electrochemistry test.

Acknowledgements

Funding for this work has been provided by the UK Department of Trade & Industry Cleaner Coal Programme.

References

[1] Stringer J and Wright IG (1995) – 'Current limitations of high-temperature alloys in practical applications' Oxidation of Metals 44 (1/2) pp265-308.
[2] Bakker WT (1995) – 'Mixed oxidant corrosion in non-equilibrium syngas at 540 °C' EPRI Report TR-104228, March 1995.
[3] D M Lloyd (1989) in Research and Development of High Temperature Materials for Industry, ed. E Bullock, pp339-359, Elsevier.
[4] J Stringer (1984) in High Temperature Materials Corrosion in Coal Gasification Atmospheres, ed. J F Norton, Elsevier.
[5] F Gesmundo, in High Temperature Materials for Power Engineering 1990, eds. E Bachelet et al, pp67-90, Kluwer, (1990).

[6] F Gesmundo, Advanced Materials for Power Engineering Components: The Corrosion of Metallic Materials in Coal Gasification Atmospheres - Analysis of Data from COST 501 (Round 1) Gasification Subgroup. EUCO/MCS/08/1991 (1991).
[7] WT Bakker, in Proceedings of Seventh EPRI Annual Conference on Coal Gasification, EPRI, Palo Alto, California, USA (1987).
[8] Proc. First International Workshop on Materials for Coal Gasification Power Plant, Petten, The Netherlands, June, 1993, in Materials for Coal Gasification Power Plant, Special Issue of Materials at High Temperature, 11 (1993).
[9] Erosion/Corrosion of Advanced Materials for Coal-Fired Combined Cycle Power Generation, Final and Summary Reports on JOUF-0022 (1994).
[10] Simms NJ, Lowe TM, Scott INS and Oakey JE (1997) – 'Materials for gasifier hot gas path components in advanced combined cycle power plants' Final Report No R106 UK Cleaner Coal Technology Programme 1997.
[11] Bakker WT (1993) – 'Effect of gasifier environment on materials performance' Materials at High Temperature 11 (1-4) pp81-89
[12] Perkins RA, Marsh DL and Sarosiek AM (1988) – 'Downtime corrosion in syngas coolers of entrained slagging gasifiers' EPRI report AP-5996.
[13] Simms NJ, Bregani F, Huijbregts WMM, Kokmeijer E and Oakey JE – 'Coal gasification for power generation: materials studies' In Proceedings of the 6th Liege Conference on Materials for Advanced Power Engineering 1988, Part II. Eds. Lecomte-Beckers J, Schubert F and Ennis PJ, pp663-679.
[14] Huijbregts WMM, Kokmeijer E and van Zuiten HG (1993) – 'Sulphidation, down-time corrosion and corrosion-assisted cracking on high alloys materials in synthetic coal gasifier environments' Materials at High Temperature 11 pp58-64.
[15] Norton JF, Maier M and Bakker WT (1999) – 'Corrosion of heat exchanger alloys exposed to a non-equilibrated co-based sulfididizing environment at 550°C' Paper No 99069 NACE '99, San Antonio, Texas, USA. 25 (7) pp27-33.
[16] Kihara S, Nakagawa K, Ohtomo A, Kato M (1987) – 'Corrosion resistance of high-chromium steels in coal gasification atmospheres' Materials Performance 26 (6) pp 9-17
[17] Saunders SRJ, Gohil DD and Osgerby S (1997) – 'The combined effects of downtime corrosion and sulphidation on the degradation of commercial alloys' Second International Workshop on Corrosion in Advanced Power Plants, Tampa, Florida, USA, 3-5 March 1997, Materials at High Temperatures 14 (3) pp237-243
[18] Norton JF, Maier M and Bakker WT (1997) – 'Corrosion of 12% Cr alloys with varying Si contents in a simulated dry-feed entrained slagging gasifier environment' Second International Workshop on Corrosion in Advanced Power Plants, Tampa, Florida, USA, 3-5 March 1997, Materials at High Temperatures 14 (2) pp81-91.
[19] Simms NJ, Nicholls JR and Oakey JEO (2001) – 'Materials Performance in Solid Fuel Gasification Systems' Materials Science Forum, 369-372 pp947-954.
[20] John RC, Fort WC and Tait RA (1993) - Materials at High Temperature, 11 pp124-132.
[21] Oldfield JW (1987) – 'Test techniques for pitting and crevice corrosion of stainless steels and nickel-base alloys in chloride-containing environments' International Materials Reviews 32 (3).
[22] Haynes AG (1992) – 'Duplex and high alloy corrosion resisting steels' Lloyd's Register Technical Association, London.
[23] ASTM G46 – Standard Practice for 'Examination and Evaluation of Pitting Corrosion'
[24] ASTM G61 - Standard Practice for 'Conducting Cyclic Potentiodynamic Polarization Measurements for Localized Corrosion'

PERFORMANCE OF GAS TURBINE MATERIALS IN 'DIRTY FUEL' ENVIRONMENTS

N J Simms, A Encinas-Oropesa, P Kilgallon and J E Oakey

Power Generation Technology Centre, Cranfield University, Cranfield, MK43 0AL, UK

Abstract

Gas turbines are critical components in the combined cycle power systems being developed to generate electricity from solid fuels, such as coal and biomass. The use of such fuels to produce fuel gases introduces the potential for significant corrosive and erosive degradation of gas turbine blades and vanes.
Series of laboratory and burner rig tests have been carried out to investigate the performance of current and candidate gas turbine materials in environments anticipated in gas turbines fired on coal and biomass derived gases. Depending on the composition of the solid fuel(s) and their mix, these gas turbine component environments include a range of levels and pressures of SO_X and HCl gases, as well as ranges of Na, K, Pb and Zn. These fuel dependent differences in the component environments will result in significantly different deposit compositions and deposition fluxes onto the components. The candidate materials have included IN738LC and CMSX-4 with overlay MCrAlY, diffusion (Pt-Al) and thermal barrier (APS and EB-PVD) coatings. The laboratory tests have been carried out using controlled atmosphere furnaces and the deposit re-coat test method. This type of testing permits the detailed control of the corrosive environment of test samples. The burner rig tests have been carried out using a natural gas fired burner rig that allows the controlled injection of contaminants in the form of gaseous (i.e. SO_X and HCl) and liquid/vapour (i.e. Na, K, Pb, Zn). In both types of testing, data on the performance of the materials has been obtained using dimensional metrology: pre-exposure contact measurements and post-exposure measurements of features on polished cross-sections. These measurement methods allow distributions of damage data to be determined and fit in with the COST522 move towards standardised methods of data collection and presentation. In addition, the types of damage observed have been characterised using standard scanning electron microscopy/ energy dispersive X-ray analysis and optical microscopy to characterise the types of degradation observed and investigate the roles of difference contaminants in the observed hot corrosion damage to the gas turbine materials.

Keywords: gas turbines; solid fuels; hot corrosion; laboratory tests; burner rig tests

Introduction

Many of the solid fuel fired advanced power generation systems currently being developed are combined cycle systems, utilising both gas and steam turbines, based on the gasification and/or combustion of solid fuels [1,2]. These power systems were originally developed to enable coal to be used to generate electricity with greatly increased efficiency and much lower environmental emissions (specifically CO_2, SO_x, NO_x and particulates) than with conventional pulverised coal systems. It has subsequently been found that many such systems can also be co-fired with various biomasses offering the advantage of further reducing net emissions by partially using these renewable CO_2 neutral fuels. In all such combined cycle systems the performance of the gas turbine is vital to the overall plant efficiency and economic viability. However, within these systems hot corrosion and/or erosion can be life limiting for gas turbine vanes and blades, in addition to the creep and fatigue processes that limit their lives in the longer term. For new fuels to be used in gas turbines, it is necessary that these critical components are manufactured from appropriate materials and that these materials give predictable in-service performance.

The environments found within the hot gas paths of gas turbines depend on the contaminants present in the fuel and air entering the turbine, as well as the turbine operating conditions.

Industrial gas turbines have been developed to fire on a wide variety of fuels, ranging from natural gas to sour gases and heavy fuel oils. The degradation of materials in such systems has been the subject of many investigations during the past 40 years, as operating conditions have developed and/or fuels have changed, and the potential problems which many be encountered in gas and oil fired gas turbines have been well characterised [3,4]. Many similar types of materials degradation can be expected in gas turbines using solid fuel derived fuel gases, as some of the contaminant species are the same as for oil and/or gas fired systems. However, the levels of contamination are different, there are additional as well as absent species and the sources/forms of the contaminant species also differ. Fuel gases derived from solid fuels such as coal, biomass and their mixes have the potential to cause both erosion and corrosion damage to gas turbine hot gas path components. Fuel derived particles can cause either erosion damage or deposition depending on the particles' size and composition, as well as aerofoil design and operating conditions. Corrosion can result from the combined effects of gaseous species (e.g. SO_x and HCl) and deposits formed by condensation from the vapour phase (e.g. alkalis and other trace metal species) and/or particle impaction and sticking. The corrosion damage mode is highly dependent on the local component environment. Conventionally, the metal vapour species of most concern were alkalis (mainly sodium) in gas turbines fired on clean fuels (either as fuel contaminants or via the combustion air) or vanadium from heavy fuel oils. In coal fired systems, as well as significant levels of both SO_X and HCl, combustion derived gases tend to have significant levels of alkali metals (sodium and potassium), whereas gasifier derived fuel gases (when used with hot gas cleaning processes) have higher levels of heavy metals, e.g. lead and zinc [5]. Co-firing with biomass or waste fuels changes the levels of all the contaminants, e.g. for trace metals, wheat straw has higher potassium levels and sewage sludges have higher zinc levels [5]. The effects of different fuels on the levels of contaminant vapour phase species, deposition fluxes and deposit compositions (e.g. melting points) requires careful consideration for each process and fuel. Thus, fuel and air quality standards produced for gas turbines fired on more traditional fuels [e.g. 6] need to be thoroughly reviewed and revised [7,8], to take into account the significant differences with these new fuel compositions, as well as the damage rates that will be acceptable for these new power systems.

This paper reports some of the results obtained in laboratory and burner rig hot corrosion tests that form the latest parts of an on-going systematic investigation of the effect of realistic levels of contaminants and other exposure parameters on the corrosion of candidate gas turbine materials for use in solid fuel fired systems. Initially these studies were targeted at conditions anticipated in gas turbines in coal combustion systems [9,10], but more recent and on-going tests have targeted gas turbines fired on fuel gases derived from gasified coal and biomass [12,13]. One of the aims of this test work is generate materials performance data suitable for inclusion in a database and for the development of empirically based predictive models of the corrosive degradation of gas turbine materials in 'dirty' gas conditions [9-13]. To generate such data it is necessary to carry out dimensional metrology on the test samples before and after their exposure to quantify the materials degradation in terms of accurate and statistically useful metal losses [9-14]. This approach to dimensional metrology is now becoming more widely adopted and has been accepted as the approach to use in the current European COST522 activities. It also formed part of the basis for the EU sponsored TESTCORR activity aimed at developing guidelines for high temperature corrosion testing [15].

Experimental Methods

Laboratory

Four series of laboratory tests have been carried out using the well established 'deposit replenishment' technique [9-13,16] to systematically investigate the effects of different 'deposit' compositions and gas partial pressures on the corrosion behaviour of gas turbine materials (Tables 1 and 2). The tests have used increasingly complex 'deposit' compositions, which have now covered mixes of Na_2SO_4 (10-90 mol%), K_2SO_4 (3-90 mol%), $ZnCl_2$ (0-55 mol%) and $PbCl_2$ (0-60 mol%), as well as wider ranges of gas partial pressures, SO_X = 20–3500 vpm, HCl = 10–4200 vpm. 'Deposition fluxes' of up to 500 $\mu g/cm^2/h$ have been used, with exposures being carried out in ceramic lined controlled atmosphere autoclaves at temperatures of 650, 700, 800 and 900°C. Exposure periods of up to 2000 hours have been used, with temperature cycling every 20 or 100 hours to replenish the surface 'deposits' (depending on the 'deposition flux' required).

The latest series of tests have been mainly targeted at effects of complex deposits with fluxes of up to ~15 $\mu g/cm^2$/hour, investigating the effects of varying potassium levels (as a result of straw type biomass additions) and the effects of introducing lead and zinc into these deposits at the lower metal temperatures (650 and 700°C). A range of base alloys and coatings have been used in these tests (e.g. Tables 3 - 5). IN738LC and RT22 coated IN738LC have been used as the reference materials throughout the all the series of tests. Throughout all these series of tests, solid cylindrical samples have been used and a common metrology method adopted (see below), in order to produce materials performance data suitable for modelling purposes [9-13].

Table 1 Exposure Conditions for Laboratory Tests

Temperature	650, 700, 800, 900°C
Exposure times	100, 200, 300, 500, 1000, 2000
Gas composition	
SO_X	20-3500 vppm
HCl	10-4200 vppm
$O_2 - CO_2 - N_2$	Balance
Deposit compositions	A – N (see Table 2)
Deposition fluxes	0.15 – 500 $\mu g/cm^2$/hour
Deposit re-coat intervals	20 or 100 hours

Table 2 Deposit Compositions

Deposit species	Deposit Identification / composition (mole %)													
	A	B	C	D	E	F	G	H	I	J	K*	L*	M	N*
Na_2SO_4	80	90	50	10	40	40	40	40	60	32	12	20	25	32
K_2SO_4	20	10	50	90	10	10	10	10	15	8	3	20	25	8
$ZnCl_2$					20	30	50				55		50	40
$PbCl_2$					30	20		50	25	60	30	60		20

* $Pb(NO_3)_2$ instead of $PbCl_2$

Table 3 Materials used in latest series of laboratory and burner rig tests

Base alloy	Corrosion resistant/ bond coating	Thermal barrier coating (application route)
IN738LC	-	-
IN738LC	RT22	-
IN738LC	Amdry 995	YPSZ (atmospheric plasma sprayed)
CMSX4	-	-
CMSX4	CN91	-
CMSX4	CN91	YPSZ (electron-beam physical vapour deposition)

Table 4 Nominal Compositions of Alloys (wt-%)

Alloy	Ni	Cr	Co	Mo	W	Ta	Nb	Al	Ti	C	Others
IN738LC	Bal	16.0	8.5	1.7	2.6	1.7	0.9	3.4	3.4	0.11	0.01 B, 0.05 Zr
CMSX-4[#]	Bal	6.5	10.0	0.6	6.0	6.0	-	5.6	1.0	-	0.1 Hf, 2.9 Re

[#] = single crystal

Table 5 Coatings

Coating	Composition	Application Route
Corrosion Resistant Coatings/Bond Coats		
RT22, CN91	Pt–Al	Electrodeposited Pt followed by over aluminising (different conditions for RT22 and CN91) and heat treatment
Amdry 995	CoCrAlY	Low pressure plasma spray
Thermal Barrier Coatings		
APS TBC	7-8% Y_2O_3 stabilised ZrO_2	Air plasma sprayed TBC on top of bond coat
EB-PVD TBC	7-8% Y_2O_3 stabilised ZrO_2	Electron beam physical vapour deposited TBC on top of bond coat

Burner Rig

A natural gas fired burner rig has been used for deposition and hot corrosion testing under continuous flux conditions. Previous test work carried has shown that realistic deposition and hot corrosion conditions can be successfully simulated in this test facility by carefully controlling the exposure conditions [9,12,13].

The fully automated burner rig, Figure 1, consists of a natural gas fired burner capable of producing combusted gas temperatures up to 1400°C, using a combustion air flow rate for up to 0.6 kg/s. For these corrosion/deposition tests, samples were exposed on probes within a test section that was designed to operate with hot internal wall faces and allows up to 24 individually controlled air-cooled probes to be exposed simultaneously. Contaminants were fed into the rig just upstream of the outer edge of the burner flame. The gaseous contaminants required, SO_2 and HCl, are supplied from individual drums of liquefied gases via pressure let-down and gas mass flow control systems. The vapour phase contaminants were supplied as a solution in water, which was fed into the test rig as a spray via an atomising nozzle.

The corrosion/deposition tests were carried out in this rig at gas temperatures of ~1180°C with vapour contaminant levels in the ranges sodium ≤300 ppb, potassium ≤ 300 ppb, lead

≤4ppm and zinc ≤900ppb, and gaseous contaminant levels of $SO_x \approx 300$ vpm, HCl ≈ 500vpm. Sample surface metal temperatures were maintained at different temperatures in the range 650-900°C. The tests have been carried out for periods of up to ~4000 hours, but mostly up to ~1000 hours, with intermediate shut-downs to retrieve/exchange shorter exposure time samples. In all these tests hollow cylindrical samples have been used (to permit sample cooling) and a common metrology method adopted (see below). The same range of materials as in the laboratory tests were included in these tests.

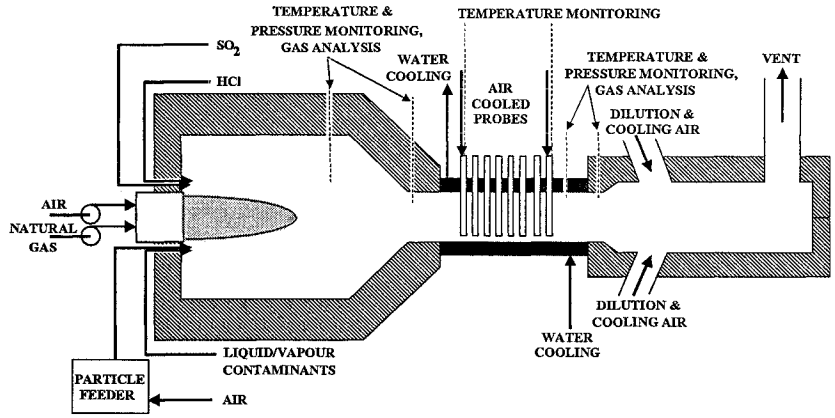


Figure 1 Cranfield University Burner Rig

Metrology

The aim of the sample metrology and analysis process is to produce a set of metal loss data for each sample exposed in the laboratory and burner rig tests. The development and application of this metrology method has been reported previously [e.g. 10-13]. The methodology is based on the accurate measurement of sample dimensions before and after exposure. For the cylindrical samples used in both the laboratory and burner tests, prior to exposure the sample dimensions were measured at particular orientations around a central plane using an accurately calibrated micrometer (±2μm). After exposure, polished cross-sections were prepared close to and parallel to the pre-exposure measurement plane. The polished cross-sections were measured using an optical microscope/image analysis system with an accurately calibrated x-y stage (±2μm). The post-exposure measurements included the position of the metal surface and other features of the corrosive degradation, e.g. internal corrosion in type I corrosion [12]. These methods were selected to allow for semi-automation so that large numbers of data points (i.e. > 24 for laboratory samples, >50 for burner rig samples and >100 for plant samples) could be collected and statistically analysed, before being used in model development or validation. During the post exposure metrology process, optical and SEM/EDX checks were made to determine which corrosion mechanism was operating to ensure that consistent corrosion models were developed.

Results and Discussions

Laboratory Tests

The results obtained from these tests show a complex interaction of the different exposure variables. It has been found that the deposition fluxes, deposit compositions and SO_X partial pressures dominate the corrosion behaviour of the materials, with less effect of HCl partial

pressures. The effect of the number, and frequency, of the thermal cycles that are an intrinsic part of this type of corrosion testing was limited to the number of initiation sites of the corrosive damage after short exposure times, and had no significant effect on the performances of the materials in the longer term.

Visual Appearance
After exposure, samples with metallic surfaces (either base alloy or coating) were dark and showed evidence of adherent deposit/scale formation (as expected). CMSX-4 samples often showed considerable spallation of deposit/scale during the thermal cycles carried out to replenish the deposit. Samples with TBC coated surfaces showed little external evidence of corrosion damage, though the EB-PVD coatings were often stained with a lilac colour.

Weight change results
Whilst the main aim of the test work was to produce to produce dimensional data on materials performance, the weighing measurements needed to recoat samples with the correct levels of 'deposit' to achieve the targeted 'deposition fluxes' allow the monitoring of sample weight changes throughout the tests (e.g. Figure 2). For the complex deposits, such graphs can be misleading if it is wished to equate weight gain to metal damage as the 'deposit' composition (and hence weight) changes on heating and in reactions with the surrounding controlled gas atmospheres. For example, lead nitrates will decompose and the deposit mix will react with the SO_X and HCl to form a sulphate/chloride mix depending on the gas composition, in line with thermodynamic predictions for gas phase transport/vapour deposition reactions. This also means that some species from the artificial 'deposits' will be volatile under certain gas composition, pressure and temperature combinations.

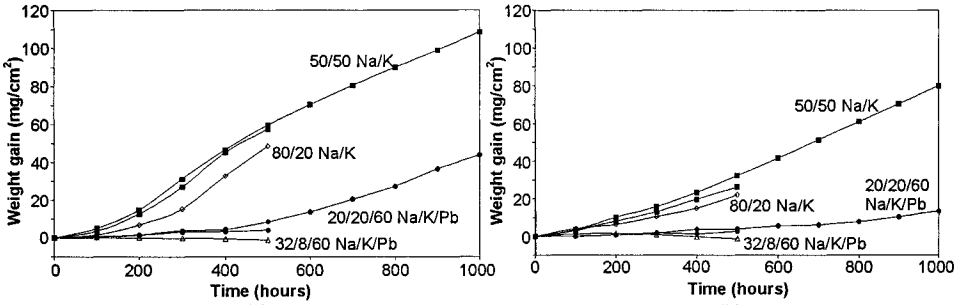


Figure 2 Weight change results for (a) IN738LC and (b) RT22 coated IN738LC samples exposed at 700°C in air 100 vpm SO_X, 100 vpm HCl with deposits A, C, J and L at a flux of 15 μg/cm²/hour

Time Dependency of Hot Corrosion Damage and Effect of Deposit Compositions
The corrosion damage observed on IN738LC in the hot corrosion tests at 650 and 700°C varied, as anticipated, between localised pitting, developing at low values of 'deposition flux' and more broad front corrosion damage at higher values of 'deposition flux'.

These effects can be illustrated by plotting the measured corrosion damage data in the form of probability plots. In this form of plot, the measured damage data are ordered and then plotted as a function of their probability of not being exceeded [14]. Figure 3 illustrates the results

found for a series of samples exposed to a 'deposit' mix of 80/20 mole % $(Na/K)_2SO_4$, at 700°C with deposition fluxes of 1.5 and 5 $\mu g/cm^2$/hour. The data in Figure 3(a) show relatively low uniform damage for the first 300 hours and then the development of a number of deeper pits. This is a clear indication of an incubation time for the development of the pitting damage at this low 'deposition flux'. It also illustrates the erroneous results that would be gained from using a weight gain method, which gives an average value of corrosion damage, to assess the corrosion damage that occurs at low 'deposition fluxes'[16]. The data in Figure 3(b) show a uniform distribution of corrosion damage developing around the samples from the start of the exposures. In this case there is no evidence of an incubation period. The difference between the maximum measured damage and the median damage, whilst significant (at ~16% after 1000 hours exposure) is not as large as for the samples exposed at low 'deposition fluxes' (at ~216% after 1000 hours exposure).

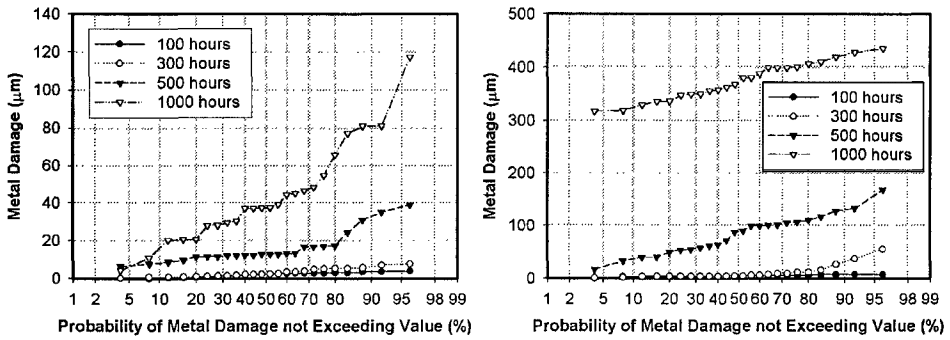


Figure 3 Evolution of the distribution of metal loss measurements from IN738LC exposed at 700°C, SO_X= 260 vpm, HCl = 300 vpm, flux of 80/20 mole % $(Na/K)_2SO_4$ = (a) 1.5 $\mu g/cm^2$/hour and (b) 5 $\mu g/cm^2$/hour [12]

This type of effect of 'deposition flux' on the development of hot corrosion damage in terms incubation has been observed all the 'deposit' compositions tested, but there are significant differences between the effects of the various deposits. This is illustrated in Figure 4 for a 'deposition flux' of 5 $\mu g/cm^2$/hour, in which 'maximum' (= damage with a 4% probability of being exceeded) corrosion damage values are plotted as a function of exposure time. The samples with this 'deposition flux' at 700°C have a clear incubation period for all the various deposit compositions. However, this incubation period is significantly shorter for the lead / zinc containing deposits, than the alkali sulphate deposits, though there are still significant differences in damage with varying Na/K ratios in these 'deposits' after 2000 hours testing. At higher 'deposition fluxes', there are still significant differences between the effects of the various 'deposit' compositions, with clear differences observed in the damage levels found with varying Na/K ratios in the alkali sulphate 'deposits'. Again, the Pb and Zn containing 'deposits' are more aggressive than those just contain alkali sulphate, but in all cases the development of the 'maximum' hot corrosion damage is approximately linear with time.

These results show that it is important to carry out hot corrosion tests for at least 500-1000 hours in order to be able to evaluate the different stages in the development of the hot corrosion damage, especially for the more realistic lower deposition flux exposure conditions.

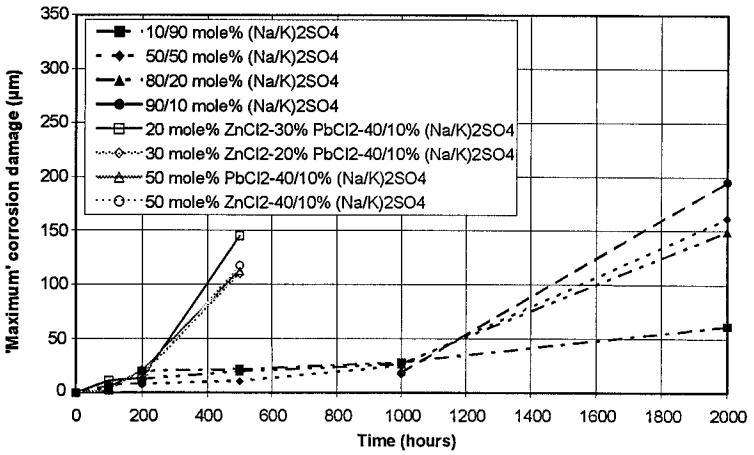


Figure 4 Effect of different deposit compositions on 'maximum' corrosion damage to IN738LC at 700°C (deposition flux = 5 µg/cm^2/hr, SOx = 2000vpm, HCl = 350 vpm) [12]

Effect of Deposition Fluxes

The 'maximum corrosion damage' results obtained for IN738LC at 700°C with a range of 'deposition fluxes' of a 'deposit' mix of 80/20 mole % $(Na/K)_2SO_4$ are illustrated in Figure 5. These results are typical of the response of gas turbine materials, with the dependence of corrosion rate on deposition flux being approximately sigmoidal with three distinct behaviour regimes [13]:

- for low deposition fluxes there were low corrosion rates;
- at intermediate deposition fluxes, much faster corrosion rates were found with a dependence on deposition flux close to linear;
- at high deposition fluxes, a thick scale/deposit layer was found which effectively creates 'a buried in ash' scenario and slightly reduces the corrosion rate with further increases in flux.

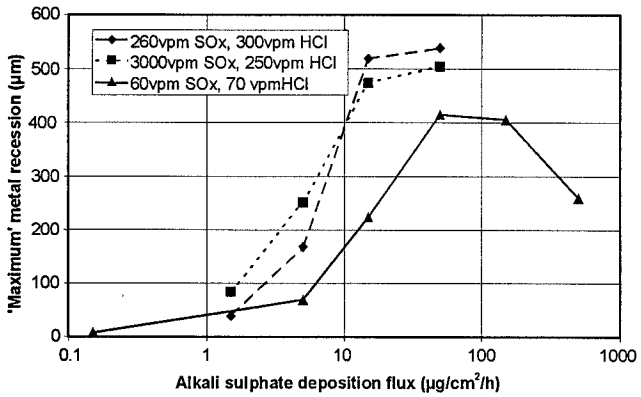


Figure 5 Effect of alkali sulphate flux and gaseous reactants on 'maximum' metal damage recession of IN738LC at 700°C [13]

Effect SO_X and HCl Concentrations

The effect of varying SO_X and HCl concentrations on the hot corrosion damage of IN738LC at 650 and 700°C were evaluated from a series of tests in which each of these contaminants was varied for the same 'deposit' composition (80/20 mole % $(Na/K)_2SO_4$) and a series of 'deposition fluxes'. It was found that the effect of SO_X levels was much more significant than HCl. The corrosion damage (whether expressed as 'maximum' or median values) increased with increasing SO_X levels, but the relationship was not linear, it was closer to logarithmic, with changes between lower levels (e.g. 60 to 300 vpm) being more significant than changes between higher levels (e.g. 300 to 3000 vpm). In addition, the effect was more pronounced at lower values of 'deposition flux', as illustrated in Figure 5.

Burner Rig Tests

As expected samples exposed on the lower metal temperature probes (~650 and ~700°C) showed type II hot corrosion damage, whilst those exposed on the higher temperature probes (~900°C) showed type I hot corrosion and oxidation damage. At intermediate temperatures (~800°C) mixed mode (i.e. types I and II) hot corrosion is evident on some materials. Thicker deposits were observed on the lower metal temperature probes, with these deposits containing all the trace elements (sodium, potassium, lead and zinc) introduced into the combustion gas stream. This emphasises the need to consider all the trace elements passing through a gasifier fuel-gas path in assessing the life of the downstream gas turbine and not just the alkali metals assessed for coal combustor derived gases. Low levels of deposition were observed on the higher temperature probes, in line with the previous rig operation and predictions from deposition models.

Direct comparison of results from the burner rig tests with those obtained from the laboratory tests is not possible due to the different exposure environments within these two test systems. However, models of materials degradation have been produced from laboratory studies [e.g. 12,13] that can be used to predict the corrosion behaviour of samples exposed in the burner rig and then these predictions compared to the observed behaviour. This is illustrated for IN738LC at 650 and 700°C in Figure 6, which shows that there is generally good agreement between the predicted and measured damage. In addition observations on polished cross-sections showed that similar morphologies of corrosive damage were generated.

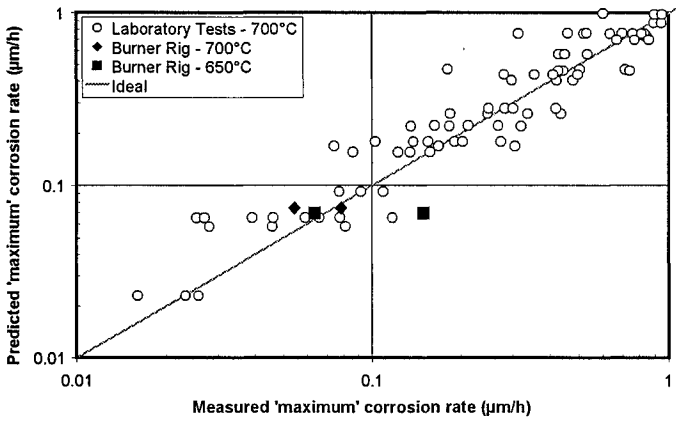


Figure 6 Comparison of measured and predicted damage for burner rig exposures

Summary
Series of laboratory and burner rig tests have been carried out to investigate the performance of current and candidate gas turbine materials in environments anticipated in gas turbines fired on coal and biomass derived gases. These controlled atmosphere tests have investigated the effects of a range of SO_X and HCl levels, as well as deposition fluxes and deposits containing Na/K/Pb/Zn sulphates/chlorides, at realistic metal temperatures. In both types of testing, data on the performance of the materials has been obtained using dimensional metrology that allows distributions of damage data to be determined, suitable for use in modelling materials performance and compiling into materials performance databases.

Acknowledgements
Funding has been provided by British Coal Corporation, UK Department of Trade and Industry (Clean(er) Coal Programme contracts C/05/00135 and C/05/00266), European Commission JOULE programme (contract JOUF-0022), European Coal and Steel Community programme (contracts 7220-ED/069 and 7220-PR/053).

References
1. W. Schlachter and G. H. Gessinger., *in* High Temperature Materials for Power Engineering 1990, E Bachelet et al Eds, (Kluwer, 1990) pp. 1-24.
2. Proc. Corrosion in Advanced Power Plants, Materials at High Temperatures 14 (1997).
3. C.T. Sims., N. S. Stoloff and W.C. Hagel, "Superalloys II", Wiley (1987)
4. "Hot Corrosion Standards, Test Procedures and Performance", High Temperature Technology 7 (4) (1989)
5. "Co-gasification of Coal/Biomass and Coal/Waste Mixtures", Final Report EC APAS Contract COAL-CT92-0001, University of Stuttgart, Germany (1995)
6. ASTM D2880, Standard Specification for Gas Turbine Fuel Oils (1990)
7. M. Decorso, D. Anson, R. Newby, R. Wenglarz and I. G Wright, Int. Gas Turbine and Aeroengine Congress, Birmingham, UK, ASME Paper 96-GT-76 (ASME, 1996)
8. I.G. Wright, C. Leyens and B.A. Pint, *in* Proc. ASME TURBOEXPO 2000, Munich, Germany, ASME Paper 2000-GT-0019 (ASME 2000)
9. N. J. Simms, J. E. Oakey, D. J. Stephenson, P. J Smith and J. R. Nicholls, Wear **186-187** (1995) 247-255
10. N. J. Simms and J. E. Oakey, *in* Microscopy of Oxidation 3, (The Institute of Materials, 1997) pp. 647-658
11. N. J. Simms, J. E. Oakey and J. R. Nicholls, Materials at High Temperature **17** (2) (2000), pp355-362
12. N.J. Simms, P.J. Smith, A. Encinas-Oropesa, S. Ryder, J.R. Nicholls and J.E. Oakey, in Lifetime Modelling of High Temperature Corrosion Processes, Eds M. Schütze et al, EFC No. 34 (Maney Publishing, London, 2001) pp246-260
13. N. J. Simms, J. R. Nicholls and J.E. Oakey, in *Materials Science Forum* Vol 369-372 (2001), pp 833-840
14. J. R. Nicholls and P. Hancock, *in* High Temperature Corrosion, RA Rapp, Ed, (NACE, 1983) pp. 198-210
15. 'Draft Code of Practice for Discontinuous Corrosion Testing in High Temperature Gaseous Atmospheres', EC Project SMT4-CT95-2001, ERA Technology, UK (2000)
16. C. Leyens, I. G. Wright, B. A. Pint and P. F. Tortorelli, in 'Cyclic Oxidation of High Temperature Materials', Eds M Schütze and W J Quadakkers, EFC No. 27 (Institute of Materials, London, 1999), pp169-186

LOW CYCLE FATIGUE IN AGGRESSIVE ENVIRONMENTS - A NEW TESTING METHOD USING CONTROLLED ATMOSPHERES

Henrik C. M. Andersson[1], Joakim Lindblom[2]

[1] Swedish Institute for Metals Research, Drottning Kristinas v. 48, S-114 28 Stockholm, SWEDEN
[2] JL Integration AB, Lorensbergsgatan 1A, S-117 33 Stockholm, SWEDEN

Abstract

The stainless steel 347 commonly used in pressurised fluidised bed combustion (PFBC) applications has been tested under low cycle fatigue (LCF) conditions. The test rig in which the testing was performed has been developed to allow for LCF testing at elevated temperatures and in controlled environments of aggressive gases.

The testing was carried out in air and in a mixture of SO_2 gas and humidified air at a temperature of 600 °C. One specimen was tested in SO_2 and dry air, and six specimens in SO_2 and humid air. The results show that the fatigue life is reduced when conducted in SO_2 compared to tests conducted in plain air. No difference in fatigue life was detected between dry and humid SO_2. Specimens pre-exposed to the aggressive gas for 100 hours at 600 °C showed no significant difference in fatigue life compared to specimens that had not received the pre-exposure.

Oxides formed on the specimens tested in air consist of a mixture of chromia and spinel oxides. For specimens tested in SO_2 iron sulphides are also found. Corrosion products cover the surface of the specimen and the opened microcracks. Some penetration of the corrosion products into grain boundaries is also observed.

Keywords: LCF, 347, SO_2, waste incineration, aggressive environments, test methodology

Introduction

The use of biomass and household waste as fuels for power production plants means that the materials have to withstand an increased chemical attack in comparison to conventional fuels. Waste products often contain compounds that produce SO_2 and other aggressive gases when burned. These gases give a more severe chemical attack than the relatively cleaner fuels such as oil and natural gas. A comprehensive study of the problem can be found in [1].

An example is pressurised fluidised bed combustion (PFCB) used in power production facilities. The effect of the chemical attack on the mechanical properties of materials used is unknown since most testing is conducted as either static corrosion tests or mechanical tests in normal air. The results are then superimposed and conclusions concerning remaining lifetimes of the material in service are drawn. This is not satisfactory since it is probable that the chemical attack decreases the fatigue life of the material. The present work aims at studying this effect by performing low cycle fatigue (LCF) tests on the stainless steel 347 in both normal air and various mixtures of gases containing SO_2.

Experimental

The test equipment used has been specially modified to allow for testing in controlled environments. The base is an Instron 1380 load frame equipped with a 30 kN load cell and a SFL SF892A split furnace. The maximum temperature of the furnace is 850 °C. and the test is controlled by a newly developed TestPoint procedure. Normal tests in air are run with three internal extensometers and one external, whereas tests in controlled atmosphere are performed with only the external extensometer. Thus a test series in controlled atmosphere is always accompanied by a test series of the same material at the same temperature in air that is used to calibrate the extensometers. The test setup with the internal extensometers is given in Figure 1.

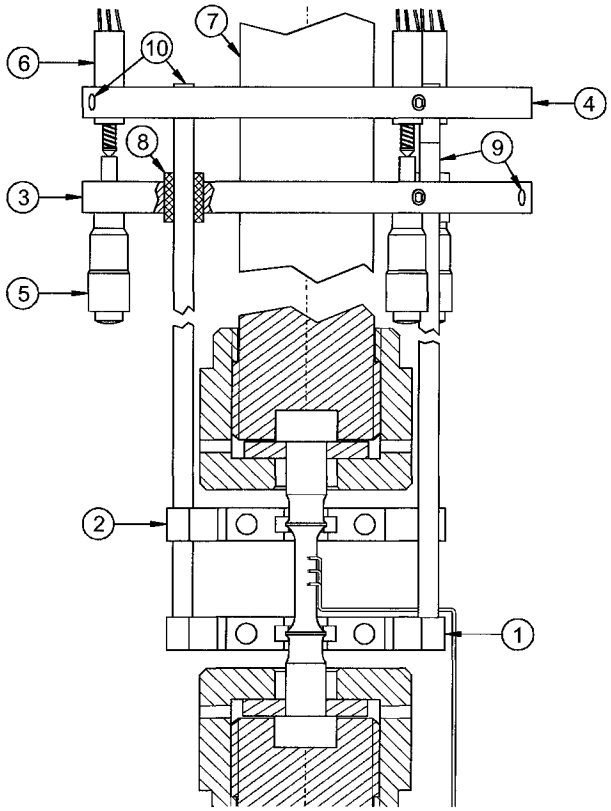


Figure 1 *Schematic drawing of the extensometer setup for testing in air. 1 and 2 are the knife-edge holders, 3 and 4 the extensometer holders, 5 is the adjustment micrometer, 6 the transducer, 7 the loading rod, 8 a bushing and 9 and 10 various adjustment screws.*

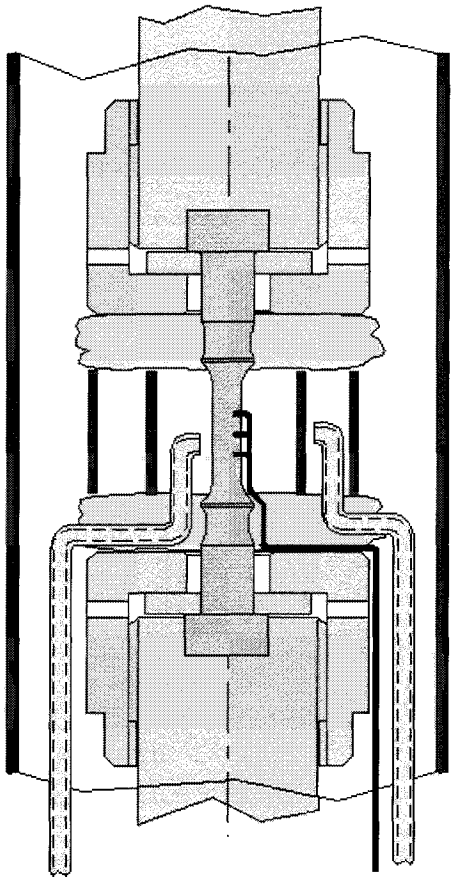


Figure 2 *Schematic drawing of the equipment setup for testing in controlled environments. The glass tubes and glass fibre padding seals can be seen around the specimen. The inlet gas flow tube end up in the inner chamber next to the specimen and the outlet gas tube can be seen in the middle chamber. Placement of the thermocouples can also be seen on the specimen.*

To make testing in controlled environments possible the internal extensometers are removed and three quartz glass tubes are inserted. The outermost tube is a snug fit against the furnace and sealed by cooled stainless steel bellows at both ends. During testing this tube is filled with argon under a slight overpressure. The two innermost tubes are sealed by glass-fibre padding at both ends and the aggressive gas is led into the innermost tube through a small diameter quartz tube. It is possible to insert three such tubes for a test series. Between the inner and the middle tube a chamber is formed and the gas outlet is placed here. Since both the argon and the aggressive gas are introduced under slight overpressure, the excess gas seeps into this chamber through the glass-fibre padding and it is the led out of the test setup through a quartz tube. A schematic drawing of the setup is given in Figure 2.

Both the inlet and outlet tubes have to pass through the watercooled lower bellows holder, which means that the corrosive gases will condense on the walls of the tube, and if there is a leak in this area the holder will be damaged. This problem has been handled in three ways. If the gas in question is dry, such as 1% SO_2 in dry air, a normal seal is used. If the gas contains water vapour, such as the humidified air used in this experiment, the gas is fed through a heated double walled tube to keep it from condensing as it passes through the cool holder. Thirdly, the outlet is made of one single-piece quartz tube that is continuous through the holder, ensuring that the gas will condense on the tube, but since it is the exhaust it does not matter and since the tube is unbroken no gases or liquids will escape.

The material for all of the tests came from a bar of the stainless steel 347 (heat number 437184) and was delivered by AB Sandvik Steel. The nominal composition of the steel is given in Table 1. The tests in this study were carried out either in air or in an atmosphere of 1% SO_2 and synthetic air. After an initial test had been carried out in a mixture of SO_2 and dry air with no apparent difference to the tests in air, the rest of the SO_2 tests were performed out with humidified air (3% H_2O) but the SO_2-content was kept at 1%. Three specimens were pre-exposed to the 1% SO_2 and humid air mix at 600 °C for 100 hours before the test was started. No strain was applied to these specimens before the 100 hours had passed, i.e. no cracks had been opened on the surface of the material during the pre-exposure.

Table 1 Chemical composition of the stainless steel 347 in wt%. Heat number 437184.

Material	C	Si	Mn	Cr	Ni	Nb	P	S
347	0.05	0.61	1.7	17.61	11.1	0.81	0.026	0.01

Most specimens were allowed to rupture and the number of cycles to crack initiation (N_i), the number of cycles to 10% load drop (N_{90}) and the numbers of cycles to final failure (N_f) were noted for each specimen. The strain rate used was 0.0001 /s. A stable hysteresis loop taken before crack initiation was also evaluated for each test and the elastic, plastic and inelastic strain ranges were noted as well as the stress range. To make the raw data possible to evaluate the measured strain from the external extensometer was reduced by the test rig compliance factor, after which the data was further adjusted for the geometrical effect of the gauge length with radii on the ends. A representation of the specimen design can be found in Figure 1. The adjustment for geometrical effects was performed according to [2].

After testing the specimens were cut along the centre-line and mounted in resin. The specimens were then ground, polished and etched in warm Aqua Regia. Metallography was carried out in a light optical microscope (LOM), and the corrosion products on the surface of the specimens and in the cracks were also analysed by microprobe analysis.

Results

LCF testing

Examples of the load drop curves obtained for the tests is given in Figure 3. Figure 4 shows the results given as total mechanical strain versus the number of cycles to 10% load drop, N90. The dotted lines in the curve correspond to the sum of the Coffin-Manson and the Basquin relation, which are usually written as:

Coffin-Manson $$\Delta\varepsilon_p = AN_{90}^{\alpha} \quad (1)$$

Basquin $$\Delta\varepsilon_e = BN_{90}^{\beta} \quad (2)$$

The coefficients from these equations evaluated for the tests performed are given in Table 2. Since no significant difference was detected between pre-exposed and not pre-exposed specimens with respect to the fatigue life. They have therefore been treated as a single test series in the following evaluation.

The inelastic strain range shows a crossover between specimens tested in SO_2 and specimens tested in air at the lower strain ranges tested, see Figure 5.

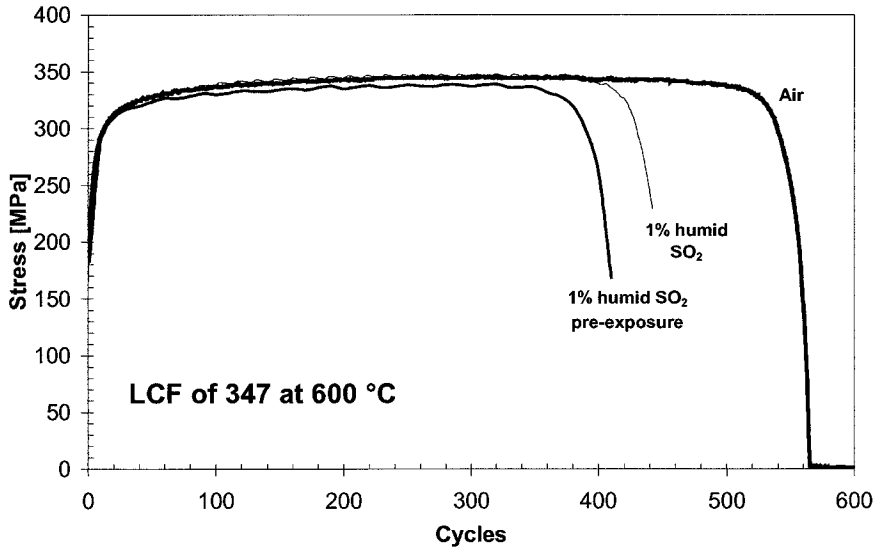


Figure 3 *Examples of load drop curves. The target strain range for these tests were ± 1%. The difference between pre-exposed and not pre-exposed tests shown in this graph is within the scatter of the experiments.*

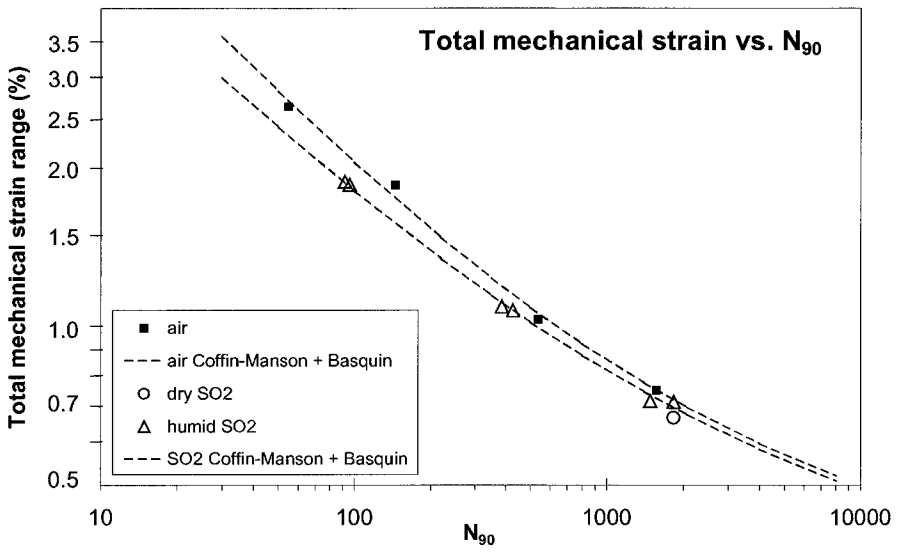


Figure 4 *Total mechanical strain vs. the number of cycles to 10% load drop, N_{90}.*

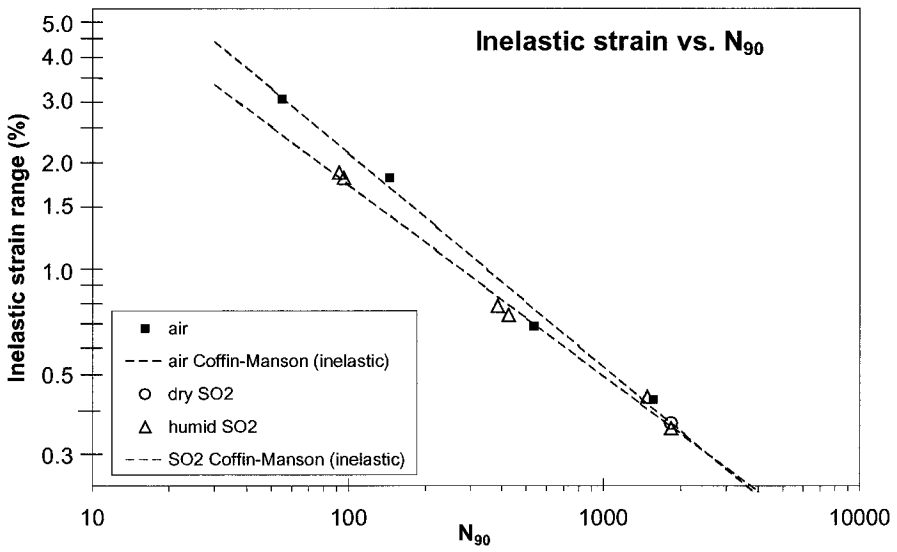


Figure 5 *Inelastic strain vs. the number of cycles to 10% load drop, N_{90}.*

Table 2 *Coefficients from the Coffin-Manson and Basquin relations, Eqns (1) and (2).*

Material	Environment	A	α	B	β
347	air	40.3	-0.636	0.82	-0.082
	humid SO_2*	26.6	-0.586	0.82	-0.088

* Note that the tests performed in humid SO_2 is treated the same irrespective of whether the specimens had been pre-exposed or not.

Examples of the hysteresis loops obtained are shown in Figure 6 and Figure 7. The horizontal part of the loop after elastic unloading and plastic deformation suggests a fair amount of creep since the stress level is constant even though the strain increases. No difference in the general shape of the loops obtained in air and in SO_2 could be observed for loops of similar strain range.

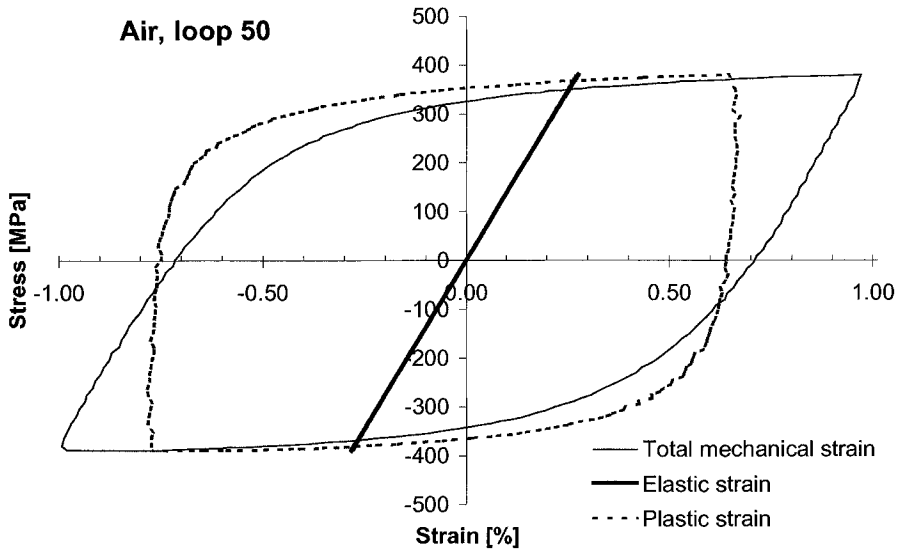


Figure 6 *Example of a stress-strain hysteresis loop for a specimen tested in air at 600 °C. Large strain range*

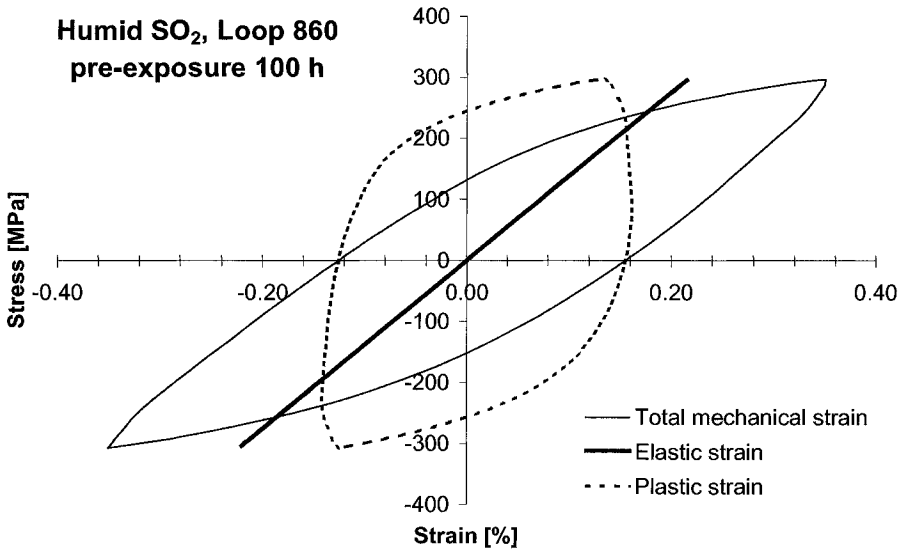


Figure 7 *Example of a stress-strain hysteresis loop for a specimen tested in SO_2 after pre-exposure 100h. Temperature 600 °C. Small strain range*

Metallography

A visual inspection of the specimens after testing showed no evidence of heavy corrosion. The specimens tested in air actually showed more oxidation than the specimens tested in SO_2 did for short exposure times. Tests at longer times showed more corrosion/oxidation but no build-up of a deposit on the surface of the specimen was present on any of the specimens.

A thin oxide layer covered specimens tested in air after testing. When exposed to air at 600 °C a stainless steel containing about 17% Cr develops an oxide layer consisting of a mix of chromium oxide (Cr_2O_3) and spinel (M_3O_4), [3]. The appearance of the oxide in microscope and the darkish colour of the specimen after testing suggest that the oxide formed is a mixture of these two compounds. A pure chromium oxide usually exhibits a more greenish tint. The surface of the specimen also exhibited a number of small cracks that had originated on grain boundaries, and the final fracture was transgranular. No other damage such as sub-surface microcracks or voids could be observed.

Specimens tested in SO_2, either dry or humid, exhibited a relatively thicker layer of corrosion products on the surface than the specimens tested in air. Microprobe analysis showed that this corrosion product contained 0.4% sulphur. The concentration of sulphur did not vary with exposure time but the specimens with longer exposure times had a thicker layer of corrosion products. The literature suggests that the scale formed is the same as the mixture of chromium oxide and spinel oxide formed in air, with the addition of iron sulphides.

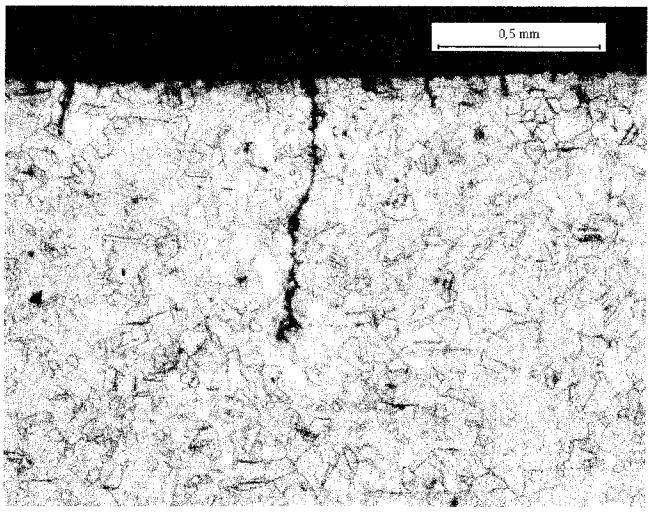


Figure 8 *Corroded crack on the surface of a specimen tested in humid SO_2. (Strain range 2.41%, 105 cycles, exposed for 17 hours at 600 °C.)*

The corrosion product also decorated the cracks that had formed in the material, Figure 8 and Figure 9, and had in some instances penetrated along grain boundaries, Figure 10.

The failure mechanism was crack initiation on the surface of the gauge length and transgranular crack propagation into the material. No other damage such as microcracks or voids was observed in the gauge length and the cross-section reduction due to the corrosion was negligible.

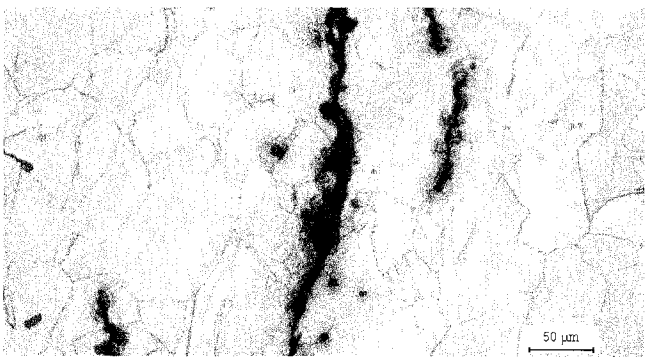


Figure 9 *Close-up on a corroded crack in a specimen tested in humid SO_2. (Strain range 2.41%, 105 cycles, exposed for 17 hours at 600 °C.)*



Figure 10 *Penetration of sulphur containing corrosion products along a grain boundary. Specimen tested in dry SO_2. (Strain range 0.71%, 1900 cycles, exposed for 158 hours at 600 °C.)*

Discussion

As can be seen from Figure 4 there is a detrimental effect on the fatigue life from the SO_2 environment. The effect is more distinct at high than at low strain ranges, but it can be seen over the whole test range. The reason for the more pronounced effect at higher strain ranges is probably related to the greater number of microscopical cracks formed when compared to lower strain ranges. The corrosion products containing sulphur, which are probably embrittling the material, increase the crack initiation and propagation rate and leads to shorter lifetimes. This effect can also be seen in the relatively low number of corroded grain boundaries found, see Figure 10. It might be argued that any grain boundary attacked in this way should crack during straining and thus form a crack. A possible explanation would be that for the low strain ranges, the strain applied to the material is too low to open up a crack from a corroded grain boundary.

This does not mean that there is no effect at even longer exposure times. Studies have shown [3] that the oxide grows thicker and penetrates deeper into the material at longer exposure times. The strain needed to open up heavier, more corroded, grain boundaries should therefore be lower and thus the fatigue lives shorter. The longest exposure times used in this study has been around 250 hours but to obtain the corrosion results needed for a significant impact at low strain ranges it is estimated that at least a few thousand hours are needed. Significantly longer test times are needed for a comprehensive study of the mechanisms involved. Another possibility of conducting these tests that will allow for more tests in a shorter period of time is to cycle each specimen in SO_2 for about 100 cycles with a relatively large strain range. The specimens are then removed and statically exposed to the corrosive atmosphere for an extended period of time, and finally reinserted in the test rig and tested to failure. In this way a greater number of specimens could be tested in a short time, but the direct comparability with service-like conditions would be lost.

In actual power plants it has also been found that a corrosive deposit of aggressive residues form on the material. This deposit can consist of a number of elements but usually some sort

of low melting salts are included, often containing zinc [1]. In this test series this compound was not simulated. Static tests of corrosion using simulated deposits have been performed using various methods, [4, 5]. This should be included in future low cycle fatigue experiments to make the investigations as complete as possible.

Few simultaneous mechanical and corrosion tests have previously been reported. The investigation reported in [6] use a different experimental approach than in this work. Exhaust gases from a turbine combustion chamber is directed to a specimen to simulate the kind of exposure a turbine blade or vane experience during service. Creep-fatigue tests performed on SAF 2205 and 316 reported in [7] show greater aggressive attack than in the present work. The atmosphere in that case was 3% SO_2 and argon, which meant that the passive film had no way of re-establishing itself after being penetrated. One should note that the same fatigue life relationship between specimens tested in air, argon and SO_2 as was found in the present investigation was found in this work. Other experiments where the lower part of the LCF specimen has been immersed in a bath of melted salt has also been reported [8].

The experimental setup used in this work has been shown to work in a standard LCF test frame and is expected to be more flexible for variations in the test conditions.

Conclusions

In this work the fatigue behaviour of the stainless steel 347 has been studied in aggressive environments.

- The aggressive atmosphere, dry or humid SO_2, reduces the fatigue life of the material. The effect is more pronounced at high strain ranges than at low strain ranges.
- The cracks initiated at the grain boundaries and propagated transgranularly in specimens tested in both air and SO_2.
- Corrosion products have been observed at the surface of the specimens and inside surface cracks.
- Corrosion products formed at the surface of specimens tested in SO_2 contain sulphur, probably in the form of sulphides.
- Corrosion products have been found to penetrate into the material along grain boundaries to a certain extent.
- Future investigations should be focused on longer exposure times and simulation of the corrosion residue formed in service on power plants.

Acknowledgements

The membership program at the Swedish Institute for Metals Research has financed this work. The member companies are thanked for their support. The steering committee, listed below, is also thanked for their patience and support during the project. The steering committee was Bo Ivarsson (AvestaPolarit), Karin Törnblom (Birka Service, Elforsk), Erik Skog (Sycon, Elforsk) and Pamela Henderson (Swedpower, Elforsk)

References

1 Melin L., "Material related problems in waste fired incinerators - A literature study", Master Thesis KTH/AMT-205, Department of Materials Technology, Royal Institute of Technology, S-100 44 Stockholm, SWEDEN (2001)

2 Day M.F., Harrison G.F., "Design and calibration of extensometers and transducers", Symp. on Measurement of high temperature mechanical properties of materials, National Physical Laboratory, Teddington, UK, pp 225 - 240, 3 - 5 June (1981)

3 Spiegel M., "Hochtemperaturkorrosion niedrig- und hochlegierter Stähle unter simulierten Müllverbrennugns-bedingungen", ISSN 0178-952X, VDI-Verlag GmbH, Düsseldorf (1994)

4 Nicholls R.J., Saunders S.R.J, "Testing methods in high temperature corrosion" Proc. Surface Stability. Oxidation -Corrosion-Erosion-Wear, London, UK, 6 September (1989)

5 Simms N.J., Oakey J.E., Nicholls J.R., "Development and application of a methodology for the measurement of corrosion and erosion damage in laboratory burner rig and plant environments", Materials at High Temperature, vol 17, no 2, pp. 355-362 (2000)

6 Kloos K.H., Granacher J., Struth U., "Environmental Effects and Protection--Combined Stress--Environmental Effects", High Temperature Alloys for Gas Turbines and Other Applications, 1986. II, Liege, Belgium, 6-9 Oct., pp. 1279-1293 (1986)

7 Aghion E., Molaba. C.A., "Creep-Fatigue Failure of SAF 2205 and 316 Stainless Steels in Ar + 3% SO_2 Environment at 700 deg C", J. Mater. Sci., vol. 29, no. 7, pp. 1758-1764 (1994)

8 Whitlow G.A., Johnson R.L., Pridemore W.H., Allen J.M., "Intermediate Temperature, Low-Cycle Fatigue Behavior of Coated and Uncoated Nickel-Base Superalloys in Air and Corrosive Sulfate Environments", Proc of Advances in Life Prediction Methods, Albany, N.Y., U.S.A., 18-20 Apr., pp. 269-276 (1983)

CHLORINE CORROSION OF THERMALLY SPRAYED COATINGS AT ELEVATED TEMPERATURES

M.A. Uusitalo, P.M.J. Vuoristo, and T.A. Mäntylä,

Tampere University of Technology, Finland.

Abstract

Superheaters of power plants utilizing chlorine-containing fuels face serious corrosion problems frequently. Chlorine accelerates corrosion in oxidizing and in reducing conditions. Coatings with high chromium content are considered as a potential solution to reduce chlorine-induced corrosion at elevated temperatures. High temperature corrosion tests were performed on 5 HVOF coatings, a diffusion chromized coating, a laser melted HVOF coating, and boiler steels. The tests were performed in oxidizing and reducing atmospheres. The test temperature was 550°C, and all atmospheres contained 500 ppm HCl. The reducing atmosphere contained also hydrogen sulphide and carbon monoxide. Dense coatings with high chromium content performed well in both atmospheres. Some of the tested coatings were penetrated and corrosive species attacked the substrate via an interconnected network of voids and oxides at splat boundaries.

Keywords: coatings, corrosion, chlorine, superheater

Introduction

The significance of biofuels and other chlorine-containing fuels in electricity and steam production is growing rapidly. However, many problems associated with fouling, slagging and corrosion arise when fuels with high chlorine content are combusted. Biomass, [1-4] waste, [5-7] and high-chlorine coals [8] are reported to cause severe materials wastage in combustors. Corrosion in combustors can take place either in the gas phase or below the ash deposits. Ash deposits accelerate corrosion remarkably [4]. Reducing conditions caused by unburned carbon or low NOx combustion further enhances corrosion [9]. Also a large amount of water vapor in flue gases can accelerate corrosion processes [10].

Corrosion problems caused by low-quality fuels are mostly solved by decreasing the steam temperature in superheaters, but the lower steam temperature drastically decreases the efficiency of electricity production. The boilers burning low-chlorine coals operate with steam temperatures up to 570°C [11], whereas boilers with high-chlorine fuels, like waste [12] or black liquor [13] operate with steam temperatures below 500°C. Biofuels are sometimes combusted with steam temperature of 530°C, but unacceptable corrosion rates have occurred [14].

High-temperature corrosion caused by combustion environments is usually accelerated oxidation or sulphidation. In oxidizing environments chlorine accelerates oxidation by a mechanism of active oxidation [15]. Low-alloy boiler steels have poor resistance against chlorine-bearing gases at elevated temperature. Chromium and nickel increase corrosion resistance of steels. Nickel-based materials are more resistant than iron-based materials [16]. An addition of molybdenum has a positive effect on corrosion resistance of alloys in chlorine-containing environments [17].

In reducing environments boiler steels are susceptible to sulphidation [18]. Chlorine in flue gases accelerates sulphidation [19]. Sulphidation resistance is also increased by addition of

chromium. Nickel-based materials are also more resistant to sulphidation, if the chromium content is high enough [20].

Corrosion resistant materials for combustion environments are highly alloyed, and thus expensive. Also mechanical properties of corrosion resistant alloys may not meet the requirements of structural components [21]. The problems associated with workability and high material price can be solved by means of coatings. Structurally consisting of load bearing ferritic steel tube, and highly alloyed and corrosion resistant outer layer, coated components provide an attractive solution for superheaters. There are several methods for producing coated tubes for boilers. Tubes are produced by means of co-extrusion [21], weld overlaying [22], pack-cementation [23], thermal spraying [24], and laser coating [25].

High velocity oxy-fuel (HVOF) spraying is a competent method for producing coatings. HVOF coatings applied in power plants are usually nickel-based coatings with high chromium content. Additional alloying with silicon, molybdenum and other minor elements may also be used. Intermetallic Fe_3Al coatings have also been reported to perform well in combustion environments [26]. HVOF coatings are considered as homogeneous and dense coatings [27]. They are used for corrosion protection in combustors [12, 17]. Despite the apparent homogeneous nature of HVOF coatings, they always contain some oxides and porosity at splat boundaries [28]. These inhomogeneities affect corrosion resistance of the coatings. Because of the porosity, there have been doubts over the corrosion resistance of HVOF coatings [27]. Coating microstructure can be homogenized for improved corrosion resistance by various post-spray treatments, like annealing [29] or laser treatment [30]. There has been little discussion of corrosion testing on thermally sprayed coatings applied to boiler steels in literature. Even then, corrosion tests are often performed on the coating layer itself, and the ability of the coating to protect the steel substrate is not evaluated [27]. Only few experiments in combustors or simulated combustion atmospheres are reported for such coated steel components. Long-term exposures with characterization of failure mechanisms are essential for estimating the shielding capability of the coating.

In present study, corrosion resistance of several HVOF coatings, laser treated HVOF coatings, diffusion coatings, and boiler steels in chlorine containing atmospheres was studied. Special attention was paid to the effect of the coating composition and coating structure on corrosion. Corrosion tests were performed in two simulated biofuel combustion atmospheres. One atmosphere was oxidizing and the other atmosphere was reducing.

Materials and methods

Materials

One ferritic steel, one austenitic steel, 5 thermally sprayed coatings, one laser melted thermally sprayed coating, and a diffusion chromized coating were tested. The nominal compositions of the tested steels and coating powders are presented in **Table 1**.

The ferritic steel tested contained 2.25 % chromium and 1 % molybdenum. This type of steel is often used as water wall tubes or superheaters in boilers. The temperature limit for this steel is 590°C because of low alloy content. This steel was also used as a substrate for all the coatings.

Table 1. Nominal compositions of tested steels and spray powders.

	Material	Nominal comp.	Type
1	Ferritic steel	Fe-2.25Cr-1Mo	Bulk
2	Austenitic steel	Fe-27Cr31Ni3.5Mo	Bulk
3	Ni-50Cr	Ni-50Cr2Si	HVOF
4	Ni-57Cr	Ni-57CrMoSiB	HVOF
5	Ni-21Cr-9Mo	Ni-21Cr9MoFe	HVOF
6	Fe_3Al	Fe-15Al-2Cr	HVOF
7	Ni-50Cr	Ni-50Cr	Excalibur HVOF
8	Ni-57Cr +laser	Ni-57CrMoSiB	HVOF+laser
9	Chromized ferritic steel	Fe-2.25Cr-1Mo+Cr	Chromized steel

Austenitic steels are considerably more expensive than ferritic steels. Tested steel contained high amounts of chromium, nickel and molybdenum. In boilers they are used only if ferritic steels cannot resist the temperature, load or corrosive environment. Also the thermal conductivity of austenitic steels is considerably lower than that of ferritic steels.

Coatings 3, 4, 5, and 6 were produced by a Diamond Jet Hybrid 2700 HVOF system. The structures were typical for metallic HVOF coatings. The splats were flattened and coatings contain low amounts of oxides and porosity. Coatings 3, 4, and 5 were nickel-based coatings, whereas coating 6 was a Fe_3Al coating. The aluminum content of the spray powder was 14.7 wt%, that equals to intermetallic Fe_3Al composition. The Fe_3Al coating was degraded during spraying, because of evaporation of aluminum, and the Al content of the coating was only 8.5 wt%.

Coating 7 had similar nominal composition than that of coating 3, but it was produced by Metalspray Inc. with the Excalibur HVOF spraying system. This coating contained considerably larger amount of oxides. Especially chromium was oxidized extensively. The coating was extremely dense and splats were wide and flat. On the basis of high oxide content and splat shape, it can be estimated that the temperature of powder particles had been higher than in conventional HVOF spraying. Also the compositions of splats varied a lot.

Coating 8 was coating 4 melted with a laser beam. Laser melting enhanced the coating homogeneity and decreased the porosity. The interconnected network of porosity and oxides had been removed by laser treatment. The coating was locally covered with a layer of chromium oxide because of oxidation during the laser treatment.

Coating 9 was diffusion chromized ferritic steel. The chromium content in the surface layer was very high, but the chromium-enriched layer was thin.

Samples

The sample dimensions were 10x8x6 mm. HVOF coatings were produced on ferritic steel plate, and samples were cut with diamond disk. Coatings were tested in the as-sprayed condition to avoid blocking of porosity or initiation of new cracks by grinding the coated surface.

Sides of bulk steel samples were ground with 1200 grid SiC paper. The thickness of the steel samples and diffusion chromized samples were measured with an accuracy of 0.01 mm.

Corrosion tests

Corrosion exposures were carried out at 550°C in a vertical three-zone furnace. More detailed information of the furnace can be found elsewhere [31].

Two synthetic atmospheres, oxidizing and reducing, were created for the tests. The flow rate was 240 ml/min for the oxidizing gas and 232 ml/min for the reducing gas. The compositions of the test gases are presented in **Table 2**. Both atmospheres contained HCl and plenty of H_2O. The reducing atmosphere contained also H_2S and CO to simulate combustion with an understoichiometric amount of air. It must be noted that reducing combustion atmosphere may still contain some oxidizers. For example, the test atmosphere contains plenty of water vapor. For a corrosion engineer, this atmosphere is oxidizing with reference to the partial oxygen pressure needed for oxide formation.

Table 2. Compositions of atmospheres.

Oxidizing atmosphere	Ar-20%H_2O-14%CO_2-3%O_2-500vppmHCl
Reducing atmosphere	Ar-20%H_2O-5%CO-0.06%H_2S-500vppmHCl

Every material was tested in both atmospheres for 100, 400, and 1000 h. All the samples were exposed in individual alumina crucibles. After placing samples into furnace, the furnace was evacuated and backfilled with argon five times. Similar procedure was carried out with test gas. Then furnace was heated to test temperature at an average rate of 200°C/hour. Premixed gases were used. HCl was added just prior the entry to furnace to avoid corrosion in the gas lines. Test was interrupted at 100 h intervals for weighting the samples and adding/removing samples. The samples were cooled down in stagnant active gas. Then furnace was cleaned by evacuating and backfilling five times with argon, followed by flowing argon for at least 1 h before opening the furnace.

Examination of exposed samples

After the exposures, the samples were weighted and molded in resin. The cross-sections were cut, ground and polished without any water-based lubricants. Microstructural examination and thickness loss measurements were performed by optical microscopy. Then samples were carbon coated and SEM studies were performed with Philips XL-30 SEM equipped with EDS (EDAX DX 4). The corrosion product layers, corrosion mechanisms, possible internal attack, changes in coating microstructure and coating/substrate interface were investigated.

Results

Corrosion damages were studied by means of weight change and SEM/EDS examinations. Only small amounts of chlorine were detected in corrosion scales. However, corrosion was very severe. The severity of corrosion, and appearance of corrosion scales indicate, that chlorine has actively taken part in corrosion processes.

The weight change is not considered as a reliable measure of the corrosion processes for coated samples that are coated on one face, because most of the weight change is due to corrosion of the substrate material in non-coated areas. In case of steels the weight change illustrates the character of corrosion process. The weight changes of steels are presented in **Fig. 1**. The shapes of the weight change curves indicate that protective corrosion scales did not form.

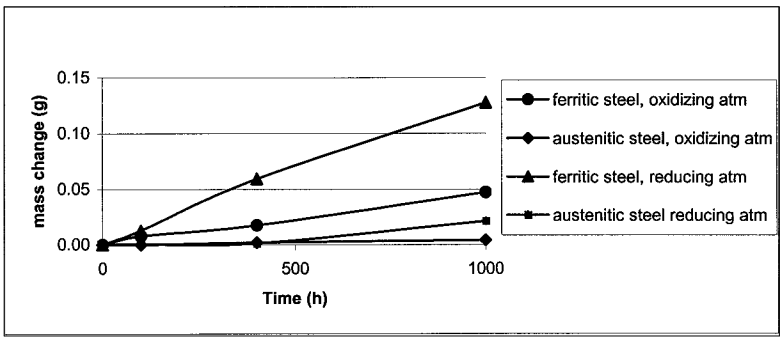


Fig.1. Weight changes of steels samples.

Ferritic steel experienced linear weight gain in both atmospheres. The thickness of the oxide layers was 100 μm in oxidizing atmosphere and 200 μm in the reducing atmosphere. In the oxidizing atmosphere corrosion products were lamellar and porous. Oxide layers on ferritic steel after 1000 h exposure in oxidizing atmosphere are presented in **Fig. 2**. Such corrosion scales are typical for active oxidation. Scales contained mostly iron oxides, but some chromium and molybdenum were also detected in layers adjacent to metal surface. Severe spalling of sulphide layers occurred in the reducing atmosphere. Corrosion was more severe in the reducing atmosphere, as expected. Lamellar scales were formed also in the reducing atmosphere. Outer layers of scales consisted mostly of iron sulphides whereas inner layers contained more chromium and oxygen.

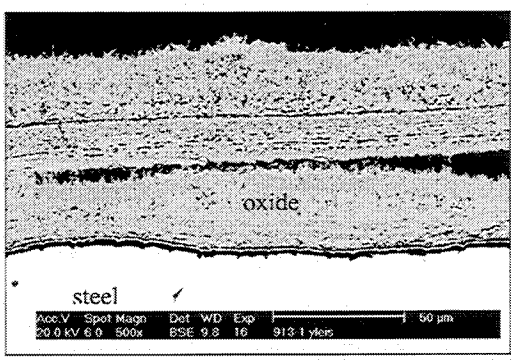


Fig. 2. Austenitic steel, 1000 h exposure in oxidizing test atmosphere.

Austenitic steel suffered less corrosion damages than the ferritic steel, as expected. Two-layered corrosion products were detected after 1000 h exposure. Discontinuous and cracked up to 20 μm thick chromium oxide layer was detected adjacent to metal surface. Porous outer corrosion product layers were partially spalled, with maximum thickness of 50 μm. The compositions of the outer oxide varied a lot. Chlorine contents up to 5 at% were detected in the outer scale. In reducing conditions corrosion was more severe. The outermost scale with maximum thickness of 20 μm, consisted mainly of iron and sulfur. Thin but continuous chromium rich layer was detected adjacent to steel. The outer part of the chromium rich layer contained plenty of sulfur, but the inner part of the chromium rich layer contained plenty of

oxygen and only few percentages sulfur. The continuous chromium rich layer was locally cracked and internal oxidation, sulfidation and also chloridation were detected. If the chromium rich layer was continuous, only chromium rich oxides were detected beneath the continuous chromium rich layer. Iron and nickel were depleted in the surface layer down to depth of 20 μm. Corrosion scales on austenitic steel after 1000 h exposure are presented in **Fig. 3**. Scales rich in sulfur appear lighter and scales rich in oxygen appear darker in the backscattering electron (BSE) image.

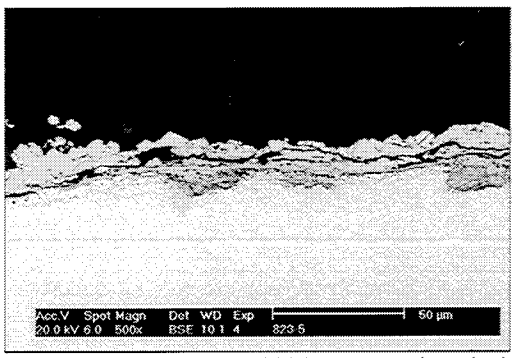


Fig. 3. Austenitic steel, 1000 h exposure in reducing test atmosphere.

The Ni-50Cr HVOF coating, material no. 3 performed well in the oxidizing atmosphere. No internal attack was detected. The coating was able to protect the substrate material. The coating/substrate interface of Ni-50Cr HVOF coating after 1000 h exposure in oxidizing atmosphere is presented in **Fig. 4**. In reducing conditions corrosion products containing chromium and sulphur were detected. The thickness of these layers was less than 30 μm. Some internal attack on coating was also detected. Minor amounts of chlorine were found at splat boundaries to a depth of 250 μm. However, no corrosion attack of the substrate material was detected.

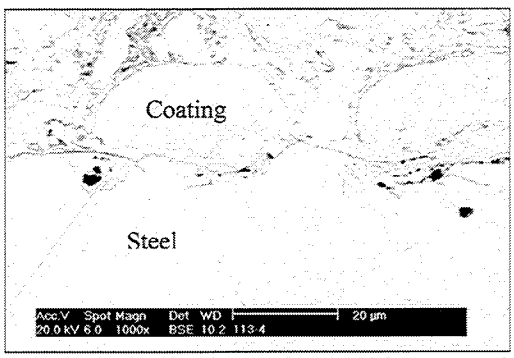


Fig. 4. Ni-50Cr HVOF coating, 1000 h exposure in oxidizing test atmosphere.

Ni-57Cr HVOF coating, material no. 4, did not suffer any corrosion damage itself. However, it was not able to protect the substrate. Corrosive species attacked the substrate via the voids and oxides, which existed at splat boundaries. In oxidizing conditions oxides were locally detected at coating/substrate interface. Ni-57Cr HVOF coating after 1000 h exposure in the

oxidizing atmosphere is presented in **Fig. 5**. The thickness of this oxide layer was less than 5 μm. In reducing conditions also chlorine and sulphur were detected at the interface. Also oxides of iron were detected in pores inside the coating. This indicates formation of iron chlorides at the interface.

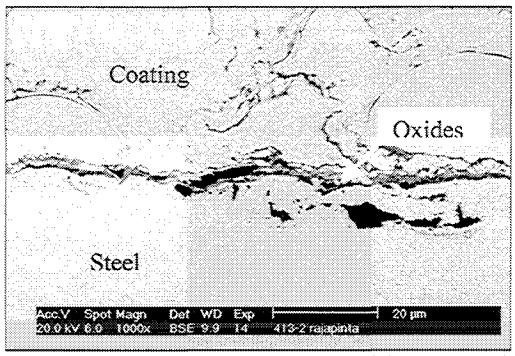


Fig. 5. Ni-57Cr HVOF coating, 1000 h exposure in oxidizing test atmosphere.

Ni-21Cr9MoFe HVOF coating, material no. 5 performed worse than the other Ni-based HVOF coatings. In the oxidising atmosphere oxides of chromium, nickel and molybdenium were found at the surface and also inside the coating. Oxides were detected to a depth of 50 μm. Oxides were detected also at coating/substrate interface. In reducing conditions a continuous layer of corrosion products were detected on top of the coating after 400 h. The outer layer consisted of nickel and sulphur, whereas the inner layer contained also chromium and oxygen. After 1000 h most of the corrosion products consisted of chromium and sulphur. Outer layer of corrosion products was very porous, which indicates formation of volatile corrosion products. Corrosion scales on Ni-21Cr9MoFe HVOF coating after 1000 h exposure in reducing atmosphere are presented in **Fig. 6**. The maximum thickness of the corrosion products was 100 μm. Sulphur was detected also inside the coating, and continuous corrosion products were found also at the coating/substrate interface.

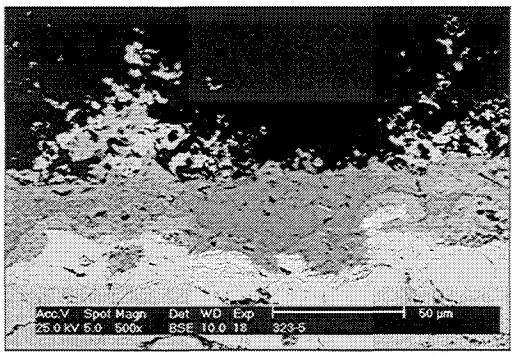


Fig. 6. Ni-21Cr9MoFe HVOF coating, 1000 h exposure in reducing test atmosphere.

Fe_3Al HVOF coating, material 6, suffered most corrosion damage of all tested coatings. In the oxidising atmosphere the outer layer of corrosion products consisted of iron and oxygen. The inner layer contained also some aluminum. Both layers were 30 μm thick. Beneath these

layers the coating was intensively oxidised to more than 500 μm, and also the substrate was corroded. In reducing atmospheres the thickness of the corrosion products was more than 200 μm. The outer layer consisted of iron and sulphur. The inner layer contained also some aluminum and oxygen. The outer corrosion layers were partially spalled. Corrosion damages were found throughout the coating and chlorine was detected also in the substrate.

Ni-50Cr coating, coating no. 7, was produced with Excalibur HVOF equipment. Corrosion resistance of this coating material was excellent. Some oxides were formed in the oxidising atmosphere and some sulphides in reducing atmosphere. Some of these coatings were severely cracked. Fractures penetrated all the way through the coating. Substrates were attacked through these fractures. Despite excellent corrosion resistance, this coating was not able to protect the substrate because of these through cracks. This kind of fractured structure is very hazardous, because formation of corrosion products at the interface may lead to spallation of the coating.

Laser melted Ni-57Cr HVOF coating, material no. 8, did not suffer any corrosion in these tests. The coating was partially covered with oxides formed during the laser treatment. These oxides contained small amounts of chlorine after the tests. These oxides may have further increased corrosion resistance of this coating. Areas without surface oxides were also examined. No signs of corrosion were detected in those areas. Laser melted Ni-57Cr HVOF coating after 1000 h exposure in oxidizing atmosphere is presented in **Fig. 7**.

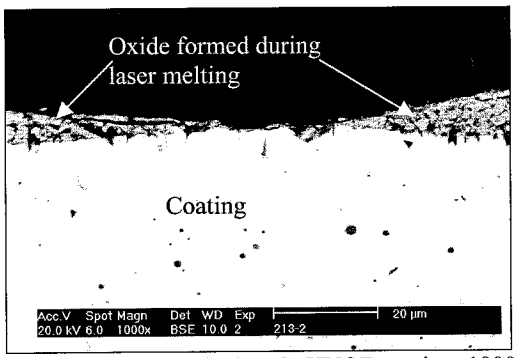


Fig. 7. Laser melted Ni-57Cr HVOF coating, 1000 h exposure in oxidizing test atmosphere.

Diffusion chromized coating, material no. 9, had very high chromium content at the surface. In the oxidizing atmosphere corrosion was not detected. The surface layer with high chromium content was brittle, and some cracks were detected. In the reducing environment corrosion products containing chromium, iron, sulphur, oxygen and chlorine were detected. Corrosion products were fragile and contained fractures. The diffusion chromized layer was very thin beneath the corrosion products. Some chlorine was also detected beneath the chromium rich diffusion layer.

Discussion

Effect of atmosphere

The temperature in the tests was 550°C. Low-alloy steels are normally used at this temperature, when clean fuels are combusted. Tests simulated combustion of chlorine containing fuels, and the corrosion rate of low-alloy steel was high in both atmospheres. In the oxidising atmosphere Cl, and in the reducing atmosphere Cl, H_2S, and low partial pressure of oxygen induced high corrosion rates. Chlorine itself was rarely detected in corrosion products, but formation of porous, layered corrosion products and high and linear corrosion rates indicate, that chlorine has actively taken part in corrosion reactions. Sulphides and also some oxides were formed in reducing conditions. The formation of oxides is due to presence of water vapor in atmosphere. Partial pressure of oxygen is high enough for oxide formation, if enough water vapor is present.

Effect of structure

Steels, laser melted coating and diffusion chromized coating were homogenous and dense in comparison with HVOF coatings. These materials suffered mainly uniform corrosion. Some grain boundary attack was detected on the low-alloy steel and also the diffusion coating was locally corroded through the thin diffusion layer. The corrosion resistance of these materials depends mostly on composition.

HVOF coatings are inhomogeneous. They consist of splats, which are separated by oxide films and voids formed during spraying process. Even the splats themselves are inhomogeneous, because they are solidified rapidly after impacting the substrate. Basically every splat is covered with a layer of oxides and voids that may act as a fast diffusion path for corrosive species through the coating. Voids and porosity form an interconnected network, which has a dominant role in corrosion resistance of the coating.

Although all the HVOF coatings were dense, the structures varied a lot. Excalibur HVOF coating contained plenty of oxides. The temperature during spraying must have been high as the porosity of the coating is low. Splats in this coating are very flat. This is a desired structure, when corrosion resistant coatings are produced. The distance from coating surface to coating/substrate interface along splat boundaries is very long. [32] Penetration of the corrosive species along splat boundaries was apparently non-existent. The drawback of heavily oxidized structure is, that the coating is very brittle. Fractures penetrated through the coating, and totally destroyed the protection capability of this coating.

The splats of the other HVOF coatings were less flattened. The distance from coating surface to coating/substrate interface along the splat boundaries was much shorter than in Excalibur HVOF coating. These coatings contained also more voids because of lower spraying temperature. As a result, protecting capability of the coating was dictated by the corrosion resistance of splat boundaries. Chlorine is known to attack oxides at elevated temperatures. It can be assumed, that chlorine also attacked the oxides on splat boundaries of tested HVOF coatings. Further optimization of spraying parameters is needed. Dense structure, highly flattened splats, and low oxide content are desired features for corrosion resistant coatings.

Laser melting is an effective method to homogenize the structure of HVOF coatings and improve corrosion resistance. Laser melted coating, that did not contain network of oxides and voids, protected the substrate much better than equivalent HVOF coating.

Effect of composition

The corrosion rate of the ferritic steel was very high in both atmospheres. Porous oxide, and sulphide layers were formed and these were not protective. The environment was too harsh for the ferritic steel, as anticipated before tests.

The corrosion resistance of austenitic steel was much better than the corrosion resistance of the ferritic steel, as expected. The partial pressure of chromium and nickel chlorides is lower than partial pressure of iron chlorides at elevated temperatures [16]. However, the shape of the weight change curve indicates, that a protective corrosion product layer did not form.

The corrosion resistance of nickel-based coatings varied with compositions. All materials performed well in oxidizing conditions. Higher chromium content seemed to increase corrosion resistance, especially in reducing conditions. The effect of minor additions cannot be estimated on the basis of these tests.

The corrosion resistance of Fe_3Al coating was very poor in both atmospheres. Adequate aluminum content, higher chromium content and pre-oxidation of the coating might have helped.

The corrosion resistance of chromium-rich diffusion chromized coating was superior to all other tested materials. However, chromium rich layer was thin and fragile, and applications must be carefully considered.

Conclusions

Dense materials with high chromium content performed well in corrosion tests. The corrosion resistance of nickel-based coatings was superior to corrosion resistance of ferritic steel. The best HVOF coatings were able to totally protect the surface material in these test conditions.

Corrosion attacked the substrate material through cracks and the interconnected network of pores and oxides at splat boundaries. The structure of HVOF coating is of major importance for corrosion resistance. Further optimization of spraying parameters is needed for maximum corrosion resistance.

Laser melting increased the corrosion resistance of HVOF coating by homogenizing the structure.

Acknowledgements

The National Technology Agency of Finland (TEKES), Kvaerner Pulping Oy, Fortum Power and Heat Oy, and Telatek Oy are acknowledged for financial support.

References

[1] S. Collins: Biomass-fired plants face down near-term challenges. Power, (1993), pp 51/53.
[2] K. Salmenoja: Field and laboratory studies on chlorine-indused corrosion in boilers fired with biofuels. Dissertation, Åbo Akademi, Finland, (2000).
[3] D.J. Gooch: Materials issues in renewable energy generating plants. International Materials Reviews, 45 (2000), pp. 1/14.
[4] H.P. Nielsen, F.J. Frandsen, K. Dam-Johansen and L. L. Baxter: The implications of chlorine-associated corrosion on the operation of biomass-fired boilers. Progress in Energy and Combustion Science, 26 (2000), pp. 283/298.
[5] M. Spiegel: Salt melt induced corrosion of metallic materials in waste incineration plants. Materials and Corrosion, 50 (1999), pp. 373/393.
[6] H.H. Krause and I.G. Wright: Boiler tube failures in municipal waste-to-energy plants. Materials Performance, 35 (1996), pp. 46/54.
[7] H.J. Grabke, E. Reese and M. Spiegel: The effects of chlorides, hydrogen chloride, and sulfur dioxide in the oxidation of steels below deposits. Corrosion Science, 37 (1995), pp. 1023/1043.
[8] J.E. Oakey, A.J. Minchener and N.J. Hodges: The use of high-chlorine coals in industrial boilers. Journal of the Institute of Energy, 64 (1991), pp. 3/11.
[9] W.T. Bakker and J. Stringer: Mixed oxidant high temperature corrosion in gasifiers and power plants. Materials at High Temperatures, 14 (1997), pp. 101/108.
[10] P. Kofstad: High Temperature Corrosion. (1988).
[11] K. Natesan: Applications of coatings in coal-fired energy systems, Surface and Coatings Technology, 56 (1992), pp. 185/197.
[12] Y. Kawahara: Development and application of high-temperature corrosion-resistant materials and coatings for advanced waste-to-energy plants. Materials at High Temperatures, 14 (1997), pp. 261/268.
[13] H.N. Tran, D. Barham and M. Hupa: Fireside corrosion in kraft recovery boilers--an overview. Materials Performance, 27 (1988), pp. 40/44.
[14] K. Salmenoja, K. Mäkelä, M. Hupa, R. Backman: Superheater corrosion in environments containing potassium and chlorine. Journal of the Institute of Energy, 69 (1996), pp. 155/162.
[15] M.J. McNallan, W.W Liang, S.H Kim and C.T. Kang: Acceleration of the high temperature oxidation of metals by chlorine in: R.A. Rapp (ed.) High Temperature Corrosion. 1981. San Diego California, pp. 316/321.
[16] A. Zahs, M Spiegel and H.J. Grabke: Chloridation and oxidation of iron, chromium, nickel and their alloys in chloridizing and oxidizing atmospheres at 400-700°C. Corrosion Science, 42 (2000), pp. 1093/1122.
[17] Y. Kawahara, N. Orita, M. Nakamura, S. Ayukawa, T. Hosoda: Application of new corrosion-resistant superheater tubings for a 500°C, 100 Kgf/cm2*g high-efficiency waste-to-energy plant. Corrosion/99, (1999), Paper 91, pp. 1/19.
[18] I.G. Wright: Hot corrosion in coal- and oil-fired boilers. Metals Handbook, 13 (1987), pp. 995/996.
[19] P.L. Daniel, J.M. Tanzosh and R. Hubinger: Estimating effects of chloride on fireside corrosion of furnace walls on coal-fired boilers. Materials Performance, (1989), pp. 41/45.
[20] B.O. Skrifvars, Chemical equilibrium analysis in the study of corrosion, Dissertation, Åbo Akademi, Finland, (2000).

[21] E.P. Latham, D.B Meadowcroft and L. Pinder: Coextrusion cladding for oxidation protection. Materials Science and Technology, 5 (1989), pp. 813/815.
[22] U. Brill and G.K. Grossmann: Corrosion behavior of weld overlays of the new alloy 50. Corrosion/2001, (2001), paper 170, pp. 1/11.
[23] S.C. Kung and R.A. Rapp: Recent development on corrosion-resistant diffusion coatings. Corrosion/99, (1999), paper 267, pp. 1/11.
[24] E.J. Morgan-Warren: Thermal spraying for boiler tube protection. Welding and Metal Fabrication, 60 (1992), pp. 25/31.
[25] M.S. Brennan and R.C. Gassmann: Laser cladding of nickel and iron base alloys on boiler waterwall panels and tubes. Corrosion/2000, (2000), paper 235, pp. 1/10.
[26] K. Luer, J. Du Pont, A. Marder: High temperature sulfidation of Fe_3Al and NiCr thermal spray coatings at 600°C. Corrosion, 56 (2000), pp. 189/198.
[27] L.N. Moskowitz: Application of HVOF thermal spraying to solve corrosion problems in the petroleum industry--an industrial note. Journal of Thermal Spray Technology, 2 (1993), pp. 21/30.
[28] V.V. Sobolev and J.M. Guilemany: Oxidation of coatings in thermal spraying. Materials Letters, 37 (1998), pp. 231/235.
[29] C.H. Lee and K.O. Min: Effects of heat treatment on the microstructure and properties of HVOF-sprayed Ni-Cr-W-Mo-B alloy coatings. Surface and Coatings Technology, 132 (2000), pp. 49/57.
[30] J. Tuominen, P. Vuoristo, T. Mantyla, M. Kylmalahti, J. Vihinen, P.H. Andersson: Improving corrosion properties of high-velocity oxy-fuel sprayed Inconel 625 by using a high-power continuous wave neodymium-doped yttrium aluminum garnet laser. Journal of Thermal Spray Technology, 9 (2000), pp. 513/519.
[31] J.R Nicholls: Discontinuous Measurements of High Temperature Corrosion. In H.J. Grabke and D.B. Meadowcroft (eds.) Guidelines for methods of testing and research in high temperature corrosion. European federation of corrosion publications, (1995), pp. 18.
[32] S.T. Bluni and A.R. Marder: Effects of thermal spray coating composition and microstructure on coating response and substrate protection at high temperatures. Corrosion, 52 (1996), pp. 213/218.

HIGH TEMPERATURE CORROSION IN STRAW FIRED POWER PLANTS: INFLUENCE OF STEAM/METAL TEMPERATURE ON CORROSION RATES FOR TP347H.

Melanie Montgomery[1], Ole Biede[2], Ole Hede Larsen[3]

[1]IPL – Materials and Process Technology, Building 204, Technical University of Denmark.
[2]Energi E2, Lautruphøj 5, 2750 Ballerup, Denmark.
[3]ELSAM A/S, Fynsværket, Havnegade 120, 5100 Odense, Denmark.

Abstract

The corrosion in straw-fired boilers has been investigated at various straw-fired power plants in Denmark. Water/air-cooled probes, a test superheater and test sections removed from the actual superheater have been utilised to characterise corrosion and corrosion rates. This paper describes the corrosion rates measured for the TP347H type steel. The corrosion morphology at high temperature consists of grain boundary attack and selective attack of chromium. The corrosion rate increases with calculated metal temperature (based on steam temperature), however there is great variation within these results. In individual superheaters, there are significant temperature variations i.e. higher temperature in middle banks compared to the outer banks, higher temperature in leading tubes, which have a high impact on corrosion. In a single loop the assumption that heat uptake (and heat flux) is linear with respect to tube length is an oversimplification. It has been observed that corrosion is higher at certain areas of the loop, presumably due to the localised high heat flux. In addition, the corrosion rate was also seen to decrease from one year to the next, although steam temperatures were the same. The difference in the results could be traced back to a lower flue gas temperature on one side of the boiler. Although metal temperature is the most important parameter with respect to corrosion rate, flue gas temperature also plays an important role. Efforts to quantify the effect of flue gas temperature on corrosion rate are on going.

Keywords: biomass, deposit corrosion, steam/metal temperature, heat flux, TP347H

1. Introduction

In Denmark, biomass (straw and/or wood) is utilised increasingly for generating energy in power plants. Straw combustion is coupled with corrosion problems that are not encountered in coal-fired plants. During combustion, potassium chloride and SO_2 are released in the flue gas and through condensation and deposition processes they will result in the formation of superheater deposits rich in potassium chloride and potassium sulphate. Many studies have been conducted, both in the field [1-7] and laboratory [8-10] to investigate corrosion due to straw-firing. Both the deposit composition (potassium chloride and potassium sulphate) and the flue gas composition affect the corrosion rates through synergistic effects. Corrosion models based on chlorination have been suggested. Laboratory tests show that metal temperature has primary importance in pure gaseous corrosion and the gas temperature is insignificant. However with deposit corrosion, the gas temperature and the temperature that this imparts to the deposit is also a significant parameter [9]. This paper will highlight some of the corrosion results for TP347H (18-8 steel) at various steam and flue gas conditions.

2. In situ corrosion exposures for straw-fired power plants

Corrosion exposures have been undertaken at the power stations Rudkøbing, Masnedø, Ensted and Maribo Sakskøbing. The boilers are all grate-fired boilers and their fuel is predominantly straw. The aim of the corrosion test programmes was to a) measure accurately corrosion rates of the existing superheater and b) measure corrosion rates of possible

alternative materials at higher temperatures. The type of exposures investigated were (i) metal rings on water/air cooled probes, (ii) sections in the existing test superheater and (iii) test tubes in a test superheater which is at higher temperatures than the actual superheater (Masnedø). Corrosion rates were calculated by measuring specimens before and after exposure. The "original metal thickness" minus "sound metal" was used to calculate the depth of corrosion attack, see schematic in Figure 1. In all corrosion investigations undertaken, the steam temperatures and surface metal temperatures have been either measured or calculated reasonably accurately. However flue gas temperatures have been more incidental and the measured temperatures show sizeable variation. i.e. in the order of 100°C.

3. Corrosion morphology

The mechanism of corrosion and various corrosion morphologies with respect to temperature has been described in detail [7].

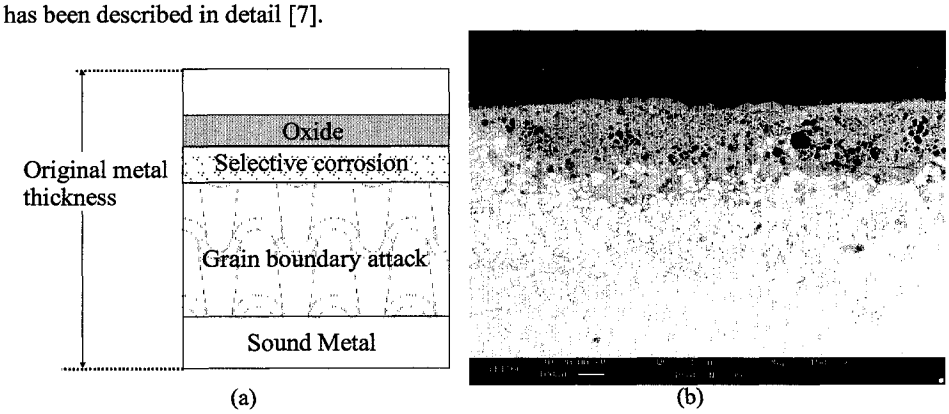


Figure 1: High temperature corrosion attack for TP347H a) schematic shows method to calculate depth of attack b) micrograph

Figure 1 shows a typical micrograph of the type of corrosion attack observed. Corrosion attack via grain boundaries occurs first, and then there is a selective depletion of chromium in the attacked grains, i.e. the metal grains that are surrounded by oxide in the middle of the micrograph contain only iron and nickel.

4. Corrosion rates with respect to calculated metal temperature

The results from the test superheater at Masnedø show that corrosion rate is low at the lower temperatures. As the temperature increases, the corrosion rate increases catastrophically (Figure 2). Since a linear corrosion rate is seen at the higher temperatures as the oxide formed is non protective, all corrosion rates have been converted to units of mm/1000 hours. Both the coarse-grained (CG) and fine-grained (FG) TP347H were investigated however there was no significant difference in corrosion rates at the higher temperatures. In this paper, surface metal temperatures and not steam temperatures are used, as it is more correct to compare corrosion rates with surface metal temperatures. The surface metal temperatures calculated from steam temperatures are based on measured inlet and outlet steam temperatures, pressure, steam flow, thickness of the tubes and thermal conductivity of the metal and inner oxide [11]. The results for TP347H from the four straw-fired plants are seen on an Arrhenius type plot in Figure 3.

Although the results show a clear trend that corrosion rate is dependent on metal temperatures, the spread of results is large. An undoubtedly significant parameter that has not been taken into account is the flue gas temperature, and this has shown itself significant in other studies [12,13]. The flue gas temperature will affect the surface temperature of the tube where corrosion occurs, and also affect the flue gas chemistry, especially the chloride-sulphur-alkali chemistry.

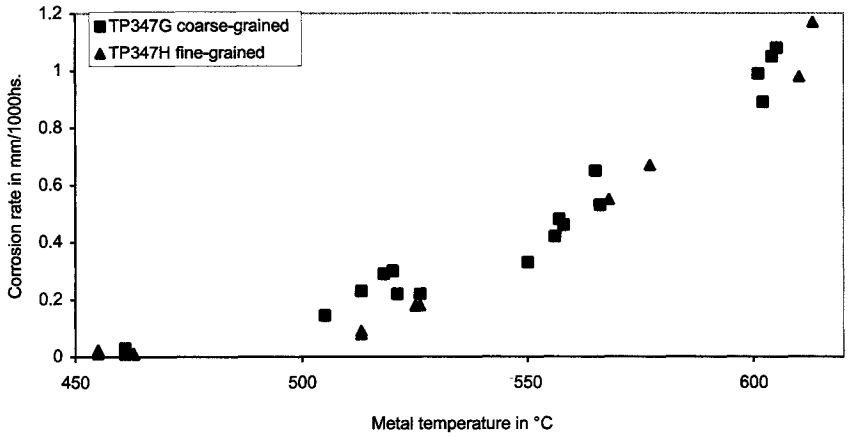


Figure 2: The effect of metal temperature, as measured on the test superheater at Masnedø CHP plant, on corrosion rate.

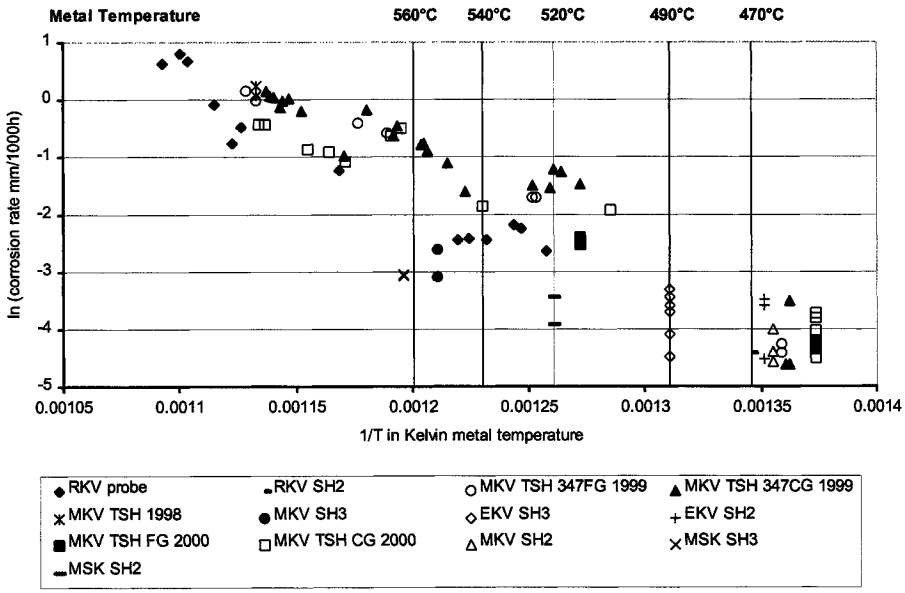


Figure 3: Corrosion rates for TP347H in various straw-fired plants illustrated on an Arrhenius type plot.

5. Effect of flue gas temperature

This section gives examples of how variation in the flue gas influences steam and metal temperatures and subsequent corrosion rates.

5.1. Measured temperature variations at Maribo Sakskøbing

Figure 4 is a schematic diagram of Masnedø CHP plant; Maribo Sakskøbing is very similar.

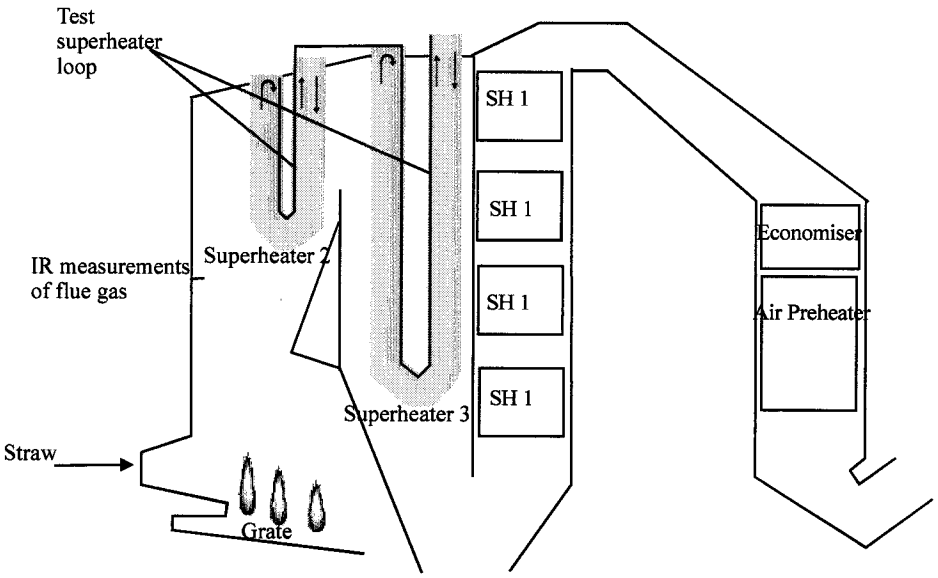


Figure 4: Schematic of Masnedø combined heat and power plant.

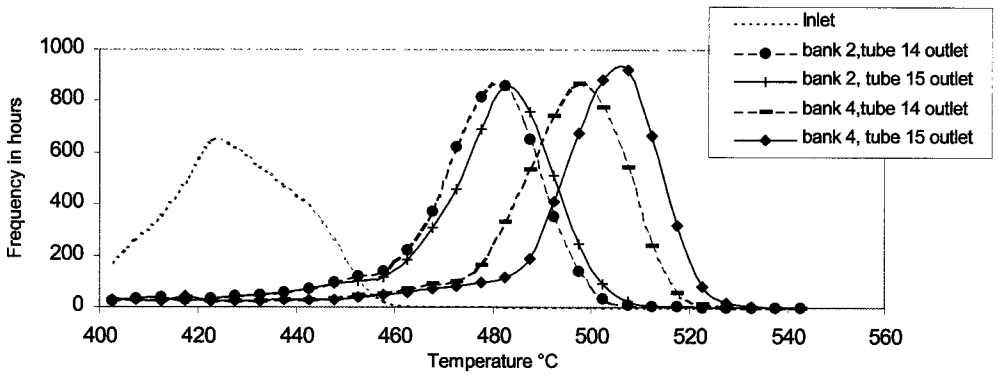


Figure 5: Temperature variation due to tube and bank position at Maribo Sakskøbing, superheater 2.

At Maribo Sakskøbing for superheater 2 and 3, steam temperatures have been measured in the penthouse for different tubes in different banks. Each superheater section consists of 8 banks with 15 tubes. The outermost and innermost tube is Tube 1 and 15 respectively. For superheater 2, despite the similar inlet temperatures for the eight banks, the outlet temperatures for example bank 4 and bank 2 can differ by 25°C, and this must be due to differences in heat flux because of different flue gas temperatures (Figure 5). Similarly for superheater 3, the outlet temperature differs by 15°C from the middle to outer banks. There is clearly a higher outlet temperature variation in the superheater 2 region as this is located in the first pass over the combustion zone. In addition, the innermost and outermost tubes in a bank incur the highest temperatures i.e. in this case both tube 1 and 15 can be designated as leading tubes. These tubes are only shielded on one side and therefore are more exposed to the effect of flue gas (Figure 5).

5.2. Results from test superheater at Masnedø showing effect of flue gas temperature

At Masnedø for the periods 1998-1999 and 1999-2000, a test superheater loop was built in as the innermost loop as shown in Figure 4. The final loop of this test superheater was situated in the superheater 2 region in bank 4 and had an inlet temperature of 500°C and an outlet temperature of 585°C. The inlet and outlet steam temperatures as measured online for the final loop in the two periods concerned were similar. Some interesting trends in corrosion rates were revealed by this final loop.

5.2.1. Variation of corrosion rates over a single loop

It would be expected that the residual metal thickness decreases the closer one comes to the outlet due to increasing temperature. External diameter measurements using a Vernier gauge show the profile in Figure 6. Due to the positioning of test sections, the external diameter was not measured for the whole loop in 1998-9. A similar trend with respect to external diameter was observed for the two periods.

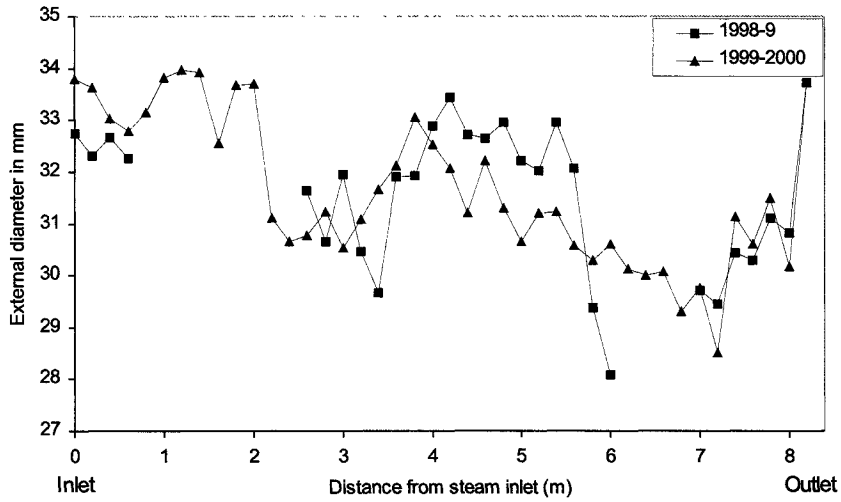


Figure 6: Post exposure external diameter along the length of the final loop in the test superheater, Masnedø.

The external diameter did not decrease evenly along the loop as would be expected but was significantly thinner about 3 metres from the inlet (described as "section 3 area" in this paper) after which the external diameter was higher.

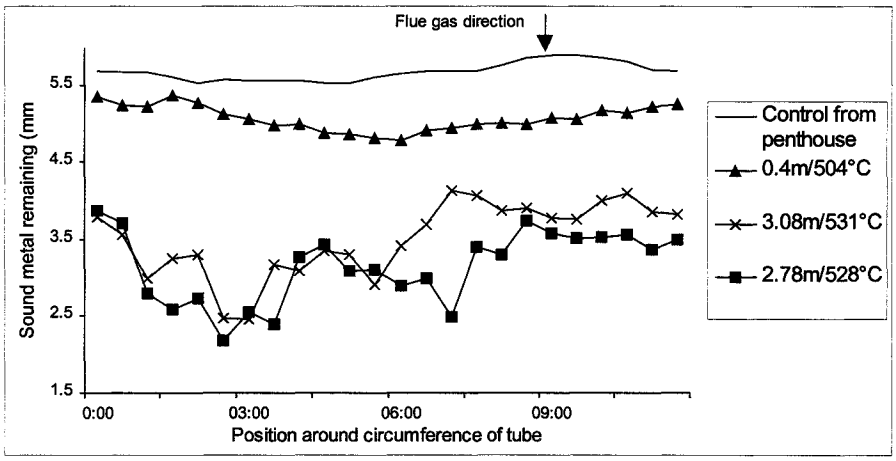
The correct corrosion rate cannot however be assessed by the external diameter measurement, but by a measurement of sound metal remaining due to the amount of selective and/or grain boundary corrosion that occurs as seen in Figure 1. Therefore for selected specimens in the loop from 1999-2000, the corrosion rates were measured using light optical microscopy at 24 positions around the circumference of the specimen. The measurements are given in Figure 7.

The legend on the diagrams shows the distance from the inlet in metres and the steam temperature. The steam and metal temperature through the test superheater loop was calculated in a simple way, assuming a constant heat flux on all parts of the superheater. Thus the calculated steam temperature increases linearly with superheater length and in all positions, the metal temperature is 36°C higher than the steam temperature. The control specimen used is from the penthouse: the tube dimensions were not measured before exposure. Variations in wall thickness of the control specimen were 0.4 mm. The first diagram is for the first part of the loop where steam flow is downwards. The next diagram is for the second part of the loop where steam flow is upwards. This shows that the corrosion rate increases at about three metres from the inlet, and then decreases to increase again in the last metre from the outlet (see curves for the 7.1m and 7.36 m specimens).

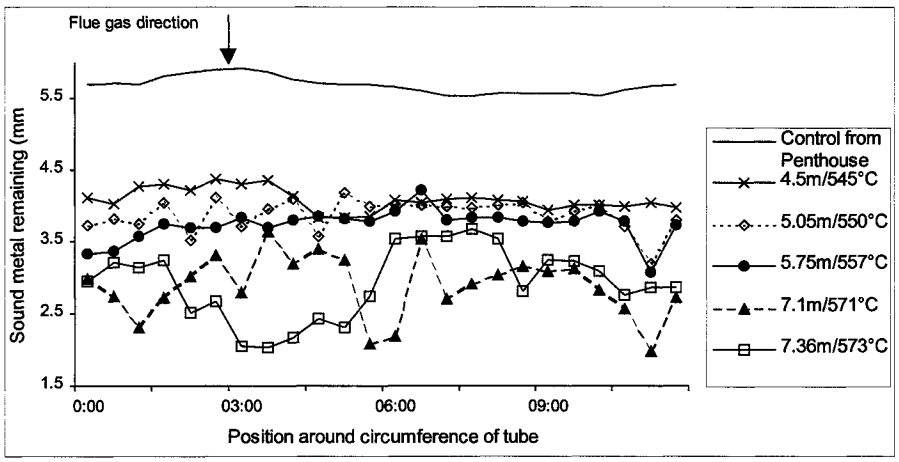
In addition, the corrosion rate varies over the circumference of the specimen. As shown on Figure 4, the test superheater loop is the innermost loop of the superheater and thus on the first part, the tube is shielded from the flue gas by the other tubes. The top figure in Figure 7 shows that in the area approximately 3 metres from the inlet, corrosion rate is highest on the opposite side of the flue gas direction, that is on the unshielded side. A difference of 1.5 mm in residual wall thickness is observed between the shielded and unshielded side. This effect is not seen near the steam inlet.

On the second part of the tube with upward steam flow, only the tube side opposite to the flue gas direction is shielded. In this area, the circumferential variations in wall thickness are not consistent, but a trend is seen with highest corrosion rates on the tube sides and partly on the tube front. This again indicates a higher corrosion rate on unshielded tube parts, where the deposit on the tube front partly has a shielding role. An exception is the specimen from 4.5 m which has similar corrosion rates around the circumference, indicating that the same amount of shielding given by the presence of an adjacent tube is also given by the deposit.

The assumption of constant heat uptake and heat flux over the length of the superheater loop is a simplification. To obtain a better understanding of the influence of flue gas temperature and heat flux on the surface temperature of the tube, the steamside oxide is being investigated. Based on steamside oxide thickness, a more accurate value for heat flux and thus a more precise metal temperature can be calculated.



a) Sound metal remaining from the first part of the loop. (i)



b) Sound metal remaining from the second part of the loop. (ii)

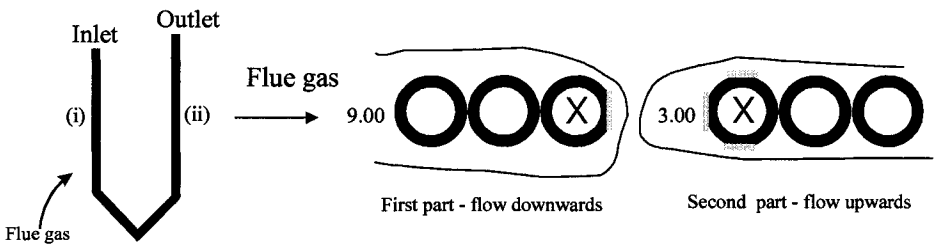


Figure 7: Sound metal remaining around circumference of the tube for the final loop in the test superheater, Masnedø.

5.2.2. Variation over two time periods

The corrosion rates for the 1998-9 and 1999-2000 periods were compared on an Arrhenius type plot (Figure 8).

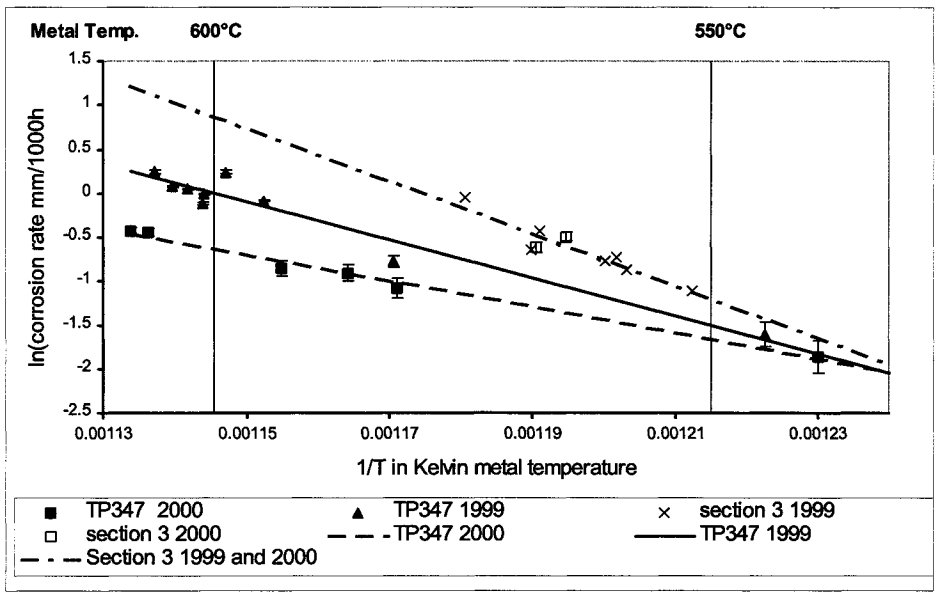


Figure 8: Comparison of corrosion rates for TP347H on test superheater for two consecutive years.

The values given are from an average worst case – i.e. the average of the highest quartile of results. The error bars show the variation in the control specimen. The corrosion rate over the main part of the loop and certainly for the areas which should have had a high steam temperature (based on inlet and outlet temperatures and assuming linear heat uptake over the length of the tube) shows differences from the first year to the next, actually a reduction in corrosion rate of approx. 50% at the highest metal temperatures. However the area which is 3 metres from the inlet (section 3 area) has similar high corrosion rates for the two periods. In the same way, the specimens just after the inlet close to the ceiling of the boiler have similar corrosion rates.

The inlet and outlet steam temperatures over the two periods varies by only a few degrees. Figure 9 compares the flue gas temperatures as measured by infrared sensors in the position shown in Figure 4. Two sets of measurements were conducted: IR 1 is positioned below banks 1-2 and IR 2 is positioned below banks 4-5. The specimens investigated were in bank 4. The IR 1 temperature for both periods was similar i.e. 1000°C however, IR 2 temperature was 800-900°C in 1999-2000, whereas it was around 1050°C in the first period. It is assumed that this lower flue gas temperature below banks 4-5 has resulted in the lower corrosion rates observed in 1999-2000. No other explanation has been found to explain the lower corrosion rates. It is worth noting that the "section 3" area has maintained high corrosion rates in both periods. No explanation for this has been achieved yet.

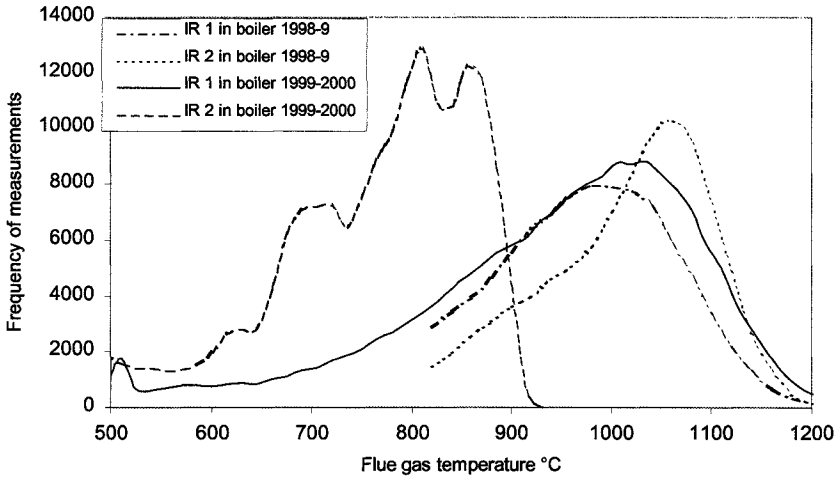


Figure 9: Flue gas temperatures in first pass measured at Masnedø 1998-99 and 1999-2000.

5.3.3. Re-evaluation of corrosion rates

Using the observations from the loop, an attempt has been made to classify the corrosion rates as being from a high or low flue gas temperature area (Figure 10).

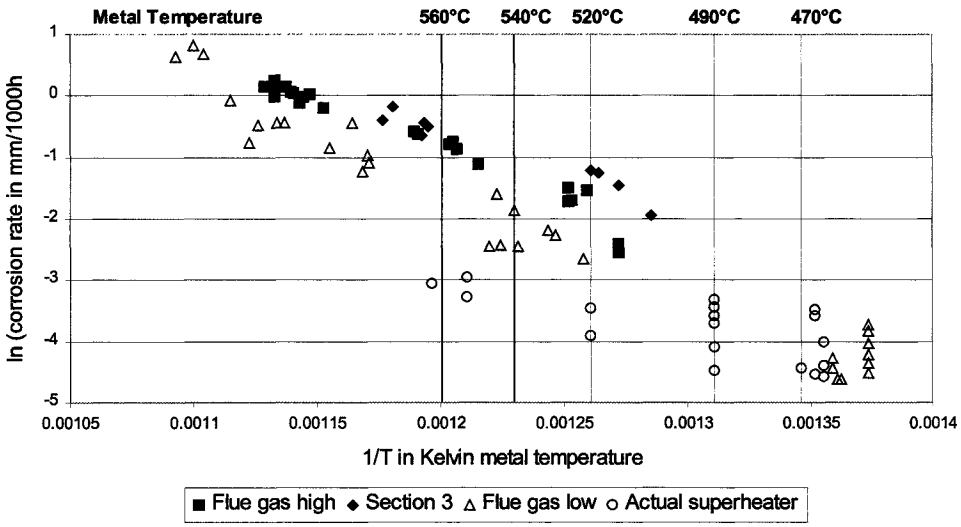


Figure 10: Corrosion rates of TP347H classified in high and low flue gas temperatures.

High flue gas designation is given for the first pass where temperature is higher than 900°C and in the area approx. 3 metres from the inlet (section 3 area). Low flue gas designation is given as lower than 900°C, areas close to the ceiling of the chamber and in the 2nd pass. The black symbols are high flue gas and the white symbols are low flue gas. From this a clear

effect of flue gas temperature on the corrosion rates is observed. However there is still a scatter in the results, for example, results from the actual superheater, and the "section 3 area".

6. Conclusions

Variations in flue gas conditions influence corrosion rates significantly when steam temperatures are also high. Based on temperature measurements it is seen that the inner and outermost tubes in the middle of the boiler have the highest steam temperatures due to the effect of flue gas temperature. A change in flue gas temperature from one year to the next also is believed to have reduced corrosion rates for specimens at high steam temperatures. The effect of flue gas direction is more significant for certain locations in the loop. Variations in corrosion rates are observed around the circumference of an individual tube indicating the effect of shielding from the other tubes. When assessing corrosion rates, it is important to be aware of areas where metal temperature is especially affected by flue gas temperature.

The flue gas temperature will affect the surface temperature of the tube where corrosion occurs. In the straw-fired plant, the deposit is important with respect to the corrosion mechanism. Flue gas temperature will affect the composition of the deposit and thus the microenvironment that is adjacent to the corroding surface. It will also influence the thickness and compactness of the deposit. These factors affect the temperature within the deposit adjacent to the metal and the possibility of melt formation, which leads to fast corrosion rates. Efforts to quantify the effect of the flue gas temperature on corrosion rates are ongoing.

Acknowledgements
PSO funding from ELTRA and Elkraft systems.

References

[1] O.H. Larsen and N. Henriksen: Proc. Power Plant Technology, Kolding 4-6 Sept. (1996) 7.1-7.18.
[2] N. Henriksen et al: VGB Conference Corrosion and Corrosion protection in Power plants 1995.
[3] F.J. Frandsen, H.P. Nielsen, P.A. Jensen et al: Paper from Eng. Found. Conf. "The Impact of mineral impurities in solid fuel combustion" Kona, Hawaii 1997.
[4] M. Montgomery and A. Karlsson: Materials and Corrosion 50, (1999) 579-584.
[5] M. Montgomery, FJ Frandsen, A. Karlsson, OH Larsen: "Effects of coal quality on Power Plant Management: Ash problems, Management and Solutions" United Engineering Foundation Inc., New York, NY and EPRI, Palo Alto, CA: 2001. 1001402. pp 3.37-3.49.
[6] M. Montgomery, B. Carlsen, O. Biede, OH Larsen, Paper 02379 presented at Corrosion NACE 2002, Denver.
[7] M. Montgomery, A. Karlsson, OH Larsen Materials and Corrosion 53 (2) 2002
[8] M. Montgomery and E Maahn: Proc. Eurocorr 1997 Trondheim.
[9] M. Montgomery in: Materials for Advanced Power Engineering (Eds. J.Lecomte Beckers, F. Schubert, PJ Ennis). Kluwer 1998.
[10] H.P Nielsen: Ph.D. Thesis, Technical University of Denmark 1998.
[11] N. Henriksen, O.H. Larsen, R. Blum:, Proc. Power Plant Technology, Kolding 4-6 Sept. 1996 pp 6.2.
[12] E. Häggblom, J. Mayrhuber. Conf. Proc. Materials for Advanced Power Engineering pp.91-109 1990.
[13] Y. Kawahara, M. Nakamura, T. Hosoda et al: NACE Corrosion 99 Paper 91.

SECTION 2

FUEL ISSUES AND NOVEL COMPONENTS

2.2. Miscellaneous Topics

EROSION CORROSION OF STEEL TUBES IN THE LOOP SEAL OF A BIOFUEL FIRED CFB PLANT.

Anna Nafari and Anders Nylund
Department of Materials Science and Engineering, Chalmers University of Technology
SE-412 96, Göteborg, Sweden

Abstract

Erosion corrosion during biomass combustion was studied through installation of a test superheater in the loop seal of the 30 MW_t Nässjö CFB boiler. The superheater tubes considered were made from the following alloys; X10 (Fe8.8Cr), Esshete 1250 (Fe15Cr9Ni6Mn), 347H (Fe17Cr11Ni) and AC66 (Fe27Cr32Ni). After one firing season (exposure time; 5242 h) the tube bundle was removed from the boiler. However, some tubes were reinstalled for a further firing season (total exposure time; 11392 h). Using metallography and Auger spectroscopy the exposed tubes were analysed with regard to material loss and corrosion products.

The degradation of the tube surface depended on material, temperature and position in the superheater. However, extending the exposure time with one firing season did not give a linear increase in material loss. The material suffering the hardest corrosion attack was X10 on which a continuous oxide scale formed around the periphery of the tube. On the other materials the corresponding oxide layer was thinner. The oxide structure on all four materials was the same consisting of one inner layer of Fe- and Cr-oxide and one outer layer of Fe-oxide. The three most alloyed materials also suffered from internal oxidation the degree of which was largest on the AC66 alloy.

Keywords: *loop seal, CFB-boliler, biomass, superheater, erosion corrosion.*

Introduction

To generate heat and electricity there has in recent years (in Sweden) been a move away from burning fossil fuels to biomass. Biomass has the advantage that it is considered carbon dioxide neutral and therefore is environmentally acceptable. However, due to the contents of alkali, chlorine, sulphur etc., the fuel is rather corrosive on the materials used in the power plants. During combustion, HCl and SO_2 are released in the flue gas and fly-ash deposits containing potassium chlorides and sulphates are formed on the material surfaces.

It is expected that the corrosion problems can be minimized if the cooling areas are located in the loop seal, of a Circulating Fluidised Bed (CFB), where the chlorine concentration is considered low [1]. Further, the heat transfer per unit area of tube surface is about 5-10 times more effective compared to that in the primary superheaters [2]. The superheater can then be made more compact which leads to savings in material and labour costs thus creating an economical space for using high alloyed and more sophisticated materials in the construction. The presence of fluidising particles in the loop seal can however increase the erosion problems.

The aim of this paper is to report results from an exposure of some ferritic and austenitic steels tubes which have been used in a superheater installed in the loop seal of a biomass fired thermal plant. Besides the corrosive atmosphere, the superheater tubes will be exposed to the incoming sand flow and deposits transferred with particles coming in from the cyclone. Steam temperatures around 500° C will generate material temperatures around 600 °C.

Experimental

A test superheater was installed in the loop seal of the 30 MW CFB-boiler in Nässjö (Sweden). The samples were 50 cm long tubes, welded together in a tube bundle. Before installation the wall thickness on each tube was measured with a micrometer gauge at the 30° intervals illustrated in Figure 1. The tubes were positioned in the tube bundle in such a way that the measurement could be repeated in the same point after exposure.

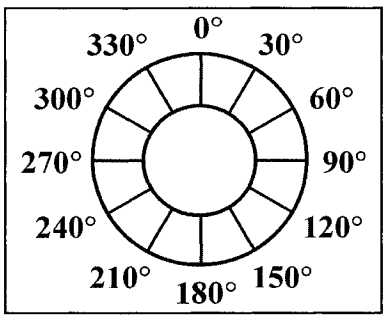


Figure 1. Positions for measurement of the tube wall thickness. 0°-180° coincides with the × direction in Fig.2.

After one firing season (5242h) the superheater was removed from the boiler and a new one was installed. Some of the tubes were then rewelded into the new one in order to study the effect of a long time exposure. The second firing season was 6150 h. The steam temperatures in the tubes at the inlet and outlet of the superheater were 470°C and 540° C, respectively. The corresponding material temperatures were estimated to be about 50-100° C higher. The examined materials and the alloy compositions are given in Table 1. Figure 2 shows their position in the tube bundle. The particles separated in the cyclone are coming in from the right on their way back to the combustion chamber. Fluidisation of the bed is achieved by air blown in from nozzles in the area below the superheater.

Table 1. Composition of the alloys (wt%) used in this study.

Alloy	Composition	Diameter × Wall thickness (mm)
347H	Fe17Cr11Ni0.05C1.6Mn0.8(Nb+0.5Ta)	33.7 × 5.6
AC66	Fe27Cr32Ni0.05C0.5Mn0.2Si0.01Al0.8(Nb+Ce)	33.7 × 4.5
Esshete 1250	Fe15Cr9Ni0.10C1Mo1Si6Mn1.3(V+Nb)0.005B	33.7 × 5.6
X10	Fe8.8Cr0.2Ni0.11C1.0Mo0.02Al0.36Si0.45Mn 0.3(V+Nb)	33.4 × 6.4

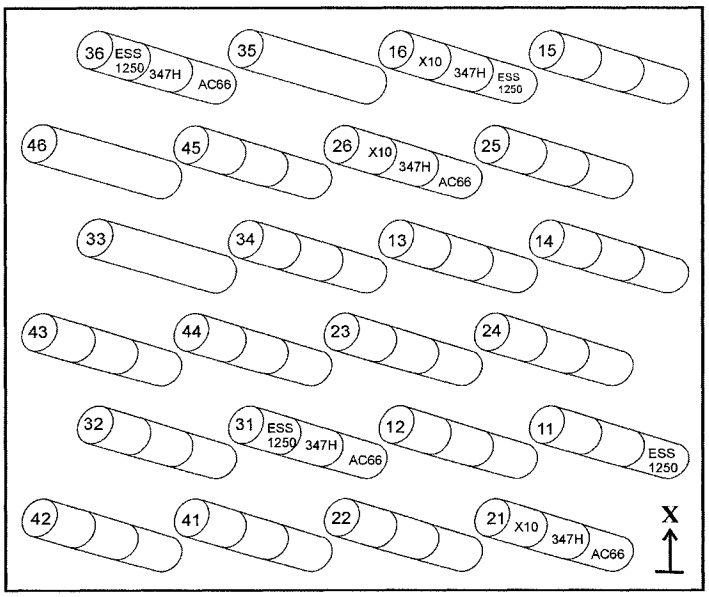


Figure 2. The position of the tubes in the tube bundle.

Samples for metallographic examination were prepared by cutting rings from the tubes, grinding on SiC-paper (1200 mesh) and polishing with diamond paste down to 1 μm. The thickness of the unattacked metal phase, as shown in Fig. 3, was then measured using an optical microscope, a modified Digital Microhardness tester FM-1 (Future-Tech Corp) with Digimatic Outside Micrometer (Mitutoyo).

The chemical composition of the corroded layers was determined by cutting samples from the rings and analysing with Auger spectroscopy (PHI 600). Some samples were prepared without the use of water or other polar liquids during cutting and polishing, which prevented the dissolution of any salt or sulphate particles in the oxide layers.

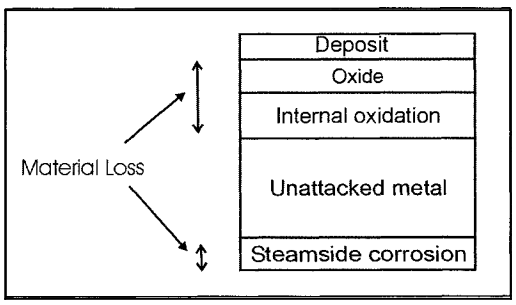


Figure 3. Schematic diagram showing the different layers in the tube wall after exposure.

Results

Chemical analysis performed at different occasions during the firing season gives that the biofuel used had a moisture content of 45-50 wt%, while the concentrations of Na, K and Ca in the dry ash were 0.6-1 wt%, 7-11 wt% and 12-22 wt%, respectively. Fourier Transform Infra Red (FTIR) Spectroscopy was used to estimate the gas composition. The concentration of the corrosive components H_2O, HCl and SO_2 were 5,6%, 7,2 ppm and 6,9 ppm, respectively. Deposits covered the exposed tubes on the leeward side, while in the direction of the particle flow they were eroded away. Their chemical composition was determined by collecting deposits on probes inserted into the loop seal. The subsequent Energy Dispersive X-ray analysis (EDX) showed that these contained K, Cl, Ca and S suggesting the presence of KCl and $CaSO_4$.

Table 2. The metal loss on the tubes examined. The angular intervals where the degree of material loss on the tube has been largest are indicated (see Fig.1 for definition).

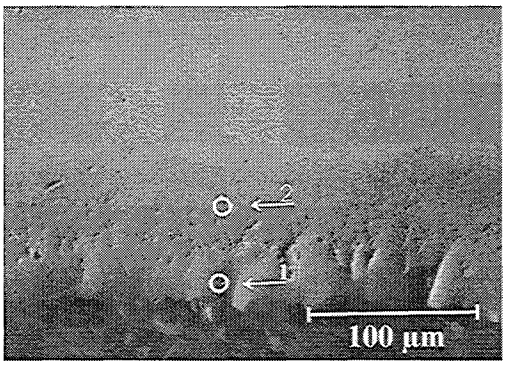
Tube number	Material	Exposure time (h)	Average material loss (µm)	Material loss, worst case (µm)	Internal oxidation (µm)
211	X10	5242	112	160 (285°-315°)	-
261	X10	5242	154	277 (195°-225°)	-
113	Esshete 1250	5242	47	82 (195°-225°)	Traces around the tube
163	Esshete 1250	5242	69	89 (345°-15°)	Traces around the tube
311	Esshete 1250	11392	36	98 (195°-225°)	Traces around the tube
361	Esshete 1250	11392	89	106 (165°-195°)	Traces around the tube
212	347H	5242	51	73 (285°-315°)	Traces around the tube
262	347H	5242	67	144 (105°-135°)	Traces around the tube
312	347H	11392	42	82 (285°-315°)	Traces around the tube
362	347 H	11392	100	180 (45°-75°)	Traces around the tube
213	AC66	5242	17	41 (195°-225°)	-
263	AC66	5242	45	113 (225°-255°)	54 (120° -240°)
313	AC66	11392	34	87 (165°-195°)	35 (120° -240°)
363	AC66	11392	38	118 (195°-225°)	43 (90°-210°)

Table 2 shows the corrosion attack as calculated by taking an average of the initial metal thickness and subtracting the average of unattacked metal thickness after exposure. A worst case has also been determined from the point of maximum material degradation. After one

firing season the average material loss is largest on X10 while the lowest was measured on AC66. On comparison the average material losses on Esshete 1250 and 347 H are about the same and just slightly larger than on AC66. However, Table 2 shows a difference in material loss between the average and worst cases. For the Esshete 1250, 347 H and AC66 alloys this is due to the fact that a large part of the surface region is unaffected. Corrosion has only taken place at certain points where the oxide products have grown into the metal phase. The phenomenon is especially pronounced on 347 H. The table also indicates the region where the material loss has been largest. This is probably coupled to the flowing conditions in the loop seal, which due to the presence of sintered particle bodies in the tube bundle have been complicated even further. Traces of internal oxidation are observed on the 347 H and more clearly on Esshete 1250, while AC66 showed a large degree of internal corrosion in the part of the tubes directly subjected to the particle flow. The internal oxidation entirely overlapped with the areas of worst metal loss.

Extending the exposure time to two firing seasons (tubes 31 and 36) does not give a linear increase in material loss. The results show that this is almost the same as for the tubes exposed for just one firing season. Thus, the erosion-corrosion rate is not constant. It is also clearly seen that the erosion-corrosion rate is influenced by the material temperature. Compared to tubes 21 and 31, the material temperature has been 70 °C higher on tube 26 and 36 for which the material loss is much larger.

An oxide formed by steam corrosion was observed on the inside wall of the tubes. The degree of attack was uniform around the tube wall. However, on AC66 it could only be detected after two firing seasons.



Apparent. at%

Point	O	Fe	Cr
1	71	29	-
2	69	24	7

Figure 4. SEM micrograph showing erosion corrosion attack on X10 (tube 161)

A scanning electron microscope (SEM) micrograph of the surface region on X10 is shown in Fig. 4. The oxide formed consists of two separate layers. From the atomic concentration table it is seen that the outer scale (point 1) consists of iron oxide while the inner part is a mixture

of Fe and Cr oxide (point 2). Chlorine Auger mappings have been recorded on the X10 oxide scales, Fig.5. The bright areas in Fig. 5b indicate Cl presence. It is clearly seen that Cl is enriched in the pores and at the metal/oxide interface between the metal and the oxide.

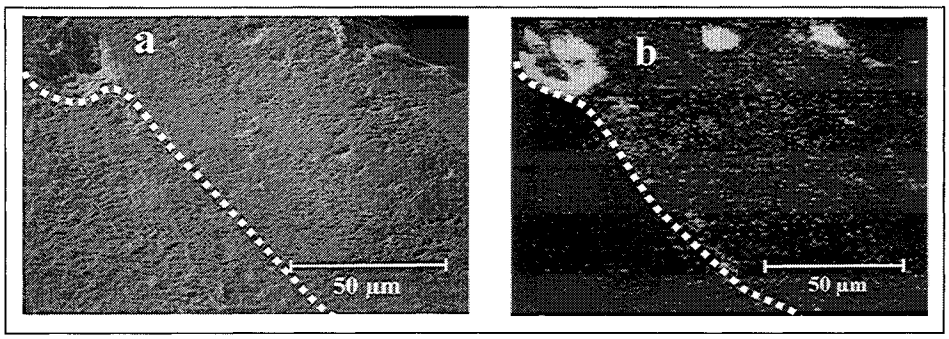
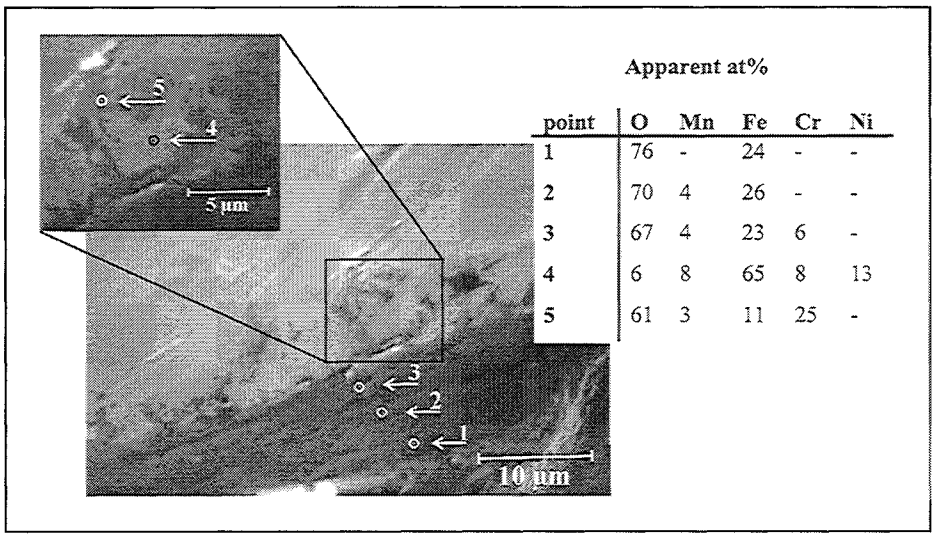


Figure 5. SEM micrograph (a) and chlorine Auger map (b) of oxide layer on X10 (tube 261). The oxide/metal interface is indicated by the dashed lines.



	Apparent at%				
point	O	Mn	Fe	Cr	Ni
1	76	-	24	-	-
2	70	4	26	-	-
3	67	4	23	6	-
4	6	8	65	8	13
5	61	3	11	25	-

Figure 6. SEM micrograph showing erosion corrosion attack on Esshete 1250 (tube 113).

The corroded layer formed on Esshete 1250, Fig. 6, is not uniform in composition. In the outer region it mainly consists of iron oxide, but in some points Mn is also detected (point 2). Chromium is only present in the inner region of the oxide (point 3) closest to the oxide/metal interface. In the region investigated some internal oxidation has taken place also. The analysis shows that Cr is depleted from the metal phase closest to the oxide (point 4) while the internal oxide is enriched in Cr (point 5).

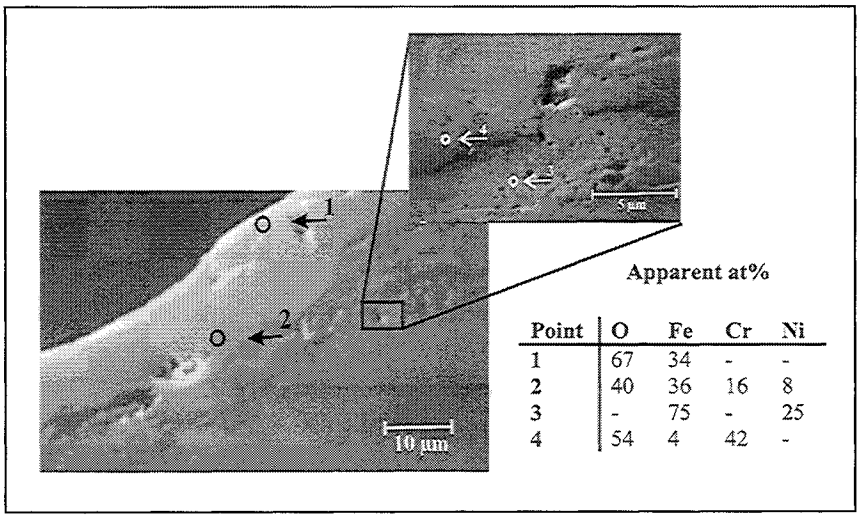


Figure 7. SEM micrograph showing the erosion corrosion attack on 347H, (tube 112).

Figure 7 shows the results received from Auger analyses of the corroded region on 347 H. The oxide layer mainly is a mixture of Cr- and Fe-oxides (point 2), only the outermost part showed any presence of a pure Fe oxide (point 1). Also on this alloy traces of internal oxidation were found. The internal oxide is again almost entirely composed of Cr oxide (point 4), while the surrounding metal phase was totally depleted of Cr (point 3).

AC66 was the alloy, suffering most from internal oxidation. This is clearly seen from Fig 8. Apparent atomic concentrations as determined from Auger analysis gives that the outermost part of the corrosion product predominantly consists of Fe oxide (point 1), while the underlying part is composed from a mixture of Cr and Fe oxide (point 2). The Cr concentration then increases even more in the internal oxide (points 5 and 7). The metal phase remaining closest to the outer continuous oxide layer is depleted in both Cr and Fe and consists of pure Ni (point 4). (The oxygen recorded arises from absorption on the sample during handling in the atmosphere.) However, the metal phase surrounding the innermost internal oxide phase is only depleted in Cr and contains both Fe and Ni (point 6).

The oxide layer has been mapped with respect to Cl as shown in Fig. 9. It is seen that Cl is strongly enriched in the pores. Further, Cl is also present in the outer parts of the oxide.

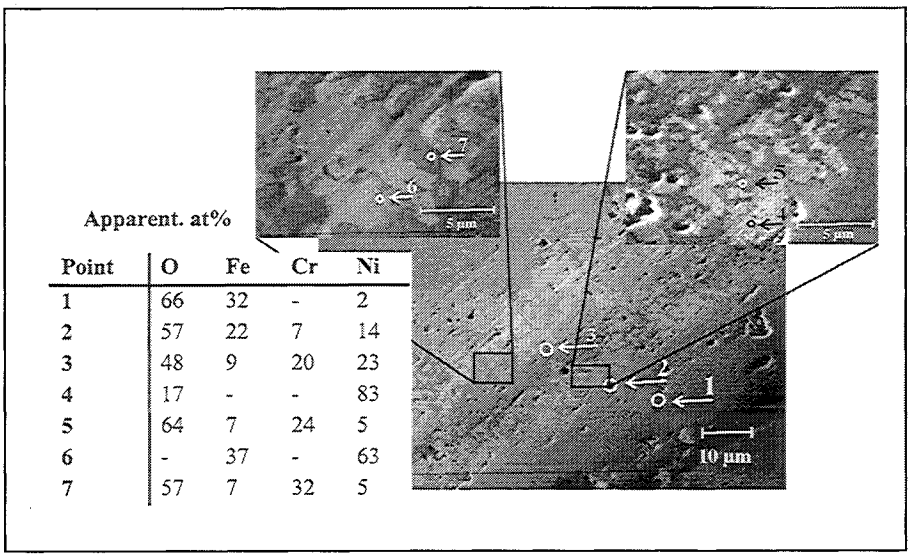


Fig. 8. SEM micrograph showing erosion corrosion attack on AC66 (tube 263).

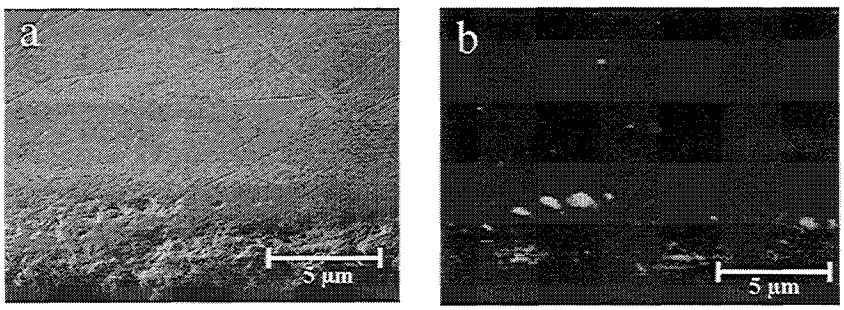


Figure 9. SEM micrograph (a) and chlorine Auger map (b) of oxide layer on AC66 (tube 263)

Discussion

Erosion-corrosion studies of superheater tubes exposed in the loop seal of a biomass fired CFB boiler showed that the material degradation is relatively low. The largest average corrosion attack measurment after one firing season was about 100-150 µm on the simplest

alloy, X10, and 20-50 μm on the high-alloyed AC66. However it should be considered that the materials subjected to long time exposure are all high alloyed and thus expected to show a good resistance towards high temperature erosion-corrosion. The corrosion rate increases with material temperature. In the case of X10, the average material loss was about 40 μm larger where the steam temperature had increased by 70°C. The tubes exposed for two firing seasons did not show any significant increase in material wastage. Thus, the oxide growth kinetics in the loop seal environment is non-linear and the oxide probably reaches its final thickness after a relatively short-term of exposure. The result shows that the erosion mechanism plays a minor part in the degradation process and that the materials are subjected almost entirely to pure corrosion rather than erosion corrosion. The particle flow pattern through the loop seal is very complex and not yet fully understood. Further, the fluidisation is also disturbed by sintered sand lumps in the decimetre range present in the tube bundle.

The observed corrosion products usually consist of two layers, one internal mixture of Cr- and Fe-oxide and one outer Fe oxide. Auger analysis has shown that Cl is present at the metal/oxide interface and in the pores of the oxide. Further K and S have also been detected in the same areas as the Cl. The chlorides from the deposits react with SO_2 and Fe_2O_3 to form chlorine gas, which then migrates through the oxide [3]. At the metal/oxide interface volatile metal chlorides are released according to eqs.(1) and (2);

$$Fe(s) + Cl_2(g) \rightarrow FeCl_2(s,g) \quad (1)$$
$$Cr(s) + Cl_2(g) \rightarrow CrCl_2(s,g) \quad (2)$$

The metal chlorides then migrate outwards and form metal oxides by reacting with oxygen in the regions with a higher oxygen partial pressure, according to eqs. (3) and (4).

$$2FeCl_2(g) + 3/2O_2 \rightarrow Fe_2O_3(s) + 2Cl_2(g) \quad (3)$$
$$2CrCl_2(g) + 3/2O_2 \rightarrow Cr_2O_3(s) + 2Cl_2(g) \quad (4)$$

The formation of the Fe oxide on top of the mixed Fe-Cr-oxide is explained by the lower equilibrium pressure of $CrCl_2$ in comparison with $FeCl_2$ [4]. Iron chloride will then migrate more readily out of the corrosion product and form Fe oxide at higher partial pressures of oxygen.

The corrosion resistance of Esshete 1250 is very good in spite of the fact that the content of alloying elements is lower than for 347 H and AC66. It can be speculated that sulphur from the base metal reacts with Mn instead of Cr, so that more Cr is available for the formation of a protective oxide scale [5]. This is underlined from S found in the oxide scale during Auger analysis.

In the areas of internal corrosion there is a strong depletion of Cr, the degree of which is largest on the alloy most rich in Cr, AC66. It has been observed [6, 7] that during combustion with biomass the selective corrosion increases with the Cr content of austenitic stainless steels. Earlier work has suggested that this effect is due to preferential attack of Cr carbides in the grain boundaries [8].

Conclusions

From exposure of four steel qualities in a superheater positioned in the loop seal of a biomass fired CFB plant the following conclusions have been drawn;

- The corrosion product usually consists of two layers; one outer Fe oxide and one internal mixture of Fe and Cr oxide.
- The degree of internal corrosion is largest on the alloy with the highest Cr content, AC66.
- The corrosion rate is larger on the tubes subjected to a higher steam temperature.
- The oxide growth kinetics in the loop seal environment is non-linear, after initial attack it stabilises at an approximate constant thickness.

Acknowledgements

KME (Consortium for Material Technology directed towards Thermal Energy Processes) is acknowledged for financing the project. The following industrial partners are also acknowledged for financing and supporting the project; Vattenfall AB for disposal of their plant in Nässjö, use of microscopy equipment and for environmental analysis in the loop seal, Kvaerner Pulping AB and AB Sandvik Steel for supplying the steel tubes. The department of environmental inorganic chemistry at Chalmers is also acknowledged for chemical analysis of the fuel.

References:

1. B-Å. Andersson, Kvaerner Pulping AB, Private communication (2002).
2. P. J. Henderson, P. Ljung, P Kallner and J. Tollin, "Fireside Corrosion of Superheater Materials In a Wood-Fired Circulating Fluidised Bed Boiler", Proc. Conf. Eurocorr 2000, London, Sept. 2000.
3. H. J. Grabke, E. Reese and M. Spiegel, "The Effects of Chlorides, Hydrogen Chloride, and Sulfur Dioxide in the Oxidation of Steels Below Deposits", Corrosion Science, Vol 37, No7 (1995) 1023-1043.
4. O. Knacke, O. Kubaschewski and K. Hesselmann (Eds), "Thermochemical Properties of Inorganic Substances", Verlag Stahleisen Gmbh, (1991).
5. P.H. Wihelmsson, "A New Sulfidation Resistant Austenitic Alloy for Fossil-fired Systems" Proc. Conf. Stainless Steels 84, London 1985, 541-547.
6. N. Henriksen and O H Larsen, "Corrosion in ultra supercritical boilers for straw combustion", Materials at High Temperatures, 12 (1997) 157-166.
7. M. Montgomery and A Karlsson, "In-Situ Corrosion Investigation at Masnedo CHP Plant- a Straw-Fired Plant", Materials and Corrosion, 50 (1999) 579-584.
8. D.A. Berztiss, M. Spiegel, H. Viefhaus and A. Schneider, "Role of Carbides in the High Temperature Corrosion of Austenitic Stainless Steels in HCl Containing Atmospheres", Proc. Conf. Eurocorr 97, Trondheim Sep1997, vol II, 29-34.

PERFORMANCE OF EROSION CORROSION RESISTANT COATINGS IN DIFFERENT COMBUSTION ENVIRONMENTS

Anders Hjörnhede and Anders Nylund
Dept. of Materials Science & Engineering, Chalmers University of Technology
SE – 412 96 Göteborg, Sweden

Abstract

Coated tubes of a low alloyed steel were exposed in three different types of combustion power plants; MultiBed Combustion (MBC), Circulating Fluidised Bed (CFB) and Pressurised Fluidised Bed Combustion (PFBC). The power plants were fired with $^2/_3$ biomass + $^1/_3$ coal, biomass and coal, respectively. In addition to laser coating two thermal coating techniques were used; arc-spray (air and nitrogen as carrier gas) and High Velocity Oxy Fuel (HVOF). In the MBC and PFBC plants the samples were located in the bed while in the CFB they were placed at the entrance to the cyclone. The material temperatures were 420°C, 550°C and 400°C in the MBC, CFB and PFBC, respectively. The corresponding exposure times in the three plants were 8000h, 3600h and 3300h.

On each tube the reduction in coating thickness was measured after exposure. Metallography was made on cross-sections of every coating. The chemical composition of the corrosion products and deposits formed was determined by EDX and Auger spectroscopy. The Ni-based coating Duroc 17x1%C showed the best overall performance in all power plants. Co - and Fe – based coatings had a good corrosion resistance in power plants fired with coal. However, in biomass fired plants a 100μm thick corrosion layer developed on the Fe – based coatings while Co – based coatings were subjected to a large degree of erosion – corrosion. Cavities were formed in all TiC – containing laser coatings. It is suggested that TiC oxidises with the formation of non-erosion resistant TiO_2. The HVOF – coatings containing Cr_3C_2 and WC also oxidised and peeled off the tubes.

Keywords: erosion – corrosion coatings, combustion power plant, thermal spray, laser cladding

Introduction

High temperature erosion corrosion is the major source for material wastage in combustion power plants. It is known that the synergy between erosion and corrosion can increase the degradation rate by an order of two magnitudes [1]. The influence of the erodent is governed by the size distribution, shape and hardness of the eroding particles as well as the composition, hardness and structure of the exposed material [2]. The oxidising/reducing properties of the surrounding atmosphere are strongly determined by the fuel used. This is also coupled to the release of HCl and SO_2 in the flue gas and KCl and K_2SO_4 in the fly-ash deposits. These components can give rise to varying degrees of accelerated corrosion [3].

Low alloyed steels give acceptable mechanical properties, but have poor erosion corrosion resistance at high temperatures. The lifetime of steel components can be increased by providing the surface with protective coatings [4]. The aim of this study is to evaluate the performance of coated steel tubes in three different types of combustion power plants. The coatings investigated were deposited with arc-spray, HVOF and laser techniques.

Experimental

Commercial coatings deposited on low-alloyed steel tubes with laser, HVOF and arc-spray (air or N_2 as carrier gas) were used in this study. The coatings and their chemical compositions are listed in Table 1. The coating thicknesses were in the range 0.8 -1.5 mm for

laser, 0.5 – 0.8 mm for arc-spray and 0.4 - 0.6 mm for HVOF. No pretreatment of the coating surface was performed before exposure.

The samples were exposed in three different power plants under different conditions (see Table 2 for details). In Värtaverket (Pressurised Fluidised Bed Combustion, PFBC) and Hallsberg Kraftvärmeverk (MultiBed Combustion, MBC) the test tubes were welded into the existing tube sets. The boiler tubes in Värtaverket (VV) in total consist of 25 loops with that

Table 1. Coatings used in this study; compositions, coating techniques and exposure plants.

Coating	**Composition**	**Coating technique**	**Värta-Verket (VV)**	**Nässjö Energiverk (NE)**	**Hallsberg Kraft-värmeverk (HK)**
Metcoloy 2	Fe12.4Cr0.6Ni0.4Mn 0.5Si0.36C	Arc-spray (air)	-	NE	HK
Metcoloy 2	Fe12.4Cr0.6Ni0.4Mn 0.5Si0.36C	Arc-spray (N_2)	-	NE	HK
Metcoloy 2	Fe12.4Cr0.6Ni0.4Mn 0.5Si0.36C	HVOF	-	NE	HK
Metcoloy 2	Fe12.4Cr0.6Ni0.4Mn 0.5Si0.36C	Laser	VV	NE	HK
Duroc 17x1%C	Ni25Cr8.8Mo1.9Fe 1.9Nb1.0C0.7Si	Laser	VV	-	HK
Stellite 6	Co28.5Cr4.2W1.1C 1.0SiNi<2.0Fe<1.5	Laser	VV	NE	HK
Duroc 17x1%C +TiC	85(Ni25Cr8.8Mo 1.9Fe1.9Nb1.0C0.7Si) 15TiC	Laser	VV	-	HK
Stellite 21 + TiC	85(Co27.0Cr5.5Mo 2.8Ni0.9Si0.25C Fe<2.0)15TiC	Laser	VV	NE	HK
Stellite 6 + TiC	85(Co28.5Cr4.2W1.1 C1.0SiNi<2.0Fe<1.5) 15TiC	Laser	VV	-	HK
Metco 3007	$80Cr_3C_2$16Ni4Cr	HVOF	-	NE	HK
Amperit 526	83WC17Co	HVOF	-	NE	-
Amdry 5843	86WC10Co4Cr	HVOF	-	-	HK

next to the air inlets defined as number one (i.e. the bottom of the boiler). Each coating quality was deposited on four different tubes positioned in loops 6,7,10 and 11. The test tubes in Hallsberg Kraftvärmeverk (HK) were located in the lowest loop of the boiler tubes, about 40 cm above the bottom nozzles. Thermal (arc-spray and HVOF) and laser coatings had been deposited on two separate tubes, respectively. The samples exposed in Nässjö Energiverk (Circulating Fluidised Bed, CFB) were deposited on a probe mounted at the cyclone entrance where the erodent is considered to be mainly fly ash with a high velocity. The temperature of the probe surface was regulated by water cooling of the interior tube wall and measured *in-situ* with four attached thermocouples. The temperatures of the coatings in VV and HK as

given in Table 2 are only estimations based on previous measurements. The fuel in Nässjö Energiverk (NE) consisted of wood chips, in HK it was a mixture of forest wastage and 30% coal while VV was fired with Polish coal powder. Mixing the latter with 20% water makes a larger condensation for district heating production possible. Dolomite was added in order to bind sulphur from the coal. Recirculation of ash caused a more complete combustion. Due to limited space, all coatings were not tested in all power plants.

After exposure an optical inspection was made in order to determine the location, colour and thickness of any deposits formed on the coatings. The roundness of the tubes was measured in a roundness profilometer (Mitutoyo Roundtest RA – 116). If possible, any deposits were then brushed off and the roundness was remeasured. The deposits collected were analysed by means of X-Ray Diffractometry, XRD (Bruker D8 Advance). The thickness and porosity of the remaining coating was optically measured on cross-sections of the tubes at every 30:th degree. The cross-sections were prepared by dry sectioning and dry grinding which prevented from any dissolution of the corrosion products. To avoid spallation of the surface products during sample preparation, the tubes were plated with Ni or coated with epoxy around selected areas. Perpendicular to the circular cross sections of the tubes new cross sections were dry cut and dry polished from the region of the incoming erodent. From these, the erosion corrosion products were determined by Auger spectroscopy (PHI 660) and EDX Energy Dispersive X-Ray analysis (LEO 1550 Gemini).

Table 2. Data from the field exposures.

Thermal Power Plant	**Värtaverket**	**Nässjö Energiverk**	**Hallsberg Kraftvärmeverk**
Boiler concept	PFBC	CFB	MBC
Exposure time	3342 h	3600 h	8172 h
Combustion temperature	850°C	850°C	-
Material temperature	380-420°C	550°C	400 - 450°C
Fuel	100% Coal	100% Biomass	70% Biomass, 30% Coal
Location	Evaporator	Cyclone entrance	Lower part of the boiler
Particle size	0.8 mm	Ash (<0.1 mm)	0.25 mm
Tube diameter	33.7 x 6.3 mm	43 x 3.7mm	50.8 x 6.35 mm
Tube composition	Fe1.5Cr0.3Mo	Fe1.0Cr0.5Mo	Fe1.3Cr0.44Mo
Total length of exposed coatings	3.5 m	0.22 m	5 m
Erodent velocity	0.9 m/s	-	>1 m/s

Results

The results received from the roundness measurements on the coatings exposed in VV are schematically shown in Fig. 1. The maximum material wastage takes place in the area subjected to the incoming erodent stream. Compared to the non TiC-containing coatings the TiC- containing ones suffer from an increased degradation in this position.

At an angle of ±(70°±30°) from the erodent angle of incidence deposits with a low adhesion to the coating surface formed. The colour of the deposits was different shades of grey. XRD-analysis showed that the deposits mainly consisted of gypsum ($CaSO_4$) and an oxide including the main alloying element of the coating, e.g. CoO on the Stellite 6 coating. The appearance of the Metcoloy 2 coating differed from the others. It was not covered with any deposits and the red/brown surface was uniformly degraded around the tube periphery.

The probe exposed in NE was completely covered with a several millimetre thick deposit. The colour varied from brown to grey with exception of that on the Metco 3007 coating which had a green appearance, probably due to the presence of Cr_2O_3. The deposits seemed to have been in a molten state at higher temperatures and their adhesion to the coating surface was very strong. Thereby only a minor part could be brushed away and no roundness measurements were possible.

No deposits formed on the coatings exposed in HK. The Fe-based coatings were subjected to corrosion on both the wind and leeward sides. In the same positions the carbide containing coatings Metco 3007 and Amdry 5843 peeled off. The peeling was observed to be more extensive on the latter.

Laser deposited Ni-coatings which do not contain TiC are basically defect and pore free and show a modest degree of corrosion after exposure in all power plants. Cobalt based Stellite 6 shows the same behaviour in VV but a 100μm grain boundary corrosion layer is detected in the surface region in NE and HK. An optical micrograph of a Duroc 17x1%C coating exposed in VV is shown in Fig. 2a. The coating/substrate interface is seen at the lower left of the figure. The microstructure is homogenous in the whole coating around the tube. However, the introduction of TiC as a hard phase results in formation of large pores and cavities during exposure as seen from Fig. 2b. The defects are concentrated around the impact area of the erodent and are suggested to originate from oxidation of TiC-particles. However, some unaffected TiC-particles dispersed in the coating matrix can also be seen from the microstructure.

In Fig. 3a a laser deposited Metcoloy 2 coating exposed in HK is shown. Irrespective of surface position a 50 - 200 μm thick corrosion layer is observed in the outer part of the coating (the dark area). The same type of corrosion layer is formed on arc-sprayed Metcoloy 2 coatings exposed in NE and HK. Metcoloy 2 coatings deposited with HVOF corrodes in NE and partially spalls in HK. EDX-analysis was performed in the areas shown in Fig. 3b. From the atomic concentrations estimated, Table 3, it is seen that areas 2 and 5 adjacent to the unaffected coating, are enriched in Cr while area 3 is depleted in Cr. Thus the corrosion scale consists of

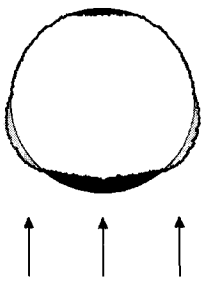


Figure 1. Cross section of an eroded tube. Black indicates erosion and grey deposits. The direction of the erodent stream is indicated by the arrows.

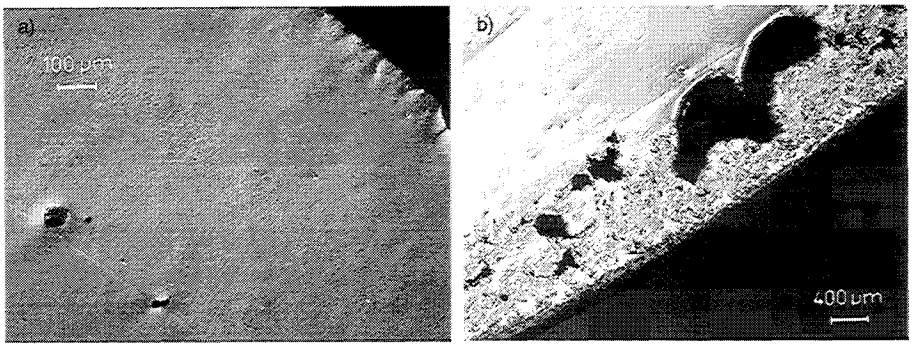


Figure 2. Optical micrographs of laser deposited a) Duroc 17x1%C and b) Duroc 17x1%C + TiC, coatings exposed in Värtaverket.

an outer Fe oxide rich layer and an inner layer with a larger Cr content. Further, K, Cl, Na and S are detected in parts of the oxide suggesting the presence of alkali chlorides from the biofuel.

The micrograph of the Metco 3007 coating shown in Fig. 4a is taken from an area close to the windward side of the tube. (The Ni-layer on top of the coating originates from the Ni-plating.) Auger analysis gives that the darker part mainly consists of Cr-oxide. A SEM micrograph of an Amperit 526 coating exposed in NE is shown in Fig. 4b. EDX-analysis in the marked points reveals that the original coating has totally vanished during exposure, no W or Co at all is detected, Table 4. Spectra 2, 4 and 5 are recorded from Fe-oxide rich areas. The penetration of Ni, spectrum 3 and C, spectra 4 and 5 from the Ni-plating and epoxy, respectively into the oxide, shows that this has a large degree of porosity.

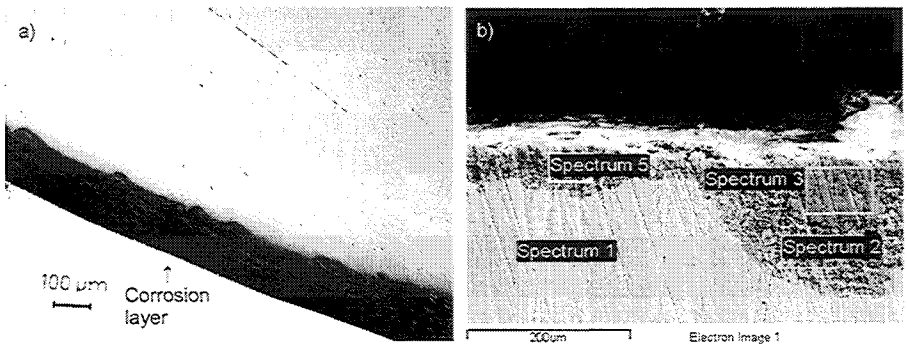


Figure 3. Laser deposited Metcoloy 2 coating exposed in Hallsberg Kraftvärmeverk. **a)** Optical micrograph. **b)** Areas selected for EDX analysis of the corrosion layer.

Table 5 summarises the elements found in selected coatings by means of Auger- and EDX-analysis. Calcium, K and S, detected in the laser deposited Metcoloy 2 coating in VV, probably reflects the presence of $CaSO_4$ and K_2SO_4. In the same way it is suggested that the corrosion layer on the Metco 3007 coating, exposed in NE, contains KCl, NaCl and WO_3. The biofuel is the source of the alkali chlorides. WO_3 originates from degradation of the Amperit 526 coating which was adjacent to the Metco 3007 coating on the probe. KCl was also found in the arc-sprayed Metcoloy 2 coating and on all samples exposed in HK due to the use of biofuel.

Table 3. EDX-analyses of selected areas in Fig. 3

Spectrum	O	Na	S	Cl	K	Cr	Fe	Others
Spectrum 1	0.00	0.00	0.00	0.00	0.00	12.49	86.63	0.88
Spectrum 2	23.60	0.00	0.13	0.21	0.58	19.84	54.03	1.60
Spectrum 3	27.07	0.00	2.31	0.22	0.00	4.60	64.92	0.88
Spectrum 5	26.57	0.52	0.17	0.34	0.43	19.12	51.44	1.40

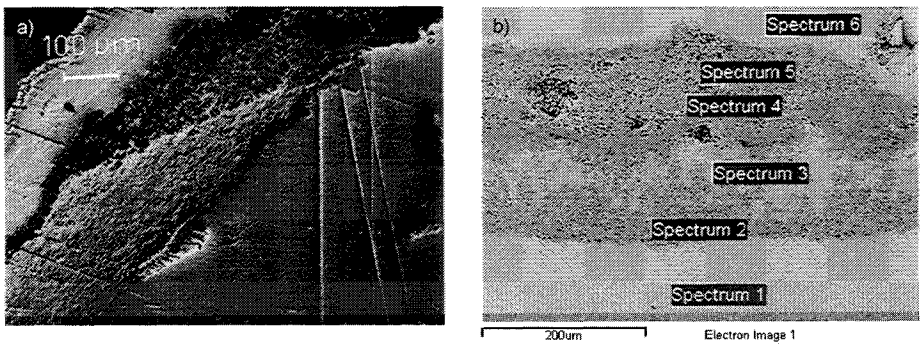


Figure 4. HVOF deposited coatings exposed in Nässjö Energiverk **a)** Metco 3007 where part of the coating has transformed into Cr-oxide. **b)** EDX-analysis of the steel tube from which the Amperit 526 coating has vanished.

In Figs. 5a-c the relative thickness of the coating remaining after exposure is shown for tubes exposed in VV, NE and HK, respectively. The largest remaining coating thickness was set to 1, even if erosion had occurred at that position. The leeward side was defined as 0° and the angle of incidence for the incoming erodent stream as 180°. From Fig. 5a it is seen that the Duroc 17x1%C and Stellite 6 coatings show the best performance in VV while the TiC-containing coatings are more eroded in the area subjected to the incoming erodent stream (140 - 220°).

Table 4. EDX-analyses of selected areas in Fig. 4

Spectrum	C	O	Cr	Fe	Ni	Mo
Spectrum 1	0.00	0.00	1.44	98.56	0.00	0.00
Spectrum 2	8.82	51.66	1.09	37.66	0.00	0.77
Spectrum 3	0.00	0.00	1.17	84.16	13.53	1.14
Spectrum 4	17.47	48.61	4.24	27.87	1.46	0.35
Spectrum 5	22.08	45.16	0.43	29.83	1.96	0.54
Spectrum 6	0.00	0.00	0.00	27.73	72.27	0.00

In NE the most severe erosion takes place in the region 120 - 240°, Fig. 5b. HVOF deposited Metcoloy 2 and laser deposited Stellite 21 + TiC and Stellite 6 coatings show the weakest performance while the degradation of the Metcoloy 2 coating arc-sprayed in N_2 is low. However, there has been a temperature gradient throughout the probe where the three most eroded coatings were subjected to material temperatures above 550°C while the temperature on the other two was below 550°C. Figure 5c shows that in HK the laser coated Duroc 17x1%C has the best erosion resistance. Metcoloy 2 arc-sprayed in air and the laser deposited Stellite 6 show a pronounced material wastage in the region 100 -230°, while Metcoloy 2, arc-sprayed in N_2, has a slightly better resistance towards degradation. However, the position for maximum material wastage varied between the coatings indicating different erosion conditions/mechanisms.

Table 5. Elements recorded during Auger and EDX analysis of the oxide in selected coatings. Elements written in italic are present in minor concentrations.

Coating	Värtaverket	Nässjö	Hallsberg
Metcoloy 2, laser	C, Ca, Cr, Fe, *K*, O, S	-	C, *Ca*, Cl, Cr, Fe, K, *Na*, O, S
Metco 3007	-	C, Cl, Cr, K, *Na*, O, S, W	C, *Ca*, Cl, Cr, Fe, K, O, S
Metcoloy 2, arc-sprayed, air	-	C, Cl, Cr, Fe, K, O, S	C, Cl, Cr, Fe, K, *P*, O, S

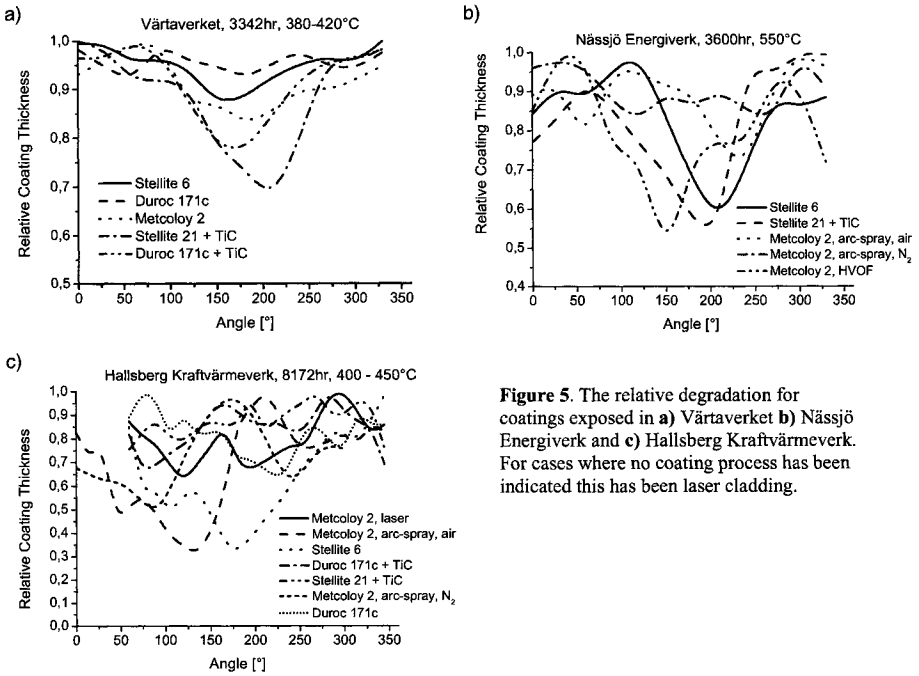


Figure 5. The relative degradation for coatings exposed in **a)** Värtaverket **b)** Nässjö Energiverk and **c)** Hallsberg Kraftvärmeverk. For cases where no coating process has been indicated this has been laser cladding.

Figure 6 shows the absolute degradation measured as the difference between the maximum and minimum thicknesses of the remaining coatings after exposure. The corrosion layers have not been taken into account. It is clearly seen that TiC-containing coatings exposed in VV and NE have degraded more than those containing no TiC. Further, in NE the thermally sprayed Metcoloy 2 coatings show a larger degradation resistance compared to the laser deposited ones. A similar result is seen from HK with exception of the Duroc 17x1%C coating. The Stellite 21 + TiC coating also shows a good performance but includes big pores and cavities. The larger absolute degradation in HK, compared to the same coatings exposed in VV and NE is due to the longer exposure time.

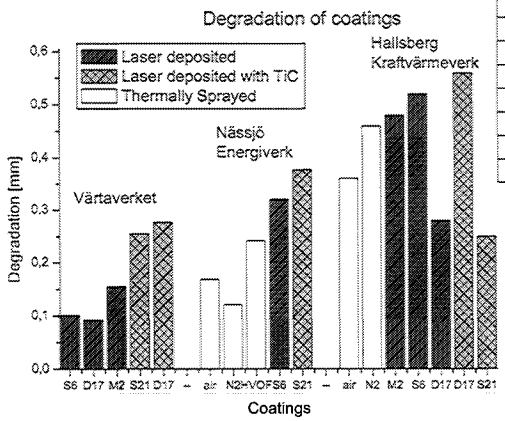
Discussion

This field test aimed to compare the erosion-corrosion resistance of various coatings on steel tubes in three different power plants. The results of the study are summarised in Table 6. The Ni-based coating, Duroc 17x1%C, deposited with laser showed the best overall performance. The Co-based Stellite 6 - and Fe-based Metcoloy 2 coatings exposed in power plants fired with biomass, suffer from grain boundary corrosion and severe overall corrosion, respectively but are more resistant in coal fired power plants. The grain boundary corrosion affected zone on Stellite 6 will enhance the material degradation due to erosion. This is clearly seen from the material wastage in the direction of the erodent stream in NE and HK. The thickness of the corrosion layer on Metcoloy 2 can be up to 200μm. The corrosion product mainly consists of Fe oxide, but Cr is enriched in the internal part of the oxide. Chloride is present in the corrosion layer for coatings exposed in biomass fired power plants. The formation and structure of the relatively thick porous oxide can be explained by recycling of $Cl_{2(g)}$ [5]. Potassium chloride condenses on the tube surface and reacts with SO_2 and Fe_2O_3 to form $Cl_{2(g)}$. The Cl_2 released then migrates through the oxide and reacts with the metal phase according to;

$Cr_{(s)} + Cl_{2(g)} \rightarrow CrCl_{2(s,g)}$ (1)

$Fe_{(s)} + Cl_{2(g)} \rightarrow FeCl_{2(s,g)}$ (2)

The metal chlorides formed are volatile at this temperature and move out through the oxide. As the O_2 partial pressure increases closer to the oxide/gas interface metal oxides are formed according to;



Abbreviation	Coating/technique
Air	Metcoloy 2, arc-sprayed in air
D17	Duroc 17x1%C, laser
HVOF	Metcoloy 2, HVOF
M2	Metcoloy 2, laser
N2	Metcoloy 2, arc-sprayed in N_2
S6	Stellite 6, laser
S21	Stellite 21, laser

Figure 6. The absolute material wastage for coatings exposed in the three power plants.

$2CrCl_{2(g)} + {}^3/_2O_{2(g)} \leftrightarrow Cr_2O_{3(s)} + 2Cl_{2(g)}$ (3)
$2FeCl_{2(g)} + {}^3/_2O_{2(g)} \leftrightarrow Fe_2O_{3(s)} + 2Cl_{2(g)}$ (4)

Table 6. The major degradation mechanisms of the tested coatings.

Coating	Värtaverket	Nässjö Energiverk	Hallsberg Kraftvärmeverk
Metcoloy 2, arc-spray, air	---	Corrosion	Corrosion
Metcoloy 2, arc-spray, N_2	---	Corrosion	Corrosion
Metcoloy 2, HVOF	---	Corrosion	Delamination
Metco 3007, HVOF	---	Delamination	Delamination
Amperit 526/ Amdry 5843, HVOF	---	Total oxidation of WC	Delamination
Metcoloy 2, laser	Erosion	---	Corrosion
Duroc 17x1%C, laser	Erosion	---	Erosion
Stellite 6, laser	Erosion	Erosion-corrosion	Erosion-corrosion
Stellite 21 + TiC, laser	Oxidation of TiC	Oxidation of TiC	Oxidation of TiC
Duroc 17x1%C + TiC, laser	Oxidation of TiC	---	Oxidation of TiC

The formation of the Fe – oxide outside the Cr – oxide is due to the lower equilibrium pressure of $CrCl_2$ in comparison with $FeCl_2$ [6]. Thus, $FeCl_2$ will move more readily out of the oxide layer and form Fe – oxide at higher partial pressures of oxygen. The absence of Cl in VV results in much thinner oxides and erosion is the major mechanism for material degradation. No differences in the thicknesses of the corrosion layers among the deposition techniques were observed.

All coatings containing carbides, Duroc 17x1%C + TiC, Stellite 6 + TiC, Metco 3007 (Cr_3C_2) and Amdry 5843/ Amperit 526 (WC), have failed completely independently of the power plant in which they where tested. TiC has oxidised to a large degree resulting in the formation of cavities and TiO_2. The WC-containing coatings partially spalled in HK and had totally vanished in NE, where the material temperature was higher, while the Metco 3007 coating partially spalled in HK and partially transformed to Cr-oxide in NE. XRD-analysis of TiC-powder exposed in air at 480°C for 2h showed that the vast majority of the TiC has formed TiO_2. Tests performed with WC-powder exposed in air for 17h at 500°C also showed that WC has almost completely reacted to WO_3. Exposure of Cr_3C_2-powder, under similar conditions, gave no indications of Cr-oxide formation.

It is suggested that the following reactions take place; $TiC_{(s)} + O_{2(g)} \leftrightarrow TiO_{2(s)} + CO_{2(g)}$ (ΔG^{800K} = -1018.3 kJ/mole), $2WC_{(s)} + 5O_{2(g)} \leftrightarrow 2WO_{3(s)} + 2CO_{2(g)}$ (ΔG^{800K} = -1988.6 kJ/mole) and $4Cr_3C_{2(s)} + 17O_{2(g)} \rightarrow 6Cr_2O_{3(s)} + 8CO_{2(g)}$. ($\Delta G^{800K}$ = -8357.8 kJ/mole). Thermodynamically, all three carbides will form an oxide both at room temperature and 500°C, since the Gibbs free energy, ΔG, is negative [7]. However, the reactions are kinetically governed and a high temperature is necessary to exceed the activation energy required for breaking the covalent bonds in the carbides.
The adhesion of the laser and arc-sprayed coatings to the tube surfaces is very good. However, HVOF-deposited coatings delaminated to a large extent, except for Metcoloy 2

exposed in NE. Contradictory to what is expected the adhesion strength of HVOF-deposited coatings in this case is lower compared to the arc-sprayed and laser deposited coatings [8]. The low adhesion strength in combination with the corrosive environment then easily results in coating delamination.

Conclusion

Coatings deposited on low alloyed steel tubes with arc-spray (air or nitrogen as carrier gas), HVOF and laser have been tested in three different types of combustion power plants. The conclusions are drawn as follows;

- Ni-based coatings have good erosion – corrosion resistance in both biomass and coal fired plants.
- Co – based coatings have good corrosion resistance in power plants fired with coal, but are subjected to erosion corrosion in biomass fired plants.
- Fe-based coatings have a good corrosion resistance in power plants fired with coal, but are subjected to corrosion in biomass fired plants.
- Carbide containing coatings are subjected to oxidation and a large degree of delamination in all power plants.

Acknowledgement

Professor Ingemar Olefjord is acknowledged for initiating the project and conducting parts of the evaluation. KME (Consortium for Material Technology directed towards Thermal Energy Processes) is acknowledged for financing the project. The following industrial partners are also acknowledged for financing and supporting the project; Midroc Metalock AB and Duroc AB for production of the coatings, Höganäs AB for production of powder, Kvaerner Pulping AB for supplying the steel tubes and Alstom Power Sweden AB, Birka Energi AB, Sydkraft AB, and Vattenfall AB for the disposal of their thermal plants.

References

1 A. Hjörnhede, R. Norling and I. Olefjord, "Proc. Int. Conf. EUROMAT 99, Munich, Germany, Sept. 27-30, 1999. Vol. 7, P. Neumann, D. Allen and E. Teuckhoff, Eds., (2000) 411-416.
2 A. Misra and I. Finnie, "On the Size Effect in Abrasive and Erosive Wear", Wear, Vol. 65 (1981) 359-373.
3 N. Henriksen and O. H. Larsen, "Corrosion in Ultra Supercritical Boilers for Straw Combustion", Material at High Temperatures, 12 (1997) 157-166.
4 Y Liu and A. V. Levy, "Erosion and Erosion-Corrosion Behavior of Chromized-Aluminized Stainless Steels at Room and Elevated Temperatures", Surface and Coatings Technology 43 – 44 (1-3) (1990) 836-847.
5 H. J. Grabke, E. Reese and M. Spiegel, "The Effects of Chlorides, Hydrogen Chloride, and Sulphur Dioxide in the Oxidation of Steels below Deposits", Corrosion Science, Vol. 37, No 7 (1995) 1023-1043.
6 O. Knacke, O. Kubaschewski and K. Hesselmann (Eds.), "Thermochemical Properties of Inorganic Substances", Verlag Stahleisen mbh (1991).
7 I. Barin, "Thermochemical data of pure substances", VCH, (1993).
8 A. Hjörnhede and A. Nylund, "Adhesion Testing of Erosion Corrosion Resistant Coatings", To be published.

HAFNON – A POTENTIAL CERAMIC MATERIAL FOR LIQUID SLAG REMOVAL IN PRESSURIZED PULVERIZED COAL COMBUSTION ?

Michael Müller, K. Hilpert, L. Singheiser

Forschungszentrum Jülich, IWV-2, D-52425 Jülich

Abstract

The corrosion behaviour of hafnon and a commercial Cr_2O_3-containing ceramic for comparison was investigated under simulated Pressurized Pulverized Coal Combustion (PPCC) conditions at 1450 °C in the presence of liquid slag. Cr_2O_3 containing ceramics show sufficient corrosion resistance because Cr_2O_3 has a miscibility gap with SiO_2 and there are no low melting mixtures with most of the slag components. The $(Cr,Al)_2O_3$ corundum phase is stable in the liquid slag, but other components of the ceramic, e.g. ZrO_2, are dissolved into the slag. The main disadvantage is the remarkable vaporisation of toxic Cr(VI)-species. Although hafnon ($HfSiO_4$) should be stable in the slag because of its phase diagram with SiO_2, it decomposes into the oxides depending on the SiO_2-concentration in the slag. The solubility of hafnon in the slag is not negligible, but there is less consumption per MWh thermal power of hafnon by dissolution than of Cr_2O_3 by vaporisation. Specimens of hafnon show relative good corrosion resistance. Only in a small outer penetration zone the silicate decomposes into the oxide. The thickness of this penetration zone depends on the homogeneity of the ceramic material and the SiO_2 content of the slag.

Keywords: hafnon, ceramic, slag, corrosion, pressurized pulverized coal combustion

Introduction

The limitation of fossil fuel resources and the urgency of reducing CO_2-emissions require the increase of the efficiency of power plants by using combined cycle power stations. Up to now efficiencies in excess of 50 % are only achievable using ash free fuels for example natural gas or oil. Coal constitutes 80 % of the world's total fossil fuel resources. By now coal fired power plants only reach efficiencies below 50 %, so that further development is essential. The Pressurized Pulverized Coal Combustion (PPCC) is a coal fired combined cycle concept which is able to achieve efficiencies in excess of 50 % [1].

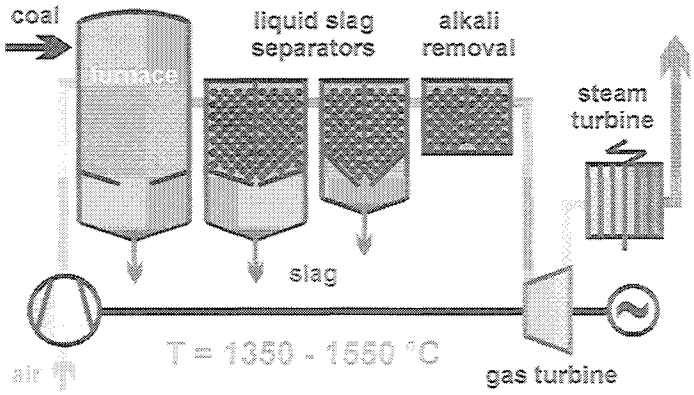


Fig. 1: Flow diagram of Pressurized Pulverized Coal Combustion (PPCC)

Gas cleaning related to fly ashes and alkalis is a necessary prerequisite for the direct use of combustion gas in advanced gas turbine systems. In case of PPCC the flue gas is routed through a column of ceramic balls as a slag separation unit and an alkali removal unit at an average temperature of 1450 °C before entering the gas turbine and the steam cycle (Fig. 1) [2]. In the liquid slag separator the liquid ash droplets deposit at the balls. The slag forms a thin film of molten slag at the surface of the ceramic balls and flows down the column. Thus, the ceramics are always exposed to a flowing film of slag and no solidified film of slag can be formed to protect the ceramic. The highly corrosive slag can react with the ceramic balls and corrosion takes place. Liquids from coal combustion contain high concentrations of SiO_2, Al_2O_3, Fe_2O_3, and alkali and alkali earth oxides which penetrate the refractory structure forming low-melting eutectic mixtures. These conditions in the slag separator system demand the following properties of the ceramics: high corrosion resistance in flue gas at T > 1400 °C, thermodynamic stability in the liquid slag, low or slight solubility in the liquid slag, no formation of low-melting eutectic mixtures with slag components, as well as low porosity, high density, and high homogeneity.

In the field of commercial ceramics only Cr_2O_3-containing ceramics show sufficient corrosion resistance in the PPCC test facility [3]. These refractories also showed a high corrosion resistance against coal slags in reducing coal gasifier atmospheres [4]. The main disadvantage in the oxidising atmosphere in PPCC is the remarkable vaporisation of toxic Cr(VI)-species [5, 6]. Thermodynamic calculations showed that especially the alkali oxides increase the Cr vaporisation. Prikhodovsky calculated that about 1 kg Cr_2O_3 evaporates per 1 MWh thermal power [6]. So, if Cr_2O_3 ceramics are used, an additional cleaning unit is needed. Therefore, other ceramic materials containing no Cr_2O_3 must be developed. In our investigations hafnon showed relative good corrosion behaviour in the field of IIIB-, IVB- and rare earth silicates [7].

Experimental

The corrosion behaviour of hafnon ($HfSiO_4$) and a commercial Cr_2O_3-containig ceramic (ICP-OES measurement: 31.0 % Cr_2O_3, 27.0 % Al_2O_3, 22.1 % ZrO_2, 11.7 % SiO_2, 1.4 % Fe_2O_3, 0.6 % MgO, 0.2 % TiO_2) which is in use in the PPCC test facility in Dorsten, were investigated. Hafnon was prepared by repeated milling and sintering the pure oxides.

The tests were conducted in Pt crucibles, in which 0.3 g ceramic powder or ceramic specimens (∅ 8 x 3 mm, one dimensional pressed and sintered at 1500 - 1700 °C) were covered with 2.1 g slag from a PPCC test facility (ICP-OES measurement: 36.2 % SiO_2, 27.0 % Al_2O_3, 14.4 % Fe_2O_3, 9.1 % CaO, 2.5 % MgO, 2.1 % Na_2O, 1.2 % K_2O) or a model slag with the same composition but 41.5 % SiO_2. Figure 2 shows a schematic representation of the experimental set-up. The ceramics were exposed to the slag at 1450 °C in pure oxygen under atmospheric pressure for 50 or 500 h. Pure oxygen was used because Fe_2O_3 is the stable oxide under typical conditions in a PPCC at a total pressure of 16 bar. The test temperature is much higher than the melting point of the slag. After tests with specimens, the crucibles were turned upside down and heated up to 1450 °C again so that the molten slag could drop down from the specimen. The slag was investigated by XRD and chemical analysis (ICP-OES). The ceramic powders were investigated by XRD. The ceramic specimens were investigated by ceramography, XRD, microscopy, and SEM.

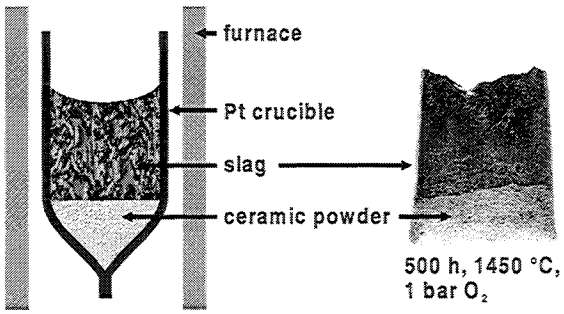


Fig. 2: Experimental set-up for the corrosion tests of different ceramics in liquid coal slag

Results and Discussion

Commercial Cr_2O_3-Ceramic

For comparison the corrosion behaviour of a commercial Cr_2O_3 ceramic which shows high corrosion resistance in the PPCC test facility was investigated. One reason for the corrosion resistance of Cr_2O_3 can be found in the phase diagram of the Cr_2O_3 - SiO_2 - Al_2O_3 system at 1700 °C [8]. It shows only solid phases and inmiscibility of Cr_2O_3 and SiO_2. There are also no low melting eutectic mixtures with the other main components of the slag. Our powder tests confirm the stability of the $(Cr,Al)_2O_3$ corundum phase (Fig. 3). Only the fraction of Al_2O_3 in the corundum phase decreases which can be shown by the shift in the lattice parameters. The chemical analyses of the slag shows that most of the ZrO_2 is dissolved in the slag. Up to 6 % ZrO_2 but only 0.2 % Cr_2O_3 is soluble in the slag. In case of a ceramic body the dissolution takes place much more slowly because of the relative small surface. Fig. 4 shows a one dimensional pressed specimen after 50 h exposure to original slag and its cross-section. The contour of the specimen is not damaged. But there is an up to 1 mm thick penetration zone in which the ZrO_2 is completely dissolved out of the ceramic body by the slag. Because this refractory is normally manufactured from the molten state and therefore very dense with very few pores at the surface, it shows very high corrosion resistance in the PPCC test facility although it contains high amounts of good soluble components such as ZrO_2 and Al_2O_3.

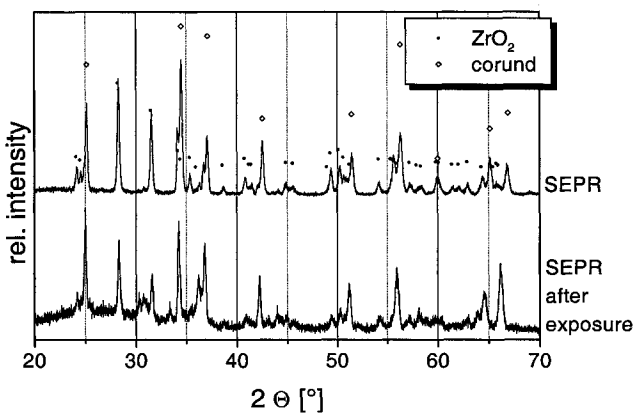


Fig. 3: XRD plot of Cr_2O_3-ceramic powder before and after 50 h exposure to slag at 1450 °C

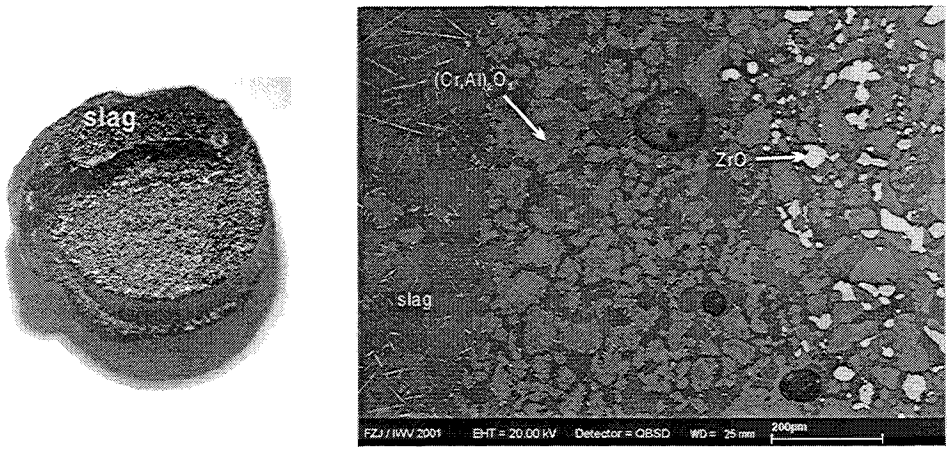


Fig. 4: Cr_2O_3-ceramic after 50 h exposure to original slag at 1450 °C, a) photo of the specimen, b) SEM picture (BSE) of the cross-section

Hafnon

The phase diagram of HfO_2 and SiO_2 [9] shows a miscibility gap of $HfSiO_4$ with SiO_2. Hafnon is the stable phase up to 1750 °C. With most of the other slag components no new phase or high melting phases are formed. Our powder tests show that the stability of hafnon in coal slags depends on the SiO_2 content of the slag (Fig. 5). In the original slag with about 36 % SiO_2 hafnon is not the stable phase, it decomposes completely into HfO_2. In the model slag with 41 % SiO_2 hafnon is nearly completely stable. Only a small amount decomposes. Using the oxide can be a problem because there is a change from monoclinic to tetragonal lattice below 1600 °C depending on purity of the oxide, which leads to inner stresses and fracture of the refractories. Stabilised ceramics cannot be used because the stabilising elements are dissolved selectively out of the ceramic.

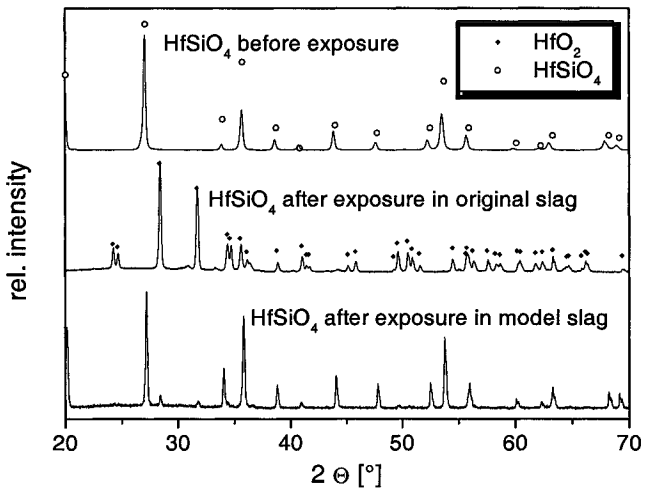
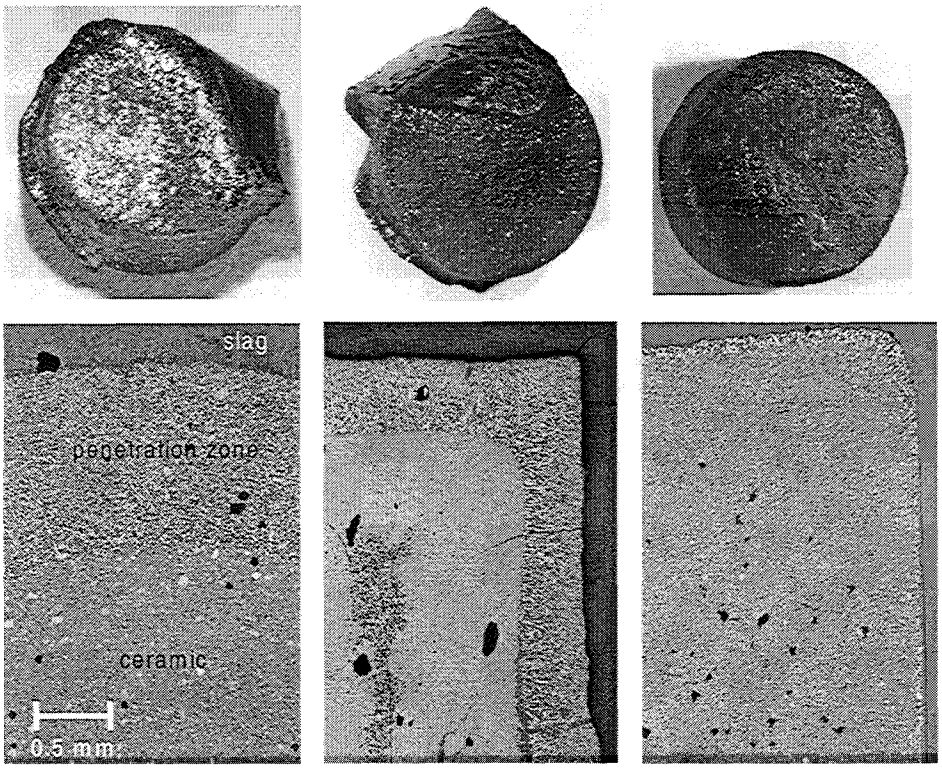


Fig. 5: XRD plot of hafnon powder before and after 500 h exposure to slag at 1450 °C

After the powder tests the original slag contains 0.4 % HfO_2 and the model slag 2,2 % HfO_2. So it has a higher solubility in the slag than Cr_2O_3. But the main mass loss of the Cr_2O_3 is caused by vaporisation. Therefore one should compare the maximum consumption of ceramic material per MWh calculated from thermodynamic data (assumption: coal with 30 GJ/t, 8 % ash, 10 % of the ash into the separator). If thermodynamic equilibrium is reached less than 0.03 kg $HfSiO_4$ per MWh_{th} is consumed by dissolution but about 1 kg Cr_2O_3 by vaporisation. With hafnon ceramics with optimised surface and microstructure thermo-dynamic equilibrium should not be reached so that the consumption of ceramic will decrease.



sintered at 1600 °C original slag | sintered at 1700 °C original slag | sintered at 1700 °C model slag

Fig. 6: One dimensional pressed hafnon specimens and their cross-sections after 50 h exposure to coal slag at 1450 °C.

Therefore, one dimensional pressed ceramic specimens of hafnon were exposed to the original and the model slag for 50 h. Figure 6 shows the hafnon specimens and their cross-sections after the corrosion test. The contours of the hafnon specimens are not damaged. The surfaces of the ceramics got a bit more rough due to the slag attack. The cross-sections show that the specimens which were sintered at 1700 °C have a finer and more homogeneous microstructure. They have also a higher density. The 1600 °C specimen has a density of 4.7 g/cm^3 (68 % relative density). The 1700 °C specimens have densities of 5.9 g/cm^3 (84 %

relative density). After exposure in original slag the hafnon specimen with rough microstructure has a penetration zone of about 1 – 1.5 mm, that with fine microstructure one of about 0.5 mm. So, a more homogeneous microstructure leads to less penetration and therefore to higher corrosion resistance. XRD measurements and SEM investigations (Fig. 7 and 8) in combination with EDX analysis show that in the penetration zone the silicates decompose into oxides. In the inner zone the silicates are stable. But there is also little corrosion attack. The grains are rounded. Slag elements, e.g. Fe, can be identified in the whole ceramic body. But this does not seem to have any influence on the mechanical stability of the ceramic at this time. This gives us hope that further improving of the ceramics by developing more homogeneous microstructure, higher density, and lower porosity, will lead to sufficient corrosion resistant refractories with sufficient lifetime.

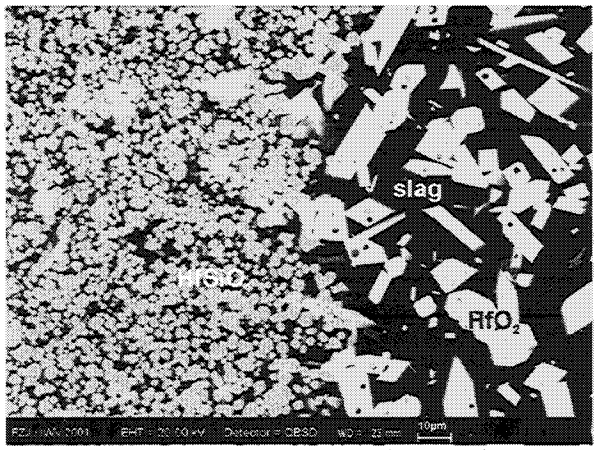


Fig. 7: SEM pictures (BSE) of the cross-sections of hafnon specimens after 50 h exposure to original slag at 1450 °C.

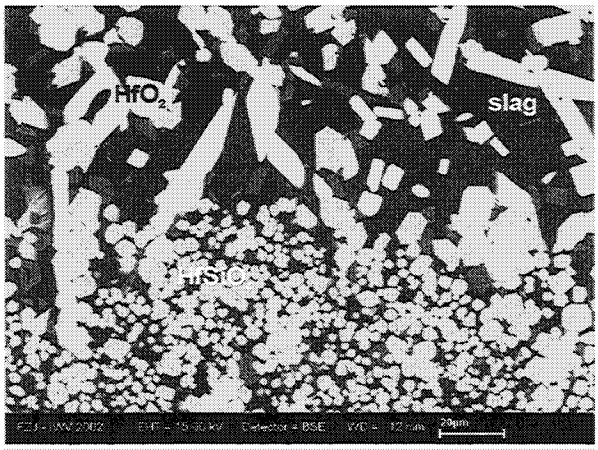


Fig. 8: SEM pictures (BSE) of the cross-sections of hafnon specimens after 50 h exposure to model slag at 1450 °C.

The specimen which was exposed to the model slag with higher amount of SiO_2 has a penetration zone of maximum 0.1 mm, because hafnon is nearly stable in this slag. In contrast to the specimens exposed to original slag in the penetration zone of the specimen exposed to model slag the silicate is not completely decomposed into the oxide. Figure 7 shows that at nearly every oxide grain a small amount of silicate is left. This confirms the great influence of the composition of the slag, especially the SiO_2 activity, which was found in the powder tests. But this also shows that the stability of a refractory, especially hafnon, last but not least depends on the coal quality. Monitoring and conditioning of coal quality is another problem which cannot be discussed in this paper.

Conclusions

The corrosion behaviour of hafnon and a commercial Cr_2O_3-ceramic were investigated in the presence of molten slag from a PPCC test facility in pure oxygen at 1450 °C.

Cr_2O_3 containing ceramics show sufficient corrosion resistance. The phase diagram of the Cr_2O_3 - SiO_2 system shows a miscibility gap. There are no low melting mixtures with most of the slag components. XRD measurements after exposure of the commercial ceramic to molten slag confirm the expected stability of the $(Cr,Al)_2O_3$ corundum phase. Other components, e.g. ZrO_2, are dissolved out of the refractory. The main disadvantage is the remarkable vaporisation of toxic Cr(VI)-species.

The phase diagram of the HfO_2 - SiO_2 system shows hafnon as a stable phase which has a miscibility gap with SiO_2. XRD measurements of hafnon powder after exposure to molten slag show that hafnon decomposes into the oxide when it is in contact with liquid slag containing 36 % SiO_2 and is stable in contact with slag with 41 % SiO_2. Chemical analysis of the slags show that hafnon has a relative low solubility (0.4 – 2.2 %) in the slag. In comparison to commercial Cr_2O_3-ceramics there is less consumption per MWh thermal power of hafnon by dissolution than of Cr_2O_3 by vaporisation. One dimensional pressed specimens of hafnon show relative good corrosion resistance. Only in a small outer penetration zone the silicate decomposes into the oxides. The thickness of the penetration zone depends on the microstructure of the ceramic and the composition of the slag, especially the amount of SiO_2. An improved microstructure of hafnon leads to higher corrosion resistance. So, further improving of the ceramic material should lead to sufficient corrosion resistant refractories.

One disadvantage of hafnon refractories which should be mentioned is the high price of hafniumoxide. But by now it is not possible to estimate the total refractory costs because the price and consumption of industrial manufactured refractories is still unknown. This information is needed to decide if hafnon is usable as refractory for this application.

Acknowledgement

The project is supported by BMWi, FKZ 0326844E

References

[1] K. Hannes, F. Neumann, W. Thielen, M. Pracht: "Kohlenstaub-Druckverbrennung", VGB-Kraftwerkstechnik 77 (1997), p. 393 - 400.

[2] K.W. Hannes: "Pilot Plant Test Results of Pressurized Pulverized Coal Combustion", Proc. of the EU Seminar: Status of development and market penetration of clean coal technologies (CCT) for power generation, Düsseldorf (1998), paper 18.

[3)] D. Pavone, W. Christmann, M.E.C. Foerster: "Ceramic Materials in a Pressurized Coal Combustion Process - a Survey", Proceedings of the 10th international IUPAC conference High Temperature Materials Chemistry, Jülich (2000), p. 13 – 19.

[4] J. Rawers, J. Kwong, J. Bernett: "Characterization of Coal-Gasifier Slag-Refractory Interactions", Materials at High Temperatures 16 [4] (1999), p. 219 - 222.

[5] P. Biedenkopf, T. Karwath, D. Kobertz, M. Rane, E. Wessel, K. Hilpert, L. Singheiser: "Vaporisation and Corrosion of Refractories in the Presence of Pressurized Pulverized Coal Combustion Slag", J. Am. Ceram. Soc., 84 [7] (2001), p. 1445-52.

[6] P. Biedenkopf, K. Hilpert, A. Prikhodovsky, L. Singheiser: "Forschung für die DKSF-Entwicklung am Forschungszentrum Jülich", Zweites Seminar Druckflamm, Aachen (2000).

[7] M. Müller, K. Hilpert, L. Singheiser: "High Temperature Ceramic Materials for Liquid Ash Removal in Pressurized Pulverized Coal Combustion", Proccedings of Euromat 2001, Rimini, Italy (2001), CD-Rom: 232.doc

[8] P.L. Roeder, F.P. Glasser, E.F. Osborn: "The System Al_2O_3-Cr_2O_3-SiO_2", Am. Ceram. Soc. Bull., 43 [4] (1964), p. 303.

[9] V.N. Parfenenkov, R.G. Grebenshchikov, N.A. Toropov, "Phase equilibriums in the hafnium dioxide-silicon dioxide system", Dokl. Akad. Nauk SSSR, 185 [4] (1969), p. 840-842.

HEAT RESISTANT SILICON NITRIDE CERAMICS WITH RARE-EARTH SILICON OXYNITRIDE

T. Nishimura, S. Guo*, N. Hirosaki, Y. Yamamoto, and M. Mitomo

National Institute for Materials Science, Advanced Materials Laboratory,
1-1 Namiki, Tsukuba, Ibaraki 305-0044, Japan
*Institute of Industrial Science, University of Tokyo
4-6-1 Komaba Meguro-Ku, Tokyo 153-8505,Japan

Abstract

Mechanical properties of silicon nitride ceramics with $Yb_4Si_2O_7N_2$ were investigated. Bending strength was 893 MPa at 1200°C and 711 MPa at 1400°C. Weight gain was 0.12 mg/cm^2 after oxidation at 1400°C for 100 h. Minimum creep rate was 4.9 x 10^{-9} s^{-1} at 1400 °C under 250 MPa of compressive stress in a nitrogen atmosphere. The present material showed higher heat resistance than previously reported silicon nitride ceramics. As a result of tensile creep test in air, the material did not fracture at 1300°C under 200 MPa for 636 h, which indicating that it can be practically applied up to 1300°C.

Keywords: silicon nitride, $Yb_4Si_2O_7N_2$, strength, oxidation, creep.

Introduction

Silicon nitride ceramic is a candidate for high-temperature structural applications, e.g., for gas turbine components, because of its high toughness and high-temperature strength. High-temperature properties must be improved, however, for efficient applications. Silicon nitride is a typical covalent material and dense ceramics cannot be obtained by sintering its pure powder. The silicon nitride ceramics are usually fabricated by liquid phase sintering technique. The liquid phase is formed by reacting oxide additives with SiO_2 on the surface of silicon nitride powder during heating. Rearrangement of silicon nitride particles and mass transfer occurs through the liquid phase, which remains as a grain boundary phase, usually amorphous, after sintering. The high-temperature properties of silicon nitride are determined by the grain boundary phase. Controlling grain boundaries is thus important in improving the high-temperature properties.

Silicon nitride sintered with Y_2O_3 retains high strength at high temperatures because Y_2O_3 forms a highly viscous grain boundary phase [1], but complete densification of the material is difficult. Crystallization of the amorphous grain boundary has been investigated by controlling chemical composition of additives and post-sintering heat treatment. A crystalline phase is chosen in a phase diagram of the Si_3N_4-SiO_2-RE_2O_3 system (RE: Sc, Y, lanthanide) because SiO_2 usually exists on the surface of silicon nitride raw powder. Crystallization of the grain boundary as $RE_2Si_2O_7$ was recently studied, because $RE_2Si_2O_7$ has a high melting point and oxidation resistance [2-4], e.g., the melting point of $Y_2Si_2O_7$ is 1775°C and that of $Yb_2Si_2O_7$ 1850 °C [5, 6]. It can exist with silicon nitride at equilibrium (Fig. 1) [7, 8], but long heat treatment is required to crystallize $RE_2Si_2O_7$. Even after long heat treatment, only the central part of multigrain junctions crystallized, while the interface

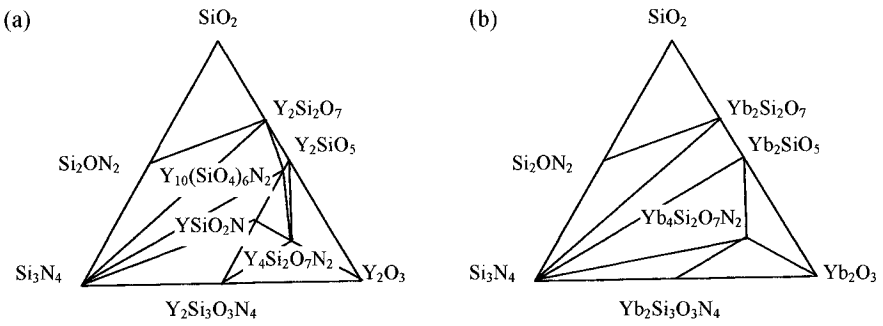


Fig. 1 Phase relationships in the system Si_3N_4-SiO_2-Y_2O_3 (a) and Si_3N_4-SiO_2-Yb_2O_3 (b).

between the grain boundary phase and silicon nitride grains remained amorphous [2, 4]. The room-temperature strength of heat-treated material was lower than that of as-sintered material. The strength of materials with $Yb_2Si_2O_7$ at 800 °C decreased over 30% [3]. This decrease is mainly due to residual stress from the thermal expansion mismatch between the silicon nitride and grain boundary phase, or by microcracking induced by volumetric change in the grain boundary phase during heat treatment [3, 9]. Rare earth silicon oxynitride, which contains nitrogen, has a closer chemical composition to silicon nitride than $RE_2Si_2O_7$. Problems with the residual amorphous phase, thermal expansion mismatch, and microcracking are expected to be solved by forming a rare earth silicon oxynitride as the grain boundary phase. In the system Si_3N_4-Y_2O_3-SiO_2, $Y_2Si_3O_3N_4$, $Y_{10}(SiO_4)_6N_2$, and $YSiO_2N$ can exist with Si_3N_4 at equilibrium (Fig. 1 (a)). The melting point of $Y_{10}(SiO_4)_6N_2$ and $YSiO_2N$ is low, so silicon nitride with $Y_2Si_3O_3N_4$ was studied. Si_3N_4 had sustained high strength at a high temperature [10] but low temperature oxidation was reported [11]. In the system Si_3N_4-Yb_2O_3-SiO_2, $Yb_4Si_2O_7N_2$ can coexist with silicon nitride (Fig.1 (b)), and its melting point is 1870°C [8], higher than that of $Yb_2Si_2O_7$ (1850°C) [6]. Silicon nitride with $Yb_4Si_2O_7N_2$ had high strength [12] and high creep resistance [13].

Research on heat-resistant metal and ceramics is on-going, mainly in applications to gas turbine components, in the High-Temperature Materials 21 Project at the National Institute for Materials Science (NIMS). Silicon nitride ceramics are used to attain a target of research, which is the development of a ceramic material that retains 1000 h creep life under 137 MPa at 1500°C. As mentioned above, silicon nitride with $Yb_4Si_2O_7N_2$ is heat-resistant and may be a reasonable candidate for this target. In the present work, the mechanical properties of silicon nitride with $Yb_4Si_2O_7N_2$ are measured.

Experimental procedure

Material

Powders of α-rich Si_3N_4 (SN-E10, UBE Industries, Tokyo, Japan), SiO_2 (99.9% purity, High

Purity Chemicals Co., Ltd., Saitama, Japan), and Yb_2O_3 (99.9% purity, Shin-etsu Chemical Co., Ltd., Tokyo, Japan) were mixed in ethanol for 2 h using a Si_3N_4 pot and balls, and dried in a rotation evaporator. The powder composition was Si_3N_4-2.4 mol% $Yb_4Si_2O_7N_2$. The dried powder was die-pressed into a rectangular-shaped powder compact, 80 mm x 45 mm x 13 mm, at room temperature under 20 MPa. The compact was then placed in a BN-coated graphite die and sintered for 1 h at 1800°C under 20 MPa, in a 1 MPa dry N_2 atmosphere, using a gas sintering furnace (FVPHR-R-10, FRET-40, Fujidempa Kogyo Co., Ltd., Osaka, Japan). The sintered specimen contained 11.95 wt% Yb_2O_3 and 0.46 wt% SiO_2. Grain boundary phases were determined by X-ray diffraction (XRD).

Measurement

Hot-pressed plates were cut into smaller pieces, 40 mm x 4 mm x 3 mm, for use as bending test specimens. Each bending test specimen was polished and edges were chamfered. A four-point bending test was conducted in a dry N_2 atmosphere at 1200°, 1400°, and 1500°C with a constant cross-head speed of 0.5 mm/min (inner span: 10 mm, and outer span: 30 mm).

To measure slow crack growth behavior, a surface flaw was introduced at room temperature using Vickers indentation at the center of the tension surface of the bending specimen. An indentation load of 98 N was used to produce initial cracks. Pre-cracked specimens were then annealed at 1200°C in a dry N_2 atmosphere for 5 h to eliminate residual stress. The four point bending test was conducted in a dry N_2 atmosphere at 1400°, and 1500°C with constant cross-head speeds of 0.5, 0.05, 0.025, 0.01 and 0.005 mm/min.

Oxidation tests were conducted at 1200°, 1400° and 1500 °C over 100 h in ambient air. Before and after oxidation, specimens were weighed using an analytical balance with an accuracy of ±0.001 mg. After oxidation, specimens were analyzed by X-ray diffraction (XRD) to identify oxidation products. The flexural strength of post-oxidized specimens was measured in four-point bending tests at room temperature.

A compressive creep test was conducted on a 3 mm x 3 mm x 10 mm specimen under 250, 300, 350, and 400 MPa at 1400°, 1450° and 1500°C in a N_2 atmosphere. Tensile creep was measured at 1300° and 1400°C under a stress of 125 to 200 MPa in the air as described elsewhere [14].

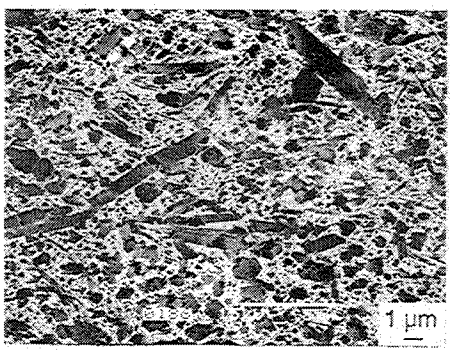


Fig. 2 Typical microstructure of sintered silicon nitride with.

Results and discussion

Material

Density, ρ, of sintered Si_3N_4 was 3.41 Mg/m^3, measured by the Archimedes method, and the relative density was

98.7%. In a typical microstructure of sintered Si_3N_4 ceramic after plasma etching (Fig. 2), the dark part is silicon nitride grain and the bright part is grain boundary phase. Elongated Si_3N_4 grains observed in the fine Si_3N_4 grains matrix, are called an "in-situ composite" microstructure. The fraction of the grain boundary appears very high, about half (Fig. 2), but it must be less than 10 %, calculated from raw powder composition. A long time is required to etch the elongated grain sufficiently, because the silicon nitride grain is etched in plasma etching. Finer grains completely disappear under this etching condition, which explains the reason for the apparently high fraction of the grain boundary.

The primary phase was β-Si_3N_4 according to XRD analysis, $Yb_4Si_2O_7N_2$ and Yb_2SiO_5 were also identified. The compositional reaction of $Yb_4Si_2O_7N_2$ and Yb_2SiO_5 is as follows:

$$2Yb_2O_3 + 1/2Si_3N_4 + 1/2SiO_2 \rightarrow Yb_4Si_2O_7N_2 \quad (1)$$

$$Yb_2O_3 \quad + \quad SiO_2 \quad \rightarrow Yb_2SiO_5 \quad (2)$$

Crystallization of the grain boundary phase occurred during sintering. Similar crystallization of the grain boundary amorphous phase was previously reported in Si_3N_4 ceramics, under the same compositions, hot-pressed at 1750°C [12, 13]. Yb_2SiO_5 formed in our experiments. An oxygen impurity exists as SiO_2 on the surface of Si_3N_4 raw powder, so the mixed powder composition is in the Si_3N_4-$Yb_4Si_2O_7N_2$-SiO_2 triangle, not on the Si_3N_4-$Yb_4Si_2O_7N_2$ tie line. Hot pressing was conducted in 1 MPa nitrogen and SiO_2 vaporization was inhibited, crystallizing Yb_2SiO_5.

Young's modulus was 328 GPa and the shear modulus 129 GPa when measured using pulse-echo method, typical of sintered silicon nitride. Fracture toughness measured by indentation technique [15] was 7.4 $MPam^{1/2}$, also typical of silicon nitride with an in-situ composite microstructure.

Strength

Flexural strength (Fig. 3) decreased with increasing temperature, averaging at 711 MPa at 1400°C and 500 MPa at 1500°C [16]. The strength of silicon nitride ceramics with $Yb_2Si_2O_7$ was 567 MPa at 1300°C [17] and that of with $Yb_2Si_2O_7$ + Yb_2SiO_5 520 MPa at 1350°C [9]. The strength at 1500°C reported for Y_2O_3-doped silicon nitride was 500 MPa [18]. The high-temperature strength of our material is comparable to heat-resistant silicon nitride ceramics reported previously [3, 9, 10, 15, 17, 18].

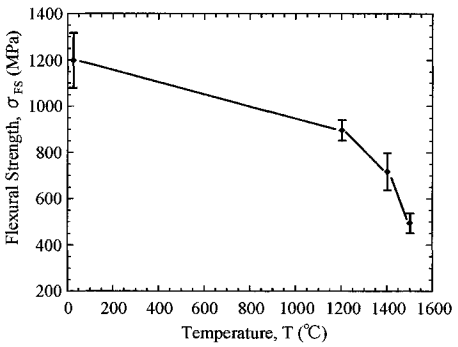


Fig. 3 Flexural strength of sintered silicon nitride.

The load-displacement curve (Fig. 4) at 1200°C is linear and that at 1400° and 1500°C non-linear, indicating that slow crack growth dominated fracture behavior at 1400° and 1500°C. To clarify this, we studied slow crack growth behavior by measuring the strength of a specimen with an artistic crack at different stressing rate at 1400° and 1500°C. The fracture stress decreases with decreasing stressing rate (Fig. 5). The decrease in fracture stress at 1500°C is greater than that at 1400°C. This dependence of fracture stress is attributed to slow crack growth at 1400° and 1500°C.

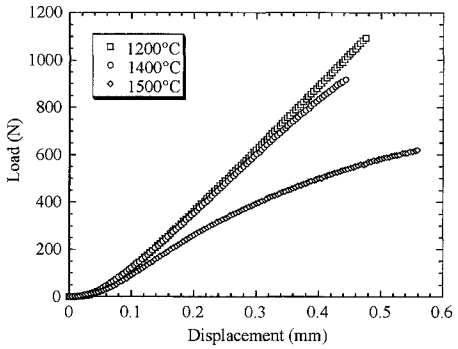


Fig. 4 Load-displacement curves for silicon nitride ceramics.

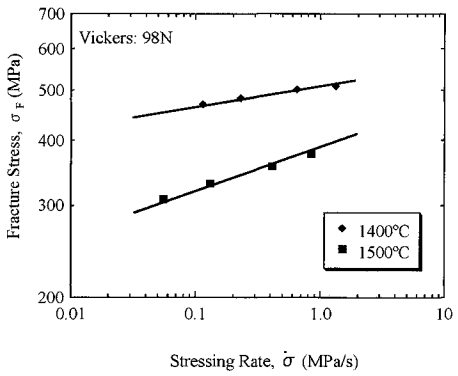


Fig. 5 Dependence of fracture stress on stressing rate.

Oxidation

The high-temperature strength and slow crack growth were measured in a nitrogen atmosphere. Oxidation resistance must be determined for applying the material to gas turbine and or other high-temperature use. Practically speaking, oxidation behavior in a wet, fuel vapor or exhausted gas should be also determined, but in the present work, oxidation in dry air was measured as the first step of the evaluation. Weight change in oxidation of the present material at 1400°C is shown in Fig. 6 with oxidation data on silicon nitride with $RE_2Si_2O_7$ (RE = La, Y and Yb) [19, 20]. The present material has higher oxidation resistance than silicon nitride with $RE_2Si_2O_7$ at 1400°C.

We studied oxidized surface using XRD, identifying crystalline β-$Yb_2Si_2O_7$ and SiO_2 (α-cristobalite) as major oxidation products, together with some β-Si_3N_4 and trace amounts of $Yb_4Si_2O_7N_2$ and Yb_2SiO_5. Beta-Si_3N_4 (excluding the maximum peak) and $Yb_4Si_2O_7N_2$ peaks decreased with increasing oxidation temperature, indicating these signals were from the bulk ceramic beneath the oxidized surface. Previous studies [21, 22] show that Si_3N_4 and $Yb_4Si_2O_7N_2$ phases were oxidized simultaneously to form SiO_2 and Yb_2SiO_5, based on the following equations, when $Yb_4Si_2O_7N_2$-Si_3N_4 bulk material was exposed to air at high

temperatures:

$$Si_3N_4(s) + 3O_2(g) = 3SiO_2(s) + 2N_2(g) \quad 3(a)$$

$$2Yb_4Si_2O_7N_2(s) + 3O_2(g) = 4Yb_2SiO_5(s) + 2N_2(g) \quad 3(b)$$

The Yb_2SiO_5 phase (oxidation product of $Yb_4Si_2O_7N_2$ or originally present at the grain boundary) reacted with SiO_2 (oxidation product of Si_3N_4) to form the $Yb_2Si_2O_7$ phase as follows [21, 22]:

$$Yb_2SiO_5(s) + SiO_2(s) = Yb_2Si_2O_7(s) \quad (4)$$

Figure 7 shows the effect of oxidation time and temperature on room temperature flexural strength, σ_F, of hot-pressed Si_3N_4 [23]. Flexural strength decreases based on the oxidation temperature, decreases gradually after oxidation below 1200°C for 100 h, but a significant decrease in flexural strength is seen in specimens oxidized at 1400° and 1500°C. Flexural strength of the present material was much higher than that of $Y_2Si_2O_7$-Si_3N_4 [24] after oxidation at the same temperatures. The strength after oxidation at 1500°C for the studied material was comparable to that of $Y_2Si_2O_7$-Si_3N_4 after oxidation at 1400°C. After oxidation for 100 h, the average reduction in flexural strength from that before oxidation is about 10% at 1200°C, about 30% at 1400°C and about 45% at 1500°C. The material was damaged by oxidation at and above 1400°C, suggesting that creep life is short at and above 1400°C.

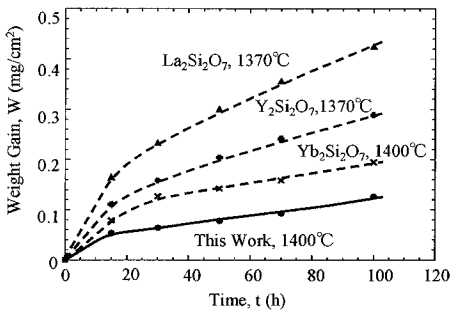


Fig. 6 Weight change of silicon nitride by oxidation [19, 20].

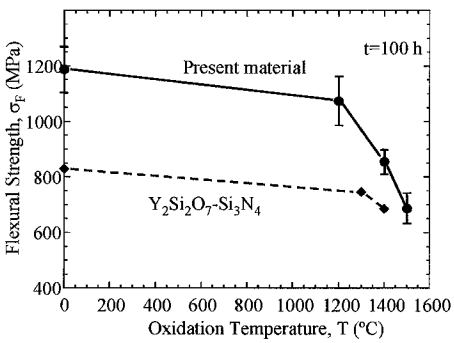


Fig. 7 Room-temperature strength of oxidized silicon nitride.

Creep

In relationships between applied stress and minimum strain rate of silicon nitride ceramics [14, 16] (Fig. 8), minimum strain rate in the tensile test is much larger than that in the compression test at the same temperature because

cavitation occurs under tensile stress. The minimum strain rate of hot-isostatically-pressed silicon nitride, SN281 (Kyocera Corp., Kyoto, Japan), is 10^{-9}-10^{-8} /s under 100-200 MPa tension at 1400°C. That of gas-pressure-sintered silicon nitride, SN88M (NGK Insulator Co., Ltd., Nagoya, Japan), is 10^{-7}-10^{-6} /s under 100-200 MPa tension at 1400°C [25]. Creep resistance of the present material, which was hot-pressed, falls in between the two materials. The creep life of the present material was longer than 600 h under 200 MPa in tension at 1300°C. At 1400°C, all samples tested at 125 – 160 MPa broke within 80 h [14]. These results suggest that the present material resists breakage for 1000 h under 137 MPa at 1300°C.

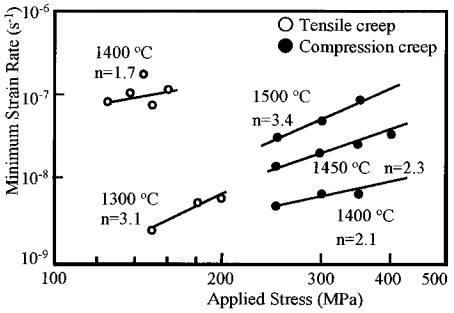


Fig. 8 Stress dependence of the minimum strain rate of silicon nitride ceramics.

Conclusion

Silicon nitride ceramics were fabricated by hot-pressing a powder mixture of Si_3N_4-2.4 mol% $Yb_4Si_2O_7N_2$. The $Yb_4Si_2O_7N_2$ and Yb_2SiO_5 crystallized during sintering. The present material has the advantage of easy grain boundary phase crystallization. Its high temperature strength, oxidation resistance, and creep resistance were comparable at the same level as or higher than those of heat-resistant silicon nitride reported previously. Creep life under 137 MPa is expected to be retained 1000 h at 1300 °C, but was within 80 h at 1400°C. To attain our target of 1000 h creep life under 137 MPa at 1500°C, we must, however, control the grain boundary more precisely.

References

[1] G. E. Gazza, J. Am. Ceram. Soc., 56, (1973) 662.
[2] M. K. Cinibulk, G. Thomas and S. M. Johnson, J. Am. Ceram. Soc., 75, (1992) 2037.
[3] M. J. Hoffmann, Tailoring of Mechanical Properties of Si_3N_4 Ceramics, Kluwer Academic Publishers, the Netherlands (1994), 233.
[4] J. S. Vetrano, H.-J. Kleebe, E. Hampp, M. J. Hoffmann, M. Rühle and R. M. Cannon, J. Mater. Sci., 28, (1993) 3529.
[5] E. M. Levin, C. R. Robbins and H. F. McMurdie, Phase diagram for Ceramists 1969 Supplement, The American Ceramic Society, Ohio (1969) 107.
[6] E. M. Levin, C. R. Robbins and H. F. McMurdie, Phase diagram for Ceramists 1969 Supplement, The American Ceramic Society, Ohio (1969) 108.
[7] F. F. Lange, S. C. Singhal, R. C. Kuznicki, J. Am. Ceram. Soc., 60, (1977) 249.
[8] T. Nishimura, M. Mitomo, J. Mater. Res. 10, (1995) 240.

[9] M. H. Lewis, Silicon Nitride Ceramics: Scientific and Technological Advances (Mater. Res. Soc. Symp. Proc. 287), Pittsburgh, PA (1993) 159.
[10] A. Tsuge, K. Nishida, and M. Komatsu, J. Am. Ceram. Soc. 58, (1975) 323.
[11] K. H. Jack, Non-oxide Technical and Engineering Ceramics, Elsevier Applied Science, London, UK (1986) 1.
[12] T. Nishimura, M. Mitomo and H. Suematsu, J. Mater. Res. 12, (1997) 203.
[13] H. Yoshida, Y. Ikuhara, T. Sakuma, T. Nishimura and M. Mitomo, Proceedings of the Seventh International Conference on Creep and Fracture of Engineering Materials and Structures, (1997) 653-662.
[14] J.-W. Cao, A. Okada, N. Hirosaki, J. Euro. Ceram. Soc., 22 (2002) 769.
[15] G. R. Anstis, P. Chantikul, B. R. Lawn, D. B. Marshall, J. Am. Ceram. Soc., 64, (1981) 533.
[16] S. Guo, N. Hirosaki, T. Nishimura, Y. Yamamoto, M. Mitomo, J. Mater. Res., submitted.
[17] M. K. Cinibulk, G. Thomas and S. M. Johnson, J. Am. Ceram. Soc., 75, (1992) 2050.
[18] J. T. Smith, and C. L. Quackenbush, Am. Ceram. Soc. Bull. 59, (1980) 529-532, 537.
[19] D. Mieskowski, W. Sanders, J. Am. Ceram. Soc., 68 (1985) C160.
[20] M. K. Cinibulk, G. Thomas and S. M. Johnson, J. Am. Ceram. Soc., 75, (1992) 2044.
[21] H. Park, H. W. Kim, H.E. Kim, J. Am. Ceram. Soc., 81 (1998) 2130.
[22] H. J. Choi, J. G. Lee, Y. W. Kim, J. Euro. Ceram. Soc., 19 (1999) 2757.
[23] S. Guo, N. Hirosaki, T. Nishimura, Y. Yamamoto, M. Mitomo, Phil. Mag. A, submitted.
[24] H. W. Kim, Y. H. Koh, H. E. Kim, J. Mater. Res., 15 (2000) 1478.
[25] F. Lofaj, A. Okada, Y. Ikeda, H. Kawamoto, Key Engineering Materials vols. 171-174 (2000) pp.747.

SECTION 3

ADVANCED STEAM POWER PLANT

SECTION 3

ADVANCED STEAM POWER PLANT

Invited Papers

BENEFIT OF ADVANCED STEAM POWER PLANTS

Rudolph Blum[1)] and John Hald[2)]
[1)]M. Sc., Elsam A/S Chemistry, Materials & Environment, Skærbæk, Denmark
[2)]M.Sc. Elsam/EnergyE2/IPL-MPT, TU Denmark, Lyngby, Denmark

Abstract

The development of advanced USC coal fired power plant should be continued, in order to secure future electricity supply and integration of renewable energy sources. Five years of operation experiences with USC power plants have already demonstrated the success of the "600°C generation" power plants. The development of a 700°C steam power plant to operate on coal in combination with biomass will enable a 40% reduction of CO_2 emission compared with the most advanced USC power plants. The 700°C steam power plant offer a flexible technology based on coal , and the demanded production flexibility in order to incorporate a high amount of unpredictable renewable energy input. The technical realisation of a 700°C steam power plant depends on a successful development and qualification of advanced ferritic, austenitic and Ni based alloys.

Keywords: Clean coal, USC Power plant, , 700°C power plant, materials development.

Introduction

Electricity generation based on clean coal technology is still an important item despite the recent worldwide trend to substitute coal with other less CO_2-intensive energy sources. The growing demand for electric energy in the fast growing economies in Asia is at present the main driver. In the USA a growth in the demand for coal for electricity production is still foreseen and even in Europe the forecasts for energy supply for the coming decades maintain coal as a major energy source for electricity production, fig.1.

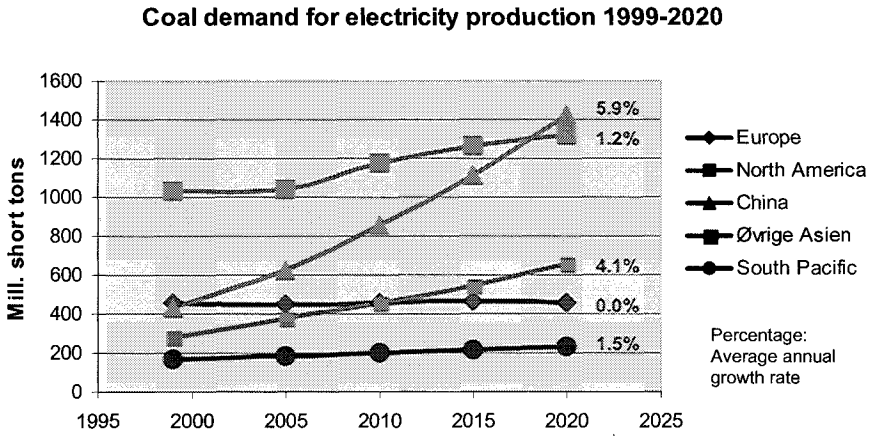


Figure 1.

Source: Energy Information Administration, DOE 2000

Renewables

Much effort has been put into the development of renewable energy sources, especially wind, biomass and solar energy. Today 16% of the electricity production in Europe is covered by renewable sources, fig 2. However, the most important renewable source, hydro power covering 14% of the electricity production, is already fully exploited. The present goal for the EU is that up to 24% of the generated electricity should be based on renewable sources in 2010. This is a very ambitious goal, because it has to rely on further development of wind, biomass and solar energy. Consequently it will most probably be associated with very high costs.

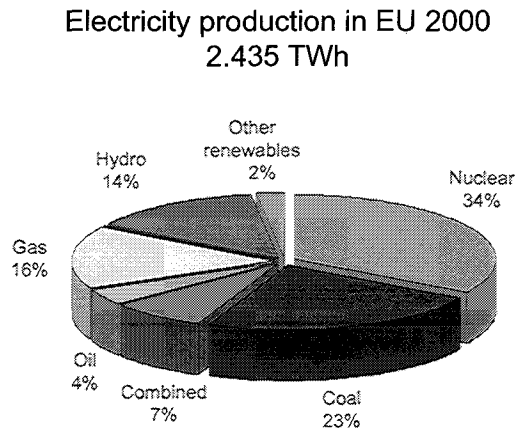


Figure 2

Source: EURELECTRIC, Eurprog 2001/ VGB

In countries like Denmark, where the potential for wind energy is large this energy source has been widely developed and exploited. The wind power production capacity is close to 50% of the peak demand in west Denmark, and this result in 15% of the annual electricity consumption from wind power. A planned increase of wind production capacity is foreseen to make it possible to cover up to 20% of the annual consumption. This high amount of unpredictable energy production has given serious regulations problems. A well developed grid and a high flexibility of the fossil fired production units are necessary to back-up the large variation of the output from the wind turbines. Most of the fossil-fired power units in Denmark are operating as combined heat and power plants. This leads to substantial overload problems when a high demand for district heating linked to the equivalent power production appears at maximum wind power output. Further development of wind power in Denmark will intensify these problems as well as the need for back-up capacity to maintain a stable grid. Sites for new wind turbines are going to be limited so only offshore installations can be realised in the future. In total these complexities increase the production cost of wind electricity, which today is more than 50% in excess of the production price of a coal fired USC unit. These costs include investments, but exclude additional cost for back-up capacity and stabilisation of the grid with significant wind power supply. On this background, a 20% share of the annual electricity consumption produced by wind power can only be regarded as possible for countries with a large potential for wind power.

For most of the European countries the wind intensity is smaller, and only figures below 20% will be realistic. In many countries massive increase of wind power necessitates large investments in the grid, which will negatively affect the economy.

The use of biomass has been an important issue during the last decade. In Denmark approximately 4% of the electricity production is based on biomass, and a doubling is foreseen in the next decade. Biomass is either used in small biomass fired units or in combination with coal in large power boilers where the share of biomass has been up to 20%. Combined coal and biomass firing seems to be the most profitable solution for the future, with respect to both generation costs and possibilities for reuse of the fly ash. The limit for biomass-produced electricity is mostly depending on the available amount of biomass in combination with fuel prices. The Danish experiences with co-firing of coal and biomass have shown that increased use of biomass should be linked with coal fired plants, and thereby the future prospects for coal fired power plants may be improved.

Solar energy is another potential energy source for the future, but a major breakthrough in efficiency and production cost for such systems is still needed before this energy supply can be of major interest. At present production prices from solar panels is four to five times higher than from coal fired USC power plants. Only if a sudden breakthrough is coming the overall situation could change dramatically and a complete restructuring towards a distributed generation system must be foreseen.

Nuclear

Nuclear energy, the only CO_2-free alternative to the renewable sources, is currently out of discussion in most European countries. Even though one third of the electricity production in Europe today is depending on nuclear energy, this energy source is foreseen to be reduced during the next decades. Such reduction will result in need for new generation capacity to replace the decommissioned nuclear units, but there do not seem to be a clear policy for the appropriate technology.

Fossil fuels

Currently there is surplus generating capacity in Europe, an very little new capacity is being installed. However, with reference to VGB [1] 400.000 MW of new production capacity is needed in Europe before 2020 to cover the increasing demand for electricity and to replace decommissioned fossil fired units built in the 1960ies and 70ies. These figures do not fully cover the consequences if a major reduction of nuclear capacity is going to happen.

In order to secure reliable electricity supply for the next decades, it is necessary to consider new fossil-fired power plants. However, as the reduction in CO_2 emission is of major concern, it is mandatory that fossil-based production be done as efficient as possible and with the highest effort to obtain low emission levels in the stack and in the drains.

Gas fired combined cycle units offer the highest efficiencies today and by far the lowest emissions of CO_2 and other unwanted species. But with a share of 16% of the electricity production in Europe the potential for gas fired units seems to have reached its limits based on

available gas resources. From an economical point of view gas based production capacity is less favourable to meet the future demands.

The largest and the most reliable fossil energy resource to meet the future challenge is coal. However, if an acceptable CO_2-emision from electricity production is to be obtained efficiency improvements of coal fired power plants must be demonstrated.

Compared with gas fired combined cycle units coal fired steam power plants require higher investments and longer time for investment returns. However, the coal fired units has demonstrated higher load flexibility and better part load efficiency, which are important for the overall economy when a high amount of unpredictable renewable energy sources has to be integrated. Furthermore, combined firing of coal and biomass should be considered in order to bring down the resultant CO_2 emission by increased use of biomass.

Therefore it is vital both to secure electricity supply and integration of renewable energy sources that the development of advanced USC coal fired power plant be continued. The present standstill in the power market should be used to intensify this development of USC plants so new advanced installations can be ready for the expected increased demand for new constructions.

Materials development - present state

Efficiency improvements in ultra supercritical (USC) power plants can only be obtained by increasing the steam parameters, which is dependent on the availability of improved high temperature materials for critical steam cycle components.

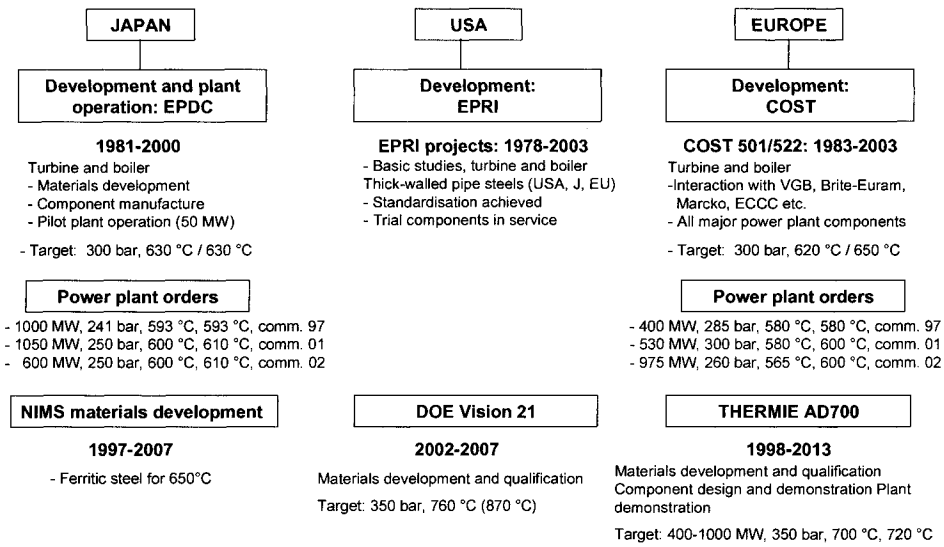


Figure 3

The international materials development projects over the last two decades has resulted in the qualification of a number of new alloys for steam boilers and turbines, figure 3. This means that a coal fired USC power plant with steam parameters of 325bar/610°C and an efficiency of about 50% can be built today. The new alloys include 2½Cr steels for furnace panels such as the HCM2S and 7CrMoVTiB1010, 18Cr austenitic steels for superheaters such as the fine grained TP347HFG and the Super 304Cu, new 9-12%Cr steels such as the P92 for steam pipes and 10Cr forging and casting steels for turbine rotors and casings. A large number of coal, lignite or gas fired USC power plants with capacities between 400 MW and 1000 MW are already commissioned or are under construction using these new materials at steam parameters up to 300 bar and 600°C.

The experiences from the newest USC power plants have already demonstrated satisfactory performance with respect to reliability, flexibility, emission control and economy, figure 4. The plants are based on major use of newly developed boiler and turbine component designs, and wide use of the newly developed high performance materials, but the availability has been as good as less advanced power plants. The additional investment costs have been marginal, and is fully returned by the efficiency increase. Therefore the overall production costs have shown the expected figures. On this background it can be concluded that the "600°C generation" of USC power plant will end up as a true success.

Power station	Cap. MW	Steam parameters	Fuel	Year of Comm.	Eff. %	Boiler/steam line materials	Turbine materials
Matsuura 2	1000	255bar/598°C/596°C	PC	1997		Super304H/P91	TMK1
Skærbæk 3	400	290bar/580°C/580°C/580°C	NG	1997	49	TP347FG/P91	COST 501 F
Haramachi 2	1000	259bar/604°C/602°C	PC	1998		Super304H/P91	HR1100
Nordjylland 3	400	290bar/580°C/580°C/580°C	PC	1998	47	TP347FG/P91	COST 501 F
Nanaoota 2	700	255bar/597°C/595°C	PC	1998		TP347H/P91	Toshiba 12Cr
Misumi 1	1000	259bar/604°C/602°C	PC	1998		Super304H/HR3C/P91	TMK2/TMK1
Lippendorf	934	267bar/554°C/583°C	Lignite	1999	42.3	1.4910/P91	COST 501 E
Boxberg	915	267bar/555°C/578°C	Lignite	2000	41.7	1.4910/P91	COST 501 E
Tsuruga 2	700	255bar/597°C/595°C	PC	2000		Super304H/HR3C/P122	Toshiba 12Cr
Tachibanawan 2	1050	264bar/605°C/613°C	PC	2001		Super304H/P122/P92	TMK2/TMK1
Avedøre 2	400	300bar/580°C/600°C	NG	2001	49.7	TP347H/P92	COST 501 E
Niederaussen	975	265bar/565°C/600°C	Lignite	2002	>43	TP347FG/E911	COST 501 E
Isogo 1	600	280bar/605°C/613°C	PC	2002		Super304H/P122	COST 501 E

Materials guide

Superheater	TP347FG: Fine Grain 18Cr10NiMoNb	Super304H: 18Cr9Ni3Cu	HR3C:25Cr20Ni	1.4910: 18Cr12Ni2½Mo
Steam lines & headers	P91: 9CrMoVNb	P92: 9Cr½Mo2WVNb	E911: 9CrMoWVNb	P122: 11Cr½Mo2WCuVNb
Turbine rotors	COST 501 F: 12CrMoVNbN101 TMK1: 10Cr1.5Mo0.2VNbN	COST 501 E: 12CrMoWVNbN1011 TMK2: 10Cr0.3 Mo2W0.2VNbN		HR1100: 1 11Cr1.2 Mo0.4WVNbN Toshiba: 11Cr1Mo1WVNbN

Figure 4. USC Power plants in service or under construction.

Future development

Further efficiency improvements of USC power plants are aimed for in worldwide development projects. In the European R&D project: "Thermie Advanced ("700°C") PF Power Plant" [2] steam temperatures up to around 700°C are aimed for. With scheduled efficiencies of about 52 – 54% and with the option to replace part of the coal with biomass such a plant will enable a reduction of CO_2 emission of around 40% compared with the most advanced USC power plants operating today. These targets bring the emissions from a combined coal-biomass fired 700°C power plant close to the figures of gas fired combined cycle plants. The project aims to demonstrate such a power plant within the next decade.

In order to realise a 700°C USC power plant extensive materials development is necessary including the use of Ni based superalloys in the most severely exposed components. These developments can be categorised into four groups reflecting the key components of such a power plant i.e:

- Furnace panels
- Superheaters
- Thick section boiler components and steam lines
- Turbine rotors, casings, valves and bolts

For furnace panels steam temperatures above 500°C must be foreseen. An interesting candidate material for such conditions might be the 12Cr steel HCM12. This material has well proven mechanical properties as well as sufficient corrosion and oxidation resistance. The main target to prove its applicability in furnace panels is to demonstrate good weldability with no need for post weld heat treatment. Demonstration tests comprising large test panels and one full boiler construction of HCM12 have shown excellent service performance, but they indicate that some work is still needed to develop a welding procedure, which guarantees unproblematic production of gas tight furnace panels. An alternative to HCM12 could be IN617, but this would lead to a very expensive construction.

For superheater tubing the aim is to develop an improved austenitic tube material with sufficient strength and flue gas corrosion resistance to operate at steam temperatures around 650°C, and to develop a Ni base superalloy to fill the gap up to 700°C steam temperature. Intensive development work is ongoing in the Thermie project to demonstrate a suitable austenitic tube material with 100.000 hour rupture strength of about 100 MPa at 700°C and a Ni based tube material with 100.000 hour rupture strength of 100 MPa at 750°C. Corrosion and oxidation resistance of both materials have been tested in laboratory and will later be validated in in-plant test rigs. Results so far have been encouraging, and commercial scale production of both materials is foreseen in the second half of 2002.

For thick section boiler components and steam lines there are two goals for the development. An improved ferritic/martensitic 9-12%Cr steel is needed to expand the present temperature range for ferritic steels up to app. 650°C. A Ni-based superalloy with a 100.000 hour rupture strength of 150 MPa at 700°C is needed to allow construction of outlet headers and main steam lines with acceptable wall thicknesses, figure 5.

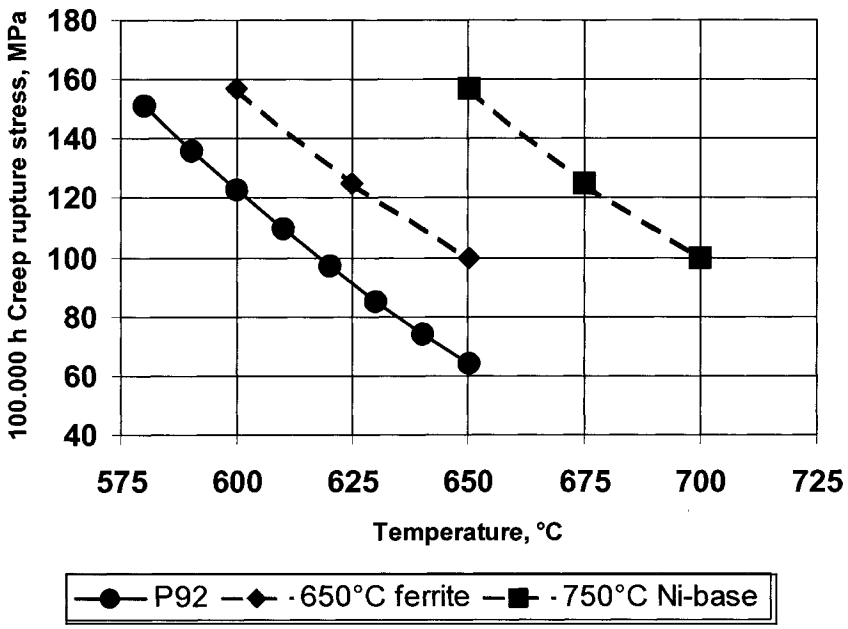


Figure 5. Future prospects for thick section boiler components and steam line materials.

The task to improve the 9-12%Cr steels on top of the impressive developments in the last two decades has proven to be very difficult. In the recent five years worldwide research has resulted in a large number of new alloys being announced, and from short-term tests they seemed very promising. However, in long term tests the strength fall off and so far no ferritic alloy has demonstrated long-term creep strength better than steel P92. In order to be able to improve the strength a fine-tuning of the composition is needed based on a thorough understanding of recent developments. Recent advances in microstructure characterisation techniques and thermodynamically based microstructure models may prove to be the only way to go further in the development of improved ferritic steels.

Alloy 263 or an improved version of IN617 may meet the demands for outlet headers and steam lines at 700°C steam temperature. Long-term creep data and demonstration of fabricability – pipe production, hot bending and welding – is needed before a 700°C power plant can be realised. Alloy 263 is under investigation in the "Thermie Advanced ("700°C") PF Power Plant" project and the improved version of IN617 is investigated by the German national project MARCKO DE2. In the second half of 2002 commercial scale production of Alloy 263 and IN617 pipe is foreseen. The products will be used for qualification of the materials.

Recent results of the developments of 9Cr boron alloyed steels in Europe support the expectations that ferritic turbines can operate up to app. 625°C steam temperature. But similar

to the ferritic steels for thick section boiler components a substantial understanding of the microstructures is needed to fine tune the chemical composition for optimum strength performance.

For turbine constructions above 625°C steam temperature a suitable Ni based superalloy is sought amongst existing gas turbine disc materials. Long-term creep data are under developed and the fabricability of full-scale turbine components will be demonstrated during the next phases in the "Thermie Advanced ("700°C") PF Power Plant"

Conclusions

It is vital both to secure electricity supply and integration of renewable energy sources that the development of advanced USC coal fired power plant be continued.

Five years of operation experiences with USC power plants have already demonstrated that the "600°C generation" power plants will end up as a true success.

The development of a 700°C steam power plant to operate on coal in combination with biomass will enable a reduction of CO_2 emission of around 40% compared with the most advanced USC power plants operating today. This will bring the emissions from a combined coal-biomass fired 700°C power plant close to the figures of gas fired combined cycle plants.

The 700°C steam power plant offer a flexible technology with minimised CO_2-emission based on coal - the most reliable energy source in the world. Further, it gives the demanded production flexibility in order to stabilise a grid with a high amount of unpredictable renewable energy input.

The technical realisation of a 700°C steam power plant depends on a successful development and qualification of advanced ferritic, austenitic and Ni based alloys. With respect to austenitic and Ni based alloys promising results have been achieved.

The economic criterion for the realisation of a 700°C steam power plant is a realistic budget price. The consumption of large quantities of expensive Ni based alloys has significant influence in this respect, and a successful development of an improved ferritic steel to be used at temperatures up to 650°C would improve the situation.

References

[1] Dr. Gerd Jäger, VGB-Kongress Kraftwerke 2001, Brüssel

[2] http://www.AD700.dk

DESIGN AND MATERIALS FOR TURBOSETS IN ADVANCED STEAM POWER PLANTS

K. Wieghardt, Siemens Power Generation, Muelheim, Germany
T.-U. Kern, Siemens Power Generation, Muelheim, Germany

The demands of the power plant market have changed dramatically during the last 10 years. This fact is demonstrated by the tendency towards much more flexible and efficient Steam Power Plants (SPP) and requirements for fewer service inspections and life-times ≥ 200,000h, not to mention a combined-cycle application. These new demands have resulted in an increased effort to significantly improve both design and materials.

A possible way in this direction is to install Super Critical SPP's, with live steam temperatures of T ≥ 580°C and to optimise the steam cycle path. However, new challenges have arisen throughout the design process. To answer these concerns, the design strategies implemented by Siemens Power Generation are based on a vast amount of experience with Ultra Super Critical SPP's, built in the 1960's, for steam parameters of up to 650°C/320bar, com-plemented by new technology developed over the last 10 years, *Tab 1.*

Number of units	Rating range MW	Main steam conditions °C / bar	Year of commissioning
2	107	600 / 221	1959
1	11	605 / 158	1956
1	7	615 / 173	1957
2	29	615 / 181	1957
1	85	615 / 196	1957
1	19	620 / 323	1956
1	12	625 / 157	1951
1	14	650 / 153	1962
1	15	650 / 177	1955
1	21	650 / 178	1964
2	15 - 21	650 / 177	1957/58

Tab.1: Reference list of Siemens USC SPP's in the 1960's with temperatures ≥ 600°C

The main difference between these USC SPP's and the requirements imposed by today's market are as follows:

- all machines previously were base load units,
- the power range output formerly varied from only 7 to 107 MW,
- the demand for flexibility during operation was lower in the past than it is today.

These restrictions also resulted from the materials used for the critical components made in Austenites. Nevertheless, proven design issues can be transferred to the current turbosets. Some of these features include the following characteristics:

- the use of material properties as a function of the steam parameters realised by material combinations (welded, or bolted, rotor and/or casing),
- the application of cooling techniques (external or internal, with steam or other medium),
- the protection of critical functional areas by special surface treatment or coatings.

An example of an external cooling technique currently designed is given in *Fig.1* for a single flow IP turbine [1].

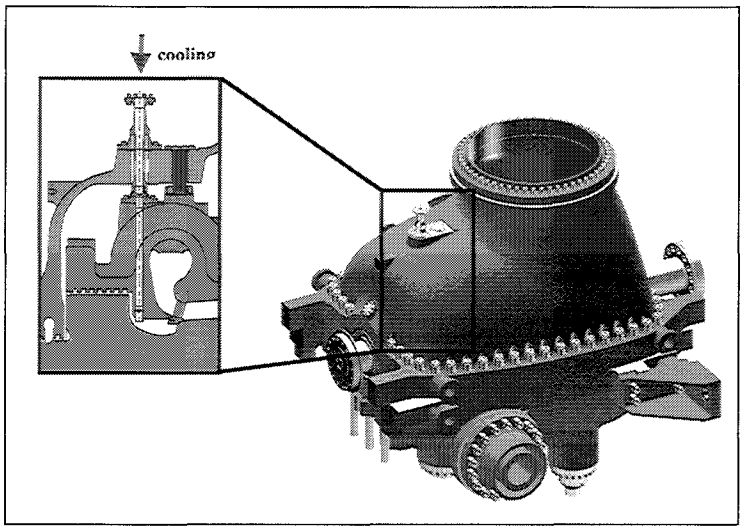


Fig. 1: Single flow IP turbine with cooling steam [1]

The realisation of critical components for USC SPP's in use today will require improved materials. Different material development programs have been initiated world-wide. In Europe, the COST program, launched in 1986, has been very successful in the introduction of new 10%Cr martensitic steels in the power plant industry. This steel class offers the possibility for cost-effectiveness and flexibility during operation.

Towards this goal, the expertise gained by Siemens in using the new 9-10%Cr steels during different applications has proved positive throughout. The design requirements for high temperature components have been fully met, without exception.
Moreover, Siemens is applying the 9-10%Cr steels in the current design, not only for very high temperature machines, but also in an effort to increase the performance of highly stressed components for steam parameters $T \geq 540°C$. It can be stated that Steam Power Plants with temperatures of up to 620-630°C can be supplied for today's customer by applying a special design and the newly developed 9-11% CrMoV steels.

Despite many successes, additional challenges have arisen in the strides towards 700°C technology. In this area of technological advancement, new design approaches and materials are being required. Design and material concerns must be jointly considered in this process. A European co-operative R&D project currently underway, THERMIE 700, combines the knowledge and experience of the European turbine manufacturer and steel-makers, with the aim of developing solutions in the energy market for the near future. Progress is being made towards this ambition. However, more work is necessary if we are to overcome the challenges in reaching this goal.

[1] Feldmueller, A.; Kern, T.-U.:
Design and Materials for Modern Steam Power Plants. 5th Intern. Charles Parsons Conf. 2000 –Advanced Materials, 3-7 July 2000, Cambridge, UK.

BOILER DESIGN AND MATERIALS ASPECTS FOR ADVANCED STEAM POWER PLANTS

Qiurong Chen and Günter Scheffknecht

ALSTOM Power Boiler GmbH, Stuttgart, Germany

Abstract

Since the late 80s great efforts have been made to increase the efficiency of coal-fired power plants. The main development trend is the increase of the steam parameters with supercritical pressures and higher temperatures at boiler outlet. This is realised by means of the well-known and since the 60s commercially used once-through technology which avoids the introduction of a new clean coal technology with some substantial risks. Only material selection and dimensioning of the pressure parts have to be adapted to the new requirements, and the design and construction have to consider the limitations on the material side.

The increase of the steam conditions is limited on the boiler side by water walls, tubing of the final superheaters and reheaters as well as the thick-walled components, mainly the high-pressure outlet headers and the piping to the turbine. Several boiler materials with improved mechanical properties have been developed in the last years. Some new materials are still in the stage of development. Besides the aspects of strength and workability of the materials, attention must be paid to the corrosion behaviour at high temperatures. In order to investigate the suitability of the various tube materials in high-temperature areas, several test installations are now in operation to forecast the corrosion properties at high temperatures.

The paper shows the design aspects and materials needs for advanced steam power plants. It reviews the available boiler materials with respect to mechanical and corrosion properties and gives limitations on the maximum achievable steam conditions. Finally, a forecast for further increase of the steam conditions considering pending and future material developments will be given.

Keywords: material development, boiler design principles, supercritical boiler, high steam parameters, advanced power plant

Introduction

The world-wide abundance of coal guarantees a stable fuel supply for the next centuries and contributes to the selection of pulverised coal-fired power plant technology as the preferred option for many utilities. Additional reasons for a preference of this technology include:

- the reliability of a technology which has evolved in incremental steps,
- high levels of availability and operational flexibility,
- high levels of fuel flexibility ensuring a secure and economic fuel source,
- high efficiencies and low generation costs.

An improvement in the thermal efficiency of the plant does not only reduce the fuel costs but also reduces the release of SO_2, NO_x and CO_2 emissions. Despite its long history, coal-fired power plant technology is still evolving, and efficiency has been improved significantly since the late 80s and will be improved still further. The increase of steam parameters to ultra- supercritical conditions is the main development trend to improve the power plant efficiency. **Fig. 1** shows the evolution of the efficiency improvement of the power plants. In **Fig. 2**, contributions of different measures for the efficiency increase are summarised. In order to realise the supercritical conditions, the well-known and since the 60s commercially used once-through technology has to be applied to the boiler design. As the components of the power

plants being operated with this technology are well-proven, higher steam conditions do not lead to a new boiler design. Only material selection and dimensioning of the pressure parts have to be adapted to the new requirements. **Fig. 3** shows a typical bituminous coal-fired once-through boiler with supercritical conditions and a power output of 900 MW.

Most bituminous coal-fired units which were built in the 80s were characterised by moderate steam conditions. The steam parameters of the power plants which are currently realised are most supercritical with much higher steam temperatures. In Germany, a lignite-fired power plant with steam parameters of 275 bar / 580 °C / 600 °C is currently being built [1]. In Denmark, two power plants with steam parameters of 290 bar / 582 °C / 580 °C / 580 °C (double reheat system) have been built [2]. In Japan, some new power plants with steam parameters up to 250 bar / 600 °C / 610 °C have been commissioned in recent years [3]. For the next years, different development programs in Europe and Japan will lead to the planning and erection of ultra-supercritical power plants with steam pressures of about 300 bar and steam temperatures above 600 °C.

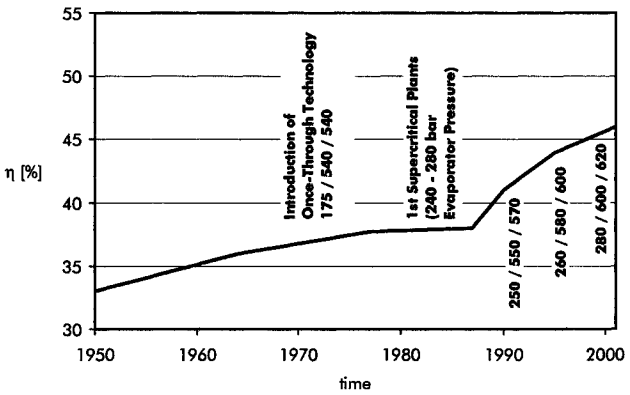


Fig. 1: Efficiency Development of Power Plants in Europe

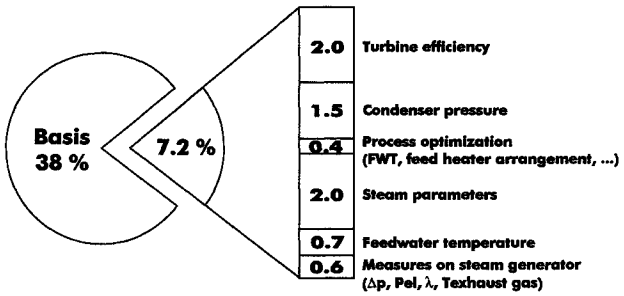


Fig. 2: Efficiency Improvement of Steam Power Plants

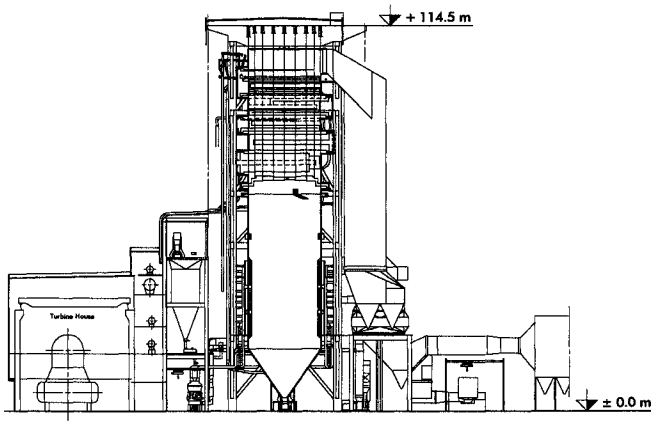


Fig. 3: A Coal-Fired Once-Through Boiler

In an on-going research project within the framework 5 (former THERMIE) programme which is funded by the European Commission, investigations are performed for an advanced power plant with the maximum steam parameters of 375 bar / 700 °C / 720 °C which are significantly higher in comparison with the state-of-the-art power plants. The efficiency of the advanced power plants will be increased from the recent range of 43 - 47 % to above 50 %. Due to the higher thermal efficiency of the power plants, the fuel consumption and emissions will be reduced by almost 15 % compared with the best plant currently available.

By increasing the steam parameters, the design margin for some boiler components will be more and more exhausted. A further increase of steam conditions is limited especially by the following components:

- water walls,
- the tubing of the final superheaters and reheaters
- and the thick-walled components, mainly the high-pressure outlet headers and the piping to the turbine.

Several boiler materials with improved properties have been developed in the last years. The requirements for the materials in the boiler application are described for example in [4]. The use of the materials for the boiler with advanced steam parameters will be first limited by the relevant creep strength specifications. The range of application of the materials for water walls and thick-walled components is additionally restricted by the manufacturing aspects. For superheater and reheater heating surfaces, further restriction results from the risk of flue gas side high-temperature corrosion and steam-side oxidation. For advanced steam conditions, new materials with higher strength, higher corrosion resistance and good weldability and formability are required.

Water Walls

The water wall as flue gas-tight enclosure of the furnace and the heat exchanger section is a very important component of the boiler. The conventional water wall materials used so far are low-alloy CrMo steels like 15Mo3 and 13CrMo44 (T12) which are characterised by an excellent workability for the manufacturing of the membrane walls.

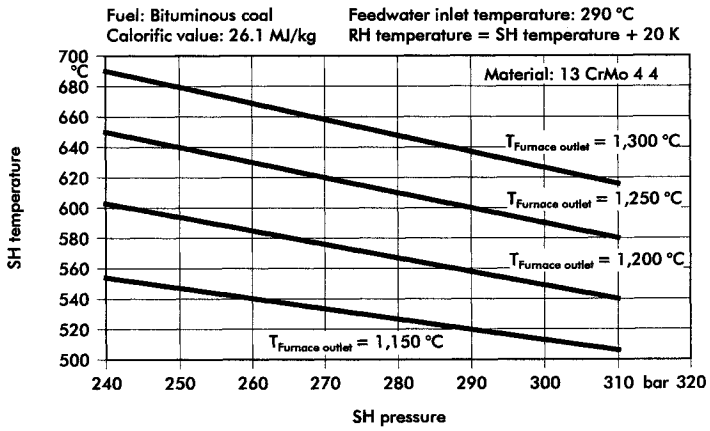


Fig. 4: Steam Parameter Limits at specified Wall Outlet Temperature for the Material 13 CrMo 44 (Pressure and Temperature refer to Operating Conditions at Boiler Outlet)

Fig. 4 shows the application limit of the material 13CrMo44. Based on a furnace outlet temperature of 1,250 °C and certain fuel properties, the steam conditions up to 290 bar / 600 °C

(SH outlet) can be realised. This corresponds to a water wall outlet temperature of about 460 °C which is shown in **Fig. 5**.

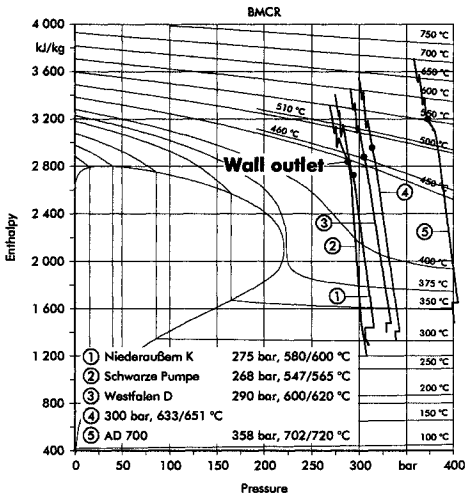


Fig. 5: h,p-Diagram of Different Boilers

From a design point of view, two aspects can be considered for higher steam conditions:

1. A possibility to reduce the steam temperature on the water wall is the increase of the furnace outlet temperature. If the furnace outlet temperature is increased to 1,300 °C, the limit of steam parameters is increased to 300 bar / 620 °C (SH outlet). As a consequence, however, the range of the applicable coals would have to be limited.
2. Another possibility to shift the heat absorption from the water wall to the convective heating surfaces is the application of flue gas recirculation. A cold flue gas recirculation of 10 % leads to a reduction of the wall outlet temperature of approximately 20 K. This method leads, however, to very large air preheaters or it may be even impossible to reach the desired low exhaust gas temperature.

On the material side, new water wall materials with much higher creep strengths can be used for higher steam conditions. With regard to the manufacturing and erection aspects, materials which do not need any post-weld heat treatment should be preferred. In this case, the maximum hardness levels in the as-welded condition have to be limited to avoid any risk of hydrogen-induced stress-corrosion cracking.

Table 1 shows the chemical composition of the candidate water wall materials in comparison with conventional ones. The 100,000 h creep rupture strengths of the materials are shown in **Fig. 6**.

Table 1: Chemical composition of water wall materials

Material	C	Cr	Mo	W	Ti	Co	Others
1 % Cr-steels:							
13CrMo44 (T12)	0.10 - 0.18	0.70 - 1.10	0.45 - 0.65	-	-	-	-
2 - 2.5 % Cr-steels:							
10CrMo910 (T22)	0.08 - 0.15	2.00 - 2.50	0.90 - 1.20	-	-	-	-
T23	0.04 - 0.10	1.90 - 2.60	max. 0.30	1.45 - 1.75	-	-	V, Nb, N, B
T24	0.05 - 0.10	2.20 - 2.60	0.90 - 1.10	-	0.05 - 1.10	-	V, N, B
9 - 12 % Cr-steels:							
HCM12	max. 0.14	11.0 - 13.0	0.80 - 1.20	0.80 - 1.20	-	-	V, Nb
Ni-based alloys:							
Alloy 617	0.05 - 0.10	20.0 - 23.0	8.0 - 10.0	0.80 - 1.20	0.20 - 0.50	10.0 - 13.0	Ni, Al

With the material 10CrMo910 (T22), the steam parameters cannot be increased considerably. A substantial improvement of the creep strength with limited hardness levels in as-welded conditions can be reached by the newly developed 2 - 2.5 % chromium steels. The typical examples of this group of steels are the material T23 (HCM2S) and T24 (7CrMoVTiB1010) which were developed on the basis of the conventional steel 10CrMo910 (T22). The creep rupture strengths of the new steels are much higher than the conventional ones (see **Fig. 6**). Both steels have been investigated by different German research programs. The aims of these projects are the qualification of both steels through welding tests with optimised welding procedure and weld metals to reduce the hardness level in the heat-affected zone and the long-term creep tests to get strength design values. The steels have shown a good workability. The hardness of approximately 350 HV achieved in the unannealed condition in the heat-affected zone, with hardness peaks of up to approximately 370 HV, is at an acceptable level (**Fig. 7**). Therefore, a post-weld heat treatment is not necessary for the manufacturing of the water walls. Sufficient ductility has been demonstrated by bending tests [5]. Meanwhile, the strength design values, both for base metal and for welds, can be seen as sufficiently examined and confirmed. Both steels have already been standardised and are available for commercial application.

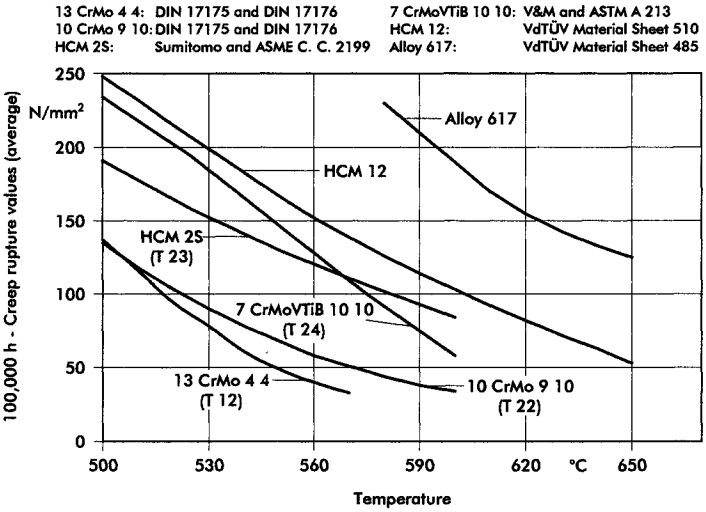


Fig. 6: 100,000 h Creep Rupture Strength for Water Wall Materials

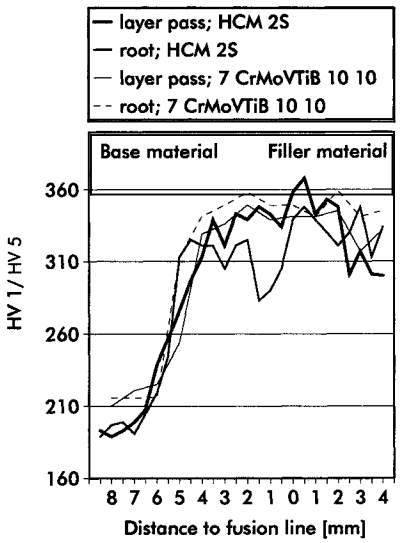


Fig. 7: Hardness Levels of the New Water Wall Materials in As-Welded Condition

By use of the newly developed 2 - 2.5 % chromium steels which have the similar weldability and workability but a much higher creep rupture strength than conventional ones, the steam temperature limit at the water wall can be increased by approximately 50 K. **Fig. 8** shows the new limit of the steam conditions for the material T24 in relation to the furnace outlet temperature. For a furnace outlet temperature of 1,250 °C, the steam conditions of

300 bar / 640 °C (SH outlet) can be realised. The application limit of the material T23 and T24 is also shown in **Fig. 5**.

For very high steam conditions such as 375 bar and 700 °C at boiler outlet with maximum metal temperatures of above 600 °C in the water wall, the 2 - 2.5 % chromium steels are not adequate. The creep strength of the materials is not sufficient. Another critical point is the lower corrosion and oxidation resistance of the steels. Due to higher metal temperatures, the magnetite deposits on the inside of the tube grow rapidly which could raise the temperature further and cause creep damage. On the outside of the tubes, the risk of corrosion increases with increasing steam temperature. In order to fulfil the strength and corrosion requirements, higher-alloyed materials are needed.

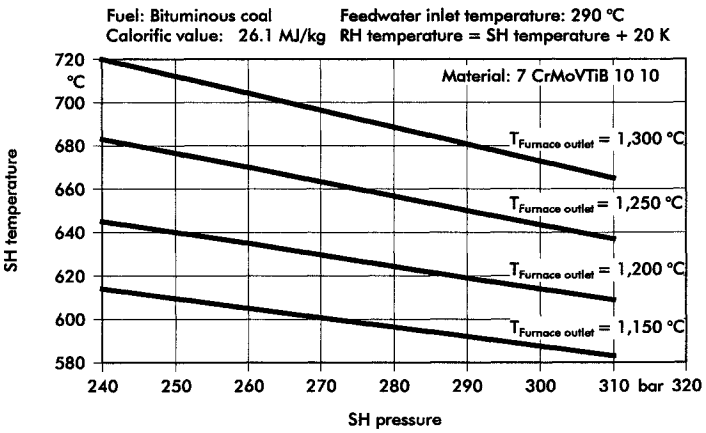


Fig. 8: Steam Parameter Limits at Specified Wall Outlet Temperature for the Material 7 CrMoVTiB10 10
(Pressure and Temperature refer to Operating Conditions at Boiler Outlet)

The austenitic steels cannot be used as candidate water wall materials because of their large thermal expansion coefficient which inhibits a welded joint between austenitic and ferritic water wall sections.

The candidate materials can be first selected from the group of modified 9 - 12 % chromium steels like T91, E911, T92 and HCM12 which have been mostly investigated up to now. Under the European COST program, it was demonstrated that the material T91 can be fabricated into water walls. However, a post-weld heat treatment is required which is difficult to perform in the field. The steels E911 and T92 have the same difficulty in welding as T91. Additionally, the 9 % Cr steels have a worse corrosion and oxidation resistance than 12 % Cr steels. Therefore, the material HCM 12 is more promising in that it has a sufficient creep strength and higher corrosion and oxidation resistance, and the hardness value in as-welded condition is the lowest among the 9 - 12 % chromium steels. Under the COST program, hardness values of below 380 HV without post-weld heat treatment have been reached under optimised conditions. However, it has to be investigated in more detail whether a post-weld heat treatment is needed for the manufacturing of the water walls. Another group of candidate materials for the water wall are the nickel-based alloys for which a post-weld heat treatment is not necessary. A well-examined nickel alloy is the material Alloy 617 which was originally developed for gas turbine applications. The alloy is used in the solution-treated condition and has the advantage of being relatively easy to weld without any requirement for complex post-weld heat treatment. Other advantages of this material are very high creep rupture strengths, high corrosion and oxidation resistance and similar heat expansion coefficients as martensitic steels.

However, the Ni-based alloys are expensive. In the new framework 5 programme, an evaporator panel made of HCM12 and Alloy 617 will be manufactured and installed in an existing boiler to gather the manufacturing and operating experience.

Superheater and Reheater Tubes

For superheater and reheater tubes, the creep strength of the used materials should be high enough at the relevant pressure and temperature range. In addition to this requirement for high strength, the corrosion resistance of the materials both on the flue gas side and on the steam side has to be considered. The oxide layer on the inside of the tube leads to higher material temperatures and could cause creep damage. External high-temperature corrosion on the flue gas side reduces the effective wall thickness of the tubes.

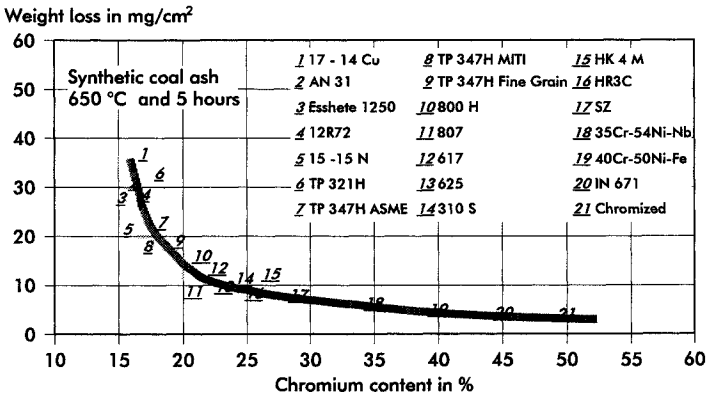


Fig. 9: High Temperature Corrosion Behaviour in Relationship with Chromium Content of the Material

In the design of boilers with very high temperatures, it should be considered that the reheater outlet group is more critical regarding the corrosion and oxidation risk due to the often higher steam temperatures and the lower heat transfer coefficients. Therefore, it should be arranged on the flue gas side downstream of the final SH heating surfaces.

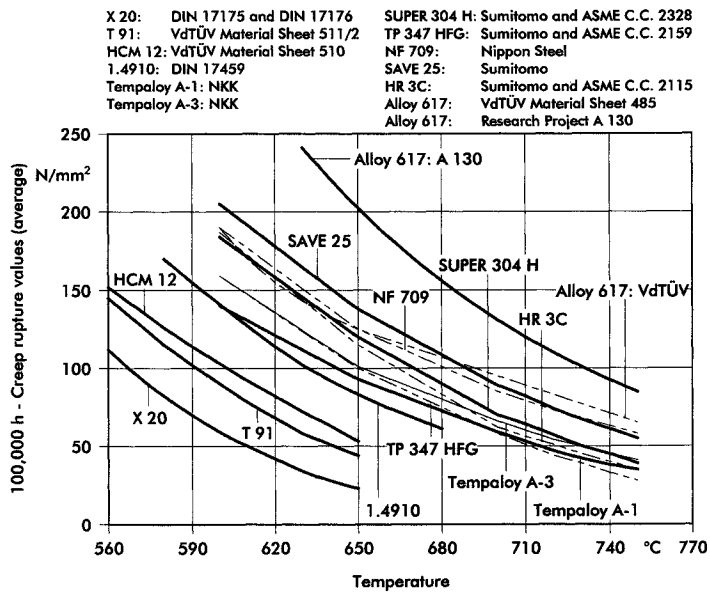


Fig. 10: 100,000 h Creep Rupture Strength for Superheater and Reheater Materials

On the material side, the chemical composition, especially the

chromium content has a large influence on the flue gas side corrosion rate which is indicated in **Fig. 9**. The resistance against corrosion increases with increasing chromium content. The chromium content of the used materials also plays the most important role as a protection against oxidation on the steam side.

Table 2 gives the chemical composition of some typical superheater materials. The 100,000 h creep rupture values of the materials which are taken from the relevant standards or based on manufacturer's specifications are shown in **Fig. 10**.

Table 2: Chemical composition of superheater and reheater materials

Steel	Cr	Ni	Mo	Nb	Ti	Co	Others
Martensitic steels:							
X20CrMoV121	10.0 - 12.5	0.30 - 0.80	0.80 - 1.20	-	-	-	V
T91	8.0 - 9.5	max. 0.40	0.85 - 1.05	0.06 - 0.10	-	-	V, N
HCM12	11.0 - 13.0	-	0.80 - 1.20	max. 0.20	-	-	V
Austenitic steels:							
X3CrNiMoN1713	16.0 - 18.0	12.0 - 14.0	2.0 - 2.8	-	-	-	N
AC66	26.0 - 28.0	31.0 - 33.0	-	0.60 - 1.00	-	-	Ce, Al
Super304H	17.0 - 19.0	7.5 - 10.5	-	0.30 - 0.60	-	-	Cu, N
Tempaloy A-1	17.5 - 19.5	9.0 - 12.0	-	max. 0.40	max. 0.20	-	-
TP347HFG	17.0 - 20.0	9.0 - 13.0	-	max. 1.0	-	-	-
NF709	18.0 - 22.0	22.0 - 28.0	-	0.10 - 0.40	0.02 - 0.20	-	N, B
Tempaloy A-3	21.0 - 23.0	14.5 - 16.5	-	0.50 - 0.80	-	-	N, B
SAVE25	21.0 - 24.0	15.0 - 22.0	-	0.30 - 0.60	-	-	W, Cu, N
HR3C	24.0 - 26.0	17.0 - 23.0	-	0.20 - 0.60	-	-	N
Ni-based alloy:							
Alloy 617	20.0 - 23.0	rest	8.0 - 10.0	-	0.20 - 0.50	10.0 - 13.0	Al

Both due to the requirement for creep strength and corrosion resistance, the martensitic steels can be only used up to steam temperatures of approximately 560 - 570 °C. Due to the higher corrosion resistance, the 12 % chromium steels are preferred to the 9 % chromium steels. For higher steam temperatures, higher-alloyed austenitic steels have to be used.

Fig. 11 shows the evolution of austenitic steels for boiler application (based on [6]). For convenience, austenitic steels can be classified as those containing less than 20 % chromium content and those containing more than 20 % chromium content.

A typical austenitic material in the DIN and TRD area is the steel X3CrNiMoN1713 (1.4910) with a chromium content of 17 % which has been used in high-temperature plants of the chemical industry in Germany for a long time. A steel with a much higher chromium content is AC66 which was developed originally for the coal gasification plants. Due to the high chromium content (27 %) and nickel content (32 %), an excellent corrosion resistance can be achieved.

In the area of ASME or in the Japanese MITI code, some very interesting developments should be mentioned here. In the group of 18 % chromium steels, the steels TP347HFG, Tempaloy A-1 and Super304H are new developments. All three steels have higher creep strengths than the conventional 18Cr-8Ni steels. The steam oxidation resistance at the tube

inside is also increased due to a fine-grained structure. For even higher steam temperatures, the 18 % chromium steels could be insufficient in view of strength and corrosion resistance. In this case, higher-alloyed materials with chromium contents above 20 % for which typical examples of the newly developed steels are HR3C, Tempaloy A-3, NF709 and SAVE25 should be used.

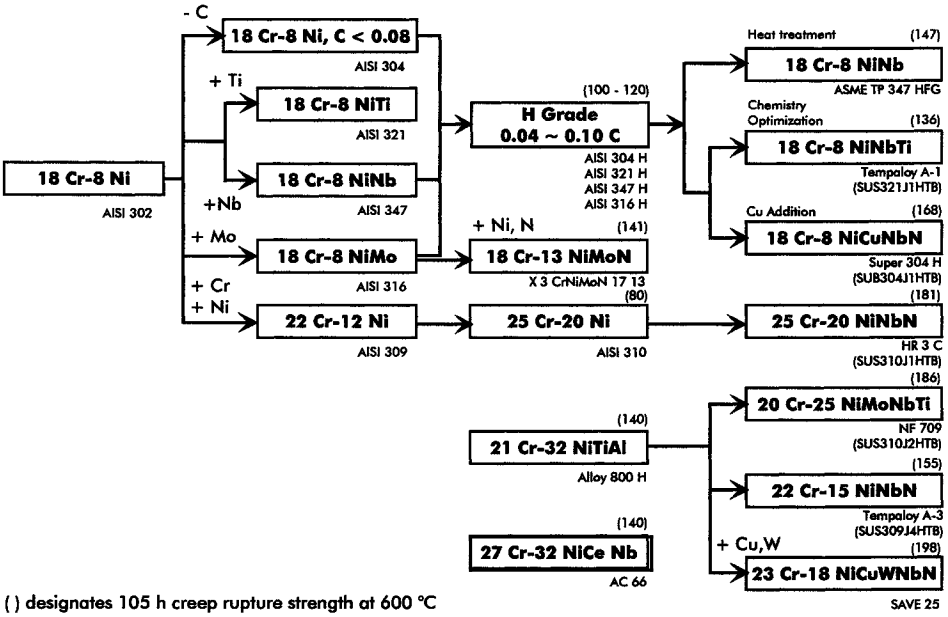


Fig. 11: Evaluation of Austenite Steels for Boiler Applications (based on Masuyama [6])

For very high steam conditions such as 375 bar and 700 °C at boiler outlet the austenitic steels are not adequate due to insufficient creep strengths. Here, nickel-based alloys are needed. The well-examined Alloy 617 can be used. In an on-going German research project, this material should be further optimised in the chemical composition to achieve higher creep strength values. Parallel to this project, a new nickel-based alloy with the name Alloy 4020 will be developed in the on-going European framework 5 project on the basis of the material Alloy C263 which must be aged after solution treatment to produce the strengthening dispersion and thus needs more complex post-weld heat treatment. The aim is to have an average 100,000 h creep strength value of 100 MPa at 750 °C.

The limit of steam conditions which can be realised with the materials from the point of view of creep strength is given in **Fig. 12.** In this diagram, a corrosion allowance of 15 % of the wall thickness has been considered. Besides the creep strengths, the application limits of the materials due to the corrosion and oxidation risk should also be considered in the design calculation.

A topic which shows significant uncertainties is the corrosion and oxidation mechanism, especially at high steam temperatures above 600 °C. On the flue gas side, not only the material

aspect, but also the operational aspects play an important role. The flue gas temperature, steam temperature, the flue gas and ash composition, the dynamic behaviour of the plant are all factors of influence. On the steam side, the oxidation growth rate, the physical properties of the oxide layer can have an effect on the material temperature increase. The lack of knowledge in these areas can be only improved by operating tests in existing boilers which should be carried out at high steam temperatures and over a long operating time.

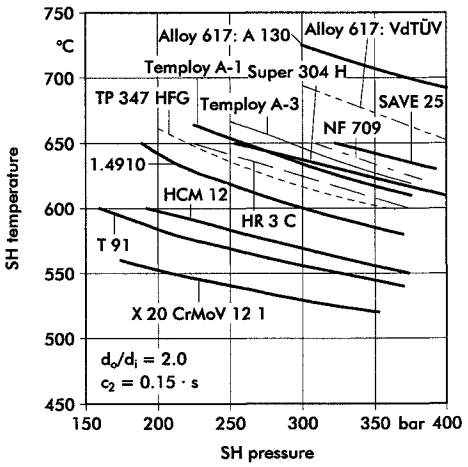
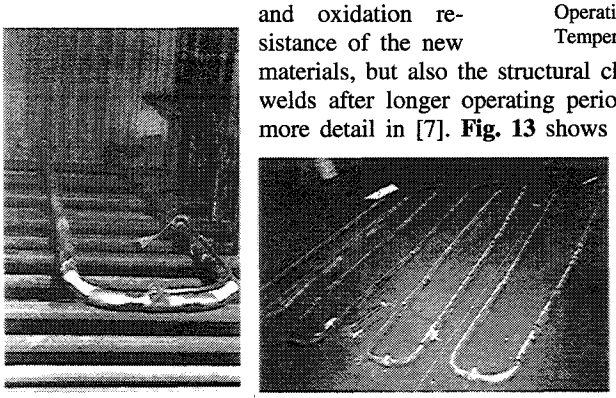


Fig. 12: Steam Parameter Limits for Different Superheater Materials from the Strength Point of View (Pressure and Temperature refer to Operating Conditions at Boiler Outlet, Design Temperature = Operating Temperature + 35K)

Such a test has been performed in the Danish Power Plant Vestkraft Unit 3 since 1995. Many test superheaters made up of a number of material samples have been installed in the boiler. The goal of the project is not only the investigation of high-temperature corrosion and oxidation resistance of the new materials, but also the structural change of base materials and the welds after longer operating periods. The project is described in more detail in [7]. **Fig. 13** shows a photo of a part of test superheaters. The test results of the first phase which was funded by the European Commission within the Brite Euram programme are given in [8]. In the next phases which were undertaken without public funding more advanced boiler materials will be tested at different temperature levels. The maximum steam temperature at the outlet of the test loop reaches up to 700 °C.



before dismantling after dismantling

Fig. 13: Test Superheater for Investigation of Corrosion and Oxidation Behaviour of the New Boiler Materials

High-Pressure Outlet Headers and Piping

By increasing steam parameters, the wall thickness of pressure parts will increase. The large wall thickness of thick-walled components limits the allowable rate of temperature change. This leads to disadvantages in the operation of the power plants.

A possibility to reduce the wall thickness of high-pressure outlet headers and piping is the increase of parallel lines of the headers to reduce the inside diameter.

From the material point of view, the wall thickness can be reduced by use of materials with higher creep strengths.

As candidate materials for thick-walled components, main attention has been paid up to now to the improvement of the modified 9 - 12 % chromium steels. The main reason is to avoid using austenitic steels for steam parameters which are expected in the near future. **Table 3** gives the chemical composition of the new materials in comparison with conventional ones. The 100,000 h creep rupture values are shown in **Fig. 14.**

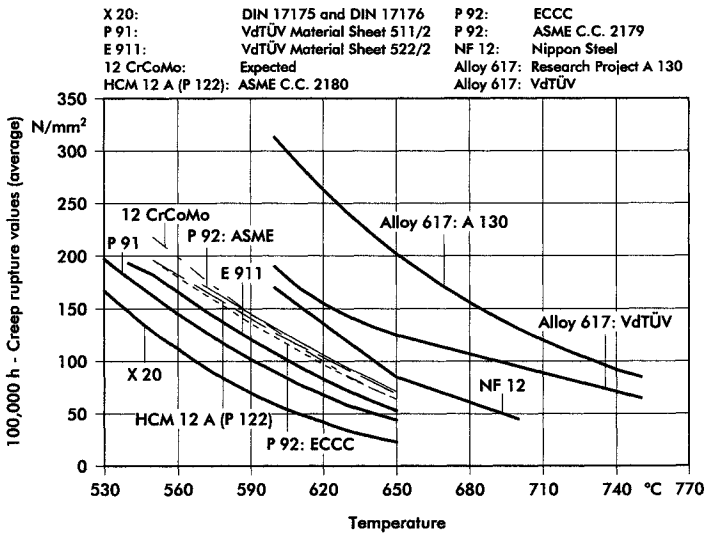


Fig. 14: 100,000 h Creep Rupture Strength for Pipe and Header Materials

Table 3: Chemical composition of header and pipe materials

Steel	C	Cr	Mo	W	Co	Others
Martensitic steels:						
X20CrMoV121	0.17 - 0.23	10.0 - 12.5	0.80 - 1.20	-	-	V
P91	0.08 - 0.12	8.0 - 9.5	0.85 - 1.05	-	-	V, Nb, N
P92 (NF616)	0.07 - 0.13	8.5 - 9.5	0.30 - 0.60	1.5 - 2.0	-	V, Nb, N, B
E911	0.09 - 0.13	8.5 - 9.5	0.90 - 1.10	0.9 - 1.1	-	V, Nb, N, B
P122 (HCM12A)	0.07 - 0.14	10.5	0.25 - 0.60	1.5 - 2.5	-	V, Nb, N, B, Cu
NF12	0.08 - 0.11	10.6 - 11.1	0.10 - 0.20	2.5 - 2.7	2.4 - 2.8	V, Nb, N, B
SAVE12	0.08	10.0	0.15	3.0	2.5	V, Nb, N, B, Cu
12CrCoMo		~12.0	~1.50		~1.0	
Ni-based alloys:						
Alloy 617	0.05 - 0.10	20.0 - 23.0	8.0 - 10.0	-	10.0 - 13.0	Ti, Ni

Fig. 15 shows the evolution of the 9 - 12 % chromium steels (based on [6]). In Europe, the conventional steel for thick-walled components has been for a long time X20CrMoV121. Extensive operating experience is available in the steam temperature range up to 560 °C. With an increase of the steam parameters, the limit of the steel X20CrMoV121 is quickly reached. In order to have higher strengths, new materials have been developed. The next development in this area led to the application of the material P91 which can be meanwhile regarded as well-examined material. In a further development, the creep rupture values of the new steels are further improved through the addition of tungsten. The typical materials from this new development are the tungsten-alloyed chromium steels E911, P92 and P122 (HCM12A). The

steel E911 developed during the European research project COST is standardised in a VdTÜV material sheet. For other steels P92 and P122, ASME code has been approved.

The recent developments on the martensitic steels are the 12Cr-Co steels NF12 , SAVE12 and the 12CrCoMo steel (type F or G) which is being developed by COST 522 programme. All materials are in a very early development stage. For all materials, even higher strength values than the above mentioned 9 - 12 % chromium steels can be expected. But no long-term strength values are available up to now.

For the very high steam conditions of 375 bar / 700 °C, nickel-based alloys like Alloy 617 and Alloy 4020 are needed. For such high steam parameters, the load change rate of the thick-walled component is very low. The power plants should be operated preferably as base-load units.

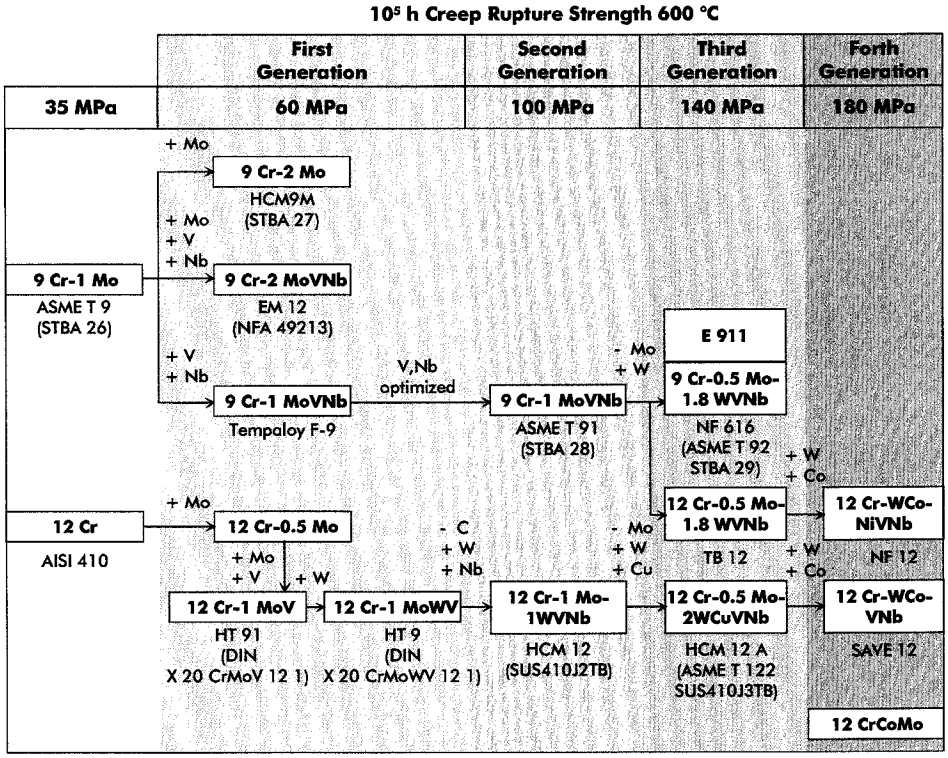


Fig. 15: Evaluation of 9 - 12 % Chromium Steels for Boiler Application (based on Masuyama [6])

Fig. 16 shows the wall thickness of the final SH outlet header for different materials at a pressure of 300 bar. If the wall thickness is limited by 100 mm which represents an outer diameter to inner diameter ratio of 2, the steam parameter limit lies approximately at 300 bar / 610 °C (SH outlet) by using the material P92 or P122 and at 300 bar / 700 °C by using Alloy 617 (based on the current VdTÜV values). If the wall thickness should be smaller, the maximum

steam conditions are accordingly lower. After upgrading of the Ni-based alloy 617, the wall thickness of the headers can be reduced by approximately 30 % at the same steam parameters.

Summary

In order to increase the power plant efficiency, once-through technology with advanced steam parameters can be used for pulverised coal-fired boilers. The critical components at high steam conditions are the water walls, the final stages of superheater and reheater tubes as well as high-pressure outlet headers and piping.

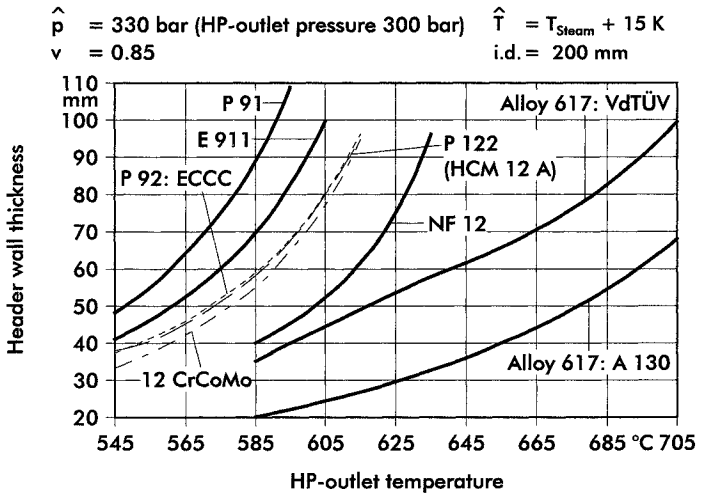


Fig. 16: Wall Thickness of Header Materials for Different Steam Conditions (Pressure and Temperature refer to Operating Conditions at Boiler Outlet)

Fig. 17 shows the different material development stages and related steam parameter limits. By use of the newly developed materials which have been qualified in the 90s, coal-fired power plants with the steam parameters 290 bar / 600 °C / 620 °C can be realised. Various on-going R&D projects like COST 522 etc. will push the steam conditions to higher than 600 °C.

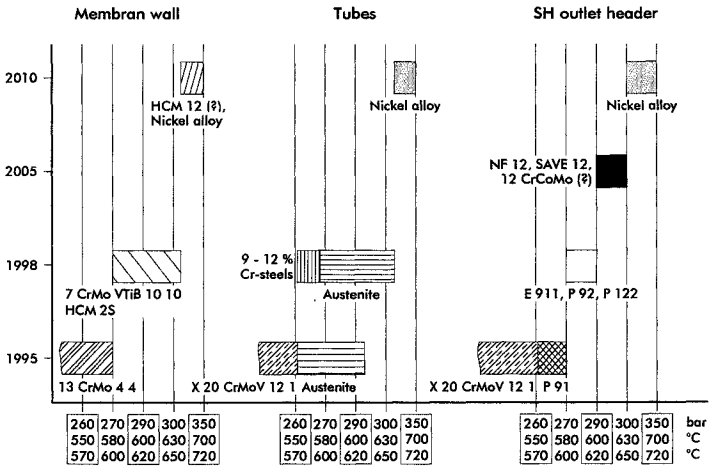


Fig. 17: Material Development Stages and related Steam Parameter Limits

It should be mentioned that for the steam parameters 300 bar / 630 °C / 650 °C currently no candidate materials can be regarded as promising materials for the SH outlet headers and piping system. The 12 % Cr-steels NF12, SAVE 12 and 12CrCoMo could have sufficient creep rupture strength (no long-term material properties are up to now available), but the oxidation resistance of these materials may not be high enough at such high temperature level.

A completely new perspective is opened with the application of Ni-based alloys which marks the next development step for advanced coal-fired power plants. **Fig. 18** shows that a major efficiency increase can be reached through a significant rise of steam parameters from the currently available 280 bar / 600 °C / 620 °C to 350 bar / 700 °C / 720 °C. The realisation of such an advanced 700 °C power plant can be expected in the next 5 to 10 years.

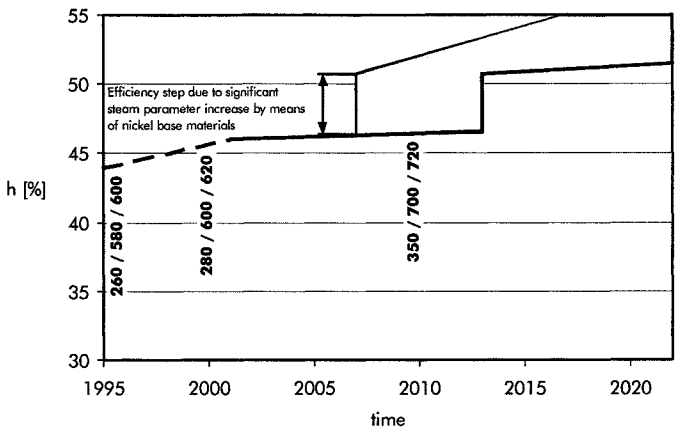


Fig. 18: Efficiency Development of Power Plants

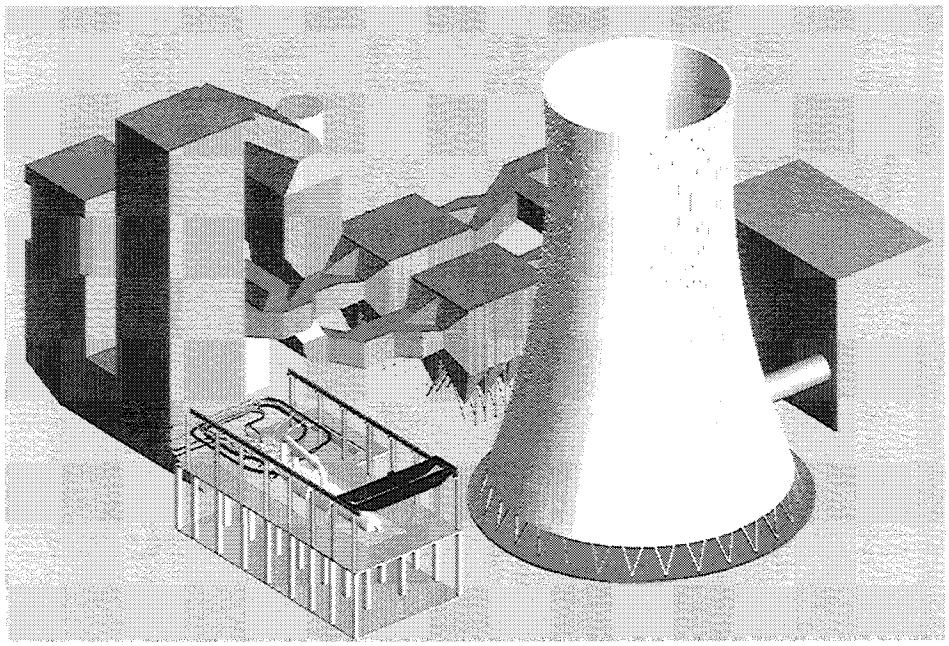


Fig. 19: Advanced Power Plant in Compact Design with an Inverse Twin Tower Boiler

The economic evaluation has shown that for an advanced 700 °C power plant the fuel costs will be reduced by roughly 15 % due to higher efficiency, while the investment costs will be increased by 10 % compared with a state-of-the-art power plant [9]. The economics can be further improved if a compact design which aims to reduce the amount of the expensive

superalloys will be introduced. **Fig. 19** shows a power plant layout based on an inverse twin-tower boiler with downward firing in the left tower and heating surfaces in the right tower. The final outlet headers are located very closely to the turbine to save expensive steam piping in superalloys.

References

[1] R. Heitmüller, H. Fischer, J. Sigg, R. Bell, N. Hartlieb: Lignite-fired Niederaußem K aims for efficiency of 45 per cent and more. Modern Power Systems, May 1999, pp. 53 - 66.

[2] Elsam: Highest supercriticality for Skaerbaek and Nordjylland. Modern Power Systems. March 1995.

[3] K. Muramatsu: Development of Ultra Supercritical Plant in Japan. In "Advanced Heat Resistant Steels for Power Generation" R. Viswanathan, J. W. Nutting, Ed.; IOM Communications Ltd., London, pp. 543 - 559, 1999.

[4] G. Scheffknecht, Q. Chen, A. Kather: Dampferzeuger mit fortschrittlichen Dampfparametern. VDI-GET Conference „Entwicklungslinien der Energie- und Kraftwerkstechnik" 10./11. Sept. 1996, Siegen/Germany.

[5] R.-U. Husemann, W. Bendick, K. Harrmann: The new 7CrMoVTiB1010 (T24) material for boiler waterwalls. IJPGC – International Conference on Power Engineering – 99, 25 - 28 July 1999, San Francisco/USA

[6] F. Masuyama: New developments in steels for power generation boilers. In "Advanced Heat-Resistant Steels for Power Generation" R. Viswanathan, J. W. Nutting, Ed.; IOM Communications Ltd., London, pp. 33 - 48, 1999.

[7] G. Scheffknecht, R. Blum, Q. Chen, A. Vanderschaeghe: Ein Vorhaben zur Ermittlung der Hochtemperaturkorrosionseigenschaften verschiedener Dampferzeugerwerkstoffe unter Betriebsbedingungen und Dampftemperaturen bis 620 °C. VGB Kraftwerkstechnik 76 (1996), pp 856 - 862.

[8] R. Blum, Q. Chen, C. Coussement, J. Gabrel, C. Testani, L. Verelst: Betriebsversuche von Überhitzerwerkstoffen bei hohen Dampftemperaturen in einem steinkohlegefeuerten Dampferzeuger. VGB-Conf. "Research for Power Station Technology 2000", 10 - 12 Oct. 2000, Düsseldorf/Germany.

[9] S. Kjaer, F. Klauke, R. Vanstone, A. Zeijseink, G. Weissinger, P. Kristensen, J. Meier, R. Blum, K. Wieghardt: The advanced supercritical 700 °C pulverised coal-fired power plant. To be presented in Power-Gen Europe 2001, 29 - 31 May 2001 in Brussels/Belgium.

ALLOY DESIGN AND MICROSTRUCTURAL CONTROL FOR IMPROVED 9-12%Cr POWER PLANT STEELS

R W Vanstone
ALSTOM Power Ltd, Rugby, UK
COST 522 Metallography and Alloy Design Group co-ordinator

Abstract

Historical developments of 9-12%Cr steels and developments in the COST 501 programme are briefly reviewed. The nature and status of investigations into the microstructural evolution of these steels and of attempts to model this evolution and the mechanical properties which follow from it are described. The alloy design philosophy being applied in COST 522 is explained and the steels being investigated in the project detailed. Finally challenges for future alloy development are outlined.

Keywords: Alloy design, microstructure, 9-12%Cr martensistic steels

The historical development of advanced 9-12%Cr steels

Creep resistant 9-12%Cr alloys were first developed for gas turbine applications in the 1950s. Steels like the 12%CrMoVNb alloys developed in the UK and the X19CrMoVNbN 11 1 alloy developed in France and Germany have high alloy content giving them high hardenability so that on cooling after solution treatment martensite is formed even in thick section and at relatively low cooling rates. This martensitic matrix contains a dense network of dislocations which is stabilised by a dispersion of carbides formed during tempering. These steels contain high levels of C which combines with large amounts of carbide-forming elements like Mo and V but especially Nb. Although these steels have very high creep strength for durations of 10,000 hours, appropriate to jet engine application, at temperatures above about 550°C their creep strength falls rapidly as durations are extended towards the 100 000 hours which is the typical basis of power plant design (Figure 1). In addition, these steels were not generally considered appropriate for the large forgings and castings required for steam turbines, being susceptible to segregation and having poor forgeability, poor weldability and limited fracture toughness.

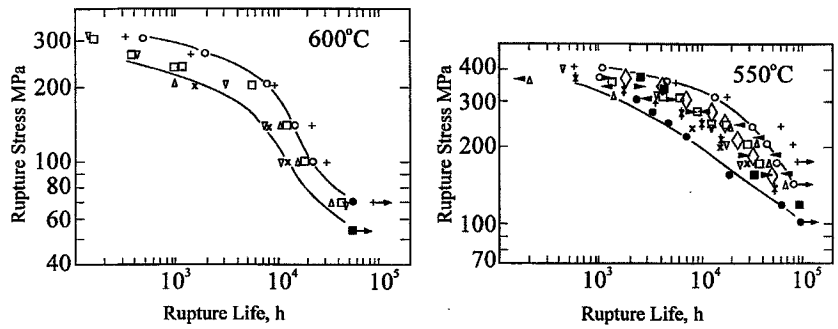


Figure 1: Rupture strength of 12CrMoVNb. At 550°C rupture strength falls rapidly beyond about 30,000 hours. At 600°C this fall occurs earlier, after about 10,000 hours.

In the mid 1970s ORNL was charged by the US Department of Energy with the development of a ferritic steel with high creep strength and good weldability for application in fast breeder

reactors. The 9%Cr1%Mo alloy used for tubing in the UK was taken as the basis and modified through additions of V, Nb and N. The resultant alloy, known as modified 9%Cr1Mo, bore a superficial resemblance to the earlier generation 12%CrMoVNb steels but it differed in certain key respects. Nb content was reduced drastically, from levels of 0.3% and above to less than 0.1%. Carbon content was also reduced, to about 0.1%. The optimisation of alloy content resulted in improved fracture toughness and weldability and more stable long term creep properties [1]. At 600°C the 100,000 hour creep strength of the new alloy proved to be around 50% greater than that of the previous generation of 12%CrMoVNb steels. This alloy, developed as a wrought material, has also been successfully applied to castings [2, 3].

Around the same time that modified 9%Cr1Mo was being developed in the USA, work began in Japan on materials suitable for rotor forgings. The steels developed were similar in concept to modified 9%Cr1Mo but with slightly more Cr (about 10%) and C (about 0.14%) and either higher Mo content or additions of W [4, 5]. The increase in C content, together with adoption of lower tempering temperatures, enabled yield strengths greater than 700 MPa to be achieved while at the same time retaining a high level of fracture toughness. At 600°C the 100 000 hour creep strength of these alloys was similar to, or slightly greater than, that of modified 9%Cr1Mo.

Alloy development in COST 501

In Europe a collaborative project to develop improved high temperature materials for power plant began in the early 1980s under the auspices of COST 501. It involved all the main turbine makers and boiler makers who were supported by material suppliers and research institutes. The methodology was essentially empirical. At first a large number of small scale melts (typically 50kg) in different alloys and different heat treatment conditions were assessed. This assessment involved tensile and impact testing, both in the as-received conditions and after long time ageing at service temperatures (480-650°C to assess potential embrittlement or softening), and most importantly of all, creep testing. In addition the forgeability of the alloys was assessed, typically through high temperature tensile testing. An attempt to simulate the condition of the alloys at end of life was made by accelerated thermal exposures. Material was heat treated at 700°C for 200 hours in an attempt to simulate exposure at around 600°C for 100,000 hours and the tensile, impact and creep properties in this condition were also investigated. The results of all of these tests were assessed, typically when creep data of at least 10,000 hours was available and the most promising materials were applied to the manufacture of prototype rotor forgings and valve chest castings. The properties of these prototypes were then confirmed by sectioning the components and carrying out further mechanical tests, creep testing then continuing for much longer durations.

The initial trial alloy selection was largely governed by:

- Reviews of the literature (at that time a large literature was already available on the development of modified 9CrMo, on the extensive investigations of Fujita, and on the early applications of his work by Japanese forgemasters and turbinemakes to develop alloys applicable to high temperature rotor forgings)
- Experience of the forgemasters in balancing the composition of the major elements (Cr, Mo, Ni, Mn etc) to achieve zero or low levels of delta ferrite and hot workability, largely

through the application of concepts like the Schaeffler diagram defining acceptable compositions in terms of Ni and Cr equivalents.
- Experience of the forgemasters in controlling levels of the minor elements (Al, Si, S) to achieve de-oxidation and acceptable levels of hot workability.

.

The early developments were certainly not based on any fundamental considerations of microstructure or creep mechanisms. Indeed any microstructural investigations would have been limited to materials in the as-received condition. It was simply not possible to investigate the evolution of microstructure during creep without first carrying out the creep tests. Nonetheless these early developments were impressively successful. Three alloys in particular (a 10%Cr1%Mo1%WVNbN alloy designated Steel E and a 10%Cr1.5%MoVNbN designated Steel F as rotor forgings and a 10%Cr1%Mo1%WVNbN steel designated CT as castings) have been applied in a generation of operating power stations [6, 7]. The application of these steels in place of the low alloy steels conventionally used has enabled an increase in operating temperatures resulting in increased power generation efficiency, lower fuel consumption and lower emissions.

Microstructural investigations and model development in COST 501/3 and COST 522

The successes of the early work in COST 501 led to further attempts to achieve even better properties. It was anticipated that a greater understanding of the microstructure of these steels and its evolution would enable improved alloy design. Within Work Package 11 (Critical Components for Advanced Steam Cycles) of Round III of COST 501, which began in January 1993 and was completed in December 1998, fourteen organisations from eight different countries were involved in detailed microstructural investigations, this activity being co-ordinated by the author [8].

Microstructural investigations were now possible on the wide range of alloys produced as small scale melts and tested in the earlier phases of the project. Material from these investigations were available in the as heat treated condition and after long term exposure to stress and elevated temperature. Materials were available from the most successful melts and also from the less successful steels. Tests on the experimental alloys had included creep tests at 600 and 650°C for up to 60,000 hours. Examination of both the head and gauge length of these creep specimens was carried out to enable the effect of creep strain in the gauge length to be established in comparison with the unstrained material in the head of the specimen and both these conditions were compared with the as heat treated condition.

Microstructural characterisation of each of these conditions and locations involved determination of the following parameters:

- hardness
- grain size
- primary phase description:
  - phase (martensite, delta ferrite etc.)
  - chemical composition
- secondary phase description:
  - species ($M_{23}C_6$, MX, Laves phases etc.)
  - size distribution
  - location (intra-granular, sub-grain boundaries etc.)

  - chemical composition
  - inter-particle spacing
- dislocation structure:
  - sub-grain size and shape
  - dislocation density

Determination of these parameters involved the use of optical microscopy, scanning and transmission electron microscopy, electron diffraction, energy dispersive spectroscopy, residual phase analysis and automated image analysis. The first phase of the investigation involved establishment of a qualitative description of these parameters. The second phase of the investigation involved their quantitative description. Detection and identification of all second phase particles is often difficult, especially when particles are small, dislocation densities high and the specimen orientation not optimised for contrast of the particle in the bright field image. Confident identification of particles has typically involved analysis of diffraction patterns. Advances in electron microscope technology are being increasingly applied to overcome such difficulties, for example energy filtering transmission electron microscopy (EFTEM) produces images giving high contrast to all particles and also, by revealing their chemical composition, enables their rapid identification [9].

Quantitative microstructural characterisation is a lengthy, painstaking process and the assessment of a wide range of alloys makes collaboration essential. Such collaboration has been one of the strengths of the COST 501 project but experience has revealed significant difficulties in comparing the results reported by one laboratory with those reported by another [10]. For example, variations of a factor of 2 were reported when different laboratories measured mean subgrain width in the same material. Investigation into the source of such variation, through a series of round-robin investigations, suggested that much of it arose from the use of different image analysis procedures and packages. Despite these difficulties, the observations made in the project have enabled significant insights into microstructural evolution in these steels and its relationship with mechanical properties. In addition, the project drew together a group of experts constituting an unrivalled forum for the discussion and assimilation of work from outside of the project.

In addition to purely microstructural investigations, the COST 501 project incorporated the development of models to predict both microstructure and the properties which follow.

Models have been developed which go some way to explaining and predicting the observed microstructural changes and their effect on creep strength. During creep the steels evolve towards thermodynamically more stable conditions. Computer models have been developed which use available thermochemical data to predict the most thermodynamically stable combination of phases in the steel, the equilibrium condition where free energy is at a minimum. Equilibrium phase diagrams are produced which predict the phases present and their fraction as a function of temperature. The chemical composition of each phase can also be predicted. An example is shown for COST steel E in Figure 2 which shows that at typical tempering temperatures just above 700°C the presence of only $M_{23}C_6$ and MX is predicted. At temperatures representing likely service temperatures for this steel, around 600°C, the phase diagram predicts the presence of Laves phase in addition to these phases. This is consistent with metallographic observations. Laves phase is not present after heat treatment but after long term exposure it does precipitate, in line with the predicted equilibrium. Thus many of

the microstructural observations can be explained on the basis of evolution towards a state of minimum free energy.

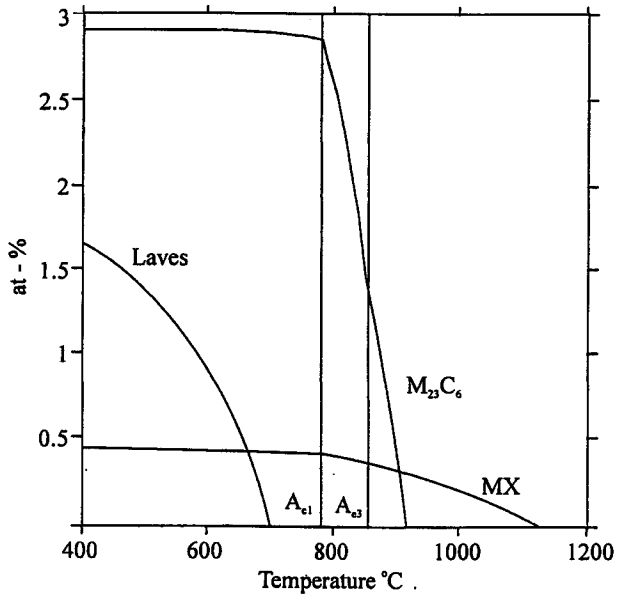


Figure 2: Equilibrium phase diagram for 10%Cr1%Mo1%WVNbN steel

Microstructure evolves only slowly towards the state of equilibrium because of the slow kinetics governing many of the processes of this evolution. In order to understand and predict the rate of evolution, models describing microstructural kinetics are required. Major efforts in modeling the kinetics of precipitate nucleation and growth were made. The model developed by Robson and Bhadeshia [11] uses thermochemical data in combination with models for nucleation and growth to predict the sequence in which phases precipitate, their fraction as a function of time and the distribution of particle size for each phase.

Understanding and predicting microstructural evolution is not a goal in itself. The link between microstructure and creep strength must be modeled. Only then can modeling be used to predict creep strength and thus provide a powerful tool for alloy development. Models describing the accumulation of creep strain as a function of microstructural parameters are also being developed. For example, the composite model of Straub et al [12] predicts creep strain as a function of particle size, dislocation density and subgrain size. Therefore many of the elements are in place for a combined model which will predict creep strength from a knowledge of chemical composition and heat treatment (Figure 3). However no models are yet available which describe the evolution of dislocation density and subgrain size. This input to a combined model must currently be made through empirical observation.

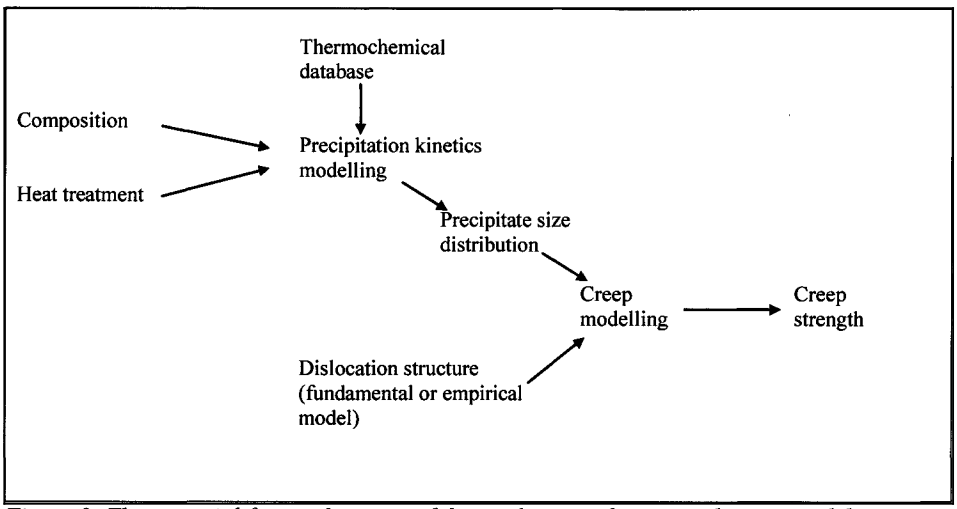


Figure 3: The potential for combination of thermodynamic, kinetic and creep modeling to predict creep strength.

The success of the COST 501 microstructural and modeling studies encouraged an extension of this work in COST 522. A group of 21 partners is currently working on a series of parallel projects to investigate different aspects of microstructural development within particular alloys (Table 1). The work has been extended to include investigations of more recent alloys developed in COST 501, new alloys being developed in COST 522, and alloys from outside the project, such as P92 and P122. The work remains quantitative but, in recognition of the difficulties encountered in comparing results across different laboratories, the work of each partner has been designed so that independent conclusions can be reached by each partner, each partner's conclusions nonetheless contributing to a greater understanding of the generic behaviour of these steels. Modeling studies include further work on the kinetics of second particle precipitation, growth and coarsening, including an extension of the Robson and Bhadeshia model to advanced austenitic alloys being developed for boiler applications. Other work is focussing on precipitation behaviour at boundaries [13]. Martensitic steels contain an enormous area of sub-grain and prior austenite grain boundaries and the majority of particles are precipitated on these boundaries. Thus improved understanding of the influence on particle nucleation and growth of these disordered zones, where diffusion coefficients, surface energies and nucleation barriers are all significantly different from the matrix, is essential to a complete understanding of these steels.

The approach to alloy design

The objective of alloy design is to define a composition and heat treatment which leads to a material which meets several requirements:

- It must have high long term creep strength coupled with resistance to isothermal softening and embrittlement.
- It must be resistant to the high temperature environment. In the turbine and boiler this implies resistance to steam oxidation but in the boiler, resistance to flue gas corrosion is also required.

Technische Universität Graz	Graz, Austria
Austrian Research Centers Seibersdorf	Seibersdorf, Austria
SKODA Research Plzen Ltd.	Plzen, Czech Republic
Institute of Physics of Materials Czech Academy of Sciences	Brno, Czech Republic
Vitkovice Research & Development	Ostrava, Czech republic
Alstom Power Support GmbH	Mannheim, Germany
MPA Stuttgart Staatliche Materialprüfungsanstalt	Stuttgart, Germany
ELSAM / ENERGY E2 Technical University of Denmark	Lyngby, Denmark
EDF Industry Branch R&D Division/Dept.Etude des Materiaux	Moret sur Loing, France
CEA Commissariat à l'Energie Atomique	Crif/Yvette, France
Tampere University of Technology Materials Science	Tampere, Finland
Centro Sviluppo Materiali	Roma, Italy
University of Mining and Metallurgy (AGH)	Krakow, Poland
Institute for Ferrous Metallurgy Dept. of Mat. Science	Gliwice, Poland
Department of Experimental Physics Chalmers University of Technology	Göteborg, Sweden
Dept. Materials Science & Engineering Royal Instituteof Technology	Stockholm, Sweden
VUZ, Welding Research Institute Dept. of physical metallurgy	Bratislava, Slovakia
Innogy	Swindon, United Kingdom
University of Cambridge Dept. of Mat.Science & Metallurgy	Cambridge, United Kingdom
Loughborough University IPTME	Loughborough, United Kingdom
Alstom Power Ltd.	Rugby, United Kingdom

Table 1: Participants in COST 522 Metallography and Alloy Design Group

- It must be capable of manufacture in economic product forms, as large forgings for rotor manufacture and as castings for components such as valve chests and cylinder casings and as pipes and tubes for boiler manufacture.
- These product forms must be ultrasonically inspectable to enable the absence of critical defects to be confirmed.
- Where appropriate for component manufacture, the materials must be weldable. This applies especially to pipes, tubes and castings but can also be a requirement for forgings for welded rotors.

The alloy design philosophy currently being followed in COST 522 draws on evidence from several different bases:

1. Empirical analysis of the results of the creep tests on the many trial melts and prototype components produced in the COST 501 programme has led to several conclusions. For example:
- Increasing Mo content from 1% to 1.5% leads to an increase in creep strength.
- In product forms representing large section turbine rotors and castings, attempts to increase creep strength through substitution of some Mo by W have resulted in no increase in long term creep strength and when W additions of around 2% or more were made such additions led to instability in long term creep strength.
- Additions of boron have been observed to lead to the highest creep strengths in the alloys tested.
- Raising tensile strength through tempering at lower temperatures gives some benefit in long term creep strength at lower temperatures but as temperatures rise towards 600°C the long term creep strengths of materials with different initial tensile strength levels tend to converge.
2. Review of the literature has yielded similar conclusions. Excellent reviews have recently been published by Mayer [14] and by Viswanathan and Bakker [15, 16]. The positive effect of boron is most vividly illustrated in the alloy TAF where levels of around 400ppm lead to 100,000 hour creep strength at 600°C of around 160MPa. Unfortunately attempts to add such high levels of boron to the large ingots required for rotor forgings have led to segregation problems.
3. Thermodynamic modeling has enabled the prediction of phase diagrams so that alloys can be designed to be free of delta ferrite and to have reasonably extensive high temperature single phase austenite fields to facilitate forging operations.
4. The results of metallographic investigations, coupled with fundamental consideration of the mechanisms of creep deformation, have enabled the identification of ideal microstructures and have also helped to clarify the role of different elements so that alloying additions can be made with higher confidence about their impact on alloy microstructures and properties:
- A fully martensitic microstructure is desirable. The high dislocation density and large sub-grain boundary area characteristic of such a structure provide a high density of nucleation sites for particle precipitation so that dispersion hardening is enhanced. In addition the complex dislocation structure itself provides barriers to dislocation glide and climb. A fully martensitic structure may be achieved by addition of an appropriate level of Cr, generally greater than 9%. Cr has the additional benefit of increasing resistance to oxidation. However if too much Cr is added, perhaps greater than 11%, the phase diagram is modified so that at high temperatures the alloy becomes two-phase (austenite and ferrite) leading to processing difficulties during forging. Furthermore on quenching the austenite transforms to martensite but the ferrite phase remains so that the complete martensitic structure cannot be achieved. Nonetheless higher levels of Cr can be accommodated if elements such as Co or Cu are added to stabilise and expand the austenite field at high temperatures.
- The sub-grain structure formed during tempering of the martensite needs to be stable for maximum creep strength. Sub-grain boundaries are pinned by precipitation of $M_{23}C_6$ particles. The dominant element in this carbide is Cr so additions of C and Cr are essential.
- Inside the sub-grains dislocation movement can be restricted by the introduction of elements in solid solution, especially larger atoms such as Mo or W which strain the lattice to create elastic fields acting against dislocation movement, or by the precipitation

of particles. V plays an important role in this dispersion hardening, reacting with N to lead to a dispersion of VN particles which typically nucleate on and pin intra-granular dislocations.

- The structure described above needs to be maintained for as long as possible during long periods of high temperature service. Investigations have shown that additions of boron stabilise these microstructures. Atom-probe investigations have shown that boron segregates to $M_{23}C_6$ particles [17] and it is observed that the coarsening rate of these particles is reduced in boron containing steels. Thus the effectiveness of $M_{23}C_6$ particles in pinning sub-grain boundaries is maintained over a longer time. The presence of boron restricts the amount of nitrogen which can be added without forming undesirable, low melting point boron nitrides so in boron containing steels the level of nitrogen is reduced to around 0.02% compared with the 0.05% levels found optimum in boron free steels. To maintain the level of interstitial elements, carbon content may be increased to compensate for the lower nitrogen content.
- Microstructures from materials tempered at lower temperatures initially contain higher dislocation densities and smaller particles. However this microstructure appears less stable than microstructures arising from tempering at higher temperatures so that in the long term at high temperatures the microstructures of initially low and high tensile strength materials converge.
- Other threats to the long term stability of the optimum microstructure arise from the precipitation of new species. Nucleation of such species during tempering may be inhibited for thermodynamic or for kinetic reasons. However these particles may precipitate slowly over many thousands of hours during the long service life of the alloys. Nucleation sites are few so the particles are typically large, contributing little to dispersion hardening. Steels containing high levels of Mo and W form Laves phase (Fe_2Mo,W) during long periods of service. This precipitation removes Mo and W from solid solution and this loss is more severe in the W containing steels. High levels of V and Nb encourage the formation of the coarse Z phase at the expense of the strengthening VN precipitate and additions of Ni accelerate this precipitation and can also lead to the formation of M6C [18]. For these reasons Ni content should be restricted as far as possible and additions of V and Nb should not exceed those levels required for the positive influences described above. Attempts to restrict particle coarsening can also be made via additions to reduce matrix diffusion rates. These rates are related to Curie temperature so additions of alloys which raise this temperature, such as Co, can be considered.
- Large components in the steels must be safe from short-term fracture as well as demonstrating long term creep strength. Fracture toughness is improved by limiting grain size and a finer grain size also reduces ultrasonic attenuation so that smaller defects may be resolved during non-destructive examination. Finer grain size is achieved by adding Nb which forms carbides insoluble at the solution temperatures applied and which therefore act to pin grain boundaries and restrict grain growth during such solution treatments.

An example of the targeted microstructure is given in Figure 4.

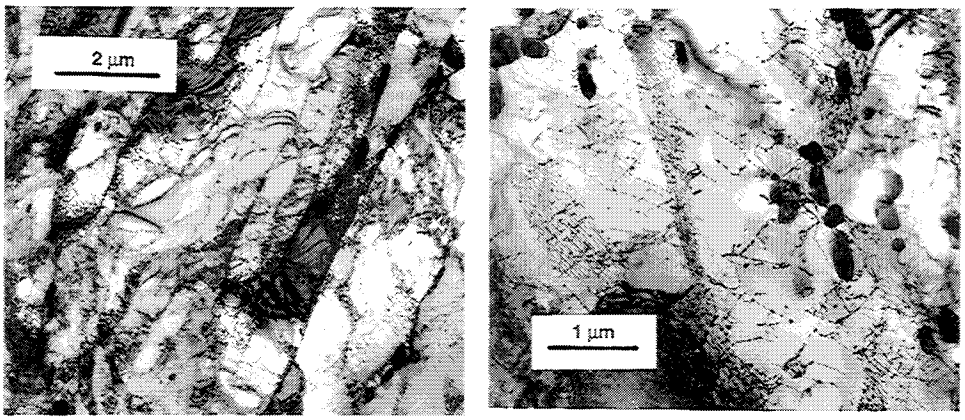


Figure 4: Microstructures for maximum creep strength are designed to contain a network of low-angle sub-grain boundaries stabilised by $M_{23}C_6$ particles with a fine dispersion of VN particles inside the subgrains to pin free dislocations.

Alloys investigated in COST 522

The insights into optimum microstructure and alloy design described above have formed the basis of the alloys being investigated in COST 522. Trade-offs are clearly required. For example both boron and nitrogen increase creep strength but when added in combination they form undesirable nitrides so when boron is added, the level of nitrogen must be limited. Difficulties in controlling segregation of high levels of boron in large ingots also leads to practical limitations on the level of boron to around 100ppm. Vanadium also enhances creep strength but if too much is added, the formation of Z phase is encouraged. Higher solution temperatures lead to increased creep strength but can also lead to coarser grain size, threatening integrity against short term fracture. Economic factors must also be considered. Higher Cr contents increase oxidation resistance but can also lead to the formation of delta ferrite and although this may be controlled by additions of Co this element is extremely expensive.

Taking all of these factors into account the alloys listed in Table 2 were designed for investigation in the COST 522 Turbine Group. The alloys are essentially based on a 10%Cr3%Co1.5%MoVNbN alloy stabilised with additions of 100ppm boron. Ni is minimised to increase long term stability. Higher Cr levels are investigated for improved oxidation resistance and two carbon levels are investigated to explore the optimum level for carbide formation. In FB9 additional Co is added to investigate the potential of Co to reduce diffusion rates by raising Curie temperature. Small amounts of W were added to FB10 and FB11 to investigate the possibility of improved solid solution strengthening at low levels of this element. These alloys are being investigated in both cast and forged product forms and the results of these investigations are described by following papers in this conference. Other alloys designed according to similar principles have been investigated in the Boiler Group.

The insights into alloy behaviour gained during COST 501 and 522 have influenced not only the alloy design philosophy but also the testing approach. As described earlier, in COST 501 an attempt was made to simulate the microstructures present after long times in service by

accelerated heat treatments at higher temperatures. However with the benefit of microstructural studies we now know that such treatments fail to bring about the precipitation of Laves phase which is an important feature of microstructural evolution at service temperatures. Therefore this approach has been abandoned. The greater knowledge of microstructural development also conditions the selection of test temperatures for long term creep testing.

	C	Cr	Mn	Mo	Ni	B	Co	N	Nb	V	W
FB 5	0.12	10	0.1	1.5	0.2	0.010	3	0.02	0.07	0.2	0
FB 6	0.12	11	0.1	1.5	0.2	0.010	3	0.02	0.07	0.2	0
FB 7	0.16	10	0.1	1.5	0.2	0.010	3	0.02	0.07	0.2	0
FB 8	0.16	11	0.1	1.5	0.2	0.010	3	0.02	0.07	0.2	0
FB 9	0.16	11	0.1	1.5	0.2	0.010	6	0.02	0.07	0.2	0
FB 10	0.12	10	0.1	0.9	0.2	0.007	3	0.02	0.07	0.2	0.4
FB 11	0.16	11	0.1	0.9	0.2	0.007	3	0.02	0.07	0.2	0.4

Table 2: Alloys investigated in COST 522 Turbine Group

Future challenges

Looking beyond the current round of activities in COST 522, further challenges for alloy development and alloy modeling must be faced.

- It is clear that higher levels of boron would lead to improved creep strength. The challenge for material suppliers is to control boron segregation in large components when boron contents are increased significantly beyond 100ppm.
- Advances in quantitative metallography are still required if results are to be repeatable and transferable between different laboratories. Physically based models describing mechanical properties will never be reliable if the microstructural parameters on which they are based cannot be measured reliably and repeatably.
- Models of thermodynamic behaviour and their underlying thermochemical database need to be improved. One area currently being tackled is the more accurate prediction of Laves phase solution temperature in Mo containing alloys. Models describing creep behaviour need to be refined, becoming more physically based to reflect the complex microstructural evolution taking place.
- Ultimately the creep strength of 9-12%Cr steels is probably limited by the volume fraction of precipitates which can be generated. Using conventional steelmaking approaches, this is limited by the solubility of elements in these steels. Other mechanisms of introducing stable dispersions of particles into these steels should be considered.

Acknowledgements

Acknowledgement is made to the various national governments who have supported the technical work of COST 522 and to the European Commission's support of its management activity. In particular the author acknowledges the support of his own government through the UK Department of Trade and Industry's Cleaner Coal Programme.

References

1. V.K. Sikka, M.G. Cowgill, B.W. Roberts, 'Creep properties of modified 9Cr-1Mo steel', Proc. Conf. 'Ferritic alloys for use in nuclear energy technologies', Snowbird, Utah, June 1983.
2. D.V. Thornton and R. Hill, 'The fabrication and properties of high temperature, high strength steel castings', Proc. of 3rd EPRI Int. Conf. on Improved Coal-Fired Power Plants (ICPP), San Francisco, April 1991.
3. K.H. Mayer and W. Gysel, 'Modified 9%CrMo cast steel for casings in improved coal-fired power plants', ibid.
4. Y. Nakabayashi et al 'Advanced 12Cr steel rotor (TMK1) for EPDC's 50MW high temperature turbine step 1 (593°C/593°C)', Proc. of 1st EPRI Int. Conf. on Improved Coal-Fired Power Plants (ICPP), Palo Alto, November, 1986.
5. A. Kaplan and M. Miyazaki, 'Advanced 12Cr steel for high temperature rotors', Proc. of 2nd EPRI Int. Conf. on Improved Coal-Fired Power Plants (ICPP), Palo Alto, November, 1988.
6. D.V Thornton and M.Taylor, 'Experience in the manufacture of steam turbine components in advanced 9-12%Cr steels', Proc. of IMechE Conf. Advanced Steam Plant, London, May 1997.
7. K.Miyashita, 'Overview of advanced steam plant development in Japan', ibid.
8. R.W. Vanstone, Progress in understanding microstructure-property relationships in advanced 9-12%Cr steels, Proceedings of 6th Liege conference, Materials for Advanced Power Engineering, Liege, September 1998 pp139-154.
9. H. Cerjak, P. Hofer, B. Schaffernak, K. Spiradek and G. Zeiler, VGB Kraftwerkstechnik 77 (1997) Heft 9 p762.
10. A. Strang, Factors affecting the quantitative evaluation of microstructures in 9-12%Cr martensitic power plant steels, Proceedings of 6th Liege conference, Materials for Advanced Power Engineering, Liege, September 1998 pp171-192.
11. J.D. Robson, H.K.D.H. Bhadeshia, 'Modeling precipitation sequences in power plant steels', Materials Science and Technology, **13**, 631-644 (1997).
12. S. Straub, P. Polick and W. Blum, 'Simulation of the creep behaviour of 9-12%CrMoV steels on the basis of microstructural data', Proc. Institute of Materials Conf. Microstructural Stability of Creep Resistant Alloys for High Temperature Plant Applications, March 1997.
13. Y Yin et al, A new modelling approach to microstructural evolution in ferritic steels, this conference
14. K-H Mayer, Advanced heat resisting steels, from Advanced Energy Conversion Materials, published by Nova Science Publisher Inc, USA, 2001.
15. R. Viswanathan and W T Bakker, Materials for Ultrasupercritical Coal Power Plants - Boiler Materials: Part 1. Journal of Materials Engineering and Performance, Vol. 10, No 1, 2001, pp 81 to 95.

16.R Viswanathan and W T Bakker, Materials for Ultra Supercritical Coal Power Plants Part 2: Turbine Materials, from PowerPlant Chemistry 2001, 3(8), pp446-451.
17.M Hattesrand, H O Andren, Boron distribution in 9-12%chromium steels, Materials Science and Engineering A270 (1999) 33-37
18.V Vodarek and A Strang, Z phase characteristics in martensitic 12CrMoVNb steels, this conference.

THE EUROPEAN EFFORT IN DEVELOPMENT OF NEW HIGH TEMPERATURE ROTOR MATERIALS UP TO 650°C – COST 522

T.-U. Kern, Siemens Power Generation, Muelheim/R, Germany
M. Staubli, Alstom Power, Baden, Switzerland
K.H. Mayer, Alstom Power Nuernberg, Germany
K. Escher, Saarschmiede Voelklingen, Germany
G. Zeiler, Boehler Schmiedetechnik, Kapfenberg, Austria

Abstract

Improved ferritic-martensitic 9-12%Cr steels are under development worldwide. In COST 501/522 the European turbine manufacturers have defined the development goals in terms of required material properties, fabrication techniques (forging, casting, welding) and non-destructive examination for application of temperatures of up to 650°C.

In the first step, trial melts for 620/630°C were developed on the basis of alloying concepts including the addition of Co, B and W. Testing was performed. The most favourable outcome has shown a Cobalt-Boron containing steel without Tungsten. Full-size trial rotors with this composition have been produced and are currently under investigation. In the second step, improved microstructural modelling tools have supported the actual selection of chemical compositions for 650°C. The alloys do not exceed the already available 620°C materials in creep rupture strength but offer a potential for improvement in oxidation resistance for T >600°C. Further trial melts are in production with lower complexity of composition.

Keywords: design, materials, high temperatures, 10Cr steels, COST 522

1 Introduction

Energy is the source of general well-being and the standard of living in each country. The energy production itself is faced with the introduction of increasingly stringent emission regulations to safeguard health and preserve the environment for future generations.

In the decades to follow, there will continue to be heavy reliance on fossil fuels, such as coal, oil and natural gas. Because the reserves of oil and natural gas are unlikely to be sufficient to satisfy fully the projected increased power demands coal may be the only fuel available in substantial quantities around the world globe. This will force power plant utilities to increase the efficiency of their power plants.

Today the market for electricity generation is dominated by combined cycle power plants based on natural gas. However, in the near future the demand for coal-fired power plant will continue to expand due to the indigenous deposits of coal in large developing countries like India and China. In Europe, coal or lignite will also play an important role in the foreseeable future, and although the requirements for new plant will be limited, there will be a substantial market for up-grading or replacement of existing plants.

The improvement in efficiency of modern steam power plants is related to raising the temperature, as well as the pressure of the steam generated in the boiler. To withstand these advanced operating conditions, materials are required with improved high-temperature capability. In order to minimise investment costs (which also influence the effective cost of electricity generation), the greatest possible use must be made of martensitic steels for all major components in both the boiler and turbine. Specifically, steels of the 9 to 12%Cr class are required with high long term creep strength and oxidation resistance in steam, along with ease of fabrication for large forgings, castings and pipe sections.

2 Requirements to Rotor Materials

The components in steam power turbo-sets like rotors, casings, valves, bolts, blades and pipes have to meet different design requirements. Depending on the customer's specifications, several basic steam turbine types with the following characteristic are possible for power ranges up to 1000MW:
- High pressure turbines (HP) with high temperature and pressure (≥ 530°C/180bar);
- Intermediate pressure (IP) with high temperature and reduced pressure (≥ 530°C/30bar),
- Low pressure (LP) turbines (≤ 350°C/10bar).

Combined HP-IP and IP-LP turbines for the smaller power range for Combined Cycle Power Plants (CCPP), in monoblock or welded rotor design, are an additional solution for power generation.
The material properties of the steam turbine components under consideration are taking into account steam pressure and the surrounding medium depending on the applied steam and component metal temperature, *Tab. 1.*

Requirements	HP- & IP-Rotors	LP-Rotors, LP-Discs	HP- & IP-Casings	HP- & IP-Blades	LP-Blades	HP- & IP-Bolts
Static strength:						
tensile strength	●	●	●	●	●	●
Creep rupture strength:						
creep behaviour	●		●	●		●
Toughness:						
fracture toughness	●	●	●	●	●	●
Fatigue properties:						
Low cycle fatigue (LCF)	●	●	●	●	●	●
High cycle fatigue (HCF)	●	●		●	●	
Crack growth:						
static - Creep CG	●		●			●
alternating - Fatigue CG	●	●	●			●
Corrosion						
local corrosion		●		●	●	●
stress corrosion cracking		●			●	●
corrosion fatigue		●			●	
Erosion behaviour	●	●	●	●	●	
Oxidation behaviour	●		●	●		●

HP = High Pressure turbine IP = Intermedium Pressure turbine LP = Low Pressure turbine

Table 1: Design requirements and material properties for turbine components

As shown, the HP and IP rotor forgings, which can reach diameters of up to 1200mm, need to be made in well selected material in order to meet all property requirements.
The creep behaviour plays an important role for areas, such as the rotor centre and the blade attachment, whereas the fatigue resistance is mainly considered in the surface regions.
A material class which incorporates many of advantageous properties and which maintains the potential for further improvements is identified in the 9-12%CrMoV steels.

They are characterized by the following points:
- A good through hardenability up to 1200mm diameter;
- Balance in strength and toughness (long and short term);
- Weldability;
- Potential for high oxidation resistance;
- Lower cost than Austenites and Ni-base alloys;
- Ease in fabrication.

The mechanical and physical property profile of these 9-12%CrMoV steels has opened the way to further increase the application temperature up to T ≥ 600°C. The aim of the material development programs in Europe was defined as follows:

- 100,000 h creep rupture strength at 620°C/600°C of about 100 MPa;
- good creep rupture ductility (>10% elongation) and no notch sensitivity;
- through-hardening up to at least 1200 mm diameter;
- minimum yield strength of 600 or 700 MPa;
- other properties such as toughness and susceptibility to embrittlement should not be worse than with conventional 12%CrMoV and 1%CrMoV rotor steels.

On the basis of the experience with the 9-12%CrMoV steels in manufacturing, operation and service the joint European material development activities started many years ago with the aim of 600/620 for the time being, and 650°C material solutions for the near future.

3 Materials development in Europe

In Europe the efforts to improve the available 9-12%CrMoV steels are concentrated in the COST programmes. **COST** (**Co**-operation in the field of **S**cience and **T**echnology) is a long established European programme aimed at co-ordinating pre-competitive research activities in numerous areas of science and technology. Participants include turbine and boiler makers, manufacturers of forgings, castings, pipework and welding consumables, as well as testing institutes and utilities. The work has spanned the entire range, from basic research and development, through nondestructive and destructive testing of small experimental batches and large scale components, to standardization of specific steels and full-scale practical application in currently operating power plants.
COST 501 (1986-1997) has established a strong trans-European network in this field. The current action COST 522 (1998-2003) was founded on the success of earlier related COST 501 action [1]. The effectiveness of the past COST actions is exemplified by the introduction of newly developed ferritic steels for forgings, castings and pipework from the COST 501 action, "Materials for Power Engineering." These improved steels are in commercial operation in advanced European power stations and have made it possible to increase the operating steam temperatures from 530-565°C to 580-600°C with a corresponding increase in thermal efficiency.
The close co-ordination of activities related to turbine and boiler components within COST have led to the successful development of advanced materials for application in the turbine, as well as in the boiler. This effort has helped to meet the common requirements with respect to steam parameters. The development, properties and application of the new boiler steel E911, which was developed in COST 501, are reported in [2-4].

3.1. Experience with Rotor Materials for 600°C Application / COST 501 Round 2

During the COST 501 three different alloy types were identified with the potential to meet the requirements for 600°C long term application. The difference to the conventional 12%CrMoV steels lies mainly in the reduced contents of C, Cr, V and the addition of Nb and N. The compositions [5] can be divided into the groups

a) 9Cr-1,5Mo-100ppm Boron type;
b) 10Cr-1Mo-1W type;
c) 10Cr-1,5Mo type.

Three full-size rotors, each with its own specified composition, were produced and fully tested. A rotor forging with 840mm diameter was manufactured from the B-type steel (designated rotor 'B'), and two rotors with 1200mm diameter were fabricated from 1W-1Mo-type steel (designated rotor 'E') and Mo-type steel (designated rotor 'F') respectively.

A comparison of the 100,000h creep rupture strength of the conventional and new steels is given in *Fig. 1.*

steel	C	Cr	Mo	W	V	Nb	N	B	(weight%)
1CrMoV	0.28	1.0	0.9	-	0.30	-	-	-	
12CrMoV	0.21	12.0	1.0	-	0.30	-	-	-	
10CrMoV	0.12	10.0	1.5	-	0.20	0.05	0.05	-	
10CrMoWV	0.12	10.0	1.0	1.0	0.20	0.05	0.05	-	
9CrMoVB	0.18	9.0	1.5	-	0.25	0.05	0.02	0.010	

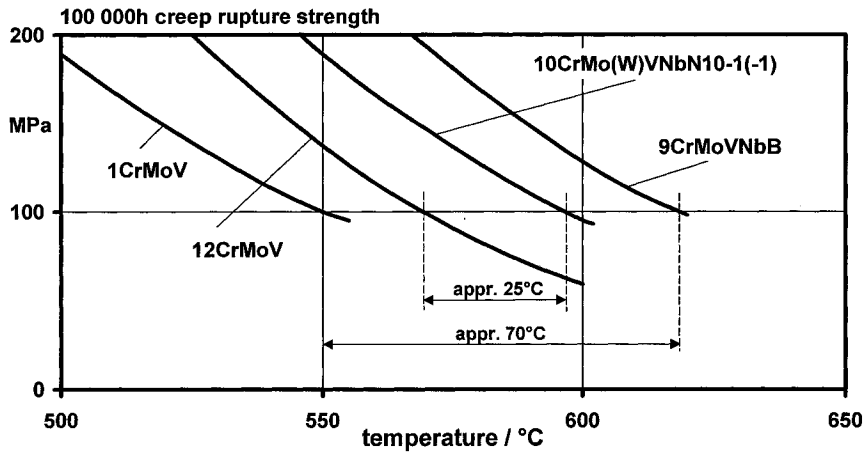


Figure 1: The 100,000h creep rupture strength of the newly developed European 600°C steels

There is significant gain in application temperature for these new rotor materials as compared with traditional rotor materials. The same creep rupture strength of 100MPa is achieved at temperatures of about 600°C for the W/Mo and Mo type steel, whereas the potential of B-steels goes up to 620°C.

The confidence to the extrapolated 100,000h long term data is based on very long creep rupture tests which have reached now times of >80,000h at 600°C for all the three materials described above.

The improved creep rupture strength does not, however, prejudice other design-relevant material properties, such as fracture toughness or low cycle fatigue behaviour. Additionally, the new materials provide benefits in medium-load and peak-load power plant operation on account of their favourable physical properties, such as reduced thermal expansion as compared to low alloyed steels. This also results in the benefit of shorter start-up times [6].
The detailed evaluation of the rotor and test melt programme given in [7] shows agreement in properties between trial melts and up-scaled components.
In order to confirm the long-term properties of the improved steel grades for 600°C application and to establish a comprehensive database for these materials, a programme was launched with the support of VGB in Germany involving the investigation of commercial components. The test programme includes 24 heavy components manufactured from the new cast and forged steels (W-bearing and W-free) and produced by different suppliers including the use of different production routes [8-10]. The creep tests have reached >40,000 hours and show a strong correlation between the creep properties of these production components and the trial components tested within COST [11].
The production experience of the new alloy types W/Mo and Mo is positive throughout [12-14]. The gained knowledge of qualified suppliers and the close co-operation within the COST group guarantees the turbine makers the required quality level of their components.

3.2. Materials for 620°C Application / COST 501 Round 3

The careful analysis of the long term test data, the results of microstructural investigations of the 600°C-materials within the metallography and alloy design working group of COST 501 and the use of new microstructural stability calculation models have led to the definition of a further five alloy compositions including:

- Reduction of the Ni-content;
- Alloying with Co;
- Addition of Boron and modifying the N-content;
- Increase of the Cr-content in order to improve the oxidation resistance at application temperatures of up to 620°C;
- Variation of the proven and investigated elements such as Mo, W, B and N on the basis of a C-Cr-Co-Nb matrix.

The required property level, as agreed for the 600°C materials, was adapted to the increase in application temperature from 600°C to 620°C.
Five trial melts were produced within weights ranging from 100 to 500kg and heat treated to simulate the centre of a large rotor forging [7, 15]. The chemical composition was designed with various goals in mind. Boron, Cobalt and Tungsten were added in special amounts to increase the creep rupture strength. The increasing Cr content belongs to the idea of improvements in the oxidation behaviour, *Tab. 2.* The main composition for FN2-FN3-FN4-FN5 is based on the proven advantage of using Mo and W for the 600°C materials with a further distinctive additive of Boron. The FB2 type follows the positive experience with the B-containing, W-free Trial rotor 'B' of the previous round COST 501. The alloys were heat treated with a cycle of 1100°C/570°C/air, 685 - 735°C/air to achieve the required two 0,2YS levels of >700MPa resp. >600MPa. After austenitisation, the cooling rate was held at 2K/min to simulate the centre of a rotor with 1200mm diameter.

Parameter		FB2	FN2	FN3	FN4	FN5
	C	0.13	0.13	0.13	0.12	0.11
Chemical	Si	0.05	0.12	0.08	0.06	0.06
Composition	Mn	0.82	0.96	0.96	0.86	0.55
(wt%)	Cr	9.32	10.2	10.2	11.5	11.2
	W	-	1.91	1.85	1.81	2.63
	Mo	1.47	0.54	0.47	0.48	0.26
	Co	0.96	-	1.98	1.90	2.66
	Ni	0.16	0.25	0.24	0.275	0.40
	V	0.20	0.23	0.22	0.21	0.22
	Nb	0.05	0.065	0.062	0.065	0.065
	N	0.019	0.042	0.041	0.060	0.027
(ppm)	B	85	47	58	49	100

Table 2: Chemical composition of the trial melts for 620°C application

The expected influences by the change in alloy composition are summarised in *Tab. 3.*

Improvement expected in	rotor E, F COST501	FN2	FN3	FN4	FN5	rotor B2 COST501	FB2
creep rupture strength	↔	↔	↔	↔	↔	↔	↔
hardenability		↔	↔	↔	↔	↔	↔
oxidation resistance			↔	↔	↔		
→ How ?	basis	+ B	+ Co	+ Cr	B ↑ W ↑ Co↑ Cr ↑	basis	- C + Co

Table 3: Summary of the expected changes in properties for the 620°C trial melts

A large test programme has been carried out with the melts of Tab. 2. The creep tests have reached times of 20,000 to 55,000 hours. A ranking of these trial melts with respect to long term properties is given in *Tab. 4.*

The best creep strength with the potential to meet the target of 100MPa at 625°C for 100,000h is expected for the melt FB2 with actual testing times of 55,000 hours, *Fig. 2.*

property	FB2	FN2	FN3	FN4	FN5
Creep Strength					
• 600°C	++	+	+	—	—
• 625°C	++	+	+	—	—
• 650°C	++	+	+	—	—
Exposure, Strength & Toughness					
• 600°C/ 650°C	++	++	++	+	—

Table 4: Ranking of the long term properties of the 620°C trial melts

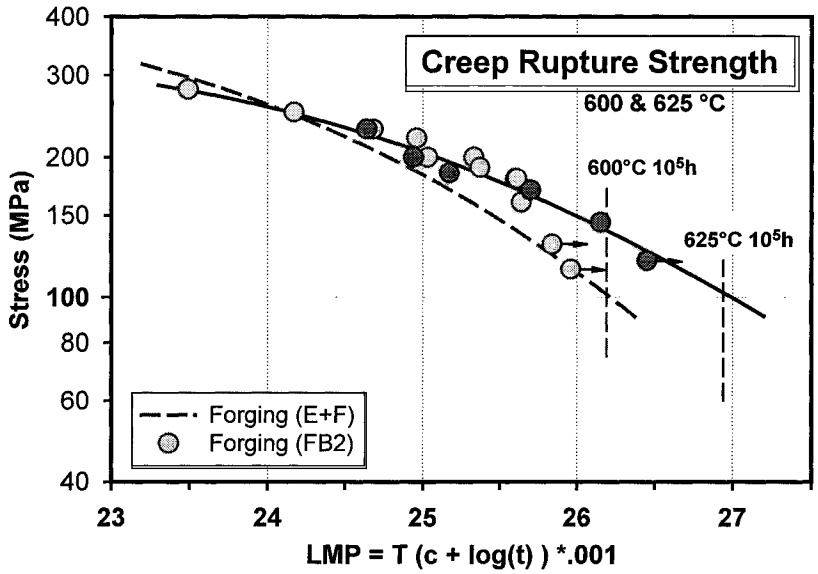


Figure 2: Creep rupture strength of the trial melt FB2 compared to 600°C materials

FN2 and FN3 have shown similar creep strength despite the difference in Co-addition but they offer no improvement over rotor B as shown in *Fig. 3.* Also their Cr-content is still too low to increase the oxidation resistance at T ≥600°C.
The two melts with the increased Cr-content i.e. FN4 and FN5 showed a decrease in creep strength with longer testing time and do not even meet the level of rotor B.

The inferences that have been drawn conclude that the chosen alloy compositions based on W did not indicate the expected advantage of a Co-addition, and the applied increase in the Cr-content for the W-variants was not well-balanced with the main composition.

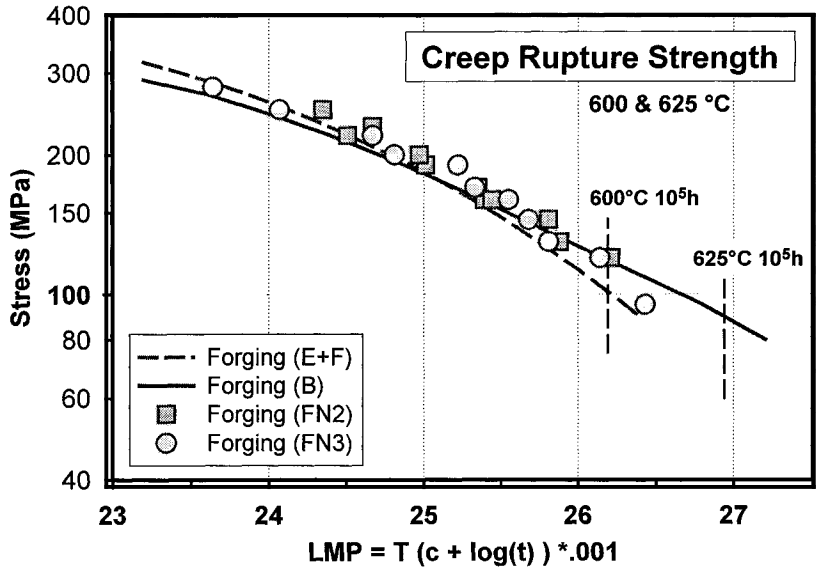


Figure 3: Creep rupture strength of the trial melts FN2 and FN3

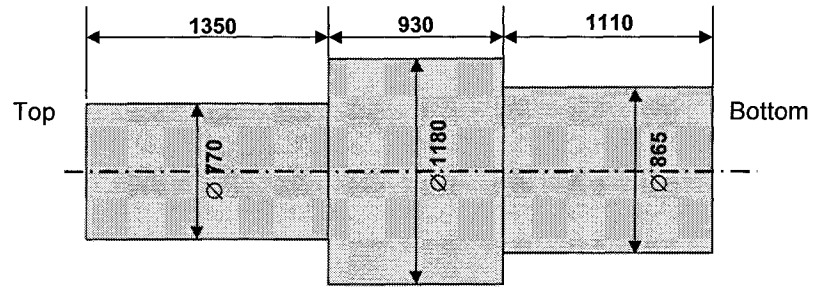
The long term stability of toughness and strength after exposure at 600°C and 650°C in the most promising melt FB2 is better than for conventional 12%Cr steel at 530°C [15].
Based on these results, the manufacture of a full-size rotor forging with the composition of FB2 has been decided.

Trial rotor forgings in FB2

Boehler/Austria has made a full-size rotor forging with a final weight of 17to. The steel making process was Boehler-BEST, a pouring process with special measures to improve the homogeneity of the ingot [16]. The final ingot was forged and heat treated. Despite the application of this process (not ESR), the chemical composition is very homogeneous at the surface positions 1-4, *Fig.4.*
The quality heat treatment was performed on the basis of the knowledge gained in the COST 501 Project and the German VGB 10Cr program [17] in which a large rotor forging in COST 501, Rotor B composition was made:

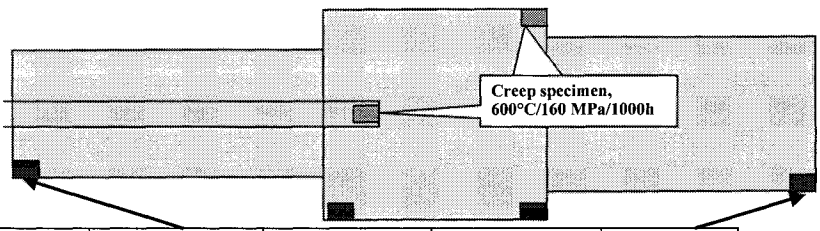
- Austenitizing: 1100°C / 10h / water-air spraying;
- Pre-tempering: 590°C / 22h / air;
- ` Final annealing: 700°C / 22h / air.

The NDT results show a minimum detectable flaw size of 1,2-1,8mm, depending on the rotor location. The quality of the rotor forging was inspected by determining the basic strength and toughness values at different positions, *Fig. 5.*
In addition, short term creep tests at 600°C were performed with $t \geq 1{,}000$h to make a first check of the achieved microstructure. The results up to now are better than for the trial melt FB2. The rotor forging is currently under investigation. The mechanical properties are examined at different surface and centre positions. These are the static and fatigue strength, toughness, creep rupture and long term stability. Preliminary results will be available soon.



wt%	1	2	3	4
C	0,13	0,13	0,12	0,13
Si	0,10	0,10	0,10	0,09
Mn	0,33	0,33	0,33	0,34
Cr	9,03	9,03	9,06	9,02
Mo	1,42	1,41	1,42	1,42
Ni	0,16	0,16	0,16	0,16
V	0,22	0,22	0,22	0,22
Co	1,28	1,28	1,29	1,27
Nb	0,054	0,053	0,054	0,054
B	0,0083	0,0077	0,0078	0,0081
N	0,023	0,023	0,023	0,023

Figure 4: Dimensions and composition of the trial rotor forging FB2-Boehler



At RT:				
UTS [MPa]	835	825	824	834
0,2YS[MPa]	713	700	702	715
EL [%]	15	17	16	16
RA [%]	56	61	56	56
Charpy [J]	30, 35, 30	35, 33, 31	37, 40, 28	31, 56, 35
FATT [°C]	+52	+36	+49	+48
At 620°C				
UTS [MPa]	443	427	439	413
0,2YS[MPa]	362	341	353	332
EL [%]	24	25	28	25
RA [%]	70	78	76	72

Figure 5: Mechanical properties at different positions of FB2-Boehler

A second full-size trial rotor forging with the composition of FB2 was made in Italy by SdF Terni. The applied steelmaking process was VCD with an ingot of 53to.
The aim of the investigations by the Italian COST 522 sub-group is to qualify the steelmaking process for this class of Boron containing 10CrMoCoVB alloys.
One of the main tasks is to answer the question of how much homogeneity in composition is achievable and what are the properties of the final rotor forging. The dimensions are representative for IP shafts. The investigations are presently under way.

Trial rotor forging in COST 501-B2 composition
The attained results of the last COST 501 rounds have confirmed that of the presently available metal compositions, the melts of type B with 9Cr-1,5Mo-100ppm Boron indicate the best long term strength behaviour. The COST 501 included a trial rotor forging manufacture (rotor B2), but due to capacity restrictions at the steelmaker Boehler/Austria the dimensions, were only 840mm diameter/ 15to ingot weight, so a simulated heat treatment for 1200mm diameter was performed. The steel making process was ESR.
In the frame of the German VGB program for 10%Cr steels Saarschmiede Voelklingen, Germany took on the challenge of installing their own steel making process for adding a defined Boron content, homogeneously distributed, to the class of the advanced 9-12%CrMoV-steels. The processing was successfully implemented, and sufficient experience was gained to produce large rotor forgings [18]. The technology was applied to make a full-size rotor with 1200mm diameter within the VGB program. The processing in forging and heat treatment was extensively investigated, and further potentials for optimisation have been identified.
To increase the knowledge base for the transfer conditions from small trial melts (100kg) to large rotor forgings (30,000kg) and introduce the latest results of the long term creep rupture tests and the microstructural understanding, the COST 522 group took the decision to manufacture a third full-size rotor with 1200mm diameter, based on the composition of COST 501-rotor B2. The steelmaker and forgemaster Saarschmiede has applied the ESR process with an ingot diameter of 1300mm. The composition is described in *Tab. 5.*

Parameter	FB4-SRD			
	C	0.19	V	0.27
Chemical	Si	0.07	N	0.016
Composition	Mn	0.28	Nb	0.065
of the ingot	Cr	9.21	P	0.005
(wt%)	Mo	1.49	S	0.001
	Ni	0.18	Al	0.006
(ppm)	B	98	Sn	0.003

Table 5: Chemical composition of the full-size rotor from Saarschmiede, type Rotor 'B'

The dimensions are shown *Fig. 6.* The rotor forgings quality heat treatment has been agreed to, which Saarschmiede is going to perform shortly. After the preliminary mechanical tests, including short term creep tests with $t \geq 1{,}000h$, the rotor forging will be released for the investigations within the COST 522 group. The first results will be available shortly.

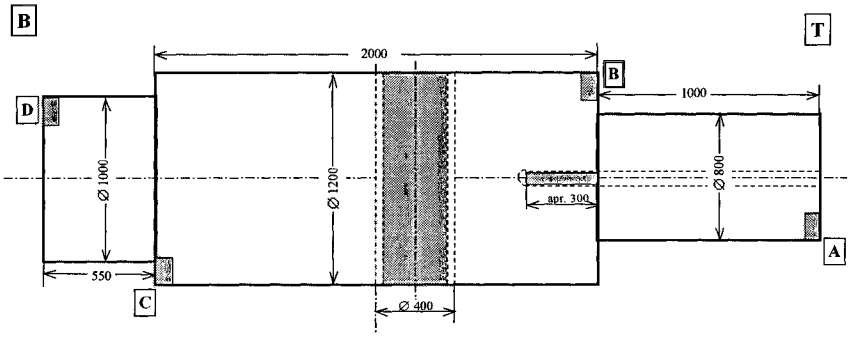


Figure 6: Dimensions of the full-size rotor from Saarschmiede

3.3. Materials for 650°C Application / COST 522

The results available so far from the previous activity show it to be unlikely that any of the trial materials investigated may have the potential to fulfil the requirements for an application at 650°C. Therefore further improvement of these ferritic-martensitic grades was necessary with respect to creep strength but under consideration of the increased oxidation occurring at this temperature level.

The development work is based on the knowledge acquired under the COST 501 programme especially the intensive microstructural investigations, the commercially available computing tools such as ThermoCalc and Dictra and the newly developed calculation methods of the equilibrium transformation temperature as well as the diffusion parameters of potential candidate test materials.

Experience has shown that steels with higher microstructural stability also show higher long-term creep strength. The overall stability depends on the stability of the precipitates against growth and coarsening and on the stability of the matrix phase against recovery, recrystallisation and depletion of main alloying elements. The transformation temperature has been identified as one of the stability parameters. It can be expected that higher Ael transformation temperatures and lower atomic mobilities result in an improved creep behaviour. $M_{23}C_6$ carbides stabilise the subgrain boundaries. Therefore, a higher amount of these precipitates should also improve the material [19, 20].

On the basis of the promising composition FB2, modifications were made in the C-, Cr-, Co-contents and by the addition of W in some cases. The low W-content of 0.5% is expected not to precipitate extensively during long-term creep exposure.

Seven trial melts have been produced with a weight of approx. 150kg, forged into bars and heat treated to simulate the centre position of a heavy forging. The compositions of these melts are given in *Tab. 6.* Different heat treatments have been carried out to investigate the influence of the austenitizing temperature on the long term properties. From the compositions FB5 and FB6 up-scaled melts of 1to have also been produced .

An extensive test programme has been started, which includes metallographic investigations, short-term and long-term mechanical properties, and oxidation tests.

The short-term results, i.e. tensile and impact tests, are shown in *Fig. 7.*

Designation New Forged Trial Melts	C wt%	Cr	Mn	Mo	Ni	B ppm	Co	N	Nb	V	W
FB 5	0.13	10.1	0.09	1.46	0.15	100	2.85	0.017	0.06	0.20	0
FB 6	0.14	11.2	0.10	1.45	0.15	100	2.93	0.016	0.08	0.22	0
FB 7	0.16	10.2	0.08	1.54	0.17	90	2.97	0.019	0.07	0.20	0
FB 8	0.17	11.1	0.09	1.46	0.20	100	2.94	0.023	0.07	0.21	0
FB 9	0.18	11	0.08	1.48	0.13	90	6.03	0.017	0.06	0.20	0
FB 10	0.12	10.3	0.12	0.90	0.17	70	3.02	0.030	0.07	0.21	0.42
FB 11	0.19	11.2	0.10	0.90	0.17	70	3.03	0.020	0.07	0.21	0.42
FB5 AD	0.12	9.86	0.02	1.54	0.18	68	2.94	0.013	0.07	0.19	0
FB6 AD	0.12	10.9	0.02	1.54	0.17	89	2.95	0.017	0.08	0.20	0

Table 6: Product analysis of new forged 650°C trial melts in COST 522

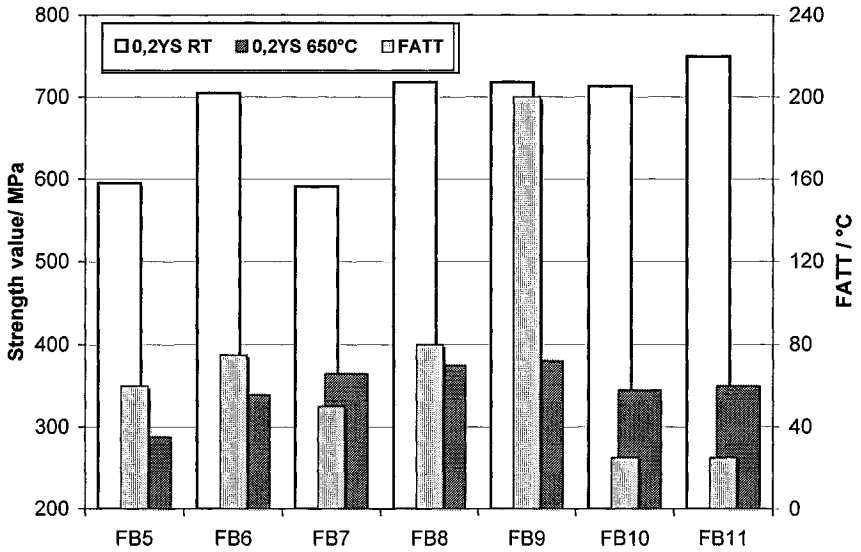


Figure 7: Yield strength at RT, 650°C and FATT of the trial melts for 650°C

The creep tests which have been started recently have currently reached durations of 15,000h, and are planned to reach 100,000 hours. Since the strength level of the new trial melts is in the same range as the previously tested materials, the current status of creep tests is still influenced by strength level. It is yet too early to draw initial conclusions, but a central tendency has been noted. None of the new melts offers a clear improved behaviour compared to melt FB2. On the other hand melts like FB6 and FB8 with a Cr-content of >11% and therefore an expected improved oxidation resistance, are still better than the 600°C-materials

with 1W/1Mo resp. 1,5Mo (Rotors 'E' & 'F'). The potential for the melt FB8 is to reach a 100,000h creep rupture strength at 600°C of 120 MPa resp. 90MPa at 620°C, *Fig. 8.*

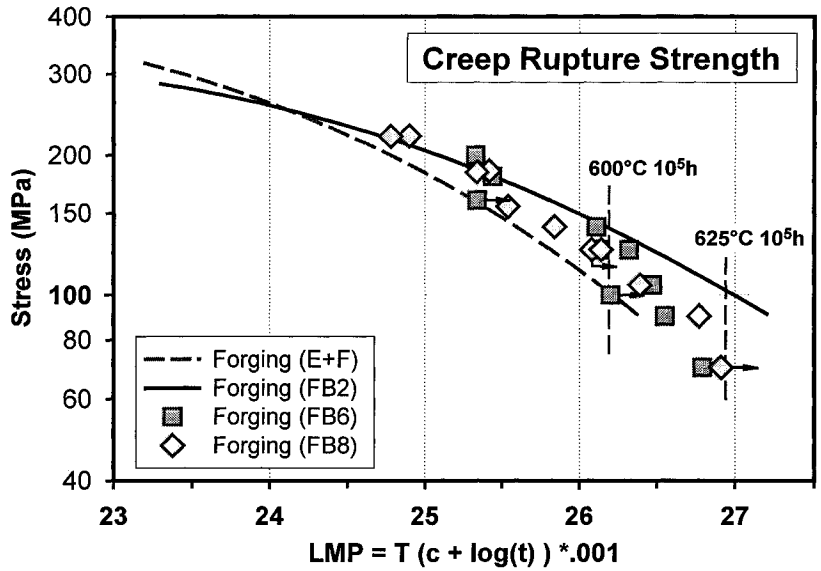


Figure 8: Creep rupture strength of the best 650°C trial melts with 11%Cr

4 Future work

The knowledge and experience gained with the new alloy types underlines the conclusion that the further increase of the application temperature above 620/630°C for ferritic-martensitic steels has become a difficult aspect, thus making it clear that the limit could be near.
The achieved complexity in composition, element balance, melting route, forging procedure and heat treatment of these 9-11%CrMoV alloys is forcing current endeavors to review the design philosophy.
The addition of Cobalt does not give a clear picture of advantageous qualities for creep and overall behaviour. The long term effect of Tungsten is under review, including the aspect of rupture ductility. The increase of Cr above 10% has up to now not been successfully re-balanced by other elements. There is no doubt that the 9-10%Cr alloys have been improved by the addition of Boron, Nitrogen, Vanadium and Niobium.
The heat treatment has to be regarded in its entirety, beginning all the way from the first stages of the forging process, including preliminary and quality heat treatment.
The effort needs to be concentrated more on the interaction of heat treatment, element homogeneity in the ingot, and the final component size. Alloy compositions with closest manufacturing windows introduce the question of reproducibility. The applicability for large rotor forgings with their gradients in such aspects as temperature during heat treatment, is presenting great challenges to today's researchers.

The COST 522 group has made the decision to leave the issue of highest complex alloy types and to go forward with employing already proven alloying elements like C, Cr, Mo, B, N, V and Nb. A matrix for new trial melts was installed. The production has been started, *Tab. 7.*

Type	C wt%	Si	Mn	Cr	Mo	Ni	V	Nb	N	B ppm
FT 1	0.20	0.30	1.0	10.0	1.5	0.10	0.27	0.06	0.02	100
FT 2	0.20	0.30	1.0	10.0	1.5	0.10	0.27	0.06	0.02	200
FT 3	0.20	0.30	1.0	10.0	1.5	0.10	0.27	0.06	0.02	270
FT 4	0.20	0.30	1.0	11.5	1.5	0.10	0.27	0.06	0.02	100
FT 5	0.20	0.30	1.0	11.5	1.5	0.10	0.27	0.06	0.02	200
FT 6	0.20	0.30	1.0	11.5	1.5	0.10	0.27	0.06	0.03	200
FT 7	0.20	0.30	1.0	11.5	1.5	0.10	0.27	0.06	0.03	270

Table 7: Alloy proposal for new 650°C trial melts in COST 522

The planned investigations are going to show the potential for overcoming the 620/630°C borderline for ferritic-martensitic 9-12%CrMoV steels.

5 Summary and Conclusions

- By concentrating the European efforts in the COST 501/ 522 programmes, materials with improved properties were successfully manufactured and tested.
- The recently developed 600°C-materials with improved properties are already being applied in several European power plants and will additionally be used in power plants currently under construction. The manufacturing experience gained with the new 600°C-materials is positive throughout.
- Potential alloy compositions for 620°C application have been identified. Three full-size prototype rotor forgings are currently under investigation.
- Based on commercial tools like ThermoCalc & Dictra, phase stability calculations and consideration of parameters such as transformation temperatures, a series of new compositions was identified. The data show that no clear improvement in creep rupture strength is expected compared to the 620°C alloys. The potential for better oxidation resistance at a high creep rupture strength level was identified with two melts.
- The high complexity in composition, element balance, melting route, forging procedure and heat treatment of the new developed 9-11%CrMoV alloys mean that a new consideration of design philosophy must be taken.

6 Acknowledgements

The authors are grateful to their collegues and partners in the program for their contributions and many discussions during the course of this endeavor. Many thanks are also extended to

the COST Management Committee for their guidance in the program and to the national funding bodies for their financial support of the individual national projects.

7 References

[1] Staubli M.; Mayer K.H.; Kern T.-U.; Vanstone R.W.:
The European Joint Development Program COST522,
5th International Charles-Parsons Conference, 03.-07. July 2000, Cambridge, UK.

[2] Staubli M., Bendick W., Orr J., Deshayes F., Henry C.:
European Collaborative Evaluation of Advanced Boiler Materials,
6th COST Conference, 05-07. October 1998, Liège, Belgium.

[3] Cerjak H., Letofsky E., Staubli M.:
The Role of Welding for Components made from Advanced 9-12% Cr Steels,
6th COST Conference, 05-07. October 1998, Liège, Belgium.

[4] Bendick W., Haarmann K., Zschau M.:
E911- Ein neuer Werkstoff für Dampfleitungen im Kraftwerksbau,
VGB Conference, Materials and Welding Technology in Power Plants 1998,
14.-15. October 1998, Hannover.

[5] Berger C., Scarlin R.B., Mayer K.H., Thornton D.V., Beech S.M.:
Steam Turbine Materials: High Temperature Forgings,
5th Liège COST Conference, 03.-06. October 1994, Liège, Belgium.

[6] Kern T.-U., Wieghardt K.:
The Application of High Temperature 10Cr Materials in Steam Power Plants,
VGB-ESKOM International Materials Conference,
18.-20. September 2000, Pretoria, South Africa.

[7] Kern T.U., Scarlin R.B., Vanstone R.W., Mayer K.H.:
High Temperature Forged Components for Advanced Steam Power Plants,
6th COST Conference, 05-07. October 1998, Liège, Belgium.

[8] Staubli M., Bendick W., Kern T.-U., Mayer K.H., Scarlin R.B.:
Neue Werkstoffe für kritische Komponenten in fortschrittlichen Dampfkraftwerken,
VGB Conference, Materials and Welding, Technology in Power Plants 1998,
14.-15. October 1998, Hannover.

[9] Mayer K.H., Kern T.-U., Staubli M., Tolksdorf E.:
Long-Term Investigations of Specimens of 24 Production Components Manufactured from the Advanced Martensitic 10%Cr-Steels for 600°C Steam Turbines,
5th International Charles Parsons Conference, 03-07. July 2000, Cambridge.

[10] Mayer K.H., Kern T.-U., Schoenfeld K.H., Staubli M., Tolksdorf E.:
Long-Term Investigations of Specimens of 8 Production rotors Manufactured of the Advanced Martensitic 10%Cr Steels X12CrMo(W)VNbN10 1 (1),
14th Intern. Forgemasters Meeting, 03-08. September 2000, Wiesbaden, Germany.

[11] Mayer K.H., Blum R., Hillenbrand P., Kern T.-U., Staubli M.:
Development Steps of New Steels for Advanced Steam Power Plants,
7th Liège COST Conference, 29. September-02. October 2002, Liège, Belgium.

[12] Thornton D.V., Mayer K.H.:
New Materials for Advanced Steam Turbines, 4th International Charles Parsons Conference, Proceedings, 04.-06. November 1997, Newcastle upon Tyne, UK.

[13] Schoenfeld K.H., Wagner H.:
Experience in Manufacturing and Mechanical Properties of Turbine Rotor Forgings and Disks in Improved 10%CrMoWVNbN-Steel, Advanced Heat Resistant Steels for Power Generation, 27.-29.April 1998, San Sebastian, Spain.

[14] Mayer K.H., Cerjak H., Kern T.-U., Staubli M., Thornton D.V.:
Present Status of Ferritic Steel Development for USC Plants in Europe, Int. Workshop on the Innovation Structural Materials and Infrastructure in the 21st Century, ULTRA STEEL 2000, 11.-14. January 2000, Tsukuba, Japan.

[15] Kern T.-U., Cerjak H., Mayer K.H, Staubli M., Vanstone R.:
Development and Qualification of Rotor Steels for 600 to 650°C Application in COST501/ COST522,
14th Intern. Forgemasters Meeting, 03.-08. September 2000, Wiesbaden, Germany.

[16] Meyer W., Zeiler G., Bauer R.:
Recent Developments on 9 to 12 Chromium Steels Open Die Forgings for Steam and Gas Turbine Applications at Boehler,
14th Intern. Forgemasters Meeting, 03.-08. September 2000, Wiesbaden, Germany.

[17] Mayer K.H., Kern T.-U., Staubli M.:
VGB Research Project No. 158: Neue Werkstoffe für Dampfturbinen 1996-2001, Final Report, 2001, Germany.

[18] Blaes N., Langner K.:
Melting of Boron Alloyed 10% Cr-Steel for Power Generation Machinery,
13th Intern. Forgemasters Meeting, Pusan, Korea, 12.-16.October 1997.

[19] Cerjak H., Hofer P., Schaffernak B.:
The Influence of Microstructural Aspects on the Service Behaviour of Advanced Power Plant Steels, 1999 ISIJ, P.874ff.

[20] Cerjak H., Hofer P., Schaffernak B., Spiradek K., Zeiler G.:
The Main Parameters Influencing the Creep Resistance of Advanced 9-12%Cr-Steels for Power Plant Application,
6th COST Conference, 05-07. October 1998, Liège, Belgium.

Development of Creep Resistant Cast Steels within the European Collaboration in Advanced Steam Turbine Materials for Ultra Efficient, Low Emission Steam Power Plant / COST 501-522

M. Staubli[1)], K-H. Mayer[2)], W. Giselbrecht[3)], J. Stief[4)], A. DiGianfrancesco[5)], T-U.Kern[6)]

1) Alstom, Baden, Switzerland
2) Alstom Power, Nürnberg, Germany
3) Voestalpine Giesserei Linz GmbH, Austria
4) PHB Stahlguss, St.Inbert-Rohrbach, Germany
5) Centro Sviluppo Materiali, Rome, Italy
6) Siemens PG, Mülheim a.d.R, Germany

Abstract

Today's state of the art for large fossil-fired steam turbines comprises live steam conditions of up to 610°C/300bar and re-heat temperatures of up to 630°C. These ultra super critical (USC) steam parameters significantly increase the plant efficiency and, at the same time, reduce the fuel consumption, thereby reducing the emissions of CO_2. These advanced steam conditions yield heat rate improvements of up to 8% as compared with conventional standard power plants. The class of the 9-12% Cr steels is currently used for the critical components in such plants since the demand for high operational flexibility of large units requires ferritic materials due to their physical properties.
Significant work to increase the application temperature of these steels was carried out during the last 15 to 20 years under different international research programmes.
In Europe these efforts were concentrated in the COST 501/522 programmes and led to improved materials, which are already successfully applied in a number of European high temperature power plants as forged and cast components and as pipework.
Cast parts such as casings and valves are critical components in USC HP and IP turbines. The development and evaluation of new high Cr cast steels from trial melts to pilot components and further extended investigation of production parts is demonstrated. These cast steels still offer some further potential regarding the creep strength although the oxidation resistance must be carefully taken into consideration at temperatures in the range 600 to 650°C. A series of new ferritic-martensitic compositions, which have been designed on the basis of the positive experience from the previous activity as well as on the results of advanced thermodynamic calculation tools, will be evaluated in the current COST 522 activity and is presented in this paper.

Keywords: Cast steel, creep resistance, experience, weldability

1. Introduction

The demand for lower production costs on the one hand and reduced noxious emissions on the other hand is the driving force for utilities to increase the efficiency of their plants. Although the immediate future will see a further increase in the market share for combined cycle plants, there is still a significant share for fossil fired steam power plants mainly in countries rich in coal or lignite. Nevertheless there is also a substantial market for the up-grading or replacement of existing older plants.
Increased efficiency for steam turbine plants means that the steam parameters have to be raised to supercritical conditions. Such an advanced power plant with steam parameters of 600°C/300bar and double reheat provides savings of approximately 8% in the heat rate and a corresponding CO_2 reduction in comparison with a conventional single reheat power plant operating typically at 540°C/180bar. If the steam temperature is further increased to about 650°C, the heat rate is reduced by more than 10% ensuring even lower CO_2 emission and fuel consumption [1].

A further major increase of efficiency is expected at steam temperatures of 700°C and above. These conditions however will require the use of nickel-base materials for a major part of critical components. This is because 700°C is outside the application range of ferritic-martensitic steels regarding steam oxidation resistance and also creep strength. No nickel-base materials are considered in the present work except for bolting applications although there have been activities launched worldwide for 700°C steam power plants [2].
The COST 501/522 programmes are focused on 9-12% Cr ferritic-martensitic steels although austenitic materials that meet the requirements for 650°C steam temperature are known. Austenitics have already been used in the 60s in power plants with similarly high steam parameters but the operating experience gained with these steels was unsatisfactory. This was mainly because of their physical properties, such as thermal expansion and thermal conductivity, which considerably restrict the operational flexibility.
Despite the fact, that cast components represent roughly 60% by weight of the HP and IP sections of a modern steam turbine, the worldwide efforts on the further development of 9-12% Cr steels are focused mainly on forged materials and pipework.

2. International Test Programmes

2.1. Research Programmes in Japan

The research programmes initiated and supported by EPDC (Electrical Power Development Company) in Japan led to a number of new steels with improved creep properties at 600°C and even higher temperatures. EPDC has ordered several power plants in which new materials are used [3]. The steam temperature in the power plants ordered recently is 610°C but material tests for steam parameters up to 650°C/350bar are currently being carried out.

2.2. Research Programmes in U.S.

In the United States EPRI launched as early as 1978 a study for more economical coal-fired plants. The study was followed in 1986 by a widely supported, extended programme in which not only American but also European and Japanese companies took part [4]. This RP1403 programme was focused on the development of materials for thick-walled boiler components and the steels NF616/P92, HCM12A/P122 and TB12M were validated and partly ASME approved. Components manufactured from these materials were subsequently applied in several advanced European power plants.
Projects 1403-15 & 1403-23 within this EPRI programme were dealing with the qualification of a 9% Cr cast steel for large steam turbine components. These projects were led and carried out by European companies and resulted in the qualification of grade 91 steel for large cast components [5].

2.3. Research Programmes in Europe

In Europe the development activities were concentrated in the COST 501 programme (1986-1997), aimed at developing and qualifying materials for application in high temperature power plants. The target temperature was 600°C in the first phase and 620°C in the second phase.
A series of ferritic steels for forgings, castings and pipework has been evaluated within COST 501. These steels are commercially in operation in advanced European power stations.
Synergies were realizable due to the contemporary activities regarding the development of improved cast materials in the EPRI 1403 and in the COST 501 programmes.

The current programme is titled „COST 522 – Energy generation in the 21st century; ultra-efficient, low emission plants“ and started in spring 1998 having a planned duration of 5

years. The overall programme is focused on the development of suitable materials, coatings and surface treatments for

- Steam power plants with inlet temperatures of up to 650°C
- Gas turbines with combustion temperature of up to 1450°C and NO_x emissions <10ppm

The sub-project „Steam Power Plant" involves a large number of partners (suppliers, manufacturers, utilities and institutes) from 15 European countries.

It is noteworthy to state that the following steps in the development of new materials are considered in the COST 501/522 programmes in order to ensure a reliable application in power plants:

- Selection of new compositions based on the experience of existing materials and based on results of advanced thermodynamic calculation tools
- Production of selected trial melts to identify promising candidate materials by means of mechanical properties, physical properties and manufacturability
- Upscaling for promising materials up to real size pilot components to investigate the influence of production route, size effects, heat treatment effects, quality assurance issues
- Investigation of production parts in order to investigate the scatter in properties due to various production technologies, different suppliers, size and shape of products, variation of chemical composition within the specification, etc.

A close collaboration between the turbine and boiler sub-groups within COST led to the successful development of new materials for application in the turbine as well as in the boiler sectors. This is in order to meet the common requirements with respect to steam parameters. The development, properties and application of the new boiler steel E911, which was developed in COST, have been reported [6,7,8]. The activities with respect to the development of new forged steels have also been reported [9,10].

3. Improved Cast Steel Grades for Application up to 600°C

The development of new ferritic-martensitic cast steel grades was closely connected to the COST research work for rolled and forged products for the same application temperatures and synergies were realized with the contemporary EPRI 1403 programme [11]. Table 1 gives details of the different developments of cast materials within COST and EPRI.

3.1 Evaluation of GX10CrMoVNbN9-1 within EPRI 1403-15

Based on comparative results from a pre-programme where modifications in the contents of C, Cr, Mo, Nb, N and the addition of boron were investigated, the composition for the main programme was selected corresponding to the range for T91 (ASTM A213). A 28t AOD heat was produced and used to cast the following test materials:

- 1 Valve body (upper part of a HP valve chest) approx. 5t
- 1 Stepped block, steeps of 150, 300 & 500mm approx. 5t
- 4 Plates 100mm thick for weld tests approx. 250kg each

In addition 4 small induction furnace (IF) heats were used to cast 100mm thick plates of approx. 250kg each with slight variations in the chemical composition.
All these test materials were given the same heat treatment as follows:

1040°C/12h/forced AC to RT + 760°C/12h/AC + 750°C/8h/FC (<25K/h)

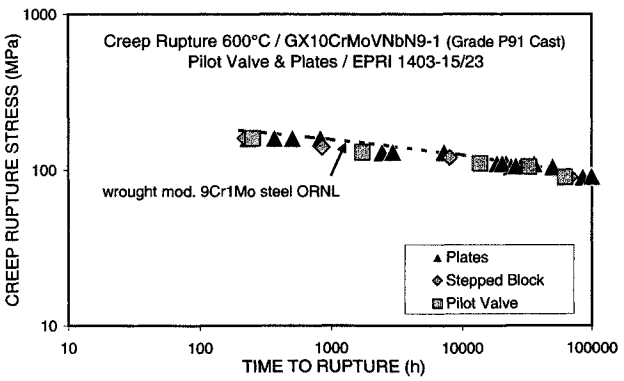
The last step at 750°C was given to simulate a PWHT.

Basic Steel	GX22CrMoV12-1 (ex DIN 17245)	X10CrMoVNbN9-1 (P91)	X7CrCoMoVNb11-6 (Firth Vickers FV535)
Modification	Boron	Mo; Mo/W	WNB, CoB, CoWNB
COST501 / I (1983-85)	Mod: C,Cr,Mo,V, plus B GX10CrMoVNbB9-1 GX19CrMoVNbB9-1		
COST501/II (1986-92)		Mod: C, Cr, plus 1%W H.T. variations GX12CrMoVNbN10-1 GX12CrMoWVNbN10-1-1	
EPRI 1403-15 (1986-92)	GX10CrMoVNbB9-1 GX20CrMoVNbB10-1	GX10CrMoVNbN9-1 Production of plates and Valve Body	
EPRI 1403-23 (1993-95)		GX10CrMoVNbN9-1 H.T. variations	
COST 501/III (1993-97)		GX12CrMoWVNbN10-1-1 Production of Valve Body	W: 1-2%/B:40-110ppm Mod. C, Mn, Ni, Co,N CB1:GX12CrMoCoVNbNB9-1 CD2:GX12CrWCoMoVNbNB9-2-1 CE2:GX12CrCoMoWVNbN9-2-1 CF2:GX10CrMoCoVNbN10-1 CB2:GX12CrMoCoVNbNB9-1
COST 522 (1998-2003)	GX20CrMoVNbNB10-1 GX20CrMoVNbNB12-1		Base CB2; mod. C,Cr,Co,W CB5:GX13CrCoMoVNbNB10-3-1 CB6:GX13CrCoMoVNbNB11-3-1 CB8:GX17CrCoMoVNbNB11-3-1 CB9:GX17CrCoMoVNbNB11-5-1 CB10:GX13CrCoMoWVNbNB10-3-1 CB11:GX17CrCoMoWVNbNB11-3-1

Table 1 *Development of cast materials within COST 501/522 and EPRI 1403*

Product	Heat	C (wt%)	Mn (wt%)	Cr (wt%)	Ni (wt%)	Mo (wt%)	V (wt%)	Nb (wt%)	N (wt%)	Al (wt%)	Rp0.2 (MPa)
Valve	90588	0.10	0.50	9.25	0.12	0.92	0.22	0.068	0.048	0.011	452
St.block	90588	0.09	0.51	9.36	0.12	0.94	0.22	0.073	0.044	0.012	432
IF Plate	70972	0.12	0.50	9.24	0.27	0.99	0.22	0.074	0.053	0.021	491
IF Plate	70975	0.09	0.41	8.93	0.21	0.99	0.19	0.074	0.041	0.011	463
IF Plate	70983	0.10	0.43	9.05	0.26	0.94	0.21	0.077	0.048	0.037	485
IF Plate	70986	0.09	0.47	9.30	0.16	0.94	0.22	0.078	0.045	0.009	472

Table 2 *Cast P91 (GX10CrMoVNbN9-1) heats creep tested under EPRI 1403*



An extended test programme was carried out within EPRI-1403 comprising NDT, mechanical tests, long-term exposure, creep, LCF and weld tests [12].

Figure 1
Creep rupture at 600°C; pilot valve & plates / EPRI 1403-15/23

The creep properties at 600°C i.e. the temperature of main interest for application are given in Figure 1 for specimens from the pilot valve, the stepped block and the 4 induction furnace heats as listed in the Table 2.
Creep tests have reached up to > 100 000h and are compared with the line for wrought mod. 9Cr1Mo steel given by ORNL. All results were found within a relatively narrow scatter-band and are approaching the line for wrought materials at about 30 000h; the lower strength in the short-time range is explained by the lower strength of the cast material as compared to wrought products due to the longer tempering (and additional simulated PWHT).

3.2. Evaluation of Cast Steels within COST 501 / 2nd Round

In the COST programme an attempt was made to further increase the creep rupture strength of the P91-type cast steel GX10CrMoVNbN9-1 from the EPRI programme by modifying the chemical composition and the heat treatment [13]. The C, Cr and Ni contents were raised and the influence of 1%W was examined additionally. Two trial melts were produced by induction furnace melting and cast in the form of 100mm thick plates with/without W on the basis of the same master melt. After preliminary tests the heat treatments as given in Table 3 were fixed :

Test material (designation)	Austenitising	Pre-Tempering	Tempering	Sim. PWHT	Rp0.2 (MPa)	Impact (J)
1% W (BT)	1100°C/12h/ac		730°C/12/ac	720°C/9h/fc	592	51
1% W (CT)	1100°C/12h/ac	550°C/20h/ac	730°C/12/ac	720°C/9h/fc	592	42
No W (B)	1100°C/12h/ac		730°C/12/ac	720°C/9h/fc	597	96
No W (C)	1100°C/12h/ac	550°C/20h/ac	730°C/12/ac	720°C/9h/fc	582	93
Pilot Valve	1100°C/12h/ac	550°C/20h/ac	730°C/12/ac	720°C/9h/fc	573	41

Table 3 H.T. conditions of GX12CrMo(W)VNbN10-1-(1) trial melts and Pilot Valve

As compared to the EPRI material the increased austenitising temperature and the reduced tempering resulted in an increase of yield strength by ca. 100MPa. An influence of the pre-tempering or the W-content was not observed for the yield strength but for the impact energy. However the reduced toughness level of the W-bearing material still is within the requirements. The composition of these COST materials is given in Table 4.

Product	Heat	C	Mn	Cr	Ni	Mo	V	Nb	N	W
IF Plate / no W	60504	0.13	0.57	10.5	0.86	1.01	0.21	0.079	0.049	0
IF Plate / 1%W	60504	0.13	0.54	10.5	0.85	1.02	0.22	0.066	0.049	1.01
Pilot Valve	81374	0.12	0.62	10.51	0.93	0.99	0.22	0.080	0.048	0.99

Table 4 Compositions of GX12CrMo(W)VNbN10-1-(1) creep tested in COST

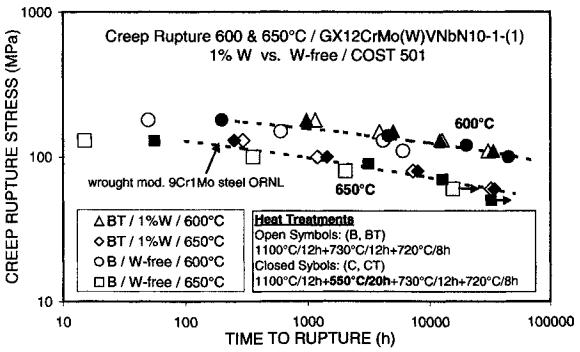


Figure 2 Creep rupture at 600 & 650°C;1%W vs. W-free / COST501

Creep tests for all versions were carried out at 600°C and 650°C as shown in Figure 2 up to >44000h. After the completion of these creep tests it is obvious that:

- The W-bearing version is in line with wrought P91 independent of the pre-tempering at 550°C (BT and CT)

- The W-free version without pre-tempering (B) is below the W-bearing material and below the line for wrought P91
- Pre-tempered W-free material (C) is also in line with wrought P91

However the decision for the main programme was made before these creep tests had reached durations in excess of 10 000h and the W-bearing version was selected for the production and evaluation of a pilot valve body.

A pilot valve body of approx. 5t and plates with 100mm thickness were made from an AOD melt. The composition of the valve, the heat treatment and some mechanical properties are included in tables 3 and 4.

Sections with different wall thickness from this valve were creep tested up to ca. 60 000h as shown in Figure 3. The results are in a narrow scatter-band together with the creep strength of the W-bearing plate (CT) mentioned above. However the creep strength at 600°C for the valve drops slightly below the line for wrought P91 after about 30 000 hours while at 650°C all results are on or above the line for wrought material.

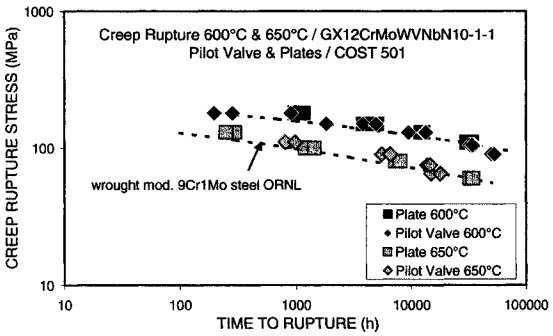


Figure 3 *Pilot valve & plates; 600 & 650°C*

As compared to conventional cast steel grades such as 1CrMoV (G17CrMoV5-10) and 12CrMoV (GX23CrMoV12-1) (EN10213) a significant improvement in creep strength is reached corresponding to an increase of the application temperature of 30 to 50°C.

The direct comparison of the creep strength at 600°C of the two valves from the EPRI and COST programmes is shown in Figure 4. Despite the differences regarding the C, Cr and W contents and the heat treatment (see tables 2, 3 and 4) after the completion of the long-term tests it can be concluded, that the creep rupture strength is similar for the two valves.

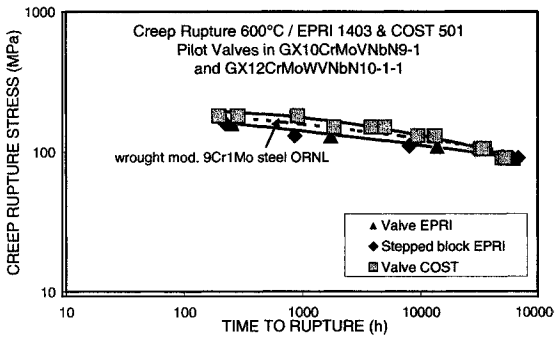


Figure 4 *Pilot valves; 600°C, both alloys*

However the higher creep strength of the COST valve measured up to 10 000h initiated at that time an additional investigation of heat treatment effects on the EPRI material. Thus test material from the stepped block was re-heat treated according to the parameters used within COST (see table 3) except the simulated PWHT at 720°C, which was omitted. As expected, the yield strength was measured to be higher than in the 1040°C/760°C/750°C condition; tests up to >20'000h also show an improvement in creep strength at 600°C. The EPRI steel and the COST steel without W both heat treated at 1100°C/550°C/730°C show no significant difference in creep strength at 600 & 650°C as demonstrated in Figure 5.

From todays data one can conclude that

- both newly developed cast materials have about the same creep rupture strength at 600°C independent of W-addition

- the positive short-term strength effect of a modified heat treatment is lost during long term creep tests at 600°C
- the increased strength level however will result in higher creep strength at lower temperatures in the range 500-600°C.

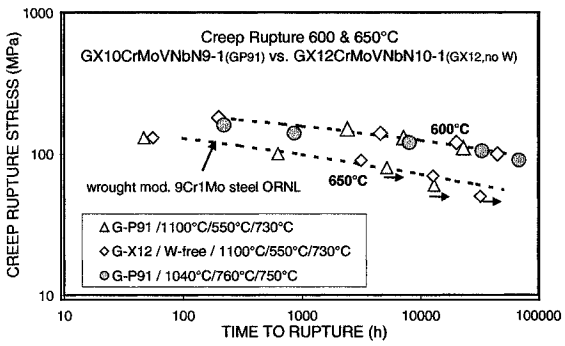


Figure 5 *Creep rupture; 600°C;1%W vs. W-free*

It is also important to note that the higher creep strength of the new cast steel grades is not accompanied by a lower fracture toughness or by reduced low cycle fatigue strength. With respect to impact energy, the new W-bearing cast steel is comparable to the widely used GX22CrMoV12-1. The toughness of the W-free steel is considerably higher and exceeds the values of the low alloyed cast steel G17CrMoV5-10.

3.3. Manufacturing Experience and Investigation of Production Components

In a series of new European power plants the newly developed cast steels are applied to achieve elevated steam parameters. Plants with live steam conditions of up to 597°C/283bar and 618°C re-heat temperature are currently under discussion or contracted. The experience that the manufacturers of these plant components have gained so far is very positive. The acceptance of the new cast steels is also demonstrated by the number of manufactured and installed power plant components. Six foundries have successfully produced some 350 castings with the weight ranging from 1 to 60 tonnes, which are already applied in more than 14 European power plants. A welcome synergy effect is proved by the fact that these materials, originally developed for steam turbines, are also currently used in other turbine applications [14,15].

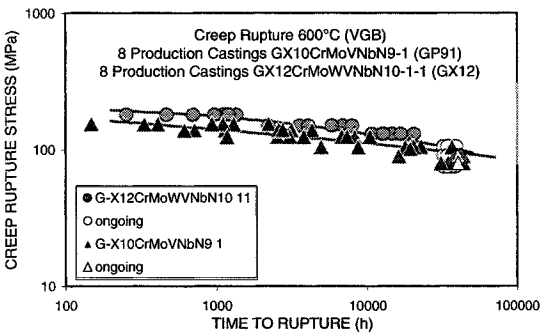


Figure 6 *600°C; cast & forged production parts*

In order to confirm the long-term properties of the new steel grades and to establish a comprehensive database for these materials, a programme was launched with the support of VGB in Germany involving the investigation of 24 commercial cast and forged components.

16 castings with weight up to 41t manufactured from W-bearing (COST) and W-free (EPRI) steels were produced by different suppliers including the use of different production routes [16, 17]. The VGB test programme includes creep testing in the temperature range 500-600°C up to 100 000 hours, tensile tests and LCF tests at different temperatures. The current status of the creep tests at 600°C with durations up to >35 000h is given for the W-bearing and W-free cast steels in Figure 6. For both steel grades results available so far from these production components confirm the good properties measured earlier on pilot

components. However the W-free steel shows a larger scatter and for the current test duration still a somewhat lower creep strength.

4. Further Development of Cast Steels for Application up to 620°C

Extensive microstructural investigations have been carried out within the metallography & alloy design sub-group in order to ascertain the causes of the differences in properties observed and to provide support for further alloy modifications [18,19]. Based on these microstructural efforts and on the careful evaluation of already available long term test data, an alloy concept for the further modification of cast steels was formulated including

- Nickel content limited to max. 0.20%
- Addition of Co of up to 1.5%
- Addition of B up to 110ppm and modifying simultaneously the N content
- Variation of the proven and investigated elements such as Mo, W, B and N on the basis of a C-Cr-Co-Nb matrix
- W content 0% to 2% and corresponding modification of Mo content

Five trial melts were cast as plates (up to 200mm thick) and 5t stepped blocks (up to 500mm thick) and were subject to a large test programme. The compositions, heat treatments and some mechanical properties are given in Table 5.

	Type CB1	Type CB2	Type CD2	Type CE2	Type CF2	Type CB2P
(wt%)	Step block 5t	Plate 200mm	Step block 5t	Plate 150mm	Step block 5t	Valve 5t
C	0.12	0.12	0.06	0.11	0.10	0.11
Mn	0.94	0.88	0.88	0.86	0.77	0.85
Cr	9.42	9.20	9.54	9.39	9.60	9.14
W	-	-	1.94	0.97	-	0.03
Mo	1.50	1.49	0.43	0.98	1.32	1.44
Co	0.93	0.98	1.07	1.52	0.93	0.96
Ni	0.14	0.17	0.10	0.15	0.22	0.22
V	0.24	0.21	0.21	0.22	0.23	0.19
Nb	0.08	0.06	0.04	0.05	0.06	0.062
N	0.02	0.02	0.045	0.05	0.04	0.021
B (ppm)	40	110	40	-	-	112
Austenitising	1050°C	1100°C	1100°C	1100°C	1100°C	1100°C
Tempering	730°C	730°C	730°C	730°C	730°C	740°C
Sim.PWHT	730°C	730°C	730°C	730°C	730°C	2x 730°C
Rp0.2 (MPa)	483	547	512	513	553	550
FATT (°C)	20	32		10	33	32

Table 5 Details of trial cast melts within COST 501/3rd Round and pilot valve

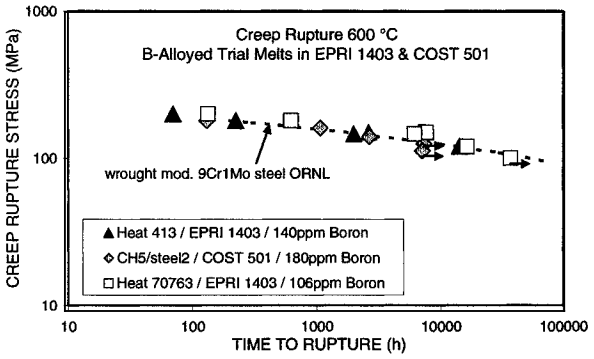


Figure 7 600°C; B-alloyed trial melts in EPRI & COST

It is noteworthy that already in a very early phase of both the COST 501 and the EPRI 1403 programmes Boron alloyed melts were produced and tested. Table 6 shows details of three melts with B levels up to 180ppm. Creep tests at 600°C are available for these melts up to more than 10'000h and the creep rupture strength is in line with wrought P91 (Figure 7). Despite these promising results further effort in both

programmes was concentrated to the modifications of P91 due to in-consistency of B effects in different test melts (most probably due to segregation) and the observed sigmoidal creep behaviour, which was not explained and led to unfavourable creep strength at durations around 10 000h.

Heat	Prog.	C	Mn	Cr	Ni	Mo	V	Nb	N	B ppm	Heat treatment	Rp0.2 (MPa)
413	EPRI	0.11	0.39	8.88	0.19	0.94	0.21	0.078	0.028	140	1050°C/730°C	551
70763	EPRI	0.19	0.44	10.6	0.14	1.50	0.23	0.147	0.019	106	1050°C/730°C	549
CH5	COST	0.19	0.41	9.56	0.11	1.65	0.26	0.07		180	1080°C/780°C	456

Table 6 Details of early Boron alloyed melts tested in EPRI and COST

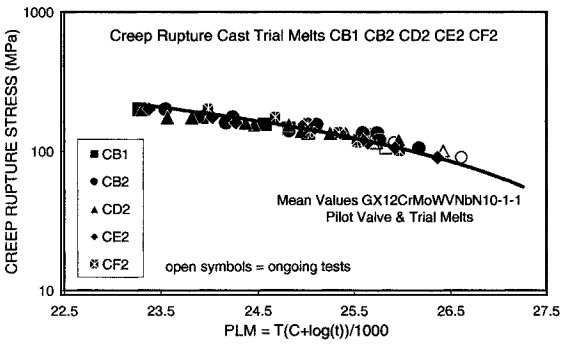


Figure 8 Cast trial melt CB1, CB2, CD2, CE2 & CF2

The test programme for the trial melts CB1 to CF2 is completed apart from the creep tests which have reached >50 000 hours. Two trial melts in particular exhibit promising creep results as shown in Figure 8 i.e. melt CB2 alloyed with 100ppm of B and melt CD2 (corresponding to Nf616 apart from the additional 1%Co) [20]. Table 7 gives an evaluation of the mechanical properties of these 5 trial melts.

	CB1	CB2	CD2	CE2	CF2
Creep strength 600°C	+	++	+	--	--
Creep strength 625°C	+	++	++	--	--
Creep strength 650°C	--	++	--	--	--
Exposure 600& 650°C/ Strength & Toughness	--	++	--	+	+

Table 7 Evaluation of mechanical properties of trial melts

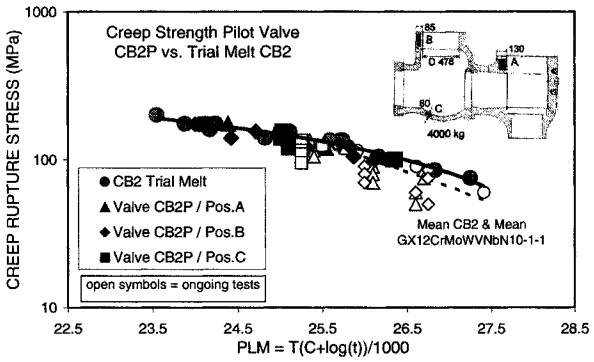


Figure 9 Pilot valve CB2P vs. trial melt CB2

A pilot valve with composition CB2P has been cast and positions with different wall thickness are under evaluation within the COST 522 programme. Composition, heat treatment and mechanical properties of this 5t pilot valve are also given in table 5 and are well in agreement with the corresponding trial melt CB2. The limited creep data up to approx. 10 000h are compared to the trial melt in Figure 9. These results are in line for the positions with equal strength level (A & C) and slightly lower for position B with somewhat reduced initial strength.

The newly developed cast steel type CB2 shows a significant improvement in creep strength over the grades GX10CrMoVNbN9-1 (EPRI 1403) and GX12CrMoWVNbN10-1-1 (COST) developed earlier, which corresponds to another increase of the application temperature of 20-25°C. However it must be considered that CB2 has only 9.2% Cr and therefore no improvement in steam oxidation resistance may be expected.

5. Development of Cast Steels for Applications at 625-650°C (COST 522)

The target steam inlet temperature of up to 650°C is expected to lead to an efficiency of approx. 50%. Wherever possible, this goal should be reached through the use of ferritic-martensitic steels in order to allow a flexible operating mode in medium-load and peak-load operation of these power plants.
A further improvement of the cast ferritic-martensitic grades is seen to be necessary with respect to creep strength but under consideration of the increased oxidation occurring at this temperature level. The results available from the previous activity show it to be unlikely that any of the trial materials investigated may have the potential to fulfil all the requirements for an application at 650°C.
The development work is based on the knowledge acquired under the previous programme especially the intensive microstructural investigations, the commercially available computing tools such as ThermoCalc and Dictra and the newly developed calculation methods of the equilibrium transformation temperature as well as the diffusion parameters of potential candidate test materials. Experience has shown that steels with higher microstructural stability also show higher long-term creep strength. The overall stability depends on the stability of the precipitates against growth and coarsening and on the stability of the matrix phase against recovery, recrystallisation and depletion of main alloying elements. The transformation temperature has been identified as one of the stability parameters. It can be expected that higher Ae1 transformation temperatures and lower atomic mobilities result in an improved creep behaviour [21]. Modifications were made on the basis of the promising composition CB2 with respect to the C, Cr and Co contents and by the addition of W in some cases. The low W-content of 0.5% is expected not to precipitate extensively during long-term creep exposure. Since it was considered that the relevant alloying aspects with respect to creep strength may be valid for both cast and forged materials, new compositions showing a strong similarity were investigated for forged and cast trial melts [10].

5.1. Evaluation of cast trial melts, 1st batch

On the basis of these considerations 6 cast trial melts have been produced as plates of 100mm thickness and were given a common heat treatment. The compositions are shown in Table 8.

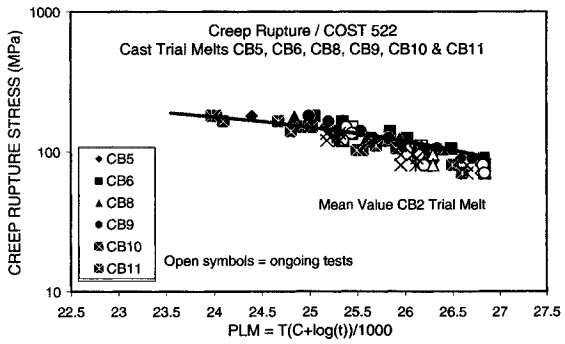


Figure 10 *Cast trial melts CB6, CB8, CB9, CB10 & CB11*

For these cast trial melts an extended test programme has been started including metallographic investigations, short-term and long-term mechanical properties, oxidation tests, evaluation and qualification of filler metals for the new cast steels and the investigation of production welds on the components. Early short-term results have been reported in [9].

The creep tests have reached durations in the range of 7000h to 18 000h and are compared in Figure 10 to the mean value of trial melt CB2. As shown in the preliminary evaluation in Table 9 only CB5 and CB6 exhibit higher creep strength than CB2 in the range 600-625°C but are similar at 650°C. However the Cr content is clearly increased and therefore an increased steam oxidation resistance may be expected at a similar creep strength level.

	Type CB5	Type CB6	Type CB8	Type CB9	Type CB10	Type CB11
(wt%)	Plate 100mm	Plate 100mm	Plate 100mm	Plate 100mm	Cast block	Cast block
C	0.13	0.13	0.17	0.17	0.13	0.17
Mn	0.20	0.19	0.20	0.19	0.25	0.17
Cr	10.1	10.9	10.85	10.9	10.24	10.71
W	-	-	-	-	0.41	0.38
Mo	1.58	1.57	1.54	1.66	0.91	0.84
Co	2.90	2.90	2.90	5.85	3.14	2.85
Ni	0.16	0.15	0.16	0.16	0.16	0.20
V	0.20	0.20	0.21	0.20	0.22	0.22
Nb	0.063	0.065	0.065	0.063	0.058	0.054
N	0.035	0.025	0.025	0.022	0.023	0.031
B (ppm)	110	109	103	108	84	120
Austenitising	1100°C	1100°C	1100°C	1100°C	1100°C	1100°C
Tempering	730°C	730°C	730°C	730°C	730°C	730°C
Sim.PWHT	730°C	730°C	730°C	730°C	730°C	730°C
Rp0.2 (MPa)	544	568	552	593	574	604
FATT (°C)	25	34	26	22		

Table 8 Trial Cast Melts investigated within COST 522

	CB5	CB6	CB8	CB9	CB10	CB11
Test duration max.	17'000	18'000	18'000	17'000	7'000	11'000
Comparison to CB2 at 600°C	+	+	+	+	+/--	--
Comparison to CB2 at 625°C	+	+	+/--	--	+/--	--
Comparison to CB2 at 650°C	+/--	+/--	+/--	+/--	+/--	--

Table 9 Preliminary evaluation of creep properties of new cast trial melts

5.2 Production of pilot components

The W-free, high Cr melt CB6 shows a promising creep strength level despite the increased Cr content of about 11%. This composition therefore was selected for the production of upscaled industrial melts for pilot components. Two foundries recently produced the components described in Table 10. Two levels for the Al-content were selected and successfully reached in the two large melts. Manufacturing experience is reported in [22] and an impression of the produced components for which a large test programme has been established is also given.

5.3 Cast trial melts 2nd batch

Only some of the melts with high contents in Cr, Co and B (CB5 to CB11) show the expected improvement in creep strength although the materials are relatively costly. On the other hand promising data are measured for a forged material investigated in an early phase of COST i.e. rotor "B" material, which is W-free and Co-free and contains ca. 100-180ppm Boron. Meanwhile several B-bearing casts have been produced and the B-segregation seems to be under control by the suppliers, hence the Boron alloyed material from early phase of COST should be considered. Bearing in mind the higher application temperature the Cr-content is raised from 9.5% to 10-11.5%. The composition of two proposed new heats (GT3 & GT7) is given in Table 11 along with the chemistry of two B-type forged rotors and the B-alloyed cast melt (see also table 6) from the early phase of COST.

The two compositions GT3 & GT7 are currently manufactured as small melts of ca. 100kg and will be subjected to a test programme.

Component (wt%)	Trial melt CB6 Plate 100mm	Range for CB6	Large melt CB6 by Lucchini / Lovere, IT 1 Pilot Valve / 29 t 2 Stepped blocks / 5t 4 Plates 100mm	Large melt CB6 by VOEST / Linz, AT 1 Pilot Valve / 5t 1 Stepped Block / 5t 4 Plates 100/50mm 1 Flange / 1t
C	0.13	0.12 to 0.14	0.12	0.13
Mn	0.19	0.15 to 0.25	0.16	0.19
Cr	10.9	10.7 to 11.3	10.87	10.35
Mo	1.57	1.45 to 1.55	1.54	1.45
Co	2.90	2.9 to 3.1	2.90	2.95
Ni	0.15	0.1 to 0.2	0.16	0.18
V	0.20	0.18 to 0.22	0.21	0.21
Nb	0.065	0.05 to 0.07	0.065	0.077
N	0.025	0.015 to 0.030	0.025	0.029
Al	0.021	max 0.01 / 0.025	0.005	0.011
B (ppm)	109	80 to 150	130	140

Table 10 Composition and components; large melts in CB6

Heat	C	Mn	Cr	Ni	Mo	V	Nb	N	B Ppm
Proposal GT3	0.20	1.0	10.0	0.10	1.5	0.27	0.06	0.02	200
Proposal GT7	0.20	1.0	11.5	0.10	1.5	0.27	0.06	0.03	300
B-type rotor / B0	0.10	0.55	9.21	0.11	1.50	0.23	0.063	0.02	180
B-type rotor / B2	0.17	0.06	9.34	0.12	1.55	0.27	0.064	0.015	100
Cast melt / CH5	0.19	0.41	9.56	0.11	1.65	0.26	0.07		180

Table 11 Composition of proposed new cast alloys

6. Weldments of the New Cast Steels

For the fabrication and application of components in the new high strength cast steel grades, the availability of a suitable weld metal is mandatory. In both programmes, EPRI 1403 and COST 501, filler metals have been developed in collaboration with electrode manufacturers.

6.1 EPRI 1403, Investigation of welds GX10CrMoVNbN9-1

Welding procedure qualification was carried out on 100mm thick plates welded by the SMAW process. Matching filler metal was used and two different PWHT were performed i.e. full re-heat treatment after welding and only stress relieving. The compositions of the base material & the weld metal, the applied PWHT and some mechanical properties are given in Table 12.

Heat	C	Mn	Cr	Ni	Mo	V	Nb	N	Al	Heat treatment	Rp0.2 (MPa)
90588 base material	0.09	0.31	9.36	0.12	0.94	0.22	0.073	0.044	.007	1040°C/760°C 750°C	432
Electrode Cromocord 9M / 4mm	.095	0.51	8.94	0.09	0.94	0.23	0.075	0.059	.0014	Full heat treatm. 1040/760/750°C 750°C/8h/FC	471 554

Table 12 Weldments of G-X10CrMoVNbN9 1 investigated in EPRI 1403

The long-term crossweld creep rupture strength at 550 & 600°C is compared in Figure 11 for the fully re-heat treated and the only stress relieved plates with results for the base material and with the mean and –20% lines for cast GX10CrMoVNbN9-1.

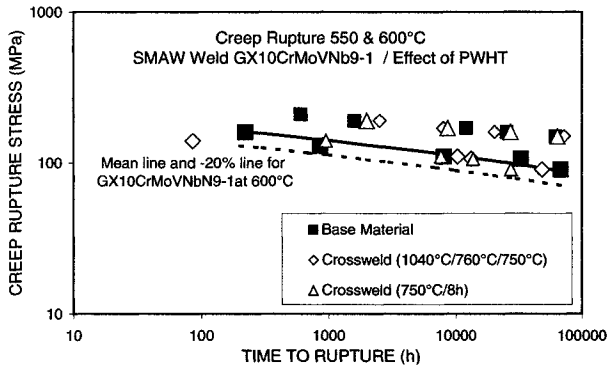


Figure 11 *SMAW weld; 550 & 600°C; effect of PWHT*

At 550°C the crossweld specimens exhibit the same creep strength as the base material independent of the PWHT i.e. full re-heat treatment or only stress relieve at 750°C/8h/FC. At 600°C the crossweld strength in the stress relieved condition after long time was found about 15% below the base material; the strength of the fully re-heat treated crossweld specimens is not significantly below the base material even for long time tests. The failure of crossweld specimens was reported in the HAZ of the base material. Reduction of area was rather low (about 4-5-%) for the weld metal independent of the PWHT. The creep properties of welds in GX10CrMoVNbN9-1 thus are found

- to have equal strength levels to the base material at 550°C independent of the PWHT
- to exhibit at 600°C a stress reduction of about 15% for the stress relieved welds
- to exhibit failure in the HAZ of base material i.e. type IV failures

Due to the low reduction of area and the high strength of the weld metal, it was recommended to modify the filler metal composition (table 12) by lowering the contents of C, V and Nb towards the lower bound of the P91 specification.

6.2. COST 501, Investigation of welds GX12CrMoWVNbN10-1-1

Similar welding procedure qualification was carried out within COST [23]. Matching filler metal (W-bearing) and W-free electrodes as given in Table 13 were used and again two different PWHT were performed i.e. full re-heat treatment after welding (1100°C+ 730°C/10h +730°C/12h) and only stress relieving (730°C/12h).

Material	C	Mn	Cr	Ni	Mo	W	V	Nb	N	Al
Base Material	0.12	0.84	9.6	0.64	0.95	0.93	0.22	0.070	0.046	.009
W-bearing Electrode	.094	0.64	9.00	0.75	0.92	1.05	0.25	0.047	0.063	.003
W-free Electrode	.11	0.69	8.63	0.60	0.95	0.04	0.21	0.05	0.035	

Table 13 *Weldments of GX12CrMoWVNbN10-1-1 investigated in COST 501*

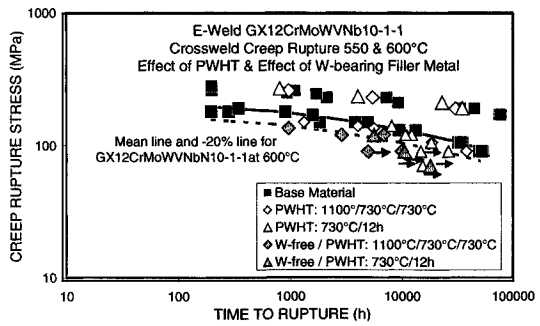


Figure 12 *E-weld; 550 & 600°C; effect of W-bearing filler*

The long-term crossweld creep rupture strength at 550 & 600°C is given in Figure 12 for the fully re-heat treated and the only stress relieved plates respectively and for W-bearing and W-free filler metals as compared to the results for the base material and to the mean and minus 20% lines for cast GX12CrMoWVNbN10-1-1. At

550°C the crossweld specimens exhibit about the same creep strength as the base material independent of the PWHT i.e. full re-heat treatment or stress relieve only. At 600°C the crossweld strength in the stress relieved condition after long time is approaching the -20% line of the base material; the strength of the fully re-heat treated crossweld specimens falls about 10% below the base material for long time tests. Although tests for W-free welds are still ongoing, early results for both PWHT conditions are on the -20% line of the base material.

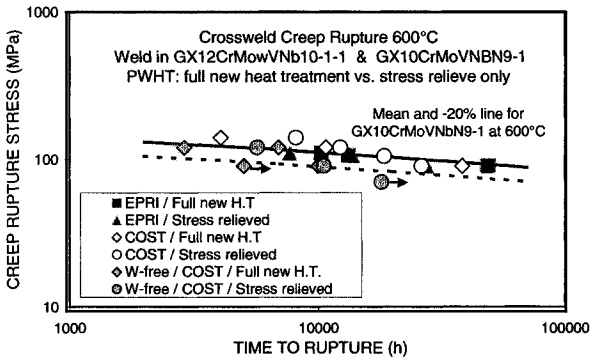


Figure 13 *Crossweld 600°C; effect of PWHT*

The direct comparison of the crossweld creep strength of both GX10CrMoVNbN9-1 and GX12CrMoWVNbN10-1-1 at 600°C is given in Figure 13 in comparison to the mean and the -20% lines of GX10CrMoVNbN9-1. In the longterm range a clear advantage of the full new heat treatment is obvious for both welds and no variant is falling below the -20% line up to now.

6.3. COST 522, Investigation of welds for new trial melts CB5 & CB11

Two of the cast trial melts were welded using new Co-modified electrodes from two suppliers. The WB5 type electrodes correspond to the CB5 type cast material; Thermanit WB5 was used to weld CB5 while Cromocord WB5 was used to weld CB11 despite the difference in composition with respect to W, Mo, C and Cr contents. The compositions of the base materials and the all weld metals are given in Table 14; detailed information regarding welding procedure and properties are reported in [24].

	C	Mn	Cr	Ni	Mo	Co	V	Nb	W	N	B	Al
Base mat. CB5	0.13	0.20	10.10	0.16	1.58	2.90	0.20	0.063		0.035	.0110	0.021
Base mat. CB11	0.17	0.17	10.71	0.20	0.84	2.85	0.22	0.054	0.38	0.031	.0120	0.017
Thermanit WB5	0.13	0.65	10.40	0.69	1.42	2.60	0.21	0.049		0.018	.0080	.001
Cromocord WB5	0.10	0.57	10.80	0.71	1.42	2.90	0.20	0.047			.0060	

Table 14 *Compositions of base material and all weld metal investigated in COST 522*

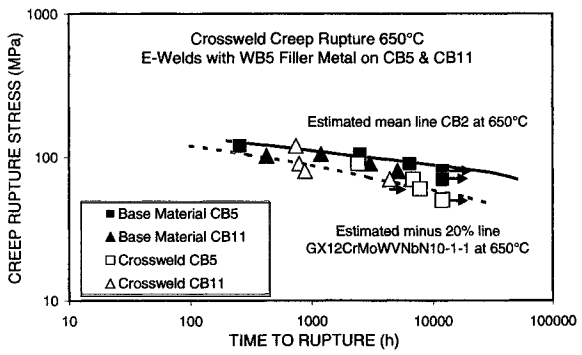


Figure 14 *Crossweld 600°C; welds on CB5 & CB11*

PWHT was carried out for both welds at 730°C/8h/FC and creep tests at 650°C have been started for all weld metal specimens and crossweld specimens. The current status is given in Figure 14 with the corresponding base material results. A preliminary evaluation shows:

- crossweld specimens from the CB5 weld fall clearly below the base material; after ca. 10 000h a

strength reduction due to welding of about 40% is observed.
- Crossweld specimens from the CB11 weld show large scatter; at longer duration the base material level may be reached; however base material CB11 exhibits much lower creep strength than CB5.

Co-modified filler metals are available, although they need further development regarding their creep strength; currently these values are only at the level of the -20% line for base material GX12CrMoWVNbN10-1-1.

7. Summary and Conclusions

- The various improvements of 9-12% Cr steels during the last 15-20 years enables thermal power plants with live steam parameters of 610°C/300bar and re-heat temperatures of up to 630°C to be realised, offering an increase in efficiency by about 8% and a related massive reduction in CO_2 emissions.
- The further development of ferritic-martensitic materials for application temperatures up to 650°C is the target of the sub-project „Steam Power Plant" in the COST 522 programme.
- By concentrating the European efforts in the COST 501/ 522 programmes, in which about 70 organisations from 15 countries take part, materials with improved properties could be successfully manufactured and tested.
- The contemporary developments within EPRI 1403-15/23 and COST 501 resulted in two cast steel grades with very similar creep strength level at 600°C and a gain in application temperature of 30-50°C as compared to cast steels applied hitherto.
- Both newly developed cast materials are already applied in several European power plants and will be used in power plants currently under construction. The manufacturing experience gained with these materials is decidedly positive.
- The broadly-based verification of the component properties demonstrates the reproducibility of the characteristic mechanical properties and increases the confidence in these new materials.
- Matching filler metals and welding procedures have been developed and the crossweld properties are satisfactory; the strength reduction due to welding is similar to that for the cast materials used previously.
- Recent developments with higher Co, Cr, and B contents showed limited improvement in creep strength above 625°C, although the higher Cr content may be beneficial for steam oxidation resistance.

8. Acknowledgement

The authors wish to thank their partners in the entire COST 522 working group for their contributions and the discussions during the course of the work. Thanks are also extended to the COST management committee and to the national funding bodies for financial support of the individual, national projects in particular to the German Ministry.

References

[1] Mayer K.H., Bendick W., Husemann R.U., Kern T., Scarlin R.B., New Materials for Improving the Efficiency of Fossil-fired thermal Power Stations, VGB Power Tech 1/98

[2] Vanstone R.W., Advanced 700°C Pulverised fuel power Plant, Proceedings of the 5th Int. Charles Parsons Turbine Conf., 3-7 July 2000, Cambridge, UK

[3] Miyashita K., Advanced Power Plant, I.Mech.E.Conference Transaction (1997) p.17-30, May 1997, London

[4] Touchton G., EPRI Improved Coal-fired Power Plant Project, 1st Int. Conf. on Improved Coal-Fired Plants, 19-21 November 1986, Palo Alto, US

[5] Mayer K.H., Gysel W., Cast Components of Steam Turbines for Improved Coal-Fired Plants, 1st Int. Conf. on Improved Coal-Fired Plants, 19-21 November 1986, Palo Alto, US

[6] Staubli M., Bendick W., Orr J., Deshayes F., Henry C., European Collaborative Evaluation of Advanced Boiler Materials, 6th COST Conference, 5-7. October 1998, Liège, Belgium

[7] Bendick W., Haarmann K., Zschau M., E911- Ein neuer Werkstoff für Dampfleitungen im Kraftwerksbau, VGB Conference, Materials and Welding Technology in Power Plants 1998, 14/15th October 1998, Hannover

[8] DiGianfrancesco A., Tassa O., Casali D., Cumino G., Creep Behaviour and Microstructural Evolution of E911 for Boiler Components, Proceedings of the 5th Int. Charles Parsons Turbine Conf., 3-7 July 2000, Cambridge, UK

[9] Staubli M., Mayer K.H., Kern T.U., Vanstone R.W., Hanus R., Stief J., Schönfeld K.H., COST522-Power Generation into the 21st Century-Advanced Steam Power Plant, Proceedings of the 3rd Conf. on Advances in Materials Technology for Fossil Power Plants, 5/6th April 2001, University of Wales, Swansea, UK

[10] Kern T.U., Staubli M., Donth B., Zeiler G., The European Effort in Development of New high Temperature Rotor Materials up to 630°C-COST522, 7th COST Conference, 30.9.-3.10.2002, Liège, Belgium

[11] Mayer K.H., Gysel W., Modified 9Cr-1Mo Cast Steels for Casings of improved Coal-fired Power Plants; 3rd International EPRI-Conference on Improved Coal-Fired Power Plants, 2-4. April 1991, San Francisco, CA

[12] Mayer K.H., Bakker W.T., New Ferritic Steels Increase the Thermal Efficiency of Steam Turbine, Int. Joint Power Generation Conf., October 1996, Huston, Texas

[13] Scarlin R.B., Berger C., Mayer K.H., Thornton D.V., Beech S.M., Steam Turbine Materials-High Temperature Castings, 5th Liège COST Conference, 3-6. October 1994, Liège, Belgium

[14] Mayer K.H., Hanus R., Kern T.U., Staubli M., Thornton D.V., High Temperature Cast Components for Advanced Steam power Plants, 6th COST Conference, 5-7. Oct. 1998, Liège,

[15] Hanus R.,Schönfeld K.H., Wagner H., Transformation of Knowledge and Technology from R&D to the Commercial Production of Heavy Steel Castings and Forgings for Power Engineering, 5th Int. Charles Parsons Conference, 3-7. July 2000, Cambridge UK

[16] Mayer K.H., KernT.U., Staubli M., Tolksdorf E., Long-Term Investigations of specimens of 24 Production Components manufactured from the Advanced Martensitic 10%Cr-Steels for 600°C Steam Turbines, 5th Int. Charles Parsons Conference, 3-7. July 2000, Cambridge UK

[17] Mayer K.H., Blum R., Hillenbrand P., Kern T.U., Staubli M., Development Steps of New Steels for Advanced Power Plants; 7th Liège COST Conference, 30.9-3.10. 2002, Liège, B

[18] Vanstone R.W., Cerjak H., Foldyna V., Hald J., Spiradek K., Microstructural Development in Advanced 9-12%Cr Creep Resistant Steels - A Collaborative Investigation in COST 501/3 WP11, 5th Liège COST Conference, 3-6. October 1994, Liège, Belgium

[19] Spiradek K., Bauer R., Zeiler G., Microstructural changes during the Creep Deformation of 9% Cr Steel, 5th Liège COST Conference, 3-6. October 1994, Liège, Belgium

[20] Mayer K.H., Cerjak H., Kern T.U., Staubli M., Thornton D.V., Present Status of Ferritic Steel Development for USC Plants in Europe, Int. Workshop on the Innovation Structural Materials and Infrastructure in the 21st century, ULTRA STEEL 2000, 11-14.Jan.2000, Tsukuba, Japan

[21] Cerjak H., Hofer P., Schaffernak B., The Influence of Microstructural Aspects on the Service Behaviour of Advanced Power Plant Steels, 1999 ISIJ, P.874ff

[22] Contessi A.,Delvecchio D., Ghidini A.,Valenti S., Carosi A., DiGianfrancesco A., Ielpo F.M., The first Industrial Cast of CrMoCoB Advanced Steel for Cast Turbine Components, 7th COST Conference, 30.9.-3.10.2002, Liège, Belgium

[23] Cerjak H., Letofsky E., Staubli M., The Role of Welding for Components made from Advanced 9-12% Cr Steels, 6th COST Conference, 5-7. October 1998, Liège, Belgium

[24] Cerjak H., Letofsky E., Jochum C., Nies H., Weldability and Weld Properties for Advanced Power Plant Materials, 7th COST Conference, 30.9.-3.10.2002, Liège, Belgium

WELDABILITY AND WELD PROPERTIES FOR ADVANCED POWER PLANT MATERIALS

H. Cerjak[1], E. Letofsky[1], C. Jochum[2], H. Nies[3]

1 Graz University of Technology, Graz, Austria
2 Thyssen Schweißtechnik, Hamm, Germany
3 Oerlikon Schweißtechnik, Eisenberg, Germany

Abstract

This paper shows the contributions of the suppliers of consumables, foundries and research institutes to the European COST program 522 for the development of new Co modified 9-12% Cr-steels.
The characterisation of welded joints in advanced high creep resistant steels is of decisive importance in the design of modern power stations. The key to solve these takes in the understanding of the metallurgical behaviour of the different microstructures appearing in the welded joint – base material, heat affected zone and weld deposit under creep exposure conditions.

Keywords: weldability, mechanical properties, creep properties

Introduction

The demand for lower production costs on the one hand and reduced noxious emissions on the other hand is the driving force for utilities to increase the efficiency of their plants. Increased efficiency for steam turbine plants means that the steam parameters have to be raised to supercritical conditions. If the steam temperature is further increased from 600°C to 650°C at 300 bar, the heat rate is reduced by more than 10% ensuring even lower $C0_2$ emission and fuel consumption. These advanced steam parameters require, however, materials with adequate creep strength and resistance to oxidation. The worldwide efforts are therefore presently focused on the further development of ferritic-martensitic 9-12% Cr steels [1].

In large castings for steam turbine components manufacturing and fabrication welds are standard procedures in manufacturing process. The knowledge of the behaviour of welds during long time service of the castings is of great importance.

The development of new ferritic-martensitic cast steel grades was closely connected to the research work for rolled and forged products for the same application temperature. In Europe the P91-type cast steel G-X12CrMoVNb 9.1 was qualified within the frame of an EPRI project. In the COST program an attempt was made to further increase the creep rupture strength on this basis by modifying the chemical composition and the heat treatment. In a first step within COST501-Round 2 the C, Cr and Ni contents were raised and the addition of 1%W was examined. In the next step within COST501-Round 3 the influence of B and N in addition to Co was tested. In the last years within COST522 new trial melts with higher C and Cr contents with Co and B was investigated. Table 1 gives details of the different developments of cast materials within COST.

Basic Steels	**G-X22CrMoV12 1** (DIN 17245)	**X10CrMoVNbN9 1** (P 91)	**X7CrCoMoVNb11 6** (Firth Vickers FV535)
Modification / Type	**Boron-Type**	**Mo, MoW-Type**	**WNB, CoB, CoWNB, CoWB-Type**
COST 501 Round 1 (1983-85)	Plus: B: 250 ppm NB : 0.08% Mod: C, Cr, Mo, V G-X10CrMoVNbB 9 1 G-X19CrMoVNbB 9 1 **Creep test max. 10.000 h**		
COST 501 Round 2 (1986-92)		Plus: W: 1% Mod: C, Cr, Heat Treatment C: G-X12CrMoVNbN 10 1 CT: G-X12CrMoWVNbN 10 1 1	
COST 501 Round 3 (1993-97)		C: G-X12CrMoVNbN 10 1 CT: G-X12CrMoWVNbN 10 1 1 **Best Candidate: CT**	Plus: W: 1-2%; B: 40-110ppm Mod: C, Mn, Ni, Cr, Co, V, Nb, (N) CB1: G-X12CrMoCoVNbB 9 1 CD1: G-X12CrWCoMoVNbNB 9 2 1 CE2: G-X12CrCoMoWVNbN 9 2 1 CF2: G-X10CrMoCoVNbN 10 1 CB2: G-X12CrMoCoVNbB 9 1 **Creep test max. 30.000 h**
COST 522 (1998-2002)		CT: G-X12CrMoWVNbN10 1 1 **Creep test max. 60.000 h**	**Best Candidate CB2** Base CB2: Mod: C, Cr, Co, W CB5: G-X13CrCoMoVNbB 10 3 1 CB6: G-X13CrCoMoVNbB 11 3 1 CB8: G-X17CrCoMoVNbB 11 3 1 CB9: G-X17CrCoMoVNbB 11 5 1 CB10: G-X13CrCoMoWVNbB 10 3 1 CB11: G-X17CrCoMoWVNbB 11 3 1

Table 1: European 9-12%Cr cast steel development within COST501/522, [1].

Description of COST522 SPP – Common Activity "Welding Subgroup"

The new program, titled COST522 – Energy generation in the 21st century; ultra-efficient, low emission plants, officially started in spring 1998. The action has a planned duration of 5 years. The sub-project dealing with steam power plant application is sub-titled "Materials for highly loaded components at steam inlet temperature of up to 650°C". The steam power plant working group within COST522 is again sub-divided into a Turbine and a Boiler group but a close collaboration between these two groups will ensure the use of synergies whenever possible. For special objects 5 subgroups for common activities were installed. The "Welding Subgroup – CA2" will be occupy with welding, processing and development of consumables. On the basis of intensive discussion within the Welding Subgroup four sub-programmes were defined:

- Weld Filler Material: optimisation of weld metal and the standardisation of weld metal;
- Casting Programme: properties of similar welds and the effect of welding processes;
- Boiler Programme: properties of similar welds of 2½Cr-1%Mo (T/P23 and T/P24) and dissimilar welds of different combination between T/P23, T/P24, P91, E911, P92 and austenitic steel;
- Matching Programme: properties of under matching, matching and over matching welds.

Throughout the whole action 37 steel producers, welding consumables producers, material suppliers, boiler and turbine manufacturers and research institutes or organisations from 14 European countries were involved.

Materials Manufactured and Tests Performed

In the framework of the turbine group different cast materials (CB2P, CB5, CB6, CB8, CB9, CB10, CB11) were produced and tested. In the framework of the welding subgroup welding consumables for Co modified 9-12%Cr steels (WB2 and WB5) were produced and investigated. These compositions are similar to those of the cast base materials (CB2 and CB5). Also welded joints were manufactured on CB2P, CB5, CB11. On tubes and pipes of these new Co modified 9-12% Cr steels different welds will be performed in the next year.

PHB had to manufacture a 4 tons housing according to the chemical composition of abbreviation CB2P. VOEST-Alpine Foundry manufactured in a first step test plates of CB5 and Acciaieria Fonderia Cividale SPA had to test the trial melt CB11. The range of the chemical composition of these three cast materials are given in table 2.

The chemical composition of the filler metals WB2 and WB5 are given in table 3. Both filler metals have been produced in different diameters: 3.2; 4.0; 5.0 mm and they have been delivered to several partners to carry out their welding program.

CB2P	C	Si	Mn	Cr	Mo	Ni	V	Al	B	Co	N	Nb	Ti
min	0.11	0.20	0.80	9.00	1.40	0.10	0.18		0.008	0.90	0.015	0.05	
max	0.14	0.30	1.00	9.60	1.60	0.20	0.22	0.020	0.015	1.10	0.030	0.07	0.010

CB5	C	Si	Mn	Cr	Mo	Ni	V	Al	B	Co	N	Nb	Ti
min	0.12	0.20	0.10	9.90	1.40	0.10	0.18	0.010	0.008	2.80	0.015	0.05	
max	0.14	0.30	0.30	10.50	1.60	0.20	0.22	0.020	0.015	3.20	0.030	0.07	0.010

CB11	C	Si	Mn	Cr	Mo	Ni	V	Al	B	Co	N	Nb	W
min	0.16	0.20	0.10	10.70	0.80	0.10	0.18	0.010	0.008	2.80	0.015	0.05	0.30
max	0.18	0.30	0.30	11.30	1.00	0.20	0.22	0.020	0.015	3.20	0.030	0.07	0.50

Table 2: Requirement on the chemical composition, cast material of CB2 [2], CB5 [3] and CB11 [4].

WB2	C	Si	Mn	Cr	Mo	Ni	V	Al	B	Co	N	Nb	Ti
min	0.12	0.20	0.40	10.00	1.40	0.60	0.18		0.006	0.90	0.015	0.04	
max	0.14	0.30	0.60	10.50	1.60	0.80	0.22	0.01	0.008	1.10	0.020	0.06	0.010

WB5	C	Si	Mn	Cr	Mo	Ni	V	Al	B	Co	N	Nb	Ti
min	0.12	0.20	0.40	10.50	1.40	0.60	0.20		0.006	2.80	0.015	0.04	
max	0.14	0.30	0.60	11.00	1.60	0.80	0.23	0.01	0.008	3.20	0.020	0.06	0.010

Table 3: Requirement on the chemical composition, all weld metal of WB2 and WB5, [5].

The actual chemical composition of the welded joint CB5 - WB5 is given in table 4 and of CB11 - WB5 in table 5.

CB5 - WB5	C	Si	Mn	Cr	Mo	Ni	V	Al	B	Co	N	Nb
product	0.13	0.28	0.20	10.10	1.58	0.16	0.20	0.025	0.010	2.90	0.035	0.063
weld	0.13	0.45	0.65	10.40	1.42	0.69	0.21	0.001	0.008	2.60	0.018	0.049

Table 4: Requirement on the chemical composition, product CB5 and weld Thermanit WB5, [3].

CB11 - WB5	C	Si	Mn	Cr	Mo	Ni	V	Al	B	Co	N	Nb
product	0.13	0.28	0.20	10.10	1.58	0.16	0.20	0.025	0.010	2.90	0.035	0.063
weld	0.098	0.19	0.57	10.80	1.42	0.714	0.20		0.006	2.90		0.047

Table 5: Requirement on the chemical composition, product CB11 and weld Cromocord WB5, [4].

Results of the COST522 Welding Subgroup

Selected results from the programmes carried out in the COST522 Welding Subgroup will be discussed below.

Welding tests with alloying type Cromocord WB 2 showed, that C is increased distinctly in the weld metal in position PF, which is obviously due to the reduced welding current, i.e. lower C burn-off in the arc, compared to position PA. By consequence the elongation was reduced and the tensile specimens broke by showing a 45° shear fracture. By reduction of the C content the elongation could be increased. An elongation > 17% in weld metal produced in position PF has finally been reached again after a PWHT at 730°C for 20 h. The replacement of stick electrodes using unalloyed core wire by a partly alloyed wire took place to reduce the addition of C, Cr, Mo and N by the coating. After this replacement new coated electrodes are available for welding Co, B alloyed casts.

In addition, the influence of Ni in the filler metal Thermanit WB2 was tested, after different PWHT´s 760°C/2h; 740°C/4h; 730°C/12h (see figure 1). As it can be seen, the Ni content in WB2 has only little influence on toughness, but little more on the strength properties of the all weld metal (see figure 2). Comparing the different heat treatments, at present time 740°C/4h show best results, at least for the weld metal.

In order to optimize the mechanical properties and especially the toughness properties, several tests have been carried out using different PWHT's. The results of these tests can be seen in table 6.

For the alloy with 1% Co (Thermanit WB2) it can be seen that a PWHT at 740 °C and > 4 h can increase toughness to a level of about 40 to 45 Joule. A double PWHT 2 x 730 °C / 10 h will also produce a toughness of about 40 to 45 Joule. The elongation varies always in the range of about 15 to 19 %.

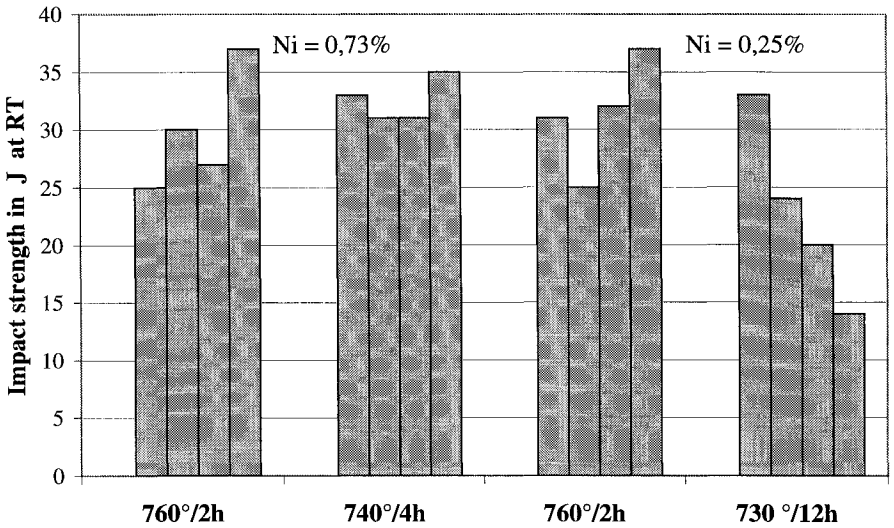


Figure 1: Effect of PWHT and Ni content in Type WB2 on toughness, [5].

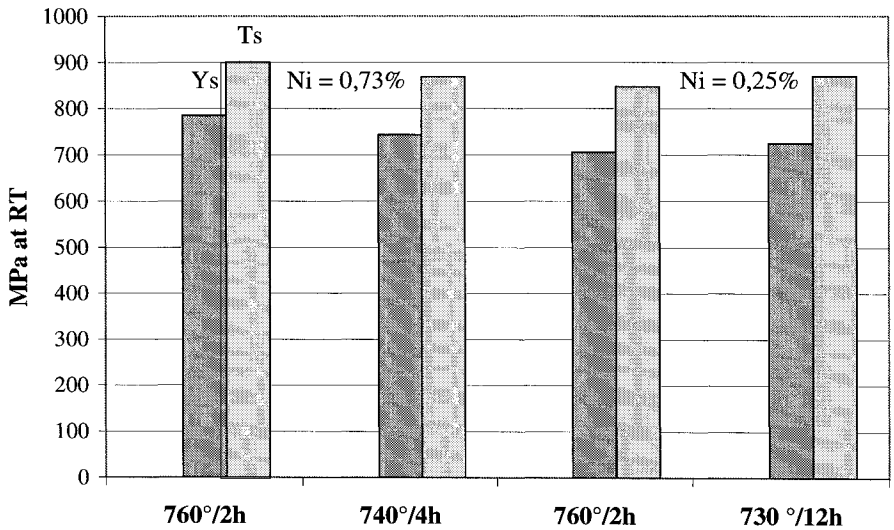


Figure 2: Effect of PWHT and Ni content in Type WB2 on strength, [5].

For the alloy with 3 % Co (Thermanit WB5) the toughness is in general on a lower level even after the optimised PWHT. At present time the requirements of > 27 Joule is at the same time the maximum achievable level. The strength properties are higher compared to that of Thermanit WB2. Again the elongation varies between 15 and 18 %.

In order to find the limits of the weldability (max. possible heat input) and to find the influence of different heat inputs on the mechanical properties a test program was carried out

producing all weld metal with increasing heat input. Table 7 shows the results for Thermanit WB2 using different heat inputs (standard: 15 to 18 kJ, pos. PA; increased heat input: 25 kJ, 33 kJ, 40 kJ, all pos. PF), PWHT was 730 °C / 20 h.
In all cases toughness was on a level clearly above 27 Joule and elongation was in the range of about 17 %.

WB2 Testtemp.	PWHT	Rp0.2 MPa	Rm MPa	A5 %	Z %	Toughness J	Heat input kJ/cm
RT	760°C/2h	784	901	16.5	55	25 30 27 37	15 - 18
	740°C/4h	743	869	19.0	61	33 31 31 35	15 - 18
	740°C/6h	722	856	15.5	56	37 40 39	15 - 18
	760°C/10h	699	835	16.2	57	42 46 40	15 - 18
	2x: 730°C/10h	673	814	17.7	55	42 44 35	15 - 18

WB5 Testtemp.	PWHT	Rp0.2 MPa	Rm MPa	A5 %	Z %	Toughness J	Heat input kJ/cm
RT	760°C/2h	766	899	15.8	56	24 29 31 22	15 - 18
650°c		292	362	23.0	78		
RT	730°C/12h	785	913	16.4	56	17 21 18 14 40	15 - 18
650°C		307	410	20.0	75		

Table 6: Mechanical properties, all weld metal of WB2 and WB5, test results of a 4.0mm electrode, Pos. PA, [5]

Heat Input kJ/cm	Welding position	PWHT	Rp0.2 MPa	Rm Mpa	A5 %	Z %	Toughness J
15 – 18	PA	2x: 730°C/10h	673	814	17.7	55	42 44 35
25	PF	730°C/20h	690	828	17.2	60	37 22 40
33	PF	730°C/20h	679	820	18.1	62	35 38 40
40	PF	730°C/20h	664	805	17.1	62	48 31 43

Table 7: Influence of heat input on the mechanical properties, all weld metal of WB2, test results of a 4.0mm electrode, at room temperature, [5]

The same program was carried out for a Thermanit WB2-alloy without Boron. The results are given in table 8. In all cases the toughness of the Boron free variant is on a higher level (50 to 55 Joule) and in all cases elongation is about 18 %.

Heat Input kJ/cm	Welding position	PWHT	Rp0.2 MPa	Rm Mpa	A5 %	Z %	Toughness J
25	PF	730°C/20h	637	796	18.7	56.2	57 56 52
33	PF	730°C/20h	588	749	17.2	55.0	54 55 52
40	PF	730°C/20h	616	773	18.8	61.4	41 51 53

Table 8: Mechanical properties, all weld metal of WB2 without Boron, test results of a 4.0mm electrode, room temperature, [5]

Caused by an observed ductility problem at PHB Stahlguss by using the WB2 weld metal produced by both Thyssen and Oerlikon, a kind of "Round Robin" test with the electrodes has been performed. Additional tests have been carried out by other project partners. All results of mechanical testing of the all weld metal lay in the same range as reported above.

After all these tests new electrodes of type WB2 have been delivered to PHB Stahlguss to carry out their welding job. This type of electrodes has been slightly modified with respect to the C-content. As observed during several tests before, there is a slight increase of carbon when welding in the vertical up position. For this reason, the C-content of the all weld was reduced to 0,10 - 0,12% (former: 0,12 – 0,14 %). These data refer to the all weld metal, produced in flat position. When welding in out of position, C-content will again increase to the former 0,12–0,14 % range. The modification of the chemical requirements is given in table 9.

WB2	C	Si	Mn	Cr	Mo	Ni	V	Al	B	Co	N	Nb	Ti
min	0.10	0.20	0.40	10.00	1.40	0.60	0.18		0.006	0.90	0.015	0.04	
max	0.12	0.30	0.60	10.50	1.60	0.80	0.22	0.01	0.008	1.10	0.020	0.06	0.010

Table 9: Requirement on the chemical composition, all weld metal of modified WB2, [5].

First test welds were carried out by VOEST-Alpine Foundry (CB5 – Theramit WB5) and by Acciaieria Fonderia Cividale SPA (CB11 – Cromocord WB5). The macro and microstructure of CB5 – WB5 is shown in figure 3.

The test samples were placed in and transverse to the weld metal. The fracture location for all test samples was in the base material. In tables 10 and 11 the results of toughness tests and tensile tests, carried out at room temperature and at 650°C are shown. CB11 shows a slightly higher toughness level than CB5. The toughness in the HAZ is higher than in the all weld position.

Steel	Cond.	Rp0.2 MPa	Rm MPa	A5 %	Z %	Fracture Location	Toughness J
CB5	Q+T [RT]	707	844	8.4	15		20 22 21
	2xSR (730°C) [RT]	544	730	16.8	42		33 36 38
all weld	RT	655	808	17.9	41		14 10 28
	650°C	248	350	29.0	79		
cross weld	RT	618	760	10.2	39	base material	HAZ
	RT	563	740	12.3	44	base material	43 30 29
	650°C	304	334	11.0	69	base material	
	650°C	280	345	20.0	71	base material	

Table 10: Mechanical properties, base material CB5, all weld metal Thermanit WB5 and cross weld CB5-WB5, test results of a 4.0mm electrode, Pos. PA, heat input ~ 10 kJ/cm, [3]

Steel	Cond.	Rp0.2 MPa	Rm MPa	A5 %	Z %	Fracture Location	Toughness J
CB11	RT	621	750	16.1	41.1		66 61 69
	650°C	261	339	28.6	79.1		
all weld	RT	638	789	17.4	38.0		28 33 39
	650°C	253	361	27.8	68.0		
cross weld	RT	609	748	10.9	37.0	base material	HAZ
	RT	601	752	11.1	39.0	base material	43 45 43
	650°C	290	348	16.2	68.0	base material	
	650°C	293	342	15.9	67.0	base material	

Table 11: Mechanical properties, base material CB11, all weld metal Cromocord WB5 and cross weld CB11-WB5, test results of a 4.0mm electrode, Pos. PF, heat input ~ 15-18 kJ/cm, [4]

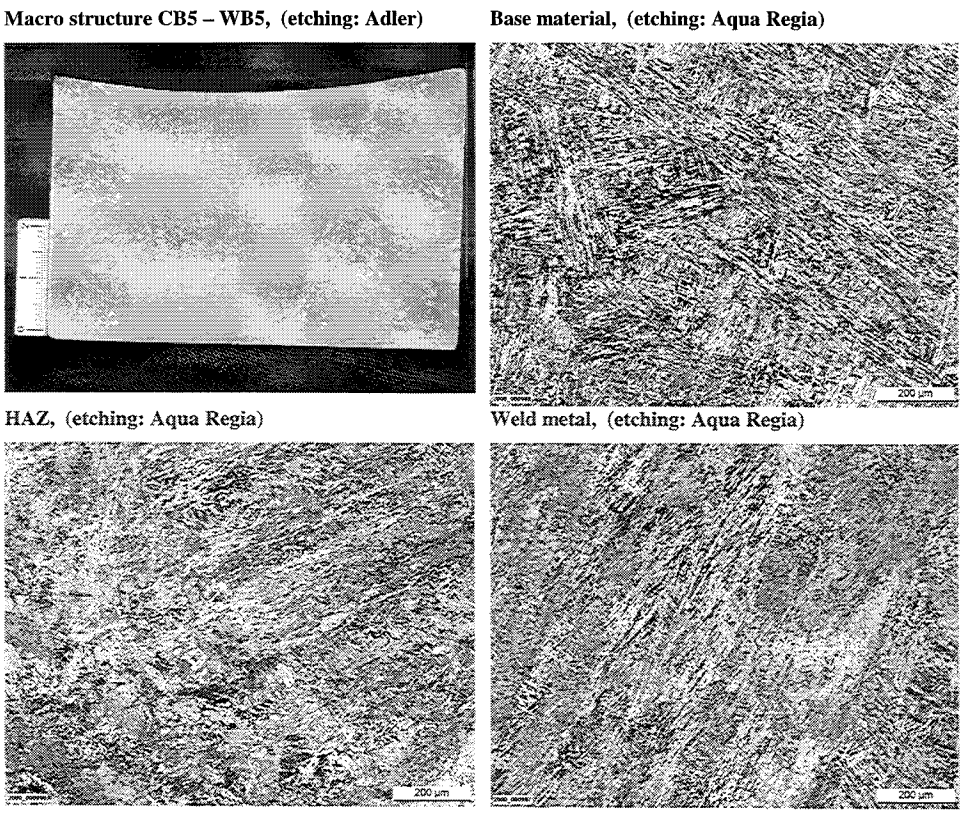


Figure 3: Macrograph from the SMAW girth weld in the CB5 test plate, microstructure of the base material, HAZ and all weld metal, [3].

The current status of creep test for the welded joint CB5 – WB5 compared with the base material CB5 and the pure weld metal WB5 at 650°C with a testing time of 12.000 hours is shown in figure 4. The results for the cross weld samples lay under the base material.

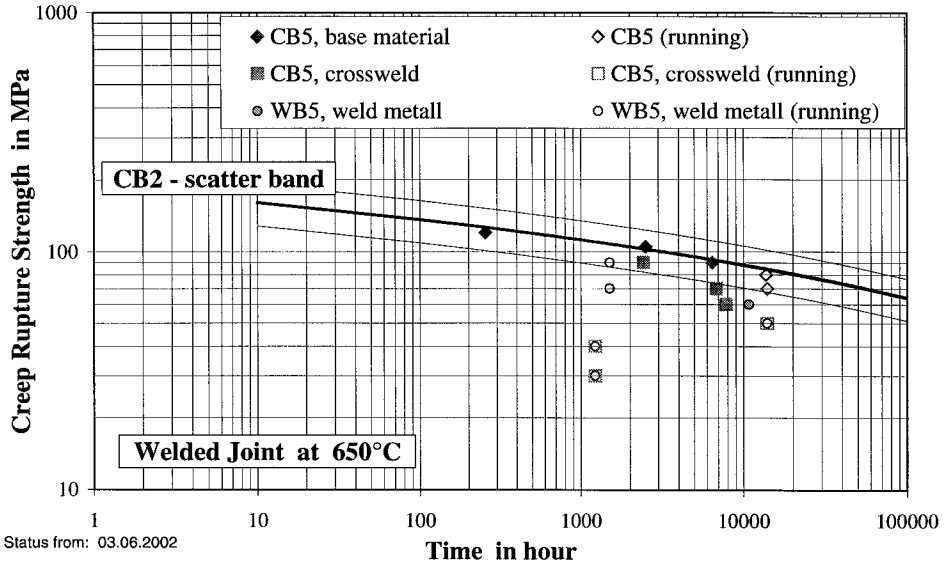


Figure 4: Creep rupture strength of parent material CB5, cross weld specimens CB5 – WB5 and all weld metal CB5 at 650°C.

Some more investigations were done on 9-12% Cr welding consumables for screening the influence of different alloying elements by Metrode Welding Consumables, ESAB Group UK and TWI.

Conclusions

As a result of all these welding tests and in accordance between Thyssen Welding (Hamm) and Oerlikon Schweißtechnik (Eisenberg) welding recommendations regarding heat input for welding of alloying types WB 2 and WB 5 have been worked out.

All future welding jobs (laboratory or productions conditions) should be carried out using a heat input and welding parameter given in table 12.

Basic covered electrode with good welding properties in all positions except vertical down. Almost free of spatter. Easy slag removal. For good mechanical properties gentle weaving technique is recommended, max. 3 times the electrode's core wire diameter. Make flat beads with a maximum thickness of 2,5 mm. Controlled heat input is very important. PWHT: heating/cooling rate above 300°C; 50 - 100 °C/h. Redrying conditions: 2h / 300 - 350 °C

dia. mm	polarity	T_{pre} °C	$T_{intp.}$ °C	Is A	Us V	Heat input kJ/cm	Heat input kJ/cm
WB2						**Pos. PA**	**Pos. PF**
2.5 x 250	=+	230 – 270	250 – 280	70 – 100	23 – 26	max. 10	max. 15
3.2 x 350	=+	230 – 270	250 – 280	90 – 140	23 – 26	max. 15	max. 25
4.0 x 350	=+	230 – 270	250 – 280	130 – 180	23 – 26	max. 18	max. 30
5.0 x 450	=+	230 – 270	250 – 280	170 - 240	23 – 26	max. 20	

Table 12: Welding parameter for weld metal WB2 and WB5, [5]

More results will be presented in individual reports of the COST partner of the COST522 – SPP: CA2 "Welding Subgroup".

Acknowledgement

The authors express their appreciation and acknowledgement to all individual members of the COST522-SPP-CA2 "Welding Subgroup" who supported unconditionally the basic intention of this successful COST action.

References

[1] M. Staubli, K.H. Mayer, T.U. Kern, R.W. Vanstone: COST501/COST522 – The European Collaboration in Advanced Steam Turbine Materials for Ultra Efficient, Low Emission Steam Power Plant, in Parsons 2000 Advanced Materials for 21st Century Turbines and Power Plant, edited by A. Strang et al., IOM Communications Ltd, (2000), pp. 98-122
[2] J. Stief: PHB Stahlguss, COST partner, private communication, (2000)
[3] R. Hanus: VOEST-Alpine Fondry Linz, COST partner, private communication, (2000)
[4] A. Valduga, A. Di Gianfrancesco: Acciaieria Fonderia Cividale and Centro Sviluppo Materiali S.p.A., COST partner, private communication, (2001)
[5] C. Jochum: Tyssen Welding, COST partner, private communication, (2000)
[6] H. Nies: Oerlikon Schweißtechnik, COST partner, private communication, (2001)

NEW BOILER MATERIALS FOR ADVANCED STEAM CONDITIONS

Brendon Scarlin and G.N. Stamatelopoulos
ALSTOM Power
Baden, Switzerland and Stuttgart, Germany

Abstract

A steady increase in operating data of steam power plant has been observed in terms of increasing temperature and pressure, in order to achieve improved thermal efficiency. Critical boiler components, which are subjected to these conditions, include water walls, superheater tubes and thick walled components such as main steam pipes and headers. Requirements include ease of manufacturing, including welding, forming and heat treatment, along with improvements in oxidation resistance and mechanical properties:

- Oxidation resistance must be sufficient to ensure that oxide growth does not lead to unacceptable temperature increase in heated tubes with the possibility of creep failure or of excessive spalling of hard solid particles
- Mechanical properties must be such as to ensure longterm operation at high temperatures (creep strength) along with flexibility of operation and load cycling (low cycle fatigue resistance).

Within the boiler group of the COST 522 programme systematic alloy development and qualification work has been carried out for the range of materials from low-alloyed steels (2.25%Cr steels), ferritic-martensitic steels (9 to 12%Cr steels) and austenitic steels. This paper reports results from the COST programme along with additional results for these and other similar materials from the literature. These results along with field experience obtained with the new materials provide a sound basis for a move to higher steam conditions.

Keywords: Boiler, ferritic steels, austenitic steels, creep strength, oxidation resistance, welding.

Introduction and Background

Economic Aspects

The building and operation of power plants is a highly competitive business in which low cost of electricity produced and high reliability of the electricity supply are key factors. In addition the availability of a longterm reliable source of fuel, at a stable price level, is essential to ensure that the economic viability of the plant is not jeopardised. Recent figures [1] have compared the known stocks of fossil fuels. Whereas coal supplies adequate for the next 250 years have been found, the supply of natural gas is currently only sufficient for 60 years. Further supplies will certainly be found, but they are likely to be increasingly difficult and expensive to extract. In this respect coal is widely distributed around the globe, whereas natural gas supplies are in only a few countries.

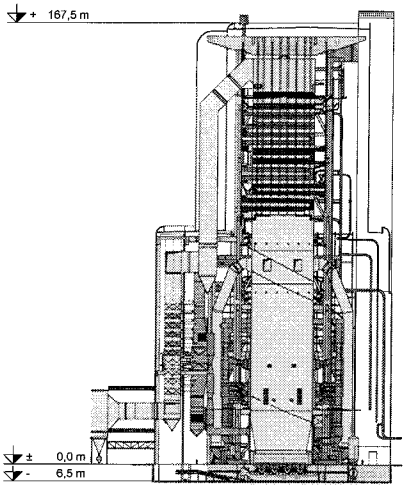
The cost of electricity is most dependent on power plant investment costs and fuel price. In this respect natural gas burning combined cycle plants benefit from low investment costs (and short construction times) but suffer from higher (and more volatile) fuel prices. On the other hand coal burning steam power plants have a balanced Cost of Electricity (CoE) structure, as investment costs, O&M costs and fuel costs contribute almost the same to the total CoE.

For the combined cycle power plant with natural gas, fuel costs are responsible for about 75 % of the CoE, rendering thus the combined cycle power plant more vulnerable to fuel cost variations.

For Germany [1] the current predictions assume that 20% more electrical power will be generated in 2020 using about the same amount of fuel as now and that over 50% of the power will come from coal and lignite burning steam power plant. Many of these will be new. Also countries with the greatest expected increase in demand for electrical supply in the next decade, such as China and India, have their own supplies of coal, which will constitute the main fuel for their power plants.
Due to the unfavourable C/H ratio of coal, concerning CO_2 emissions, the only way to keep them low is to increase the efficiency, mainly by increasing the steam parameters. The efficiency increase reduces also the fuel costs and saves the fuel resources. For this reason a series of R&D materials projects started in recent years in Europe, the USA and Japan aiming at the qualification and testing of new materials for advanced steam parameters.
The power plant owner's interest in high equipment reliability is based on his need to obtain a quick financial return on his investment and on his contractual obligation to supply his customers with electrical power. From this point of view the plant owner will favour well proven technology in terms of well-established design concepts and materials which have been extensively tested and validated, encompassing long-term testing of new materials and validation of component manufacturing processes e.g. casting, forging, forming, welding.

The boiler represents the largest "component" in a steam power plant. Consequently key issues are the reliability of critical components, including water walls, superheater tubes and thick walled components such as main steam pipes and headers as well as the search for more economical materials and fabrication processes.
Fig.1 shows a longitudinal section of the Niederaussem K boiler with steam parameters of 290 bar and 580 / 600 °C, which is planned to start operation in 2002 in Germany. Niederaussem K is lignite-fired with an installed capacity of 1000 MWel and an efficiency of over 43 % (NCV, net). For the last stages of the superheater and reheater the austenite X3CrNiMoN1713 (1.4910) is used. The selection of materials for the key high-temperature components is shown in Fig.2. Concerning the thick walled components in Niederaussem K the material E911 is used for the superheater and reheater outlet headers, as well as for the live steam and hot reheat pipe.

Materials Issues
The availability of suitable materials has limited the development of steam power plants to higher temperatures and hence higher efficiencies. Whereas for the steam turbine the critical high-temperature components are rotors, casings, turbine blades and bolts [2], the key components on the boiler side are thin-walled water wall, superheater and reheater tubes (typically with up to 8 mm wall thickness) and thick-walled steam pipes and headers (with up to 90 mm wall thickness).



Steam parameters:

SH	290 bar/580	°C
RH	80 bar/600	°C
Steam capacity	2,620	t/h
Feedwater temperature	294	°C

Fuel data:

NCV	9,200	kJ/kg
Ash	6	%
Moisture	53.3	%

Fig.1: Longitudinal section of the Niederaussem K boiler with steam parameters of 290 bar and 580/600°C

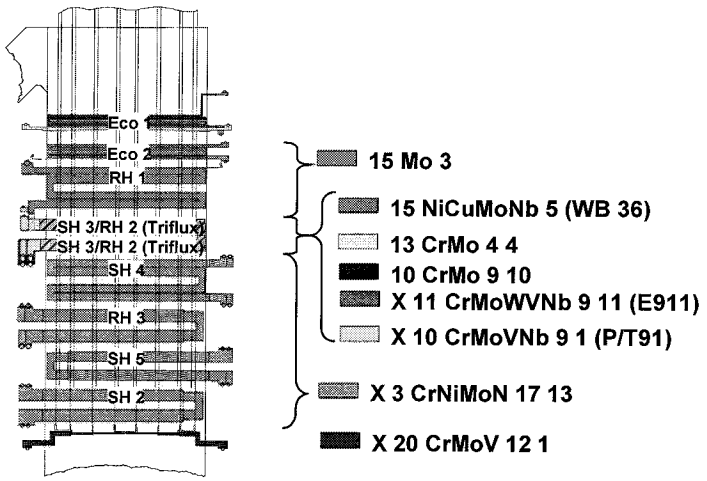


Fig.2: Materials selection for key components for the Niederaussem K boiler

Current state-of-the-art power plant operate up to live steam conditions of typically 580°C at 270 bar and reheat steam of 600°C. Under these conditions operation temperature for the key components is:

- water walls up to 520°C (metal temperature)
- thick-walled pipes and headers up to 600°C (metal temperature)
- superheaters and reheaters up to 630°C (metal temperature).

Requirements for each of these components include ease of manufacturing, including welding, forming and heat treatment, along with improvements in oxidation and corrosion resistance and mechanical properties:

- Oxidation resistance must be sufficient to ensure that steam-side oxide growth does not lead to unacceptable temperature increase in heated tubes (water walls, superheaters and reheaters) with the possibility of creep failure or of excessive spalling of hard solid particles which will cause erosion in the steam turbine
- Corrosion resistance must be high enough to ensure minimal loss of material on the fireside, for the grade of coal generally used in each power plant
- Mechanical properties must be such as to ensure long-term operation at high temperatures (creep strength) along with flexibility of operation and load cycling (low cycle fatigue resistance)

For satisfactory operation of these components in the temperature ranges indicated and with minimal costs for materials and manufacturing, it is usual to employ 2.25%Cr steels for water walls, 9-12%Cr steels for thick-walled pipes and austenitic steels for superheater and reheat tubes. Considerable development activity of materials in these classes has been ongoing for the last 25 years.

State of the Art of Boiler Steels (see Table 1)

- 2.25%Cr 1%Mo steels are best able to satisfy financial constraints and have been greatly improved, by analogy with the 9%Cr steels, by the substitution of almost all of the 1%Mo by 1.6%W. The improved material HCM2S has been standardised in ASTM as **T23**, a thin-walled tube suitable for water-wall applications. It benefits greatly from the fact that it does not need either preheat or post weld heat treatment. In the temperature range up to 550°C it has similar creep strength to higher alloyed steels such as T91 and is preferred due to the ease of welding. At higher temperatures a 9 to 12%Cr steel must be used, along with the increased difficulty of welding and of performing post weld heat treatment of large water wall panels on site. As a consequence of the high creep strength at intermediate temperatures, there is interest in using the tungsten-containing 2.25%Cr steel also for thick-walled piping.

- 9-12%Cr steels provide an excellent combination of creep strength and oxidation resistance, along with the other necessary attributes in terms of fabricability of thin-walled and thick-walled components and good resistance to thermal fatigue (good thermal conductivity and low coefficient of thermal expansion). Starting from the European 12%Cr steel **X20 CrMoV 12 1**, widely used since the '60s, further developments led in the '80s in the USA to the production of **T91 and P91**, a 9%Cr steel with lower carbon content, thereby combining good weldability and toughness with a greatly increased creep strength. On this basis developments in Japan led to **P92**, a 9%Cr steel with addition of 2%W, and in Europe to **E911**, a 9%Cr steel containing 1% each of Mo and W. Both modifications of T/P91 again improved the creep strength, without significant loss of toughness or weldability. All these steels are in widespread use.

  Although the 9%Cr steels show improved creep strength, their oxidation resistance in steam is reduced in comparison with the 12%Cr steels, to the extent that they may not be acceptable at the highest temperatures [3].

As shown in Fig.3, steam oxidation resistance of the 9%Cr steels at 650°C is significantly worse than that of the 12%Cr steel. The W-containing P92 is also inferior to P91.

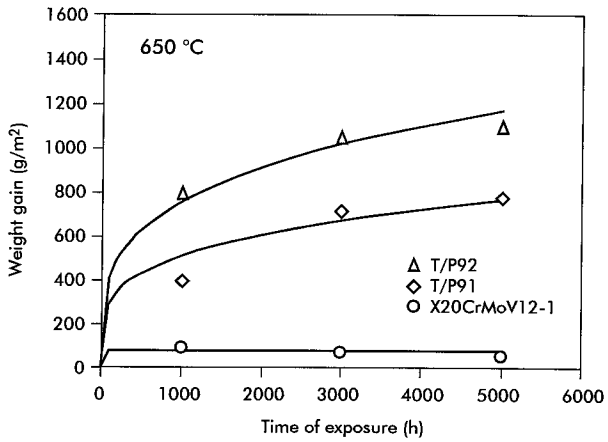


Fig.3: Oxidation behaviour of 9-12%Cr steels in a steam atmosphere

Hence newest developments have concentrated on the 12%Cr steels:
HCM12 which is alloyed with W and Mo, but contains up to 30% δ ferrite
HCM12A which has increased W and decreased Mo, and 1%Cu to avoid δ ferrite
A series of new steels in the ongoing COST 522 programme, which additionally contain different levels of Co and B.

- Austenitic steels provide the best combination of creep strength and oxidation resistance for thin walled components, at only slightly higher cost than for the 9-12%Cr steels. A wide range of steels is available with satisfactory creep, oxidation and welding properties. Development trends are towards cost reduction through reducing the amounts of expensive alloying elements, while maintaining satisfactory properties.

Steel		Chemical Composition (wt.%)												
		C	Si	Mn	Ni	Cr	Mo	W	V	Nb	Ti	B	N	others
2Cr	T22	0.12	0.3	0.45	--	2.25	1.0	--	--	--	--	--	--	--
	P23	0.06	0.2	0.45	--	2.25	0.1	1.6	0.25	0.05	--	0.003	--	--
9Cr	P91	0.10	0.4	0.45	0.8	9.0	1.0	--	0.20	0.08	--	--	0.05	--
	E911	0.12	0.2	0.51	0.25	9.0	0.9	0.9	0.20	0.06	--	--	0.06	--
	P92	0.07	0.06	0.45	--	9.0	0.5	1.8	0.20	0.05	--	0.004	0.06	--
12Cr	HCM12	0.10	0.3	0.55	--	12.0	1.0	1,0	0.25	0.05	--	--	0.03	--
	P122	0.11	0.1	0.60	--	12.0	0.4	2.0	0.20	0.05	--	0.003	0.06	1.0Cu
15Cr	Esshete 1250	0.12	0.5	6.0	10.0	15.0	1.0	0.2	1.0	--	0.06	--	--	--
20Cr	NF 709	0.15	0.5	1.0	25.0	20.0	1.5	--	--	0.2	0.1	--	--	--

Table 1: Nominal compositions of selected tube and pipe steels

Alloy Design Principles

In recent years significant progress has been made in discovering how the composition and the microstructure of the steels influence the short and longterm properties. For example for 9-12%Cr steels there is now a general (qualitative) understanding of the complex strengthening mechanisms and principles of alloy design [4]:

- Chromium (11 to 12%) provides superior oxidation resistance
- Carbon (0.1 to 0.2%) for the formation of $M_{23}C_6$ precipitates
- Molybdenum and Tungsten (each 1 to 2%) provide solid solution strengthening
- Vanadium (about 0.25%) to form MX precipitates
- Niobium (about 0.06%) to stabilise grain size during austenitising
- Boron (about 0.01%) to reduce the coarsening rate of $M_{23}C_6$ precipitates

There is also increasing understanding of the degradation processes, whereby Mo and W in solid solution are precipitated out in the form of large Laves phase particles, and whereby MX particles are transformed to rapidly coarsening M_6X or Z phase [5,6]. Nevertheless a great deal of the alloy development work performed in the past has been on a trial and error basis. Alloy design is now supported by powerful electron microscope methods to quantitatively analyse precipitate distributions and coarsening rates and by computer aided techniques, based on physical understanding of the processes of phase transformations and precipitate nucleation and growth. Further models to predict creep strength on the basis of microstructural features, such as martensite lath size and precipitate distributions are also being developed and validated [7].

Long-term creep strength is dependent on various parameters, all of which are dependent on the chemical composition of the steel:

- diffusion rates of substitutional elements control coarsening rates of particles – this in turn is controlled by the Curie temperature, which is positively affected by additions of Co and C and negatively by Ni, Si, Mn and Cr.
- precipitate stability and bond strength are related to orbital energy of the alloying elements and thereby also to the chemical composition [8]
- programmes such as THERMOCALC and DICTRA [9,10] are able to predict equilibrium phase diagrams of multi-component alloys and thermodynamic and diffusion parameters – on this basis compositions have been selected for investigation in the COST 522 programme. The target has been a high $\alpha \rightarrow \gamma$ transformation temperature along with a low diffusion rate.

Whereas these techniques can provide valuable insights and indicate directions in which improved creep strength may be obtained, requirements in terms of high oxidation resistance and good forming and welding properties are not addressed. There is also no general agreement as yet on the benefit obtainable through the addition of high W levels, which have the potential disadvantage of Laves Phase precipitation. The best levels of B and N addition are also not clarified, since B stabilises $M_{23}C_6$ precipitates and N contributes to MX precipitation, but there is also the potential of precipitation of rapidly coarsening BN particles. Hence it is still necessary to perform manufacturing trials and long-term tests.

Materials Qualification

Within the COST programme a stepwise approach to alloy development, validation and introduction into power plant was agreed. This approach is shown in Fig. 4.

1) On the basis of experience with earlier materials and the results of phase stability predictions, compositions are selected and a number of small laboratory melts are manufactured. These are produced in an appropriate product form, representative of the components in question (e.g. castings, forgings, bars, tubes or pipes) and are subjected to a standardised testing programme. The screening programme includes heat treatment trials, followed by tensile and impact energy testing, short and longer term stress rupture and creep testing, thermal exposure tests for times up to 10'000 hours to check for embrittlement or softening and tests in flowing steam at elevated temperature to check for adequate resistance to oxidation and spalling of the oxide layers.
2) After typically 10 to 20 thousand hours of testing the results for the melts of different compositions are analysed and further small melts may be produced within the same nominal specification range for the variants showing the best combinations of properties. These results provide a better overview of the statistical scatter in properties which can be expected for a certain nominal composition.
3) As a next stage larger melts will be made of size representative of the components in question in order to check the upscaling potential. They are subjected to the same investigation programme.
4) Further manufacturing technologies, such as welding, nondestructive inspection and bending are demonstrated on these "components".
5) The final step comprises order, construction and operation of a high temperature steam power plant, making use of the new high temperature materials. In the first place the new materials may be used at temperatures below their full capability, in order to obtain further practical experience before taking full advantage of the improved temperature capabilities of the new steel.

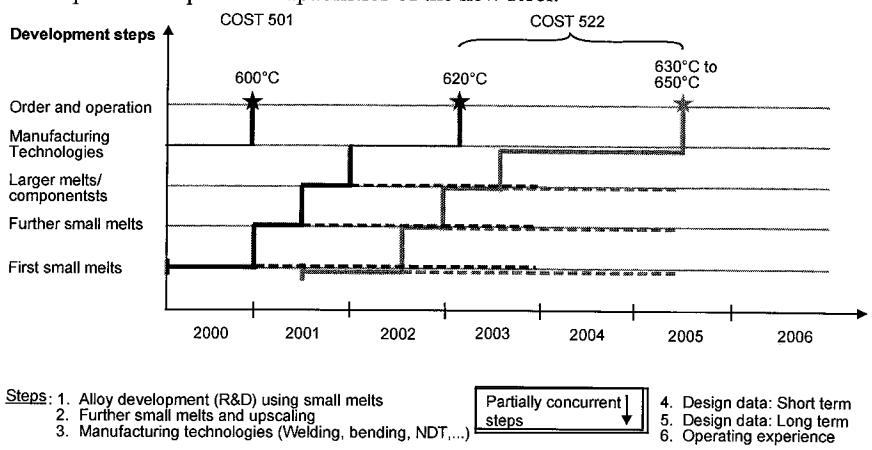


Fig.4: Steps in the qualification and introduction of new power plant steels.

Whereas the COST programme has been primarily concerned with the development and testing of new steels for the key components in boilers and turbines, other national and international programmes have had a complementary function (statistical evaluations, investigation of properties of welds or performance of field tests)

Ongoing National and International Boiler Materials Programmes.

Several programmes in Europe, and elsewhere, are concerned with specific aspects of the development of new steels for boiler applications:

COST 501 and 522
The COST 501 programme examined primarily the mechanical properties and weldability of the W-alloyed version of P91, designated E911. It was produced and tested in various product forms. The large database produced was sufficient to apply for and obtain ASME/ASTM approval [11]. Components of the new steel are already in service in operating power stations, for example as thick walled components in Niederaussem K, as mentioned before. For comparative purposes products of the steel P92 were also manufactured and tested. P92 is also commercially used, for example in the live steam pipe of the Danish power plant Avedore and the RH outlet header of the German power plant Kiel.

The ongoing COST 522 programme is investigating the use of T23 and P23 for water walls and pipe sections, new 11%Cr steels for pipe applications and new austenitic steels for reheaters and superheaters.

Komet650
Investigations are focussed on steam oxidation testing in the bypass of the Westfalen B power plant. Samples of 9 to 12%Cr steels (such as E911, P91, P92 and P122), austenitics and nickel-based alloys are being exposed for up to 24'000 hours at both 620 and 650°C. At intermediate times samples are removed for metallographic examination to determine the rate of oxidation and the tendency to oxide spalling [12]. The effectiveness of coatings as protection against steam oxidation is also under investigation. Currently testing times have exceeded 12'000 hours.

PIPPE
Uniaxial and multiaxial similar and dissimilar cross-weld tests were performed on E911 welded with different consumables and welding processes. Both as-manufactured and service-exposure simulated specimens were tested. Observations of failure locations and creep strength reductions factors permit the determination of long-term design stresses [13].

VESTKRAFT
In the Danish power plant Vestkraft 3 ALSTOM installed in cooperation with ELSAM and EdF three test loops for the testing of advanced materials. The first one was installed in 1995 for temperatures up to 620 °C and the project was partially funded by the EU in the framework of the BRITE-EURAM program [14]. The subsequent two loops for temperatures up to 635 °C and 700 °C were installed respectively in 1998 and 2000. For these two test loops no public funding was requested and the 700 °C loop is a joint cooperation of ELSAM and ALSTOM only. In the 700 °C test loop the following materials are tested:

Martensites:	T24
	T92
	HCM12A

Austenites:	TP347HFG
	Tempalloy A3
	Super304H
	Super304H (shot-blasted)
	HR3C
	NF709
	SAVE25
Ni-Based Alloys:	Alloy 617
	Alloy 4020

The project aims at the investigation of the steam oxidation and the high temperature corrosion resistance of the new materials, as well as the metallographic change of base material and welds after long term operation.

VGB

Tests specimens have been removed from several cast and forged production pieces of the W-free and W-containing 10%Cr steels investigated in COST 501. Compositions of the W-conaining steels correspond closely with that of E911. Statistical evaluation of long-term creep and low cycle fatigue tests provide a reliable estimate of the scatter in mechanical properties, from which design lines can be determined [15].

In addition programmes:

- the European Creep Collaborative Committee has carried out an extensive compilation and evaluation of the long-term creep properties of E911 and its cross-weld properties [16]
- multiaxial creep testing of E911 has been carried out in the LICON project [17]
- the German Steel Application Group P297 has investigated the creep properties of E911 similar welds and has published reduction factors for the cross-weld creep strength [18]

EPRI

This 4 –year programme was directed towards the qualification of new 9 to 12%Cr steels for thick-walled pipes with a better capability than P91 and able to operate up to 620°C [19]. The work involved the fabrication of representative components and long-term mechanical testing of base materials and both similar and dissimilar welds. The results led to the ASME Code Case approval of P92 and P122.

Thermie / Marcko

THERMIE AD700 is a phased long-term project funded by the EU with a very wide participation of European manufacturers, utilities and institutes that started in 1998 and aims at the demonstration of an ultra supercritical coal-fired power plant with parameters of 350 bar and 700/720/720 °C and efficiency of over 50 %. The first phase dealt with the conceptual feasibility and the design of such a power plant and the results gained allowed the continuation into a second phase, started in 2002, where the basic design and testing of critical components for boiler, turbine and piping will be carried out. The project will be completed with the construction and operation of an ultra supercritical coal-fired power plant. Especially for the boiler side evaporator panels for high temperatures will be tested during the current second phase. As mentioned before the waterwall of the boiler is a critical component, when increasing the steam parameters.

Therefore a test evaporator panel made of new materials will be manufactured (with accompanying welding and bending tests) and installed in a Danish power plant owned by ENERGI E2 . After service exposure the test rig will be dismantled and analysed [20].
The MARCKO program focuses on the Alloy 617 and its application for the 700 °C range. The material is known from its application and use in the GT technology. In the framework of MARCKO the composition is optimised in order to achieve a 100 MPa creep rupture strength at 10^5 hours and 730 °C. The project is funded by the German steel research foundation (AVIF) and is carried out by boiler manufacturers (ALSTOM, BBP) and institutes (MPA, TU Stuttgart).

Programme	Activities	Participants	Countries	Duration
COST 501 and 522	Development and qualification of new steels for all key components (water walls, superheaters, pipes and headers) to 650°C	Boilermakers, steelmakers, universities & research institutes	EU	Until 2003
Komet650	Oxidation testing of pipe materials (ferritic and austenitic) in power plant steam bypass at 620 and 650°C	Boilermakers & research institutes	DE/CH	Until 2004
PIPPE	Creep testing of similar and dissimilar (austenitic) welds of steel E911 at 625°C	Boilermaker, utility & steelmaker	UK	Until 2001
VESTKRAFT	Long-term exposure of tube materials to steam oxidation in high temperature superheater sections of steam power plants (2.25%Cr, 12%Cr, nickel alloys)	Boilermaker, utility & research institute	DE/FR/DK /BE/IT	Until 2004
VGB	Long-term mechanical testing of samples from several production pieces of 10%Cr steel (castings and forgings) for statistical analysis	Utilities, turbinemakers, research institutes	DE/CH	Until 2005
EPRI	Manufacture, testing and qualification of P92 and P122 for thick-walled boiler components up to 620°C.	Utilities, boilermakers, steelmakers & research institutes	US	Completed in 2000.
Thermie (EU) & Marcko (DE)	Qualification of materials for water walls, superheaters and thick-walled pipes for reheat temperatures up to 720°C.	Utilities, boilermakers, steelmakers & research institutes	EU	Until 2010
DoE	Qualification of advanced materials for ultra supercritical conditions	EPRI, boilermakers, research institutes	US	Until 2006

Table 2: Ongoing boiler materials development programmes

Department of Energy (DoE) Project

Recently the DoE started an advanced Materials Programme having the following objectives:

- Identify limiting materials performance issues
- Identify improved alloys, fabrication processes and coating methods for steam temperature up to 760 °C
- Lay groundwork for ASME approval
- Define issues to reach 870 °C

The duration of the program will be five years (2001-2006) and will be funded by DoE with 21 M US$. It will be carried out by a consortium coordinated by EPRI and including the major American boilermakers (ALSTOM, B&W, FW, BBP).

As described above and summarised in Table 2, the programmes differ significantly in terms of the specific aims, activities, types of participants involved (industrial, academic, research institutes, etc.), national involvement and source of financing (national, European or private), but nonetheless complement one another in terms of generating all information required for application of the new materials.

Status of the COST 522 Boiler Programme

The COST 501 boiler materials programme was focussed primarily on testing and qualification of the thick-walled pipe material E911 (in comparison with P92). E911 is now in operation at temperatures up to 600°C.
For COST 522 the temperature targets were raised by a further 25 to 50 °C. Major efforts are on

1) validation of T/P23 for higher application temperatures, both for water walls and thick-walled pipes
2) new 11 to 12%Cr steels with a good combination of creep strength and oxidation resistance
3) new more economical austenitic steels with good creep strength and oxidation resistance.

The participants in the boiler and welding groups are shown in Table 3 along with their primary activities:

- manufacturing of steel bars or pipe/tube components
- production of welding consumables or welded joints
- mechanical testing of as-received or thermally exposed material
- steam oxidation and corrosion testing.

T/P23
Creep and other mechanical properties of thin-walled tube material are well documented. In order to determine the permissible area of application of T/P23, it was considered necessary

- to manufacture thicker walled material to verify that mechanical properties are still acceptable
- to manufacture similar welds and dissimilar welds (to P91) and subject them to mechanical testing
- to carry out steam oxidation testing to ensure this does not limit high temperature applications.

Continuous Cooling Transformation (CCT) diagrams, such as the one shown in Figure 5, are used as the basis for determining heat treatment schedules. They permit the determination of the minimum cooling rate (appropriate quenching methods) from the austenitising temperature and hence the maximum pipe wall thicknesses which can be produced without the occurrence of ferrite / pearlite in the microstructure. Such heat treatment simulation trials have been performed within the COST 522 programme for material produced by Vallourec & Mannesmann.

Table 3 shows that 43 partners from 16 European countries are involved, i.e. 6 boilermakers, 2 utilities, 10 suppliers of steel melts, tubes and pipes and 25 universities and testing organisations.

Partner	Country	Material supply	Welding	Mechanical Testing	Thermal Exposure	Oxidation / Corrosion
Technical University, Graz	AT		X	X		
Belgian Group : BWI, Laborelec	BE		X	X		
Skoda Research	CZ			X		
Czech Academy of Science, Brno	CZ			X		
Vitkovice Research and Development	CZ			X		
SVUM, Prague	CZ			X		
Vallourec & Mannesmann – Germany	DE	X		X		
Fraunhofer Institute, Freiburg	DE			X		
Siemens, Mülheim	DE			X	X	
Research centre, Jülich	DE					X
Alstom Power, Stuttgart and Baden	DE/CH		X	X	X	X
Babcock-Borsig Power, Oberhausen	DE			X		
Oerlikon Welding Technology, Eisenberg	DE	X				
Böhler Thyssen Welding Technology, Hamm	DE	X				
Siempelkamp, Dresden	DE			X		X
MPA, Stuttgart	DE			X		
ELSAM / ENERGY E2, Lyngby	DK			X		
Institute Technology Aerospace, Madrid	ES			X		X
EDF, Moret sur Loing	FR			X		
Vallourec & Mannesmann – France	FR	X		X		
Tampere University of Technology, Tampere	FI			X		
VTT Manufacturing Technology,	FI			X		X
Metso Powdermet, Tampere	FI	X		X		
Technical University of Budapest	HU			X		
Centro Sviluppo Materiali, Rome	IT			X		
Ansaldo Ricerche, Genova	IT			X		X
CESI, Milano	IT			X		X
Dalmine	IT	X				
Dutch Group: KEMA, TNO	NL			X		X
Krakow University of Technology	PL			X		
Instutute for Ferrous Metallurgy, Gliwice	PL			X	X	
Institute of Welding, Gliwice	PL		X	X	X	
RAFAKO, Raciborz	PL		X	X		
Sandvik Steel, Sandviken	SE	X				
Welding Research Intitute, Bratislava	SK		X	X		
SES, Tlmace	SK		X	X		
Mitsui-Babcock Energy, Renfrew	UK			X		
TWI, Abington	UK		X			
Corus Group, Rotherham	UK	X		X		
National Physical laboratory, Teddington	UK					X
Powergen, Ratcliffe-on-Soar	UK			X	X	
Esab Group, Waltham Cross	UK	X	X			
Metrode Products, Chertsey	UK	X	X			

Table 3: Participants in the COST 522 Groups Boiler Materials and Welding

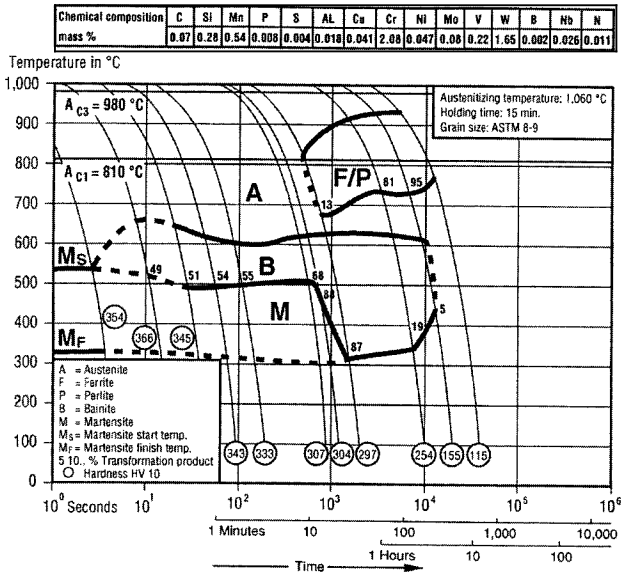


Fig. 5: Continuous Cooling Transformation diagram for T/P23.

In addition pipes with both 30 and 47mm wall thickness have been manufactured and mechanically tested. Chemical composition and mechanical properties were in accordance with the ASTM Code Case 2199. Heat treatment was with austenitising at 1050-1060°C followed by water quenching and tempering for 1 or 2 hours at 760-770°C. There is little effect of wall thickness on tensile properties, with all values lying above the prescribed minima. As shown in Fig 6, impact energy is also rather insensitive to wall thickness and heat treatment schedule.

For welding trials P23 (and P91) with the nominal dimensions 219mm OD and 30mm wall thickness was manufactured by Vallourec & Mannesmann (France) and provided to the partners for further mechanical testing and welding trials. Similar welds have been manufactured with matching (P23) consumables and dissimilar welds have been produced both with low alloy (P23) and high alloy (P91) consumables. Both GTAW and SMAW procedures have been employed. Post-weld heat treatment of 2 hours at 750°C has been used. Tensile, impact, creep and long-term thermal exposure tests up to 10'000 hours are ongoing. Fig. 7 shows results of impact energy measurement made at room temperature for the 2.25%Cr 15%Mo 0.25%V, 1.5%W weld metal compared with that with 9%Cr1%Mo weld metal.
For the former the impact energy is lowest in the HAZ of the P91, but even here it lies in the acceptable range. Use of the P91 weld metal, as required by German standards, leads to very low impact energy values in the weld metal. Values can be increased by increasing the temperature or time in the PWHT, but then weld metal strength values may fall below acceptable minimum values. An improvement can also be achieved through attention to the oxygen and nitrogen levels in the weld metal.

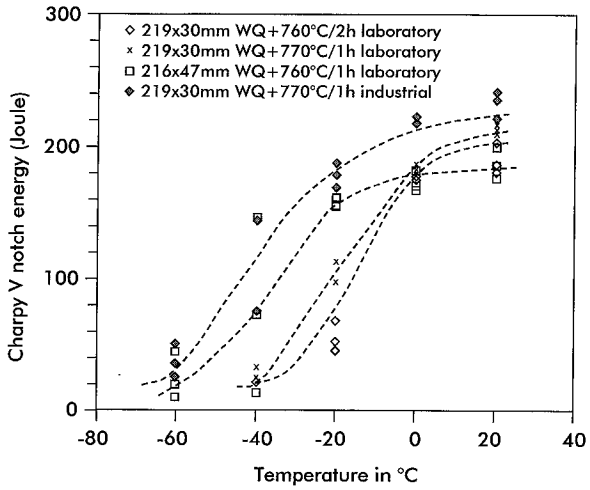


Fig.6: Charpy impact energy of P23 for different wall thicknesses and heat treatment schedules

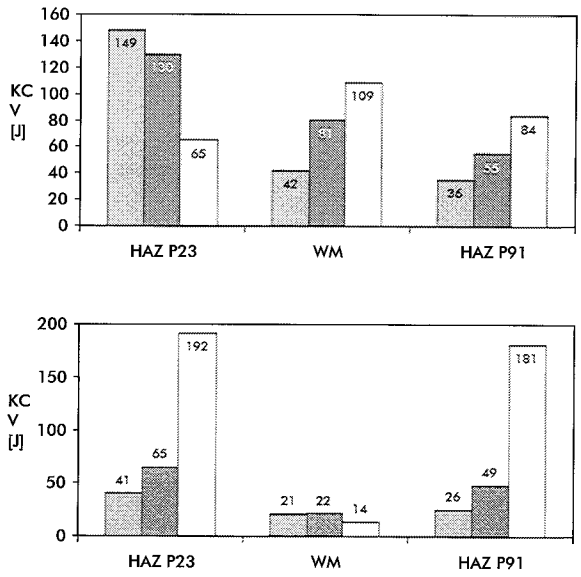


Fig.7: Impact energy results of investigation of dissimilar P23-P91 welds (top: 2.25% Cr weld metal/bottom: 9% Cr weld metal)

Weld simulation trials are also ongoing to study the different regions of the heat affected zone.

Complementary tests are ongoing in the ECCC programme on P23, using material of 360mm OD and 60mm wall thickness from Sumitomo. Testing is being performed for base material and cross-weld specimens.

As shown in Table 3, steam oxidation testing is being performed in several laboratories under carefully controlled conditions. The effects of temperature, time, pressure and flow rate are being investigated on the growth rate and spalling tendency of the oxide layers. Consistency between the testing laboratories was first ensured by round-robin testing in which each laboratory performing oxidation tests on samples from a single batch of P92 material.
The proceedings of this conference also contain 5 further individual contributions from the COST 522 programme and 2 further contributions from Japan on steels of the 2.25%Cr class.

New 11 to 12%Cr Steels
Chemical compositions of steels have been proposed based on the results of oxidation and mechanical tests of other steels in this group and on predictions made on the basis of the alloy design principles described above. Further account is taken of the Ac_1 temperature, which should be as high as possible, and of the position of the steel in the Schäffler Diagram, which should ensure freedom from significant amounts of δ ferrite. Several small melts have been produced by Vallourec & Mannesmann and by Corus. All contain at least 11%Cr to promote oxidation resistance along with Co of up to 3% to reduce the tendency to δ ferrite formation. Ni and Mn contents are in all cases each below about 0.5%. Specific differences in W (0 to 2%) and Mo (0.3 to 1.5%) are under investigation. Similarly B content is varied systematically. Al content is generally low. Compositions are given in Table 4.

11%Cr Steels		Chemical Composition (wt.%)												
		C	Si	Mn	Ni	Cr	Mo	W	Co	V	Nb	Al	B	N
Designation	Manufacture													
A	V&M	0.19	0.10	0.50	0.20	11.6	1.48	-	-	0.26	0.06	0.005	0.003	0.015
B	V&M	0.18	0.10	0.51	0.25	11.5	1.48	-	-	0.26	0.06	0.010	0.004	0.047
C	V&M	0.16	0.09	0.53	0.26	11.2	1.46	-	0.90	0.25	0.05	0.012	0.006	0.063
D	V&M	0.16	0.10	0.50	0.26	11.4	1.48	-	1.06	0.25	0.06	0.008	0.012	0.063
E	V&M	0.13	0.10	0.49	0.28	11.3	1.44	-	3.06	0.25	0.06	0.010	0.007	0.051
F	V&M	0.12	0.49	0.35	0.29	11.5	0.29	1.50	1.62	0.26	0.05	0.008	0.005	0.065
G	V&M	0.14	0.29	0.49	0.18	11.4	1.30	-	1.53	0.24	0.05	0.005	0.007	0.072
BGF1	Corus	0.16	0.15	0.09	0.14	11.0	1.04	0.32	2.12	0.26	0.06	0.008	0.009	0.059
BGF2	Corus	0.16	0.30	0.22	0.43	11.1	1.04	0.32	2.16	0.27	0.07	0.007	0.011	0.060
BGF3	Corus	0.17	0.35	0.22	0.44	11.2	0.50	2.10	2.15	0.26	0.07	0.007	0.009	0.063
BGF4	Corus	0.18	0.36	0.21	0.43	11.0	1.03	0.33	2.15	0.35	0.03	0.006	0.008	0.078

Table 4: Nominal compositions of new 11%Cr steels under investigation in the COST 522 programme.

The positions of the steels in the Schäffler diagram [3] are shown in Fig. 8.

Longest creep and thermal exposure tests of the new melts have reached durations of up to 15'000 hours. The most promising melts show creep rupture strength values in the upper part of the scatterband for E911 and oxidation resistance is expected to be better on account of the significantly higher Cr content. Steam oxidation and fireside corrosion tests are in progress.

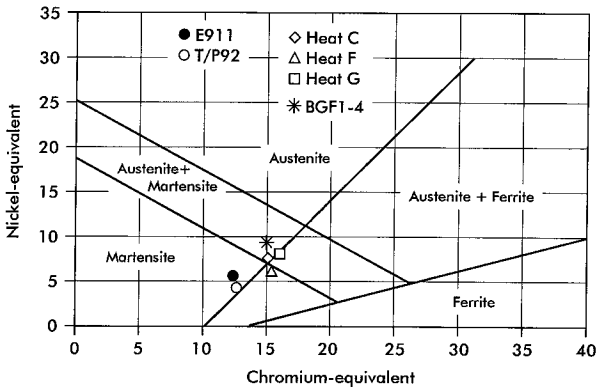


Fig.8: Positions of new 11%Cr steels in the Schäffler diagram (modified by H.Schneider)
Cr_{Eq} = Cr + 2Si + 1.5Mo + 5V + 5.5Al + 1.75Nb + 1.5Ti + 0.75W
Ni_{Eq} = Ni + Co + 0.5Mn + 3'0C + 0.3Cu + 25N

20ton melts of the steels F and G have already been manufactured and testing has started. It is proposed to manufacture an 80 ton melt before the end of 2002. Pipe manufacturing and weld tests will be started shortly on the variants which show the best combination of long-term creep strength, resistance to embrittlement and oxidation resistance.

The proceedings of this conference also contain 25 further contributions from the COST 522 programme, 3 contributions from other European projects and 21 contributions from Japan on steels of the 10-12%Cr class.

New Austenitic Steels

Four new austenitic steels have been manufactured by Corus with a base composition similar to that of Esshete 1250 but with increased content of Cr to improve oxidation resistance and in certain cases with addition of Cu. Melts have been produced and rolled down to bar. Heat treatment is as for Esshete 1250 (1100°C/20min./air cool). ASTM grain size is 8 to 10 and the δ ferrite content is <0.5%. A fine dispersion of second phase particles is seen in the matrix.
NF709 and Esshete 1250 will be taken as reference material in order to judge the success of the new materials in terms of reduced costs and improved properties. Compositions are given in Table 5.

Creep screening tests have reached durations of up to 5'000 hours. Steam oxidation and fireside corrosion tests are in progress.Again pipe manufacturing and weld tests will be started on the variants which show the best combination of long-term creep strength, resistance to embrittlement and oxidation resistance.

Austenitic Steels		Chemical Composition (wt.%)											
		C	Si	Mn	Ni	Cr	Mo	W	Cu	V	Nb	B	N
Designation	Manufacture												
BGA1	Corus	0.11	0.64	6.3	15.2	23.1	1.0	-	-	0.29	0.19	0.005	0.095
BGA2	Corus	0.11	0.54	9.7	13.0	23.2	1.0	-	-	0.30	0.57	0.005	0.180
BGA3	Corus	0.11	0.55	6.2	15.0	23.1	1.0	-	3.0	0.30	0.57	0.006	0.180
BGA4	Corus	0.10	0.54	6.1	14.9	22.8	0.2	1.4	3.0	0.29	0.57	0.006	0.190

Table 5: Nominal compositions of new austenitic steels under investigation in the COST 522 programme.

The proceedings of this conference also contain 4 further contributions from European projects and 2 contributions from Japan on austenitic steels.

Conclusions and Outlook

The increase of the efficiency and the reduction of both fuel costs and CO_2 emissions are directly linked with the increase of the steam parameters of coal-fired power plants and consequently with the use of advanced materials. The critical boiler components were identified as the waterwall, the last stages of the superheater and reheater heating surfaces and the thick-walled components, such as headers and connecting pipes. COST 522 addresses material issues for these critical components that can cover temperatures up to 620 °C. Not only mechanical properties, such as creep rupture strength, are addressed, but also fabricability and weldability aspects, as well as steam oxidation at high operating temperatures. For a further major increase in the steam parameters the use of Ni-based alloys for some critical components seems inevitable.

With coal reserves currently forecast to last four times longer than those of oil and gas and with a secure supply structure, coal is expected to increase its share in electricity production worldwide. This expectation is enhanced by the advantages pulverised coal-fired power plant technology offers, such as the high level of availability and operational flexibility, the high efficiency and the low generation costs.
Through efficiency increase and application of Clean Coal Technologies coal-fired power plants can make a major contribution in the reduction of CO_2 and other primary pollutants. In the context of efficiency increase the development of advanced materials for ultra supercritical conditions is of crucial importance and will be systematically pursued also in the future by power plant manufacturers.

Acknowledgements

The authors would like to thank the Management Committee of the COST 522 action for their support and the national funding bodies for their financial contributions.

References

[1] W.A.Benesch, Planning new coal-fired power plants, VGB Power Tech, 6/2001, p.37-44.

[2] K.Wieghardt, T.U.Kern, Design and materials for turbosets in advanced steam power plants, 7th Liege Conference on Materials for Advanced Power Engineering 2002, 29th Sept. – 2nd Oct. 2002.

[3] W.Bendick, J.Gabrel, J.C.Vaillant, B.Vandenberghe, Development of a new 12%Cr steel for tubes and pipes in power plants with steam temperatures up to 650°C, Liege conference on Materials for Advanced Power Engineering 2002, 29th Sept. – 2nd Oct. 2002.

[4] Z.Kubon, V.Foldyna, V.Vodarek, Optimised chemical composition of 9-12%Cr steels with respect to maximum creep resistance, 6th Liege COST Conference on Materials for Advanced Engineering 1998, p. 311-320.

[5] K.Kimura, H.Kushima, F.Abe, K.Suzuki, S.Kumai, A.Satoh, Microstructural change and degradation behaviour of 9Cr-1Mo-V-Nb steel in the long term, Parsons 2000, Advanced Materials for 21st century turbines and power plant, 3-7 July 2000, p.590-602.

[6] S.H.Ryu, J.Yu, B.S.Ku, Effects of alloying elements on the creep rupture strength of 9-12%Cr steels, ibid, p. 472-484.

[7] W.Blum, S.Straub, P.Polcik, K.-H.Mayer, Quantitative investigation of microstructural evolution of two melts of the martensitic rotor steel X12CrMoWVNbN 10 1 1 during long-term creep, VGB Power Tech 4/2000, 59-66.

[8] M.Morinaga, R.Hashizume, Y.Murata, An electronic approach to the deign of ferritic steels for power plants, 5th Liege COST Conference, Materials for Advanced Power Engineering 1994, P.319-328.

[9] B.Sundmann, in F.H.Hayes ed., User aspects of phase diagrams, Institute of Metals, London, 1991, p.130.

[10] J.O.Anderson, L.Höglund, B.Jönnson, J.Angren, Fundamentals and applications of ternary diffusion, ed. By G.R.Purdy, Pergamon Press, New York, (1990), p-153.

[11] M.Staubli, W.Bendick, J.Orr, F.Deshayes, C.Henry, European collaborative evaluation of advanced boiler materials, 6th Liege COST Conference, Materials for Advanced Power Engineering 1998, p.87-103.

[12] C.Köster, P.Moser, H.Bergmann, J.Jacobs, VGB Power Tech 9/2000, p.64.

[13] D.J.Allen, A.Fleming, Creep performance of similar and dissimilar E911 steel weldments for advanced high temperature plant, Parsons 2000, Advanced Materials for 21st century turbines and power plant, 3-7 July 2000, p.276-290.

[14] R.Blum, Q.Chen, C.Coussement, J.Gabrel, C.Testani, L.Verelst, Operational tests of superheater materials at high steam temperatures in a hard coal fired steam generator, VGB Power Tech 10/2001, p.86-91

[15] K.H.Mayer, T.U.Kern, M.Staubli, E.Tolksdorf, Long-term investigation of specimens of 24 production components manufactured from advanced martensitic 10%Cr steels for 600°C turbines, Parsons 2000, Advanced Materials for 21st century turbines and power plant, 3-7 July 2000, p.372-385.

[16] D.V.Thornton, Activities of the European creep collaborative committee, Parsons 2000, Advanced Materials for 21st century turbines and power plant, 3-7 July 2000, p.123-128.

[17] P Auerkari, S R Holdsworth, J H Rantala, R C Hurst, C Coussement & R Hack; 'Modelling the development of creep damage', Proc. Baltica Conf. on Condition and Life Management for Power Plants, Helsinki, June 2001.

[18] H.Heuser, W.Bendick, B.Melzer, M.Zschau, H.Cerjak, E.Letofsky, Determination of the long-term properties of matching weld metals for creep resistant steels, Research report of German Steel Application Group P297, Dec.2000 (in German).

[19] E.Metcalfe and W.T.Bakker, EPRI project RP1403-50 "Advanced 9Cr/12Cr materials for thick section boiler components", EPRI/National Power Conference 11th May 1995, London p.1-7.

[20] Kjaer, S.; Klauke, F.; Vanstone, R.; Zeijseink, A.; Weissinger, G.;Kristensen, P.; Meier, J.; Blum, R.; Wieghardt, K. : The advanced supercritical 700 °C pulverised coal-fired power plant, Power-Gen Europe 2001, Brussels, Belgium

MATERIALS FOR ULTRA-SUPERCRITICAL COAL-FIRED POWER PLANT BOILERS

R. Viswanathan
EPRI
3412 Hillview Avenue
Palo Alto, CA 94304
Ph/Fax: (650) 855-2450/x1026
E-mail: rviswana@epri.com

R. Purgert
Energy Industries of Ohio
Park Center, Suite 200
6100 Oak Tree Blvd.
P.O. Box 31274
Independence, OH 44131
Ph/Fax: (216)-2952/2901
E-mail: Purgert@msn.com

U. Rao
USDOE, NETL
626 Cochrans Mill Road
P.O. Box 10940
Pittsburgh, PA 15236-0940
Ph/Fax: (412) 386-4743/x5917
E-Mail: Rao@netl.doe.gov

Abstract

The U.S. Department of Energy (DOE) and the Ohio Coal Development Office (OCDO) have recently initiated a project aimed at identifying, evaluating, and qualifying the materials needed for the construction of the critical components of coal-fired boilers capable of operating at much higher efficiencies than current generation of supercritical plants. This increased efficiency is expected to be achieved principally through the use of ultra-supercritical steam conditions (USC). The project goal is to increase the main steam temperature initially to 760°C (1400°F), while attention also is given to identifying the materials issues involved in service at temperatures up to 870°C (1600°F) in the longer term. The project is intended to complement alloy development and evaluation programs now being carried out in Europe and Japan. Those programs have identified ferritic steels capable of meeting the strength requirements of USC plants to approximately 620°C (1150°F) and nickel base alloys suitable up to 732°C (1350°F). In this project, the maximum temperature capabilities of these and other available high-temperature alloys are being assessed to provide a basis for materials selection and application under a range of conditions prevailing in the boiler, for 38.5 MPa/760°C (5500 psi/1400°F) main steam conditions. This paper provides a brief review of current alloy capabilities and describes the scope of the DOE/OCDO sponsored projects.

Keywords: Efficiency, Boilers, Ultra supercritical, Materials, Coal

1.0 Introduction and Background

The goal of improving the efficiency of pulverized coal (PC) power plants, by increasing the temperature and pressure of the working fluid (steam) has been pursued for many decades. Table 1 illustrates actual or expected efficiencies corresponding to various steam cycles. The goal for increased efficiencies has acquired special urgency due to environmental and global warming concerns in recent years. The U.S. Department of Energy has identified this as a key component of their clean coal technologies in their Vision 21 plans. A major challenge in constructing ultra-supercritical (USC) plants has been in the area of materials technology. While materials suitable for metal temperatures up to 565°C (1050°F) were available even 20 years ago, further developments were needed to achieve 593°C (1100°F) and beyond. Intense R&D efforts were carried out in Japan, USA and Europe with an intermediate goal of 620-630°C (1150°F-1166°F)/30 MPa (4200 psi). More recently, the Thermie project in Europe has been addressing 700°C (1297°F) 37.5 MPa (5400 psi) main steam conditions.[1] This has been partly made possible by some very exciting progress in developing highly creep resistant 9 to 12%Cr ferritic steels and some Ni base alloys. The objective of this paper is to review developments in materials technology related to boilers and to describe the scope of a new project sponsored by OCDO and the USDOE. Detailed reviews of materials for supercritical boilers may be found in References 2–7.

2.0 Boiler Materials Requirements

The key components whose performance is critical for ultra-supercritical (USC) plants are high-pressure steam piping and headers, superheater tubing and waterwall tubing. Steam pipes carry high-pressure high-temperature steam from the boiler to the turbine. Headers are also pipes, but contain numerous tube penetrations which either bring in/take out steam to/away from the header. Since they operate at high temperatures, these components have to meet creep strength requirements. In addition, pipes and headers, being heavy section components, are subject to fatigue induced by thermal stresses. Ferritic/martensitic steels are preferred because of their lower coefficient of thermal expansion and higher thermal conductivity compared to austenitic steels. Many of the early problems in the USC plants were traceable to the use of austenitic steels which were very prone to thermal fatigue. Research during the last decade has, therefore, focused on developing cost-effective, high-strength ferritic steels that could be used in place of austenitic steels. This has resulted in ferritic steels capable of operating at metal temperatures up to 620°C (1150°F), with good weldability and fracture toughness.

Superheater and reheater (SH/RH) tubing application calls for high creep strength, thermal fatigue strength, weldability, resistance to fireside corrosion/erosion and resistance to steamside oxidation and oxide spallation. Thermal fatigue resistance as well as cost considerations would dictate the use of ferritic/martensitic steels. Unfortunately, the strongest of these steels which can be used up to metal temperature of 620°C (1150°F)*, purely from a creep strength point of view, are still further limited by fireside corrosion to metal temperature of 593°C (1100°F). This

* All temperatures cited in the paper are steam temperatures unless otherwise specified. For header and piping, metal temperature is nearly equal to the steam temperature. For tubing, the metal temperature is generally higher than the steam temperature by up to 28°C (50°F).

Table 1
Estimated Plant Efficiencies for Various Steam Cycles
(Ref. P. Weitzel and M. Palkes)*

		Efficiency Net HHV	
Description	Cycle	Reported at European Location (LHV/HHV)	Converted to U.S. Practice[4] HHV
Subcritical	16.8 MPa/538°C/538°C[3]		37
Supercritical	24.5 MPa/565°C/565°C/565°C[3]		40.9
ELSAM (Nordjylland 3)	28.9 MPa/580°C/580°C/580°C	47/44	42
State of the Art Supercritical (LEBS)	31.5 MPa/593°C/593°C/593°C[3]		42.3
EPRI/Parson	35 MPa/649°C/649°C/649°C		42.7
Thermie	38 MPa/700°C/720°C/720°C	50.2/47.7	46.43
EPRI/Parson	37.8 MPa/700°C/700°C/700°C		44
DOE/OCDO USC Project	38.5 MPa/760°C/760°C 38.5 MPa/760°C/760°C/760°C		46.5 47.5–48

3. Eastern bituminous Ohio coal. Lower Heating value, LHV boiler fuel efficiency is approximately 4.2% higher than higher heating value, HHV boiler fuel efficiency. For example, an LHV net plant heat rate at 6205.27 Btu/kWh with the LHV net plant efficiency of 55% compares to the HHV net plant heat rate at 6494.85 Btu/kWh and HHV net plant efficiency of 52.55%.
4. Reported European efficiencies are generally higher compared U.S. due to differences in reporting practice (LHV vs HHV), coal quality, auxiliary power needs, condenser pressure and ambient temperature and many other variables. Numbers in this column for European project numbers are adjusted for US conditions to facilitate comparison.

* Personal communication from Paul Weitzel, Babcock & Wilcox, Barberton, OH and Mark Palkes, Alstom Power Co., Windsor, CT, May 24, 2002.

corresponds to a steam temperature of about 565°C (1050°F) since SH/RH metal temperature can exceed the steam temperature by as much as 28°C (50°F) to 39°C (70°F). Excessive corrosion of ferritic steels caused by liquid iron-alkali sulfates in the tube deposits is an acute concern in the USA, where high sulfur corrosive coals are used more frequently than elsewhere. Therefore high strength ferritic steels such as T-91 are infrequently used in the U.S. The standard practice in conventional plants is to use T-22 for the lower temperatures and SS304H or SS347 for the highest temperatures.

With respect to waterwall tubing, the concern is twofold. High supercritical pressures and the use of high heat release furnaces will increase the waterwall temperatures to the point that easily

weldable low alloy steels such as T-11* (1.25Cr, 0.5Mo) have insufficient creep strength. Higher strength steels such as T-91 are available, but require postweld heat treatments. The second concern is corrosion. Recent results in the USA on boilers retrofitted with low NOx burner systems, using overfire air, indicate that the present low alloy steels can suffer from excessive corrosion, as high as 2 mm/yr. Weldable high strength alloys clad or overlaid with high Cr alloys have to be utilized to reduce or eliminate excessive corrosion[2].

2.1 Historical Evolution of Steels

Masuyama has presented an excellent historical perspective on the development of steels for power plants as shown in Table 2[8]. The table shows 10^5h creep rupture strength at 600°C (1112°F) by year of development and classifies the ferritic steel development in terms of 4 generations.[8] His paper serves as a key resource for industry and has been used extensively in preparing this paper.

In the field of austenitic steels, efforts were made from the 1970's to the early 1980's to improve conventional 18Cr-8Ni series steels originally developed as corrosion resistant materials for chemical use, mainly with respect to their creep strength. Another goal pursued from the 1980's to the early 1990's was to improve the creep strength of conventional 20-25Cr series steels having superior oxidation and corrosion resistance.

2.1.1 Evolution of Ferritic Steels

Ferritic steel developments are mostly aimed at their use for thick section pipes and headers. Table 3 shows the chemical compositions of ferritic steels for power boilers.[8] The systematic evolution of these steels has been thoroughly reviewed by Masuyama, as shown in Figure 1[8]. Among the most recent 9%Cr steels fully commercialized, the P91 steel has been used as a material for headers, steam pipes and superheater tubes in supercritical plants operating up to 593°C (1100°F). Alloy NF616 (P-92), developed by substituting part of the Mo in P91 by W, has an even higher allowable stress and can be operated up to temperatures of 620°C (1150°F) purely from creep considerations. E911 is a European alloy similar in composition to NF616 with similar capabilities. Oxidation and fireside corrosion may limit their application still further.

Among the 12%Cr steels, HT91 has been widely used for tubing, headers and piping in Europe. Use of the steel in Japan and US has been limited due to its poor weldability. HCM12 is an improved version of HT91 with 1% W and 1% Mo, having a duplex structure of δ-ferrite and tempered martensite with improved weldability and creep strength. Further increases in creep strength by substituting more of the Mo with W and addition of Cu has resulted in alloy HCM12A (P-122), which can be used for header and piping up to 620°C (1150°F). It has capabilities similar to P92, with slightly increased resistance to steam oxidation due its higher chromium content. Two alloys NF12 and SAVE12 having an even higher creep strength than HCM12A are in the developmental stage. NF12 contains 2.5%Co, 2.6%W and slightly higher B compared to HCM12A. SAVE12 contains 3% Co, 3% W, and minor amounts of Ta and Nb. These latter elements contribute to strengthening by producing fine and stable nitride precipitates. HCM2S (T-23) a low carbon 2-1/4Cr-1.6W steel with V and Nb is a cost-effective steel with

* ASME boiler code steel designation, equivalent pipe steels are designated as P-11, 92, etc., while forgings are designated F-11, 91, etc.

Table 2
Evolution of Four Generations of Ferritic Steels (Based on Reference 8)

Generation	Years	Alloy Modifications	Strength 10^5 hr Creep Rupture Achieved MPa at 600°C	Example Alloys	Maximum Metal Use Temp. °C*
1	1960-70	Addition of Mo or Nb, V to simple 12Cr and 9Cr Mo steels	60	EM12, HCM9M, HT9, Tempaloy F9, HT91	565
2	1970-85	Optimization of C, Nb, V	100	HCM12, T91, HCM2S	593
3	1985-95	Partial substitution of W for Mo	140	P-92, P-122, P-911 (NF616, HCM12A)	620
4	Emerging	Increase of W and addition of Co	180	NF12, SAVE12	650

*Based on 100 MPa/10^5h

Table 3
Nominal Chemical Compositions of Ferritic Steels for Boiler (8)

	Steels	Specification		Chemical Composition (mass%)											
		ASME	JIS	C	Si	Mn	Cr	Mo	W	Co	V	Nb	B	N	Others
2Cr	T22 (2.25Cr–1Mo)	T22	STBA24	0.12.	0.3	0.45	2.25	1.0	–	–	–	–	–	–	–
	HCM2S (2.25Cr–1.6WVNb)	T23	STBA24J1	0.06	0.2	0.45	2.25	0.1	1.6	–	0.25	0.05	0.003	–	–
9Cr	T9(9Cr–1Mo)	T9	STBA26	0.12	0.6	0.45	9.0	1.0	–	–	–	–	–	–	–
	HCM9M(9Cr–2Mo)	–	STBA27	0.07	0.3	0.45	9.0	2.0	–	–	–	–	–	–	–
	T91(9Cr–1MoVNb)	T91	STBA28	0.10	0.4	0.45	9.0	1.0	–	–	0.20	0.08	–	0.05	–
	NF616(9Cr–0.5Mo–2WVNb)	T92	STBA29	0.07	0.06	0.45	9.0	0.5	1.8	–	0.20	0.05	0.004	0.06	–
	Tempaloy F–9(9Cr–1MoVNb)	–	–	0.06	0.5	0.60	9.0	1.0	–	–	0.25	0.40	0.005	–	–
	EM12 (9Cr–2MoVNb)	(NFA49213)	–	0.10	0.4	0.10	9.0	2.0	–	–	0.30	0.40	–	–	–
12Cr	HT91(12Cr–1MoV)	(DIN X20CrMoV121)	–	0.20	0.4	0.60	12.0	1.0	–	–	0.25	–	–	–	0.5Ni
	HT9(12Cr–1MoWV)	(DIN X20CrMoWV121)	–	0.20	0.4	0.60	12.0	1.0	0.5	–	0.25	–	–	–	0.5Ni
	HCM12(12Cr–1Mo–1WVNb)	–	SUS410J2TB	0.10	0.3	0.55	12.0	1.0	1.0	–	0.25	0.05	–	0.03	–
	HCM12A(12Cr–0.4Mo–2WCuVNb)	T122	SUS410J3TB	0.11	0.1	0.60	12.0	0.4	2.0	–	0.20	0.05	0.003	0.06	1.0Cu
	NF12(11Cr–2.6W–2.5CoVNbB)	–	–	0.08	0.2	0.50	11.0	0.2	2.6	2.5	0.20	0.07	0.004	0.05	–
	SAVE12(11Cr–3W–3CoVNbTaN)	–	–	0.10	0.3	0.20	11.0	–	3.0	3.0	0.20	0.07	–	0.04	0.07Ta 0.04Nd

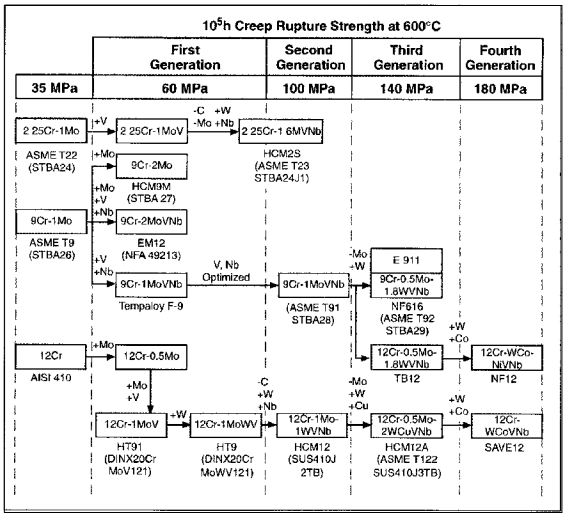


Figure 1
Evolution of ferritic steels for boilers[8]

higher creep strength than T22. Because of its excellent weldability without pre- or post-weld heat treatment it is a good candidate for waterwall tubing.

2.1.2 Evolution of Austenitic Steels

Austenitic steels have been used primarily in the finishing stages of superheater/reheater tubing, where, oxidation resistance and fireside corrosion become important in addition to creep strength. From a creep strength point of view, T91 is limited to 565°C (1050°F) steam (metal 593°C [1100°F]) and NF616, HCM12A and E911 are limited to 593°C (1100°F) steam (metal 620°C [1150°F]). Even the strongest ferritic steel today is limited to 593°C (1100°F) (metal temperature) from an oxidation point of view. At temperatures above these, austenitic steels are required. Hence there has been considerable development with respect to austenitic stainless steels. In conventional plants in the U.S. SS304H and SS347 are widely used instead of T-91 in superheater applications, mainly because they are easier to weld, while the cost difference is relatively small.

Table 4 includes a list of the compositions of various high strength stainless steels for SH/RH tube applications. The steels fall into four categories: 15Cr, 18Cr, 20-25Cr and higher Cr stainless steels. The various stages in the evolution of these steels have consisted of initially adding Ti and Nb to stabilize the steels from a corrosion point of view, then reducing the Ti and Nb content (understabilizing) to promote creep strength rather than corrosion, followed by Cu

additions for increased precipitation strengthening by fine precipitation of a Cu rich phase, and heat treatment modifications. Further trends have included austenite stabilization using 0.2% nitrogen and W addition for solid solution strengthening. This development sequence is illustrated in Figure 2[8]. The highest creep strength is achieved in SAVE 25, but the fireside corrosion resistance of the alloy is controversial.

2.2 Choice of Materials for Headers and Steam Pipes

Material-property requirements for headers and steam pipes are likely to be similar, and hence they have been grouped together. Some minor differences exist which may affect material selection. The steam temperature is likely to be much more uniform in steam pipes, but subject to time-dependent and location-dependent fluctuations in headers. Hence, the thermal-fatigue-strength requirements are greater for headers than for steam pipes. Self-weight-induced stresses are less important for headers than for steam pipes, permitting heavier-wall construction and an attendant higher temperature/pressure capability for a given material when used in headers. One of the most important differences is that headers have many welded attachments to inlet stub tubes from reheaters and superheaters and intersections of outlet nozzles connecting pipework. Depending on the selection of materials for the superheater/reheater tubes and the header piping, dissimilar-metal welded joints may be required. The integrity of such austenitic-to-ferritic welds when 9 to 12%Cr steels form the ferritic components needs to be more thoroughly investigated.

Headers and pipes have traditionally been made from low alloy steels such as P11 and P22 in the USA. Even in conventional boilers, such headers can fail due to thermal fatigue cracking, caused by cycling. A common failure mode is the cracking of the ligaments between the tube boreholes[9]. The use of higher temperatures and pressures can only increase the problem. Previous attempts to use austenitic steels have not been successful due to high thermal expansion of these steels.

As shown in Table 2 ferritic steels can be used up to the temperature limits indicated. The most creep resistant steels, P92, P122 and P911 can be used for heavy section applications up to 620°C (1150°F), although steamside oxidation may lower their applicability to lower temperatures. At temperatures exceeding 620°C (1150°F) and up to about 675°C (1250°F) austenitic steels may be needed. Beyond 675°C (1250°F) up to 788°C (1450°F) nickel base alloys may be used.

Figure 3 shows a plot of the allowable stress at various temperatures for ferritic steels[8]. The figure clearly shows the enormous advances in the materials technology which have been made in the last 20 years. Especially at the higher temperatures, the most advanced steels show allowable stresses that are nearly 2.5 to 3 times that of the workhorse steel in conventional plants, i.e., 2-1/4Cr-1Mo steel (P22). The layering of the alloys into the different generations described earlier is also evident. HCM12A (P122), NF616 (P92) and E911 emerge as the three highest strength alloys suitable for ultra supercritical plants up to 620°C, followed by T91, HCM12, EM12 and HT91 suitable for intermediate temperatures up to 593°C (1100°F) followed by T22 for use up to 565°C (1050°F). NF12 and SAVE12 are still developmental. Alloy HCM2S has much higher strength than P22, is weldable and therefore suitable for application as a replacement for P22. More recently, Fujita has reported on a modified version of NF12 with aluminum content below 20 ppm and Ni content below 0.1%, which has creep properties higher than NF12. This alloy is believed to have adequate strength for 650°C applications [10].

Table 4
Nominal Chemical Compositions of Austenitic Steels for Boiler (mass %) (8)

	Steels (JIS)	C	Si	Mn	Ni	Cr	Mo	W	V	Nb	Ti	B	Others
18Cr–8Ni	ASME TP304H (SUS304HTB)	0.08	0.6	1.6	8.0	18.0	–	–	–	–	–	–	–
	Super 304H (SUS304J1HTB)	0.10	0.2	0.8	9.0	18.0	–	–	–	0.40	–	–	3.0Cu, 0.10N
	ASME TP321H (SUS321HTB)	0.08	0.6	1.6	10.0	18.0	–	–	–	–	0.5	–	–
	Tempaloy A–1 (SUS321J1HTB)	0.12	0.6	1.6	10.0	18.0	–	–	–	0.10	0.08	–	–
	ASME TP316H (SUS316HTB)	0.08	0.6	1.6	12.0	16.0	2.5	–	–	–	–	–	–
	ASME TP347H (SUSTP347HTB)	0.08	0.6	1.6	10.0	18.0	–	–	–	0.8	–	–	–
	ASME TP347 HFG	0.08	0.6	1.6	10.0	18.0	–	–	–	0.8	–	–	–
15Cr–15Ni	17–14CuMo	0.12	0.5	0.7	14.0	16.0	2.0	–	–	0.4	0.3	0.006	3.0Cu
	Esshete 1250	0.12	0.5	6.0	10.0	15.0	1.0	–	0.2	1.0	0.06	–	–
20–25Cr	ASME TP310 (SUS310TB)	0.08	0.6	1.6	20.0	25.0	–	–	–	–	–	–	–
	HR3C (SUS310J1TB)	0.06	0.4	1.2	20.0	25.0	–	–	–	0.45	–	–	0.2N
	Alloy 800H (NCF800HTB)	0.08	0.5	1.2	32.0	21.0	–	–	–	–	0.5	–	0.4Al
	Tempaloy A–3 (SUS309J4HTB)	0.05	0.4	1.5	15.0	22.0	–	–	–	0.7	–	0.002	0.15N
	NF709 (SUS310J2TB)	0.15	0.5	1.0	25.0	20.0	1.5	–	–	0.2	0.1	–	–
	SAVE25	0.10	0.1	1.0	18.0	23.0	–	1.5	–	0.45	–	–	3.0Cu, 0.2N
High Cr–High Ni	CR30A	0.06	0.3	0.2	50.0	30.0	2.0	–	–	–	0.2	–	0.03Zr
	HR6W	0.008	0.4	1.2	43.0	23.0	–	6.0	–	0.18	0.08	0.003	–

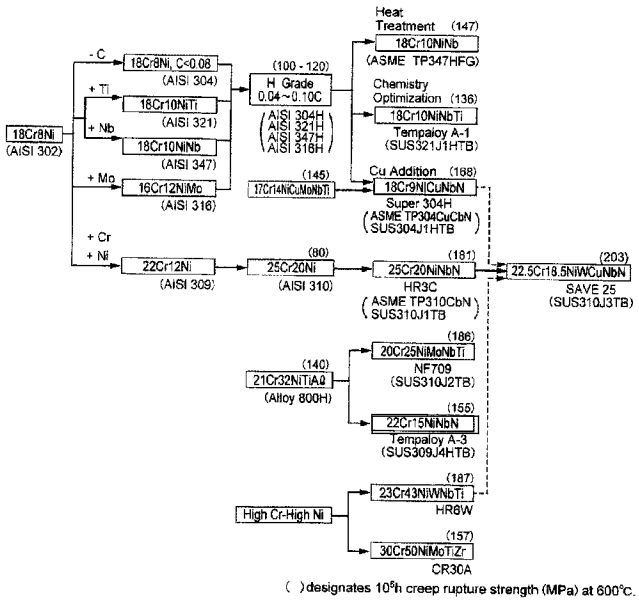


Figure 2
Development Progress of Austenitic Steels for Boiler(8)

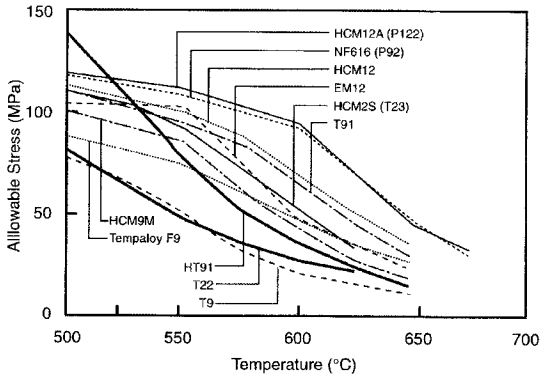


Figure 3
Comparison of allowable stresses of ferritic steels for boiler
(Based on Reference 8)

Some additional design considerations in applying the advanced ferritic steels are as follows:

1. The high temperature strength of the advanced alloys, e.g. NF616, HCM12A and E911 (P-92, P-122, E911) is essentially the same as that of low-end austenitic alloys. But oxidation resistance is less than that of austenitic alloys. This parameter of advanced 9 to 12Cr alloys must be more fully evaluated prior to application to high temperature parts.
2. Post weld heat treatment (PWHT) is always required for welded joints of advanced 9 to 12 Cr alloys to ensure minimal stress and optimal ductility. Design must be made to reduce field heat treatment as much as possible to keep production and PWHT costs minimal.
3. In the weldment of dissimilar alloys, material selection must be based on consideration of PWHT temperature. For example, the 9Cr-1Mo alloy and 1Cr-0.5Mo steel would not be acceptable materials for the case of joints in a longitudinal direction; measures must be taken to consider the behavior of welded joint creep rupture strength.
4. Last but not least, is the apparent susceptibility of ferritic steel welds to Type IV cracking, which occurs at the edges of fine grained HAZ material adjacent to unaffected parent material. Susceptibility to this has been clearly demonstrated for 1/2CrMoV, 2-1/4Cr-1Mo and 9Cr-1Mo (T91) steels. Safety margins of 10 to 20% are sometimes adopted to provide for this mechanism. Since the problem in girth welds is primarily associated with bending stresses, the problem can be overcome by proper plant design and maintenance. This issue has therefore been generally glossed over.

Figure 4 is a plot of the allowable stresses vs temperatures for comparing the temperature capabilities of ferritic alloys with austenitic steels and Ni base alloys.[11] The Figure also shows

the actual stresses at several steam pressures. The Ni base alloys are superior to the austenitic steels, which, in turn are better than ferritic steels. The nickel base alloys Inco740, Haynes 230, IN625, IN617, HR6W and HR120 have much higher temperature capability, in decreasing order as listed compared to austenitic steels, followed by the ferritic steels. Purely from the creep strength point of view, at a pressure of 5500 psi for a 2" x 0.5" tube (stress 8.6 ksi), ferritic steels are useful up to about 620°C (1150°F) (metal temperature), austenitic steels up to about 675°C (1250°F). At metal temperatures higher than about 675°C (1250°F), nickel base alloys (see Table 5) are needed. The alloy Inco740 appears capable of reaching 788°C (1450°F). Since the thick walled components are used over a range of conditions, all of the above categories of materials area likely to be used at different locations in an ultra supercritical plant.

2.3 Choice of Materials for Superheater/Reheater Tubes

The superheater tubes in the boiler are likely to undergo the most severe service conditions and must meet stringent requirements with respect to fire-side corrosion, steamside oxidation, creep rupture strength and fabricability. In addition, they must be cost-effective. Based on these issues candidate materials for various steam conditions have been summarized in Table 6. The rationale for these selections is discussed in the following sections.

2.3.1 Creep Rupture Strength

In terms of creep rupture strength, application for tubes follow the same logic as for the headers/pipes discussed earlier. The principal difference is that in the tubes, the inside metal temperature can be higher than the steam temperature by as much as 25 to 39°C (50 to 70°F). Thus, tubes made of T22 should be limited to steam temperature of 538°C (1000°F); Alloys T91, HCM12, EM12, HCM9M and HT91 limited to steam temperature of 565°C (1050°F); Alloys T-92, P-122 and E911 limited to steam temperature of 593°C (1100°F) (or metal temperature of 620°C [1150°F]), while the developmental ferritic alloys NF12 and SAVE12 may permit steam temperatures up to 620°C (1150°F). Under corrosive conditions however, even the best ferritic steel may be limited to 565°C (1050°F) temperature and austenitic steels are needed in the metal temperature range 620-675°C (1150-1250°F). Above 675°C (1250°F) nickel base alloys are needed.

For convenience, austenitic steels can be classified as those containing less than 20% Cr and those containing more than 20% Cr. Alloy modifications based on the 18Cr-8Ni steels, such as TP304H, 316H, 347H, and Tempaloy A-1, and alloys with lower chromium and higher nickel contents, such as 17-14 CuMo steel, Esshete 1250, and Tempaloy A2, fall into the classification of steels with less than 20% Cr. The allowable tensile stresses for steels in this class are intermediate between ferritic steels and high Cr austenitic stainless steels. Several high-creep-strength alloys containing more than 20% Cr, such as NF707, NF709, HR3C, and SAVE 25 have been developed, and offer low-cost alternatives to Incoloy 800 for use in the temperature range from 620 to 675°C (1150 to 1250°F). Clearly, SAVE 25, NF709, HR3C and Super304H are leading candidates for use in the highest-temperature applications. At temperatures exceeding 675°C (1250°F) nickel base alloys are candidates (see Table 7). The highest temperature capability at a given stress is exhibited by Inco740, Haynes 250, HR6W and Inco617 in

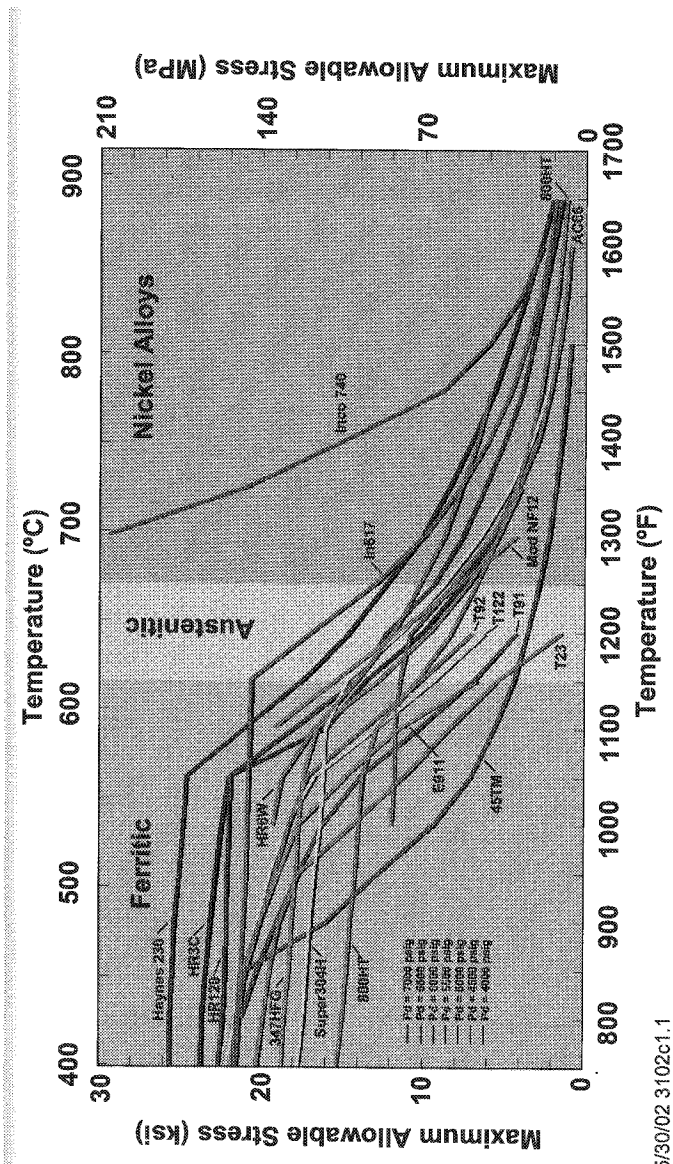
Table 5
Nominal Chemical Composition of Ni Base Alloys for USC Boilers

Alloy	Fe	Ni	Cr	Co	Mo	W	Ta	Nb	Al	Ti	Mn	Si	C	B	Zr	Other
IN 617	–	54	22	12.5	9	–	–	–	1	–	–	–	0.07	–	–	–
IN 625	2.5	61	21.5	–	9	–	–	3.6	0.2	0.2	0.2	0.2	0.05	–	–	–
HR 230	3	Bal	22	5	2	14	–	–	0.3	–	–	0.4	0.1	–	–	0.2 La
HR 120	33	37	25	3	2.5	2.5	–	0.7	0.1	–	0.7	0.6	0.05	0.004	–	0.2 N
HR 160	4	Bal	28	27	–	–	–	–	–	–	–	2.75	0.05	–	–	–
800	40	30/35	19/23	–	–	–	–	–	0.15/0.6	0.15/0.6	1.5	1.0	0.1	–	–	0.75 Cu
800HT	40	30/35	19/23	–	–	–	–	–	0.5	0.5	1.5	1.0	0.08	–	–	(Al + Ti) 0.85-1.2
INCO 740	0.7	48	25	20	0.5	–	–	2	0.9	2	0.3	0.5	0.06	–	–	–
45TM	23	45	27.5	–	–	–	–	–	–	–	1.0	3.0	0.08			0.3 Cw

Table 6
Candidate Alloys for USC Plants

TRADE DESIGNATION	NOMINAL COMPOSITION	ASME Code/ Code Case	Preferred Application	Temp. of Application (metal)
Ferritic Steels				
HCM2S	2-1/4Cr-1.5W-V	2199	WW*	
Tempaloy F-2W	2Cr-1W-Mo-V-Nb		WW	
HCM12	12Cr-1Mo-1W-V-Nb		WW	
NF12	11Cr-2.6W-2.5Co-V-Nb-N		H	Up to 650°C (1200°F)
SAVE 12	12Cr-W-Co-V-Nb-N		H	
NF 616 (P-92)	9Cr-2W-Mo-V-Nb-N	2179	H	
HCM12A (P-122)	12Cr-1.5W-Mo-V-Nb-N-Cu	2180	H	Up to 620°C (1150°F)
E911	9Cr-1Mo-1W-V-Nb-N		H	
Austenitic Steels				
SAVE25	23Cr-18Ni-Nb-Cu-N		T	
NF709	20Cr-25Ni-NB-Ti-N		T	
HR3C	25Cr-20Ni-Nb-N	2113	T	620°C–675°C (1150°F–1250°F)
Super304A	18Cr-8Ni-W-Nb-N		T	
347HFG	18Cr-10Ni-Nb	2159	T	
800HT	21Cr-32Ni-Al-Ti	1987	T	
HR120	Ni-33Fe-25Cr-N	2315	T	
Ni Base Alloys				
INCO740	25Cr-20Co-2Ti-2Nb-V-Al		P, T	
230	22Cr-14W-2Mo-La	2063	P, T	675°C–788°C (1250°F–1450°F)
Marco Alloy				
625	21.5Cr-9Mo-5Fe-3.6Nb-Al-Ti	1409	P, T	
617	22Cr-12.5Co-9Mo-1.2Al	1956	P, T	
HR6W	23Cr-6W-Nb-Ti		P, T	
45TM	27Cr-23Fe-2.75Si	2188	P, T	

**WW - water wall; T - superheater/reheater tubes; P - pipes and headers



5/30/02 3102c1.1

Figure 4
Boiler Materials for USC Plant(11)

decreasing order. A new alloy "Marco" is reported to have been developed in Germany as a modified version in IN617, possessing higher strength than IN617.

2.3.2 Fire-side Corrosion

Fireside corrosion results from the presence of molten sodium-potassium-iron trisulfates. Because resistance to fire-side corrosion increases with chromium content, the 9 to 12% Cr ferritic steels are more resistant than the 2-1/4Cr-1Mo steels currently used. The 12% Cr steel in turn shows better corrosion resistance than 2-1/4% Cr steel and 9% Cr steel. Stainless steels and other superalloys containing up to 30% Cr represent a further improvement. Increasing the chromium content beyond 30% results in a saturation effect on the corrosion resistance at least in the laboratory, as shown in Figure 5[12]. For practical purposes, when corrosive conditions are present, fine distinctions between ferritic steels may be academic, and it is usually necessary to use austenitic steels containing chromium in excess of 20%.

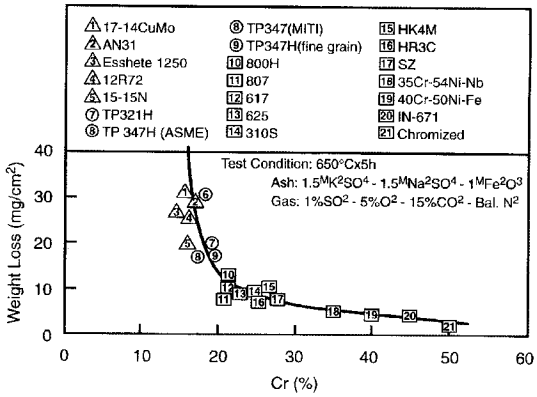


Figure 5
Relationship between hot-corrosion weight loss and chromium content for various alloys[12]

A ranking of the performance of various austenitic alloys in the presence of trisulfates has been provided by Ohtomo *et al*[13] on the basis of short-term laboratory tests (see Figure 6). The plots of weight loss versus temperature exhibit a bell-shape curve. At temperatures below 600°C (1110°F), corrosion is believed to be low because the trisulfate exists in solid form. Above 750°C (1380°F), corrosion rates are once again low, as the trisulfates vaporize. The worst corrosion problem is in the range 600 to 750°C (1110 to 1380°F). The data indicate that the high-chromium alloys such as type 310 stainless steel and Incoloy 800H are superior to the other alloys tested, and that Inconel 671 (Ni-50Cr) or its matching weld metal IN72 are virtually immune to attack. Lower-chromium stainless steels, such as type 316H, type 321H, and Esshete 1250, show considerable susceptibility to attack. The alloy most susceptible to attack seems to be the 17-14 CuMo alloy used in the Eddystone 1 plant. Results of field probe studies confirm the following ranking of alloys in increasing order of corrosion resistance: T91, HCM12, type 347 stainless steel, Incoloy 800, and Inconel 671[14]. In addition to alloy selection, other

"fixes' to minimize fire-side corrosion, such as shielding of the tubes coatings and claddings may also be applied, if economical[15].

Results of extensive field tests have also been reported by Blough[16]. This was based on a collaborative study by EPRI, IHI and F-W who carried out extensive laboratory and field tests in 3 boilers, two of them fueled with somewhat corrosive Eastern bituminous US coal, one fueled with a supposedly non-corrosive Western low sulfur sub-bituminous coal. The experiments were carried out using air cooled, retractable probes, inserted in finishing superheater or reheater areas. Metal temperatures were maintained in the 600-690°C range (1250-1300°F). Exposure time was 16,000 hrs with samples removed after 4000, 12,000 and 16,000 hrs. Figure 7 shows metal losses observed in one of the boilers, using an Eastern bituminous coal, Figure 8 those observed in the boiler using subbituminous Western coal. The losses observed were about the same but the corrosion mechanisms were different. Tubes from the boilers using eastern bituminous coals showed the classic liquid ash corrosion in the 10 and 2 o'clock positions of the tube, where sulfur rich fly ash impacts on the tube. Potassium rich sulfate was found in the ash deposits, and metal wastage was caused by internal oxidation and sulfidation, because a fully protective Cr_2O_3 scale could not form in the presence of sulfur rich deposits. With increasing Cr content in the alloy the Cr_2O_3 scale became more protective, but in all alloys internal oxidation and sulfidation occurred in Cr depleted zones below the scale.

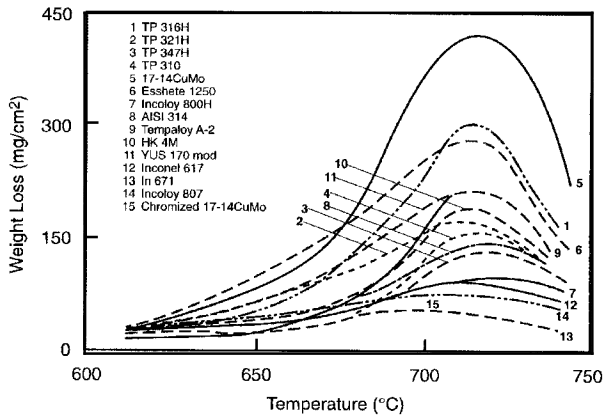


Figure 6
Comparison of fire-side corrosion resistance of various alloys[13]

The corrosion morphology of the tubes from the boiler using Western subbituminous coal was similar, but the area of major attack was on the side of the tube facing away from the flue gas stream, where deposits rich in very fine $CaSO_4$ were found.

From the results presented above, it may be concluded that substantial superheater corrosion can occur, especially in high strength austenitic alloys with a low chromium content. For most coals, high strength modified Alloy 800 type alloys such as NF709, will probably have sufficient corrosion resistance, while for more corrosive coals modified SS 310 type alloys, e.g. HR3C, should give an extra margin of safety. It is of interest to note here that the T-91 sample exposed in the low sulfur coal fueled boiler had a corrosion loss similar to SS 347, which is considerably less than that of SS 304 and 17-14CuMo. A probable reason is that scales and deposits usually adhere tight to ferritic/martensitic steels, but spall readily from all austenitic steels.

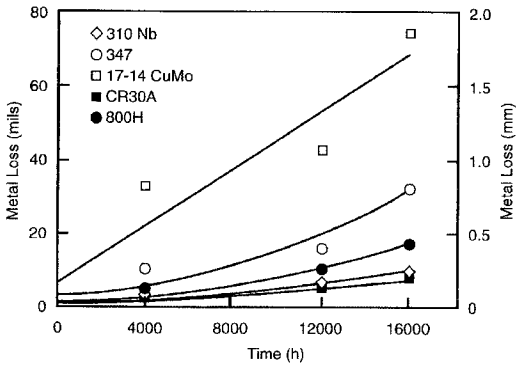


Figure 7
Metal losses of various superheater steels in a boiler using bituminous eastern U.S. coals[16]

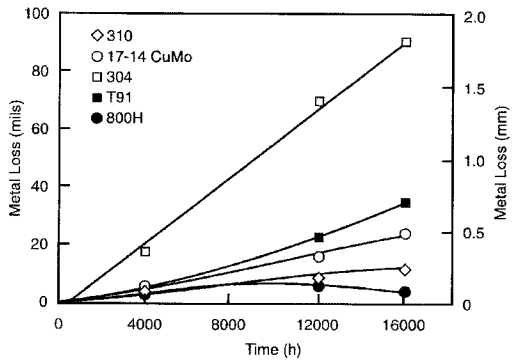


Figure 8
Metal losses of various superheater steels in a boiler subbituminous western U.S. coals[16]

Based on the favorable results from the air-cooled probes in one of the plants, the SS304M reheater, which suffered from severe alkali sulfate corrosion was replaced by one made from SS310 NbN (HR3C).[17] Test sections of other alloys were built into the reheater and carefully monitored. It was found that 310NbN (HR3C) was a satisfactory material for 90% of the reheater, with less than 0.25 mm/yr (10 mils/yr) corrosion. However in one area, about 10 tubes wide and 10 ft (3m) high, corrosion rates ranged from 0.5 – 1.25 mm/yr (20-50 mils/yr). Here the corrosion resistance of SS310 was about the same as that of SS347 and alloy 800H. Only a Cr-Ni steel (Cr30A) with 30% Cr had significantly lower corrosion rates, ranging from 0.125 – 0.5 mm/yr (5 – 20 mils/yr). It is concluded that increasing the Cr content of the alloy from 18-20% to 23-25% will only significantly increase corrosion resistance, when the corrosivity of the deposits is moderate, i.e. ≤ 0.5 mm/yr (20 mils/yr for 18-8 stainless steels). For more corrosive conditions, co-extruded tubes or weld overlay claddings containing at least 40% Cr are strongly recommended. For metal temperatures exceeding 675°C (1250°F), nickel base alloys such s INCO740, Haynes 230, INCO 617 and HR6W need to be considered.

Extensive field experience at EPRI and TVA has shown fireside corrosion is very local, even with very corrosive coals. Thus 20% Cr alloys are generally suitable as the main material of construction. Local areas where severe corrosion is predicted by combustion modeling or found after initial operation can then be made more corrosive resistant by high chromium weld overlays. These overlays, using weld metal In72 (44Cr, balNi) and In671 (48Cr, balNi), are commercially available, although improved application methods and reduced costs are desirable. Candidate alloys for tubing after transitions from Ni alloys are the austenitic steels followed by the ferritic.

2.3.3 Steam-side oxidation

Steam-side oxidation of tubes and exfoliation of the oxide scale and its consequence in terms of solid-particle erosion damage to the turbine are well known. This problem is expected to be more severe in advanced steam plants, because the much higher steam temperatures employed are likely to cause more rapid formation of oxide scale.

Very limited data are available regarding the steam-side scale-growth characteristics of the ferritic tubing alloys. In a study by Sumitomo Metal Industries[18], the oxide growth in steam for alloys T22 (2-1/4Cr-1Mo), T9, HCM9M, and the modified 9Cr-1Mo (T91) were compared based on 500 hr tests. Results showed the superiority of the T91 alloy over the other alloys. Masuyama *et al* compared alloys HCM12, HCM9M, 321H, and 347H in field tests in the temperature range 550 to 625°C (1020 to 1155°F) over a period of one year[19]. Samples were inserted in the tertiary and secondary superheaters and reheaters. From the results, they concluded that the resistance to steam oxidation of HCM12 is superior to those of 321H and HCM9M and comparable to that of fine-grained 347H for exposure to the high-temperature region of the reheater. Subsequent monitoring over a period of three years has borne out their earlier conclusions[20]. In addition to the inherent resistance of HCM12M steel to steam-side oxidation, Masuyama *et al* suggest that the tendency toward exfoliation of oxide scale would also be less for this alloy than for austenitic steels[19,20]. Additional improvements in 9 to 12% Cr steels may be possible by extending the chromizing[21,22] and chromate conversion treatments[23] that currently are applied to lower-alloy steels, grain refinement during heat treatment has been shown to be clearly beneficial as well. Internal shot blasting is also known to improve the steam oxidation resistance of 300 series stainless steels by enhancing chromium diffusion. It is therefore anticipated that these steels would be used in the fine-grain and shot-peened conditions. Results of steam oxidation tests at 650°C (1200°F) for times up to 2000 h have been reported for several austenitic steels[24]. Steamside oxidation results on Ni base alloys are not available and the upper temperature limits have not been defined.

2.4 Choice of Materials for Waterwalls

2.4.1 Metal Temperature Concerns

This issue has been discussed originally by Blum[25]. In boilers operating at 625°C/32 MPa, maximum midwall temperatures can be as high as 500-525°C, depending on magnetite deposits at the inside of the tube. This means that the creep resistance of standard low-alloy ferritic steels such as T-11 is not adequate. Originally T-91 steel was the only suitable substitute. Under the COST program[26] it was demonstrated that this material can be fabricated into waterwalls. However a postweld heat treatment is required, which is difficult to do in the field. Two steels containing 2.5 and 12Cr% respectively developed by Sumitomo and MHI are more promising in that they do not require preheat or postweld heat treatment.[25-27] Both steels have creep strength in the same range as T-91 and use similar precipitation strengthening mechanisms. Especially the 2.5%Cr steel appears promising for this

application. It also has recently been approved by the ASME boiler code committee as T-23. Test panels are now in service in various boilers.

2.4.2 Waterwall Corrosion Concerns

Recent reductions in NOx emissions, mandated by the Environmental Protection Agency in the USA have led to the introduction of deeply staged combustion systems, in which the air/fuel ratio is significantly less than 1, and additional combustion air is added above the burners via overfire air ports. Several boilers in the USA retrofitted with such systems have reported severe corrosion of low alloy steel waterwalls, with metal losses in the 1-3 mm/yr (40-120 mil/yr) range. Supercritical units are generally more severely affected than subcritical units and severe corrosion is generally limited to coals with more than 1%S. However above 1%S there is no strict correlation between S and corrosion rate. The highest corrosion losses are found in regions where H_2S rich substiochiometric flue gas mixes with air from the overfire air ports. Laboratory studies indicate that the high corrosion rates cannot be explained by the presence of H_2S and CO in the flue gas alone. Work by Kung[28] has shown that corrosion rates in gas mixtures, actually found in boilers, containing 500-1500 pm H_2S and 5-10% CO, are generally less than 0.5 mm/yr (20 mils/yr) at 450°C. More recently it was shown that the presence of FeS deposits can greatly increase the corrosion rate, but only under alternating oxidizing/reducing conditions or oxidizing conditions alone. When corrosion is a problem there is no alternative to overlay coatings or cladding with high Cr alloys such as IN671 or IN72.

The temperature of waterwalls is driven by the steam pressure. Present maximum waterwall temperatures are in the 470°C range for steam pressures of 24.5 MPa (3500 psi). If this is increased to 35 MPa (5000 psi), the expected maximum waterwall temperature will increase by 50 to 75°C (to 500–525°C [932–977°F]). Alloy T23 is deemed sufficient for this application from a creep standpoint. Qualification and field trials of this alloy are needed to allow routine commercial application.

3.0 U.S. Project on Boiler Materials for USC Plants

Table 1 illustrates the efficiency advantages to be gained by going to higher steam conditions. Compared to the efficiency of subcritical steam plants of 37% and that by conventional supercritical plants of 40.9%. The steam conditions of 5500 psi/1400°F/1400°F envisaged in the DOE/OCDO project offers an efficiency of 46.5% (HHV); For a double reheat cycle it is increased to 47.5 (HHV). It is to be noted however that efficiency is a function of numerous variables and the values reported in Europe are generally higher compared to the U.S by 3 to 4 points. An attempt has been made to achieve an apples-to-apples comparison as described in the Table.

This project was initiated about 6 months ago around October 2002 and is of 5 years' duration. It is funded by the USDOE/National Energy Technology Labs (15.2 Million US$), and the Ohio Coal Development Office of the Ohio Department of Development (2.0 Million US$). The participants also provide cost sharing to the tune of 2.7 Million US$.

The goals of the project include: identification of advanced materials that achieve cost competitive, environmentally acceptable coal based electric power generation that includes the use of high sulfur coals; and to enable domestic boiler manufacturers to globally compete for the construction and installation of high efficiency coal fired power plants.

The specific objectives of the Ultra Supercritical Materials Project are to:

- Identify materials performance issues that limit operating temperatures and thermal efficiency of coal-fired electricity generating plants;

- Identify improved alloys, fabrication processes and coating methods that will permit boiler operation of steam temperatures up to 760°C or 1400°F and steam pressures up to 5500 psi;
- Work with alloy developers, fabricators, equipment vendors and power generation plants to develop cost targets for the commercial deployment of alloys and processes developed;
- Define issues impacting designs that can permit power generation at temperatures greater than or equal to 870°C or 1600°F;
- Lay the groundwork for ASME Code approval.

The alloys that will be evaluated under the Ultrasupercritical Materials Program will have direct application in all advanced fossil-based power generation technologies that incorporate the Rankine steam cycle. This program will have an impact on ultrasupercritical coal combustion systems, integrated gasification combined cycle plants, hybrid cycles incorporating partial gasification and fluid bed combustion, and gasification fuel-cell/turbine systems. The near term benefits this research program could solve high-temperature materials problems in present power generation systems. The long term benefit would be the development of new high temperature materials capable of providing for higher efficiency cycles critical to the success of the Vision 21 concept pioneered by the USDOE.

The scope of work involves conceptual design, economic studies, and evaluation of candidate alloys' mechanical properties, steamside oxidation resistance, fireside corrosion resistance, weldability and fabricability. Coating and cladding technologies will also be evaluated. Detailed reviews of the State-of-the-Art with respect to alloy selection, mechanical properties, oxidation and coatings will be conducted right at the start. The impact of these technologies on code development will also be explored.

The consortium of members performing the various tasks include Alstom Power, Babcock Borsig Power, Babcock & Wilcox Co./McDermott Technologies, Foster Wheeler Development Corp. and the Electric Power Research Institute (EPRI). EPRI also oversees and manages the technical direction, while the Energy Industries of Ohio (EIO) is the prime contractor that has the overall management responsibilities. The Oak Ridge National Labs (ORNL) is informally part of the consortium structure as they provide complementary input to this project through a parallel contract.

4.0 Summary and Conclusions

Literature pertaining to materials technology for boilers in ultra supercritical pulverized coal power plants has been reviewed. Extensive development in strengthening of 9 to 12% ferritic steels have resulted in temperature/pressure capabilities well over the conventional framework of 538°C/17 MPa (1000°F/2400 psi) for the steam. Nearly two dozen plants have been commissioned worldwide with main steam temperatures of 585 to 600°C (1080-1112°F) and pressures of 24 to 30 MPa (3400-4200 psi). Specific materials developments with respect to key components are as follows:

For heavy section components such as pipes and headers, minimizing thermal fatigue has been a major driver in addition to achieving high creep strength. For this reason, alloy development has focused on ferritic steels containing 9-12% Cr. Optimization of C, Nb, Mo and V and partial substitution of W for Mo in the 9-12% Cr ferritic steels has resulted in three new alloys HCM12A, NF616 and E911 (P122, P92 and E911) capable of operating up to 620°C (1150°F) (metal temperature) at steam pressures up to 34 MPa (4800 psi). Beyond 620°C oxidation resistance may become an additional limiting factor, especially for the 9% containing steels. A newer class of 12% Cr alloys NF12 and SAVE12, containing cobalt and additional Cr is being evaluated for possible 650°C (1200°F) application. It appears from preliminary results that austenitic steels or Nickel alloys would be needed

for metal temperatures exceeding 675°C (1250°F). Candidate alloys for heavy section applications and the applicable limiting temperatures are shown in Table 7.

For SH/RH tubes, steamside oxidation resistance, and fireside corrosion resistance are major drivers in addition to creep resistance. Furthermore, tube metal temperatures often exceed the steam temperature by as much as 28-39°C (50-70°F) It is unlikely that any ferritic steels can be used in the finishing stages of SH/RH circuits at steam temperatures exceeding 565°C (1050°F). Austenitic steels need to be used at these higher temperatures. Depending on the corrosivity of the coal used, higher Cr steels or clad steels may be required. For 620°C (1150°F) application, Super 304H, Tempalloy Al, Eshete 1250 and 17 Cu-MO are acceptable under non corrosive conditions while 20-25% Cr alloys such as HR3C, NF709, 347HCG, SAVE 23 and cladding with IN72 are recommended for more corrosive conditions. Several candidate alloys Inconel 617, NF709 and Cr30A and alloys clad with Inconel 671 (50% Cr) are available for use at 650°C.

For both header and SH/RH applications close to 760°C Ni base alloys Inco740, Nimonic 230 and modified Alloy 617 are being evaluated. Additional cladding with high Cr alloys may be needed for tubing.

For upper waterwall sections, two new steels containing 2.5 and 12% Cr known as HCM2(T23) and HCM 12 respectively are very promising in terms of creep strength and weldability. They are suitable for use in the range of 595-650°C steam conditions purely from a creep strength point of view. When fireside corrosion in low NOx boilers is an issue, these alloys will have to be clad or weld overlaid with alloys containing more than 18-20% Cr.

A new consortium project sponsored by USDOE and OCDO aims to evaluate materials for a USC boiler operating at 30.9 MPa (5500 psi)/760°C (1400°F)/760°C (1400°F). Details of the project are described.

5.0 References

[1] R.W. Vanstone, "Advanced (700°C) Pulverised Fuel Power Plants", *Proc. Parsons 2000 Advanced Materials for 21st Century Turbines and Power Plant*, A. Strang et al. Ed.; Book 736, IOM Communications Ltd., London, 2000, pp. 91-98.

[2] R. Viswanathan and W.T. Bakker, *Materials for Ultra Supercritical Coal Power Plants, Boiler Materials: Part 1, and Turbine Materials: Part 2*, Journal of Materials Engg. and Performance, ASM, Vol. 10(1), Feb 2001, pp. 81-100.

[3] W.T. Bakker, "Materials for Advanced Boilers", in Advanced Heat Resistant Steels for Power Generation, R. Viswanathan and J.W. Nutting, Ed.; IOM Communications Ltd., London, pp 435-455, 1999.

[4] R. Blum, "Materials Development for Power Plants With Advanced Steam Parameters—Utility Point of View", in *Materials for Advanced Power Engg.*, D. Coursouradis et al. Ed.; Part 1, 15-30, Kruwer Academic Publishers, Netherlands, 1994.

[5] F. Starr and A. Shibli, "Fundamental Issues in the Development of Austenitic and Nickel Based Alloys for Advanced Supercritical Steam Systems", same publications as Reference 1, pp. 459-471.

[6] G. Schaffknecht and Q. Chen, "Materials Issues for Supercritical Boilers", same publication as Reference 1, pp. 249-265.

[7] L.A. Ruth and N. Birks, *Materials Needs for High Efficiency Coal Fired Boiler Plants,* International Symposium on Ultra-High Temperature Materials, Tajimi, Japan, 1995.

[8] F. Masuyama, "New Developments in Steels for Power Generation Boilers", in Advanced Heat Resistant Steels for Power Generation, R. Viswanathan and J.W. Nutting, Ed.; IOM Communications Ltd., London, pp 33-48, 1999.

[9] R. Viswanathan, "Damage Mechanisms and Life Assessment of High-Temperature Components", ASM International, Metals Park, OH, 1989.

[10] T. Fujita, Personal Communication, January 2002.

[11] B. Vitalis, Babcock Borsig Power Co., Personal communication, 2002.

[12] T. Ikeshima, *Bull. Japan Inst. Metals*, Vol. 22 (No. 5), 1983, p 389.

[13] Ohtomo *et al*, High Temperature Corrosion Characteristics of Superheater Tubes, Ishikawajima Harima Industries, *Engg. Rev.*, Vol. 16 (No. 4), Oct 1983.

[14] A.L. Plumley and W.R. Roczniac, Coal Ash Corrosion Field Testing of Advanced Boiler Tube Materials, in *Proceedings of the Second International Conference on Improved Coal-Fired Power Plants*, Electric Power Research Institute, Palo Alto, CA, Nov 1-4, 1988.

[15] A.F. Armor, R.I. Jaffee and R.D. Hottenstine, "Advanced Supercritical Power Plants – The EPRI Development program, Proc. of American Power Conference, Vol. 46, 1984, p 70.

[16] J.L. Blough *et al*, "Superheater Corrosion – Field Test Results", Report TR-103438, EPRI, Palo Alto, Nov 1993.

[17] J.L. Blough *et al*, "Superheater Corrosion in Ultra Supercritical Power Plants, Long-Term Field Exposure at TVA's Gallatin Plant", EPRI Report TR-111239, EPRI, Palo Alto, 1999.

[18] "Properties of Super 9Cr Steel Tube (ASTM) A 213-T 91," Report 803 F-No. 1023, Sumitomo Metal Industries, July 1983.

[19] F. Masuyama, H. Haneda, T. Daikoku, and T. Tsuchiya, "Development and Applications of a High Strength, 12% Cr Steel Tubing with Improved Weldability", Technical Review, Mitsubishi Heavy Industries, Ltd., Japan, Oct. 1986, p 229-237.

[20] F. Masuyama, H. Haneda, K. Yoshikawa, and A. Iseda, Three Years of Experience with a New 12% Cr Steel in Superheater, in *Advanced in Materials Technology for Fossil Fuel Power Plants*, R. Viswanathan and R.I. Jaffee, Ed., American Society for Metals, Metals Park, OH, 1987, p 259-266.

[21] A.J. Blazewicz and M. Gold, "Chromizing and Turbine Solid Particle Erosion", ASME Paper No. 78, JPGC PWR-7, Joint ASME/IEEE/ASCE Power Generation Conference, Dallas, September 1978.

[22] P.L. Daniel *et al*, "Steamside Oxidation Resistance of Chromized Superheater Tubes", CORROSION 80, NACE Conference, Chicago, May 1980.

[23] J.M. Rehn *et al*, "Controlling Steamside Exfoliation in Utility Boiler Superheaters and Reheaters", Paper No. 192, CORROSION 80, NACE Conference, Chicago, May 1980.

[24] K. Kubo, S. Murase, M. Tamura, and T. Kanero, Application of Boiler Tubing Tempalloy Series to the Heat Exchanger of Advanced Coal-Fired Boilers, in *Proceedings of the First International Conference on Improved Coal-Fired Power Plants*, A.F. Armor, W.T. Bakker, R.I. Jaffee, and G. Touchton, Ed., Report CS-5581-SR, Electric Power Research Institute, Palo Alto, CA, 1988, p 5-237 to 5-254.

[25] R. Blum, "Materials Development for Power Plants with Advanced Steam Parameters. Utility Point of View", *Proc. Materials for Advanced Power Eng.*, 1991, 3-6 Oct. 1994, Liege, Belgium, Kluwer Ac. Publ. Dordrecht, The Netherlands, 15.

[26] C.J. Franklin and C. Henry, "Materials Development and Requirements for Advanced Boilers", Reference 31, 89.

[27] F. Masuyama, Y. Sawaragi *et al*, "Development of a Tungsten Strengthened Low Alloy Steel with Improved Weldability", Reference 31, 173.

[28] S.K. Kung, "Prediction of Corrosion Rate for Alloys Exposed to Reducing/Sulfidizing Combustion Gases", *Corrosion 97*, NACE 1997, 97-136.

Acknowledgments

This Review was sponsored by the Department of Energy under Grant DE-FG26-01NT-41175 and by the Ohio Coal Research Office under Grant D-00-20.The encouragement and support of the program managers R. Romanosky and H. Johnson are very much appreciated.

THE STEAM OXIDATION RESISTANCE OF 9-12% CHROMIUM STEELS

P J Ennis and W J Quadakkers

Research Centre Juelich (FZJ)
Institute for Materials and Processes in Energy Systems IWV2
D-52425 Juelich, Germany

Abstract

The steam oxidation resistance of commercial steels and developmental steels in the COST 522 Action has been investigated. Tests were carried out at various laboratories participating in the COST Action, each laboratory using, in the absence of a standard oxidation test, its own test technique. Each laboratory included the benchmark material, a commercial heat of P92, so that inter-laboratory scatter could be assessed and related to the particular test technique used. In spite of the differences in the test procedures of the participating laboratories, the results were in relatively good agreement.
Regarding the experimental cast and forged steels examined in the COST Action, the results have confirmed that a significant reduction in steam oxidation rates can be achieved by increasing the chromium content. However, there are other alloying additions that play an important role in the formation of protective oxide scales. It is recommended that at least 11% Cr and 0.3% Si should be specified for the steels in order to obtain improved steam oxidation resistance.

Keywords: P92 steel, steam oxidation, 11% Cr steels

Introduction

There have been over the last twenty years significant improvements in the mechanical properties of 9% chromium steels, with the result that these steels may now be considered for applications at temperatures of 600°C and even higher [1-3]. Although the creep rupture strength is satisfactory, the strongest steel of this category P92 having a 100 000 h stress rupture strength of 100 MPa at 615°C [4], corrosion testing revealed that the oxidation rates in steam-containing environments were very much higher than in air [5, 6]. It appears that the presence of only small amounts of water vapour in the service or test environment causes severe degradation of the normally protective oxide scale, resulting in unacceptably high oxidation rates. Not only is the metal wastage high, resulting in the loss of load bearing cross-section and possible early failure, but also the thick oxide scales themselves are of concern. For heated tubes, the thick scales would reduce the heat transfer across the tube wall and lead to over-heating and subsequent mechanical failure. Spalled oxide particles may also become entrained in the flowing steam, causing potential erosion problems in the turbine.

A principal aim of the COST Action 522 working group for steam power plant materials is therefore to develop new steel compositions having similar strength to the commercial advanced 9% chromium steels (P91, P92 and E911) but with significantly improved steam oxidation resistance. The approach is to increase the chromium content and to off-set the increased tendency for ferrite formation by additions of Co, the only element that extends the austenite field in the Fe-Cr alloy constitutional diagram to higher Cr levels without decreasing the α/γ transformation temperature. By this means, a fully martensitic microstructure can be achieved during cooling down after the austenitisation heat treatment, in spite of the higher Cr content. The

new steels selected at the start of the COST 522 Action contained either 10.5 or 11.5% Cr, 1.5% Mo, 3% Co and 0.03% N, together with the carbide/nitride formers 0.2% V and 0.04% Nb. Based on earlier mechanical testing results, the steels also contained 0.01 % B [2] and one steel was made with a higher Co addition of 6%. Both forged and cast versions of the steels were investigated.

Experimental programme

Test materials

Table 1 lists the chemical compositions of the steels for the wrought (FB series) and the cast (CB series) products. As several laboratories participated in the evaluations of the steam oxidation resistance of the new steels, each participant included a benchmark material, a heat of P92 manufactured by the Nippon Steel Corporation, in their exposure tests, in order to enable comparisons to be made between the laboratory data. Details of this heat are also shown in Table 1

Table 1
Compositions of new Cr steels and P92 benchmark heat

Steel	C	Cr	Mo	W	Co	Nb	V	N	B
FB5	0.13	10.10	1.46	-	2.85	0.060	0.20	0.017	0.010
FB6	0.14	11.20	1.45	-	2.93	0.080	0.22	0.016	0.010
FB7	0.16	10.20	1.54	-	2.97	0.070	0.20	0.019	0.009
FB8	0.17	11.10	1.46	-	2.94	0.070	0.21	0.023	0.010
FB9	0.18	11.00	1.48	-	6.03	0.060	0.20	0.017	0.009
FB10	0.12	10.34	0.90	0.42	3.02	0.070	0.21	0.030	0.007
FB11	0.19	11.15	0.90	0.42	3.02	0.070	0.21	0.020	0.007
CB5	0.13	10.10	1.58	-	2.90	0.063	0.20	0.035	0.0105
CB6	0.13	10.90	1.57	-	2.90	0.065	0.20	0.025	0.0109
CB8	0.17	10.85	1.54	-	2.90	0.065	0.21	0.025	0.0106
CB9	0.17	10.90	1.66	-	5.85	0.063	0.20	0.022	0.0105
CB10	0.13	10.24	0.91	0.41	3.14	0.058	0.22	0.023	0.0084
CB11	0.17	10.71	0.84	0.38	2.85	0.054	0.22	0.031	0.012
P92	0.12	8.85	0.42	1.85	-	0.07	0.20	0.042	-

The specific contributions of the various participants to the overall programme are shown in Table 2, together with information concerning the test atmospheres used; more detailed results of some of these investigations are reported elsewhere in the Proceedings.

Evaluation procedures

The oxidation behaviour was generally characterised by the time-dependent mass change in discontinuous tests and post-exposure metallographic examination of the oxide scales. For a further indication of the steam oxidation resistance of the experimental steels, comparisons of the oxidation rate with that of the low alloy steel 1Cr0.5Mo at 550°C were made. This steel has been successfully used in power plant construction at service temperatures up to 550°C and there is considerable long-term service experience. The steam oxidation data at 550°C may therefore serve as a useful indicator of an acceptable level of oxidation resistance.

Table 2
List of partners and their contributions to steam oxidation testing of the new steels

Partner*	Materials tested	Test temperatures, °C	Test environment	Remarks
ALSD	FB, CB, P92	600, 650	flowing steam	
ANSA	FB6, P92	650	flowing steam	
CESI	CB6, P92	650	flowing steam	steam conditioned
FZJ	FB, CB, P92	600, 625, 650	Ar-50% steam	
FZJ	P92	600, 650	static steam	240 bar
INTA	P92	650	flowing steam	
KEMA	P92	600	flowing steam	provided data from earlier tests at 60 bar steam pressure
NPL	P92	600	flowing steam	
SPGG	CB, P92	650	static steam	
SVUM	FB2, 10, 11, CB6, P92, Fe24Cr	600, 650	Ar-50% steam	

* ALSD: Alstom Power, Mannheim, Germany – R Knoedler
ANSA: Ansaldo Ricerche, Genoa, Italy – D Casali
CESI, Milan, Italy – L Torri
FZJ: Forschungszentrum Juelich IWV-2, Juelich, Germany – P J Ennis
INTA: Instituto de Técnica Aeroespacial, Madrid, Spain – A Aguero
KEMA: NV KEMA Power Generation & Sustainables, Arnhem, the Netherlands – R van Vulpen
NPL: National Physical Laboratory, Teddington, UK – S Osgerby
SPGG: Siempelkamp Prüf- und Gutachter-Gesellschaft, Dresden, Germany – P Seliger
SVUM: SVUM Research Centre Bechovice, Prague, Czech Republic – J Cizner

Each laboratory used its own technique for assessing the steam oxidation resistance of the new steels in comparison with P92. As can be seen from Table 2, the exposure conditions varied between the laboratories, mainly with respect to the test gas atmosphere, some using carrier gas saturated with water vapour, others using pure or conditioned steam. The only stipulation for all laboratories was the surface finish of the test coupons, which was specified at 1200 grit finish.

Comparison of the results for the benchmark steel P92

The results obtained for the benchmark heat of the P92 steel are summarised in Figures 1 and 2, which show the mass changes measured after 1000 h exposure in steam-containing atmospheres and the oxide scale thickness, respectively. Included in the Figure 2 are data determined at high steam pressure supplied by KEMA for a different heat of P92 and data from a field trial at Willemshafen Power Station. In spite of the differences in the testing techniques and test environments, the results up to 2000 h exposure exhibit remarkably good agreement, perhaps with the exception of the CESI result. Some more detailed evaluation of the CESI results is required to establish the reason for the difference. The low mass gains for the CESI experiments and the relatively large differences found after 5000 h may be due to spalling of the oxide scales.

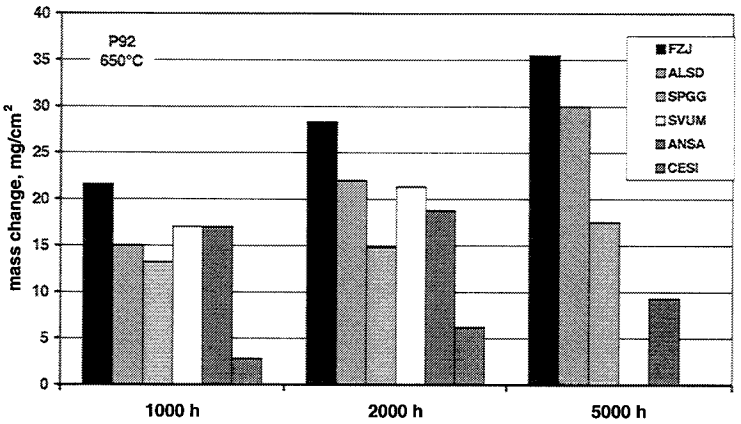


Figure 1
Inter-laboratory comparison of mass changes for the benchmark steel P92 exposed in steam-containing atmospheres at 650°C for 1000, 2000 and 5000 h

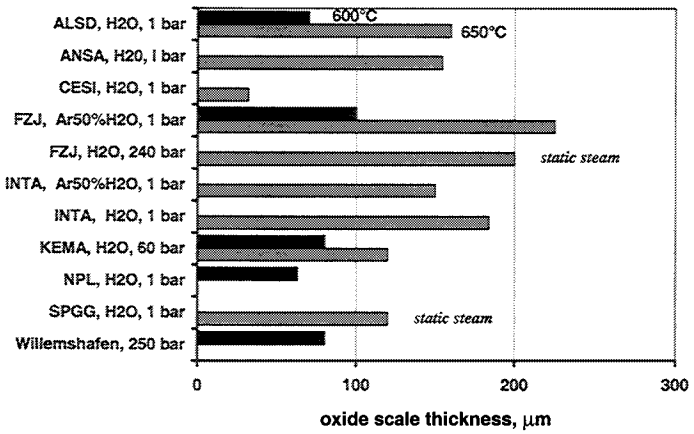


Figure 2
Oxide scale thickness on P92 steel after 1000 h at 600 and 650°C in steam-containing atmospheres

Steam oxidation resistance of new forged steels (FB series)

The results of the steam oxidation testing of the new FB steels are summarised in Figure 3.

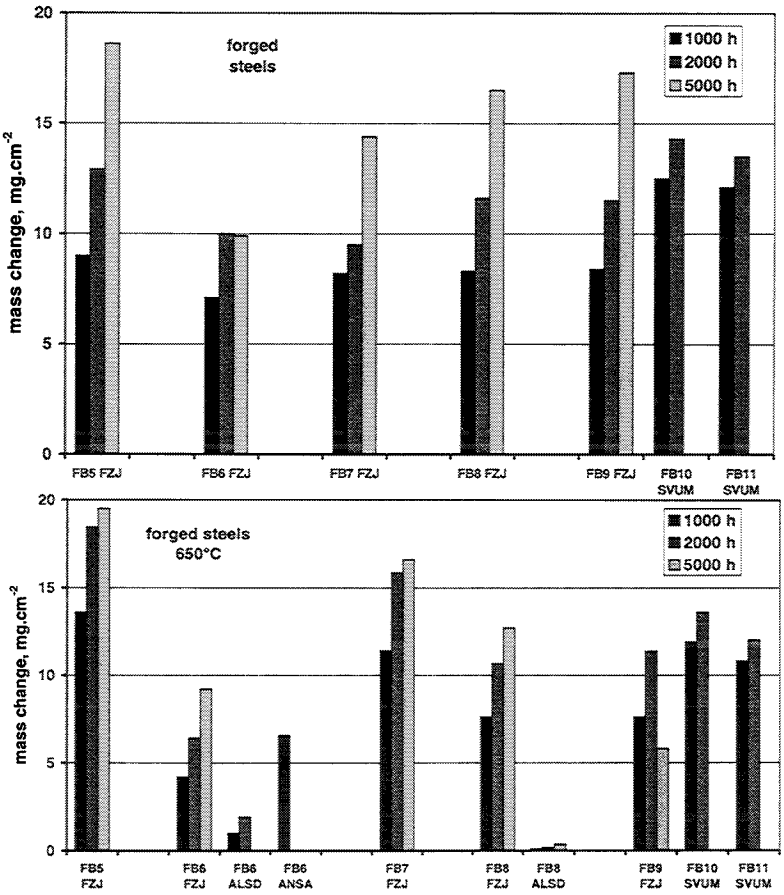


Figure 3
Mass changes for the new FB series of forged steels at 600 and 650°C
in steam-containing atmospheres

The highest mass gains after 5000 h are significantly lower than the highest mass gain for P92 of 30-35 mg/cm^2, indicating the improvement obtained by increasing the highest Cr content. From the Figure 3b, it can be seen that there are some large differences in the data from different laboratories, in contrast to the data for P92. One reason for the differences in the mass changes is that in some tests the oxide scale has spalled off.

The mass changes determined at FZJ are shown in Figure 4 as a function of exposure time. Here again the tendency of some compositions (FB6 at 600°C and all the FB steels at 650°C) can be observed.

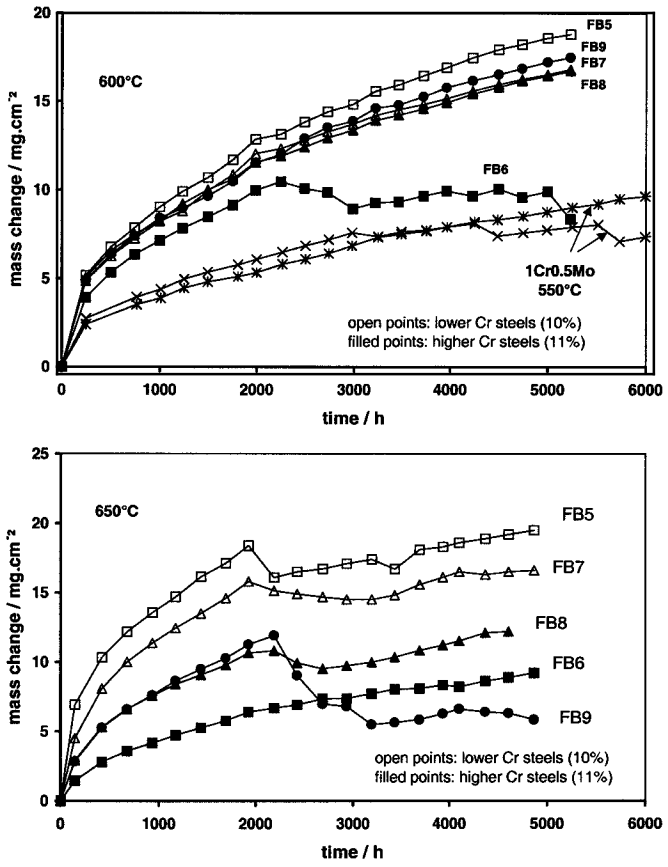


Figure 4
Mass changes for the new forged steels (series FB) in Ar-50% H_2O at 600 and 650°C, with comparative data for 1Cr0.5Mo determined at 550°C

The mass change data for the steel 1Cr0.5Mo steel at 550°C included in Figure 4 indicate a steam oxidation resistance that is acceptable from a practical point of view; there being extensive long-term experience with this steel at this temperature in power generation plant. It is clear that none of the FB steels exposed at 600-650°C can match the steam oxidation resistance of the 1Cr0.5Mo steel at 550°C.

Steam oxidation resistance of the new cast steels

The results obtained for the new cast steels (CB series) are shown in Figure 5. Two of the laboratories (ALSD and FZJ) recorded particularly low mass gains for the CB steels. The much higher values found by SPGG may be attributed to the fact that these tests were carried out in a static atmosphere [6]; the high mass gains observed by SVUM require more detailed consideration. However, the highest values observed for the cast steels were more or less the same as the mass changes seen for the forged steels.

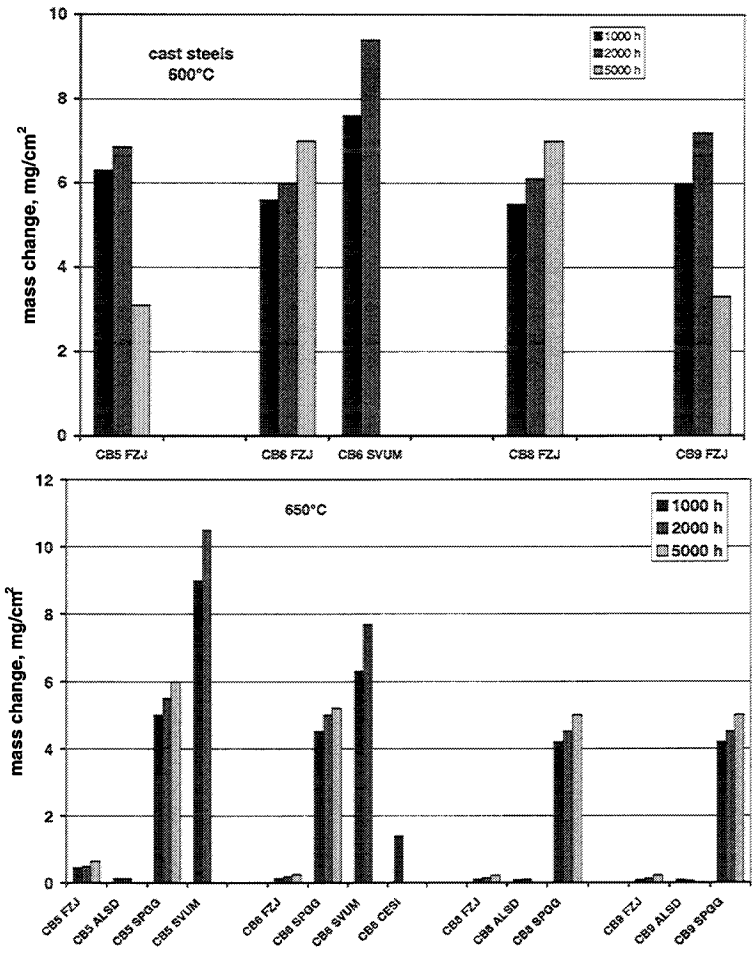


Figure 5
Mass changes for the cast steel (series CB) exposed in steam-containing atmospheres at 650°C

Figure 6 shows the time dependence of the oxidation process; these curves were determined by FZJ. The oxide scales appeared to spall after relatively short exposure times and low mass gains for the steels CB5 and CB9 at 600°C. At 650°C, all the CB steels exhibited very low mass gains, and performed significantly better than 1Cr0.5Mo at 550°C.

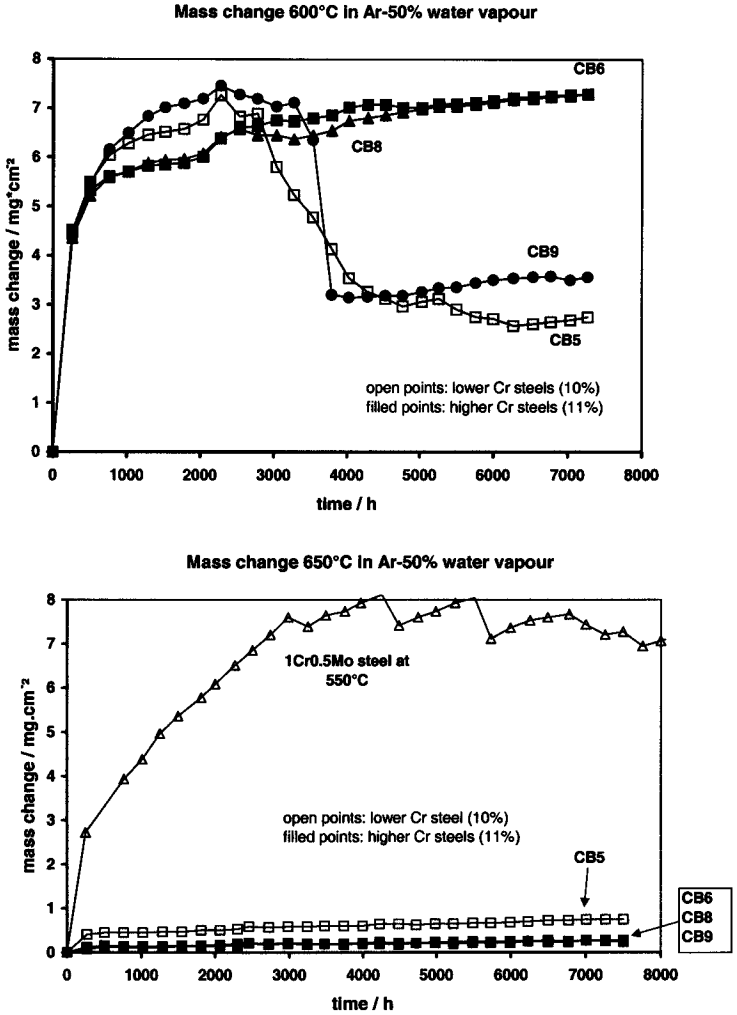


Figure 6
Mass change of cast steels (series CB) as a function of exposure time in Ar-50%H_2O with comparative values for 1Cr0.5Mo at 550°C – FZJ data

Temperature dependence of steam oxidation resistance

The results presented show that in many cases the steels show better steam oxidation resistance at 650°C than at 600°C. A bell-shaped temperature dependence of the steam oxidation rate has been reported [5] and the effect is attributed to the increased incorporation of Cr in the scale. As the test temperature is increased, Cr diffuses more rapidly and the scale becomes more protective. The temperature dependence of the steam oxidation of the new steels is presented in Figure 7, confirming that this effect is also present in the new steels. It is therefore important that oxidation testing should not only be carried out at the highest application temperature; the highest oxidation rates may be found at lower temperatures.

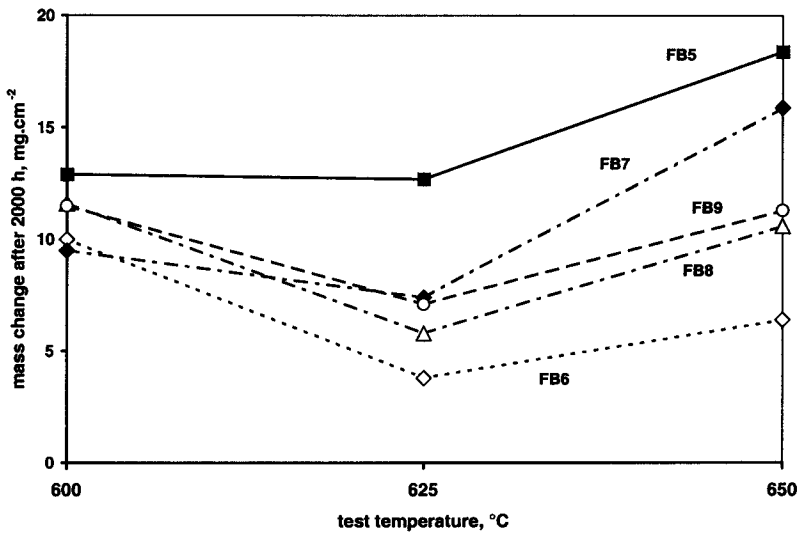


Figure 7
Temperature dependence of oxidation mass gain for forged steels series FB
(filled points, low Cr; open points high Cr)

Influence of alloying additions on steam oxidation behaviour

The aim of the new steel development was to obtain improved steam oxidation resistance, principally by increasing the Cr content of the steels. This objective has in general been met, the new cast and forged steels exhibiting better oxidation resistance than P92. There was evidence that the cast steels were superior to the forged versions of the steels. To show the beneficial effect of the increased Cr contents, the mass changes at 600 and 650 after exposure for 2000 h in steam-containing environments are plotted in Figure 7 as a function of Cr content. The diagram clearly shows the dominating influence of Cr content on the steam oxidation resistance. The tendency for the cast versions to be better than the forged steels is also apparent from the Figure 7. It is, however, known that the minor alloying additions can affect the oxidation rate

and the adherence of the oxide scale. In Figure 8, the results are re-plotted with the Si and Mn contents differentiated into low, medium and high level ranges.

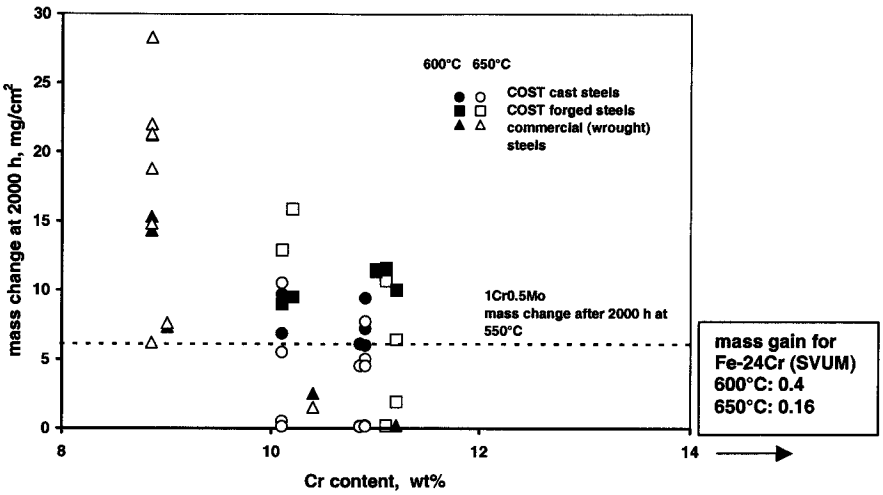


Figure 8
Mass changes for high Cr steels after exposure in steam-containing atmospheres as a function of Cr content

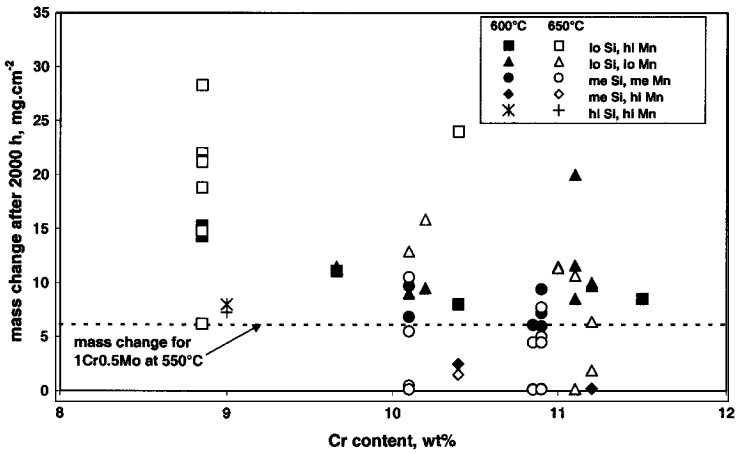


Figure 9
Same results as in Figure 8 with some additional data from model alloys [7]; data are differentiated according to Si and Mn contents;
Si: low <0.13, medium 0.2 – 0.3, high 0.3 – 0.4
Mn: low <0.1, medium 0.15 – 0.3, high 0.35 – 0.56

Figure 9 shows that the lowest mass gains for a given Cr content were generally found for steels with Si contents above 0.2% (points indicated by circles and diamonds), and

all the cast versions of the new steels were in this category. The low Si steels which included the forged versions of the new steels and the commercial P92 and E911 steels, indicated in the diagram by triangles and squares, exhibited the highest mass gains. Concerning the other alloying additions, the steels examined in the COST Action did not allow an evaluation of the effect of Co on the steam oxidation resistance. Experiments with model steel compositions [8] have, however, indicated that additions of Co promote the formation of Cr_2O_3 scales at 600 – 650°C, although Co itself is not incorporated into the scales.

The effect of Si additions has been investigated in the high Cr steels [9] and together with the data presented in this paper, the results indicate that it would be beneficial for the steam oxidation resistance to have at least 11% Cr and 0.3% Si present. The addition of Co to provide a fully martensitic microstructure at the higher Cr contents is not expected to have any deleterious effect and may indeed be beneficial.

Mechanisms of steam oxidation

The mechanisms of steam oxidation in ferritic steels have been investigated in [8] in which a two-stage process was proposed. The first stage involves the formation of gaseous $Fe(OH)_2$ and the second stage is the formation of H_20/H_2 bridges [9]. The first stage reaction may be pressure dependent and this would explain the results obtained for P92 in high pressure steam environments. It will be important to carry out steam oxidation exposures at high pressure in the further development of high Cr steels for service in steam at 600-650°C.

Future steel development

The results have clearly shown the beneficial effects of increasing Cr content on the steam oxidation resistance. The mechanical properties of the new COST 522 steels are being investigated and some results are presented in other papers in these proceedings (see, for example Kern et al: The European Effort in Development of New High Temperature Rotor Materials up to 650°C – COST 522, and Staubli et al: Development of Creep Resistant Cast Steels Within the European Collaboration in Advanced Steam Turbine Materials for Ultra Efficient, Low Emission Steam Power Plant – COST 501 and 522). It was clearly going to be difficult to obtain in a single composition the highest creep strength and the optimum steam oxidation resistance, and therefore some compromise will be necessary. One way ahead that is under consideration is the application of coatings for protection against steam oxidation. The COST 522 efforts in this direction are reported elsewhere in these proceedings (Aguero et al: Coatings for Steam Power Plant Under Advanced Conditions) and some promising results have been obtained.

The problem of extrapolating the steam oxidation data to service lifetimes is made difficult by the propensity of the scales to spall off. The spalling behaviour is being examined and spalling maps which indicate at which thickness and under which cooling rates the scales spall are being developed (see Osgerby and Mccartney: Steam Oxidation of 9-12% Martensitic Steels: Characterisation and Modelling the Spalling Behaviour).

Conclusions

1. For steels required to operate at temperatures of 600-650°C in steam environments, at least 11% Cr and 0.3% Si appear to be necessary.

2. There was fairly good agreement between the results from the different participating laboratories in short-term exposures in steam. The tendency for spalling led to somewhat larger scatter of the data after longer exposure times.

Acknowledgments

The authors wish to thank all the partners in the COST 522 Oxidation and Protective Systems Group for the excellent co-operation. Thanks are also due to Dr V Shemet who supervised the steam oxidation testing in Jülich.

References

[1] ASTM Standard A335-P91 Standard Specification for Seamless Ferrite Steel Pipe for High Temperature Service, American Society for Testing of Materials, 1986
[2] M Staubli, W Bendick, J Orr, F Deshayes, C Henry; European Collaborative Evaluation of Advanced Boiler Materials, in Materials for Advanced Power Engineering 1998, ed J Lecomte-Beckers, F Schubert, P J Ennis, ISBN 389336 228-2, Forschungszentrum Julich, Energy Technology Series, Volume 5, 1998, Part I, 87-103
[3] T Fujita; Advances in 9-12% Cr Heat Resistant Steels for Power Plants, in Advances in Material Technology for Fossil Power Plants, ed R Viswanathan, W T Bakker, J D Parker, EPRI Report 1001462, Institute of Materials Book 0770, 2001, ISBN 1-86125-145-9, 33-65
[4] P J Ennis; The Long-Term Creep Rupture Strength of 9-12% Chromium Steels, in Advances in Turbine Materials, Design and Manufacturing, ed A Strang, W M Banks, R D Conroy, M J Goulette, Institute of Materials, Book 689, ISBN 1 86125 053 3, 1997, 296 - 308
[5] P J Ennis, W J Quadakkers; The Oxidation Behaviour of Ferritic and Austenitic Steels in Simulated Power Plant Service Environments, as ref 2, 123-138
[6] M Thiele, H Teichmann, W Schwarz, W J Quadakkers, H Nickel; VGB Power technology, 2/97, 1997, 129-134
[7] J C Nava-Paz, R Knoedler; Steam-Side Oxidation of Ferritic Steels, as ref 2, 451-459
[8] J Ehlers, W J Quadakkers; Oxidation of Ferritic 9-12% Cr Steels in Steam-Containing Atmospheres at 550 to 650°C, doctoral thesis (in German), Report of the Forschungszentrum Jülich Jül-3883, June 2001, ISSN 0944-2952
[8] Y Fukuda, K Tamura, K Suzaki; in Proc Int Symposium Aging and Life Prediction of Corrodible Structures, Sapporo, Japan, 1997, 835
[9] A Rahmel, J Tobolski; Influence of Water Vapour and Carbon Dioxide on the Oxidation of Iron in Oxygen at High Temperatures, in Corrosion Science, Vol 5, 1965, 333-346

"COATINGS FOR STEAM POWER PLANTS UNDER ADVANCED CONDITIONS"

Alina Agüero and Raul Muelas
Instituto Nacional de Técnica Aeroespacial (INTA)
Ctra. Ajalvir Km. 4
28850 Torrejón de Ardoz (Madrid)
SPAIN

Brendon Scarlin / Reinhard Knoedler
ALSTOM
Baden, SWITZERLAND / Mannheim, GERMANY

Abstract

To achieve higher power generation efficiency in steam turbines, operating temperatures are expected to rise from 550°C to 650°C. Two approaches are being followed in COST 522 in order to accomplish this goal: 1) the development of new materials and 2) for the first time in Europe, the use of oxidation resistant coatings on currently available materials with higher creep strength but inferior steam oxidation resistance, which is the object of this work.

This presentation covers the efforts carried out while exploring the suitability of coatings for steam turbine components. In the initial stages of this work, commercially available materials, known to have good high temperature oxidation resistance, were applied by different deposition techniques. These techniques were chosen on the basis of being potentially appropriate for coating very large components: the application of aluminium slurries, the deposition of Al, Cr, Co, Fe and Ni alloyed materials by thermal spray and the application of electroless nickel. The aluminium slurry coating was deposited by brushing, and a series of post-heat treatments were evaluated in order to generate a uniform and stable diffusion coating. Thermal spray coatings were deposited by High Velocity Oxygen Flame (HVOF) spraying and optimisation to minimise porosity and maximise adhesion was carried out. Electroless nickel coatings were applied using commercial procedures.

The coatings were characterised by metallography, SEM-EDS and XRD and steam oxidation laboratory testing was carried out at 650° C. The preliminary findings showed that some of the studied coatings are very promising.

Results of the initial preliminary testing carried out for 10,000 h. will be presented. Finally, mechanisms of protection as well as degradation for the different coatings will also be discussed.

Keywords: Steam power plant, high temperature, efficiency, ferritic steels, oxidation resistance, coatings.

1. Introduction and Background

Future coal-fired steam power plant will be required to operate with high efficiency and thereby at high temperatures. As a consequence key high temperature components will require not only high creep strength but also a high resistance to oxidation in a steam environment. In particular, components such as steam pipes as well as turbine rotors, casings and blades must be resistant to the growth and also to the exfoliation of oxides.

Whereas alloy development activities have been very successful in improving the creep strength (for example the replacement of X20CrMoV 12 1 by P92 or E911), this has generally been achieved

through lowering the chromium content. The consequence has been a worsening of the resistance to steam oxidation [1].

At 650°C the oxidation of ferritic Cr-steels in steam is much more pronounced than in air [2, 3] and the critical amount of Cr required to form protective Cr_2O_3 or $(Cr, Fe)_2O_3$ scales increases [4, 5]. It has been suggested that H_2O reduces the stability of Cr_2O_3 or causes it to decompose. Other workers suggest that steam causes the dissolution of H+ in Cr_2O_3, enhancing its ionic conductivity and resulting in a deterioration of its protective properties [6]. A third group suggest that the formation of volatile species such as CrO_2OH or $CrO_2(OH)_2$ are responsible for the breakdown of the scale [7- 9]. On ferritic steels with a Cr content lower that 10 w%, very thick oxide scales form consisting of a top layer of Fe_2O_3 and Fe_3O_4 and an inner zone mainly $(Fe,Cr)_3O_4$ spinels. These scales spall causing metal cross-section loss, component blockage and erosion of components located down-stream and also produce a thermal insulating effect resulting in overheating [10-12].

A possible solution may be provided by enhancing the surface oxidation resistance through the application of coatings. The conditions to be satisfied by such coatings are not only high resistance to oxidation growth and spalling during service, but also:

- ease of application also for large or complex components
- good adhesion to the substrate and no need for thermal treatments above the normal tempering temperature
- resistance to erosion by solid particles
- repairability on site
- low cost.

Earlier work has been performed in this area in an EPRI programme [13] particularly for boiler tubes of 2.25%Cr steels and austenitic stainless steels. The range of coatings and surface treatments investigated included chromising from an aqueous chromate solution, application of a Cr_2O_3 ceramic coating, and application of a layer of aluminium, electroless nickel or silicon. Oxidation testing was typically carried out for 2500 hours in a closed-loop steam testing rig at 650°C. For coatings applied using these specific techniques and for these specific testing conditions it was concluded that the only satisfactory behaviour was achieved using the chromising technique. However there is increasing resistance to use of chromate coating processes due to the health and environmental hazards involved, so that alternatives are being sought. In the EPRI investigation it was noted that application conditions were not ideal, so that a continuous defect-free layer was not achieved for all coatings. For example, where the electroless nickel coating was defect free, local behaviour was very good. It was pointed out that "some type of nickel coating may be an effective diffusion barrier". Other work also covered the deposition of Cr by pack cementation [14] but this process is carried out at temperatures too high (> 800°C) for the ferritic steels currently employed in the manufacture of steam turbine components

In a recent initial feasibility study carried out by our group within the framework of the COST 522 action, a number of commercially available coatings were explored for steam oxidation protection [15, 16]. These included materials known to have good oxidation resistance and deposited by techniques that can be employed to coat large steam turbine components either at the plant or at their location of manufacture, and also taking into consideration economical aspects. The promising results motivated further work and field testing of selected coatings.

This work includes the overall results of the joint efforts carried out at INTA in Spain and at ALSTOM Power in Germany and Switzerland. It covers the most promising and/or interesting results obtained when commercially available coatings obtained at INTA or from commercial sources were tested both in the laboratory or in a bypass of a steam turbine. The results have provided some information regarding the mechanism of protection and/or failure of the studied systems.

2. Experimental

2.1 Materials

Specimens of P92 (C: 0.1, Mn: 0.5, Si: 0.03, Cr: 8.8, Ni: 0.06, Mo: 0.4, W: 1.8, V: 0.20 w%) were obtained from Nippon Steel Corporation (15x15x1 mm). Specimens of E911 (Cr: 9, Mn: 0.5, Ni: 0.2, W: 1, Mo:1, V: 0.2, Nb: 0.08, N: 0.05, C: 0.1, Si: 0.2 w%) were obtained from the COST 501 programme. Both were sand blasted, ground (Struers 1200) and vapour degreased prior to coating. The Al slurry and the powders for thermal spraying were obtained from commercial sources.

2.2 Slurry Coatings

At INTA Process Technology Laboratories, the Al slurry was applied by brush and the coated samples were subjected to a "curing heat treatment" at 350ºC for 30 minutes under air. Diffusion heat treatment was performed under argon flow at 700ºC for 10 h. The Si aluminide coatings were prepared in the same manner by adding Si powder to the commercial slurry before application and ensuring thorough homogenisation of the modified slurry. The commercially applied Al slurries (Sermetel) were obtained from Sermatech, USA.

2.3 Thermal Spray Coatings

At INTA Process Technology Laboratories, coatings were deposited by a Sulzer Metco Diamond Jet Hybrid HVOF unit (A-3120) mounted on a 6 axes robot (ABB) and fed by a twin rotation powder feeder.

Special (proprietary) stellite and carbide coatings for field tests were applied by commercial HVOF sprayers.

2.4 Electroless Coatings

Electroless nickel with a P-content of 12% were applied to different base materials with a thickness of about 50 μm by Degussa, Schwäbisch Gmünd, Germany.

2.5 Characterisation

Sample characterisation was carried out by optical and electron microscopy (JEOL JSM-840 equipped with a KEVEX EDS microanalyser) of metallographically polished cross sections before and after exposure and by XRD (PHILLIPS PW 3710).

2.6 Steam Oxidation Laboratory Testing

Two similar steam oxidation rigs were employed both at INTA and at ALSTOM Power. The design of the rig is shown in figure 1. The oxygen content in the water must be kept to values below the 10 ppb level as the presence of oxygen favours the growth of hematite instead of magnetite. This is achieved by permanently bubbling N_2 into de-ionized, distilled water. The water is re-circulated by means of a condenser connected to the reservoir. Prior to testing, air is displaced from the testing chamber by means of N_2 which is kept flowing while heating up to the test temperature takes place (approximately 600ºC/h). Once the test temperature is achieved, the N_2 flow is cut and the water re-circulation pump is turned on. To carry out weight measurements or to remove samples, the samples are cooled to about 300ºC under N_2 and removed from the furnace. The reheat cycle (from 300ºC to the test temperature) is also carried out under N_2.

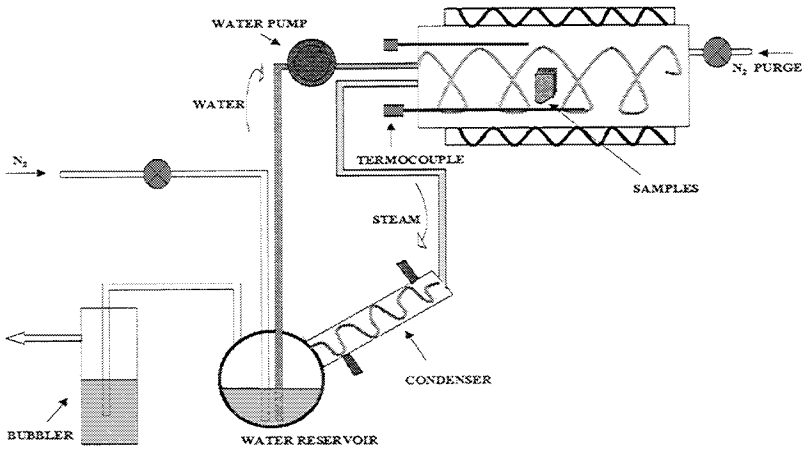


Figure 1: Design of the laboratory set-up of the pure steam oxidation rig.

2.7 Field Testing

Field tests were carried out in a steam bypass in the Westfalen power plant within the Komet 650 project [17]. Several alloys as well as coatings are currently under test at nominally 620 and 650 °C. Selected results after 6500 h will be presented.

3. Results

Several coatings applied on P92 specimens by three different techniques have been studied and were laboratory tested at 650°C under pure flowing steam. Commercially available materials containing protective oxide formers (Al, Cr, and Si) were selected also on the basis of good high temperature oxidation resistance (in air). Three families of coatings were studied: slurry aluminides, thermal spray coatings and electroless Ni coatings.

Moreover, in the Komet 650 programme, which is coordinated by the RWE Power AG and VGB PowerTech, investigations are focussed on steam oxidation testing in the bypass of the Westfalen B power plant. Samples of 9 to 12%Cr steels (such as E911, P91, P92 and P122), austenitic steels and nickel-based alloys are being exposed for times ultimately up to 24,000 hours nominally at both 620 and 650°C. At intermediate times samples are removed for metallographic examination to determine the rate of oxidation and the tendency to oxide spalling. The effectiveness of some coatings as protection against steam oxidation is also under investigation. Currently testing times have exceeded 12,000 hours.

3.1 Slurry aluminides

3.1.1 As deposited coatings characterisation

A commercially available aluminium slurry applied on P92 following the manufacturer's recommendations was heat treated at 700°C under flowing Ar. The resulting structure is shown in figure 2. Electron diffraction carried out in a Transmission Electron Microscope [18] confirmed the presence of an outer Fe_2Al_5 matrix and inner and thinner FeAl layer as illustrated in the figure.

Samples were also obtained directly coated from a coating vendor using also a slurry aluminium. Their structure was similar to that obtained in the laboratory.

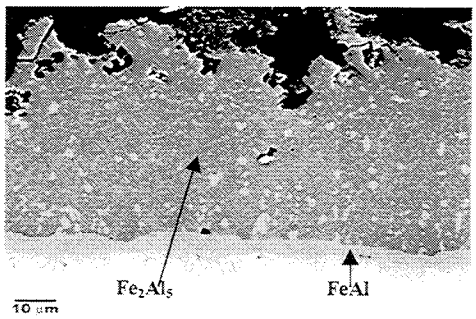


Figure 2: Slurry aluminide coating on P92 heat-treated at 700°C

The same Al slurry was modified by adding Si powder in different weight percentages. Si addition may stabilise the coating from inward diffusion, one of the main causes of aluminide coatings failure due to the loss of Al near the surface. Small amounts of Si on steel are also known to reduce the steam oxidation rate. The "as coated samples" were also heat treated at 700°C under flowing Ar. The microstructure of the 20 w% Si aluminide coating is shown in figure 3 where at least 5 phases can be observed. On the basis of EDS semiquantitative analysis the following phases are proposed: phase I near the surface could be $Fe_2(Al, Si)_5$ with some Cr in solution (36 w%Al, 3 w% Cr, 20 w%Si, 40 w%Fe), next to it, in the inwards direction a lighter coloured phase (II) can be attributed to Fe(Al, Si) also with some dissolved Cr (20 w%Al, 3 w% Cr, 22 w%Si, 55 w%Fe) while the next one of darker colour could be Fe_2Al_5 (46 w%Al, 2 w% Cr, 1 w%Si, 46 w%Fe) since it is poorer in Si. In phase III some precipitates (IV) of $Cr(SiAl)_2$ (12 w%Al, 48 w% Cr, 16 w%Si, 15 w%Fe) can be observed and finally a last lighter colour phase can be attributed to FeAl (20 w%Al, 4 w% Cr, 5 w%Si, 71 w%Fe).

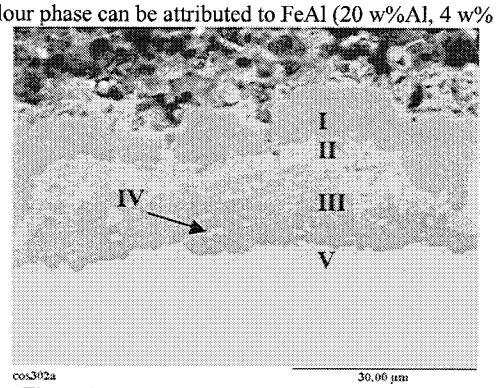


Figure 3: Slurry 20 w% Si aluminide coating on P92 heat treated at 700°C. I: $Fe_2(Al, Si)_5$; II: Fe(Al, Si); III: Fe_2Al_5; IV: $Cr(Si, Al)_2$ and V: FeAl

3.1.2 Steam Oxidation Laboratory Testing and characterisation of exposed samples

Figure 4 shows the mass variation as a function of time during steam oxidation testing. P92, has also been included for comparison purposes. Some of the coated aluminide samples experience an initial weight loss due to losses of undiffused slurry. Thoroughly ground samples did not lose weight. All of the tested coatings showed weight gains considerably lower than that of P92, the base material.

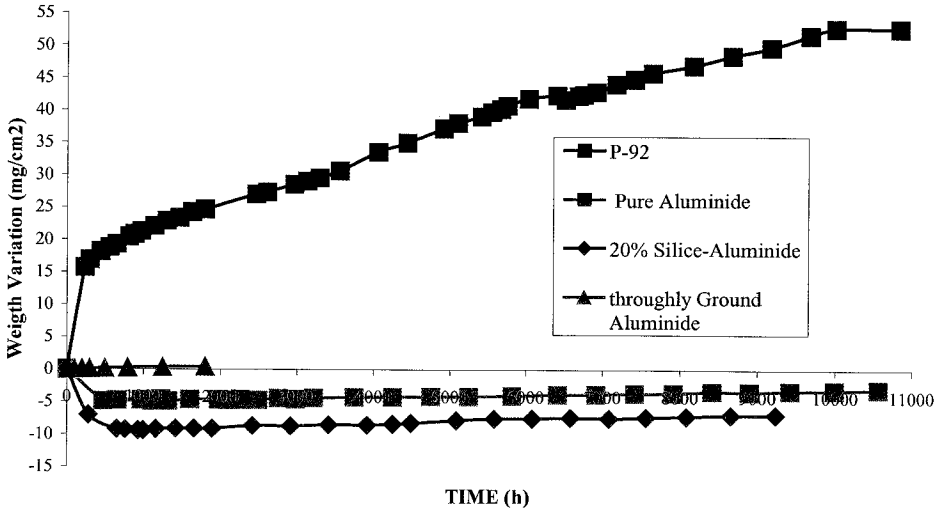


Figure 4: Mass variation of slurry coatings exposed to steam at 650°C

P92 experienced a large oxide scale growth as shown in figure 5, with an outer growing layer of Fe_2O_3-Fe_3O_4 and inner growing Fe, Cr spinels. There was little evidence of scale spallation up to 10000 h of exposure.

The cross-section of the pure aluminide coating after 10000 h of steam exposure is shown in figure 6. The coating microstructure has evolved to pure FeAl, probably by inward diffusion of Al with a surface content of Al 15 w%. Examination of intermediate time samples showed that the higher aluminide phase disappeared only after 2000-2500 hours. A zone with dark

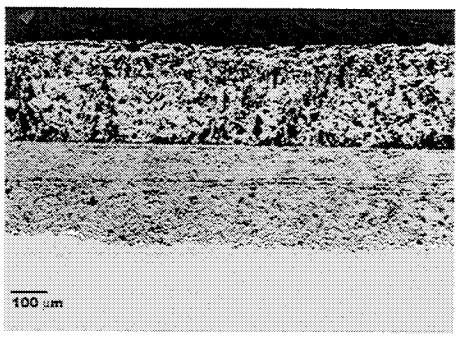


Figure 5: Cross section of a P92 specimen exposed to 5000 h of steam oxidation at 650°C

"needle like" precipitates of an unidentified phase rich in Al are also present beneath the coating and within the substrate. This zone was present from the beginning in the unexposed heat treated (for 10 hours) coating and grew in thickness from about 4 µm to 65 µm after 10000h of exposure.

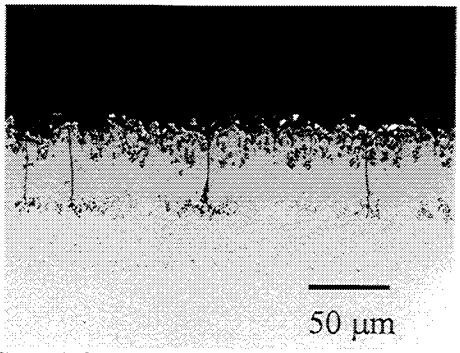


Figure 6: Cross section of a slurry aluminide coating on P92, exposed to 10000 h of steam oxidation at 650°C

Cracks perpendicular to the coating surface were present but never reached the substrate up to the tested period. Thermal cycling associated with the quite brittle Fe aluminides phases is probably causing these cracks. XRD of these coatings confirmed the presence of αAl_2O_3 scale, the most protective of its phases, as shown in figure 7.

The steam oxidation behaviour of the samples containing less than 5 % Si was not too different from the pure aluminide coatings, whereas for contents of 10 w% or higher the diffusion rate was modified significantly. For instance, the microstructure of the 20 w% Si aluminide coating tested for 6500 h also showed signs of diffusion but to a much lesser extent (figure 8). Phase I, tentatively identified as $Fe_2(Al, Si)_5$ and the closest to the surface has disappeared while II, the next one, Fe(Al, Si) has grown in thickness. Moreover, the thickness of phase III (Fe_2Al_5) has decreased considerably, while phase V (FeAl) has grown in thickness.

The coating is much richer in Al than a pure aluminide exposed to steam for the same period of time and the Al rich precipitate zone only reached 10 μm (at the same exposure, the precipitation zone of the pure aluminide coating was already 60 μm). As with the pure aluminide coating, perpendicular

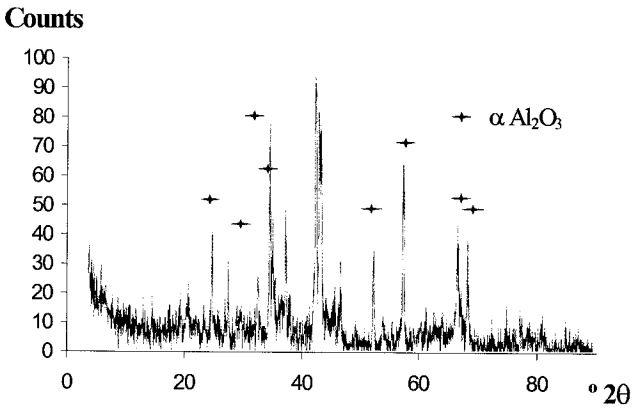


Figure 7: XRD of the surface of a pure aluminide coating Exposed to pure steam at 650°C

cracks develop, but again never reaching the substrate. However, a very thin unidentified phase surprisingly rich in Mn (10-20 w%) and W (6-8 w%) appeared at the coating / substrate interface. Although P92 has 0.5 w% Mn, such as high concentration is difficult to explain. A similar observation of a high Mn concentration in an oxide layer has been recently reported [19]. This layer seems to behave as a diffusion barrier. No signs of coating spallation could be observed for the tested period.

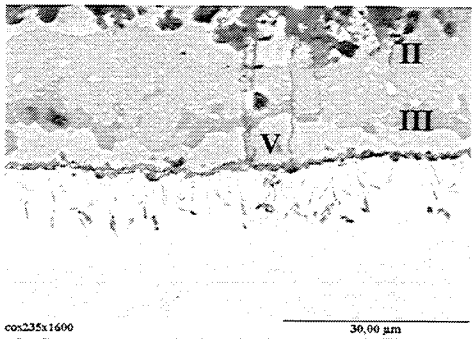


Figure 8: Cross section of a 20 w% Si slurry aluminide coating on P92, exposed to 6400 h of steam oxidation testing at 650°C

3.1.3 Diffusion studies

In order to determine if the changes in the pure aluminide coatings are due to spallation, interdiffusion with the substrate or both, aluminide coated P92 specimens were held at 650°C under flowing N_2. The samples showed similar behaviour to those exposed to steam, developing cracks and diffusing inwards. After 5500 hours, both N_2 and steam exposed samples had a remaining coating thickness of 40 µm and an interdiffusion zone of 55 µm. These results clearly indicate that the coating degradation takes places due to interdiffusion with the substrate and not to spallation. Employing diffusion barriers or adding elements (such as Si) that reduce interdiffusion should therefore ensure longer lives for this type of aluminide coating operating under steam at 650°C.

3.1.4 Field Tests

In the field test carried out at Westfalen, spallation was often observed in the uncoated samples as shown in figure 9 for P92.

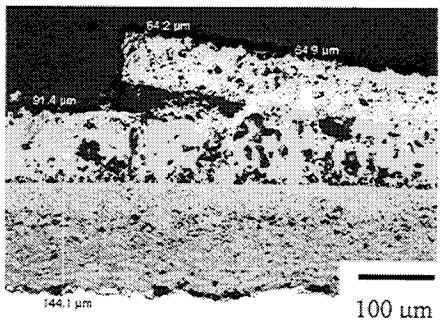


Figure 9: Cross sections of P92 steel exposed at 642°C for 6500 h in a steam bypass in the Westfalen power plant (about 280 µm scale)

This difference from the spallation behaviour observed in the laboratory tests might be attributed to different operating regimes (thermal cycles), to the higher pressure or due to the higher steam velocity in the field. In addition there are some indications, that a higher oxygen concentration is present in the field, which can lead to formation or hematite instead of magnetite. However, these observations must be confirmed by further testing.

Al slurry coatings showed only a very thin scale of aluminium oxide on top of the coating after 6500 h at 642 °C in the steam bypass (figure 10). Below the coating, a diffusion zone of about 60 µm forms, where Al has diffused into the base alloy as with the samples tested in the laboratory. The diffusion zone has not increased significantly with respect to the observations after 3300 h. Also the oxidised cracks did not increase neither in number nor in depth. Unprotected E911 develops an oxide layer of about 200 µm after this time.

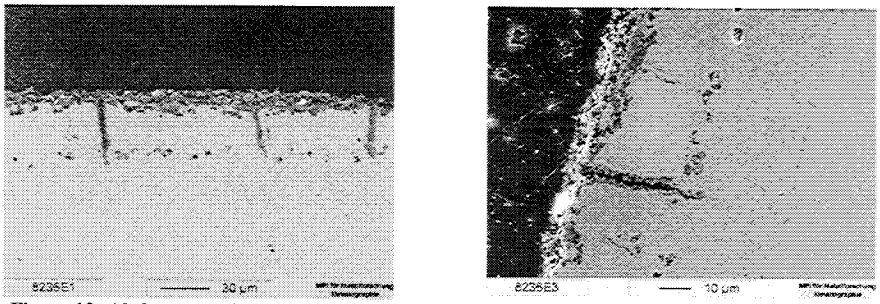


Figure 10: Al slurry coatings on E911 after 6500 h at 642 °C in a steam bypass in the power plant at Westfalen. The aluminium oxide scale is < 10 µm thick.

3.2 Thermal Spray Coatings

Although thermal spray coatings are rather expensive as compared to slurry aluminides, their life may be longer and therefore, their use justified in some specific components. Several commercial powders containing Co, Ni, Fe, Al and Cr were chosen and were deposited by HVOF.

3.2.1 As deposited HVOF coatings characterisation

NiCr (Sulzer-Metco), FeCrAl (TAFA) and AlCoFeCr (SNMI), were deposited on P92 by HVOF.

NiCr, was chosen for its high content of Cr (20 w%) and the microstructure of the as-deposited coating is illustrated in figure 11. SEM-EDS analysis showed a 19.8 w% Cr content.

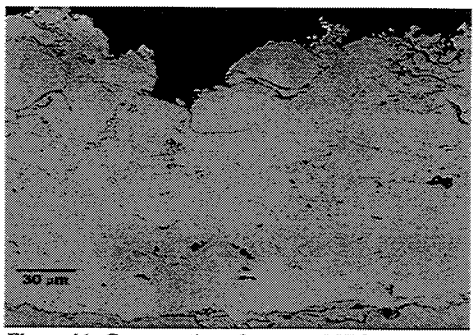


Figure 11: Cross section of as coated NiCr deposited by HVOF on P92

FeCrAl with an even higher Cr content (30 w%) and 5 w% Al showed less initial porosity as shown in figure 12. SEM-EDS analysis indicated 27.5 w% Cr and 5.9 % Al .

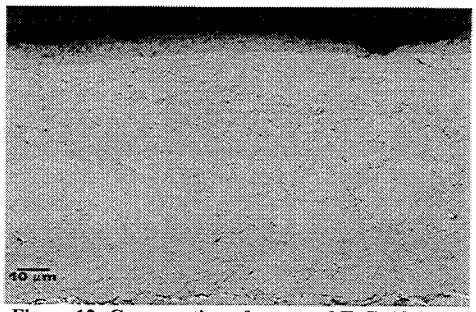


Figure 12: Cross section of as coated FeCrAl deposited by HVOF on P92

AlCoFeCr is a brittle quasicrystalline alloy with a very low thermal conductivity (2.3 W/m°K), close to that of traditional thermal barrier coatings based on yttria stabilised zirconia. Tests carried out at INTA have previously shown high resistance to oxidation (air) at 1000°C and to hot corrosion

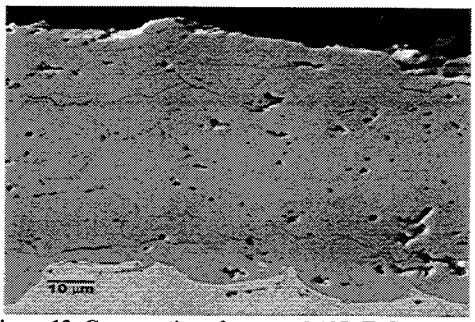


Figure 13: Cross section of as coated AlCoFeCr deposited by HVOF on P92

at 900°C [20]. However, at these temperatures, coating-substrate interdiffusion is important resulting in the transformation of the quasicrystalline phases and therefore forming materials with thermal conductivities typical of metallic alloys. AlCoFeCr deposited by HVOF resulted in a 75 µm layer showing some micro-cracks and porosity as can be seen in figure 13. The SEM-EDS analysis indicated a composition of 58.4 w% Al, 20.13 w% Co, 11.1 w% Fe and 10.4 w% Cr.

3.2.2 Steam Oxidation Laboratory Testing and characterisation of exposed samples

Figure 14 shows the mass variation of the thermal spray coatings as a function of time during steam oxidation testing. The three coatings experienced very little weight gain during 10,000 h of exposure.

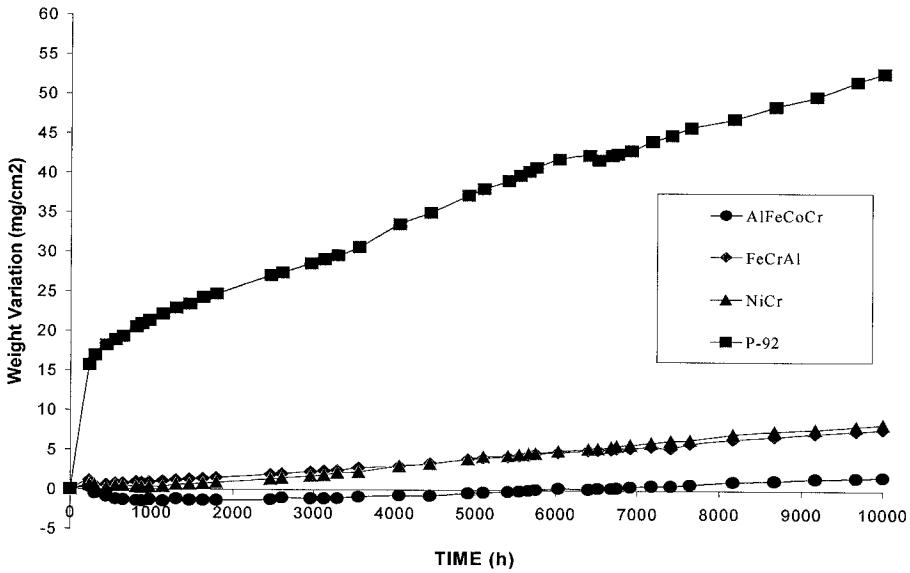


Figure 14: Mass variation of HVOF coatings exposed to steam at 650°C

The cross section micrograph of NiCr exposed to 10000 h is shown in figure 15 along with the EDS mapping of the principal elements. A very thin oxide scale has developed on its surface.

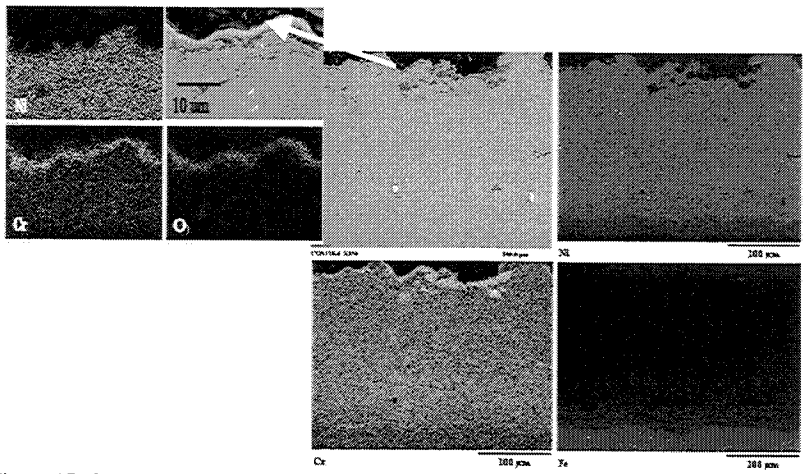


Figure 15: Cross section of NiCr deposited by HVOF exposed to steam for 10,000 h at 650°C

EDS analysis shows this layer is probably a chromium oxide. As can be seen, there is no significant thickness loss and the Cr content remains unchanged except in the zone near the substrate interface where some coating-substrate interdiffusion has taken place.

The FeCrAl coating remained totally unaffected as shown in figure 16. No changes in the coating composition or evidence of coating-substrate interaction could be observed. An even thinner oxide layer rich in Al could be seen at the coating surface, but in this case the EDS point analysis does not allow differentiation between Al oxide or perhaps an Al, Cr spinel.

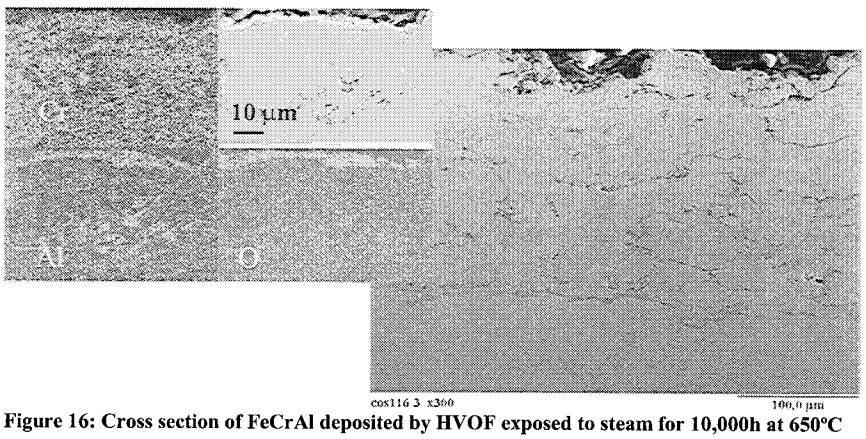


Figure 16: Cross section of FeCrAl deposited by HVOF exposed to steam for 10,000h at 650°C

AlCoFeCr, the thermal barrier candidate, did show evidence of coating-substrate interdiffusion as seen in figure 17. No initial quasicrystalline coating is left. Instead, an outer layer with a much lower Al concentration (30 w%) and Kirkendall porosity is present, on top of a second layer, richer in Fe. These two layers are probably the result of Al inward diffusion, leaving a depleted layer on top and forming an Fe aluminide at the coating-substrate interface. Moreover, Al rich needle-like precipitates, identical to those observed in the slurry aluminide coatings are present in the substrate immediately adjacent to the coating. However, no signs of substrate oxidation could be observed.

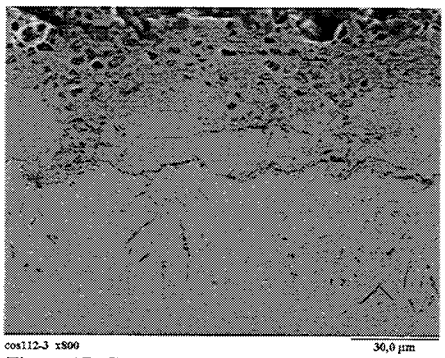


Figure 17: Cross section of AlCoFeCr deposited by HVOF exposed to steam for 10,000h at 650°C

3.2.3 Field Tests

A few proprietary coatings were applied by HVOF spraying onto E911 and exposed to steam in the bypass at the power plant in Westfalen. These coatings proved to be very oxidation resistant similar to the results obtained in the laboratory for the HVOF coatings, and only very thin oxide scales could be observed (figures 18a and b).

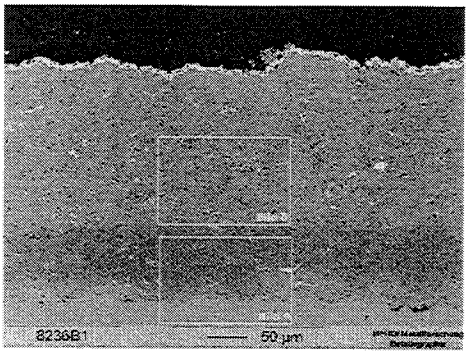


Figure 18a: Chromium carbide containing nickel coating on E911 after 6500 h at 642°C at the Westfalen power plant.

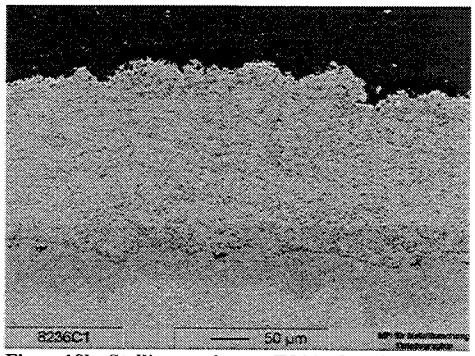


Figure18b: Stellite coating on E911 after 6500 h at 642 °C at the Westfalen power plant.

3.3 Electroless nickel coatings

Electroless nickel with a P-content of 12% was applied onto E911 with a thickness of 40 – 60 µm. After exposure times of up to 5000 h in the laboratory at 600 and 650 °C the oxidation stability of these coatings is seen to be very high although the presence of cracks that reached the substrate was observed. Figure19 shows that only thin oxide layers (predominantly Fe-oxides) grow on top of the coating.

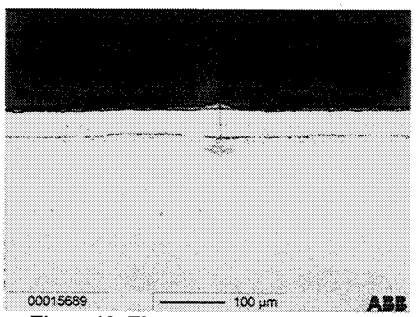


Figure 19: Electroless nickel on E911 after 4350 h at 600 °C exposed to steam. Near the crack thin oxide scales can be seen.

This is most pronounced in the vicinity of cracks in the nickel coating, as the mapping shows in detail in figure 20. It is therefore important for future work to make efforts to avoid such cracks. At the interface between nickel and base alloy also thin oxides has been formed around the crack. These inner oxides are formed by Fe-, Ni- and Cr –oxides

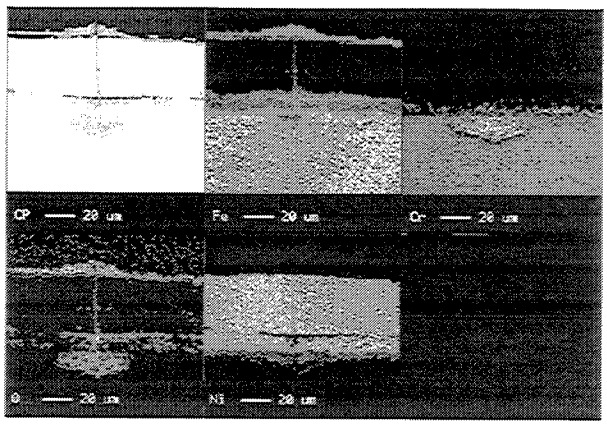


Figure 20: EDS mapping of an electroless Ni coating on E911 exposed to steam for 4350 h at 600°C

4. Discussion

The principal coating degradation mechanism observed for the alumina-former coatings, both slurry aluminide or HVOF deposited AlCoFeCr coatings is the loss of Al content due to coating-substrate interdiffusion since there is no evidence of scale spalling or degradation. αAl_2O_3 seems therefore to form despite the relatively low temperature and to be inert to steam under the testing conditions. Longer exposure will reveal if the pure aluminide slurry coatings will be protective during the expected 100,000 h of service or if more stable coatings such as the Si aluminides will be required. In these Si aluminide coatings, the presence of Si has caused the formation of a diffusion barrier layer at the coating substrate interface. This layer is rich in Mn and its phase composition will be determined by means of electron diffraction and TEM microanalysis. Moreover longer term effect of cracks needs to be determined.

As mentioned, the HVOF deposited AlCoFeCr coating intended to be used as a thermal barrier coating, was not stable at 650°C since Al inward interdiffusion took place. Thus, the initial coating gains thermal conductivity as it loses its quasicrystalline phases.

Regarding the chromia formers, some interesting results have been observed as chromia formed on NiCr (20 w%Cr) seems to be very stable to steam oxidation. No evidence of scale degradation nor Cr depletion near the scale could be observed and the coating did not seem to experience changes during the 10,000 h steam exposure period, other than a very limited degree of coating-substrate interdiffusion (and at a zone remote from the surface). A possible explanation for this observation may be in the role of Fe in the degradation mechanism of chromia. Its absence in NiCr may prevent the formation of less stable (Fe, Cr) spinels. This hypothesis needs to be explored in more detail.

Results seem to indicate that the FeCrAl coating formed alumina instead of chromia despite the relatively low temperature, as well as the low Al content (5 w% as opposed to 30 w% of Cr). There is however some precedent in this selective Al oxidation for Fe-13Cr-4Al alloys as I. Kvernes and collaborators observed the formation of Al_2O_3 on this alloy at 940°C when exposed to air with up to a 2 v% in moisture. At lower temperature, the oxidation resistance of this alloy was also excellent but only Cr_2O_3, Fe_2O_3 and $(Fe, Cr)_2O_3$ were observed [21]. Further analysis will be carried out in order to determine the composition of the oxide formed under the present testing conditions, that is if it is pure Al- oxide or an Al, Cr spinel.

Electroless nickel coatings suffer from iron diffusion through the nickel layer. As a consequence, iron oxides are formed at the nickel/steam interface. This is most pronounced in the vicinity of cracks in the nickel coating. However, since the iron oxide scale is very thin, even after longer times, electroless nickel could serve as protective coating, especially if the coating can be applied almost crack –free.

The field test results so far obtained are in agreement with the laboratory tests regarding the behaviour of the slurry aluminide coatings. However, uncoated materials spalled in the field testing whereas under laboratory conditions spalling was seldom observed for samples of equal exposure time even though the oxide scale thickness was similar in both samples. Higher flow rates as well as high pressure may be the cause of this difference. Differences in steam chemistry may also play a role (oxygen content of feedwater).

5. Conclusions and Outlook

The use of coatings on steam turbine components can greatly reduce steam oxidation at 600-650°C for durations in excess of 10,000 h. Longer exposure testing is ongoing, both in the laboratory and under operating conditions.

The principal mechanism of the slurry aluminide coating degradation is coating-substrate interdiffusion and efforts have already begun in order to prevent or retard it.

Thermal spray coatings are more stable than slurry aluminides. Their higher cost may be justified by longer lifetime for certain components. Chromia formed in alloys not containing Fe is very stable and formation of volatile chromium oxide or hydroxide containing species does not seem to occur in these alloys. Evaporation of chromium volatile species in Cr-containing steels under steam may be rather due to Cr, Fe spinels instead of chromium oxide. Further studies will be carried out in order to validate this hypothesis.

Nickel coatings can also be a viable solution. The oxidation rate is greatly diminished by nickel coatings. However, it is not clear whether the necessary freedom from cracking can be achieved. It must also be tested in longterm experiments, whether the thin iron oxide layers, which form at the interface nickel/steam tend to spall off.

Quasicrystalline AlCoFeCr can not be employed as a thermal barrier coating at 650°C since it degrades due to coating substrate interdiffusion. Traditional thermal barrier coatings will be deposited on P92 and tested under steam at 650°C

There are few results with Al-coatings available from field tests. These tests show a good correlation with the laboratory tests, although spallation in field tests is more pronounced than in the laboratory. Thus, coating can avoid both excessive oxide growth and spallation. This helps to achieve a higher power plant lifetime and efficiency by avoiding damage of turbine components by spalled particles and by providing better heat transfer conditions (thinner scales).

Acknowledgements

AA and RM (INTA) wish to acknowledge A. Del Olmo and T. Atance for their invaluable technical assistance, M.C. García for her contribution to the XRD work and A. Sánchez for supporting this project. RK (ALSTOM) wishes to thank G. Scheffknecht, G. Stamatelopoulos and Q. Chen for their support of the project and for valuable discussions.
The authors would like to thank the Management Committee of the COST 522 action and the national funding bodies for financial support.

References

[1] R. Knödler, P.J. Ennis, BALTICA V Conference, Porvoo, June 2001, Proceedings p. 355
[2] J.P.T. Vossen, P. Gawenda, K. Rahts, M. Röhrig, M. Schorr, M. Schütze, Materials at High Temperatures 14 (1997) 3.
[3] K. Zabelt, Technische Überwachung 39 (1998) 11C.
[4] I. Kvernes, M. Oliviera and P. Kofstad, Corros. Sci., 17 (1977) 2371
[5] S. Jianian, Z. Longjiang and L. Tiefan, Oxid. Met., 48 (1997) 347
[6] T. Norby, J. Phys. 3 (1993) 99
[7] H. Asteman, J.-E. Svensson, M. Norelli, L.-G. Johansson, Oxidation of Metals 54 (2000), 11
[8] H.C. Graham and H.H. Davies, J. Am Ceram. Soc., 54 (1971) 89
[9] C. A. Stearns, F.J. Kohl and G.C: Fryburg, J. Electrochem. Soc., 121 (1974) 945.
[10] C. Berger C., R.B. Scarlin, K.H. Mayer., D.V. Thornton and S.M. Beech *in Materials for Advanced Power Engineering*, D. Coutsouradis et al Eds., (Kluwer Academic Publ., Dordrecht, Boston, New York, 1994) Part I, pp 47
[11] W.J. Quaddakers, P.J. Ennis, Materials for Advanced Power Engineering 1998, Part I, Liege, Belgium, J. Lecomte-Beckers, F. Schubert and P.J. Ennis, Eds., (Forschungszentrum Jülich Gmbh, 1998), pp.123
[12] Y. Fufuda, K. Tamura and T. Sato, Materials for Advanced Power Engineering 1998, Part I, Liege, Belgium, J. Lecomte-Beckers, F. Schubert and P.J. Ennis, Eds., (Forschungszentrum Jülich Gmbh, 1998), pp.461
[13] EPRI Report CS-1811, Project 644-1, Corrosion problems in coal-fired boiler superheater tubes: Steam-side oxidation and exfoliation, April 1981
[14] J. Stringer , Surface and Coating Technology, 108-109 (1998) 1
[15] A. Agüero, F.J. García de Blas, R. Muelas, A. Sanchez y S. Tsipas, Materials Science Forum, 369-372 (2001) 939-94
[16] A. Agüero R. Muelas and A. Román., Surface Modification Technologies XIV, T. S. Sudarshan and M. Jeandin Eds., (ASM Inernational, Materials Park, Ohio, 2001), pp. 92
[17] Köster, P. Moser, H. Bergmann, J. Jacobs, VGB Power Tech 9 (2001),64
[18] P. Vallés, INTA, Madrid, 2001, Unpublished Results
[19] R.J. Ehlers, W.J. Quadakkers, Oxidation of ferritic 9-12%Cr steels in steam-containing atmospheres at 550 to 650°C, Jülich Report 3883, ISSN 0944-2952, 2001 (in German)
[20] Sánchez A., Garcia de Blas F.J., Algaba J.M., Alvarez J, Garcia Poggio M.C., Agüero A., Proceedings of Materials Research Society 1998 Fall Meeting, J.M. Dubois, P.A. Thiel, A.P. Tsai and K. Urban Eds., Boston, Massachussets, November 1998, pp 447-458.
[21] I.Kvernes, M.Oliveira and P.Kofstad, Corrosion Science, 17 (1977) 237.

SECTION 3

ADVANCED STEAM POWER PLANT

3.1. Microstructure

MARTENSITIC/FERRITIC SUPER HEAT-RESISTANT 650°C STEELS – MICROSTRUCTURE

R. Agamennone and W. Blum
Universität Erlangen-Nürnberg, Technische Fakultät, Institut für Werkstoffwissenschaften LS 1, Martensstrasse 5, D-91058 Erlangen, Germany

Abstract

The model alloys DT4-1 (3% W), DT4-2 (4% W) and DT4-13 (3% W, 0.2% Ta) were microstructurally investigated after heat treatment and after compression creep at 650°C for up to 3000 h with stepwise increase in stress. The subgrain size in the annealed martensite did not change significantly during creep in accordance with the laws of subgrain evolution. In the initial state after heat treatment the precipitates in DT4-1 and -2 consisted mainly of $M_{23}C_6$. In DT4-13 TaC was additionally present in a fine distribution. Creep resulted in massive precipitation of Laves phase. The evolution of the precipitate structure was consistent with the results of thermodynamic calculations of equilibrium phases using the program Thermocalc. The observed precipitates explain the high creep resistance of the model alloys which increases in the sequence DT4-1, -2 and -13.

Keywords: 12% chromium steel, creep, subgrain, precipitates

1. Introduction

The present contribution is part of a cooperative project aiming at developing new super heat-resistant steels for use in power plants at 650°C and 300 bar. A selected number of model alloys produced within the project were microstructurally investigated to understand their creep properties which are comparable or superior to those of the commercial steel P92.

2. Experimental

Model alloys were produced as small ($\approx$ 0.5 kg) laboratory casts and heat treated and tested in creep at the Max-Planck-Institut für Eisenforschung, Düsseldorf [1, 2]. The model alloys investigated in this work were DT4-1 (with 3% W), DT4-2 (with 4% W) and DT4-13 (with 3% W, 0.2% Ta). Their chemical composition is given in table 1.

Alloys		Cr	Si	C	N	W	V	Ta	Co	Cr_{eq}
DT4-1	3W	12.70	0.192	0.083	0	3.13	0.213	0	4.82	7.93
DT4-2	4W	12.60	0.147	0.081	0	4.14	0.215	0	5.61	7.6
DT4-13	0.2Ta	12.70	0.209	0.135	0.0098	3.07	0	0.212	2.05	9.3

Table 1: Designation and chemical composition of the investigated model alloys (mass-%)

The heat treatment consisted of austenization for 0.5h at 1070°C followed by air cooling and tempering for 2h at 780°C followed by air cooling. The microstructural investigations

were done in the initial state after heat treatment and in the state after compressive creep at 650°C. From each material thin steel foils and extraction replicas were prepared. The steel foils were thinned by jet electropolishing of discs with 3 mm diameter and 60-80 μm thickness, using a mixture (volume ratio 10:1) of acetic and perchloric acid at 283 K and 20 V. Replicas were prepared by selective matrix etching in Vilella etchant to isolate the precipitates, vaporizing with carbon and separating the carbon film from the matrix in acid (volume ratio HNO_3 : HCl : H_2O = 10 : 1 : 10).

The mean size w of subgrains was determined by scanning transmission electron microscopy (STEM) of thin steel foils using the line intersection technique with test lines drawn at 45° to the direction of elongation of the martensite laths [3]. Size distribution and volume fraction of precipitates were evaluated combining EDX-analysis and size determination in STEM of extraction replicas. Linear montages of STEM micrographs (Fig. 1) were prepared to minimize systematic errors by subjective choice of object [4, 5]. Following the procedure described in [4, 5], each micrograph was taken twice, firstly with optimum resolution to enable determination of the equivalent precipitate diameters and secondly in combination with semiautomatic determination of the EDX-spectrum of each potential precipitate. For each type $k = 1, 2, ...$ of precipitates the size distribution and the average size $d_{\mathrm{p},k}$ were determined by hand-marking the circumferences of precipitates followed by image analysis with the software Image C. The volume fractions $f_{\mathrm{p},k}$ of precipitates were determined as [6]:

$$f_{\mathrm{p},k} = \frac{N_{A,k} \cdot \phi_k \cdot V_{\mathrm{p},k}}{t_{\mathrm{foil}} + d_{\mathrm{p}}} \tag{1}$$

where ϕ_k is the numerical fraction and $V_{\mathrm{p},k}$ the mean volume of precipitates of type k and t_{foil} the thickness of the investigated volume, approximated as 100 nm in agreement with [4, 5]. The error bars given in this work for w, d_{p} and f_{p} represent the standard deviation of ≥ 3 individual values measured for different samples, neglecting systematic errors, e.g. due to deviations of t_{foil} from the estimated value.

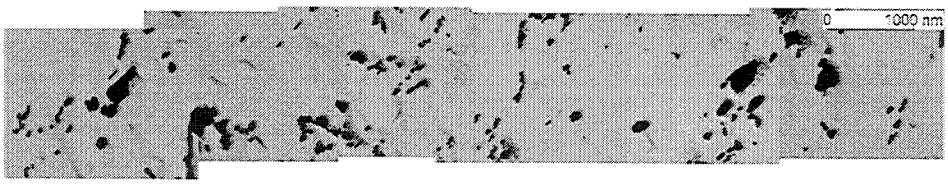


Figure 1: Montage of STEM pictures of extraction replica of DT4-1 after heat treatment

3. Results

The microstructure of the model alloys consisted of tempered martensite with small amounts of δ-ferrite [2]. Creep tests have been carried out by Knezevic et al. [1] in compression of specimens of aspect ratio of about 2 at 650°C with stepwise increase in load. Figure 2 a to c (upper part) show the variation of the creep rate $\dot{\epsilon}$ with strain ϵ in these tests. The $\dot{\epsilon}$-ϵ curves were obtained by evaluation of the measured strain

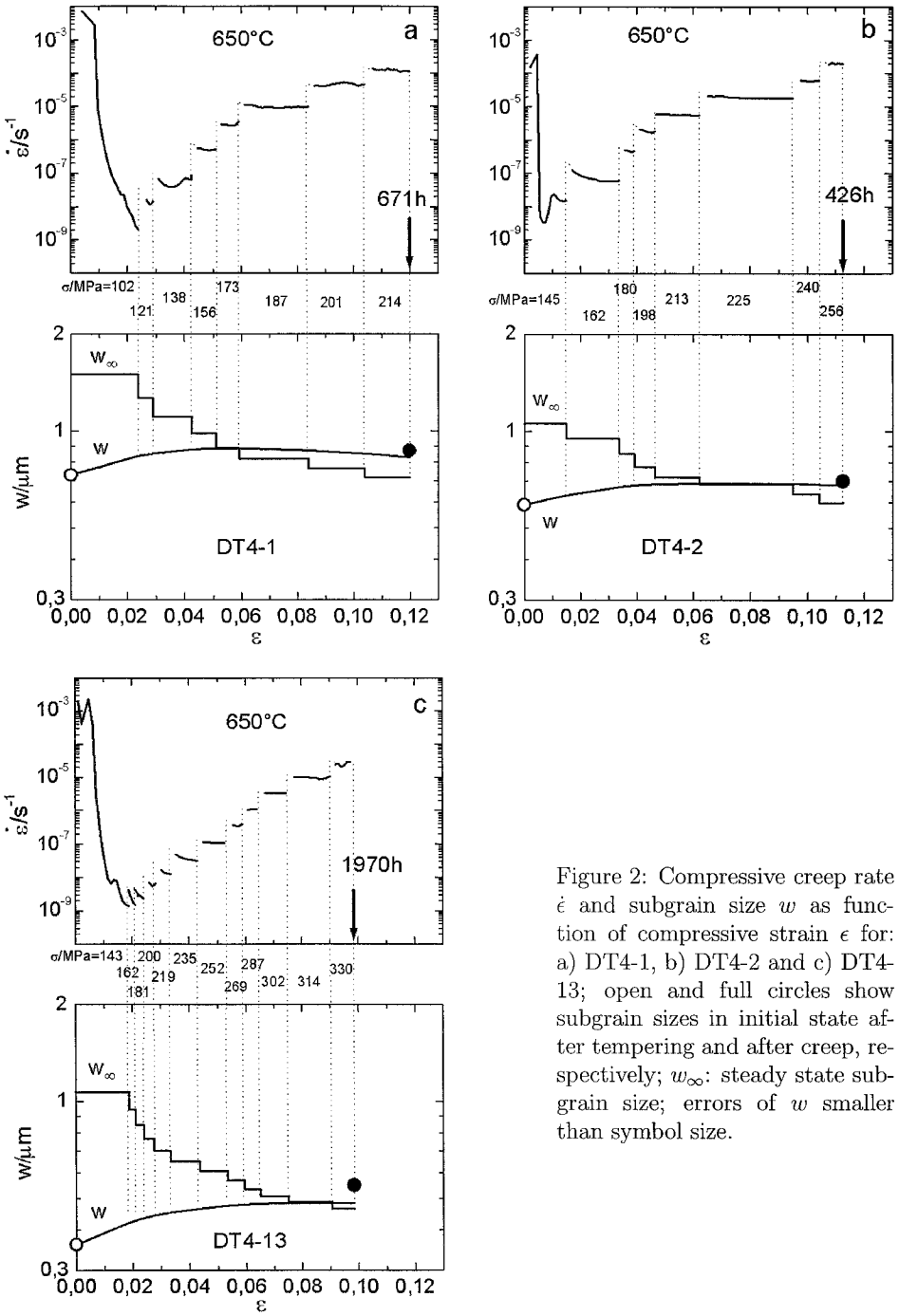


Figure 2: Compressive creep rate $\dot{\epsilon}$ and subgrain size w as function of compressive strain ϵ for: a) DT4-1, b) DT4-2 and c) DT4-13; open and full circles show subgrain sizes in initial state after tempering and after creep, respectively; w_∞: steady state subgrain size; errors of w smaller than symbol size.

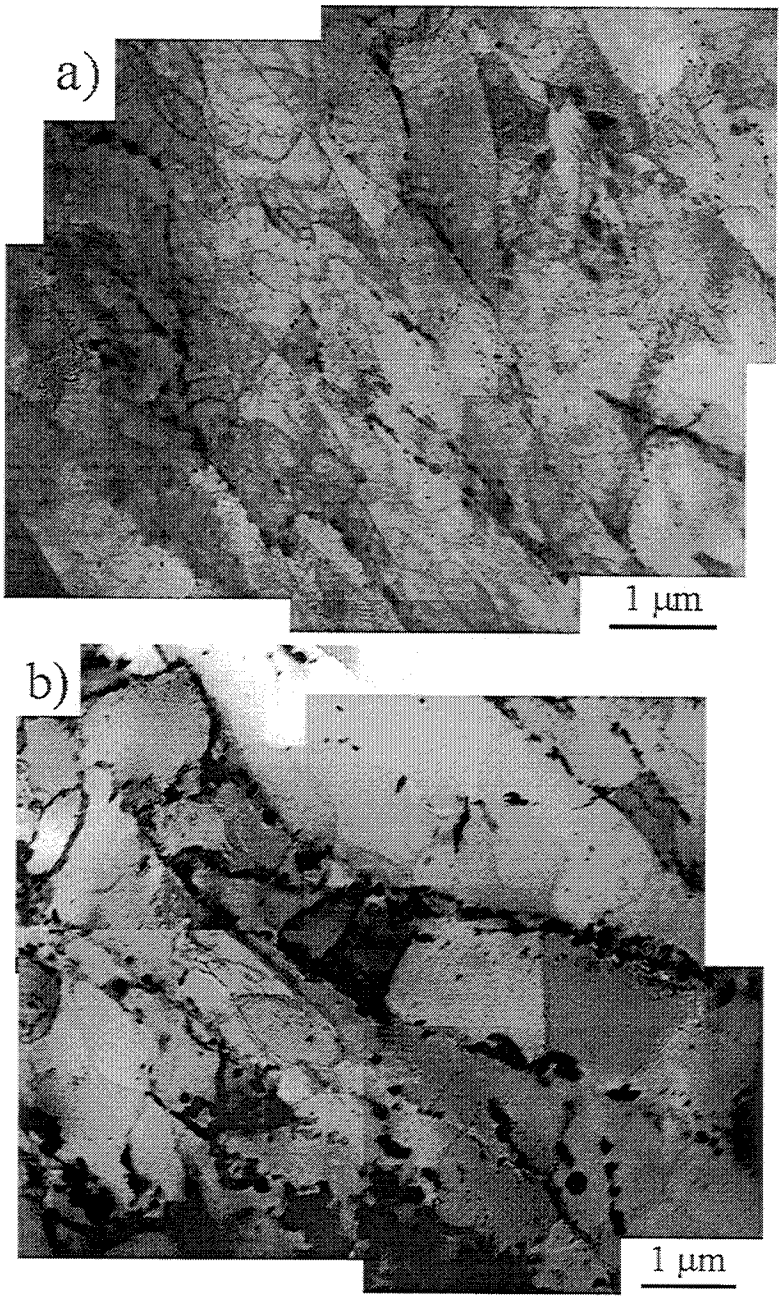


Figure 3: Subgrain structure of DT4-13 (0.2% Ta) a) in initial state after heat treatment, b) at end of creep test in Fig. 2c (650°C, 330 MPa, $\epsilon = 0.098$, 1970 h); bright field TEM.

ϵ-time t data with appropriate averaging to determine the creep rate as $\dot{\epsilon} = \Delta\epsilon/\Delta t$ with $\Delta\epsilon > 10^{-3}$, i.e. sufficiently large compared to the experimental error of strain determination. σ is the stress (load per average cross section) at the point of load increase. The $\dot{\epsilon}$-ϵ curves clearly show that the minimum (secondary) creep rate $\dot{\epsilon}_{\min}$ has not been attained in the initial portions of the tests. The corresponding data points are marked in Fig. 4 by an arrow. The lower parts of Fig. 2 a to c display the subgrain sizes measured before and after creep. Examples of the subgrain structure are shown for DT4-13 in Fig. 3. The initial subgrain size w_0 after tempering increases in the order DT4-13, DT4-2 and DT4-1. The continuous w-ϵ-curves starting at w_0 at $\epsilon = 0$ were calculated from the subgrain evolution law given in [3, 6]:

$$\frac{d\log w}{d\epsilon} = -\frac{\log w - \log w_\infty}{k} \tag{2}$$

with k being approximated as 0.12. w_∞ is the steady state value of the subgrain size which depends on stress σ normalized by the shear modulus G according to [3, 6, 8]:

$$w_\infty = \frac{C \cdot G \cdot b}{\sigma} \tag{3}$$

where $b = 0.248$ nm is the Burger vector and $C = 10$; due to the stepwise increases in load, w_∞ is a stepwise decreasing curve. The increasing w-evolution curves and the decreasing w_∞-curves approach each other with increasing strain so that the difference between the two becomes relatively small meaning that the subgrain size remains virtually unaltered. Consistent with the relative constancy of w, the transients following the stress increases are quite limited in the later portions of the tests. This indicates that the creep rates in these portions can be identified with the secondary rates for the respective stresses.

The secondary creep rates $\dot{\epsilon}_{\min}$ determined in this manner are displayed in Fig. 4. The figure includes data for the steel P92 (9% Cr, 2% W) taken from the literature [9]. The alloy DT4-1 (with 3% W) exhibits a stress dependence of the secondary creep rate similar to that of P92. This is remarkable as the subgrains in DT4-1 are distinctly coarser ($\approx$ 700 nm, Fig. 2) compared to P92 ($\approx$ 300 nm [7]) so that there is less subgrain strengthening in DT4-1 in relation to P92. The increase of W in DT4-2 (with 4% W), balanced by Co to keep the chromium equivalent constant [1], leads to improved creep resistance. With the addition of 0.2% Ta, the curve of DT4-13 (with 3% W) shifts to even higher stresses. After tempering all alloys contain $M_{23}C_6$ precipitates which are mainly located at subgrain boundaries (Fig. 3a). In addition, TaC is present in DT4-13 in relatively homogeneous, fine distribution. There are also few coarse Laves phase precipitates present in the tempered state of DT4-2. Typical EDX spectra of the three kinds of precipitates are given in Fig. 5. Figures 6 to 8 present the evolution of the mean sizes and the volume fractions of the precipitates as a function of time spent during creep at 650°C. Dotted lines indicate the f_p-values determined by Vilk and Inden [10] as a result of calculations with the software Thermocalc. The initial d_p-values of $M_{23}C_6$ are in approximate agreement with the calculated values. The initial sizes of $M_{23}C_6$-precipitates are about 100 nm. It is noted that the $M_{23}C_6$-precipitates were frequently lying in close contact so that the separation of different precipitates was somewhat subjective causing an error of unknown magnitude.

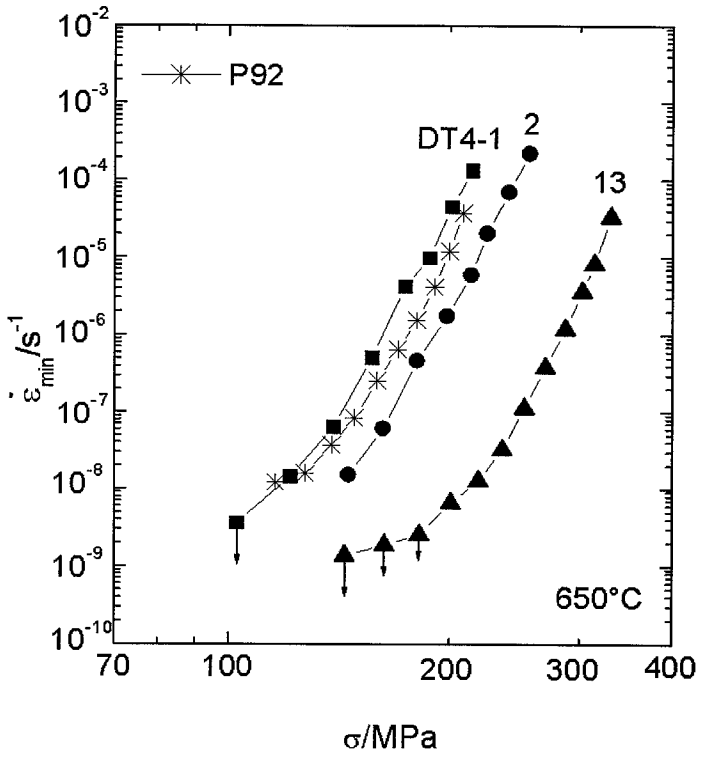


Figure 4: Secondary creep rate of DT4-1, DT4-2, DT4-13 as a function of applied stress at 650°C; data for P92 from [9]. Arrows indicate $\dot{\epsilon}$ values measured in the primary range of creep.

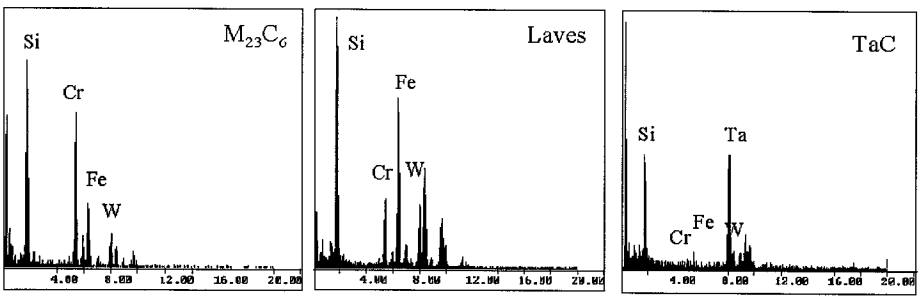


Figure 5: EDX spectra of precipitates: a) $M_{23}C_6$ (rich in Cr), b) Laves phase (rich in Fe and W), c) TaC (rich in Ta).

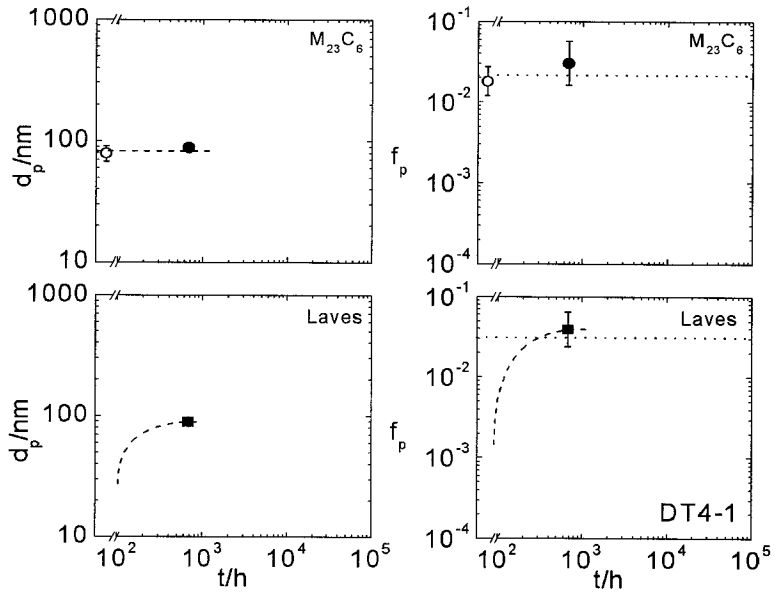


Figure 6: Mean precipitate sizes d_p and volume fraction f_p of $M_{23}C_6$ and Laves phase in DT4-1 as a function of time t at 650°C. Open symbols: after tempering, full symbols: after creep, small symbols: <3 individual values. Dotted lines from Thermocalc.

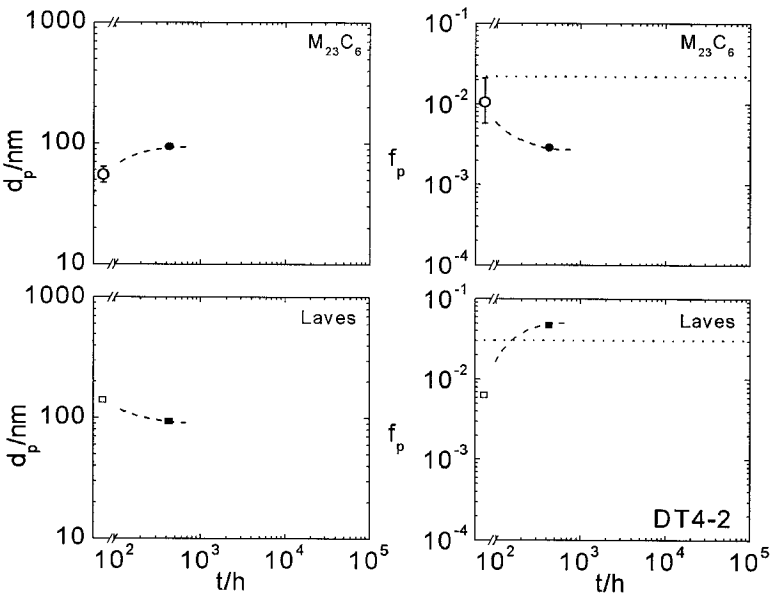


Figure 7: As Fig. 6 for DT4-2.

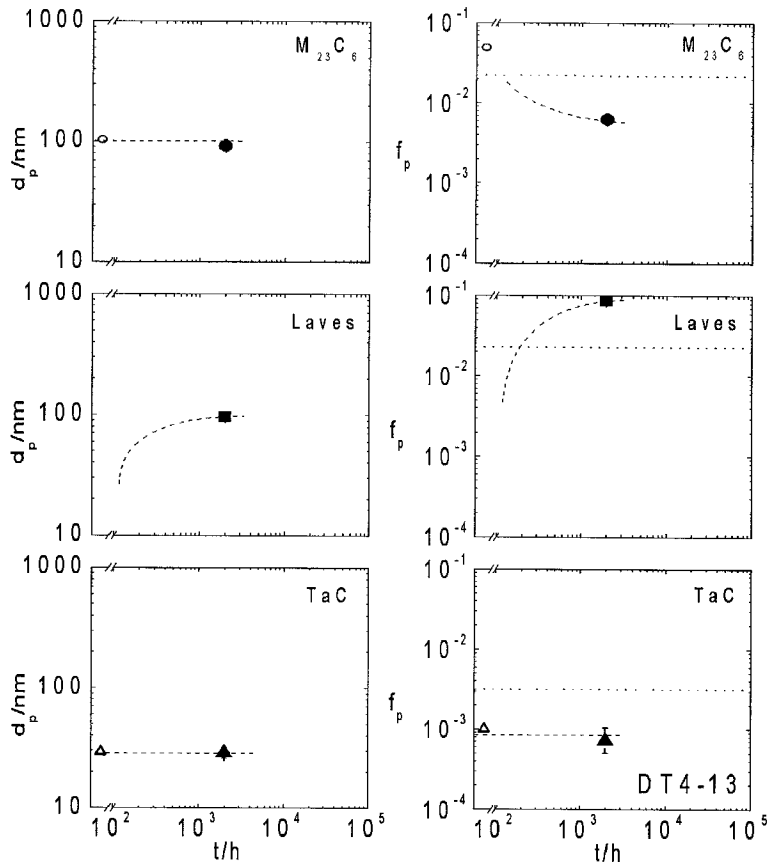


Figure 8: Mean precipitate sizes d_{p} and volume fraction f_{p} of $M_{23}C_6$ and Laves phase in DT4-1 as a function of time t at 650°C. Open symbols: after tempering, full symbols: after creep, small symbols: <3 individual values. Dotted lines from Thermocalc.

For TaC the measured f_{p} values are smaller than calculated, but still in the right order of magnitude. There was no significant coarsening of either phase during creep. The initial volume fraction of Laves phase was in all cases quite small or even negligible. However, there was a massive precipitation of Laves phase occurring at the temperature of creep raising its volume fraction to values equal to or even higher than the initial values for $M_{23}C_6$. This agrees with the Thermocalc calculations. In agreement with [11], Laves phase was observed to nucleate at $M_{23}C_6$ precipitates during creep, possibly for the enrichment of silicon (see Fig. 5) which is of importance in the formation of the Laves phase. The observation of strong decrease of the volume fraction of $M_{23}C_6$ being coupled with strong increase of the volume fraction of Laves phase may be related to the spatial proximity of both phases, in that Laves phase grows at the expense of $M_{23}C_6$.

5. Summary

Within the range of creep rates measured in this work there is a tendency for the model alloys to be strengthened by increasing W content. DT4-1 with 3% W has similar creep properties at 650°C as P92, although its initial subgrains are coarse in relation to those of P92. DT4-2 with 4% W is significantly stronger than P92 in spite of relatively large initial subgrains. DT4-13 with 3% W and addition of Ta is strongest. This may be explained by the addition of hardening by initial subgrains of relatively small (360 nm) size and hardening of the subgrain boundaries by $M_{23}C_6$ and Laves phase plus hardening of the subgrain interior by TaC. The present results thus indicate a potential to reach sufficient creep resistance for application at 650°C.

Acknowledgment

Thanks are due to the Deutsche Forschungsgemeinschaft for funding this work.

References

[1] V. Knezevic and G. Sauthoff. Martensitic/ferritic super heat-resistant 650°C steels - Design of model alloys. In *Materials for Advanced Power Engineering* (2002).

[2] R. Agamennone, C. Berger, W. Blum, J. Ehlers, J. Granacher, G. Inden, V. Knezevic, G. Sauthoff, A. Scholz, L. Singheiser, J. Vilk, and Y. Wang. Martensitic/ferritic super heat-resistant 650°C steels. In *Materials for Advanced Power Engineering* (2002).

[3] S. Straub, M. Meier, J. Ostermann, and W. Blum. Entwicklung der Mikrostruktur und der Festigkeit des Stahles X 20 CrMoV 12 1 während Zeitstandbeanspruchung und Glühung. In *VGB-Konferenz "Restlebensdauer 1992", 6. und 7. Juli 1992, Mannheim, VGB-TB 520, Vortrag 7*, VGB Technische Vereinigung der Großkraftwerksbetreiber e.V. (1992) 7.1–7.29.

[4] G. Götz, Y. Qin, and W. Blum. Investigation of precipitation in cast martensitic annealed steel X12 CrMoVWNbN 10-1-1 by semiautomatic EDX-analysis in the scanning transmission electron microscope. In R. Viswanathan, W.T. Bakker, and J. D. Parker, editors, *Advances in materials technology for fossil power plants, Proc. of the 3rd Conference held at University of Wales Swansea, 5th April - 6th April 2001*, The Institute of Materials, London (2001) 155–163.

[5] G. Götz and W. Blum. Mikrostruktur und Kriechwiderstand der Stähle G- X12CrMoWVNbN10-1-1 und X12CrMoWVNbN10-1-1. In *Langzeitverhalten warmfester Stähle und Hochtemperaturlegierungen, Beiträge zur 24. Vortragsveranstaltung der Arbeitsgemeinschaft für warmfeste Stähle und der Arbeitsgemeinschaft für Hochtemperaturwerkstoffe am 30. November 2001 in Düsseldorf*, Verein Deutscher Eisenhüttenleute VDEh, Düsseldorf (2001) 18–25.

[6] P. Polcik. Modellierung des Verformungsverhaltens der warmfesten 9-12%Chromstähle im Temperaturbereich von 550–650°C. D29 (Dissertation Universität Erlangen-Nürnberg). Shaker Verlag, Aachen (1999).

[7] D. Henes, S. Straub, T. Sailer, P. Polcik, W. Blum, and K.H. Mayer. Zeitstandbedingte Änderungen der Mikrostruktur in dem japanischen Stahl NF616 mit 9%Cr, 0.5%Mo,

1.8%W, Nb, V. In *Langzeitverhalten warmfester Stähle und Hochtemperaturwerkstoffe, 20. Vortragsveranstaltung der Arbeitsgemeinschaft Warmfeste Stähle und der Arbeitsgemeinschaft Hochtemperaturwerkstoffe, 11.1997*, Verein Deutscher Eisenhüttenleute, Düsseldorf (1997) 42–55.

[8] S. Straub. *Verformungsverhalten und Mikrostruktur warmfester martensitischer 12%-Chromstähle.* Fortschr.-Ber. VDI Reihe 5 Nr. 405. VDI Verlag, Düsseldorf (1995).

[9] P. J. Ennis, A. Zielinska-Lipiec, O. Wachter, and A. Czyrska-Filemonowicz. Microstructural Stability and Creep Rupture Strength of the Martensitic Steel P92 for Advanced Power Plant. *Acta mater.* 45 (1997) 4901–4907.

[10] J. Vilk and G. Inden. Martensitic/ferritic super heat-resistant 650°C steels - thermodynamics and kinetics of precipitation reactions. In *Materials for Advanced Power Engineering* (2002).

[11] M. Hättestrand. *Precipitation Reactions at High Temperature in 9-12% Chromium Steel.* PhD thesis, Department of Experimental Physics, Chalmers University of Technology, Göteborg University (2000).

PRECIPITATION OF Z-PHASE AND DEGRADATION BEHAVIOUR OF Mod.9Cr-1Mo STEEL

K. Kimura*, K. Suzuki**, Y. Toda*, H. Kushima* and F. Abe*

* National Institute for Materials Science
1-2-1 Sengen, Tsukuba-shi, Ibaraki 305-0047, Japan
** Interdisciplinary Graduate School of Science and Engineering,
Tokyo Institute of Technology
4259 Nagatsuta, Midori-ku, Yokohama, Kanagawa 226-8502, Japan

Abstract

Changes in precipitates and microstructure during creep deformation at 873 and 923K have been investigated on a modified 9Cr-1Mo steel, in conjunction with degradation behaviour. Three types precipitates of $M_{23}C_6$, Nb(C,N) and V(C,N) have been observed in the as tempered condition and in the creep ruptured specimens. Precipitation of Laves phase (Fe_2Mo) has been detected in the specimens creep ruptured at 873K. Moreover, precipitation of Z-phase which is a complex nitride in a form of Cr(Nb,V)N, has been found in the specimens creep ruptured after long-term creep deformation for more than about 10,000h and 5,000h at 873K and 923K, respectively. Precipitation of Z-phase preferentially takes place at the vicinity of prior austenite grain boundary (PAGB), as a result of presence of coarse primary MX type carbonitride particles on PAGB. The coarsening rate of Z-phase is larger than those of $M_{23}C_6$ and MX, and it is much faster at 923K than that at 873K. Tendency of decrease in the number density of MX particles has been observed with progress in precipitation and coarsening of Z-phase. It has been concluded that precipitation of Z-phase is one of the reasons which promote a preferential recovery at the vicinity of PAGB during long-term creep exposure.

Keywords: mod.9Cr-1Mo steel, microstructure, recovery, precipitate, nitride, carbide, Laves-phase, Z-phase creep strength, prior austenite grain boundary

1. Introduction

Improvement of energy efficiency of fossil power plant is strongly demanded, in order to save energy resources such as oil, coal and natural gas and to suppress the emission of CO_2 gas. From such point of view, a lot of researches and developments on high strength ferritic creep resistant steels have been carried out [1]-[4]. Mod.9Cr-1Mo steel [5] has been widely used in power plant for high temperature structural components such as header and main steam pipe. Many investigations have been performed on the relationship between microstructure and strength property of a Mod.9Cr-1Mo steel [6]-[15]. Recently, it has been reported by Kimura et al. [13] that degradation of Mod.9Cr-1Mo steel during long-term creep deformation has been caused by heterogeneous recovery of tempered martensite microstructure preferentially occured at the vicinity of prior austenite grain boundary (PAGB), in contrast to homogeneous progress in recovery at the higher stress condition. Moreover, precipitation of Z-phase [16] has been found in the Mod.9Cr-1Mo steel after long-term creep exposure for 10,000h and more and it has been supposed that the precipitation of Z-phase may affect on a preferential recovery at the vicinity of PAGB [14], [15]. In this study, changes in microstructure and precipitates after heat treatment and during long-term creep exposure have been investigated on a Mod.9Cr-1Mo steel and the effect of precipitation of Z-phase has been discussed, in order to understand a degradation mechanism of preferential recovery occurred at the vicinity of PAGB.

2. Experimental procedure

A Mod.9Cr-1Mo steel (ASME SA-213 T91) which is the same material used in the previous studies [13]-[15] has been used in this study. Chemical composition (mass%) and heat treatment condition are shown in Table 1. Creep specimen with 6mm in diameter and 30mm in gauge length have been taken from a boiler and heat exchanger tube with about 8mm in wall thickness.

Microstructural observation was conducted on thin foils that were prepared from the steel in the as tempered condition, the crept specimens for 3,000h and 7,900h at 873K-120MPa and the creep ruptured specimen after 12,858.6h at 873K-120MPa. Analysis of the precipitates was conducted on carbon extracted replicas which were prepared from the steel in the as tempered condition and the creep ruptured specimens at 873K and 923K, creep exposure times are up to about 34,000h and 41,000h, respectively, using a field emission transmission electron microscope (FE-TEM) with an energy dispersive X-ray spectroscopy (EDX).

Table 1: Chemical composition (mass%) and heat treatment condition of the Mod.9Cr-1Mo steel studied.

C	Si	Mn	P	S	Ni	Cr
0.09	0.29	0.35	0.009	0.002	0.28	8.70
Mo	Cu	V	Nb	Al	N	Fe
0.90	0.032	0.22	0.072	0.001	0.044	Bal.

Normalizing : 1,323K/10min. → Air cooling
Tempering : 1,038K/30min. → Air cooling

3. Results and discussion

3.1 Changes in microstructure during creep exposure

Figure 1 shows schematic illustration on the effect of heterogeneous recovery on creep deformation behaviour of a Mod.9Cr-1Mo steel proposed by Kushima et al. [13]. It has been supposed that recovery of tempered martensite microstructure progressed homogeneously at the higher stress condition in the short-term region, however, heterogeneous recovery preferentially occured at the vicinity of PAGB promote the onset of accelerating creep stage at the lower stress condition in the long-term region.

Bright field TEM images on (a) a steel in the as tempered condition, the specimens crept for (b) 3,000h and (c) 7,900h at 873K-120MPa and (d) the specimen creep ruptured after 12,858.6h at 873K-120MPa are shown in Figure 2. Creep exposure periods of 3,000h and 7,900h at 873K-120MPa correspond to A point, at the onset of accelerating creep stage, and B point, in the accelerating creep stage, shown in Figure 1, respectively. Typical tempered martensite microstructure is observed in the as tempered condition (Fig.2 (a)), the lath width is about 0.3μm and the dislocation density is very high. In the creep ruptured specimen (Fig.2 (d)), significantly recovered microstructure which is wholly covered with coarse subgrain with a few μm in diameter is observed. On the other hand, progress in recovery is observed

only at the vicinity of PAGB in the specimen crept for 3,000h (Fig.2 (b)) and the microstructure within grain is still fine similar to that in the as tempered condition. In the specimen crept for 7,900h (Fig.2 (c)), extension of recovered region at the vicinity of PAGB is observed. Progress in recovery was observed only at the vicinity of PAGB at the onset of accelerating creep stage and heterogeneous progress in recovery during accelerating creep stage was clearly demonstrated by the extension of recovered region.

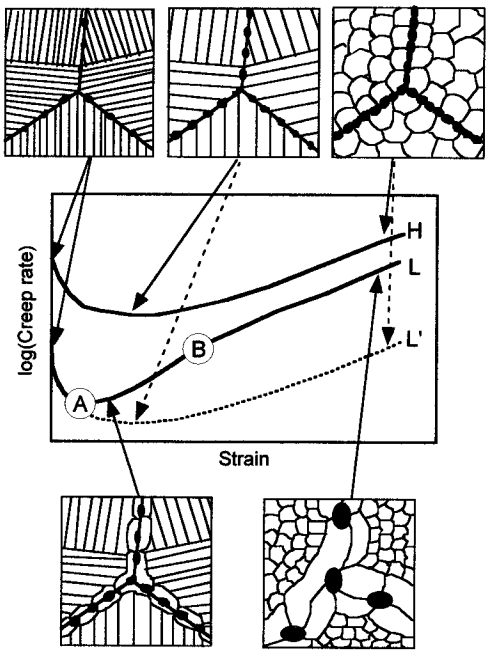


Figure 1: Schematic illustration on the effect of heterogeneous recovery on creep deformation behaviour of Mod.9Cr-1Mo steel.

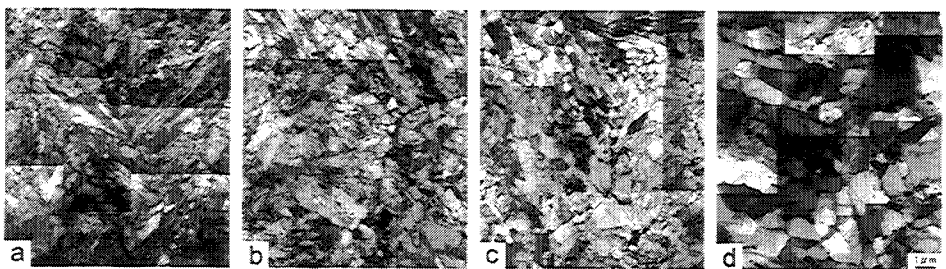


Figure 2: Bright field TEM images of Mod.9Cr-1Mo steel (a) in the as tempered condition, crept for (b) 3,000h and (c) 7,900h, (d) creep ruptured after 12,858.6h at 873K-120MPa.

3.2 Changes in precipitates

Species of the precipitates identified by EDX analysis on the steel in the as tempered condition and the specimens creep ruptured at 873K and 923K are summarized in Figure 3. Three types precipitates of $M_{23}C_6$ carbide, Nb or V dominant MX type carbonitrides of Nb(C,N) and V(C,N) were identified in the as tempered condition. Laves phase (Fe_2Mo) precipitates during short-term creep deformation at 873K, but not at 923K. Precipitation of Z-phase was detected after several thousands hours of creep exposure at the both temperatures. Precipitation of Z-phase was found more frequently at the vicinity of PAGB than within grain. Moreover, tendency to decrease in number of MX type carbonitride particles with increase in creep exposure time has been observed, especially at 923K, and Nb dominant MX of Nb(C,N) has not been found in the specimen creep ruptured after 41,425.2h at 923K-50MPa.

Changes in average chemical composition of the $M_{23}C_6$ carbide with increase in creep exposure time at 873K and 923K are shown in Figure 4. Increase in Cr content from about 60 to 70mass% instead of decrease in Fe content from about 30 to 20mass% with increase in creep exposure time is observed at the both temperatures. A little increase in Mo content instead of decrease in Cr content with increase in creep exposure time at 873K has been also observed on Laves phase. However, such obvious change in average chemical composition with increase in creep exposure time has not been observed on Nb(C,N), V(C,N) and Z-phase.

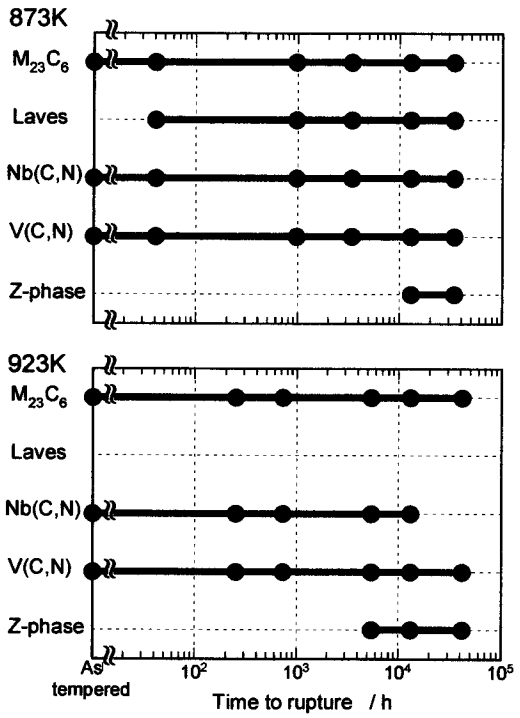


Figure 3: Changes in precipitates with increase in creep exposure time at 873 and 923K.

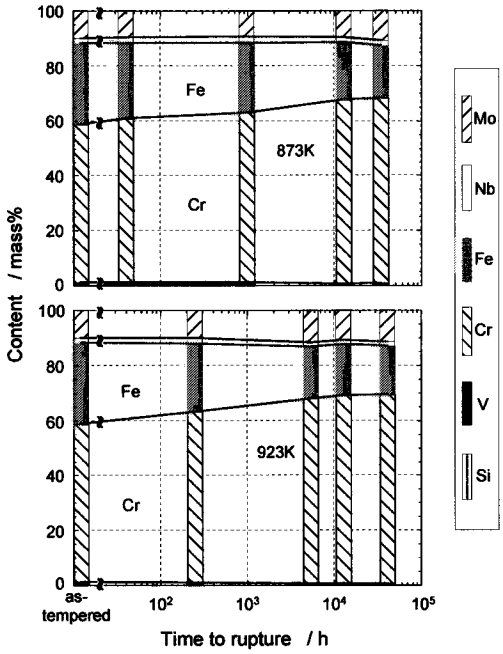


Figure 4: Changes in chemical composition of $M_{23}C_6$ carbide with increase in time to rupture at 873 and 923K.

Changes in number fraction of the two MX type carbonitrides of V(C,N) and Nb(C,N) with increase in creep exposure time at 873K and 923K are shown in Figure 5. No obvious change in number fraction of those is observed at 873K, however, it shows tendency to decrease in a number fraction of Nb(C,N) with increase in creep exposure time at 923K. Number fraction of Nb(C,N) particle to the total number of MX type carbonitride particles is about 30% in the as tempered condition and it decreases with increase in creep exposure time at 923K to 0% in the specimen creep ruptured after 41,425.2h. Decrease in total number of fine MX precipitates was also observed with increase in creep exposure time at 923K. It seems that a decrease in number fraction of Nb(C,N) particles means not increase in a number of V(C,N) particles, but an earlier disappearance of Nb(C,N) than V(C,N) with decrease in total number of MX particles, due to a small amounts of Nb(C,N) particles.

Changes in mean diameter of the precipitates with increase in creep exposure time at 873K and 923K are shown in Figure 6. Mean diameters of Nb(C,N) and V(C,N) were described as MX in the lump, since no significant difference in size of those two precipitates was observed. Mean size of the $M_{23}C_6$ carbide is larger than that of the MX carbonitride and the coarsening rate of all the precipitates are accelerated by increase in temperature from 873K to 923K, especially on the Z-phase. Coarsening of the Z-phase at 923K is very fast in comparison with those of the other precipitates, since precipitation of it starts after thousands hours of creep exposure. Such significant rapid coarsening of Z-phase should affect the distribution of MX

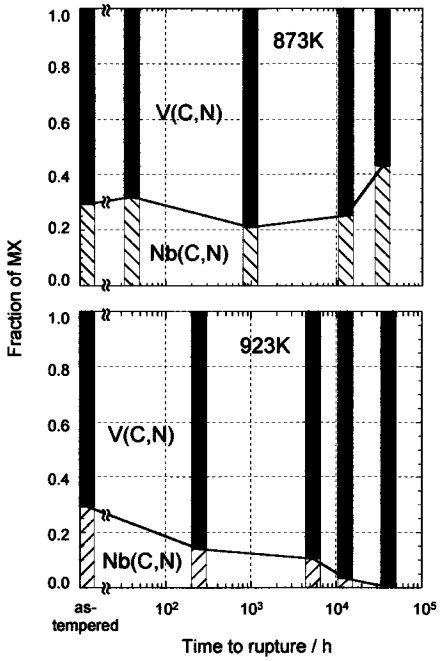


Figure 5: Changes in fraction of Nb(C,N) and V(C,N) with increase in time to rupture at 873 and 923K.

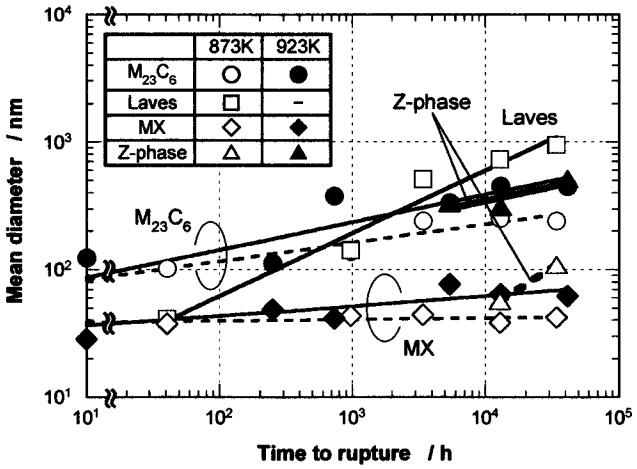


Figure 6: Changes in mean diameter of the precipitates with increase in time to rupture at 873 and 923K.

precipitates, since Z-phase is a complex nitride in a form of Cr(Nb,V)N [16] and, therefore, coarsening of Z-phase requires resolving of MX precipitates. Consequently, decrease in a number of MX particles and disappearance of Nb(C,N) with increase in creep exposure time at 923K is thought to be caused by precipitation and rapid coarsening of Z-phase.

3.3 Precipitation of Z-phase

Bright field TEM images of the carbon extracted replica prepared from the specimen in the as normalized condition are shown in Figure 7. Image of Fig.7 (b) is the enlarged one on the area indicated by square in the image of Fig.7 (a). Aligned coarse precipitates with a size of 50 to 150nm and a lot of fine particles are observed. It seems that the aligned coarse particles are the primary precipitates which exist at the normalizing temperature of 1,323K on the prior austenite grain boundary and a lot of fine particles precipitate during cooling from the normalizing temperature.

Results of EDX analysis on the each precipitates in the as normalized condition are shown in Figure 8. All the precipitates consist of mainly niobium and vanadium and $M_{23}C_6$ type carbide has not been observed. Therefore, it has been cleared that the precipitate exists in the as normalized condition is only MX type carbonitride and $M_{23}C_6$ type carbide precipitates during tempering. MX type carbonitride observed in the as tempered condition and after creep exposure has been reported to be clearly divided into two groups of niobium dominant type or vanadium dominant one by the concentration of niobium and vanadium [14], [15]. However, the results of EDX analysis on the precipitates in the as normalized condition indicates gradual change in the chemical composition from niobium dominant to vanadium dominant. Such continuous change in chemical composition of the MX type carbonitride has not been observed on the steel in the as tempered condition and the specimens subjected to creep exposure.

Correlation between niobium content and diameter of each precipitates in the as normalized condition are shown in Figure 9 for intergranular precipitates (○) and intragranular one (●).

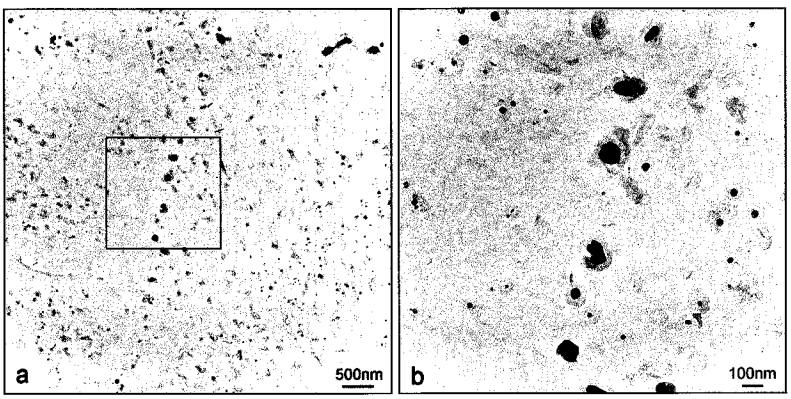


Figure 7: Bright field TEM images of the carbon extracted replica taken from the steel in the as normalized condition. (b) is the enlarged image of the area indicated by square in (a).

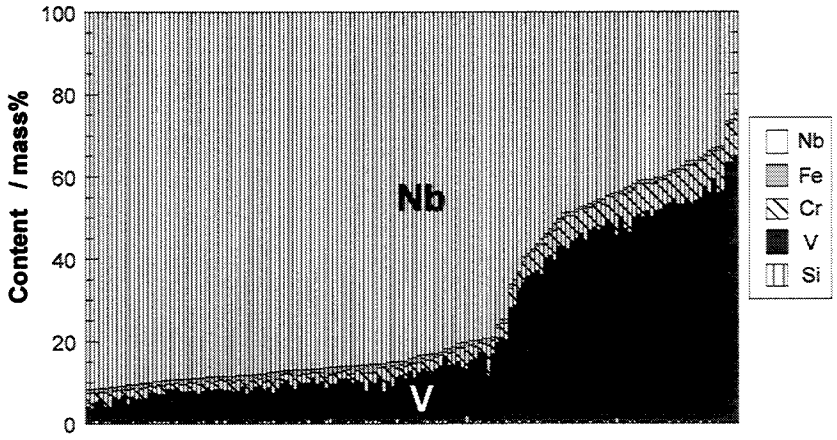


Figure 8: Results of EDX analysis on the precipitates in the as normalized condition.

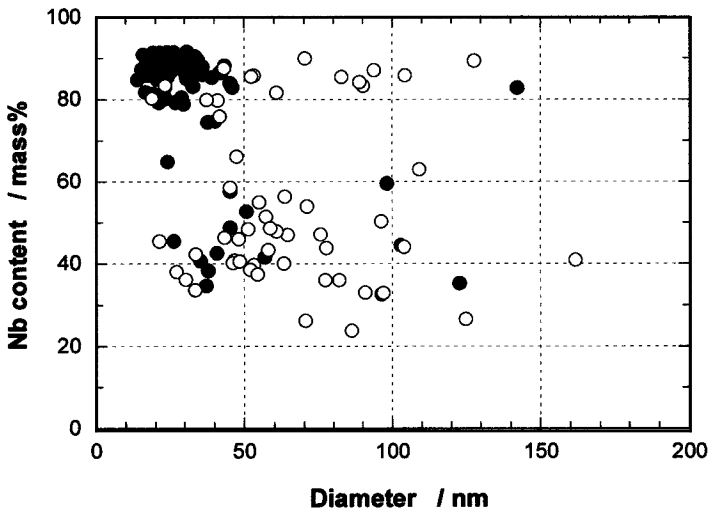


Figure 9: Correlation between Nb content and size of the precipitates in the as normalized condition. ○: intergranular, ●: intragranular

Almost of all the intragranular precipitates are fine particles with a diameter of less than 50nm and contain relatively high niobium concentration of 80 to 90mass%. On the other hand, diameters of the intergranular precipitates are relatively larger than those of the intragranular one and varies considerably in the wide range from 20 to 160nm. Moreover, niobium content of the intergranular precipitates also indicates a large spread from 20 to 90mass%. Although

the diameter and the niobium content of the intragranular precipitates are almost the same as those of Nb(C,N) in the as tempered condition [14], [15], the intergranular one are not equivalent to MX precipitatesobserved in the as tempered condition and the specimens subjected to creep exposure. It has been supposed that there is a complete solid solution system between Nb(C,N) and V(C,N) at the normalizing temperature of 1,323K, and, consequently, chemical composition of the primary MX precipitates varies in the wide range. Moreovery, such primary MX precipitates should be decomposed during tempering into niobium dominant and vanadium dominant MX carbonitrides of Nb(C,N) and V(C,N) [17].

From the above observation on the microstructure in the as normalized condition, the presence of coarse primary precipitates of MX type carbonitride on the PAGB has been revealed. Such primary precipitates are supposed to be decomposed into Nb(C,N) and V(C,N) during tempering and a precipitation density of the MX type carbonitrides is higher at the vicinity of PAGB than that within grain. Consequently, niobium and vanadium which are the main constituents of Z-phase exist at the vicinity of PAGB with the higher concentration than that within grain. As a result of such localized distribution of niobium and vanadium may promote the precipitation of Z-phase at the vicinity of PAGB. It has been concluded that precipitation of Z-phase which tends to occurr at the vicinity of PAGB due to higher precipitation density of MX type carbonitrides, may be one of the important factors which promote a preferential recovery at the PAGB during long-term creep exposure of a Mod.9Cr-1Mo steel.

4. Conclusions

Changes in microstructure and precipitates after heat treatment and during long-term creep exposure have been investigated on a Mod.9Cr-1Mo steel in order to discuss the effect of Z-phase precipitation on a degradation mechanism of preferential recovery at the vicinity of prior austenite grain boundary and the following results are obtained.

1. Preferential recovery at the vicinity of PAGB and heterogeneous progress in such recovered region were observed at the onset of accelerating creep stage and in the accelerating creep stage during creep exposure at 873K-120MPa.
2. Decrease in number of MX type carbonitrides with progress in creep exposure and disappearance of Nb(C,N) after long-term creep exposure were observed at 923K.
3. Although the coarsening rate of the precipitates are accelerated by increase in temperature, coarsening of Z-phase at 923K has been found to be very rapid in comparison with those of the other precipitates of $M_{23}C_6$ and MX.
4. Precipitation of Z-phase tends to take place at the vicinity of PAGB rather than within grain as a result of higher precipitation density of Nb(C,N) and V(C,N) due to a presense of a lot of coarse primary precipitates of MX carbonitride on PAGB.
5. It has been concluded that precipitation and rapid coarsening of Z-phase which occurred more frequently at the vicinity of PAGB is one of the important factors of a preferential recovery at the vicinity of PAGB during long-term creep exposure of a Mod.9Cr-1Mo steel.

References

[1] F. Abe, M. Igarashi, N. Fujitsuna, K. Kimura and S. Muneki. "Research and

Development of Advanced Ferritic Steels for 650°C USC Boilers." Proc. 6th Liege Conf., Materials for Advanced Power Engineering, Vol.1 (1998), p.259.

[2] E. Metcalfe and B. Scarlin. "Advanced High Efficiency Steam Power Plant." Proc. 6th Liege Conf., Materials for Advanced Power Engineering, Vol.1 (1998), p.35.

[3] M. Igarashi, S. Muneki, H. Kutsumi, T. Itagaki, N. Fujitsuna and F. Abe. "A New Concept for Strengthening of Advanced Ferritic Steels for USC Power Plant." Proc. 5th International Charles Parsons Turbine Conference, Cambridge, (2000), p.334.

[4] K. Kimura, K. Seki, Y. Toda and F. Abe. "Development of High Strength 15Cr Ferritic Creep Resistant Steel." ISIJ International, Vol.41 (2001), p.S121.

[5] V. K. Sikka. "Development of Modified 9Cr-1Mo Steel for Elevated-Temperature Service." Proc. Topical Conf. on Ferritic Alloys for Use in Nuclear Energy Technologies, Pennsylvania, (1984), p.317.

[6] K. Hamada, K. Tokuno and T. Takeda. "Dispersion hardening effects of Nb-V precipitates in Mod.9Cr-1Mo steels." Nuclear Engineering and Design, Vol.139 (1993), p.277.

[7] A. Tooyama and Y. Minami. "Creep Rupture Strength and Long Term Aging Properties of 9Cr-1Mo-Nb-V Heat Resistant Steel." Report of the 123rd Committee on Heat-Resisting Metals and Alloys, Vol.34 (1993), p.23.

[8] F. Masuyama and N. Nishimura. "Effect of Structures and Residual Elements on Creep Behavior of Modified 9Cr-1Mo Steel." Strength of Materials, The Japan Institute of Metals, Sendai, (1994), p.657.

[9] K. Sawada, K. Maruyama, R. Komine and Y. Nagae. "Microstructusal Changes during Creep and Life Assessment of Mod.9Cr-1Mo Steel." Tetsu-to-Hagané (in Japanese), Vol.83 (1997), p.466.

[10] A. Orlova, J. Bursik, K. Kucharova and V. Sklenicka. "Microstructural development during high temperature creep of 9% Cr steel." Materials Science and Engineering, Vol.A245 (1998), p.39.

[11] E. Cerri, E. Evangelista, S. Spigarelli and P. Bianchi. "Evolution of microstructure in a modified 9Cr-1Mo steel during short term creep." Materials Science and Engineering, Vol.A245 (1998), p.285.

[12] S. Spigarelli, E. Cerri, P. Bianchi and E. Evangelista. "Interpretation of creep behaviour of a 9Cr-Mo-Nb-V-N (T91) steel using threshold stress concept." Materials Science and Technology, Vol.15 (1999), p.1433.

[13] K. Kimura, H. Kushima and F. Abe. "Heterogeneous Changes in Microstructure and Degradation Behaviour of 9Cr-1Mo-V-Nb Steel During Long Term Creep." Key Engineering Materials, Vols. 171-174 (2000), p.483.

[14] K. Kimura, H. Kushima, F. Abe, K. Suzuki, S. Kumai and A. Satoh. "Microstructural Change and Degradation Behaviour of 9Cr-1Mo-V-Nb Steel in the Long Term Region." Proc. 5th International Charles Parsons Turbine Conference, Cambridge, (2000), p.590.

[15] K. Kimura, K. Suzuki, S. Kumai, H. Kushima and F. Abe. "Precipitation of Z-phase and Its Effect on Creep Strength of Mod.9Cr-1Mo Steel." Proc. Creep Resistant Metallic Materials, Prague, (2001), p.186.

[16] A. Strang and V. Vodarek. "Z phase formation in martensitic 12CrMoVNb steel." Materials Science and Technology, Vol.12 (1996), p.552.

[17] K. Inoue, N. Ishikawa, I. Ohnuma, H. Ohtani and K. Ishida. "Calculation of Phase Equilibria between Austenite and (Nb, Ti, V)(C,N) in Microalloyed Steels." ISIJ International, Vol.41 (2001), p.175.

DISTRIBUTION OF MX CARBONITRIDES AND ITS EFFECT ON CREEP DEFORMATION IN 9Cr-0.5Mo-1.8W-VNb STEEL

K. Sawada, K. Kubo, T. Hara and F. Abe
National Institute for Materials Science
1-2-1, Sengen, Tsukuba, Ibaraki 305-0047, JAPAN

Abstract

The effect of the coarsening behavior and precipitation sites of MX carbonitrides on creep behavior was investigated for P92(9Cr-0.5Mo-1.8W-VNb) steel by conventional TEM observations of replica films and by elemental mapping of thin films in energy filtered TEM(EF-TEM), respectively. The MX carbonitrides precipitate not only inside lath grains but also on lath boundaries, and pin lath boundary migration during creep. The stress exponent n of minimum creep rate decreases with increasing temperature. At 750 ℃, creep rupture strength abruptly decreases due to the decrease of the n value and the quick increase of creep rate in tertiary stage. The coarsening of MX carbonitrides at 650 ℃ to 750 ℃ corresponds to an early stage of Ostwald ripening and is accelerated by creep deformation. The decrease of stress exponent n with increasing temperature is caused by decreasing Orowan stress due to the coarsening of precipitates, $M_{23}C_6$, MX and Laves phase. At 750 ℃, the coherent strain between the MX carbonitrides inside lath grain and matrix significantly reduces at long term, leading to a quick increase of creep rate in tertiary stage.

Keywords : 9Cr steel, creep behavior, MX carbonitrides, EF-TEM

1 Introduction

Plant operation under ultra super critical steam (USC) conditions improves power generating efficiency. P92(9Cr-0.5Mo-1.8W-VNb) steel is used for the critical components of boilers in the USC power plants. The microstructure of the steel consists of a tempered martensitic lath structure with a high dislocation density and several kinds of precipitates. An increase of lath width and a decrease of dislocation density occurs during creep deformation, resulting in a decrease of creep strength.[1,2] Since $M_{23}C_6$ carbide and Laves phase are distributed on lath, packet and block boundaries, the microstructural degradation during creep is retarded by their pinning effects.[3,4] However, the precipitates coarsen during creep deformation, leading to a decrease of the pinning effects at long-term region. Abe[5] reported that the addition of W retards the coarsening of $M_{23}C_6$ during creep deformation, resulting in a increase of creep strength in terms of the pinning effect.

The creep rupture strength of modified 9Cr-1Mo steel is markedly improved by the addition of V, Nb and N, which form MX carbonitrides.[6] The coarsening process of MX carbonitrides has been reported in several high chromium ferritic steels.[7,8] However, the effects of the coarsening on creep behavior are not well understood because of a low coarsening rate of MX carbonitrides during creep at typical operating temperature. In addition, although the precipitation sites of MX carbonitrides are not clear because of the complexity of tempered martensitic microstructure, MX carbonitrides are usually assumed to retard a free dislocation movement inside lath grain during creep. To reveal the strengthening mechanism of MX carbonitrides, it is necessary to investigate the coarsening process and precipitation

sites.

The purpose of this paper is to clarify the effect of MX coarsening on creep behavior and the precipitation sites of MX carbonitrides for P92 steel. In the steel, the $M_{23}C_6$ carbides are distributed along prior austenite grain boundaries and lath boundaries while most of the MX carbonitrides is assumed to distribute inside lath.[9] The Laves phase precipitates on prior austenite grain boundaries and lath boundaries after creep deformation.[9,10]

2 Experimental procedure

The chemical composition of the steel studied is listed in Table 1, where normalizing and tempering conditions are also given. After the heat treatments, the steel gained tempered martensitic lath structure but no δ-ferrite. The gauge length and diameter of the creep specimens were 50 and 10 mm, respectively. Uniaxial creep tests were performed under constant loads at 550, 600, 650, 700 and 750 ℃ in air for up to about 10,000 hours. Some tests at 750 ℃ were interrupted at several creep strains to investigate the coarsening process of the MX carbonitrides during creep under constant load.

Table 1 : Chemical composition(in mass%) and heat treatment condition of the steel studied.

C	Si	Mn	P	S	Ni	Cr	Mo	V	Nb
0.11	0.10	0.45	0.012	0.003	0.17	8.82	0.47	0.19	0.06
W	N	Al	B	Normalizing			Tempering		
1.87	0.047	0.01	0.002	1070℃, 2h A.C.			780℃, 2h A.C.		

The specimens for TEM (200 kV, JEOL 2010F) observations were cut longitudinally from the head and gauge portions of crept samples. The specimens from head portions were used to determine the effects of thermal ageing. Extracted carbon replicas were prepared in order to avoid matrix effects in the case of chemical analysis of the precipitates. The cross section of specimens was mechanically polished by emery papers and 0.05 μm aluminum oxide powder, and then etched using a solution of 3 ml hydrochloric acid and 1 g picric acid in 100 ml of ethanol. The etched specimens were carbon coated, and the replicas were released with a solution containing 5 pct HNO_3 and 90 pct ethanol. The size distribution and mean radius of the MX carbonitrides were evaluated by taking fifteen bright field images in TEM, corresponding to 150~250 particles per specimen. In P92 steel, the composition of the MX (M = V, Nb, X = C, N) carbonitrides is readily distinguished from that of the $M_{23}C_6$ (M = Fe, Cr, W, Mo) carbides and Laves phase $(Fe, Cr)_2(W, Mo)$.[9,10] Therefore the MX carbonitrides were identified by energy dispersive X-ray spectrometer (EDS) analysis.

To reveal the distribution of the MX caronitrides in thin film, elemental mapping in energy filtered TEM (EF-TEM) was gained for as tempered and crept specimens.

3 Results and Discussion

3.1 Precipitation sites of MX carbonitrides

Figure 1 shows a bright field image and energy filtered images of chromium and vanadium in

the as tempered specimen. The chromium map and vanadium map demonstrate the distributions of Cr-rich($M_{23}C_6$) and V-rich(MX) precipitates, respectively. The $M_{23}C_6$ and MX carbonitrides are distributed mainly on lath boundaries. However, it is reported that the MX carbonitrides precipitate inside lath grain and act as obstacles to free dislocations inside lath grain during creep.[11] The size of the MX carbonitrides observed in Fig. 1 is relatively larger than that of previous works.[12] In this study, EF-TEM method did not detect the smaller MX carbonitrides presumably inside lath grain. The results in Fig. 1 and the previous works suggest that the MX carbonitrides precipitate inside lath grains and on lath boundaries. This is why it is expected that the MX carobinitrides retards not only the movement of free dislocations but lath boundary migration during creep.

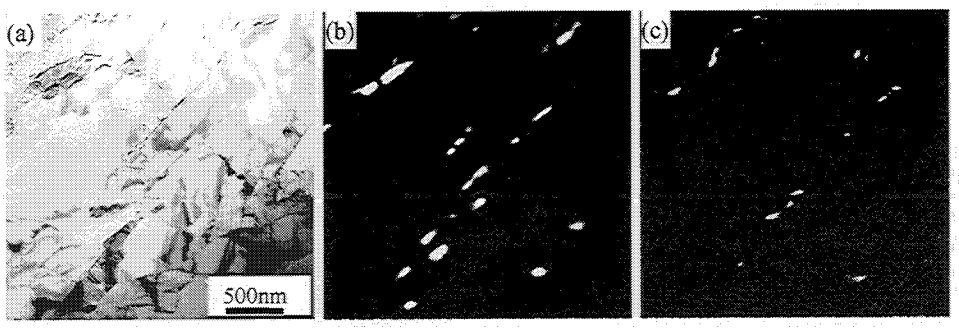


Figure 1 : Bright field image (a) and EF-TEM images in as tempered specimen.(b)elemental mapping of Cr, (c)elemental mapping of V

TEM micrographs showing the interaction between lath boundary and the MX carbonitrides in a crept specimen is shown in Fig. 2. It was confirmed by EDX analysis that the particle pinning lath boundary was V-rich, meaning the MX carbonitrides. The MX carbonitrides also pins lath boundary and contribute to creep strengthening although the $M_{23}C_6$ pins lath boundary during creep.[3]

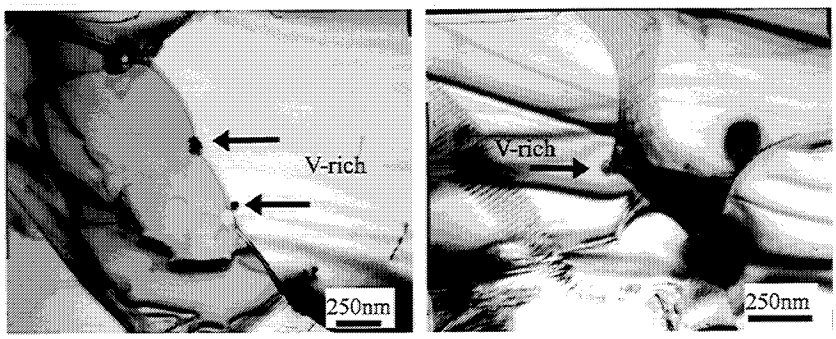


Figure 2 : TEM micrographs showing interaction between lath boundary and MX(V-rich) carbonitrides in ruptured specimen. 750℃, 20MPa, t_r = 5713 h

3.2 Creep properties

Figure 3 shows creep rupture strength at various temperatures. The rupture strength at 750 ℃ decreases quickly at rupture lives longer than 1000 h, although the rupture strength at 550 ℃ to 700 ℃ do not decrease pronouncedly even at long term region.

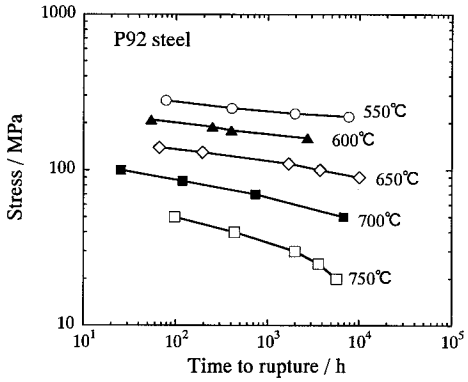


Figure 3 : Stress versus time to rupture for the P92 steel.

Figure 4 demonstrates the relationship between minimum creep rate and stress at 550 ℃ to 750 ℃. The stress exponent n decreases with increasing temperature. The value n is known to be 4-6 and large up to 40[13] for single phase alloys and complex alloys consisting of several phases, respectively. The present results mean that precipitation strengthening due to $M_{23}C_6$, MX and Laves phase becomes small with increasing temperature. At 750 ℃, the n value is 5.7 which is approximately the same as that for single phase alloys, indicating the precipitation strengthening is very small at the temperature. Figure 5 shows the Monkmann-Grant relationship between minimum creep rate and rupture time at 550 ℃ to 750 ℃. The relationship is represented by a straight line irrespective of creep conditions. However, the data at 750 ℃ deviate from the line at long term region.

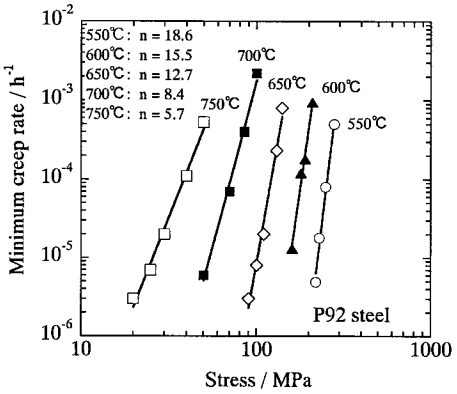


Figure 4 : Minimum creep rate as a function of stress

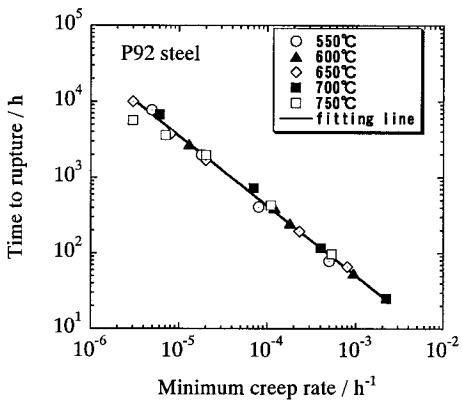


Figure 5 : Relationship between minimum creep rate and time to rupture.

This result means that contribution of a decrease in minimum creep rate to an increase in creep rupture time becomes small at long term region. In short, a creep rate increases quickly in tertiary stage at long term region.

Consequently the precipitation strengthening becomes small at higher temperature (low value of n) due to the coarsening of the precipitates. In addition, at 750 ℃, the creep rupture strength abruptly decreases at long term due to the quick increase of creep rate at tertiary stage. The coarsening rate of MX carbonitrides is 1/10 of that of $M_{23}C_6$.[14] At 750 ℃, Orowan stress from the $M_{23}C_6$ is much lower than that of MX carbonitrides since Orowan stress is inversely proportional to inter-particle spacing. In short, the MX carbonitrides strongly contribute to creep strength. Therefore, it will be effective for well understanding of effect of the MX carbonitrides on creep behavior to investigate the coarsening process of the MX carbonitrides mainly at 750 ℃.

3.3 Coarsening process of the MX carbonitrides during ageing and creep

Figure 6 shows the TEM micrographs of extraction replica of the specimen head portion under no stress, after creep rupture testing. The arrows indicate the MX carbonitrides consisting of V, Nb, N and C confirmed by EDX analysis. About 70 pct of the MX carbonitrides analyzed were V-rich, meaning that most of the MX carbonitrides were VN.

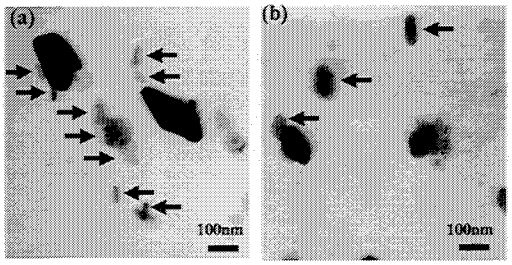


Figure 6 : TEM micrographs of extraction replica in ruptured specimens. (a) 650℃, 110MPa, t_r = 1689.1h (b)700℃, 60MPa, t_r = 1995.7h Arrows indicate MX carbonitrides.

The mean radius of the MX carbonitrides is plotted against ageing time in Fig. 7. The mean radius was evaluated from equivalent circle diameter of measured particles. The mean radius was 15.4 nm before ageing. It is seen that the coarsening rate of the MX carbonitrides is larger at higher temperature. Figure 8 shows the change of amount of V and Nb in extracted residue as a function of aging time. The amount of V and Nb is kept constant during aging, meaning that the additional precipitation of the MX carbonitrides does not occur during aging. This means that the MX carbonitrides coarsen under the mechanism of Ostwald ripening [15,16] described by the following equation ;

$$r^m - r_0^m = k \cdot t \qquad (1)$$

where r and r_0 are the mean particle radius at the time t and 0, respectively, k is the rate constant, and m is the exponent describing the controlling process of coarsening. It is reported that the value m in 9Cr-1Mo-VNb(T91) [8] steel and 12Cr steel [7] are 3 and 5, respectively. However, the value m in Fig. 7 is evaluated to be 8 to 15 which are much larger than the

exponent for lattice (m = 3) [15,16] and pipe (m = 5) [17] diffusion. The data in Fig. 7 may correspond to an early stage of Ostwald ripening since the MX carbonitrides are thermally stable and can not coarsen easily for up to 10,000 h at 650 ℃ to 750 ℃. This is the reason for the larger value m in Fig. 7. Indeed, it is reported that the coarsening process of the $M_{23}C_6$ corresponds to an early stage of Ostwald ripening.[5,18]

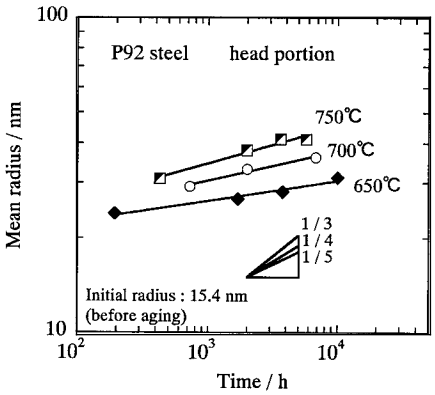


Figure 7 : Coarsening of the MX carbonitrides at 650℃ to 750℃.

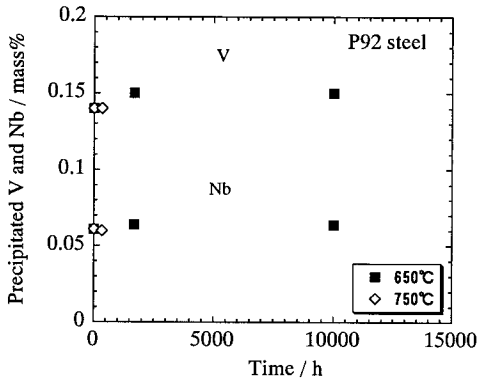


Figure 8 : Amount of V and Nb in the extracted residue with ageing time.

Figure 9 demonstrates the size distribution curve of the MX carbonitrides after ageing and creep. The size distribution in gauge portion of crept specimen (t = 1761 h) is broader than that in head portion at almost the same time (t = 1994 h), indicating creep deformation accelerates the coarsening of the MX carbonitrides. Figure 10 shows the comparison of mean radius of the MX carbonitrides between after ageing and creep. The data for the gauge portion at 650 ℃ and 750 ℃ are obtained from ruptured and interrupted specimens, respectively. The mean radius in gauge portion is larger than that in head portion.

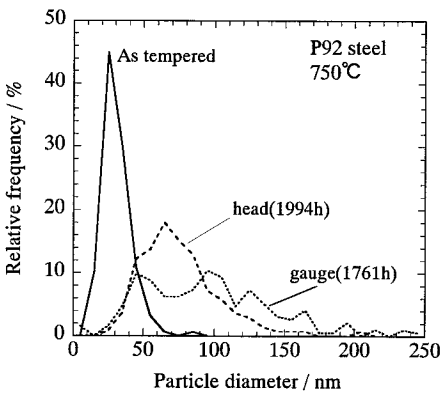


Figure 9 : Change of size distribution curve of MX carbonitrides during ageing and creep.

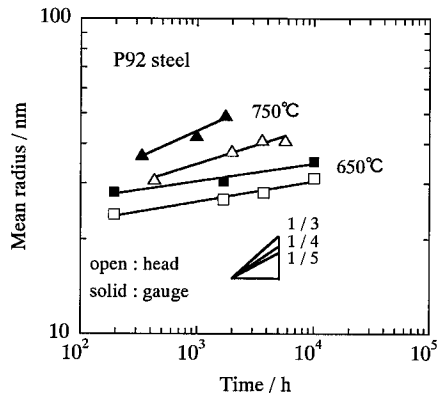


Figure 10 : Effect of creep deformation on coarsening process of MX carbonitrides.

3.4 Effect of the coarsening of the MX carbonitrides on creep behavior

The inter-particle spacing of $M_{23}C_6$, MX and Laves phase all increases with increasing temperature and creep time due to the coarsening of the particles, resulting in a decrease of Orowan stress. The MX carbonitrides coherently precipitate inside lath grains, and a coherent strain can be resistance to free dislocation motion. The coherent strain markedly reduces, when the mean MX carbonitrides radius is larger than 40 nm.[19] The mean radius in the gauge portion at 650 ℃ are kept smaller than the critical value 40 nm during creep shown in Fig. 10, meaning that the coherent strain is kept high and effective as a resistance to free dislocation motion inside lath grain at the temperature. On the other hand, the mean radius in the gauge portion reduces to the critical value at about 550 h at 750 ℃ as shown in Fig. 10. In short, the coherent strain of the MX carbonitrides reduces negligibly small at a short time of 550 h during creep at 750 ℃. Figure 11 exhibits the relationship between creep rate and time at 750 ℃. The time to reach minimum creep rate at 20 and 25 MPa are more than 550 h, indicating the coherent strain of the MX carbonitrides is very small at secondary and tertiary stages. Therefore, the resistance of the MX carbonitrides to free dislocation motion decreases and creep rate abruptly increases at tertiary stage as shown in Fig. 5.

Consequently the decrease of the coherent strain due to the coarsening of the MX carbonitrides also contributes to a decrease of creep rupture strength at long term.

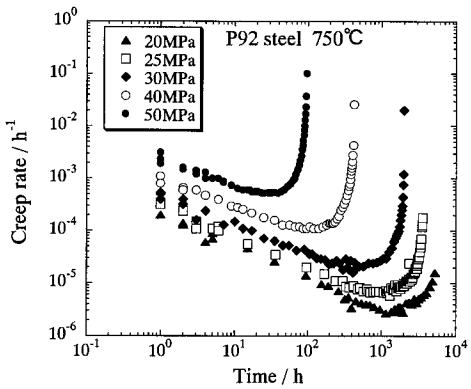


Figure 11 : Creep rate as a function of time at 750 ℃.

4 Conclusions

Distribution of the MX carbonitrides and its effect on creep behavior were studied using EF-TEM method and investigating the coarsening process of the MX carbonitrides during creep. The results are summarized as follows.

1. The MX carbonitrides precipitate not only inside lath grains but also on lath boundaries, and pin lath boundary migration during creep.
2. The stress exponent of minimum creep rate decreases with increasing temperature. At 750 ℃, creep rupture strength abruptly decreases at long term, and creep rate quickly increases in tertiary stage at long term region.

3. The coarsening of the MX carbonitrides is controlled by the mechanism of Ostwald ripening, and is accelerated by creep deformation.
4. The coherent strain of the MX carbonitrides becomes negligibly small at longer than 550 h at 750 ℃. This means that resistance to free dislocations inside lath grain is very small in tertiary stage of 20 and 25 MPa at 750 ℃, indicating creep rate quickly increases and creep rupture strength abruptly decreases at long term.

5 References

1. S. Straub, P. Polcik, W. Besigk, W. Blum, H. König and K.H. Mayer : *Steel Res.*, **66** (1995), 402.
2. G. Eggeler : *Acta Metall.*, **37** (1989), 3225.
3. F. Abe and S. Nakazawa : Metall. Trans. A **23A** (1992), 3025.
4. K. Sawada, M. Takeda, K. Maruyama, R. Ishii, M. Yamada, Y. Nagae and R. Komine : *Mater. Sci. Eng.*, **A267** (1999), 19.
5. F. Abe : Proc. The fourth Int. Conf. on Recrystallization and Related Phenomena, Tsukuba, July (1999), The Japan Institute of Metals, 289.
6. V. K. Sikka : Proc. Topical Conf. on Ferritic Alloys for Use in Nuclear Energy Technologies, Warrendale PA, (1984), TMS-AIME, 317.
7. Y. Kadoya, B. F. Dyson and M. McLean : Proc. 6th Liege Conf. on Materials for Advanced Power Engineering Part I, Liege, October (1998), Forschungszentrum Jülich GmbH, 593.
8. S. Spigarelli, E. Cerri, P. Bianchi and E. Evangelista : *Mater. Sci. Tech.*, **15** (1999), 1433.
9. J. Hald : *Steel Res.*, **67** (1996), 369.
10. P. J. Ennis, A. Zielinska-Lipiec, O. Wachter and A. Czyrska-Filemonowicz : *Acta mater.*, **45** (1997), 4901.
11. K. Hamada, K. Tokuno, Y. Tomita, H. Mabuchi and K. Okamoto : *ISIJ Int.*, **35** (1995), 86.
12. A. Zielinska-Lipiec, A. Czyrska-Filemonowicz, P. J. Ennis, O. Wachter : Proc. 6th Liege Conf. on Materials for Advanced Power Engineering Part I, Liege, October (1998), Forschungszentrum Jülich GmbH, 559.
13. R. W. Lund and W. D. Nix : Acta Metall., **24** (1976), 469.
14. J. Hald and S. Straub : Proc. 6th Liege Conf. on Materials for Advanced Power Engineering Part I, Liege, October (1998), Forschungszentrum Jülich GmbH, 155.
15. I. M. Lifshitz and V. V. Slyozov : *J. Phys. Chem. Solids*, **19** (1961), 35.
16. G. Wagner : *Z. Elektrochem.*, **65** (1961), 581.
17. M. Kreye : *Z. Metallk.*, **61** (1970), 108.
18. G. Götz, Y. Qin and W. Blum : Prc. of the 3rd Conf. on Advances in Material Technology for Fossil Power Plants, Swansea, April (2001), The Institute of Materials, London, 155.
19. M. Igarashi, S. Muneki and F. Abe : *Key Eng. Mater.*, **171-174** (2000), 505.

THE EFFECT OF MICROSTRUCTURAL STABILITY ON LONG-TERM CREEP BEHAVIOUR OF 9-12%Cr STEELS

Vaclav Sklenicka[1], Kveta Kucharova[1], Lubos Kloc[1], Milan Svoboda[1] and Marc Staubli[2]

[1)]Institute of Physics of Materials, Academy of Sciences of the Czech Republic, Zizkova 22, CZ-616 62 Brno, Czech Republic
[2)]ALSTOM Power (Switzerland), Ltd., Dept. GTEMD, Haselstrasse 16, CH-5401 Baden, Switzerland

Abstract

A comparison is made between the creep characteristics of two modified 9-12%Cr chromium steels (P91 and P92) in both the as-received state and after isothermal ageing at 650°C for 10 000 h in an effort to obtain more complete description of the role of microstructural stability in high temperature creep of these steels. Constant load tensile creep tests and creep tests by means of the helicoid spring specimen technique were carried out at temperature of 600°C. The results show the creep resistance of the aged steels is considerably deteriorated by comparison with steels in the as-received state in the dislocation creep region i.e. at applied stresses $\sigma \geq 100$ MPa. It is suggested that a decrease in the creep strength arises mainly from the change of dislocation substructure. By contrast, no significant effect of microstructural stability on creep behaviour was found in a regime of viscous creep ($\sigma \leq 100$ MPa).

Keywords: modified 9-12%Cr steels, creep, microstructural stability, creep strength, creep life

1. Introduction

Creep behaviour and degradation of creep properties of creep-resistant materials are phenomena of major practical relevance, often limiting the lives of components and structures designed to operate for long periods under stress at elevated temperatures [1,2]. Therefore, with modern power plants designed for lives over 30 years, procedures are required to allow the results obtained in short-term creep tests of high temperature materials to be extrapolated to provide accurate long-term design date.

The long-term creep data required for design of large-scale components and structures for power stations are usually derived by extrapolation of short-term stress-rupture properties. Unfortunately, the short-term data for 9-12%Cr steels are characterized by wide a scatter band which arises from uncertainties of testing methods, material inhomogenities and microstructural instabilities. The influence of microstructural variability on creep properties is mechanism dependent, therefore, evaluation of the scatter caused by microstructural changes is only possible if the precise creep mechanisms of the material are known.

The present investigation was conducted on two modified 9-12%Cr steels (P91 and P92) in an effort to obtain more complete description and understanding of the role of microstructural and deformation processes in high temperature creep. In order to accelerate some microstructural changes and thus to simulate long-term service conditions, isothermal ageing at 650°C for 10 000 h was applied to both steels in the as-received states. The standard tensile creep tests and the creep tests by means of helicoid spring specimens were performed at 600°C on both steels in the as-received state and after long-term isothermal ageing.

2. Experimental Procedures

The tempered martensite ferritic steel P91 (produced by Vitkovice Steel, Czech Republic) with the following chemical composition (in wt%) 0.09C, 0.56Mn, 0.20Si, 0.021P, 0.009S, 0.05Cu, 0.46Ni, 8.36Cr, 0.86Mo, 0.20V, 0.06Nb, 0.065N and 0.007Al was subjected to the two stage heat treatment: 1060°C/1h/air + 750°C/2h/air. Flat creep specimens having a 50 x 5 x 3.2 mm gauge section were machined from the heat treated blank whereas helicoid spring specimens were machined from a seamless tube fabricated from the same heat.

The P92 material was received in the form of a seamless pipe produced by Nippon Steel Corporation with the following bulk chemical analysis (in wt%): 0.08C, 9.0Cr, 0.5Mo, 1.8W, 0.2V, 0.06Nb, 0.05N, 0.003B, <0.04Al with the following heat treatment: 1065°C/2h/air + 770°C/2h/air. Cylindrical creep specimens of 5 mm diameter were machined from a seamless pipe with OD 350 mm and wt 50 mm. Both P91 and P92 steels were investigated in as-received state (i.e. after heat treatment) and after isothermal annealing at 650°C up to 10 000 hours.

Constant load tensile creep tests were carried out using the flat creep specimens at temperature of 600°C with the testing temperature continuously monitored and maintained constant to within ± 0.5C of the desired value [3]. The applied stresses ranged from 120 to 250 MPa. Creep tests were performed in purified argon in tensile creep machines. The creep elongations were measured using a linear variable differential transducer (the strain was measured with a sensitivity of 5 x 10^{-6}) and they were continuously recorded digitally and computer processed. All of the tensile creep specimens were run to final fracture.

Short-term creep tests were performed on the P91 steel at temperature of 600°C and at stresses below 100 MPa by means of the helicoid spring specimens technique [4,5] . Optical measurements of individual coil spacings were performed periodically and the creep strains were derived. Since the stress and strain in helicoid spring are essentially shear ones, they were transformed to the equivalent tensile quantities using the known relations $\sigma = \sqrt{3}\tau$ and $\varepsilon = \gamma\sqrt{3}$, where σ is tensile stress, τ is shear stress, ε is tensile strain and γ is shear strain.

3. Experimental Results

Figures 1 and 2 show selected creep curves for steel P91 and steel P92 for uniaxial tensile creep tests conducted at 600°C under comparable levels of the applied stress σ. As demonstrated by the figures, significant differences were found in the creep behaviour of both steels in the as-received state when compared to their after ageing state. First, the standard ε vs. t curves (Figs. 1 and 2) appear to show the long-term isothermal ageing of the steels leads to an increase in the creep plasticity, which is proved in particular by the values of the total strains to fracture for the aged steels crept at low stresses (Figs. 1d and 2d). Second, the aged steels exhibit markedly shorter time to fracture than the steels in the as-received state over the entire stress range used. Third, the shapes of creep curves for both the as-received state and aged state of the steels differ considerably. It is important to note that the standard creep curves shown in Figs. 1 and 2 do not clearly indicate individual stages of creep. However, these standard ε vs t curves can be easily replotted in the form of the instantaneous strain rate $\dot{\varepsilon}$ versus time t as shown in Fig. 3a,b. It is clear that neither curve exhibits a well-defined

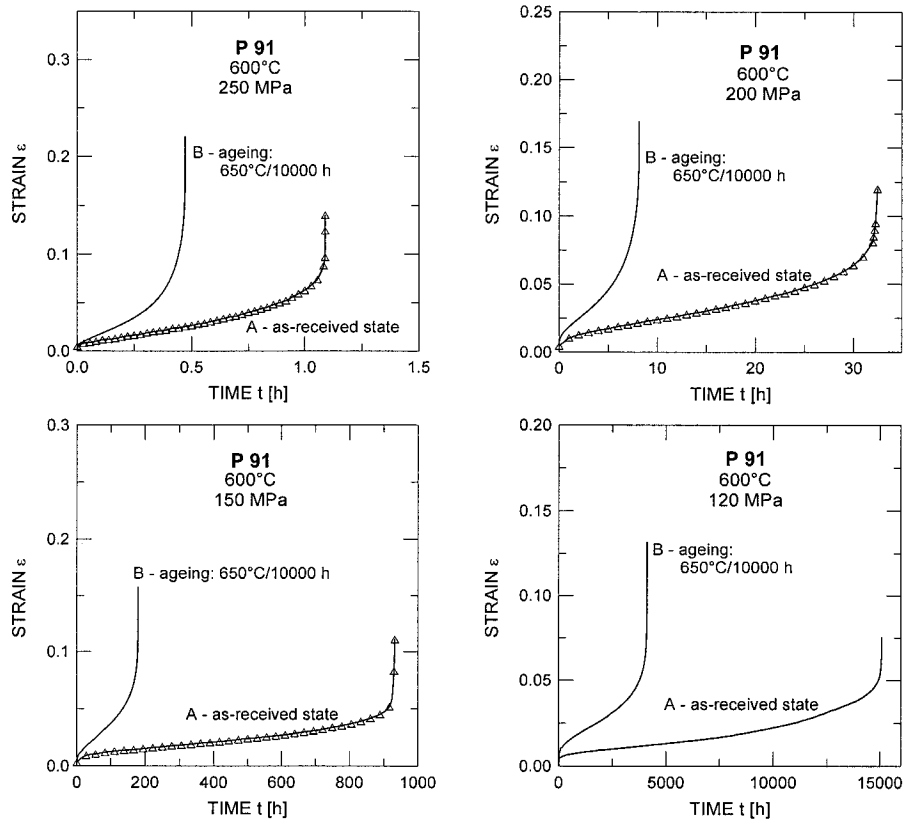


Figure 1. Creep curves of the P91 type steel in two states (A and B) at 600 °C and four levels of applied stress: 250 MPa (a), 200 MPa (b), 150 MPa (c) and 120 MPa (d).

steady state. In fact, this stage is reduced to an inflection point of the $\dot{\varepsilon}$ versus t curve. Despite this similarity, the occurence of a primary stage followed by a tertiary stage of creep in the as-received state is in striking contrast to the nature of the creep curves in the aged state. The latter curves (B in Fig. 3a,b) show the primary stage is fairly extensive and covers practicaly a half of the whole duration of creep exposure and a minimum in the creep rate is not well-defined. A further comparison between creep behaviour of the different states of steels P91 and P92 follows from Fig. 4a,b where the data are replotted as the instantaneous strain rate $\dot{\varepsilon}$ against strain ε. Inspection suggests that creep in both states is dominated by a fairly extensive tertiary stage. On the other hand, very short primary creep is terminated by an attainment of the minimum creep rate. It is important to note that the strain at which the minimum creep rate is reached ($\varepsilon \cong 0.025$) does not depend significantly on the state of steel.

In Fig. 5a,b the minimum creep rates $\dot{\varepsilon}_m$ are plotted against the applied stress σ on a logarithmic scale. Inspection of Fig. 5 leads to two observations. First, the steels in the as-received state exhibit better creep resistance than those after long-term ageing over the entire

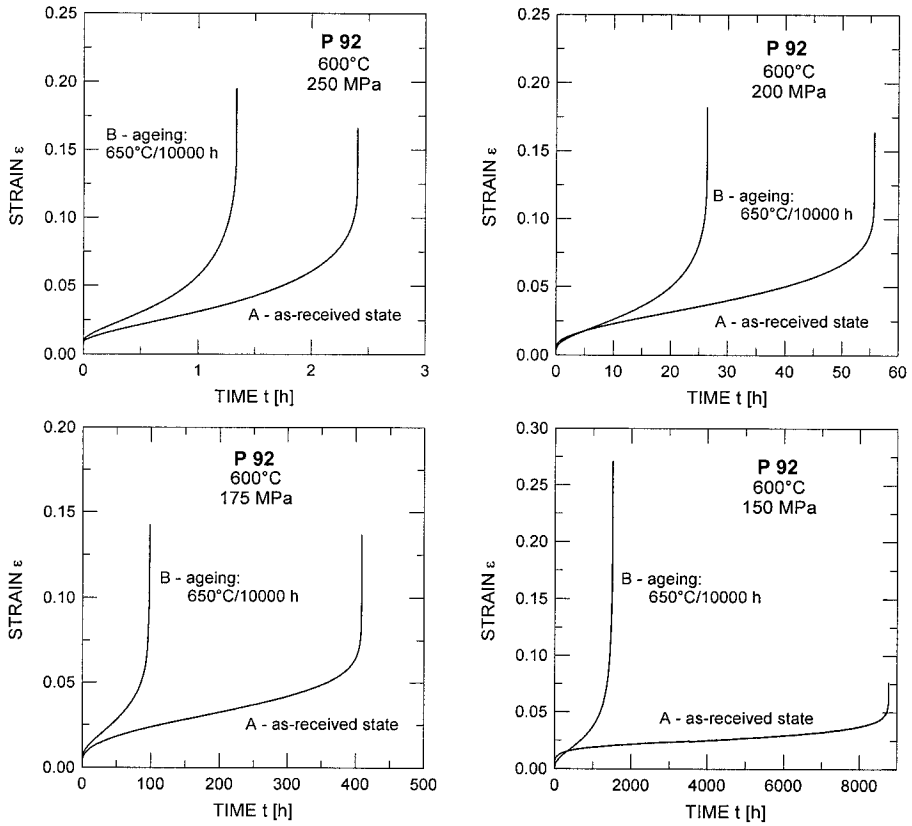


Figure 2. Creep curves of the P92 type steel in two states (A and B) at 600 °C and four levels of applied stress: 250 MPa (a), 200 MPa (b), 175 MPa (c) and 150 MPa (d).

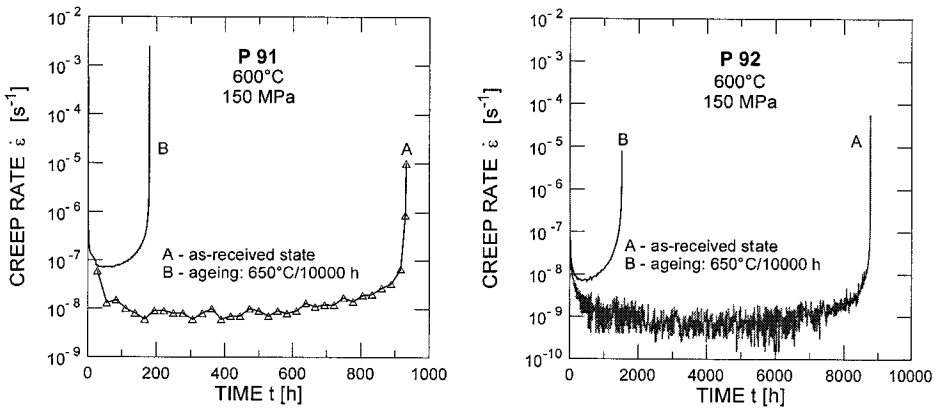


Figure 3. Creep rate versus time plots for P91 (a) and P92 (b) steels.

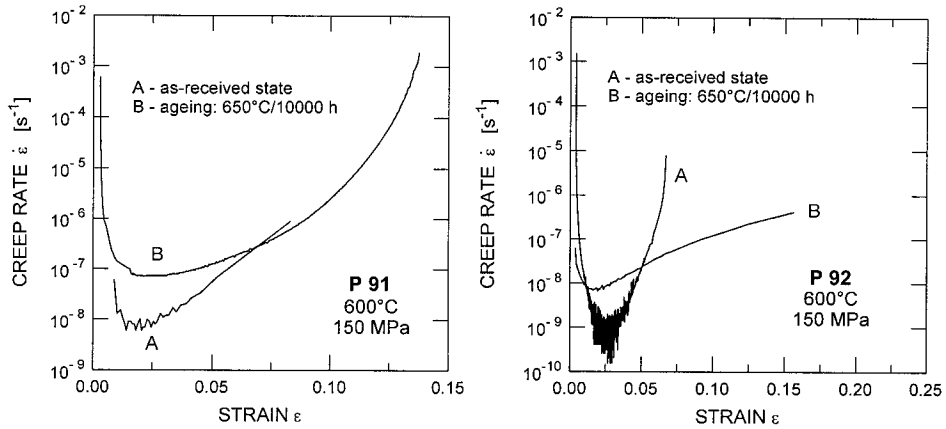


Figure 4. Creep rate versus strain plots for P91 (a) and P92 (b) steels.

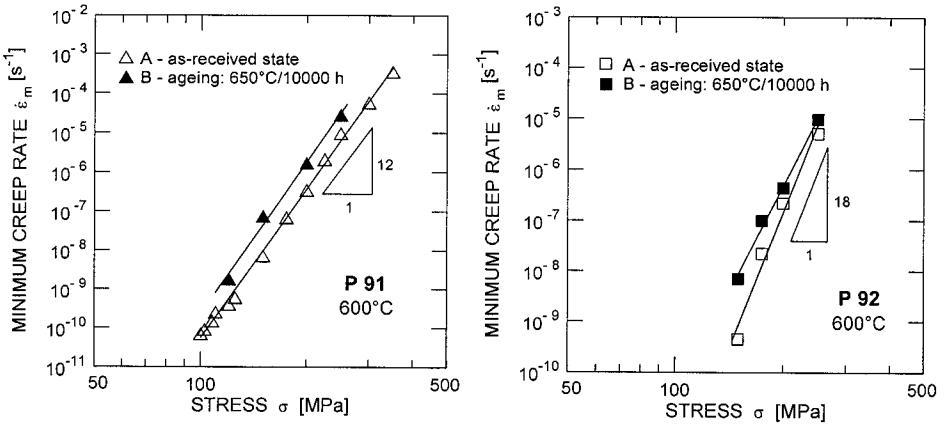


Figure 5. Stress dependences of minimum creep rate for P91 (a) and P92 (b) steels.

stress range used; the minimum creep for steel P91 in the as-received state is about order of magnitude less than that of the aged P91 steel. The stress dependences of the minimum creep rates for steel P92 are different in trend. While the slope and therefore the apparent stress exponents of creep rate $n = (\partial \ln \dot{\varepsilon} / \partial \ln \sigma)_T$ are the same for steel P91 (Fig. 5a) the slope and the stress exponent n for steel P92 depends on its state; the difference for the state after ageing increases with decreasing applied stress (Fig. 5b). For both steels, the double logarithmic plot of the time to fracture t_f as a function of applied stress are shown in Fig. 6. It is clear from these plots that the creep life of steels in the as-received state is longer than the aged steels. While the difference for steel P91 is independent of applied stress (Fig. 6a) for steel P92, this difference consistently decreases with increasing applied stress, with a tendency at the higher stresses towards no effect of the state of steel on the lifetime. A variation of the strain to fracture ε_f with stress and the state of steels is shown in Fig. 7. This figure indicates no clear effect of stress and/or materials state on the strain to fracture. The strains to fracture are

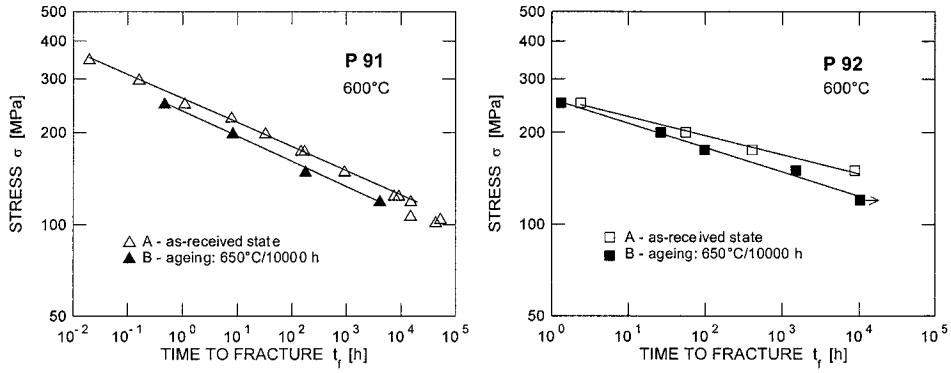


Figure 6. Stress dependences of time to fracture for P91 (a) and P92 (b) steels.

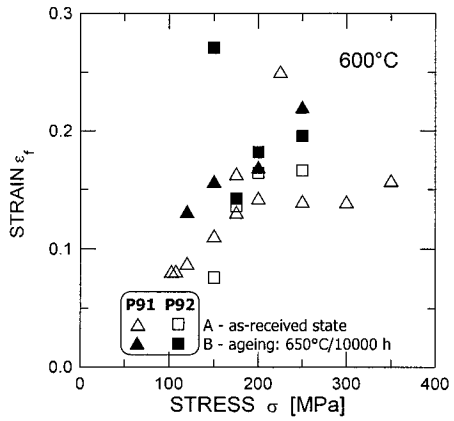


Figure 7. Stress dependences of strain to fracture for P91 and P92 steels.

typically 15 – 20%; a decrease in ε_f at low stresses can be connected with the occurrence of intergranular creep cavitation and fracture.

Creep testing by means of the helicoid spring specimens was performed at the applied stress ranging from 1 to 100 MPa and at 600°C on steel P91 in both the as-received and aged states. The minimum creep rates $\dot{\varepsilon}_{min}$ ranging from 8 x 10^{-4} to 8 x $10^{-13}s^{-1}$ correspond to these loading conditions – Fig. 8. Inspection of this figure suggests that the minimum creep rates are proportional to applied stress up to about 100 MPa ($n \cong 1$). Mutual comparison of the creep results obtained by the helicoid spring specimen technique with the results of standard uniaxial tensile creep tests on the steel investigated has shown very good coherency of both creep testing techniques [4]. The transition from power-law creep (dislocation creep) with the stress exponent of the creep rate n of about 12 to the viscous creep ($n = 1$) was found at stresses around 100 MPa at 600°C – Fig. 8. It should be stressed that any extrapolation from the power-law creep regime to stress below 100 MPa may lead to serious underestimation of the creep rate predicted. No substantial effect of long-term ageing was found for the viscous

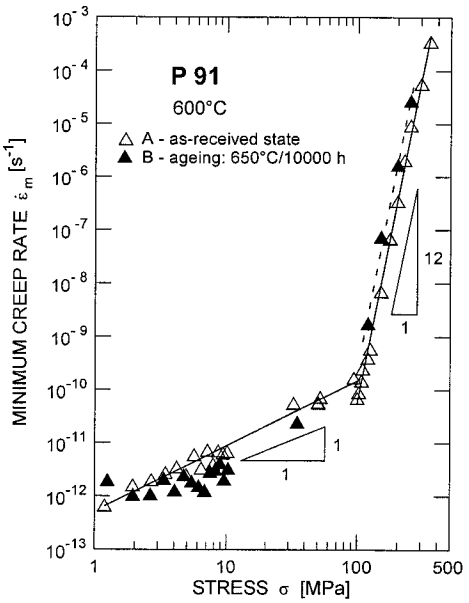


Figure 8. Stress dependences of minimum creep rate for P91 steel in both power-law ($\sigma \geq 100$ MPa) and viscous ($\sigma \leq 100$ MPa) regimes obtained by tensile creep testing ($\sigma \geq 100$ MPa) and the helicoid spring specimens testing ($\sigma \leq 100$ MPa).

creep. The creep rate for the aged state seems to be a slightly lower than those for the as-received state.

4. Discussion

A power plant may have a life of 40 years. If a total creep strain of 1 pct is permissible, the creep rate is about $10^{-11}s^{-1}$. Extrapolation to this rate from rates measurable in the standard laboratory creep testing is perilous (Fig. 8), and we need to understand the physical processes involved. At these low rates of creep deformation the transport of matter occurs by migration of vacancies rather than by the glide of dislocations. These creep processes are usually classified as viscous creep [6]. Viscous creep can be proceeded by Nabarro-Herring [7-9] (the vacancies diffuse through the bulk of the grain) and/or Coble [7-10] (diffusion is mainly along the grain boundaries) diffusion creep or by Harper-Dorn creep [7-11] (vacancies diffuse from edges of dislocations with Burgers vectors parallel to the tensile axis to the edges of dislocations with Burgers vector normal to the tensile axis). The existence and theoretical interpretation of viscous creep in pure metals are well established; by contrast, the understanding of viscous creep in materials hardened by precipitates is very incomplete at present.

At the lower stresses in Fig. 8, the experimental points appear to lie along a line having a slope of n = 1. It can be shown theoreticaly that there is a value of n = 1 for all viscous mechanisms [12]. Thus, the low stress region of n = 1 in Fig. 8 can be attributed to viscous creep. However, it is less easy to distinguish experimentally between the occurence of

Nabarro-Herring, Coble and/or Harper-Dorn creep giving the same value of n. The main difference between these mechanisms consists in the grain size dependence of the creep rate [12]. Since the steel P91 of only one grain size was used, the present results do not provide any basis for the creep mechanisms identification.

In a precipitate – hardened alloy, the accumulation of precipitate particles on grain boundaries parallel to a tensile axis during diffusion creep (H – N creep, Coble creep) could reduce the rate of creep. Two mechanisms are involved. First, diffusion creep is necessarily coupled with grain boundary sliding, and the presence of precipitates in a grain boundary inhibites sliding. Second, there is much evidence that the interface between a matrix and a hard precipitate is a much less effective source and since of vacancies than a boundary between two grains of the matrix [7]. No detailed understanding of the kinetics of creep in the diffusional regime is available. The original theory assumed that all grain boundaries would be ready sources and sinks of vacancies. It is now clear that this is not the case. Further, precipitates in the grain boundaries can introduce a threshold stress. Finally, diffusion creep could results in an increase in the area of the grain boundary leading to an increase in surface energy. All the above factors can lead to a reduction in the creep rate.

Understanding of Harper-Dorn creep is much less satisfactory than that of N – H and Coble creep. The process occurs within grain, and there is no accumulation or depletion of matter at the grain boundaries. Unlike other creep processes, H – D creep is characterized by dislocation density that is independent of the applied stress. Under the creep loading conditions used in this work the pipe diffusion should control the dislocation Harper-Dorn creep mechanism.

Although no coherent explanation of the creep behaviour of the P91 steel in the low stress region (Fig.8) can be given along the lines discussed above it can be concluded that no significant effect of microstructural stability on creep behaviour may be expected at low strain rates in which a regime of diffusion creep and/or Harper-Dorn creep dominates.

To determine the rate-controlling process(es) in creep in the high stress region ($\sigma \geq 100$ MPa), the slopes of the minimum creep rates were determined at temperature of 600°C for both P91 and P92 steel in the as-received and aged states (Fig. 5a,b and Fig. 8). The stress dependence of the creep rate can be described by an equation of the power-law form:

$$\dot{\varepsilon}_{min} \alpha A\sigma^n$$

where A and n are constants at a given temperature. The observed high values of the stress exponent $n >> 1$ indicate the presence of the power-law or dislocation creep [3]. The stress exponent n changes from 12 (steel P91, Fig. 5a and 9) to 18 (steel P92, Fig. 5b and 8). Similar values for n have been frequently reported in the literature. Fig. 6 shows the stress dependence of the time to fracture t_f. Here again the straight-line approximation good fit to the data, providing that the power-law relationship of the type

$$t_f \alpha B\sigma^{-m}$$

is obeyed. The observed values of the stress exponent m are very similar to the values for stress exponent n. This can be explained by the fact, that both the creep deformation and fracture are controlled by the same mechanism. This suggestion is further supported by Fig. 9. In this figure values of t_f are plotted against the minimum creep rate $\dot{\varepsilon}_m$ in double logarithmic coordinates. The slope of the straight line in these coordinates is almost exactly equal to 1

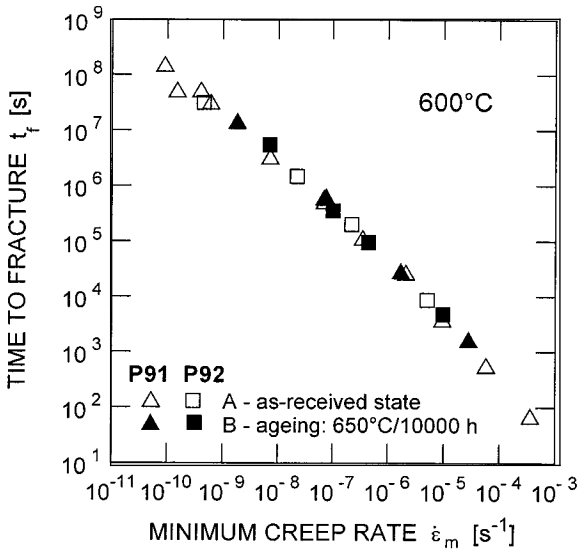


Figure 9. Dependence of time to fracture on minimum creep rate (the Monkman-Grant relationship) for P91 and P92 steels.

(independently of the steel and its state) so that the well known Monkman-Grant relationship [12,13] $\dot{\varepsilon}_m t_f = \text{const}$, holds.

At present we are still some distance from a more complete description and understanding of significant microstructural features and deformation mechanisms responsible for the enhanced creep strength of tempered martensite ferritic 9-12%Cr steels in dislocation (power-law) creep. The movement of dislocations through the matrix is at first resisted by (a) the dislocation substructure distribution (dislocation strengthening mechanism), (b) intragranular particles, mainly MX (particle strengthening), and (c) the strain fields associated with elements in solid solution (solid solution strengthening). As creep progresses the dislocation substructure changes to form subgrains whose boundaries are stabilized by $M_{23}C_6$ and MX particles and possibly also by Laves phases. However, as these particles form and coarsen they denude the surrounding matrix of elements in solid solution, thus reducing the contribution of solid solution strengthening to creep resistance. Thus it seems likely that, as these changes progress, creep resistance becomes less and less dependent on resistance to the movement of individual dislocations through the matrix and more and more dependent on the resistance to subgrain growth through boundary migration.

Recently, Sklenicka et al [3,14] and Cadek et al [15] reported extensive studies and analyses of creep behaviour and microstructure of the P91 steel in the region of power-law creep. The analyses suggested strongly that (i) the creep rate is not recovery controlled, (ii) neither is the creep rate controlled by dislocation climb around carbide particles provided no interaction of dislocations with carbide particle takes place and finally (iii) the Rősler-Artz model [16] assuming an attractive interaction of dislocations with dispersed particles and thermally activated detachment of the dislocations from the particles failed to account for the creep data

of the P91. A metallographic analysis had shown that the effect of the rearrangement of dislocations and subgrain coarsening on creep is more important than the effect of precipitation strengthening [3,14]. However, some evidence has been found for suppression or retardation of subgrain growth, suggesting a pinning of subgrain boundaries by the particles. A similar conclusion has also been convincingly demostrated by Kucharová and co-workers [17] using a novel approach in which creep specimens of P91 steel (in the as-received state) were subjected to additional thermo-mechanical treatments to change the subgrain and particle structures. The creep strength of resulting microstructures was tested under reference creep conditions (at 650°C and at 150 MPa). It has been found that the creep rate under reference conditions can consistently be accounted for by the density of subgrain boundary particles or, equivalently, by the area swept out by dislocations between two stops at subgrain boundary carbides. This area is a product of the minimum subgrain size and the spacing between two subgrain boundary particles [17].

The contributions of the various microstructural features (dislocation density, subgrain size, carbide, carbonitride and intermetallic precipitates) to the creep strength of P92 steel were extensively studied [18]. Ennis [19] reported that in P92 steel, during the first 3000 h of exposure at 600 – 650°C a rapid reduction in the dislocation density and increase in size of $M_{23}C_6$ precipitates occurs. The fine carbides, nitrides and carbonitrides are stable and do not coarsen significantly. Decreasing the dislocation density before testing by high temperature tempering reduces creep strength. If the martensitic transformation is suppressed by appropriate heat treatment, P92 steel exhibits very low creep strength. It is therefore important that an initial 100% martensitic microstructure is obtained [19]. It should be stressed that the priority element having determined the original subgrain size and shape is the initial lath martensitic microstructure. Hättestrand and Andren [20] studied a isothermally aged P92 and found that coarsening of $M_{23}C_6$ carbides is accelerated by the strain, while the effect of strain on VN precipitates is insignificant. According these authors MX (mainly VN) precipitates appear to be relatively stable at temperatures 600°C and 650°C up to 10 000 h of ageing. With $M_{23}C_6$ precipitates the situation is different. At 600°C, no coarsening appears to take place during 10 000 h of ageing, while in creep the particles coarsen to about 20% larger size. At 650°C particle coarsening takes place in both aged and creep tested material. The role of tungsten (P92 steel has the addition of 1.8 wt% tungsten in comparison with P91 steel) was studied by Hald [18]. It was found that W precipitates as intermetallic Laves phase during creep exposure, but the loss of tungsten from solid solution does not seem to affect long-term creep stability. Subgrains in steel P92 grow as a function of creep strain and stress following a general function for all 9-12%Cr steels, which indicates that the precipitate stability may control the creep strength of the steels of the inherent. While MX (VN) particles coarsen very slowly during creep exposure, precipitation of new MX particles during creep could not be confirmed.

From the above discussion it can be concluded that the creep behaviour and creep strength in the power-law creep region are controlled by the coexistence of dislocation substructure and precipitates, the latter mainly acting as subgrain stabilizer. Thus, the role of dislocation substructure dominates the role of precipitation strengthening due to carbide particles. Figure 4 gives an additional support for a decisive role of dislocation substructure in creep behaviour of the steels investigated; independently of the type of steel and its state and/or microstructure the minimum creep rate is reached in all cases at practically the same strain ($\varepsilon \cong 0.025$).

Consequently, a decrease of the creep resistance of the aged steels may be explained by taking account of the change of dislocation substructure during isothermal ageing.

5. Conclusions

The creep resistance of two modified 9-12%Cr steels (Grades P91 and P92) is shown to be considerably influenced by microstructural changes and microstructure stability during long-term ageing and/or creep over a range of dislocation (power-law) creep. It is suggested that the change in the dislocation substructure dominates over indirect effects caused by particle evolution. By contrast, no significant effect of microstructural stability on creep was found in a regime of viscous creep which is inherent to real service loading conditions of the steels of interest. It is generally claimed that the particle dispersions inhibit vacancy generation and annihilation at grain boundaries, but current diffusional theories have not been modified to provide estimates of the creep rates displayed at low stresses with particle-hardened alloys.

6. Acknowledgements

Financial support for this work was provided in part by the Grant Agency of the Czech Republic under Contract No. 106/02/0608, and in part by the Ministry of Education of the Czech Republic under Contract No. OC 522.40 (COST 522).

7. References

[1] H.K.D.H.Bhadeshia, Estimation of the microstructure and properties of ferritic creep-resistant steam pipe steels. In: Modelling of microstructural evolution in creep resistant material, eds. A. Strang and M. McLean, IOM, London 1999, pp. 15-38.

[2] A.Strang, V.Vodarek and H.K.D.H.Bhadeshia, Modelling of microstructural degradation in creep resistant 12%Cr power plant steels, ibid, pp. 129-150.

[3] V.Sklenicka, K.Kucharova, A.Dlouhy and J.Krejci, Creep behaviour and microstructure of a 9%Cr steel. In: Materials for advanced power engineering, eds. D. Coutsouradis et al., Kluwer Academic Publishers, Dordrecht 1994, pp. 435-444.

[4] L.Kloc and V.Sklenicka, Transition from power-law to viscous creep behaviour of P91 type heat-resistant steel. Mater. Sci.Eng., A234-236, (1997), pp. 962-965.

[5] L.Kloc, V.Sklenicka and J. Ventruba, Comparison of low stress creep properties of ferritic and austenitic creep resistant steels, Mater. Sci. Eng., A319-321, (2001), pp. 774-778.

[6] O.D.Sherby, O.A.Ruano and J. Wadsworth, Deformation mechanisms in crystalline solids and newtonian viscous behavior. In: Creep behavior of advanced materials for the 21st century, eds. R.S.Mishra et al., TMS, Warrendale, 1999, pp. 397-411.

[7] F.R.N.Nabarro, Creep at very low rates. Metal. Mater. Trans., 33A, (2002), pp. 213-218.

[8] T.G.Langdon, Creep processes at low stress levels. In: Creep deformation: Fundamentals and Applications, eds. R.S.Mishra et al., TMS, Warrendale 2002, pp. 41-50.

[9] F.A.Mohamed, Creep behavior at very low stresses, ibid, pp.71-83.

[10] R.L.Coble, A model for boundary diffusion controlled creep in polycrystalline materials. J. Appl. Physics, 34, (1963), 1679-1705.

[11] F.A.Mohamed and J. Wolfenstine, Harper-Dorn creep in materials. In: Hot deformation of aluminium alloys, eds. T. Langdon et al., TMS, Warrendale, 1991, pp. 223-230.
[12] J.Cadek, Creep in metallic materials. Elsevier, Amsterdam, 1988.
[13] F.C.Monkman and N.J.Grant, Proc. ASTM, 56, (1956), p. 593 – cited in [12].
[14] A.Orlova, J.Bursik, K.Kucharova and V.Sklenicka, Microstructural development during high temperature creep of 9%Cr steel, Mater.Sci.Eng., A245, (1998), pp. 39-48.
[15] J.Cadek, V.Sustek and M.Pahutova, An analysis of a set of creep data for a 9Cr-1Mo-0.2V (P91 type) steel, Mater.Sci.Eng., A225, (1997), pp.22-28.
[16] J.Rösler, N.Bäker and C.Tiziani, Dual scale particle strengthened alloys for high temperature application: Creep behaviour and fundamentals of design. In: Creep deformation fundamentals and applications, eds. R.S.Mishra et al., TMS, Warrendale, 2002, pp. 185-193.
[17] K.Kucharova, J.Nemec and A.Dlouhy, Microstructure and creep strength of tempered martensite ferritic steel. In: Creep and fracture of engineering materials and structures, eds. J.C.Earthman and F.A.Mohamed, UC Irvine, 1997, pp. 79-88.
[18] J.Hald, Microstructure stability of steels P92 and P122. In: Advances in material technology for fossil power plants, eds. R. Wiswanathan et al., The Institute of Materials, London, 2001, pp. 115 – 124.
[19] P.J.Ennis, Creep strengthening mechanism in high chromium steels, ibid, pp. 187-194.
[20] M.Hättestrand and H.-O.Andren, Evaluation of particle size distributions of precipitates in a 9% chromium steel using energy filtered transmission electron microscopy. Micron, 32, (2001), pp. 789-797.
[21] J.Hald, Materials comparisons between NF 616, MCM 12A and TB 12M – III. Microstructural stability and ageing. In: New steels for advanced plant up to 620°C, ed.E. Metcalfe, EPRI, 1995, pp. 152-173.
[22] P.J.Ennis, A.Zielenska-Lipiec, O.Wachter and A. Czyrska-Filemonowicz, Microstructural ability and creep rupture strength of the martensitic steel P92 for advanced power plant. Acta mater., 45, (1997), pp. 4901-4907.
[23] M. Hatterstrand, M.Schwind and H.-O.Andren, Microanalysis of two creep resistant 9-12% chromium steels. Mat.Sci.Eng., A250, (1998), pp. 27-36.

SYSTEM FREE ENERGY APPROACH TO THE PRECIPITATION OF THE LAVES PHASE IN Fe-Cr-W-C QUATERNARY STEELS

Y. Murata[(1)], T. Koyama[(2)], M. Morinaga[(1)], R. Hashizume[(3)], T. Miyazaki[(4)] and M. Doi[(5)]

(1) Department of Materials Science and Engineering, Graduate School of Engineering, Nagoya University, Furo-cho, Chikusa-ku, Nagoya 464-8603, Japan
TEL & FAX : +81 52 789 3232 E-mail : murata@numse.nagoya-u.ac.jp
(2) National Institute for Materials Science (NIMS), Japan
(3) Technical Research Center, The Kansai Electric Power Co. Inc., Japan.
(4) Emeritus Professor of Nagoya Institute of Technology, Japan.
(5) Department of Materials Sci. and Engineering, Nagoya Institute of Technology, Japan.

Abstract

In order to elucidate the microstructure evolution in advanced high Cr heat resisting ferritic steels, a time-composition-temperature diagram of Fe-10mass%Cr-W-C quaternary steels is calculated on the basis of the system free energy theory proposed by Koyama and Miyazaki. The microstructures are predictable using such a system free energy consisting of chemical free energy, interface energy and strain energy between the matrix and precipitates in the steel. In this study, our attention is focused on the Laves phase as the precipitate, because this phase is formed in recently developed heat resisting ferritic steels and affects their creep strength largely. The calculations conducted in the Fe-Cr-W-C quaternary steels lead to the following findings; (i) The Laves phase is not formed in those steels containing less than 0.4mol%W(about 1.4mass%W) even after a long term aging at 923K. (ii) Only granular Laves phase precipitates in the steel containing 0.4mol%W to 1.05mol%W (about 3.5mass%W) even in the early stage of aging at 923K. (iii) The morphological change of the Laves phase from the fine coherent precipitate to the granular one occurs in a regular aging sequence in the steel if it contains more than 1.05mol%W. (iv)Coherent precipitation line for the Laves phase is determined in the quasi-binary phase diagram as a function of the W content. These findings obtained theoretically are consistent with experimental results.

Keywords: ferritic steel, Laves phase, system free energy, microstructure evolution

1. Introduction

There has been a strong need to develop advanced ferritic steels which can be utilized even under the ultra super critical (USC) conditions of power plants. In those plants, there is a trend of raising the steam temperature up to 923K (650°C). Therefore it has been requested strongly to develop advanced high Cr ferritic steels which are tolerable under such severe operating conditions of power plants. High Cr heat resistant ferritic steels are composed generally of the martensite phase, MX carbonitride, $M_{23}C_6$ carbide and intermetallic compounds such as the Laves phase, the μ phase, the z phase, etc [1,2]. From the complexity of the microstructure in these steels, it is difficult to predict the microstructure evolution at high temperatures, although the prediction is important in understanding creep strength of the ferritic steels.

In recent advanced heat resistant ferritic steels containing a high amount of refractory elements such as Mo, W, Re, etc., the Laves phase is believed to precipitate in the boundaries of martensite lath, block, packet and some prior austenite grains, while keeping

granular in shape. However, a number of fine Laves-phase precipitates are found to exist even inside the martensite lath in the tempered steels containing 10mass%Cr and 4.6mass%W [3]. There is a room to debate on the contribution of the Laves phase to creep strength, but the fine Laves phase must contribute to the creep strength. Then it is important to make clear the morphological change of the Laves phase for understanding the creep strength of those steels.

The objective of this study is to elucidate the microstructure evolution of the Laves phase in advanced high Cr heat resistant ferritic steels following the system free energy theory [4]. This is the first-step for predicting the whole microstructure evolution of high Cr ferritic steels.

2. Theory of System Free Energy

A general explanation of the system free energy

Following the previous report [4], the concept of system free energy is explained below. Figure 1 is a schematic illustration of free energy changes during phase decomposition. When a supersaturated solid solution of the composition X_0 separates into two phases of the compositions X_1 and X_2, it has usually been considered that the free energy decreases from G_S to G_0. However, since the phase decomposition inevitably causes additional free energies such as elastic strain energy E_{str} and an interfacial energy E_{surf}, the free energy of the microstructure is not G_0 but G_{system}. Consequently the free energy change associated with the phase decomposition is only G_s-G_{system}, and the remaining G_{system}-G_0 gradually decreases during the subsequent structural evolution such as the coarsening of the precipitates. Therefore it is expected that the evaluation of G_{system} in the progress should make it possible to predict the progress of microstructure evolution.

The total free energy of the microstructure should be given by the sum of a chemical free energy, G_0, an elastic strain energy, E_{str}, an interfacial energy, E_{surf}, and an elastic interaction energy, E_{int}, and then a possibility of predicting the microstructure development is treatable on the basis of the total free energy. The total free energy is called as system free energy, G_{system} $(=G_0+E_{str}+E_{surf}+E_{int})$.

System free energy for the Fe-Cr-W-C system

The Fe-Cr-W-C quaternary system is employed in order to perform the simulation of the advanced heat resisting steels, and special attention is directed towards the morphological evolution of the Laves phase. In this case, as shown in Fig.2, the relationship between the microstructure evolution and the free energy change can be drawn by analogy with Fig.1. The existence of $M_{23}C_6$ carbide is also being considered in this simulation. But this carbide precipitates incoherently even in the as-tempered state in high Cr ferritic steel, and the morphological change of $M_{23}C_6$ carbide is smaller than that of the Laves phase. Therefore, the contribution of both elastic strain energy and interfacial energy generated from this carbide to the change of system free energy is disregarded in this study. Also, volume fractions of both the Laves phase and $M_{23}C_6$ carbide are small, and hence the interaction

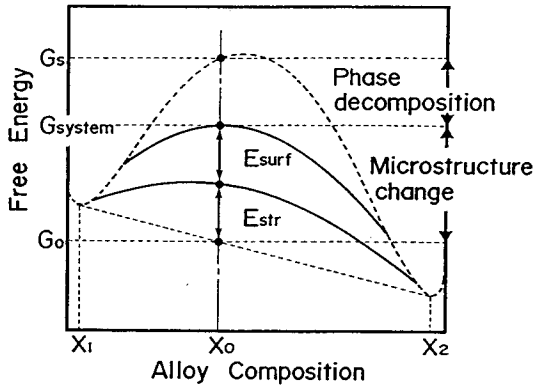


Fig. 1 Schematic drawing of the free energy change with phase decomposition and microstructure change. The dotted curve is the chemical free energy of solid solution, E_{surf} is the interfacial energy and E_{str} is the elastic strain energy.

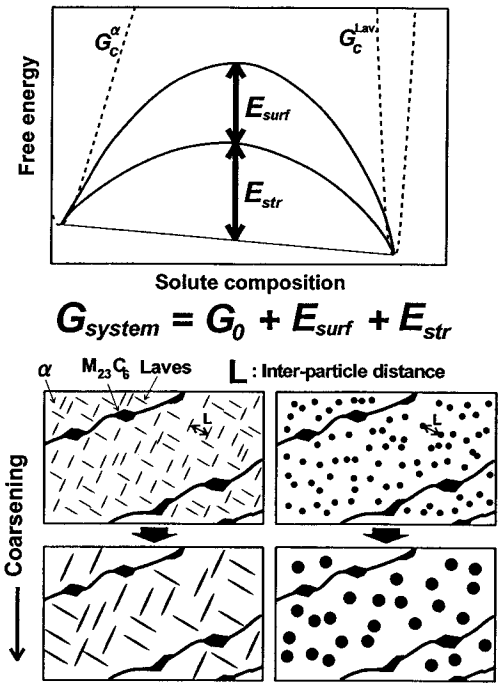


Fig.2 Relationship between the free energy change and the microstructure evolution in Fe-Cr-W-C steels. The free energy change is associated with the morphological change from the coherent fine Laves phase to the granular incoherent Laves phase.

energy E_{int} in G_{system} is set to be zero in this simulation. Furthermore, MX type carbonitrides are not considered to influence the microstructure evolution of the Laves phase, because the carbonitrides scarcely change during aging at about 1000K due to their high stability in the ferritic steels. As a result, the system free energy is estimated by the sum of chemical free energy, G_0, elastic strain energy, E_{str}, and interfacial energy, E_{surf}, in Fe-Cr-W-C quaternary steels.

Chemical Free Energy G_0 for Fe-Cr-W-C Quaternary System

The chemical free energy for Fe-Cr-W-C alloys is evaluated as,

$$G_0 = f_\alpha G^\alpha + f_{M_{23}C_6} G^{M_{23}C_6} + f_{Laves} G^{Laves}. \tag{1}$$

Here, G^α, $G^{M_{23}C_6}$ and G^{Laves} are the chemical free energy for the α phase, for $M_{23}C_6$ carbide, and for the Laves phase, respectively. f_i is the volume fraction of i phase. Furthermore, G^α is separated into the following two parts, i.e., one is the paramagnetic term and the other is the term of ferromagnetic excess free energy.

$$G^\alpha = [G^\alpha]^{para} + [\Delta G^\alpha]^{ferro} \tag{2}$$

According to the sub-lattice model, $[G^\alpha]^{para}$ is expressed as,

$$[G^\alpha]^{para} = \frac{1}{a + cy_C^{II}} \begin{bmatrix} y_{Va}^{II}(Y_{Fe}^{I} {}^{\circ}G_{Fe:Va}^{\alpha} + Y_{Cr}^{I} {}^{\circ}G_{Cr:Va}^{\alpha} + Y_{W}^{I} {}^{\circ}G_{W:Va}^{\alpha}) \\ +y_C^{II}(Y_{Fe}^{I} {}^{\circ}G_{Fe:C}^{\alpha} + Y_{Cr}^{I} {}^{\circ}G_{Cr:C}^{\alpha} + Y_{W}^{I} {}^{\circ}G_{W:C}^{\alpha}) \\ +a\begin{Bmatrix} Y_{Fe}^{I}Y_{Cr}^{I}(y_{Va}^{II}L_{Fe,Cr:Va}^{\alpha} + y_C^{II}L_{Fe,Cr:C}^{\alpha}) \\ +Y_{Fe}^{I}Y_{W}^{I}(y_{Va}^{II}L_{Fe,W:Va}^{\alpha} + y_C^{II}L_{Fe,W:C}^{\alpha}) \\ +Y_{Cr}^{I}Y_{W}^{I}(y_{Va}^{II}L_{Cr,W:Va}^{\alpha} + y_C^{II}L_{Cr,W:C}^{\alpha}) \end{Bmatrix} \\ +cy_{Va}^{II}y_C^{II}(Y_{Fe}^{I}L_{Fe:Va,C}^{\alpha} + Y_{Cr}^{I}L_{Cr,Va,C}^{\alpha} + Y_{W}^{I}L_{W:Va,C}^{\alpha}) \\ +aRT(Y_{Fe}^{I}\ln Y_{Fe}^{I} + Y_{Cr}^{I}\ln Y_{Cr}^{I} + +Y_{W}^{I}\ln Y_{W}^{I}) \\ +cRT(y_{Va}^{II}\ln y_{Va}^{II} + y_C^{II}\ln y_C^{II}) \end{bmatrix}. \tag{3}$$

Here, a and c are the number of sub-lattices for the substitutional sites and the number of sub-lattices for the interstitial sites, respectively. Va represents the atomic vacancy. y_{Va}^{II} and y_C^{II} are atomic fractions of vacancy and carbon in the sub-lattice II for interstitial elements, respectively. Y_i^I is the atomic fraction of i element in the sub-lattice I for substitutional elements, ${}^{0}G_{Xi:Va}^{\alpha}$ is the molar Gibbs free energy for a $(X_i)_a$:$(Va)_c$ type compound, ${}^{0}G_{Xi:C}^{\alpha}$ is the molar Gibbs free energy for a $(X_i)_a$:$(C)_c$ type compound. Also, $L_{Fe,X_i:Va}^{\alpha}$ is a molar interaction energy between Fe atom and X_i atom when all the sub-lattices for interstitial elements are occupied by vacancies, $L_{Fe,X_i:C}^{\alpha}$ is a molar interaction energy between Fe atom and X_i atom when all the sub-lattices for interstitial elements are

occupied by carbon atoms, and $L^{\alpha}_{X_i:Va:C}$ is a molar interaction energy between carbon atom and vacancy when all the sub-lattices for substitutional elements are occupied by X_i atoms. R is the gas constant and T is the temperature. The molar Gibbs free energy and the molar interaction energy are given in the Thermo-Calc database.

Temperature dependence of the excess free energy associated with magnetic energy is employed as the following formula proposed by Hillert and Jarl [5].

$$[\Delta^{\circ}G^{\alpha}_{Fe}(T)]^{ferro} = RT\ln(\beta+1)\cdot f(\tau)\ . \tag{4}$$

Here, β is the number of the Bohr magneton, and τ is the reduced temperature, T/T_c. Also, $f(\tau)$ is the function representing by the power series of τ. On the basis of the sub-lattice model, the Curie temperature T_c and the number of the Bohr magneton β_c for Fe-C-Cr-W quaternary steels are given as,

$$\begin{aligned}T_C = {} & Y^I_{Fe}y^{II}_{Va}{}^{\circ}T_{Fe:Va} + Y^I_{Fe}y^{II}_{C}{}^{\circ}T_{Fe:C} + Y^I_{Cr}y^{II}_{Va}{}^{\circ}T_{Cr:Va} + Y^I_{Cr}y^{II}_{C}{}^{\circ}T_{Cr:C} + Y^I_{W}y^{II}_{Va}{}^{\circ}T_{W:Va} + Y^I_{W}y^{II}_{C}{}^{\circ}T_{W:C} \\ & + aY^I_{Fe}Y^I_{Cr}(y^{II}_{Va}{}^{\circ}T_{Fe,Cr:Va} + y^{II}_{C}{}^{\circ}T_{Fe,Cr:C}) \\ & + aY^I_{Fe}Y^I_{W}(y^{II}_{Va}{}^{\circ}T_{Fe,W:Va} + y^{II}_{C}{}^{\circ}T_{Fe,W:C}) \\ & + aY^I_{Cr}Y^I_{W}(y^{II}_{Va}{}^{\circ}T_{Cr,W:Va} + y^{II}_{C}{}^{\circ}T_{Cr,W:C}) + cy^{II}_{Va}y^{II}_{C}(Y^I_{Fe}{}^{\circ}T_{Fe:Va,C} + Y^I_{Cr}{}^{\circ}T_{Cr:Va,C} + Y^I_{W}{}^{\circ}T_{W:Va,C}),\end{aligned} \tag{5}$$

$$\begin{aligned}\beta_C = {} & Y^I_{Fe}y^{II}_{Va}{}^{\circ}\beta_{Fe:Va} + Y^I_{Fe}y^{II}_{C}{}^{\circ}\beta_{Fe:C} + Y^I_{Cr}y^{II}_{Va}{}^{\circ}\beta_{Cr:Va} + Y^I_{Cr}y^{II}_{C}{}^{\circ}\beta_{Cr:C} + Y^I_{W}y^{II}_{Va}{}^{\circ}\beta_{W:Va} + Y^I_{W}y^{II}_{C}{}^{\circ}\beta_{W:C} \\ & + aY^I_{Fe}Y^I_{Cr}(y^{II}_{Va}{}^{\circ}\beta_{Fe,Cr:Va} + y^{II}_{C}{}^{\circ}\beta_{Fe,Cr:C}) \\ & + aY^I_{Fe}Y^I_{W}(y^{II}_{Va}{}^{\circ}\beta_{Fe,W:Va} + y^{II}_{C}{}^{\circ}\beta_{Fe,W:C}) \\ & + aY^I_{Cr}Y^I_{W}(y^{II}_{Va}{}^{\circ}\beta_{Cr,W:Va} + y^{II}_{C}{}^{\circ}\beta_{Cr,W:C}) + cy^{II}_{Va}y^{II}_{C}(Y^I_{Fe}{}^{\circ}\beta_{Fe:Va,C} + Y^I_{Cr}{}^{\circ}\beta_{Cr:Va,C} + Y^I_{W}{}^{\circ}\beta_{W:Va,C}).\end{aligned} \tag{6}$$

The meanings of superscripts and subscripts in Eqs.(5) and (6) are the same as those in Eq.(3).

The chemical free energy of $M_{23}C_6$ is also calculated on the basis of the Thermo-Calc database using a formula of $(Fe,Cr)_{20}(Fe,Cr,W)_3C_6$ [6], and then it is given as,

$$G^{M_{23}C_6}_{c} = \frac{1}{29}\begin{bmatrix} Y^I_{Fe}Y^{II}_{Fe}G^{M_{23}C_6}_{Fe:Fe:C} + Y^I_{Fe}Y^{II}_{Cr}G^{M_{23}C_6}_{Fe:Cr:C} + Y^I_{Fe}Y^{II}_{W}G^{M_{23}C_6}_{Fe:W:C} + Y^I_{Cr}Y^{II}_{Fe}G^{M_{23}C_6}_{Cr:Fe:C} + Y^I_{Cr}Y^{II}_{Cr}G^{M_{23}C_6}_{Cr:Cr:C} + Y^I_{Cr}Y^{II}_{W}G^{M_{23}C_6}_{Cr:W:C} \\ +20\left(Y^I_{Fe}Y^I_{Cr}Y^{II}_{Fe}L^{M_{23}C_6}_{Fe,Cr:Fe:C} + Y^I_{Fe}Y^I_{Cr}Y^{II}_{Cr}L^{M_{23}C_6}_{Fe,Cr:Cr:C} + Y^I_{Fe}Y^I_{Cr}Y^{II}_{W}L^{M_{23}C_6}_{Fe,Cr:W:C}\right) \\ +3\begin{pmatrix} Y^I_{Fe}Y^{II}_{Fe}Y^{II}_{Cr}L^{M_{23}C_6}_{Fe:Fe,Cr:C} + Y^I_{Fe}Y^{II}_{Fe}Y^{II}_{W}L^{M_{23}C_6}_{Fe:Fe,W:C} + Y^I_{Fe}Y^{II}_{Cr}Y^{II}_{W}L^{M_{23}C_6}_{Fe:Cr,W:C} \\ Y^I_{Cr}Y^{II}_{Fe}Y^{II}_{Cr}L^{M_{23}C_6}_{Fe:Fe,Cr:C} + Y^I_{Cr}Y^{II}_{Fe}Y^{II}_{W}L^{M_{23}C_6}_{Fe:Fe,W:C} + Y^I_{Cr}Y^{II}_{Cr}Y^{II}_{W}L^{M_{23}C_6}_{Fe,Cr,W:C} \end{pmatrix} \\ +RT\left\{20(Y^I_{Fe}\ln Y^I_{Fe} + Y^I_{Cr}\ln Y^I_{Cr}) + 3(Y^{II}_{Fe}\ln Y^{II}_{Fe} + Y^{II}_{Cr}\ln Y^{II}_{Cr} + Y^{II}_{W}\ln Y^{II}_{W})\right\} \end{bmatrix}. \tag{7}$$

Also, according to the formula of $(Fe,Cr)_2(W,Mo)$, chemical free energy for the Laves phase, G_c^{Laves}, is expressed as,

$$G_c^{Laves} = \frac{1}{3}\begin{bmatrix} Y_{Fe}^I Y_W^{II} G_{Fe:W}^{Laves} + Y_{Cr}^I Y_W^{II} G_{Cr:W}^{Laves} + 2Y_{Fe}^I Y_{Cr}^I Y_W^{II} L_{Fe,Cr:W:C}^{Laves} \\ +RT\{2(Y_{Fe}^I \ln Y_{Fe}^I + Y_{Cr}^I \ln Y_{Cr}^I) + Y_W^{II} \ln Y_W^{II}\} \end{bmatrix}$$

$$= \frac{1}{3}\begin{bmatrix} Y_{Fe}^I G_{Fe:W}^{Laves} + Y_{Cr}^I G_{Cr:W}^{Laves} + 2Y_{Fe}^I Y_{Cr}^I L_{Fe,Cr:W:C}^{Laves} \\ +2RT(Y_{Fe}^I \ln Y_{Fe}^I + Y_{Cr}^I \ln Y_{Cr}^I) \end{bmatrix}. \quad (8)$$

Elastic Strain Energy for Fe-Cr-W-C Quaternary System

In general, elastic strain energy is generated in alloy when a coherent precipitate having a different lattice constant with the matrix exists in the alloy. From this sense, we take into account only the elastic strain energy generated from the coherent fine Laves phase in Fe-Cr-W-C quaternary steels. The strain energy is given by,

$$E_{str} = Af(1-f)(c_{Laves} - c_\alpha)\eta^2 Y_{<100>}$$
$$Y_{<100>} = \frac{E}{1-\nu} \quad . \quad (9)$$

Here, A is a constant, and f is the volume fraction of the precipitate. We assumed the elastic strain energy E_{str} for the fine Laves phase to be about 20% of the value for the coherent precipitate in Fe-W binary system [7]. Then A is set to be 0.2 in this simulation. c_{Laves} and c_α are chemical compositions of the Laves phase and the ferrite phase, respectively. $\eta(c_{Laves} - c_\alpha)$ is the lattice mismatch between the α phase and the Laves phase in the coherent plane [8]. E and ν are the Young's modulus and the Poisson's ratio, respectively, and the values of pure iron are used in this study.

Interfacial Energy for Fe-Cr-W-C Quaternary System

Interfacial energy E_{surf} between the Laves phase and the matrix is evaluated in both coherent and incoherent states by using the following equation.

$$E_{surf} = S_V(p)\gamma_S, \quad (10)$$

where $S_V(p)$ is interfacial area per unit volume and it is expressed as,

$$S_V(p) = \frac{S(p)}{V} = \frac{fS(p)}{V\{(p(r_0)\}}$$
$$= \frac{\pi r_0^2 p^{-2/3}[2+g(p)]}{\frac{4}{3}\pi r_o} = \frac{3fp^{-2/3}[2+g(p)]}{4r_o} \quad . \quad (11)$$

Here, V is a volume of the steel, f is the volume fraction of the precipitate, r_0 is a radius of

the sphere having the same volume of ellipsoid of the aspect ratio, p, and $V\{p(r_0)\}$ is the volume of the precipitate. $g(p)$ is a function representing a shape of ellipsoid. There are three possible types of $g(p)$ depending on the aspect ratio of p, and they are represented as

$$g(p)=\frac{2p^2}{(1-p^2)^{1/2}}\log\left[\frac{1+(1-p^2)^{1/2}}{p}\right], \qquad (p<1)$$

$$g(p)=2, \qquad (p=1) \qquad (12)$$

$$g(p)=\frac{2p^2}{(1-p^2)^{1/2}}\tan^{-1}(p^2-1)^{1/2}. \qquad (p>1)$$

In Eq.(10), the surface interfacial energy, γ_s, and the aspect ratio, p, are set to be the following values in this study.

(i) for the fine Laves phase : $\gamma_s=\gamma_c=0.1J/m^2$, and p=0.1,

(ii) for the granular Laves phase : $\gamma_s=\gamma_i=0.468J/m^2$, and p=1.

Here, γ_c and γ_i are the coherent- and the incoherent-interface energy, respectively. This incoherent-interfacial energy, γ_i, is the value for the grain-boundary energy-density of the δ phase [9].

3. Results and Discussion

Calculated results

Figure 3(a) shows the changes in the system free energy at 800K with the size of the Laves phase in an Fe-10mass%Cr-9.35mass%(3mol%)W-0.11mass%C steel (notice: W coordinate shown in Fig.3 is represented in mol%). The three horizontal lines in the figure correspond to three energy levels, which are the free energy of the supersaturated solid solution of 3mol%W steel (G_c^{α}), the free energy of the microstructure precipitating the coherent Laves phase ($G_0+E_{str}^{coh}+E_{surf}$), and the free energy of the microstructure precipitating the incoherent Laves phase ($G_0+E_{str}^{incoh}$). In Fig.3(a), the full line represents the case of coherent Laves phase and the broken line shows the case of the incoherent (granular) Laves phase. When the size is small, the system free energy for the fine coherent Laves phase is lower than that for the incoherent one. The critical size of the coherent-to-incoherent transition is estimated from Fig.3(a) to be about 8nm for the 3mol%W steel. It is noted here that this value is a radius of the sphere having the same volume of ellipsoid of an aspect ratio, p. Therefore, when the shape is ellipsoid, the long diameter of the ellipsoid is much larger than the critical value shown in Fig.3.

A series of calculations similar to Fig.3(a) is carried out using steels with various W contents. As a result, Fig.3(b) is obtained. This figure exhibits the stable morphology of the Laves phase at 800K in Fe-10Cr-W-0.11C(mass%) quaternary steels. In this figure, the phase boundary between the coherent and the granular Laves phases at 3mol%W

corresponds to the critical size shown in Fig.3(a). In Fig.3, the size scale is able to convert into the time scale following the equation, $r^m - r_{t=0}{}^m = kt$, where k and m are constants and $r_{t=0}$ is the size at t=0.

Figure 4 shows the calculated results exhibiting the stable morphology of the Laves phase which changes with the W content, the size and the temperature in Fe-10Cr-W-0.11C (mass%) alloys. Three bottom figures show stable regions for the coherent and the granular (incoherent) Laves phases at 900, 1000 and 1100K. These calculated results leads to the following findings; (i) The Laves phase is not formed in those steels containing less than 0.4mol%W(about 1.4mass%W) even after a long term aging at 923K. (ii) Only granular Laves phase precipitates in the steel containing 0.4mol%W to 1.05mol%W (about 3.5mass%W) even in the early stage of aging at 923K. (iii) The morphological change of the Laves phase from the fine coherent precipitate to the granular one occurs in a regular aging sequence at 923K in the steel containing more than 1.05mol%W.

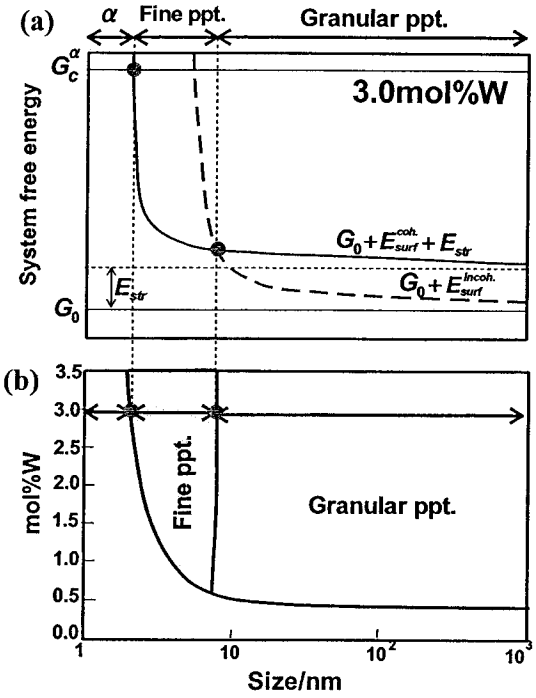


Fig. 3
(a) Changes in the system free energy at 800K with the size of the Laves phase in an Fe-10mass%Cr-9.35mass% (3mol%)W-0.11mass%C steel (notice: W coordinate shown in mol%).
(b) Stable morphology of the Laves phase in Fe-10Cr-W-0.11 C(mass%) quaternary steels.

A series of calculations similar to the bottom figures in Fig.4 is conducted at various temperatures. As a result, a quasi-binary phase diagram for the Laves phase is obtained as shown in the upper figures of Fig.4. It is found that the critical W concentration at which the Laves phase changes the shape from fine to granular one increases with increasing temperature. The fine coherent Laves phase exists in the region of the higher W contents

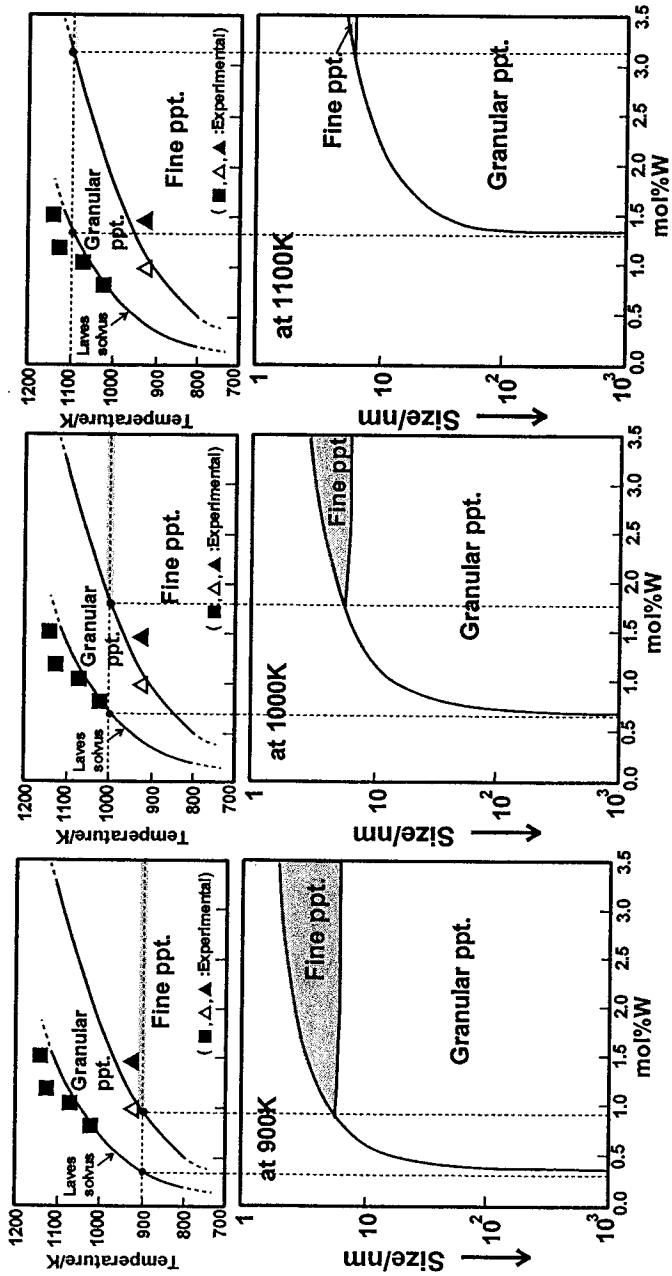


Fig.4 Calculated results exhibiting the stable morphology of the Laves phase in Fe-Cr-W-C alloys. Square and triangle marks plotted in the upper figures are experimental results. The open triangles and solid triangles show the positions where the granular Laves phase and the fine coherent Laves phase are observed, respectively.

and the lower temperatures in this quasi-binary phase diagram.

Comparison between the calculated results and experimental results

In the upper figures of Fig.4, experimental data are also plotted using square and triangle marks which are obtained at 923K in Fe-10Cr-0.1C-W-Co-V-Mo (mass%) ferritic steels. The square marks show the solid-solubility for the Laves phase. On the other hand, the open triangle and solid triangles show the positions, where the granular Laves phase and the fine coherent Laves phase are observed, respectively. By comparing these experimental data with the calculated phase boundaries, it is found that the prediction from the system free energy agrees well with the experimental results.

The system-free-energy calculations supported by a few experimental results will serve as a powerful method for predicting the microstructure evolution in high Cr ferritic steels with complicated microstructures.

4. Conclusion

The concept of system free energy is applied to the prediction of the morphological change of the Laves phase in high Cr ferritic steels containing W. It is shown that the critical W concentration for the transition from coherent-to-incoherent Laves phase in the Fe-Cr-W-C system is predicted on the basis of the system free energy. Coherent precipitation line for the Laves phase is determined in the quasi-binary phase diagram as a function of the W content. The prediction from the system free energy agrees well with the experimental results of high Cr heat resistant ferritic steels.

Acknowledgement

This work is supported in part by the Grant-in-Aid for Scientific Research of Japan Society for the Promotion of Science (JSPS), Japan.

References

[1] T.Fujita: ISIJ International, 32 (1978) 175.

[2] A.Strang and V.Vodarek: Materilas Sci., Techonogy, 12(1996), 552.

[3] Y.Murata, M.Morinaga, R.Hashizume, K.Takami, T.Azuma, Y.Tanaka and T.Ishiguro: Materials Sci. and Engineering, A282 (2000) 251.

[4] T.Miyazaki, T.Koyama: Materials Sci. and Engineering, A136 (1991), 151.

[5] M.Hillert and M.Jarl: CALPHAD, 2(1978), 227.

[6] P.Custafson: Met. Trans. A, 19A(1988),2547.

[7] T.Koyama:Doctoral Thesis (Nagoya Institute of Technology, 1996, Nagoya, Japan)

[8] Y.Murata, T.Takami, M.Kamiya, M.Morinaga, R.Hashizume, K.Miki, T.Azuma and T.Ishiguro; Tetsu-to-Hagane, 88(2002) 214.

[9] L.E.Murr: *"Interfacial Phenomena in Metals and Alloys"*, Addison-Wesley Publishing Co. Inc., (1975), p.131.

MICROSTRUCTURAL PHYSICALLY BASED CREEP MODELLING ON 9-12% CR STEELS

Peter Weinert

Institute for Materials Science, Welding and Forming
Graz University of Technology
Austria

Abstract

In this contribution a hierarchical creep model for the description of the creep behaviour of complex ferritic / martensitic 9-12%Cr steels over all creep regimes is introduced. For the microstructural induced creep the model of Ghoniem et al. has been refined and extended, considering the essential changes in the microstructure and the influence of different second phases. To model the microstructural changes and the related strain-rate behaviour during the uniaxial testing of those materials, accepted concepts and physical formulations for the processes have been used. Due to the general character of the microstructure model related phenomena like recovery can be modelled too. To extend the modelling to the tertiary creep regime damage formulations have been incorporated with special focus on the continuous nucleation of intragranular pores and the growth in the constrained mode according to the observed kinetic of damage under typical test conditions. For the elasto - mechanical influence of damage, a Kachanov type formulation has been used. To consider instability phenomena and effects on a creep specimen, iterative elasto / visco-plastic finite element formulations have been used for the description of the thereby altered elastic stresses and deformations. Verification calculations on Cr steels are shown. Finally a critical review of the model is performed in order to evaluate the applicability.

Keywords: model, creep, 9-12% Cr steels, microstructure, damage

Introduction

The current status of understanding the creep behaviour of complex steels is well reflected by the still used common trial and error procedure to optimise ferritic / martensitic 9-12% Cr steels respectively to raise the creep rupture strength $\sigma_{100/10E5}$ up to 625-650 [°C].
Beside the principally not constant stationary creep rate behaviour (see e.g. [1,26]), the change in the creep fracture mode from ductile to brittle [8] (see also Figure 2 (d)), lowering the stresses, is covered up in the case of precipitation hardened steels by precipitation sequences, coarsening and growth of second phases [3,32]. These processes are imposing further degradation mechanisms to such materials. Due to that reliable prognostication of the high temperature behaviour at low stresses based on short time creep experiments is not possible seriously (see Figure 1). Within the european research initiative COST 501 much effort have been put on the investigation of the microstructure in order to quantify the microstructural changes controlling the creep behaviour (e.g. [3,2,27]). Accompanying attempts to model the creep behaviour based on a single process cannot consider the coupling to the rest of the microstructural constituents and interactions. Thereby it was not possible to address and quantify the influence of the different strengthening contributors, e.g. different precipitates or dislocations, accurately.
Considering a schematic creep curve, as shown in Figure 2, the time related principal processes can be identified as a prerequisite, in order to model the complete creep behaviour.

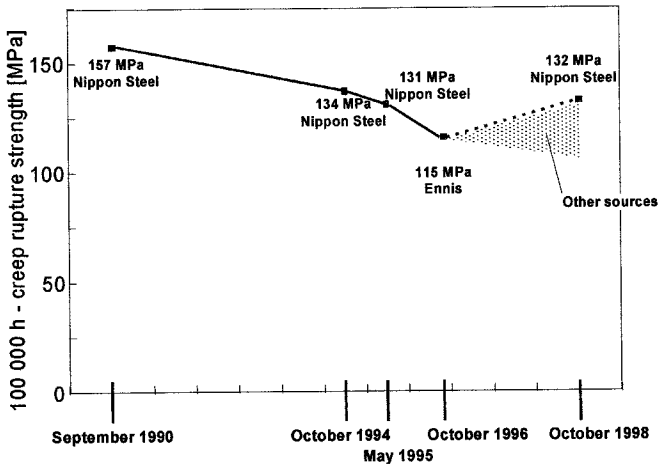


Figure 1: Extrapolated creep rupture strength $\sigma_{1E05/600}$ of the steel NF616 based on short time creep rupture data [3].

By that, the complex problem is treated here with a subdivision into three main parts:

(1) The microstructure model to describe the kinetics of the microstructure in form of several dislocation densities, the subgrain radius and the uniaxial true strain rate behaviour basing on the model of Ghoniem et al. [7].

(2) The damage kinetics for the nucleation and growth of intragranular voids (transgranular voids have been neglected); Coupling of the void kinetic to continuum damage parameters (CDM), treatable within finite element formulations (FE).

(3) Approach to consider an evolving instability with an onset in the secondary creep regime in form of a geometric neck (ductile creep fracture) or a localised damage without a pronounced geometric necking of a creep - specimen (brittle creep fracture).

Model

Microstructure Model

Numerous creep models have been published restricted to pure metals and a limited range of stress and temperature e.g. recovery or glide models (for a review see [4]). Beside the most named approach, the composite model of Vogler and Blum [5] and related approaches e.g. from Orlova et al. [6], Ghoniem et al. [7] published a novel, physical approach. Therein the representative microstructure consists out of subgrains, approximated by area equivalent circles, the boundary of subgrains constituted out of dislocations, and the area of subgrains with mobile dislocations (see Figure 3). The microstructural evolution is considered by the description of single mechanisms, e.g. for thermal and dynamic recovery of dislocations, interaction of mobile dislocations with a subgrain boundary (SGB) and growth of subgrains. The evolutionary equation for one microstructure parameter, in form of an ordinary differential equation, results by the assumption of the additivity of mechanisms, similar to approaches for the modelling of the flow curve. Basing microstructure attributes are the mean value of the subgrain radius, mobile, SGB and static dislocations (see Figure 3). Highlights of Ghoniems approach are the considered transition in the stress exponent up to values of $n \sim 20$

(power-law breakdown) by incorporating the mechanism of dynamic recovery of mobile dislocations, the formulations for the thermal recovery of dislocations and for interaction processes (knitting) of dislocations with the boundary of a subgrain. To verify the model of

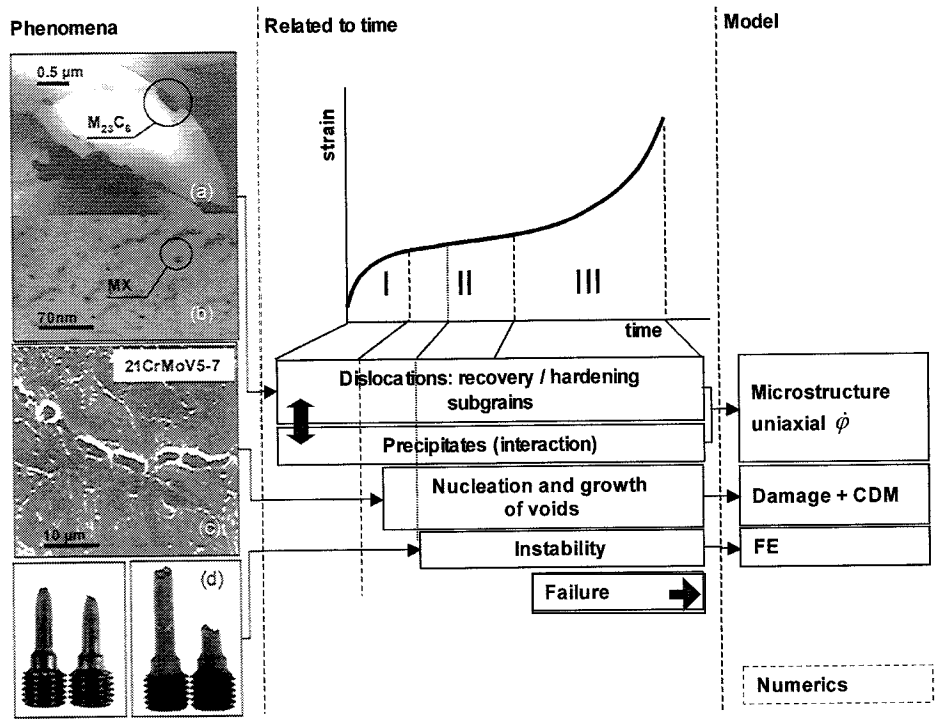


Figure 2: Typical observed phenomena in the area of high temperature deformation of steels – time related processes and main constituents of the complete creep model: (a) and (b) - interactions of precipitates in the steel G-X12CrMoVNbN10-1-1 [3] (c) intragranular voids [8] and (d) broken creep specimens G-X12CrMoVNbN10-1-1 [3].

Ghoniem et al., their approach has been tested on modelling of pure thermal recovery of zone melted iron, using the experimental work of Michalak and Paxton [9] and the modelling

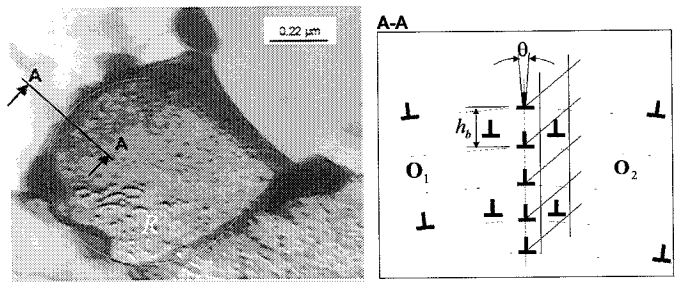


Figure 3: Unit cell used in the model of Ghoniem et al. with θ as misorientation angle, O_1 and O_2 as orientation of neighboured subgrains and h_b as the dislocation distance in the boundary.

of creep of α-iron at 700 °C / 14 MPa under constant stress basing on the work of Karashima et al. [10]. By that strategy it was possible to check formulations for single mechanisms. By that the following parts of the model have been exchanged:

- New formulation for growth of subgrains [11,17],
- Glide kinetic for pure metals and precipitation hardened steels including the transition respectively the low stress range (see e.g. [15])
- Use of the composite approach from Vogler and Blum [5] respectively Nix [12].

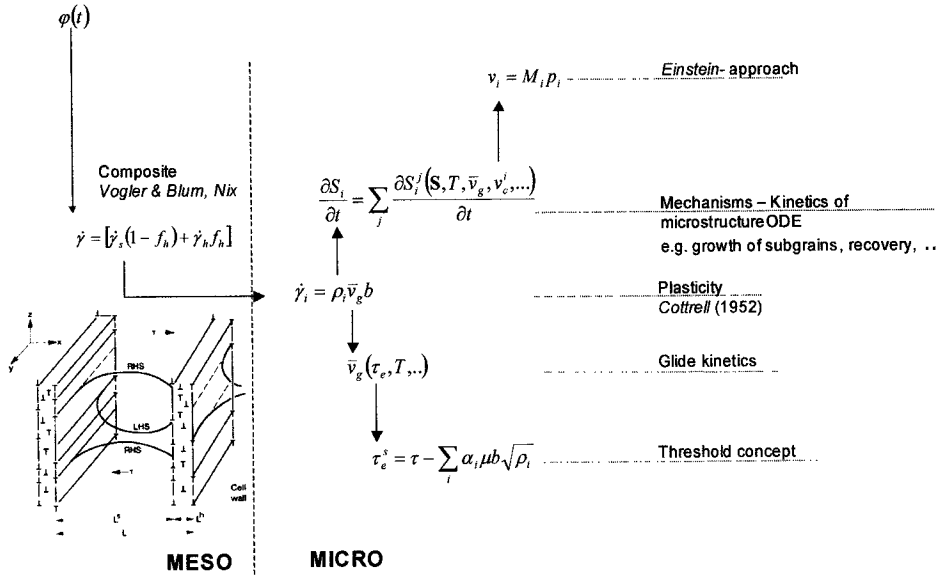


Figure 4: Sketch of the modified uniaxial microstructure model; v_g and v_c are denoting the glide and climb velocity of dislocations, S a microstructural parameter e.g. the radius of a subgrain.

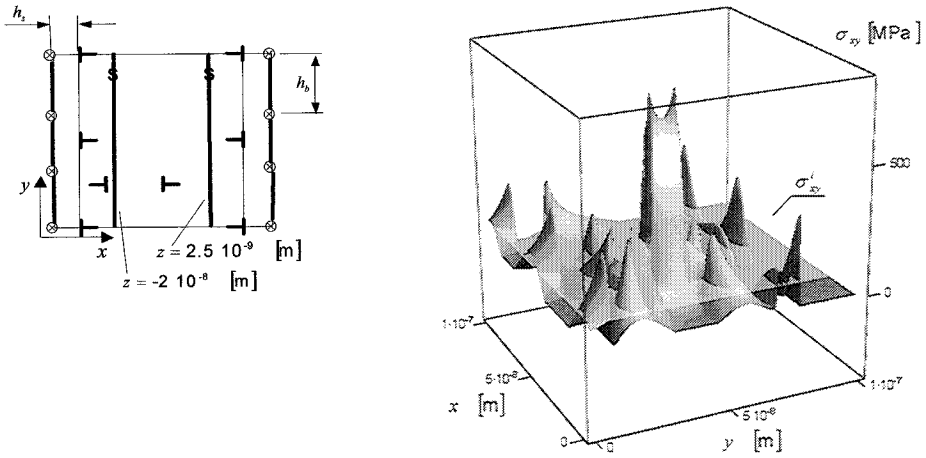
In order to rely on a physical base, formulations for the velocities (climb and glide) are using physical diffusion parameters, which can be estimated, by use of thermodynamic software ThermoCalc (SGTE-database) [13]. Within the model for the description of the strain rate (see Figure 4), the effective stress τ_e plays a key role controlling the velocity of dislocations respectively the strain-rate. Phenomenological the influence of dislocations on the effective stress can be modelled by use of Taylor formulas (see eq. 1) whereby the Taylor factor α scales the threshold contribution. In order to estimate α for each specific dislocation population, adequate configurations of dislocations have been assumed similar to Roters and Raabe [14], the stress field calculated and the Taylor factor estimated according to

$$\tau_e = \tau - \sum_i \alpha_i \mu b \sqrt{\rho_i} \tag{1}$$

$$\tau_i = \alpha_i \mu b \sqrt{\rho_i} = \alpha_i \mu b \frac{1}{\lambda} \tag{2}$$

$$\alpha_i = \left| \frac{\sigma_{xy}}{\mu b (\rho_i)^{0.5}} \right|. \tag{3}$$

The therefore principal applied procedure is illustrated in Figure 5.



(a) (b)

Figure 5: (a) Assumed 3D distribution of dislocations and (b) resulting, calculated stress distribution for σ_{xy} [17]; σ'_{xy} denotes the mean threshold stress of the configuration.

Precipitation Hardened Steels

Nevertheless real materials are exhibiting different second phases playing a different role in the stabilization of the microstructure. Additionally precipitates are undergoing dissolution, growth and coarsening [3,2,26]. Within the model statistically distributed phases, e.g. fine MX ((V,Nb)(C,N)), and nonstatistically distributed precipitates like $M_{23}C_6$ ($(Cr,Fe,Mo)_{23}C_6$) are considered. The influence on the strain rate over the complete stress range has been described by the use of the approach from Rösler and Arzt [15] for non-interacting particles. Their model considers the dislocation bypassing by over climbing. One essential attribute in their approach is the considered transition to the Orowan mechanism in the stress regime $\tau < \tau_o$, basing on the idea of Ashby and Arzt [16]. Herein the transition has been described by a rule of non-linear mixture for the climbing and Orowan bypassing [17]. According to the composite approach the contribution to the strain rate contribution from the hard zone has been considered. The influence of non-statistically distributed precipitates on the strain rate of the hard zone has been treated as threshold stress and their effect on the growth of subgrains by a Zener formulation. By the lack of an adequate modelling of the precipitation, available experimental data for ferritic / martensitic Cr steels for the different precipitation species have been used for the modelling studies of the creep behaviour.

Damage

In order to suffice the experimental observations concerning intragranular damage in heat resistant steels under typical service conditions the following items have been considered:

- Continuous nucleation approach [8]

$$J = \alpha\beta\dot{\varphi}_v \exp\left(-\frac{t}{\tau_{inc}}\right) \tag{4}$$

with subsequent growth causing a size distribution of voids.

- Growth of intragranular voids by use of the unconstrained / constrained formulation of Riedel [8].

- Intragranular damage is observed on grain boundary facets predominately normal to the first principal stress. This is considered by use of a stereological approach [17] and by the approximation of the grain structure by octahedra to relate the area density of voids to the inner grain boundary surface. Stable martensite laths undergoing intragranular damage have been neglected.

- Continuum damage mechanics [18] by relating the void density and size to a phenomenological damage parameter D.

Details of the damage approach will be published in detail.

Instability
To estimate the date of the onset in a creep experiment the criteria of Hähner [19] has been used. Afterwards the non-linear deformation and altered stresses have been computed by utilizing an elasto / visco-plastic iterative FE procedure [20].

Studies

Creep of X20CrMoV12-1
The following studies on the creep behaviour of the steel X20CrMoV12-1 have been performed:

- T = 873 K / σ = 160 MPa – based on the experimental work of Eggeler et al. (in [21]) for the creep behaviour and of Nilsvang et al. (in [21]) on the precipitation.
- T = 823 K / σ = 165 MPa - based on the work of Straub et al. [22]

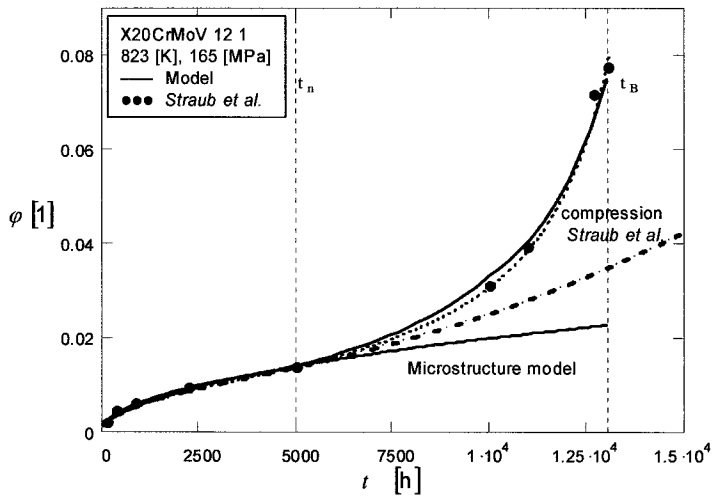


Figure 6: Measured and calculated creep behaviour of X20CrMoV 12 1 - T = 823 K / σ= 165 MPa.

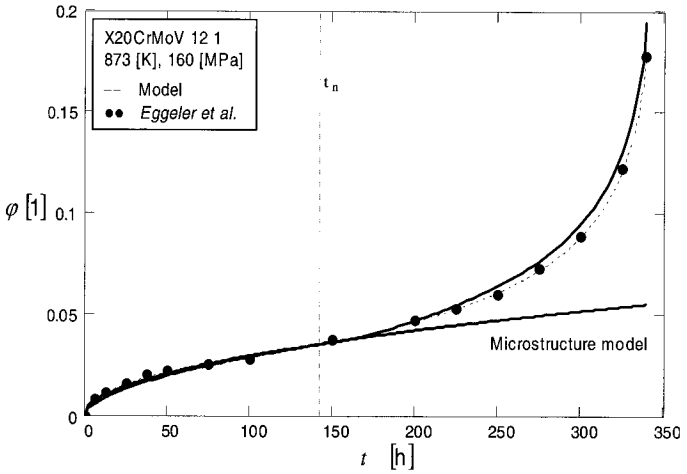


Figure 7: Measured and calculated creep behaviour of X20CrMoV 12 1 - T = 873 K / σ = 160 MPa.

The modelled creep curves are shown in Figure 6 and Figure 7. Therein the pure calculated uniaxial creep behaviour is shown for comparison. The date of the onset of the instability t_n, estimated by the experimental creep curve and the criteria of Hähner can be seen too. Interestingly, the study performed for the lower temperature shows a computed specimen geometry in accordance with the observed brittle fracture behaviour from Poeppel and Hildebrandt [23] (see Figure 8 (b)) at similar conditions.

Creep of NF616 (P92)

The role of the Laves-Phase in the steel NF616, or principally in 9-12% Cr steels, has been discussed intensively to explain the creep behaviour of the NF616 in terms of the microstructure and its stability. TEM - investigations revealed that the Laves-phase is not exclusively statistically distributed in the microstructure. Therefore in the simulation for the creep behaviour at T = 873 K and σ = 145 MPa under constant force, the Laves- Phase has been assumed to have a strengthening effect in the interior of subgrains (see Figure 10 (a)). Phase - data for the volume fractions and diameters as a function of the time have been taken from Hättestrand [27] and Zielinska-Lipic [24]. The input data for the starting structure have been taken from Ennis et al. [26]. In principal the model is able to describe the creep behaviour, but a strong deviation in the late tertiary regime appears due to a numerical instability in the FE-model (see Figure 9). For the evaluation of the influence of the Laves-phase a complementary study has been preformed neglecting the Laves-phase. Thereby a reasonable enhanced transition creep is predicted by the model as shown in Figure 10 (b).

Discussion and Summary

The results on the modeling of pure iron have been published in [25] whereby the model meets the real behavior without unnecessary scaling. Although it was not possible here to introduce the model in detail, it has to be mentioned that for the modeling of the creep behavior of ferritic / martensitic steels the model has to be scaled in order to meet the reality in the form of the creep curve and in the microstructural evolution. The basing assumption of

a mean, isotropic subgrain structure is in contradiction to experimental observations as shown exemplarily in Figure 11. Due to the martensitic transformation an anisotropic, non-uniform structure is formed which transforms under enhanced temperatures to a polygonal structure. In the case of incoherent precipitates which are obeying an orientation relationship, the anisotropic effects are maybe enhanced due to the retarding effect on subgrain growth and the deformation. By that the use of analytical, nevertheless physically based models for this specific problem is questionable. In the opinion of the author the current status of discrete models for the kinetics of inner surfaces e.g. cellular automata, network models or Monte-Carlo approaches, are adequate to use such approaches also in order to set up a base for the physically based modeling of the precipitation e.g. which needs an estimate for specific surface energies for incoherent precipitates. Further, the generation of "modern" 9-12% Cr steels reveal a strong inhomogenity in the dislocation density, which have not been considered up to now.

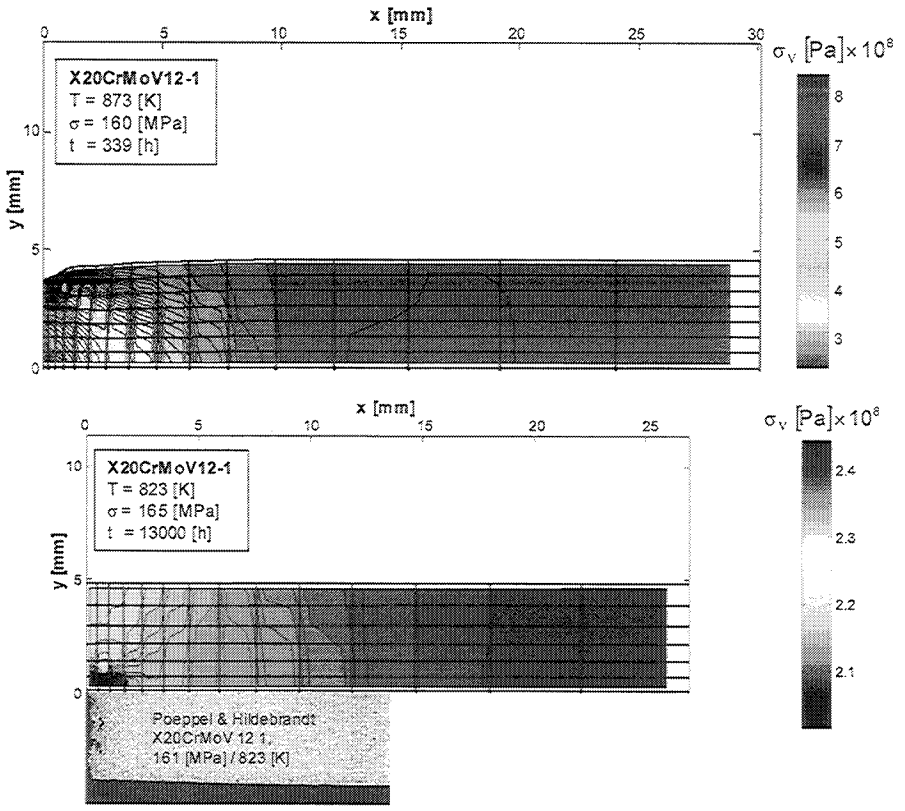


Figure 8: Calculated distributions of the equivalent von Mises stress σ_v and geometry of specimens (quarter of creep sample) - X20CrMoV12-1: (a) 873 K, 160 MPa at 339 h and (b) 823 K, 165 MPa at 13000 h (constant force) – image of a broken creep sample - X20CrMoV12-1 loaded at 823 K / 161 MPa from Poeppel & Hildebrandt [23].

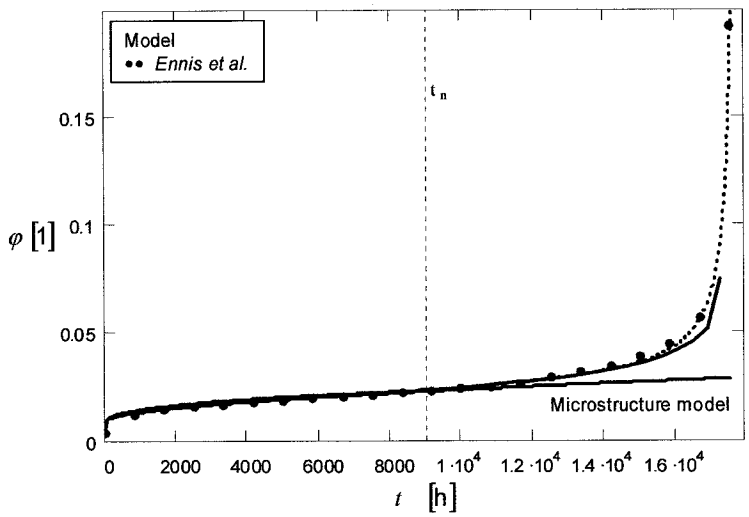


Figure 9: Comparison of computed and experimental [26] creep behaviour of NF616 - YAT - 873 K, 145 MPa under constant force.

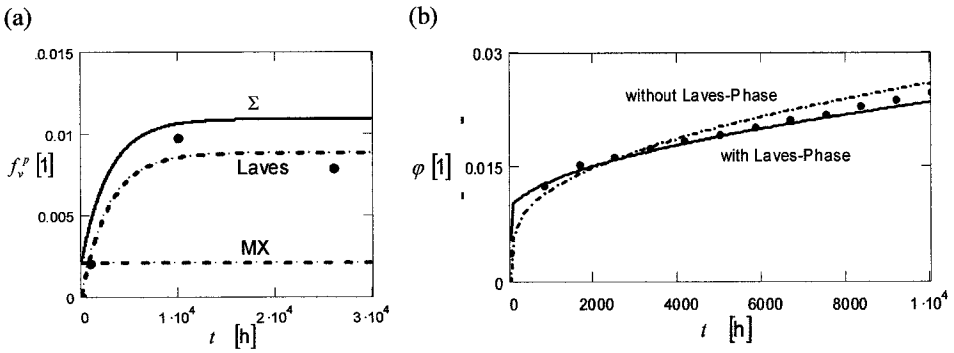


Figure 10: (a) Considered volume fractions of precipitates f_v^p acting in the subgrain interior [24,26,27]; Σ designates the sum of the volume fractions of the Laves and the MX-phase; (b) comparison of the calculated creep behaviour in the transition creep range (873 K - 145 MPa) with and without consideration of the Laves-Phase.

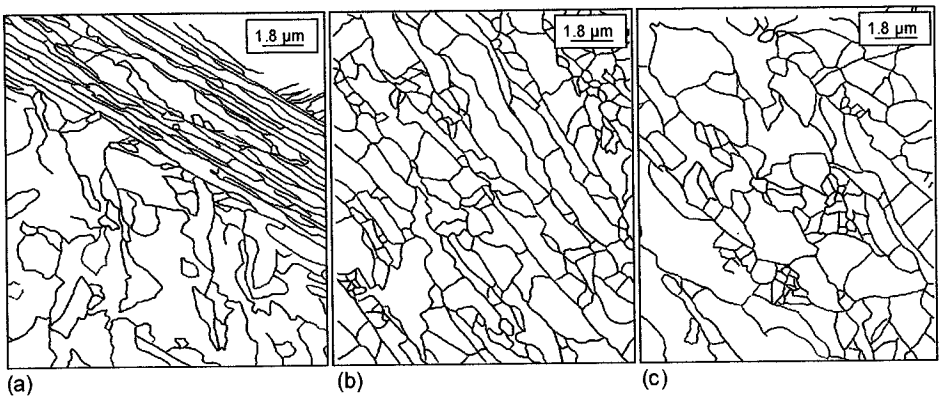


Figure 11: Redrawn substructure from TEM bright field images heat treated and broken creep samples (shaft) of the G-X12CrMoWVNbN10-1-1: (a) as-received (heat - treated) (b) $T = 600$ °C, $\sigma = 130$ MPa and $t = 12118$ h and (c) $T = 650$ °C, $\sigma = 80$ MPa and $t = 7959$ h [28].

Acknowledgement. The authors gratefully acknowledge the funding of this work by the Austrian research fund FWF - "Fonds zur Förderung der wissenschaftlichen Forschung" – contract SO 68-5.

References

[1] G.Dimmler, P.Weinert, B.Schaffernak, H.Cerjak, and R.Hanus, Proc.: Baltiva V – International Conference on Condition and Life Time Management for Power Plants, Helsinki, 2001.

[2] P.Polcik, (Ph.D. thesis, Erlangen University), Shaker, 1999.

[3] P.Hofer, (Ph.D. thesis, Institute for Materials Science, Welding and Forming, Graz University of Technology), 1999.

[4] W.Blum, Zeitschrift für Metallkunde, 68 (7) (1977), 277-284.

[5] W.Blum et al., Acta metall., 37 (1989), 2439-2453.

[6] A.Orlava, K.Miclicka and F.Dobes, Materials Science and Engineering, A194 (1995), 9-16.

[7] N.M.Ghoniem, J.R.Matthews and R.J.Amodeo, Res Mechanica, 29 (1990), 179-219.

[8] H.Riedel, High Temperature Fracture, (Springer, 1988).

[9] J.T.Michalak and H.-W.Paxton, Trans. Of the Metallurgical Society of AIME, 221 (1961), 850-857.

[10] S.Karashima, Trans. JIM, 12 (1971), 369-274.

[11] T.O.Saetre, O.Hunderi and N.Ryum, Acta metall.,37(5) (1989), 1381-1387.

[12] W.D.Nix, J.C.Gibeling and D.A.Hughes, Metallurgical Transactions A, 16 (1985), 2215-2226.

[13] B.Schaffernak, (Ph.D. thesis, Institute for Materials Science and Welding, Graz University of Technology), 2000.

[14] F.Roters and D.Raabe, Materials Science and Technology, 12 (1996), 281-289.

[15] J.Rösler and E.Arzt, Acta metall., 36(4) (1988), 1043-1051.

[16] E.Arzt and M.F.Ashby, Scripta Metallurgica, 16 (1982), 1285-1290.

[17] P.Weinert, (Ph.D. thesis, Institute for Materials Science, Welding and Forming, Graz University of Technology), 2001.

[18] A.C.Cocks and M.F.Ashby, Progress in Materials Science, 27 (1982), 189-244.

[19] P.Hähner, Acta metall.mater., 43 (11) (1995), 4093-4100.

[20] T.J.R.Hughes and R.L.Taylor, Computers & Structures, 8 (1978), 169-173.

[21] W.Blum, in Plastic Deformation and Fracture of Materials (Vol.6), (VCH, 1983), 359-406.

[22] S.Straub et al., VGB Kraftwerkstechnik, 73(8) (1993), 646-653.

[23] W.Poeppel and U.Hildebrandt, Prakt. Metallographie, 26 (1989), 141-153.

[24] A.Zielinska-Lipic et al., Conf.-Proc. : "Proc. of the 6th Liege - Conference: Materials for Advanced Power Engineering 1998", Liege, (1998), 559-566.

[25] P.Weinert and B.Buchmayr, Proc.: Creep Resistant Metallic Materials – Prague, (April 2001), 268-277.

[26] P.Ennis, Acta metall.,45(12) (1997), 4901-4907.

[27] M.Hättestrand and H.-O.Andren, Brinell Workshop - Report, Stockholm, (2000).

[28] P.Hofer, (Diploma thesis, Institute for Materials Science, Welding and Forming, Graz University of Technology), 1994.

Z PHASE CHARACTERISTICS IN MARTENSITIC 12CrMoVNb STEELS

Vlastimil Vodarek and Andrew Strang[a]

VITKOVICE – Research and Development, 706 02 Ostrava , Czech Republic

[a] Department of Engineering, University of Leicester, Leicester, United Kingdom

Abstract

Precipitation of Z phase contributes significantly to degradation of creep properties of 12CrMoVNb steels because its precipitation is accompanied by dissolution of finely dispersed nitrides and carbonitrides which initially hardened the material. The kinetics of Z phase precipitation are accelerated by increases in the nickel content of the steels. The orientation relationship between Z phase and the martensitic/ferritic matrix was determined as: $(001)_Z$ // $(001)_\alpha$, $[010]_Z$ // $[010]_\alpha$. Prolonged thermal/creep exposure is accompanied by recrystallisation of the matrix and this orientation relationship is destroyed. Nevertheless Z phase particles preserve the form of thin plates. Z phase is a nitride which is rich in vanadium, niobium and chromium and its composition depends on the temperature of precipitation. The composition of Z phase does not change during long term exposure at the original precipitation temperature. Furthermore the composition of Z phase is also dependent on the initial chemical composition of steels.

Keywords: Martensitic 12CrMoVNb steels; microstructural evolution; Z phase; orientation relationship; composition changes of precipitates.

1. Introduction

The modified martensitic 9-12%Cr steels are regarded as candidate materials for the critical components in the advanced fossil-fired power plants [1]. The long term creep strength and the oxidation resistance in steam are the major criteria for such materials. Significant work to increase the application temperature of these steels has been carried out during the last decades under different international research programmes [1,2]. Long term creep rupture tests carried out on experimental alloys have generated a valuable archive of material for microstructural investigations. The objective of detailed metallographic studies is to improve understanding of microstructural evolution in these alloys, to relate microstructures to observed creep properties and to gain insights to facilitate development of improved materials.

The 12CrMoVNb steels were originally developed for gas turbine applications [3]. Although these alloys have very high creep strength for durations of 10 000 hours, appropriate to jet engine applications, at temperatures above about 550°C their creep strength falls rapidly as durations are extended towards the 100 000 hours which is the typical basis of power plant design. This phenomenon, which is generally referred to as „sigmoidal behaviour", is closely associated with microstructural instabilities [4]. Investigations on minor phase evolution in 12CrMoVNb steels using X-ray diffraction on extracts of minor phase

particles revealed diffraction lines corresponding to $M_{23}C_6$ and MX phases and an additional single strong asymmetric diffraction peak corresponding to an interplanar spacing of d = 0.226 nm [5]. This peak was found to be present only in records related to long term exposures at testing temperatures of 550°C and 600°C. The presence of this additional strong diffraction peak indicated that a substantial amount of another minor phase had formed in these steels during long term thermal/creep exposure. Detailed analytical electron microscopy (AEM) studies revealed that this phase was a complex nitride called Z phase [6,7]. It was shown that precipitation of modified Z phase, which was accompanied by dissolution of the fine matrix M_2X and/or MX phases, contributed significantly to the reduction in the creep rupture strength of these alloys [6,8]. Subsequently the formation of Z phase has also been observed in some modern niobium containing 9-12%Cr steels [9-12].

This paper reports the results of studies on crystallography and chemical composition of Z phase in 12CrMoVNb steels during thermal exposure at temperatures 475°C, 550°C and 600°C up to 100 000 hours. The orientation relationship between Z phase and the martensitic/ferritic matrix has been determined. The results of Z phase composition studies are discussed in terms of their potential as an in service temperature history indicator of the material.

2. Materials and Experimental Procedure

The metallographic studies were carried out on three commercial casts of a 12CrMoVNb steel. Details of chemical compositions of these steels are shown in Table1. Creep rupture tests on these casts with different nickel contents were conducted at temperatures 475°C, 550°C and 600°C for durations up to 100 000 hours [6,8].

Table 1 Chemical compositions of the 12CrMoVNb steels (wt-%)

Cast Identity	C	Si	Mn	Ni	Cr	Mo	V	Nb	N-total
A	0.16	0.28	0.74	0.52	11.20	0.61	0.28	0.29	0.074
B	0.14	0.37	1.00	0.76	11.10	0.57	0.36	0.32	0.062
C	0.14	0.13	0.88	1.15	11.74	0.50	0.29	0.30	0.064

AEM studies were carried out on carbon extraction replicas and thin foils using a Philips CM20 TEM equipped with an EDAX PV 9900 EDX system. The thin foils were prepared by twin jet electropolishing in a solution of 5% $HClO_4$ in glacial acetic acid at room temperature and a voltage of 80V. Minor phases were identified using a combination of SAD and qualitative EDX analysis. Quantitative analyses on Z phase particles were carried out on carbon extraction replicas using PMTHIN software with calculated k-factors. Corrections for X-ray absorption and fluorescence were not applied. In order to achieve consistent results analyses were only carried out on particles which were not strongly diffracting and did not overlap with other particles.

The results reported in this paper were obtained on the heads of the creep rupture testpieces where the microstructural changes corresponded mainly to the effects of thermal exposure.

3. Results and Discussion

Results of detailed investigations on minor phase evolution in the 12CrMoVNb steels during both quality heat treatment and subsequent creep/thermal exposure were published elsewhere [6,8]. It was proved that particles of Z phase formed in all three casts only during long term exposure at testing temperatures. The kinetics of Z phase precipitation were accelerated by increases in the nickel content of the steels, Fig. 1. Z phase formed coarse thin plates of an irregular shape, Fig. 2.

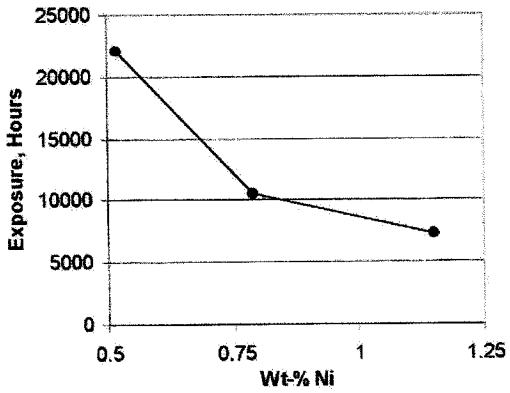


Fig. 1 The first appearance of Z phase in Casts A, B and C during thermal exposure at 600°C.

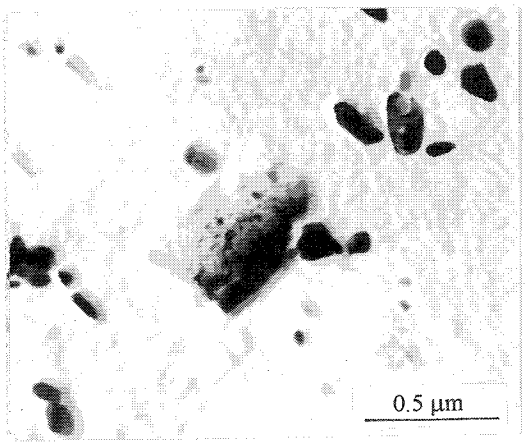


Fig. 2 TEM micrograph showing an irregular thin Z phase plate, carbon extraction replica, Cast A, 600°C / 30 770 hours

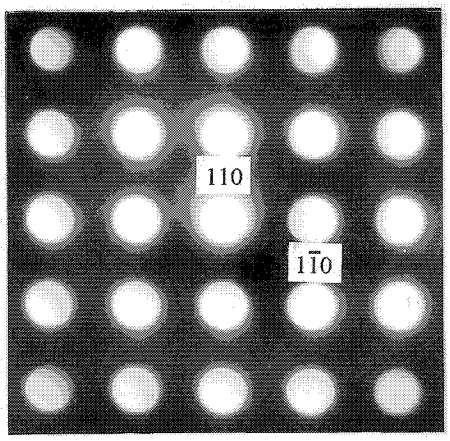


Fig. 4 [001] SADP of Z phase

The ideal composition of Z phase (the space group P4/nmm) with the lattice parameters $a_Z = 0.3037$ nm and $c_Z = 0.7391$ nm has been reported to be CrNbN [13]. Detailed

AEM studies on 12CrMoVNb steels proved that Z phase was rich in nitrogen, vanadium, niobium and chromium, Fig. 3 and had a tetragonal unit cell with the average lattice parameters $a_o = 0.286$ nm and $c_o = 0.739$ nm [6,7]. It is worth noting that the a_o parameter is very close to the unit cell size of the ferrite (a_α = 0.2861 nm). In accordance with the extinction rules for the space group P4/nmm analysis of [001] zone axis revealed the absence of {hk0} reflections consistent with the condition h + k = 2n + 1, where n is an integer, Fig. 4. The principal difference between modified Z phase in the 12CrMoVNb steels and the ideal Z phase (NbCrN) is considered to be the partial substitution of niobium by vanadium. This substitution can qualitatively explain deviations in unit cell dimensions on the basis of differences in the relative atomic radii of these atoms, $r_{Nb} = 0.146$ nm and $r_V = 0.135$ nm [14].

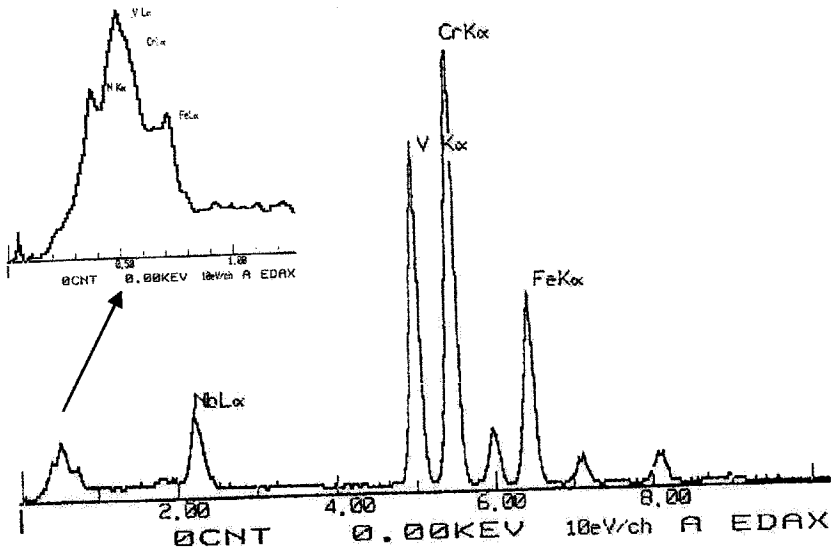
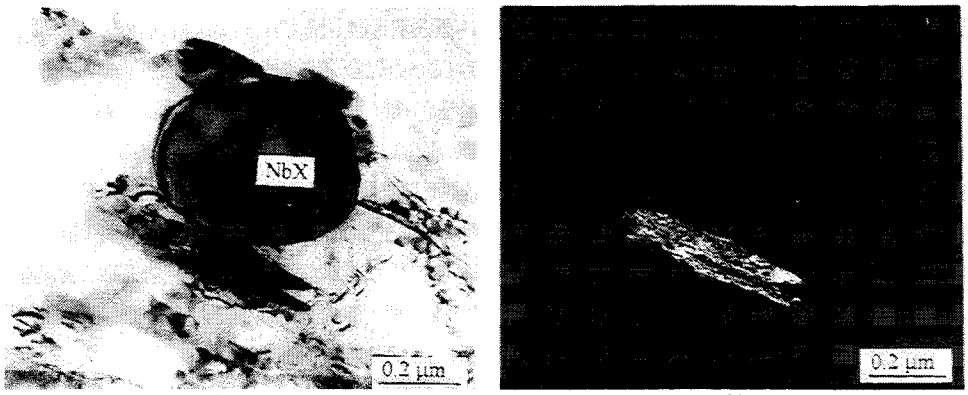


Fig. 3 An EDX spectrum of Z phase

Z phase particles were often closely associated with the primary NbX particles which gradually dissolved during long term exposure at testing temperatures. Quantitative X-ray diffraction studies on minor phases electrolytically extracted from Cast A demonstrated that the overall content of NbX phase after 94 000 hours creep exposure at 600°C was reduced to approximately 50% of that measured in the as received condition [5]. Furthermore precipitation of Z phase was accompanied by total dissolution of fine nitrides of M_2X and/or secondary (V,Nb)N phases which initially hardened the material. Figs. 5a,b show a plate-like Z phase particle which nucleated on the primary NbX particle. Furthermore, in the close vicinity of Z phase particles were frequently observed $M_{23}C_6$ carbides. It can be supposed that at least some of these carbides precipitated during exposure at testing temperatures due to carbon release from dissolving NbX particles.



a) b)

Fig. 5 Precipitation of Z phase on the NbX particle, Cast C, 600°C / 7 247 hours,
a) bright field image,
b) dark field image taken using 102_Z reflection.

3.1 The orientation relationship

An orientation relationship between Z phase and the martensitic/ferritic matrix was studied on samples corresponding to early stages of Z phase precipitation in individual casts. Based on the analysis of the composed symmetrical selected area patterns (SADP's), the orientation relationship was determined as:

$$(001)_Z \,//\, (001)_\alpha$$
$$[010]_Z \,//\, [010]_\alpha \qquad (1)$$

The composed SADP $[010]_Z + [010]_\alpha$ is shown in Figs. 6a,b. The easy growth of Z phase particles in the plate-like form takes place on cube planes of the ferritic/martensitic matrix due to a small degree of misfit in the $\{001\}_\alpha$ and $(001)_Z$ planes. Taking into account the orientation relationship and the appropriate lattice parameters of both phases the transformation matrix [15] can be expressed as:

$$(Z\mathbf{T}\alpha) = \frac{a_\alpha}{a_Z}\begin{pmatrix} 1 & 0 & 0 \\ 0 & 1 & 0 \\ 0 & 0 & \frac{a_Z}{c_Z} \end{pmatrix} = \begin{pmatrix} 1 & 0 & 0 \\ 0 & 1 & 0 \\ 0 & 0 & 0.387 \end{pmatrix} \qquad (2)$$

This transformation matrix can be used for calculations of parallel atomic directions and planes in both phases:

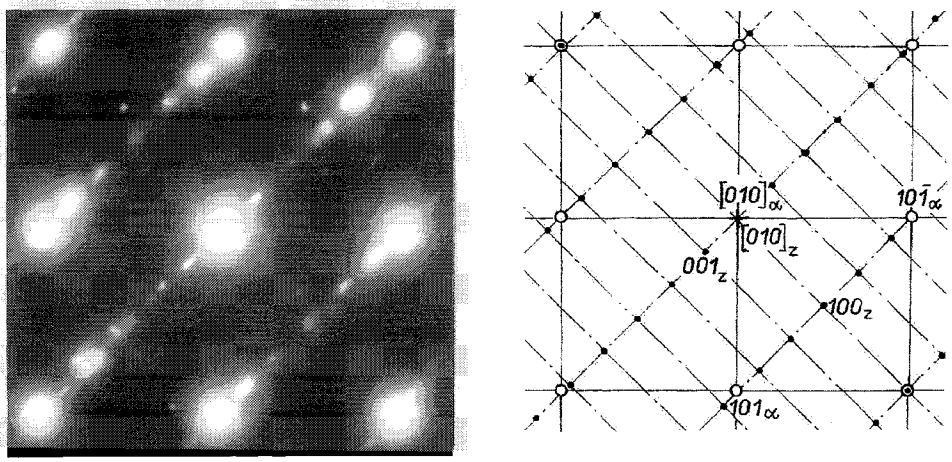
$$[Z,\mathbf{t}] = (Z\mathbf{T}\alpha)\,[\alpha,\mathbf{r}] \qquad (3)$$

$$[\alpha^*,\mathbf{n}] = (Z\mathbf{T}\alpha)^T [Z^*,\mathbf{k}] \quad (4)$$

The orientation relationship has three variants because $(001)_Z$ plane can be parallel to any of the crystallographically equivalent $\{001\}_\alpha$ planes:

$$(Z\mathbf{T}\alpha)_n=(Z\mathbf{T}\alpha)\ \mathbf{R}^{'\varphi}_{[111]} \quad (5)$$

where n = 1,2,3 and $\mathbf{R}^{'\varphi}_{[111]}$ is the rotation matrix of the ferritic crystal around [111] axis for the angle $\varphi=0^\circ$, 120° and 240°.



a) b)

Fig. 6 The composed SADP of Z phase and the ferritic matrix,
a) experimental pattern,
b) key diagram.

It has to be noted that during prolonged thermal/creep exposure the above orientation relationship was destroyed due to recrystallisation of the matrix. Nevertheless the plate-like form of Z phase particles was preserved.

3.2 Chemical compositions of Z phase

The formation of alloy carbides and nitrides in steels involves considerable diffusion and precipitates have compositions which are close to equilibrium [16]. The results shown in Fig. 7 demonstrate that chemical composition of Z phase does not change during long term exposure at the original precipitation temperature.

The high standard deviation values in these results strongly suggest that the Z phase composition is not homogeneous. Chemical inhomogeneity would result in variations in the values of the lattice parameters and is probably the cause of the asymmetric form of $(102)_Z$ (d = 0.226 nm) diffraction peak observed in the X-ray diffraction records [5]. However Figs. 8 and 9 show that the average composition of Z phase is dependent on the initial composition of the steel. Although the niobium contents of each cast are similar, the average niobium content

of Z phase increases with increasing nickel content in the casts investigated. Furthermore the average chemical composition of Z phase in the 12CrMoVNb steels depends on the temperature of precipitation, Fig. 10.

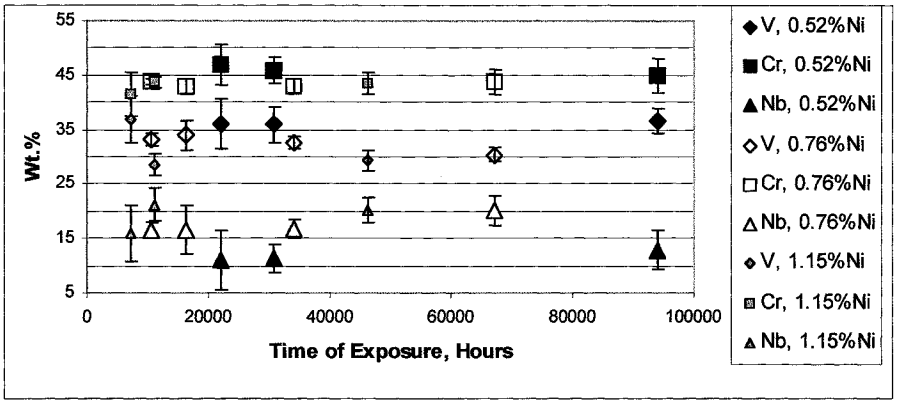


Fig. 7 Changes of Cr, V and Nb contents of Z phase formed during thermal exposure at 600°C

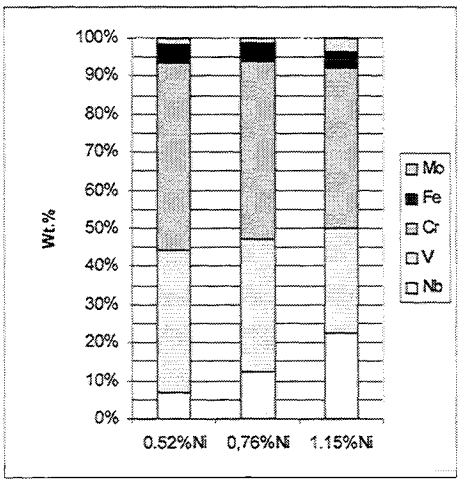


Fig. 8 The average chemical compositions of Z phase in Casts A, B, C at 550°C

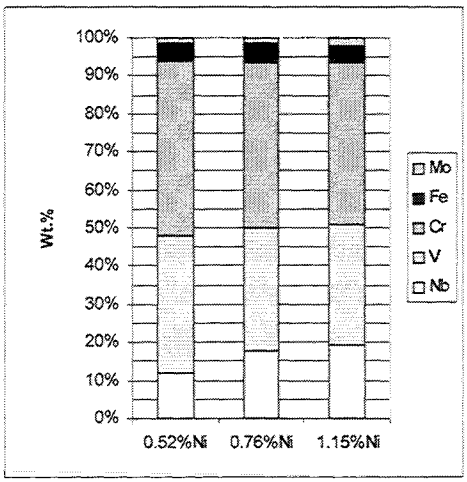


Fig. 9 The average chemical compositions of Z phase in Casts A, B, C at 600°C

The average composition of Z phase does appear to be unique for each temperature of formation and as such a relationship between the composition of Z phase and its temperature of formation may be able to be used as a temperature exposure indicator for the 12CrMoVNb steels. However since the composition of Z phase is also dependent on the initial composition of the steel it will also be necessary to know the composition for any given cast of the steel or

any other niobium containing 9-12%Cr steel before the composition of Z phase can be used with confidence for this purpose [17].

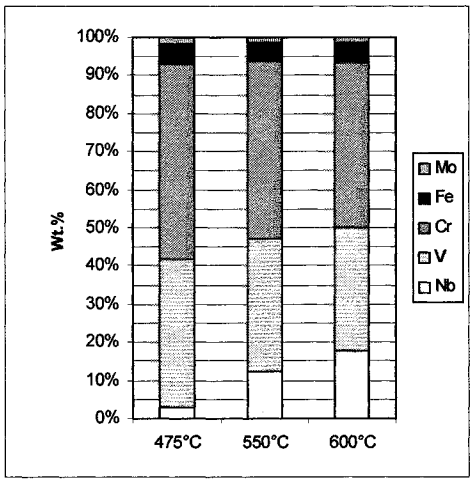


Fig. 10 The average chemical compositions of Z phase in Cast B at 475°C, 550°C and 600°C

4. Conclusions

Precipitation of Z phase represents a significant mechanism of creep strength degradation in 12CrMoVNb steels. The kinetics of Z phase precipitation were accelerated by increases in the nickel content of the steels. The orientation relationship between Z phase and the ferritic matrix was determined as: $(001)_Z$ // $(001)_\alpha$, $[010]_Z$ // $[010]_\alpha$. During further thermal/creep exposure this orientation relationship was destroyed due to recrystallisation of the matrix. Nevertheless the plate-like shape of Z phase particles was preserved. The average chemical composition of Z phase does appear to be unique for each temperature of formation. Furthermore the composition of Z phase is also dependent on the initial chemical composition of steels.

References

[1] Staubli M.E., Mayer K.H., KernT.U. and Vanstone R.W., „COST501/COST522 – The European Collaboration in Advanced Steam Turbine Materials for Ultra Efficient, Low Emission Steam Power Plant", Proc. PARSONS 2000, Advanced Materials for 21st Century Turbines and Power Plant, Cambridge July 2000, edited by A.Strang et al., Institute of Materials, London, 2000, pp. 98-122.

[2] Thornton D.V. and Mayer K.H., „ New Materials for Advanced Steam Turbines", Proc. Advances in Turbine Materials, Design and Manufacturing", Newcastle upon Tyne, November 1997, edited by A.Strang et al., Institute of Materials, London, 1997, pp. 203-226.

[3] Vanstone R.W., „Microstructure in Advanced 9-12%Cr Steam Turbine Steels", Proc. Quantitative Microscopy of High Temperature Materials, Sheffield, November 1999, edited by A.Strang and J.Cawley, Institute of Materials, London, 2001, pp. 355-372.

[4] Strang A., Foldyna V., Jakobova A., Kubon Z., Vodarek V. and Lenert J., „Factors Affecting the Prediction of the Long Term Creep Rupture Properties of Microstructuralle Unstable 9-12%Cr Power Plant Steels", Proc. Advances in Turbine Materials, Design and Manufacturing, Newcastle upon Tyne, November 1997, edited by A.Strang et al., Institute of Materials, London, 1997, pp. 603-612.

[5] Chickwanda H.K., „Microstructural Stability of 12CrMoVNb Power Plant Steels", PhD Thesis, Imperial College, London, 1994.

[6] Strang A. and Vodarek V., „Microstructural Stability of High Chromium Ferritic Power Plant Steels", Proc. Microstructural Development and Stability in High Chromium Ferritic Power Plant Steels, Cambridge, June 1995, edited by A.Strang, Institute of Materials, London,1997, pp. 31-51.

[7] Strang A. and Vodarek V., Mater. Sci. Technol., 12 (1996) 552-556.

[8] Strang A. and Vodarek V., „Microstructural Stability of Creep Resistant Martensitic 12%Cr Steels", Proc. Microstructural Stability of Creep Resistant Alloys for High Temperature Plant Applications, Sheffield, March 1997, edited by A. Strang, J. Cawley and G.W.Greenwood, Institute of Materials, London, 1998, pp. 117-133.

[9] Bursik J. and Merk N., „Quantitative Microstructural Assessment of P91 Ferritic Steel after Long Term Creep at High Temperature", Proc. Mechanical Behaviour of Materials at High Temperature, September 1995, Sesimbra, NATO Advanced Study Institute, 1995, pp. 1-12.

[10] Kimura K., Kushima H., Abe F., Suzuki K., Kumai S. and Satoh A., „Microstructural Change and Degradation Behaviour of 9Cr-1Mo-V-Nb Steel in the Long Term Region", Proc. PARSONS 2000, Advanced Materials for 21st Century Turbines and Power Plant, Cambridge July 2000, edited by A.Strang et al., Institute of Materials, London, 2000, pp. 590-602.

[11] Hofer P., „Mikrostrukturelle Analyse als Basis für die Entwicklung neuer Kraftwerkstoffe am Beispiel von G-X12CrMoWVNbN 10-1-1", Doctoral Thesis, TU-Graz, Graz, 1999.

[12] Cerjak H., Letofsky E., Hanus R., Heuser H. and Jochum C., „The Behaviour of Weldings in Large 9%Cr Alloy Castings", Proc. PARSONS 2000, Advanced Materials for 21st Century Turbines and Power Plant, Cambridge, July 2000, edited by A.Strang et al., Institute of Materials, London, 2000, pp. 386-398.

[13] Jack D.H. and Jack K.H., JISI (1972) October, 790-792.

[14] Rothery-Hume W. and Raynor G.V., The Structure of Metals and Alloys, Fourth Edition, Institute of Metals, London, 1972.

[15] Schumann H., Kristallgeometrie, Deutscher Verlag für Grundstoffindustrie, Leipzig, 1980.

[16] Bhadeshia H.K.D.H., Strang A. and Gooch D.J., Int. Mater. Reviews, 43 (1998) No.2, 45-69.

[17] Vodarek V. and Strang A., Mater. Sci. Technol.,16 (2000) 1207-1213.

MICROSTRUCTURAL ISSUES IN THE DESIGN OF AUSTENITIC AND NICKEL BASED MATERIALS FOR SUPERHEATER SYSTEMS IN 700°C STEAM PLANT

F. Starr and A. Shibli
European Technology Development
2 Warwick Gardens, Ashtead, Surrey UK.

Abstract

Analysis of published long term stress rupture data of a wide range of commercial austenitic and nickel based tube materials suggests that whatever the type of strengthening precipitate, the dominant strengthening mechanism is that of dislocation climb. More surprisingly, in all cases, the stress exponent is close to four. Using a correlation based on these results, a table is given showing the likely practical limits for stress rupture strength of superheater tubing over the range 600°-1200°C. It should therefore be possible to develop a material with a 100 kh stress rupture strength of just under 100 MPa at 750°C. This is broadly in line with superheater needs for ultra supercritical plant with steam temperatures in the 700°C range

Keywords: Austenitic, nickel based, tube alloys, ultra supercritical, stress rupture

1. Introduction

Current steam generating power plants are limited to efficiencies of the order of 43-47% when burning coal, with steam temperatures ranging between 540 and 580°C. Efficiencies of around 50% will be achievable within the next 10 years using 9-12 Cr ferritic alloys [1,2,3]. The prospects for the successful development of superheater materials for steam plant with an efficiency of 55% will require the use of advanced alloys of the austenitic and nickel based type. Ideally, these would be materials that are supplied in the hot formed condition, and which derive long term strength from in-service precipitation hardening mechanisms. This paper looks at the possibility of achieving the necessary stress rupture targets, with such materials, using correlations based upon the Lagneborg equation.

2. High Temperature Strength Targets

To establish rational stress rupture/temperature targets for superheater materials we need to estimate likely tube temperatures and stresses in plants that will have an efficiency of 55%. To obtain such efficiency will require a very high combination of steam temperatures and pressures. Figure 1 was plotted, by the authors, using steam temperature and pressure data from power plants of various vintages. This is perhaps the simplest way of showing that there is an exponential relationship between these two functions, so that at temperatures above 450°C pressures increases very rapidly. This exponential trend results from the need to get an adequate expansion across the turbines to ensure that the temperature of the steam entering the condenser is as close to ambient as possible. There are complicating factors, which in part account for the scatter in the graph. The use of reheat, to improve plant output and efficiency, tends to push plant pressures upwards. Conversely, the abstraction of steam from the turbines, for feed heating, also to improve efficiency, reduces the need to operate at very high pressures. The disadvantage of feed heating is that plant output is reduced. Other factors, which influence the scatter, include turbine efficiency and condenser temperature.

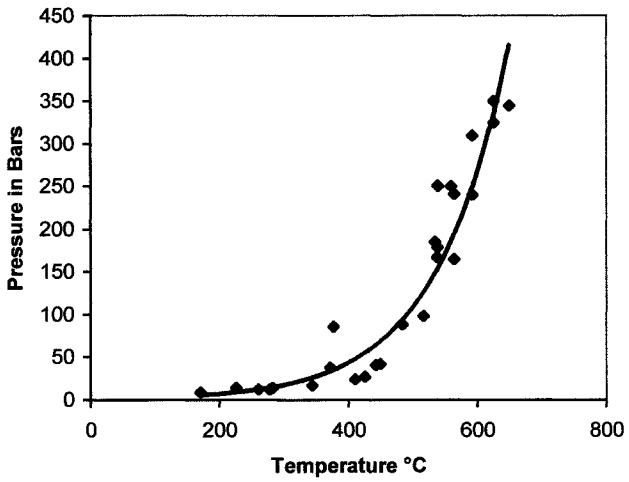


Fig 1. Steam Turbine Pressure Versus Temperature

Judging from European, Japanese and American data, steam conditions of approximately 700-740°C and 350-400 bar will be needed for an efficiency of 55% [1-4]. Using data from a paper by Birks and Smith, the hoop stress, in a typical heavy-gauge austenitic superheater tube, can be taken as 1.89 times the internal pressure [4]. This suggests that the hoop stress would be 66 MPa at 350 bar, or 75 MPa at 400 bar steam pressure. Since, for a 100 000 tube life, the stress rupture properties of tube materials would need to be some 1.3-1.5 times greater than the hoop stress, superheater material strength would be in the range 90-115 MPa. This strength would have to be available at a metal temperature some 30-40°C hotter than the steam, so that tube skin temperature would be in the range 730-780°C. Of course, it may be possible to reduce stresses to a small extent by an increase in wall thickness. Regrettably, the lower thermal conductivity and higher expansion coefficients of austenitic and nickel based alloys, compared to the ferritics, implies a greater tendency to thermal fatigue in heavy section pipework, so that there are limits to this approach.

3. Dislocation Climb and Stress Rupture Properties

What are the prospects for the development of improved and lower cost materials? Figure 2 was plotted by the authors using stress rupture data of a wide variety of wrought and spun cast austenitic and nickel base alloys, and shows the 100 000 hour log rupture stress as a function of temperature for each of these alloys. Only a limited number of alloys can be shown of the ones plotted in the original spreadsheet, because of colour restrictions, but the values for all the alloys fall within a fairly tight band. It is therefore possible to take an average of the stress rupture values at any given temperature and plot a straight line that runs through the centre of the band.

As can be seen from Fig. 2, the gradient of the log stress-temperature relationship for most alloys is remarkably similar to that of the average line. For much of their length, the lines for individual alloys are parallel to the average line, suggesting that there is a fundamental underlying relationship. The authors suggest that such a relationship results from the fact that creep in high-temperature materials is principally due to the climb of dislocations over precipitates. At constant stress, the rate of dislocation climb is governed by the alloy diffusion rate and by the shear modulus of the alloy matrix. The effect of diffusion rate is a very strong function of temperature; the effect of modulus due to a change in temperature is not so marked.

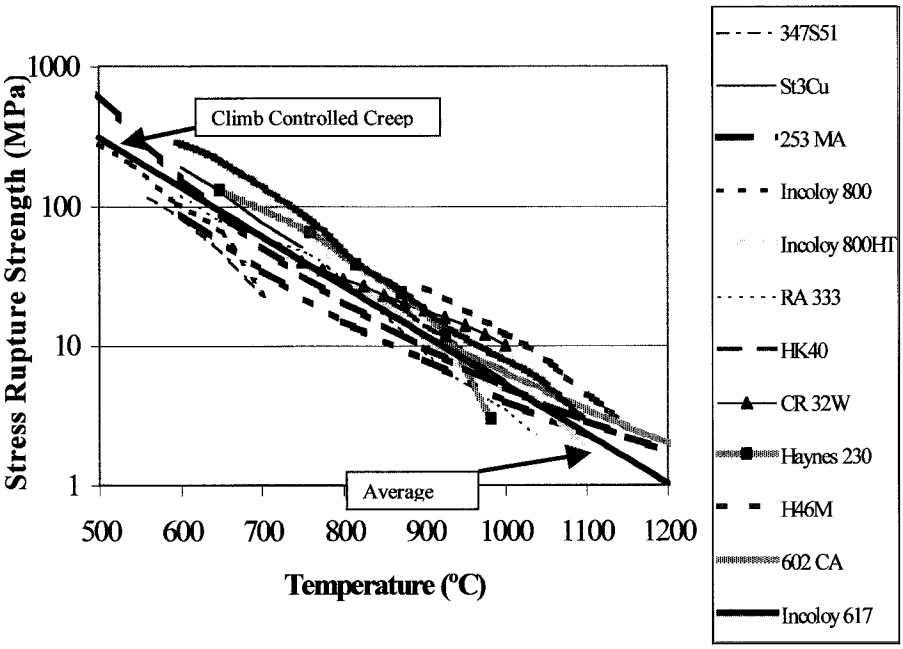


Fig 2: 100 000 Hour Log Stress v. Temperature

For conventional alloys, the strengthening precipitates are intermetallic compounds. These can only form when temperature is at an optimum. Below this temperature, diffusion is too slow to permit the necessary aggregation of elements that make up the strengthening intermetallic. Hence precipitate formation is extremely sluggish and the alloy is relatively weak. At temperatures somewhat above the optimum, the intermetallic precipitate grows so quickly that it loses coherency. At even higher temperatures the precipitate will be thermodynamically unstable, so strength will drop off even more rapidly. Figure 3 shows this effect schematically.

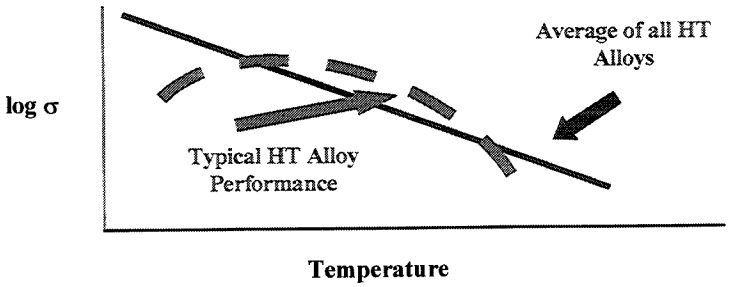


Figure 3. Typical HT Alloy Stress Rupture Behaviour on Log Stress v. Temperature Plot

Here it should be noted that we are discussing long term precipitation reactions which only stabilise after some thousands of hours after a material has entered service. All commercial high temperature FCC type alloys make use of one or more strengthening precipitates, such as TiC, M_6C, $M_{23}C_6$, in older materials, and nitride and CuTi phases in some of the newer ones. At the intended service temperature, diffusion in the alloy should be fast enough to permit the precipitate to form, but not so fast that the precipitate overages within the design lifetime. Increasing the quantity of refractory metals in an alloy will tend to slow down diffusion rates and increase the modulus. Accordingly the higher temperature alloys have higher proportions of these elements.

Lagneborg proposed a modification of the well known Weertman equation, which relates the creep rate to a power function of the shear stress, the assumption being that the creep mechanism is due to dislocation climb [5]. The equation can be written as follows:

$$d\varepsilon/dt = (2b^2 LD\theta /kT) (\sigma/\alpha Gb)^n \quad \ldots\ldots(1)$$

Where $d\varepsilon/dt$ is the creep rate and:

b= Burgers Vector

n= Stress Coefficient

L = Mean Free Path of Dislocations

θ = Dislocation Line Tension

D= Matrix Diffusion Coefficient

k = Boltzmanns Constant

T = Absolute Temperature

σ = Stress

α = Factor Related to Dislocation Interaction Stresses

G= Shear Modulus

INCORPORERMaking the assumption that the Burgers vector, mean free paths of dislocations etc. are constant, for all high temperature FCC alloys that form strengthening precipitates in service, this equation can be simplified as follows:

$$d\varepsilon/dt = A(D/T) (\sigma/G)^n \quad \ldots\ldots(2)$$

The equation can be further simplified by assuming that the creep rate of these alloys is constant. In practice this will be close to $1.10^{-11}.s^{-1}$, or just under 1% creep in 100 000 hours.

We can also use the elastic or Young's modulus E rather than the shear modulus G, these assumptions simply altering the value of the constant A in equation 2. This equation can now be rearranged so that we are able to plot the variation of stress against temperature.

$$\sigma = E\,(AT/D)^{1/n} \quad \ldots\ldots\ldots\ldots\ldots\ldots\ldots\ldots (3)$$

We can now use this equation to calculate the variation in stress rupture value against temperature for climb-controlled creep.

A curve of this type is plotted in Fig. 2 along with the data for real materials. In order to normalize the results, and to eliminate the effect of the constant A, the high-temperature end of the climb-controlled creep line was "anchored" so as to give a stress rupture value of 1.75 MPa at 1200°C. The climb controlled creep line has a curved form so that, at the low-temperature end of the graph, it is steeper than the "straight-line average" curve, but somewhat less steep at the high-temperature end.

The value of the stress coefficient that gave the closest fit to the straight line average was 4. It is of particular note that when the stress coefficient is 4, the Lagneborg equation assumes a dimensionless form. In this condition all the units in the equation need to be put into the correct SI units, so that, for example, the Burgers vector is stated in metres, dislocation line tension in Newtons, Boltzmanns Constant in $N.m.K^{-1}$, etc.

4. Normalised Creep Strength Ratio v.Temperature

The data that was plotted in Fig. 2 can also be used to show the relative changes in alloy properties with temperature. To obtain this relative or *Normalized Creep Strength Ratio* the stress rupture strength of an alloy at a given temperature is divided by the average strength of all the materials at that temperature.

For a material with only one strengthening precipitate, the normalized creep strength would be expected to be low at low temperatures. It would then peak at intermediate temperatures, before falling away at an even higher temperature. As stated earlier this is the result of limited precipitation at the lower temperature, because of the slow rate of diffusion. Again to reiterate the point, at high temperatures, the normalised creep strength would fall away due to over-aging effects. Only at intermediate temperatures would the alloy perform well in comparison to the average. Figure 4 shows this schematically. Note that, by definition, the "average" in Figure 2, when plotted on the normalised creep strength graph is unity at all temperatures, and is shown by the horizontal black line on Figure 4.

In many modern high-temperature alloys a variety of precipitation processes will take place, so that as one type of precipitate begins to overage, another begins to form. In this way, the normalized creep strength can be held reasonably constant over a wide temperature range. Figure 5 shows the temperature-dependence of this parameter for a number of alloys. As might be expected, the higher-alloyed materials, such as Inconel ® 617, and Paralloy® H46 have normalised strengths well in excess of one. But no alloy found so far has a normalised strength above 2.4.

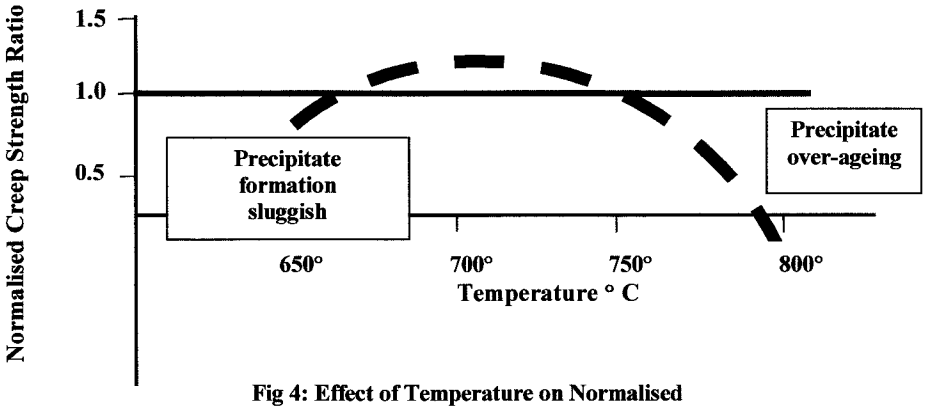


Fig 4: Effect of Temperature on Normalised Creep Strength Ratio

It should be noted that although some materials improve as temperature increases, such as 253MA® and 602CA®, this simply means that compared to the average value, which by definition is unity, the fall-off in strength is not so rapid.

5. Probable Limits to Alloy Development

Having established the basic reasons for the inexorable drop off in strength of high temperature materials, it becomes possible to estimate what are the probable limits in terms of the development of high temperature alloys. Inspection of Figure 5 shows that in general the best of the alloys offer, over a limited range of temperatures, strengths up to 2.2 to 2.4 times this average. Using a value of 2.4 times the average, Table 1 can be used to estimate what are the probable upper limits for alloy strength at any temperature. Significant numbers in the context of a steam plant operating at an efficiency of 55% are those at 750°C of 97.2 MPa and at 800°C of 64.8 MPa. It suggests that superheater metal temperatures will need to be limited to about 750-770°C if acceptable tube strengths and tube lives are to be achieved, even with a good deal of materials development.

Table 1 also shows likely maximum strength levels for wrought and spun cast materials over the temperature range 800°-1200°C. These figures should be helpful in assessing heat exchanger design issues in indirect fired gas turbine cycles or other innovative energy conversion systems.

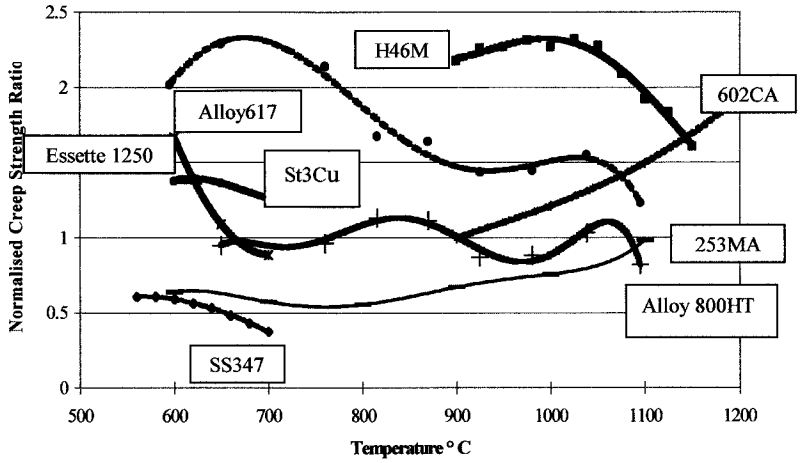


Fig 5: Normalised Creep Srength Ratio v.Temperature

Table 1

Average and Probable Upper Limits to 100000 Hour Stress Rupture Strength

Temperature°C	Average Stress Rupture Value of All Alloys (MPa)	Probable Upper Limits (MPa)
600	**137.7**	**330.5**
650	**91.6**	**219.9**
700	**60.9**	**146.2**
750	**40.5**	**97.2**
800	**27.0**	**64.8**
850	**17.9**	**43.0**
900	**11.9**	**28.6**
950	**7.9**	**20.0**
1000	**5.3**	**12.7**
1050	**3.5**	**8.4**
1100	**2.3**	**5.5**
1150	**1.5**	**3.6**
1200	**1.0**	**2.4**

6. Summary and Conclusions

These correlations and the underlying theoretical basis for them indicate that there are reasonable prospects of developing materials which will enable plant to reach 55% efficiency target, at the same time maintaining sensible tube wall thicknesses as indicated in the Birks and Smith paper. Nevertheless, there is little margin in hand. The results of this analysis also suggest that design should be done on a superheater life of 100 000 rather than 250 000 hours, as is the norm for current ultra supercritical plant. Equation 3 indicates that, using a stress exponent of four, achievable stress levels would be down by about 20% compared to the values stated in Table 1.

Acknowledgment

The authors wish to thank P J Ennis of the Research Centre Juelich, Germany, for providing data and for valuable discussions.

References

1. E. Metcalf and B. Scarlin, 'Advanced High Efficiency Steam Power Plant', Materials for Advanced Power Engineering, ed. J. Lecomte-Beckers, F. Schubert and P J. Ennis, Energietechnik 1998.pp 35-52

2. F. Abe, M. Igarashi, N. Fujitsuna, K. Kimura, and S. Muneki, 'Alloy Design of Advanced Ferritic Steel for 650°C USC Boilers', Advanced Heat Resistant Steels for Power Generation, ed. R. Viswanathan and J. Nutting, Book 708 IOM Communications 1999 pp 84-95

3. K. Muramatsu, 'Development of Supercritical Plant in Japan', Ibid. pp 543-559

4. N. Birks and C R. Smith, 'Factors in the Selection of Advanced Alloys for Advanced Heat Exchangers', Materials Issues in Heat Exchangers and Boilers Conference, Proceedings ed. F.Starr and B. Meadowcroft, IOM, London, 1997. pp 51-61

5. R. Lagneborg, 'Creep: Mechanisms and Theories', Creep and Fatigue in High Temperature Alloys, ed. J. Bressers, Applied Science, 1981.pp 41-71

PRECIPITATION OF INTERMETALLIC PHASES DURING MARTENSITE AGING IN STEELS CONTAINING 10% Cr

G.D. Pigrova

Central Boiler and Turbine Institute

Politechnicheskaya 24, 194021 St.Petersburg, Russia

Abstract

Phase formation processes in maraging steel over the range from 300 to 650^{0}C have been studied by a phase analysis method. Different intermetallic phases, i.e. R-phase, Laves phase and Ni_3Ti-type have been found to appear during long-term aging(for up to 5000h). Both the stability regions for intermetallics of the R-phase, Laves phase and Ni_3Ti-type and phase reactions depending on heat treatment procedure and aging temperature-time characteristics have been found. The relationships between the type of phases precipitated and their alloying element contents are established. Matrix segregation along with chromium rich solid solution precipitation have also been observed to occur over the range from 400 to 450^{0}C. Some effect on the character of phase transformations in the steel is shown to have been exerted by the temperature of prior-to-aging tempering.

Keywords: maraging steel, phase formation, intermetallics

1 Introduction

The maraging stainless steels find increasing use in machine engineering owing to their higher strength properties at reasonable level of ductility. The progressively complicated composition of maraging steels attracts enhanced interest to the investigations of steel phase composition, mainly, of a quantitative nature.

The objective of the present work is to study the structures, compositions and amounts of phases that form in 10Cr-2Mo-0.7Ti steel during long-term aging (up to 5000 h) at temperatures from 300 to 650^{0}C.

2 Experimental details

The work has been carried out by using a physical-chemical method of phase analysis. To isolate phases from 10Cr-2Mo-O.7Ti steel (10.3% Cr; 9.6% Ni; 2.1% Mo; 0.66% Ti; 0.014% C; 0.17% Si; 0.08% Mn) the electrolytes of the following compositions have been used: 1) methanol with HCl, 2) H_3PO_4 agueous solution. The phase structures have been examined by an X-ray method. It should be noted that the phases formed during low-temperature aging are highly dispersed ones, and X-ray analysis is frequently insufficient for identifying their type. This is responsible for the ambiguous interpretation of the results obtained in the studies of compounds in maraging steels. That is why much attention in this work is given to the chemical analysis of the isolated phases.

The heat treatment of the steel before aging included quenching from a temperature of 950^{0}C for 1 h followed by tempering at 500, 550 or 600^{0}C for 3 h. It has been found that different cooling rate after quenching does not affect the phase composition of a steel during aging. Besides martensite, a cubic titanium carbonitride with a lattice parameter of 0.427nm is observed in steel after quenching. During cooling after quenching, the intermetallic phases –a Laves phase $Fe_2(Mo,Ti)$ and χ-phase FeCrMoTi may also appear, though in a very small quantity(less than 0.2% with respect to the weight of steel). Since a titanium carbonitride is the major dispersed phase and intermetallic phases in some specimens are formed in small quantities, it may be considered not necessary for the intermetallics to be present in as-quenched steel.

3 Results and discussion

The 10Cr-2Mo-0.7Ti steel over the aging temperature range from 300 to 650^{0}C is a multiphase system (see Table 1), in which the following phases are formed: 1) a simple titanium carbonitride M(C,N), 2) an intermetallic R-phase having a rombohedral symmetry with 53 atoms in the elementary cell and belonging to the type of TCP (topologically close packed) phases [1], 3) chromium-based solid solution, 4) Ni_3Ti phase with a cubic(•- Ni_3Ti) or hexagonal (•- Ni_3Ti) symmetry; 5) a Laves •-phase $Fe_2(Mo, Ti)$.

Table 1. Phase composition of 10Cr-2Mo-0.7Ti steel

Aging		Tempering for 3 h at T, ^{0}C		
T, ^{0}C	Time, h	500	550	600
300	1000	M (C,N)	M (C,N)	M (C,N), Ni_3Ti*
300	5000	M (C,N)	M (C,N)	M (C,N), Ni_3Ti*
350	1000	M (C,N)	M (C,N)	Ni_3Ti*
350	5000	M (C,N)	M (C,N)	Ni_3Ti*
400	1000	R*, Cr*	R*, Cr*	Ni_3Ti*
400	5000	R*, Cr*	R*, Cr*	Ni_3Ti*
450	1000	R*, Cr*	R*, Cr*	R*, Ni_3Ti
450	5000	R, Cr*	R, Cr*	R*, Ni_3Ti
500	1000	R, β- Ni_3Ti	R, β- Ni_3Ti	R,β-Ni_3Ti,η-Ni_3Ti
500	5000	R, η- Ni_3Ti	R, η- Ni_3Ti	R, η- Ni_3Ti
550	1000	R, η- Ni_3Ti	R, η- Ni_3Ti	R, η- Ni_3Ti»
550	5000	R, η- Ni_3Ti	R, η- Ni_3Ti	R, η- Ni_3Ti
600	1000	η- Ni_3Ti, λ	η - Ni_3Ti, λ	η- Ni_3Ti, λ
650	1000	λ	λ	λ

- from chemical analysis of a precipitate

The R-phase isolation from steel has been performed using electrolyte 1. The R-phase only is isolated from specimens aged at 500 and 550^{0}C in this electrolyte, and that made it possible to

determine a phase composition which proved to be identical for both temperatures. The temperature of preliminary tempering, does not affect the R-phase composition, which in steel is $(Fe, Ni)_{26}Cr_8(Mo, Ti)_{15}$, and this is close to the R-phase composition of $(Fe, Co, Ni)_{17}Cr_8Mo_{10}$ in Fe-14Cr-9Co-5Ni-5Mo steel [2]. The amount of Ni and Ti present is insignificant, the major elements being Fe and Mo, and the change in their amounts in the precipitate composition with aging temperature may indicate the R-phase formation.

The R-phase occurrence has been determined from X-ray diffraction patterns after aging for 1000 h at 500^{0}C only (see Table). From the chemical analysis of the precipitate it is found that during aging for 1000 h the R-phase appears even at 400^{0}C after preliminary tempering in the range from 500 to 550^{0}C and at 450^{0}C after tempering at 600^{0}C. With aging time extending to 5000 h, the R-phase is found by X-ray analysis at 450^{0}C (preliminary tempering at 500-550^{0}C). The comparison of element contents in the precipitate depending on aging temperature shows that the R-phase formation may be identified by an increase in Mo and Fe contents. After tempering in the range from 500 to 550^{0}C, the R-phase is observed to occur at 400^{0}C when still no diffraction lines can be distinguished on X-ray diffraction patterns because of small particles sizes. The phase starts to nucleate extensively at 450^{0}C (Fig.1), and the further increase in aging temperature leads basically to a R-phase particle coarsening rather than to an increase in phase quantities. After tempering at 600^{0}C, the R-phase is not observed to form at 400^{0}C, and at 450^{0}C its quantity is much lower than at 500 to 550^{0}C.

Increasing aging temperature up to 600 and 650^{0}C does not lead to the R-phase appearance - at temperatures above 550^{0}C it seems to be unstable. To confirm this, the specimen has been aged at 650^{0}C. The R-phase has been obtained in the specimen by the previous long-term aging at 500^{0}C. After aging at 650^{0}C, the R-phase is completely absent in the specimen. The R-phase in this steel seems to exist in the range from 400 to 550^{0}C. Low levels of R-phase in the steel and small particle sizes due to low temperature of phase stability precluded obtaining a phase X-ray diffraction patterns suitable for use in calculating lattice parameters. An alloy corresponding to a specified R-phase composition has therefore been manufactured. The alloy has proved to be a single-phase one, which confirms the valid determination of R-phase composition. Lattice parameter predictions based on the X-ray diffraction patterns yielded the following: a=1.096 nm, c=1.950 nm, and c/a=1.78.

The chromium content in the precipitate obtained in electrolyte 1 depends on the aging temperature (Fig.1) most strongly in the range from 400 to 450^{0}C at the temperatures of tempering between 500-550^{0}C. After tempering at 600^{0}C, the Cr content in the precipitate varies monotonically with an increase in aging temperature and corresponds to an increase in the R-phase quantity. The maximum Cr release during aging in the range from 400 to 450^{0}C after tempering at 500 to 550^{0}C can not be associated with the R-phase formation, as Cr level in known R-phases [3,4] does not exceed 20 to 30%, whereas in this case at 400^{0}C Cr is the major element in the precipitate. Along with other Cr-based steels, the steel under study is prone to segregate and separate a Cr-based phase. The most intensive segregation is observed to occur after tempering at 500^{0}C, less intensive – at 550^{0}C no segregation whatever occurs at tempering above 600^{0}C. The Cr-rich lines on X-ray diffraction patterns have not been found because of small particle sizes and phase quantities. The chemical analysis data on the isolated precipitate show the Cr-rich phase occurrence in the range from 400 to 450^{0}C.

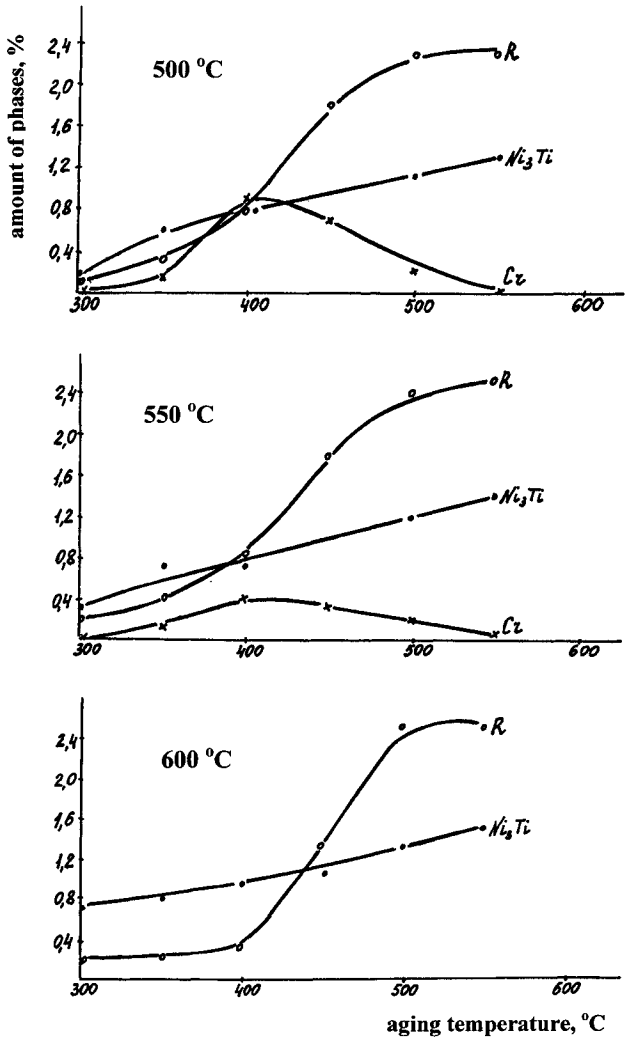


Fig.1. Amount of phases in steel as a function of aging temperature. Tempering at 500, 550 and 600 °C.

During aging at 500^{0}C for more than 1000 h, a hexagonal η- Ni_3Ti- phase has been shown by X-ray diffraction patterns only after tempering at 600^{0}C, the X-ray line being quite blurred due to a high level of phase dispersity. During aging for the same time, but at higher temperatures of 550 and 600^{0}C, the η-phase has been found to occur independently of the temperature of previous tempering. Extending aging time to 5000 h results in the η- phase appearance regardless of the tempering temperature. At aging temperature below 500^{0}C the η - phase is not observed to occur. This is confirmed by the chemical analysis data on the

precipitate obtained in electrolyte 2. If the temperature is below 500^0C, the η- phase is present only in a such a quantity, as that was formed during preliminary tempering at 600^0C. The Ni_3Ti phase in this steel may also be formed with a different structure – as a cubic β- Ni_3Ti phase. The β- Ni_3Ti phase is revealed by the X-ray analysis during aging at 550^0C for 1000 h regardless of the temperature of the previous tempering and has a rough composition of $(Ni_{0.5}Fe_{0.5})Ti$. The cubic β- Ni_3Ti seems to be a metastable phase in this steel. Ni_3Ti is formed in several steps: Ni and Ti-rich regions, cubic β- Ni_3Ti, and stable hexagonal η- Ni_3Ti.

Steel specimens aged at 650^0C showed the absence of Ni_3Ti phase which is not observed to form at temperatures above 600^0C, and the only stable phase is the Laves phase. From the chemical analysis, the Laves phase composition may be written as $(Fe_{0.8}Cr_{0.1}Ni_{0.1})\ Mo_{0.6}Ti_{0.4}$, and its amount does not depend on the tempering temperature and is about 4% after aging for 1000 h at 650^0C.

The contents of Ni and Cr in the Laves phase are insignificant, whereas Fe, Mo and Ti are its predominant elements. Note, that the Laves phase has as much of the bonded Ti and Mo as was present in the composition of η- Ni_3Ti and R-phase at 500-550^0C, i.e., with increasing temperature, the alloying elements in the same quantity seem to go over into a phase which is more stable at the given temperature. It should also be stressed that there is some structural affinity between the λ- and R-phases. Aging at 650^0C causes the dissolution of R- and η- Ni_3Ti phases formed as a result of the previous extended aging of the specimens at lower temperatures and the formation of the Laves phase in a quantity similar to that obtained after tempering at any temperature. The phase equilibrium in a steel at 650^0C seems to be established after aging for 1000 h regardless of the specimen heat treatment history, and the only phase observed under these conditions is a Laves phase which is realized owing to steel alloying with Ti and Mo.

A study of the steel phase composition during aging at temperatures between 300 and 650^0C has shown a rather intricate process of intermetallic phase formation in this case(Fig.2) The X-ray analysis reveals the existence of R-phase only after 450^0C when the phase content is 1.3-1.8%, but, as it follows from the chemical analysis of the isolated precipitate, the phase may form also at lower temperatures. The tempering temperature does not affect the mere fact of the R-phase appearance during further aging, but it determines the rate of precipitation and the phase quantity. The Ni_3Ti may appear both as a cubic β- Ni_3Ti and hexagonal η- Ni_3Ti structure. The η- Ni_3Ti has been found to occur in the range from 500 to 600^0C and R- phase
- from 400 to 550^0C. At 600^0C the Laves phase of $Fe_2(Mo,Ti)$ composition is a stable phase in the steel.

In addition to the intermetallic phase formation, a process of matrix segregation has been observed to occur, resulting in the formation of a Cr-rich phase(it is essentially Cr with a small amount of Fe). The above process is considerably affected by the tempering temperature(Fig.2). Tempering at 500^0C leads to most intensive matrix segregation during further aging, whereas after tempering at 600 no matrix segregation with Cr-rich solid solution precipitation has been observed. The Ni_3Ti phase appearance at 600^0C seems to reduce the degree of steel alloying, which results in the absence of Cr precipitate and inhibits the R-phase nucleation at 400 to 450^0C.

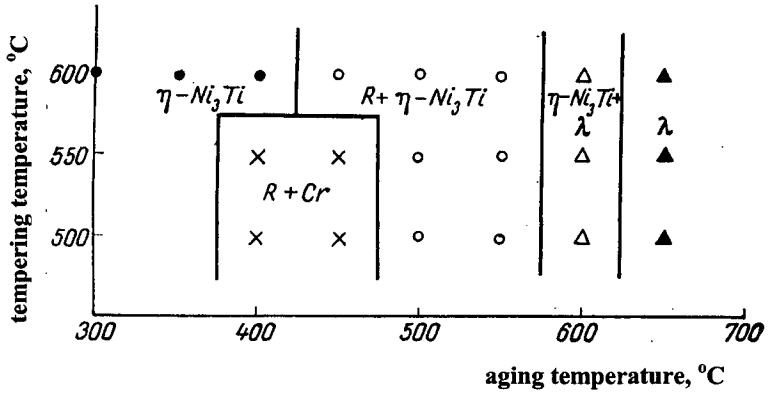


Fig.2. Phase diagram of steel for aging temperature 300-650 °C after tempering at 500, 550 and 600°C

The comparison of phase transformations in this steel and its mechanical properties shows that the highest level of strengthening corresponds to the initial stage of R-phase and Cr-rich solid solution precipitation. This may be also responsible for a reduced ductility property. The proper choice of the preliminary tempering temperature may to some degree affect the course of phase transformations during further aging at temperature up to 500^{0}C and thus provide the necessary level of properties. At temperatures above 500^{0}C the steel phase composition is independent of the temperature of previous tempering.

4 Conclusions

Thus, the study of the phase composition of maraging alloy steel shows that the intermetallic phases of different type may form during long-term aging over the temperature range from 400 to 650^{0}C. The precipitates in this steel are intermetallics: the R-phase, the Ni_3Ti –type and Laves phase Fe_2Mo-type. The intermetallic R-phase precipitation occurs in the context of matrix segregation and Cr-rich solid solution precipitation at temperature between 400 and 450^{0}C.

5 References

[1] Y. Komura, W.G. Sly and D.P. Shoemaker. The crystal structure of the R-phase. Acta Cryst., 13, 1960, p.575.

[2] N. F. Lashko and L.V. Zaslavskaja. Metallovedenie i termicheskaia obrabotka metallov, 10, 1974, p.39.

[3] F.A.Thomson and D.R.F. West, Intermetallic compound precipitation in a 10Cr-13Co-5Mo alloy. JISI, 210, 1972, p.691.

[4] H. Hughes and S. R. Keown, Precipitation of a transition intermetallic compound (R-phase) in steels. JISI, 206, 1968, p.275.

A NEW MODELLING APPROACH TO MICROSTRUCTURAL EVOLUTION IN FERRITIC STEELS

You Fa Yin and Roy G Faulkner

IPTME, Loughborough University, Loughborough, Leicestershire, LE11 3TU, UK

Abstract

A new technique based on Monte Carlo random sampling has been proposed to simulate the precipitation kinetics in alloys. The new approach employs time-dependent nucleation, growth and coarsening theory, and Fick's diffusion laws, considers both inter-granular and intra-granular precipitation and also combines inter-granular precipitation kinetics with inter-granular segregation. The simulation can be used not only to predict the average size of precipitate phase particles, but also to predict particle size distributions, volume fraction and inter-particle spacing. The new approach overcomes the shortcomings of model calculations where only the average size of the precipitate phase is considered. In addition, the proposed simulation overcomes the difficulty of connecting Monte Carlo steps to real time found when using the Metropolis algorithm. The approach has been used to simulate $M_{23}C_6$ precipitation kinetics in a creep-resistant steel, P92: the results are in good agreement with published experimental measurements.

Key Words: Computer simulation, Carbide, Precipitation, Ferritic steels, Grain boundaries

Introduction

Computer modelling of precipitation kinetics provides a useful tool for the prediction of microstructural evolution in alloys. In recent years, there is increasing interest in the modelling of precipitation kinetics in alloys, especially in power plant steels [1-4]. The widely used method is the model calculation of precipitation. Here modelling is based on equations derived from fundamental principles using Avrami relationships with some simplifications. Examples of such models include models developed by Bhadeshia's group [1-2] and the model used in the DICTRA software [5]. Recently, these models have been developed to deal with multi-component systems [6]. However, these models mainly deal with intra-granular precipitates. Faulkner *et al.* have developed a grain boundary precipitation model where grain boundary precipitation is combined with grain boundary segregation [7-8]. However, in all these models, only the average size and spacing of the precipitates is considered.

A different approach is the Monte Carlo Metropolis sampling simulation [9-10]. The simulation starts with assigning energies to the matrix and the precipitate phase and then sampling the phase transformation using the Metropolis sampling algorithm. Detailed information of precipitation, including particle size distributions may be obtained. However, it is difficult to connect the Monte Carlo steps to the real time during the phase transformation.

Here we propose a new simulation technique based on the Monte Carlo random sampling technique. The model is applied to simulation of precipitation kinetics in a power plant steel, P92, and the results are compared with experimental measurements reported in the literature.

The model and simulations

Basic theories

The theories on which the new simulation approach is based are briefly reviewed below.

Grain boundary segregation

Segregation of solute atoms to grain boundaries results in the redistribution of solute atoms in the material, and this affects the nucleation site density. Two segregation mechanisms exist [11]. (1) Non-equilibrium segregation (NES) takes place when the material is quenched from the solution heat treatment temperature or heat treated and quenched at temperatures higher than about 0.55 times the absolute melting temperature and can still be present during subsequent ageing and service. (2) Equilibrium segregation (ES) of solute takes place during heat treatments at lower temperatures, such as tempering and ageing. The solute concentration profile due to NES and ES can be found in references [4,11] and will not be discussed further here.

Nucleation

The nucleation rate can be described by the following equation [12]:

$$I = Z\beta^* \left(\frac{N}{x_\theta}\right) \exp\left(-\frac{\Delta G^*}{kT}\right) \exp\left(-\frac{\tau}{t}\right) \tag{1}$$

where N is the number of a particular type of atomic site, x_θ is the molar fraction of solute atoms in the nucleus phase, k the Boltzmann constant, T the absolute temperature, ΔG^* the energy required to form the critical nucleus, t the time and τ the incubation time for nucleation. The two coefficients Z and β^* are as follows

$$Z = \frac{V_\theta (\Delta G_V)^2}{8\pi\sqrt{kTK_j\sigma_{\alpha\theta}^3}}, \quad \beta^* = \frac{16\pi\sigma_{\alpha\theta}^2 D x_\alpha L_j}{a^4 (\Delta G_V)^2} \tag{2}$$

where V_θ is the volume occupied by one atom in the nucleus, ΔG_V the free energy change per unit volume of nucleus, $\sigma_{\alpha\theta}$ the interfacial free energy, D the diffusivity, x_α the solute concentration in the matrix, a the lattice parameter, L_j and K_j are defined by

$$V = \frac{4}{3}\pi r^3 K_j, \quad S = 4\pi r^2 L_j \tag{3}$$

In these two equations, V and S are volume and surface area of the nucleus respectively and r the radius or a characteristic length parameter of the particle. The incubation time $\tau = \frac{8kT\sigma_{\alpha\theta}a^4}{V_\theta^2 (\Delta G_V)^2 D x_\alpha}$ is usually very small, so that the term $\exp\left(-\tau/t\right)$ in Equation (3) can be assumed as unity.

Growth and coarsening

The formed nuclei can either grow or dissolve depending on the size of the nuclei and the solute concentration in the matrix. At early stages of precipitation, the solute concentration in the matrix is high and it is probable that the solute concentration in the matrix is higher than the solute concentrations at surfaces of all precipitates (Figure 1). Therefore, all precipitates grow. However, as the concentration gradient in the vicinity of the smaller particles is lower than that of the larger particles, smaller particles grow at lower rates. This process is growth. When the concentration in the matrix decreases to such a level that the concentration in the matrix is higher than that at the surface of some large particles but lower than some smaller particles, then there is a concentration gradient between small and large particles as shown in Figure 1. In such circumstances, the larger particles continue to grow at the cost of the dissolution of smaller particles. This is referred to as coarsening.

The solute concentration at the surface of a particle with radius of curvature of r, C_r, can be described by the Gibbs-Thomson equation:

$$C_r = C_\infty \exp\frac{2\sigma_{\alpha\theta}V_\theta}{RTr} \quad (4)$$

where C_∞ is the equilibrium solute concentration, V_θ the molar volume of the precipitate phase, R the universal gas constant. The equilibrium solute concentration is determined using the following equation [8]

$$C_\infty = \left[\frac{1}{C_c}\exp\left(\frac{-\Delta H}{RT}+\frac{\Delta S}{R}\right)\right]^{X_E} \quad (5)$$

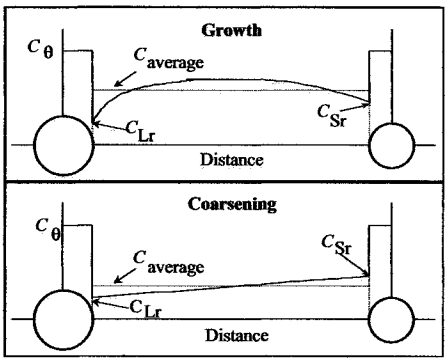


Figure 1. Growth and coarsening mechanism of precipitation.

where C_C is the concentration of the non rate controlling element, X_E the ratio of the number of non rate controlling to rate controlling atoms in the precipitate phase. ΔH and ΔS are the enthalpy and entropy of solution of the precipitate respectively.

When the solute concentration gradient in the vicinity of a particle surface is known, the rate of its growth or dissolution can be calculated using Fick's first law of diffusion:

$$J = DS\frac{dC}{dZ} \quad (6)$$

where J is the diffusion flux, D the diffusivity, S the surface area of the particle and $\frac{dC}{dZ}$ is the concentration gradient in the direction normal to the particle interface.

The simulation approach

This section presents the details of the new simulation approach.

The simulation cell

As in all Monte Carlo simulations, the process is simulated in a simulation cell. One of the simplest forms of simulation cell is shown in Figure 2. The material can be constructed with the periodic boundary conditions applied to the cell. In this way, the structure and properties of the cell can be taken as representative of the structure and properties of the real material.

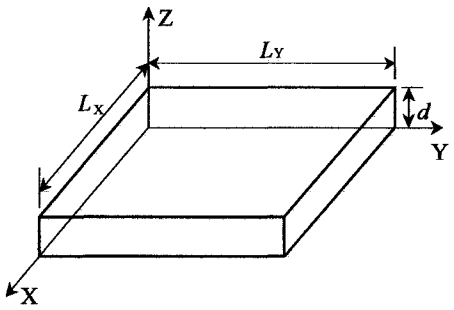


Figure 2. The simplest simulation cell. The surface of the cell is the grain boundaries.

In this paper, the cell can be regarded as a grain and the surface of the cell is the grain boundary, though we acknowledge that the actual grain may have different and irregular shape. The size of the grain is characterised by its length in X, Y and Z directions, namely L_X, L_Y and d as shown in Figure 2. In ferritic steels, we take d as a measure of the grain size and L_X, L_Y are much larger than d to represent a lath plate.

Segregation

Segregation of solute atoms to grain boundaries is considered in the new approach in two ways. (1) As most power plant steels are solution heat treated or normalised at temperatures around 1060 °C and then either quenched or air cooled, the non-equilibrium segregation model is employed to predict the segregation effects during the quench. This gives the initial solute concentration distribution in grain boundaries and the matrix within the simulation cell. (2) The time-dependent segregation model is employed to give solute distributions during subsequent tempering and ageing of the alloys of concern.

Nucleation

Two types of nucleation sites are considered in this paper. One is the intra-granular precipitate. In this case, homogeneous nucleation and spherical particles are assumed. In the case of inter-granular or grain boundary precipitates, cap shaped particles are assumed (Figure 3). In both cases, the critical nucleus size and the activation energy for nucleation can be determined using the following equations:

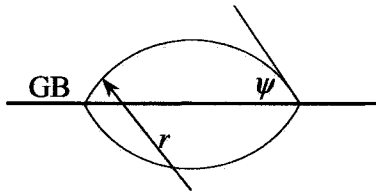


Figure 3. Grain boundary cap shaped precipitate. GB stands for grain boundary, ψ is the contact angle and r is the radius of the sphere from which the cap is cut.

$$r^* = -\frac{2\sigma_{\alpha\theta}}{\Delta G_V},\ \Delta G^* = \frac{16\pi\sigma_{\alpha\theta}^3}{3\Delta G_V^2} K_j \qquad (7)$$

For spherical particles, r is the radius and thus K_j and L_j (Equation (3)) are unity. For cap shaped particles, r is the radius of the cap and K_j and L_j is related to the contact angle by:

$$K_j = \frac{1}{2}\left(2 - 3\cos\psi + \cos^3\psi\right),\ L_j = 1 - \cos\psi$$

In this paper, it is assumed that $\psi = 57°$, as in reference [7] for $M_{23}C_6$ particles in austenitic steels. It is found that the simulation results fit the experimental observations well when the interfacial energy, $\sigma_{\alpha\theta}$, equals 0.51 J m^{-2}.

ΔG_V in Equations (2) and (7) is determined as a function of temperature and matrix composition using MTDATA [13] for the actual system. The equilibrium solute concentration in Equations (4) and (5) is also determined using MTDATA.

The simulation treats the tempering and ageing of the steel consecutively. The whole tempering and ageing process is divided to many small time intervals, Δt. At each time interval $t \sim t + \Delta t$, sets of random numbers (x, y, z) are generated to locate the critical nucleus both in the grain boundaries and in the matrix. At present, we assume a nucleation is successful when the generated nucleus does not overlap with others. The total number of nuclei accepted in any time interval $t \sim t + \Delta t$ is controlled by Equation (1), *i. e.*,

$$\Delta N(t) = Z\beta^* \left(\frac{N}{x_\theta}\right) \exp\left(-\frac{\Delta G^*}{kT}\right) \Delta t \qquad (8)$$

where $\Delta N(t)$ is the number of nuclei generated in the simulation cell during the time interval. No particular size distribution of the nuclei is introduced here. The nucleation rate decreases with time because the matrix solute concentration decreases due to the formation of precipitates as discussed in the next section (Equation (9)).

Growth and coarsening

When the number of generated nuclei at any time interval $t \sim t + \Delta t$ reaches the value determined by Equation (8), generation is stopped. When the next time interval is considered, the appropriate number of new nuclei are generated according to Equation (8), with adjusted parameters for β^* and ΔG^* because of the changed matrix composition. All particles generated before this time interval are assumed to be in the growth/coarsening regime. Then, the average matrix solute concentration is determined from the initial composition of the material and the volume fraction of precipitates. Assuming that the initial concentration of solute is C_g and the volume fraction of precipitates at time t is V_f, then the corresponding average solute concentration would be:

$$\overline{C}_t = 1 - \frac{V_f \rho_\theta N_r}{\rho_\alpha C_g} \tag{9}$$

ρ_α and ρ_θ are the molar density of the matrix and the precipitate phase respectively and N_r is the number of rate controlling atoms in the precipitate molecule. Thus the concentration gradient at the surface of a particle at time t can be estimated using a mean field approximation

$$g = \frac{\overline{C}_t - C_r}{\overline{d}} \tag{10}$$

where $\overline{d}$ is the average inter-particle spacing. If g>0 the particle grows and if g<0 the particle dissolves. Thus, the increase of the volume of a particle, ΔV, in time interval $t \sim t + \Delta t$ is

$$\Delta V = DSg \frac{\rho_\theta}{C_\theta \rho_\theta - C_r \rho_\alpha} \Delta t \tag{11}$$

For inter-granular particles, S is divided into two parts: one within the matrix and the other in the grain boundary to allow both volume and grain boundary diffusion of solute atoms to or from the formed precipitates. The latter is determined by the precipitate size and the grain boundary width. At each time step, concentration gradient and then volume increase are calculated for each individual particle. The average concentration in the matrix is re-calculated when any one of the particles changes its volume. To ensure a random sampling, a random number is generated to pick up a particle. Then the volume change of this particle is calculated according to Equation (11) and consequently the average concentration in the matrix is calculated according to Equation (9). This process is repeated in each time interval for all existing particles.

The simulation loop

The simulation process is summarised in Figure 4. After the establishment of the simulation cell, the inter-granular segregation models are used to calculate the initial solute distribution within the cell. Then the heat treatment time is divided into tens of thousands of small time intervals. Within each time interval, segregation model is used to calculate solute concentration distribution, then positions of a certain number of nuclei are generated randomly and all particles are individually allowed to either grow or dissolve. The process is looped until the required ageing time is reached and simulation results are then written to a file.

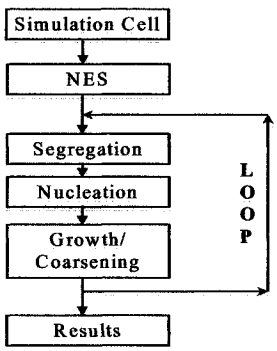


Figure 4. The simulation loop shows the main steps in the simulation proposed. NES stands for Non Equilibrium Segregation.

Particle size distribution data is also saved to a file. Main parameters used in the simulation of precipitation kinetics in this paper are summarised in Table1.

Table 1 Main parameters used in the simulation of precipitation kinetics.

Parameter		Unit	Value	Reference
a	lattice parameter	nm	0.2866	[14]
V_θ	molar volume, precipitate	$m^3\ mol^{-1}$	1.82×10^{-4}	[14]
V_α	molar volume, matrix	$m^3\ mol^{-1}$	9.05×10^{-6}	[15]
D_{b0}	grain boundary Cr diffusion Pre-exponential term	$m^2\ s^{-1}$	502	[16]*
Q_b	grain boundary Cr diffusion Activation energy	$kJ\ mol^{-1}$	283.1	[16]
D_{V0}	Cr volume diffusion pre-exponential term	$m^2\ s^{-1}$	8.5×10^{-4}	[17]
Q_V	Cr volume diffusion Activation energy	$kJ\ mol^{-1}$	240	[17]
ψ	contact angle	degree	57	[7]
ΔH	enthalpy of solution	$kJ\ mol^{-1}$	102.9	§
ΔS	entropy of solution	$J\ mol^{-1}\ K^{-1}$	-109.3	§

* calculated from triple product taking $\delta = 5\times10^{-10}$m and $k = 1$.
§ calculated using MTDATA

The material and heat treatment

P92 is a creep resistant 9% chromium steel used in power plant. Many microstructural investigations have been performed on this steel and thus a relatively good microstructural picture of the material at different heat treatment conditions has been established [5,18-20]. The composition of the steel is shown in Table 2 [18]. The steel is austenitised at 1070 °C for two hours and air cooled, followed by tempering at 770°C for two hours and then air-cooling. Typical ageing or creep test conditions reported in the literature are 600°C and 650°C for up to a few tens of thousands of hours.

Table 2. Chemical composition of steel P92 [18] in wt% (Fe balance)

Cr	Mn	Ni	Mo	W	V	Nb	C	B	N	Si	P
8.96	0.46	0.06	0.47	1.84	0.20	0.07	0.11	0.001	0.05	0.04	0.008

We apply our simulation to $M_{23}C_6$ precipitates in this material at the heat treatment conditions reported in the literature, *i. e.* P92 solution heat treated at 1070°C, tempered at 770°C for two hours and then aged at 600°C and 650°C for up to 100 000 hours.

Results and discussion

Precipitate size

The simulated average $M_{23}C_6$ precipitate size as a function of tempering and ageing time at 600 °C and 650 °C is shown in Figure 5. The equivalent circle radius is defined as the radius of a circle whose area is the same as the area shown in Figure 3 for cap shaped precipitates. This facilitates the comparison with experimental observations. For intra-granular spherical particles, the equivalent circle radius is equal to the radius of the sphere. The time axis starts

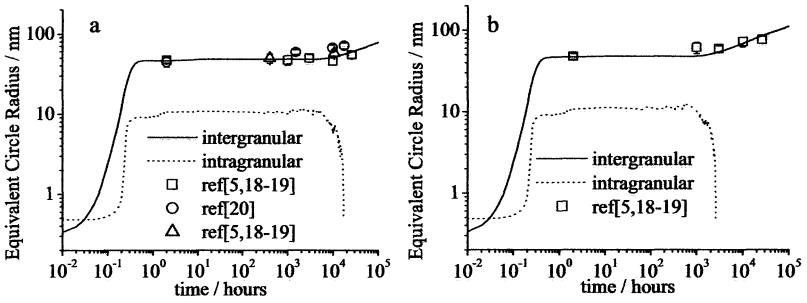


Figure 5. Simulated $M_{23}C_6$ precipitation kinetics in P92, together with experimental measurements reported in the literature. The material is tempered at 770 °C for two hours and then aged at (a) 600 °C and (b) 650 °C. Squares are measurements made on isothermally aged samples, others are on creep tested samples.

from the beginning of tempering, therefore the time from $t = 0$ to $t = 2$ represents the tempering process and $t > 2$ hours represents the ageing process (the same time axis is employed for all following figures). The solid and dotted lines are simulated inter- and intra-granular precipitation respectively. Also plotted in the figures are experimental measurements of $M_{23}C_6$ particle size in P92 reported in the literature [5, 18-20]. In Figure 5(a), the triangles and circles are measurements on samples creep tested at 600 °C. The remaining data points are from measurements on samples isothermally aged at 600 °C and 650 °C. It is clear that the simulated results are in good agreement with measurements at both 600 °C and 650 °C. Intra-granular precipitates virtually make no contribution to the overall average particle size due to the number of particles being very small.

As shown in Figure 5, particles grow slowly at the beginning of tempering. Then they grow rapidly and reach a semi-stable state at about $t = 0.2$ hours. The average size of the particles only changes slightly during the next few thousand hours. Then the size of inter-granular particles increases sharply again while intra-granular particle size decreases steeply due to coarsening. From Figure 5, we can see (1) Intra-granular particles are much smaller than inter-granular particles. (2) Appreciable coarsening effects can be observed only after a few thousand hours. (3) The effects of ageing temperature on the coarsening of the particles are two-fold. First, the higher the ageing temperature, the earlier an appreciable coarsening effect can be observed. As Figure 5 shows, the onset time for the second sharp increase of particle size is about 5000~6000 hours at 600 °C and only about 1000 hours at 650 °C. Second, coarsening rate is much higher at 650 °C than 600 °C.

Inter-particle spacing

Inter-particle spacing is an important parameter in determining the mechanical properties of precipitate hardened steels. In the simulation, the inter-particle spacing is determined from the number of inter-granular particles at the boundary and the grain boundary area. The simulated average inter-particle spacing in P92 aged at 600 °C and 650 °C is shown in Figure 6 for inter-granular $M_{23}C_6$ particles. The inter-particle spacing decreases sharply, corresponding to the sharp increase in the number of precipitates nucleated, at the beginning of

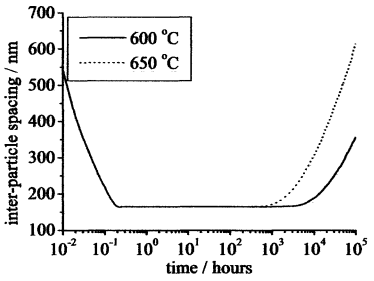


Figure 6. Inter-particle spacing of inter-granular particles in P92 as a function of

tempering. The minimum inter-particle spacing is about 165 nm, ~4 times the equivalent circle radius at the end of tempering. The inter-particle spacing increases sharply after a few thousand hours as a result of coarsening. The effects of higher ageing temperature on coarsening rate is also clearly demonstrated here with a much earlier and sharper increase in inter-particle spacing at 650 °C than at 600 °C.

Precipitate volume fraction

The simulated $M_{23}C_6$ particle volume fraction in P92 aged at 600 °C and 650 °C is shown in Figure 7 as a function of time. It is clear that the volume fraction of $M_{23}C_6$ particles at the beginning of tempering is very low and increases slowly, though a considerable number of particles may have been nucleated. However, the volume fraction increases very steeply after about 0.2 hours and reaches a maximum in a very short time. The maximum is kept until the end of tempering. When ageing starts, there is a marked increase in the volume fraction of particles. Then it reaches another maximum and the volume fraction hardly changes on further ageing.

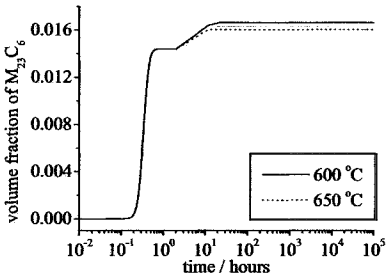


Figure 7. Simulated volume fraction of $M_{23}C_6$ particles in P92 as a function of ageing time.

The marked increase of volume fraction at the early stage of ageing is a result of the decrease in temperature from tempering to ageing. Decreases in temperature cause a decrease in solute solubility in the matrix, thus decreasing the equilibrium solute concentration. This gives rise to the increase of solute for precipitation and therefore increases the volume fraction of precipitates. For the same reason the volume fraction of the precipitates at 600 °C is higher than at 650 °C, as demonstrated in Figure 7. This effect is a direct output of the simulation with no prejudgement about the actual value of volume fraction, except the solubility as a function of temperature calculated using MTDATA. In addition, this result is confirmed to some extent by Hättestrand and Andrén's work [18], where relative increases were observed in VN particle volume fraction in P92 of 18.5% and 11.1% (relative to volume fraction in the as-received, *i. e.* tempered material) for ageing at 600 °C and 650 °C respectively. Figure 7 shows relative increases of 15.6% and 11.4% of $M_{23}C_6$ volume fraction for ageing at 600 °C and 650 °C respectively. The simulated volume fraction is also in good agreement with the equilibrium volume fraction (~0.019) calculated using MTDATA.

Particle size distribution

The simulated $M_{23}C_6$ particle size distributions in P92 after tempering at 770 °C for two hours, and ageing at 600 °C for 10000 and 100000 hours are shown in Figure 8. A relatively narrower size distribution is found after tempering. As the ageing time increases, the distribution gets broader and the peak shifts to larger particle sizes, because the larger particles grow and smaller particles dissolve. The shape of the particle size distributions is reasonable. However, the simulated particle size distribution is not in a good agreement with Gustafson and Hättestrand's results, where the size distributions are skewed to smaller particle sizes [5,18]. Therefore, further validation of the model is required.

Monte Carlo random sampling methodology

The simulation approach proposed here is different from both analytical model calculations of precipitation and the Monte Carlo Metropolis sampling simulation. Compared to analytical

modelling, this new approach has a number of advantages. (1) It can give more detailed information, especially about particle size distributions and particle spatial distributions. (2) In the new simulation technique, some physical phenomena are spontaneously described. For example, the switch from growth to coarsening is an automatic process in the simulation proposed here. (3) The proposed simulation approach can deal with more complicated systems. For example, with the random sampling technique employed here, factors such as grain boundary heterogeneity can easily be taken into account.

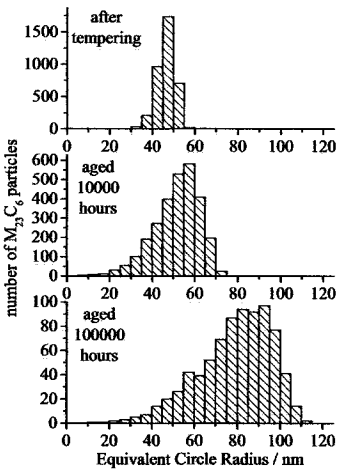


Figure 8. Simulated particle size distribution of $M_{23}C_6$ in P92 at different stages of ageing. The ageing temperature is 600 °C.

The simulation approach is less computationally demanding than Monte Carlo Metropolis sampling simulations. Thus this technique enables precipitation processes within larger simulation cells to be simulated. The transformation of tens of thousands of second phase particles may be followed. Therefore, more representative particle size distributions can be obtained. In addition, the approach here simulates the precipitation kinetics in the real time scale by using the diffusion law. Thus the results can be easily compared with experimental observations.

The proposed approach is being developed to enable the simulation of simultaneous and consecutive precipitation of different precipitates in different alloys. Further experimental validations of the technique are also being carried out.

Conclusions

A new simulation approach to the modelling of precipitation kinetics of chromium carbide in ferritic steels based on a Monte Carlo random sampling technique has been proposed. The technique automatically predicts the transition from growth to coarsening. For the first time, the technique simultaneously simulates inter-granular and intra-granular precipitation kinetics. The application of the proposed approach to a ferritic power plant steel P92 shows good agreement with experimental observations reported in the literature.

Acknowledgement

We would like to thank the Engineering and Physical Science Research Council (EPSRC) for funding (Grant number GRN 13074), and Powergen and Innogy for co-funding the project.

References

[1] J. D. Robson, H. K. D. H. Bhadeshia, Modelling precipitation sequences in power plant steels .1. Kinetic theory, *Mater. Sci. Tech.*, **13**(8), 1997, 631-639.

[2] J. D. Robson, H. K. D. H. Bhadeshia, Modelling precipitation sequences in power plant steels .2. Application of kinetic theory, *Mater. Sci. Tech.*, **13**(8), 1997, 640-644.
[3] Å. Gustafson, Coarsening of TiC in austenitic stainless steel - experiments and simulations in comparison, *Mater. Sci. Eng. A*, **287**(1), 2000, 52-58.
[4] R. G. Faulkner *et al.*, Forecasting Grain Boundary Precipitation Kinetics in Austenitic Steels, in Microstructural Stability of Creep Resistant Alloys for High Temperature Plant Applications, in Microstructural Stability of Creep Resistant Alloys for High Temperature Plant Applications (ed. Strang, A. *et al.*), IOM, 1998, 431-443.
[5] Å. Gustafson, and M. Hättestrand, Coarsening of Precipitates in an Advanced Creep Resistant 9% Chromium Steel - Quantitative Microscopy and Simulations, paper VI in PhD thesis (Hättestrand, M.), Göteborg University, Sweden, 2000.
[6] G. Ghosh, and G. B. Olson, Simulation of paraequilibrium growth in multicomponent systems, *Metall. Mater. Trans. A*, **32**(3), 2001, 455-467.
[7] R. A. Carolan, and R. G. Faulkner, Grain Boundary Precipitation of M23C6 in an Austenitic Steel, *Acta Metall.*, **36**(2), 1988, 257-266.
[8] H. Jiang, and Faulkner R. G., Modelling of Grain Boundary Segregation, Precipitation and Precipitate-Free Zone of High Strength Aluminium Alloys - I. The Model, *Acta. Mater.*, **44**(5), 1996, 1857-1864.
[9] Y. Saito, Monte Carlo simulation of grain boundary precipitation, *Mater. Sci. Eng. A*, **223**(1-2), 1997, 125-133.
[10] J. M. Liu, A Monte-Carlo simulation of decomposition kinetics in fine-grained binary alloys, *Mater. Sci. Eng. A*, **254**(1-2), 1998, 45-52.
[11] R. G. Faulkner, Segregation to Boundaries and Interfaces in Solids, *Intern. Mater. Rev.*, **41**(5), 1996, 198-208.
[12] W. C. Johnson *et al.*, Influence of Crystallography on Aspects of Solid-Solid Nucleation Theory, *Metall. Trans. A*, **6A**, 1975, 911-919.
[13] R. H. Davies, A. T. Dinsdale, T. G. Chart, T. I. Barry, and M. H. Rand, Application of MTDATA to the modelling of multicomponent equilibria, *High Temp. Sci.*, **26**, 1990, 251.
[14] W. B. Pearson, A handbook of Lattice Spacings and structures of metals and alloys, Pergamon Press, London 1958.
[15] E. A. Brandes and G. B. Brook, Smithells Metals Reference Book, Butterworth-Heinemann, Oxford, 1992.
[16] Z. Tőkei, K. Hennesen, H. Viefhaus and H. J. Grabke, Diffusion of chromium in ferritic and austenitic 9-20 wt-% chromium steels, *Mater. Sci. Tech.*, **16**, 2000, 1129-1138.
[17] T. Gladman, Principles of Microstructural Stability in Creep Resistant Alloys, in Microstructural Stability of Creep Resistant Alloys for High Temperature Plant Applications (ed. Strang, A. *et al.*), IOM, 1998, 49-68.
[18] M. Hättestrand, and H. -O. Andrén, Evaluation of particle size distributions of precipitates in a 9% Cr-steel using energy filtered transmission electron microscopy, Paper V in PhD thesis (Hättestrand, M.), Göteborg University, Sweden, 2000.
[19] M. Hättestrand, and H. -O. Andrén, Influence of Strain on Precipitation Reactions During Creep of an Advanced 9% Chromium Steel, Paper VII in PhD thesis (Hättestrand, M.), Göteborg University, Sweden, 2000.
[20] P. J. Ennis *et al.*, Quantitative Comparison of the Microstructures of High Chromium Steels for Advanced Power Stations, in Microstructural Stability of Creep Resistant Alloys for High Temperature Plant Applications (ed. Strang, A. *et al.*), IOM, 1998, 135-143.

AUTHOR INDEX

A

Abe F., II.1171, II.1181, III.1379, III.1397, III.1469, III.1561, III.1571, III.1581, III.1591, III.1629, III.1639, III.1691
Agamennone R., II.1161, III.1279
Agüero A., II.1143
Ahmaniemi S., I.449
Allen D., I.5, I.283, III.1487, III.1661
Andersson H.C.M., II.933
Angella G., I.167
Arai M., III.1269
Archer N.J., I.523
Arrell D., II.605, II.633
Artinger I., III.1701
Azuma T., III.1269, III.1497

B

Backes G., II.751
Bacos M.-P., I.429
Bakker W., II.815
Bale D.W., I.73, I.149
Banks J.P., I.577
Barbezat G., I.511
Baxter D., I.73, I.523
Beck T., III.1419
Bendick W., III.1361
Berger C., I.89, III.1279, III.1409, III.1551
Bezençon C., I.503
Bianchi P., I.449, I.523
Biede O., II.957
Blough J., II.815
Blum R., II.1009, III.1385
Blum W., II.1161, III.1279
Boßmann H.P., II.871
Bohn D.E., I.107
Bontempi P., I.149, III.1621
Bordenet B., II.871
Böttger B., I.89, I.315, III.1333
Brozda J., III.1711
Brückner U., I.217
Buckthorpe D., II.759
Buenaventura A., II.759
Burlet H., I.419
Bursik J., III.1521
Busquin P., III.1806
Busso E.P., I.23, I.283

C

Cabibbo M., III.1453
Cailletaud G., I.23
Carosi A., III.1731
Cerjak H., II.1081, III.1539
Cernuschi F., I.449
Chen Q., II.1019, III.1333
Chen W.Y., I.187
Chi B.H., III.1681
Cizner J., II.785
Contessi E., III.1731
Couturier R., I.419, II.759
Cremer R., II.663
Cui C.Y., II.595
Czyrska-Filemonowicz A., I.149

D

Danciu D., I.227, I.235
Daniel R., I.293
Dassios C.G., II.769
Davis C., II.785, II.893
De Beer A.J., III.1783
Del Puglia P., II.769
Del Vecchio D., III.1731
Di Gianfrancesco A., II.1065, III.1731
Dimmler G., III.1539
Dlouhý A., II.605
Doi H., III.1269
Doi M., II.1201
Dubiel B., I.139, I.149
Dubiez S., I.419
Ducki K.J., I.401
Dupin N., I.315

E

Ehlers J., III.1279
Emura S., II.643
Encinas-Oropesa A., II.923
Ennis P.J., II.1131, III.1279
Epishin A., I.217
Escher K., II.1049
Evangelista E., III.1453

F

Faulkner R.G., II.1247
Foldyna V., III.1477
Formanek B., II.785
Frahm J., I.543
Friedrich B.-C., II.759
Fries S.G., I.315, III.1333
Fritscher K., I.483
Frommert M., II.673
Fujita T., III.1269, III.1311
Fujiyama K., I.345
Fukui Y., III.1269
Fukuyama Y., I.255, II.733

G

Gabrel J., III.1343, III.1361
Gallet S., II.633
Garcia Oca C., II.711
Gasser A., II.751
Ghidini A., III.1731
Giannozzi M., I.493
Gil I., II.703
Giorni E., I.493, I.523
Girard B., I.429
Giselbrecht W., II.1065
Goransson K., II.785
Gottstein G., II.673
Granacher J., III.1279
Guardamagna C., I.149, III.1621
Guétaz L., I.419
Guo J.T., II.595
Guo S., II.997

H

Haase H., III.1409
Hagiwara M., II.643
Hakl J., II.615
Hald J., II.1009
Hamano S., III.1351
Hara T., II.1181
Harada H., I.159, II.197, I.303, II.733
Harada N., I.245
Hashizume R., II.1201, III.1497
Hayakawa H., III.1445
Hecht U., I.315
Heckmann S., I.561
Hede Larsen O., II.957
Henderson M., I.139, I.149, I.293, II.633
Henderson P.J., II.785, II.883
Herzog R., I.543, I.551, I.561
Hetmanczyk M., I.401
Heuser H., III.1671
Hillenbrand P., III.1385
Hilpert K., II.989
Hino T., I.303
Hirosaki N., II.997
Hjörnhede A., II.979
Höbel M., I.503
Högberg J., II.883
Horn A., II.743
Hornak P., I.365, I.375
Hovsepian P. Eh., I.465
Hu W., II.673

I

Ielpo F.M., III.1731
Igarashi M., III.1397, III.1469, III.1561, III.1591, III.1639
Ikeda K., III.1371
Imai H., I.535
Inden G., III.1279, III.1299
Innocenti M., I.523, II.769
Ishiguro T., III.1497
Ishii R., III.1371
Ishitsuka T., III.1321
Isobe S., III.1351

Itagaki T., III.1397, III.1629, III.1639
Ito S., I.255
Izumi T., II.693

J

Jacobs M., II.833
Jakobová A., III.1477
Jirikovsky K., I.569
Jochum C., II.1081, III.1671
Josso P., I.429
Judkins R.R., II.853

K

Kadoya Y., III.1351
Kakehi K., I.207
Kaneko J., III.1371, III.1721
Kang S.T., III.1505
Karada H., I.395
Karlsson A., II.785
Karlsson B., II.605
Kawai H., III.1351
Kaysser W.A., I.483
Kelbassa I., II.751
Kern T.-U., II.1017, II.1049, II.1065, III.1385
Keutgen S., II.751
Kilgallon P., II.903, II.913, II.923
Kim B.J., III.1505, III.1681
Kim J.T., III.1505
Kimura K., II.1171, III.1397, III.1571, III.1581
Kimura M., III.1515
Klabbers J., I.139, I.227, I.385
Kloc L., II.1189, III.1531
Knezevic V., III.1279, III.1289
Knödler R., II.1143, III.1601
Kobayashi K., III.1515
Kobayashi T., I.159, I.197, I.303, I.395
Koizumi Y., II.197, I.303, I.395
Kolkman H., I.149
Komatsubara S., III.1311
Kondo Y., I.245
Kong B.O., III.1681
Kong C.N., I.273
Konter M., I.503
Koolloos M.F.J., II.633
Kopp R., I.325
Kostopoulos V., II.769
Koyama T., II.1201
Kratochvil P., II.615
Krejcí J., I.569
Kreutz E.W., II.743, II.751
Kroupa A., III.1477, III.1521
Kubo K., II.1181, III.1691
Kubon Z., III.1477
Kuc D., I.401
Kucharova K., II.1189
Kung S., II.815
Kurz W., I.503
Kushima H., II.1171, III.1571, III.1581
Kutsumi H., III.1629, III.1639

L

Lapin J., II.605, II.623
Layne A.W., I.121
Lee K.W., III.1681
Lee S.Y., III.1505, III.1681
Lefebvre Bo., III.1343
Letofsky E., II.1081
Lewis D.B., I.465
Leyens C., I.465
Li G.S., II.595
Li H., I.167
Lim B.S., III.1681
Lindblom J., II.933
Link T., I.217
Löhe D., III.1419
Lorenzoni L., I.449
Lukas P., I.139, I.149
Luo Q., I.465
Lupinc V., I.43, I.167, I.409, II.605, II.683

M

Ma D., I.315
Magoshi R., III.1351
Mai Y.-W., I.187
Majerus P., I.551
Maldini M., I.139, I.167, I.409

Mäntylä T.A., I.449, II.945
Mao C., II.845
Marchionni M., II.683
Martinez C., II.663
Masuyama F., III.1767
Matsui M., III.1691
Matsuo T., I.177, I.245
Mattsson M., II.883
Mayer K.H., II.1049, II.1065, III.1385, III.1521
Mc Cartney L.N., III.1613
McColvin G., II.833
Meriggi M., I.439
Merluzzi M., I.493
Metz Ch., I.523
Miki K., III.1497
Mimura H., III.1321
Minami Y., III.1445
Mitomo M., II.997
Miura N., I.245
Miyazaki T., II.1201
Mohrmann R., III.1651
Monteiro A., I.475
Montgomery M., II.957
Moormann R., II.759
Morinaga M., II.1201, III.1497
Morris D.G., II.703, II.711
Muelas R., II.1143
Müller M., II.989
Mulvihill P., I.149, III.1261
Munasinghe D., II.833
Muneki S., III.1469, III.1561, III.1591
Munoz-Morris M.A., II.703, II.711
Münz W.-D., I.465
Murakami H., I.535
Murakumo T., I.159
Murata Y., II.1201, III.1497

N

Nafari A., II.969
Nakamoto Y., I.177
Nakazawa S., I.159, I.197
Nam S.W., III.1681
Narita T., II.693
Nazmy M., I.43, II.605, II.683
Neuschütz D., II.663
Nicholls J.R., I.57
Nies H., II.1081
Nikbin K., II.605
Nishimoto T., II.693
Nishimura T., II.997
Noda T., III.1351
Norreys A., I.523
Norton J.F., II.913
Nylund A., II.969, II.979

O

O'Dowd N.P., I.283
O'Driscoll J., II.833
Oakey J.E., I.73, II.785, II.801, II.903, II.913, II.923
Obrtlik K., I.149
Odaka T., II.733
Okada H., III.1397, III.1469, III.1561, III.1591
Okayama A., I.355
Okubo H., III.1469, III.1561, III.1591
Olsha Z., III.1783
Onay B., I.355
Ono H., I.395
Onofrio G., II.683
Osgerby S., II.801, III.1261, III.1613

P

Palm M., II.653
Palumbo G., III.1453
Pappas Y.Z., II.769
Park S.H., III.1681
Pasternak J., III.1711
Pelachová T., II.623
Penkalla H.J., I.89, I.227, I.235, I.335
Peters M., I.465
Pigrova G.D., II.1241
Pinder L.W., II.893
Pirch N., II.751
Podstranska I., III.1521
Pollock T.M., I.263

Portella P.D., I.217
Portinha A., I.475
Pratesi F., I.493
Purgert R., II.1109

Q

Qi Y.H., II.595
Quadakkers J.W., II.1131, III.1279

R

Rademakers P., II.785
Rae C.M.F., I.207
Rantala H., II.759
Rao U., II.1109
Rau K., III.1419
Reed R.C., I.207
Regino G.M., I.283
Reichert K., II.663, II.673
Ricci N., III.1621
Rinaldi C., I.439
Rio C., I.429
Riou B., II.759
Ro Y., II.197
Rösler J., I.89
Rozsavölgyi Z., III.1701
Ruth L.A., III.1745
Ryu S.H., III.1505, III.1681

S

Saeki H., II.733
Saito D., I.255, I.345
Sandström R., III.1431
Sato M., I.395
Saunders S.R.J., I.577, II.801
Sauthoff G., II.653, III.1279, III.1289,
Sawada K., II.1181, III.1379
Scarlin B., II.1091, II.1143, III.1601
Scarpellini R., II.845
Scheffknecht G., II.1019
Schneider A., III.1299
Schnell A., I.503
Scholz A., III.1279, III.1409, III.1551
Schubert F., I.235, I.335, I.385, I.543, I.551, I.561
Schulz U., I.483
Schwienheer M., III.1409
Seitisleam F., III.1431
Seitz W., II.815
Semenak J., I.375
Servetto C., III.1487, III.1661
Shibli A., II.1233
Simms N.J., I.73, II.801, II.903, II.913, II.923
Singheiser L., I.561, II.989, III.1279
Sklenicka V., II.1189, III.1521, III.1531
Spigarelli S., III.1453
Spiradek K., III.1459
Stamatelopoulos G.-N., II.1091
Starr F., II.1233
Staubli M., II.605, II.683, II.1049, II.1065, II.1189, III.1385
Steen M., II.769
Steinbach I., III.1333
Steinbrech R.W., I.543, I.551, I.561
Stief J., II.1065
Stocker Ch., III.1459
Stöver D., I.475, I.511
Strang A., II.1223
Strunz P., I.365
Sundman B., III.1333
Suzuki A., I.535
Suzuki K., II.1171
Svejcar J., I.569
Svoboda M., II.1189, III.1521

T

Tabuchi M., III.1397, III.1691
Tamaki H., I.355
Taneike M., III.1379
Tang F., II.643
Teixeira V., I.475
Terada Y., I.177
Thoma A., III.1551
Tin S., I.263
Tinga T., I.293
Toda Y., II.1171, III.1571

Tohyama A., III.1445
Tohyama H., III.1571
Toji A., III.1311
Tomasi A., II.683
Torri L., III.1621
Toulios M., I.5, I.23
Tsuda Y., III.1371, III.1721

U

Uehara T., III.1311
Ueta S., III.1351
Uusitalo M.A., II.945

V

Vaillant J.-C., III.1343, III.1361
Valarani M., II.845
Valenti S., III.1731
Van der Schaaf B., II.759
Vandenberghe B., III.1343, III.1361
Vanstone R.W., II.1035, III.1261
Vaßen R., I.475, I.511
Vilk J., III.1279, III.1299
Vippola M., I.449
Viswanathan R., II.1109
Vitusevych V., I.315
Vlachos D., II.769
Vlasák T., II.615
Vodarek V., II.1223, III.1477
Vrchovinsky V., I.365, I.375
Vuoristo P., I.449
Vuoristo P.M.J., II.945

W

Wagnière J.-D., I.503
Wahl G., I.523
Wang C.H., I.187
Wang Y., III.1279
Wangyao P., I.375
Wanikawa S., III.1397
Ward T.J., I.293
Warnken N., I.315
Watanabe T., III.1691
Weinert P., II.1211, III.1539
Wen K.Y., II.673
Wessel E., I.385
White P.S., I.273, II.723
Wiedenmann A., I.365
Wieghardt K., II.1017
Wilcock I.M., I.139
Willach J., II.743
Wing R., I.57, I.523
Wolske M., I.89, I.325
Wosik J., I.335
Wu F., I.535
Wu R., III.1431

Y

Yamada K., III.1469, III.1561, III.1591
Yamada M., III.1371, III.1721
Yamaguchi K., III.1397, III.1515
Yamamoto R., III.1351
Yamamoto Y., II.997
Ye L., I.187
Yeatman J., I.523
Yin Y.F., II.1247
Yokokawa T., II.733
Yoshida T., II.733
Yoshinari A., I.355
Yoshioka Y., I.255, I.303, I.345
Yu J., III.1505

Z

Zeiler G., II.1049, III.1459
Zeman M., III.1711
Zhang X.P., I.187
Zhou H., II.197
Zhou L.Z., II.683
Zonfrillo G., I.493
Zrnik J., I.365, I.375

KEYWORD INDEX

γ' phase: I.245, I.255
[001] orientation: I.177
0.2 % proof stress: III.1581
10 % Cr steel: II.1049, III.1385
11% Cr steels: II.1131
12 % Cr steel: II.1161, III.1269, III.1279, III.1289, III.1299, III.1361
2.25 % Cr1.7 % NiMoVNbW steel: III.1721
700°C power plant: II.1009
8 wt.% YSZ: I.543
9 % Cr steel: II.1171, II.1181, III.1691
9-12 % Cr steel: II.1035, II.1189, II.1211, III.1505, III.1539, III.1409, III.1459, III.1681, III.1731
A-286 alloy: I.401
Advanced 700C class steam turbine: III.1351
Advanced power plant: II.1019
Ageing: I.335, I.493
Agressive environnements: II.933
AISI 316L: III.1419
Al: I.523
Al + Y: I.523
Alloy 122: III.1261
Alloy design program: II.733
Alloy development: I.89, III.1333, III.1351, III.1361, III.1745
AMDRY 995 coatings: I.439
Anisotropy: I.293
Annealing: I.569, II.711
APS: I.57
Austenitic: II.1233
Austenitic stainless 353 MA: III.1431
Austenitic stainless steel: III.1445
Austenitic steels: II.1091
Autocatalytic electroless deposit: I.429
Back-stress concept: III.1539
Bayonet tubes: II.845
Biomass: II.903, II.957, II.969
Blade: I.523
Boiler: II.1091, II.1109
Boiler design principles: II.1019
Boiler tube: III.1321, III.1445
Bond coat: I.551
Bucket: I.255
Burner rig tests: II.923
Carbides: I.227, I.263, II.1171, II.1247, III.1477
Carbon free: III.1469
Carbon-free martensitic alloys: III.1629
Casing: III.1371
Cast component: I.89, II.605, III.1385, III.1731
Cast steel: II.1065
Cavitation: III.1431
Ceramic: II.845, II.989, III.1745
Ceramic matrix composites: II.769
Ceria-stabilized zirconia: I.483
CFB-boiler: II.969
Chaboche: III.1651
Chlorination: II.815
Chlorine: II.893, II.945
Chromium steels: II.893, III.1521
Clean coal: II.1009
CM186: I.285
CM186LC: I.5, I.139, I.149, I.227, I.293, I.355
CM247: II.871
CMSX-2: I.255
CMSX-4: I.5, I.227, I.235, II.871
Coal: II.785, II.903, II.1109
Coal-fired boilers: II.815
Coating: I.57, I.465, I.493, I.523, I.577, II.945, II.979, II.1143
Cobalt: III.1311
Cold bending: III.1343
Combined cathodic arc/unbalanced magnetron sputtering: I.465
Combined cycle power plant: I.107, III.1721
Combustion liner: I.345
Combustion power plant: II.979
Composite: II.673, II.853
Composition: II.643
Composition changes of precipitates: II.1223
Computer simulation: II.1247
Constitutive models: I.23
Cooled blade design: I.23
Cooling holes: I.385, II.743
Cooling technology: I.107

Corrosion: I.73, I.107, II.785, II.801, II.883, II.945, II.989
Corrosion resistance: I.57, III.1279
Cost 522: I.57, II.1035, II.1049, III.1487
Cr content: III.1497
Cr_2N: III.1571
Creep: I.5, I.43, I.89, I.139, I.159, I.167, I.177, I.197, I.207, I.217, I.273, I.293, I.365, I.375, I.409, I.419, I.551, II.595, II.605, II.623, II.723, II.997, II.1161, II.1189, II.1211, III.1361, III.1379, III.1397, III.1431, III.1453, III.1459, III.1469, III.1487, III.1497, III.1521, III.1531, III.1561, III.1621, III.1661
Creep behaviour: II.615, II.1181, III.1539, III.1551
Creep crack growth: I.89
Creep equations: III.1409, III.1551
Creep fatigue: III.1409
Creep fracture: II.623
Creep life: II.1189, III.1521
Creep strength: I.303, I.395, II.1065, II.1081, II.1091, II.1189, III.1269, III.1289, III.1311, III.1321, III.1371, III.1409, III.1445, III.1505, III.1521, III.1571, III.1691, III.1711, III.1767
Creep-fatigue: III.1397, III.1515
CrVN: III.1321
Crystallographic models: I.283
CVD: I.523
Cyclic oxidation: I.57, I.493
Damage: I.375, II.1211, III.1409
Database: I.73, II.801
Deformation/damage behaviour: I.385
Degradation: I.345, III.1477
Depletion: I.493
Deposits: II.913, II.957
Design: I.121, II.1017, II.1049
Diffusion: I.569
Diffusion Barrier: I.535
Directional solidification: I.355
Dislocations: II.711
Double layer: I.511
Downtime corrosion (DTC): II.913
DS superalloy: I.395
Ductility: III.1571
Ductility normalized strain-range partitioning method: III.1515
Duplex microstructure: II.605
E911: III.1487
EB-PVD: I.57, I.483, I.535
EFCC plants: II.845
Efficiency: II.1109, II.1143
EF-TEM: II.1181
Elastic behaviour: I.543
Elastic modulus: I.561
Electric power plants: III.1745
Electrochemical particle isolation: III.1459
Energy: III.1806
Engine: I.429
Erosion corrosion: II.969
ESR method: III.1269
European commission: III.1806
Experience: II.1065
Extrapolation: II.723
Extrapolation of creep rupture time: III.1539
Fatigue: I.43, I.375
FATT: III.1505
FEM: I.293, I.325, III.1731
FePd: III.1561
Ferrite matrix: III.1571
Ferritic steel: II.1091, II.1143, II.1201, II.1247, III.1311, III.1379, III.1397, III.1487, III.1515, III.1561, III.1581, III.1591, III.1601, III.1621, III.1629, III.1639, III.1661
Fiber coating: II.663
Filler metals: III.1671
Fireside corrosion: II.893
Forging: I.89, I.325
Fraction of precipitates: I.159
Fractography: II.633
Fracture: I.577, III.1431
Gamma TiAl: I.43, II.605, II.633
Gas: II.759
Gas separation process: II.853
Gas turbine: I.57, I.303, I.345, II.923
Gas turbine coatings: I.73
Gas turbine design program: II.733
Gasification: II.903
Gasifier: II.913
Grain boundary: II.1247, III.1453
Graphite: II.759
Growth behaviour: I.187
Hafnon: II.989
Hastelloy X: I.345
HAZ: III.1661, III.1691
Heat exchanger: II.801, II.845, II.913
Heat flux: II.957

Heat input: III.1701
Heat resistance: II.997
Heat resistant steel: III.1269, III.1321, III.1445, III.1767
Heat treatment: I.227
High cycle fatigue: II.633
High steam parameters: II.1019
High temperature: I.409, II.1049, II.1143, III.1431
Hold time: I.375
Homogeneous deformation: III.1469
Homogenisation: I.283
Hot corrosion: I.355, I.395, II.871, II.923, III.1445
Hot deformation: I.401
HP-LP single cylinder steam turbine rotor: III.1721
HTGR: III.1783
HTR: II.759
IGCC: III.1767
Impact: III.1505, III.1701
IN 738: I.871
Inconel 617: I.335, I.385
Inconel 706: III.1551
Industrial gas turbine: I.5, I.139, I.149
In-situ SEM fatigue: I.187
Interfaces: II.673
Intermetallic: I.43, II.595, II.633, II.653, II.1241
Intermetallic compound: II.673, II.703, II.711, III.1469, III.1571
Intermetallic matrix composite: II.663
Iron aluminides Fe_3Al: II.615
Irradiation: II.759
Ir-Ta coating: I.535
Johnson-Mehl-Avrami: III.1651
Kinetics: III.1299
$L1_0$ type ordered intermetallic phase: III.1561
Laboratory tests: II.923
Laser cladding: I.503, II.751, II.979
Laser drilling: II.743
Laser thermal shock: I.439
Laves: II.1171, II.1201, III.1289, III.1459, III.1497
LCF: I.5, I.149, I.273, II.933, III.1621, III.1681
Life prediction: I.375, III.1409
Liquid metal cooling: I.263
Long-term: III.1279, III.1497, III.1571, III.1581
Loop seal: II.969
Low activity Al pack cementation process: I.535
Low alloy steel: II.893, III.1343, III.1371
Low NOx combustors: II.815
Low thermal expansion: III.1351
LPPS and HVOF coatings: I.439
$M_{23}C_6$: III.1571
Magnetic field: III.1591
Magnetron sputtering: II.663
Manufacturing: III.1731
Maraging steel: II.1241
Martensitic steel: II.1223, III.1379, III.1397, III.1613, III.1701
Material development: II.1019, II.1009
Material science: I.107
Materials: I.121, II.759, II.1109, II.1049, II.1017, III.1745
MCrAlY: I.57, I.429, I.551, II.871
Mechanical properties: I.73, II.615, II.643, II.683, II.703, II.711, II.833, II.1081, III.1261, III.1385, III.1671, III.1681, III.1731
Medium rating thermal power plant: III.1721
Microporosity: I.217
Microstructural stability: II.1189, III.1279
Microstructurally short crack: I.187
Microstructure: I.159, I.167, I.177, I.227, I.235, I.245, I.335, I.365, I.395, I.401, I.429, I.503, I.569, II.595, II.623, II.633, II.643, II.703, II.1035, II.1171, II.1211, III.1261, III.1505, III.1521, III.1561, III.1681, III.1731
Microstructure evolution: II.1201, II.1223
Microstructure simulation: I.315, I.325
Modelling: I.273, II.801, I.409, II.1211, III.1613
Modified Garofalo equation: III.1551
Multi-scale modelling: I.23
MX carbonitrides: II.1181, III.1289
Nanocomposite ceramic coatings: I.475
Nanolayer: I.475
Nearly lamellar microstructure: II.605
Neutron diffraction: I.365
NiAl base alloy: II.595, II.653
Ni-Al coating: II.663, II.693
Ni-Al-Cr-Ta-W: I.315
Ni-base SC superalloy: I.263, I.535, II.733

Ni-base superalloy: I.159, I.167, I.177, I.197, I.207, I.227, I.409, I.419, II.1233, III.1351
Nitride: II.1171
No-destructive evaluation: II.769
Non-isothermal model: III.1651
Non-linear finite element analyses : I.283
Notch behaviour: III.1409
ODS Alloys: II.833
Orientation relationship: II.1223
Oxidation: I.569, II.683, II.693, II.997, II.1091, II.1143, III.1397, III.1621
Oxidation resistant nitride coating: I.465
Oxide/oxide: II.769
Oxide scales: III.1601
P 23: III.1671
P 24: III.1671
P92 steel: II.1131
Palladium: III.1639
Particulate composites: II.643
PD 6605: III.1487
Phase formation: II.1241
Phase transformation: I.89, III.1651
Phase-field: I.315, III.1333
Physical properties: I.73
Pipe: III.1361
Plasma sprayed TBC: I.543
Plasma-spraying: I.511
Platinum aluminising: I.57
Post-weld heat treatment: III.1701
Powder metallurgy: I.419
Power generation: III.1711, III.1783
Power plant: II.743, III.1767
Precipitation: II.1161, II.1171, II.1247, III.1299, III.1691
Precipitation strengthening: III.1351, III.1379, III.1477, III.1571
Prediction: III.1581
Pressurized pulverized coal combustion: II.989
Prior austenite grain boundary: II.1171
Processing: II.615
Protective oxide layer: III.1629, III.1639
PVD: I.57, I.475
PWA1480: I.245
PWHT: III.1671
Rafted structure: I.245
Rafting: I.159, I.167, I.255, I.303
Recovery: II.1171, III.1497
Regression analysis: I.395
Reheater: II.893
Relaxation: I.551
Research: III.1806
Rhenium: I.207
Rupture: II.595
SANS: I.365
Scale fracture: III.1613
Sealing: I.449
Shaping: II.743
Shear test: I.551
Short cracks: I.385
Silicon carbide: II.845
Silicon nitride: II.997
Simulation: III.1333
Single crystal: I.5, I.23, I.139, I.149, I.167, I.177, I.187, I.197, I.235, I.255, I.273, I.283, I.293, I.303
Single crystal coating: I.503
Slag: II.989
Slip bands: I.187
SO_2: II.933
Solid fuels: II.801, II.923
Solid solution: III.1459, III.1477
Solidification: I.315
Solution heat treatment: I.355
Spallation: III.1601, III.1613
Specific heat: I.449
Sputtering: I.475
Stabilised zirconia: I.475
Stacking fault energy: I.207
Stainless steel: III.1321
Stationary creep rate: III.1539
Steam chest: III.1261
Steam oxidation: II.1131, III 1445, III.1601, III.1613, III.1629, III.1639
Steam plant: II.1143, III.1681
Steam turbine: III.1371
Steam/metal temperature: II.957
Steel: II.759, III.1531
Straw: II.785
Stress exponent: III.1531
Stress range partitioning method: III.1581
Stress rupture: II.1233
Subgrain: II.1161
Sulfidation: II.815
Superalloy: I.89, I.217, I.315, I.325, I.355, I.365, I.569, II.723, II.751, III.1333

Supercritical boiler: II.1019
Superheated steam: III.1621
Superheater: II.785, II.883, II.893, II.945, II.969
System free energy: II.1201
T and P 23: III.1343
TBC: I.57, I.449, I.483, I.511, I.561
TEM: I.235, II.673
Temperature capability: I.511
Tensile: I.235
Tensile strength: I.43
Test: I.577, II.759, II.933
Thermal barrier: I.543
Thermal conductivity: I.449
Thermal cycling: I.511
Thermal diffusivity: I.449
Thermal efficiency: III.1767
Thermal exposition: I.365
Thermal mechanical fatigue: I.577
Thermal spray: II.979
Thermal stability: I.475
Thermally grown oxide: I.483
Thermocalc: III.1477
Thermodynamic modelling: I.315, II.871, II.903, III.1299, III.1333, III.1477
Thermo-mechanical fatigue: I.197, I.273, I.439, III.1419
Thermomechanical heat treatment: III.1591
Thermo-mechanical properties: II.769
Ti-Al-Ni phase diagram: II.693
TiAl: II.623, II.683
Time dependant deformation: I.561
Titanium alloy: I.465, II.643, II.751
Titanium aluminides: II.623, II.693
TP347H: II.957
Trace contaminants: II.903
Transition piece: I.345
Tube: III.1361
Tube alloys: II.1233
Tungsten: III.1311
Turbine blade: I.245, I.429
Turbine components: I.419, II.751, II.769, III.1269
Turbines: II.743
Type 347: II.933
Type IV cracking: III.1661
Udimet 720: I.419
Under deposit corrosion: II.815
USC: II.1009, II.1109, II.1233, III.1311, III.1397, III.1469, III.1515, III.1591, III.1629, III.1639, III.1767
Valve: III.1371
Virtual gas turbine system: II.733
Visco-plastic: I.561, III.1651
Viscous creep: III.1531
Vision 21: III.1745
Waspaloy: I.335, III.1551
Waste: II.785, II.933
Weldability: II.1065, II.1081, III.1711
Welded joint: III.1397, III.1661, III.1691, III.1711
Welding: II.1091, III.1343, III.1671, III.1681, III.1701
Wood: II.785, II.883
Workability: I.325
$Yb_4Si_2O_7N_2$: II.997
Z phase: II.1171, II.1223
Zener-Hollomon parameter: I.401
Zirconia: I.449

Schriften des Forschungszentrums Jülich
Reihe Energietechnik/Energy Technology

1. **Fusion Theory**
   Proceedings of the Seventh European Fusion Theory Conference
   edited by A. Rogister (1998); x, 306 pages
   ISBN 3-89336-219-3

2. **Radioactive Waste Products 1997**
   Proceedings of the 3rd International Seminar on Radioactive Waste Products
   held in Würzburg (Germany) from 23 to 26 June 1997
   edited by R. Odoj, J. Baier, P. Brennecke et al. (1998), xxiv, 506 pages
   ISBN 3-89336-225-8

3. **Energieforschung 1998**
   Vorlesungsmanuskripte des 4. Ferienkurs „Energieforschung"
   vom 20. bis 26. September 1998 im Congrescentrum Rolduc und
   im Forschungszentrum Jülich
   herausgegeben von J.-Fr. Hake, W. Kuckshinrichs, K. Kugeler u. a. (1998),
   500 Seiten
   ISBN 3-89336-226-6

4. **Materials for Advances Power Engineering 1998**
   Abstracts of the 6th Liège Conference
   edited by J. Lecomte-Beckers, F. Schubert, P. J. Ennis (1998), 184 pages
   ISBN 3-89336-227-4

5. **Materials for Advances Power Engineering 1998**
   Proceedings of the 6th Liège Conference
   edited by J. Lecomte-Beckers, F. Schubert, P. J. Ennis (1998),
   Part I xxiv, 646, X pages; Part II xxiv, 567, X pages; Part III xxiv, 623, X pages
   ISBN 3-89336-228-2

6. **Schule und Energie**
   1. Seminar Energiesparen, Solarenergie, Windenergie. Jülich, 03. und
   04.06.1998
   herausgegeben von P. Mann, W. Welz, D. Brandt, B. Holz (1998), 112 Seiten
   ISBN 3-89336-231-2

7. **Energieforschung**
   Vorlesungsmanuskripte des 3. Ferienkurses „Energieforschung"
   vom 22. bis 30. September 1997 im Forschungszentrum Jülich
   herausgegeben von J.-Fr. Hake, W. Kuckshinrichs, K. Kugeler u. a. (1997),
   505 Seiten
   ISBN 3-89336-211-8

Schriften des Forschungszentrums Jülich
Reihe Energietechnik/Energy Technology

8. **Liberalisierung des Energiemarktes**
   Vortragsmanuskripte des 5. Ferienkurs „Energieforschung"
   vom 27. September bis 1. Oktober 1999 im Congrescentrum Rolduc und
   im Forschungszentrum Jülich
   herausgegeben von J.-Fr. Hake, A. Kraft, K. Kugeler u. a. (1999), 350 Seiten
   ISBN 3-89336-248-7

9. **Models and Criteria for Prediction of Deflagration-to-Detonation Transition (DDT) in Hydrogen-Air-Steam-Systems under Severe Accident Conditions**
   edited by R. Klein, W. Rehm (2000), 178 pages
   ISBN 3-89336-258-4

10. **High Temperature Materials Chemistry**
    Abstracts of the 10th International IUPAC Conference, April 10 - 14 2000, Jülich
    edited by K. Hilpert, F. W. Froben, L. Singheiser (2000), 292 pages
    ISBN 3-89336-259-2

11. **Investigation of the Effectiveness of Innovative Passive Safety Systems for Boiling Water Reactors**
    edited by E. F. Hicken, K. Verfondern (2000), x, 287 pages
    ISBN 3-89336-263-0

12. **Zukunft unserer Energieversorgung**
    Vortragsmanuskripte des 6. Ferienkurs „Energieforschung"
    vom 18. September bis 22. September 2000 im Congrescentrum Rolduc und
    im Forschungszentrum Jülich
    herausgegeben von J.-Fr. Hake, S. Vögele, K. Kugeler u. a. (2000),
    IV, 298 Seiten
    ISBN 3-89336-268-1

13. **Implementing Agreement 026**
    For a programme of research, development and demonstration on advances fuel cells
    Fuel Cell Systems for Transportation
    Annex X. Final Report 1997 - 1999
    edited by B. Höhlein; compiled by P. Biedermann (2000), 206 pages
    ISBN 3-89336-275-4

14. **Vorgespannte Guß-Druckbehälter (VGD) als berstsichere Druckbehälter für innovative Anwendungen in der Kerntechnik**
Prestressed Cast Iron Pressure Vessels as Burst-Proof Pressure Vessels for Innovative Nuclear Applications
von W. Fröhling, D. Bounin, W. Steinwarz u. a. (2000) XIII, 223 Seiten
ISBN 3-89336-276-2

15. **High Temperature Materials Chemistry**
Proceedings of the 10th International IUPAC Conference
held from 10 to 14 April 2000 at the Forschungszentrum Jülich, Germany
Part I and II
edited by K. Hilpert, F. W. Froben, L. Singheiser (2000), xvi, 778, VII pages
ISBN 3-89336-259-2

16. **Technische Auslegungskriterien und Kostendeterminanten von SOFC- und PEMFC-Systemen in ausgewählten Wohn- und Hotelobjekten**
von S. König (2001), XII, 194 Seiten
ISBN 3-89336-284-3

17. **Systemvergleich: Einsatz von Brennstoffzellen in Straßenfahrzeugen**
von P. Biedermann, K. U. Birnbaum, Th. Grube u. a. (2001), 185 Seiten
ISBN 3-89336-285-1

18. **Energie und Mobilität**
Vorlesungsmanuskripte des 7. Ferienkurs „Energieforschung“
vom 24. September bis 28. September 2001 im Congrescentrum Rolduc und im Forschungszentrum Jülich
herausgegeben von J.-Fr. Hake, J. Linßen, W. Pfaffenberger u. a. (2001),
205 Seiten
ISBN 3-89336-291-6

19. **Brennstoffzellensysteme für mobile Anwendungen**
von P. Biedermann, K. U. Birnbaum, Th. Grube u. a. (2002)
PDF-Datei auf CD
ISBN 3-89336-310-6

20. **Materials for Advances Power Engineering 2002**
Abstracts of the 7th Liège Conference
edited by J. Lecomte-Beckers, M. Carton, F. Schubert, P. J. Ennis (2002),
c. 200 pages
ISBN 3-89336-311-4

Schriften des Forschungszentrums Jülich
Reihe Energietechnik/Energy Technology

21. **Materials for Advances Power Engineering 2002**
Proceedings of the 7th Liège Conference
edited by J. Lecomte-Beckers, M. Carton, F. Schubert, P. J. Ennis (2002),
Part I c. 600 pages; Part II c. 600 pages; Part III c. 600 pages
ISBN 3-89336-312-2

Schriften des Forschungszentrum Jülich
Reihe Energietechnik / Energy Technology Volume 21, Part III

Forschungszentrum Jülich GmbH
Institut für Werkstoffe und Verfahren der Energietechnik

Jacqueline Lecomte-Beckers, Marc Carton,
Florian Schubert and Philip J. Ennis (Editors)

Materials for Advanced Power Engineering 2002

Proceedings of the 7th Liège Conference
Part III

EUROPEAN COMMISSION
UNIVERSITE DE LIEGE

Schriften des Forschungszentrum Jülich
Reihe Energietechnik / Energy Technology Volume 21, Part III

ISSN 1433-5522 ISBN 3-89336-312-2

Die Deutsche Bibliothek- CIP-Einheitsaufnahme

Materials for advances power engineering 2002 : proceedings of the 7th Liège Conference / ed.: Jacqueline Lecomte-Beckers ... - Jülich : Forschungszentrum, Zentralbibliothek

(Schriften des Forschungszentrums Jülich : Reihe Energietechnik ; Vol. 21)
ISBN 3-89336-312-2
Pt. 3 . - (2002)

Publisher and Distributor:	Forschungszentrum Jülich GmbH Central Library 52425 Jülich Phone +49 (0) 24 61 61 53 68 · Telefax +49 (0) 24 61 61 61 03 e-mail: zb-publikation@fz-juelich.de Internet: http://www.fz-juelich.de/zb
Cover Design:	Grafische Betriebe, Forschungszentrum Jülich GmbH
Printer:	Grafische Betriebe, Forschungszentrum Jülich GmbH
Copyright:	Forschungszentrum Jülich 2002

Printed on environmentally friendly paper.

The editors cannot accept any responsibility or liability for the accuracy of any statements or information given in the papers.

Schriften des Forschungszentrum Jülich
Reihe Energietechnik / Energy Technology, Volume21, Part 3

ISSN 1433-5522
ISBN 3-89336-312-2

Neither this book nor any part of it may be reproduced or transmitted in any form or by any means, electronic or mechanical, including photocopying, microfilming, and recording, or by any information storage and retrieval system, without permission in writing from the publisher.

FOREWORD

The European Co-operation in the field of Scientific and Technical Research (COST) is now a well established organisation for the co-ordination of national research and development programmes on a European level. This series of Liège Conferences was initiated in order to disseminate the results of the materials related COST Actions, beginning with COST 50 which was mainly concerned with materials for gas turbines and then moving to COST 501 in which materials for power generation plant were investigated. The results of the current COST Action 522 'Ultra Efficient, Low Emission Power Plants' are presented at this, the Seventh Liège Conference. The work is focused on materials for the components that have a decisive influence on the enhancement of power plant performance and efficiency.

Reliable energy supply at reasonable cost is one of the most important factors in the development of the modern industrialised society, but we are becoming increasingly concerned about the environmental impact of energy production and of the need to conserve valuable energy resources for future generations. Therefore, the emphasis is on a sustainable energy supply and the development of advanced energy conversion and power generation technologies taking into account the need for fuel conservation and environmental protection is essential. Although new and emerging energy technologies are of great interest, fossil fuel will continue to make a significant contribution well into the 21st century. Because a by-product of the conversion of fossil fuels is CO_2, the key factor is the thermal efficiency of plant; the higher the efficiency, the lower will be the levels of CO_2 produced for a given energy output. Power plant can be made more efficient by increasing the temperatures and pressures of the process, resulting in the general requirement for improved materials and components that can operate reliably for long times at higher temperatures and pressures.

The materials research and development activities required for the critical components of power generation plant have been based on the principle of work-sharing, bringing together materials scientists, design engineers, alloy producers and component manufacturers, reflecting the need to match materials properties and component behaviour. In order to put the European efforts into a world context, there are several invited review papers covering power plant materials development in the USA, Japan and South Africa. In addition there are over 130 contributions (presented as posters at the Conference) from 26 countries.

The Conference Proceedings reflect the Conference Technical Programme. They are divided in three volumes and the contents are as follows:

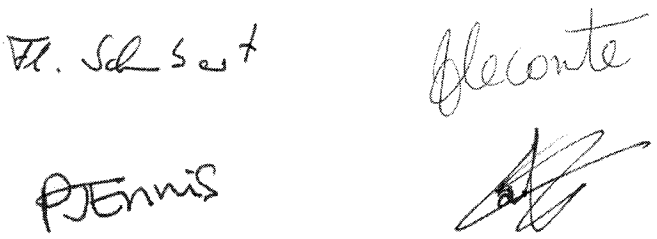
Part I : ADVANCED GAS TURBINE MATERIALS I
Invited Papers
1.1. Single Crystal
1.2. Ni Base Superalloys
1.3. Coatings

Part II : ADVANCED GAS TURBINE MATERIALS II
1.4. Intermetallics
1.5. Miscellaneous Topics
FUEL ISSUES AND NOVEL COMPONENTS
Invited Papers
2.1. Hot Gas Corrosion
2.2. Miscellaneous Topics
ADVANCED STEAM POWER PLANT I
Invited Papers
3.1. Microstructure

Part III: ADVANCED STEAM POWER PLANT II
3.2. Alloy Development
3.3. Mechanical Properties
3.4. Steam Oxidation and Coatings
3.5. Welding
3.6. Applications
OUTLOOK
Invited Papers

As in previous Liège Conferences, many people have made significant contributions to the success of this Conference. The Technical and Editorial Board would like to thank all the members of the COST 522 Management Committee both for their supervision and co-ordination of the considerable research effort in their own countries and across national boundaries, and for their help in the reviewing of the contributed papers.

September 2002



International Advisory Board

Aguero, A.	INTA	Spain
Allen, D.	Alstom Power	UK
Artinger, I.	TU Budapest	Hungary
Auerkari, P.	VTT	Finland
Berger, C.	TU Darmstadt	Germany
Bosansky, J.	Welding Research Inst	Slovenia
Bregani, F.	CESI	Italy
Cerjak, H.	TU Graz	Austria
Czyrska-Filemonowicz, A.	AGH Krakow	Poland
Delannay, F.	UC Louvain	Belgium
Déroulède, A.	DGXII	CEC
Engelen, B.	Min Economic Affairs	Belgium
Ennis, P.J.	FZ Jülich	Germany
Geipel, D.	MBF	Germany
Germain, A.	Université de Liège	Belgium
Hald, J.	TU Denmark	Denmark
Harada, H.	NIMS	Japan
Härkegård, G.	NUST	Norway
Henderson, P.J.	Vattenfall	Sweden
Khan, T.	ONERA	France
Kern, T.U.	Siemens PG	Germany
Koslowski, R.	TU Krakow	Poland
Legros, W.	Université de Liège	Belgium
Lecomte-Beckers, J.	Université de Liège	Belgium
Lupinc, V.	CNR-IENI	Italy
Masuyama, F.	Mitsubishi HI	Japan
Mayer, K.H.	Alstom Energie	Germany
McLean, M.	Imperial College	UK
Oakey, J.	Cranfield University	UK
Perez-Trujillo, F.	UC Madrid	Spain
Pomeroy, M.	University of Limerick	Ireland
Rademakers, P.	TNO	The Netherlands
Sánchez-Pasqual, A.	INTA	Spain
Schubert, F. (Chairman)	FZ Jülich	Germany
Seitz, E.	DGXII	CEC
Singheiser, L.	FZ Jülich	Germany
Sklenicka, V.	Academy of Sciences	Czech Republic
Spiradek-Hahn, A.	ÖFZ Seibersdorf	Austria
Staubli, M.	Alstom Power	Switzerland
Teixeira, V.M.	University of Minho	Portugal
ten Hoeven, H.J.	NRL	The Netherlands
Tiainen, T.	TU Tampere	Finland
Toulios , M.	NTU Athens	Greece
van Duysen, J.C.	EDF	France
Viswanathan, R.	EPRI	USA
Wright, I.	ORNL	USA
Zrnik, J.	TU Kosice	Slovakia

Technical and Editorial Board

J. Lecomte-Beckers (chief editor)	Université de Liège	Belgium
D. Allen	Alstom Power	UK
M. Carton	Université de Liège	Belgium
H. Cerjak	TU Graz	Austria
A. Déroulède	DGXII	CEC
P. J Ennis	FZ Jülich	Germany
H. Nguyen-Dang	Université de Liège	Belgium
J. Oakey	Cranfield University	UK
R. B. Scarlin	Alstom Power	Switzerland
F. Schubert	FZ Jülich	Germany
E. Seitz	DGXII	CEC
M. Staubli	Alstom Power	Switzerland
M. Toulios	NTU Athens	Greece

Organisation of Sessions

Advanced Gas Turbine Materials :	D. Allen
Fuel Issues and Novel Components :	J. Oakey
Advanced Steam Power Plant :	M. Staubli

Local Organisation Committee

F. Schubert (chairman)	Jülich
J. Lecomte-Beckers (vice-chairman)	Liège
P. J. Ennis, R. Herzog	Jülich
M. Carton, Y. Greday	Liège
B. Krahl-Urban (co-ordinator)	Jülich

Conference Secretaries

E. Wittig, Y. Abdel-Fatah, S. Stassar	Jülich
R. Pirson	Liège

The 7th Liège Conference has been organized by the Forschungszentrum Jülich and the Université de Liège.

TABLE OF CONTENTS

PART I

Foreword iii

Table of Contents vii

SECTION 1 – ADVANCED GAS TURBINE MATERIALS

Invited Papers

THE MECHANICAL BEHAVIOUR OF A CLASS OF RHENIUM BASED SX SUPERALLOYS FOR INDUSTRIAL GAS TURBINE APPLICATIONS I.5
Toulios M., Allen D.H.

CONSTITUTIVE MATERIAL FORMULATIONS AND ADVANCED LIFE ASSESSMENT METHODS FOR SINGLE CRYSTAL GAS TURBINE BLADES I.23
Busso E.P., Toulios M., Cailletaud G.

GAMMA TiAl INTERMETALLICS FOR TURBOMACHINERY APPLICATIONS I.43
Nazmy M., Lupinc V.

ADVANCES IN COATING SYSTEMS FOR UTILITY GAS TURBINES I.57
Nicholls J.R., Wing R.

ENVIRONMENTAL DEGRADATION OF GAS TURBINE COATINGS: TOWARDS STANDARDISED TESTING AND DATABASES I.73
Simms N.J., Bale D.W., Baxter D., Oakey J.E.

WROUGHT Ni-BASE ALLOYS FOR ADVANCED GAS TURBINE DISC AND USC STEAM TURBINE ROTOR APPLICATIONS I.89
Rösler J., Böttger B., Wolske M., Penkalla H.J., Berger C.

NEW MATERIALS AND COOLING SYSTEMS FOR HIGH TEMPERATURE, HIGHLY LOADED COMPONENTS IN ADVANCED COMBINED CYCLE POWER PLANTS I.107
Bohn D.E.

OVERVIEW OF US-DOE PROGRAM IN HIGH EFFICIENCY ENGINES AND TURBINES I.121
Layne A.W.

1.1. Single Crystal

THE CREEP BEHAVIOUR OF AS-CAST SX CM186LC AT INDUSTRIAL GAS TURBINE OPERATING CONDITIONS I.139
Wilcock I.M., Lukas P., Maldini M., Klabbers J., Dubiel B., Henderson M.B.

THE LOW CYCLE FATIGUE BEHAVIOUR OF AS CAST SINGLE CRYSTAL CM186LC I.149
Bale D.W., Henderson M., Dubiel B., Czyrska-Filemonowicz A., Guardamagna C., Bontempi P., Mulvihill P., Lukas P., Obrtlik K., Kolkman H.

CREEP BEHAVIOUR OF THE THIRD GENERATION Ni-BASE SINGLE CRYSTAL SUPERALLOY TMS-75 AND ITS γ/γ' TIE-LINE ALLOYS I.159
Murakumo T., Kobayashi T., Nakazawa S., Harada H.

CREEP BEHAVIOUR AND γ' EVOLUTION OF A NEW NICKEL BASE SUPERALLOY FOR SINGLE CRYSTAL BLADE APPLICATIONS I.167
Maldini M., Lupinc V., Li H., Angella G.

CREEP OF [001]-ORIENTED Ni-20 MASS %Cr SINGLE CRYSTALS I.177
Terada Y., Nakamoto Y., Matsuo T.

CHARACTERIZATION OF THE PROPAGATION BEHAVIOR OF SHORT FATIGUE CRACKS IN NICKEL-BASED SINGLE CRYSTAL SUPERALLOY SC16 I.187
Zhang X.P., Wang C.H., Chen W.Y., Ye L., Mai Y.-W.

EFFECT OF γ' VOLUME FRACTION ON THIRD-GENERATION SINGLE-CRYSTAL SUPERALLOYS I.197
Zhou H., Harada H., Ro Y., Koizumi Y., Kobayashi T., Nakazawa S.

ON THE EFFECT OF RHENIUM ON THE EXTENT OF PRIMARY CREEP IN ADVANCED Ni-BASED SUPERALLOYS I.207
Rae C.M.F., Kakehi K., Reed R.C.

INVESTIGATION OF POROSITY IN SINGLE-CRYSTAL NICKEL-BASE SUPERALLOYS I.217
Epishin A., Link T., Brückner U., Portella P.D.

INVESTIGATION AND COMPARISON OF THE MICROSTRUCTURE OF THE NICKEL-BASE SUPERALLOYS CMSX-4 AND SX CM186LC I.227
Danciu D., Klabbers J., Penkalla H.J.

DISLOCATION MICROSTRUCTURE OF CMSX-4 AFTER TENSILE TESTING WITH DIFFERENT STRAIN RATES AT 700 AND 1000°C I.235
Danciu D., Penkalla H.J., Schubert F.

MORPHOLOGICAL CHANGE IN γ' PHASE IN DIFFERENT PORTIONS OF FIRST STAGE HIGH PRESSURE TURBINE BLADE OF PWA1480 I.245
Miura N., Harada N., Kondo Y., Matsuo T.

METALLURGICAL ANALYSIS OF IN SERVICE *CMSX-2* SINGLE CRYSTAL GAS TURBINE BUCKETS I.255
Yoshioka Y., Saito D., Ito S., Fukuyama Y.

CARBIDE PRECIPITATION IN SINGLE CRYSTAL Ni-BASE SUPERALLOYS I.263
Tin S., Pollock T.M.

MODELLING OF HIGH TEMPERATURE TMF TESTS OF SINGLE CRYSTALS BY A PURE CREEP LAW I.273
White P.S., Kong C.N.

A MULTISCALE CONSTITUTIVE APPROACH TO MODEL THE MECHANICAL BEHAVIOUR OF INHOMOGENEOUS SINGLE CRYSTAL SUPERALLOYS: APPLICATION TO AS-CAST SX CM186LC I.283
Regino G.M., Busso E.P., O'Dowd N.P., Allen D.

DEFORMATION MODELLING OF THE SINGLE CRYSTAL SUPERALLOY CM186LC I.293
Daniel R., Tinga T., Henderson M.B., Ward T.J.

TMS-82+: A HIGH STRENGTH Ni-BASE SINGLE CRYSTAL SUPERALLOY I.303
Hino T., Yoshioka Y., Koizumi Y., Kobayashi T., Harada H.

1.2. Ni Base Superalloys

MICROSTRUCTURE OF A 5-COMPONENT Ni-BASE MODEL ALLOY: EXPERIMENTS AND SIMULATION I.315
Warnken N., Böttger B., Ma D., Vitusevych V., Hecht U., Fries S.G., Dupin N.

ALLOY DESIGN FOR ULTRA HIGH TEMPERATURE STEAM TURBINE APPLICATIONS : SIMULATION OF MICROSTRUCTURE DURING FORGING I.325
Kopp R., Wolske M.

MICROSTRUCTURE AND STRUCTURAL STABILITY OF CANDIDATE MATERIALS FOR TURBINE DISC APPLICATIONS BEYOND 700°C I.335
Penkalla H.J., Wosik J., Schubert F.

MATERIAL DEGRADATION AND DAMAGE ASSESSMENT FOR GAS TURBINE COMBUSTION COMPONENTS I.345
Saito D., Yoshioka Y., Fujiyama K.

EFFECT OF SOLUTION HEAT TREATMENT ON THE HOT CORROSION RESISTANCE OF A SECOND GENERATION DS SUPERALLOY I.355
Tamaki H., Okayama A., Onay B., Yoshinari A.

CREEP PROPERTIES DEGRADATION IN A LONG-TIME THERMALLY EXPOSED NICKEL BASE SUPERALLOY I.365
Zrnik J., Strunz P., Vrchovinsky V., Hornak P., Wiedenmann A.

EFFECT OF TENSILE HOLDS ON THE DEFORMATION BEHAVIOUR OF A NICKEL BASE SUPERALLOY SUBJECTED TO LOW CYCLE FATIGUE I.375
Zrnik J., Semenak J., Wangyao P., Vrchovinsky V., Hornak P.

IN-SITU OBSERVATIONS OF THE DEFORMATION AND DAMAGE BEHAVIOUR AROUND LASER-DRILLED COOLING HOLES IN INCONEL ALLOY 617 USING THE SCANNING ELECTRON MICROSCOPE I.385
Klabbers J., Wessel E., Schubert F.

DESIGN OF Ni-BASE DS SUPERALLOYS FOR INDUSTRIAL GAS TURBINES I.395
Sato M., Koizumi Y., Kobayashi T., Karada H., Ono H.

THE INVESTIGATIONS OF DEFORMABILITY AND STRUCTURE OF A-286 ALLOY AT HIGH TEMPERATURE DEFORMATION I.401
Ducki K.J., Hetmanczyk M., Kuc D.

MODELLING THE CREEP BEHAVIOUR OF A WROUGHT NICKEL BASE SUPERALLOY IN A WIDE RANGE OF STRESS/TEMPERATURE CONDITIONS I.409
Maldini M., Lupinc V.

CREEP BEHAVIOUR OF A POWDER METALLURGY UDIMET 720 NICKEL-BASED SUPERALLOY I.419
Dubiez S., Couturier R., Guétaz L., Burlet H.

1.3. Coatings

MCrAlY COATING BY AN ELECTROCHEMICAL ROUTE I.429
Bacos M.-P., Girard B., Josso P., Rio C.

EVALUATION OF THERMOMECHANICAL FATIGUE RESISTANCE OF COATED SUPERALLOYS BY A LASER THERMAL SHOCK SYSTEM I.439
Meriggi M., Rinaldi C.

THERMOPHYSICAL AND MICROSTRUCTURAL CHARACTERISATION OF MODIFIED THICK YTTRIA STABILISED ZIRCONIA THERMAL BARRIER COATINGS I.449
Bianchi P., Cernuschi F., Lorenzoni L., Ahmaniemi S., Vippola M., Vuoristo P., Mäntylä T.

ADVANCED NITRIDE COATINGS FOR OXIDATION PROTECTION OF TITANIUM ALLOYS I.465
Leyens C., Hovsepian P.Eh., Münz W.-D., Peters M., Lewis D.B., Luo Q.

HIGH TEMPERATURE NANOLAMINATE CERAMIC COATINGS PREPARED BY PVD TECHNIQUES I.475
Teixeira V., Monteiro A., Portinha A., Vaßen R., Stöver D.

CYCLIC LIFETIME OF PYSZ AND CESZ EB-PVD TBC SYSTEMS ON VARIOUS Ni-SUPERALLOY SUBSTRATES I.483
Schulz U., Fritscher K., Kaysser W.A.

CHARACTERISATION OF SIX OVERLAY COATINGS I.493
Giannozzi M., Giorni E., Merluzzi M., Pratesi F., Zonfrillo G.

SINGLE CRYSTAL COATING OF SX TURBINE BLADES BY A LASER CLADDING TECHNIQUE I.503
Bezençon C., Wagnière J.-D., Höbel M., Schnell A., Konter M., Kurz W.

COMPARISON OF THERMAL CYCLING LIFE OF YSZ AND $LA_2ZR_2O_7$-BASED THERMAL BARRIER COATINGS I.511
Vaßen R., Barbezat G., Stöver D.

DEPOSITION OF ALUMINIUM + YTTRIUM ON THE INTERNAL SURFACES OF COMPLEX COOLED INDUSTRIAL TURBINE BLADES I.523
Innocenti M., Giorni E., Wing R., Norreys A., Archer N.J.,Yeatman J., Bianchi P., Baxter D., Wahl G., Metz Ch.

CHARACTERIZATION OF THE BOND-COAT MATERIALS FOR THE SUPER HIGH EFFICIENCY GAS TURBINES I.535
Suzuki A., Wu F., Murakami H., Imai H.

ELASTIC BEHAVIOUR OF PLASMA SPRAYED THERMAL BARRIER COATINGS I.543
Steinbrech R.W., Frahm J., Herzog R., Schubert F.

DEFORMATION BEHAVIOUR OF A LOW PRESSURE PLASMA SPRAYED NiCoCrAlY BOND COAT UNDER SHEAR LOADING AT TEMPERATURES ABOVE 750°C I.551
Majerus P., Steinbrech R.W., Herzog R., Schubert F.

VISCO-PLASTIC PROPERTIES OF SEPARATED THERMAL BARRIER COATINGS UNDER COMPRESSION LOADING I.561
Heckmann S., Herzog R., Steinbrech R.W., Schubert F., Singheiser L.

STRUCTURE IN THE SURFACE LAYER OF COATED Ni-BASED SUPERALLOYS DURING ANNEALING IN OXYDATION ENVIRONMENT I.569
Svejcar J., Jirikovsky K., Krejcí J.

MEASUREMENT OF THE DUCTILE BRITTLE TRANSITION TEMPERATURE AND THERMAL MECHANICAL FATIGUE RESISTANCE OF COATINGS USED IN GAS TURBINE ENGINES I.577
Saunders S.R.J., Banks J.P.

AUTHOR INDEX I

KEYWORD INDEX VII

PART II

SECTION 1 – ADVANCED GAS TURBINE MATERIALS

1.4. Intermetallics

MICROSTRUCTURE AND TENSILE CREEP BEHAVIOR OF MULTIPHASE NiAl EUTECTIC ALLOYS MODIFIED WITH Zr OR Hf II.595
Guo J.T., Qi Y.H., Cui C.Y., Li G.S.

CREEP STRENGTH AND MICROSTRUCTURE OF Ti-46Al-2W-0.5Si BASE ALLOYS II.605
Dlouhý A., Arrell D., Karlsson B., Lapin J., Lupinc V., Nazmy M., Nikbin K., Staubli M.

HIGH TEMPERATURE DEFORMATION OF THE Fe28Al3Cr IRON ALUMINIDE MODIFIED WITH ADDITIVES II.615
Hakl J., Vlasák T., Kratochvil P.

MICROSTRUCTURE AND CREEP OF γ-TIAL BASED INTERMETALLIC ALLOY II.623
Lapin J., Pelachová T.

HIGH CYCLE FATIGUE BEHAVIOUR OF INTERMETALLIC γ-TiAl BASED ALLOYS II.633
Koolloos M.F.J., Arrell D.J., Henderson M.B., Gallet S.

Ti_2AlNb-BASED TITANIUM INTERMETALLIC ALLOYS FOR HIGH TEMPERATURE APPLICATIONS II.643
Hagiwara M., Emura S., Tang F.

MANUFACTURING AND TESTING OF A NOVEL ADVANCED NiAl-BASE ALLOY FOR GAS TURBINE APPLICATIONS II.653
Palm M., Sauthoff G.

HIGH-RATE SPUTTER DEPOSITION OF NiAl ON SAPPHIRE FIBERS II.663
Reichert K., Martinez C., Cremer R., Neuschütz D.

INTERFACIAL THERMAL STABILITY IN BN-COATED CONTINOUS Al_2O_3 FIBER REINFORCED NiAl COMPOSITES II.673
Wen K.Y., Reichert K., Hu W., Frommert M., Gottstein G.

MECHANICAL PROPERTIES AND OXIDATION BEHAVIOUR OF A CAST TiAl INTERMETALLIC II.683
Lupinc V., Marchionni M., Nazmy M., Onofrio G., Staubli M., Tomasi A., Zhou L.Z.

COATING OF Ni-ALUMINIDES ON TiAl INTERMETALLICS THROUGH UP-HILL DIFFUSION II.693
Izumi T., Nishimoto T., Narita T.

INFLUENCE OF MICROSTRUCTURAL EVOLUTION ON HARDNESS OF A γ TiAl INTERMETALLIC CONTAINING W AND Si II.703
Munoz-Morris M.A., Gil I., Morris D.G.

STRENGTHENING MECHANISMS IN DUCTILE FeAl INTERMETALLIC PROCESSED BY MECHANICAL ALLOYING II.711
Morris D.G., Garcia Oca C., Munoz-Morris M.A.

1.5. Miscellaneous topics

EXTRAPOLATION OF LIMITED CREEP DATA BY PARALLEL FITTING WITH DATA FOR SIMILAR MATERIALS II.723
White P.S.

DEVELOPMENT OF A VIRTUAL TURBINE SYSTEM FOR NEW MATERIALS DESIGN II.733
Saeki H., Fukuyama Y., Yokokawa T., Odaka T., Yoshida T., Harada H.

DRILLING OF COOLING HOLES AND SHAPING OF BLOW-OUT FACILITIES IN TURBINE BLADES BY LASER RADIATION II.743
Willach J., Horn A., Kreutz E.W.

REPAIR AND (RE)CONDITIONING OF COMPRESSOR AND TURBINE BLADES BY CO_2 AND Nd: YAG LASER RADIATION II.751
Kelbassa I., Gasser A., Backes G., Keutgen S., Kreutz E.W., Pirch N.

HIGH TEMPERATURE REACTOR (HTR) MATERIALS II.759
Buckthorpe D., Couturier R., Van der Schaaf B., Riou B., Rantala H., Moormann R., Buenaventura A., Friedrich B.-C.

PROPERTIES OF OXIDE/OXIDE CMCs FOR HIGH TEMPERATURE APPLICATIONS IN GAS TURBINES II.769
Innocenti M., Del Puglia P., Pappas Y.Z., Dassios C.G., Steen M., Kostopoulos V., Vlachos D.

SECTION 2 - FUEL ISSUES ANS NOVEL COMPONENTS

Invited Papers

IN-SITU FIRESIDE CORROSION TESTING OF ADVANCED BOILER MATERIALS WITH DIVERSE FUELS II.785
Henderson P.J., Karlsson A., Davis C., Rademakers P., Cizner J., Formanek B., Goransson K., Oakey J.

DEGRADATION OF BOILER AND HEAT EXCHANGER MATERIALS: DATA GENERATION, DATABASES AND PREDICTIVE MODELLING II.801
Saunders S.R.J., Simms N.J., Osgerby S., Oakey J.E.

COMPLEX FIRESIDE CORROSION MECHANISM IN BOILERS USING STAGED COMBUSTION SYSTEMS II.815
Bakker W., Kung S., Blough J., Seitz W.

FABRICATION OF A GAS TURBINE COMBUSTION HARDWARE IN ODS FERRITIC MATERIALS II.833
McColvin G., Munasinghe D., O'Driscoll J., Jacobs M.

DESIGN, CONSTRUCTION AND TESTING OF A CERAMIC HIGH TEMPERATURE HEAT EXCHANGER FOR AN EXTERNALLY FIRED CYCLE PLANT II.845
Mao C., Scarpellini R., Valarani M.

ELECTRICAL SWING ADSORPTION FOR CO_2 SEPARATION AND CAPTURE II.853
Judkins R.R.

2.1. Hot Gas Corrosion

HIGH TEMPERATURE CORROSION IN GAS TURBINES: FUEL MODEL AND EXPERIMENTAL RESULTS II.871
Bordenet B., Boßmann H.P.

REDUCTION OF FIRESIDE CORROSION OF SUPERHEATER MATERIALS IN A BIOMASS-FIRED CIRCULATING FLUIDISED BED BOILER II.883
Henderson P.J., Högberg J., Mattsson M.

EFFECT OF FUEL TYPE ON THE FIRESIDE CORROSION OF BOILER MATERIALS FOR ADVANCED CLEAN COAL TECHNOLOGIES II.893
Pinder L.W., Davis C.J.

FATE OF TRACE CONTAMINANTS FROM BIOMASS FUELS IN GASIFICATION SYSTEMS II.903
Kilgallon P., Simms N.J., Oakey J.E.

MATERIALS FOR GASIFIER HEAT EXCHANGERS II.913
Kilgallon P., Simms N.J., Norton J.F., Oakey J.E.

PERFORMANCE OF GAS TURBINE MATERIALS IN "DIRTY FUEL" ENVIRONMENTS II.923
Simms N.J., Encinas-Oropesa A., Kilgallon P., Oakey J.E.

LOW CYCLE FATIGUE IN AGGRESSIVE ENVIRONMENTS –A NEW TESTING METHOD USING CONTROLLED ATMOSPHERES II.933
Andersson H.C.M., Lindblom J.

CHLORINE CORROSION OF THERMALLY SPRAYED COATINGS AT ELEVATED TEMPERATURES II.945
Uusitalo M.A., Vuoristo P.M.J., Mäntylä T.A.

HIGH TEMPERATURE CORROSION IN STRAW FIRED POWER PLANTS: INFLUENCE OF STEAM/METAL TEMPERATURE ON CORROSION RATES FOR TP347H II.957
Montgomery M., Biede O., Hede Larsen O.

2.2. Miscellaneous Topics

EROSION CORROSION OF STEEL TUBES IN THE LOOP SEAL OF A BIOFUEL FIRED CFB PLANT II.969
Nafari A., Nylund A.

PERFORMANCE OF EROSION CORROSION RESISTANT COATINGS IN DIFFERENT COMBUSTION ENVIRONMENTS II.979
Hjörnhede A., Nylund A.

HAFNON – A POTENTIAL CERAMIC MATERIAL FOR LIQUID SLAG REMOVAL IN PRESSURIZED PULVERIZED COAL COMBUSTION ? II.989
Müller M., Hilpert K., Singheiser L.

HEAT RESISTANT SILICON NITRIDE CERAMICS WITH RARE-EARTH SILICON OXYNITRIDE II.997
Nishimura T., Guo S., Hirosaki N., Yamamoto Y., Mitomo M.

SECTION 3 – ADVANCED STEAM POWER PLANT

Invited Papers

BENEFIT OF ADVANCED STEAM POWER PLANTS II.1009
Blum R., Hald J.

DESIGN AND MATERIALS FOR TURBOSETS IN ADVANCED STEAM POWER PLANTS II.1017
Wieghardt K., Kern T.-U.

BOILER DESIGN AND MATERIALS ASPECTS FOR ADVANCED STEAM POWER PLANTS II.1019
Chen Q., Scheffknecht G.

ALLOY DESIGN AND MICROSTRUCTURAL CONTROL FOR IMPROVED 9-12% Cr POWER PLANT STEELS II.1035
Vanstone R.W.

THE EUROPEAN EFFORT IN DEVELOPMENT OF NEW HIGH TEMPERATURE ROTOR MATERIALS UP TO 650°C – COST 522 II.1049
Kern T.-U., Staubli M., Mayer K.H., Escher K., Zeiler G.

DEVELOPMENT OF CREEP RESISTANT CAST STEELS WITHIN THE EUROPEAN COLLABORATION IN ADVANCED STEAM TURBINE MATERIALS FOR ULTRA EFFICIENT, LOW EMISSION STEAM POWER PLANT / COST 501-522 II.1065
Staubli M., Mayer K.-H., Gieselbrecht W., Stief J., DiGianfrancesco A., Kern T.-U.

WELDABILITY AND WELD PROPERTIES FOR ADVANCED POWER PLANT MATERIALS II.1081
Cerjak H., Letofsky E., Jochum C., Nies H.

NEW BOILER MATERIALS FOR ADVANCED STEAM CONDITIONS II.1091
Scarlin B., Stamatelopoulos G.N.

MATERIALS FOR ULTRA-SUPERCRITICAL COAL-FIRED POWER PLANT BOILERS II.1109
Viswanathan R., Purgert R., Rao U.

THE STEAM OXIDATION RESISTANCE OF 9-12% CHROMIUM STEELS II.1131
Ennis P.J., Quadakkers W.J.

COATINGS FOR STEAM POWER PLANTS UNDER ADVANCED CONDITIONS II.1143
Agüero A., Muelas R., Scarlin B., Knoedler R.

3.1. Microstructure

MARTENSITIC/FERRITIC SUPER HEAT-RESISTANT 650°C STEELS –MICROSTRUCTURE II.1161
Agamennone R., Blum W.

PRECIPITATION OF Z-PHASE AND DEGRADATION BEHAVIOUR OF MOD.9Cr-1Mo STEEL II.1171
Kimura K., Suzuki K., Toda Y., Kushima H., Abe F.

DISTRIBUTION OF MX CARBONITRIDES AND ITS EFFECT ON CREEP DEFORMATION IN 9Cr-0.5Mo-1.8W-VNb STEEL II.1181
Sawada K., Kubo K., Hara T., Abe F.

THE EFFECT OF MICROSTRUCTURAL STABILITY ON LONG-TERM CREEP BEHAVIOUR OF 9-12%Cr STEELS II.1189
Sklenicka V., Kucharova K., Kloc L., Svoboda M., Staubli M.

SYSTEM FREE ENERGY APPROACH TO THE PRECIPITATION OF THE LAVES PHASE IN Fe-Cr-W-C QUATERNARY STEELS II.1201
Murata Y., Koyama T., Morinaga M., Hashizume R., Miyazaki T., Doi M.

MICROSTRUCTURAL PHYSICALLY BASED CREEP MODELLING ON 9-12 % Cr STEELS II.1211
Weinert P.

Z PHASE CHARACTERISTICS IN MARTENSITIC 12CrMoVNb STEELS II.1223
Vodarek V., Strang A.

MICROSTRUCTURAL ISSUES IN THE DESIGN OF AUSTENITIC AND NICKEL BASED MATERIALS FOR SUPERHEATER SYSTEMS IN 700°C STEAM PLANT II.1233
Starr F., Shibli A.

PRECIPITATION OF INTERMETALLIC PHASES DURING MARTENSITE AGING IN STEELS CONTAINING 10% Cr II.1241
Pigrova G.D.

A NEW MODELLING APPROACH TO MICROSTRUCTURAL EVOLUTION IN FERRITIC STEELS II.1247
Yin Y.F., Faulkner R.G.

AUTHOR INDEX I

KEYWORD INDEX VII

PART III

SECTION 3 – ADVANCED STEAM POWER PLANT

3.2. Alloy development

EVALUATION OF A NEW 11 % Cr STEEL FOR STEAM CHESTS III.1261
Bates P., Vanstone R.W., Osgerby S., Mulvihill P.

DEVELOPMENT OF HIGH WCoB-CONTAINING 12Cr ROTOR STEELS FOR USE AT 650C IN USC POWER PLANTS III.1269
Arai M., Doi H., Fukui Y., Azuma T., Fujita T.

MARTENSITIC/FERRITIC SUPER HEAT-RESISTANT 650°C STEELS III.1279
Agamennone R., Berger C., Blum W., Ehlers J., Ennis P.J., Granacher J., Inden G., Knezevic V., Quadakkers J.W., Sauthoff G., Scholz A., Singheiser L., Vilk J., Wang Y.

MARTENSITIC/FERRITIC SUPER HEAT-RESISTANT 650°C STEELS – DESIGN OF MODEL ALLOYS III.1289
Knezevic V., Sauthoff G.

MARTENSITIC/FERRITIC SUPER HEAT-RESISTANT 650°C STEELS – THERMODYNAMICS AND KINETICS OF PRECIPITATION REACTIONS III.1299
Vilk J., Schneider A., Inden G.

IMPROVEMENT OF CREEP RUPTURE STRENGTH OF HIGH STRENGTH 12Cr FERRITIC HEAT-RESISTANT STEEL III.1311
Uehara T., Toji A., Komatsubara S., Fujita T.

DEVELOPMENT OF A NEW 18Cr-9Ni AUSTENITIC STAINLESS STEEL BOILER TUBE III.1321
Ishitsuka T., Mimura H.

ALLOY DESIGN FOR ULTRA-HIGH TEMPERATURE STEAM TURBINE APPLICATIONS: PHASE FIELD SIMULATION OF THE REMELTING PROCESS III.1333
Böttger B., Steinbach I., Fries S.G., Chen Q., Sundman B.

WORKABILITY AND DEVELOPMENT OF T/P23 (2.25 % Cr-1.6W-Nb-V STEEL) FOR FOSSIL BOILER AND COMBINED CYCLE APPLICATIONS III.1343
Gabrel J., Lefebvre Bo., Vaillant J.-C., Vandenberghe B.

NEW WROUGHT Ni-BASED SUPERALLOYS WITH LOW THERMAL EXPANSION FOR 700C STEAM TURBINES III.1351
Yamamoto R., Kadoya Y., Kawai H., Magoshi R., Noda T., Hamano S., Ueta S., Isobe S.

DEVELOPMENT OF A NEW 12% Cr-STEEL FOR TUBES AND PIPES IN POWER PLANTS WITH STEAM TEMPERATURES UP TO 650°C III.1361
Bendick W., Gabrel J., Vaillant J.-C., Vandenberghe B.

HIGH PERFORMANCE LOW ALLOY STEEL CASTING FOR STEAM TURBINE III.1371
Ishii R., Tsuda Y., Yamada M., Ikeda K., Kaneko J.

DEVELOPMENT OF HIGH STRENGTH 9Cr STEEL BY COMBINATION OF FINE MX-TYPE NITRIDES AND NO CARBIDE III.1379
Taneike M., Sawada K., Abe F.

DEVELOPMENT STEPS OF NEW STEELS FOR ADVANCED STEAM POWER PLANTS III.1385
Mayer K.H., Blum R., Hillenbrand P., Kern T.-U., Staubli M.

GUIDING PRINCIPLES FOR DEVELOPMENT OF ADVANCED FERRITIC STEELS FOR 650°C USC BOILERS III.1397
Abe F., Okada H., Wanikawa S., Tabuchi M., Itagaki T., Kimura K.,
Yamaguchi K., Igarashi M.

3.3. Mechanical Properties

LONG TERM CREEP AND CREEP FATIGUE PROPERTIES OF THE MARTENSITIC STEELS OF TYPE (G)X12CrMoWVNbN10-1-1 III.1409
Schwienheer M., Haase H., Scholz A., Berger C.

TWO SPECIMEN COMPLEX THERMAL-MECHANICAL FATIGUE TESTS ON THE AUSTENITIC STAINLESS STEEL AISI 316 L III.1419
Rau K., Beck T., Löhe D.

CREEP PROPERTIES OF AUSTENITIC STAINLESS 353 MA AT 1100°C AND 1200°C III.1431
Wu R., Seitisleam F., Sandström R.

PROPERTIES AND EXPERIENCES WITH A NEW AUSTENITIC STAINLESS STEEL (TEMPALOY AA-1) FOR BOILER TUBE APPLICATION III.1445
Minami Y., Tohyama A., Hayakawa H.

IMPROVEMENTS IN THE SHORT TERM CREEP STRENGTH OF AISI 304L BY MEANS OF GRAIN BOUNDARY DESIGN AND CONTROL III.1453
Spigarelli S., Cabibbo M., Evangelista E., Palumbo G.

MICROSTRUCTURAL FEATURES INFLUENCING THE CREEP PROPERTIES OF 9-12 % Cr-STEELS FOCUSING ON LAVES-PHASE PRECIPITATION III.1459
Stocker Ch., Spiradek K., Zeiler G.

CREEP PROPERTIES OF PRECIPITATION STRENGTHENED CARBON FREE MARTENSITIC ALLOYS III.1469
Muneki S., Okubo H., Okada H., Yamada K., Igarashi M., Abe F.

MICROSTRUCTURE AND PROPERTIES OF MODIFIED 3% Cr STEELS III.1477
Foldyna V., Jakobová A., Vodárek V., Kroupa A., Kubon Z.

AN ASSESSMENT OF CREEP RUPTURE DATA ON STEEL E911 III.1487
Allen D.J., Servetto C.

EFFECT OF Cr CONTENT ON THE CREEP STRENGTH AND MICROSTRUCTURAL CHANGE IN HIGH Cr HEAT RESISTANT STEEL III.1497
Miki K., Azuma T., Ishiguro T., Hashizume R., Murata Y., Morinaga M.

THE EFFECT OF THE ELEMENT CARBON ON THE TOUGHNESS AND THE CREEP RUPTURE STRENGTH IN 12Cr HEAT RESISTANT STEELS III.1505
Ryu S.H., Kim M.S., Lee Y.S., Kang S.T., Kim J.T., Yu J.

STRAIN RANGE PARTITIONING ANALYSIS FOR CREEP-FATIGUE LIFE OF FERRITIC HEAT-RESISTING MATERIALS III.1515
Kimura M., Kobayashi K., Yamaguchi K.

HIGH TEMPERATURE CREEP BEHAVIOUR AND MICROSTRUCTURAL CHANGES OF TAF 650 STEEL III.1521
Svoboda M., Bursik J., Podstranska I., Kroupa A., Sklenicka V., Mayer K.-H.

STRESS CHANGE EXPERIMENTS IN LOW STRESS CREEP REGIME OF P-91 TYPE STEEL III.1531
Kloc L., Sklenicka V.

INVESTIGATIONS AND ANALYSIS ON THE STATIONARY CREEP BEHAVIOUR OF 9-12 % CHROMIUM FERRITIC MARTENSITIC STEELS III.1539
Dimmler G., Weinert P., Cerjak H.

ALLOY DESIGN FOR ULTRA HIGH TEMPERATURE STEAM TURBINE APPLICATIONS: CREEP BEHAVIOUR AND MODELLING OF CREEP III.1551
Thoma A., Scholz A., Berger C.

EFFECT OF ALLOYING ELEMENTS ON CREEP PROPERTIES OF Pd ADDED 9Cr FERRITIC STEELS III.1561
Okada H., Muneki S., Yamada K., Okubo H., Igarashi M., Abe F.

IMPROVEMENT OF CREEP STRENGTH OF PRECIPITATION STRENGTHENED 15Cr HEAT RESISTANT FERRITIC STEELS III.1571
Toda Y., Tohyama H., Kushima H., Kimura K., Abe F.

LONG-TERM CREEP STRENGTH PREDICTION OF HIGH Cr FERRITIC CREEP RESISTANT STEELS III.1581
Kushima H., Kimura K., Abe F.

EVALUATION OF CREEP PROPERTIES AND MICROSTRUCTURES ON THERMO-MECHANICAL AND MAGNETIC TREATED 9Cr FERRITIC STEELS III.1591
Okubo H., Muneki S., Okada H., Yamada K., Igarashi M., Abe F.

3.4. Steam Oxidation and Coatings

OXIDATION OF ADVANCED FERRITIC/MARTENSITIC STEELS AND OF COATINGS IN FLOWING STEAM AT 650°C III.1601
Knödler R., Scarlin B.

STEAM OXIDATION OF 9-12Cr MARTENSITIC STEELS: CHARACTERISATION AND MODELLING THE SPALLING OF OXIDE SCALE III.1613
Osgerby S., Mc Cartney L.N.

MECHANICAL AND OXIDATION TESTING OF ADVANCED MATERIALS FOR STEAM POWER PLANTS III.1621
Bontempi P., Guardamagna C., Ricci N., Torri L.

IMPROVEMENT OF STEAM OXIDATION RESISTANCE FOR FERRITIC HEAT RESISTANT STEELS III.1629
Kutsumi H., Itagaki T., Abe F.

STEAM OXIDATION OF HIGH CHROMIUM FERRITIC STEELS CONTAINING PALLADIUM III.1639
Itagaki T., Kutsumi H., Igarashi M., Abe F.

3.5. Welding

DESCRIPTION OF THE MATERIAL BEHAVIOUR IN GIRTH WELDS DURING WELD FABRICATION AND FOR HIGH TEMPERATURE SERVICE III.1651
Mohrmann R.

AN ASSESSMENT OF CREEP RUPTURE DATA ON E911 STEEL WELDMENTS III.1661
Servetto C., Allen D.J.

CHARACTERIZATION OF MATCHING FILLER METALS FOR NEW FERRITIC-BAINITIC STEELS LIKE T/P23 AND T/P24 III.1671
Heuser H., Jochum C.

EVALUATION OF THE WELDED JOINTS IN P92 AND P122 PIPE STEELS III.1681
Ryu S.H., Lee K.W., Chi B.H., Lee Y.S., Kong B.O., Park S.H., Nam S.W., Lim B.S., Kim B.J.

CREEP STRENGTH AND MICROSTRUCTURES FOR HAZ OF WELDMENTS OF HIGH Cr FERRITIC STEELS III.1691
Matsui M., Tabuchi M., Watanabe T., Kubo K., Abe F.

RESEARCH AND DEVELOPMENT OF NEW MARTENSITIC STEELS III.1701
Artinger A., Rozsavolgyi Z.

3.6. Applications

THE FIRST SUPERCRITICAL POWER UNIT IN POLAND. WELDABILITY EVALUATION OF NEW MARTENSITIC CHROMIUM STEELS WITH TUNGSTEN ADDITIONS AND PROPERTIES OF WELDED JOINTS III.1711
Brózda J., Zeman M., Pasternak J.

APPLICATION OF A NEW ROTOR STEEL FORGING FOR MEDIUM RATING SINGLE CYLINDER STEAM TURBINES III.1721
Yamada M., Tsuda Y., Kaneko J.

THE FIRST INDUSTRIAL CAST OF CrMoCoB ADVANCED STEEL FOR CAST TURBINE COMPONENTS III.1731
Contessi E., Del Vecchio D., Ghidini A., Valenti S., Carosi A., Di Gianfranceso A., Ielpo F.M.

OUTLOOK

Invited Papers

MATERIALS DEVELOPMENT FOR ADVANCED VISION 21 POWER PLANTS III.1745
Ruth L.A.

TRENDS IN POWER ENGINEERING IN JAPAN AND REQUIREMENTS FOR IMPROVED MATERIALS AND COMPONENTS III.1767
Masuyama F.

POWER GENERATION IN SOUTHERN AFRICA III.1783
De Beer J.A., Olsha Z.

ENERGY RESEARCH IN THE SIXTH FRAMEWORK PROGRAMME III.1801
Busquin P.

ADDENDUM

DEGRADATION OF EB-PVI) THERMAL BARRIER COATINGS DURING THERMAL CYCLING III.1809
Sun X.F., Li M.H., Zhang Z.Y., Guan H.R

AUTHOR INDEX I

KEYWORD INDEX VII

Part III

SECTION 3

ADVANCED STEAM POWER PLANT

SECTION 3

ADVANCED STEAM POWER PLANT

3.2. Alloy Development

EVALUATION OF A NEW 11%CR STEEL FOR STEAM CHESTS

P Bates[1], R W Vanstone[2], S Osgerby[3] and P Mulvihill[4]

[1] Sheffield Forgemasters Engineering Ltd, Sheffield, UK
[2] Alstom Power, Rugby, UK
[3] NPL Materials Centre, Teddington, UK
[4] Powergen, PTC, Nottingham, UK

Abstract

Full size steam chests have been fabricated successfully in alloy 122 by casting and forging routes. Initial integrity and microstructural evaluation showed that the components were sound and homogeneous. The material is currently being characterised in terms of its microstructure and mechanical and oxidation behaviour. This paper reports progress on assessing the required properties eg impact, tensile, creep, LCF and oxidation, and demonstrates the continued confidence in this material for potential use for steam chests in the next generation of turbines.

Keyword: Steam Chest, Alloy 122, Microstructure, Mechanical Properties

Introduction

The steam chest is one of the most demanding applications for materials in steam turbine technology. This component is exposed to the highest operating temperatures and pressures with no practical scope for cooling. Operating temperatures of around 600 °C represent the practical upper limit for 9%Cr steels but the next generation of turbines will require materials with adequate creep and steam oxidation resistance at higher temperatures. An 11%Cr alloy, designated alloy 122, is a candidate material for this application and has already been demonstrated to have superior properties to 9%Cr materials in tubing and pipework.

The initial work on these components has been reported previously [1]. The current paper updates that report to include recent test results.

Component Manufacture

Two production routes, casting and forging, are being evaluated. The preferred production route is casting as this is generally more economic, however this route has the potential for segregation in large components and may result in inferior properties compared to forged components.

The material was produced from high grade, low residual scrap that was melted in a basic electric arc furnace as a 50 tonne charge. The liquid metal was tapped into a ladle where slag and alloying additions were added. Subsequently the melt was degassed in the SFEL vacuum argon degassing secondary steelmaking unit and then deoxidised using a combination of aluminium and vacuum carbon deoxidation. The final cast analysis is given in Table I. The melt was then split with approximately 35 tonnes teemed into a steeply tapered 60 inch diameter, multi-fluted mould and the balance transferred to the foundry to produce the cast steam chest, Figure 1. The casting was left in the mould to slow cool for 14 days and was

stripped only after the temperature had dropped below 300 °C. The casting was then cleaned out and heated to 970 °C with the feeder heads still attached, annealed and slow cooled with a total cycle time of 4.5 days. Finally the casting was heated to 200-300 °C and the feeder heads removed by oxy-parting.

Table I Cast Analysis, wt%

C	Si	Mn	P
0.12	0.20	0.68	0.009
S	Cr	Mo	Ni
0.007	11.07	0.35	0.31
Al	Cu	Co	N
0.005	1.01	0.011	0.055
B	V	W	Nb
0.002	0.22	1.94	0.054

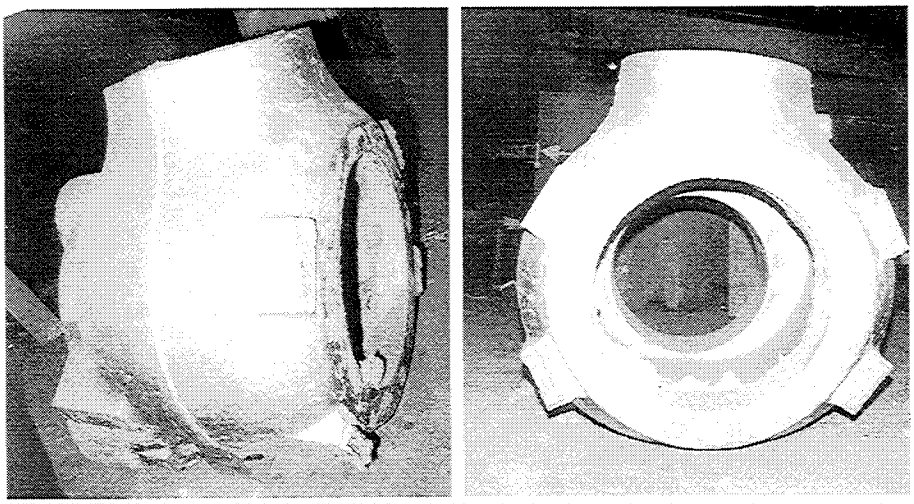


Figure 1 Steam chest casting

After an extended cooling time the 60 inch diameter ingot was stripped and transferred to the forge. The ingot was pre-heated to 650 °C, then heated slowly to the forging temperature of 1200 °C and soaked for 20 hours. The ingot then underwent the forging sequence shown in Figure 2. No problems were encountered during this process and a correctly shaped forging, which was free of surface cracks, was achieved. An isothermal transformation heat treatment was carried out at 700 °C prior to machining to the final shape, Figure 3.

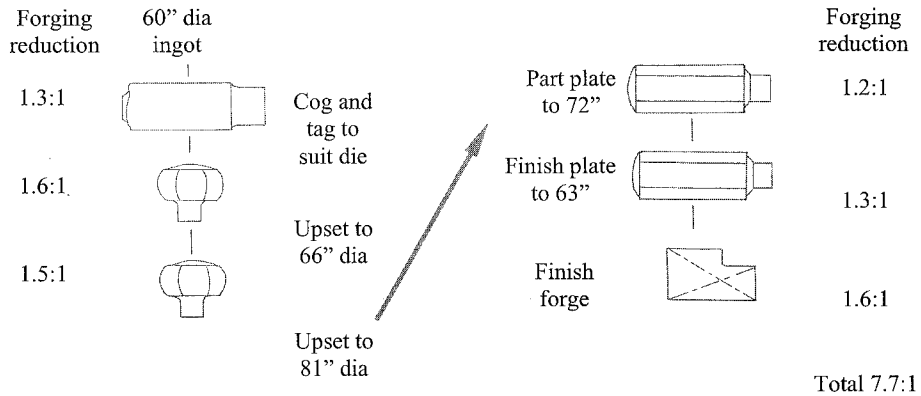


Figure 2 Forging sequence

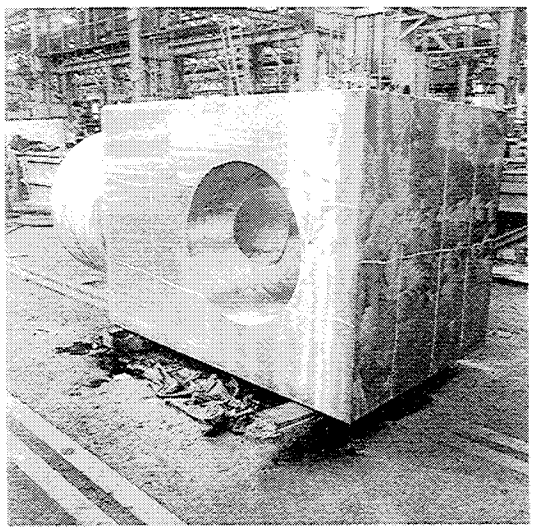


Figure 3 Forged steam chest after machining

Extensive heat treatment trials were conducted to determine the optimum quality heat treatment schedule for the two components. The schedule detailed in Table II was chosen to achieve the required tensile and impact properties.

Table II Quality Heat Treatment Schedules for Forged and Cast Components

Forging	Casting
1050 °C / 8 h / air cool	1050 °C / 8 h / air cool
670 °C / 14 h / furnace cool	670 °C / 8 h / air cool
760 °C / 14 h / furnace cool	760 °C / 8 h / air cool

Both components were examined for defects using visual, magnetic particle and ultrasonic techniques. No significant surface defects were observed in the forged component and any subsurface defects were well within the levels acceptable for steam turbine forgings. Some areas of tearing and centre line shrinkage were observed in the cast component but at a level typical of castings in conventional alloys.

Microstructure

Microstructural investigations were carried out on material taken from both components using optical and transmission electron microscopy.

As-received condition

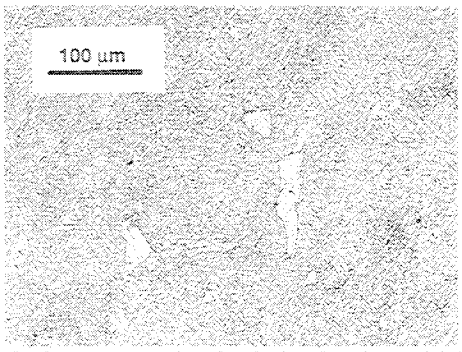
Optical microscopy revealed that the microstructure of the forging consisted of tempered martensite and a small amount of δ-ferrite (Figure 4a). The content of δ-ferrite was less than 1.0%.

Electron microscopy showed that tempering of the forging resulted in the formation of subgrains inside the martensitic matrix and a reduction in dislocation density. Undissolved primary particles of NbX phase were randomly distributed throughout the matrix. Relatively coarse $M_{23}C_6$ particles were observed along prior austenite and subgrain boundaries (Figure 4b) while much finer secondary MX particles, rich in V and Nb, were observed on dislocations inside subgrains as well as in the subgrain boundaries (Figure 4c). Fine particles of this phase contribute significantly to the high level of creep resistance of the advanced 9-12%Cr heat resistant steels. No Laves phase was observed in the martensitic matrix.

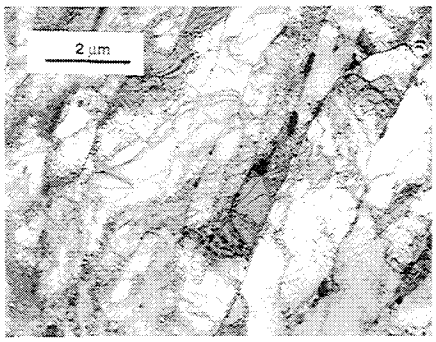
The islands of δ-ferrite contained a large amount of small precipitates and δ/α interfaces were decorated by a network of coarser particles, mostly $M_{23}C_6$. (Figure 4d). Precipitation reactions in the δ-ferrite were significantly modified due to differences in chemical composition, the islands of δ-ferrite being significantly enriched in chromium, vanadium, molybdenum and tungsten. As a result the amount of precipitation in the δ-ferrite was much higher than in the martensitic matrix. Tempering during quality heat treatment resulted in precipitation of secondary MX, $M_{23}C_6$ and tungsten rich Laves phase particles. Laves phase formed as needle-like as well as blocky particles.

No ε-Cu particles were found in any of the phases so it is concluded that Cu remains in solid solution during heat treatment.

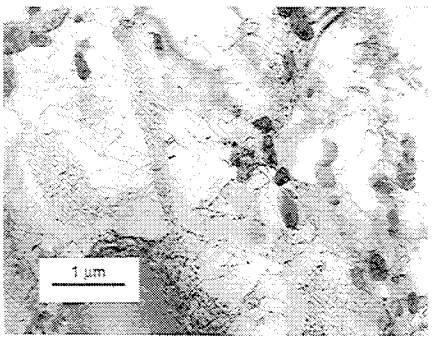
Optical microscopy revealed that the casting microstructure consisted of tempered martensite and δ-ferrite as in the case of the forging. However the amount of δ-ferrite in the microstructure was higher than in the forging, generally being around 2.5% but rising to around 6% in the middle of the thinner section (Figure 5). Nonetheless, no continuous network of δ-ferrite was observed in any area. Primary grain boundaries, formed during solidification, were decorated by a network of coarse carbides.



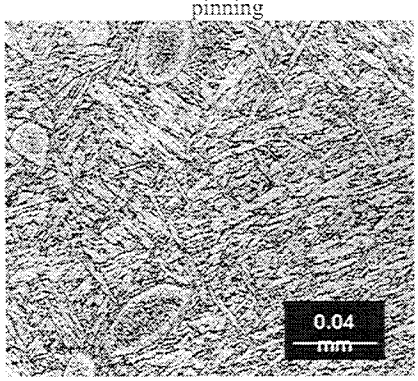
a) optical microstructure showing isolated regions of delta ferrite

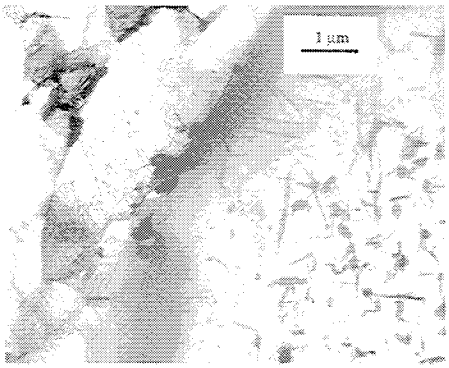


b) subgrain structure with $M_{23}C_6$ boundary pinning



c) MX particles inside subgrains





d) Delta ferrite/martensite boundary decoration

Figure 4 Microstructure of the forging in the as-received condition

Electron microscopy revealed microstructures and phases similar to those observed in the forging ie no Laves phase in the martensitic matrix and no Cu particles. However, interdendritic segregation in the casting resulted in more pronounced heterogeneity of precipitate distribution than in the forging.

The average grain size was similar in the casting and the forging, being around 150 microns (ASTM 2.5 – 3.0). However occasional grains in the casting were as large as 500 microns.

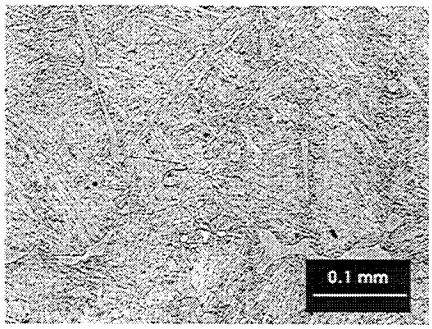


Figure 5 Microstructure of the cast material in the as-received condition

Aged conditions

Optical microscopy revealed no change in the martensitic matrix of specimens which had been aged at 550-650 °C for 1700 hours. However some coarsening of precipitates at the α/δ interface was observed, especially at 600 and 650 °C.

Electron microscopy revealed tungsten-rich Laves phase precipitation within the martensitic matrix of all aged conditions (Figure 6). Particles of Laves phase in specimens aged at 550 and 600 °C were predominantly needle like but in specimens which had been aged at 650 °C blocky Laves phase particles were also observed.

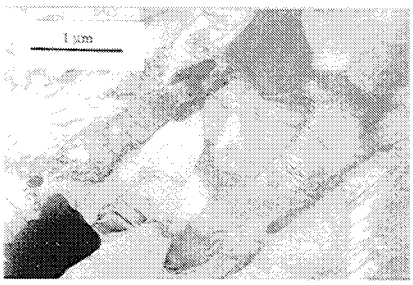


Figure 6 Laves phase in the forging after ageing at 650°C – TEM image

No ε-Cu particles were found in any of the specimens investigated so that over the ageing times investigated Cu remains in solid solution.

Mechanical Properties

Tensile and Impact

Room temperature tensile and impact properties of the two materials in the conditions corresponding to the quality heat treatment and a simulated post-weld heat treatment are given in Table III.

Table III Room Temperature Mechanical Properties after simulated PWHT

Material	Simulated PWHT	$R_P0.2$ MPa	R_m MPa	Elongation %	R A %	Cv J
Forging	10 h at 760 °C	511	697	24	51	20/33/38
Casting (80mm section)	16 h at 760 °C	523	712	23	54	17/19/22
Casting (120mm section)	16 h at 760 °C	506	686	22	51	16/17/24

Material is currently being exposed for extended durations at 600 and 650 °C. Tensile and impact data after these exposures will be needed to confirm the long-term stability of the material.

Creep

Creep tests have been carried out in the temperature range 550 – 650 °C for durations up to 10000 h. Rupture data are summarised in Figure 7. The properties of the cast and forged material are essentially identical and show a temperature advantage of ~20 °C over modified 9Cr1Mo material, the alloy currently applied to high temperature steam chests. Testing to extend the dataset to 30000 h durations is in progress.

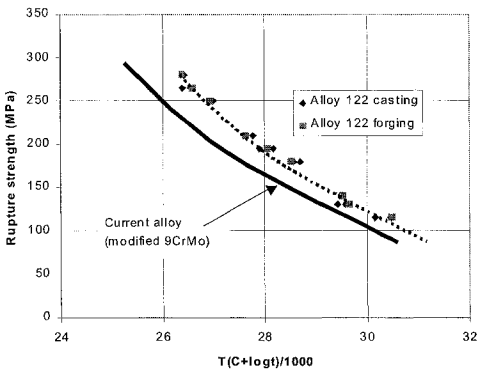


Figure 7 Summarised creep properties of cast and forged material

LCF

Cast and forged materials were tested at 600 °C under continuous cycling and with cycles that included a 0.5 h hold period at maximum tensile strain. The forged material shows superior

LCF resistance to the cast material at high strains but at lower strains their behaviour is similar. The introduction of tensile hold periods produces a small decrease in cycles to crack initiation for the forged material (Figure 8). Similar tests on the cast material are in progress.

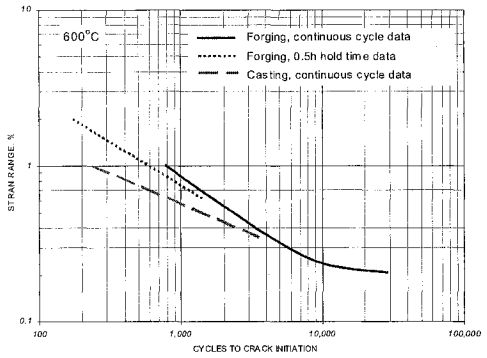


Figure 8 Low cycle fatigue properties

Further Work

An extended test programme is in progress including:

- Thermal ageing to 10000 h, to assess stability
- Creep tests to 30000 h duration
- Oxidation in steam environments to 10000 h duration
- Creep crack growth on as-received and thermally aged material
- Creep performance of welded joints

Conclusions

Cast and forged steam chests have been manufactured successfully using alloy 122. The components have been demonstrated to have acceptable component integrity, microstructure and short term mechanical properties. Testing is continuing to extend the range of data in order to demonstrate further the potential for using alloy 122 in this application.

Acknowledgements

The financial support of the UK Department of Trade and Industry is gratefully acknowledged.

References

[1] P Bates, I Nicholls, D V Thornton and R W Vanstone, Forged and Cast Steam Chests in New 11%Cr Steel, in Parsons 2000: Advanced Materials for 21st Century Turbines and Power Plant, eds A Strang, W M Banks, R D Conroy, G M McColvin, J C Neal and S Simpson, IOM Communications, 2000 pp 157-170

DEVELOPMENT OF HIGH WCoB-CONTAINING 12Cr ROTOR STEELS FOR USE AT 650C IN USC POWER PLANTS

M. Arai*, H. Doi*, Y. Fukui*, T. Azuma** and T. Fujita***

* Hitachi, Ltd., 7-1-1 Omika-cho, Hitachi-city, 319-1292, Japan

** The Japan Steel Works, Ltd., 4 Chatsu-machi, Muroran, 051-8505, Japan

***Emeritus Professor, The University of Tokyo, Japan

Abstract

A new WCoB12%Cr ferritic rotor material (HR1200: Hitachi Rotor 1200F) has been studied for application in future high efficiency ultra-supercritical-pressure steam (USC) power plants designed to operate under the steam condition of 650C. Addition of W, Co and B has been found to improve creep rupture strength at elevated temperatures. Reduction of Ni and Al impurities, on the other hand, has suppressed degradation of long-time creep rupture properties at about 650C. Both 20 and 80-ton trial rotor shafts were forged and tested, especially, for their long-time creep rupture properties. The results showed that the alloy has satisfactory properties to be a candidate material for turbine rotor shaft, under 650C steam condition, in USC power plants.

To verify the reliability of this material, a model turbine rotation test was performed in an R&D program initiated by the Electric Power Development Co., Ltd. (EPDC) of Japan. The test was conducted for 500 hours at 650C. Investigation of the mechanical properties of the rotor material, after the rotation test, confirmed the reliability of this material.

Keywords: heat resistant steels, turbine rotors, 12Cr steels, ESR method, creep properties

1. Introduction

Preservation of the natural environment and fossil fuel resources has become a global concern. Electric power consumption will increase in the future as more electrical devices are used all around the world. Since coal is the major energy source among fossil fuels, coal fired thermal power plants will continue to be the main energy supply system from the viewpoint of economical performance and operational characteristics. However, for further reduction in CO_2 emissions and fossil fuel consumption, it is necessary to develop a new USC power generation system with higher efficiency than conventional plants. Realization of the new USC system depends more on materials development than on new plant design, and the improvement of creep resistance of materials is one of the key technologies for the new system. Thus, development of better heat resistant steels are being pursued globally [1-5].

Recently, deterioration of long-time creep rupture properties, after about 10,000 hours, of high W-containing 12%Cr steels has been reported [6,7]. These studies showed that improvement of long-time creep rupture properties is the most important issue for the development of new 12%Cr steels for USC Plants.

This paper focuses on the investigation of the effect of chemical composition and manufacturing process to improve long time creep rupture properties, and on the evaluation of the creep rupture strength of WCoB12%Cr steel (HR1200) trial rotor forgings. The technology of alloy design to improve long-time creep rupture properties of this steel is discussed based on the reduction of Ni and Al impurities, and material property evaluations conducted for the trial rotor forgings. To verify the reliability of this material, a model turbine rotation test was performed in an R&D program initiated by the Electric Power Development Co., Ltd. (EPDC) of Japan. The test was conducted for 500 hours at 650C. Investigation of the mechanical properties of the rotor material, after the rotation test, confirmed the reliability of this material.

2. Alloy design

Research on WCoB12%Cr steel (HR1200) for steam turbine rotor shaft has been conducted for some time in the authors' laboratory. It is known that common alloying elements; Mo, V, Nb in heat resistant 12%Cr steel are ferrite-formers which improve the creep rupture strength of ferritic steels. V and Nb form carbides and influence precipitation hardening. V and Nb can not be added to steel in large amounts because of their low solubility. However, increased solubility of these elements in steel is required for better creep resistance. On the other hand, Mo has an effect on solution hardening of the steel matrix and suppresses the recovery of martensite phase caused by dislocation migration. W behaves similar to Mo. Regression analysis done for the effect of Mo and W content on creep rupture strength of conventional 12%Cr steels at 500C and 550C gave the following relations:

$$\sigma_{500C}\ (\text{MPa}) = 195.15 + 67.37\ (\%\text{Mo}) + 55.90\ (\%\text{W}) \quad (1)$$

$$\sigma_{550C}\ (\text{MPa}) = 117.19 + 29.32\ (\%\text{Mo}) + 82.96\ (\%\text{W}) \quad (2)\ [8]$$

At 550C, W had a larger coefficient than Mo. It was thus concluded that W imparts higher creep resistance to steel than Mo at high temperatures. Fujita [9] pointed out that the optimum Mo equivalent value is 1.5, which is given by the relation (Mo-eq.) = (%Mo) + 0.5(%W). For HR1200, the optimum additions of Mo and W were determined to be 0.2 mass% and 2.6 mass%, respectively.

Although increasing the ferrite-former content improves creep strength of steels, the excess amount of ferrite-former addition may deteriorate mechanical properties because of δ-ferrite formation. Suppression of δ-ferrite formation in steel can be estimated from the value of Cr equivalent which is expressed by the following equation:

$$\text{Cr-eq.} = (\%\text{Cr}) + 6(\%\text{Si}) + 4(\%\text{Mo}) + 1.5(\%\text{W}) + 11(\%\text{V}) + 5(\%\text{Nb}) - 40(\%\text{C}) - 2(\%\text{Mn}) - 4(\%\text{Ni}) - 2(\%\text{Co}) - 30(\%\text{N}) \quad (3)$$

Since ferrite-formers all have positive coefficients in equation (3), Cr-eq. value which shows the tendency for δ-ferrite formation must be reduced by the addition of austenite-formers to 12%Cr steels. However, addition of most of the austenite-formers may deteriorate creep

rupture strength of 12%Cr steels.

Optimum amounts of Co, B and N for this steel were investigated using 50kg ingots prepared by vacuum induction melting. The δ-ferrite phase disappeared after 1 mass% Co addition. Effects of Co, B and N on creep resistance of 12%Cr steels are shown in Fig.1(a)-(c). As shown in Fig. 1(a), a continuous increase in creep rupture strength was observed for Co additions up to 1 mass%. As much as 1 mass% Co addition was required to eliminate δ-ferrite and to increase creep rupture strength.

As shown in Fig. 1(b), B was added to WCo12%Cr steels in amounts as much as 300 ppm. Although details of the mechanism of creep strength improvement by B addition has not been made clear, a continuous increase in creep rupture strength was observed for B additions up to 100 ppm. At higher B levels, a plateau in creep rupture strength was reached. The small amount of B addition to WCo12%Cr steels improved hardenability.

In case of B-containing steels, formation of BN and the consequent reduction of the effect of B and N on steel properties are matters of concern. A peculiar behavior was observed during an investigation of B-free and B-added WCo12%Cr steels. Unlike conventional 12%Cr steels, creep rupture strength and N content of WCoB12%Cr steel was found to have an inverse dependency. It is thought that the excess N addition possibly promoted BN formation which negated effects of both B and N on this steel's properties. It was shown in Fig. 1(c) that the optimum N addition was less than 200 ppm.

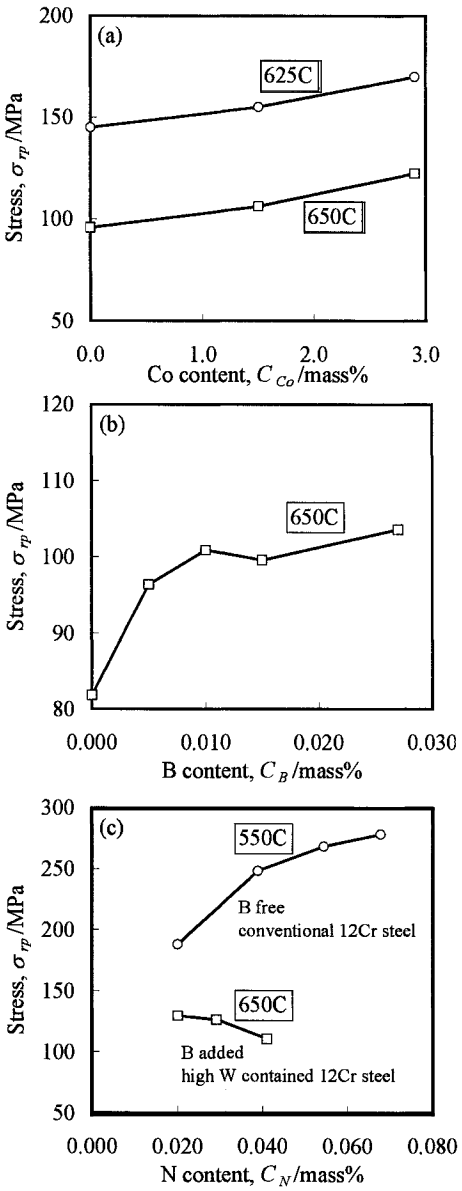


Fig.1 10^5h hours creep rupture strength as a function of (a)Co, (b)B and (c)N content

3. Trial rotor forging

3.1 Manufacturing of HP rotors

Trial manufacturing of 1000 MW-class HP turbine rotor for which the ingot weight was about 20 tons, was carried out for the evaluation of its mechanical properties. Table 1 shows the

Table 1 Chemical composition of trial HP-rotor forging

(mass%)

Steel	C	Si	Mn	Ni	Cr	Mo	W	Co	V	Nb	N	B	Al(ppm)	Cr-eq.
A (20 ton)	0.09	0.02	0.53	0.51	11.0	0.23	2.66	2.53	0.22	0.07	0.020	0.018	50-90	6.44

1050C OQ, 570C AC, 700C AC

chemical composition and heat treatment of trial rotor forging. Chemical composition of the HP rotor was analyzed for bottom, medium and top sections of the drum portion at diagonal positions. Although gravitational segregation of W and B was suspected during steel making process due to their significantly different atomic densities compared to Fe, such a segregation was not detected in the trial rotors. Thus, it was concluded that ESR (Electro Slug Remelting) method can be successfully utilized for manufacturing ingots with a homogeneous distribution of all the alloying elements throughout the entire body of rotor. The manufactured 20-ton rotor shaft forging is shown in Fig.2. Creep rupture strength of the rotor was evaluated by using specimens prepared from the HP rotor girth.

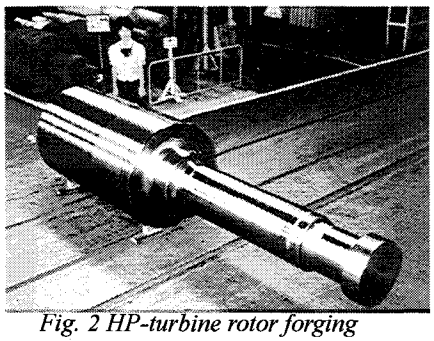


Fig. 2 HP-turbine rotor forging (20-ton class)

3.2 Manufacturing of a 40-ton ingot

If the steam temperature of both high and intermediate pressure turbines are designed to be the same, the manufacturing process is more difficult for the intermediate pressure turbine rotor because of its larger size which weighs about 80 tons. Thus, investigation of segregation of alloying elements and the simulation for upset

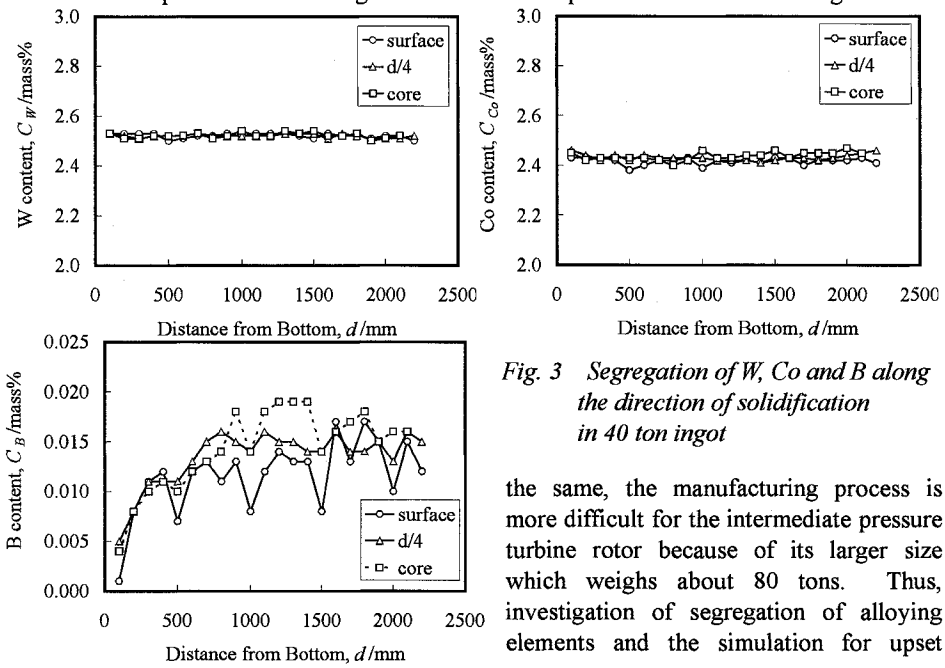


Fig. 3 Segregation of W, Co and B along the direction of solidification in 40 ton ingot

forging using small test pieces was carried out by a half size long ESR ingot of 40 tons (ϕ1800 x 2250). The ESR ingot was sectioned in half along the boring section. Segregation profile along the boring direction is shown in Fig.3 for W, Co and B. According to Fig.3, segregation of W and Co was not present. However, B content was not homogeneously dispersed throughout the whole ingot.

3.3 Manufacturing of IP rotors

After evaluating creep rupture strength of the HP rotor, chemical composition of the IP rotor was revised and its Ni content was reduced as shown in Table 2. The slag composition during ESR was modified to achieve a homogeneous B dispersion. Total weight of the IP- rotor shaft was about 80 tons. Upset forging was performed 4 times. Each upset forging required heating of the ingot. The final shape of the 80-ton rotor shaft forging is shown in Fig.4.Creep rupture strength was evaluated using specimens prepared from the IP rotor girth.

Table 2 Chemical composition of trial IP-rotor forging

(mass%)

Steel	C	Si	Mn	Ni	Cr	Mo	W	Co	V	Nb	N	B	Al(ppm)	Cr-eq.
B (80 ton)	0.10	0.06	0.46	0.25	10.2	0.14	2.51	2.44	0.21	0.07	0.017	0.013	19	6.24

1050C OQ, 570C AC, 700C AC

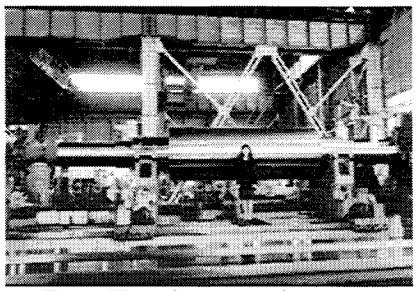


Fig. 4 IP-turbine rotor forging (80-ton class)

3.4 Creep rupture strength of trial rotor forgings

Specimens prepared from both the HP (steel A) and IP (steel B) rotor girth were used to evaluate creep rupture strength of steels. Fig.5 shows the results of the creep rupture tests. Creep rupture strength of steel A was observed to deteriorate rapidly after 10,000 hours especially at 650C. However, for steel B, such a deterioration was not observed even after 20,000 hours. Fig.6 shows ductility of steel specimens crept at 650C. Ductility of steel B was better than steel A at all test

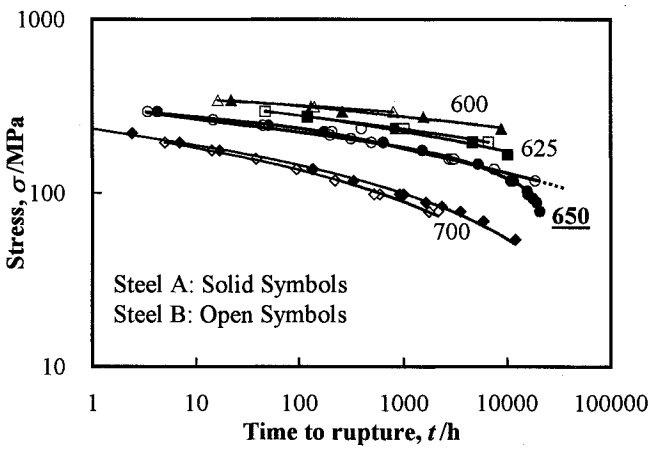


Fig.5 Creep rupture properties of 12%Cr steel ingots

temperatures. As shown in Fig.5, RA (Reduction of Area) of steel A decreased after 10,000 hours but recovered later to values observed after shorter times. This recovery of RA must be the result of a softening phenomenon in these steels. It is concluded that the rapid deterioration of creep strength after long times observed in Fig.5, especially at 650C, was caused by softening. In the case of steel B, the decrease of RA was observed at about 20,000 hours. Rapid deterioration of creep rupture strength did not occur for steel B because recovery of RA, i.e. softening, had not started yet. It is concluded that creep rupture strength of steel B satisfies the target value of 100 MPa at 650C after 100,000 hours estimated by the Larson-Miller Parameter with a constant C of 40.

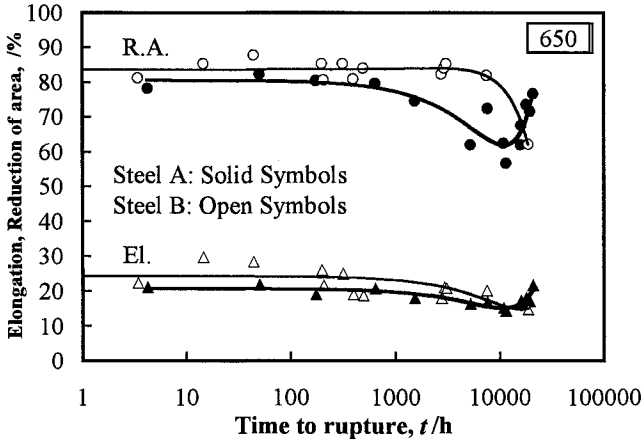


Fig.6 Ductilities of 12%Cr steel ingots

3.5 Microstructure observations

Specimens for TEM observations were prepared from both steels A and B after heat-treatment and creep test at 650C. As shown in Fig.7, tempered martensite was observed in heat-treated

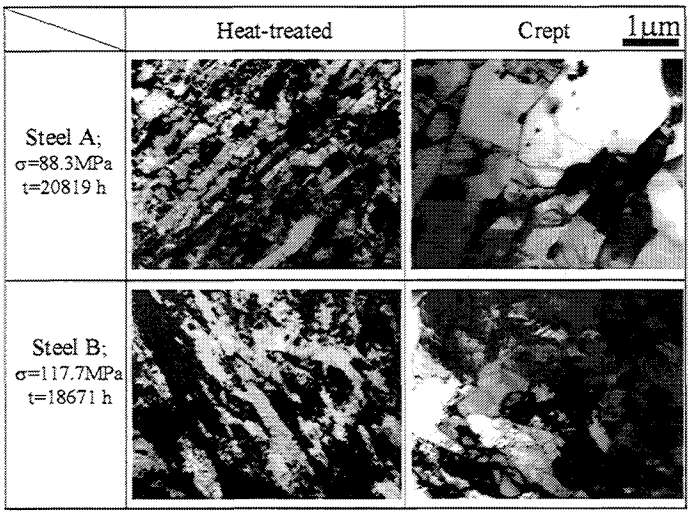


Fig.7 TEM microstructures of creep test specimens (650C)

specimens. Width of lath martensite in steel B was narrower than in steel A. In steel A, growth of sub-grains and recovery of dislocations during creep rupture test was observed clearly. In steel B, partial recovery was observed and the lath martensite structure with high-density dislocations was maintained.

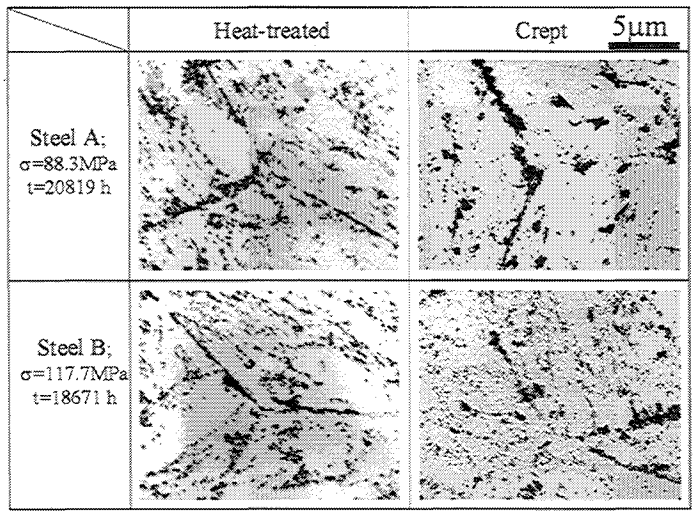


Fig.8 TEM microstructures of extraction replica of creep test specimens (650C)

Fig.8 shows the TEM observations conducted on extraction replica of specimens. $M_{23}C_6$ carbides and $Fe_2(W,Mo)$ laves phases were observed at former γ grain boundaries and lath boundaries both in heat-treated and crept specimens. Only $M_{23}C_6$ carbides were observed within the lath structures. Size of precipitates observed at each site was summarized in Table 3. Although the size of precipitates in heat-treated A and B steels were almost the

Table 3 Size of precipitates as measured from extraction replicas

(μm)

		$M_{23}C_6$		Laves Phase	
		Heat treated	Crept at 650C	Heat treated	Crept at 650C
Former g	Steel A	0.05-0.3	0.1-1	0.3-0.5	1
G.B.	Steel B	0.05-0.3	0.1-0.5	0.3-0.5	0.5-1
Lath	Steel A	0.05-0.3	0.1-0.5	0.2-0.5	0.5-1
Boundary	Steel B	0.05-0.3	0.1-0.3	0.3	0.1-0.5
Within	Steel A	0.05-0.2	0.1	-	-
Lath	Steel B	0.05-0.2	0.1	-	-

same, growth of precipitates in crept samples was observed at former γ grain boundaries and lath boundaries but not within the lath structure. Compared to steel B, growth of precipitates during the creep test was observed more clearly in steel A, especially at former γ grain boundaries. Since creep rupture strengths of steels A and B were comparable after short

times (Fig.4), it was expected that the effect of the width of the lath structure and the size and density of precipitates on short time creep rupture strength were not different for both steels.

Therefore, it was considered that the observed difference between the long-time creep rupture properties of these steels were caused by their structural changes during creep rupture tests. With respect to their chemical compositions, steel A and B had different Ni and Al contents. It is probable that Ni and Al content of these steels affected their long-time creep rupture strength. It is considered that reduction of Ni and Al suppresses the growth of precipitates and improves stabilization of the microstructure. In steel B, reduction of Al to less than 20 ppm was highly effective in improving the long-time creep rupture strength. This new WCoB12%Cr steel (steel B) had better creep properties and was successfully utilized for the manufacturing of trial rotor forging. The test results showed that this new steel has satisfactory properties to be a candidate material for turbine rotor shafts of 650C-steam generating USC power plants.

4.Turbine rotating test

To verify the reliability and practicability of this material, a model turbine rotation test was performed in the R&D program initiated by the EPDC of Japan for a target steam temperature of 630C. The test was conducted for 500 hours at 650C. The high-pressure and the intermediate-pressure first-stage blades installed in the experimental rotors had the same shape as those on the 1000 MW steam turbine. Fig.9 shows the rotating test apparatus. Investigation of the mechanical properties of the rotor material, after the rotation test, confirmed the reliability of the material.

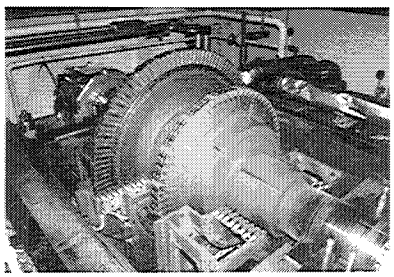


Fig.9 Turbine rotating test apparatus

5. Future rotor materials

Reduction of Ni and Al impurities in the developed steel suppressed deterioration of its long-time creep rupture properties at 650C. Effects of other austenite formers; Mn and Co on the long-time creep strength of this 12%Cr steel are expected to be the same as those of Ni. As for Co, it was added as a strengthening element but its effect on the long-time stabilization of microstructure is not clear. Since reducing Ni, Mn and Co contents will enhance δ-ferrite formation as indicated by equation (3), an effective method to suppress formation of δ-ferrite is the reduction of Cr-eq. by adding C to the steel in amounts up to 0.14 mass%.

The new 12%Cr alloy is designed to have stable long-time creep properties by reducing Ni, Mn and Co, and increasing C contents. Composition and heat-treatment conditions of the small ingot prepared to investigate long-time creep rupture strength of the new 12%Cr alloy were summarized in Table 4.

Table 4 Chemical composition of the newly designed steel (mass%)

Steel	C	Si	Mn	Ni	Cr	Mo	W	Co	V	Nb	N	B	Al(ppm)	Cr-eq.
E	0.14	0.03	0.15	0.10	10.1	0.18	2.41	1.45	0.20	0.07	0.018	0.011	≦10	7.41

1050C OQ, 570C AC, 700C AC

6. Conclusions

A new 12%Cr rotor material has been developed for application in future high-efficiency USC power plants designed to operate at 650C steam. Both 20 and 80-ton trial rotor shafts were forged and tested especially for their long-time creep rupture properties. A model turbine rotation test was also performed. The results obtained in the present study are as follows;

(1) The new steel has satisfactory properties to be a candidate material for turbine rotor shafts of 650C-steam generating USC power plants.
(2) Manufacturing of trial rotor forgings was successful.
(3) Stabilization of long-time creep rupture properties of the new steel was confirmed.
(4) Reduction of Ni and Al impurities in steel suppressed deterioration of its long-time creep rupture properties at 650C. Growth of precipitates and recovery of the microstructure were delayed by this reduction of impurities.
(5) The reliability of the material was confirmed after a model turbine rotating test.

References

[1] K. Hidaka, Y. Fukui, S. Nakamura, R. Kaneko, Y. Tanaka and T. Fujita, : Development of Heat Resistant 12%CrWCoB Steel Rotor for USC Power Plant, Advanced Heat Resistant Steels for Power Generation, EPRI, San Sebastian, Spain, 27-29 April 1998, pp. 418-429.
[2] K. Hidaka, M. Shiga, S. Nakamura, Y. Fukui, N. Shimizu, R. Kaneko, Y. Watanabe, N. Morisada, Y. Tanaka and T. Fujita, : Development of large-scale 12Cr ferritic steel turbine rotor aiming the application of ultra supercritical steam power plant at 650C, Materials Engineering in Turbines and Compressors, Newcastle upon Tyne, UK, 25-27 April 1995, Vol.1 pp.191-200.
[3] K. Hidaka, M. Shiga, S. Nakamura, Y. Fukui, N. Shimizu, R. Kaneko, Y. Watanabe and T. Fujita, : Development of 12Cr rotor steel for 650C USC steam turbine rotors, Materials for Advanced Power Engineering, Belgium, 3-6 October 1994, Part I, pp. 281-290.
[4] M. Miyazaki, M. Yamada, Y. Tsuda and R.Ishii, : Advanced heat resistant steels for steam turbines, Advanced Heat Resistant Steels for Power Generation, EPRI, San Sebastian, Spain, 27-29 April 1998, pp. 574-585.
[5] Y. Kadoya, R. Magoshi, H. Kawai, I. Tsuji, T. Tsuchiyama, S. Takeuchi and Y. Yasumoto, : Alloy design and production of an advanced 12Cr steel rotor applicable to elevated steam temperatures, Fifth International Conference on Clean Steel, Hungary, 2-

4 June 1997, Vol.2, pp. 167-177.

[6] K. H. Mayer, H. Cerjak, T.Kern, M. Staubli and D. V. Thornton, : Present status of ferritic steel development for USC power plant in Europe, International Workshop on the Innovative Structural Materials for Infrastructure in 21st. Century, Tsukuba, Japan, 12-13 January 2000, pp. 65-88.

[7] K. Sawada, M. Takeda, K. Maruyama, R. Ishii and M. Yamada, : Dislocation structure degradation during creep of martensitic heat-resisting steels with and without W, Materials for Advanced Power Engineering, Julich, September 1998, Part I. pp. 575-583.

[8] M. Shiga, : Doctoral Thesis, Hokkaido University, 1995, pp. 102-124.

[9] T. Fujita, : Current progress in 9-12%Cr ferritic heat resistant steels, Materials Engineering in Turbines and Compressors, Newcastle upon Tyne, UK, 25-27 April 1995, vol.2, pp. 493-516.

MARTENSITIC/FERRITIC SUPER HEAT-RESISTANT 650°C STEELS

R.Agamennone[1], C.Berger[2], W.Blum[1], J.Ehlers[3], P.J.Ennis[3], J.Granacher[2], G.Inden[4], V.Knezevic[4], J.W.Quadakkers[3], G.Sauthoff[4], A.Scholz[2], L.Singheiser[3], J.Vilk[4], Y.Wang[2]

[1] IWW-LS1, Universität Erlangen-Nürnberg, D-91058 Erlangen, Germany
[2] IfW, TU Darmstadt, D-64283 Darmstadt, Germany
[3] IWV2, Forschungszentrum Jülich GmbH, D-52425 Jülich, Germany
[4] Max-Planck-Institut für Eisenforschung GmbH, D-40237 Düsseldorf, Germany

Abstract

World-wide demand for higher steam parameters of Ultra Super Critical (USC) Power Plants has led to developments of new materials with improved high-temperature properties. A new project aims at new ferritic creep-resistant steels for application at 650°C and 300bar. The critical issues are improvement of long-term creep strength as well as oxidation and corrosion resistance.

The aim of the present research is to design new super heat-resistant martensitic/ferritic 9-12%Cr steels using basic principles and concepts of physical metallurgy, to test and optimise model alloys and to investigate and clarify their behaviour under long-term creep conditions with emphasis on microstructural stability and corrosion resistance. Model alloys have been designed, produced and tested with respect to deformation and corrosion. The design of model alloys has been supported by theoretical simulations and transmission electron microscopy investigations. First results for various modified 12%Cr model steels are reported, which indicate a high potential for reaching sufficient creep and corrosion resistance at 650°C. The work with further optimisation of composition and microstructure is in progress.

Keywords: Ferritic heat-resistant 12%Cr steels, microstructural stability, long-term creep, corrosion resistance

1. Introduction

The demand for reduction of monetary and environmental costs of electricity generation has resulted in the development of a new class of coal-fired plants – Ultra Super Critical (USC) Power Plants. The operating temperature and pressure of the new plants are higher than those in conventional ones in order to reduce consumption of fuel, improve thermal efficiency and reduce CO_2 emission. For this, materials with adequate creep properties and corrosion resistance are needed. There are world-wide activities in research and development of new ferritic/martensitic 9-12%Cr steels (always mass %) [1, 2]. A new German project (within the frame of the MARCKO program) has been initiated to develop a new ferritic steel for application at 650°C and 300bar in conventional power plants. The aim of the present research is to design new high-strength super heat-resistant martensitic/ferritic 9-12%Cr steels using basic principles and concepts of physical metallurgy, to test and optimise model alloys and to investigate and clarify their behaviour under long-term creep conditions with emphasis on microstructural stability and corrosion resistance. The present paper outlines the project and reports some first results. For details the reader is referred to the more specific reports on the various subprojects [3, 4, 5, 6].

2. Project structure

Five research groups cooperate as is shown in Figure 1.

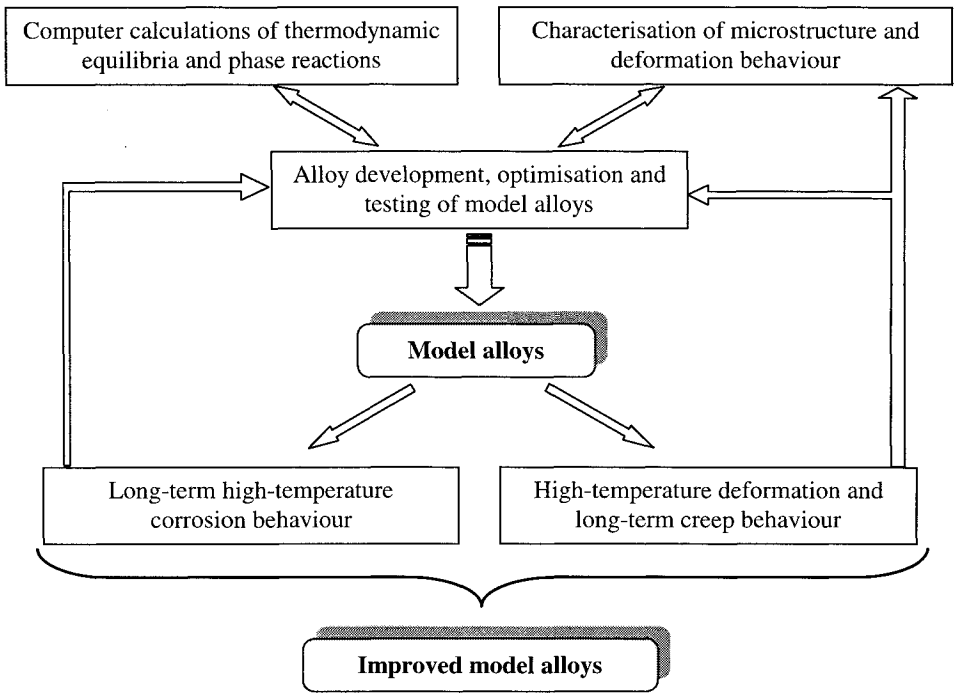


Fig.1. Development of new ferritic heat resistant 12%Cr steels.

In view of the world-wide developments of 9-12%Cr steels for application at higher temperatures, especially in Japan, the starting point has been a screening of available data, which has been supported by thermodynamic computer calculations of expected phase equilibrium and simulations of growth of precipitates [4]. Small laboratory casts of model alloys with systematically varied compositions to provide sufficient creep strength and corrosion resistance have been prepared for microstructural investigation as well as mechanical and corrosion testing [3]. The results of these investigations will form a database, which will allow estimation of the potential of the various alloy modifications and by this to reduce the number of alloys to be studied. The present study is directed at improved model alloys for further more detailed studies.

3. Design concept

The most important design parameter is a 10^5h creep rupture strength of approximately 100MPa at 650°C, as well as sufficient steam oxidation resistance. Additionally, the new material must show sufficient toughness, good fabricability, hot workability, and weldability.

The mechanical properties and their changes during service of ferritic high-Cr steels depend on chemical composition and initial microstructure as well as on service conditions. An advantageous initial microstructure of the 9-12%Cr steels is tempered martensite with or without δ-ferrite, which is formed during the final normalising and tempering heat treatment. This microstructure consists of ferrite subgrains with a high density of dislocations and distributions of more or less fine stable precipitates which block movement of subgrain boundaries ($M_{23}C_6$ carbide and Laves phase particles) and dislocations (MX carbonitride particles) and decelerate the coarsening of the microstructure [7]. During exposure to elevated temperatures and creep stress, pronounced microstructure development occurs with dislocation recovery, grain and subgrain coarsening and precipitate coarsening by diffusion processes, which all deteriorate the mechanical properties. To achieve sufficient creep resistance during the entire service life, it is necessary to stabilise the microstructure by alloying with elements which provide enough solid solution and precipitate strengthening and slow down diffusion. For this, the effects of relevant alloying elements and different types of stable precipitates on the long-term deformation behaviour as well as the oxidation resistance in steam are to be investigated systematically. Coarse intermetallic phases – in particular the Laves phase – preferentially with precipitation during service are to be used to provide enhanced creep resistance during service besides finely distributed carbides. Three series of model alloys have been prepared in order to investigate the effects of different combinations of precipitate particles on the creep resistance. The first series is to reveal the effect of various Laves phase precipitates on strengthening after precipitation of $M_{23}C_6$. A second series of alloys has been designed with not too high W content and various MX forming elements. A third series of alloys contains increased amounts of W, Ti and Ta as MX forming elements with additional microalloying with B. More details are given in [3].

To achieve a microstructure with evenly distributed particles, it is necessary to have an initially 100% martensitic microstructure and avoid formation of δ-ferrite, which deteriorates the mechanical properties. The ability to form a fully austenitic and hot-workable microstructure during normalising depends on the proper balance of the austenite and ferrite forming elements. To characterise the tendency to δ-ferrite formation, the chromium equivalent (Cr_{eq}) according to the empirical Schaeffler and Schneider diagrams together with the more reliable thermodynamic Thermocalc calculations are used. In particular, the M_s temperature should be sufficiently high to provide a complete martensitic transformation, and a high A_{c1} temperature is targetted to raise the upper limit of the tempering temperature. Additional model alloys are designed to study the effects of various austenite-forming elements.

The minimisation of particle coarsening by Ostwald ripening, which causes creep softening, is a further important topic. In view of the rate constant for Ostwald ripening, minimisation of particle coarsening means a low interface energy of the precipitated phase, i.e. coherent or semicoherent particle interfaces, a low solubility of the precipitated phase in the matrix and a low effective diffusion coefficient for the diffusive transport of solute in the matrix to and from the precipitate particles.

The necessary oxidation and corrosion resistance is obtained by increasing the Cr content to 12% and using small amounts of Si.

3. Thermodynamic computer calculations of phase equilibrium and precipitate growth

The computer program Thermocalc with a validated database of Gibbs free energies for the thermodynamic calculation of phase equilibrium has become a new powerful tool for a more accurate evaluation of phase stability [8-9]. The new ferritic steels are very complex multi-component systems with sometimes even more than 10 alloying elements. In particular, Cr, V, Nb, Mn, W, Ni, Co, Ti, Ta, N, B are usually added. The elements Ta and B are not yet included in the thermodynamic database. These missing data have to be implemented. This kind of calculation provides very useful data for the design of alloys.

The amount and composition of equilibrium phases as a function of temperature is calculated using the Thermocalc software and database, with chemical composition as the only input. Figure 2 shows the calculated equilibrium phase fractions for the model alloy DT4-30 (12Cr-0.2Si-0.15C-0.05N-4W-0.2Ta-2.85Co). This alloy was designed such that δ-ferrite formation does not occur at the austenitization temperature (right dotted line), and to have $M_{23}C_6$, Laves phase and Ta–MX carbonitrides as equilibrium phases at a service temperature of 650°C (left dotted line). Most of the Ta-MX carbonitrides are precipitated in low-temperature ferrite (arrows).

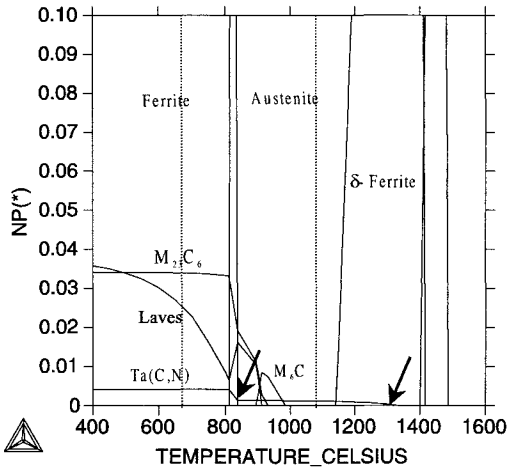


Fig.2. Calculated types and mole fractions (NP) of phases as a function of temperature for model alloy DT4-30 (12Cr - 0.2Si - 0.15C - 0.05N - 4W - 0.2Ta - 2.85Co).

Such calculations help to define the composition window of pure austenite at given temperatures. The Thermocalc results clearly show that the situation is more complex than is described by the traditional Cr and Ni equivalents in the empirical diagrams of Schaeffler and Schneider.

The obtained microstructures represent metastable states, which tend to transform towards more stable states. Materials development thus has to deal with the problem of stability of microstructure under complex service conditions, e.g. elevated temperature and stress. Although the amount of some of the alloying elements may seem to be negligibly small, this small quantity may still have a strong effect on the kinetics of phase reactions and thus on the formation and further evolution of the microstructure. The kinetic parameters of alloying elements vary by orders of magnitude in different phases, e.g. in ferrite (α) compared to

austenite (γ). Likewise the mobilities of substitutional (e.g. Mn, Cr, Ni...) elements and interstitial elements (C, N) differ enormously. As a result of these differences, various reaction regimes may occur as a function of time and heat treatment temperature before equilibrium is attained. It is also possible that, because of fast kinetics, metastable phases appear at intermediate stages consuming a large part of the available driving force. The time to reach equilibrium will then be drastically increased, often far beyond tolerable time scales. The consequences will then be revealed by a degradation of creep properties during long-term service of such material.

Once the thermodynamic data of the systems considered is available, the kinetics of precipitate growth can be calculated. The calculation of thermodynamic properties allows definition of the driving forces for reactions and to be taken of account the coupling (for the most part of thermodynamic origin) between kinetic parameters, in particular, diffusivities. It is only with the aid of numerical techniques that the complex growth kinetics can be taken into account in a quantitative way for the multi-component model alloys in question. For this the software DICTRA is used. For details the reader is referred to [10-15].

The complex behavior of such multi-component alloys is exemplified by the case of $M_{23}C_6$ precipitation in a ferritic steel, the composition of which corresponds to the alloy DT4-1, i.e. Fe-12.7Cr-4.82Co-0.213V-0.83C. Figure 3 shows the calculated results at 1053K (780°C). The Cr-profile within the $M_{23}C_6$ particle varies strongly as a function of time indicating the particle growth. This shows that the boundary condition at the moving interface is by far not constant. According to the thermodynamic database Co practically does not enter the carbide particle. It is rejected into the ferrite matrix and concentrates in front of the moving boundary. The kinetics of reaction are then controlled by the diffusion of Co into the ferrite matrix. Similar data are obtained for the other elements.

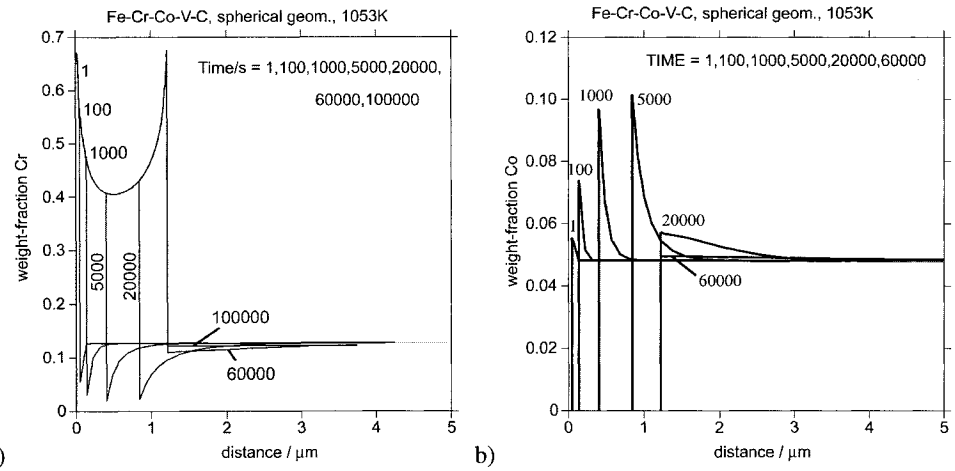


Fig. 3. Calculated Cr content (a) and Co content (b) in a growing $M_{23}C_6$ particle and in the ferrite matrix as a function of distance from the particle centre in alloy DT4-1 at various times.

This type of calculation is presently performed for various alloys and includes also the Laves phase. In addition the growth of two competing phases will be calculated by considering two coupled cells of ferritic matrix, one with a $M_{23}C_6$ precipitate particle, the other with a Laves particle. This type of calculation will give information on the kinetics of coupled competitive growth and of Ostwald ripening effects under long-term service conditions.

4. Microstructural investigations

The microstructure has been investigated in the heat-treated condition (after standard heat treatment with austenitization (1070°C/0.5h/air cooling) and annealing (780°C/2h/air cooling) and after mechanical testing. The relevant microstructural elements are examined qualitatively and, whenever possible, quantitatively by suitable combination of microscopic methods, including transmission electron microscopy (TEM) which is indispensable for revealing the structural details in the submicrometer range.

The qualitative investigations of the initial heat-treated microstructure have shown fully or almost fully tempered martensitic microstructures. Figure 4 shows an example of tempered martensitic microstructure with a small amount of δ-ferrite. The martensite lath boundaries are decorated by carbides ($M_{23}C_6$), which have precipitated preferentially at the boundaries during heat treatment. The more detailed investigation of TEM thin foils (Fig.5) reveals fine substructures in the ferritic matrix with very small subgrains with a high dislocation density and fine precipitates inside subgrains as well as on grain and interphase boundaries, indicating interactions between the precipitates and the dislocation substructure. The low-angle and high-angle boundaries as well as the finer microstructural details, namely the dislocations, precipitates and solute atoms within the subgrains, are considered to contribute to hardening.

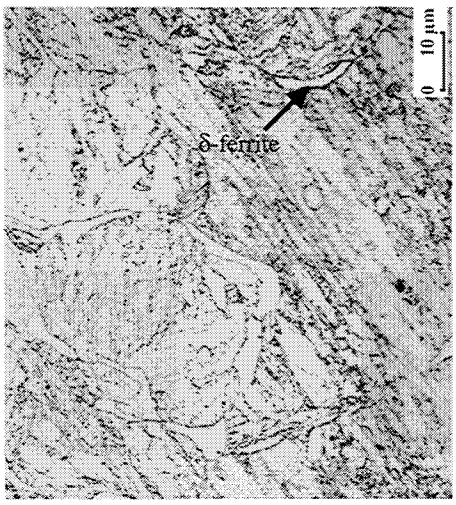


Fig. 4. Optical micrograph of model alloy DT4-1 (12Cr-0.2Si-0.10C-3W-0.2V-4.7Co) after heat treatment: martensite lath structure with a small amount of δ-ferrite ($M_{23}C_6$-hardened).

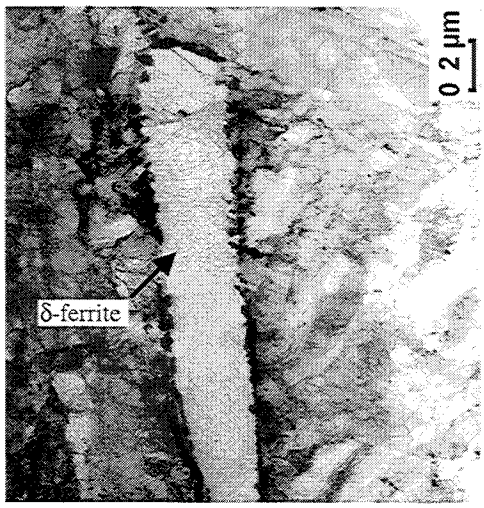


Fig. 5. TEM micrograph of model alloy DT4-1 (12Cr-0.2Si-0.10C-3W-0.2V-4.7Co) after heat treatment: martensite lath structure with a small amount of δ-ferrite ($M_{23}C_6$-hardened).

In Figure 6 typical examples of precipitates in the model alloys are shown. They have been identified by EDX. From this, it can be derived that $M_{23}C_6$ carbides as well as Laves phase are acting as obstacles for the movement of subgrain boundaries (Fig. 6a), i.e. there is "particle-stabilized subgrain hardening". Typical MX particles are smaller than $M_{23}C_6$ or Laves phase particles and react with dislocations. However, detection and identification of all precipitates in the ferrite matrix is difficult, especially when particles are small, dislocation densities high and contrast in the bright field image low. For better quantification and characterisation of the precipitates by size and chemical composition (using EDX), selective etching is applied to isolate the precipitates and extract them from the matrix, Fig. 6b.

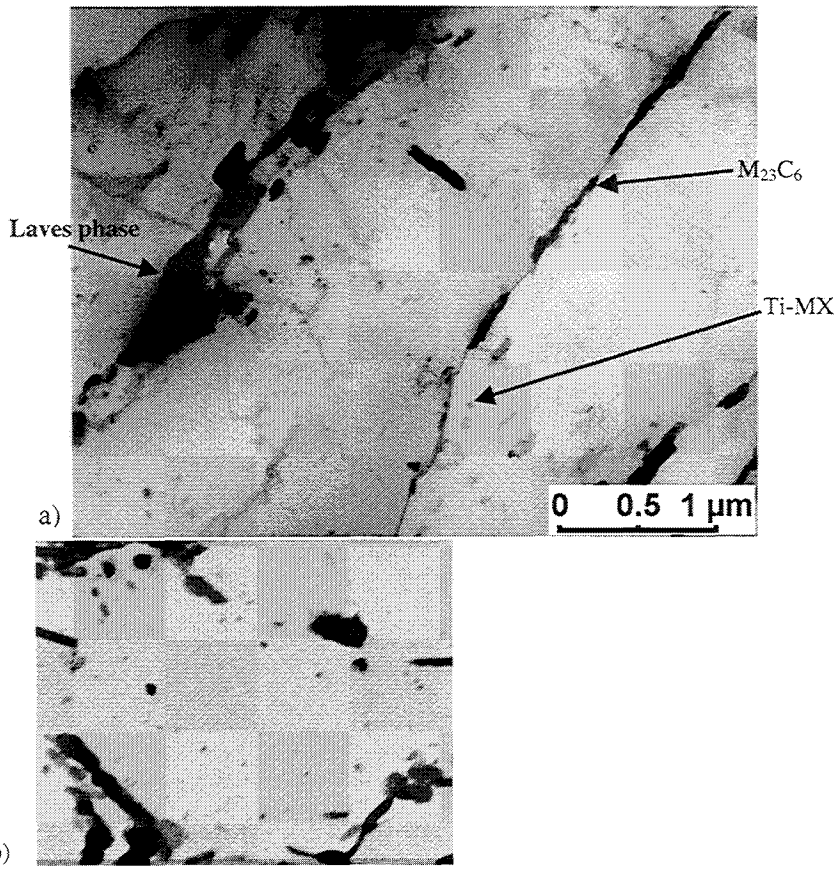


Fig.6. Precipitates in model alloy DT4-9 (12Cr-0.2Si-0.15C-3W-0.2Ti-3.05Co) after creep for 337 h at 650 °C: a) TEM micrograph of thin foil, b) TEM micrograph of extraction replica (same magnification as in (a)).

More work is needed to quantify the magnitudes of the various hardening contributions under conditions of creep when the dislocation density tends to decrease and the particles tend to coarsen. More and quantitative details on the microstructure of the 650°C-steels are reported in [5].

5. Mechanical testing

Tensile and compression tests of heat-treated alloys at room temperature and at 650°C have been performed in order to determine yield strength and ductility. Charpy tests have been used to characterise the impact properties. The results have shown the expected strengthening effects as well as sufficient ductility and toughness.

Screening creep tests are performed at temperatures between 600°C and 700°C in two regimes: in compression with stepwise loading (to characterise the stress dependence of secondary creep) and in tension with constant loading (for the preliminary characterisation of the creep strength). The results of compression creep tests for higher stress levels have indicated a high potential for reaching a sufficient creep resistance at 650°C, Figure 7. The results together with the first results of constant loading tests are used for the selection of model alloys for more detailed studies. In particular, long-term creep testing up to 20000h has been started.

The long-term creep tests of selected model alloys are to be performed with materials with three different heat-treatments in view of components in USC power plants, i.e. pipes and turbine rotors (core and surface). This research is still in progress.

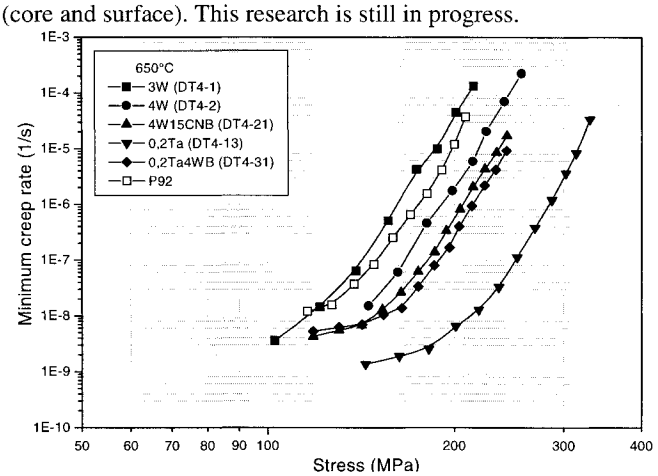


Fig. 7. Stress dependence of the compressive minimum creep rate at 650°C for selected alloys.

The estimation of long-term creep strength by extrapolation from experimental short-term data for evaluation of improvement of creep behaviour of the new alloys is an important topic. Various approaches by means of the Larson-Miller parameter or the Monkman-Grant parameter have been used. A problem is the complexity of the model alloys as well as the microstructural changes by ageing under service conditions.

6. Corrosion

The corrosion properties are a matter of primary concern in the development of steels for USC power plants. Steam-side corrosion can produce very thick oxide scales, which can lead

to overheating and which may spall and cause failure of particular components. Additionally, the reduction in metal cross-section associated with the formation of thick oxide scales will reduce the load-bearing capability, which is very critical for thin-section components.

In this study, steam oxidation tests in simulated service environments are carried out at temperatures between 600 and 650°C. The understanding of the mechanisms of oxidation including investigation of scale formation kinetics with effects of alloying elements on oxidation and effects of oxidation on service life is the subject of this part of the project [6].

The first results of long-term corrosion tests indicate the improved corrosion behaviour of 12%Cr steels compared with a commercial 9%Cr steel, Figure 8, especially at higher temperatures. In particular, alloys with Nb and Ta have exhibited extremely low corrosion rates.

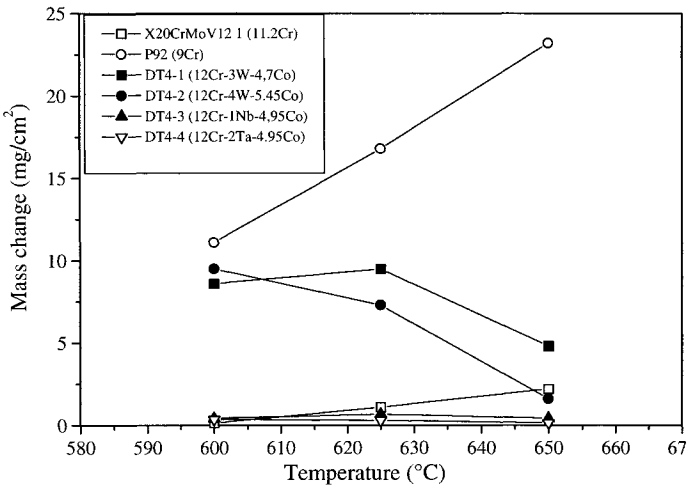


Fig.8. Mass change of 9-12%Cr steels as a function of temperature during exposure in Ar-50Vol.% H_2O for 1000h.

7. Perspectives

The investigation of the material behaviour of the considered model alloys and further more detailed studies are continued to clarify the prospects for optimising composition and pre-treatment. The interpolation and extrapolation of the observed microstructure behaviour is to be based on the theoretical calculations and microstructural investigations. It is expected that a sufficient long-term creep resistance can be achieved by optimising the content of MX forming elements and increasing the W content, together with microalloying with B.

Acknowledgment

The financial support by the Deutsche Forschungsgemeinschaft is gratefully acknowledged.

8. References

[1] K.H.Mayer, H.Cerjak, T.Kern, M.Staubli, D.V.Thornton, *Present status of ferritic steel development for USC plants in Europe*, International Workshop on the Innovation Structural Materials for Infrastructure in the 21st Century, ULTRA STEEL 2000, Tsukuba, 2000.

[2] F.Abe, M.Igarashi, S.Wanikawa and others, *R&D of advanced ferritic steels for 650°C USC Boilers*, Proceedings of the Fifth International Charles Parson Turbine Conference PARSON 2000 "Advanced Materials for 21st Century Turbines and Power Plant", IOM London, (2000)129-142.

[3] V.Knezevic, G.Sauthof, *Martensitic/ferritic super heat-resistant 650°C steels – Design of model alloys*, Materials for Advanced Power Engineering 2002.

[4] J.Vilk, G.Inden, *Martensitic/ferritic super heat-resistant 650°C steels – thermodynamics and kinetics of precipitation reactions*, Materials for Advanced Power Engineering 2002.

[5] R.Agamennone, W.Blum, *Martensitic/ferritic super heat-resistant 650°C steels – Microstructure*, Materials for Advanced Power Engineering 2002.

[6] J.Ehlers, P.J.Ennis, J.W.Quadakkers, L.Singheiser, *Oxidation Behaviour of Super Heat-Resistant Ferritic Steels in Environments Containing Water Vapour at 650°C*, Materials for Advanced Power Engineering 2002.

[7] H.Cerjak, P.Hofer, B.Schaffernak, *The influence of microstructural aspects on the service behaviour of advanced power plant steels*, ISIJ International, 39(1999)874-888.

[8] SGTE (Scientific Group Thermodata Europe), *Solution Database of Jan. 1994.*

[9] B. Sundman, B. Jansson and J.-O. Andersson, *The THERMOCALC database system*, CALPHAD 9(1985)153-190.

[10] S. Crusius, G. Inden, U. Knoop, L. Höglund and J. Ågren, *On the numerical treatment of moving boundary problems*, Z. Metallk., 83 (1992), 673-678.

[11] S. Crusius, L. Höglund, U. Knoop, G. Inden and J. Ågren, *On the growth of ferrite allotriomorphs in Fe-C*, Z. Metallk., 83(1992)729-738.

[12] G. Inden and P. Neumann, *Simulation of diffusion controlled phase transformations in steels*, Steel research, 67(1996)401-407.

[13] P. Franke and G. Inden, *Diffusion Controlled Transformations in Multi-Particle Systems*, Z. Metallk., 88(1997)917-924.

[14] G. Inden, *Cinétique de transformation de phases dans des systèmes polyconstitués - aspects thermodynamiques*, Entropie, 202/203(1997)6-14.

[15] A. Borgenstamm, A. Engström, L. Höglund and J. Ågren, *DICTRA, a Tool for Simulation of Diffusional Transformations in Alloys*, J. Phase Equilibria, 21(2000)269-280.

MARTENSITIC/FERRITIC SUPER HEAT-RESISTANT 650°C STEELS – DESIGN OF MODEL ALLOYS

V. Knezevic, G.Sauthoff

Max-Planck-Institut für Eisenforschung GmbH, D-40237 Düsseldorf, Germany

Abstract

Tempered martensitic/ferritic 9-12%Cr steels are now recognized to be the most potential materials for 650°C Ultra Super Critical (USC) Power Plants. The degradation of long-term creep strength, as a result of microstructural changes during long-term exposure at the elevated temperature, is the main problem for this group of steels. Therefore, to achieve sufficient creep resistance during the entire service life it is necessary to stabilize the microstructure by alloying with elements which provide enough solid solution and precipitation strengthening and slow down diffusion.

The aim of the present study is to investigate the effect of different types of precipitates as well as alloying elements on mechanical long-term properties of new ferritic 12%Cr steels. Fine distributions of stable precipitates which block the movement of subgrain boundaries ($M_{23}C_6$ carbides, Laves phase) and dislocations (MX carbonitrides) and delay coarsening of microstructure is the key to high creep strength of such steels. Furthermore, additional Laves phase, which precipitates during service, is to strengthen the alloys when $M_{23}C_6$ particles become less effective. Addition of Co is to achieve an initially 100% martensitic microstructure and moreover to slow down diffusion processes and consequently coarsening of particles. The partial substitution of Co by Cu and Mn is also investigated to reduce costs. The first results of mechanical tests of the studied model alloys have shown positive effects of the addition of W as Laves phase forming element, as well as of the MX forming elements Ta and Ti. Alloying with Co has also shown beneficial effects on the creep strength of model alloys. Further optimisation of composition and microstructure is in progress.

Keywords: 12%Cr steels, Laves phase, MX carbonitrides, creep resistance

1. Introduction

The demands for higher steam parameters of USC power plants with enhanced thermal efficiency, lower costs and reduced emission of environmentally damaging gases have resulted in advanced alloy-development programs aiming at new materials with improved long-term high-temperature properties [1]. The new martensitic/ferritic 9-12%Cr steels are an alternative for widely used high-strength austenitic stainless steels. Their favourable physical properties (such as advantageous thermal conductivity and lower thermal expansion coefficient together with higher thermal shock resistance) and lower price are the main advantages of austenitic stainless steels, especially for construction of thick-section components and components with large diameters. The critical issues are the improvement of long-term creep strength as well as oxidation and corrosion resistance.

As is well known, the increased temperature accelerates all degradation processes in the steels, such as migration of atoms and dislocations, recovery and recrystalisation, grain and subgrain coarsening, precipitation coarsening, corrosion etc. Therefore, under service conditions (elevated temperature and pressure) pronounced microstructural changes occur, leading to the degradation of long-term creep strength [2]. Hence, improvement of

microstructural stability is the key for decelerating degradation processes and obtaining excellent long-term creep strength. For this it is necessary to slow down the recovery of microstructure, provide enough solid solution and precipitation strengthening and slow down precipitation coarsening. The aim of the present study is to investigate the effect of different types of precipitates ($M_{23}C_6$, MX, Laves phase) as well as alloying elements on creep behaviour of new super heat-resistant 12%Cr steels. This paper describes the alloy design philosophy and the present status of steel development.

2. Experimental material and procedure

Small laboratory casts (~0.5kg mass) with systematically varied compositions with respect to relevant alloying elements are vacuum induction melted. For achieving the needed initial microstructure, standard heat treatments with austenitization at 1070°C for 0.5h, subsequent air cooling and annealing for 2h at 780°C are used.

The microstructures of the model alloys in the initial state and after mechanical testing are qualitatively and quantitatively analysed by light (LM) and transmission electron (TEM) microscopy [3]. The microstructure observations are compared not only with the predictions of the empirical Schaeffler diagram, but also with theoretical simulations using the computer program Thermocalc [3].

Yield strength, ultimate strength and fracture strain are determined in tension at room temperature whereas yield strength at 650°C is determined in compression. Screening creep tests are performed at temperatures between 600°C and 700°C in compression with stepwise loading and in tension with constant loading under stresses ranging from 40 to 240MPa.

3. Results

3.1. Design of model alloys

The present development aims at new alloys with a 10^5h creep rupture strength of 100MPa at 650°C. For this it is necessary to provide the formation of stable precipitates, avoid δ-ferrite formation, slow down diffusion rates and minimise particle coarsening (Ostwald ripening), maintain and possibly increase M_s and A_{c1} temperature and obtain high steam oxidation resistance, but also provide sufficient toughness, good weldability and sufficient hot workability.

Figure 1 shows the alloy design concept for the new martensitic/ferritic super creep resistant 12%Cr steels.

The contents of Cr and Si were fixed at 12% and 0.2%, respectively, to obtain the necessary oxidation and corrosion resistance. It was reported earlier that 9%Cr steels cannot be used in a temperature range above 625°C because of oxidation and corrosion problems and too high contents of Si have negative effects on creep properties [4].

The key for achieving an extended creep life of this class of steels, besides solid-solution strengthening, is the production of fine distributions of stable precipitates which block the movement of subgrain boundaries ($M_{23}C_6$ carbides, Laves phase) and dislocations (MX carbonitrides) and delay coarsening of microstructure. The aim is to produce a sequence of

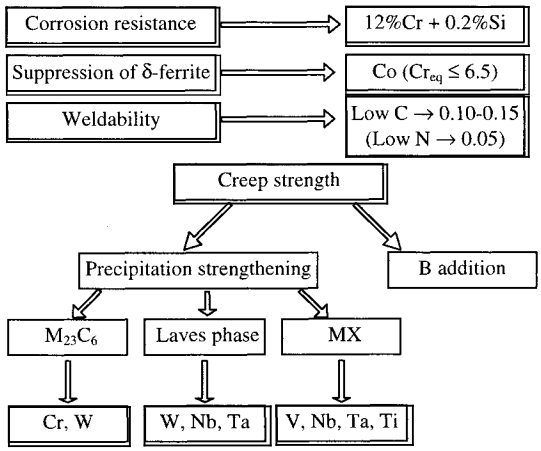


Fig.1. Alloy design concept for new martensitic/ferritic 12%Cr model alloys.

precipitates with different kinetics, i.e. when the first precipitate ($M_{23}C_6$) overages the second precipitate (Laves phase) comes into operation. In view of the minimisation of the particle coarsening by Ostwald ripening, precipitation of coherent or semicoherent MX particles with low solubility in the matrix is strongly desirable. Therefore relatively high amounts of carbide, nitride and Laves phase forming elements - Cr, W, Nb, V, Ta, Ti together with C and N – are to be added to form stable precipitates. However, C and N are to be restricted to retain weldability.

These alloying elements are ferrite-forming elements. δ-ferrite is an undesirable phase and has a negative effect on creep resistance, ductility and impact energy. Hence, the addition of Co is to balance ferrite-forming elements and to achieve an initially 100% martensitic microstructure. For quantification of the tendency of δ-ferrite formation the chromium equivalent (Cr_{eq}) has been used, the upper limit of which has been chosen as 6.5 [5]:

$$Cr_{eq} = Cr+6Si+4Mo+1.5W+11V+5Nb+12Al+2.5Ta+8Ti-40C-2Mn-4Ni-2Co-30N-Cu \quad (1)$$

Moreover, Co has almost no effect on the A_{c1} temperature, increases the M_s temperature and Curie temperature and is expected to slow down diffusion processes and consequently coarsening of particles, it shows high solubility in ferrite and almost no solubility in the Laves phase. The partial substitution of Co by Cu and Mn is studied in view of cost reduction. For further improvement of creep properties, addition of B is to be used.

According to this concept 4 series of model alloys have been prepared, Tables 1-4. The first series is used to study the effects of variation of Laves phase precipitation on strengthening after precipitation of $M_{23}C_6$, Table 1. Based on the alloy with 3%W from the first series and the experiences with the 9%Cr steels, which contain fine MX carbides and carbonitrides, the second series of alloys has been designed using V, Nb, Ti and Ta as MX forming elements to investigate effects of different types of carbonitrides on creep properties, Table 2. The increased amount of W (4%) and Ti and Ta, which are the most promising MX forming elements in view of the high stability and the low solubility of the respective MX phases, is the base for the design of the third series of alloys, Table 3. It is expected that a proper balance of these two types of precipitates leads to sufficient creep strength at 650°C. In addition, the effect of boron microalloying is to be checked. Table 4 shows the designed

Table 1. Nominal composition (wt.%) of series 1 alloys (Laves phase alloys).

Alloys	Cr	Si	C	N	W	V	Nb	Ta	Co	B
W-Laves phase	12,00	0,20	0,10-0,15	0,0-0,05	3,0-4,0	0,20			2,95-5,45	0-0,003
Nb-Laves phase	12,00	0,20	0,10			0,20	1,00		4,95	
Ta-Laves phase	12,00	0,20	0,10			0,20		2,00	4,95	

Table 2. Nominal composition (wt.%) of series 2 alloys (MX phase alloys)

Alloys	Cr	Si	C	N	W	V	Nb	Ta	Ti	Co
V-MX	12,00	0,20	0,15	0,05	3,00	0,30-0,40				3,50-5,45
Ti-MX									0,01-0,35	2,65-5,45
Nb-MX							0,20-0,40			2,35-2,85
Ta-MX								0,20-0,80		2,10-5,45

Table 3. Nominal composition (wt.%) of series 3 alloys (MX + Laves phase alloys)

Alloys	Cr	Si	C	N	W	Ta	Ti	Co	B
W-Laves phase + Ti-MX	12,00	0,20	0,15	0,05	4,00		0,35	4,00	0-0,003
W-Laves phase + Ta-MX						0,20-0,80		2,85-5,45	
W-Laves phase + Ta-Ti-MX						0,10-0,50	0,01-0,20	3,525-4,00	

Table 4. Nominal composition (wt.%) of alloys with reduced Co content.

Alloys	Cr	Si	C	N	W	V	Co	Other
Co+C	12,00	0,20	0,20	0,05	4,00	0,20	2,70-4,45	
Co+Mn			0,15					1,00Mn
Co+Cu							3,20-4,45	1,00Cu

chemical compositions of additional alloys in which Co in the alloy with 4%W is replaced partially by C, Cu and Mn in order to study the effect of different austenite-forming elements on creep.

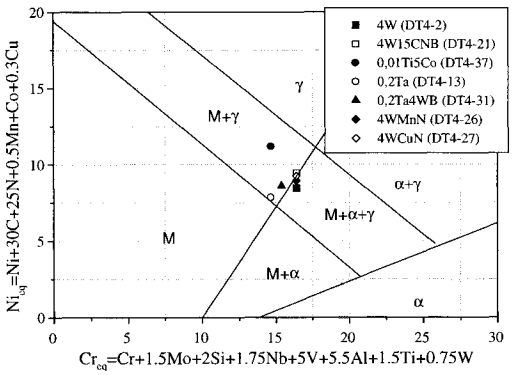


Fig.2. Schaeffler diagram for selected alloys of the various series.

According to the Schaeffler diagram (Fig.2.) the designed alloys are near the line which separates the fields with and without δ-ferrite and therefore no δ-ferrite is expected in the heat-treated alloys of all series. This is confirmed by thermodynamic calculations which predict the absence of δ-ferrite for most alloys [3]. $M_{23}C_6$ carbide and Laves phase are equilibrium phases at 650°C, as well as at the temperature of annealing (780°C). In alloys with MX forming elements the MX carbonitride is expected at both temperatures of interest. With the optimisation of the amounts of alloying elements it is possible to obtain an alloy in which precipitation occurs mostly in the low-temperature ferrite.

3.2. Chemical composition and microstructure

The chemical analyses of the prepared model alloys have shown deviations from nominal compositions, in particular higher amounts of Cr and W and lower contents of C and N, causing an increase of the Cr_{eq} values and shifting the alloys in the Schaeffler diagram toward the ferrite field. The microscopic examinations have confirmed the tendency for δ-ferrite formation, but still fully or almost fully tempered martensitic microstructures have been obtained initially, Fig. 3. The more detailed TEM analyses have confirmed the presence of limited amounts of δ-ferrite in some alloys, as well as very fine subgrain structures in the martensitic matrix [3]. Table 5 gives an overview of particles detected by EDX-analyses in

heat-treated and crept microstructures of selected model alloys from the first and the second series. Relatively coarse $M_{23}C_6$ particles have been found on grain and subgrain boundaries in the initial state, a few coarse Laves phase particles have also been observed in the second alloy and the fine, homogeneously distributed TaX particles have precipitated inside subgrains in the last alloy. A distinct coarsening of the subgrains, as well as of $M_{23}C_6$ carbides, and a pronounced precipitation of Laves phase has been observed in all three alloys. TaX particles in alloy DT4-13 grow only very slowly as was expected.

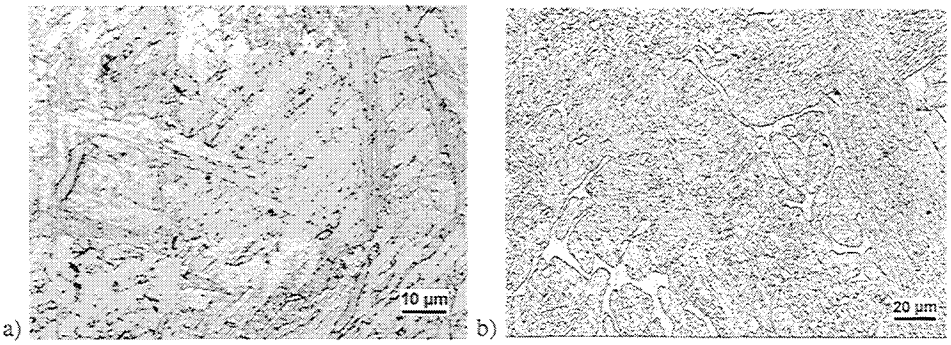


Fig.3. LM micrographs of alloys a) DT4-2 and b) DT4-31 after heat treatment.

Table 5. Precipitates in selected model alloys from different series.

Alloy	Precipitates	
	"heat-treated" state	"crept" state
DT4-1 (12Cr-0.2Si-0.10C-3.0W-0.2V-4.7Co)	$M_{23}C_6$	$M_{23}C_6$ + Laves phase
DT4-2 (12Cr-0.2Si-0.10C-4.0W-0.2V-5.45Co)	$M_{23}C_6$ + Laves phase	$M_{23}C_6$ + Laves phase
DT4-13 (12Cr-0.2Si-0.15C-0.05N-3.0W-0.2Ta-2.1Co)	$M_{23}C_6$ +Ta-MX	$M_{23}C_6$ +Ta-MX + Laves phase

3.3. Mechanical properties

3.3.1. Yield and ultimate strength

The ultimate tensile strength at room temperature of all selected alloys from the three series, Fig. 4, are on the same level or higher than the minimum specified value for P92 (600MPa [6]). The increased amounts of W and C and addition of N and B on the one hand, and addition of MX forming elements on the other hand increase both yield strength and ultimate

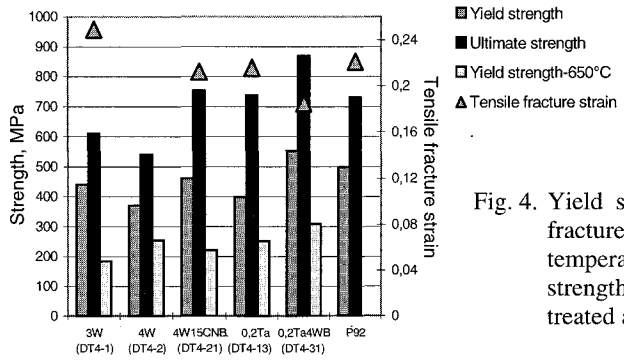


Fig. 4. Yield strength, ultimate strength and fracture strain in tension at room temperature and compressive yield strength at 650°C for selected heat-treated alloys of the three alloy series.

tensile strength by up to 35% and 39%, respectively. The ductility decreases, but the fracture strain is still of the order of 20%. Increasing the testing temperature from room temperature to 650°C lowers the strength, but again increases of W and C and addition of N and B lead to higher yield strengths at 650°C.

3.3.2. Impact toughness

Results of impact tests for selected model alloys are shown in Fig. 5. The brittle-to-ductile transition temperature (temperature for medium energy between lower and upper level of impact energies) is about –35°C and –22°C for alloys DT4-7 and DT4-13, respectively, and about –20°C for the other 3 alloys. High impact energy values (77J/cm^2 and 74J/cm^2 for the first two alloys and about 60J/cm^2 for the last three alloys) are reached at 30°C and 60°C, respectively.

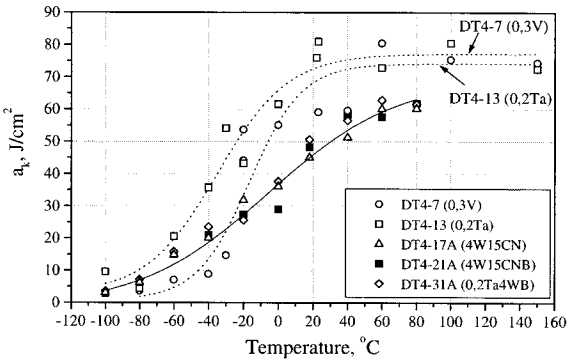


Fig. 5. Temperature dependence of impact energy for selected model alloys (heat-treated state).

3.3.3. Creep

The results of compression creep tests with stepwise loading for higher stress levels at 650°C and 675°C for selected alloys from series 1-3 are shown in Figures 6 and 7. The base alloy DT4-1 exhibits a stress dependence of secondary creep at 650°C similar to that of P92, whereas all others exhibit lower minimum creep rates, Fig. 6. The increased W content as well as addition of MX forming elements and B shifts the stress-creep rate curves to higher stresses. Alloy DT4-13 with 0,2Ta has shown the lowest minimum creep rate at 650°C. As usual the stress dependence of $\dot{\varepsilon}_{min}$ can be described by Norton´s power law:

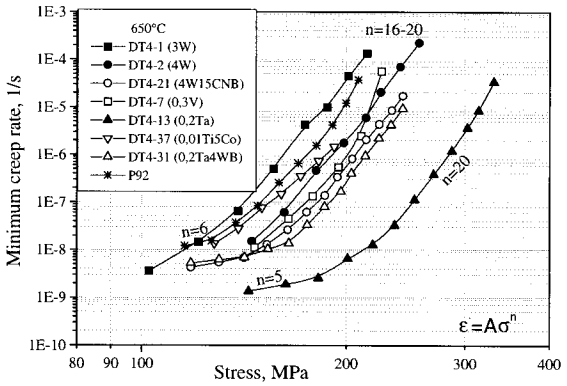


Fig.6. Stress dependence of the compressive minimum creep rate at 650°C for selected alloys.

$$\dot{\varepsilon}_{min} = A\,\sigma^n, \qquad (2)$$

where n is the stress exponent and A is a factor of proportionality depending on microstructure and temperature. The slope of the σ-$\dot{\varepsilon}_{min}$ plot for alloy DT4-13 decreases from a high value (n=20) for stresses > 210MPa to a low value (n=5) for lower stresses. A similar behavior has been observed for other alloys: n takes high values (n=16-20) in the high-stress region and decreases to low values in the low-stress region, indicating the effect of precipitate hardening.

The change in the slope of the σ-$\dot{\varepsilon}_{min}$ curves was also found at 675°C, Fig.7. At this temperature the first results for alloy DT4-21 (12Cr-0.2Si-0.15C -0.05N -4.0W - 0.2V-3.7Co-0.003B) suggest that an increase of carbon content and addition of N and B can significantly improve creep properties (compared to both model alloy DT4-2 and commercial alloy P92, tested under the same conditions). Moreover, even for alloy DT4-15 (12Cr-0.2Si-0.15C-0.05N-3.0W-0.8Ta-2.85Co), which has lower creep strength at 675°C than P92, a higher content of W and alloying with B improves the creep properties with levels higher than for P92.

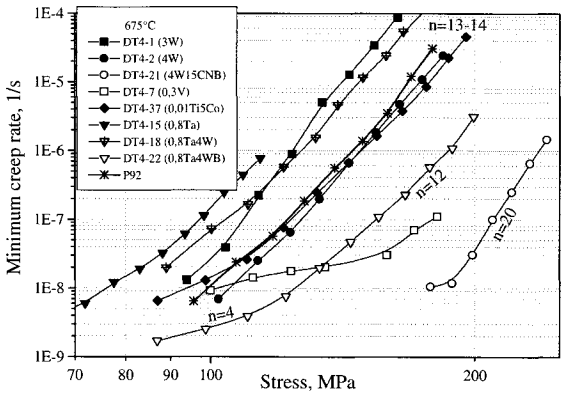


Fig.7. Stress dependence of the compressive minimum creep rate at 675°C for selected alloys.

The results of iso-stress tests over a range of stresses from 60 to 150MPa at 650°C for alloys DT4-1 and DT4-2 are shown in Figure 8. The creep rate vs. time curves (Figs. 8a and b) show that both alloys exhibit similar creep rates in the initial stage of creep, whereas the primary creep of alloy DT4-2 extends to longer times than that of the alloy DT4-1, resulting in a lower minimum creep rate and longer rupture time. The longer duration of primary creep is believed to result from the higher amount of Laves phase precipitates on boundaries in alloy DT4-2. It should also be noted that at higher stresses (120 - 150MPa) the creep minimum is observed for higher strain levels (for alloy DT4-1 in the strain range 0.015- 0.02 and for alloy DT4-2 – up to 0.05), Figures 8c and d. At lower stresses (60 to 100MPa), however, the creep minimum is reached at small strains less than 0.01. Thus the transition from primary creep to tertiary creep occurs at relatively small strains compared with creep at higher stresses.

Addition of MX-forming elements reduces the creep rate in the primary stage and shifts the strain for minimum creep rate to lower values, although the effect on creep life, compared with base alloy DT4-1, is less pronounced, Figures 9a and b. Still alloy DT4-2 with increased amount of W exhibits the lowest creep rate and the longest creep life.

The first results of series 3 alloys have shown a beneficial effect of the simultaneous effects of the increase of W content and addition of MX forming elements as well as addition of B, Fig.10a and b. The creep rate in the primary stage is significantly reduced and the resultant creep life is almost double that of alloy DT4-2.

The analysis of data according to the familiar Monkman-Grant equation leads to a linear dependence of the minimum creep rate on time to rupture in the double-logarithmic plot, Figure 11. The slope of the lines and the constants for alloys DT4-1 and DT4-2 are very close to literature data [6]. This type of creep data evaluation can be used to predict the rupture lives for specimens being tested at low stresses, which have not yet ruptured, as well as for determination of the secondary creep rate for 10^5h rupture life.

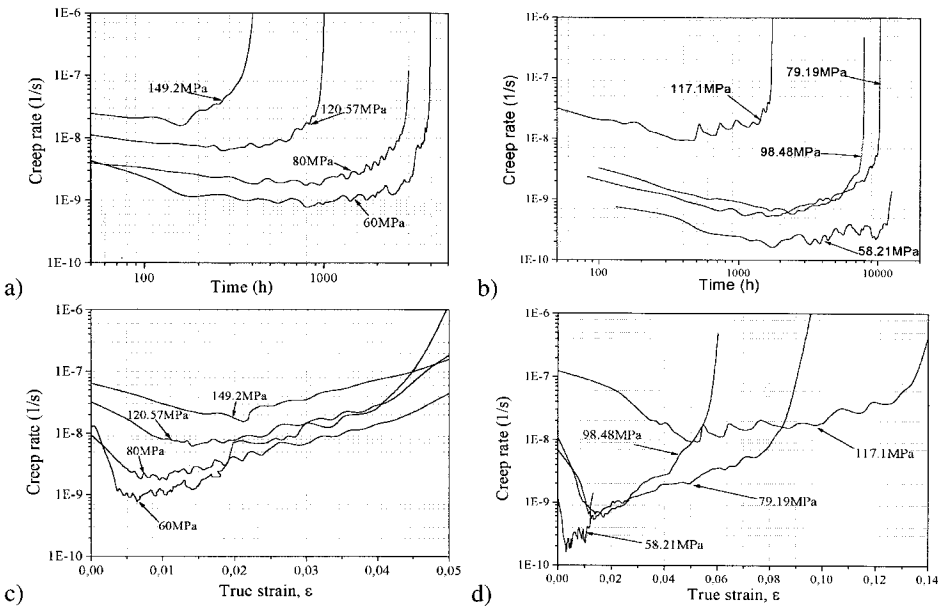


Fig. 8. Tensile creep curves for alloys DT4-1 (a, c) and DT4-2 (b, d) at 650°C.

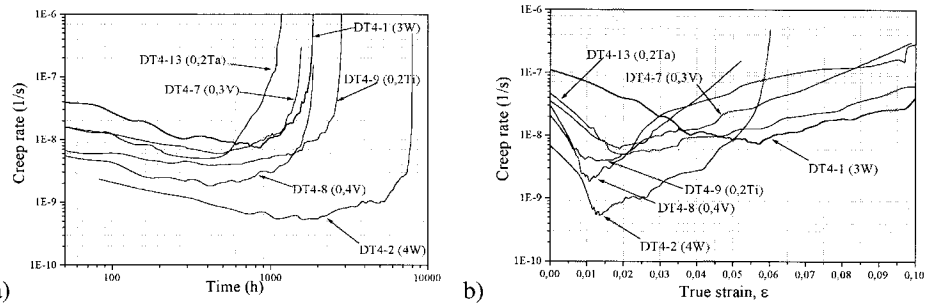


Fig.9. a) Creep rate vs. time and b) creep rate vs. creep strain curves for selected alloys at 650°C (stress level 100MPa)

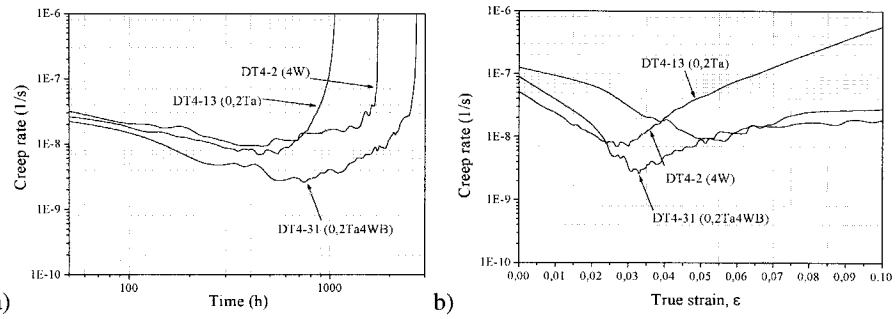


Fig.10. a) Creep rate vs. time and b) creep rate vs. creep strain curves for selected alloys at 650°C (stress level 120MPa).

The iso-stress data for selected alloys in the temperature range 625-700°C, Figure 12, again demonstrate the considerable strengthening effect of increased W and Co contents which is not restricted to 650°C. It is noted that the apparent temperature dependence of the minimum creep rate does not correspond to a simple Arrhenius-type relation which is believed to be caused by microstructure changes as a function of temperature.

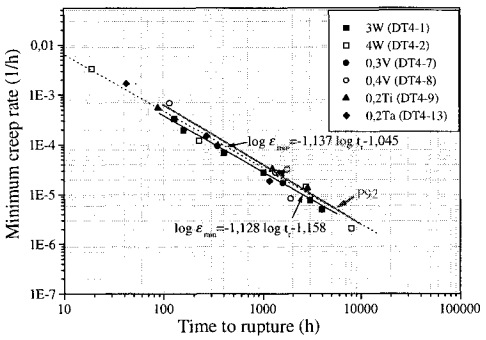


Fig.11. Minimum creep rate as a function of rupture life time for selected alloys (Monkman-Grant analysis).

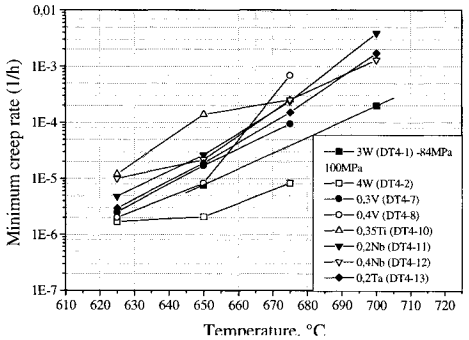


Fig.12. Minimum tensile creep rate at 100MPa as a function of temperature for selected alloys.

4. Discussion

The present results for various 12%Cr model alloys have indicated a high potential for reaching a sufficient creep resistance at 650°C.

In spite of the deviation from the nominal compositions and hence higher Cr_{eq} than 6.5, the addition of Co to 12%Cr steels, which balances the effect of the ferrite-forming elements, indeed prevents δ-ferrite formation and produces martensitic microstructures without lowering the A_{c1} and M_s temperatures too much. The first results of the partial substitution of Co by Cu are rather promising. This is being studied in more detail. Alloying with W for producing the Laves phase and with MX forming elements has shown the expected effects on precipitation kinetics and creep strengthening. The volume fraction of Laves phase seems to depend only on W content. The amount of MX phase depends sensitively on the N content. Further work is concentrated on the careful balance of alloying elements for producing a precipitation sequence of MX phase and Laves phase, which is supported by theoretical calculations.

The ultimate tensile strength, yield strength and ductility at room temperature as well as at 650°C of the studied model alloys are on the same level or higher than for alloy P92 [6]. Even toughness, which is usually the main problem of creep resistant steels, is still satisfactory.

According to first results the MX particles with Ta exhibit negligible coarsening during creep, which is a prerequisite for maintaining a high creep resistance. The addition of MX-forming elements and N in the second series of model alloys has not produced the expected positive effects, Fig. 9. The low N level in the studied model alloys is believed to be the reason for the still low strengthening effect of the MX precipitates in the present alloys. Table 6 summarises

the observed effects. The higher content of N and Co as well as precipitation of fine MX phase in the solid state obviously led to better creep properties, together with increased W content. The further optimisation of the amount of the MX forming elements - in particular Ta and Ti as the most promising elements in view of their low solubility in ferrite - with the proper amount of N together with the optimisation of the Co content is expected to result in alloys with a satisfactory creep resistance at 650°C. The first results of creep tests for the third series of alloys have confirmed the feasibility of this aproach. This is subject of further work, which is in progress.

Table 6. Composition of N and Co in selected alloys from series 1 and 2 and characteristics of MX particles (according to thermodynamic calculations [5]).

	Alloy					
	DT4-2	DT4-8	DT4-9	DT4-13	DT4-7	DT4-1
$\dot{\varepsilon}_{min}$	5,05 E-10	1,76 E-09	3,82 E-09	4,58 E-09	5,95 E-09	7,16 E-09
N content (wt.%)	-	0,0093	0,0210	0,0098	0,0015	-
Co content (wt.%)	5,6	3,9	2,5	2,05	3,6	4,8
Precipitation of MX	-	in solid state	from liquid phase	in solid state	in solid state	-

5. Conclusions

The creep strength of ferritic/martensitic 12%Cr heat resistant steels can be improved by:
- increase of W content (from 3% to 4%) for providing enough Laves phase strengthening during high-temperature exposure when coarsened $M_{23}C_6$ becomes less effective,
- addition of MX forming elements, especially Ta and Ti, for delaying dislocation recovery,
- microalloying with B, and
- increase of Co content for stabilising $M_{23}C_6$ and Laves phase particles and producing initially 100% martensitic microstructures.

The proper balance of these elements should lead to satisfactory creep strength. The more detailed investigation of the observed effects is in progress.

6. References

[1] F. Masuyama, *History of Power Plants and Progress in Heat Resistant Steels*, ISIJ International, 41(2001)612-625.

[2] H.Cerjak, P.Hofer, B.Schaffernak, *The influence of microstructural aspects on the service behaviour of advanced power plant steels*, ISIJ International, 39(1999)874-888.

[3] R.Agamennone, C.Berger et al., *Martensitic/ferritic super heat-resistant 650°C steels*, Materials for Advanced Power Engineering 2002.

[4] F. Masuyama, *New developments in steels for power generation boili*, Proceedings of the International Conference on Advanced Heat Resistant Steels for Power Generation in San Sebastian (Spain), IOM, London.

[5] Y.Kadoya, R.Magoshi et al., *Alloy design and production of an advanced 12Cr steel rotor applicable to elevated steam temperatures*, Fifth International Conference on Clean Steel, Balatonfüred, Hungary, 1997.

[6] O.Wachter, P.J.Ennis, *Investigation into the properties of the 9% chromium steel 9Cr-0.5Mo-1.8W-V-Nb with a view to ist application as steel for pipework and boilers operating at elevateed temperatures – Part 1: Microstructure and mechanical properties of the basis steel*, VGB Kraftwerkstechnik, 77(1997)699-713.

MARTENSITIC/FERRITIC SUPER HEAT-RESISTANT 650°C STEELS – THERMODYNAMICS AND KINETICS OF PRECIPITATION REACTIONS

J.Vilk, A. Schneider and G.Inden

Max-Planck-Institut für Eisenforschung GmbH, Max-Planck Straße 1, 40237 Düsseldorf, Germany

Abstract

The aim of the present study is to support the design of 12%Cr steels for application in 650°C Ultra Super Critical (USC) Power Plants in view of achieving a highly stable microstructure with initially 100% martensite which is strengthened by different types of phases ($M_{23}C_6$, MX, Laves phase). Thermodynamic calculations of phase equilibria in these new ferritic 12%Cr super-heat resistant steels are performed using Thermo-Calc. The complex multicomponent alloys, which contain some non-typical alloying elements, require modifications of the original database with additional thermodynamic data, for example for systems containing Ta. The high creep strength of this type of steel results from finely distributed precipitates in a tempered martensitic microstructure. Increased service temperatures and creep deformation favour degradation processes, which decrease the strength of the steels. Therefore, the diffusion controlled precipitation processes are simulated using DICTRA.

Keywords: ferritic heat-resistant 12%Cr steels, precipitation, thermodynamics, kinetics

1. Introduction

Within this project 9-12% Cr steels with fully martensitic microstructure are considered. The alloying elements have to be chosen such that after the heat treatment (austenitisation – cooling – tempering) the microstructure consist of tempered martensite. After tempering a lath martensitic structure is obtained with precipitates in the laths and on the lath boundaries. This microstructure still does not correspond to an equilibrium state.

The essential precipitates are carbides or carbonitrides, $M_{23}C_6$, MX and Laves phase. As a result of the high Cr content, the possibility of δ-ferrite present being at the austenitization temperature is high. δ-ferrite present in the martensitic structure deteriorates the physical properties like toughness, creep-strength, rupture, hot workability [1], [2]. The suppression of unwanted δ-ferrite in chromium steels is of paramount importance and thus a major aspect of the thermodynamic calculations.

In order to establish a given microstructure by an adequate heat treatment it is necessary to have an idea about the kinetics of formation of the various phases. The kinetics are controlled (a) by the diffusivities of the elements which may vary by orders of magnitude, and (b) by differences in the solubility. If elements are higly soluble they have to be transported to the growing phases by diffusion, if they are not soluble they have to be rejected ahead of the growth front into the matrix. Based on the thermodynamic data it is possible to calculate the diffusion controlled kinetics.

The basis for the equilibrium calculations is the software THERMOCALC [3] together with the database SSOL [4] .

2. Equilibrium calculations

The new ferritic steels are very complex multicomponent steels. Up to now model alloys have been considered and analyzed. They may be divided into four groups. The equilibrium calculations were performed with these alloys. In this report the results of selected alloys (given in Table 1) are presented.

Alloy		Cr	Co	W	Si	V	C	Nb	Ti	N
DT4-1	3W	12.00	4.70	3.00	0.20	0.20	0.10			
DT4-7	03V	12.00	3.50	3.00	0.20	0.30	0.15			0.05
DT4-9	0.2Ti	12.00	3.05	3.00	0.20		0.15		0.20	0.05
DT4-10	0.35Ti	12.00	3.95	3.00	0.20		0.15		0.35	0.05
DT4-11	0.2Nb	12.00	2.35	3.00	0.20		0.15	0.20		0.05

Table 1: Chemical compositions

The elements Ta and B could not be included in the thermodynamic calculations since Ta is not yet implemented in the database. The element B is included. However, the corresponding thermodynamic data are either incomplete or not correct. The calculations including B gave absurd results (e.g. liquid stable at very low temperatures). Preliminary calculations including the systems Ta-C and Ta-C-N could be performed with a non-public database obtained in co-operation with Dr. Ales Kroupa [15] who assessed data for ferrite, austenite and MX-carbide.

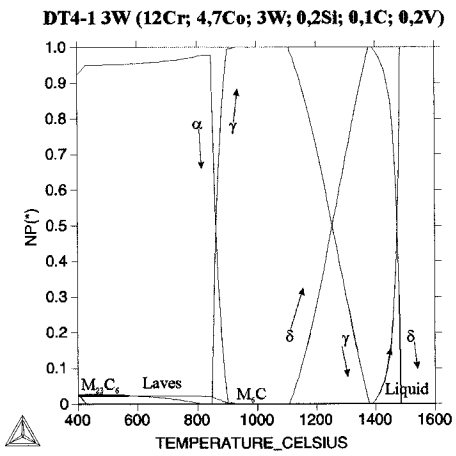


Figure 1a

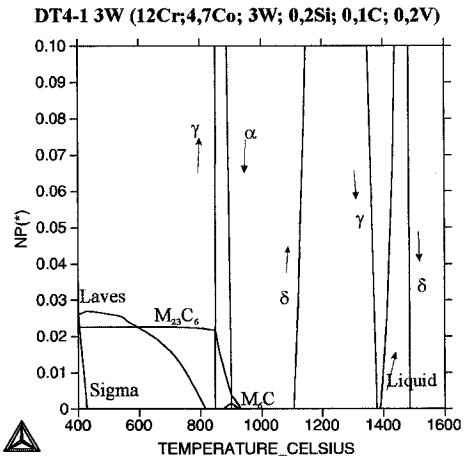


Figure 1b

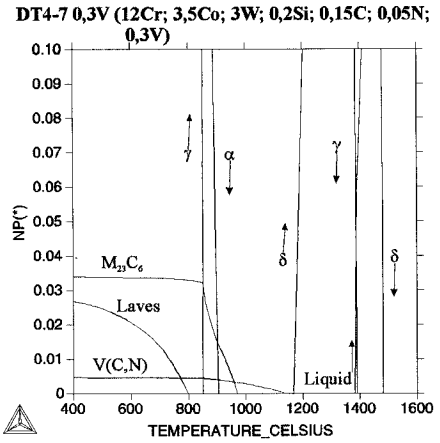


Figure 1c

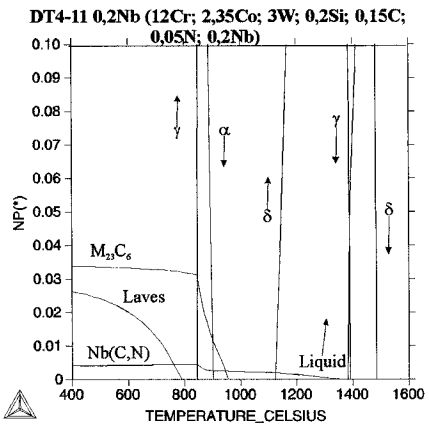


Figure 1d

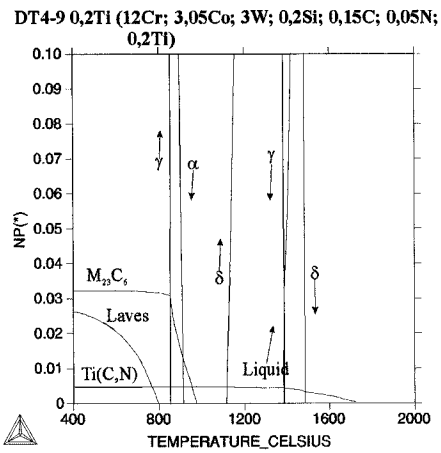


Figure 1e

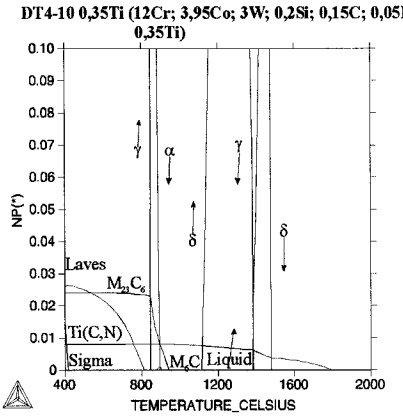


Figure 1f

Figure 1 a-f: Thermodynamic calculations for alloys from Table 1 (NP(phase) = amount of the phase in mole fractions of formula unit. The formula is defined for 1 mole of atoms, e.g. $M_{0,793}C_{0,207}$ instead of $M_{23}C_6$).

The results from thermodynamic calculations for model alloys from Table 1 are shown in Figure 1. The diagrams show the mole fractions of coexisting phases as a function of temperature. At the austenitization temperature of 1070°C the alloys are austenitic as required. At the tempering temperature 780°C, $M_{23}C_6$ and the Laves phase are stable in the ferritic matrix. Adding W increases the amount of Laves phase and stabilizes it to higher temperatures, Figure 1a, 1b. These phases precipitate mainly on subgrain boundaries where they block the movement of these boundaries [13].
The next series of model alloys introduces V, Nb, Ti and Ta as MX forming elements. The experiments with 9% Cr steels containing fine MX carbides show that the MX particles are very small producing a strong precipitation strengthening effect.

The calculated phase equilibria are shown in Figure 1c-1f. The diagrams show the temperature range of δ-ferrite free zone around the austenitization temperature. At the temperature of tempering, the carbides $M_{23}C_6$, MX and Laves phase are stable.
The elements M=V, Ti, Nb stabilize the M(C,N) carbonitride. This carbonitride may be so stable that that it precipitates already in the liquid phase, Figure 1e,1f. Precipitation in the liquid phase is unwanted since it will lead to coarse particles which do not improve the mechanical properties.

3. Effect of alloying elements on the ferrite/austenite phase boundaries

It is common practice to classify the elements according to their stabilizing effect on various phases, e.g. ferrite or austenite stabilizer. The stabilizing effect of an element is determined by its effect on the phase boundaries. If adding the element leads to a widening of the ferrite (austenite) phase field, the element is called a ferrite (austenite) stabilizer. The effect is scaled relative to reference elements, Cr for ferrite stabilizers, and Ni for austenite stabilizers. So-called "Cr-equivalents" and "Ni-equivalents" are introduced as axes such that, instead of having many component axes, multi-component property diagrams are projected into a plane with the two axes, Cr and Ni equivalents. One such diagram is the Schaeffler diagram, originally invented to characterize the effect of alloying elements on the microstructure of steel welds. Such diagrams have also been used in the development of ferritic steels in order to determine limits for the occurrence of δ-ferrite after an austenitization treatment. An example of such a Schaeffler diagram is shown in Figure 2.

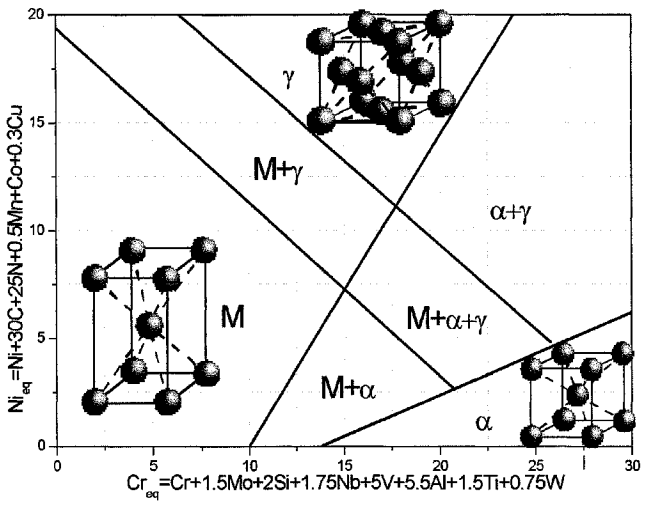


Figure 2: Schaeffler diagram characterizing microstructures in ferritic 9-12%Cr steels after austenitisation, according to [19]. On the axes Cr- and Ni-equivalents are plotted which are supposed to bring the boundaries of an Fe-X-Y system into coincidence with Fe-Cr-Ni.

Such diagrams are very attractive in view of their simplicity. The question remains, whether or not such diagrams can be supported by thermodynamic calculations. Two questions shall be answered: (a) is it justified to assume the same equivalence factor for both ferrite and

austenite boundaries; (b) are the calculated values of the equivalence factor in agreement with the values proposed in Figure 2.

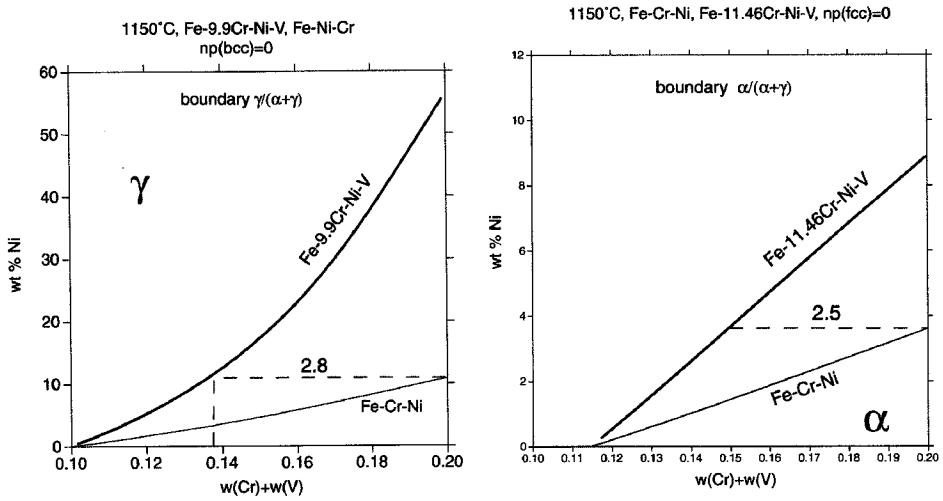


Figure 3: Calculated effect of V on the solubility limits of ferrite and austenite relative to the effect of Cr, T=1150°C. The factors 2.8 and 2.5 are the Cr-equivalent factors of V. Multiplying the V-content by these factors brings the two boundaries almost to coincidence in a limited composition range. On the abscissa the sum of weight fractions Cr+V is plotted.

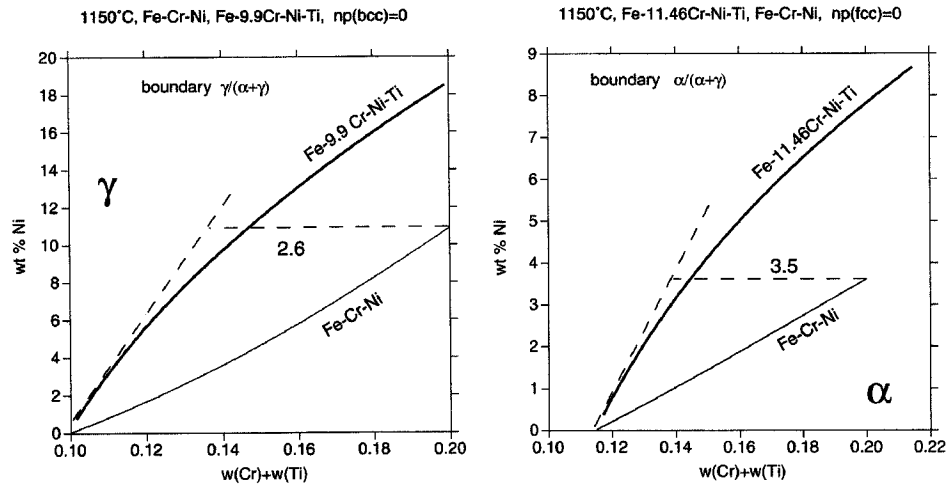


Figure 4: Calculated effect of Ti on the phase boundaries ferrite and austenite compared to the effect of Cr, T=1150°C. The factors 2.6 and 3.5 are the Cr-equivalent factors. Multiplying the Ti-content by these factors brings the two boundaries almost to coincidence. On the abscissa the sum of weight fractions Cr+Ti is plotted.

Of course, the Schaeffler diagram is supposed to give information after quenching. However, in the case of ferritic steels austenite transforms fully into martensite during cooling and δ-ferrite is present only if it was present before cooling at the austenitization temperature. Therefore, in this particular case, an equilibrium calculation can deal with this question.
If no other elements than Cr and Ni are considered the boundaries (α+γ) in Figure 2 correspond to the phase boundaries α/γ and γ/α of the ternary Fe-Cr-Ni system at a certain temperature. According to the calculations this temperature is close to 1150°C.
The effect of V on the phase boundaries is shown in Figure 3. The Cr-equivalents required to shift the phase boundaries to obtain coincidence with the Fe-Cr-Ni system are indicated. They turn out almost the same, 2.8 and 2.5, but they are only half the value proposed in Figure 2. The effect of Ti is shown in Figure 4. In this instance, the Cr-equivalents are less close together and again about half the value proposed in Figure 2. For Mo the factors 1.3 and 1.26 are obtained, see Figure 5: These values are close together and close to the value proposed in Figure 2. In the case of Al a Cr-equivalent can only be defined for very low contents, Figure 6.

The situation becomes much less satisfactory when austenite stabilizers are considered. There is no way to get Ni-equivalents for C close to each other for the two boundaries, see Figure 7. The Ni-equivalents are 18 and 71, respectively, and have to be compared with 30 proposed in Figure 2. The effect of Mn is shown in Figure 8 by a superposition of the two isothermal sections Fe-Cr-Ni and Fe-Cr-Mn. At this temperature Mn opens the ferrite field rather than the austenite field as required for an austenite stabilizer. Thus, it is not possible to give a Ni-equivalent to Mn. Similar results have been obtained for Co.

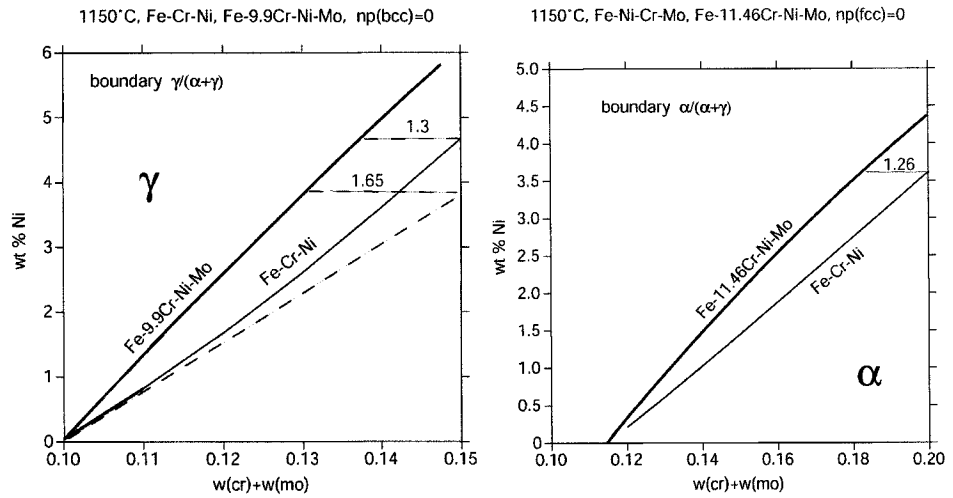


Figure 5: Calculated effect of Mo on the phase boundaries ferrite and austenite compared to the effect of Cr, T=1150°C. The factors 1.3 and 1.26 are the Cr-equivalent factors. Multiplying the Mo-content by these factors brings the two boundaries almost to coincidence. On the abscissa the sum of weight fractions Cr+Mo is plotted.

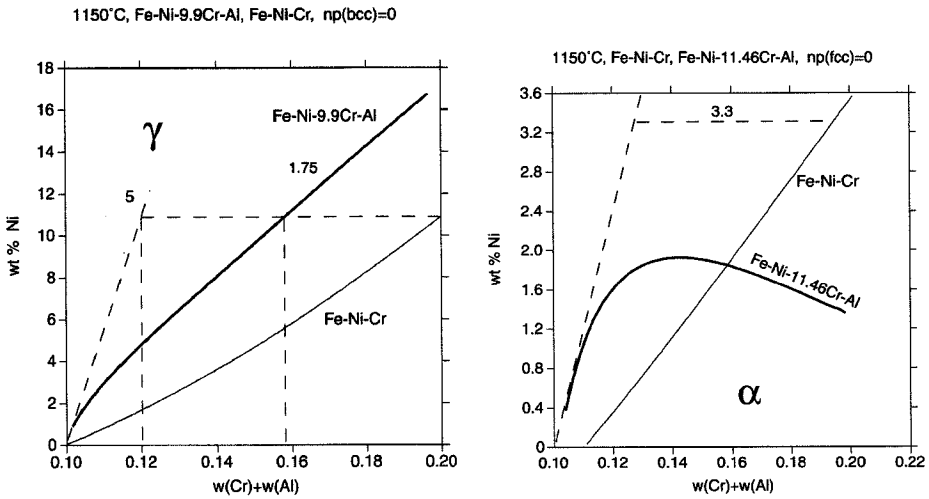


Figure 6: Calculated effect of Al on the phase boundaries ferrite and austenite compared to the effect of Cr, T=1150°C. Depending on the concentration range a factor of 5 or 1.75 applies to the γ/(γ+α)–boundary, while for the α/(α+γ) boundary a factor 3.3 can only be used for low concentrations. On the abscissa the sum of weight fractions Cr+Al is plotted.

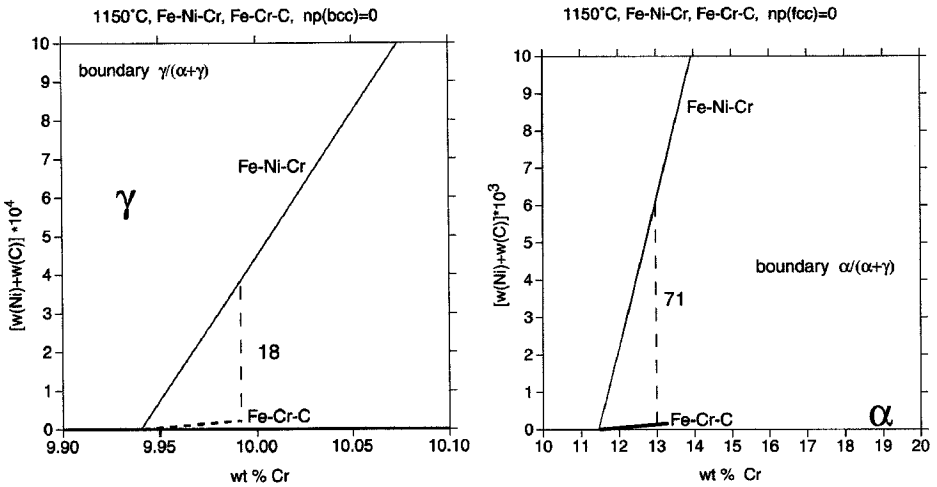


Figure 7: Calculated effect of C on the phase boundaries ferrite and austenite compared to the effect of Ni, T=1150°C. A factor of 18 applies to the γ/(α+γ)-boundary, while for the γ/(α+γ)-boundary a factor 71 holds. On the ordinate the sum of weight fractions Ni+C is plotted.

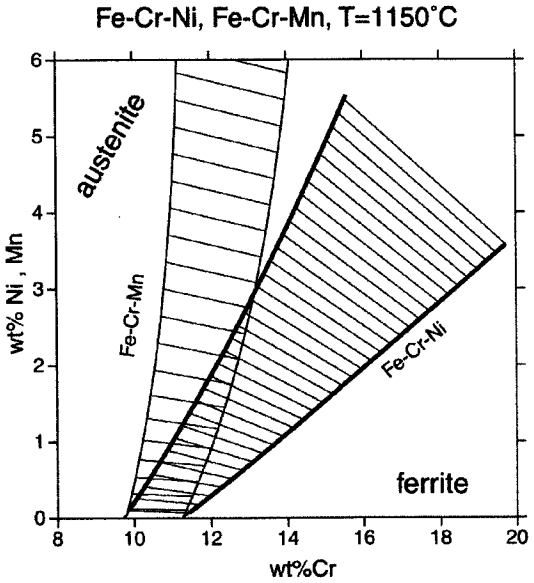


Figure 8: Superposition of the phase diagrams Fe-Cr-Ni and Fe-Cr-Mn showing the effect of Mn on the position of the phase boundaries. At this temperature Mn stabilizes ferrite instead of austenite.

Although the simplified approach with Schaeffler diagrams may have been used with some success as a guide line, the limitations become transparent with thermodynamic calculations. It appears that even on a qualitative level there are serious deficiencies, the major deficiency being the lack of any predictive capability.

4. Kinetics of transformation

The thermodynamic data of the systems considered being available, it is natural to move from equilibrium towards transformations. The calculation of thermodynamic properties allows definition of driving forces for reactions and hence of the coupling (for the most part of thermodynamic origin) between kinetic parameters, e.g. diffusivities. The fundamentals are well known, but the complexity of the multi-component systems, of the associated kinetic parameters and of thermal treatments represent an almost insurmountable barrier. It is only with the aid of numerical techniques that this complexity can be taken into account quantitatively. The software DICTRA is the result of more than a decade of development emerging from a co-operation between the Royal Institute of Technology (Stockholm) and the Max-Planck-Institute for Iron Research (Düsseldorf) started by a 5 years project in 1988. For details the reader is referred to [5]-[11].

There are several fundamental concepts forming the basis of the treatment:

1. The movement of an interface is controlled by the mass balance obtained from the fluxes of the diffusing elements across the interface [6].
2. Local equilibrium is assumed at moving interfaces. In a binary system this equilibrium determines the compositions on either side of the boundary in terms of the tie-line of the two-phase equilibrium. In multi-component systems the operating tie-line varies with time. It is determined by the condition that the mass balance of every diffusing

element gives the same interface velocity. The local equilibrium may be subject to constraints such as a finite interface velocity. The local equilibria are calculated using THERMOCALC as a subroutine [7].

3. Diffusion is treated considering true thermodynamic driving forces, i.e. chemical potential gradients. This is essential in multi-component systems where diffusion may take place against the composition gradient.
4. The thermodynamic driving forces imply that the kinetic parameters must be the mobilities rather than diffusivities. A kinetic database has been established covering a large number of elements and phases [16]-[18].
5. Transformation and diffusion are treated in geometries with only one space co-ordinate (linear, ellipsoidal etc.) [7]. Space may be subdivided into "cells" with one or more different phases [9]. Within each phase the space coordinate is discretized by grid points. Boundary conditions are to be imposed to define the interaction between the cells.

The complex behaviour of phase transformations in multi-component systems becomes already transparent in the case of $M_{23}C_6$ precipitation in a ferritic steel. The composition selected corresponds to the alloy DT4-1, i.e. Fe-4.82%Co-12.7%Cr-0.213%V-0.83%C. The temperature of calculation is 1053K or 780°C. The growth of $M_{23}C_6$ carbide within a spherical cell of 5μm radius is shown in Figure 9.

The Cr-profile within the growing $M_{23}C_6$ particle varies strongly as a function of its size, or equivalently of time and distance, Figure 10a. This shows that the boundary condition at the moving interface is by far not constant. The corresponding Cr-activity profile is shown in Figure 10b. A very similar composition and activity profile was obtained for V. The situation is different for Co. According to the thermodynamic database Co practically does not enter the carbide particle. Co is thus rejected into the ferrite matrix and concentrates in front of the moving boundary, as shown in Figure 10c. The kinetics of reaction is very much dependent on the volume diffusion of Co into the ferrite matrix and on the diffusion of Cr and V.

The C-activity profile is shown in Figure 10d. It is interesting to see a hump developing in front of the moving interface during the early stages of reaction. This finding needs a more careful analysis. It has to do with the fact that for the composition selected it is not possible to find a tie-line with a C-activity close to that of the bulk material. This is a necessary condition for a slow reaction controlled by Cr, Co, V diffusion. The other possibility obviously selected by the program is a tie-line which defines a C-activity slightly higher than in the bulk. The total C-flux at the interface is then the result of a flux difference. The two opposite flux components are due to (a) the activity drop towards the carbide particle and (b) due to the activity gradient towards the bulk.

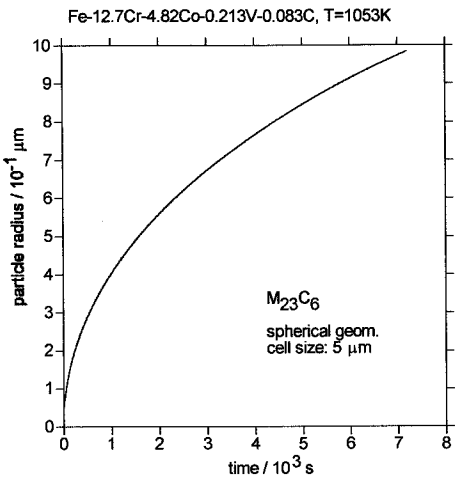


Figure 9a Radius of the $M_{23}C_6$ particle as a function of time during the early growth regime.

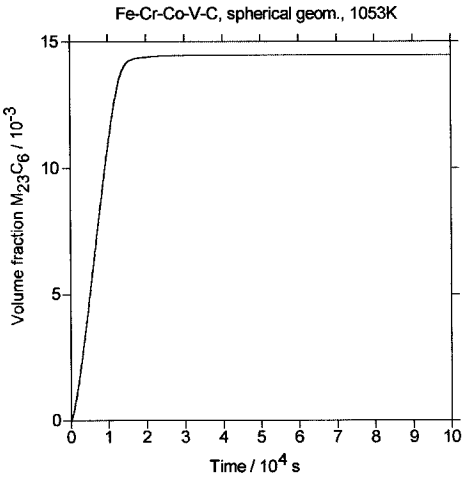


Figure 9b Volume fraction of $M_{23}C_6$ carbide as function of reaction time. After about 20 ks the precipitation reaction is practically complete.

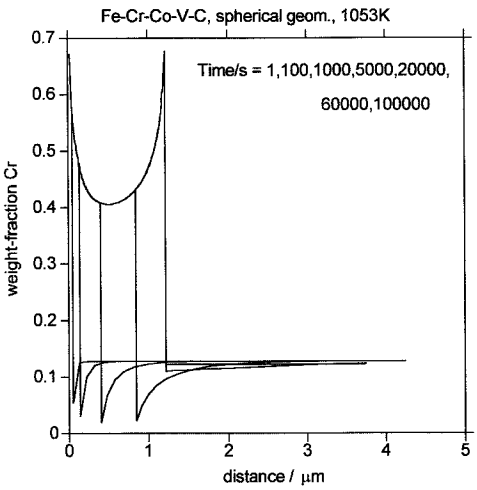


Fig. 10a Calculated Cr-profile in a growing $M_{23}C_6$ particle and in the ferrite matrix vs distance in alloy DT4-1 at different time steps.

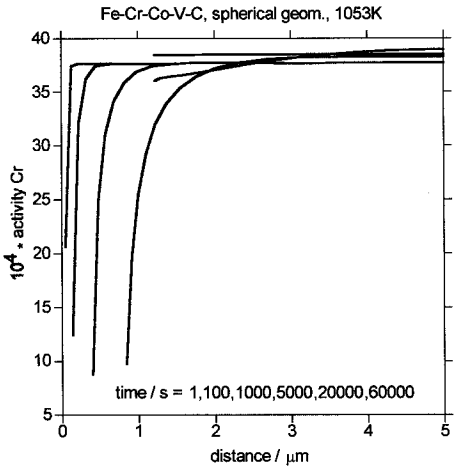


Fig. 10b Calculated Cr-activity profile in the ferrite matrix, ahead of the growing $M_{23}C_6$ particle, vs distance in alloy DT4-1 at different time steps.

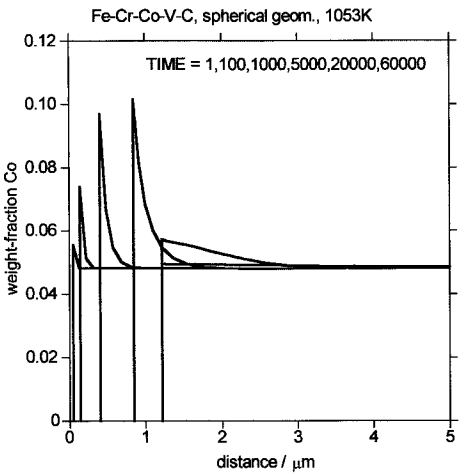


Fig. 10c Calculated Co-profile in a growing $M_{23}C_6$ particle and in the ferrite matrix vs distance in alloy DT4-1 at different time steps.

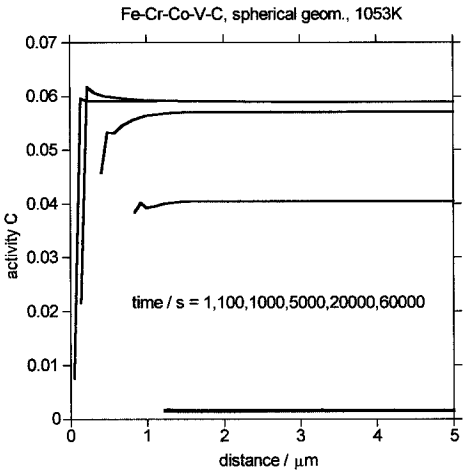


Figure 10d Calculated C-activity profile in the ferrite matrix, ahead of the growing $M_{23}C_6$ particle, vs distance in alloy DT4-1 at different time steps.

This type of calculation is presently performed for various alloys and includes also the Laves phase. One step further will be the calculation with two coupled cells of ferritic matrix, one with $M_{23}C_6$ precipitation, the second with Laves phase precipitation. This type of calculation shall give information about the kinetics of coupled growth and of ripening effects during long term service conditions.

References

[1] Blum, R; Hald, J.; Bendick, W.: Newly developed high temperature ferritic – martensitic steel from USA, Japan and Europe, Internationale VGB- Konference: Fossilbefeuerte Dampfkraftwerke mit forgeschnittenen Auslegugsparametern, Kolding, 1993

[2] Abe, F.; Araki, H.: Matrials Science and Technology, Vol.8, 1992, pp. 767-773

[3] B. Sundman, B. Jansson and J.-O. Andersson, The THERMOCALC databank system, CALPHAD 9 (1985), 153-190

[4] SGTE (Scientific Group Thermodata Europe), Solution Database of Jan. 1994,

[5] DICTRA software developed within the project COSMOS (Computer Supported Modelling of Steel Transformations), funded by Volkswagen-Stiftung and Land Nord-Rhein-Westfalen (1988-1993)

[6] S. Crusius, G. Inden, U. Knoop, L. Höglund and J. Ågren, "On the numerical treatment of moving boundary problems", Z. Metallk. 83 (1992), 673-678

[7] S. Crusius, L. Höglund, U. Knoop, G. Inden and J. Ågren, "On the growth of ferrite allotriomorphs in Fe-C", Z. Metallk. 83 (1992), 729-738

[8] G. Inden and P. Neumann, "Simulation of diffusion controlled phase transformations in steels", steel research 67 (1996) 401-407

[9] P. Franke and G. Inden, "Diffusion Controlled Transformations in Multi-Particle Systems", Z. Metallk. 88 (1997) 917-924

[10] G. Inden, "Cinétique de transformation de phases dans des systèmes polyconstitués - aspects thermodynamiques", Entropie 202/203 (1997), 6-14

[11] A. Borgenstamm, A. Engström, L. Höglund and J. Ågren, "DICTRA, a Tool for Simulation of Diffusional Transformations in Alloys", J. Phase Equilibria 21 (2000), 269-280

[12] Knezevic, V.; Sauthoff, G.: Martensitic/ferritic super heat resistant 650°C steels- Design of model alloys, Materials for Advanced Power Engineering, Liege, 2002

[13] Agamennone, R.; Blum, W.: Martensitic/ferritic super heat resistant 650°C steels- Microstructure, Materials for Advanced Power Engineering, Liege, 2002

[14] Inden, G.; Vilk, J.: Superwarmfeste ferritische Stähle für umweltschonende kohlbefeuerte Dampfkraftwerke mit Dampfeintrittstemperaturen von ca. 650°C – Termodynamische und kinetische Berechnungen von Ausscheidungsreaktionen, Düsseldorf, 2001

[15] Dr. Ales Kroupa, Institute of Physics of Materials, Academy of Science, Zizkova 22, 61662 Brno, Czech Republic

[16] J.-O. Andersson and J. Ågren, J. Appl. Phys. 72 (1992) 1350-1355

[17] B. Jönsson, Z. Metallk. 85 (1994) 498-509

[18] A. Engström and J. Ågren, Z. Metallk. 87 (1996) 92-97

[19] H. Schneider, Foundry Trade J. 108 (1960) 562-563

IMPROVEMENT OF CREEP RUPTURE STRENGTH OF HIGH STRENGTH 12CR FERRITIC HEAT-RESISTANT STEEL

Toshihiro Uehara*, Akihiko Toji*, Shugo Komatsubara*, and Toshio Fujita**

*Hitachi Metals, Ltd., 2107-2 Yasugi-cho, Yasugi-shi, Shimane-ken, 692-8601, Japan
**Emeritus Professor of the University of Tokyo, Japan

Abstract

Recently, steam temperature in USC(ultra super critical) power plant has been increasing in order to improve the efficiency. Superior high temperature mechanical properties such as creep rupture strength are required for materials applied for turbine blades and bolts of USC power plant above 600-650℃. A high strength 12% chromium ferritic heat-resistant steel, TAF650, which contains W, Co, and B, was developed for these applications. Chemical compositions of TAF650 were determined to make the microstructure stable at elevated temperatures. But the creep rupture strength of TAF650 at longer time than 1,000 hours deviated from the estimation from Larson-Miller curve obtained from the data within 2,000 hours. The present study is aimed at improving the long time creep rupture strength of TAF650 at 600-650℃. The effect of the contents of Ni, Co, B, etc. on the creep rupture strength of TAF650 was investigated. It is found that the decrease of the austenite forming elements such as Co and Ni and the increase of B suppress the degradation of long time creep rupture strength of TAF650.

Keyword : ferritic heat-resistant steel, creep rupture strength, tungsten, cobalt, USC

Introduction

Recently, high efficiency of USC power plants is required for reduction of CO_2 emissions from the viewpoint of protecting global environment. High strength at elevated temperature of heat-resistant steels applied for turbine blades and bolts has been needed in order to improve the efficiency of steam turbines. Therefore 12Cr ferritic heat-resistant steel with high creep rupture strength at 600–650℃, TAF®650, was developed [1]. Alloy design approach to stabilize the microstructure at elevated temperature was carried out, and long time creep rupture strength was estimated by means of Larson-Miller fitting from the results of creep rupture tests within a relatively short time of about 2,000 hours when TAF650 was developed. But it was found that creep rupture strength of TAF650 measured after long time creep rupture tests was lower than estimated from results of short time creep rupture tests. Therefore, improving the long time creep rupture strength of TAF650 is required. In this study, the effect of alloying elements on the long-time creep rupture strength such as Ni, Co, and B was investigated in order to improve the long time creep rupture strength of TAF650.

Experimental procedures

Alloy Design

Typical chemical composition of TAF650 is shown in Table 1. Since it is well known that long time creep rupture strength of 12% Cr ferritic heat-resistant steels at 600-650℃ is improved by adding W rather than Mo, TAF650 contains 2.6 mass% W, which is a much higher content than in conventional ferritic heat-resistant steels. Moreover, for stabilization of microstructure at elevated temperature for a long time, amounts of C and N which cause microstructural change of carbides and nitrides during heating for a long time are reduced to a

relatively low level. And 2.9 mass% Co is added in TAF650 for suppression of delta-ferrite formation due to the small amounts of C and N and addition of W. Such alloy design enabled TAF650 to achieve high creep rupture strength.

However it was found that microstructure of TAF650 changed easily during a short time exposure at elevated temperature after a long time creep rupture tests, which is different from our estimation. This seems mainly to be attributed to the recovery of martensite matrix which is caused by the decrease of solution strengthening effect of matrix due to the reduction of amount of W in the matrix which occurs simultaneously with precipitation of Laves phase(Fe_2W) during long time creep tests.

Therefore, the effect of reduction of austenite-forming elements such as Co and Ni, which contributed to suppression of Laves phase precipitation, on improvement of long time creep rupture strength was investigated. Reduction of austenite-forming elements such as Co and Ni, however, increases tendency to formation of delta-ferrite phase. In order to estimate the potential of forming delta-ferrite phase, the value of Cr-equivalent which is expressed by the following equation was used :

$$Cr.eq=\%Cr+6x\%Si+4x\%Mo+1.5x\%W+11x\%V+5x\%Nb -40x\%C-2x\%Mn-4x\%Ni-2x\%Co-30x\%N \quad (1)$$

Previous studies indicated that delta-ferrite phase did not form at the values of Cr-equivalent of 9.51[2], 6.44 and 6.24[3], although it varied with ingot sizes. On the other hand, it is well known that B is an effective element for improving long time creep rupture strength, and TAF650 already contains about 0.015 mass% of B. The effect of increase of B content was also investigated in this study.

Materials and experimental procedures

Chemical compositions of alloys used in this study are shown in Table 1. The three improved alloys contain smaller amounts of Co and Ni than TAF650. Co content was reduced to 1.2 mass% in TAF650LCO, and to about 2-2.2 mass% in TAF650R and TAF650B. Moreover, B was increased to 0.025 mass% in TAF650B although it was 0.014 mass% in TAF650R. Al content was suppressed to a low level in these alloys, which was 0.009 mass% in TAF650 and 0.001 mass% in TAF650R and TAF650B, although it was 0.033 mass% in TAF650LCO, which was higher than those in the other alloys. The values of Cr equivalent of experimental alloys are also shown in Table1. The values of Cr equivalent of improved alloys, TAF650LCO, TAF650R, and TAF650B, are larger than that of TAF650, and it is supposed that improved alloys are apt to form delta-ferrite. These improved alloys were vacuum induction melted and cast into ingots of 10-150kg. TAF650R and TAF650B were hot-forged to 30mm square bars, although TAF650LCO was forged to 30mm x 90mm rectangular bar. Sample of TAF650 was cut from 70mm round commercially produced bar. They were austenitized at 1100℃ for 1 hour, followed by oil quenching and then tempered at 700℃ for 2 hours followed by air cooling.

Table1 Chemical compositions of specimens (mass%)

Specimen	C	Si	Mn	Ni	Cr	W	Mo	V	Co	Nb	Fe	N	B	Al	Cr.eq
TAF650	0.10	0.09	0.50	0.51	10.88	2.55	0.14	0.19	2.90	0.10	bal.	0.0250	0.013	0.009	4.81
TAF650LCO	0.13	0.03	0.18	0.11	10.51	2.40	0.14	0.23	1.17	0.07	bal.	0.0230	0.011	0.033	8.70
TAF650R	0.12	0.05	0.10	0.11	10.20	2.52	0.15	0.21	2.29	0.08	bal.	0.0229	0.014	0.001	6.94
TAF650B	0.12	0.06	0.09	0.10	10.18	2.56	0.15	0.21	2.05	0.08	bal.	0.0297	0.025	0.001	7.26

Microstructure was observed with an optical microscope in the longitudinal cross section. Creep rupture tests were carried out at temperatures in the range of 600 and 700℃. Some crept specimens were used for transmission electron microscopy(TEM). Thin disks were cut from the region about 10mm from fracture surfaces, because it was supposed that these sites were hardly strained. Thin foils were prepared by electropolishing. Chemical compositions in the matrix were analyzed by EDS in TEM at 5 points for 1 sample.

Results and discussions

Fig.1 shows the results of creep rupture tests of TAF650. The relation between stress and time to rupture remained almost linear within about 1,000 hours, but then the creep rupture strength deteriorated rapidly, especially after about 6,000 hours at 600℃, after about 2,500 hours at 625℃, and after about 1,000 hours at 650℃, respectively. It is supposed that precipitation of Fe_2W was promoted due to addition of 0.51 mass% Ni and 2.9 mass% Co and then solution strengthening effect of W in matrix was reduced and recovery of martensite matrix occurred rapidly. At 700℃, however, rapid decrease of creep rupture strength did not occur because Fe_2W did not precipitate very much.

Fig.2 shows microstructures of improved alloys, compared with that of conventional TAF650. Delta-ferrite does not exist in TAF650(2.9 mass% Co), TAF650R(2.29 mass% Co), and TAF650B(2.05 mass% Co), although delta-ferrite exists in TAF650LCO(1.17 mass% Co). The tendency to form delta-ferrite increases with decreasing Co and Ni contents. With regard to Cr equivalent, delta-ferrite does not form when the values of Cr equivalent are 6.94(TAF650R) and 7.26(TAF650B), but does form when the values of Cr equivalent is 8.7(TAF650LCO).

Fig.3 shows the phase diagram calculated by Thermo-Calc, which indicates the effect of Co content on the formation of delta-ferrite. It is found that the region of austenite phase extends with increasing Co content (Fig.3). In case of being quenched from 1100℃, the addition of more than about 1.5 mass% Co is necessary to suppress the formation of delta-ferrite. Furthermore, increase of Co content does not influence the region of $M_{23}C_6$ type carbide, but extends the region of Laves phase(Fe_2W).

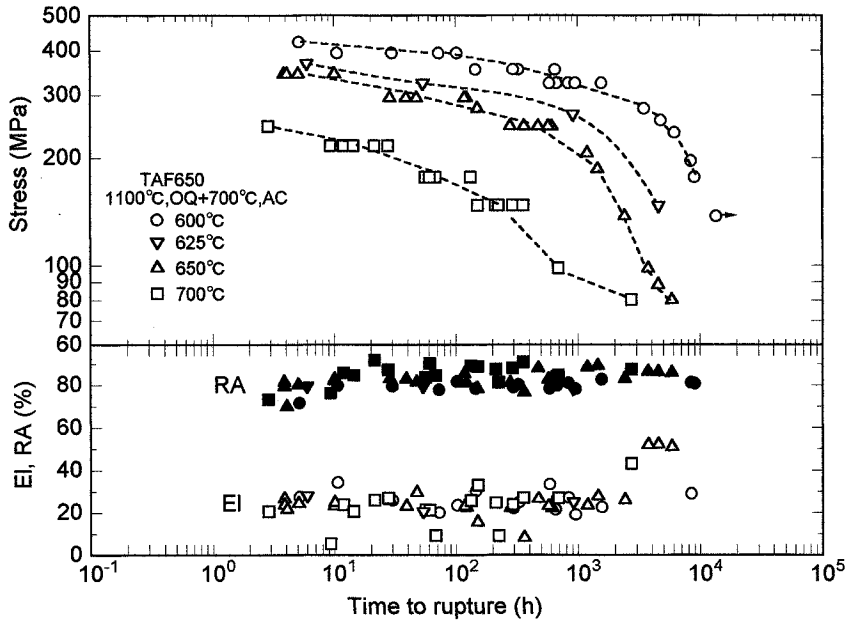


Fig.1 Result of creep rupture tests of TAF650.

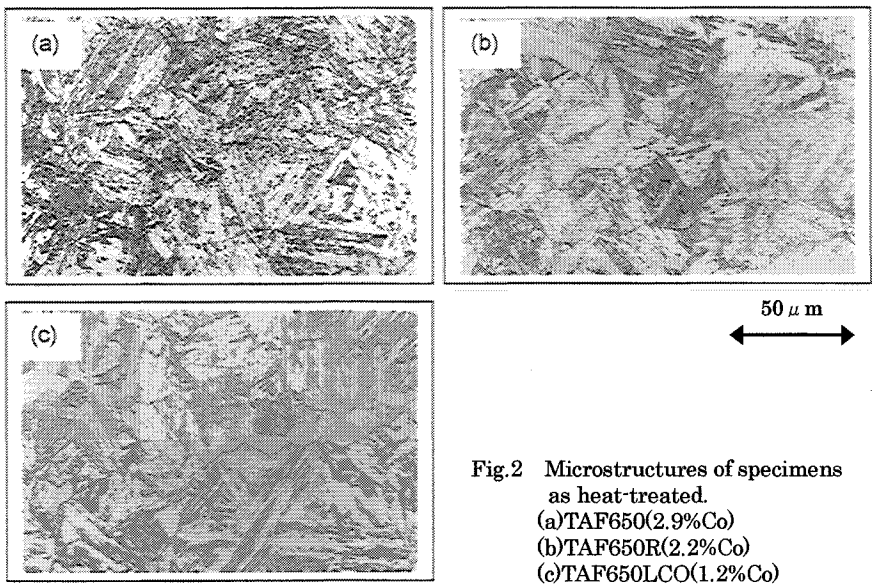


Fig.2 Microstructures of specimens as heat-treated.
(a)TAF650(2.9%Co)
(b)TAF650R(2.2%Co)
(c)TAF650LCO(1.2%Co)

Creep rupture strength of improved alloys is shown in Fig.4, compared with that of conventional TAF650. Within about 1,000 hours, creep rupture strength of improved alloys is equivalent to that of TAF650, but is significantly improved after about 1,000 hours. Particularly, TAF650R and TAF650B containing Co of about 2.1 to 2.3 mass% have higher creep rupture strength after about 1,000 hours than TAF650LCO containing Co of about 1.2 mass%. It is supposed that the reason why creep rupture strength of TAF650LCO was not improved sufficiently is due to both the existence of delta-ferrite and the high Al content. Since it is known that Al content of more than about 0.02 mass% promotes softening of 12% Cr steel at 650℃[3], it is necessary to reduce Al content as impurity. For rupture lives of greater than 1,000 hours, the improved TAF steels provide for a given stress at 25℃ increase in temperature capability ; the rupture life of the improved TAF steels for a given stress at 650℃ is similar to that of TAF650 at 625℃.

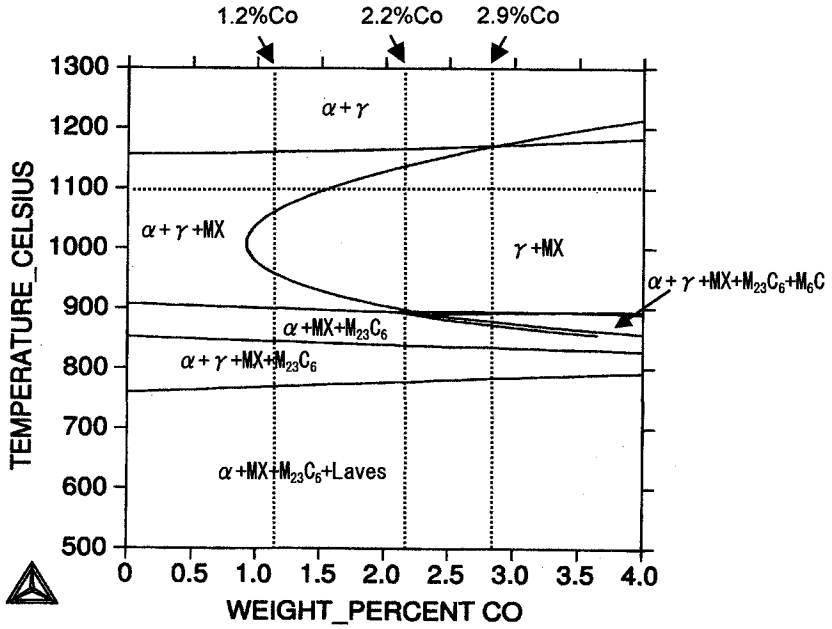


Fig.3 Calculated phase diagram of
0.1C-0.1Mn-0.1Ni-10.5Cr-2.6W-0.15Mo-0.2V-0.08Nb-xCo-0.025N-bal.Fe.

Creep rupture strength of TAF650B containing high B content is higher than that of TAF650R which has similar chemical compositions to TAF650B except for B. Increase of B content is effective in improving long-time creep rupture strength. Since increase of B applied for large-scale products might cause reduction of impact toughness to some extent, however, more evaluation tests are necessary to increase B content in TAF650.

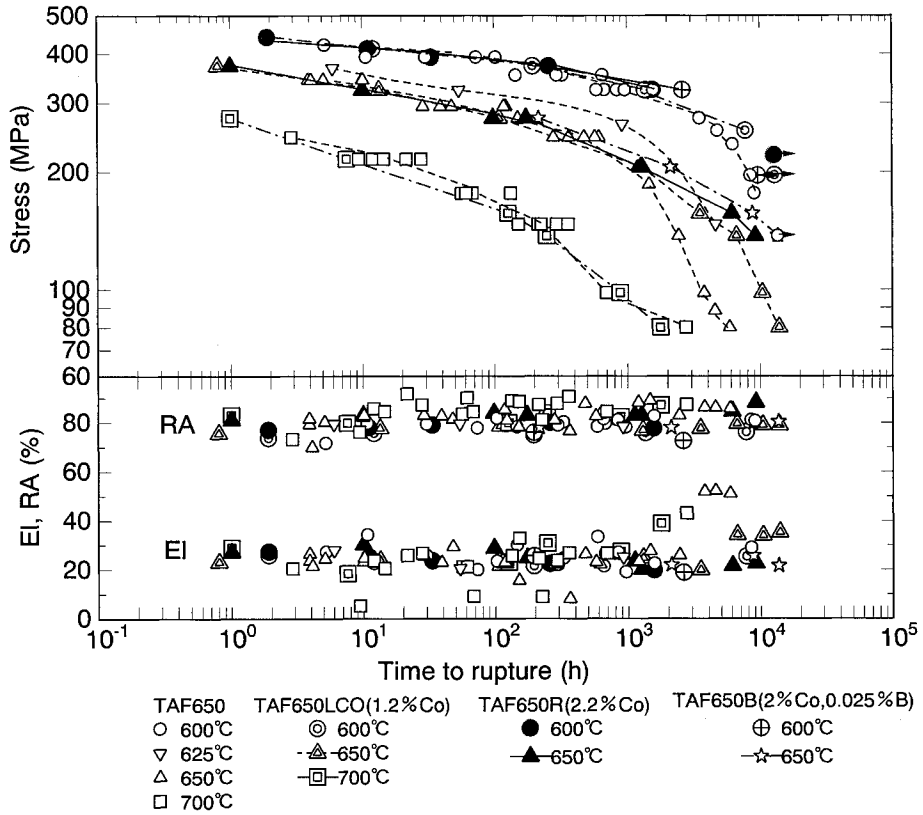


Fig.4 Creep rupture strength of improved alloys, compared with that of conventional TAF650.

Typical transmission electron micrographs of TAF650 and TAF650B as heat-treated and after creep are shown in Fig.5. The microstructure of both alloys as heat-treated is lath martensite structure with high dislocation density, small amount of small carbides. On the other hand, microstructure of gauge section of both alloys (except for localized reduction of area) after creep at 650℃ and 137MPa still maintains elongated lath morphology, but the width of laths is much larger than that as heat-treated and the recovered ferrite structure has a low dislocation density. Equi-axed subgrain structure is observed partially. Moreover, a large amount of large precipitates are observed, which precipitate mainly along prior austenite grain boundary, block boundary, and lath boundary. TAF650B has a similar microstructure to TAF650, but indicates longer time to rupture than TAF650, that is, time to rupture is 2415 hours for TAF650 and 13611 hours for TAF650B. It seems to be difficult for microstructure of TAF650B to recover, since TAF650B takes more time to recover than TAF650.

Fig.6 shows the result of EDS analysis of solution elements in matrix using TEM. Particularly, W content in matrix of TAF650, TAF650R, and TAF650B decreases after creep at 650℃, compared with the as heat-treated condition. It is supposed that decrease of W content in matrix after exposed at 650℃ for a long time is attributed to precipitation of Laves phase (Fe_2W).

For improved alloys containing small addition of austenite formers, such as Co and Ni which have higher long-time creep rupture strength than TAF650, the decrease of solid solution elements, particularly W, is small, and solid solution strengthening is maintained for a long time at elevated temperatures. This seems to be one of the main reasons for the higher long-time creep rupture strength of improved alloys. However, the change of morphology, amount, size, and so on of precipitates after long-time exposure at 650℃ must also be investigated to clarify the mechanism of improving creep rupture strength.

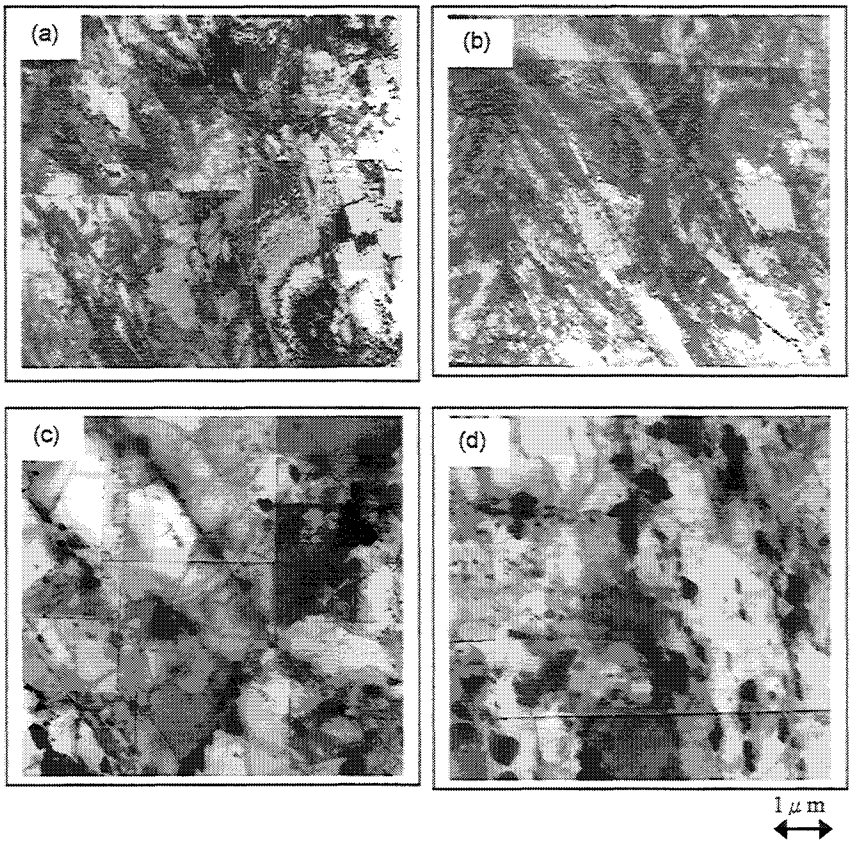


Fig.5 Typical transmission electron micrographs of TAF650 and TAF650B as heat-treated and after crept.
(a) TAF650, as heat-treated, (b) TAF650B, as heat-treated
(c) TAF650, crept at 650℃, 137MPa, 2415.7 hrs,
(d) TAF650B, crept at 650℃, 137MPa, 13611.4hrs.

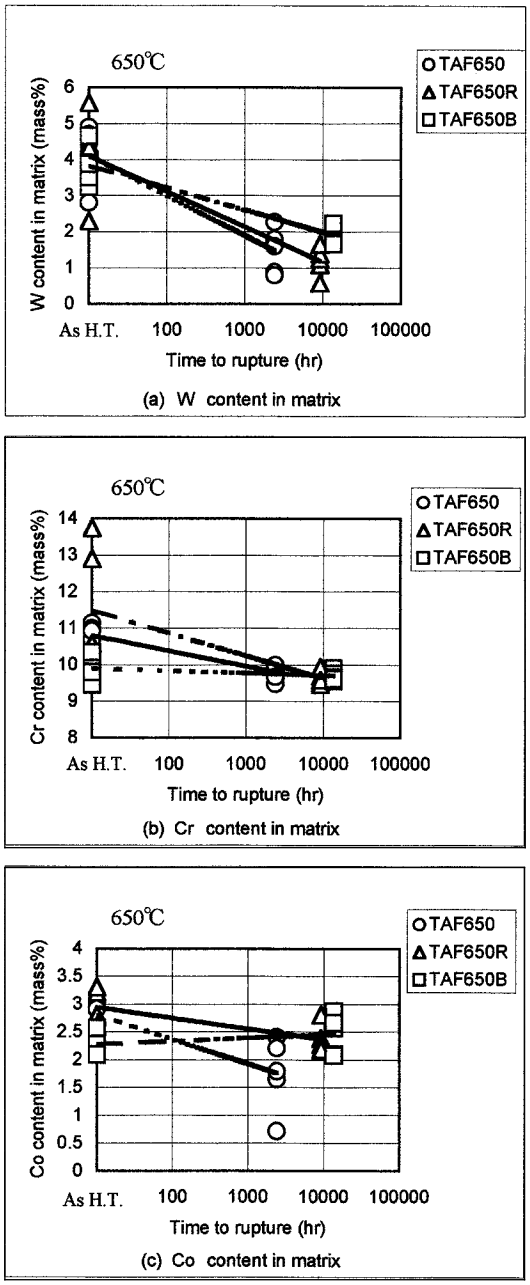


Fig.6 Result of EDS analysis of solution elements in matrix as heat-treated and after crept at 650℃ using TEM.

Conclusions

Decrease of austenite formers such as Co and Ni was carried out for suppressing deterioration of long-time creep rupture strength of 12Cr ferritic heat-resistant steel TAF650 containing 2.9 mass% Co and 0.5 mass% Ni. It is necessary to add more than about 1.5 mass% Co for suppressing the formation of delta-ferrite. Reduction of austenite formers such as Co and Ni is very effective for increasing long-time creep rupture strength at around 600 – 650℃. Modified alloys, which are TAF650R with about 2.2 mass% Co and 0.1 mass% Ni and TAF650B with about 2.0 mass% Co, 0.1 mass% Ni, and 0.025 mass% B have improved long-time creep rupture strength.

References

[1] T. Uehara, T. Ohno, R. Watanabe, and T. Fujita : Development of high strength 12% Cr Ferritic heat-resistant steel, Materials Engineering in Turbines and Compressors, Newcastle upon Tyne, UK, 25-27 April 1995, Vol.2, 391.

[2] K. Hidaka, Y. Fukui, S. Nakamura, T. Onoda, Y. Tanaka, and T. Fujita : Development of 12%CrWCoB steel turbine material for USC power plant, Report of the 123rd committee on heat-resisting materials and alloys, Japan society for the promotion of science, Vol.39(1998), No.3, 295.

[3] M. Arai, H. Doi, Y. Fukui, R. Kaneko, T. Azuma, and T. Fujita : Improvement of long time creep rupture properties of high WCoB containing 12Cr rotor steels for use at 650C in USC power plants, proceedings of the 3rd EPRI conference on technology for fossil power plants, Swansea, UK, April 2001, 1.

DEVELOPMENT OF NEW 18Cr-9Ni AUSTENITIC STAINLESS STEEL BOILER TUBE

Ishitsuka Tetsuo* and **Mimura** Hiroyuki**

*: Nippon Steel Corporation, Steel Research Laboratories,
20-1 Shintomi, Futtsu, Chiba 293-8511, Japan
**: Nippon Steel Corporation, Hikari R&D Laboratories,
3434 Shimata, Hikari, Yamaguchi 743-8510, Japan

Abstract

A new austenitic stainless steel boiler tube, 18Cr-9Ni-Nb-V-W-N (XA704), has been developed. The high temperature mechanical properties and corrosion resistance of the steel were investigated. The creep rupture strength of the developed steel is about 1.5 times that of type 347H (JIS SUS347HTB), and is almost the same as that of NF709 at 650°C. This excellent creep strength of the steel is mainly due to precipitation strengthening by CrVN, and solid solution strengthening by tungsten. These effects are stable for a long term. The carbon content of the steel is reduced to 0.03% to improve the intergranular corrosion resistance. The steam oxidation resistance and the high temperature corrosion resistance of the tube are almost the same as those of fine-grained type 347H. The hot cracking susceptibility in weld of XA704 is lower than that of type 304H and type 310. Thus XA704 is suitable for use as a material for superheater and reheater tubes of thermal power boilers.

Keywords: Boiler tube, Heat resistant steel, Stainless steel, CrVN, Creep strength

1. Introduction

Coal-fired power plants with steam temperatures of 600 °C and below still have an important role in generating of electricity, though high-efficiency liquid natural gas combined cycle power plants are increasingly being constructed. However, it is strongly required that construction cost, including material cost, of coal-fired power plants be reduced, as a result of shrinkage in the market and consequent severe competition.

There are several ways of reducing material and fabrication cost. One way is to select materials with high-performance and comparably reasonable cost . For example, applying a material with higher creep strength than conventional materials to boiler tubes, can reduce the wall thickness of boiler tubes and consequently their weight . If the material's price is not so expensive compared with those of conventional materials, the material cost may be reduced.

Another way is adopting materials with improved workability. For example, conventional high-strength austenitic stainless steel boiler tubes usually have high susceptibility to intergranular corrosion because of their high carbon contents, and require special cost-increasing care after post-weld heat treatment for dissimilar welded joints with ferritic steel tubes. Applying a high-strength austenitic stainless steel tube with no susceptibility to intergranular corrosion can result in leaving out such special care like the painting of welded portions or inserting well-stabilized austenitic stainless steel tubes between high strength austenitic stainless tubes and ferritic steel tubes. Therefore high creep strength austenitic steel tubes with low susceptibility to intergranular corrosion and reasonable prices are required.

To respond to these requirements, the authors have developed a 0.03C-18Cr-9Ni-0.35Nb-0.3V-2W-0.2N steel (XA704) for application to superheater tubes. This steel has excellent creep strength, is inexpensive and has no susceptibility to intergranular corrosion. The creep rupture strength of the steel is about 1.5 times that of type 347H (JIS SUS347HTB, 18Cr-

14Ni-0.8Nb), and is almost the same as that of NF709 (20Cr-25Ni-1.5Mo-0.35Nb-N) [1] at 650°C, owing to precipitation strengthening by nitrides of niobium and vanadium, and solid solution strengthening by tungsten and nitrogen. This paper introduces the properties of XA704 steel and the precipitation behaviour of its alloying elements at elevated temperatures.

2. Alloy design concept of 0.03C-18Cr-9Ni-W-Nb-V-N (XA704) steel

The alloy design concept of XA704 is shown in Fig. 1.

- As the basic chemical composition, 18%Cr-9%Ni was selected in consideration of material cost and high temperature corrosion resistance. As the target application of the steel is superheater tubes for coal-fired power plants with steam temperatures of 600 °C and below and metal temperatures of 650 °C and below, 18%Cr is enough with respect to hot corrosion and steam oxidation resistance.
- The carbon content of the steel was decreased to less than 0.05% to improve intergranular corrosion resistance. The value of carbon is quite low compared with that of conventional high strength heat resistant austenitic stainless steels. To compensate for the reduction of high-temperature strength and austenite phase stability caused by the reduction of carbon, a substantial amount of nitrogen was added instead. Nitrogen is effective for both precipitation strengthening and solution strengthening.
- Niobium was added to XA704 steel for the precipitation strengthening by nitrides. Niobium is a common alloying element for heat resistant austenitic stainless steels to improve high-temperature strength, and it also makes the grains of the base metal fine, which is beneficial for steam oxidation resistance.
- Vanadium was also added to the steel, though vanadium is seldom contained in conventional heat resistant austenitic stainless steels except for Esshete1250 (15Cr-10Ni-1.5Mo-1Nb-0.2V) [2]. Vanadium has been thought not to be effective for creep strength of austenitic alloys because vanadium carbide tends to coarsen at an early stage of the creep tests. However, the authors have confirmed that vanadium is effective in the low carbon and high nitrogen steel designed here, since vanadium precipitates as nitride [3].
- Tungsten is contained in the steel to enable solid solution strengthening. Though molybdenum also has the same effect, it reduces coal ash corrosion resistance [4]. For this reason, tungsten is selected for the developed steel.
- The toughness after aging and hot cracking susceptibility of the weld are affected by the stability of the austenite phase. When austenite is unstable, σ phase tends to precipitate during long-term use, and then toughness decreases remarkably. On the other hand, excessively stable austenite causes hot cracking at the weld. Therefore, optimum phase

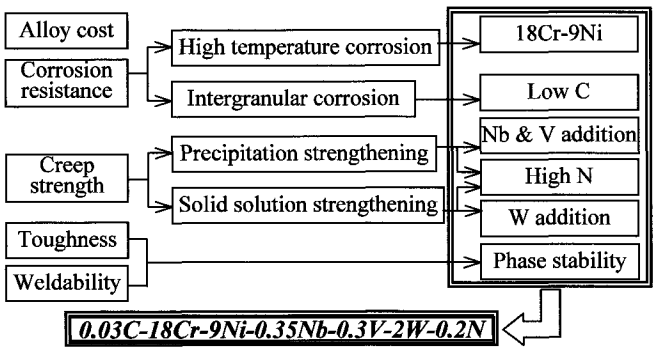


Fig. 1 Alloy design concept of the newly developed XA704 steel.

stability was considered.

As a result of these considerations, the final chemical composition of XA704 was decided as 0.03C-18Cr-9Ni-0.35Nb-0.3V-2W-0.2N.

3. Properties

3.1 Test materials

The chemical compositions of XA704 used in this study are shown in Table 1. Six heats of tubes were manufactured by an electric furnace melting – continuous casting – hot extrusion – cold drawing – solution heat treatment process. Eleven heats of plates were manufactured in the laboratory by a vacuum induction melting – hot rolling – solution heat treatment process. These test materials were evaluated in terms of microstructure, tensile properties at elevated temperatures, creep rupture properties, corrosion resistance, toughness after aging and weldability.

3.2 Microstructure

Figure 2 shows the microstructure of the tube F. The structure consists of an austenite phase with fine precipitates in the grains.

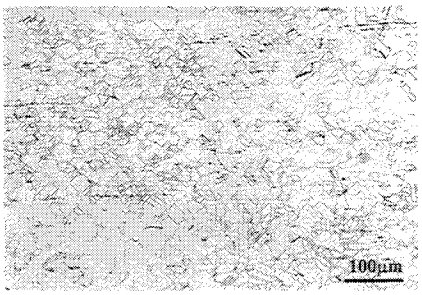


Fig. 2 Optical microstructure of XA704 steel tube F.

3.3 Tensile properties

The tensile properties of the developed steel are shown in Fig. 3. The tensile strength at each temperature of the steel was higher than that of JIS SUS347HTB [5] due to the solution strengthening by tungsten and nitrogen. The tensile ductility of the steel was high enough for use as boiler tube.

Table 1 Chemical compositions of test materials (mass %).

Designation	Size(mm)	C	Si	Mn	P	S	Ni	Cr	Nb	V	W	N
Specification		≦ 0.05	≦ 1.00	≦ 2.00	≦ 0.04	≦ 0.03	8.00 / 11.00	17.00 / 20.00	0.25 / 0.50	0.20 / 0.50	1.50 / 2.60	0.10 / 0.25
A	ϕ*50.8-t**8.0	0.030	0.33	1.50	0.019	0.0007	9.14	18.13	0.33	0.31	2.47	0.21
B	ϕ50.8-t8.0	0.029	0.33	1.47	0.017	0.0019	8.87	17.85	0.36	0.31	2.48	0.19
C	ϕ44.5-t6.0	0.029	0.34	1.20	0.026	0.0007	9.42	18.07	0.37	0.33	2.29	0.19
D	ϕ50.8-t8.0	0.033	0.27	1.66	0.026	0.0024	9.75	18.43	0.36	0.33	2.05	0.18
E	ϕ63.5-t4.0	0.030	0.26	1.64	0.027	0.0005	9.84	18.40	0.38	0.30	2.01	0.24
F	ϕ50.8-t8.0	0.028	0.27	1.69	0.025	0.001	9.85	18.45	0.37	0.30	2.13	0.23
G	W***120-t15	0.030	0.22	1.45	0.022	0.0008	8.88	17.82	0.35	0.29	2.43	0.19
H	W120-t15	0.031	0.29	1.48	0.023	0.0009	8.96	17.97	0.35	0.30	2.55	0.20
I	W120-t15	0.032	0.29	0.98	0.021	0.0007	9.02	17.60	0.35	0.29	2.41	0.22
J	W120-t15	0.015	0.29	1.46	0.023	0.0015	9.09	17.49	0.35	0.28	2.41	0.21
K	W120-t12	0.029	0.32	1.47	0.026	0.0017	9.37	18.25	0.36	0.30	2.41	0.20
L	W120-t12	0.029	0.31	1.44	0.025	0.0008	9.68	17.99	0.30	0.30	1.59	0.18
M	W120-t12	0.030	0.34	1.47	0.027	0.0009	9.82	18.08	0.35	0.29	2.07	0.20
O	W120-t12	0.030	0.28	1.44	0.024	0.0014	9.83	19.98	0.37	0.29	2.02	0.23
P	W120-t12	0.016	0.31	1.42	0.027	0.0012	9.51	18.58	0.36	0.29	2.02	0.19
Q	W120-t12	0.027	0.31	1.81	0.024	0.0020	9.81	18.64	0.38	0.29	2.08	0.19
R	W120-t12	0.027	0.29	1.81	0.023	0.0020	9.78	18.73	0.39	0.31	2.08	0.21

*ϕ: outside diameter, ** t: thickness, *** w: width

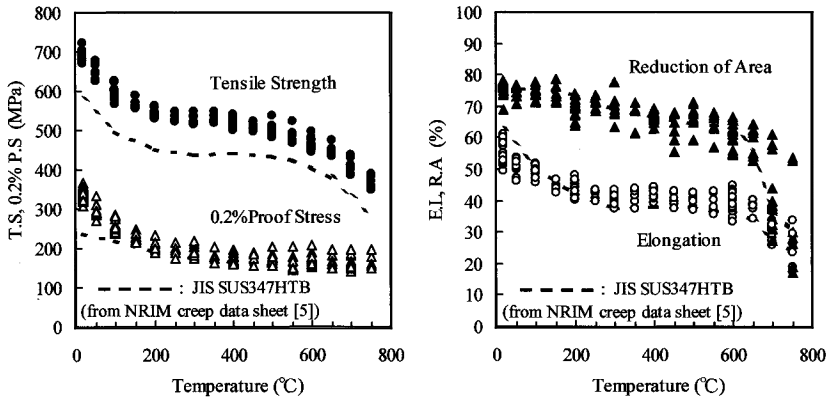


Fig. 3 Tensile properties of XA704 steel tubes D and F

3.4 Creep rupture properties

Figure 4 shows the creep rupture strength of XA704 at every 50°C from 600° to 800°C. The longest rupture time was about 40,000 h at 700°C. There is no tendency for a rapid decrease in rupture strength to occur at longer times of up to 40,000 h and higher temperatures. From the figure, the creep rupture strength for 100,0000 h at 650°C is estimated at 120 MPa from the Larson-Miller parametric analysis. This value is about 1.5 times that of SUS347HTB [5]. The maximum allowable stress curve for the developed steel calculated from the tensile and creep rupture data compared with that of the conventional steels is shown in Fig. 5. XA704 has much higher maximum allowable stress than that of conventional 18Cr-8Ni austenitic stainless steel such as SUS347HTB, and is almost the same as that of NF709 [1] at around 650°C.

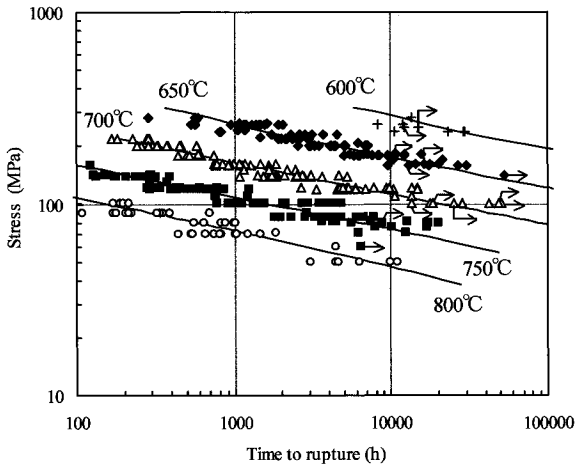


Fig. 4 Creep rupture strength of XA704 steel.

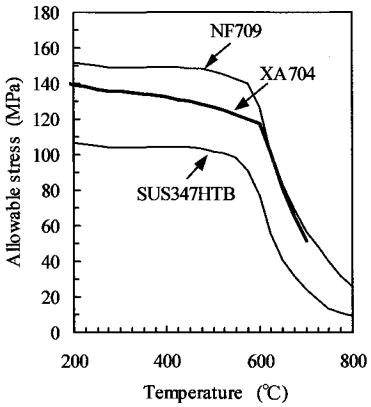


Fig. 5 Comparison of maximum allowable stress of XA704 with SUS347HTB and NF709.

3.5 Corrosion resistance

Hot corrosion

The vanadium attack and the coal ash corrosion resistance of XA704 were evaluated with synthetic ash. As shown in Fig. 6, XA704 has almost the same hot corrosion resistance as SUS347HTB at 600° to 700°C.

Steam oxidation

Steam oxidation tests were conducted for XA704 and SUS347HTB at 600°, 650° and 700°C for 3,000 h. The average ASTM grain size number of each material was 7.9 and 8.3, respectively. Specimens with the original inside surface of the tube were used for the tests. Optical micrographs of cross sections of steam oxidation scales after the tests are shown in Fig. 7. XA704 had almost the same steam oxidation scale thickness as SUS347HTB, maybe because the former material had almost the same grain size and chromium content as the latter material.

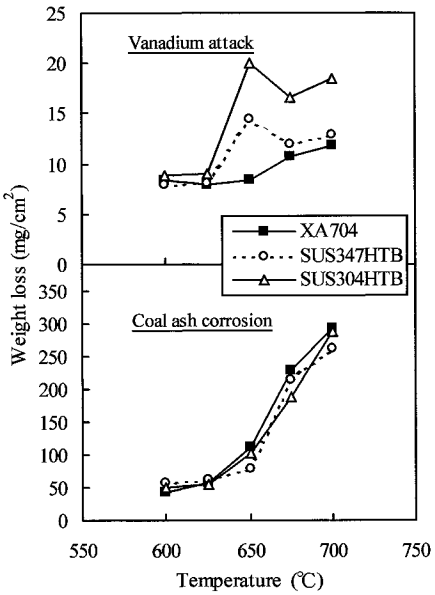


Fig. 6 Hot corrosion resistance of XA704 steel tubes C and D with synthetic ash.
Vanadium attack test Ash: V_2O_5:Na_2SO_4=85:15 (mass), Gas: air, Test time: 20 h
Coal ash corrosion test Ash: Na_2SO_4:K_2SO_4:Fe_2O_3=1.5:1.5:1 (mol)
Gas: 5%O_2+15%CO_2+0.5%SO_2+balN_2, Test time: 100 h

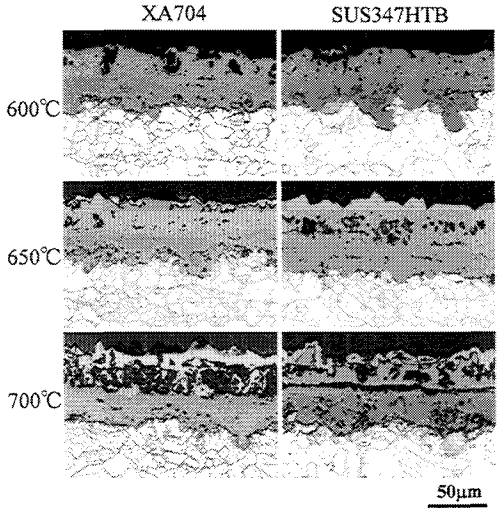


Fig. 7 Cross sections of steam oxidation scales grown on XA704 (tube E) and SUS347HTB exposed for 3,000 h.

Intergranular corrosion

The intergranular corrosion resistance of XA704 was examined by the Strauss test (ASTM A262 Practice E) with specimens heated at 550° to 850°C for 0.1 to 1,000 h. The results along with the results of SUS347HTB (0.07C-18Cr-11Ni-0.7Nb) and type 304H (JIS SUS304HTB, 0.06C-18Cr-9Ni) are shown in Fig. 8. Though SUS347HTB and SUS304HTB cracked respectively at over 0.1 h and at over 10 h heating condition, XA704 did not crack within these heating conditions. The low intergranular corrosion susceptibility of XA704 results

from the low content of carbon compared with that of conventional austenitic stainless steel boiler tubes.

3.6 Toughness after aging

Figure 9 shows the Charpy impact test results of XA704 aged at 600°, 650° and 700°C for up to 10,000 h. Though the impact value decreased gradually with increasing aging time and aging temperature, the value is still high enough to allow the steel to be used as a boiler tube, even after aging for 10,000 h.

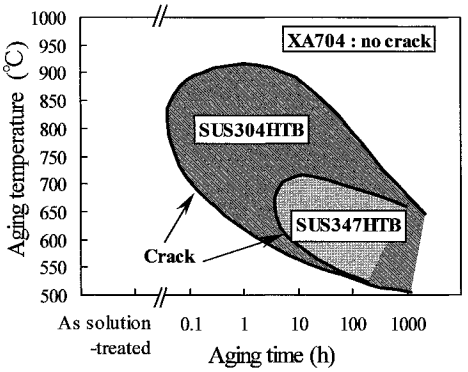


Fig. 8 Results of Strauss test of heated XA704 (Tube B), SUS347HTB and SUS304HTB.

3.7 Weldability

The weldability of XA704 was evaluated compared with SUS304HTB and type 310 (JIS SUS310TB, 25Cr-20Ni) by a varestraint test. The total weld metal crack length was applied for the evaluation. The results are shown in Fig. 10. XA704 has lower hot cracking susceptibility than SUS304HTB and SUS310TB.

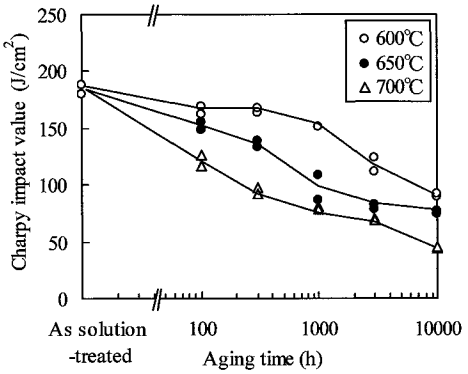


Fig. 9 Change in Charpy impact value at 0°C after aging (Tube D).
Specimens: 5 mm sub-size 2 mm V-notch

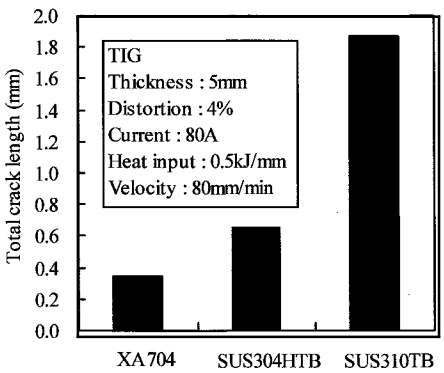


Fig. 10 Results of varestraint test of XA704, SUS304HTB and SUS310TB.

4. Precipitation behaviour

4.1 Objective

The excellent high temperature strength of XA704 is probably due to precipitation strengthening by nitrides of niobium and vanadium, and solution strengthening by tungsten and nitrogen. Coarsening of the nitrides and precipitation of solute tungsten may affect the high temperature strength. Therefore, the precipitation behaviour of alloying elements was examined in detail to evaluate long-term stability of the high temperature strength of XA704.

4.2 Experiment

Tube D was aged at 600°, 650° and 700°C for 100, 300, 1,000, 3,000 and 10,000 h. The precipitates were extracted electrolytically from aged and non-aged (as-solution-treated) tubes. X-ray diffraction and elemental analysis were conducted for the extracted precipitates. In addition, the precipitates were observed by Transmission Electron Microscope (TEM) with the use of extracted replica specimens.

4.3 X-ray diffraction

X-ray diffraction result of the precipitates extracted from as-solution-treated tube D is shown in Fig. 11. CrNbN and NbN were identified. Though diffraction peaks of CrNbN were higher than those of NbN in the case of tube D, the opposite was sometimes true in the case of the other heats [3].

Figure 12 shows a change in the X-ray diffraction profiles of the precipitates extracted from tube D aged at 600°, 650° and 700°C. At every temperature, diffraction peaks of CrNbN and NbN remained as they were even after aging for 10,000 h as a solution-treated condition. Diffraction peaks of $M_{23}C_6$ appeared at every temperature at 100 to 1,000 h, depending on the temperature, and became stronger with time.

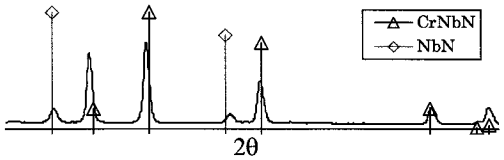


Fig. 11 X-ray diffraction results of the precipitates extracted from as-solution-treated tube D. Diffraction peaks of NbN and CrNbN quoted from Joint Committee of Powder Diffraction Standard (JCPDS) are also indicated together.

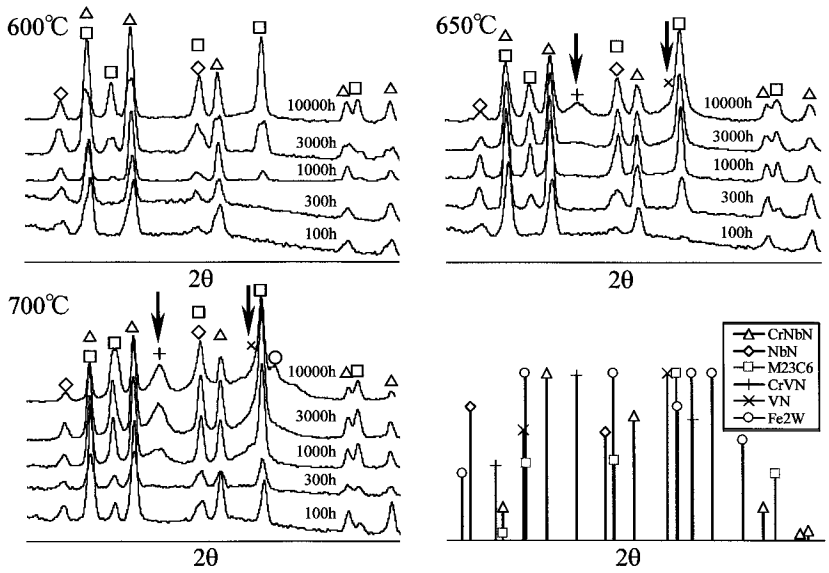


Fig. 12 X-ray diffraction profiles of the precipitates extracted from aged tube D. Diffraction peaks of some compounds quoted from JCPDS are also indicated.

A broad diffraction peak, indicated by " + ", appeared at 650° and 700°C, respectively at 3,000 h and 1,000 h. The peak was identified as CrVN (Z phase) [6]. Another broad diffraction peak, indicated by " × ", appeared at 650° and 700°C, respectively at 3,000 h and 1,000 h. Although the peak corresponds to **200** spot of VN, the existence of VN is not so apparent from the diffraction profiles because diffraction peaks of VN and $M_{23}C_6$ overlap each other. The broad diffraction peak probably means that the precipitates were very fine, and they must play an important role in precipitation strengthening of XA704.

A peak of Fe_2W which is indicated by "O" appeared only at 700°C at 10,000 h. No diffraction peaks of σ phase appeared in these aging conditions.

4.4 TEM observation

Figure 13 shows extracted replica images of precipitates observed by TEM. The specimens were taken from tube D in solution-treated condition and aged for 10,000 h.

As a solution-treated state, a few particles with diameters of 1 to 2 μm existed in the grain as shown in photo (a). The particles still remained in the grain even after 10,000 h at each temperature. These precipitates were identified as CrNbN and NbN by Transmission Electron Diffraction (TED) and Energy Dispersive X-ray Spectrometry (EDS).

Many large precipitates grew on the grain boundaries during aging as shown in photos (b), (c) and (d). These were confirmed to be $M_{23}C_6$ by TED and EDS. These results correspond to the results of X-ray diffraction.

Very small precipitates shaped like strings were observed everywhere in the grains after aging. The string-like precipitates look like thin strings at 600°C, thick strings at 650°C and shredded strings at 700°C from the photos (b), (c) and (d). However, higher magnification photos (e), (f) and (g) reveal different features. Photo (e) shows that the width of the string-like precipitates grown at 600°C is less than 50 nm. At 650°C, many wing-like precipitates had grown from the 'strings' perpendicular to those as seen in photo (f). At 700°C, the 'strings' decreased and the 'wings' increased. Photo (g) shows that many wing-like precipitates are apart from 'strings' and dispersed in the grains with high density.

The wing-like precipitate was identified as CrVN by TED pattern analysis, as shown in Fig. 14. Since the crystal system of CrVN is tetragonal and has a long c-axis of 0.739 nm [6], it can be clearly distinguished from the other kinds of precipitates when an electron beam direction is perpendicular to the c-axis. EDS spectrum showed that the precipitate consisted of chromium and vanadium. This supports the results of the TED pattern analysis. A small amount of niobium was also contained in the precipitate. The string-like precipitate has not been identified clearly yet. EDS spectra of the string-like precipitate showed that it consisted of chromium and vanadium with a few niobium like wing-like precipitates. However, the TED pattern usually corresponded to CrVN (Z phase) and/or VN (MX type (Cr,V)N). A further analysis must be conducted to clarify the identity of the string-like precipitates. In photo (h) of Fig.13, much larger precipitates than the wing-like precipitate were observed. These were identified as Fe_2W by TED and EDS.

4.5 Elemental analysis

Figure 15 shows the change in the amounts of alloying elements in the precipitates of tube D with aging. The precipitation amounts are indicated by mass percent relative to the amount of an electrolysed matrix. The amount of each element added in the steel is also indicated in the figure. Though precipitation was accelerated as aging time and temperature increased for each element, the precipitation behaviour differed for every element.

Iron content in the precipitates was relatively high. Most precipitating iron was probably contained in $M_{23}C_6$. The rapid increase of iron content in the precipitates from 3,000 to 10,000 h at 700°C might be attributed to growth of Fe_2W. Chromium precipitated more significantly than iron. As shown in Fig. 10, the initial precipitation of chromium was as CrNbN. During aging, chromium also precipitated as $M_{23}C_6$ and CrVN. However, Cr_2N was not identified by X-ray diffraction. Precipitation of nickel was very little compared with iron and chromium.

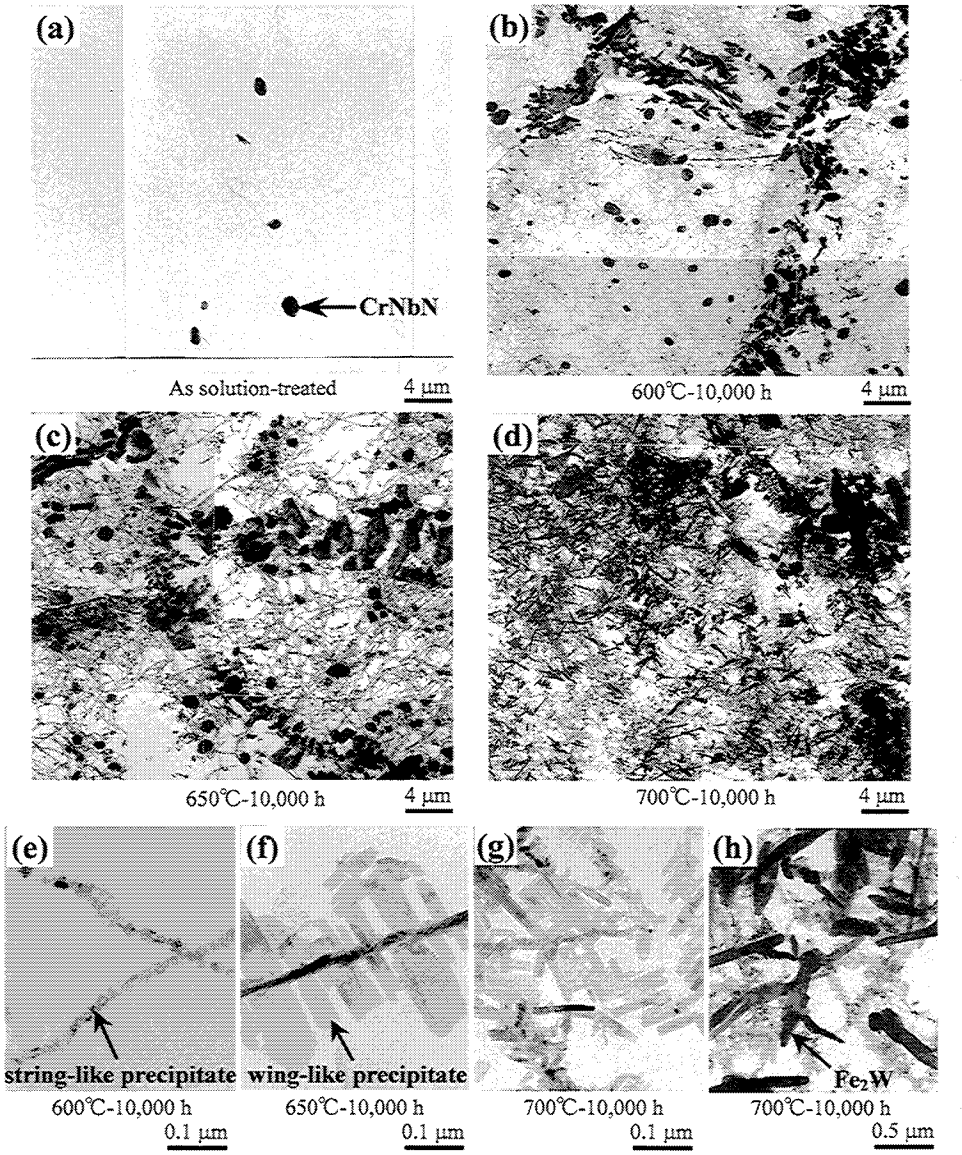


Fig. 13 Extracted replica images of precipitates of tube D observed by TEM.

More than a half of the added niobium had already precipitated in the solution-treated condition as CrNbN and NbN. During aging, niobium precipitated in CrVN as shown by TEM observation. Almost all niobium had precipitated at around 10,000 h at 700°C. On the other hand, vanadium dissolved entirely in the solution-treated condition, and precipitated more slowly than niobium as aging time increased. About a quarter of the total vanadium added in the steel still dissolved even after aging for 10,000 h at 700°C, and the precipitation was not saturated.

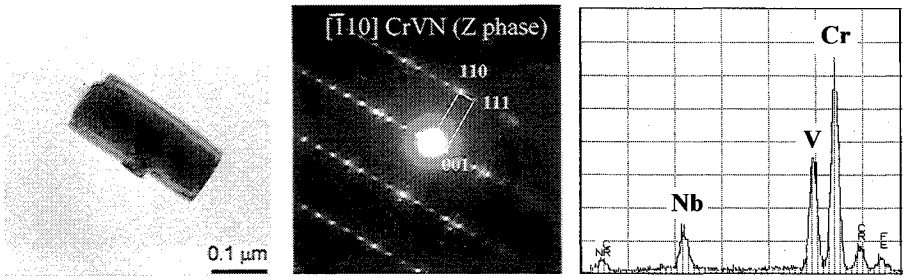


Fig. 14 Results of identification of a wing-like precipitate.

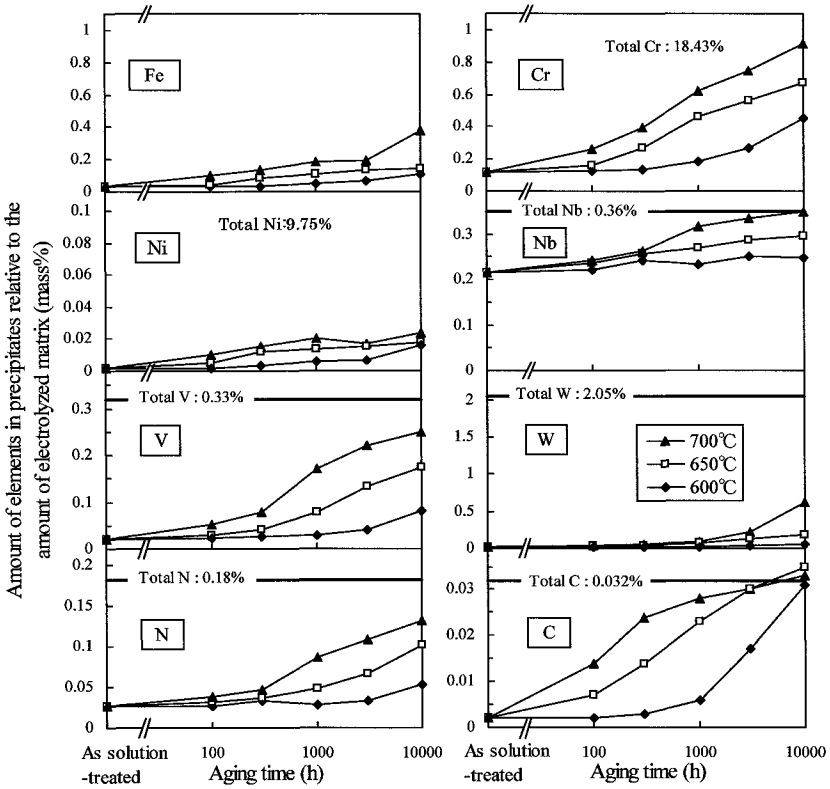


Fig. 15 Elemental analysis of precipitates in the aged tube D.

Tungsten also dissolved entirely in the solution-treated condition, and precipitated gradually as aging time increased. The precipitation rate was very slow at 600° and 650°C. Almost all tungsten added in the steel still dissolved even after 10,000 h aging. Although a little precipitation of tungsten occurred at 700°C, about seventy percent of the total tungsten still dissolved after 10,000 h. This means that solution strengthening by tungsten is effective for 10,000 h or more. Precipitating tungsten after 10,000 h at 700°C was probably Fe_2W.

About fifteen percent of the total nitrogen had already precipitated as CrNbN and NbN after it was solution-treated, and the amount of nitrogen in the precipitates increased gradually as aging time increased. About thirty percent of the total nitrogen still dissolved in the steel after 10,000 h at 700°C. Thus, nitrogen contributes to both solution strengthening and precipitation strengthening for a long time. Almost all carbon added in the steel had already precipitated as $M_{23}C_6$ in 10,000 h at each temperature. The result of Electron Probe Microanalysis indicated that the amount of carbon taken in nitrides such as CrNbN or CrVN was very small [7].

4.6 Discussion

As the results of the above analysis, several kinds of precipitates were found in XA704. The initial precipitates which remain just after solution heat treatment were CrNbN and/or NbN. These precipitates are needed for XA704 to obtain steam oxidation resistance since they are effective for restraining grain coarsening in the solution treatment. However, as shown in Fig. 13, these initial precipitates tended to be too large to have an effect on creep strength. On the other hand, the effect of niobium on creep rupture strength results from the fine precipitates of niobium precipitating in use. TEM observation indicated that niobium precipitating in use was taken into chromium-vanadium nitrides which were like strings and/or wings and were fine enough to improve creep strength. However, a further addition of niobium will only result in the increase of large initial CrNbN and NbN, and thus have no effect on creep strength.

Since almost all added vanadium dissolved in the matrix just after solution heat treatment, vanadium compounds found in XA704 had precipitated in use. Vanadium was detected only in the string-like precipitates and the wing-like precipitates. Although there is little experimental evidence, the initial precipitate of vanadium is thought to be VN and the origin of the string like precipitate. VN will grow while taking chromium in, and the chromium content in VN will increase with time. When the chromium content becomes nearly equal to vanadium, CrVN (Z phase) probably begins to grow like wings from VN perpendicular to the string. The string shrinks in size with growth of CrVN, and finally, CrVN disperses in the grain with high density. Moreover, TEM observation showed that CrVN kept its size very fine even after aging at 700°C for 10,000 h. Thus, CrVN is probably very effective in improving the creep rupture strength for a long term. Higher addition of vanadium may increase these small precipitates and consequently increase the creep strength. However, an excessive addition of vanadium results in nucleation of δ ferrite, vanadium content must be restricted within an adequate amount.

Solution strengthening by tungsten was probably effective for a long term because almost all tungsten dissolved in the matrix even after 10,000 h at 600° and 650°C. Although a little Fe_2W was observed after 10,000 h at 700°C, rapid deterioration of creep strength did not occur in the creep rupture tests at least until 40,000 h at 700°C as shown in Fig 4. TEM observation showed that the size of Fe_2W was larger than that of CrVN but was smaller than 1 μm, and the spacing of each Fe_2W was less than 1 μm. Thus, Fe_2W may contribute to the precipitation strengthening, and may compensate for the decrease of the solution strengthening.

As a result of the above consideration, it can be concluded that stable and fine precipitates of CrVN with niobium and a large amount of solute tungsten give XA704 remarkably high creep strength for a long term.

5. Conclusions

The newly developed austenitic stainless steel boiler tube XA704 was evaluated in terms of tensile strength at elevated temperatures, creep strength, corrosion resistance, toughness after aging and weldability. Moreover, precipitation behaviour was examined in detail.
The results are summarized as follows:

1) The maximum allowable stress values of XA704 are much higher than those of SUS347HTB, and almost the same as those of NF709 at 650°C.
2) The hot corrosion resistance and the steam oxidation resistance of XA704 are comparable to those of SUS347HTB.
3) The intergranular corrosion resistance of XA704 is much better than that of SUS347HTB and SUS304HTB. XA704 is not sensitized for inter granular corrosion after heating at 550° to 850°C for 0.1 to 1,000 h.
4) Although the toughness after long-term aging decreases gradually with increasing aging time and aging temperature, the impact value after aging for 10,000 h at 700°C is still high enough to allow the developed steel to be used as a material for a boiler tube.
5) The hot crack susceptibility of XA704 is superior to that of SUS304HTB and SUS310TB.
6) Fine and stable CrVN which precipitates in use and a large amount of solute tungsten contribute to the high creep strength of XA704. These effects are maintained for a long term.
7) Thus, it can be concluded that XA704 has high strength, good corrosion resistance and is inexpensive, and thus is suitable for use as a material for superheater and reheater tubes of thermal power boilers.

References

[1] Takahashi, T., Sakakibara, M., Kikuchi, M., Araki, S., Ogawa, T., Nagao, K. and Fujita, T., "Development of a high-strength 25Ni-20Cr steel for tubes in ultra-supercritical power boilers," EPRI Second Int. Conf. on Improved Coal-fired Power Plants, (1989), p.41_3-41_17.
[2] Orr, J. and Nileshwar, V. B., "'Esshete 1250':an advanced austenitic stainless steel for power station tubes, pipes and headers," Stainless Steels '84, Göteborg, (1984), p.533-540.
[3] Ishitsuka, T. and Mimura, H., "Development of 18Cr-9Ni-W-Nb-V-N Austenitic Stainless Steel Tube for Thermal Power Boilers," JSME. Int. J., A 45 (2002), p.110
[4] Kihara, S., Nakagawa, K., Ohtomo, A., Aoki, H. and Ando, S., "Simulating test results for fireside corrosion of superheater & reheater tubes operated at advanced steam condition in coal-fired boilers," High. Temp. Corros. Energy. Syst., (1985), p.361-376.
[5] "Data sheets on the elevated-temperature properties of 18Cr-12Ni-Nb stainless steel for boiler and heat exchanger seamless tubes (SUS347HTB)," NRIM Creep Date Sheet, No.28A (1983).
[6] Strang, A. and Vodarek, V., "Z phase formation in martensitic 12CrMoVNb steel" Mater. Sci. Technol, 12 (1996), p.552
[7] Ishitsuka, T. and Mimura, H., under preparation.

ALLOY DESIGN FOR ULTRA–HIGH TEMPERATURE STEAM TURBINE APPLICATIONS: PHASE–FIELD SIMULATION OF THE REMELTING PROCESS

B. Böttger, I. Steinbach, S. G. Fries
ACCESS e. V., Intzestraße 5, D–52072 Aachen, Germany

Q. Chen, B. Sundman
Department of Material Science and Engineering,
Royal Institute of Technology, S–10044 Stockholm, Sweden

Abstract

A multiphase–field model coupled to thermodynamic databases is presented which is able to handle multicomponent and multiphase structural evolution on microscopic scale. Databases assessed according to the CALPHAD approach are connected online to the phasefield code using the thermodynamic software package Thermo–Calc and a fortran interface. Multi–binary extrapolation is used to make simulations of realistic systems viable. A unit cell approach is used to apply this model to the remelting process, which locally is simulated as a directional solidification under high thermal gradients.
The model is applied to remelting of the three Ni–base superalloys IN706, IN617 and Waspaloy, respectively, which are used as a starting point for the development of new alloys for ultra–high temperature steam turbine applications. From the results secondary phase formation, incipient melting as well as homogenisation times and temperatures can be predicted. Additionally an alloy–specific freckle criterion is calculated from the simulation results, which allows the estimation of the freckle risk under typical remelting conditions.

Keywords: phase–field, simulation, thermodynamic coupling, superalloys, alloy development

Introduction

In the design process of new alloys for steam turbine applications, the remelting process, being the first step in the lifecycle, is of special importance. The production of high quality ingots from Ni–based superalloys by vacuum arc (VAR) or electroslag remelting (ESR) is not in all cases as straightforward as e.g. for IN706, where even large ingot sizes are obtained in industrial practice. One typical problem is the formation of freckles, which arise from liquid density inversion in the mushy zone. This effect is a direct consequence of the microscopic segregation process and can completely prohibit the use of a specific alloy as it is the case for large Waspaloy ingots. Further problems can be caused by precipitation of brittle phases which can not be removed easily by homogenisation treatment.

Simulation tools are needed which are able to predict the remeltability as well as the quality and properties of the ingot for promising alloy compositions without the necessity of expensive solidification experiments. Simulation has to be done at a microscopic scale as composition primarily affects the microsegregation behaviour and macrosegregation is successfully prevented by modern remelting techniques. Even the freckles which usually extend over larger distances are eventually caused by segregation inside the mushy zone.

A steep increase in complexity arises from the fact that commercial Ni–based superalloys are multicomponent systems which cannot be successfully described without using sophisticated thermodynamic software packages like Thermo–Calc [1] together with extended thermody–

namic databases. Today several databases for Ni–based superalloys are available [2], which are assessed from a high number of experimental informations using the CALPHAD method [3] and which permit extrapolation of the thermodynamic behaviour to the desired alloy compositions.

In this paper a two–dimensional unit cell model is presented which describes dendritic solidification in industrial remelting processes. Microstructure and secondary phase formation is simulated using the multiphase–field method [4,5] which is online coupled to thermodynamic databases. This combination of tools, as described in this paper, allows the effective prediction of the remeltability of new alloys.

Multiphase–Field Model Coupled to Realistic Thermodynamic Data

The phase field method is a powerful tool for describing the spacial evolution of interfaces between different phases. Several phase–field models have been presented in literature which differ in terms of the free energy density in the interfacial region as well as in the way how they were derived [6–8].

The following approach is based on a multiphase–field concept which has been published earlier [4,5]. The development of the phase–field parameter ϕ_i of a phase i in a multiphase system is described as the sum of the pair–wise interactions with all other phases j (in the case of a double well potential):

$$d\phi_i/dt = \sum_j^N \mu_{ij}\left[\sigma_{ij}\left(\phi_i\nabla^2\phi_j - \phi_j\nabla^2\phi_i + \frac{36}{\eta_{ij}^2}\phi_i\phi_j(\phi_i-\phi_j)\right) + \frac{6}{\eta_{ij}}\phi_i\phi_j\Delta G_{ij}\right] \quad (1)$$

Here μ_{ij} is the interface mobility, σ_{ij} the surface energy, η_{ij} the interface thickness, N the number of coexisting phases and ΔG_{ij} the driving force for the transformation between the phases i and j.

A distinctive feature of the multiphase–field model presented here regards the coupling to the diffusion equation. In contrast to the Wheeler–Boettinger model [6] instead of the overall composition c^k the phase compositions c_i^k and c_j^k are used to determine the driving force ΔG_{ij}. This makes the model more suitable for the input of realistic thermodynamic data. Multiphase diffusion for a component k is then given as the sum of the fluxes in the individual phases which are calculated from the composition gradients ∇c_i^k using the diagonal terms D_i^k of the diffusivity matrix:

$$dc^k(\vec{x},t)/dt = \nabla\left(\sum_{i=1}^N \phi_i D_i^k \nabla c_i^k\right) \quad (2)$$

The thermodynamic calculation now has to provide three informations from the database, a) the relation beween the phase compositions c_i^k which are in contact, b) the thermodynamic driving force ΔG_{ij} in eq. (1) and c) some nucleation conditions for secondary phases.
For diffusion–controlled processes like those simulated in this paper a pseudo–equilibrium approach can be applied which assumes local equilibrium at the interface. The driving force ΔG_{ij} results from a slight deviation from equilibrium which we get by construction of a common tangent to the gibbs energy functions f_i and f_j ($a^k = df^k/dc^k$ is the slope of the Gibbs energy curve which has to be identical for both phases):

$$\Delta G_{ij}=f_i-f_j+a^k(c_i^k-c_j^k) \tag{3}$$

Eq. (3) must be true for all compontents simultaneously, regarding as additional condition the conservation of composition at each interface point:

$$\sum_i \phi_i c_i^k=c^k \tag{4}$$

This is done in a pair–wise manner for all phase interactions *ij*. Eq. (3) is solved by use of the software package Themo–Calc [1] which has been enhanced by an extra routine in order to meet also eq. (4). Together with a realistic database even complex multicomponent and multi–phase problems can be solved in this way.

Multi–Binary Extrapolation

Even though the above description provides a complete solution within the local equilibrium approximation immense calculation times would be needed to include the thermodynamic calculations for multicomponent alloys in each time step and for all interface gridpoints. Therefore, together with the equilibrium calculation the slopes m_{ij}^k and m_{ji}^k of the liquidus (solvus) and the solidus plane are extracted at the equilibrium compositions $c_i^{0,k}$ and $c_j^{0,k}$ respectively in the directions of every component k. By this procedure we get a number of linearized phase diagrams for each interface cell. These phase diagrams are additionally shifted by the temperature equivalent ΔT_{ij}^{off} of the calculated equilibrium deviation ΔG_{ij} from eq. (3) if ΔS_{ij}^{trans} is the transformation entropy :

$$\Delta T_{ij}^{off}=\Delta S_{ij}^{trans}\Delta G_{ij} \tag{5}$$

From the local phase diagrams we get a good interpolation of the thermodynamic behaviour and time–consuming "real" equilibrium iterations have to be done only from time to time, when local compositions or the temperature show considerable deviation from the conditions at the last linearisation.

From the interpolation of the equilibrium temperatures

$$T_{ij}^{eq}=T_{ij}^{0,eq}+T_{ij}^{off}+\sum_k^{N-1} m_{ij}^k(c_i^k-c_{ij}^{0,k}) \tag{6}$$

(or the analogue expression using the solidus slopes m_{ji}^k) we obtain the interpolated driving force, if T is the actual temperature at this gridpoint:

$$\Delta G_{ij}^*=-\Delta S_{ij}^{trans}(T-T_{ij}^{eq}) \tag{7}$$

Using eq. (6) and the analogue formulation with m_{ji}^k together with eq. (4) finally the interpolated local phase compositions can be calculated:

$$c_i^{*k}=\frac{c^k-\Sigma_j\phi_j(c_{ji}^{0,k}-c_{ij}^{0,k}m_{ji}^k/m_{ij}^k)}{\Sigma_j\phi_j m_{ji}^k/m_{ij}^k} \tag{8}$$

The Unit Cell Approach

In industrial remelting processes local solidification conditions are characterised by high thermal gradients and low cooling rates. This leads to dendritic morphology which is close to the cellular–dendritic transition region, i.e. tertiary arms are weakly developed, and due to grain

selection the dendrite trunks are oriented in the direction of the thermal gradient. Under such conditions segregation can be described in a isothermal two–dimensional cut through the primary dendrite [9–11] better than between secondary arms like in plate models.

Fig. 1 shows the unit cell used in the simulation throughout this paper. As dendrites often show fourfold shapes the dendritic cross section is assumed to be of such symmetry within a regular dentritic array. Due to this symmetry only a quarter of one dendritic cross section is included into the unit cell. The third dimension along the dendrite axis corresponds in this unit cell approach to the time variable which describes growth inside one fixed cross section or at the same time the gradient along the mushy zone. The side length of the unit cell is correlated to the dendritic primary spacing λ_1 and can be estimated from the thermal gradient G and the solidification velocity v using the theory of Hunt [12]:

$$\lambda_1 = K G^{-1/2} v^{-1/4} \tag{9}$$

According to Goldschmidt [13] the factor K can be considered as a unique constant for superalloys. Alternatively K can be estimated from experiments.

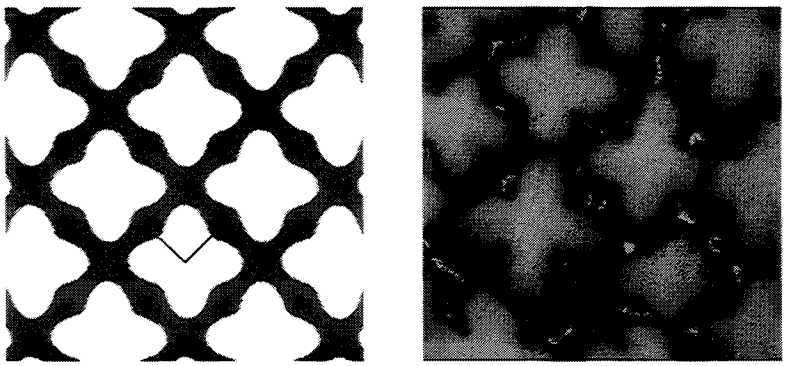


Fig. 1: Comparison of the dendritic array given by the unit cell approach to a real dendritic array (CMSX–6). The small quadratic area indicated by the black square is the unit cell which is included into the simulation.

Freckle Criterion

In this paper a freckle criterion is derived which does not describe the effects of the solidification process parameters as done by other authors [14–17], but focuses on the specific tendency of the alloys for freckle formation. This tendency can be assessed from the composition distribution along the mushy zone which can be calculated using the unit cell model together with the multiphase–field approach described above. The composition change in direction of the temperature gradient is reconstructed from the time evolution of the average liquid composition calculated in the unit cell. The liquid density ρ is determined using the empirical approach of Sung et al. [18]:

$$\rho^{-1} = \sum_k \frac{c_{liq}^k}{\rho_{Ref}^k + \Lambda^k (T - T_{Ref}^k)} \tag{10}$$

According to this approximation ρ is calculated from the densities of the pure element melts ρ^k_{Ref} and the thermal expansion coefficients Λ^k given at a reference temperature T^k_{Ref} by molar volume averaging with the molar compositions c^k_{liq}. Now for all positions h in the mushy zone a buoyancy force $f_B(h)$ is calculated. This is done by integration of the liquid density differences in the melt between this point and the top of the mushy zone weighted with the liquid fraction:

$$f_B(h)=\int_{z=0}^{h} f_L(z)\ (\rho(z)-\rho(0))\,dz \tag{11}$$

In order to get a freckle criterion which is independent from the temperature gradient integration is done over the temperature T instead of the height h:

$$f^*_B(T)=\int_{T=T^{Liq}}^{T(h)} f_L(T)\ (\rho(T)-\rho(T^{Liq}))\,dT \tag{12}$$

The formation of a freckle will be initiated at the point where the value of f^*_B is maximum, defining the freckle parameter f_{FR}:

$$f_{FR}=max(f^*_B(T)) \tag{13}$$

If no liquid density inversion occurs at all the value of f^*_B is arbitrarily taken at the temperature where the fraction liquid is 0.5.

Results

a) Simulation of IN706 Solidification:

For simulation of IN706 solidification under remelting conditions a 7 component equivalent composition has been chosen which includes all elements which play an important role in the solidification process. This composition is shown in tab. 1. Input parameters for calculation are the primary dendrite spacing λ which according to experimental findings was set to 200 μm and a typical cooling rate of 0.5 K/s. Diffusion constants for the liquid phase were estimated as 1.0×10^{-5} cm²/s for Carbon and 5.0×10^{-6} cm²/s for the other elements. The temperature–dependent diffusion coefficients for fcc (the primary phase) are given in tab. 2. Due to the lack of literature data these values were also used in the secondary phases. All thermodynamic data were taken from the 11 component database nifedata [8] provided from Thermotech by online coupling to Thermo–Calc during simulation.

Tab. 1: Composition used for IN706 simulation

	Ni	Fe	Cr	Ti	Nb	Al	C
at%	bal	37.7	17.1	1.83	1.8	0.55	0.05

Tab. 2: Temperature dependent diffusion coefficients in the fcc phase expressed as $D=D^0\ x\ exp(-Q/RT)$ [19,20]

	Fe	Co	Cr	Mo	Ti	Nb	Al	B	C
D^0 (cm²/s)	10	1.8	5.2	1.3	4.1	0.01	1.87	0.0066	14.2
Q (kJ/mol)	269	282	289	283	275	201	268	96	194.8

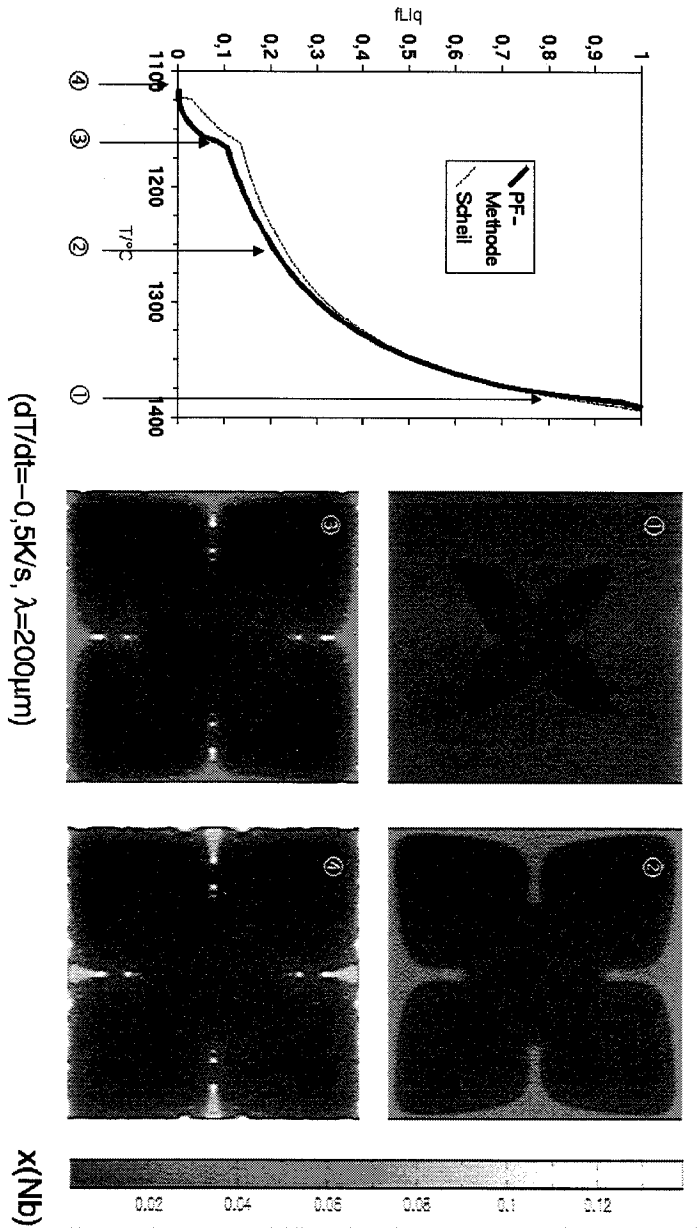


Fig. 2: Left side: Comparison of the fraction solid vs. temperature curve for the phasefield simulation (bold line) and a Thermo–Calc Scheil calculation. Right side: Corresponding microstructure evolution represented by the Nb composition in the unit cell. In frame 4 complete solidification is reached.

Fig. 2 shows the solidification progress predicted from simulation. In the diagram at the left side the fraction solid vs. temperature dependence for simulation is compared to the results of a Scheil Calculation done by Thermo–Calc using the same thermodynamic database. The differences between the two curves are relatively small at the beginning and get considerably large at the end of the solidification process. This is mainly due to back diffusion which is taken into account by our phase–field model. Another slight difference at the very beginning is caused by an initial undercooling of the dendrite (tip undercooling) which was set to 2 K in our model.

On the right side of fig. 2 the microstructure during solidification is shown for 4 timesteps, which are also indicated in the fraction–solid curve. Displayed is the Nb distribution within the isothermal cross–section through the dendritic unit cell. As can be seen the primary dendrite is growing according to the fourfold symmetry of the unit cell. Approaching the end of solidification secondary phases are formed which can be identified by their increased Nb composition (timesteps 3 and 4).

In fig. 3 the composition distribution after complete solidification is shown for all elements. In addition to a strong microsegregation for almost all elements, three different secondary phases can be distinguished: The small MC carbides which are forming first during solidification can be identified by their high carbon content. The Laves phase covers a bigger area in the cross–section and is relatively high in Nb. Just before freezing of the remaining liquid, η appears as third phase, indicated by its low content of Fe and Cr.

b) Homogenisation:
More important than their formation is the sissolution of these phases during the production process of steam engine parts, especially if brittle phases are involved. As secondary phase formation during solidification is a metastable process most of them can be dissolved by heating at a temperature just below the melting point. This homogenisation treatment can also be of importance because it increases the melting temperature which directly after solidification can be very low due to strong segregation. If this temperature is exceeded during forging, the material can be destroyed by incipient melting.

Homogenisation can be observed also in simulation, where this process is demonstrated for IN706 (fig. 4). In this calculation the temperature after solidification was raised to 1093°C for several hours. As can be seen the Laves and η phase is vanishing slowly due to the diffusion process while MC carbides are stable and show only ripening after 33 hours. In reality transformation to $M_{23}C_6$ would be expected, which has not been taken into account here.

c) Prediction of the Freckle Risk:
As shown above the freckle risk can be estimated from the liquid density inversion which is caused by segregation during solidification. The resulting freckle number has been calculated from phase–field simulations for the three candidate alloys IN706, Waspaloy and IN617, which have been chosen as a reference for the development of new steam turbine alloys [21].

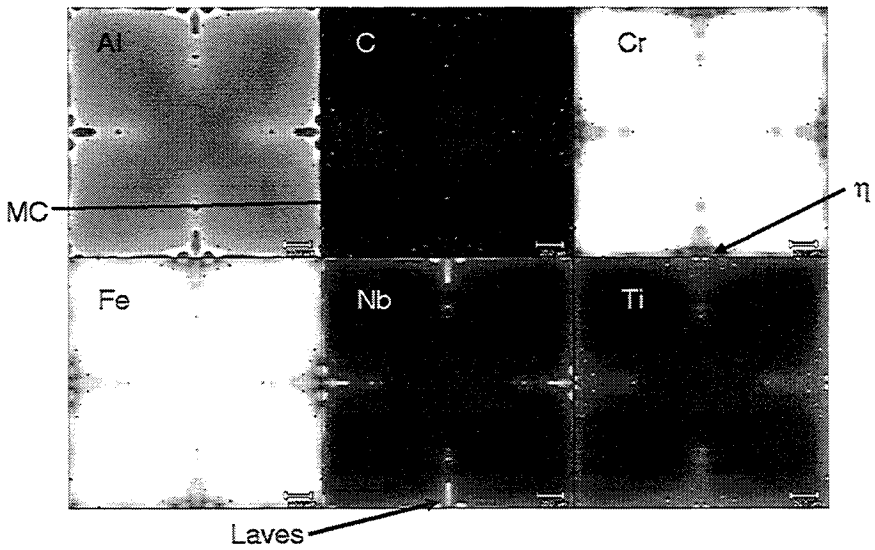


Fig. 3: Microstructure after solidification represented by the distribution of the different alloying elements in the unit cell. The secondary phases MC, Laves and η can be distinguished by their characteristic compositions.

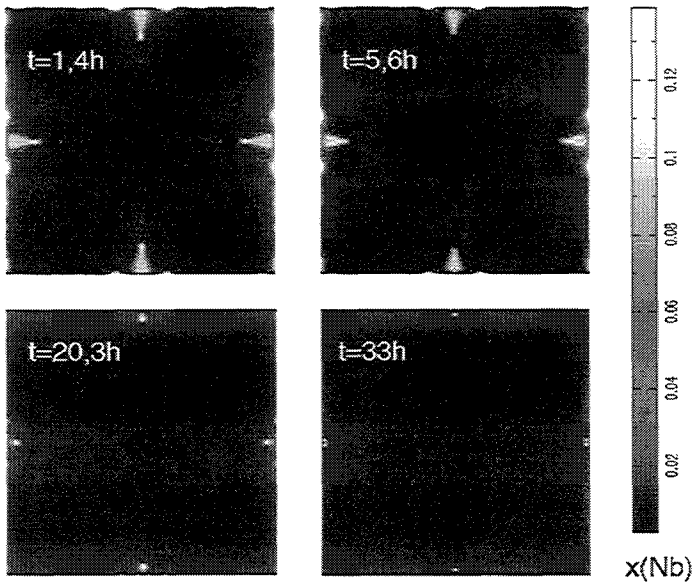


Fig. 4: Secondary phase dissolution by heat treatment at 1093°C. Shown is the Nb composition in atomic percent.

Tab. 3 summarizes the compositions and tab. 4 the calculated freckle numbers for the three alloys. The negative values for IN706 and IN617 demonstrates that no density inversion is observed at all. At the contrary Waspaloy shows a positive freckle number. The results are in good agreement with practical experience: While IN706 and IN617 can be used for production of even large ingots, Waspaloy is known to be very critical with respect to freckle formation so that the remelting of ingots bigger than 1 meter in diameter is effectively impossible. From the freckle calculations also a modified Waspaloy composition has been proposed for use in steam turbines [21].

Tab. 3: Compositions of Waspaloy and IN617

at%	*Ni*	*Fe*	*Co*	*Cr*	*Mo*	*Ti*	*Nb*	*Al*	*B*	*C*
IN617	bal	0.55	12.7	24.6	5.48	0.67	–	2.39	–	0.29
Waspaloy	bal	0.58	13.5	21.2	2.68	3.73	0.006	2.58	0.03	0.16

Tab. 4: Calculated freckle numbers

alloy	*IN617*	*Waspaloy*	*IN706*
freckle number [gKcm^{-3}]	–0.224	0.069	–0.354

Conclusion

It has been shown that the multiphase–field model coupled to thermodynamic databases is a powerful tool for the prediction of microstructural evolution at a microscopic scale. The pragmatic multi–binary extrapolation of the local phasediagrams allows the application to complex multicomponent and multiphase problems like Ni–based superalloys and precipitation of secondary phases at reasonable calculation times.
Using a unit cell approach for dendritic solidification under remelting conditions the tool was applied to the prediction of the remeltability of potential ultra high temperature steam turbine alloys. While in the paper results for the commercial alloys IN706, Waspaloy and IN617 are shown, the future potential consists in the application to modified alloy compositions. Important parameters like brittle phase formation, incipient melting temperatures and heat treatment cycles needed for homogenisation can be estimated without need for expensive experiments. The risk of freckle formation during remelting is evaluated by an alloy–specific freckle criterion. For the three model alloys a good coincidence between this criterion and industrial experience has been found.

Acknowledgment

The authors wish to thank the DFG (Deutsche Forschungsgesellschaft) for financial support under grant number He2700/4–5

References

[1] B. Sundman, B. Jansson and J. O. Anderson, "The Thermo–Calc Databank System", CALPHAD, 9 (1985) 153–190.

[2] N. Saunders, "Phase Diagram Calculations for Ni–Based Superalloys", Superalloys 1996, (Warrendale, PA: Met. Soc. AIME., 1996), 101–110.
[3] N. Saunders and A. Miodownik: CALPHAD, Calculation of Phase Diagrams, A Comprehensive Guide; Elsevier S. Ltd. 1998, ISBN 0–08–042–129–6.
[4] I. Steinbach et al., "A Phase Field Concept for Multiphase Systems", Physica D, 94 (1996) 135–147.
[5] J. Tiaden, B. Nestler, H. J. Diepers, I. Steinbach, "The multiphase–field model with an integrated concept for modelling solute diffusion", Physica D 115 (1998) 73–86.
[6] A. A. Wheeler, W. J. Boettinger and G. B. McFadden, Phys. Rev. A 45, (1992) 7424.
[7] G. Caginalp and W. Xie, Phys. Rev. E 48, (1993) 1897.
[8] S. G. Kim, W. T. Kim, T. Suzuki,"Phase–field model for binary alloys", Phys. Rev. E 60, (1999) 7186.
[9] B. Böttger, U. Grafe, D. Ma, S. G. Fries, "Simulation of microsegregation and microstructural evolution in directionally solidified superalloys", Mater. Sci. Tech. 16 (2000) 1425–1438.
[10] B. Böttger, U. Grafe, D. Ma, A. Schnell, "Prediction and Measurement of Microsegregation and Microstructural Evolution in Directionally Solidified Superalloys", Superalloys 2000, (Warrendale, PA: Met. Soc. AIME., 2000), 313–322.
[11] D. Ma, "Modellierung des Dendritenwachstums und der Mikroseigerung bei gerichteter Erstarrung, Teil I: Entwicklung eines analytischen Mikromodells", Gießereiforschung, 1 (1998) 29–34.
[12] J. D. Hunt, "Cellular and primary dendrite spacings", Solidification and Casting of Metals, Vol. 192 (1979) 3–9. The Metal Society, London.
[13] D. Goldschmidt, "'Einkristalline Gasturbinenschaufeln aus Nickelbasis–Legierungen, Teil I", Mat.–wiss. u. Werkstofftech., 25 (1994) 311–320.
[14] P. Auburtin, S. L. Cockcroft and A. Mitchell, "Liquid density inversions during the solidification of superalloys and their relationship to freckle formation in castings", Superalloys 1996, (Warrendale, PA: Met. Soc. AIME., 1996), 443–450.
[15] R. Schadt, I. Wagner, J. Preuhs, P. R. Sahm, "New aspects of freckle formation during single crystal solidification of CMSX–4", Superalloys 2000, (Warrendale, PA: Met. Soc. AIME., 2000), 211–218.
[16] C. Beckermann, J. P. Gu and W. J. Boettinger, "Development of a freckle predictor via Rayleigh number method for single–crystal nickel–base superalloys", Metall. Mater. Trans. A, 31 (2000) 2545–2557.
[17] P. Auburtin, T. Wang, S. L. Cockcroft and A. Mitchell, "Freckle formation and freckle criterion in superalloy castings", Metall. Mater. Trans. B, 31 (2000) 801–811.
[18] P. K. Sung, D. R. Poirier and E. McBridge, "Estimating densities of liquid transition–metals and Ni–base superalloys", Mat. Sci. Eng. A, 231 (1997) 189–197.
[19] Z. Minamino, H. Yoshida, S. B. Jung, K. Hirao, T. Yamane, "Diffusion of Platinum and Molybdenium in Ni and Ni_3Al", Defect and Diffusion Forum Vols. 143–147 (1997), pp 257–262.
[20] J. Cermak, H. Mehrer; "Tracer Diffusion of ^{14}C in Austenitic Ni–Fe–Cr Alloys", Acta metall. mater. Vol. 42 (1994), No.4, pp. 1345–1350.
[21] J. Rösler et al.; "Wrought Ni–Base Alloys for Advanced Gas Turbine Disc and USC Steam Turbine Rotor Applications", this conference

WORKABILITY AND DEVELOPMENT OF T/P23 (2.25%Cr-1.6W-Nb-V STEEL) FOR FOSSIL BOILER AND COMBINED CYCLE APPLICATIONS

J. Gabrel[1], Bo. Lefebvre[2], J.C. Vaillant[3], B. Vandenberghe[4]

[1] Vallourec Research Center, Aulnoye-Aymeries, France
[2] Vallourec and Mannesmann Tubes, Saint-Saulve, France
[3] Vallourec and Mannesmann Tubes, Boulogne-Billancourt, France
[4] Vallourec and Mannesmann Tubes, Düsseldorf, Germany

Abstract

The improvement of thermal efficiency by raising temperature and pressure of power plants has recently led to the development of new steels. The Grade ASTM A213-T23 (2,25%Cr-1,6W-Nb-V steel), initially developed in Japan is included in these new steels. It is produced world-wide for fossil boiler tube applications with a maximum operating metal temperature up to 580°C.

A213-T23 is used instead of the previous 2,25%Cr-1%Mo as T22 (10CrMo9-10 according to prEN 10216-2: January 2002) with large advantages. In fact it appears to combine a good workability with a strong creep behavior:

- The workability, namely cold bending, hot bending and different welding processes is improved thanks to a low Carbon content. The maximum Vickers hardness as welded, less than 350HV, avoids the post heat treatment (PWHT) with a good toughness
- Very high creep properties close to T91
- Good thermal fatigue resistance due to a smaller designed wall thickness.

T23 is also a good candidate to replace, in some conditions of temperature, the A213-T91 (X10CrMoVNb9-1 according to prEN 10216-2 January 2002) steel, with a very competitive price.
If T23 steel was firstly developed as an ideal candidate for waterwall panel applications in Ultra Super Critical Boiler (USCB), it is now used more frequently for superheaters and reheaters of conventional boilers. This steel is also adequate for Heat Recovery Steam Generator (HRSG) in combined cycle.

Thanks to its experience, VALLOUREC & MANNESMANN TUBES has now a world-wide T23 reference. Besides, in order to support to the design of boiler components with homogeneous steel grade and then to propose ASTM A335-P23 grade, V&M is developing piping with heavy wall thickness.

Keywords: Low alloyed steel – T and P 23 – Welding – Cold bending

Introduction :

The improvement of thermal efficiency by raising temperature and pressure of power plants has recently led to the development of new steels. The Grade ASTM A213-T23 (2,25%Cr-1,6W-Nb-V steel), initially developed in Japan is included in these new steels. It is produced world-wide for fossil boiler tube applications with a maximum operating metal temperature up to 580°C [1].

Development of T23 steel grade :

Chemical composition and mechanical properties :
This new ferritic micro-alloyed W-modified 2.25%Cr steel has a very low Carbon content which improves fabricability (welding , bending, ...) by reducing hardenability. The partial substitution of Molybdenum by Tungsten increases the creep behaviour by strengthening, the Vanadium and Niobium (Cb) improve creep strength by precipitation of carbides and the Boron addition allows to obtain a microstructure more homogeneous and participate to the very high creep properties.
Chemical composition and mechanical properties are given in the following tables 1 and 2

Standard	C	Mn	P	S	Si	Cr	Mo	V	W	Nb	B	N	Al
	%	%	%	%		%	%	%	%	(Cb)	%	%	%
prEN 10216-2	0.08	0.30	max.	max.	max.	2.00	0.90	n.s.	n.s.	n.s.	n.s.	n.s.	max.
10CrMo9-10	0.14	0.70	0.025	0.020	0.50	2.50	1.10	n.s.	n.s.	n.s.	n.s.	n.s.	0.040
A 213	0.04	0.10	max.	max.	max.	1.90	0.05	0.20	1.45	0.02	0.0005	max.	max.
Grade T23	0.10	0.60	0.030	0.010	0.50	2.60	0.30	0.30	1.75	0.08	0.006	0.030	0.030

Table 1 : Chemical composition

Standard	Y.S.	U.T.S.	Elong.	Hardness
	MPa (ksi)	MPa (ksi)	2" - %	HB
prEN 10216-2	min.	480	min.	
10CrMo9-10	280	630	22	
A 213	min.	min.	min.	max.
Grade T23	400 (58)	510 (74)	20	220

Table 2 : Mechanical properties

Grade T23 shall be normalized at 1040°C (1,900°F) minimum and tempered at 730°C (1,350°F)minimum as a final heat treatment.

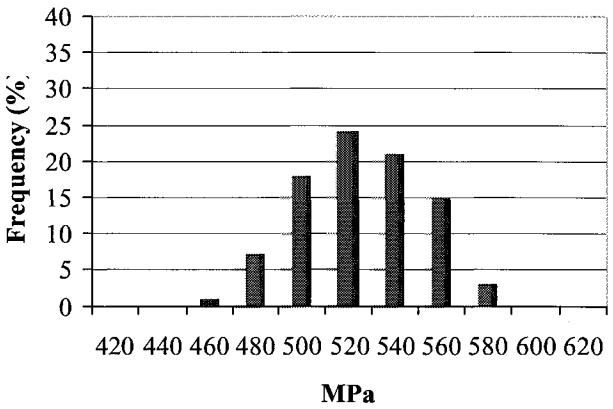


Fig: 3 Yield strength

The figures 3 and 4 show the yield and tensile strength distribution for industrial products.

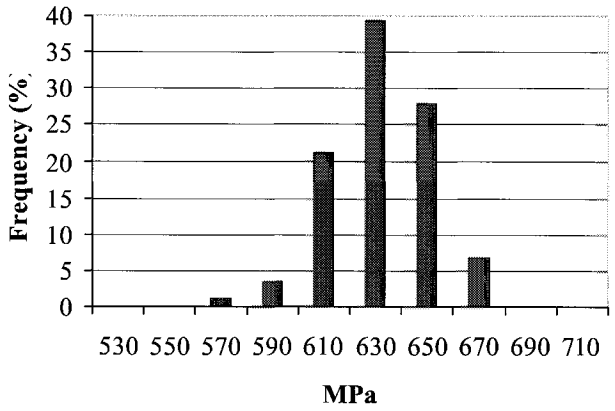


Fig: 4 Tensile strength

The figure 5 demonstrates the good behavior of the mechanical properties at high temperatures (up to 600°C)

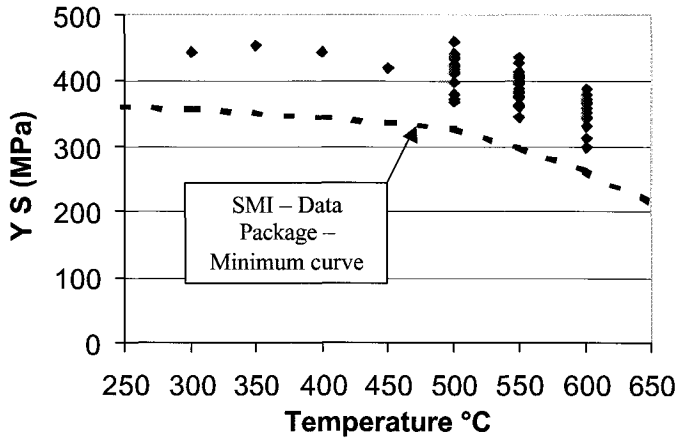


Fig: 5 Yield strength at elevated temperatures

Creep properties :
Creep tests have been performed on tubes from 5 different industrial heats, at different temperatures between 500°C and 650°C. The cumulated creep test duration is about 416,000 hours and individual tests have duration up to 25,000 hours.

All results are plotted with the Larson-Miller parameter; the constant C was taken equal to 20. As we can see in the above curve (figure 6), the V&M extrapolated results are close to the average values from the ASME Code.

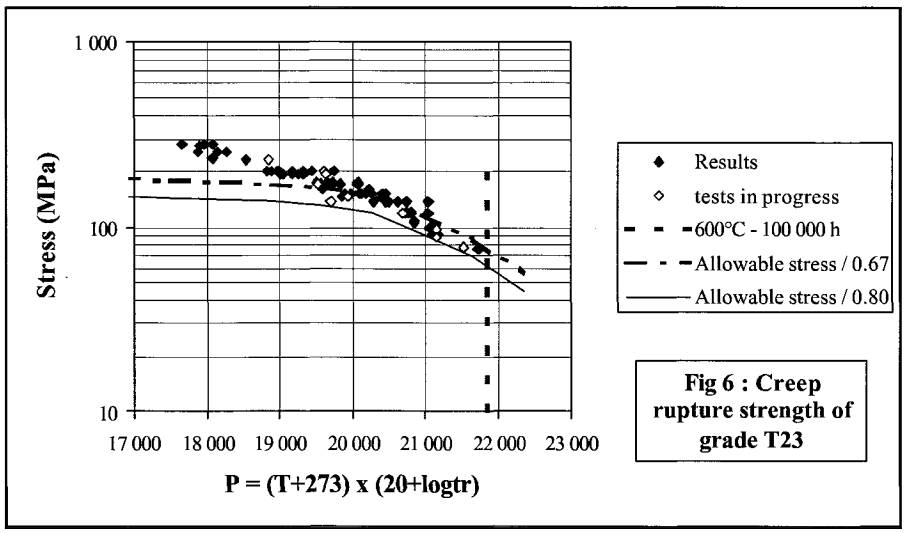


Fig 6 : Creep rupture strength of grade T23

V&M manufacturing and main references :

Power station	Size of tube OD x WT mm (in.)	Component	Operating condition of boiler component	Tons	Tube delivery
Cordemais V France	33.7 x 5.0 (1.3 x 0.2)	Waterwall	405°C (760°F) steam temperature 200 bar (2.9 ksi)	3	1997
Jorf Lasfar Morocco	50.8 x 4.6 (2 x 0.18)	Superheater	542°C (1,010°F) steam temperature 182 bar (2.6 ksi)	42	End of 1998
Foster Wheeler China	44.5 x 5.6	Superheater	> 500°C	30	1999
Deltak USA Combined Cycle	38.6 x 2.7 38.6 x 3.2	Superheater	500°C Low pressure	23	End 1999
Formosa Heavy Industry	44.5 x 6.6 44.5 x 5.08	Superheater	600 °C (1122 °F) 148 bar (2.1 ksi)	35	2000
Deltak USA Combined Cycle	38.6 x 2.7	Superheater		30	End 2000
Foster Wheeler Canada	38 x 4.19	Superheater		25	End 2000
Daekyung Machinery Korea	60.3 x 3.43 50.8 x 6.1 63.5 x 3.05	Superheater		190	End 2000
Deltak USA Tenaska	31.8 to 50.8	Superheater		235	mid 2001
Alstom TVA Bull Run	28.6 x 3.2 cold drawn	Superheater		78	End 2001
Alstom Steward I and II	44.5 x 4.19	Superheater		100	2002

Table 7 : Main reference of T23 tubes in power plants

In the table 7 the actual state of fabrication and operating experience is shown.

Since the end of 1998, the production of T23 tubes has increased regularly.
If T23 steel was firstly developed as an ideal candidate for waterwall panel applications in Ultra Super Critical boiler, it is now used more frequently for superheaters and reheaters of conventional boilers [2]. This steel is also adequate for HRSG in combined cycle.

Today, VALLOUREC & MANNESMANN TUBES produces a complete range of tubes in accordance with ASME.

Weldability
The tests performed after TIG butt welding (bend, tensile, Charpy V notch, hardness tests and micrographic examinations) give satisfactory results with and without preheating [3]. In both cases the maximum hardness is 313HV (195HV for base material). Therefore, there is no need for preheating and Post Welding Heat Treatment (PWHT) according to the French NFE32-107, European EN288-3 and German ADHP 2/1 Codes. For the ASME Code, it is mandatory to perform PWHT, nevertheless for the tube range it is possible to replace PWHT by preheating.
Some other tests performed on SMAW process also give good results.

Creep rupture tests were launched on welded joint with specimens machined across the weld in order to test at the same time base material, heat affected zone and weld deposit. The ruptures occur where the base material has been softened by welding cycles i.e. mainly in base material.

Cold bending
After bending and heat treatment with a radius between 1 OD and 3 OD, the hardness values are presented in the table 8 :

HV		R=1 OD=51mm	R=1.3 OD=66mm	R=3 OD=153mm
Base material		200	200	200
As bent	Intrados	262	253	240
	Extrados	254	248	245
Tempered 730° / 15min	Intrados	236	236	219
	Extrados	230	230	225
Tempered 730° / 60min	Intrados	202	212	209
	Extrados	221	223	204

Table 8 : Evolution of the hardness (HV10)

Cold bending could generate high cold working in extrados (tension) and in intrados (compression). The hardness values in as bent conditions and after stress relieving tempering (Post Bending Heat Treatment-PBHT) are 62HV higher than the base material hardness values. Therefore the PBHT is not mandatory in accordance with French and German Codes. Some deformation tests were performed in order to simulate high level of cold working. This was made on plates cold rolled in laboratory with high level of wall thickness reduction ratio of 15, 20 and 35%. The analysis of the results shows that for very severe deformation ratio (>20%) the structure could be softened by recristallization effects during the PBHT. In such cases we could observe a detrimental effect on the creep behavior. Consequently for very severe deformation ratio we would recommend to perform a complete heat treatment of the bend (normalizing and tempering). For usual deformation ratio (R> 1.7 OD) no detrimental effect was observed, therefore no PBHT is necessary.

Development of P23 steel grade

Our experience on thicker tubes helped us in the development of heavy wall pipes. For such dimensions the heat treatment is the key point to obtain good properties and suitable toughness. Thanks to several trials the necessity of accelerated cooling was pointed out. The best condition for this heat treatment is :

- Austenitizing which provides dissolution of most precipitates.
- Water quenching to obtain bainitic-martensitic structure [4].
- Tempering which allows the precipitation of Chromium carbides and fine Vanadium and Niobium (Cb) carbonitrides which improves the creep behavior.

VALLOUREC & MANNESMANN TUBES have successfully manufactured some pipes with a wall thickness up to 30 mm with the following heat treatment :

- Austenitizing 1060°C
- Water quenching
- Tempering 760–770°C

We have obtained the following results :

Heat treatment	Y.S. Mpa	U.T.S. MPa	Elong (2") %
Austenitization 1060°C + Water Quenching + Tempered 760°C	510	608	25.1

Table 9 : Mechanical properties at room temperature

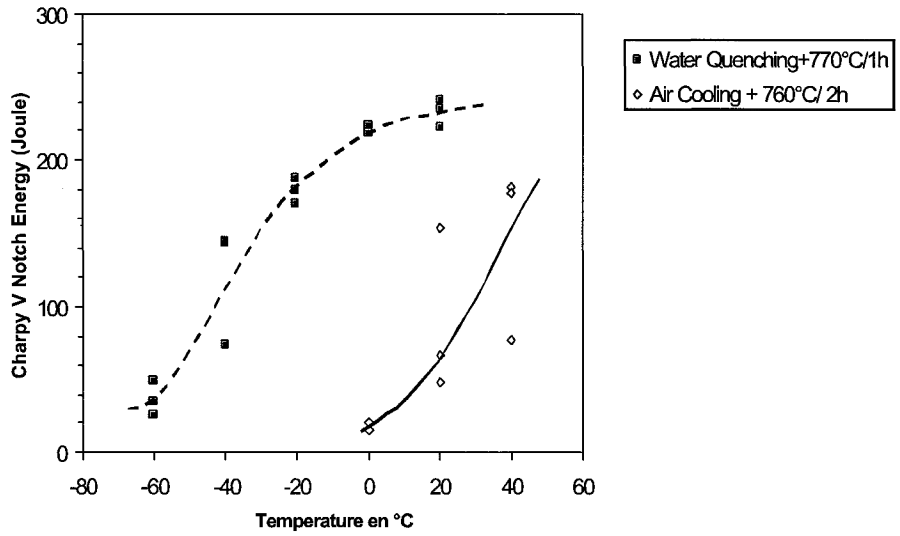


Fig : 10 Influence of the cooling rate after austenitization on impact tests

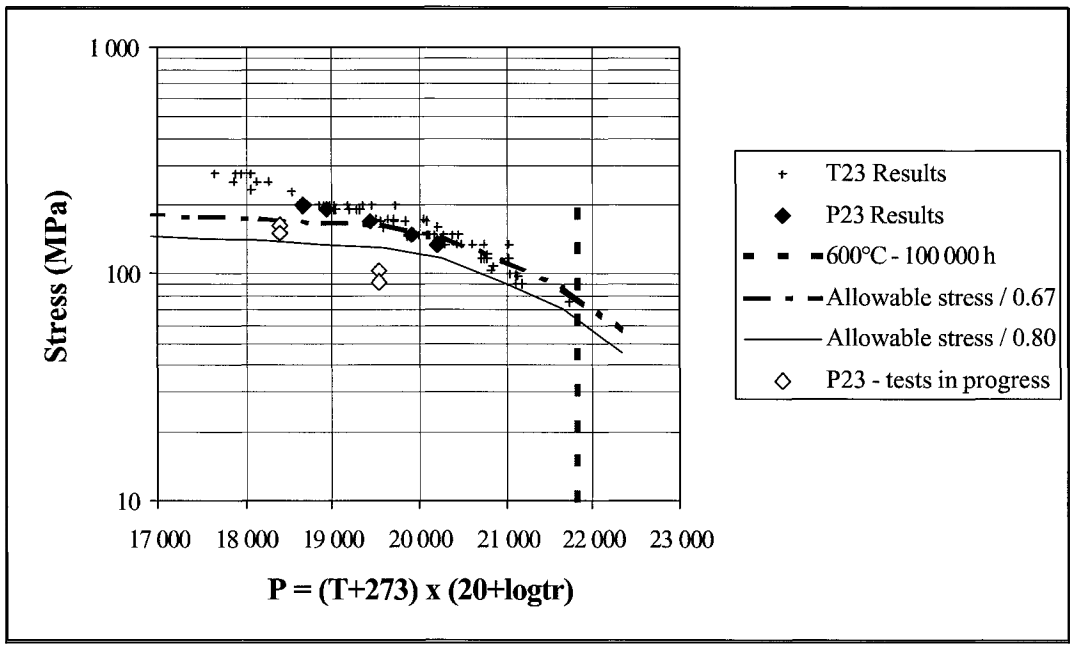


Fig 11 : Comparison between T23 and P23 creep rupture strength

The first tests , performed on these pipes are satisfactory, mainly the base material creep tests give values in the scatter band, but slightly lower than T23 tubes results.
Other rolling tests are planned this year on heavier wall thickness up to 50 mm.
An important program has been launched with the COST 522. The pipe from V&M TUBES has been delivered and is undergoing full characterization and welding qualification. As welding consumables are available on the market V&M TUBES has started its own welding program. Weld joints were successfully performed and characterization is in progress.

Conclusions

The good weldability and cold bending allow, thanks to a low Carbon content, to avoid PWHT and PBHT in most cases.
These excellent properties and an efficient mastering of industrial manufacturing of tubes have opened three main applications :

- Construction of waterwall panels for USCB
- Manufacturing of superheaters for conventional boilers or HRSG
- Repair jobs in old boilers

Moreover the first results on P23 pipes open an interest in piping material. High creep strength allows a considerable reduction in wall thickness compared to heavy wall thickness of P22 components.

Reference

[1] VALLOUREC & MANNESMANN TUBES, The T23/T24 Book – New Grades for Waterwalls and Superheaters, 1998
[2] F. Deshayes, W. Bendick, K. Haarmann, J-C. Vaillant, New 2-3%Cr Steel Grades for Waterwall panels and Superheaters
[3] A. Arbab, Grade T23 with improved creep strength, weldability and cold bending, COST 522 Steam Power Plant, Progress Report N°1, 2000-03.
[4] N. Komai, T. Imazato, F. Masuyama, Continuously Cooled Microstructure and Creep Rupture Strength of Low C-2.25Cr-1.6W-V-Nb Steel, ISIJ International, Vol. 41 (2001), Supplement, pp. S91-S96.

NEW WROUGHT NI-BASED SUPERALLOYS WITH LOW THERMAL EXPANSION FOR 700C STEAM TURBINES

Ryuichi Yamamoto*, Yoshikuni Kadoya*, Hisataka Kawai**, Ryotaro Magoshi***, Toshiharu Noda****, Shuji Hamano****, Shigeki Ueta**** and Susumu Isobe****

* Takasago Research and Development Center, Mitsubishi Heavy Industries, Ltd., 2-1-1 Shinhama Arai-cho, Takasago, Hyogo, 676-8686, Japan.
** Takasago Machinery Works, Mitsubishi Heavy Industries, Ltd., 2-1-1 Shinhama Arai-cho, Takasago, Hyogo, 676-8686, Japan. (now Osaka Yakin Kogyo Corporation, Ltd., 25 Tomoe, Bessho-machi, Miki, Hyogo, 673-0443, Japan)
*** Takasago Machinery Works, Mitsubishi Heavy Industries, Ltd., 2-1-1 Shinhama Arai-cho, Takasago, Hyogo, 676-8686, Japan.
**** Research and Development Laboratory, Daido Steel Co., Ltd., 2-30 Daido-cho, Minami-ku, Nagoya, 457-8545, Japan.

Abstract

Advanced 700C class steam turbines require austenitic alloys to replace conventional ferritic 12Cr steels, which lose creep strength and oxidation resistance above 650C. The austenitic alloys, however, possess a higher thermal expansion coefficient than ferritic 12Cr steels. Therefore, Ni-based superalloys were tailored to reduce their coefficients to the level of 12Cr steels. A regression analysis of commercial superalloys proves that Ti, Mo and Al decrease the coefficient quantitatively in this order, while Cr increases it so significantly that Cr should be limited to 12wt% to secure oxidation resistance. The newly designed Ni-18Mo-12Cr-1.1Ti-0.9Al alloy is strengthened by gamma-prime [Ni_3(Al,Ti)] and also Laves [Ni_2(Mo,Cr)] phase precipitates. It bears a RT/700C mean expansion coefficient equivalent to that of 12Cr steels and far lower than that of low-alloyed heat resistant steels. It surpasses a current turbine alloy, Refractaloy 26, in tensile strength at RT to 700C and SCC life in 330C deaerated pure water. Its creep rupture life at 700C is equivalent to that of Refractaloy 26. The developed alloy will be suitable for fasteners and/or blades in steam turbines at present and future USC power plants.

Keyword: advanced 700C class steam turbine, Ni-based superalloy, low thermal expansion, alloy design, precipitation hardening

1. Introduction

In recent power plants, the maximum steam temperature has been raised to boost the net efficiency and reduce CO_2 emission, fuel consumption and investment cost, up to 700C for a PF power plant [1]. Such advanced 700C class steam turbines require austenitic alloys to replace ferritic Super 12Cr steels, which lose creep strength and oxidation resistance above 650C. Most of the conventional austenitic superalloys, however, possess such large coefficients of thermal expansion when compared with those of ferritic 12Cr steels that it is difficult to substitute superalloys for 12Cr steels easily.

Among austenitic alloys, the Invar-types such as INCOLOY alloy 783 have lower coefficients [2, 3]. Unfortunately, their Cr content is limited to only 3%Cr to sustain the magnetic Invar effect and so they lack oxidation resistance in steam [4].

Therefore, the oxidation resistant Ni-based superalloys were tailored to reduce their coefficients of thermal expansion to the level of 12Cr steels for present and future USC power plants.

2. Experimental Procedures

The experimental alloys were melted in a vacuum induction furnace and cast into 50 kg ingots, 138 mm round and 380 mm high. They were forged down into 50 mm square bars at 1180C. The bars were solution treated at 1050C for 2 hrs and water cooled, and then aged in various conditions and air cooled.

The primary characters of the alloys were referred from available data on a current turbine alloy, Refractaloy 26 (Ni-20Co-16.2Fe-18Cr-3.2Mo-2.6Ti).

3. Results and Discussions

3.1. Alloy Design for Ni-Based Superalloys with Low Thermal Expansion

In order to design a suitable alloy, the effect of each major alloying element was extracted from the database on commercial wrought Ni-based superalloys [5]. At first, Fig. 1 shows the effect of Fe on the mean coefficients of thermal expansion (α). In low or non Cr Invar-type alloys, Fe obviously decreases the coefficients, while in non-magnetic alloys it tends to increase them. This reveals that Fe should be eliminated from the system to reduce the coefficients.

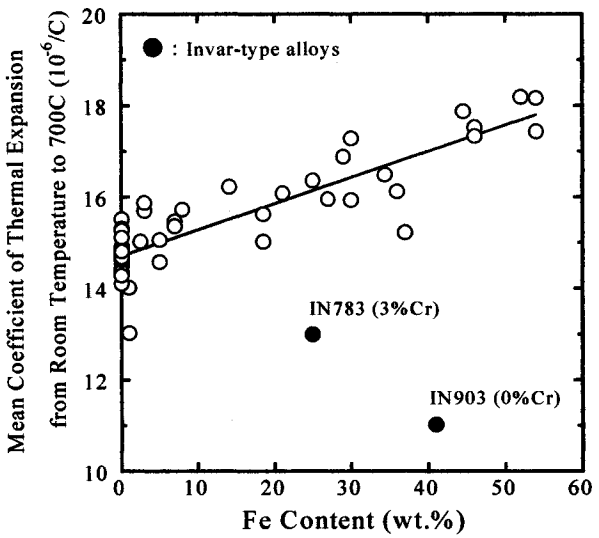


Fig. 1 The effect of Fe content on the mean coefficients of Ni-based superalloys

Employing the data on superalloys practically without Fe (less than 5% as an impurity), a regression analysis was carried out to deduce the contribution of each element to the coefficients of thermal expansion. Fig. 2 shows the obtained factors, by which the content of each element is multiplied to calculate the mean coefficients from RT to 538C(1000F), 600C and 700C, respectively. Eq. 1, below, is for the coefficient to 700C,

$$\alpha = 13.8732 + 7.2764\times10^{-2}\times Cr + 3.751\times10^{-2}\times(Ta + 1.95Nb) + 1.9774\times10^{-2}\times Co + 7.3\times10^{-5}\times Co\times Co - 1.835\times10^{-2} Al - 7.9532\times10^{-2}\times W - 8.2385\times10^{-2}\times Mo - 1.63381\times10^{-1}\times Ti \quad (1)$$

where α is the mean coefficient in 10^{-6}/C and the symbols of each element are the contents in weight percent.

According to Fig. 2 and Eq. 1, Ti, Mo, W and Al reduce the coefficient, while Cr, Ta+Nb and Co increase it. Among the latter, Cr around 12% is an indispensable alloying element for oxidation resistance in steam [6], and therefore Ta, Nb and Co were discarded when designing superalloys with lower thermal expansion.

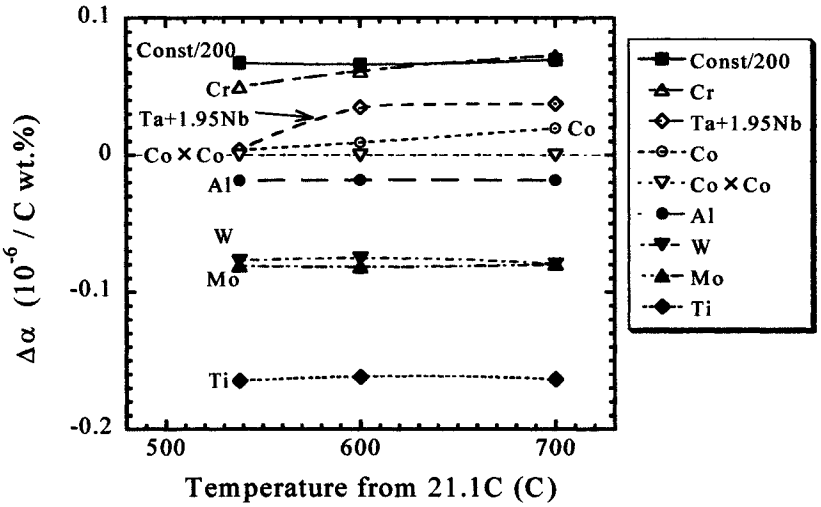


Fig. 2 Obtained factors to calculate the mean coefficients from alloy composition

Table 1 Chemical composition (wt.%) and mean coefficients of the preliminary alloys

Experimental	Ni	Mo	W	Al	Ti	Cr	α (10^{-6}/C to 700C)	
							Predicted	Measured
D-31	Bal.	8.1	13.2	0.54	3.9	12.3	12.4	12.5
D-4	Bal.	7.1	14.1	0.45	4.1	12.2	12.4	12.6
D-52	Bal.	7.6	13.9	1.5	3.2	10.7	12.4	12.5
D-62	Bal.	8.0	13.6	1.8	3.0	9.2	12.3	12.5

The validity of Eq. 1 above was ascertained by the preliminary work on some experimental alloys, as shown in Table 1, with lower Cr compared with conventional superalloys. Judging from Thermo-Calc, the amount of Mo and W in D-31 and D-4, and Al in D-52 and D-62 is to be the upper limit for completely dissolving sigma or alpha-W and gamma-prime in the solution treatment respectively and for guaranteeing sufficient hot-workability. In Table 1, the measured coefficients are so close to the predicted values that Eq. 1 is sufficiently employable for calculating the coefficient from the alloy composition.

Table 2 shows the other experimental alloys prepared to optimize the essential elements, Mo, Ti and Al, in Ni-based alloys with the lower coefficients equivalent to those of 12Cr steels. The alloy system was designed to be strengthened by both phases, gamma-prime [$Ni_3(Al,Ti)$] and Laves [Ni_2 (Mo,Cr)] precipitating at aging. As mentioned above, Mo is essential for suppressing the thermal expansion and also for strengthening the system; therefore, another useful element, W, was discharged from the system to assure the phase stability.

Table 2 Chemical composition (wt.%) of the experimental alloys and Refractaloy 26

Alloy	Ni	Cr	Mo	Al	Ti	Co	Fe
LTA1	Bal.	12.1	17.9	1.22	1.60	-	-
LTA5	Bal.	12.0	18.2	0.92	1.14	-	-
LTA6	Bal.	12.0	18.2	0.66	0.86	-	-
LTA7	Bal.	12.0	20.0	0.93	1.15	-	-
LTA8	Bal.	12.0	20.0	0.68	0.86	-	-
LTA9	Bal.	12.0	19.9	0.53	0.70	-	-
LTA10	Bal.	10.0	22.0	0.30	0.41	-	-
LTA11	Bal.	10.1	22.0	0.62	0.80	-	-
Refractaloy 26	Bal.	18	3.2	-	2.6	20	16.2

3.2. Precipitation Hardening in the System

The hardness after aging is shown in Fig. 3. The higher Al+Ti alloys, LTA1, LTA5 and LTA7, are hardened by aging at 650C to 800C, while the higher Mo, LTA11, is aged at 650C. The former are strengthened by gamma-prime and the latter by Laves, which precipitates at lower temperatures [7]. The other 4 alloys, even the higher Mo, LTA10, are not hardened by aging. This suggests that the precipitation of Laves is triggered or accelerated by gamma-prime.

The above interaction was traced by the double aging for LTA5, Fig. 4. The single 24 hrs aging at 650C hardens the alloy only to 24HRC, while the same occurs after 750C aging up to 35HRC, which is higher than the 29HRC obtained by the single aging at 750C for 24 hrs. Similar results were obtained from LTA1 and LTA7. This proves that the double aging at higher and then at lower temperatures is effective for accelerating Laves precipitation with preceding gamma-prime.

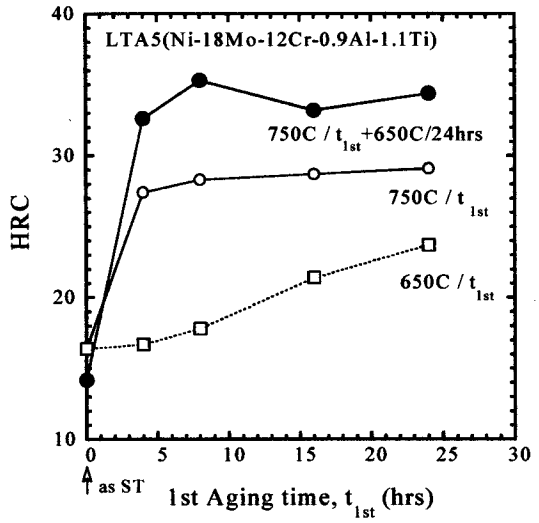


Fig. 3 The effect of aging temperatures on hardness

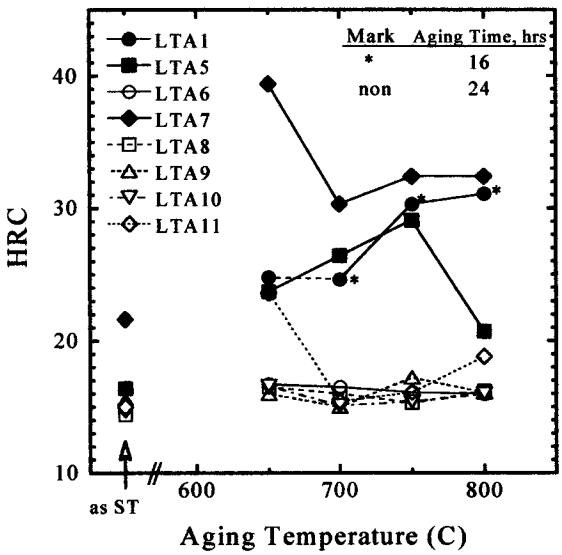
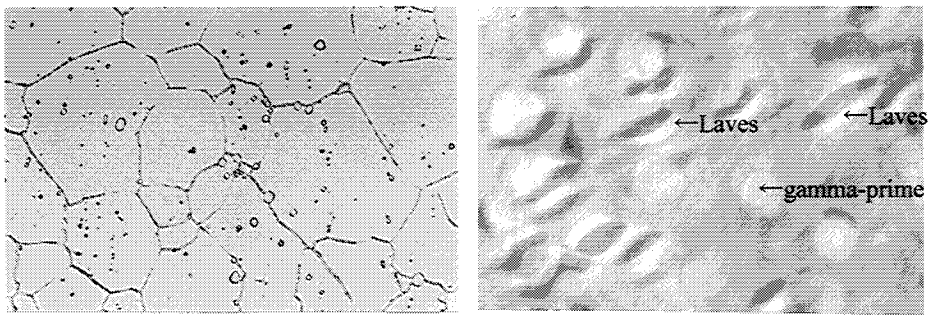


Fig. 4 Hardening in the single and the double aging

Among the age-hardenable experimental alloys, LTA5 contains the least amount of Al, Ti and Mo, and also bears the attractive combination of hot-workability and strength at elevated temperatures as mentioned later. Therefore, LTA5 was designated as LTES700, which is

named after Low Thermal Expansion Superalloys for 700C steam turbines. Its nominal composition is Ni-18Mo-12Cr-1.1Ti-0.9Al in wt%. It is hardened by the double aging of 750C/16 hrs AC and then 650C/24 hrs AC.



(a) Optical (b) TEM

Fig.5 Microstructures of LTES700 double-aged

3.3. Microstructure of LTES700

The micrographs of the double-aged LTES700 are shown in Fig. 5. The blocky precipitates in the optical photo are the retained eta carbides, M_6C, undissolved in the solution treatment.

The TEM photo shows the densely populated gamma-prime phases square in shape and discal Laves phases, which were observed in high Mo alloys [8, 9, 10]. They precipitate during the double aging in this order.

3.4. Mean Coefficients of Thermal Expansion for LTES700

The mean coefficients from RT to given temperatures are shown in Fig. 6 including conventional steels and an alloy for steam turbines[5]. The RT/700C coefficient for LTES700 is 13.2×10^{-6}/C as predicted by Eq. 1. On the whole, LTES700 possesses a coefficient much lower than those of Refractaloy 26, Nimonic 80A and 2.25Cr steel, close to that of conventional 12Cr steels and between those of 2.25Cr steel and advanced 12Cr steels. This demonstrates that LTES700 is sufficiently compatible in thermal expansion with 12Cr steels in steam turbines.

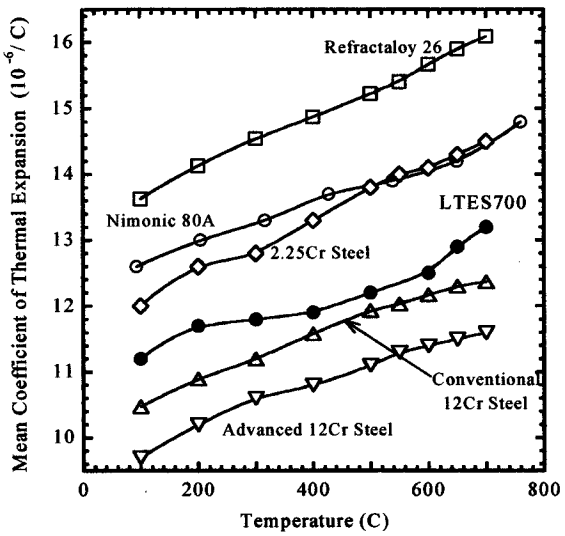


Fig. 6 Mean coefficients of LTES700, heat resistant steels and superalloys[5]

3.5. Tensile Properties of LTES700

The strength and the ductility at RT and elevated temperatures are shown in Fig. 7. Compared with Refractaloy 26, LTES700 has the higher strength, especially 0.2%PS and the larger elongation up to 500C. The additional strengthening by Laves is attributed to the higher strength of LTES700 with lower Al+Ti than Ti of Refractaloy 26.

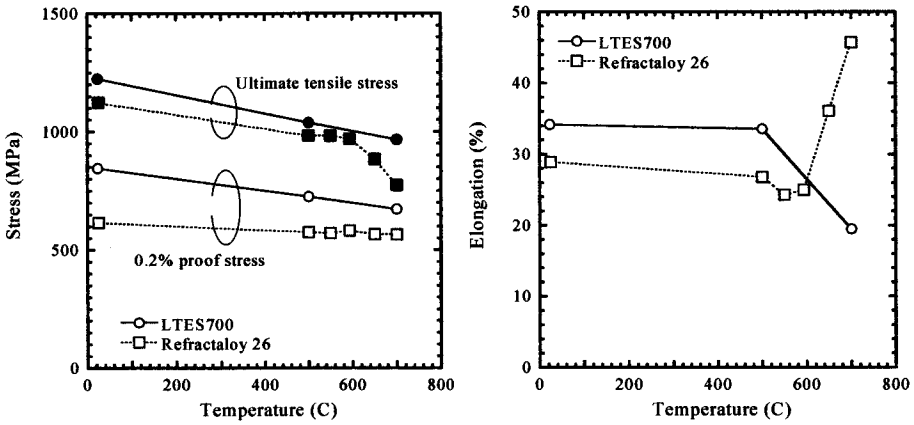


Fig. 7 RT and high temperature tensile properties of LTES700 and Refractaloy 26

3.6. Creep-Rupture Strength of LTES700

The stress to rupture is plotted against Larson-Miller parameters in Fig. 8. In smooth specimens, LTES700 at 700C carries strength equivalent to that of Refractaloy 26. The notched specimens in LTE700 show longer lives than those of the smooth. This reveals that LTES700 is insensible to notches and so it is durable as threaded fasteners.

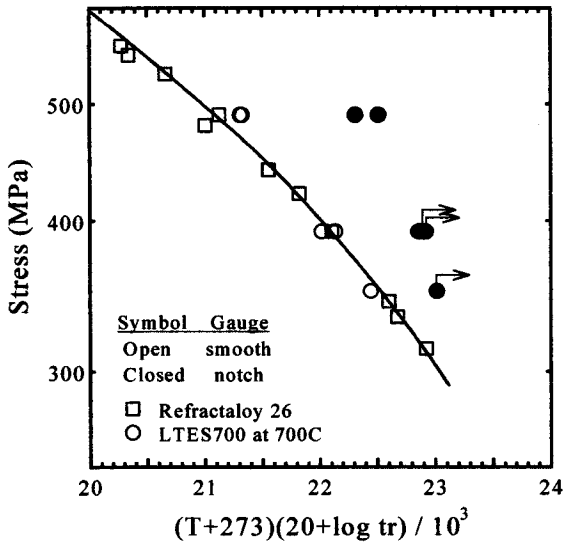


Fig. 8 Smooth and notched creep-rupture strength of LTES700 at 700C and Refractaloy 26

3.7. Stress Corrosion Cracking Resistance of LTES700

The configuration of specimens is shown in Fig. 9. The static stress at the notch bottom is applied by cramping the legs by 3.5mm at the end with an inserted screw bolt. The cramped specimens are immersed in 330C deaerated pure water (DO_2<5ppb) in a batch-type autoclave. The autoclave is opened once a month and the side surfaces of the specimens are inspected to measure the crack length from the notch bottom. The time to failure is defined as the total immersion period for one of the cracks to propagate to 1mm.

As shown in Fig. 10, the two specimens in LTES700 exceeded 4,000 hrs without failure, while one of two in Refractaloy 26 failed

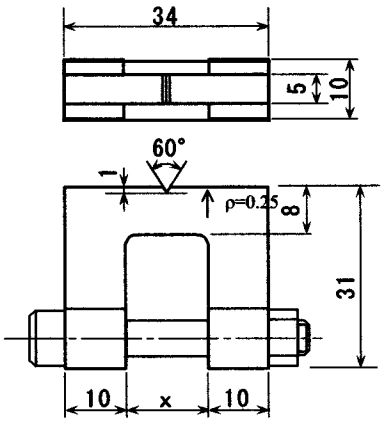


Fig. 9 A specimen for SCC test in pure water (Unit: mm)

around 2,000 hrs. This shows that LTES700 has SCC resistance equal or superior to that of Refractaloy 26.

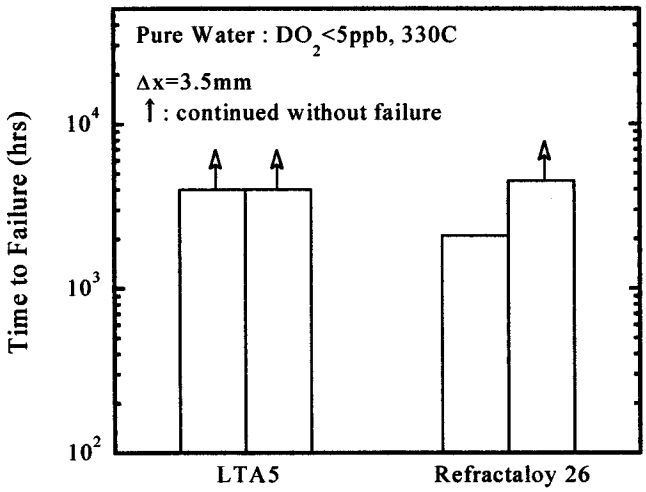


Fig. 10 SCC lives of LTES700 and Refractaloy 26

4. Conclusions

(1) Through a regression analysis of the database on conventional austenitic Ni-based superalloys, a linear equation was derived to calculate the coefficients of thermal expansion from alloy composition. It proved valid enough to predict the coefficients for newly designed alloys.

(2) According to the above, Ti, Mo and Al all reduce the coefficient for Ni-based alloys in this order. Employing them as main alloying elements, a new austenitic alloy LTES700, Ni-18Mo-12Cr-1.1Ti-0.9Al, was designed to reduce the coefficient to the level of ferritic 12Cr steels.

(3) LTES700 is strengthened by two types of precipitates, gamma-prime [Ni_3(Al, Ti)] and Laves [Ni_2(Mo, Cr)] phases, which precipitate during the double aging.

(4) The double-aged LTES700 possesses tensile strength at RT to 700C and SCC life in 330C deaerated pure water superior to those of a current turbine alloy Refractaloy 26 and has at 700C an equivalent creep-rupture life.

The new superalloy, LTES700, with low thermal expansion will be suitable for fasteners and/or blades in steam turbines for present and future USC power plants.

5. References

[1] R. W. Vanstone, Advanced ('700C') Pulverized Fuel Power Plant, Proc. 5th Inter. Charles Parsons Turbine Conf., (2000), 91.

[2] D. F. Smith and J. S. Smith, Superalloys 1984, Conf. Proc., TMS AIME, (1984), 591.

[3] K. A. Heck, J. S. Smith and R. Smith, ASME Turbo Wxpo. '96, 96-GT-380, (1996)

[4] R. Yamamoto, T. Kadoya, R. Magoshi, H. Kawai, T. Noda and S. Isobe, Effects of Cr and Mo on Properties of Ni-Fe-Co-Cr-Al Invar alloys, Report of the 123rd Committee on Heat-Resisting Materials and Alloys, **40** (1999), 161.

[5] INCO, High Temperature High Strength Nickel Base Alloys, (1977)

[6] R. Yamamoto, T. Kadoya, R. Magoshi, H. Kawai, T. Noda and S. Isobe, Design of Ni-Based Superalloys with Low Thermal Expansion (I), CAMP-ISIJ, **14** (2001), 1322.

[7] M. Kumar and V. K. Vasudevan, Ordering Reactions in an Ni-25Mo-8Cr Alloy, Acta Mater., **44** (1996), 1591.

[8] M. Sundararaman, L. Kumar, G. E. Prasad, P. Mukhopadhyay and B. Banerjee, Precipitation of Intermetallic Phases with Pt_2Mo-Type Structure in Alloy 625, Metal. Mater. Trans. A, **30A** (1999), 41.

[9] N. S. Mishra and S. Ranganathan, Electron microscopy and diffraction of ordering in a Ni-25wt%Mo alloy, Mater. Sci. Eng., **A150** (1002), 75.

[10] S. K. Srivastava and B. E. Lewis, The Ni_2(Mo, Cr) ORDERING TRANSFORMATION IN A NI-MO-CR ALLOYS, Kinetics of Ordering Transformations in Materials, (1992), 141.

DEVELOPMENT OF A NEW 12% CR- STEEL FOR TUBES AND PIPES IN POWER PLANTS WITH STEAM TEMPERATURES UP TO 650°C

W. Bendick[1)], J. Gabrel[2)], J.-C. Vaillant[3)] and B. Vandenberghe[4)]

1) Mannesmann Forschungsinstitut, D-47251 Duisburg, Germany
2) Centre de Recherche Vallourec, F-59620 Aulnoye, France
3) V&M France, F-92103 Boulogne-Billancourt Cedex, France
4) V&M Deutschland, D-40435 Düsseldorf, Germany

Abstract

Presently martensitic 9% Cr-steels, e.g. E911 and P92, are used for power plants with advanced steam parameters. While these materials have the highest creep rupture strength values of ferritic steels, their oxidation resistance is lower than 12% Cr-steels, such as X20CrMoV12-1. With increasing steam temperature the lifetime of components made of 9% Cr-steel becomes limited not only by creep but also by oxidation. A steam temperature of 650°C has been the target for the development of a new martensitic steel with high creep rupture strength and improved oxidation resistance. The basis was a 12% Cr-steel in order to meet the requirements for oxidation resistance. Other elements were necessary to stabilise the phase structure and to achieve a high creep rupture strength. The influence of different elements, like cobalt, tungsten and boron, has been investigated by seven different lab heats. Creep tests > 10000 h indicate that a creep rupture strength comparable to T/P92 can be achieved by the new steel grade. An industrial heat with optimised composition has been made. Tubes and pipes have been produced successfully and the product qualification has started. A program for future work is outlined.

Keywords: alloy development, 12% Cr steel, creep, tube, pipe

Introduction

The American development of a modified 9% chromium steel called T/P91 in the early eighties has terminated a long period of standstill in material development for power plant application [1]. Due to its higher creep rupture strength this steel allowed the start of building a new generation of advanced plants with higher efficiencies being enabled by an increase of steam parameters, mainly the steam temperature. The following development of steels like E911 and T/P92 allowed a further enhancement of temperature to presently about 610°C for live steam and 625°C for hot reheat steam [2, 3]. This is achieved by an increase of creep rupture strength of roughly 20%. World-wide activities aim at further improvement of plant efficiency by increasing the steam temperature. As an example the European research program COST 522 has set a target of developing new materials which allow steam temperatures up to 650°C.

Principles of alloy design

Presently martensitic 9% Cr-steels, e.g. P91, E911 and P92, are used for power plants with advanced steam parameters. While these materials have the highest creep rupture strength values of ferritic steels, their oxidation resistance is considerably inferior to 12% Cr-steels, such as X20CrMoV12-1. As an example Figure 1 shows test results in steam at 650°C. That is

why with increasing steam temperature the lifetimes of components made of 9% Cr-steel become limited not only by creep but also by oxidation [4].

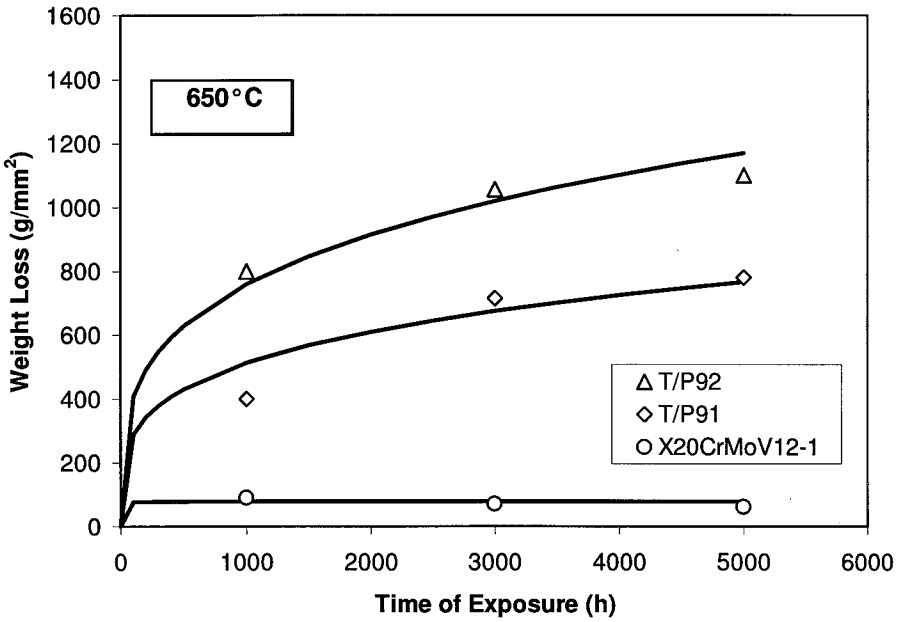


Figure 1: Oxidation behaviour of 9-12% Cr-steels in steam atmosphere

The aim of the R&D project initiated by Vallourec & Mannesmann Tubes (V&M) was to develop a new 12% Cr-steel with improved oxidation resistance in order to allow an application up to 650°C. In addition to improved oxidation resistance, the strength properties of the new steel should be comparable to or better than P92. Also hot workability and weldability should be acceptable and, if possible, as good as P91 or P92.

In a first step a total of seven lab heats have been produced and tested at CEV (Centre de Recherche Vallourec) and MFI (Mannesmann Forschungsinstitut). The chemical compositions are given in Table 1. All heats have a chromium content higher than 11% in order to meet the requirement of good oxidation resistance. Vanadium, niobium and nitrogen have been added in quantities similar to the 9% Cr-steels in order to achieve precipitation strengthening by MX particles. Other strengthening elements like molybdenum, tungsten and boron have been varied. As indicated by the Schaeffler diagram in Figure 2, the phase stability is affected by increasing the chromium content from 9 to 11% in steels like E911 and P92. A fully martensitic structure can only be obtained by simultaneously increasing the nickel equivalent. This has been done by adding cobalt to the lab heats. Another possibility is to increase the C-content from 0.10 to about 0.20% (heats A and B). However, an increase of carbon content has an adverse effect on fabricability. Because of the high price of cobalt

combinations of medium Co- and medium C-contents have also been tested. Heat C can be regarded as prototype of this variant. The composition of heat G is similar to heat C except for the higher B-content, which follows the results of alloy development of a rotor steel in COST 501 [5]. While heats C and G are tungsten-free with a Mo- content of 1.5%, heat F is a tungsten bearing steel with 1.4% W and only 0.3% Mo. Heat F uses the strengthening effect of Laves phase precipitation similar to E911 and P92.

	Heat A	Heat B	Heat C	Heat D	Heat E	Heat F	Heat G
C	0.190	0.184	0.158	0.160	0.129	0.110	0.163
Si	0.10	0.10	0.09	0.10	0.10	0.45	0.10
Mn	0.52	0.51	0.53	0.50	0.49	0.20	0.50
P	0.012	0.012	0.006	0.008	0.009	0.013	0.009
S	0.001	0.001	0.001	0.001	0.001	0.002	0.001
Al	0.005	0.010	0.012	0.008	0.010	0.015	0.006
Cu	0.020	0.023	0.013	0.013	0.014	0.013	0.014
Cr	11.64	11.54	11.25	11.42	11.29	11.50	11.44
Ni	0.20	0.25	0.26	0.26	0.28	0.23	0.27
Mo	1.48	1.48	1.46	1.48	1.44	0.28	1.46
W						1.40	
V	0.26	0.26	0.25	0.25	0.25	0.24	0.25
Nb	0.058	0.058	0.047	0.058	0.057	0.065	0.044
Co	0.006	0.007	0.90	1.06	3.06	1.30	1.49
B	0.0035	0.0039	0.0062	0.0117	0.0068	0.0030	0.0081
N	0.015	0.047	0.063	0.063	0.051	0.056	0.050

Table 1: Chemical composition of 12% Cr-laboratory heats (mass - %)

The chromium and nickel equivalent for heat C, F and G have been calculated and plotted into Figure 2 in order to allow a rough estimation on the phase stability of the heats. All heats are situated near the point where martensite, austenite, and ferrite meets. According to the figure heat F may show some δ- ferrite, whereas heats C and G might contain a small amount of austenite. However, neither δ- ferrite nor retained austenite were observed in the 3 heats after final heat treatment.

Properties of laboratory heats

After preliminary tests on all materials, heats C, F and G were chosen as candidate material and were investigated in more detail. The program included the determination of mechanical

properties as well as tests on hot workability. Some of the most important test results are given below.

Mechanical properties

At first the optimum heat treatment conditions had to be found out. Normalisation was carried out at 1060°C, following the usual treatment for E911 and P92. Afterwards the optimum tempering conditions were investigated by a tempering diagram (Figure 3).

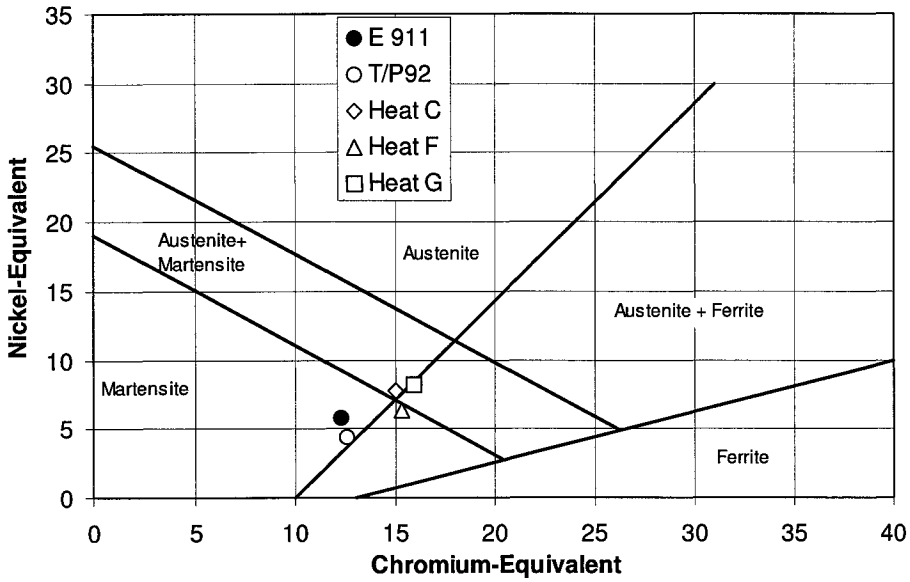


Figure 2: Schaeffler diagram modified acc. to H. Schneider

$Cr_{Eq} = Cr + 2Si + 1.5Mo + 5V + 5.5Al + 1.75\ Nb + 1.5Ti + 0.75W$

$Ni_{Eq} = Ni + Co + 0.5Mn + 30C + 0.3Cu + 25\ N$

The maximum tempering temperature is limited by the A_{C1b} point which varied between 810°C for heat C and 830°C for heat F. Optimum properties are achieved by tempering in the range 760-800°C. Details on heat treatment and mechanical properties are given in Table 2. While the tensile and impact properties are comparable for heat C and F, heat G reveals higher strength and lower ductility values. This has to be attributed to the rather low tempering temperature. The values in Table 2 are also comparable to P92 with the exception of toughness. Toughness is distinctly lower, although it was no problem to reach the specified minimum of 41 J. Yield and tensile strength values at elevated temperature are represented in Figure 4. All values lie distinctly above the minimum curve for P92 as given in the ASME data package.

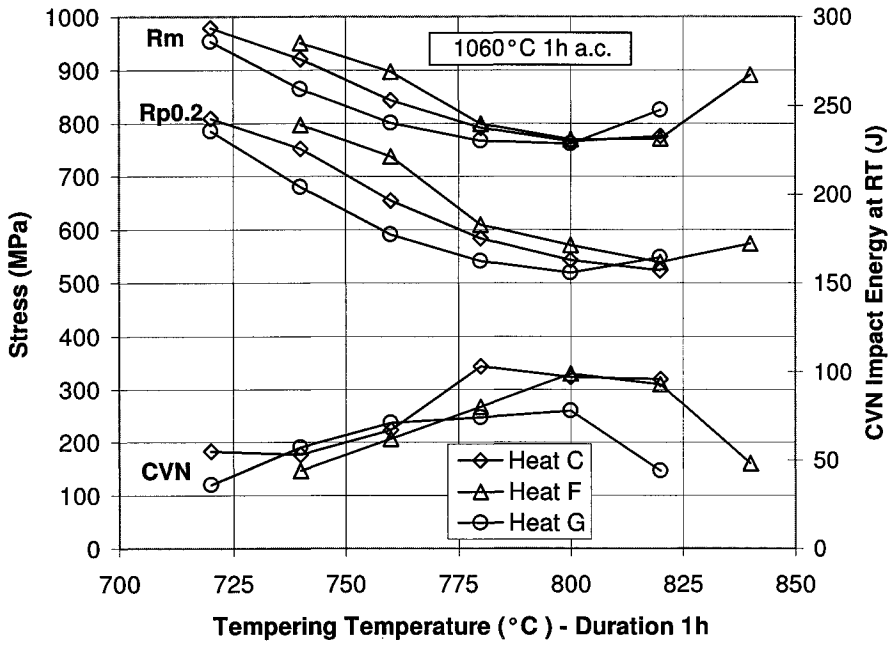


Figure 3: Influence of tempering on the RT properties of laboratory heats C, F and G

Material	Heat Treatment	Yield Strength MPa	Tensile Strength MPa	Elongation %	Hardness HV10	Impact Energy CVN (J)
Heat C	1060°C 1h a.c. + 780°C 2h a.c.	571	796	21.3	261	107
Heat F	1060°C 20' a.c. + 800°C 30' a.c.	559	749	25.0	236	118
Heat G	1060°C 1h a.c. + 760°C 2h a.c.	622	817	17.8	253	68

Table 2: Mechanical properties of selected 12% Cr-laboratory heats at RT (mean values)

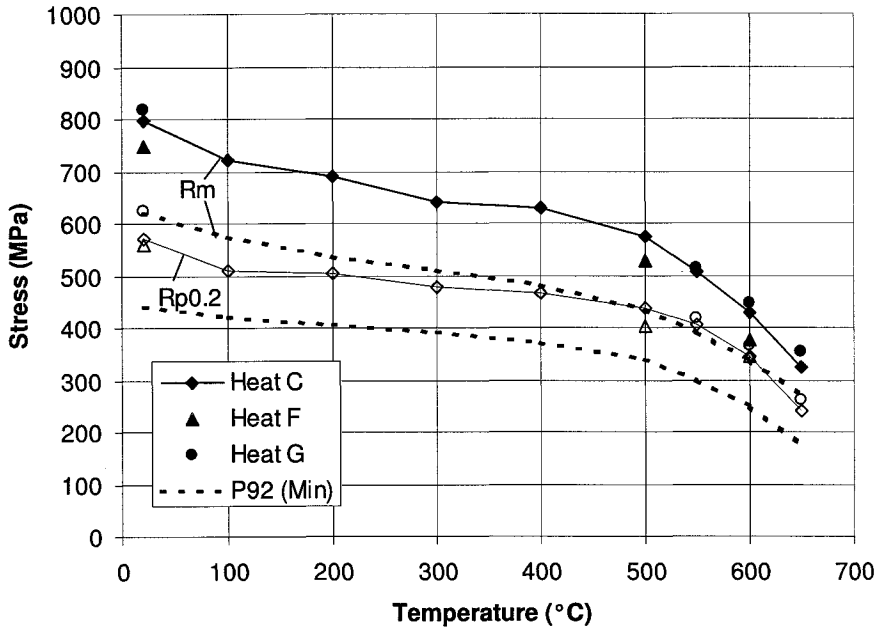


Figure 4: Yield and tensile strength of laboratory heats at elevated temperatures

Creep test results

Creep tests were carried out at 600, 625 and 650°C. The current status of testing for heats C, F and G is represented in Figures 5 to 7. Included for reference are the P92 scatterbands with the mean lines corresponding to the ECCC evaluation of 1999 [6]. The tests have reached times up to 15000 h. All rupture points and running tests are situated within the scatterbands. While the rupture points of heats F and G are close to the P92 mean curves, heat C seems to have a slightly lower creep rupture strength.

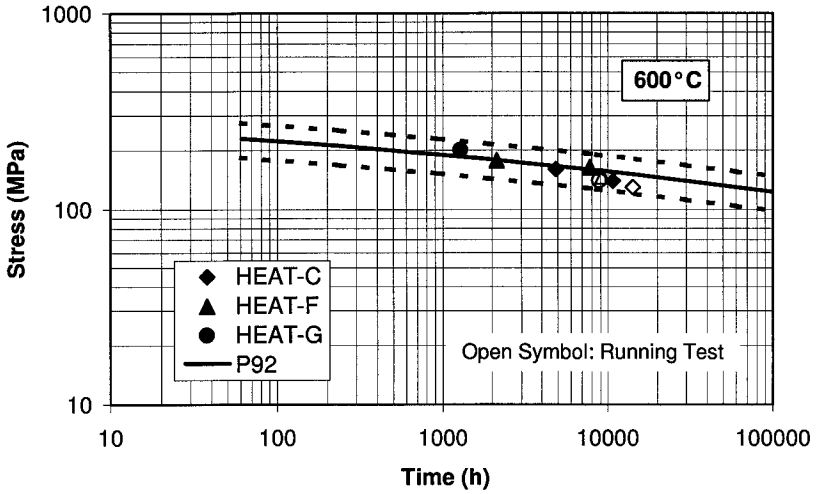


Figure 5: Creep test results on laboratory heats C, F and G at 600°C

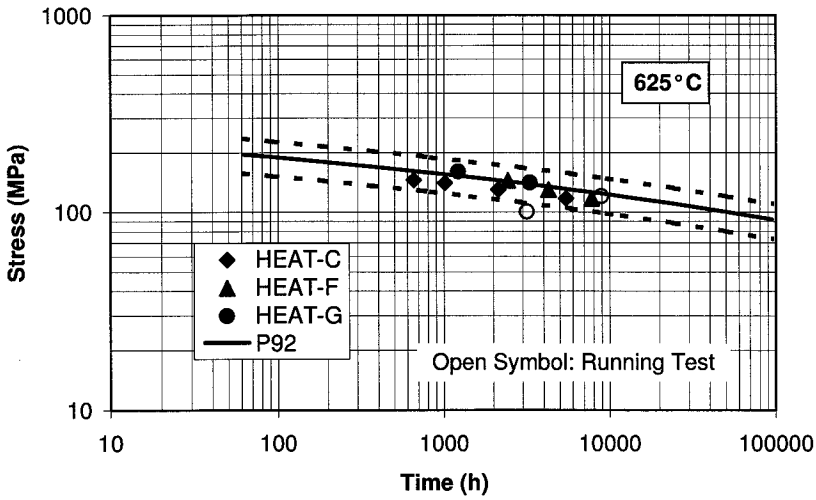


Figure 6: Creep test results on laboratory heats C, F and G at 625°C

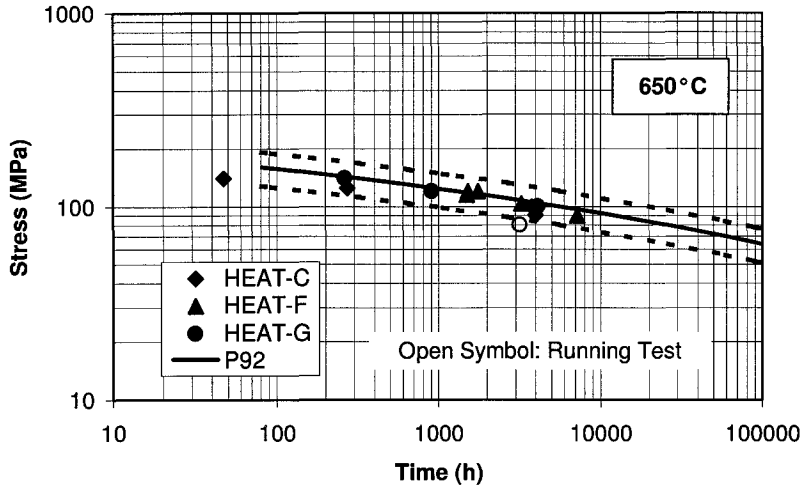


Figure 7: Creep test results on laboratory heats C, F and G at 650°C

Production of tube and pipe

Based on the positive results of the lab heats, V&M decided in 2001 to take the next step of alloy development, i.e. industrialisation of the new steel grade. The best properties were provided by heats F and G. Because of only small differences between the heats and in view of unknown behaviour during tube and pipe production, it was decided to order two heats of 20 tons each. The chemical compositions of the industrial heats are given in Table 3.

	C	Si	Mn	P	S	Al	Cu	Cr
Heat 1 (Type F)	0.115	0.49	0.35	0.018	0.001	0.008	0.08	11.50
Heat 2 (Type G)	0.140	0.29	0.49	0.017	0.001	0.005	0.07	11.45

	Ni	Mo	W	V	Nb	Co	B	N
Heat 1 (Type F)	0.29	0.29	1.50	0.26	0.050	1.62	0.0049	0.065
Heat 2 (Type G)	0.18	1.30	0.06	0.24	0.048	1.53	0.0070	0.072

Table 3: Chemical composition of 12% Cr-industrial heats (mass - %)

Small changes with respect to the lab heats have been made intentionally as a further step of optimisation. Ingots have been rolled to tubes of size 60.3 OD x 8.8 mm by the continuous mandrel rolling process and pipes of size 406.4 OD x 35 mm by the pierce and pilger rolling process. No problems occurred during production. Both materials revealed a comparable rolling behaviour. First results of the material properties at RT are given in Table 4. The microstructure is fully martensitic in both cases. Further qualification work is in progress.

Material	Heat Treatment	Yield Strength MPa	Tensile Strength MPa	Elongation %	Hardness HV10	Impact Energy CVN (J/cm^2)
Heat 1 Tube	1060°C 20' a.c. + 780°C 2h a.c.	606	779	21.3	236	191
Heat 1 Pipe	1060°C 1h a.c. + 780°C 2h a.c.	587	784	22.8	247	128
Heat 2 Tube	1060°C 20' a.c. + 780°C 2h a.c.	617	807	20.7	247	214
Heat 2 Pipe	1060°C 1h a.c. + 780°C 2h a.c.	574	785	22.5	247	105

Table 4: Mechanical properties of 12% Cr-industrial heats at RT (mean values)

Future work

In a first phase both industrial heats will receive a basic qualification of material properties in short-term tests, also including oxidation tests in steam and basic tests on weldability. This phase will be finished in mid-2002. Based on an assessment of all test results, a decision will be taken on the material to be followed up for full qualification by long-term creep and ageing tests. In parallel the development of welding consumables and welding procedures will be pursued by partner companies. For further qualification and industrialisation a second large heat is planned for production in 2002.

Acknowledgement

Part of this work is funded within the frame of the European COST 522 project by the German BMBW under project no. 0327071J.

References

[1] Bendick, W., Haarmann, K., Ullmann, K., and Zschau, M.:
Use of P91 in Europe and overseas. Proc. ASME Joint International Power Generation Conference, Phoenix, Az, USA, Oct. 2-6, 1994, 94-JPGC-PWR-35

[2] Bendick, W., Deshayes, F., Haarmann, K., and Vaillant, J.-C.:
New 9-12% Cr steels for boiler tubes and pipes – Operating experiences and future developments. Proc. EPRI Conf. Advanced Heat Resistant Steels for Power Generation, San Sebastian, Spain, 27-29 April, 1998

[3] Richardot, D., Vaillant, J.-C., Arbab, A., and Bendick, W.:
The T92/P92 Book. Vallourec & Mannesmann Tubes, 2000

[4] Ennis, P.J.:
The long-term creep rupture properties of 9-12% chromium steels. Proc. 4th Int. Charles Parsons Turbine Conference, Newcastle, UK, 4-6 Nov, 1997, pp. 296-308

[5] Kern, T.-U., Scarlin, B., Vanstone, R.W., and Mayer, K.H.:
High temperature forged components for advanced steam power plants. 6th Liège Conference on „Materials for Advanced Power Engineering", Liège, Eds. J. Lecomte-Beckers, F. Schubert and Ph. Ennis, Forschungszentrum Jülich 1998, pp. I.53-I.70

[6] ECCC Data Sheets 1999
Ed. by D.G. Robertson, ERA Technology Ltd, Leatherhead, UK, 1999

HIGH PERFORMANCE LOW ALLOY STEEL CASTING FOR STEAM TURBINE

Ryuichi Ishii [1], Yoichi Tsuda [1], Masayuki Yamada [1],
Kazuaki Ikeda [2] and Joji Kaneko [2]

[1] Power and Industrial Systems R&D Center, Toshiba Corporation
[2] Keihin Product Operations, Toshiba Corporation
2-4, Suehiro-cho, Tsurumi-ku, Yokohama, Japan

ABSTRACT

A low alloy steel casting added tungsten has been developed for thick wall components of steam turbine. In order to maximize the solid solution elements in the matrix, the contents of tungsten and molybdenum were determined based on the stable values reached after long-term exposure at high temperature. Most of trial melts with various chemical compositions revealed tempered bainitic structure without α-ferrite formation. The creep rupture strength of several trial melts were superior to that of conventional 1%CrMoV steel casting and the toughness remarkably increased. Based on these investigations, 2%CrMoWVB steel casting was selected for manufacturing the prototype model casing. The castability and weldability of the steel casting were equivalent to 1%CrMoV steel casting. The mechanical properties of base metal and welded joint were sufficient for high temperature components. This steel casting is useful for structural optimization of thick wall components such as turbine casing, valve body and so on.

Keywords : steam turbine, casing, valve, low alloy steel casting, creep rupture strength

Introduction

An increase in operating temperature and/or pressure improves the thermal efficiency of fossil-fired power plants. The enhanced operating condition, however, requires the advanced material with high creep rupture strength for high temperature components. 1%CrMoV steel castings have been widely used in power plants as thick wall components such as turbine casing, valve body and so on. The application of 1%CrMoV steel forging or 12%Cr steel casting [1] made it possible to make the design easy, when these components are to be subject to more severe conditions. Current tendency of fossil-fired power plants, however, reveal that stronger materials than 1%CrMoV steel casting are required and less expensive steels than 1%CrMoV steel forging or 12%Cr steel casting. The authors have developed a 2%CrMoWVB steel casting which has superior creep rupture strength to 1%CrMoV steel casting due to solid solution strengthening by tungsten, and precipitation strengthening by carbides. This paper describes the evaluation results of trial melts and manufacturing results of prototype model casing.

Optimization of chemical composition

Trial melts

In order to determine the chemical composition, the evaluation of 30kg trial melts was carried out. Seventeen kinds of 2%Cr steel casting were manufactured using the vacuum induction melting process to investigate the effect of alloying elements. These steel

castings have varied chemical composition of carbon, manganese, niobium, titanium, tungsten and boron as shown in Table 1. Compared with 1%CrMoV steel casting, the feature of chemical composition of trial melts is mainly as follows:

- Lower molybdenum content
- Addition of tungsten and boron

After casting and preliminary heat treatment, all melts were austenitized at 1050°C for 3 hours. Afterwards, tempering were performed at the range from 660°C to 720°C for 20 hours.

Table 1 Chemical composition of steel castings studied. (mass%)

	C	Si	Mn	Ni	Cr	Mo	V	W	Nb	N	B	Fe
No.1 -No.5	0.068 / 0.074	0.20 / 0.22	0.20	0 / 0.29	2.34 / 2.36	0.49 / 1.00	0.25	0.97 / 2.50	0.050	0.010	0 / 0.006	Bal.
No.6 -No.10	0.10 / 0.16	0.19 / 0.20	0.02 / 0.22	0.15 / 0.16	2.25 / 2.34	0.48 / 0.50	0.26	2.00 / 2.53	0 / 0.047	0.021 / 0.022	0.004 / 0.005	Bal.
	C	Si	Mn	Ni	Cr	Mo	V	W	Ti	N	B	Fe
No.11 -No.16	0.19 / 0.22	0.18 / 0.25	0.20 / 0.80	0.15 / 0.53	2.22 / 2.35	0.49 / 0.70	0.26 / 0.27	1.80 / 2.48	0 / 0.021	0.017 / 0.022	0.004 / 0.005	Bal.
No.17	0.26	0.19	0.21	0.15	2.26	0.50	0.26	2.01	-	0.020	0.0048	Bal.

Effect of alloying elements on mechanical properties

Hardness measurement, tensile test, Charpy impact test and creep rupture tests were conducted with trial melts.

Figure 1 shows the effect of carbon content on the hardness after quenching. Good hardenability is required in case of thick wall components such as turbine casings.

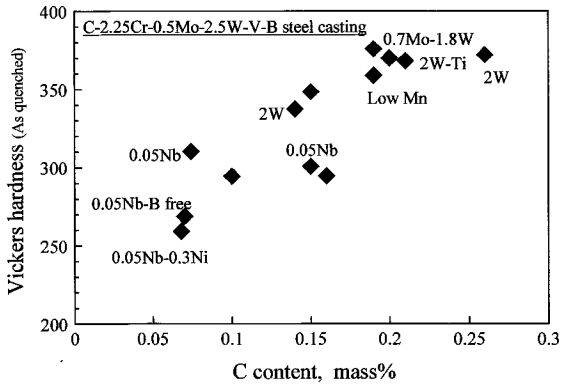


Figure 1 Effect of carbon content on Vickers hardness after quenching.

The increasing of carbon content from 0.07 mass% to 0.26 mass% had favorable effect on hardenability. However, the hardness of the low carbon steel castings classified No.1-No.5 in Table 1 was insufficient to thick wall components. On the other hand, the susceptibility to cracking increases and the weldability becomes worse with increasing carbon content. Therefore, the desirable carbon content was determined to be approximately 0.15mass % that is equivalent to 1%CrMoV steel casting.

In order to maximize the amount of solid solution elements in the matrix, the content of tungsten and molybdenum was determined based on the data for aged 2.25Cr-1Mo steel and 2.25Cr-1.6W steel [2]. Both steels show the depletion of the molybdenum and tungsten content in the matrix down to approximately 0.4 mass% and 1.0 mass% for more than 10,000h at 600°C, respectively. Therefore, molybdenum and tungsten content are required at least exceed these values.
A little quantity addition of boron improves the creep rupture strength. The weldability, however, becomes worse with increasing boron content. The desirable boron content was determined to be less than 0.005 mass%.

Tensile strength and elongation of trial melts were determined in the range from 650MPa to 750MPa and from 20% to 30%, which are equivalent to or slightly higher than those of 1%CrMoV steel casting.

Figure 2 shows one of the creep rupture test results of the trial melts, which contains sufficient molybdenum and tungsten, compared with 1%CrMoV steel casting [3]. The molybdenum and tungsten content are represented by molybdenum equivalent in the figure for convenience. Compared with 1%CrMoV steel casting, Larson-Miller parameter of trial melts except for low carbon steel castings increased with increasing the molybdenum equivalent. The desirable molybdenum equivalent requires at least 1.5.

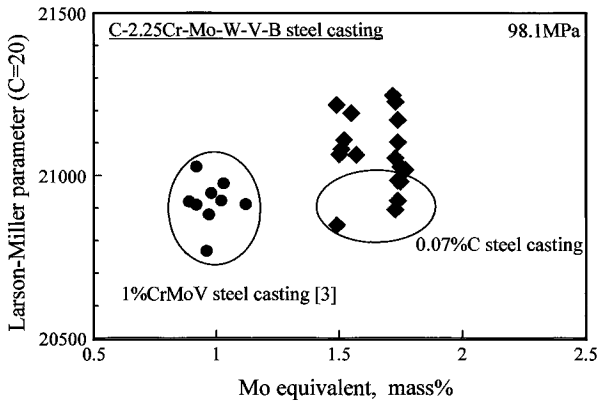
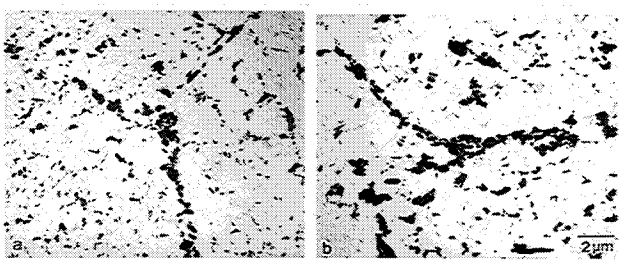


Figure 2 Effect of molybdenum equivalent on Larson-Miller parameter.

Microstructure

Figure 3 shows the carbon extracted replicas of as tempered and crept 0.15C-2Cr-0.5Mo-2W-0.25V-0.004B steel casting. Many M_7C_3, M_3C, M_2X and MX type precipitates were identified in as tempered specimen. The main metallic constituents of the particles located at grain boundaries were classified into two groups, namely Fe-Cr-W and Cr-Fe. The main metallic constituents of the fine particles within grain were W-Mo-Cr and V. Although the number of the coarsen precipitates increased in the crept specimen, the density of fine precipitates within grain remained as good as before creep. These observations revealed that the change in the precipitation morphology was scarcely

recognized during creep.
Based on the test results, 0.16C-2Cr-0.5Mo-2W-0.25V-B steel casting was selected to be the proper composition for the prototype casting.



a) As tempered b) Crept at 630°C-98.1MPa (tr = 2913.3h)
Figure 3 Carbon extracted replicas of trial steel casting.

Manufacture and evaluation of Prototype model

A prototype model was manufactured by Japan Steel Works, LTD. on the basis of knowledge obtained so far. The purpose of the manufacturing is to confirm the castability, mechanical properties and weldability.

Product
The chemical composition of the prototype model is shown in Table 2. Other minor constituents were added to this prototype steel casting. In order to reduce impurities as far as possible, the ladle refining was carried out after basic electric furnace melting. This steel casting was cast into about 10 ton casing model as shown in Figure 4. The product was normalized at 1,050°C for 12 hours, and then tempered at 690°C for 12 hours. In addition, stress relieving was performed at 680°C or 690°C for 12 hours.

Table 2 Chemical composition of the prototype model.

C	Si	Mn	Cr	Mo	V	W	B	Fe
0.16	0.22	0.59	2.06	0.54	0.25	1.98	0.0042	Bal.

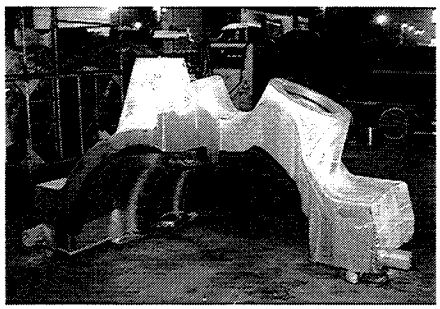


Figure 4 A protoptype model after surface treatment.

Producibility

Castability of this steel casting was equivalent to the 1%CrMoV steel casting. The number of casting defect was equivalent to 1%CrMoV steel casting, and no macro- and micro-segregation were confirmed in various portion of the prototype model. Distribution of each element was almost homogeneous in various locations.

Microstructure

Figure 5 shows the optical micrograph of thick wall portion of the prototype model. It revealed the tempered bainitic structure without α-ferrite and nonmetallic inclusion formation. The prior austenitic grain size number (ASTM) was about No.5.

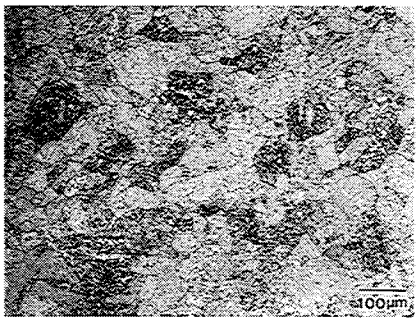


Figure 5 Optical micrograph of thick wall portion of the prototype model.

Mechanical properties

Figure 6 shows the tensile test results of the prototype model and average strength of 1%CrMoV steel casting [3] in the curved line. Tensile strength of the prototype model was equivalent to the 1%CrMoV steel casting. The model has enough ductility.

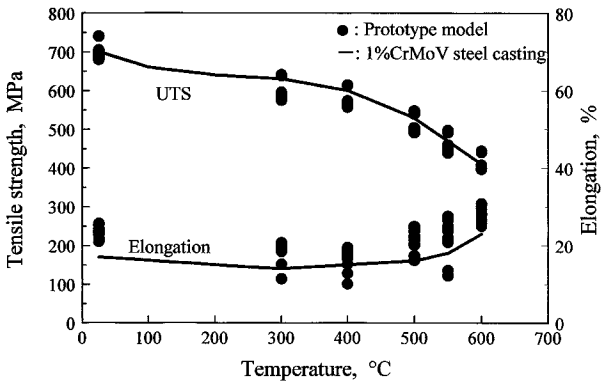


Figure 6 Tensile strength and elongation of various portion of prototype model.

Figure 7 shows the Charpy impact test results for the various portion of the prototype model. The initial absorbed energy for the model was higher, and the fracture appearance transition temperature, which ranged from 30°C to 50°C, was remarkably lower than that of 1%CrMoV steel casting.

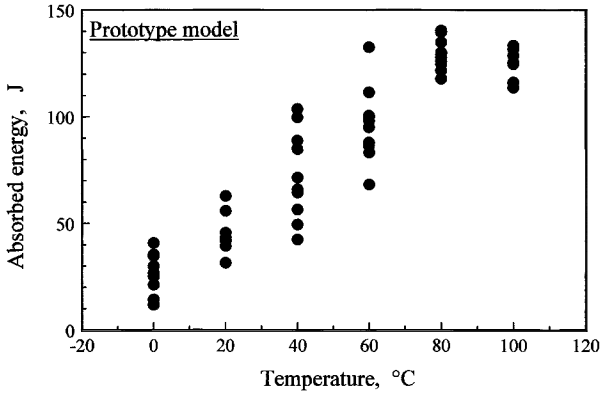


Figure 7 Charpy impact test results for the prototype model.

Figure 8 shows the creep rupture strength of various portion of prototype model tested at 630°C. The longest testing time plotted in this figure is about 8,000h. The prototype model showed slightly lower strength than that of trial melt with similar composition in the higher stress region. The good results, however, were obtained in the lower stress region compared with trial melts and 1%CrMoV steel casting.

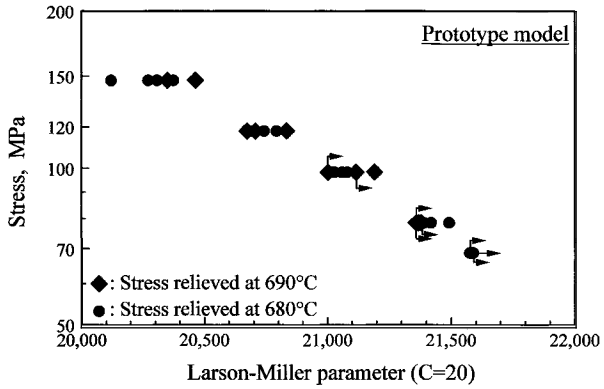


Figure 8 Creep rupture test results of prototype model.

Welding

The results of the fundamental investigation on the weldability conducted using trial melts with various chemical compositions revealed that the weldability of them was

equivalent to that of 1%CrMoV steel casting in case of using covered electrode for 2.25%Cr steel. No special precautions were necessary in welding of prototype model. Although further investigation on the post weld heat treatment condition is required, the mechanical properties of welded joint were superior to those of 1%CrMoV steel casting.

CONCLUSION

In order to improve the mechanical properties of 1%CrMoV steel casting, trial melts with various chemical compositions were manufactured and evaluated. Sufficient mechanical properties required for thick wall components were shown in several trial melts. A 0.16C-2Cr-0.5Mo-2W-V-B steel casting was selected as the preferable composition and the successful results on producibility and weldability were confirmed throughout the manufacturing of the prototype model casing. Although the chemical composition of new steel casting should be still more modified, the results offered a good prospect to the application to the thick wall components such as high pressured 566°C class steam turbine casing, valve body and so on in the future.

REFERENCES

[1] Y. Tsuda, M.Yamada, R.Ishii and O.Watanabe, Proc. of the 4th Inter. Charles Parsons Turbine Conf., (1997), p.283
[2] K. Miyata, M. Igarashi and Y. Sawaragi, Proc. of the ICOPE-97, Vol.2, (1997), p.77
[3] NRIM CREEP DATA SHEET, No.31B, NRIM, (1994)

DEVELOPMENT OF HIGH STRENGTH 9CR STEEL BY COMBINATION OF FINE MX-TYPE NITRIDES AND NO CARBIDE

Masaki Taneike, Kota Sawada and Fujio Abe

Structural Materials Research Center, Materials Engineering Lab.,
National Institute for Materials Science
1-2-1 Sengen, Tsukuba 305-0047, Japan

Abstract

The improvement of creep strength has been achieved for 9Cr steel by optimized distributions of fine MX-type nitrides. The creep test was carried out for 9Cr-3W-VNb-N steels containing 0.002 and 0.08 mass%C at 923K and 160MPa for up to about 10^4h. The creep rupture strength is much larger for the extremely low carbon steel (0.002mass%C) than for the steels containing carbon of 0.08 mass%. The creep life of the extremely low carbon steel at 923K and 160MPa is about ten times as large as that of the steel containing 0.08 mass%C. The microstructures of the steels examined are observed to be tempered martensite. A large number of fine MX identified as nitrides having a size of 2 - 20 nm are distributed on grain boundaries as well as on lath boundaries in the extremely low carbon 9Cr steel after tempering. A combination of the removal of any carbide whose coarsening rate is much larger than that of nitrides and the fine distributions of MX-type nitrides is significantly effective for the stabilization of a high density of dislocations as well as a variety of boundaries in the martensitic 9Cr steel for up to long times at 923K.

Keywords: creep, martensite, precipitation strengthening, ferritic heat resistant steel

1 Introduction

Ferritic heat resistant steels have attracted strong interest in applications for boilers and turbines of ultra super critical power plants. These steels are used for a long period over ten years and hence the improvement of the more long-term creep strength is strongly demanded. Recently, development of the steel which can be used at a temperature of 923K or more has been furthered[1]. For these steels, the temperature of 923K is very high for a long-term use because it is higher than a half of melting temperature and microstructure evolution significantly takes place. In order to maintain a high level of creep strength for up to long times at high temperature, it is required to stabilize the microstructure for up to long times. Especially, coarsening of precipitation strengthening particles promotes the microstructure evolution, which causes a significant decrease of creep strength [2]. Various researches for the stabilization of the particles during high temperature creep were carried out by taking account of the stabilization of microstructure near prior austenite grain boundaries for tempered

martensitic 9Cr steels[3]. For example, Igarashi et.al [4] studied an application of fine FePd intermetallic compound of L_{10} type as precipitation strengthening particles. Horiuchi et.al [5] reported that the long-term creep strength was improved by adding boron, which stabilizes the microstructure near prior austenite grain boundaries through the stabilization of $M_{23}C_6$. However, it seems that the improvement of long-term creep strength at 923K is not still insufficient. Therefore, it is necessary to search innovative methods for the sufficient microstructure stabilization and further improvement of long-term creep strength at 923K.

In conventional 9 - 12 Cr steel, both $M_{23}C_6$ and MX particles precipitate during tempering and intermetallic compounds such as Laves phase precipitate during creep. The $M_{23}C_6$, constituting of mainly iron and chromium, precipitates as a large particle of about 200 – 300 nm on the prior austenite grain boundaries and lath boundaries. $M_{23}C_6$ carbides act as obstacles for migrating lath boundaries, but they tend to coarsen easily during creep. The MX carbonitrides of niobium and vanadium precipitate as fine particles of about 2 - 20 nm mainly on dislocations in the matrix. The MX is more stable during creep than the $M_{23}C_6$, because it precipitates coherently with the matrix and the solubility of constituents, niobium and vanadium, is quite low [6]. Many researches for using both particles effectively have been carried out until now. However, no attempt has been examined for 9 - 12 Cr steels to eliminate the $M_{23}C_6$ carbides and to stabilize the microstructure only by the MX nitrides.

The purpose of the present research is to investigate the distribution of MX nitrides consisting of vanadium and niobium in a 9Cr steel containing extremely low carbon and its effect on creep strength at 923K. The fine distribution of the MX nitrides along prior austenite grain boundaries and lath boundaries is shown to be very effective for the microstructure stabilization and the improvement of long-term creep strength.

2 Experimental procedure

Chemical compositions of steels studied are Fe-9Cr-3W-0.06Nb-0.2V-0.05N with carbon of 0.002 and 0.08 mass%. The steels are named 0C steel and 008C steel, accordingly to the carbon concentration. These steels were normalized at 1373K for 1h, cooled in air, and tempered at 1073K for 1h. Vickers hardness of the tempered steels were almost the same, about 230. The microstructures of the steels were observed to be tempered martensite. Creep tests were carried out at 923K under stress conditions between 140 and 180MPa. Microstructure of the steels was observed by optical and transmission electron microscopes. The precipitates were observed by using carbon extraction replicas and were identified by EDS analysis. The concentration of alloying elements contained in the precipitates was

measured by ICP analysis of electrolytically extracted residues.

3 Results and discussions

Creep rupture strength

Figure 1 shows stress vs. time to rupture curves at 923K. The results of 9Cr-0.5Mo-2W-V-Nb (ASME P92) are also shown by the dotted line for comparison. The creep life of the 0C steel is about ten times as long as that of the 008C steel and about one hundred times as long as that of the P92 steel. It should be emphasized that the creep strength of the 0C steel is excellent from a short time to a long time about 10^4h.

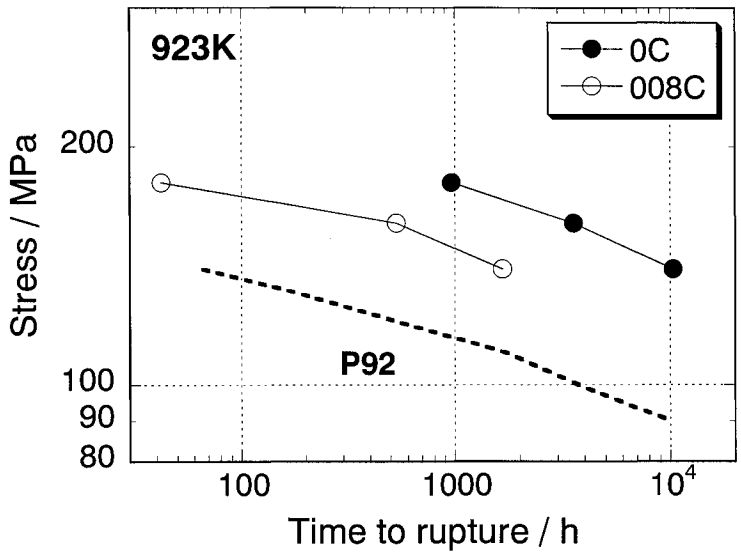


Figure 1: Stress vs. time to rupture curves of the present studied steels and the conventional steel NF616 at 923 K

Microstructure of the steels

Figure 2 shows the results of TEM observations of the steels after tempering. In conventional 9Cr steel, the $M_{23}C_6$ carbides precipitate on lath and block boundaries and prior austenite grain boundaries, and the MX carbonitrides precipitate within lath mainly. As shown in Fig.2, the microstructure of the 008C steel is similar to that of the conventional steel. On the other hand, in the 0C steel, almost no $M_{23}C_6$ particle precipitates and the fine precipitates having a size of 2 - 20 nm are densely distributed along prior austenite grain boundaries and lath

boundaries. The fine precipitates are identified as MX nitrides consisting of vanadium and niobium, as will be described later. The distribution of the MX nitrides within lath is not clear because of limited resolution, but it seems that the number of MX particles within lath in the 0C steel is fewer than in the 008C steel because more MX particles precipitate along boundaries in the 0C steel. Thus the distribution of precipitates greatly differs between the two steels.

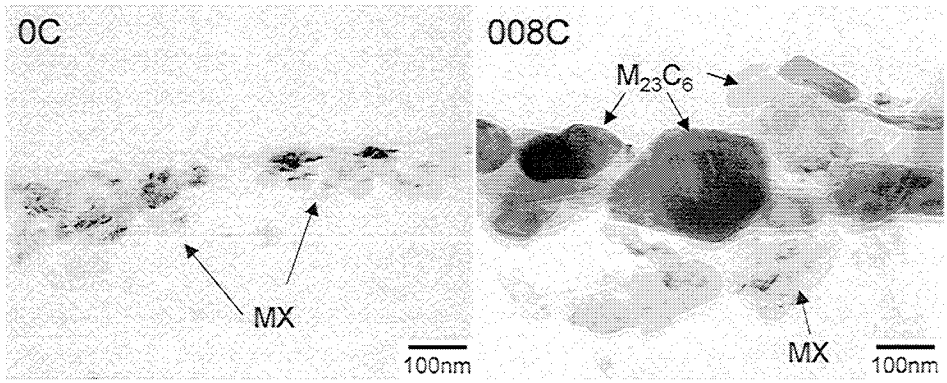


Figure 2: Precipitates along prior austenite grain boundaries in the 0C and 008C steels after tempering

The higher creep rupture strength of the 0C steel at a short time of 1000h than the others (Fig.1) results from a fine dispersion of the MX nitrides. The maintainance of a high level of creep rupture strength of the 0C steel for up to long times suggests that the fine MX nitrides are stable during long-term creep and that the recovery of lath martensitic microstructure is effectively suppressed during creep. The present results suggest that the fine distribution of the MX nitrides alone along lath boundaries is preferable for the stabilization of lath martensitic microstructure during creep than the distribution of both the $M_{23}C_6$ carbides and the MX carbonitrides. Then, it is considered that to stabilize the microstructure near the boundary it is most important in order to increase resistance for creep deformation.

Concentration of alloying elements contained in precipitates

In order to estimate quantitatively the amount of precipitates in the steels, the measurement of extracted residue of the steels after tempering is shown in Figure 3. The amount of chromium, iron and tungsten, which consist of $M_{23}C_6$, is much lower in the 0C steel than in the 008C steel. This result agrees with the results of the TEM observations showing substantially no $M_{23}C_6$ in the 0C steel. In the 008C steel, a large amount of chromium, iron and tungsten

precipitate as $M_{23}C_6$, reducing in the matrix. Among these elements, tungsten is regarded as an element causing large solid solution strengthening because of its large misfit to the matrix [7]. The amount of precipitated tungsten is about 0.2 mass% smaller in the 0C steel than in the 008C steel. This indicates that solid solution strengthening due to dissolved-tungsten is larger in the 0C steel than in the 008C steel. However, during creep deformation, tungsten precipitates as Fe_2W Laves phase, which is an intermetallic compound. As a result, tungsten in the matrix in equilibrium scarcely differs between the two steels. Accordingly, it should be regarded that a difference of solid solution strengthening by tungsten among the steels remained only in an early stage of creep. On the other hand, the concentration of dissolved chromium in the matrix differs between the two steels even in equilibrium. Chromium is regarded as an element causing little effect of solid solution strengthening. However, chromium may cause solid solution strengthening by the formation of a pair with nitrogen, for example. At present, it is difficult to explain the observed large creep strength of the 0C steel only by the difference of the concentration of solute elements causing solid solution strengthening. In the 0C steel, it is considered that precipitation strengthening by fine MX nitrides explains a great part of the improvement of creep rupture strength and that solid solution strengthening by tungsten acts more effectively than in the 008C steel only in an early stage of creep deformation. The detailed analysis should be made in future research.

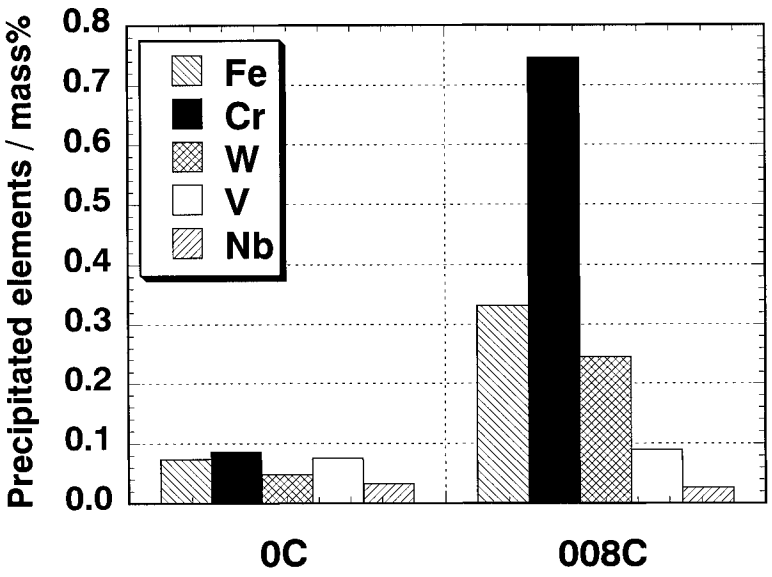


Figure 3: Concentration of the elements in precipitates of the steels after tempering

4 Conclusions

(1) The creep life of the steel containing almost no carbon is about ten times as long as that of the steel containing 0.08 mass%C and about one hundred times as long as that of the P92 steel at 923K.
(2) In the 0C steel, there is almost no $M_{23}C_6$ particle and the fine precipitates having a size of 2 - 20 nm are densely distributed along prior austenite grain boundaries and lath boundaries. The present results suggest that the fine distribution of the MX nitrides alone along lath boundaries is preferable for the stabilization of lath martensitic microstructure during creep than the distribution of both the $M_{23}C_6$ carbides and the MX carbonitrides.
(3) In the 0C steel, it is considered that precipitation strengthening by fine MX nitrides explains a great part of the improvement of creep rupture strength and that solid solution strengthening by tungsten acts more effectively than in the 008C steel only in an early stage of creep deformation.

5 Acknowledgement

The authors wish to thank the members of NIMS for performing the long-term tests.

6 References

[1]F.Masuyama: Materials for Advanced Power Engineering 1998, Part, eds.By J.Lecomte-Becker et al., Forschungzentrum Julich, Germany, (1998),1807
[2] K.Kimura: Materia, 35(1996), 535
[3] H.Kushima, K.Kimura, F.Abe: Tetsu-to-Hagane, 85(1999),841
[4] M.Igarashi, S.Muneki, H.Kutsumi, T.Itagaki, N.Fujitsuna and F.Abe: Proc. PARSONS 2000 Advanced Materials for 21ST Century Turbines and ower Plant, ed. by A.Strang et al., The Institute of Materials, (2000), 334-347
[5] T.Horiuchi, M.Igarashi and F.Abe: PRoc. International Workshop on the Innovative Structural Materials, NRIM, (2001), 176-179
[6] A.Iseda, Y.Teranishi, F.Masuyama: Tetsu-to-Hagane, 76(1990), 1076
[7] Y.Kadoya, E.Shimizu: Tetsu-to-Hagane, 86(2000), 189

DEVELOPMENT STEPS OF NEW STEELS FOR ADVANCED STEAM POWER PLANTS

K.H. Mayer[1)], R. Blum[2)], P. Hillenbrand[3)], T.-U. Kern[4)] and M. Staubli[5)]

1) ALSTOM Power, Nuremberg, Germany
2) ELSAM ENERGY, Frederica, Denmark
3) VGB PowerTech, Essen, Germany
4) Siemens Power Generation, Muelheim, Germany
5) ALSTOM Power, Baden, Switzerland

Abstract

A multicity of influencing factors must be taken into account in the development of heat-resistant steels for highly stressed power station components. A factor of major significance in the manufacture of relatively small test melts with the weight of rougly 50-100kg is a respresentative simulation of the condition which can exist during the manufacture of a full-size component with a weigth of up to 60t. Consequently the research programmes should include the manufacture and thorough examination of full-size pilot components up to a minimum of 35 000h to check the transfer conditions of the results obtained with small test melts. If the transfer condition are positive the materials can be released for the manufacture of full size components for new but lower stressed power plants. Pursuant to this, it is equally important to gather further experiences by making a representative checkup on a number of production components, encompassing a large number of steel works and foundries with their specific technologies in the field of melting, casting, forging and heat treatment. The paper focuses this development way of about 15 years on investigations under the European joint programmes COST501/522 and on subsequent investigations carried out on 24 large components of new European advanced steam power stations under a research programme sponsored by the German utility organisation VGB PowerTech.

Keywords : advanced 10%Cr steels, manufacturing rotors and cast components, mechanical and creep properties

1. Introduction

Under the joint European program COST 501 with partners from power station manufacturers, steelworks, power station operators and research institutes, the past 17 years have seen the development and qualification of ferritic-martensitic 9-10% Cr-steels which permit the manufacture of fossil-fired thermal power stations operating at live steam and reheat steam temperatures of 600/625°C and supercritical live steam pressures of up to approximately 300 bar [1].

Based on these steam parameters it will be possible – in comparison with conventional thermal power stations with steam admission temperatures of roughly 540°C, to improve the thermal efficiencies by up to about 6-8% and thus reduce the CO_2 emissions by up to 15-20% [2].

The focal point of the research work was the development of ferritic-martensitic 10% Cr-steels with a 100 000 h creep rupture strength of roughly 90 – 100 MPa at the maximum design temperatures of 600 and 625°C. In addition, a steel quality had to be found with characteristics suitable for the successful manufacture of power station components and with

properties required for safe and flexible plant operation, i.e., favourable properties for the production processes of melting, casting, forging, heat treatment and welding on the one hand, and adequate ductility, toughness and low-cycle fatigue strength on the other. These characteristics have to correspond at least with those of the steels hitherto used up to about 540°C (2%CrMo,1%CrMoV and 12%CrMoV).

The new steels were developed on the basis of a thorough examination of a large number of test melts. Subsequently, the successful candidate steels were used to manufacture pilot components which were dimensioned according to the size of real turbine components, such as rotor shafts and valve chests. After verification under the research and development program and additional investigations by the manufacturers in long-term tests over a period of 30 000 h, the pre-requisites had been established for the manufacture of 14 European thermal power stations to operate at advanced steam parameters and at outputs of up to 950 MW. Table 1 shows the type of fuel and the major design data of these plants:

Steam Plant	Fuel	Output MW	Live Steam bar/°C	Reheat Steam °C	Thermal Efficiency %
Skaerbaek	Gas	400	290/582	580/580	49[1)]
Nordiyland	Coal	400	290/582	580/580	48[1)]
Avedore	Biomass, Coal	530	300/582	600	47
VALA	Coal	260	180/536	570	
Schkopau A,B	Lignite	450	285/545	560	40
Sch.Pumpe A, B	Lignite	800	268/545	565	40,6
Boxberg Q,R	Lignite	818	268/545	583	41,7
Lippendorf R,S	Lignite	900	268/554	583	42,3
Niederaußem	Lignite	950	268/580	600	>43

1) sea water cooling

Table 1: European Advanced Steam Power Plants

The steam parameters were increased from 540°C to 600°C in steps so that the strength potential of the newly developed steels was not exhausted for the first plants to be manufactured.

Unexpectedly, no exceptional problems were encountered in the manufacture of the highly stressed components, such as the turbine rotors, the valve chests and the turbine casings for these plants. Reports on experience are positive throughout [3 to 7].

Under a research scheme sponsored by the VGB [8] and covering an initial period of 8 years, a joint effort has been launched by the turbine manufacturers and power station operators with the aim of subjecting a large number of specimens of 24 large and highly stressed components of the power stations listed in Table 1 to long-term creep rupture tests as well as low-cycle fatigue tests and hot tensile tests in order to increase the wealth of experience and the data basis and, if possible, to identify specific hitherto unknown production and size influences for further development work.

Table 2 outlines the scope of the investigations. The test stresses of the creep rupture tests were selected to reach rupture times of up to at least 100 000 h.

Turbine Components	Newly developed Steels	Hot Tensile Test at °C			Creep Test at °C			LCF Test at °C	
		500	550	600	500	550	600	RT	600
4 Rotors	X12CrMoVNbN 10 1	X	X	X	X	X	X	X	X
4 Rotors	X12CrMoWVNbN 10 1 1	X	X	X	X	X	X	X	X
4 Casings	G-X12CrMoVNbN 9 1	X	X	X	X	X	X	X	X
4 Valves	G-X12CrMoVNbN 9 1	X	X	X	X	X	X	X	X
5 Casings	G-X12CrMoWVNbN 10 11	X	X	X	X	X	X	X	X
3 Valves	G-X12CrMoWVNbN 10 11	X	X	X	X	X	X	X	X
24 Components	Number of Property Curves : ⇐	24	24	24	9	14	30	16	16

Table 2: Scope of the Investigated Steam Turbine Components

A report is given hereunder on the steels and components covered by this investigation and on the results.

2. Upscaling

A multiplicity of influencing factors must be taken into account in the development of heat-resistant steels for highly stressed power station components. A factor of major significance in the manufacture of relatively small test melts with a weight of roughly 50-100 kg is a representative simulation of the conditions which can exist during the manufacture of a full-size component with a weight of up to 60 t and a diameter of up to 1200 mm. Figure 1 demonstrates the involved sizes of the small bars of the test melts, the relevant sizes of the used pilot rotor and the forging size of a typical HP/IP rotor. Special significance of the manufacturer technology is, for instance to consider:

- the melting operation (purity, de-oxidation, segregation, homogenity of the properties)
- the casting operation (degasification, solidification, segregation, homogenity of the properties)
- the forging operation (forging rate, forging temperature, grain size)
- pre-heat treatment (e.g. normalizing, heating/cooling rate, tempering)
- heat treatment (austenitizing, heating/cooling rate, hold time)
- post-weld heat treatment (heating/cooling rate, stress relieving, hold time)

The production processes of the test melts, duly allowing for these production factors, must be established in a manner ensuring that the simulation of the production and geometrical conditions of the full-size components is largely taken into account and that the results obtained for the test melts are achieved for the complete full-size component, i.e., from the rim zones to the core zones.

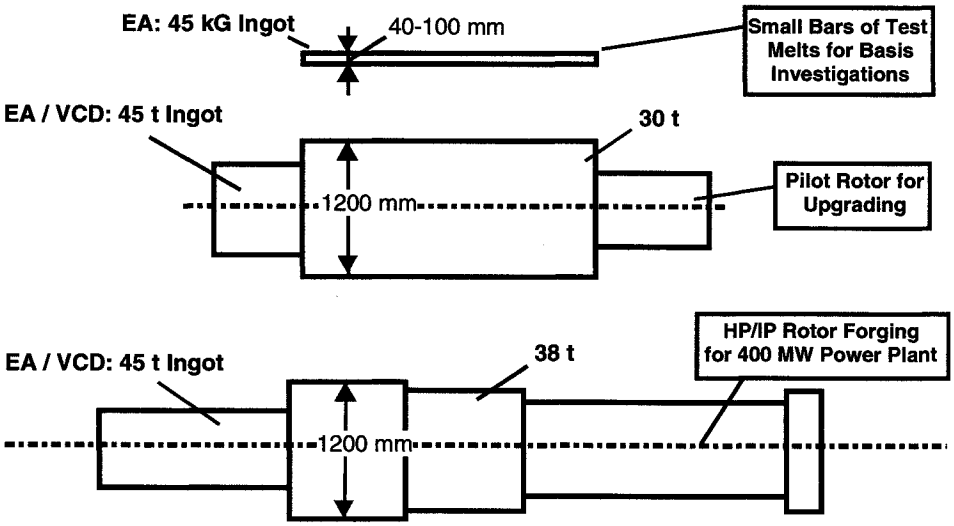


Figure 1 : Up-scaling at rotor steel development

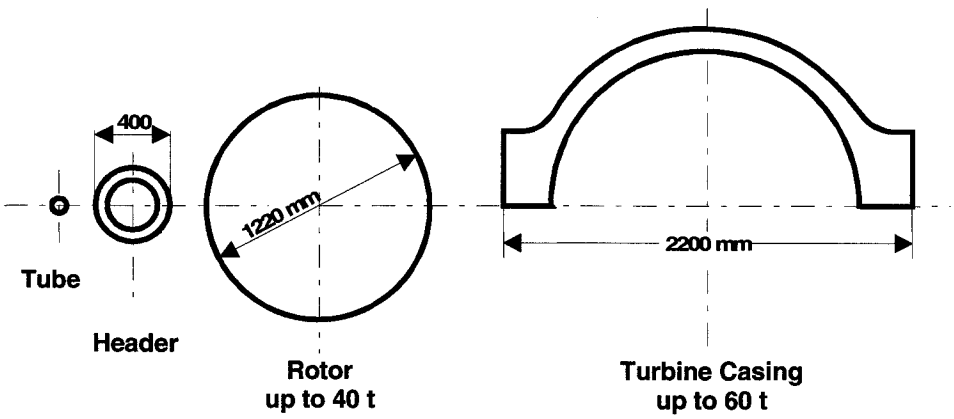


Figure 2 : Comparison of Sizes and Shapes of Steam Plant Components

Figure 2 illustrates the sizes and the shapes of main steam plant components which are to realize with the new developed steels.

While simulating the conditions of the full-size components another factor which must be taken into account is that only such production processes are adopted which ensure that the component is manufactured with adequate attenuation behaviour for non-destructive examination as well as freedom from cracks.

Consequently, owing to these reasons, the research programs include the manufacture and thorough examination of full-size pilot components to check the transfer conditions of the results obtained with small test melts. If the transfer conditions are positive the materials can be released for the manufacture of full-size components for a new plant.

Pursuant to this, it is equally important to gather further experience by making a representative checkup on a number of production components, encompassing a large number of steelworks and foundries with their specific technologies in the fields of melting, casting, forging and heat treatment.
Figure 3 gives an overview of the development and manufacturing steps versus time between literature survey of the planned development programme and the realization of 350 castings by 6 foundries for 14 new power stations after about 10 years of intensive research work and the following checkup of 16 new castings by creep tests of specimens of representative locations of these components.

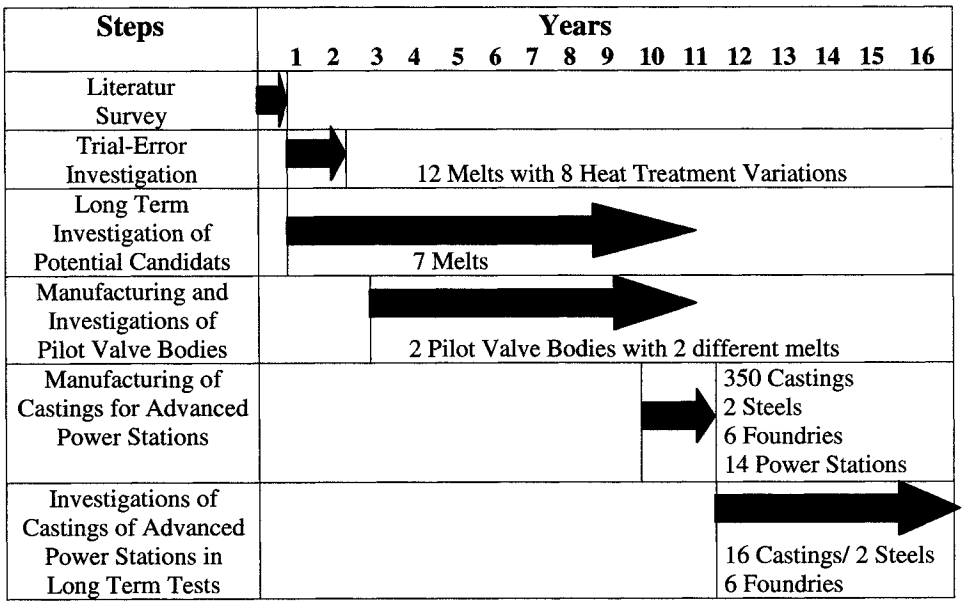


Table 3: Steps of steel development and of manufacturing of components for advanced steam power stations

3. Investigated Components

3.1 Rotor Forgings

The investigation is being carried out on 4 rotors each of the steels X12CrMoVNbN 10 1 and X12CrMoWVNbN 10 1 1, manufactured by 4 different forgemasters. Table 4 shows the applied melting technologies, the sizes of the ingots and the rotor forgings.

No	Material	Melting Method	Weight of Melt t	Weight of Ingot t	Weight of Rotor t	Rotor Diameter mm
1	X12CrMoVNbN 10 1	EA/VAD	108	108	22	1 200
2	X12CrMoVNbN 10 1	EA/VCD*		31	21	917
3	X12CrMoVNbN 10 1	EA/VCD	97	45	38	1 200
4	X12CrMoVNbN 10 1	EA/VCD	97	45	38	1 200
5	X12CrMoWVNbN 10 1 1	ESR	105	102	38	850
6	X12CrMoWVNbN 10 1 1	ESR	86	84	38	850
7	X12CrMoWVNbN 10 1 1	ESR	159	159	6,8	1 000
8	X12CrMoWVNbN 10 1 1	ESR	159	159	4,5	780

*BEST: Boehler Electro Slag Topping Process

Table 4 : Manufacturing Data of the Rotor Forgings

4 rotors were manufactured by the ESR method, 3 rotors by EA/VCD and 1 rotor by the EA/VAD melting method. The weights of the melts and the ingots are within the range of 31 to 108 t. Substantially lower are the weights of the rotor forgings at 4.5 up to 38 t. The maximum forging diameter of the rotors is between 780 and 1220 mm.

The chemical composition, the heat reat treatment condition and the mechanical properties of the investigated rotors is published in [9].

All mechanical properties established for the production rotors are in agreement with the test values of the pilot rotors E and F of the COST 501-2 Programme [10].

3.2 Turbine Casings and Valve Chests

The investigation covers a total of 9 turbine casings and 7 valve chests, with 8 components of the tungsten-free cast steel version G-X12CrMoVNbN 9 1, which in its chemical composition is largely in keeping with the forging and rolling steel P 91. This cast steel grade was subjected to a detailed investigation under EPRI Program RP 1403-9 and qualified for use in the manufacture of steam turbines [11 to 14]. The 8 other components are manufactured of the tungsten-carrying version G-X12CrMoWVNbN 10 1 1, which roughly agrees in its chemical composition with the tungsten-carrying rotor steel X12CrMoWVNbN 10 1 1 [10]. The castings were manufactured by 6 different European foundries.
Table 5 shows the method of melting, the weights and the global dimensions of the components.

No	Component	Cast Steel	Melting Method	Weight of Piece t	Outer Dimension of Piece and Wall Thick. mm *
1	VHP Inner Casing	G-X12CrMoVNbN 9 1	LD/LRF	9.8	1600x2720
2	HP/IP Inn. Casing	G-X12CrMoVNbN 9 1	LD/LRF	15.2	2000x4050
3	VHP Valve Chest	G-X12CrMoVNbN 9 1	EA/AOD	4.5	1000x1800
4	HP Valve Chest	G-X12CrMoVNbN 9 1	EA/LRF	5.6	1300x1850
5	IP Valve Chest	G-X12CrMoVNbN 9 1	EA/VAD	16.2	2200x2650
6	VHP Inner Casing	G-X12CrMoVNbN 9 1	LD/LRF	9.8	1600x2720
7	HP/IP Inn. Casing	G-X12CrMoVNbN 9 1	LD/LRF	15.2	2000x4500
8	VHP Valve Chest	G-X12CrMoVNbN 9 1	EA	4.5	1000x1800
9	Inner Casing	G-X12CrMoWVNbN 10 1 1	LD/LRF	35	2700/S=70
10	Inner Casing	G-X12CrMoWVNbN 10 1 1	LD/LRF	41	2700/S=70
11	Valve Chest	G-X12CrMoWVNbN 10 1 1	EA/AOD	13.4	1340/S=100
12	Valve Chest	G-X12CrMoWVNbN 10 1 1	EA/AOD	13.2	1340S=100
13	Valve Chest	G-X12CrMoWVNbN 10 1 1	EA/AOD	10.7	1340/S=100
14	HP Inner Casing	G-X12CrMoWVNbN 10 1 1	LD/LRF	9.8	1980x3170
15	IP Inner Casing	G-X12CrMoWVNbN 10 1 1	LD/LRF	23.5	2750x4220
16	IP Inner Casing	G-X12CrMoWVNbN 10 1 1	LD/LRF	25	2750x4220

- S= Wall Thickness

Table 5: Melting Methods, Weights and Dimensions of the Investigated Cast Components

With the exception of Casting No. 8, all castings were manufactured according to a specific secondary metallurgy (LRF, AOD and VAD). Primary melting was carried out either in an LD converter or in an electric arc furnace.

The weights of the castings are within a range of 4.5 to 41 t. The IP inner casings, Nos. 15 and 16, have the largest dimensions.

The chemical composition, the heat treatment condition and the mechanical properties of the investigated castings are published in [9].

The chemical composition, the heat treatment and the mechanical properties are in accordance with the specifications and the conditions and results of the aforementioned research programmes.

4. Results of the Creep Tests

Test results are currently available up to about 40 000 h. By way of example, Figures 3 to 6 show the creep rupture strength determined at 600°C for the rotor steels X12CrMoVNbN 10 1 and X12CrMoWVNbN 10 1 1 and also for the cast steel grades G-X12CrMoVNbN 9 1 and G-X12CrMoWVNbN 10 1 1. In each case the results are compared with the results of the investigated pilot components of the research programmes.

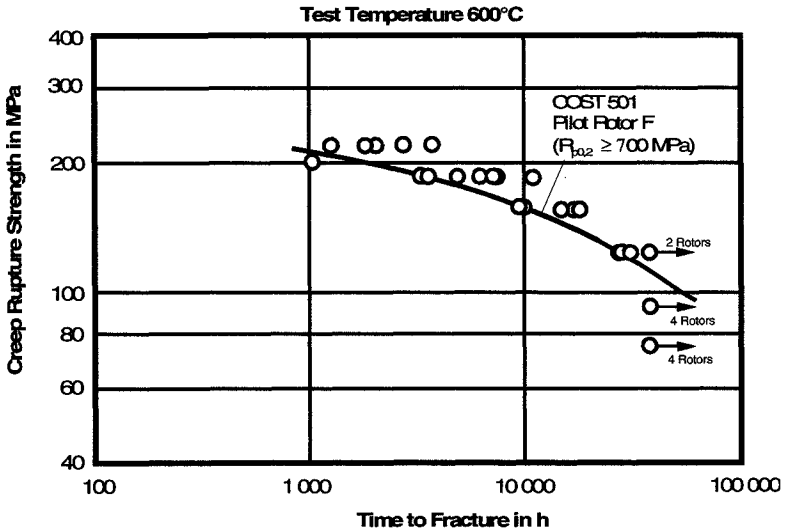


Figure 3: Creep Rupture Strength of Rotor Steel X12CrMoVNbN 10 1 at 600°C

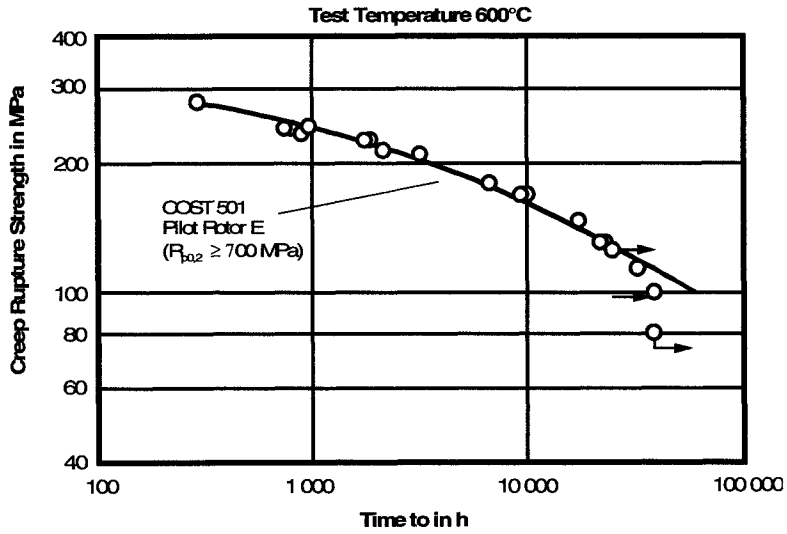


Figure 4: Creep Rupture Strength of Rotor Steel X12CrMoWVNbN 10 1 1 at 600°C

For all rotors the results currently available are equal to or better than the mean-value curves of the pilot rotors. As a rule, the creep test specimens, originating from the rotors with a higher initial strength at room temperature, also exhibit a longer life span. A noticeable fact in connection with the results of the rotor specimens is the relatively small scatter band of approximately plus/minus 6%.

A comparison between the results of the tungsten-carrying and the tungsten-free versions of the production rotors shows that during the test period both types of material have roughly the same creep rupture strength. This result also coincides with the results of both pilot rotors "E" (tungsten-carrying) and "F" (tungsten-free) of the COST 501 program at 600°C.

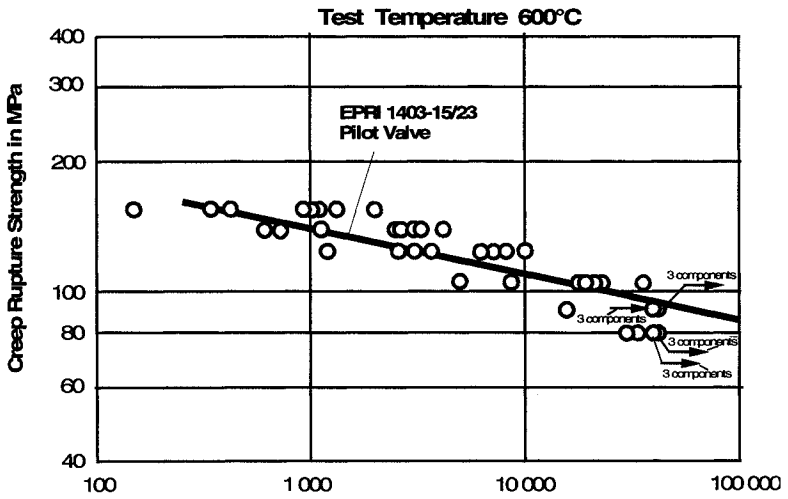


Figure 5: Creep Rupture Strength of Cast Steel G-X12CrMoVNbN 9 1 at 600°C
(Results of 8 cast components manufactured by 5 different foundries)

The measured values of the specimens from the castings scatter about the mean-value curves of the pilot components of the EPRI and COST programs. However, the scatter of the specimens of the tungsten-free version (Fig. 5) is substantially higher than for the tungsten-carrying version (Fig.6) and also higher than for the investigated rotors. This is presumably attributable to the larger circle of suppliers (5 different foundries) and to the specific production methods of the individual foundries involved. Thus, for instance, the castings with the higher aluminium contents of 0.020 and 0.021% reveal the lowest creep rupture strength. This finding is in good agreement with observations and investigations by V. Foldyna et al.[15] , who found that in the presence of higher Aluminium contents there was a lower content of dissolvable nitrogen for the formation of Vanadium-Nitrogen precipitation of type MX and M_2X. As substantiated by numerous tests, these Vanadium precipitations contribute greatly to improving the creep rupture strength of the newly developed 9-10%CrMoVNbN steels.

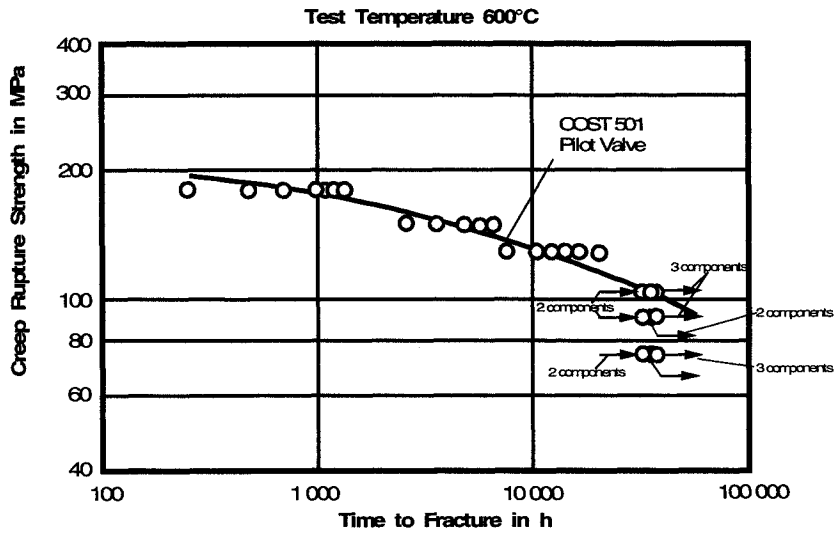


Figure 6: Creep Rupture Strength of Cast Steel G-X12CrMoWVNbN 10 1 1
(Results of 8 cast components manufactured by 2 foundries)

A comparison between the present results of the two cast steel grades G-X12CrMoVNbN 9 1 and G-X12CrMoWVNbN 10 1 up to about 40 000 h shows that, as a rule, the castings of the tungsten-carrying version have a higher creep rupture strength. The cause presumably lies in the higher initial strength. This finding coincides with the results of EPRI Program 1403 and COST Program 501. Based on the present research results, expectations are that in the long term both cast steel grades will roughly exhibit about the same creep rupture strength at 600°C.

5. Summary and Conclusion

Under the joint European Programs COST 501 and EPRI RP 1403-9 with partners from power station builders, steelworks, power station operators and research institutes, the past 20 years have seen the development and qualification of ferritic-martensitic 9-10% Cr-steels which permit the manufacture of fossil-fired thermal power stations operating at live steam and reheat steam temperatures of 600/625°C and supercritical live steam pressures of up to approximately 300 bar.

A multiplicity of influencing factors have been taken into account in the development of the new heat-resistant steels for highly stressed power station components. A factor of major significance in the manufacture of relatively small test melts with a weight of roughly 50-100 kg is a representative simulation of the conditions which can exist during the manufacture of a full-size component with a weight of up to 60 t and a diameter of up to 1200 mm.

Consequently the research programs include the manufacture and thorough examination of full-size pilot components to check the transfer conditions of the results obtained with small test melts. Due to the positiv transfer conditions the materials have been released for the manufacture of full-size components for 14 advanced European thermal power stations.

Unexpectedly, no exceptional problems were encountered in the manufacture of the highly stressed components, such as turbine rotors, casings and valves.

Under a research scheme sponsored by the VGB a joint effort has been launched by the turbine manufacturers and power station operators with the aim of subjecting a large number of specimens from 24 large production components of the new power stations to long-term creep rupture tests as well as low-cycle fatigue tests and hot tensile tests in order to increase the wealth of experience and the data basis and, if possible, identify specific hitherto unknown production and size influences for further development work.

The large components with weights up to approximately 60 t were manufactured by 5 different forgemasters and 6 different foundries, so as to cover a wide spectrum of production and size influences.

Results are in good agreement with the results of the investigations of test melts and pilot components under the research programmes.

Acknowledgement

The authors of this contribution express their gratitude to the VGB and the sponsoring member companies for financing the investigations and for their approval to publish this contribution.

References

[1] M. Staubli, K.H. Mayer, T.U. Kern and R.W. Vanstone:'COST 522; Power Generation into the 21st Century; Low Emission Plant Advanced Steam Power Plant', 5th International Charles Parsons Turbine Conference, Cambridge UK, 3-7 July 2000

[2] K.H.Mayer, W. Bendick, R.-U. Husemann, T. U. Kern and R.B. Scarlin:'New Materials for Improving the Efficiency of Fossil-Fired Power Stations', VBG PowerTech 1/98, pages 22 to 27.

[3] M. Taylor and D.V. Thornton:'Experience in the Manufacture of Steam Turbine Components in Advanced 9-12% Chromium Steels', International Conference on Advanced Steam Plant – New Materials and Plant Design and their Implications for Future CCGT and Conventional Power Stations, London, UK, 21-22 May 1997,

[4] M.A. Walsh:'Manufacture of 10%CrMoVNbN Turbine Rotors for Supercritical Applications', 13th International Forgemaster Meeting Advanced Heavy Forgings, Pusan, Korea, 12-16 October 1997, Volume I, pages 399-416,

[5] K.-H. Schönfeld and H. Wagner:'Experience in Manufacturing and Mechanical

Properties of Turbine Rotor Forgings and Discs in improved 10%CrMoWVNbN Steel',EPRI Conference Advanced Heat resistant Steels for Power Generation, San Sebastian, Spain, 27-29 April 1998, Conference Pre-Print

[6] F.A.Schuster and H. Cerjak:'Steel Castings made from newly developed 9-12%Cr-Steels for Advanced Power Generation', ASME Cogen-Turbo Power Conference, Vienna, Austria, 23-25 August 1995, 95-CTP-54,

[7] R. Hanus, F. Schuster, A. Buberl and H. Cerjak:'Investigations on Large Turbine Casings and Valve Bodies made of new 9-12%Cr-Cast Steels and Improvements of Casting Technique and Quality Performance', 6th Liège COST Conference Materials for Advanced Power Engineering 1998, Liège, Belgium, September 1998, Proceedings Part I, pages 193-204,

[8] VGB Research Project No. 158/:'Neue Werkstoffe für Dampfturbinen', 1996-2004,

[9] K.H. Mayer, T.U. Kern, M. Staubli and E. Tolksdorf: „ Long-term Investigations of Specimens of 24 Production Components manufactured from Advanced Martensitic 10%Cr-Steels for 600°C Steam Turbines", 5th International Charles Parsons Turbine Conference, 3.-7. July 2000, Cambridge, UK

[10] T.U.Kern, K.H.Mayer, R.B. Scarlin and R.W. Vanstone :'High Temperature Forged Components for Advanced Steam Power Plant', 6th Liège COST Conference Materials for Advanced Power Engineering 1998, Liège, Belgium, September 1998, Proceedings Part I, pages 53-70,

[11] K.H. Mayer and W. Gysel:'Modified 9%CrMo Cast Steel for large Cast Components of 1100°F Coal-Fired Power Plants – EPRI Project 1403-15/23', International EPRI Symposium on Improved Technology for Fossil Power Plants – New & Retrofit Applications, Washington, D.C. USA, 1-3 March 1993

[12] K.H.Mayer and W.T. Bakker:'New Ferritic Steels increase the Thermal Efficiency of Steam Turbines', International Joint Power Generation Conference, Houston, Texas, USA, October 1996,

[13] K.H. Mayer, R. Hanus, T.U. Kern M. Staubli and D.V. Thornton: 'High Temperature Cast Components for Advanced Steam Power Plant';6th Liège COST Conference Materials for Advanced Power Engineering 1998, Liège, Belgium, September 1998, Proceedings Part I, pages 71-85,

[14] K.H.Mayer, H. König, J .Granacher and M. Schwienheer: "Zeitstandverhalten der Stahlgußsorte GX12CrMoVNbN 9 1", 21. 23. Information Conference of German Creep Committee, Düsseldorf, Germany, 1. December 2000

[15] Foldyna, Z. Kubon, V. Vodárek and K.H. Mayer:'The Influence of Chemical Composition on the Creep Rupture Properties of 9-12%Chromium Steels', 21. Information Conference of German Creep Committee, Düsseldorf, Germany, 27 November 1998,

GUIDING PRINCIPLES FOR DEVELOPMENT OF ADVANCED FERRITIC STEELS FOR 650°C USC BOILERS

Fujio Abe*, Hirokazu Okada*, Shuji Wanikawa*, Masaaki Tabuchi*,
Takehiko Itagaki*, Kazuhiro Kimura*, Koji Yamaguchi* and Masaaki Igarashi**
* National Institute for Materials Science, 1-2-1 Sengen, Tsukuba 305-0047, Japan
** Sumitomo Metal Industries Ltd., 1-8, Fuso-cho, Amagasaki 660-0891, Japan

Abstract

In order to improve long term creep strength, we have been trying to stabilize lath martensitic microstructure in the vicinity of prior austenite grain boundaries by the addition of boron to stabilize $M_{23}C_6$ carbides at lath boundaries, by the elimination of $M_{23}C_6$ carbides to distribute fine MX nitrides homogeneously along lath boundaries and prior austenite grain boundaries, and by the elimination of $M_{23}C_6$ carbides and MX carbonitrides to distribute intermetallic compounds homogeneously along prior austenite grain boundaries as well as within the grain. A new attempt has been also demonstrated for a full-annealed ferrite matrix 15Cr steel. The newly developed steels exhibit much higher creep rupture strength than T91 and P92. A combination of Pd addition and surface straining causes the formation of protective Cr-rich oxide scale on the surface of 9Cr steel, which significantly improves the oxidation resistance in steam at 650 °C. Decreasing the width of heat affected zone by EB welding is effective for the extension of creep life of welded joints but the brittle Type IV fracture appears even in the EB welded joints at low stress and long time conditions.

Key Words: ferritic steel, martensitic microstructure, USC boiler, creep, creep-fatigue, oxidation, welded joint

1. Introduction

The National Institute for Materials Science (formerly, National Research Institute for Metals) has been conducting the research and development of advanced ferritic steels for application to thick section boiler components such as main steam pipe and header of ultra-supercritical (USC) power plant at 650 °C [1]. Critical issues for the development of ferritic steels for 650 °C USC boilers are the improvement of oxidation resistance as well as long-term creep rupture strength. The resistance to Type IV cracking strength loss in welded joints is also serious for construction of thick section boiler components. Furthermore, the thermal cycling capabilities of thick section components in USC plant would be severely restricted by fatigue damage. Under these circumstances, our project involves the improvement of creep strength, oxidation resistance and creep-fatigue properties for high-Cr ferritic steels, including welded joints. This paper describes an outline of the alloy design philosophy and the present status of steel development. Several types of high-Cr ferritic steels having higher creep rupture strength than ASME-P92 (9Cr-0.5Mo-1.8W-VNb) have been developed. The guidelines for improving oxidation resistance in steam at 650 °C are also presented.

2. Alloy Design Philosophy Based on Microstructure Stabilization Near Prior Austenite Grain Boundaries

The analysis of long term creep data of Mod.9Cr-1Mo steel in the NIMS Creep Data Sheets suggests that special attention should be paid to stabilize the microstructure in the vicinity of prior austenite grain boundaries for the improvement of long term creep strength [2]. The critical issues for the development of advanced 9 to 12Cr steels are to stabilize lath martensitic microstructure, especially in the vicinity of prior austenite grain boundaries, and to prevent the formation of AlN, M_6X and Z-phase, which promote inhomogeneous microstructural evolution. We have been trying to stabilize lath martensitic microstructure in

the vicinity of prior austenite grain boundaries by the addition of boron to stabilize $M_{23}C_6$ carbides at lath boundaries, by the elimination of $M_{23}C_6$ carbides to distribute fine MX nitrides homogeneously along lath boundaries and prior austenite grain boundaries, and by the elimination of $M_{23}C_6$ carbides and MX carbonitrides to distribute intermetallic compounds homogeneously in the vicinity of prior austenite grain boundaries as well as within the grain. Boron is known to segregate at grain boundaries, which reduces the rate of microstructural evolution. However, it is also reported that excess addition of boron and nitrogen promotes the formation of boron-nitrides at grain boundaries, which offsets the benefit due to boron and nitrogen [3]. Therefore, in the present work, the addition of a large amount of boron exceeding 0.01 wt% is examined in combination with no nitrogen addition. In order to avoid the formation of AlN, residual Al is minimized to a low level as low as 20-30 ppm. A new attempt for the stabilization of microstructure has been also demonstrated for a full-annealed ferrite matrix 15Cr steel.

3. New Steels with Improved Creep Strength

The creep rupture data for the newly developed steels at 650 °C is shown in Figure 1, where the results for conventional steels, ASME-T91 (9Cr-1Mo-VNb) and ASME-P92 are also shown for comparison. Although only the creep rupture data for up to about 10,000 h are available at present, the developed steels exhibit higher creep rupture strength than T91 and P92. The 9Cr-3.3W-1Pd-VNb steel was alloy-designed to obtain homogeneous precipitation of Fe-Pd intermetallic compound having $L1_0$ type ordered structure [4]. Pd is promising as a potential element to form fine precipitates of Fe-Pd $L1_0$ as well as an austenite-stabilizing element which can substitute for Ni and Co. The detailed creep behavior of the new steels is described in the following.

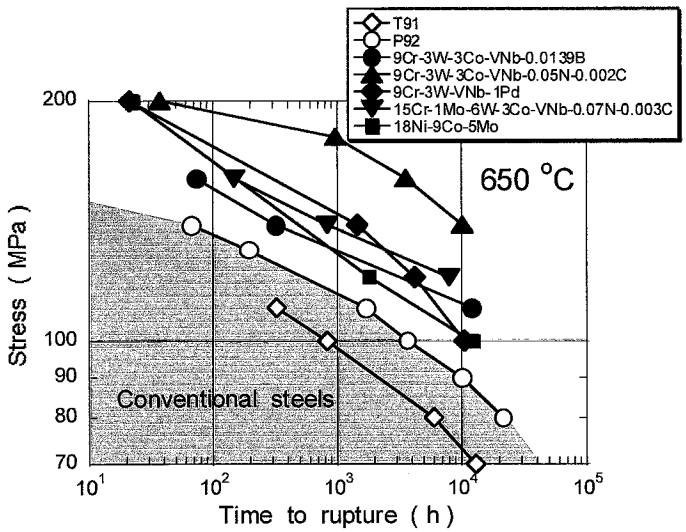


Figure 1 Creep rupture data for the developed steels comparing with those for conventional steels T91 and P92 at 650 °C.

3.1 Stabilization of lath martensitic microstructure near grain boundaries by boron addition

The improvement of creep rupture strength by the addition of small amount of boron has been examined for a 0.08C-0.3Si-0.5Mn-9Cr-3W-0.2V-0.05Nb-3Co steel with 0.0139 wt% boron [5] which is denoted as 9Cr-3W-3Co-VNb-0.0139B in Figure 1. Residual nitrogen in the steel was analyzed to be 30 ppm. Figure 2 shows the creep rate versus time curves of the steel at 650°C, together with those of the steels with 0 and 0.0092 wt% boron. According to the concentration of boron, the steels are denoted as 0B, 0.0092B and 0.0139B. It should be noted that the transient creep region of the steels with boron continues up to longer times than that of the steel without boron, resulting in the lower minimum creep rate and longer rupture time. The longer duration of transient creep region in the steel containing boron results from the stabilization of lath martensitic microstructure up to longer times through the stabilization of $M_{23}C_6$ carbides in the vicinity of prior austenite grain boundaries by an enrichment of boron, as shown schematically in Figure 3.

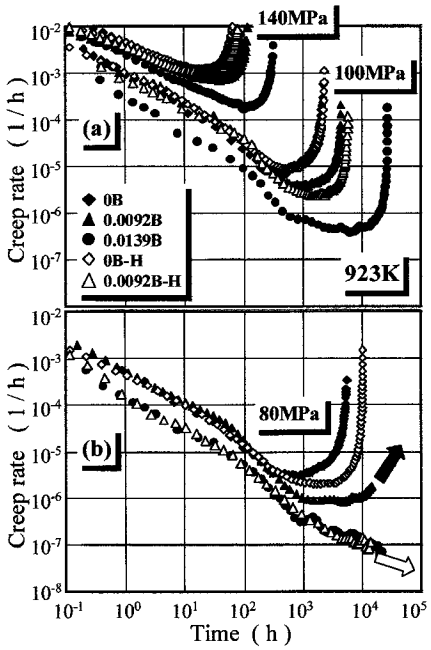


Figure 2 Creep rate versus time curves of 9Cr-3W-3Co-VNb steel with and without boron.

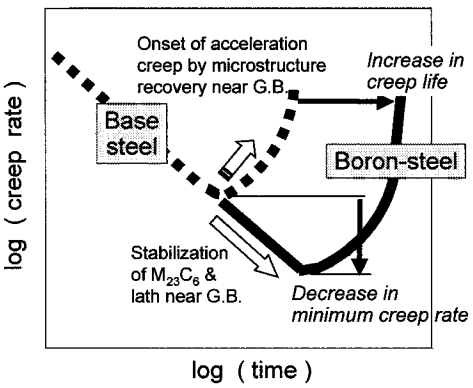


Figure 3 Schematic creep rate versus time curves, showing decrease in minimum creep rate and increase in creep life.

Field Emission Auger Electron Spectroscopy (FE-AES) shows that boron is enriched in the $M_{23}C_6$ carbides, which is more significant in the vicinity of prior austenite grain boundary, as shown in Figure 4. The $M_{23}C_6$ carbides are distributed mainly along prior austenite grain boundaries and along lath, block and packet boundaries inside grain. No evidence was found for the enrichment of boron in the Fe_2W Laves phase. Hattestrand and co-workers [6] already reported an enrichment of boron in $M_{23}C_6$ carbides for 12Cr steels by Atom Probe Field Ion Microscopy. But they did not specify whether the $M_{23}C_6$ carbides where boron was enriched were located in the vicinity of prior austenite grain boundaries or not.

It should be also noted that most of added boron in the 0.0092B and 0.0139B steels have already precipitated as large inclusions of tungsten boride during heat treatment before creep test. The tungsten borides are dissolved by high-temperature normalizing at 1150°C for the 0.0092B steel. The 0B and 0.0092B steels subjected to the high-temperature normalizing are denoted as 0B-H and 0.0092B-H steels, respectively, in Figure 2. Figure 5 shows the average boron concentration in the $M_{23}C_6$ carbides of the 0.0092B and 0.0092B-H steels after tempering, where the $M_{23}C_6$ carbides are roughly divided into 2 groups; those existing within 2μm from prior-austenite grain boundaries (near GB) and those existing more than 2μm away from grain boundaries (inside G). The result for the 0.0139B steel near GB is also represented in Figure 5 for comparison. The boron content in the $M_{23}C_6$ carbides is significantly increased in the 0.0092B-H steel to about the same extent as the 0.0139B steel. The high-temperature normalizing results in lower minimum creep rate and hence longer time to rupture as shown in Figure 2, especially at low stress and long time conditions. The present results indicate that the amount of effectively utilized boron is essential to improve long term creep strength and that high-temperature normalizing can increase it.

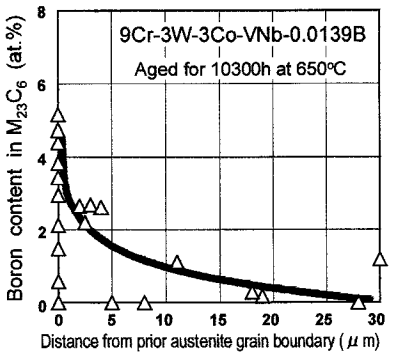


Figure 4 Boron content in $M_{23}C_6$ in the 9Cr-3W-3CoVNb steel with 0.0139 wt % boron, as a function of distance from prior austenite grain boundary.

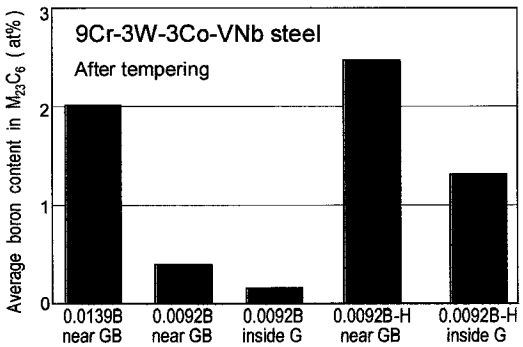


Figure 5 Average boron content in $M_{23}C_6$ within 2μm from grain boundaries and inside grain more than 2μm away from grain boundaries.

3.2 Effect of fine MX nitrides along prior austenite grain boundaries and lath boundaries combined with no $M_{23}C_6$

The improvement of creep strength has been also achieved for a tempered martensitic 9Cr-3W-3Co-0.2V-0.05Nb-0.05N-0.002C steel by optimizing the distribution of fine MX nitrides. No carbon was added in this steel to eliminate $M_{23}C_6$ carbides [7]. The steel is denoted as 9Cr-3W-3Co-VNb-0.05N-0.002C in Figure 1. The creep rupture strength of this steel is much larger than that of the other steels, as can be seen in Figure 1. The TEM observations show that a large number of fine MX nitrides having a size of 2 - 20 nm are distributed along prior austenite grain boundaries as well as along lath boundaries but no $M_{23}C_6$ after tempering because of extremely low carbon concentration. The MX nitrides consist of vanadium nitrides, mainly. The present results suggest that the fine distribution of

the MX nitrides but no $M_{23}C_6$ alone along lath boundaries is preferable for the stabilization of lath martensitic microstructure for up to long times at 650°C. In conventional ferritic steels, the $M_{23}C_6$ carbides usually exhibit a large coarsening during creep, which promotes inhomogeneous microstructure evolution and hence causes a decrease in creep strength. The precipitation of Fe_2W Laves phase takes place during creep in the present steel, which may contribute additionally to the stabilization of lath martensitic microstructure. It should be noted that solid solution strengthening due to dissolved tungsten in the matrix is not important in the present steel, because the concentration of dissolved tungsten decreases considerably as the Fe_2W Laves phase precipitates during creep.

3.3 Homogeneous distribution of intermetallic compounds in a carbon-free Fe-18Ni-9Co martensitic alloy

The creep deformation behavior of the carbon-free Fe-12Ni-9Co martensitic alloy is completely different from that of the tempered martensitic 9Cr-3.3W-VNb base steels [8]. Conventional 9-12Cr steels usually exhibit a steeper decrease of creep rate with strain in the transient creep region, giving a smaller strain for minimum creep rate at which the acceleration creep starts. On the other hand, the carbon-free martensitic alloy, 18Ni-9Co-5Mo in Figure 1, exhibits gradual change in creep rate with strain both in the transient and acceleration creep regions, and gives a large strain to reach a minimum creep rate. This suggests that the creep deformation in the present alloy takes place homogeneously even at low stress and long time conditions. It should be also noted that the 12Ni-9Co-10W alloys with 2Pd or 5Cr, exhibit higher creep rupture strength than JIS SUS 304HTB austenitic stainless steel at a higher temperature of 700°C (Figure 6) [8]. The transient creep region of the carbon-free 12Ni-9Co-10W alloys with 2Pd or 5Cr continues for up to longer times, which decreases the minimum creep rate. The present results indicate that the carbon-free martensitic alloy exhibits a very small decrease in creep rupture strength with increasing temperature. Therefore, the carbon-free martensitic alloy is promising as one of candidates for structures of high temperature plants such as 700 °C USC plant.

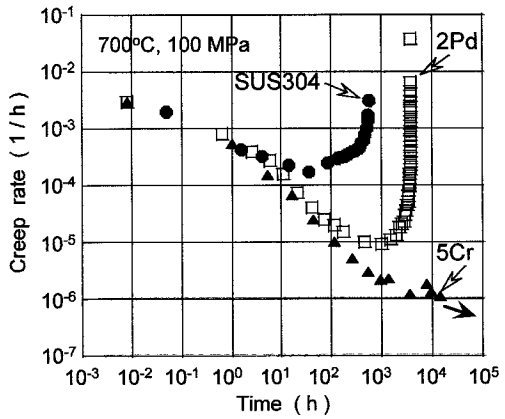


Figure 6 Creep rate versus time curves of carbon-free 18Ni-9Co-10W alloys with 2Pd and 5Cr at 700°C and 100 MPa, compared with JIS SUS304HTB austenitic steel.

3.4 Full-annealed ferrite matrix 15Cr steel

In order to improve creep strength at very long times, another attempt has been also demonstrated for a full-annealed 15Cr steel with ferrite matrix containing very low density of dislocations; 15Cr-1Mo-6W-3Co-VNb-0.07N-0.003C steel in Figure 1 [9]. Combined addition of W and Co decreases the creep rate at the beginning of creep and drastically decreases the creep rate during transient creep region, resulting in a significant decrease in minimum creep rate. Strengthening effect of W and Co in the steel is thought to be obtained by a precipitation strengthening that is mainly supported by fine particles precipitated during creep deformation. It should be also noted that higher Cr concentration in the present steel than in the conventional ferritic heat resistant steels containing 9 - 12Cr is advantageous in oxidation resistance at high temperature.

4. Oxidation Resistance in Steam

Figure 7 compares the weight gain in steam at 650 °C among the steels [10]. The sheet specimens having a size of 10x20x2 mm were cut from bulk materials, which were already heat treated, ground on a SiC paper of 320 grit, rinsed in acetone and then supplied to the oxidation test in steam. Comparing the data on the 9Cr-3WVNb and 9Cr-1.5MoVNb steels, one can see that the substitution of W for Mo increases the weight gain by about 1.3 times. The lower weight gain in Mod.9Cr-1Mo (9Cr-1MoVNb) than in P92 (9Cr-0.5Mo-1.8WVNb) steels results mainly from the higher Mo and lower W concentrations in Mod.9Cr-1Mo than in P92. The lower weight gain in P122 (11Cr-0.4Mo-2WCuVNb) than in P92 is considered to result mainly from the higher Cr concentration in P122 than in P92. The weight gain of the 9Cr-3WVNb steel with 3%Pd is significantly lower than that of other steels examined. The thin scale of Cr-rich oxide, presumably Cr_2O_3, forms on the specimen surface of the 9Cr-3WVNb steel with 3%Pd in steam at 650°C, while thick scale consisting of magnetite in the outer layer and Fe-Cr spinel oxides in the inner layer forms in the other steels. No evidence is found for the formation of Fe_3O_4 magnetite type oxide scale nor any oxide

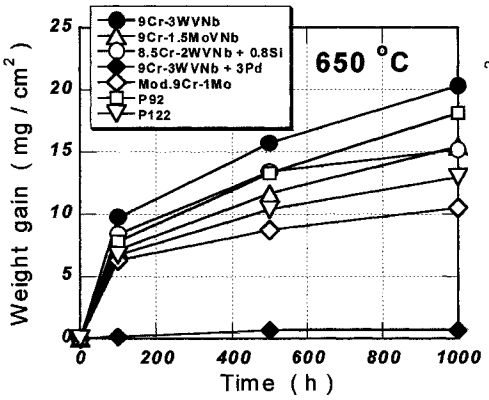


Figure 7 Weight gain of the steels in steam at 650 °C.

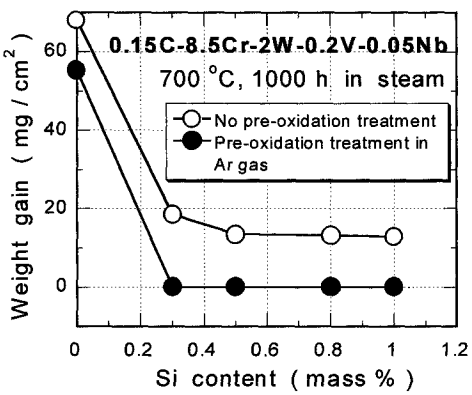


Figure 8 Improvement of oxidation resistance by pre-oxidation in argon gas.

containing Pd in the 9Cr-3WVNb steel with 3%Pd. The TEM observations show that the surface grinding on a SiC paper produces strained region with a high density of dislocations about 1 μm beneath the specimen surface. The oxidation test of the 9Cr-3WVNb steel with 3%Pd after additional annealing at 750°C for 50 h in vacuum for strain release exhibits a large weight gain and the formation of thick scale consisting of two layers similar as those in the other steels. The buff-polishing instead of the surface grinding on a SiC paper also exhibits a large weight gain and the formation of thick scale. The present results suggest that a combination of Pd addition and surface straining promotes the formation of protective Cr-rich oxide scale, which significantly improves the oxidation resistance in steam at 650 °C.
The formation of protective Cr-rich oxide scale is also achieved by pre-oxidation treatment in argon gas containing small amount of oxygen [15]. This is shown in Figure 8 for a 0.15C-8.5Cr-2W-0.2V-0.05Nb steel. The addition of Si decreases the weight gain of the steel, but the pre-oxidation treatment in argon gas further decreases the weight gain during subsequent oxidation in steam at 650°C. The decrease in weight gain by the pre-oxidation treatment is considered to result from the formation of Cr-rich oxide scale during pre-oxidation.

5. Creep-Fatigue Life

We have carried out creep-fatigue tests at 650°C for various kinds of 9-12Cr ferritic steels including oxide dispersion strengthened (ODS) ferritic steels, using cylindrical specimens with 8 mm diameter and 18 mm parallel-sided region in the center [11]. The creep-fatigue tests were performed under total axial strain control using side-contacting extensometry with a 16 mm gauge length. A trapezoidal strain wave with a strain hold on the tension side was used. The total strain range of the wave was 0.6 and 1%. The holding time was 1 and 3 h for total strain range of 0.6 and 1%, respectively. At a total strain range of 1%, the

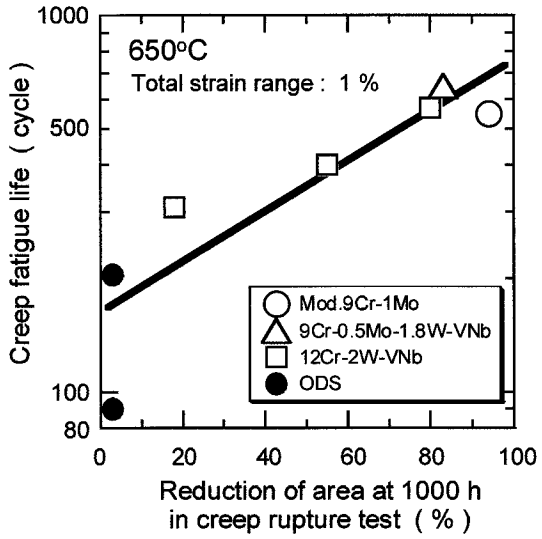


Figure 9 Relationship between creep-fatigue life a total strain range of 1% and reduction of area at 1000 h in creep rupture test for the ferritic steels at 650°C.

creep-fatigue life is proportional to the reduction-of-area in creep rupture test but not to the creep strength, as shown in Figure 9. This suggests that enough reduction-of-area would be required for the steels for application to USC boilers. The boron addition to the 9Cr-3W-3Co-VNb steel improves the reduction of area as well as the long term creep strength. On the other hand, with reducing total strain range to 0.6%, the creep-fatigue life of the ODS ferritic steels significantly increases. Although the creep ductility is very low for the ODS ferritic steels, the creep strength is very high and hence the accumulation of plastic strain during cyclic loading is very low at a small total strain range.

6. Creep Strength of Simulated-HAZ and Welded Joints

In order to clarify the mechanisms of Type IV crack in welded joints, the relationship between creep strength and microstructure has been investigated for P92 and P122 after heat treatments simulating heat affected zone (HAZ) of welded joints [12]. The prior austenite grain size decreased with increasing peak temperature up to 950 °C, indicating that the A_{C3} heating resulted in much more fine grains than the base material and A_{C1} heating. The creep rupture time has its minimum after heating the specimens to the temperature near A_{C3}, while the hardness has its minimum after heating to the temperature near A_{C1}. Therefore, the softening pronounced by the A_{C1} heating does not explain the minimum time to rupture. The present results indicate that the fine grains produced by the A_{C3} heating are responsible for the minimum time to rupture.

Indeed, the creep rupture time of conventional gas-tungsten-arc (GTA) welded joints is approximated by that of the A_{C3}-simulated HAZ specimens at low stresses as shown in Figure 10 for P122. In Figure 10, the creep rupture data for the base metal, weld metal and electron beam (EB) welded joints are also shown for comparison. The creep rupture tests of the welded joints were carried out using plate specimens of 18 x 5 mm cross section in gauge portion, while those of the base metal, weld metal and A_{C3}-simulated HAZ specimens were carried out using rod specimens with 10 mm in gauge diameter and 50 mm in gauge length.

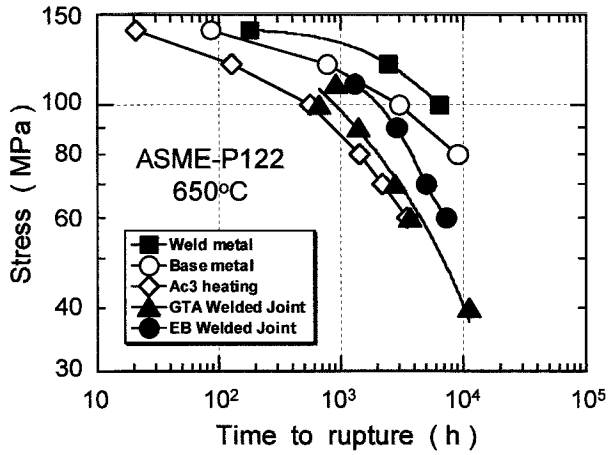


Figure 10 Creep rupture data for weld metal, base metal, A_{C3}-simulated HAZ, GTA and EB welded joints of ASME-P122 at 650°C.

The width of HAZ was successfully reduced by means of EB welding. The width of HAZ was 2.5 and 0.5mm for the conventional GTA and EB welded joints, respectively. The creep rupture data of the GTA and EB welded joints are located between those of the base metal and A_{C3}-simulated HAZ specimens. It should be noted that the rupture times of the EB welded joints are longer than those of the GTA welded joints by about 2 times. The present results indicate that decreasing the width of HAZ is effective for the extension of creep life but that the brittle Type IV fracture appears even in the EB welded joints at low stress and long time conditions.

Figure 11 compares the creep rupture time of A_{C3}-simulated HAZ specimens for the several steels at 650°C and 110 MPa, where the results of base metal are also shown for comparison. The ratio of the creep rupture time of A_{C3}-simulated HAZ to that of base metal is ranging from about 20 to 30%. Therefore, the creep rupture time of A_{C3}-simulated HAZ is proportional to that of base metal, suggesting that the improvement of creep strength for base metal contributes to the improvement of creep strength for welded joint. Because the fine grains produced by the A_{C3}-heating contain a large number of prior austenite grain boundaries, the stabilization of microstructure in the vicinity of prior austenite grain boundaries would be severely required for the improvement of creep strength for welded joint.

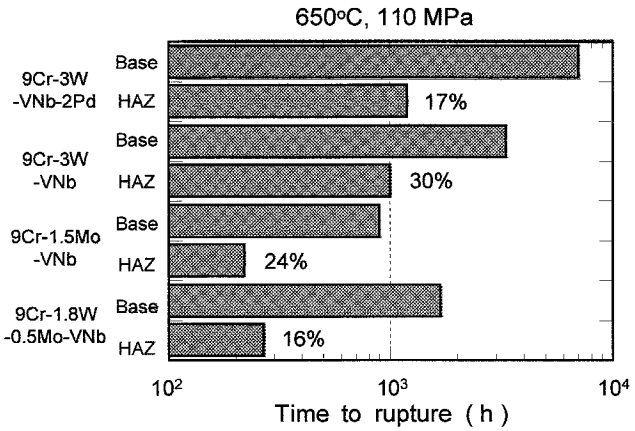


Figure 11 Creep rupture data of base metal and A_{C3}-simulated HAZ for the steels at 650°C and 110 MPa.

5. Summary

(1) Based on the alloy design philosophy that special attention should be paid to stabilize the microstructure in the vicinity of prior austenite grain boundaries for the improvement of long term creep strength, several types of high-Cr ferritic steels having much higher creep rupture strength at 650°C than P92 have been developed. The newly developed steels are tempered martensitic 9Cr steels strengthened by boron, MX nitrides and Fe-Pd $L1_0$, a carbon-free martensitic alloy and a full-annealed ferrite matrix 15Cr steel.

(2) A combination of Pd addition and surface straining promotes the formation of protective Cr-rich oxide scale, presumably Cr_2O_3 scale, on the surface of a 9Cr-3W-VNb steel,

which significantly improves the oxidation resistance in steam at 650 °C. The formation of protective Cr-rich oxide scale is also achieved by pre-oxidation treatment in argon gas containing small amount of oxygen.

(3) The creep-fatigue life is proportional to the reduction-of-area in the creep rupture test but not to the creep strength at a total strain range of 1%. The boron addition to the 9Cr-3W-3Co-VNb steel improves the reduction of area as well as the long term creep rupture strength. With reducing total strain ranges below 0.6%, the creep-fatigue life of the ODS ferritic steels significantly increases.

(4) Fine grains produced by the A_{C3} heating are responsible for Type IV cracking strength loss in welded joints. Decreasing the width of HAZ is effective for the extension of creep life of welded joints but the brittle Type IV fracture appears even in the EB welded joints at low stress and long time conditions. Further improvement of creep strength of welded joints can make it possible to use the present steels as thick section boiler components of 650°C USC plant.

References

[1] F. Abe, M. Igarashi, S. Wanikawa, M. Tabuchi, T. Itagaki, K. Kimura and K. Yamaguchi, Proceedings of the 3rd EPRI Conference, p.79, eds. by R. Viswanathan, W.T. Bakker and J. D. Parker, Swansea, UK, (2001).

[2] K. Kimura, K. Suzuki, Y. Toda, H. Kushima and F. Abe, this proceedings (Proceedings of the 7th Liege Conference), in press, (2002).

[3] K. Hidaka, Y. Fukui, S. Nakamura, R. Kaneko, Y. Tanaka and T. Fujita, Advanced Heat Resistant Steels for Power Generation, eds. by R. Viswanathan and J. Nutting, p.418, The Institute of Materials, (1999).

[4] M. Igarashi, S. Muneki, H. Hasegawa, K. Yamada and F. Abe, ISIJ International, **41**, S101 (2001).

[5] T. Horiuchi, M. Igarashi and F. Abe, ISIJ International, **42**, in press (2002).

[6] M. Hattestrand and H. O. Andren, Mater. Sci. Eng., **A270**, 33 (1999).

[7] M. Taneike, K. Sawada and F. Abe, this proceedings (Proceedings of the 7th Liege Conference), in press, (2002).

[8] S. Muneki, H. Okada, K. Yamada, H. Okubo, M. Igarashi and F. Abe, Proceedings of 4th Pacific Rim International Conference on Advanced Materials and Processing (PRICM4), p.2691, Hawaii, (2001).

[9] K. Kimura, H. Toyama, Y. Toda, H. Kushima and F. Abe, Report of the 123rd Committee on Heat-Resisting Materials and Alloys, p.33, Japan Society for the Promotion of Science, **43** (2002). (in Japanese)

[10] T. Itagaki, H. Kutsumi, M. Igarashi and F. Abe, this proceedings (Proceedings of the 7th Liege Conference), in press, (2002).

[11] M. Kimura and K. Yamaguchi, Proceedings of the 7th International Conference on Creep and Fatigue at Elevated Temperatures, p.481, Japan Society of Mechanical Engineers, (2001).

[12] M. Matsui, M. Tabuchi, T. Watanabe, K. Kubo, J. Kinugawa and F. Abe, ISIJ International, **41**, S126 (2001).

SECTION 3

ADVANCED STEAM POWER PLANT

3.3. Mechanical Properties

LONG TERM CREEP AND CREEP FATIGUE PROPERTIES OF THE MARTENSITIC STEELS OF TYPE (G)X12CrMoWVNbN10-1-1

M. Schwienheer, H. Haase, A. Scholz and C. Berger
Institute of Materials Technology
Darmstadt University of Technology

Abstract

A key feature of the future development of power plants is materials for heavily loaded high temperature turbine components, such as rotors and castings. Martensitic 600°C steels of type (G)X12CrMoWVNbN10-1-1, which were developed in COST 501, show high creep properties, ductility and low cycle fatigue properties. These steels are also easy to produce and cost-effective. In order to employ the full potential of these steels the knowlege of their mechanical long term behaviour close to service conditions is essential. Along with the creep rupture behaviour the creep behaviour is of special interest for turbine component design. The creep behaviour can be described by a modified Garofalo equation which permits description of the primary, secondary and tertiary creep. Start-up and shut-down phases lead to cyclic loading at the heated surface of heavy components. Creep fatigue life can be predicted on the basis of the generalized damage accumulation rule. Software tools are available for industrial application for scatterband assessment (programme DESA), creep curves (KARA) and creep fatigue life prediction (SARA). The influence of notches was analysed in order to apply uniaxial material behaviour to multi-axial loading.

Key words: 9-12% Cr steels, creep rupture, creep equations, creep fatigue, damage accumulation, life prediction, notch behaviour

1. Introduction

Increasing fuel costs and the pressure to reduce environmental pollution drive the worldwide development of fossil-fired power plants. With ultra super critical steam parameters with more than 600°C/300 bar a significant increase of the plant efficiency, and at the same time, a reduction of the CO_2 emission is possible [1]. Therefore the materials for highly loaded high temperature turbine components, such as rotors and castings are of special interest for the development since this aim can only be achieved by further material develpoment with improved creep and ductility behaviour [2]. With regard to good long term properties and manufacturing qualities new ferritic-martensitic 9-12% Cr-steels were developed during the last 20 years under international joint research programs and in Europe exceptionally in COST [3]. The steels of type (G)X12CrMoWVNbN10-1-1 show good creep rupture strength and also good ductility properties [4]. They are suitable for manufacturing large components and they also show a better fatigue limit in comparison with materials used up to now [4]. In order to exploit the full potential of these steels, the knowlege of their mechanical long term behaviour close to service conditions is essential. For the design of turbine components not only the creep rupture behaviour is of special interest but also the creep strain behaviour. Because of start-up and shut-down phases, which lead to cyclic loads at the heated surface of heavy components the knowledge of the long term creep behaviour is necessary for safe operation of the turbine. While the creep and fatigue descriptions specify the uniaxial material behaviour, investigations of notch behaviour support the transfer of characteristic values to multiaxial loaded turbine components.

Within the framework of the German MARCKO-DT1/2 resarch projekt, funded by the German ministry of economics and the turbine industry, the steels X12CrMoWVNbN10-1-1 (material identifier 1A) and GX12CrMoWVNbN10-1-1 (2A) were investigated (Table 1).

No.	Steel	Chemical Composition (wt %)							
		C	Cr	Mo	W	Ni	V	Nb	N
1A	X12CrMoWVNbN10-1-1	0,12	10,0	1	1	0,8	0,2	0,05	0,05
2A	GX12CrMoWVNbN10-1-1	0,12	10,0	1	1	0,8	0,2	0,05	0,05
		Heat Treatment							
1A	X12CrMoWVNbN10-1-1	1 050°C 7h/oil + 570°C 10,25h/air + 690°C 10h/air							
2A	GX12CrMoWVNbN10-1-1	1070°C 12 h/air + 730°C 12h/air + down to 300°C 10 h/furn.							

Table 1. Chemical composition (standard values) and heat treatment of the test materials.

An expansion to tungsten-free heats is planned. The aim of this joint venture is to determine well-assured long term values and descriptions of the material behaviour under service conditions. The work performed at the IfW is given below and concerns the creep, the fatigue and the notch behaviour of the steels containing tungsten. The rotor steel 1A was produced as a rod of ø 400 mm and 6 500 mm long and the cast steel 2A as plates of 500 x 350 x 300 mm^3. The manufacturing conditions of the test material were similar to those of real turbine components. Before starting the main investigations the homogenity of the two steels were examined with creep rupture tests up to 3000 h duration. On the basis of these tests, a correlation of specimen location and creep properties at specific material zones is possible.

2. Creep

2.1 Creep rupture behaviour

For the design of high temperature components long term values are needed especially the creep rupture strength and characteristic time-to-strain values. In this case the mean behaviour of the material type and its behaviour at the lower scatterband is of special interest. Therefore creep tests on the rotor steel 1A and the cast steel 2A were performed at the main test temperature 550 and 600 °C and also at 625 and 650 °C for extrapolation purposes. The tests at 600 °C reached about 20 000 h duration. In addition creep data of other heats from other sources [5, 6, 7] of the corresponding steel types were included to assure the scatterband and additional creep tests at these heats were supplemented. On this basis first scatterband assessments for the material type X12CrMoWVNbN10-1-1 and GX12CrMoWVNbN10-1-1 were carried out.

Those assessments will often be made on the basis of a time-temperature parameter P(T,t). It is supposed to permit combination of the isothermal time rupture and time-to-strain curves for different temperatures each to one master curve. For a numerical solution a model function for the master curve must be found. A decisive problem concerning assessments of this type is the evaluation of the quality of a model function. The quality concerns the interpretation of the basis test results. For the purpose of the computer-aided scatterband assessment the IfW developed the software DESA which provides a versatile and robust methodology for multi-heat creep rupture data and supports the user to come to an optimum model function with moderate effort [8].

The actual status of the creep tests for both steel types offers an inhomogeneous contribution of data assignment concerning stresses, temperatures and test duration. The time temperature relation is unusally complex within the considered range of temperature. Hence in a preliminary version the more flexible graphical scatterband assessment method was used. With longer test durations a numerical assessment will be performed. The result of the graphical assessment (Fig. 1) shows an acceptable scatterband for both steel types. As expected the cast steel features a lower creep rupture strength than the rotor steel in the considered time range.

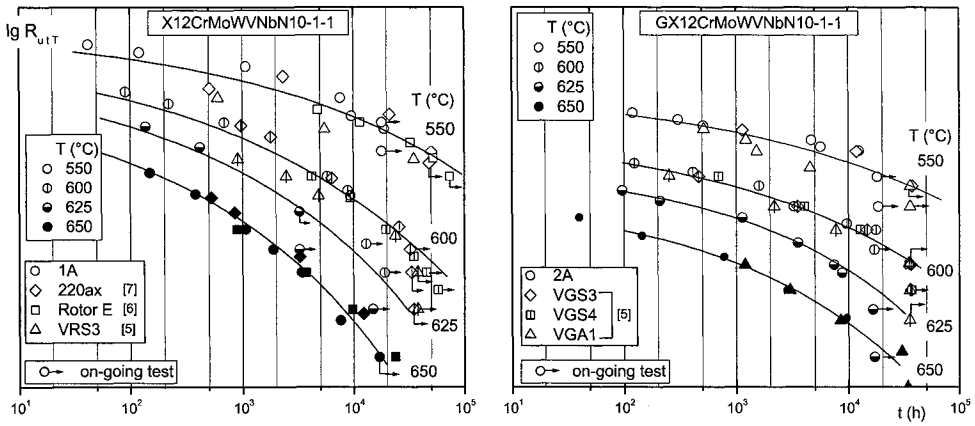


Fig. 1. Results of the graphical scatterband assessment for the creep rupture strength R_{utT} of the steel type X12CrMoWVNbN10-1-1 and GX12CrMoWVNbN10-1-1

2.2 Creep strain behaviour

To determine the time dependent deformation of high temperature components creep equations are very important. Simple equations of Norton Bailey type or others are often used to obtain a quick estimate of stress redistribution or relaxation in components. On the other hand, constitutive equations coupling deformation, hardening and damage processes are the general tool for the design of components under variable tensile and compression conditions. In between these solutions, phenomenological equations are available which are easier to establish and describe primary, secondary and tertiary creep [9]. Within different phenomenological models, such as the Graham Walles equation [10] and the Thata projection method [11], the modified Garofalo equation [12,13] is of special interest. Experience in creep modelling [8,14] shows that this equation often forms the best solution [9]. It describes the permanent strain

$$\varepsilon_{per} = \varepsilon_i + \varepsilon_{f1} + \varepsilon_{f2} + \varepsilon_{f3} = \varepsilon_i + \varepsilon_{f1max} \cdot \left[1 - e^{-D(t/t_{12})^u}\right] + \dot{\varepsilon}_{pmin} \cdot t + C_{23} \cdot (t / t_{23})^f \qquad (1)$$

and approximates the basic creep processes (Fig. 2). It delivers stable solutions which do not strongly depend on the available data sets as in the case of other equations [9].

With the experimental strain values according to Fig. 2 the modified Garofalo equation models the initial plastic strain ε_i, and the primary, secondary and tertiary creep ε_{f1}, ε_{f2}, ε_{f3}. The modelling of equation (1) is performed by stepwise regression analyses [13,15].

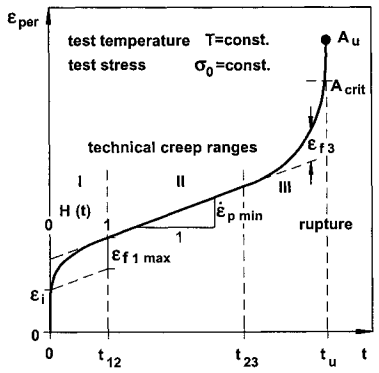


Fig. 2. Schematic diagram of a linear creep curve which can be interpreted by the modified Garofalo equation (1)

As soon as a partial equation is modelled it is used to represent the corresponding quantity for the subsequent regression analyses. This delivers a stable solution. For the application of the creep equations the IfW developed the software KARA and KARA F, which are tools to represent and modify available creep equations and to calculate stress redistribution of components in the creep range with Finite Element programs [8].

In order to model creep behaviour of rotor steel 1A, first of all a time and stress dependent description of the initial plastic strain ε_i was derived with test results of hot tensile tests and continuous creep tests. With the calculated values of the initial plastic strain the creep strain $\varepsilon_f = \varepsilon_{per} - \varepsilon_i$ can be determined while neglecting the recovery strain ε_r. The values of the minimum creep rate $\dot{\varepsilon}_{pmin}$, the maximum value of primary creep $\varepsilon_{f1\,max}$ and the transition times t_{12}, t_{23} are derived from linear creep curves. By iteration, the interpretation of the linear creep curves is improved until both quantities $\dot{\varepsilon}_{pmin}$ and $\varepsilon_{f1\,max}$ present continuous functions of stress and temperature [9]. The determined minimum creep rate $\dot{\varepsilon}_{pmin}$ and its interpretation by established model functions, which were enhanced with temperature dependent functions, is given in Fig. 3.

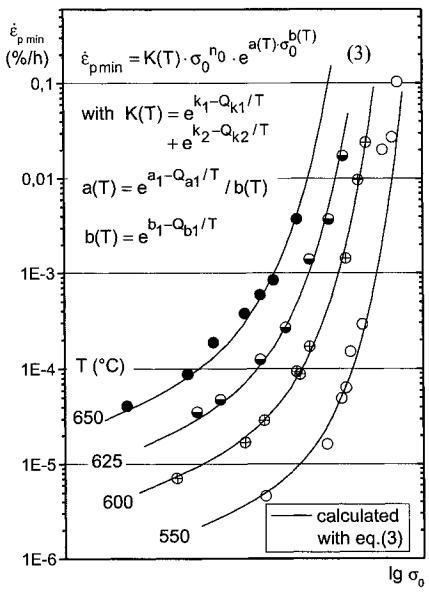


Fig. 3. Mininum creep rate $\dot{\varepsilon}_{pmin}$ of steel X12CrMoWVNbN10-1-1/1A

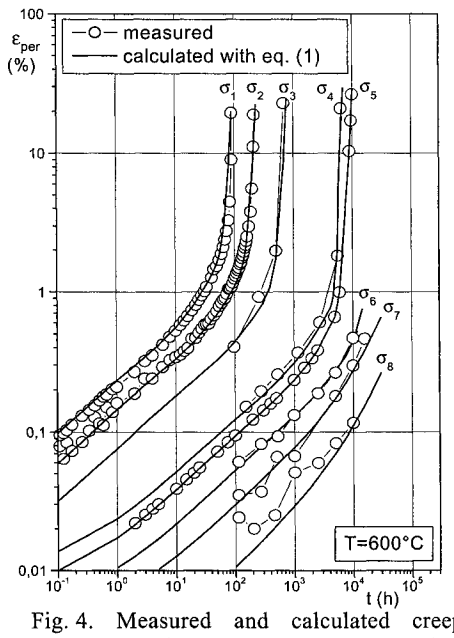


Fig. 4. Measured and calculated creep curves of steel X12CrMoWVNbN10-1-1/1A

In the next step the coefficients D and u of the time function of primary creep ε_{f1} were determined from a plot of $\log(-\ln(1-\dot{\varepsilon}_{p\,min} \cdot t) / \varepsilon_{f1\,max}))$ against $\log(t/t_{12})$. Finally the constants C_{23} and f of tertiary creep are derived from a plot of the quantities $\log(\varepsilon_f-\varepsilon_{f1}-\varepsilon_{f2})$ against $\log(t/t_{23})$. A comparison of the measured creep curves with the results from the modeled creep curves for T=600 °C (Fig. 4) shows a relatively good agreement. For the cast steels 2A a similarly good solution is expected. In future work an expansion to creep equations for both steel types is planned, rather than creep equations for individual materials.

3. Creep Fatigue

3.1 Conventional Creep Fatigue Behaviour

At the heated surface of turbine components temperature transients cause strain cycling with variable thermal (secondary) stresses. In addition, pressure loading and, for rotors, centrifugal loading, leads to quasistatic (primary) stresses. As a consequence, strain cycling can be a critical loading condition at the heated surface of large components. Because of the intended service life of more than 200 000 h for these components, long term creep fatigue values are essential for design purposes [17]. In order to simulate creep fatigue loading conventional fatigue and creep fatigue tests with hold time ($t_{Ht} = t_{Hc}$ = 3 min or 20 min) at the main test temperature 550 and 600 °C were carried out (Fig. 5 and 6). The tests were performed with the laboratory-typical strain rate at the ramps of $\dot{\varepsilon}_r$ = 6 %/min. The fatigue life values, number of cycles to failure N_f, agree well with the data from other sources. Short hold times of 3 min. in tension and compression reduce creep fatigue life by a factor of about 3. A much smaller reduction in number of cycles to failure N_f can be observed by an increase of hold time up to 20 min. This is due to stress relaxation behaviour of these steels at the test temperatures given above close to the highest service temperature. Decrease of temperature by a step of 50 °C reduces significantly the amount of stress relaxation. Both steels show typical cyclic softening behaviour, whereby the cyclic stresses for the cast steel are a factor of about 20 % lower compared to the rotor steel (Fig. 5).

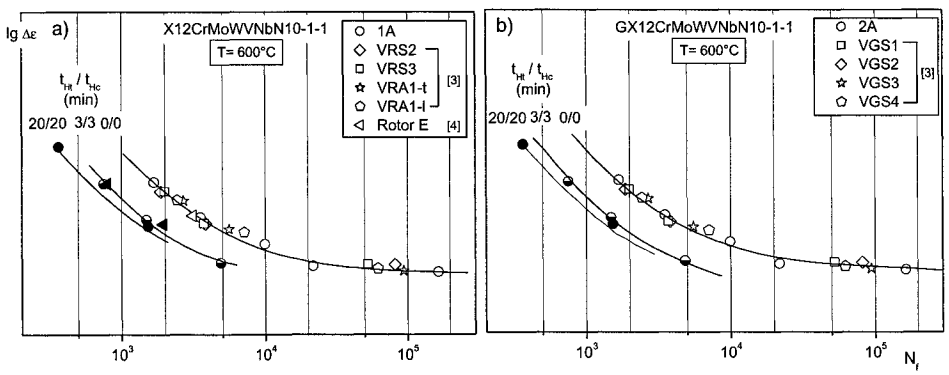


Fig. 5. Fatigue and creep fatigue behaviour at 600°C for the steels of type X12CrMoWVNbN10-1-1 (a) and GX12CrMoWVNbN10-1-1 (b)

Increasing total strain range leads to higher softening effects. For the rotor steel the effect of hold time is found to be much smaller compared to the cast steel. The stress-strain path can be modelled by the Ramberg-Osgood-equation [18, 19] as

$$\varepsilon = \sigma / E + (\sigma/K')^{1/n'}. \quad (4)$$

The parameters E, K' and n' are temperature and strain-rate dependent as well as dependent on the ratio N/N_f. The effect of hold time on cyclic strength is somewhat smaller for the rotor steel compared to the cast steel.

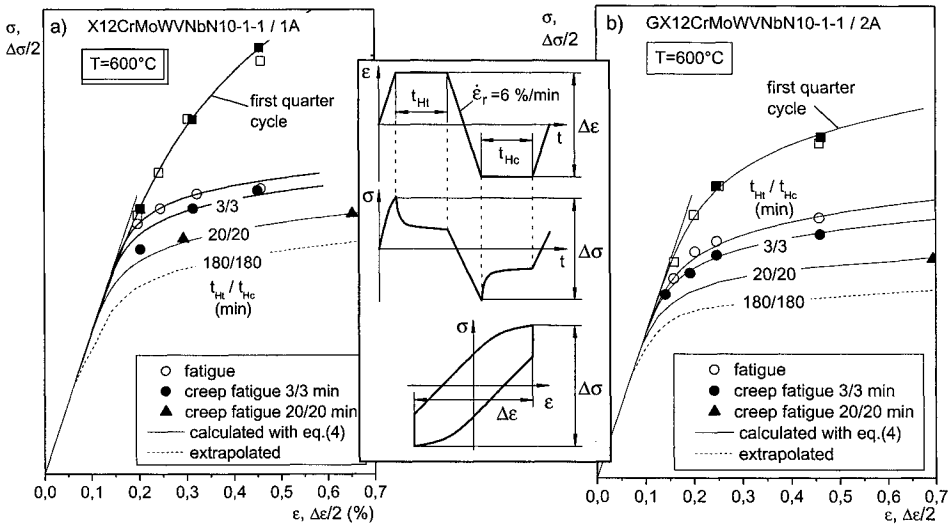


Fig. 6. Cyclic stress-strain curve at mid term cycle (N/N_f =0.5) for fatigue and creep fatigue, steel X12CrMoWVNbN10-1-1/1A (a) and GX12CrMoWVNbN10-1-1/2A (b)

3.2 Service-type Creep Fatigue

Besides conventional creep fatigue behaviour service-type strain cycling is of specific design interest. Therefore a single-stage service-type strain cycle (Fig. 7) was developed, which is characterized by a compressive strain hold phase 1 simulating start-up conditions, a zero strain hold phase 2 approximating temperature equilibrium during constant loading and a tensile strain hold phase 3 simulating shut-down conditions.

Due to the simpler testing procedure most of the service-type strain cycle tests are carried out isothermally. On the other hand thermal-mechanical fatigue (TMF) testing is closer to service conditions. However, in former investigations on 1- and 12-%CrMoV rotor steels anisothermal tests lead to insignificantly higher number of cycles to failure than isothermal testing [16]. Isothermal service-type creep fatigue tests on steel X12CrMoWVNbN10-1-1 and GX12CrMoWVNbN10-1-1 investigated here, exeeded longest times to failure of 11 000 h and 6 000 h respectively and will be continued up to 30 000 h. The influence on fatigue life of altering temperature during anisothermal tests is still under investigation.

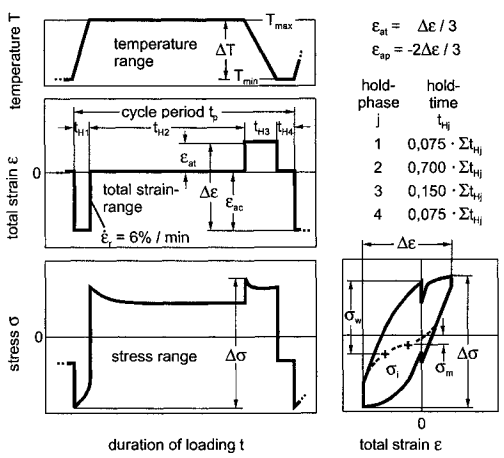


Fig. 7. Service-type cycle for the simulation of the heated surface of heavy components [16]

Of high practical relevance are multi-stage service-type strain cycling tests, that demonstrate typical loading conditions for cold start, warm start and hot start cycles. Such elementary cycles were arranged to a loading sequence presenting each of the three different ranges of temperature and total strain. Hereby, frequencies of one cold start, three warm starts and 16 hot starts were identified as typical for a medium-loaded power plant. Three-stage service-type strain cycling tests on both steels have exceeded 10 000 h.

The creep fatigue life analysis is based on the generalized damage accumulation rule

$$\Sigma\, N/N_{fo} + \Sigma\, \Delta t/t_r = D_{krit} \qquad (5)$$

which combines the Miner-rule for fatigue damage and the life fraction rule for creep damage. The procedure developed contains some features different from conventional damage rules [16, 17, 19, 20]. Regarding the accumulation of fatigue damage, the number of cycles to failure N_{fo} in eqn. (5) is taken from the corresponding life curve for standard strain cycling with a chracteristic hold time $t_{h\,sta}$, which increases with decreasing total strain range $\Delta\varepsilon$. Furthermore the influence of mean stress σ_m on N_{fo} is taken into consideration by applying the Smith, Watson and Topper parameter. For the accumulation of the creep damage, the rupture time t_r is determined for the effective stress σ_{eff}, the hold times $t_{h\,sta}$ in phases 1 and 3 are omitted and the cyclic softening behaviour is considered.

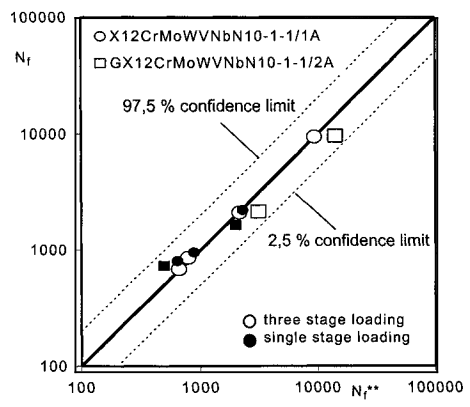


Fig. 8. Results of creep fatigue life prediction by PC programme SARA

As a result of the creep fatigue life analysis, the creep fatigue damage value D for both steels varies between 0.53 to 0.80 with mean values of $\overline{D} = 0.71$ in case of the rotor steel and $\overline{D} = 0.65$ in case of the cast steel [19,20].

In order to predict life time under multi-stage creep fatigue loading a PC-programme SARA was developed. In a first step SARA calculates stress-strain hysteresis loops for all cycles of a multi-stage loading sequence. In a second step, SARA calculates fatigue damage and creep fatigue damage (eq. 5) for all individual cycles. The calculation is completed, when a critical creep fatigue

damage value D_{crit} is exceeded. By the use of the above mean values ($D_{crit} = \overline{D}$) the predicted number of cycle to failure N_f** agrees with experimental results N_f within a factor 2 which is acceptably for such complex loading (Fig. 8).

4. Notch Behaviour

The service life of components depends on start-up and shut-down conditions as given above, but is also influenced by notches of components, which can not be avoided generally. With respect to a complete calculation of components the application of the finite element method is necessary [19, 20, 21]. Hereby, the knowledge of material laws for creep (eq. (1)) and cyclic conditions (eq. (4)) are needed. The development of Finite Element subroutines to calculated stress relaxation in the notch and the cyclic stress-strain path are in progress. Further, the creep laws developed here are necessary to verify the constitutive models developed by the partners within the MARCKO project.

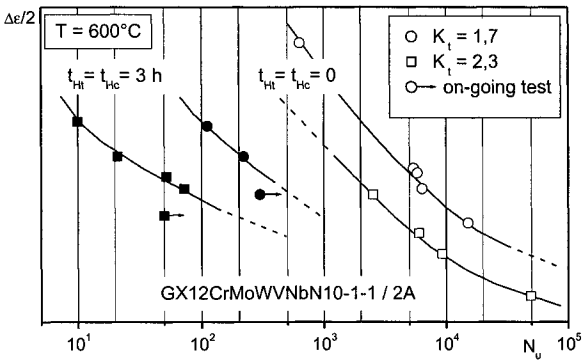


Fig. 9. Influence of two different notch geometries on rupture life N_u under fatigue and creep fatigue loading, steel GX12CrMoWVNbN 10-1-1 /2A

Of fundamental interest is the study of the influence of different notch geometries ($K_t = 1.7$ and 2.3) on life under constant loading and under cyclic loading. Creep rupture tests on rotor steel 1A and the cast steel 2A reached 20 000 h and show notch strengthening behaviour. This corresponds with the fact that the reduction of the elongation at creep rupture was not observed in the range of test duration. The cyclic notch behaviour of the steels 1A and 2A was investigated by load-controlled fatigue tests and creep fatigue tests with 3 h hold times in tension and compression. The total strain range $\Delta\varepsilon$ was estimated using the Neuber rule. As expected, a clear influence of long hold time on the number of cycles to rupture N_u was observed (Fig. 9). Also the sharper notch geometry causes shorter life time by a factor of up to one hundred.

5. Conclusions

For the "600 °C" steels X12CrMoWVNbN10-1-1 and GX12CrMoWVNbN10-1-1 for modern power plant applications basic knowledge under static and cyclic long term loading including notch influences was obtained. The main results and industrial benefit of these investigations are:

- Generation of long term static and cyclic design data including notch effects
- Modelling of creep by a modified Garofalo creep equation to be applied to finite element calculations of notch components

- Modelling of cyclic stress strain behaviour
- Assessment of creep fatigue damage by the damage accumulation rule modified by features considering service-type loading
- Application of a user PC-programme SARA to predict creep fatigue life.

6. Acknowledgement

The authors would like to thank the German Bundesministerium für Wirtschaft (BMWi) and the German Arbeitsgemeinschaft industrieller Forschungsvereinigungen (AiF) for funding and the companies working in the research groups for funding and technical support.

7. Literature

[1] Staubli, M., K.H. Mayer, T.U. Kern, R.W. Vanstone, COST 501/COST522 - The European Collaberation in Advanced Turbine Materials for Ultra Efficient, Low Emission Steam Power Plant, Proceedings of the 5th International Charles Parson Turbine Conference, Cambridge, UK, 2000, p. 98-122.

[2] Berger, C, K.H. Mayer, R.B. Scarlin, Neue Turbinestähle zur Verbesserung der Wirtschaftlichkeit von Kraftwerken, VGB Kraftwerkstechnik 71 (1991), Heft 7, page 689-699 (in german).

[3] Mayer, K.H., T.U. Kern, K.H. Schönfeld, M. Staubli and E. Tolksdorf, Long-term investigations of specimens of 8 production rotors manufacturers of the Advanced Martensitic 10 % Steels X12CrMo(W)VNbN10-1(1), Proc. of the 14th International Forgemasters Meeting, 3-8 Sep. 2000, Wiesbaden, Germany, p. 277-282.

[4] Mayer, K.H., T.U. Kern und M. Staubli, Stand der Entwicklung moderner thermischer Energieerzeugungsanlagen unter Berücksichtigung der eingesetzten Werkstoffe, Proceedings of the 6th material conference "Werkstoffe für die Kraftwerkstechnik an der Schwelle zum 21. Jahrhundert" TU Graz, 16. April 1999, Graz, Austria (in German).

[5] Final report of the VGB-Programm No. 158, "Neue Werkstoffe für Dampfturbinen", joint venture research programme of the VGB-Fachausschußes "Werkstoffe konventionell" and the turbine manufactors ALSTOM Power and Siemens Power Generation, march 2001 (in German).

[6] Final report of the sub-projekt of the European COST 522 research programme "Energieerzeugung im 21. Jahrhundert - Kraftwerke mit ultrahohem Wirkungsgrad und geringen Emissionen", BMWi- Föderkenzeichen 0327071A, Dezember 2000 (in German).

[7] Final report of AVIF-research programme "Verhalten warmfester Stähle bei regelloser Zeitstandbeanspruchung", A 123, Forschungshefte Forschungskuratorium Maschinenbau e.V. (FKM), Heft 269 (2002), (in German).

[8] Granacher, J., M. Monsees, P. Hillenbrand, C. Berger: Software for the assessment and application of creep and rupture data, Nuclear Engineering and Design 190 (1999), p. 273-285

[9] Granacher, J., H. Moehlig, M. Schwienheer, C. Berger, Creep Equations for High temperature Materials, Creep 7, the seventh International Conference on Creep and Fatigue at Elevated Temperatures, June 3 - 8, 2001, NRIM, Tsukuba, Japan, Proceedings p. 609-616.

[10] Graham, A. and Walles, K.F.A., Relations between long and short time properties of commercial alloys, J. Iron and Steel Inst. 179 (1955) p. 205-290.

[11] Evans, R.W., Parker, J.D. and Wilshire, B., An extrapolation procedure for long-term creep strain and creep life prediction with special reference to ½Cr½Mo¼V ferritic steel, in: Recent advances in creep and fracture of engineering materials and structures, Eds.: Wilshire, B. and D.R.J. Owen, Swansea (1982) p. 135-167.

[12] Garofalo, F., Fundamentals of Creep and Creep-rupture in Metals, Macmillan, New York, 1965.

[13] Kloos, K.H., Granacher, J. and Monsees, M., Creep equations for heat resistant steels, steel research 69 (1998) p. 447-453.

[14] Kloos, K.H., J. Granacher and M. Monsees: Optimization and verification of creep equations for heat resistant steels, steel research 69 (1998) No. 10+11, pp. 454-462.

[15] Kloos, K.H., Granacher, J. and Pfenning, A., Creep equations for high temperature alloys on the basis of a parametric assessment of multi-heat data, steel research 67 (1996) p. 106-110.

[16] Granacher, J.; A. Scholz, H. Möhlig, C. Berger, Prediction of Long Term Behaviour of Heat Resistant Power Plant Steels under Variable Loading Conditions, Contribution to the 8th Japanese-German Joint Seminar on Structural Integrity and NDE in Power Engineering, Mai 31 - June 1, 2001, Tokyo, Japan, p. 209-224.

[17] Härkegård, G., Designing steam turbines for transient thermal loading, High Temperature Structual Design, ESIS12 (L. H. Larsson, ed.), 1992, Mechanical Engineering Publication, London, p. 21-40.

[18] Ramberg, W. and W.R. Osgood: Description of Stress-Stair Curves by three Parameters, NACA TN 902 (1943).

[19] Haase, H. A. Scholz, J. Granacher, C. Berger, Mehrstufiges betriebsähnliches Kriechermüdungsverhalten der neuen Hochleistungsstähle, Vortrag auf der 23. Vortragsveranstaltung der Arbeitsgemeinschaft für warmfeste Stähle und Hochtemperaturwerkstoffe, 01. Dezember 2000 in Düsseldorf, Germany, Proceedings, Ed.: VDEh Düsseldorf, 2001, p. 50-63 (in German).

[20] Haase, H., A. Scholz and C. Berger, Simulation of multistage creep fatigue behaviour, 8th International Fatigue Congress, FATIGUE 2002, Proceedings of the Eighth International Fatigue Congress, Ed. A. F. Blom, Stockholm, Sweden, June 2002, p. 3133-3140.

[21] Mao., T.S., J. Granacher, C. Berger, Life Calculation of Creep loaded notched Parts with different Geometries, 14th International Forgemasters Meeting, 3 - 8 September 2000, Wiesbaden, Germany, IFM 2000, p. 221-227.

TWO SPECIMEN COMPLEX THERMAL-MECHANICAL FATIGUE TESTS ON THE AUSTENITIC STAINLESS STEEL AISI 316 L

K. Rau, T. Beck, D. Löhe

Universität Karlsruhe (TH), Institut für Werkstoffkunde I, Kaiserstr. 12, D-76131 Karlsruhe, Germany

Abstract

Complex thermal mechanical fatigue (CTMF) tests were performed on the austenitic stainless steel AISI 316 L which is a candidate material for blades and vanes in the hot sections of advanced steam turbines. The tests were carried out on a two specimen CTMF testing system. The first specimen represents a volume element near the surface, the second an element inside a thermally loaded component, e. g. a solid steam turbine blade. To each specimen individual temperature cycles are applied in order to simulate the thermal loading at the respective locations within the blade. The earlier and faster heating up and cooling down of the surface with respect to the core of the component is simulated by a phase shift of the temperature cycles which have the same maximum and minimum temperatures, identical heating and cooling rates and dwell times of 45s at the maximum temperature.

The interaction between both specimens is achieved by two loading conditions which are implemented into the 4-channel digital controller of the two servohydraulic load units and the respective heating and cooling equipment:

- Identical total strains at every point of time, which means that no thermally induced bending occurs in the simulated component.
- The sum of the forces on both specimens is zero all the time.

The cyclic deformation behaviour of the material under these loading conditions is represented by the hystereses of the nominal stress versus the total mechanical strain and the plastic strain. From these hysteresis loops, cyclic deformation curves were taken. Generally, cyclic hardening occurs. Cyclic creep towards negative total strains is observed, which is due to the fact that in both specimens the temperatures at which compressive loading occurs are higher than those at which tensile stresses develop and, accordingly, the resulting compressive plastic deformation in each cycle is more pronounced than the tensile re-deformation. The cyclic creep rate strongly increases with increasing phase shift between the temperature cycles.

1 Introduction

In many components used for high temperature applications, such as steam and gas turbines, internal combustion engines or heat exchangers, start-stop processes and load changes cause non steady-state and inhomogeneous temperature fields which induce complex cyclic mechanical loading [1, 2]. Fig. 1 shows a schematic sketch of the temperature-time sequences and the respective mechanical loading occuring within a solid turbine blade during a start-stop cycle. When heated by the indicated gas flow with a temperature T_G, the temperature of the volume element 1 at the surface of the turbine blade firstly rises and then reaches the service temperature. After stopping the gas flow, the temperature decreases. The temperature of volume element 2 shows a similar *T-t* path which is phase shifted against the *T-t* path of element 2. As a consequence, there is a temperature difference between the volume elements 1 and 2 during heating up until volume element 2 has reached the service temperature and also during cooling down. Until the steady state is reached, the thermal strain of the volume element 1 is partially constrained by the colder regions of the component, which are represented by the volume element 2. This results in compressive loading at the position 1 and in tensile loading at 2. If the deformation during heating up is purely elastic, the mechanical

loading becomes zero as soon as the temperature is homogenous within the component. During cooling down at the end of the service cycle, tensile loading occurs in volume element 1 and compressive loading in 2. Repeated start-stop cycles result in so called „thermal fatigue" (TF), which is often responsible for the initiation of fatigue cracks in turbine blades, vanes and discs [1, 2]. Trying to assess the lifetime of TF-loaded components by using results from isothermal fatigue (IF) tests can result in strongly non-conservative results, because under TF loading other deformation- and damage mechanisms occur than in the case of isothermal fatigue [2 - 5]. Due to that, thermal-mechanical fatigue (TMF) tests are carried out in total strain control. These tests simulate the thermally induced loading arising at critical locations of a component in specimens that are loaded uniaxially and homogenously. This leads to more realistic results concerning the cyclic deformation, lifetime and damage behaviour than IF tests [1 - 5]. However, because a fixed total strain - time sequence is applied to the specimen, such conventional TMF tests ignore the interaction between different volume elements on the hot and cold side of a component, which can result in a redistribution of the occurring stresses as well as in cyclic creep of the whole component. Furthermore, neither in IF nor in TMF tests a superposition of the thermally induced stresses by mechanical stress states, e. g. due to centrifugal forces, can be simulated. These effects are taken into account by so called Complex Thermal-Mechanical Fatigue (CTMF) tests carried out with a two specimen testing system as described in detail in [2, 6]: One specimen represents the hot and the other a cold volume element in a thermally loaded component (see Fig. 1), each with its individual temperature-time path. The interaction of both elements is realised by keeping the total strains of both specimens at identical values which means that no thermally induced bending of the considered component occurs. The results of such CTMF experiments on AISI 316 L are given in the present paper. The development of stress-strain hystereses and the respective cyclic deformation curves are presented and discussed.

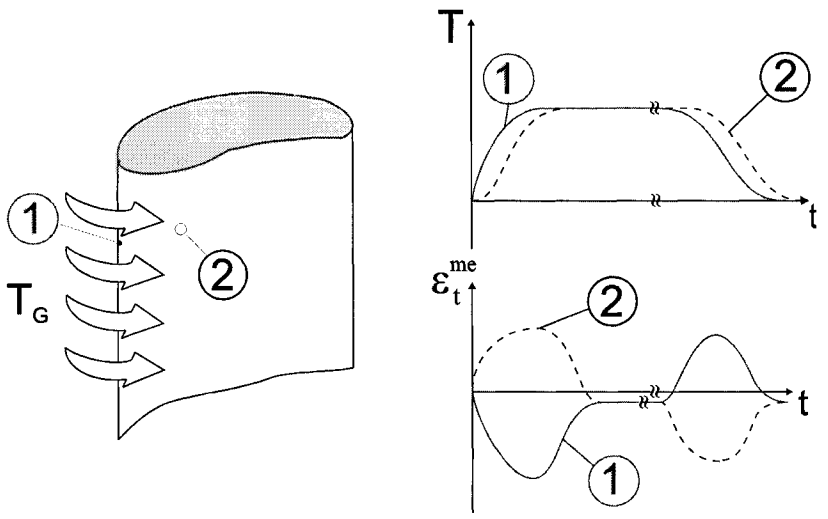


Fig. 1: Thermal and mechanical loading in solid turbine blades (schematic sketch)

2 Test Material and Specimen Geometry

The tests were carried out on the austenitic stainless steel AISI 316 L (X2 CrNiMoN 17 12) with a content of δ-ferrite below 1,0 Vol.-%. The material was supplied as plates with a thickness of 40 mm which were solution annealed in vacuum at 1100 °C. An optical micrograph of the material in the as-received state is given in Fig. 2. The austenite grains with an average size of ASTM 4 have a relatively high twin density.

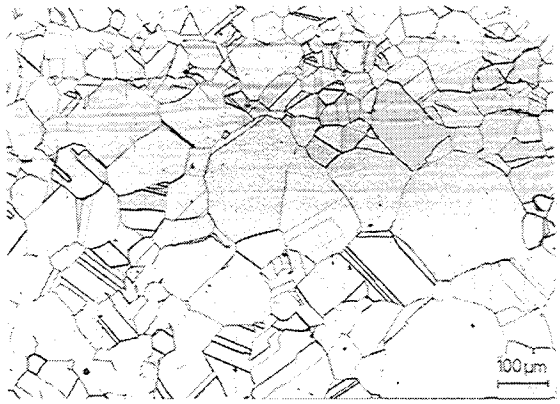


Fig. 2: Optical micrograph of AISI 316 L (X2 CrNiMoN 17 12) in the as-received state

The chemical composition of the material is given in Table 1.

Fe	C	Cr	Ni	Mo	N	Mn	Si	Cu
Bal.	0.019	17.14	12.6	2.4	0.053	1.796	0.3	0.138

Table 1: Chemical composition of AISI 316 L (X2 CrNiMoN 17 12)

The nitrogen content increases the yield strength at moderate temperatures and decreases significantly the content of brittle χ and σ phases [7]. Fig. 3 shows the geometry of the solid round test pieces as used for the CTMF-experiments.

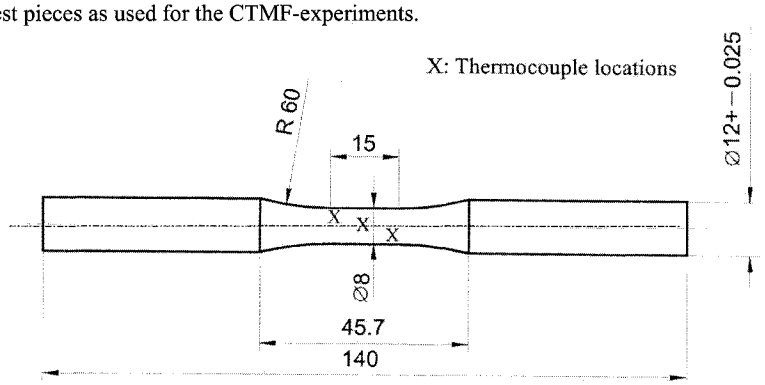


Fig. 3: Specimen geometry

The temperature value within the gauge length and its homogeneity were determined by three type K (Ni-CrNi) thermocouples which were spot welded at the positions as drawn in Fig. 3. The spot welding process was optimised in order to get a minimal influence on the microstructure and to avoid damage which would lead to an accelerated crack initiation at the thermocouple locations.

3 Experimental Details

The CTMF tests were carried out on a two specimen testing facility which is sketched in Fig. 4. It mainly consists of two servohydraulic load frames with a nominal force of 100 kN, two inductive furnaces and a four-channel MTS TestStar device which controls the complete system [2, 6].

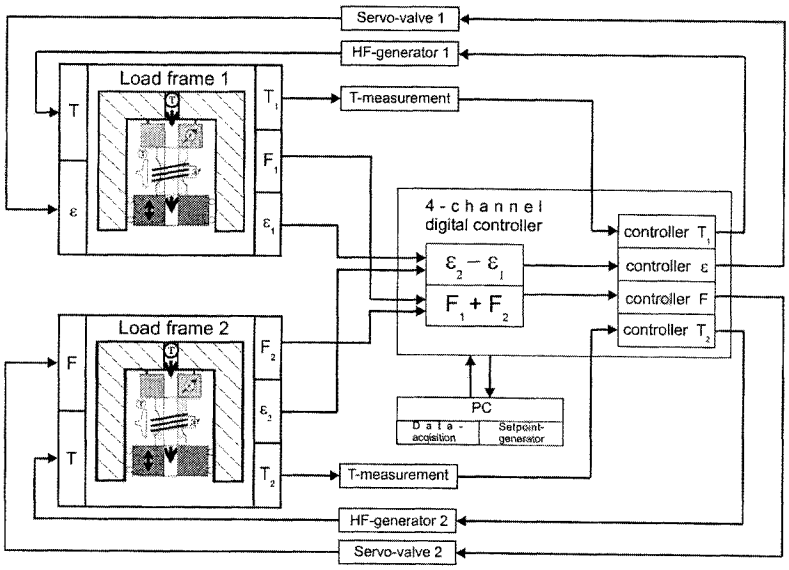


Fig. 4: Experimental setup (schematical sketch)

The specimens are fixed by hydraulic water cooled grips. The strain is measured directly at each specimen by air cooled high temperature extensometers. The specimens are heated by two 5 kW high frequency generators. The respective induction coils are adapted to the specimen geometry in such a way that the temperature differences within the gauge lengths are below ± 5 °C. Cooling of the specimens is achieved by the heat flux into the water cooled grips and, if necessary, by proportionally controlled air jets blowing radially upon the specimen surfaces.
The following conditions are realised by closed-loop control circuits:

- Separate temperature-time-sequences for specimen 1 and specimen 2 (Consideration of different thermal loading at the surface and at the core of the component)

- Freely selectable sequence of the sum of the forces on both specimens as a function of time (In the present study this quantity is generally zero corresponding to thermal fatigue without external force)
- Equal total strains at specimen 1 and specimen 2 at every point of time (The constraint between both specimens producing different mechanical strains originates from this boundary condition. Furthermore, it means that there is no thermally induced bending within the component)

These relationships can be summarised as follows:

$$T_1 = f_1(t) \tag{1}$$

$$T_2 = f_2(t) \tag{2}$$

$$F = F_1 + F_2 = 0 \tag{3}$$

$$\varepsilon_t = \varepsilon_{1,t} = \varepsilon_{2,t} \tag{4}$$

At given numbers of cycles, the forces, total strains and temperatures of both specimens were stored as a function of time with a sample rate of $1\,s^{-1}$. At the beginning of each test, the thermal strain ε^{th} was determined as a function of the temperature by a polynomial of 2nd order for each specimen from experimental data obtained during five „reference cycles" without any mechanical loading. Youngs modulus $E(T)$ as a function of the temperature was also determined in separate tests and subsequently approximated by a polynomial of 3rd order. To get the total mechanical strain ε_t^{me} the equation

$$\varepsilon_t = \varepsilon_t^{me} + \varepsilon^{th} \tag{5}$$

was used. The plastic strain ε_p was calculated for each cycle using the equation:

$$\varepsilon_t^{me} = \varepsilon_e + \varepsilon_p = \frac{\sigma_n}{E(T)} + \varepsilon_p \quad , \tag{6}$$

where ε_e is the elastic strain. Plotting the total mechanical strain and the plastic strain against the nominal stress σ_n hystereses were obtained and evaluated to get cyclic deformation curves of the maximum and minimum stress σ_{max} and σ_{min} as well as the maximum and minimum strain $\varepsilon_{t,max}$ and $\varepsilon_{t,min}$ and the plastic strain amplitude $\varepsilon_{a,p}$ versus the number of cycles N.

All tests were carried out with equal temperature-time paths which were phase shifted between specimen 1 and specimen 2 as shown below. The minimum temperatures of both specimens was T_{min}= 200°C, the respective maximum temperature was T_{max}= 650°C. The cycle times generally were 180 s with a dwell time at maximum temperature t_d=45 s. Phase shifts of t_{ph} = 11.25 s, 22.5 s, 33.75 s and 45 s were applied. The sum of the forces F_S was zero. The discussion of the results in the present paper is focused on a phase shift of 22.5 s. Accordingly, the respective results are emphasised in the following diagrams.

4 Results and Discussion

Fig. 5a) gives the temperature – time sequences of both specimens. In Fig. 5b) the resulting total strains $\varepsilon_t = (\varepsilon_{1/2}^{th} + \varepsilon_{1/2,t}^{me})$ in the first CTMF cycle are plotted as a function of the time. ε_t is identical at both specimens at any time according to eq. (4). The corresponding paths of the nominal stresses σ_n versus t are shown in Fig. 5c). The total strain – time path develops at a phase shift t_{ph} = 22.5 s as follows: At the beginning of the cycle, specimen 1 is heated up with a temperature rate of 10K/s while specimen 2 stays at 200°C within the first 22.5 s. During

this period ε_t rises with decreasing rate up to a value of 0.12 %. As soon as T_2 also starts to increase (t = 22.5s) ε_t rises more steeply until specimen 1 reaches T_{max} after 45 s. Then, ε_t continues to increase at a reduced rate until specimen 2 also has reached T_{max}= 650°C at t = 67.5 s. As expected, a constant value of ε_t = 0.85 % is observed while both specimens remain at T_{max}. The $\varepsilon_t - t$ path during the cooling phase of the cycle follows immediately from the corresponding relationships. At the end of the first cycle when both specimens are at T_{min} = 200°C, a remaining total strain of ε_t= –0.2 % is measured. This means that a "shortening" of the CTMF system, which consists of both samples and is governed by eq. (1) – (4), has occurred. The reason for that effect are compressive plastic deformations of at least one of the specimens, which are not completely compensated by the tensile deformations which also occur in both samples as becomes obvious from Fig. 5c). The stress-time paths given there indicate that at t < 22.5 compressive stresses develop with increasing temperature in specimen 1 which have a peak value of –160 MPa. During 22.5 s < t < 45 s the absolute value of the stresses in both specimens decreases by about 30 MPa in spite of a constant temperature difference and therefore constant total mechanical strains because Youngs modulus of both specimens decreases with increasing temperature. During the first half of the dwell time of specimen 1 (45 s < t < 67.5 s) T_2 still rises from 425°C to 650°C. The resulting increase of ε_2^{th} while ε_1^{th} is constant combined with the condition $\varepsilon_{1,t} = \varepsilon_{2,t}$ leads to a change of σ_1 from compression to tension with a final value of σ_1 = 100 MPa when specimen 2 reaches T_{max}. This value remains constant until the cooling of specimen 1 starts. At that moment σ_1 further increases to a peak value of about 150 MPa which occurs when specimen 1 reaches T_{min}. During the dwell time at the minimum temperature of specimen 1, specimen 2 further cools down from 425 °C to 200 °C. At the same time σ_1 changes to negative values. When specimen 2 reaches the minimum temperature, a constant value of σ_1 = –160 MPa appears. Because of the condition $F_1 + F_2 = 0$ which means $|\sigma_1| = |\sigma_2|$ the stress – time path in specimen 2 is axial symmetric to that in specimen 1.

The stress – total mechanical strain as well as the stress – plastic strain hystereses of specimen 1 during the first CTMF cycle are given in Fig. 6a) and b). In Fig. 6c) and d) the respective hystereses of specimen 2 are plotted. During the first 22.5 s of the cycle when T_1 has risen and T_2 is constant, continuously increasing compressive stresses and strains arise in specimen 1 combined with a pronounced plastic deformation. At the same time a nearly elastic tensile deformation of specimen 2 occurs. At the end of this phase of the cycle, shortly before $\sigma_{2,max}$ is reached, weak tensile plastic deformation is also observed at sample 2. Then, as discussed before, the magnitudes of both stresses slightly decrease during 22.5s < t < 45s and subsequently, as soon as the dwell time of specimen 1 begins while the other sample is still heated up, the stresses change their sign combined with an elastic-plastic deformation of both test pieces.

After both specimens have reached T_{max}, σ_1 and σ_2 remain constant until t = 90 s. The following decrease of T_1 while T_2 still remains at 650°C leads to a further increase of the absolute stress values combined with a more pronounced compressive plastic deformation of specimen 2 with respect to the tensile deformation of specimen 1 that occurs at the same time. This is due to the fact that specimen 2 is loaded in compression with the same absolute stress value, but at a higher temperature than specimen 1 in tension. As soon as T_2 starts to decrease, $|\sigma_1|$ and $|\sigma_2|$ increase because both temperatures decrease and thus Youngs modulus increases. When specimen 1 has reached T_{min} , the further cooling of specimen 2 causes once more a change from tensile to compressive stresses and vice versa which is combined with an elastic-plastic deformation of specimen 1 in compression and of specimen 2 in tension.

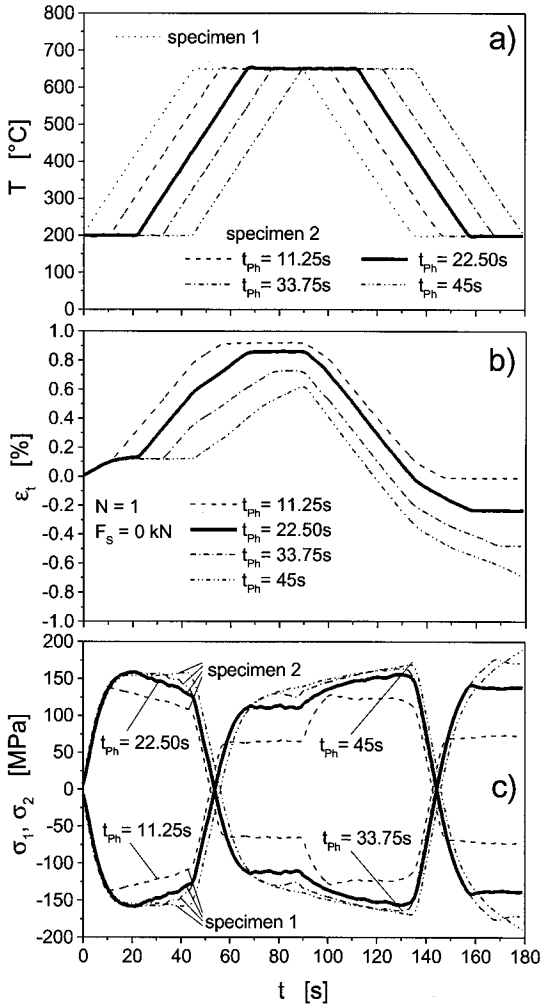


Fig. 5: Temperature, total strain and nominal stress of both specimens versus time at N=1

As becomes obvious from the discussion above, compressive stresses generally occur at higher temperatures than the tensile stresses with identical absolute values that develop in the other specimen at the same time. Therefore, the compressive plastic deformation of both specimens is larger than their tensile plastic deformation. This results in a remaining compressive strain of the system consisting of both samples with a value of –0,2 % at the end of the first cycle.

As becomes obvious from Fig. 5 increasing, (decreasing) phase shifts lead to a shorter (longer) duration of the period of the dwell time with both specimens being at a constant temperature of 650°C. For t_{ph} = 45 s this state is only reached at one point of time (t = 90s).

Accordingly, the duration of the periods with constant total strains and stresses in Fig. 5b) and c) become shorter with increasing t_{ph}. Additionally, the maximum difference between T_1 and T_2 is the higher the larger the phase shift is (see Fig. 5a)).

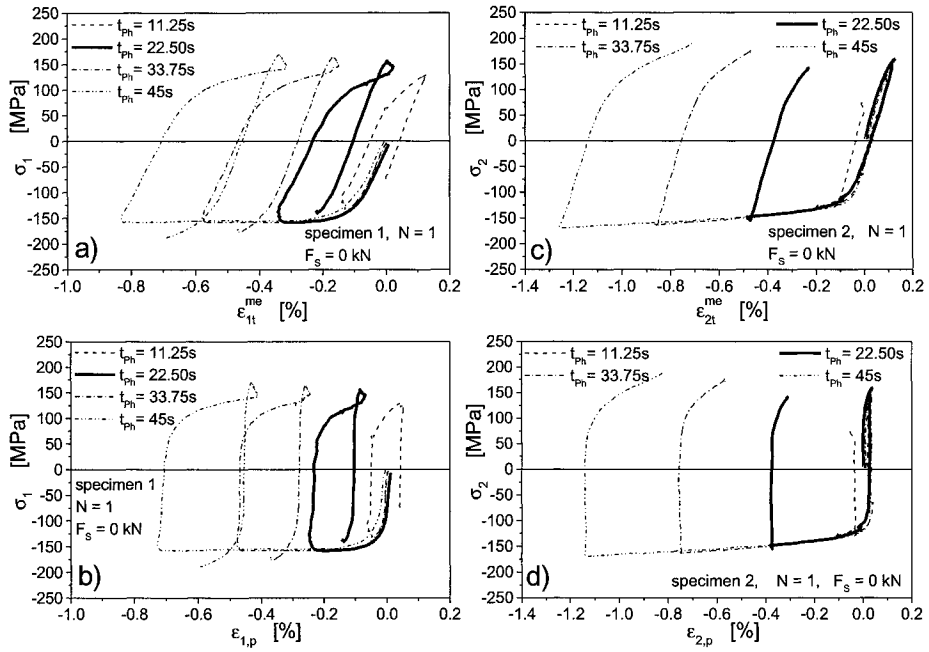


Fig. 6: Stress – total mechanical strain and stress - plastic strain hystereses of both specimens during the first cycle

However, in spite of strongly increasing total mechanical strain amplitudes, especially at $t_{ph} >$ 22.5 s this only leads to a weak increase of the peak stresses because the stress – strain path of AISI 316 L is relatively flat and therefore the possible peak stresses are limited. Accordingly, as becomes obvious from Fig. 6, an increasing phase shift results in a very strong increase especially of the compressive plastic deformation of specimen 1 during the first 45 s of the cycle and of specimen 2 after having passed the dwell time. The respective tensile plastic deformations also increase with t_{ph} but not to the same extent as the plastic strains in compression. Due to these facts, the remaining compressive strain at the end of the first cycle is the larger the higher t_{ph} is.

Fig. 7 gives an overview of the cyclic deformation behaviour occurring at all investigated phase shifts. In Fig. 7a) the the maximum and minimum stresses of specimen 1 $\sigma_{1,max}$ and $\sigma_{1,min}$ are plotted versus N. As is concluded from eq. (3), the respective values of specimen 2 are $\sigma_{2,max} = -\sigma_{1,min}$ and $\sigma_{2,min} = -\sigma_{1,max}$. Fig. 7b) shows the corresponding peak values of the total strain which are equal at both samples according to eq. (4). Fig. 7c) and d) show the paths of the plastic strain amplitudes $\varepsilon_{1,ap}$ and $\varepsilon_{1,ap}$, both versus N.

At t_{ph} 11.5 s $\sigma_{1,max}$ increases very weakly during the complete test starting at a value of 130 MPa, whereas $\sigma_{1,min}$ decreases from –130 MPa to –160 MPa within the first three cycles and then remains constant up to N=1000. Larger phase shifts result in higher peak stresses at the first cycle and in a continuous increase of $\sigma_{1,max}$ which is the more pronounced the higher t_{ph} is. For t_{ph} 45 s $\sigma_{1,max}$ starts at 170 MPa in the first cycle and reaches a value of 280 MPa at N = 18.

The maximum and minimum values of the total strain $\varepsilon_{t,max}$ and $\varepsilon_{t,min}$, which are plotted versus N in Fig. 7b), remain constant throughout the test at t_{ph} 11,25 s. Larger phase shifts result in a continuous decrease of $\varepsilon_{t,max}$ and $\varepsilon_{t,min}$ which is the more pronounced the higher t_{ph} is. The cyclic creep rate does not decrease until the end of the test. If the peak strain – time paths in Fig. 7b) are plotted versus N in a linear scale, it becomes obvious that after the first cycles approximately constant creep rates occur. The reason for that behaviour is, as already discussed in connection with Fig. 6, the fact that generally the compressive stresses which occur at one specimen act at higher temperatures and therefore against a lower resistance to plastic deformation than the tensile loading with the same absolute value occurring at the other test piece at the same time. The absolute values of these stresses and therefore the cyclic creep rate are the larger the higher t_{ph} is. The experiments with t_{ph} = 33.75 s (45 s) had to be stopped at N = 60 (18) because the minimum strain reached the limit of the extensometer range.

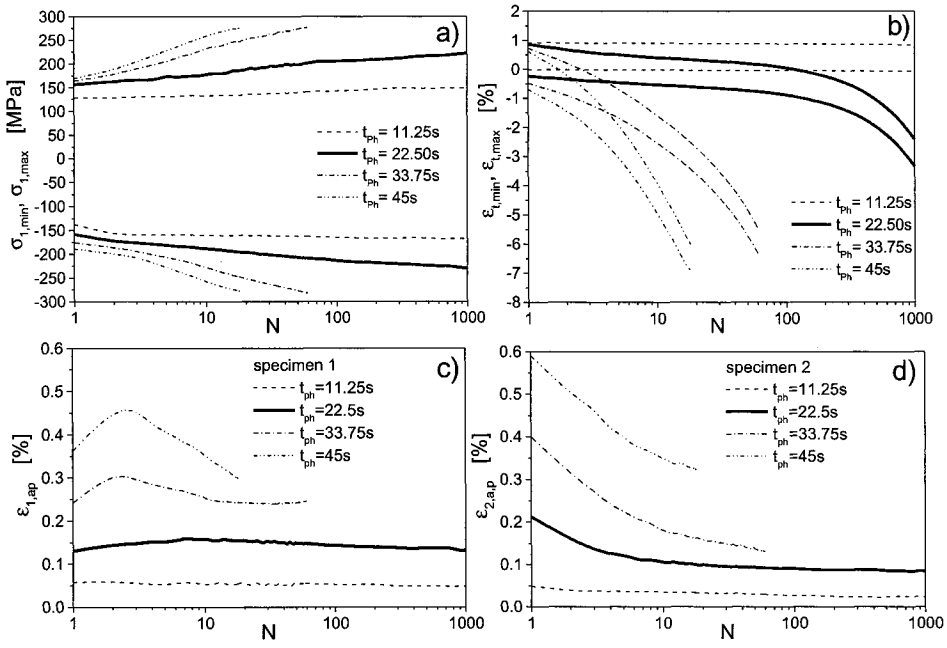


Fig. 7: Cyclic deformation curves of the peak stresses and strains as well as of the plastic strain amplitudes versus N

At first glance, the paths of the peak stresses as a function of N seem to indicate simultaneous cyclic hardening of both samples which is the more pronounced the higher t_{ph} is. But, a closer look at Fig. 7b), c) and d) shows that a more sophisticated interpretation of the cyclic deformation behaviour is necessary. In fact, specimen 2 shows a continuous decrease of the plastic strain amplitude with increasing N which is the more pronounced the larger t_{ph} is. In the case of t_{ph} = 22.5 s, saturated values of $\varepsilon_{2,ap}$ are approached at $N \sim$ 200. The other way round, at t_{ph} = 22.5 s the plastic strain amplitudes of specimen 1 increase within the first cycles and afterwards show a significantly weaker decrease than the respective values of specimen 2. At t_{ph} = 11.25 s, $\varepsilon_{1,ap}$ stays nearly constant up to N = 1000. The increase of $\varepsilon_{1,ap}$ within the first cycles can be explained using Fig. 6 as follows: The first cycle starts with a compressive elastic-plastic deformation of specimen 1 at an initial stress of zero resulting in the σ_n - $\varepsilon_{1,p}$ path as plotted in Fig. 6b). The second cycle does not start at σ_1=0 but at a stress σ_1 = -150 MPa at t_{ph} = 22.5 s and even at higher compressive stresses in the case of larger phase shifts. Accordingly, at specimen 2 tensile stresses with the same absolute values occur at the beginning of the 2nd cycle. Therefore, as soon as specimen 1 begins to be heated up again, extensive compressive plastic deformation takes place in this sample, whereas specimen 2 is to a smaller extent plastically deformed in tension due to the lower temperature occurring at this test piece. As a result of these other starting conditions compared with the first cycle, the plastic strain amplitude in specimen 1 increases up to N = 2 at t_{ph} = 33.75 s and up to N = 10 at t_{ph} = 22.5 s. Afterwards, cyclic hardening occurs which results in a strong decrease of $\varepsilon_{1,ap}$ at t_{ph} = 33.75 s until the end of the test. At t_{ph} = 22.5 s the cyclic hardening is less pronounced but leads to a nearly constant plastic strain amplitude at N>100. In the case of t_{ph} = 11.25 s $\varepsilon_{1,ap}$ remains constant throughout the test.

Except from the first cycles where, as discussed above, a more differenciated view of the interaction of both specimens in the CTMF testing system that is governed by the conditions given in eq. (1) - (4) is necessary, cyclic hardening occurs in both specimen which is proven by the increase of the stress amplitude occurring at the same time with constant or decreasing plastic strain amplitudes. As shown in previous publications concerning another kind of CTMF cycle carried out at AISI 316 L [8, 9], mainly dynamic strain ageing processes due to plastic deformations while heating up or cooling down the material at temperatures above 300°C, which lead to diffuse dislocation arrangements, are responsible for this behaviour.

5 Summary and Conclusions

CTMF experiments give the opportunity of a greatly simplified simulation of complex thermally induced loading, e. g. in solid turbine blades, considering a two - body model. Although the multiaxiality of the loading in a real component is neglected and the temperature cycles are extremely simplified, CTMF tests are able to provide a deep basic understanding of the complex interactions between mechanically coupled volume elements in components that undergo service cycles which result in inhomogeneous and non steady-state temperature fields. Furthermore, CTMF tests allow a direct measurement of the materials reactions in terms of stress – total mechanical strain hysteresis loops and cyclic deformation curves, respectively, which is not possible in thermal fatigue experiments carried out on components.

The presented experiments were carried out on the austenitic stainless steel AISI 316 L which is a candidate material for blades and vanes of high temperature steam turbines. In order to simulate the interaction between volume elements at the surface and inside a solid turbine blade during start stop processes, identical temperature cycles with dwell times at T_{max} =

650°C and T_{min} = 200°C were chosen and the T - t path of specimen 2 was phase shifted with respect to the one of specimen 1.
The influence of that phase shift on the cyclic deformation behaviour which is completely different to the results of strain controlled isothermal fatigue and thermal mechanical fatigue tests on one specimen can be summarised as follows:

- Cyclic creep to negative total strains is observed which is the more pronounced the higher the phase shift between both temperature cycles is
- After an initial phase, cyclic hardening occurs which increases when the phase shift between the $T-t$ cycles is increased
- In the case of large phase shifts, this cyclic hardening does not result in significant decrease of the cyclic creep rate with increasing N
- The occurrence of cyclic hardening correlates well with the microstructural changes under CTMF loading without phase shifts carried out in a previous study [8, 9]

Acknowledgement
The financial support of the Deutsche Forschungsgemeinschaft (DFG) is gratefully acknowledged. The authors also give special thanks to the Institut für Materialforschung II of the Forschungszentrum Karlsruhe for the supply of the test material.

6 References

[1] A. Weronski, T. Hejwowski, Thermal fatigue of metals, Marcel Dekker Inc, New York, (1991)

[2] G. Pitz: Ermüdungsverhalten metallischer Hochtemperaturwerkstoffe unter komplexer thermisch-mechanischer Beanspruchung, PhD-thesis, Universität Karlsruhe, 1997

[3] K.-H. Lang, T. Beck, B. Flaig, R. Hallstein, D. Löhe: Einfluß von Haltezeiten auf das Lebensdauerverhalten von Zylinderkopfwerkstoffen unter thermisch-mechanischer Ermüdungsbeanspruchung, VDI-Bericht 1472 zur Tagung „Werkstoff und Automobilantrieb", Dresden, 28.-29. 10. 99, VDI-Verlag Düsseldorf, 1999, pp. 437-454

[4] G. Pitz, T. Beck, K.-H. Lang, D. Löhe: Thermisch-mechanisches und isothermes Ermüdungsverhalten der Nickelbasis-Superlegierung IN792CC, Mat.-Wiss. u. Werkstofftechn. 28 (1997), pp. 142-148

[5] T. Beck, G. Pitz, K.-H. Lang, D. Löhe: Thermal-mechanical and isothermal fatigue of IN 792 CC, Materials Science and Engineering A234-236 (1997), pp. 719-722

[6] L. Angarita, G. Pitz, K.-H. Lang, D. Löhe, Realization of Complex Thermal-Mechanical Fatigue by a Two-Specimen Testing System, 3rd Symposium on Thermo-Mechanical Fatigue Behaviour of Materials, ASTM STP 1371, West Conshohocken, PA, USA, 1998, pp. 304-318

[7] G. Steinbeck, P. H. Cyris, W. Heimann, W. Weißling, Stand und Entwicklungstendenzen auf dem Gebiet der nichtrostenden Stähle, VDI Berichte Nr. 1150, (1994), pp. 1-25

[8] T. Beck, K.-H. Lang, O. Vöhringer, D. Löhe: Experimental Analysis of the Interaction of "Hot" and "Cold" Volume Elements during Thermal Fatigue of a Cooled Component made from AISI 316 L Steel, Zeitschrift für Metallkunde, Vol. 92, 08/2001, pp. 875-881

[9] K. Rau, T. Beck, D. Löhe: Isothermal-, Thermal-Mechanical- and Complex Thermal-Mechanical Fatigue Tests on AISI 316 L Steel- A Critical Evaluation, Materials Science and Engineering (2001), in review

CREEP PROPERTIES OF AUSTENITIC STAINLESS 353 MA AT 1100°C AND 1200°C

Rui Wu, Facredin Seitisleam and Rolf Sandström

Swedish Institute for Metals Research
Drottning Kristinas väg 48, S-114 28 Stockholm, Sweden
Email: ruiwu@simr.se

Abstract

Creep tests at 1100°C and 1200°C are performed on the austenitic stainless 353 MA hot rolled plate and extruded tube. Pre- and post-test metallography are carried out to study microstructural variation and creep damage development. The results show that the hot rolled plate has a longer time to 1% and 2% creep strain, in comparison to the extruded tube. At rupture, the tube gives both higher creep strength and ductility than the plate. The Norton law and the Monkman-Grant correlation are found to be valid for both materials. Post-test metallography shows that intergranular and transgranular failure is dominant for the plate and the tube, respectively. Creep damage in the plate is more extensive than that in the tube. Oxide is frequently detected on the surface of specimen, especially for the long time tests at 1200°C. Associated with oxide, cracks initiate on the surface and propagate intergranularly into the material. The nitride, Cr_2N, and possibly Cr_3Si, precipitate after approximately 2000 hours at both 1100°C and 1200°C.

Keywords: Austenitic stainless 353 MA, creep, high temperature, cavitation, fracture

1. Introduction

Demands for efficiency increase and economic performance for petrochemical and power plants lead often to an increased operating temperature and pressure in components such as gas turbines, nozzles, heat exchangers, and heat treatment equipment. Under such conditions, thermal stability, oxidation, corrosion, and erosion resistance, as well as creep properties are of great concern. The developed and applied alloys must show satisfactory resistance to microstructural degradation, aggressive environment and premature failure.

The heat resisting austenitic stainless steel 353 MA is a further development of its previous generation 253 MA. 353 MA has a high chromium content and an approximately tripled nickel content. Higher chromium and nickel contents result in an increased oxidation resistance and an increased resistance against carbon and nitrogen pick-up, respectively [1]. Nitrogen is added to improve the mechanical strength at both room and elevated temperatures without impairing the ductility. Also, addition of nitrogen reduces the susceptibility to embrittling sigma phase formation. Moreover, an increased silicon content and the addition of rare earth metals (REM) improve the oxidation resistance and enhance the oxide adherence.

Studies of high temperature corrosion and oxidation on 353 MA have been carried out, e.g. in [2-4] and are summarised in [1]. It has been found that elevated temperature performance of 353 MA in laboratory corrosion testing is as good as expected under carburising and nitriding conditions and unexpectedly good in sulphur containing atmospheres.

Apart from good corrosion resistance, 353 MA exhibits excellent creep strength even at temperatures up to 1000°C [1]. To use 353 MA at temperatures as high as 1200°C, which is slightly above its spalling temperature of 1175°C, the creep strengths at temperatures up to

1200°C must be known. However, no creep data at temperatures above 1100°C are available.

The *purposes* of this paper are to investigate creep properties of 353 MA in hot rolled and extruded conditions at 1100°C and 1200°C, to study creep damage distribution and development, and to compare the creep results with those obtained from 253 MA.

2. Experiments

2.1 As-received material

A hot rolled plate and an extruded tube, both made of 353 MA, are used in the present investigation. The chemical compositions (in wt%) of both materials, together with product form, heat treatment and dimension, are given in Table 1. Mechanical properties at room temperature for the hot rolled plate are: proof strength is 316 MPa, tensile strength 705 MPa, elongation 57%, and hardness (HRB) 83. Both plate and tube consist of austenite with twins. The grain size in the plate is somewhat mixed. The fine grains have a size of about 39 μm and the coarse grains 167 μm, giving a mean grain size of 80 μm. The grain size in the tube is fairly uniform and it is about 55 μm.

Table 1 Chemical composition (wt%), product form, heat treatment and dimension

Product form	Heat Treatment	Dimension (mm)	C	Si	Mn	P	S	Cr	Ni	Mo	N
Hot rolled plate	1120°C, quenched in water	20 × 1500 × 3000	0.05	1.3	1.34	0.007	0.001	24.8	34.9	0.13	0.18
Extruded tube		Ø90 × 12*	0.05	1.49	1.42	0.013	0.001	24.8	34.8	0.17	0.17

** Outer diameter is Ø90 mm and wall thickness 12 mm*

2.2 Creep specimens and testing

Two series of the creep specimens are taken from the hot rolled plate and from the extruded tube. The specimens from the tube are taken longitudinally. Cylindrical specimens, with threaded ends with ∅14 mm diameter and 50 mm gauge length, are used.

All the specimens were uniaxially tested in air in a dead weight lever creep machine at 1100 and 1200°C at stresses from 2.5 to 8 MPa. The maximum temperature variations with time are controlled within ±2°C. Details on creep testing at very high temperatures are given in [5].

2.3 Post-test metallography

The failed specimens are metallographically examined using a light optical microscope (LOM). The mid-thickness of the specimens which is perpendicular to the fracture is sectioned, ground and polished to 1 μm before etched in a solution containing 10 ml HNO_3, 100 ml HCl and 100 ml H_2O. Cross section (the section parallel to the fracture) and the head (threaded end) of a few specimens are metallographically examined as well.

3. Results and comparison

3.1 Creep testing results and comparison

Examples of creep curves, where the creep strain is plotted against time, are presented in Fig. 1 for the hot rolled plate at 1100°C. It is seen that the creep curves show generally an insignificant primary creep, a pronounced secondary creep, and a dominant tertiary creep.

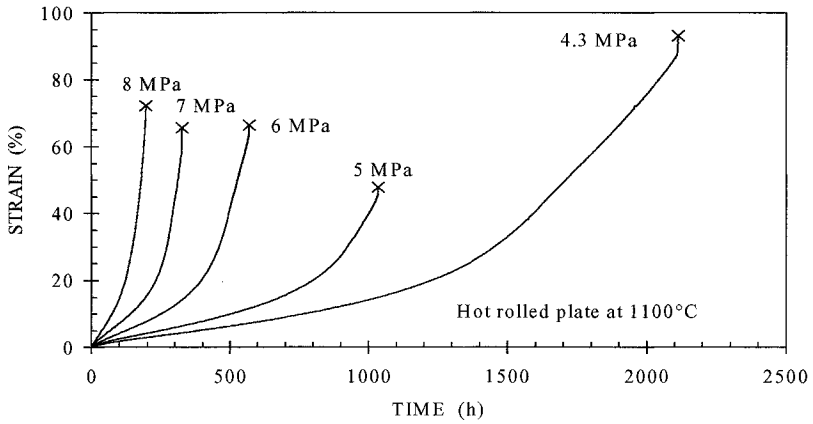


Fig. 1 *Creep strain versus time for the hot rolled plate at given stresses at 1100°C.*

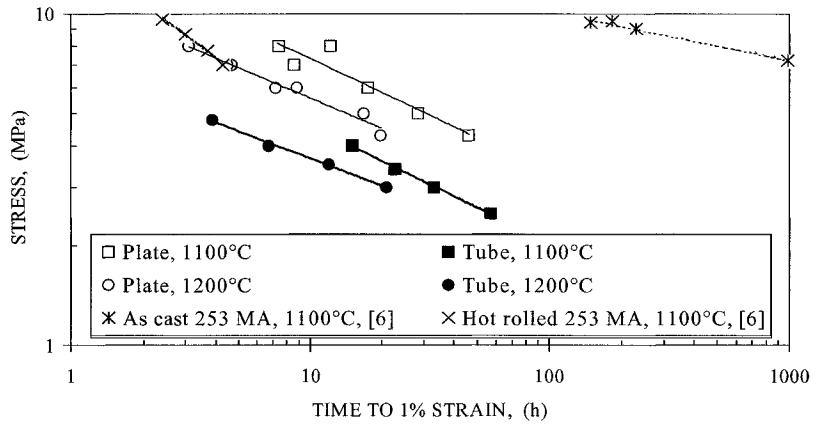


Fig. 2 *Stress versus time to 1% creep strain for the hot rolled plate and the extruded tube at 1100°C and 1200°C. Data for the as-cast and the hot rolled 253 MA at 1100°C [6] are included for comparison.*

Stress as a function of time to 1% creep strain is shown in Fig. 2. Data for the as-cast and the hot rolled 253 MA at 1100°C [6] are included for comparison. It is noted that the as-cast and the hot rolled 253 MA contain 0.39% and 0.09% carbon, respectively. It is seen that time to 1% strain for the hot rolled plate is longer than that for the extruded tube at the same temperature and stress. Time to 1% strain for the hot rolled 253 MA at 1100°C is similar to that for the extruded tube of 353 MA, but shorter than that for the hot rolled plate of 353 MA. The as-cast 253 MA shows the longest time to 1% strain at 1100°C, in comparison to other series. This is also true for time to 2% strain.

Stress against time to rupture t_R is given in Fig. 3 for both the hot rolled plate and the extruded tube at 1100 and 1200°C. Data for the as-cast and the hot rolled 253 MA at 1100°C [6] are also included for comparison. It is seen that at the same temperature the tube material shows a longer t_R than the plate material does at the same stress. This is true for the tests at both 1100 and 1200°C. For the same material at the same given stress t_R is longer at 1100°C than that at 1200°C. The as-cast 253 MA gives a longer t_R than the other three series at 1100°C. t_R for the hot rolled 253 MA is fairly similar to that for the hot rolled tube of 353 MA.

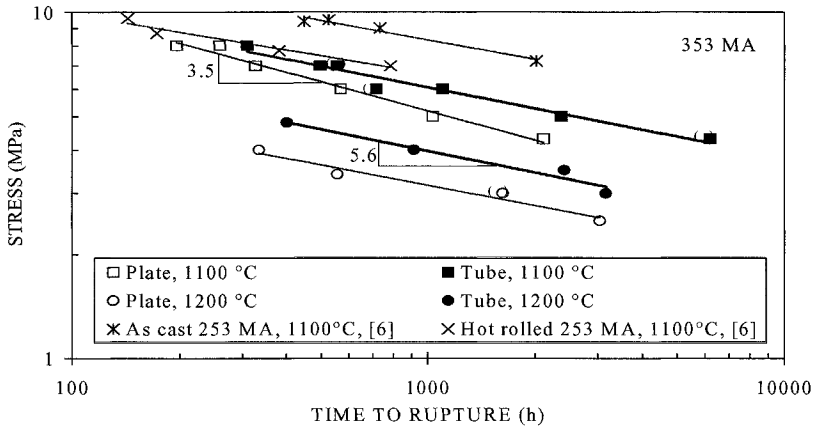


Fig. 3 *Stress versus time to rupture for the hot rolled plate and the extruded tube at 1100°C and 1200°C. Data for the as-cast and the hot rolled 253 MA at 1100°C [6] are included for comparison. Data in brackets refer to the tests interrupted due to furnace failure.*

With double logarithmic scales, t_R increases linearly with decreasing stress for all the series at the given temperatures, c.f. Fig. 3, and this relation can be described as

$$t_R = c \cdot \sigma^{-\upsilon} \qquad (1)$$

where c and ν are empirically determined constants and their values are given in Table 2. ν at 1100°C is somewhat smaller than that at 1200°C. At the same temperature ν for the plate is smaller than that for the tube.

Elongation at rupture is given as a function of time to rupture in Fig. 4. Data for the as-cast and the hot rolled 253 MA at 1100°C [6] are also included for comparison. It can be seen that the tube material exhibits a better creep ductility than the plate at both 1100°C and 1200°C. Elongation for the tube is usually lager than 100% with a maximum value of 145%. For the plate material, elongation is usually smaller than 80% with a minimum value of 45%. There is no distinct dependence of elongation on time. In comparison to 353 MA material, the as-cast 253 MA gives the lowest elongation ranging from about 20% to 40%. The hot rolled 253 MA shows a creep ductility between the plate and tube 353 MA.

Table 2 Experimentally determined constants

Series	Stress, (MPa)	C, $h \times (MPa)^{v}$	v	b, $1/h \times (MPa)^{-n}$	n	δ	C_{MG} $1/h \times (h)^{\delta}$
Hot rolled plate of 353 MA at 1100°C	4.3 - 8	3.25×10^{5}	3.5	5.11×10^{-6}	2.2	-0.94	0.147
Extruded tube of 353 MA at 1100°C	2.5 - 4	5.27×10^{6}	4.8	4.23×10^{-7}	3.8		
Hot rolled plate of 353 MA at 1200°C	4.3 - 8	2.99×10^{5}	5.0	2.46×10^{-10}	11		
Extruded tube of 353 MA at 1200°C	3 - 4	2.54×10^{6}	5.6	2.93×10^{-8}	7.0		
Hot rolled 253 MA at 1100°C	7 – 9.6	3.58×10^{7}	5.6	5.29×10^{-11}	7.7		
As-cast 253 MA at 1100°C	7.2 - 9.5	6.00×10^{7}	5.2	4.51×10^{-10}	4.4	-0.62	0.000357

C and v are defined in eqn. (1). b and n are defined in eqn. (2). δ and C_{MG} are defined in eqn. (3).

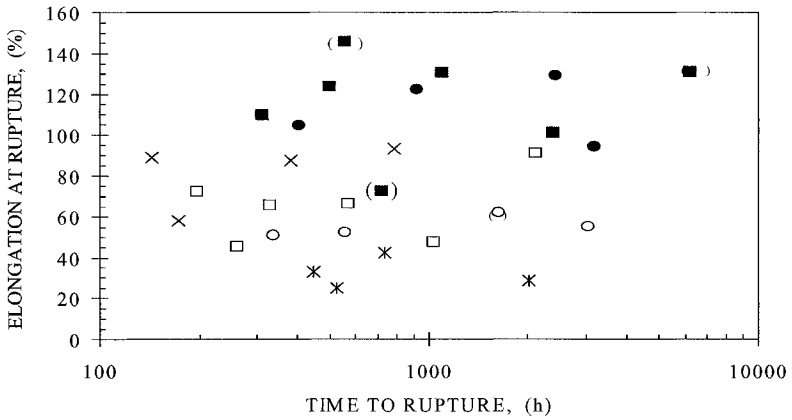


Fig. 4 Elongation at rupture versus time to rupture for the hot rolled plate and the extruded tube at 1100°C and 1200°C. Data for the as cast and the hot rolled 253 MA at 1100°C [6] are included for comparison. Data in brackets refer to the tests interrupted due to furnace failure. Figure legends are the same as those in Fig. 3.

Reduction of area at rupture is given as a function of time to rupture in Fig. 5. Data for the as-cast and the hot rolled 253 MA at 1100°C [6] are also included for comparison. Reduction of area for the tube and for the plate is between 80% to almost 100% and between 30% to 40%, respectively. This is independent of temperature and time. Reduction of area for the as-cast 253 MA is similar to that of the 353 MA plate. Reduction of area for the hot rolled 253 MA lays between the 353 MA plate and tube materials.

The minimum creep strain rate, $\dot{\varepsilon}_{min}$, is shown against stress in Fig. 6. Data for the as-cast and the hot rolled 253 MA at 1100°C [6] are also included for comparison. $\dot{\varepsilon}_{min}$ at 1200°C is higher than that at 1100°C at the same stress. This is true for both the plate and tube 353 MA

materials. At the same temperature, $\dot{\varepsilon}_{min}$ for the plate and for the tube is fairly identical. Comparing to the as-cast 253 MA at 1100°C, 353 MA gives about two orders of magnitude higher $\dot{\varepsilon}_{min}$ at the same stress. $\dot{\varepsilon}_{min}$ for 353 MA is approximately the same as that for the hot rolled 253 MA at higher stresses. As stress decreases, higher $\dot{\varepsilon}_{min}$ is found in 353 MA.

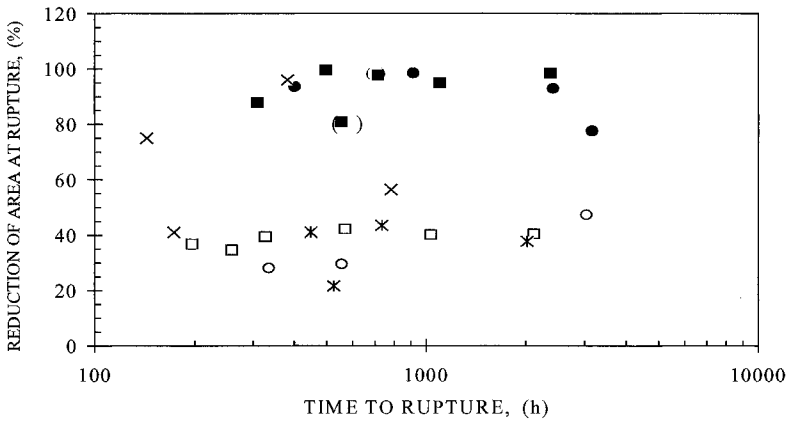


Fig. 5 *Reduction of area at rupture versus time to rupture for the hot rolled plate and the extruded tube at 1100°C and 1200°C. Data for the as cast and the hot rolled 253 MA at 1100°C [6] are included for comparison. Data in brackets refer to the tests interrupted due to furnace failure. Figure legends are the same as those in Fig. 3.*

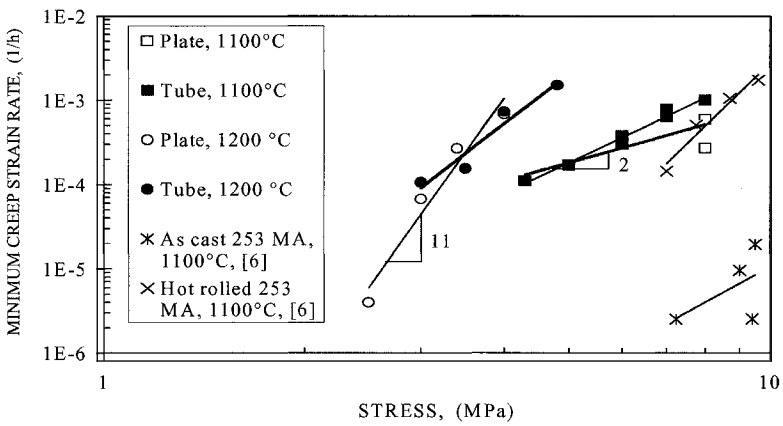


Fig. 6 *Minimum creep strain rate versus stress for the hot rolled plate and the extruded tube at 1100°C and 1200°C. Data for the as-cast and the hot rolled 253 MA at 1100°C [6] are included for comparison.*

From Fig. 6 it is seen for all the series at both 1100°C and 1200°C that $\dot{\varepsilon}_{min}$ decreases with decreasing stress σ and $\dot{\varepsilon}_{min}$ - σ follows Norton's law

$$\dot{\varepsilon}_{min} = b \cdot \sigma^n \qquad (2)$$

where b is a constant and n the stress index. The values of b and n are given in Table 2. n is larger at higher temperature.

$\dot{\varepsilon}_{min}$ versus time to failure t_R is shown in Fig. 7. It can be seen that $\dot{\varepsilon}_{min}$ decreases linearly with increasing t_R. All the data, except those for the as-cast 253 MA at 1100°C, fall in a narrow band. This relation between $\dot{\varepsilon}_{min}$ - t_R is the Monkman-Grant correlation

$$t_R^{\delta} \cdot \dot{\varepsilon}_{min} = C_{MG} \qquad (3)$$

where the constant C_{MG} = 0.147 and the exponent δ = 0.94 for 353 MA and the hot rolled 253 MA, see Table 2. For the as-cast 253 MA the constant C_{MG} = 0.000357 and the exponent δ = 0.62, see also Table 2. δ is usually close to unity.

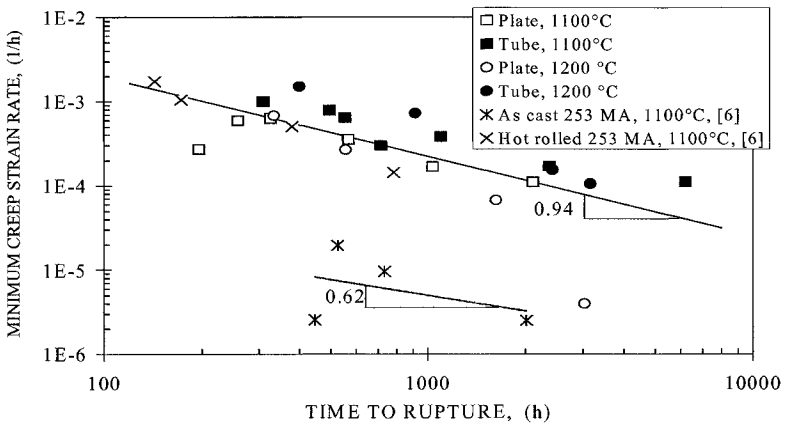


Fig. 7 *Minimum creep strain rate versus time to rupture for the hot rolled plate and the extruded tube at 1100°C and 1200°C. Data for the as cast and the hot rolled 253 MA at 1100°C [6] are included for comparison.*

3.2 Post-test metallography

Rupture mode and creep damage development and distribution on the specimens taken from the hot rolled plate at 1100°C are intergranular, see Fig. 8a. This is independent of stresses and rupture times. Close to the fracture, intergranular cracks and cavities are frequently observed. In some cases, cavities inside the grain are seen. For the hot rolled plate consisting of mixed grains, severe creep damage are often found either in the region where fine grains are dominant, or at the boundary between the coarse and the fine grains, see also Fig. 8a. The creep damage distribution appears across the whole gauge length of the specimen. For instance, extensive cavities and cracks can be observed 20-25 mm from the fracture, see Fig. 8b. For the specimen having the longest rupture time of 2113 hours in this series, precipitates

appear at the grain boundaries, twins, and inside the grains, see Figs. 8a and 8b. These precipitates are not seen on the specimens having shorter rupture times.

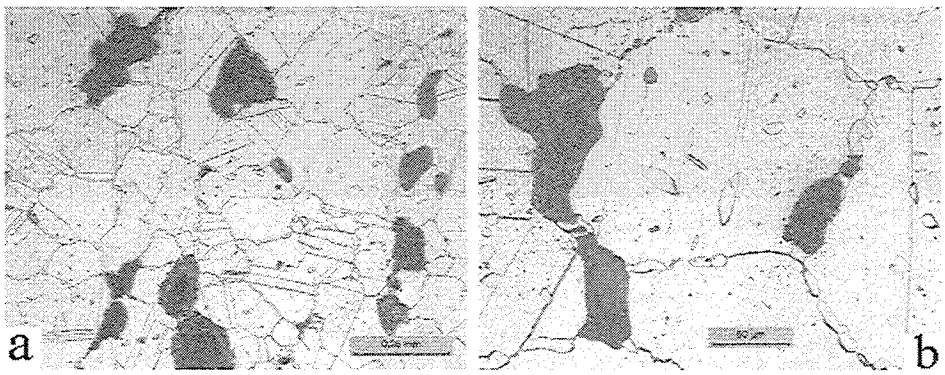


Fig. 8 *LOM micrograph from hot rolled plate at 1100°C/4.3 MPa. Rupture time t_R = 2113 hours and elongation at rupture ε_R = 91.3%. Stress direction is horizontal. a) Adjacent to the fracture. b) 20 mm from the fracture.*

For the hot rolled plate at 1200°C, the rupture mode and creep damage development and distribution are analogous to that at 1100°C. Insensitive to stresses and rupture times, intergranular fracture is dominating, see Fig. 9a. Extensive intergranular cavities and cracks are found both adjacent to the fracture and far away from the fracture. Again, cavities inside the grains are seen. Frequently, serious creep damage are concentrated to the fine grain region, see also Fig. 9a. Precipitates occur at the grain boundaries, twins, and inside the grain, on the specimens exposed to long time testing. Surface cracks are found to propagate intergranularly into the material, see Fig. 9b. On the surface of the long time exposed specimens, oxide can be seen, see also Fig. 9b.

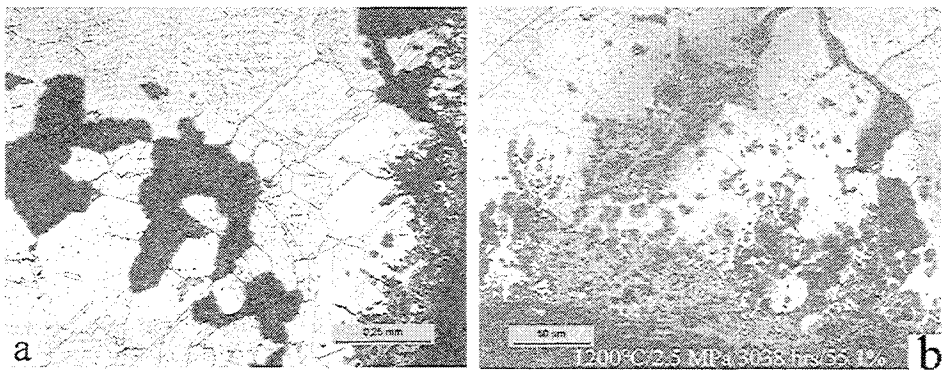


Fig. 9 *LOM micrograph from hot rolled plate at 1200°C. Stress direction is horizontal. a) At 4 MPa, t_R = 335 hours and ε_R = 50.9%. Fracture. b) At 2.5 MPa, t_R = 3038 hours and ε_R = 55.1%. 15 mm from the fracture.*

Independent of stresses and rupture times, failure is predominantly transgranular for the extruded tube at 1100°C, see Fig. 10a. Extensive cavities are often observed close to the fracture. Extent of cavities decreases with increasing distance from the fracture, *e.g.* only few cavities are found about 10-20 mm from the fracture, see Fig. 10b. Surface cracks are found to propagate intergranularly into the material. Cavities are sometimes observed inside the grains. Precipitation takes place at the grain boundaries, twins, and inside the grain for the specimens exposed to long time testing, not only within the gauge length, see Fig. 10b, but also in the head of the specimen (threaded ends). More precipitates are found within the gauge length than in the head.

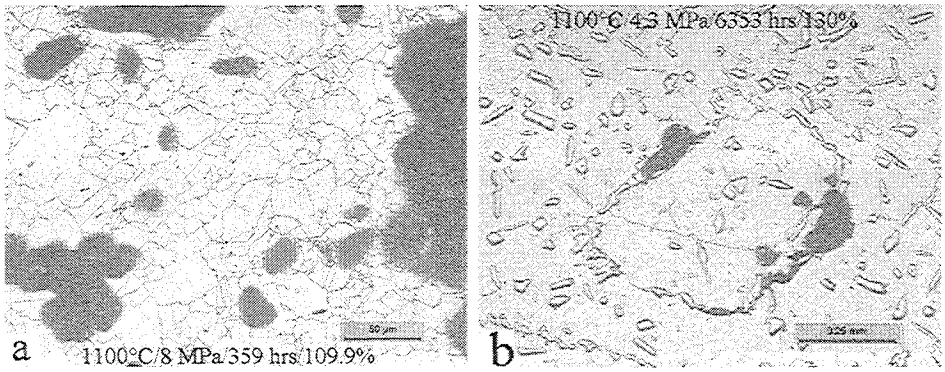


Fig. 10 *LOM micrograph from extruded tube at 1100°C. Stress direction is horizontal. a) At 8 MPa, t_R = 359 hours and ε_R = 109.9%. b) At 4.3 MPa, t_R = 6353 hours and ε_R = 130%.*

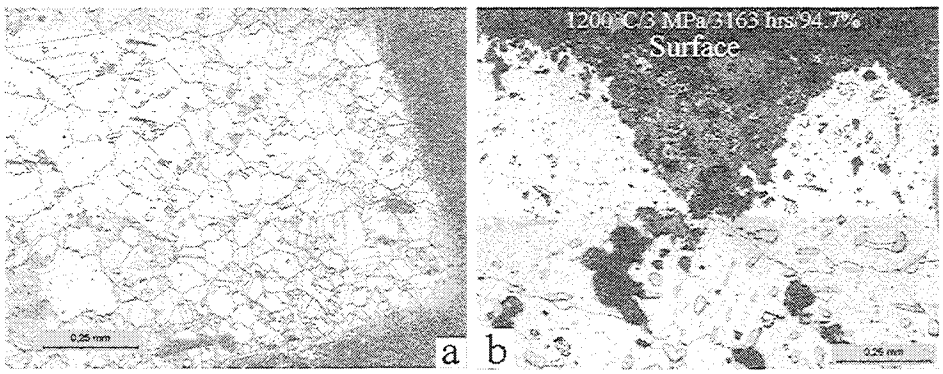


Fig. 11 *LOM micrograph from extruded tube at 1200°C. Stress direction is horizontal. a) At 4.8 MPa, t_R = 401 hours and ε_R = 104.6%. Fracture. b) At 3 MPa, t_R = 3163 hours and ε_R = 94.7%.*

Rupture mode, creep cavitation development and distribution, as well as characteristics of precipitates for the extruded tube at 1200°C are similar to those at 1100°C. Independent of rupture times, transgranular failure is dominant and separate cavities are visible close to the

fracture, see Fig. 11a. No cavitation can be found as distance from the fracture increases to about 10 mm. On the surface, microcracks surrounded by cavities and oxide are frequently observed, see Fig. 11b. Precipitates appear at the grain boundaries, twins, and inside the grain for the long time exposed specimen, see also Fig. 11b.

4. Discussion

4.1 Creep properties

From Fig. 2 it can be seen that, at the same stresses, time to 1% creep strain for the hot rolled plate is longer than that for the extruded tube, although time to rupture for the hot rolled plate is shorter than that for the extruded tube, c.f. Fig. 3. This is because the hot rolled plate creeps slower than the extruded tube in the beginning of the tests, or during primary creep. Slower creep deformation on the plate continues into the secondary creep. This is more notable at 1100°C. The extent of the secondary and tertiary creep are more pronounced for the tube than for the plate. As a result of pronounced secondary and tertiary creep as well as better creep ductility, the tube gives longer time to rupture than the plate.

In comparison to the plate material, the tube material shows both better creep ductility and longer creep life, although the chemical compositions for the plate and the tube are nearly identical, see Table 1. This finding is actually in agreement with a previous study of 253 MA [7], which reported that material having higher creep ductility also gave longer creep life.

As a result of much higher carbon content (0.39%) in the as-cast 253 MA, it gives the longest rupture time, see Fig. 3, but the lowest ductility, see Fig. 4, compared to other series. This indicates that creep strength increases with increasing carbon content. Meanwhile, increased carbon content will reduce creep ductility.

The relations between stress, time to rupture, and minimum creep strain rate, namely the Norton law and the Monkman-Grant correlation, c.f. eqns (1), (2) and (3), respectively, are found to be valid for 353 MA in the present study in which testing temperatures are very high, even higher than its spalling temperature of 1175°C. These relations have been found for many alloys at normal creep conditions. The combination and utility of these findings may open an opportunity for extrapolation, thereby lifetime prediction.

4.2 Fracture and creep damage

Examination of rupture mode reveals that transgranular and intergranular fracture dominate in the extruded tube and in the hot rolled plate, respectively, see Figs. 8a, 9a, 10a and 11a. This is independent of temperature, stress, and rupture time. This is expected to be due to the difference in rupture ductility. Lower and higher ductility are associated with intergranular and transgranular fracture, respectively.

Extensive creep damage in terms of cavities and cracks are often observed on both plate and tube at given testing conditions, especially adjacent to the fracture, see Figs. 8a, 9a, 10a, 11a and 11b. At such high temperatures, both diffusion and grain boundary sliding take place more easily, leading to extensive cavities and cracks.

For the plate, extensive creep damage can be found far away from the fracture and it distributes across the whole gauge length at both 1100°C and 1200°C, see Figs. 8b and 9b.

Severe creep damage are often found to be concentrated to either the fine grain dominated region, or at the boundary between the coarse and the fine grains, see Figs. 8a, 9a and 11a. This is independent of temperature and rupture time. The concentration of creep damage in the fine grain region is probably because there are more possible sites for damage generation due to grain boundary sliding.

For the tube, extent of creep damage decreases with increasing distance from the fracture at 1100°C, i. e. only few separate cavities are observed about 10 mm or more from the fracture, see Fig. 10b. At 1200°C, damage is only concentrated to the fracture. About 10 mm or more away from the fracture there is no cavitation at all.

Apparently, intergranular fracture, extensive creep damage development and distribution, as well as mixed grain size may result in reduced creep ductility and shorten creep life for the hot rolled plate, in comparison to the extruded tube.

Cavities occur usually at grain boundaries and interfaces between particle and matrix. In the present investigation, however, cavities are frequently observed inside the grain, see Fig. 11a, although boundary cavities and cracks are predominant. Cavities inside the grain have also been reported for 253 MA at 1100°C [6]. It is stated in [6] that the hot rolled 253 MA undergoes grain growth during creep testing. Since there are no other phases than austenite, grain coarsening could easily occur at such high temperatures. Consequently, cavities initially located at grain boundaries may be left behind the boundaries and positioned inside the grains. In addition to grain growth, cavities are found to occur at twins and the interface between precipitate and matrix. This can also explain why cavities are found inside the grains.

4.3 Oxide

Oxide formed on the surface of the specimen, see Figs 9b and 11b. This is more significant at 1200°C and long time tests. Oxide is also detected for 253 MA at 1100°C [6]. The reasons for oxidation could be i) too high temperature, e.g., 1200°C for 353 MA is higher than its spalling temperature of 1175°C, and ii) carbide precipitation and nitrogen pick-up which reduce oxidation resistance [1]. It is difficult, however, to measure the thickness of oxide since oxide was broken and fell when rupture took place and specimen was removed from the holder.

Cracks surrounded by cavities are associated with oxide. After initiated on the surface, the cracks propagate intergranularly into the material, see Figs. 9b and 11b. Intergranular crack propagation can be a consequence of the carbide precipitation, e.g. the formation of $Cr_{23}C_6$, in the neighbour of the grain boundary which results in a chromium depleted zone [1, 6].

4.4 Precipitation

A large number of particles precipitate after approximately 2000 hours both in the plate and in the tube material, see Figs. 8a, 8b, 10b and 11b. It seems that the precipitation is time controlled rather than strain controlled, since it occurs both along the gauge length and in the head of the specimens. The head should not be subjected to stress. Similar precipitation has been observed in 253 MA at 900°C [8] and at 1100°C [6] after long time testing, although in one case the precipitates were found already after 734 hours at 1100°C [6]. The precipitate has been identified as Cr_2N [6, 8]. In the present investigation, Cr_2N appears at the grain boundaries and twins, and inside the grains. In the previous study [6], however, Cr_2N is concentrated to fracture and cracks.

With the help of thermodynamical databases [10] the amount of different equilibrium phases can be computed. Thermo-Calc predicts that 2.5 at % Cr_3Si and 0.2 at % Cr_2N should be present at 1100°C after a sufficient long time for 353 MA. Surprisingly, no precipitates are obtained at 1200°C. Evidently the system underestimates the precipitation at 1200°C, which could be caused by segregation or inaccuracies in the thermodynamic data. Anyhow, Cr_3Si is a clear candidate for the precipitates also at 1200°C.

The presence of Cr_2N and possibly Cr_3Si precipitates is likely to have a beneficial influence on creep strength and ductility since there is no apparent indication of degraded creep strength and ductility at long times which can be due to the precipitation, see Figs. 3-5. It is well known that transgranular, and to some extent also intergranular precipitates contribute to an increased creep strength [1]. In the present case, the reduced tertiary creep rate on the plate at 1200°C/2.5 MPa could be due to precipitation strengthening. On the other hand, because of carbon and nitrogen pick-up, the formation of carbides and nitrides can embrittle the material and reduce the oxidation resistance due to a reduction of the amount of chromium in solid solution [1, 9].

5. Conclusions

Creep tests are carried out on austenitic stainless 353 MA at 1100°C and 1200°C. Materials in the form of hot rolled plate and the extruded tube are tested.

1) The hot rolled plate shows longer time to 1% and 2% creep strain than the extruded tube. The tube exhibits longer rupture time and better creep ductility than the plate.

2) The Norton law and the Monkman-Grant correlation are valid for both the plate and the tube at given testing conditions.

3) Independent of testing conditions, intergranular and transgranular failure is dominant for the plate and the tube, respectively.

4) Extensive creep damage in terms of cavities and cracks is found on both the plate and the tube materials. This is more pronounced adjacent to the fracture. For the plate, severe creep damage is detected across the whole gauge length and it is usually concentrated to the fine grained region. For the tube, the extent of creep damage decreases with increasing distance from the fracture. At 1200°C, no damage could be observed about 10 mm or more from the fracture.

5) Oxide is frequently detected on the surface of specimen. This is more significant at 1200°C and after long time testing. Associated with oxide, cracks surrounded by cavities initiate on the surface and propagate intergranularly into the material.

6) Nitrides, Cr_2N, and possibly Cr_3Si precipitate after approximately 2000 hours at both 1100°C and 1200°C. They appear at the grain boundaries, twins, and inside the grains. They are observed both within the gauge length and in the head of the specimen. It is likely that the precipitation has a beneficial influence on the creep strength and ductility, which can explain the good long term creep properties for 353 MA and 253 MA.

ACKNOWLEDGEMENT

This work was performed at the Swedish Institute for Metals Research (SIMR). The financial support from the participating companies, see below, and from the Consortium for Materials Science in Thermal Energy Processes, KME, is gratefully acknowledged. AvestaPolarit AB and AB Sandvik Steel are thanked for providing test material and relevant technical data. The late Dr Lars Lindé, SIMR, initiated the project. Prof. Rolf Sandström, SIMR, is thanked for comments and discussions. Mr. Anders Mårtenson, SIMR, is thanked for literature collection.

The members of research committee are thanked for comments and suggestions: Pamela Henderson, Vattenfall Utveckling AB; Maria Sundqvist, AB Sandvik Steel; Tage Johansson, Alstom Power Sweden; Bo Ivarsson, AvestaPolarit AB; Karin Törnblom, Birka Värme; Per-Olof Persson, CSM Materialteknik AB; Erik Skog, Sycon; and Thomas Hansson, Volvo Aero Corporation.

References

1. Segerbäck M., Ivarsson, B. G., Johansson R. and Kelly J. C; Avesta Sheffield 353 MA® - a Material for Very High Temperatures and Harsh Environments, ACOM Avesta Sheffield Corrosion Management and Application Engineering, 4-1995, (1995)
2. Johansson R., Hamer J., Redmond J. D. and Davison R.; Oxidation and high temperature corrosion resistance of REM-treated austenitic stainless steel, Proc. Int. Conf. Corrosion 90, Paper no. 294, Las Vegas, USA, April 23-27, (1990)
3. Harper M. A., Ducasse M. and Young D. J.; Cyclic oxidation plus carburization of heat-resistant alloys, Corrosion, Vol. 51, No. 3, (1995), p. 191-200
4. Tjokro K., Young D. J., Johansson R. E. and Ivarsson B. G.; High temperature sulfidation-oxidation of stainless steels, J. de Physique IV, Vol. 3, C9, (1993), p. 357-364
5. Lindblom J., Seitisleam F. and Henderson P. J.; Creep testing of steels at very high temperatures, JTEVA, Vol. 24, No. 5, September, (1996), p. 329-332
6. Lindblom J., Lofti A., Lindé L. and Seitisleam F.; Creep testing of the austenitic stainless steel 253 MA in cast and hot-rolled condition at 1100°C, Swedish Institute for Metals Research, IM-1999-013, April, (1999)
7. Yu M. D. and Sandström R.; Influence of Cerium on the creep properties of the austenitic stainless steel 253 MA, High Temperature Technology, Vol. 6, No. 3, (1988), p. 153-157
8. Yu M. D. and Sandström R.; Influence of carbon and nitrogen content on the creep properties of the austenitic stainless steel 253MA, Scand. J. Metallurgy, Vol. 17, (1988), p. 156-167
9. Data sheet and technical information, Sandvik stainless high temperature grades, S-130-ENG, http://www.sandvik.com, February, (2001)
10. Sundman B., Jansson B. and Andersson J-O.; The Thermo-Calc Databank System, Calphad, vol. 9, no. 2, (1985), p. 153-190

PROPERTIES AND EXPERIENCE WITH A NEW AUSTENITIC STAINLESS STEEL (TEMPALOY AA-1) FOR BOILER TUBE APPLICATION

Yusuke Minami
Materials & Processing Research Center
NKK CORPORATION
Kawasaki, JAPAN
Akira Tohyama and Hitoshi Hayakawa
NKKTUBES
Kawasaki, JAPAN

Abstract

A new austenitic stainless steel (TEMPALOY AA-1:0.1C-18Cr-10Ni-3Cu-Ti-Nb) has been developed. The allowable tensile stress of this steel is more than 30% higher compared with that of ASME SA-213 Grade TP347H in the temperature range 600-700℃. This superior creep rupture strength is caused by the precipitation of MC and $M_{23}C_6$ carbides, and Cu-rich phase. The hot corrosion resistance and long term aging properties of this steel are at the same level as 18Cr-8Ni stainless steels. The steam oxidation resistance can be achieved by a shot-blasting method.
Two years practical service as the superheater tubes in a boiler has revealed that the mechanical properties and environmental resistance of this steel are sufficient as boiler material. This steel has been already approved by METI standard in Japan as METI SUS321J2HTB.

Keywords: Creep rupture strength, austenitic stainless steel, boiler tubing, hot corrosion, steam oxidation

1 Introduction

Recently, the steam conditions of boilers for thermal power generation have become higher in temperature and pressure. The severe steam condition essentially requires the use of steels having superior high temperature strength than those of conventional steels. The resistance to steam oxidation and fuel ash corrosion is required for superheater and reheater tubes materials. It is also important that materials are easy to weld or fabricate, that they can be used for a long time at high temperature without their material properties deteriorating, and that their costs are low enough for plant economy.
The effects of various alloying elements on the creep rupture strength of 18-8 stainless steel were examined. As a result, TEMPALOY AA-1 (0.1C-18Cr-10Ni-3Cu-Ti-Nb) has been developed [1]. The allowable tensile stress of this steel is more than 30% higher compared with that of ASME SA-213 Grade TP347H in the temperature range 600-700℃. This superior creep rupture strength is caused by the precipitation of MC and $M_{23}C_6$ carbides, and Cu-rich phase. This report describes the properties of this new steel (TEMPALOY AA-1:0.1C-18Cr-10Ni-3Cu-Ti-Nb) and the results of two years practical service as superheater tubes.

2 Chemical composition and properties

2.1 Chemical composition

The chemical composition of TEMPALOY AA-1 is shown in Table 1. The base composition of this steel is 18%Cr and 10%Ni. The small amount of Ti and Nb are added from the viewpoint of creep rupture strength. Also, 3%Cu is added in order to increase the creep rupture strength [2]. The heat treatment is solution treatment and the structure is fully austenite phase as shown in Figure 1.

Table 1 Chemical composition of TEMPALOY AA-1 (mass%)

C	Si	Mn	P	S	Cu	Ni	Cr	Ti	Nb	B
0.07- 0.14	Max. 1.00	Max. 2.00	Max. 0.040	Max. 0.010	2.50- 3.50	9.00- 12.00	17.50- 19.50	0.10- 0.25	0.10- 0.40	0.0010- 0.0040

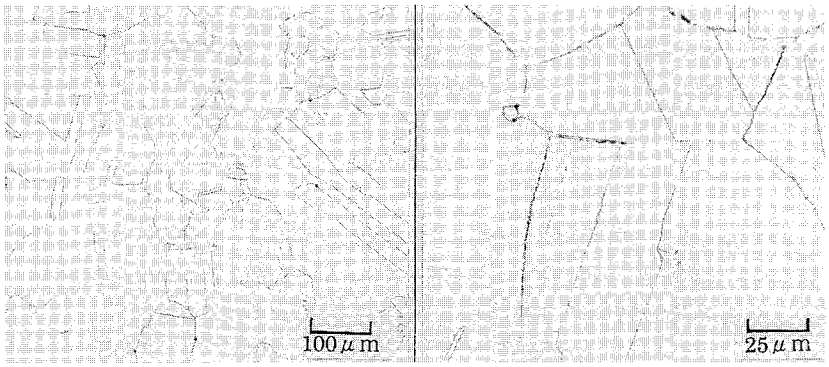


Figure 1 Microstructure of solution treated steel

2.2 Mechanical properties

The specification of the mechanical properties is given in Table 2. The tensile properties at elevated temperature of this steel are shown in Figure 2. The tensile strength and ductility are at the same level as conventional 18-8 stainless steels.

Table 2 Mechanical properties

0.2%Proof stress (MPa)	Tensile strength (MPa)	Elongation (%)
≧205	≧500	≧35

2.3 Creep rupture strength

The creep rupture strength of this steel is shown in Figure 3. The stress-rupture curves of this steel are stable in the temperature range from 600℃ to 800℃ and do not indicate any drop in rupture strength at longer period. The allowable tensile stress of TEMPALOY AA-1 is more than 30% higher compared with that of ASME SA-213 Grade TP347H in the temperature range 600-700℃.

2.4 Aging behavior

The charpy impact properties of this steel after aging are shown in Figure 4. Impact test temperature is 0℃. The impact value of this steel is over 100J/cm^2 after aging for 10,000h in the temperature range from 650℃ to 750℃.

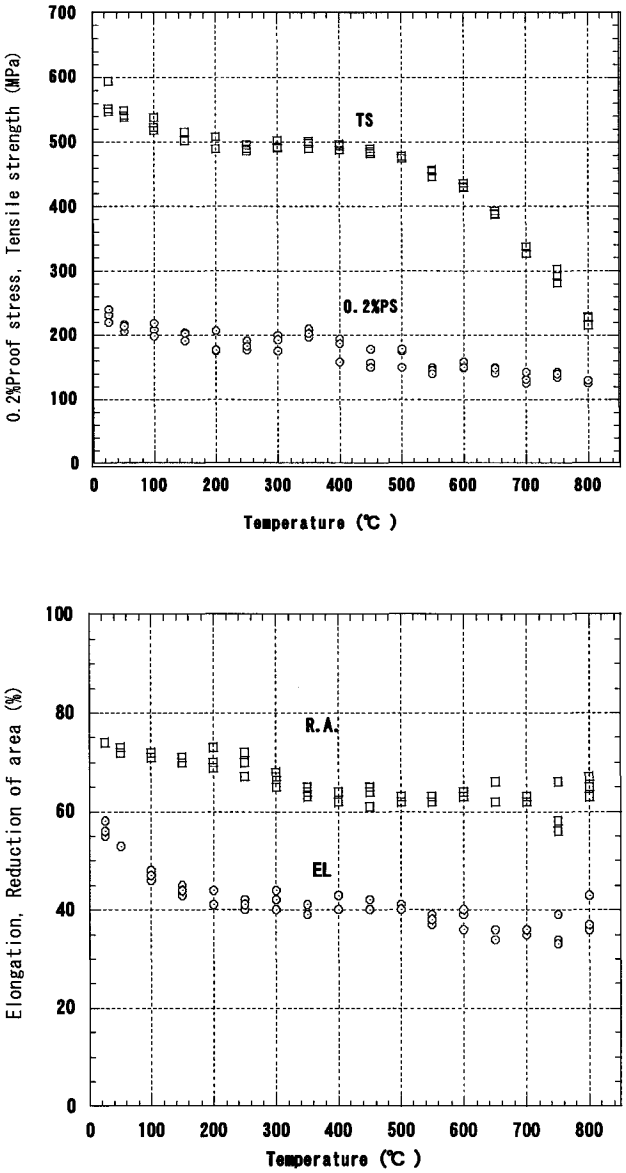


Figure 2 Tensile properties at elevated temperature

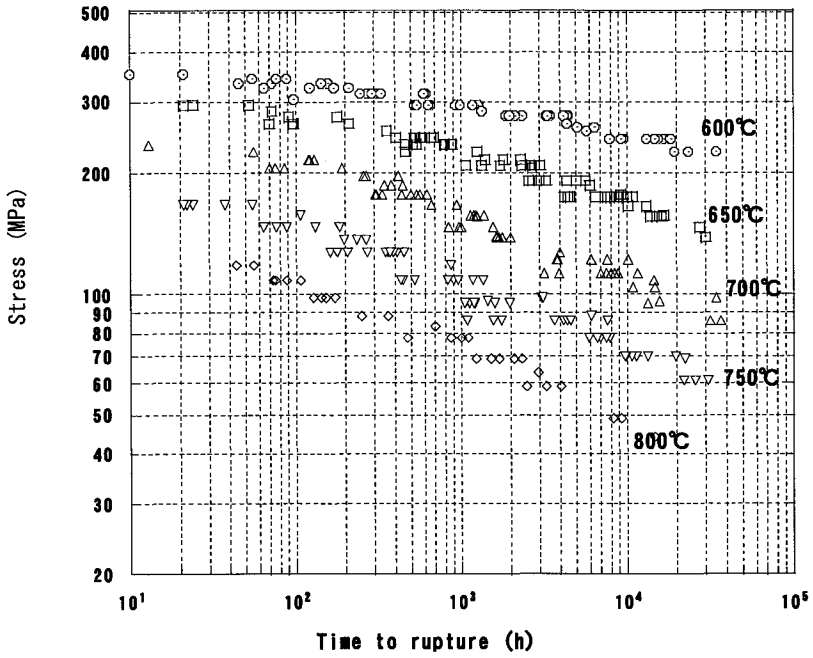


Figure 3 Creep rupture strength of TEMPALOY AA-1

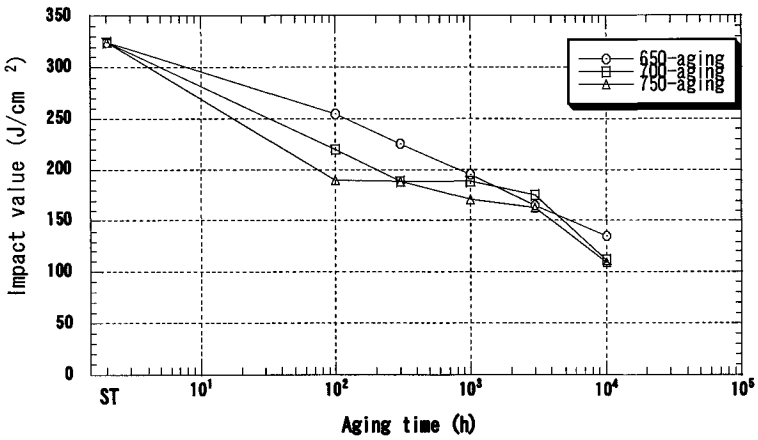


Figure 4 Charpy impact properties after aging

2.5 Corrosion resistance

The hot corrosion and steam oxidation tests were carried out. The results of these tests are shown in Figure 5 and Figure 6 respectively. The hot corrosion resistance of this steel is at the same level as SUS321H (18Cr-10Ni-0.4Ti) steel in coal-ash simulated environment. The steam oxidation resistance is also equal to SUS321H. There is no difference in hot corrosion and steam oxidation properties between TEMPALOY AA-1 and SUS321H because these properties primarily depend on the Cr content in the steel. The scale thickness of shot-blasted TEMPALOY AA-1 by steam oxidation is under 10 μm even at 750℃ for 1000h. The excellent steam oxidation resistance produced by shot-blasting was reported in other papers [3]-[4].

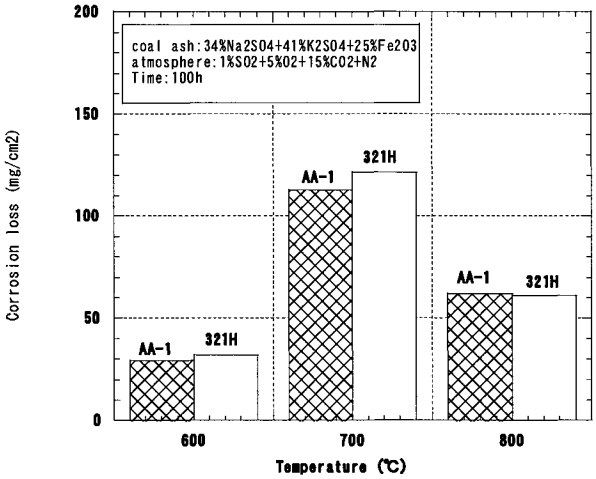


Figure 5 Hot corrosion properties

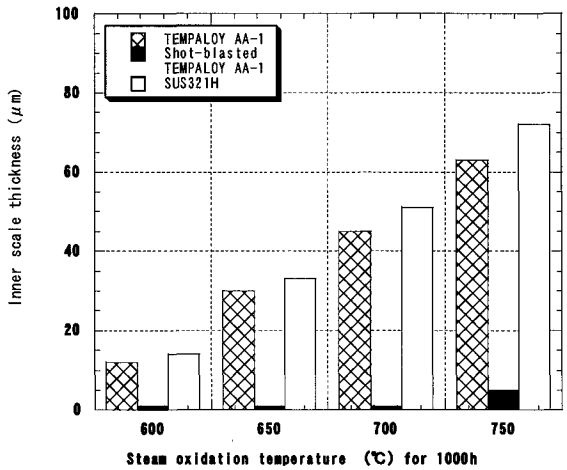


Figure 6 Steam oxidation properties

3 Field service experience

3.1 Tube and field condition

The chemical composition of the tube for field service is shown in Table 3.

Table 3 Chemical composition of the tube (mass%)

C	Si	Mn	P	S	Cu	Ni	Cr	Ti	Nb	B
0.10	0.29	1.57	0.025	0.004	2.87	10.37	17.92	0.19	0.27	0.0024

The dimension of the tube is outer diameter 57.1mm and wall thickness 11.9mm. The field service duration is two years. The tube was installed as the secondary superheater in the boiler. The operation condition of the boiler is listed in Table 4. The steam condition is sub-critical pressure.

Table 4 Operation condition of the boiler

Boiler	NKK Ohgishima Power Station No.1 Boiler
Steam Pressure	13.2/2.86 MPa
Steam Temperature	541/541℃
Amount of Main Steam Flow	410T/H
Service Period	1997.4～1999.3 (two years)

3.2 Appearance and dimension

The outer surface of the tube shows red brown color. The fuel ash is not deposited on the outer surface. The local corrosion by fuel ash is not detected. The inner surface of the tube shows blue gray color. The exfoliation of the scale by steam oxidation on the inner surface is not observed.

The dimension of the tube was measured after removing the deposit on the outer surface and the scale on the inner surface. There is no difference in outer diameter and wall thickness between before and after using the tube.

3.3 Microstructure

The optical microstructure of the tube after two years service was observed. Although there are fine carbides along the grain boundary, no sigma phase is observed on the triple points of the grain boundary. The microstructural change of this tube is sufficient for long time use.

3.4 Mechanical properties

The tensile properties of the tube were examined both at room temperature and elevated temperature. There is no difference in tensile strength and proof stress of the tube between before and after use, and the ductility is also at the same level. Charpy impact test was performed at 0℃. The average value of three specimens of the used tube is 190J. This value is enough for a superheater tube.

3.5 Creep rupture strength

The results of creep rupture test for used tube are shown in Fig.7. The specimens were sampled from the flame and the rear side on the tube. The creep rupture strength of both sides is at the same level and equal to the strength of new tubes. This result shows that this steel has sufficient creep rupture strength as a superheater tube after long time use.

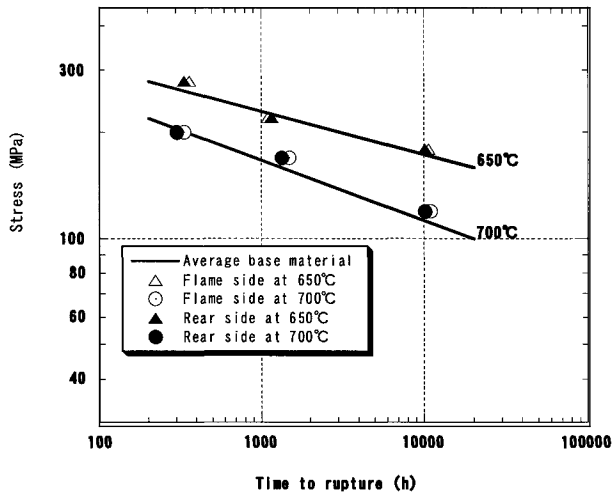


Figure 7 Creep rupture strength of the tube after two years service

4 Conclusions

A new austenitic stainless steel TEMPALOY AA-1 has been developed. This steel shows adequate properties as boiler tubing.
(1) The allowable tensile stress of this steel is more than 30% higher compared with that of ASME SA-213 Grade TP347H in the temperature range 600-700℃.
(2) The hot corrosion resistance and long term aging properties of this steel are at the same level as 18Cr-8Ni stainless steels.
(3) The steam oxidation resistance of this steel is also equal to conventional 18Cr-8Ni stainless steels. The excellent resistance to steam oxidation can be achieved by shot-blasting.
(4) Two years practical service as the superheater tubes in a boiler has revealed that the mechanical properties and environmental resistance of this steel are sufficient as boiler material.
(5) This steel has been already approved by METI standard in Japan as METI SUS321J2HTB.

References

[1] A.Tohyama, M.Miyauchi and Y.Minami, "DEVELOPMENT OF 18Cr-10Ni-3Cu-Ti-Nb STAINLESS STEEL FOR ULTRA SUPER CRITICAL BOILERS", Materials for Advanced Power Engineering 1994, Part1, p.495
[2] Y.Minami and H.Kimura, "THE EFFECT OF Cu ADDITION ON THE CREEP RUPTURE STRENGTH OF 17Cr-14Ni-Cu-Mo STAINLESS STEEL", International Conference on Creep, Tokyo (1986), p.221
[3] Y.Minami, A.Tohyama, M.Seki, K.Nonaka and K.Koga, "Steam-Oxidation Resistance of Shot Blasted Stainless Steel Tubing After 10-Year Service", NKK

TECHNICAL REVIEW No.75 (1996)
[4] M.Miyauchi, A.Tohyama and Y.Minami, "Steam-oxidation Property of the Shot-blasted Stainless Steel Tubing for 10 years Service", ICOPE-93, JSME-ASME International Conference on Power Engineering (1993), p.53

IMPROVEMENTS IN THE SHORT TERM CREEP STRENGTH OF AISI 304L BY MEANS OF GRAIN BOUNDARY DESIGN AND CONTROL

S.Spigarelli*, M.Cabibbo*, E.Evangelista* and G.Palumbo**

* INFM/Department of Mechanics, University of Ancona, Via Brecce Bianche I-60131 Ancona, Italy
** Integran Technologies Inc., 1 Meridian Road, Toronto, Ontario, M9W 4Z6, Canada

Abstract

The creep response of an AISI 304 L steel with a high fraction of low-Σ boundaries was investigated at 853 and 923 K. The analysis of the experimental data showed that in the low stress regime the minimum creep rate of the investigated material was two orders of magnitude lower than that measured in another AISI 304 L with conventional grain boundaries. The stress exponent was close to 10 and 15 at 923 and 853 K respectively, while the activation energy was 594 and 698 kJ/mol at 230 and 200 MPa respectively. The increase in creep strength was attributed to the intrinsic nature of grain boundaries, in particular to their almost complete immunity from carbide precipitation. It was thus supposed that the low C content was preserved for further precipitation on dislocations during creep exposure.

Keywords: grain boundary control, creep

Introduction

The concept of grain boundary design and control was introduced in 1984 by Watanabe [1], who identified the potential benefits, in term of improved properties, that could be obtained by manipulating the nature of grain boundaries in metallic materials. The grain boundary nature can be described by means of the Coincidence Site Lattice (CSL) model, based on the misorientation of adjoining crystals [2]. A three-dimensional sublattice, with points common to both crystals, in fact, can be obtained and the reciprocal of the volume fraction of coincidence sites, relative to the unit cell of a single crystal lattice, gives the Σ-parameter. It is thus clear that increasing Σ-values correspond to a greater degree of disorder at interfaces of adjacent grains; low-Σ boundaries, on the other hand, naturally occur, but their frequency depends on the thermomechanical history of the material [3]. As a result, conventional materials exhibit a low (<25%) population of low-Σ boundaries. This is a clear disadvantage, since low-Σ boundaries exhibit special chemical and mechanical properties, including a high resistance to sliding, cavitation and fracture, as well as a relative immunity to corrosion and sensitisation. Several studies [3-4], for example, demonstrated that low-Σ alloys show reduced susceptibility to impurity segregation and high resistance to intergranular corrosion, aspects of great industrial relevance for a structural material like the austenitic stainless steel AISI 304 L [5]. In this context, the analysis of other aspects related to the mechanical response at high temperature of low-Σ structural materials, for example of the creep strength, could provide the opportunity for a more accurate lifetime prediction. The aim of the present study

is precisely to evaluate the short term creep behaviour of a low-Σ AISI 304 L steel, and to make a comparison with the data available in the literature for other materials of similar composition but with high Σ.

Material and experimental procedure

The AISI 304 L (carbon content 0.017% in weight) was supplied by Integran Technologies Inc. (Ontario, Canada). The steel has 63% low-Σ boundaries, and an average grain-size of 15 μm. Constant load short-term creep tests were carried out at 853 and 923 K on samples of 25 mm gauge length and with 3.2 mm x 3.2 mm section. The majority of the tests were carried out to rupture, even if the tests under the lower stresses were interrupted after the beginning of the tertiary stage.

Results

Figure 1 plots the shape of the creep curves obtained by testing the AISI 304 L at 923 K; the curves exhibits a well defined primary stage, followed by a secondary or a minimum creep rate range, and by an extended tertiary region.

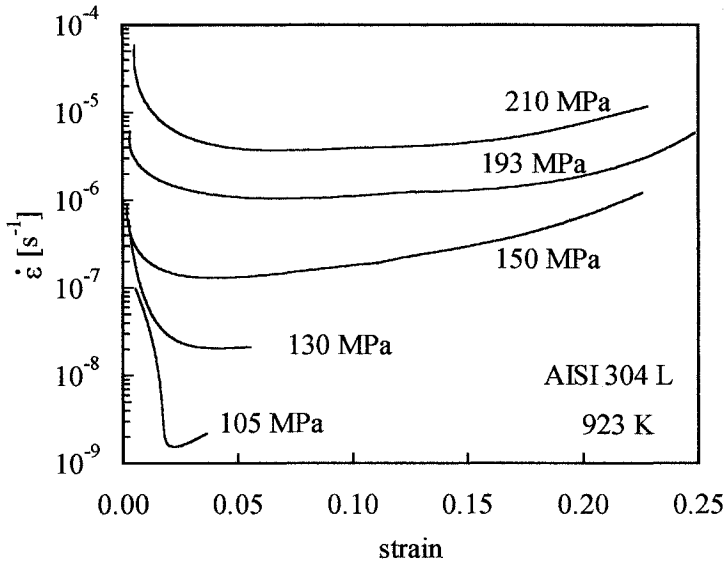


Figure 1 Shape of the creep curves obtained by testing the low-Σ AISI 304 L at 923 K. The tests at 130 and 105 MPa were interrupted.

Figure 2 plots the minimum (or secondary) creep rate ($\dot{\varepsilon}_m$) as a function of applied stress. The data were described by means of the conventional power-law equation:

$$\dot{\varepsilon}_m = A\sigma^n \qquad (1)$$

where A is a temperature dependent parameter, and n is the stress exponent (n=10.4 and 15.6 at 923 and 853 K respectively). The apparent activation energy for creep, defined by the relationship

$$Q = R \ln\left(\frac{\dot{\varepsilon}_{m2}}{\dot{\varepsilon}_{m1}}\right)\frac{T_1 T_2}{T_2 - T_1} \qquad (2)$$

with T_1=853 K and T_2=923 K, was estimated, from the lines in Fig.2, as 594 and 698 kJ/mol under applied stress of 230 and 200 MPa.

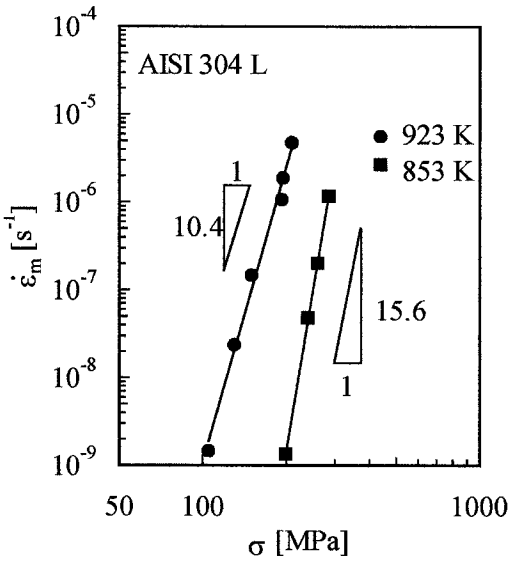


Figure 2. Minimum strain rate as a function of applied stress.

Figure 3 plots the relationship between the time to fracture / strain to fracture ratio (t_r/ε_c) and the minimum creep rate; the figure clearly demonstrates that the Dobes-Milicka relationship [6]

$$\frac{t_r \dot{\varepsilon}_m}{\varepsilon_r} = \text{const} \qquad (3)$$

is satisfied; for comparison purpose, the data obtained by Gold et al. [7] by testing a conventional AISI 304 (C=0.08% max.) have been included in the figure. The two materials exhibit the same behaviour, an indication of the same deformation dependence of rupture processes [6].

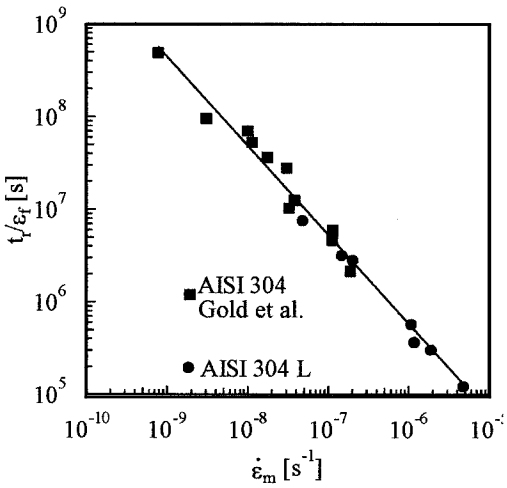


Figure 3. Dependence of ratio of time to fracture to total creep strain on minimum creep rate.

Figure 4 plots the hardness, measured along the gauge length of fractured samples, as a function of time to rupture. Since the changes in hardness are the result of the variation of dislocation density as well as of the precipitation hardening due to $M_{23}C_6$, the lines connecting data points in Fig.4 do not represent the time-

dependence alone, as in the case of ageing studies. Nevertheless, Figure 4 suggests that precipitation hardening should play a relevant role. It is well know, in fact, that an increase in applied stress corresponds to a substantial increase in free dislocation density and to a parallel decrease in subgrain size, that in any case remain constant during the secondary and tertiary stages of each test [8,9]. Thus, it should be concluded that the effect of a decrease in stress (i.e. an increase in time of exposure) corresponds to a monotonic variation in hardness. The peak in hardness in Fig.4 should be more likely associated with differences in carbide size and distribution, a result of dynamic precipitation during creep. For comparison purposes Fig.4 includes the data obtained by testing an AISI 304 H [10]. The higher HV values in AISI 304 H can be easily explained by the higher C content (C=0.07%) available for both grain boundary and intragranular carbide precipitation.

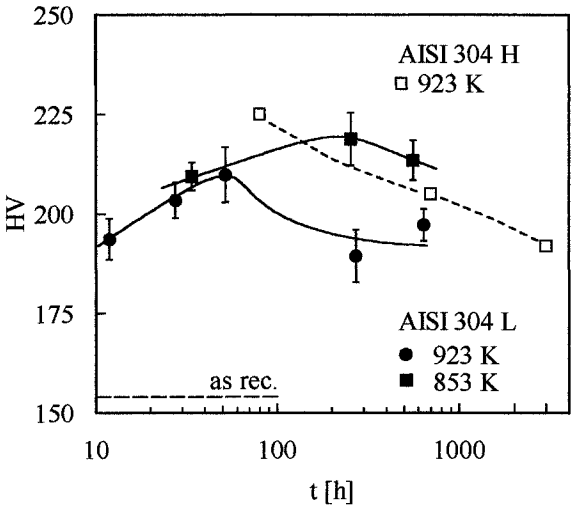


Figure 4. Hardness measured along the gauge length of fractured crept samples. For comparison purpose the data on an AISI 304 with 0.07% C [10] have been included.

Discussion

A comparative analysis of the data of the present study with those available in the literature unambiguously indicates that both the stress exponent and the apparent activation energy for creep are substantially higher for the low-Σ AISI 304 L. This "anomalous" behaviour is clearly illustrated in Table I and Figure 5. In particular, Figure 5 clearly shows that the low-Σ steel exhibits the lowest values of minimum creep rate of the whole set of steels considered in this study, with the exception of the AISI 304 investigated by Gold et al. [7]. A direct comparison between the times to rupture observed in this study, and those reported in ref.[7], confirms that the two materials do not simply exhibit similar minimum creep rate values, but have also an equivalent creep strength.

Table I. Resume of literature data on minimum creep rate dependence on applied stress for AISI 304 and AISI 304 L steels. The activation energy for self diffusion in austenite is close to 270 kJ/mol [11]

steel	C content (Wt.%)	n	Q (kJ/mol)	ref.
AISI 304	-	5.6 (973 K) 5.9 (923 K) 6.5 (873 K)	385 (at 104 MPa) 334 (at 240 MPa)	[11]
AISI 304 L	0.015	6 (923 K)	285 (at 108.1 MPa)	[12]
AISI 304	0.056	8 (923 K)	326 (at 123.5 MPa)	[12]
AISI 304 L	0.017	10.4 (923 K) 15.3 (853 K)	594 (at 230 MPa) 698 (at 200 MPa)	this study

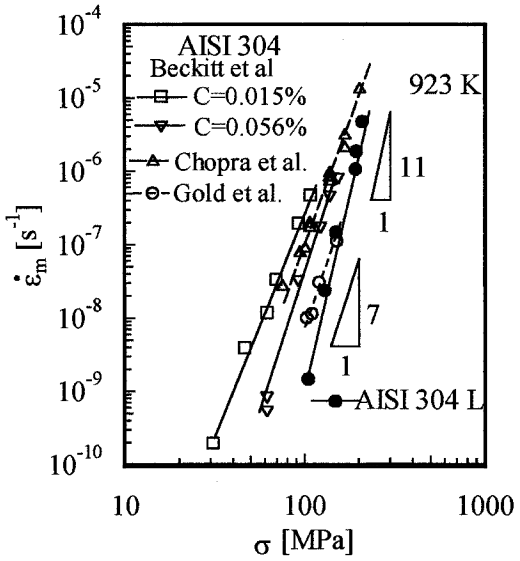


Figure 5. Comparison between the minimum creep rate dependencies on applied stress for different AISI 304 steels (see also Table I for details and references)

The differences observed when comparing different heats of materials with similar composition but different C content have been usually explained by the effect of dynamic precipitation of $M_{23}C_6$ during creep [11,12]. It is well known that precipitation occurs during high temperature exposure preferentially along grain boundaries [13,14] and twin boundaries. These particles, which do not interact with dislocations, can raise hardness but have a minor effect on creep strength. At 923 K precipitation on dislocations occurs only for relatively long times (well above 500 h) of exposure [13]. In this sense, the observation that AISI 304 L exhibits, in general, the highest minimum creep rate, at a given stress, can be easily explained by considering the very limited C-content available for precipitation. Yet, this picture cannot be reconciled with the data obtained in the present study, unless it is supposed that all C is retained in solid solution until it precipitates on dislocations, restricting dislocation mobility. Very high values of the stress exponent and of the apparent activation energy for creep like

those reported herein are usually considered an indication of a threshold-like behaviour [15], generated by the interaction between precipitates and dislocations. Additionally, it has been recently demonstrated that low-Σ boundaries are immune from precipitation [5,14]. If precipitation on grain boundaries is suppressed, or at least strongly reduced, it can be reasonably supposed that a considerable fraction of the low C content is indeed maintained in solid solution and precipitates after sufficiently long times of exposure. In any case it is obvious that this theory needs to be further supported by additional experimental evidence based on a careful analysis of the microstructure after creep exposure, since other mechanisms, also related to the intrinsic nature of grain boundaries, may significantly influence the creep response.

Conclusion

The creep response of an AISI 304 L steel with a high population of low-Σ grain boundaries was investigated at 853 and 923 K. The analysis of the experimental data showed that in the low stress regime the minimum creep rate of the investigated material was two orders of magnitude lower than that measured in another AISI 304 L with conventional grain boundaries. Additionally, the stress exponent n and the apparent activation energy for creep were found to be substantially higher than those of other general (i.e., high-Σ) materials with similar compositions. This behaviour was related to the intrinsic nature of grain boundaries, in particular with their almost complete immunity from carbide precipitation. It was thus supposed that the low C content was preserved for further precipitation on dislocations during creep exposure.

Acknowledgements
The authors greatly acknowledge Integran Technologies Inc. for providing material.

References

1] T.Watanabe, Res. Mechanica, 11 (1984) 47.
2] M.L.Kronberg and F.H.Wilson, Trans. TMS-AIME, 185 (1949) 501.
3]G.Palumbo, E.M.Lehockey and P.Lin, JOM, 50 (1998) 40.
4] G.Palumbo and K.T.Aust, in Materials Interfaces, D.Wolf and S.Yip Eds., Chapman and Hall, London, 1992, 190.
5] Y.Zhou, K.T.Aust, U.Erb and G.Palumbo, Scripta Mater., 45 (2001) 49.
6] F.Dobes and K.Milicka, Metal Sci., 11 (1976) 382.
7]M.Gold, W.E.Leyda and R.H.Zeisloft, Journ. Eng.Mater.Techn., 10 (1975) 305.
8] M.E.Kassner, Journ.Mat.Sci., 25 (1990) 1997.
9] M.E.Kassner and M.-T.Terez Prado, Progress in mat.Sci, 45 (2000) 48.
10] H.Tanaka, M.Murata, F.Abe and H.Irie, Mater.Sci.Engng., A319 (2001) 788
11] G.K. Chopra and K.Natesan, Metall. Trans., 8A (1977) 633.
12] F.R.Beckitt. T.M.banks and T.Gladman, in "Creep strength in Steel and High Temperature Alloys", The Metals Society, London, 1974, 71.
13] C.J.Novak, in Handbook of Stainless Steels, D.Peckner and I.M.Bernstein Eds., cGraw-Hill, New york, 1977, p.4-38.
14] H.U.Hong, B.S.Rho and S.W.Nam, Mater. Sci.Engng., A318 (2001) 285.
15] J.Cadek, Creep of Metallic Materials, Elsevier, 1988, 80.

MICROSTRUCTURAL FEATURES INFLUENCING THE CREEP PROPERTIES OF 9 – 12% CR – STEELS FOCUSING ON LAVES PHASE PRECIPITATION

Ch. Stocker[1)], K. Spiradek[1)], G. Zeiler[2)]

[1)] Austrian Research Centres Seibersdorf GmbH
Department of Materials Technology
A-2444 Seibersdorf, Austria

[2)] BOEHLER-Edelstahl GmbH
PO box 96
A-8605 Kapfenberg, Austria

Abstract

Due to environmental and economical demands concerning the reduction of emissions and increase of the efficiency of coal fired power stations further materials development was necessary in the past few years. Especially in the frame of the European research activities COST 501 and COST 522 significant steps forward have been made in understanding and identifying the main microstructural features that are responsible for the good/negative creep properties of 9 – 12% Cr – steels.
In this paper a modified 9% Cr – steels with additions of boron is introduced by presenting its superior creep behaviour and structural stability compared to conventional Cr – alloyed material. The microstructural features responsible for these outstanding high temperature properties will be presented and especially the role/effect of the Laves Phase precipitation on the mechanical high temperature properties will be stressed out. In this connection quantitative results describing the amount of Laves Phase depending on temperature, stress and time are presented and correlated with the creep test data. Further the growth rate and the chemical composition of this intermetallic compound is estimated and the results of a detailed investigation on a broken creep specimen will draw a picture of a possible damage mechanism occurring in the tertiary creep range.

KEYWORDS: 9% Cr steel, Laves Phase, electrochemical particle isolation, solid solution strengthening, creep

1. Introduction

The 9%Cr steel with boron developed in the frame of European COST 501 (and following rounds) program exhibit an excellent creep behaviour in the temperature range of 600-650°C [1]. The high degree of microstructural stability is a key to reach these properties. The microstructure of the steel is relatively complex, exhibiting the tempered martensitic structure with imbedded precipitates of MX and $M_{23}C_6$ in the as-received condition (forged component, austenitizing and two steps tempering) [2]. After a very long testing time changes in microstructure occur which influence the creep behaviour of the material. Beside the reduction of the dislocation density and subgrains formation (recovery processes), coarsening of $M_{23}C_6$ is going on and the precipitation of Laves-phase starts accompanied by compositional changes of both, the ferritic/martensitic matrix and the precipitates. Boron incorporated in $M_{23}C_6$ positively influences the creep strength, lowering the ripening rate of these particles which extends the precipitation strengthening at the beginning of the creep deformation and delays the recovery processes (by pinning of subgrain boundaries) in the later creep phases [3, 4].
The VN precipitates distributed within the martensite laths are rather stable during the creep acting as barriers for the dislocation movement [5].

A very important aspect is the contribution of the Laves-phase (Fe_2Mo) to the creep strength of the 9%Cr-steel with boron. The Laves-phase is known to reduce the ductility of steels (at

least at low temperatures) [6] due to its brittleness and the large size. In the literature one can find a very confusing information about the effect of the Laves-phase on the mechanical properties at elevated temperatures especially on the creep behaviour. Therefore systematic investigations were carried out to get an impression about the precipitation and coarsening processes of this phase during the long-term creep deformation. The results are correlated to the creep behaviour of the steel and discussed with respect to the effect on the creep properties.

2. Experimental Details

2.1 Material

The B – added 9% Cr – steel *B2* was manufactured by BÖHLER Edelstahl GmbH in Kapfenberg / Austria applying the electro – slag – remelting – secondary metallurgical process. The chemical composition (in weight-%), the heat treatment parameters and the obtained yield strength values of this material are specified in Table 1 and Table 2.

C	Si	Mn	P	S	Al	Cr	Mo	Ni	V	Nb	N	B
0,17	0,07	0,06	0,008	0,001	0,016	9,3	1,55	0,12	0,27	0,064	0,015	0,010

Table 1: Chemical composition of the investigated steel B2

Austenitizing		1st Tempering		2nd Tempering		Yield Strength
T [°C]	t [h]	T [°C]	t [h]	T [°C]	t [h]	[MPa]
1100	2	590	8	700	16	651

Table 2: Heat treatment parameters and yield strength values of the tested material

2.2 Experimental Procedure

To study and characterise the precipitation process of Laves-phase at 600°C detailed investigations on material extracted from creep specimens (head section: no stress (σ) influence; gauge length: combined influence of temperature (T) and stress (σ)) have been performed.

To estimate the volume - fraction of Laves-phase microstructural investigations were carried out with transmission electron microscope (TEM) (Philips CM 20 STEM with an acceleration voltage of 200 kV) applying TEM, STEM and SE techniques. Thin foils were prepared by mechanically grinding and electrolytically polishing in a solution of 10% perchloric acid and 90% acetic acid. The precipitated phases in general were identified by selected area electron diffraction in combination with EDX – analysis. The quantitative particle parameters (equivalent circle diameter, area - and volume fraction) were evaluated by image analysis using the software package ANALYSIS 2.11 provided by Soft – Imaging – Software GmbH.

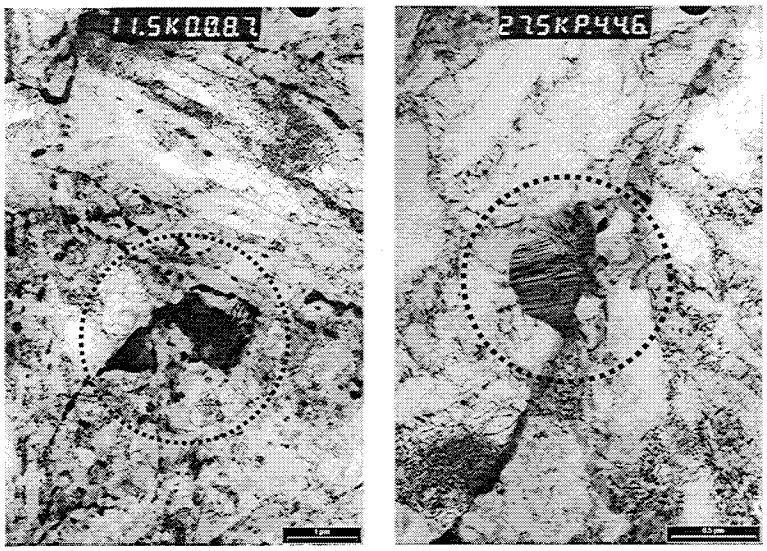
To crosscheck the results from the TEM analysis the method of electrochemical isolation of particles and the selective dissolution of Laves-phase respectively was used as well to measure the quantity of this intermetallic compound. The steel matrix was dissolved anodically in an electrolyte during a potentiostatic electrochemical process. Details of this method are given in [7]. The remaining residuals contain all precipitated phases (carbides, carbonitrides, Laves-phase,..) of this steel. In relation to the amount of matrix that has been dissolved their weight fraction can be estimated. As an additional advantage of this procedure

the chemical composition of Laves-phase (and other particles) can be revealed by EDX in TEM without the influence of the surrounding matrix. In order to quantify its amount the isolated phases were treated with a solution in which Laves-phase exclusively dissolves. Due to the fact that the other types of precipitates are not affected the share of this intermetallic compound can be determined.
To study the creep degradation processes that are related to the presence of Laves-phase the microstructure of a broken creep specimen (600°C, 160 MPa, 16703h, A_U = 16,9%) was investigated in the necked area near the fracture surface. Therefore one half of the broken sample was cut into two parts along its axis, mechanically grinded, polished and afterwards etched for 15 seconds in Villela – solution (1g picric acid, 5 ml HCl and 100 ml Ethanol). The following analysis were carried out using a Field Emission Gun (FEG) – Environmental Scanning Electron Microscope (ESEM) (Philips XL-30 FEG ESEM) at an acceleration voltage of 30 kV.

3. Results

3.1 Distribution of Laves-phase

In the as received condition the microstructure of the steel B2 is free of Laves-phase and the total quantity of precipitated phases in terms of weight fraction was found to be 3,47% (acc. to the electrochemical particle isolation). After a longer period of time at 600°C Laves-phase precipitates in this steel mainly on former austenite grain – and ferritic/martensitic lath boundaries (fig.1). Due to the fact that nearly all of the modern 9 – 12% Cr – steels that are used for applications at higher service temperatures are alloyed with significant amounts of Mo and/or W this kind of intermetallic compound can be observed in most of these materials.



a) b)

Fig.1: Laves-phase in steel B2 (after about 60 000h at 600°C) on a) lath boundaries and b) along former austenite grain boundaries

3.2 Identification of Laves-Phase

Laves-phase (type Fe_2Mo, hexagonal, structure type C14) was identified by selective area electron diffraction (SAD) in combination with EDX – analysis (fig.2).

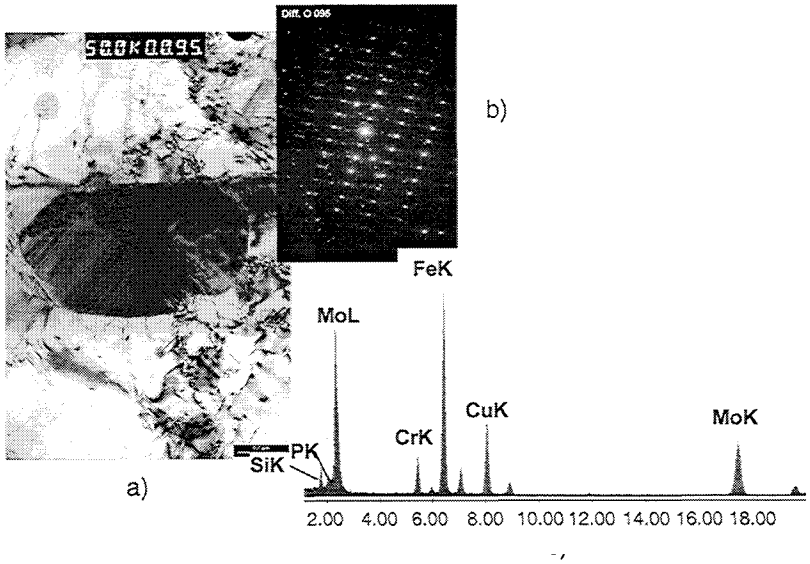


Fig.2: a) Laves-phase particle, b) selective area diffraction pattern of Laves-phase, c) corresponding EDX – spectrum (Cu – peak from copper containing specimen holder)

3.3 Chemical Composition of Laves-Phase

The chemical composition of Laves-phase was determined by energy dispersive X-ray analysis (EDX) of electrochemically extracted particles. A number of samples after different ageing times at 600°C (with and without the influence of stress) were analysed. These measurements revealed no significant changes of the chemical composition neither with time (t) nor due to the influence of stress (σ). The mean value of the chemical composition is given in Table 3. It is evident that Fe is substituted by Cr to a significant extent.

Weight - %				
Fe	**Mo**	**Cr**	**Si**	**P**
40,1 ± 1,5	46,6 ± 2,3	11,1 ± 2,7	1,7 ± 0,7	0,5 ± 0,1
At. - %				
Fe	**Mo**	**Cr**	**Si**	**P**
48,0 ± 1,9	32,6 ± 2,1	14,2 ± 3,3	4,1 ± 1,0	1,2 ± 0,3

Table 3: Chemical Composition of Laves-Phase in weight - and atomic - %

3.4 Amount of Laves-phase and Precipitation Kinetics

The amount has been estimated on material extracted from the head – and gauge length section of creep specimen in terms of area or volume fraction respectively. The measurements were carried out using SE techniques in transmission electron microscope. From these results the weight fraction of Laves-phase was calculated taking the mean chemical composition and the densities of the incorporated elements into account. On the other hand the weight fraction has been directly measured from the electrochemically isolated particles after selective dissolution of Laves-phase. Figure 3 summarises the obtained results and also presents the total amount of precipitates as measured with electrochemical particle extraction.

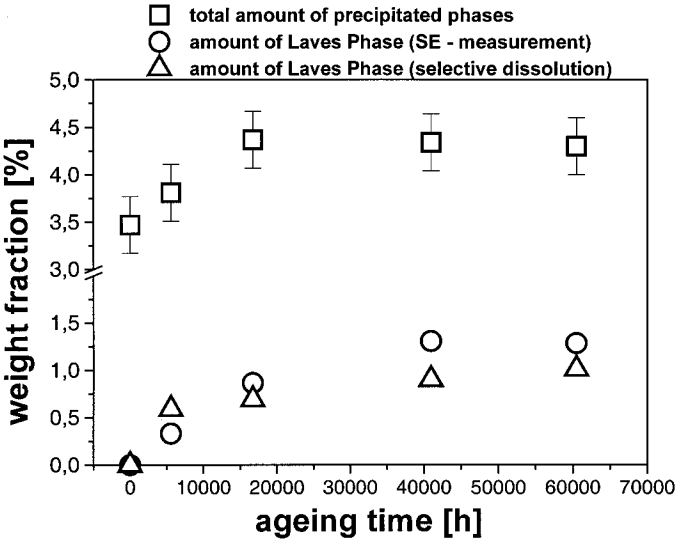


Fig. 3: Total amount of precipitated phases (electrochemical particle extraction) and weight fraction (acc. to SE – measurements and the method of selective dissolution) of Laves-phase depending on ageing time

It is obvious that the increase of the total amount of precipitated phases with ageing time can be attributed to the precipitation and growth of Laves-phase. A very important information is the fact that its fraction remains constant after about 40000h at 600°C. Therefore it can be assumed that the equilibrium condition has been reached after this time.

In material additionally exposed to stress (gauge length of the creep specimens) the weight fraction of Laves-phase seemed to be slightly higher but the difference is rather small.

The size of these particles has been measured using TEM and can be described in terms of equivalent circle diameter (ECD). The comparison of the values obtained in material extracted from the head section (t, T) and the gauge length (t, T, σ) of creep samples is shown in Figure 4.

According to these results Laves-phase grows with time up to about 40000h. A further coarsening of these precipitates after approximately 60000h has not been observed.

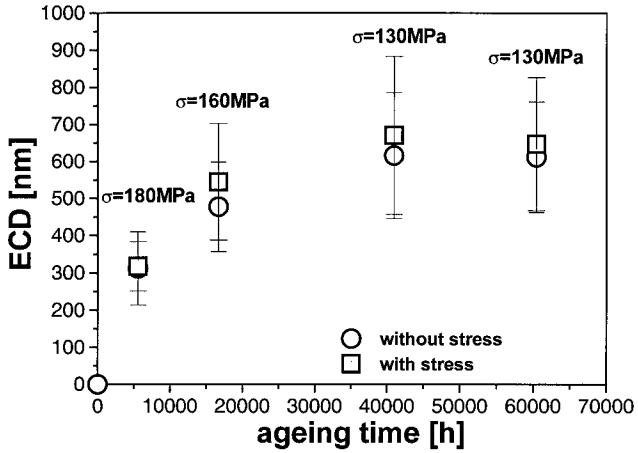


Fig. 4: Size of Laves-phase particles (Equivalent Circle Diameter) depending on ageing time at 600°C: with and without the influence of stress

Taking these results into account the precipitation kinetics of Laves-phase (without the influence of stress) can be described with an adjusted Johnson – Mehl – Avrami – type of equation (Figure 5):

$$f_L(t) = (1 - e^{-(\frac{t}{t_0})^n}) * f_L(t \rightarrow \infty)$$

$f_L(t)$.....	volume fraction of Laves-phase at a certain time
t_0.....	time constant
$f_L(t \rightarrow \infty)$.....	equilibrium amount of Laves-phase (volume fraction)
n.....	time exponent

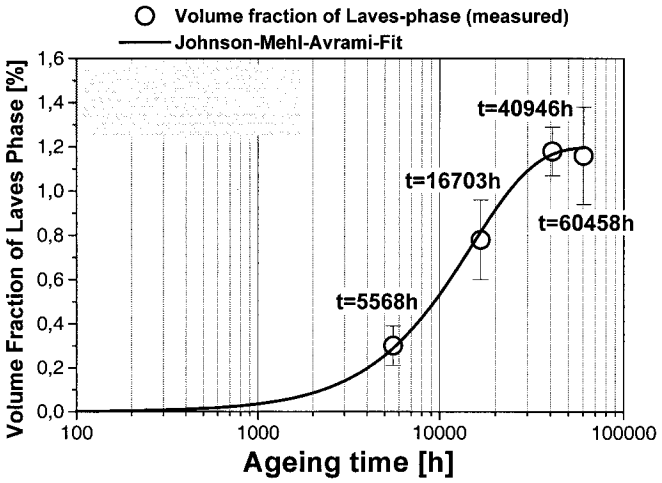


Fig. 5: Kinetic of the Laves-phase precipitation (Johnson – Mehl – Avrami – Fit)

3.5 Role of Laves-phase in Creep Damage Processes

In order to identify the effect of Laves Phase on the high temperature degradation processes the microstructure of a broken creep specimen (600°C, 160 MPa, 16703h, A_U = 16,9%) was investigated by SEM in the necked area near the fracture surface. No fractured Laves-phase particles could be found in this area. Only on the interface between Laves-phase and the surrounding ferritic matrix void formation could be observed in some cases (figure 6). It indicates that these precipitates have the similar effect on creep damage as the other particles of the same size (coarse $M_{23}C_6$, primary NbC).

Due to such behaviour the reduction of ductility of the steel could be expected. The higher the amount of coarse (~ >0,5 µm) particles in the microstructure (independent of the type of phase) the more voids may form (mainly in the tertiary creep range) leading to a reduction of the effective cross-section of the sample and to lowering of the creep rupture elongation .

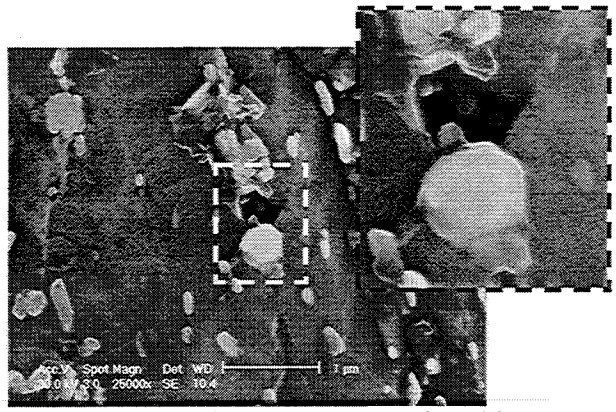


Figure 6: Void formation on the interface between Laves-phase / ferritic matrix in the necked area of a broken creep specimen (600°C, 160MPa, 16703h, A_U = 16,9%)

3.2.5 Reduction of Mo-Content in Solid Solution Due to the Precipitation of Laves-phase

In the as received condition of the material, Mo was measured in solid solution, in primary MX particles (to a small extend) and in $M_{23}C_6$ precipitates. This could be revealed by EDX – analysis. Taking into account the weight fraction (~ 3,3 %) and the chemical composition of $M_{23}C_6$ it can be estimated that after the final heat treatment about 1/3 (~0,5 weight %) of the Mo in this steel is incorporated in these type of particles. The rest stays in solid solution. During the precipitation of the Mo – rich Laves-phase the content of Mo in the ferritic matrix reduces continuously down to a final value of about 1/3 of the total amount of molybdenum (1,55 weight %) in this steel (Figure 7).

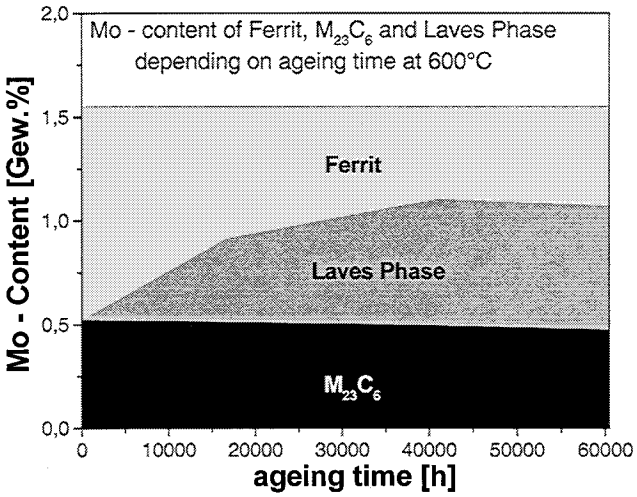


Fig. 7: Distribution of the total amount of Mo (1,55 weight %) in the microstructure of the investigated steel depending on ageing time at 600°C (without the influence of stress).

4. Summary and Discussion

In the steel B2 (9% Cr steel with 1,55% Mo and additions of B) at 600°C Laves-phase ($(Fe,Cr)_2Mo$, hexagonal, structure type C14) appears/precipitates after a few thousand hours mainly on former austenite grain – and ferritic/martenistic lath boundaries. The kinetics of this precipitation process can be described by an adjusted Johnson – Mehl – Avrami type of equation. The equilibrium condition is established after about 40000h of ageing at 600°C. After this time the precipitated volume fraction of Laves-phase of ~ 1,2 % remains constant. Stress seems to accelerate this precipitation process but has no significant influence on the equilibrium amount of this compound. The size of Laves-phase increases with the time up to the mean ECD – values of ~ 0,6 µm after 40000h. A further coarsening of these particles has not been observed which may be related to the relatively high values of interparticle spacing and the low diffusion rates (in the ferritic matrix) of the elements forming this phase (Fe, Mo, Cr). Additionally, due to its incorporation in $M_{23}C_6$ particles and as a result of appearance and growth of Laves-phase the content of Mo in solid solution (ferritic matrix) is continuously reduced during ageing at 600°C. Only approximately 1/3 of the total amount of Mo in this steel remains in solid solution after the equilibrium amount of $(Fe, Cr)_2Mo$ has precipitated. The correlation of these findings with the creep test results gives the impression that there is no significant detrimental influence on solid solution strengthening. In such a case the creep rates due to the reduction of the inner stresses should increase [8]. This effect however has not been observed. The main deformation process in the steel B2 at 600°C in the stress range between 100 and 180 MPa has been identified as climb controlled dislocation creep with a stress exponent n in the Norton creep equation ($(d\varepsilon/dt)_{min} = A * \sigma^n$) of approximately 5 [9]. Considering the fact that the climb of dislocations is diffusion controlled and that there are indications that the diffusion coefficient of Mo in Fe at this temperature is even slightly higher than the self-diffusion coefficient of α – iron [10] the solid solution strengthening effect of molybdenum (at 600°C) should be rather poor.

Concerning the influence of the Laves-phase on damage mechanisms caused by combined influence of temperature and stress, the investigation has shown that the void formation can be generally observed in the vicinity of different coarse (~ > 0,5 μm) particles not only of Laves-phase but also $M_{23}C_6$ and primary NbC. These occurrences influence rather negatively the material's ductility. The higher the amount of coarse particles the more voids will form and therefore the corresponding loss of ductility could be expected. In fact, the creep rupture elongation values of steel B2 decrease as the time to rupture increases [9] provided the same creep mechanism is dominant. Nevertheless this reduction of creep rupture elongation of steel B2 is not very pronounced and it can be assumed that the amount and/or the size of Laves-phase is obviously not high enough to cause a tremendous effect. On the other hand the fraction of coarse particles is increasing at a very slow rate due to the low growth rate of $M_{23}C_6$ precipitates (caused by the incorporation of B). So the ductility values of the steel can be expected to remain in an acceptable range throughout the whole life-time of the material.

5. Conclusions

- Laves Phase $(Fe, Cr)_2Mo$ precipitates in steel B2 at 600°C after a few thousand hours of ageing. The equilibrium condition is established after approximately 40000h. After this time a further increase of the amount or size of Laves-phase has not been observed.

- Despite its brittleness at room temperature no fractured Laves-phase – particles have been found in broken creep specimen. Void formation could be observed on the interface between the ferritic matrix and Laves-phase (and other coarse particles).

- After long periods of ageing at 600°C only 1/3 of the total amount of Mo in steel B2 remains in solid solution. At 600°C no significant reduction of solid solution strengthening caused by precipitation of Mo-rich Laves-phase will be expected. It is due to the fact that there are indications that the diffusion coefficient of Mo in α – iron at this temperature is slightly higher than the self-diffusion coefficient of Fe in ferrite.

6. Acknowledgements

The experimental work was done in the frame of the European COST 501 and 522 programs. The authors would like to thank The National Research Foundation of Austria for the financial support. The authors appreciated the creative discussions with Prof. Degischer, Institute of Materials Science and Testing, Vienna University of Technology.

7 References

[1] Staubli M.; Vanstone R.W.; Kern T.U.; Mayer K.H.: COST 501/COST 522 The European Collaboration in Advanced Steam Turbine Materials for Ultra Efficient, Low Emission Steam Power Plant, in: Proc. of the 5th Int. Charles Parsons Turbine Conf., 2000, A. Strang, W. Banks, R. Conroy, G. McColvin, J. Neal and S. Simpson (Ed.), (2000), 98 - 122

[2] Spiradek K., Bauer R., Zeiler G.: Microstructural Changes During the Creep Deformation of 9% Cr-Steel; in: Proc. of Materials for Advanced Power Engineering, Part 1, Liege , 1994, Courtsouradis D., Dividson J.H., Ewald J., Greenfield J., Khan T., Malik, M, Meadowcroft D.B., Regis V., Scarlin R.B., Schubert F., Thornton D.V. (Ed.), Kluwer Academic Publishers, Dordrecht/Boston/London, (1994), 251 - 262

[3] Nowakowski P., Straube H., Spiradek K., Zeiler G.: Microstructural Evolution During Creep of a New Modified 9% Cr-Steel with Boron and Cobalt; in: Proc. of Materials for Advanced Power Engineering, Part 1, Liege , 1998, J. Lecomte-Beckers, F. Schubert, P.J. Ennis (Ed.), Schriften des Forschungszentrum Jülich, (1998), 567 - 574

[4] Spiradek-Hahn K.; Nowakowski P.; Zeiler G.: Boron Added 9% Cr Steels for Forged Components in Advanced Power Plants; in: Proc. of the 9th Int. Conf. on Creep and Fracture of Engineering Materials and Structures in Swansea, 2001, J. D. Parker (Ed.); Institute of Materials, London :, (2001), 165 - 175

[5] V. Foldyna; "Microstructural Stability of Ferritic 9 – 12% Chromium Steels"; COST 501, Summarising Report, (1994)

[6] S. Kunimitsu, Y. You, N. Kasuya, Y. Sasaki and Y. Hosoi; "Effect of thermo-mechanical treatment on toughness of 9Cr-W ferritic – martensitic steels during aging"; Journal of Nuclear Materials 179-181, (1991), 689 – 692

[7] W. Koch; "Metallkundliche Analyse"; Verlag STAHLEISEN m.b.H., Düsseldorf (1965)

[8] R. Bürgel; "Handbuch Hochtemperatur-Werkstofftechnik"; Vieweg Verlag, Braunschweig/Wiesbaden, (1998), 130

[9] Ch. Stocker; "Effect of Laves Phase Precipitation on the Creep Behaviour of a new 9% Cr Steel with Mo and Additions of B"; PhD Thesis in progress to be submitted at the end of (2002).

[10] J. Fridberg, L.E. Törndal and Mats Hillert; "Diffusion in Iron"; Jernkont. Ann., 153, , (1969), 263 – 276

CREEP PROPERTIES OF PRECIPITATION STRENGTHENED CARBON FREE MARTENSITIC ALLOYS

Seiichi Muneki, Hiroshi Okubo, Hirokazu Okada, Katsumi Yamada, Masaaki Igarashi and Fujio Abe
Materials Creation Research Group, Materials Engineering Laboratory
National Institute for Materials Science
1-2-1, Sengen, Tsukuba, Ibaraki, 305-0047, Japan

Abstract

A new attempt has been demonstrated using carbon free Fe-Ni-Co martensitic alloys strengthened by μ-phase such as Fe_7W_6 or Fe_7Mo_6 and Laves phase such as Fe_2W or Fe_2Mo to achieve homogeneous creep deformation at high temperatures and low stress levels. Creep behavior of the alloys was found to be completely different from that of the conventional high-Cr ferritic steels. The alloys exhibited gradual change in the creep rate with strain both in the transition and acceleration creep regions, and give a larger strain for the minimum creep rate. In these alloys, the creep deformation took place very homogeneously and no heterogeneous creep deformation was enhanced even at low stress levels. The fine precipitates were found stable even at 973K and the minimum creep rate effectively decreased much lower than that of 304 stainless steel. Moreover, superior creep resistance was achieved by the addition of 5% Cr to the alloy.

Keywords: creep, USC boiler, carbon free, intermetallic compound, homogeneous deformation

1. Introduction

High Cr ferritic steels have successfully been used for large diameter and thick section boiler components such as main steam pipe and header in super critical (SC) boilers in fossil-fired power plants [1]. Recent trend to utilization of clean energy leading to protection of global environment has been accelerating application of ultra super critical (USC) boilers, which are operated with higher efficiency in power generation than in conventional ones and thus release less amount of carbon dioxide etc [2,3]. The USC boiler requires heat resistant materials with improved creep rupture strength at elevated temperatures over 873K, because of increase in operating temperature and pressure of the steam used. The expected goal of the steam condition for USC boilers is, however, now considered to be 903K and 30MPa[3], which might be the applicable limit of the conventional ferritic steels regarding their creep strength and the steam-oxidation resistance.

Creep deformation of the ferritic steels is controlled by recovery and softening process of the tempered martensite, which strongly depends on the constitution of the microstructure and its change with time [4,5].

To achieve long-term stability of the tempered martensite is considered to be the key to increase the creep resistance of the steels at elevated temperatures over 873K.

It is also noted that the creep behavior of the Fe-Ni-Co alloys is completely different from that of the conventional high-Cr ferritic steels. The Fe-Ni-Co alloys exhibit gradual change in the creep rate with strain both in the transition and acceleration creep regions, and give a larger strain for the minimum creep rate [6]. The addition of Pd and Cr to the carbon free Fe-Ni-Co alloy enhances much the creep resistance at elevated temperatures over 923K [7]. In this paper, the effect of Cr and Cr-Si additions to the alloy on the creep properties over 923K is discussed.

2. Experimental Procedure

Table 1 Chemical composition of the alloys used (mass%).

	C	Si	Mn	Ni	Co	W	Cr	Ti	Al
Base	0.0014	0.01	0.47	12.18	9.04	10.06		0.2	0.14
5Cr	0.0005	0.02	0.46	12.08	8.96	9.9	5.04	0.16	0.09
5Cr-1Si	0.0006	0.99	0.48	11.95	8.99	9.95	5.09	0.18	0.11
9Cr	0.0003	0.04	0.45	12.06	9.04	10.1	8.66	0.16	0.09

	N	B	Fe
Base	0.0006	0.0047	Bal.
5Cr	0.0005	0.0052	Bal.
5Cr-1Si	0.0016	0.0055	Bal.
9Cr	0.0006	0.0051	Bal.

The chemical compositions of the alloys used in this study are given in Table 1. They were melted as 10kg-ingots in a vacuum induction furnace. The ingots were pressed and rolled to 16mm square bars after heating for 1h at 1473K. They were aged for 1h between 773K and 1113K after solution treatment for 0.5h at 1273K. To examine the long-term stability of the microstructure of these alloys, specimens were aged for 1 to 1,000h at temperatures of 923 and 973K. Creep rupture testing was conducted in the range of temperatures from 923 to 1023K and in the range of stresses from 60 to 200MPa using a 6mm diameter and 30mm gauge length tensile specimen in the as solution treated condition. The microstructure of the alloys was examined using an optical microscopy and a field emission scanning electron microscopy. Transformation temperatures of A_s, A_f, M_s and M_f were measured with dilatometry by the following procedure. The specimens were induction heated from room temperature to 1273K at the heating rate of 10K/min, kept for 10min at 1273K, and then cooled to room temperature with the cooling rate of 10K/min.

3. Results and Discussion

Fig.1 shows the effect of additional elements on the transformation temperatures of A_s, A_f, M_s and M_f measured by dilatometry on heating and cooling with the rates of 10K/min. A_s and A_f temperatures of the base alloy were 1005K and 1077K, respectively. On the other hand, those of 5Cr and 5Cr-1Si alloys were identified about 200K lower than those of the base alloy. M_s and M_f temperatures were also decreased drastically by about 300K by the addition of 5% Cr. No transformation behavior was observed for 9Cr alloy. It was considered that too much addition of Cr decreased M_s and M_f temper-

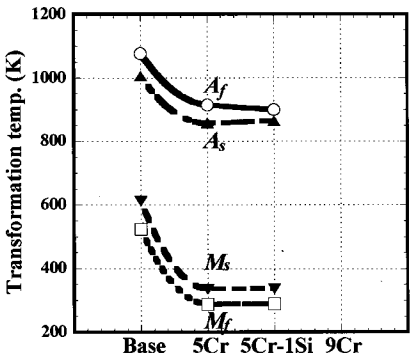


Fig.1 Change of transformation temperatures by additional elements of Fe-12Ni-9Co-10W alloy.

ature further so that the austenitic structure remained at room temperature.

Fig.2 shows hardness change of all four alloys after aging for 1h at the temperatures between 773K and 1113K. The three martensitic alloys: Base, 5Cr and 5Cr-1Si showed equivalent initial hardness of about HV320. Austenitic alloy 9Cr was softer than the three martensitic alloys and the hardness showed little change due to the aging. Whereas the three martensitic alloys were hardened by the 1h-aging especially at temperatures around 850K.

Fig.3 shows the time dependence of the hardness of the alloys aged until 1,000h at 923K(marked with open symbol in the figure) and 973K (marked with solid symbol in the figure). The three martensitic alloys were hardened immediately by the aging and then softened with the aging duration. However, the hardness of these alloys after 1,000h aging was equal or harder than that of solution treated condition. Whereas hardness of 9Cr alloy did not show any remarkable change even by the long-term aging.

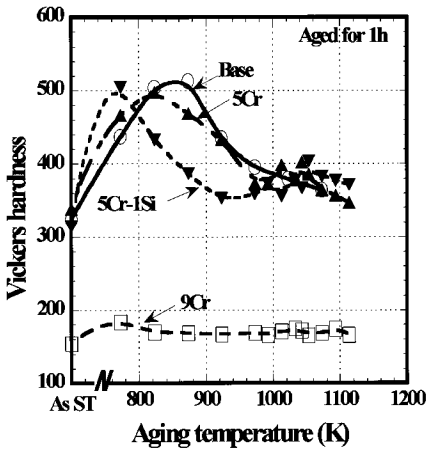


Fig.2 Hardness change of the alloys after aging for 1h at the temperatures between 773K and 1113K.

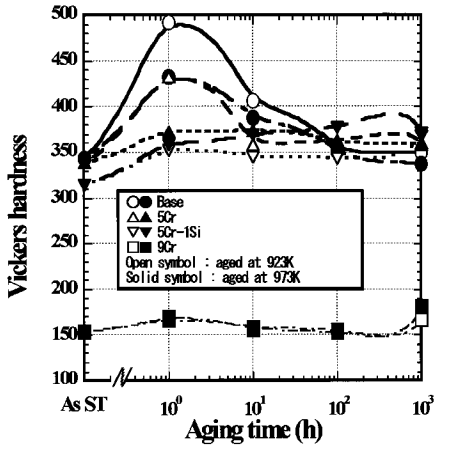


Fig.3 Time dependence of hardness on the alloys aged at 923K and 973K.

Fig.4 shows typical creep curves of all four alloys crept at 923K and 200MPa. Time to rupture of the base alloy was about 140h. Creep resistance was remarkably improved by the Cr addition, as shown in fig. 4. Especially time to rupture of the 5Cr alloy was about 20 times longer than that of the base alloy. Addition of Si to 5Cr alloy did harm to creep resistance of the alloy.

Fig.5 shows the creep rate vs. time curves of the alloys crept at 923K and 100MPa, which is half of the stress condition shown in Fig.4.

Only Base alloy ruptured at about 2,300h after passing the following process of the transition creep region, showing minimum creep rate, 2.7 x 10^{-5}(1/h) and the acceleration of creep. Tests of the other three alloys are still continuing over 20,000h and these curves do not have reached the minimum values of creep rate so far.

Fig.6 shows stress dependence of the time to rupture at 973K. For the base steel, logarithmic time to rupture increased linearly with decrease of logarithmic stress from about 220h at 120MPa to 4,100h at 60MPa. Creep strength at 973K was also increased by the addition of Cr. Among them the 5Cr alloy exhibited the most superior creep life and the creep tests at 100MPa and 80MPa continue over 20,000h.

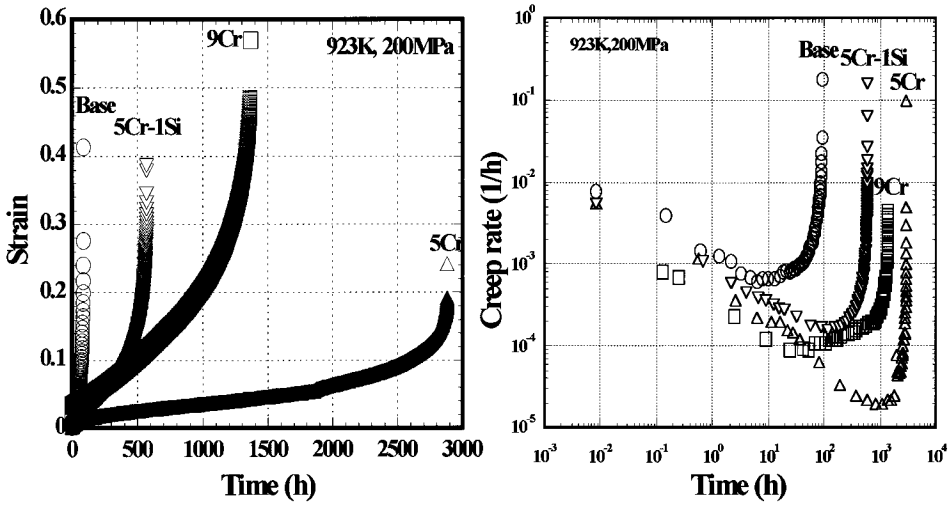


Fig.4 Creep strain vs.time and creep rate vs.time curves of the alloys crept at 923K and 200MPa.

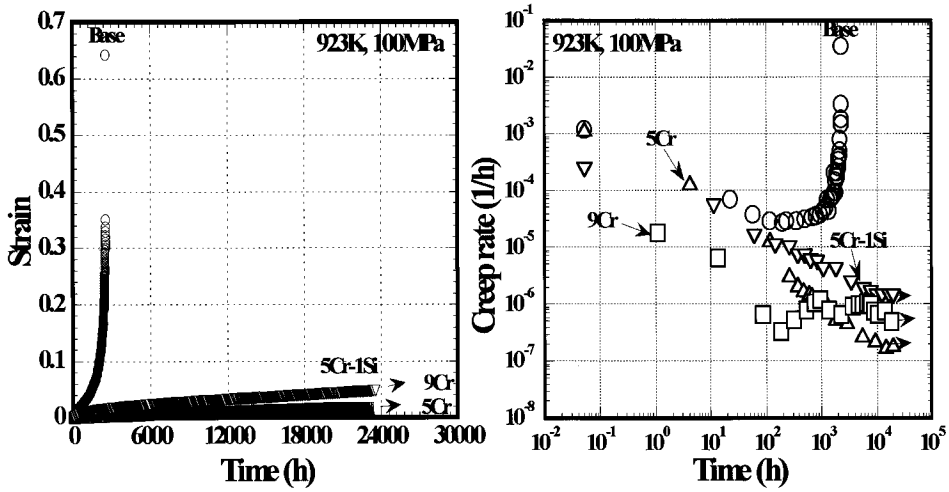


Fig5 Creep strain vs.time and creep rate vs. time curves of the alloys crept at 923K and 100MPa.

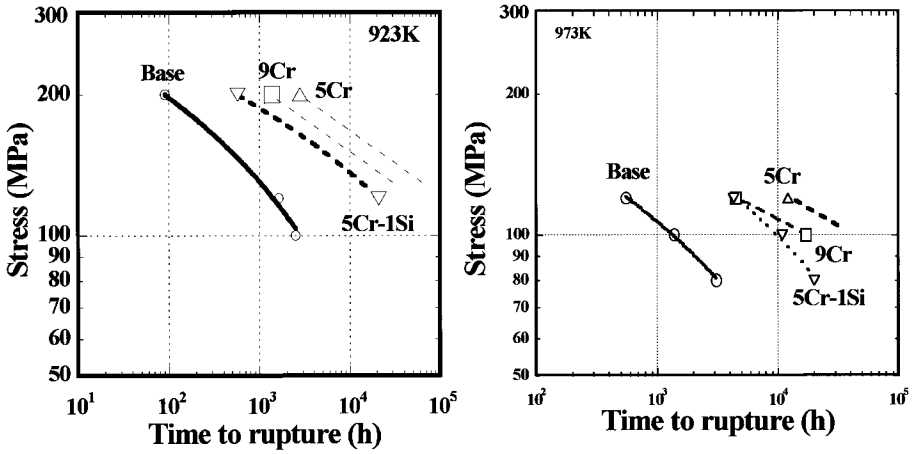


Fig.6 Stress dependence of time to rupture of the alloys crept at 923K and 973K.

Fig.7 shows the creep rate vs. time curves of the 5Cr alloy and 304 stainless steel crept at 973K and 100MPa [8]. Creep rates of these alloys were almost equivalent at the beginning of the creep test, but the creep rate of the 5Cr alloy remarkably decreased as compared with that of the 304 stainless steel during the transition creep region.

The minimum creep rate of the 5Cr alloy was about two orders in magnitude lower than that of the 304 stainless steel.

Fig.8 shows the creep rate vs. strain curves of the two alloys corresponding to Fig.7. In conventional high-Cr ferritic steels, at long-term creep region, heterogeneous deformation along prior austenite grain boundary is frequently observed and causes the transition to the acceleration creep at a small strain. In the case of modified 9Cr-1Mo steel crept at 873K and 100MPa, the transition strain to acceleration creep is less than 0.01 [9]. On the contrary, steady state creep of the 5Cr alloy still continues at the strain of 0.03, as shown in Fig. 8.

Fig.9 shows back scattered electron images of the 5Cr alloy after 1,000h aging at 923K(a) and 973K(b), respectively.

Primary austenite grain boundary were decorated semi-continuously with intermetallic compounds of μ (Fe_7W_6) and Laves (Fe_2W) phases. Such intermetallic compounds are also distributed finely and uniformly inside the grain with a large amount, as shown in Fig. 9. Even though the precipitations after aging at 973K showed some growth as compared to the aging at 923K, fine precipitates less than 100nm were still distributed uniformly. It was suggested that such fine and stable precipitations prevented the dislocation migration and improved the creep strength remarkably.

Fig.10 shows the SEM micrographs showing the changes in the microstructure of the head portion of the specimen crept at 973K and 100MPa. It is seen that the marked differences are the size and distribution of the m and Laves phases inside the grain even after the creep

test at about 12000h in the 5Cr alloy.

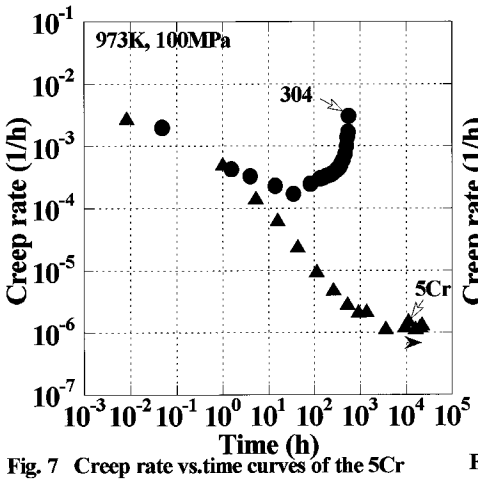


Fig. 7 Creep rate vs.time curves of the 5Cr alloys and 304 crept at 973K and 100MPa.

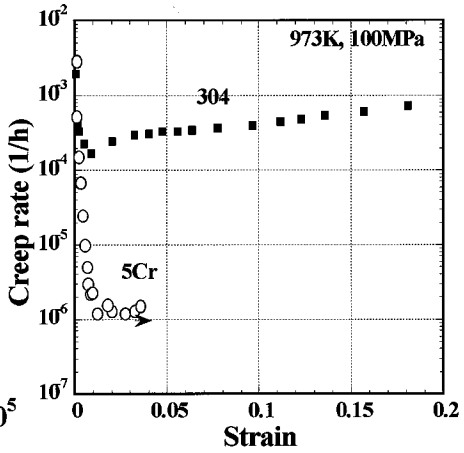


Fig.8 Creep rate vs. strain curves of the 5Cr alloy and 304 crept at 973K and 100MPa.

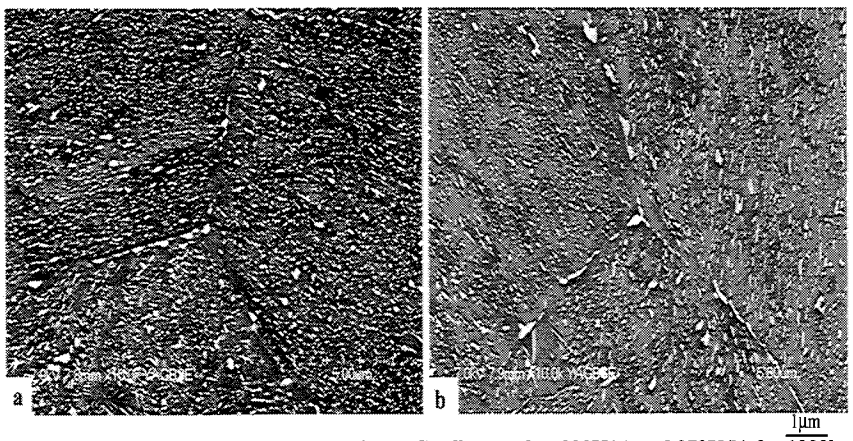


Fig.9 Back scattered electron images of the 5Cr alloy aged at 923K(a) and 973K(b) for 1000h.

Fig.11 shows the creep rate vs. time curves of the alloys crept at 1023K and 100MPa. Even at 1023K, creep resistance of the alloy was drastically increased by the addition of 5% Cr. Namely, the 5Cr alloy ruptured at 6,800h.

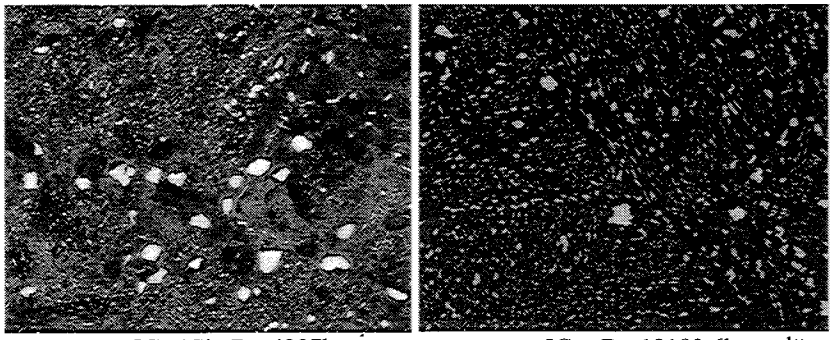


Fig.10 SEM micrographs showing the changes in the head portion of the specimens crept at 973K and 100MPa.

Thus it was concluded that the addition of Cr to the carbon-free Fe-12Ni-9Co martensitic alloys enhances the creep resistance at elevated temperatures in the range of 923 to 1023K due to fine dispersion strengthening and the homogeneous creep deformation, although further detailed phase identification may be necessary to clarify how Cr affects the formation of these fine precipitates.

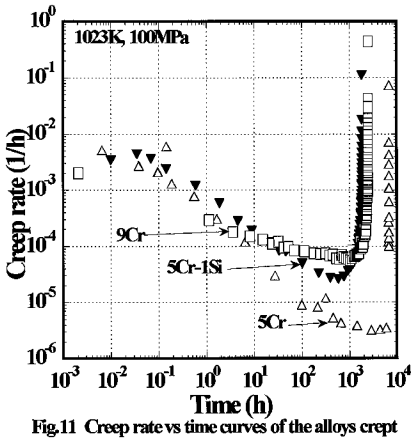


Fig.11 Creep rate vs time curves of the alloys crept at 1023K and 100MPa.

4. Conclusion

A new attempt has been demonstrated using carbon free Fe-12Ni-9Co martensitic alloys strengthened by μ and Laves phases such as Fe_7W_6 and Fe_2W to achieve homogeneous creep deformation at high temperatures and low stress levels. The addition of Cr to the carbon free Fe-12Ni-9Co alloy improved the creep resistance remarkably at elevated temperatures over 923K. Especially the 5Cr alloy exhibited a homogeneous creep deformation even in the long-term creep region contrary to the conventional high-Cr ferritic steel and showed superior creep resistance to the austenitic stainless steel 304.
Uniformly distributed fine and stable intermetallic precipitation is one of the reasons of this excellent creep property.

Acknowledgement

The authors would like to express their sincere gratitude to Mrs. Wakako Moriiwa and Mrs.

Toshiko Ishizuka for their sincere collaboration in experiments.

REFERENCES

[1] V.K.Sikka, C.T.Ward and K.C.Phomas, "Modified 9Cr-1Mo Steel - An Improved Alloy for Steam Generator Application", in ASM Int.Conf. Production, Fabrication, Properties and Application of Ferritic Steels for High Temperature Applications, Warren, PA. Oct.6-8 (1981).
[2] F.Masuyama, I.Ishihara, T.Yokoyama and M.Fujita, "Application of Tungsten Strengthened 9-12% Cr Boiler Steel Pipes", The Thermal and Nuclear Power, 46, (1995), 498.
[3] K.Muramatsu, "Development of Ultra-Super Critical Plant in Japan", in Proc. Advanced Heat Resistant Steels For Power Generation, 27-29 April, Miramar Palace, San Sebastian, Spain, (1998), 543.
[4] M.Igarashi, S.Muneki, H.Kutsumi, T.Itagaki, N.Fujitsuna and F.Abe, "A new concept for strengthening of advanced ferritic steels for USC power plant", Proc. of 5th Inter. Charles Parsons Turbine Conf, July 3-7, Cambridge, 2000.
[5] M.Igarashi, K.Yamada, S.Muneki and F.Abe, "Long-term creep deformation characteristics of α " precipitation hardened ferritic steels", in Proc. 4th Workshop on Innovative Structural Materials for the Infrastructure in the 21st Century, Tsukuba, 12-13 January 2000, p.106, (*in Japanese*).
[6] S.Muneki, H.Okada, K.Yamada, H.Okubo, M.Igarashi and F.Abe, "Creep Characteristics in Carbon Free New Martensitic Alloys", in Proc. 4th Pacific Rim Int. Conf. on Advanced Materials and Processing (PRICM4), Ed. by S.Haneda, Z.Zhong, S.W.Nam and R.N.Wright, JIM, (2001), 2691.
[7] S.Muneki, M.Igarashi and F.Abe, "Effect of Mo and W on Creep Characteristics of Precipitation Hardened Carbon Free Martensitic Alloys", Tetsu-to-Hagane, 88(2002), 45 (*in Japanese*).
[8] NRIM Creep Data Sheet, No.4B, (1986)
[9] K. Kimura, H. Kushima and F. Abe, "Heterogeneous Changes in Microstructure and Degradation Behavior of 9Cr-1Mo-V-Nb Steel During Long Term Creep", Key Engineering materials, Trans Tech Publications, Switzerland, 171-174 (2000), 483

MICROSTRUCTURE AND PROPERTIES OF MODIFIED 3%Cr STEELS

V.Foldyna[1, now 2], A.Jakobová[1], V.Vodárek[1], A.Kroupa[3],Z.Kuboň[1]
[1]VÍTKOVICE Research and Development Ltd., Ostrava, Czech Republic
[2]JINPO PLUS a.s.,Research and Development, Ostrava, Czech Republic
[3]Institute of Physics of Materials, Academy of Sciences of the Czech Republic, Brno, Czech Republic

ABSTRACT

Precipitation strengthening in steels investigated is predominantly affected by vanadium carbide. It is not practical to increase the Mo and /or W content in solid solution. Higher Mo and/or W content leads to formation of Mo and/or W rich M_6C carbide and dissolution of MX particles decreasing precipitation strengthening. Therefore increase overall Mo and/or W content in the steel over this limit does not offer any advantage. It has been shown that increasing V content up to stoichiometric ratio may improve creep resistance due to higher precipitation strengthening.

Keywords: precipitation strengthening, solid solution, carbide, thermodynamic equilibrium, degradation, THERMOCALC

1. Introduction

The efficiency of power plants can be improved by increasing the steam temperature and/or pressure. The development of more creep resistant steels has been driven by requirements of higher efficiency of power plants.

For several decades a permanent effort has been devoted to the improvement of the creep resistance of modified 9 to 12% Cr steels. The really promising way how to improve the creep resistance of these steels is based on raising nitrogen content in the steel to about 0.08%.

Requirement on reduction of power generators cost have led to the development of cheaper low alloy steels with higher creep resistance and better weldability compared to the conventional 2.25Cr-1Mo steel.

The aim of the present paper is to point out the most important strengthening and degradation processes during creep exposure with respect to chemical composition, microstructure and properties at elevated temperatures. The attention will be focused on advanced low alloy steels.

2. Microstructure, strengthening and degradation mechanisms

The creep properties of ferritic steels are controlled by the chemical composition and microstructure of these steels. Given a certain chemical composition, microstructure of steels depends on the heat treatment, temperature and time of creep exposure.

The fundamental knowledge of microstructural evolution during creep exposure, strengthening and degradation mechanisms are a prerequisite for successful development of ferritic heat resistant steels with different chromium contents.

2.1. Strengthening mechanisms

The most potent strengthening mechanisms operating during high temperature creep exposure in low alloy and chromium modified steels are precipitation strengthening and solid solution strengthening [1,2,3].

2.1.1.Precipitation strengthening

Precipitation strengthening in low alloy CrMo(W)V steels is predominantly affected by vanadium carbide or carbonitride. Precipitation strengthening in the modified 9 to 12% chromium steels is predominantly controlled by $M_{23}C_6$ and VN. It has been shown that both the proof stress at room temperature and the creep rupture strength at high temperatures increase, while the creep rate decreases [1,4,6] with decreasing interparticle spacing of secondary phases.

2.1.2. Solid solution strengthening

It was frequently supposed that significant solid solution strengthening of ferritic steels can be attained by increasing Mo and/or W contents in the steel. Nevertheless, the beneficial effect of these elements can be attained only if they remain in the solid solution. Therefore, when assessing how the creep resistance depends on the Mo and/or W contents in the steel, we must take into account the decreasing solid solution concentration of these elements during creep exposure. Precipitation of Mo and /or W rich phases, such as M_6X and /or Fe_2Mo, depletes the Mo and /or W from the solid solution and decreases solid solution strengthening [4,12,13].

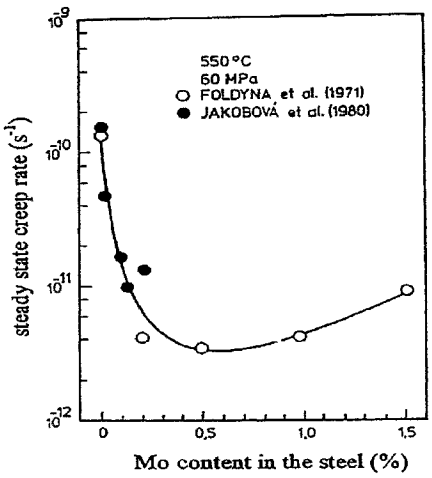


Fig. 1 Dependence of creep rate on Mo content in low alloy 0.5Cr-0.3V steels

It has been found that it is not practical to increase the overall Mo_{eq} content (Mo_{eq} = %Mo + 0.5%W) over solid solution solubility limit which depends on the temperature and the chemical composition of the steel. In low alloy CrMoV steels containing about 0.12%C, 0.5%Cr and 0.3%V the creep resistance increases only up to about 0.5%Mo [3,14,16].

The most pronounced drop of creep rate at temperature 550°C and load 60 MPa was observed when molybdenum content was changed from 0 to 0.20%, Fig.1. In steels with more than 0.5%Mo a slight increase in creep rate was observed. In 9% Cr steels, long time creep rupture tests (up to about 10^5 hours) did not confirm the beneficial effect of Mo addition on the creep rupture strength of 9%Cr steels with Mo content higher than about 1%. The solubility of Mo has a limit (in 9%Cr steels lies at 600°C well below 1%) and therefore there is no advantage, from the point of solid solution strengthening, to increase Mo content in 9%Cr steels above 1% [10,15].

2.2. Degradation mechanisms

Degradation of creep resistance is the consequence of long term high temperature service or creep exposure when microstructural changes lead to decrease of precipitation strengthening and/or solid solution strengthening.

The coarsening of secondary phases increases the mean diameter of particles, decreases number of particles per unit volume while the volume fraction remains constant. Therefore the average interparticle spacing increases.

In the low alloy CrMoV steels the precipitation strengthening is affected mainly by V_4C_3 or VCN while in low alloy CrMo steels especially Mo_2C and Cr_7C_3 phases are important. The dimensional stability of carbides precipitating in CrMo steels is much smaller than the dimensional stability of vanadium carbonitrides in CrMoV steels [14].

In 9-12%Cr modified steels containing Mo(W), V(Nb) and N the most important coarsening processes are related to $M_{23}C_6$, while secondary MX particles are dimensionally more stable.

Precipitation of M_6X in all ferritic steels is detrimental. Precipitation of this phase is accompanied by Mo and/or W depletion of the matrix and results in decreasing of solid solution strengthening. Moreover, precipitation of M_6X particles is accompanied by dissolution of fine MX particles and causes further deterioration of precipitation strengthening mechanism.

3. Development and properties of advanced low alloy chromium steels

Advanced low alloy chromium steels T23 and T24 were developed during the eighties in Japan [5,18,19] and Germany [7,11], respectively. Steel TEMPALOY F-2W was proposed later on [8]. Chemical compositions of the mentioned advanced steels are shown in Table I.

Table I - Chemical compositions of advanced 2 – 3%Cr steels

Steel	C	Mn	Si	Cr	Mo	V	W	Nb	Ti	N	B
T23	0.04	0.10	max.	1.90	0.05	0.20	1.45	0.02	-	max.	0.0005
	0.10	0.60	0.50	2.60	0.30	0.30	1.75	0.08		0.030	0.0060
T24	0.05	0.30	0.15	2.20	0.90	0.20	-	-	0.05	max.	0.0015
	0.10	0.70	0.45	2.60	1.10	0.30			0.10	0.012	0.0070
F-2W	0.10	0.51	0.60	1.91	0.60	0.37	0.33	-	0.14	-	0.0046

The comparison of creep rupture strength of advanced steels is shown in Fig.2. The creep rupture strength of all new steels is significantly higher than that of the steel 2.25Cr-1Mo at temperatures from 500 to 600°C.

The development of advanced tungsten bearing steel containing about 2.3% chromium (T23) has been performed in Japan on the following assumptions [5,19]:

- the carbon content should be lowered to less than 0.1% in order to improve the weldability

- using the basic composition 2.25Cr-0.25V-0.05Nb, of which the vanadium and niobium have been optimized by numerous studies on 9 to 12%Cr steels. The W and Mo contents have been optimized to 1.6% and around 0.1%, respectively
- it was supposed that addition of W and/or Mo increases solid solution strengthening, while V and Nb were added as precipitation strengthening elements
- the addition of B improves the creep rupture strength
- fully bainitic structure in the normalised condition leads to sufficient toughness after tempering

Another approach for improving creep rupture strength of 2.25Cr-1Mo was proposed in Germany [7,11] where tungsten free steel T24 has been developed. This steel contains 1%Mo as solid solution strengthening element, while V and Ti are added as precipitation strengthening elements. It was also considered that B addition improves creep rupture strength.

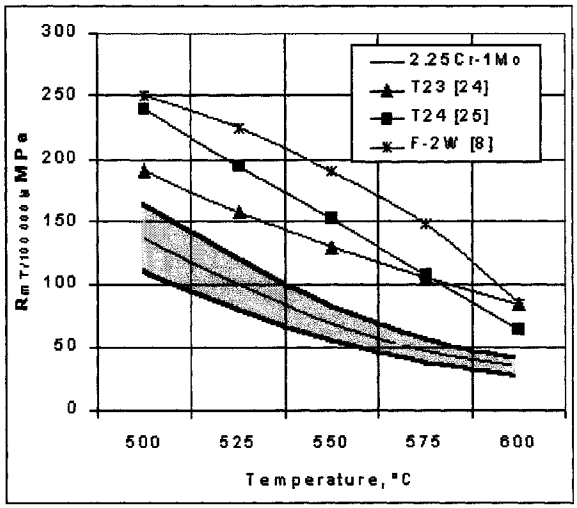


Fig. 2 Temperature dependence of creep rupture strength in 10^5 hours

Steel TEMPALOY F-2W containing 2% Cr has been recently developed in Japan [8]. It was supposed that Mo and W can more significantly increase solid solution strengthening when Mo content is higher (about 0.6%) than W content (about 0.3%).

The proposed molybdenum equivalent (Mo_{eq} = %Mo + 0.5%W) for this steel is lower (about 0.75%) than in both above mentioned advanced steels (about 1%). Vanadium and titanium are added as precipitation strengthening elements. Boron is again added to improve creep rupture strength, but nitrogen is not specified.

3.1. Microstructural investigations on a T23 steel

Microstructural investigations were performed on a tube Ø51 x 6.3 mm. The quality heat treatment consisted of normalising at 1060°C followed by tempering at 760°C. Chemical composition of the investigated tube is shown in Table II.

Table II. Chemical composition of the tube, wt. %

C	Si	Mn	P	S	Cr	Mo	V	Al	Ti	Nb	N	B	W
0.09	0.23	0.43	0.012	0.001	2.03	0.09	0.22	0.022	0.05	0.06.	0.007	0.0016	1.57

Microstructure of the tube was fully bainitic. Electron microscopy investigations were performed by using both carbon replicas and thin foils. Minor phases were identified by electron diffraction and X-ray microanalysis. A typical example of minor phase distribution is shown in Fig.3. The prior austenite grain boundaries were decorated by a discontinuous network of coarse particles. Furthermore, many fine particles decorated bainite lath boundaries and were also precipitated inside bainitic laths. Individual rings in diffraction patterns corresponded to MX phase. EDX analyses revealed in most fine particles the simultaneous occurrence of vanadium, titanium and niobium. These fine particles precipitated during tempering (secondary MX particles). Also some primary MX particles were observed randomly distributed in the bainitic matrix.

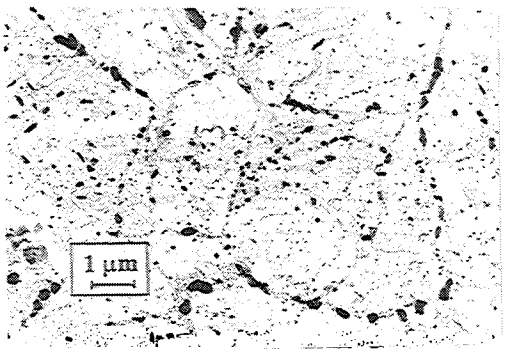


Fig. 3 Distribution of secondary phases. Prior austenite grain boundaries are decorated with coarse particles

EDX analyses on these coarse MX particles revealed titanium and a small amount of niobium, reflecting the Ti content of 0.05% although this element is not specified in the T23 steel grade. EDX studies on coarse particles along prior austenite grain boundaries proved that these particles were rich in iron, chromium and tungsten. The Fe/W ratio corresponded to that reported for the $M_{23}C_6$ phase [22].

Furthermore, particles rich in chromium and iron were found . These particles are chromium carbides. During diffraction studies intensive streaking was observed in spot diffraction patterns. This is typical for carbides of M_7C_3 type.

3.2. Thermodynamic modelling

The calculation of thermodynamic equilibrium has been performed using THERMOCALC software [20]. The specialised database Steel 13, developed by one of the authors [21] was used for the calculations. The vertical sections of investigated systems are shown in Fig. 4a and 4b. Stable secondary phases MX, M_6C and M_7C_3 can be expected in the temperature range 500 to 700°C in alloys containing 1.45 to 1.75%W and 0.1%Mo (corresponding to the steel T23) – see Fig. 4a. All above mentioned secondary phases can be expected also in the equilibrium of tungsten free alloys containing 0.9 to 1.1Mo – corresponding to the steel T24 – see Fig. 4b.

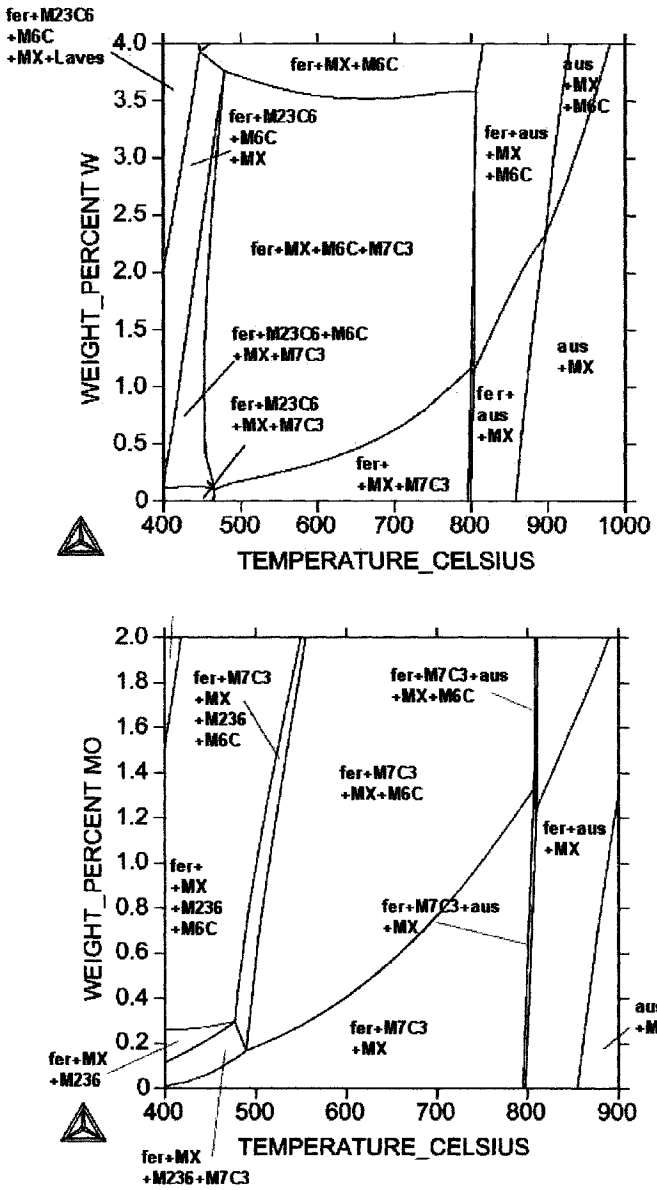


Fig. 4 Temperature-concentration equilibrium phase diagram for the systems:
a) 2.5Cr-0.3V-0.1C-0.1Mo-0.025N-W
b) 2.5Cr-0.3V-0.1C-0.025N-Mo

The equilibrium at 550 and 600°C of Mo in solid solution and V bound in VC at 550 and 600°C have been calculated using thermodynamical data [21] (Figs. 5, 6).

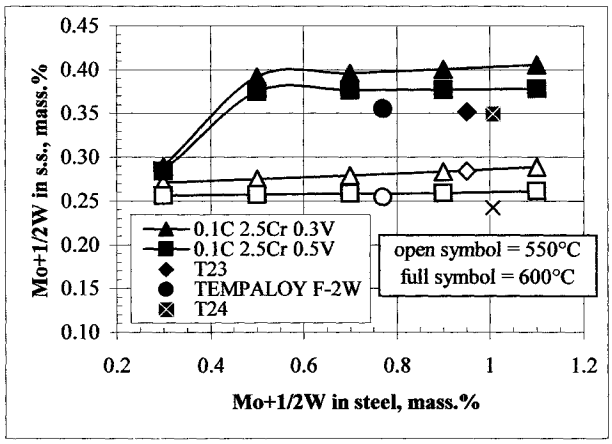


Fig. 5 The dependence of Mo_{eq} equilibrium level in solid solution on overall Mo_{eq} content in the steel

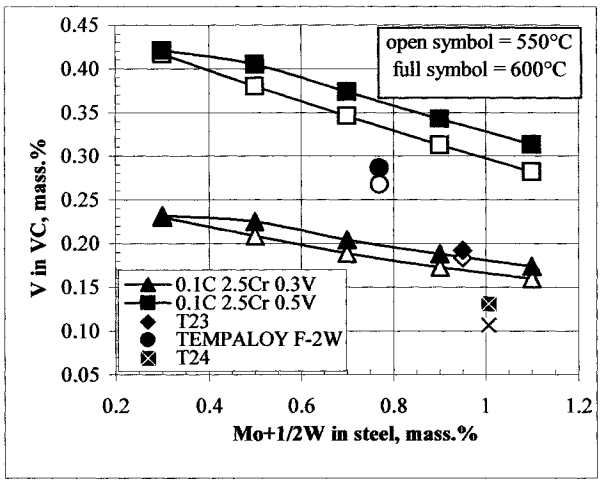


Fig. 6 The dependence of the equilibrium level of V in VC on the overall Mo_{eq} content in the steel

Molybdenum content in solid solution at 600°C increases with increasing overall Mo content in the steel only up to about 0.5%Mo in the steel. The Mo content in solid solution remains unchanged in the steel with further increasing Mo content in the steel due to precipitation of M_6C carbide. Mo in solid solution at 550°C is lower in comparison with 600°C and remains practically unchanged in the whole investigated region from 0.3 to 1% Mo in the steel (Fig. 5). The vanadium content bound in VC decreases slowly with increasing Mo content in the steel. Higher V content bound in VC has been observed in alloys with higher V content in the model alloy (Fig. 6). In Fig. 6 are also shown experimental results attained on advanced steels containing different V content (T23 – 0.28%V, T24 – 0.19%V, TEMPALOY F-2W – 0.37%V).

4. Discussion

Behaviour of ferritic creep resistant low alloy steels and modified 9 to 12% chromium steels at elevated temperatures shows great similarities, but as well there are some significant differencies.

It is well known, that low alloy CrMoV steels are precipitation strengthened by vanadium carbide and/or carbonitride particles. The precipitation of vanadium carbide is impossible in modified 9 to 12% Cr steels due to high solubility of VC. Therefore it is important to keep the stoichiometric ratio V:N in these chromium steels to attain desirable precipitation strengthening.

The way how to improve creep rupture strength of the steel 0.5Cr-0.5Mo-0.3V is to increase the overall vanadium content to stoichiometric ratio V:C. The effect of V:C ratio on the time to rupture is shown in Fig. 7. Due to increasing V content, the amount of V(C,N) increases and the interparticle spacing decreases [3].

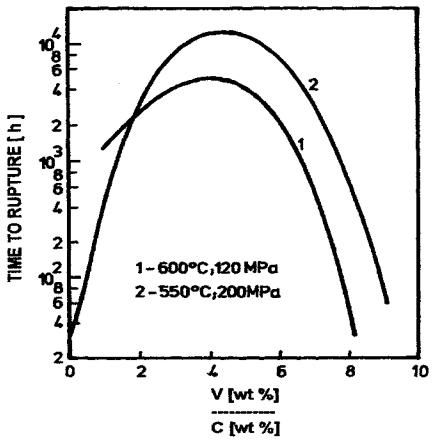


Fig. 7 How time to rupture depends on the ratio V:C at two testing conditions

The precipitation of vanadium carbide can be expected in low alloy steels with Cr content up to 3% Cr. Therefore it seems to be reasonable to keep the stoichiometric ratio V:C.

The theoretical modelling has shown, that in model alloys with 0.5%V the amount of vanadium bounded in VC increases. Due to higher amount of VC particles interparticle spacing decreases and creep rupture strength increases.

It seems to be reasonable,, in accordance with the thermodynamic analyses, to decrease Mo or Mo_{eq} in all discussed steels.

Modelling of equilibrium content of Mo in solid solution has shown that there is no advantage to increase the overall Mo content in these steels over 0.5%. It is not possible to increase Mo content in solid solution over the solubility limit. The solubility limit of molybdenum in solid solution is at 600°C about 0.5%. Increasing Mo_{eq} contents increase the probability of M_6C formation. Results of thermodynamic modelling demonstrate that in the T23 steel stable minor phases are MX, M_6X and M_7C_3. Neverthelles, the appearance of M_6X in this steel after quality heat treatment (tempering at 760°C) is not probable due to kinetic factors. Experimental results indicate that M_6X particles form during subsequent creep and/or thermal exposure at the expense of metastable $M_{23}C_6$ [22]. The undesirable phase M_6C has been found in the steel TEMPALOY F-2W after creep exposure at 550°C for 12 338h [19] and in the steel 3Cr1Mo0.25V after annealing 10 000h at 600°C [17,23]. M_6C carbides have grown at the expense of surrounding carbides. Presence of M_6C can not be excluded after shorter time of creep or annealing in the range 550 to 600°C.

In modified 9% Cr steels containing Mo_{eq} = 1.5 it has been found, that decline of Mo_{eq} in solid solution during creep exposure is faster in steels containing higher W content [9].

New V-alloyed steels (2.25Cr-1Mo-0.25V and 3Cr-1Mo-0.25V) for pressure vessels forged components of hydroprocessing reactors have been developed recently[17].
Available creep data have shown that creep rupture strength of all mentioned new 3% Cr advanced steels is greater than that of the steel 2.25Cr-1Mo, but we should take into account that creep behaviour of these steels responds very sensitively to the structure changes occurring during high temperature exposure which makes difficult the prediction of creep properties using relatively short-term creep tests [23].
All new steels (T23, T24, Tempaloy F-2W, 2.25Cr1Mo0.25V and 3Cr1Mo0.25V) have confirmed higher creep resistance compared to the conventional 2.25Cr1Mo steel. Small differencies in established creep properties can be attributed not only to differencies in chemical composition , but also to the uncertainty of creep rupture estimation using relatively short time creep rupture test and especially different ways of creep rupture estimation.

5. Conclusion

With respect to the results of thermodynamic modelling the overall Mo or Mo_{eq} content in all investigated new steels should be lowered to about 0.5%, to prevent the precipitation of M_6C carbide. To increase precipitation strengthening overall V content should be increased to stoichiometric ratio V:C.

6. Acknowledgement

This work was supported by the Grant Agency of the Czech Republic under project No. 106/00/0860 and 106/00/0855 and by the Czech Academy of Sciences under the project S2041105.

References

[1] Foldyna,V., Purmenský,J.:Role of dispersed phase in creep of ferritic steel, Czechoslovak Journal of Physics, 39, 1989, p.1133
[2] Foldyna,V., Kuboň,Z.,Vodárek,V.: Long term creep resistance and microstructural stability of of ferritic heat resistant steel, Proc. of the Fifth Workshop on the Ultra-Steel, 2001, Tsukuba, Japan, p.150
[3] Purmenský,J., Foldyna,V., Kuboň,Z.: Creep resistance and structural stability of low-alloy CrMo and CrMoV steels, Proc.of the 8th Int. Conf. on Creep and Fracture of Engineering Materials and Structures, Ed. T.Sakuma and K.Yagi, 1999, Tsukuba, Japan, p.419
[4] Foldyna,V.,Jakobová,A.,Vodárek,V.,Kuboň,Z.: Chromium modified steels metallurgical understanding, Proc.of the 5th Liege Conf. Materials for Advanced Power Engineering 1994, Ed.:D.Coetsouradis et al, 1994, Liege, Belgium, p.453
[5] Masuyama,F. et al.: Development of tungsten strengthened low alloy steel with improved weldability, ibid [4], p.173
[6] Kuboň,Z., Foldyna,V., Vodárek,V.: Optimized chemical composition of 9-12%Cr steels with respect to maximum creep resistance, Proc.of the 6th Liege Conf. Materials for Advanced Power Engineering 1998, Ed.:J.Lecomte-Beckers, F.Schubert and P.J.Ennis, 1998, Liege, Belgium, p.311
[7] Deshayes,F.,Bendick,V., Haarmann,K., Vaillant,J.C.: New 2-3% Cr steel grades for waterwall panels and superheaters, ibid [6], p.501
[8] Tohyama,A.,Minami,Y.: Development of 2Cr-Mo-W-Ti-V-B ferritic steel for ultra critical boilers, ibid [6], p.431

[9] Vanstone,R.W.: Progress in understanding microstructure-property relationship in advanced 9-12% Cr steels, ibid [6], p.311
[10] Foldyna,V., Kuboň,Z., Jakobová,A., Vodárek,V.: Microstructural stability of advanced 9-12% chromium steels, Proc.of the 9 Int.Symp. Creep Resistant Metallic Materials, 1996, Hradec n.M., Czech Republic, p.203
[11] Bendick,W., Haarmann,K., Ring,M., Zschau,M.: Assessment of creep rupture strenght of new steels for advanced power plant piping and and tubing, ibid [10], p.276
[12] Foldyna,V. et al.: Einfluss des Molybdengähaltes auf die Zeitstandfestigkeit von Chrom-Molybdän-Vanadin-Stählen mit niedrigen Kohlenstoffgehalt, Archiv für das Eisenhüttenwessen, 42, 1971, p.927
[13] Jakobová,A., Foldyna,V., Prnka.: Einfluss des Molybdängehaltes auf die Zeitstandfestigkeit von Chrom-Molybdän-Vanadin-Stählen mit unterschiedlicher Streckgrenze bei Raumtemperatur, Archiv für das Eisenhüttenwessen, 43, 1972, p.55
[14] Foldyna,V.,Purmenský,J.,Kuboň,Z.: Development of low alloy and 9-12% chromium steels, Proc.of the 1st Int. Conf. on Component Optimalisation, Ed.: W.J.Evans, R.W.Evans, M.R.Bache, 1999, Swansea, UK, p.187
[15] Foldyna,V.,Jakobová,A.,Říman,R.,Gemperle,A.: Effect of structure factors on the creep properties of modified chromium steels, steel research 62, 1991, p.453
[16] Jakobová,A.,Foldyna,V.,Vodárek,V., Kuboň,Z.: Creep resistant ferritic steels containing 0.5 to 12%Cr, Proc.of the10th Int.Conf. Creep Resistant Metallic Materials, 2001, Praha, Czech Republic, p.117
[17] Di Gianfrancesco,A. et al.: Creep properties and microstructural evolution of 2.25Cr-1Mo-0.25V and 3Cr-1Mo-V modified steels for pressure vessel forget components, Proc.of the 14th International Forgemasters Meeting, Ed. VDEh, 2000, Wiesbaden, Germany, p.215
[18] Komai,N. et al.:Development and application of 2.25Cr-1.6W (HCM2S) steel large diameter and thick section pipe, Proc. of the Conf. Advanced Heat Resistant Steels for Power Generation, 1998, San Sebastian, Spain, Section 1A:Steel Development
[19] Sawaragi,Y. et al.:Properties after service exposure of 2.25Cr-1.6W-V,Nb (HCM2S) and 12Cr-0.4Mo-2W-1Cu-V,Nb (HCM12A) steel tubes in a power boiler, ibid [16], Section 1B: Service Experience
[20] Kroupa,A., Unucka,P.: Internal Report Steel 13.tdb, IMP Brno, Czech Republic, 2001
[21] Sundman,B.: Thermo-Calc, version L, Royal Ins. of Technol., Stockholm, 1997
[22] Miyata,K. et al.: Effect of trace elements on creep properties of 0.06C-2.25Cr-1.6W-0.1Mo-0.25V0.05Nb steel, Proc. of ICOPE-97, 1997, Tokyo, Japan
[23] Di Gianfrancesco,A. et al.: Microstructural evolution and creep behaviour of 2.25Cr-1Mo-0.25V and 3Cr-1Mo-0.25V modified steels for pressure vessel forged components, Proc.of the 3rd EPRI Conf. on Advances in Materials Technology for Fossil Power Plants, Swansea, UK, 2001
[24] The T23/T24 Book, Vallourec & Mannesmann Tubes, 1998
[25] Vd TÜV, Warmfester Stahl 7CrMoVTiB 10-10, Werkstoff-Nr. 1.7378, 2001

AN ASSESSMENT OF CREEP RUPTURE DATA ON STEEL E911

David J. Allen*
Chiara Servetto**

(*) Powergen UK plc, Power Technology Centre - Nottingham, UK
(**) Istituto Italiano della Saldatura - Genova, Italy

Abstract

This paper reports an investigation of the BS PD 6605 methodology and ECCC guidelines for the assessment of creep rupture data. The COST project data set on E911 steel was selected as a basis for collaborative development by IIS and Powergen. The work was carried out at Power Technology and supported by an ECCC (European Creep Collaborative Committee) technical interchange programme.

The effects of alternative approaches to data selection, censoring techniques, post assessment testing and preferred model selection were explored by carrying out a series of assessments. Critical evaluation indicated that more reliable long term extrapolation may be obtained when short term data is excluded from assessment, with care to avoid bias in censoring. The work also showed that whilst traditional parametric models can be too sensitive and hence liable to extrapolation error, the more robust models used in PD 6605 can be too insensitive and hence liable to reproduce complex data trends poorly. Post assessment test evaluation should therefore concentrate on identifying the most probable data trend for extrapolation of long term rupture strength values. A separate analysis is recommended when the objective is instead to obtain the best short and medium term data fit.

Keywords: creep, ferritic steel, E911, COST, PD 6605

Introduction

The assessment of creep rupture data to determine extrapolated long term strength values plays a key role in design and materials selection for high temperature plant. The subject is controversial for reasons which include differences of philosophy, objectives, and techniques. Graphical methods offer flexibility, but can be subjective and dependent on individual interpretation of the best curve fit to data points that are both bunched and scattered. Time-temperature parameter methods often prove too optimistic, indicating that short term trends at high temperatures are not a good guide to long term trends at lower temperatures. Techniques using higher-order stress polynomials [1] tend to fit data well but perform poorly in extrapolation, their over-sensitivity leading to faults such as turnback in the rupture life plot.

The statistical methodology developed as BSI PD 6605 [2], incorporating European Creep Collaborative Committee (ECCC) guidelines and implemented using GLIM software, offers a number of advantages. It applies a number of semi-empirical curve fitting models in turn and allows the assessor to select the best. Its mathematical basis promises to reduce subjectivity, improve data fitting, and provide an objective framework to compare different assessments. It also offers a number of post – assessment (PAT) tests for physical realism, goodness of fit, robustness and extrapolation performance, while allowing the assessor to judge their significance and choose which model to apply.

This paper reports an investigation of the principles of creep rupture data assessment, based on PD 6605. The work was carried out at Power Technology, UK, as part of an ECCC

technical interchange which supported the secondment of one author (CS). The investigation was based on the large, well-characterised COST data set on E911 steel as supplied to ECCC for assessment. A previous PD 6605 assessment by VTT [3] provided a useful starting point.

Preassessment

The data set consisted of 325 failed and 23 unfailed data points from 13 casts tested at 550 - 650 °C. Isothermal plots for the best – tested casts were used as recommended [2] to indicate the basic shape of the rupture curve. This suggested a slightly sigmoidal (reverse S curve) trend at lower stresses, Figure 1.

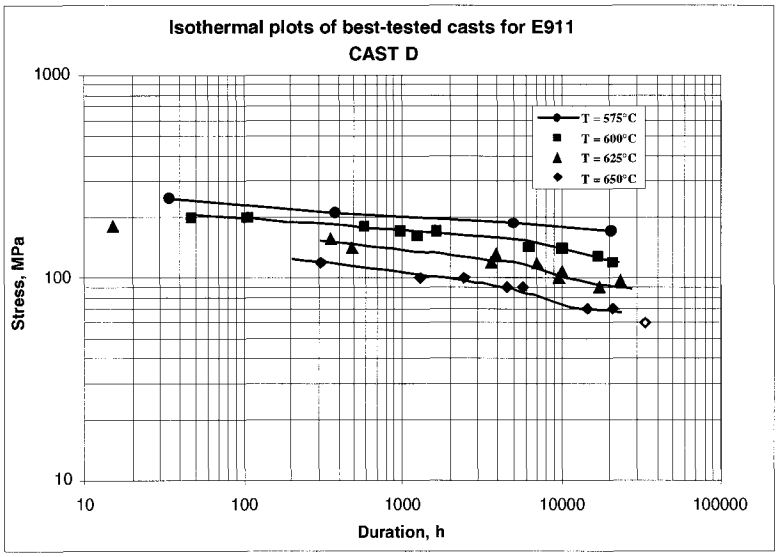


Figure 1. Typical isothermal plot for a best-tested cast.

A question raised by VTT [3] was the admissibility of short term data. PD 6605 suggests exclusion ("censoring") of test data below 10 hours, which may relate to tensile rather than true creep failure. VTT noted that the short term data were out of line with longer term test results, and adopted a somewhat more stringent cut-off, discarding data points below 100 hours.

Assessment Trials

The VTT assessment on data points with rupture lives exceeding 100 hours was replicated at Power Technology, with essentially identical results. A series of ten further assessments was then carried out to explore the effects of changes in factors such as the inclusion or exclusion of a weaker cast and the treatment of unfailed data. In particular, attention was directed to "left censoring" techniques, i.e. the inclusion or exclusion of short and / or medium term data.

Figures 2 and 3 show isothermal plots of the data at 600°C and 650°C respectively, together with the replicated VTT "100 hour" assessment curve and alternative data fit curves from the

present work. It is notable that at both temperatures, the great majority of the data points representing rupture lives below 1000 hours fall below and to the left of the "100h" curve. Hence, the 100h curve is not a good fit to these shorter term data.

For data points above 1000 hours, the 100h curve seems a reasonable fit. Indeed, all the curves on each of these Figures seem to fit the data adequately, thus providing a clear illustration of just how difficult it really is to select the best curve fit by eye alone. However, the 100h curve is logically questionable. If that curve attempts a best fit to the 100 – 1000 hour data, but clearly fails to achieve it, then its shape must be an imperfect compromise between the differing short and long term trends. Hence, it also cannot be expected to be the best fit curve for long term data fitting and extrapolation.

This suggests that, when short term data follow a different trend from the medium term data, the best way to determine the most probable long term data extrapolation may simply be to discard the short term data. Alternative assessments with different cut-off times of 100h, 1000h and 5000h were therefore carried out. These were also compared with assessments based on applying a maximum cut-off in stress, instead of a minimum cut-off in time. In principle, stress limits are preferable because they provide an unbiased means of censoring the data set, whereas time limits favour stronger casts which (for a given stress) record longer lives and hence escape the cut-off.

PD 6605 provides a simple procedure to obtain stress cut-off limits that are broadly related to a chosen time limit. The cut-off stress to be applied at a given temperature is defined in PD 6605 as the lowest stress for which any data point at that temperature lies below the specified time limit. This procedure works well when large numbers of data points exist at each temperature, but can give arbitrary results or break down when there are few data points at a particular temperature. A refinement was therefore devised for this work. For a chosen time limit, the PD 6605 stress limit was determined for each temperature at which more than 10 data points existed. A linear best fit to the plot of PD 6605 stress limit values versus temperature was then used to define the actual stress limits to be applied.

Results

The PAT tests showed that two algebraic models, the "Soviet" SM1 model and the "Minimum Commitment" MC model, produced the best results. Parametric models using fourth-order polynomials gave well-fitting but physically unrealistic results, whilst the simpler results obtained with second-order polynomials achieved adequate realism and robustness at the expense of a poor data fit. While MC gave the better data fit, SM1 showed better robustness. This is a measure of the risk involved in using a model which is too sensitive to the addition or removal of a few longer term data points, and hence potentially unreliable in extrapolation. Following the adverse experience with high-order polynomial fits, robustness is given prominence in PD 6605.

Cut-off Criteria

For a chosen time limit (e.g. 1000h), the time - based cut-off procedure consistently produced long term extrapolated strength values which were lower than or equal to those obtained using the stress - based cut-off procedure. That a technique biased towards strong casts in censoring short term data should produce weaker long term values seems paradoxical, but can be

explained. The assessment curve naturally tends to pivot about the central data values, so that if short term strength is artificially raised, projected long term strength will correspondingly tend to fall. The bias was negligible for the 100h criteria, but substantial for the stringent 5000h cut-off criteria. The safest practice is therefore to adopt a stress cut-off approach and eliminate any risk of bias.

Results at 600°C and 650°C for the 100h, 1000h-stress based, and 5000h-stress based cut-off criteria are shown in Figures 2-5 for the SM1 and MC models respectively. Generally, the more stringent (1000h or 5000h) cut-off criteria produce steeper curves. These fit the medium and long term data better, and hence produce significantly lower estimates of long term extrapolated creep strength than those obtained in previous work.

Considering the choice of cut-off criterion, the 100h-stress, 1000h-stress and 5000h-stress criteria reduce the analysed data set to 275, 194, and 103 points respectively. The stringent 5000h-stress criterion discards well over half of the data points and reduces the range of variation in rupture life to barely an order of magnitude, making it rather sensitive to data scatter. The 1000h-stress criterion, Table 1, was therefore preferred. While this discards 44% of the data points, these represent only 5% of the total test duration. By contrast, an uncensored PD 6605 assessment would allocate 44% of the overall weighting to these data points. Even for cases where there is no obvious difference between short term and longer term data trends, therefore, it is suggested that an uncensored PD 6605 assessment places undue weighting on short term data.

TEMP	TOTAL		TEST DURATION										$t_{r[max]}$	$\sigma_{o[min]}$	$\sigma_{o[max]}$
°C	DATA		<10kh		10-20kh		20-30kh		30-50-kh		50-70kh		[h]	[Mpa]	[Mpa]
	B	UB	B	UB	B	UB	B	UB	B	UB	B	UB	B	B	B
550	6	3	3		1		2					3	23,415	200	220
575	17	2	7		4	1	3		2	1	1		54,570	150	195
600	54	4	25		20		6	1	3	2		1	38,306	105	165
612	2		1		1								15,294	120	145
620	4				2		1		1				33,602	100	120
625	32	4	23	3	6		2		1	1			31,126	90	131
630	3		3										8,574	100	120
635	5		5										8,244	100	120
640	4		3		1								11,704	100	100
650	46	8	30	5	12		2	1	2	2			44,872	52	100
totals	173	21													

Table 1. Summary of the data used in assessment

Model Selection

The PAT test results did not clearly determine which should be the preferred model. However, a careful examination of the data fit proved more effective.

The MC model (Figures 4 and 5) predicted slightly sigmoidal curve shapes, in line with the individual cast data of Figure 1. However, the SM1 model (Figures 2 and 3) produced simpler curves with a continual gentle increase in slope with increasing life. This is, in fact, a natural consequence of the mathematics. The SM1 equation contains only two terms in stress. Hence, it is only capable of predicting a simple monotonic strength - life curve. The MC equation, however, contains three stress terms. This allows it to predict a curve of varying curvature, and hence to model sigmoidal behaviour effectively. The MC model also gave a

better data fit, and its predictions were less sensitive to changes in the selected cut-off criterion, Figures 2-5. Hence, it was chosen as the preferred model.

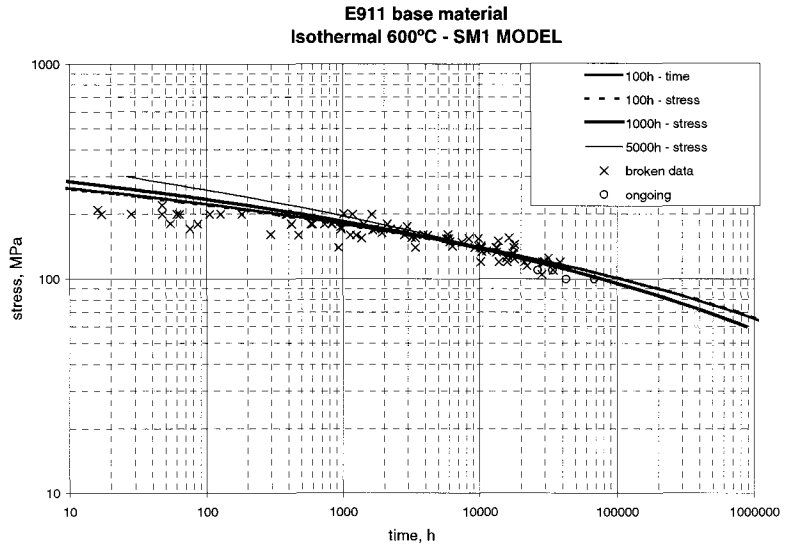


Figure 2. 600°C - SM1 model.
Comparison of cut-off criteria at 100h - time, 100h – stress, 1000h-stress, and 5000h-stress

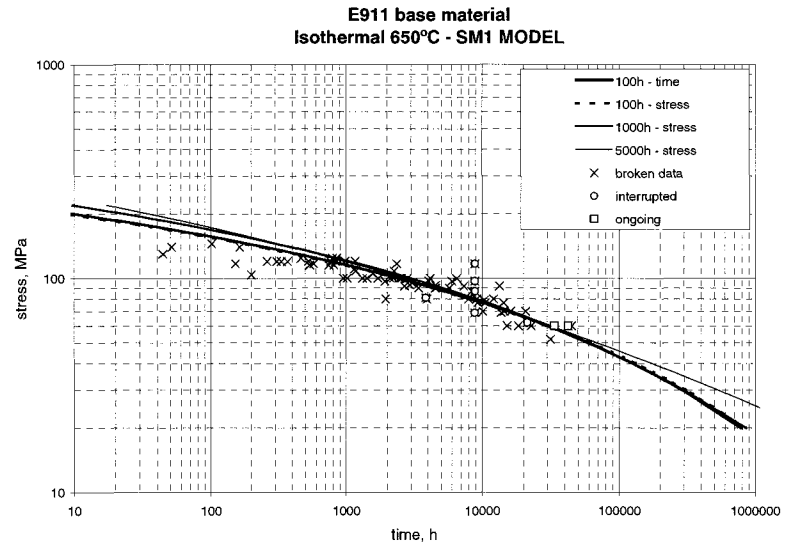


Figure 3. 650°C - SM1 model.
Comparison of cut-off criteria at 100h - time, 100h – stress, 1000h-stress, and 5000h-stress

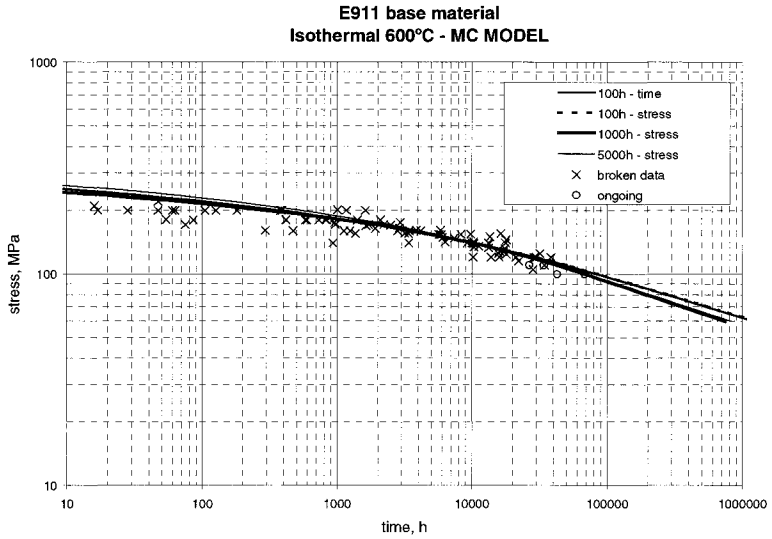


Figure 4. 600°C - MC model.
Comparison of cut-off criteria at 100h - time, 100h – stress, 1000h-stress, and 5000h-stress

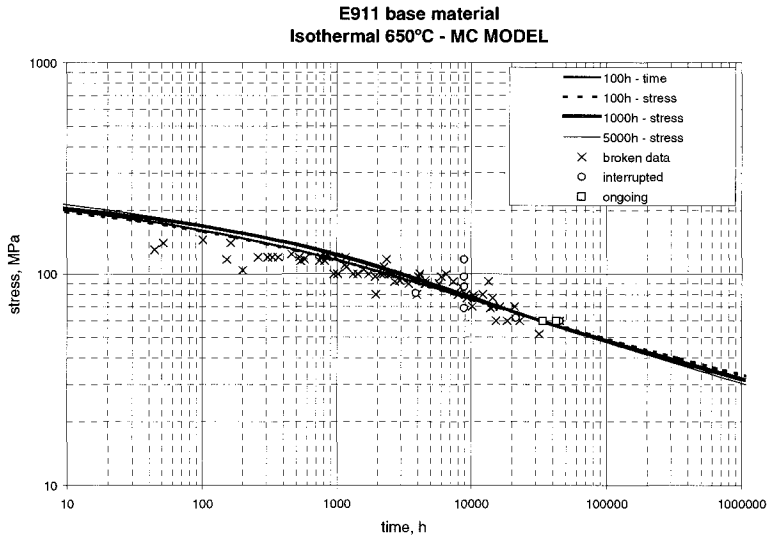


Figure 5. 650°C - MC model.
Comparison of cut-off criteria at 100h – time, 100h – stress, 1000h - stress, and 5000h-stress

There is clearly a trade-off between robustness and sensitivity. Higher order polynomial functions fit the data well, but are over-sensitive and hence liable to excessive curvature outside the data range. At the opposite extreme, a straight line fit is highly robust, but insensitive and inaccurate. A compromise is therefore required. Over-reliance on robustness criteria should not be allowed to impose a poor model which does not correctly identify the basic shape of the data trend.

Creep Strength Predictions

The VTT assessment [3] predicts the 100,000 hour mean creep strength of E911 at 600°C to be 101 MPa, in line with or somewhat below previous assessments based on uncensored data. However, the present assessment predicts a value of 92 MPa. For comparison, use of the SM1 model would have produced 95 MPa. Adopting a 5000h-stress cut-off would have yielded values of 93 MPa with the MC model and 94 MPa with SM1. Thus, the lower creep strength prediction is mainly due to the exclusion of short term, high stress data which do not conform with the long term trend. Other factors, such as the precise cut-off criterion and the choice of model, are less important.

The result reflects the common finding that high alloy ferritic steels show long term changes in the shape of the stress rupture plot. This behaviour is not specific to E911. Data on competitor steels should therefore be assessed similarly.

Post Assessment Tests

A crucial test of any assessment is its ability to predict the long term data trend. PD 6605 PAT test 2.1 provides an objective check in which predicted life is plotted against actual life for each data point. The present model fails the test as laid down in PD 6605, but it does so only because of its tendency to overestimate life in short term testing. A more appropriate PAT test may be based solely on the long term data above 5000 hours, Figure 6. The present model then performs well, the gradient of 0.97 being close to the ideal value of unity. However, the 100h (VTT) model obtains a gradient value of 1.11, demonstrating that models which do not exclude all the short term data tend to over-predict long term creep strength.

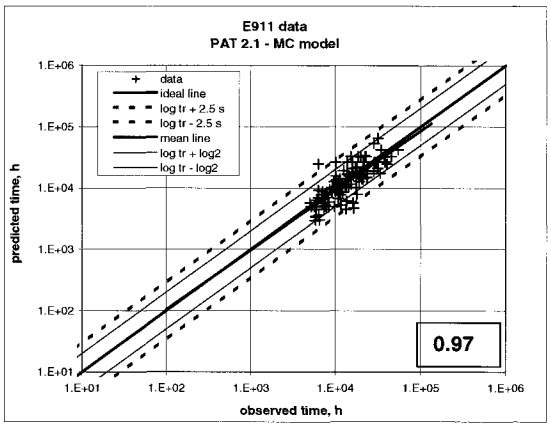


Figure 6. Modified "PAT 2.1" test for data points exceeding 5000 hours

The modified PAT test described here is not solely a measure of the model applied. It also determines whether the data set itself can reliably be assessed. For example, suppose that the data set includes just a very few results beyond x0,000 hours, and these appear to suggest a sudden drop in strength after that time. Any model would then be liable to fail the modified PAT test and (apparently) over-predict long term life. Such a result would indicate a need for caution in extrapolation until more long term data are available.

Discussion

Data censoring – Not valid, or essential?

A simple physical model can be suggested to explain the flattening of the strength – life curve at high stresses observed in this work and elsewhere. As the applied stress increases toward the flow stress, creep deformation processes may be augmented by additional tensile deformation mechanisms. The gradual transition from a time-dependent thermally activated creep regime toward an (almost) time-independent plastic flow regime takes place over a range of stresses. Within this range, the overall deformation rate increases very rapidly with stress. Consequently, the rupture life correspondingly falls rapidly. This corresponds with the flattened trend of the short term data points in Figures 2-5.

If this model is correct, it follows that the best way to assess long term creep behaviour is to censor the data, and eliminate the high stress test results. As these short term data points are influenced by factors that are not relevant to longer term behaviour, they are simply misleading. Hence, when the most accurate long term assessment is needed, and longer term data are available, it is best to discard the short term data.

An alternative approach would be to seek mathematically better models which could adapt to fit both the short and long term trends without loss of robustness. This could be useful for limited data sets lacking longer term data. However, it is argued that when sufficient long term data are available, censoring out the short term data is not merely an expedient procedure, but is actually a better approach in principle.

Long term rupture strength assessment for design

The philosophy adopted in this paper is that an assessment should aim to determine the most probable long term extrapolated creep strength values, based on trends identifiable from the existing data. Several difficult points arise in considering how this aim should be interpreted. For example, suppose that we are given three sequential data values 17, 16 and 15 generated by an unknown process, and we are asked to forecast the next value. Clearly, there is a sense in which 14 is the "correct", i.e. intuitively most probable, prediction. There is also a sense in which, for example, 16 (oscillatory behaviour) might be described as an equally valid prediction. Values such as 11 (a "break in the weather" - or an unexpected long term drop in creep strength) are of course also quite possible. The viewpoint adopted here is that every effort should be made to identify the true long term trend, and thus minimise the risk of surprise results when longer term data are eventually obtained. However, since there is no way that such surprises can be excluded with certainty, an assessment result can claim no more than that it represents the most probable extrapolated long term strength values.

Medium term data assessment for steel development

What has to be sacrificed, in this approach, is the possibility of a single optimal data fit to the entire rupture curve. In Figures 2-5, the improved extrapolation obtained with a 1000h - stress cut-off is at the expense of an even poorer fit to the (excluded) short term data. In some applications, for example when providing a comparison baseline for new steel developments, it is the short and medium term properties that are important.

The results obtained here suggest that very short term rupture test data may be unduly influenced by factors which affect tensile strength (e.g. variations in heat treatment, levels of elements such as manganese and silicon), and hence unreliable as an indicator of long term creep properties. However, rupture test durations of about 1000 hours and above produce data which do follow the long term trend line, and thus appear to be genuinely representative of true creep behaviour.

A minimum requirement for the evaluation of a newly developed experimental alloy should, therefore, be the provision of sufficient rupture data from 1000 hours upwards to establish reasonable first estimates of creep strength and its longer term trend. An order of magnitude variation in life should be sufficient to indicate the trend. Hence, a recommendation that arises naturally from this work is that candidate development alloys should initially be tested across a rupture life range of about 1,000 to 10,000 hours. This is in line with common practice. It also follows that if an established steel such as E911 is to provide a baseline for comparison, the baseline should be obtained by making a separate assessment of the comparable short and medium term rupture data on the established steel.

Short term data for welding consumable evaluation

In many high temperature applications, the creep properties of the parent material and the weld heat-affected zone are critical, while those of a weld metal which is not used in a fully load-bearing configuration may be less important. Nevertheless, a grossly undermatching weld metal would be at risk of failure. Limited testing may therefore be warranted to establish that the weld metal properties are adequate. What is required is an approximate measure of weld metal creep strength which can be compared that of the parent material. This work would suggest that testing out to no more than about 1000 hours should be sufficient to obtain suitably representative creep strength values for this purpose. This is in line with current proposals for the new CEN Standard on conformity evaluation of welding consumables for operation in the creep range.

Steel requirements for high temperature plant

What the plant manufacturer and end user need are steels with well characterised and realistically assessed long term high temperature properties. The need is to design components with confidence that they will achieve their anticipated lives. That need is poorly met today by advanced steels worldwide. All too often, values recommended for design purposes are based on secretive, subjective, and suspiciously optimistic assessments that fail to command confidence. It may not be far-fetched to claim that this is an area in which Europe can offer leadership.

Conclusions

1. A modified PD 6605 assessment of the COST E911 parent material creep rupture database shows that censoring short term data may be necessary to achieve the best fit to the long term data and hence obtain the most appropriate extrapolated strength values.

2. This approach results in an approximately 10% reduction in the predicted 100,000 hour rupture strength at 600°C.

3. The lower long term creep strength identified in this way reflects the common finding that many high alloy ferritic steels show long term changes in the shape of the stress rupture plot. The behaviour is not specific to E911, and a similar assessment approach should therefore be applied to competitor steels.

4. The PD 6605 approach offers many advantages over current alternatives, but further developments in modelling and post-assessment testing may be worthwhile.

5. A final assessment to determine the most probable extrapolated long term creep strength values should be based on the selection of the best censoring criterion following a number of trial assessments.

6. A separate assessment of the short and medium term data may be required when determining a baseline for comparison with newly developed steels and welding consumables for which only shorter term data are available.

References

[1] PD 6525, 1990, "Elevated temperature properties for steels for pressure purposes: Part 1. Stress rupture properties", BSI.

[2] PD 6605-1:1998, "Guidance on methodology for assessment of stress-rupture data – Part 1: Procedure for derivation of strength values", BSI.

[3] Holmstrom, S, Auerkari, P, "Modelling of creep rupture strength and stress reduction factors for welded 9%Cr steel", Proc. Conf. "Baltica V", Vol.2, pp.621-633, publ. VTT, Espoo, 2001.

EFFECT OF Cr CONTENT ON THE CREEP STRENGTH AND MICROSTRUCTURAL CHANGE IN HIGH Cr HEAT RESISTANT STEEL

Kazuhiro Miki[*1], Tsukasa Azuma[*1], Toru Ishiguro[*2], Ryokichi Hashizume[*3], Yoshinori Murata[*4] and Masahiko Morinaga[*4]
*1 : Muroran Research Laboratory, The Japan Steel Works, Ltd., Hokkaido, Japan
*2 : Steel Business Division, The Japan Steel Works, Ltd., Tokyo, Japan
*3 : Technical Research Center, The Kansai Electric Power, Hyogo, Japan
*4 : Dept. of Mater. Sci. & Eng., Nagoya Univ., Aichi , Japan

Abstract

The effect of the Cr content on the creep strength at the 650°C of high Cr heat resistant steel containing 3.5%W, 3%Co and 0.01%B for steam turbine rotor was examined. The amount of Cr was varied from 8.5% to 11.5%. The tensile strength at room temperature and the creep rupture strength in the short time at 650°C increased with increase of Cr content. However the remarkable degradation of creep rupture strength occurred at early stage with increase of Cr content, and the highest rupture strength in 98MPa were shown at the 9%Cr steels. The precipitation quantity of W was almost same regardless of the Cr content so that solid solution strengthening effect by W is same regardless of the Cr content. The formation of subgrain is early in the 10.5-11.5%Cr steels crept at 650°C under the lower applied stress, and Laves phase precipitated within the lath disappeared earlier, whereas the lath structure in the 8.5-9.5%Cr steels recovered slowly. Therefore, it was guessed that the coarsening of precipitates were promoted and the recovery could not be suppressed in the higher Cr steels.

Keywords : Cr content, creep, long term stability, recovery, Laves

1. Introduction

Recently, high Cr heat resistant steels, with significantly improved high temperature creep strength were developed as materials for the steam turbine rotor in USC pressure power plant [1]-[4]. In these ferritic heat resistant steels for use at 650°C, the improvement of the long-term creep strength is most important. However in the high Cr ferritic heat resisting steels containing 9 to 12%Cr with the tempered martensitic structure, it is known that the creep strength under the lower stress condition at 650°C is often shorter than the predicted creep strength. The degradation of creep strength within 10000h has been discussed by relating to the precipitation of Laves phase consisting of Fe, Cr, Mo and W[5]-[7], in addition, the formation of a recovery zone along grain boundary is proposed[8]. However, the cause has not yet been clarified. The effect of the Cr content on the creep strength at the 650°C in high Cr heat resistant steel containing 3.5%W, 3%Co and 0.01%B for steam turbine rotor material was examined. The amount of Cr was varied from 8.5% to 11.5%, and then, the effect of Cr on the stability of the precipitate in the high temperature range was investigated.

2. Experimental procedure

Table 1 shows chemical composition of the laboratory heats containing 3.5%W, 3%Co and 0.01%B. The amount of Cr was varied from 8.5% to 11.5%. The 50kg ingots of the tested materials were cast by vacuum induction melting and forged into plates of 35mm thickness. They were normalized at 1100°C for 5h followed by tempering at 720°C for 20h. The quality heat treatment was performed on austenitizing at 1070°C for 5h and controlled cooling at 100°C/h corresponding to the cooling rate on the center of turbine rotor, followed by 1st tempering at 570°C for 20h and 2nd tempering at 680°C for 20h. The microstructure of these steels was homogeneous tempered martensitic structure except for 11.5% Cr steel which had approximately 3% delta ferrite in small areas.

Tensile tests at room temperature and 600°C, aging and creep tests at 650°C were performed. The microstructural observation by transmission electron microscopy (TEM), X-ray diffraction and the chemical analysis of extraction residue were carried out by using aged or crept materials. In addition, tempering heat treatment was performed after austenitizing at 1070°C for 5h, at the temperature from 450°C to 780°C for 50h in order to evaluate the effect of Cr content on tempering softening resistance.

Table 1 Chemical composition of tested steels. (mass%)

steel	C	Si	Mn	Ni	Cr	Mo	V	Nb	W	Co	B	N
8.5%Cr	0.10	0.03	0.01	0.20	8.56	0.11	0.15	0.07	3.45	2.99	0.009	0.020
9.0%Cr	0.09	0.03	0.01	0.21	9.04	0.11	0.15	0.06	3.55	2.98	0.009	0.020
9.5%Cr	0.10	0.03	0.01	0.21	9.51	0.11	0.15	0.06	3.58	2.99	0.009	0.020
10.0%Cr	0.09	0.03	0.01	0.21	10.06	0.11	0.15	0.06	3.55	3.02	0.011	0.020
10.5%Cr	0.10	0.03	0.01	0.20	10.50	0.10	0.15	0.06	3.54	3.00	0.010	0.021
11.5%Cr	0.10	0.03	0.01	0.21	11.59	0.11	0.15	0.07	3.60	3.04	0.010	0.020

3. Results and discussion

3.1 Mechanical properties

The change of tensile strength of the tempered steels against Cr content is shown in Fig.1. With increasing Cr content, the ultimate tensile stress at RT and 600°C increased. The behavior of tempering softening resistance also shows a similar tendency, and then, the hardness becomes higher with increasing Cr content at tempering temperatures from 600°C to 780°C as shown in Fig.2.

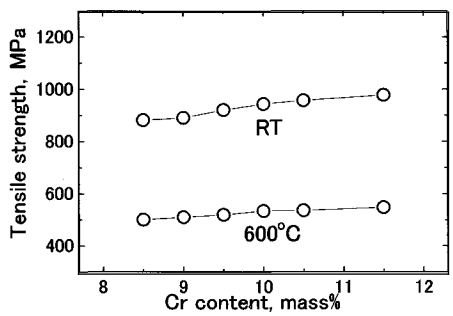


Fig.1 Effect of Cr content on the mechanical properties

Fig.3 shows the creep curves at 650°C-157MPa. In the transient creep area, the strain became smaller with increasing Cr content and this behavior correlates with the tensile strength. However the onset of accelerating creep of highest and lowest Cr steels occurred at an early stage and ruptured after relatively short times. This result indicates that there is a optimum Cr content for the creep strength.

Fig.4 shows the creep rupture curves at 650°C. In the high stress region, the rupture time increases with increasing Cr content, but in the low stress region the rupture time decreases from as Cr increases. The relationship of the rupture time versus Cr content is shown in Fig.5. The rupture time of the 11.5%Cr steel was the longest at 300MPa, the peak rupture time shifted gradually to the lower Cr side with decreasing applied stress. At 98MPa, the longest rupture time was obtained at 9%Cr.

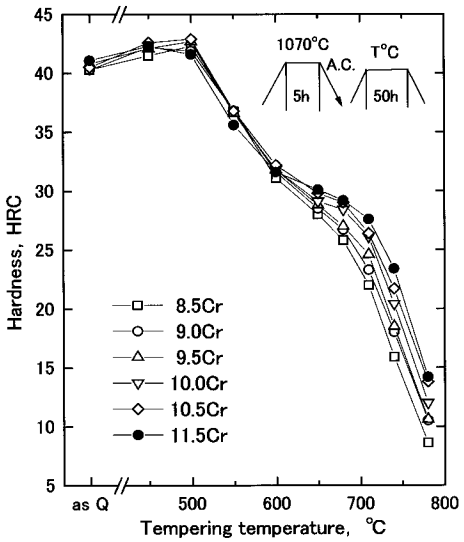


Fig.2 Tempering hardness of 8.5–11.5%Cr steels

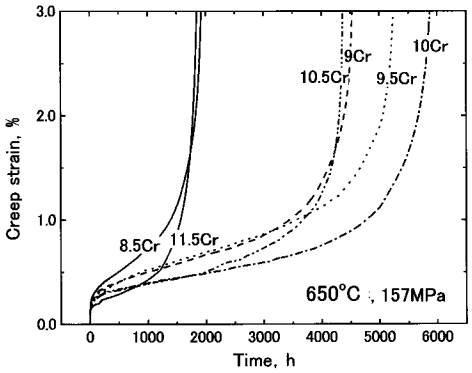


Fig.3 Creep curves of 8.5–11.5%Cr steels at 650°C. 157MPa

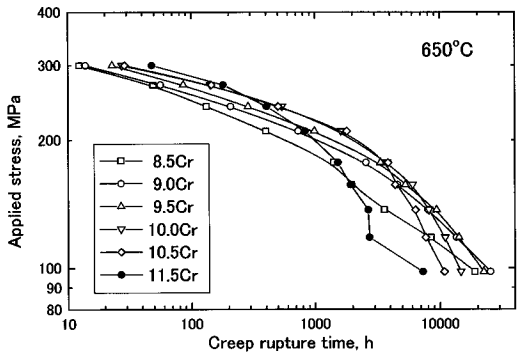


Fig.4 Creep rupture curves at 650°C of high Cr steels including 3.5%W

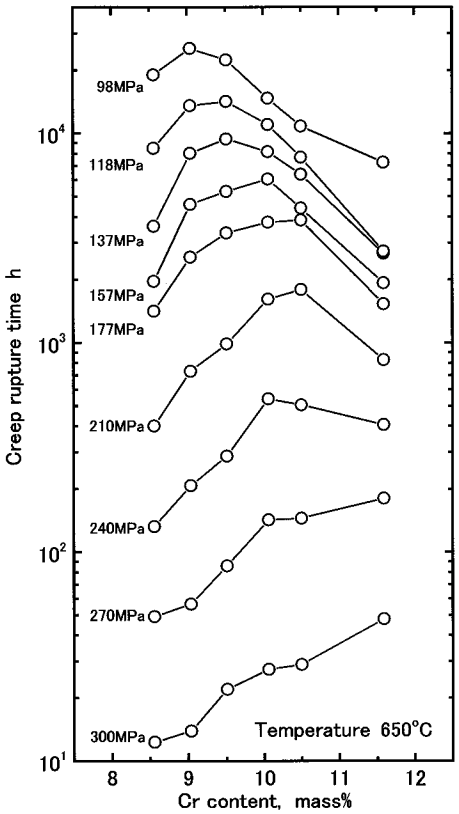


Fig.5 Effect of Cr content on the creep rupture time

The hardness after aging at 650°C and creep properties are shown in Fig.6. The behavior of hardness during aging is similar to that of creep curve, that is, the creep strength or hardness decrease in the short time as the Cr content is increasing. The ductility increases

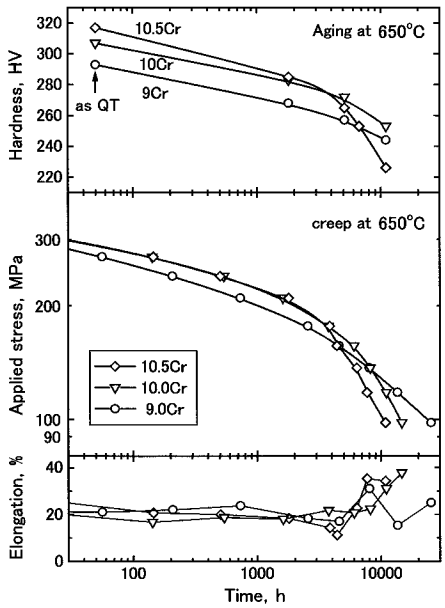


Fig.6 Aging and creep properties at 650°C of the high Cr steels containing 3.5%W

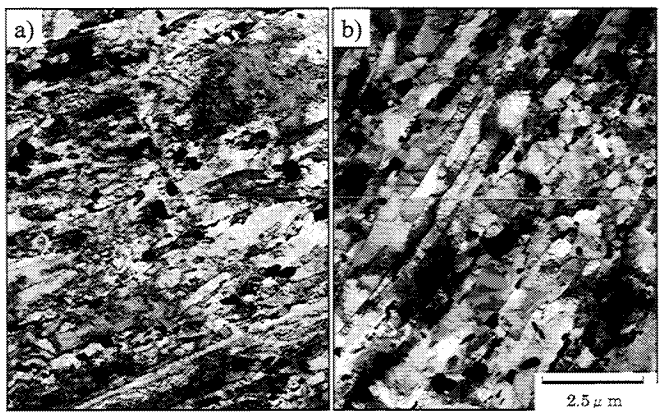


Fig.7 Transmission electron micrographs of a) 9%Cr steel and b) 10.5% Cr steel aged at 650°C for 11000h

with decreasing creep rupture strength, and it corresponds to softening of the steels aged at 650°C. Therefore the degradation of the creep strength within 10000h does not depend on the creep brittleness, but on the softening.

TEM micrographs of 9%Cr and 10.5%Cr steel after aging at 650°C for 11000h are shown in Fig.7. Comparing with the 9%Cr steel, lath width increases and dislocation density decreases in 10.5%Cr steel. It was indicated that the recovery of higher Cr steel was occurred at an early period and that the microstructural stability was low.

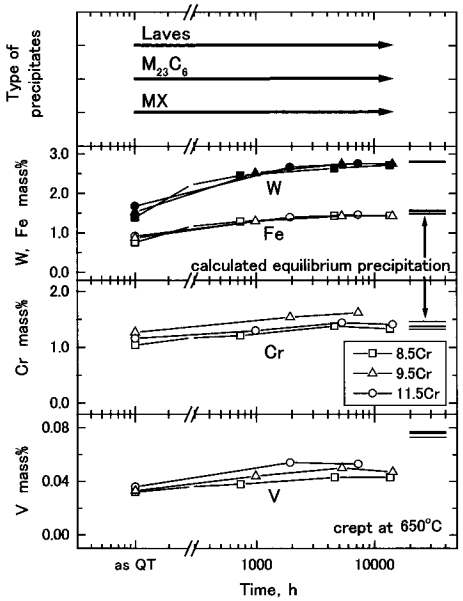


Fig.8 X-ray diffraction and chemical analysis of the extracted residue in the crept specimens containing 3.5%W

3.2 Microstructure after creep

The results of X-ray diffraction and quantitative chemical analysis of extraction residue on the crept specimens are shown in Fig.8. $(Fe,Cr)_2W$-Laves phase, $M_{23}C_6$ carbide and MX carbonitride precipitated in as tempered, and the peaks against each precipitate was detected in all steels crept for 10000h. Precipitation quantity of each alloying element increased with the progress for the rupture time, and it respectively reached a constant value within 5000h. These values agree with the equilibrium precipitation quantity of W, Fe, Cr calculated by Thermo-Calc. As precipitation quantity of each alloying element was almost same regardless of the Cr content, it is suggested that there is no difference in the solid solution strengthening by W.

TEM micrographs of 9.5%Cr and 11.5%Cr as tempered steels are shown in Fig.9. Both steels also show the martensite structure in which dislocation density is very high. Laves phase precipitate on various boundaries and in lath coherently[9] as well as $M_{23}C_6$ precipitates on the boundaries. TEM micrographs of specimens crept at 650°C-157MPa of the 9.5%Cr and 11.5%Cr steels are shown in Fig.10. Rupture time was 5289h at 9.5%Cr steel and 1928h at 11.5%Cr steel respectively. In the 11.5%Cr steel, the dislocation density decreased, subgrains have been formed, and the fine Laves phase which had precipitated coherently in lath can be hardly observed. In the 9.5%Cr steel, on the other hand, the lath width remained narrow and dislocation density was high, besides a lot of fine Laves phase coherently precipitated in lath.

The difference in such recovered microstructure at 650°C was observed in both crept and aged specimens. The recovery of the lath structure was slow in 9 to 9.5%Cr steels, whereas the progress of subgrain formation was early and fine Laves phase in lath disappeared in the 10.5 to 11.5%Cr steel at 650°C. Therefore it was concluded that the increase of growth rate of the precipitates such as the Laves phase accelerated the recovery with increasing Cr content.

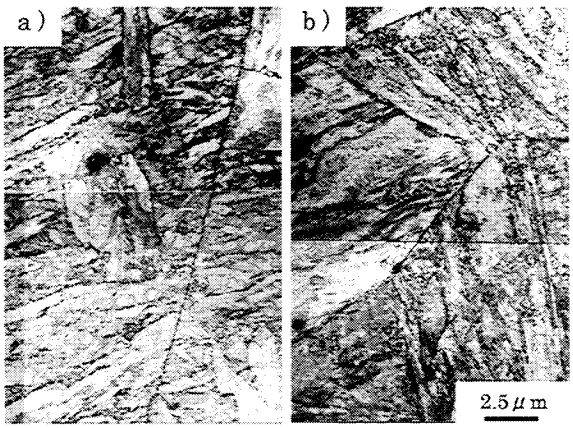


Fig.9 Transmission electron micrograph of a) 9.5%Cr steel and b) 11.5%Cr steel as tempered

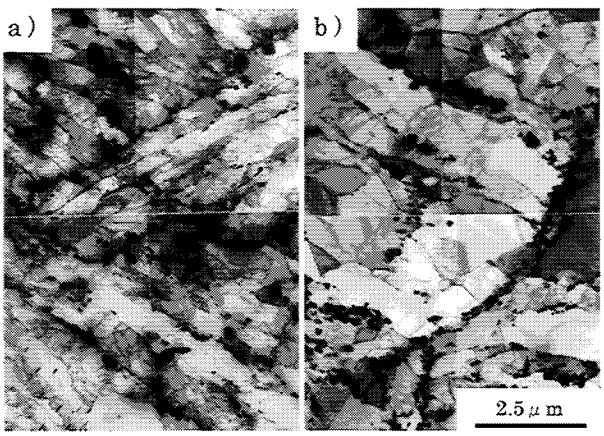


Fig.10 Transmission electron micrograph of a) 9.5%Cr steel and b) 11.5%Cr steel crept at 650°C, 157MPa

3.3 Transformation temperature

The transformation temperatures of the test materials are shown in Fig.11. The Ac1 temperature was approximately 815°C regardless of Cr content, and the Ac3 temperature increased from 882°C to 937°C with increasing Cr content. The ferrite phase may be stable rather high Cr materials than lower Cr materials. Ms temperature and Mf temperature were decreased with increasing Cr content. Although the dislocation density of as tempered materials was too high to measure, it is presumed that dislocation density of as quenched materials is almost the same, because hardness of as quenched materials was the same as shown in Fig.2.

Fig.12 shows the solvus temperature of Laves phase estimated by X-ray diffraction of the residue of the crept or aged materials at various temperature for 1 to 10000h. In the range of 10 to 11.5%Cr steel the solvus temperature of Laves phase rises with increasing Cr content. In the steels containing more than 10%Cr, however, Laves phase may be coarsen easily at 650°C which is considerably lower than its solvus. In fact, Laves phase coarsened and lath microstructure recovered early in higher Cr steels as shown in Fig.7 and Fig.10, although precipitate quantity of Laves phase is the same regardless of Cr content as shown in Fig.8. It was concluded that the coarsening of precipitates such as Laves phase were promoted and the recovery of microstructure could not be suppressed in the higher Cr steels.

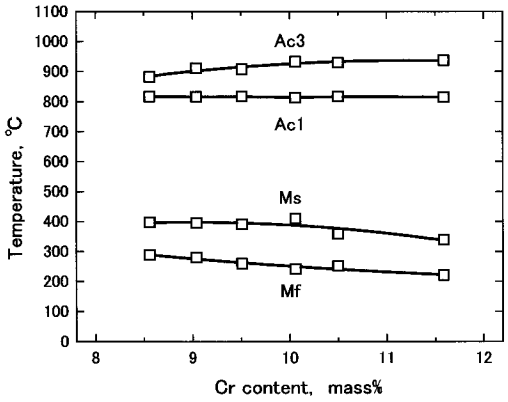


Fig.11 Transformation temperature of 8.5–11.5% Cr steels

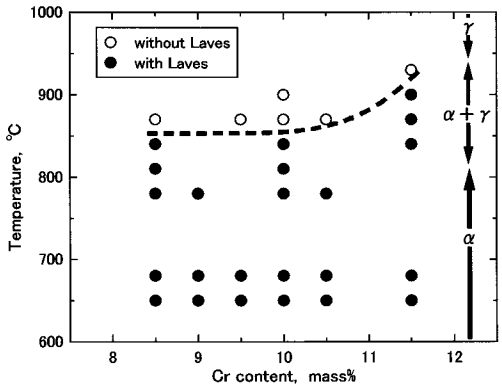


Fig.12 Solvus temperature of 8.5–11.5% Cr steels containing 3.5%W

4. Conclusion

The effect of the Cr content on the creep strength at 650°C of high Cr heat resistant steel containing 8.5-11.5%Cr, 3.5%W, 3%Co and 0.01%B for USC turbine rotor material was examined. The tensile strength at room temperature and the creep rupture strength in the short time at 650°C increased with the increase of Cr content. However the remarkable degradation of creep rupture strength occurred at early stage with increasing Cr content. Solid solution strengthening effect by W is the same regardless of the Cr content. The formation of subgrain is early in the 10.5-11.5%Cr steels crept at 650°C under the lower applied stress condition, and Laves phase precipitated within the lath disappeared earlier, whereas the lath structure in the 8.5-9.5%Cr steels recovered slowly. Therefore, it was concluded that the coarsening of precipitates such as Laves phase was promoted and the recovery of microstructure could not be suppressed in the higher Cr steels.

It is clarified that 9%Cr content was desirable for suppressing creep strength degradation in lower stress at 650°C of heat resistant steel containing high W. In the future, further improvement is necessary in order to improve simultaneously steam oxidation and long-term creep strength.

References

[1] T.Fujita : "Development of High Chromium Ferritic Heat Resistant Steels for Power Plants", Thermal and Nuclear Power, 42 (1991), p.1485.

[2] Y.Tsuda, M.Yamada, R.Ishii, Y.Tanaka, T.Azuma and Y.Ikeda : "Development of High Strengthening 12%Cr Ferritic Steel for Turbine Rotor Operating Above 600°C", 13th International Forgemasters Meeting, Oct. 12-16(1997), Pusan, Korea, p.417

[3] R.Kaneko, S.Nakamura, Y.Watanabe and Y.Tanaka : "Development of Steam Turbine Materials at Target Temperature 650°C", Thermal and Nuclear Power, 46(1995), p.968.

[4] C.Berger, E.Potthast, R.Bauer and G.A.Honeyman : "Development of High Strength 9-12% CrMoV Steels for High Temperature Rotor Forging", 11th International Forgemasters Meeting, June 11-14(1991), Terni/Spoleto, Italy, IX.5

[5] Y. Hasegawa, T. Muraki, M. Ohgami and H. Mimura : "Optimum Tungsten Content in High Strength 9 to 12% Chromium Containing Creep Resistant Steels ", Proceedings of 8th International Conference on Creep and Fracture of Engineering Materials and Structures, November 1-5 (1999), p.427

[6] F. Abe : "Contribution of Tungsten to Microstructure Stabilization and Improvement of Creep resistance in Simple 9Cr-W Steels", Proceedings of 8th International Conference on Creep and Fracture of Engineering Materials and Structures, November 1-5 (1999), p.395

[7] J. Hald : "Microstructure Stability of Steels P92 and P122 ", Proceedings of 3rd Conference on Advances in material technology for fossil power plants, April 5-6 (2001), p.115

[8] H. Kushima, K. Kimura and F. Abe : "Degradation of Mod.9Cr-1Mo Steel during long-term Creep Deformation", Tetsu-to-Hagane, 85 (1999), p.841

[9] Y. Murata, M. Morinaga, R. Hashizume, K. Takami, T. Azuma, Y. Tanaka and T. Ishiguro : "Effect of carbon Content on the mechanical Properties of 10Cr-5W ferritic steels", mat. Sci. and Eng., A282 (2000), p.251

THE EFFECT OF THE ELEMENT CARBON ON THE TOUGHNESS AND THE CREEP RUPTURE STRENGTH IN 12Cr HEAT RESISTANT STEELS

S. H. Ryu *, M. S. Kim *, Y. S. Lee *, S. T. Kang *, J. T. Kim *, Jin Yu **

* Doosan Heavy Industries & Construction Co., Ltd., Changwon, Korea
** Korea Advanced Institute of Science and Technology, Taejon, Korea

Abstract

The effect of the element carbon on the toughness and the creep rupture strength has been investigated in 9~12%Cr rotor alloys with 0.01~0.20%C and 2.5~3.5%W.

The packet size of the alloys with higher carbon content was finer than that of the alloys with lower carbon content. The cleavage facet size and the unit cleavage crack path were closely related to the martensite packet size without respect to the chemical compositions. The concurrent improving trend of the strength and the transition temperature with increasing carbon content resulted from the refinement of martensite packet size. The increment of 0.01% in the carbon content resulted in the increase in the tensile strength by about 10 MPa and the decrease in the $FATT_{50}$ by about 7.4°C.

The carbon increment from 0.1% to 0.2% decreased the creep rupture strength. However, the long-term creep rupture strengths of the alloys with higher carbon content showed some possibility crossing over those of the alloys with lower carbon content because of the low tendency of Laves phase precipitation.

Keywords: 9-12% Cr Steels, Impact Toughness, Creep Rupture Strength, FATT, Microstructure,

1. Introduction

To improve the thermal efficiency of the fossil power plant, there is a drive to develop 9 to 12 wt% Cr ferritic steels, which can be applied up to 650°C. It has been known that the strong precipitate forming elements, W, Mo, V, Nb, B and Cr, are essential for the creep rupture strength and for the corrosion and oxidation resistance.

However, it is possible to improve the creep rupture strength at the expense of the toughness. Alloying elements to significantly improve the creep rupture strength clearly reduce the toughness with increased content. To improve the toughness without the reduction of creep rupture strength, Si and Mn contents are lowered as much as possible and Ni is intentionally added up to about 1 %. However the toughness in ferritic steels with higher W and lower C contents is not increased readily as expected.

The alloys containing 2~3.5% W and approximately 3% Co indicate the lower long-term creep rupture strength especially at 650 °C due to the premature precipitation of Fe_2W Laves phase [1]. Incidentally, the existence of Laves phase has an effect on the toughness as well as on the long-term creep rupture strength. Therefore, it can be presumed that in the ferritic steels with W content above about 2%, the reduction in the forming tendency of Laves phase contributes to the improvement of the long-term creep rupture strength and the toughness.

According to J. Z. Briggs et al. [2], the formation of Fe_2Mo Laves phase is considered to require an atomic ratio Mo:C of five or higher. As the same principle as Fe_2Mo, Fe_2W Laves phase is expected to be formed at above the certain value of atomic ratio of W:C. It is clear that carbon has a big effect on the microstructure related to the creep rupture strength

and the toughness at the same time because the increase of carbon content decreases the forming tendency of Laves phase as well as delta-ferrite [3][4] and the martensite packet size [5][6][7]. Therefore, it will be a task to investigate the variation of the creep rupture strength and the toughness with the addition of carbon. It is known that in the 9-12%Cr ferritic steels, the carbon content indicating the highest creep rupture strength at 600°C is around 0.1% [8] [9]. Many heat resistant 9-12% Cr steels with about 0.1% carbon have been developed in recent years. However, there are insufficient researches for the optimum carbon content and the effect of carbon on the creep rupture strength and the toughness when the higher W content is present together with Co, Cu, B and N in the 9-12%Cr ferritic steels.

In this study, we investigated the effect of the element carbon in the range from 0.01 to 0.20%C on the toughness and the creep rupture strength in the ferritic steels containing alloying elements, such as 10.5~12% Cr, 2.5~3.5% W, 3% Co, 1~2% Cu and so forth.

2. Experimental Procedure

Trial melts containing 0.01~0.20% C with Cr, W, B, V, Nb, N and so forth were produced by vacuum induction melting. The chemical compositions are given in Table 1. Ingots, 50~100 kg each, were forged to rectangular bars with 45 mm x 100 mm at 1150 ~ 950 °C. Forged bar were austenitized at 1100°C for 4 hours, cooled to room temperature with a cooling rate of 110°C per hour to simulate the thermal histories at the center of rotor forgings with diameter 1200mm and subsequently tempered at 700°C for 10 hours followed by furnace cooling.

Table 1. Chemical compositions of 10~12%Cr heat resistant alloys studied (wt%).

Alloy ID	Alloy Group	C	Si	Mn	Ni	Cr	Mo	W	V	Nb	B *	N *	Co	Cu	Al
BC1	MnNi-2.5W	0.01	0.02	1.05	0.90	11.26	0.09	2.61	0.23	0.05	119	385	-**	-	0.076
BC2	"	0.07	0.02	1.03	0.88	10.80	0.09	2.59	0.19	0.05	88	350	-	-	0.080
BC3	"	0.13	0.02	1.03	0.84	11.03	0.10	2.56	0.22	0.05	82	403	-	-	0.074
BC4	"	0.18	0.02	1.01	0.87	10.88	0.10	2.54	0.22	0.05	80	357	-	-	0.060
CK1	MnNi-3.0W	0.19	0.05	1.01	0.83	10.99	0.08	2.98	0.19	0.06	85	316	-	-	0.004
CW30B2	"	0.11	0.02	0.98	0.84	10.86	0.09	3.06	0.2	0.05	76	356	-	-	<0.01
CK2	NiMn-3.0W	0.20	0.08	0.50	1.05	10.92	0.07	2.96	0.18	0.05	80	226	-	-	0.003
BW30Cr1	"	0.11	0.03	0.49	1.05	10.8	0.07	3.07	0.20	0.05	75	256	-	-	0.010
CoC1	Co-2.5W	0.05	0.04	0.05	0.13	11.25	0.08	2.55	0.21	0.06	13	376	3.00	-	0.005
CoC2	"	0.09	0.03	0.05	0.13	11.27	0.10	2.55	0.21	0.07	13	380	2.99	-	0.006
CoC3	"	0.13	0.03	0.05	0.13	11.40	0.11	2.55	0.21	0.06	14	394	2.99	-	0.005
CK3	Co-3.5W	0.19	0.06	0.13	0.52	11.01	0.09	3.45	0.21	0.055	100	332	2.97	-	0.004
CoW35B2	"	0.09	0.04	0.05	0.50	11.26	0.10	3.51	0.21	0.06	76	397	3.02	-	0.007
CK4	Cu-3.5W	0.18	0.10	0.09	0.50	10.75	0.06	3.45	0.18	0.05	90	337	-	2.0	0.004
CuW35B2	"	0.12	0.14	0.08	0.50	11.26	0.08	3.58	0.23	0.07	93	425	-	1.93	0.006
CK5	Cu-3.0W	0.21	0.04	0.04	0.01	11.88	0.09	3.03	0.19	0.05	100	65	-	1.32	0.004

* ppm , ** no addition

The tensile and the creep test specimens with the gage dimension of 6.5mm OD x 50mm Length were machined along the longitudinal direction parallel to forging direction. The full-sized 10 x 10 mm Charpy V-notch specimens were also cut off from the same direction as the tensile test specimen. Tensile and Charpy impact tests were conducted at the ambient temperature and at the temperatures of -70 ~ 140°C respectively. Creep tests were performed at 600, 650 and 700 °C in normal atmospheric conditions under constant loads.

SEM micrographs of the fracture surface were used to measure the martensite packet size equivalent to the effective grain size. Microstructures were observed on the plane perpendicular to Ni-plated cleavage fracture surface in order to investigate the cleavage crack path. The TEM investigations for thin foils and carbon extraction replicas and the X-ray analysis for the electrolytically extracted precipitates were conducted by the same method as reference [1].

3. Results

3.1 Microstructure

Fig.1 shows the change of the microstructure with carbon content in MnNi-2.5W alloy group shown in Table 1.

The delta ferrite was formed up to approximately 41 volume % on the tempered martensite microstructure in the BC1 alloy with 0.01 % C and was not indicated in the BC3 alloy with 0.13 % C. The fraction of delta ferrite in the tempered martensite in 9~12% Cr ferritic steels containing W and B could be predicted by the chromium equivalent (Cr_{eq}) suggested by Ryu et al. [4]. In this study, delta ferrite preferentially was formed along grain boundaries or grain boundary triple junctions under the condition of Cr_{eq} above 10%. The prior austenite grain size with a small amount of delta ferrite was finer than that with the 100% tempered martensite structure, while the carbon content hardly had a large effect on the prior austenite grain size in the alloys with the fully tempered martensite.

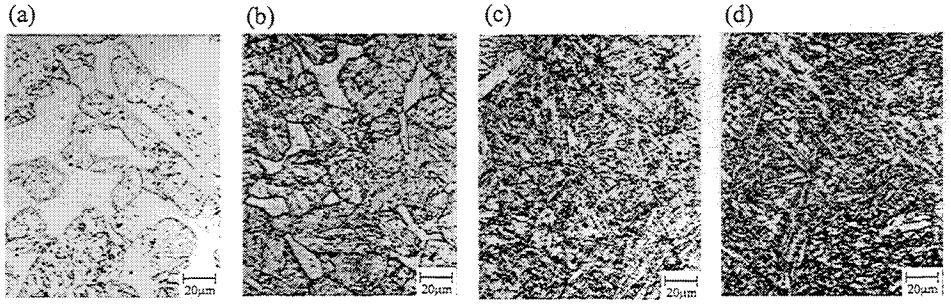


Fig.1 Variation of the microstructures with carbon content in (a) the BC1 alloy with 0.01%, (b) the BC2 alloy with 0.07%C, (c) the BC3 alloy with 0.13%C and (d) the BC4 alloy with 0.18%C.

3.2 Tensile properties

Fig.2 (a) shows the variation of the tensile strength with carbon content. It has been known that the strength in the martensite structure increases in proportion to the 0.33~1.00 power of the carbon content [10]. In this study, the tensile strength increased in proportion to the square root of carbon content within the range from 0.01% to 0.20% C, which was in good agreement with the suggestion by M. Cohen [11].

For a fixed carbon content, the tensile strength increased with increasing W content due to the formation of precipitates containing W element. At a given W content, the tensile strengths of the alloys with Co was superior to those of the alloys with austenite stabilizing elements, such as Cu, Ni and Mn. In this study, the tensile strength and the yield strength increased to

the extent of about 10 MPa and about 8.4 MPa respectively per the increment of 0.01% C.

The dashed line shown in Fig.2 (a) is the minimum tensile strength required at the center of the conventional 11CrMoVNbN rotor forgings [12]. Therefore, the carbon content has to be over 0.07~0.10% C to meet the tensile strength requirement for rotor forgings according to the content of W and the austenite stabilizers.

3.3 Charpy impact energy

Fig.2 (b) shows the relationship between carbon content and Charpy impact energy. The impact values increased with increasing C content in the studied range. The increase of the toughness was especially remarkable at the alloys with about 0.2% C compared to the alloys with carbon below about 0.1%.

For a fixed carbon content, the toughness increased with decreasing W content. It is known that in the alloys with bainitic structure, the tensile strength increased and the toughness decreased with the increase of carbon content. In these alloys with tempered martensite structure, the toughness was improved with increasing carbon content.

The criterion of the Charpy impact energy at room temperature for the high-pressure rotor forgings is indicated with a dashed line in Fig.2 (b). The toughness value called for the conventional 11CrMoVNbN rotor forgings is over approximately 14 J/cm^2 at room temperature and about 55 J/cm^2 at 135°C after tempering.

In the studied alloys with low carbon and Co and W above 3.0% each, the criterion of the Charpy impact energy for rotor forgings could not be satisfied readily in spite of the tempering at the high temperature around 700°C. Therefore, the alloys with low carbon content were in need of the tempering treatment at temperatures higher than 700°C within the consideration of yield strength or the carbon content above about 0.13~0.15%.

In the MnNi-3.0W, NiMn-3.0W and Co-3.5W alloy groups with W above 3.0%, USE (upper shelf energy) were in the range of 65~80 J/cm^2. There was no change nearly in the USE with the variation of carbon content to the extent of 0.1%. While, in the Co-2.5W alloy group, the USE decreased from 137 J/cm^2 to 115 J/cm^2 with increasing carbon content and increased from 76 J/cm^2 to 126 J/cm^2 with decreasing W content from 3.5% to 2.5%. It seemed that W and N content had a large effect on the USE rather than the carbon content in alloys studied even though it is known that the increasing carbon content decreased the USE in the alloys with bainitic structure [13].

3.4 Fracture appearance transition temperature

Fig.2 (c) shows the variation of the 50% fracture appearance transition temperature ($FATT_{50}$) as a function of carbon content. In the same way as the Charpy impact energy, it is known that the $FATT_{50}$ value increases with increasing carbon content in bainitic structure. However, in these alloys, the $FATT_{50}$ was improved with increasing carbon content. That is, the transition temperature was lowered to room temperature when carbon content increased to around 0.2 %.

According to B. Cina et al. [14], the increment of 0.01% in the carbon content increases the transition temperature by 5.8°C in the 3%Cr-Mo steel with 0.18~0.30% C. While, for the

case of the 10~12%Cr-W alloys with 0.01~0.20%C studied, the transition temperature was lowered by 7.4°C per the increment of 0.01%C.

It is suggested that Ni addition lowers the transition temperature by the strengthening of matrix structure and the reduction of precipitation [15][16]. Among the studied alloys, the Ni content in the CK3 alloy was 0.5% higher than that in the CK2 alloy, the $FATT_{50}$, however, was similar to each other. Ni addition up to around 1% seemed not to be effective to the improvement of the transition temperature in the 10~12%Cr-W alloys. The criterion of the $FATT_{50}$ in conventional 11CrMoVNbN rotor forgings is below 79°C as shown in the Fig.2 (c). The carbon content to satisfy this criterion is more than 0.13%.

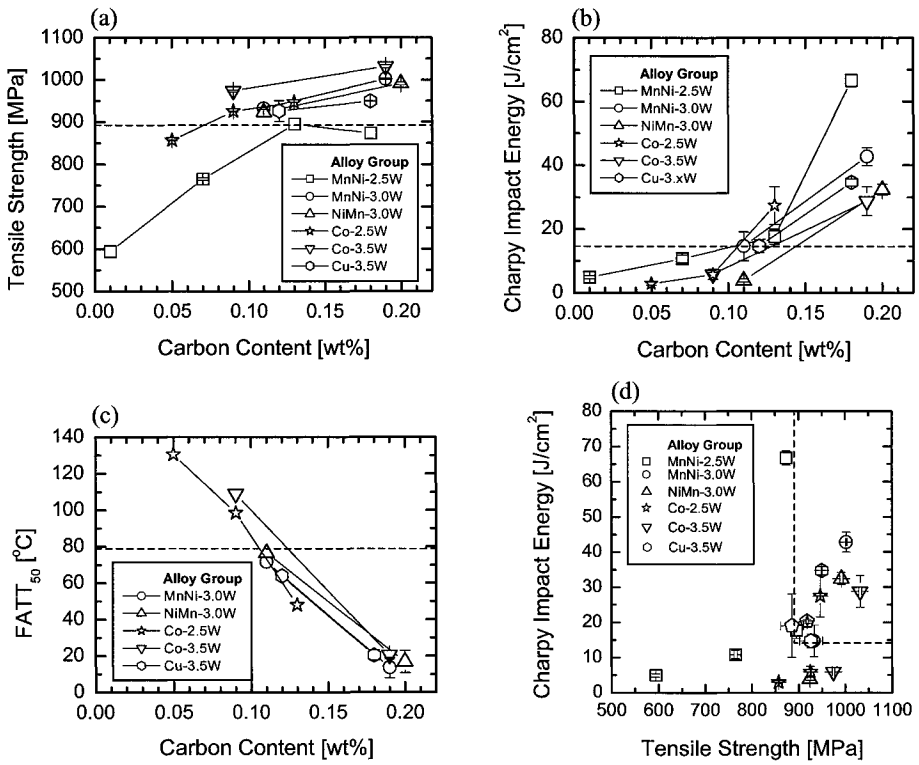


Fig.2 The effect of carbon content on (a) the tensile strength at RT, (b) the Charpy impact energy at RT, (c) The $FATT_{50}$ and (d) The relationship between tensile strength and Charpy impact energy.

3.5 Creep rupture strength

Fig.3 shows the comparison of the creep rupture strengths in the alloy with similar alloying composition except for carbon. Although the creep rupture strength of the MnNi-2.5W alloy group indicated a very low creep rupture strength compared to those of the other alloys studied due to the high aluminum content, it showed a trend that the creep rupture strength

increased with increasing carbon content up to 0.13%C (BC3 alloy) and then decreased by the additional increment of carbon content (BC4 alloy).

In the NiMn-3.0W alloy groups with 3.0%W, the creep rupture strengths at the temperatures of 600~700°C decreased when the carbon content increased from 0.10% to around 0.20%. These decreases of the creep rupture strength were somewhat remarkable at 650°C rather than 600°C.

In the Cu-3.5W and Co-3.5W alloy groups containing around 3.5% W, the creep rupture strength decreased in accordance with the increase of carbon content from 0.10% to 0.20%. On the contrary, the long-term creep rupture strength of the alloys with higher carbon content showed some possibility crossing over those of the alloys with lower carbon content although it was still unclear because of insufficient test data at this stage.

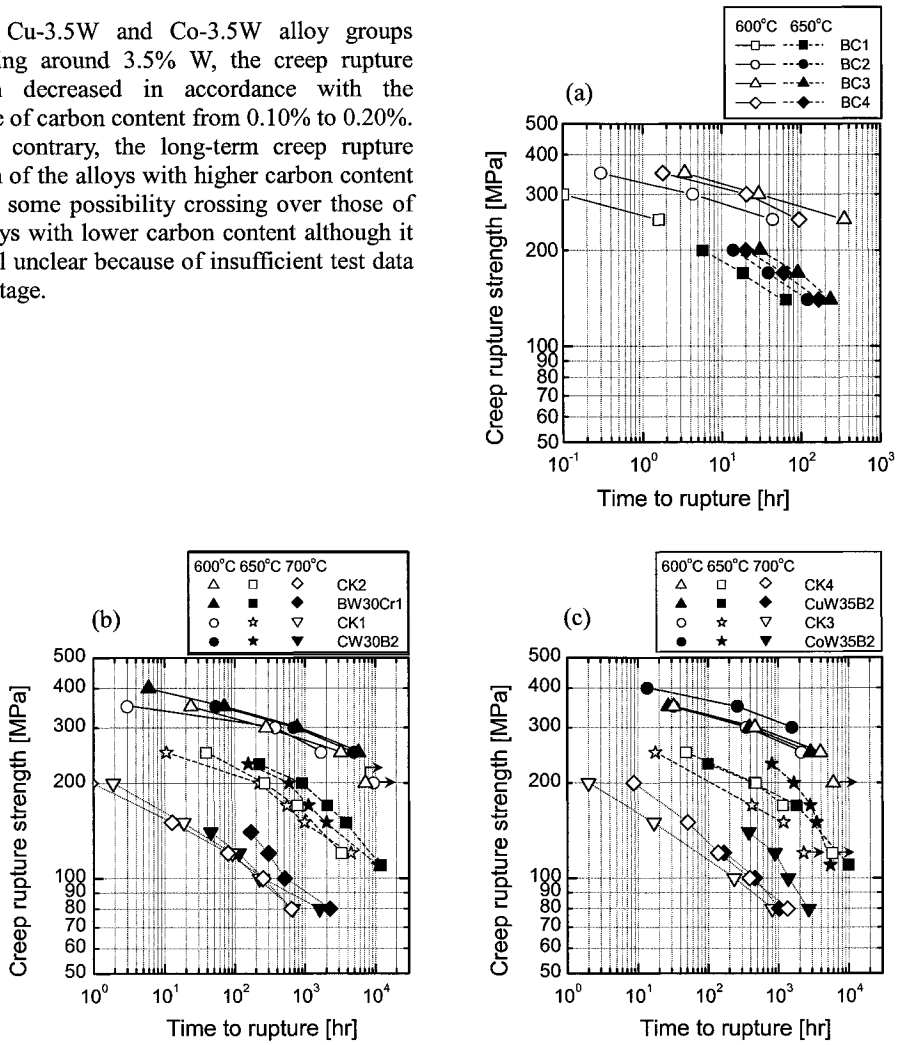


Fig.3 Comparison of the creep rupture strengths at 600°C, 650°C and 700°C with carbon content in (a) MnNi-2.5W group alloys, (b) MnNi-3.0W and NiMn-3.0W group alloys and (c) Co-3.5W and Cu-3.5W group alloys.

4. Discussion

4.1 The effect of carbon content on the toughness

It has been known that the prior austenite grain size, the packet size [5][6][7] and lath width [17][18][19] of martensite structure have an influence on the Charpy impact energy and $FATT_{50}$ in tempered martensitic structure.

Fig.4 shows the fracture surface of the Charpy impact specimen fractured at cleavage fracture region (liquid nitrogen temperature). BW30Cr1 and CK2 alloys belong to the NiMn-3.0W alloy group with the same chemical composition except for carbon content. In Fig.4, it is found out that the cleavage facet size is similar to the packet size of martensite and the cleavage facet size of the CK2 alloy with 0.2% C is finer than that of the BW30Cr1 alloy with 0.1% C.

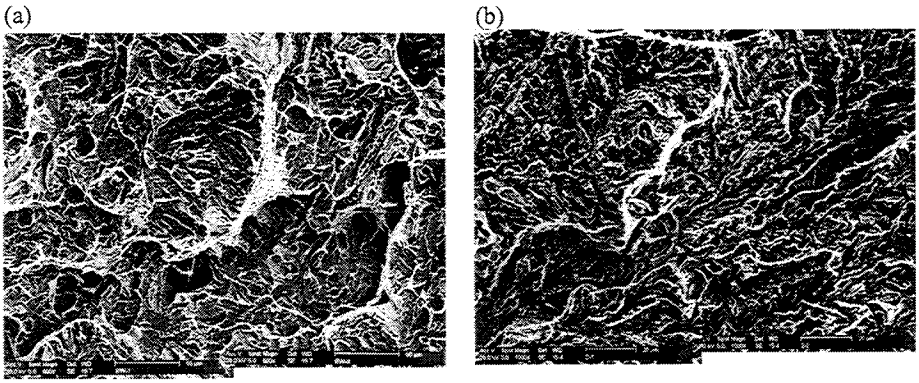


Fig.4 The comparison of the cleavage facet size on the fracture surface of the Charpy impact test specimens with carbon content in (a) the BW30Cr1 (x500) and (b) the CK2 alloys (x1000).

Fig.5 shows the relationship between the unit cleavage crack path and the packet size in the martensite structure. It was observed on the perpendicular section to fracture surface shown in Fig.4. The Ni-layer was plated on the fracture surface to make the observation of unit crack path easy. The cleavage crack paths of NiMn-3.0W group alloys are shown in Fig.5 (a) and (b). The unit cleavage crack path was similar to the packet size of martensite structure. The BW30Cr1 alloy with 0.11%C had a longer unit cleavage crack path compared with that of the CK2 alloy with 0.20%C. The same result as above was occurred in the CoW35B2 and CK3 alloys as shown in Fig.5 (c) and (d). It is found out that the cleavage fracture is closely related to the packet size of martensite structure without respect to the chemical compositions.

In the range of alloying compositions studied, the increase of carbon content had an influence on the packet size of martensite structure. The packet sizes of the BW30Cr1 and CoW35B2 alloys with approximately 0.1%C were 17 μm and 21 μm respectively. While, CK2 and CK3 indicated the packet size around 9 μm and 10 μm respectively. That is, the packet sizes of the alloys with higher carbon content were finer than those of the alloys with lower carbon

content. This observation was in agreement with the results of G. R. Speich et al. [20], who suggested that the martensite packet size was related to the carbon content.

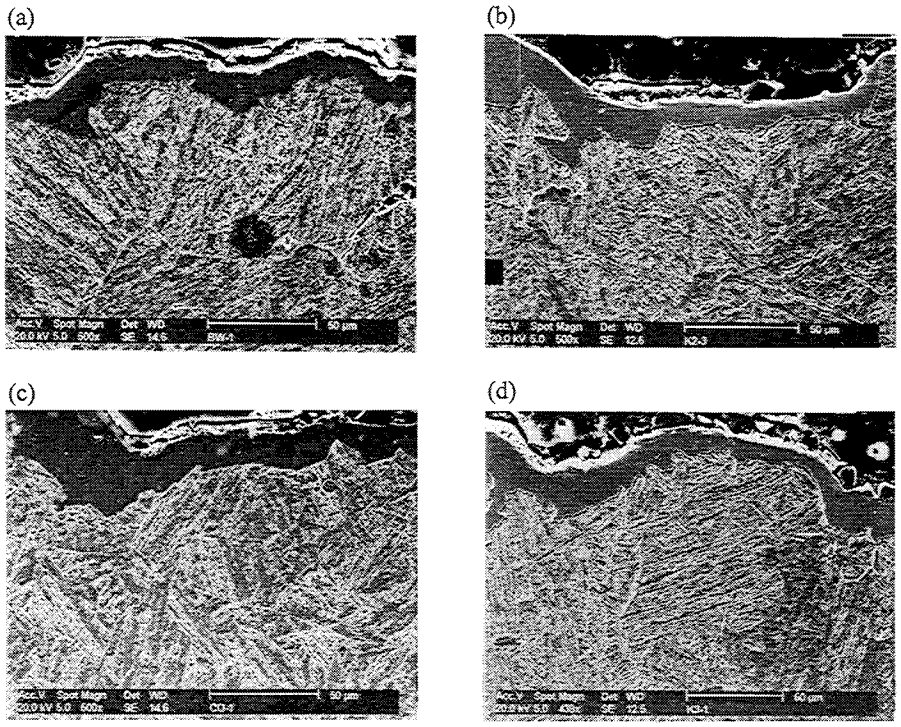


Fig.5 Shapes of the cleavage crack paths indicated at the plane perpendicular to the cleavage fracture surface of the Charpy impact test specimen in (a) the BW30Cr1, (b) the CK2, (c) the CoW35B2 and (d) CK3 alloys.

The finer martensite packet decreases the transition temperature because lots of high angle packet boundaries caused by finer packet size act as effective barrier to cleavage crack propagation. The cleavage crack suffers from the resistance of microstructural barriers and changes its path at packet boundaries.

In accordance with the increase from 0.1%C to 0.2%C, the precipitation of Laves phase were changed. In the BW30Cr1 and CoW35B2 alloys, Laves phase had already occurred at the tempering stage due to the high W content and the low C content, while Laves phase was hardly observed in the CK2 and CK3 alloys. Therefore, the higher toughness in the CK2 and CK3 alloys were affected by the reduced forming tendency of Laves phase as well as the refinement of martensite packet size compared to that of the BW30Cr1 and CoW35B2 alloys.

The martensite packet size exerts an effect on the strength as well. The yield strength increases with decreasing martensite packet size and can be expressed to the square root of the martensite packet size [21]. Therefore, it is sure that the concurrent improving trend of the strength and the transition temperature resulted from the refinement of martensite packet

size with increasing carbon content.

In the studied alloying composition, the Charpy impact energy, the $FATT_{50}$ and the strength were improved at the same time with increasing carbon content. That is, the increment in carbon content of 0.01% results in the increase in the tensile strength by about 10 MPa and the decrease in the $FATT_{50}$ by about 7.4°C.

4.2 The effect of carbon content on the creep rupture strength

The BC3 and BC4 alloys with 0.13%C and 0.18%C respectively showed very similar microstructure except for the amount of precipitates after tempering. The amount of the extracted precipitates in the BC3 and the BC4 alloys were 2.57wt% and 3.77wt% respectively at the as-tempered condition. The reduction in the creep rupture strength of the BC4 alloy compared to that of the BC3 alloy might be caused by the excessive precipitation of $M_{23}C_6$ at the tempering stage.

Fe_2W Laves phase precipitates at the as-tempered condition or after creep exposure depending on W contents. In the BW30Cr1 and the CoW35B2 alloys, Laves phase was already precipitated at lath boundaries, prior austenite grain boundaries and the interface between delta ferrite and martensite and within delta ferrite. The fine Laves phase contributes to the improvement of the creep rupture strength at shorter time. However it coarsens very rapidly and then loses the precipitation strengthening effect. In the CoW35B2 alloy, the rapid decrease of the creep rupture strength especially at 650 °C in shorter time can be accounted for the premature precipitation of Laves phase and thus the depletion of W in matrix [1].

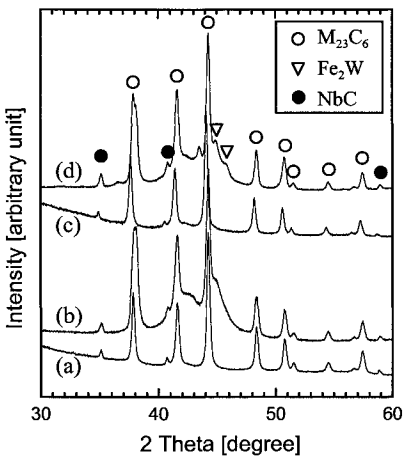


Fig.6 XRD profiles of the precipitates extracted electrolytically after tempering in (a) the CK3, (b) CoW35B2, (c) CK4 and (d) CuW35B2 alloys.

Carbon might play an important role in the reduced forming tendency of Laves phase by means of the control of the atomic ratio of W:C. As in the CoW35B2 and the CK3 alloys, the carbon content increases from 0.09% to 0.19%, the atomic ratios of W:C are decreased from 2.5:1 to 1.1:1. Fe_2W Laves was formed in the CoW35B2 alloy after tempering as shown in Fig.6 (b). On the contrary, in the CK3 alloy, Laves phase was hardly observed in spite of the same chemical composition as the CoW35B2 alloy except for carbon content. Therefore, it seems that the increase of carbon content from 0.10% to 0.20% somewhat lower the tendency of Laves phase precipitation for a fixed W content and hence the rapid declining tendency of the creep rupture strength at 650 °C

5. Conclusion

In the 9~12%Cr alloys for rotor forgings with 0.01~0.20%C, 2.5~3.5%W, Co, Cu and so forth, the effects of carbon content on the creep rupture strength and the toughness are summarized

as follows.

- The increase of carbon content had effect on the martensite packet size rather than the prior austenite grain size. The packet size of the alloys with higher carbon content was smaller by half of the size than that of the alloys with lower carbon content.
- The cleavage facet size and the unit cleavage crack path were closely related to the martensite packet size without respect to the chemical compositions.
- The concurrent improving trend of the strength and the transition temperature with increasing carbon content resulted from the refinement of martensite packet size.
- The increment of 0.01% in the carbon content resulted in the increase in the tensile strength by about 10 MPa and the decrease in the $FATT_{50}$ by about 7.4°C.
- The carbon increment from 0.1% to 0.2% decreased the creep rupture strength. However, in the Co added alloys, the long-term creep rupture strengths at 650°C of the alloys with higher carbon content showed some possibility crossing over those of the alloys with lower carbon content because of the reduction in the forming tendency of Laves phase.

References

[1] S. H. Ryu, Jin Yu and B. S. Ku, Effects of alloying elements on the creep rupture strength of 9-12% Cr steels, Proceedings of the 5th International Charles Parsons Turbine Conference, 3-7 July 2000, Churchill College, Cambridge, UK, pp.472-484.
[2] J. Z. Briggs and T. O. Parker, The super 12% Cr steels, Climax Molybdenum Co., New York, 1965.
[3] D. L. Newhouse, C. J. Boyle and R. M. Curran, Preprint of the 68th ASTM Annual Meeting, Purdue University, Lafayette, IN, June 13-18, 1965.
[4] S. H. Ryu and Jin Yu, A new equation for the Cr equivalent in 9 to 12 pct Cr steels, Met. and Mat. Trans. A, Vol. 29A, June 1998, pp.1573-1578.
[5] H. Ohtani, F. Terasaki and T. Kunitake, Trans. Iron Steel Inst. Jap. 12, 1972, p.118.
[6] L. A. Norstrom, Scand. J. Met. 5, 1976, p.159.
[7] J. P. Naylor and P. R. Krahe, Met. Trans. 5A, 1974, p.1699.
[8] T. Fujita, Y. Nakabayashi, A. Suzuki and A. Hizume, Proc. of COST-EPRI Workshop about 9-12% Cr Steel for Power Generation, Schaffhausen, Schwej, Oct. 13-14, 1986, pp.1-7.
[9] T. Fujita, Advanced Materials & Processes 4, 1992, pp.42-47.
[10] F. B. Pickering, Material Science and Technology Vol.7, VCH Publishers Inc., New York, 1992, p.70.
[11] M. Cohen, Trans. AIME 224, 1962, p.638.
[12] High chromium alloy steel turbine rotor forgings, GE Power Generation Engineering, 1994.
[13] H. Nakajima and T. Araki, Tetsu-to-Hagane, Vol.58 No.14, 1972, pp.1993-2004.
[14] B. Cina and P. Jubb, Factors affecting the transition temperatures of forgings used in power-generating equipment, J. Iron Steel Inst. 193, 1959, p.329-349.
[15] T. Araki, M. Shin and R. Sagawa, Tetsu-to-Hagane, Vol.61 No.7, 1975, pp.972-990.
[16] H. Nakajima and T. Araki, Tetsu-to-Hagane, Vol. 61 No.15, 1975, pp.3119-3128.
[17] J. P. Naylor and P. R. Krahe, Met. Trans. 6A, 1975, p.594.
[18] J. P. Naylor and R. Blondeau, Met. Trans. 7A, 1976, p.891.
[19] Y. Ohmori, H. Ohtani and T. Kunitake, Tetsu-to-Hagane, Vol.58 No.8, 1972, pp.1076-1085.
[20] G. R. Speich and H. Warlinont, J. Iron Steel Inst. 206, 1968, p.385.
[21] J. A. Whiteman, Low carbon steels for the eighties, London, The Institute of Metallurgists, Series 3, No. 6, p.I-1.

STRAIN RANGE PARTITIONING ANALYSIS FOR CREEP-FATIGUE LIFE OF FERRITIC HEAT-RESISTING MATERIALS

Megumi Kimura, Kazuo Kobayashi and Koji Yamaguchi
National Institute for Materials Science
1-2-1, Sengen, Tsukuba 305-0047, Japan

Abstract

Creep-fatigue interaction of several ferritic steels such as Mod.9Cr-1Mo, 9～12Cr-2W, newly produced Pd-added 9Cr-1Mo-1.5Pd and 9Cr-3W-0.7Pd steels, extremely high strength oxide dispersion strengthened (ODS) ferritic steels and a precipitation hardened carbon-free martensitic steel, were investigated. For these ferritic steels it was clarified that there were two points to improve the creep-fatigue life. One is to keep the creep ductility high, and the second is to decrease the plastic strain drastically in new high strength steel. From the viewpoint of an evaluation of the creep-fatigue life, the analysis by ductility normalized strainrange partitioning method explained well the effect of creep ductility and the strength of the materials on the creep-fatigue life.

Key words: Creep-fatigue interaction, Ferritic heat-resisting steels, Ultra supercritical power plant, Ductility normalized strainrange partitioning method

1.Introduction

New ferritic heat-resisting steels for ultra supercritical (USC) power plant have been developing in Japan, Europe and USA[1]. The fossil fuel power plants operate under daily start-up and shut-down so thermal stresses are induced. The environment and thermal history of USC power plants under high pressure steam at 650°C are very severe to the steels. Creep-fatigue interaction, as well as creep rupture strength, is an important factor for the strength design of the components. Tensile tests, creep rupture tests and creep-fatigue interaction tests were carried out for commercial and newly produced ferritic steels.

2. Materials and Test Methods

Chemical composition of the materials used in this study are shown in Table 1. Mod.9Cr-1Mo is selected as a base material because it is the most popular and widely used one in high strength ferritic steels. 9Cr-2W and 12Cr-2W steels are the maximum strength ferritic steels at present in the commercial base ferritic steels[2]. Pd-added 9Cr-1 Mo-1.5Pd or 9Cr-3W-0.7Pd ferritic steels hardened by FePd $L1_0$ orderd phase, carbon free Fe-Ni-Co martensitic steel strengthed by Fe_7M_6(μ phase) and Fe_2M(Laves phase), and oxide dispersion strengthened(ODS) ferritic steels, were newly produced by Igarashi[3], Muneki[4] and Wanikawa[5] of NIMS, respectively. Product forms of the 12Cr-2W are three types, plate, tube and pipe.

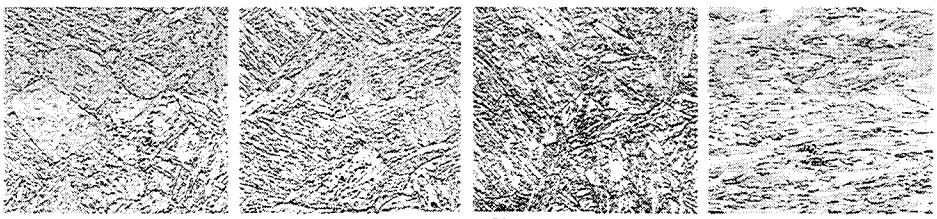
Table 2 is the processing details. Thickness of the plates is from 25 to 30 mm. Size of the pipe of 12Cr-2W steel is as follows; outer diameter is 600mm and inner diameter is 360mm. Reduction ratio of this pipe is small as compared with the plates or tube as shown in Table2.

Table 1 Chemical composition of the materials used in this study (mass%).

Material	Shape	C	Si	Mn	Cu	Ni	Cr	Co	W	Mo	V	Nb	Ti	Al	N	Pd	Y	B	Re
Mod.9Cr-1Mo	plate	0.08	0.34	0.49	0.02	0.09	8.34	-	-	0.89	0.23	0.07	-		0.059	-	-	-	-
9Cr-2W	plate	0.09	0.18	0.46	-	0.14	8.87	-	1.89	0.45	0.21	0.07	-		0.05	-	-	-	-
12Cr-2W	plate	0.12	0.28	0.63	0.98	0.35	10.7	-	1.9	0.36	0.22	0.06	-		0.076	-	-	-	-
12Cr-2W	tube	0.11	0.27	0.59	0.82	0.33	12.1	-	1.82	0.34	0.19	0.06	-		0.07	-	-	-	-
12Cr-2W	pipe	0.14	0.26	0.65	0.74	0.4	11.03	-	1.95	0.29	0.2	0.07	-		0.06	-	-	-	-
9Cr-1Mo-1.5Pd	plate	0.12	0.03	0.5	-	-	9.0	-	-	1.3	0.30	0.05	-		0.003	1.5	-	0.008	-
9Cr-3W-0.7Pd	plate	0.10	0.03	0.35	-	-	9.0	-	3.0	-	0.2	0.05	-		0.03	0.7	-	0.005	0.5
ODS-A	bar	0.062	0.02	0.13	-	0.02	11.9	-	2.39	<0.01	<0.01	0.01	0.38		0.016	-	0.28	-	-
ODS-B	bar	0.062	0.02	0.13	-	0.02	11.9	-	2.39	<0.01	<0.01	0.01	0.38		0.016	-	0.28	-	-
C-Free-M	bar	0.0005	0.02	0.46	-	12.08	5.04	8.96	9.9	-	-	-	0.12	0.06	0.0005	-	-	0.0052	-

Table 2 Processing details of the materials.

Material	Shape	Thickness (mm)	Reduction ratio	Normalizing	Tempering	PWHT
Mod.9Cr-1Mo	plate	25	8	1050℃/10min AC	770℃/1h AC	740℃/1h FC
9Cr-2W	plate	25	8.7	1060℃/1h AC	770℃/2h AC	
12Cr-2W	plate	25	28	1050℃/100min AC	770℃/360minAC	
12Cr-2W	tube	9	84	1050℃/10min AC	790℃/180minAC	
12Cr-2W	pipe	120	4.5	1050℃/60min AC	780℃/360minAC	
9Cr-1Mo-1.5Pd	plate	25	-	1100/4hr AC	500/4hr AC→770/4hr AC	
9Cr-3W-0.7Pd	plate	25	-	1100/4hr AC	500/4hr AC→770/4hr AC	
ODS-A	bar	20□	7	HIP、Grooved rolling 930℃、Annealing 930℃		
ODS-B	bar	20□	7	HIP、Grooved rolling 930℃、Annealing 1250℃		
C-Free-M	bar	20□	-	1000℃,30min As solution treatment		



(a) 12Cr-2W(plate) (b) 12Cr-2W(pipe) (c) 9Cr-3W-0.7Pd (d) ODS-A(bar)

Fig. 1 Typical microstructures of the materials.

Typical microstructures are shown in Fig.1. 12Cr-2W steel plate is tempered-martensitic as shown in Fig.1(a). Mod.9Cr-1Mo, 9Cr-2W steel plates and 12Cr-2W steel tube and pipe are also tempered-martensitic, but the pipe has large grain size shown in Fig.1(b). Pd added steel has also tempered martensite as shown in Fig.1(c). ODS is ferritic structure as shown in Fig.1(d). The carbon free Fe-Ni-Co martensitic steel is a lath-martensitic structure.

Creep-fatigue tests were conducted at 650℃. The wave shape of the creep-fatigue test was a trapezoidal one with 3 hr or 1 hr hold at tension side. Total strain range of the wave shape is 1.0, 0.6 and 0.4%. The specimen is machined to cylindrical smooth with a diameter of 8 mm from the product form along a rolling direction or longitudinal direction.

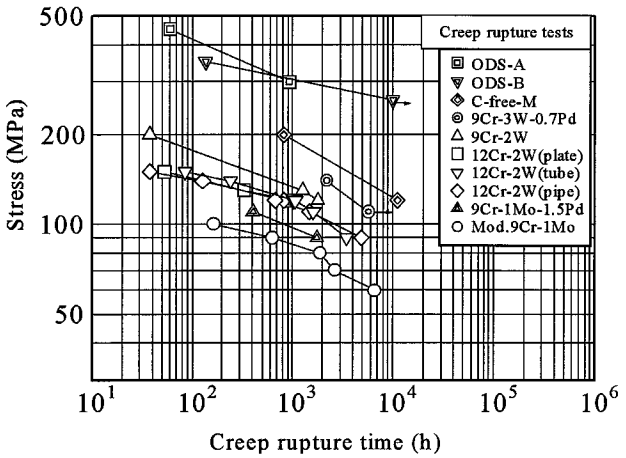


Fig.2 Creep rupture strength for the ferritic steels at 650℃

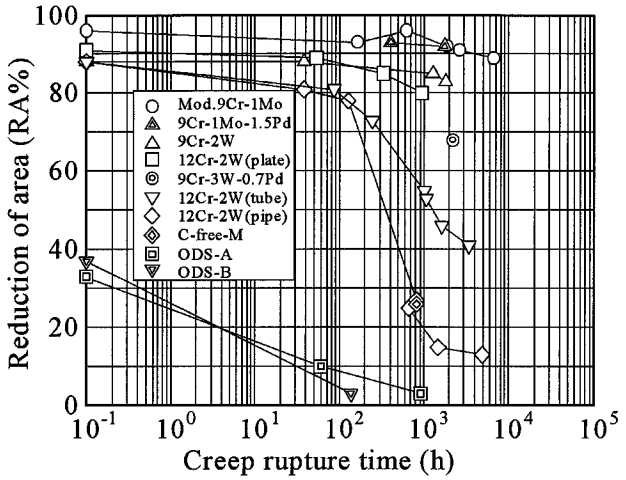


Fig.3 Reduction of area for the ferritic steels at 650℃.

3.Results and Discussion

3.1 Results of creep rupture tests

Creep rupture strength and reduction of area depending on the creep rupture time are shown in Fig.2 and Fig.3, respectively. As for the creep strength, base Mod.9Cr-1Mo steel is the weakest. The next stronger are 9Cr-1Mo-1.5Pd and 12Cr-2W steel plate, tube and pipe. And the next are 9Cr-2W and 9Cr-3W-0.7Pd steel plates. The carbon free martensite and ODS materials are extremely strong.

On the other hand, the order of reduction of area is opposite. Both ODS have the lowest reduction of area. The nexts higher are 12Cr-2W steel pipe and tube. These reductions of area are decreasing with the creep rupture times. 12Cr-2W and 9Cr-2W steel plates have

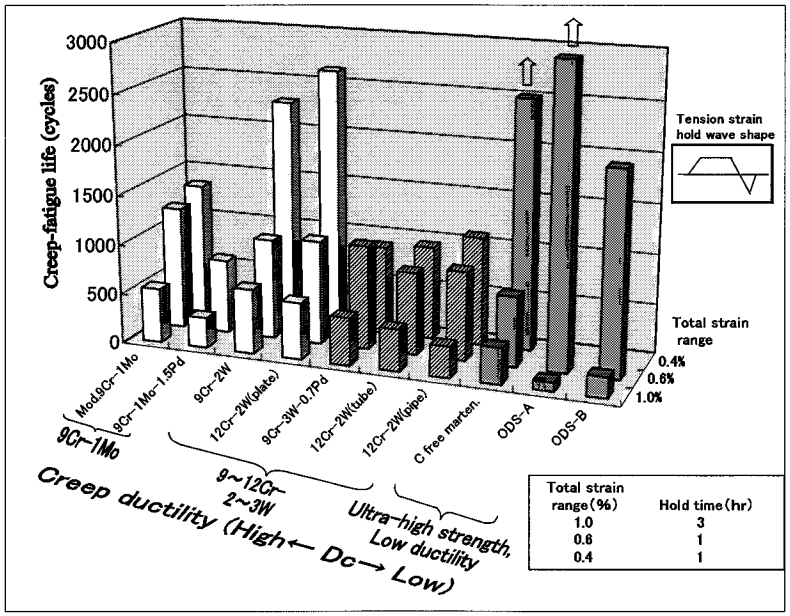


Fig.4 Creep-fatigue lives for the ferritic steels at 650℃.

high reductions of area, and Mod9Cr-1Mo and 9Cr-1Mo-1.5Pd steel plates have the highest ones.

3.2 Results of creep-fatigue tests

Number of cycles to failure for the creep-fatigue test (creep-fatigue life) is shown in Fig.4. The lives are clearly dependent on the kind of materials. The order of materials on the side axis in Fig.4 is the order of reduction of area at 1,000 hr of creep rupture time, and the materials are divided into three groupes such as 9Cr-1Mo group, W-strengthed group and Ultra high-strength group, as shown on the side axis of Fig.4. In addition, as for the dependency of the reduction of area on the rupture time, the materials are also divided into three group such as high reduction of area group, decreasing reduction of area with the time group and low reduction of area (low ductility) group as shown in vertical axis of Fig.4 by darkness tone.

In Fig.4 there are two remarkable regions which show extremely long creep-fatigue life, the first is 9Cr-2W and 12Cr-2W steel plates and the second is cabon free martensite and ODS steels at small total strain range of 0.4% or 0.6%. The former materials have higher creep strength and the same high ductlility as compared with the base Mod. 9Cr-1Mo steel. The latter materials have ultra-high strength and low ductility. The ultra-high strength means that there is only a little plastic strain in the hysteresis loop in the cyclic test as shown in Fig.5, because the hysteresis loop is very narrow compared with the base Mod.9Cr-1Mo steel.

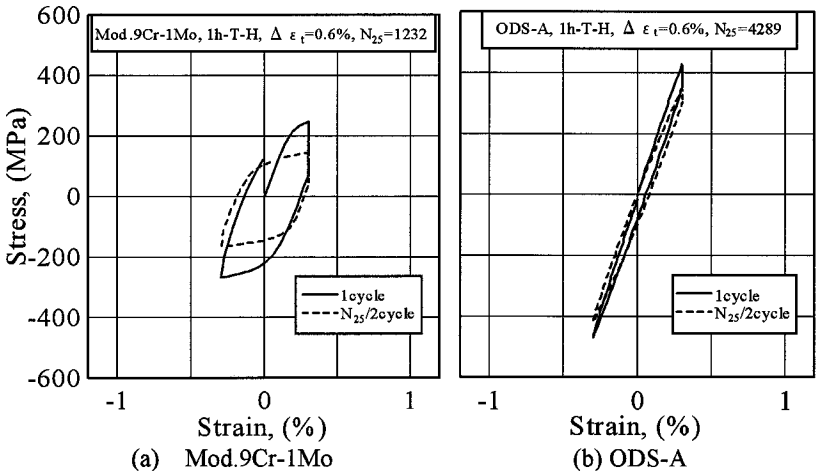


Fig.5 Comparison of representative stress-strain hysteresis loops on creep-fatigue test.

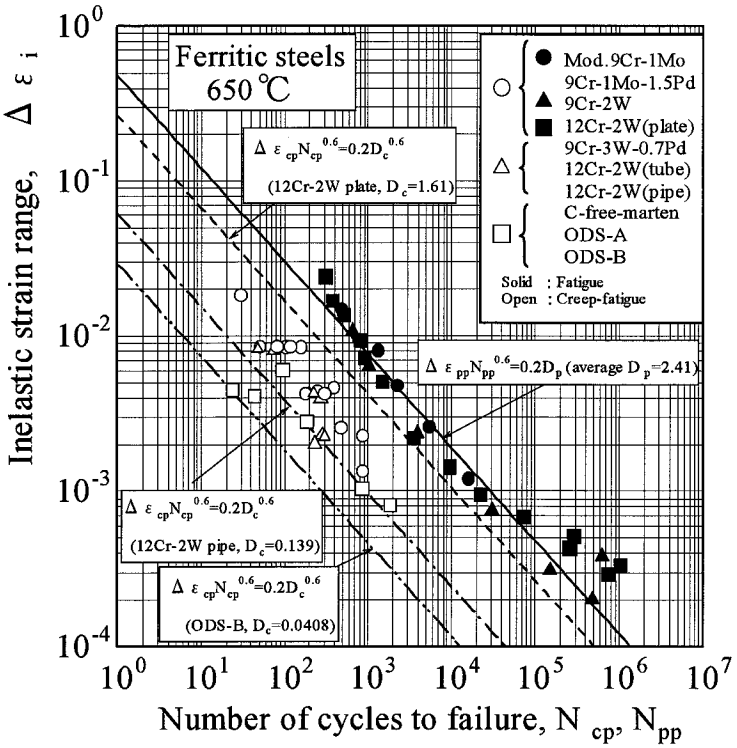


Fig. 6 Analysis result by strainrange partitioning method for the ferritic steels.

3.3 Analysis by ductility normalized strainrange partitioning method

From the above section it was clarified that there were two points to improve the creep-fatigue life. One is to keep the creep rupture ductility high, and the second is to decrease the plastic strain of cyclic deformation in new high strength steel. From the viewpoint of an evaluation of the creep-fatigue life, the analysis by ductility normalized strainrange partitioning method may be available. This method is based on plastic strain range and ductility of the materials.

Halford and et al [6] proposed the following equations,

$$\Delta \varepsilon_{pp} N_{pp}^{0.6} = 0.5 D_p \quad \cdots\cdots\cdots\cdots\cdots\cdots (1)$$

$$\Delta \varepsilon_{cp} N_{cp}^{0.6} = 0.2 D_c^{0.6} \quad \cdots\cdots\cdots\cdots\cdots\cdots (2)$$

For these ferritic steels, the result of the analysis is shown in Fig.6. As for equation (1), the constant 0.5 was modified to 0.2 to fit the equation (1) to the triangular fatigue test data of solid symbols. As for the equation (2), three dotted prediction lines were drawn as a parameter of the value of D_c of the matereials. One is a dotted line of 12Cr-2W steel plate as a representative of high ductility materials. The second is a dotted line of 12Cr-2W steel pipe as a representative of decreasing ductility materials. The third is a dotted line of ODS-B as a representative of low ductility ultra-high strength materials.

From Fig.6 the analysis by ductility normalization strainrange partitioning method explains well the effect of creep ductility and the strength of the materials on the creep-fatigue life.

4.Summary

Creep-fatigue interaction of several ferritic steels were investigated. For the ferritic steels it was clarified that there were two points to improve the creep-fatigue life. One is to keep the ductility high, and the second is to decrease the plastic strain drastically in new high strength steel. From the viewpoint of an evaluation of the creep-fatigue life, the analysis by ductility normalized strainrange partitioning method explained well the effect of creep ductility and the strength of the materials on the creep-fatigue life.

Reference

[1] The EPRI/National Power Conference, New Steels for Advanced Plant up to 620℃, Ed. By E.Metcalfe, (1995).
[2] F.Masuyama, ASME Code Approval for NF616 and HCM12A, The EPRI/National Power Conference, New Steels for Advanced Plant up to 620℃, Ed. By E.Metcalfe, (1995)98.
[3] M.Igarashi, S.Muneki and F.Abe, Report 123 Committee, J Soc. Promo. Sci., Vol.39, No.3(1998)355.
[4] S.Muneki, M.Igarashi and F.Abe, Tetsu-to-Hagane, 88(2002)45.
[5] S.Wanikawa, unpublished work.
[6]G.R.Halford, J.F.Saltsman and M.H.Hirschberg, Proc. Conf. Environmental Degradation of Eng.Mater., Blacksburg, (1977)599.

HIGH TEMPERATURE CREEP BEHAVIOUR AND MICROSTRUCTURAL CHANGES OF TAF 650 STEEL

Milan Svoboda[1)], Jiri Bursik[1)], Ivana Podstranska[1)], Ales Kroupa[1)], Vaclav Sklenicka[1)] and K.-H. Mayer[2)]

[1)] Institute of Physics of Materials, Academy of Sciences of the Czech Republic, Zizkova 22, CZ-616 62 Brno, Czech Republic
[2)] Alstom Power, D-90208 Nuernberg, Germany

Abstract

The microstructure of W, Ni and Co containing high chromium martensitic steel TAF 650 was quantified by transmission electron microscopy and image analysis. Samples were studied in the as-received state and after creep loading to fracture at 650 °C for approx. 4000 and 6000 h where marked decrease in the time to fracture has been found. Additional creep investigation of this steel reveals substantially longer time to fracture at lower stresses than was expected from previous results. In order to find out microstructural features responsible for such improvement in the creep properties, microstructural investigations of TAF 650 steel after 18 700 hours creep exposure at temperature 650 °C was performed. The results show that the synergetic effect of fine MX precipitates decreases due to Z-phase precipitation together with higher amount of Laves phase particles found in creep specimens compared to isothermally aged material is responsible for the creep strength. The prediction of creep behaviour based on a comparison of experimentally determined secondary phases and chemical composition with equilibrium values obtained by THERMO-Calc calculations are also provided.

Keywords: creep, chromium steels, microstructure, creep lifetime, creep strength

1. Introduction

Improved ferritic steels are required to minimise the costs for high temperature steam power plants and to provide high flexibility of their operation. For this reason there are worldwide activities in research and development for the 9-12%CrMoV steel class. These steels have tempered martensitic lath structure and are strengthened by precipitates and solute atoms. Classical steels of this type have attained their high creep strength by the addition of V, Nb and N, which form fine precipitates. The creep strength of high Cr ferritic steels has been improved further by replacing part of Mo by W. Recently, new trial melts for 620/630°C application were developed on the basis of the new alloying concepts like the addition of cobalt and boron. These alloying concepts have been applied to various well-established steels; for example the TAF 650 steel was derived from the TAF-steel, exploited around 1980 [1]. In this steel part of Mo was replaced by W, and Co and Ni were added. This new steel exhibited higher creep rupture strength at higher stresses (for short rupture times) than the original TAF steel. However, the difference between creep rupture strength of the steels decreased with decreasing stress. Finally, the creep rupture strength of TAF 650 is below that of TAF at low stresses. This marked decrease seems to be slowed down at the lowest stresses as can be seen in Fig. 1.

The steel in the as-received state and the creep specimens from the region of marked decrease in creep lifetime, denoted as Z4 and Z5 in Fig. 1, has been examined by the authors of this paper earlier [2,3]. It was found that the microstructure of TAF 650 is not homogeneous in the

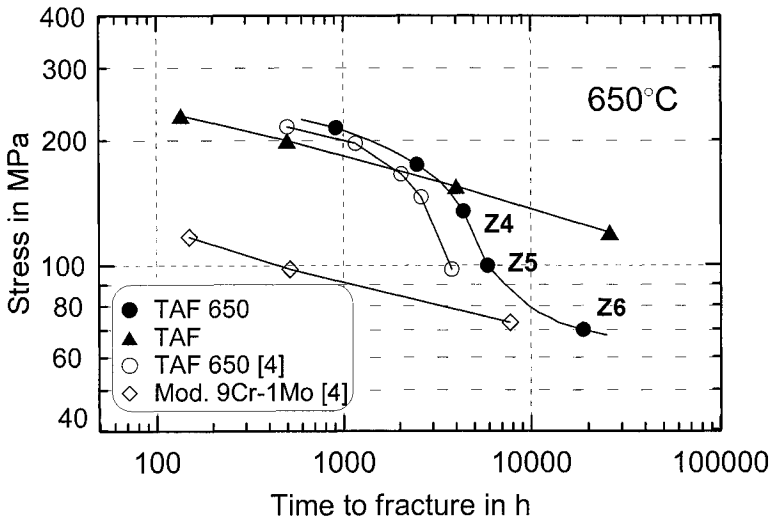


Fig. 1 The comparison of stress vs time to fracture curves at 650 °C for various ferritic steels (for steels composition see Table 1).

as-received state and that the pronounced precipitation of Laves phase Fe_2W occurs during both annealing and creep exposure. The decrease of creep rupture strength was tentatively attributed to these two reasons.

The several studies recently appeared dealing with TAF 650 steel itself [4] or the 9Cr steels containing W and Ni and/or Co, e.g. [5,6] suggested that above mentioned effects are not the only reasons for the decrease in the creep rupture strength. Sawada [4] studied effect of W on recovery of lath structure during creep on two steels with (TAF 650 steel) and without (Mod. 9Cr-1Mo steel) W. He reported the similar creep rupture strength behaviour for TAF 650 steel, as can be seen in Fig. 1 where his results are indicated by open symbols. In his work nevertheless, he did not provide any explanation for observed abrupt decrease of creep rupture strength of TAF 650 steel. Hasegawa et al. [5] studied optimal tungsten content in 9-12%Cr steels. It is interesting to note that among various steels with different tungsten content only that with Ni and/or Co addition showed an abrupt decrease of creep rupture strength in the temperature interval from 600 to 700 °C. Hasegawa explains in his paper, that due to the higher Cr content of the steels G and H more Laves phase precipitates which causes the drop of the creep rupture strength. Recently, Abe [6] published a study on the creep deformation behaviour of simple 9Cr-W and solute modified 9Cr-WVTa steels containing no N (only 0.003%). He did not encounter any abrupt decrease of creep rupture strength as a result of W addition to the steel and Fe_2W Laves phase precipitation contrary to Hasegawa conclusions.

The specimen Z6 creep tested for the longest time, see Fig. 1, was supplied for this study so it was possible acquire additional data to those published previously [2,3]. Taking into account the creep data for specimen Z6 it can be expected from Fig. 1 that TAF 650 steel may exhibit a sigmoidal behaviour in creep rupture test. Such a behaviour has already been described by Vodarek and Strang [7] for 12CrMoVNb steel containing nickel, creep tested at temperatures

550 and 600 °C. They found that the precipitation of Z-phase occurs in the steel. In the frame of above mentioned findings the question naturally arises if the presence of Z-phase could contribute to the creep rupture strength decrease in TAF 650 steel. Therefore the aim of this work was to perform careful microstructural investigation of the specimen Z6 tested for the longest time, i.e., 18 870 h at 650 °C. An attempt to include Z-phase as an equilibrium phase into thermodynamic modeling by means of THERMO-Calc is also presented.

2. Experimental procedures

Chemical compositions of the steels TAF 650 and TAF are given in Table 1. However, only TAF 650 steel has been used in this study.

Table 1. Chemical composition of TAF and TAF 650 steels in wt.%

steel	C	Si	Mn	Cr	Mo	Ni	W	V	Nb	N	B	Co
TAF 650	0.10	0.07	0.55	10.84	0.14	0.55	2.63	0.19	0.06	0.016	0.019	2.86
TAF	0.21	0.41	0.89	10.53	1.59	-	-	0.19	0.20	0.02	0.037	-

The material in the as-received state (virgin condition), and three specimens crept at 650 °C were available for microstructural investigation. The heat treatment of material in the as-received state was 1100 °C/1 h/oil + 750 °C/2 h/air. The parameters of creep tests are summarized in Table 2. As already mentioned main attention was paid to the specimen Z6 in this work.

Table 2. Parameters of creep tests performed at 650 °C

Specimen	Stress [MPa]	Time to rupture [h]
Z4	135	4 379
Z5	100	5 888
Z6	70	18 870

For each creep specimen two different areas were examined. The perpendicular section from the specimen *head*, where pure annealing occurs, and the section perpendicular to the longitudinal axis of the *gauge length* approx. 7 mm apart the necked region where the final fracture occurs.

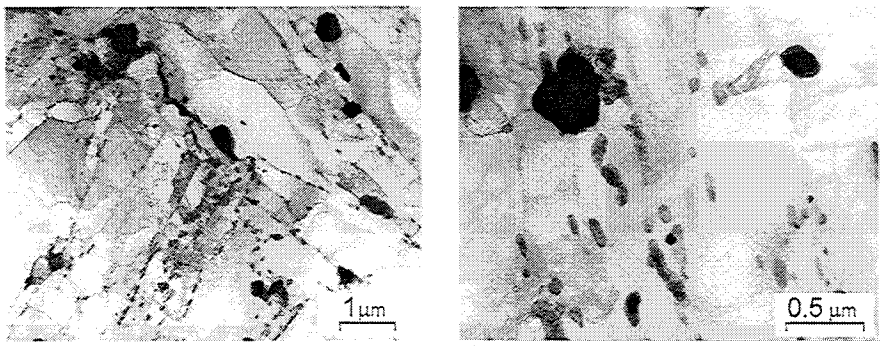
Thin foils were prepared by mechanical grinding to 80 μm thickness followed by twin jet electrochemical polishing. The latter operation was carried out at about 12 °C and 100 V dc in an electrolyte composed in volume by 95% acetic acid and 5% perchloric acid. Carbon extraction replicas were prepared by classical one step method. Line drawings of subgrains or particles on transparency were prepared from TEM micrographs. These were scanned into binary images and analyzed by PC based automatic image analysis system DIPS, as described in [8]. The energy dispersive X-ray analysis (EDS) of the precipitates was performed on extraction replicas in scanning mode of TEM (STEM). The metallic composition of precipitates was derived from X-ray spectra using EDAX technique for thin samples. No absorption or fluorescence corrections were applied. TEM investigation was conducted using a Philips CM12 TEM/STEM microscope equipped with EDAX Phoenix analyzer.

The software THERMO-Calc was used for the calculation, together with thermodynamic database, developed for such complex materials by one of the authors [9]. This database incorporates data for lower order systems found in literature with some data obtained and published by authors [10]. Such procedure allows the calculation of phase equilibria in complex systems very closely describing experimentally studied steels, using known thermodynamic interactions.

3. Results

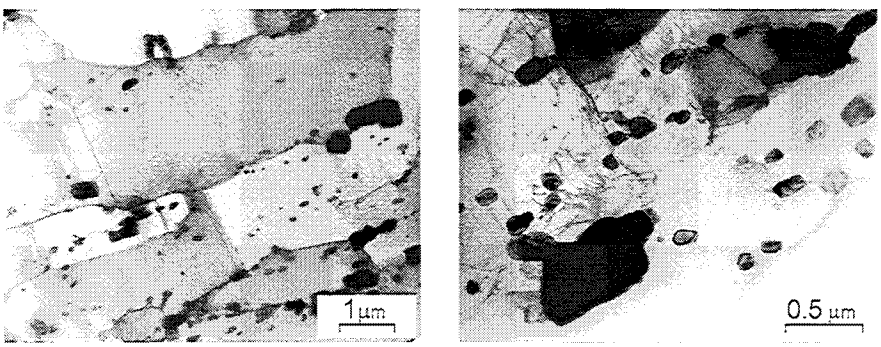
3.1 Microstructure

Figures 2 and 3 show the examples of microstructure morphology of specimen Z6 in its head and gauge parts. The microstructure of aged martensite with recognizable subgrains and relatively high density of dislocations were observed in the head part of specimen. The formation of an equiaxed subgrain structure with very low dislocation density and the presence of large particles of secondary phases were main features of microstructure in the gauge length part.



a b

Fig. 2 TEM micrographs of TAF 650 steel after creep, specimen Z6 head part: a) subgrains and b) particles.



a b

Fig. 3 TEM micrographs of TAF 650 steel after creep, specimen Z6 gauge length part: a) subgrains and b) particles.

The results of quantitative characterization of subgrain and particle sizes are summarized in Table 3. The subgrain size increases markedly in both, head and gauge parts of Z6 specimen compared to Z4 and Z5 ones. By contras, secondary particles size increases only slightly in gauge length part of Z6 specimen. The cumulative distribution curves of particle and subgrain sizes are shown in Fig. 4.

Table 3. Quantitative characterization of microstructural parameters

specimen	position	Subgrain d_{eqv} [μm]	Particle d_{eqv} [nm]
as received		0.45	75
Z4	head	0.44	88
	gauge	0.66	106
Z5	head	0.33	112
	gauge	0.77	112
Z6	head	0.59	103
	gauge	1.44	118

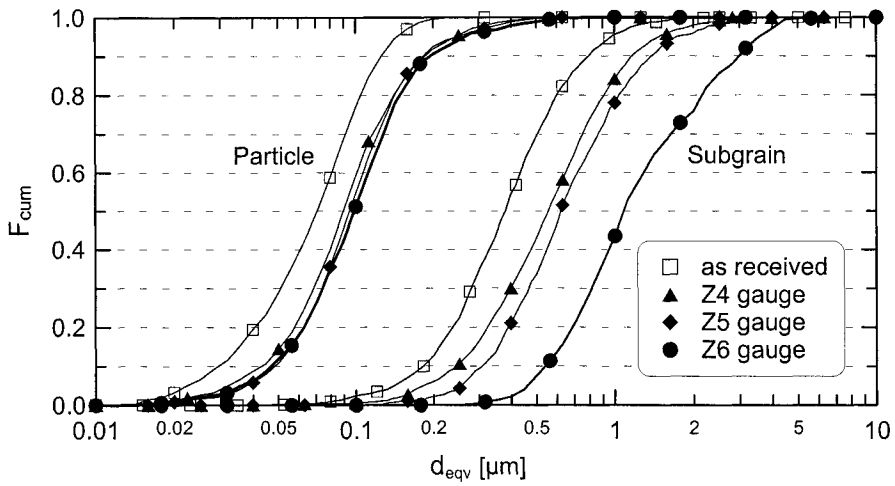


Fig. 4 Cumulative distribution curves of particle and subgrain equivalent diameters for TAF 650 steel in as received state and after creep tests at 650 °C: gauge length of specimens Z4, Z5, and Z6.

3.2. Secondary phase particles

The Cr-rich $M_{23}C_6$ carbides, Laves phase Fe_2W particles, and (Cr, Nb and V) rich particles of Z-phase were found in both head and gauge length parts of Z6 specimen. No systematic difference in chemical composition between particles in head and gauge length parts was found. The determined chemical composition of secondary phases found in Z6 specimen of

steel investigated is summarized in Table 4. The verification of Z-phase was done by selected area electron diffraction, Fig. 5.

Table 4. Experimentally determined chemical composition of phases in TAF 650 steel after 18 700 h at 650 °C, normalized wt.%

Phase	Fe	Cr	W	Mn	V	Mo	Si	Nb
$M_{23}C_6$	19.4	57.1	16.6	0	0.6	2.0	3.2	1.2
Laves	23.8	5.7	57.8	0.3	0.1	2.8	7.7	1.7
Z-phase	4.3	40.5	2.4	0.1	23.3	1.9	1.4	26.1

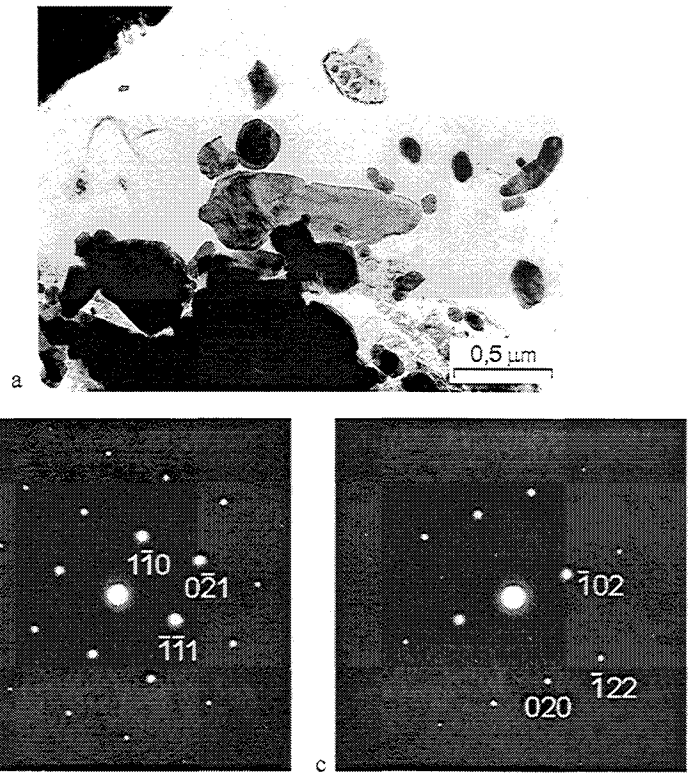


Fig. 5 TEM image of extraction replica and SAD patterns from Z-phase: a) Z-phase is light grey particle in the middle of image, b) B = [112] and c) B = [201].

The crystallography of Z-phase was taken according to [11] as a complex nitride phase possessing tetragonal unit cell with a = 0.286 nm and c = 0.739 nm. The particles giving the X-ray signal high enough to perform EDS analysis were $M_{23}C_6$ carbides but we can not exclude that there is a small amount of very tiny particles of the type MX mainly in head part of the specimen. The main features of secondary particle population can be stated as follows:

There is a substantial amount of relatively large particles of $M_{23}C_6$, Fe_2W Laves phase and Z phase whereas the tiny particles are very rare.

3.3. Thermodynamic calculation

The temperature dependence of the phase composition in TAF 650 steel, taking $M_{23}C_6$, Laves phase and MX carbides as equilibrium phases, has been published in [2]. The calculated amount of phases and their chemical compositions at 650 °C are given in Table 5.

Table 5. Equilibrium chemical composition of phases in TAF 650 at 650 °C, THERMO-Calc calculation without Z-phase, normalized wt.%.

Phase	Amount, %	Fe	Cr	Co	W	Mn	Ni	V	Mo	Si	Nb
Matrix	96.01	84.9	9.9	3.0	0.83	0.57	0.53	0.12	0.08	0.07	0.001
$M_{23}C_6$	2.10	17.1	73.3	0	7.5	0.7	0.1	0.7	0.8	0	0
Laves	1.68	30.2	7.9	0	59.9	0	0	0	1.92	0	0
MX	0.21	0	1.8	0	0	0	0	52.0	0	0	46.2

An attempt was made to calculate the equilibrium chemical composition of phases present in TAF 650 steel at 650 °C, regarding the Z-phase as the equilibrium one in this work. The results are summarized in Table 6.

Table 6. Equilibrium chemical composition of phases in TAF 650 at 650 °C, THERMO-Calc calculation, Z-phase included, normalized wt.%.

Phase	Amount, %	Fe	Cr	Co	W	Mn	Ni	V	Mo	Si	Nb
Matrix	95.92	85.0	9.8	3.0	0.83	0.56	0.53	0.13	0.08	0.07	0.001
$M_{23}C_6$	2.04	17.4	73.3	0	7.0	0.71	0.06	0.83	0.77	0	0
Laves	1.68	30.2	7.9	0	59.9	0	0	0	1.91	0	0
MX	0.05	0	0.28	0	0.85	0	0.03	11.8	0	0	87.2
Z-phase	0.18	0	46.3	0	0	0	0	35.2	0	0	18.5

Thermodynamic data for Z-phase are very scarce and therefore the results given in Table 6 are only approximate. Nevertheless, the two clear conclusions follow from a mutual comparison of Tables 5 and 6; considerable decrease of MX amounts on the behalf of Z-phase and change of equilibrium composition of MX.

4. Discussion

4.1. Microstructure evolution

The determined subgrain size in gauge length of specimen Z6, i.e., 1.4 μm (see Table 3), agree well with the value for martensite lath width of approx. 1.6 μm reported by Sawada [4] for TAF 650 steel creep tested at 650 °C (the value taken from figure). Further, from the time dependence of lath width in Sawada work [4] it can also be derived that a large acceleration of subgrain growth takes place after approx. 3000 h duration of creep test. The same dependence can be derived from cumulative distribution curves in Fig. 4 where the curve for the Z6 specimen is shifted to markedly higher values of equivalent diameter. It should be noted here that Sawada [4] found the same dependence for Mod. 9Cr-1Mo steel. Similar dependence also

results from subgrain width as determined by Ennis et al. [12] for P92 steel after creep test at 600 °C. In this case the subgrain width increased from 0.7 μm after 1500 h to 1.4 μm after 10 000 h of creep exposure. Neither Mod. 9Cr-1Mo nor P92 steels exhibit marked decrease on creep rupture strength curves. Therefore the substantial subgrain size growth in TAF 650 steel found in this work cannot be directly connected with creep rupture strength drop. Inspection of Fig. 4 also shows that there is only slight increase of particle diameters in specimen Z6 compared to specimens Z4 and Z5.

4.2. Z-Phase

In this work the Z-phase was found in TAF 650 steel after creep test running for 18 700 h at 650 °C. Z-phase has been frequently detected in austenitic stainless steels containing niobium and nitrogen, see e.g., [13]. Recently it has also been found in 9-12Cr ferritic steels by several authors [11,14-16]. Bursik and Merk [14] and Kimura et al. [16] found this phase in P91 steel in specimens tested at 650 °C. Strang and Vodarek [11] found Z-phase in 12CrMoVNb in specimens after long-term annealing at 600 °C (longer than 22 000 h) and 550 °C annealed for 79 200 h. Hatterstrand and Andren [15] found the small amount of relatively coarse particles of a phase rich in chromium and vanadium, which was considered to be Z-phase, in P92 steel aged for 26 000 h at 600 and 650 °C. The Z-phase is a complex nitride phase described by the formula CrNbN. The part of Nb is replaced by V in Z-phase found in 9-12Cr ferritic steels and this phase is therefore referred to as modified Z-phase Cr(Nb,V)N. The chemical composition of Z-phase, determined in this work, both experimentally and by means of THERMO-Calc together with chemical composition of Z-phase taken from the literature is summarized in Table 7, for comparison. It can be seen that the determined chemical composition of Z-phase agrees reasonably well with these data.

Table 7. Chemical composition of Z-phase, normalized wt.%

Wt.%	Fe	Cr	W	V	Mo	Si	Nb
This work, experimental	4.3	40.6	2.4	23.3	1.9	1.4	26.1
This work, THERMO-Calc	0	46.3	0	35.2	0	0	18.5
Bursik and Merk [14]	4.6	38.4	-	27.3	2.5	0.6	27.2
Strang and Vodarek [11]	4.4	44.9	-	36.6	1.6	-	12.9
Kimura et al. [16]	4.6	38.0	-	30.9	-	-	26.4

4.3. Creep behaviour

Correlation between long-term creep rupture strength and microstructure was studied by Park and Fujita [17] within the research work of the steel TAF. The relatively small amount of MX particles during the subgrain growth stage of microstructure evolution is proposed as a reason for a marked drop in creep rupture strength in Park and Fujita paper. There is direct microstructural evidence for a decrease in the amount of tiny MX precipitates due to Z-phase precipitation in papers [7,11] and the results of thermodynamic calculation performed in part 3.2. of this work. It can be clearly seen from Tables 5 and 6 that introduction of Z-phase into calculations leads to substantial decrease of MX precipitate amount while the amount of precipitates of the type $M_{23}C_6$ and Laves phase is affected only slightly. These facts together with direct microstructural observation of small density of tiny particles in this work leads to following explanation of the shape of the creep rupture strength curve for the TAF 650 steel at 650 °C. The creep strength is high up to 3000 h due to high dislocation density and presence

of tiny precipitates of MX and relatively small $M_{23}C_6$ and Laves phase particles. After that time the precipitation of Z-phase starts, which leads to a decrease in the MX amount in steel. According to Vodarek and Strang [7] Z-phase should not be present in as received state because the precipitation of this phase take place only after prolonged periods of exposure at testing temperature. In the meantime coarsening of $M_{23}C_6$ carbides and growth of Laves phase particles occur and their precipitates lose the ability to hinder dislocation motion. Moreover the growth of Laves phase Fe_2W decreases the content of tungsten in the matrix and contributes to a decrease of the creep rupture strength by weakening of substitutional hardening. Once the substantial part of equilibrium amount of Z-phase precipitates, the decrease in the amount of tiny MX particles slows down and the steepness of the creep strength curve is reduced.

It is well known that a lot of various types of intermetallic phases exist in austenitic steels. Thus it should be expected that additions of austenite forming elements into ferritic steel could pronounce intermetallic phase formation. On the other hand these austenite forming elements are added to ferritic Cr steels to make the suitable tempering treatment possible. Ennis et al. [12] showed that the martensite transformation is required to produce a high initial dislocation density and after recovery a stable subgrain structure on which the long creep strength depends. This trade off in austenite elements effect cannot be easily overcome. The most promising way seems to be the thermodynamic modeling, both equilibrium and kinetic approaches, which could provide a promising design of chemical composition of steels to be approved experimentally.

5. Conclusions

Microstructural examination of subgrain and particle sizes, dislocation density and particles type determination in high temperature creep resistant martensitic steel TAF 650 after creep test performed at temperature 650 °C, with stress 70 MPa and time to rupture 18 870 hour have lead to following conclusions:

- Substantial difference exists between subgrain sizes in head and gauge length part of creep specimens.
- The $M_{23}C_6$ carbides, Laves phase Fe_2W particles and (Cr, Nb and V) rich Z-phase were found in both head and gauge length parts of specimen. The difference between particle sizes in both parts is insignificant.
- The formation of Cr, Nb and V rich modified Z-phase occurs at the expense of tiny (Nb,V)X particles responsible for the stabilization of lath martensitic microstructure.
- The thermodynamic modeling of phase equilibria in TAF 650 steel gave chemical composition of Z-phase in reasonable agreement with experimentally determined compositions even though available thermodynamic data are incomplete.
- Both the synergetic effect of fine MX precipitates decreases due to Z-phase precipitation and tungsten depletion of solid solution due to Fe_2W Laves phase precipitation could be the reason for sigmoidal shape of creep strength curves of TAF 650 steel.

Acknowledgement

Financial support for this work was provided by the Grant Agency of the Czech Republic under Grants No. 106/00/0855 and No. 106/02/0608 and by the Academy of Sciences of the Czech Republic under Grant No. S2041105.

References

[1] T. Fujita, T. Sato, N. Takahashi, Effect of Mo and W on long term creep rupture strength of 12%Cr heat-resisting steel containing V, Nb and B, Trans. ISIJ, 18, 1978, 115-124
[2] M. Svoboda, A. Dlouhy, I. Podstranska, V. Sklenička and K. H. Mayer, Microstructural changes in creep of TAF 650 steel at 650 °C, In: Proceedings of Metallurgical Conference METAL 2000, TANGER, spol. s r.o., Ostrava, 2000, on CD, paper nr. 714, 8 pp.
[3] M. Svoboda, I. Podstranska, A. Kroupa, V. Sklenicka and K. H. Mayer, Creep resistance and microstructural stability of TAF 650 steel, In: Creep Resistant Metallic Materials, VITKOVICE - Research and Development Ltd., Ostrava, 2001, 196-203
[4] K. Sawada, M. Takeda, K. Maruyama, R. Ishii, M. Yamada, Y. Nagae and R. Komine, Effect of W on recovery of lath structure during creep of high chromium martensitic steels, Mat. Sci. Engng., A267, 1999, 19– 25
[5] Y. Hasegawa, T. Muraki, M. Ohgami and H. Mimura, Optimum Tungsten Content in High Strength 9 to 12% Chromium Containing Creep Resistant Steels, Key Engineering Materials, 171-174, 2000, 427– 436
[6] F. Abe, Creep rates and strengthening mechanisms in tungsten-strengthened 9Cr steels, Mat. Sci. Engng, A319-321, 2001, 770– 773
[7] V. Vodarek and A. Strang, Compositional changes in minor phases present in 12CrMoVNb steels during thermal exposure at 550°C and 600° C, Mater. Sci. Technol., 16, 2000, 1207– 1213
[8] K. Kucharova, J. Nemec and A. Dlouhy, Microstructure and creep strength of tempered martensite ferritic steels, Metals & Materials Society, 1997 , 79-88
[9] P. Unucka, A. Kroupa, M. Svoboda and R. Foret, The modelling of phase diagrams in complex Cr-Mo steels, submitted for publication,
[10] A. Kroupa, J. Havrankova, M. Coufalova, M. Svoboda and J. Vrestál, Phase Diagram in the Iron-Rich Corner of the Fe-Cr-Mo-V-C System below 1000 K, J. of Phase Equilibria, 22, 2001, 312– 323
[11] A. Strang and V. Vodarek, Z phase formation in martensitic 12CrMoVNb steel, Mater. Sci. Technol., 3, 1996, 552– 556
[12] P. J. Ennis, A. Zielińska-Lipiec and A. Czyrska-Filemonowicz, Influence of heat treatments on microstructural parameters and mechanical properties of P92 steel, Mater. Sci. Technol., 16, 2000, 1226– 1232
[13] H. Hughes, Complex nitride in Cr-Ni-Nb steels, J. Iron Steel Inst. , 205, 1967, 775– 778
[14] J. Bursik and N. Merk, Quantitative microstructural assessment of P91 ferritic steel after long term creep at high temperature, In: Mechanical Behaviour of Materials at High Temperature, C. Moura Branco et al. (eds.), Kluwer Academic Publisher, Netherlands, 1996, 299-307
[15] M. Hattestrand and H.-O. Andren, Evaluation of particle size distributions of precipitates in a 9% chromium steel using energy filtered transmission electron microscopy, Micron, 32, 2001, 789– 797
[16] K. Kimura, K. Suzuki, H. Kushima and F. Abe, Precipitation of Z-phase and its effect on creep strength of mod.9Cr-1Mo steels, In: Creep Resistant Metallic Materials, VITKOVICE - Research and Development Ltd., Ostrava, 2001, 186-195
[17] I. M. Park and T. Fujita, Long-term creep rupture properties and microstructure of 12% Cr heat resisting steels, Trans. ISIJ, 22, 1982, 830-837

STRESS CHANGE EXPERIMENTS IN LOW STRESS CREEP REGIME OF P-91 TYPE STEEL

Luboš Kloc and Václav Sklenička

Institute of Physics of Materials
Academy of Sciences of the Czech Republic
Žižkova 22, CZ-61662 Brno, Czech Republic

Abstract

Transition from the power-law to viscous creep behaviour has been recently reported for both martensitic and austenitic creep resistant steels just under conditions corresponding to the industrial applications of these steels. The observed creep behaviour could not be simply related to any of the known theories of the viscous creep, like the diffusional creep or the Harper-Dorn creep.

In the present work, the high sensitivity helicoid spring specimen creep technique was modified to allow stress changes during the low stress, low strain rate experiments. The results obtained on the P-91 type modified martensitic 9% Cr steel support the previous observations of the change of the creep deformation mechanism at low stresses. However, the creep behaviour at low stresses and the mechanisms involved are still not fully understood. At present, therefore, more effort should be directed to investigate the creep of high temperature structural materials at low stresses.

Keywords: viscous creep; power-law creep; stress exponent; steel

Introduction

The design of components and structures loaded at elevated temperatures requires reliable long-term creep data. Such data used to be derived by an extrapolation from the short-term creep experiments. The extrapolation procedures are limited by the microstructural stability, as well as possible changes in the creep deformation mechanisms.

There are many experimental evidences in the literature that the metallic materials behave differently under creep conditions at low applied stresses [1–5]. The term "low stresses" is strongly dependent on the material. For both austenitic and martensitic creep resistant steels, it has been shown that the transition stress from the high stress creep regime to the low stress creep regime occurs just at conditions corresponding to the service loading of the steels [4,5]. Thus, the low stress creep regime in the creep resistant steels is of great practical relevance.

The main difference in creep behaviour under low stresses consists in the much weaker dependence of the creep rate on stress. When expressed due to stress exponent n, the constant stress experiments lead to the value of about 1 under low stresses, while the values from 7 to 12 or even more used to be reported under a high stress regime. Concurrently, the differences in creep rates between various types of steel and pure iron are much less under low stresses. It indicates that the strengthening microstructural elements are much less efficient as obstacles to the deformation process.

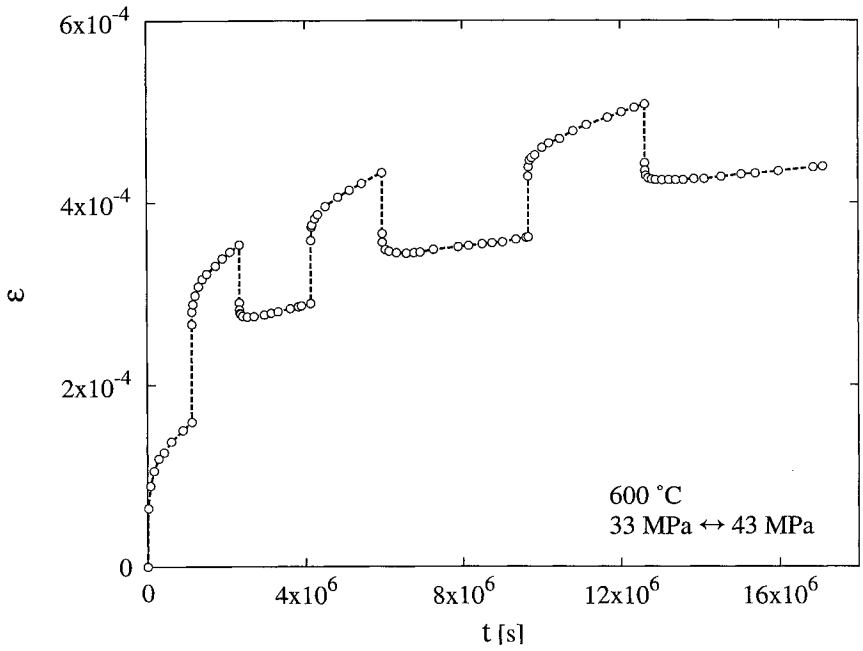


Fig. 1: *Creep curve of the stress change experiment*

Nevertheless, the observed creep properties of the steels under low stresses cannot be clearly related to any known creep mechanism [6,7]. The stress change experiments are convenient to provide more data needed for the identification of the involved creep deformation mechanisms.

Experimental material and procedures

The P-91 type ferritic-martensitic creep resistant steel has been used for the present experiments. The steel has been supplied by the Vítkovice steel a.s. in the form of "ready to use" pipes. The chemical composition is shown in the Table I.

Cr	Mo	Si	Mn	V	Ni	Nb	C	N	Al	P	S	Fe
8.5	0.88	0.43	0.40	0.23	0.10	0.10	0.10	0.045	0.018	0.015	0.006	bal.

Tab I: *Chemical composition of the used P-91 type steel in wt. %*

Helicoid spring specimen technique [8,9] has been used for the creep testing. The technique was modified to allow stress changes within the protective atmosphere of purified argon. Coil spacing has been measured optically. Helicoid spring specimens have been made by machining from the pipe to preserve original microstructure. Specimens have been aged by long term annealing at 650 °C for 10,000 h before the creep test. The resulting microstructure is described elsewhere [10].

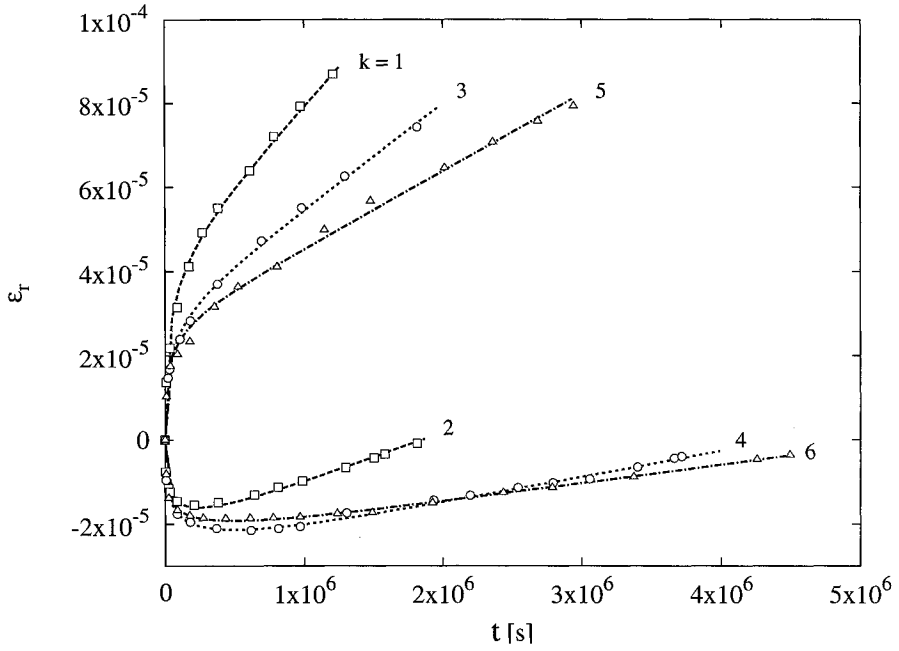


Fig. 2: *Individual parts of the creep curve recorded after stress changes. Elastic strain is eliminated.* k *is sequential number of the preceding stress change*

Creep tests were then conducted at 600 °C stabilized within ±1 °C . One specimen has been crept at initial stress of 33 MPa and the stress was raised to 43 MPa and back several times. For comparison, another specimen has been crept at the constant stress of 35 MPa. Since the stress and strain in the testing technique are essentially the shear ones, they were recalculated to the equivalent tensile quantities using the von Mises criterion, i.e. $\sigma = \sqrt{3}\tau$ and $\varepsilon = \gamma/\sqrt{3}$.

Results

The creep curve recorded in the stress change experiment is shown in the figure 1. It is clear that every change of the applied stress is followed by the transient effect resembling the primary stage of the standard constant stress creep curve, but the strain rate after the stress decrease is negative.

The individual segments of the creep curve are depicted in the figure 2, where the segments are denoted by the number k corresponding to sequential number of the preceding stress change. In the figure, the elastic strain corresponding to the stress change is eliminated.

Each segment of the creep curve is fitted by the equation derived by Li [11] for the primary

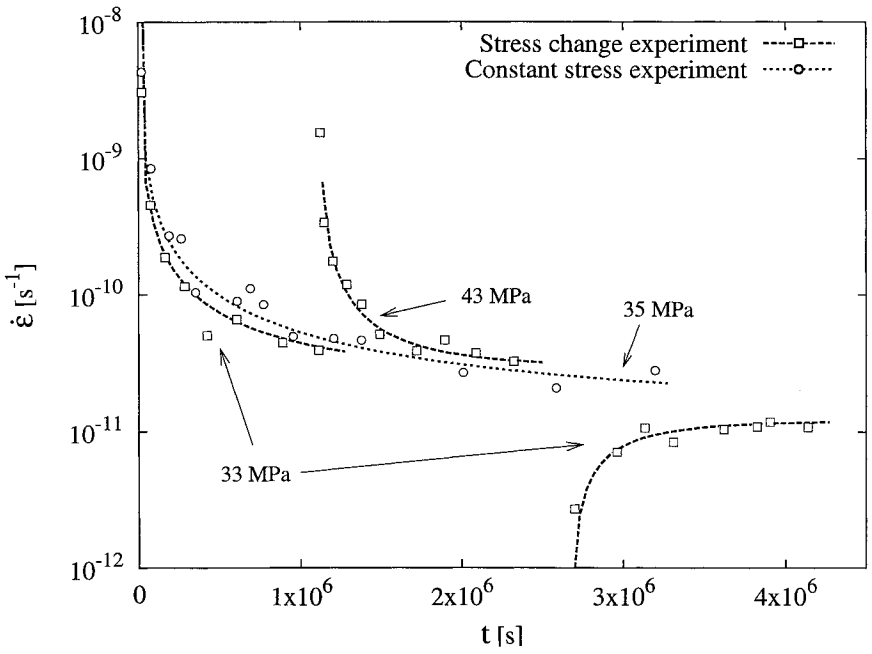


Fig. 3: *The first three segments of the creep curve with the stress changes compared to the constant stress creep curve, plotted as the creep rate against the time*

stage of the creep curve, expressed in the form

$$\varepsilon = \dot{\varepsilon}_s t \pm \dot{\varepsilon}_s \tau \ln\left(1 + \left(\exp\left(\frac{\varepsilon_t}{\dot{\varepsilon}_s \tau}\right) - 1\right)\left(1 - \exp\left(\frac{-t}{\tau}\right)\right)\right)$$

where $\dot{\varepsilon}_s$, ε_t and τ are parameters meaning the steady state creep rate, the total transient strain and the relaxation period of the transient process, respectively.

The rough estimation of the initial strain rate $\dot{\varepsilon}_i$ can be done from the fitted parameters. The results show that for each segment the relation $\dot{\varepsilon}_i/\dot{\varepsilon}_s \approx 10^3$ holds.

Discussion

Influence of the stress changes to the creep rate

The creep rate after the stress increase and decrease back to original value tends to reach considerably lower level than that obtained by the constant stress test, as it can be seen in the figure 3. This indicates that some kind of strengthening occurs during the period of the higher stress. On the other hand, it is not possible to find any changes in the microstructure before and after creep test by the standard methods of the optical and electron metallography. This is not surprising, because the total strain reached in this type of experiments is too low to cause visible changes. Under such condition, any conclusions concerning the strengthening

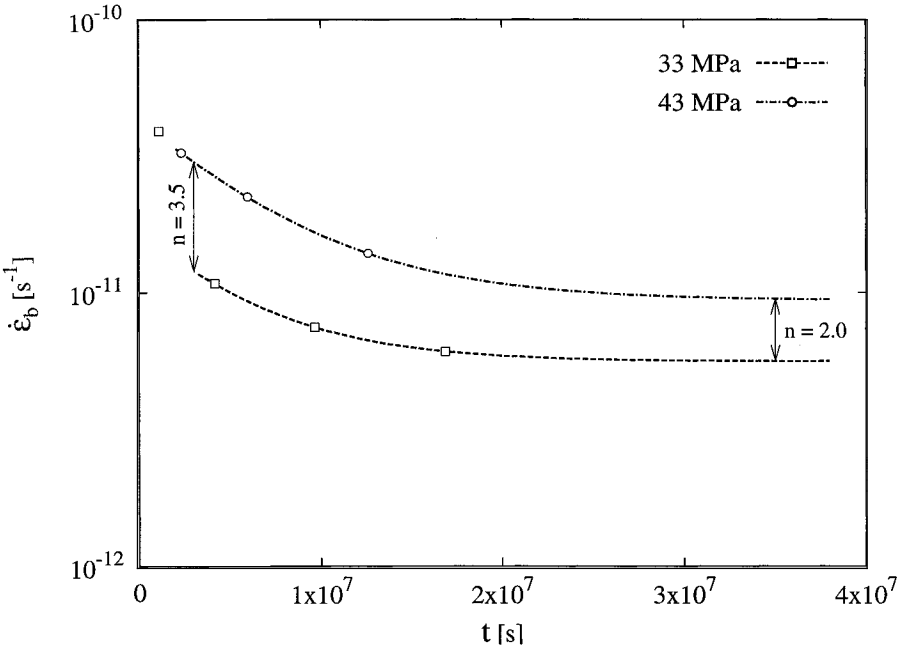


Fig. 4: *The creep rate before the stress change plotted against the time of corresponding stress change. Simple exponential decay is used for extrapolation*

mechanism could be only speculative.

Stress exponent

The stress exponent n, describing the dependence of the creep rate on the applied stress and defined as

$$n = \frac{\Delta \log (\dot{\varepsilon}_s)}{\Delta \log (\sigma)}$$

is considered as a main indicator of the creep regime and its corresponding creep mechanism, at least in classical creep theories. Its value had been reported close to one, when calculated from the constant stress experiment in the low stress regime of structural steels [5]. By contrast, when the stress exponent is calculated from the present stress change experiment, it reaches the value decreasing from about 3.5 to about 2, as can be seen in the figure 4. In the figure, the measured creep rates just before the stress change $\dot{\varepsilon}_b$ are plotted; in fact, these values are almost identical to that obtained by the curve fitting and denoted $\dot{\varepsilon}_s$ in the previous section. The value of n is much greater than that obtained from the constant stress experiments. On the other hand, it is much lower than the values reported for the high stress creep regime. This confirms the previous conclusion, that the creep behaviour of structural steels under low stresses is very different from that at high stresses and extrapolations from the high stress creep regime to lower stresses are unreliable. Different situation arises in the speculations on the creep mechanism dominating the low stress creep regime. The viscous creep mechanisms, like a diffusional creep

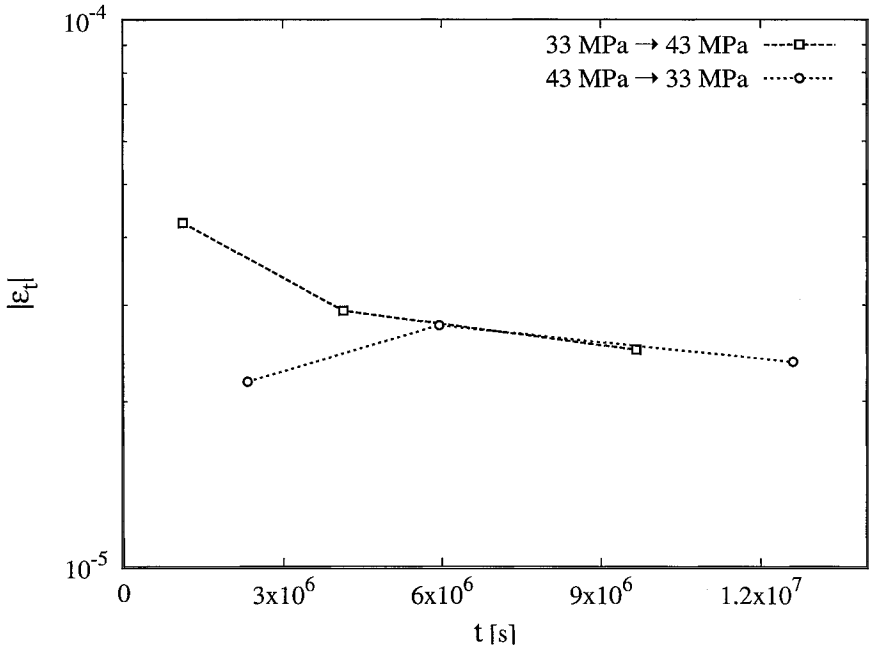


Fig. 5: *The total transient strain plotted against the time of corresponding stress change*

and Harper-Dorn creep are not able to explain the observed results. In the authors' opinion, it is necessary to collect much larger set of experimental results in the region of low stress creep regime before a theory with some reasonable level of probability can be proposed.

Transient effects

Transient stages after each stress change can be described by the total transient strain ε_t and the relaxation period τ. Both parameters are plotted against the time of the corresponding stress change in the figures 5 and 6. The parameters are more or less constant, their changes throughout the experiment are comparable with the error of their estimation. The total transient strain has the same value for the stress increase and decrease, while the relaxation period is visibly longer for the stress decrease changes. The potential microstructure evolution, which can be deduced from the strengthening effect described above, has little influence on the transient stage. The transient strain should be then probably assigned to the stress redistribution [12], which assumes the large stress concentrations around some microstructural elements. The elastic modulus for the steel at 600 °C is reported as $G = 97.4\,\mathrm{GPa}$ [13]. The equivalent elastic deformation corresponding to the applied stress change is then about $\varepsilon_e \approx 4 \times 10^{-5} \geq \varepsilon_t$, what makes the above assumption acceptable.

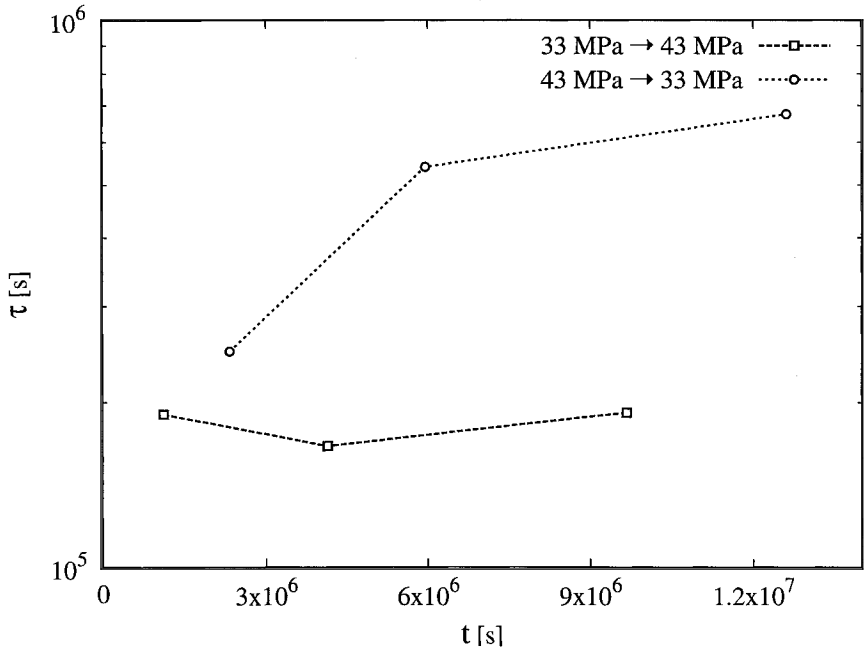


Fig. 6: *The relaxation period of the transient process plotted against the time of corresponding stress change*

Conclusion

The modified helicoid spring specimen technique has been used for creep test of the 9% chromium (P-91 type) creep resistant steel at 600 °C and the applied stress changing from 33 MPa to 43 MPa and back. The results confirm the creep behaviour being strongly different of that observed at higher stresses. On the other hand, the stress exponent is approaching the value of about 2. Thus, the simple mechanisms of the viscous creep, proposed previously, are not applicable. Every stress change is followed by the large transient stage, most probably caused by the stress redistribution and indicating large stress inhomogeneity in the microscale.

Acknowledgment

This work was supported by the Grant Agency of the Academy of Sciences of the Czech Republic under contract no. A2041101 and the Grant Agency of the Czech Republic under Grant no. 106/02/0608.

References

[1] T. Sritharan and H. Jones: The creep of type 304 stainless steel at low stresses, Acta Metall. 28 (1980), 1633

[2] T. Sritharan and H. Jones: Creep of type 316 stainless steel at low stresses, Metal Sci. 15 (1981), 365

[3] S. J. Dobson, H. Jones and G. W. Greenwood: Creep of stabilized stainless steel at low stresses, in: J. Beech (ed.), Perspectives of metallurgical development, the Metals Society, London 1984, p. 291

[4] J. Fiala, L. Kloc and J. Čadek: Creep in Metals at Intermediate Temperatures and Low Stresses - A Review, Mater. Sci. Eng. A 137, (1991), 163

[5] L. Kloc, V. Sklenička and J. Ventruba: Comparison of low stress creep properties of ferritic and austenitic creep resistant steels, Mater. Sci. Eng. A319-321 (2001), 774

[6] L. Kloc, J. Fiala and J. Čadek: Diffusional Creep and Harper-Dorn Creep at Intermediate Temperatures, in: R. S. Mishra, A. K. Mukherjee and K. L. Murty (eds.): Creep Behavior of Advanced Materials for the 21st Century, TMS, Warrendale, PA, USA 1999, p. 471

[7] L. Kloc and V. Sklenička: Primary Creep of Metallic Materials at Low Stresses and Intermediate Temperatures, in: R. S. Mishra, A. K. Mukherjee and K. L. Murty (eds.): Creep Behavior of Advanced Materials for the 21st Century, TMS, Warrendale, PA, USA 1999, p. 495

[8] B. Burton and G. W. Greenwood: The contribution of Grain-Boundary Diffusion to Creep at Low Stresses, Metal. Sci. J. 4 (1970), 215

[9] J. Fiala and J. Čadek: Diffusional creep in iron at homologous temperatures in the vicinity of 0.53, Metal. Mater 20 (1982), 277

[10] V. Sklenička, K. Kuchařová, L. Kloc, M. Svoboda and M. Staubli: The effect of microstructural stability on long-term creep behaviour of 9 – 12 % Cr steels, in this proceedings

[11] J. C. M. Li: A dislocation mechanism of transient creep, Acta Metall. 11 (1963), 1269

[12] G. S. Daehn: Primary creep transients due to non-uniform obstacle sizes, Mater. Sci. Eng. A319-321 (2001), 765

[13] J. Čadek and V. Šustek: An analysis of a set of creep-strain-rate and time-to-creep fracture data for a 9Cr-1Mo-0.2V steel, High Temp. Mater. Proc. 16 (1997), 97

INVESTIGATIONS AND ANALYSIS ON THE STATIONARY CREEP BEHAVIOUR OF 9-12% CHROMIUM FERRITIC MARTENSITIC STEELS

G. Dimmler, P. Weinert and H. Cerjak

Institute for Materials Science, Welding and Forming
Graz University of Technology
Austria

Abstract

This contribution deals with the description of the creep behaviour in the stationary creep regime in order to enable a more detailed and exact description of the creep rupture strength on basis of the Monkman-Grant relation. Special focus is given therein on microstructural aspects. In general the stationary creep behaviour has been investigated by evaluating the creep rate and the change of stress exponent of already established grades of high temperature creep resistant steels.

Keywords: creep behaviour, back-stress concept, stationary creep rate, extrapolation of creep rupture time, 9-12% Cr steels

Introduction

Extrapolation of the rupture time based on the results of short time creep tests are an important aspect for the design and the reliability of new heat resistant steels. Thereby the stress dependence of the creep rate and the time to rupture as basis for extrapolation of the rupture time have been frequently investigated in the case of precipitation strengthened low alloy and modified Cr steels. Exemplarily, the minimum creep rate vs. the stress curves of the steels NF616 and P91 are shown in fig. 1. As it can be seen, the creep rate shows obviously different stress dependences at high and low stress regimes. This transition in the stress dependence indicates a change in the creep mechanism.

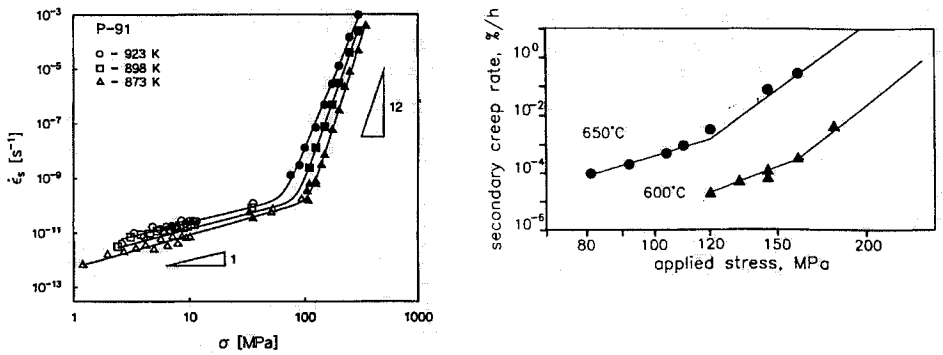


Fig. 1: Stress dependence of measured and experimentally evaluated $\dot{\varepsilon}_{ss}$ by Kloc and Sklenicka [1] of the steel P91 (left) and by Ennis et al. of the steel NF616 [15] (right)

Thereby, extrapolation methods based on creep rates from "power-law"-stress regions to stress levels below designing limits of approx. 100 MPa would lead to clearly underestimated creep rupture strength. Due to time consuming and cost intensive creep tests, only limited creep data at these low stress-levels are available. To generate creep rate data in this low stress region, Kloc and Sklenicka [1] used a special testing method known as "helicoidal-spring-technique" [2, 3, 4].

Stress dependence of secondary creep

Based on the experimental results different approaches are used to describe the stress dependence of the minimum creep rate. At low stresses creep is controlled by diffusion (diffusion creep). At higher stress regions, creep is controlled by dislocation movement (dislocation creep) [5], which can be described by power laws [6, 7] as the well known Norton relationship

$$\dot{\varepsilon}_{ss} = A_0 \cdot \sigma^n \qquad (1)$$

where A_0 is a constant and σ is the applied stress. The stress exponent n is typically about 3..5 in the power law regime for pure metals and mono-phase materials [8]. At low stresses a stress exponent of about n~1 can be measured [9]. This behaviour is described as "Harper-Dorn" creep [10], which will be explained in more detail later in this paper[1]. At high stresses, values for the stress exponent up to $n \geq 20$ have been measured [11]. This behaviour is understood as "power-law-breakdown" or exponential creep [12, 13]. In the range of exponential relationship between creep rate and stress, an extrapolation of the creep rate to lower stress-levels is acceptable (fig. 1). Thereby, an extrapolation of the time to rupture t_B, based on the well known Monkman-Grant relation [14]

$$\log t_B + \log \dot{\varepsilon}_{SS} = const \text{ or } \dot{\varepsilon}_{SS} \cdot t_B = C_{MG} \qquad (2)$$

will be possible. The Monkman-Grant constant C_{MG} can be evaluated as a result from short time creep tests, assuming an independent damage kinetics mainly controlled by the strain. It should be mentioned again at this point, that an extrapolation of the secondary creep rate is only allowed in the region of constant stress dependence. The results of Kloc and Sklenicka have illustrated in fig. 1 that a change in the creep-mechanism is taking place for the steel P91 in the region of 100 MPa. Ennis et al. [15] investigated the creep behaviour on the steel NF616 and distinguished also two regions, with an exponent n = 16 at high stresses and n = 6 at lower stresses. Compared to the investigations on P91 (fig. 1), creep data at stress regions with dominant diffusional creep behaviour (low stress regions with an exponent n = 1) are not available. On the other side, there are less data published in the region between 10 MPa to 100 MPa for the steel P91 (fig. 1). From this, it is imaginable, that there are three stress regions characterised with different stress exponents, as it is shown schematically in fig. 2. Fig. 2 illustrates the problems of extrapolation based on the stationary behaviour. Most of the creep tests are running at stress levels in the power-law breakdown region because of their short testing time. The operating stress levels are below and a change in creep mechanism lies between. To guarantee reliable results, an extrapolation is only allowable within a constant stress exponent. One way, to find out these breakpoints, are serial numbers of creep tests, which are time intensive.

[1] Notice, that "Harper-Dorn" creep is often miss-understood as diffusion-creep in literature [1].

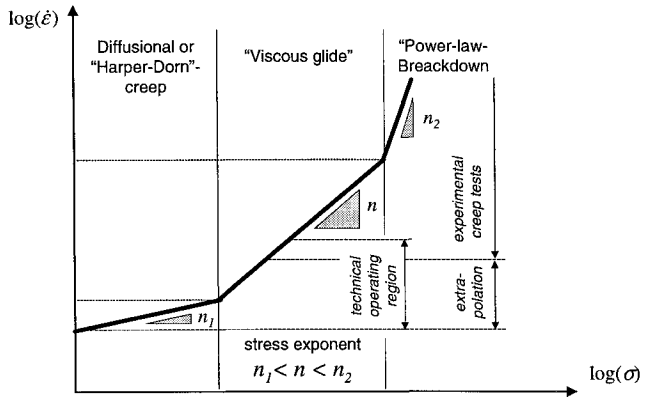


Fig. 2: Schematic illustration of the stress dependence of $\dot{\varepsilon}_{SS}$ (source: [16] in [34])

Alternatively it is proposed to estimate the transition by a physically based model to understand this change of the mechanism, and to calculate these corresponding stress levels. Such a model is known in the literature as back-stress-concept. This model will be explained in detail below.

Back-stress concept

Alloys with enhanced creep properties earn their strength partly from precipitation hardening. These materials often show values for the stress exponent n ≥ 20 [17] in the stress regions of power law breakdown. Nowick & Machlin and Cotrell & Aytekin [18] explained this high values by an enhanced inner stress σ_i , compared to pure materials. This inner stress σ_i is mainly constructed by second phases τ_{part} [19, 20] and the dislocations τ_{disl} [21]:

$$\sigma_i = M \cdot (\tau_{disl} + \tau_{part}) \tag{3}$$

where M is the Taylor-Factor. In the following calculations, a Taylor-Factor of M = 3 was used. Thereby, incorporating the inner stress into the Norton approach equation (1) can be adapted to

$$\dot{\varepsilon} = A(S) \cdot (\sigma - \sigma_i)^n \tag{4}$$

with a modified stress exponent n. According to Taylor [22], the back-stress from dislocations can be calculated by

$$\tau_{disl} = \alpha \cdot G \cdot b \cdot \sqrt{\rho_{f,\infty}} \tag{5}$$

with the elastic interaction-constant α, the shear modulus G, the Burgers vector b and the stationary mobile dislocation density $\rho_{f,\infty}$. To measure the dislocation density, expensive and time intensive TEM-investigations are necessary and the resulting scatterband of the experimental evaluated data leads to uncertain results. Investigations of the microstructural development in 9-12% Cr steels have shown that the dislocation spacing approaches steady

state values depending on the applied stress with increasing strain ε . This value is given by the dislocation density, over a wide range of alloy compositions that reaches the stationary value of

$$\rho_{f,\infty} = \frac{1}{3{,}9} \cdot \left(\frac{\sigma}{G \cdot b} \right)^2 \tag{6}$$

where G is the shear modulus, b the Burgers vector and σ is the applied stress. The back stress from particles for precipitation hardened materials can be derived by using the approach of Ashby [23] for the Orowan-stress τ_O

$$\tau_0 = \tau_{part} = C \cdot \frac{G \cdot b \cdot \sqrt{f_v^{part}}}{r_{part}} \cdot \ln\left(\frac{2 \cdot r_{part}}{r_0} \right) \tag{7}$$

with the constant $C = 0.14$ for screw-dislocations or $C = 0.093$ for edge-dislocations. G is the shear modulus and b the Burgers vector, f_v^{part} is the volume fraction of precipitates, r_{part} the precipitate radius and r_0 the „cut-off"-radius of the dislocations ($r_0 \sim 30 \cdot b$). It has been found further that the precipitates positioned on dislocations delay the below described microstructural development during creep exposure and thereby the development of strain in time, by blocking the movement of dislocations. Therefore, the microstructural stability and thereby the creep strength of the 9-12% Cr steels is controlled by the stability of the precipitates.

Beside the change of the dislocation density during creep exposure, also a change of the radius and the volume fraction of the precipitates have been investigated in a 10% Cr steel using the EFTEM-Method by Hofer et al. [24, 25]. These investigations have further shown that there are several different types of precipitates present. They differ in their occurrence time, position within the microstructure, size or growth rate and result in different softening effects under creep exposure. For example, these detailed microstructural investigations on the steel G-X12CrMoWVNbN 10 1 1 [25] have shown that the Laves-phase decreases the solid solution strengthening effect of the matrix by depleting the matrix from Mo and W. The appearance of the Z-phase coincided clearly with a decrease of the number of the substructure stabilising $M_{23}C_6$ and VN precipitates.

The significant influence of the changing microstructure on the particle strengthening effect can be directly estimated by equation (7) and can be seen in fig. 3. In the field of low applied stresses, the creep-mechanism shows the features that are characteristic for diffusional creep (Newtonian viscous behaviour). This linear relationship between stress and strain-rate (stress exponent n = 1), known as Harper-Dorn (H-D) creep, has been confirmed in aluminium and its alloys [26, 27]. The scarcity of data in the low stress H-D regime has limited the number of detailed analyses of this mode of creep. It is well established however, that the mechanism of deformation in H-D creep is diffusion-controlled dislocation motion. Thus, dislocation substructure, grain size and density are important microstructural variables influencing H-D creep [26, 27]. Several dislocation mechanisms have been proposed for H-D creep, which are described in the literature [34, 28]. With increasing stress-levels, dislocation by-pass particles by climbing and a change in the particle-parameter has a less detrimental effect to the inner stress compared to high stress regimes, where dislocations can by-pass particles by the Orowan-process. This process is proportional to the applied stress up to a "critical applied

stress σ_c". Above this critical stress σ_c, the Orowan-process is stress independent, which means that the Orowan-stress indicates an threshold-stress (back-stress) of the particles τ_{part} to the dislocation movement (fig. 3).

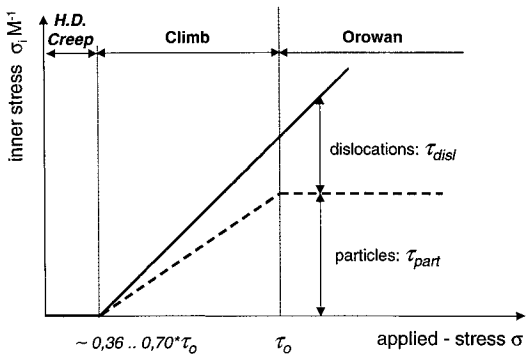


Fig. 3: Scheme of the inner stress σ_i as a function of the back-stress of particles τ_{part} and the dislocations τ_{disl} [29]

Below the Orowan-stress, dislocations can by-pass a group of particles by local climb or by general climb [31, 33]. This threshold-stress follows from the requirement to create a new length of dislocation during the intersection between particles and dislocations. Particles can be climb-by-passed with a smaller increase in dislocation length when climb is general, thus, the general climb is associated with much smaller threshold-stresses. This has been estimated by Blum & Reppich [30] depending for the volume fraction range (from 1% to 10%) as a function of the Orowan-stress τ_O [31, 32]

$$\tau_{cl} \cong 0{,}03..0{,}08 \cdot \tau_O . \tag{8}$$

A statistical based approach to describe the threshold of local climb is also given by Blum & Reppich as a function of the Orowan-stress τ_O [29, 31 ,33]. Further refinements alter the results of $\tau_{cl} \cong 0{,}36 \cdot \tau_O$ by less than a factor of 2, so that the threshold is given by

$$\tau_{cl} \cong 0{,}36..0{,}7 \cdot \tau_O \tag{9}$$

The scatter in experimental data is usually larger than this [31]. For more detailed information concerning the climb-threshold see Cadek [34].

Validation of the back-stress concept by experimental data

Up to this point, the main contributors to the inner stress σ_i have been discussed. It has been shown roughly, that changes in the kind of interaction between dislocations and second phases are reflected in differing characteristic threshold stresses. Spinning the wheel further, the principal questions arises: Are the macroscopic transition stresses in the minimum creep rate vs. stress curves mainly controlled by the precipitates? This question will be validated on experimental data of established representatives of heat resistant steels, listed in tab. 1.

Tab. 1: Chemical composition of validated heat resistant steels

	C	Mn	Cr	Ni	Mo	V	Nb	W	B	N	Si
P91	0.1	0.45	8.75	0.4	0.95	0.215	0.08	-	-	0.05	0.35
G-X12CrMoWVNbN1011	0.13	0.52	10.5	0.86	1.03	0.23	0.066	1.01	-	0.049	0.33
NF616 (P92)	0.124	0.47	9.07	0.06	0.46	0.19	0.063	1.78	0.003	0.043	0.02
X20CrMoV121 (1.4922)	0.17 0.23	max. 1.0	10.0 12.5	0.3 0.8	0.8 1.2	0.25 0.35					max. 0.5

As a first example, the back-stress concept is validated on published, experimental data of the steel NF616 (P92 after ASME Code Case 2179). For this steel, creep rate data in the stress regime of the expected mechanism-change have been published by Ennis et al. [15] and detailed microstructural investigations of the size of precipitation and volume fraction for the temperatures 873K and 923K have been performed by Hättestrand et al. [35].

Fig. 4 show the calculated back-stresses of the main precipitates (ordered in their contribution to the Orowan-stress: $M_{23}C_6$, MX, Laves-Phase) of the steel NF616 as a function of the creep exposure time. Due to the microstructural changes during creep, the total Orowan-stress of the steel NF616 at 873K lays in the range of 110MPa after short time and decreases slightly approximately to 100 MPa with increasing creep exposure time due to the softening effects. Based on these data, the inner stress σ_i can be calculated using equation (3). Therefore, the scatterband of the applied-stress, where the moving dislocations can by-pass the particles dominantly by Orowan-mechanism, can be quantitatively evaluated. For the steel NF616, this threshold-stress scatterband has been calculated at the temperatures 923 K and 873 K, and are shown in fig. 5.

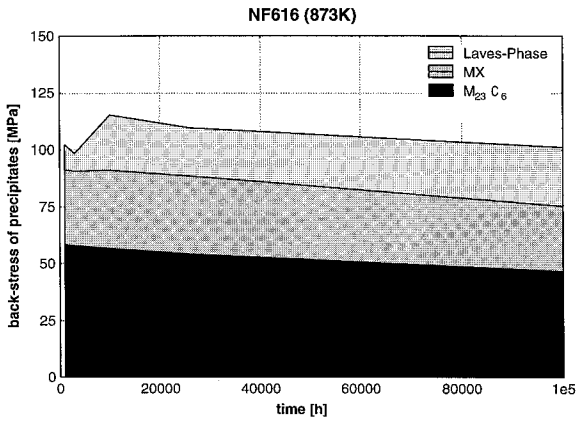


Fig. 4: Calculated back-stress of the precipitates ($\tau_p = \tau_o$) in the steel NF616 vs. creep exposure at 873 K

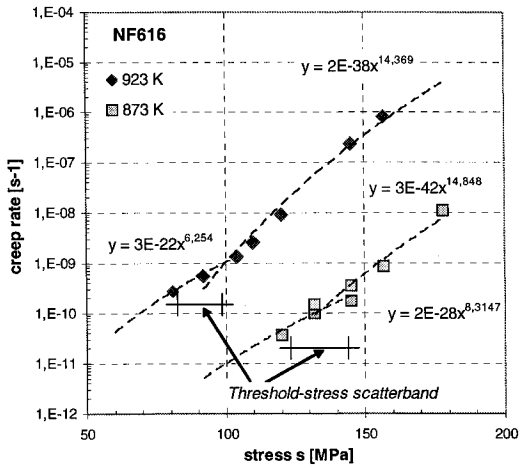


Fig. 5: Measured creep-rate vs. applied stress σ of the steel NF616 at 873K and 923K in comparison to the calculated back-stress scatterband

Additionally to the threshold-stress scatterband, the creep rates of the steel NF616 are plotted over a wide stress range in fig. 5. As published by Ennis et al. [15], a change in the deformation mechanism is indicated by a different stress exponent n of the Norton equation. The stress exponent n has been evaluated as exponent using a power-law regression model (in fig. 5). Compared to the experimental creep rates the "calculated" threshold-stress seems to indicate the expected change in the deformation mechanism, visible by different slopes in fig. 5. To check this correlation, further calculations and validations for typical representatives of 9-12% Cr-steels as the steels G-X12CrMoWVNbN 10 1 1, P91 (X10CrMoVNb 9 1) and X20CrMoV 12 1 have been performed (chemical composition see tab. 1). The sources of the published data, used in the following calculations are summarized in tab. 2 and the results are exemplarily given in the following figures.

Tab. 2: Sources of published data used for evaluation of the back-stress concept

Steel	Main Precipitates	Microstructural data	Creep data
NF616 (P92)	$M_{23}C_6$ MX Laves-Phase	Hättestrand et al. [35]	Ennis et al. [15]
G-X12CrMoWVNbN 10 1 1	$M_{23}C_6$ MX Laves-Phase Z-Phase *)	Hofer et al. [24, 25] Polcik [36]	Hofer [25]
P91 (X10CrMoVNb 9 1)	$M_{23}C_6$ MX	Polcik [36]	Spigarelli et al. [37] Taylor et al. [38] Sklenicka et al. [39] Polcik [36]
X20CrMoV 12 1	$M_{23}C_6$	Polcik & Straub [36]	Polcik [36]

*) was not considered for the calculations

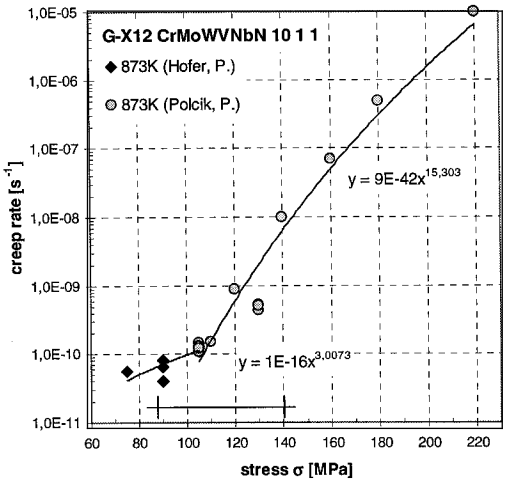


Fig. 6: Creep-rate vs. applied stress σ of the steel G-X12CrMoWVNbN 10 1 1 at 873K in comparison to the calculated back-stress scatterband (Sources of data are listed in brackets)

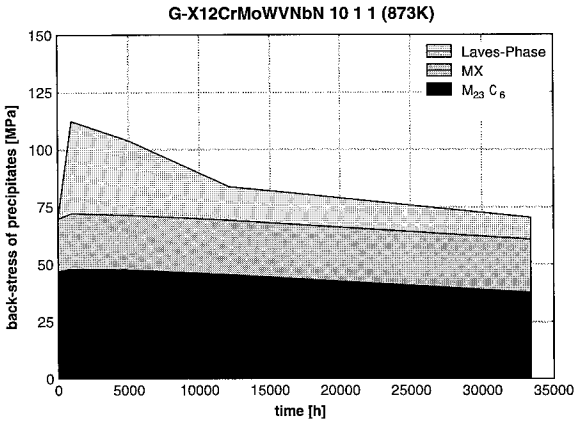


Fig. 7: Calculated back-stress of the precipitates ($\tau_p = \tau_o$) in the steel G-X12CrMoWVNbN 10 1 1 vs. creep exposure at 873 K

The scatterband of the threshold-stress for the steel G-X12CrMoWVNbN 10 1 1 in fig. 6 is wider and lower than the scatterband of the steel NF616. One explanation is the rapid coarsening of the Laves-Phase and as a consequence the decreasing contribution to the Orowan-stress at long exposure times as it is shown in fig. 7 based on the experimental data of Hofer [25] for the kinetics of the precipitates. Detailed microstructural investigations and creep rates down to very low stresses (see fig. 1) are published by Sklenicka et al. [1] for the steel P91 (X10CrMoVNb 9 1). At these low stress-levels diffusional or "Harper-Dorn"-creep with a stress exponent of n = 1 is expected. That means, that there are three stress regions with

roughly constant stress exponent n. The first mechanism-change at higher stresses has been described with a threshold-stress based on the total Orowan-mechanism under contribution of the dislocation barrier behaviour. Below the Orowan-stress it is considered that a dislocation can by-pass particles via a climb-mechanism as mentioned already above. Due to the surface energy, a local-climb behaviour can be expected for incoherent or semi-coherent particles, as the precipitates $M_{23}C_6$ in the steel P91. The coherent particles – as the MX precipitates in the steel P91 - show general-climb behaviour, which can be neglected because of their less interaction with the dislocations as it is theoretically described in equation (8). By that, the climb-threshold follows the barrier behaviour of incoherent precipitates and can be calculated using equation (9).

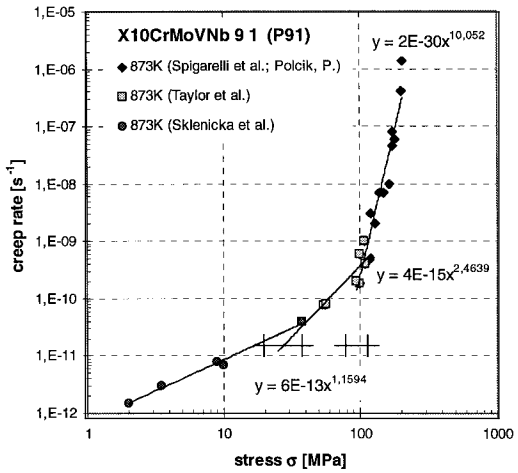


Fig. 8: Creep-rate vs. applied stress σ of the steel P91 at 873K in comparison to the calculated back-stress scatterband

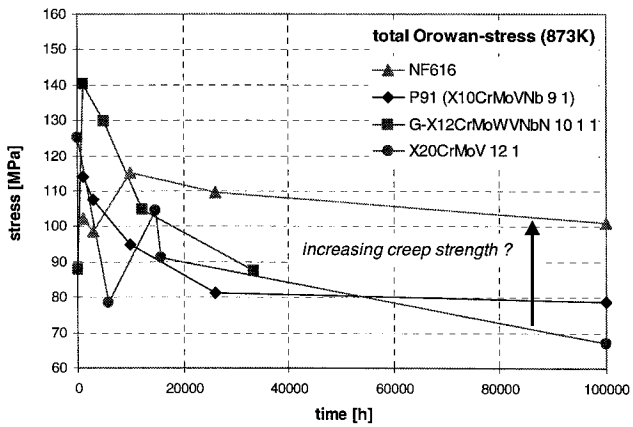


Fig. 9: The devolution of the total back-stress of precipitates under creep exposure.

The calculated climb-threshold for the steel P91 beside the Orowan-threshold is shown in fig. 8 (Notice the logarithmic scaled X-axis!). Because of non available or published data at low stresses, a further validation of the above described assumption is not possible. Therefore creep experiments on the steel G-X12CrMoWVNbN 10 1 1 at very low stress levels have been started, to enable an evaluation of the creep rates down to low stresses. Fig. 9 gives an overview of the calculated Orowan-threshold of the heat resistant steels listed in tab. 1. It should be pointed out here, that as far as data are available, the steels with higher creep strength show a higher total Orowan-stress at long times.

Another possibility to determine the threshold-stress was published by Peterseim and Sauthoff [40]. Reviewing equation (4), the data can be plotted as $\dot{\varepsilon}_{ss}^{\frac{1}{n}}$ versus σ, and a linear regression of the data gives an estimate for the unknown parameter A and the threshold-stress. Using the creep rates of the steel NF616 and P91 only a stress exponent of approximately n = 3 leads to useful values concerning the threshold stresses, as it is shown in fig. 10. Using the above described method of Peterseim and Sauthoff on the available data of the steel P91, again, only a stress exponent of approx. n = 3 yields acceptable values for the threshold-stress. Up to now, there is no explanation for the gap between the stress exponent evaluated by the slope of the creep (n~13; fig. 5) and the stress exponent n~3 determined exemplarily in fig. 10.

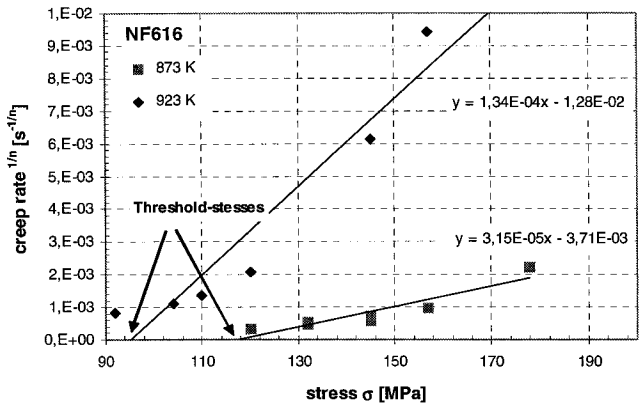


Fig. 10: Secondary creep rate as a function of stress at 873K and 923K for the steel NF616.

Conclusions

Hofer et al. [24] showed a method for the quantification of the microstructural changes like the precipitation diameter or the volume fraction of a precipitation-population during creep exposure. Based on this data, a way has been found, to calculate or estimate microstructural controlled threshold-stresses. Although a scatterband has to be considered, these threshold-stresses gives a good correlation with the stress levels of the expected mechanism-changes based on experimentally creep data. This method can help to support the quantification of creep-rate based rupture time extrapolation methods like the Monkman-Grant relation. These threshold-stresses limit the range of an experimentally based extrapolation of the creep rate.

Being able to calculate these thresholds, the stress levels for creep tests can be optimised, and the effectiveness of creep experiments can be increased.

Outlook

For a better evaluation of this back-stress approach on the 9-12% Cr steels, further complete creep-specimen-series especially at low stress levels are necessary. This contribution deals with the describing and validation of the stationary creep behaviour. A major influence to the rupture time and so to the extrapolation-methods has of course the damage behaviour. Investigations concerning the kinetic of the damage as the nucleation and growth of cavities will be continued.

These investigations could be performed in the framework of the European action COST 522.

Acknowledgments

The authors gratefully acknowledge the funding of this work by the Austrian research fund FWF - "Fonds zur Förderung der wissenschaftlichen Forschung" – contract FWF P13802 TEC.

References

[1] Kloc, L.; Sklenicka, V.: Transition from power-law to viscous creep behaviour of P-91 type heat-resitant steel, Materials Science and Engineering, (1997), pp. 962-965

[2] Burton, B. & Greenwood, G.W.: Metal. Sci. J., 4 (1970), p. 215

[3] Fiala, J. and Cadek, J.: Metall. Mater., 20 (1982), p. 277

[4] Novotný, J.; Fiala, J. and Cadek, J.: Metall. Mater., 23 (1985), p. 329

[5] Frost, H.J.; Ashby, M.F.: Deformation Mechanism Maps; Pergamon Press; Oxford 1982, Chapter 2

[6] Blum, W.; Ilschner, B.: Phys. Stat. Sol., 20 (1967), pp. 629-642

[7] Norman, E.C.; Duran, S.A.: Acta Met., 18 (1970), pp. 723-731

[8] Cannon, W.R. and Sherby, O.D.: High Temperatur Creep Behaviour of Class I and Class II Solid Solution Alloys, Metallurgical Transactions, 1 (1970), pp. 1030-1034

[9] Ruano, O.A.; Wadsworth, J.; Sherby, O.D.: Harper Dorn Creep in Pure Metals, Acta Metallurgica, 36 (1988), pp. 1117-1128

[10] Harper, J.G. and Dorn, J.E.: Acta Metall., 5 (1957), p. 654

[11] Wilcox B.A, Clauer A.H., Trans. Met. Soc. AIME, 236, 1966, p.570-580

[12] Krausz, A.S.; Krausz, K.: Unified Constitutive Laws of Plastic Deformation, Academic Press, (1966)

[13] Vollertsen, F.; Vogler, S.: Werkstoffeigenschaften und Mikrostruktur, Hanser Studien-Bücher- Carl Hanser Verlag, München-Wien, (1989)

[14] Monkman, F.C. and Grant, N.J.: Proc. ASTM, 56 (1956), p. 593

[15] Ennis, P.J.; Zielinska-Lipiec, A.; Wachter, O.; Czyrska-Filemonowicz A.: Acta mater. Vol. 45, No. 12, pp.4901-4907, 1997

[16] Yavari, P. and Langdon, T.G.: Acta Metall., 30 (1982), p. 2181

[17] Arzt, E.: Res Mech., 31, 4, (1991), pp. 399-453

[18] Ilschner, B., Hochtemperatur-Plastizität, Springer-Verlag, Berlin 1973

[19] Lagneborg, R.: Bypassing of Dislocations past Particles by a Climb Mechanism, Scripta Metallurgica, 7 (1973), pp. 605-614

[20] London, T.G.: A Method of Distinguishing Between Diffusion Creep and Harper-Dorn Creep at Low Stress Levels, Scripta Metallurgica, 35 (1996), pp. 733-737

[21] Kocks, U.F.: Metall. Trans, 1 (1970), p. 1121

[22] Taylor G.; Proc. R. Soc., 145 A (1934), p.362-404

[23] Verhoeven, J.D.: Fundamentals of Physical Metallurgy, John Wiley & Sons, New York, first edition, 1975

[24] Hofer, P., Cerjak, H.; Warbichler, P.: Materials Science and Technology, October 2000, Vol. 16, pp. 1221

[25] Hofer, P.: Microstructural Analysis as Basis of the Development of New Materials for Power Plants Conducted an G-X12CrMoWVNbN 10-1-1; PhD-Thesis, Graz (1999)

[26] Barrett, C.R.: Muehleisen, G.C. and Nix, W.D.: Mater. Sci. Engng 10, 33 (1972)

[27] Mohamed, F.A. and Ginter, T.G.: Acta metal. 30, 1869 (1982)

[28] Ruano, O.A.; Wadsworth, J. and Sherby, O.D.: Acta metal. Vol. 36, No. 4 pp. 1117-1128, (1988)

[29] Brown L.M, Ham R.K., Strengthening methods in crystals, Appl.Science Publ., London, 1971, p.75

[30] W. Blum, B. Reppich, Creep of particle-strengthened alloys, Pineridge press Ltd., Creep behaviour of crystalline solides, 1985, p.83-135

[31] Arzt, E.; Ashby, M.F.: Scripta Metallurgica, 16 (1982), pp. 1285-1290

[32] Hausselt, J.H. and Nix, W.D.: Acta Met., 25 (1977), p. 1491

[33] Shewfelt, R.S.W. and Brown, L.M.: PHIL: Mag: 35 (1977), p. 945

[34] Cadek, J.: Creep in Metallic Materials, Elsevier, Amsterdam, 1988

[35] Hättestrand, M: Precipitation Reactions at High Temperatures in 9-12% Chromium Steels, PhD-Thesis 2000, Göteborg, Sweden

[36] Polcik, P.: Modellierung des Verformungsverhaltens der warmfesten 9-12% Chromstähle im Temperaturbereich von 550-650°C, PhD-Thesis 1998, Erlangen; Shaker Verlag

[37] Spigarelli, S.; Cerri, E.; Evangelista, E. And Bianchi, P: Materials for Advanced Power Engineering 1998 as Proceeding of the 6th Liége Conference Pt. 1. , p.539-548, Liége, Belgium, 1998

[38] Taylor, N.; Bontempi, P.; Maciga, C.; Livraghi, M.: in Materials for Advanced Power Engineering, D. Coutsouradis et al, editors, p. 341, Kluver Academic Publisher, Netherlands (1994)

[39] Kloc, L.; Sklenicka, V.: Materials Science and Engineering, A234-236 (1997), p.962-965

[40] Peterseim, J.; Sauthoff, G.: steel research 57 (1986) No.1, pp 19-23

ALLOY DESIGN FOR ULTRA HIGH TEMPERATURE STEAM TURBINE APPLICATIONS: CREEP BEHAVIOUR AND MODELLING OF CREEP

A. Thoma, A. Scholz, C. Berger

Institute for Materials Technology (IfW D),
Darmstadt University of Technology

Abstract

Nickel base alloys are possible materials for use in future steam turbines operating at or above 700 °C. The investigations of a joint research program are focused on requirements for the use as rotor materials in steam turbines. These requirements are castability, forgeability, long term stability of microstructure, sufficient creep behaviour and creep crack growth resistance for large diameters. Of special interest are the model materials Inconel 706 and Waspaloy.
The investigations at IfW D deal with the assessment and determination of long term creep and creep rupture behaviour of different model alloys. As a result, important long term data up to 15 000 h have been generated. Further, creep behaviour can be modelled by the modified Garofalo creep equation in the whole relevant temperature and stress range. The established creep equations were also used for the modelling of creep crack growth behaviour as a part of a partner's investigations in this joint research program. Similar investigations are planned for new defined improved 700 °C-alloys.

Keywords : creep behaviour, creep equations, modified Garofalo equation, Waspaloy, Inconel 706

1. Introduction

Previous steam power plants work at parameters of temperature and pressure of about 540 °C and 180 bar, according to a total efficiency of approximately 38 %. Modern steam power plants that were built in the 1990s are working at temperatures just below 600 °C and pressure of approximately 250 bar. For future plants temperatures up to 700 to 720 °C and pressure up to 360 bar are of high interest, whereby a total efficiency of approximately 55 % is aspired. The use of ferritic steels is limited to temperatures of about 620 °C. Thus, nickel base alloys are necessary to bear the required temperature and pressure. In a DFG (Deutsche Forschungsgemeinschaft) joint research program nickel base alloys are investigated for the use as rotor materials in steam turbines at temperatures of 700 to 720 °C and service durations up to 200 000 h. In this context castability and forgeability, the long term stability of microstructure, the mechanical long term behaviour and the creep crack growth resistance for large diameters of forged nickel base alloys are important criterions. In order to study these requirements different partners take part on this comprehensive investigations.
This paper depicts the determination of creep and creep rupture properties of the two investigated model alloys Inconel 706 (NiCr 16 Fe 37 Nb 3 TiAl) and Waspaloy (NiCrCo 57 19). Both materials are in the focus to be further developed combining the efforts and results of all partners. Besides the generation and assessment of long term

creep and creep rupture data the establishment of creep equations is necessary to describe creep in the whole relevant temperature and stress range of the provided application. These creep equations also support the work of a partner modelling the creep crack growth resistance.
From the large number of existing creep equations the well proved modified Garofalo equation [1, 2, 3] was taken, i.e.

$$\varepsilon_p = \varepsilon_i + \varepsilon_{f1\max} \cdot H(t) + \dot{\varepsilon}_{p\min} \cdot t + \varepsilon_{f3} \quad (1)$$

with initial plastic strain ε_i, maximum amount of primary creep strain $\varepsilon_{f1\ max}$, a time function H(t) of primary creep strain, the minimum creep rate $\dot{\varepsilon}_{p\ min}$ and the tertiary creep strain ε_{f3} (Fig. 1). The development of a creep equation of this type is exemplified for Waspaloy.

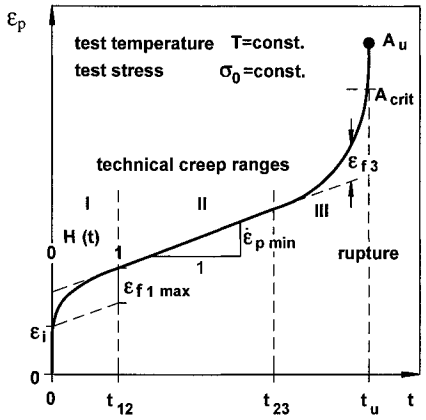


Fig. 1. Linear creep curve and components of equation (1)

2. Experimental

In the first step of the joint research program different types of nickel base alloys were identified as so called model materials. Of special interest are the following alloys :

- Inconel 706, representing a γ' / γ''-strengthened material and
- Waspaloy, representing a γ'-strengthened material.

The alloy Inconel 706 [4] was examined in two different heat treatment conditions (Table 1). The first version (material identifier 1A) has γ' and γ''-phase. The second version 1B additionally has η-phases which decorate the grain boundaries. This is due to

Material	Heat treatment	Microstructure	Condition	No
Inconel 706	980°C 2h air	γ + γ' / γ''	new n)	1An
	+ 720°C 8h / 1K/min to 620°C 8h/F	γ + γ' / γ'' + η *)	aged a)	1Aa
	980°C 3h / 4K/min to 820°C 10h/F	γ + γ' / γ'' + η +)	new n)	1Bn
	+ 720°C 8h / 1K/min to 620°C 8h/F	γ + γ' / γ'' + η +)	aged a)	1Ba
Waspaloy	1080°C 4h / 4K/min to 700°C / air	γ + γ'	new n)	3An
	+ 850°C 4h /air + 760°C 16h / air	γ + γ'	aged a)	3Aa
*) in the matrix +) at grain boundaries a) 750°C 5000 h n) after heat treatment				

Table 1. Details of the considered model materials

a special heat treatment with a direct cooling procedure [5, 6]. This heat treatment was originally suggested by Shibata as a heat treatment for large components of Inconel 706, it is assumed to be an economic heat treatment procedure [7]. The material Waspaloy

contains besides coherent γ'-precipitations also $M_{23}C_6$-precipitations at the grain boundaries. Two different types of γ'-precipitations have been observed [8]. These are great primary γ'-precipitations with sizes of particles of approx. 200 nm and small secondary γ'-precipitations. The secondary γ'-precipitations are distributed fine in the matrix and disappear after ageing the material. Both materials are tested in two different conditions. These are a new condition "n" after heat treatment and an aged condition "a" after additional ageing of 5 000 h at 750 °C. This aged condition approximates a so called mid-of-life-condition of 100 000 h at 700 °C obeying the Larson-Miller parameter. The creep rupture tests are achieved according to DIN EN 10 291. They are mainly performed by an interrupted testing procedure and partly by an uninterrupted testing procedure. Some of the uninterrupted tests are performed until a certain time or plastic strain has been reached and then continued in the interrupted mode until rupture [9]. The tests on alloy Inconel 706 cover a temperature range of 600 to 750 °C, tests on alloy Waspaloy a temperature range of 600 to 800 °C. The criterion of evaluation is the capability to obtain a creep rupture strength $R_{u\,t\,T}$ of more than 100 MPa for 100 000 h and 700 °C. In addition to the model materials discussed above optimized versions are defined with changes in composition and microstructure. The experimental work of the optimized materials is in progress.

3. Assessment of Creep Rupture Data

The results of the creep rupture tests are assessed by the usual graphical method that is based on plastic strain-time-diagrams (Fig. 2) and stress-time-diagrams (Fig. 3). The standard assessment includes plots of the plastic strain ε_p against time of all available tests. The results of tests are plotted e.g. at the main temperature of 700 °C for the material Waspaloy in condition new, 3An (Fig. 2). The values of the creep rupture strength $R_{u\,t\,T}$ and the creep strength $R_{p\varepsilon\,t\,T}$, that is the stress to produce a certain plastic strain ε_p during a time t at temperature T, are determined by crossplotting e.g. for the material Waspaloy at 700 °C. Also the results

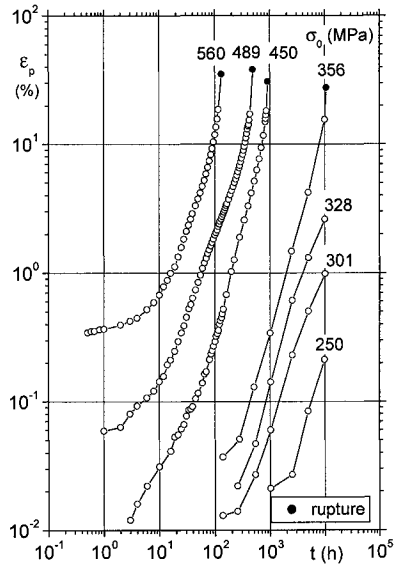


Fig. 2. Strain-time-diagram of material Waspaloy, 3An at 700 °C

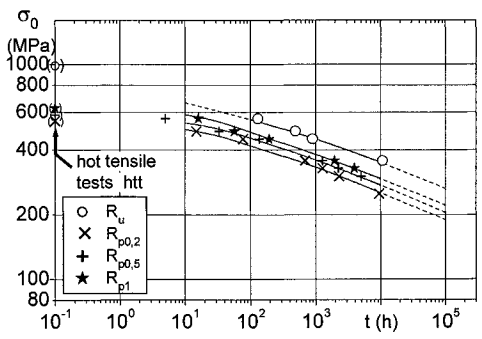


Fig. 3. Stress-time-diagram of material Waspaloy, 3An at 700 °C

of the hot tensile tests (htt) are plotted in the stress-time-diagram in the usual technical manner as an approximation of the test duration t ≈ 0.1 h. In addition the stress values are plotted against temperature T and with equibalancing of all this mentioned plots finally balanced creep rupture curve families are established. As a result, the described graphical crossplotting leads to stress-time-diagrams with creep rupture strength R_{utT} and creep strength $R_{p\varepsilon tT}$ of all available temperatures. Alloy Inconel 706, 1Bn shows a strong decrease of creep rupture strength R_{utT} with increasing temperature (Fig. 4). On the contrary, material Waspaloy shows values of creep rupture strength R_{utT} that are clearly higher than the required limit of 100 MPa for 700 °C and 100 000 h.

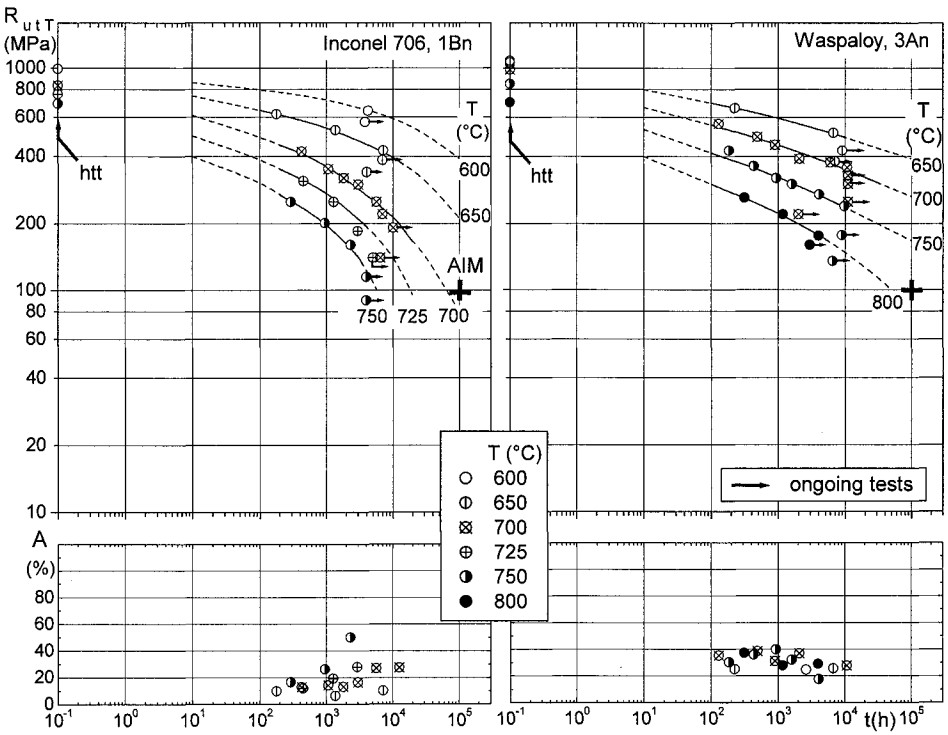


Fig. 4. Creep rupture strength R_{utT} and rupture elongation A_{utT} of the alloys Inconel 706, 1Bn and Waspaloy, 3An

Creep rupture strength values for 100 000 h / 700 °C could be estimated with an extrapolation time ratio q_e of less than 10. The final experimental aim is to reach test durations of up to 30 000 h. As a consequence, the extrapolation time ratio q_e can be reduced up to $q_e \approx 3$ which is in accordance to DIN EN 10 291. Values of the creep rupture strength for 100 000 h will be obtained by the end of the project.
A special assessment has been conducted in order to compare the estimated 100 000 h–values with the restriction of an extrapolation time ratio $q_e \approx 10$. Both alloys, Inconel 706

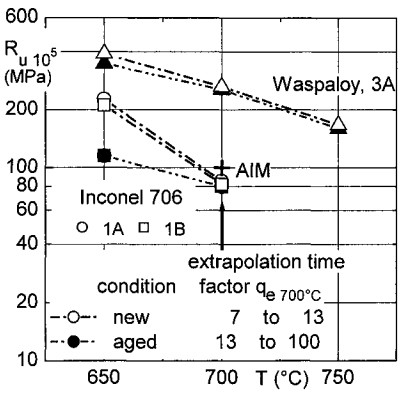


Fig. 5. Estimated 100 000 h values of creep rupture strength R_u plotted against temperature T from the graphical assessment.

in the heat treatment conditions A and B and Waspaloy are compared in the new condition as well as in the aged condition (Fig. 5). For material Waspaloy a creep rupture strength $R_{u\,t\,T} \approx 260$ MPa for 700 °C and 100 000 h can be derived. The course against the temperature also behaves very stable and the ageing treatment shows only small effect on the creep strength. Alloy Inconel 706 appears with relatively high values of creep rupture strength $R_{u\,t\,T}$ up to 650 °C in both heat treatment conditions. However, with increasing temperature a considerable loss of creep rupture strength is found. There are nearly no differences of creep rupture strength $R_{u\,t\,T}$ between both heat treatment conditions, but a strong decrease in both aged conditions is observed. This contradicts to a long term stability of alloy Inconel 706 in both heat treatment conditions.

Further, it should be mentioned that relatively low values of rupture elongation are observed for this alloy in condition new, especially in version 1An. Values of only 3 to 4 % at 650 °C were found [10]. Slightly higher values are measured for alloy 1Bn of approx. 6 to 10 % also at 650 °C (Fig. 4).

4. Modelling of Creep for Waspaloy

As already mentioned above conventional creep equations are of industrial need to describe creep in the relevant temperature and stress range. For this purpose the modified Garofalo equation [11] is assumed to be suitable (eq. 1). This equation is close to reality and describes primary, secondary and tertiary creep and can be modelled relatively easy [1, 2, 3]. They are well adapted to calculate the time dependent stress and strain distribution of components or test pieces which are subjected to quasistatic loading conditions. The modelling of such an equation is demonstrated in the following for the example of the material Waspaloy, 3An. The experimental basis includes creep data of less than 15 000 h at the main temperature of 700 °C and creep data of approx. 8 000 h at temperatures of 650 and 750 °C. The tests at 600 °C have been started later and have exceeded a duration of 2 000 h. The parameter identification of the creep equation starts with modelling the initial plastic strain ε_i, followed by the modelling of the quasistatic creep range. A special behaviour is pointed out for Waspaloy in the quasistatic range. Finally the parameter identification is completed with defining primary and tertiary creep.

Initial plastic strain

The initial plastic strain ε_i is taken from hot tensile tests but additional data points from uninterrupted creep tests are also considered (Fig. 6). High values of stress σ_0 are observed for initial plastic strain ε_i at the uncertainty of measurement ± 0.01 %. The equation for the description of the initial plastic strain ε_i contains a constant c_i in dependence on temperature T to describe the stress σ_0 in the range of

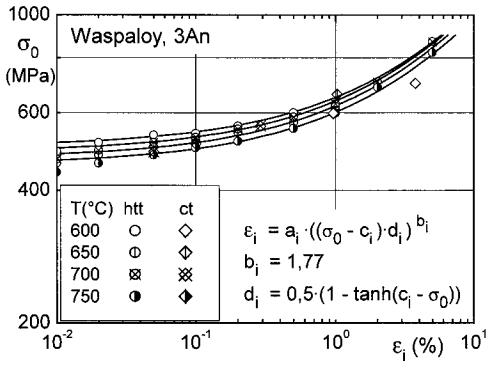


Fig. 6. Initial plastic strain ε_i from hot tensile test (htt) and creep test (ct) and recalculation

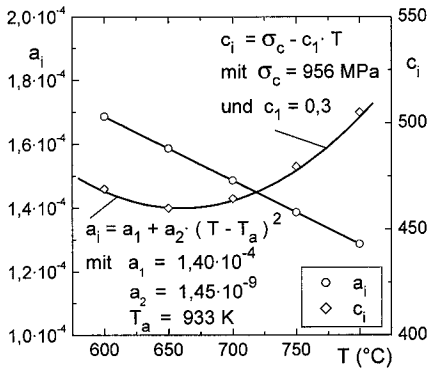


Fig. 7. Constants a_i and c_i to describe dependence of temperature T of initial plastic strain ε_i

the uncertainty of measurement. This again causes a constant d_i also depending on temperature T. The constant d_i assures the necessary condition of $\sigma_0 - c_i \geq 0$. Also the condition of $\varepsilon_i \rightarrow 0$ for $\sigma_0 \rightarrow 0$ is fulfilled with an equation of that type. The determination of the constants a_i and c_i is shown in Fig. 7.

With the initial plastic strain ε_i the data points $\varepsilon_f(T, \sigma_0, t) = \varepsilon_p(T, \sigma_0, t) - \varepsilon_i(T, \sigma_0)$ could be determined to plot linear creep curves $\varepsilon_f(t)$ of the type of Fig. 1. From these curves the values of the minimum creep rate and the maximum amount of primary creep strain ε_{f1max} as well as the transition times e.g. t_{12} are graphically determined in the following.

Determination of secondary creep

The modelling of the secondary creep range shows an individual material behaviour of Waspaloy. This alloy shows a slightly different behaviour than demonstrated in Fig. 1. Passing through the initial plastic strain and the primary creep range, the secondary creep (quasistatic creep) can be divided formally into two parts, a first part with a smaller amount of minimum creep rate $\dot{\varepsilon}_{p\,min\,1}$ and a second part with a greater amount of minimum creep rate $\dot{\varepsilon}_{p\,min\,2}$. This behaviour is illustrated in a plot of a linear creep curve from an uninterrupted creep test at the main temperature of 700 °C (Fig. 8). The two minimum creep rate values obey the condition $\dot{\varepsilon}_{p\,min\,1} < \dot{\varepsilon}_{p\,min\,2}$.

The transition times are defined as

- ▷ t_{12} : time of transition between primary and secondary creep,
- ▷ t_{23} : time of transition between the two secondary creep ranges and
- ▷ t_{34} : time of transition between secondary and tertiary creep range.

Plots of

- $\varepsilon_{f\,1max}$ against stress σ_0
- $\dot{\varepsilon}_{p\,min\,1}$ against stress σ_0
- $\dot{\varepsilon}_{p\,min\,2}$ against stress σ_0
- transition time t_{12} against $\dot{\varepsilon}_{p\,min\,1}$
- transition time t_{23} against $\dot{\varepsilon}_{p\,min\,1}$
- transition time t_{23} against $\dot{\varepsilon}_{p\,min\,2}$
- transition time t_{34} against $\dot{\varepsilon}_{p\,min\,2}$

are established and checked for consistence in a complex procedure of equibalancing all of these plots. These plots offer the opportunity to check if the determined values for different stresses and temperatures are well correlated. If it is necessary, slightly adjusted values may improve the continuous course of the minimum creep rates $\dot{\varepsilon}_{p\,min\,1}$, $\dot{\varepsilon}_{p\,min\,2}$ and the maximum amount of primary creep $\varepsilon_{f\,1max}$. The modelling of the maximum amount of primary creep $\varepsilon_{f\,1max}$, the two minimum creep rates $\dot{\varepsilon}_{p\,min\,1}$ and $\dot{\varepsilon}_{p\,min\,2}$ and the transition times are the important next steps and are accomplished with the above mentioned plots. Here, determination of $\dot{\varepsilon}_{p\,min\,2}$ is described. From a plot of $\log \dot{\varepsilon}_{p\,min\,2}$ against $\log \sigma_0$ (Fig. 9) a simultaneous dependence of stress σ_0 and temperature T became obvious. The family of curves can be interpreted by an equation of the type

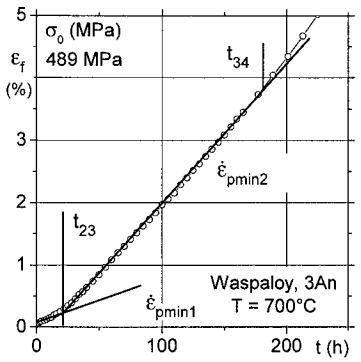


Fig. 8. Linear time-strain-diagram as example of two secondary creep ranges of Waspaloy, 3An.

$$\dot{\varepsilon}_{pmin2} = K_2(T) \cdot \sigma_0^{n_{02}} \cdot e^{c \cdot \sigma_0^c / d} \qquad (2)$$

with constants n_{02} , c, d and the temperature function $K_2(T)$. To model eq. (2) the generalized Norton-exponent

$$n_{\sigma 2} = \frac{\delta \log \dot{\varepsilon}_{pmin2}}{\delta \log \sigma_0} \qquad (3)$$

is determined from the isothermals in Fig. 9 and is plotted against stress σ_0 (Fig. 10).

From this diagram the coefficient n_{02} is determined and values of $n_{\sigma 2} - n_{02}$ could be calculated and plotted against stress σ_0 in a

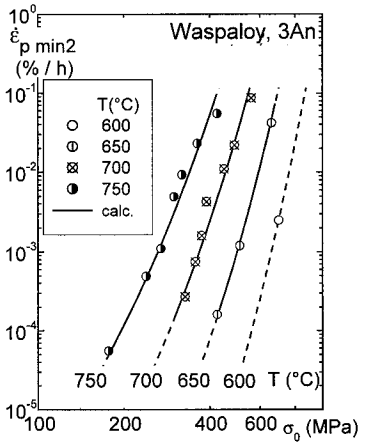


Fig. 9. Minimum creep rate $\dot{\varepsilon}_{p\,min\,2}$ of Waspaloy, 3An

double logarithmic diagram (Fig. 11). From there the coefficients of an equation

$$n_{\sigma 2} - n_{02} = c \cdot \sigma_0^{\,d} \tag{4}$$

are determined. The integration of eq. (4) via eq. (3) delivers eq. (2) with an integration constant $K_2(T)$. That constant is modelled with the aid of a simple Arrhenius equation [1, 10] (Fig. 12). If the minimum creep rate $\dot{\varepsilon}_{p\,min\,2}$ is recalculated with eq. (2) and the determined coefficients, the measured data points are well interpreted in the range of temperature and stress (Fig. 9). The minimum creep rate $\dot{\varepsilon}_{p\,min\,1}$ is determined in the same way.

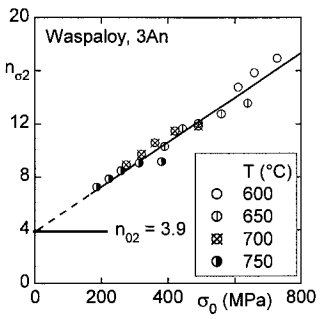


Fig. 10. Stress and temperature dependence of exponent $n_{\sigma 2}$

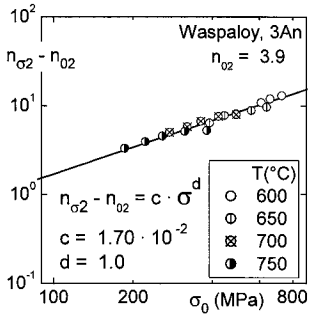


Fig. 11. Stress dependence of quantity $n_{\sigma 2} - n_{02}$

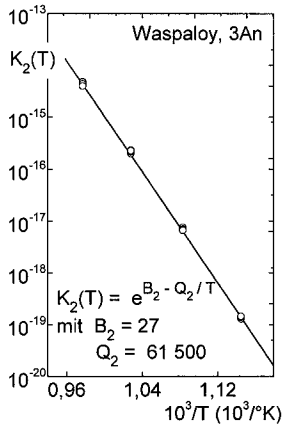


Fig. 12. Integration constant $K_2(T)$ of equation (2)

Determination of primary and tertiary creep

The primary creep strain obeys to

$$\varepsilon_{f1} = \varepsilon_{f1max} \cdot H(t) \tag{5}$$

with its maximum amount $\varepsilon_{f\,1max}$ and a time function H(t). The variable $\varepsilon_{f\,1max}$ can be described by

$$\varepsilon_{f\,1max} = a_I \cdot \sigma_0^{\,b_I} + \left(\sigma_0 / \sigma_I^{\,*}\right)^{b_I^{\,*}} \tag{6}$$

with coefficients a_I, b_I, $\sigma_I^{\,*}$, $b_I^{\,*}$ (Fig. 13). The transition time t_{12} is determined in Fig. 14 as example for determination the transition times. The time function H(t) was described in the usual way [2, 3, 10] by

$$H(t) = 1 - e^{-D \cdot (t/t_{12})^u} \tag{7}$$

with constants u, D and the transition time t_{12}.

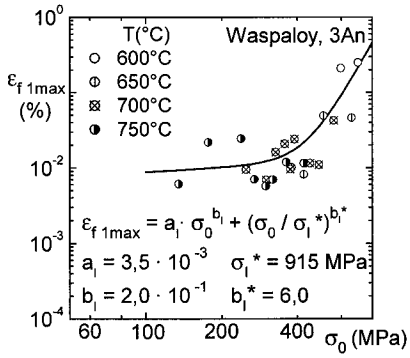


Fig. 13. Maximum amount of primary creep strain $\varepsilon_{f\,1max}$

Generally the principle is considered that all terms of the creep equation that have already been modelled have to be used for the determination of the following constants.
The establishment of the preliminary creep equation of material Waspaloy is completed with the description of tertiary creep that obeys [3, 10]

$$\varepsilon_{f3} = C_3 \cdot \left(t / t_{34} \right)^f . \qquad (8)$$

Evaluation of the established creep equation

The grade of this established preliminary creep equation of material Waspaloy is checked by recalculation of the measured creep data points in the whole relevant and interesting range of temperature (Fig. 15). Recalculated creep values meets the experimental results within an acceptable scatter band.
Finally, "rough" provisional courses of the recalculated creep curves have been observed at the transitions t_{23} (Fig. 16). This can be improved by implementing a time function $H_2(t)$ e.g. in the form

$$H_2(t) = \alpha_2 \cdot e^{-\beta_2 \cdot \left(t - t_{23} / t_{23} \right)^2} \qquad (9)$$

into the established preliminary creep equation, so that a smooth transition between the two ranges of secondary creep will be obtained.

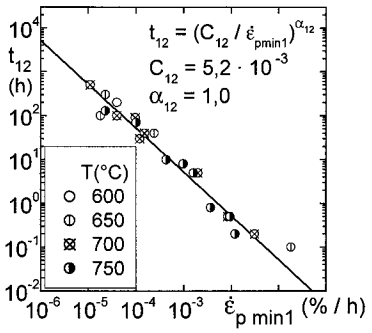


Fig. 14. Dependence of transition time t_{12} from minimum creep rate $\dot{\varepsilon}_{p\,min\,1}$, material Waspaloy, 3An

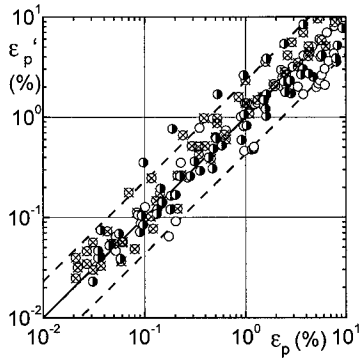


Fig. 15. With the developed creep equation calculated plastic strain ε_p' and measured data points of plastic strain ε_p of material Waspaloy, 3An

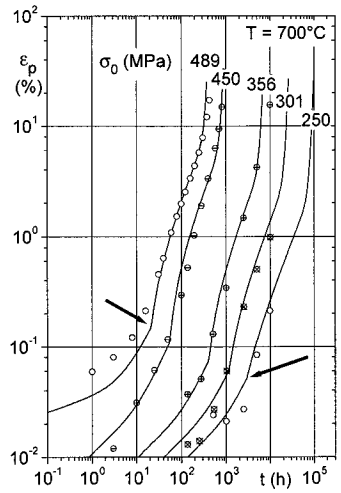


Fig. 16. Experimental 700°C-creep data points and recalculated creep curves with the creep equation of Waspaloy, 3An

5. Summary

The creep and creep rupture behaviour of the alloys Inconel 706 and Waspaloy have been investigated in a joint DFG-research program. These materials have been examined under two material conditions, a condition „new" and a condition „aged" which is generated by additional annealing at 750 °C for 5 000 h to approximate 100 000 h at 700 °C. Alloy Inconel 706 is tested in a temperature range of 600 to 750 °C and Waspaloy in a temperature range of 600 to 800 °C.

The main results can be summarized as follows :

- Long term creep and creep rupture data have been generated in a wide range of temperatures and stresses up to 15 000 h.
- An assessment of this data basis followed by an extrapolation leads to 100 000 h / 700 °C values of creep rupture strength of 260 MPa for Waspaloy, which exceeds the industrial requirement of 100 MPa clearly. Inconel 706 shows a significantly lower value.
- Creep of material Waspaloy has been modelled by a modified Garofalo creep equation. This alloy shows an individual creep behaviour in the quasistatic creep range. An improvement of this creep equation can be expected by the numerical interpretation of the two secondary creep ranges, which can be observed here.

In cooperation with the other partners of the joint research work, the investigations will be continued and extended to modified alloy types.

Thanks are due to the Deutsche Forschungsgemeinschaft for the promotion of the work

6. References

1) Preußler, T.: Numerical description of the creep behaviour of superalloys; Dr.-Ing. Thesis Darmstadt, Germany D17 (in German).
2) Granacher, J., M. Monsees, P. Hillenbrand, C. Berger : Software for the assessment and application of creep and creep rupture data; Nuclear Engineering and Design 190, 1999, pp. 273-285.
3) Kloos, K.H., J. Granacher, A. Pfenning : Creep equations for high temperature alloys on the basis of a parametric assessment of multi-heat data; steel research 67 No 3, 1996.
4) Inconel 706, brochure from Huntington Alloys Inc., Huntington WV, 1974.
5) Müller, S., J. Rösler : On the Creep Crack Growth Behaviour of Inconel 706; Presented at Inter. Congress on Advanced Materials and Processes EUROMAT99, Sept., 27-30, 1999.
6) Rösler, J., B. Böttger, M. Wolske, H.J. Penkalla, C. Berger : Wrought Ni-Base Alloys for Advanced Gas Turbine Disc and USC Steam Turbine Rotor Applications, Proc. 7th Liège Conference, 2002.
7) Shibata, T. et al. : Effect of Cooling Rate from Solution Treatment on Precipitation Behavior and Mech. Properties of Alloy 706, Superalloys 718, 625, 706, Ed. E.A. Loria, Pittsburgh, TMS 1997
8) Penkalla, H.J., J. Wosik, F. Schubert : Microstructure and Structural Stability of Candidate Materials for Turbine Disc Applications beyond 700 °C, Proc. 7th Liège Conference, 2002.
9) Granacher, J., M. Oehl, T. Preußler : Comparison of interrupted and uninterrupted creep rupture tests; steel research 63 (1992) pp. 39-45.
10) Berger C., J. Granacher, A. Thoma : Creep Rupture Behaviour of Nickel Base Alloys for 700 °C-Steam Turbines, in Superalloys 718, 625, 706 and Derivatives, Pittsburgh, PA, TMS 2001
11) Garofalo, F.: Fundamentals of creep and creep-rupture in metals, Macmillan, New York (1965).

EFFECT OF ALLOYING ELEMENTS ON CREEP PROPERTIES OF Pd ADDED 9Cr FERRITIC STEELS

Hirokazu Okada, Seiichi Muneki, Katsumi Yamada,
Hiroshi Okubo, Masaaki Igarashi and Fujio Abe
Materials Creation Research Group, Materials Engineering Laboratory
National Institute for Materials Science
1-2-1, Sengen, Tsukuba, Ibaraki 305-0047, JAPAN

Abstract

Owing to the fine precipitations of FePd $L1_0$ type ordered phase α ", Pd addition to 9Cr ferritic heat resistance steel improves the creep strength by not only reducing the creep rate but also extending the creep rupture life. In this study, effects of alloying elements on creep properties of Pd added 9Cr ferritic steels have been evaluated with 10kg-ingots in order to search the substitutional element for the precious metal Pd. Among the metals from VIIA to IB except Fe and Tc, some elements were found to harden the steels aged at around 823K, which is the precipitation temperature of α ". Corresponding to the hardness change, some elements were found to improve the creep properties also. Among such elements, especially Re addition prevented the growth of Laves phase and remarkably reduced the minimum creep rate at lower stress levels. From these results, pipe fabrication and welding tests were performed on Pd and Re-added 9Cr steel using 180kg-ingots. It was found that this steel could easily be welded by gas tungsten arc welding and formed into pipe without harmful defects.

Keywords: ferritic steels, FePd, $L1_0$ type ordered intermetallic phase, creep, microstructure

1 Introduction

High Cr ferritic steels such as ASME P91 steel have been successfully used for large diameter and thick section boiler components such as main steam pipe and header in super critical boilers in fossil-fired power plants [1]. Recent trend to utilization of clean energy leading to protection of global environment has been accelerating application of ultra super critical (USC) boilers, which are operated with higher efficiency in power generation than conventional ones and thus release less amount of carbon dioxide [2,3]. The USC boilers require new steels with improved creep strength and steam-oxidation resistance at elevated temperatures over 873K, because of the increase in operating temperature and pressure of the steam. Addition of W to the steel has been found to be effective to increase creep rupture strength at high temperatures and has already been used in some newly developed steels such as P92 and P122 for the USC boilers [4].

A typical initial microstructure of these steels consists of tempered lath-martensite matrix with dislocation density of the order of $10^{14}/m^2$ [5,6] and $M_{23}C_6$ (M: Cr, Fe, Mo, W etc.) type carbides along prior austenite grain boundary as well as packet, block and lath boundaries [7]. MX (M: V, Nb etc. and X: C, N) type carbonitrides are considered to form mainly inside lath, although some are found to form along the boundaries because of the preferential nucleation on the dislocations during tempering [8,9]. The addition of W to the steels sometimes enhances precipitation of intermetallic phases such as Laves and μ phases mainly along prior austenite grain boundaries and lath boundaries, and also inside the grains during long-term exposure at high temperatures [10]. FePd-based $L1_0$ type ordered phase α " has recently been found to form coherently inside the grains in the steels with Pd and to be useful to increase the creep resistance like MX carbonitride [11].

In this study, effects of alloying elements on creep properties of Pd added 9Cr ferritic steels have been evaluated in order to search for substitutional elements for the precious metal Pd. Then pipe fabrication and welding test were done to confirm the possibility to apply Pd added 9Cr steel to large diameter and thick boiler components.

2 Experimental Procedure

Fundamental Test

Table 1 shows the chemical compositions of the tested steels. Pd concentrations were varied from 0 to 1.5 mass%: B1 to B4. 0.5% Pd steel: B2 was selected as base steel, and various metals, from VIIA to IB except Fe, Tc and Pd, were added with 0.5 mass % to the base steel: B5 to B7, C1 to C6, D1, D2 and D4. 10kg-ingots were prepared by vacuum induction melting. The ingots were hot forged and rolled into 16mm square bars. All bars were normalized at 1373K for 0.5h.

Table 1 Chemical compositions of the steels for the fundamental test. [mass%]

Mark	C	Si	Mn	Cr	W	V	Nb	N	B	Pd	Others
B1	0.07	0.29	0.47	8.9	3.2	0.19	0.05	0.06	0.005	-	-
B2	**0.07**	**0.32**	**0.49**	**8.8**	**3.2**	**0.19**	**0.05**	**0.05**	**0.005**	**0.56**	-
B3	0.08	0.31	0.50	9.0	3.2	0.19	0.05	0.06	0.005	**1.12**	-
B4	0.08	0.31	0.50	9.0	3.3	0.19	0.05	0.06	0.005	**1.62**	-
B5	0.08	0.27	0.49	8.8	3.2	0.18	0.04	0.06	0.005	0.59	**Co: 0.49**
B6	0.08	0.32	0.50	8.8	3.2	0.19	0.05	0.06	0.005	0.56	**Ni: 0.50**
B7	0.08	0.31	0.50	9.0	3.3	0.18	0.05	0.05	0.005	0.56	**Cu: 0.50**
C1	0.08	0.27	**0.98**	8.9	3.3	0.19	0.05	0.06	0.005	0.58	**(Mn)**
C2	0.08	0.31	0.50	9.0	3.3	0.19	0.05	0.06	0.005	0.56	**Ru: 0.47**
C3	0.08	0.30	0.50	9.1	3.3	0.19	0.05	0.06	0.005	0.56	**Rh: 0.54**
C4	0.08	0.30	0.50	9.0	3.2	0.19	0.05	0.06	0.005	0.56	**Re: 0.47**
C5	0.08	0.30	0.49	9.0	3.2	0.19	0.05	0.06	0.007	0.56	**Os: 0.49**
C6	0.08	0.30	0.50	9.0	3.2	0.19	0.05	0.06	0.005	0.56	**Ir: 0.48**
D1	0.08	0.31	0.50	9.0	3.1	0.19	0.05	0.07	0.005	0.56	**Au: 0.52**
D2	0.08	0.30	0.49	8.8	3.2	0.19	0.05	0.06	0.005	0.56	**Pt: 0.41**
D4	0.08	0.28	0.49	9.0	3.3	0.19	0.05	0.06	0.006	0.57	**Ag: 0.28**

Softening behaviors of the steels were examined with tempering from 773 to 1113K for 1 to 20h. After tempering at 1043K for 4h, creep tests were conducted at 923K with 120 and 100MPa. The dimension of the creep test specimen was 8mm in diameter and 42mm in gauge length. Microstructure of the steels in the tempered and the creep-ruptured conditions were examined under scanning electron microscope (SEM). The amount of precipitates for the creep-ruptured specimens was estimated by the quantitative chemical analysis of extracted residues.

Demonstrational Test

Table 2 shows the chemical compositions of the steels for this demonstration. From the fundamental test results, 0.5mass% of Re was added to 9Cr-0.3Mn-9Cr-3W-0.7Pd-V, Nb, N, B steel: MC1 and MC2. Mod. 9Cr-1Mo steel: MA1 and the steel equivalent to B1: MB1 and MB2 were also prepared to the test as the references. Three 180kg-ingots, MA1, MB1 and MC1, were hot forged and rolled into 25mm wall thickness plate. Two 180kg-ingots, MB2 and MC2, were hot forged and hot extruded into pipes. The dimension of the pipe is 84mm in outside diameter and 12.5mm in wall thickness. All plates and pipes were normalized at 1373K for 4h. MA1, MB1 and MB2 were tempered at 1043K for 4h and other were tempered at 823K for 4h followed by tempering at 1043K for 4 h. This double tempering, combination of low temperature aging and high temperature tempering, is reported

to give the optimum initial microstructure consisting of fine dispersion of the α" phase and MX carbonitride inside lath decorated with $M_{23}C_6$ along lath, block and packet boundaries of martensite as well as along the prior austenite grain boundaries [12]. In order to evaluate the applicability of Pd bearing steel to the thick-walled pipes of fossil fired power plants, following tests were conducted. High strain rate tensile tests were performed on the plates with a condition of a heating rate of 100 $K \cdot min^{-1}$, a holding time of 30 min, a temperature range from 1273 to 1548 K and a strain rate of 1 sec^{-1}. The plates were also welded with AWS ER Ni Cr-3 filler wire by gas tungsten arc welding (GTAW) and the properties of welded joints were examined. Figure 1 shows the cross section of beveling. The welding conditions are summarized in Table 3.

Table 2 Chemical compositions of the steels for the demonstrational test. [mass%]

Mark	C	Si	Mn	Cr	W	V	Nb	N	B	Pd	Others
MA1	0.10	0.34	0.43	8.7	-	0.23	0.08	0.04	0.0001	-	Mo: 0.98
MB1	0.08	0.30	0.51	9.0	2.9	0.20	0.05	0.05	0.005	-	-
MB2	0.08	0.30	0.51	9.0	2.9	0.20	0.05	0.05	0.005	-	-
MC1	0.10	0.04	0.36	9.0	2.9	0.19	0.05	0.03	0.005	0.70	Re: 0.49
MC2	0.10	0.04	0.37	9.1	2.9	0.19	0.05	0.03	0.004	0.69	Re: 0.49

Note: MB2 and MC2 were for pipes. Others were for plates.

Table 3 Welding conditions for the plates

Item	Condition
Method	Gas Tungsten Arc Welding
Filler Wire	AWS ER Ni Cr-3 equivalent
Arc Current	1 through 6th pass: 70 - 160A after 7th pass: 180 -200A
Arc Voltage	8 - 16V
Welding Speed	about 80 mm/min
Pre Heating	minimum 373K
Sealing Gas	Ar (99.9%)
Post Welding Heat Treatment	1013K for 4h, air cooling

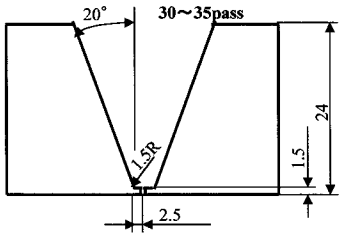


Fig.1 A cross section of weld groove for welding joints.

3 Results and Discussion

Fundamental Test

Figure 2 shows the tempering parameter dependence of the hardness for Pd-added and Pd-free steels. Pd addition hardened the steel at the temperature around 823K and the hardness depended on the Pd concentrations. Figure 3 shows the secondary electron image of 1.5%Pd steel: B4 after tempering at 823K for 20h. About 100nm-length precipitates, arranged in specific directions were observed inside martensite lath. This is because Fe-Pd $L1_0$ type ordered phase: α" precipitates coherently and disk-likely

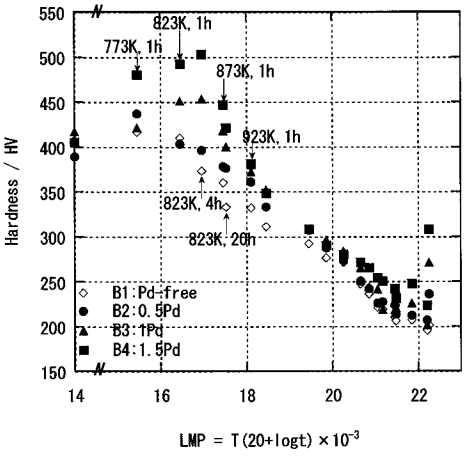


Fig. 2 Tempering parameter dependence of hardness showing the precipitation hardening around 823K.

inside the ferrite matrix: α with the following crystallographic relationship; {001} α //{001} α ", <100> α //<110> α " [11]. Hardness after 20h tempering at 823K of the tested steels is summarized in Fig.4. 0.5 mass% addition of Mn, Ru, Rh, Re, Os, Ir, Au or Pt hardened the 0.5%Pd steel to the 1%Pd steel level. These metals were expected to dissolve in α " and to increase the volume fraction of α " comparing to that of 0.5%Pd steel.

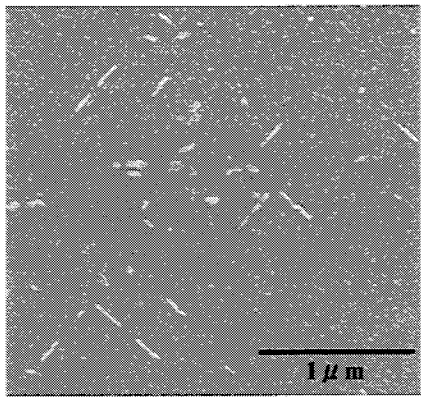


Fig. 3 Secondary electron image of B4 steel after temperingfor 20h showing the Fe-Pd $L1_0$ ordered phase which is precipitated coherently to the bcc matrix.

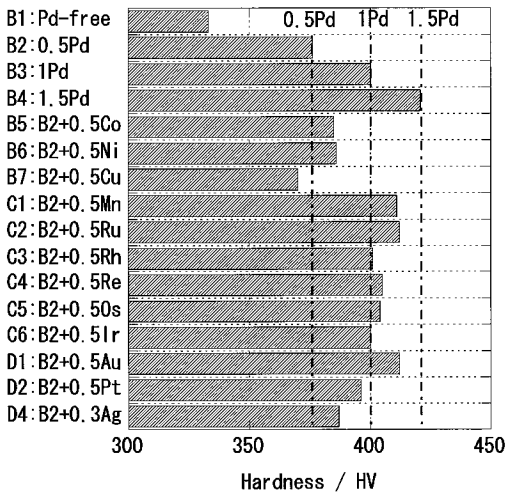


Fig. 4 Comparison of hardness after 20h tempering at 823K for the tested steels.

Figures 5(a) and (b) show the effect of alloying elements on the time to rupture and the minimum creep rate crept at 923K with 120 and 100MPa, respectively. Minimum creep rate axis is reversed so that the data correspond to the time to rupture. Corresponding to the

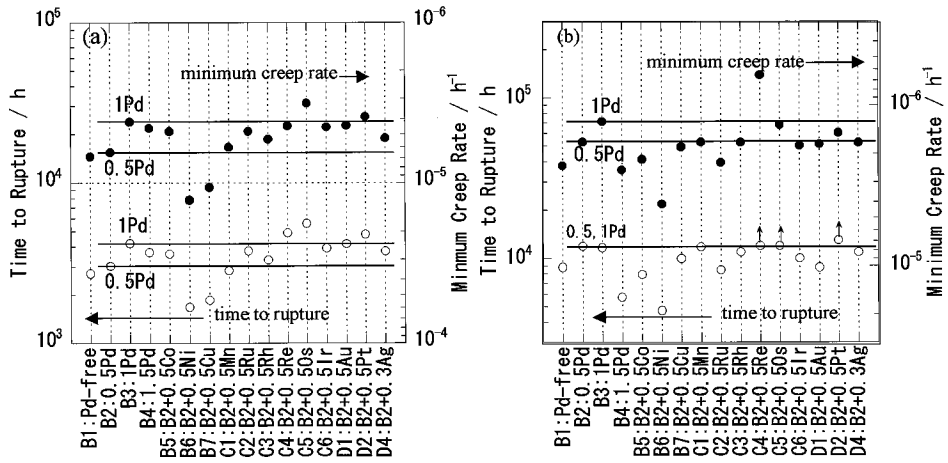


Fig.5 Time to rupture and minimum creep rate of the tested steels crept at 923K with 120MPa: (a) and 100MPa: (b). note: C4, C5 and D2 in fig.5(b) are still testing.

changes of the hardness, additions of Ru, Re, Os, Ir, Au or Pt decreased the minimum creep rate and increased the creep rupture life to the level of 1%Pd steel, as shown in Fig. 5(a). Figure 6 shows the time dependence of creep rate for C1, C4 and C5 comparing with B1, B2 and B3. Addition of Re or Os not only decreased the minimum creep rate but also delayed the acceleration of creep and prolonged the creep rupture life. Furthermore, C4 showed superior creep resistance to other steels under lower stress condition, as indicated by the smallest minimum creep rate in Fig. 5(b). Whereas, although increase of Mn concentration hardened the steel after aging at 823K, no improvement of creep resistance was observed. True strain vs. creep rate curve of C1 steel is shown in Fig. 7. Increase of Mn decreased the creep rate at the early stage of primary creep to the level of B3, but the creep rate came close to B2 at the minimum creep and rapidly increased at the end of the tertiary creep.

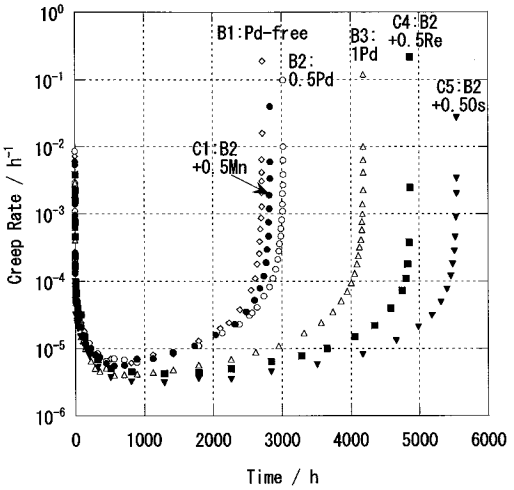


Fig. 6 Typical time vs. creep rate curves of the tested steel crept at 923K and 120MPa.

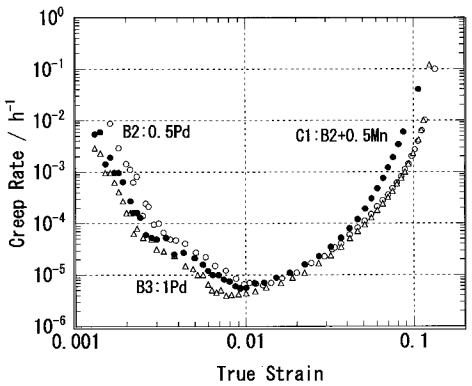


Fig. 7 True strain vs. creep rate curve of C1 steel comparing with B2 and B3 steels.

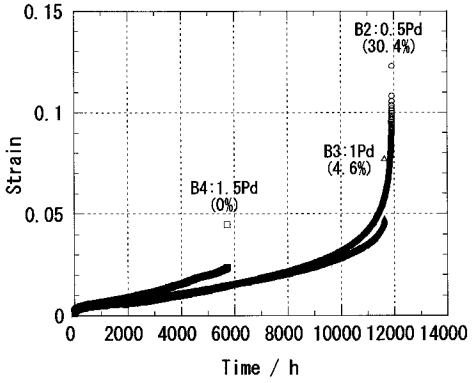


Fig. 8 Effects of Pd concentration on time-strain curves crept at 923K and 100MPa. Reduction of area is also indicated in the figure.

B4 steel showed the degradation of creep properties by excess addition of Pd, as shown in Fig. 5(b). Figure 8 shows the time-strain curves of B2, B3 and B4 crept at 923K with 100MPa. A sudden rupture at the early stage of tertiary creep was observed in B4 steel. It was suggested that too much addition of fine precipitation such as α " and MX carbonitride deteriorated the creep ductility resulting in the reduction of creep rupture life.

Paying attention to C1 and C4, precipitation behavior of these steels was evaluated by quantitative analysis of extracted residue and microstructural observation by SEM. Figure 9 shows the amount of precipitates of B1, B2, B3, C1 and C4 after crept at 923K and 120MPa. The amount of Mn in precipitates depended on that of Pd in precipitates, suggesting the Mn dissolution in α". The Pd to Mn ratio in precipitates was about 0.5 so that the amount of Mn in precipitates was limited to only 0.2mass%, which was less than the concentration of Mn in B2 steel, in the case of 0.5%Pd steel. It was suggested that the Mn addition promoted the precipitation of α ", but in the saturated condition the amount of α " for C1 was almost equivalent to that for B2. As a result, C1 showed superior creep resistance to B2 in the early stage of primary creep but came close to B2 on the way to the minimum creep.

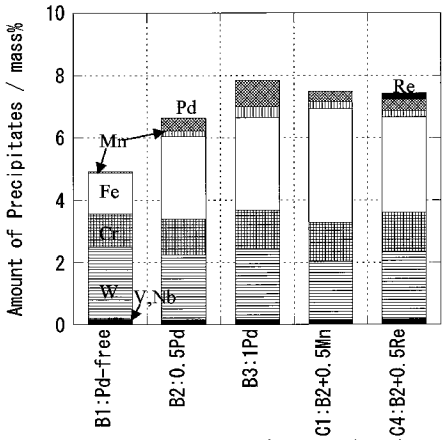


Fig. 9 Amount of precipitates for ruptured specimens crept at 923K and 120MPa.

Figure 10 shows the back scattered electron images of ruptured specimen crept at 923K with 120MPa for B2, B3, C1 and C4. Prior austenite, packet and block boundaries of B2

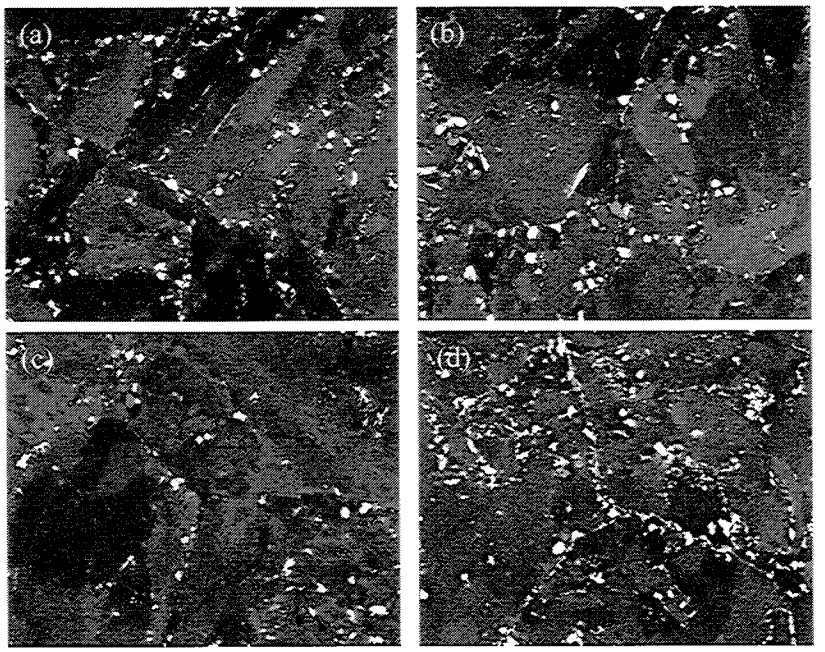


Fig.10 Back scattered electron images of crept specimen. (a): B2, t_R=3021h, (b): B3, t_R=4182h (c): C1, t_R=2829h (d):C4, t_R=4857h

and B3 were decorated with $M_{23}C_6$ (gray precipitates in Fig. 10) and Laves phase (bright one in Fig. 10). And there was no clear difference in boundary decoration between B2 and B3. Poor boundary decoration was observed in Mn increased steel. On the contrary, continuous precipitation along boundaries and fine Laves phase inside lath were observed in Re-added steel. It was assumed that the growth of the precipitations in C1 accelerated the tertiary creep, as shown in Fig. 7, and the continuous precipitations in C4 delayed the transition to tertiary creep, as shown in Fig. 6, by stabilizing the boundaries. It was also assumed that the fine Laves precipitates in C4 reduced the minimum creep rate remarkably, as shown in Fig. 5(b).

Demonstrational Test

From the fundamental test results, C4 steel was selected for demonstrational test. Chemical composition of MC1 and MC2 was slightly modified from C4, as shown in table 2, concerning the improvement of creep properties. N was decreased to 0.03mass% to decrease fine precipitation of MX instead of α" in order to increase the creep ductility. Mn was decreased slightly to prevent the growth of precipitations such as Laves phase. C, Si and W were also changed slightly to get the fully martensitic structure.

First, high temperature ductility was evaluated to judge the possibility of pipe fabrication by hot forging and extrusion process. Figure 11 shows the high strain rate tensile test results for MA1, MB1 and MC1. Reduction of area for MC1 kept more than 70% around hot forming temperature, which was considered to be enough to fabricate pipes, and the tensile strength was not remarkably higher than that of modified 9Cr-1Mo steel. From these results, pipe fabrication was done and succeeded without harmful defects.

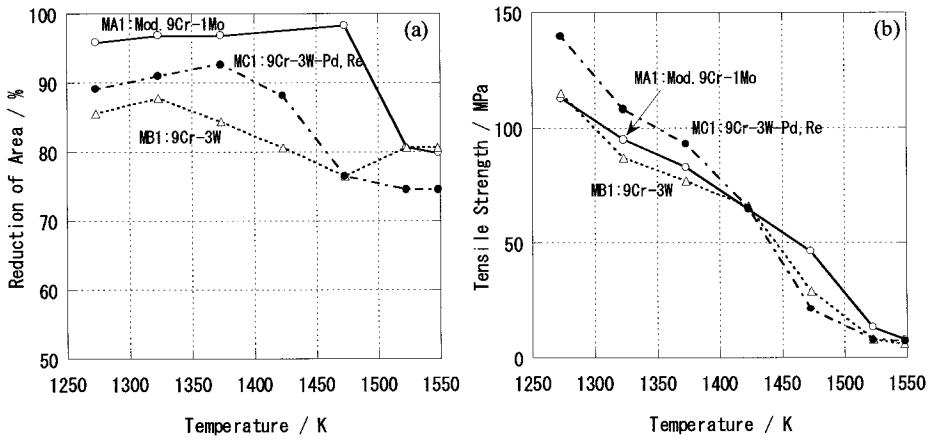


Fig. 11 High strain rate tensile test results, reduction of area; (a) and tensile strength; (b), for three kinds of steel plates.

Then, the plates were welded by gas tungsten arc welding. All plates were also welded successfully without defects, as shown in figure 12. The Charpy impact properties of the welded joints were shown in figure 13. Although the values of absorbed energy of the MC1 joint were lower than that of modified 9Cr-1Mo steel joint, the values still fulfill the

requirements for the practical use.

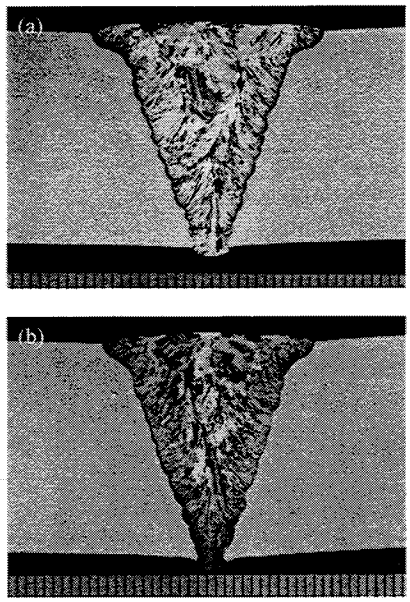


Fig. 12 Macro structure of welded joints for MB1; (a) and MC1; (b) after post welding heat treatment.

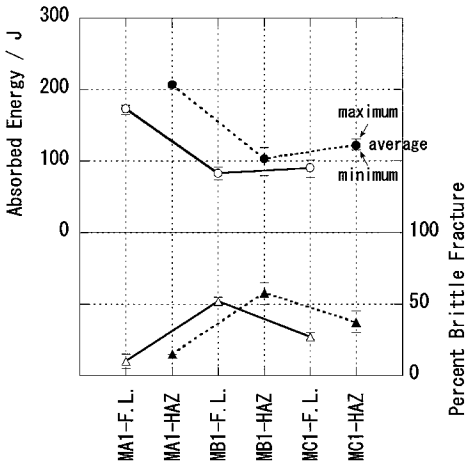


Fig. 13 Charpy impact properties of welded joints. 2mm-V notch is on the fusion line (F.L.) or heat affected zone (HAZ) of 10 × 10 × 55 mm specimen.

4 Conclusion

In order to search for substitutional elements for the precious metal Pd, effects of alloying elements on creep properties of Pd-added 9Cr ferritic steels have been evaluated. Following results were acquired:

(1) Addition of Ru, Re, Os, Ir, Au or Pt hardened the 0.5Pd steel after tempering at precipitation temperature of α " and also improve the creep property to the 1%Pd steel level.

(2) Increase of Mn concentration promoted the precipitation of α " but did not increase the amount of α ", resulting in no improvement of creep properties.

(3) Re addition prevented the growth of precipitation such as $M_{23}C_6$ and Laves phase, resulting in improving the creep properties at lower stress levels.

From the above fundamental test results, demonstrational pipe fabrication and welding tests were performed for Pd and Re added steel. Pd and Re added steel was successfully formed into pipe and welded without harmful defects.

Detailed creep properties of fabricated plates and pipes will be reported in near future.

5 Acknowledgement

The authors would like to thank Sumitomo Metal Technology for carrying out this demonstrational experiment.

6 References

[1] V. K. Sikka, C. T. Ward and C. Thomas, "Modified 9Cr-1Mo Steel - An Improved Alloy for Steam Generator Application", ASM Int. Conf. Production, Fabrication, Properties and Application of Ferritic Steels for High-Temperature Applications, ASM, Washington D.C., (1981)
[2] F. Masuyama, I. Ishihara, T. Yokoyama and M. Fujita, "Application of Tungsten Strengthened 9-12% Cr Boiler Steel Pipes", The Thermal and Nuclear Power, 46(1995), 498.
[3] K. Muramatsu, "Development of Ultra-Super Critical Plant in Japan", Proc. Advanced Heat Resistant Steels For Power Generation, edited by R. Viswanathan and J. Nutting, The University Press, Cambridge, (1998), 543.
[4] F. Masuyama: Proc. Advanced heat Resistant Steels For Power Generation, edited by R. Viswanathan and J. Nutting, The University Press, Cambridge, (1998), 33.
[5] K. Sawada, M. Takeda, K. Maruyama, R. Ishii and M. Yamada, "Dislocation Substructure Degradation during Creep of martensitic Heat-resisting Steels with and without W", Proc. the 6th Liege Conf. on Materials for Advanced Power Engineering, edited by J. Lecomte-Beckers, F. Schubert and P. J. Ennis, Forshungs-zentrum, Julich GmbH, (1998), I.575-583.
[6] H. Nakashima, "Strength and Structure Change of 9Cr-3W-3Co Martensitic Steel During High Temperature Deformation", Proc. Int. Workshop on the Innovative Structural materials for Infrastructure in 21st Century, NRIM, Tsukuba, (2000), 21.
[7] M. Igarashi, S. Muneki and F. Abe, "Microstructure Control of Martensitic Phase Matrix in Advanced Ferritic Steels for USC Boilers to Achieve Long Term Stability", Proc. the 6th Liege Conf. on Materials for Advanced Power Engineering, edited by J. Lecomte-Beckers, F. Schubert and P. J. Ennis, Forshungs-zentrum, Julich GmbH, (1998), I.673-646.
[8] M. Igarashi, K. Yamada, S. Muneki and F. Abe, "Long-Term Creep Deformation Characteristics of α" Precipitation Hardened Ferritic Steels", Proc. Int. Workshop on the Innovative Structural materials for Infrastructure in 21st Century, NRIM, Tsukuba, (2000), 106, *(in Japanese).*
[9] K. Yamada, S. Muneki, M. Igarashi and F. Abe, "Precipitation Behavior of MX in High-Cr Ferritic Steels", Proc. Int. Workshop on the Innovative Structural materials for Infrastructure in 21st Century, NRIM, Tsukuba, (2000), 114, *(in Japanese).*
[10] M. Igarashi, S. Muneki, H. Kutsumi, T. Itagaki, N. Fujitsuna and F. Abe," A New Concept for Strengthening of Advanced Ferritic Steels for USC Power Plant", Proc. 5th Inter. Charles Persons Turbine Conf., edited by A. Strang, W. M. Banks, R. D. Conroy, G. M. McColvin, J. C. Neal and S. Simpson, The University Press, Cambridge, (2000), 334.
[11] M. Igarashi, S. Muneki and F. Abe: Report of 123rd Committee on Heat-Resisting Metals and Alloys, Jpn. Soc. for the Promotion of Sci., 39 (1998), 355-362 *(in Japanese).*
[12] M. Igarashi, S. Muneki, H. Hasegawa, K. Yamada and F. Abe, "Creep Deformation and the Corresponding Microstructural Evolution in High-Cr Ferritic Steels", ISIJ International, 41 (2001), Supplement, S101-S105.

IMPROVEMENT OF CREEP STRENGTH OF PRECIPITATION STRENGTHENED 15CR HEAT RESISTANT FERRITIC STEELS

Yoshiaki Toda[(a)], Hideaki Tohyama[(b)],
Hideaki Kushima[(a)], Kazuhiro Kimura[(a)], Fujio Abe[(a)]

[(a)]National Institute for Materials Science
1-2-1 Sengen, Tsukuba-shi, Ibaraki 305-0047, Japan
[(b)]Interdisciplinary Graduate School of Science and Engineering,
Tokyo Institute of Technology
4259 Nagatsuta, Midori-ku, Yokohama, Kanagawa 226-8502, Japan

Abstract

Effects of C and N on strength properties and microstructure of fully annealed and precipitation strengthened 15Cr ferritic steels with ferrite matrix have been investigated, and possibility of improvement in long-term creep strength of the steels has been discussed. Creep rupture life of the steel has been extended by about 10 times with the addition of 0.07mass% N and a combination of 0.05mass% C and 0.03mass% N. Creep rupture lives of those steels are longer than that of the conventional ferritic creep resistant steel of NF616. The long-term creep strength of the studied 15Cr steel is significantly improved with the addition of optimum amounts of C and N. Rod or plate type fine precipitates identified as intermetallic compounds of Laves phase, μ-phase and χ-phase, chromium nitride (Cr_2N) and chromium carbide ($M_{23}C_6$) have been observed within the grains with high density in the creep ruptured specimens. Rupture elongation of the steels are lower than those of the conventional ferritic creep resistant steels. It has been pointed out that a balance between creep strength and ductility should be improved in order to construct large scale high temperature structural components with the studied 15Cr steel.

Keywords: creep strength, long-term, ferrite matrix, precipitation strengthening, intermetallic compound, Cr_2N, $M_{23}C_6$, ductility

1. Introduction

Recently, improvement of energy efficiency in fossil fired power generations has been requested from a global environmental point of view in order to reduce CO_2 emission and save energy resources. For that reason, creep strength of high temperature structural components in power plants should be advanced, and steam temperature and pressure must be increased. Consequently, many efforts have been conducted on research and development of new high strength heat resistant materials[1]. Ferritic steel, that is one of the high strength heat resistant materials, possesses higher thermal conductivity and lower thermal expansion coefficient than those of austenitic heat resistant steels and Ni base super alloys. So, it is necessary to develop in particular ferritic heat resistant steels in order to improve the energy efficiency in fossil fired power plants which are operated for peak load demand with frequent start-and-stop.

Usually, the microstructure of conventional high strength ferritic creep resistant steels is tempered martensite. However, the creep strength of these materials is strongly influenced by degradation during long-term service at the elevated temperatures, since the tempered martensitic microstructure is unstable during long-term service at the elevated temperatures.

For example, preferential recovery in the vicinity of prior austenite grain boundaries and expansion of it has been pointed out as a degradation mechanism of a modified 9Cr-1Mo steel[2, 3]. Suppression of degradation through the improvement of stability of the microstructure is a main concept to obtain high creep strength in the long-term[4].

On the other hand, Kimura et al. have investigated effects of initial microstructure on long-term creep strength of a 0.5Cr-0.5Mo steel, and it has been pointed out that the long-term creep strength of fully annealed ferrite and pearlite microstructure is higher than those of tempered martensite or bainite microstructures[5]. It has been supposed that the highest long-term creep strength of fully annealed microstructure is attained by its low dislocation density. That result has indicated that fully annealed microstructure possesses advantages for long-term creep strength under service conditions in power generation[5]. Furthermore, Kimura and Toda et al. investigated the creep strength properties of fully annealed 15Cr-1Mo-3W-V-Nb ferritic steels with ferrite matrix at 923K, and found that increase in W and Co content could improve the creep strength as much as that of the conventional ferritic heat resistant steels through the distribution of fine precipitates identified as intermetallic compounds and carbide with high density[6-10]. In addition, it was pointed out that higher Cr content than those of the conventional ferritic creep resistant steels is suitable for not only ferrite microstructure but also better oxidation resistance[6-10]. However, slopes of the stress vs. time to rupture curves of these steels were relatively large, and the long-term creep strength of the steels decreased remarkably compared with the conventional ones[6-10].

Therefore, the aim of the present study is to investigate the effects of C and N on the long-term creep strength and microstructure of the precipitation strengthened 15Cr ferritic steels and to discuss a possibility of improvement in long-term creep strength of the steels. Since the faster diffusion rates of C and N elements are supposed to significantly influence the stability of microstructure at the elevated temperatures, the objective has been focused on the effects of C and N on the long-term creep strength in this study,

2. Experimental procedure

Chemical compositions of the steels used in the present study are shown in **Table 1**. C and N free 15Cr-1Mo-6W-0.2V-0.05Nb-3Co-0.003B (mass%) is a base composition. Four other kinds of steels, which contain 0.07mass%N (0C-7N steel), 0.1mass%C (10C-0N steel), a combination of 0.05mass%C and 0.03mass%N (5C-3N steel) and a combination of 0.1mass%C and 0.08mass%N (10C-8N steel) have been investigated. 10C-8N steel, which has been referred to as 6W-3Co steel, had the highest creep rupture strength in the previous study[6-10]. These steels were prepared in a vacuum induction furnace. The ingots with a weight of 10kg were hot forged into bars with a diameter of about 15mm and annealed for 30min at 1473K followed by furnace cooling.

Table 1 Chemical compositions (mass%) of the steels studied.

	C	Cr	Mo	W	V	Nb	Co	N	B
base	**0.001**	14.91	1.01	6.03	0.19	0.045	2.96	**0.0018**	0.0031
0C-7N	**0.003**	14.91	1.01	6.00	0.19	0.045	2.96	**0.066**	0.0028
10C-0N	**0.10**	14.88	1.01	6.01	0.19	0.045	2.96	**0.0019**	0.0028
5C-3N	**0.046**	15.00	1.00	6.07	0.19	0.043	2.97	**0.033**	0.0030
10C-8N	**0.096**	15.10	0.99	5.94	0.18	0.064	3.00	**0.082**	0.0027

Dimensions of creep specimens were 6mm in gauge diameter and 30mm in gauge length according to JIS (Japan Industrial Standard) Z 2201 Type II[11]. Creep tests were conducted at a range of temperatures from 873 to 973K and a range of stresses from 50 to 200MPa up to about 10,000h in air. Creep deformation was measured using an extensometer attached to the gauge portion of the specimens.

Microstructure of the steels in the as-annealed condition and creep ruptured specimens were examined under a scanning electron microscope (SEM). Identification of precipitates was conducted on electrolytically extracted residues that were taken from the specimens isothermally aged for 1000h at 923K by means of X-ray diffraction analysis.

3. Results and Discussion

3.1 Creep strength property

Stress vs. time to rupture curves of the steels at 923K are shown in **Fig. 1**. The curves of a 9Cr-1Mo-V-Nb (Mod. 9Cr-1Mo) steel[12] and a 9Cr-0.5Mo-2W-V-Nb (NF616) steel[13], which are conventional ferritic creep resistant steels, are also shown in the same figure. Creep rupture strength of 10C-8N steel was the highest among the precipitation strengthened 15Cr ferritic steels in the previous study[6-10]. Times to rupture of all the present studied steels are longer than that of a Mod. 9Cr-1Mo steel. Time to rupture of 10C-0N steel, to which is added 0.10mass%C and N free, is as long as that of C and N free base steel. So, the addition of C solely is little effective in the improvement of creep rupture strength of the steels. On the other hand, the addition of N solely and a combination of C and N improve the creep rupture strength. Creep rupture lives of 0C-7N, 5C-3N and 10C-8N steels are longer than that of NF616 steel at higher stresses than 120MPa.

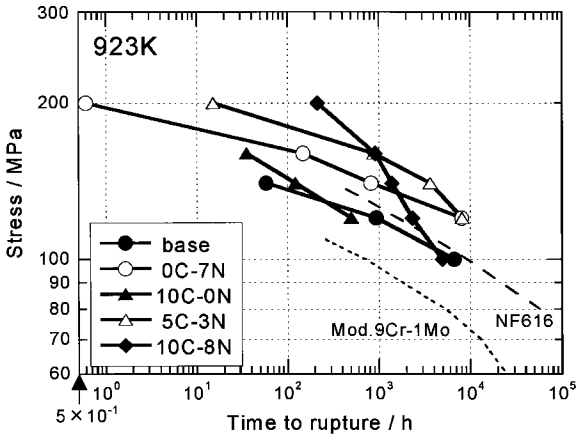


Fig. 1. Stress vs. time to rupture curves of the 15Cr steels and two conventional ferritic creep resistant steels[12, 13] at 923K.

It is also observed that the slopes of stress vs. time to rupture curves of 10C-0N, 5C-3N and 10C-8N steels, which contain carbon, increase with decrease in stress, but those of C free base and 0C-7N steels are small regardless of stress condition. 10C-8N steel possesses the highest creep strength at short-term and higher stress condition among the five 15Cr steels. However, the time to rupture of this steel is shorter than that of C free steels in the longer-term than 5,000h and the stresses lower than 100MPa. In the previous study, it has been reported that the slopes of the stress vs. time to rupture curves of Co free steels were smaller than that of Co added steels, and the long-term creep strength of Co free steels was higher than that of Co added steels[10]. It has been supposed that the above mentioned creep strength properties of Co added steels are due to a coarsening of $M_{23}C_6$ carbide and loss of precipitation strengthening effect[10]. For that reason, the small slopes of the stress vs. time to rupture curves of base and 0C-7N steels are supposed to be related to no presence of carbide.

Fig. 2 shows stress vs. minimum creep rate curves of the steels. The creep tests of 0C-7N and 10C-0N steels at 100MPa have not yet been ruptured and those data are shown by the open points and the dashed lines. The curve of N free 10C-0N steel is similar to that of base steel. Although the minimum creep rates of 5C-3N and 10C-8N steels are small at high stress condition of 200MPa, they are the same as or higher than that of base steel at a low stress condition of 100MPa. On the other hand, the stress exponent of C free 0C-7N steel is large through the stress range investigated. Although the minimum creep rate of this steel is several hundreds times higher than that of 10C-8N steel at 200MPa, that is one hundred times lower than that of 10C-8N steel at 100MPa. The stress exponent of 0C-7N steel tends to decrease at the low stress condition, however the minimum creep rate of this steel is much lower than that of the other steels at stresses lower than 120MPa.

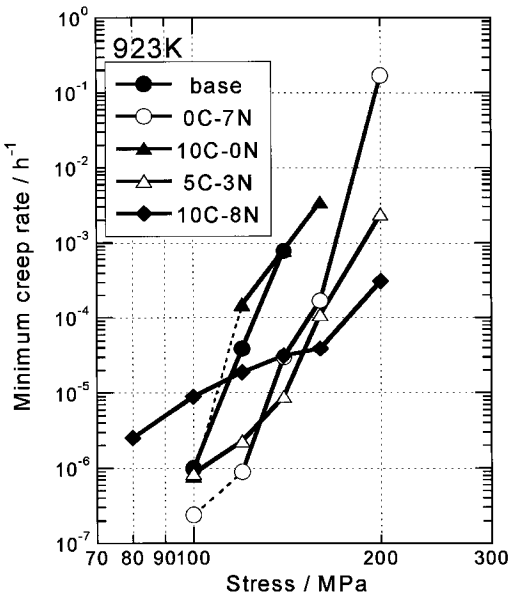


Fig. 2. Minimum creep rate vs. stress curves of the steels at 923K.

Fig. 3 shows creep rate vs. time curves of (a) 0C-7N and (b) 5C-3N steels at 923K and various stresses from 100 to 200MPa. The creep rupture lives of these are the longest among the present 15Cr steels at 120MPa. The creep rates of both 0C-7N and 5C-3N steels decrease drastically after several tens of hours of creep deformation. Although in (b) 5C-3N steel, the minimum creep rate decreases with decrease in stress, onset time of the accelerating creep stage are from about 1000 to 5000h, and the increase in creep rupture life with decrease in stress is not as much as the decrease in the minimum creep rate. On the other hand, in (a) 0C-7N steel, the onset time of the accelerating creep stage and the creep rupture life are extended with decrease in stress, with decrease in minimum creep rate. It has been reported in the previous study that the precipitation strengthening by intermetallic compounds is more effective than that by carbide for improving long-term creep strength of the 15Cr ferritic steel[10]. It is likely that the above difference in the creep deformation behavior between 0C-7N and 5C-3N steels is due to the difference in the long-term stability of the strengthening effects due to intermetallic compound and carbide. Moreover, 0C-7N steel may be expected to possess better long-term creep rupture strength than that of 5C-3N steel at the stresses lower than 100MPa.

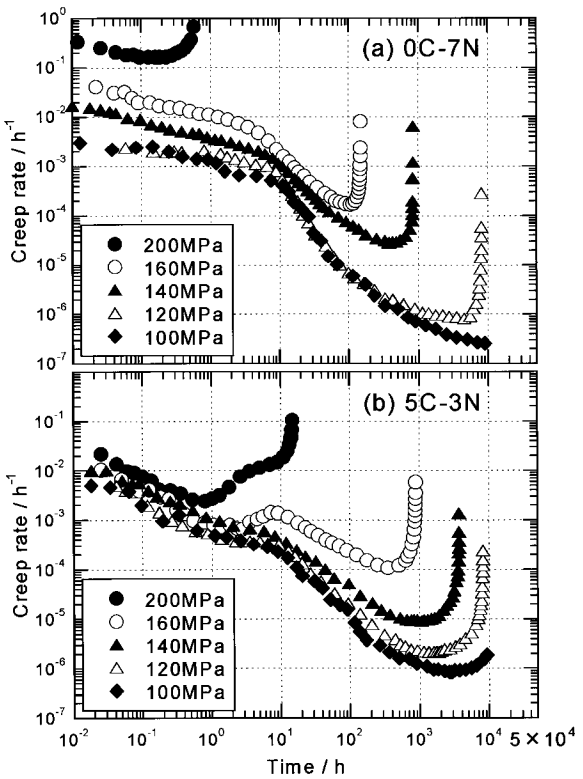


Fig. 3. Creep rate vs. time curves of (a) 0C-7N steel and (b) 5C-3N steel at 923K for various stresses.

Fig. 4 shows creep rupture elongations of the steels creep ruptured in the range of temperatures from 873K to 973K. The creep rupture elongation tends to decrease with the increase in time to rupture in all steels. Especially, the creep rupture elongations of 0C-7N and 5C-3N steels, which show the high creep rupture strength in the present study, decrease to smaller than 10%.

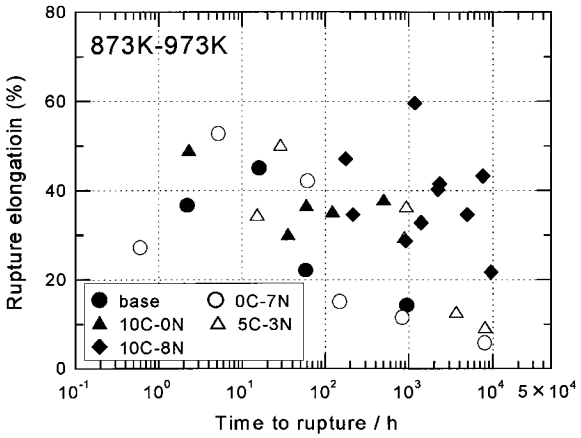


Fig. 4 Rupture elongation of the steels at 873~973K.

It has been concluded from the above results that the long-term creep strength of the fully annealed 15Cr ferritic steel is significantly improved with the addition of optimum amounts of C and N. However, the creep rupture elongation decreases with increase in the creep rupture life. Therefore, improving a balance between creep strength and ductility should be attained in the future study in order to apply the fully annealed 15Cr ferritic steels for practical use.

3.2 Microstructural change

Fig. 5 shows SEM micrographs of (a) base; (b) 0C-7N; (c) 10C-0N; (d) 5C-3N and (e) 10C-8N steels in the as-annealed condition. A few precipitates with about 1μm in size are observed in (a) base steel, (b) C free 0C-7N and (c) N free 10C-0N steels. And coarse block type precipitates with several μm in size are observed on the grain boundary in (d) 5C-3N and (e) 10C-8N steels. These precipitates appear to be formed during furnace cooling. Almost all of the matrix of every steel is ferrite phase.

Fig. 6 shows SEM micrographs of the steels creep ruptured at 923K and 120MPa. t_r values indicated in each micrograph are times to rupture. In (d) 5C-3N and (e) 10C-8N steels, the block type precipitates which are observed on the grain boundary of the steels in the as-annealed condition have coarsened to several tens of μm in size. In every steel, rod or plate

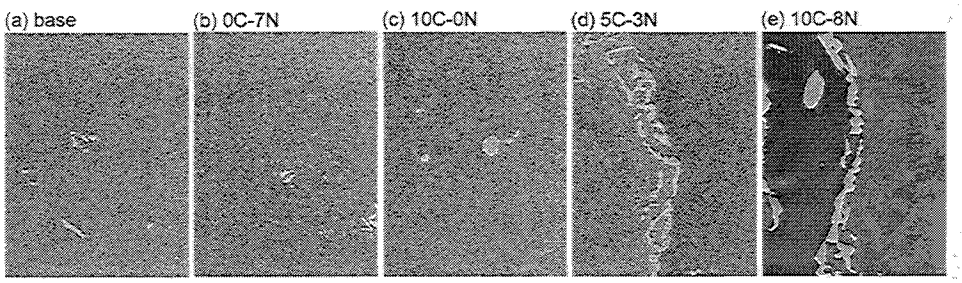


Fig. 5. SEM micrographs of (a) base; (b) 0C-7N; (c) 10C-0N; (d) 5C-3N and (e) 10C-8N steels in the as-annealed condition.

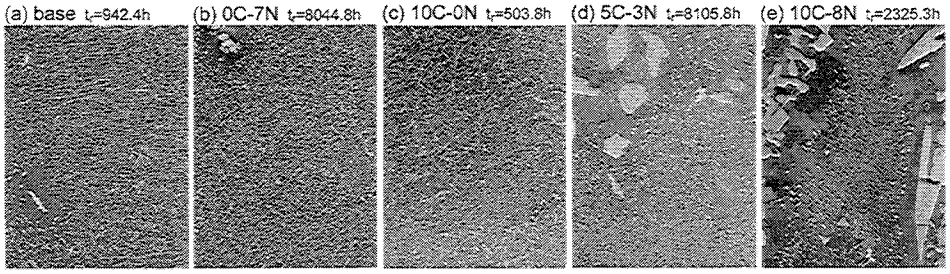


Fig. 6. SEM micrographs of (a) base; (b) 0C-7N; (c) 10C-0N; (d) 5C-3N and (e) 10C-8N steels creep ruptured at 923K and 120MPa. The value of t_r inserted into each photo stands for time to rupture.

type fine particles with several hundreds of nm in length are observed within grains with high density. Especially, in (b) 0C-7N and (d) 5C-3N steels, which possess excellent creep rupture strength, it is recognized that the precipitates within the grain remain still fine even after about 8,000 hours of creep exposure. It seems that the growth rate of these particles in the 0C-7N and 5C-3N steels are extremely small.

In order to identify the precipitates shown in Fig. 6, X-ray diffraction analysis was conducted on the electrolytic residue taken from the specimens isothermally aged for 1,000h at 923K. **Fig. 7** shows X-ray diffraction profiles of (a) base; (b) 0C-7N; (c) 10C-0N; (d) 5C-3N and (e) 10C-8N steels. The results obtained by comparing these profiles with the JCPDS cards are as follows; the peaks in the profile of (a) base steel are identified as those from Laves phase (Fe_2W) and μ-phase (Fe_7W_6), which are intermetallic compounds classified into topologically close packed (TCP) phase[14], and the peaks in (b) 0C-7N steel coincide with that of Cr nitride (Cr_2N) in addition to Laves phase and μ-phase. The peaks of (c) 10C-0N; (d) 5C-3N and (e) 10C-8N steels, which contain C, are identified as those from χ-phase ($Fe_{36}Cr_{12}W_{10}$), which are also an intermetallic compound classified into TCP phase, and carbide ($M_{23}C_6$) besides Laves phase and μ-phase. Therefore, most of the precipitates observed in SEM micrographs are identified as three kinds of intermetallic compounds, Cr

nitride and carbide. It has been supposed that the excellent long-term creep strength of 0C-7N and 5C-3N steels may be obtained by distribution of many fine particles of TCP phases and slow growth rate of those precipitates during long-term creep exposure.

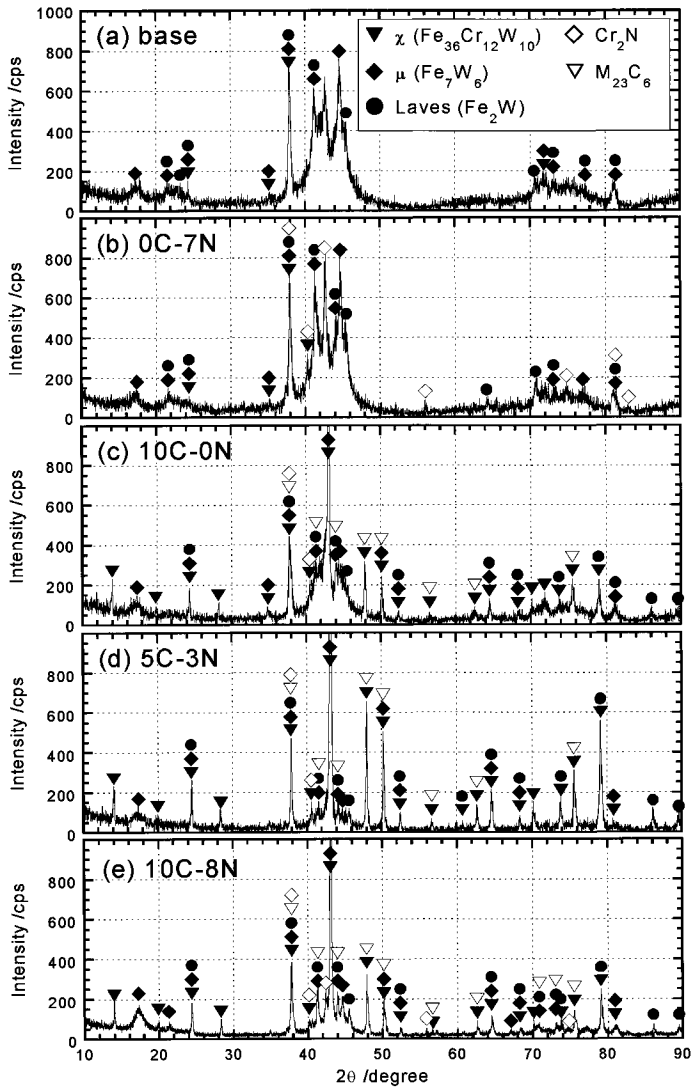


Fig. 7 X-ray diffraction profiles of the electrolytically extracted residues taken from (a) base; (b) 0C-7N; (c) 10C-0N; (d) 5C-3N and (e) 10C-8N steels aged for 1,000h at 923K.

4. Conclusion

The effects of C and N on the creep strength properties and microstructure of the fully annealed and precipitation strengthened 15Cr ferritic steels are investigated. The obtained results are as follows:

(1) The time to rupture of 10C-0N steel is as long as that of C and N free base steel and the addition of C solely is little effective in the improvement of creep rupture strength of the steel. On the other hand, the addition of N solely and a combination of C and N improve the creep rupture strength. The creep rupture strengths of 0C-7N and 5C-3N steels are higher than that of the conventional ferritic creep resistant steel of NF616. The creep rupture strength of 10C-8N steel is also higher than that of NF616 steel, however the strength decreases drastically with decrease in stress in the long-term.

(2) The rupture elongation of the steels decreases with increase in time to rupture. Especially, the rupture elongations of 0C-7N and 5C-3N steels that possess the highest creep strength among the present studied steels are smaller than 10%.

(3) The rod or plate type fine particles are precipitated within the grain with high density in the creep ruptured steels. The growth rates of these particles are very small in 0C-7N and 5C-3N steels. The stability of precipitates, therefore, the precipitation strengthening effects strongly depend on the C and N contents.

(4) Laves phase and μ-phase are precipitated in the isothermally aged C and N free base steel. Besides these phases, Cr nitride is observed in 0C-7N steel. Moreover, χ-phase and $M_{23}C_6$ carbide are observed in 10C-0N steel and the steels containing both C and N.

(5) The main contribution of this paper is the finding on possibility of improvement in the long-term creep strength of the fully annealed and precipitation strengthened 15Cr ferritic steels by controlling the amounts of C and N contents through the stabilizing of microstructure during long-term creep exposure at the elevated temperatures. In the future, it is necessary to improve a balance between creep strength and ductility in order to apply the fully annealed 15Cr ferritic steels for practical use.

References

[1] F. Masuyama, History of Power Plants and Progress in Heat Resistant Steels, ISIJ Int., Vol. 41, 2001, 612.
[2] K. Kimura, H. Kushima, F. Abe, K. Suzuki, S. Kumai and A. Satoh, Microstructural Change and Degradation Behaviour of 9Cr-1Mo-v-Nb Steel in the Long Term, Proc. of the 5th Int. Charles Parsons Turbine Conf., ed. by A. Strang et al., Cambridge, 2000, 590.
[3] K. Suzuki, S. Kumai, H. Kushima, K. Kimura and F. Abe, Changes in Precipitates of Modified 9Cr-1Mo Steel During Long-term Creep Deformation at 873K and 923K, Proc. of the 7th Int. Conf. on Creep and Fatigue at Elevated Temperatures, ed. by Y. Asada, Tsukuba, 2001, 335.
[4] K. Maruyama, K. Sawada and J. Koike, Strengthening Mechanisms of Creep Resistant Tempered Martensitic Steel, ISIJ Int., Vol. 41, 2001, 641.
[5] K. Kimura, H. Kushima, E. Baba, T. Shimizu, Y. Asai, F. Abe and K. Yagi, Effect of

Initial Microstructure on the Long Term Creep Strength of a Low Alloy Cr-Mo Steel, Proc. of the 5th Int. Charles Parsons Turbine Conf., ed. by A. Strang et al., Cambridge, (2000), 558.

[6] K. Kimura, K. Seki, Y. Toda and F. Abe, Development of High Strength 15Cr Ferritic Creep Resistant Steel with Addition of Tungsten and Cobalt, ISIJ Int., Vol. 41, 2001, Supplement, S121.

[7] K. Kimura, K. Seki, Y. Toda and F. Abe, Creep Strength Property of Precipitation Strengthened 15Cr Ferritic Creep Resistant Steel, Proc. of the 3rd Conf. on Advanced in Material Technology for Fossil Power Plants, ed. by R. Viswanathan, W. T. Bakker and J. D. Parker, Swansea, 2001, 403.

[8] K. Kimura, K. Seki, Y. Toda and F. Abe, Development of Precipitation Strengthened 15Cr Ferritic Creep Resistant Steel, Proc. of the 7th Int. Conf. on Creep and Fatigue at Elevated Temperatures, ed. by Y. Asada, Tsukuba, 2001, 437.

[9] Y. Toda, K. Seki, K. Kimura, and F. Abe, Effects of W and Co on the Microstructure and Creep Strength of the Precipitation Strengthened 15Cr Ferritic Steels, JSME Int. J., Vol. A45, 2002, 25.

[10] Y. Toda, K. Seki, K. Kimura, and F. Abe, Microstructure and Strength Property of the Precipitation Strengthened 15Cr Ferritic Heat Resistant Steels with Addition of W and Co, ISIJ Int., **received**.

[11] Japanese Industrial Standard, Test Pieces for Tensile Test for Metallic Materials JIS Z 2201, Japanese Standard Association, (1998).

[12] NRIM Creep Data Sheet No.43, Data Sheets on the Elevated-temperature Properties of 9Cr-1Mo-V-Nb Steel Tubes for Boilers and Heat Exchangers (ASME SA-213/SA-213M Grade T91) and 9Cr-1Mo-V-Nb Steel Plates for Boilers and Pressure Vessels (ASME SA-387/SA387M Grade 91), National Research Institute for Metals, Tsukuba, (1996).

[13] Data Package for NF616 Ferritic Steel (9Cr-0.5Mo-1.8W-Nb-V), 2nd Edition, Nippon Steel Corporation, (1994).

[14] F. C. Frank and J. S. Kasper, Complex Alloy Structures Regarded as Sphere Packings. I. Definitions and Basic Principles, Acta Cryst., Vol. 11, 1958, 184.

LONG-TERM CREEP STRENGTH PREDICTION OF HIGH CR FERRITIC CREEP RESISTANT STEELS

H.Kushima, K.Kimura and F.Abe
National Institute for Materials Science
1-2-1 Sengen, Tsukuba-shi, Ibaraki 305-0047, JAPAN

Abstract

Creep rupture strength property of high Cr ferritic creep resistant steels have been investigated, in conjunction with degradation and creep deformation behaviour, for the purpose of improving the accuracy of long-term creep strength prediction. Strain at the onset of accelerating creep stage decreases with decrease in stress in a stress range of less than about 200MPa. Boundary condition between short-term region and long-term one where the slopes of the stress vs. time to rupture curves become steeper corresponds to a stress condition where the onset strain of accelerating creep stage is about 0.012. Moreover, stress level of such boundary is almost the same as 50% of the 0.2% proof stress at the temperatures. Prediction of long-term creep strength using by a Larson-Miller parameter with a best fit parameter constant gives dangerous results of overestimation in the long-term. On the other hand, similar prediction with the creep rupture data under the stress conditions lower than 50% of the 0.2% proof stress at the temperatures and a parameter constant of 20 has produced better results. It has been concluded that short-term creep rupture data under the stress conditions higher than 50 % of the 0.2% proof stress at the temperatures, should be excluded for a prediction of long-term creep strength property of high Cr ferritic creep resistant steels.

Keywords : long-term creep strength, prediction, high Cr ferritic creep resistant steel, 0.2% proof stress, stress range partitioning method

1 Introduction

Improvement of energy efficiency of fossil fired power plant is strongly demanded, in order to save energy resources such as oil, coal and natural gas and to suppress the emission of carbon dioxide [1]. Many efforts have been conducted on research and development of high strength ferritic creep resistant steel that makes possible an increase in operating steam conditions of temperature and pressure [2]. High efficiency thermal power plants have been constructed with a Mod.9Cr-1Mo steel and have been already operated for 10 years and more. In the last decade, high chromium ferritic creep resistant steels of NF616 [3], HCM12A [4] and E911 [5] whose creep strength are higher than that of a Mod.9Cr-1Mo steel have been developed. Such high strength high chromium ferritic creep resistant steels have been already applied to construction of large scale structural components such as headers and main steam pipes of modern thermal power plants. Some problems on an overestimation of long-term creep strength have been pointed out on such high chromium ferritic creep resistant steels [6], since relations between stress and time to rupture of those steels display inflections in the long-term which results in large drop in long-term creep strength. In order to improve accuracy of long-term creep strength prediction, several methods have been proposed, as follows.

1. The short-term creep rupture data should not be used for a long-term life prediction.
2. Creep rupture data should be divided into two groups of higher stress, short-term region and lower stress, long-term one according to difference in slope of stress vs. time to rupture curves [6].

However, a criterion for the short-term data which should be excluded from a life prediction has not yet been established for the former method. For the latter one, since long-term creep rupture data must be obtained to define a boundary between short-term region and long-term one, therefore, it is not useful for a life prediction from short-term creep data.

Recently, Kimura et al. [7] have investigated the degradation behaviour of a Mod.9Cr-1Mo steel during long-term creep exposure and reported that long-term creep strength is reduced by heterogeneous recovery preferentially occurred at the vicinity of prior austenite grain boundary, in contrast to homogeneous progress in recovery observed in the specimen creep ruptured in the higher stress and short-term region. Moreover, a change in creep deformation behaviour with increase in duration of creep deformation has been also observed on a Mod.9Cr-1Mo steel. It has been also pointed out that a boundary between short-term region and long-term one may be defined by considering such change in creep deformation behaviour. In the present study, defining method of a boundary between short-term region and long-term one has been investigated on high chromium ferritic creep resistant steels from a viewpoint of creep deformation and degradation behaviour, and an improvement of long-term creep strength assessment has been discussed.

2 Experimental Procedure

A Mod.9Cr-1Mo steel (ASME SA-213 T91) [8] (A) and a 12Cr-2W-0.4Mo-VNbCuB steel (B) were used in the present study. Chemical compositions and heat treatment conditions of the steels are shown in Table 1 and Table 2, respectively. Creep deformation and creep rupture data up to about 60,000h for a Mod.9Cr-1Mo steel and about 20,000h for a 12Cr-2W-0.4Mo-VNbCuB steel were used. Creep tests were conducted under constant load condition over a temperature range from 550 to 750°C in air.

Microstructure was examined using a Hitachi HF-2000 transmission electron microscope on a Mod.9Cr-1Mo steel in the as tempered condition and after creep rupture. A Larson-Miller parameter and a modified θ projection method [9] were employed for long-term creep rupture life prediction. A new prediction method of long-term creep strength with higher accuracy has been discussed by means of a Larson-Miller parameter.

Table 1: Chemical compositions (mass%) of the steels studied.

Steel	C	Si	Mn	Cr	W	Mo	V	Nb	N	Cu	B
A	0.09	0.29	0.35	8.70	-	0.90	0.22	0.072	0.044	-	-
B	0.11	0.27	0.59	12.10	1.82	0.34	0.19	0.06	0.066	0.82	0.003

Table 2: Heat treatment conditions of the steels studied.

Steel	Normalizing	Tempering
A	1,050°C, 10min. / Air cooling	765°C, 30min. / Air cooling
B	1,050°C, 10min. / Air cooling	790°C, 180min. / Air cooling

3 Results and Discussion

Heterogeneous Recovery

Stress vs. time to rupture curves of the Mod.9Cr-1Mo steel tested over a range of temperatures from 550 to 700°C are shown in Figure 1. The rupture lives predicted from the short-term creep rupture data whose rupture lives are less than 20,000h using a Larson-Miller parameter with a best fit parameter constant of 38, are also indicated by the dotted lines in Figure 1. Slopes of the stress vs. time to rupture curves increase monotonously with decrease in applied stress. Since creep rupture strength decreases significantly in the long-term over about 10,000h at 600 and 650°C, 100,000h creep rupture strength at these temperatures are extremely overestimated. Corresponding to large decreases in creep rupture strength, significant decrease in rupture elongation is also observed in the long-term over about 10,000h.

Creep rate vs. strain curves of the Mod.9Cr-1Mo steel tested over a range of stresses from 100 to 200MPa at 600°C are shown in Figure 2. Creep deformation consists of transient and accelerating creep stages and no obvious steady state stage is observed. In the higher stress region from 140 to 200MPa, minimum creep rate is observed in the relatively large strain range from 0.02 to 0.03. On the other hand, creep rate shows minimum value at small strain less than 0.01 and the accelerating creep stage onsets at the relatively small strain in the lower stress region from 100 to 120MPa, in comparison with those in the higher stress region. Consequently, significant decrease in creep rupture strength in the long-term may be caused by onset of accelerating creep stage at the relatively early stage of the creep deformation.

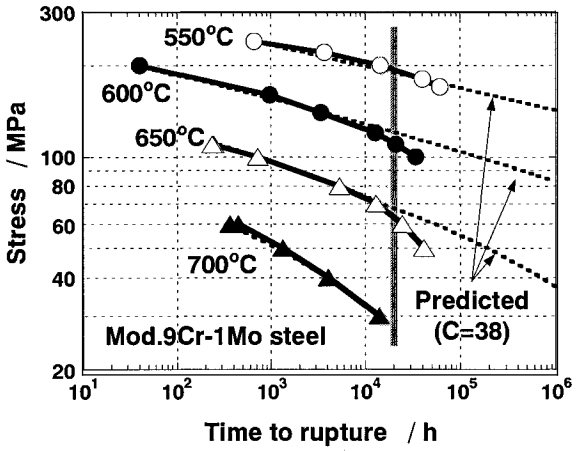


Figure 1: Stress vs. time to rupture curves of a Mod.9Cr-1Mo steel and the creep rupture life predicted from the short-term data whose rupture lives are less than 20,000h using a Larson-Miller parameter with a best fit parameter constant of 38.

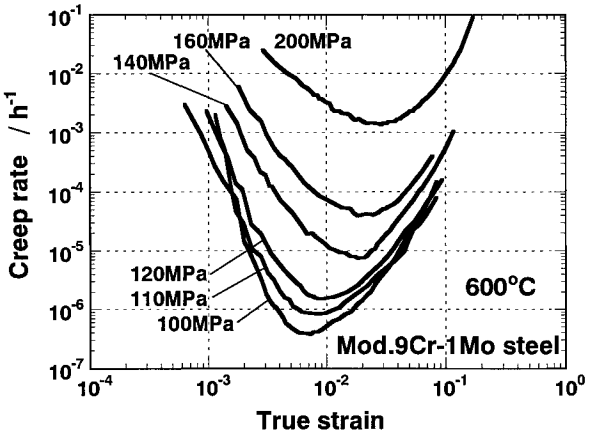


Figure 2: Creep rate vs. strain curves of a Mod.9Cr-1Mo steel at 600°C.

Bright field TEM images of the Mod.9Cr-1Mo steels (a) in the as tempered condition and the specimens creep ruptured at 600°C after (b) 971.2h at 160MPa, (c) 12,858.6h at 120MPa and (d) 34,141.0h at 100MPa are shown in Figure 3. Typical tempered martensite microstructure is observed in the as tempered condition (Fig. 3 (a)). Dislocation density of the steel in the as tempered condition is very high and the lath width is about 0.3 μm. Slightly recovered microstructure with increases in lath width and subgrain size and decrease in dislocation density is observed in the specimen creep ruptured after 971.2h at 600°C-160MPa (Fig. 3 (b)). Significant progress in recovery of the tempered martensite microstructure and annihilation of martensite lath structure is observed in the specimen creep ruptured after 12,858.6h at 600°C-120MPa (Fig. 3 (c)). On the other hand, features of the microstructure in the specimen creep ruptured after 34,141.0h at 600°C-100MPa (Fig. 3 (d)) are different from those of the other creep ruptured specimens. Significantly recovered region is observed along the prior austenite grain boundary (PAGB), however, the microstructure within grain is still fine in comparison with that in the vicinity of PAGB. Although time to rupture under the stress of 100MPa (34,141.0h) is about three times longer than that under the stress of 120MPa (12,858.6h), the subgrain size within grain of the former specimen is smaller than that of the latter one. Heterogeneous progress in recovery of tempered martensite microstructure is observed at low stress condition in contrast to homogeneous one at higher stresses. Bimodal distribution of the subgrain size was clearly observed only in the specimen creep ruptured at 600°C- 100MPa [10].

A similar phenomenon of preferential recovery in the vicinity of PAGBs has been also reported on a 1Cr-1Mo-0.25V turbine rotor steel as a degradation mechanism during long-term creep exposure [11]. It has been supposed that a preferential recovery occurred in the vicinity of PAGBs may promote the onset of accelerating creep stage and result in significant decrease in creep strength in the long-term. Therefore, if the stress dependence of the onset strain of accelerating creep stage observed for a Mod.9Cr-1Mo steel (Fig. 2) is a common feature for high chromium ferritic creep resistant steels, such changes in onset strain of accelerating creep stage may be available to define a boundary between short-term region and long-term one.

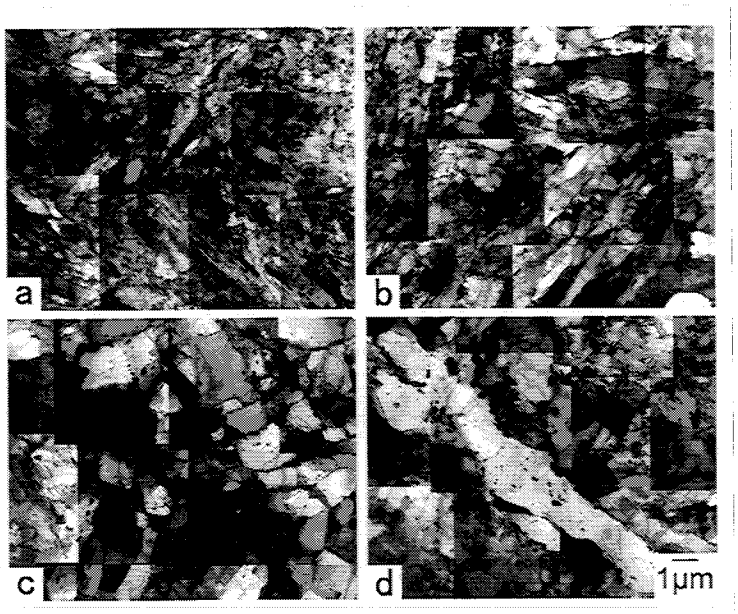


Figure 3: Bright field TEM images of the Mod.9Cr-1Mo steels (a) in the as tempered condition and the specimens creep ruptured at 600°C after (b) 971.2h at 160MPa, (c) 12,858.6h at 120MPa and (d) 34,141.0h at 100MPa.

Creep Strength Properties of a 12Cr-2W-0.4Mo-VNbCuB steel

Stress vs. time to rupture curves of a 12Cr-2W-0.4Mo-VNbCuB steel tested over a range of temperatures from 550 to 750°C are shown in Figure 4. The creep rupture lives predicted by a modified θ projection method [9] from the short-term creep rupture data indicated by the solid symbols whose rupture lives are less than about 1,000h, are shown by the dotted lines in Figure 4. Inflections of the relations between stress and time to rupture which result in overestimation of the predicted long-term creep rupture strength are clearly observed at the temperatures from 600 to 700°C.

Creep rate vs. strain curves of a 12Cr-2W-0.4Mo-VNbCuB steel tested over a range of stresses from 55 to 150MPa at 650°C are shown in Figure 5. Similar stress dependence of the creep deformation behaviour as shown in Figure 2 on the Mod.9Cr-1Mo steel is observed. Creep deformation of a 12Cr-2W-0.4Mo-VNbCuB steel also consists of transient and accelerating creep stages and the onset strain of the accelerating creep stage decreases with decrease in applied stress from about 0.03 at 150MPa to about 0.0025 at 55MPa.

Stress dependences of the onset strain of accelerating creep stage of a 12Cr-2W-0.4Mo-VNbCuB steel over a range of temperatures from 550 to 750°C are shown in Figure 6. Although the onset strain of accelerating creep stage increases with decrease in stress in the stress region higher than about 200MPa, it decreases with decrease in stress in the wide stress region lower than about 200MPa. Same stress dependence of the onset strain of accelerating creep stage has been reported on the similar high

chromium ferritic creep resistant steels [12]. Consequently, it has been supposed that decrease in the onset strain of accelerating creep stage with decrease in stress in the wide stress range is a common phenomenon for high chromium ferritic creep resistant steels.

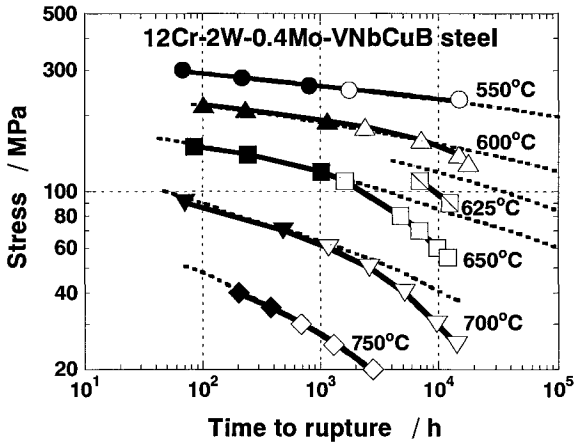


Figure 4: Stress vs. time to rupture curves and the creep rupture lives predicted by a modified θ projection analysis of a 12Cr-2W-0.4Mo-VNbCuB steel.

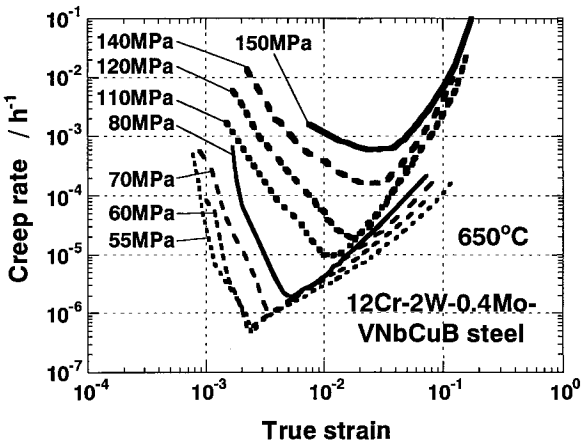


Figure 5: Creep rate vs. strain curves of a 12Cr-2W-0.4Mo-VNbCuB steel at 650°C.

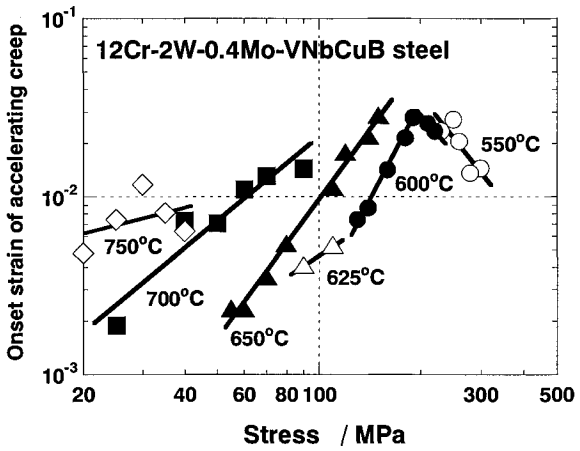


Figure 6: Stress dependence of the onset strain of accelerating creep stage of a 12Cr-2W-0.4Mo-VNbCuB steel.

Inflection of Stress vs. Time to Rupture Curve

Kimura et al. [7] have reported that recovery of tempered martensite microstructure of a Mod.9Cr-1Mo steel proceeds heterogeneously in the lower stress and long-term region, in contrast to homogeneous progress in the higher stress and short-term region. Recovery at the vicinity of prior austenite grain boundary is promoted by concentrated internal strain introduced by martensitic transformation, rapid diffusion rate and faster coarsening of precipitates on grain boundary, in contrast to those within grain. With increase in applied stress, however, recovery within the grain is also accelerated and the locally recovered region at the vicinity of the prior austenite grain boundary is easily extended within the grain with the assistance of higher external stress. Consequently, creep strength in the higher stress condition is significantly lowered with increase in applied stress. Such effect of applied stress on creep strength is thought to be a main factor which causes an inflection of stress vs. time to rupture curve. Moreover, stress condition where the stress vs. time to rupture curve indicates an inflection should correlate with strength property such as proof stress, and the correlations between those have been investigated.

Stress vs. time to rupture curves of a 12Cr-2W-0.4Mo-VNbCuB steel tested over a range of temperatures from 550 to 750°C are shown in Figure 7, with the stress conditions where the onset strain of accelerating creep stage is 0.012 and half of the 0.2% proof stresses at the temperatures. Good correspondence between not only the stress conditions where the onset strain of accelerating creep stage is 0.012 and half of the 0.2% proof stress, but also these stress conditions and the inflections of the stress vs. time to rupture curves are clearly observed. Consequently, a boundary between short-term region and long-term one in a stress vs. time to rupture diagram can be evaluated as a half of the 0.2% proof stress at the temperatures. It has been supposed that the reason for such good correspondence between half of the 0.2% proof stress and inflection of the curve is an occurrence of local plastic deformation as a result of micro scale yielding under a half of the 0.2% proof stress at the temperature. But the precise mechanism and the physical meaning of it should be investigated in the future.

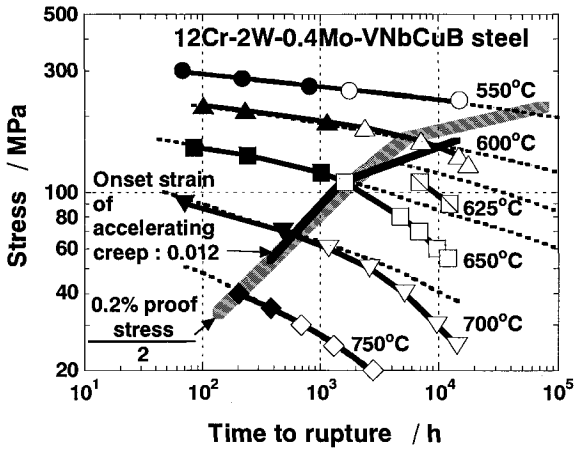


Figure 7: Comparison between the stress condition where the onset strain of accelerating creep stage is 0.012 and a half of the 0.2% proof stress of a 12Cr-2W-0.4Mo-VNbCuB steel.

Creep Life Prediction by Stress Range Partitioning Method

The boundary between short-term region and long-term one in a stress vs. time to rupture diagram where a slope of the relation between stress and time to rupture is small and large, respectively, can be estimated by considering a half of the 0.2% proof stress, and creep rupture data can be divided into two groups. In this section, long-term creep life prediction based on such stress range partitioning method will be discussed.

Long-term creep rupture life prediction method has been investigated using a Larson-Miller parameter on a Mod.9Cr-1Mo steel with the following four sets of the creep rupture data.

(1) All the creep rupture data
(2) Creep rupture data whose rupture life is less than 20,000h
(3) Creep rupture data whose rupture life is less than 20,000h and the applied stress is less than a half of the 0.2% proof stress at the temperatures
(4) Creep rupture data whose rupture life is longer than 1,000h and less than 20,000h and the applied stress is less than a half of the 0.2% proof stress at the temperatures

By comparing the predicted long-term creep rupture lives for the above four data sets with the best fit parameter constant of 32 to 38 and the constant value of 20, most proper result was obtained with the data set of (4) and a parameter constant of 20. Predicted creep rupture lives for the Mod.9Cr-1Mo steel using a Larson-Miller parameter with a parameter constant of 20 from all the creep rupture data and the proposed selected data indicated by large circles (data set of (4)) based on a stress range partitioning method are shown in Figure 8, described by fine dotted lines and bold broken lines, respectively. Although the long-term data up to about 60,000h are used for the prediction from all the creep rupture data, predicted 100,000h creep rupture strength are significantly overestimated (fine dotted lines).

On the other hand, 100,000h creep rupture strength are adequately evaluated from the proposed selected data (bold broken lines), even when the number of data used for prediction is only seven. From the above results, creep rupture data should be divided into two groups of higher stress, short-term region and lower stress, long-term one, by considering a half of the 0.2% proof stress at the temperatures for the proper long-term creep strength prediction of high chromium ferritic creep resistant steels. It has been concluded that the accuracy of long-term creep strength prediction of high chromium creep resistant steels can be improved by applying a stress range partitioning method based on a ratio of applied stress to a 0.2% proof stress and a Larson-Miller parameter with a constant of 20.

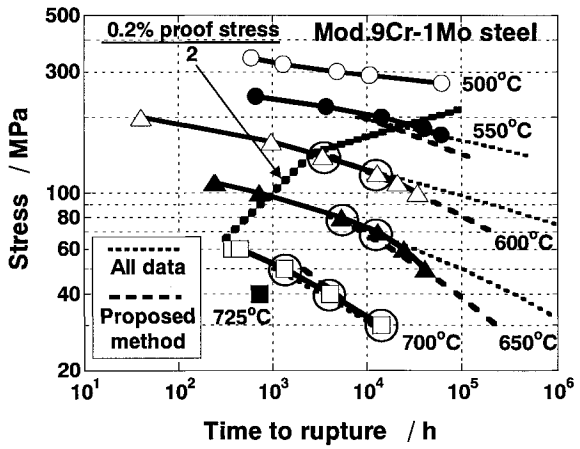


Figure 8: Predicted creep rupture lives of a Mod.9Cr-1Mo steel by a conventional method with all the creep rupture data (fine dotted lines) and a proposed one with the selected data indicated by large circles based on a stress range partitioning method (bold broken lines).

4 Conclusions

A defining method for a boundary between short-term region and long-term one in a stress vs. time to rupture diagram and improvement of long-term creep strength prediction of high chromium ferritic creep resistant steels have been investigated and the following results are obtained.

1. Corresponding to large drops in long-term creep strength, heterogeneous progress in recovery has been observed on a Mod.9Cr-1Mo steel.
2. The onset strain of accelerating creep stage of a 12Cr-2W-0.4Mo-VNbCuB steel decreases with decrease in stress in the wide stress region lower than about 200MPa.
3. Good correspondence between not only the stress conditions where the onset strain of accelerating creep stage is 0.012 and half of the 0.2% proof stress at the temperatures, but also these stress conditions and the inflections of the stress vs. time to rupture curves has been observed.
4. Good correspondence between half of the 0.2% proof stress and inflection of the stress vs. time to

rupture curve has been supposed to be caused by local plastic deformation as a result of micro scale yielding under a half of the 0.2% proof stress at the temperatures.

5. Proper prediction of long-term creep strength using a Larson-Miller parameter has been attained with the creep rupture data in the stress condition less than a half of the 0.2% proof stress and a parameter constant of 20 rather than a best fit value, which produces a serious overestimation.
6. It has been concluded that the accuracy of long-term creep strength prediction of high chromium ferritic creep resistant steels can be improved by applying a stress range partitioning method based on a ratio of applied stress to a 0.2% proof stress and a Larson-Miller parameter with a constant of 20.

5 References

[1] A. Nitta. "Energy Problem and High-Temperature Materials Technology in the 21st Century." Report of the 123rd Committee on Heat-Resisting Metals and Alloys, Japan Society for the Promotion of Science, Vol. 28, No. 3 (1997), p.157.

[2] F. Masuyama. "History of Power Plants and Progress in Heat Resistant Steels." ISIJ International. Vol. 41, No. 6 (2001), p.612.

[3] M. Ohgami, S. Araki, H. Naoi, T. Ogawa, H. Yasuda, H. Masumoto, and T. Fujita. "Development of a 9Cr-0.5Mo-1.8W Steel for Boiler Tubes." Tetsu-to-Hagané. Vol. 76, No. 7 (1990), p.1124.

[4] A. Iseda, A. Natori, Y. Sawaragi, K. Ogawa, F. Masuyama, and T. Yokoyama. "Development of High Strength and High Corrosion Resistance 12%Cr Steel Tubes and Pipe (HCM12A) for Boilers." The Thermal and Nuclear Power. Vol. 45, No. 8 (1994), p.900.

[5] M. Staubli, W. Bendick, J. Orr, F. Deshayes, and Ch. Henry. "European Collaborative Evaluation of Advanced Boiler Materials." Proceedings of the 6th Liège Conference on Materials for Advanced Power Engineering 1998, Liège, Vol. 5, Part 1 (1998), p.87.

[6] V. Foldyna, Z. Kubon, A. Jakobová, and V. Vodárek. Microstructural Development and Stability in High Chromium Ferritic Power Plant Steels. London, The Institute of Materials (1997), p.73.

[7] K. Kimura, H. Kushima, and F. Abe. "Heterogeneous Changes in Microstructure and Degradation Behaviour of 9Cr-1Mo-V-Nb Steel During Long Term Creep." Key Engineering Materials. Vols. 171-174 (2000), p.483.

[8] NRIM Creep Data Sheet. Tokyo, National Research Institute for Metals, No. 43 (1996).

[9] K. Maruyama, C. Harada, and H. Oikawa. "Formulation of Creep Curves and Rupture Lives for Long-term Creep Property Prediction with Special Reference to a 12 Cr (H46) Steel." Transactions ISIJ. Vol. 26 (1986), p.212.

[10] K. Kimura, H. Kushima, F. Abe, K. Suzuki, S. Kumai, and A. Satoh. "Microstructural Change and Degradation Behaviour of 9Cr-1Mo-V-Nb Steel in the Long Term Region." Proceedings of the Fifth International Charles Parsons Turbine Conference on Advanced Materials for 21st Century Turbines and Power Plant, Cambridge, U.K., July (2000), p.590.

[11] T. Matsuo, K. Kimura, R. Tanaka, and M. Kikuchi. "Degradation of 1Cr1Mo1/4V Steel at High Temperatures." Proceedings of the Fourth International Conference on Creep and Fracture of Engineering Materials and Structures, Swansea, U.K., April (1990), p.477.

[12] H. Kushima, K. Kimura, and F. Abe. "Long-term Creep Strength and Changes in Creep Deformation of High Cr Ferritic Creep Resistant Steels." Proceedings of the CAMP-ISIJ, Fukuoka, Japan, September, Vol. 14, No. 6 (2001), p.1289.

EVALUATION OF CREEP PROPERTIES AND MICROSTRCTURES ON THERMO-MECHANICAL AND MAGNETIC TREATED 9Cr FERRITIC STEELS

Hiroshi Okubo, Seiichi Muneki, Hirokazu Okada, Katsumi Yamada, Masaaki Igarashi and Fujio Abe
Materials Creation Research Group, Materials Engineering Laboratory
National Institute for Materials Science
1-2-1, Sengen, Tsukuba, Ibaraki, 305-0047,Japan

Abstract

Effect of thermomechanical and magnetic treatment on creep characteristics of advanced heat resistant ferritic steels for USC power plants has been investigated to explore fundamental guiding principles for improving creep rupture strength at elevated temperatures over 873K. A model steel with a composition of Fe-0.08C-9Cr-3.3W-3Co-0.2V-0.05Nb-0.05N-0.005B-0.3Si-0.5Mn (in mass%) has been prepared by vacuum induction melting. Creep tests and microstructural observations were performed on the thermomechanical and magnetic treated specimen after tempering. New thermomechanical treatment without magnetic field showed some improvement in creep strength comparing with ordinally normalized and tempered specimen. Further improvement was observed in the specimen that had been exposed to a magnetic field during transformation into martensite. From the results of microstructural observation, it was found that the finely distributed precipitates such as MX and $M_{23}C_6$ caused this improvement. And it was suggested that the magnetic treatment at martensitic transformation increase the precipitation sites during tempering, resulting in increasing the amount and preventing the growth of the precipitations.

Keywords: USC power plant, thermomechanical heat treatment, magnetic field, heat resistant ferritic steel

1. Introduction

High Cr ferritic steels such as 9Cr-1MoVNb steel (ASME SA335 P91) have successfully been used for large diameter and thick section boiler components such as main steam pipe and header in super critical (SC) boilers in fossil-fired power plants [1]. Recent trend to utilization of clean energy leading to protection of global environment has been accelerating the application of ultra super critical (USC) boilers, which are operated with higher efficiency in power generation than conventional ones and thus release less amount of carbon dioxide etc. [2,3]. The USC boiler requires heat resistant materials with improved creep rupture strength at elevated temperatures over 873K, because of the increase in operating temperature and pressure of the steam used. Addition of W to the steel has been found to be effective to increase creep rupture strength at high temperatures and has been already used in some developed steels for the USC boilers [3].

Many researches and developments have been actively performed to achieve further improvement of high Cr Ferritic steels [4,5,6]. But these attempts were mainly by alloying design. And there were a few attempts to improve high Cr ferritic steels by thermomechanical heat treatment [7,8]. Effect of ausforming and marforming processes on creep properties were reported to give fine distribution of the precipitates such as MX (M: V, Nb etc) and $M_{23}C_6$ (M: Cr, Fe, W, Mo, etc) but suppress strong texture resulting in reduction of creep rupture life [8]. In this paper, new thermomechanical processes with magnetic field were applied to a 9Cr-3.3W-3Co-Nb-V-B model steel to control the initial microstructure.

Next, creep tests for thermomechanically treated samples are performed after tempering. Then, effects of thermomechanical and magnetic treatment on creep properties and microstructure are discussed.

2. Experimental Procedure

A 9Cr-3.3W-3Co-Nb-V-B model steel used in this study was melted as a 100kg ingot in a vacuum induction furnace. The chemical composition of the steel is given in Table 1.

Table 1 Chemical composition of the steel used (mass%).

C	Si	Mn	Cr	W	Co	V	Nb	N	B	Fe
0.08	0.3	0.5	9.0	3.3	3.0	0.2	0.05	0.05	0.005	Bal.

The ingot was homogenized for 4h at 1473K and reheated at 1273K for pressing and rolling to 16mm square bars. DSC (Differential Scanning Calorimetry) measurement was conducted on heating and cooling between the ambient temperature and 1373K at a rate of 10K/min to analyze the transformation and precipitation behavior of the steel. The relevant transformation temperatures, A_{c1}, M_s and M_f determined are 1096, 658 and 521K, respectively. Thermomechanical and magnetic treatment (TMMT) was carried out by using the equipment with superconducting magnet, as shown in Fig.1. The round bar type specimen as shown in Fig.2 was used for TMMT.

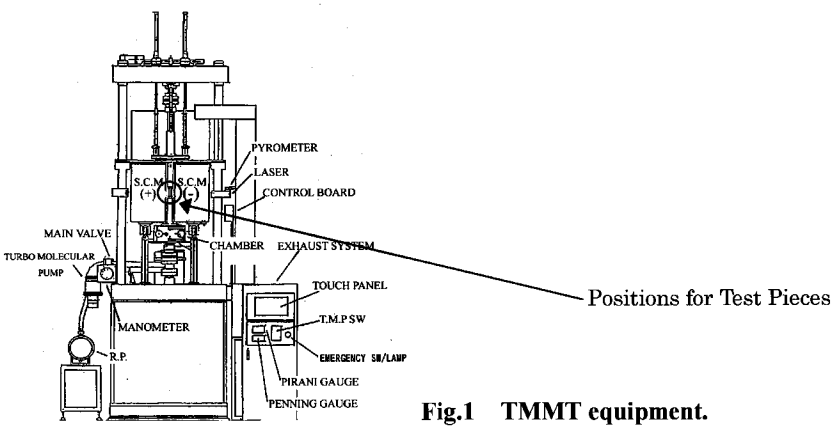


Fig.1 TMMT equipment.

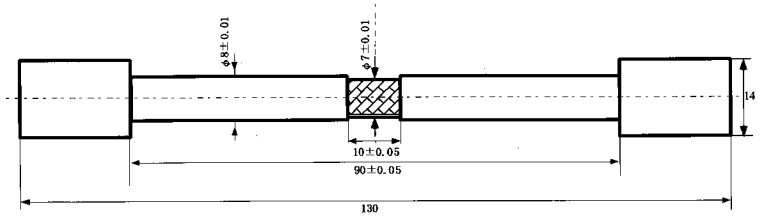


Fig.2 Geometry of specimen for TMMT (mm).

Several treatments were performed on the basis of the following diagram in Fig.3.

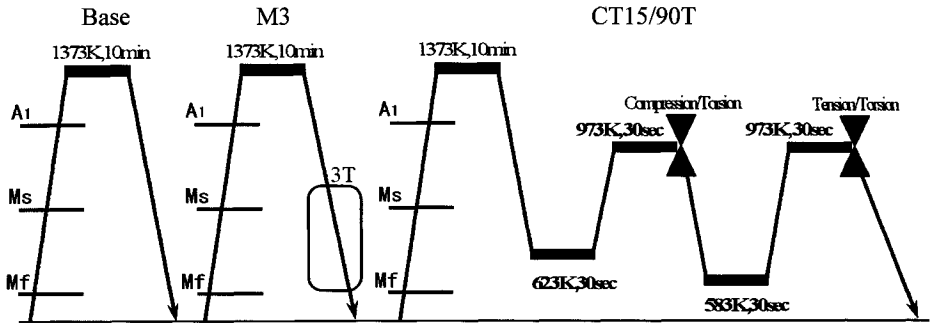


Fig.3 Schematic drawing of several kinds of heat treatments in TMMT.

At first all samples were normalized at 1373K for 10min. Base was given only normalization without the effect of magnetic field and deformation. M3 was given magnetic field of 3 T on cooling stage during martensitic transformation. CT15 and 90T were thermomechanically treated samples. After normalization, as a first step samples were cooled down to below M_s temperature: 623K for partially transformation to martensite, next reheated to 973K and then deformed. This series of partial martensitic transformation and deformation at 973K was repeated, as shown in Fig. 3. The temperature of second martensitic transformation was 40K lower than that of the first one. First and second deformations were reversed in order to prevent the conspicuous change of shape of the prior austenite grain. CT15 was compressed for 15% at first and then elongated for 15%. 90T was given clockwise torsion for 90 degrees and then given counter-clockwise torsion for 90 degrees.

Specimens for creep tests were cut out from the TMMT specimen after tempering at 1043K for 4h, as shown in Fig. 4. The creep tests were carried out at 923K with 120MPa. The microstructures of the steel were examined using an optical microscopy and a field emission scanning electron microscopy (FE-SEM) operated with 10kV acceleration voltage.

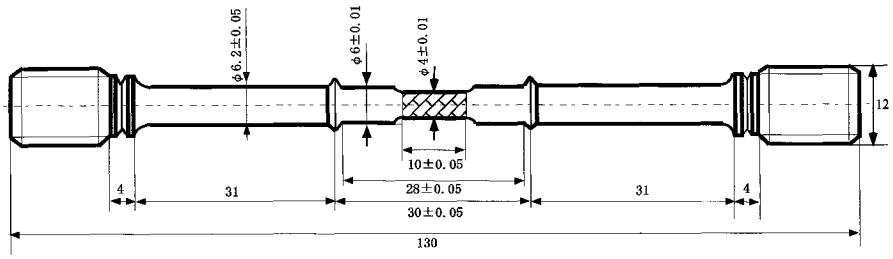


Fig.4 Geometry of specimen for creep tests (mm).

3. Results and Discussion

Fig.5 shows typical optical micrographs of Base and M3 samples before tempering. Both samples show fully martensitic structure without δ ferrite. Prior austenite grain sizes of Base and M3 samples were about 70 and 90 μ m in diameter, respectively.

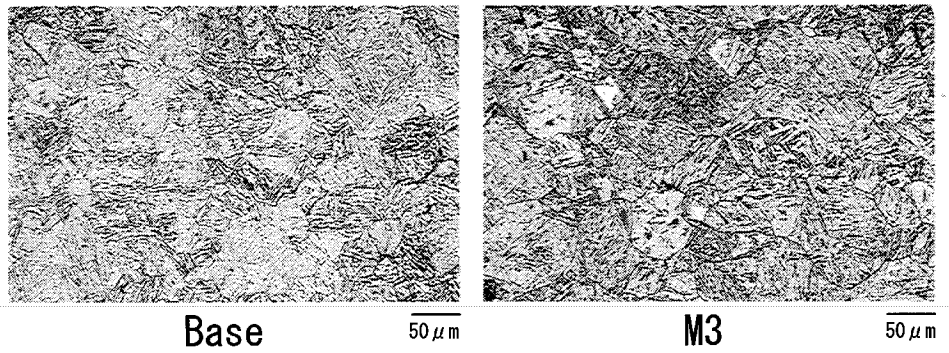


Fig.5 Optical micrographs showing the effect of magnetic field after normalization.

Figs.6 (a) and (b) show creep curves of Base, CT15 and M3 samples and the corresponding creep rate vs. time curves of them crept at 923K with 120MPa. Base ruptured at about 2000h i.e. half of the creep life of CT15. Creep strength of M3 was remarkably improved only by the effect of magnetic field. Initial creep rates of all three specimens exhibited similar values, but the creep rates in the transition creep region and the minimum creep rates decreased with time from Base, CT15 to M3 in order, as shown in Fig.6 (b). As a result the creep life of M3 drastically increased about three times as long as that of Base.

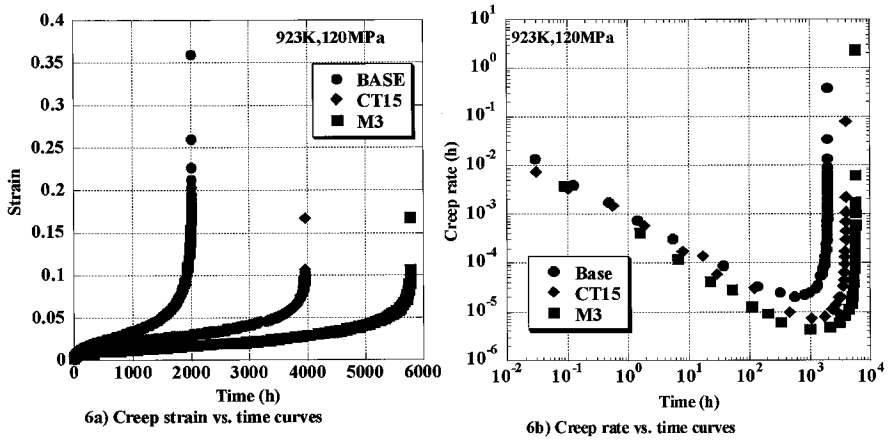
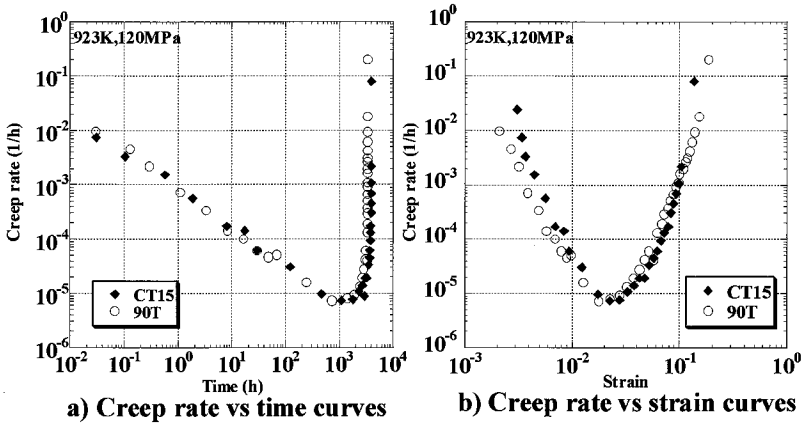


Fig.6 Creep curves of the specimens crept at 923K with 120MPa.

Figs.7 (a) and (b) show the effect of deformation mode on the creep curves. As clearly shown in these figures, there was no clear effect on creep properties by the difference of the deformation mode: compression- tension (CT15) and clockwise-counterclockwise torsion (90T). Both samples showed similar trend from the transition to acceleration creep.



a) Creep rate vs time curves **b) Creep rate vs strain curves**

Fig.7 Effect of deformation mode on creep properties the specimens at 923K with 120MPa.

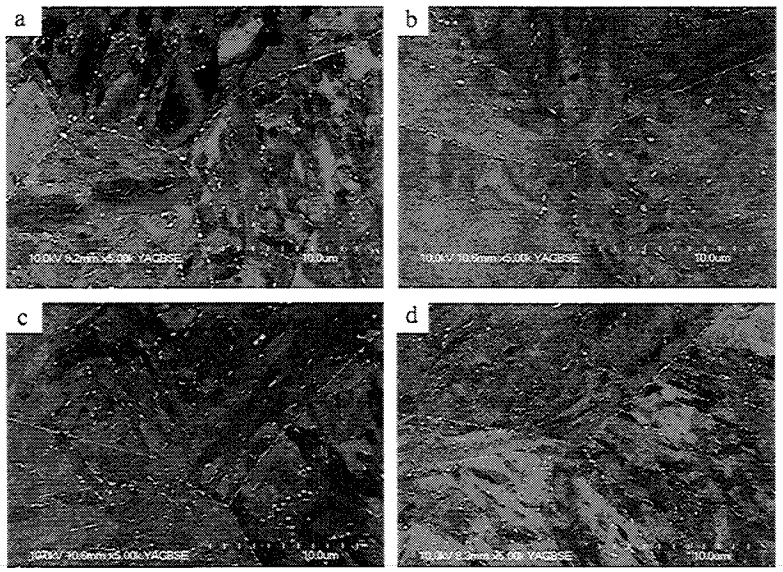


Fig.8 Back scattered electron images of Base(a),CT15 (b),90T(c) and M3(d) after tempering at 1043K for 4h.

Fig.8 shows the back scattered electron images of the specimens after tempering. In these

micrographs the rough distribution of individual blocks or packets can be identified from the channeling contrast. Although the aim of this thermo-mechanical and magnetic treatment was to control the martensite sub-structure and to get fine distribution of precipitates such as MX and $M_{23}C_6$, there was no clear difference between the four samples in size of blocks or packets. Further investigation using techniques such as orientation imaging microscopy is needed to identify the effect of thermo-mechanical and magnetic treatment on martensite sub-structure. Anyway, in this paper, to identify the effects of the treatment on precipitation behavior, SEM observation on precipitates and quantitative analysis of extracted residue were conducted on Base and M3, which showed most superior creep resistance.

Fig.9 shows secondary electron images of the specimen after tempering. There is no clear different in size and distribution of $M_{23}C_6$ that precipitated along prior austenite grain boundaries between Base and M3, as shown in Figs.9 (a) and (b). On the other hand, finer and more homogeneous distribution of $M_{23}C_6$ was found in M3 rather than Base at lath, block or packet boundaries by comparing Figs.9 (c) and (d).

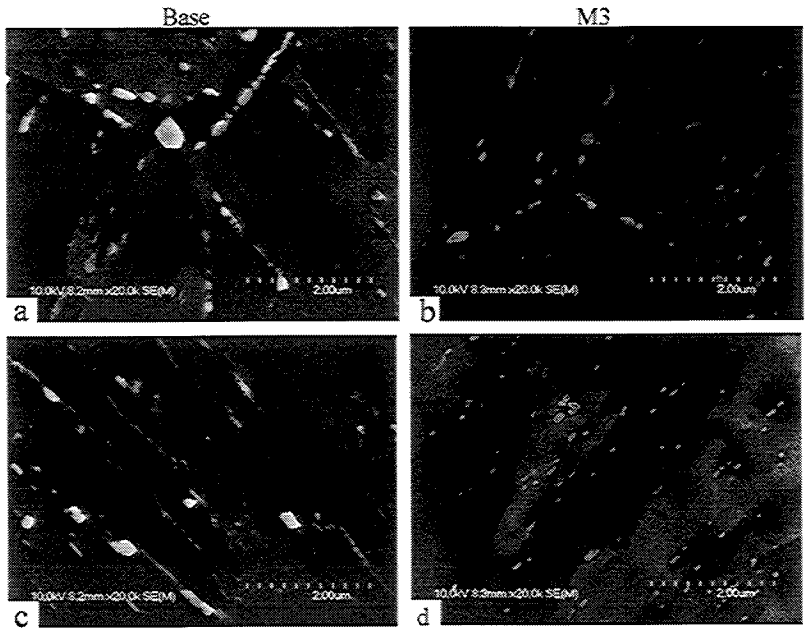


Fig.9 Secondary electron images of Base: (a) and (c) , and M3: (b) and (d) after tempering at 1043K for 4h.
(a) and (b) show the images for prior austenite grain boundary.
(c) and (d) show the images for inside the grain.

Figs.10 (a) and (b) show the results of quantitative analysis of the extracted residue for Base and M3 before and after tempering at 1043K for 4h. The analyzed elements were divided

into two groups: Fig.10 (a) for V, Nb and Fig.10 (b) for Fe, Cr, W corresponding to MX and $M_{23}C_6$, respectively. As for Fe, Cr and W, the precipitates before tempering were considered to be not $M_{23}C_6$ but Fe_3C, because the Fe was enriched in the precipitates. There was little difference in amount of MX and $M_{23}C_6$ precipitates between the two samples before tempering. Precipitation of both MX and $M_{23}C_6$ mainly occurred during tempering and total amount of precipitates of M3 was about 7% larger than that of Base. Thus it was suggested that the magnetic field during martensitic transformation does not directly influence the precipitation at martensitic transformation but increase the precipitation sites, resulting in finer distribution and larger amount of precipitations during tempering.

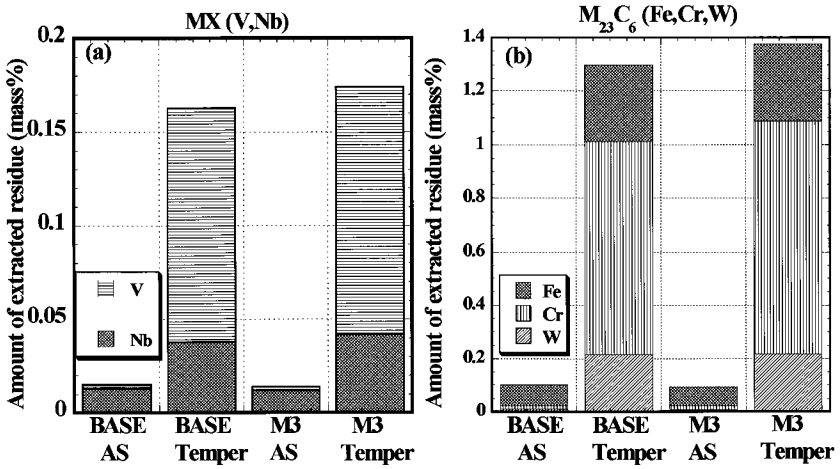


Fig.10 Amount of extracted residue of (a) MX and (b)$M_{23}C_6$ before and after tempering at 1043K for 4h.

4. CONCLUSION

To explore the further improvement in creep rupture strength over 873K of advanced heat resistant ferritic steels for USC power plants, several kinds of thermomechanical and magnetic treatments on a model steel of Fe-0.08C-9Cr-3.3W-3Co-0.2V-0.05Nb-0.05N-0.005B-0.3Si-0.5Mn have been examined in order to obtain different initial microstructures from the conventional normalization and tempering treatment. New thermomechanical treatments without magnetic field showed drastic improvement in creep strength comparing with normalized and tempered specimen.

Further improvement was observed in the only magnetic treated specimen.
From the results of microstructural observation, it was found that the finely distributed precipitates such as MX and $M_{23}C_6$ inside the grain caused this improvement. And it was suggested that the magnetic treatment at martensitic transformation increased the precipitation sites during tempering, resulting in increasing the amount and preventing the growth of the precipitations during tempering.

Evaluation of the creep properties of the samples with complex thermomecanical and magnetic treatments are in progress and will be reported in near future.

ACKNOWLEDGMENT

The authors would like to express their sincere gratitude to Mrs. Wakako Moriiwa and Mrs. Toshiko Ishizuka for their sincere collaboration in experiments.

REFERENCES

[1] V.K.Sikka, C.T.Ward and K.C.Phomas, "Modified 9Cr-1Mo Steel - An Improved Alloy for Steam Generator Application", in ASM Int. Conf. Production, Fabrication, Properties and Application of Ferritic Steels for High Temperature Applications, Warren, PA. Oct.6-8 (1981).

[2] K.Muramatsu, "Development of Ultra-Super Critical Plant in Japan" , in Proc. Advanced Heat Resistant Steels For Power Generation , 27-29 April, Miramar Palace, San Sebastian, Spain, (1998), 543.

[3] F.Masuyama, "New Developments in Steels for Power Generation Boilers", in Proc. Advanced Heat Resistant Steels For Power Generation , 27-29 April, Miramar Palace, San Sebastian, Spain, (1998), 33.

[4] M.Igarashi, S.Muneki and F.Abe, "Microstructure Control of Martensitic Phase Matrix in Advanced Ferritic Steels for USC Boilers to Achieve Long Term Stability", in Proc. of the 6th Liege Conf. on Materials for Advanced Power Engineering, Oct., Liege, Belgium, (1998), I.637-646.

[5] M.Igarashi, S.Muneki, H.Kutsumi, T.Itagaki, N.Fujitsuna and F.Abe, "A new Concept for Strengthening of Advanced Ferritic steels for USC Power Plant", in Proc. of 5th Int. Charles Parsons Turbine Conf., July, Cambridge,(2000),334

[6] F.Abe, T.Horiuchi, M.Taneike, S.Muneki and H.Okada, "Microstructure Design near Grain Boundaries for Creep Resistant Tempered-Martensitic 9Cr Steels for 650℃ USC Boilers", Creep Deformation: Fundamentals and Applications, Edited R.S.Mishra, J.C.Earthman and S.V.Raj, TMS,(2002),341

[7] A.Matsuzaki, Y.Saito, O.Watanabe, C. Shiga and I.Nakagawa, "Effect of Thermo-Mechanical Control Process on Mechanical Properties of 9Cr-1Mo-V-Nb Steel", Tetsu-to-Hagane, 7 (1990), 68 *(in Japanese)*

[8] S.Muneki, M.Igarashi, K.Yamada and F.Abe, "Effect of Thermomechanical Heat Treatment Through Multiple Pass Rolling on Creep Characteristics of High Cr Ferritic Heat Resistant Steels", in Proc. 1st Int. Conf. on Advanced Materials Processing, IMEA, November, Rotorua, New Zealand,(2000),283-288

SECTION 3

ADVANCED STEAM POWER PLANT

3.4. Steam Oxidation and Coatings

1600

OXIDATION OF ADVANCED FERRITIC / MARTENSITIC STEELS AND OF COATINGS IN FLOWING STEAM AT 650 °C

Reinhard Knödler
Alstom Power Support, 68309 Mannheim, Germany

Brendon Scarlin
Alstom Power, 5401 Baden, Switzerland

Abstract

Highly efficient, advanced power plants must operate at high steam temperatures of up to 650 °C. It is necessary at such temperatures to use materials with high creep strength and sufficient oxidation resistance in the service environments. Several high Cr steels have been developed which have good mechanical properties at > 600 °C (e.g. E911, HCM12A, P92). However, at these temperatures, the materials suffer from rapid oxidation in steam which reduces the load-bearing cross-section. Furthermore, the thick oxide scales tend to spall, leading to erosion damage of turbine blades.

Within the COST522 programme the oxidation of new ferritic / martensitic steels with different compositions and of coatings were tested in flowing steam. In addition, mechanisms of steam oxidation were investigated and ways to improve oxidation resistance were outlined. The new steels developed in COST 522 and also some coatings showed very low oxidation rates. Preliminary results are reported on the effect of temperature and time of exposure. The analysis of the morphology and composition of oxide scales enables clarification of steam oxidation mechanisms. Special attention was paid to the spallation behaviour of the steels and the role of operating conditions (thermal cycling).

The results obtained from laboratory tests and from field trials in operating power plants are in good agreement.

Keywords: Steam oxidation, ferritic steels, spallation, oxide scales

Introduction

Highly efficient, advanced power plants will operate at high steam temperatures of up to 650 °C. It is necessary at such temperatures to use materials with high creep strength and sufficient oxidation resistance in the service environments. Several high Cr steels have been developed which have good mechanical properties at > 600°C (e.g. E911, HCM12A, P91, P92). However, at these temperatures, the materials suffer from rapid oxidation in steam which reduces the load-bearing cross-section. Furthermore, thick oxide scales tend to spall, leading to erosion damage of turbine blades.

Materials with high creep strength and high oxidation resistance are important for supercritical boilers [1, 11], as well as for turbines [2, 13]. Tests have been carried out in different experimental arrangements [3, 4, 6]. Field tests in power plants are under way and first results have been obtained [8, 9,12].
It is obvious from several papers, that oxidation of ferritic Cr-steels in steam is much more pronounced than oxidation in air [5, 8]. This was proposed to be due to the formation in water vapour of chromic acid [7], which is volatile at 650 °C. This, in turn, causes a depletion in chromium, which accelerates oxidation. A comprehensive summary of the literature published so far is [15].

Within the European COST 522 project a number of participants from different countries formed an „oxidation subgroup“ which aims at determining oxidation rates of conventional and new ferritic / martensitic steels. Together with creep tests, welding tests, metallographic analysis and other tests, this will help to reach the goal of COST 522: to develop advanced steels for higher temperatures.

In the following, results of tests are reported on oxidation of advanced alloys, developed in COST 522. In addition, scale morphologies and spallation characteristics were investigated. Comparisons with field tests conclude this paper. Preliminary results were presented in [10].

Experimental and test materials

The samples were exposed to superheated steam using a re-circulating arrangement. It operates at ambient pressure at 650 °C. The steam has a flow velocity between 150 and 300 ml/h, which corresponds to about 4 - 8 cm/s (0.01 kg /m^2 s). De-ionized water with no additives was used. By continuous bubbling nitrogen through the reservoir, the oxygen content of the steam was kept below 20 ppb. The arrangement is shown in fig. 1.

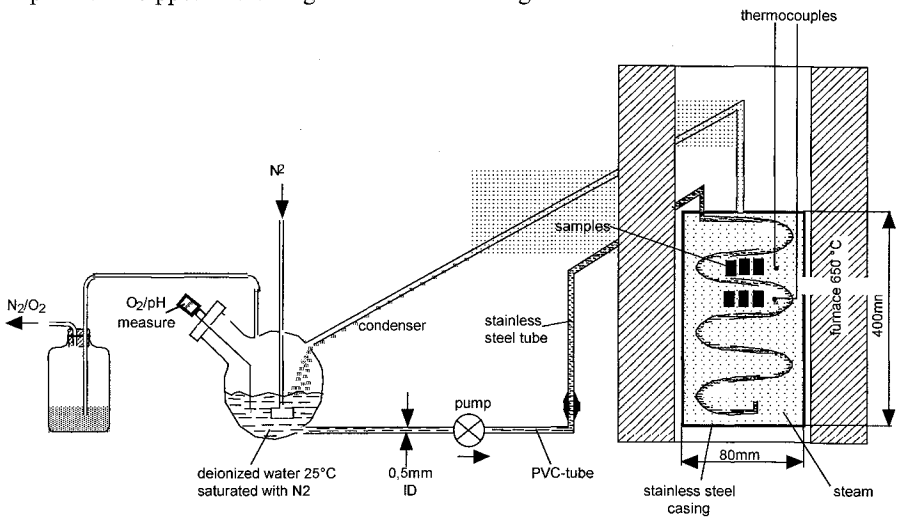


Fig. 1: Experimental arrangement for testing in circulating steam

The samples had a surface area of about 6 cm^2 and were fine-ground with 1200 Struers. In order to measure the oxygen uptake, the weight of the samples was determined after about every 300 h. For this purpose, they were cooled down slowly in the furnace and again slowly heated up. In special experiments rapid cooling was applied by removing the samples from the hot furnace directly into ambient air.

The thickness of the oxide scale after exposure was determined on metallographic cross sections. In the case of Cr steels the scale consists of an outer magnetite scale (Fe_3O_4) and an inner Cr-Fe- spinel. The interface between the two scales remains unchanged during oxide growth. Thus, the magnetite grows at the interface to the steam by iron ions migrating through

the two scales and taking-up oxygen from the steam. The spinel grows at the interface to the alloy by taking-up oxygen which migrates through the two scales.

The compositions of the materials tested is given in table 1.

Table 1: Compositions of steels investigated

ALLOY	Cr	Mn	Ni	Co	W	Mo	V	Nb	N	C	Si	Al
FB2	9.3	0.8	0.16	1	0	1.5	0.2	0.05	0.02	0.13	0.05	0.005
ST22	2.2				1.5	0.1					0.3	
P92	9	0.4	0.2		2	0.5				0.13	0.4	
E911	9	0.5	0.2		1	1	0.2	0.08	0.05	0.1	0.2	
FB6	11.3	0.1	0.15	3	0	1.5	0.2	0.07	0.02	0.15	0.13	0.003
FB8	11.1	0.09	0.1	3	0	1.5	0.2	0.07	0.02	0.18	0.1	0.005
CB8	10.8	0.2	0.1	3	0	1.5	0.2	0.06	0.02	0.17	0.26	0.023
1.4541	18	< 2	10							0.1		
1.4562	27	< 2	30			6				0.01		

P92 was taken as reference material which all participants of the oxidation subgroup will test. This ensures that the testing equipment of the different laboratories are compatible with each other.

Results

Relationship between weight change and scale thickness

A linear relationship between scale thickness and weight gain was obtained, if no spallation occurred. This is shown in fig. 2. It can be seen that a factor of 10 exists between scale thickness in µm and weight increase in mg/cm2. The density of the oxides can be calculated from this to be about 3.6 g/cm^3, corresponding to a porosity of roughly 30 %.

The diamonds in fig. 2 represent data for our usual operation mode (samples cooled down every 335 h). They match quite well the dotted line. However, if the operation mode is completely isothermal (no cooling during exposure), the circled values are obtained. They are clearly above the dotted line, which signifies a higher density of the "isothermal" oxide scale. In turn, this means that with the thermally cycled samples (represented by the diamonds) spallation starts. For the 2% Cr-steel ST22 spallation is so strong that it can be seen even visually. This can be seen from the comparably low weight increase (i.e. loss of scale).

Morphology of oxide scales on 9% Cr steels

As shown in fig. 3, scales consist essentially of 2 types of layers: a Cr-Fe-spinel phase at the interface to the base metal and a magnetite phase on top of the spinel. For "short" exposure times the original surface is still visible as a boundary between the spinel and the magnetite. However, after longer times, this boundary moves into the base material because the oxide layers spall. Spallation usually starts in the magnetite layer, as can be seen in fig. 3, where part of the magnetite will spall off soon. However, it is not unusual that the complete magnetite spalls. Very rarely is the spinel layer observed to spall. It can be assumed, that after spallation of the magnetite layer the remaining spinel layer will be gradually transformed into magnetite.

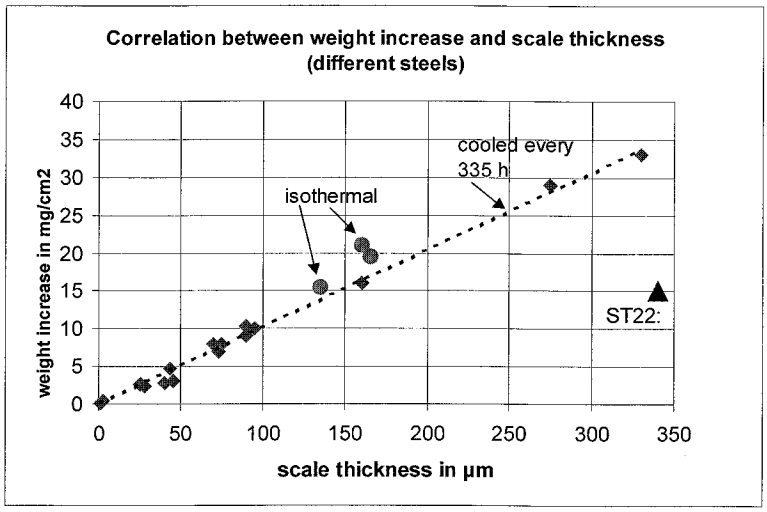


Fig. 2: Correlation between scale thickness (spinel + magnetite) and weight gain for 9-12% Cr-steels and on 2% Cr-steel. Diamonds and dotted line: samples cooled down every 335 h. Circles: isothermal operation. ST22: strong spallation.

Hematite instead of magnetite could be found sometimes in field tests. The reason for this undesired compound (because of its poor adherence properties) could be the steam chemistry with too much oxygen. However, these effects are still in the process of investigation.

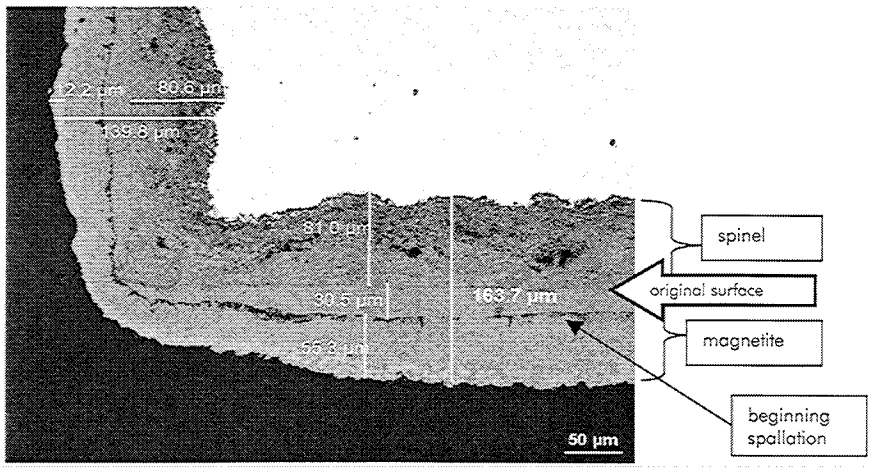


Fig. 3: Oxide scale on E911 after 3600 h at 650 °C.

Spallation behaviour

Spallation is a serious problem, because the spalled hard particles can cause damage downstream to the turbine components. Most alloys are sensitive to spallation, because the thermal expansion coefficients of the scales differ considerably from the respective base material. This is shown in fig. 4:

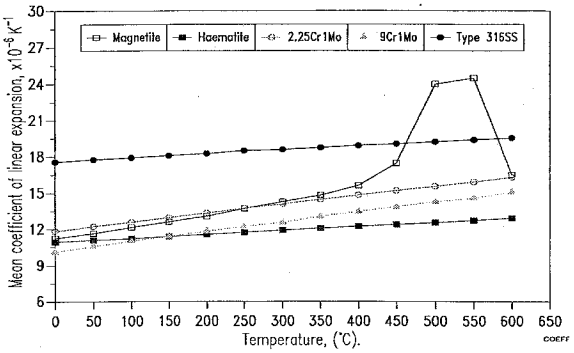


Fig. 4: Thermal expansion coefficients of magnetite, hematite and alloys (J. Armitt, D.P. Holmes, et.al., EPRI Report No. FP-686 (1978

The influence of thermal cycling and of operation time on the spallation was investigated for the isothermal mode and after quenching the samples in water (to induce spallation). Fig. 5 shows the behaviour of ST22 and fig. 6 the behaviour of P92 after relatively short exposure times (742 h – 1820 h). It can be seen that:

- with the 2% Cr-steel there is strong spallation with no difference between the isothermal and the thermal cycling mode.
- with the 9% Cr-steel P92 no spallation occurred up to the exposure time of 1820 h, neither under isothermal nor under thermal cyclic conditions.

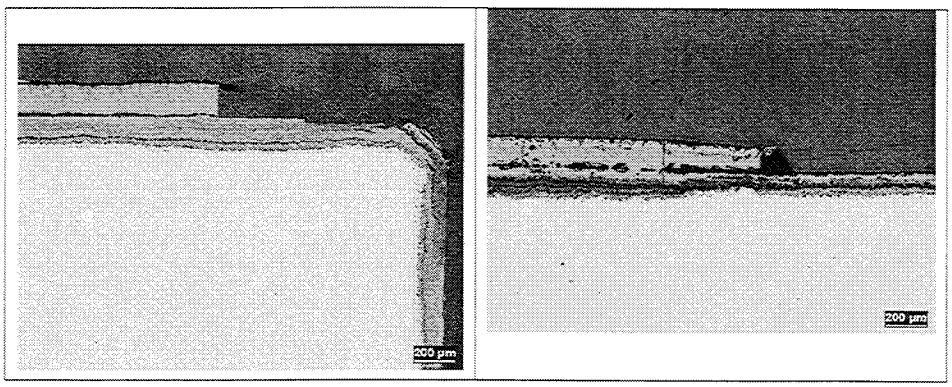


Fig. 5: Spallation of ST22 at 650 °C. Left: isothermal exposure for 1440 h, scale thickness max. 320 µm. Right: quenched in water after 742 h, scale thickness max. 280 µm

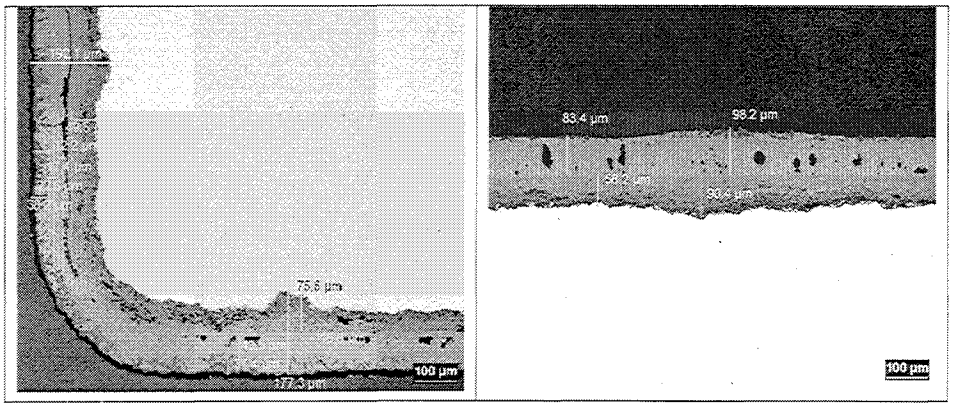


Fig. 6: Exposure of P92 at 650 °C. No spallation observed. Left: isothermal exposure for 1440 h, scale thickness about 165 µm. Right: quenched in water after 742 h and 1820 h, scale thickness about 180 µm. Please note the different scale as compared to fig. 5.

However, after longer exposure times spallation could be observed to begin also with the 9% Cr-steels. These effects could only be seen after careful preparation of cross sections, using vacuum infiltration to preserve the loose sections of the scale. Fig. 7a and 7b shows areas of spallation with P92 after 3600 h at 650 °C.

Long-time oxidation characteristics of P92 and ST22

Fig. 8 shows the kinetics of oxidation of the reference material P92 and (as comparison) for the 2% Cr-steel ST22. It can be seen, that the oxidation rate of ST22 is higher than P92 by at least a factor of 3. The rate law of P92 is parabolic until about 2000 h and then deviates towards a slower rate. This behaviour can be a sign of spallation of small parts of the outer scale.

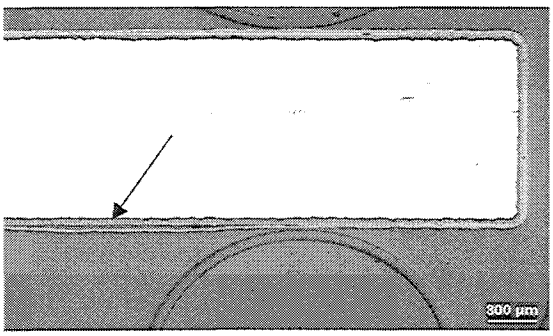


Fig. 7a: Beginning of spallation of P92 after 3600 h at 650 °C (see arrow). Thermal cycling every 1000 h.

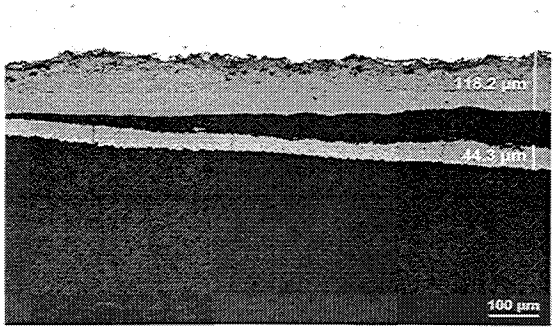


Fig. 7b: Magnified section of fig. 7a, showing spallation of part of the outer magnetite layer.

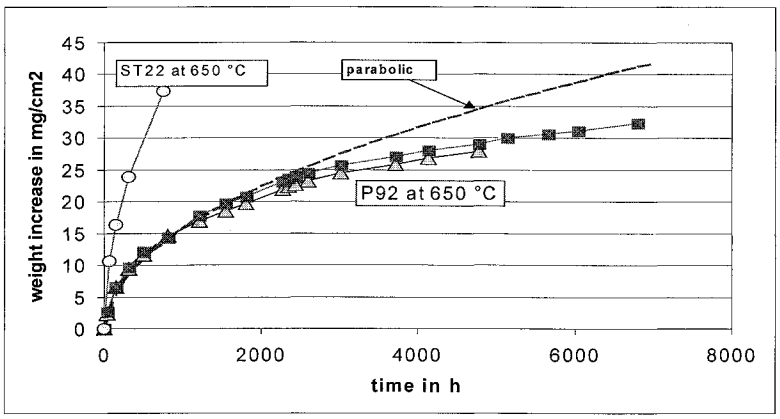


Fig. 8: Weight increase of P92 and ST 22 at 650 °C. According to fig. 2 a weight increase of 30 mg/cm2 corresponds to a scale thickness of about 300 µm.

Oxidation characteristics of new alloys

Some of the newly developed alloys have been tested in steam atmosphere at 650 °C for more than 5000 h. The results are shown in fig. 9 together with the reference P92.

It can be seen, that the new 11% Cr- alloys FB8 and CB8 exhibit only about 1% of the oxidation rate of P92. By applying the correlation of fig. 2 , this means that after about 10.000 h FB8 will show a scale thickness of only about 8 µm. The rate law is nearly parabolic, as it is with P92.

FB2 with 9% Cr shows higher values which tend to come near those of P92 after longer times. FB6 with 11% Cr is still lower than P92, however, not as low as FB8 and CB8, despite the same Cr-content. It is not yet clear, what causes this mismatch, but the higher Al-content of FB8 and CB8 could be an explanation. It is also not clear why FB6 and FB2 are different in the rate law, which is almost linear.

For P92 and FB8 – for which parabolic growth was obtained – the rate constants are $2.6*10^{-7}$ $g^2/cm^2/h$ and $1.5*10^{-11}$ $g^2/cm^2/h$, respectively. For CB8 the rate constant is obviously $< 10^{-11}$.

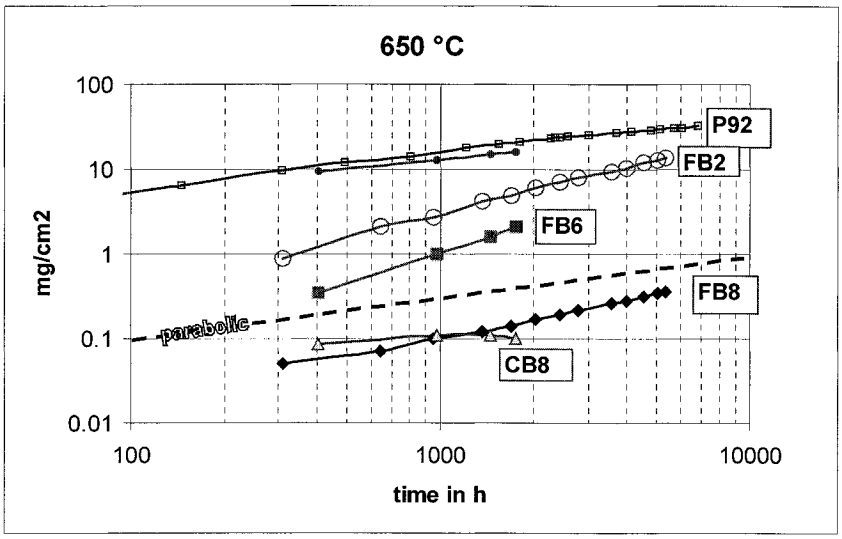


Fig. 9: Oxidation rates of new alloys at 650 °C. As reference P92 is plotted (two different runs, to show the scatter). The dashed line represents a parabolic behaviour. Samples were air-cooled at every data point.

Oxidation kinetics of nickel coatings on low-alloyed steels

Oxidation resistant coatings on 9% Cr-steels can be a viable solution to the oxidation problem. Such coatings can be applied on steels with high creep strength , which have usually poor oxidation resistance. Coating materials investigated so far are aluminium and electroless nickel. The work on aluminium will be presented elsewhere [14]. In the following the nickel work is described.

Electroless nickel with a P-content of 12% was applied to different base materials with a thickness of about 50 µm. After exposure times of up to 5000 h the oxidation stability of such components turned out to be very high. Fig. 10 shows the weight change , compared to P92. It can be seen that all of the coatings are oxidized with considerably lower rate than uncoated P92. Even if the plain, non-alloyed steel St37 is coated, only negligible oxidation is observed. Please notice, that at each data point in fig. 10 the samples were cooled down.

The rate law is clearly non-parabolic, which points to an oxidation process which is not controlled by diffusion. One of the reason could be cracks in the coating, which allows oxidation products from the base material to come to the surface. As example a cross section is shown in fig. 11. A thin oxide scale – consisting of iron oxides - on top of the nickel coating (about 10 µm after 3600 h at 650 °C) and at the interface to the base material can be seen. This

is especially pronounced in the vicinity of the crack , where oxide growth is increased. This could lead to the observed non-parabolic growth rate. If crack formation can be reduced or avoided by proper application and optimisation of the coating, the rate of oxide growth can be further improved, also for long time service.

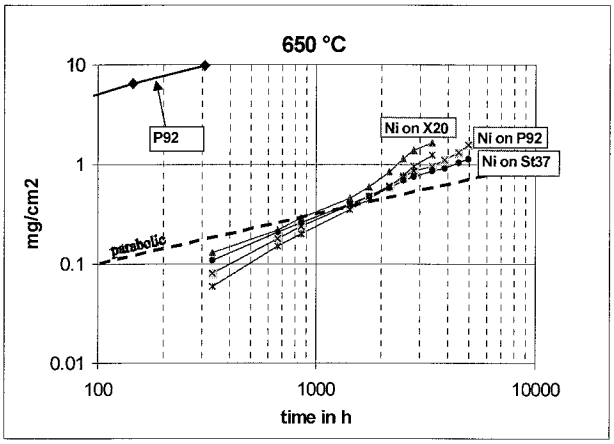


Fig. 10: Weight change of nickel coated samples at 650 °C. Base alloys are X20, P92 and St37. Uncoated P92 is plotted as reference. The parabolic behaviour is indicated as dashed line. Thermal cycling was performed at each data point.

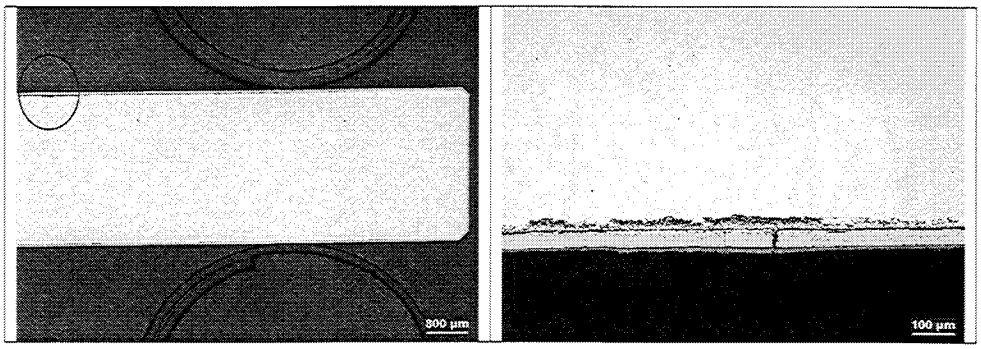


Fig. 11: Micrographs of nickel-coated X20 samples after 3600 h at 650 °C. Left: Overview, showing that the nickel coating is still complete. Circle: Crack in the coating, which leads to increase oxidation, as shown on the right micrograph using a greater magnification

Comparison of laboratory results with field tests

In order to compare different data with each other, it is necessary to calculate the rate constants, based on the usual equation for parabolic (diffusion based) growth:

$$D = \sqrt{K * t},$$

where D is the oxide thickness in µm, t the time in h and k the rate constant in $\mu m^2/h$. Although the time law in our experiments shows some deviations from parabolic behaviour, the calculation of rate constants can be accepted for shorter times and for the absence of spallation.

Fig. 12 shows a comparison of field data from the Vestkraft plant [9] with laboratory data [4] and our own data.

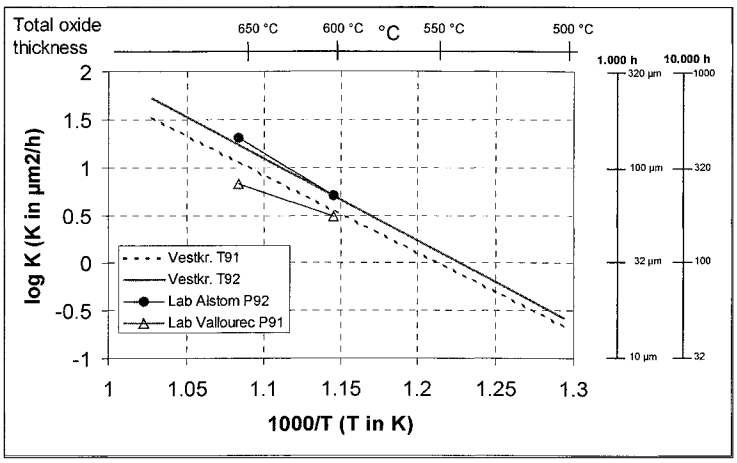


Fig. 12: Comparison of field data and lab data for 9% Cr-steels. Alstom data are based on 7.700 h, Vallourec on 8.000 h and Vestkraft on 23.000 h. Oxidation rate is given for the total oxide thickness (magnetite and spinel), assuming a parabolic law. The scales on the right indicate oxide thicknesses for 1.000 and 10.000 h

It can be seen from fig. 12, that the field data are in good agreement with lab data. However, this is valid probably only for relatively short exposure times, because for longer times spallation effects play an essential role, which could be influenced by steam chemistry and operation conditions.

Conclusions

- The spallation behaviour of scales depends on exposure time, operation modes and steam chemistry. Spallation is generally more pronounced in field tests than in lab tests.
- New alloys from COST 522 showed very low oxidation rates compared to P92. Especially FB8 and CB8 are very promising.
- Electroless nickel coatings show high oxidation stability, provided that there are no defects in the coating.
- Data of field tests, which were published in the open literature, showed good agreement with lab data (for limited operation time)

References

[1] G. Scheffknecht, Q. Chen, 5th Intl. Parsons Conf., July 2000, Cambridge
[2] C. Berger, R.B. Scarlin, K.H. Mayer, D.V Thornton, S.M Beech, Materials for Advanced Power Engineering, Liege, 1994, Kluwer Academic Press, Dordrecht, Part I, 47
[3] J.C. Nava-Paz, R. Knödler, Materials for Advanced Power Engineering, Liege , Nov. 1998
[4] V. Lepingle, G. Louis, D. Petelot, B. Lefebre, J.C. Vaillant, Eurocorr Conference London, Sept. 2000
[5] J.P.T. Vossen, P. Gawenda, K. Rahts, M. Röhrig, M. Schorr, M. Schütze, Materials at High Temperatures 14 (1997), 387
[6] P.J. Ennis, A. Zielinska-Lipiec, O. Wachter, A. Czyrska-Filemonowicz, Acta mater. 45 (1997), 4901
[7] H. Asteman, J.-E. Svensson, M. Norelli, L.-G. Johansson, Oxidation of Metals 54 (2000), 11
[8] K. Zabelt, Technische Überwachung 39 (1998), 11
[9] R. Blum, Q. Chen, C. Coussement, J. Gabrel, C. Testani, L. Verelst, VGB Kongreß Essen, Okt. 2000, VGB Power Tech 10 (2001), 86
[10] R. Knödler, P.J. Ennis, BALTICA V, June 2001, Porvoo, Finland
[11] F. Abe, M. Igarashi et. al., 3rd EPRI Conf., Swansea, UK, April 2001
[12] C. Köster, P. Moser, H. Bergmann, J. Jacobs, VGB Power Tech 9(2001), 64
[13] R. Viswanathan, W.T. Bakker, Power Plant Chemistry 2001, 3(8)
[14] Alina Agüero, Liege conference, Sept. 2002
[15] I.G. Wright, B.A. Pint, NACE CORROSION, Denver, CO, April 8-11, 2002

STEAM OXIDATION OF 9-12CR MARTENSITIC STEELS: CHARACTERISATION AND MODELLING THE SPALLING OF OXIDE SCALE

S Osgerby and L N McCartney
NPL Materials Centre, National Physical Laboratory, Teddington, Middlesex TW11 0LW, United Kingdom

© Crown Copyright

Abstract

A model has been developed to predict the onset of cracking and spallation in multi-layered oxide scales. This model has been validated using the 9-Cr steel, P92, oxidised in flowing steam at 600 and 650 °C. The input parameters for the model, with a single exception, have been measured independently or obtained from published literature. The one parameter that cannot be obtained directly is the fracture energy of the magnetite layer in the scale: this parameter is used to 'train' the model at a single scale thickness from where the temperature drop to cause cracking in thicker scales can be calculated.

Measurements of the temperature drop required to cause cracking have been made using acoustic emission. These data have been used to validate the model.

Keywords: Martensitic steel; steam oxidation; modelling, scale fracture, spallation

Introduction

For many components, operating at high temperatures in steam environments, metal wastage due to oxidation is one of the main causes of failure. While the growing oxide is protective, the rate of metal loss decreases with time and can be predicted with reasonable confidence. Problems arrive when this 'safe' situation is disturbed and the oxide is rendered non-protective by crack formation and/or spallation, usually during a temperature change.

Characterisation of Scale Failure

Specimens of the 9%Cr martensitic steel, P92, were oxidised in flowing steam at atmospheric pressure at 600 and 650 °C for durations up to 2000 h. The specimens were then cooled at a linear rate of 100 °C h^{-1} whilst being monitored for acoustic emission (AE). A typical AE record during cooling is shown in Figure 1. Two distinct peaks in AE activity are observed. The first of these is interpreted as the initial cracking of the oxide scale and the second can be interpreted as the actual spallation event.

After cooling, the specimens were electroplated with Ni to ensure edge retention, sectioned, mounted, polished to a final finish with OPS and examined under an optical microscope. The oxidation product formed was multi-layered with a thin outer haematite scale, a thicker layer of magnetite, another relatively thick layer of spinel and a region of internal oxidation. This is consistent with previous observations of scale grown under these conditions [1]. Haematite was present due to the high level of dissolved oxygen present in the water used to generate the steam atmosphere. Several types of failure events were detected in the oxide and these are shown in Figure 2. The most common type of failure observed was tensile through-thickness cracking in the magnetite layer, Figure 2b. Other types of failure observed arose

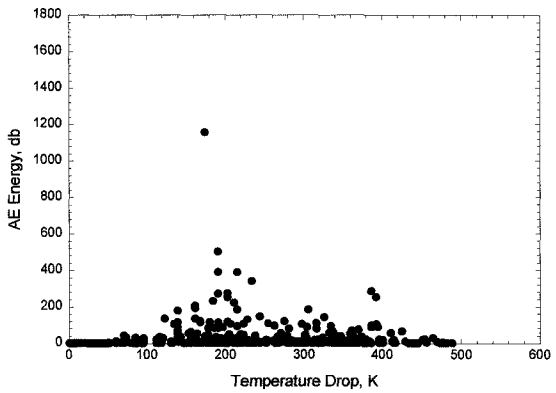


Figure 1 AE activity during cooling at 100 °C h-1 of P92 after oxidation in flowing steam for 500 h at 600 °C.

(a) (b)

(c)

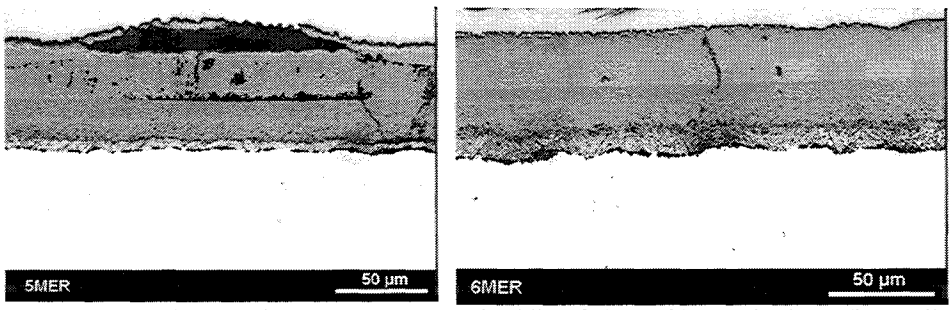
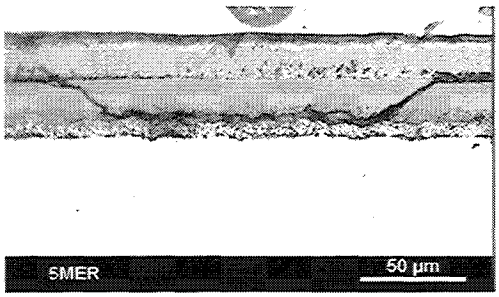


Figure 2 Examples of oxide scale damage (a) buckling failure of haematite layer (b) tensile cracking in magnetite (c) compressive shear crack and delamination in spinel.



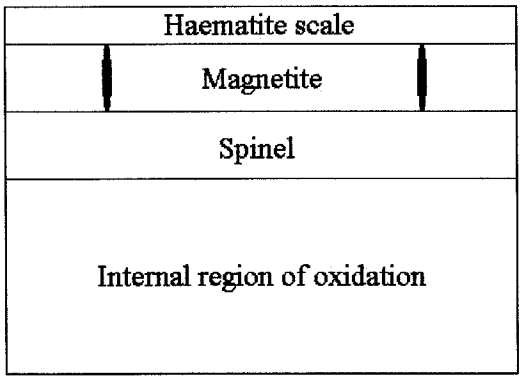
from compressive strain causing buckling in the haematite (Figure 2a) or shear cracks in the spinel (Figure 2c) layers.

Model Development

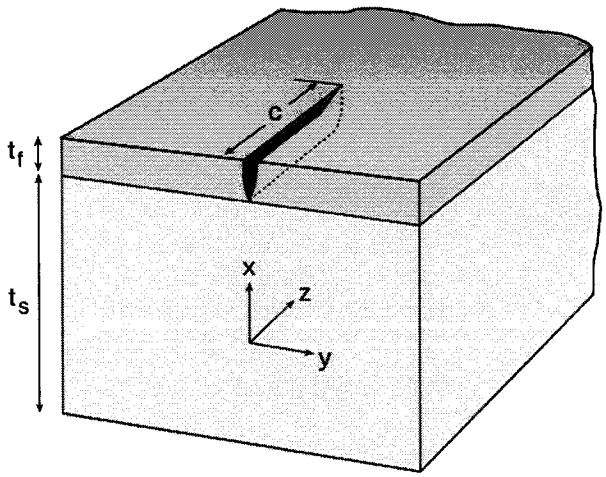
The model used was based upon a concept that was originally developed to predict tensile cracking in polymer composites [2]. The basis of the model, when applied to multi-layered coatings, is shown in Figure 3. The specimen is first divided into several layers representative of the geometry of the system that is being modelled (Figure 3a). Each layer in the system is attributed specific properties characteristic of the material in that layer. Under the action of a tensile stress, one or more of the layers can form cracks (Figure 3a shows cracks only in the layer beneath the external surface). Analytical methods of solving the linear elastic stress analysis problem are used to predict the stress and displacement distributions everywhere in each layer of the system. Numerical methods are needed to solve the fourth order ordinary differential equations that govern stress transfer between layers in the presence of cracks. The modelling technique has been extensively validated by comparing model predictions with the results of FEA. The analytical model has been shown to be the equal of, if not better than, the FEA approach, and is a much more rapid solution technique. Energy methods that are fully consistent with linear elastic fracture mechanics are then used to predict the conditions of loading for which it is energetically favourable for cracks to form in specific layers. Figure 3b illustrates the fracture mechanics approach applied to the steady propagation of a crack in a surface layer. When performing the analysis it is essential that the through-thickness dependences of the stress and displacement fields are accurately predicted. This is achieved by subdividing each layer into sets of layer elements each having the same properties. In those regions of layer interfaces where a crack tip might be located the layer elements on either side of such an interface are divided successively, usually about three times. This achieves a layer refinement that is able to model the singularities in the stress field at the crack tips. Ultimately, progressive loading of the system leads to the through-thickness cracks initiating delaminations and spallation along the interface.

During cooling, stresses in the oxide scales are generated due to the different thermal expansion coefficients of each material layer. Thermal expansion coefficients as a function of temperature for haematite, magnetite, spinel and 9Cr1Mo steel have been collated from the literature [3, 4] and are presented in Figure 4. It can be seen that haematite and the substrate, having the lower coefficients of thermal expansion than the other layers, will tend to be subjected to compressive stresses during cooling whilst the magnetite layers, having higher thermal expansion coefficients, will be subjected to tensile stresses during cooling. The spinel layer may be subjected to either tensile or compressive stresses depending upon the relative influence of the magnetite and substrate surrounding it.

The Young's modulus and Poisson's ratio of haematite have been measured by Robertson and Manning [5] together with the Poisson's ratio for iron-chromium spinel. The Young's modulus of the P92 substrate was reported by Mimura et al [6]. The Young's modulus of the spinel was measured by nanoindentation during the course of this work. The values for the elastic parameters are given in Table I. In this preliminary modelling activity these parameters have been taken as independent of temperature as any effects of temperature dependency are expected to be minor.



(a)



(b)

Figure 3 Basis of cracking model (a) definition of layered structure with fracture sites in one layer (b) crack propagation in specific layer

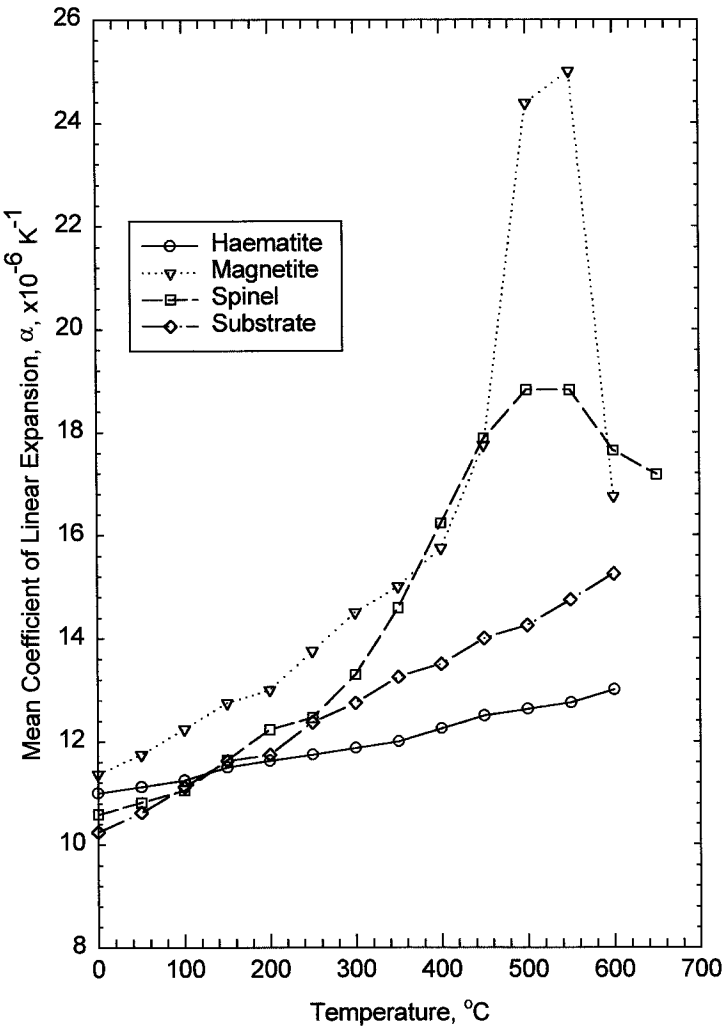


Figure 4 Thermal expansion coefficients of the different layers in 9%Cr steel oxidised in steam.

Table I: Elastic parameter of oxide scales and substrate

	Young's Modulus GPa	Poisson's Ratio
Haematite	220	0.19
Magnetite	210	0.29
Spinel	233	0.31
P92 Substrate	227	0.3 (assumed)

A simulated cooling test was carried out using a constant cooling rate of 100 °C h^{-1} and a fracture energy was assigned to the magnetite layer whose value predicted the first crack of this layer at the temperature drop that had been observed experimentally. The data chosen to fit the model was the shortest initial exposure viz 500 h at 600 °C. The model predictions for the critical temperature drop for cracking reproduced the experimental data when a value of 10.24 J m^{-2} was assigned as the fracture energy of magnetite. This value equates to a fracture toughness of 1.52 MN $m^{-1.5}$, which is similar to published values [7,8] of 1.07 and 1.82 MN $m^{-1.5}$

It should be emphasised that the fracture energy parameter is the only input to the model that cannot be measured independently – all the other inputs are obtained from experimental data or are previously published values.

At this stage the model is not capable of predicting interfacial crack growth and final spallation. Therefore a pragmatic criterion for spallation was invoked viz that spallation occurred after a further 200 °C temperature drop after first cracking of the magnetite. Further development of the model to incorporate the ability to predict interfacial crack growth is planned.

The evolution of the individual layers within the scale with time has been determined in accordance with the following rules. These were developed through observation of the scales that were formed during a series of exposures at 600 °C for times up to 2000 h:

- the outer haematite layer remains at a constant thickness of 4.7 μm
- the magnetite and spinel layers grow at rates such that the ratio of their thickness' remains constant at 1.05

Metallography of exposed specimens has shown that these rules describe the growth of oxide scale on this material under the experimental conditions used in this work to a reasonable degree. A short modelling exercise has also shown that, except when the total scale thickness is very low, the temperature drop to initiate cracking in the magnetite layer is insensitive to the thickness of haematite.

Using the above rules, model predictions of the temperature drop to initiate cracking and spallation of the magnetite as a function of the total scale thickness, after oxidation at 600 °C and cooling at 100 °C h^{-1}, have been made. These are shown in Figure 5 together with data from controlled cooling tests. It can be seen that the model represents an adequate description of this limited dataset although further refinements to the model, e.g. fitting the model to one of the other data points to obtain a slightly different (higher) value for fracture energy, would improve the overall fit.

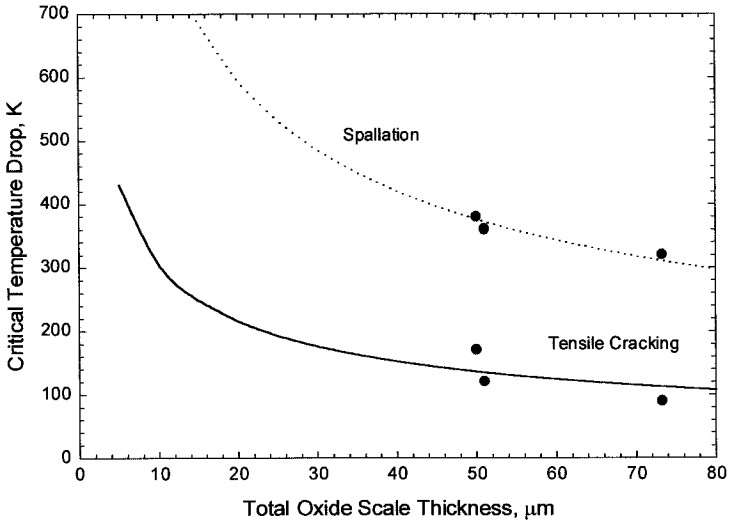


Figure 5 Comparison of Model Predictions and Data from Controlled Cooling Experiments
• Data —Model prediction for cracking ····· Model prediction for spallation

Future Work

The current model allows only for stress evolution in the oxide scale layers due to differences in thermal expansion coefficient. These stresses may be relaxed by creep in one or more of the layers. This mechanism will be included in future model development.

A more robust method of predicting spallation will also be developed. This will incorporate crack growth along the magnetite/spinel interface.

Conclusions

A model for predicting cracking and spallation in oxide scales, grown under a steam atmosphere, on 9%Cr martensitic steels has been developed. The model has been benchmarked against experimental data on scales grown on P92 steel at 600 °C.

Acknowledgements

This work was carried out under the Degradation of Materials in Aggressive Environments Programme, a programme of underpinning research funded by the United Kingdom Department of Trade and Industry.

The authors are grateful to Mr M U Sheriff, who carried out much of the experimental work.

References

[1] E Metcalfe, in Proc. Surface Stability, Oxidation-Corrosion-Erosion-Wear, ed T N Rhys-Jones, Inst Met, London 1989, pp 145-185

[2] L N McCartney, *Composites Science and Technology* **58** 1998 1069-1081

[3] J Armitt, D R Holmes, M I Manning, D B Meadowcroft and E Metcalfe, The Spalling of Steam-Grown Oxide from Superheater and Reheater Tube Steels, Electric Power Research Institute, EPRI Report No FP-686, 1978

[4] F Eberle and J H Kitterman in 'Behaviour of Superheater Alloys in High Temperature, High Pressure Steam' Ed G E Lien, ASME 1968 67-113

[5] J Robertson and M I Manning, *Mater. Sci. Technol.* **6** 1990 81

[6] H Mimura, M Ohgami, H Naoi and T Fujita, Materials for Advanced Power Engineering 1994, Eds D Coutsouradis, J H Davidson, J Ewald, P Greenfield, T Khan, M Malik, D B Meadowcroft, V Regis, R B Scarlin, F Schubert, D V Thornton, Kluwer Academic Publishers, Dordrecht, 1994 361-372

[7] M M Nagl, PhD Thesis, M M Nagl, University of Glamorgan, UK, (1992), "Identification of the mechanisms of oxide scale fracture, and its correlation with strain using AE"

[8] P Hancock and J R Nicholls, Mater. Sci. Technol. **4**, 1988 398-406

MECHANICAL AND OXIDATION TESTING OF ADVANCED MATERIALS FOR STEAM POWER PLANTS.

Paolo Bontempi, CristinaGuardamagna, Noemi Ricci, Lucia Torri

CESI – Via Reggio Emilia, 39 - 20090 Segrate (Milano) – Italy

Abstract

In the frame of the COST522 programme, Steam Power Plant Working Group, CESI is carrying out an experimental programme in order to evaluate boiler and turbine innovative materials suitable for applications up to 650°C.
In this paper results from Low Cycle Fatigue, creep and oxidation-corrosion testing are presented.
LCF tests at T=600°C have been performed on a new cast steel (CB6), evaluating also the effect of hold time period. The preliminary creep results at T=625°C on four new 11%Cr ferritic steels for piping are presented: the experimentation is still in progress.
The steamside corrosion - oxidation test results at T=600°C and T=650° till now obtained on both boiler and turbine innovative materials are shown.

Keywords: ferritic steel, low cycle fatigue, creep, oxidation, superheated steam

Introduction

Energy saving and reduction in CO_2 emissions are the requirements for developing new power production technologies with improvements in efficiency. In steam power plants these results can be reached increasing the steam temperature and the pressure to achieve Ultra Super Critical (USC) conditions: as a consequence, higher creep strength and oxidation corrosion resistance are required for the materials used in plant components [1].
In the frame of the COST522 programme, Steam Power Plant Working Group, CESI is carrying out an evaluation on boiler and turbine innovative materials suitable for applications up to 650°C. The CESI programme involves the following items:

- assessment of Low Cycle Fatigue (LCF), Fatigue Crack Growth (FCG) behaviour, and oxidation kinetics of rotor and casing materials for steam turbines;
- assessment of creep properties and corrosion (fireside and water/steamside) resistance of materials for boiler tubes and pipes.

The mechanical properties assessment for rotor and casing materials has been focussed till now on the LCF characterisation at 600°C of one cast steel (CB6). The effect of hold time period (20 min. in tension and 20 min in compression) on the LCF behaviour of this material has been also investigated. For advanced boiler material, CESI is involved in the creep characterisation of new 11%Cr ferritic steels carrying out creep testing at 625°C: preliminary results are presented here.
The steamside corrosion - oxidation activity undertaken by CESI is aimed to study the effect of steam conditioning (All Volatile Treatment – AVT- and Combined Water Treatment – CWT-), steam temperature and temperature cycling over the resistance of the tested materials. Oxidation tests are now in progress in AVT superheated steam at two different temperatures (600 and 650°C) with a cycle time of 1000 hours over a wide range of materials. Both low alloy and new high Cr ferritic steels are currently under exposure and their behaviour is compared with the reference P22 and P92 steels; innovative cast material (CB6) for rotor casing is also under exposure.

Materials

Table 1 shows the chemical composition of all the tested material: a new cast rotor steel with high cromium level (CB6) with 2.9% Co, four trial melts ferritic steels new 11% Cr (H1F35÷38) for piping, with different levels of W, Si, Mn, Ni, Mo and Nb and a new martensitic steel 12%Cr (pipe G-1550) with 1.5% Co. P92 steel has been used as reference steel in oxidation tests.

Experimental

Low Cycle Fatigue Tests

LCF tests have been performed on a cast rotor steel (CB6) using cylindrical specimens (ϕ =6,35 mm), according to ASTM E 606 – 92 "Standard Practice for Strain-Controlled Fatigue Testing" under deformation control and with the following test parameters:
Temperature: 600°C; Strain Range: 1.4; 1.2; 1.0; 0.8; 0.5%; Strain Rate: 1E-03 1/s;
R (ε_{min} / ε_{max}): -1; Waveform: triangular; Hold Time: 0 min (6 tests with continuous cycle) and 20 min tensile and 20 min compression (5 tests Hold Time).
The overall test matrix has been reported in Table 1, together with the results.

Table 1: CB6 steel LCF tests matrix and results at 600°C.

Spec.Code	N_f (**) [Cycl. Fail.]	Strain (*) Total (@) [%]	Plastic [%]	Elastic [%]	Stress (*) Total [MPa]	Tens. [MPa]	Tens.Relax. [MPa]	Comp.Relax [MPa]	Mod.Elast [GPa]
Continuous tests									
CB6-14	710	1.4001	0.9760	0.4241	526.9	259.8	n.a.	n.a.	124 (+)
CB6-12	980	1.2000	0.8475	0.3525	523.5	259.0			156 (+)
CB6-1	1300	0.9998	0.6637	0.3361	512.1	253.3			152 (+)
CB6-08	1340	0.7998	0.4901	0.3097	501.6	247.9			162 (+)
CB6-08a	2060	0.7998	0.4764	0.3234	498.0	246.4			154 (+)
CB6-05	5800	0.4998	0.2099	0.2899	464.9	230.9			160 (+)
Tests with hold time 20 min tensile/20 min compression									
CB6-14ht	317	1.4764	1.2920	0.1844	520.9	265.3	83.7	91.4	145 ($)
CB6-12ht	380	1.2208	1.0880	0.1328	481.0	238.4	74.4	81.8	144 ($)
CB6-12hta	650	1.2171	1.1000	0.1171	440.5	214.0	64.9	87.5	144 ($)
CB6-1ht	750	1.0186	0.8880	0.1306	419.2	208.2	92.6	83.3	145 ($)
CB6-08ht	1115	0.8238	0.6631	0.1607	435.5	215.5	96.2	111.7	159 ($)

(*) mid-life values (**) 25% tensile load drop below the stationary condition
(@) controlled total strain (measured)
(+) calculated by $E = \Delta\sigma/\Delta\varepsilon_{el}$ ($) calculated by hysteresis elastic slope

LCF test results with continuous cycle has been fitted according to the Manson -Coffin relationship:

$$\Delta\varepsilon_t = (C_1 \cdot N_f^{\alpha 1})_{el} + (C_2 \cdot N_f^{\alpha 2})_{pl}$$

where N_f is the number of cycles to failure and $\Delta\varepsilon_t$ is the total strain range.
The coefficients C_1, C_2, α_1 and α_2 listed below, have been calculated by a least square regression of mid-life values from Table 1.

Elastic component		*Plastic component*	
C_1	α_1	C_2	α_2
0.9972	*-0.1476*	*119.83*	*-0.7328*

The following figure 1 shows the Manson- Coffin curve together with the elastic and plastic components.

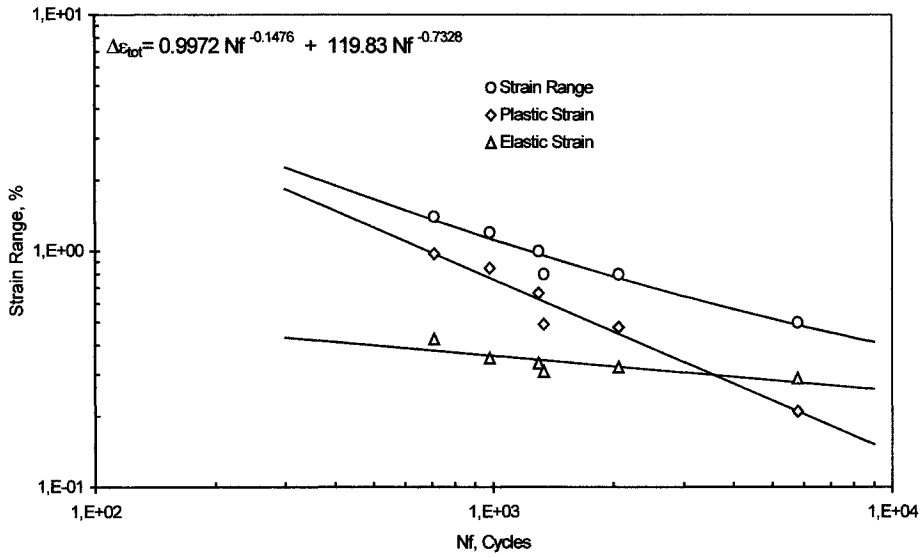


Figure 1: Manson-Coffin curve for CB6 cast steel LCF tested at T=600°C.

The LCF test results (T=600°C) with hold time (20 min. compression and 20 min. tension) are shown in figure 2: there is, as expected, a reduction in fatigue resistance of about a factor of 2 due to the creep –fatigue interaction. A general comparison between LCF behaviour at T=600°C of CB6 steel and other ferritic steels with high chromium content is shown in figure 3. In LCF tests without hold time, CB6 steel shows a behaviour very similar to P92, E911, P91; in LCF tests with hold time the CB6 steel behaviour is similar to X-10 (COST 501 WP3) steel.

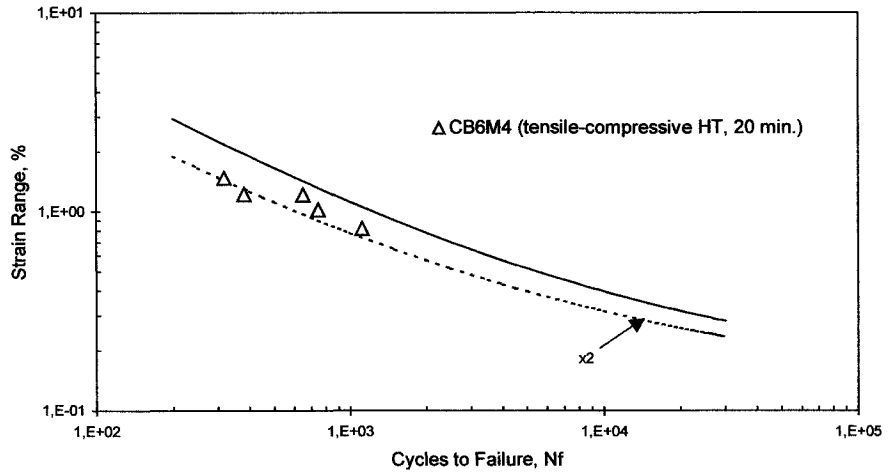


Figure 2: Comparison between LCF results with and without hold time: the dashed line corresponds to a reduction by a factor of 2.

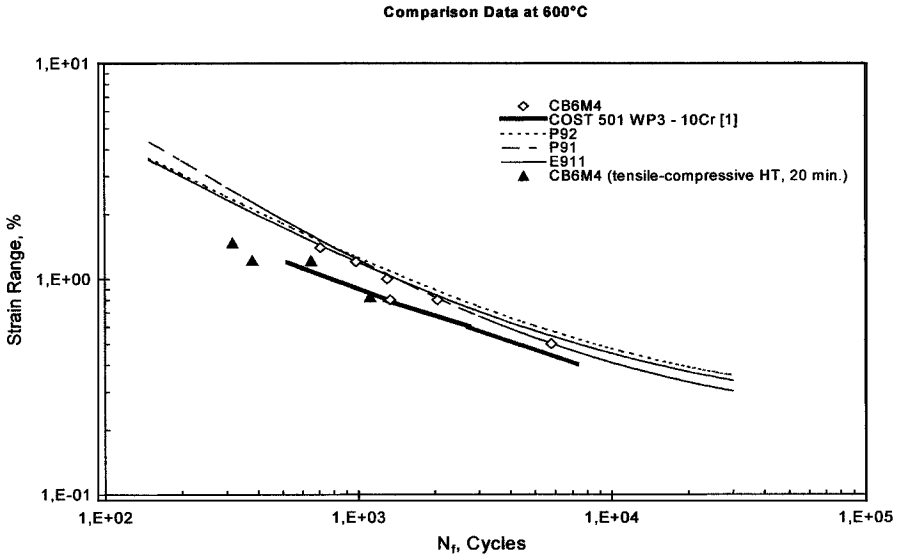


Figure 3: Comparison of LCF behaviour at T=600°C between CB6 steel and other ferritic steels with high Chromium content [2].

Creep Tests

Creep tests are now in progress on four new trail melts of new 11% ferritic steel for piping. Tests are performend according to ASTM E 139-95. For all the materials the test temperature is T= 625°C. The whole test matrix and preliminary results are shown in Table 2

Table 2: Creep tests matrix and preliminary results.

Specimen	Stress [MPa]	Time to Rupture [hours]	Time to 0,2% [hours]	Time to 0,5% [hours]	Time to 1,0% [hours]	Elongation [%]	Reduction of Area [%]	Minimum creep rate [%/hours]	Status
H1F35-C1-1	155	731.4	5	30	110	9.2	67.1	4.06E-03	broken
H1F35-C1-2	140	*739.9*	10	122	706	*1.0*			in prog.
H1F35-E1-1	125								
H1F35-E1-2	110								
H1F36B1-1	155	783.8	5	9	60	13.8	48.4	3.02E-03	broken
H1F36B1-2	140	*405*	6	130		*0.8*			in prog:
H1F36F1-1	125								
H1F36F1-2	110								
H1F37B1-1	155	*1680.1*	7	90	635	*1.6*			in prog:
H1F37B1-2	140	*400*	15	222		*0.6*			in prog.
H1F37H1-1	125								
H1F37H1-2	110								
H1F38G1-1	155	246.3	0.3	2.0	10.0	29.5	78.1	2.37E-02	broken

In figure 4 are reported the creep curves till now obtained: the worst behaviour at 155Mpa is shown by the trail melt with the lower W and Nb contents, while the melt with the higher W content (2.03%W) has shown the longest creep life.

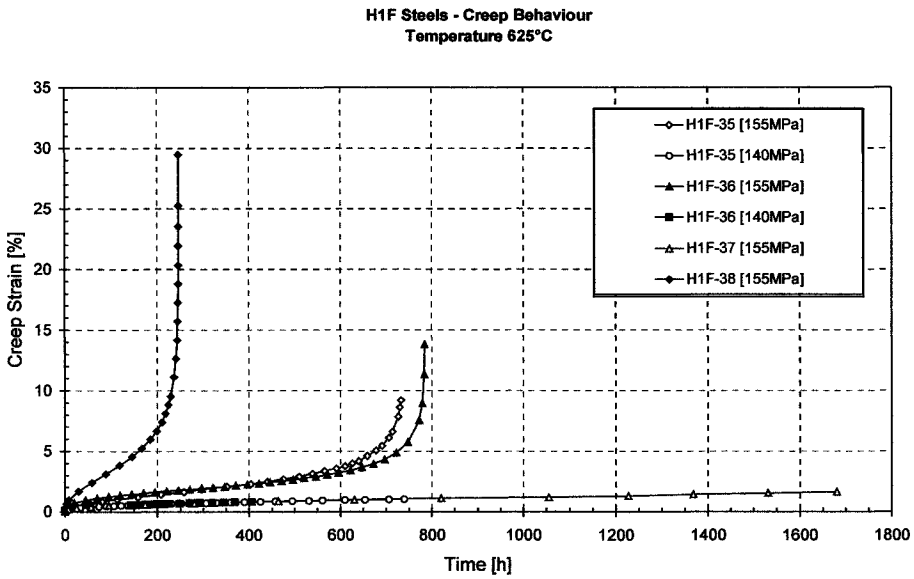


Figure 4: Creep strain vs time for new 11 % Crferritic steels.

Oxidation Tests

The oxidation tests, both on turbine and boiler materials (reference P92, CB6, H1F35-38 and PipeG-1550 listed in tab.1), have been performed in superheated steam at T=600°C (±3°C) and T= 650°C (±5°C). The steam is produced by heating demineralized water, pretreated in a mixed anionic and cationic resins bed until its conductivity is lower than 0.1 μS/cm. Then the water is deoxygenated with N_2 to have dissolved oxygen content <5 ppb. After the deoxygenation period ammonia is added to water to reach the pH value of about 9. A dosimetric pump with flow rate <0.5 kg/h feeds the water into two test autoclaves made in Inconel. The specimens, ground all over the surfaces, are held in vertical position. For each material and for each temperature level 3 exposure cycles of 1000 hours are scheduled.
Table 3 shows the oxidation test matrix and the overall results both in terms of weight changes and thickness of the oxide scale (outer and inner).

Table 3: Overall oxidation tests matrix and results.

Material	Temp. [°C]	Time exp. [hours]	ΔW_{th} [mg/cm^2]	Oxide thick. [μm]	First layer oxide thick. [μm]	Second layer oxide thick. [μm]
CB6	600	1000	0.11	-	-	-
CB6	650	1000	1.41	6.77	2.58	3.78
P92	650	1000	2.84	22.48	20.08	5.51
P92	650	2000	6.22	46.80	39.50	9.23
H1F35	600	1000	2.67	17.06	6.31	9.78
H1F35	650	1000	2.98	29.98	12.83	16.49
H1F36	600	1000	1.02	13.58	5.86	7.97
H1F36	650	1000	1.72	19.51	7.61	11.11
H1F37	600	1000	1.60	18.16	6.98	11.04
H1F37	650	1000	2.42	27.64	10.29	16.58
H1F38	600	1000	0.90	10.72	2.78	6.39
H1F38	650	1000	1.59	17.59	6.81	10.52
PipeG-1550	600	1000	-	32.37	29.38	5.97
PipeG-1550	650	1000	10.01	79.82	39.83	40.96

In figure 5 the weight changes of P92 reference steel and the four new 11%Cr ferritic steeels H1F materials versus the chromium equivalent content are shown after 1000 hours exposure at 650°C.
The oxidation resistance increases with the chromium equivalent content; the H1F37 material, which has a content in Mo that is the half in comparison with the other three material H1F (0.5% instead of about 1%) shows an oxidation rate a little higher than expected [3].
All the four new 11%Cr ferritic steels show a double layer oxide growth, as shown in figure 6: the inner oxide layer is very compact, while the outer oxide layer is more porous. Moreover, the inner oxide layer is more evident after the tests at 650°C.
The PipeG-1550 material shows a very high oxidation both at 600 and 650°C only after 1000 hours: this could be attributed to its low Si content (0.1%).
In figure 7 is shown the P92 after 1000 hours and 2000 hours at 650°C. Signs of spallation could be seen after 2000 hours exposure. For all the materials after only 1000 hours of exposure there is no evidence of spallation [4,5].

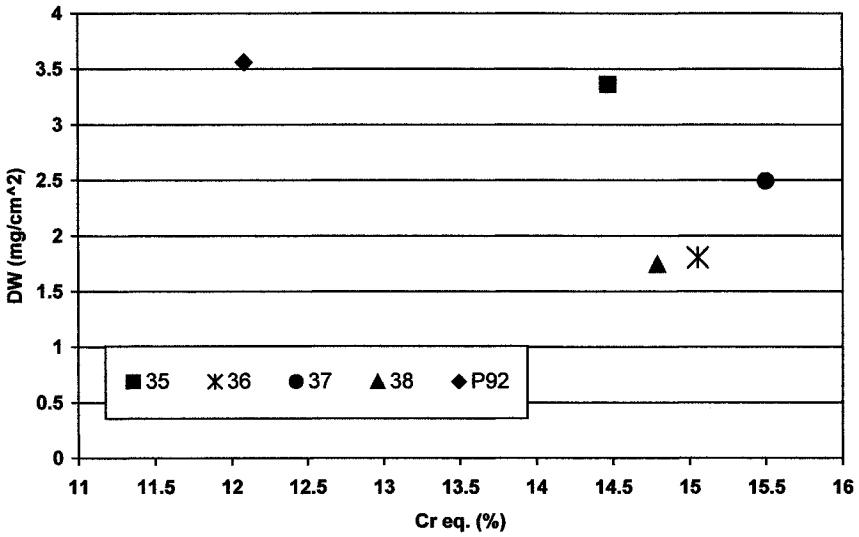


Figure 5: Oxidation resistance of new ferritic steels vs Cr equivalent (%).

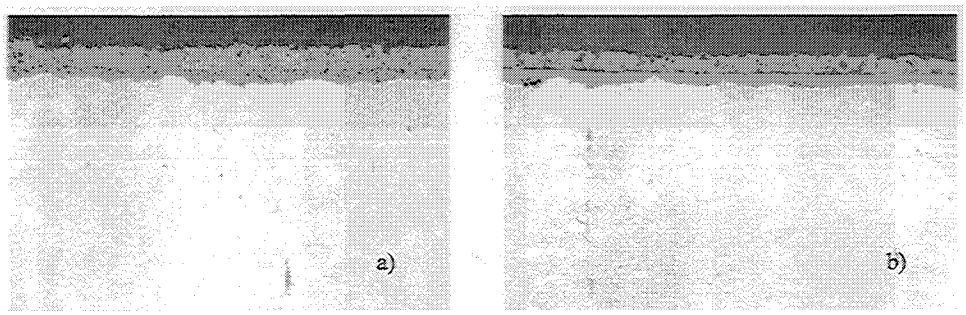


Figure 6: New 11% Cr steel (H1F36) after 1000 hours exposure a)600°C, b) 650°C (400X).

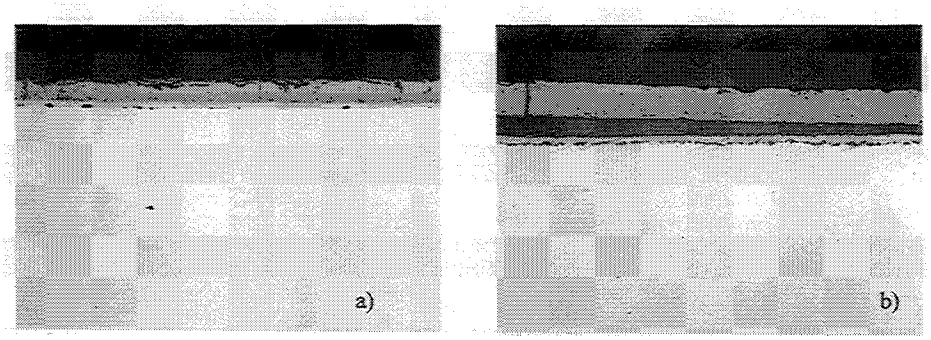


Figure 7: P92 reference steel at 650°C a) for 1000 hours; b) for 2000 hours (200 X)

Conclusions

In this paper some preliminary results on mechanical and oxidation-corrosion properties on innovative materials for advanced steam turbines and boilers have been presented.
The LCF behaviour at T=600°C of the CB6 cast steel (11% Cr) IS comparable with the P92, E911, P91 steels. The presence of hold time period, as expected, produces a reduction in fatigue resistance of about a factor of 2, due to the creep-fatigue interaction.
The preliminary creep results (T=625°C) on new 11%Cr ferritic steels have also been presented; the oxidation resistance for these steels increases with their Cr equivalent content; the steel with the lower Mo content shows an oxidation rate a little higher than expected.
Signs of spallation have been detected after 2000 hours exposure on P92; there is no evidence of spallation for all the tested materials after 1000 hours of exposure.

Acknowledgements

This activity was performed in the frame of the Programme "Ricerca di Sistema", D-L- MICA 26-01-2000. Thanks are also extended to the COST Management Committee for their guidance of the programme.

References

[1] W.T.Bakker:" Materials for Advanced Boilers" Proc. of Advanced Heat Resistant Steels for Power Generation Conf., Ed. R. Viswanathan and J.Nutting, 1998 pp.435-444.

[2] B.Scarlin, K.H.Mayer, C.Berger, "COST 501 Round II – New Steel and Manufacturing Processes for Critical Components in Advanced Steam Power Plant", Final Report, June 1994.

[3] J.L.Blough et al.: "Superheater corrosion: field test results" EPRI Rep. TR-103438 Nov.1993.

[4] P.J. Ennis, Y. Wouters e W.J. Quaddakkers, "The Effects of Oxidation on the Service Life of 9-12% Chromium Steels", Advanced Heat Resistant Steels for Power Generation, 27-29 April 1998, San Sebastian, pp.457-467.

[5] G. Lai, "Oxidation", High-Temperature Corrosion of Engineering Alloys, ASM 1990, pp.22.

IMPROVEMENT OF STEAM OXIDATION RESISTANCE FOR FERRITIC HEAT RESISTANT STEELS

Hiroyuki Kutsumi, Takehiko Itagaki and Fujio Abe

National Institute for Materials Science
1-2-1 Sengen, Tsukuba-shi, Ibaraki 305-0047, Japan

Abstract

In order to make clear the effect of alloying elements except for Cr and Si, the authors have made a fundamental study on the oxidation behavior for a variety of ferritic heat resistant steels in steam; six heat of T91 with different S contents, five kinds of 9Cr-W/Mo steels with different W/Mo where the Mo equivalent was kept to 1.5 mass % and twelve kinds of carbon free Fe-Ni-Co base martensitic alloys. This paper describes how to improve steam oxidation resistance for ferritic heat resistant steels. The oxidation tests were carried out in steam at 773-1023K for up to 1000 hours. Small amounts of sulfur in T91 improved the steam oxidation resistance. Addition of molybdenum was more effective than tungsten for the steam oxidation resistance. The steam oxidation characteristics of carbon free Fe-Ni-Co base martensitic alloys over 973K was improved by the increase of the Ni content, and the weight gain of the 12Ni alloy was about half of that of T91 at 973K and 1023K. When surface strained high-Cr ferritic steels with small amounts of Pd was oxidized in steam at 923K, protective and thin Cr-rich oxide layer was formed in the steel surface. The steam oxidation resistance was dramatically improved by this protective oxide layer. In addition, pre-oxidation in flowing Ar over 723K was made to high-Cr ferritic steel without Pd in order to form similar protective oxide layer.

Keywords : Steam oxidation, High-Cr ferritic steel, Carbon-free martensitic alloys, Protective oxide layer, USC boiler

1. Introduction

Considering recent global environmental problems, it seems to be an important problems to restrain carbon dioxide discharged from thermal power plants which use fossil fuels such as coal and petroleum. Therefore, heat resistant steels for ultra-supercritical (USC) plants have been developed. Therefore, large-diameter tubes, as main steam tubes for USC boilers, are required to withstand high temperatures of more than 873K over long periods[1]. Targeted steam conditions have been increased up to 903K, 30MPa[2]. Thus, it is necessary to develop new steels whose creep strength and steam oxidation resistance will be superior to those of the conventional high Cr ferritic steels.

While many investigators have reported on oxidation behavior of existing steels, such as ASME SA 335-P122、ASME SA 335-P92 and so on, in a steam atmosphere [3-7], the oxidation mechanism or the effect of trace elements have not been sufficiently elucidated. In order to make clear the effect of alloying elements except for Cr and Si, the authors have made a fundamental study on the oxidation behavior for a variety of ferritic heat resistant steels in steam. We have obtained a very significant result through investigating the effect of Mo, W and trace amounts of S on the steam oxidation resistance, and wish to provide herein a summary of our findings.

On the other hand, Dr. S. Muneki successfully developed carbon free martensitic alloys by removing influence of carbide and then strengthening only intermetallic compounds'

precipitation. Consequently, we found it efficient for improving creep resistance at high temperatures over 923K to strengthen Fe-Ni-Co martensitic alloys by Laves and μ-phase[8]. Nevertheless, there have been no investigations on steam oxidation behavior of precipitation the C-free martensitic alloys. This report also summarizes the experimental results of steam oxidation at high temperature of the C-free martensitic alloys.

Then, Dr. M. Igarashi developed new steels based on new strengthening theory[9,10], which have the $L1_0$ type FePd-base intermetallic compound precipitated in the ferrite matrix. This kind of reinforcement functions additively with the reinforcement by precipitation of MX type carbonitride, $M_{23}C_6$ type carbide, and the Laves phase. We studied the steam oxidation of palladium-containing high-Cr ferritic steel at high temperatures of around 650°C. As a result, an unusual oxidation behavior, different from that of usual high-Cr heat-resistant ferritic steels, was found in this study. In addition, we observed the similar phenomenon, when the pre-oxidation in Ar flow over 723K was conducted to usual high-Cr ferritic steels without pd, and also wish to provide herein a summary of our findings.

2. Experimental

In this study, five kinds of 9Cr-W/Mo steels with different W/Mo where the Mo equivalent was kept to 1.5 mass %(A series alloys) [11], ASME SA 335-P122(S1), ASME SA 335-P92(S2) and 9Cr2W(T6B) steel (B series alloys), six heats of Mod.9Cr1Mo(T91) with different S contents(C series alloys) [12], twelve kinds of carbon free Fe-Ni-Co base martensitic alloys(D series alloys), two kinds of 9Cr-3.3W steels with 3mass% Pd(P3) and without Pd(B2)(E series alloys) and three kinds of 8.5-12Cr-2W steels with different Si and Cr contents (F series alloys) were used. Chemical compositions of the alloys are given in **Table 1**. A, D and E series alloys and T6B were prepared in our laboratory, while S1, S2 and C series alloys were commercial steels. The specimens except for D series alloys for oxidation test were cut into a coupon shape of 10×20×2 mm by electrical-discharge machining from the bulk material treated with normal tempering and normalizing. The specimens of D series alloys were also similarly cut after solution treatment for 1.8Ks at 1273K. Finally the specimens were finished up with SiC abrasive papers of 320 grit.

Schematic illustration of steam oxidation test apparatus is shown in **Fig. 1**. Steam generated from pure water, whose dissolved oxygen was under 10 ppb and whose electric conductivity was under 8.0 μS/m, was introduced into a test reactor. The flow rate of steam was controlled by limiting the water supply to the steam generator to 0.17 ml/s. The specimen in a ceramic crucible was set in the testing apparatus after it was washed with methanol and acetone in the ultrasonic bath. We discharged air from the testing chamber with a vacuum pump and filled it with argon gas with dew point of 208 K and oxygen content of 0.3 ppm and heated the testing chamber up to 473K. The gas in the chamber was then exchanged with steam and then continued to be heated at oxidation temperature. The total heating operation took about 3 hours. The time for oxidation was defined as the time period from reaching oxidation temperature to shutting down the power.

Oxidation tests were performed in a steam atmosphere at four different temperatures from 873 K to 1023 K, with a 50 K interval, for up to 3.6 Ms (1000 h). The cross section of the oxidized specimens was observed by optical microscope and scanning electron microscope (SEM). Element analysis of the near surface area was performed by EDX and WDX. The

Table 1 Chemical compositions of the alloys (mass %)

Series	Alloy	C	Si	Mn	Cr	W	Mo	V	Nb	B	Al	Cu	Ni	N	S	P
A	T1B	0.08	0.3	0.50	8.95	3.05	-	0.23	0.051	0.0031	0.009	0.049	0.003	0.049	-	-
	T2B	0.08	0.30	0.51	8.94	2.79	0.10	0.22	0.051	0.0036	0.010	0.047	0.003	0.047	-	-
	T3B	0.08	0.30	0.52	9.04	2.51	0.33	0.21	0.053	0.0032	0.010	0.050	0.003	0.050	-	-
	T4B	0.08	0.3	0.52	8.98	1.85	0.62	0.22	0.049	0.0031	0.010	0.049	0.003	0.049	-	-
	T5B	0.08	0.3	0.50	9.08	-	1.54	0.20	0.045	0.0034	0.010	0.049	0.004	0.049	-	-
B	S1	0.12	0.3	0.6	10.50	2.05	0.36	0.21	0.06	0.003	0.005	0.97	0.34	0.069	0.001	0.018
	S2	0.09	0.2	0.5	8.97	1.89	0.45	0.21	0.06	0.002	-	-	0.13	0.050	0.001	0.010
	T6B	0.08	0.3	0.5	8.34	2.00	-	0.23	0.069	-	0.008	0.020	0.09	0.059	-	-
C	ModA	0.10	0.4	0.40	8.53	-	0.96	0.21	0.076	-	0.010	0.022	0.12	0.050	0.001	0.015
	ModB	0.09	0.3	0.5	8.51	-	0.90	0.21	0.076	-	0.020	0.026	0.20	0.042	0.001	0.015
	ModC	0.09	0.3	0.4	8.70	-	0.90	0.22	0.072	-	0.001	0.032	0.28	0.044	0.002	0.009
	ModD	0.08	0.3	0.5	8.34	-	0.89	0.23	0.070	-	0.011	0.020	0.09	0.059	0.004	0.005
	ModE	0.08	0.3	0.5	8.34	-	0.89	0.23	0.070	-	0.011	0.020	0.09	0.059	0.004	0.005
	ModF	0.10	0.2	0.4	8.74	-	0.94	0.21	0.076	-	0.014	0.012	0.04	0.058	0.001	0.005

Series	Alloy	Ni	Co	Mo	Pd	W	Ti	Al	Cr	N	B	C	Si	Mn
D	P5	11.82	8.92	-	-	9.82	0.20	0.14	-	0.0006	0.0047	0.0003	0.90	0.49
	P6	11.10	9.01	-	1.99	10.00	0.18	0.10	-	0.0005	0.0049	0.0002	0.02	0.46
	P7	12.08	8.96	-	-	9.90	0.12	0.06	5.04	0.0005	0.0052	0.0005	0.02	0.46
	P8	12.06	9.04	-	-	10.10	0.16	0.09	8.66	0.0006	0.0051	0.0003	0.04	0.45
	P9	11.95	8.99	-	-	9.95	0.18	0.11	5.09	0.0016	0.0055	0.0006	0.99	0.48
	X1	17.5	8.9	4.92	-	-	0.18	0.07	-	0.0012	0.0050	0.0009	0.01	0.45
	X2	12	9	4.94	-	-	0.18	0.09	-	0.0011	0.0048	0.0021	0.01	0.45
	X3	6.05	9	4.95	-	-	0.21	0.09	-	0.0010	0.0052	0.0022	0.02	0.46
	X4	12.2	9	-	-	10.06	0.20	0.09	-	0.0015	0.0050	0.0014	0.01	0.47
	X5	11.6	8.6	-	-	4.90	0.20	0.09	-	0.0014	0.0049	0.0015	0.01	0.45
	X6	18.4	7.8	3.04	-	-	0.21	0.12	-	-	-	0.0029	<.005	0.0004
	X7	12	-	2.86	-	-	0.20	0.11	4.98	-	-	0.0028	<.005	0.0017

Series	Alloy	C	Si	Mn	Cr	W	V	Nb	Pd	B	N
E	P3	0.08	0.3	0.5	9.0	3.3	0.2	0.051	3.0	0.005	0.05
	B2	0.08	0.31	0.5	9.0	3.3	0.2	0.051	-	0.005	0.050
F	A0	0.15	-	-	8.5	2.0	0.2	0.051	-	-	-
	A3	0.15	0.8	-	8.5	2.0	0.2	0.051	3.0	0.005	0.05
	B2	0.15	0.5	-	12.0	2.0	0.2	0.051	-	0.005	0.050

oxide layer was analyzed by thin film X-ray diffraction (XRD), XPS, and TEM. In the XRD procedure, Cr-Kα irradiation of an incident angle of 1° was used. The diffracted X-rays were collected in the 2θ region between 10° and 120°. The thin film specimens for TEM observation were prepared by Ar ion-milling and observation was performed at a voltage of 200 kV.

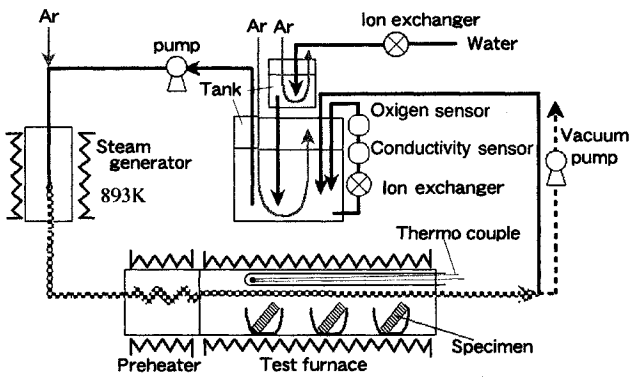


Fig.1 Steam oxidation test apparatus.

3. Results and Discussion

Effect of Mo, W and trace amounts of S on steam oxidation behavior of high-Cr ferritic heat resistant steels

Fig. 2 shows weight gain of the five kinds of 9Cr-W/Mo steels with different W/Mo where the Mo equivalent was kept to 1.5 mass % (A series alloys) oxidized in steam atmosphere for 3.6Ms. With composition of 2.8W-0.1Mo or 2.5W-0.3Mo, weight gain had a small maximum value. However, as W addition was decreased, that is, as Mo addition was increased, weight gain became smaller. At all given temperatures, ranging 873 K to 1023 K, with composition of 0W-1.5Mo, the smallest weight gain was obtained. It was shown from this that W, rather than Mo, tends to lower the steam oxidation resistance of alloys.

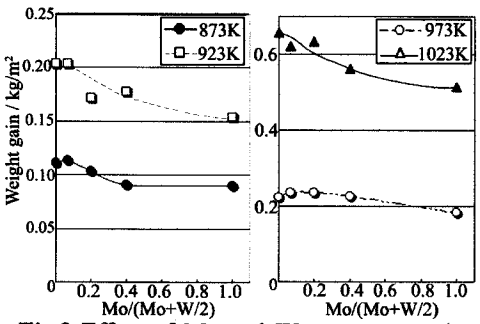


Fig.2 Effect of Mo and W contents on the steam oxidation behavior.

Fig.3 shows weight gain of six kinds of Mod.9Cr-1Mo steels (the C series alloys) oxidized in steam for 3.6Ms. For comparison, it also shows weight gain of ASME SA 335-P122 (S1), ASME SA 335-P92 (S2) and 9Cr2W(T6B) which were generated by substituting Mo of Mod.9Cr-1Mo steel for W. At 873 K, irrespective of different heat, no difference of weight gain was found among six kinds of Mod.9Cr1Mo steels, showing less weight gain than that of S1. Also, T6B had the most weight gain among the nine kinds of steels. It is suggested that T6B should include less Cr and more W than S1 and S2 to be inferior to them regarding its steam oxidation resistance. On the other hand, ranging between 923 K to 1023 K, weight gain of Mod.9Cr-1Mo steels greatly differed depending on the given heat, so it is supposed that there should be a point at which oxidation behavior drastically changes, near 923 K. Over 923 K, while ModD's and ModE's weight gains were notably small to show better steam oxidation behavior than S1, other alloys' weight gains were equal or inferior to S1. Furthermore, even ModA, which had the most weight gain, had less weight gain than S2 and T6B. Analyzing chemical compositions shown in Table 1, there was no significant difference between main elements with each heat; yet, ModD and ModE included only S more, by 20 ppm to 30 ppm, than other alloys. Thus, trace amounts of S are suggested to have a certain contribution to oxidation resistance.

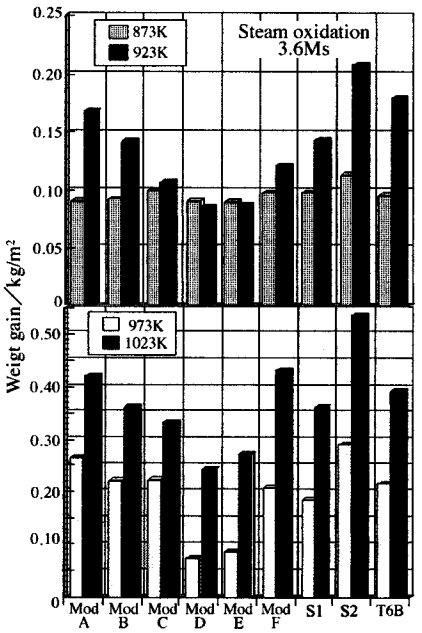


Fig.3 Weight gain of B and C series steels exposed in steam for 3.6Ms

Moreover, for the purpose of investigating the difference of scales more in detail, by using X-ray micro-analyzer, element analyses were performed to cross-sections of scales of ModA, ModE, and ModF, which were exposed to steam oxidation at 923 K and 973 K for 3.6 Ms. Results of Mod.E is shown in **Fig. 4**. S is found to enrich near interface between the inner oxide layer and the base metal of the alloy. Though the mechanism has not been elucidated, it is supposed that segregation of S near surface of alloy should promote segregation of Mn, which has a high affinity for S, and resultant surface segregation of Cr and Si. It is suggested that in the earlier stages of oxidation, Cr and Si should enrich near interface between the inner layer and base metal, and present an obstacle to oxygen's inner diffusion. Thus, inner oxidation and resultant scale growth should be restrained to make a difference in oxidized scales' structures.

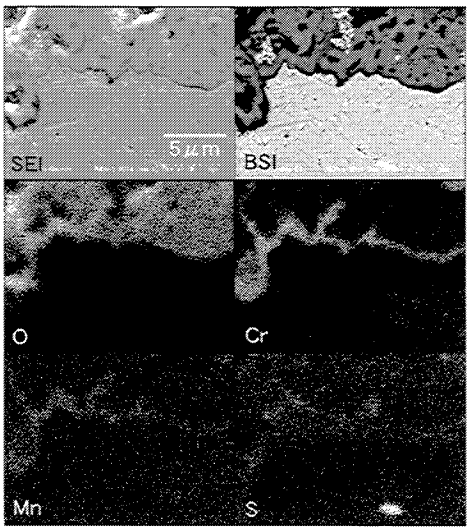


Fig.4 Characteristic X-ray map of each element in the oxide scale formed on ModE exposed in steam at 923K for 3.6Ms.

Steam oxidation behavior of carbon-free Fe-12Ni-9Co base martensitic alloys

Fig. 5 shows the weight gain obtained by exposing six kinds of the D series alloys in steam atmosphere at 873 and 923K for 3.6Ms. They include a base alloy of Fe-12Ni-9Co-10W-0.5Mn, four kinds of alloys, having the same fundamental composition as the base steel, with only one element added, 1mass% Si, 2mass% Pd, 5mass% Cr, or 9mass% Cr, respectively, and an alloy, whose fundamental composition was Fe-12Ni-0Co-10W-0.5Mn, with both 5mass% Cr and 1mass% Si added. Si, Cr, and Pd, though efficient in conventional high-Cr ferritic heat resistance steels, was found to make no contribution to improving oxidation characteristics of precipitation hardening type C-free martensitic alloys.

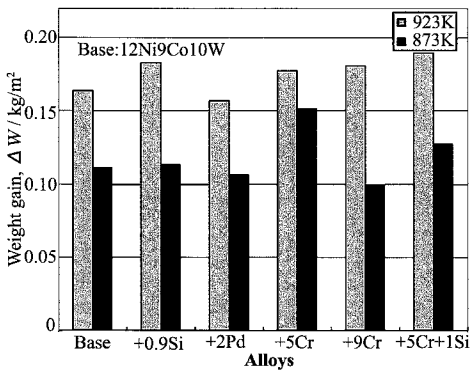


Fig.5 Effect of Cr, Si, and Pd contents on the steam oxidation behavior of alloys by exposing them to steam atmosphere at 873 and 923K for 3.6Ms.

Fig. 6 shows the oxidation weight gain obtained by exposing three alloys (12Ni9Co5Mo, 12Ni9Co5W and 12Ni9Co10W) in steam atmosphere at 873 to 1023K for 3.6Ms. At 1073K, weight gain of the alloy whose Mo was substituted for W increased by almost 200%, demonstrating that W must deteriorate oxidation resistance.

Fig. 7 shows weight gain obtained by exposing the alloy of Fe-xNi-9Co-5Mo, whose Ni content was varied from 6 to 18mass%, in steam atmosphere at 873 to 1023K for 3.6Ms. Below 923K, no influence of Ni content on weight gain was found. On the other hand, when oxidized at 973K and 1023K, for Ni contents over 12%, weight gain was remarkably decreased. Especially at 1023K, weight gain of 12Ni alloy is about 50% of that of 6Ni alloy.

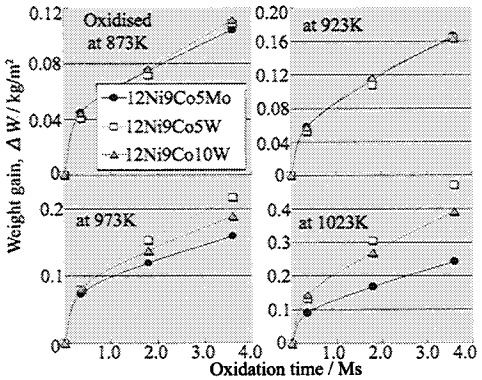


Fig.6 Effect of Mo and W contents on the steam oxidation behavior of alloys by exposing them to steam atmosphere at 873-1023K for 3.6Ms.

Fig. 8 contrasts oxidation weight gains of alloys of 12Ni and 18Ni at 873K and 973K with those of three conventional steels (ASME SA 335-P122, ASME SA 335-P92 and Mod.9Cr-1Mo steel) at 873K. It shows that the weight gain due to steam oxidation of alloy with 12 and 18Ni at 973K is approximately the same as that of three commercial 9-12Cr ferritic steels at 873K. From the perspective of steam oxidation, it is suggested that the C-free martensitic alloys, including Ni of over 12mass%, should be sufficiently durable at the high temperature of 973K in that these three conventional steels were put into practical use at 873K.

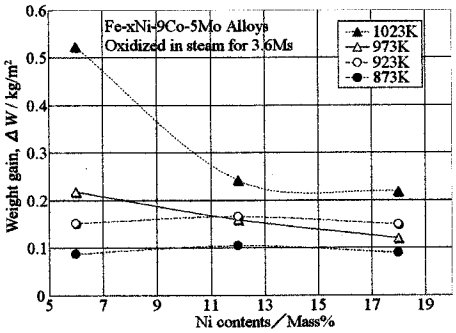


Fig.7 Effect of Ni contents on the steam oxidation behavior of alloys by exposing them to steam atmosphere at 873-1023K for 3.6Ms.

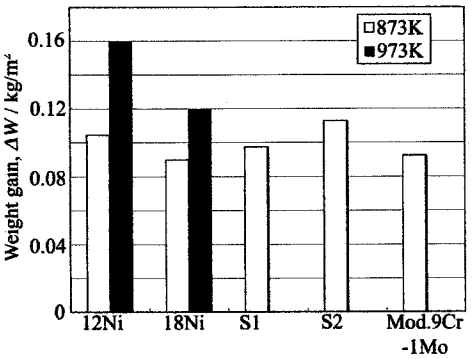


Fig.8 Comparison of weight gains by exposing 12Ni-alloy, 18Ni-alloy and three commercial high-Cr ferritic heat resistance steels in steam at 873K and at 973K for 3.6Ms .

Fig. 9 shows the element mapping of scales obtained by exposing the alloy of Fe-18Ni-9Co-5Mo in a steam atmosphere at 973K for 3.6Ms. Its scale was a monolayer of Fe oxide, including no other elements. Around the pores right under the scale, while Fe was exhausted and Ni was relatively enriched, no inner oxidized layers were detected.

Fig.10 shows the X-ray diffraction pattern of scales of 18Ni-9Co-5Mo alloys oxidized at 973K for 3.6Ms. With a micro beam X-ray of 50 μ mϕ, X-ray diffraction patterns were

measured at each point of scale (a), Fe exhaustion layer (b), and base metal (c). It followed from this that even if each diffraction pattern included the other patterns, the scale was magnetite and there was austenitic alloy layer between the scale and base ferritc metal.

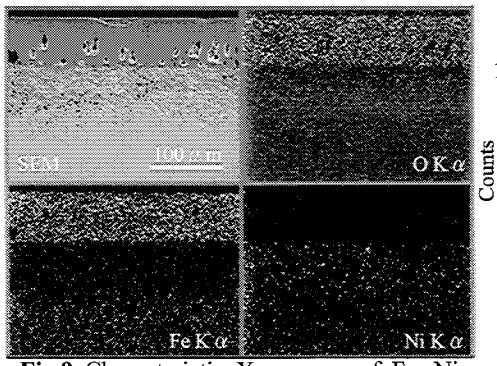


Fig.9 Characteristic X-ray map of Fe, Ni and O in the oxide scale formed on Fe-18Ni-9Co-5Mo alloy exposed in steam at 973K for 0.36Ms

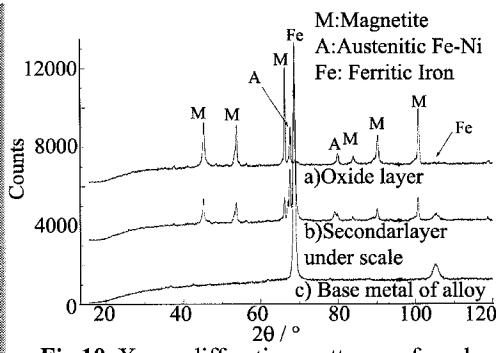


Fig.10 X-ray diffraction patterns of scale and secondary layer formed on surface of Fe-18Ni-9Co-5Mo alloy exposed in steam at 973K for 0.36Ms.

It is suggested that as scales are formed by Fe diffusion in high temperature steam, Fe concentration is diluted and, in turn, Ni concentration is relatively inspissated; then the alloy is transformed into an austenitic alloy. Because the austenitic layer is made just under the scale, the Fe diffusion rate is slowed down to restrain scale growth.

The formation of protective and thin Cr-rich oxide layer

Fig. 11 shows the optical microscopic observation of the cross section of the oxidized specimens, showing the difference in oxidation between the three alloys. Specimens were pretreated either by surface finishing with a SiC paper of 320 grit or by annealing at 973K for 180ks in vacuum for strain releasing. Then the specimens were oxidized in steam at 923K for 360ks. The oxidation of the P3 specimen finished with SiC paper was suppressed remarkably by the formation of the thin oxide layer, while in the specimen treated by vacuum annealing its oxidation was accelerated to form a thick oxide scale consisting of two layers. Also in buff-polished specimens thick two layered scale similar to those of the vacuum annealed specimens was observed.

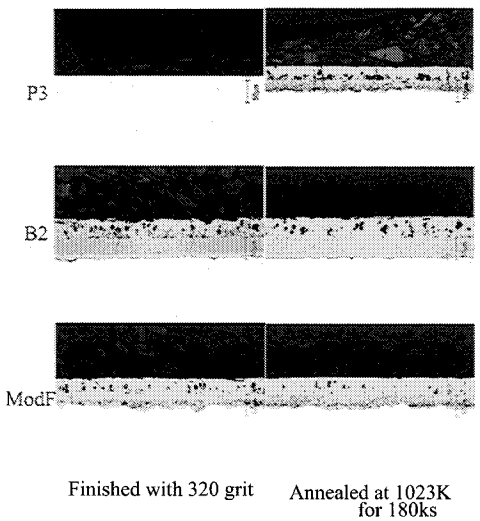


Fig.11 Influence of surface finishing in the steam oxidation of 9Cr ferritic steels

Fig. 12 shows the cross section of the steam-oxidized surface of the 9Cr-ferritic steel sputtered with palladium or platinum. Similar to the P3 specimen shown in Figure 8, a

protective oxide layer was observed only in the specimen strained by surface processing. In addition, pre-oxidation in Ar flow over 923K to high-Cr ferritic steel without pd was made to form similar protective oxide layer.

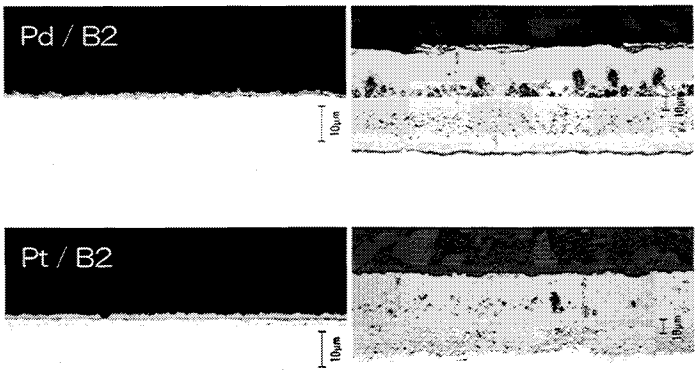


Fig.12 Influence of surface straining in the steam oxidation of 9Cr ferritic steel coated with Pd or Pt

Fig. 13 shows the optical microscopic observation of the cross section of five kinds of specimens (F series alloys, S1, S2 and ModF) oxidized in steam atmosphere after pre-oxidation treatment in Ar flow at 923K for 10.8ks. The oxidation of the specimen with 0.8mass% Si was suppressed remarkably by the formation of the thin oxide layer, while other specimens' oxidation were accelerated to form a thick oxide scale consisting of two layers.

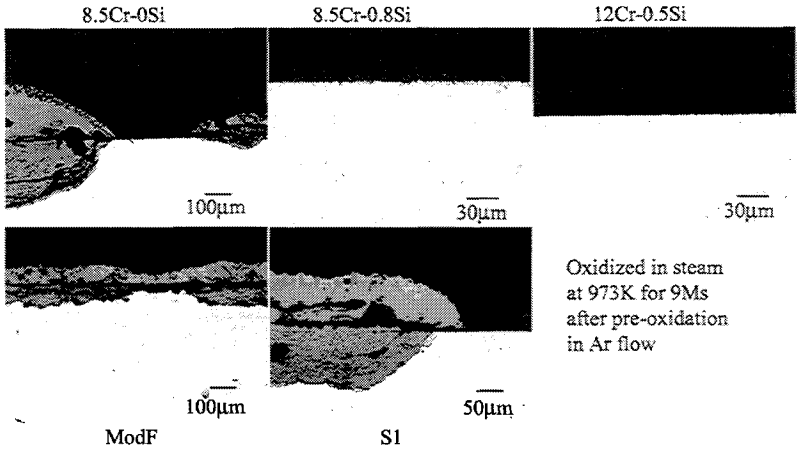


Fig.13 Effect of pre-oxidation treatment on the steam oxidation scales.

Fig. 14 shows the element mapping of the P3/320grit specimen by STEM-EDS analysis. Fe is dense in the center of the oxide grains, while Cr is dense in the grain boundary, surfaces

and the interfaces between the scale and substrate. It seems to have a kind of substructure at the surface and inside the oxide grain, which was observed as apparently one phase by TEM. The protective oxide layer on the surface of the Pd-added steel formed by steam oxidation is considered to be $(Fe,Cr)_2O_3$. The oxide layer is Fe_2O_3 in early stage of oxidation. The Cr concentration in the layer increases with time and the composition of the oxide changes finally to that of Cr_2O_3. Cr is supplied through the defects in the metal substrate, such as grain boundary, dislocation, and slip plains, while Pd is considered to have the role of increasing the activity of Cr in steam oxidation.

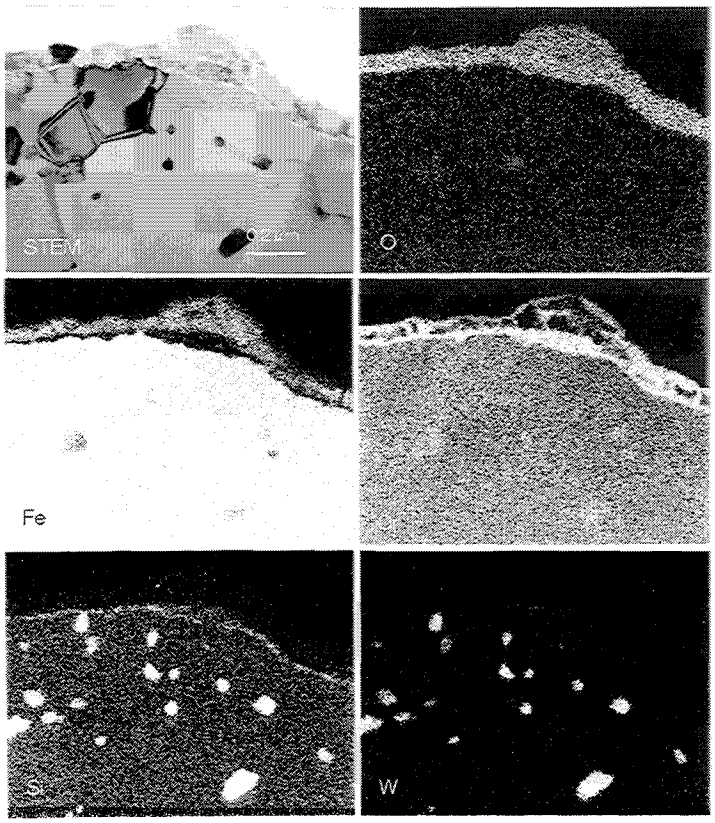


Fig.14 STEM-EDS analysis of protective oxide layer on P3/320 grit specimen

4. Conclusion

Steam oxidation of a variety of ferritic heat resistant steels was studied and the following conclusions were obtained.

1. molybdenum was more effective than tungsten for the steam oxidation resistance of high-Cr ferritic heat resistant steels.
2. Small amounts of sulfur in high-Cr ferritic heat resistant steels improved the steam oxidation resistance for high-Cr ferritic heat resistant steels.
3. Tungsten must deteriorate oxidation resistance of carbon free Fe-Ni-Co base martensitic alloys.
4. The steam oxidation characteristics of carbon free Fe-Ni-Co base martensitic alloys over 973K was improved by the increase of the Ni content, and the weight gain due to steam oxidation of alloy with 12 and 18Ni at 973K is approximately the same as that of three commercial 9-12Cr ferritic steels at 873K.
5. When surface strained high-Cr ferritic steels with small amounts of Pd was oxidized in

steam at 923K, protective and thin Cr-rich oxide layer was formed in the steel surface. And steam oxidation resistance was dramatically improved by this protective oxide layer.

6. pre-oxidation in Ar flow over 723K to high-Cr ferritic steel without Pd was made to form similar protective oxide layer.
7. The protective oxide layer on the surface of the Pd-added steel formed by steam oxidation is considered to be $(Fe,Cr)_2O_3$.

Acknowledgement

The author would like to thank Mr. K. Yokokawa, Dr. S. Muneki and Dr. M. Igarashi for preparation of test specimens and their valuable advice and comments on the analysis of the oxidized scales.

References

[1] V.K. Sikka, C.T. Ward and K.C. Thomas: ASM Int. Conf. Production, Fabrication, Properties and Application of Ferritic Steels for High Temperature Applications, Warren, PA.Oct.6-8(1981)

[2] F. Masuyama, I. Ishihara, T. Yokoyama, and M. Fujita: Thermal and Nuclear Power, **46**(1995), 498

[3] Y. Watanabe, T. Kondo, T. Kishinami, M. Inui, Y. S. Yi : Report of 123rd Committee on Heat-Resisting Metals and Alloys, Jpn. Soc. for the Promotion of Sci, **39**(1998), p.389

[4] Y. S. Yi、Y. Watanabe, T. Kondo, M. Sato : Report of 123rd Committee on Heat-Resisting Metals and Alloys, Jpn. Soc. for the Promotion of Sci,**39**(1998), p.53

[5] K. Tamura, K. Suzuki, Y. Fukuda、K. Mitsuhara、H. Yamanouchi: Proc. 2nd International Conference on Heat-Resistant Materials, Gatlinburg, TN, (1995), p.33

[6] Y. Fukuda、K. Tamura、K. Suzaki: Proc. International Symposium on Plant Aging and Life Prediction of Corrodible Structures, Sapporo, Japan, (1997), p.835

[7] Y. Komai, F. Masuyama, Y. Sawaragi, A. Iseda: Report of 123rd Committee on Heat-Resisting Metals and Alloys, Jpn. Soc. for the Promotion of Sci., **41**(2000), p.239

[8] S. Muneki, M. Igarashi, F. Abe: TETSU-TO-HAGANE, **88**(2002), 45

[9] M. Igarashi, S. Muneki and F. Abe: Report of 123rd Committee on Heat-Resisting Metals and Alloys, Jpn. Soc. for the Promotion of Sci., **39**(1998), 355

[10] M. Igarashi, S. Muneki, H. hasegawa, K. Yamada and F. Abe: ISIJ International, **41**(2001), Supplement, S101

[11] K. Yokokawa, O. Kanemaru, H. Miyazaki, T. Ohba, F. Abe: CAMP-ISIJ, **12**(1999), 439

[12] NRIM Creep Data Sheet. Tokyo: National Research Institute for Metals, September 1996. No.43

[13] H. Fujikawa and N. Otsuka: Nippon Kagaku Kaishi, 1988, No.1, 45

STEAM OXIDATION OF HIGH CHROMIUM FERRITIC STEELS CONTAINING PALLADIUM

Takehiko Itagaki*, Hiroyuki Kutsumi*, Masaaki Igarashi** and Fujio Abe*

* National Institute for Materials Science
** Sumitomo Metal Industries Ltd.

Abstract

The steam oxidation behavior of 9Cr ferritic steel containing palladium was studied in comparison with that of Mod.9Cr-1Mo steel (P91). It was found that the oxidation of 9Cr steel containing 3 mass% Pd, the surface of which was finished with SiC paper of 320 grit, was suppressed by the formation of a protective oxide layer when it was exposed to steam at 650°C. This experimental result is unusual in high-Cr ferritic steels, including Mod.9Cr-1Mo. A similar suppression of oxidation was also observed in specimens of Mod.9Cr-1Mo steel which were coated with palladium or platinum. When the steel containing palladium was exposed to steam at 650°C for 50 h, the thickness of the oxide layer became about 0.3 μm. The analyses of the oxide layer by thin film X-ray diffraction, TEM, and electron diffraction suggest that the protective layer is made of $(Fe, Cr)_2O_3$ with a rhombohedral structure. A supply of chromium from the metal matrix due to the residual strain in the surface region of specimen and an increase of the chromium activity due to palladium may contribute to the formation of the protective oxide layer.

Keywords : Steam oxidation, High-Cr ferritic steel, Palladium, Protective oxide layer, USC boiler

1. Introduction

Reduction of CO_2 emission has been recognized strongly as a counter-measure against the greenhouse effect. The improvement of efficiency of coal power plants helps the solution of exhaustion of energy resources and to stop the greenhouse effect. The research and development of next-generation ultra-supercritical (USC) power plants have been performed in European countries and Japan[1,2]. Heat-resistant ferritic steels such as P92 and P122 have already been developed as parts of large and thick pipes for the main steam pipes and headers. It is necessary to develop new heat-resistant ferritic steels with high strength and anti-corrosive property in order to realize further improved fuel efficiency and to construct flexible power plants with changeable output depending upon the change in demand[3,4]. We have been developing high-Cr heat-resistant ferritic steel for large & thick pipes that can be used in a next-generation USC power plant in operation at 650°C and 350 atm. We developed new steels based on new strengthening theory[5,6], which have the $L1_0$ type FePd-base intermetallic compound precipitated in the ferrite matrix. This kind of reinforcement functions additively with the reinforcement by precipitation of MX type carbonitride, $M_{23}C_6$ type carbide and the Laves phase.

Since steam at high temperature seems to accelerate the oxidation of steels, anti-oxidation property against high-temperature steam becomes more important for the USC power plant class in operation at 650°C. We studied the steam oxidation of palladium-containing high-Cr ferritic steel at high temperatures of around 650°C. As a result, an unusual oxidation behavior, different from that of usual high-Cr heat-resistant ferritic steels, was found in this study.

2. Experimental

Table 1 lists the chemical compositions of the alloys used in this study. The alloy (P3) added with palladium and the alloy (B2) without palladium were prepared in our laboratory, while the Mod.9Cr-1Mo steel (ModF) was commercial steel plate. The specimens for oxidation test were cut into a coupon shape of 10×20×2 mm by electrical-discharge machining from the bulk material treated with normal quenching and annealing. Finally the specimens were finished up with SiC abrasive papers of 320 grit. Some specimens were treated either by buff-polishing for removing their process-strained layer in the near-surface region or vacuum annealing at 750°C for 50 h for strain releasing. Sputter coating of palladium or platinum on B2 and ModF were attempted to investigate the effect of palladium on the steam oxidation behavior of the ferritic steels. Before the sputtering, the substrates of the B2 and ModF specimens were finished with SiC paper of 320grit and then washed. Then palladium or platinum was sputtered with a magnetron sputtering apparatus for a layer of about 1 μm in thickness. The sputtered specimens were heat treated by diffusive permeation at 750°C for 50h in vacuum. Subsequently the sputtered specimens were process strained by hammering on SiC paper of 320grit, in order to avoid removing the surface coated layer by grinding. The hammering was repeated until the virgin surface had faded away completely. The hammering was confirmed by microscopic observation.

Table 1 Chemical compositions of the alloys (mass %)

P3	Fe-0.08C-0.31Si-0.5Mn-9.0Cr-3.3W -0.2V-0.05Nb-3.0Pd-0.005B-0.05N
B2	Fe-0.08C-0.31Si-0.5Mn-9.0Cr-3.3W -0.2V-0.05Nb -0.005B-0.05N
ModF	Fe-0.10C-0.24Si-0.5Mn-8.7Cr-0.94Mo-0.2V-0.08Nb -0.05N
Pd/B2, Pd/ModF	Pd sputter coating / Substrate
Pt/B2, Pt/ModF	Pt sputter coating / Substrate

Fig. 1 shows the setup of the testing apparatus for steam oxidation. The quality of the water in the water tank was kept with concentration of oxygen less than 10 ppb and electrical conductivity less than 8.0 μS/m. The flow rate of steam was controlled by the water supply to the steam generator, which was 10 cm^3/min. The test specimen in a ceramic crucible was set in the testing apparatus after it was washed with methanol and acetone in the ultrasonic bath. The testing chamber with specimens in it was evacuated, and then argon gas with dew point of –65°C and oxygen content of 0.3 ppm was filled and heated up to 200°C. The gas in the chamber was then exchanged with steam and then continued to be heated at oxidation temperature. The total heating operation took about 3 hours. The time for oxidation was defined as the time period from reaching oxidation temperature to shutting down the power.

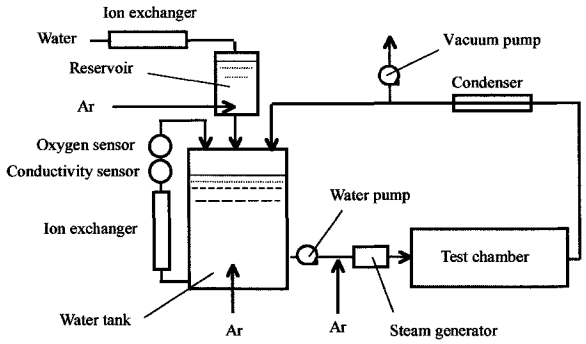


Fig. 1 Schematic illustration of steam oxidation apparatus

The cross section of the oxidized specimens was observed by optical microscope and

scanning electron microscope (SEM). Element analysis of the near surface area was performed by EPMA. The oxide layer was analyzed by thin film X-ray diffraction (XRD), XPS, and TEM. In the XRD procedure, Cr-Kα irradiation of an incident angle of 1° was used. The diffracted X-rays were collected in the 2θ region between 10° and 120°. The thin film specimens for TEM observation were prepared by Ar ion-milling and observation was performed at a voltage of 200 kV.

3. Results and Discussion

Steam oxidation of high-chromium ferritic steels and effect of palladium addition

Fig. 2 shows the optical microscopic observation of the cross section of the oxidized specimens, showing the difference in oxidation between the three alloys. Specimens were pretreated either by surface finishing with a SiC paper of 320 grit or by annealing at 750°C for 50 h in vacuum for strain releasing. Then the specimens were oxidized in steam at 650°C for 100 h. The oxidation of the P3 specimen finished with SiC paper was suppressed remarkably by the formation of the thin oxide layer, while in the specimen treated by vacuum annealing its oxidation was accelerated to form a thick oxide scale consisting of two layers. Also in buff-polished specimens thick two layered scale similar to those of the vacuum annealed specimens was observed.

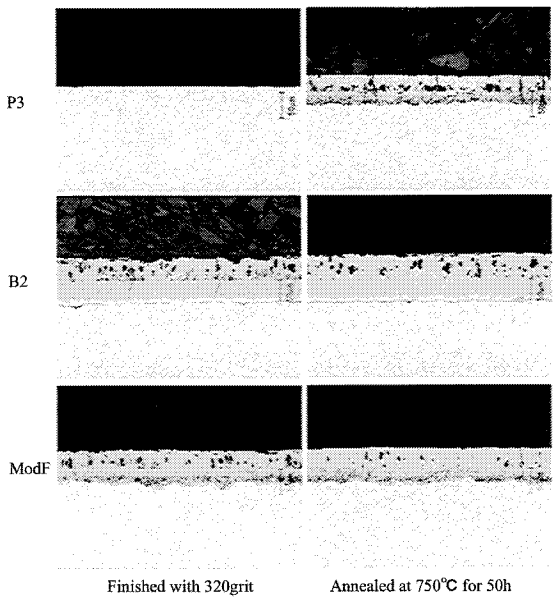


Fig.2 Influence of surface finishing in the steam oxidation of 9Cr ferritic steels

It is clear that the change in oxidation behavior of P3 alloy finished with SiC paper is dependent upon the presence of the strained surface region . On the other hand, the B2 and ModF specimens formed two layered thick scales, irrespective of surface finishing conditions. The total thickness of the two-layered oxide scale was about 60 μm in the P3 annealed specimen, while it was about 100 μm for the B2 alloy. For the two layered scale, it was believed that the outer layer was magnetite (Fe_3O_4) and the inner layer was a spinel-type oxide of Fe and Cr, respectively[7].

Fig. 3 shows the elemental map of the cross section of the oxidized P3 specimen finished with SiC paper of 320 grit. This picture was obtained by long time exposure of electron beam in EPMA because the existence of any oxide layer could not be found by optical microscope. A thin oxide film with high concentration of Cr can be seen on the surface of the P3 specimen. Si was concentrated as islands in the interface between the thin Cr-rich layer and metal matrix.

The Cr content seems to decrease slightly in the region up to 2μm from the surface. The Pd-rich phase in the metal matrix is found to be the FePd-base intermetallic compound. The FePd phase is absent in the low-Cr region near the surface. As there is no segregation of Pd in the surface layer, the possibility that the solubility of Pd increases in this region may be reasonable. The SEM observation analyzed that the oxide layer is about 0.3 μm in thickness, mainly consisting of Cr and Fe with the intensity ratio of Cr:Fe = 95:25 by EDS analysis.

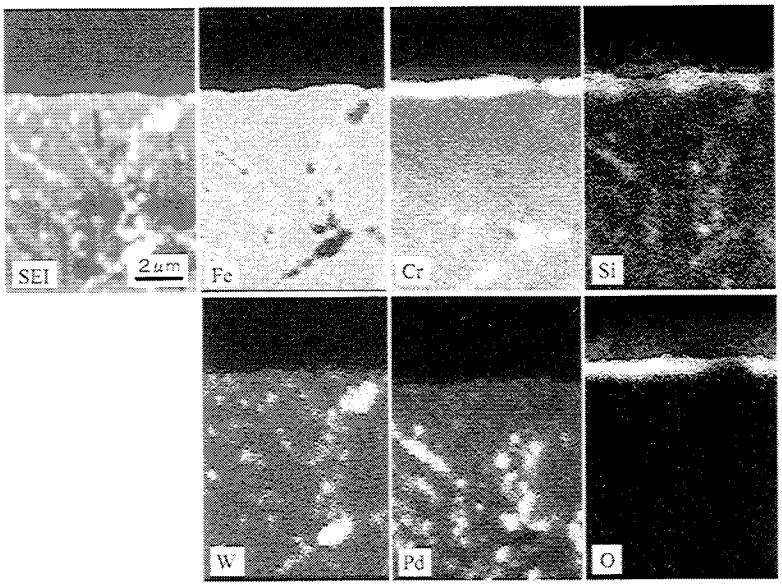


Fig.3 EPMA analysis of a near surface area of the Pd-added alloy finished with 320 grit SiC paper

Fig. 4 shows the XRD patterns of the steam-oxidized surface of the P3 alloy. Magnetite (Fe_3O_4) and Hematite (Fe_2O_3) were detected in the surfaces of the specimens which were vacuum annealed and buff-polished before steam oxidation. A thin whitish layer can be seen in the outermost surface of the outer oxide layer, suggesting the Hematite structure by XRD analysis. On the other hand, a phase similar to the Cr_2O_3 structure, Magnetite and (110) reflection of metal matrix (α-Fe) were observed in the P3 specimen whose surface was finished by 320grit SiC paper before

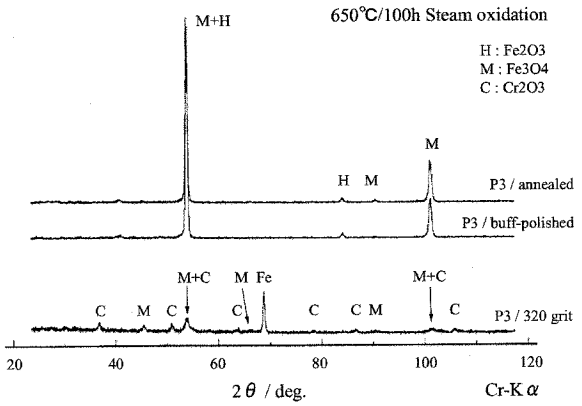


Fig. 4 Thin film X-ray diffraction of the Pd-added alloy(P3) oxidized in steam

oxidation. The phase noted as "C:Cr_2O_3" in Figure 4 is very similar to the Eskolaite (Cr_2O_3) with rhombohedral structure. Since the results of EPMA mapping and SEM-EDS analysis indicate that there is a high concentration of Cr in the surface layer, this phase may have the same structure as Cr_2O_3 but has a slightly different element composition. As the (110) peak of metal matrix (α-Fe) is detected, the oxide layer seems to be very thin.

Oxidation behavior of 9Cr ferritic steel sputter-coated with Pd or Pt

Fig. 5 shows the cross section of the steam-oxidized surface of the 9Cr-ferritic steel sputtered with palladium or platinum. Similar to the P3 specimen shown in Figure 2, a protective oxide layer was observed only in the specimen strained by surface processing. The same trend of formation of the scales was observed in the sputtered specimens as for B2 and ModF substrates. Both the palladium or platinum sputtered, but not surface processed, B2 specimens exhibited total thickness of the two layered scales about 80% of the thickness in the B2 specimen without sputtering. So the effect of sputtering of palladium or platinum on the oxidation behavior is negligible qualitatively. Surface processing by SiC paper of 320grit after sputtering helped the formation of protective oxide layers. But the protective oxide layers on the sputtered specimen were thick compared to that of the P3 alloy. As the soundness of the protective oxide layer on the sputtered specimen is low, the oxide layer is often broken to form the thick two layered scales. The main reason for the low stability of the scale on sputtered specimens, compared to that of the alloyed specimen P3, may be due to the inhomogeneities of the sputtered layer and also the surface processing. It seems that the inhomogeneity of surface processing is more responsible for the inhibition of a better oxide layer formation than that of sputtering because the EPMA analysis clarifies qualitatively that Pd or Pt concentration in the sputtered surface becomes several tens mass%, which is

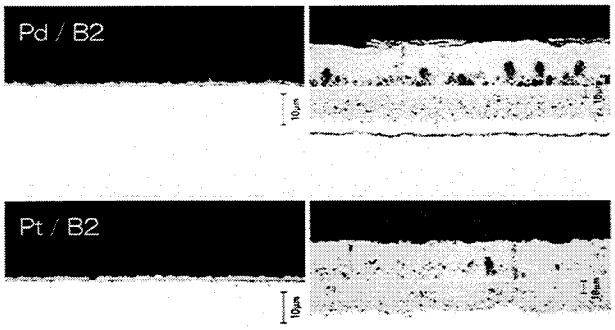


Fig.5 Influence of surface straining in the steam oxidation of 9Cr ferritic steel coated with Pd or Pt

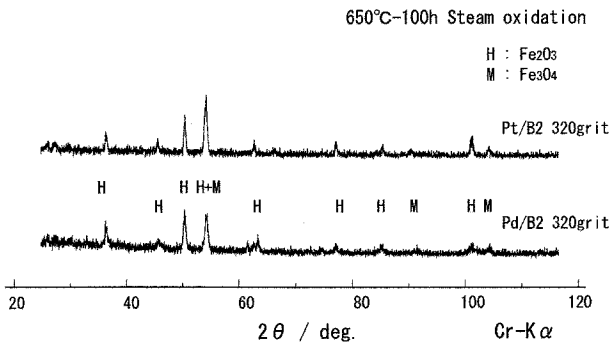


Fig.6 Thin film X-ray diffraction of the coated specimen oxidized in steam

much larger than the 3 mass% palladium in the P3 alloy. The oxide layer of the Pd-sputtered specimen was more stable than that of the Pt-sputtered specimen.

Fig. 6 shows the XRD profiles of the specimens steam-oxidized at 650°C for 100 h in which the specimens had been sputtered with Pd or Pt and then surface processed. Both the Pd and Pt sputtered specimens showed only the diffraction peaks due to Hematite and Magnetite. Peaks due to Cr_2O_3 and α-Fe could not be observed. The EPMA mapping exhibited the scale consisting of two layered oxide. Unfortunately the exact structure of the scale could not be revealed, but a Cr-rich layer having a structure similar to Cr_2O_3 and a layer of ferric oxide may be formed in the inner and outer layers, respectively.

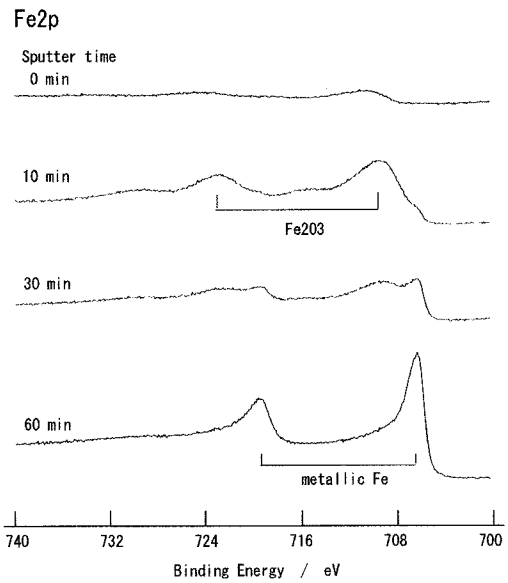


Fig.7 XPS analysis of the protective oxide layer on P3/320grit specimen

Analysis of protective oxide layer

The XPS analysis was performed for the 0.3 μm thick Cr-rich oxide layer, which was formed by steam oxidation at 650°C for 100h of the P3 alloy finished with 320 grit SiC paper. Fig. 7 shows the change in peak of the Fe-2P3/2 and 2P1/2. The information of substrate can be obtained by Ar-sputtering for 30 min. The position of the 2P3/2 peak is located at about 710 eV, being near the position of FeO, but the possibility of being Fe_2O_3 is strong because the peak difference between 2P3/2 and 2P1/2 peaks is 13.6 eV. In the case of Cr, the peak did not agree with one of the Cr_2O_3, but the energy difference between the two peaks was 9.7eV, and it agreed with the standard data of Cr_2O_3. Palladium was not detected in the scale, but the peak corresponding to substrate was obtained after Ar-sputtering for 60 min. Tungsten was detected as WO_3 only before the Ar-sputtering, and Si was detected as the peak of SiO_2 after the Ar-sputtering for 30 min. According to the results of the XPS analysis, the main portions of the protective oxide may be composed of the materials very close to Fe_2O_3 or Cr_2O_3. The WO_3 peak is included in the outermost surface, and SiO_2 is located between the oxide layer and substrate, while Pd may be located only in the metal matrix.

The change in surface before and after the steam oxidation of the P3 alloy at 650°C for 50h was measured by TEM, in order to observe the initial state of formation for the protective oxide layer. Fig. 8(a) shows the outermost surface of the specimen before the oxidation, indicating the surface region processed by 320grit finishing about 0.3 μm in width, and showing high dislocation density in the region about 1 μm beneath the surface. The effect of processing by machining seems to reach the deep region of about 3-5 μm beneath the surface, which is why an entanglement of dislocation lines is clearly observed. Fig. 8(b) shows the texture of the surface of the steam-oxidized material. The crystalline granules of the oxide were observed in a protective surface layer about 0.1 μm thick, showing the granules oriented

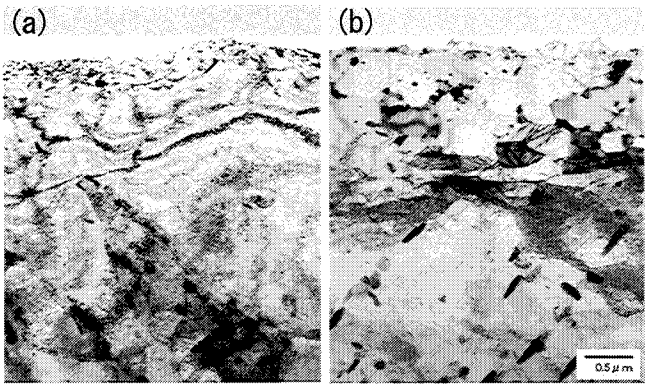


Fig.8 TEM texture of the near-surface layers of the P3/320grit specimen
(a) before oxidation, (b) after steam oxidation

in a layer. The metal substrate in the region about 1μm below the surface was observed as equiaxed fine grains with no dislocation (0.5μm in diameter) because of recrystalization. Since the dislocation lines were observed to be dense in the intermediate region 2-3 μm below the outermost surface, the heating condition of steam oxidation in this study suggests conditions insufficient for recrystalization in usual sense.

Fig. 9 shows the element mapping of the specimen by STEM-EDS analysis. Fe is dense in the center of the oxide grains, while Cr is dense in the grain boundary, surfaces and the interfaces between the scale and substrate. It seems to have a kind of substructure at the surface and inside the oxide grain, which was observed as apparently one phase by TEM. Fig. 10 indicates the result of the P3/320grit specimen by line analysis, indicating the high concentration of Cr in the surface and interfaces of the oxide grains. Fig. 11 shows a highly magnified photograph and the electron diffraction of the P3/320grit specimen. Since there is an arrangement of atoms matched to the spots of electron diffraction and a contrast based only on azimuthal difference is observed, except at the interface between the scale and substrate, this scale seems to be formed with an arrangement in a layer of single crystal grains without a substructure. The electron diffraction analysis suggests that the oxide grains have

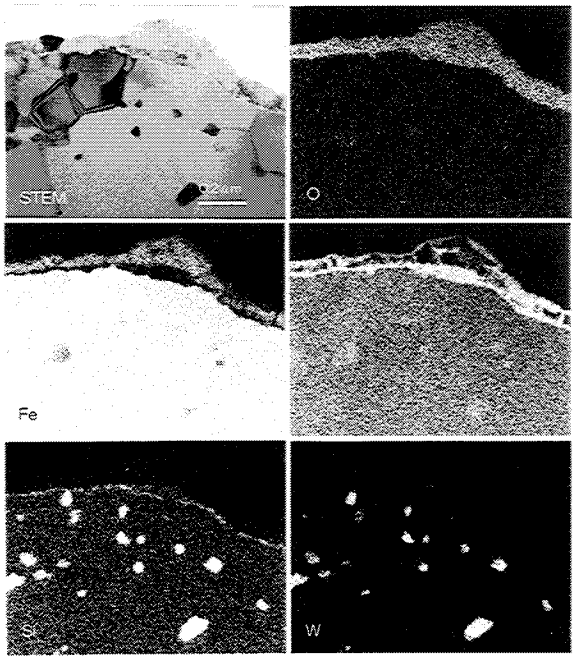


Fig.9 STEM-EDS analysis of protective oxide layer on P3/320grit specimen

rhombohedral structure and have a lattice constant intermediate between Fe_2O_3 and Cr_2O_3. If the (0110) spot is supposed due to either pure Cr_2O_3 or Fe_2O_3, this spot should be extinctive due to the extinction rule. The direction of irradiation (zone axis) of electron ray was [0001].

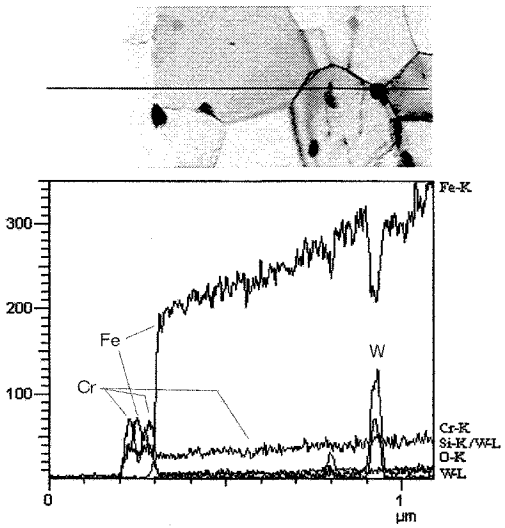


Fig.10 Line analysis of the protective oxide layer on P3/320grit specimen

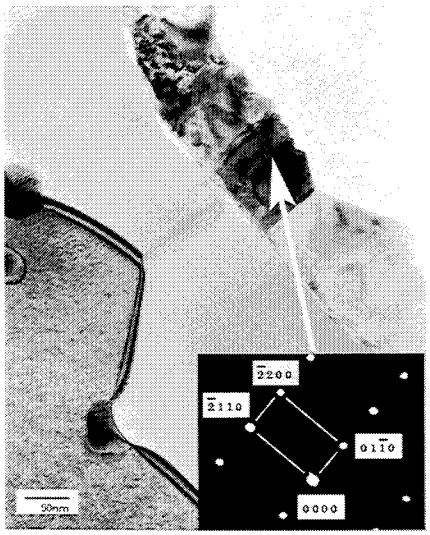


Fig.11 Electron diffraction of the protective layer on P3/320grit specimen

It can be speculated as follows. In the initial stage of oxidation, ferric oxides with lower valence such as FeO and Fe_3O_4 are formed, and then Cr oxide is formed at interface between the ferric oxide layer and metal matrix. Then the ferric oxides change into Hematite (Fe_2O_3) because the supply of Fe from substrate is obstructed by Cr oxide. Then only Cr is supplied from the substrate, and covers the outermost surfaces of the scales due to the diffusion of Cr through the boundaries of the Fe_2O_3 grains. Though the structure of the scale is close to one of Fe_2O_3 in early stage of oxidation, according to the gradual increase of Cr atoms, finally it reaches close to Cr_2O_3 in composition. Since Hematite and Eskolite have the same rhombohedral structure, and the lattice constants of the former are a = 5.02480 Å, c = 13.71630 Å and those of the latter are a = 4.95876 Å, c = 13.59420 Å, both structures are able to change continuously with each other. Neither pure Hematite nor pure Eskolite shows (0110) diffraction due to the extinction rule. The appearance of the (0110) spot in Figure 11 can be explained by diffraction of $(Fe,Cr)_2O_3$, in which Fe atoms are exchanged partly into Cr atoms. Although the average composition of the scale at 50h oxidation is Cr:Fe = 1:1, or deflected to rich Fe side, the composition of the scale after 100 h oxidation is shifted predominantly to the Cr-rich side. The experimental fact supports the change of $Fe_2O_3 \rightarrow Cr_2O_3$.

Since the phenomenon of the formation of a protective Cr-rich oxide layer on the surface of austenitic steels during steam oxidation is well known, it is utilized as improving anti-oxidation of boiler tubes by shot peening or grain refinement[8,9,10]. The mechanism

of oxidation is not clear presently, and the structure of the oxide layer is not completely clarified, but there are common recognitions such as 1) the defect structures such as residual strains and grain boundaries induce the formation of a Cr-rich protective oxide layer by increasing paths of Cr diffusion, 2) the anti-oxidation treatments are not effective in the high temperature region above 700°C, 3) this phenomenon is not observed in the ferritic steels with less Cr content than austenitic steels.

The phenomenon that addition of Pt in the Fe-Cr alloy decreases the oxidation rate was known earlier[11], and the effect of elements of platinum group on the anti-oxidative properties of steel has been studied widely in U.S.S.R.[12]. Muramatsu et al[13] reported the increase of the anti-oxidative property of W-Cr sintered alloy with an addition of small amounts of Pd. He claimed that the α-Pd appearing in the grain boundary supplies the paths for Cr diffusion and then accelerates the formation of a Cr-rich oxide layer. Delport et al[14] studied by Auger analysis the initial oxidation behavior of Fe-40Cr alloy added with a small amount of Pd, and he found that Pd oxides are formed in the initial stage of oxidation. He speculated that the protective layers are prepared by high-speed diffusion of Cr over the Pd oxides. Wolff et al[15] reported that protective layers of Al oxides are formed on Fe-35Cr-5Al alloy by adding a small amount of Ru. At present, it is clear that the elements of platinum group increases selectively the rate of diffusion of Cr or Al, and then assists the formation of protective layers, although the controlling mechanism of oxidation is not completely clarified.

It is necessary to clear the state of palladium after oxidation, in order to clarify the role of palladium. We failed to detect Pd atoms in the surface regions in this experiment. But it is possible to interpret that Pd or Pt atoms contribute to the formation of protective layers by increasing the Cr activity, because the protective oxide layer similar to the austenitic steels is formed in the steam when the surface of ferric steels containing Pd or coated with Pd or Pt were process strained. The unusual oxidation behavior of the P3 alloy in steam is considered to occur by the formation of a Cr-rich protective oxide layer due to the two factors of accelerative diffusion of Cr by process strain in the surface layers and an increase of activity of Cr by addition of Pd.

4. Conclusion

Steam oxidation of Pd-added 9Cr ferritic steel at 650°C was studied and the following conclusions were obtained.

1. The formation of a Cr-rich protective oxide layer suppresses remarkably the oxidation of 9Cr ferritic steel added with Pd of 3 mass% when the steel is processed with surface straining and then exposed to steam at 650°C.
2. When the same material is either vacuum annealed at 750°C for 50 h or the surface strained layer is removed by buff-polishing, the specimen is oxidized more quickly to form two-layered scale in which the outer and inner layers are Magnetite and Fe-Cr spinel, respectively. At high temperatures above 700°C, the stability of the protective oxide layer decreases and is not observed at 800°C.
3. The steam oxidation at 650°C of 9Cr ferritic steel without Pd was accelerated to form the two-layered scale. Surface straining of the materials does not suppress the oxidation.
4. Surface straining of the 9Cr ferritic steel sputtered with Pd or Pt suppresses the oxidation of the steel by forming a protective layer, similar to the case of the steel added with Pd of 3 mass%.

5. The protective oxide layer on the surface of the Pd-added steel formed by steam oxidation is considered to be $(Fe,Cr)_2O_3$.
6. The oxide layer is Fe_2O_3 in early stage of oxidation. The Cr concentration in the layer increases with time and the composition of the oxide changes finally to that of Cr_2O_3. Cr is supplied through the defects in the metal substrate, such as grain boundary, dislocation, and slip plains, while Pd is considered to have the role of increasing the activity of Cr in steam oxidation.

Acknowledgement
The author would like to thank Dr. T. Abe, Dr. M. Ohnuma and Dr. K. Ymada for their valuable advice and comments on the analysis of the protective surface layer, role of Pd in the oxidation mechanism, and analysis of protective oxide layer.

References
[1] K. Muramatsu: Proc. Advanced Heat Resistant Steels for Power Generation, edited by R. Viswanathan and J. Nutting, The University Press, Cambridge, 1998, 543
[2] T. Kikuchi: Report of 123rd Committee on Heat-Resisting Metals and Alloys, Jpn. Soc. for the Promotion of Sci., vol.39(1998), 255 (in Japanese)
[3] M. Igarashi and Y. Sawaragi: Proc. Int. Conf. on Power Engineering-97, JEME, Tokyo, Japan, 1977, vol.2, 107
[4] Y. Fukuda, K. Tamura and T. Sato: in Proc. of the 6th Liege Conf. on Materials for Advanced Power Engineering, 5-7 October, Liege, Belgium, 1998, vol.I, 461
[5] M. Igarashi, S. Muneki and F. Abe: Report of 123rd Committee on Heat-Resisting Metals and Alloys, Jpn. Soc. for the Promotion of Sci., vol.39(1998), 355 (in Japanese)
[6] M. Igarashi, S. Muneki, H. hasegawa, K. Yamada and F. Abe: ISIJ International, vol.41(2001), Supplement, S101
[7] H. Fujikawa and N. Otsuka: Nippon Kagaku Kaishi, 1988, No.1, 45 (in Japanese)
[8] N. Otsuka: Sumitomo Metals, vol.44 (1992), No.3, 45 (in Japanese)
[9] H. Ichinose, T. Kanero, Y. Minami and Y. Tsuchiya: Report of 123rd Committee on Heat-Resisting Metals and Alloys, Jpn. Soc. for the Promotion of Sci., vol.28(1977), 167 (in Japanese)
[10] Y. Teranishi, K. Yoshikawa, H. Fujikawa and M. Kubota: Report of 123rd Committee on Heat-Resisting Metals and Alloys, Jpn. Soc. for the Promotion of Sci., vol.24(1983), 395 (in Japanese)
[11] P. Monnartz: Metallurgie, vol.8(1911), 161
[12] N. D. Tomashov: Protection of Metals, vol.17(1981), 11
[13] Y. Muramatsu and T. Takeda: Trans. Natl Res. Inst. Metals, vol.24(1982), 15
[14] W. E. Delport and J. P. Roux: Corrosion Science, vol.26(1986), 407
[15] I. M. Wolff, L. E. Iorio, T. Rumpf, P. V. T. Scheers and J. H. Potgieter: Materials Science and Engineering, vol.A241(1998), 264

SECTION 3

ADVANCED STEAM POWER PLANT

3.5. Welding

DESCRIPTION OF THE MATERIAL BEHAVIOUR IN GIRTH WELDS DURING WELD FABRICATION AND FOR HIGH TEMPERATURE SERVICE

Ralf Mohrmann

Fraunhofer-Institut für Werkstoffmechanik
D-79108 Freiburg, Wöhlerstrasse 11, Germany

Abstract

A non-isothermal model was developed including viscoplastic deformation, phase transformations and their interactions. The model was applied to a 12% chromium steel for temperatures between RT and 1600K. Austenite transformation, martensite transformation and the constitution of carbides were identified to affect the mechanical behaviour of the martensitic steel investigated. A generalized Johnson-Mehl-Avrami equation and the Koistinen-Marburger equation were used to describe these phase transformations.
Viscoplastic deformations were modelled with an isothermal Chaboche-type model which was extended to non-isothermal conditions. Tensile, cyclic and relaxation test data were used to identify the model parameters.

Keywords: non-isothermal model, viscoplastic deformation, phase transformation, Johnson-Mehl-Avrami, Chaboche

1 Introduction

Finite element simulations of the weld fabrication process and of the post weld heat treatment require material models describing the mechanical behaviour and phase transformations. Those models should be applicable to multiaxial stress states, valid in the temperature domain considered, and should incorporate effects of phase transformations on the mechanical behaviour.

2 Phase Transformations in Steel X20CrMoV 12 1

2.1 Considered Phase Transformations

Phases and phase transformations of the 12% chromium steel X20CrMoV 12 1 during austenitization and tempering were investigated experimentally by Petri et al. [1] and Straub [2]) and with thermodynamic calculations by Hald and Straub [3] and Strang [4]. In order to model the mechanical behaviour it is necessary to take at least those phases into account that affect the mechanical behaviour. The austenite phase, the martensite phase and a phase built by precipitated carbides were identified to affect the mechanical behaviour.
The relative mass proportions of the martensite phase z_M and of the austenite phase z_A (i.e. the mass proportion of metal atoms in a bcc lattice and in a fcc lattice, respectively) were defined. The unit cells of these phases have different volumes. Therefore, a martensite or austenite transformation will cause a volume change.
The relative mass proportions of carbon dissolved in austenite c_A and in martensite c , or precipitated as carbides c_P were defined. For simplicity only one type of carbide was included. The volume change caused by the interchange of carbon was neglected.

2.2 Modelling Phase Transformations in the Steel X20CrMoV 12 1

The phases to be modelled (z_A, z , c_A ,c and c_P) obey obvious conservation laws

$$z_A + z_M = 1 \quad \text{and} \quad c_A + c_M + c_P = 1 \,. \tag{1}$$

Basically, one has to consider the exchange rate of the austenite $\leftrightarrow$ martensite tranformation $\dot{z}_A$ and the exchange rates of the carbon kinetics $\dot{c}_A$, $\dot{c}_M$ and $\dot{c}_p$, which are defined by (with $\dot{c}_A + \dot{c}_M + \dot{c}_p = 0$)

$$\dot{c}_M = \dot{c}_{M\leftrightarrow P} - \dot{c}_{M\leftrightarrow A}, \quad \dot{c}_A = \dot{c}_{A\leftrightarrow P} + \dot{c}_{M\leftrightarrow A}, \quad \dot{c}_P = -(\dot{c}_{M\leftrightarrow P} + \dot{c}_{A\leftrightarrow P}) \,. \tag{2}$$

$\dot{c}_{M\leftrightarrow P}$ and $\dot{c}_{A\leftrightarrow P}$ represent the rate of carbon that is interchanging between the precipitated and the dissolved state (in the martensite lattice or the austenite lattice). $\dot{c}_{M\leftrightarrow A}$ represents the amount of dissolved carbon that is being exchanged between martensite and austenite (in the domain where these phases coexist).

Austenitization and the processes represented by $\dot{c}_{M\leftrightarrow P}$ and $\dot{c}_{A\leftrightarrow}$ are governed by nucleation and growth. Concepts that treat this process have been developed by Johnson, Mehl and Avrami ([5], [6]). The generalized form based on the approach of Fortunier and Leblond [7] was used, here outlined for z_A:

$$\dot{z}_A = \begin{cases} mf(T)\cdot(z_{A,eq}(T) - z_A)\left(\ln\dfrac{z_{A,eq}(T)}{z_{A,eq}(T) - z_A}\right)^{\frac{m-1}{m}} & \text{if } z_{A,eq}(T) \geq z_A \\ f(T)\cdot(z_{A,eq}(T) - z_A) & \text{else} \end{cases} . \tag{3}$$

where m is a temperature independent parameter. The kinetic parameter f and the equilibrium proportion of austenite $z_{A,eq}$ are appropriate functions of the temperature.

The martensite transformation is instantaneous. According to Koistinen and Marburger [8] the proportion of martensite at temperatures below the martensite starting temperature M_S is a function of temperature. The austenite proportion z_A is defined

$$z_A(T) = \exp\left(-a(M_S - T)\right) \text{ with } a \approx 1.10\cdot 10^{-2} \text{ 1/K.} \tag{4}$$

For the carbon dissolved in the austenite or martensite phase it was assumed that this carbon remains dissolved during austenite or martensite transformation, respectively

$$\dot{c}_{M\leftrightarrow A} = \begin{cases} \dfrac{\dot{z}_A}{1 - z_A} c_M & \text{für } \dot{z}_A \geq 0 \\ \dfrac{\dot{z}_A}{z_A} c_A & \text{für } \dot{z}_A < 0 \end{cases} . \tag{5}$$

Further information about the parameter identification, the experimental data base and the phase transformations is given in Gantert [9].

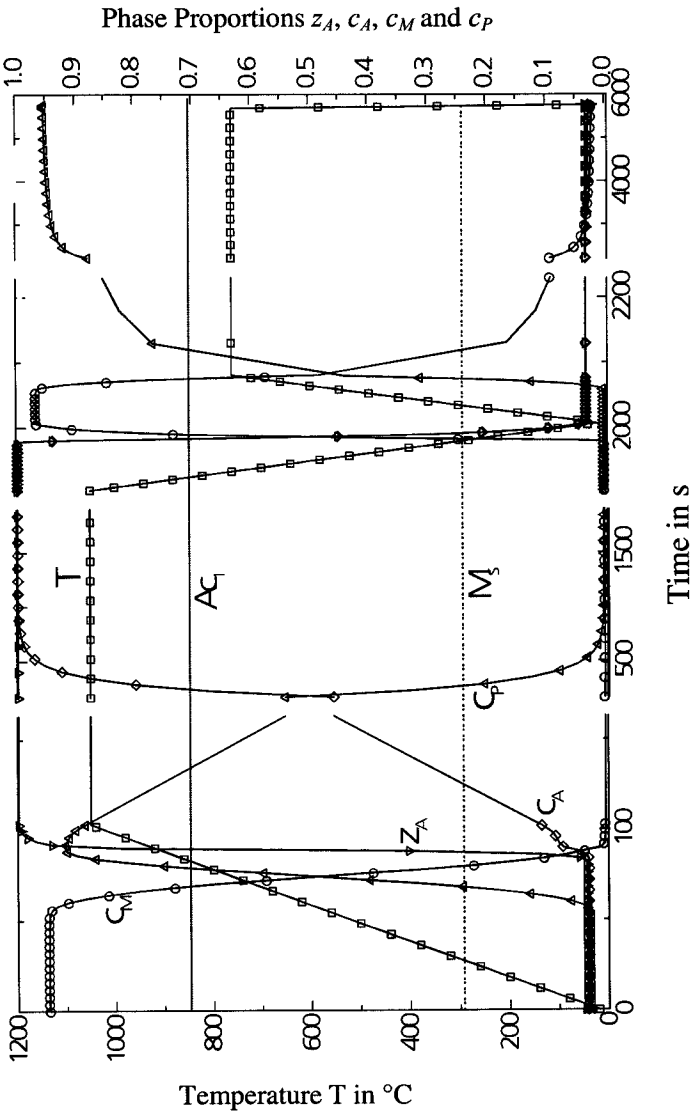


Figure 1: Phase evolution during a complete heat treatment: temperature and phase proportions are plotted versus time.

2.3 Simulation of an Industrial Heat Treatment

The present model was verified by the simulation (see figure 1) of a typical heat treatment defined in the industrial standard [10]: normalizing at 1050°C for ½ h, followed by air cooling and tempering at 760°C for 1 h, followed by air cooling. Figure 1 gives the temperature-time cycle of the simulated heat treatment.

Any initial material state should lead finally to a high proportion of martensitic lattice (z_A small) and almost all carbon precipitated as carbides (c_P almost 1). The evolution of phases is shown in figure 1. Heating and cooling rates are 10°C/s. The entire procedure can be described by the material behaviour within certain time intervals (compare Fig. 1):

Section I: The temperature has not reached austenite starting temperature A_{c1}. The dissolved carbon precipitates partly.

Section II: 1050°C is reached. The material is completely austenitized and carbides start to dissolve.

Section III: During cooling M_S is reached. Austenite transforms quickly into martensite. Therefore, the proportion of carbon dissolved in austenite turns into a high proportion of carbon dissolved in martensite (see eq. 5).

Section IV: The tempering temperature of 760°C is reached. Carbon content precipitates almost completely as carbides.

Section V: The heat treatment is finished. The material consists of 3% of austenite and 96% of the carbon is precipitated as carbide.

3 The Mechanical Model

3.1 Model Definition

The mechanical model is based on the work of Chaboche ([11], [12] and [13]). The definition of the one-dimensional form of the model is given by:

$$\dot{\varepsilon}_{vp} = \underbrace{\left\langle \frac{|\sigma - a| - k}{Z} \right\rangle^{n}}_{\dot{p}} \operatorname{sgn}(\sigma - a) \tag{6}$$

$$a = a_1 + a_2 \tag{7}$$

$$\dot{a}_i = H_i \dot{\varepsilon}_{vp} - D_i a_i \dot{p} \quad for \quad i = 1,2 \qquad a_i(t=0) = 0 \tag{8}$$

$$\dot{k} = 0, \qquad k(t=0) = k_0 \; . \tag{9}$$

$\dot{\varepsilon}_{vp}$ is the viscoplastic strain rate. The kinematic hardening variables a_1 and a_2 and the isotropic hardening variable k are internal variables. The parameters for the yield stress, k_0, the stress exponent, n, the viscosity, Z, the kinematic hardening, H_1 and H_2, the dynamic recovery, D_1 and D_2, describe the behaviour for one temperature at a certain phase state. The mentioned parameter depends on temperature and phase variables (z_A, c_P, c_M and c). For every temperature and for every phase state mechanical data (tensile, tension/compression,

relaxation tests) were needed to determine the parameters. It is obvious that this enormous experimental effort needs simplification. For the present work, mechanical data for three states:

- tempered martensite ($z_A \approx 0$, $c_P \approx 1$, $c_A \approx c_M \approx 0$),
- quenched martensite ($z_A \approx 0$, $c_M \approx 1$, $c_A \approx c_P \approx 0$) and
- austenite ($z_A = 1$, $c_A = 1$, $c_P = c \quad = 0$)

were available. The tempered martensite data were used to determine the parameters in the temperature range between room temperature and 800°C. Since there were few experiments performed in the state of high proportion of austenite only, following assumptions and simplifications were made arbitrarily, in order to reduce the flexability of the mechanical model:

- Both, tempered martensite and austenite have individual yield stress parameter $k_{0,M}(T)$ and $k_{0,A}(T)$. It is assumed that they become identical at high temperatures.
- A factor $b = \min\left(\frac{k_{0,A}(T)}{k_{0,M}(T)}, 1\right)$ is introduced. b is used to scale $z_A(T) = b \cdot z_M(T)$ and $H_{i,A}(T) = b \cdot H_{i,M}(T), i = 1,2$.

All other austenite parameters are identical to the tempered martensite ones: $n(T) = n_A(T) = n_M(T)$ and $D_i(T) = D_{i,A}(T) = D_{i,M}(T)$.

No plasticity can be detected from the quenched martensite data, because the material is brittle and fractures before yielding. We assume a quasi-elastic model by adding the term $c_M \cdot \Delta k_M$ (Δk_M = 1000 MPa) to the tempered martensite yield stress parameter $k_{0,M}(T)$.

The parameter values depending on the phase proportion are linearly interpolated with respect to the relative proportion of austenite z_A between the states of tempered martensite and austenite. The dependence of the isotropic hardening rate $\dot{k}$ and the initial value of k on the phase proportions are

$$\begin{aligned} \dot{k} &= \left((1-z_A)\frac{\partial k_{0,M}}{\partial T} + z_A \frac{\partial k_{0,A}}{\partial T}\right)\dot{T} + \left(k_{0,A}(T) - k_{0,M}(T)\right)\dot{z}_A + \Delta k_M \, \dot{c}_M \\ k(t=0) &= (1-z_A)k_{0,M}(T) + z_A \, k_{0,A}(T) + \Delta k_M \, c_M \end{aligned} \qquad (10)$$

The interpolations of the viscosity parameter Z and the hardening moduli H_i are given in the equations 11 and 12, respectively:

$$Z(T) = (1-z_A)Z \quad (T) + z_A Z_A(T) \qquad (11)$$

$$H_i(T) = (1-z_A)H_{i,M}(T) + z_A H_{i,A}(T) \quad for \quad i = 1,2 \; . \qquad (12)$$

Since the von-Mises criterion has been used, the model can easily be generalized to a multiaxial form and applied for future implementations in finite element programs.

3.2 Temperature Dependence of Model Parameters

The mechanical model was extended to non-isothermal conditions: First, the parameters for tempered martensite were determined for each temperature separately. Then, appropriate functions to approximate these parameters have to be identified. These functions depend on parameters themselves. Finally, these parameters are fitted to the whole set of given experiments.

Figure 2 illustrates this process for the parameters k, Z, and n. The symbols are the parameter values at RT, 200°C, 400°C, 600°C, 700°C, 800°C, 850°C, and 900°C. The lines are analytical functions fitted to these values. The dashed lines show the parameter values after fitting the parameter functions to all given experiments. These parameter values (dashed lines in Fig. 2) are used in the next section to discuss experimental and modelling results.

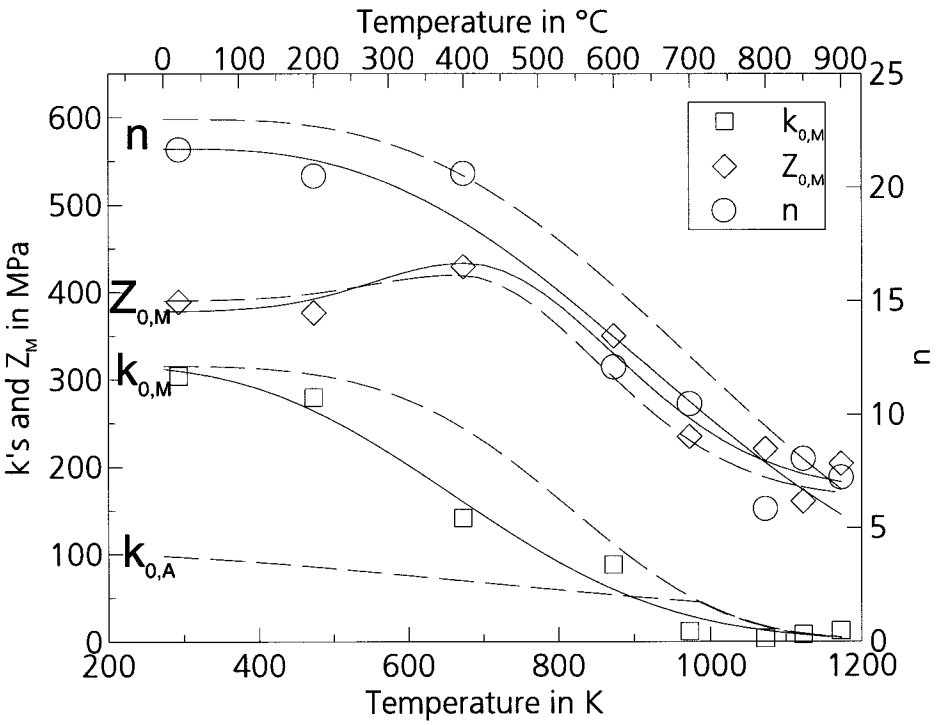


Figure 2: Temperature dependence of model parameters: The symbols represent isothermal fits, the lines are analytical functions fitted to these parameters and the dashed lines are the parameter functions fitted to the whole set of experiments.

3.3 Results

In figures 3 and 4 part of the experimental and modelling results are shown. Further results can be found in Gantert [9]. In figure 3, tensile tests with similar loading rates and different temperatures are depicted. The material shows the expected decreasing of yield stress for increasing temperature. The yield stress changes most at about 600°C which is in accordance with the parameter change in this temperature domain (see figure 2).

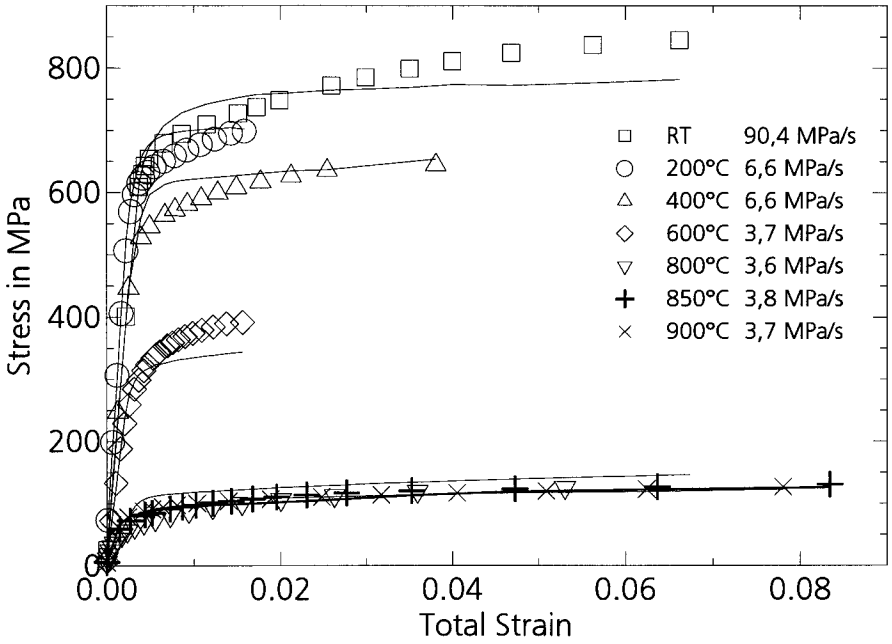


Figure 3: Tensile test and modelling results for X20CrMoV 12 1: Stress is plotted versus total strain. Symbols represent experimental data, lines represent the corresponding model result.

Furthermore, the tensile tests at 800°C, 850° and 900°C show virtually no difference, although one would expect, that a temperature difference of 100K and a change of the equilibrium proportion of austenite between 0 and 81% austenite should have an effect. The microstructures were equilibrated at the test temperature before the tensile tests were run. Figure 4 gives results for tension/compression tests. The model describes the experimental data reasonable well.

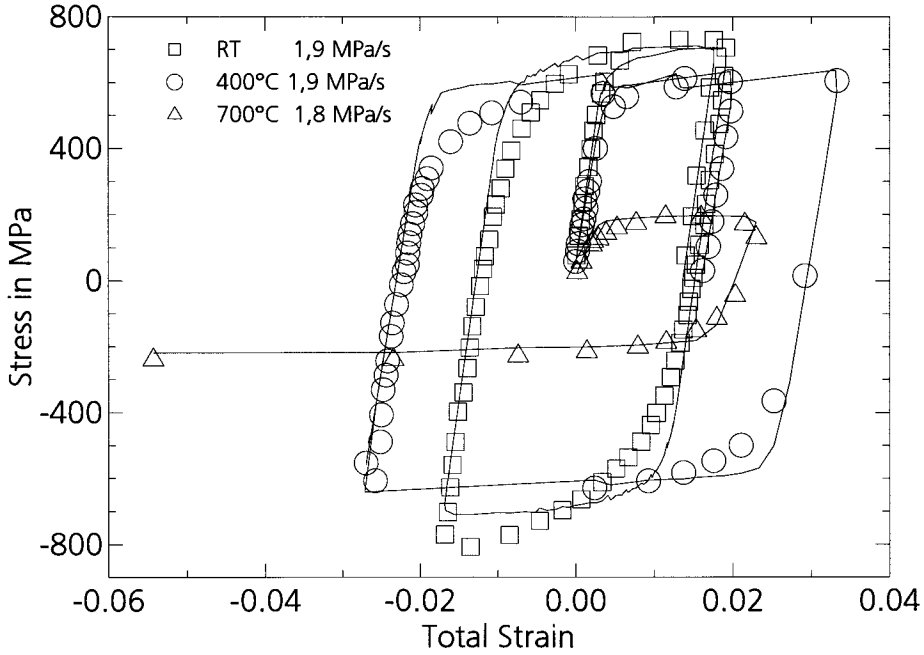


Figure 4: Tension/compression tests and modelling results for X20CrMoV 12 1 at room temperature, 400°C and 700C°: All experiments start at zero stress and strain. Stress is plotted versus total strain. Symbols represent experimental data, lines represent the corresponding model result.

4 Conclusion

The presented material model is based on a Chaboche-type viscoplastic deformation model, a generalized Johnson-Mehl-Avrami equation describing austenite transformation and carbon kinetics and the Koistinen-Marburger equation describing martensite transformation.
The transformations between the tempered, quenched and austenitized states of steel X20CrMoV 12 1 were modelled well. These transformations are relevant for the mechanical behaviour of X20CrMoV 12 1. The martensitic and the austenitic proportions of the material and their carbon content were modelled well. This was verified by a simulation of an industrial heat treatment.
Based on the transformation behaviour of steel X20CrMoV 12 1 the Chaboche model was fitted to mechanical data of austenite and martensite phases, respectively. In order to describe temperature dependent parameter functions were determined. For the martensitic and the austenitic state the model reproduces the experiments reasonably well.

5 Acknowledgement

We gratefully acknowledge the support of Dr. A. Rosselet, SULZER Innotec, Switzerland for supplying the huge data base and for fruitful discussions.

6 References

[1] Petri, R., Schnabel, E., Schwaab, P., „Zum Legierungseinfluß auf die Umwandlungs- und Ausscheidungsvorgänge bei der Abkühlung warmfester Röhrenstähle nach dem Austenitisieren, II. 12%ige Chromstähle", *Archiv des Eisenhüttenwesens* **52** (1981) 27

[2] Straub, S., „Verformungsverhalten und Mikrostruktur warmfester martensitischer 12%-Chromstähle", Fortschrittsberichte VDI, Reihe 5: Grund- und Werkstoffe, Nr. 405, VDI Verlag, 1995

[3] Hald, J., Straub, S., „Microstructural Stability of 9%-12%CrMo(W)VNbN-Steels", preprint

[4] Strang, A.. (Hrsg.), „Microstructural Development and Stability in High Chromium Ferritic Steels", Article in Book "Microstructural development and stability in high chromium ferritic power plant steels", Cambridge University Press, 1997

[5] Johnson, W., A., Mehl, R., F., „Reaction Kinetics in Processes of Nucleation and Growth", *Transactions of the American Institute of Mining, Metallurgical, and Petroleum Engineers* **135** (1939) 416

[6] Avrami, M., Kinetics of Phase Change I, *Journal of Chemical Physics* **7** (1939) 1103

[7] Fortunier, R., Leblond, J.-B., „Recent advances in the numerical simulation of simultaneous diffusion and precipitation of chemical elements in steels", Framasoft+CSI, 10 rue Juliette Récamier, 69456 Lyon Cedex 06, France

[8] Koistinen, D., P., Marburger, R., E., *Acta Metallurgica* **7** (1959) 59

[9] Gantert, C., "Modelle für das temperaturabhängige Verformungsverhalten von Hochtemperaturwerkstoffen und Anwendung auf Kraftwerksstähle", 1999, Technical Report, Fraunhofer IWM, Freiburg, Germany

[10] DIN 17 175, Nahtlose Rohre aus warmfesten Stählen, 5/1979

[11] Chaboche, J.-L., Rousselier, G., „On the Plastic and Viscoplastic Constitutive Equations Part I: Rules Developed with Internal Variable Concept", *Journal of Pressure Vessel Technology* **105** (1983) 153

[12] Chaboche, J.-L., „Time-Independent Constitutive Theories for Cyclic Plasticity", *International Journal of Plasticity* **2** (1986) 149

[13] Chaboche, J.-L., Lemaitre, J., „Mechanics of Solid Materials", Cambridge Univ. Press, 1990

AN ASSESSMENT OF CREEP RUPTURE DATA ON E911 STEEL WELDMENTS

Chiara Servetto [(*)]
David J. Allen [(**)]

[(*)] Istituto Italiano della Saldatura - Genova, Italy
[(**)] Powergen UK plc, Power Technology Centre - Nottingham, UK

Abstract

This paper describes an assessment of cross-weld creep rupture data from the COST project data set on E911 steel weldments. The work was undertaken as a collaborative development by IIS and Powergen, carried out at Power Technology and supported by an ECCC technical interchange programme.

The BS PD 6605 assessment methodology was applied, with modifications as described in a companion paper at this Conference. In line with previous assessments of this data set, the results suggest a substantial long term weld strength reduction, to a plateau value of around 60% of the parent material creep strength under conditions appropriate to long term service at high temperature. Longer term testing is required to confirm these findings, which rely on considerable extrapolation. However, they clearly suggest that the temperature limit for advanced plant design should primarily depend on the long term risk of weld HAZ failure, and should not solely be based on parent material design parameters.

Further analysis also shows that the weld strength factor can be evaluated as a simple function of applied stress, largely independent of time and temperature. Its value rises toward 100% at high stress, but falls to the plateau value of about 60% at low stresses. Alternatively, weld strength factor may be evaluated as a function of the Larson-Miller time-temperature parameter, showing that the plateau value is applicable to long term service. Hence, confidence in the extrapolation is improved.

Keywords: creep, ferritic steel, weld, HAZ, Type IV cracking

Introduction

Experience with previous generations of power plant has shown that creep data on parent steels may not be the most important consideration in high temperature materials selection. Premature creep cracking at weldments can bring major costs in terms of periodic inspection and repair. The main creep failure mechanism experienced in UK plant has been "Type IV" cracking at the outer edge of the weld heat-affected zone (HAZ) in CrMoV steel pipework and, more recently, in high alloy ferritic steels. In addition to characterising the creep properties of parent materials, therefore, there is a need to quantify the creep strength of welded joints, and hence determine suitable weld strength factors (WSF) for use in the design of welded components operating in the creep range.

This paper describes an assessment of E911 steel cross-weld creep rupture test data from the COST project database, carried out as for the parent material [1] in accordance with the PD 6605 procedure [2]. Further studies have also been performed, and a new correlation identified between the weld strength factor and the applied stress. The work was carried out at Power Technology, UK, as part of a European Creep Collaborative Committee (ECCC) technical interchange programme which supported the secondment of one of the authors (CS).

Assessment

The full data set includes 110 broken and 6 unbroken data points on a total of 5 casts tested mainly at 600°C, 625°C and 650°C, with a maximum rupture life of 16087 hours. To restrict consideration to HAZ cracking, tests that failed in parent or weld metal were excluded from assessment. The data points with unspecified fracture locations were retained because they fell within the HAZ failure scatter band, figures 1-2.

A cut-off procedure was also applied to exclude short term data, since these appear to follow a substantially different trend from the longer term data. As described in the companion paper on parent material assessment [1], a 1000h stress-based cut-off criterion was applied. Essentially, this excludes the results at those test stresses for which some or all the rupture lives were below 1000h. Information on the assessed data points is given in table 1.

TABLE 1 – information on the data set (after cut-off and pre-assessment)

TEMP °C	TOTAL DATA		TEST DURATION <10kh		10-20kh		20-30kh		30-50-kh		$t_{r[max]}$ [h]	$\sigma_{o[min]}$ [Mpa]	$\sigma_{o[max]}$ [Mpa]	TOTAL	%B of TOTAL
	B	UB	B	UB	B	UB	B	UB	B	UB	B	B	B		
575	3	2	2		1			2			12,096	165	190	5	6%
600	19	2	16		3			2			14,131	100	161	21	39%
625	14	2	12		2			2			16,087	60	120	16	29%
630	1		1								562	120	120	1	2%
645	1		1								145	100	100	1	2%
650	11		9		2						10,250	45	100	11	22%
totals	49	6												**55**	

$t_{r[max]}$ = maximum time to rupture
$\sigma_{o[min]}$ = minimum test stress
$\sigma_{o[max]}$ = maximum test stress

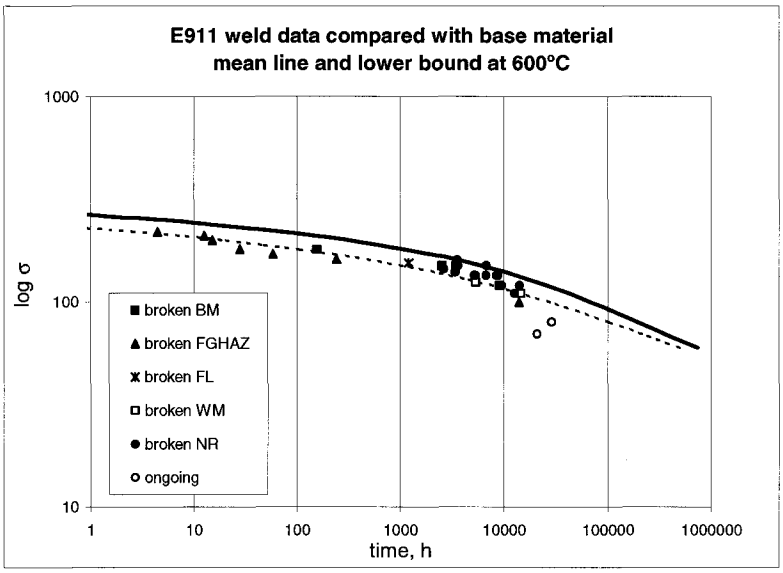
B = broken data
UB = unbroken data

The PD 6605 post-assessment (PAT) tests found three potentially acceptable models, but as the most "robust" of these also gave the poorest data fit, PAT testing alone did not clearly identify the best choice. However, examination of the 625°C and 650°C isothermal data plots indicates a slightly sigmoidal, reverse S type of curve shape at lower stresses. The "Soviet" SM1 model cannot generate such a complex curve shape, as it contains only two stress terms, and hence produced a poor data fit. The third-order Manson-Haferd model produced what appeared to be a different artefact, in this case a strongly sigmoidal curve outside the data range which showed no correspondence with the real evidence. Fortunately, the Minimum Commitment (MC) equation:

$$\ln t^* = \beta_0 + \beta_1 \log\sigma + \beta_2\sigma + \beta_3\sigma^2 + \beta_4 T + \beta_5/T$$

predicted a mildly sigmoidal curve with good data fitting, and was chosen as the preferred model.

As this assessment is mainly based on only 2 casts, the extrapolated values fail to conform with the strict validity requirements of the ECCC guidelines [3], while data beyond 16000 hours are clearly needed to establish the true long term trend. Hence, this assessment must be considered provisional.



(BM = base material, FGHAZ = fine grained HAZ, FL = fusion line, WM = weld metal, NR = not recorded)

Figure 1

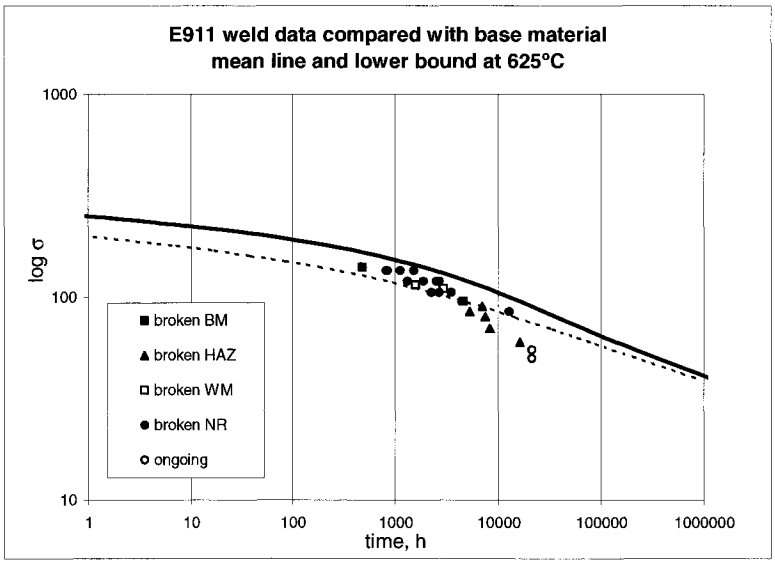


Figure 2

Weld strength factor (WSF)

Figures 3-4 show the isothermal cross-weld data plots at 600°C and 625°C and compare the mean assessment lines with those previously obtained [1] for the parent steel. The strength reduction of welds increases with both time and temperature. Predicted values of the mean weld strength factor (WSF), defined as the ratio of mean weld strength to mean parent strength, are given in table 2 and plotted against rupture life for a range of temperatures in figure 5. These results are broadly similar to those of a previous assessment [4], with slight differences arising mainly from the respective parent material assessments.

TABLE 2 – Weld strength factors for E911 welds

Temp. [°C]	Duration (h)					
	1000	3000	10000	30000	50000	100000
550			*0.96*	**0.94**	*0.94*	*0.92*
560		*0.97*	**0.96**	**0.94**	*0.92*	*0.90*
570		*0.97*	**0.95**	**0.92**	*0.90*	*0.86*
580	*0.98*	**0.96**	**0.94**	**0.89**	**0.86**	*0.80*
590	**0.97**	**0.95**	**0.91**	**0.84**	**0.80**	*0.73*
600	**0.96**	**0.93**	**0.87**	**0.78**	**0.73**	*0.70*
610	**0.94**	**0.89**	**0.80**	**0.71**	**0.68**	*0.66*
620	**0.91**	**0.84**	**0.73**	**0.66**	**0.65**	*0.64*
630	**0.86**	**0.77**	**0.67**	**0.63**	*0.63*	
640	**0.79**	**0.69**	**0.63**	*0.61*		
650	**0.71**	**0.63**	**0.60**	*0.59*		
660	**0.64**	**0.59**				
670	**0.58**	**0.56**				

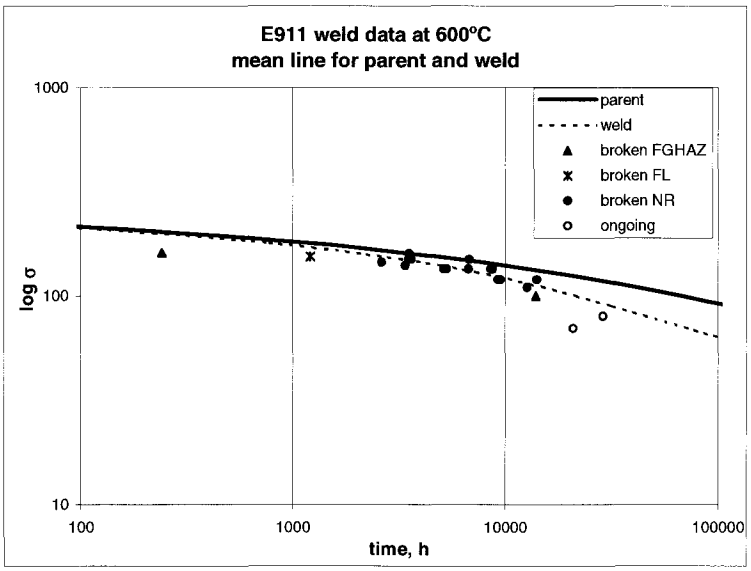


Figure 3

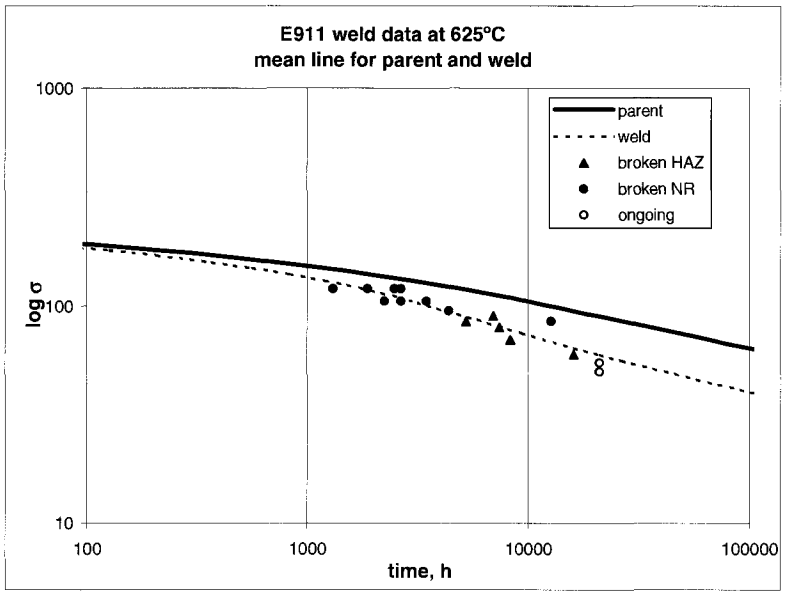


Figure 4

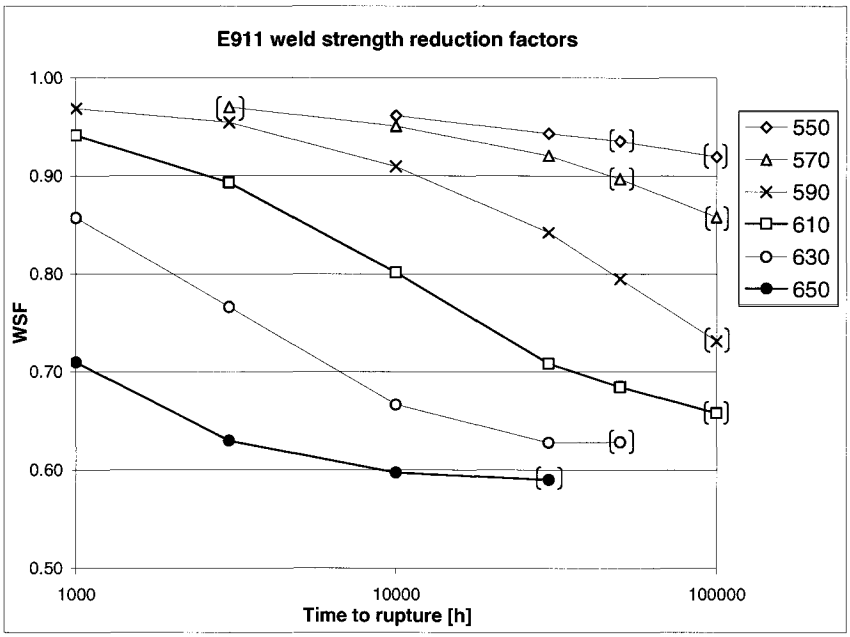


Figure 5

WSF versus stress

A replot of the weld strength factor against parent material rupture strength, figure 6, shows interesting results. The predictions for different temperatures all fall onto virtually the same single curve, showing a smooth decrease in WSF as the parent stress decreases. The WSF is close to 1.0 for parent strength values above about 150 MPa, corresponding to the stress range within which cross-weld test failures take place in the parent material. However, WSF falls to 0.70 and below at lower stresses, below 100 MPa. While the plot suggests a slight residual dependence of WSF on temperature, this could simply be due to minor assessment inaccuracies. Hence, it seems reasonable to plot an approximate single best fit curve relating WSF to parent material stress.

The plot also suggests that the WSF curve flattens out at lower stresses, and falls asymptotically towards a constant "plateau" value of about 0.6. This is a provisional conclusion, as the bracketed points in figure 6 represent extrapolation beyond the weld data range. Examination of the raw data suggests that the sigmoidal trend identified is realistic and that the "plateau" effect is, therefore, probably real. However, a "worst-case" extrapolation is also sketched in figure 6 to illustrate the alternative possibility that the WSF curve does not flatten out at all.

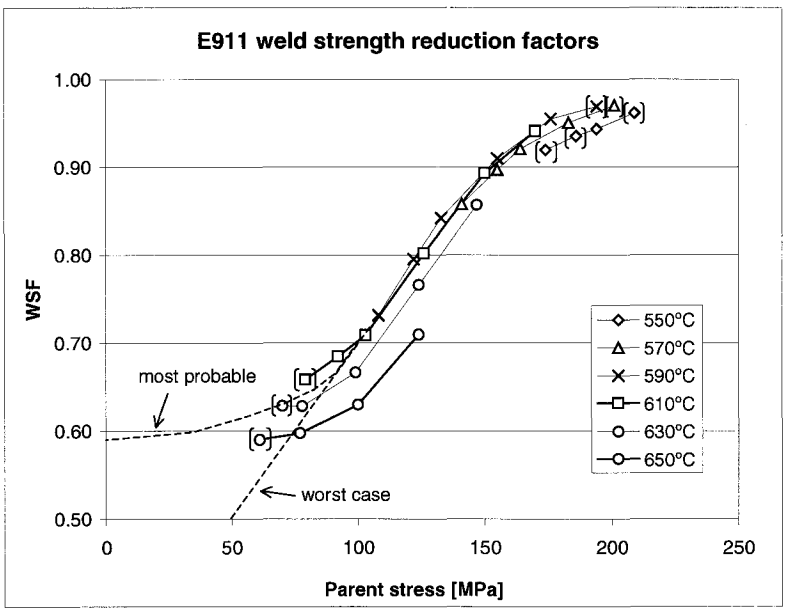


Figure 6 – WSF versus stress

The broad conclusions are not, in fact, very dependent on whether the "most probable" or "worst case" extrapolation is correct. For design stresses of the order of 50 MPa, the WSF is either around 0.6 or, on the worst case hypothesis, slightly lower. In either case, only small system loads would be required to ensure that circumferential weld HAZ failure should precede parent pipe material failure in operating plant. Hence, the high temperature limit for

plant design with E911 should primarily be determined in relation to the long term risk of weld HAZ failure, and not solely in relation to the parent material design parameters.

Different considerations apply to components operating at lower temperatures and higher stresses. Thus, parent material design stresses above 125 MPa imply WSF values above 0.8, with much lower risks of premature weld failure. The WSF - stress relationship can thus be applied to design and operate components at lower temperatures without undue conservatism.

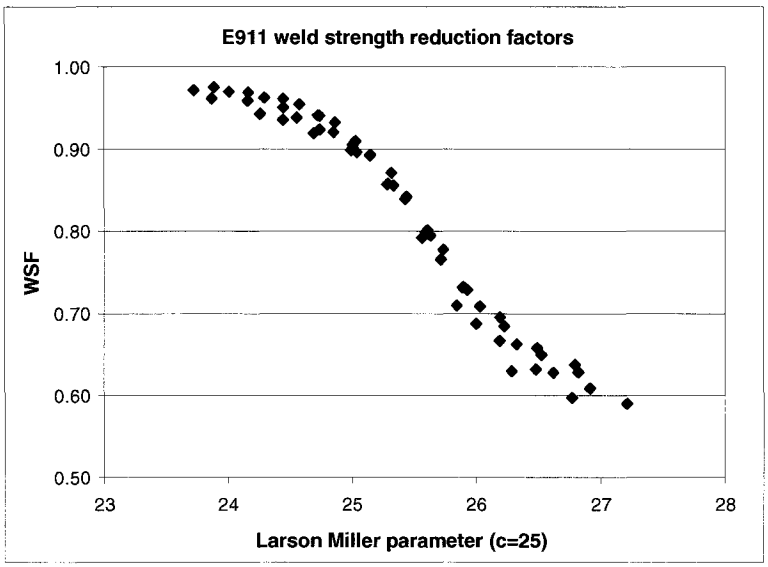
The reasons why WSF should obey such a simple correlation with parent material stress require further investigation. The MC model, used here for both weld and parent data, predicts life in terms of separate stress and temperature functions. For such a model, a WSF - stress correlation arises naturally, provided the weld and parent data show similar temperature dependence. This proviso requires only that the activated processes controlling creep behaviour in a parent material and its own HAZ are similar, and applies quite well for E911, where (despite apparently major differences in the fitting factors) the predicted effects of a temperature change (such as 650°C to 550°C) on parent life (increased x 1419) and weld life (increased x 1620) are similar.

PD 6605 also offers alternative models which include stress / temperature interaction terms, for example SM1. Models of this type would not need to predict a simple WSF – stress relationship, and might therefore naturally be preferred if and when such a relationship does not apply. However, an unpublished assessment of dissimilar weld data by the authors found that although SM1 gave the best fit, WSF was again a simple function of parent stress alone. This suggests that approximately temperature-independent WSF - stress relationships could prove to be quite widely applicable to ferritic steel welds in general, irrespective of the methods used to assess the data.

WSF versus time - temperature parameters

The good correlation between WSF and stress suggests the possibility of a parallel correlation between WSF and a time-temperature parameter. This was investigated, and very good results were obtained using the Larson - Miller (LMP) parameter. Predicted WSF values for the 550°C - 650°C range of temperatures were replotted against LMP, using a constant c = 25 (with T in °K and t in hours) to minimise scatter, figure 7. Again, this indicates a plateau WSF value of around 0.6 or below, reached at an LMP value of about 27. This equates to e.g. 170,000 hours at 620°C, and is therefore reasonably typical of anticipated end-of-life conditions for high temperature E911 plant.

The WSF - stress and WSF - LMP correlations may both find application in plant design and long term operation. Both provide similar information. WSF - stress is well suited to design considerations, whereas WSF - LMP may be useful e.g. in considering plant life extension.



PLM = T[K]·(logt+c)/1000

Figure 7

Cast specific WSF assessment

To investigate the behaviour of individual casts, the individual strength ratios between each actual data point and the predicted mean line have been calculated for both parent data (R_{BM}) and cross-weld data (R_W). Average R_{BM} and R_W values at each test temperature have thence been derived as simple measures of the relative strengths of each cast, Table 3, and used to calculate cast-specific average WSF values at each temperature.

TABLE 3 – Weld strength factors for individual casts

		BASE MATERIAL		WELDS	
cast	temperature [°C]	R_{BM} $\sigma_{oBM}/\sigma^*_{BM}$	No of data	R_W σ_{oW}/σ^*_W	No of data
D	625	1.03	7	1.10	1
D	650	0.98	6	1.12	2
F	600	1.07	7	0.91	2
F	625	1.06	4	0.94	4
F	650	1.07	7	1.02	5
J	600	0.96	7	1.01	15
J	625	1.00	6	1.01	9
J	650	0.98	5	0.91	3

Legend:

σ_{oBM}	actual stress value of creep test on base material at t_{R_BM}
σ^*_{BM}	predicted stress obtained from the base material mean line at t_{R_BM}
σ_{oW}	actual stress value of creep test on welds at t_{R_WM}
σ^*_W	predicted stress obtained from the weld mean line at t_{R_WM}

The results, though limited, show remarkably poor correlation between cross-weld and parent creep strength. Cast D, with parent strength close to mean, consistently showed cross-weld strength well above the mean. Cast F, by contrast, showed relatively poor cross-weld strength, despite its consistently better than mean parent material strength. Insofar as these data indicate any correlation between cross-weld and parent creep strength, therefore, it is inverse. In the absence of better information, reasonable conservative estimates on the cross-weld performance of a weak parent cast may be obtained by multiplying the cast-specific parent strength values by the all-data average weld strength factor.

Summary and conclusions

An assessment of the E911 cross-weld creep rupture database was carried out using the PD 6605 approach. Provisional weld strength factor values for HAZ failure were determined using the MC equation to model sigmoidal behaviour, and a substantial weld strength reduction was predicted for long term, high temperature performance. Additional analysis also showed that:

1. For E911, WSF can essentially be predicted as a simple function of stress alone, independent of temperature. The value of WSF falls from 1 at high stresses, when cross-weld tests fail in the parent material rather than the HAZ, down to an apparent minimum "plateau" value of about 0.6 at low stresses.

2. WSF can, alternatively, be equally well predicted as a simple function of the Larson-Miller time-temperature parameter. This similarly indicates that WSF falls to a plateau value close to 0.6 under conditions appropriate to long term service at high temperature.

3. Whilst the predicted long term values of WSF are subject to uncertainty because of the shortage of data and extended extrapolation, the uncertainty can be bounded within reasonable limits. A "worst case" prediction for WSF, ignoring the evidence of sigmoidal behaviour and thus presuming that no minimum "plateau" exists, would indicate WSF values falling to about 0.5 at a stress of 50 MPa. At practical stress levels, therefore, the best estimate WSF prediction is not greatly higher than the "worst case" estimate.

4. These results indicate that the temperature limit for plant design with E911 should primarily be determined in relation to the long term risk of weld HAZ failure, and not solely in relation to the parent material design parameters.

5. There is no clear correlation between the cast - specific parent and cross-weld rupture strengths. Instead, there is evidence that an above-mean strength parent cast can have below-mean cross weld strength.

References

[1] Allen, D J, Servetto, C, "An assessment of creep rupture data on steel E911", 7th Liege Conference on Materials for Advanced Power Engineering, 2002.

[2] PD 6605, "Guidance on methodology for assessment of stress-rupture data", BSI, 1998.

[3] ECCC Recommendations Volume 5, 'Guidance for the assessment of creep rupture, creep strain and stress relaxation data, ECCC Document 5524/MC/38, Issue 4, ed. Holdsworth, S.R., 2001.

[4] Holmstrom, S, Auerkari, P, "Modelling of creep rupture strength and stress reduction factors for welded 9%Cr steel", Proc. Conf. "Baltica V", Vol.2, pp.621-633, publ. VTT, Espoo, 2001.

CHARACTERIZATION OF MATCHING FILLER METALS FOR NEW FERRITIC-BAINITIC STEELS LIKE T/P 23 AND T/P 24

Dr.-Ing. H. Heuser and Dr. rer. nat. C. Jochum
Thyssen Welding Germany, Hamm

Abstract

New welding consumables for welding HCM 2 S and 7 CrMoVTiB 10-10 have been developed. This paper shows the contribution of a manufacturer of filler metals to the European COST research program 522 and the actual stage of filler metal development.

Keywords: Filler metals, welding, PWHT, mechanical properties, P 23, P 24

Introduction

Creep resistant steels for high temperature service are a vital part in the construction of power stations. In the last decades, the steel 2 1/4 % Cr -1%Mo (ASTM: T 22/P22) has been used world wide with greatest success, based on excellent operating behavior. The increase of steam parameters requires the development of new high strength and creep resistant materials. However the possibility to increase steam parameters is restricted if pressure and temperature in the membrane waterwalls cannot be increased simultaneously. Conventional ferritic-bainitic steels such as ASTM A 213 T12 (13CrMo4-4) and ASTM A 213 T22 (10CrMo9-10) do not have enough creep strength for the use as membrane waterwalls of U.S.C.B. (Ultra Super Critical Boilers). The creep strength of the new materials such as T 23 and T 24 is much higher than that of T 22 and is on a level between X 20 and P 91 **(fig. 1).** In addition, the maximum hardness in HAZ of these new steels is below 350 HV, so that a PWHT is not necessary, at least when tube materials are welded. The new grades T23 and T24 with high creep behavior and with low hardness in the as-welded condition are potential material candidates for water wall components as well as for thick walled pipes.

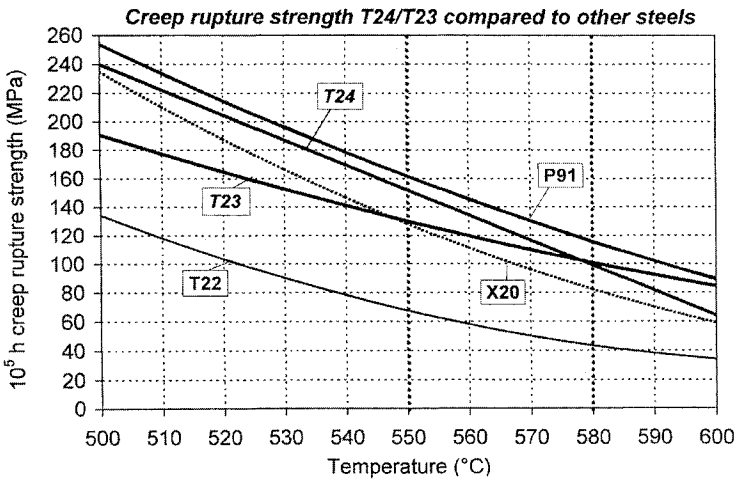


Figure 1: Comparison of Creep strength of water wall materials

During the work of the European research program COST 522 – Energy generation in the 21st century; ultra-efficient, low emission plants - , which started in 1998, the development of new filler metals for these two new candidates was first focused only on thin walled tube material as it is used for water wall fabrication. But during research work it soon became clear, that these new materials are also of great importance for thick walled components. For this reason new filler metals were required, and not only for GTAW, but also for SMAW and for SAW welding processes.

The present paper will show the current stage of development of new filler metals for welding of new materials like T/P 23 (HCM 2S) and T/P 24 (7CrMoVTiB10-10).

Chemical composition of Base Material and Filler Metals

Chemical compositions of steel grades, per ASME Code Case 2199 (HCM 2S) and T24 (7CrMoVTiB10-10), per ASTM A 213 (draft) are compared in **table 1** to other standard steel grades (T22, T91) used for high temperature application in power plants. So far, the requirements for chemical composition of the new filler metal for welding T 23 and T 24 material are related to those of the base material. Modifications as done with the filler metal for welding P 91 material (Ni, Nb) are not necessary.

T/P 22 2 1/4 Cr-1 Mo		C	Si	Mn	Cr	Mo	Ni	V	W	Al	B	N	Nb	Ti
ASTM A 387	min.	.05	.00	.30	2.0	.90	-	-	-	-	-	-	-	-
Gr 22 Cl 2	max.	.15	.50	.60	2.5	1.10	-	-	-	-	-	-	-	-

T/P23 HCM 2 S		C	Si	Mn	Cr	Mo	Ni	V	W	Al	B	N	Nb	Ti
ASTM A 213	min.	.04	-	.10	1.9	.05	-	.20	1.45	-	.0005	-	.02	-
code case 2199	max.	.10	.50	.60	2.6	.30	-	.30	1.75	.030	.0060	.030	.08	-

T/P24 7CrMoVTiB10-10		C	Si	Mn	Cr	Mo	Ni	V	W	Al	B	N	Nb	Ti
ASTM A 213	min.	.05	.15	.30	2.2	.90	-	.20	-	-	.0015	.030	-	.05
draft	max.	.10	.45	.70	2.6	1.10	-	.30	-	.020	.0070	.070	-	.10

X10CrMoVNb 91		C	Si	Mn	Cr	Mo	Ni	V	W	Al	B	N	Nb	Ti
ASTM A 213	min.	.08	.20	.30	8.0	.85	-	.18	-	-	-	.030	.06	-
P 91	max.	.12	.50	.60	9.5	1.05	.40	.25	-	.040	-	.070	.10	-

Table 1: Chemical composition of ferritic creep resistant base material and of martenstic P 91.

To develop grade T/P23 the basic composition of 2 1/4 Cr 1 Mo grade was modified by the addition of tungsten (1.6 %), by the reduction of molybdenum (0.20 %) and of carbon (0.04-0.10 %) and small additions of vanadium, niobium, nitrogen and boron. Thanks to these specific additions after proper heat treatment (N + T or Q + T), creep strength values and the resulting allowable stresses are significantly improved **(see fig. 1)**. The carbon content was intentionally lowered with regards to weldability: no PWHT is necessary on thin walled components. Thanks to a modern steel melting practice, residual elements are strictly limited to ensure consistent behavior during manufacturing, fabrication and uniform creep resistance.

For grade T 24, which is closer to the basic composition of (modified) 2 ¼%Cr 1% Mo, vanadium, titanium and boron additions have led to an improvement in creep rupture strength

compared to grade T22. The optimization of the chemical composition includes a considerable reduction of the carbon content as an important step towards achieving low hardness values in the as-welded heat affected zone.

Table 2 compares the values of mechanical properties proposed in the ASTM/ASME standards for T23 and T24 respectively with other grades commonly used [1].

Grade	YS MPa	TS MPa	Elong. %	CVN J
T/P 22 2 1/4 Cr-1 Mo ASTM A 387 Gr 22 Cl 2	> 310	515 - 690	> 18	-
T/P23 HCM 2 S ASTM A 213 code case 2199	> 400	> 510	> 20	-
T/P24 7CrMoVTiB ASTM A 213 draft	> 450	585	> 20	> 41
X10CrMoVNb 91 ASTM A 213 P 91	> 415	> 585	> 20	> 41

Table 2: Requirements for mechanical properties of some ferritic creep resistant steels and for P 91 at RT

Development of filler metals for new base materials

When developing new base material, one of the basic questions today is concerning the corresponding filler metal. What kind of filler metal and welding processes will be needed and what are the requirements. The manufacturers of filler metals think about wether a new filler metal has to be developed or wether a similar welding consumable is already available. In case there are micro alloying elements in the base material it is of importance, that these elements are also inside the wire used as filler metal. Especially elements like Ti, B or Nb will have a considerable burn off during welding. For this reason it is of importance to have these elements already inside the wire and not only inside the coating of the electrode. Both filler metals for welding the new grades T/P 23 and T/P 24 are based on matching wire composition.

Table 3 shows the chemical composition of the GTAW-filler and the test results for the all weld metal acc. to DIN EN 32525/T1 of Union I CrMoVTiB and for the joint. The tests have been carried out with and without PWHT, and test temperature were RT, 550 and 600 °C. As it can be seen, toughness is, even without PWHT for the all weld metal on an extremely high level close to the maximum of 300 J. This is probably supported by welding thin layers. In the joint at the 6 o´clock position toughness is without PWHT still in the range of 45 J. Hardness is on a level below max. 322 HV10, without PWHT.

a) **Chemical composition of GTAW filler metal Union ICrMoVTiB (wire and all weld metal) 2.5 mm∅**

	C	Si	Mn	P	S	Cr	Mo	V	B	Co	N	Nb	Ti
wire	,061	,24	,53	,003	,002	2,39	1,01	,24	,0037	,01	,016	,008	,073
all weld metal	,061	,23	,49	,002	,002	2,29	1,00	,24	,0020	-	,014	,007	,034

b) **Mechanical properties, all weld metal**

Testtemp.	PWHT °C / h	YS MPa	TS MPa	Elong. %	Red. A %	CVN J	Hardness HV 10
RT	no PWHT	664	803	19,1	80,6	298 298 298	269
600 °C		457	561	18,6	83,8	-	-
RT	740 / 2	595	699	20,3	78,9	264 280 292	-
RT	740 / 4	540	642	22,1	78,0	278 299 299	-
550 °C	740 / 4	396	436	19,8	78,9	-	-

c) **Mechanical properties of the joint at RT** **Pipe: P 24; 159 mm x 20 mm**

PWHT °C / h	Weld. pos.	YS MPa	Ts MPa	Elong. %	Location of Fracture	CVN J	Hardness HV 10	Side Bend Test
740/2	PA	471	600	30,8	BM	284 287 292	206 - 236	180°
	PF	489	599	31,0	BM	261 298 270		180°
	PE	459	594	32,0	BM	299 298 296		180°
no PWHT	PE	-	-	-	-	35 49 48	297 - 322	-

d) **Welding parameter for welding the joint:**

∅ 2.5 mm	Polarity	Preheat temp. °C	Interpass temp. °C	Is A	Us V
root	=-	200	200 - 250	130 - 160	17
filler & cap	=-	200	200 - 250	180 - 190	22

Table 3: Chemical composition and mechanical properties of Union I CrMoVTiB

Matching filler metal for welding 7CrMoVTiB 10-10 (T / P 24)

For T / P 24 material filler metals for GTAW, SMAW and for SAW welding processes are available. The following tables will show a summary of test results and mechanical properties of all weld metal and of a joint with P 24 material (159 mm outer ∅; and 20 mm in wall thickness). These tests are partly used for qualification tests according the German TÜV regulation. As for girth welding of thin walled tubes (like it is done when welding water walls) no PWHT is required, some of the tests have been carried out with and without PWHT.

Table 4 shows chemical composition of the covered electrode. As it can be seen, there is a small burn-off of the elements like Ti and B. This loss can be compensated by adding B- and Ti-components to the coating, but only to a certain extend and in combination with other elements (like e.g. Silicon. That is, f. ex., the reason for the Si-increase in the weld metal). The test results of the all weld metal have been taken at RT and at 600 °C, which is the max. allowable service temperature for the base material 7CrMoVTiB 10-10 according to VdTÜV-Data sheet 533. Mechanical properties have also been tested after a PWHT at 740°C for 15 h. Such a heat treatment is necessary for qualifying the filler metal for welding pipes up to

unlimited wall thickness. A joint of a pipe was welded with GTAW for the root and first filler. Remaining fillers have been SMA-welded with the 2,5 and 3,2 mm electrodes. As already mentioned above, again the influence of layer thickness in the different welding positions (12, 3 and 6 o'clock) can be demonstrated with different toughness levels. Best properties can be observed in the 3 o'clock position. In addition toughness has been tested in the overhead position without PWHT. Even under these test conditions toughness is sufficient. Hardness is always below 350 HV10.

a) Chemical composition of SMAW filler metal Thyssen CrMoVTiB (all weld metal) 4.0 mm ∅

	C	Si	Mn	P	S	Cr	Mo	Ni	V	B	N	Nb	Ti
wire	,061	,24	,53	,004	,002	2,39	1,01	-	,24	,0037	,016	,008	,073
all weld metal	,064	,47	,56	,008	,006	2,38	,97	,13	,24	,0030	,035	,008	,043

b) Mechanical properties, all weld metal

Testtemp.	PWHT °C / h	YS MPa	TS MPa	Elong. %	Red. A %	CVN J	Hardness HV 10
RT	no PWHT	702	860	16,8	59,1	16 18 14 12 16	320
600 °C		524	613	15,8	66,4	-	-
RT	740/ 2	507	626	21,9	75,0	163 166 110 178 155	233
600 °C		306	366	25,6	76,9	-	-
RT	740/ 15	478	605	24,0	74,0	167 186 170	206
550 °C		348	410	21,4	76,1	-	-
600 °C		276	336	21,8	84,0	-	-

c) Mechanical properties at RT of a joint P 24; root: Union I CrMoVTiB ; filler: Thyssen CrMoVTiB

PWHT °C / h	Weld. pos.	YS MPa	TS MPa	Elong. %	Location of fracture	CVN J	Hardness HV 10	Side Bend Test
740/2	PA	453	597	31,9	BM	49 53 94	221 - 236	180°
	PC	444	591	30,7	BM	104 79 120		180°
	PF	452	588	28,9	BM	35 65 48		180°

d) Welding parameter

	∅ mm	Polarity	Preheat temp. °C	Interpass temp. °C	Is A	Us V
TIG root	2,5	= -	200	200 - 250	130-160	17
TIG 1. Pass	2,5	= -	200	200 - 250	190	22
SMAW	2,5	= +	200	200 - 250	70-90	23
SMAW	3,2	= +	200	200 - 250	120	24

Table 4: Chemical composition and mechanical properties of Thyssen CrMoVTiB

Table 5 shows test results of SAW filler metal. In case of SAW welding the lowest B- and Ti contents in the weld metal had been found. This may be the reason for the relatively high toughness values. SAW is used only for heavy wall components. Therefore a PWHT of at least 2 h at 740°C is generally required. Hardness is in that case at about 230 HV10.

Figure 2 shows a picture of the macro structure of a joint of the 20 mm thick P 24 pipe with GTAW filler metal Union I CrMoVTiB after PWHT of 740°C/2h. The position taken for this picture is at the 9 o'clock, welding was carried out in the vertical up position. **Figure 3** shows the corresponding hardness profiles of this section in the root and in the cap-layer without and with a PWHT. The hardness of the base material is on a level of about 190 HV10. In the as

welded condition hardness in the root is a little bit higher compared to the hardness in the cap layer. The maximum hardness of the weld metal is 351 HV10. In the HAZ the max. value is at a level of 366 HV10. After a PWHT at 740°C/2h hardness can be reduced by about 100 HV10 units to a value of about 230 HV10. Again the hardness of the root is slightly higher than in the cap. This is probably caused by annealing effects.

a) Chemical composition of filler metal Union S 1 CrMoVTiB, all weld, 4.0 mm ∅
Flux: UV 430 TTR-W

	C	Si	Mn	P	S	Cr	Mo	V	B	N	Nb	Ti
wire	,061	,24	,53	,004	,002	2,39	1,01	,24	,0037	,016	,008	,073
all weld metal	,058	,24	,75	,003	,002	2,26	1,01	,22	,0008	,010	,007	,027

b) Mechanical properties at RT, all weld metal; welding with AC

PWHT °C / h	YS MPa	TS MPa	Elong. %	Red. A %	CVN J	Hardness HV 10
740 / 2	633	713	15,7	57,9	170 175 181	230

c) Welding parameter

Polarity	Preheat temp. °C	Interpass temp. °C	Is A	Us V	Vs cm/min	Heat input kJ/cm
AC	180	200 - 220	550	31	55	18,6

Table 5: Chemical composition and mechanical properties of Union S 1 CrMoVTiB

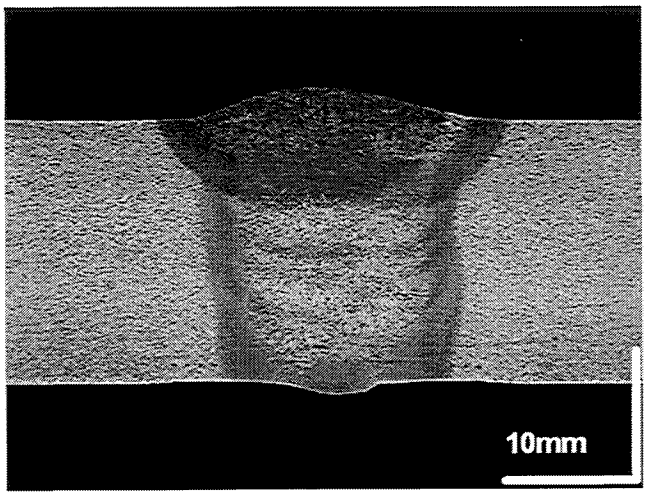


Figure 2: Macro graph of the joint P 24 with Union I CrMoVTiB

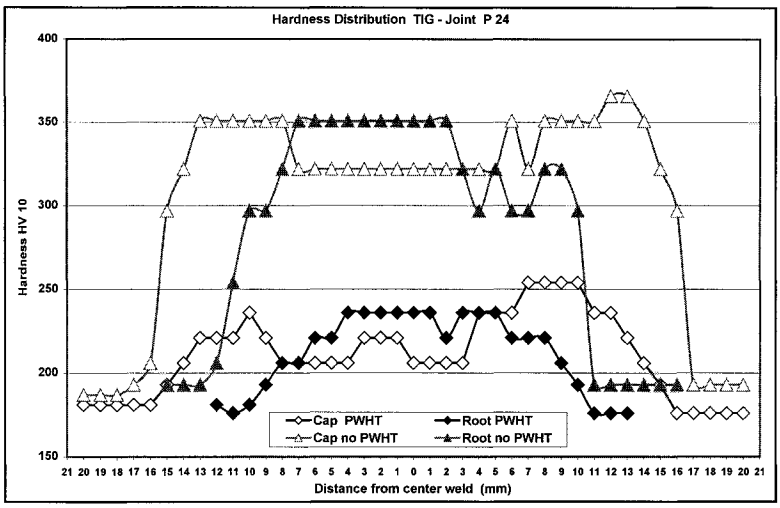


Figure 3: Hardness profiles through the joint P 24 with Union I CrMoVTiB (see fig. 2)

Matching filler metal for welding HCM 2 S (T / P 23)

While pipe material testing was carried out for the P 24 material, for the T/P 23 material only tube welding were carried out so far. Up to now only little pipe material had been delivered to the project partners of the COST program. Qualification tests are running now with the filler metals mentioned below.

Table 6 gives an overview of the chemical composition of the GTAW-filler metal and the mechanical properties of all weld metal and of a test of a tube joint. It can be seen, that the strength properties are on a similar level like T/P 24 filler metal. In the as welded condition strength is higher, probably caused by the slightly higher C content in this wire. And it seems to be a tendency for less toughness with the T/P 23 material at least in the as welded condition, due to the high tungsten and carbon content. The matching GTAW-filler for T/P 24 has remarkable high toughness values.

With automatic orbital GTAW equipment a tube (OD = 50,8 mm; Width = 7,1 mm) was welded using a 0,8 mm wire [1]. The welding parameters are given in **table 6d** Welding has been carried out using two different preheat conditions. As seen in part **c** of **table 6** the mechanical properties of this joint fulfill the requirements of the base material. There is no difference in the properties after welding with or without preheat temperature and toughness is in the range of about 75 J/cm². As the hardness is below 313 HV10 all requirements for water wall welding of T 23 material are fulfilled.

Tables 7 gives information about chemical composition of the electrode and the mechanical properties after PWHT of the T/P23 SMAW fillers. A PWHT at 740 °C (10 °C below the max. allowable temperature) produce good toughness properties. As already mentioned for the electrode Thyssen CrMoVTiB, here again a long term PWHT for 15 h was carried out. Mechanical properties of the electrode are comparable to those of P 24 filler.

a) Chemical composition of wire and GTAW filler metal Union I Cr 2 WV, all weld, 2.5 mm ∅

	C	Si	Mn	P	S	Cr	Mo	V	W	B	N	Nb
wire	,081	,27	,54	,009	,004	2,10	,08	,21	1,58	,0010	,016	,033
all weld metal	,075	,27	,51	,007	,002	2,10	-	,21	1,57	-	,014	,032

b) Mechanical properties, all weld metal

Testtemp.	PWHT °C / h	YS MPa	TS MPa	Elong. %	Red. A %	CVN J	Hardness HV 10
RT	as welded	857	951	19,2	74,0	30 46 38	332
	730 / 0,5	682	761	19,5	76,0	256 207 242	-
	730 / 2	621	708	21,0	77,0	218 192 222	-
	740 / 4	520	620	20,2	83,1	299 286 261	-
450 °C	as welded	760	888	16,2	69,0	-	-
500 °C	as welded	696	814	14,6	66,0	-	-

c) Mechanical properties at RT of a T 23 joint (Tube dimension: 50.8 mm x 7.1 mm)

Preheat °C	YS MPa	TS MPa	location of fracture	CVN (J) BM	CVN (J) HAZ	CVN (J) WM	CVN (J/cm²) BM	CVN (J/cm²) HAZ	CVN (J/cm²) WM	Hardness HV 10
no	491	607	B.M.	100	94	31	248	232	77	max. 313
175	495	611	B.M.	103	87	29	258	217	73	-

d) Welding parameter for GTA orbital welding

∅ mm	Polarity		Is A	Pulsed Intens. A/ms	Heat Input kJ/cm	Shielding gas
0,8	=-	root	100	140A / 5ms 60 / 50	11,4	Ar
0,8	=-	fillers	100	140A / 5ms 60 / 50	11,4	Ar

Table 6: Chemical composition and mechanical properties of Union I Cr 2 W V

a) Chemical composition of SMAW filler metal: Thyssen Cr 2 WV, all weld, 3.2 mm ∅

	C	Si	Mn	P	S	Cr	Mo	Ni	V	W	B	N	Nb
wire	,060	,26	,50	,011	,002	2,13	,07	,13	,21	1,77	,0010	,015	,062
all well metal	,050	,21	,50	,016	,006	2,30	,06	,12	,23	1,58	-	,017	,038

b) Mechanical properties, all weld metal

Testtemp.	PWHT °C / h	YS MPa	TS MPa	Elong. %	Red. A %	CVN J	Hardness HV 10
RT	740 / 2	509	625	19,0	71,9	128 140 136	227
RT	740 / 15	421	553	25,0	74,0	156 156 160	192
600 °C		280	319	22,4	81,6	-	-

c) Welding parameter

∅ mm	Polarity	Preheat temp. °C	Interpass temp. °C	Is A	Us V
3,2	=+	200	200 - 250	130	24

Table 7: Chemical composition and mechanical properties of Thyssen Cr 2 W V

The SAW process requires a PWHT. The CVN-values of the all weld metal at RT in the as welded condition are below 15 J. **Tables 8** show the results of the all weld metal tests after three different PWHT´s at 650°, 705° and 740°C. It is obvious that a PWHT-temperature of 650 °C is to low and toughness is not higher than without any heat treatment. Furthermore it can be seen that there is a scatter band for the CVN-values, if PWHT is not sufficient (see at 705/10 h). Best toughness properties are observed after PWHT of 740/2h.

a) Chemical composition of SAW filler metal: Union S 1 Cr 2 WV; Flux: UV 430 TTR-W

	Ø mm	C	Si	Mn	P	S	Cr	Mo	Ni	V	W	Al	B	N	Nb	Ti
wire	4,0	,060	,26	,50	,011	,002	2,13	,07	,13	,21	1,77	,01	,0010	,005	,062	,04
all weld metal	4,0	,045	,27	,94	,013	,003	2,04	,11	,09	,19	1,61	-	-	,007	,043	,07

b) Mechanical properties at RT, all weld metal

PWHT °C / h	YS MPa	TS MPa	Elong. %	Red. A %	CVN J	Hardness HV 10
650/10	713	795	16,1	50,2	18 21 25	236
705/10	612	700	19,1	57,9	98 150 100	236
740 / 2	615	702	18,1	59,1	204 187 208	237

c) Welding parameter

Ø mm	Polarity	Preheat temp. °C	Interpass temp. °C	Is A	Us V	Vs cm/min	Heat input kJ/cm
4,0	≈	180	220	550	31	55	18,6

Table 8: Chemical composition and mechanical properties of Union S 1 Cr 2 W V

Conclusions

For new base materials like HCM 2 S and 7CrMoVTiB 10-10, which will be used in future power plant construction, the corresponding filler metals have been developed. Although these base materials should be used in the main application for thin walled water wall construction, thick walled pipe material have to be connected, too. For this reason, filler metals for all kind of conventional welding processes are needed. During the research program COST 522 the manufacturers have started to develop these filler metals and due to hard research work all consumables are available now. In this paper it could be demonstrated, that all kind of filler metals will fulfil all requirements, even in the as welded condition without a PWHT, if necessary.

Acknowledgement

The authors express their appreciation and acknowledgement to all individual members of the "COST 522 welding group and boiler group" who supported the successful COST action and the present research work.

References

[1] Arndt, J.; Haarmann, K.; Gottmann, G.; Vaillant, J. C.; Bendick, W.; Deshayes, F.: The T23/T24 Book, New Grades for Waterwalls and Superheaters, 1998 Vallourec & Mannesmann Tubes

EVALUATION OF THE WELDED JOINTS IN P92 AND P122 PIPE STEELS

S. H. Ryu *, K. W. Lee *, B. H. Chi *, Y. S. Lee *, B. O. Kong *
S. H. Park **, S. W. Nam **, B. S. Lim #, B. J. Kim #

* Doosan Heavy Industries & Construction Co., Ltd., Changwon, Korea
** Korea Advanced Institute of Science and Technology, Taejon, Korea
# Sungkyunkwan University, Suwon, Korea

Abstract

SAW and SMAW processes in P92 and P122 pipe steels have been investigated for the application to the main steam pipe and the header components of boiler in the domestic thermal power plant.
P92 steel indicated the higher weld metal toughness compared to P122 steel. The double PWHT was more beneficial to the weld metal toughness than the single PWHT with the same tempering parameter. Determined from the weld metal toughness and the economic point of view, the PWHT conditions of the P92 and the P122 steels were 750°C for 5hrs and 760°C for 5hrs respectively.
The continuous low cycle fatigue (LCF) life was similar for both P92 and P122 irrespective of the test temperatures and the position of cross weld. The continuous LCF and the creep-fatigue interaction (CFI) tests also indicated very similar fatigue life in the base metal regardless of the holding time. On the other hand, in the weld metal, the CFI life caused a reduction in cycles to failure lower by a factor of 2 ~ 4 than the continuos LCF life, and the extent of reduction was increasing with increasing test temperatures.
There was an indication of dependence of crack growth rate on temperature in the P92 and the P122. The slope of the Paris plot (m) had also a trend towards the higher values at the higher temperatures. The crack growth rate in the weld metal was slightly slower than that in the base metal. The HAZ showed the fastest growth rate and the highest value over m ~ 4 in the cross weld. The crack growth rates in the base metal of the P122 were faster than those of the P92 at temperatures of 600~700°C.

Keywords: 9-12% Cr Steels, Steam Plant, Welding, Mechanical Properties, Microstructure, Low Cycle Fatigue

1. Introduction

Material selection for boiler systems with advanced steam conditions is determined by considering many factors. For thick-section components, such as headers and pipes, fabricability, weldability and resistance to thermal fatigue are necessary consideration as well as creep rupture strength.

Ferritic steels are usually preferred for this type of environment due to higher thermal properties and fatigue strength than those of austenitic steels. Among 9-12% Cr ferritic steels, 9Cr-2W (P92) and 12Cr-2W (P122) steels have been widely used at advanced steam conditions because of the possibilities of reducing the wall thickness of piping for given steam conditions due to their high creep rupture strength. For the base metals of the P92 and the P122, sufficient database, such as mechanical properties, creep rupture strength, low cycle fatigue and creep-fatigue properties, are available. However, in the welded joints, there are insufficient database for the mechanical properties and the failure behaviors, such as low cycle fatigue and fatigue crack growth.

In this study, effects of the welding processes and the post weld heat treatment on mechanical properties and failure behaviors have been investigated in the P92 and the P122. The results will be utilized to develop a life assessment system for boiler components in thermal power plants.

2. Welding Procedure

The chemical compositions of the P92 and the P122 pipe steels and the welding consumables are given in Table 1. The dimensions of pipes are OD 304mm and WT 62mm for the P92 and OD 395mm and WT 50mm for the P122. Table 2 shows the mechanical properties of the as-received materials for the P92 and the P122 steels.

Table 1. Chemical compositions of the as-received materials (base metal) and the matching welding electrodes for the P92 and the P122 steels.

Element	Base Metal		Welding Electrode						
			P92				P122		
	P92 [1]	P122 [2]	GTAW [3]	SMAW [3]	SAW [3]	FCAW [4]	GTAW [5]	SMAW [5]	SAW [6]
C	0.10	0.13	0.10	0.11	0.09	0.11	0.07	0.08	0.11
Si	0.22	0.31	0.36	0.22	0.30	0.23	0.32	0.33	0.19
Mn	0.48	0.59	0.44	0.54	0.52	0.49	0.48	0.79	1.18
P	0.017	0.020	0.012	0.014	0.009	0.009	0.006	0.010	0.023
S	0.006	-	0.005	0.005	0.001	0.007	0.003	0.004	0.004
Ni	0.18	0.34	0.72	0.59	0.48	0.57	1.12	0.94	1.20
Cr	9.11	10.57	8.89	8.50	8.59	8.41	10.54	10.01	10.69
Mo	0.47	0.33	0.41	0.50	0.39	0.55	0.34	0.19	0.11
W	1.71	1.79	1.75	1.45	1.61	1.65	1.48	1.44	1.83
Cu	-	0.96	-	0.06	0.05	0.02	1.48	1.50	0.46
V	0.18	0.21	0.23	0.20	0.15	0.22	0.21	0.16	0.21
Nb	0.056	0.060	0.069	0.02	0.038	0.062	0.05	0.02	0.04
B	0.003	0.002	-	0.002	-	-	-	0.002	0.020
N	0.041	0.060	0.052	0.041	0.046	0.040	0.040	0.039	0.025

1) and 2) were supplied by V&M Tubes Co. and Sumitomo Metal Industries, Ltd. respectively. 3), 4), 5) and 6) were supplied by Thyssen Krupp Stahlunion GMBH, ESAB SëAH Corp., Sumikin Welding Industries, Ltd. and Kobe Steel respectively.

Table 2. Dimensions and mechanical properties of the as-received materials for the P92 and the P122 steels.

Steel	Dimension (mm)	Heat treatment [1]	Mechanical Properties			
			TS (MPa)	YS (MPa)	EL (%)	HRB
P92	OD304 x WT 62	N : 1050°C x 1hr, AC T : 760°C x 3hr, AC	674	506	23.6	-
P122	OD 395 x WT 50	N : 1050°C x 0.5hrs, AC T : 770°C x 6hr, AC	758	591	24	221

1) N : Normalizing, T: Tempering, AC : Air cooling from austenitizing temperature.

The welding processes used in this study consisted of SMAW (Shielded Metal Arc Welding) and SAW (Submerged Arc Welding). GTAW (Gas Tungsten Arc Welding) was employed for the root pass welding. The details of the welding conditions are shown in Table 3. They are basically similar to those applied to the P91. The welded joints were subjected to PWHT (Post Weld Heat Treatment) with the conditions of 740 ~ 760°C for 2~65 hours.

3. Test Results

3.1 Microstructure

Macrostructure of the longitudinal section across the circumferential butt welded joint is given in Fig.1. Defects were not observed in the weld metal and the HAZ. Microstructures of the weld metal in the P92 and the P122 were tempered martensitic structures with a delta ferrite content below 1 percent. In the weld metal of the P122, especially a small amount of retained austenite below about 4% was indicated.

Table 3. Welding parameters for GTAW, SMAW and SAW processes in the P92 and the P122 steels.

Welding Process	Steel	Matching Filler Metal		Welding Condition				
		Brand Name	Dia. (mm)	Layers	Current (A)	Voltage (V)	Speed (cm/min)	Preheat / Inter Pass Temp.
GTAW	P92	THERMANIT MTS616 [1]	ϕ2.4	1~3	120~150	12~16	8~15	200 ~ 300 °C
	P122	T-HCM12A [2]	ϕ2.4					
SMAW	P92	THERMANIT MTS616 [1]	ϕ4.0	4~30	140~160	22~26	6~15	
	P122	#HCM12A [2]	ϕ4.0					
SAW	P92	THERMANIT MTS616 [1],[4]	ϕ2.5	4~50	250~350	25~35	35~45	
	P122	8LB004 [5]	ϕ2.4					
FCAW	P92	DSB9W [3]	ϕ1.2	-	200~210	25~26	-	

1) Thyssen Krupp Stahlunion GMBH. 2) Sumikin Welding Industries, Ltd.. 3) ESAB SëAH Corp.. 4) SAW flux : MARATHON 543. 5) Kobe Steel, Ltd..

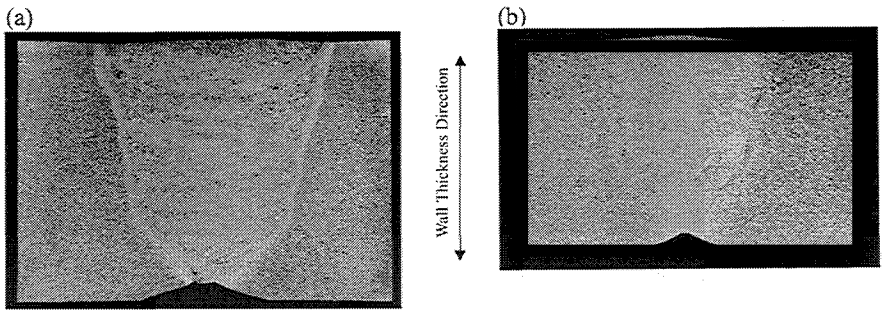


Fig.1 Macrosections of multipass weld produced by SMAW using a U groove in the P92 and the P122 steels. (a) The P122 steel (WT=62mm). (b) The P92 steel (WT=50mm).

3.2 Tensile Properties

The weld metal samples were machined along the circumferential weld seam. The cross weld samples were removed across the seam so that the gage length comprised the base metal, the HAZ and the weld metal. The dimensions of the gage part in all test samples were 6.25mm OD x 25mm Length. Tensile tests were conducted at room temperature and 600°C.

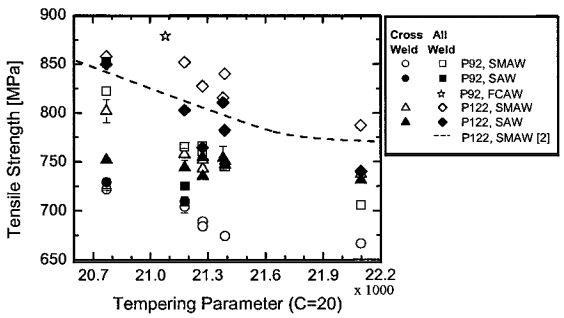


Fig.2 Variation of the tensile strength at RT with PWHT conditions in the SMAW and SAW welded ioints of P92 and P122 steels.

Fig.2 gives the variations of the tensile strength in the cross weld and the weld metal as a function of the PWHT conditions and the welding processes with reference data. The fracture location for all cross weld samples was in the base metal. The tensile strengths in the P122

were higher than those in the P92 at a fixed PWHT condition and welding process as expected from the as-received properties. As comparing the welding processes, the tensile strengths of the SAMW process were superior to those of the SAW in the P122 steel but similar to those of the SAW in the P92 steel at the cross weld and the weld metal. The FCAW process showed the highest weld metal tensile strength in the welding processes studied.

3.3 Impact Toughness

The full-sized 10 x 10 mm Charpy V-notch specimens were obtained across the circumferential weld seams. A V-notch was placed in the base metal, the HAZ and the center of weld deposit respectively. Impact tests were conducted at room temperature.

The base metal of the P92 and the P122 exhibits relatively lower toughness level compared with the low alloy steels due to the alloying elements added to improve creep rupture strength. However, it is known that their toughness is restored to the extent of approximately 80~180 J/cm^2 after tempering at about 760°C carried out at mill makers. Therefore, the problem with the shortage of toughness is limited only to the weld metal and the HAZ region.

The HAZ toughness was restored up to the similar or higher value compared with the base metal by the PWHT of 750°C for 5 hours (TP=21175) in the both materials without respect to the welding processes (Fig.3 (a)). The weld metal toughness became different with welding processes and materials as shown in Fig.3 (b).

SMAW

The weld metal toughness of the P92 was higher than that of the P122 at all PWHT conditions. It achieved an average toughness being about 58 J/cm^2 after the PWHT of 750°C for 5 hours. For the P122, the weld metal toughness was no more than approximately 23 J/cm^2 at TP=20768 (750°C for 2 hours), but it increased with the increasing tempering parameter and came to about 48 J/cm^2 at TP=22096 (740°C for 65 hours).

SAW

The SAW process showed a lower weld metal toughness compared with the SMAW regardless of the material types and the PWHT conditions. In the P92 steel, the weld metal toughness indicated the very low value being 12 J/cm^2 after the PWHT of 750°C for 2 hours. However, they are recovered up to the average toughness of 34 J/cm^2 after the PWHT for 5 hours at the same temperature, while the P122 steel still indicated a very low toughness value, about 31 J/cm^2 at TP=22096, even at a high tempering parameter. Generally, the toughness of SAW weld metal lowers due to the higher oxygen content and heat input introduced during welding process. In this study, it seems that the retained austenite included in the weld metal has an effect on the decrease of the weld metal toughness in addition to the oxygen content. The weld metal toughness of P122 increased up to about 44 J/cm^2 by means of the double PWHT of 740°C for 5 hours (TP=21273), which can take a role to change the fresh martensite formed at the first PWHT into the tempered martensite at the second PWHT.

In the FCAW process, the weld metal toughness of the P92 steel was similar to that of the SMAW in spite of the higher value of the tensile strength. When being compared with the weld metal toughness achieved by other researches [1][2], the current results indicate quite low values in spite of similar compositions of weld metal due to the difference of welding parameters such as heat input.

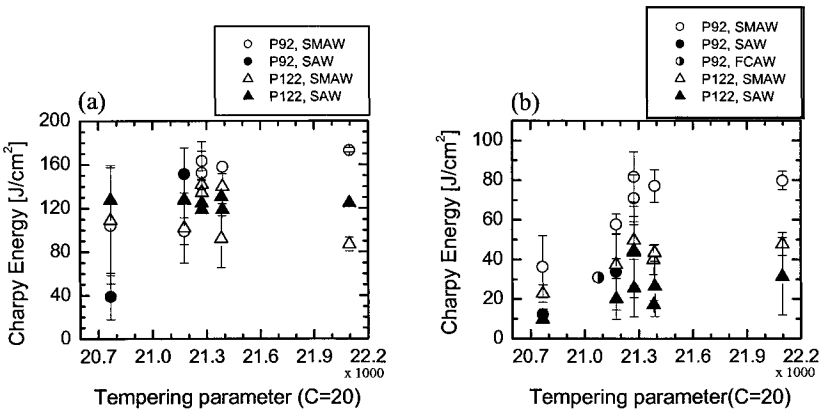


Fig.3 Variation of the Charpy impact energy with the PWHT conditions in the SMAW and the SAW welded joints of the P92 and the P122 steels. (a) The HAZ, (b) The weld metal.

3.4 Low Cycle Fatigue (LCF)

All test samples were machined across the circumferential weld seam of the SMAW process. The weld metal and the base metal samples included only weld deposit and base metal at the gage part respectively. The HAZ samples were drawn and machined in such a way that the center of HAZ was placed at the specimen gage center so that the gage length comprised with the base metal, the HAZ and the weld metal. The dimensions of gage part of all test samples were 7mm OD and 8mm Length.

For all LCF tests, uniaxial strain control push-pull tests were performed at a strain rate of 4 x 10^{-3} s^{-1} with total strain range of ±1.5 ~ ±3.0% at normal atmospheric conditions. A symmetrical continuous triangular loading waveform was used for LCF test. Creep-fatigue interaction (CFI) tests for the P122 were performed with strain-hold of 10 minutes at tensile peak strains under the same temperature conditions as the LCF test.

The continuous LCF life plotted as a function of the plastic strain ranges is given in Fig.4. Fatigue life was generally dependent on the test temperature and the position of cross weld. In the ranges studied, however, the fatigue lives were similar for both the P92 and the P122 irrespective of the test temperatures and the position of cross weld. They were in the similar range with the data for the base metals of P91, P92 and P122 reported by M. Sato et al. [3].

The results of CFI tests with 10 minutes hold for the P122 are given in Fig.5 with the continuous LCF. In the base metal, the continuous LCF and CFI tests indicated nearly similar fatigue life regardless of the holding time. The CFI life in the weld metal caused a reduction in cycles to failure lower by a factor of 2 ~ 4 than that of the continuous LCF and the extent of reduction was more pronounced with increasing test temperatures. This means that holding time has a severe effect on the microstructural changes in the weld metal more than in the base metal

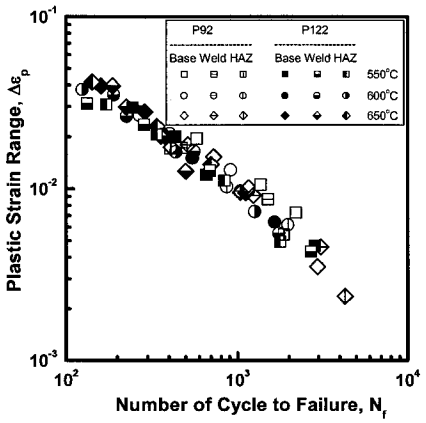


Fig.4 Coffin-Manson plots of the base metal, the HAZ and the weld metal under the continuous low cycle fatigue at various test temperature in P92 and P122 steels.

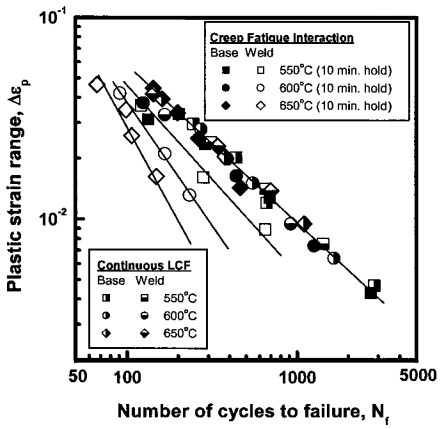


Fig.5 Coffin-Manson plots of the base metal, the HAZ and the weld metal under the continuous LCF and the creep-fatigue with 10 minutes hold time at various test temperature in P122 steels.

Fig.6 indicates the variations of the tensile peak stress as a function of normalized fatigue life with the plastic strain range during the continuous LCF and the CFI tests. The typical cyclic softening behavior occurred in the tempered martensitic structure was observed in all of the base metal and the weld metal throughout the CFI test with holding time and they were increased with increasing test temperature. The decreasing trend in the tensile peak strength was similar for both the base metal and the weld metal. The plastic strain range occurred seriously in the weld metal more than in the base metal from early stage of test. Therefore, the damage accumulated in the weld metal was increased with the increasing cycles beyond that in the base metal and gave rise to the reduction of fatigue life in the weld metal.

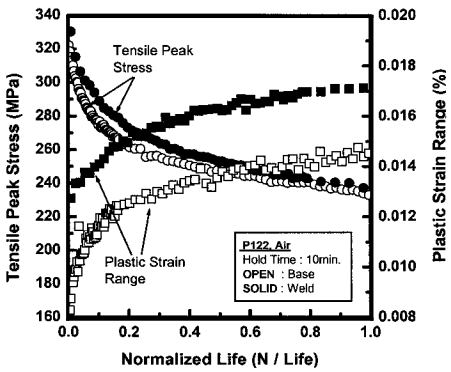


Fig.6 Variation of the tensile peak stress and the plastic strain range in the weld metal with the normalized fatigue life at 1.5% total strain range condition under the continuous LCF and the creep-fatigue with hold time.

When comparing the microstructural evolutions developed in the weld metal with that in the base metal during CFI test, the recovery of lath structure and the formation of subgrain structure were locally produced seriously in the weld metal more than in the base metal (Fig.7). It was presumed that the local accelerated recovery and recrystallization resulted from the intrinsic non-homogeneity and the loose structure of the weld metal compared with the base metal. Therefore, the additional microstructural evolutions caused by the creep

deformation during holding time offered the large plastic strain and led to the decrease of fatigue life in the weld metal during the CFI test.

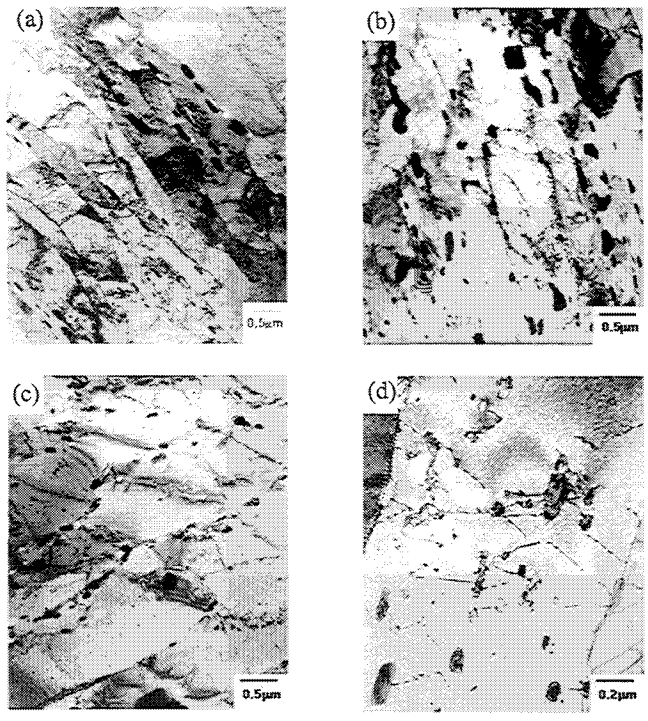


Fig.7 Comparison of TEM microstructures in the base metal and the weld metal before and after creep-fatigue test at 650°C with 10 minutes hold time and $\Delta\varepsilon_t$=1.5% in the P122 steel. (a) The as-received base metal before test. (b) The base metal after creep-fatigue test. (c) and (d) The weld metal after creep-fatigue test.

3.5 Fatigue Crack Growth

The compact tension specimens with 6.9mm in thickness and 38mm in width were cut off across the circumferential weld seam of the SMAW process. The notches in all specimens were placed in the base metal and the center of the HAZ and the weld metal. Fatigue crack growth tests were performed at 600, 650 and 700°C of normal atmospheric conditions with a stress ratio R=0.1, using a sine waveform of 20 Hz. The crack length was determined from the DCPD method and crack growth rates were calculated by the secant method.

The crack propagation rates plotted against the stress intensity range are given in Figs.8 to 10. In the P92 steel, there was an indication of dependence of crack growth rate on temperature, in good agreement with the results by P. J. Cotterill et al. [4]. It showed a clear trend that crack growth rate increased with the increasing temperature in the base metal and the weld metal except for the HAZ. The slope of the Paris plot (m) had also a trend towards the higher values at the higher temperatures. The crack growth rate in the weld metal was slightly slower than that in the base metal, but the difference was small. In the weld metal,

the crack growth rate at 700°C was 2 times faster than that at 600°C. The HAZ indicated the fastest growth rate and the highest value over m ~ 4 in the cross weld.

In the P122 steel, although there was an indication of dependence of crack growth rate on temperature for the case of 600°C and 700°C, the difference in rate between 600°C and 650°C was negligible. The crack growth rate was low in the weld metal rather than the base metal.

The crack growth rates in the base metal of the P122 were faster than those of the P92 at all test temperatures. At 600°C, the crack growth rate in the weld metal of P122 was faster by a factor of approximately 3.8 compared with that in the P92.

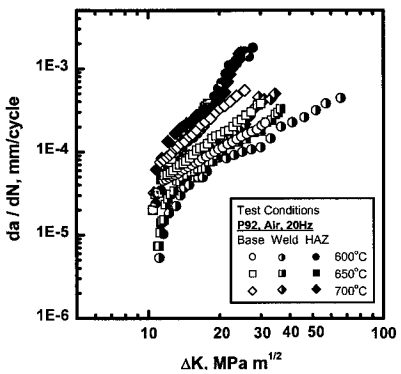


Fig.8 Variation of crack growth rates in the base metal, the HAZ, and the weld metal with ΔK at various temperatures in the P92 steel.

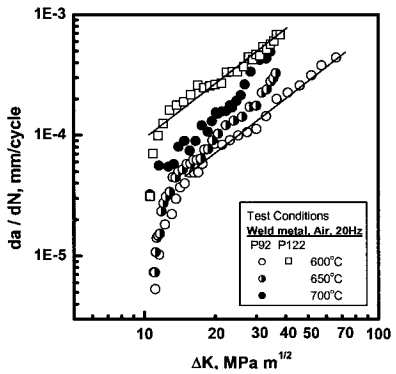


Fig.9 Comparison of crack growth rates in the weld metal with ΔK at various temperatures in the P92 and P122 steels.

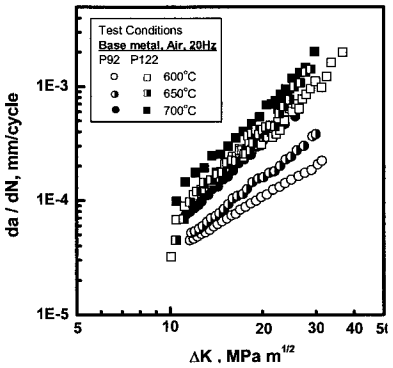


Fig.10 Comparison of crack growth rates in the base metal with ΔK at various temperatures in the P92 and P122 steels.

4. Discussion

4.1 Effects of weld metal compositions on the weld metal toughness

It is recognized that weld metal toughness can be improved with the strengthening of matrix

structure and the reduction of precipitation for Ni addition and a role of deoxidant for Mn [5]. However the combined additions of Ni and Mn is limited to below about 1.5% because the excessive content of Ni+Mn lowers the Ac1 temperature and give rise to degradation of weld metal toughness [6] and creep rupture strength [7] [8]. Therefore it seems that an optimum selection of Ni and Mn content is necessary to guarantee weld metal toughness, higher PWHT temperature and creep rupture strength in the weld metal at the same time.

In this study, Ni and Mn were preferably controlled up to levels of 2 times higher than the base metal compositions, while W and Nb were controlled to lower levels as much as possible within the considerations of the creep rupture strength. Especially, the weld metal of the P122 contained higher levels of Ni and Mn compared to those of the P92 in order to compensate the deterioration of toughness caused by the additional additions of Cr and Cu. The Ni+Mn content in the SAW electrode of the P122 was increased to the extent of 2.38%.

PWHT temperature and soaking time to restore the weld metal toughness become different with the weld metal compositions and the welding parameters. The higher weld metal toughness can be achieved with the higher PWHT temperatures or longer soaking times. But the higher PWHT temperature can result in exceeding the Ac1 temperature. The Ac1 temperatures of the P92 and the P122 base metals are about 835°C and 805°C respectively [9][10]. Some additional Ni and Mn content added in the weld metal of the P92 and the P122 steels have a strong influences on the Ac1 temperatures and hence a permissible PWHT temperature because the additions of 1wt% of Ni and Mn in a 0.1C-12Cr steel lower Ac1 temperatures by 30°C and 25°C respectively [11]. The Ac1 temperatures of the weld metals of the P92 and the P122 steels were, therefore, determined at 760~780°C [12]. It is important to set the PWHT temperature with leaving sufficient margin against Ac1 temperature because of the risks of austenite reformation to the fresh martensite in the P92 and the P122 weld metals. However, the high tempering resistance of the P92 and the P122 steels calls for the PWHT at a high temperature close to Ac1, and the selection of the PWHT temperature is limited to the narrow ranges below the Ac1 temperature from a commercial point of view.

In this study, among the various conditions of 740~760°C for 2~65 hours, PWHT conditions of the P92 and the P122 were 750°C for 5hrs and 760°C for 5hrs respectively, which were determined from the weld metal toughness, the Ac1 temperature and a commercial point of view. Therefore, there was a special attention to ensure that the PWHT temperature did not exceed Ac1 temperature because they were so close to Ac1 point.

5. Conclusion

The characteristics of the welded joints with the welding processes and the PWHT conditions in the P92 and P122 steels can be summarized as follows.

- A small amount of delta ferrite and retained austenite occurred in the weld metal of the P92 and the P122 steels.
- The weld metal toughness of the P92 was superior to that of the P122. The double PWHT was beneficial to weld metal toughness compared to the single PWHT with the same tempering parameter.
- The optimum PWHT conditions of the P92 and the P122 steels were 750°C for 5hrs and 760°C for 5hrs respectively. However, a special attention was necessary for ensuring that the PWHT temperatures did not exceed Ac1 temperature because they were so close

to Ac1 temperature.

- The continuous low cycle fatigue life was similar for both P92 and P122 at all test temperatures and the position of cross weld. The continuous LCF and the CFI tests also indicated nearly similar fatigue life in the base metal regardless of the holding time. In the weld metal, the CFI life caused a reduction in cycles to failure lower by a factor of 2 to 4 than the continuous LCF life.
- The local accelerated recovery and recrystallization caused by the intrinsic non-homogeneity and the loose structure of the weld metal offered the large plastic strain and led to the decrease of fatigue life of the weld metal during the CFI test.
- There was an indication of dependence of crack growth rate on temperature in the P92 and the P122 steels. The crack growth rate in the weld metal was slightly slower than that in the base metal. The HAZ indicated the fastest growth rate and the highest value over $m \sim 4$ in the cross weld. The crack growth rates in the base metal and weld metal of the P122 were faster than those in the P92 at 600°C.

References

[1] Doc. No. 96130, SMAW electrode for HCM12A steel, Sumitomo Metal Ind., Ltd..
[2] Doc. No. 041999-T008, The development of SAW electrode for adv. 12Cr steels, Kobe Steel, Ltd., May 1999.
[3] M. Sato, H. Kimura, M. Abe, M. Yamauchi and M. Fujita, Creep-fatigue characteristics of advanced high strength Cr-W steels for power boiler applications, Advanced Heat Resistant Steel for Power Generation, Edited by R. Viswanathan and J. Nutting, IOM Communications Ltd., 1999, pp. 298-308.
[4] P. J. Cotterill and J. F. Knott, Effects of temperature and environment on fatigue crack growth mechanisms in a 9% Cr 1% Mo steel, Acta Metall. Mater. Vol.40, No. 10, 1992, pp.2753-2764.
[5] Z. Zhang, A. W. Marshall, and J. C. M. Farrar, Recent developments in welding consumables for P(T)91 creep-resisting steels, Int. Conf. on Integrity of High-Temperature Welds, the Institution of Mechanical Engineers 1998, pp. 77-91.
[6] D.Richardot, J. C. Vaillant, A. Arbab, and W. Bendick, The T92/P92 Book, V & M Tubes, 2000, p.40.
[7] S. H. Ryu, Jin Yu and B. S. Ku, Effects of Alloying Elements on the Creep Rupture Strength of 9-12% Cr Steels, Proceedings of the fifth International Charles Parsons Turbine Conference, 3-7 July 2000, Churchill College, Cambridge, UK, pp.472-484.
[8] F.Masuyama, M.Matsui and N. Komai, Key Engineering Materials Vols. 171-174 (2000), 2000 Trans Tech Publication, Switzerland, p.99-108, 2000.
[9] D.Richardot, J. C. Vaillant, A. Arbab, and W. Bendick, The T92/P92 Book, V & M Tubes, 2000, p.15.
[10] Report No. 907 F-No.3255, Sumitomo Metal Ind., Ltd., Feb. 1997.
[11] W. Betteridge, Cobalt and Its Alloys, Ellis Horwood Limited, Market Cross House, Cooper Street, Chichester, West Sussex, PO19 1EB, England, 1982, p. 100.
[12] S. Matsumoto, Information about #HCM12A (SMAW electrode) for HCM12A, Private Communication, Sumikin Welding Industries, Ltd., Aug. 2000.

CREEP STRENGTH AND MICROSTRUCTURES FOR HAZ OF WELDMENTS OF HIGH CR FERRITIC STEELS

Masakazu Matsui, Masaaki Tabuchi, Takashi Watanabe, Kiyoshi Kubo and Fujio Abe
Materials Engineering Laboratory, National Institute for Materials Science

Abstract

In ferritic 9-12%Cr heat resistant steels , higher metal temperatures accelerate creep damage especially in welded joints and sometimes result in serious cracks in heat affected zone (HAZ). In this study, the simulated HAZ specimens are prepared by heating with varying peak-temperature from1123 to 1273K, for three kinds of steels with the same Mo equivalents, 9Cr-3W, 9Cr-1.5Mo and 9Cr-1.8W-0.5Mo (P92), in order to investigate the effect of W and Mo contents. In creep tests at 923K, the rupture time of simulated HAZ for each steel shows a minimum value by heating just below Ac3 temperature. In the Ac3 simulated HAZ specimens, the creep rupture time shows longer value in the order of 9Cr-3W, 9Cr-1.8W-0.5Mo and 9Cr-1.5Mo steel, which has the same tendency as that in base metal. The Ac3 simulated HAZ specimens do not have a lath martensitic microstructure and coarsening of precipitates, $M_{23}C_6$, is observed before creep. The Ac3 simulated HAZ specimen of each steel contains higher density of dislocations than base metal. The faster recovery of high density of dislocations and the sparse distribution of large $M_{23}C_6$ carbides during creep promote the formation of coarse subgrains, which accelerates eventual creep fracture.

Key words: creep rupture strength, welded joint, 9%Cr ferritic steel, heat affected zone, precipitates

1. Introduction

Recently several types of advanced 9-12%Cr ferritic steels strengthened by W have been developed in order to improve the thermal efficiency of power plants. 9Cr-0.5Mo-1.8W-VNb(P92) and 11Cr-0.4Mo-2W-CuVNb (P122) steels are being now performed for application to boiler components of ultra-supercritical (USC) power plants operating at 898 K[1]. National Institute for Materials Science has been conducting a research and development project on advanced ferritic steels for USC boilers at 923K since 1997[2].

The resistance to creep cracking in the heat affected zone (HAZ) of welded joints is one of the problems for these 9 - 12%Cr ferritic steels for construction of thick section boiler components [3-5]. It is reported on 9Cr-0.5Mo-1.8W-VNb (P92) steel that the degradation of creep rupture strength of welded joint becomes more significant with increasing temperature, especially above 873 K [6].

Creep rupture strength of 9-12%Cr steels which contains various contents of W have been studied[7,8]. Little has been studied, however, concerning creep properties of welded joints and the simulated HAZ specimen for these 9-12%Cr steels strengthened by W.

In this study, the creep tests of the simulated HAZ specimens for three kinds of steels, 9Cr-3W, 9Cr-1.5Mo and 9Cr-1.8W-0.5Mo (P92) were carried out at 923K. The relationship between microstructure and creep deformation behavior was investigated on these steels. Some mechanisms for the degradation of creep strength in HAZ were discussed.

2. Experimental procedure

Table1 shows the chemical compositions of test materials. To investigate the effect of W and Mo in 9%Cr, the amount of W and Mo was varied as 3%W-0%Mo, 0%W-1.5%Mo and 1.8%W-0.5%Mo , which is P92. The normalizing and tempering conditions of each steel were also shown in Table1. Ac1 and Ac3 were measured by using high frequency induced heating device.

Figure1 shows the heat treatment conditions for the preparation of the simulated HAZ samples. Each sample was heated up and kept for 180s at the various peak temperatures between 1123 and 1273 K and then cooled in air. Finally, PWHT was carried out for each sample including the base metal at 1013K. In this paper, the specimens subjected to heating up to the various peak temperatures followed by PWHT are called simulated HAZ specimens.

Creep test was carried out at 923 K, using specimens of 6mm gauge diameter and 30 mm gauge length for the simulated HAZ specimens. The microstructure of the creep specimen was observed by scanning electron microscopes (SEM) and transmission electron microscopes (TEM).

Table 1 Chemical compositions (wt%) and heat treatment of test materials

	C	Si	Mn	Cr	W	Mo	V	Nb	N	Heat treatment	
3W- 0Mo	0.076	0.32	0.50	8.95	3.05	0.003	0.23	0.051	0.0490	1373K×0.5h+ 1073K×1h	
0W-1.5Mo	0.078	0.32	0.50	9.08	<0.01	1.540	0.20	0.045	0.0487	1373K×0.5h+ 1073K×1h	
1.8W-0.5Mo	0.09	0.16	0.47	8.72	1.87	0.45	0.21	0.06	0.050	1343K× 2h+ 1053K×2h	P92

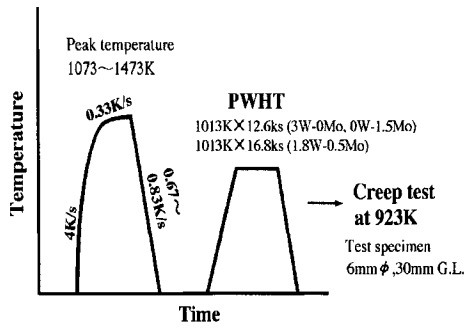


Fig.1 Conditions of heat treatment of simulated HAZ

3. Results and discussion

3.1 Creep strength of the simulated HAZ specimen

Figure2 shows the creep rupture data [9] of the welded joint, the base metal, the Ac1 and Ac3 simulated HAZ specimens at 923 K for P92. The welded joints were prepared by means of Gas Tungsten Arc (GTA) welding using the filler metal [10] with matching composition of 11Cr-0.4Mo-2W-CuVNb steel. The difference of creep rupture strength between welded joint and base metal was comparatively small at high stress and short time conditions. But the creep rupture strength of the welded joint decreases rapidly and then it becomes almost the same as that of the Ac3 simulated HAZ specimen at low stress and long time conditions because it frac-

tured in Type Ⅳ mode. Similar behavior was also observed for 11Cr-0.4Mo-2W-CuVNb steel [11]. The creep rupture strength of the Ac1 simulated HAZ specimen seems to coincide with that of the same heat of base metal (plate) at long times.

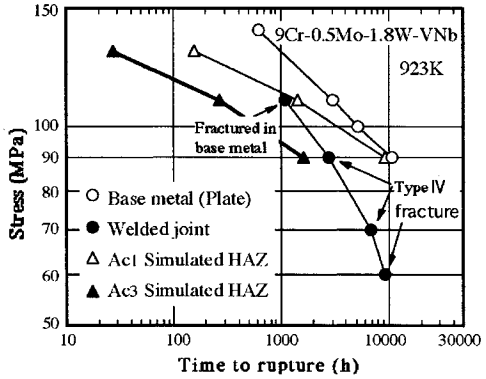


Fig.2 Creep rupture time of base metal, welded joints of 9Cr-0.5Mo-1.8W-VNb steel

Figure3 shows the relationship of creep rupture time and peak temperature in the simulated HAZ specimen of 3W-0Mo, 0W-1.5Mo and 1.8W-0.5Mo steel tested at 923K for 110MPa. The rupture time of each steel shows a minimum value at just below Ac3. In base specimen, the rupture time shows longer value in the order of 3W-0Mo, 1.8W-0.5Mo and 0W-1.5Mo steel, and it also shows the same order in the simulated HAZ specimen. The creep rupture time of the simulated HAZ specimen heated to Ac3 is about one-fifth that of the base metal for each steel.

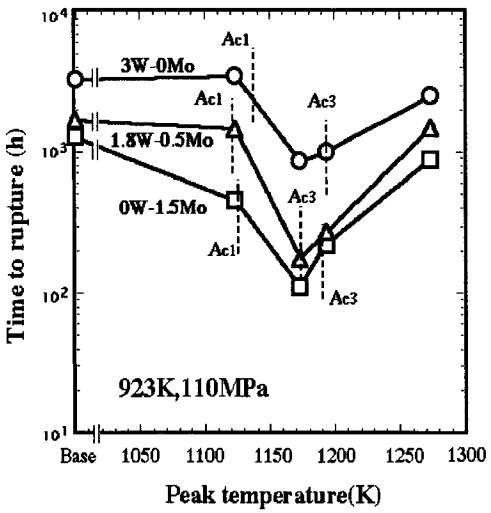


Fig.3 Change of creep rupture time as a function of peak temperature

Figure4 shows the creep curves at 923K for 110MPa of base specimen and the Ac3 simulated HAZ specimen of each steel. The rupture time in base metal of 3W-0Mo steel is longer than that of any other steel. By the effect of W contents, the transient creep region, where the creep rate decreases with time, continues for up to longer times. In the Ac3 simulated HAZ specimen, rupture time of 3W-0Mo steel is longer than that of any other steels. The Ac3 simulated HAZ specimen has a fine-grained structure and shorter transient creep region and therefore the rupture time of the Ac3 simulated HAZ specimen is shorter than that of base metal. The longer

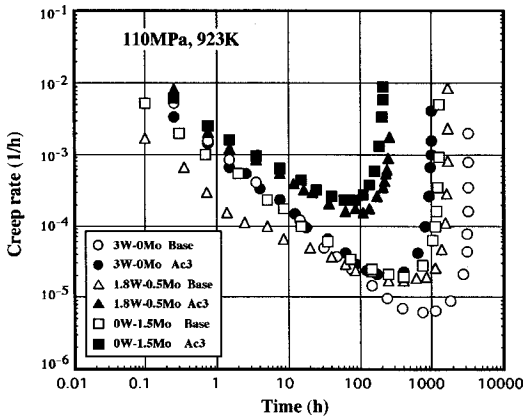


Fig.4 Creep curves of base metal and simulated HAZ specimens heated to Ac3

3.2. Precipitates of the simulated HAZ specimens before creep

Figure5 shows the extracted residue amount of simulated HAZ specimens of 3W-0Mo, 1.8W-0.5Mo and 0W-1.5Mo steels. The amount of precipitates, mainly $M_{23}C_6$ carbides, in each steel of simulated HAZ specimen are decreased one-third that of base metal because some precipitates are solved to matrix by heating up to Ac3. The amount of precipitates for the simulated

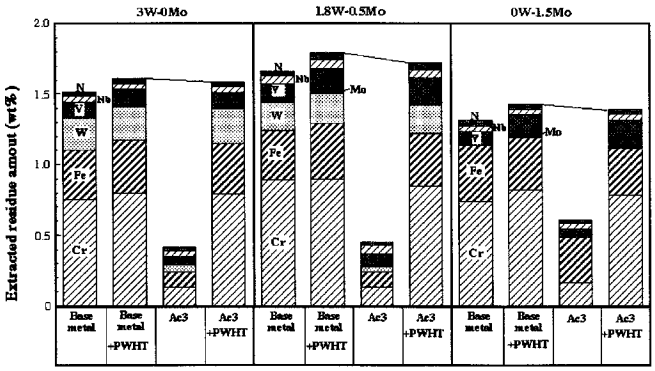
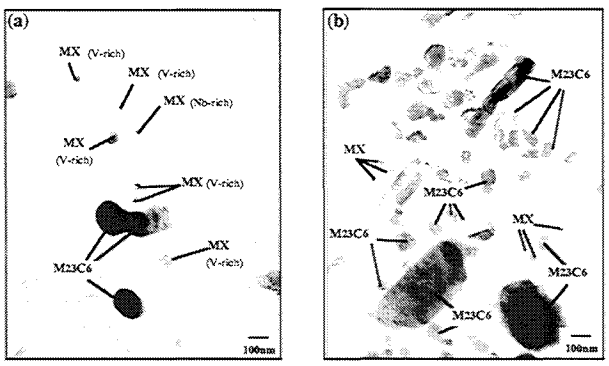


Fig.5 Extracted residue amount of simulated HAZ specimens for 3W-0Mo, 1.8W-0.5Mo and 0W-1.5Mo steel

HAZ specimen is increased by PWHT to nearly as same level as that for base metal. Total amount of precipitates of the Ac3 simulated HAZ specimen after PWHT is larger in the order of 1.8W-0.5Mo, 3W-0Mo and 0W-1.5Mo

TEM micrographs of extraction replicas of the Ac3 simulated HAZ specimen of 1.8W-0.5Mo steel before and after PWHT are shown in Fig.6. By heating up to Ac3 in a short time, most of precipitates dissolve in the matrix, however, some of the precipitates are still remained. These undissolved precipitates are coarsened during PWHT. The large size of $M_{23}C_6$ carbides above 500nm can be observed in Fig.6(b). In addition to these coarsened $M_{23}C_6$ carbides, small size $M_{23}C_6$ carbides below 100nm are newly precipitated. The size of MX seems to be not changed during PWHT. It can be considered that this coarsening of $M_{23}C_6$ carbides will have some relation to the degradation of creep rupture time of simulated HAZ specimen.



before PWHT after PWHT

Fig.6 TEM micrographs of extraction replicas of simulated Ac3 HAZ specimens before and after PWHT

Figure7 shows the SEM microstructures after PWHT, namely before creep, of base metal and simulated Ac3 HAZ specimens of 3W-0Mo, 1.8W-0.5Mo and 0W-1.5Mo steel. The base metal of each steel exhibits clear lath martensitic microstructure. On the other hand, in the Ac3 simulated HAZ specimen of each steel, the lath microstructure cannot be observed. The grain size is smaller than base metal and it is about 7 μ m. Some precipitates in the Ac3 specimens are larger than those in base metal. This reason was mentioned above. The region where precipitates are scarcely observed, also becomes larger especially in the Ac3 specimens of 0W-1.5Mo steel. From these results, it can be considered that the creep rupture time of the simulated HAZ specimens has its minimum after heating nearly to Ac3.

3.3. Microstructures and precipitates of simulated HAZ specimen after creep

Generally speaking, the recovery of dislocations occurred and some of precipitates are coarsened during creep. The SEM microstructures of base metal and simulated Ac3 HAZ specimens

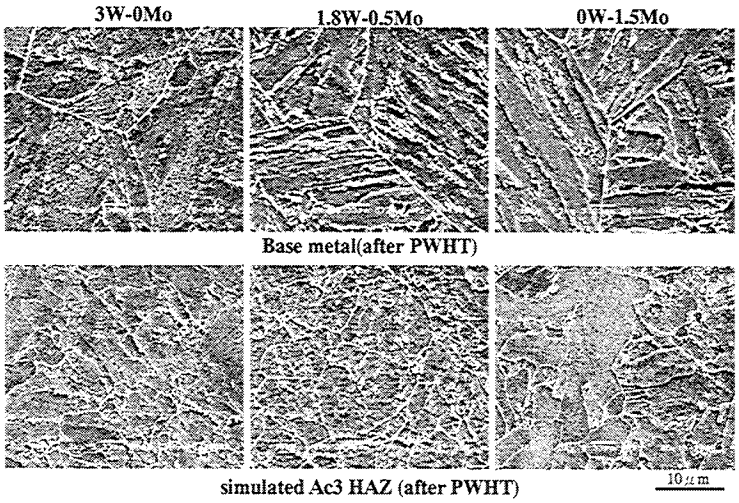


Fig.7 SEM microstructures of base and simulated Ac3 HAZ specimens of 3W-0Mo,1.8W-0.5Mo and 0W-1.5Mo steel before creep

of 1.8W-0.5Mo before and after creep are shown in Fig.8. In the base specimen before and after creep, both of them have clear lath martensitic microstructures. On the other hand, in the Ac3 simulated HAZ specimen after creep, the lath martensite microstructure is not observed as shown in Fig.8. In base metal and simulated Ac3 HAZ specimen crept at 923K and 90MPa, the precipitates at the grain boundaries are coarsened and some transgranular precipitates disappeared.

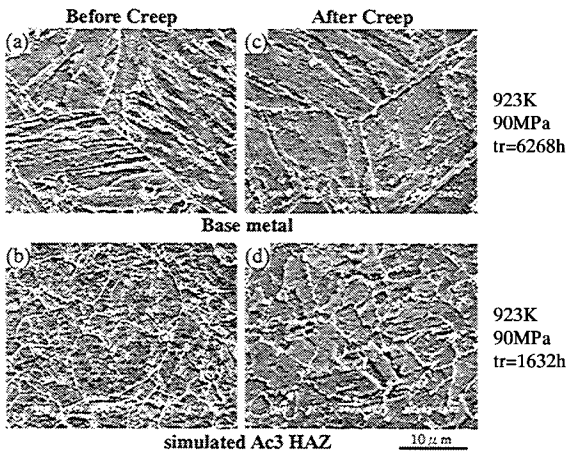


Fig.8 SEM microstructures of base and simulated Ac3 HAZ specimens of 1.8W-0.5Mo steel before and after creep.

Figure9 shows TEM micrographs of thin foils of 3W-0Mo steel after creep. The dislocation density of the Ac3 specimen before creep is higher than that of base metal. However, it decreased rapidly during creep and therefore the recovery rate of the Ac3 specimen is faster than that of base metal. The coarsened subgrains,which have few dislocations, in the Ac3 specimen crept at 923K for 1632h are observed in comparison with the microstructure of base metal crept for 6268h.

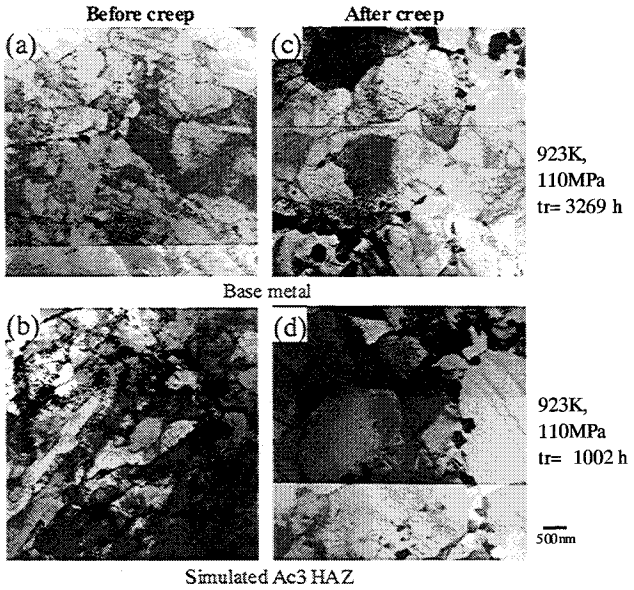


Fig.9 TEM micrographs of thin foils 3.0W-0Mo steel before and after creep at 923K, 110MPa.

The changes of precipitates in 3W-0Mo steel before and after creep are investigated. The TEM micrographs of extraction replicas of 3W-0Mo steel are shown in Fig.10. The rupture time of Ac3 simulated HAZ specimen, 1002h at 923K and 110MPa, is about one-third of that of base metal. Before creep in the Ac3 simulated HAZ specimen, as shown in Fig10(b), the size of $M_{23}C_6$ carbides is larger than that in the base metal. (Fig.10(a)). After creep (Fig.10(c)and (d)), some $M_{23}C_6$ carbides become larger and large Laves phases, which are newly precipitated during creep, are observed. The size of $M_{23}C_6$ carbides and Laves phase after creep are above 500nm. It is well known that the coarsening rate of Laves phase is relatively faster than that of $M_{23}C_6$ carbides during creep. The coarsening rate of precipitates, $M_{23}C_6$ carbides and Laves phases, in the Ac3 HAZ simulated specimen is faster than that in the base metal. The size of MX carbonitrides, which is very fine of 10 to several tens nm, is nearly the same for both base metal and simulated HAZ specimens and scarcely changes during creep.

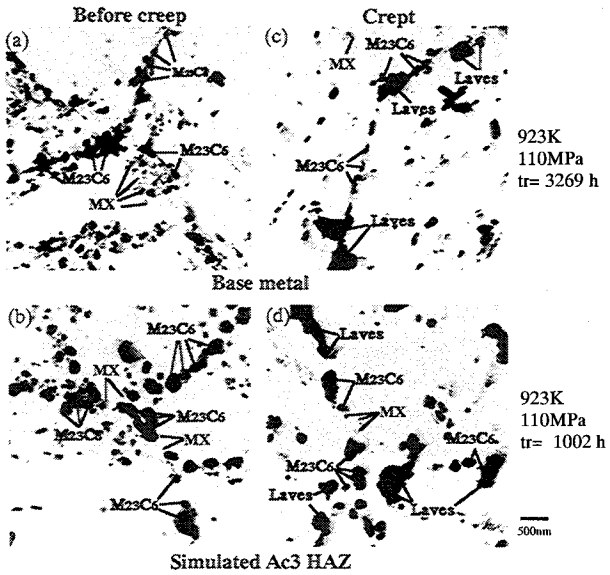


Fig.10 TEM micrographs of extraction replicas of 3W-0Mo steel before and after creep.

3.4. Effect of W content in the simuated HAZ specimen

Tungsten, which has been regarded as one of the solid solution elements, is alloyed for better creep strength in current high Cr steels. The report [7] about base metal of 9%Cr steels with various W contents has shown that subsitituting W for a part of Mo has benefical effects on creep rupture strength at 923K and that the substitution reduces the coarsening tendency of precipitates. It is also reported that fine Laves phases, which precipitate in martensitic lath during creep on W containing steel, has the pinning effect [8]. It is considered that the creep rupture time of base metal in Fig.4 shows longer values in the order of 3W-0Mo, 1.8W-0.5Mo and 0W-1.5Mo steel because Tungsten addition has the effect of solution strengthening and precipitation strengthening by fine Laves phases. In the Ac3 simulated HAZ specimens, the rupture time has the same tendency as that in base metal as shown in Fig.3. As a result from this, the effect of solution strengthening by addition W keeps the microstructure stable during creep in the Ac3 specimen.

As shown above in Fig.5, 3W-0Mo steel heated up to Ac3 has less residual precipitates than the other steels. After PWHT, however, 3W-0Mo steel in the Ac3 specimen has more precipitates than that of 0W-1.5Mo steel. From this result, it is considered that the size of $M_{23}C_6$ carbides of the simulated HAZ specimen for 3W-0Mo steel after PWHT is smaller than that for the other steels. It shows that the growth rate of Laves phases in 3W-0Mo steel is smaller than those in 0W-1.5Mo steel during creep. In addition, the region where precipitates are scarcely

observed in the Ac3 simulated HAZ specimen is larger in 0W-1.5Mo steel after PWHT than any other steels as shown in Fig.7.

The Ac3 simulated HAZ specimen of each steel, however, does not have lath martensitic structure. It can be considered that the morphology of precipitates during creep in the Ac3 simulated HAZ specimen is different from that of base metal which has clear lath martensitic structure. The changes in size and distribution of precipitates during long-term creep test should be more investigated.

4.Conclusions

The creep test was carried out for the simulated HAZ specimens of three kinds of steels with the same Mo equivalents, 9Cr-3W, 9Cr-1.5Mo and 9Cr-1.8W-0.5Mo (P92).

(1) On creep tests at 923K, the rupture time of each steel showed a minimum value of simulated HAZ specimens heated to just below Ac3 temperature. The creep rupture time of the Ac3 simulated HAZ specimens of each steel was about one-fifth of that of base metal.

(2) The Ac3 simulated HAZ specimens did not have lath martensitic microstructure and significant coarsening of precipitates, $M_{23}C_6$ carbides, was observed before creep. The growth rate of Laves phase and $M_{23}C_6$ carbides of Ac3 simulated HAZ specimens was larger than that of base metal during creep.

(3) The Ac3 simulated HAZ specimen of each steel before creep contained a higher density of dislocations than base metal. The dislocations of the Ac3 simulated HAZ specimen decreased rapidly and coarsening of $M_{23}C_6$ carbides and Laves phases during creep and therefore the recovery rate of the Ac3 specimen was faster than that of base metal.

(4)In the Ac3 simulated HAZ specimens, the creep rupture time showed a longer value in the order of 3W-0Mo, 1.8W-0.5Mo and 0W-1.5Mo steel, which showed the same tendency as that in base metal. It could be considered that the effect of solution strengthening by W addition kept the microstructure stable during creep in the Ac3 simulated HAZ specimen.

References

[1]K.Muramatsu: 'Development of Ultra-Super Critical Plant in Japan.'Advanced Heat Resistant Steels for Power Generation, ed. by R.Viswanathan and J.Nutting, The University Press, Cambridge, (1999), 543.

[2]F.Abe, M.Igarashi, S.Wanikawa, M.Tabuchi, T.Itagaki, K.Kimura and K.Yamaguchi: 'Improvement of Creep Strength of Ferritic Steels for 650℃ USC Boilers', Proc. of the 7th International Conference on Creep and Fatigue at Elevated Temperatures (Creep 7), (2001),433.

[3]F.Masuyama: 'New Developments in Steels for Power Generation Boilers.'Advanced Heat Resistant Steels for Power Generation, ed. by R.Viswanathan and J.Nutting, The University Press, Cambridge, (1999),33.

[4]H.Cerjak and E.Letofsky: 'Behaviour of Advanced 9-12Cr Steels and its Weldments in Short and Long Term Tests.' Advanced Heat Resistant Steels for Power Generation, ed. by R.Viswanathan and J.Nutting, The University Press, Cambridge,(1999),611.

[5] F.Masuyama, M.Matsui and N.Komai: 'Creep Rupture Behavior of Advanced 9-12%Cr Steel Weldment', Proc. of 8th Intern.Conf. on Creep and Fracture of Engineering Materials and Structures (CFEMS-8), Key Engineering Materials, Tsukuba, Japan, (2000), 99.

[6] Y.Hasegawa, M.Ohgami and Y.Okamura: 'Creep Properties of Heat Affected Zone of Weld in W Containing 9-12% Chromium Creep Resistant Martensitic Steels at Elevated Temperature', Advanced Heat Resistant Steels for Power Generation, ed. by R.Viswanathan and J.Nutting, The University Press, Cambridge, (1999),655.

[7] K.Ryuu and T.Fujita:'Effect of W on Mechanical Properties and Microstructure of a High strength 9%Cr Heat Resisting Steel',Tetsu-to-Hagane, (1987),1034.

[8] R.Ishii,Y.Tsuda,M.Yamada and M.Miyazaki:'The Effect of Tungsten on Creep Properties of High Chromium Steels for Steam Turbine', ed. by R.Viswanathan and J.Nutting, The University Press, Cambridge, (1999),277.

[9]M.Matsui, M.Tabuchi, T.Watanabe, K.Kubo, J.Kinugawa and F.Abe:'Degradation of Creep Strength in Welded Joint of 9%Cr Steel', ISIJ International,41(2001)S126.

[10] K.Ogawa, A.Iseda, Y.Sawaragi, S.Matsumoto and F.Masuyama: 'Development of High Strength 12%Cr Steel Pipe and Tubes for Boilers(2)-Properties of Similar Weld Metal of HCM12A Steel and its Welded Joint', Sumitomo Metals, Japan, (1995), 39.

[11]M.Tabuchi, T.Watanabe, K.Kubo, J.Kinugawa and F.Abe: 'Mechanical Properties of 11Cr-0.4Mo-2W-CuVNb Steel Welded Joints at Elevated Temperatures',Int. J. of pressure vessel,(2002),521.

RESEARCH AND DEVELOPMENT OF NEW MARTENSITIC STEELS

Artinger István[1], Rózsavölgyi Zsolt[2]

[1] Budapest University of Technology and Economics
Department of Material Science and Engineering
H-1521 Budapest, Műegyetem rkp. 1-3., Hungary

[2] AGMI Material Testing and Quality Control Co. Ltd.
Mechanical Laboratory
H-1751 Budapest, P.O.-Box: 114., Hungary

Abstract

The welding technology is one of the most important research aspects in the development of the creep resistant 9–12 % Cr-modified steels. To ensure the long-term high temperature strength and the stability of the microstructure, the initial material properties have to be controlled and known precisely. This paper briefly introduces the requirements, application and manual metal-arc welding technology of these steels and examines the effects of the heat input and post weld heat treatment on the weld metal.

Keywords: martensitic steels, welding, heat input, post weld heat treatment, impact energy

1 Introduction

The driving force for development in the power generation industry is raising the efficiency of the thermal cycle, reducing the emission of the greenhouse gases and producing electric and heat energy in a more economical way. One internationally accepted way to satisfy these requirements is building supercritical (SC) power plants with the operating conditions of 280 bar and 580 °C live steam parameters and 600 °C reheat temperature. Raising the thermal parameters of the heat carrying agent up to these values 45 % efficiency can be achieved. The next step of the development is targeting the 48–50 % efficiency by building ultra-supercritical (USC) power plants with operating conditions: 340 bar / 650 °C / 670 °C.

Material properties strongly affect the upper limit of the use. The constructional materials have to be suitable for the complex requirements to withstand the loads and stresses. Corrosion and heat resistance combined with adequate strength are the most important from the aspects of dependability. The designed 200 000 hours of lifetime requires high creep resistance and microstructural stability of the steels. During the construction of the equipments weldability and formability are also important factors in choosing the right material.

Current progress of material application in the energy industry is reducing the amount of the high-alloyed heat resistant austenitic steels. The newly developed and commercially sold 9-12 % Cr-modified high temperature strength steels are very good candidates for components such as boiler membrane walls, steam pipes and turbine rotors or casings. Their manufacturing costs are lower, thermal and mechanical properties are better than the austenitic steels in the 500–600 °C temperature interval, and the use of these steels allows

more flexible operation of the power plant. The disadvantage of this type of steel is that relatively little operational experience is available, it takes a long time to obtain experience of the creep and ageing properties of the steels.

Steel types like P91 (developed in USA), NF 616 (Japan) and E911 (Europe) are well known and used more and more widely in power generation. A strongly developing area of the whole research is the question of weldability of these materials. Filler material, welding technology, long term properties of the weld material are in the focus, because the welding itself is a critical point in an operating system and from the aspect of reliability this part is weaker that the base material.

2 Investigation of the Weld Metals

The Department of Material Science and Engineering at the Budapest University of Technology and Economics takes part in the development within the activities of the COST programme sponsored by the European Commission. During the COST 501 and 522 programmes the research was focused on ageing the base material, examining the change in the mechanical properties and understanding the process resulting the degradation. Another important research field of the Department is the studying of new welding materials, examining the effects of the heat input (Q_{in}) and post weld heat treatment (PWHT) on the mechanical properties [1].

The prescriptions of the standards No. MSZ EN 1597-1:2000 (Welding Consumables. Test Methods. Part 1: Test Piece for All-weld Metal Test Specimens in Steel, Nickel and Nickel Alloys) and MSZ EN 1597-2:2000 (Welding Consumables. Test Methods. Part 2: Preparation of Test Piece for Single-run and Two-run Technique Test Specimens in Steel) were taken into consideration during the planning of the test series.

The electrodes were supplied by the Department of Material Science and Engineering, the welding and the heat treatments were performed at the Welding Plant of the Alstom Power Hungary Co. Ltd. The manufacturing and testing of the specimens were carried out at the AGMI Material Testing and Quality Control Co. Ltd.

Two chemically different composition covered electrodes (∅4 × 450) were tested (Table 1). The electrodes were deposited with controlled different heat inputs (Q_{in} = 0.8–2.2 kJ/mm) and two different PWHTs (730 °C / 12 h and 750 °C / 2 h) were performed on the plates to examine the behaviour of the weld metal.

Mark	Chemical Composition [wt %]												
	C	Si	Mn	P	S	Cr	Mo	Co	Ni	V	Nb	B	N
Electrode 1	0.12	0.22	0.52	0.009	0.010	10.42	1.44	2.85	0.72	0.19	0.048	0.0064	0.016
Electrode 2	0.11	0.19	0.55	0.009	0.010	10.24	1.50	1.02	0.75	0.21	0.048	0.0058	0.018

Table 1: The chemical composition of the deposited electrodes

Fig. 1 and 2 show the macroscopic image and the microstructure of one weld.

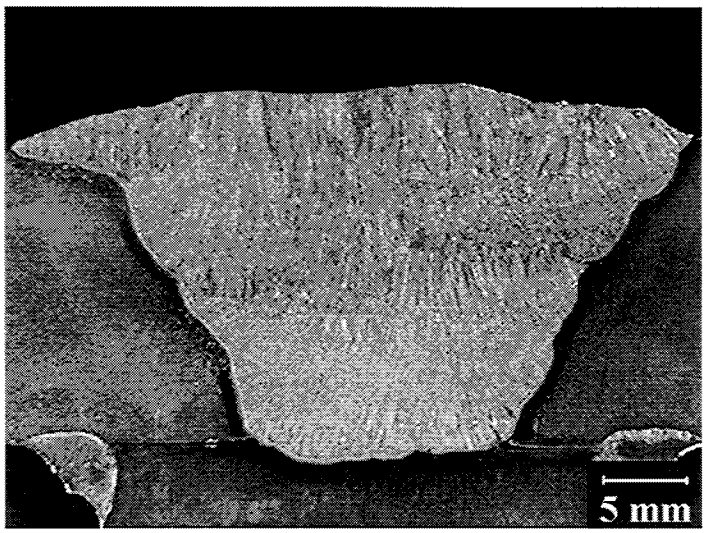


Fig. 1: Macroscopic image of the weld

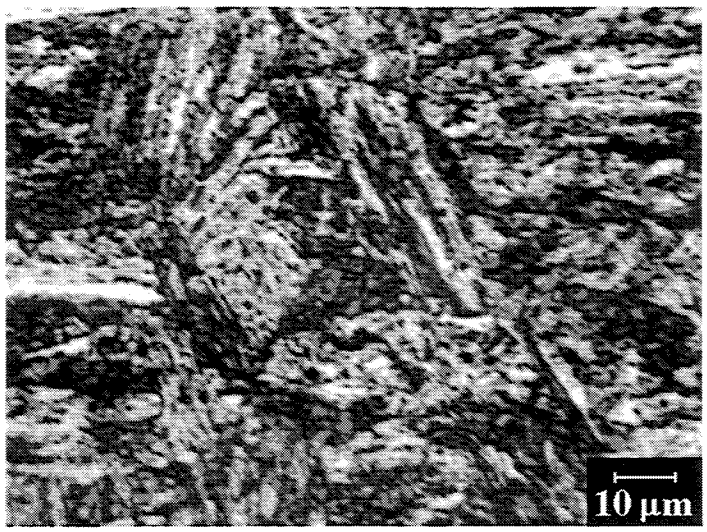


Fig. 2: Microstructure of the weld

Mechanical tests were carried out on the weld metal. The tensile test was done at room temperature (RT) and the standard Charpy V-notch impact test at 3 temperatures (20, 50 and 100 °C). Table 2 contains the results of the tensile test and Fig. 3–6 show the Charpy impact test results.

Heat Input Q_{in} [kJ/mm]	Heat Treatment [temp. / time]	Yield Strength $R_{p0.2}$ [N/mm^2]	Tensile Strength R_m [N/mm^2]	Elongation A [%]	Hardness HV 10
Electrode 1					
0.8	750 °C / 2 h	738	886	13.1	279
0.8	730 °C / 12 h	714	846	14.7	272
1.3	750 °C / 2 h	767	885	14.3	289
1.3	730 °C / 12 h	676	796	15.1	257
2.2	730 °C / 12 h	668	835	14.3	278
Electrode 2					
1.1	730 °C / 12 h	608	766	16.7	268
2.3	730 °C / 12 h	608	742	17.1	262

Table 2: The mechanical properties of the deposited weld metal at RT

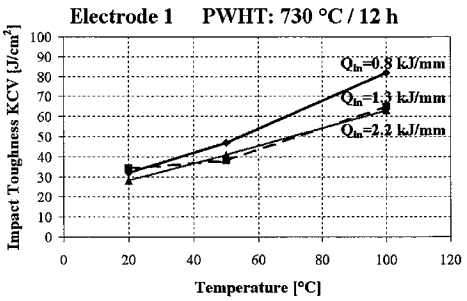


Fig. 3: Charpy impact test results of Electrode 1

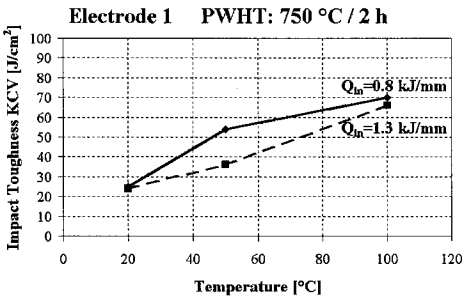


Fig. 4: Charpy impact test results of Electrode 1

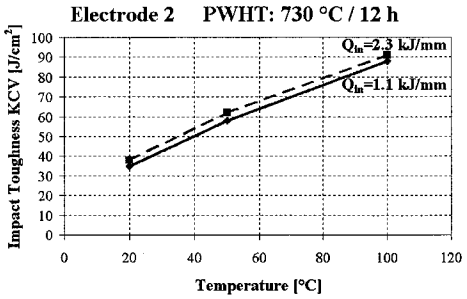


Fig. 5: Charpy impact test results of Electrode 2

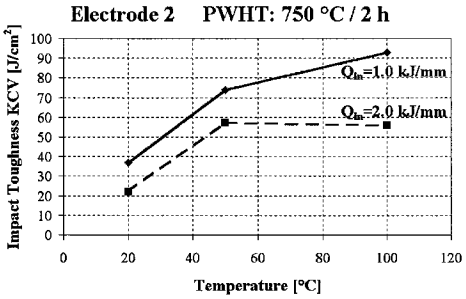


Fig. 6: Charpy impact test results of Electrode 2

3 Discussion

The alloy content and the microstructure of the steels have key importance in ensuring the good mechanical properties. Chromium is the most important element in the steels, it gives the appropriate heat and corrosion resistance against the effects of the superheated steam. Molybdenum raises creep resistance, improves ductility and weldability. Carbon content of the alloys is low (~0.1 %) to ensure weldability and ductility and to minimize the risk of welding cracks. Vanadium and boron are microalloying elements and beneficial to the formation of the thermally stable carbides and carbo-nitride precipitates. The composition of the welding materials slightly differs from the base material with regard to niobium and nickel contents. Niobium content is reduced to ~0.04 % while nickel content is raised to ~0.7 % to improve ductility and weldability [2].

The effects of cobalt and boron are under investigation, these 2 chemical elements raise the transition temperatures, improve the long-term high temperature properties of the materials.

The welding was performed in martensitic state of the material because of the high alloy content and short cooling times. It is very important to determine the correct pre-heat temperature to minimize the risk of hot cracks (too high pre-heat temperature) or cold cracks (too low pre-heat temperature). By choosing the optimum temperature the austenite / martensite ratio can be controlled during the welding process. Test and literature data show that the optimal pre-heat temperature is in the range of M_s-(80–100 °C), where M_s can be calculated on the basis of chemical composition [3].

To reach the required mechanical properties PWHT has to be carried out on the weldments. It is very important to develop the homogeneous martensitic structure before the heat treatment with cooling down the material near 100 °C. Heat treatment changes the microstructure from martensite into tempered martensite, the final size and distribution of the strengthening $M_{23}C_6$, M_7C_3 carbides and MX-type carbo-nitride, -boride precipitations forms during the treatment. Generally the lower temperature but long time heat treatment is more advantageous for the long term structural stability of the steel than the applied higher temperature and shorter time heat treatments used in mass production. In industrial conditions this latter is accepted and used very often.

Research results show that the application of low heat input results in higher ductility of the weld metal. Curved, low thickness welded layers were deposited, utilizing the advantages of that during the welding the upper row heat treats the previous row in its full cross section. This phenomenon is very useful especially in welding relatively thin walled plates or pipes. The effect of the 730 °C / 12 h PWHT is better from the aspect of ductility but results in a slightly lower strength.

The creep properties of martensitic base materials are well known, but the critical point in a construction is always the welding, especially the heat affected zone (HAZ). Investigating the long-term high temperature properties of the new filler materials is a very important research area. Literature data [4] shows that the creep resistance of the weldments is 20–30 % lower compared to the base material. The creep rupture strength of the weld materials decreases with increasing temperature and time to rupture compared to the base material.

The solution of keeping the initial mechanical properties is to preserve the original dislocation network and to form thermally stable precipitations. Numerical methods and thermodynamic models are applied during the design of an alloy by calculating phase diagrams, phase transitions and precipitation behaviour. The results correlate with research data [5], showing that the size, distribution and composition of the precipitated phases change, new phases (Laves phase, σ-phase) form at high temperature resulting in the degradation of the initial mechanical properties.

4 Summary

Newly developed martensitic steels are good candidates for substituting the austenitic heat resistant steels in the range of 550–600 °C. In Europe under the COST programme, in the USA the Electric Power Research Institute (EPRI) and in Japan the Electric Power Development Corporation (EPDC) support the research for developing steels with better quality, properties and performance [6]. The welding of martensitic steels has key importance, international research together with the electrode manufacturers is unfolding. The task of this development is to create steels which keep their advantageous initial mechanical properties and minimise the embrittlement caused by the operating conditions and flexible operation.

The Department of Material Science and Engineering at the Budapest University of Technology and Economics takes part in the activities of the COST 501 and 522 programmes, examining the changes in the mechanical properties after ageing or a welding and PWHT procedure.

Test results show that in case of manual metal-arc welding of thin wall plates or tubes with using low heat input and thin deposited layers result in higher absorbed impact energy than applying high heat input during the welding process. The ratio of tensile / yield strength is high, combined with adequate elongation.

One retarding factor of the application of new Cr-modified steels is the relatively low operational experience. Material tests have to be carried out to find the optimal chemical composition and metallurgical state of the material for the given load.

5 Acknowledgements

I am grateful to my teachers and professors at the Department of Material Science and Engineering for helping me to plan and organize the research and also to my colleagues at the AGMI Material Testing and Quality Control Co. Ltd. for their support in performing the tests.

6 References

[1] I. Artinger: Effect of Welding and Ageing on Properties of New 9–12 % Steels (Materials for Advanced Power Engineering 1998. Proceedings of the 6th Liége Conference, Belgium, p. 363–372)

[2] H. Heuser, C. Jochum: Azonos fajtájú hegesztési hozaganyagok konvencionális erőművek újszerű melegszilárd krómacéljaihoz (Gép Vol. 6 (2000), p. 3–8)

[3] L. Béres, A. Balogh, W. Irmer: A repedésérzékenység és az előmelegítés kapcsolata az X 10 CrMoVNb 9 1 jelű acél mertensites hegesztésekor (Gép Vol. 6. (2000), p. 22–24)
[4] A. Jakobová, V. Vodárek, K. Hennhofer, V. Foldyna: Microstructure and Creep Properties of P91 Steel and Weldments (Materials for Advanced Power Engineering 1998. Proceedings of the 6th Liége Conference, Belgium, p. 373–382)
[5] B. Schaffernak, P. Hofer, H. Cerjak: Description of the Precipitation Behaviour of Advanced 9-12 % Cr Steels for Power Plant Applications (Materials for Advanced Power Engineering 1998. Proceedings of the 6th Liége Conference, Belgium, p. 519–527)
[6] T. Fujita: Current Progress in 9–12 % Cr Ferritic Heat Resistant Steels (Central European & World Connection Electric Power Industry Forum 95, Kraków, Poland, p. 1–24)

SECTION 3

ADVANCED STEAM POWER PLANT

3.6. Applications

THE FIRST SUPERCRITICAL POWER UNIT IN POLAND. WELDABILITY EVALUATION OF NEW MARTENSITIC CHROMIUM STEELS WITH TUNGSTEN ADDITIONS AND PROPERTIES OF WELDED JOINTS.

Jerzy Brózda, Marian Zeman[1)], Jerzy Pasternak[2)]

[1)] Instytut Spawalnictwa, ul. Bł. Czesława 16/18, 44-100 Gliwice, Poland
[2)] Fabryka Kotłów RAFAKO S.A., ul. Łąkowa 33, 47-400 Racibórz, Poland

Abstract

Short characteristics of the out-of-date Polish power generation system are given, which shows that in the near future there will be a shortage of electrical energy and the necessity to build supercritical power units. A lignite fired boiler will be build at the RAFAKO Boiler Plant. Supercritical operating parameters require new creep resisting steels to be applied for the boiler and pipe systems. Therefore at the Institute of Welding weldability examinations have been performed on selected Cr-W heat resisting steels. Welding thermal cycles have been simulated on steels: HCM2S (T23/P23), HCM12A, T92/P92 and E911. The influence of $t_{8/5}$ cooling times on Charpy V notch toughness, HV10 hardness and microstructure of simulated HAZ's is presented in the form of graphs and prints of microstructures. By means of simulation technique the susceptibility to reheat cracking of the HCM12A steel has been evaluated. At REMAK- Opole (Enterprise for the Modernisation of Power Installations) and RAFAKO tube/pipe test joints were welded, to select proper fabrication conditions. Mechanical properties of the welded test joints, KV notch toughness of weld metals and HAZ's and microstructures were examined and are presented.

Keywords: power generation, creep resisting steels, weldability, welded joints.

Short characteristics of the Polish power industry and the first supercritical boiler

The Polish power generation system is to a great extent out of date. 40 units with a power rating of 200 MW have reached in the year 2000 the age of 25÷38 years. In spite of running pro-ecological investments by many power plants [1, 2], quite a large number of units is of low effectiveness and does not comply with the standards of allowable NO_x, SO_2 and CO_2 emission. In many cases a further decrease of the already low efficiency and availability factor is observed, as well as the increase of breakdowns and maintenance costs. In 1995 the net efficiency of the best Polish power plants was 33 % on the average [3], while the world average is 36 %, and for new units it is in the range of 42÷46 %. Specialists from the power generation branch agree, that contemporary plants will be able to meet the power demands in Poland only until the years 2007-08, under assumption of a steady modernisation of power units with a total power rating of 2000 MW yearly. For the energy consumption forecast three assumptions were made: survival version – for a 4 % average GNB growth rate, basic version – when the average GNB growth rate will be 5.5 %, and progress version – for an 8.4 % average GNB growth rate (Fig. 1). In any case there will be a demand for electrical energy and the reconstruction of completely exploited lignite fired power units should be accomplished by building supercritical units.
The first supercritical boiler for the Pątnów II power unit has been designed as a monotube boiler, characterized by the following parameters: live steam temperature 560 °C, re-superheated steam temperature 568 °C, design pressure of the primary circuit 295÷335 bar, design pressure of the secondary circuit 66 bar.

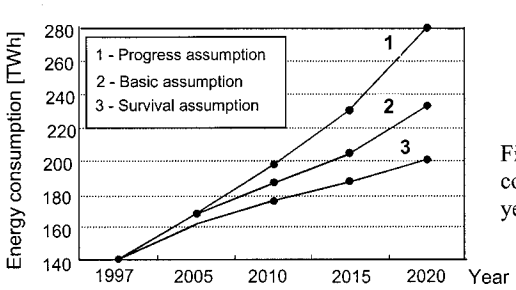


Fig. 1. Prognosis of electric power consumption in Poland up to the year 2020 [2]

The supercritical operating parameters require new creep resisting steels to be applied for the boiler and pipe systems. To prepare our power industry for the new task, weldability examinations have been performed on selected Cr-W heat resisting steels at the Institute of Welding. At RAFAKO and REMAK- Opole tube/pipe test joints have been welded, heat treated and properties of the weldments determined to select proper fabrication conditions. Some results are presented on the following pages.

Weldability evaluation of new martensitic Cr-W steels

Examined steels

In recent years some investigations have been made at the Institute of Welding on weldability evaluation of martensitic steels with W additions [4, 5]. Chemical composition and mechanical properties of the examined steels are given in tables 1 and 2.

Table 1. Chemical composition of examined steels

Steel		C	Si	Mn	P	S	Cr	Mo	W	V	B	N	Nb	Al
HCM2S (T23) ϕ 63.5 x 9.8 mm		0.06	0.24	0.18	0.017	0.005	2.18	0.07	1.50	0.25	0.0055	0.007	0.04	0.003
P23 ϕ 219 x 30 mm		0.07	0.28	0.54	0.008	0.004	2.08	0.08	1.65	0.22	0.0020	0.011	0.03	0.018
Specifi-	min.	0.04		0.10			1.90	0.05	1.45	0.20			0.02	
cation	max.	0.10	0.50	0.60	0.030	0.010	2.60	0.30	1.75	0.30	0.006	0.030	0.08	0.030
T92 ϕ 51.0 x 7.0 mm		0.09	0.22	0.45	0.017	0.002	8.81	0.45	1.64	0.23	0.004	0.042	0.06	0.017
P92 ϕ 219 x 20 mm		0.11	0.21	0.43	0.013	0.006	8.93	0.49	1.65	0.19	0.005	0.055	0.05	0.008
Specifi-	min.	0.07		0.30			8.50	0.30	1.50	0.15	0.001	0.030	0.04	
cation	max.	0.13	0.50	0.60	0.020	0.010	9.50	0.60	2.00	0.25	0.006	0.070	0.09	0.040
E911 ϕ 405 x 60 mm		0.12	0.17	0.47	0.016	0.003	8.62	0.94	0.93	0.20	0.0018	0.067	0.08	0.007
Specifi-	min.	0.09	0.10	0.30			8.50	0.90	0.90	0.18	0.0005	0.050	0.06	
cation	max.	0.13	0.50	0.60	0.020	0.010	9.50	1.10	1.10	0.25	0.005	0.090	0.10	0.040
HCM12A [1] ϕ 38 x 6.3 mm		0.10	0.27	0.58	0.017	0.002	12.10	0.25	1.84	0.19			0.09	
HCM12A [2] ϕ 355 x 45 mm		0.13	0.31	0.60	0.014	0.001	10.65	0.35	1.92	0.22			0.06	
Specifi-	min.	0.07					10.00	0.25	1.50	0.15			0.04	
cation [3]	max.	0.14	0.70	0.50	0.020	0.010	12.50	0.60	2.50	0.30	0.0050	0.010	0.10	0.010

[1] 0.85 %Cu. 0.35 %Ni; [2] 0.94 %Cu. 0.35 %Ni; [3] 0.30-1.70 %Cu. max. 0.50 %Ni

Table 2. Mechanical properties of examined steels

Steel	$R_{0.2}$ [MPa]	R_m [MPa]	A (2") [%]	Steel	$R_{0.2}$ [MPa]	R_m [MPa]	A_5 [%]
HCM2S (T23) ϕ 63.5 x 9.8 m	483	595	44				
P23 ϕ 219 x 30 mm	496	597	23.3	E911 ϕ 405 x 60 mm	512	725	20
Specification	min. 400	min. 510	20	Specification	min. 450	620-850	min. 19
T92 ϕ 51.0 x 7.0mm	523	693	27	HCM12A ϕ 38 x 6.3 mm	620	830	27
P92 ϕ 219 x 20 mm	566	731	25.5	HCM12A ϕ 355 x 45 mm	610	800	25
Specification	min. 440	min. 620	min. 20	Specification	min. 430	min. 630	min. 25

Properties of simulated HAZ's

On specimens extracted from the examined steels welding thermal cycles characterised by the maximum temperature T_{max}=1250 °C and cooling times $t_{8/5}$=6, 24, 60 and 300 seconds were simulated by a computer controlled thermal and stress-strain simulator. Microstructure. hardness and notch toughness were determined for the simulated HAZ's.

By means of a special dilatometric device [6] transformation temperatures have been determined on small cylindrical specimens and TTT- diagrams for welding purposes (austenitizing temperature 1250 °C) were constructed for selected steels. Examination results are presented in Figures 2-9.

HCM2S (T23) and P23 steels

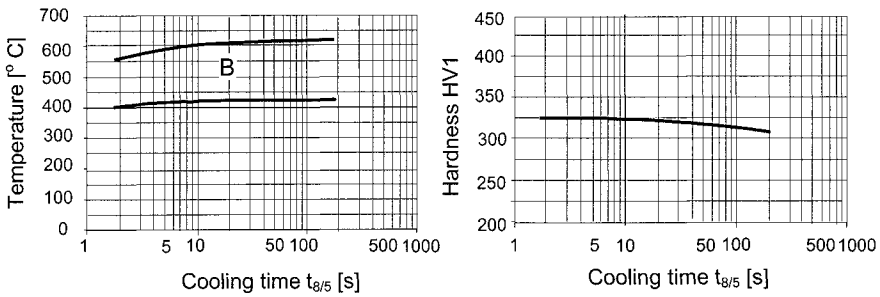


Fig. 2. TTT – diagram for the HCM2S steel

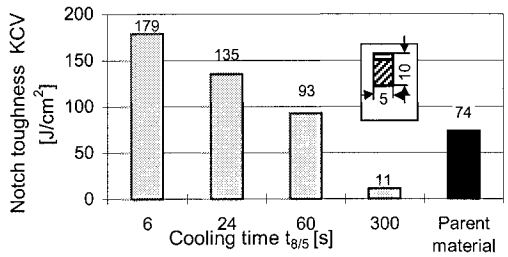


Fig. 3. Notch toughness KCV of simulated HAZ's for various cooling times of HCM2S steel. Maximum temperature of welding thermal cycles T_{max} = 1250 °C.

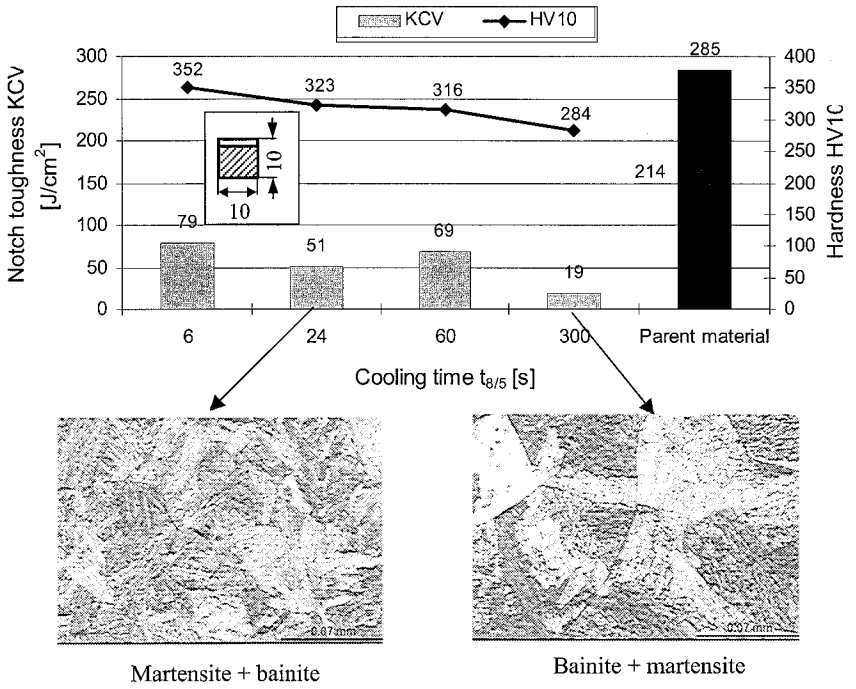


Fig. 4. Notch toughness KCV and hardness HV10 of simulated HAZ's for various cooling times of P23 steel. Maximum temperature of welding thermal cycles T_{max}=1250 °C.

T92 und P92 steels

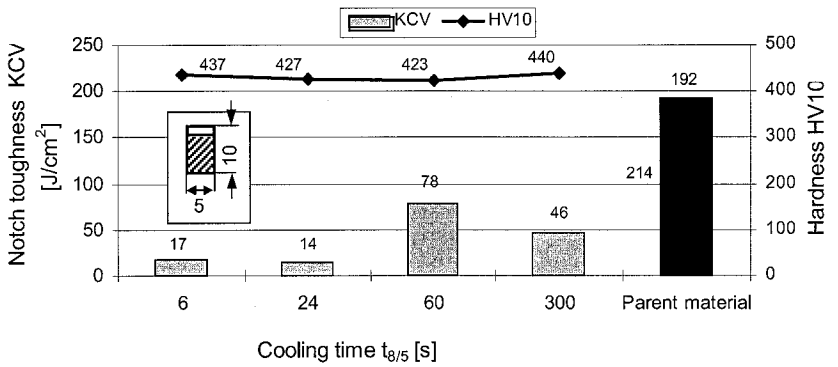


Fig. 5. Notch toughness KCV and hardness HV10 of simulated HAZ's for various cooling times of T92 steel. Maximum temperature of welding thermal cycles T_{max}=1250 °C.

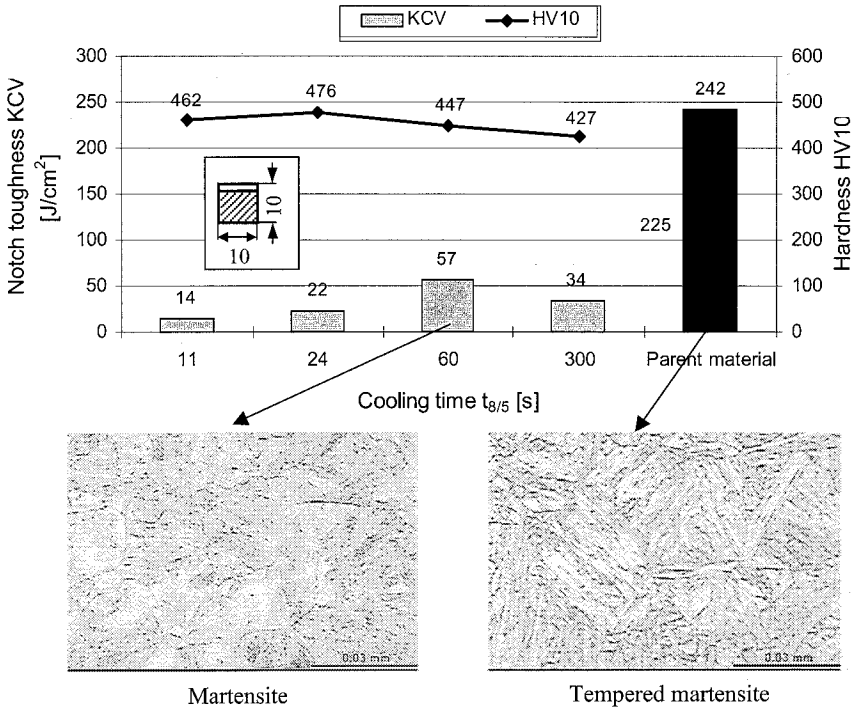


Fig. 6. Notch toughness KCV and hardness HV10 of simulated HAZ's for various cooling times of P92 steel. Maximum temperature of welding thermal cycles T_{max}=1250 °C.

E911 steel ,

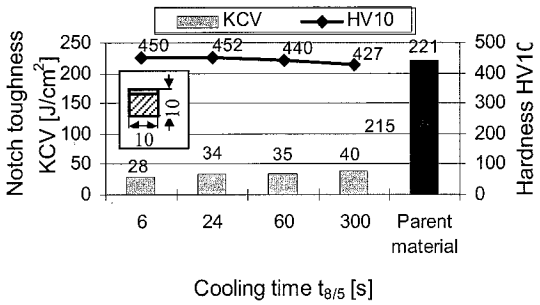
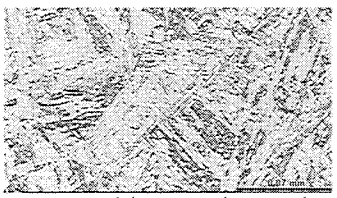
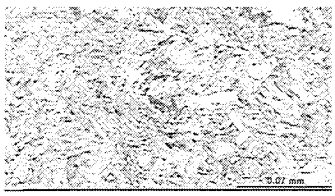


Fig. 7. Notch toughness KV and hardness HV10 of simulated HAZ's for various cooling times of E911 steel. Maximum temperature of welding thermal cycles T_{max} = 1250 °C.



Parent material, tempered martensite



Simulated HAZ, $t_{8/5}$=24 s, martensite

HCM12A steel

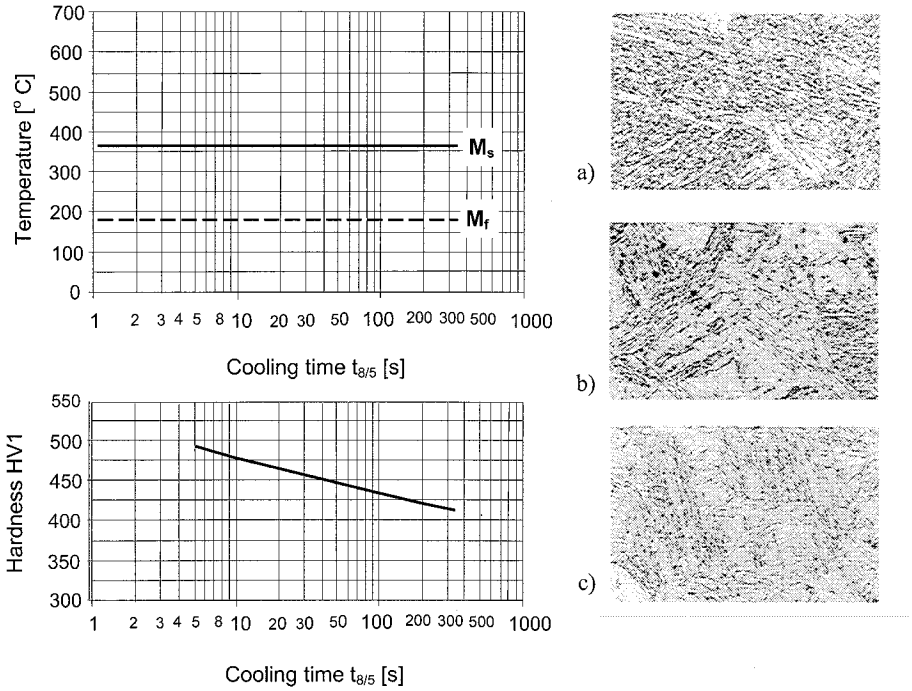


Fig. 8. TTT – diagram for HCM12A steel. Microstructures: a) parent material – tempered martensite, b) $t_{8/5}$=6 s, c) $t_{8/5}$=300 s – martensite. $FeCl_3$ etched, 200 x.

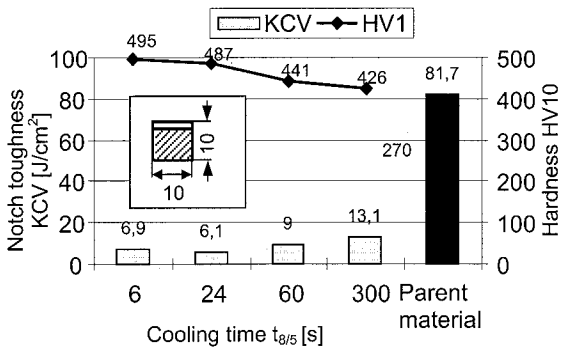


Fig 9. Notch toughness KV and hardness HV10 of simulated HAZ's for various cooling times of HCM12A steel. Maximum temperature of welding thermal cycles T_{max} = 1250 °C.

Susceptibility to reheat cracking

Susceptibility to reheat cracking of welded joints has been evaluated by the method given in [7]. Specimens treated by simulated thermal cycles with a maximum temperature of 1250 °C

and cooling times $t_{8/5}$=6 s, 60 s and 600 s were tensile tested at temperatures in the range of 400÷850 °C, after soaking during 30 minutes. The strain rate was 0.5 mm/min. The measure of susceptibility to reheat cracking is reduction of area Z. A steel with Z > 20 % is considered as not susceptible to reheat cracking. Test results for the HCM12A steel (ϕ 355 x 45 mm, table 1) are presented in Fig. 10.

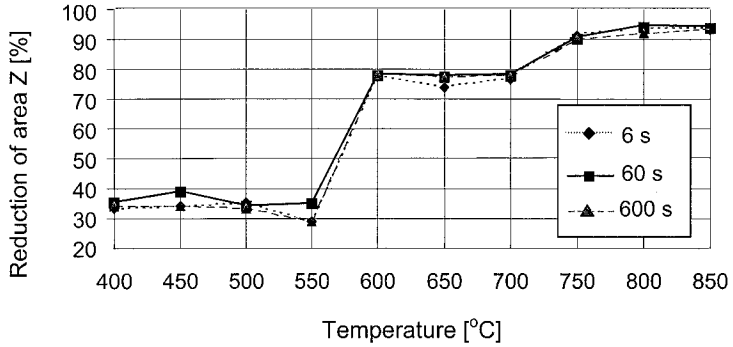


Fig. 10. Effect of tensile test temperature on reduction in area Z of simulated HAZ's (T_{max}=1250 °C, $t_{8/5}$=6, 60 and 600 s) of HCM12A steel.

Welded joints and their properties

At REMAK butt joints made of steel T92 (tube ϕ 51.0 x 7.0 mm) and E911 (pipe ϕ 405 x 60 mm) have been welded in the fixed position with horizontal and vertical tube/pipe axis.

T92 tube joints

The T92 steel tube was welded by the TIG process (pulsed arc) using P92-IG Böhler wire ϕ 2.4 mm, at a preheat temperature of 210÷250 °C and welding parameters: 120/80÷125/100 A, 14 V. After radiographic inspection, which did not reveal unacceptable imperfections, metallographic examinations, hardness and mechanical tests were performed on the welded joints. Results of Vickers hardness test and metallographic examination are shown in Figures 11 and 12.

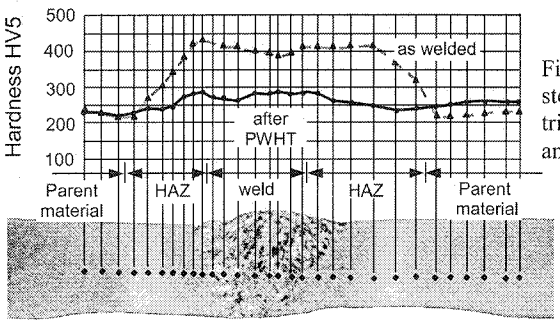
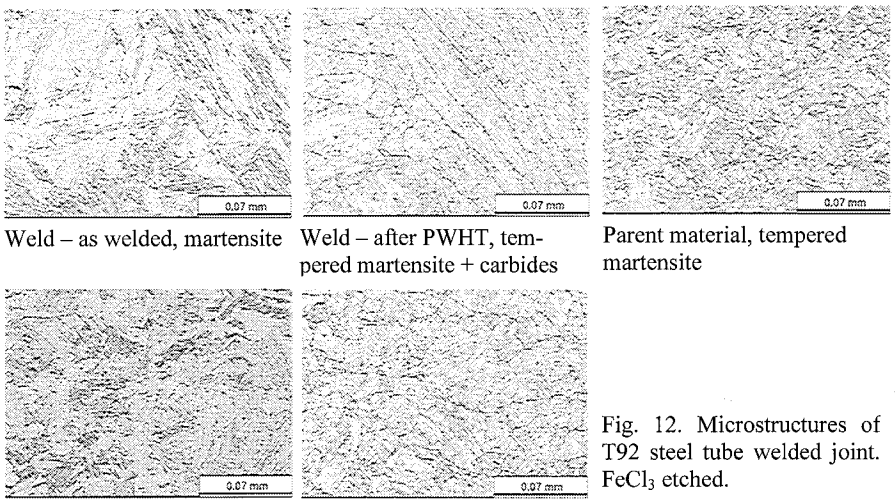


Fig. 11. Macrostructure of T92 steel weldment and hardness distribution in the as welded joint and after PWHT (760 °C, 1h)



Weld – as welded, martensite | Weld – after PWHT, tempered martensite + carbides | Parent material, tempered martensite

HAZ– as welded, martensite | HAZ– after PWHT, tempered martensite

Fig. 12. Microstructures of T92 steel tube welded joint. $FeCl_3$ etched.

The tensile strength of welded joints, tested according to the standards PN-EN 895:1997 and PN-EN 10002-1+AC1:1998, was in the range of 655÷695 MPa, which is higher than the minimum value 620 MPa required for the T92 steel (table 2). All specimens ruptured in the HAZ. In the bend test, performed according to PN-EN 910:1999 (plunger ϕ 21 mm), all specimens reached the bend angle 180 °. Notch toughness tests have been performed according to PN-EN 10045-1:1994 on 10.0 x 5.0 mm Charpy V specimens. The following KCV mean values from 9 specimens were received: 119 J/cm^2 and 182 J/cm^2 - respectively for the weld metal and fusion boundary of the tube joints welded in the fixed horizontal position; 85 J/cm^2 and 185 J/cm^2 - respectively for the weld metal and fusion boundary of the joints welded in the fixed vertical position.

E911 pipe joints

Two butt joints have been welded on pipes ϕ 405 x 60 mm in the fixed positions with horizontal and vertical pipe axis. The following Böhler fillers were used: C9 MVW-IG wire (ϕ 2.4 mm) - for the root pass, and FOX C9 MVW stick electrodes (ϕ 2.5 and 3.2 mm) - for the filling passes. The heat input did not exceed 20 kJ/cm. The welded joints were preheated by an induction device to a temperature of 200 °C, the interlayer temperature was maintained below 300°C. After welding the joints were stress relieved (760 °C/3h).

After positive results of ultrasonic examination, the following mechanical tests and examinations have been performed on the pipe joint welded in the horizontal fixed position: transverse tensile tests, side bend tests, impact tests on specimens located at 3 depth of wall thickness, macro- and micro-examinations, hardness measurements on joint cross section.

All transverse tensile tests ruptured in the parent material and the tensile strength (R_m=686÷706 MPa) was higher than the minimum value required for the E911 steel (620 MPa – table 2). All side bend test results were positive. The impact absorbed energy for the tested regions of the pipe butt joint was as follows (mean values of 9 results): 60 J/cm^2 – weld metal, 160 J/cm^2 – fusion boundary and 185 J/cm^2 – HAZ (2 mm).

Macro- and microstructures of the welded joint are shown in Figures 13 and 14.

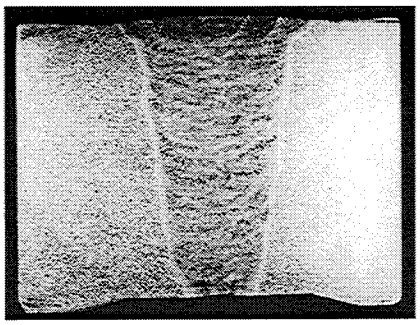
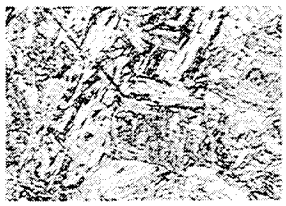
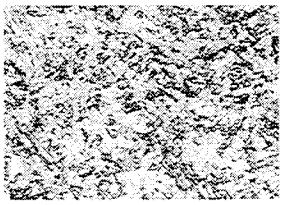


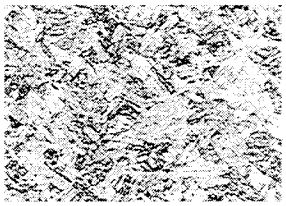
Fig. 13. Macrostructure of the E911 steel pipe joint (ϕ 405 x 60 mm) welded in the fixed horizontal position. Quality level B



Parent material.
Tempered martensite,
210 HV10



HAZ close to the weld
Tempered martensite,
265 HV10

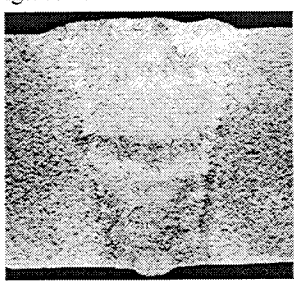


Weld metal
Tempered martensite,
250 HV10

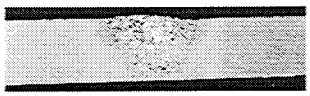
Fig. 14. Microstructures of the butt joint of E911 steel pipe (ϕ 405 x 60 mm) welded in the fixed horizontal position. $FeCl_3$ etched, 250 x.

HCM12A tube and pipe joints

The joints have been welded at the RAFAKO Boiler Plant. The tube joints ϕ 38 x 6.3 mm were TIG welded using T-HCM12A ϕ 1.6 mm Sumitomo wire with a preheating temperature of 250 °C. For welding pipe joints ϕ 355 x 45 mm the same wire was used for the root pass (TIG) and Sumitomo stick electrodes HCM12A ϕ 2.4 and ϕ 4.0 mm – for filling passes. Welded joints were heat treated for 5 h at the temperature of 740 °C (tubes) and 760 °C (pipe). During the tensile test of tube welded joints, performed according to PN-EN 895:1997, the specimens ruptured in the parent material (R_m=772 MPa). Bend tests showed good plastic properties (130 °, plunger ϕ 20 mm). Charpy V notch toughness (specimens 10.0 x 5.0 mm) was as follows: 94 J/cm^2 – parent material, 90 J/cm^2 – weld metal, 91 J/cm^2 – HAZ. Macrostructure of pipe and tube welded joints is presented in Fig. 15 and microstructures of the tube joint – in Figures 16 and 17.



1:1



2:1

Fig. 15. Macrostructure of HCM12A steel welded joints



Fig. 16. Parent material HCM12A. Tempered martensite + δ ferrite (235 HV10). $FeCl_3$ etched, 500 x

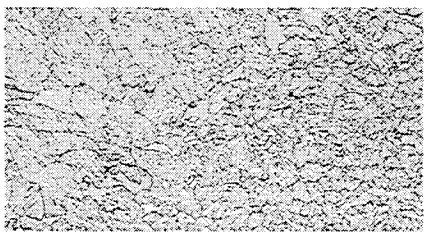


Fig. 17. Transition zone: weld - tempered martensite + carbides (max. 271 HV10), HAZ - tempered martensite + δ ferrite, (max. 270 HV10). $FeCl_3$ etched, 200 x

Discussion

Simulation tests have shown that welding thermal cycles produce in the HAZ of Cr-W steels martensitic microstructures with high hardness, exceeding 450 HV for short cooling times. In steels with high chromium content (T92/P92, E911 and HCM12A) hardness does not fall below 400 HV even for longer cooling times ($t_{8/5}$=300 s, Figs. 5, 6, 7 and 9), which is the result of the transformation characteristics (TTT- diagram Fig. 8). High hardness values were also measured in the as welded T92 steel joint (Fig. 11).
There is an evident notch toughness decrease of simulated HAZ's in comparison with the parent material, especially for steels with high Cr content. PWHT restores the notch toughness. Welded joints after PWHT show KCV values in the HAZ in the range of 74÷185 J/cm^2 and 43÷90 J/cm^2 – in the weld metal.
Tube and pipe joints of the new martensitic Cr-W steels, welded with proper filler materials, according to proven welding and PWHT procedures, have good mechanical properties and satisfactory brittle fracture resistance.

References

[1] Development study of the electric energy production subsystem up to the year 2020. Polish Electric Networks S.A., Warszawa , 1994 (in Polish)
[2] The Energy Market Agency S.A.: Assumptions for the Polish energy politics up to the year 2020. Working draft –version 2. Warszawa, 1999 (in Polish).
[3] Pasternak J., Hernas A., Miliński P.: New martensitic steels for supercritical boilers. Energetyka No 4, 1997 (in Polish).
[4] Zeman M., Brózda J., Pasternak J.: Weldability evaluation of the HCM12A steel assigned for elements of supercritical power boilers. Przegląd Spawalnictwa Nr 6, 1999, p. 1-7 (in Polish).
[5] Brózda J.: Weldability characteristics and welding technology guidelines of the advanced heat resisting steels. COST 522 Progress Report No 1 (12.03.2001) and No 2 (28.09.2001).
[6] Brózda J., Łomozik M., Malczewski K.: A modernized technique for examining phase transformations in metals during simulated welding thermal cycles. Proceedings of International Symposium of Physical Simulation. Delft, 1992, p. 185-189.
[7] Coussement C., Dhooge A.: Evaluation weldability using weld simulation testing. Ibid, p. 149-156..

APPLICATION OF A NEW ROTOR STEEL FORGING FOR MEDIUM RATING SINGLE CYLINDER STEAM TURBINES

Masayuki Yamada[1], Yoichi Tsuda[1] and Joji Kaneko[2]

[1]Chief specialist and senior specialist, respectively, Power and Industrial Systems R&D, Toshiba Corp., 2-4, Suehiro-cho, Tsurumi-ku, Yokohama, 230-0045 Japan
[2]Chief specialist, Keihin Product Operations, Toshiba Corp., 2-4, Suehiro-cho, Tsurumi-ku, Yokohama, 230-0045 Japan

Abstract

The demand of the 80-300MW class medium rating steam turbines has been recently increasing specially for combined cycle plants and IPP (Independent Power Producer) plants. The compact structure is needed for the effective use of grounds, the saving of raw materials and the reduction of exhausted CO_2 in these steam turbines.

For these viewpoints, a new 2.25%Cr1.7%NiMoVNbW steel forging has been developed for the high pressure (HP)-low pressure (LP) single cylinder steam turbine rotor. The principal technological features of this rotor steel are as follows:
(1) The optimization of chemical composition for the increasing of tensile strength, toughness and creep rupture strength.
(2) The application of differential heat treatment condition for HP and LP rotor portions.
(3) The application of ESR (Electroslag Remelting) process for the reduction of carbon segregation in the center portion of the rotor ingot.

This new steel shows a good creep rupture strength equivalent to the conventional 1%CrMoV HP rotor steels and the excellent proof stress and toughness which is the supreme level in single cylinder turbine rotors. Twelve rotor forgings have been already produced for the commercial HP-LP single cylinder steam turbines and have been operated without any problem.

The development of this new rotor steel forging has contributed for the extension of single cylinder steam turbine rating and the increasing of turbine efficiency due to the application of longer blades.

Keywords: 2.25%Cr1.7%NiMoVNbW steel, HP-LP single cylinder steam turbine rotor, combined cycle power plant, medium rating thermal power plant

Introduction

Steam turbines generally consist of plural cylinders. However, when a rotor forging with a good combination of creep rupture strength, proof stress and toughness is available, the steam turbine can be designed as a single cylinder type, which makes the unit compact and simple. 1%CrMoV steel rotor forgings currently used at high temperature are excellent in creep rupture strength but poor in toughness, while 3.5%NiCrMoV steel rotor forgings used at low temperature are excellent in toughness but poor in creep rupture strength. It is required for HP-LP single cylinder turbine rotor forgings to have both high creep rupture strength and good toughness which are mutually contradictory properties as a rule. The 1%CrMoVNiNb steel forging is one of this kind of turbine rotor forging [1]. However, it would be applicable only for the turbine rotors of 100MW or smaller units with its last stage blades up to 660 mm (26 inches) in length because of inadequate proof stress and toughness of this forging. The demand of the 80-300MW class medium rating steam turbines has been recently increasing

specially for combined cycle plants and IPP plants.

The last stage blades might range in length from 850 mm (33.5 inches) to 1070 mm (42 inches) in this kind of medium rating HP-LP single cylinder turbines. Therefore, higher proof stress and toughness than those of the conventional HP-LP single cylinder turbine rotor forgings are required for the new HP-LP single cylinder rotor forging to withstand the increased centrifugal stress. FIG. 1 shows the development history for the new HP-LP single cylinder steam turbine rotor forging.

This paper covers the outline of R&D process on the development of a new HP-LP rotor forging and the production and evaluation of commercial rotor forgings.

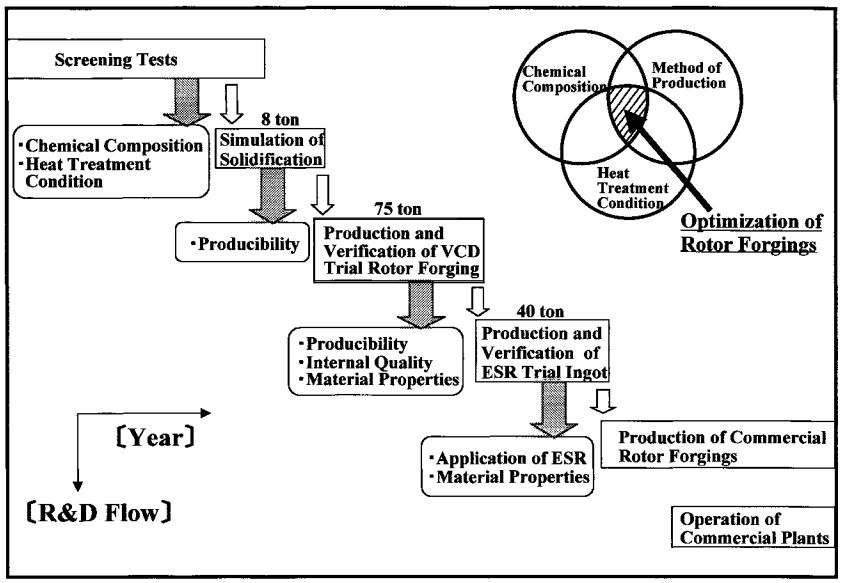


FIG. 1 Development history of the new rotor forging for the medium rating single cylinder steam turbines

OPTIMIZATION OF CHEMICAL COMPOSITION AND HEAT TREATMENT CONDITION

Screening tests for the optimization of chemical composition and heat treatment condition for a new HP-LP rotor steel have been performed with a lot of small size laboratory heats [2], [3], [4]. The important results on chemistry of this rotor steel are as follows:

(a) Higher chromium and nickel content than those of conventional 1%CrMoV HP rotor steel and conventional 1%CrMoVNiNb HP-LP single cylinder rotor steel is very useful for the improvement of toughness.

(b) Addition of niobium is very effective for the refining of grain size and the improvement of toughness.

(c) Addition of tungsten is useful for the maintaining good creep rupture strength in the steel containing higher chromium and nickel.

(d) 2.25%Cr1.7%NiMoVNbW steel is very favorable for the advanced HP-LP single cylinder

rotor forging.

On the other hand, the principal results on heat treatment condition of this rotor steel are as follows:

(a) The application of differential heat treatment method in which the respective heat treatment conditions are applied to HP and LP portions, is desirable in order to obtain the required mechanical properties .

(b) 970°C was selected as the austenitizing temperature for the HP portion of rotor forging from the viewpoints of keeping the good creep rupture strength.

(c) 900°C was selected as the austenitizing temperatures for the LP portion of rotor forging in order to obtain the required proof stress and toughness.

PRODUCTION AND EVALUATION OF VCD TRIAL ROTOR FORGING

Production of Trial Rotor Forging

A product-size trial rotor forging was produced on the basis of knowledge obtained from the fundamental study. The drum diameter of the trial rotor forging was 1750 mm in LP portion and 1000 mm in HP portion. The diameter of this rotor is large enough for covering HP-LP single cylinder rotors for turbines of 300MW plants. The target of chemical composition for the trial rotor forging was 0.24%C-lowSi-0.5%Mn-2.25%Cr-1.7%Ni-1.1%Mo-0.2%V-0.015%Nb-0.2%W-Fe (Bal.). It was decided from the viewpoints of mechanical properties and the reduction of chemical segregation, in reflection of the preliminary solidification test result with the superclean process (ultra-low level of Mn content) using a 8 ton Ingot [5]. Impurities such as phosphorus, sulphur, arsenic, tin and antimony were determined to be suppressed to the industrial lowest levels.

The ladle refining was carried out after the basic electric furnace melting and the VCD (Vacuum Carbon Deoxidization) process was applied during vacuum pouring for obtaining a sound 75 ton ingot. A differential heat treatment method was applied for this trial rotor forging. The HP portion was austenitized at 970°C and afterwards forced air cooled. The LP portion was austenitized at 900°C and afterwards water spray cooled. Consequently, the double tempering was employed to remove residual austenitic structure for improving the proof stress. The first tempering was carried out at 580°C and the differential second tempering at 640°C and at 625°C were applied for HP and LP portions respectively. Thereafter, stress relieving was performed at 600°C over the whole rotor.

Evaluation of Trial Rotor Forging

The result of ladle analysis was approximately consistent with the target composition. Meanwhile, carbon content tended to be gradually more concentrated approaching the top side from the bottom one of the ingot, that is, the slight carbon segregation was observed in the center portion of the ingot (FIG. 2).

Tensile and Charpy impact properties in the center portion of the fully heat-treated (after stress relief) trial rotor forging are shown in FIG. 3. In the center core of the LP portion (position D), FATT of 23°C and 0.02% proof stress of 655 MPa were obtained.

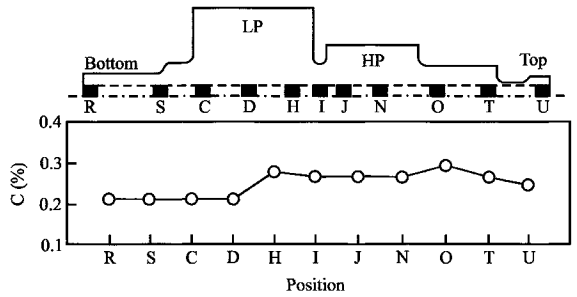


FIG. 2 Distribution of carbon content in the center portion of VCD trial rotor forging

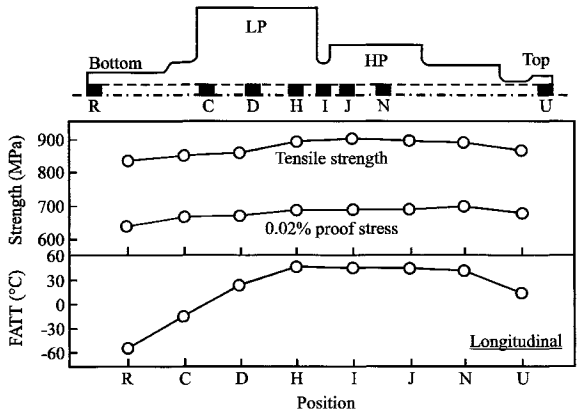


FIG. 3 Tensile and impact properties in the center portion of VCD trial rotor forging

MODIFICATION OF MANUFACTURING PROCESS

In order to reduce the chemical segregation in the center of ingot and to improve the toughness of LP center portion, the application of ESR process, a little modification of chemical composition and the accompanied optimization of the heat treatment condition (austenitizing temperature) were considered [6] [7].

Chemical Composition

The modified chemical composition for the next step is shown in TABLE 1. Nb content was increased to 0.030% in order to refine the grain size. Mn content was reduced to the ultra-low level (superclean) from the viewpoint of the suppression of temper embrittlement during long time operation.

TABLE 1 Target of the chemical composition of ESR trial ingot (mass%)

	C	Si	Mn	Ni	Cr	Mo	V	Nb	W
ESR trial ingot	0.24	< 0.03	< 0.05	1.70	2.25	1.10	0.20	0.030	0.20
VCD trial rotor	0.24	< 0.03	0.50	1.70	2.25	1.10	0.20	0.015	0.20

Metallurgical Evaluation of ESR Ingot

The application of ESR process was considered to reduce the chemical segregation in the center of ingot. The ESR trial ingot was 40 tons in weight and 1800 mm x 2290 mm in size. Several metallurgical investigations were performed in the longitudinal and the transverse cross sections of the ESR ingot. The ESR ingot had excellent cleanliness (the percentage of area occupied by the non-metallic inclusions such as sulphides, silicates, alumina, etc.) of 0.004% to 0.01%. The apparent eutectic Nb(C, N) was not observed also in the center of ingot. The macrostructure of the ESR ingot was fairly fine and heavy carbon segregation was not observed. As for the other alloying elements, the degree of chemical segregation was similarly low and a relative homogeneous ingot was obtained.

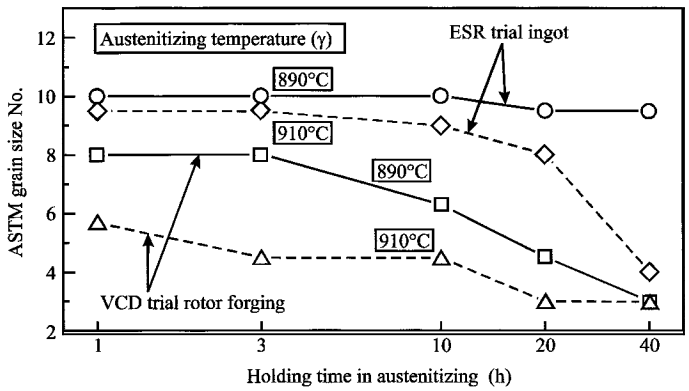


FIG. 4 Grain growth behavior during austenitizing

Heat Treatment

In the VCD trial rotor forging, the toughness was below the estimation obtained by the preliminary simulation test due to the difference of holding time in austenitizing. The holding time was 3 hours in the simulation test and 40 hours in manufacturing of the trial rotor forging respectively. In order to clarify this difference of toughness, the investigation was performed concerning the grain growth behavior using the materials sampled from the VCD trial rotor forging and the ESR trial ingot (FIG. 4). The grain was more refined compared with the VCD trial rotor forging by the increasing of Nb content and the application of the superclean process. Moreover, the grain size could be maintained at the refined condition even in the austenitizing temperature of 890°C.

The test block sampled from the center portion of the ESR ingot was forged with the forging ratio of 4 and heat-treated nearly in accordance with the heat treatment condition of LP portion of turbine rotor forgings. The austenitizing temperature was determined to be 890°C in which the grain size was not changed during a long holding time. The grain size number of these test specimens was 8.2 (average of ASTM No.) that was fairly fine. The correlation between FATT and 0.02% proof stress of the test specimens is shown in FIG. 5 compared with the results of VCD trial rotor forging. The test specimens show a good combination of FATT and proof stress superior to those of VCD steel forging. It is estimated that the improvement of toughness in the ESR ingot is due to the refinement of grain size by the in-

creasing of Nb content from 0.015% to 0.030% and the change of quenching temperature from 900°C to 890°C.

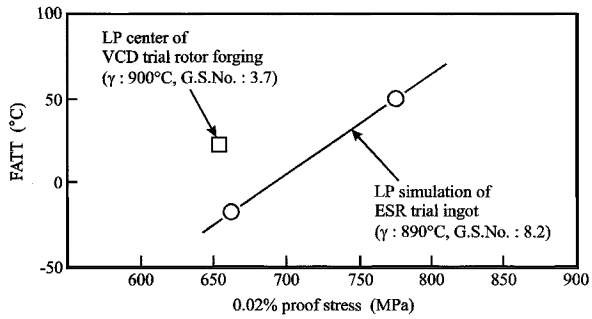


FIG. 5 The correlation between FATT and proof stress

PRODUCTION AND EVAUATION OF ROTOR FORGINGS FOR COMMERCIAL POWER PLANT

From the above mentioned results, the improvement of toughness would be obtained by the reduction of chemical segregation using the application of ESR process and the refinement of grain size by the increasing of Nb content with the accompanied optimization of austenitizing temperature. Moreover, it would be anticipated that the application of the ESR process made it possible to get a superclean material, and to suppress the temper embrittlement during long time operation.

Twelve rotor forgings have already been produced with the modified manufacturing process for the steam turbines of the principally advanced combined cycle power plants. FIG. 6 shows one example of the appearance of HP-LP rotor forging after completion of attachment of blades for the commercial single cylinder steam turbine.

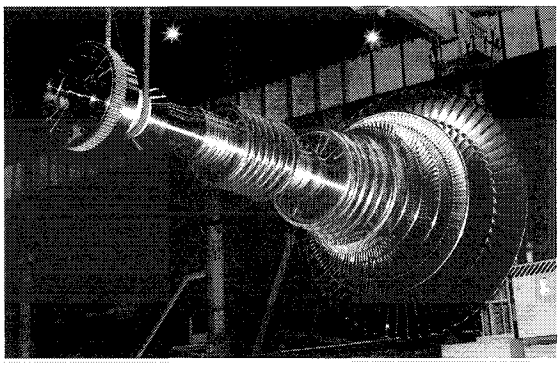


FIG. 6 The appearance of commercial HP-LP rotor forging

Production of Rotor Forgings

The typical shapes of the rotor forgings are shown in FIG. 7. The maximum diameter of LP

portion is ϕ 1750 mm among twelve commercial rotor forgings. The ladle analysis results of these rotor forgings are listed in TABLE 2. The result of ladle analysis was approximately consistent with the target value. The quality heat treatment was performed with the differential heat treatment method. The HP and LP portions were austenitized at 970°C and at 890°C, respectively. Thereafter, double tempering and stress relieving were performed.

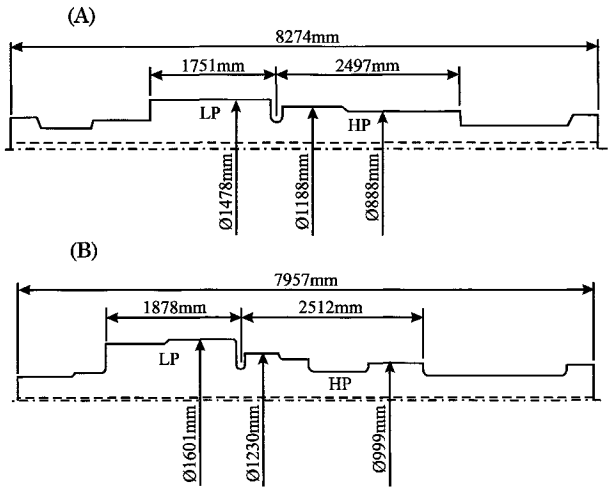


FIG. 7 The shapes of rotor forgings for commercial power plants

TABLE 2 Ladle analysis result of commercial rotor forgings (mass%)

	C	Si	Mn	P	S	Ni	Cr	Mo	V	Nb	W
Target	0.24	< 0.03	< 0.05	< 0.003	< 0.0015	1.70	2.25	1.10	0.20	0.030	0.20
Commercial rotor forgings	0.21 - 0.26	0.02 - 0.06	0.03 - 0.04	0.003 - 0.004	0.001	1.67 - 1.84	2.21 - 2.28	1.08 - 1.14	0.19 - 0.21	0.024 - 0.029	0.19 - 0.20

Evaluation of Rotor Forgings

Non-destructive inspection

No indications were detected by non-destructive inspection tests such as ultrasonic and magnetic particle methods. It was confirmed that these commercial rotor forgings had excellent quality.

Chemical composition

FIG. 8 shows the distribution of carbon and niobium in the center portion of the commercial rotor forging(A). Although the carbon segregation was slightly observed here, the degree of this segregation was significantly lower compared with that of the VCD trial rotor forging. The application of the ESR process seems to be very effective for the reduction of carbon segregation in the center portion of the rotor forgings.

Metallography

The macrostructure of the center core bar revealed no apparent segregation. The microstructure in various regions of the rotor forging(A) was tempered bainite that is typical of low alloy rotor forgings and no apparent Nb(C, N) was found. Quite fine grain was obtained at the LP portion caused by the austenitizing temperature of 890°C. ASTM grain size numbers for the rotor forging(A) were 4.3 and 10.4, respectively in the center core regions of HP and LP portions.

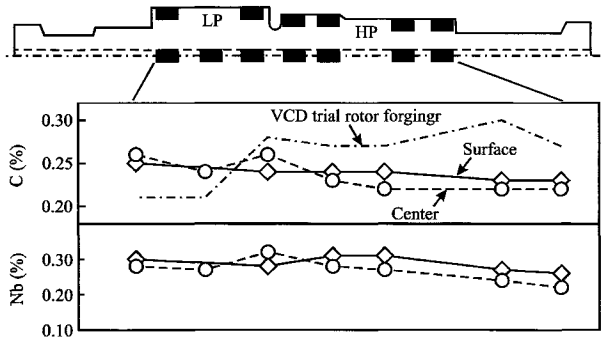


FIG. 8 The distribution of carbon and niobium in center portion of commercial rotor forging(A)

Tensile and impact properties

FIG. 9 shows the tensile and Charpy impact properties in the center portion of several commercial rotor forgings. All the test results showed required properties. The FATT in LP portion of these rotor forgings was about 25°C lower than that of the VCD trial rotor forging. The application of ESR process, a little modification of chemical composition and the optimization of heat treatment condition seem to be very effective for the improvement of toughness in the center portion of the rotor forgings.

FIG. 10 shows the correlation between the FATT and the 0.02% proof stress compared with other low alloy steel rotor forgings. The new HP-LP rotor forgings showed good combination of room temperature strength and toughness which is superior to that of the conventional HP-LP rotor forging and close to that of the 3.5%NiCrMoV LP rotor forging.

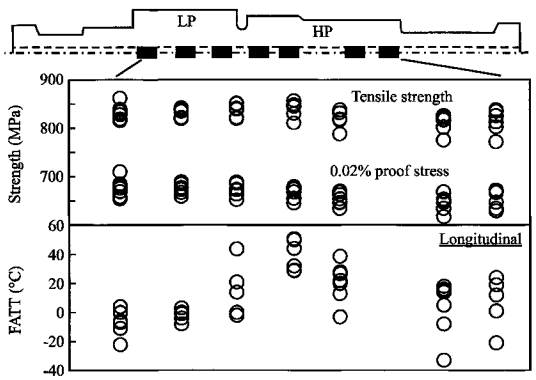


FIG. 9 Tensile and impact properties of commercial rotor forgings

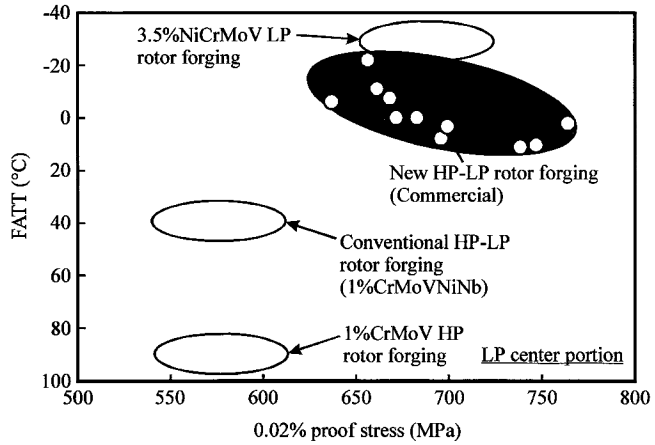


FIG. 10 FATT and 0.02% proof stress of commercial rotor forgings

Creep rupture strength

FIG. 11 shows the creep rupture strength of several commercial rotor forgings. Good creep rupture strength equivalent to that of the 1%CrMoV HP rotor forging was obtained.

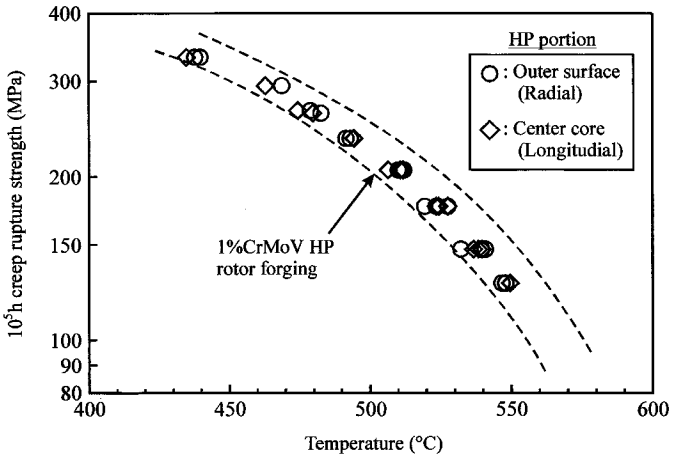


FIG. 11 Creep rupture strength of commercial rotor forgings

SUMMARY

A new forging steel, 2.25%Cr1.7%NiMoVNbW has been developed for 80-300MW class medium rating HP-LP single cylinder steam turbine rotors by improving of the chemical composition and the heat treatment condition. This steel shows a good creep rupture strength equivalent to the conventional 1%CrMoV HP rotor steels and good proof stress and toughness close to those of the conventional 3.5%NiCrMoV LP rotor forgings.

The most suitable manufacturing process was established by the study of the VCD trial rotor forging and the ESR trial ingot. The feature of the process is the application of ESR process and the accompanied modification of chemical composition and heat treatment condition in order to reduce the chemical segregation and to improve the toughness.

Twelve rotor forgings have already been produced for the commercial HP-LP single cylinder steam turbines principally of the advanced combined cycle power plants. Excellent mechanical properties have been obtained and homogeneous contents of alloying elements have also been obtained in the center core of these rotor forgings. It can be considered that the new rotor forging steel will be applied for a lot of medium rating steam turbines for advanced combined cycle plants and IPP plants.

Trial and commercial rotor forgings have been produced in co-operation with The Japan Steel Works, LTD.

REFERENCES

[1] M. Yamada, M. Miyazaki, O. Watanabe and M. Kawai, "Development of Integral High-Pressure Low-Pressure Combination Rotor Forgings" ASTM STP903 Steel Forgings, 1986, pp. 59

[2] O. Watanabe, M. Yamada, Y. Tsuda and M. Miyazaki, "Improved CrMoV Steel Rotor Forgings for HP-LP Single Cylinder Steam Turbines" Symposium on Materials for Combined Cycle Power Plant, 1991, pp. 60

[3] M. Yamada, Y. Tsuda, O. Watanabe, M. Miyazaki, Y. Tanaka, T. Takenouchi and Y. Ikeda, "HLP Single Cylinder Steam Turbine Rotor Forgings for Combined Cycle Power Plants" R. I. Jaffee Memorial Symposium on Clean Materials Technology, ASM TMS Materials Week, 1991, pp. 161

[4] Y. Tsuda, M. Yamada, O. Watanabe, M. Miyazaki, Y. Tanaka, T. Takenouchi, and Y. Ikeda, "Development of Advanced HLP Single Cylinder Steam Turbine Rotor Forgings" JSME-ASME International Conference on Power Engineering-93, 1993, pp. 91

[5] H. Yamada, T. Takenouchi, M. Funazaki, T. Takahashi, T. Iwadate and S. Nakada, "Effect of Alloying Elements on Macrosegregation of Super Clean CrMoV Steel" TETSU-TO-HAGANE, Vol. 81, 1995, pp. 82

[6] M. Yamada, Y. Tsuda, M. Miyazaki, Y. Tanaka, T. Azuma and Y. Ikeda, "A New Superclean High Pressure-low Pressure Rotor Steel for Advanced Combined Cycle Power Plants" EPRI Workshop on Clean Steel: Superclean Steel, 1995, pp. 109

[7] Y. Ttsuda, M. Yamada, J. Kaneko, Y. Tanaka and Y. Ikeda, "Application of a New Rotor Steel Forging for Single Cylinder Steam Turbines" The 13th International Forgemasters Meeting, Pusan, Korea, Volume 1, 1997, pp. 343

THE FIRST INDUSTRIAL CAST OF CrMoCoB ADVANCED STEEL FOR CAST TURBINE COMPONENTS

E. Contessi (*), D. Delvecchio (*), A. Ghidini (*), S. Valenti (*),
A. Carosi (**), A. Di Gianfrancesco (**), F. M. Ielpo (**)
(*) Lucchini Sidermeccanica Lovere, BG, Italy
(**) Centro Sviluppo Materiali, Rome, Italy

Abstract

Higher efficiency in the new fossil fuel fired plant for power generation, in order to reduce the emissions, needs increase in temperature and pressure service and, consequently, development of new steel grades with improved creep performances. Castings, as well as, tubes, pipes, and forged components used in the hottest part of the plant, play a relevant role. In fact, the highly loaded component in the high and intermediate pressure section of the steam turbine, such as inner, outer and valve casing, pipes and elbows, are very stressed both thermally and mechanically.
This paper shows the preliminary results, obtained on the first experimental industrial cast produced by Lucchini Sidermeccanica in Lovere, using the new CrMoCoB steel, developed in the frame of COST 522. The components have been designed by FEM code analysis, to optimise filling, pouring and solidification. The set up of heat treatment on base and PWHT material, simulating the repairing, as well as the mechanical properties and the microstructures obtained on a test block, are discussed.

Keywords: 9-10%Cr steel casting, cast turbine components, foundry, manufacturing, FEM modelling, mechanical properties, microstructure.

1 Introduction

Development of 9-12%Cr martensitic steels grades for power generation components has been a significant feature, since the 1980s. However, steels with the basic compositions of 9Cr1Mo have been widely used for many years. The driving force for new developments has been the need to increase the temperature and pressure of the steam circuit. The next generation of ultra supercritical power plant will have service temperatures in the range 600-650°C and very high pressure; hence the performance of materials for castings, pipes and tubes for boilers and rotors has to be increased. This means the replacement of the GS17CrMoV 5 11 ferritic-bainitic and GX22CrMoV 12 1 ferritic-martensitic steels grades, used up to 565°C all over the world. Also the G-X12CrMoVNbN 9 1 (Grade 91) and the G-X12CrMoWVNbN 10 11 (Grade 911), developed in Europe in the COST 501 Round I and II, for temperature up to 600°C cannot guarantee the 100 000 h creep rupture strength of 100 MPa at 620-650°C. Therefore, a large number of new ferritic-martensitic steel grades have been developed, on the basis of the results obtained from the previous round, in the frame of the new European Program COST 522 – Power Generation, into the 21st Century "Advanced Steam Power Plant". The most promising of these new compositions has been produced as full industrial cast in Lucchini Sidermeccanica - Lovere Plant, in Italy.

2 COST 522 Programme

Lucchini Sidermeccanica, leader in the field of castings and forgings, produces steel grades for cast turbine components for the energy field in its foundry at Lovere.
Since 2001, Lucchini Sidermeccanica, jointly with Centro Sviluppo Materiali, has actively worked in the European Programme COST 522 - Advanced Power Plant, with the aim to optimise the new steel grades required.
In the cast programme, starting from CB2, as reference material, 6 new trial melts have been produced as experimental plates (table 1) and have been heat treated with the same parameters (1).
The CB6 composition, which had showed the best performances, has been selected in the Turbine Group for the production of an industrial scale cast.

3 Production and Manufacturing Process

In the COST 522 activities, Lucchini Sidermeccanica has produced the first prototype "Full-Scale" casting, made by 50 tons of liquid CB6 steel grade. The new heat has been carefully designed, in each process route, in order to achieve the aimed chemical analysis from COST 522 (table 2), with special emphasis for the very low Al content. Due to very restricted amounts of P, Sn, As, Ti and Cu residuals, specially selected scrap has been melted in an electric arc furnace (EAF), followed by the addition of the main alloying elements (Cr = 11%, Co = 3%, Mo = 1.5%) in a ladle furnace (LF). In order to avoid contamination, the Co and Cr amounts have been added as pure metallic ferroalloys. The stirring of the liquid bath and the aimed pouring temperature have been guaranteed by Ar blowing from the pouring plug at the ladle bottom and by heating devices.

The aimed Nb and B contents, due to high affinity with O_2 and N_2 (the latter is required in the range 150 - 300 ppm), balanced with Al and Ti as low as possible (< 0.01%), required a calibrated deoxidation with Al, before and during vacuum degassing (V.D.) by the tank degassing plant. The additions of Nb and B have been made at the end of the mentioned deoxidation process. The results of heat and product chemical analyses are shown in Table 2. The main target with a very low Al content (50 ppm), as well as reduced contents of P, S, Sn, As, Cu and Ti has been reached.

4 Components design activities

FEM code analysis has been used to simulate the manufacturing processes of the following components:

- two 4-ton test blocks, one of which has been instrumented by thermocouples, in order to calibrate the thermal model
- one 12-ton flange for turbine casing
- one 6-ton forging ingot

Two FEM code softwares have been used and their results compared:

- MAGMAsoft, installed at Lucchini Sidermeccanica,
- PROCAST, at Centro Sviluppo Materiali.

The foundry process simulations, made by MAGMAsoft, accurately represent the dynamic, fluid and thermal fields of the casting-mould system, using control volumes. Critical zones of castings and particular processes can be assessed in the

design stage, using suitable physical factors, such as solidification times, thermal gradients, cooling rates. These provisional models give information necessary for optimisation, in order to avoid zones affected by defects such as porosity, shrinkage and crack.

The foundry processes can be separated and the main stages analysed:
- Casting of the molten steel into the mould
- Filling the mould
- Solidification (in a well defined temperature range depending on steel composition)
- Cooling (taking in account transformations of steel in solid phase)

Each of the above mentioned stages is associated with phenomena of mass transport, conservation of energy and motion quantity, which can be suitably assessed as a function of time (t) and space (x, y, z), through differential equations (Navier-Stokes equations for the fluid dynamics calculation and Fourier equations for the thermal flow calculation).
To obtain reliable, physico-mathematical modelling, it is necessary:
- to define carefully design parameters, namely: heat temperature, casting dimensions, configuration of the casting-mould-gates system, melted steel flows;
- to know exactly the thermo-physical and chemical properties of the materials (liquidus and solidus temperatures, viscosity, density, conductivity, thermo-physical characteristics of any cooling plates, sands, refractory materials, heat transfer coefficients between the various different used materials). Some of these values have been evaluated by THERMOCALC analysis.

The knowledge of the "thermal field" of the system mould-cast allows to analyse the microstructural evolution of the steel, which is directly tied to the thermal history of the strained piece and to the chemical composition of the steel (CCT and TTT diagrams). The simulation codes were validated by experimental tests from the real process. In fact, there are various "solidification parameters" which, singly or suitably combined, prove useful in predicting any zone, subject to microporosity due to shrinkage:
- number of Nyama N ($G/\varepsilon^{0,5}$ with $N_{crit} = 1$)
- feeding parameter associated to the ability of the material feeding
- maximum thermal gradient G to the end of solidification (°C/cm)
- solidification speed V (cm/s)
- instantaneous cooling speed E (°C/s)
- solid fraction F_s (%)
- time of local solidification T_f (s)

These parameters are visualized with "three-dimensional chromatic mappings", constructed on casting geometry, describing the thermal and fluid dynamic field evolution of the whole system. An example of the simulation results is shown in Figure 1.

In order to evaluate the values of the coefficients used in the predictive models, one test block has been instrumented by 20 thermocouples, located in the steel and in the refractory layers, as show in Figure 2. Other experimental tests have been

carried out in order to evaluate the thermal conductivity of cromite-sand-resin, silica, cromite-material insulators.

The results of the simulation, verified after the pouring and solidification, confirmed the software improvements, and at the same time, they indicated some limits. A careful search of "true" coefficients, taking in to account the chemical and physical characteristics of the used materials, is very important because these values are functions of the process. The differences between the calculated values and the values from the producer's literature can be quite large, probably because they are related to single, unmixed and uncompacted material.

Regarding the use of the mathematical models two important aspects have been verified:

- the convective movement and the fluid dynamics calculation have to be taken in account and used during the solidification simulation, not only during the pouring; this makes the calculation times long.
- the values of the heat transfer coefficients at the interfaces between the materials (mould-steel, steel-atmosphere) are critical and the transfer between the pipe and the external air has to be taken into account, also in the presence of insulating powder.
-

Figure 3 shows an example of the solid fraction calculated during the simulation process by Procast software and Figure 4 illustrates the cast components produced in CB6 steel grade.

5 Material characteristics and properties

Two plates have been used for the heat treatment set up and preliminary characterizations. The critical transformation temperatures in steel heating and cooling have been measured by dilatometry (table 3).

To set up the best heat treatment conditions in terms of austenitising and tempering temperature, the following matrix has been adopted:

Austenitising temperature (°C):	960 – 1000 – 1050 – 1070 – 1100
Tempering temperature (°C):	710 – 730 – 750

The holding time was set at up to 1 h/inch for austenitising and 0.5 h/inch for tempering. Figure 5 shows the microstructures, after austenitising at various temperatures from 960°C to 1100°C. In the range 1050-1100°C a fully recrystallised structure was observed without abnormal grain growth.

Mechanical tests, such as tensile testing at RT and at 600°C, notch impact toughness and hardness tests have been carried out, in order to select the optimum austenitizing and tempering temperatures. Figures 6 to 9 show the results. It is possible to observe that the best compromise between tensile and impact properties is austenitising at 1100°C and tempering at 730°C. This condition is in agreement with the experience made with the experimental cast in previous COST activities. A second tempering at 730°C will be carried out, to simulate the PWHT(Figure 10), applied after repairing and joint of the components; however, detrimental effects on the final mechanical properties are not expected.

6 Conclusions

A new CrMoCoB steel has been cast and various components will be heat treated using the thermal conditions selected on the basis of the results obtained on plates treated in the laboratory. A large programme for material qualification has been scheduled:

- tensile, impact, creep, fatigue testing
- creep crack growth testing
- microstructural analysis by TEM in order to evaluate the microstructure and precipitate evolution of the material after heat treatment and ageing.

New Cast	C	Cr	Mn	Mo	Ni	B	Co	N	Nb	V	W
CB 2	0.12	9.2	0.88	1.49	0.17	0.0113	0.98	0.020	0.06	0.21	0.02
CB 5	0.13	10.1	0.20	1.58	0.16	0.0110	2.90	0.035	0.06	0.20	0
CB 6	0.13	10.9	0.19	1.57	0.15	0.0110	2.90	0.025	0.07	0.20	0
CB 8	0.17	10.9	0.20	1.54	0.16	0.0110	2.90	0.025	0.07	0.21	0
CB 9	0.17	10.9	0.19	1.66	0.16	0.0110	5.85	0.022	0.06	0.20	0
CB 10	0.13	10.2	0.25	0.91	0.16	0.0080	3.14	0.023	0.06	0.22	0.41
CB 11	0.17	10.7	0.17	0.84	0.2	0.0120	2.85	0.031	0.05	0.22	0.38

Table 1: Product analysis of New Cast Melts Developed for COST 522 (mass pct) (1)

Element	COST Analysis		Industrial limits		Lucchini Analysis	
	Min.	Max.	Min.	Max.	Cast	Product
C	0.12	0.14	0.12	0.15	0.123	0.12
S		0.005		0.01	0.008	0.007
P		0.01		0.015	0.008	0.007
Mn	0.15	0.25	0.1	0.3	0.17	0.16
Cr	10.7	11.3	10.5	11.5	10.77	10.87
Ni	0.1	0.2	0.1	0.3	0.14	0.14
Mo	1.45	1.55	1.4	1.6	1.48	1.51
Cu		0.1		0.1	0.06	0.06
Si	0.2	0.3	0.15	0.35	0.26	0.26
V	0.18	0.22	0.17	0.23	0.2	0.193
Al		**0.01**		**0.01**	**0.007**	**0.005**
Sn		0.01		0.01	0.007	0.008
As		0.01		0.01	0.004	0.003
B	0.008	0.015	0.008	0.015	0.014	0.013
Nb	0.05	0.07	0.05	0.08	0.057	0.056
Ti		0.01		0.01	0.003	0.003
N_2	0.015	0.03	0.015	0.03	0.0238	0.0245
Co	2.9	3.1	2.8	3.2	2.97	3.08
H_2		0.0005		0.0005	<0.0005	<0.0005
O_2		0.0005		0.0005	<0.0005	<0.0005

Table 2: Heat and product chemical analyses

Property	
Specific Weight (g/cm^3)	7.85
Young Modulus (MPa)	206000
Coefficient of linear expansion (mm/mm/°C)	11.6
Thermal Conductivity (W/(m °C) at 73°C	27.26
A_{C1} (°C)	845
A_{C3} (°C)	950
A_{R1} (°C)	390
A_{R3} (°C)	220

Table 3: Physical properties of CB6 casting

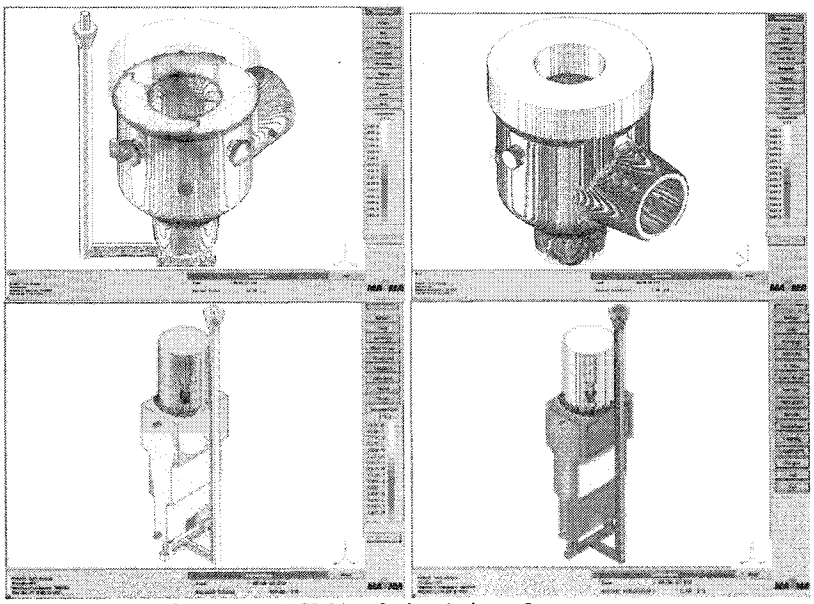


Figure 1: MAGMAsoft simulation of components

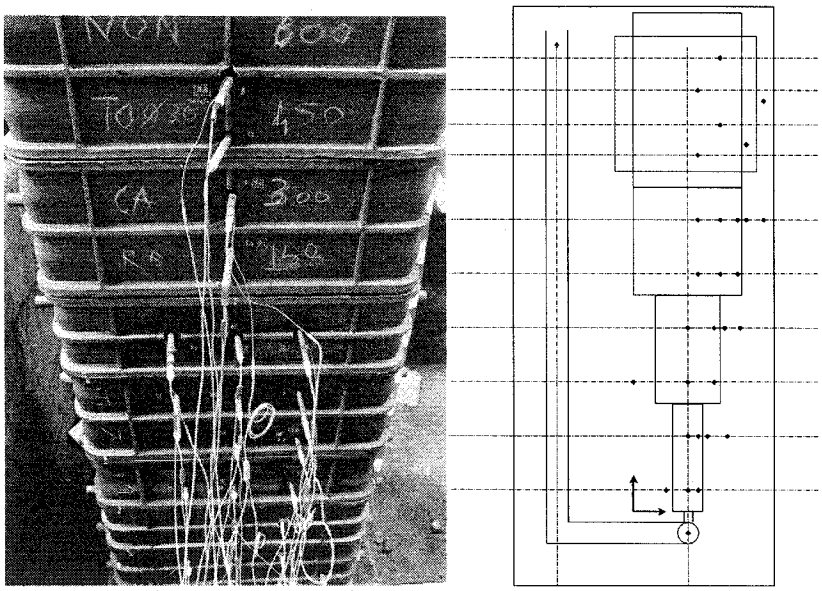


Figure 2: Step block instrumented with thermocouples

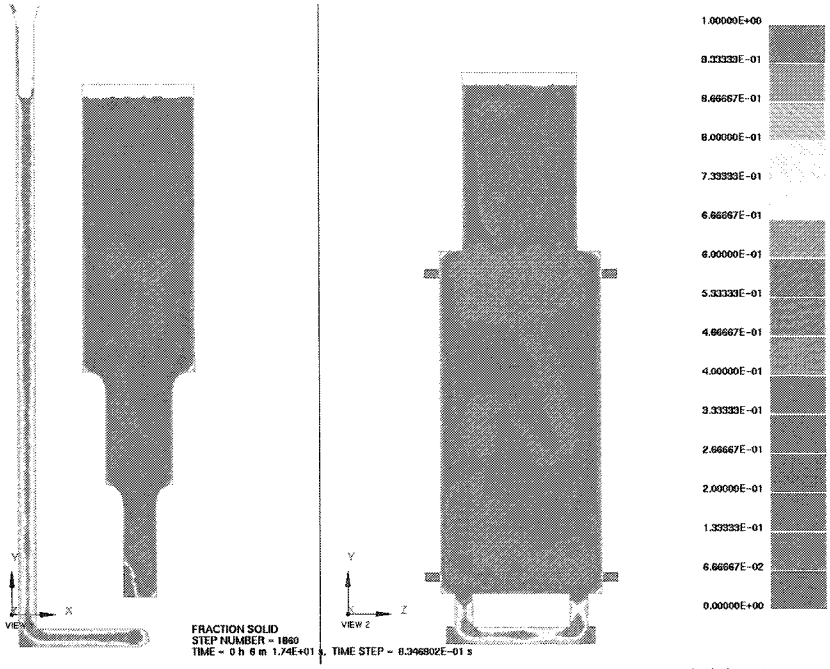


Figure 3: Example of fraction of solid material calculated during the solidification by Procast software

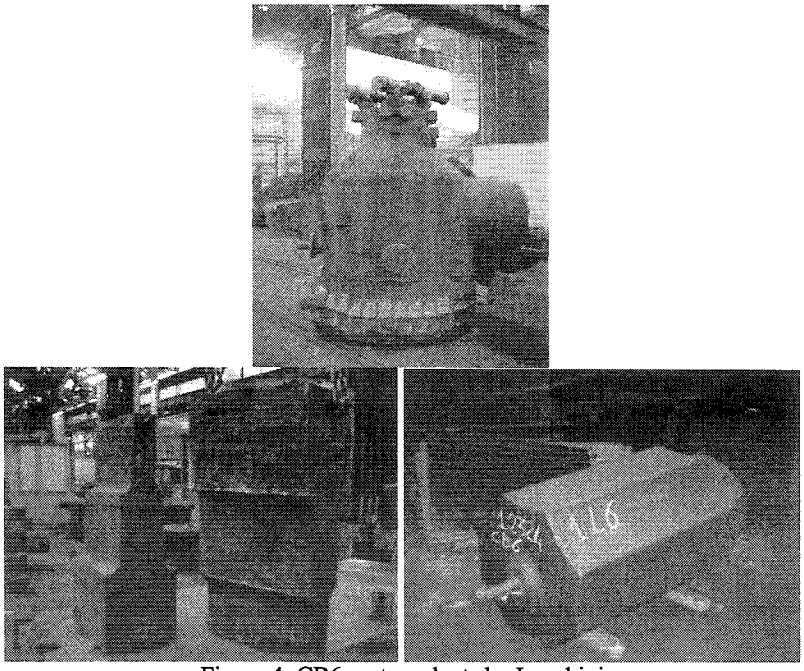


Figure 4: CB6 cast products by Lucchini

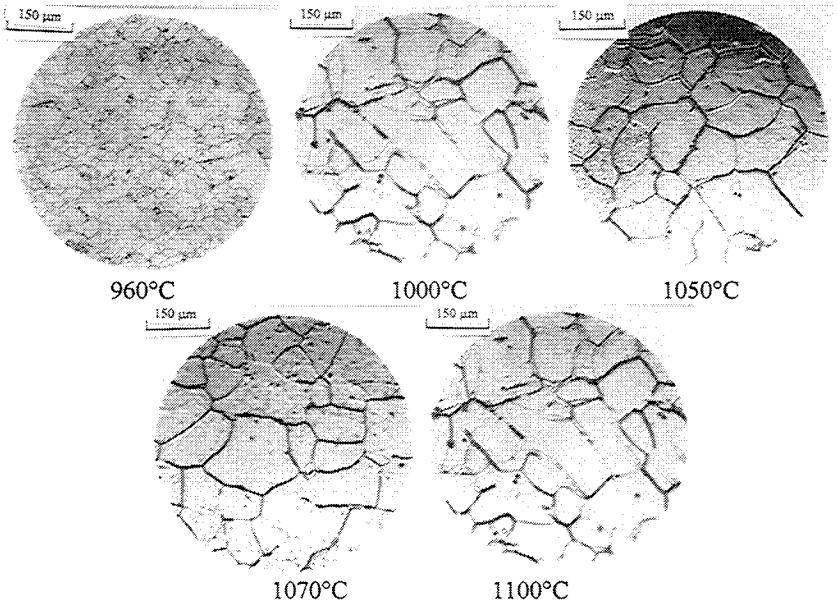


Figure 5: Microstructure of CB6 material, after austenitising at different temperatures

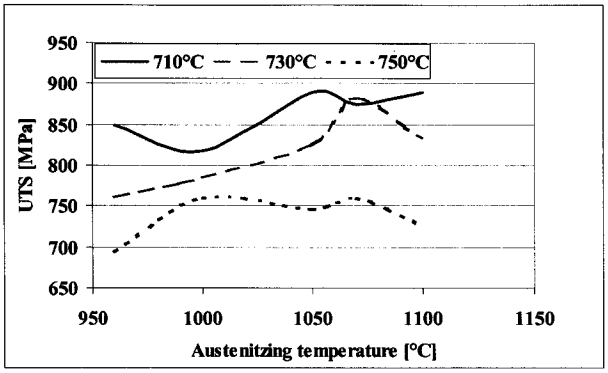


Figure 6: Ultimate tensile strength at room temperature versus austenitising temperature for various tempering temperatures

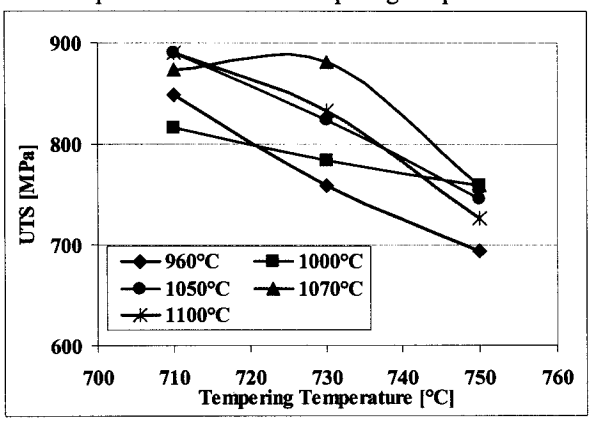


Figura 7: Ultimate tensile strength at room temperature versus tempering temperature for various austenitising temperatures

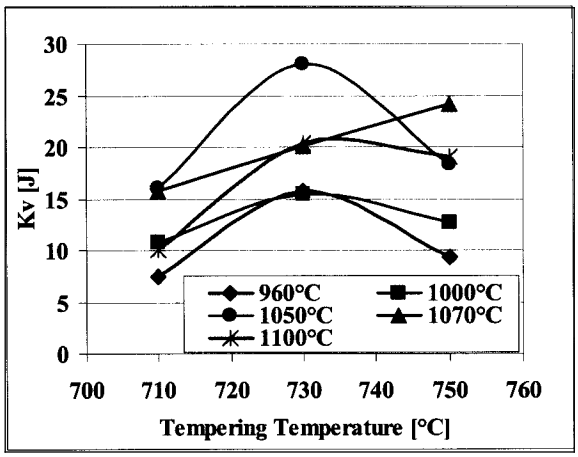


Figure 8: Room temperature Charpy-V impact toughness versus tempering austenitising temperature for various austenitising temperatures

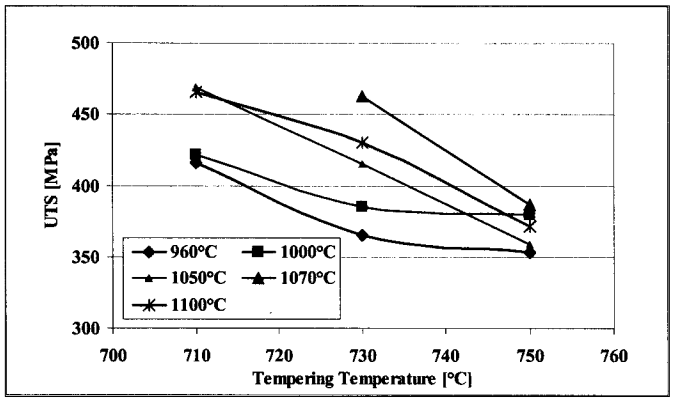


Figure 9: Ultimate tensile strength at 600°C versus tempering temperature

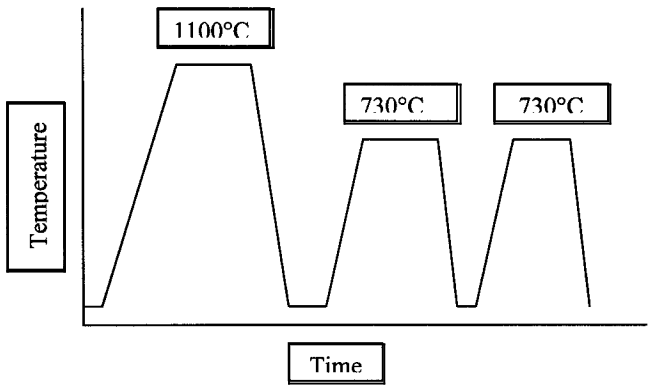


Figure 10: Heat treatment procedure (cooling is made in still air)

Reference

1) M.Staubli, K-H. Mayer, T.U. Kern, R.W.Vanstone, R. Hanus, J. Stief, K-H. Schonfeld: COST 522 – Power Generation into the 21st Century; Advanced Steam Power Plant: EPRI Conference, Swansea April 2001

OUTLOOK

OUTLOOK

Invited Papers

MATERIALS DEVELOPMENT FOR ADVANCED VISION 21 POWER PLANTS

Lawrence A. Ruth

National Energy Technology Laboratory
United States Department of Energy
Pittsburgh, Pennsylvania, U.S.A.

Abstract

Vision 21 is the U.S. Department of Energy's (DOE's) initiative for developing the technology needed for near-zero emission 21st century energy plants. The goal of Vision 21 is to effectively remove, at affordable costs, environmental concerns associated with the use of fossil fuels for producing electricity and other valuable energy products. To achieve this goal, DOE's National Energy Technology Laboratory (NETL) has begun an intensive, long-range, 15-20 year research and development effort involving industry, academia, and government.

Vision 21 focuses on developing the key technologies that will be needed to design Vision 21 energy plants. Among the most critical of these technologies is materials technology. Advanced structural materials are needed that can withstand the high temperatures and corrosive conditions typical of coal combustors and gasifiers, steam generators, air heaters, and gas turbines. Functional materials are required for applications including gas separation membranes, gas filters, and fuel cells. Classes of materials being considered for these applications include advanced ferritic and austenitic alloys, oxide dispersion-strengthened alloys, intermetallics, advanced ceramics and composites, single crystal superalloys, and thermal barrier coatings.

This paper summarizes the activities that are currently underway to develop advanced materials for Vision 21 applications. Many of these activities are conducted in the DOE Fossil Energy Advanced Research Materials Program.

Keywords: materials research, alloys, ceramics, electric power plants, Vision 21

Introduction

Vision 21 is the U.S. Department of Energy's (DOE's) initiative to develop the technology for new generations of ultra-clean 21st century energy plants. The goal of Vision 21 is to effectively remove, at affordable costs, environmental concerns associated with the use of fossil fuels for producing electricity and other valuable energy products. The environmental concerns include "traditional" air pollutants such as sulfur and nitrogen oxides and particulate matter; liquid and solid discharges; and gases associated with global climate change, primarily carbon dioxide. In order to achieve this ambitious goal, DOE's National Energy Technology Laboratory (NETL) has implemented an intensive, long-range research and development collaboration among industry, academia, and government aimed at providing substantial advances in fossil energy-related technologies.

The fundamental driving force behind Vision 21 is the growing world energy demand. While continued growth in the use of renewable energy forms is expected, along with a potential resurgence in nuclear power, there will be a powerful economic driving force for major and expanded use of fossil fuels, including coal –the most plentiful fossil fuel– over the coming decades. World wide and in the U.S., fossil fuels currently account for 85 percent of total energy consumed [1,2]. Our long-range energy plans need to include fossil fuels and we have no choice but to resolve all of the environmental issues, including impacts on global climate change, associated with their use.

Vision 21 stresses innovation and revolutionary technologies in order to create the technology basis for 21st century energy plants with unprecedented levels of efficiency and environmental performance. Evolutionary improvements to existing technologies will be inadequate if Vision 21 is to be successful. A suite of technology subsystems, or "modules," is being developed that will become the building blocks of Vision 21 plants (Figure 1). These modules will be interconnected in the configurations needed to utilize fossil fuels and "opportunity" feedstocks and produce market-driven products. The feedstocks, products, plant configurations and sizes, and environmental controls will be site specific and determined by prevailing market conditions. At this time, DOE believes it is important to avoid a prescriptive approach that favors certain feedstocks, products, technologies, or specific configurations of modules in order to avoid the real risk of mistakenly emphasizing technologies that ultimately will not be used. Further, it is important to emphasize that the Vision 21 plant is not an "energyplex." Vision 21 plants are likely to produce electricity only although additional products, such as clean transportation fuels, could be made when such production is supported by favorable economics. A Vision 21 plant might produce power during the day and fuels at night, for example. The size, complexity, and cost of energy plants that produce a multiplicity of products is likely to be prohibitive, especially in the U.S. and other developed nations.

Vision 21 is an industry-driven program. Industry involvement, beginning at the planning stages, was actively sought in order to build the commitment needed for a long-range program and to help ensure market relevance of new technologies that are pursued. The collaborative efforts of industry, academia, and government in the planning process have resulted in the Vision 21 Technology Roadmap. The Roadmap, which is available at www.netl.doe.gov/coalpower/vision21/v21rdmp.pdf, identifies ten key technology areas and two methodologies that are believed to be critical for the Vision 21 energy plant and outlines 15-year R&D strategies that include objectives, barriers to achieving objectives, and strategies for overcoming barriers. These key technologies and methodologies are:

Technologies:

- Combustion & high-temperature heat exchange
- Gasification
- Gas purification
- Gas separation
- Turbines
- Fuel cells
- Syngas conversion to fuels & chemicals
- Environmental control technology
- Sensors and controls
- Materials

Methodologies:

- Computational modeling and virtual simulation
- Systems analysis and integration

Materials technology may be the most critical of the key Vision 21 technologies because materials technology is enabling, to a greater or lesser extent, for each of the other key Vision 21 technologies.

Vision 21 Energy Plant

Figure 2 shows the performance targets, including costs and timing, for Vision 21 energy plants. Targets are clearly very aggressive, especially since the Technology Roadmap calls for designs of commercial-scale plants to be available in only 15 years. Certain benefits from Vision 21, called "spinoffs," should begin to be realized sooner, before 2005. Spinoffs include low-cost gas separation technology (e.g., H_2 from syngas and O_2 from air), better gas purification/cleaning processes, improved catalysts for producing clean fuels and chemicals from low-valued raw materials, more efficient and lower cost environmental control technology, high-temperature heat exchangers, and improved materials for service under high-temperature conditions. The spinoffs are expected to have applications beyond the electric power and energy industries.

Figure 3 shows an artist's rendition of a possible configuration of a Vision 21 energy plant. Again, it must be stressed that Figure 3 is illustrative only; there is no intent to imply that multiple products are likely to be made at a given plant. The gasifier produces a fuel (synthesis) gas that is cleaned and used to produce power from gas turbines and fuel cells as well as clean transportation fuels and chemicals. The plant features modular design and makes a market-driven product slate. Coal and "opportunity" feedstocks are gasified using oxygen produced with a low-cost air separation membrane. The fuel gas is cleaned and a second membrane is used to separate hydrogen. Carbon monoxide in the fuel gas may be shifted to CO_2, which can be sequestered if necessary. Electricity is generated with a fuel cell using the hydrogen and a gas turbine using the energy in the fuel cell exhaust. Heat remaining in the gas turbine exhaust is used to generate steam for process heating. A portion of the fuel gas is diverted for the production of clean liquid fuels and high-value chemicals.

It needs to be noted that, while Vision 21 is concerned with all fossil fuels, coal receives a substantial share of attention because of the formidable environmental challenges associated with coal use. The U.S. has the largest coal reserves of any country, about a 250-year supply at current use rates, and coal-fired power plants generate approximately 55 percent of the U.S. electricity [3]. Major increases in coal use are expected in developing countries, particularly India and China.

Vision 21 Materials Development

To achieve the performance targets of the Vision 21 energy plant will require advanced materials with capabilities beyond those now available. Vision 21 materials can be grouped into four categories:

- new alloys
- ultra-high performance materials
- coatings
- functional materials

New alloys are being developed for use as structural materials that will need to withstand severe environmental conditions, including high temperatures, corrosive and/or erosive atmospheres, and elevated pressures. Structural materials comprise iron- and nickel-based alloys, intermetallic compounds, oxide-dispersion-strengthened alloys, and single crystal alloys. Example applications include gas turbine airfoils and combustor components and high-temperature heat exchange components such as high-pressure tubing for steam superheaters, reheaters, and air heaters.

Ultra-high performance materials are alloys and ceramics being developed for applications such as high-efficiency turbine components, and thermowells for slagging coal combustion and gasification systems, at temperatures in the 1000-1700°C (1800-3100°F) range.

Coatings are used to provide corrosion protection to underlying structural components and may be either metallic or ceramic materials. Research to demonstrate and confirm the efficacy of conventional gas turbines in a coal-derived synthesis gas system is being addressed. Hot-gas environments that result from syngas combustion differ from those resulting from natural gas combustion and there is a dearth of long-term performance data for syngas environments. Priorities include the selection and verification testing of turbine hot-path component materials and protective coatings.

Important functional materials can be either alloys or ceramic materials for applications such as gas filters to remove particulate to levels required for gas turbines or other sensitive downstream equipment, catalysts for fuel synthesis or other reactions, fuel cell electrodes, and gas separation membranes.

Materials research supporting Vision 21 is largely conducted in the DOE Fossil Energy Advanced Research Materials Program. The Program is funded at approximately $7 million annually, and includes activities at Oak Ridge National Laboratory (ORNL), at other National Laboratories including internal projects at NETL in the Office of Science and Technology (Pittsburgh, PA, and Morgantown, WV), as well as projects at universities and with industry.

The balance of this paper provides descriptions of current materials development support for Vision 21. More detailed information on specific projects can be found in the

references, many of which are from the Proceedings of the 15th Annual Conference on Fossil Energy Materials, held in Knoxville, TN, from April 30-May 2, 2001. A copy of the Proceedings is available on the ORNL Internet site at www.ornl.gov/fossil.

New Alloys

The theme of this work is to determine how composition and microstructure affect alloy properties, and to apply this knowledge to the development of new alloys that have both improved environmental resistance and high-temperature strength. Applications of particular interest include ultra-supercritical steam cycle superheaters and reheaters that operate at steam temperatures to 760°C (1400°F) or higher and pressures to 35 MPa (5000 psi). Boosting steam temperature and pressure is key to increasing the efficiency of Rankine cycle steam-electric plants in the absence of a low-temperature heat sink (such as the Baltic Sea).

Austenitic and Ferritic Alloys for Supercritical Coal Plants

To qualify advanced steels for use with ultra-supercritical steam plants and to seek routes for higher-temperature alloy capabilities, DOE, through NETL, is providing $10.5 million over the next five years to a consortium of four major boiler manufacturers (Alstom, McDermott Technologies with its affiliate Babcock & Wilcox, Foster Wheeler, and Babcock Borsig), EPRI, the Ohio Coal Development Office, and ORNL [4]. The consortium will provide an additional $4.8 million. NETL will manage the effort, act as a liaison between the consortium and the utility industry, and advise the consortium on environmental and systems issues. The project goals are to measure alloy property and performance data where needed to supplement those generated by on-going programs elsewhere, and to examine the barriers to increasing the temperature capabilities of these alloys. The immediate goal is the identification of alloys for boiler tubes capable of operation with steam at temperatures and pressures up to 760°C (1400°F) and 35 MPa (5000 psi). The current state-of-the-art is limited to about 600°C (1100°F) and 30 MPa (4300 psi).

This new DOE effort will build on alloy development work in progress. For example, a European consortium partially funded by the European Union under the "Thermie" program is developing steam generator technology for steam temperatures up to 700°C (1300°F). The DOE approach will be to identify and qualify ferritic steels that have the maximum temperature capability for this class of materials, and nickel-base superalloys for higher-temperature components. A large part of the program effort will involve the measurement of mechanical property data required by the various structure-property-performance and life prediction models that will be used to qualify the alloys. Other efforts will address fabrication and welding issues, as well as the mode and rate of degradation in both the fireside and steam-side environments to define the alloy temperature limits imposed by corrosion considerations. In addition, the barriers to increasing the temperature capabilities of these alloys will be examined, and the issues involved in developing materials for service at temperatures as high as 870°C (1600°F) will be identified. The overall result of this program is intended to provide the means for U.S. boiler manufacturers to build more efficient coal-fired power plants using advanced steam cycles.

In a separate project, structural alloys are being evaluated for high-temperature components of advanced coal combustion systems used with combined-cycles and other Vision 21 applications. ORNL and Special Metals Corporation (Huntington, WV) have jointly developed a modified type 803 alloy with dramatically improved tensile strength, creep strength and rupture resistance at 820°C (1500°F) relative to the standard, unmodified base alloy [5]. The improvements were accomplished through microstructural design and control and minor alloying element changes. Resistance to oxidation, carburization, and sulfidation of the modified Fe-25Cr-35Ni alloy is not diminished.

Oxide-Dispersion-Strengthened Alloys and Iron Aluminide Intermetallics

Oxide-dispersion-strengthened (ODS) alloys are produced by mechanical alloying of a fine dispersion of an inert oxide into the base alloy. They are a promising class of alloys primarily because of their outstanding high-temperature creep strength compared with conventional alloys. Prototype ODS alloys have already demonstrated the ability to operate at metal temperatures of 1100°C (2000°F) in heat exchanger applications: ODM751 in an earlier COST program [5a], and MA754 in the U.S. HiPPS program [5b].

ORNL is addressing the materials-related barriers to expediting the use of ODS alloys in components that will be required for Vision 21 plants [6]. Specific objectives are to develop detailed knowledge of ODS alloy behavior useful to component designers and plant operators, including fabrication and joining, service performance, and modes of failure. The scope of the effort includes development of ODS iron-aluminum alloys with superior resistance to high-temperature sulfidation and carburization attack compared to the best FeCrAl alloys, while attaining strength levels comparable to commercially available ODS FeCrAl alloys, such as Inconel MA956. First steps have been taken towards developing an analytical description of observed high-temperature oxidation behavior. The goal is to quantify and model the oxidation behavior of ferritic ODS alloys to provide a means of accurately predicting service life, which likely will be governed more by consumption of Al as a result of the formation of protective oxide scale than by strictly mechanical considerations. In a companion project, the University of California at San Diego is exploring routes for modifying ODS alloy microstructure to tailor the mechanical properties for specific applications [7]. Lengths of tubing have been made from ODS-Fe_3Al alloy via a proprietary single step extrusion consolidation process and the process parameters, i.e., extrusion ratios, temperature, can design, etc., prescribed. Inherent material- and processing-induced anisotropies in ODS-Fe_3Al-base alloys will be exploited to improve mechanical properties.

Tubing made from ODS alloy retains its strength at very high temperatures but its application is limited by poor weldability and relatively poor circumferential creep strength compared to longitudinal strength. Special Metals Corporation and its partners are modifying the alloy grain structure to increase circumferential strength so that ODS alloy tubes may be used reliably at high pressures and temperatures to 1100°C (2000°F) [8]. Improved joining methods are also being developed and high-temperature corrosion limits are being established.

The Special Metals project is focusing on MA956, which has the nominal composition (in weight percent) of Fe, 20Cr, 4.5Al, 0.5Ti, 0.05C, $0.5Y_2O_3$. Various thermal-mechanical processing parameters, including extrusion ratio and temperature, amount of cold work, and recrystallization temperature and time, are being manipulated to produce an alloy tube with the desired microstructure and strength properties. The joining methods being investigated include friction welding, explosive bonding, magnetic impulse welding, and transient liquid-phase bonding. Tubing specimens will be corrosion tested both by exposure to flue gas and simulated ash deposits in laboratory furnaces, and to conditions in a coal-fired boiler at temperatures up to 1200°C (2200°F) for 10,000 hours.

In other ODS alloy-related activities, TWI (Cambridge, England) has been involved in investigation of friction welding as a method for joining ODS iron aluminide tubes to other iron aluminide tubes and to austenitic alloys [9]. The University of Liverpool (Liverpool, England) is conducting experiments to determine the sources of processing defects in ODS alloys and their effects on recrystallization behavior, as well as to recommend methods for reducing them [10].

Alloys based on the cast and wrought version of the iron aluminide intermetallic, Fe_3Al, are low in basic materials cost, are lighter than stainless steels and, most importantly, have excellent high-temperature oxidation and sulfidation resistance owing to the formation of an external, protective alumina scale. Their use, however, has been limited by relatively poor low-temperature ductility and poor strength and creep resistance above 600°C (1112°F).

Idaho National Engineering and Environmental Laboratory (Idaho Falls, ID) has been involved in determining the influence of processing on the high-temperature mechanical properties and environmental resistance of Fe_3Al [11]. ODS-Fe_3Al alloys were fabricated by reaction synthesis and the response of the microstructure to deformation at elevated temperature and subsequent annealing was characterized. Creep properties were studied in detail and compared to current theories for creep strengthening by oxide dispersions.

West Virginia University (Morgantown, WV) is evaluating the intrinsic and extrinsic fracture behavior of iron aluminides in terms of defect concentrations, dislocation mobility, and solute effects [12]. Work also involves an experimental study of environmentally assisted crack growth of Fe_3Al at room and elevated temperatures. The combined modeling and experimental activities are expected to elucidate the mechanisms controlling deformation and fracture of Fe_3Al in various environments.

The Colorado School of Mines (Golden, CO) is determining the role of microstructure in the intergranular cracking of aluminides, with special emphasis on cracking susceptibility [13]. The weldability of Fe_3Al-X alloys is being evaluated and correlated with composition, phase equilibria, grain size and morphology, domain size, and degree of long-range order.

Ultra-High Performance Materials

Ultra-high performance materials such as Cr-based alloys, Mo-Si intermetallics, and ceramic composites, are being developed for applications at temperatures above those possible with conventional materials: 1000-1700°C (1800-3100 °F). Current findings suggest that some intermetallics with very high melting points might be used as alternatives to ceramics in high-temperature applications.

Alloys and Intermetallics

Work on ultra-high performance intermetallics is focusing on Cr- and Mo-based alloys that show a promising combination of mechanical properties and environmental resistance at very high temperatures. ORNL and Tennessee Technological University (Cookeville, TN) are developing high-strength, oxidation- and corrosion-resistant Cr_2Ta-reinforced Cr alloys for use in Vision 21 energy plant components, including process monitoring equipment (e.g., thermowells), structural components, and protective coatings [14]. These alloys are particularly suited for applications involving aggressive, high-temperature slag environments, such as those encountered in gasification systems. Successful development is expected to improve thermal efficiency through increased operating temperatures, decreased cooling requirements, and improved process control. The key challenge is to overcome inadequate room-temperature toughness, with the best Cr-Cr_2Ta alloys exhibiting only modest toughness. Although MgO dispersions have been claimed to improve the room-temperature mechanical properties of unalloyed Cr, efforts to introduce the effect in Cr-Cr_2Ta-MgO alloys were not successful. Significant modification of the Cr matrix phase in the Cr-Cr_2Ta by microalloying may be necessary to improve room-temperature properties. Interestingly, preliminary attempts at microalloying with Fe resulted in an increase in room-temperature toughness of about 50 percent.

Silicide intermetallics can have outstanding oxidation resistance due to the formation of a protective silica scale. $MoSi_2$, for example, is widely used in heating elements for high-temperature furnaces but it has very low fracture toughness at room temperature. Reducing Si concentration below that of $MoSi_2$ likely increases fracture toughness but decreases oxidation resistance. Optimization of Mo-Si-B alloys, which have excellent oxidation resistance, is thus a tradeoff between fracture toughness and oxidation resistance. Creep resistance is also an issue since it is also affected by composition changes.

ORNL, Ames National Laboratory, and Iowa State University (Ames, Iowa) are developing ultra-high temperature, corrosion-resistant components based on the Mo-Si system [15,16]. For non load-bearing applications such as coatings, burner and heat exchanger components, and certain gas turbine components, these materials may be ideally suited. It has been shown that high-temperature Mo-Si-B-based components, especially those containing high volume fractions of molybdenum silicides and borosilicides, offer the potential for operating at temperatures to at least 1600°C (2900°F) in air. Current work is investigating the ability of these materials to resist aggressive combustion environments. Results indicate that the oxidation rate at 1000-1100°C (1800-2000°F) is accelerated by the presence of water vapor due to the formation of volatile

silicon oxy-hydroxide species. ORNL is determining fracture toughness, creep properties, and oxidation resistance of different compositions of Mo-Si-B alloys.

Ceramics and Refractories

Ceramics, ceramic composites, and refractories have numerous Vision 21 applications including liners for gasification and combustion systems, high-temperature heat exchangers, and turbine components. For example, indirectly fired coal combustion systems use heat exchangers to transfer heat from hot combustion gases to the clean air that drives the turbines. For high efficiencies, the air temperature at the turbine inlet needs to exceed approximately 1100°C (2010°F), and preferably about 1450°C (2650°F). These heat exchangers will operate under pressure and experience thermal and mechanical stresses during startup, shut-down, and transients. For directly fired turbines, Vision 21 performance targets are a rotor inlet temperature of 1600°C (2900°F) with component lifetimes of 50,000 hours. Turbine combustor liners and transitions may need to operate with gas temperatures as high as 1700°C (3100°F). Silicon carbide-matrix composites appear promising for these applications because of their high strength at elevated temperature, low weight, thermal and mechanical shock resistance, damage tolerance, and oxidation and creep resistance.

Activities are focusing on scaling up chemical vapor infiltration of tubular and other practical shapes of fiber-reinforced silicon carbide. Research emphasizes understanding the nature of the fiber matrix interface with the aim of developing interfaces that have the desired mechanical properties and yet are resistant to oxidation.

Argonne National Laboratory is developing non-destructive evaluation (NDE) acoustic and radiographic techniques that can be used to characterize structural ceramics and detect flaws in the early stages of processing as well as in the final densified state [17,18]. The NDE techniques include three-dimensional computed tomography, thermal imaging, and air-coupled ultrasound.

Improved refractory materials for coal gasifier linings are needed because severe slag attack on current linings has resulted in unacceptably short lifetimes for both refractory liner and thermocouple assemblies. To address this problem, Albany Research Center (Albany, Oregon) is developing improved materials and fabrication techniques with the aim of extending the lifetime of refractory linings in slagging gasifier systems to at least three years [19]. The short service lives of these linings is a result of severe operating conditions, including temperatures to 1650°C (3000°F), thermal cycling, alternating reducing and oxidizing conditions, and the presence of corrosive gases and slags. Simulated gasifier conditions are being used to characterize refractory-slag interactions as a first step towards improving refractory linings.

Silicon carbide whiskers and short fibers, called fibrils, have been shown to provide excellent toughening of ceramics, such as alumina, and whiskers are presently used in high-speed cutting lathe tools. A significant manufacturing problem is that whiskers are respirable and present potential health hazards; however, fibrils are sufficiently long (up to 2-3 cm) that they are non-respirable and so represent a significant breakthrough for this

class of materials. Single crystal silicon carbide fibrils have exhibited good oxidation resistance to 1600°C (2900°F). A manufacturing process with the potential for low-cost and high-volume fibril production is needed. ReMaxCo Technologies (Oak Ridge, TN) is developing innovative approaches for producing silicon carbide fibrils with the potential for low-cost and high-volume fibril production [20]. Slow growth of the fibrils and excessive waste of raw materials have been the major impediments.

Coatings and Corrosion Protection

Coatings and protective barriers can be useful for protecting metallic and ceramic materials that offer the requisite mechanical properties for application in advanced coal combustion and gasification systems but have insufficient resistance to degradation in aggressive environments. Several materials, such as iron aluminide alloys and mullite ceramics, have been found to have remarkable resistance to erosion and corrosion in coal combustion and gasification environments. Research was implemented to take advantage of these properties by applying coatings to conventional and developmental substrate materials.

Coatings

ORNL is working to establish coating compositions and microstructures necessary for long-term, high-temperature corrosion protection in harsh environments [21]. The overall objective is to determine the relationship of composition, microstructure, and application method to coating performance and service lifetime. Yttria-stabilized zirconia (YSZ) is widely used in thermal barrier coatings (TBCs), e.g., for gas turbine engine blades, because of its low thermal conductivity, high thermal stability, and relatively high coefficient of thermal expansion. One of the current technologies for deposition of YSZ on high-performance turbine blades utilizes electron-beam physical vapor deposition, which produces a characteristic columnar coating structure, resulting in excellent strain tolerance during thermal cycling. However, there are issues with respect to cost, long-term stability, and environmental degradation of these coatings. In the ARM program, a chemical vapor deposition (CVD) process to produce YSZ coatings that utilizes organo-metallic precursors flowing over a heated substrate is being explored as an alternative for the current process.

Tennessee Technological University is investigating iron-aluminum coatings using CVD to provide good control over the processing parameters and the coating composition, structure, and thickness. Evaluation of the coatings addresses issues concerning coating performance and service life, including the influence of duty cycle length and operating temperature on the oxidation behavior of coatings relevant to conditions experienced in fossil-fueled processes [22]. Coatings have been applied to examples of different classes of steels, including an austenitic stainless steel (304L) and a ferritic steel (Fe-9Cr-1Mo). The initial coatings were uniform in composition, purity, and microstructure. In cycling tests at 800°C (1500°F) in H_2S-H_2O-H_2-Ar, the coatings on both substrates exhibited protective behavior and uniform attack.

Water wall corrosion in coal-fired steam-generators (especially those operating with supercritical steam conditions) using low-NOx burners with separated over-fire air ports

has recently become a significant problem in the U.S. One remedy used in practice is to apply weld overlay coatings of a Ni-Cr-Mo-based alloy (Inconel 625). Lehigh University (Bethlehem, PA) is investigating the use of weld overlay coatings of iron aluminide alloys; such alloys with 10 percent or more Al are attractive candidates for this application because they have good corrosion resistance in sulfidizing environments and are expected to be significantly less expensive than Inconel 625 [23]. They are easily weldable with aluminum concentrations up to 10 weight percent, but higher Al contents are problematical. Lehigh is determining if acceptable corrosion resistance can be achieved at aluminum concentrations below 10 percent by adding alloying elements such as Cr and Ti. Initial results show that Cr addition can be beneficial in mixed oxidizing-sulfidizing environments but that Al concentrations of 10 percent are needed to form a continuous protective scale.

The University of Pittsburgh (Pittsburgh, PA) is beginning work to improve the durability of turbine blades and to allow the use of fuels with impurities, including sulfur, alkali metals, and vanadium [24]. A dense overlay of Al_2O_3 will be deposited on a YSZ thermal barrier coating using physical vapor deposition and sol-gel methods. YSZ coatings have limited durability for advanced gas turbine applications when dirty fuels are burned. The hot corrosion resistance of the Al_2O_3-protected system will be compared with that of the YSZ-only system.

Argonne National Laboratory (Argonne, IL) (ANL) is evaluating mechanisms of oxidation, sulfidation, and ash attack on structural alloys and coatings exposed to combustion and gasification environments [25]. Corrosion behavior for low-alloy steels, 310 stainless steel, alloy 800, and coatings that include chromizing, aluminizing, and iron aluminide is being studied in laboratory corrosion experiments. Information is being developed on corrosion rates, on microstructural characteristics of the corrosion products, on the mechanical integrity and cracking of scales, and on the role of sulfur and deposits. Additional work is concerned with evaluating and better understanding the protection offered by oxide scales, examining the reliability of corrosion-resistant ceramics being developed as protective overcoats and/or structural materials, and identifying and evaluating compositions and synthesis routes for producing materials with damage-tolerant scales and coatings.

ANL is also developing NDE methods for high-temperature coatings, including elastic optical methods based on detection of polarized back-scattered laser light and thermal imaging based on a time-temperature surface response from a flash thermal pulse [26]. For TBC systems, for instance, it is important to know if and when a coating is nearing a condition where spallation is likely, if its thickness has been reduced to minimum levels, or if the coating properties have changed. In both approaches, information is needed about the optical transmission characteristics of the coatings, and these characteristics have been determined for air-plasma-sprayed and electron beam-physical vapor deposition TBC systems. NDE results have shown that with proper specific spectral frequency exitation, both the elastic optical scatter and thermal imaging methods can be used to detect regions of non-uniform coating and regions that can potentially spall.

NETL (Pittsburgh, PA) and the University of North Dakota Energy & Environmental Research Center (EERC) have developed pilot-scale systems capable of creating conditions of corrosion and erosion similar to those occurring in large-scale power systems [27]. NETL operates the fossil fuel-fired Combustion and Environmental Research Facility (CERF), a 150 kW (thermal) test facility that can fire gaseous, liquid, or solid fuels, including coal. The CERF has been used to expose ceramic and alloy samples at pressures from ambient to 1.4 MPa (200 psig) for tubes and temperatures from 800-1430°C (1500-2600°F) with exposure times exceeding 1000 hours. In addition, EERC has two pilot-scale solid-fuel systems available for exposure of materials coupons. ORNL provides analytical support by analyzing fuels, deposits, and corrosion products.

Functional Materials

Functional materials include gas filters, gas separation membranes, and solid-state electrolyte materials for fuel cells. Activities related to functional materials include development of advanced fabrication processes.

Vision 21 has stringent gas cleaning requirements that are needed to protect sensitive components downstream of combustion or gasification systems from harmful substances originating in the plant feedstock. In may cases, gas purity requirements for turbines, fuel cells, and fuels/chemicals synthesis reactors exceed environmental emissions requirements. Table 1 shows example gas purity requirements for these applications.

Highly efficient, reliable gas filtration systems are needed for advanced coal-based power generation systems such as pressurized fluidized bed combustion (PFBC) and integrated gasification combined cycle (IGCC). Removing particulate sizes down to about one micron is critical to minimizing corrosion, erosion, and deposition of downstream turbine components. Early work on filters for removal of particulate matter from gas streams focussed on cleaning the combustion gases from a PFBC prior to expansion in a turbine. Filter elements were silicon carbide "candle" filters and operating temperatures were about 815°C (1500°F). Subsequent test work at the U.S. Department of Energy's Power Systems Development Facility showed that for combustion applications the maximum operating temperature to avoid filtration difficulties was 760°C (1400°F) [28]. In IGCC, filtration temperatures can probably be reduced without substantial losses in thermal efficiency. In commercial gasification systems, the filter operating temperature will likely be below 540°C (1000°F), where metallic filters may be preferred over ceramic elements. Engineering and economic evaluations seem to show that warm gas filters (<540°C operating temperature) are more reliable than hot gas filters (~815°C/1500°F operating temperature), and that the efficiency penalty at the lower temperatures is minor.

Vision 21 will require lower cost, more efficient gas separation systems to produce oxygen for combustors and gasifiers; hydrogen for fuel cells, turbines, and process applications; and carbon dioxide for sequestration. In an IGCC plant, for example, the air separation system can account for 15-20 percent of the capital cost of the plant and consume 15-20 percent of the power output. Improvements in air separation technology can have a substantial impact on IGCC economics. For combustion-based applications, the availability of low-cost oxygen will also enable the use of oxygen-enriched

combustion in "sequestration-ready" systems that produce a concentrated stream of CO_2. The goal is to produce oxygen at, perhaps, one-half the cost of current cryogenic technology. Low-cost technology for separating hydrogen from synthesis gas would create significant opportunities in fuel cell power and chemicals synthesis and in other areas. Ion-electron conducting membranes and other new materials are being explored for oxygen and hydrogen separation. One novel approach for CO_2 separation is the use of CO_2 hydrates. This technology offers a low-temperature means to produce CO_2 and high-purity hydrogen from a "shifted" synthesis gas produced by the gasification of carbon-based feedstocks. Another new approach is based on carbon fiber molecular sieves.

Achieving the efficiency target for Vision 21 energy plants will likely require the use of fuel cells. High-temperature fuel cells, e.g., solid oxide (SOFC) and molten carbonate (MCFC), are leading candidates for Vision 21 applications because of their high efficiencies and because their high operating temperatures (900-1000°C/1650-1830°F for SOFCs and 650-700°C/1200-1300°F for MCFCs) allow ready integration with gasification-based Vision 21 plants. DOE program objectives are to develop fuel cell stack modules with 80,000 hour minimum operating lives and capital costs of $100-200/kW. New technologies will be needed to achieve these targets.

Conventional SOFCs are operated at high temperature in order to attain reasonable power density. Materials problems associated with high-temperature operation include electrode sintering, interfacial diffusion between electrolyte and electrode, and mechanical stresses due to different thermal expansion coefficients. These problems have limited the commercial development of SOFCs. Because it would be desirable to operate a SOFC at reduced temperatures (600-850°C/1110-1560°F) while still maintaining the power densities achieved at high temperatures, much attention is being given to research and development to reduce the operating temperatures. However, as temperature is lowered, resistive losses across the solid electrolyte increase and over-potentials at the air and fuel electrode are similarly magnified. Still, lower temperature operation allows a wider choice of interconnect materials, including metal alloys, as well as decreasing electrode sintering and minimizing electrolyte-electrode interfacial diffusion.

Scale-up of fuel cells to sizes larger than 30 MW will be a major challenge. Fuel Cell Energy (Danbury, CT) and Siemens-Westinghouse Power Corporation (Pittsburgh, PA) are developing molten carbonate and solid oxide fuel cells, respectively. Activities range from component development through the eventual construction and demonstration of full-scale megawatt-capacity fuel cell power plants. It is hoped that this work will lead to the development of fuel cells that can compete in the market for use in Vision 21 plants.

Filters

Ames National Laboratory is developing sintered metallic filters and evaluating the corrosion resistance of filter materials in combustion and gasification atmospheres in order to determine the optimum alloy composition and filter structure [29]. The binder-assisted powder processing and sintering techniques being developed will permit additional filter design capability, e.g., highly controlled filter porosity and permeability

with greatly simplified processing, thus enabling more efficient and effective filtration. Filter alloys have been based on Ni-Cr-Al-Fe powder mixtures that have been sintered and exposed as solid coupons to simulated combustion atmospheres at temperatures to 850°C (1560°F).

Solid State Electrolyte Systems

Improving the performance and reducing the cost of SOFCs is an important Vision 21 objective. Activities include development of alternative solid electrolyte, electrode, and interconnect compositions, and effective seals and fuel-conditioning devices necessary for SOFC applications. ORNL is developing infrared plasma processing as a method to rapidly sinter YSZ electrolytes on porous supports composed of lanthanum manganite or YSZ/NiO composites [30]. The goal is to reduce cycle times and costs for fuel cell fabrication. Also, models will be formulated for stresses that develop within the electrode/electrolyte layer as a direct result of sintering. Pacific Northwest National Laboratory has investigated SOFCs that use cathodes made from substituted lanthanum ferrite and ferrite/cerate composites intended for operation at 600-850°C (1110-1560 °F) [31]. Losses at the cathode/electrolyte interface are among the principal barriers to SOFC operation in this temperature range. For a given ferrite composition, the best performance was obtained for composite electrodes, which provided mixed electronic and ionic conductivity, while the poorest performance was obtained for electrodes with no ceria barrier layer. Ceria composite electrodes were less susceptible to cracking during thermal cycling than similar structures with a ceria barrier layer.

Gas separation membranes

Projects are underway to develop more efficient, lower cost technology for separating oxygen from air and hydrogen from syngas. Siemens-Westinghouse Power Corporation and Praxair, Inc. (Tonawanda, NY) are developing zero-emissions power plants that integrate SOFCs with oxygen transport membranes (OTMs) [32]. The exhaust products of the SOFC will consist of only steam and CO_2 that can be easily recovered for sequestration. OTM technology provides a more efficient method of supplying the oxygen necessary to oxidize the fuel remaining in the SOFC exhaust than conventional air separation technology. In addition, the comparable operating temperatures of SOFCs and OTMs allow for efficient and cost-effective integration.

Several types of membrane systems for separating hydrogen are being developed. Los Alamos National Laboratory (Los Alamos, NM) is investigating the use of palladium [33]. Pd alloys are attractive materials for use as membranes because of their high permeability and relative robustness; however, the high cost of Pd makes its use on thin metal films (<20 microns) supported by hydrogen porous substrates imperative. Because Pd is also catalytic for reactions such as methane-steam reforming and water-gas shifting, both of which produce hydrogen, reactors have been designed in which hydrogen removal through the membrane allows the reactions to proceed completely to products. Recent advances have been made in achieving thinner membranes; a composite membrane with Pd thickness as low as 0.5 micron has been developed. However, if Pd membranes are to become viable technology for energy applications, sulfur tolerance

must be improved, hydrogen fluxes must be increased, and membrane lifetimes and costs must be improved.

Hybrid organic-inorganic materials are being developed at Sandia National Laboratories (Albuquerque, NM) [34]. Polysilsesquioxanes have good thermal and chemical stability and can be easily processed into defect-free films. They can be prepared from the hydrolysis and condensation of monomers with bridging organic groups and coated onto the mesoporous surface of alumina ceramic supports. Such membranes have been shown to have good selectivity for helium over methane and carbon dioxide.

Ceramic ion-conducting membranes, being non-porous, produce pure hydrogen. Protons and electrons, catalytically produced from molecular hydrogen at the membrane surface, are conducted through the membrane where they are recombined to hydrogen at the other surface. The driving force is the differential hydrogen partial pressure. Conduction occurs between 600 and 800°C (1100-1500°F). The main development issues are achieving satisfactory transport rates, membrane stability in aggressive environments, and designing effective seals and manufacturing procedures. Eltron Research (Boulder, CO) and its partners are optimizing membranes comprising proton-electron conducting metal oxides and cermets (metal oxide/metal composites) [35]. Hydrogen fluxes of 0.1-1.0 cm^3/cm^2-min have been achieved, which is probably about one order of magnitude below commercially viable fluxes. ITN Energy Systems (Littleton, CO) is developing composite membrane structures that will be fabricated into monolithic modules [36]. The membranes are fabricated from cermets in which the metal serves as the electron conductor and a doped cerate as the proton conductor.

The Inorganic Membrane Technology Laboratory at East Tennessee Industrial Park (Oak Ridge, TN) is developing methods of producing porous alumina membranes having ultra-micro pores (0.5-3 nanometers) that can separate gases based on molecular size [37]. Apparently defect-free membranes are being routinely fabricated and permeance measurements have been made for helium in heavier gases at pressures of 1-2 atmospheres and temperatures from 25 to 250°C (77-480°F). The successful development of defect-free membranes should lead to economic manufacturing processes for membranes that can separate hydrogen from other gases.

Emission of CO_2 from fossil fuel burning is, of course, a key issue in global climate change. Sequestration, or long-term storage of CO_2 in the ground or ocean, has been proposed as a management strategy. However, there are substantial energy and cost penalties associated with sequestration, particularly with capture and separation of CO_2 from the gases issuing from the energy plant. More efficient, lower cost methods are needed to separate CO_2.

A novel carbon adsorbent, called a "carbon fiber composite molecular sieve," has been developed by ORNL and the University of Kentucky [38]. Separation of CO_2 from air and mixed streams, such as reformed fuels, has been demonstrated. The material has a continuous carbon skeletal structure and is, therefore, electrically conductive. Desorption of an adsorbed gas, such as CO_2, can be accomplished by applying a low voltage across

the adsorbent. The system pressure and temperature do not have to be altered as in other processes such as pressure swing adsorption. The new desorption process has been named "electrical swing adsorption." The technology will be employed by ZeTek Power Company for CO_2 scrubbers used in alkaline fuel cell systems.

Conclusions

A wide range of improved structural and functional materials will be needed for Vision 21 energy plants. Materials will be called on to perform at higher operating temperatures in more corrosive and erosive environments and to perform specialized functions such as separating particulate from gas streams or a single component gas from gas mixtures. Critical applications for improved materials include:

- high-temperature heat exchangers for advanced steam systems and air heaters
- ultra-high temperature alloys, ceramics, and refractories for gasification and combustion applications
- hot-gas filters
- gas-separation membranes (e.g., for hydrogen, oxygen, carbon dioxide)
- turbine components including airfoils, shrouds, and combustor parts
- fuel cell components including electrodes and electrolytes

Developing acceptable materials for coal-based systems will be challenging since the performance requirements proposed are increasingly pushing the limits of capability of most available materials. The maintenance of a strong research and development program is essential. Classes of materials that currently show promise for structural applications include advanced iron- and nickel-based alloys, oxide-dispersion-strengthened alloys, intermetallics (including iron aluminides), and fiber-reinforced ceramic composites. Protective coatings and claddings will become an increasingly important part of the materials systems required for operation in high-temperature, corrosive, and erosive environments. Effective and durable materials will be essential for the operation of some of the proposed gas separation processes, and the focus currently is on ion-electron conducting ceramics and the carbon fiber composite molecular sieve. Research and development activities will continue to be a cooperative effort among the national laboratories in the U.S., universities, and industrial developers and users of advanced materials.

Acknowledgement

The author expresses his appreciation to Dr. Udaya S. Rao of NETL's Office of Project Management for his assistance in providing useful information about the Advanced Research Materials Program, and to Dr. Ian G. Wright of ORNL for his thoughtful suggestions.

References

Note: Proceedings of the Annual Fossil Energy Materials Conferences are available at www.ornl.gov/fossil/.

[1] Energy Information Administration, *"International Energy Outlook 2000,"* U.S. Department of Energy, Washington, DC 20585 (March 2000) pp. 10-11.

[2] Energy Information Administration, *"Annual Energy Outlook 2001,"* U.S. Department of Energy, Washington, DC 20585 (December 2000) pp. 3-4.

[3] Energy Information Administration, *"International Energy Outlook 2000,"* U.S. Department of Energy, Washington, DC 20585 (March 2000) p. 69.

[4] Viswanathan, R., and Bakker, W., "Materials for Ultrasupercritical Coal Power Plants," *Journal of Materials Engineering and Performance,* 10 (2001) pp. 81-95.

[5] Maziasz, P.J., Swindeman, R.W., Harper, M.A., Smith, G.D., "Development of Modified Alloy 803 with Improved Creep Resistance Above 800°C," *Proc. 15th Annual Conference on Fossil Energy Materials* (2001).

[5a] Starr, F., White, A.R., Kazimierzak, B., in *Materials for Advanced Power Engineering 1994*, D. Coutsouradis, et al., Eds., (Kluwer Academic Publishers) pp. 1393-1412 (1994).

[5b] Seery, D.J., Sangiovanni, J., "Engineering Development of a Coal-Fired High-Performance Power Generating System," Paper no. 1.7 in *Proc. Advanced Coal-Based Power and Environmental Systems '98 Conference*, Morgantown, West Virginia, July 21-23, 1998, DOE/FETC-98/1072 (1998).

[6] Wright, I.G., McKamey, C.G., Pint, B.A., "Oxide-Dispersion-Strengthened Alloy Development," *Proc. 15th Annual Conference on Fossil Energy Materials* (2001).

[7] Kad, B.K., McKamey, C.G., Sikka, V.K., Wright, I.G., "High-Temperature Performance of ODS Fe_3Al-Based Alloy Tubes," *Proc. 15th Annual Conference on Fossil Energy Materials* (2001).

[8] Harper, M.A., "Oxide-Dispersion-Strengthened Heat Exchanger Tubing," *Proc. Vision 21 Program Review*, U.S. DOE, National Energy Technology Laboratory, Morgantown, WV, November 6-7, 2001.

[9] See National Energy Technology Laboratory Project Fact Sheet at: www.netl.doe.gov/coalpower/advancedresearch/material_pages/Project_Files/TWI2.pdf

[10] Ritherdon, J., Jones, A.R., "Defect Reduction in ODS Fe_3Al," *Proc. 15th Annual Conference on Fossil Energy Materials* (2001).

[11] See National Energy Technology Laboratory Project Fact Sheet at: www.netl.doe.gov/coalpower/advancedresearch/material_pages/Project_Files/INEEL2.pdf

[12] See National Energy Technology Laboratory Project Fact Sheet at: www.netl.doe.gov/coalpower/advancedresearch/material_pages/Project_Files/WVU2.pdf

[13] See National Energy Technology Laboratory Project Fact Sheet at: www.netl.doe.gov/coalpower/advancedresearch/material_pages/Project_Files/CSM2.pdf

[14] Brady, M.P., Zhu, J.H., Liu, C.T., Tortorelli, P.F., and Walker, L.R., "Oxidation Resistance and Mechanical Properties of Laves Phase Reinforced Cr In-situ Composites," *Intermetallics,* 8 (2000) pp. 1111-1118.

[15] Schneibel, J.H., and Easton, D.S., "Oxidation Resistance, Fracture Toughness, and Creep Strength of Mo-Si-B Alloys Containing alpha-Mo," *Proc. 15th Annual Conference on Fossil Energy Materials* (2001).

[16] Kramer, M.J., Degirmen,O., Thom, A.J., and Akinc, M., "Novel Processing of Mo-Si-B Intermetallics for Improved Efficiency Power Systems," *Proc. 15th Annual Conference on Fossil Energy Materials* (2001).

[17] Stinson, M.C., Lee, W.O., Stockenrider, J.S., and Ellingson, W.A , "Recognition of Subsurface Defects in Machined Ceramics by Application of Neural Networks to Laser Scatter Patterns," *NDT & E International,* 30 (1997) p. 334.

[18] Ellingson, W.A., Koehl, E.R., Budzynski, B., and Carroll, J. "Development of NDE Technology for Hot Gas Filters," *Proc. 14th Annual Conference on Fossil Energy Materials*, Knoxville, TN (2000).

[19] Dogan, C.P., Kwong, K-S., Bennett, J.P., and Chin, R.E., "Refractory Failure in IGCC Fossil Fuel Power Systems," *Proc. 15th Annual Conference on Fossil Energy Materials*, Knoxville, TN (2001).

[20] Nixdorf, R.D., and Kimrey, H., "Development of a Commercial Process for the Production of Silicon Carbide Fibrils," *Proc. 15th Annual Conference on Fossil Energy Materials*, Knoxville, TN (2001).

[21] Besmann, T.M., and McLaughlin, J.C., "Atmospheric Pressure CVD of YSZ Using Stagnation Flow for Thermal Barrier Coatings," *Proc. 15th Annual Conference on Fossil Energy Materials*, Knoxville, TN (2001).

[22] Pint, B.A., Tortorelli, P.F., Haynes, J.A., and Wright, I.G., "Evaluation of Iron-Aluminide CVD Coatings for High Temperature Corrosion Protection," *Proc. 15th Annual Conference on Fossil Energy Materials*, Knoxville, TN (2001).

[23] Regina, J.R., DuPont, J.N., and Marder, A.R., "Sulfidation Resistance of Fe-Al Based Alloys with Cr and Ti Additions," *Proc. 15th Annual Conference on Fossil Energy Materials*, Knoxville, TN (2001).

[24] See National Energy Technology Laboratory Project Fact Sheet at: www.netl.doe.gov/coalpower/advancedresearch/material_pages/Project_Files/PITT1.pdf

[25] Nateson, K., and Kraus, C., "Corrosion Performance of Structural Alloys and Coatings in the Presence of Deposits," *Proc. 15th Annual Conference on Fossil Energy Materials*, Knoxville, TN (2001).

[26] Ellingson, W.A., et al., ibid.

[27] Hurley, J.P., Crocker, C.R., Mathur, M.P., Freeman, M.C. and Cole, N.C. "Corrosion Testing of Advanced Materials in Pilot-Scale Coal-Fired Power Systems," *Proc. 14th Annual Conference on Fossil Energy Materials*, Knoxville, TN (2000).

[28] Longanbach, J.R., and Pinkston, T.E., "Development and Demonstration of Advanced Power Generation System at the Power Systems Development Facility," *Proc. Int'l. Coal Utilization and Fuel Systems Conf.,* Clearwater, FL, March 6-9, 2000.

[29] Anderson, I.E., and Terpstra, R.L., "Progress in Development of High Temperature Metallic Filters for Advanced Fossil Energy Systems," *Proc. 15th Annual Conference on Fossil Energy Materials*, Knoxville, TN (2001).

[30] Armstrong, T.R., Armstrong, Vodraska, C., Forrest, M.E., Engleman, P.G., Harper, D.D., and Blue, C.A., "High Density Infrared Sintering Process," *Proc. 2000 Fuel Cell Seminar*, Courtesy Assoc., Portland, OR (2000) p. 566.

[31] Pederson, L.R., Chou, Y-S., Coffey, G.W., Hardy, J.S., Kerstetter, K.J., Rieke, P.C., and Thompson, E.C., "Solid Oxide Electrolyte Systems," *Proc. 15th Annual Conference on Fossil Energy Materials*, Knoxville, TN (2001).

[32] Bessette, N., "Zero Emission Power Plants," *Proc. Vision 21 Program Review*, U.S. DOE, National Energy Technology Laboratory, Morgantown, WV, November 6-7, 2001.

[33] Paglieri, S.N., and Birdsell, S.A., "Palladium Alloy Composite Membranes for Hydrogen Separations," *Proc. 15th Annual Conference on Fossil Energy Materials*, Knoxville, TN (2001).

[34] Loy, D.A., Cornelius, C.J., Lean, J.T., and Schneider, D.A., "Development of New Hybrid Organic-Inorganic and Inorganic Materials for Membranes at Sandia National Laboratories," *Proc. 15th Annual Conference on Fossil Energy Materials*, Knoxville, TN (2001).

[35] Roark, S.E., Mackay, R., and Sammells, A.F., "Hydrogen Separation Membranes for Vision 21 Fossil Fuel Plants," *Proc. Vision 21 Program Review*, U.S. DOE, National Energy Technology Laboratory, Morgantown, WV, November 6-7, 2001.

[36] See National Energy Technology Laboratory Project Fact Sheet at: www.netl.doe.gov/publications/factsheets/project/proj142.pdf.

[37] Fain, D.E., Marshall, B.B., Raj, T., Adcock, K.D., and Powell, L.E., "Ceramic Membranes for High Temperature Hydrogen Separation," *Proc. 15th Annual Conference on Fossil Energy Materials*, Knoxville, TN (2001).

[38] Burchell, T., Judkins, R., Gabbard, A., Omatete, O., and Rogers, M., "Development of Novel Activated Carbon Composites," *Proc. 15th Annual Conference on Fossil Energy Materials*, Knoxville, TN (2001).

Table 1. Gas Purity Requirements for Vision 21 Subsystems

	Turbines	Fuel Cells*	Fuels/Chemical Production
Sulfur	to meet environmental target (~5 ppm)	<0.1 [<0.5] ppm	<60 ppb
Alkali	0.1-0.5 ppm		
Halides (HCl)	0.6-3.0 ppm	<1 [<0.5] ppm	<10 ppb
NH_3		<5000 [<10,000] ppm	<10 ppb
V	0.05-0.2 ppb		
AsH_3		[<1 ppm]	
HCN			<10 ppb
Iron carbonyl			<10 ppb
Nickel carbonyl			<10 ppb
C_2H_2			<10 ppb
Particulate matter	<1.0 ppm (0 ppm>10 microns)		

* Figures without [ ] are for solid oxide fuel cells, figures with [ ] are for molten carbonate fuel cells

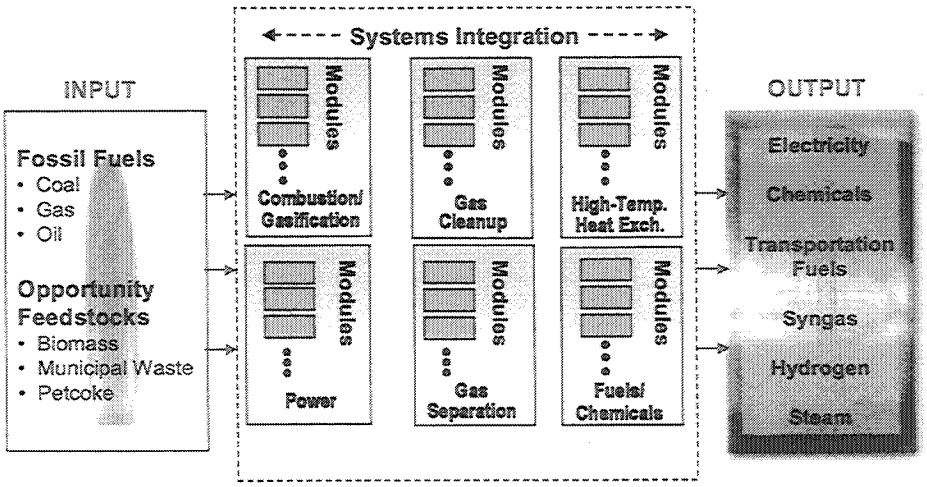


Figure 1. Technology Modules Form the Building Blocks of Vision 21 Energy Plants

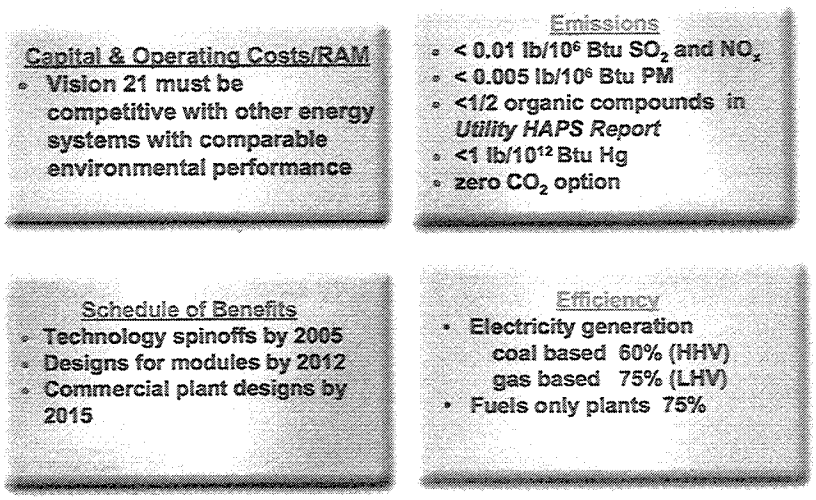


Figure 2. Performance Targets for Vision 21 Energy Plants

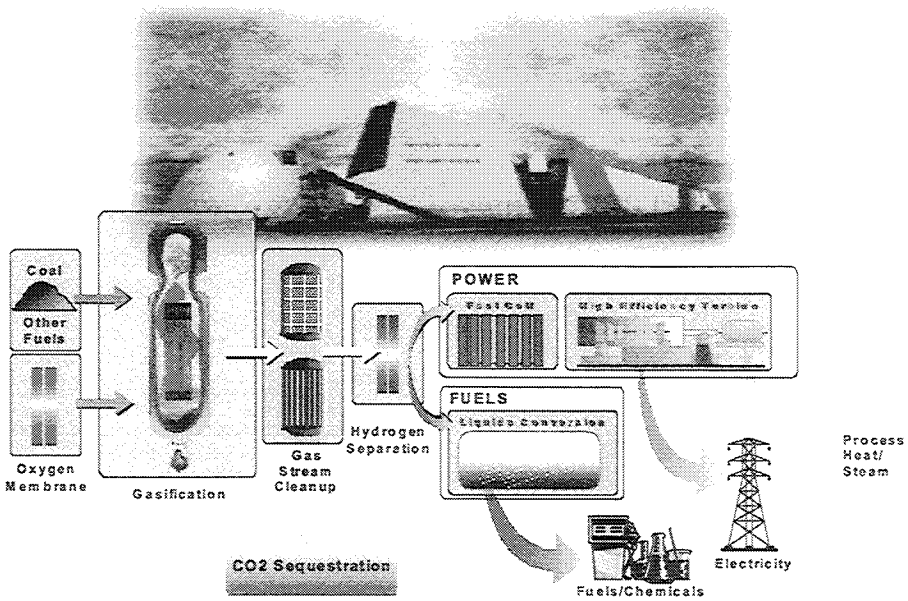


Figure 3. Example Configuration of a Vision 21 Energy Plant

TRENDS IN POWER ENGINEERING IN JAPAN AND REQUIREMENTS FOR IMPROVED MATERIALS AND COMPONENTS

Fujimitsu Masuyama

Mitsubishi Heavy Industries, Ltd.
Nagasaki Research and Development Center
5-717-1, Fukahori-machi, Nagasaki 851-0392
Japan

Abstract

From the viewpoint of Japan's energy security and energy supply structure, the diversification of energy sources, the improvement of thermal efficiency, and the reduction of cost for power generation are highly important. Environmental protection, mainly by reducing CO_2 emissions, is also a global issue requiring urgent consideration. Coal has a higher carbon content than other fossil fuels, and is disadvantageous from the standpoint of CO_2 emissions. Nevertheless, reserves are plentiful and it will continue to be an important energy source into the near future. Accordingly, major development efforts have been undertaken in Japan as national projects for ultra supercritical (USC) pressure plants, pressurized fluidized bed combustion (PFBC) plants and integrated coal gasification combined cycle (IGCC) plants in order to obtain improved thermal efficiency. In the case of USC plants, steam temperature and pressure have recently been increased so as to improve thermal efficiency from those for conventional supercritical power plants. In Japan steam conditions with a temperature of 600℃ have already been adopted for newly constructed plants, and a 610～630℃ class is expected to be realized depending on orders in the near future. The main components of advanced steam parameter plants, such as main steam line pipes and turbine rotors, are made of newly developed high strength 9-12%Cr steels. Newly developed high strength and anti-corrosion austenitic steels are also used for superheaters and reheaters. High strength and high performance heat resistant materials are needed for superheaters and other components in the furnaces of PFBC and IGCC plants, and these can be based on existing ferritic and austenitic steels developed for USC plants.

Keywords: Power plant, heat resistant steel, creep strength, thermal efficiency, USC, IGCC

Introduction

The number of thermal power plants in Japan expanded rapidly from around 1955, becoming the main source of electric power. Since then, major efforts have been directed towards lower power generating costs through expanded capacity, as well as improved efficiency by means of higher temperature and pressure, also resulting in ongoing reductions in CO_2 emissions. Extensive work has also been aimed at the reduction of pollution, including reductions in gaseous emissions and ash from the combustion of fossil fuels, and the purification and treatment of water used in power stations. Conservation of resources and the environment is of global importance, and efforts such as these must be continued. In particular, improved performance is required for power plant materials that can be used under rigorous conditions in order to achieve greater reliability and performance. This paper presents a trend overview of power engineering and materials development particularly for

ultra supercritical (USC) power plants, which are in turn contributing to environmentally motivated efforts at higher temperature and pressure conditions for high-temperature equipment.

Environmental Aspects and Efficiency of Power Generation Systems

As exemplified by the Environment Basic Law effected in 1993 and the Kyoto Protocol of 1997, environmental regulations are being applied increasingly strictly to fossil-fired power plants, which account for 30% of Japanese CO_2 emissions. Possible response measures consist either of a) improvements in thermal efficiency that consequently serve to reduce the amount of fuel used and therefore to reduce emissions of CO_2 and pollutants, or b) exhaust gas purification and ash treatment methods that directly reduce the regulated substances. Technologies for higher efficiency have been extensively studied in various power generation systems, serving to increase generating capacities as shown in Fig. 1[1]. These are of course environmentally relevant, but the most effective approach for fossil-fired power systems is to utilize relatively clean fossil fuels that result in lower amounts of CO_2 and ash, i.e., natural gas. For the equivalent amount of power generated, the amount of the carbon in natural gas is about 70% of that in coal, and about 90% of that in oil. Natural gas is accordingly being used to a greater extent, and attention is focusing on gas turbine combined cycle (GTCC) generation that features a combination of steam and gas turbines. Large numbers of these facilities have been built in recent years. Efficiency is 47% at a gas turbine inlet temperature of 1,300℃, or 50% at 1,500℃. Although the latter case requires improved performance of the Ni base super alloys and their coatings used in the gas turbine, the steam turbine and heat recovery steam generator operates at a maximum temperature of about 570℃, such that low alloy steel or 9%Cr steel can be used.

Higher efficiency is being investigated for various other systems in addition to GTCC. In particular, while coal has higher carbon content than natural gas or oil, and is therefore

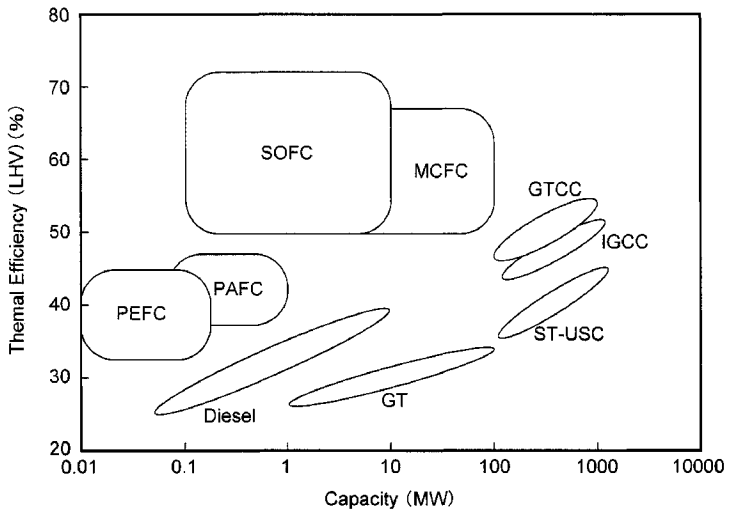


Fig. 1 Efficiency-capacity diagram for power generation systems

disadvantageous from the standpoint of CO_2 emissions, reserves are plentiful and it will continue to be an important energy source well into the future. Research aimed at cleaner and higher efficiency use is thus being pursued from a variety of view points. Attention has been drawn to integrated coal gasification combined cycle (IGCC) and pressurized fluidized bed combustion (PFBC) systems, which are expected to deliver efficiency close to 50%. High strength heat resistant materials are needed for superheaters and other components in the furnaces of IGCC and PFBC systems, and existing austenitic steels developed for USC power boilers can be used.

The higher efficiencies accompanying adoption of the above-noted new systems will necessitate elevated steam temperature and pressure for USC power plants, continuing the trend line that has been seen for conventional power generating systems. This makes higher strength and higher performance essential for in-furnace components and steam piping, and various efforts have been undertaken from the standpoint of materials. Progress has been especially evident from the 1980s onward in terms of the development and use of high strength heat resistant materials, progress that is still continuing. The efficiency of conventional supercritical pressure power plants was formerly below 40%, but that of USC power plants fueled by natural gas or coal has risen to around 45%, which has become the standard for thermal power plants currently planned or under construction.

Trends in Coal-Fired Power Technology

Japan is almost completely reliant on imports for its primary energy needs, making the Japanese energy supply structure quite weak indeed. Accordingly, diversification of energy sources and limitation of energy consumption are both highly important. In addition, the issue of environmental protection and the concomitant need to reduce CO_2 emissions make it increasingly imperative to boost the efficiency of coal-fired power plants[2]. Fig. 2[2]

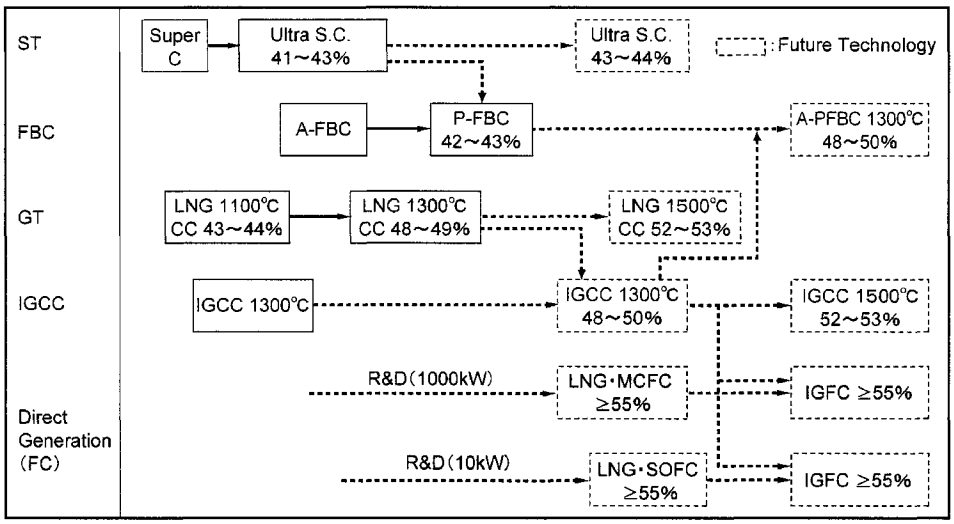


Fig. 2 Progress in power generation systems

illustrates the outlook for the progress in power generation systems with high efficiency generating technology.

Coal contains higher amounts of sulfur than other fossil fuels, also problematic from an environmental perspective, but coal is widely and plentifully distributed throughout the world, and is therefore advantageous from the standpoints of economy and security. At present, pulverized coal-fired (PCF) power plants account for 1,000MW in Japan, and coal is an important element of Japanese electric power supply. The PCF approach is a single steam cycle system that involves the combustion of coal in a boiler, with the resulting steam used to drive a steam turbine. Accordingly, thermal efficiency is governed by the steam conditions, which have been improved in the past from sub-critical pressure, to super critical pressure, and then to USC pressure, which is already in current use.

Meanwhile, in the area of coal combustion, atmospheric pressure fluidized bed combustion (AFBC) technology has been developed in addition to PCF. With AFBC, coal is combusted in a fluidized bed, and the placement of steam generator and superheater tubes within this fluidized bed enables a substantial rise in the heat transfer coefficient. In addition to allowing a more compact boiler design, the use of limestone as a fluidized bed material also enables in-furnace desulfurization. AFBC also features a lower combustion temperature than PCF, contributing to lower NOx. The system makes use of either a bubbling type or a circulating type fluidized bed, and a 350MW class bubbling type AFBC plant (the world's largest) began operations in Japan in 1995.

The steam conditions of PCF power plants have been reaching maximum levels, and, as AFBC is also a single steam cycle system, it will be difficult to achieve further improvements in efficiency. As a result, it is anticipated that the future direction of high efficiency generating technology will shift towards combined cycle generating systems such as liquid natural gas combustion turbine combined cycle. These systems feature the combination of steam and gas turbines to enable higher thermal efficiency. PFBC and IGCC technologies are also being extended to coal combustion combined cycle systems in order to utilize coal.

With PFBC, a fluidized bed boiler is placed in a pressure vessel, and coal is combusted under high pressure conditions to drive an expansion turbine. This means that desulfurization can be accomplished within the furnace, and that combustion efficiency is raised due to the elevated partial pressure of oxygen. Generally speaking, since coal gas and combustion gases contain greater amounts of impurities such as dust and SOx than GTCC, these substances are considered more difficult to apply to a high temperature gas turbine such as in the case of GTCC technology. Accordingly, it has been proposed that a comparatively lower temperature at the gas turbine inlet is more practical when using coal, which is one of the reasons for pursuing PFBC technology. Efforts following this logic have incorporated a relatively low gas turbine inlet temperature of 850℃, with a steam line output ratio approximately 80% higher, such that generating efficiency is governed by steam conditions. In response, research on advanced PFBC (or A-PFBC) has begun, seeking to elevate the gas turbine inlet temperature and to simultaneously increase the amount of heat input into the turbine, thereby boosting efficiency. The first commercial introduction of PFBC with 85MW was accomplished in 1998 at Tomato-Atsuma Unit 3 of Hokkaido Electric Power Co., and successful operation has continued to the present. The facility is equipped with full capacity ceramic filters which operate at 850℃[3].

With IGCC, coal is converted to flammable gas (CO, H_2, etc.) in a coal gasifier, and is then combusted in a combustion gas turbine. The fact that the fuel is burned at the gas turbine inlet means that issues such as high temperature and pressure piping encountered with PFBC

technology are reduced in importance, thus making the system optimal for higher gas turbine inlet temperature, associated with higher efficiency. The conversion of coal into flammable gas makes it possible to use the same cycles as for GTCC technology, and generating efficiency approaching that of GTCC is anticipated. Development of IGCC in Japan has reached a stage approaching a final decision for construction of a demonstration plant. Fig. 3 [4] shows IGCC capacity scale-up plans in Japan. Research and development to confirm a technological scale-up from a 200 t/d pilot plant to a 1,700 t/d demonstration model began as a national project in 1997 aimed at the targets specified in Table 1[5]. This 250MW air-blown IGCC demonstration project is presently being conducted by Clean Coal Power R&D Co. Ltd. (CCP) established in 2001 by the nine regional utility companies of Japan, Electric Power Development Co. (EPDC), and the Central Research Institute of Electric Power Industry (CRIEPI). Plant construction will start in 2004 followed by operations testing through 2009[5]. A pressurized 24 t/d gasifier has been built, and scale-up

Table 1 Major specifications of IGCC demonstration plant

Capacity	Rated Power Output	250MW (1700t/d)
Targets of Thermal Efficiency (LHV Basis)	Gross Efficiency	48%
	Net Efficiency	42%
Plant System	Gasifier	Air-Blown, Entrained Flow Gasifier, Dry Coal Feed
	Gas Clean-up	Amine Absorption, Limestone-Gypsum Method for Sulfur Recovery
	Gas Turbine	1200°C Class TIT
Flue Gas Emission Target	SOx	8ppm
	NOx	5ppm
	Dust	4mg/m^{3}N

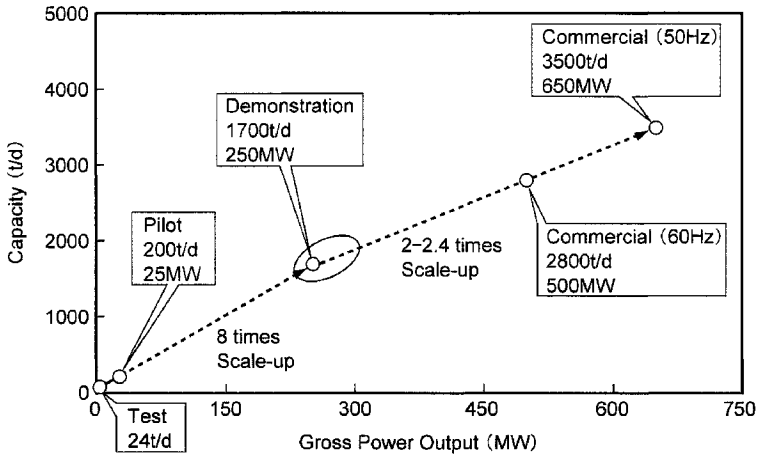


Fig. 3 Capacity scale-up in IGCC plant

technology and the performance of porous filters have been verified. Stable operation was accordingly achieved under the design operating conditions for the demonstration plant. Gasification calculation was accurate and the performance of porous filters met the requirements[6][7].

The major development efforts being undertaken as national projects in this conjunction are USC, PFBC, and IGCC. USC technology will contribute directly to the improved efficiency of steam turbines, and large-scale (1,000MW per unit) pulverized coal-fired power plants are being planned and constructed. Since PFBC technology allows more compact boilers due to the combustion of coal under pressure, it is particularly suited for replacement of existing power plants where space is a constraint, and commercial plants have been constructed. IGCC is considered to be the highest efficiency technology available for near-term implementation, and, as it serves to reduce the issue of coal ash treatment, there is a strong possibility that IGCC will become the leading coal-fired power technology in thefuture. However, technological development is still in progress, and cost-related problems remain.

Other technologies include those for direct power generation, such as molten carbonate fuel cells (MCFC), solid oxide fuel cells (SOFC), and magneto hydrodynamics (MHD) generation. These technologies are currently being developed mainly based on the use of liquid natural gas (LNG) fuel. However, as coal is still being viewed as a major energy source for the future due to plentiful reserves, security and other considerations, efforts are gradually being steered in this direction. It will therefore be highly important to establish basic technology for the use of coal in new power generation technologies.

Materials Technology for USC Power Plants

Steam conditions of fossil-fired power plants

In Japan, as shown in Fig. 4 steam pressure and temperature rose sharply after 1950. Meanwhile, thermal power generation overtook hydroelectric generation to become the leading source of energy by 1960, although still using domestic coal as the primary fuel.

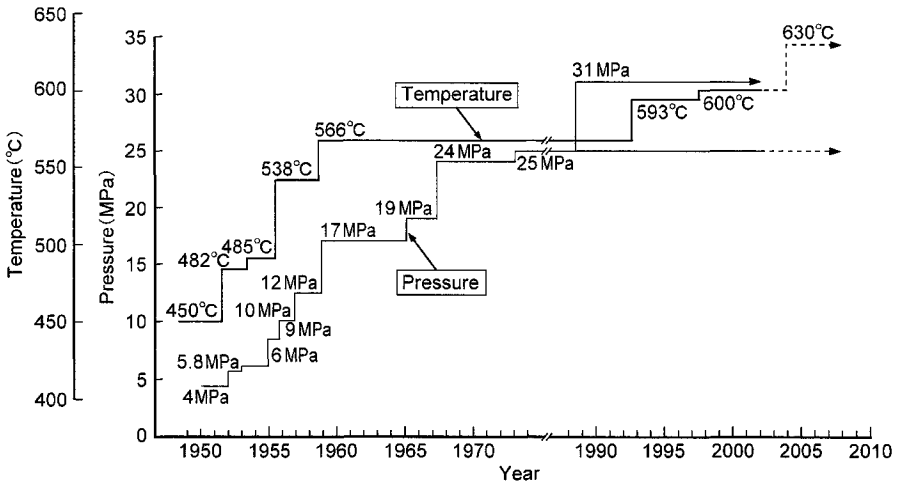


Fig. 4 Trends of steam conditions of power plants in Japan

However, contemporary thermal efficiency was only about 30%, rather lower than the figures of approximately 40% that were delivered by subsequent supercritical pressure (24MPa, 538℃) plants. Because petroleum, which began to be imported into Japan in large quantities from around 1965, was found to be more cost effective, thermal power plants that had been using mainly Japanese domestic coal were converted for the firing of imported heavy crude oil. These plants were again converted in the wake of the oil crises of 1973 and 1978, this time for the use of imported coals.

From around 1975, frequent starts and stops of fossil-fired power plants have been increasingly been required for load adjustments, accompanied by the expansion of nuclear power generation and changes in patterns of electricity demand. Steam conditions had been fixed at combinations of 24MPa and 538℃ or 19MPa and 566℃, with no additional elevation, despite progressive enlargement of plant scale over the 20 year period from the late 1960s. However, the oil crises triggered a call for further elevation of steam conditions, leading to the appearance of the first USC sliding pressure plant (31MPa, 566℃) in 1989. This represented the first increase in steam pressure and temperature in more than 20 years. Conditions for subsequent new plants have been successively raised beyond conventional limitations, and current temperatures are 593 or 600℃ at pressures of 24.1-25MPa, while the use of 630℃ is being studied for the next stage of advance. Of the 41 units with operation starts scheduled from 1990 through 2003, 24 units feature a temperature of at least 593℃ for main and/or reheat steam, with the majority of these advanced units commencing operations from 1997 onwards. Fig. 5[8] shows the relationship among steam pressure, temperature and thermal efficiency. It is clear from the figure that raising the steam pressure and temperature reduces turbine cycle heat consumption, thereby raising turbine efficiency. An efficiency increase of approximately 6% could be gained, provided that steam parameters are raised from the conventional 583℃ at 24MPa to the target of EPDC Phase-2, 630℃ at 30MPa.

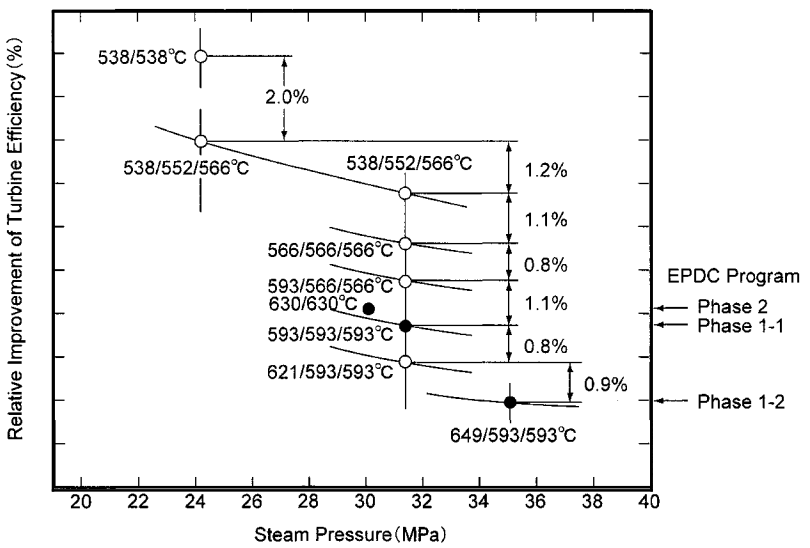


Fig. 5 Relation between steam conditions and efficiency

Modern USC power plants and the future

Modern USC power plants are already in service and under construction in Denmark, Germany and Japan. Table 2[8] lists the USC power plants in Japan with steam parameters in the range of 24.1-25MPa and 31MPa in pressure, and of 538℃ to 600℃ in superheater steam temperature, including in-service, under construction, and designed plants.

Fig. 6 [9] shows steam parameter plots for USC power plants at past, present and future

Table 2 Ultra supercritical pressure power plants in Japan

Main Steam		Hot Reheat Steam Temperature (°C)	Number of Units	Unit Belonging to the Group
Pressure (MPa)	Temperature (°C)			
24.1~25.0	538	566	XX	Not Referred to
	538	593	1	(1)
	566	566	3	(2)
	566	593	4	(3)
	593	593	6	(4)
	600	600	3	(5)
	600	610	3	(6)
31.0	566	566/566	2	Kawagoe 1&2

Name of the Units
(1) Hekinan 3
(2) Tsuruga 1, Reihoku 1, Shiriuchi 2
(3) Nosiro 2, Nanao-Ohta 1, Haramachi 1, Tachibanawan, Maizuru 1&2
(4) Matsuura 2, Nanao-Ohta 2, Tsuruga 2, Reihoku 2
(5) Misumi 1, Haramachi 2, Hitachinaka 1
(6) Tachibanawan 1&2, Isogo 1

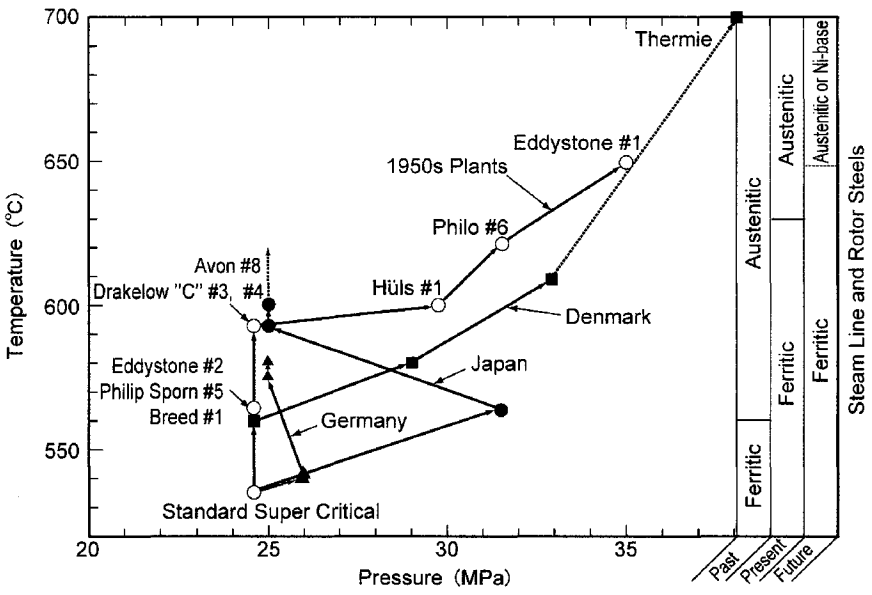


Fig. 6 Steam parameter plots for ultra supercritical pressure power plants

points on a graph of pressure versus temperature. Time-wise service temperature ranges are also indicated on this graph for ferritic and austenitic steels for heavy section components such as steam line pipe and turbine rotors. The upper temperature limit for ferritic steels has thus far risen from around 560℃ to 630℃, and will increase to 650℃ in the future.

Material development for power plants applications

Figs. 7 and 8 respectively show development progress for ferritic and austenitic boiler steels with the 100,000 hours creep rupture strength at 600℃, for materials developed to date. Regarding ferritic steels, low alloy steels or 9-12%Cr steels at about 40MPa of 10^5h creep d rupture strength had been used for many years. Nevertheless, there was a problem of cost increases because, especially in the case of superheaters and the reheaters, there was an alloy "gap" between the low alloy steels and the 18%Cr-8%Ni steels, arising as a result of temperature elevation. Accordingly, development of high strength 9-12%Cr steels was initiated in order to fill this gap, and the materials for 60MPa class (first generation) were developed over the period from 1960 to 1970. Further developments were pursued, ancreep rupture strength reached the 100MPa class (second generation) in the 1980s, with the 140MPa class (third generation) achieved in the 1990s. Materials for the 180MPa class, the next generation, are expected to emerge. The outside diameter and wall thickness of pipes and tubes can be greatly reduced through elevation of the creep rupture strength. The thermal stresses can accordingly be reduced, and construction will be possible for fossil-fired power plants capable of load sliding operation under steam conditions of further elevated pressure and temperature. In order to use austenitic steels for superheater and reheater tubes for USC power boilers, several materials have already been developed that are sufficient to meet the steam temperature of 650 ℃, taking cost-effectiveness into consideration. 22.5Cr-18.5Ni-1.5W-3CuNbN steels[10] represent a typical high performance tubing material with 203MPa creep rupture strength at 600℃ and 100,000 hours.

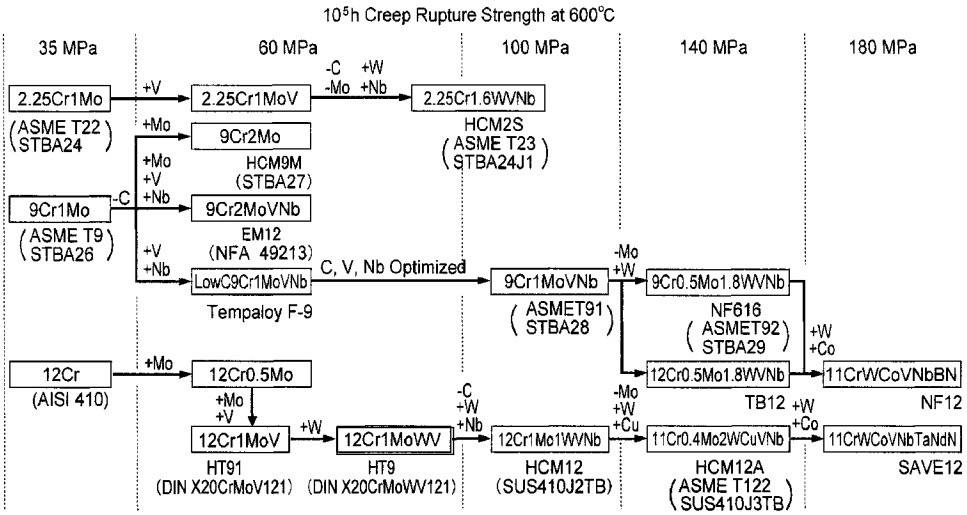


Fig. 7 Development progress of ferritic steels for boiler

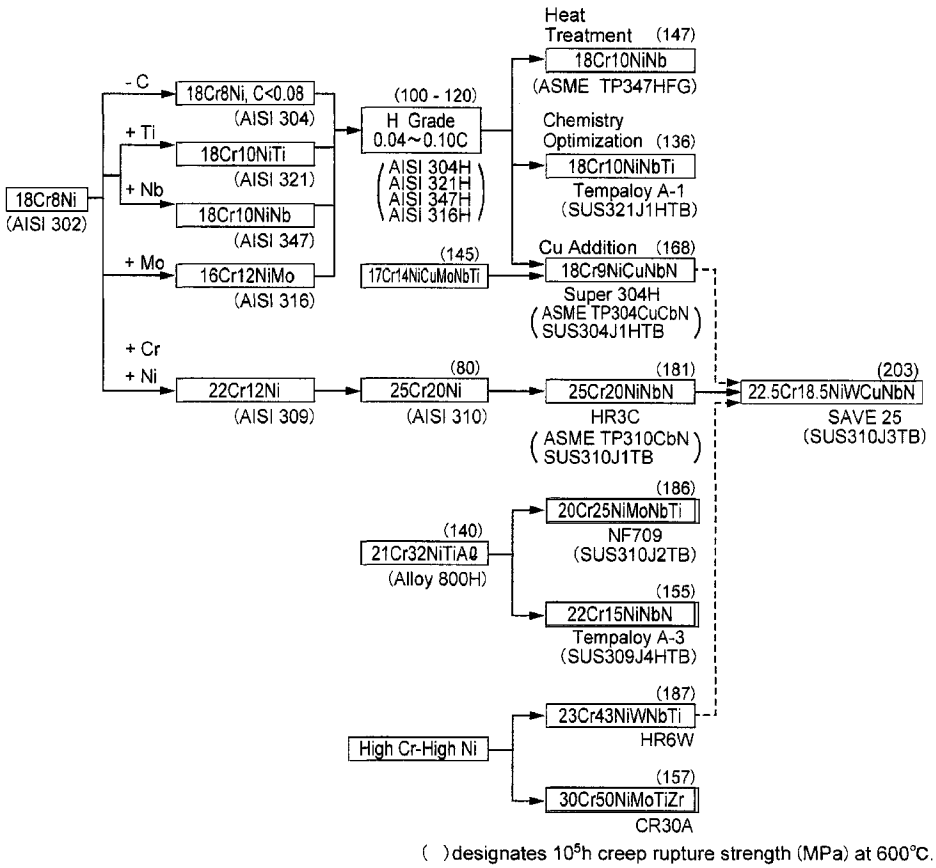


Fig. 8 Development progress of austenitic steels for boiler

The development progress of turbine steels for small components, rotors and casings, is shown in Fig. 9, although their comparison may not be especially useful. The H46[11] is an original high strength 12%Cr steel developed around 1950 and contains V, Nb and N. The C contents in turbine steels have risen to higher values because these steels are not used in components for welded structures except cast steels, and because their strengths at room and intermediate temperatures must be enhanced. Turbine rotors[12] and gas turbine disks[13] were developments based on this steel, reducing Cr content to around 10.5% with additions of N, Nb, N and B. Chemical compositions employed for these two types of steels had a great influence on the development of high temperature and pressure turbine rotor and casing materials, initiated in the early 1980s. Consequently creep strengths were increased by slightly decreasing the C content and using optimized contents of V, Nb and N. Furthermore, in the context of application at even higher temperatures or for further elevation of strength, Mo alloy steels appeared to have already reached a limit, and development of steels using W as an alloy element was needed in 1980s to 1990s. Several steels were proposed as rotor steels for 593℃ to 621℃[14], and W was added at levels of 0.3% or 1.0%. Chemical

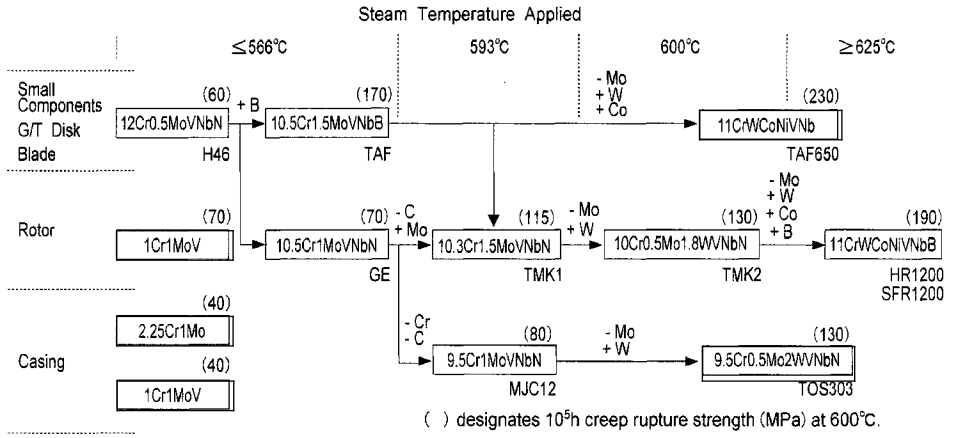


Fig. 9 Development progress of 9-12%Cr turbine steels

compositions were then developed for potential use as rotor steel for 621℃, with Mo decreased to 0.5% and W increased to 1.8%, or Mo decreased to 0.2% with W increased to 2.5%. For all of these materials, the 100,000 hours creep rupture strength at 600℃ exceeded the 100MPa objective. For temperatures above 621℃, 10-11%Cr rotor steels with 2-6W, 3Co and B[15] and 0.7Mo, 1.8W, 3Co and B[16] have been developed which contain further increased W and additions of Co and B. These development efforts are being undertaken in view of accommodating up to 650℃, and the goal is for 100,000 hours of creep rupture strength at 650℃ in excess of 100MPa.

Application studies on USC power plant materials

In Japan, research into the use of USC conditions for fossil-fired power plants was initiated in order to obtain data on practical material properties and reliability of heat resistant steels through field tests in utility power plants. This was because there was a background in Japan of existing developments in 9-12%Cr steels and austenitic steels, which have excellent creep strength and corrosion resistance for their costs. Table 3 presents the USC power plant development objectives. In Phase-1 of the development project for USC power plants, initiated by the Ministry of International Trade and Industry (MITI, now the Ministry of the Economy, Trade and Industry) and conducted by EPDC during the period 1981-1993, boiler and turbine element tests and field demonstration tests were carried out at temperatures of 593℃ and 649℃. The Phase-1 program targeted the development of double reheat steam conditions of 31.4MPa and 593℃/593℃/593℃ with the use of ferritic 9-12%Cr steels, and 34.3MPa and 649℃/649℃/649℃ for austenitic steels[8] During the period 1994-2001 the Phase-2 program was conducted for the development of single reheat steam conditions of 30MPa and 630℃/630℃ with ferritic steels. Both programs have basically been conducted by using existing newly developed heat resistant steels. Concurrently, the National Research Institute for Metals (NRIM, now the National Institute for Material Science) has been conducting a research and development project since 1997 aimed at ferritic heat resistant steels applicable for 650℃ class steam conditions.

Table 3 EPDC USC program target

			Conventional	Phase-1		Phase-2
				Step-1	Step-2	
Main Component Material			Ferritic	Ferritic	Austenitic	Ferritic
Steam Parameter	Pressure	(MPa)	24.1	31.4	34.3	30.0
	Temperature	(℃)	538/566	593/593/593	649/593/593	630/630
Gross Thermal Efficiency		(%)*	42.1	44.2	44.9	44.2
Relative Efficiency Improvement		(%)	Base	5.0	6.5	4.8
Annual Coal saving		(ton)*	Base	96000	175000	95000
Annual CO_2 Reduction Per Year		(10^6Nm^3)*	Base	117	152	112

* : Based on a 1000MW Unit

In the case of the EPDC USC program, relative improvements in thermal efficiency at the generator terminal through higher temperature and pressure over conventional supercritical plants were anticipated to be 5% from Step-1, 6.5% from Step-2, and 4.8% from Phase-2. Savings in coal consumption are also facilitated, with consequent reductions in CO_2 emissions. USC can thus be viewed as an effective means of cutting CO_2 output. Recent large-scale coal fired power plants in Japan, such as EPDC's Matsuura Unit 2 represent the adoption of Step-1 of Phase-1 temperature conditions, with steam temperature of 593℃ and higher.

In boiler tests, high tensile strength steels with greater additions of the alloy elements Cr, Mo and Cu than current carbon and low alloy steels were applied for a) low temperature components tests for economizers, and b) intermediate temperature components such as waterwalls, as well as for the original tests focusing on high temperature components for superheaters and reheaters. This was to limit the wall thickness and reduce the boiler weight of low and intermediate temperature components. The most important task was development of ferritic steel for use in high temperature large diameter piping such as final superheater outlet headers and main steam pipes. Four steels were chosen, three of which consisted of tungsten alloyed NF616 (P92)[17], HCM12A (P122)[18], and Tempaloy F-12M[19], the strongest ferritic steel in current use. The fourth steel was NF12[20], strengthened by adding tungsten and cobalt. Five steels were used for the high temperature superheaters and reheaters, consisting of SAVE12[21] strengthened by means of tungsten and cobalt addition, and the four steels adopted for the above-mentioned steel pipe. Four austenitic stainless steels for tubing were also installed in the high temperature superheaters and reheaters.

With respect to turbine rotor steels, turbine manufacturers are currently pursuing development of new 12%Cr steels that will be applicable for 630℃ class equipment, and HR1200[15] and SFR1200[22] with enhanced creep rupture strength were used as turbine rotor steels. Turbine blade steels were TAF650[15], which was the blade version of HR1200 rotor steel, and new 12%Cr steel for SFR1200.

In order to ascertain the material properties of the Phase-2 test steels and establish the fabrication procedures, tests were conducted with respect to weldability and bending formability. Weldability was confirmed to be satisfactory, as sound joints were produced for both similar and dissimilar metal welds. In terms of bending formability, deformation was found to be within the allowable range, and no abnormal changes were observed in the

microstructures. A full-scale fabrication trial was performed to verify whether economizers, waterwalls, superheaters, headers, and main steam pipes could be fabricated for 1,000MW class coal fired USC boilers operating at Phase-2 steam conditions. Full-scale components were constructed, and verification was conducted with respect to fabricability, material properties, and the soundness of pressurized components.

Cost based strength and component design

Allowable stress is a measure of the high temperature strength of heat resistant steels, and is often determined by creep rupture strength under actual operating conditions. In order to improve the reliability of high temperature components, it is therefore necessary to ascertain creep rupture strength up to 100,000 hours (the basis for fixing allowable stress), or to make an accurate estimate of this, and to fully appreciate the relationship between the changes in creep rupture strength and structures over long periods of time.

Both high temperature strength and economy must be considered in the selection of materials. In general, higher cost materials have greater high temperature strength. Fig. 10 shows the relationship between the allowable temperature at an allowable stress of 49MPa and the relative material cost for various boiler tube steels, including newly developed ones. The relative material cost has been determined based on a steel tube of normal dimensions ($D/T \geqq 2.5$; T=tube thickness, D=tube diameter) and an allowable stress of 49MPa was chosen in consideration of the prevailing steam pressures in ultra-supercritical pressure power plants.

Although the standard and newly developed steels cover a wide scatter band, the figure confirms that the allowable temperature increases with the material cost for the same allowable stress conditions. For each group of materials, i.e., those with similar relative

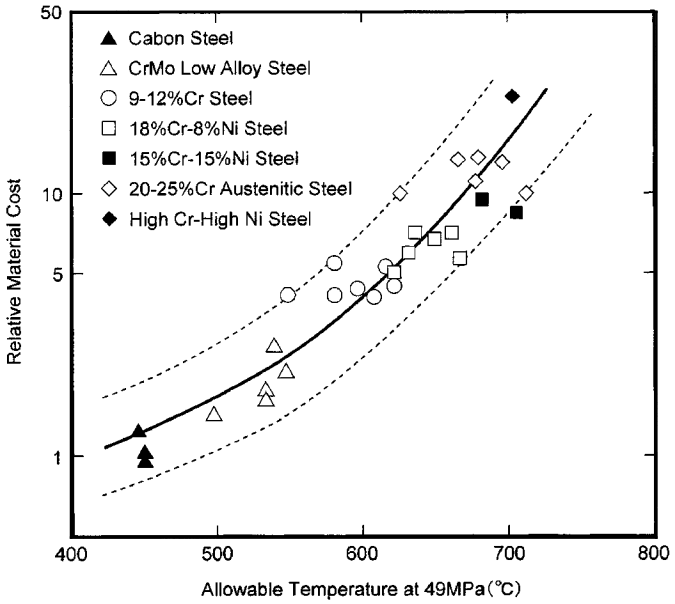


Fig. 10 Relation between allowable metal temperature and the allowable stress of 49MPa and the relative material cost

costs, it is necessary to raise the high temperature strength so that they fall as nearly as possible to the bottom of the band. Fig. 11 illustrates the sectional profile of a superheater outlet header designed for steam conditions of 30MPa and 630℃ using upgraded steels having improved creep strength against P91 as a base material. Advanced steels bring great reduction of pipe diameter and weight as shown in Fig. 11, which strongly affect the cost performance of the pipe work.

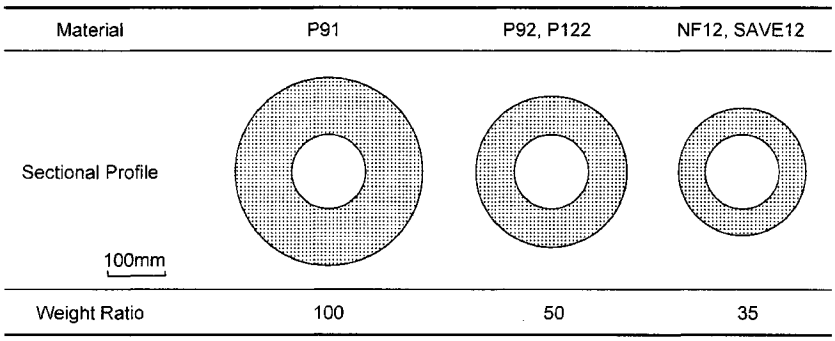


Fig. 11 Sectional profile and weight ratio for superheater outlet header used advanced steels

Future issues for material development solutions

The development of heat resistant materials for thermal power plants has a long history, and many of the high strength heat resistant steels that have been developed are currently in service in high temperature and pressure USC power plants. However, the mechanisms underpinning the high creep strength that has been obtained are not fully understood. Material design during research and development has been based mainly on creep rupture test results, but further analysis is required in order to elucidate the creep deformation behaviour.

Also, while efforts are being made to obtain data for long periods in the laboratory (in view of the fact that the effects of stress are felt in actual use over a duration of 100,000 hours at high temperatures), tests surpassing several tens of thousands of hours are extremely rare. In particular, the strength of materials tempered at lower temperatures such as 9-12%Cr steel declines rapidly beyond a few hundred thousand hours, i.e., sigmoidal curvature is seen on stress-time to rupture diagrams. This kind of complex creep behaviour needs to be predicted in the shortest possible test duration, with strength accurately assessed beyond 100,000 hours.

Materials anticipated for development and future power plant application include ferritic steels that can be used up to 650℃, and, from the standpoint of cost, inexpensive carbon steels or low alloy steels with substantially improved strength and corrosion resistance, as well as high strength austenitic steels.

In terms of their actual use, newly developed steels must also provide satisfactory weldability and fabricability, so as to be able to undergo various heat and process histories. Accordingly, the accumulation of large amounts of data is required with respect to material properties and how they are affected by other factors. Such data will naturally be essential to the establishment of design and fabrication standards for equipment using newly developed materials.

Summary

The major development efforts being undertaken in Japan are GTCC, PFBC, IGCC and USC. Gas turbines for GTCC are already commercially operated at inlet temperatures of 1,500℃ class to achieve high efficiency of 50%. This requires improved Ni-based super alloy and thermal barrier coating for gas turbine blades, although the steam cycles of this system require only low alloy steels and 9%Cr steels for operation at a maximum of about 570℃.

Commercial operations commenced in 1998 for a PFBC plant with a capacity of 85MW, while an IGCC demonstration plant with 250MW is now under design for the start of operation in 2008 reflecting the pilot plant test conducted for about 10 years until 1996. For those plants, existing ferritic and austenitic steels developed for USC plants over the last several decades can be used satisfactorily.

Steam conditions for conventional power plants have recently been raised in order to respond to environmental protection and energy conservation concerns. In Japan steam conditions with a temperature of 600℃ have already been adopted for newly constructed plants, and pending orders, a 610-630℃ class is expected to be realized in the future. The next goal will be a 650℃ class with ferritic steels. Since 1960 numerous studies on heat resistant steels for boiler and turbine applications have been conducted. Among the various steels developed for advanced steam cycles, major progress has been seen in 9-12%Cr steels for boiler pipe work and turbine components, and in austenitic steels for superheater and reheater tubing. In particular, recently developed ferritic 9-12%Cr steels are stronger than conventional austenitic stainless steels. The most recent 9-12%Cr steels have a creep rupture strength of 100MPa at 650℃ for 100,000 hours. Such enhancement in creep strength is achieved by alloying with tungsten to reduce some of the molybdenum. Strengths of 180MPa at 600℃ or 130MPa at 650℃ are anticipated in the near future for ferritic steels. Significant improvements are also being achieved in austenitic steels for boiler superheater and reheater tubing, and development is now being oriented towards high-performance and low-cost steels capable of superior resistance to oxidation/corrosion in high temperature environments.

Acknowledgements

The author would like to acknowledge advice and numerous helpful discussions with Mr. Shozo Kaneko, Executive Vice President of Clean Coal Power R&D Co., Ltd., Japan.

References

[1] Agency of Natural Resources and Energy, Energy 2002, (2001), p.181
[2] Ministry of Economy, Trade and Industry, Report on Development of Coal-Fired Power Technology for The 21st Century, (1988)
[3] S. Kaneko, K. Tsukagoshi, S. Uchida, M. Kinoshita and K. Tokuda, Mitsubishi Juko Giho, Vol.35 (1998)
[4] S. Kaneko, Y.Ishibashi and J. Wada, Conf. Gasification Technology 2001, San Francisco, California, Oct. 7-10, (2001)
[5] Ministry of Economy, Trade and Industry, Report on Demonstration of IGCC Plants, (2000)

[6] S. Sato, K. Ohta, T. Furuya, Y. Koyama and A. Hashimoto, Mitsubishi Juko Giho, Vol.37 (2000), p.10
[7] S. Sato, Y. Kobyashi, K. Ohta, O. Shinada and A. Hashimoto, Mitsubishi Juko Giho, Vol.38 (2001), p.64
[8] K. Muramatsu, Advanced Heat Resistant Steels for Power Generation (Ed. By R. Viswanathan and J. Nutting), IOM Communications, Ltd. UK., (2001), p.543
[9] F. Masuyama, ISIJ International, Vol.41 (2001), p.612
[10] H. Senba, M. Igarashi and Y. Sawaragi, Proc. Int. Conf. Power Engineering –'97, Vol.2, JSME, Tokyo Japan, (1977), p.125
[11] D. A. Oliver and T. Harris, Iron and Steel Inst. Special Report No.43, (1952), p.46
[12] D. L. Newhouse, C. I. Boyle and R. M. Curram, 68th ASTM Annual Meeting, Lefayette, Indiana, (1965)
[13] T. Fujita, Trans. Japan. Inst. Metals, Vol.9 (1968), p.167
[14] F. Ito, K. Kuwabara, M. Miyazaki, Y. Fukui and Y. Takeda, 1st Int. Conf. Improved Coal-Fired Power Plants, Palo Alto, California, (1986)
[15] K. Hidaka, Y. Fukui, R. Kaneko and T. Fujita, IMechE Conf. Trans. 1997-2, Advanced Steam Plant, IMechE, London, (1997), p.99
[16] Y. Tsuda, R. Ishii, M. Yamada, T. Azuma, Y. Tanaka and Y. Ikeda, Proc. Int. Conf. Power Engineering- '97, Vol.2, JSME, Tokyo, Japan, (1997), p.131
[17] M. Sakakibara, H. Masumoto, T. Ogawa, T. Takahashi and T. Fujita, Thermal and Nuclear Power, Vol.38 (1987), p.84
[18] A. Iseda, Y. Sawaragi, S. Kato and F. Masuyama, 5th Int. Conf. Creep of Materials, Lake Buena Vista, Florida, (1992)
[19] K. Hayahi, T. Kojima, Y. Minami, M. Hayashida and Y. Yamazaki, Thermal and Nuclear Power, Vol.40 (1998), p.736
[20] M. Ohgami, Y. Hasegawa, H. Naoi and T. Fujita, IMechE Conf. Trans. 1997-2, Advanced Steam Plant, IMechE, London, UK., (1997), p.115
[21] M. Igarashi and Y. Sawaragi, Proc. Int. Conf. Power Engineering-'97, Vol.2, JSME, Tokyo, Japan, (1997), p.107
[22] Y. Arai, K. Tamura, F. Masuyama, I. Kajigaya, R. Kaneko and T. Omori, Thermal and Nuelear Power, Vol.52 (2001), p.32

POWER GENERATION IN SOUTHERN AFRICA

JA de Beer
Z Olsha

Eskom Enterprises
South Africa

Abstract

This paper outlines the main characteristics of power generation in Southern Africa, in terms of primary energy resources, existing and projected power supply and demand, types and location of power plants, regional integration, and environmental management aspects. Various options for future development of power generation are presented as part of an overall Integrated Resource Planning (IRP) process for the power industry. These include coal and natural gas based options, hydro power and other renewable energy, and nuclear power plants. A specific option, the Pebble Bed Modular Reactor (PBMR), under development by Eskom Enterprises and other international and local partners, is described in terms of overall design parameters, inherent safety features, economics and environmental aspects. Included is a high level discussion on the selection of materials for the design of this PBMR plant, an advanced design version of a High Temperature Gas Reactor (HTGR).

1. Introduction – Regional Energy Overview

Southern Africa region, which includes the 14 countries of the Southern Africa Development Community (SADC), like other Africa sub-regions with the exception of East Africa, is a net energy exporter (coal by South Africa and oil by Angola). In 1999, the SADC countries collectively consumed 5.14 Quads (10^{15} Btu) of commercial energy (1.3% of total world consumption) and produced 7.62 Quads (2.0% of total world production). Also in 1999, SADC members generated 112.8 million metric tons of carbon emissions (1.8% of the world total). In 1999, the region's dominant economy, South Africa, accounted for 85.4% (4.39 Quads) of SADC energy consumption, 72.8% (5.54 Quads) of SADC energy production, and 88.1% (99.45 million metric tons) of SADC carbon emissions.

SADC commercial energy resources are diverse, and significant reserves of coal (67 billion t), petroleum (6 billion barrels), uranium (600 000 t) and to a lesser extent natural gas (8.5 tcf) can be found in the region. Electricity in the region is generated through thermal or hydroelectric resources, with one nuclear facility in South Africa. Natural gas is becoming more significant to the SADC energy sector as large gas fields off Mozambique, South Africa and Namibia are developed. In spite of the country's continuing civil war, Angola continues to attract oil sector investment and to increase oil production.

Due to the region's relatively small urban population, access to commercial energy sources is limited. The majority of the SADC population still relies on the use of bio-fuel (wood) as its primary source of energy. Bio-fuel accounts for 75% of total final demand in the region. The countries with the highest rates of bio-fuel consumption are Tanzania, Mozambique, Zimbabwe, Zambia and Malawi.

2. Power Generation in Southern Africa

2.1 Overview

SADC's total installed electric generating capacity (breakdown shown in Table 1) was 46700 megawatts (MW) at 2000, the majority of which is thermal. Total electricity production for the region in 1999 was some 219 000 GWh. Net hydroelectric generation was some 21 000 GWh with Zambia (7600 GWh) and the Democratic Republic of Congo (5160 GWh) being the largest generators. In 1998, total SADC electricity consumption was 204 000 GWh led by South Africa's 174500 GWh (85%). Zimbabwe (8400 GWh, 4%), Zambia (6400 GWh, 3%) and the Democratic Republic of Congo (5500 GWh, 3%) were the next largest electricity consumers.

Table 1: SADC Power Market

Country	Installed Capacity [MWe]	Production [GWh]	Utility Peak Demand [MWe]
Angola	**397**	**1480**	**291**
Botswana	**132**	**610**	**316**
Dem. Rep. Congo	**1800**	**5270**	**900**
Lesotho	**75**	**NA**	**83**
Malawi	**308**	**1030**	**196**
Mauritius	**365**	**1260**	**300**
Mozambique	**2000**	**2300**	**704**
Namibia	**400**	**NA**	**344**
Seychelles	**28**	**160**	**NA**
South Africa	**36000***	**191 000**	**30600**
Swaziland	**51**	**380**	**155**
Tanzania	**763**	**2250**	**570**
Zambia	**2436**	**7640**	**1180**
Zimbabwe	**1961**	**5780**	**2175**
SADC Total	**46715**	**219160**	**37814**

* Net capacity, excluding 3800 MWe of mothballed plant
Source: SAPP Plan Report July 2001, EIA CABS Report 2000.

2.2 South Africa – a Major Regional Player

South Africa has a gross installed electric generating capacity of some 42 011 MWe, including 3800 MWe of mothballed plant (Camden, Grootvlei, Komati) and a net (sent-out) capacity of 36 208 MWe. Conventional thermal (coal fired) plants generate the majority (90%) of South Africa's electricity. The Koeberg nuclear power plant (2 x 950 MWe) generates some 6%, two conventional hydroelectric plants and two pumped-storage plants are also utilized to generate 4% as peaking plants.

2.2.1 Eskom

South Africa's parastatal electric utility, Eskom, is the largest utility in the region (and in Africa) and is one of the largest (7th) electric utilities in the world, in terms of

generation capacity. In addition to serving the domestic market, Eskom imports power from the DRC, Mozambique and Zambia and exports power to Botswana, Lesotho, Namibia, Swaziland and Zimbabwe, and to an aluminium smelter in Mozambique.

Eskom embarked on an unprecedented electrification programme under which it has provided power to 2.2 million homes since 1995. Eskom's 24 generation plants and transmission grid performance, in terms of reliability and availability, have continuously exceeded international best quartile performance. Eskom is one of the lowest-cost producers of electricity in the world (with a wholesale power tariff of 1.2 USc/kWh) and yet has maintained its financial health. Eskom is making a considerable effort and progress in improving technical performance, financial governance, managing environmental impacts, adding value to customers and developing new business opportunities. At the Financial Times Global Energy Awards Ceremony in December 2001, Eskom was presented with the award for best Power Company of the Year.

2.2.2 Eskom Enterprises

Eskom is mindful of the development taking place within a globalising world. Its strategic intent envisages pre-eminence in Africa, as well as global stature. Eskom, through its wholly owned subsidiary, Eskom Enterprises, (established in January 1999) has embarked on a growth and diversification strategy that includes investment in, and delivery of, products and services in the power, primary energy, telecommunication and IT sectors in Africa and, on a selective basis with local partners, participating in related activities in other parts of the world. Today Eskom Enterprises activities spread over some 30 countries in Africa, as well as in the Middle East and Latin America, The nature of such activities include investment, partnerships, concessions, operation, management, consulting, and supply and construction/rehabilitation contracts. In many ways Eskom Enterprises is pioneering the rollout of the African Renaissance through its promotion and implementation of projects related to the New Partnership for Africa Development (NEPAD).

The primary strategic objective of Eskom Enterprises is to maximise the value of non-regulated business activities of Eskom, and to develop competitive new business related to the energy supply industry. Its significant investment – along with other local and international partners in developing the innovative Pebble Bed Modular Reactor (PBMR), confirms the company's long term positioning as a developer and purveyor of leading-edge technologies.

3. Regional Co-operation – The Southern African Power Pool

Southern African Power Pool (SAPP) aims to link SADC member states into a single electricity grid. The Southern African Power Pool (SAPP) was created in 1995 when twelve countries within the Southern half of the African continent presented on the map of Figure 1, decided to pool their electricity supply resources for their mutual benefit. Twelve utilities signed the Inter-Utility Memorandum of Understanding (IUMOU) of the SAPP: SNEL (Democratic Republic of Congo), TANESCO (Tanzania), ESCOM (Malawi), ZESCO (Zambia), ENE (Angola), NAMPOWER (Namibia), BPC (Botswana), ZESA (Zimbabwe), EdM (Mozambique), SEB (Swaziland), ESKOM (South Africa) and LEC (Lesotho).

The main interconnections between the twelve utilities and their respective forecast peak load in the year 2000 are shown on Figure 1. Three utilities are not interconnected to the SAPP network yet, Escom, Tanesco, and ENE. The first two are expected to be connected to ZESCO and EdM within a few years, while the timing of the interconnection between SNEL, ENE and Nampower depends on the resolution of the conflicts in Angola and in the Democratic Republic of Congo. The total peak load in the SAPP was about 37 814 MWe in the year 2000 with a load factor of about 72 %. Eskom's customers in South Africa require about 80 % of the peak load of the SAPP. The total generating capacity of the SAPP at present is about 46715 MWe , 88 % of which is provided by thermal plant, mostly coal-fired, and mostly located in the south of the SAPP, and the remainder by hydroelectric plant, mostly located in the northern part. There is a 1800 MW nuclear power plant in Cape town.

The main goal of the SAPP is the co-ordination and co-operation in the planning and operation of the various systems to minimise costs while maintaining reliability, and the equitable sharing of the resulting benefits. Amongst the benefits expected from the pool is a reduction in the required generating capacity, a reduction in fuel costs, and an improved utilisation of hydro energy capacity.

The SAPP is managed by five committees, an executive committee in charge of the overall pool policy, a management committee responsible for the power pool itself, and three subcommittees in charge of technical issues namely: planning, operating, and environmental.

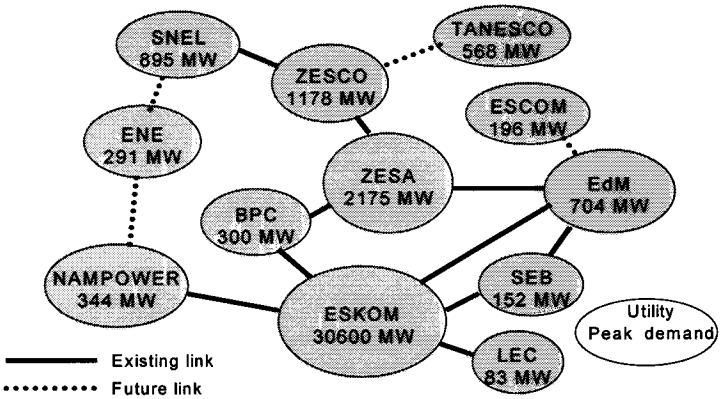


Figure 1: SAPP interconnections and peak demands (2000)

The SAPP is a loose pool, where each utility keeps full authority over, and responsibility for, its own generation and transmission system. There is no central dispatching of power, and most of the exchanges of power are performed in terms of long term (5 to 20 years) bilateral or multilateral agreements between utilities for the sale of firm power. A co-ordination centre located in Harare (Zimbabwe) monitors compliance of the SAPP utilities with the various operating rules of the SAPP, and administers a short term energy market, which is a day-ahead market for exchange of surplus energy at a low price, which started in the year 2001.

In addition to the exchanges of firm power and short term energy, the SAPP transmission network is used to provide mutual assistance between utilities in case of emergency, which is essential to maintaining the reliability and quality of the power supply to the SAPP customers. This enabled the SAPP in the year 2000 to reduce its capacity reserve requirement from 18 % to 10 % of peak demand.

In the year 2001, the SAPP Planning Subcommittee prepared an optimal generation and transmission capacity expansion plan over the next 20 years, which identifies the priority projects for the development of the power pool, and assesses the benefits of co-ordinated planning. This plan is purely indicative, and each SAPP utility remains free to develop its power system as it wishes.

An important current issue in the SAPP is the tariff for wheeling power over the SAPP network, presently between 7.5 % to 15 % of the tariff for the wheeled power, which is often low due to the existence of excess generating capacity in the pool. The SAPP management is presently considering a proposal for basing the wheeling tariff on the cost and usage of the assets used for wheeling, which will lead to a higher wheeling tariff. This may significantly reduce the trade in short term energy. However, this may also encourage the development of the SAPP network for the bilateral trade in firm power.

Another issue is the membership of the SAPP, which is presently reserved to the national electrical power utilities. Independent Power producers (IPP's) such as Hidroelectrica de Cahora Bassa (HCB) and the Copperbelt Energy Consortium (CEC) or independent Transmission Producers (ITP's) can only attend SAPP committees meetings as observers. Since a few utilities may also be unbundled in the near future, the SAPP may have to broaden its membership to include IPP's and ITP's to retain its influence on power trading in the region.

In the long term, the SAPP vision is to transform itself from a co-operative pool to a competitive pool where each end user in any SADC country will be allowed to choose a supplier of its choice in any SADC country, and wheel its purchased power to its point of consumption.

4. The Pan-African Transmission Grid

Generating one's own power was always thought to be the key to energising a nation, but a change in mindset is spreading across Africa with a new focus being placed on transmission. With this approach it is possible to generate at a common point or at a point where energy resources allow a low cost generation, and transmit and distribute the power through a particular region or indeed over a continent.

Developing cross-border electricity links in many cases could make sound business sense. North Africa is trading electricity and is planning to further this pattern with greater integrated system development with the Middle East and Europe. A well developed Southern Africa Power Pool allows trading between most of the SADC countries. At the end of 1999, representatives from 11 member countries of the Economic Community of West African States (Ecowas) deliberated on a plan for the regional development of generation facilities and concluded by expressing their desire to implement a West African Power Pool. An East African Power Pool linking Kenya,

Uganda and Tanzania has been proposed and terms of reference for an energy master plan have been agreed.

The huge hydro-power potential which exists in countries like Angola, Mozambique, DRC, Zambia, Nigeria, and even Zimbabwe (some 100 000 MWe all together for the continent), the large natural gas reserves in North and West Africa and Angola, and the huge coal and uranium reserves in Southern Africa all give rise to ambitious medium to long-term plans to interconnect these resource-rich countries with the rest of the continent and further to transmit power to Europe. The attached African grid map shows the various existing and planned, local and regional power grids.

5. Future Power Generation Options

Southern Africa has been blessed with a diverse base of primary energy resources. A vast majority of the region's people does not have access to electricity. Plans to supply power throughout the regions will have to include both grid and non-grid options and implementation of renewable energy options on an appropriate scale. Coal, oil, natural gas, hydro-power, nuclear, solar energy, wind power, and bio-mass, may all be regarded as applicable options for the region.

The challenge of identifying and quantifying the impact of various electricity generation options on the physical, societal, economic and geo-political environment cannot be underestimated, specifically in the developing world. Among the large-scale options under consideration in the region are the development of the hydro potential on the Zambezi river (Mepanda-Uncua, Kafue Lower, Itezhi-Tezhi, Batoka Gorge), on the Inga (Congo) river (Inga II and III), and in Angola/Namibia (Epupa Dam), the development of gas fields and associated generation plant in Namibia, Mozambique and South Africa, and the development of coal fired plant in Zimbabwe and Mozambique.

At a conservative annual growth rate of some 4% for the region (6% is required, according to UN estimate, to reach poverty reduction targets - reduce the number of people living on less than 1 $/day by half by 2015), means an annual increase of some 1400 MWe. This presents a significant challenge in terms of optimising the development of generation options to limit financial strain on some of the region's poor economies.

Integrated Resource Planning has been applied, mainly in South Africa by Eskom, with a view to optimize the mix of future supply and demand side options. Eskom's strategic planning is supported by its research and development programme, with an annual budget of some R 300 million, which includes the development of pilot/demonstration plants for clean coal technologies, environmental impact mitigation options, renewable energy (solar, wind, bio-mass) options, energy storage technologies, and the development of a safe and economic nuclear generation option – a new and improved version of the High Temperature Gas Reactor (HTGR) - the Pebble Bed Modular Reactor.

The development of a commercial scale pilot/demonstration plant is aimed at providing a cost effective, safe and environmentally benign option, to facilitate plant siting, and to provide flexibility for decision making.

6. The Nuclear Option - The Pebble Bed Modular Reactor (PBMR)

6.1 Background

The Pebble Bed Modular Reactor represents a significant advance in reactor safety as well as a substantial reduction in the cost of nuclear power generation. In the case of "conventional" power reactors, the probability of a large release of radio-activity is minimal and the associated risk to nearby populations is several orders of magnitude less than non-nuclear risks accepted without question in daily life. The PBMR carries no risk of a major release of radioactivity – short of total destruction of the plant by an outside agency. Because the PBMR is, to a large extent, inherently safe, there is less need for the sophisticated and costly engineered safety systems of today's large power reactors. It therefore also promises significantly cheaper electrical power than its predecessors.

6.2 History of project development in South Africa

Development in South Africa - In the late 1980's, the Atomic Energy Corporation (now NECSA, the Nuclear Energy Corporation of South Africa) was designing an indigenous power reactor of the pressurized-water reactor (PWR) type. It was also developing a small, similarly based marine reactor. Both projects were terminated in 1989 following which some key personnel of the design team joined the high-tech 'Integrator of System Technology' (IST) in Pretoria. In 1990, Armscor invited IST to carry on with the marine reactor project and then, in the following year, changed the focus and asked for a 5-MW power unit for remote inland locations.

By that time, IST had been made aware by former AEC personnel of a promising German experience with a small reactor, known as the "pebble bed" because of its billiard-ball-like fuel "pebbles". A report was presented to the armaments manufacturer, Armscor, in 1992 – and was shelved. It presented a conceptual system design of a small power reactor based on the German core concept, with a direct helium thermodynamic cycle for power conversion.

In a remarkable act of faith, IST pursued the small reactor project at its own expense. Mining organizations were approached, there being known mineral deposits in southern Africa that cannot be exploited due to lack of power supply. None of the organizations approached was prepared to be the first to commit to such a novel power technology. Eskom, the national electricity utility company, was formally approached in 1993 and at first rejected the idea. The nuclear world believed in economy of scale. The reactors of the nuclear power station at Koeberg, north of Cape Town, were each designed to generate 921MW. Elsewhere, 1400 and 1500-MW reactors were being developed. The idea of a 50-MW modular unit offered by IST seemed less than sensible.

Over the next few years, however, possible commercial advantages (discussed below) of making such a mental leap downwards became increasingly apparent. Following enthusiastic lobbying within the organization, Eskom added the PBMR to the list of renewable and other power generation technologies being investigated for future investment. The promise of the PBMR system survived these further investigations. Given the necessary approvals, construction of a first module could begin in 2004.

Reactor design is not a core business for Eskom. Accordingly, in 1999, a separate entity known as PBMR (Pty) Ltd was established, as a subsidiary of Eskom Enterprises, initially to develop the design and to establish beyond doubt the technical and commercial feasibility of the project. The technical staff, which now numbers 200 engineers and scientists based in Centurion, near Pretoria, was drawn from organizations such as Eskom, IST, Denel (SA aviation and arms developers) and the former AEC.

One of the conditions imposed by Eskom to assure itself of the international viability of the PBMR concept was that the project should proceed only if credible foreign nuclear organizations saw sufficient potential in it to bear part of the development cost. As discussed below, the required interest was quickly manifested.

6.3 Technology Development - Plant Design

6.3.1 Systems Engineering

The PBMR reactor is contained in a vertical steel pressure vessel approximately 22 m high with an internal diameter of 6.2 m. The wall thickness is approximately 120mm resulting in a mass of some 724 t. The reactor pressure vessel is thus very much larger than those of the 921-Mwe reactors at Koeberg. Within the vessel, the slim cylindrical pebble core is contained within the core cavity, surrounded by a graphite "reflector". This reflector takes the form of a 36-sided right prism (diameter 5.5 m, height 15 m). The core cavity within it has a diameter of 3.5 m and is 9 m high. Some 330 000 fuel spheres and about 110 000 pure graphite spheres of the same diameter are loaded into this cavity to form the reactor core. The fuel spheres are loaded around the periphery with pure graphite spheres in the centre. The active part of the core thus takes the form of a vertical hollow cylinder 8.5 m tall with external and internal diameters of 3.5 m and nearly 1 m, respectively. This annular arrangement of uranium-bearings spheres, unique to the PBMR technology, spreads power generation more evenly across the core and limits the temperatures in the centre of the core in the event of a loss-of-cooling accident. The function of the graphite reflector, other than to contain the core and to transmit heat outwards, is to improve neutron efficiency by reflecting errant neutrons back into the core. The reflector is penetrated by a ring of 35 vertical holes to accommodate the reactivity control and reserve shutdown systems as described below.

In the helium-cooling circuit, "cold" helium at 500°C and 7 MPa enters the reactor pressure vessel through ducts at the bottom of the vessel and is led up through the reflector to above the height of the core. It then flows downward through the pebble bed and emerges at 900°C through a large duct in the bottom of the reactor pressure vessel. Thermodynamically, the system constitutes a recuperated Brayton cycle with a closed-circuit, water-cooled inter-cooler and a pre-cooler.

Expansion of the working gas (helium) drives three gas-turbines in series. The first two smaller turbines are coupled to compressors while the third drives the power generator. All three have vertical shafts supported by magnetic bearings. The gas gives up much of its residual energy in the recuperator heat-exchanger before being recompressed and recirculated to the reactor pressure vessel. The pre-cooler and inter-cooler heat exchangers are cooled, via closed intermediary water loops, by an external heat sink (water body or air).

The power output of the module is controlled by raising and lowering the helium pressure. Raising the system pressure by introducing more helium into the gas circuit increases the mass flow of helium passing through the core and, to some extent, lowers the fuel temperature. The Doppler effect (described below) causes the power level to rise to a new equilibrium level. Reducing the gas inventory has the reverse effect.

Alternatively, rapid changes in power level can be made by means of bypass valves or by moving the control rods suspended in the vertical holes in the reflector. Inserting these rods reduces the number of neutrons reflected back into the core and thus reduces the reactivity of the core and the power level. An entirely separate and diverse reserve shut-down system utilizes the remaining holes in the reflector.

Refueling is carried out continuously with the reactor at power. Fuel spheres are released from the bottom of the reactor, monitored to determine the degree of burn-up and, if there is useful energy left in them, recycled pneumatically to the top of the reactor. At equilibrium, some 372 new pebbles are added to the vessel each day and a similar number discharged into the spent fuel silos. The annual full-power fuel requirement is thus about 26 t. On average, during 850 day period in the reactor, a single pebble will circulate through the core six times. "Burnt-out" pebbles rejected by the system are diverted into silos in the basement of the reactor building. These tanks have sufficient capacity to hold all spent fuel spheres generated throughout the 40 year design life of the reactor. Thereafter they remain in the decommissioned reactor building for a further decade or more before ultimate disposal.

6.3.2 The Fuel

The starting material for the manufacture of the fuel is uranyl nitrate solution enriched to contain 8% uranium-235. Falling droplets of the solution are transformed by chemical engineering techniques into "kernels" of enriched uranium oxide (UO_2), approximately 0.5 mm in diameter. These kernels are coated successively with porous graphite, dense pyrolytic graphite, silicon carbide, and finally a further shell of pyrolytic graphite. The shells so formed are respectively 90, 40, 35 and 40 microns thick to give a final coated-particle diameter of just less than one millimeter.

The coating technique floats the UO_2 kernels on a stream of argon in a small fluidized-bed furnace. Appropriate organic gases are then introduced to the argon stream. The important silicon carbide shell, for example, is formed in a three-hour process by decomposing gaseous CH_3SiCl_3, into HCl as well as the required SiC, which deposits on the floating kernels. The process is relatively straightforward.

The innermost shell of porous carbon accommodates both swelling of the uranium oxide kernel under irradiation and fission product gases (isotopes of xenon and krypton), which diffuse from or recoil out of the kernel during operation. A build-up of pressure which might otherwise rupture the outer containment shells is thereby avoided. The first pyrolytic graphite shell protects the kernel from chemical attack during the formation of the silicon carbide shell. The highly stable and mechanically strong silicon carbide shell forms a miniature pressure boundary, which retains essentially all fission products formed during operation. Its stability is the key to the PBMR safety. Finally, the outer pyrolytic carbon layer protects the silicon carbide

shell from physical damage during the subsequent manufacturing processes that form the spherical fuel element.

These processes consist of compacting a mixture of some 15 000 coated particles together with resin-coated graphite dust into a sphere 50 mm in diameter, pressing this sphere into 5-mm thick hemispherical shells of pure graphite, and heating the sphere so formed to 900°C under vacuum to decompose the resin binder and to degas the final product. The pebble is finally machined to produce a near-perfect sphere with a diameter of 60 mm.

The product is a smooth, tough sphere which handles very much like a large black billiard ball. Each such 200-g "billiard ball" contains 9 g of enriched uranium. During operation, the graphite acts as the moderator, slowing fission neutrons born in the uranium kernels with energies around 2 MeV down to the "thermal" energies around 0.02 eV, at which energy further uranium-235 fission takes place. The pebbles are thus both fuel and moderator. The fuel will be made at Pelindaba in South Africa, by NECSA using the German technology. Extensive testing of irradiated fuel made in Germany showed that fewer than two granules in 100 000 have been damaged or had defective silicon carbide shells.

The ability to retain fission products within the coated particles at high temperature is the key to the safety of high temperature gas reactor. The increasing release rate of fission product krypton-85 from the coated particles, with temperature and with annealing time at high temperature, signals progressive failure of the silicon carbide shell. The fuel suffers progressive degradation with temperature, but only at temperatures above 1600°C. There can be no significant release of fission products at temperatures below 1600°C. As discussed below, even under accident conditions the fuel temperature can never reach that level.

6.3.3 Materials Selection for the Main Power System (MPS)

Materials selection for each component is addressed in the PBMR integrated design process. The iterative process involves critical evaluation of the operating conditions, safety classification, design codes, maintenance, costs etc. The overall philosophy is also to use well-qualified material that ought to reduce overall costs, assist in the licensing process and ensure a wide base of manufacturability. The materials currently designated for the MPS, consisting of the Reactor Unit (RU), the Primary Pressure Boundary (PPB) and the Power Conversion Unit (PCU), is described and is applicable to a core gas inlet temperature of 500°C and a gas outlet temperature of 900°C. The designs of structural components are for 35 effective full power years (300 000 operating hours) while the rotating components are designed for selective parts replacement at maintenance intervals (50 000 operating hours).

6.3.3.1 Reactor Unit (RU)

The reactor unit consists of a core structure of graphite, contained within the core barrel that in turn is supported by the RPV (part of the PPB). The designated graphite is a medium grained, extruded, near isotropic nuclear grade graphite. This will be used to form the bottom, side and top reflectors that contain the bed of fuel spheres. The side reflector is restrained against movement due to hydraulic and pebble bed forces by a system of restraining bands, currently designed to be carbon-carbon composite straps. The carbon-based components are exposed to helium gas streams at

temperatures ranging from 500°C to 900°C and would experience fast neutron fluences at end-of-life ranging from $1x10^{18}n/cm^2$ to $2x10^{22}n/cm^2$. The design of these components takes account of in-service degradation mechanisms like neutron irradiation induced changes to physical and mechanical strength properties, helium corrosion effects and the effect of air ingress events. The extensive database of irradiation-induced changes in various graphite grades have been utilized to predict the expected changes in the PBMR grades of graphite, and this will be supplemented by a materials testing programme. Provision is made for partial graphite reflector replacement after about 24 years of operation.

The core barrel and support structure provides gas flow paths, supports the graphitic core and dissipates heat during normal and abnormal conditions. The material is currently Type 316 austenitic stainless steel and the design is being performed in accordance with ASME Section III, Division 1, Subsection NG – Core Support Structures. Normal operating temperature is about 500°C, increasing to about 700°C during abnormal operating conditions. The mechanical design is well within current design experience. An area of development is the assurance of emissivity of the core barrel to ensure the required heat dissipation and removal and thus the cooling down of the fuel.

6.3.3.2 Primary Pressure Boundary(PPB)
The primary pressure boundary separates the helium circuit from atmosphere and consists essentially of two parts, namely the RPV and the PCU pressure boundary.

- Reactor Pressure Vessel(RPV)

The RPV is designed in accordance with ASME Section III, Division 1, Subsection NB – Class 1 Components. The RPV wall temperature is conditioned to be at about 300°C, to keep the irradiation embrittlement due to fast neutrons within the known database provided by the extensive operation of pressurized water reactors (PWR's). It is also for this reason that the designated material is SA 508, Grade 3 – a forging material commonly used for the construction of pressure vessels. During abnormal operating conditions the RPV wall temperature will increase to between 400°C and 500°C, for a limited period. The end-of-life fast fluence level experienced by the RPV wall is an order of magnitude less than that of PWR's.

- Power Conversion Unit (PCU) Pressure Boundary

The PCU pressure boundary is exposed to helium at a maximum temperature of 150°C and insignificant levels of fast neutron dose. The current material designation is a combination of SA 508 (forgings) and SA 533 (plates).

6.3.3.3 Power Conversion Unit(PCU)
The PCU consists of the two turbo-compressor units, the power turbine-generator, the recuperator, the pre-cooler, the inter-cooler and connecting pipe-work.

- Turbo-compressors and Power Turbine

The High Pressure Turbine (HPT) and Low Pressure Turbines (LPT) drive the respective compressors via integral shafts. The gas inlet temperature (900°C for HPT, 800°C for the LPT and 690°C for the Power Turbine) dominates the material choice of the helium-wetted components, i.e. rotating and stationary blades, discs & casings. Cooling is minimized to ensure optimum efficiency and for this reason the high Ni-

alloys and super-alloys are utilized to obtain the desired design life. The un-cooled blades are designated to be of directionally solidified and equiaxed casting materials (MGA1400DS and MGA2400CC) - containing significant amounts of nickel, chromium and cobalt to ensure the high temperature strengths required. The design of the HPT also has to cater for significant levels of neutron streaming from the reactor unit as well as fission product plate-out. Due to the foreseen maintenance on the turbo-units, the dose rates from these components due to the activation and contamination are to be kept as low as possible.

• Recuperator

The recuperator has a normal operating temperature of about 500°C and the inlet temperature can increase to about 700°C for short periods during transient conditions. The current design is a plate-fin configuration of a stabilized austenitic stainless steel (Type 347). The recuperator is predicted to be the main location for fission product plate-out and low maintenance and repair requirements are to be catered for in the design.

• Pre-cooler/Inter-cooler

The pre-cooler and inter-cooler are water-to-gas heater exchangers with gas temperatures of around 140°C and water inlet temperatures of 28°C. The current design utilizes integrally finned carbon steel U-tubes in a carbon steel shell-and–tubesheet arrangement.

• Hot Piping

The piping that directs the helium flow from the reactor unit to the PCU components, between the respective PCU components and back to the reactor unit is of similar design. The pipe design consists of an internal metallic liner that is in contact with the high temperature helium. The liner is then insulated from the pressure-retaining pipe with SiO_2- and Al_2O_3-fibrous material. The liner material is designated to be Alloy 800H, a nickel-iron-chromium alloy. For the core return piping, between the recuperator and the reactor unit, the internal sleeve material is designated to be Type 321 stainless steel, a stabilized austenitic stainless steel, due to the lower required operating temperatures. The pressure-retaining pipes are nominally exposed to helium at temperatures of 150°C and are currently designated to be low-alloy steel (16Mo3).

6.3.3.4 Materials selection - Conclusion

The current PBMR design strives to utilize established, well-qualified materials. Certain areas have been identified where data are lacking in regard to assuring optimal design life and designing for replacement; conducting supplemental materials testing will address these deficits. Material advances and qualification of properties in the following areas will benefit the design of future PBMR's:

- High strength, isotropic, irradiation resistant graphite materials.
- Irradiation resistant carbon fibre based materials.
- Low-activation, high strength metallic materials.

6.3.4 Nuclear Safety Aspects

Nuclear safety is dominated by two phenomena of reactor physics: fission product decay heating and the nuclear Doppler effect. They are respectively a curse and a blessing.

While a reactor is operating, approximately 94% of the heat generated arises instantaneously in the fission process. The remaining 6% is heat generated by the radioactive decay of fission product debris from earlier fissions. This decay heat does not "switch-off" when the reactor is shut down; initially 6%, it falls to 1.4% in the hour following shut-down, and to 0.5% one day later. In a large power reactor, however, even 0.5% may amount to 15 MW and has the potential to melt the core, so, to achieve the required high degree of safety, it is necessary to install highly reliable, duplicated emergency and shut-down cooling systems driven by correspondingly reliable stand-alone duplicated or triplicated emergency power supplies. These must be designed, manufactured and maintained to the highest and therefore costliest quality assurance requirements. Furthermore, it has been deemed prudent from the outset to house the reactor and associated equipment in the familiar cylindrical or spherical containment buildings.

At Three Mile Island ITMI) in 1979, a pressure relief valve opened as designed but it failed to re-seat, thereby creating a loss-of-coolant accident – an event foreseen in the design. Largely because of inappropriate training, however, the operators misinterpreted what was going on, interfered with the as-designed plant response and cancelled the emergency cooling system. Decay heat melted much of the core. The step-change in safety inherent in the modular pebble bed reactor is that such a meltdown is impossible. Not only will its type of fuel not melt, but also there appear to be no circumstances in which the fuel can reach temperatures at which coated-particle degradation leading to significant fission product release can occur.

The fission product decay heat-rate of each relatively small PBMR module is approximately 10 times less than that at TMI. The core and the pressure vessel, on the other hand, are physically relatively big. The net result is that, even if all forced cooling of the core were lost, and if all control rods were held out of the core, natural processes would soon be removing heat form the pressure vessel faster than decay heat can generate it. As a result, the central fuel temperature would peak at below 1600°C and then slowly decline. As described above, there can be no fuel degradation and therefore no fission product release below that temperature, and only a slowly escalating release at temperatures substantially higher. Even following total failure of the helium circuit, therefore, the operators would have nothing to do for several hours. They could walk away. The validity of this scenario in respect of the 15-Mwe AVR reactor in Germany was demonstrated at least twice when all forced cooling was deliberately removed from the core, all control rods were fully withdrawn, and the evolution of the core and vessel temperatures was observed.

The Doppler effect is the second effect mentioned. Uranium-238 has a resonance capture peak in the epi-thermal neutron energy range. This peak broadens as the fuel temperature rises. As a result, neutrons are absorbed increasingly readily by uranium-238 before they can be slowed down by the moderator to thermal energies at which fission in uranium238 takes place. The reactivity of the core is thus reduced by the increase in temperature and the core level must fall.

Most power reactors exhibit a net negative feedback to temperature and power changes due to this mechanism. In certain conditions in certain reactor, however, the negative Doppler feedback effect can be overwhelmed by other factors and an increase in temperature or reactor power can feed on itself, accelerating the rate of

increase. Fast-acting control systems are needed to control this type of feedback. At Chernobyl, the control system did not respond quickly enough. The control room staff disregarded operating rules in trying to operate the reactor at very low power in the positive feedback condition. The reactor design was seriously flawed in that it was physically possible for them to do so.

In the PBMR, the negative Doppler feedback is dominant under all possible conditions. Core damage due to reactivity accidents also, therefore, appears to be impossible. Fire is clearly another aspect of fundamental safety importance. Photographs of the exposed and burning Chernobyl core remain clearly in the memory. To date, however, the safety analyses for the PBMR have revealed no circumstances in which sufficient oxygen can reach the fuel to sustain a graphite fire.

In summary, no situation has been identified in which sufficient radioactive material can be released from the site to necessitate any off-site protective action. There should therefore be no need for any off-site emergency plan or for any restriction on local population development adjacent to the site. In practice, It may well be considered prudent for early units to be located in relatively sparsely populated areas. It is hoped that such a requirement, if imposed, will fall away as confidence in the system grows. In respect of other safety considerations such as radioactive effluents and the exposure to radiation of operator and maintenance personnel, past experience of High Temperature Gas Reactors (HTGRs) has been excellent. There remains the emotive issue of the long-term disposal of the spent fuel. The reasons for industry confidence that deep geological disposal will provide ample safety for future generations are beyond the scope of this article. Suffice it to say here that the silicon carbide shell around each granule will afford excellent containment long after other engineered barriers to ground-water contamination have crumbled. The "problem" of spent fuel disposal will therefore be less of an issue for the PBMR than for other reactors. It is not the intention to reprocess the fuel to recover unused uranium or plutonium.

The safety analyses are currently being scrutinized by the National Nuclear Regulator (NNR) and its consultants abroad as part of the nuclear safety licensing process. The statement made here, while they reflect the views of PBMR (Pty) Ltd and of the other major participants, must therefore be regarded to some extent as *sub judice*.

6.4 Economic and Commercial Aspects

No nuclear project will succeed unless the public and decision-makers see a clear need for it and trust it. More specifically, it must be perceived to be a low cost and very safe. The PBMR will have a low cost because, owing to its intrinsic safety, the sophisticated safety systems built around today's large reactors are not needed. As a result, after the early units, the PBMR construction cost is expected to fall to the target of around U.S. $1000 per kilowatt, or about $120 million per 120-MW module. This is little more expensive than the likely cost to Eskom of new coal-fired plant at about $900 per kW. The nuclear fuel cost, less significant in the equation than the cost of coal, is expected to be comparable with coal costs even at the pit-head power stations in South Africa (Mpumalanga Province). Carriage of coal to the coast, where the first PBMR modules are likely to be located, is now unthinkably expensive.

South Africans enjoy the cheapest electricity in the world. If the PBMR can be shown to be economically competitive here, as it currently appears that it will be, it will compete anywhere. Further, it emits no greenhouse gases. We therefore have the unexpected and entertaining possibility of reactors being exported by South Africa or built overseas under licence to a South African organization. The world market for new power stations is estimated to be $85 billion per year. Another facet of the commercial case is the short construction time. Power purchased in large blocks – perhaps R30 billion for a 4000-MW coal station, or even more for a twin unit 3000-MW nuclear station – involves massive expenditure throughout the decade prior to the required commercial operation date. If the demand growth projections are over-optimistic, as in RSA in the 1970s and 1980s, there can be massive over-expenditure. If the analyses are unduly pessimistic, there will be power shortages. With an estimated 24-month construction period, PBMR modules can be added to the grid as and where required. Moreover, the PBMR system has great operational flexibility. Modules can be brought on and off load or the power output of individual modules can be varied rapidly to accommodate fluctuating loads on the grid.

The PBMR has much else in its favour. The ongoing EIA cannot but conclude that is environmentally sound and far less objectionable than gas-fired and, in particular, coal-fired generation. Furthermore, as indicated above, there will be no technical need to site PBMR modules in remote locations although, initially, there may be a "political" need to do so. Because the yearly fuel requirement is only 26 t per module, and because the very mildly radioactive fuel pebbles are easily transported, modules can, given public acceptance, be sited exactly where the power is needed. Communities need no longer depend on power transmitted expensively over great distances from massive central power stations.

6.5 Project Status

As indicated above, PBMR (Pty) Ltd was established in 1999, as a subsidiary of Eskom Enterprises. Local share capital is provided by Eskom (30%) and the Industrial Development Corporation (IDC) (25%). The foreign interest, the sine qua non stipulated at the outset by Eskom, is represented by British Nuclear Fuels (BNFL) Ltd (22.5%) and the large American electricity supply utility, Excelon (12.5%). The remaining 10% is reserved for black empowerment investment. Eskom is itself a technically strong organization, being, with some 42 000 MW of installed capacity, the seventh largest supply utility in the world. Conditional upon results achieved by the demonstration PBMR module, it ahs undertaken to order 10 further modules. This demonstration of faith is essential for the export potential to be realized. Excelon is the largest utility in the US with a mixed portfolio of power stations totalling 22 500 MW. Its annual revenue exceeds $12 billion. It is rapidly expanding its nuclear interests by buying operating nuclear station in the U.S. It has announced that it expects next year to apply to the U. S. Nuclear Regulatory Commission for a licence to build a first PBMR module there.

BNFL is also a major player on the nuclear stage, providing products and expertise to the nuclear industry worldwide. Its activities cover fuel manufacture and nuclear services, nuclear power generation, spent fuel management and decommissioning. It operates in 15 countries and employs more than 23 000 people. The IDC has operated successfully in this country since its inception in 1940. Its mandate is to promote

economic growth in southern Africa by financing sustainable, competitive industries in accordance with sound business principles.

In terms of a contract with HTR GmbH, Eskom has for some years enjoyed generous access to German HTGR technology. HTR GmbH is the successor organization to those involved in the German pebble bed reactors and in subsequent design studies for the once proposed, fully commercial update. Negotiations with other major industrial organizations are now in hand. Mitsubishi Heavy Industries of Japan, for example, which could build reactor pressure vessels, has made public its interest in participating. Three major studies are currently under way or, in the case of the detailed feasibility study (DFS), have recently been completed. A principal objective of the DFS was to make progress on the design to the point at which the future generation cost, and therefore the likely competitiveness of the plan, could confidently be determined to within 10% on the basis of firm prices quoted by equipment suppliers. The report now is under scrutiny by the local and foreign partners and by government. The SA Department of Minerals and Energy has assembled an experienced review panel.

The second major study is the Environmental Impact Assessment (EIA) that includes the important public participation process. The contract to perform the work was won by group of companies led by the Pretoria-based organization, Poltech. The EIA is financed, but in no way controlled, by Eskom as the owner of the proposed plant. The study has been in progress for more than a year, during which time public attention focused largely on the preparation of the Scoping Report. This report, which is the vehicle provided to satisfy the public that all aspects needing to be addressed in a nuclear EIA are being addressed, was drafted following a series of public meetings. It has been made available for further public comment at Koeberg and, mainly, in public libraries in appropriate centres. Everyone who asked to be registered as an "interested and affected party" was given a list of these centres.

Since Koeberg already has the necessary infrastructure, available space, and abundant cooling water, it is Eskom's preferred site for the first unit. To minimize fuel transportation distances, however, the Department of Environmental Affairs and Tourism (DEAT) required that issues relevant to Pelindaba, the envisaged fuel manufacturing site, as a possible site also be included in the report. The report's authors, however, still believe that Koeberg remains the better site. Naturally the EIA report will not satisfy everyone. Nuclear opponents have already reserved their position by declaring the EIA process flawed. Every effort is being made to meet their objections. Meanwhile, the work in the field has progressed. The complete EIA report is scheduled to be presented to DEAT and again to the public in the first half of 2002. Nuclear safety aspects have been excluded for the EIA process. The National Nuclear Regulator (NNR) has the responsibility to establish nuclear safety standards and to ensure that installations subject to a nuclear licence meet those standards, so the simultaneous inclusion of nuclear safety in the EIA studies would involve unwarranted duplication. It is clearly recognized, however, that safety is a key public concern. In accordance with legislation, therefore, the National Nuclear Regulator (NNR) intends to hold public meetings on nuclear safety issues. This work constitutes the third major ongoing study.

In July 2000, Eskom submitted its formal application to the NNR for a nuclear installation licence. A multi-volume Safety Analysis Report describing the plant and dealing with nuclear safety issues in as much detail as is possible at this stage, has been compiled by PBMR (Pty) Ltd and is to be presented by Eskom to the NNR in the near future. The document is intended to give the NNR sufficient confidence to authorize construction. Several important stands must therefore come together before government can approve the construction:

- The several partners in the project and the minister of mineral and energy affairs must be assured, on the basis of the now completed DFS, that the project is technically and commercially sound.
- The minister of environmental affairs and tourism must accept the final EIA reports for the construction and operation of the plant, for the manufacture of the fuel at Pelindaba, and for the transport of materials for fuel manufacture and the transport of the manufactured fuel itself.
- The chief executive officer of the NNR, subject to NNR board approval, must be prepared, principally on her staff's review of the Safety Analysis Report, to issue the construction licence. This licence will probably stipulate further hold points.
- Other agencies, not least the NNR, must also signify approval on the basis of information supplied by Eskom.

Given these approvals, construction may begin in 2004, followed by a long commissioning period to test every aspect of plant performance. The target date for commercial operation is 2008.

7. Conclusion

Southern Africa should have a mix of generating technologies. Coal may continue to play a large part in the south (RSA) through the application of clean coal technologies and hydro-power potential in the central Africa (DRC) offers vast supply and should be pursued if political difficulties can be overcome. Natural gas reserves in the region (Namibia, Mozambique and Angola) are not large in world terms. Gas is an excellent chemical feedstock and provides low cost and clean heat for industrial purposes. Solar and wind power should be encouraged, especially as small-scale off-grid application for energising remote communities. Nuclear power offers clean, safe, reliable electricity on a large scale and can be sited where required, close to demand centres. The region's nuclear fuel reserves are practically unlimited (20% of world reserve). Nuclear power could therefore be a significant part of the future power generation mix in Southern Africa.

Bibliography

1. Development of power pooling in Southern Africa, K Sithole, Journal of Energy in Southern Africa, August 1997.
2. Southern African Power Pool, Inter Utility Memorandum of Understanding, 8 December 1995.
3. Southern African Power Pool, Annual Review Report, April 1997-March 1999.
4. Proposed generation capacity reserve criterion for the Southern African Power Pool, JL Pabot and GPWG, EAPIC 2000 conference, October 2000, Uganda.

5. Optimal Generation Capacity Expansion Plan (Pool Plan) for the Southern African Power Pool, JL Pabot and GPWG, EAPIC 2001 conference, October 2001, Ethiopia.
6. Southern African Power Pool, Annual Report 2001.
7. Energy in Africa, December 1999, DOE/EIA-0633(99), US Department of Energy.
8. Eskom's Integrated Electricity Plan, IEP6, 1999
9. Southern African Development Community, Country Brief Analysis (CABS), February 2001, USA DOE, Energy Information Administration
10. African Electricity Infrastructure Interconnections and Electricity Exchanges, T.J. Hammons, B.K. Blyden et al., IEEE Transactions on Energy Conversion, Vol 15, No 4, December 2000.
11. Southern African Power Pool, Pool Plan report, Volumes 1-4, July 2001.
12. A fresh, green look at nuclear power, Andrew Kenny, Third Sub- Saharan Power Conference, February 2002, Midrand, South Africa
13. Eskom's Annual Report 2001
14. Eskom Enterprises Annual Report 2001
15. The Pebble Bed Modular Reactor, D.R. Nicholls, South African Journal of Science (98), January/February 2002
16. The Lighting Up of Africa, JA deBeer, New African, February 2001

ENERGY RESEARCH IN THE SIXTH FRAMEWORK PROGRAMME

Philippe Busquin

Member of the European Commission

Abstract

This paper presents the content of the 6th Framework Programme of the European Commission for technology research and development in the field of energy. These energy research activities are put in the more general context of energy policy and research policy. From this point of view, the paper also explains how this contributes to and constitutes an essential element of the more general European Research Area initiative, in its attempt to solve the problems of fragmentation and duplication of efforts of research and technology development in Europe. Concentrating on energy research, it shows how the priorities selected for the sixth Framework Programme can make a contribution to a smooth transition towards a sustainable energy future.

Keywords: research, energy, European Commission.

Introduction

Energy is the basis of economic development. Even if the energy intensity of our societies is decreasing, energy consumption is increasing, only more slowly than development measured by GDP per capita.

Many regions in the world will undergo socio-economic development which will both be sustained by, and give rise to increased energy consumption. As an example, it should be recalled that over two billion people still do not have access to modern electricity services.

Energy has today to cope with an ever-increasing socio-economic demand, but must also satisfy more and more stringent environmental criteria. The key word is sustainability, our energy usage today also impact on the environment and should not prevent future generations having access to energy services as well, and therefore sustain their own development. A major challenge is to de-couple energy use from economic growth.

Although the energy industry is characterised by long term investments in infrastructures, it must be an ever-changing industry, always in transition, another key word.

Our policies these days should aim at ensuring a smooth transition from the present situation, mainly depending on fossil fuels, to a future situation, with the necessary diversification of primary energy supply sources, including renewable energy sources, as well as maybe some sustainable nuclear options. In this transition, fossil fuels can of course play a role provided we can cost-effectively dispose of the damaging greenhouse gas derived from their use.

Against this background, I would like to begin by addressing a number of relevant energy policies before I address research policy, and more specifically its energy aspects, but let us begin by taking a look at projections.

Energy Outlook to 2020

The "*Green paper*" on energy security of supply and "*Energy Outlook to 2020*" indicate that, taking into account the various policies already in place:

- Total world energy consumption would increase by 20% per annum from now to 2020, whilst energy intensity would decrease by 1.4% p.a. in the same period.
- The world dependence on fossil fuels would still be close to 90% by 2020.
- Natural gas usage is expected to grow rapidly in some regions of the world.
- In the EU, over the same period, the energy consumption would grow at 1% p.a., whilst the EU energy intensity would decrease by 1.5% p.a..
  The EU dependency on imported fuels would go from under 50% now to more than 65% in 2020.
- In the EU, gas would have the largest increase and coal the largest decrease.

Presentation of General Energy Policies

Some of these trends are regarded as not acceptable, because they do not go in the direction of sustainability, for instance from a security of supply point of view. Policy actions are therefore required to try to challenge these trends.

A first issue is climate change.
This is where sustainability takes its full meaning; the use of energy today should not jeopardise the chances of future generations. Under the Kyoto Protocol, the EU is set to decrease GHG emissions in the period 2008-2012 by 8% compared to 1990. This has been translated into a so-called "burden-sharing" agreement whereby the specificities of the different countries are taken into account. The latest report from the European Environment Agency indicated that the EU as a whole is on target so far, however, with wide discrepancies between the member states. The Commission has established the European Climate Change Programme to help identify the most environmentally and cost effective ways of enabling the EU to meet its target. Energy Research and the diffusion of more efficient technologies are obviously two of the essential ways.

A second issue is the energy security of supply for the EU.
One of the key messages of the Commission's Communication on Europe strategy for the security of energy supply, which we call "the Green Paper", is a necessary diversification, against a rising import dependency. There is no single perfect energy option. This necessary diversity should be reflected in all the other energy policies and in our research priorities.
A third issue is the strengthening of renewable energy sources.
A Directive aims at doubling the share of RES from 6% to 12% by 2010, and the share of RES in electricity generation from 14% to 22% by the same date. This will be achieved through the setting of national targets, the encouragement of national support schemes and a guaranteed access to transmission and distribution for green electricity.

A Communication from the Commission indicates that biofuels, methane and hydrogen (from renewables) should each increase their share to 5% of the total of fuels sold for transport by 2020. This has been translated for biofuels into a proposal for a directive, setting a first objective of 2% of biofuels by 2005, and 5.75% by 2010.

A fourth issue is energy efficiency and demand side management.

It is the key to try to de-couple economic growth from energy usage. The Commission has issued a communication in 2000 on this topic. It is also one of the elements of the "*Green paper*". This lists a potential for energy efficiency improvement of 18% from 1995 to 2010. This potential is equivalent to 160 Mtoe, roughly the total final energy demand of Austria, Belgium, Denmark, Finland, Greece and the Netherlands combined. Three groups of action were proposed:

- Measures to better integrate energy efficiency into non-energy Community policies.
- Measures to enhance existing Community energy efficiency policies.
- New common and co-ordinated policies and measures.

A Commission proposal for a directive to increase the use of co-generation in the EU is part of this.

There is no need to say how useful energy research can be in the improvement of energy efficiency.

Everything will have to take into account the context of the further integration and opening of the energy markets.
This was stressed at the Barcelona summit in March 2002. The Commission had presented in March 2001 a Communication on how to complete the internal energy market. It should however be a concern that this general policy is compatible with the other ones, which is not always obvious. It has for instance been observed that liberalisation has had detrimental effects on the introduction of co-generation in some member states.

Research Policy

The European Research Area was approved by the Heads of State and of Governments at the Lisbon Summit.

The awareness of the fragmentation and duplication of our efforts in the field of research and technological development formed the basis of the proposal for the creation of the European Research Area. The Union invests 1.9% of its GNP in research and technological development, much less than the United States (2.6%) and Japan (2.9%). The exploitation of scientific results is often inadequate.

The integration of research at a European level is not simply a step forward, but a change of paradigm. We envisage an area in which projects and programmes of research can be conceived and carried out in a truly European context and where research workers can benefit from development prospects and mobility throughout Europe. To fully exploit the considerable research potential of Europe, the various actors should be able to benefit from

greater fluidity, transparency and accessibility of the European work area and from real possibilities of co-operation.

The European Research Area will permit an enhanced performance of our scientific system for the benefit of society and the European economy alike. This new concept led us to reconsider deeply the main financial instrument, which the EU uses to support European research, which we call the Framework Programme. This instrument, endowed with 17.5 billion Euro over 4 years, must facilitate the integration of European research as its primary objective. Please allow me to underline three of its principal elements:

- New financial support instruments, such as networks of excellence and integrated projects, will enable those involved in European research to develop strategic co-operation, result in structuring/integrating effects, with more autonomy and flexibility than in the past;

- The European Framework programme has to play the role of catalyst. This is why European support will concentrate on those topics where it is essential to have a critical mass sufficient to generate new knowledge enabling real progress and support for new industrial activities;

- It is time for the European Union to establish a genuine networking of research policies and programmes, whether they are national or regional, and to avoid fragmentation and the duplication of effort. This is why the programme proposal envisages direct support for co-operation and for the more coherent implementation of national and regional research programmes and activities.

This will result in the mobilisation of a critical mass of resources to give a genuine structuring effect to European actions.

It is with this spirit in mind that we have to analyse the priorities of energy research.

Energy Research More Specifically

The proposals for research in the energy field include activities for both the short and the long term.

The short-term actions are aimed at the efficient use of energy, as well as the validation and demonstration of new and renewable energy technologies and their integration into existing networks in combination with conventional power plant. Improvements in the competitiveness and reliability of these new methods are also covered.

For the longer term actions, the objective is to prepare the conditions for the development of alternative sources and methods of energy transformation and transport which have a large potential to provide a break-away from an energy supply system strongly dependent on fossil fuels. This is true in particular in the fields of transport and the decentralised production and distribution of electricity and heat. The choice covers fuel cells and hydrogen, as well as renewable sources that have a large potential, such as biomass and photovoltaics. An

additional priority is also set on the mitigation of CO_2 emissions in association with cleaner fossil fuel plants.

Further to this, materials research is an important topic for a number of on-going FP5 projects, notably the 700°C supercritical power plant development, now in its second phase, and in the gas turbine sector, where there is for example ongoing research on ceramic matrix composites and long life coatings.

In FP6, materials research will undoubtedly be an essential component of the actions undertaken on most of the priorities. This will be the case from fuel cells and hydrogen, to CO_2 capture and storage plants, through biomass and photovoltaïcs.

As indicated by the expressions of interest that we have recently received for integrated projects and networks of excellence in energy, the future activities will generally consider materials research and development in their fields of activity.

As far as nuclear energy is concerned:
The principles proposed for the new EURATOM programme also stress the concentration on a limited number of strategic objectives to strengthen collaboration between Member States. A major priority concerns waste management, the principal problem today affecting the use of nuclear fission for electricity production. There is significant public and private European research effort on the development of technologies for the treatment and storage of nuclear waste. The action of the Union in this field makes it possible to strengthen and ensure the consistency of the strategies adopted by waste management organisations and related industrialists. Moreover, the debate on the structures of our energy supply after 2020 perhaps necessitates concerted research effort at the international level on a new generation of fission reactors.

Concerning research on controlled thermonuclear fusion, Europe has already invested significant amounts on research efforts. Fusion is now inbetween two generations of experimental installation. The JET reactor permitted significant progress, but experts agree that the continuation of the development of fusion by magnetic containment towards its ultimate goal, electricity production, requires the construction of a more powerful installation, the ITER.

Conclusion

I have been taking you through the various energy policies of the EU, concentrating on the energy research policy. As a conclusion, I would simply like to stress once more the only fundamental objective underlying all this: to provide our society with affordable energy to sustain its future well-being and development. That will be achieved if we can ensure a smooth transition to a sustainable energy future.

I hope that you are convinced that energy research plays a critical role in that respect.

Bibliography

- Energy Outlook to 2020 – EC DG TREN

- COM (2001) 125 Final "Completing the internal energy market"
- Promotion of green electricity – Presentation of the new Directive – Commission
- COM (2000) 769 Final - Green Paper "Towards a European strategy for the security of energy supply"
- COM (2000) 247 Final "Action plan to improve energy efficiency in the European Community"
- COM (2001) 547 Final "Communication on alternative fuels for road transportation and on a set of measures to promote the use of biofuels" and COM (2001) 265 (COD) "Proposal for a directive on the promotion of the use of biofuels for transport".
- ECCP Report, June 2001, EC DG Environment.
- COM (2000) 6 - Towards a European Research Area.
- Decision no 2002/xxx/ec of the European parliament and of the Council concerning the sixth framework programme of the European community for research, technological development and demonstration activities, contributing to the creation of the European research area and to innovation (2002-2006).
- FP6 – Proposal for the specific programmes, EC DG RTD

ADDENDUM

DEGRADATION OF EB-PVD THERMAL BARRIER COATINGS DURING THERMAL CYCLING

X. F. Sun, M. H. Li, Z. Y. Zhang, H. R. Guan
Institute of Metal Research, Chinese Academy of Sciences, Shenyang, 110016, P. R. China

Abstract

Yttria partially stabilized zirconia (YPSZ) ceramic top coat was deposited on NiCrAlY bond coat by electron beam physical vapor deposition (EB-PVD). Thermally cyclic test was performed at 1050℃. The experimental characterization of thermal barrier coating (TBC) specimens was conducted using scanning electron microscopy (SEM), equipped with energy dispersion X-ray spectroscopy (EDAX), and X-ray diffraction (XRD). It was shown that microcracks initiated preferentially in the YPSZ top coat along columnar grain boundaries and then penetrated through the whole top coat down to the thermally grown oxide (TGO) layer, accelerating the oxidation of bond coat. The TGO growth stress due to the rapid formation of NiO and spinel and the thermal stress due to the mismatch of thermal expansion coefficient are the main reasons for ceramic top coat spallation. The degradation mode of EB-PVD TBC is that ceramic top coat spalls at the interface between bond coat and TGO, with TGO scale still adhering to YPSZ.

Keywords: EB-PVD, TBCs, TGO, thermal cycling, degradation

Introduction

Thermal barrier coatings (TBCs) are applied in hot parts of gas turbines to increase the engine's efficiency by elevating the operation temperature or reducing the amount of cooling air. The present state-of-the-art TBCs are yttria-partially-stabilized zirconia (YPSZ) coatings deposited by atmospheric plasma spraying (APS) or electron beam deposition (EB-PVD)[1,2]. It has been reported that EB-PVD TBCs have superior properties to APS TBCs [3]. The unique columnar microstructure of EB-PVD ceramics exhibits a higher strain tolerance, but failure still occurs by spallation. The tenacious thermally grown oxide (TGO) plays a key role in the adhesion of the ceramic layer of the TBC. Lou and Wang [4,5] reported that the micro- or nano-structural coating forms a very thin, compact and adherent scale. In this work, bond coats were applied by magnetron sputtering to obtain a nano-structure and ceramic top coats were prepared by electron beam physical vapor deposition. The cyclic oxidation behavior of the TBC system was investigated.

Experimental procedure

Superalloy substrate discs (5mm× Φ15mm) were machined from Ni-base single-crystal bars, whose composition was mainly Ni with small amount of Cr, Al, W, Mo and Ta. After rounded and grit-blasted, the discs were cleaned in an ultrasonic bath and then put into a magnetron sputtering system for the overlaying of a NiCrAlY bond coat. The partially yttria (7wt.%)-stabilized zirconia top coat was deposited by a 120 kW EB-PVD coater. Thermal cycling test was conducted in a programmable, automated furnace at 1050℃. Thermal cycles consisted of a 5 min heating the specimens to 1050℃ and maintaining that temperature for 40 min, followed by forced air cooling for 20 min to room temperature. The microstructures of as-deposited and thermal cycled TBCs were investigated with scanning electron

microscopy (SEM), equipped with energy dispersive microanalysis and X-ray spectroscopy (EDAX). X-ray diffraction (XRD) analysis was used to identify phases of the inside surface for the spalled specimens.

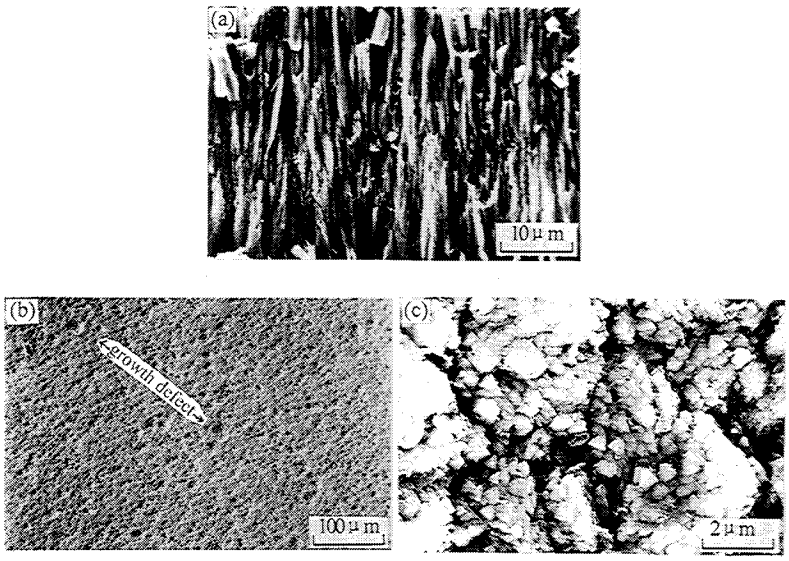


Fig.1 SEM images of as-deposited ceramic coatings (a) for cross-section, (b) and (c) for surface

Results

As-deposited ceramic coating

The as-deposited ceramic top coat exhibits a columnar-grained microstructure (Fig.1a). The columnar grains form dense clusters, but there are gaps or holes among the grain clusters (Fig.1b), which allow the lateral expansion and contraction of the ceramic columnar grains and allow free expansion of the substrate over a relatively large range. In this way, the ceramic top coat has the capacity for a high degree of expansion, exceeding that of the bulk material, and reduces the stress concentration resulted from the mismatch of the thermal expansion coefficient between the ceramic top coat and the substrate. The roughness of the as-deposited ceramic top coat is relatively low, but some spots of prominent growth defects can be observed (Fig.1c). Such defect is a bundle of zirconia columns. The outer surface diameters of these defects are in the range of 10~60μm.

Morphology of ceramic coatings after thermal cycling

The surface of the as-deposited ceramic top coat is dense. During thermal cycling, the gaps among grain clusters became wide, and some of which connected with one another and developed into microcracks. With the thermal cycles increasing, microholes could be observed in the relatively dense grain clusters, and microcracks further extended and became apparent (Fig.2a). After 300 cycles, some growth defects were surrounded by macrocracks

that were developed from microcracks (Fig.2b) and some had been spalled from the bond coat.

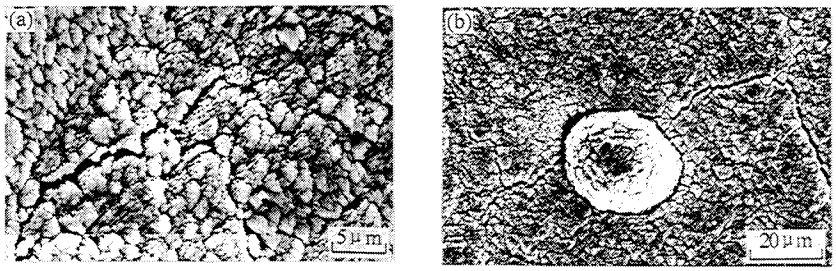


Fig.2 Surface SEM images of TBCs after thermal cycling at 1050℃ for (a)200 cycles and (b)300 cycles

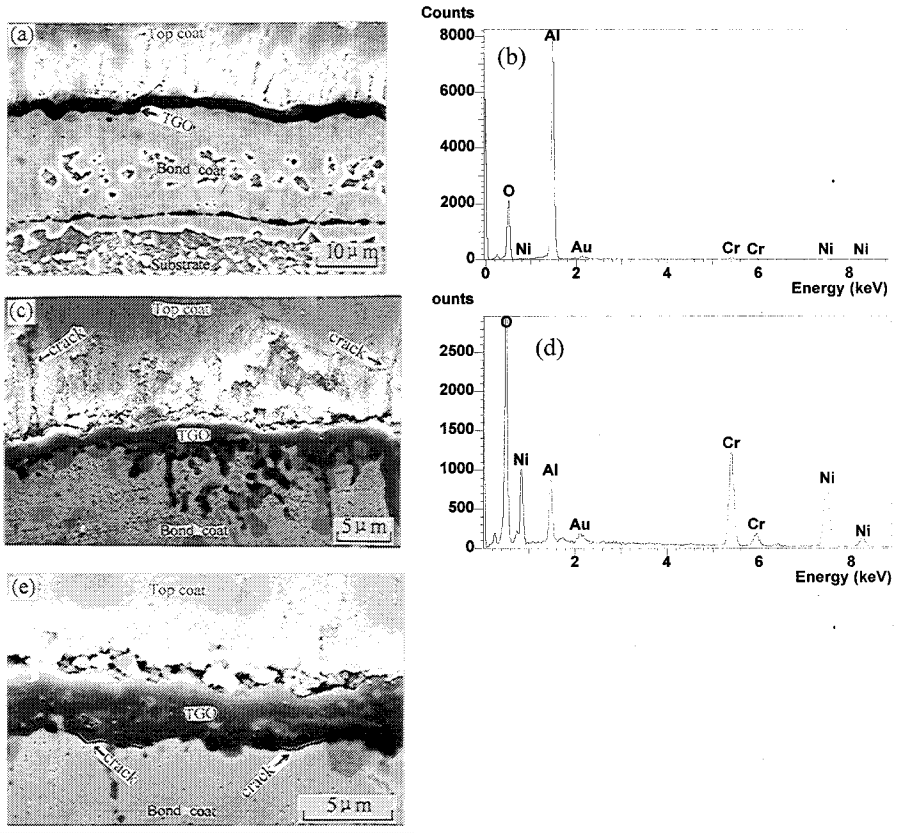


Fig.3 Cross-sectional SEM images and TGO EDS results of TBCs after thermal cycling at 1050℃ for (a) and (b) 100cycles, (c), (d) and (e) 300 cycles

Oxidation of bond coat

The cross-section SEM images and EDAX results of TGO for TBC specimens after thermal cycling are shown in Fig.3. It can be seen that after 100 thermal cycles the TGO layer is about 2μm in thickness (Fig.3a) and consists of only Al_2O_3 oxide (Fig.3b). Severe inner oxidation is observed in many locations after 300 cycles, where oxidation products extend into the NiCrAlY bond coat (Fig.3c). Although Al_2O_3 is the major phase of TGO, nickel-rich and chromium-rich oxides were detected near the interface of TGO/bond coat (Fig.3d), which are presumably NiO or $Ni(Cr,Al)_2O_4$ spinel. From the section, microcracks were observed along the columnar grain boundary in YPSZ, which started inside the top coat and was normal to the interface between ceramic top coat and bond coat (Fig.3c). Considering that ceramic top coat is subjected to tensile stress when heated, microcracks between columnar grains can be easily produced. These microcracks, which can reduce concentration of the stress resulted from the effect of thermal expansion coefficient mismatch between the ceramic top coat and substrate, will favor prolonging the thermal cycling lifetime of TBCs by releasing stresses in the top coat if they do not extend any further. However, if the cracks propagate the whole ceramic top coat along the columnar direction, air goes through these large cracks easily and accelerates the oxidation of the bond coat. Several cracks were also observed at the interface between the TGO layer and the bond coat (Fig.3e).

The fracture surface is shown in Fig.4, which reveals the uneven bare bond coat. EDAX confirmed that the surface, where TBC had been spalled off, was bare bond coat. Examination of the underside of the TBC spalled from the sample revealed that it was dark gray. According to XRD analysis, the underside of the spalled TBC consisted principally of NiO, α -Al_2O_3, and spinel with a trace of ZrO_2(Fig.5).

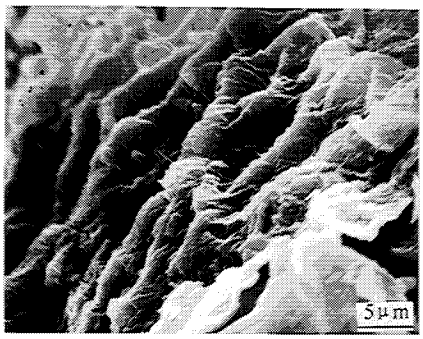


Fig.4 Surface SEM image of the specimen where the ceramic top coat fell off

Discussion

The oxidation of bond coat plays a significant role in the degradation of TBCs when operated at elevated temperature. The bond coat might be oxidized not only by the ionic transportation of oxygen through the zirconia top coat lattice but also by the gaseous diffusion of oxygen which penetrates through microcracks. After the specimens exposed at 1050℃ for

100 cycles, the TGO consisted only of the oxide α -Al_2O_3. When they were cycled to 300 cycles, a large amount of spinel and NiO were detected. This indicates that the formation of Al_2O_3 scale is very fast at the initial stage of oxidation because of the higher affinity of aluminum to oxygen, which gives rise to the selective oxidation of aluminum. In addition, the average grain size of the sputtered NiCrAlY bond coat is less than $100nm$ [6], which can accelerate the selective oxidation of aluminum [5]. With the formation of more Al_2O_3, the bond coat was aluminum-depleted near the TGO/bond coat interface [7]. When the aluminum content of the bond coat is not sufficient to provide the critical aluminum content for forming the only Al_2O_3 oxide, other oxide phases such as NiO and Ni (Cr, $Al)_2O_4$ may also grow. Furthermore, with the microcracks in the YPSZ top coat developing into macrocracks and penetrating through the whole ceramic coat along grain boundary, the inward transport of oxygen is accelerated, promoting the oxidation of the bond coat. The formation of more NiO and spinel may result in a rapid volume increase in TGO.

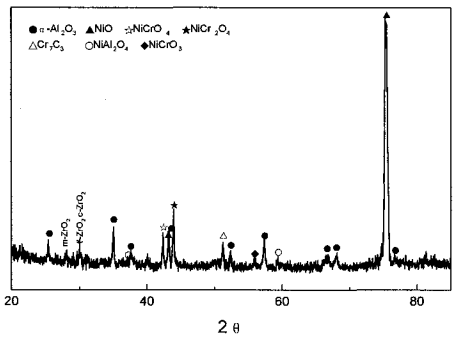


Fig.5 X-ray diffraction pattern of the inner surface of TBCs after 300 cycles at 1050℃

Moreover, during thermal cycling, strain developed at the bond coat/TGO interface due to the difference of thermal expansion coefficients. It can be given by expression:

$$\Delta E = \Delta\alpha \cdot \Delta T \qquad (1)$$

Where ΔE is the developed strain, $\Delta\alpha$ is the difference in coefficient of thermal expansion, and ΔT is the change in temperature. The combination of the oxide growth and the thermal expansion mismatch strain develops high in-plane stresses in TGO. Out-of-plane stress is generated when in-plane stresses create a stress component normal to the interface [e.g. by geometry changes (buckling)], thus providing a driving force for oxide spallation. As the interface of the bond coat/TGO is not perfectly flat, out-of-plane stresses easily build up. When the severe oxidation of the bond coat occurs, the oxide scale grows more rapidly, and the bond coat/TGO interface becomes irregular. The irregularities can act as stress concentrators. All these accelerate the build-up of out-of-plane stresses. When exceeding the interfacial strength of the bond coat/TGO interface, the out-of-plane stresses separate the TGO from the bond coat and result in cracking at the interface of bond coat/TGO. As the thermal cycling goes on, crack propagates by the extension of a buckled region followed by cracking at the ridge of the buckle or the production of kink cracks in the TGO. Once kink

cracks are initiated in the TGO and penetrate through the whole ceramic top coat, the coating detaches and the EB-PVD TBC spalls at the interface of TGO/bond coat.

Summary

Based on the experimental investigation, the failure mode of EB-PVD TBCs is considered to be following:

During thermal cycling, microcracks, which first form in the ceramic top coat along the columnar grain boundaries and then grow to penetrate the whole ceramic top coat in columnar direction, accelerate the oxidation of the bond coat. As a result of aluminum-depletion in bond coat, NiO and spinel oxides are formed near the interface of TGO/bond coat, which gives rise to a rapid increase of the TGO volume. The combination of TGO growth stress and thermally induced stress due to the mismatch of thermal expansion coefficient results in cracking at the interface of TGO/bond coat. As the thermal cycling goes on, crack propagates by the extension of a buckled region followed by cracking at the ridge of the buckle or the production of kink cracks in the TGO. Once kink cracks are initiated in the TGO and penetrate through the whole ceramic top coat along columnar grain boundaries, the coating is then free to detach, and the ceramic coat spalls at the interface of TGO/bond coat, with the TGO scale still adhering to YPSZ.

Acknowledgments

The authors thank Prof. H.Y.Lou for sputtering NiCrAlY bond coat, Prof. S.K.Gong for electron beam-physical vapor depositing ceramic top coat and Prof. T.F.Li for his suggestion.

References

[1] S.Bose, J.DeMasi-Marcin, Thermal Barrier Coating Experience in Gas Turbine Engines at Pratt & Whitney, Journal of Thermal Spray Technology, 6(1)(1997) 99-104

[2] W.A.Nelson, R.M.Orenstein TBC Experience in Land-Based Gas Turbines, Journal of Thermal Spray Technology, 6(2)(1997) 176-180

[3] R.A.Miller, Thermal Barrier Coatings for Aircraft Engines: History and Directions, Journal of Thermal Spray Technology, 6(1)(1997) 35-42

[4] H.Lou, F.Wang, B.Xia, L.Zhang, High-temperature oxidation resistance of sputtered micro-grain superalloy K38G, Oxidation of Metals, 38(3/4)(1992) 299-307

[5] F. Wang, The effect of nanocrystallization on the selective oxidation and adhesion of Al_2O_3 scales, Oxidation of Metals, 48(1997) 215-224

[6] M.H.Li, Z.Y.Zhang, X.F.Sun, W.Y.Hu, H.R.Guan, Investigation of Morphology and Phase Structure Feature of TBC, Materials Review 15 (2001) 71-73(in Chinese)

[7] M.H.Li, X.F.Sun, Z.Y.Zhang, S.K.Gong, W.Y.Hu, H.R.Guan, Z.Q.Hu, Oxidation and Phase Structure of the Bond Coat in EB-PVD Thermal Barrier Coatings during Thermal Cycling, Acta Metallurgica Sinica, 38(1)(2002)79-83

AUTHOR INDEX

A

Abe F., II.1171, II.1181, III.1379, III.1397, III.1469, III.1561, III.1571, III.1581, III.1591, III.1629, III.1639, III.1691
Agamennone R., II.1161, III.1279
Agüero A., II.1143
Ahmaniemi S., I.449
Allen D., I.5, I.283, III.1487, III.1661
Andersson H.C.M., II.933
Angella G., I.167
Arai M., III.1269
Archer N.J., I.523
Arrell D., II.605, II.633
Artinger I., III.1701
Azuma T., III.1269, III.1497

B

Backes G., II.751
Bacos M.-P., I.429
Bakker W., II.815
Bale D.W., I.73, I.149
Banks J.P., I.577
Barbezat G., I.511
Baxter D., I.73, I.523
Beck T., III.1419
Bendick W., III.1361
Berger C., I.89, III.1279, III.1409, III.1551
Bezençon C., I.503
Bianchi P., I.449, I.523
Biede O., II.957
Blough J., II.815
Blum R., II.1009, III.1385
Blum W., II.1161, III.1279
Boβmann H.P., II.871
Bohn D.E., I.107
Bontempi P., I.149, III.1621
Bordenet B., II.871
Böttger B., I.89, I.315, III.1333
Brozda J., III.1711
Brückner U., I.217
Buckthorpe D., II.759
Buenaventura A., II.759
Burlet H., I.419
Bursik J., III.1521
Busquin P., III.1806
Busso E.P., I.23, I.283

C

Cabibbo M., III.1453
Cailletaud G., I.23
Carosi A., III.1731
Cerjak H., II.1081, III.1539
Cernuschi F., I.449
Chen Q., II.1019, III.1333
Chen W.Y., I.187
Chi B.H., III.1681
Cizner J., II.785
Contessi E., III.1731
Couturier R., I.419, II.759
Cremer R., II.663
Cui C.Y., II.595
Czyrska-Filemonowicz A., I.149

D

Danciu D., I.227, I.235
Daniel R., I.293
Dassios C.G., II.769
Davis C., II.785, II.893
De Beer A.J., III.1783
Del Puglia P., II.769
Del Vecchio D., III.1731
Di Gianfrancesco A., II.1065, III.1731
Dimmler G., III.1539
Dlouhý A., II.605
Doi H., III.1269
Doi M., II.1201
Dubiel B., I.139, I.149
Dubiez S., I.419
Ducki K.J., I.401
Dupin N., I.315

E

Ehlers J., III.1279
Emura S., II.643
Encinas-Oropesa A., II.923
Ennis P.J., II.1131, III.1279
Epishin A., I.217
Escher K., II.1049
Evangelista E., III.1453

F

Faulkner R.G., II.1247
Foldyna V., III.1477
Formanek B., II.785
Frahm J., I.543
Friedrich B.-C., II.759
Fries S.G., I.315, III.1333
Fritscher K., I.483
Frommert M., II.673
Fujita T., III.1269, III.1311
Fujiyama K., I.345
Fukui Y., III.1269
Fukuyama Y., I.255, II.733

G

Gabrel J., III.1343, III.1361
Gallet S., II.633
Garcia Oca C., II.711
Gasser A., II.751
Ghidini A., III.1731
Giannozzi M., I.493
Gil I., II.703
Giorni E., I.493, I.523
Girard B., I.429
Giselbrecht W., II.1065
Goransson K., II.785
Gottstein G., II.673
Granacher J., III.1279
Guardamagna C., I.149, III.1621
Guétaz L., I.419
Guo J.T., II.595
Guo S., II.997

H

Haase H., III.1409
Hagiwara M., II.643
Hakl J., II.615
Hald J., II.1009
Hamano S., III.1351
Hara T., II.1181
Harada H., I.159, II.197, I.303, II.733
Harada N., I.245
Hashizume R., II.1201, III.1497
Hayakawa H., III.1445
Hecht U., I.315
Heckmann S., I.561
Hede Larsen O., II.957
Henderson M., I.139, I.149, I.293, II.633
Henderson P.J., II.785, II.883
Herzog R., I.543, I.551, I.561
Hetmanczyk M., I.401
Heuser H., III.1671
Hillenbrand P., III.1385
Hilpert K., II.989
Hino T., I.303
Hirosaki N., II.997
Hjörnhede A., II.979
Höbel M., I.503
Högberg J., II.883
Horn A., II.743
Hornak P., I.365, I.375
Hovsepian P. Eh., I.465
Hu W., II.673

I

Ielpo F.M., III.1731
Igarashi M., III.1397, III.1469, III.1561, III.1591, III.1639
Ikeda K., III.1371
Imai H., I.535
Inden G., III.1279, III.1299
Innocenti M., I.523, II.769
Ishiguro T., III.1497
Ishii R., III.1371
Ishitsuka T., III.1321
Isobe S., III.1351

Itagaki T., III.1397, III.1629, III.1639
Ito S., I.255
Izumi T., II.693

J

Jacobs M., II.833
Jakobová A., III.1477
Jirikovsky K., I.569
Jochum C., II.1081, III.1671
Josso P., I.429
Judkins R.R., II.853

K

Kadoya Y., III.1351
Kakehi K., I.207
Kaneko J., III.1371, III.1721
Kang S.T., III.1505
Karada H., I.395
Karlsson A., II.785
Karlsson B., II.605
Kawai H., III.1351
Kaysser W.A., I.483
Kelbassa I., II.751
Kern T.-U., II.1017, II.1049, II.1065, III.1385
Keutgen S., II.751
Kilgallon P., II.903, II.913, II.923
Kim B.J., III.1505, III.1681
Kim J.T., III.1505
Kimura K., II.1171, III.1397, III.1571, III.1581
Kimura M., III.1515
Klabbers J., I.139, I.227, I.385
Kloc L., II.1189, III.1531
Knezevic V., III.1279, III.1289
Knödler R., II.1143, III.1601
Kobayashi K., III.1515
Kobayashi T., I.159, I.197, I.303, I.395
Koizumi Y., II.197, I.303, I.395
Kolkman H., I.149
Komatsubara S., III.1311
Kondo Y., I.245
Kong B.O., III.1681
Kong C.N., I.273
Konter M., I.503
Koolloos M.F.J., II.633
Kopp R., I.325
Kostopoulos V., II.769
Koyama T., II.1201
Kratochvil P., II.615
Krejcí J., I.569
Kreutz E.W., II.743, II.751
Kroupa A., III.1477, III.1521
Kubo K., II.1181, III.1691
Kubon Z., III.1477
Kuc D., I.401
Kucharova K., II.1189
Kung S., II.815
Kurz W., I.503
Kushima H., II.1171, III.1571, III.1581
Kutsumi H., III.1629, III.1639

L

Lapin J., II.605, II.623
Layne A.W., I.121
Lee K.W., III.1681
Lee S.Y., III.1505, III.1681
Lefebvre Bo., III.1343
Letofsky E., II.1081
Lewis D.B., I.465
Leyens C., I.465
Li G.S., II.595
Li H., I.167
Lim B.S., III.1681
Lindblom J., II.933
Link T., I.217
Löhe D., III.1419
Lorenzoni L., I.449
Lukas P., I.139, I.149
Luo Q., I.465
Lupinc V., I.43, I.167, I.409, II.605, II.683

M

Ma D., I.315
Magoshi R., III.1351
Mai Y.-W., I.187
Majerus P., I.551
Maldini M., I.139, I.167, I.409

Mäntylä T.A., I.449, II.945
Mao C., II.845
Marchionni M., II.683
Martinez C., II.663
Masuyama F., III.1767
Matsui M., III.1691
Matsuo T., I.177, I.245
Mattsson M., II.883
Mayer K.H., II.1049, II.1065, III.1385, III.1521
Mc Cartney L.N., III.1613
McColvin G., II.833
Meriggi M., I.439
Merluzzi M., I.493
Metz Ch., I.523
Miki K., III.1497
Mimura H., III.1321
Minami Y., III.1445
Mitomo M., II.997
Miura N., I.245
Miyazaki T., II.1201
Mohrmann R., III.1651
Monteiro A., I.475
Montgomery M., II.957
Moormann R., II.759
Morinaga M., II.1201, III.1497
Morris D.G., II.703, II.711
Muelas R., II.1143
Müller M., II.989
Mulvihill P., I.149, III.1261
Munasinghe D., II.833
Muneki S., III.1469, III.1561, III.1591
Munoz-Morris M.A., II.703, II.711
Münz W.-D., I.465
Murakami H., I.535
Murakumo T., I.159
Murata Y., II.1201, III.1497

N

Nafari A., II.969
Nakamoto Y., I.177
Nakazawa S., I.159, I.197
Nam S.W., III.1681
Narita T., II.693
Nazmy M., I.43, II.605, II.683
Neuschütz D., II.663
Nicholls J.R., I.57
Nies H., II.1081
Nikbin K., II.605
Nishimoto T., II.693
Nishimura T., II.997
Noda T., III.1351
Norreys A., I.523
Norton J.F., II.913
Nylund A., II.969, II.979

O

O'Dowd N.P., I.283
O'Driscoll J., II.833
Oakey J.E., I.73, II.785, II.801, II.903, II.913, II.923
Obrtlik K., I.149
Odaka T., II.733
Okada H., III.1397, III.1469, III.1561, III.1591
Okayama A., I.355
Okubo H., III.1469, III.1561, III.1591
Olsha Z., III.1783
Onay B., I.355
Ono H., I.395
Onofrio G., II.683
Osgerby S., II.801, III.1261, III.1613

P

Palm M., II.653
Palumbo G., III.1453
Pappas Y.Z., II.769
Park S.H., III.1681
Pasternak J., III.1711
Pelachová T., II.623
Penkalla H.J., I.89, I.227, I.235, I.335
Peters M., I.465
Pigrova G.D., II.1241
Pinder L.W., II.893
Pirch N., II.751
Podstranska I., III.1521
Pollock T.M., I.263

Portella P.D., I.217
Portinha A., I.475
Pratesi F., I.493
Purgert R., II.1109

Q

Qi Y.H., II.595
Quadakkers J.W., II.1131, III.1279

R

Rademakers P., II.785
Rae C.M.F., I.207
Rantala H., II.759
Rao U., II.1109
Rau K., III.1419
Reed R.C., I.207
Regino G.M., I.283
Reichert K., II.663, II.673
Ricci N., III.1621
Rinaldi C., I.439
Rio C., I.429
Riou B., II.759
Ro Y., II.197
Rösler J., I.89
Rozsavölgyi Z., III.1701
Ruth L.A., III.1745
Ryu S.H., III.1505, III.1681

S

Saeki H., II.733
Saito D., I.255, I.345
Sandström R., III.1431
Sato M., I.395
Saunders S.R.J., I.577, II.801
Sauthoff G., II.653, III.1279, III.1289,
Sawada K., II.1181, III.1379
Scarlin B., II.1091, II.1143, III.1601
Scarpellini R., II.845
Scheffknecht G., II.1019
Schneider A., III.1299
Schnell A., I.503
Scholz A., III.1279, III.1409, III.1551
Schubert F., I.235, I.335, I.385, I.543, I.551, I.561
Schulz U., I.483
Schwienheer M., III.1409
Seitisleam F., III.1431
Seitz W., II.815
Semenak J., I.375
Servetto C., III.1487, III.1661
Shibli A., II.1233
Simms N.J., I.73, II.801, II.903, II.913, II.923
Singheiser L., I.561, II.989, III.1279
Sklenicka V., II.1189, III.1521, III.1531
Spigarelli S., III.1453
Spiradek K., III.1459
Stamatelopoulos G.-N., II.1091
Starr F., II.1233
Staubli M., II.605, II.683, II.1049, II.1065, II.1189, III.1385
Steen M., II.769
Steinbach I., III.1333
Steinbrech R.W., I.543, I.551, I.561
Stief J., II.1065
Stocker Ch., III.1459
Stöver D., I.475, I.511
Strang A., II.1223
Strunz P., I.365
Sundman B., III.1333
Suzuki A., I.535
Suzuki K., II.1171
Svejcar J., I.569
Svoboda M., II.1189, III.1521

T

Tabuchi M., III.1397, III.1691
Tamaki H., I.355
Taneike M., III.1379
Tang F., II.643
Teixeira V., I.475
Terada Y., I.177
Thoma A., III.1551
Tin S., I.263
Tinga T., I.293
Toda Y., II.1171, III.1571

Tohyama A., III.1445
Tohyama H., III.1571
Toji A., III.1311
Tomasi A., II.683
Torri L., III.1621
Toulios M., I.5, I.23
Tsuda Y., III.1371, III.1721

U

Uehara T., III.1311
Ueta S., III.1351
Uusitalo M.A., II.945

V

Vaillant J.-C., III.1343, III.1361
Valarani M., II.845
Valenti S., III.1731
Van der Schaaf B., II.759
Vandenberghe B., III.1343, III.1361
Vanstone R.W., II.1035, III.1261
Vaßen R., I.475, I.511
Vilk J., III.1279, III.1299
Vippola M., I.449
Viswanathan R., II.1109
Vitusevych V., I.315
Vlachos D., II.769
Vlasák T., II.615
Vodarek V., II.1223, III.1477
Vrchovinsky V., I.365, I.375
Vuoristo P., I.449
Vuoristo P.M.J., II.945

W

Wagnière J.-D., I.503
Wahl G., I.523
Wang C.H., I.187
Wang Y., III.1279
Wangyao P., I.375
Wanikawa S., III.1397
Ward T.J., I.293
Warnken N., I.315
Watanabe T., III.1691
Weinert P., II.1211, III.1539
Wen K.Y., II.673
Wessel E., I.385
White P.S., I.273, II.723
Wiedenmann A., I.365
Wieghardt K., II.1017
Wilcock I.M., I.139
Willach J., II.743
Wing R., I.57, I.523
Wolske M., I.89, I.325
Wosik J., I.335
Wu F., I.535
Wu R., III.1431

Y

Yamada K., III.1469, III.1561, III.1591
Yamada M., III.1371, III.1721
Yamaguchi K., III.1397, III.1515
Yamamoto R., III.1351
Yamamoto Y., II.997
Ye L., I.187
Yeatman J., I.523
Yin Y.F., II.1247
Yokokawa T., II.733
Yoshida T., II.733
Yoshinari A., I.355
Yoshioka Y., I.255, I.303, I.345
Yu J., III.1505

Z

Zeiler G., II.1049, III.1459
Zeman M., III.1711
Zhang X.P., I.187
Zhou H., II.197
Zhou L.Z., II.683
Zonfrillo G., I.493
Zrnik J., I.365, I.375

KEYWORD INDEX

γ' phase: I.245, I.255
[001] orientation: I.177
0.2 % proof stress: III.1581
10 % Cr steel: II.1049, III.1385
11% Cr steels: II.1131
12 % Cr steel: II.1161, III.1269, III.1279, III.1289, III.1299, III.1361
2.25 % Cr1.7 % NiMoVNbW steel: III.1721
700°C power plant: II.1009
8 wt.% YSZ: I.543
9 % Cr steel: II.1171, II.1181, III.1691
9-12 % Cr steel: II.1035, II.1189, II.1211, III.1505, III.1539, III.1409, III.1459, III.1681, III.1731
A-286 alloy: I.401
Advanced 700C class steam turbine: III.1351
Advanced power plant: II.1019
Ageing: I.335, I.493
Agressive environnements: II.933
AISI 316L: III.1419
Al: I.523
Al + Y: I.523
Alloy 122: III.1261
Alloy design program: II.733
Alloy development: I.89, III.1333, III.1351, III.1361, III.1745
AMDRY 995 coatings: I.439
Anisotropy: I.293
Annealing: I.569, II.711
APS: I.57
Austenitic: II.1233
Austenitic stainless 353 MA: III.1431
Austenitic stainless steel: III.1445
Austenitic steels: II.1091
Autocatalytic electroless deposit: I.429
Back-stress concept: III.1539
Bayonet tubes: II.845
Biomass: II.903, II.957, II.969
Blade: I.523
Boiler: II.1091, II.1109
Boiler design principles: II.1019
Boiler tube: III.1321, III.1445
Bond coat: I.551
Bucket: I.255
Burner rig tests: II.923
Carbides: I.227, I.263, II.1171, II.1247, III.1477
Carbon free: III.1469
Carbon-free martensitic alloys: III.1629
Casing: III.1371
Cast component: I.89, II.605, III.1385, III.1731
Cast steel: II.1065
Cavitation: III.1431
Ceramic: II.845, II.989, III.1745
Ceramic matrix composites: II.769
Ceria-stabilized zirconia: I.483
CFB-boiler: II.969
Chaboche: III.1651
Chlorination: II.815
Chlorine: II.893, II.945
Chromium steels: II.893, III.1521
Clean coal: II.1009
CM186: I.285
CM186LC: I.5, I.139, I.149, I.227, I.293, I.355
CM247: II.871
CMSX-2: I.255
CMSX-4: I.5, I.227, I.235, II.871
Coal: II.785, II.903, II.1109
Coal-fired boilers: II.815
Coating: I.57, I.465, I.493, I.523, I.577, II.945, II.979, II.1143
Cobalt: III.1311
Cold bending: III.1343
Combined cathodic arc/unbalanced magnetron sputtering: I.465
Combined cycle power plant: I.107, III.1721
Combustion liner: I.345
Combustion power plant: II.979
Composite: II.673, II.853
Composition: II.643
Composition changes of precipitates: II.1223
Computer simulation: II.1247
Constitutive models: I.23
Cooled blade design: I.23
Cooling holes: I.385, II.743
Cooling technology: I.107

Corrosion: I.73, I.107, II.785, II.801, II.883, II.945, II.989
Corrosion resistance: I.57, III.1279
Cost 522: I.57, II.1035, II.1049, III.1487
Cr content: III.1497
Cr_2N: III.1571
Creep: I.5, I.43, I.89, I.139, I.159, I.167, I.177, I.197, I.207, I.217, I.273, I.293, I.365, I.375, I.409, I.419, I.551, II.595, II.605, II.623, II.723, II.997, II.1161, II.1189, II.1211, III.1361, III.1379, III.1397, III.1431, III.1453, III.1459, III.1469, III.1487, III.1497, III.1521, III.1531, III.1561, III.1621, III.1661
Creep behaviour: II.615, II.1181, III.1539, III.1551
Creep crack growth: I.89
Creep equations: III.1409, III.1551
Creep fatigue: III.1409
Creep fracture: II.623
Creep life: II.1189, III.1521
Creep strength: I.303, I.395, II.1065, II.1081, II.1091, II.1189, III.1269, III.1289, III.1311, III.1321, III.1371, III.1409, III.1445, III.1505, III.1521, III.1571, III.1691, III.1711, III.1767
Creep-fatigue: III.1397, III.1515
CrVN: III.1321
Crystallographic models: I.283
CVD: I.523
Cyclic oxidation: I.57, I.493
Damage: I.375, II.1211, III.1409
Database: I.73, II.801
Deformation/damage behaviour: I.385
Degradation: I.345, III.1477
Depletion: I.493
Deposits: II.913, II.957
Design: I.121, II.1017, II.1049
Diffusion: I.569
Diffusion Barrier: I.535
Directional solidification: I.355
Dislocations: II.711
Double layer: I.511
Downtime corrosion (DTC): II.913
DS superalloy: I.395
Ductility: III.1571
Ductility normalized strain-range partitioning method: III.1515
Duplex microstructure: II.605
E911: III.1487
EB-PVD: I.57, I.483, I.535
EFCC plants: II.845
Efficiency: II.1109, II.1143
EF-TEM: II.1181
Elastic behaviour: I.543
Elastic modulus: I.561
Electric power plants: III.1745
Electrochemical particle isolation: III.1459
Energy: III.1806
Engine: I.429
Erosion corrosion: II.969
ESR method: III.1269
European commission: III.1806
Experience: II.1065
Extrapolation: II.723
Extrapolation of creep rupture time: III.1539
Fatigue: I.43, I.375
FATT: III.1505
FEM: I.293, I.325, III.1731
FePd: III.1561
Ferrite matrix: III.1571
Ferritic steel: II.1091, II.1143, II.1201, II.1247, III.1311, III.1379, III.1397, III.1487, III.1515, III.1561, III.1581, III.1591, III.1601, III.1621, III.1629, III.1639, III.1661
Fiber coating: II.663
Filler metals: III.1671
Fireside corrosion: II.893
Forging: I.89, I.325
Fraction of precipitates: I.159
Fractography: II.633
Fracture: I.577, III.1431
Gamma TiAl: I.43, II.605, II.633
Gas: II.759
Gas separation process: II.853
Gas turbine: I.57, I.303, I.345, II.923
Gas turbine coatings: I.73
Gas turbine design program: II.733
Gasification: II.903
Gasifier: II.913
Grain boundary: II.1247, III.1453
Graphite: II.759
Growth behaviour: I.187
Hafnon: II.989
Hastelloy X: I.345
HAZ: III.1661, III.1691
Heat exchanger: II.801, II.845, II.913
Heat flux: II.957

Heat input: III.1701
Heat resistance: II.997
Heat resistant steel: III.1269, III.1321, III.1445, III.1767
Heat treatment: I.227
High cycle fatigue: II.633
High steam parameters: II.1019
High temperature: I.409, II.1049, II.1143, III.1431
Hold time: I.375
Homogeneous deformation: III.1469
Homogenisation: I.283
Hot corrosion: I.355, I.395, II.871, II.923, III.1445
Hot deformation: I.401
HP-LP single cylinder steam turbine rotor: III.1721
HTGR: III.1783
HTR: II.759
IGCC: III.1767
Impact: III.1505, III.1701
IN 738: I.871
Inconel 617: I.335, I.385
Inconel 706: III.1551
Industrial gas turbine: I.5, I.139, I.149
In-situ SEM fatigue: I.187
Interfaces: II.673
Intermetallic: I.43, II.595, II.633, II.653, II.1241
Intermetallic compound: II.673, II.703, II.711, III.1469, III.1571
Intermetallic matrix composite: II.663
Iron aluminides Fe_3Al: II.615
Irradiation: II.759
Ir-Ta coating: I.535
Johnson-Mehl-Avrami: III.1651
Kinetics: III.1299
$L1_0$ type ordered intermetallic phase: III.1561
Laboratory tests: II.923
Laser cladding: I.503, II.751, II.979
Laser drilling: II.743
Laser thermal shock: I.439
Laves: II.1171, II.1201, III.1289, III.1459, III.1497
LCF: I.5, I.149, I.273, II.933, III.1621, III.1681
Life prediction: I.375, III.1409
Liquid metal cooling: I.263
Long-term: III.1279, III.1497, III.1571, III.1581
Loop seal: II.969
Low activity Al pack cementation process: I.535
Low alloy steel: II.893, III.1343, III.1371
Low NOx combustors: II.815
Low thermal expansion: III.1351
LPPS and HVOF coatings: I.439
$M_{23}C_6$: III.1571
Magnetic field: III.1591
Magnetron sputtering: II.663
Manufacturing: III.1731
Maraging steel: II.1241
Martensitic steel: II.1223, III.1379, III.1397, III.1613, III.1701
Material development: II.1019, II.1009
Material science: I.107
Materials: I.121, II.759, II.1109, II.1049, II.1017, III.1745
MCrAlY: I.57, I.429, I.551, II.871
Mechanical properties: I.73, II.615, II.643, II.683, II.703, II.711, II.833, II.1081, III.1261, III.1385, III.1671, III.1681, III.1731
Medium rating thermal power plant: III.1721
Microporosity: I.217
Microstructural stability: II.1189, III.1279
Microstructurally short crack: I.187
Microstructure: I.159, I.167, I.177, I.227, I.235, I.245, I.335, I.365, I.395, I.401, I.429, I.503, I.569, II.595, II.623, II.633, II.643, II.703, II.1035, II.1171, II.1211, III.1261, III.1505, III.1521, III.1561, III.1681, III.1731
Microstructure evolution: II.1201, II.1223
Microstructure simulation: I.315, I.325
Modelling: I.273, II.801, I.409, II.1211, III.1613
Modified Garofalo equation: III.1551
Multi-scale modelling: I.23
MX carbonitrides: II.1181, III.1289
Nanocomposite ceramic coatings: I.475
Nanolayer: I.475
Nearly lamellar microstructure: II.605
Neutron diffraction: I.365
NiAl base alloy: II.595, II.653
Ni-Al coating: II.663, II.693
Ni-Al-Cr-Ta-W: I.315
Ni-base SC superalloy: I.263, I.535, II.733

Ni-base superalloy: I.159, I.167, I.177, I.197, I.207, I.227, I.409, I.419, II.1233, III.1351
Nitride: II.1171
No-destructive evaluation: II.769
Non-isothermal model: III.1651
Non-linear finite element analyses : I.283
Notch behaviour: III.1409
ODS Alloys: II.833
Orientation relationship: II.1223
Oxidation: I.569, II.683, II.693, II.997, II.1091, II.1143, III.1397, III.1621
Oxidation resistant nitride coating: I.465
Oxide/oxide: II.769
Oxide scales: III.1601
P 23: III.1671
P 24: III.1671
P92 steel: II.1131
Palladium: III.1639
Particulate composites: II.643
PD 6605: III.1487
Phase formation: II.1241
Phase transformation: I.89, III.1651
Phase-field: I.315, III.1333
Physical properties: I.73
Pipe: III.1361
Plasma sprayed TBC: I.543
Plasma-spraying: I.511
Platinum aluminising: I.57
Post-weld heat treatment: III.1701
Powder metallurgy: I.419
Power generation: III.1711, III.1783
Power plant: II.743, III.1767
Precipitation: II.1161, II.1171, II.1247, III.1299, III.1691
Precipitation strengthening: III.1351, III.1379, III.1477, III.1571
Prediction: III.1581
Pressurized pulverized coal combustion: II.989
Prior austenite grain boundary: II.1171
Processing: II.615
Protective oxide layer: III.1629, III.1639
PVD: I.57, I.475
PWA1480: I.245
PWHT: III.1671
Rafted structure: I.245
Rafting: I.159, I.167, I.255, I.303
Recovery: II.1171, III.1497
Regression analysis: I.395
Reheater: II.893
Relaxation: I.551
Research: III.1806
Rhenium: I.207
Rupture: II.595
SANS: I.365
Scale fracture: III.1613
Sealing: I.449
Shaping: II.743
Shear test: I.551
Short cracks: I.385
Silicon carbide: II.845
Silicon nitride: II.997
Simulation: III.1333
Single crystal: I.5, I.23, I.139, I.149, I.167, I.177, I.187, I.197, I.235, I.255, I.273, I.283, I.293, I.303
Single crystal coating: I.503
Slag: II.989
Slip bands: I.187
SO_2: II.933
Solid fuels: II.801, II.923
Solid solution: III.1459, III.1477
Solidification: I.315
Solution heat treatment: I.355
Spallation: III.1601, III.1613
Specific heat: I.449
Sputtering: I.475
Stabilised zirconia: I.475
Stacking fault energy: I.207
Stainless steel: III.1321
Stationary creep rate: III.1539
Steam chest: III.1261
Steam oxidation: II.1131, III 1445, III.1601, III.1613, III.1629, III.1639
Steam plant: II.1143, III.1681
Steam turbine: III.1371
Steam/metal temperature: II.957
Steel: II.759, III.1531
Straw: II.785
Stress exponent: III.1531
Stress range partitioning method: III.1581
Stress rupture: II.1233
Subgrain: II.1161
Sulfidation: II.815
Superalloy: I.89, I.217, I.315, I.325, I.355, I.365, I.569, II.723, II.751, III.1333

Supercritical boiler: II.1019
Superheated steam: III.1621
Superheater: II.785, II.883, II.893, II.945, II.969
System free energy: II.1201
T and P 23: III.1343
TBC: I.57, I.449, I.483, I.511, I.561
TEM: I.235, II.673
Temperature capability: I.511
Tensile: I.235
Tensile strength: I.43
Test: I.577, II.759, II.933
Thermal barrier: I.543
Thermal conductivity: I.449
Thermal cycling: I.511
Thermal diffusivity: I.449
Thermal efficiency: III.1767
Thermal exposition: I.365
Thermal mechanical fatigue: I.577
Thermal spray: II.979
Thermal stability: I.475
Thermally grown oxide: I.483
Thermocalc: III.1477
Thermodynamic modelling: I.315, II.871, II.903, III.1299, III.1333, III.1477
Thermo-mechanical fatigue: I.197, I.273, I.439, III.1419
Thermomechanical heat treatment: III.1591
Thermo-mechanical properties: II.769
Ti-Al-Ni phase diagram: II.693
TiAl: II.623, II.683
Time dependant deformation: I.561
Titanium alloy: I.465, II.643, II.751
Titanium aluminides: II.623, II.693
TP347H: II.957
Trace contaminants: II.903
Transition piece: I.345
Tube: III.1361
Tube alloys: II.1233
Tungsten: III.1311
Turbine blade: I.245, I.429
Turbine components: I.419, II.751, II.769, III.1269
Turbines: II.743
Type 347: II.933
Type IV cracking: III.1661
Udimet 720: I.419
Under deposit corrosion: II.815
USC: II.1009, II.1109, II.1233, III.1311, III.1397, III.1469, III.1515, III.1591, III.1629, III.1639, III.1767
Valve: III.1371
Virtual gas turbine system: II.733
Visco-plastic: I.561, III.1651
Viscous creep: III.1531
Vision 21: III.1745
Waspaloy: I.335, III.1551
Waste: II.785, II.933
Weldability: II.1065, II.1081, III.1711
Welded joint: III.1397, III.1661, III.1691, III.1711
Welding: II.1091, III.1343, III.1671, III.1681, III.1701
Wood: II.785, II.883
Workability: I.325
$Yb_4Si_2O_7N_2$: II.997
Z phase: II.1171, II.1223
Zener-Hollomon parameter: I.401
Zirconia: I.449

Schriften des Forschungszentrums Jülich
Reihe Energietechnik/Energy Technology

1. **Fusion Theory**
   Proceedings of the Seventh European Fusion Theory Conference
   edited by A. Rogister (1998); x, 306 pages
   ISBN 3-89336-219-3

2. **Radioactive Waste Products 1997**
   Proceedings of the 3rd International Seminar on Radioactive Waste Products
   held in Würzburg (Germany) from 23 to 26 June 1997
   edited by R. Odoj, J. Baier, P. Brennecke et al. (1998), xxiv, 506 pages
   ISBN 3-89336-225-8

3. **Energieforschung 1998**
   Vorlesungsmanuskripte des 4. Ferienkurs „Energieforschung"
   vom 20. bis 26. September 1998 im Congrescentrum Rolduc und
   im Forschungszentrum Jülich
   herausgegeben von J.-Fr. Hake, W. Kuckshinrichs, K. Kugeler u. a. (1998),
   500 Seiten
   ISBN 3-89336-226-6

4. **Materials for Advances Power Engineering 1998**
   Abstracts of the 6th Liège Conference
   edited by J. Lecomte-Beckers, F. Schubert, P. J. Ennis (1998), 184 pages
   ISBN 3-89336-227-4

5. **Materials for Advances Power Engineering 1998**
   Proceedings of the 6th Liège Conference
   edited by J. Lecomte-Beckers, F. Schubert, P. J. Ennis (1998),
   Part I xxiv, 646, X pages; Part II xxiv, 567, X pages; Part III xxiv, 623, X pages
   ISBN 3-89336-228-2

6. **Schule und Energie**
   1. Seminar Energiesparen, Solarenergie, Windenergie. Jülich, 03. und
   04.06.1998
   herausgegeben von P. Mann, W. Welz, D. Brandt, B. Holz (1998), 112 Seiten
   ISBN 3-89336-231-2

7. **Energieforschung**
   Vorlesungsmanuskripte des 3. Ferienkurses „Energieforschung"
   vom 22. bis 30. September 1997 im Forschungszentrum Jülich
   herausgegeben von J.-Fr. Hake, W. Kuckshinrichs, K. Kugeler u. a. (1997),
   505 Seiten
   ISBN 3-89336-211-8

Schriften des Forschungszentrums Jülich
Reihe Energietechnik/Energy Technology

8. **Liberalisierung des Energiemarktes**
   Vortragsmanuskripte des 5. Ferienkurs „Energieforschung“
   vom 27. September bis 1. Oktober 1999 im Congrescentrum Rolduc und
   im Forschungszentrum Jülich
   herausgegeben von J.-Fr. Hake, A. Kraft, K. Kugeler u. a. (1999), 350 Seiten
   ISBN 3-89336-248-7

9. **Models and Criteria for Prediction of Deflagration-to-Detonation Transition (DDT) in Hydrogen-Air-Steam-Systems under Severe Accident Conditions**
   edited by R. Klein, W. Rehm (2000), 178 pages
   ISBN 3-89336-258-4

10. **High Temperature Materials Chemistry**
    Abstracts of the 10th International IUPAC Conference, April 10 - 14 2000, Jülich
    edited by K. Hilpert, F. W. Froben, L. Singheiser (2000), 292 pages
    ISBN 3-89336-259-2

11. **Investigation of the Effectiveness of Innovative Passive Safety Systems for Boiling Water Reactors**
    edited by E. F. Hicken, K. Verfondern (2000), x, 287 pages
    ISBN 3-89336-263-0

12. **Zukunft unserer Energieversorgung**
    Vortragsmanuskripte des 6. Ferienkurs „Energieforschung“
    vom 18. September bis 22. September 2000 im Congrescentrum Rolduc und
    im Forschungszentrum Jülich
    herausgegeben von J.-Fr. Hake, S. Vögele, K. Kugeler u. a. (2000),
    IV, 298 Seiten
    ISBN 3-89336-268-1

13. **Implementing Agreement 026**
    For a programme of research, development and demonstration on advances fuel cells
    Fuel Cell Systems for Transportation
    Annex X. Final Report 1997 - 1999
    edited by B. Höhlein; compiled by P. Biedermann (2000), 206 pages
    ISBN 3-89336-275-4

Schriften des Forschungszentrums Jülich
Reihe Energietechnik/Energy Technology

14. **Vorgespannte Guß-Druckbehälter (VGD) als berstsichere Druckbehälter für innovative Anwendungen in der Kerntechnik**
Prestressed Cast Iron Pressure Vessels as Burst-Proof Pressure Vessels for Innovative Nuclear Applications
von W. Fröhling, D. Bounin, W. Steinwarz u. a. (2000) XIII, 223 Seiten
ISBN 3-89336-276-2

15. **High Temperature Materials Chemistry**
Proceedings of the 10th International IUPAC Conference
held from 10 to 14 April 2000 at the Forschungszentrum Jülich, Germany
Part I and II
edited by K. Hilpert, F. W. Froben, L. Singheiser (2000), xvi, 778, VII pages
ISBN 3-89336-259-2

16. **Technische Auslegungskriterien und Kostendeterminanten von SOFC- und PEMFC-Systemen in ausgewählten Wohn- und Hotelobjekten**
von S. König (2001), XII, 194 Seiten
ISBN 3-89336-284-3

17. **Systemvergleich: Einsatz von Brennstoffzellen in Straßenfahrzeugen**
von P. Biedermann, K. U. Birnbaum, Th. Grube u. a. (2001), 185 Seiten
ISBN 3-89336-285-1

18. **Energie und Mobilität**
Vorlesungsmanuskripte des 7. Ferienkurs „Energieforschung“
vom 24. September bis 28. September 2001 im Congrescentrum Rolduc und im Forschungszentrum Jülich
herausgegeben von J.-Fr. Hake, J. Linßen, W. Pfaffenberger u. a. (2001),
205 Seiten
ISBN 3-89336-291-6

19. **Brennstoffzellensysteme für mobile Anwendungen**
von P. Biedermann, K. U. Birnbaum, Th. Grube u. a. (2002)
PDF-Datei auf CD
ISBN 3-89336-310-6

20. **Materials for Advances Power Engineering 2002**
Abstracts of the 7th Liège Conference
edited by J. Lecomte-Beckers, M. Carton, F. Schubert, P. J. Ennis (2002),
c. 200 pages
ISBN 3-89336-311-4

Schriften des Forschungszentrums Jülich
Reihe Energietechnik/Energy Technology

21. **Materials for Advances Power Engineering 2002**
Proceedings of the 7th Liège Conference
edited by J. Lecomte-Beckers, M. Carton, F. Schubert, P. J. Ennis (2002),
Part I c. 600 pages; Part II c. 600 pages; Part III c. 600 pages
ISBN 3-89336-312-2